LA-12004-C
Conference

LA--12004-C

DE91 009298

UC-910 and UC-414
Issued: March 1991

Proceedings of the 1990 Linear Accelerator Conference

September 10–14, 1990

Albuquerque Hilton
Albuquerque, New Mexico

DISTRIBUTION OF THIS DOCUMENT IS UNLIMITED

MASTER

Los Alamos
NATIONAL LABORATORY
Los Alamos New Mexico 87545

MESSAGE CENTER
C D E F G H I

st Ballroom

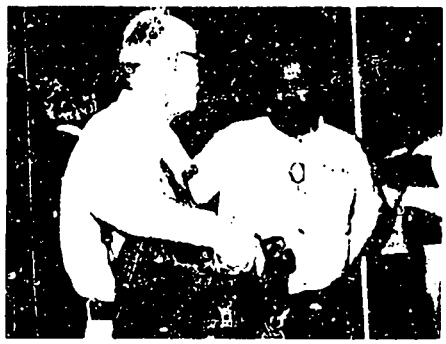

TABLE OF CONTENTS

Foreword i
S. O. Schriber
LANL

Conference Organization iii

Conference Schedule iv

Summary of the 1990 Linear Accelerator Conference v
Pierre Grand

Session MO1 --- Monday, September 10, 1990 **Chairman: R. Hardekopf**

The Stanford Linear Collider 3
J. T. Seeman
SLAC

Status of CERN Linear Collider Studies 8
G. Guignard
CERN

The Japan Linear Collider 13
K. Takata
KEK

SESSION MO2 --- Monday, September 10, 1990 **Chairman: D. Young**

CEBAF Progress Report 21
B. K. Hartline
CEBAF

The Fermilab Linac Upgrade 26
R. J. Noble
FERMI

The SSC Linac 31
J. M. Watson
SSC

SESSION MO4 --- Monday, September 10, 1990 **Chairman: S. Yu**

RFQ Lens for Low Energy Ion Beam Focusing 39
D. A. Swenson, D. D. Gillings, W. J. Hoffert, and S. R. Schmidt
SAIC

New Vanes for RFQ1 42
B. G. Chidley, F. P. Adams, G. E. McMichael, T. T. Ngoc, and T. S. Bhatia
AECL

Study of High Strength Coppers for RFQ1's New Vanes 45
T. T. Ngoc and R. M. Hutcheon
AECL

Components for CW RFQ's 48
T. T. Ngoc, G. E. McMichael, G. M. Arbique, and F. P. Adams
AECL

Modeling of the End Regions of RFQ's Using the 3-D SOS Code 51
I. S. Lehrman and C. Warren
Grumman, Mission Research Corp.

RF Parameters and Scaling Relations for Four-Chamber RFQ Cavities 54
V. V. Paramonov
INR USSR

The π-Mode Stabilizing Loop for Four-Vane Type RFQs 57
A. Ueno, T. Kato, and Y. Yamazaki
KEK

RF Field Measurement of an RFQ Cold Model Cavity for the JHP 60
A. Ueno, Y. Mori, A. Takagi, C. Kubota, and Y. Yamazaki
KEK

Azimuthal Stabilization of the Radio-Frequency Quadrupole with Loop-Coupled TEM Lines 63
G. Spalek, J. Rose, and A. Klapetzky
Grumman, LANL

A Coaxial Line Azimuthal Field Stabilizer for Radio Frequency Quadrupoles 67
G. Spalek and A. Klapetzky
LANL

Coupled Radio-Frequency Quadrupoles as Compensated Structures 70
M. J. Browman and L. M. Young
LANL

Electrical Characteristics of a Short RFQ Resonator 73
I. Ben-Zvi, A. Jain, H. Wang, and A. Lombardi
SUNY, INFN-LNL-Italy

First Tests of a Superconducting RFQ Structure 76
J. R. Delayen and K. W. Shepard
ANL

Design and Application Possibilities of Superconducting Radio-Frequency Quadrupoles 79
A. Schempp, H. Deitinghoff, J. R. Delayen, and K. W. Shepard
ANL, Goethe Univ.

Application of RF Superconductivity to High-Brightness Ion Beams Accelerators 82
J. R. Delayen, C. L. Bohn, and C. T. Roche
ANL

Experimental Results in Superconducting Niobium Resonators for High-Brightness Ion Beam Acceleration 85
J. R. Delayen, C. L. Bohn, and C. T. Roche
ANL

Design of a Superconducting Interdigital Accelerator Structure for Radioactive Heavy Ions 88
J. S. Fraser and H. R. Schneider
TRIUMF

Radio Frequency Superconducting Structures Development Laboratory Capability at Los Alamos National Laboratory 91
B. Rusnak, E. R. Gray, R. J. Houlton, G. P. Lawrence, E. A. Meyer, D. L. Schrage,
A. Klapetzky, A. H. Shapiro, G. Spalek, J. Stovall, and P. Wright
LANL

A Numerical Study of Superconducting Cavity Components 93
B. C. Yunn and J. J. Bisognano
CEBAF

Field Stabilization in the Quasi-Alvarez Structure 96
M. Vretenar and D. J. Warner
CERN

Computer Design and Dynamics of the Quasi-Alvarez Linac 99
P. Lapostolle, E. Tanke, M. Vretenar, D. J. Warner, and S. Valero
CERN, LNS-France

Conditioning of High Gradient H- Accelerating Cavities 102
T. Kroc and A. Moretti
FERMI

Mechanical Construction of the 805 MHz Side Couple Cavities for the Fermilab Linac Upgrade 105
M. P. May, J. R. Fritz, T. G. Jurgens, H. W. Miller, J. Olson, and D. Snee
FERMI

The Determination of the 805 MHz Side Coupled Cavity Dimensions for the Fermilab Linac Upgrade 108
T. G. Jurgens, H. W. Miller, A. Moretti, and P. Zhou
FERMI

Tuning Methods for the 805 MHz Side-Coupled Cavities in the Fermilab Linac Upgrade 111
H. W. Miller, T. G. Jurgens, Q. A. Kerns, R. Padilla, and Z. Qian
FERMI

Side Coupled Accelerating Structure Automated Measurement System 114
P. S. Prieto, J. Crisp, T. G. Jurgens, and T. Savord
FERMI

Stability of Field Distribution in Coupled-Cavity Structures 117
L. V. Kravchuk and G. V. Romanov
INR-USSR

A Systematic Error Study for the Bead Pull Measurements 120
Y. V. Bylinsky, I. V. Gonin, L. V. Kravchuk, P. P. Ostroumov, V. V. Paramonov, and V. A. Puntus
INR USSR

Fabrication Technique of Drift Tube with Permanent Quadrupole Magnet for the Linac of the JHP 123
Y. Iino, T. Adachi, T. Kawasumi, and M. Ozaki
Mitsubishi, KEK

Fabrication Technique of ACS Cavity for the JHP 126
K. Yamasu, T. Iwata, M. Hamaoka, T. Kageyama, Y Yamazaki, Y. Morozumi, and K. Yoshino
Mitsubishi, KEK

Evaluation of RF Seals for Resonant Cavity Applications 129
B. Rusnak, J. Rose, G. Spalek, G. O. Bolme, N. K. Bultman, A. Klapetzky, E. L. Kemp, and J. E. Stovall
LANL, Grumman

Damped and Detuned Accelerator Structures 132
H Deruyter, Z D. Farkas, H. A. Hoag, K. Ko, N. Kroll, G. A. Loew, R. H. Miller,
R. B. Palmer, J. M. Paterson, K. A. Thompson, J. W. Wang, and P. B. Wilson
SLAC

HEM_{11} Modes Revisited 135
J. W. Wang and G. A. Loew
SLAC

Structure Design for a 500 GeV S-Band Linear Collider 138
P. Hanne, N. Holtkamp, R. Klatt, and T. Weiland
Darmstadt

MACSE: Accelerating Electrons at Saclay with Superconducting Cavities 141
P. Leconte, B. Aune, S. Buhler, L. Cardman, J. M. Cavedon, J. Fagot, J. Gastebois, J. F. Gournay,
J. M. Hisleur, M. Jablonka, M. Juillard, T. Junquera, E. Klein, A. Mosnier M. Prome, and A. Veyssiere
CEN-France

High Gradient Experiment by Accelerator Test Facility for Japan Linear Collider 144
S. Takeda, M. Akemoto, H. Hayano, T. Naito, and H. Matsumoto
KEK

X-Band Accelerating Structure for Japan Linear Collider 147
T. Higo, M. Takao, M. Suetake, K. Kubo, and K. Takata
KEK

A High-Power Model of the ACS Cavity 150
T. Kageyama, Y. Morozumi, Y. Yamazaki, and K. Yoshino
KEK

Multi-Cavity Bridge Coupler 153
Y. Morozumi, T. Kageyama, and Y. Yamazaki
KEK

Design Features of the Input Coupler for the DTL 156
F. Naito, T. Kato, Y. Morozumi, E. Takasaki, Y. Takeuchi, and Y. Yamazaki
KEK

High-Power Hybrid Attenuator & Phase-Shifter Systems 159
S. Ohsawa, I. Abe, M. Yokota, Y. Ogawa, S. Anami, I. Sato, and A. Asami
KEK

R & D on an X-Band Klystron Modulator for Japan Linear Collider 162
T. Shidara, M. Akemoto, M. Yoshida, S. Takeda, K. Takata, and Linear Collider Study Group
KEK, Linear Coll. Study Group

Microwave Source Upgrade of the KEK 2.5-GeV Linac Relevant to B-Factory Project 165
T. Shidara, H. Honma, K. Nakao, S. Anami, and A. Asami
KEK

X-Band Klystron for Japan Linear Collider 168
H. Mizuno, J. Odagiri, and T. Higo
KEK

Klystron Modulators with HV Common-Bus for the JLC 171
M. Akemoto, H. Hayano, T. Kawamoto, T. Shidara, J. Urakawa, and S. Takeda
KEK

A Long-Pulse Thyristor-Switched Modulator for the JHP Proton Linac 174
S. Anami, M. Kawamura, T. Kubo, K. Kudo, M. Ono, E. Takasaki, T. Takenaka, S. Ogawa, and S. Kosek
KEK, Hitachi

Relativistic Klystron Simulations Using RKTW2D 177
R. D. Ryne and S. S. Yu
LLNL

Using Traveling Wave Structures to Extract Power from Relativistic Klystrons 180
R. D. Ryne and S. S. Yu
LLNL

Study of High Efficiency Linear Accelerator Structure 183
I. Sato and Y. L. Wang
KEK

Operation of a 473 MHz Pulsed Klystrode Power Source 186
W. W. MacKay, F. R. Huson, C. Kronke, D. Sun, and J. Zeigler
TAC

Mode Competition in High Power Gyroklystron Amplifiers 189
P. E. Latham, W. Main, S. Tantawi, W. Lawson, C. D. Striffler, J. Calame, S. M. Miller, and V. L. Granatstein
U. Maryland

Relativistic Klystrons for High-Gradient Accelerators 192
G. A. Westenskow, D. P. Aalberts, M. A. Allen, J. K. Boyd, R. S. Callin, G. A. Deis, H. Deruyter, K. R. Eppely, K. S. Fant, W. R. Fowkes, J. Haimson, H. A. Hoag, D. B. Hopkins, Houck, R. F. Koontz, T. L. Lavine, G. A. Loew, B. Mecklenburg, R. H. Miller, T. J. Orzechowski, R. D. Ruth, R. D. Ryne, A. M. Sessler, A. E. Vlieks, J. W. Wang, and S. S. Yu
LLNL, SLAC, LBL, Haimson

Operating Characteristics of a Two-Cavity X-Band Gyroklystron Experiment 195
W. Lawson, J. Calame, D. Welsh, M. E. Read, B. Hogan, M. Naiman, P. E. Latham, M. Skopec, C. D. Striffler, M. Reiser, and V. L. Granatstein
U. Maryland, Physical Sciences, Inc.

High Power Amplifiers for Accelerator Applications: The Large Orbit Gyrotron and the High Current, Space Charge Enhanced Relativistic Klystron 198
R. M. Stringfield, M. V. Fazio, D. G. Rickel, T. J. Kwan, A. L. Peratt, J. Kinross-Wright, F. W. Van Haaften, R. F. Hoeberling, R. Faehl, B. Carlsten, W. W. Destier, and L. B. Warner
LANL

L-Band High Power Amplifiers for CEBAF Linac 201
R. Nelson, R. Killion, and J. Fugitt
CEBAF

SLED-II: a New Method of RF Pulse Compression 204
P. B. Wilson, Z. D. Farkas, and R. D. Ruth
SLAC

RF Tests on the INS 25.5-MHz Split Coaxial RFQ 207
S. Shibuya, S. Aria, A. Imanishi, T. Morimoto, E. Tojyo, and N. Tokuda
Tokyo, Grad.Univ-Tsukuba

Close-Coupled RF Power Systems for Linacs 210
W. J. Hoffert, S. R. Schmidt, and D. A. Swenson
SAIC

Measurement of RF Surface Efficiency at Cryogenic Temperatures Using a Resonant Cavity 213
G. C. Bolme, G. P. Boicourt, L. L. Booth, N. K. Bultman, E. Foley, D. J. Liska, R. A. Lohsen, J. Nielsen, B. Rusnak, G. Spalek, and N. G. Wilson
LANL

Voltage Breakdown Test at 473 MHz 216
D. Sun, F. R. Huson, and W. W. MacKay
TAC

Measurement of RF Accelerator Cavity Field Levels at High Power from the Characteristic X-Ray Emissions 219
G. O. Bolme, G. P. Boicourt, K. F. Johnson, R. A. Lohsen, O. R. Sander, and L. S. Walling
LANL

Theory and 3-D Simulations of an RF Accelerating Cavity with Asymmetric Power Feed 223
T. P. Hughes, T. C. Genoni, and R. E. Clark
MRC

The Use of a Spreadsheet in the Design of Accelerator Components 226
S. K. Brown and E. A. Wadlinger
LANL

Dual Klystron Modulator 229
W. J. Johnson and W. E. Stein
LANL

A Highly Effective Deflecting Structure 232
C. Leemann and C. G. Yao
CEBAF

Improvements to the PFN Capacitors for the Klystron Modulators of the KEK 2.5-GeV Linac 235
H. Honma, T. Shidara, S. Anami, A. Asami, and H. Sakaguchi
KEK, Nichiken-Japan

Computer Determinations of the Properties of Waveguide Loaded Cavities 238
N. M. Kroll and X. Lin
UCSD, SLAC

Design Study of a Heavy Ion RF Linac for MEV Implanter 241
H. Fujisawa, Y. Iwashita, M. Inoue, and H. Takekoshi
Nissin, ICR-Kyoto, Japan

Use of TW Output Structures for High Peak Power RF Generators 244
J. Haimson and B. Mecklenburg
Haimson

The Precise Measurement of Electric and Magnetic Fields in a Resonant Cavity 247
J. Gao
ORSAY France
IHEP-PRC

MEQALAC: a 1 MeV Multichannel RF Accelerator for Nitrogen Ions 250
J. G. Bannenberg, W. H. Urbanus, R. G. Wojke, H. Klein, R. W. Thomae, A. Schempp, T. Weis, and P. W. van Amersfoort
FOM-Netherlands; GoethUniv., Frankfurt

Degradation of Niobium Superconducting RF Cavities During Cooling Time 253
B. Aune, B. Bonin, J. M. Cavedon, M. Juillard, A. Godin, C. Henriot, Ph. Leconte, H. Safa, A. Veyssiere, and C. Zylberajch
CEN

SESSION TU1 --- Tuesday, September 11, 1990 **Chairman: S. Yamada**

Review of Negative Hydrogen Ion Sources 259
C. W. Schmidt
FERMI

ECR Ion Sources and Applications with Heavy-Ion Linacs 264
R. C. Pardo
ANL

Progress in Photoinjectors for Linacs 269
R. L. Sheffield
LANL

Linacs for Free Electron Lasers 273
C. Pellegrini
UCLA

SESSION TU2 --- Tuesday, September 11, 1990 **Chairman: J. Leiss**

Design of Long Induction Linacs 281
G. J. Caporaso and A. G. Cole
LLNL

Heavy Ion Induction Linacs for Fusion 286
R. Bangerter and D. Ho
LBL, LLNL

Recent Development in Inertial Fusion Based on RF Acceleration 289
I. Hofmann
GSI

SESSION TU4 --- Tuesday, September 11, 1990 **Chairman: J. Staples**

A Scheme to Compensate the Transient Beam Loading in TW Electron Linacs 297
J. Xie and R. Zhang
BNL, IHEP-China

Beam Loading Studies at CEBAF 300
G. A. Krafft, S. Simrock, and K. Mahoney
CEBAF

Feed-Forward Compensation for Transient Beam Loading of the 805 MHz Debuncher for the Fermilab Linac Upgrade 303
J. A. MacLachlan, F. E. Mills, and T. Owens
FERMI

Cumulative Beam Breakup in Radio-Frequency Linacs 306
C. L. Bohn and J. R. Delayen
ANL

Suppression of Single Bunch Beam Breakup by BNS Damping 309
R. L. Gluckstern, F. Neri, and J. van Zeijts
Univ. Maryland

PARMTEQ Calculations on Beam Dynamics in a Frequency Variable RFQ 312
H. Deitinghoff and A. Schempp
Frankfurt

A New Dynamics Code DYNAC for Electrons, Protons and Heavy Ions in Linacs with Long Accelerating Elements 315
P. Lapostolle, F. Meot, S. Valero, and E. Tanke
CEN, CERN

Damping of Higher-Order Modes in Electron Linacs 318
P. Hulsmann, M. Kurz, H. Klein, and A. Schempp
Frankfurt

Effect of Tank Sequencing on CCL Accelerators 321
C. C. Paulson and R. A. Hartley
Grumman

RFQ Beam Dynamics Model Development 326
A. M. Todd and M. F. Reusch
Grumman

New Beam-Dynamics Design Procedure for RFQs 329
A. Ueno and Y. Yamazaki
KEK

Numerical Models of Beam Dynamics in Ion Induction Linacs 332
J. R. Freeman and J. S. Wagner
SNL

The Fermilab Upgrade Linac: Dynamics Design Process 335
L. Oleksiuk, J. A. MacLachlan, and F. E. Mills
FERMI

Beam Dynamics Design of a Pion Linac 338
S. Nath, G. R. Swain, R. W. Garnett, and T. P. Wangler
LANL

A Comparison of Beam-Dynamics Solutions for the SSC 1284-MHz Coupled-Cavity Linac 341
R. W. Garnett, G. H. Neuschaefer, T. S. Bhatia, and J. M. Watson
LANL, SSC

Error and Tolerance Estimates for the SSC CCL 344
T. S. Bhatia, R. W. Garnett, G. H. Neuschaefer, and K. Crandall
LANL, AccSys

Beam Dynamics Simulation of the LAMPF Linear Accelerator 347
R. W. Garnett, R. S. Mills, and T. P. Wangler
LANL

SSC Drift Tube Linac Physics Design 351
G. H. Neuschaefer, S. Nath, J. H. Billen, T. S. Bhatia, and J. M. Watson
LANL, SSC

Moment Methods for Simulation and Design 355
W. P. Lysenko
LANL

Emittance Growth in a Magnetic Transfer Line Caused by the Variation of Beam Neutralization 358
T. Weis, J. Wiegand, R. Dolling, J. Pozimski, H. Klein, and I. Hofmann
Goethe Univ., GSI

Beam Parameters Optimization in the Initial Part of Linac 361
N. Edamenko, D. Ovsyannikov, A. Zhabko, and V. Kabanov
Leningrad SU, MRI-USSR

First Operation of the 850 MeV C. W. Electron Accelerator 'MAMI' 362
H. Herminghaus, H. H. Braun, H. Euteneuer, F. Fiedler, A. Gauch, G. Gruber, A. Hager, R. Herr, L. Jaekel, P. Jennewein, K. H. Kaiser, R. Klein, H. J. Kreidel, U. Ludwig-Mertin, K. W. Nilles, G. Patzner, H. Scholer, A. Streun, G. Stephan, T. Weis, and P. Zinnecker
Mainz

Controlling Multi-Bunches by a Fast Phase Switching 364
F. J. Decker, R. K. Jobe, L. Merminga, and K. Thompson
SLAC

Formulas for the Twiss Beam Parameters for a Matched Beam at the Entrance to a Linac 367
G. R. Swain
LANL

Semi-Analytical Calculation of Accelerating Beam in a Photo-Injector Cavity 369
H. Takeda
LANL

MAFIA Release 3.X 372
M. Bartsch, M. Dehler, M. Dohlus, P. Hahne, R. Klatt, F. Krawczyk, Z. Min, T. Propper, P. Schutt, T. Weiland, S. Wipf, M. Marx, F. Ebeling, and B. Steffen
THD, DESY, KFA-FRG

Theoretical/Numerical Investigation of Induction Cavity Impedances for Moderate to Large Gap Widths 375
J. F. DeFord
LLNL

Modified-Yee Field Solutions in the Amos Wakefield Code 378
C. C. Shang and J. F. DeFord
LLNL

Wake Potentials and Impedances for the ATA Induction Cell 381
G. D. Craig
LLNL

Application of Linear Magnetic Loss Model of Ferrite to Induction Cavity Simulation 384
J. F. DeFord and G. Kamin
LLNL

Mutual Compensation of Wakefields and Chromatic Effects of Intense Linac Bunches 387
J. T. Seeman and N. Merminga
SLAC

New Compensation of Transverse Wakefield Effects in a Linac by Displacing Accelerating Structures 390
J. T. Seeman
SLAC

Stochastic Electron Beams in the Ion-Focused Regime 393
K. J. O'Brien and J. R. Freeman
SNL

Intense Ion Beam Transport in Neutral Gas 396
C. L. Olson
SNL

Design Studies of SSC Low-Energy-Beam-Transport System using Einzel Lenses 399
C. R. Chang
SSCL

Design Studies of Low Energy H- Beam Transport with Electrostatic Lenses 402
C. Allen, C. R. Chang, and M. Reiser
U. Maryland

HESQ, a Low Energy Beam Transport for The SSC Linac 405
D. Raparia
SSCL

Construction of a Test Magnet for JLC Final Focus 408
M. Fujii, M. Kikuchi, K. Kuno, S. Kuroda, T. Matsui, H. Nakayama, K. Oide, T. Tauchi, and N. Yamamoto
KEK, Mitsubishi

Beam Transfer Between the Coupled Cavity Linac and the Low Energy Booster Synchrotron for the SSC 411
R. K. Bhandari and S. Penner
SSCL

Measurement and Simulation of Whole Beam Brightness on the ETA II Linear Induction Accelerator 414
Y. J. Chen, J. C. Clark, A. C. Paul, W. E. Nexsen, and W. C. Turner
LLNL

Energy Sweep Compensation of Induction Accelerators 417
S. E. Sampayan, G. J. Caporaso, Y.-J. Chen, T. A. Decker, and W. C. Turner
LLNL

Characterization of Field Errors of Layer Wound Short Solonoids 420
W. E. Nexsen, Jr
LLNL

Progress in ETA-II Magnetic Field Alignment using Stretched Wire and Low Energy Electron Beam Techniques 423
L. V. Griffith and F. J. Deadrick
LLNL

Pulsed Taut-Wire Alignment of Multiple Permanent Magnet Quadrupoles 426
C. M. Fortgang, L. B. Dauelsberg, C. Geisik, D. J. Liska, and R. E. Shafer
LANL

A Small-Bore High-Field Superconducting Quadrupole Magnet 429
D. B. Barlow, R. H. Kraus, C. T. Lobb, M. T. Menzel, and P. L. Walstrom
LANL, Grumman

High Order Optics of Multipole Magnets 432
P. L. Walstrom, F. Neri, and T. Mottershead
LANL, Grumman

Reduction of Beam Corkscrew Motion on the Eta II Linear Induction Accelerator 435
W. C. Turner, S. L. Allen, H. R. Brand, G. J. Caporaso, F. W. Chambers, Y.-J. Chen, F. E. Coffield, F. J. Deadrick, T. A. Decker, L. V. Griffith, D. L. Lager, W. J. Mauer, W. E. Nexsen, A. C. Paul, V. L. Renbarger, and S. Sampayan
LLNL

'Smile' a New version for the RADLAC II Linear Accelerator 438
M. G. Mazarakis, J. W. Poukey, S. L. Shope, C. A. Frost, P. J. Pankuch, B. N. Turman, J. J. Ramirez, and K. R. Prestwick
SNL

Calculation of Time Delay Lines with Hon Modes for RF-Energy Upgrade Systems 441
B. Y. Bogdanovich, Y. K. Majorov, V.V.Rassadin, and V. A. Senyukov
MEPI-USSR

Orbit Correction Techniques for a Multipass Linac 444
A. Barry, B. Bowling, J. Kewisch, and J. Tang
CEBAF

Accelerator Deflection Mode Dampening Experiments at Argonne 447
E. Chojnacki, W. Gai, C. Ho, R. Konecny, S. Mtingwa, J. Norem, M. Rosing, P. Schoessow, and J. Simpson
ANL

Secondary Electron Methods for Ion Phase Motion Research 450
A. M. Tron
MEPI-USSR

Generation of a Rectangular Beam Distribution for Irradiation of the Accelerator Production of Tritium Target 453
B. Blind
LANL

Diagnostics for the 400 MeV FNAL Linac 456
E. S. McCrory, G. Lee, and R. C. Webber
FERMI, SSC

RFQ1 Diagnostic Devices 459
B. G. Chidley, G. M. Arbique, M. S. de Jong, G. E. McMichael, W. L. Michel, and B. H. Smith
AECL

A Flior and Wire-Shadow Diagnostic for Low-Energy Ion Beams 462
K. Saadatmand, J. D. Schneider, C. Geisik, and R. R. Stevens, Jr.
LANL

A Very Wide Bandwidth Faraday Cup Suitable for Measuring Gigahertz Structure on Ion Beams with Velocities Down to b < 0.01 465
J. M. Bogaty, R. C. Pardo, and B. E. Clift
ANL

Control System of ATF 468
H. Hayano, J. Urakawa, M. Akemoto, and T. Naito
KEK

Expert System for Diagnosis of Klystron Modulator (KMTS) 471
I. Abe, H. Hanaki, S. Anami, K. Nakahara, M. Kitamura, and A. Asami
KEK, Tohoku Univ.

Upgrading the Fermilab Linac Local Control System 474
E. S. McCrory, R. W. Goodwin, and M. F. Shea
FERMI

A New Technique for Transverse Phase Ellipse Measurement 477
P. B. Vasilev and A. M. Tron
MEPI-USSR

Calibration and Operation Schemes for CEBAF RF Control 480
S. N. Simrock, J. C. Hovater, I. Ashkenazi, G. E. Lahti, K. L. Mahoney, and J. A. Fugitt
CEBAF

The CEBAF Fast Shutdown System 484
J. Perry and E. Woodworth
CEBAF

Robust RF Control of Accelerators 487
W. J. Johnson and C. T. Abdallah
LANL, UNM

Precision, 32 Channel Power Supply System 490
N. Dobeck, J. Beaufait, E. Boettcher, G. Burtner, P. Francis, R. LaMora, M. O'Sullivan, C. Settles, and C. Sharp
CEBAF

High Stability Switching Mode Power Converters for Magnet Loads 493
O. Calvo, C. Sibley, and T. Russ
MIT Bates

Application of a Relational Database for Documenting the Ground Test Accelerator Cable Routing and Wiring Interconnections 496
D. B. Blackwell, W. L. Rogers, V. W. Brown, G. A. Ekeroth, and T. O. McGill
LANL

RF Pulse Shape Control using a Recurrent Algorithm for a FEL RF-Gun Cavity 499
P. Balleyguior and R. Dei-Cas
CEA France

SESSION WE1 --- Wednesday, September 12, 1990 **Chairman: L. Bollinger**

Superconducting RF Cavity Technology 505
H. Padamsee
Cornell

The ATLAS Positive Ion Injector 510
K. Shepard, L. M. Bollinger, and R. C. Pardo
ANL

The Pros and Cons of Cryogenic Accelerators: an Engineering Point of View 515
W. Fox
LANL

Low Beta CW Linacs for Intense Beams 516
G. E. McMichael
AECL

SESSION WE2 --- Wednesday, September 12, 1990 **Chairman: H. Klein**

Interdigital RF Structures 525
U. Ratzinger
GSI

Tuning and Stabilization of RFQ's 530
L. M. Young
LANL

Variable Energy and Heavy Ion RFQs 535
A. Schempp
Univ. Frankfurt

SESSION TH1 --- Thursday, September 13, 1990 **Chairman: P. Grand**

Development of the High Intensity Proton Linac for the Japanese Hadron Project 543
Y. Yamazaki and M. Kihara
KEK

Linear Accelerator for Production of Tritium: Physics Design Challenges 548
T. P. Wangler, G. P. Lawrence, T. S. Bhatia, J. H. Billen, K. C. Chan, R. W. Garnett, F. W. Guy, D. J. Liska, S. Nath, G. H. Neuschaefer, and M. Shubaly
LANL

New Applications for High-Power Proton Linacs 553
G. P. Lawrence
LANL

Commercial Applications of Linacs 558
R. W. Hamm
Accsys

SESSION TH2 --- Thursday, September 13, 1990 **Chairman: R. Gluckstern**

Summary of 1990 Code Conference 565
R. K. Cooper and K. C. Chan
LANL

A Heavy Ion Injector at CERN 568
H. Haseroth
CERN

Some New Methods of RF Control 573
S. P. Jachim
LANL

SESSION TH4 --- Thursday, September 13, 1990 Chairman: A. Vlieks

Linear Accelerator for Burner-Reactor 581
G. Batskikh, B. P. Murin, and A. P. Fedotov
MRI-USSR

Super High-Power RF Regotron-Type Generator for Linear Accelerator with High Mean Currents 584
B. P. Murin, A. P. Durkin, O. Y. Shlygin, and I. V. Shumakov
MRI-USSR

Operating Experience with the Impela-10/50 Industrial Linac 587
J. Ungrin, S. B. Alexander, S. T. Craig, G. Frketich, V. A. Mason, I. L. McIntyre, M. P. Simpson, D. L. Smyth, R. J. West, and B. F. White
AECL

An Electron Linac for Intraoperative Radiation Therapy 590
G. T. Konrad
Siemens

Injector System of HIMAC 593
S. Yamada, T. Hattori, A. Itano, M. Kanazawa, A. Kitagawa, T. Kohno, Y. Miyazawa, O. Morishita, K. Noda, H. Ogawa, K. Sato, Y. Sato, K. Sawada, M. Sudou, E. Takada, T. Yamada, and Y. Hirao
NIRS-Japan

Test Linac Facility at Photon Factory, KEK 596
H. Kobayashi, T. Urano, A. Enomoto, T. Oogoe, S. Ohsawa, N. Kamikubota, T. Kurihara, K. Nakamura, K. Furukawa, H. Honma, Y. Yamazaki, and A. Asami
KEK

Numerical Modelling of the CEBAF Electron Gun with EGUN 599
P. Liger and G. A. Krafft
CEBAF

LAL (Orsay) RF Gun Simulations and Model Cavity Design 602
C. Travier, J. Gao, and H. Liu
ORSAY France, IHEP-PRC

Electron Diodes and Cavity Design for the New 4-MeV Injector of the Recirculating Linear Accelerator (RLA) 605
M. G. Mazarakis, D. L. Smith, J. W. Poukey, L. F. Bennett, W. R. Olson, and B. N. Turman
SNL

Numerical Models of Injectors for High-Current Electron Linacs 608
J. W. Poukey and M. G. Mazarakis
SNL

The Linac Injector for the ANL 7 GeV Advanced Photon Source 611
A. Nassiri, W. Wesolowski, and G. Mavrogenes
ANL

The LEP Injector Linac 614
R. Bossart, J. P. Delahaye, J. C. Godot, H. B. Madsen, P. Pearce, A. Riche, and L. Rinolfi
CERN

The Injector Linac for SPring-8 617
H. Yoshikawa, N. Nakamura, H. Suzuki, M. Iizuka, T. Ishida, K. Yamada, A. Mizuno, K. Mashiko, and H. Yokomizo
JAERI

KEK 2.5-GeV Electron/Positron Linac Status and Research Activities 620
A. Asami
KEK

Present Status and Reinforcement Plan of the KEK Positron Generator 623
A. Enomoto, T. Oogoe, T. Kamitani, K. Kakihara, S. Ohsawa, I. Sato, and A. Asami
KEK

First Operation of the Superconducting 130 MeV CW-Electron-Accelerator at Darmstadt 626
K. A. Zomssen, D. Flasche, H. D. Graf, V. Huck, K. D. Hummel, G. Kalisch, C. Lutlge, J. Pinkow, A. Richter, T. Rietdorf, P. Schardt, E. Spamer, A. Staschek, A. Stiller, O. Titze, H. Weise, and W. Ziegler
TH

High Gradient Experiment of the S-Band Electron Linac 629
H. Matsumoto, M. Akemoto, H. Hayano, T. Naito, and S. Takeda
KEK

The Injector of the Superconducting Linac LISA 632
A. Aragona, C. Biscari, R. Boni, M. Castellano, N. Cavallo, F. Cevenini, V. Chimenti, G. Di Pirro, A. Gallo, A. Ghigo, F. Giacco, S. Kulinski, P. Patteri, B. Spataro, F. Tazzioli, and M. Vescovi
INFN, Rome; INFN,Napoli; INS, Poland; Univ. Rome

The Linear Superconducting Accelerator (LISA) Project at Frascati INFN Laboratories 635
A. Aragona, S. Bartalucci, C. Biscari, R. Boni, M. Castellano, N. Cavallo, F. Cevenini, V. Chimenti, G. DiPirro, S. Faini, A. Gallo, U. Gambardella, A. Ghigo, S. Kulinski, C. Marchetti, C. Milardi, L. Palumbo, P. Patteri, C. Sanelli, M. Serio, B. Spataro, S. Tazzari, F. Tazzioli, L. Trasatti, and M. Vescovi
INFN. Rome, INFN, Napoli, INS, Poland, Dip Ener. Univ., Rome

Design of a Bunching System for a High-Current Electron Linac 638
N. Nakamura, H. Yoshikawa, H. Suzuki, M. Iizuka, T. Ishida, K. Yamada, A. Mizuno, K. Mashiko, and H. Yokomizo
JAERI

Magnetic Bunchers for the Generation of High Peak Current, Low Emittance Electron Pulses at Medium Energy 641
B. E. Carlsten, B. D. McVey, E. M. Svaton, G. R. Magelssen, and L. M. Young
LANL, Rockwell Int.

Electron Gun of the Accelerator Test Facility for the JLC 644
M. Akemoto, H. Akiyama, H. Hayano, H. Kobayashi, T. Naito, H. Matsumoto, Y. Otake, and S. Takeda
KEK

Development of Polarized Electron Source Using GaAs-AlGaAs Superlattice 647
Y. Kurihara, T. Omori, Y. Takeuchi, M. Yoshioka, K. Iioga, T. Nakanishi, H. Aoyagi, M. Tsubata, T. Baba, and M. Mizuta
KEK, Nagoya Univ., NEC Corp

Design of a 10-MeV Photoinjector Accelerator for ELFA 650
A. Cucchetti and L. M. Young
LANL

Energy Flow and High Repetition Rate Issues for the ETA-II Magnetic Modulator System 653
M. Newton, D. Barrett, C. Ollis, and D. Pendelton
LLNL

Simulation of a Standing-Wave Free-Electron Laser 656
W. M. Sharp, A. M. Sessler, D. Whittum, and J. S. Wurtele
LLNL, LBL, MIT

Towards a 12 GeV Electron Accelerator for Nuclear Physics with a 100% Duty Cycle 659
B. Aune, J. L. Belmont, J. P. Didelez, G. Leleux, J. M. Loiseaux, M. Goutteffangeas, M. Prome, and A.Tkatchenko
IPN-France, ISN France, CEN-Saclay

The Energy Stabilization for the SLC Scavenger Beam 662
I. Hsu, M. Browne, T. Himel, R. Humphrey, K. Jobe, M. Ross, J. L. Pellegrin, and J. T. Seeman
SLAC

The Problems of Ion Beams Modeling in Injectors and RFQ Linacs 665
Yu. P. Vakhrushin, M. F. Vorogushin, and Yu. A. Svistunov
SRI-USSR

Induction Acceleration Module for Maryland Pulse Compression Experiment 668
J. G. Wang, D. X. Wang, E. Boggasch, D. Kehne, M. Reiser, and T. Shea
U. Maryland

Status of the BNL Toroidal Volume H- Source 671
J. G. Alessi and K. Frelac
BNL

The BNL 200 MeV H- Linac--Performance and Upgrades 674
J. G. Alessi, J. M. Brennan, A. Kponou, V. LoDestro, and P. A. Montemurro
BNL

Beam Performance and Measurements on the RFQ1 Accelerator 677
G. M. Arbique, B. G. Chidley, M. S. de Jong, G. E. McMichael, and J. Y. Sheikh
AECL

Cesium Effect on Volume H- Ion Source 680
Y. Mori, T. Okuyama, A. Takagi, and D. Yuan
KEK, TRIUMF

Deceleration of Antiprotons with a RFQ 683
A. Schempp, H. Deitinghoff, M. de Saint Simon, C. Thibault, and F. Bollo-Pilat
Frankfurt - FRG, CSNSM-France, CERN

Performance of the CERN High-Intensity RFQ 686
E. Tanke, M. Vretenar and M. Weiss
CERN

Preliminary Designs of 1.54 GeV Damping Ring and Bunch Compressor for the JLC 689
J. Urakawa, K. Egawa, T. Higo, T. Ieiri, K. Kanazawa, M. Kikuchi, H. Kimura, K. Kubo, S. Kurokawa, Y. Mizumachi, H. Nakayama, K. Oide, Y. Sakamoto, S. Sakanaka, M. Takao, S. Takeda, Y. Takeuchi, M. Tejima, N. Yamamoto, S. Yamamoto, K. Yokoya and M. Yoshioka
KEK

Ion Source and Injector Improvements at the Superhilac 692
B. Feinberg, G. Behrsing, B. Gavin, S. Ryce, K. Sihler, and D. Syversrud
LBL

Development of the DTL for the JHP 695
F. Naito, T. Kato, E. Takasaki, and Y. Yamazaki
KEK

Test of a 473 MHz Four-Rod RFQ 698
R. Kazimi, F. R. Huson, and W. W. MacKay
TAC

The Single-Beam Funnel Demonstration: Experiment and Simulation 701
K. F. Johnson, O. R. Sander, G. O. Bolme, J. D. Gilpatrick, F. W. Guy, J. H. Marquardt, K. Saadatmand, D. Sandoval, and V. Yuan
LANL

Transverse Coupling Impedance Measurement Studies of Low-Q Cavities 704
L. S. Walling, P. Allison, and A. H. Shapiro
LANL

High Current, Low-Energy RF Ion Accelerator 707
B. P. Murin, V. M. Pirozhenko, and O. V. Plink
MRI-USSR

Progress on the TAC Ion Source and LEBT 710
C. R. Meitzler, P. Datte, F. R. Huson, and P. Tompkins
TAC

Proposal of a Pulsed ECR-Source for Synchrotron Injection 713
U. Ratzinger, W. Bleuel, B. Wolf, N. Angert, and R. Geller
GSI-FRG, CEN-France

Asymptotic Analysis of the Longitudinal Instability of a Heavy Ion Induction Linac 716
E. P. Lee and L. Smith
LBL

Technique of Measuring Bunch Length by Phasing an RF Cavity 719
W. Barry, P. Kloeppel, and R. Rossmanith
CEBAF

The Delta-T Tuneup Procedure for the Fermilab Linac 721
T. Owens and E. S. McCrory
FERMI

Simulations of High Disruption Colliding Beams 724
J. R. Boyce, S. Heifets, and G. A. Krafft
CEBAF

Dispersion and Interbunch Energy Variation for an e+e- Linear Collider 727
T. L. Houck
LLNL

Design Constraints for Electron-Positron Linear Colliders 730
A. Mondelli and D. Chernin
SAIC

The CERN Linear Collider Test Facility 733
Y. Baconnier, R. Bossart, K. Geissler, J. C. Godot, K. Hubner, H. Kugler, J. H. Madsen, A. J. Riche, J. Strode, and G. Suberlucq
CERN

Computer Simulations of New Dielectric Accelerator Devices 736
K. C. Chan and P. Schoessow
ANL, LANL

A Linear Accelerator in Space---the Beam Experiment Aboard Rocket 739
P. G. O'Shea, T. A. Butler, M. T. Lynch, K. F. McKenna, M. B. Pongratz, and T. J. Zaugg
LANL

About FE Electron Loading of the Cavity with High Level RF Power 743
O. K. Belyaev, V. P. Gamarsky, A. V. Gladkov, R. Y. Ivanov, Y. G. Malynin, A. B. Masaev, S. V. Pusanov, A. N. Semizarov, V. B. Stepanov, V. A. Khmara, and Y. M. Yashnov
INR-USSR

MeV-Proton Linac 746
Y. Iwashita, M. Inoue, H. Ego, H. Okamoto, S. Kakigi, M. Sawamura, T. Shirai, H. Fujita, K. Fukunaga, and H. Takekoshi
Kyoto Univ., JAERI

A New 1.4 MeV/U Injector Linac for the Unilac 749
N. Angert, L. Dahl, J. Glatz, J. Klabunde, M. Muller, U. Ratzinger, B. Wolf, H. Deitinghoff, J. Friedrich, H. Klein A. Schempp, and R. Gelier
GSI-FRG, IAP-FRG, CEN, France

Transverse Beam Dynamics Studies of a Heavy Ion Induction Linac 752
T. Garvey, S. Eylon, T. J. Fessenden, K. Hahn, E. Henestroza, and D. Keefe
LBL

Investigation of Beam Aberrations and Beam Halo by 3-Dimensional Emittance Measurements 755
G. Riehl, J. Pozimski, and W. Barth
Frankfurt

Emittance Determination of Electron Guns by Analysis of Beam Profile Measurements 758
B. Strongin and A. Salop
Varian

Performance of the 2-MeV Microwave Gun for the SSRL 150-MeV Linac 761
M. Borland, M. C. Green, R. H. Miller, L. V. Nelson, E. Tanabe, J. N. Weaver, and H. Wiedemann
SSRL, SLAC, AET

Automation Tools for Accelerator Control a Network Based Sequencer 764
P. Clout, M. Geib, and R. Westervelt
Vista

Increasing Output Power of a 850 MHz Tetrode with a Floating Deck Modulator 767
D Rees and C. Friedrichs
LANL

Laser Interferometer for the Precise Alignment of a Linear Accelerator 770
Y. Ogawa, T. Suzuki, K. Furukawa, A. Asami, and I. Sato
KEK

Experimental Investigations of Multi-Bunch Instability by a Transverse Wake Field 773
Y. Ogawa, T. Shidara, and A. Asami
KEK

Choice of the Block-Scheme of 1-1.5 GeV 300 mA Linear Accelerator 776
I. M. Kapchinskiy
ITEP-USSR

High Current Ion Linacs for Transmutation of Long-Lived Wastes 778
P. P. Blagovolin, I. V. Chuvilo, I. M. Kapchinskiy, and N. V. Lazarev
ITEP-USSR

'ISTRA 10' Linear Proton Accelerator Start-Up 782
V. A. Andreev, V. S. Artemov, I. V. Chuvilo, I. M. Kapchinskiy, A. M. Kozodaev, A. A. Kolomiets, V. S. Kosjak, J. N. Kuzmin, R. P. Kujbida, V. V. Kurakin, N. V. Lazarev, I. M. Lipkin, A. M. Raskopin, N. I. Rybakov, V. S. Skachkov, J. B. Stasevich, N. V. Shachraj, R. M. Vengrov, and A. M. Vishnevskij
ITEP-USSR

SESSION FR1 --- Friday, September 14, 1990 **Chairman: G. Loew**

Beam Dynamics in Linear Colliders 787
R. Ruth
SLAC

Design Study for a 500-GeV Linear Collider 792
T. Weiland
DESY/THD

Diagnostics for High-Brightness Beams 797
R. E. Shafer
LANL

SESSION FR2 --- Friday, September 14, 1990 **Chairman: S. Schriber**

Wakefield Accelerators 805
J. Simpson
ANL

The BNL Accelerator Test Facility 810
K. Batchelor
BNL

List of Participants 815

List of Participants by Affiliation 823

Author Index 827

Foreword

S. O. Schriber
Conference Chairman

FOREWORD

The fifteenth Linear Accelerator Conference was held at the Albuquerque Hilton Hotel, Albuquerque, New Mexico, from September 10 through September 14, 1990. The conference had 325 participants with fifteen countries represented. A complete list of participants can be found at the end of these Proceedings.

The International Advisory Committee and the Program Committee established the program format at meetings in Chicago, Illinois, March 22, 1989; Albuquerque, New Mexico, December 6-7, 1989; Washington D. C., April 16, 1990; and Tesuque, New Mexico, May 31-June 1, 1990. It was decided to follow the successful program format that had been developed over the past years. All five morning sessions were devoted to the presentation of invited papers. Each session allowed invited speakers twenty-five minutes for their talks plus five minutes for questions. Three afternoon sessions were dedicated to the presentation of contributed papers, with the early afternoon session containing approximately 12 (five minute) oral presentations to "advertise" selected contributed poster papers.

Our Proceedings consists of 32 invited papers and 208 contributed papers that are arranged in the order of presentation.

The entertainment at the conference consisted of a banquet dinner at the Wool Warehouse Dinner Theater where the play "The Marriage-Go-Round" was enjoyed by all. A barbeque dinner at Los Amigos Ranch was held Wednesday, September 12, complete with volleyball, horseshoes, ping pong, western music, horseback riding,

duck races, and Pueblo Indian dances. We now have a champion duck racer in the accelerator community and expect Gerry McMichael to demonstrate his skills at future meetings. At a New Mexican Buffet served poolside at the Hilton Hotel Thursday, September 13, participants enjoyed Mariachi music and a one-hour performance by a Spanish dance troupe. A tour of accelerator facilities at the Los Alamos National Laboratory was held Friday afternoon. Marilyn Thomas, Lois Plato, and Brenda McKenna deserve much credit for the success of the Companion's Program that was attended by 40 people and included such activities as a "Get Acquainted Breakfast" followed by shopping in Old Town; a Santa Fe Opera tour; a fashion show; a tour of the Museum of Natural History; and a ride on the Sandia Peak Tram, complete with hike and box lunch.

On September 12, 1990, the International Advisory Committee determined that the next Linear Accelerator Conference would be hosted in 1992 by the Chalk River Nuclear Laboratories. John H. Ormrod will chair the conference that will be held in Ottawa. The 1994 meeting will be held either in Europe or Asia—-a decision will be made early in 1991.

The conference was closed by Dr. Pierre Grand, who gave a conference summary that appears following the conference schedule.

Special thanks are extended to the Local Organizing Committee; the International Advisory Committee; the Program Committee; session chairpersons; speakers and poster session presenters; Hilton Hotel staff; Publication staff and all of those who worked behind the scenes to make this a most enjoyable conference.

A final thanks to all the attendees for showing that our field consists of an exciting mixture of people with various personalities, know-how, and technical expertise.

S. O. Schriber
Conference Chairman

1990 LINEAR ACCELERATOR CONFERENCE
CONFERENCE ORGANIZATION

International Advisory Committee

S. Schriber, Chairman, LANL
J. Alessi, BNL
N. Angert, GSI
D. Boehne, GSI
J. Broberg, NIST
S. Chattopadhyay, LBL
R. Gluckstern, U. of Maryland
H. Grunder, CEBAF
H. Henke, CERN
Y. Hirao, NIRS
H. Klein, IAP
J. LeDuff, Laboratoire de l'Accélérateur Linéaire
C. Leemann, CEBAF
G. Loew, SLAC
T. Nishikawa, KEK
J. Ormrod, CRNL
R. Pardo, ANL
M. Prome, Laboratory National SATURNE/SD
A. Sessler, LBL
D. Sutter, US DOE
D. Young, FERMI
S. Yu, LLNL

Program Committee

R. Hardekopf, Chairman, LANL
N. Angert, BNL
J. Barbe, LANL
C. Beckmann, LANL
T. Bhatia, LANL
R. Gluckstern, U. of Maryland
P. Grand, AMPARO
Y. Hirao, NIRS
H. Klein, IAP
C. Leemann, CEBAF
G. Loew, SLAC
M. Lynch, LANL
G. McMichael, CRNL
R. Miller, SLAC
C. Schmidt, FERMI
S. Schriber, LANL
R. Shafer, LANL
K. Shepard, ANL
J. Staples, LBL
D. Sutter, US DOE
O. VanDyck, LANL
J. Watson, SSC
S. Yu, LLNL

Local Organizing Committee

J. Archuleta
C. Beckmann
J. Dussart
R. Hardekopf
B. Maes
R. Montoya
H. Ortega
A. Rodriguez
S. Schriber
M. Thomas
B. Rochester, Hilton Hotel
J. Barbe
M. Carpenter
A. Elliott
J. Hull
B. McKenna
S. Nicol
L. Plato
J. Sandoval
A. Shapiro
W. VanderHam

1990 LINAC CONFERENCE PROGRAM SCHEDULE

Sunday, Sept. 9		Monday, Sept. 10	Tuesday, Sept. 11	Wednesday, Sept. 12	Thursday, Sept. 13	Friday, Sept. 14
	6:30 - 8:00 a.m.	Breakfast (Rio Grande Rm)	Breakfast (Rio Grande Rm)	Breakfast (Rio Grande Rm)	Breakfast (Rio Grande Rm)	Breakfast (Rio Grande Rm)
REGISTRATION 12 Noon to 9 pm Monday 7 am Garden Room	8:00 - 10:00 Four 25-min. talks plus 5-min. Q & A New Mexico Ballroom	**MO1 INVITED** **Chair - R. Hardekopf** **8:00 S. Schriber** Welcome **8:15 J. Seeman** The Stanford Linear Collider **8:45 G. Guignard** Status of CERN Linear Collider Studies **9:15 K. Takata** The Japan Linear Collider **9:45 V. Balakin** VLEPP Linear Collider Project in the Soviet Union	**TU1 INVITED** **Chair - S. Yamada** **8:00 C. Schmidt** Review of Negative Hydrogen Ion Sources **8:30 R. Pardo** ECR Ion Sources and their Application with Heavy-Ion Linacs **9:00 R. Sheffield** Progress in Photoinjectors for Linacs **9:30 C. Pellegrini** Linacs for Free Electron Lasers	**WE1 INVITED** **Chair - L. Bollinger** **8:00 H. Padamsee** Superconducting RF Cavity Technology **8:30 K. Shepard** The ATLAS Positive Ion Injector **9:00 W. Fox** The Pros and Cons of Cryogenic Accelerators: An Engineering Point of View **9:30 G. McMichael** Low Beta CW Linacs for Intense Beams	**TH1 INVITED** **Chair - P. Grand** **8:00 Y. Yamazaki** Development of the High Intensity Proton Linac for the JHP **8:30 T. Wangler** Linear Accelerator for Production of Tritium: Physic Design Challenges **9:00 G. Lawrence** New Applications for High-Power Proton Linacs **9:30 R. Hamm** Commerical Applications of Linacs	**FR1 INVITED** **Chair - G. Loew** **8:00 R. Ruth** Beam Dynamics in Linear Colliders **8:30 R. Miller** RF Power for TeV Linear Colliders **9:00 T. Weiland** Design Study of a 500-GeV Linear Collider **9:30 R. Shafer** Beam Diagnostics for High-Brightness Beams
	10:00 - 10:30	BREAK	BREAK	BREAK	BREAK	BREAK
	10:30 - 12:00 Three 25-min. talks plus 5-min. Q & A New Mexico Ballroom	**MO2 INVITED** **Chair - D. Young** **10:30 B. Hartline** CEBAF Progress Report **11:00 R. Noble** The Fermilab Linac Upgrade **11:30 J. Watson** The SSC Linac	**TU2 INVITED** **Chair - J. Leiss** **10:30 G. Caporaso** Design of Long Induction Linacs **11:00 R. Bangerter** Heavy Ion Induction Linacs for Fusion **11:30 I. Hofmann** Recent Development In Inertial Fusion Based on RF Acceleration	**WE2 INVITED** **Chair - H. Klein** **10:30 U. Ratzinger** Interdigital RF Structures **11:00 L. Young** Tuning and Stabilization of RFQs **11:30 A. Schempp** Variable Energy and Heavy Ion RFQs	**TH2 INVITED** **Chair - R.Gluckstern** **10:30 R. Cooper** Summary of 1990 Code Conference **11:00 H. Haseroth** Heavy Ion Linacs **11:30 S. Jachim** Some New Methods of RF Control	**FR2 INVITED** **Chair - S. Schriber** **10:30 J. Simpson** Wakefield Accelerators **11:00 K. Batchelor** The BNL Accelerator Test Facility **11:30 P. Grand** Summary
	12:00 - 1:30	LUNCH (Poolside)	LUNCH (Poolside)		LUNCH (Poolside)	
		Monday, Sept. 10	Tuesday, Sept. 11	Wednesday, Sept. 12	Thursday, Sept. 13	Friday, Sept. 14
	1:30 - 2:30 Twelve 5-min. Poster Summaries New Mexico Ballroom	**MO3** **Chair - S. Yu** **ORAL POSTER SUMMARY SESSION**	**TU3** **Chair - J. Staples** **ORAL POSTER SUMMARY SESSION**	**AFTERNOON FREE**	**TH3** **Chair - A. Vlieks** **ORAL POSTER SUMMARY SESSION**	Tour to Los Alamos by previous arrangement only
	2:30 - 5:00 Southwest Ballroom	**MO4** **POSTER SESSION**	**TU4** **POSTER SESSION**		**TH4** **POSTER SESSION**	
Welcome Reception 6 to 8 pm Promenade			**Banquet Dinner** Wool Warehouse Restaurant (limited seating) First bus departs Hilton Hotel 5:15 pm	**Barbeque Dinner** Los Amigos Ranch First bus departs Hilton Hotel 4:00 pm	**New Mexico Buffet** Poolside at the Hilton Hotel 6:00 pm	

Summary of the 1990 Linear Accelerator Conference

Pierre Grand

Before addressing the highlights of this most successful Linac Conference, it is fitting at this time to look back and reminisce some. This 1990 Linac Conference is the 15th meeting of its kind, and marks the 30th anniversary of such conferences. It is indeed a milestone. What is remarkable is that after rather modest beginnings, the field of linear accelerator technology is healthier and more rewarding than ever.

John Blewett organized the first informal Linac meeting at the Brookhaven National Laboratory (BNL) in 1960. The next year he organized the second Linac Conference which I attended, also at BNL. It had about 40 participants. It was an exciting time. That period had seen the successful completion of a host of "high energy" linacs: the 10-MeV/n heavy ion linacs at Yale and Berkeley, the 40-MeV and 50-MeV 3-tanks Minnesota and PLA Rutherford machines, the 50-MeV BNL and the European Center for Nuclear Research (CERN) injectors, etc., all these were drift tube or Alvarez proton linacs. At the same time, a 300-MeV travelling wave electron linac had been constructed and successfully operated to unheard of energies of 2-GeV at the Hansen Lab, Stanford University. These machines utilized state-of-the-art technologies including such things as home-made power amplifiers, oil and mercury diffusion pumps for vacuum, etc. The design of rf cavities was arrived at analytically and by extensive use of cold models. At that time, the still recent discovery of strong focusing by Courant and Snyder, and the Smith-Gluckstern phase stability diagram for linacs answered all possible questions concerning transverse as well as longitudinal beam dynamics. In addition, Cockroft-Walton dc accelerators and duoplasmatron ion sources had pretty well established the injection system technology. In 1960 great plans were afoot for even bigger and more powerful machines. Argonne National Laboratory (ANL) was building their 50-MeV ZGS linac injector. Stanford wanted to build a 20-GeV electron linac (ludicrous!), MURA wanted to build a 200-MeV linac injector for a device known as FFAG. Yale University had started thinking of an 800-1000 MeV linac for a meson factory. These were heady days, and most of these ambitious projects have actually come to see the light, albeit, perhaps not quite as conceived. More importantly, it is with pride that this community can look back at these "then advanced projects" and remark that their operating performance actually has exceeded the expectations.

Now! to the present!

As we now review and summarize this conference in light of the last 30 years we must ask ourselves: what's new; and where will it lead? In light of these questions one can almost answer "nothing much has happened during the last 30 years." However, I would like to point to three outstanding and entirely disconnected developments which open the way for future applications of linear accelerators to higher currents and energies, and/or more compact, energy-efficient machines.

The first and perhaps most important advance for linac technology has been the very large array of numerical calculational codes and the concurrent enormous increase in computational power available today. Cooper of Los Alamos gave a good review of available 2-D and 3-D codes which can be used for almost every conceivable design problem the accelerator designer faces. Thus, transport magnets can now be modeled with a high degree of accuracy. The same can be said of accelerating cavities and finally beam dynamics codes incorporating many forces, heretofore only grossly estimated (e.g., space charge) can now accurately predict the behavior and beam losses of linacs. This was vividly demonstrated by Garnett of LANL in a poster comparing the beam transport model and the actual performance of the Los Alamos Meson Physics Facility (LAMPF), where the calculational results actually agree with reality.

The second advance that is making a real difference to the present and future of the linac technology is the invention of the Radio Frequency Quadrupole (RFQ) by Kapchinskiy and Teplyakov of Institute for Theoretical and Experimental Physics (ITEP) and Serpukov and its development to full potential at Los Alamos. The RFQ has now become a mature technology and is used in every proton linac design presented at this conference.

Evolutionary improvements are still in progress, witness the more than 25 RFQ papers presented at this meeting. The invention and realization of the RFQ has overcome a fundamental limitation of linac technology permitting on the one hand to now produce small compact, relatively inexpensive multi-MeV ion linacs that outperform cyclotrons and on the other hand permit higher currents, high-energy linacs to be designed for higher efficiency and lower beam losses. Note Weiss's poster of CERN which demonstrated acceleration of 250 mA. Thus the RFQ has spawned a company like Accyss Technology Inc. which is successfully commercializing compact proton linacs, while making plans for very large proton accelerators such as the Accelerator Transmutation of Waste (ATW) proposed by Los Alamos realizable. A remarkable RFQ test described at this meeting is the 1-MeV RFQ developed at Los Alamos (BEAR) which operated while aboard a rocket to an apogee of 240 Km.

The third and unrelated highlight of this conference is the coming of age of superconducting rf cavity technology. Many years have gone by since Schwettman first promised wonderful things at Stanford. Since much effort has been devoted to this technology with many disappointments. However, slowly but surely progress was made on a steady but continuous basis at many institutions. This effort is finally paying off as demonstrated by the daring decision at Continuous Electron Beam Accelerator Facility (CEBAF) to go superconducting. This decision is now vindicated by the successes achieved in reaching high fields (~9 MV/m) with increased reliability and reproducibility. Padamsee of Cornell gave an excellent review of the state-of-the-art of that technology while Hartline of CEBAF reported on the largest ongoing rf cavity Superconducting SC project, CEBAF, and Shepard of ANL described perhaps the most successful application of SC cavities to date, the ATLAS project at Argonne. It appears that this year has been a turning point in SC cavity technology in that it is now accepted as a viable option for many applications. Thus a number of projects are now being planned with SC cavities especially for electron storage ring upgrades. Superconducting niobium, rf cavity technology is here to stay and grow.

On the other hand, over the last few years, HiTc materials produced a great deal of enthusiasm, hope, and some snake oil in the linac community. However, it has become clear that if HiTc has applications in rf cavities, it is still far in the future. It is now recognized and accepted, thus the paucity of papers on the subject.

Now, I will try to pick from the more than 200 papers presented at this conference, those I thought worth highlighting. On the subject I polled six different attendees and asked them to give me their opinion. I received six different answers! This indicates the difficulty in choosing from the very rich menu presented at this conference. However, at the risk of missing some gems I will give my own biased comments.

On structures, the CERN Pb linac project is generating a resurgence of interest for low beta structures. Interesting work is going on at Gesellschaft Fur Schwerionenforschung (GSI) on IH structures (paper by Ratzinger) and at CERN on a DTL variation called "Quasi Alvarez" (poster by Warner et al.). As mentioned earlier, there is still a lot of activity in improving RFQs, and in Japan, spurred by the JHP program, coupled cavity structures are being further developed in view of improving their performance (coupling, mode separation, etc.). This work appears to be leading towards rather fancy, expensive solutions. At this point, it is also worth noting the total absence of papers dealing with disk-and-washer. This type of accelerating structure appears to have been abandoned as being too messy (too many overlapping rf modes).

In a different context, the recent interest in linear colliders is generating totally new approaches in accelerating structure design. Experimental and theoretical studies are being pursued at a number of major institutions: Institute for High Energy Physics (KEK), Stanford Linear Accelerator Center (SLAC), Novossibirsk, CERN, etc. Perhaps the most interesting paper on the subject was that presented by Guignard of CERN. Whether these new microwave structures have a practical future remains to be seen. Their mechanical tolerance requirements of one to two orders of magnitude better than present technology is clearly beyond state-of-the-art, but it proves the point, "linacs have always been fun." Similarly, linear collider technology is generating all kinds of new, clever ideas in microwave rf power generation. Miller of SLAC really let his imagination run in presenting a paper on the subject.

On new acceleration techniques, there was very little. Coherent acceleration techniques which a few years ago generated so much enthusiasm have pretty well disappeared from the scene. However, work on wake field acceleration is continuing albeit at a slow pace. Simpson of ANL, the champion of that technology gave a good review of the field. It's still far off!

It should be noted that the incentive for these new approaches for accelerator structures

is the potential for very high acceleration gradients (100's of MeV/m) which would make linear colliders look like a cinch. By the same token, one should note Weiland's paper of Deutsches Elektronen Synchrotron (DESY) for a 500 GeV linear collider based on existing technology. It doesn't look that preposterous! After all we have the Superconducting Supercollider! I believe that, as demonstrated by this paper, present technology and improvements thereon, can realistically do the job! It is worth pursuing.

Another strong push on electron linac technology albeit at lower energies is being generated by the Free Electron Laser (FEL) community. I counted 16 FEL projects currently in existence. FEL technology has very specific requirements for high brilliance, high peak current, very short pulses. The success of the technology is being driven by photocathode developments. There was a quite a number of good FEL presentations at this meeting, with few results however. I believe that the next conference, two years from now, will devote a larger portion to FEL technology. Watch for it!

Now, as we wrap up this meeting, I will add a few words on two applications which in the long run are, I believe, the drivers for the linac technology.

The first, near term application, is the development of linacs as neutron factories. It is clear that our future electricity generation will depend more and more on a nuclear power economy. That system, however, will be strongly influenced by safety considerations and institutional limitations. In this context, it is becoming evident that accelerators can play a role, whether as a fuel producer (ATP) or a waste burner (ATW) and replace fission reactors for specific applications, e.g., neutron scattering research! These ideas are not new, but their time may have finally come. Wangler and Lawrence of Los Alamos National Laboratory (LANL) gave two papers on the subject and several posters from the Soviet Union were presented as well.

In the same vein, I am sure, most of us remember the SNQ project at Julich. I will wager that the next generation neutron scattering sources will closely resemble that machine and worth noting is the design specification for the Japan Hadron Project (JHP) linac injector. It will be a high-energy, high-current, high-duty factor machine designed for neutron production. Yamazaki of KEK presented that design.

The second, longer term application, is the use of linacs for inertial confinement fusion. Work is continuing on the subject as described by Hoffmann of GSI and Bangerter of Lawrence Berkeley Laboratory (LBL). Progress is slow but steady. Lack of funding precludes leaps in the technology at this time. The induction linac versus the rf linac competition is still on. Which way to go is still unclear—on that, the jury is still out. What is important at this point in time is that there is no apparent showstopper and the effort on that technology should be further encouraged.

So, this brings us to the close of this conference. This summary does not do justice to the overall excellent quality and technical content of the more than 200 papers and posters presented here! It was a good meeting! Keep it up!

Monday

Session MO1
Chairman: R. Hardekopf
Invited Papers

THE STANFORD LINEAR COLLIDER*

John T. Seeman
Stanford Linear Accelerator Center, Stanford, California 94309

Abstract

The Stanford Linear Collider (SLC) has been in operation for several years with the initial particle and accelerator physics experiments just completed. A synopsis of these results is included. The second round of experiments is now under preparation to install the new physics detector (SLD) in Fall 1990 and to increase the luminosity significantly by late 1991. Collisions at high intensity and with polarized electrons are planned. Many beam dynamics and technological advances are in progress to meet these goals.

Introduction

The normal collision cycle for the SLC[1,2] is to accelerate a positron and an electron bunch extracted from their respective Damping Rings to 47 GeV in the SLAC Linac. They are then collided after passing through two Arcs and shaped to a small size by the Final Focus (see Fig. 1). The spent beams are discarded in high power dumps after a single collision. On the same acceleration cycle a third (electron) bunch is accelerated to about 30 GeV in the linac (2 km), extracted, and, then, converted to positrons in a high power target. The positrons are accelerated to 200 MeV and transported back to the beginning of the linac. When the positrons arrive, the first 100 m of the linac is pulsed and is used to accelerate the positron bunch and two new electron bunches (made by a gridded gun). These bunches are injected into the two 1.15 GeV Damping Rings where radiation damping reduces the emittances to values required for small beam spots at the final focus. This cycle is repeated at 120 Hz. The inherent instabilities of linacs in general have been compensated by the use of slow (one minute) and fast (every pulse) feedback systems (computer driven). Over seventy variables are now actively controlled.

The SLC came into full operation in 1989 producing its first Z^0 particle on April 11. During that year over 22 nb^{-1} of luminosity were logged (see Fig. 2). Over that period the luminosity was increasing linearly with time ultimately obtaining 0.26 nb^{-1} per day. The Z^0 resonance parameters were

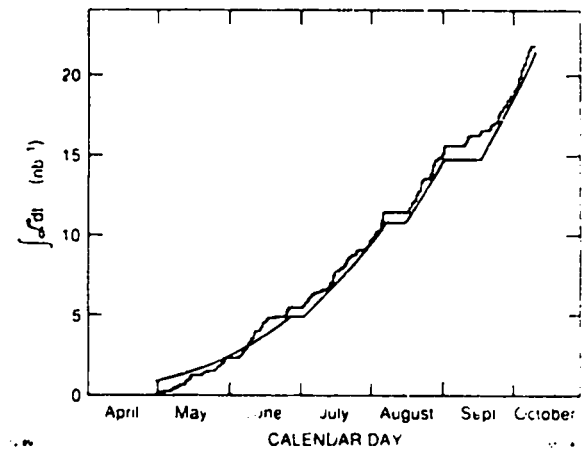

Fig. 2 Integrated luminosity with time in 1989.

measured[3]. The mass is 91.11 (+/- 0.23) GeV, the width 1.61 (+0.60/-0.43) GeV, and the number of neutrino species 2.7 (+/- 0.7). Since these measurements LEP at CERN has had a rapid turn on and presently dominates these measurements. The program of the SLC has now taken on a different direction: to produce polarized Z^0 decays and to study the accelerator physics issues required for the next linear collider. The goal[2] is to make a collision rate comparable to 100 K Z^0 per year with polarization by early 1992. The required parameters for that goal are listed in Table 1. The technological advancements being commissioned now are discussed below.

Positron Production

The old positron target was fixed in position and could handle only 2 X 10^{10} electrons per bunch at 60 Hz without cracking. This target was sufficient for collision parameters used in 1989. However, for the 1992 goals a significantly higher

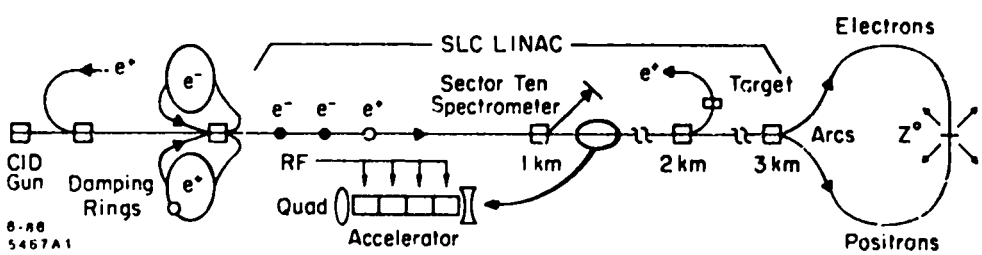

Fig. 1 Schematic view of the Stanford Linear Collider (SLC)

* Work supported by Department of Energy contract DE-AC03-76SF00515.

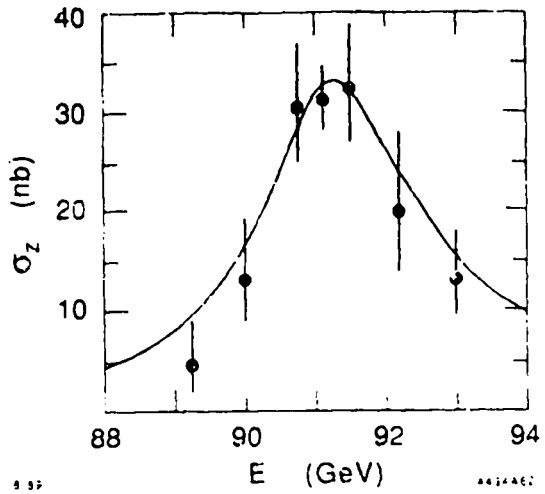

Fig. 3 Measured Z^0 mass in 1989.

incident power is required. A rotating high power target[4] has been installed in January 1990. A 120 Hz pulse rate of over 6 X 10^{10} electrons per bunch can be safely handled. The target does not let two bunches strike the same position over several seconds (see Fig. 4). This new target has been successfully placed in operation. In case of a failure an semi-remote removal system can safely pull the target out of the vault in about 30 minutes with minimal exposure to the crews.

The yield ratio of the number of targeted electrons to the number of positron exiting the positron damping ring needs to be approximately 1.1. The best yield measured is 0.9 with 0.6 as typical. The two problem areas are the momentum collimation region just downstream of the 200 MeV accelerator near the target and the region at the beginning of the two mile accelerator where the positrons are accelerated and injected into the damping ring. Extensive studies are under way to improve the local yields.

Kicker Improvements

The reliability of the damping ring injection and extraction kickers has gone from poor in 1989 to good in 1990. Several improvements including radiation hard magnet insulation, lead shielding, improved pulser design, and magnet heaters have increased the mean time to failure significantly[5]. Furthermore, the two bunch extraction kicker in the electron damping ring must provide equal deflections to the two bunches to about one part in 10^3 to avoid wakefield enlargement of the second bunch in the linac. It was too difficult to make a pulser-magnet combination to do this directly. Consequently, a pulse forming line and a pre-kicker have been added to the primary pulser to make the deflection of the second bunch adjustable (see Fig. 5).

Table 1
SLC Operating Parameters

Parameter	Achieved 1989	Achieved 1990	Desired 1992
N^- (X 10^{10}) (IP)	2.0	3.6	4.0-5.0
N^+ (X 10^{10}) (IP)	1.3	1.9	3.5-5.0
Emittance (10^{-5} r-m)	5.0-6.0	4.5-7.0	3.0-5.0
IP beam size (μm)	2.7-3.3	3.0-4.1*	1.7-2.5
Pinch enhancement	1.0	1.0	1.1-1.2
Repetition rate (Hz)	60	120	120
Efficiency (short term)	0.25	0.3	0.4-0.5
Luminosity (X 10^{29} /cm/s)	0.14	0.30	5.2-9.7

(* Increased with higher Ns.)

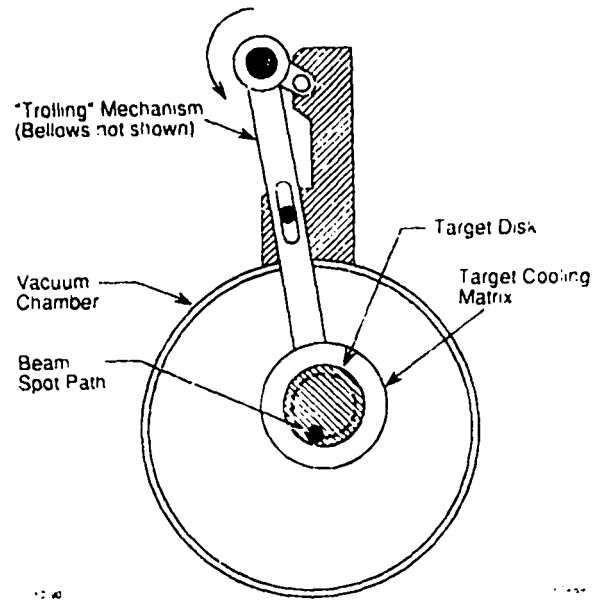

Fig. 4 New high power rotating positron target.

Wire Scanners

The measurement of beam transverse dimensions is crucial for maintaining the beam emittances generated in the Damping Rings and transported through the Linac to the Arcs and Final Focus. At beam currents above 2 X 10^{10} particles and spot sizes below 200 microns, the old SLC profile monitors (phosphor screens) become radiation damaged in tens of minutes. After that these monitors are no longer satisfactory for detailed emittance measurements. (However, they remain good for observing beam transverse tails.) Furthermore, these profile monitors are thick enough so that they generate sufficient beam spray that the machine protection systems start to trip. Systems of wire scanners were installed in the Linac and Final Focus to avoid these problems.

A schematic view of a wire scanner is shown in Fig. 6. The scanner has three wires (x,y,and u) which can be moved through the beam. A photomultiplier tube at 90 degrees and an ion chamber downstream are used to sense the number of particles striking the wire. A histogram of a measured beam shape is shown in Fig. 7. A wakefield tail on the beam can be clearly seen. The signal fall times were arranged so that bunches 60 nsec apart could be cleanly resolved. Initial problems with signal saturation and wire vibration were alleviated by reducing the number of photons reaching the photocathode and by

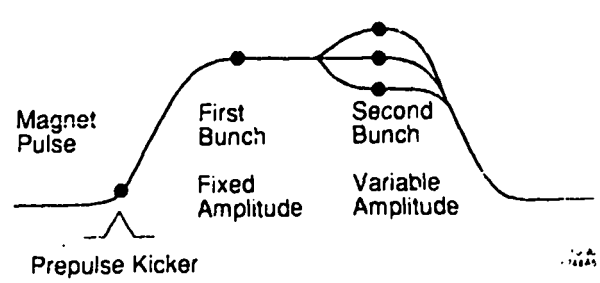

Fig. 5 Improvements to the Damping Ring extraction kicker to allow independent control of both electron bunches.

choosing the optimum scan speed, respectively. Nearby klystrons sometimes produce dark current from the accelerating structure which give a long time background signal. Reducing the accelerating gradient by about 10 % usually eliminates this noise source.

Systems of four scanners were placed over a distance of 10 m at the beginning of the linac and 50 m at the end so that different betatron phases can be sampled (for both positron and electrons). Using these four scanners complete emittance measurements including the Twiss parameters can be obtained. A complete measurement takes about one minute. An automatic computer program systematically measures the emittances every 30 minutes and makes a long term history plot. During collisions when the linac collimators are inserted, the wire scans in the linac

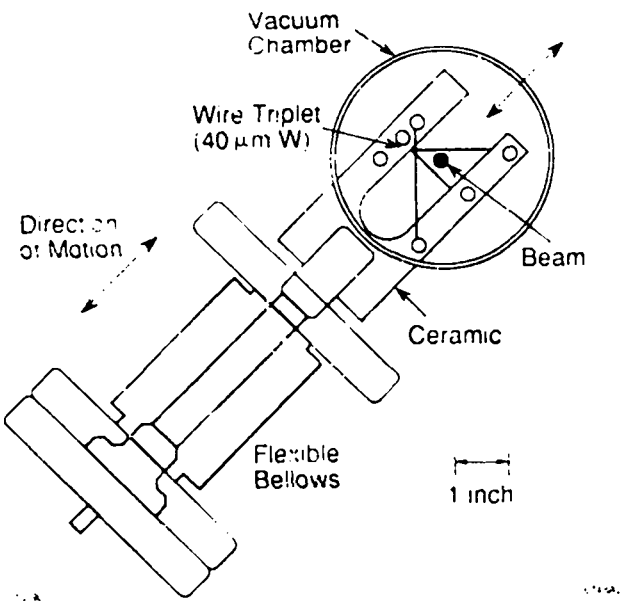

Fig. 6 New wire scanner for the SLC. The wire is made to move through a beam fixed in position.

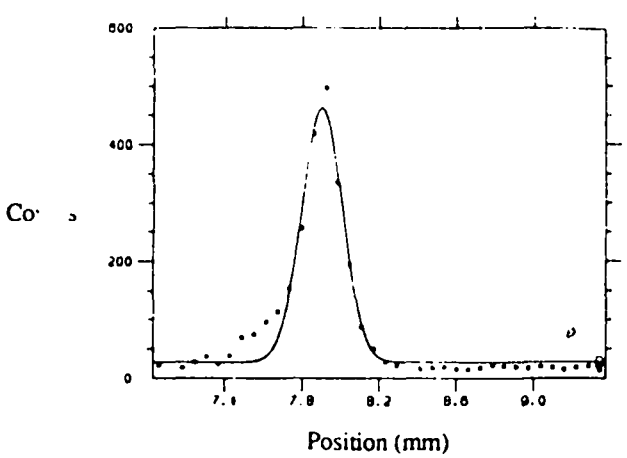

Fig. 7 Measured beam shape showing a wakefield tail. The measured beam size is 105 +/- 5 μm. The invariant emittance is measured using four separated scanners to be 5. (+/- 0.3) X 10^{-5} r-m at 3 X 10^{10} e- / bunch.

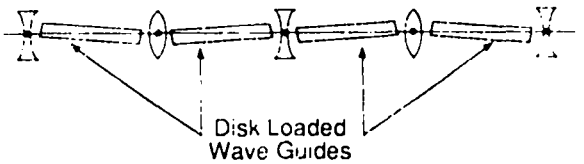

Fig. 8 Schematic view of misaligned accelerating structures.

can be performed without interruption to the physics data taking at the IP. There are twelve scanners installed at present[6]. Twelve more are due for installation in early 1991.

Emittance Control

The emittance of a beam accelerated in the linac can be enlarged by misalignments of the quadrupoles, position monitors (BPM), and accelerating structures. A beam based alignment technique using two beam trajectory information combined with different lattice strengths has reduced the quadrupole rms offsets from about 250 microns in 1988 to 100 microns in 1990. The BPM rms errors have been reduced from 150 to 75 microns. So far no successful technique has been developed to identify particular accelerator offsets (see Fig. 8) using beam data. The difficulty lies in the long distance integral of the beam over the locally generated wakefields to make a transverse tail. In addition, the energy spread introduced via transverse wakefield (BNS) damping makes filamentation more rapid and reduces the growth of a wakefield signal. From mechanical alignment data the accelerator offset errors are approximately 300 microns rms. Tracking simulations[7] with these errors have been made (see Fig. 9). The calculated emittance enlargement ranges from 20 to 150 % dominated by the structure errors. The component of the error at the betatron frequency likely dominates the emittance enlargement. The betatron component is strongly seed dependent.

Injection jitter makes the emittance change pulse by pulse. Several photographs of observed wakefield induced tails are shown in Fig. 10. Many sources of launch jitter have been found and cured. The resulting jitter is now about 35 % of the injection beam transverse sigma (= 350 microns) (mostly horizontal). The extraction kicker contributes one third; unknown sources the rest.

The history of emittance and beam current measurements

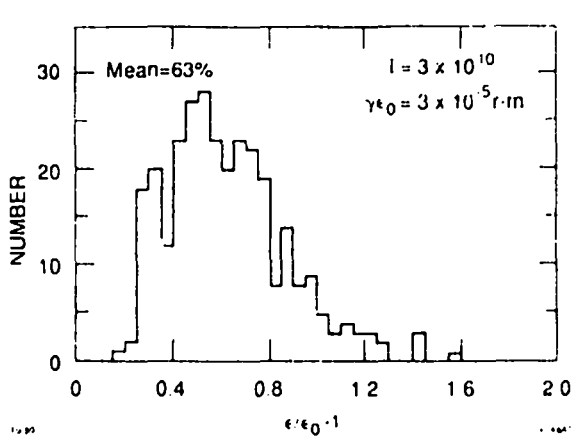

Fig. 9 Emittance growth from accelerator errors for 300 simulated linacs using 100 μm quadrupole and BPM random offsets, 300 μm accelerator errors, 2 % energy scale errors, and 2 degrees input RF phase errors.

is shown in Fig. 11 indicating that many studies[8] were completed to reduce the emittance to within a factor of two of the design. The June 1990 increase in the emittances is due to a mechanical alignment procedure error of the accelerating structure (subsequently fixed). The structure temperature was held constant during alignment but the housing doors were open allowing cold air to distort the mechanical support vertically on the order of 0.5 mm. The alignment procedure and conditions are under review.

A new method for controlling wakefield effects produced by offset accelerators has been suggested[9] where structure distortions at the betatron frequency are actively added to the linac (without damage) to counterbalance the random offsets. This technique has the hope of significantly increasing the alignment tolerance of the structure, providing on line wakefield control, and reducing the need for manual alignment in the tunnel.

SLC Arc Correction

The correction of the Arc optics is now nearly complete with the use of a new closed magnet bump. This closed trajectory distortion is used to compensate for random and systematic errors which have caused coupling of horizontal and vertical betatron motion. These errors generate increased projected emittances and betatron function mismatches. This new bump is shown in Fig. 12. With these corrections the electron and positron Arcs now have projected emittance enlargements less than 10 % and 30 %, respectively. In addition, there are optical adjustments in the Final Focus which can remove most of these projected growths.

Backgrounds and Collimation

The MKII physics detector is sensitive to several kinds of backgrounds. (1) Beam particles displaced more than four transverse sigma produce synchrotron radiation in the final quadrupole triplet. This radiation scatters from the internal masking and is mostly absorbed. However, a small fraction enters the vertex and central chambers, causing multiple hits in the sense wires. (2) Off energy particles strike the collimators in the final focus and produce muons. Finally, (3) only a few errant particles need strike the vacuum chamber in the quadrupole triplet to generate 50 GeV electromagnetic showers too near the detector to shield. A system of eight adjustable collimators was installed at the end of the linac to make a rectangular square cut in betatron space to eliminate many of these errant particles. This system (see Fig. 13) then allowed the other collimator in the Arcs and Final Focus to become secondary phase space cuts. They have been very successful. The four upstream collimators are the primary cuts placed at three sigma. The downstream jaws are set to four sigma as secondary cuts. The jaws themselves are titanium blocks with water cooling through a copper-stainless steel arm. The blocks are 1.8 radiation lengths long. Stepping motors control their positions to about 50 microns. Each jaw can withstand 7 KW of incident beam power in a 150 micron square beam.

Operation at 120 Hz

Running the SLC at 120 Hz collision rate requires full three bunch operation in which two electron bunches are

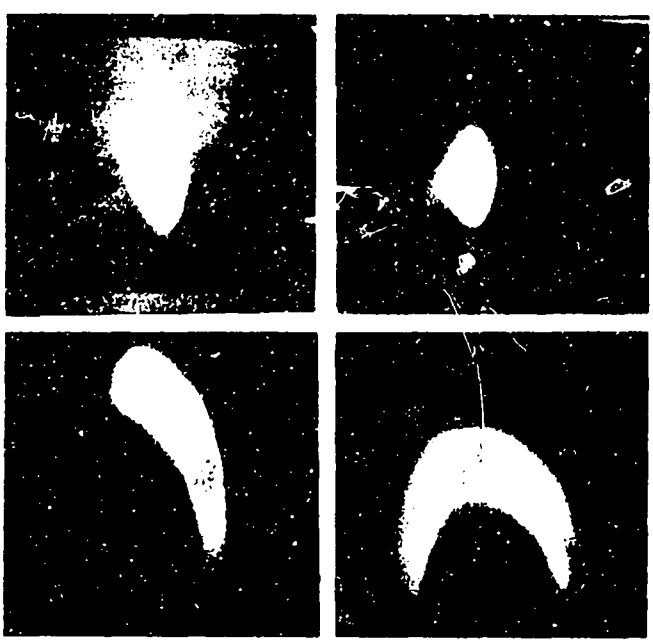

Fig. 10 Observed wakefield beam tails at 47 GeV. The upper left photo shows a well steered beam. The lower right shows a 3 X 10^{10} e- bunch with a 1 mm betatron oscillation.

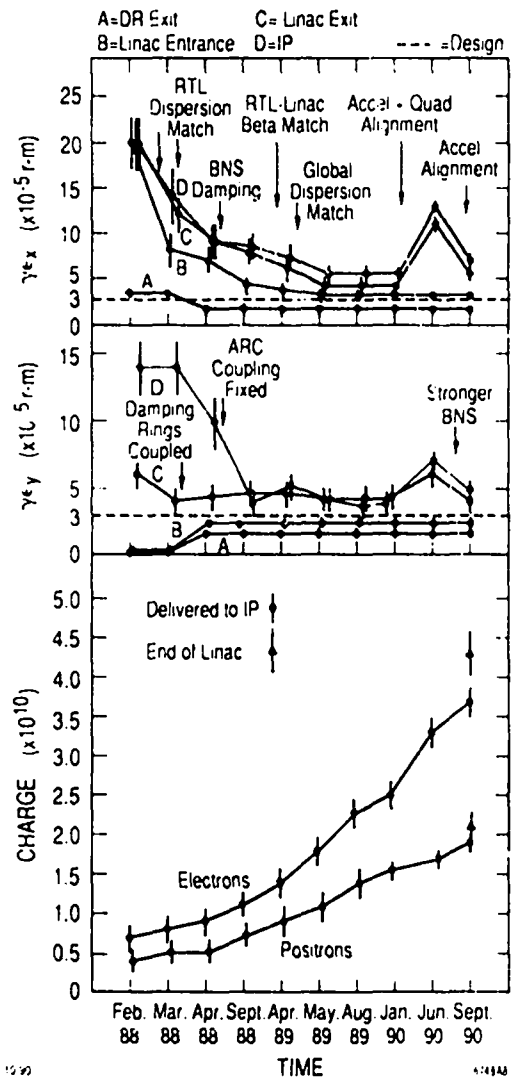

Fig. 11 History of the beam emittances and currents versus time. As the intensities have increased the emittances have been maintained through better control and alignment.

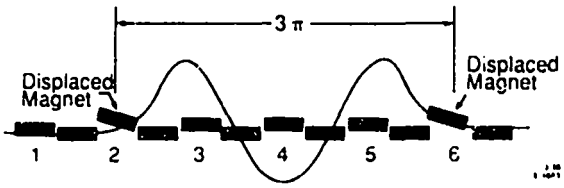

Fig. 12 Magnet 'bumps' in the SLC Arcs which have provided the final needed correction for cross plane coupling.

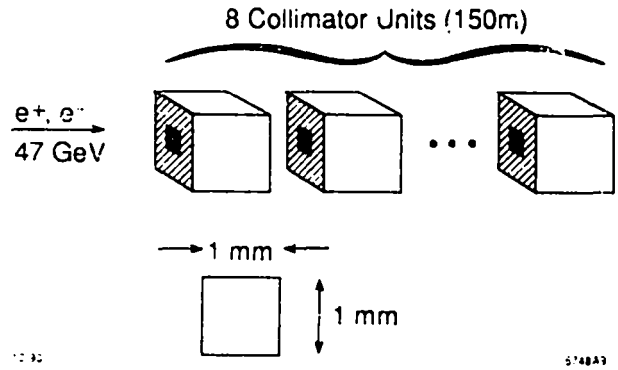

Fig. 13 Adjustable collimators at the end of the linac provide 3 σ transverse cuts on the beam tails. The eight collimators make a 1 mm square hole over 150 m through which both beams pass. Only 10 to 30 % loss of beam is typical.

produced every pulse and the positron Damping Ring contains two bunches, which alternately damp through two collision cycles. At 120 Hz rate the alternate acceleration cycles occur 180 degrees apart on the AC power cycle and have measurable differences (see Fig. 14) which affect beam tuning and detector backgrounds. Most of the differences appear as beam energy differences. Some of the sources have been identified and cured. The remaining problems are reduced by accelerating slightly (10 %) different beam currents on the alternate pulses.

Electron Polarization

A polarized electron source[10] with a 3-electrode photocathode is being prepared for use in Fall 1991 to provide longitudinally polarized electrons at the interaction point for a

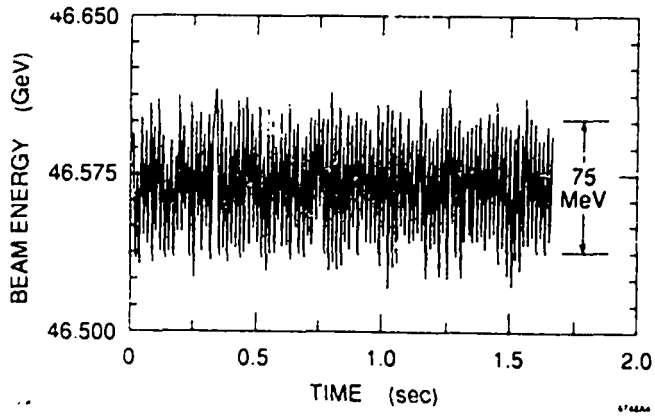

Fig. 14 Observed 'time-slot separation' of the beam energy in the final focus during operation at 120 Hz.

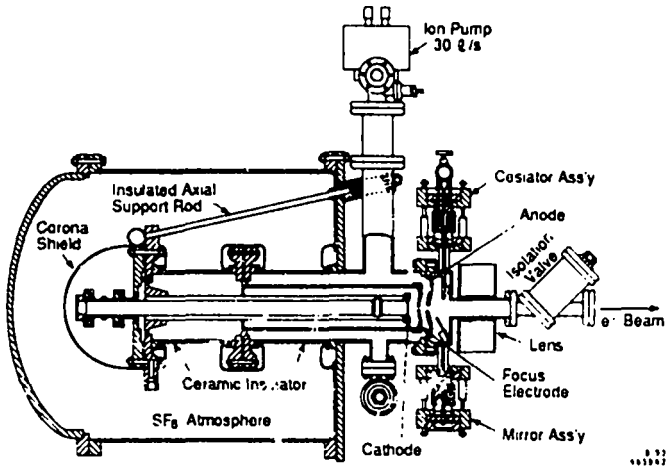

Fig. 15 New polarized electron gun using a GaAs photocathode.

precision measurement of $\sin^2\theta_W$. A second gun with an improved design is under construction (see Fig. 15). Tests to improve the lifetime, peak beam current, and vacuum properties of the first gun are underway. The three spin manipulation solenoids (superconducting) used to get the beam in and out of the Damping Ring are build. Two are installed and operational; the third is to be installed in Summer 1991. The Compton and Moller polarimeters at the end of the linac and in the final focus are installed and being tested. The source polarization is expected to be 39 % and, due to some depolarization effects in the Damping Ring and e^- Arc, the IP polarization should be 34 %.

Acknowledgments

The construction, commissioning, and operation of the SLC required the dedication, insight, hard work, and perseverance of many people at SLAC and from associated universities and laboratories. It is to their credit that significant progress in understanding the accelerator physics of linear colliders and the first observations of hadronic decays of the Z^0 have been made.

References

1. R. Erickson, Ed., "SLC Design Hand Book", SLAC Document, December (1984).
2. M. Breidenbach et al., "SLC Performance in 1991," SLAC Document, January (1990).
3. G. Abrams et al., "Initial Measurements of Z-Boson Resonance Parameters in $e^+ e^-$ Annihilation," PRL 63,7,724 (1989).
4. E. Reuter et al., "Design of a High Power Target System for the SLC Positron Source," SLAC-PUB-5369 (1990).
5. T. Mattison, private communication.
6. M. Ross et al., "SLC Wire Scanners," AIP Instrumentation Workshop Proceedings, FNAL October (1990).
7. C. Adolphsen et al., "High Current Effects in the SLC Linac," APS Washington Meeting, May (1990).
8. J. Seeman et al., "Observation and Control of Emittance Growth in the SLC Linac," 14th Int. Conf. on High Energy Accelerators, Tsukuba, ISSN 0031-2460, 1055 (1989).
9. J. Seeman, "New Compensation of Transverse Wakefields using Displaced Accelerating Structures," Linac Conference, Albuquerque, September (1990).
10. J. Clendenin, "The SLC Polarized Electron Source," Workshop on Polarized Electron Sources, Bonn, (1990).

STATUS OF CERN LINEAR COLLIDER STUDIES

G. Guignard
CERN, CH-1211 Geneva 23

Abstract

A description is given of the topics which have been the subject of studies and developments, and the status of the work on a CERN linear collider (CLIC) is summarized. Progress was made on the test facility, for investigating the critical question of generating the short and intense bunches required for the driving beam. In the drive linac, the wake fields associated with the transfer structure and the consequent stability issue are severe. Therefore, studies and calculations are carried on overmoded pipes, cylindrical with either symmetrical corrugations or combs asymmetrically placed on one side. In the main linac, the question was addressed of minimizing the energy spread by shifting the phase of the accelerating voltage, leading to requirements conflicting with those for beam stability. A prototype of high-gradient accelerating cells has been built and measured. In parallel with the design studies of the final focus system, a model of a small-aperture, high-gradient quadrupole, that could be part of the scheme, has been realized and measured.

Introduction

Research and development on a linear electron-positron collider aiming at a 2 TeV c.m. energy continue at CERN and the work done concerns hardware developments as well as fundamental problems. Prototypes of key elements and test facilities have been or are being constructed, and theoretical or conceptual studies on injection, beam optics and wake-field effects have progressed. Before reporting on these topics, let us briefly recall the main characteristics of the CLIC scheme and give a short list of the main linac parameters (Table I).

TABLE I
Main Linac Tentative Parameters

Parameters	Values	Units
Energy	1.0	TeV
Luminosity	$1.1 \cdot 10^{33}$	$cm^{-2}s^{-1}$
Gradient	80	$MV\ m^{-1}$
RF frequency	30	GHz
Repetition rate	1.7	kHz
Bunch population	$5 \cdot 10^{9}$	
V-emittance ($\gamma\epsilon_y$)	$0.5 \cdot 10^{-6}$	rad m
H-emittance ($\gamma\epsilon_x$)	$1.5 \cdot 10^{-6}$	rad m
FF aspect ratio	5	
FF beam height	12	nm
Bunch length	0.17	mm

There are two distinctive features of the CLIC scheme[1]. The first one is the 30 GHz chosen for the main linac operating frequency, because the average RF power is inversely proportional to its square. This was considered as the highest possible value when taking into account the manufacturing tolerances, beam-induced wake fields and alignment tolerances. The work done so far has now shown any impossibility even if feasibility limits are nearly reached. The success with the construction of a prototype accelerating structure and its positioning to better than 1 μm is encouraging. The second feature is the generation of the RF power by a two-beam scheme, in which the drive beam passes decelerating structures where the 30 GHz power is generated and fed to the main linac. The drive beam consists of a train of intense short bunches and receives energy from 350 MHz sc cavities. The difficult questions of generating this beam and designing transfer structures require considerable development. The test facility addressing the former is fairly advanced and concepts of travelling-wave structure are under study.

Power Generation and Test facility

The generation of a drive beam, consisting of bunches of 1 mm r.m.s. length, 1 cm spacing and 10^{12} particles requires development. It is proposed that trains of such bunches , separated by the drive linac wavelength of c/350 MHz, will be generated by a battery of complex pre-accelerators. In order to study the feasibility of these devices, an experimental CLIC test facility (CTF) is in preparation [2]. It includes an RF gun, a beam line acting as magnetic spectrometer, acceleration to ~ 60 MeV and RF power generation at 30 GHz. A pulse compressor may be added eventually. A key element of this facility is the laser-driven photocathode and a d.c. test bench has been built for testing its fabrication [3].

Fig. 1 The photocathode test bench

The photocathode test bench (Fig.1) is made up of a preparation chamber, a d.c. gun and an instrumentation beam line. The preparation chamber has three evaporators, an arm to transfer the cathode in the gun and a thickness monitor and has been upgraded recently with emission monitoring during evaporation and a new pumping system. The quantum efficiency is indeed a critical parameter (10^{-3} required for a few tenths of nC's) and the quality of the photocathodes depends strongly on the vacuum pressure. The d.c. gun field can reach 8 MV/m and the beam line contains four focusing coils, longitudinal

profile monitor, luminescent screen for image analysis and Faraday cup for recording the charge. For a 4 mm spot size and 10 ns pulses, the gun space-charge limit is at ~12A. Best results ($7 \cdot 10^{11}$ e^-) have been achieved with Cs_3Sb and 266 nm laser.

Fig. 2 The test facility RF gun

The aim of the CTF is to study the generation of very short (some ps), high-intensity (> 10 nC) bunches and of 30 GHz RF power by deceleration in a CLIC structure, whose prototype is described below. Main objectives are to learn about the guns, the bunch compressors, eventually to generate 24 MW peak power for 11 ns, to create an 80 MV/m gradient in a second structure and to test beam instrumentation. This planned performance requires an intensity of 40 nC or $2.5 \cdot 10^{11}$ particles. The adopted design is based on a one-and-a-half-cell S-band RF gun, with an operating frequency of 3 GHz. The RF gun (Fig. 2) is under test and generates up to 100 MV/m at the cathode. The transfer line, including spectrometer, instrumentation and steering or focusing elements, will be installed next. First beam will then be produced with a non-synchronized laser giving a long pulse (8 ns) and optics and instrumentation tests will be carried out. Later a laser with phase and amplitude stabilization becomes available, which can be synchronized to the RF. The RF phase at the laser pulse is an important parameter for obtaining the proper longitudinal phase space distribution for the compressor and a good survival rate of the initial charge. Numerical simulations [4] have shown that 30 nC/beam could be obtained (with optimistic cathode parameters), at the sacrifice of emittances and energy spread. To alleviate the task of the gun, trains of bunches distributed over two structure fill-times can be used. If the charge in the train per fill-time is equal to the single bunch charge (40 nC) about the same RF power is generated.

Drive Linac and Power Transfer

Energy requirements in the two-beam CLIC scheme imply an integrated gradient ratio equal to the frequency ratio. With the figures of Table 1 and a gradient in the sc cavities of the order of 10 MVm^{-1} say, the filling factor of the active part is around 10%. This gives the advantage of long distances between re-accelerating structures and the freedom of most of the tunnel from active high-power equipment other than copper structures. To induce the required 30 GHz power, the drive beam is made of four trains (distant by 2.8 ns) of ten bunches separated by 33 ps. The drain time of the transfer structure fills the gap between trains, whose number is conditioned by the fill-time of the main accelerating structure.

The design of the travelling-wave transfer structures then becomes difficult. The equilibrium between the energy loss in the structures and gain in the drive cavities implies a very low characteristic impedance (several Ω/m) and subsequently the parasitic impedances must be held to very low values also. Studies have shown that fractional wake loss per transition from structures to cavities can be kept low (10^{-4}) and the higher-mode energy loss in cavities reaches a tolerable value of ~6%. Major problems arose when computing longitudinal and transverse wake fields due to the resistive walls of transverse structures made of two parallel plates with combs. Longitudinal wakes could generate a decelerating field up to 18% of the average voltage gain and transverse wakes were so strong that stabilizing the drive beam with BNS damping would require very strong external focusing and large energy spread (~10%). To alleviate these constraints, work started on structures with increased beam-to-wall distance and reduced resistive wall effects [5]. Further developments are certainly required.

The first improved concept starts from a large circular pipe of 12 mm diameter (transverse wakes reduced by a factor 27), with a smooth inner wall. A power collecting rectangular waveguide runs along the outside of the pipe and is coupled to the inside via periodic holes. In order to fill the gap between the trains with the pulse produced, the group velocity of the wave travelling in the guide must be < c (say ~c/2) and the phase velocity then reaches ~2c. Hence, the coupling holes must be separated by two 30 GHz wavelengths (20 mm) and their dimensions adjusted to give the requisite impedance. Since a TEM field is easy to simulate, a model has been built (Fig. 3) and has shown that obtaining the 11.4 ns pulse with the right phase and amplitude might require working at lower phase velocity (~1.2 c) and coupling to a backward wave. The pipe being large, it is also overmoded and there is one accelerating mode with a cut-off below 30 GHz. It can be cancelled if its phase slip with respect to the wave in the guide is equal to π between two consecutive holes.

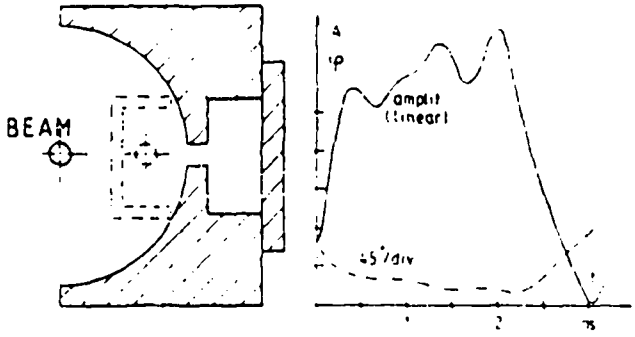

Fig. 3 Possible concept of transfer structure

Another concept of similar nature is studied numerically. It is based on an even larger pipe (22 mm diameter) with very shallow and 6 mm periodic corrugations and a rectangular waveguide on

one side. In principle, the discontinuities created by the corrugations make it possible to generate in the guide a backward wave with phase velocity equal to c and group velocity below c. Coupling is again achieved via periodic holes between the cylinder and the guide.

Energy Spread and Beam Stability

An important problem is making the final focus (FF) system accept the unavoidable energy spread of the beam, due to high single-bunch extraction and stabilization of the wake field's deflecting effects by strong BNS damping [8]. The required focusing gradient over the bunch length can be generated by a deliberate energy spread from head to tail adding to external quadrupole fields and/or actual RF quadrupoles created with asymmetric slots in a fraction (~10%) of the structure. Without RF quadrupoles, stabilization implies a 4 to 6% energy spread that is obviously in conflict with the energy acceptance of the FF, limited by chromaticity compensation to a value ten times smaller.

It now seems possible to match the beam's energy spread to FF acceptance by cancelling to higher orders the longitudinal wake with the RF voltage [6]. The resulting accelerating-gradient variation over the bunch can be flattened by adjusting the RF phase, for given bunch length and population. In this way very flat curves near the centre of the bunch have been obtained, with two maxima of about the same amplitude and one minimum. The energy distribution is deduced from such curves via the inverse of their derivatives [7] and has therefore sharp peaks related to the points with zero derivatives. In the presence of these peaks, the distribution can be centred with respect to the average value of the energy and the tail population reduced. On top of this it is reasonable to assume that a small fraction of particles with an energy below a certain limit does not contribute to luminosity.

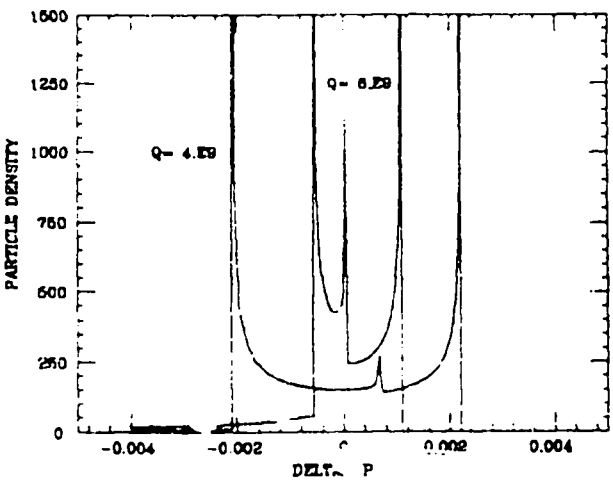

Fig. 4 Distributions reducing energy spread

With such energy distributions and "tail cuts" a minimum r.m.s. energy spread of 0.9‰ was achieved for a bunch length of 0.17 mm and $6 \cdot 10^9$ particles (14% being discarded from the tail). This optimum corresponds to the nominal parameters of Table 1, an RF phase of 8° and a total relative energy range of from +1.2 to -4‰, so as to fit the FF acceptance. Figure 4 shows the corresponding energy distribution together with that obtained with another set of parameters (0.11 mm bunch length, $4 \cdot 10^9$ particles, 7° RF phase and only 4% discarded) to indicate the range in which they can be varied. In the last case, the r.m.s. energy spread is 1.6‰ and the total range from +2.2 to -4‰ is accepted by the FF system.

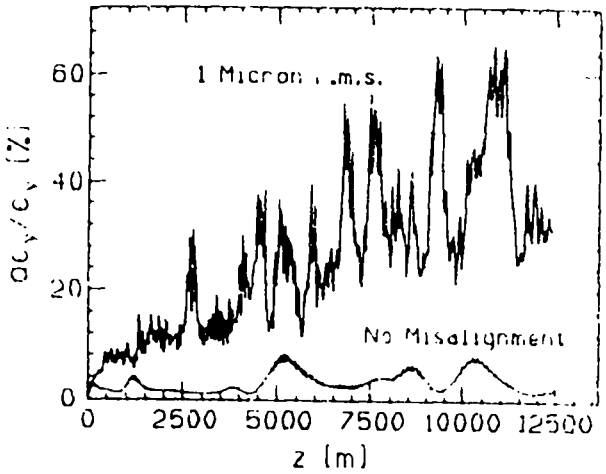

Fig. 5 Vertical blow-up with autophasing

Recently, numerical simulations were carried on with the main linac parameters about a possible higher order BNS scheme [8], called autophasing and using the wake to create coherence within a bunch. Preliminary results have shown that for a perfect linac, with only magnetic focusing of 90° phase advance and 20 m wavelength, and injection errors of 4.2 and 1 μm per plane (H and V), the emittance blow-up could be kept below 6% (Fig. 5) using four linac sections with RF phases between -35° and -10°, and an energy spread of 4.5%. In the presence of random errors in quadrupole alignment (e.g. 1 μm, r.m.s.), autophasing is more difficult. After RF phase adjustment to larger values between -40° and -16.5° (5.4% energy spread) and simple trajectory corrections, the emittance growth was about 50% (horizontal) and 30% (vertical), as is also shown in Fig. 5. Further investigations are necessary, since the tolerances are a critical question.

Structure Fabrication and Alignment

Each main linac proposed is composed of 45'750 27.32 cm long accelerator sections, with gradients of 80 MV/m, quality factor of 4224, shunt impedance of 110.6 MΩ/m and fill time of 11.1 ns. The total peak input power is 1.848 TW/linac and there would be 82 cells per section. The outer diameter of the accelerating structure, machined to ±1 μm, serves as reference for alignment. The structure is pumped by four vacuum manifolds through a series of radial holes or damping slots if incorporated. There are four 5 mm diameter holes for cooling and two 1.6 mm diameter recessed holes for dimple tuning. The cell dimensions give a measured $2\pi/3$ mode frequency of 29.985 GHz.

A prototype section [9], with only 30 cells, but otherwise complete, with reference surfaces, input and output couplers and vacuum and cooling connections has been made at CERN with the help of industry (Figs. 6 and 7). Brazing of machined copper cups was the fabrication method used. Machining tolerances

of ±2 μm (except for reference surfaces) and a surface finish to 15 nm r.m.s. roughness enabled cell-to-cell phase shift errors to be kept below 0.5° on unbrazed damped stacks of 15 cells and the Q-factor to reach 95% of the theoretical value. Since non-reproducible frequency changes could be produced by subsequent brazing operations, the 30-cell structure has been designed to require a 3° phase shift change per cell in the finished prototype section. Therefore, four dimple tuners per cell were foreseen and two actually used for final tuning. High-quality brazing of the discs is necessary to prevent excess flow of braze either on the external surface (reference) or into the cell (frequency changes). This was achieved by creating 1 mm annular copper-to-copper diffusion bond (mirror finish) at the inside and outside edges of the cup. These bonds stop braze leakage and provide electrical contact. Brazing of water and vacuum pipes was made in a second stage, after drilling out the cooling channels and milling the vacuum manifold recesses. Matching the impedance of the brazed structure with couplers is finished with phase shifts in the range +5°/-2.5°. Given the success of the prototype construction, it is now planned that two full-length sections will be fabricated for CTF.

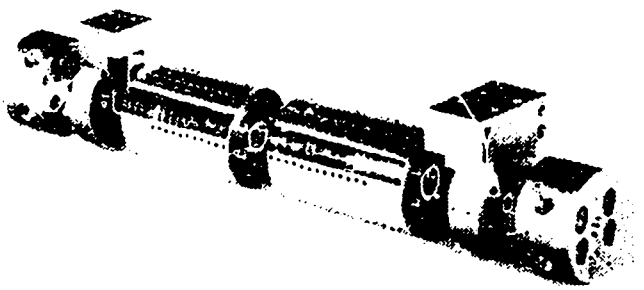

Fig. 6 Prototype section before brazing

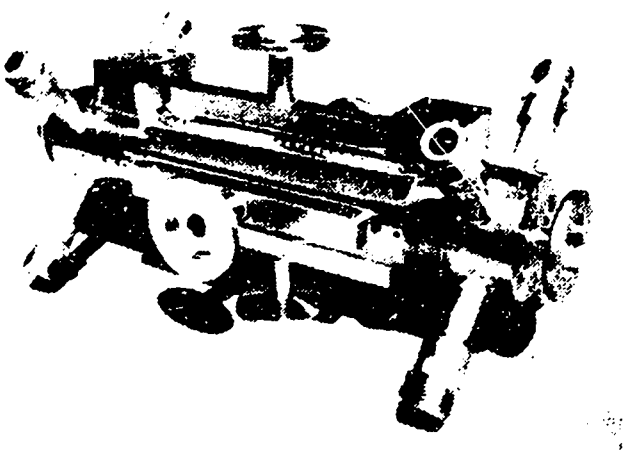

Fig. 7 Finished 30-cell prototype section

Accelerating structures with quadrupoles must be aligned within microns and an automatic alignment is mandatory. To study the question of precise positioning, a micro-movement test facility [10] has been constructed (Fig. 8) and installed on a reference granite block. It consists of two ceramic girders supported by three platforms which are each activated by three precision jacks that allow rotations in the three planes via swivel-joint link rods. Dummy accelerating sections were clamped to the ~1 m long girders via supports which have been fixed with a 3 μm precision. Commercial micromovers and capacitive-vernier transducers (0.1 μm resolution over ±4 and 5 mm) have been used. With this system, the structure could actually be displaced micron by micron, and the measured coupling between the three motions corresponds to the theoretical one. Automatic alignment also requires the beam position to be measured with micron resolution. Concept of position pick-up is based on an E_{110} mode cylindrical cavity, mounted coaxially to the main structure and working at 33 GHz to avoid interference with the RF pulse. The narrow band signal selection under development is carried out by filtering and mixing down signals in several stages.

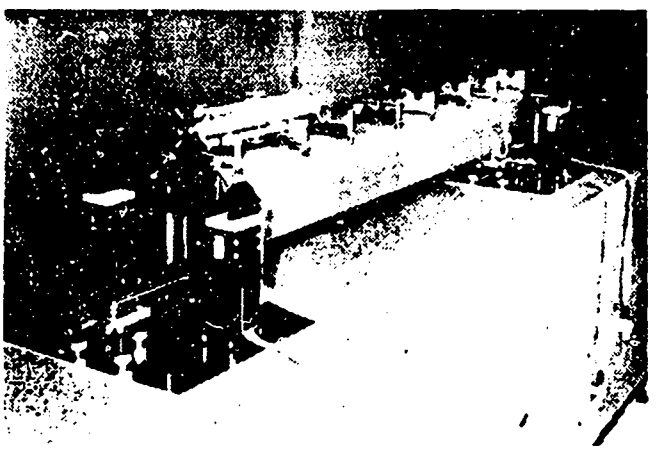

Fig.8 Micro-movement full-size model

Collision Point Requirements

The beam's transverse dimensions at the collision point must be small (nm) in order to reach the adequate luminosity. So as to avoid a centre-of-mass energy spread due to beam-beam radiation larger than 0.1 and too high a repetition rate, i.e. a beam power, the beam height is further reduced to a value corresponding to a large aspect ratio σ_x/σ_y (Table 1). Compression of the beam is provided by a four-lens telescope, with 25 × 75 de-magnification, that is 128.4 m long and optimizes the product of drifts and strengths. Large chromatic aberrations blowing up the beam are compensated in a chromatic correction section 320 m long and made of two lattices, one for horizontal and one for vertical compensation. Each lattice contains four pairs of quadrupoles for a total phase shift of 2π as well as a pair of equal-strength sextupoles, placed at the maximum of the corresponding β value and at equal dispersion. In addition, the two sextupoles of a pair are separated in phase by π and lie in both planes at a multiple of $\pi/2$ from the crossing point. With all these conditions, 2nd order geometric and chromatic aberrations created by the sextupoles themselves are cancelled, except for the two terms that correspond to the blow-up generated by the telescope and have to be compensated. The requisite dispersion is generated by weak 19 m long dipoles. The energy acceptance of this system [11]

(FF), defined as doubling the beta functions, is about ±4‰ (Fig. 9).

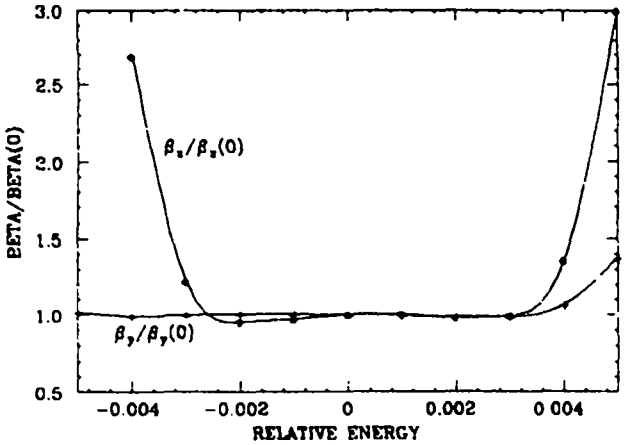

Fig. 9 Energy acceptance of Final Focus

The emittance blow-up by quantized radiation is critically dependent on the emittances (Fig. 10) for a given gradient in the last quadrupole. The effect nearly vanishes for small enough normalized emittances and this explains the revised values quoted in Table 1. The conceptual design of the damping rings has been examined again in view of these values. It is still based on the simplest lattice for small emittance, made of a FODO structure with a combined function magnet in the D-quadrupole [12]. However, to obtain these emittances with low damping times, the dipole length and the number of cells (hence the circumference) have been increased (340 cells), and the energy raised up to 3.35 GeV, which has implications on the injector complex. Luminosity not only depends on the emittances of the head-on colliding bunches, but also on the constriction of the orbits due to the bunch penetration. This important effect has been simulated numerically using non-Gaussian particle distribution as obtained by tracking and including aberrations and synchrotron radiation. It was found with the most recent parameters that the luminosity is enhanced by about 2.5 so as to reach the value of Table 1 with the beam sizes given.

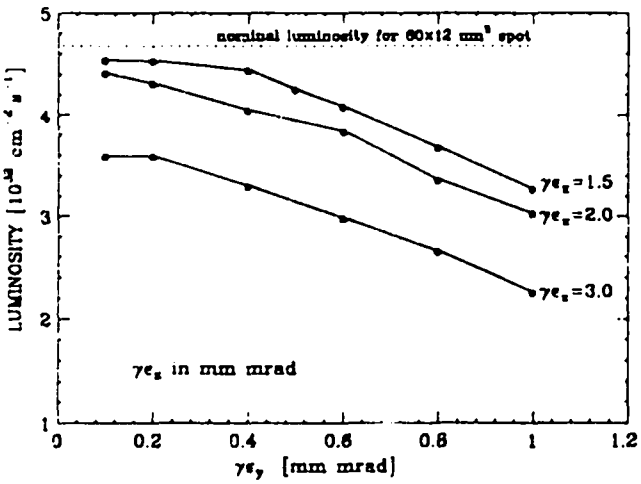

Fig. 10 Luminosity dependence on emittances

Quantized radiation also puts a limit on the useful quadrupole strength and on the interest for ultrahigh gradients. Therefore focusing in the FF system should be achieved by ferromagnetic, electromagnetic or pulsed quadrupoles with 1 mm apertures. Studies are being pursued of a quadrupole made of soft ferromagnetic poles with simple geometry for sub-micron tolerances as well as good field quality and excited by blocks of commercial permanent magnet material [13]. Pole prototypes of 25 mm long module with up to 1.4 T tip field have been built (Fig. 11) together with a precision measuring bench. In parallel, lenses made of four single, axial conductors (Fig. 12) and powered oppositely in pairs are considered and field quality was studied for different geometries [14]. To minimize the average power, these quadrupoles would be pulsed, with up to 7T on the surface, ~10 kA per conductor and 4 μs pulse length. An enlarged model has been built for low current tests.

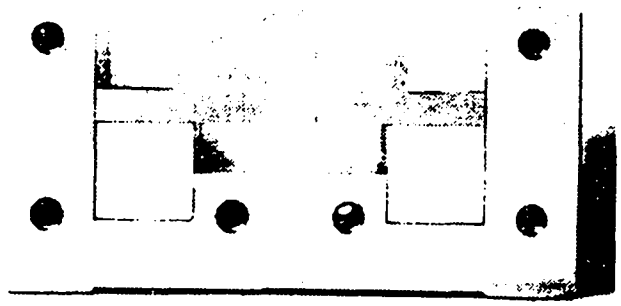

Fig. 11 Permanent half-quadrupole model

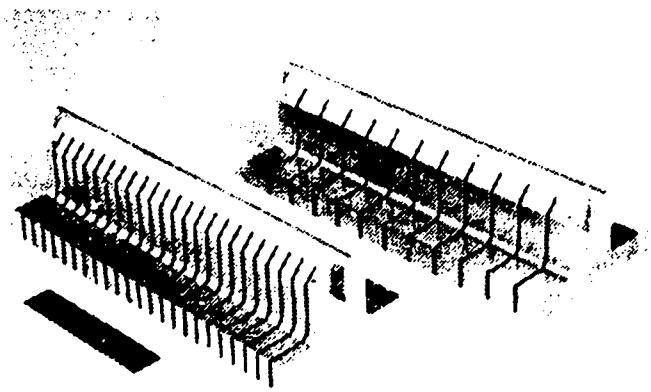

Fig. 12 Model of pulsed quadrupole conductors

References

1. W. Schnell, 1988 Linac Conf., Virginia
2. Y. Baconnier *et al.*, this Conference.
3. Y. Baconnier *et al.*, EPAC 90, Nice (1990).
4. H. Kugler *et al.*, EPAC 90, Nice (1990).
5. L. Thorndahl and E. Jensen, Private comm.
6. C. Fischer and G. Guignard, to be published.
7. K.L.F. Bane, SLAC-AP-76(1989).
8. V. Balakin, LC90 Workshop, KEK (1990).
9. I. Wilson *et al.*, EPAC 90, Nice (1990).
10. W. Coosemans *et al.*, EPAC 90, Nice (1990).
11. O. Napoly and B. Zotter, EPAC 90, Nice (1990).
12. J.P. Delahaye and J.P. Potier, PAC, Chicago (1989).
13. K. Egawa and T.M. Taylor, PAC, Chicago (1989).
14. P. Sievers, Private comm. (CLIC Note 112).

THE JAPAN LINEAR COLLIDER

Koji Takata
KEK, National Laboratory for High Energy Physics,
1-1 Oho, Tsukuba-shi, Ibaraki-ken 305, Japan

Abstract

Present status of R&D works for the proposed 1 TeV Japan Linear Collider is presented. Discussions are given about its major parameters. Summarized are high gradient experiments, X-band klystron development and accelerating structure studies at KEK. Test of the first X-band klystron with the designed output power 30 MW started and a peak power of about 10 MW has been achieved.

Introduction

The electron positron collision experiments at the energy frontier have been carried out solely with storage rings. In Japan the TRISTAN electron positron storage ring, which was commissioned November 1986, has been operated for physics experiments at the center of mass energy around 60 GeV with its highest value 64 GeV being attained in November 1989.[1] For the energy frontier physics in the 2000's, however, the center-of-mass energy is desired to be as high as 1 TeV. For such an energy range the only possible accelerator is the linear collider. In 1986 the Japan high energy physics community adopted the resolution to start R&D works for a 1 TeV linear collider in Japan, JLC (Japan Linear Collider), the construction of which is hoped to start in the end of 1990's.[2]

For a linear collider, the main electron and positron linacs extend colinearly, and accelerated electron and positron bunches collide each other at the median point. In order to enhance the luminosity, the cross section of a bunch is made as small as possible in each final focus section extending from the end of either linac to the collision point. At the entrance of the linacs, on the other hand, beam emittances are reduced to a minimum in a damping ring with a beam energy of about 1.5 GeV. The injector linac for the damping ring will be of a conventional type for each beam. For positrons, however, an electron linac with the energy being at least 10 GeV is necessary in order to convert electrons efficiently into positrons.

Since we started parameter designs for JLC in 1986, it has been our consistent policy that the main linac should be based on conventional linac technologies in which we have much experience. In particular, since the required acceleration gradient is as high as 100 MV/m, the RF power source is the key element in the JLC design. Hereupon we have been pursuing to push forward the well established klystron technologies to get very high power tubes. Regarding the RF frequency, a higher one is generally desirable because of, for instance, power saving. But we chose it at the X-band range which is not yet too high for fabrication of klystrons and disk loaded accelerating structures. Particularly it is 11.424 GHz, four times the SLAC frequency, since almost all of the conventional linacs are operated at the latter frequency and hence its integer multiple would be very convenient in the R&D works hereafter.

JLC Design

Figure 1 shows a schematic layout of JLC with its parameters listed up in Table 1.[3] The maximum luminosity would be 6.2 x 10^{33}cm^{-2}sec^{-1}. Each linac operates at a repetition rate of 200 Hz. For a linac pulse 10 bunches are accelerated at the gradient 100 MV/m. The population per bunch is 1.0 x 10^{10} particles. The normalized emittances 3 x 10^{-6} rad.m and 3 x 10^{-8} rad.m for the horizontal direction and the vertical, respectively, are assumed to be the same as those achieved in the damping ring. The beam power 1.60 MW would be 9.3 % of the RF power for the accelerating structure. The overall length of the JLC system will be around 16 km. The interaction point and the damping ring complex will be located in the KEK site. The total wall plug power should not exceed the maximum available power at KEK of 200 MW.

We assume a flat beam with an aspect ratio of 166 at the interaction point (IP). The rms beam sizes will be as small as 230 nm horizontally and 1.4 nm vertically. The rms bunch length is 76 μm which is almost equal to the vertical beta function β_x^* 50 μm. In order to avoid the background problem at IP, the electron and positron bunches collide at a small horizontal angle of 6 mrad. This angle can be coped with in the final focusing section. Therefore the electron and positron linacs can be set in a straight tunnel, to a great simplicity of its construction. But a small loss of luminosity due to the finite angle crossing is not taken into account in the figure of Table 1. The beamstrahlung parameter $\Upsilon_{av.}$ is as small as 0.49 because of the large aspect ratio and a moderate energy loss δ due to beamstrahlung. Simulations suggest that the pair creation is concentrated within a very narrow cone in the forward direction and would cause no serious background problems.

The X-band main linac for each beam will consist of 900 eight-meter-long modules as shown in Figure 2.[4] In each module eight 70 cm long accelerating structures[5] are placed with a space of 1 m with focusing quads between them. The accelerating structure is assumed to be of a constant-impedance 2π/3-mode traveling-wave type with 80 cells including the input and output couplers. With the iris radius 3.7 mm (a/λ = 0.14) and the disk thickness 2.0 mm, the computed Q value and shunt impedance are 6600 and 93 MΩ/m, respectively. With the group velocity being 2.5% of the light velocity, the filling time is 92 ns. The peak input power for the average gradient 100 MV/m becomes 120 MW. The bunch to bunch spacing is chosen to be 1.4 ns or 16 RF cycles and hence the bunch train length becomes 12.6 ns. In order to minimize the bunch to bunch energy spread due to the beam loading, some of the 900 modules are to be not completely filled with the RF pulse when the bunch train runs through.

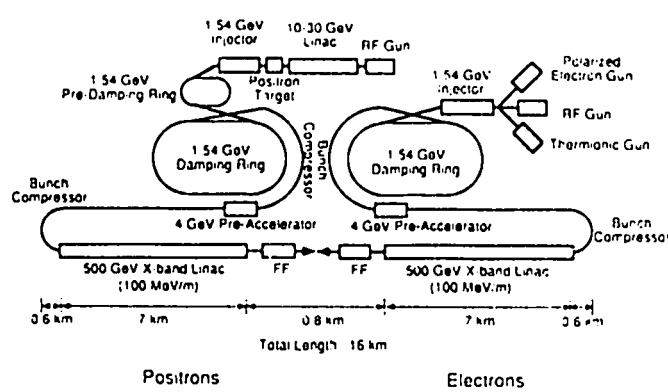

Fig. 1. Schematic layout of the JLC accelerator complex

TABLE 1
JLC Parameters

Global Parameters		
Beam energy	2E	500+500 GeV
Repetion frequency	f_{rep}	200 Hz
Number of particles/bunch	N	1.0×10^{10}
Number of bunches/RF pulse	N_b	10
Beam power per beam	P_b	1.60 MW
Normalized emittance	ε_{xn}	3×10^{-6} rad.m
	ε_{yn}	3×10^{-8} rad.m
Luminosity	L	$6.2 \times 10^{33}/cm^2 sec$
Total accelerator length		16 km
Wall plug power		200 MW max
Beam-beam Interaction		
Rms beam size at IP	σ_x^*	230 nm
	σ_y^*	1.4 nm
Aspect Ratio	R	166
Rms bunch length	σ_z	76 μm
Beamstrahlung parameter	$\Upsilon_{av.}$	0.49
Average energy loss by beamstrahlung	δ	14 %
Crossing angle	θ	6 mrad
Final Focus System		
Beta function at IP	β_x^*	14 mm
	β_y^*	0.05 mm
Total length		365 m
Distance between the last quad and IP		1.0 m
Pole tip field of the last quad	B_t	1.4 T
Aperture of the last quad	2a	1.04 mm
Main Linac		
RF frequency	f_{rf}	11.424 GHz
Accelerating gradient	G	100 MV/m
Number of structures/beam		7,200
Structure length		70 cm
Number of cells/structure		80
Q value	Q	6,600
Shunt impedance	r	93 MΩ/m
RF power/structure	P_o	120 MW
Number of klystrons/beam		1,800
Accelerating mode		2π/3
Filling time	T_f	92 nsec
Iris radius	a	3.7 mm
Disk thickness	t	2.0 mm
Group velocity	v_g/c	0.025
Attenuation parameter	τ	0.50
Normalized elastance	s_0	0.70 Vm/pC
Extraction efficiency	η_{b1}	1.65 %/bunch
Bunch spacing	t_b	1.40 nsec
Beta function	β(s)	$3.0 \sqrt{E/10GeV}$ m
Damping Ring		
Energy		1.54 GeV
Number of paticles/bunch		1×10^{10}
Number of bunches /train		10
Number of trains		8
Bunch spacing	t_b	1.40 ns
Bunch train spacing		61 ns
Circumference	C	180 m
Transverse damping time	$\tau_{x,y}$	4.8 ms
RF frequency	f_{RF}	1.428 GHz
RF peak voltage	V_{RF}	1.0 MV
Wiggler field	B_{wig}	2.0 Tesla
Wiggler pitch	λ_{wig}	42.5 cm
Length of wigglers	L_{wig}	40 m
Equilibrium emittance	ε_{xn}	3×10^{-6} rad.m
	ε_{yn}	3×10^{-8} rad.m
Equilibrium bunch length	σ_z	5.0 mm
Equilibrium energy spread	σ_ε	0.79×10^{-3}

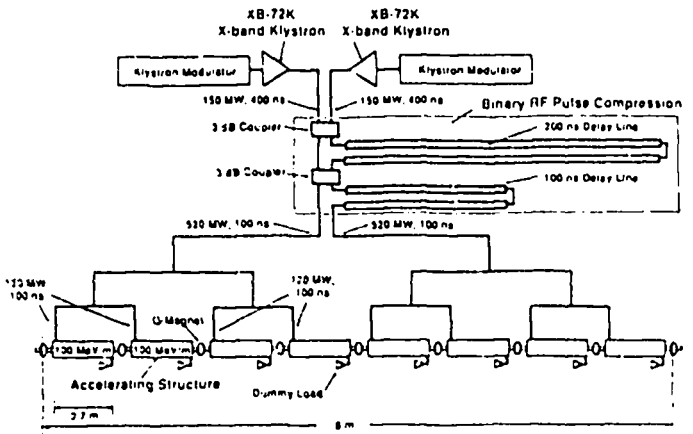

Fig.2. Unit module of X-band main linac

The single bunch longitudinal wake for the gradient 100 MV/m is expected to be -0.2% and -0.8% for the longitudinal position $-\sigma_z$ and σ_z respectively. The energy spread inside a bunch necessary for achieving the BNS damping[6] would be on the order of ± 0.5 %. We do not yet have, however, an accurate estimation of transverse wake field and hence are not able to determine the synchronous phase for the bunch. At any rate it would not deviate from the RF crest by more than ±10°.

For the multi-bunch acceleration we must solve the beam break up problem. In this case the dominant wake component would come from the TM_{110} mode. The wake potential due to a transversal offset of a preceding bunch induces also an offset for the trailing bunch. The value Δ of the latter relative to the former offset can be expressed as[7]

$$\Delta = \frac{\beta_0 e N}{G} \sqrt{\frac{E_f}{E_0}}\, W_0 \exp\left[-\frac{\omega_1 t_b}{2Q_1}\right] \qquad (1)$$

where E_0 is the injection energy (10 GeV), E_f the final energy (500 GeV), G the acceleration gradient (100 MV/m), N the number of particles per bunch (1×10^{10}) and the β_0 the beta-function at the injection energy (3.0 m) which we assume to be proportional to square root of the beam energy. For the TM_{110} wake we assume that W_0 is about 1×10^{17} V/C-m^2 as several numerical calculations show and ω_1 equal to $2\pi \times 16$ GHz. Since the bunch spacing t_b is equal to 1.4 ns, substitution of the numerical values leads to

$$\Delta = 34 \exp\left[-\frac{70}{Q_1}\right] \qquad (2)$$

From this relation we see that the Q value of the TM_{110} mode Q_1 should be so low as 10 for Δ « 1, while for Q_1 = 20, Δ is about 1. The damped cavity structure is, therefore, indispensable to suppressing the multi-bunch beam break up. Also it should be noted that for low frequency deflecting modes the wakes seem insensitive to the aperture radius a, contrary to the case of short range wakes.

For the RF power source we will employ two klystrons for each module as shown in Figure 2. The klystron

named XB-72K, now in the designing stage, would generate a peak power of 150 MW in a 400 ns long pulse.[8] The output pulses from the paired klystrons will go through a two-stage pulse compression system[9] where the pulse length is compressed to 100 ns. Taking the waveguide loss into account we expect that the designed input power 120 MW would be available for each of eight accelerating structures. In order to improve the overall efficiency, we are considering a modulator incorporating magnetic switches with which rise and fall times as short as 100 ns would be enabled.

The 1.54 GeV damping ring will be a race-track type with two FODO arcs and two wiggler sections.[10] The circumferential length is 180 m and eight batches of ten bunch trains are stored with a spacing of 6[illegible] ns which is necessary for the rise and fall times of kicker magnets. The RF frequency 1.428 GHz is one eighth of the X-band frequency and the bunches in a train are placed in every two RF buckets. Wigglers of a total length of 40 m damps transverse betatron oscillations with a time constant of 4.8 msec to the equilibrium normalized emittances as shown in Table 1. The equilibrium rms bunch length σ_z and energy spread σ_ε are 5.0 mm and 0.79 x 10^{-3}, respectively In order to increase the acceptance for the positron beam, we are considering the possible use of a pre-damping ring with a third circumference.

Accelerator Test Facility

In order to promote the R&D works for JLC, we have been establishing an accelerator test facility (ATF) in KEK. As a first step, a 1.54 GeV high gradient S-band linac is under construction. We will annex to it a test damping ring with which we will try to achieve the desired normalized emittances $\varepsilon_x/\varepsilon_y$ = 3.0 x 10^{-6} / 3.0 x 10^{-8} rad-m. The low emittance beam will be used to test the final focusing system. We also plan to construct a module of the X-band linac with which we will test the 100 MV/m acceleration using the 1.54 GeV linac beam. Novel techniques for electron and positron sources are also to be tested at ATF.

The S-band linac will consist of a 40 MeV injector and 1.5 GeV normal section. As an electron source we developed a 200 kV thermionic gun. It is to be followed by a subharmonic buncher operating at 714 MHz, a fourth of the S-band frequency, in order to get the 1.4 ns bunch spacing. The electrons will then be injected into a 1.5 m long conventional disk loaded structure. The 1.5 GeV linac will consist of twelve 3 m long disk loaded structures in which a gradient of 42 MV/m will be attained with six klystrons each generating 180 MW 1 μs pulses with the aid of the SLED system.[11]

With regard to the RF source, we had no reliable high-power S-band klystrons when we started the R&D works. Supported by the US and Japan scientific collaboration program, eight 5045 SLC klystrons[12] were delivered to KEK by SLAC. They can be operated at a rating of 100 MW output power for 1 μs pulses. Four modulators have already been set up and used for driving those tubes. We have obtained 200 MW 1 μs pulses in a single S-band waveguide line by combining the outputs of two tubes.

Besides constructing the linac, we are also undergoing tests of an S-band high gradient structure and development of X-band klystrons using the facility as described in the following sections.

S-band High Gradient Test

It is the key issue in R&D to successfully attain the high gradient 100 MV/m over a considerable length of the structure. Though tests should be carried out at the X-band frequency, there have been no high power X-band tubes available and hence experiments at KEK are restricted to only S-band structures.

Since the 30 MW klystron for the Photon Factory 2.5 GeV linac was the only available tube, an S-band resonant ring was employed to boost the peak travelling wave power. A five cell $2\pi/3$ mode travelling wave structure was tested in this ring and it was possible to attain the gradient 100 MV/m.[13] But, since the active length including the coupler cells is only 17.5 cm and the RF power has scarcely a flat top in a resonant ring, it was desired that a much longer structure should be tested with a square pulse of a sufficient peak power and flat top.

As described above, however, the peak power 200 MW has become available by using the 5045 tubes. Hence we fabricated a constant gradient 66.5 cm long $2\pi/3$ mode travelling wave structure in which the gradient 100 MV/m is to be attained for the 200 MW peak input power.[14, 15, 16] The iris diameter changes from 19.0 mm for the first cell to 15.9 mm for the last cell. The filling time is 430 ns. The disk thickness is 5.84 mm. According to Superfish calculations, the peak surface field of about 2.0 times the average acceleration gradient exists around the rounded iris. The structure is made of class-1 OFHC copper. Disks and cylinders were surface finished to the order of 0.02 μm except for the rounded iris where the roughness was one order of magnitude larger. They were brazed together with a 790°C silver alloy in a hydrogen furnace. The squeezing process for tuning the cells was carried out with a continuous flow of dry nitrogen gas inside the structure.

The experimental setup is shown in Figure 3. Since the survey of the field emission was the main purpose, faraday cups and current transformers were placed on each side of the structure. An energy analyzer was installed downstream. The conditioning started in July 1989 and continued until April 1990 when a ceramic pipe section for the current transformer cracked due to radiation damage. The integrated conditioning time was about 900 hours. The RF pulse was 1.0 μs long with a rise time of 100 ns. Its repetition rate was 25 Hz at first and then doubled. In the last stage the average gradient E_{acc} reached 92 MV/m, whereupon the peak input power was 160 MW. A considerable portion of the time was taken to improve the output coupler where breakdown occurred very often as radiation monitors and a current profile monitor suggested. It might be due to the fact that the surface finish of this area was not good enough at the initial tuning process. Application of inhomogeneous fields of about 200 gauss was very effective in speeding up the processing.

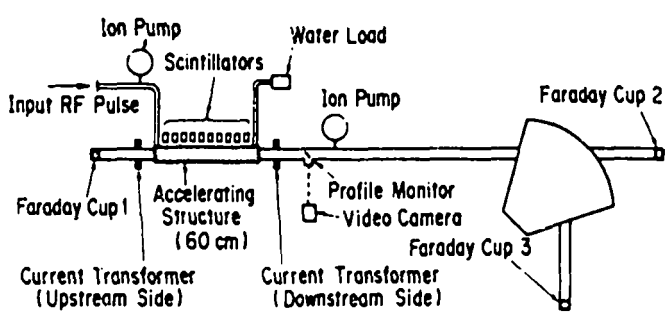

Fig. 3. Experimental set up for high gradient test of an S-band 66.5 cm long structure

The modified Fowler-Nordheim relation for the RF field is given by[17]

$$\ln\left[\frac{I}{E^{2.5}}\right] = -\frac{B\phi^{1.5}}{\beta E} + \text{constant} \qquad (3)$$

where I is the field emission in Amperes, E the peak surface RF field in V/m, β the enhancement factor, ϕ the metal work function in eV which is assumed here to be 4.65 eV of copper, and the numerical constant B is equal to 6.53×10^9.

The enhancement factor was around 90 for integrated conditioning hours from 200 to 400. But at the final stage where E reached 2.0 x 92 MV/m, β reduced to about 40. Beam acceleration was tried at acceleration gradients from 70 to 85 MV/m. At the 50 Hz repetition rate, 200 ns long beam pulses with peak currents up to 0.9 A were successfully accelerated. The beam energy spectra were consistent with the gradient calculated from the peak input power if we take into account the beam loading effect using the measured shunt impedance.

X-band Klystron

From many experiences about both S-band and UHF high power klystrons developed for the TRISTAN accelerator complex, we think that the most important is to get, for any kind of tube, a reliable electron gun which is stable and has a long life under high voltage operation. We therefore started at first fabrication of a diode tube named XB-50D[18] which has a somewhat small cathode diameter of 50 mm compared with the XB-72K tube. The designed voltage and perveance were 450 kV and 0.57 $\mu AV^{-3/2}$, respectively. For the cathode an iridium-coated barium-impregnated cathode was used. For the convenience sake, the gun electrodes were made compatible with the socket for the 5045 tubes at ATF.

The conditioning was carried out at a repetition rate of 2 Hz. It took 50 hours to reach the design voltage 450 kV. The perveance was 0.60 $\mu AV^{-3/2}$ for the cathode temperature 1020°C. The beam power was 81.5 MW. With further conditionings with 20 Hz pulses, the fault rate reduced to once per 8×10^4 pulses at the above voltage.

Employing the same gun configuration, we fabricated the first high power klystron XB-50K as shown in Figure 4.[19] The RF section was optimized by the 2.5D simulation code FCI.[20] It consists of five cavities with the drift section 8 mm indiameter between them, where an axial magnetic field of 4.5 kGauss is applied. The RF interaction length is 268 mm. The output cavity is of a pill box type 10.2 mm long and 17.2 mm in diameter with an interaction gap of 6 mm. It is coupled to the standard WR90 waveguide 22.9 mm wide and 10.2 mm high through a 9.8 mm wide inductive window. Those dimensions were determined with the codes Superfish and Mafia to obtain an optimized Q_{ext} 30. The FCI calculation gives an efficiency of 47 % or output power of 36 MW for this Q_{ext}. Though Qext larger than 40 would result in efficiencies better than 50 % as FCI simulations suggest, the surface field would be too high. Our design criterion for it was 100 MV/m, which correspond to Qext equal to 30. As the output window we chose a very simple design of a half wave-length ceramic block 4.45 mm thick with the same cross section as the waveguide. The VSWR is 1.01 at 11.4 GHz and its bandwidth at 1.05 is 90 MHz.

The conditioning of the first XB-50K tube was carried out at a repetion rate of 2 Hz. The voltage pulse width is about 2 µs, while the RF pulse width is 140 ns. After conditionings 15 hours long in total, the highest cathode voltage was 350 kV, when the tube suffered from cracks in the output window. The output power reached 11 MW with an efficiency of 27 % as shown in Fig.5. The perveance was 0.54 $\mu AV^{-3/2}$ which is close to the designed value 0.56 $\mu AV^{-3/2}$.

The XB-72K tube with the cathode diameter 72 mm is under design. According to FCI calculations, it will be operated at 600 kV with a perveance of 1.2 $\mu AV^{-3/2}$. With five cavities and drift tubes with a diameter of about 9.5 mm, 150 MW RF power is expected with an efficiency of 45 %. For the output cavity we will use a single gap pill box cavity without the nose cone to reduce the surface field gradient to 72 MV/m.[21]

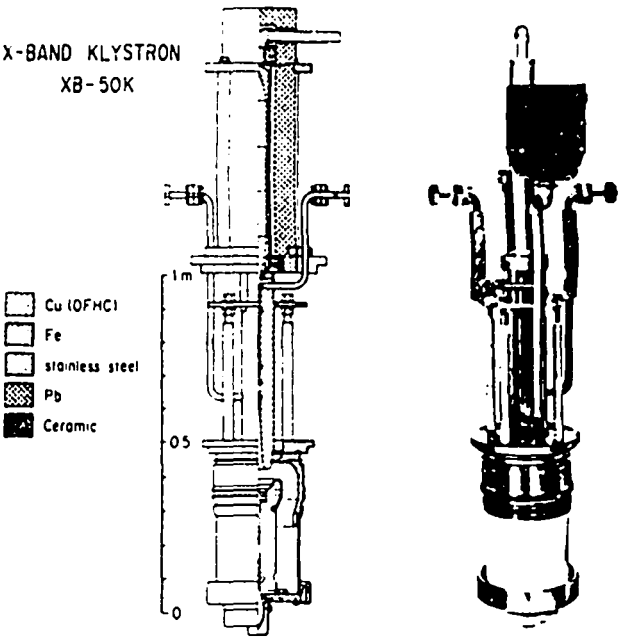

Fig. 4. First X-band klystron XB-50K

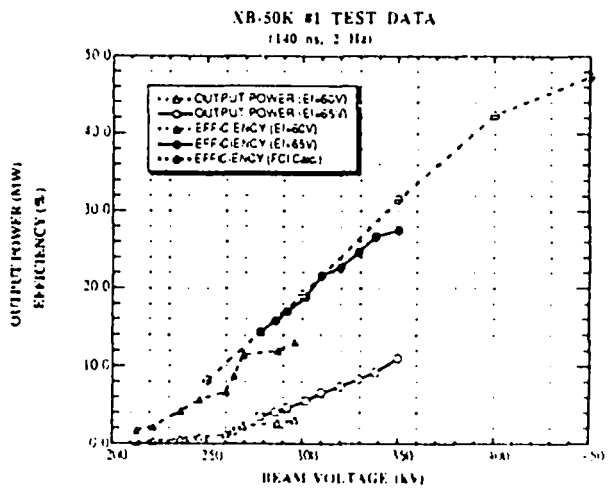

Fig.5 Conditioning of the XB-50K klystron

X-band Structure

R&D studies for X-band structures[22,23] have been covered two fields. One is to survey fabrication techniques for producing structures in the X-band scale. The other is to find damped structures with Q values on the order of 10 for deflecting modes by three dimensional calculations.

Machining tests were carried out for a cell unit scaled a fourth down from the conventional S-band disk loaded structure. It is a cuplike cylinder of 30 mm in the outer diameter and 21 mm in the inner with a 2.0 mm thick disk at an end. The disk has an aperture 6 mm in diameter with the edge rounded with a radius of

0.5 mm. Several pieces were fabricated by using a fairly good lathe. Machining accuracies for the cylindrical section were measured to be ±4 μm for the diameter dimensions and off-center within 3 μm. The outer disk surface of the cup had a flatness of 1 μm but the other side of the disk had deviations of about 5 μm. The surface roughness was on the order of 0.1 μm. Preliminary tests of brazing these pieces were also carried out.

Taking those results into consideration, we are designing an X-band structure for the high gradient test using the KB-50K klystron. It is a constant-impedance $2\pi/3$ mode 22 cell structure 19.25 cm long with the disk aperture diameter 6 mm. For an input power of 30 MW, an average gradient of 85 MV/m would be obtained with the attenuation parameter τ being about 0.33.

Calculations of damped structures have been carried out by use of Slater's formula[24] for the slots as shown in Figure 6. Two slots are cut in every other disk. The slot dimensions listed in the figure caption are the optimized ones for the TM_{110} mode. For modes with cell-to-cell phase shifts of 0 and π, the Q_{ext} values are as low as about 1 and 20, respectively. The latter is not yet low enough according to Equation 2 and additional slots may be necessary. For the accelerating mode, the slots would have a considerable amount of magnetic coupling and the dispersion relation should be carefully calculated. The Q value of the accelerating mode would be also a little go down since the slots so wide as shown in Figure 6 inevitably disturbs the cylindrically symmetric wall current.

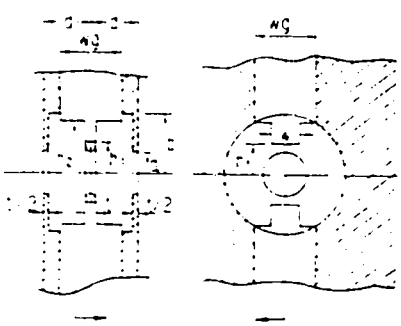

Fig. 6. X-band damped cavity calculation for the typical dimensions: cavity radius b=10.6mm, pitch d=8.75mm, aperture radius a=3.7mm, disk thickness t=2.0mm, slot heits h1=5.5mm and h2=9.0mm, slot width w=5.0mm, waveguide height/width wg=11.1mm.

Conclusions

Among many problems which should be solved by the R&D works, the key issues are the RF source and accelerating structure. As discussed above, the present status of their development are still far off from what is required for the JLC design. Particularly, if the RF source will not be fully developed, the JLC might be started with lower gradients 50 to 75 MV/m, contrary to the designed 100 MV/m acceleration. At any rate, we are stressing the klystron development most, since its test cycle usually takes much time. The other issue which should be seriously considered is to construct a test damping ring as early as possible in ATF. With low emittance beams generated by it, such urgent subjects as wake fields and beam monitors, for instance, will be experimentally pursued.

References

1. Y. Kimura, "The Performance of TRISTAN and Accelerator Development at KEK," presented at the Second European Particle Accelerator Conference, Nice, France, June 12 - 16, 1990.
2. Y. Kimura, K. Takata and M. Yoshioka, "Electron-positron Linear Collider R&D Program at KEK," Proceedings of the 1987 ICFA Seminar on Future Perspectives in High Energy Physics, Upton, USA, 1987, pp. 219.
3. K. Yokoya, "JLC Beam Dynamics," Proceedings of the First Workshop on Japan Linear Collider (JLC), KEK, October 24 - 25, 1989, pp. 26.
4. S. Takeda, "JLC Status," Presented at the Second International Workshop on Next-generation Linear Colliders, KEK, March 1990.
5. T. Higo, "X-band Accelerating Structure for Japan Linear Collider," Proceedings of this conference.
6. V. E. Balakin, A. V. Novokhatsky and V. P. Smirnov, "VLEPP: Transverse Beam Dynamics," Proceedings of 12th International Conference on High Energy Accelerators, Fermi Lab., August 1983.
7. K. Yokoya, private communication.
8. H. Mizuno and J. Odagiri, "X-band Klystron for Japan Linear Collider," Proceedings of this conference.
9. Z. D. Farkas, " Binary Power Multiplier," SLAC-PUB-3694, 1985.
10. J. Urakawa, "Preliminary Design of 1.54 GeV Damping Ring and Bunch Compressor for JLC," Proceedings of this conference.
11. Z. D. Farkas et al, "SLED: a Method of Doubling SLAC's Energy," SLAC-PUB-1453, 1974.
12. M. A. Allen et al, " Reliability and Lifetime Predictions of SLC Klystrons " SLAC-PUB-4863, March 1989.
13. H. Matsumoto et al, "RF Breakdown Studies on an S-band Disk Loaded Structure," Proceedings of the 1987 IEEE Particle Accelerator Conference, Washington, D.C., 1987, pp. 1654.
14. K. Takata, "Operational Experience of Superconducting and High Gradient RF Cavities," To be published, Proceedings of the 14th International Symposium on Discharges and Electrical Insulation in Vacuum, Santa Fe, USA, September 1990.
15. S. Takeda, "High Gradient Experiment by Accelerating Test Facility for Japan Linear Collider," Proceedings of this conference.
16. H. Matsumoto, "Experimental Study of the S-band High Gradient Linac," Proceedings of this conference.
17. G. A. Loew and J. W. Wang, "Field Emission and RF Breakdown in Copper Linac Structure," *Particle Accelerators*, 1990, Vol. 30, pp. 225.
18. H. Mizuno, J. Odagiri and T. Higo, "X-band Klystron Diode Test for Japan Linear Collider (JLC)," *Particle Accelerators*, 1990, Vol. 30, pp. 167, and also KEK Preprint 89-114, September 1989.
19. H. Mizuno, "RF Power Source for JLC," Proceedings of the First Workshop on Japan Linear Collider (JLC), KEK, October 24 - 25, 1989, pp. 76.
20. T. Shintake, "FCI- Field Charge Interaction Program for High Power Klystron Simulations," KEK Preprint 89-18, 1989.
21. T. Shintake, " High-Power Klystron Simulations using FCI - Field Charge Interaction Code," to be published on KEK report.
22. T. Higo, "Accelerating Structure," Proceedings of the First Workshop on Japan Linear Collider (JLC), KEK, October 24 - 25, 1989, pp. 91.
23. T. Higo, M. Takao et al, "X-band Accelerating Structure for Japan Linear Collider," Proceedings of this conference.
24. T. Kageyama, "A Simple Method Using MAFIA to Calculate External Q Values of Waveguide-Loaded Cavities," KEK Report 89-4.

Monday

Session MO2
Chairman: D. Young
Invited Papers

CEBAF PROGRESS REPORT*

Beverly K. Hartline†
Continuous Electron Beam Accelerator Facility
12000 Jefferson Avenue, Newport News, VA 23606

Abstract

At the Continuous Electron Beam Accelerator Facility, under construction in Newport News, Virginia, a pair of 400-MeV superconducting linacs interconnected for five-pass recirculation will provide 4-GeV, 200-μA, cw electron beams to simultaneous nuclear physics experiments in three end stations. As of August 1990, the first production-version cryomodule has been successfully tested, the injector's initial superconducting quarter-cryomodule has accelerated beam to the required 5 MeV, and industry has supplied the first production accelerating cavities, klystrons, cryomodule components, and other hardware. The first section of the 1400-m, cast-in-place, racetrack-shaped tunnel was occupied in January, the entire racetrack was completed in June, and occupancy will proceed in stages through late 1990. Installation has advanced on the helium transfer, accelerator control, and personnel safety systems. Injector installation is under way, with systems tests to 25 MeV to commence late this fall. Commissioning of the 4800-W, 2-K central helium refrigerator has begun. The Program Advisory Committee has approved initial nuclear physics experiments, the experimental equipment conceptual design is complete, the first major spectrometer components are out for bid, and end station construction has begun. Project completion is scheduled for 1993, with first physics in 1994. Construction cost is $265M.

Introduction

The 4-GeV continuous-wave (cw) superconducting recirculating electron accelerator under construction since February 1987 at the Continuous Electron Beam Accelerator Facility (CEBAF), Newport News, Virginia, serves a mission identified in a nuclear physics community consensus now more than a decade old. The 1979 Long Range Plan[1] of the DOE/NSF Nuclear Science Advisory Committee (NSAC) called for a GeV-scale, continuous-beam electron accelerator to study the quark structure of the nucleus. Succeeding NSAC long-range plans[2,3] have reiterated support for bringing CEBAF into operation to meet this scientific need.

To meet the physics requirements, CEBAF's beam performance objectives are given in Table 1. Beams will be extracted from the accelerator for simultaneous use in three experimental halls.

Table 1
Beam Performance Objectives

Energy	$0.5 \leq E \leq 4.0$ GeV
Beam current	$I \leq 200\ \mu$A
Duty factor	100%
Emittance ($\sigma^2 = \frac{1}{4}\epsilon\beta$)	$\epsilon \leq 2 \cdot 10^{-9}$ m·rad
Momentum spread	$\sigma_E/E \leq 2.5 \cdot 10^{-5}$

A cw device is the approach of choice to produce a high-quality continuous beam. Low peak current for a given average current lowers emittance, and continuously operating rf systems can be controlled quite precisely in phase and amplitude, thereby leading to small energy spread and small variations of average energy. To avoid the high capital cost of a single, long 4-GeV linac, CEBAF's beam is passed five times through a parallel pair of 400-MeV linacs connected by recirculation arcs (Figure 1).

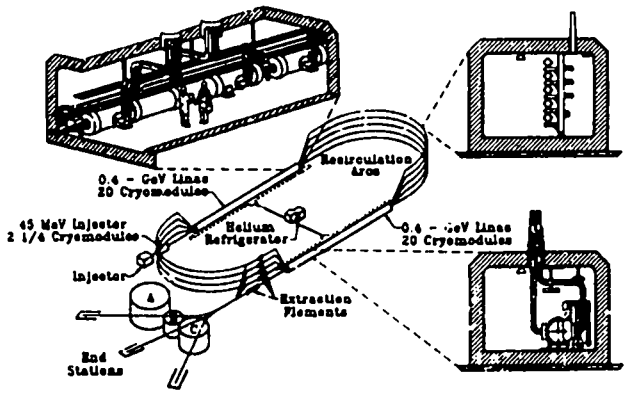

Figure 1. Schematic of the CEBAF superconducting recirculated linac.

The recirculated linac is injected with electrons at 45 MeV (β = 0.99994), sufficiently relativistic that both the newly injected beam and recirculated beams at higher energies can pass together through the linacs, all maintaining the proper phase relative to the rf field. Each beam, however, requires a separate recirculation path matched to the electron momentum to transport it between linacs.

This progress report updates the CEBAF overview presentation at the 1988 Linac Conference.[4]

Accelerator Construction Progress

In early September 1990, the construction phase of the facility was 49% complete, with an additional 20% of the work under way on contracts. First articles of most accelerator components have been delivered. The first quarter of the cast-in-place concrete tunnel was occupied in January,

* Work supported by the U.S. Department of Energy under contract DE-AC05-84ER40150.

† The author acknowledges the technical contributions of numerous CEBAF staff members.

and tunnel construction was completed in June. Construction of associated surface buildings continues, with occupancy expected in November 1990 (Figure 2). CEBAF's 4800-W, 2-K Central Helium Liquefier (CHL) is in the final stages of installation, and commissioning has begun.

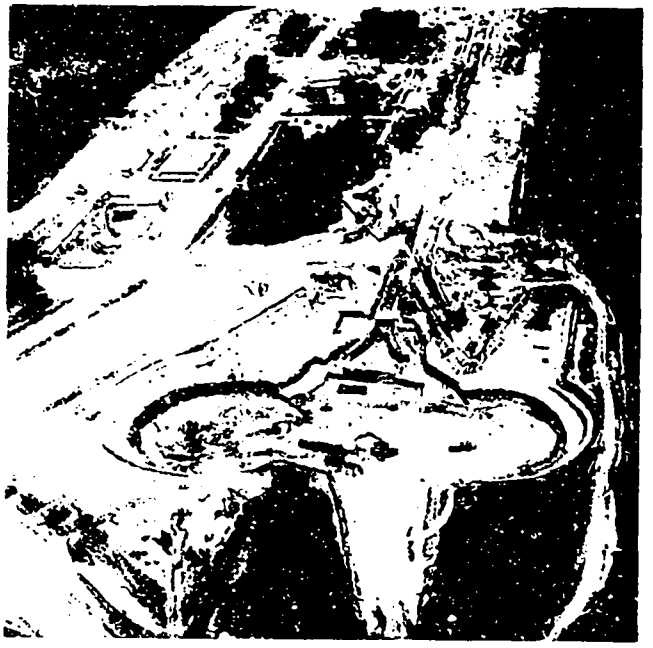

Figure 2. CEBAF civil construction progress, July 1990. End station excavation in foreground; accelerator surface buildings in background; injector service building near the center left edge.

Injector

The 5-MeV initial section of the injector has been in operation in the test lab for a year, together with components of the accelerator control system now being permanently installed. The 5-MeV section includes the electron gun, chopping and bunching cavities, a room-temperature capture section that raises the energy to 0.5 MeV, and a pair of superconducting rf cavities identical to those used in the linacs. Operation at 5 MeV has permitted extensive testing of beam diagnostic instrumentation, rf control hardware and software, and operating procedures. This section of the injector achieved a maximum energy of 5.5 MeV (10% above the design value) and a peak cw current of 550 μA (over 2.5 times the design value). Laboratory testing of the 5-MeV section ended on July 31, 1990; the hardware is now being installed in the tunnel and service buildings in preparation for 25-MeV operation (beam accelerated by ten superconducting cavities) late this fall (Figure 3). In the spring an additional accelerating module containing another eight cavities will complete the 45-MeV injector. Using the 45-MeV injector alone, CEBAF plans late next year to conduct a one-pass recirculation experiment to confirm beam breakup analyses, the reinjection scheme, and the capability to detect individual beam positions in a multipass situation. Injector operation and testing are planned to proceed in parallel with linac installation during 1991.

Figure 3. Tunnel installation of initial injector section.

Accelerating Structures

The accelerator's 1497-MHz, five-cell superconducting niobium cavity was originally developed at Cornell University[5] and later adopted for CEBAF. At one end, a waveguide acts as the fundamental rf power input coupler and as a coupler for extracting some of the higher-order modes generated by the beam current; at the other end of the cavity, two waveguides perpendicular to each other and to the beam axis serve as couplers to extract additional higher-order modes. In longitudinal section, the inner surfaces of the cells comprise elliptical segments; this elliptical shape was developed to reduce multipacting, a process that degrades the achievable electric field by leading to excessive heat loss in the cavity wall. The shape also yields good mechanical rigidity and a chemical rinsing geometry advantageous during pre-assembly processing. Table 2 gives key cavity parameters.

Table 2
Cavity Parameters

Fundamental frequency	f_0 = 1497 MHz
Shunt impedance	r/Q = 960 Ω/m
Loaded Q (@ f_0)	$Q_{ext} = 6.6 \times 10^6 \pm 20\%$
Q_{ext} (HOM)	$10^3 \leq Q_{ext} \leq 10^5$
Operating temperature	2 K
Active length	0.5 m
Performance specifications:	
Accelerating gradient	$E_{acc} \geq 5$ MV/m
Q_0 @ 2 K & 5 MV/m	$Q_0 \geq 2.4 \times 10^9$
(rf losses	≤ 11 W/m)

Cavities are chemically processed and assembled in a clean room into evacuated, hermetically sealed pairs. Each pair is inserted into a liquid-helium cryostat called a cryounit. Four cryounits are serially linked to form the accelerator's basic accelerating module, the cryomodule (Figure 4). Each linac will have 20 cryomodules, connected by warm sections of beam line containing vacuum equipment, beam monitors, and magnets to focus and guide the beam

By August 1990, 27 production cavities had been delivered as scheduled and six pairs had been prepared for cryounit assembly. In vertical pair tests, cavity maximum

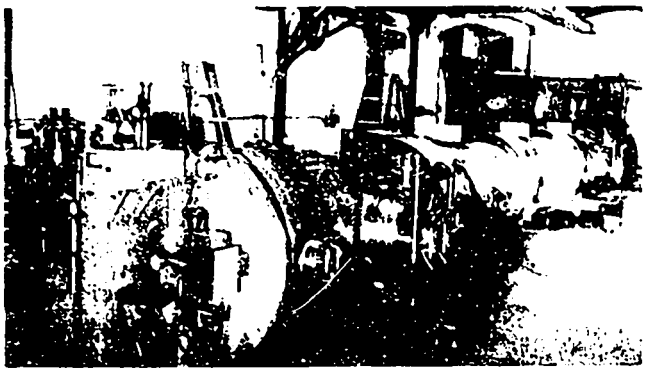

Figure 4. CEBAF cryomodule containing eight cavities for a 20-MeV nominal energy gain.

gradients averaged 9.0 MV/m (180% of spec) and Q_0 averaged 6.5×10^9 (recirculocal average; 270% of spec). The accelerator requires a total of 338 cavities, including the injector's 18.

All cryomodule parts are on contract, first articles have been received, and the first cryomodule has been installed in the tunnel. CEBAF's second cryomodule is being assembled.

RF System

Tailoring the rf system to drive superconducting cavities imposes some unusual requirements. To allow each cavity to operate at its own optimum accelerating gradient, we have implemented an individual rf amplifier and feedback chain for each cavity. The high loaded Q means that the bandwidth of the cavity is very narrow (227 Hz). Since the cavities are equipped only with slow (hours to days) mechanical tuners, the rf system has to assume the burden to correct phase and amplitude to compensate for microphonics, ponderomotive forces, and beam current fluctuations. Table 3 shows the allowable error tolerance in the rf control system.

Table 3
RF Amplitude and Phase Stability Requirements

Uncorrelated errors	
Amplitude	$\Delta V/V \leq 4.5 \times 10^{-4}$
Phase	$\Delta\phi \leq 1°$
Correlated errors	
Amplitude	$\Delta V/V \leq 2.2 \times 10^{-5}$
Phase	$\Delta\phi \leq 0.25°$

During 5-MeV operation, the rf control system achieved amplitude control $\Delta V/V \sim 10^{-4}$ and phase control $\Delta\phi \sim 0.1°$, despite microphonic amplitudes a factor of three worse than those expected in the tunnel. Moreover, it successfully regulated cavity accelerating gradients at several selected values between 0.1 MV/m and 6.8 MV/m, the maximum gradient of the cavities involved.

Instrumentation and Control

The CEBAF control computer system is a distributed system of supermini and supermicro computers which operate in a two-level hierarchy. The seven supervisory-level computers each can control and monitor a subsystem of up to 20 local-level computers. Local area networks and computer-automated measurement and control (CAMAC) interfaces enable intelligence to be extensively distributed for automated control capability at the local level. This control system provides an efficient operator interface to implement set points and to monitor and analyze status for about 30,000 input/output data points (Figure 5).

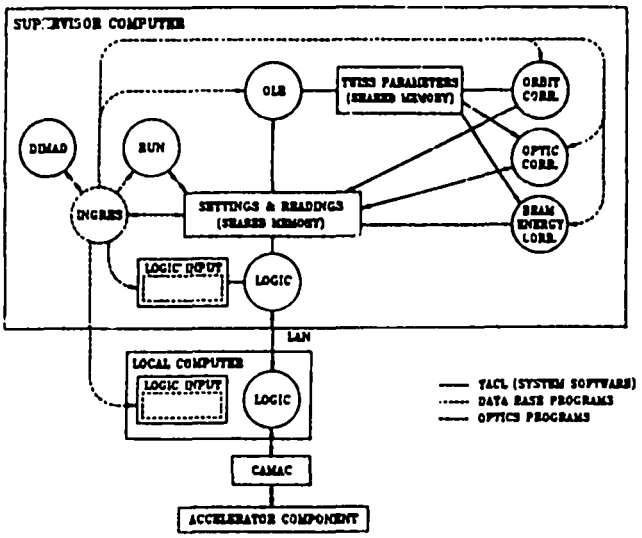

Figure 5. Accelerator control and modeling system schematic.

CEBAF has developed control system software[6] that allows control algorithms and application software to be developed efficiently by operators and physicists without extensive specialized programming skills. Control databases and displays can be modified without requesting custom software updates. The system software is complete and has been in use at CEBAF and other labs for as long as two years. Several optics and application programs have been developed. Hardware installation is underway, with about two-thirds of the computer, networking, and CAMAC equipment on site.

Among the important monitoring systems feeding the control system are the ~800 beam monitoring instruments, such as beam position monitors (BPMs), current monitors, profile monitors, viewscreens, and devices to measure energy and polarization. The workhorse units are the BPMs: a 1.5-GHz system picks up on the fundamental rf frequency, and a 100-MHz system is sensitive to a modulation imposed on the beam for a time period less than the beam recirculation time (4.3 μs). This latter system allows the positions of the beams from each pass to be monitored independently in the linacs. Beam instrumentation is in production and first articles are being installed in the injector.

Safety systems include (1) a hardwired fast-shutdown system that shuts down the injector within 20 μsec of detecting beam loss or selected other faults; (2) a fully redundant PLC-based personnel safety system; and (3) numerous hardware-protection warnings and interlocks implemented in software or hardware. Safety system installation for the injector is approaching completion.

Beam Transport

Beam transport is accomplished using a FODO lattice in the linacs and in modified form in the arcs. In the linacs, the half-cell length is 9.6 m: each half-cell contains one eight-cavity cryomodule (Figure 6). Either a focusing or a defocusing quadrupole, along with beam diagnostics and correction dipoles, is located in each 1.35-m warm region between cryomodules. In the arcs, the modified FODO lattice contains eight quadrupoles in each 63-m (45°) superperiod, and the transport channels are both achromatic and isochronous. Lattice functions have been designed to minimize emittance dilution due to synchrotron radiation effects. Bend magnets have low fields (maximum ~6 kG). Path-length correction to maintain correct phase for all of the different-energy beams is accomplished by "dog legs" in the arcs. Altogether some 2000 magnets are included in the lattice. These magnets are driven by power supplies regulated at 10^{-4} (typically); a few units require 10^{-5}.

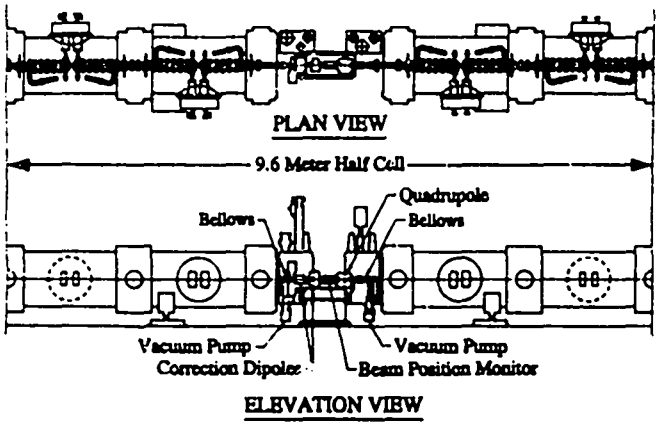

Figure 6. Linac half cell.

Contracts have been placed for the injector magnets, major bend magnets, and power supplies. Other beam transport elements are in various stages of the procurement process.

Cryogenics

CEBAF's 4800-W, 2-K Central Helium Liquefier (CHL) is located geographically in the center of the accelerator racetrack. An H-shaped distribution system feeds liquid helium and shield gas to the string of cryomodules in each linac. Within the linacs, cryomodules are supplied in parallel with liquid helium at 2.2K (2.8 atm), which is expanded through Joule/Thompson valves to reach 2.0 K inside the helium vessels in each cryomodule. The helium is returned to the CHL as gas at 2.0 K (0.031 atm). Helium gas at 40 to 50 K is distributed using the same transfer lines to cool the thermal shields. The CHL is 98% complete and being commissioned. Transfer lines are 49% fabricated and 31% installed. The CHL will be used when we begin injector commissioning in the tunnel late this fall.

Beam Delivery

The multi-user beam delivery system allows each of three experimental halls to receive beams of the desired current at different (but correlated) energies. The system has two key elements: the injector and the rf separators (deflecting cavities) in the extraction line. The injector creates three interspersed bunch trains, $k + 3N, k = 0, 1, 2$, and $N = 0, 1, 2, 3...$, where bunches with different k can have different bunch charges, i.e., currents. An rf separator in each of the west arc beam lines and in the highest-energy, fifth-pass beam line deflects the beam, optics amplify the initial deflection, and septum magnets extract beam for simultaneous delivery to all three end stations. At an operating frequency of ~1000 MHz for the rf separator and ~1500 MHz for the rf system, the separator phases are independent of N and amount to ϕ_0, $\phi_0 + 240°$, and $\phi_0 + 120°$ for bunch trains $k = 0$, 1, and 2 respectively. Of particular usefulness are the initial phases $\phi_0 = 0$, leading to 0°, 240°, 120° resulting in a straight-left-right distribution (e.g., for distributing beams of equal energy to three end stations), and, for a two-beam split, $\phi_0 = 90°$, leading to 90° 330°, 210° resulting in extraction of one beam and further recirculation of two.

Nuclear Physics Program Preparations

After endorsements from CEBAF's Program Advisory Committee (PAC) and from the DOE/NSF Nuclear Science Advisory Committee (NSAC), which met at CEBAF June 4, 1990, DOE approved CEBAF's experimental equipment plan[7] in late June. The plan includes roughly $75 million in spectrometers, detectors, and data acquisition systems matched to experiment proposals from the nuclear physics community. After reviewing 47 proposals from 253 physicists at 64 institutions requesting 47,000 hours of beam time, the PAC has recommended approval for 16 proposals, conditional approval for 13 additional proposals, and initial allocation of 8040 hours.

Two 4-GeV/c high-resolution (10^{-4}) QQDQ magnetic spectrometers in Hall A (diameter = 53 m) are planned for high-resolution charged-particle coincidence studies (Figure 7a). The spectrometer design calls for superconducting cos 2θ quadrupoles. A request for proposals has been issued for fabrication of the superconducting dipole magnet.

The CEBAF large-acceptance spectrometer (CLAS), based on a toroidal magnetic field ($\int B \cdot dl \sim 2.5$ T-m) produced by six superconducting coils, will provide multiparticle detection capability in Hall B (diameter = 30 m) (Figure 7b). Bids for CLAS torus construction were received in July 1990, and award is expected by December.

Hall C (diameter = 45 m), a multipurpose area for specialized apparatus, will have a moderate-resolution high-momentum (6 GeV/c) QQQD electron spectrometer (HMS) (Figure 7c) supplemented by other detection systems, including a short-orbit spectrometer for decaying particles (e.g., pions and kaons). The request for proposals has been issued for the HMS superconducting dipole and for the spectrometer's support carriage. The HMS superconducting design calls for superconducting cold-iron quadrupoles.

The three large end stations are partially underground, domed concrete structures. End station excavation is nearly complete (Figure 2), foundation work has begun, and some 60% of the 235 meters of beam switchyard and beam transport tunnels—connecting the racetrack accelerator tunnel with the end stations—are complete.

The experimental equipment is planned to be installed starting in late 1992, when end station construction is complete, and to be available in phases for physics research beginning in early 1994, when the Hall C HMS is to be ready for beam.

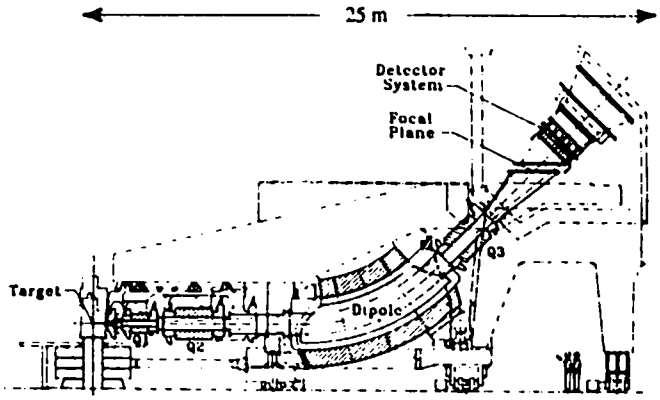

(a) Hall A

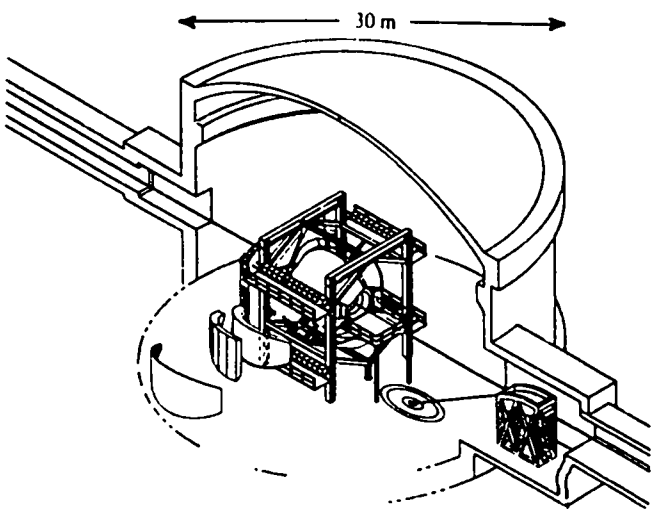

(b) Hall B

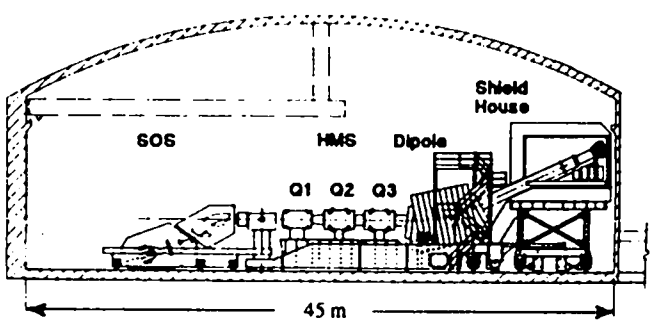

(c) Hall C

Figure 7. Experimental equipment.
(a) 4-GeV/c high-resolution spectrometer for Hall A. (b) CEBAF large-acceptance spectrometer (CLAS) for Hall B. (c) Moderate-resolution high-momentum spectrometer and short-orbit spectrometer for Hall C.

Summary and Outlook

With most major components fully designed and on order from industry, CEBAF's attention has turned to installation and commissioning. Figure 8 shows completed and upcoming milestones. Recent highlights include successful 5-MeV operation and the start of production-scale cavity pair and cryomodule assembly. Running the central helium liquefier, accelerating beam to 25 MeV in the injector, and placing orders for detector components are our major near-term goals.

The construction project is scheduled to be complete in summer 1993, and six months of commissioning are planned in preparation for the start of physics operation in mid-winter 1994.

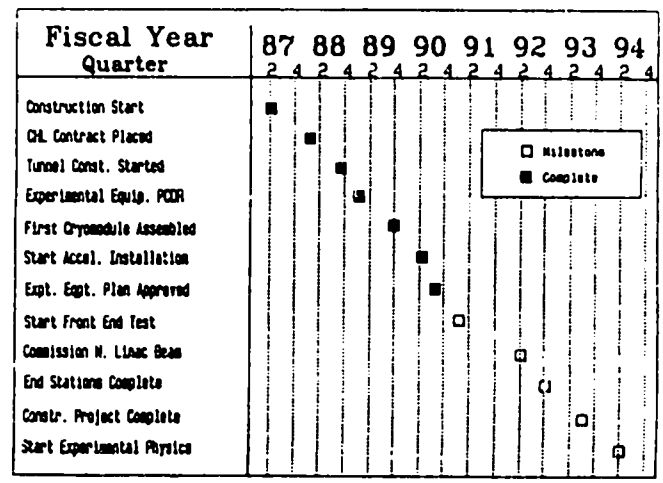

Figure 8. Major milestones.

References

1. *Long Range Plan for Nuclear Science*, DOE/NSF Nuclear Science Advisory Committee (NSAC), 1979.
2. *Long Range Plan for Nuclear Science*, DOE/NSF Nuclear Science Advisory Committee (NSAC), 1983.
3. *Nuclei, Nucleons, Quarks: Nuclear Science in the 1990s*, DOE/NSF Nuclear Science Advisory Committee (NSAC), 1989.
4. H. Grunder, "The Continuous Electron Beam Accelerator Facility," *1988 Linear Accelerator Conference Proceedings*, 3–8.
5. R. M. Sundelin, "High-Gradient Superconducting Cavities for Storage Rings," *IEEE Trans. Nucl. Sci.* **NS-32** (1985), 3570-3573.
6. R. Bork *et al.*, "CEBAF Control System," *1988 Linear Accelerator Conference Proceedings*; E. Navarro *et al.*, "Use of the TACL System at CEBAF for Control of the Cryogenic Test Facility," *Proceedings of the IEEE Real-Time System Symposium*, May 1989.
7. *Conceptual Design Report, Basic Experimental Equipment*, CEBAF, April 1990.

THE FERMILAB LINAC UPGRADE

Robert J. Noble
Fermi National Accelerator Laboratory,* Batavia, Illinois 60510

Abstract

The Fermilab Linac Upgrade is planned to increase the energy of the H^- linac from 200 to 400 MeV. This is intended to reduce the incoherent space-charge tuneshift at injection into the 8 GeV Booster which can limit either the brightness or the total intensity of the beam. The Linac Upgrade will be achieved by replacing the last four 201.25 MHz drift tube tanks which accelerate the beam from 116 to 200 MeV, with seven 805 MHz side-coupled cavity modules operating at an average axial field of about 7.5 MV/m. This will allow acceleration to 400 MeV in the existing Linac enclosure. Each accelerator module will be driven with a klystron-based rf power supply. A prototype rf modulator has been built and tested at Fermilab, and a prototype 12 MW klystron is being fabricated by Litton Electron Devices. Fabrication of production accelerator modules is in progress.

Introduction

The Fermilab 200-MeV linear accelerator has operated almost continuously since 1970 as an injector for the Fermilab chain of accelerators and as a secondary neutron producer for the Neutron Therapy Facility with a reliability approaching 99%. The purpose of the Fermilab Linac Upgrade is to increase the final kinetic energy of the beam from 200 MeV to about 400 MeV. This is expected to reduce beam emittance degradation in the 8 GeV synchrotron booster following the linac and allow beams of higher brightness (number of particles per unit emittance) to be accelerated.[1] The intended consequence of this will be to increase the collision rate in the antiproton-proton collider by a factor of three and the intensity for the fixed-target experiments by 75% if the increase in brightness can be conserved through later acceleration stages. The 400 MeV limit is dictated by H^- ion stripping considerations in the magnetic fields of the Linac-to-Booster transfer line.

The present 200 MeV drift-tube linac (DTL) consists of nine accelerator cavities operating at a frequency of 201.25 MHz. Each cavity is powered by a triode-based radio-frequency (rf) power supply rated to deliver up to 5 MW of peak power for a 125 μsec flat-top pulse. The Linac Upgrade will replace the last four cavities, which accelerate the beam from 116 MeV to 200 MeV in a length of 56 meters, with seven side-coupled cavity modules operating at a frequency of 805 MHz or four times the DTL frequency (see Figure 1). The higher frequency allows higher accelerating gradients to be achieved so that a kinetic energy of 400 MeV can be reached in the same linac enclosure. Each module will be driven with a klystron-based rf power supply rated to deliver up to 12 MW of peak power for 125 μsec at 15 Hz repetition rate. The nominal peak power requirement of each module with 35 mA of beam is about 10 MW. The new linac is designed to accelerate up to 50 mA of beam to allow for future improvements.

---

*Operated by the Universities Research Association under contract with the United States Department of Energy.

Accelerator Structure

The side-coupled accelerating structure (SCS) was selected for the Linac Upgrade because it is well understood and fully proven. The side-coupled structure was used above 100 MeV for the 805 MHz Los Alamos Meson Physics Facility (LAMPF) proton linac designed in the early 1960's (see Figure 2). This coupled cavity structure is operated in a so called TM_{010} $\pi/2$ standing wave mode in which the phase shift between an accelerating cell and an adjacent coupling cell (off the beam axis) is 90 degrees. The accelerator cell length is $\beta\lambda/2$ for particle-wave synchronism. Here β is the particle velocity divided by the speed of light, and λ is the free space wavelength of the accelerating field. The insensitivity of field amplitudes and phases to mechanical perturbations in such $\pi/2$ structures is a fundamental reason for their widespread use.

From the work done at Los Alamos National Laboratory on the SCS and the Fermilab program of design,[2] tuning,[3] prototyping[4] and full-power testing,[5] we have confidence that our design goals can be met. Because the new side-coupled (SC) linac will replace that part of the existing drift-tube linac which accelerates the beam from 116 MeV to 200 MeV, it must have a gradient about three times higher than in the DTL and make conservative use of space for beam matching, focusing and diagnostics. In particular, a Transition Section for matching the beam between the DTL and side-coupled linac and a space of about two meters at the downstream end of the linac for changes in the Linac-to-Booster transfer line are required. Other major design goals were to minimize power consumption and to keep all parameters within a range favoring dependable routine operation. Table 1 summarizes the principle design criteria and derived parameters for the new linac.

The average axial field, E_0 of 7.5 MV/m is about three times the gradient in the existing DTL. Long voltage conditioning times and an inordinately high sparking rate causing erratic beam pulses and unreliable injector operation are considered unacceptable for the new linac. For the Linac Upgrade it was considered desirable to limit the spark rate to one spark per thousand rf pulses corresponding to at most 0.1% beam loss due to cavity sparking. To investigate this constraint, full power testing has been performed on six-cell prototype cavities and a complete 16-cell accelerator section.[5] The later represents one of the 28 sections needed for the new linac. These power tests have shown that with the appropriate cavity nose-cone shape (see Figure 3) to reduce peak surface fields (37 MV/m), a spark rate of one spark per thousand rf pulses can be achieved for a complete linac after about 20 million rf pulses (125 μsec, 15 Hz) of conditioning. The spark rate continues to decrease with conditioning. Over the range of surface fields 30 to 45 MV/m, the spark rate varies as $E_s^{19.5 \pm 0.5}$.

Table 1. 400 MeV Linac Design Criteria and General Parameters

Initial kinetic energy (T_i)	116.54	MeV
Final kinetic energy (T_f)	401.46	MeV
Length, including transition section	63.678	m
Frequency of rf (f)	805.0	MHz
Beam current averaged over pulse (I_b)	50.	mA
Beam pulse length	< 100.	μs
Repetition rate	15.0	Hz
Accelerating phase (φ_s)	-32.	deg
Average axial field (E_o)	8.07-7.09	MV/m
Maximum surface field (E_{max})	36.8	MV/m
Kilpatrick limit (E_K)	26.	MV/m
Number of modules	7	
RF power/module, typical	< 12.	MW
copper loss	7.2	MW
beam power	2.0	MW
reserve and control	2.8	MW
Number of sections/module	4	
Number of rf cells/section	16	
Total number of rf cells (7 × 4 × 16)	448	
Length of bridge couplers between sections	$\frac{3}{2}\beta\lambda$	
Transverse focusing scheme	FODO	
Transverse phase advance/FODO cell, average	70	deg
Quadrupole magnetic length	8.0	cm
Quadrupole poletip field	4.6	kG
Quadrupole bore radius (r_q)	2.0	cm
Cavity bore radius (r_b)	1.5	cm

The rf properties of accelerating cells for the SC linac were calculated with the computer code SUPERFISH. Cavity dimensions were determined generally to maximize the shunt impedance for all energies. The major cavity radius R_C basically determines the shunt impedance, but several other dimensions were varied to slightly improve this parameter. A constant cavity radius of 13.455 cm was found to be adequate between 116 and 400 MeV. To reduce peak surface fields while concentrating more field into the accelerating gap, a double-radius nose-cone design was adopted.[6] Here the nose-cone outline is determined by two radii of curvature, 7 mm and 2.21 mm. The program SUPERFISH was used to calculate the effective shunt impedance ZT^2, the transit time factor T, and the ratio of the maximum surface field and average accelerating field E_{max}/E_o at several values of β corresponding to the energy range 116 to 400 MeV. The SUPERFISH values of ZT^2 (see Figure 4) are typically 15% lower in actual cavities due to the coupling slot (5% coupling) and braze imperfections.

The division of the new SC linac into seven independently excited rf modules originally resulted from three principal considerations, namely the practical size for 805 MHz klystrors, the shunt impedance of the structure and the existence of suitable penetrations from the linac utility basement into the linac enclosure. Since the original design in 1987, radiation safety considerations have mandated the need for new waveguide penetrations with the existing downstream DTL penetrations in the linac utility basement to be ultimately sealed. Uniform distribution of rf power favors feeding the modules from the center, so there is a bridge coupler at that location which can accommodate a magnetic quadrupole also. Rf defocusing requires that the quadrupoles of the FODO channel be less than two meters apart in the first modules. These conditions were satisfied by dividing the modules into four sections separated by bridge couplers of length $3\beta\lambda/2$ (see Figure 5).

The linac design proceeded interatively by using third order fits to ZT^2, T and E_{max}/E_o to calculate the length and number of cells needed to reach the design energy of 400 MeV. The design was subject to the constraints that the peak electric field not exceed 44 MV/m (1.6 Kilpatrick), the accelerating cells in each section be of constant length and that the total length of the side-coupled linac not exceed 66 meters. An acceptable design was arrived at by having 16 cells per section with peak fields of only 37 MV/m and roughly equal power dissipation in each section. Table 2 summarizes the parameters of the side-coupled linac by accelerator section. Module 0, Sections 1 and 2 are the two 805 MHz buncher cavities in the Transition Section between the DTL and new linac.

Table 2. 400 MeV Linac Parameters by Section

Module /Sect.	Grad [MV/m]	KE_{out} [MeV]	L_{cell} [m]	L_{sep} [m]	P_{cu} [MW]	P_{beam} [MW]	$\Delta\varphi_{cu}$ deg	$\Delta\varphi_{b}$ deg
0					(Transition Section)			
1	2.23	116.5	1.3613	0.6653	0.13	0.00		
2	0.00	116.5	0.3403	0.7951	0.00	0.00		
			0.0000	0.8381				
			1.7016	2.2984	0.13	0.00		
			4.0000		0.13			
1	8.07							
1		125.1	1.3814	0.1418	1.75	0.43		
2		133.8	1.4215	0.2628	1.88	0.44	77	100
3		142.3	1.4606	0.2703	1.93	0.45		
4		152.1	1.4987	0.2775	1.91	0.46	78	106
			5.7621	0.9524	7.47	1.78		
			6.7145		9.25			
2	7.85							
1		161.2	1.5353	0.2846	1.72	0.46		
2		170.6	1.5701	0.2912	1.85	0.47	40	103
3		180.2	1.6047	0.2977	1.89	0.48		
4		190.0	1.6380	0.3041	1.95	0.49	80	101
			6.3484	1.1776	7.33	1.90		
			7.5260		9.23			
3	7.66							
1		199.7	1.6700	0.3102	1.70	0.48		
2		209.5	1.7009	0.3161	1.82	0.49	81	98
3		219.6	1.7309	0.3218	1.86	0.50		
4		229.8	1.7600	0.3273	1.85	0.51	81	96
			6.8618	1.2754	7.23	1.98		
			8.1372		9.21			
4	7.48							
1		239.9	1.7881	0.3327	1.66	0.51		
2		250.1	1.8151	0.3379	1.79	0.51	81	91
3		260.5	1.8414	0.3428	1.84	0.52		
4		271.1	1.8670	0.3477	1.83	0.53	90	92
			7.3116	1.3611	7.14	2.07		
			8.6728		9.21			
5	7.34							
1		281.5	1.8917	0.3524	1.67	0.52		
2		292.1	1.9155	0.3570	1.78	0.53	80	90
3		302.8	1.9387	0.3614	1.83	0.53		
4		313.6	1.9613	0.3657	1.81	0.54	79	89
			7.7072	1.4365	7.09	2.12		
			9.1436		9.21			
6	7.20							
1		324.4	1.9830	0.3698	1.66	0.54		
2		335.2	2.0039	0.3738	1.77	0.54	79	87
3		346.1	2.0244	0.3777	1.81	0.55		
4		357.1	2.0443	0.3815	1.79	0.55	78	85
			8.0555	1.5028	7.03	2.18		
			9.5583		9.21			
7	7.09							
1		368.1	2.0635	0.3852	1.65	0.55		
2		379.1	2.0821	0.3887	1.76	0.55	77	84
3		390.2	2.1002	0.3[illegible]	1.80	0.56		
4		401.5	2.1179	0.3955	1.78	0.56	76	82
			8.3637	1.5614	6.99	2.22		
			9.9251		9.21			
Grand Total			52.1119	11.5656	50.27	14.25		
			63.6775		64.66			

For the bridge coupler, the post-stabilized design originally developed for the LAMPF accelerator has been adopted.[7] The $3\beta\lambda/2$ couplers for the Linac Upgrade range in length from about 35 cm to 55 cm and

are shorter than any used at LAMPF ($5\beta\lambda/2$ and $7\beta\lambda/2$). Bridge coupler models and MAFIA[8] computer calculations indicate that the use of two side-posts, 90 degrees apart, permits the interfering $TE_{111}(x,y)$ and $TM_{011}(x,y)$ modes to be moved out of the accelerating passband (780-830 MHz for 5% coupling). The bridge couplers will have two end-posts for tuning the fundamental TM_{010} resonance.

The DTL operates with stronger transverse focusing and weaker longitudinal focusing than the side-coupled linac. Six-dimensional phase space matching is required to preserve the brightness of the DTL beam in the new linac. The longitudinal matching is effected by placing a sixteen-cavity, 805 MHz side-coupled buncher section (E_0T = 2 MV/m) after the last drift-tube tank (Tank 5) and a four-cavity vernier buncher half-way between the sixteen-cavity buncher and first section of the new linac (see Figure 6). The last two DTL quadrupoles and three new quadrupoles separating the DTL, bunchers and new linac will control the transverse matching. The total length of the Transition Section is about four meters. The 805 MHz bunchers will probably be powered by 200 kW Varian VKP-7955 klystrons.

Radio-Frequency Power System

The 805 MHz Linac Upgrade requires seven high-power klystron and modulator systems to run the seven independent accelerator modules. Table 3 gives a complete power tabulation for an RF station assuming 35 mA of accelerated beam. This shows that only about 10 MW of peak power is needed. The klystron specifications in Table 4 apply to a 12 MW prototype klystron on order with Litton Electron Devices. The RF modulator consists of a pulse forming network (PFN) discharged into the klystron cathode through an oil-filled 20:1 step-up transformer. The PFN is charged to 18 kV from a power supply using the resonant charging technique (capacitor and charging choke) with an SCR (silicon controlled rectifier) switch to initiate the charging cycle. The power supply stores about 40 kJ but only about 6 kJ are used to charge the PFN every 66 msec (15 Hz).

Table 3. RF Power Tabulation

Nominal power, accelerating 35 mA beam (SUPERFISH shunt impedance derated by 15%)	8.6 MW
Waveguide run losses (WR975), harmonic isolator (if required)	0.6 MW
Add 10% for feedback loop regulation	0.9 MW
The cavity diameter may have to be altered slightly at some β's to avoid TM_{110} deflecting modes	0.1 MW
Estimated Total	10.2 MW

Table 4. Klystron Specifications

Peak power output	12 MW
Pulse length	125 μs
Pulse repetition rate	15 pps
Duty factor	0.1875%
Average power	22.5 KW
Efficiency	50%
Gain	50 dB
RF output	WR975 waveguide
Dimensions	108 inch height 24 inch diameter
Voltage	170 KV
Current	141 A

Project Status

The three major systems for the Linac Upgrade are side-coupled accelerator modules, rf modulators and 12 MW klystrons. The Project began construction in October 1989 and is scheduled for linac conversion to 400 MeV energy in the summer of 1992. A prototype rf modulator begun in January 1989 was successfully operating into a resistive load by December 1989. The modulator can produce up to 40 MW of power for 125 μsec pulses at 15 Hz. Some design modifications were made based on the operation of this prototype, and component procurement for the seven production modulators began in April 1990. Fabrication is scheduled to begin in November 1990 and be completed by October 1991.

Fabrication of a prototype accelerator module (four sections and three bridge couplers) began in October 1989. This prototype is electrically and mechanically equivalent to the first of seven side-coupled linac modules needed for the new linac. The first 16-cavity section was brazed at Pyromet Inc. (San Carlos, California) in January 1990 and the second section in April. The third and fourth sections were brazed simultaneously in August 1990. The first section brazed was power tested and voltage conditioned to design gradient in April 1990. Buildup of the sections and bridge couplers into a complete module began in August 1990. This prototype is now planned to be used as the first accelerator module of the new linac.

In June 1990 Class 1, OFHC copper segments for production accelerator fabrication began arriving from Hitachi Industries, Japan. Copper for one 16-cavity linac section arrives every two weeks to begin a four-month machining, tuning and brazing cycle (see Ref. 4). The segmented construction of side-coupled accelerating structure used at LAMPF has been adopted for the Fermilab linac (see Figure 7). As of September 1990 seven sections of copper had arrived and the fabrication cycle was on schedule. Two sections will be brazed every four weeks at Pyromet Inc. starting in October 1990. When brazed sections return to Fermilab, the $\pi/2$ mode is tuned to within 20 kHz of 805 MHz (as corrected for 25°C and vacuum) and the side-cells are tuned to give a 100 kHz positive stopband for thermal stability (see Ref. 3).

A prototype 12 MW klystron is on order with Litton Electron Devices, San Carlos, California. The L-5859 klystron has five cavities (input, two idlers, penultimate, output) and should operate at 2 μperv. The prototype was due in December 1989. In January 1990 while under test at the plant, the tube suffered a catastrophic arc destroying the barium-strontium coated cathode. The cathode had not been adequately processed and the tube's 1.5 liter/sec ion pump was inadequate (subsequently changed to an 8 liter/sec pump). A rebuilt klystron was delivered to Fermilab in May 1990. The tube reached 12 MW power with a gain exceeding 50 dB (see Figure 8). After about 18 hours of rf running the tube suffered a loss of vacuum. Failure analysis at Litton indicated a ceramic arc punch-through in the high-voltage cathode insulator. The tube was dissasembled and cleaned with rebuilding in progress as of September 1990. The prototype and subsequent production tubes are on the critical path for the project's completion.

References

1. S.D. Holmes, et al, "Upgrading the Fermilab Tevatron", Proc. of the 1989 Particle Accel. Conf., IEEE Trans. Nucl. Sci.

2. T.G. Jurgens, et al, "Determination of the 805 MHz Side-Coupled Cavity Dimensions for the Fermilab Linac Upgrade", 1990 Linac Conf., these proceedings.

3. H.W. Miller, et al, "Tuning Methods for the 805 MHz Side-Coupled Cavities in the Fermilab Linac Upgrade", 1990 Linac Conf., these proceedings.

4. M.P. May, et al, "Mechanical Construction of the 805 MHz Side-Coupled Cavities for the Fermilab Linac Upgrade", 1990 Linac Conf., these proceedings.

5. T. Kroc and A. Moretti, "Conditioning of High Gradient H⁻ Accelerating Cavities", 1990, Linac Conf., these proceedings.

6. A suggestion of Lloyd Young, Los Alamos National Laboratory.

7. J.M. Potter and E.A. Knapp, "Bridge Coupler Design and Tuning Experience at Los Alamos", Proc. of the 1972 Linear Accel. Conf. (Los Alamos), p. 242.

8. T. Weiland, "Computer Modelling of Two and Three-Dimensional Cavities", IEEE Trans. Nucl. Sci. NS-32, 2738 (1985).

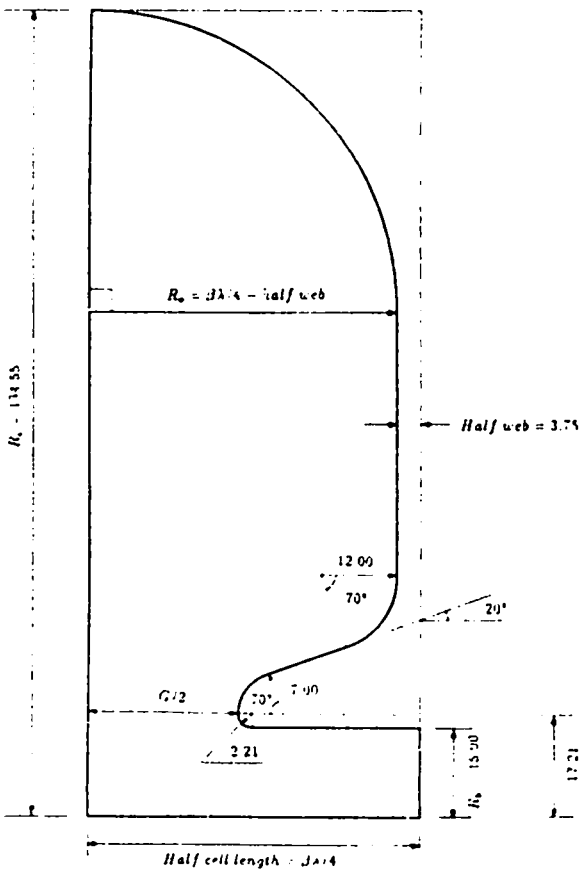

Figure 3. Fermilab 805-MHz side-coupled cavity geometry (dimensions in mm)

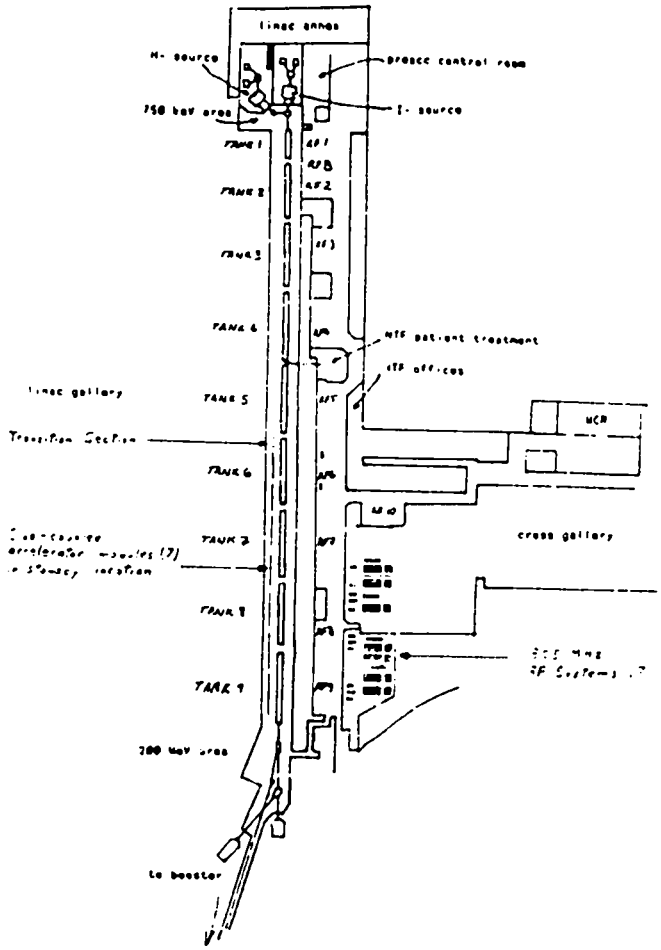

Figure 1. The Fermilab Linac (plan view)

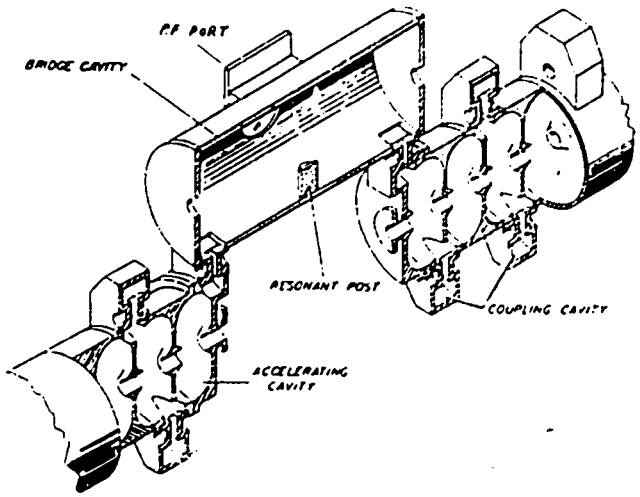

Figure 2. The LAMPF side-coupled accelerator and post-stabilized bridge coupler.

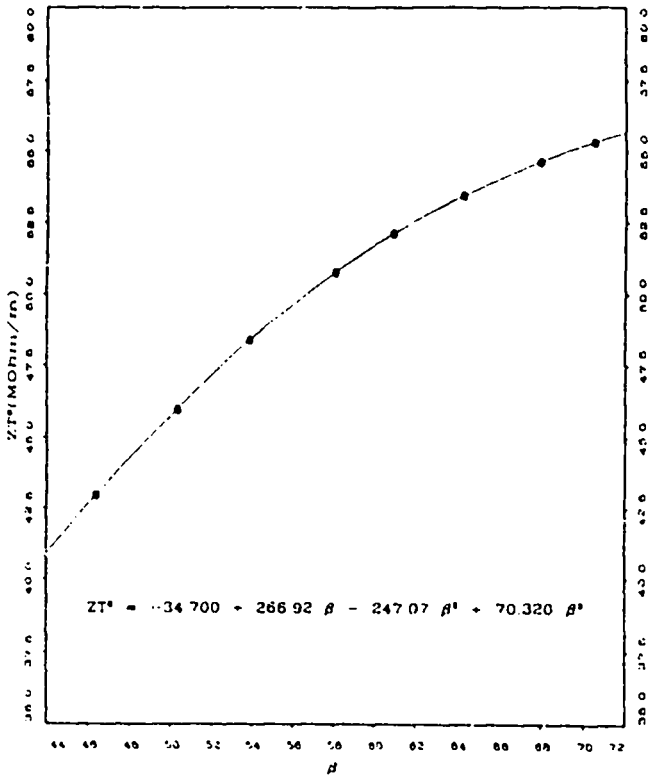

Figure 4. Effective shunt impedance versus relativistic beta for the Fermilab side-coupled linac (unadjusted SUPERFISH calculation).

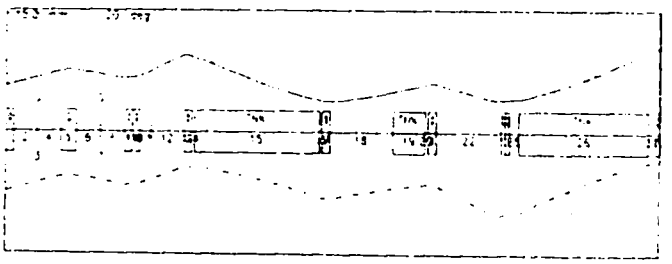

Figure 6. Transition Section beam envelopes from the center of the third from last quadrupole in DTL Tank 5 to the center of the quadrupole between Sections 1 and 2 of side-coupled Module 1. The bunch length is shown with a dotted curve, the horizontal envelope with a solid curve and the vertical envelope with a dashed curve.

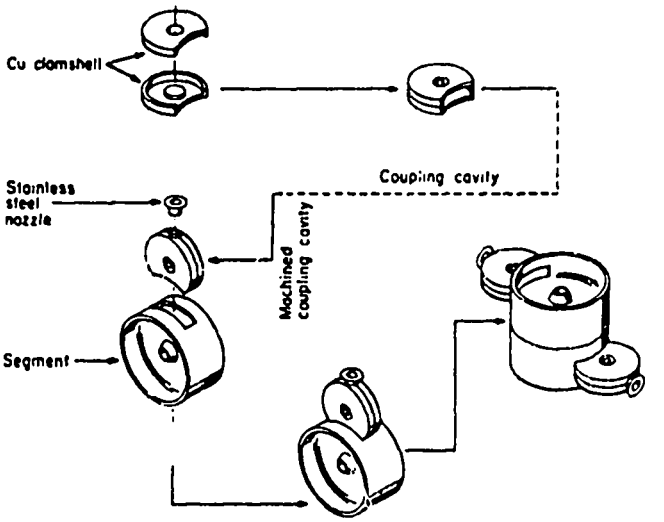

Figure 7. Segmented construction of side-coupled accelerator structure used for the LAMPF and Fermilab linacs.

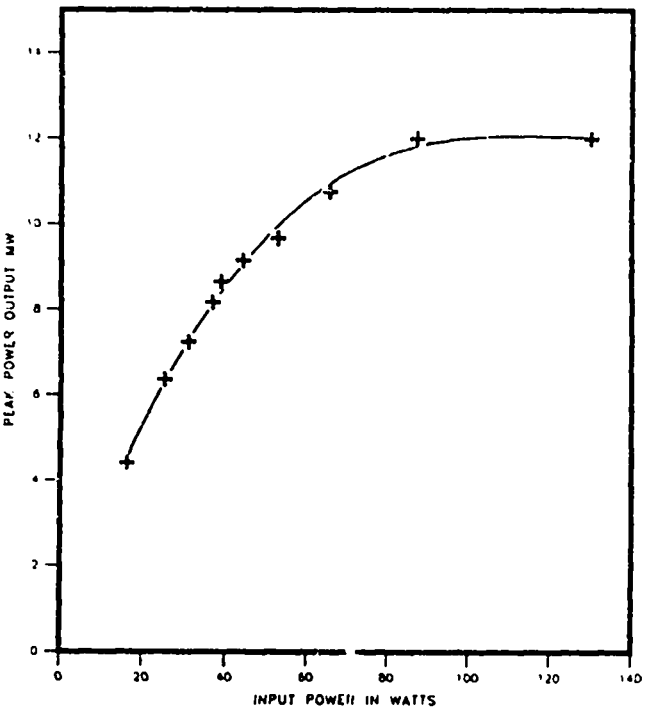

Figure 8. Peak power output versus input drive power for the Litton L-5859 805 MHz klystron.

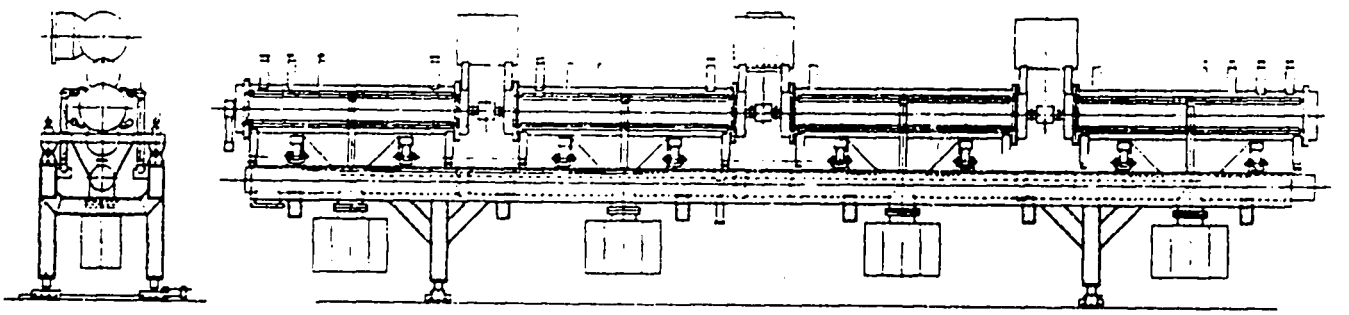

Figure 5. Fermilab side-coupled accelerator module containing four sections and three bridge couplers. Module height is approximately 2 meters, and the length varies from 6.5 to 10 meters for Modules 1 to 7.

THE SSC LINAC

J. M. Watson
Superconducting Super Collider Laboratory*, Dallas, Texas 75237

Abstract

The preliminary design of the 600 MeV H^- linac for the Superconducting Super Collider injector is described. The linac must provide a 25 mA beam during 7–35 μs macropulses at 10 Hz within injection bursts. Normalized transverse emittances of less than 0.5 π mm-mrad (rms) are required for injection into the Low Energy Booster synchrotron. Cost, ease of commissioning, and operational reliability are important considerations. The linac will consist of an H^- source with electrostatic LEBT, 2.5 MeV radiofrequency quadrupole accelerator, a 70 MeV drift-tube linac, and 530 MeV of side-coupled linac. The RFQ and DTL operate at 428 MHz and the side-coupled linac operates at 1284 MHz. A modest total length of 150 m results from the tradeoff between cost optimization and reliability. The expected performance from beam dynamics simulations and the status of the project are described.

Introduction

The design of the SSC linac is determined primarily by the requirements of the Low Energy Booster (LEB). Multiturn H^- injection into the LEB allows the use of a modest linac current with small emittance. The use of quasi-adiabatic capture in the LEB reduces the complexity of the linac front end and lowers the emittance for several reasons—the front end current is lower, a higher frequency RFQ is used, no choppers are required, and fewer turns will fill the LEB (fewer passes through the stripper).

The present design of the linac satisfies the LEB requirements and should have adequate design safety margins to provide for substantial flexibility, excellent reliability, and the potential for future upgrades. Although no inventions are required for this design, further development of several portions could improve reliability and lower construction costs of linac components. These development areas are described below within the appropriate linac component descriptions.

Nominal linac operation consists of the two modes listed in Table I—filling the collider rings and providing test beams. The linac satisfies the factor-of-five increase in LEB current for test beams by operating with a longer macropulse (increasing the number of injection turns). Since the other linac operating parameters remain unchanged, no linac tuning should be required in changing operating modes and no degradation in beam quality should occur. Of course, the option of lower current for as long as 35 μs is possible for both operating modes.

TABLE I
SSC Linac Requirements

Filling collider ring
25 mA H^- current during macropulse
6.6 μs macropulse (three-turn LEB injection)
1×10^{10} / LEB bunch
< 0.5 π mm-mrad (t, rms, norm) emittance
10 Hz repetition rate
Test beam operation
25 mA during macropulse
35 μs macropulse (16-turn LEB injection)
5×10^{10} / LEB bunch
< 4 π mm-mrad (t, rms, norm) emittance
10 Hz repetition rate

*Operated by the Universities Research Association, Inc. for the United States Department of Energy under Contract No. DE-AC02-89ER40486.

Figure 1 is a block diagram of the major components of the linac with major system parameters and simulated performance shown. It consists of an H^- source, an RFQ to bunch and initially accelerate the beam, a drift-tube linac to accelerate the particles to relativistic velocities, and a coupled-cavity linac for most of the energy gain. A substantial base of experience exists for linacs of this type with similar parameters. Based on past experience, actual linac performance can be expected to be close to the design simulations. By not departing too far from typical existing facilities, the availability requirement of 98% should be attainable after a reasonable commissioning period.[1] To provide adequate safety margins and allow future upgrades, the linac components are designed to handle twice the current with twice the emittance. Safety margins of this size are attainable with only a small impact on the cost of the linac. The frequencies are chosen to provide bunches on an harmonic of the LEB buckets at 600-MeV injection and for optimal accelerator operation. There are nine linac bunches per LEB bucket. The possible future transition to bunch-to-bucket LEB capture is therefore not forbidden by this design. Also, the harmonic relationship preserves the possibility of notching the beam to improve the efficiency of quasi-adiabatic capture.

The transfer line between the linac and LEB has also been designed and is described in these proceedings.[2] The transfer line contains an energy analyzing section, a transverse emittance measuring section, and a buncher and focusing elements for longitudinal and transverse matching onto the stripper of the LEB injection girder.

Some aspects of the linac design will probably change during the preliminary design and engineering development stages. Accelerator changes will be incorporated where performance, reliability, or cost improvements are possible over the baseline design presented here. This baseline design is within the state-of-the-art of linac performance and is a cost-effective approach.

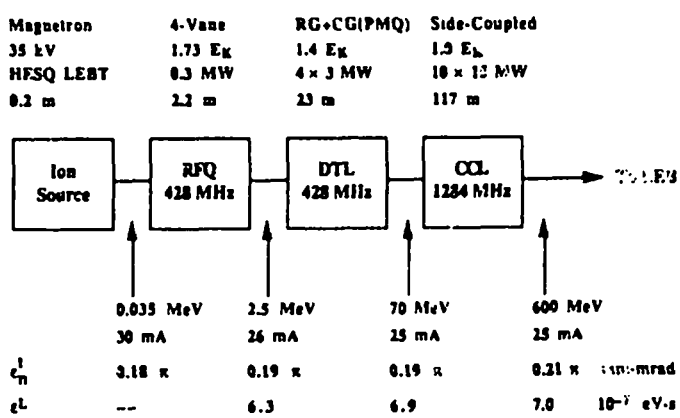

Figure 1. Linac block diagram.

Ion Source

The first component of the linac will be an H^- ion source. There are three very different ion sources that should be capable of meeting the SSC beam criteria. These are the magnetron,[3] the Penning,[4] and the non-cesium volume source.[5] All three of these sources have unique advantages that must be considered. Of the three, only the magnetron has been used at large HEP facilities where long-term operation with high availability is required. If brightness becomes an issue, the Penning source is the brightest H^- source available. The simplest source to maintain and operate is the rf-excited volume source, which also may have an additional advantage

in terms of system reliability since it can be operated without filaments or cesium injection.

The magnetron has been chosen for the baseline design since it would require little effort to optimize it to the SSC beam parameters of 30 mA at 35 keV with very low duty. A prototype has been developed and delivered to the SSCL by the Texas Accelerator Center (TAC) for installation on the linac test stand. The Penning source could also easily be developed as a production source. Due to the similar electronics and vacuum systems of the magnetron and Penning sources, it is conceivable that these sources could be used interchangeably. The rf-excited volume source has the potential of being simplest and most reliable with further improvement in reducing the gas usage and the extracted electron current. SSCL is supporting this development effort at Lawrence Berkeley Laboratory.

Low Energy Beam Transport

The beam from an ion source is relatively large in radius and divergence and must be matched to the RFQ. The section of the linac that provides this match is called the low energy beam transport (LEBT). It also usually contains source diagnostics and provides the differential vacuum pumping between the source and the RFQ. The LEBT consists of lenses that focus the beam onto the entrance of the RFQ.

Most existing LEBT systems use magnetic focusing solenoids or permanent magnet quadrupoles. These LEBT systems also utilize charge neutralization in the background gas to minimize the required focusing strengths. The neutralization time should be short compared to the pulse length; otherwise, a large fraction of the beam at the front of the pulse will be lost due to inadequate focusing. As neutralization develops, the space charge forces decrease. Consequently the beam phase space ellipse rotates, constantly changing the match into the RFQ acceptance. Additional problems arise due to beam-plasma instabilities and the interface uncertainty as the beam appears charged again as it enters into the electric fields of the RFQ that has swept away the charge neutralizing ions formed in the collisions. Improper matching at such transitions and the conversion of field energy into transverse kinetic energy associated with changes in the beam profiles may cause significant emittance growth and particle loss.

The SSC linac requires a pulse length shorter than 35 μs. This is comparable to the expected neutralization time in hydrogen gas. The beam would need to be on approximately 100 μs to become fully neutralized. The neutralization time can be reduced by introducing xenon into the LEBT; however, full neutralization will always considerably increase the pulse length required from the source. The frequency of source maintenance is therefore increased and the reliability of the RFQ is decreased because of the poorer vacuum and increased cesium deposition rate. For the short-pulse operation of the SSC linac it is best to avoid neutralization if possible.

The 30-mA operating current is small enough that several concepts using electric focusing to avoid neutralization can be considered: einzel lenses, electrostatic quadrupoles, and radiofrequency quadrupole lenses. The RFQ lens can probably transport higher currents with fewer aberrations, but it is more complex and adds another rf system. The einzel lens and helical electrostatic quadrupole (HESQ) are the leading candidates for the SSC linac. The einzel lens is probably the most mature technology for this application. However, it requires voltages similar to the source voltage and is prone to aberrations. We are presently building a dual einzel lens LEBT for evaluation on the linac test stand.[6] The helical electrostatic quadrupole is somewhat more efficient than standard electrostatic quadrupoles and should be very reliable since modest voltages are required. A prototype HESQ LEBT is presently being characterized at TAC. We are starting construction of a fully engineered HESQ LEBT with nickel electroformed electrodes for evaluation on the linac test stand.[7] The HESQ LEBT parameters are summarized in Table II.

TABLE II
HESQ Simulation Parameters

Length	22.5 cm
Voltage	7 kV
Breakdown voltage	100 kV
Pitch of helix	15 cm
Electrode spacing	1.46 cm
Bore radius	1.5 cm
Input beam	
Current	30 mA
Transverse emittance (n, rms)	0.18 π mm-mrad
Output beam	
Current	30 mA
Transverse emittance (n, rms)	0.20 π mm-mrad

RFQ Accelerator

The RFQ accelerator is currently the accelerator of choice between the source and drift-tube linac instead of the Cockcroft-Walton high-voltage column used at earlier facilities. A considerable amount of RFQ design and operational experience now exists at many laboratories around the world at several frequencies and ion species.[8] Proton and H^- RFQs have been operated at 80, 200, and 425 MHz. The RFQ provides superior acceleration and matching performance in much less physical space and with greater reliability. With the RFQ operating at the same frequency as the DTL, more than 90 percent of the continuous beam from the source can be bunched, accelerated to several MeV, and captured by the DTL within a few meters with all apparatus at ground potential except for the 35-kV source. Most of the RFQ length is required for matching the beam transversely into a narrow channel and for quasi-adiabatically bunching the beam prior to acceleration. The attention to matching and gradual bunching and acceleration pays off not only in the improved capture efficiency, but in much less growth of the emittances in this section of the accelerator. The brightness requirements of the SSC and its future upgrades should be readily achievable by the linac because of the superior performance of RFQs.

With the choice of quasi-adiabatic capture in the LEB, excellent linac performance can be achieved by using an RFQ and DTL operating at the same frequency. The higher frequency improves the RFQ longitudinal emittance and the choppers and bunchers at low energies of older systems are always a source of transverse emittance growth. The beam macropulse length and, hence, the number of injection turns, is also minimized in this design since none of the beam is intentionally discarded.

The design of the RFQ is straightforward since several devices with similar requirements have been operated. The design philosophy adopted here is to make the RFQ operationally flexible and reliable. The current should be variable from 5 to 50 mA with the source emittance degraded by as much as a factor of two. The beam position tolerances should be reasonable and the maximum peak surface fields should be less than 36 MV/m (1.8 Kilpatrick). The output energy is a tradeoff between optimal matching into the DTL and keeping the length of the RFQ reasonable. The injected energy into the DTL should be high enough so that the drift-tube lengths are long enough for adequate permanent magnet quadrupoles. Two 425-MHz drift-tube linacs using permanent magnet quadrupoles have been built and successfully operated at higher currents with a starting energy of 2 MeV. A DTL injection energy of 2.5 MeV appears to perform well in our simulations with ample design margin. The mechanical structure of the RFQ could be either 4-vane or 4-rod. The 4-vane structure is chosen for this design primarily because of its much larger experience base. A design example is presented that satisfies the above requirements and can be fabricated with little further development. This RFQ is being fabricated for SSCL by Los Alamos National Laboratory. A 4-rod RFQ is being developed at TAC as a possible second injector for the SSC linac.

The RFQ design simulation parameters are listed in Table III. The input beam is 30 mA with a normalized transverse rms emittance of 0.20 π mm-mrad. The current limit for this design example is kept large so that this RFQ could work with higher beam currents. Another significant advantage of a higher current limit is that the specified tolerances for the RFQ fabrication process can be relaxed. One pays a price in terms of slightly increased length and power. Furthermore, this design example has a large acceptance that makes it possible to accelerate injected beams with transverse emittances that are larger by a factor of 2.

TABLE III
RFQ Design Parameters

Frequency	428 MHz
Injection energy	0.035 MeV
Output energy	2.5 MeV
Injection current	30 mA
Output current	27 mA
Input trans. emittance (n, rms)	0.20 π mm-mrad
Output trans. emittance (n, rms)	0.19 π mm-mrad
Output long. emittance (rms)	0.063×10^{-5} eV-s
RFQ length	222 cm (3.17 λ)
Total peak power	283 kW
Beam peak power	77 kW
Copper peak power	206 kW
Duty factor	0.05%
Copper power (average)	103 W
MPSEF	1.73 E_K

RFQ-DTL Matching Section

The RFQ-to-DTL matching section contains four quadrupoles and two 428-MHz bunchers. The quadrupole magnets are an extension upstream of the DTL FODO lattice. The permanent-magnet quadrupoles are variable with gradients varying from 131 to 140 T/m and lengths of 3.8 mm. The bunchers are located between the first and second and the third and fourth quadrupoles. The bunchers need net voltages of only 100 and 70 kV. They are operated at -90 deg for no net energy gain. By choosing a ramped gradient drift-tube linac with initial focusing strengths similar to the output of the RFQ, this matching section was designed to be independent of the beam current. This substantially eases commissioning and improves flexibility. Space will be provided in the matching section for the diagnostics required for tuneup of the source-LEBT-RFQ front end. The diagnostics also facilitate the setup of this section to provide a properly matched input beam for the DTL. The length of this section for one RFQ is approximately 75 cm. Additional RFQs approximately double the length of the section to accommodate the bending magnets, additional quadrupoles, and one additional buncher per RFQ. For the longer matching sections it is critical to keep the transverse size of the beam small to avoid transverse emittance growth.

Drift-Tube Linac

A DTL is the accelerator of choice to accept the 2.5-MeV output of the RFQ and accelerate the H^- ions to the relativistic velocities needed by the CCL. At 2.5 MeV the ions have sufficient velocity that permanent magnet quadrupoles have ample strength to control the beam. The DTL will be contained in four tanks, each powered by a single klystron. A gradient (E_0) of 4.6 MV/m (1.4 Kilpatrick peak surface field) will be used and is considered conservative in terms of operational reliability. Isolation valves, variable quadrupoles, steering magnets, and beam diagnostic stations are placed between the tanks.

The 428-MHz DTL is similar to several others that were recently built. But it is a fairly expensive structure because of the effort involved in fabricating the drift tubes. Decreasing fabrication costs will be an active area for engineering development. At this point in the design the strategy is to start the coupled-cavity linac (CCL) at the lowest reasonable energy. Below 70 MeV the performance and efficiency of the CCL falls rapidly. The present simulations indicate that 70 MeV is probably a good compromise between cost and performance.

The DTL design presented here uses conservative parameters for electric and magnetic fields and yet accommodates a wide range of current and emittance. The permanent magnet quadrupoles in the drift tubes have a gradient of 140 T/m by using a pole-tip field of 1.1 T and a bore radius of 8 mm. Recent high-current DTLs have successfully used permanent magnet pole-tip fields as large as 1.3 T. A peak surface electric field of 1.4 Kilpatrick, which is also considered to be conservative for this type of linac, has been chosen for this design. The beam size remains small transversely and longitudinally throughout the DTL with all transitions made gradually. The gentle treatment of the bunch reduces the demands on the RFQ-DTL matching section, should simplify commissioning and operation, and naturally leads to preservation of beam quality.

The DTL parameters are linearly ramped in the first tank (2.5–14 MeV) from the output parameters of the RFQ. The longitudinal and transverse focusing strengths at the start of the DTL are forced to be nearly equal to the focusing strengths at the end of the RFQ. This ensures a smooth match into the DTL and makes the operation of the matching section nearly independent of beam current. To hold the longitudinal focusing strength constant, the accelerating field (E_0T) is ramped from 1.5 to 4.0 MV/m. The particle phase is also ramped to hold the phase width of the zero-current separatrix constant in real space. Throughout the DTL the beam size is kept small relative to the bore size (< 25 %). When realistic fabrication errors are included using PARTRACE, the edge of the beam should stay within a radius of 6 mm with 95 % confidence.[9] The last three DTL tanks will each be approximately 5.8 m in length and add approximately 19 MeV per tank. The beam will be steered back onto the axis between each tank using the two variable and movable permanent-magnet quadrupoles located 1$\beta\lambda$ apart between tanks. Simulations with up to twice the transverse emittance or three times the current also showed no beam loss and no transverse emittance growth. The parameters of the DTL are listed in Table IV.

TABLE IV
DTL Design Parameters

Frequency	428 MHz
Injection energy	2.5 MeV
Output energy	70 MeV
Injection current	25 mA
Output current	25 mA
Emittance (n, rms)	
Input transverse	0.19 π mm-mrad
Output transverse	0.19 π mm-mrad
Input longitudinal	0.063×10^{-5} eV-s
Output longitudinal	0.069×10^{-5} eV-s
DTL length	23 m
Number of cells	151
Number of tanks	4
Magnetic lattice	FODO
Synchronous phase (from peak)	-35 to -30 deg after 14 MeV
Accelerating field (E_0T)	1.5 to 4.0 MV/m after 14 MeV
MPSEF	1.4 E_K (28 MV/m)
Total rf power	12 MW

DTL-CCL Matching Section

Since the CCL operating frequency is the third harmonic of the DTL frequency, the beam must be bunched for longitudinal matching and transversely matched into the CCL magnetic lattice. The matching section must accomplish this with little beam loss and negligible emittance growth. The conceptual design for this section accomplishes these requirements in a space of 2.7 m using two 1284-MHz rf bunchers, one quadrupole singlet, and two quadrupole doublets. The quadrupole doublets are an upstream extension of the CCL lattice. The bunchers are positioned between the first and second and the third and fourth quadrupoles and will be powered by splitting rf from the first CCL klystron. Space is available for current, position, and energy diagnostics in this design. Analogous to the DTL matching, the first two tanks of the CCL have ramped gradients making the operating values of this matching section nearly current independent. The beam size remains nearly constant so the PARMILA simulations indicate no losses or emittance growth.

Coupled-Cavity Linac

A standing-wave CCL will be used for most of the energy gain provided by the linac. It is the simplest of the linac types used on the SSC, provides the highest gradient, and is the least expensive per meter to fabricate. Many CCLs of the side-coupled type have been built during the past twenty years since it was developed and used for the 800-MeV LAMPF linac. It has especially been exploited in recent years for electron accelerators used for a variety of applications including commercial medical diagnostic and therapy devices, free-electron lasers, and racetrack microtrons.[10] The side-coupled linac was recently adopted as the accelerator of choice for the Fermilab linac upgrade to 400 MeV.[11]

The CCL will operate on the third harmonic of the DTL—1284 MHz. The higher frequency was chosen to reduce structure and rf costs through a smaller, more efficient structure and to raise the voltage breakdown threshold. A harmonic higher than the third complicates the DTL-CCL matching section and leads to more emittance growth. An average gradient (E_0T) of 6.7 MV/m with a peak surface field of 32 MV/m (1.0 Kilpatrick) will be used. The ratio of peak surface field to average gradient is kept low by enlarging the outer radius of the nose of the accelerating cell at the expense of shunt impedance. This should provide very dependable operation with a brief commissioning period, yet keep the linac length short to minimize cost. After an initial conditioning period of a few days, the linac should lose a pulse due to a spark less than once per hour. The rf system and H^- source will probably cause lost pulses at a higher rate than linac sparks.

The coupled-cavity linac will be made up of cells that are brazed together into tanks. The tanks are separated to provide space for focusing and steering magnets and diagnostics. The number of cells per tank is determined by the minimum spacing permitted for the quadrupoles in the magnetic lattice. The tanks are then resonantly coupled together into modules with bridge couplers to minimize the number of klystron systems (these typically contribute nearly half of the construction costs of a high-gradient linac). The number of tanks that can be coupled together in a module with one rf source is limited by the gradient droop in the end tanks and the available peak rf power per klystron.

The side-coupled structure is the most efficient structure for low-current designs such as this where one klystron will drive many cells. If we allow a 3 % droop in the gradient from the center cell to the end cell, a side-coupled module with 128 accelerating cells would require a 5 % coupling constant between cells and would have a shunt impedance at 82 % of the SUPERFISH value. Similar performance for an on-axis module would require a 10 % coupling constant and would yield a shunt impedance at 67 % of the SUPERFISH value. An annular-ring-coupled structure with four coupling slots would require a coupling constant of 7.1 % and would yield a shunt impedance at 69 % of the SUPERFISH value. The high coupling constant available from the disk-and-washer structure does not outweigh the considerable engineering development still required and the complexity of tuning the structure to avoid the modes crossing the accelerating frequency.

The present design of the CCL from 70 to 600 MeV was simulated with 60 tanks of 22 cells/tank (20 cells/tank in the module end tanks). Ten klystrons are used to power these as 10 modules with six tanks/module. Multiple-cell bridge couplers (5 and 3 $\beta\lambda/2$) will be used to accommodate (>30 cm) the focusing quadrupole and beam diagnostics between tanks. The spacing between modules will be larger to accommodate the additional diagnostics and an isolation vacuum valve. Conventional magnet quadrupoles are used with 70-degree phase advance per cell. The bore of the linac starts with a radius of 1.27 cm and is reduced to 1 cm after the 6th module. With alignment errors simulated using CCLTRACE, the beam should always fill less than 60 % of the bore with 95 % confidence.[12] This bore size should be conservative for this low-duty linac.

At the end of the linac, 99 percent of the beam should be within a 1-MeV window and the bore-radius–to–beam-radius ratio is 3:1. The CCL design parameters are summarized in Table V. This section of the linac is expected to easily transport the beam with no losses and no emittance growth. In fact, if the transverse emittance of the source is improved by a factor of two, most of that improvement should survive the entire linac as presently designed.

TABLE V
CCL Design Parameters

Frequency	1284 MHz
Injection energy	70 MeV
Output energy	600 MeV
Injection current	25 mA
Output current	25 mA
Emittance (n, rms)	
Input transverse	0.19 π mm-mrad
Output transverse	0.21 π mm-mrad
Input longitudinal	0.06×10^{-5} eV-s
Output longitudinal	0.06×10^{-5} eV-s
CCL length	117 m
Number of modules	10
Number of tanks per module	6
Number of cells per tank	22 and 20
Magnetic lattice	FODO
Synchronous phase (from peak)	-30 deg
Accelerating field (E_0T)	6.7 MV/m
MPSEF	1.0 E_K (32 MV/m)
Total rf power	140 MW

The CCL was simulated to 1 GeV by continuing the same module and magnetic lattice structure. An additional length of 98 m was required. The beam continued to be well behaved, with no losses or emittance growth. The bore-radius–to–beam-radius ratio remained approximately 3:1, and the energy spread grew to only slightly above 2 MeV. A future upgrade of the SSC linac to 1 GeV will be straightforward since the additional tunnel length will be built during the original construction. Prior to upgrade, the extra length will contain a transport line consisting of a continuation of the CCL lattice.

Rf Requirements

As described above, the SSC linac is composed of three different accelerator structures (RFQ, DTL, and CCL) at two different frequencies (428 and 1284 MHz). The high-power rf requirements of the three systems are shown in Table VI.

TABLE VI
Linac Rf Power System Requirements

	RFQ	DTL	CCL
Frequency (MHz)	428	428	1284
Pulse length (μs)	50	50	50
Repetition rate (Hz)	10	10	10
Rated peak power (MW)	4	4	20
Operating peak power (MW)	0.3	3	15
Number of klystrons	0	4	10
Operating efficiency (%)	-	50	45

The power for the RFQ will be split from the klystron driving the first DTL tank. This is feasible for two reasons: first, the first DTL tank has 1 MW of excess power since it has a ramped gradient; and second, the beam loading of the RFQ and first DTL tank are similar. The tubes will actually be operated at 25 percent less power from their rated and factory tested values to improve reliability, shorten turn-on time, and provide control margin. A 50-μs rf pulse is chosen to provide a 35-μs linac beam pulse. The 15-μs differential will be used for cavity filltime and settling of the feedback controls.

Each rf amplifier consists of a charging supply, pulse-forming network (PFN), pulse transformer, and klystron. Since the duty factor is so low, efficiency is not an issue in operating costs; therefore, nominal klystron tube efficiencies are assumed. Klystron tubes at these power levels and pulse lengths are readily available. A PFN is the most straightforward and well-understood modulator scheme available and will work well at a pulse length of 50 μs. The dc power supplies are small because of the low duty factor.

The low-level rf systems will provide the feedback and feedforward required to maintain the fields in each tank to an amplitude constant to 0.5 % and a phase constant to 0.5 degrees.

Status and Schedule

The present SSC schedule calls for 200 GeV test beams to be available by the end of 1995. This requires the operation of the linac, LEB, and MEB. In support of this we are planning on starting the commissioning of the full linac by the end of 1994. The source and LEBT tests have already started. The RFQ will be added in early 1992 to the linac test stand at the Dallas offices. Installation of those components and the DTL at the SSC campus should begin by the end of 1992.

Cost Estimate and Procurement Plan

The base cost (no contingency, escalation, or R&D) of the SSC linac was estimated to be approximately $33 million in FY90 dollars. Approximately 90 % of the linac will be procured from industry. The DTL structures, CCL structures, and rf systems will be built by industrial partners. The source, LEBT, and RFQ are being built either internally or through collaborations with other laboratories.

Acknowledgments

The SSC Linac Group is indebted to the dedicated help of many people in arriving at the present design. We especially appreciate the assistance of Tarlochan Bhatia and his team at Los Alamos and Russ Huson and his team at TAC. We have built on the early work of many contributors from many laboratories assisting the Central Design Group.

References

[1]R. I. Cutler, "Linac Reliability Issues," Internal SSCL Report (1990).

[2]R. K. Bhandari and S. Penner, "Beam Transfer Between the Coupled Cavity Linac and the Low Energy Booster Synchrotron for the SSC," This Conference.

[3]C. W. Schmidt and C. D. Curtis, "A 50-mA Negative Hydrogen Ion Source," IEEE Trans. Nucl. Sci. NS-26 (3), 4120 (1979).

[4]H. V. Smith, et al., "Pulsed H^- Beams From Penning SPS Sources Equipped With Circular Emitters," in Proceedings of the 1988 Linac Conference (1988).

[5]K. N. Leung et al., "Optimization of H^- Production From a Small Multicusp Ion Source," Rev. Sci. Instrum. 60(4), 531 (1989).

[6]C. R. Chang, "Design Studies of SSC Low-Energy-Beam-Transport System Using Einzel Lenses," This Conference.

[7]D. Raparia, "HESQ, A Low Energy Beam Transport for the SSC Linac," This Conference.

[8]R. H. Stokes and T. P. Wangler, "Radio Frequency Quadrupole Accelerators and Their Applications," Ann. Rev. Nucl. Part. Sci. 38, 97 (1988).

[9]G. H. Neuschaefer et al., "SSC Drift Tube Linac Beam Dynamics Design," This Conference.

[10]R. K. Cooper et al., Radio-Frequency Structure Development for the Los Alamos/NBS Racetrack Microtron, Los Alamos National Laboratory Report No. LA-UR-83-95, 1983.

[11]D. E. Young et al., "400-MeV Upgrade for the Fermilab Linac," presented at the XIVth International Conference on High Energy Accelerators, Tsukuba, Japan, 22–25 August 1989 (unpublished).

[12]T. S. Bhatia et al., "Error and Tolerance Estimates for the SSC Coupled-Cavity Linac," and R. W. Garnett et al., "A Comparison of Beam Dynamics Solutions for the SSC 1284-MHz Coupled-Cavity Linac," This Conference.

Monday

Session MO4
Chairman: S. Yu
Contributed Papers

RFQ LENS FOR LOW ENERGY ION BEAM FOCUSING*

D. A. Swenson, D. D. Gillings, W. J. Hoffert, S. R. Schmidt
Science Applications International Corporation
4161 Campus Point Court, San Diego, CA 92121

Abstract

A new application for RFQ focusing has been identified, namely that of preparing low energy charged particle beams for injection into RFQ linacs. The relatively large-diameter, short-focal-length requirement of this application has proven difficult to satisfy with conventional, static, electric or magnetic, quadrupole or solenoid, lens elements. The RFQ lens offer some unique capabilities for this application: 1) being electric in nature, the RFQ lens is particularly effective for low energy ion beams, 2) being rf in nature, the RFQ lens can have arbitrarily short periods in the focal structure, which can produce near-symmetrical action on the beam in both transverse planes, and 3) being primarily two-dimensional in nature, the RFQ lens offers less aberrations to the beam than a highly three-dimensional array of quadrupole lenses. The RFQ lens, used as suggested here, may represent an important new element for low energy beam transport systems. The lens exhibits a net focusing in both transverse planes, maintains a near circular beam throughout the lens, has no frequency or phase constraint to subsequent linac structures, has acceptable surface field strengths, and is tunable, simultaneously in both transverse planes, by rf amplitude. A 10-inch-diameter, 3.5-inch-long, 300-MHz RFQ lens unit, complete with a 20-kW, close-coupled, rf power system has been designed, fabricated and tested. Features of the design, fabrication, tuning and excitation will be presented. Results of the preliminary beam tests will be described.

RFQ Lens Background

The success of RFQ linacs presents us with lower energy beams in low energy beam transport (LEBT) systems and the need for more strongly convergent beams at the entrance to linacs. Achieving the required focusing with quadrupole or solenoid lens systems has become a problem. The lower beam energies give added impetus to the use of electric, as opposed to magnetic lenses in these regions.

The RFQ lens is an electric quadrupole lens with the added advantages that no insulators are required to support the resonant electric fields in the structure and the required "alternating gradient" feature is provided by the temporal alternation in the polarity of the fields.

RFQ lenses are inherently simpler than RFQ linacs. They have been around longer than their linac counterpart, finding application in atomic physics, plasma physics, and mass spectroscopy. Prior to this initiative, however, they were thought to be too weak in focusing strength to serve the demanding application of matching low-energy ion beams into modern RFQ linacs.

A key observation, made by one of the authors (DAS), is that there are some configurations of RFQ lenses whose effect on the beam is independent of the phase of the rf excitation at the time that the particle enters the lens. This, in turn, suggests that these configurations do not have to be synchronized with the linac phase or frequency to have a useful focusing effect on the beam. In particular, it suggests that RFQ lenses could be designed to operate at a lower frequency than the linac where their strength would be substantially stronger.

Properties Of RFQ Lenses

The focusing strength for RFQ devices is proportional to $B=E\lambda^2/((m/q)r)$, where E is the surface electric field on the tip of the electrode, λ is the rf wavelength, m/q is the mass-to-charge ratio of the beam particles, and r is the radial aperture of the electrodes. If E is expressed in units of MV/m, λ in meters, m in MeV, q in multiples of the proton charge, and r in meters, the quantity B, which we will call the "B-value" or focusing strength of the RFQ, is unitless. For example, an RFQ lens with E=11.2 MV/m, λ=1.0 m, m=938 MeV, q=1, and r=0.01 m, has a B-value of 1.2.

For a given beam particle and electric surface field limit, the maximum achievable focusing strength of an RFQ lens is proportional to λ^2/r. Hence, for small apertures, small wavelengths (high frequencies) are acceptable; for large apertures, large wavelengths (low frequencies) are required.

The optimization of RFQ linacs for focusing and acceleration of small diameter particle beams essentially precluded the use of RFQ lenses, operating at the linac frequency, on the larger diameter beams in LEBTs, because of inadequate lens strength. The key observation, presented here, is that there are some configurations of RFQ lenses that do not have to be at the linac frequency in order to effect a useful transformation on the beam and, in particular,

* Work supported by U.S. Army Strategic Defense Command, Huntsville, AL.

may operate at a lower frequency where their strengths can be substantially higher.

The basic components and performance of an RFQ lens for LEBT applications are shown in Fig. 1. The lens comprises three sections, namely, the input matching section, the center section, and the output matching section. It is the proper configuration of the two matching sections that gives the all-important phase independence of the focusing action. The RFQ field strength in the two matching sections must increase smoothly from zero to full strength, or vise versa, over some minimum distance to allow the beam to adapt to the time-varying rf fields within the lens.

The beam profiles through the basic RFQ lens, as displayed by the TRACE program, are shown in the lower part of Fig. 1. The horizontal profiles are shown above the center line and the vertical profiles are shown below. The four different trajectories, seen in each profile near the center of the lens, correspond to four different phasings of the beam relative to the lens excitation.

Figure 2 shows the transverse phase spaces (the six boxes at the top of the figure) and the beam profiles (the large box at the bottom of the figure) for four beams, separated by 90° in phase, at the beginning (left), middle, and end of an RFQ lens. The phase spaces display the transverse dimensions of the beam versus the angular divergence of the beam. The beams are considered to occupy the elliptical regions in the transverse phase spaces. The A and B values in each box correspond to the α and β twiss parameters respectively for the four beams.

The phase space and profiles of the four beams are chosen to be identical at the input side of the figure. In the middle of the lens, the

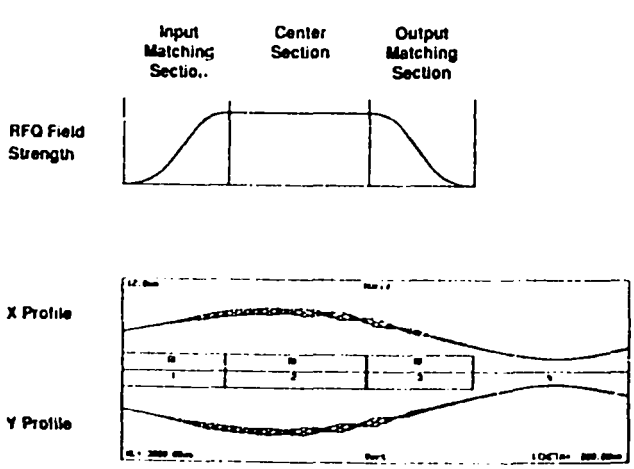

Fig. 1. Basic Components and Performance of an RFQ Lens.

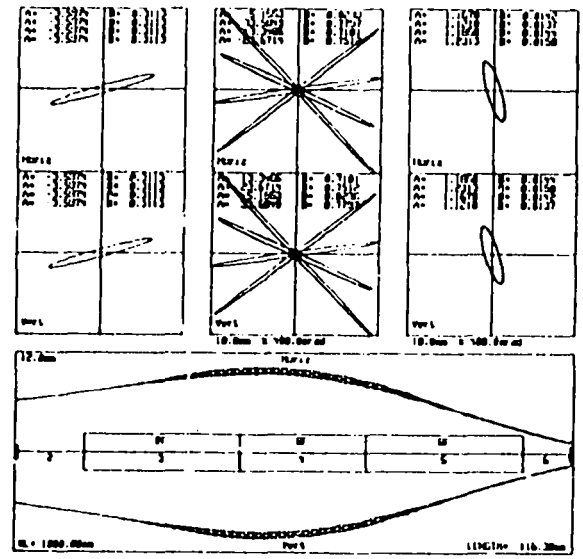

Fig. 2. Phase Space at Beginning, Middle and End of RFQ Lens.

phase spaces occupied by the four beams are dramatically different. The fact that these phase spaces and profiles coalesce at the end of the lens demonstrates that the lens action is independent of phase.

Consider a beam in a LEBT that is ten times the diameter of the beam in a 425-MHz RFQ linac. Because the radial aperture of the lens electrode must be ten times larger than that of the linac in order to accommodate the beam, the achievable RFQ lens strength in the LEBT, at the frequency of the RFQ linac, is down on order of magnitude from that in the linac. Since the focusing strength is proportional to the square of the rf wavelength, the possibility of using a 100-MHz lens, instead of a 425-MHz lens, regains that order of magnitude in strength.

A unique feature of the RFQ lens is its ability to achieve short focal lengths for large diameter beams, utilizing quadrupole focusing, while maintaining nearly circular cross-sections for the beams. This requires focal periodicities that are short relative to the diameter of the beam. This can be shown to be impractical for electrostatic or magnetostatic quadrupole lens systems and practical for the RFQ lens. In the static cases, the field limitations are longitudinal and the field pattern is highly three dimensional. In the rf case, the field limitations are transverse and the field patterns are primarily two dimensional, which may in turn reduce beam aberrations. In these geometries, the transverse field limitations are much higher than the longitudinal limits, leading to higher focusing strengths and shorter focal lengths for the RFQ lens.

A wide variety of match conditions are possible with the RFQ lens. The output of the RFQ lens has azimuthal symmetry as required by the input to RFQ linacs. Consequently, matching a beam to an RFQ linac with an RFQ lens may require only two adjustable parameters compared to the four adjustable parameters required by static quadrupole systems. The two adjustable parameters could be lens excitation and lens position. Another approach would be to have two RFQ lenses in tandem to provide the two adjustable parameters.

The RFQ lens differs from an electrostatic quadrupole lens because of the time-dependent nature of its electric fields. Unlike an electrostatic lens, it can discriminate between different ions species in a particle beam. The RFQ lens is similar to a magnetic lens in that it focuses lighter particles more strongly than heavier particles of the same charge and energy.

The choice of the optimum length and frequency for a specific application of the RFQ lens is complicated by the interplay between two competing phenomenon. The focusing effect of an RFQ lens is a complex function of its length, aperture, excitation, and resonant frequency. Longer lenses require less electric field gradient, which implies lower surface electric fields and less rf power. Larger aperture lenses require the same electric field gradient, which implies higher surface electric fields and more rf power. For systems involving highly divergent or convergent beams, longer lenses, with their lower electric field gradient will allow larger beam excursions, which, in turn, will require larger lens apertures and more rf power. This puts an upper bound on the lens lengths for some lens applications.

The input and output radial matching sections of the lens add to the total length of the lens. In these sections, the electric field gradient must increase smoothly from zero to full strength, or vice versa, to allow the beam to adapt to the time varying nature of the rf fields within the lens. Design experience tells us that these sections should each be about three particle wavelengths in length: shorter sections result in significant beam emittance growth. In some cases, lower frequencies, with their longer matching sections, will allow larger beam excursions, which, in turn, will require larger lens apertures and more rf power. This puts a lower bound on the frequencies for some lens applications.

The RFQ lens, as described here, represents an important element for low-energy beam transport systems. It offers exceptional strength for low-energy ion beams. It exhibits a net focusing in each transverse plane, maintains a near circular beam throughout the lens, may be exceptionally low in aberrations, has no frequency or phase constraint to subsequent linac structures, has acceptable surface field strengths, and is tunable, simultaneously in both transverse planes, by rf amplitude.

Design, Fabrication, and Test

An RFQ lens was designed, fabricated and tested. The goal was to focus a slightly divergent, 20-mA beam of 20-keV protons into a modern RFQ linac. Beam dynamic studies (using TRACE2D) suggested suitable parameters for this system to include a resonant frequency of 300 MHz, a lens length of 10 cm, a radial aperture of 1 cm, and a focusing strength of 1.2.

A decision was made to fabricate this RFQ lens as a very short, large-diameter, four-vane RFQ structure. The initial estimates of the transverse dimensions of the lens cavity and its rf power requirements were based on two-dimensional rf cavity calculations (SUPERFISH). These estimates suggested a cavity diameter of 25 cm, a vane-to-vane voltage of 112 kV, vane-tip electric field of 11.2 MV/m, a maximum surface electric field of 13.9 MV/m, and a peak rf power of 7.1 kW.

The outer part of the lens cavity was constructed as a heavy-walled cylinder, 10 inches in diameter and 3.5 inches long. Four vane assemblies are mounted inside this enclosure, attached to the heavy cylindrical wall by two concentric push/pull screw assemblies. Electrical contact between the vane bases and the cavity walls is based on flexed fins at the edge of the vane bases, which are designed to produce a substantial force against the wall. The vacuum requirement for the RFQ lens is simplified by surrounding the entire lens assembly with a vacuum housing that bolts directly to an RFQ linac.

The rf power is supplied by a close-coupler rf power system base on an Eimac Planar Triode, Y-690, which provides a peak rf power pulse of 26 kW at a 1% duty factor.

In the preliminary test of this RFQ lens system, no focusing action was observed. During the test, it was determined that we were low in lens strength, by a factor of 4, due to an abnormally low cavity Q value and insufficient rf power. Neither of these limitations are fundamental and further tests are planned. The RFQ lens concept still seems sound and its realization still seem practical.

NEW VANES FOR RFQ1

B.G. Chidley, F.P. Adams, G.E. McMichael, T. Tran Ngoc
AECL Research, Chalk River Laboratories
Chalk River, Ontario, Canada, K0J 1J0
T.S. Bhatia
Los Alamos National Laboratory,
Los Alamos, NM 87545 USA

Abstract

The RFQ1 accelerator was built with replaceable vanes; the option has always existed to replace the existing vanes with new ones having a revised geometry or construction. The original vanes were designed with a peak surface electric field of 1.5 times Kilpatrick, which is now viewed as being too conservative. The new design will use a peak field of 1.8 Kilpatrick and a modified tip profile to increase the output energy from 0.6 MeV to 1.3 MeV. Computer simulations have been done using PARMTEQ and RFQCOEF to assess the effects of higher order harmonics of the potential on beam losses. The vane will be machined out of GlidCop AL-15[1] (an alumina dispersion-strengthened copper) with the cooling channels gun drilled. Heating calculations have been done using MARC and MENTAT with rf currents calculated by MAFIA and SUPERFISH.

Introduction

The new vanes for RFQ1 must be designed within constraints imposed by the existing hardware. The principal changes are in the vane tip shape and modulation, but there are some changes in the vane body related to the structural material and machining techniques. The basic parameters are given in Table 1.

TABLE 1
RFQ1 Basic Parameters

Frequency	267.0 MHz
Input Energy	50 keV
Vane Length	146.88 cm
Beam Current	75 mA
Beam Emittance (rms, norm)	0.05 π cm mrad
RF Power	<200 kW
Peak Surface Electric Field	18 * Kp

The differences in shape between the new vanes, as shown in Fig. 1, and the existing ones are in the tip (which doesn't show in the figure) and in the widening or hip near the base. This hip is to accommodate cooling channels and adjust the resonant frequency to compensate for the smaller aperture.

Vane Tip Cross Section

The vane tip, as shown in Fig. 2, is the only part of the vane of interest to beam dynamics. Specifically, most of the design procedure involves finding the aperture α as a function of z. The dimensions common to the old and new tips are CL = 12.70 cm, A = 0.60 cm, and B = 11.045 cm, where CL is the distance from the vane base to the tank centre line and B is the distance from the vane base to the numerically profiled part of the tip. The dimensions to be determined are ρ and α. The radius of curvature of the tip does not directly affect beam dynamics, but is significant because it

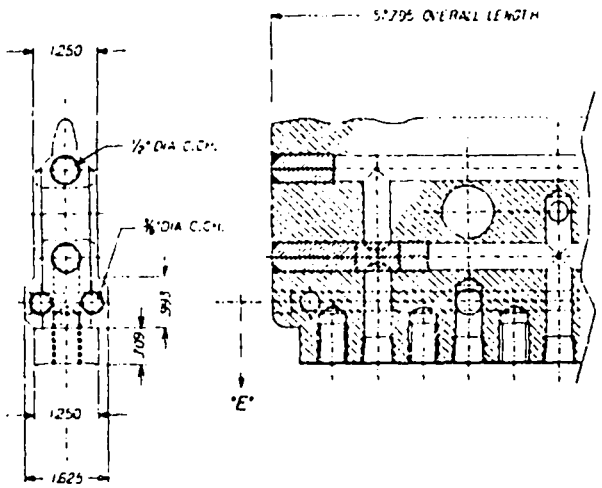

Fig. 1 New vane design.

affects the peak surface field (enhancement factor), the structure resonant frequency, and the harmonic terms of the potential near the beam axis.

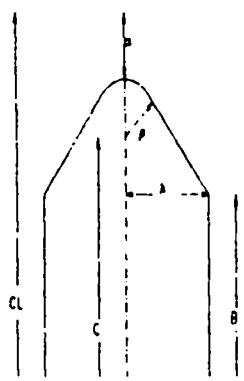

Fig. 2 Vane tip cross section.

Enhancement Factor

The enhancement factor is shown as a function of ρ/r_o in Fig. 3. The peak surface electric field is EFACT * (V/r_o), where V is the intervane voltage and r_o is the mean aperture. For highest current limit and accelerating gradient, one wants (V/r_o) to be as high as possible. However, the peak electric field is limited by sparking, so a minimum EFACT is wanted. If this were the only consideration one would choose ρ/r_o = 0.75. However, modification of the potential harmonics or a desire to maintain constant intervane capacitance may force other choices.

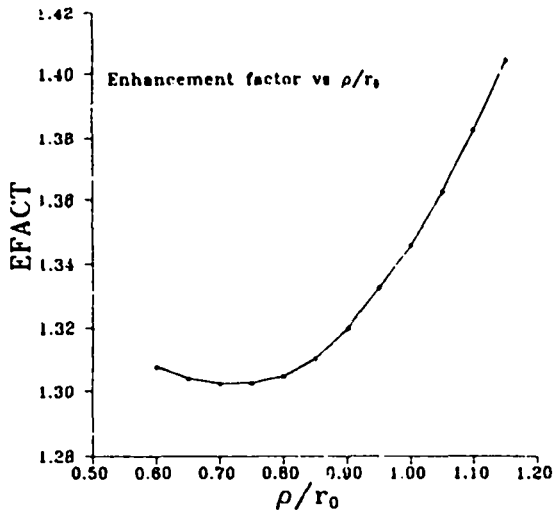

Fig. 3 Typical enhancement factor vs ρ/r_o.

Resonant Frequency Stabilization

One of the design optimizations requires a small variation in r_o with z. This will cause a change in resonant frequency and a field tilt unless compensated by some means. There are several ways to do this, but a convenient means is to vary ρ as indicated in Fig 4. This shows the variation in ρ/r_o required to maintain the resonant frequency as calculated by MAFIA as r_o is changed.

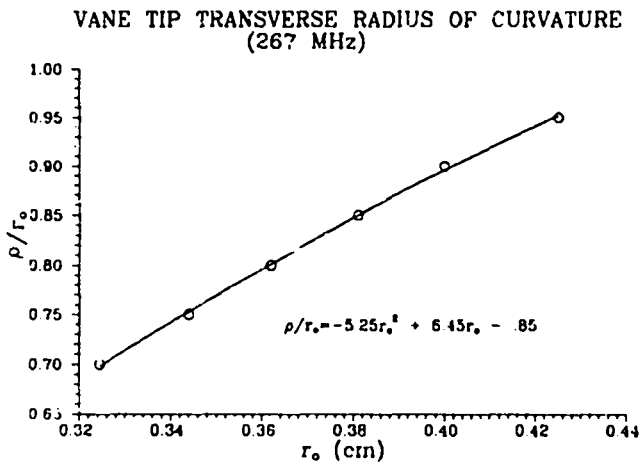

Fig. 4 Variation of ρ/r_o to maintain frequency.

Harmonic Terms of Potential

The potential in an RFQ near the beam axis may be written

$$U(r,\theta,z) = \sum_{s=0}^{\infty} C_{0s}(kr)^{\lambda} \cos(\lambda\theta) + \sum_{m=1}^{\infty} \cos(kmz) \sum_{s=0}^{\infty} C_{ms} I_{\lambda}(kmr) \cos(\lambda\theta)$$

where $k = \pi/L$

$\lambda = 4s$ for odd m

$= 4s+2$ for even m

or in the notation used by PARMTEQ :

$$\begin{aligned} U(r,\theta,z) = \; & A_{01}\, r^2 \cos(2\theta) \\ & + A_{10}\, I_0(kr) \cos(kz) \\ & + A_{03}\, r^6 \cos(6\theta) \\ & + A_{12}\, I_4(kr) \cos(4\theta) \cos(kz) \\ & + A_{21}\, I_2(2kr) \cos(2\theta) \cos(2kz) \\ & + A_{23}\, I_6(2kr) \cos(6\theta) \cos(2kz) \\ & + A_{30}\, I_0(3kr) \cos(3kz) \\ & + A_{32}\, I_4(3kr) \cos(4\theta) \cos(3kz). \end{aligned}$$

The idealized two-term potential is

$A_{10} = (V/2) * (1/r_o)^2$

$A_{01} = (V/2) * A * I_0(2\pi r/\{\beta\lambda\})$

where $A = (m^2-1)/[m^2 I_0(2\pi a/\{\beta\lambda\}) + I_0(2\pi ma/\{\beta\lambda\})]$

The actual A_{10}, A_{01} can be calculated with RFQCOEF and vary with ρ as shown in Figs. 5 and 6. Care must be taken to control the higher order terms, some of which can affect beam spill.

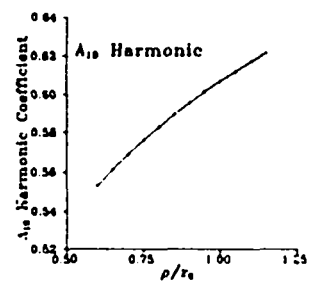

Fig. 5 A_{10} harmonic.

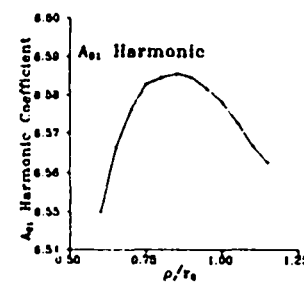

Fig. 6 A_{01} harmonic.

Vane Longitudinal Profile

The design procedure for the longitudinal profile is fairly standard, except that it includes a consideration of harmonics. The computer program CURLI is used first, using a C_z = 150 mA, and $W_g = W_i * (99.5/\phi_g)^2$. ϕ_g is the synchronous phase at the end of the gentle bunching section and is a free parameter chosen to optimize performance. W_g is the energy at this point and is calculated from the injection energy W_i. CURLI selects parameters that give a specified C_z, the longitudinal and transverse current limit. RFQUIK is then used to generate a two-term potential design with an adjustment in the accelerating section, as suggested by Wangler.[2] POTRFQ is used to calculate the harmonic coefficients, and PARMTEQ used to calculate the transmission. The choice of ρ is an iterative process requiring compromises. The final design is given in Table II.

TABLE II
Final Design Parameters

Output Energy	1.237 MeV
Output Current	75 mA
Number of Cells	120
Vane Voltage	77.4 kV
Peak Field	1.75 * Kp
Transmission	87 %

TABLE III
RFQ Parameters

CELL	a	m	Lcell	r_o	ρ	Emax	EFACT
10	0.3429	1.0243	0.581	0.3470	0.2638	27.831	1.2474
20	0.3334	1.0825	0.586	0.3467	0.2633	28.361	1.2710
30	0.3252	1.1362	0.605	0.3464	0.2626	28.719	1.2871
40	0.3180	1.1858	0.650	0.3461	0.2622	28.883	1.2945
50	0.3127	1.2224	0.728	0.3461	0.2622	28.803	1.2910
60	0.3082	1.2521	0.846	0.3462	0.2624	28.559	1.2801
70	0.2951	1.3471	1.019	0.3463	0.2625	28.284	1.2677
80	0.2478	1.7536	1.342	0.3464	0.2627	27.904	1.2515
90	0.2484	1.7978	1.769	0.3564	0.2801	27.327	1.2591
100	0.2498	1.8653	2.155	0.3697	0.3036	27.123	1.2955
110	0.2530	1.9448	2.516	0.3874	0.3350	26.562	1.3292
115	0.2558	1.9870	2.691	0.3983	0.3549	26.169	1.3471
120	0.2595	2.0303	2.862	0.4114	0.3780	25.739	1.3667

Table III shows a (minimum aperture in the cell), m (modulation), Lcell (cell length), r_o (mean aperture), and ρ (transverse radius of curvature) every 10 cells.

Note the increase in r_o and the corresponding increase in ρ above cell 100, and note that the maximum field occurs at cell 40, so the rise in enhancement factor at cell 120 is not a problem.

The variation of transmission with intervane voltage is shown in Fig. 7 and the variation with input emittance is shown in Fig. 8.

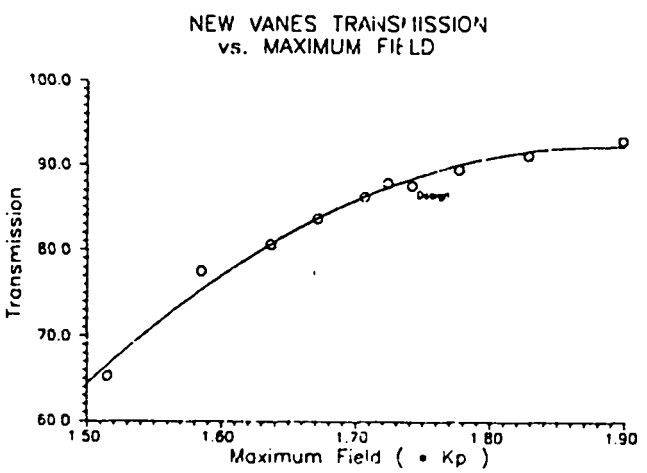

Fig. 7 Transmission vs maximum field.

Vane construction

The vanes will be machined from single pieces of GlidCop Al-15 dispersion-strengthened copper, using gun-bored cooling channels. This material has a strength comparable to mild steel and a conductivity 92% of that of OFHC copper. Tests of this material are described in a companion paper.[3]

Thermal Calculations

Calculations have been done using surface heat fluxes calculated by SUPERFISH to determine thermal distributions, thermal stresses, and deformations. The results indicate an increase in vane height at full power of 0.033 mm and an increase in length along the vane tip

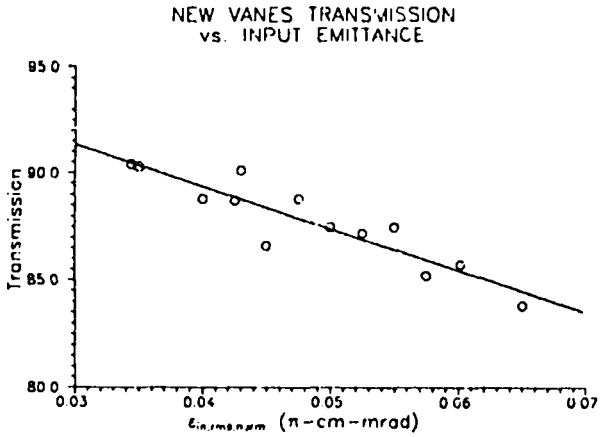

Fig. 8 Transmission vs. input emittance.

of 0.142 mm from centre to end. The most severe deformation occurs near the ends of the vane, where the height will increase by 0.076 mm. The results of the calculations are shown in Fig. 9. These deformations are small enough that they will not affect operation of the RFQ.

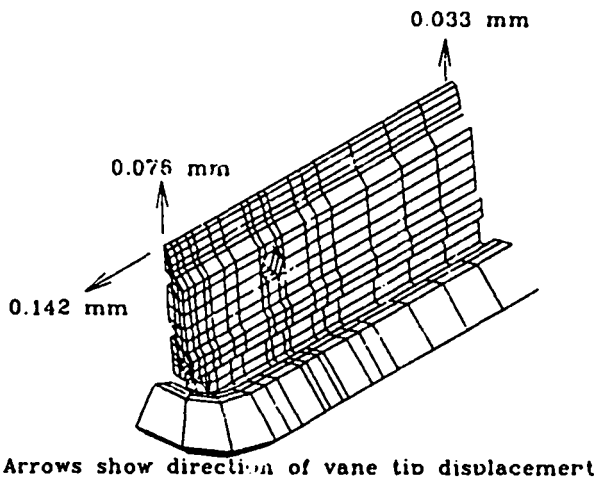

Fig. 9 Distortion of vane due to thermal stress.

References

1. GlidCop Products Information Bulletin, SCM Metal Products Inc., 1988.

2. D. Schrage et al., "A Filght-Qualified RFQ for the BEAR Project", Proc.1988 LINAC conf., Continuous Electron Beam Accelerator Facility report CEBAF-Report-89-001 (1989) 54.

3. T.Tran-Ngoc and R.M. Hutcheon, "Study of High-strength Coppers for RFQ1's New Vanes", these proceedings.

STUDY OF HIGH-STRENGTH COPPERS FOR RFQ1'S NEW VANES*

T. Tran-Ngoc and R.M. Hutcheon
AECL Research, Chalk River Laboratories
Chalk River, Ontario, Canada, K0J 1J0

Abstract

This paper summarizes a study of high-strength copper alloys to select a suitable material for new vanes on the RFQ1 accelerator. GlidCop AL-15 alumina-dispersion-strengthened copper has been chosen for its high strength, relatively high thermal and electrical conductivities and its ability to retain its strength through heating cycles. The results of a detailed test program to evaluate this material are also reported.

Introduction

In the design of the RFQ1 accelerator structure, low-carbon steel was used to provide structural strength. Inside surfaces, where appreciable rf currents flow, were copper electro-plated.[1] This design is complex, expensive to fabricate and difficult to modify. For the new vanes[2] it was decided to see if an improved design could be obtained by using a high-strength copper alloy. A test program was conducted on the selected alloy to verify some of the properties and required fabrication techniques.

Commercially Available High-Strength Coppers

Copper can be strengthened significantly by alloying, by precipitation hardening or by dispersion of a second-phase material in the copper matrix. Usually, alloying elements cause a significant loss in the electrical conductivity (e.g., brass and bronze). In the age-hardened condition, the precipitation-hardenable alloys (e.g., zirconium copper and chromium copper) offer higher strength than pure copper at room temperature and better electrical conductivity than alloyed copper.[3] However, extended exposure to temperatures above the initial aging temperature lower both the strength and conductivity. The dispersion-strengthened coppers provide both high conductivity and strength, and remain stable after exposure to high temperature.[4]

Several high-strength, high-conductivity copper alloys were considered for the RFQ1 application. Their yield and tensile strengths vary with the amount of cold-work, and are summarized in Fig. 1. Electrical conductivities are shown in Table 1.

Due to its high strength, good electrical conductivity and stability on prolonged exposure to high temperature, GlidCop AL-15 in low oxygen grade was chosen for the new vanes.

*This work was partially supported by Los Alamos National Laboratory under contract No. 9-X5D-7832D-1.

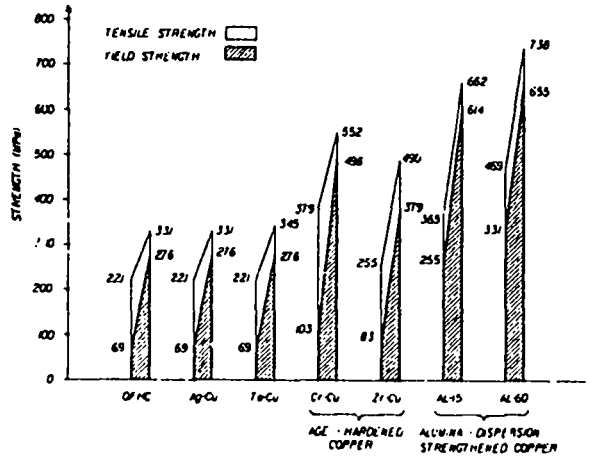

Fig. 1. Tensile and yield strength of coppers.

TABLE 1

Room Temperature Electrical Conductivity of Coppers

Material	DC Electrical conductivity (%IACS)
OFHC	101
Ag-Cu	96
Te-Cu	90
Cr-Cu	80
Zr-Cu	95
AL-15	92
AL-60	78

Evaluation of GlidCop AL-15 Copper

All our test specimens were machined from a low oxygen grade 31.75 mm (1.25") diameter AL-15 rod sample, which has a minimum yield strength of 317 Mpa (46 000 psi).

Plug Welding

In general, extensive welding of the material for joining structural components is not recommended. The large difference in density between copper and alumina will make the latter segregate in the melt and create non-uniformities in the properties of the welded

joints. In our application, it is only necessary to make small welds to plug the ends of the gun-drilled cooling channels, and these are in locations where such variation of the material properties is not important. Sound and leak-tight joints have been demonstrated using helium-shielded tungsten-arc welds with 70% Cu 30% Ni rod and OFHC copper rod as filler materials, and also with electron beam welds.

Brazing

Because of the fine grain structure of AL-15 at brazing temperature, the silver constituent of the brazing alloys diffuses very rapidly away from the joints. Nickel or copper plating is recommended as a barrier to this diffusion.[4] The higher the brazing temperature the thicker the required plating layer. Nickel plating was used and test joints were made between two pieces of AL-15, and between AL-15 and stainless steel or OFHC copper.

Due to the slow heating rate of our radiant furnace (about 3.5°C/min near the brazing temperature) we encountered the above-mentioned diffusion problem even when using the manufacturer-recommended plating thicknesses However, increasing the plating thickness and minimizing the holding time at brazing temperature to about 5 minutes yielded good results. Leak-tight joints were obtained using Cusil (liquidus = 780°C) and Palcusil 5 (liquidus = 810°C) with nickel plating thicknesses of about 0.013 mm (0.0005") and 0.025 mm (0.001"), respectively.

Mechanical Tests of the Racetrack-Shape Compressed Joint

The vacuum and rf seal between the RFQ1 vanes and tank are made by a compressed joint.[1] Tests of the strength of the sealing edge were carried out using GlidCop AL-15 samples in the as-received, highly cold-worked (deformed by a compression load of 1050 N/mm) and heat-treated (3 cycles up to a maximum of 900°C) condition, and compared with mild-steel ASTM A266 class 2.

Vacuum-tight joints were obtained for all AL-15 samples at a linear compression load of about 140 N/mm (800 lbs/in). The results of mechanical tests, performed in steps of increasing bolt torque, are illustrated in Fig. 2. The sealing edges on all samples increased in radius and were reduced in height by about the same amount, with most of the deformation taking place during the first loading cycle. Comparing the results obtained for different sample materials indicates that:

- Up to a load of 480 N/mm (2750 lbs/in), AL-15 in the as-received and heat-treated condition is comparable to mild steel,
- AL-15 in a highly cold-worked condition outperforms mild steel in the testing range, and
- The heat treatment has very little effect on the strength of AL-15.

The seal at the bottom of each RFQ1 vane is compressed by thirty-six 1/2-20 UNF alloyed-steel screws at 120 Nm (90 ft-lbs) torque. At this level copper would wear and gall; therefore, Helicoil inserts are used in all threaded holes. Such a screw was torqued to 220 Nm (160 ft-lbs) in a Helicoil insert in AL-15 with no apparent damage to the threaded hole or the screw itself.

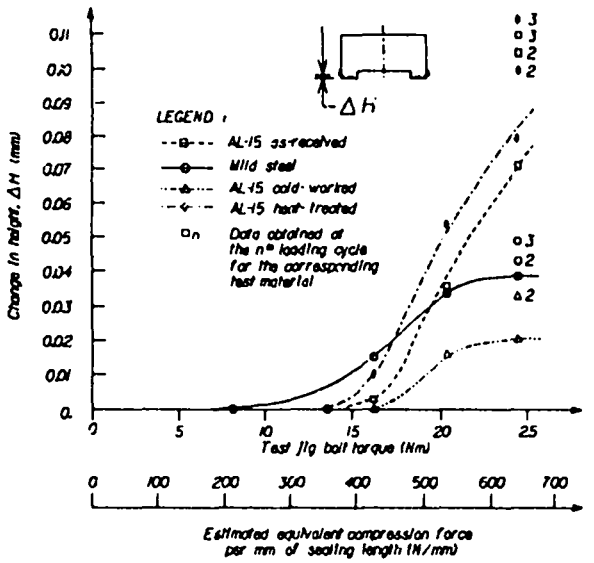

Fig. 2. Change in height of the sealing edges.

RF Conductivity Measurements

To measure the rf conductivity of AL-15 in the 300 MHz frequency range, an open circuit terminated one wavelength coaxial TEM resonator was fabricated (see Fig. 3). It comprises an OFHC copper cylindrical outer conductor (radius, r_o = 42.3 mm and 1.4 m long) and a centre conductor (radius, r_c = 12.6 mm and 1.0 m long) which is supported by two teflon discs. The test was performed by making measurements with an OFHC centre conductor and with a geometrically identical conductor made out of the test material. For this arrangement, the ratio of the conductivities as a function of the measured unloaded Q's (with the OFHC copper and with the sample centre conductors) is given by the following formula:

$$\frac{\sigma_{sample}}{\sigma_{OFHC}} = \left[\frac{Q_{OFHC}}{Q_{Sample}} \left(1 + \frac{r_c}{r_o}\right) - \frac{r_c}{r_o} \right]^{-2}$$

Measured Q's and calculated conductivities are given in Table 2.

TABLE 2

Measured Q and RF Conductivity at 290 MHz

Sample type	Measured Q	$\frac{Q_{OFHC}}{Q_{sample}}$	$\frac{\sigma_{sample}}{\sigma_{OFHC}}$
OFHC copper	5493±20	1.000	100%
AL-15	5322±20	1.032	92%
Al 6061-T6	4166±20	1.319	50%

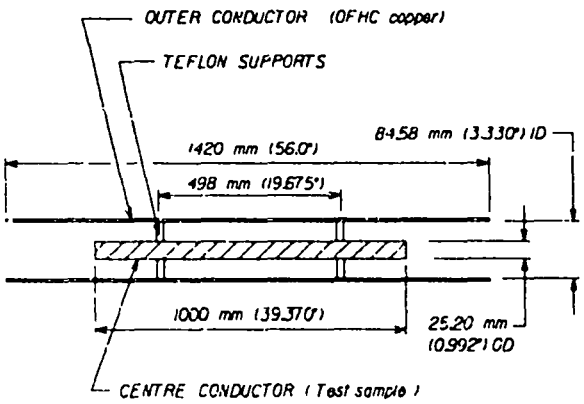

Fig. 3. Resonator structure for the Q measurements

Sparking Characteristics

To determine the rf sparking characteristics for this material would require a high-power resonant test structure. This would be as expensive to build as the new vanes, therefore this test will be part of the planned experimental program for the new vanes. However, DC sparking and conditioning characteristics are fairly easy to check and were carried out. These characteristics of AL-15 were compared with those of OFHC copper and aluminum. No significant differences were found. All could be conditioned to withstand 90 kV across a 6 mm gap and there was no sign of damage to the surfaces of the tested samples (cylindrical shape, diameter = 25.4 mm, corner radius = 3.2 mm, surface finish ≈ 0.0008 mm).

Discussion and Conclusions

The test results have confirmed that GlidCop AL-15 is a suitable high-strength copper to be used in the manufacturing of the new vanes. The use of this material will pioneer its application in the design and fabrication of accelerator components and will allow more flexibility in the RFQ experimental program.

Acknowledgments

The authors wish to thank G.E. McMichael for support and suggestions during the study and J.E. Anderchek, D.G. Hewitt, D.J. Disney, L.F. Birney, A.D. Davidson, G.W. Wood and R.A.Vokes for their help and assistance in preparing the samples and conducting the many tests.

References

1. G.E. McMichael, B.G. Chidley, R.M. Hutcheon and T. Tran-Ngoc, "RFQ1 Fabrication and Low Power RF Tuning", Proceedings of the 1987 IEEE Particle Accelerator Conference, IEEE Catalog No. 87CH2387-9, 3, 1857 (1987).

2. B.G. Chidley, G.E. McMichael, T. Tran-Ngoc and F.P. Adam, "New vanes for RFQ1", these proceedings.

3. OFHC Brand Copper News, Vol 5 No 1, June 1965, American Metal Climax Inc.

4. GlidCop Products Information Bulletin, SCM Metal Products Inc., 1988.

COMPONENTS FOR CW RFQ'S*

T. Tran-Ngoc, G.E. McMichael, G.M. Arbique and F.P. Adams
AECL Research, Chalk River Laboratories
Chalk River, Ontario, Canada, K0J 1J0

Abstract

Many components have been designed and tested in cw operation using the RFQ1 accelerator structure as a test bed. Improved VCR's (vane-coupling-rings) have been in service for over a year with no sign of deterioration. Dynamic tuners were developed and performed flawlessly at cw power levels approaching 8 W/cm^2. Recently, the design of the drive loop has been modified after some problems were encountered in operation. Calculation of the field enhancement at the end of the vane showed that the racetrack-shaped gasket, which makes the rf and vacuum joint between the tank and the vane, withstands a factor of 5 higher power density than expected.

Introduction

The RFQ1, a 75 mA cw proton accelerator, has been used as a test bed for developments aimed at building a firm technological base for the design of cw RFQ's. Components such as rf drive loops, slug tuners, vane-coupling-rings (VCR's), rf and vacuum joints have been designed, tested and improved.[1] The design features of these components, their recent performance in testing and operation, and design improvements, will be discussed in this paper.

RF Drive Loop

The drive loop, shown in Fig. 1, is mounted in one of the four centre ports of the RFQ. The inner and outer conductors of the drive loop are water cooled. The vacuum window is an air-cooled ceramic (99.9% alumina) cylinder. Mechanical clamps engage split rings seated in grooves near the ends of the ceramic cylinder to compress O-rings and make the vacuum seals. This type of removable joint permits easy disassembly of the loop for inspection or servicing.

The loop conductor is cooled by the main assembly cooling circuit. The loop body, sized to compensate for the open volume of the port, maintains the correct rf field balance and frequency for the tank.[2]

The original loop design operated without any major problems for about 2 years at cw power levels up to 175 kW. However, after a 2-month shutdown, attempts to recondition the RFQ were unsuccessful and excessive arcing was observed in the drive loop. Upon disassembly of the loop, the section of the ceramic cylinder facing the tapered portion of the inner conductor was found to be heavily coated with copper (about 0.03 mm thick) which had sputtered from the neighbouring copper surfaces on the inner and

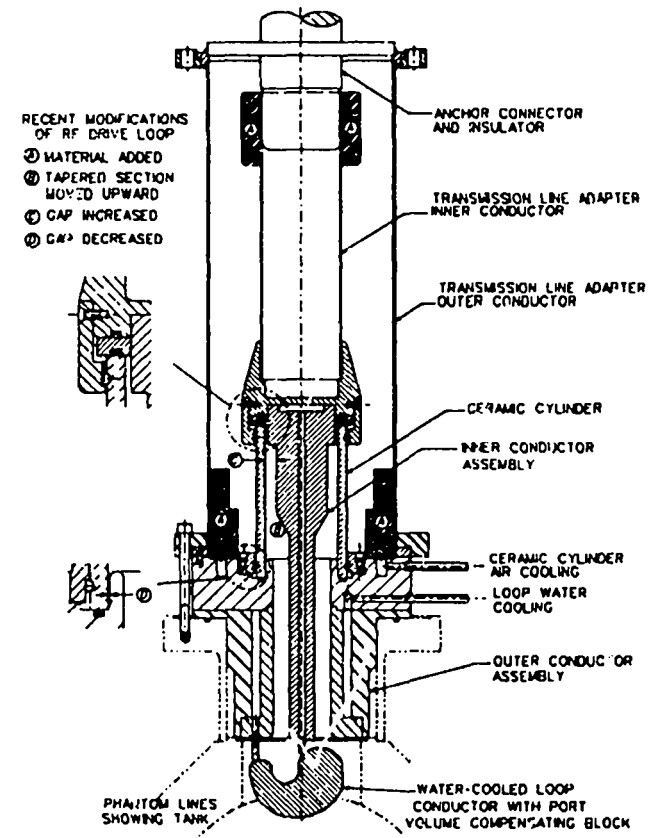

Fig. 1. RFQ1 drive loop

outer conductors. The loop was refurbished by grinding and cleaning the inside of the ceramic cylinder and smoothing the eroded copper surfaces.

When the loop was re-installed, only a few tens of watts could be delivered to the RFQ. Much higher power could be delivered without vacuum in the RFQ, indicating that multipactoring was the likely cause of the problem. The ceramic cylinder was coated with chromic-oxide to reduce secondary electron emission, but no improvement was observed. The ends of the RFQ were then opened for a thorough cleaning of the interior surfaces in the region of the end tuners and VCR's. It was then possible to break through the multipactoring levels, and a tank power of about 100 kW (80% of normal operating level) was reached before a large vacuum leak developed in the loop after more arcing. The ceramic had fractured, presumably due to thermal shock in the region where copper had again sputtered on the inner surface. The geometry of the loop conductors in this region was then modified in an attempt to decrease the field intensity. This changed the pattern of copper plating and erosion, but did not prevent the arcing or eventual destruction of the ceramic.

*This work was partially supported by Los Alamos National Laboratory under contract No. 9-X5D-7842D-1.

Most recently, the loop was modeled using the new code SEAFISH, a SUPERFISH-like code able to compute complex-valued travelling-wave rf field distributions and VSWR's.[3] The calculations showed an electric field concentration at the end of the ceramic cylinder where fracturing occurred (see Fig. 2a). They also indicated that the modifications highlighted in Fig. 1 would improve the design by: (i) giving a more uniform rf field distribution through the ceramic (see Fig. 2b), which would reduce the field stress by a factor of 2; (ii) improving the match of the loop (from a VSWR of 1.66 to 1.07) ; and (iii) eliminating standing waves between the ceramic and the loop termination. A loop with these modifications is presently being tested on RFQ1.

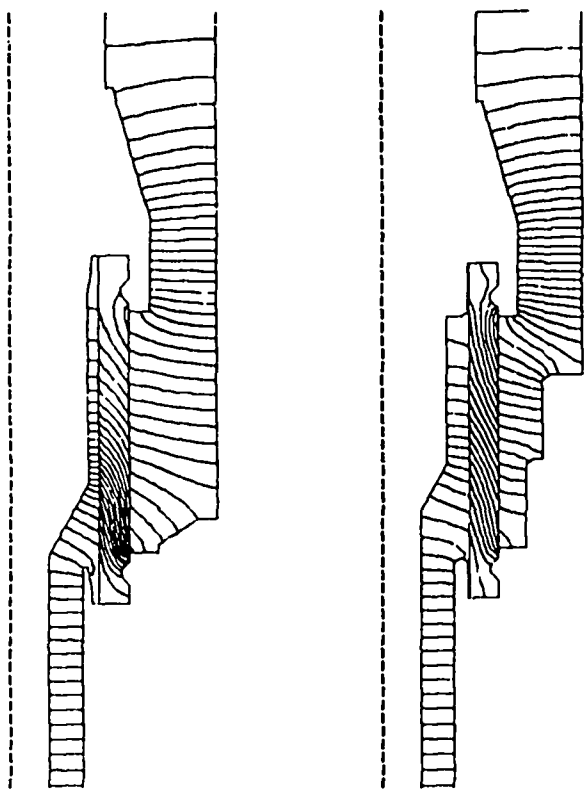

(a) (b)

Fig. 2. Rf field distribution in the gap between inner and outer conductors and through the wall of the ceramic window a) before modification b) after modification

Dynamic Tuners

One static plug-tuner is mounted in the RFQ1 centre-port directly opposite to the rf drive loop and 2 motor-driven plug-tuners (see Fig. 3) are installed in the adjacent ports. The tuning plunger diameter and the plunger-to-tank gap are 96.4 mm and 1.0 mm, respectively. The design mechanical stroke and speed of the dynamic tuners are ± 20 mm and 2.5 mm/s, respectively.

Figure "H" contact fingers are used at the plunger sliding joint. The fingers are cooled by direct conduction to the outer cylinder and plunger. Water channels in the outer cylinder and a coaxial flow

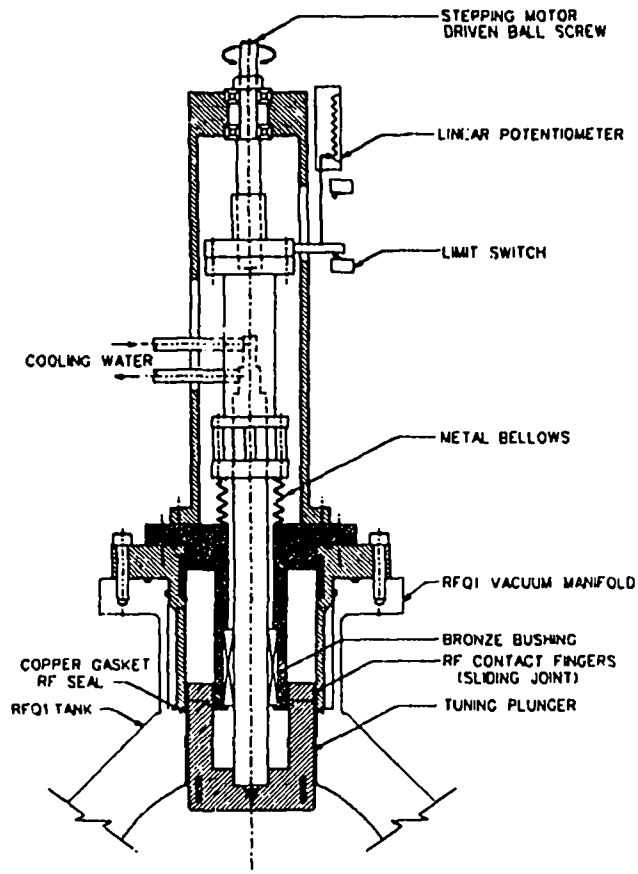

Fig. 3. RFQ1 dynamic tuner

circuit in the centre shaft of the tuner provide good cooling of all parts exposed to significant rf heating. A bronze bushing, located close to the front end of the tuner, keeps the various moving parts concentric and assures uniform compression of the sliding contact fingers. The surfaces that they contact are made of solid OFHC copper to provide good electrical conductivity. Stainless steel walls on the cavity behind the contacts attenuate any rf field that may leak past the joint. A metal bellows, remote from rf fields, forms the flexible vacuum barrier.

Positioning of the tuning plunger is by a ball nut and screw, directly driven by a stepping motor. A motion control indexer-module, a linear-potentiometer, limit-switches and a fail-safe brake are the critical components of the position control system.

During commissioning, insertions to 9.6 mm and retractions to 7.6 mm, from a position flush with the tank wall, were tested. Moved in tandem, the 2 tuners changed the tank frequency by 625 kHz. Moved in opposition (one inserted, the other retracted) a dipole field of up to 10% was introduced. The tuners performed flawlessly up to cw power levels approaching 8 W/cm^2 (1.6 Kilpatrick vane tip fields). The tuner moved smoothly under high power, with no indication of sparking. Visual inspection of disassembled components after the tests revealed no sign of damage.

VCR's

A pair of VCR's are used at each end of the RFQ1 vanes to suppress dipole components in the RFQ field.[1] These are made of 6.3 mm OFHC copper tubes, which are water cooled by bypassing the flow from cooling channels on the connected vanes. The water-to-vacuum joints are soft-soldered to allow easy removal, and we had problems with the solder melting during the first year of operation. Since then, the VCR design has been improved by: (i) increasing the joint diameter to decrease the current density; (ii) using a tin-silver solder (Mattisol-E) instead of the lower-temperature, 50/50 tin-lead solder; (iii) copper-plating the soldered joints (using a brush-plating technique) to lower surface resistance; and (iv) increasing the VCR to end-tuner-post gap to decrease the current due to the capacitance coupling. The improved VCR joints have been in service for over a year with no sign of deterioration.

RFQ1 "Racetrack" Seals

Racetrack-shaped gaskets, made from 1.5 mm thick OFHC copper, are compressed against sealing edges at the bottom of the vanes and on the tank, to make rf and vacuum joints.[4] They are cooled by conduction to cooling channels in the vanes, tank and clamps. Overheating of the gasket at the end of the vane is still a factor limiting the cw operating power on RFQ1. Recent MAFIA calculations have confirmed that overheating is due to field enhancement in the vane-end region, which was not accounted for in the original cooling design of the tank and vanes. The predicted power density at the bottom-end corner of the vane and on adjacent surfaces of the copper gasket is a factor of 5 higher than anticipated in the original design. The racetrack-shaped gaskets have thus proven they are able to withstand much higher temperatures and thermal gradients than expected.

Since replacement of the vane seals in early 1989, there has been only a minor vacuum leak at the high-energy end of one of the vanes. Torquing the three bolts nearest the end of the vane an additional 5% cured the leak and there have been no reoccurrences in the past year.

Discussion And Conclusions

RFQ1 has proven to be a valuable test bed for high-power cw RFQ components. Detailed designs for dynamic tuners, rf drive loops, VCR's and racetrack-shaped copper seals have been developed, tested and improved for cw operation up to 150 kW, 10% above design power. Although recent problems with the operation of the drive loop have interrupted operation of the facility, we are gaining a better understanding of this critical component and are establishing the utility of the SEAFISH code for rf component design and analysis.

Acknowledgments

Special acknowledgment to R.M. Hutcheon, J.C. Brown and J.Y. Sheikh for their support in rf design, to M.S. de Jong for his support in rf computer simulation, to E.C. Douglas for his assistance in mechanical design, to L.F. Birney, A.D. Davidson and B.H. Smith, who assembled, tested, and maintain the facility, and to the staff in the Accelerator Physics machine shop who built, repaired and modified the components.

References

1) G.E. McMichael, G.M. Arbique, J.C. Brown, B.G. Chidley, R.M. Hutcheon, M.S. de Jong and J.Y. Sheikh, "Exploring the Beam Parameter Space of a CW RFQ Proton Accelerator", Proc. 1989 IEEE Part. Acc. Conf., 2, 980, 1989.

2) B.G. Chidley, G.M. Arbique, R.M. Hutcheon, G.E. McMicheal and J.Y. Sheikh, "RF Tuning and Initial CW Operation of RFQ1", European Particle Accelerator Conference, Rome, Italy, June 1988.

3) M.S. de Jong, private communication.

4) G.E. McMichael, B.G. Chidley, R.M. Hutcheon and T. Tran-Ngoc, "RFQ1 Fabrication and Low Power RF Tuning", Proc. 1987 IEEE Part. Acc. Conf., 3, 1875 (1987).

MODELING OF THE END REGIONS OF RFQs USING THE 3-D SOS CODE

Ira S. Lehrman
Grumman Corporate Research Center
Princeton, NJ

Gary Warren
Mission Research Corporation
Newington, VA

Abstract

The end region of a RFQ accelerator is essentially a 3-D structure in which the ends of the vanes must be undercut to allow the electromagnetic fields to penetrate between quadrants. The dimensions of the undercuts critically affect the resonant frequency and field homogeneity in the RFQ. RFQ modeling results utilizing the 3-D SOS code are presented. Preliminary results using coarse grids have provided a rough estimate of the RFQ geometry. In the near future the dimensional resolution of the code will be significantly increased. It is expected that the final vane dimensions can be calculated precise enough that the number of machining iterations required to resonant an RFQ can be reduced.

1. Introduction

In this paper, we present modeling results utilizing the three-dimensional (3-D) SOS[1] code for the end region of an radio frequency quadrupole (RFQ) accelerator. This paper closely parallels the work of Browman *et al*[2] in which the MAFIA[3] code was used. The purpose of this work is to investigate the usefulness of the SOS code running on a mini-supercomputer for modeling of 3-D structures such as RFQs. The ultimate goal of this work is to reduce the number of machining iterations required to resonant an RFQ. The SOS code has been installed on the Grumman Stardent Titan computer. This is a relatively inexpensive (~$150K) UNIX computer with 3 CPUs, 96M of memory, and a vector processing unit. Grids on the order of 120^3 can be stored in memory. At present the largest simulations we have been successful with are 62 x 62 x 30. Though not limited by memory, enhancements are being made to the Eigenvalue solver in order to converge for finer and finer grids. In addition, upgrades to the computer's file system and CPUs are also planned.

The method for determining the dimensions of the end region of the RFQ is described in section 2. Section 3 presents modeling results to date. The conclusions of this work are given in section 4.

2. Method

The two-dimensional transverse dimensions of an RFQ are routinely determined utilizing the SUPERFISH[4] (SF) code. This code was used to design the 348 Mhz RFQ shown in Figure 1. A difficulty in modeling RFQs

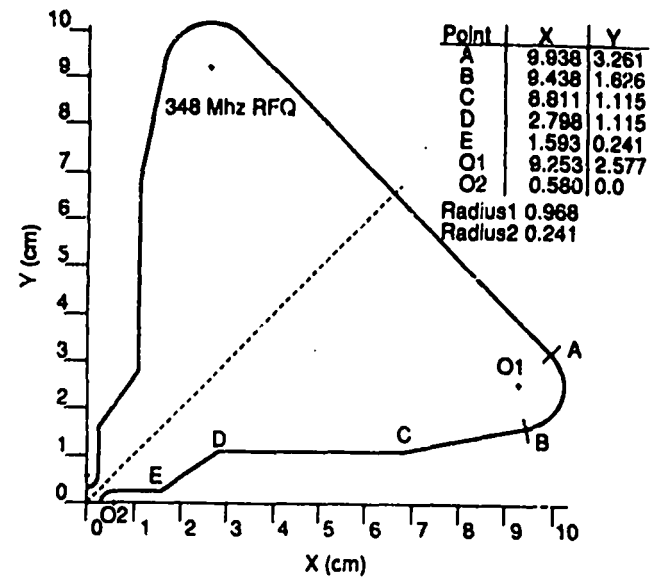

Figure 1. 348 Mhz RFQ as determined by SF.

is that the resonant frequency is critically determined by the capacitive coupling between vane tips, hence a disproportionate number of grid cells is allocated to this region. Computationally, this means that the largest frequency that the grid can support is often greater than 1000 times the resonant frequency. Hence high frequency contamination can cause the solution to converge slowly.

In order to reduce the number of iterations required for the code to converge, a preset field option has been added which allows an initial guess of the fields to be inputted. For the RFQ, the fields:

$$E_r(r,\theta) = 0 \qquad (1)$$

$$E_\theta(r,\theta) = (r + r_0)^{-1} \qquad (2)$$

have been used. r_0 is the vane tip radius. After the resonant frequency has been found, the fields are stored in a file. These files can be read in for successive runs in which slight variations in the geometry can be made.

Figure 2 shows a perspective view of the RFQ geometry. Only one quadrant of the RFQ need be modeled to determine the quadrupole modes. So called mirror boundary conditions are imposed on the transverse boundaries and the longitudinal boundary opposite the undercut region. These mirror boundary conditions ensure

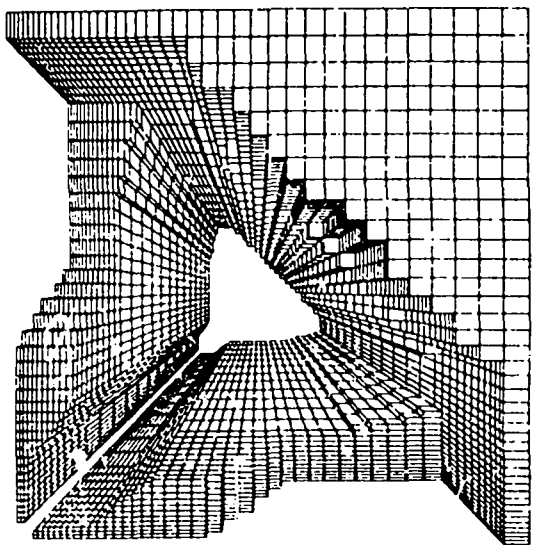

Figure 2. 3-D perspective of the SOS geometry

that the magnetic field is continuous across boundaries. If a metallic boundary was imposed on one of the transverse boundaries, the dipole modes of the RFQ could be found. At first only one cell is modeled in the longitudinal dimension and 40 x 40 in the transverse dimension. This allows the 2-D resonant frequency to be found. Since the spatial resolution of the 3-D simulations is not as fine as in SF simulations, the resonant frequency will differ. If desired, the vane tips could be moved in order to achieve a resonant frequency closest to 348 Mhz. The SOS code is then run for the full 3-D geometry (40 x 40 x 24). A longitudinal length of 30 cm was chosen. This distance must be long enough that it does not affect the resonant frequency. By contrast, the engineering test (cold) model of this RFQ was 4 m in actual length.

3. Results

The resonant frequency vs. undercut depth is plotted in Figure 3. In these simulations the locations of the start and end of the diagonal cut where keep constant. The depth of the undercut predicted by SOS is 3.3 cm (± 0.3 cm due to the spatial resolution). This is very close to the experimentally determined depth of 3.2 cm. Machining of the undercuts required 4 iterations, each of which consisted of disassembling the RFQ, machining, reassembling, and performing bead-pull measurements. In the future it is expected that the dimensional resolution of the code can be increased to predict the final dimension within ± 0.1 cm. This could possibly reduce the number of machining iterations.

The electric and magnetic fields in the undercut regions are shown in Figures 4 and 5. As expected the electric field is concentrated in the vane tip region and everywhere normal to the vanes. Magnetic field coupling between adjacent quadrants is clearly shown in Fig. 5. In

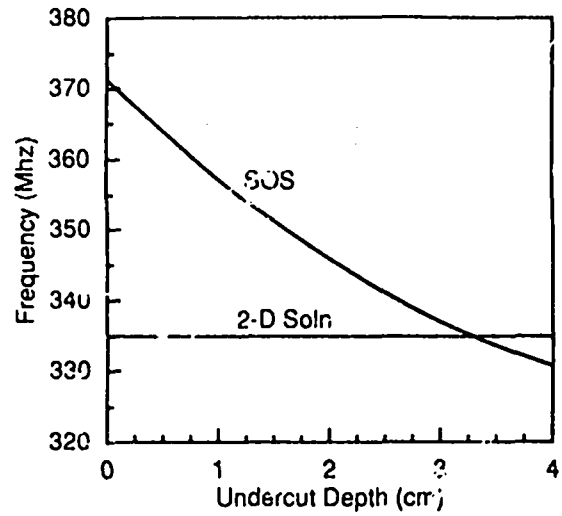

Figure 3. Frequency vs. undercut depth (30cm axial length)

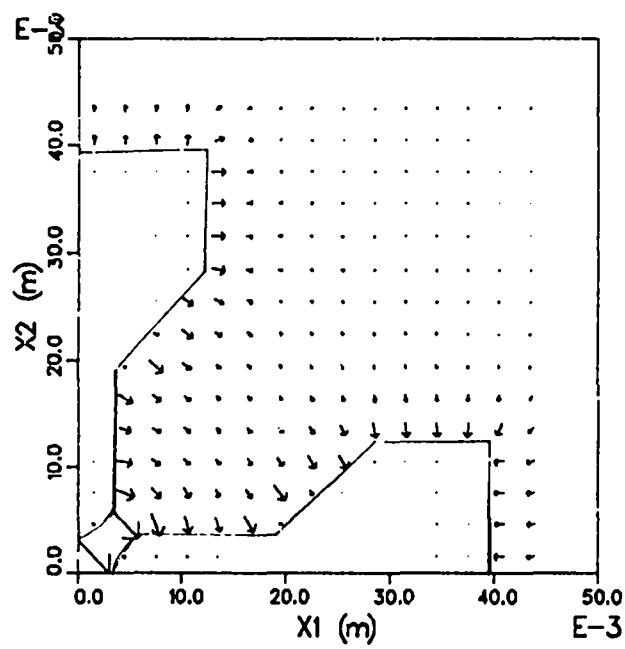

Figure 4. Electric field in the undercut region at an axial location of 2 cm.

order to determine the expected power dissipation on the vanes, the magnetic field tangential to the vane surface was determined. From the magnetic field, the power loss was calculated according to:

$$P(w/cm^2) = \frac{B^2}{\mu_0^2 \delta \sigma} \qquad (3)$$

where δ is the skin depth and σ is the conductivity. Figure 6 shows the power loss on the surface of the vane. The

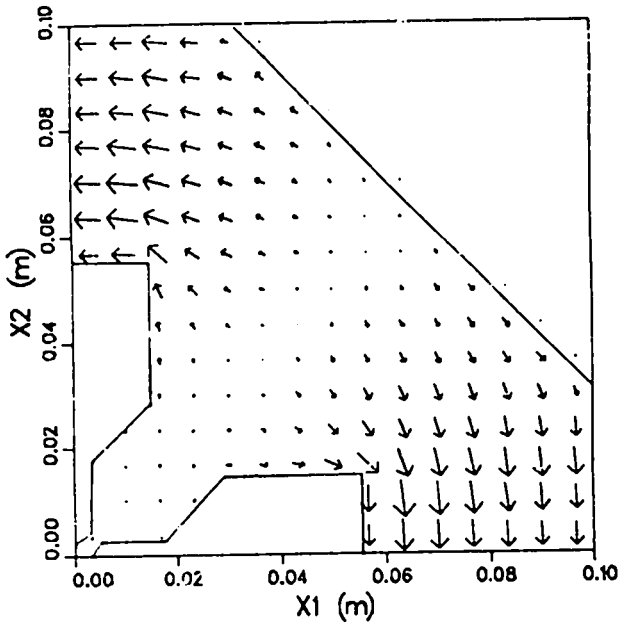

Figure 5. Magnetic field in the undercut region at an axial location of 2 cm.

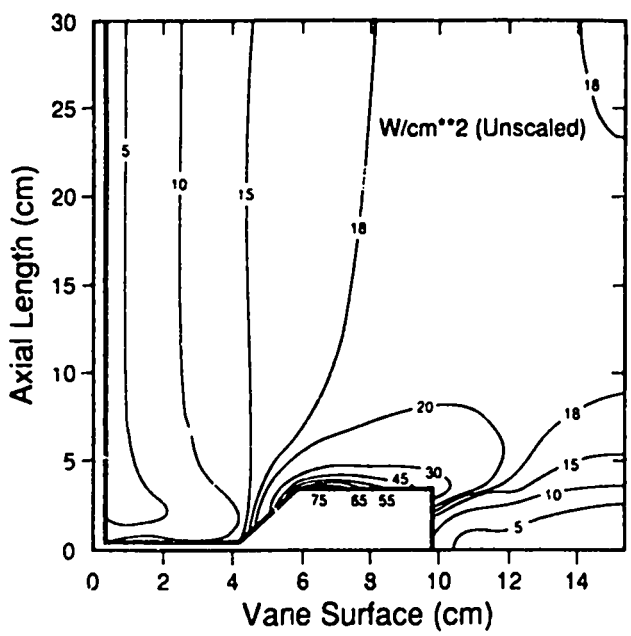

Figure 6. Power loss along the surface of the vane

ordinate is not the transverse dimension, but the arc length is moving along the vane surface to the middle of the back wall. Figure 7 shows the power loss on the end of the vane. The location of the start and end of the vane undercut is indicated. Notice that in both Figs. 7 and 8 the maximum power loss occurs in the back corner of the vane. To compare these results with the 2-D SF simulations, Fig. 8 shows the expected power loss at an axial length of 30 cm (3-D) compared to the expected power loss from SF. Notice the agreement is quite good.

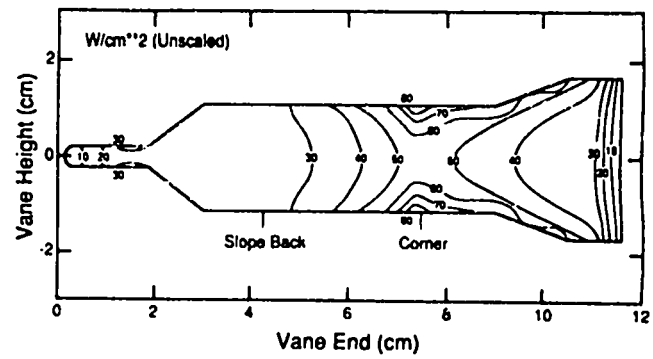

Figure 7. Power loss along the end of the vane

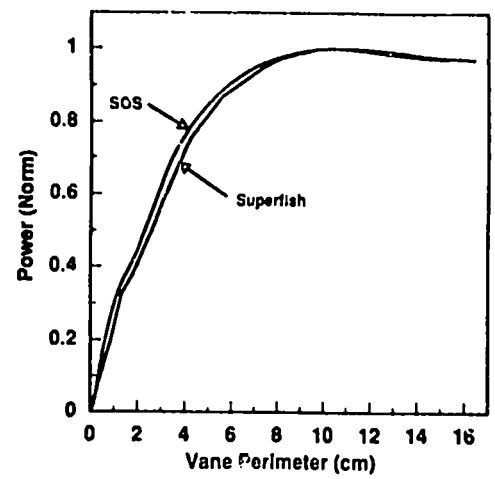

Figure 8. Comparison of the SOS and SF predicted power loss

4. Conclusions

The modeling results presented in this paper suggest that in the future the 3-D SOS code could determine the final dimensions of an RFQ precise enough that the number of machining iterations could be reduced. The 3-D modeling identifies region of high power loss. The power loss in the corner region is about 4 times larger than the peak power loss in the 2-D case, suggesting the need for 3-D modeling. Parametric studies could then be preformed in order to determine optimal geometries.

References

[1]G. Warren, *IEEE Trans. Elec. Dev.* 35 (1988) 2027.

[2]M. J. Browman, G. Spalek, T. C. Barts, "Studying the End Regions of RFQs Using the MAFIA Codes," 1988 Linear Accelerator Conference, Williamsburg, VA.

[3]R. Klatt, F. Krawczyk, W. R. Novender, et al "MAFIA - A Three-Dimensional Electromagnetic CAD System for Magnets, RF Structures, and Transient Wakefield Calculations," 1986 Linear Accelerator Conference, Stanford, CA

[4]K. Halbach, R. F. Holsinger, *Particle Accelerators* 7 (1976) 213.

RF PARAMETERS AND SCALING RELATIONS FOR FOUR CHAMBER RFQ CAVITIES.

V.V.Paramonov,

Institute for Nuclear Research of the AS of the USSR,
60-th October,Anniversary Prospect, 7a,117312,Moscow

ABSTRACT

The comparison (in 2D approximation, without taking into account end plates) of RF parameters for four chamber RFQ cavities, differing in chamber shape, is done. Using lumped parameters expressions for RF characteristics estimations are given. It is shown that per unit length capacity between electrodes depends only on the shape of the electrode and don't depend on dimension. Dependence of cavity characteristics from working frequency is considered.

INTRODUCTION

RFQ [1] cavities becomes now the necessary part of modern linear ion accelerators. Features of the structure for particle beams are now well known. There are several methods to form quadruple field distribution. Four chamber H-cavity is widely used. Differing in design, four chamber cavities have some general properties. In this paper attempt to analyze this properties is done.

DEFINITIONS OF VALUES

Numerical calculation of the RFQ cavity properties with end plates and electrode modulation in account is essentially 3D problem. But main RF characteristics of the regular part of the cavity can be estimated with using usual 2D codes, SUPERFISH [2] or MULTIMODE [3]. For consideration, let's define main parameters. Taking into account 2D approximation, we shall use all quantities divided on length of the cavity:

a) RF power dissipation

$$P_s=\frac{R_s}{2}\int_{\Gamma} H_z^2\, d\Gamma, \qquad (1)$$

b) stored energy

$$W_0=\frac{\mu_0}{2}\int_{S} H_z^2\, dS, \qquad (2)$$

c) capacity of the electrodes

$$C=\frac{2\,W_0}{U^2}, \qquad (3)$$

d) shunt resistance (for transversal focusing field)

$$R_t=\frac{U^2}{2\,P_s}, \qquad (4)$$

Voltage between electrodes and quality factor don't depend on the length

$$U_0=\omega\,\mu_0\int_{S} H_z\, dS, \qquad (5)$$

$$Q=\frac{\omega\,W_0}{P_s}, \qquad (6)$$

Here R_s is surface resistance, Γ,S are boundary and square of the chamber. To avoid misunderstanding, we shall use all quantities, mentioned above, for one chamber, so integration in (1),(2),(5) is inside one chamber. For the whole cavity, taking into account identity of all chambers, we easy find

$$P_s^{\Sigma}=4\,P_s,\ W_0^{\Sigma}=4\,W_0,\ U^{\Sigma}=U,\ C^{\Sigma}=4\,C,$$
$$R_t^{\Sigma}=R_t/4,\ Q^{\Sigma}=Q$$

All quantities, mentioned above, can be calculated during numerical simulation. But H-cavity may be considered as a device with lumped parameters. Plots of lines H_z=const on fig.1 for different shapes of chambers are shown. In 2D approximation lines H_z=const coincides with lines of the electric field. Number of lines at each plot equals 9 and H_z between lines changes at 0.1 H_{zmax}. One can see that without dependence on chamber shape electric field is concentrated in the small space between electrodes and in main part of the chamber magnetic field is approximately uniform. It allows successfully use definitions of the electrode capacitance and the chamber inductance.

DEPENDENCE OF THE CAVITY CHARACTERISTICS FROM DIMENSIONS

RF power needed to have the voltage given is defined by shunt resistance. At the same time ratio R_t/Q is defined by electrodes capacitance:

$$R_{t/Q}=\frac{U^2}{2\omega\,W_0}=\frac{1}{\omega\,C} \qquad (7)$$

Next statement is valid: for electrodes without modulation per unit length capacitance between electrodes depends only on shape and placement of electrodes and don't depend on dimensions. Suppose we have several infinitely long parallel conductors which are arbitrary placed in XY plane. To find

capacitance between i-th and j-th conductor we keep i-th conductor with potential Uo and calculate charge induced at j-th one. This conductor configuration generates distribution $U_1(x,y)$ of the potential in XY plane. Capacitance per unit length is:

$$\frac{dC}{dl} = \frac{\int \sigma \, d\Gamma}{U_0} = \frac{\int (E_n \, n) d\Gamma}{U_0} = -\frac{\int \mathrm{grad}(\, U_1(x,y)) \, d\Gamma}{U_0} \qquad (8)$$

where Uo - voltage between conductors, σ - surface charge density, E_n - electric field at the surface of the conductor. Let's change cross dimensions in ν times without changing in potentials at the conductors. If so, distribution $U_2=U_1(x/\nu, y/\nu)$ also will be the solution of the Laplas problem and dC in (8) will be the same, because changing in $d\Gamma$ will be compensated by inverse changing in grad(U_2). This property is a straight consequence of the longitudinal homogeneity of the problem. For electrodes with simple shape of the cross-section analytical relation for capacitance may be found. In this paper numerical method by using (3), which seems more flexible, was applied. For proposed in Ref. [4] electrodes with half- circular cross-section and radius of circular be equal to radius of the aperture capacitance is C = (31.3 ± 0.5) pf/m. Comparison of electrodes with different shape one can find, for example, in Ref. [5]. To have working frequency with capacitance C given it is needed to adjust inductance $\mathcal{L}$. In assumption that Hz is uniform in main part of the chamber estimation for inductance:

$$\mathcal{L} = \mu_0 \, S \qquad (9)$$

and next relations are valid:

$$U=\mu_0 \, \omega \, H_{zmax} S, \quad I=H_{zmax}, \quad P_s = \frac{R_s \, H^2_{zmax} \, L}{2},$$

$$I= U \, C \, \omega, \qquad (10)$$

where L is the length of the chamber perimeter, I is equivalent current. Taking into account these relations, we can find estimations for Q and R_t:

$$Q = \frac{1}{R_s} \sqrt{\frac{\mu}{C}} \frac{\sqrt{S}}{L} \qquad (11)$$

$$R_t = \frac{1}{R_s} \frac{\mu_0 \, S}{C \, L}$$

In formulas (11) there is geometrical formfactor - $\sqrt{S}/L$ - ratio of chamber square to chamber perimeter. For reasonable shapes of the chambers, which are shown in fig. 1 , this formfactor changes slightly and has maximum value $\sqrt{S}/L$ =0.28 for circular. It explains more high value of Q for variant, shown in fig. 1 . In table 1 calculated by MULTIMODE code values Q fnd R_t for chambers, shown in fig.1, are given. The results presented confirm the conclusion that there are no large increase in quality factor with optimization of the chamber shape. It is difficult to say, that any reasonable shape has large features in their radiotechnical characteristics and technological aspects come at first position. Results, which are presented in table 1, confirm relation (7): for the electrode shape given R_t is directly proportional to Q.

RFQ cavity must provide quadruple focusing and RF power needed to adjust gradient G of the focusing field is

$$P_s = \frac{G^2}{8} \frac{a^4}{R_t} \qquad (12)$$

Usually RFQ cavity operates with maximum possible electric field E_s at the surface of the electrodes. RF power needed is

$$P_s = \frac{E_s^2 \, a^2}{8 \, \alpha^2 R_t}, \qquad (13)$$

$$\alpha = \frac{2 \, E_s}{G \, a} = \frac{a \, E_s}{U}, \qquad (14)$$

where a is aperture radius, α - ratio of maximum electric field to middle one in the aperture. For electrodes proposed in Ref. [5] α =1.4. Relations (12),(13) are usual for systems with quadruple field distribution. Results of this chapter shows, that to decrease RF power needed it is necessary to take minimal possible aperture and electrodes with small value of the capacitance. Large improvement in R with chamber shape optimization seems not be possible.

WORKING PARAMETERS VS FREQUENCY

To estimate RF parameters of the cavity at frequency, if the same parameters are known at frequency for similar cavity, it is helpful to know there dependence vs frequency.

From relations (6) - (8) we find:

$$Q = f^{-1/2}, \quad R_t = f^{-3/2}. \qquad (15)$$

Such unusual dependence of R_t vs f is consequence of definition (4). To find maximum electric field avaluable at a given frequency one usually use Kilpatric relation. If so, for RF power in (13) we have dependence:

$$P_s = a^2 \, f^{5/2} \qquad (16)$$

Taking into account that length of the chamber perimeter decreases as f^{-1}, we see that heat loading per unit square of the camber surface. rises as $f^{7/2}$. With increasing of working frequency RFQ cavity cooling becomes severe problem.

Table 1 Calculated values of Q, R_t and frequency shifts caused by boundary displacement at 1 mm inside cavity. Working frequency is 198.2 MHz.

N	Q	R_t,kOm	df1	df2	df3	df4	df5	R, H cm
1	12300	315	-37.0	-4.7	-1.0	2.9	3.3	19.3
2	13270	340	-37.0	-4.7	-1.0	2.1	3.0	16.1
3	13500	346	-37.0	-4.7	-1.0	2.0	2.9	17.6
4	13800	354	-36.5	-4.6	-0.97	2.3	2.4	16.05
5	13830	355	-37.0	-4.6	-1.0	1.5	3.3	14.05
6	15200	390	-35.7	-4.5	-1.0	2.1	3.9	7.12

SENSITIVITY OF THE WORKING FREQUENCY TO SMALL DEVIATIONS IN CHAMBER DIMENSIONS

For usual cavity dimensionles coefficient

$$D_i = \frac{df}{dx_i}\frac{x_i}{f} \qquad (17)$$

where x_i - i - th dimension of the cavity , which depend only on cavity shape and don't depend on frequency, describes sensitivity of the working frequency to small deviation's in dimensions. Peculiarity of H- cavity is that, such description isn't valid for region near axis. Small deviations in electrode dimensions destroy geometrical similarity and capacitance becomes depending on dimensions. So, for dimension of the electrodes Di is inverse proportional to absolute values of dimensions. In table 1 frequency changes (in MHz) caused by displacement of boundary parts inside the cavity at 1 mm are given. Working frequency is 198.2 MHz radius of the aperture is equal to 6.536 mm. The parts of boundary are labeled at fig. 1c. Variants in the table 1 are in accordance with shown in fig. 1.

CONCLUSION

Some properties of the four chamber cavities, which are radiotechnical realization of the RFQ structure, are considered. It is shown that per unit length capacity between electrodes depends only on the shape of the electrode and don't depend on dimension. Some expressions for RF characteristics estimations are given. The author wish to thank I.V. Gonin for help in preparation of this work and L.V. Kravchuk for helpful discussion.

REFERENCES

1. I.M.Kapchinsky, V.A.Teplyakov. The linear accelerator with spatially uniform strong focusing. Preprint ITEP, N 673, Moscow, 1969, (in Russian)

2. K. Halbach, R.F. Holsinger, SUPERFISH- a computer program for evaluation of RF cavities with cylindrical symmetry, Particle Accelerators, v. 7, p. 213, 1976

3. A.I.Fedoseev et al., MULTIMODE- a powerfull code for frequency spectrum computation of electromagnetic fields in axially symmetric cavities and longitudinally homogeneous waveguides of arbitrary shape. Nuclear Instruments and Methods, v.227, n. 3, p. 411, 1984

4. M.L.Gusev, E.N.Daniltsev, I.M.Kapchinsky et al. Investigation of the four chamber H cavity. Preprint ITEP 49, Moscow, 1980, (in Russian).

5. S.E.Bragin et al. Investigation of the electrodes shape in the RFQ structure. Pros. of the 9-th Allunion meeting of particle accelerators, Dubna, v.1, p. 152, 1985,(in Russian).

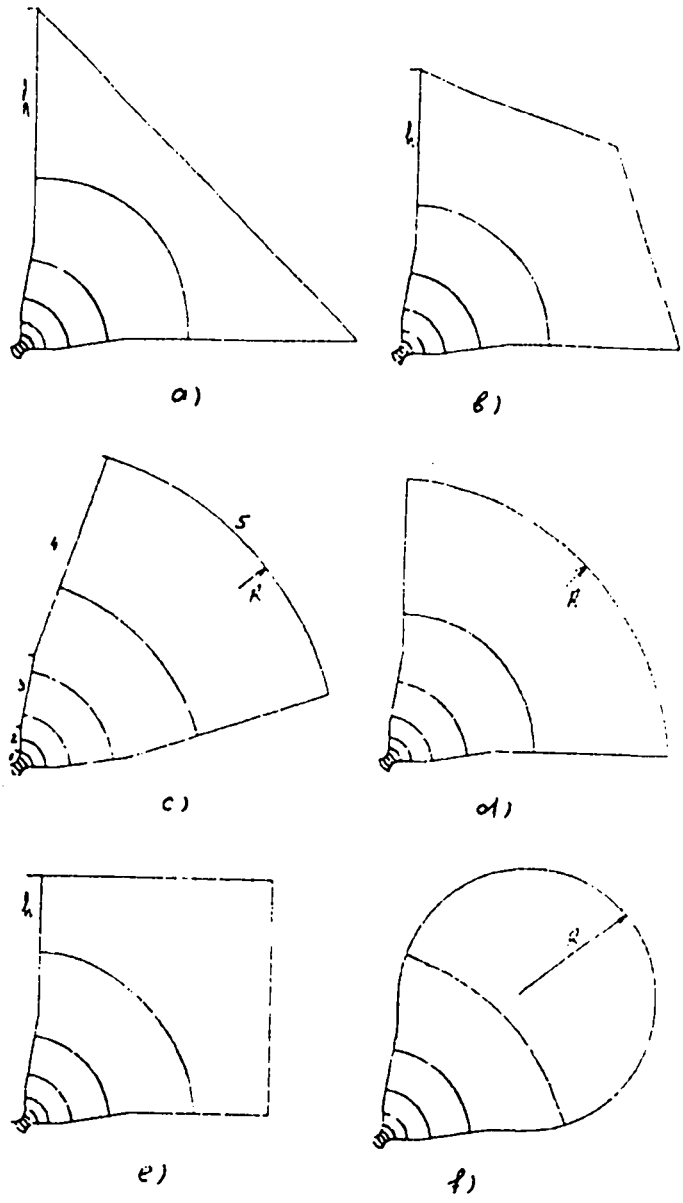

Fig. 1. Electric field distribution for different shapes of chamber.

THE π-MODE STABILIZING LOOP FOR FOUR-VANE TYPE RFQs

A. Ueno, T. Kato and Y. Yamazaki
National Laboratory for High Energy Physics
1-1 Oho, Tsukuba-shi, Ibaraki-ken, 305, Japan

Abstract

The tuning of four-vane type radio-frequency quadrupole (RFQ) linacs is difficult, mainly because dipole modes whose resonant frequencies are close to that of the accelerating mode easily mix with the accelerating mode. In order to avoid dipole mode mixing, several pairs of the vane coupling rings (VCRs), which provide periodic electrical connections between diametrically opposite vanes, have been mainly used so far. However, the VCR is difficult to fabricate and is less reliable under high-duty operation. Thus, a new field-stabilization concept has been proposed, and is referred to as a π-mode stabilizing loop (PISL). The concept is based on mode stabilization by magnetic coupling between two neighboring quadrant cavities with closed loop couplers. The results of recent calculations using the MAFIA code package with an increased number of meshes are presented.

Introduction

In a four-vane type RFQ cavity, the lowest mode is a dipole mode (TE110-mode), the magnetic field pattern of which is schematically shown in Fig. 1b) or 1c). Its resonant frequency is slightly lower than the accelerating mode of the lowest-order quadrupole mode (TE210-mode), the magnetic field pattern of which is schematically shown in Fig. 1a). An RFQ, being long compared with its rf wavelength, has many other higher-order dipole modes (TE11n-mode), the resonant frequencies of which are higher or lower than that of the accelerating mode, or sometimes close to that of the accelerating mode.[1] The dipole mode with a resonant frequency closer to that of the accelerating mode is more easily mixed with the accelerating mode by a small amount of perturbation. Since the dipole mode gives rise to beam bending, the mixing of the dipole mode reduces the acceptance of an RFQ. Also, the mixing of the other modes to the accelerating mode is a cause of accelerating field nonuniformity.

In order to increase the frequency of the lowest-order dipole mode higher than the accelerating mode, several pairs of vane coupling rings (VCRs),[2] which provide periodic electrical connections between diametrically opposite vanes, have been used in most of the successfully operating four-vane type RFQs. Although an RFQ with several pairs of VCRs is stable against the mixing of dipole modes, it is difficult to fabricate. A VCR with a complicated shape must be machined in a narrow region inside of the cavity. In particular, the cooling of the VCR and the electrical contact between the VCR and the vanes (important for the high duty operation) are very difficult.

Thus, a new field-stabilization concept has been proposed, that is based on mode stabilization by magnetic coupling between two neighboring quadrant cavities with closed loop couplers. This concept is referred to as a PISL (p-mode stabilizing loop),[3] since the quadrupole mode is considered to be a π-mode azimuthally and the PISL is effective not only for the four-vane type RFQ cavity, but also for a π-mode cavity. In ref. 3 the PISL is compared with the VCR; it is shown that the VCR can be regarded as one version of the PISL.

In this paper, the results of recent calculations are presented concerning the PISL using the MAFIA code package[4,5] with an increased number of meshes. These calculations were carried out in order to [illegible] the HPI with the PISLs for the Japanese Hadron Project (JHP).[6] A practical installation method of the PISL is also described.

Principle and Installation Method of the PISL

The principle of the PISL is detailed in ref. 3. It is briefly described by using one type of the possible PISL arrangements shown in Fig. 2, which will be used for the RFQ of the JHP. It can be seen that two closed loops made of a conductor are formed by adding two bars to a conventional four-vane type RFQ cavity. Each bar is connected to the walls of two neighboring quadrant cavities through a clearance hole bored in the vane. These loops are referred to as PISLs. The area surrounded by the PISL is shown by the hatched region in Fig.2. It is noted that the cavity wall was used as a part of the PISL.

In order to understand the principle of the PISL, it is important to note that the total magnetic flux normal to the surface surrounded by a conductive closed loop will be zero, since the tangential electric field vanishes at the surface of the conductor, as does the integral of the electric field along the closed loop. Then, the magnetic flux shown in Fig. 1a) or 1c) can enter inside of the PISLs, while the flux of Fig. 1b) cannot. Therefore, the PISLs have little effect on the field pattern and, thus, on the resonant frequency for the modes shown in Figs. 1a) and 1c). On the other hand, the magnetic flux shown in Fig. 1b) will make a detour around the loop, increasing the resonant frequency. In this way the PISL pushes up the resonant frequency of one of the dipole modes. It is noted that the hatched area is proportional to the coupling strength as the lowest-order approximation. Since the PISLs shown in Fig. 2 have little effect on the other dipole mode shown in Fig. 1c), the other pair of PISLs must be installed to remaining two vanes for suppressing this dipole mode.

A practical way to install and cool the PISLs is schematically shown in Fig. 3. The PISLs can be fabricated from outside of the cavity by inserting bars after assembling the entire four-vane cavity. It is thus expected that the fabrication of the PISL will be much easier than that of the VCR. The PISLs can be cooled by the water conducted through the pipe used as the bar. Then, the connection point of the water path can be chosen at the outside of the cavity and independently with the rf contact point. Therefore, high reliability for electrical and thermal contacts is expected.

Results of MAFIA Calculations

In order to save CPU time, a small number of meshes ($N_x \times N_y \times N_z = 20 \times 20 \times 49$) were used in calculations of ref. 3, where the shape of the cavity was rather different from the actual state. Thus, after increasing the number of meshes ($N_x \times N_y \times N_z = 34 \times 34 \times 71$) we carried out a MAFIA analysis on a realistic cavity, which has almost the same shape as the RFQ for the JHP.

At first, the resonant frequencies of the lowest-order quadrupole and dipole modes (TE210- and TE110-modes) were calculated for an ideally symmetric four-vane type RFQ cavity with infinite length. Because of its symmetry, only one-quarter of the structure was necessary for the calculation, as shown in a three-dimensional computer plot of Fig. 4. This structure, whose length L_z is 17 cm, is referred to as STD (standard). For the TE210-mode the boundary condition is given by perpendicular magnetic fields to the boundary surfaces of x=0, y=0, z=0, and $z=L_z$, while for the TE110-mode the magnetic fields perpendicular to the boundary surfaces of y=0, z=0, and $z=L_z$ and parallel to x=0.

The effects of the PISL were studied with the struc-

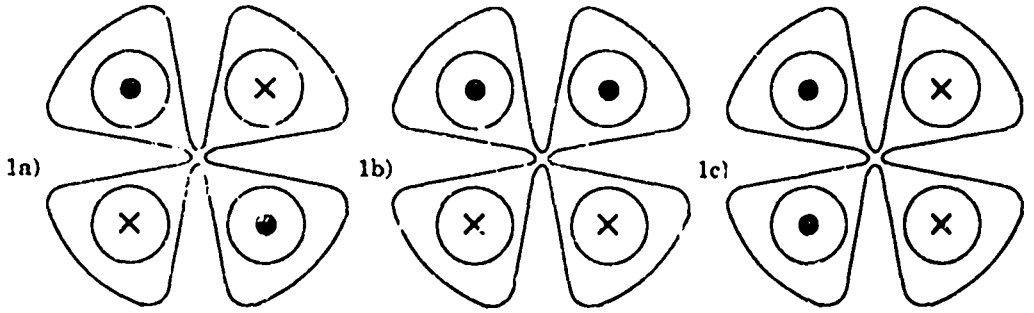

Fig. 1. Magnetic field patterns of the quadrupole mode (a) and the two degenerated dipole modes (b,c).

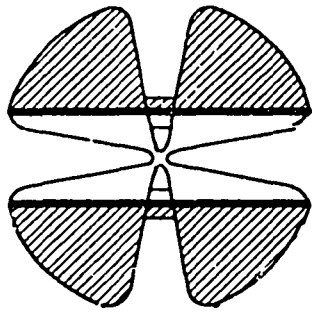

Fig. 2. Arrangement of PISL.

ture shown in Fig. 5. This structure is the same as the structure shown in Fig. 4, except for the bars, which are parts of the PISLs shown in Fig. 2c), and clearance holes through which the bars pass from one quadrant cavity to the neighboring quadrant cavity. The cross sections of the bar and the clearance hole are circles with radii of 2.5 and 7.5 mm, respectively. These values and the position of the PISL were chosen in order to satisfy such technical requirements as the cooling path and rigidity. This structure is referred to as a PISL-JHP. The obtained magnetic field patterns of the lowest-order quadrupole and dipole modes are shown in Figs. 6 and 7, respectively. The magnetic flux of the dipole mode can not enter inside of one of the PISL (see Fig. 7a)), as described above.

The results of the calculations are summarized in Table I. In order to study the accuracy of the calculations with the MAFIA we also listed the results of the two-dimensional precise calculations ($N_x \times N_y = 150 \times 150$) with SUPERFISH,[7] designated by STD-SF. The symbols of f_Q and Q_Q are the resonant frequency and Q-value of the lowest-order quadrupole mode, respectively; f_D and Q_D are those of the lowest-order dipole mode, and $\Delta f_{QD} = f_D - f_Q$.

It is noted that the dipole mode has a lower frequency than that of the quadrupole mode in the ideally symmetric four-vane type RFQ cavities (STD-SF and STD). Although the resonant frequencies, f_Q and f_D, of the STD are about 3 MHz lower than those of STD-SF respectively, the frequency difference, Δf_{QD}, of the STD is in good agreement with that of the STD-SF. Therefore, it is expected that the relative values, such as the frequency differences, are fairly reliable in calculations with the MAFIA.

In contrast to the ideally symmetric four-vane type RFQ cavity, the lowest dipole mode of PISL-JHP has about a 35 MHz higher resonant frequency than does the lowest quadrupole mode, indicating that the tuning of the four-vane type RFQ becomes easier with the PISLs. In designing an RFQ cavity with PISLs, it should be noted that the PISLs lower the Q-value by about 5 % and the resonant frequency by about 4 %, respectively.

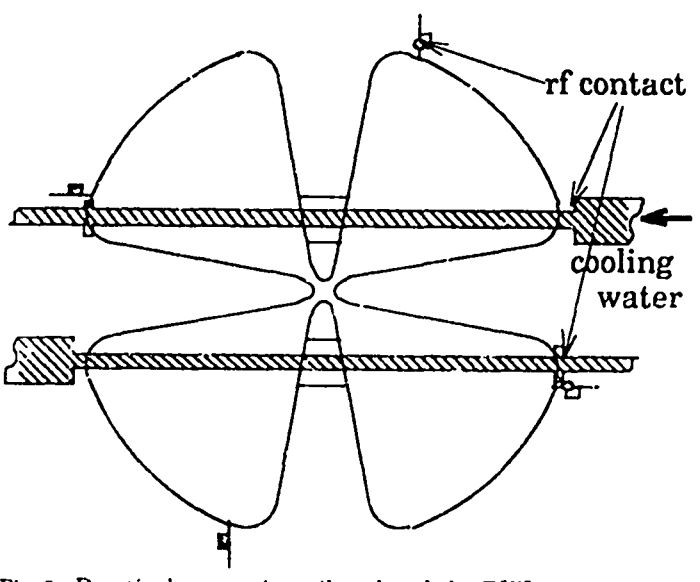

Fig. 3. Practical way to install and cool the PISLs.

Conclusion

A practical way to install and cool the PISL, which satisfies such technical requirements as the cooling path and the rigidity, are presented. The MAFIA analysis on this arrangement shows promising results: the lowest dipole mode has about a 35 MHz higher resonant frequency than does the accelerating mode, and the decrease of the Q-value caused by the PISLs is less than 5 %.

The next step of the study of the PISL is to test the performance of the PISL empirically by installing the PISLs in the cold model of the RFQ cavity for the JHP. If the results are promising, the PISLs will be installed in the RFQ linac for the JHP.

References

1. A. Ueno et al., "RF Field Measurement of an RFQ Cold Model Cavity for the JHP", this conference.
2. H. R. Schneider and H. Lancaster, IEEE Trans. Nucl. Sci., NS-30, No.4, 3007 (1983).
3. A. Ueno and Y. Yamazaki, to be published in Nucl. Inst. and Meth. A.
4. T. Weiland, Part. Accel. 17, 227 (1985).
5. R. Klatt et al., 1986 Linear Accelerator Conf. Proc., Stanford Linear Accelerator Center report SLAC-303, 276 (1986).
6. Y. Yamazaki, "Development of a High-intensity Proton Linac for the JHP", this conference.
7. K. Halbach et al., Part. Accel. 7, 213 (1976).

TABLE I
Summary of the calculations.

Structure Name	f_Q (MHz)	Q_Q	f_D (MHz)	Q_D	Δf_{QD} (MHz)
STD-SF	432.244	10014	418.810	9836	-13.434
STD	429.410	9707	416.156	9532	-13.254
PISL-JHP	412.698	9227	447.778	7243	35.080

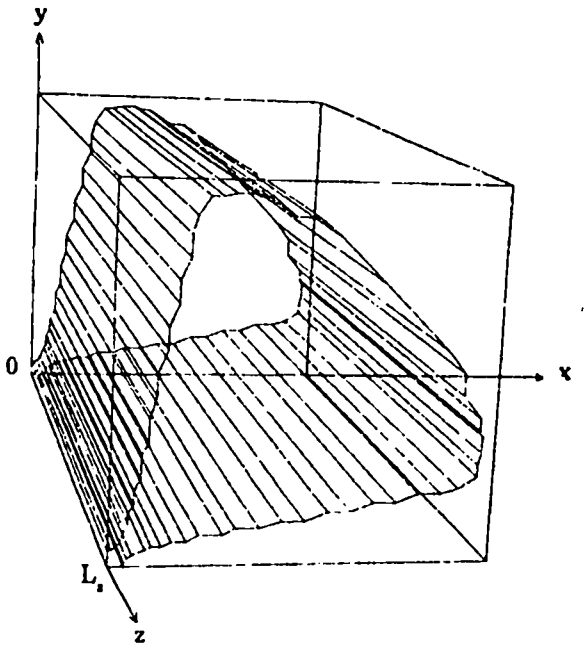

Fig. 4. Three-dimensional computer plot of the STD structure.

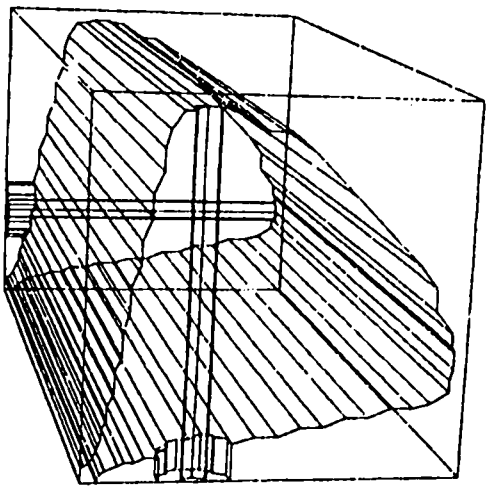

Fig. 5. Three-dimensional computer plot of the PISL-JHP structure.

6a)

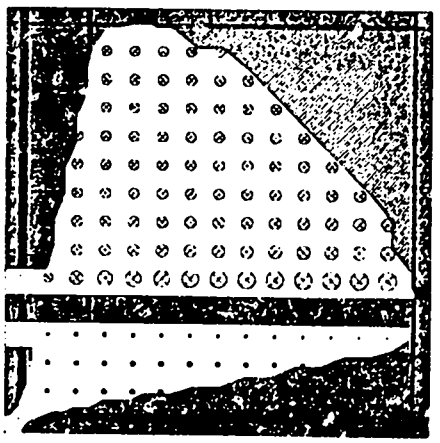

6b)

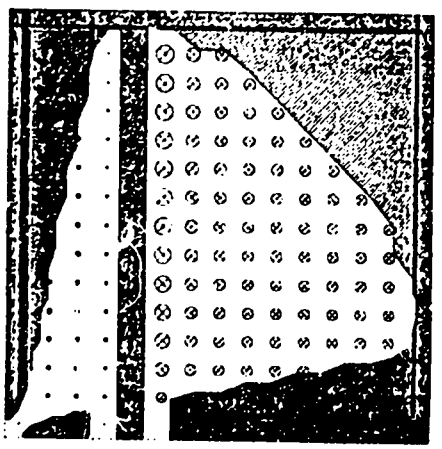

Fig. 6. PISL-JHP's magnetic field patterns of the lowest-order quadrupole mode on the surfaces of z=0 (a) and z=L_z (b).

7a)

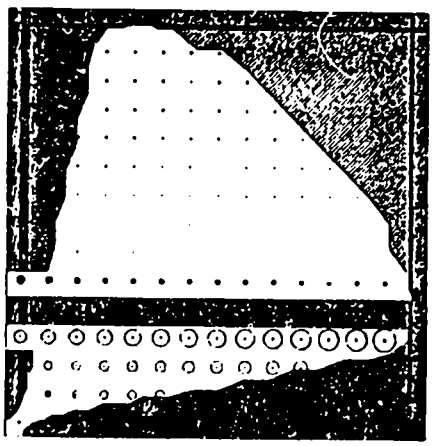

7b)

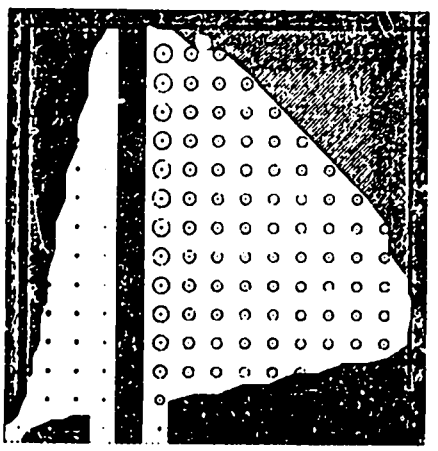

Fig. 7. PISL-JHP's magnetic field patterns of the lowest-order dipole mode on the surfaces of z=0 (a) and z=L_z (b).

RF FIELD MEASUREMENT OF AN RFQ COLD MODEL CAVITY FOR THE JHP

A. Ueno, Y. Mori, A. Takagi, C. Kubota and Y. Yamazaki
National Laboratory for High Energy Physics
1-1 Oho, Tsukuba-shi, Ibaraki-ken, 305, Japan

Abstract

A radio-frequency quadrupole (RFQ) linac will be constructed as a preinjector linac for the Japanese Hadron Project (JHP). Its resonant frequency, injection and final energies are determined from beam-optics considerations of the entire system to be 432 MHz, 50 keV and 3 MeV, respectively. In order to achieve these requirements, keeping the maximum surface electric field to less than 1.8-times the Kilpatrick limit, the RFQ becomes about 2.7 m long. In order to examine the field stability of such a long RFQ cavity, a cold model cavity without vane modulation or a side-tuner was constructed with relative intervane-distance errors of less than ±30 μm. The measurements showed that a good longitudinal and azimuthal field uniformity within ±3.5 % could be achieved by adjusting only end tuners.

Introduction

A long RFQ linac with a resonant frequency of 432 MHz and a length of 2.7 m (about four times of the rf wavelength) will be constructed as a 3-MeV preinjector linac for the Japanese Hadron Project (JHP).[1,2] Its rf duty is to be 3 %, rather higher than that of common RFQs.

In general, it is difficult to fabricate a four-vane type RFQ linac that is long compared with the rf wavelength for the following reasons.[3] Since the frequency separation between two neighboring quadrupole or dipole modes (TE21n- and TE21(n+1)-modes or TE11n- and TE11(n+1)-modes) becomes smaller for a longer cavity and the lowest-order dipole mode (TE110-mode) has a slightly smaller frequency than does the accelerating mode (TE210-mode), the frequency difference between the accelerating mode and the nearest dipole mode, or the nearest higher-order quadruple mode, becomes smaller for a longer cavity. The frequency difference between two modes is closely related to the tolerance of the machining, since a small amount of the asymmetry can mix the two modes with a small frequency separation. Therefore, the specifications for the machining accuracy become more severe for a longer RFQ. On the other hand, accurate machining naturally becomes more difficult for longer vanes.

The mixing of the dipole mode arises from the azimuthal asymmetry, resulting in non-uniform distribution of the stored energy among the four quadrant cavities. On the other hand, the mixing of the higher-order quadrupole mode is caused by a longitudinal imperfection, resulting in a longitudinal field tilt. It is noted that the mixing of the dipole mode has a worse effect on the beam than does the field tilt, since the dipole mode has a bending effect on the beam, reducing the acceptance of the RFQ.

Neither of the four-vane type RFQ with vane coupling rings (VCRs)[4] nor a four-rod type RFQ[5] that may cure the above problem of the dipole-mode mixing can easily meet the present requirements of both high duty and high frequency. On the other hand, the above mentioned difficulty with the four-vane type RFQ was not sufficiently understood quantitatively to make a final decision to choose the RFQ parameters. Thus, a cold model was fabricated in order to develop a machining method that can meet the severe specifications and to study the rf characteristics of the long RFQ cavity.

Machining Method and Errors

A cold model of the RFQ cavity (Fig. 1) was fabricated by assembling four pieces, as was originally proposed at LANL (Los Alamos National Laboratory).[6] Each piece is made of vacuum-melted oxygen-free copper pillar, to which silver is added (0.2 %) in order to strengthen the material mechanically. Each pillar was machined with formed cutters into a cross-sectional shape designed with the computer code SUPERFISH,[7] as shown in Fig. 1. This cold model is an ideal RFQ cavity without vane modulation, a radial matching section or a side-tuner, except for the vane-ends and the end plates. The vane-end cuttings are rectangular (Fig. 2a)) and their vane-end conditions can be adjusted by inserting the tuning plates shown by the hatched areas in Fig. 2b-c). Each of the end plates is equipped with four capacitive tuners (C-tuner) and four inductive tuners (L-tuner) made of copper plungers (Fig. 3). The rf field is measured with the bead-perturbation method, introducing a bead into the inside of the cavity through one of the five holes bored in each of the end plates. The five holes are located in order to measure the field at the beam axis and the stored energies of the four quadrant cavities. Loop monitors can be installed in the end plates. A photograph of the cavity is shown in Fig. 4, where the end plates are removed in order to show the inside of the cavity.

The intervane-distances could be measured when three pieces of the pillars were assembled. Deviations of the measured distances from the designed value are shown along the longitudinal position in Fig. 5. It can be seen that the relative intervane-distance errors are less than ±30 μm.

The measured resonant frequency and Q-value of the accelerating mode is 431.236 MHZ and 8000, respectively. The former is a little lower than the calculated value of 432.244 MHz. This discrepancy is understandable as a result of the dipole-mode mixing described in the next section. The latter is 80-percent of the calculated value.

RF Field Measurement

At first, the best tuning plate regarding the field distribution was chosen by varying the tuning plates, while locating the tuning plungers at the end plates on the inner surfaces of the end plates, where the effects of the tuners vanish. Among the four cases shown in Fig. 2, the best result was obtained with the tuning plates shown in Fig. 2c). Figure 6 shows the result of a field measurement for the lowest-order quadrupole mode (TE210-mode) in a form of the distribution of the squares of the magnetic fields among the four quadrant cavities. It can be seen that the distribution was already fairly uniform, even without any adjustment of the end tuners. Nevertheless, it is noted that the magnetic fields are a little drooped near the vane-ends, indicating that the local resonant frequencies near the vane-ends are slightly higher than the average. Also, the magnetic field strengths of the second and third cavities are slightly larger than those of the first and fourth cavities. This is understandable as a result of the mixing of the accelerating quadrupole mode with a dipole mode.

Keeping these indications in mind, we adjusted the positions of the end tuners, and obtained the results shown in Fig. 7. The squares of the magnetic fields are more uniformly distributed among the four quadrant cavities and along the longitudinal direction. The distributions are uniform within ±7 %. (The field uniformity is within ±3.5 %.) The measured dispersion curves of the dipole and quadrupole modes are shown in Fig. 8. The accelerating quadrupole mode (TE210-mode) is located near the middle of the two dipole modes (TE111-, TE112-modes) and fairly separated from the dipole modes, resulting in only slight mixing of the dipole modes. Also, good machining accuracy can be seen from the small breaking of the degeneracy of the dipole modes. It is noted that more mixing of the dipole modes is expected for the shorter RFQ, where the TE210-mode becomes closer to the TE111-mode. Paradoxically speaking, the field distribution of a longer RFQ will be easier to tune than that of a shorter one in this region of the length.

Although the magnetic field distribution of the TE210-

mode can be tuned fairly well, the dipole modes are still mixed, as can be seen in Fig. 7. In order to remove the mixing entirely, side tuners will be necessary in addition to the end tuners, resulting in a more difficult adjustment of the tuners. It was already fairly difficult to adjust the end tuners, probably because of the complicated relation of the TE210-mode to many other modes such as the TE110-, TE111-, TE112- and TE211-modes. Furthermore, the field distribution of the TE210-mode was slightly unstable: a few-percent change of the square of the magnetic field arose from a few-degree change of the ambient temperature. The change of the field reflected a redistribution of the stored energy among the four quadrant cavities, indicating that the amount of the mixing of the dipole modes was unstable. It should be noted that the mixing of the TE211-mode, revealed in the field tilt, was not as unstable as that of the dipole modes, although the frequency of the TE211-mode is as close to that of the TE210-mode as the dipole modes (see Fig. 8). This phenomenon can be understood as follows. If one of the vanes is bent for some reasons, by slight thermal stress for example, one intervane-distance will become narrower, while the other intervane-distance will become enlarged, resulting in a perturbation that can give rise to a mixing of the dipole modes. On the other hand, the effect of this perturbation on the local frequency of the quadrupole mode is cancelled out in a lowest-order approximation. Therefore, the amount of mixing of the dipole mode is more unstable against thermal stress, or something like that.

So far, we have been concentrating on the field distribution of the quadrupole mode. It is also interesting to see the field distribution of the lowest-order dipole mode (TE110-mode) in Fig. 9. The distribution was far from uniform. This can be understood as follows. The shape of the vane end shown in Fig. 2c) was adjusted in order to make uniform the field distribution of the quadrupole mode. The vane end, thus adjusted, simulates the open-boundary condition at the vicinity of the end plates for the quadrupole mode, but not necessarily for the other modes. The longitudinally uniform field distribution of the lowest-order dipole mode was obtained with the vane end shown in Fig. 2b). The difference between the real and ideal boundary conditions at the vane end of Fig. 2c) has another effect: the measured resonant frequency 420.114 MHz of the TE110-mode is slightly higher than the calculated value of 418.810 MHz with the SUPERFISH. This effect is larger for shorter RFQ cavities.

Conclusion

In order to examine the field stability of a 432-MHz RFQ cavity with a length of 2.7 m, a cold model without modulation or a side-tuner was constructed with relative intervane-distance errors of less than ±30 μm. A good longitudinal and azimuthal field uniformity (within ±3.5 %) was achieved by adjusting only the end tuners. It is expected that a more uniform field distribution can be obtained by installing side tuners. However, the tuning will be difficult owing to the complicated relation of the accelerating mode to many other modes. Also, the uniformity of the field distribution was slightly thermally unstable, since the mixing of the dipole modes seems to be easily modified by thermal stress in the vanes. This is not preferable under the high-duty operation necessary for the JHP. Therefore, a new field stabilizing structure, PISL,[8,9] will be adopted for the JHP.

Acknowledgement

The authors are indebted to Prof. M. Kihara for his continuous encouragement.

References

1. Y. Yamazaki, "Development of a High-intensity Proton Linac for the JHP", this conference.
2. A. Ueno and Y. Yamazaki, "New Beam-dynamics Design Procedure for RFQs", this conference.
3. F. O. Purser et al., Proc. 1984 Linear Accel. Conf., GSI-84-11, 115 (1984).
4. H. R. Schneider and H. Lancaster, IEEE Trans. Nucl. Sci., NS-30, No. 4, 3007 (1983).
5. R. Kazimi, Proc. 1988 Linear Accel. Conf., CEBAF-Report-89-001, 61 (1989).
6. D. Schrage et al., Proc. 1988 Linear Accel. Conf., CEBAF-Report-89-001, 54 (1989).
7. K. Halbach et al., Part. Accel. 7, 213 (1976).
8. A. Ueno and Y. Yamazaki, to be published in Nucl. Instr. and Meth. A.
9. A. Ueno et al., "The π-mode Stabilizing Loop for Four vane Type RFQs", this conference.

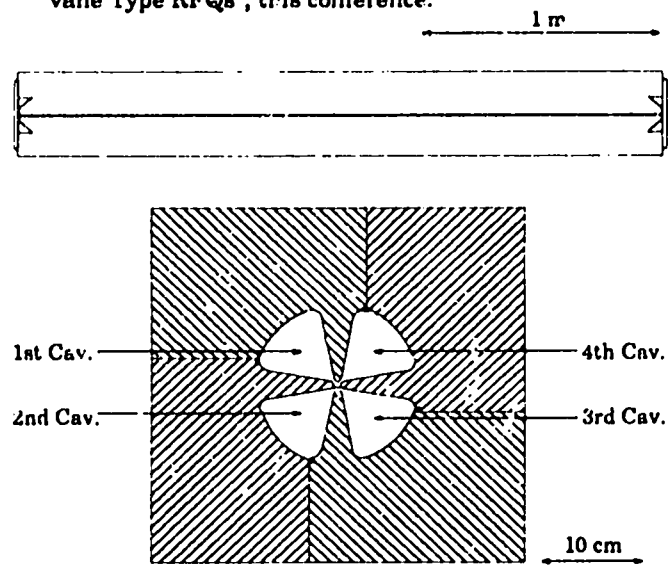

Fig. 1. Schematic of the cold mode RFQ cavity.

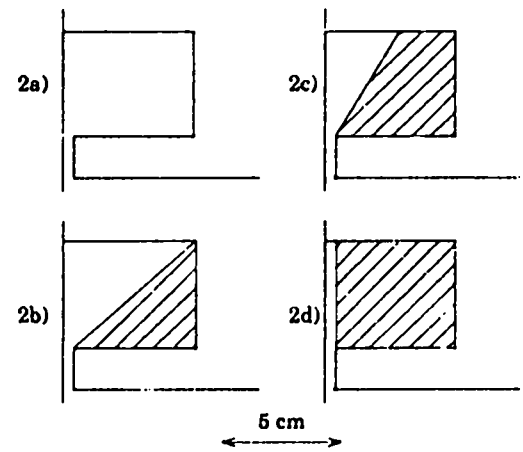

Fig. 2. Vane end cutting and tunimg plates.

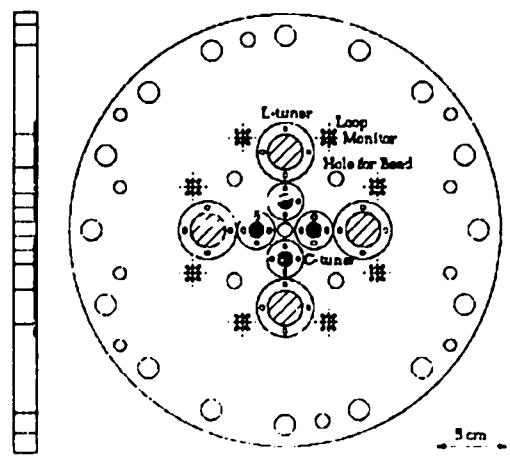

Fig. 3. Scheme of the end plate.

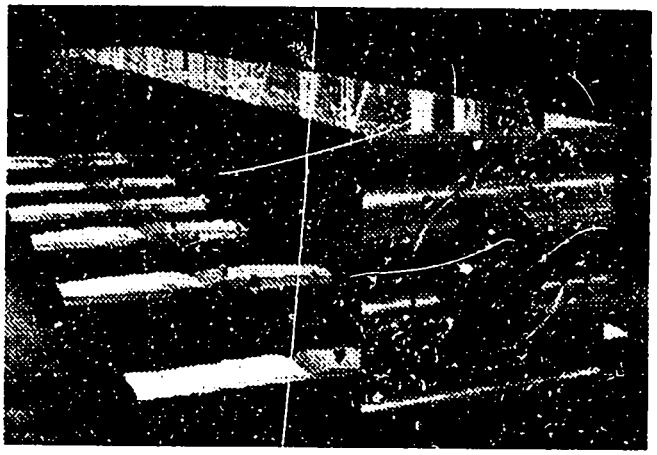

Fig. 4. Photograph of the cold model RFQ cavity.

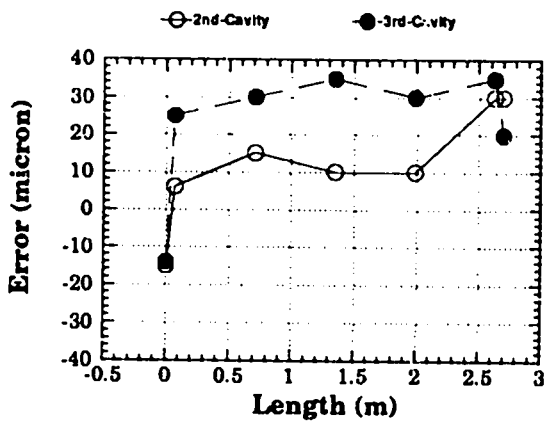

Fig. 5. Intervane-distance errors shown as functions of the longitudinal position.

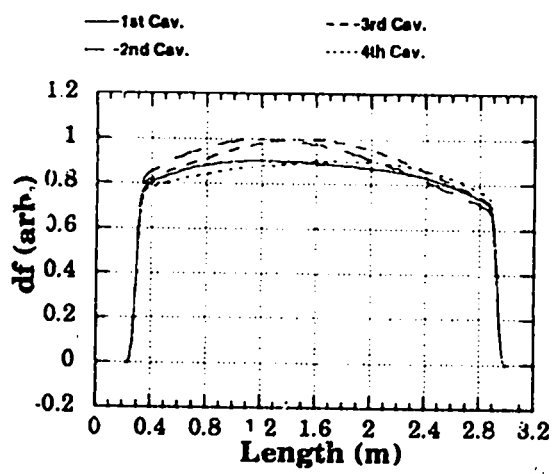

Fig. 6. Distribution of the square of the magnetic fields of the TE210-mode in the four cavities, measured by the bead perturbation method when every tuning plungers at the end plates is located on the inner surface of the end plate.

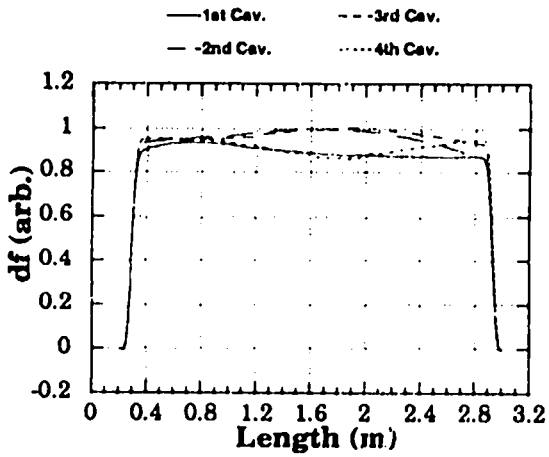

Fig. 7. Distribution of the square of the magnetic fields of the TE210-mode in the four cavities, measured by the bead perturbation method after the tuning of the end tuners.

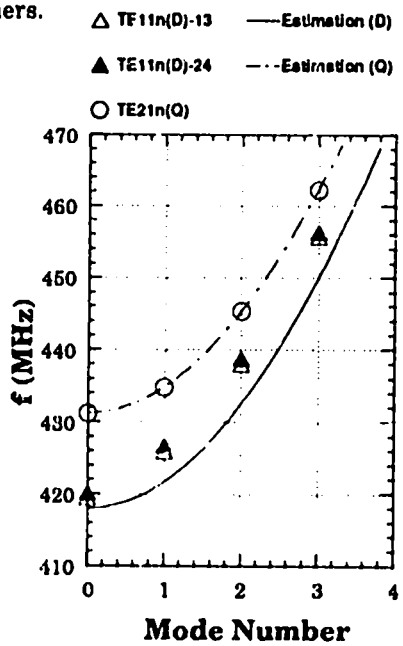

Fig. 8. Measured dispersion curves of the quadrupole and dipole modes.

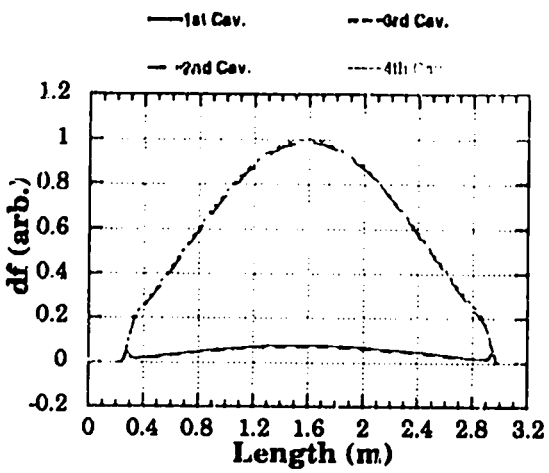

Fig. 9. Distribution of the square of the magnetic fields of the TE110-mode in the four cavities, measured by the bead perturbation method under the same condition of the measurement of Fig. 7.

AZIMUTHAL STABILIZATION OF THE RADIO-FREQUENCY QUADRUPOLE WITH LOOP-COUPLED TEM LINES*

G. Spalek, J. Rose,** and A. Klapetzky
Los Alamos National Laboratory, Los Alamos, NM 87545

Abstract

Azimuthal stabilization studies were performed on a RFQ-cold model, a low-power test cavity. The cold model was a 2.64-meter long aluminum structure, constructed in eight parts azimuthally, with four vane pieces and four skirt pieces, and two sections longitudinally. The structure was originally designed with vane coupling rings (VCRs) to resonate at 425 MHz. Without VCRs the structure resonates in the quadrupole zero mode at 436 MHz. Loop-coupled, lambda (2π) resonant coaxial transmission lines were installed, as shown in Fig. 1. This concept was initially proposed at Los Alamos.[1] The coupling loops are oriented such that opposite quadrant quadrupole fields induce equal but opposite currents leaving the stabilizer unexcited. Any imbalance in fields between the two quadrants (referred to as dipole components or simply dipoles) will induce a net current. Thus, the stabilizer will not couple to the quadrupole mode, but to the dipole mode.

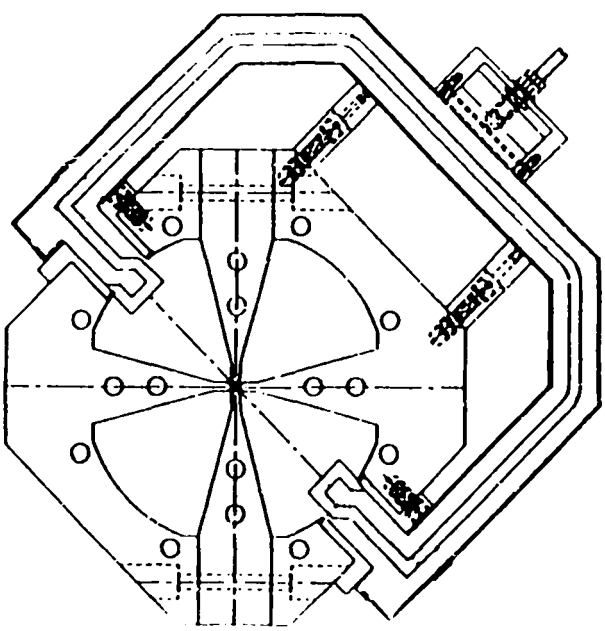

Fig. 1 Azimuthal Resonant Stabilizers

Stabilizer Design

The stabilizers are nominally 80Ω coax, fabricated from 1-inch folded copper box for the outer conductor and 1/4-inch diameter magnet wire inner conductor.

The resonant coaxial lines are designed to be lower in frequency than the quadrupole "0" mode in the RFQ. They can be tuned higher by an inductive (slug) tuner in the H-field maximum (center) of the coax. A typical range of frequencies is 430 MHz to 440 MHz, with a Q (RFQ cavity shorted) of 900, measured at the quadrupole frequency. The frequencies of the stabilizers are determined by shorting the RFQ with approximately 40 rods inserted approximately 10/quadrant and shorting the vane tips. This moves the RFQ frequency far from the stabilizer frequency, effectively decoupling the two, and a drive and pickup loop in the stabilizer is then used to determine the resonant frequency.

In tests to date, there are eight stabilizers occupying eight longitudinal positions on the RFQ-four in each plane and alternating between orthogonal positions.

The ARSs couple to the dipole fields, and the "dipole" in the RFQ and the eight stabilizers act as a two-cavity-coupled system. Figure 2 shows the mode spectra with and without stabilizers. The ARSs have coupled to the dipole at 430 MHz, and split it into two modes, one below and one above the quadrupole. The new dipole/ARS system resonates at 425 MHz and 440 MHz, and no dipole components of the field exist at the RFQ 0-mode frequency.

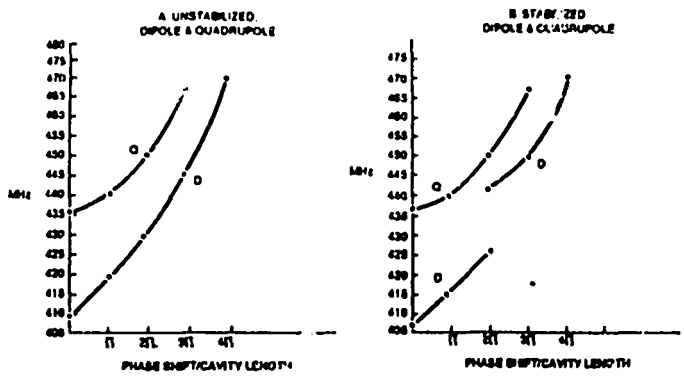

Fig. 2. Mode spectra.

Experimental Results

Relative field measurements were performed using the bead perturbation technique, with a computer analyzed beadpull test set. The cold model was tested with stabilizers in several different configurations; without vane undercuts, with vane undercuts, and with slug tuners inserted halfway for inducing field asymmetries (dipole fields).

Figures 3 and 4 show the stabilized and unstabilized [illegible] dipole fields before vane undercuts. Quadrupole [illegible]

$$Q = \frac{F_1 + F_2 + F_3 + F_4}{4}$$

$$DIPOLE\ 1 = \frac{F_1 - F_3}{2} \qquad DIPOLE\ 2 = \frac{F_2 - F_4}{2}$$

Dipole 2 has been reduced from 30% to 2%. (No attempt was made to reduce the high-energy end dipole at the 220 to 260 cm region, which is an artifact of the absence of undercuts.) The bumps are an artifact of the measurement, where the bead is drawn down the cavity near the wall and goes past the tuning slugs and stabilizer coupling loops. The magnetic field is compressed in the surface of the end plate.

TE110-mode in the four cavities, measured by the bead perturbation method under the same condition of the measurement of Fig. 7.

---

*Grumman is supporting Los Alamos National Laboratory (LANL) on the GTA Program under Contract 9-X28-7633M-1. LANL is under contract to the U. S. Army Strategic Defense Command.

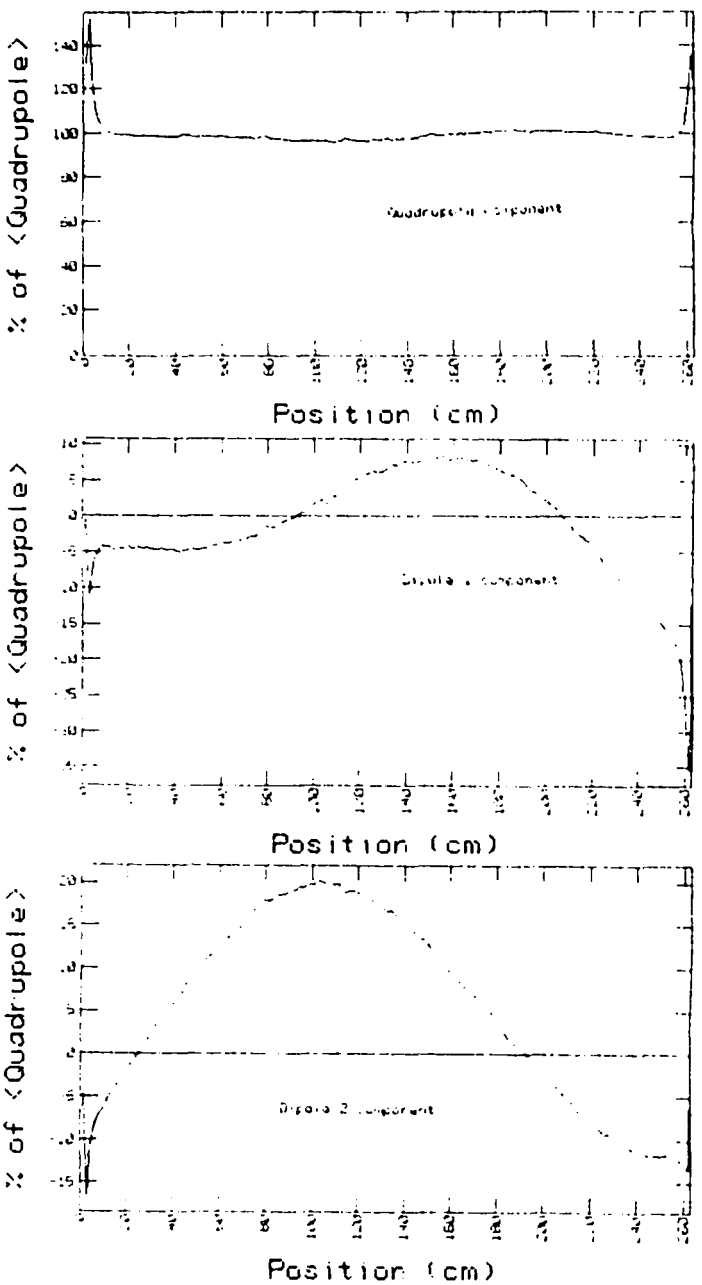

Fig. 4. Unstabilized, no undercuts.

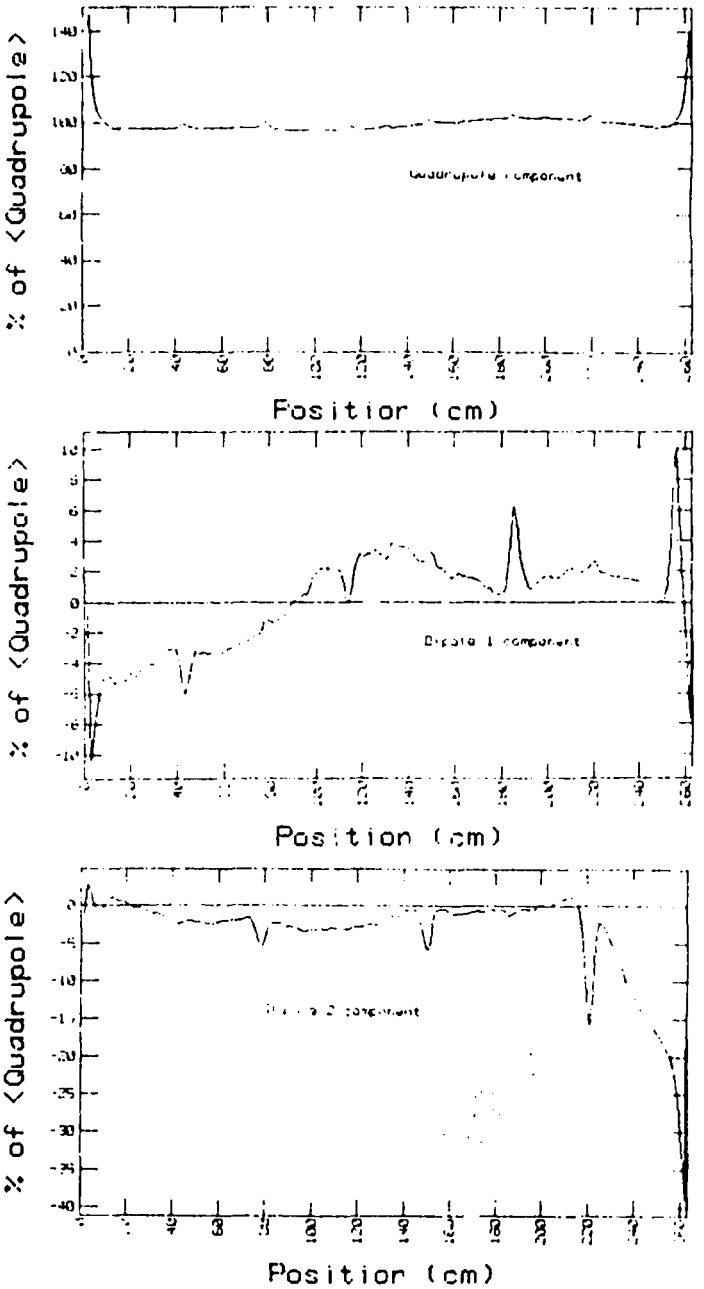

Fig. 4. Stabilized, no undercuts.

Figure 5 and 6 show the quadrupole and dipole fields after the undercuts were added. The unstabilized dipole has been reduced to approximately 10%. This is the result of two effects: first the end tuning capacitors are removed, which had tended to introduce end region asymmetries; and second the dipole mode spectrum has shifted downward, with the two nearest dipoles evenly spaced about the quadrupole zero mode, an inherently more stable configuration. This last effect is serendipitous, a function of the length of the RFQ, which is ordinarily not a free parameter to choose.

In order to perform stability measurements, all of the tuning slugs were inserted to their mid-position. This enables the introduction of a dipole field component by moving, for example, quadrant 1 slugs out producing -150 kHz local frequency shift and quadrant 3 slugs in inducing +150 kHz shift, with zero net frequency change. Figure 7 shows the unstabilized and stabilized response of the perturbations. The stabilized structure has clearly succeeded in minimizing the effect of the perturbations. It should be noted that the perturbation used here, of -150 kHz Q2 and +150 kHz Q4, is much larger and more localized than anything the RFQ would ordinarily encounter. Dipole 1 is unaffected by the perturbations in quadrants 2 and 4 (bottom plots)

Effect on Quadrupole Mode

The advantage of azimuthal resonant stabilizers vs VCRs is that they do not affect the quadrupole fields. The resonant frequency of the RFQ has been measured before and after stabilizer installation. The frequency changed from approximately 436.00 MHz to 436.00 MHz, compared to an 11-MHz frequency shift with VCRs. This simplifies the design of the RFQ considerably, since the resonant frequency of the cavity is nearly the same as that based on the SUPERFISH design using the same cross section. In addition, since the frequency of the quadrupole mode is not affected locally (or globally) by the stabilizers, the quadrupole mode is flat to within 1%. This is not the case when VCRs are used, which locally load the RFQ quadrupole mode. Since, one is forced to operate at the loaded cutoff frequency in order to obtain flat fields end to end,

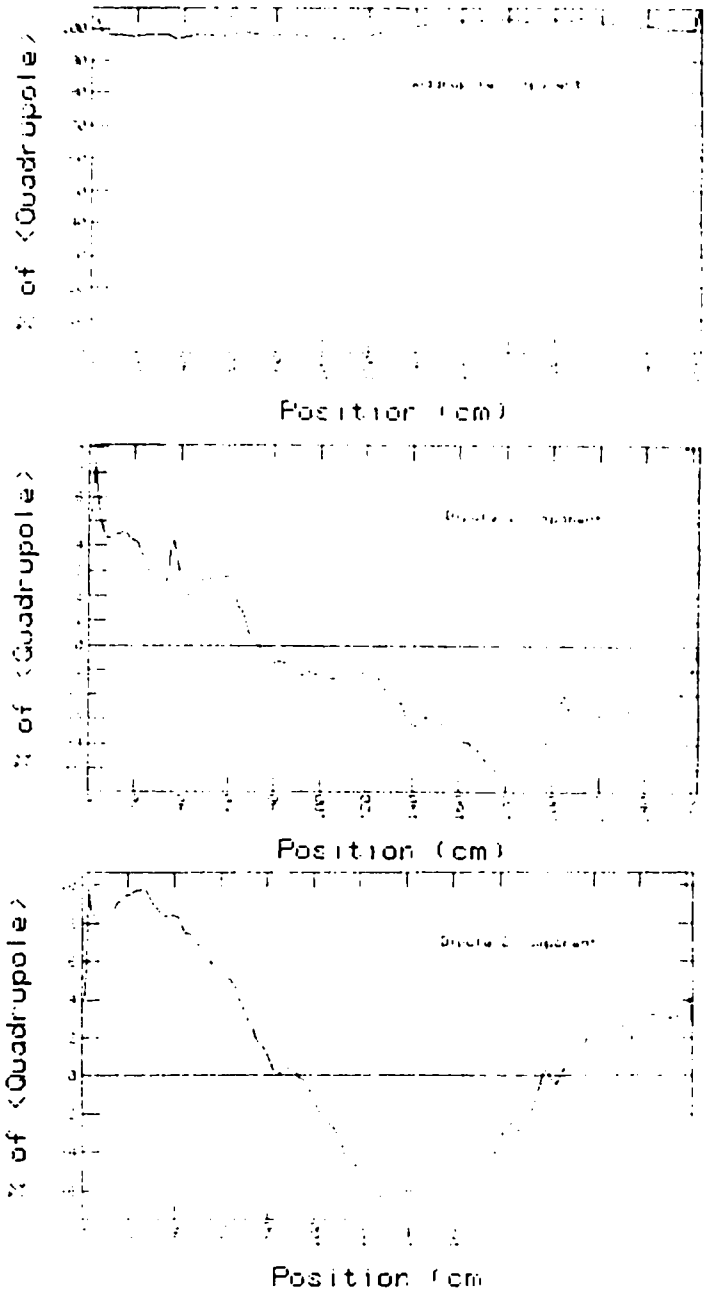

Fig. 5. Unstabilized, w/undercuts.

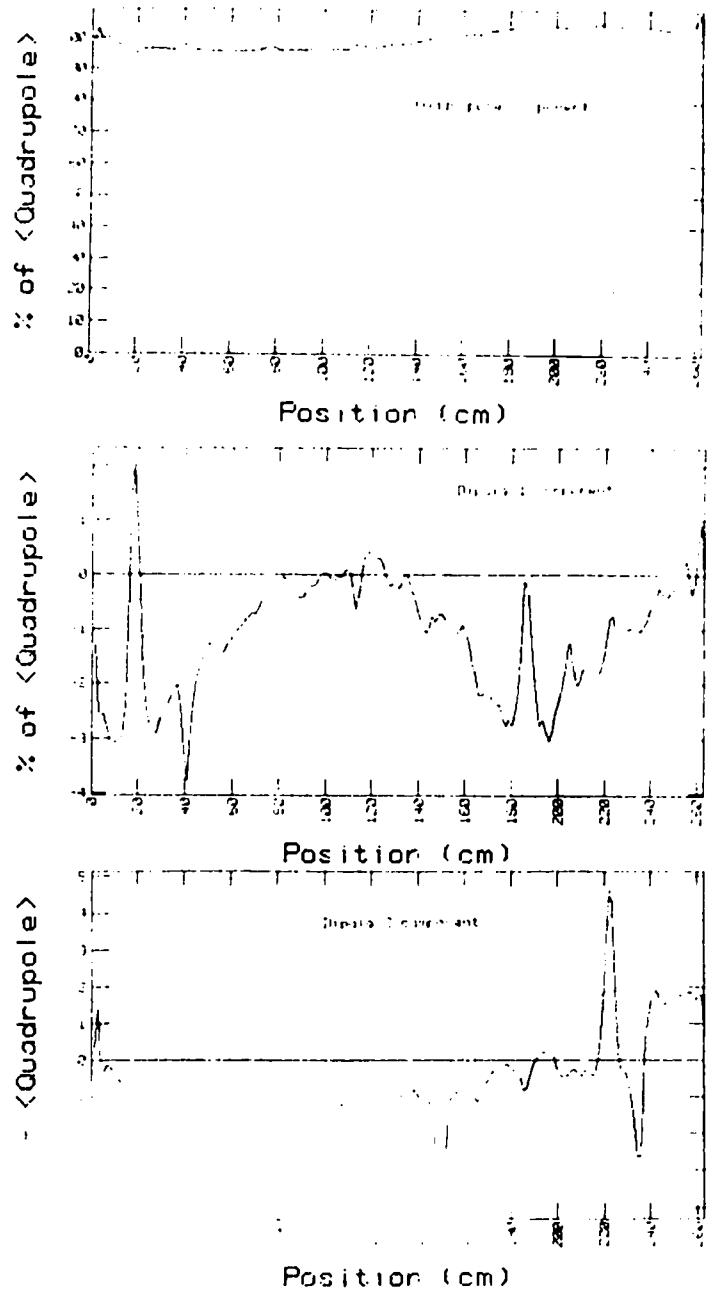

Fig. 6. Stabilized, w/undercuts.

the RFQ is operated below cutoff between VCRs, and the quadrupole 0 mode is evanescent and the field droops. Figure 8 shows the cold model quadrupole field plot with eight VCRs installed.

Stored Energy Measurements: Power Dissipated

The power dissipated in the stabilizers was measured making use of the principle that U/f is an adiabatic invariant in rf cavities.

$$U/f = \text{constant} \qquad \therefore \lambda dU + U d\lambda = 0$$
$$\therefore dU/U = df/f$$

The perturbation measurements, using the beadpull system, measures df/f. Two beadpulls are performed, one with, one without stabilizers, and the difference in total stored energy measured in kHz taken. This difference, divided by the original stored energy Unstabilized (kHz), represents the ratio of stored energy in the stabilizers relative to the RFQ. The total stored energy of the RFQ is calculated by SUPERFISH, so that the stored energy of the stabilizers can be calculated. The power dissipated can then be determined from the relation $P = \omega U/Q$, after measuring the Q of the stabilizers.

Another method that can be used is derived from the relation $Q = \omega U/P$. the total Q of the coupled system is given by

$$Q_{total} = \frac{\omega U_{total}}{P_{total}} = \frac{\omega (U_1 + U_2)}{P_1 + P_2},$$

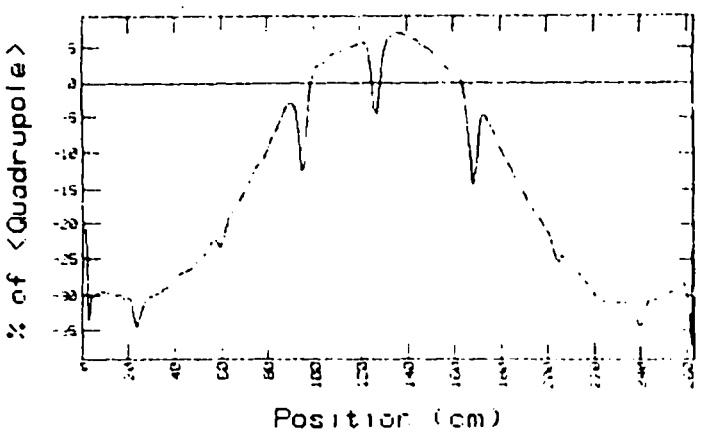

Unstabilized

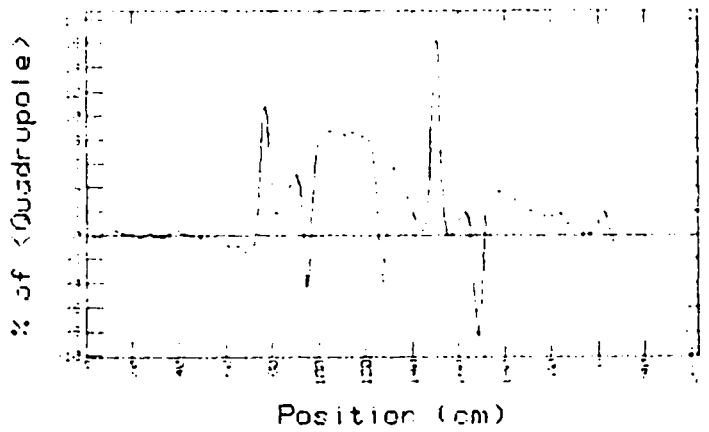

Stabilized

Fig. 7. Dipole perturbation measurements.

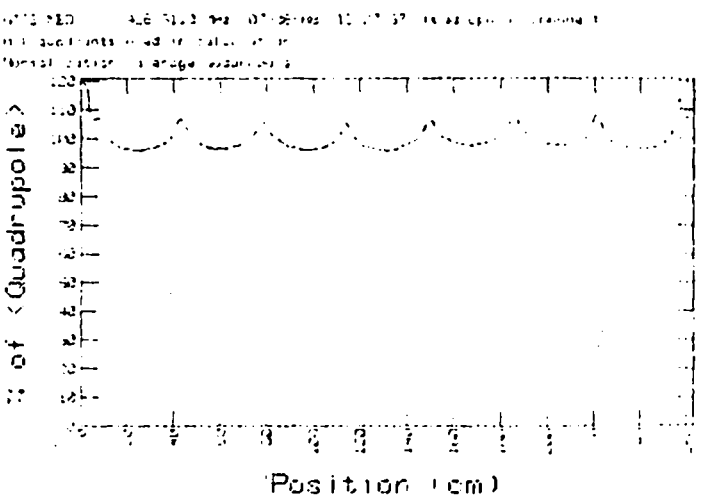

Fig. 8. Quadrupole field with VCRs.

where U_1, P_1 are the stored energy and power dissipated in the RFQ, respectively, and U_2, P_2 associated with the stabilizers. Since $P = \omega U/Q$, we can rewrite the above as

$$U_2 = U_1 \frac{\left(\frac{Q_{tot}}{Q_1} - 1\right)}{\left(1 - \frac{Q_{tot}}{Q_2}\right)}$$

Both methods are subject to relatively large errors, the first due to trying to measure differences in stored energy of a few percent, with accuracies in each measurements of approximately 1/2 percent. This leads to measurement errors of 0.7%. The second results from having to measure Q with accuracies of better than 1% for the case of the cold model.

The difference in stored energy before and after installation of stabilizers was measured by bendpulls to be 0.7%. This difference of 0.7% represents the percentage of total stored energy in the stabilizers. The SUPERFISH computed RFQ stored energy is 0.1914 J/m, times the 2.64 meters of cavity = 0.505 J, so the stored energy in the stabilizers is 0.505(.007) = 0.00354 J. The average Q of the stabilizers is 925. This was the measured Q, with the ARS installed on the RFQ and the RFQ detuned. So this represents (0.00354 J/925) (2π 435 X 10^6 rad/sec) = 10.2 kW, distributed (unevenly) over the eight stabilizers. The difference in total stored energy between the unstabilized structure and the stabilized structure with a +150 kHz perturbation in quadrant 2 and -150 kHz in quadrant 4 was measured. Similarly, the difference for -150 kHz perturbation in quadrant 2 and +150 kHz in quadrant 4 was also examined. The stored energy in the stabilizers has decreased from 0.7% to 0.5% for the first perturbation and increased from 0.7% to 2% for the second. The first perturbation has acted to correct the original dipole inherent in the RFQ and therefore reduced the stabilizer excitation. The second perturbation has acted to increase the original dipole and shows up as an increase in the excitation of the stabilizers. The amount of dipole field levels in the stabilized structure did not change appreciably. This points out the advantage of being able to tune the original dipole to zero prior to stabilizing the structure toreduce the power dissipation in the stabilizers. These measurements were performed on the cold model with vane undercuts, when there had been approximately 10% dipoles before stabilization. The power dissipated in the ARSs is determined by the stored energy, which can be reduced by slug tuneradjustment, and by improving the Q of the stabilizers. A factor of 1-1/2 to 2 in stabilizer Q improvement should be relativelysimple.The Q method of determining stored energy resulted in 1.9% of the stored energy in the stabilizers; however, because the difference in Q_{tot} and Q_{RFQ} was small, the measurement is not accurate. The Q method should be more useful with an all copper RFQ and stabilizers, where the difference in Q_{RFQ} and Q_{TOT} is more significant and could be measured easily.

Reference

1. A. Shempp, "Field Stabilization of RFQ Structures", 1984 Linac Conference, Lufthansa-Schulungs Zentrum Seeheim, F.R.G., May 7-11, 1984 p. 338.

A COAXIAL LINE AZIMUTHAL FIELD STABILIZER FOR RADIO FREQUENCY QUADRUPOLES*

G. Spalek and A. Klapetzky
Los Alamos National Laboratory, MS-H811
Los Alamos, NM 87545

Abstract

Azimuthal stabilization studies have been performed on a 1.75-m-long low-power model of a Radio Frequency Quadrupole (RFQ). The model was modified to accept seven resonant coaxial azimuthal stabilizers spaced at $\lambda/2$ intervals longitudinally and alternating in orientation between two orthogonal planes (Figure 1). The stabilizers are resonant versions of similar stabilizers proposed some years ago [1]. Measurements have shown that these stabilizers are easy to tune even in a very crudely constructed RFQ. They are fairly insensitive to asymmetries and tuning and can be used to adjust the dipole component of an RFQ.

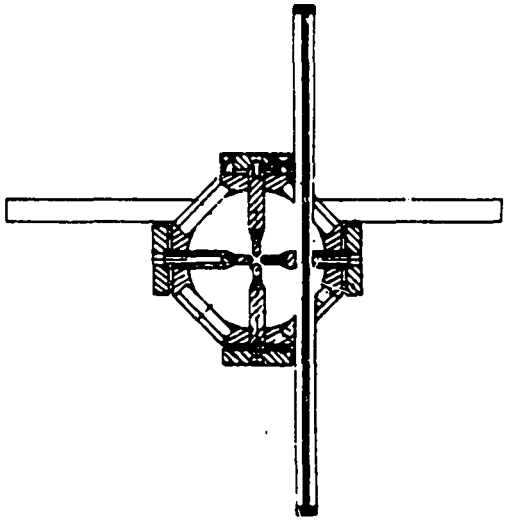

Fig. 1 RFQ model w/stabilizers.

Stabilizer Design & Principle of Operation.

As shown in Figure 1, the stabilizers consist of 41.6-Ω coaxial resonators (CRs) with shorted ends, inserted through a hole in a RFQ vane and walls. Their center conductors have a diameter of 0.64 cm. The CRs are nominally λ long at the RFQ operating frequency with provision for tuning by approximately ±20 MHz by movement of their shorted ends. They are arranged so that their electric field nodes are located at the vane center line. The areas enclosed in adjacent quadrants by the resonator center conductor, the RFQ wall, and the vane should be approximately equal. For the orientation shown in Figure 1, if no vertical dipole exists in the RFQ, the RFQ's magnetic field fluxes through the adjacent enclosed areas are equal. Voltages induced in the CR by these equal fluxes will cancel, leaving the CR unexcited. If, however, a vertical dipole is present, the fields in adjacent quadrants will be unequal. The CR will then be excited in such a way that the fields will become equal (zero dipole), acting just like the off-axis cavity in a side-coupled linac operating in π mode. Changing the position of the CR's electric field node by offsetting both shorted ends in the same direction has the same effect as changing the relative sizes of the enclosed areas. The CR then makes the fields unequal to make the fluxes equal. This offset can then be used either to introduce a dipole component into the RFQ or to correct for unequal enclosed areas caused by mechanical asymmetries.

Stabilizer Tuning

Because of the length and crude construction of the RFQ model, it was impossible to tune its end resonators to obtain a uniform quadrupole field without first installing the stabilizers. In fact, the admixture of dipole and quadrupole modes was such that the lowest quadrupole mode could not be identified from field measurements. Instead, the quadrupole was shorted at its ends and the quadrupole cut-off frequency (approximately 612 MHz) was estimated from the measured quadrupole mode dispersion diagram. The CRs were then tuned in place, to 612 MHz while the RFQ was shorted in all quadrants at $\lambda/2$ longitudinal intervals by conducting rods inserted radially to contact the vane tips. Care was taken to assure that the CR's electric field nodes were approximately at the RFQ vane center line. Then, with the RFQ unshorted, the lowest quadrupole mode (which now had very little dipole admixture) was tuned for longitudinal field uniformity by using the RFQ end tuners. Then the CRs were re-tuned to give the smallest dipole admixture with the quadrupole mode. The final frequencies were the following:

- RFQ quadrupole frequency = 610.2 MHz, and
- CR frequency (RFQ-shorted) = 611.0 MHz.

Finer adjustment of the CRs can be made by perturbing the RFQ to introduce a dipole mode and by tuning the CRs for minimum dipole component. This is a tedious procedure that was found unnecessary with these stabilizers.

Experimental Results

The CR and quadrant numbering convention is shown schematically in Figure 2. All even-numbered CRs (2,4,6) were oriented to lie in the vertical plane and penetrated quadrants 3 and 4. All odd numbered CRs were in the horizontal plane and penetrated quadrants 1 and 2. Thus the even-numbered CRs could affect only the vertical dipole D_v and the odd CRs only the horizontal dipole D_h, which are here defined in terms of the quadrant fields F_i as:

$$D_h = \frac{F_3 + F_4 - F_1 - F_2}{4} \tag{1}$$

$$D_v = \frac{F_1 + F_4 - F_3 - F_2}{4} \tag{2}$$

*Work supported by Los Alamos National Laboratory Institutional Supporting Research, under the auspices of the United States Department of Energy

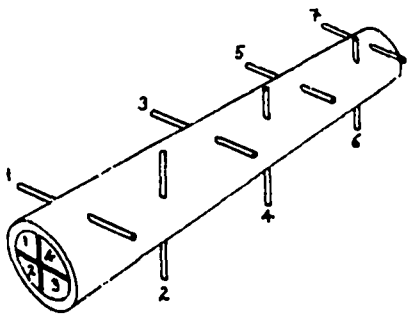

Fig. 2. Numbering convention.

The quadrupole component is defined as

$$Q = \frac{F_1 + F_2 + F_3 + F_4}{4} \quad . \tag{3}$$

Fields were measured by using the conducting bead-pull technique in the magnetic fields of the RFQ quadrants. A computer was then used to extract the dipole and quadrupole field components.

Figure 3 shows the measured quadrupole and horizontal and vertical dipole components in the as-tuned RFQ. Notice that the dipoles are less than 5% of the quadrupole component everywhere except at the ends of the RFQ where there was no stabilization and the end tuners introduced large asymmetries. The large amplitude spikes are an artifact of the measurement that occurs when the perturbing bead enters the enhanced magnetic field area near the CR center conductors. The size and polarity of these spikes is actually a measure of the stabilizers' excitation, stored energy, and therefore of their power dissipation. The on-axis fields do not exhibit these spikes. Notice that the quadrupole does not show the "clothesline" shape of a vane coupling-ring-stabilized RFQ.

To show the sensitivity of the dipole fields to offsets of the CR electric field nodes, the even CRs were moved upward by 2.5 cm while they remained tuned to 611 MHz. Only the vertical dipole field component was affected appreciably, as expected. Figure 4 shows the difference between the dipoles measured before and after the CR offset. The vertical dipole has increased by approximately 10% while the horizontal dipole has changed by only approximately 2.5%. This result indicates some mixing between horizontal and vertical dipoles caused by mechanical asymmetries.

Field stability of the RFQ with CRs relative to a partially stabilized RFQ was measured in the following manner:

1. CR 4 was detuned and the fields measured.
2. A 50-kHz perturbation was introduced into quadrant 1 at the CR 4 longitudinal position and the fields measured.
3. CR 4 was retuned to the proper frequency for stabilization and the fields measured.
4. With CR 4 properly tuned the same 50-kHz perturbation was applied to quadrant 1 and the fields again measured.
5. Differences between the dipole components of cases (1) and (2) and also between dipoles of cases (3) and (4) above were calculated.

Figure 5 shows the differences between cases (1) and (2) above with the longitudinal position of the perturbation indicated by the arrow. The horizontal dipole is not affected by the perturbation because there are horizontal stabilizers at $\lambda/2$ on either side of it. The vertical dipole is changed drastically because the nearest vertical stabilizers are at λ distance on either side of the perturbation and CR 4 is detuned.

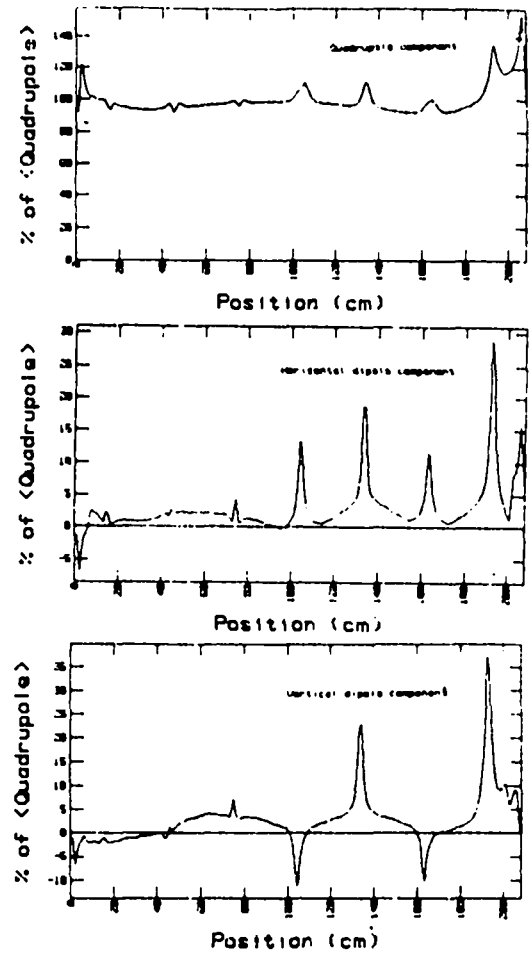

Fig. 3. As-tuned RFQ field components.

The differences between cases (3) and (4) above are shown in Figure 6. Neither the horizontal nor the vertical dipoles are affected by the perturbation when all stabilizers are correctly tuned.

Stored energies and power dissipation in the stabilizers for a given frequency perturbation were not measured. This measurement should be performed before any CW application is contemplated.

Conclusion & Comments

Coaxial resonant stabilizers appear to be promising candidates for stabilizing RFQs azimuthally. Their simple construction, ease of tuning, and tolerance to offsets makes them well suited even for cryogenic RFQ applications. However, because they are quite long, they protrude considerably from the RFQ, making the structure difficult to handle without damaging the CRs. If adjustment of the RFQ dipoles is desired without offsetting the CRs, they can be modified as shown in Figure 7. Here an axial rotation of the

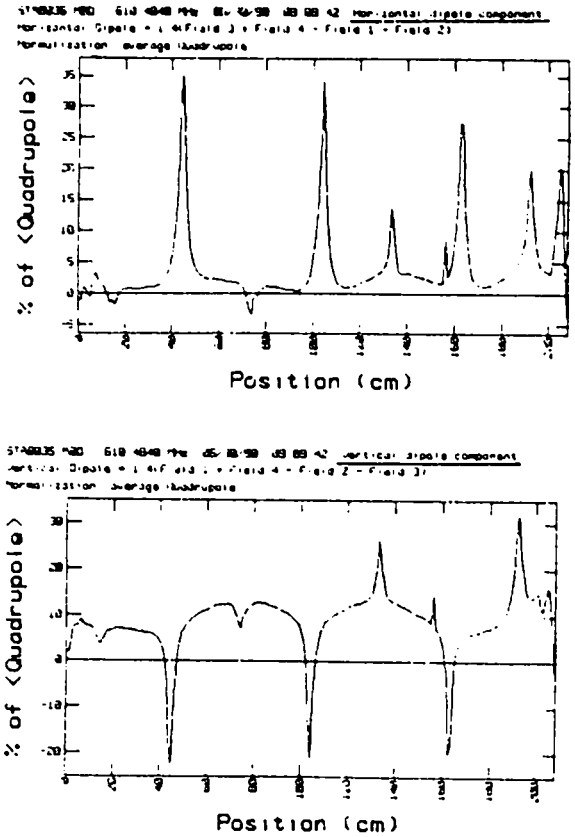

Fig. 4. CR's 2, 4, 6 offset 2.5 cm upward.

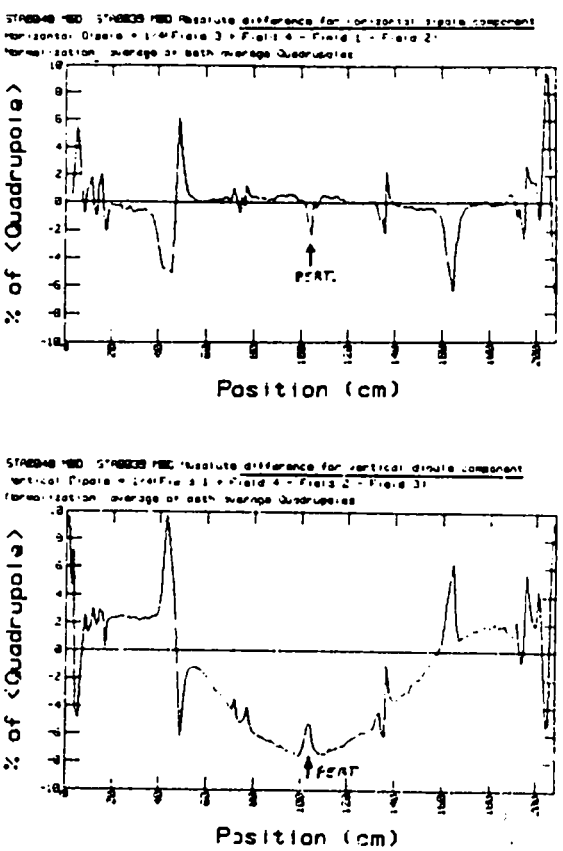

Fig. 5. 50 kHz perturbation in quadrant 1, CR 4 detuned.

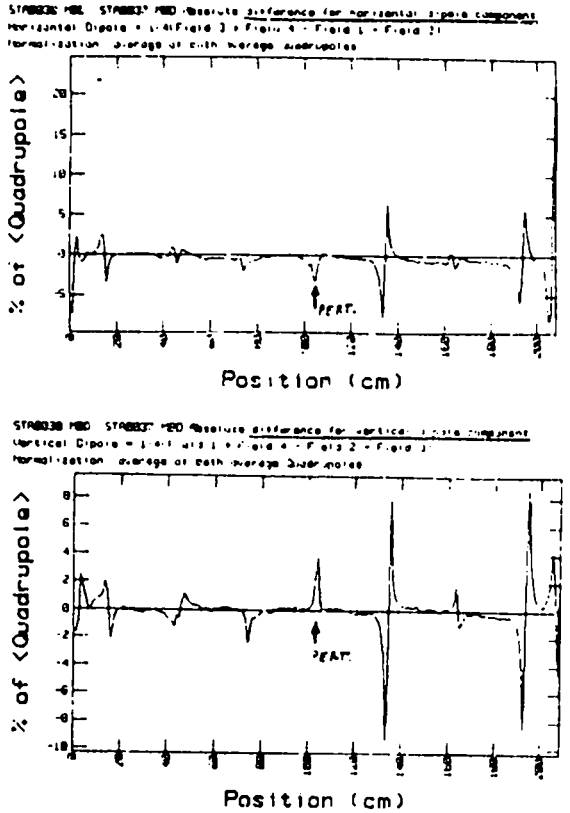

Fig. 6. 50 kHz perturbation in quadrant 1, CR 4 tuned.

CR will change the relative areas enclosed by the CR and the RFQ walls in adjacent quadrants, thus making the stabilizer behave just as if its electric field node had been displaced.

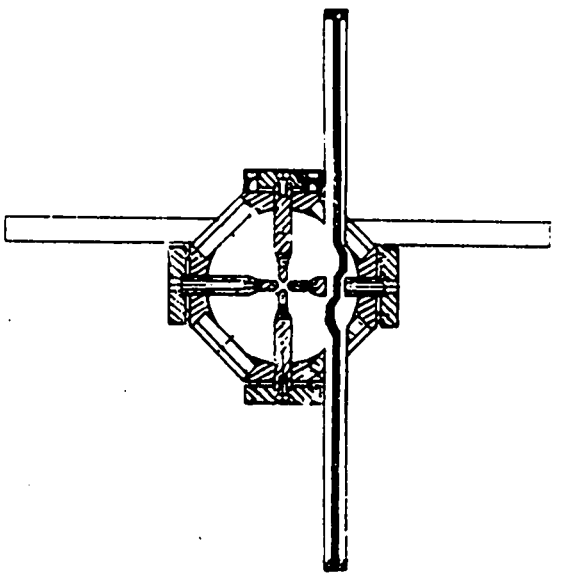

Fig. 7. Modified stabilizer.

Reference

1. A. Schempp, "Field Stabilization of RFQ Structures," 1984 Linac Conference, Lufthansa-Schulungszentrum, Seeheim, F.R.G., May 7-11, 1984, p. 338.

COUPLED RADIO-FREQUENCY QUADRUPOLES AS COMPENSATED STRUCTURES*

M. Jean Browman (AT-6) and Lloyd M. Young (AT-1)
Los Alamos National Laboratory, Los Alamos, NM 87545

Abstract

The usefulness of radio-frequency quadrupoles (RFQs) for accelerating and bunching high-current beams in a compact, lightweight structure is well known. Until now, however, RFQs have been used only for low-energy acceleration because the structure operates in the 0 mode, and problems of mode coupling and field uniformity multiply as the length of the RFQ increases. In general, significant improvements against perturbations in the 0 or π mode can be obtained by providing the structure with another passband that couples to the first to produce a non-zero slope of the dispersion curves. Such a modified structure is called a compensated structure. The three-dimensional MAFIA codes were used to study the feasibility of designing compensated RFQs by dividing long RFQs into sections coupled together by short gaps between the end regions. We found that such a structure does have improved mode spacing and longitudinal stability. Results from this study will be presented.

Introduction

This paper discusses an investigation of a scheme proposed by one of us (LY) to extend the usefulness of radio frequency quadrupoles (RFQs). RFQs use strong electrostatic focussing in a narrow channel, thus allowing high-current beams. They also combine the functions of acceleration and bunching, which means these functions can be accomplished in a compact, lightweight structure. Unfortunately, the amount of acceleration given to a particle depends upon the length of the RFQ used. Problems of mode coupling and field uniformity multiply as the length of the structure increases, so until now RFQs have been used only for low-energy acceleration. Since RFQs are operated in the zero mode, we hypothesized that coupling together short, e.g. one-meter long, sections of RFQs to make a longer compensated[1] structure could improve mode separation and longitudinal stability. We have tested this hypothesis by simulating such coupled RFQs using the MAFIA 3-D electromagnetic analysis codes.[2]

Modeling the Structure

A simulation was done of a coupled RFQ consisting of four approximately one-meter sections separated by variable (0.168 cm–0.26 cm) gaps between the overhangs and by variable-thickness (0.168 cm–0.26 cm) plates with 20.4-cm^2 holes cut in the center. Figure 1 shows a three-dimensional plot of the MAFIA model of this structure, and Fig. 2 shows a cross section of the overhang-coupling-gap region of the MAFIA model.

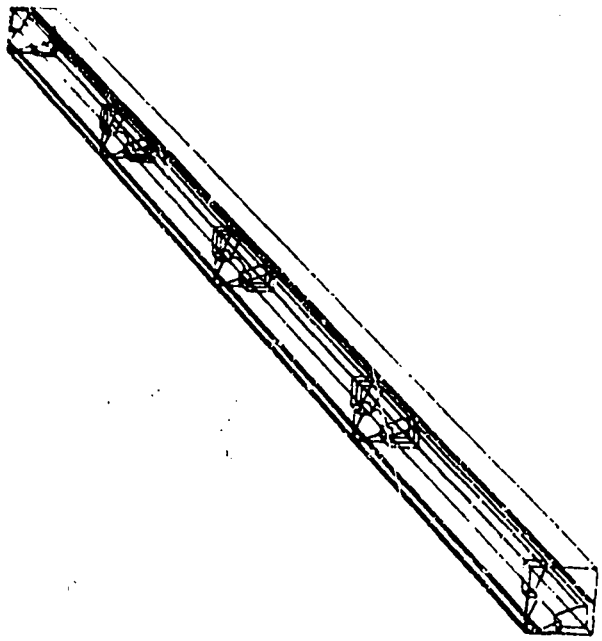

Fig. 1. A four-section coupled RFQ as modeled by MAFIA.

Because of symmetry only one-quarter of the structure needs to be generated. The boundary conditions were chosen so that only the quadrupole modes and the gap modes, i.e., TM-like modes with fields concentrated in the gaps between the RFQs, were studied.

The MAFIA region has the dimensions 7.92 cm × 7.92 cm × 399.2 cm. The MAFIA model was designed to have some of the characteristics of the Beam Experiment Aboard a Rocket (BEAR) RFQ.[4] In particular, the cross-sectional area of the MAFIA overhang and the capacitance/length and cutoff frequency of the MAFIA model were approximately that of the BEAR RFQ. Except for these criteria, the exact shape of the MAFIA cross section was not a concern; the concern was to keep the number of mesh points used as small as possible for reasons of economy. More details of the MAFIA mesh and of the comparison of the MAFIA model with the BEAR RFQ are found in Ref. 3.

An RFQ is essentially a waveguide operated at cutoff, terminated by an end region whose fields must be matched to those of the waveguide.[5–8] This matching is done by undercutting the vanes.[5] The metal that is removed is called

*Work supported by Los Alamos National Laboratory Institutional Supporting Research, under the auspices of the US Department of Energy.

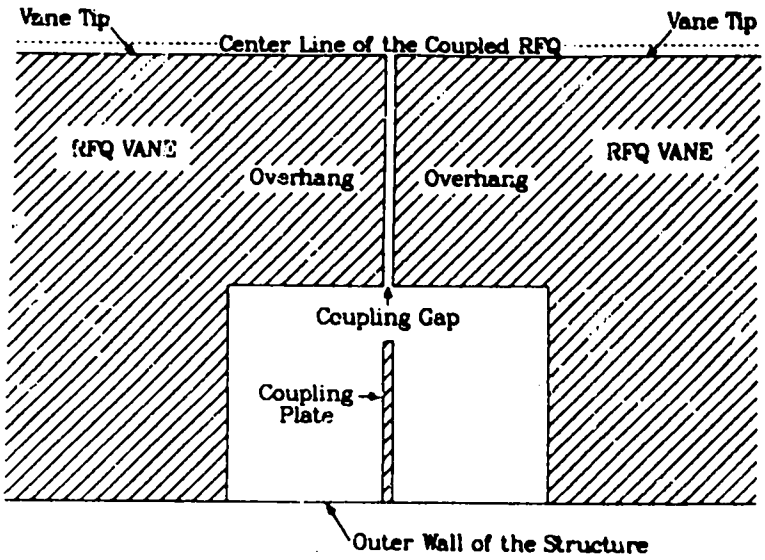

Fig. 2. A cross section of the overhang-coupling-gap region of the RFQ, taken through the center of one of the vanes.

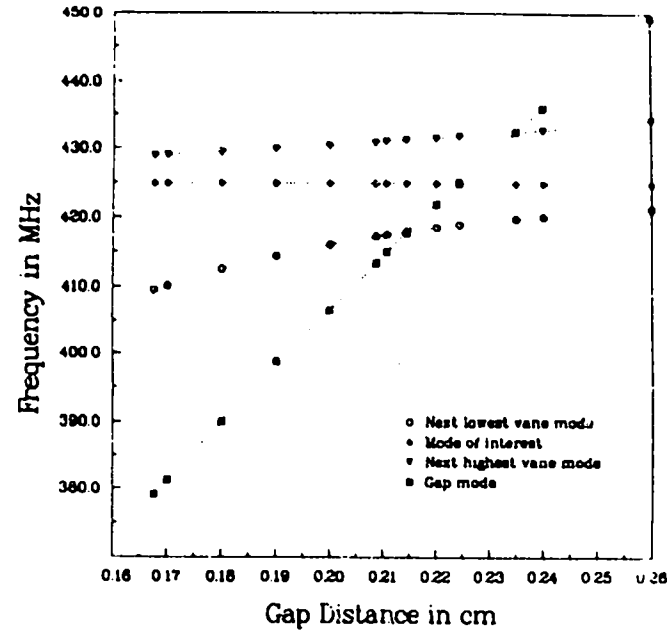

Fig. 3. Plot of frequency vs gap distance for the quadrupole RFQ mode, the nearest quadrupole modes, and the gap mode.

the undercut; the part of the vane remaining (in the region where the metal has been removed) is called the overhang. Again, see Fig. 2.

The overhangs at both the ends of the RFQs and at the gaps were adjusted to make the electric field between the vanes approximately constant along the length of the RFQ. The following overhangs were used in the MAFIA model:

Overhangs at ends of the structure	2.65 cm
Overhangs at the coupling gaps	2.83 cm

THE EFFECT OF GAP DISTANCE ON MODE SEPARATION AND ON LONGITUDINAL STABILITY

We know from the theory of compensated structures[1] that varying the gap distance will affect the mode spacing in the coupled RFQ system. Figure 3 illustrates this point. We can see that a 0.22 cm gap results in a near-optimum separation between the quadrupole modes. At this gap there is a difference of 6.5 MHz between the RFQ quadrupole mode, ω_0, and the next lowest quadrupole mode, ω_-, and 6.6 MHz between ω_0 and the next highest quadrupole mode, ω_+. By contrast, there is only a 1.9 MHz separation between ω_0 and the next highest mode in a 399.2-cm uncoupled RFQ.

A coupling gap of 0.22 cm should also be near optimum for the longitudinal stability of the structure, because the difference $(\omega_-^2 - \omega_0^2) \approx -(\omega_+^2 - \omega_0^2)$. Again, we know from the theory of compensated structures that when this condition is true the improvement against perturbations is by far greater than that due to the improved mode spacing alone[1].

In order to test this expectation, we added a 4.12 cm^3 perturbation to the end of both the coupled and uncoupled structures. Fig. 4 compares the electric field between the vanes as a function of distance along the RFQ for the two structures. The perturbation was chosen larger than what would be expected in practice in order to test the relative stability of the rf fields for the two systems. Notice that the field droops significantly more for the uncoupled RFQ and that the field of the coupled RFQ is essentially constant from cell-to-cell.

Unfortunately, as we can see from Fig. 3, for the cross-sectional geometry chosen the frequency of the gap mode is 421.8 MHz for the 0.22-cm gap, which is only 3.1 MHz different from the 424.9-MHz frequency of the mode of interest. Thus the frequency of the gap modes would be a factor in the design a real coupled RFQ.

THE EFFECT OF THE SIZE OF THE COUPLING HOLE ON TUNING AND ON LONGITUDINAL STABILITY

We also tested the possibility of tuning the individual sections of the coupled RFQ at the gaps by changing the shape of the coupling hole rather than by changing the length of the overhang.[3] We were able to show that tuning the coupling holes has the same effect on the longitudinal stability as tuning the gap overhang lengths. The equivalence of the two methods of tuning is important if coupled

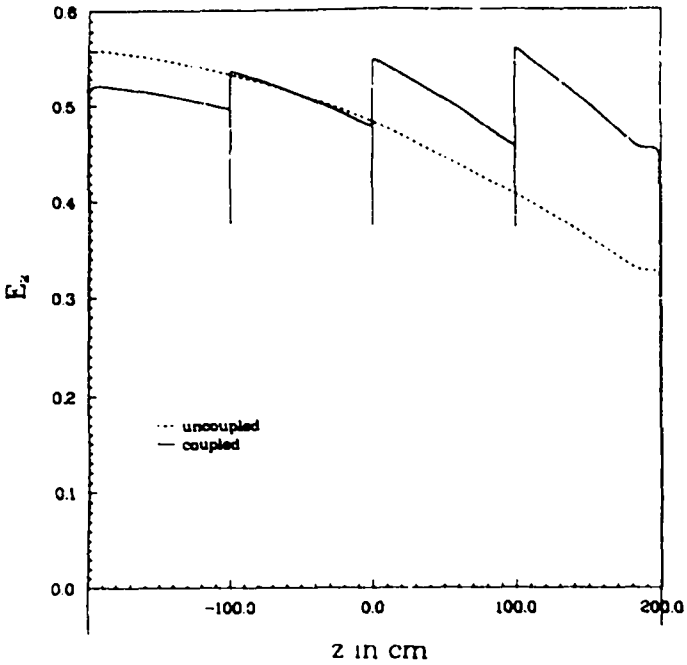

Fig. 4. Comparison of the fields between the vanes for the perturbed coupled and uncoupled RFQs.

RFQs are to be built, since it is much easier to vary the size of the coupling hole than to vary the length of overhangs.

EFFECT OF THE COUPLING PLATES ON POWER LOSS

The effect of the presence of the plates on the power loss in the structure was a concern, but the MAFIA calculations indicated that coupling the RFQs decreased the quality factor of the structure by only 0.4%.

CONCLUSIONS

As we have seen above, coupling together four approximately one-meter sections of RFQs, assuming one tuned the gap distance and either the size of the coupling holes or the length of the gap overhangs, did improve the mode separation between the quadrupole modes. Coupling the RFQs also improved the longitudinal rf stability.

The presence of the TM-like gap modes was discovered to be a problem, and the effect of the cross-sectional geometry on the frequency of these modes would need to be studied before a real coupled RFQ could be built. It should also be noted that the dipole modes were not looked at in this study, but it is expected that their mode separation would be also be improved by coupling the RFQs.

REFERENCES

1. G. Dôme, "Review and Survey of Accelerating Structures," in *Linear Accelerators*, P. M. Lapostolle and A. L. Septier, editors, 1970, pp. 665-673.

2. T. Barts, M. J. Browman, R. Cooper, C. T. Mottershead, G. Rodenz, S. G. Wipf, R. Klatt, F. Krawczyck, W.-R. Novender, C. Palm, T. Weiland, B. Steffen, "MAFIA-A Three-Dimensional Electromagnetic CAD System for Magnets, RF Structures, and Transient Wakefield Calculations," *1986 Linear Accelerator Conference Proc.*, Stanford Linear Accelerator Center Report SLAC-303, 276-278 (1986).

3. M. Jean Browman and Lloyd M. Young, "A Study of Coupled Radio-Frequency Quadrupoles Using the MAFIA Codes," Accelerator Theory Note AT-6:ATN-90-3

4. D. Schrage, L. Young, B. Campbell, J. H. Billen, T. Wangler, J. Stovall, F. Martinez, W. Clark, S. Gibbs, G Bolme, P. O'Shea, M. Lynch, J. Devenport, J. Rathke, R. Micich, J. Rose, R. Richter, and G. Rosato, "A Flight-Qualified RFQ for the BEAR Project," *1988 Linear Accelerator Conference Proc.*, CEBAF-Report-89-001, 54-57 (1989).

5. M. J. Browman, G. Spalek and T. C. Barts, "Studying the End Regions of RFQs Using the MAFIA Codes," *1988 Linear Accelerator Conference Proc.*, CEBAF-Report-89-001, 64-66 (1989).

6. M. Jean Browman and George Spalek, "Tuning the End Regions of RFQs—The Need for Vane Undercutting," Accelerator Theory Note AT-6:ATN-87-13.

7. M. Jean Browman and George Spalek, "The Effect of the End Gap Distance on Power Dissipation in the End Regions of RFQ's," Accelerator Theory Note AT-6:ATN-87-14.

8. M. Jean Browman and George Spalek, "The Effect of the Shape of Vane Undercutting on Power Dissipation in the End Regions of RFQ's," Accelerator Theory Note AT-6:ATN-87-15.

ELECTRICAL CHARACTERISTICS OF A SHORT RFQ RESONATOR[1]

I. Ben-Zvi[2] A. Jain[3] and H. Wang[4]
Physics Department, SUNY at Stony Brook, NY 11794-3800
and
A. Lombardi
INFN-LNL, Via Romea 4, Legnaro (PD) I-35020, Italy

Abstract

Electrical characteristics of a short RFQ resonator of the 'four rod' type have been studied by carrying out measurements on models and numerical simulations using the MAFIA codes. An empirical formula is obtained for the capacitance of vane-like electrodes in a four-rod RFQ resonator. It is shown that the electrode supports could account for a significant part of the total capacitance. This additional capacitance may change the circuit symmetry and give rise to a dipole component. This effect can be compensated by appropriate modifications of the support structure. The beam offset due to a dipole component is estimated.

An Improved Formula for Interelectrode Capacitance

The total capacitance is an important design parameter for any resonator. For a 4-rod RFQ structure[1], an estimate for interelectrode capacitance C is given in reference 2. Our measurements show that the formula in reference 2 *overestimates* C by about 10% for unmodulated structure ($m = 1$), and *underestimates* C by about 10% for large modulation ($m \sim 3$). If we compare a cross section of the modulated structure with that of the "equivalent" unmodulated structure with aperture $r_0 = a/\sqrt{\chi}$ it will be seen that the overall transverse dimension of the actual structure is larger. An unmodulated 4-rod structure with suitable "vane-like" extensions would be closer to the actual structure. We have measured capacitances for unmodulated 4-rod structures with and without an extension to arrive at an improved empirical formula.

The measurements were carried out using a digital LCR meter, model HP4271A. The electrodes were held in place by fixing them to a pair of plexiglass plates. It was found that typically, the fixtures contributed about 2 pF. The values reported in this work are corrected for the effect of these fixtures.

For the unmodulated structure, a fixed radius of curvature, $\rho = 1.59$ cm and a fixed length $l = 50.8$ cm were used. The measurements were carried out for $a = 2.2$, 3.5 and 4.8 cm. The extension length h was varied between 0 to 15 cm. The modulated structure had $\rho = 1.75$ cm, $l = 39.4$ cm, $a = 2$ cm and $m = 3.2$. The average value of χ (over four cells) is 0.26, giving $r_0 = a/\sqrt{\chi} = 4$ cm.

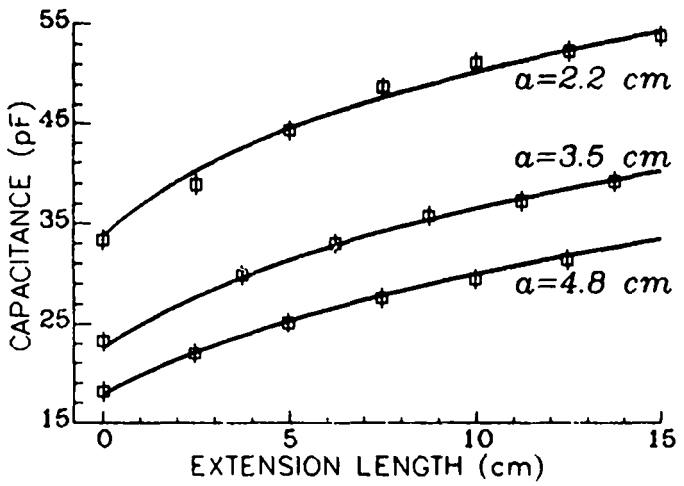

Figure 1: *Capacitance of unmodulated 4-rod structures with a=2.2, 3.5 and 4.8 cm as a function of extension length h. The solid lines are given by eq.(1).*

The variation of capacitance with the extension length h is shown in Fig.1 for the unmodulated structure. The experimental values are shown by squares and the error bars represent typical uncertainities of ± 1 pF in the measurements. The solid lines in Fig.1 represent estimates from an improved capacitance formula given by

$$\frac{C}{l} = \frac{39.37}{cosh^{-1}\left(\frac{r_0/\rho+1}{\sqrt{2}}\right)} + \frac{31.05}{r_0/\rho - \sqrt{2} + 1} + 25.28\, ln\left(1 + \frac{h}{a+\rho}\right) \quad pF/m \quad \ldots(1)$$

The first two terms on the right hand side of eq.(1) have the same form as in reference 1 with somewhat different constants, while the last term is based on an approximate analytic estimation of capacitance increase due to the extensions. For the modulated structure, the appropriate value of h is $ma - r_0$. For the $m = 3.2$ structure studied, eq.(1) gives a value of $C = 22.01$ pF, which matches exactly with the measured value of 22 pF for the modulated structure.

In a real 4-rod RFQ, the electrodes must be held in place by some support structure. This produces additional capacitance, which could be significant, particularly for short RFQs. We have measured this effect with a support in the form of a rectangular frame.

[1] Work Supported by NSF Grant No. PHY-8902923

[2] Also NSLS Department, Brookhaven National Laboratory, Upton NY 11973

[3] Permanent Address : Nuclear Physics Division, BARC, Bombay 400085, India.

[4] Permanent Address : Tandem Accelerator Laboratory, Physics Department, IAE, Beijing 102431, P.R. China.

For the unmodulated structure, the capacitance increases from 33.4 pF ($a = 2.2$ cm) without supports to 42.2 pF with supports. In the case of modulated structure, these values are 22 pF and 30.2 pF respectively. Thus the supports do add significantly to the total capacitance, and can not be neglected.

Beam Offset due to Electrical Unbalance

Dipole field components in the RFQ are the result of deviation from the basic quadrupolar symmetry which can be expressed as a voltage asymmetry or an equivalent dipole field superimposed on the quadrupole field.

The equivalent circuit of the short, four rod, RFQ resonator is shown in Figure 2. The inductive path to a pair of electrodes has an inductance $L/2$ for the common part, then L_1 and L_2 inductive arms leading to the two electrodes. The inductive unbalance δ is defined as $\delta = 2(L_1 - L_2)/(L_1 + L_2)$. The parasitic capacitance between the support arms and the electrodes results in the capacitive unbalance which is described by the parameter $\epsilon = C'/C$, where $C - C'$ is the basic inter-electrode capacitance and C' is the single arm to electrode parasitic capacitance. These unbalances can be controlled by the proper design of the resonator[2]. We define $l = (L_1 + L_2)/2$ and $\alpha = \frac{l}{2(L+l)}$. The solution of the equations of this circuit to first order in δ and ϵ results in frequencies of the two lowest modes

$$\omega_0 = \frac{1}{2\sqrt{(L+l)C}}, \quad \omega_1 = \omega_0/\sqrt{\alpha} \qquad (2)$$

Furthermore, the voltage unbalance $\Delta V/V$ at the fundamental frequency ω_0 is given by

$$\frac{\Delta V}{V} = \frac{\alpha}{1-\alpha}(\delta - \epsilon) \qquad (3)$$

Thus one may eliminate the unbalance by cancelling the capacitive term ϵ against the inductive term δ. From the measured values of capacitance for the unmodulated structure described earlier in this paper,

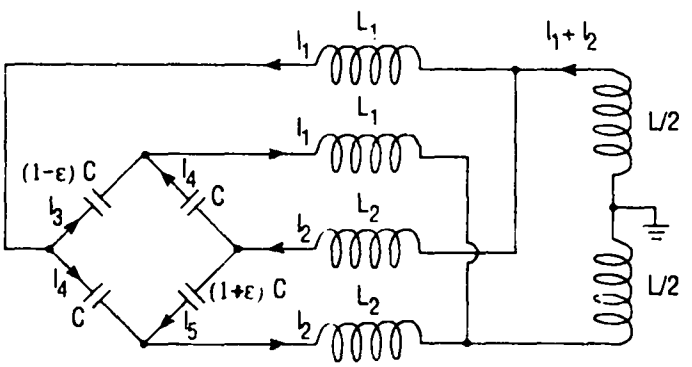

Figure 2: *The equivalent circuit of a short, four rod RFQ resonator*

we have $4(C - C') = 33.4$pF, and $4C = 42.2$pF. Under the simplifying assumptions of $L \approx L_1 \approx L_2$, eq.(3) gives a voltage unbalance of about 7%. Unbalance measured experimentally by bead-pulling is about 3%. The discrepancy in the estimate could be due to use of a simplified lumped circuit equivalent, as well as neglecting higher order terms in δ and ϵ.

By introducing a few simplifying assumptions we can estimate the effect of the dipole field on the beam. Let us use a model linac RFQ with smooth focussing and neglect acceleration. The dipole field is taken conservatively to be continuous and the result of a constant voltage asymmetry. The beam will establish a neutral axis offset from the geometrical beam axis. We wish to estimate the neutral axis offset relative to the beam size.

The transverse motion in a focussing channel is given by $x'' + k^2 x = 0$ where $k^2 = qV/(Mv_0^2 r_0^2)$. M, q and v_0 are the particle's mass, charge and velocity. Let the voltages of an electrode pair be $V + \Delta V$ and $V - \Delta V$. The motion in the dipole field is given by $x'' = qE_d/(Mv_0^2)$ We can express the dipole field as a function of the longitudinal coordinate z by

$$E_d(z) = \left(\frac{\Delta V}{a}\right) \frac{2\cos(kz + \Phi_s)}{(m+1) - (m-1)\sin kz} \qquad (4)$$

where the aperture variation between a and ma is approximated as sinusoidal. Φ_s is the synchronous particle phase. The average dipole field $\overline{E_d}$ is obtained by integrating over the RFQ period,

$$\overline{E_d} = \left(\frac{\Delta V}{a}\right) \frac{\sin\Phi_s}{\sqrt{m}} \frac{\sqrt{m}-1}{\sqrt{m}+1} \qquad (5)$$

This average dipole field in the presence of the quadrupole focussing channel results in a neutral axis offset x_0 given by

$$x_0 = r_0 \left(\frac{\Delta V}{V}\right) \frac{m+1}{2\sqrt{m}} \frac{\sqrt{m}-1}{\sqrt{m}+1} \sin\Phi_s \qquad (6)$$

This expression for x_0 can be used as a guide to the severity of the dipole effects. As long as x_0 is significantly smaller than the beam radius σ_x, the dipole effects can be neglected. The figure of merit in terms of the RFQ and beam parameters is:

$$\frac{x_0}{\sigma_x} = \left(\frac{qV}{Mc^2}\right)^{1/4} \sqrt{\frac{r_0}{\epsilon_n}} \frac{\Delta V}{V} \frac{m+1}{2\sqrt{m}} \frac{\sqrt{m}-1}{\sqrt{m}+1} \sin\Phi_s \qquad (7)$$

where ϵ_n is the normalized emittance. For a typical set of values[2] $\epsilon_n = 0.1\pi$ mm.mrad, $V = 420$ KV, $r_0 = 4$ cm, $m = 4$, $\Phi_s = 25_0$, and Pb^{35+} beam, we have $(x_0/\sigma_x) = 5.85(\Delta V/V)$.

Numerical Simulations by MAFIA Codes

The electrical characteristics of the RFQ depend on the RF field distribution in the resonator. A three

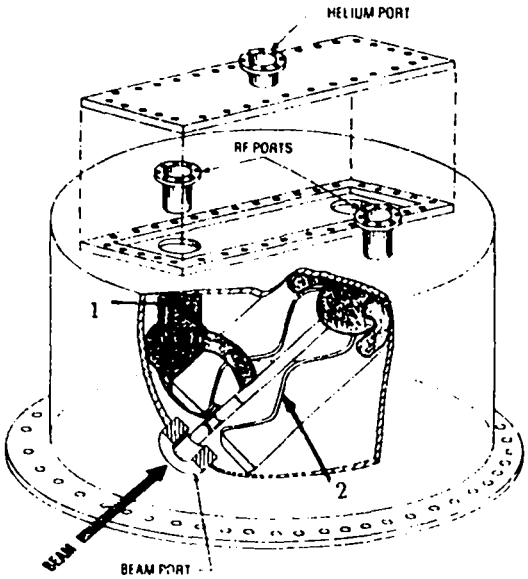

Figure 3: *A schematic view of the prototyp superconducting RFQ resonator*

dimensional electromagnetic fi as calculated using MAFIA[4] codes for the or RFQ structure.

A simpler problem was run on a VAX computer with 42,735 mesh no to simulate an aluminum model which is modulated 4-rods structure with a pair of rec r frame supports. For our superconducting RF rototype resonator design, a real structure wit *dulated* electrodes (m = 4) and a cylindrical ta (see Fig.3) was simulated and run on a vectorized I I-3090 with up to 298,125 mesh points. It is neces to have certain mesh density and large memory sp e for a good soluti f this problem.

The results of both M FIA simulations and comparisons with measureme and approximate expressions are presented in Table 1. Fig.4 is from MAFIA postprocessor plot, show g the electric field distribution in the region betw en a pair of modulated electrodes. MAFIA calc ions show that our resonator's fundamental mode is quadrupolar. Next higer frequency mode (dipole mode) is about double the fundamental frequency. The location of the peak surface magnetic field B_s is marked by arrow 1 in Fig 3. At this point the field is enhanced by a superposition of field from two conductors. The arrow 2 in Fig 3 shows the location of the peak surface electric field E_s.

The electrical unbalance on electrodes was checked b MAFIA and experiment for the unmodulated model. The difference betw en the center and end of the electrodes is due to transmission line effects. The measured values of the frequency tuning sensitivity for translation of the bottom cover in a modulated structure model was 3.3-0.7 KHz/mm for cover to electrode distance of 10-25 cm. The tuning sensitivity for the beam ports was ~60-5 KHz/mm for electrode to beam port ga of 2 to 4 cm.

Figure 4: *Electric field distribution obtained by using MAFIA codes*

Table 1. MAFIA Results vs Measurements and Approximate Expressions

	Unmodulated Model			Modulated Prototype	
Character.	MAFIA	Meas.	Approx.(1)	MAFIA	Approx.3
f (MHz)	61.9	6 .5	54.8(2)	54.7	60.8(2)
Q (Cu)	14300		13260	9952	8938
C_{total}(pF)	48.2(4)	42.2	34.2(6)	45.4(4)	24.7(6)
$E_s/V(m^{-1})$	53.3(7)		65.3(7)	62.0(9)	38.5(7)
B_s/V(G/MV)	1218(8)	1187	1322(8)	1365	1271(10)
$(E_s/E_s)_{...}$				0.114	0.101
$\Delta V/V(\%)$					
Ends	3.0	2.0	7.0	2.2	15
Centre	3.7	2.1	7.0	2.9	15

Notes:
(1) Obtained from the total stored energy.
(2) At the straight corner of ro end.
(3) At the inner top corner of rectangular support.
(4) The supports and arms were assumed to be pairs of parallel strip conductor. The inductance and resistance per unit length are[5] $\frac{L}{l} = \frac{\mu}{2\pi}[ln(b/a) + 3/2]$ (H/m) , $R/l = \frac{...}{\sigma\delta}$ (Ω/m), where a and t are width and thickness of conductors. b is the conductors' seperation. σ = conductivity, δ = skin depth.
(5) Using equation (2), and C_{total} from MAFIA calculations
(6) Using equation (1). The contribution of the supports was not included.
(7) Using $E_s/V = 1.15/r_0$ as given by reference 6.
(8) It is estimated as $B_s = \frac{B_{s-C_{total}}}{\sqrt{2}(a+c)}$ at sharp corner of conductor and contributed by the support and arm. $C_{...}$ is taken from MAFIA results.
(9) This value is higher than the approximation because the simulated electrodes have sharp edges.
(10) Using C_{total} from MAFIA calculations.

The authors thank M. Vretenar, H. Kirk and L. Moorman for help in the MAFIA calculations. and P. Paul for his keen interest in this work.

References

1. A. Schempp, M. Fersh and H. Klein, *Proc. 1987 Particle Accelerator Conference* in *IEEE Trans. Nucl. Sci* **87CH2387-9**, 267(1987).
2. R.M. Hutcheon, File No. 9022/ZEBRA-TM-67, AEC, Chalk River.
3. I. Ben-Zvi, A. Lombardi and P. Paul, submitted to *Particle Accelerators*.
4. *MAFIA User Guide*, The Mafia Collaboration, DESY, LANL and KFA, 1988.
5. G.W. Carter, *The Electromagnetic Field in its Engineering Aspects*, Elsevier, New York, 1967, p.232.
6. K.R. Crandall, R.S. Mills and T.P. Wangler, *Proc. 1983 Particle Accelerator Conference, Santa Fe NM, LA-UR 83-743*

FIRST TESTS OF A SUPERCONDUCTING RFQ STRUCTURE

J. R. Delayen
Engineering Physics Division, Argonne National Laboratory, Argonne, Illinois 60439

K. W. Shepard
Physics Division, Argonne National Laboratory, Argonne, Illinois 60439

Abstract

High surface electric fields have been obtained in the first tests of a superconducting rf quadrupole device. The rf quadrupole fields were generated between niobium vanes 6.5 cm in length, with an edge radius of 2 mm, and with a beam aperture of 6 mm diameter. In tests at 4.2 K, the 64 MHz device operated cw at peak surface electric fields of 128 MV/m. Virtually no electron loading was observed at fields below 100 MV/m. It was possible to operate at surface fields of 210 MV/m in pulses of 1 msec duration using a 2.5 kW rf source. For the vane geometry tested, more than 10 square centimeters of surface support a field greater than 90% of the peak field. The present result indicates that electric fields greater than 100 MV/m can be obtained over an appreciable area, sufficient for some accelerator applications. It also shows that superconducting rf technology may provide an extended range of options for rf quadrupole design.

Introduction

Several workers have suggested that superconducting rf technology might provide a good means for achieving cw-operable, high-field rf quadrupole (RFQ) devices.[1,2] A problem in developing such devices is that present RFQ cavity geometries are generally quite different from the geometries used for superconducting rf devices. Parameters which have proven critical in superconducting cavity development, such as maximizing mechanical stability and minimizing peak rather than rms values of surface magnetic fields, have not been the critical parameters in the development to date of normally-conducting RFQ structures.

For this initial trial, rather than take on all aspects of developing an optimized superconducting RFQ, we have modified an existing superconducting accelerating device, the Argonne niobium split-ring resonator[3], in order to use it as an rf "voltage platform" on which to mount a 7 cm long superconducting niobium RFQ vane structure. While the resulting device could with little modification be used to accelerate beam, it does not represent an optimum design as an actual accelerating structure.

The object of the experiment was not to produce the front end of an ion accelerator, but to determine, for a realistic vane geometry, the field gradients one can expect for cw operation of a superconducting RFQ device. In this way, we can begin experimentally to establish a range of parameters for the design of superconducting RFQ accelerating structures.

*Work supported by the U.S. Department of Energy under contract W-31-109-ENG-38.

Resonator Design, Construction and Calibration

The split-ring assembly from an existing ATLAS resonator was modified, as shown in Figure 1, by replacing the drift tubes with shortened drift tubes to which the RFQ vanes were attached. Both the vanes and the drift tubes were made from high-thermal-conductivity Nb. The thermal conductivity of Nb is usually specified by the residual resistance ratio[4] which was about 250 for the material used.

The vanes were first welded to the drift tubes and the drift tube assemblies were chemically polished for 15 minutes in a 2:1:1 mix of phosphoric, nitric and hydrofluoric acids. The drift

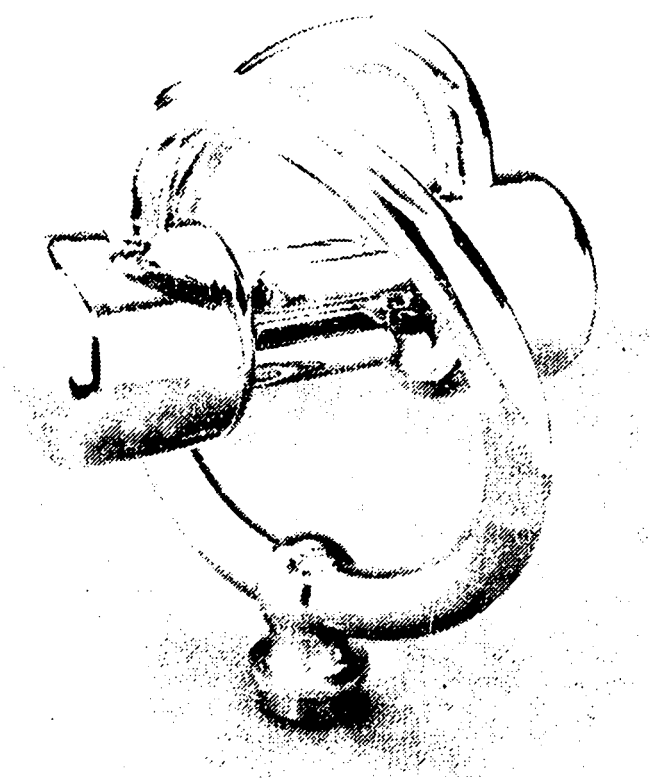

Fig. 1. Niobium split-ring assembly with RFQ vanes prior to being welding into the outer housing.

tube assemblies and the split ring arms were then annealed for 6 hours at 1190 °C. After welding was completed, the assembly (vanes, drift tubes and split-ring arms) was chemically polished again for 30 minutes. The split-ring was then welded back into the original resonator housing and the inside of the whole resonator was electropolished for 50 cycles. The resonator was assembled in a dust-free environment and then allowed to stand for three days filled with semiconductor-quality deionized water.

The resonator was drained and dried, then mounted in a test cryostat and evacuated. During pumpout, the resonator was warmed to about 50 °C for 24 hours and reached a vacuum of a few times 10^{-7} torr prior to cooldown. During the cryogenic test, rf power was coupled into the resonator through an adjustable magnetic coupling which could be varied from over-critical to very weak coupling.

The absolute rf field level was calibrated by the standard technique of measuring both the input power P while critically coupled and also the intrinsic resonator rf decay time τ. These two numbers determine the total rf energy content U of the resonator as $U = P * \tau$. The relationship between energy content and drift tube voltage was obtained by a perturbation measurement (bead pull test) which measured the electric field on axis as a function of the total rf energy content; the voltage was obtained by integrating the measured electric field from the resonator outer wall up to the face of the drift tube. Because the dimensions of the drift-tube and RFQ vane assembly are much smaller than the free-space wavelength, a quasi-static, near field approximation is quite accurate. Thus the code POISSON could be used to calculate the electric field on and near the vanes in terms of the voltage on the drift tubes.

The geometry of the quadrupole field region is shown in Figure 2. The aperture diameter is 6 mm, the vane edge radius is 2 mm and the minimum distance between vanes of opposite voltage is 3.1 mm. POISSON yields the result that, at a voltage difference of 200 kV between adjacent vanes, the peak surface electric field is 80.3 MV/m and that 10 cm^2 of area support a field greater that 90% of the peak field. We estimate the experimental error in determining the field level to be of the order of 5%.

We have not corrected the calibration for the rf-voltage drop along the vanes. The vanes can be considered as short (7 cm) sections of essentially TEM transmission lines, much shorter than the wavelength (470 cm), thus the voltage will be constant along their length to a fraction of a percent. We also have neglected any field enhancement at the end of the vanes. This field enhancement will be small since the radius at the end of the vane (10 mm) is much larger than the edge radius (2 mm). Both the above effects cause the actual fields to be higher than the quoted fields.

During a second test of the structure we measured the spectrum of the x-rays generated as a result of field emission, the cut-off in the spectrum corresponds to the intervane voltage. At the operating field the x-ray cutoff indicated an intervane voltage of 209 kV which is in agreement with a voltage of 174 kV calculated by the procedure described above.

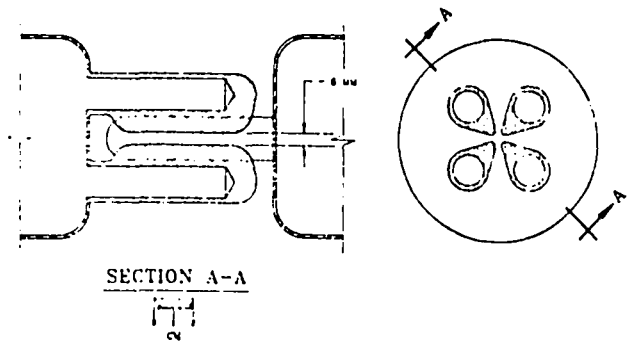

Fig. 2. Geometry of the vanes generating the rf quadrupole fields.

The peak surface magnetic field can be scaled from the value measured in the unmodified split-ring resonator by a factor which depends only on the change in frequency caused by the addition of the RFQ vanes. We estimate that for a peak surface magnetic field of 740 gauss, which is routinely achieved in cw operation of the unmodified ATLAS split-ring resonators, the peak surface electric field would be 211 MV/m. For pulsed operation, surface magnetic fields 50% higher can be sustained in the unmodified resonator. Thus, even at the field levels achieved, magnetic-field related processes should not limit the high-field performance of the present RFQ structure.

Experimental Results

Immediately upon cooldown, the structure exhibited multipacting barriers beginning at very low field levels (<10 MV/m surface field) which were conditioned completely away by the application of a few watts of rf power over a period of 2 - 3 hours. The observed multipacting behavior is typical of the unmodified ATLAS niobium split-ring resonators, and was found to be qualitatively unchanged by the addition of quadrupole vanes to the structure.

After low-power, cw conditioning to remove multipacting, the resonator was operated in a pulsed mode, using a 2500 watt rf source, at as high a field level as possible for about 30 minutes. The duty factor was one or two 10 msec pulses per second. Such high-power conditioning is the procedure currently used on the ATLAS superconducting linac to reduce high-field electron loading (presumably caused by field emission).

Figure 3 shows the resonator quality factor (Q) as a function of peak surface electric field at 4.2 K after conditioning. The qualitative behavior is typical of all split-ring resonators. The low-field Q is fairly constant and primarily determined by resistive losses associated with the rf surface magnetic field. Above 100 MV/m the losses increase rapidly with a corresponding decrease in Q. Fields of 128 MV/m could be sustained in cw operation and were limited by the inefficient cooling of the vanes. Higher fields could be achieved in pulsed operation by gradually reducing the duty factor. The maximum field was achieved using a pulsed 2.5 kW source, and 210

MV/m could be maintained for times in excess of 1 msec. The increased losses at high fields are due to electron loading (field emission), evidenced by the emission of x-rays and by the fact that the losses observed immediately on cooldown can be reduced by operating the resonator at high fields (conditioning).

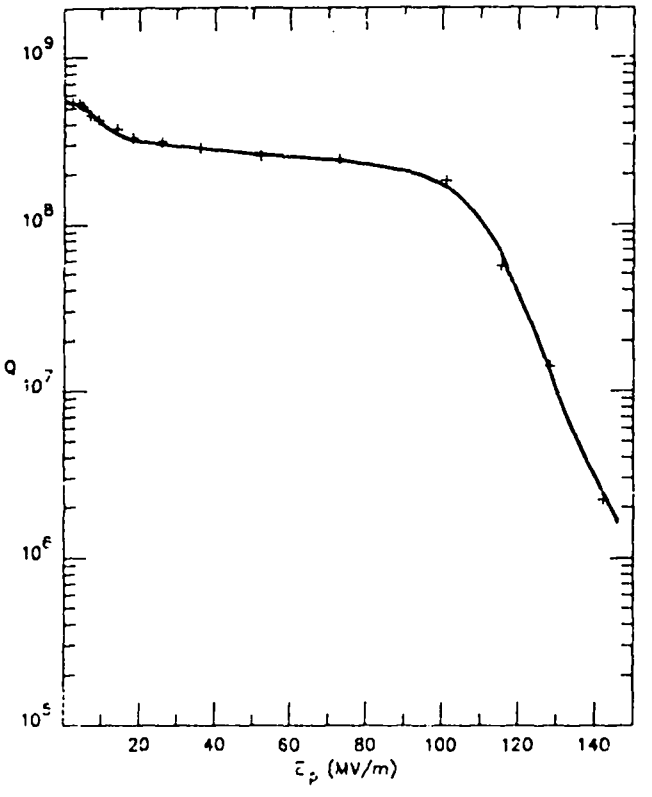

Fig. 3. Quality factor of the resonator at 4.2 K as a function of the peak surface electric field.

The cw fields which were achieved are comparable to those previously reported at higher frequency,[5] but were sustained over areas of the order of 10 cm^2 instead of a few mm^2. The pulsed surface electric fields are the highest which have been reported for superconducting niobium structures.

Electron loading is the field-limiting process in the present structure and will clearly be of prime importance in future designs. The present test demonstrates an RFQ vane structure requiring negligible rf power for surface electric field levels below 100 MV/m, 0.9 W per cm of RFQ structure at 115 MV/m, and 38 W/cm at 143 MV/m.

The RFQ structure is undergoing further testing after additional chemical polishing of the drift tubes and the vanes. Cw fields of 90 MV/m and pulsed fields of 110 MV/m have been achieved in preliminary results in this new series of tests.

Conclusions

There are several aspects of the present result that may have bearing on potential applications. The fields attained are substantially higher than expected for normally-conducting cavities of comparable frequency for either cw or pulsed operation.[6] Also, this initial superconducting RFQ device has operated at fields a factor of three higher than have been reported for cw operation of normally-conducting RFQ devices.[7] The present result indicates that superconducting rf technology may appreciably extend the range of options for RFQ design.

Acknowledgements

We thank C. Batson, C. L. Bohn, P. Markovich, and C. T. Roche for their assistance. This work was supported by the U.S. Department of Energy under contract No. W-31-109-Eng-38.

References

1. D. A. Swenson, IEEE Trans. Nucl. Sci., **NS-32**, 3240 (1985).

2. I. Ben-Zvi, Particle Accelerators, **23**, 265 (1988).

3. K. W. Shepard, IEEE Trans. Nucl. Sci., **NS-28**, 3248 (1981).

4. H. Padamsee, Proc. of the 2nd Workshop on rf Superconductivity, CERN, Geneva, Switzerland, Editor: H. Lengeler, 539 (1984).

5. D. L. Moffat, T. Flynn, K. Green, J. Kirchgessner, H. Padamsee, D. Rubin, J. Sears, Q. Shu, Proc. of the 4th Workshop on rf Superconductivity, KEK, Tsukuba, Japan, Editor: Y. Kojima, KEK Report 89-21, 445 (1990).

6. J. W. Wang, G. A. Loew, Proc. of the 1989 Particle Accelerator Conference, IEEE Catalog No 89CH2669-0, 1137 (1989).

7. S. O. Schriber, Proc. of the 1986 Linear Accelerator Conference, SLAC-Report-303, 591 (1986).

DESIGN AND APPLICATION POSSIBILITIES OF SUPERCONDUCTING RADIO-FREQUENCY QUADRUPOLES

A. Schempp, H. Deitinghoff
Institut für Angewandte Physik, J.W. Goethe Universität, 6000 Frankfurt, FRG

J. R. Delayen
Engineering Physics Division, Argonne National Laboratory, Argonne, Illinois 60439

K. W. Shepard
Physics Division, Argonne National Laboratory, Argonne, Illinois 60439

Abstract

In recent experiments,[1] cw surface electric fields in excess of 100 MV/m have been obtained in a superconducting rf quadrupole (SCRFQ) device. In this paper we explore some design and application possibilities of SCRFQs which have been opened by these results. For example, SCRFQs may be able to accelerate higher cw currents than is now possible. Also, highly-modulated SCRFQs could be designed to provide compact, high-longitudinal-gradient devices. Some conceptual designs and applications will be discussed.

Introduction

The radio-frequency quadrupole (RFQ) accelerator structure which is based on the concept of spatially homogeneous focusing[2,3] is applied in many low energy ion accelerators. It provides strong focusing and acceleration of ion beams which makes it especially attractive for the production of high-current high-brightness beams.

RFQ injectors have facilitated the introduction of new high-current ion sources, as well as electron cyclotron resonance (ECR) sources and electron beam ion sources (EBIS), for highly charged heavy ions.

Operational simplicity makes RFQ structures attractive for applications previously using electrostatic machines, e.g., neutron production and ion implanters. The main field of application, however, is high current ion accelerators in which a significant improvement in brightness has been achieved with specially designed RFQs.[3,4]

The maximum ion current that can be transported through an RFQ structure is roughly proportional to the voltage U between the RFQ electrodes. In normally-conducting RFQ structures, rf power requirements lead to pulsed operation with moderate voltages and small aperture. This approach is well suited for high current synchrotron injectors and combinations with an ECR or EBIS ion source.

*Work supported by the U.S. Department of Energy under contract W-31-109-ENG-38

Since the first proposal of the RFQ principle, attempts have been made to build a cw RFQ with high beam power. Cw RFQ accelerators have been constructed and operated at Los Alamos and Chalk River.[5] Proposals for SCRFQs have also been made in the past.[6,7]

Very high field strengths in an SCRFQ resonator have been recently obtained by two of the authors[1]. These results indicate that superconducting rf technology may appreciably extend the range of options for RFQ designs.

In the following sections some examples for conceptual SCRFQ designs will be discussed which indicate some of the new possibilities.

Design Considerations

The choice of the focusing and accelerating fields along the RFQ determines the properties of the ion beam. Generally, RFQ design has been studied in great detail to tailor the RFQ for the requirement of the specific application.[3,4]

The basic input parameters: injection energy T_i, structure frequency f, electrode voltage U, and average aperture a_m have to be chosen to match for the source emittance,the required beam emittance and ion current at the RFQ output. Other possible limits such as sparking, power density problems, rf efficiency, and mechanical stability have to be taken into account as well.

In RFQ structures the longitudinal accelerating field is roughly proportional to the frequency and, for a compact RFQs the frequency should be as high as possible. On the other hand, preserving the beam emittance requires "slow" acceleration and a comparatively long structure. This is one of the typical tradeoffs in RFQ design for which beam dynamics, rf, and mechanical design have to be balanced.[4]

A typical result of these design studies is a voltage around 100 kV, a minimum aperture radius of 1.5 to 3 mm for frequencies between 100 and 400 MHz.[8] For the 4-rod RFQ higher voltages and bigger apertures are usually chosen, which leads to shorter structures and eases rf and mechanical tolerances. At the low frequency of 27 MHz, voltages of up to

200 kV for acceleration of low charge state uranium have been proposed.[9]

Irrespective of the application, normally conducting RFQs have been designed to operate at surface fields between 1.5 and 2.5 the Kilpatrick field (E_k).[10] For high duty cycles more conservative values of 1.5 to 1.7 E_k are usually chosen.

In most RFQ designs, a majority of cells (half periods of the electrode modulation which correspond to a drift tube of a $n\lambda/2$-type accelerator) is used not for accelerating, but for transporting and bunching the ion beam: for example 200 out of 286 cells for the GSI HLI-RFQ.[11] This will not change much with higher electrode voltages. For the bunching section, higher fields can improve the design only in cases where focusing strength is the limiting factor.

High fields make significant improvements for three different cases of cw accelerators: (1) high currents and light ions (P,D), (2) highly charged heavy ions accelerators (ECR-RFQ combinations) (3) low charge state beams (e.g. radioactive beams, molecular ions, clusters).

Superconductivity brings a different set of constraints into the design process of RFQs. Sparking of the type observed in normal-conducting structures and expressed in terms of the Kilpatrick limit is usually not seen in superconducting structures. What is usually observed is a soft barrier caused by non-resonant electron emission (field emission). The dependence of the field emission limit on various parameters is not well understood, however it seems to be virtually independent of frequency.

Another limit is set by the rf critical field of the superconducting material which, for niobium, is slightly higher than 2000 gauss. Magnetic fields in excess of 1500 gauss have been achieved in actual superconducting structures. RFQs have surface magnetic field to surface electric field ratio which are smaller than usually seen in superconducting structures and, with some attention to the design to avoid current concentration, the surface magnetic field should not be a limiting factor.

For low-frequency, low-current applications, SCRFQ structures will suffer microphonic-induced phase noise similar to that previously experienced in helically-loaded SC structures.[12,13] While this is not expected to be an insuperable problem, structure design must fully consider the mechanical stability required for rf phase control.

Examples

Superconductivity is a natural solution to the problem of cw operation of accelerators. Prospects for this application are enhanced by results of the first test of a short SCRFQ structure, in which high surface electric fields (130 MV/m) and high inter-electrode voltages (300 kV) were obtained. Although these experimental results need to be confirmed in longer structures, they are most encouraging and we have developed a set of design examples based on an inter-electrode voltage of 300 kV:

1. Assuming a voltage of 300 kV between the electrodes, a 10 MeV D^+ RFQ operating at 400 MHz with a 100 mA output beam with a normalized emittance of 1 π mm-mrad could be as short as 1.8 m; its length at a frequency of 200 MHz, with even higher current, would still be very attractive (3.5 m). For a

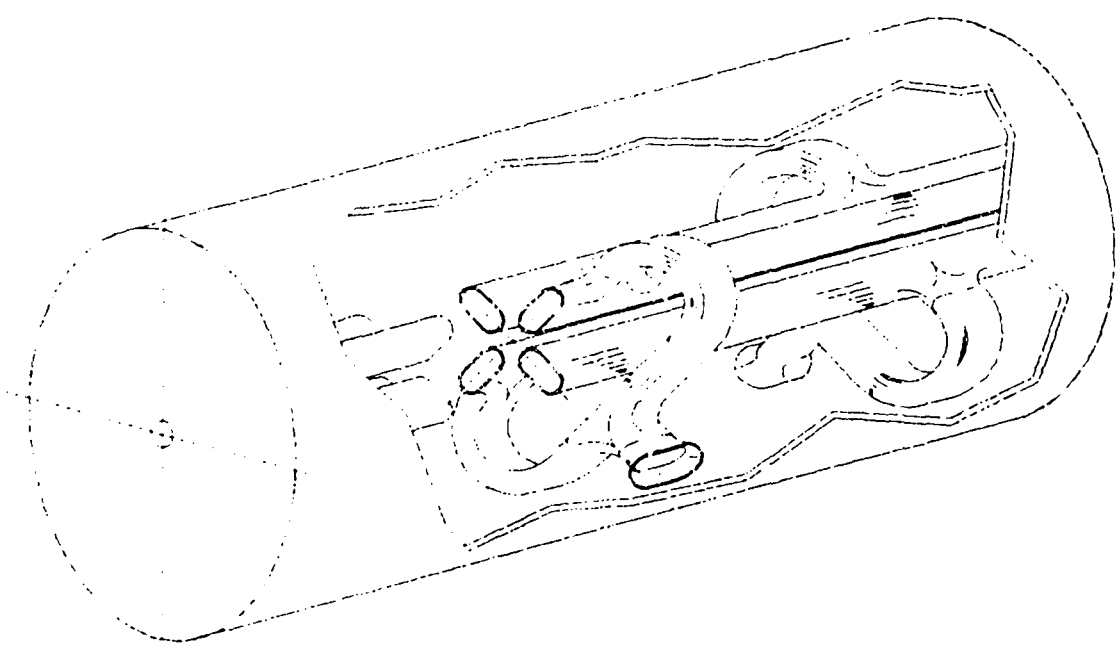

Fig. 1 Conceptual design of a low-frequency SCRFQ accelerator structure.

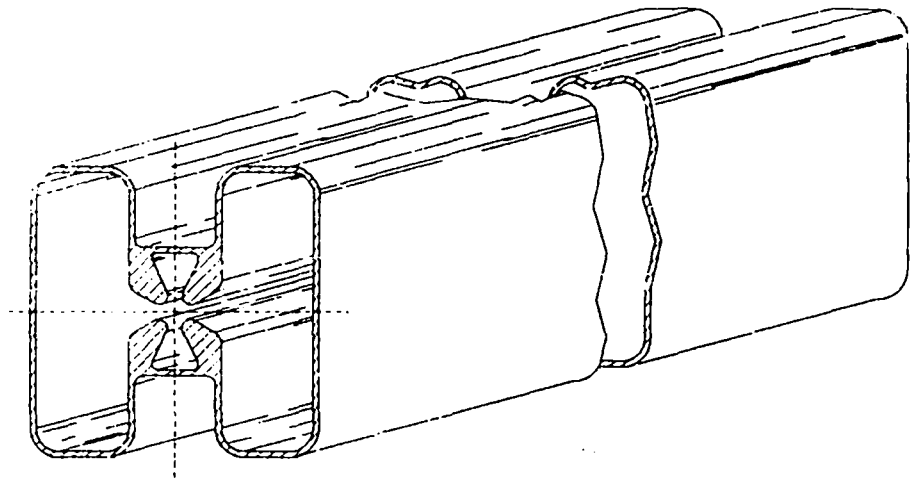

Fig. 2 Conceptual design of a high-frequency SCRFQ accelerator structure.

similar proton accelerator, the length would be 2.5 m at 400 MHz. In these examples, the RFQ has a high average accelerating field even when compared with conventional accelerating cavities. Taking into account that no lenses and cryostats have to interrupt the structure, the accelerating field of 5-8 MV/m in the structure roughly correspond to the actual "real estate gradient". By allowing a slight increase in the transverse emittance and the structure length, the current capability of such an accelerator could be as high as 500 mA.

2. Highly charged heavy ions can efficiently be produced in ECR sources.[14] Extrapolating the source development to a beam of U^{30+} and assuming ATLAS-like harmonic bunching off a 300 kV platform one avoids the need for a relatively long RFQ bunching section. With a 300 kV electrode voltage, a 100 MHz, 1 MeV/u RFQ can be relatively short: L = 2.1 m. The structure length would scale inversely with the charge to mass ratio.

3. An SCRFQ could also be very attractive for radioactive beam acceleration. One of the authors recently designed an RFQ accelerator for $^{27}Al^{1+}$ at ISOLDE.[15] This accelerator will produce 1 MeV/u, and is a machine of size similar to the pre-stripper portion of the UNILAC at GSI. Optimizing an SCRFQ for this application, again assuming 300 kV inter-electrode voltage, results in a surprisingly compact accelerator. For a frequency of 100 MHz the total RFQ length is 6.9 m. Injecting at 100 MHz and doubling the frequency at 0.4 MeV/u would reduce the total length to 5.1 m.

Conceptual designs for SCRFQs operating at low and high frequencies are shown in figures 1 and 2 respectively.

Conclusions

Compact, cw SCRFQ accelerators with high gradients and high currents can be designed for a variety of applications. Further experimental work is needed to determine with better confidence the paramoter values which can be used in the design of SCRFQs. In the case of low current applications the beam dynamics design does not require any major change from present designs. For high current applications, development would probably be required to handle the high beam power, e.g. 1 MW in example 1. Beam impingement in an important outstanding issue: solutions for radial matching must be improved, and fuller understanding of halo formation and emittance growth mechanisms is necessary.

References

1. J.R. Delayen and K.W. Shepard, these Proceedings.
2. I.M. Kapchinskij, V.A. Tepljakov, Prib. Techn. Eskp., **2**, 19 (1970).
3. K.R. Crandall, R.H. Stokes, T.P. Wangler, Proc. of the 1979 Linac Conference, BNL 51134, 205 (1979).
4. A. Schempp, Proc. of EPAC I,World Scientific Publishing Co., Singapore, 464 (1989).
5. G.E. McMichael, these Proceedings.
6. D.A. Swenson, IEEE Trans. Nucl. Sci., **NS-32**, 3240 (1985).
7. I. Ben-Zvi, Particle Accelerators, **23**, 255 (1988).
8. A. Schempp, Proc. of the 1988 Linac Conference,CEBAF-Report-89-001, 460 (1989).
9. A. Schempp, H. Deitinghoff, A. Kipper; Nuclear Instrum. and Methods, **A278**, 169 (1989).
10. W.D. Kilpatrick, Rev. Sci. Instrum., **28**, 824 (1957).
11. N. Angert, L. Dahl, J. Glatz, J. Klabunde, M. Müller, U. Ratzinger, B. Wolf, H. Deitinghoff, J. Friedrich, H. Klein, A. Schempp; these Proceedings.
12. G.J. Dick, K.W. Shepard; Proc. of the 1972 Applied Superconductivity Conference, 649 (1972).
13. G. Hochschild, D. Schulze, F. Spielbock; IEEE Trans. Nucl. Sci., **NS-20**, 71 (1973).
14. R.C. Pardo; these Proceedings.
15. H. Haas H. Ravn, A. Schempp, B.W. Allardyce, B. Jonson, C. Rolfs; Proc. of the First International Conference on Radioactive Nuclear Beams, World Scientific Publishing Co., 59 (1990).

APPLICATION OF RF SUPERCONDUCTIVITY TO HIGH-BRIGHTNESS ION BEAM ACCELERATORS*

J.R. Delayen, C.L. Bohn, and C.T. Roche
Argonne National Laboratory, Engineering Physics Division
9700 South Cass Avenue, Argonne, Illinois 60439

Abstract

A development program is underway to apply rf superconductivity to the design of cw linear accelerators for high-brightness ion beams. The key issues associated with this endeavor have been delineated in an earlier paper. Considerable progress has been made both experimentally and theoretically to resolve a number of these issues. In this paper we summarize this progress. We also identify current and future work in the areas of accelerator technology and superconducting materials which will confront the remaining issues and/or provide added capability to the technology.

I. Introduction

The motivation and issues associated with the application of rf superconductivity to linear accelerators for high-brightness ion beams have been discussed in an earlier paper.[1] The following major development work areas were identified: Resonator Geometry, Beam Impingement, Focusing, Beam Instabilities, Beam Loading/Control, and Materials. Since the publication of this paper, a number of promising experimental results have been obtained in the areas of Resonator Geometry and Materials. Niobium cavities with coaxial quarter-wave and half-wave geometries have yielded cw accelerating gradients as high as 18 MV/m. A resonator with an RFQ geometry sustained cw electric fields as high as 128 MV/m over a 10 cm^2 surface area. The rf surface resistance of a wide variety of high-T_c superconductors have been measured in the presence of high rf surface magnetic fields. The results of these experiments are summarized here. In addition, beam impingement and cumulative beam breakup have been calculated for high-brightness ion linacs, and the results are presented here.

II. Niobium Resonators

Our approach to the development of niobium resonators for the acceleration of high-brightness ion beams is based on the use of some form of resonant line with the beam traversing the high-voltage region. This approach was found to be successful in the development of existing slow-wave superconducting structures at lower frequencies.[2]

The first of these cavities to be fabricated was a 400 MHz coaxial quarter-wave structure optimized for particle velocity 0.15c.[3] It yielded an average cw accelerating gradient of 12.9 MV/m with 21 W of rf power input to the cavity. This corresponded to an energy gain of 0.820 MV per unit charge.

Subsequently a 355 MHz coaxial half-wave structure optimized for particle velocity 0.12c was fabricated.[3] It yielded an average cw accelerating gradient of 18 MV/m with 40 W power input to the cavity. This corresponded to an energy gain of 1.26 MV per unit charge. At 10 MV/m, the power dissipation was 2 W. The accelerating gradient of this cavity is the highest achieved in a low-velocity structure. Because of its promising performance, this resonator is the prototype cavity for a superconducting section which is planned for fabrication and testing with a D^- beam of energy 7.5 MeV and current 80 mA.

Work in progress includes the fabrication of a 2-gap, 850 MHz spoke resonator.[1] In addition, the 3-gap, 850 MHz spoke resonator shown in Figure 1 is planned for construction. This resonator should provide a larger real-estate gradient than is available with 2-gap structures.

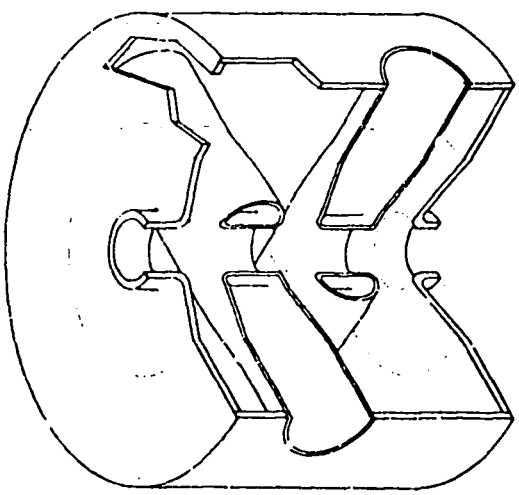

Fig. 1. Conceptual design of a 3-gap spoke resonator.

During its cryogenic tests, the first superconducting RFQ device was operated at fields a factor of three higher than have been reported for cw operation of normally-conducting RFQ structures.[4] The results suggest that rf superconductivity may appreciably extend the range of options for RFQ design. Possible applications and designs of superconducting RFQs are under study.[5]

III. Superconducting Materials

High-T_c Superconductors. We have constructed and used several apparatuses for measurements of rf surface resistance (R_s) at frequencies from 0.15 to 40 GHz and rf surface magnetic fields (B_{rf}) as high as 640 gauss.[6] The most recent to be constructed is a coaxial quarter-wave cavity designed

*Work supported by the U.S. Department of Energy under contract W-31-109-ENG-38 and the U.S. Army Strategic Defense Command.

specifically for measurements of disk-shaped samples at 820 MHz and 4.2 K, and at B_{rf} ranging to hundreds of gauss.[7] The frequency was chosen to be representative of an accelerator.

A wide variety of films on silver and dielectric substrates spanning an enormous range of materials and fabrication techniques were measured with the quarter-wave cavity.[6] Most were approximately 24 mm in diameter by 0.5 mm thick. Most of the films on silver substrates covered all surfaces of the substrate. The qualitative behavior of the surface resistance of films on silver substrates is identical for each material: R_s increases monotonically with field amplitude through a transition region characterized by a strong field dependence, and then saturates at high field at a value of a few percent of the normal-state R_s just above T_c. This is a signature of the polycrystalline nature of the films and does not reflect their intrinsic properties. For example, R_s of epitaxial films on dielectric substrates degraded at high fields, but were substantially better than R_s of the polycrystalline films at high fields. Nevertheless, the degradation in R_s needs to be mitigated by a suitable process of materials engineering before high-T_c superconductors can be of use in accelerating cavities.

In light of these results, niobium and its alloys will likely remain the materials of choice in the near future for accelerator applications.

Niobium. A "voltage platform" was constructed to determine, for a realistic (four-finger) vane geometry, the field gradients which could be expected in the cw operation of a superconducting RFQ.[4] With this vane geometry, cw fields of 128 MV/m could be sustained over a surface area of order 10 cm^2 and were limited by the inefficient cooling of the vanes. In pulsed operation, 210 MV/m could be maintained for times in excess of 1 msec. These results indicate that there is no fundamental reason preventing niobium resonators from operating at gradients substantially higher than those routinely achieved today.

An increase in achievable surface fields has been obtained by high-temperature treatment of niobium structures[8], and we are now building a facility for this. We are also beginning to investigate films of niobium alloys for applications in accelerating cavities.

III. Theoretical Considerations (U)

Beam Impingement. We study beam impingement with a model which includes heat transport both in the resonator wall and at the interface between the resonator wall and the cryogen. The model incorporates the worst-case assumption that the ions will deposit their total kinetic energy (taken to be 200 MeV) at the niobium-vacuum interface. The heat-transport problem is approximated as one-dimensional heat flow across a plane. The cryogen is assumed to be liquid helium at 4.2 K (He I).

The heat-transport problem is dominated by the interface between the resonator wall and the liquid helium. To maximize the heat flux while minimizing the temperature difference at the interface, it is necessary to operate in the nucleate-boiling regime and to avoid film boiling. This will limit the rate of heat removal to 1 W/cm^2 and the temperature difference between the wall and bath to 1 K.[9] Assuming the accelerating structure is fabricated from RRR=250 niobium, which has thermal conductivity ~1 W/cm-K at 5.2 K,[10] the temperature rise at the niobium-vacuum interface will be of order 0.2 K. Since niobium has T_c=9.2K, this temperature increase would not present a serious problem for a cavity operating at 4.2 K.

The rate of heat removal restricts the amount of beam which can be permitted to impinge on a resonator. A 2D-Gaussian beam (σ_{rms}=0.6 mm) of H^- ions with 200 MeV energy and 100 mA current is assumed. Given a perfectly centered beam and a 1 W/cm^2 heat flux, the drift tube aperture would need a minimum diameter of 6.7 mm to prevent thermal runaway. By comparison, a typical superconducting resonator such as the structures described above has an aperture of order 25 mm. Thus, we conclude that, given large apertures in the constituent resonators, beam impingement in a superconducting linac will not result in a thermal management problem. Moreover, both beam scrapers and focusing elements can be placed between the resonators to reduce beam impingement further.

If beam impingement were to occur despite these preventive measures, then cryogen would be consumed. The amount would depend on the beam flux impinging on the accelerator. As an illustration, we consider an accelerator consisting of 200 superconducting resonators each of which is being impacted by beam over a 5cm^2 area resulting in a heat flux of 1 W/cm^2. Liquid helium evaporates at a nominal rate of 1.4 l/W-hr. Therefore, in this example, the rate of liquid helium consumption would be less than 0.4 l (nominally 50 g) per second of operation.

Cumulative Beam Breakup. A section of 352 MHz niobium coaxial half-wave cavities is currently being designed for experiments with a D^- beam of energy 7.5 MeV and current 80 mA. The section is a step along ther development path toward a full superconducting high-current ion linac. We assume both the section and the full linac will provide a real-estate gradient of 4.5 MV/m. We consider cumulative beam breakup (BBU) in both cases by applying a BBU formalism developed elsewhere.[11] The notation and equations cited here correspond to the notation and equations of Ref. 11. We assume pessimistically a misaligned beam with the worst possible beam-cavity resonance, for which $\omega\tau=4\pi(1+1/2Q)$ and $p(\omega\tau)=Q/\pi$ [cf. eq. (18)], to calculate the Q of the corresponding deflecting mode needed to keep the transverse displacement below approximately twice the initial displacement at the exit aperture of the linac.

To calculate the geometry factor Γ of the deflecting modes, we model the coaxial half-wave geometry as a TEM cavity in which the inner and outer conductors have radii a and b, respectively, and the cavity has height $h=\lambda_0/2$, where λ_0 is the wavelength of the fundamental (accelerating) mode. From eq. (4), the corresponding geometry factor is

$$\Gamma = \frac{8\omega\left[si\left(\frac{\omega b}{\beta c}\right) - si\left(\frac{\omega a}{\beta c}\right)\right]^2}{\pi e_0 c^2 h \ln(b/a)} .$$

To evaluate Γ numerically, we choose b=2a and $a+b=\beta\lambda_o/2.2$, consistent with the design of slow-wave structures.[12]

We assume the section consists of five 352 MHz cavities with no focusing. The geometry factor is $\Gamma=5.97\times10^{-7}\omega\ \Omega/m^2$. The initial and final beam energies are 7.5 MeV and 10.9 MeV, respectively, for which $\beta(0)=.089$, $\gamma(0)=1.004$, and $\beta(\mathcal{L})=.107$, $\gamma(\mathcal{L})=1.006$. The section therefore provides approximately a coasting beam with $\beta=.089$, $\gamma=1$, $\langle I\rangle=.08$ A, and no net focusing. The spacing between cavities is taken to be $L=2\beta(0)\lambda_o=.152$m, and the total accelerating length is $\mathcal{L}=4L=.608$m. Given the worst-case resonance, the steady-state displacement dominates. From eqs. (2) and (17), the Q which allows transverse displacement ξ_∞ at $\mathcal{L}$ is

$$Q = \frac{2p}{\langle I\rangle Ze}\frac{\omega}{\Gamma}\frac{L}{\mathcal{L}^2}\ln^2\left(\frac{2\xi_\infty}{\xi_o}\right).$$

We find $Q\le1.9\times10^7$ assures $\xi_\infty/\xi_o\le2$. By comparison, the external Q of the accelerating mode required to couple to the high current should be $\sim10^5$. The rf coupling would probably also provide an external $Q<10^7$ for the deflecting mode and thereby control BBU.

We now consider a full linac, the basic conceptual idea of which is to extend the section to accelerate a $\langle I\rangle=100$ mA D^- beam from 5 MeV to 200 MeV, for which $\beta(0)=.0728$, $\gamma(0)=1.003$, and $\beta(\mathcal{L})=.428$, $\gamma(\mathcal{L})=1.106$. We treat this beam as nonrelativistic ($\gamma=1$) and assume a linear accelerating gradient ($d\gamma/ds=G=2.37\times10^{-3}m^{-1}$). With a 4.5 MV/m real-estate gradient, the linac length is $\mathcal{L}=43$m. We assume the cavities all have $\Gamma=5.97\times10^{-7}\omega\ \Omega/m^2$ and are spaced in the manner $L=L_o[\beta/\beta(0)]$ with $L_o=.124$m, so that the total number of cavities is $N(\mathcal{L})=\int ds/L(s)=88$. We also assume that 10T solenoids occupy 25% of the linac and are equivalent to a uniform focusing field B=5T along the whole linac. Then, from eq. (20) with $\phi=-30^\circ$, the net transverse focusing wavenumber is $k_T=k_B$. As specified, this linac provides a nonrelativistic, slowly accelerated beam with strong solenoidal focusing, and thereby fulfills the assumptions leading to eqs. (21) and (22). The strong focusing provides an oscillatory steady-state displacement, and the transient term dominates. Evaluating the maximum amplitude ξ_{max} from eq. (22) and using equations (2) and (20) for $\epsilon(0)$ and $k_B(0)$, respectively, we find that the Q which allows transverse displacement ξ_{max} at $\mathcal{L}$ is

$$Q = 2\frac{B}{\langle I\rangle N}\frac{\omega}{\Gamma}\ln\left[\frac{2\xi_{max}}{\xi_o}\sqrt{\pi\frac{\langle I\rangle N}{B}\frac{\Gamma}{\omega}Q}\right].$$

As indicated in Fig. 2, the maximum transverse displacement is a sensitive function of the Q of the deflecting mode. We find approximately $Q\le5.5\times10^6$ assures $\xi_{max}/\xi_o\le2$. Just as for the section, the rf coupling would probably provide an external Q lower than this and thereby control BBU.

The limits on Q would be larger than those calculated here if a more realistic set of assumptions were used. For example, the frequencies of the higher-order modes in coaxial half-wave structures would be substantially removed from a harmonic of the fundamental (accelerating) mode due to capacitive laoding. This means the magnitude of the resonance function $p(\omega\tau)$ would be much less than we assumed, and BBU growth would be correspondingly lower. Other mitigating factors are listed in Ref. 11.

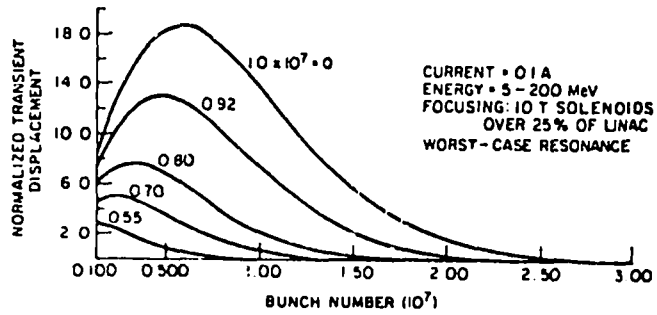

Figure 2. Normalized transient displacement ξ_M/ξ_o vs. bunch number M at the last cavity of the full D^- linac (see text). Curves correspond to different values of Q of the deflecting mode.

V. Conclusions

Recent results in the work areas of Resonator Geometry, Beam Impingement, Beam Instabilities, and Materials (i.e., niobium) make the prospects for superconducting high-brightness ion accelerators very encouraging. We are now developing a section of resonators and focusing elements to test with high current and thereby gather results in the work areas of Focusing and Beam Loading/Control. In addition, we are designing superconducting RFQs and plan eventually to explore the possibility of constructing compact linacs from RFQs for the acceleration of high-current ion beams.

References

1. J.R. Delayen, Nucl. Instrum. and Meth., **B40/41**, 892 (1989), and Proc. 1988 Linear Accelerator Conference.
2. J.R. Delayen, Proc. 4th Workshop on rf Superconductivity, KEK, ed. by Y. Kojima, 249 (1989).
3. J.R. Delayen, C.L. Bohn, and C.T. Roche, these Proceedings.
4. J.R. Delayen and K.W. Shepard, these Proceedings.
5. A. Schempp, H. Deitinghoff, J.R. Delayen, and K.W. Shepard, these Proceedings.
6. J.R. Delayen, C.L. Bohn, and C.T. Roche, J. Supercon., **3**, 243 (1990) and Proc. 1990 Applied Superconductivity Conference, Aspen, CO 24-28 Sep 90.
7. J.R. Delayen, C.L. Bohn, and C.T. Roche, Rev. Sci. Instrum., **61**, 2207 (1990).
8. Q.S. Shu, J. Graber, W. Hartung, J. Kirchgessner, D. Moffat, R. Noer, H. Padamsee, D. Rubin, and J. Sears, Cornell University Report CLNS-90/1005 (1990).
9. D. Lyon, Adv. Cryo. Eng., **10**, 371 (1965).
10. H. Elias and W. Weingarten, CERN/EF/RF 82-8 (1982).
11. C.L. Bohn and J.R. Delayen, these Proceedings.
12. J.R. Delayen, Nucl. Instrum. and Meth., **A259**, 341 (1987).

EXPERIMENTAL RESULTS IN SUPERCONDUCTING NIOBIUM RESONATORS FOR HIGH-BRIGHTNESS ION BEAM ACCELERATION

J.R. Delayen, C.L. Bohn, and C.T. Roche
Argonne National Laboratory, Engineering Physics Division
9700 South Cass Avenue, Argonne, Illinois 60439

Abstract

Two niobium resonant cavities for high-brightness ion beam acceleration have been constructed and tested. The first was based on a coaxial quarter-wave geometry and was optimized for phase velocity β_0=0.15. This cavity, which resonates at 400 MHz in the fundamental mode, operated at an average (wall-to-wall) accelerating gradient of 12.9 MV/m under continuous-wave (cw) fields. At this gradient, a cavity Q of 1.4×10^8 was measured. The second was based on a coaxial half-wave geometry and was optimized for β_0=0.12. This cavity, which resonates at 355 MHz in the fundamental mode, operated at an average accelerating gradient of 18.0 MV/m under cw fields. This is the highest average accelerating gradient achieved to date in low-velocity structures designed for cw operation. At this gradient, a cavity Q of 1.2×10^8 was measured.

I. Introduction

Most of the development work on superconducting cavities has been done in connection with high-energy electron accelerators and heavy-ion boosters for electrostatic accelerators.[1-3] While the former have accelerated beams of several mA current, the latter have accelerated beams of only μA current. The resonators described in this paper mark the first steps toward the development of compact superconducting linear accelerators for high-current, high-brightness ion beams.[4]

Most superconducting resonators for heavy-ion acceleration span a band in eigenfrequency-velocity space from roughly f=50 MHz, β=0.01 to f=200 MHz, β=0.2.[5] The most successful low-velocity structures are based on some form of resonant line with the beam traversing the high-voltage region. Thus, our development approach involves extending this resonator class to higher frequencies and velocities. In turn, we have constructed and operated a coaxial quarter-wave structure at f=400 MHz which was optimized for β_0=0.15, and a coaxial half-wave structure at f=355 MHz which was optimized for β_0=0.12.

II. Coaxial Quarter-Wave Resonator

A schematic of the coaxial quarter-wave resonator appears in Figure 1. The inner conductor was formed from 0.16-cm-thick sheet niobium of high RRR value (200-250) and was filled with liquid helium during testing. The outer conductor was fabricated from a cylinder comprised of a 0.16-cm-thick sheet of niobium which was explosively bonded to copper. The copper, a good thermal conductor, extracted heat from the niobium, a relatively poor thermal conductor, and transferred it to an adjacent liquidhelium reservoir. The bore-hole diameter was selected to be approximately 2.5 cm to reduce the likelihood of beam impingement, and the length of each gap was approximately 1.6 cm. All welds were made with an electron-beam welder. The bottom plate of the resonator was located relatively far from the inner conductor so that the rf fields at this plate would be weak. This allowed the plate to be demountable, enabling easy access to the interior surfaces of the cavity.

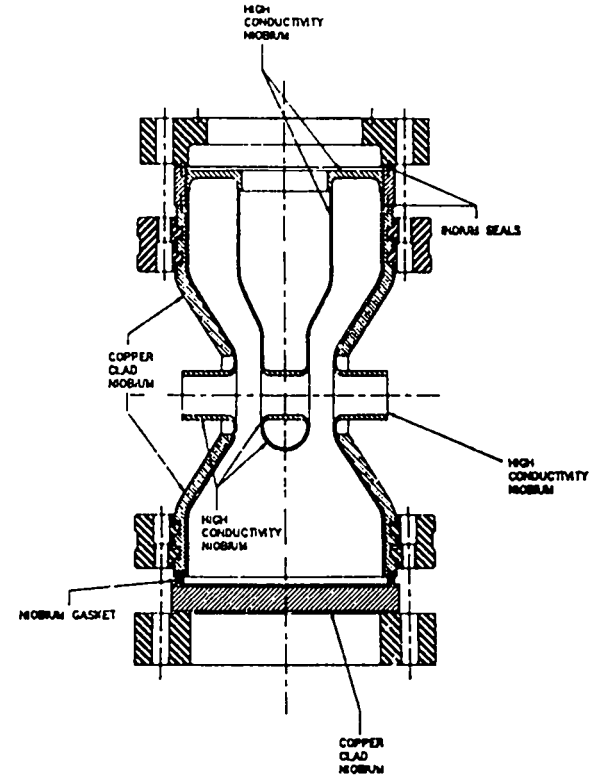

Fig. 1 400 MHz coaxial quarter-wave resonator; β_0=0.15.

Table 1. Properties of the coaxial quarter-wave resonator.

Frequency	400 MHz
β_0	0.15
Energy gain[a)]	63.5 kV
Peak surface E field[a),b)]	3.2 MV/m
Peak surface B field[a),b)]	58 G
Energy content[a)]	9.6 mJ
Geometrical factor QR_s	38.3 Ω

[a)]at an accelerating field of 1 MV/m.
[b)]calculated from Ref. 6.

*Work supported by the U.S. Department of Energy under contract W-31-109-ENG-38 and the U.S. Army Strategic Defense Command.

Special care was taken to prepare the surfaces of the inner conductor and shorting plate after these two pieces were welded together. The surface treatment began with electropolishing in a 17:3 solution of sulfuric acid and hydrofluoric acid, respectively, to remove approximately 15 μm of niobium. This was followed by annealing in a 4×10^{-7} torr vacuum for approximately 13 hours at 1200 C (5 hours at full temperature). An additional electropolishing to remove another 135 μm of niobium was then performed. Afterwards, the piece was annealed a second time and welded to the outer conductor.

A final treatment of the niobium surfaces of the whole resonator was done to remove surface imperfections generated during the welding of the inner and outer conductors (e.g. weld beads, sharp edges, etc.). The geometry of the cavity made it difficult to design electrodes for concentrated electropolishing of this weld area. Consequently, the final treatment was a chemical polish using a 2:1:1 solution of phosphoric acid, nitric acid, and hydrofluoric acid, respectively. Initially, a brief polish was done to remove approximately 25 μm from the niobium surface in the region of the closure weld with successively less material removed away from this area. The resonator was then cooled and tested using the procedure described below, and an average accelerating gradient of 5 MV/m was achieved. The cavity Q degraded sharply above this level due to the onset of a thermal instability. Subsequent examination of the resonator's inner surface with a fiber optic probe revealed what appeared to be small residual weld beads in the general vicinity of the weld connecting the shorting plate and the outer conductor. Therefore, a second chemical polish was done to remove an additional 50 μm from the surface. Subsequent testing of the resonator yielded the results described below.

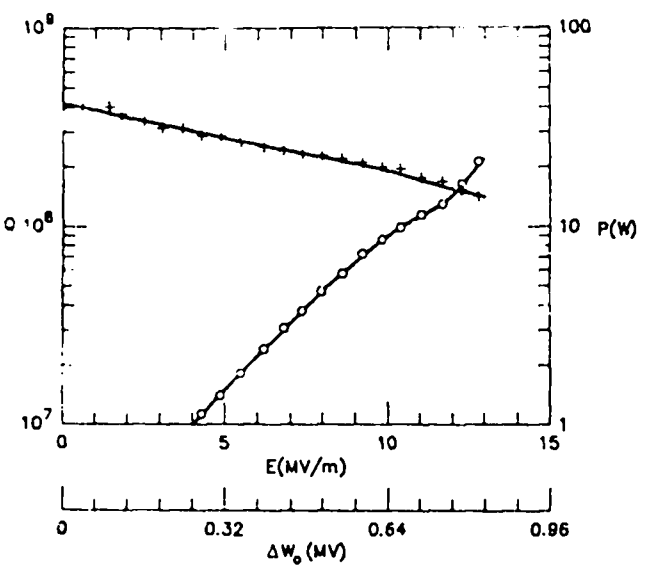

Fig. 2 Q-curve for the 400 MHz quarter-wave resonator.

At the beginning of the test, several multipacting levels appeared, they processed out rapidly, however. After multipactor processing was completed, a Q-curve was measured. As shown in Figure 4, Q varied from 4.1×10^8 at low rf field amplitude to 1.4×10^8 at the highest field achieved. Attempts to go higher in power resulted in a thermal instability in the cavity. X-ray radiation was monitored along the beam line with a detector located external to the cryostat. The maximum x-ray intensity observed was 17 mR/hr, indicating that field emission was always low. Accordingly, the power dissipated in the cavity was also low.

An average accelerating gradient of 12.9 MV/m was achieved with 21 W of rf power input to the cavity. This corresponds to an energy gain of 0.820 MV per unit charge. The associated peak surface electric and magnetic fields were approximately 41 MV/m and 750 G, respectively. Average accelerating gradients as high as 14 MV/m were achieved in the pulsed mode and were limited by a thermal instability. Because electron emission was low, no attempt was made to condition the cavity with either rf power or helium gas. The resonator was not shielded from ambient magnetic fields, so the degradation of Q with increasing field could have been due to losses from trapped flux in the superconducting niobium.

III. Coaxial Half-Wave Resonator

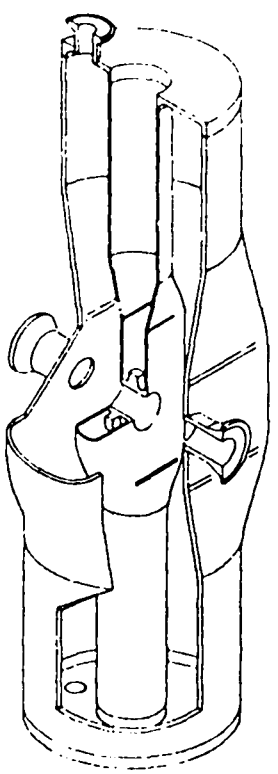

Fig. 3 355 MHz coaxial half-wave resonator; $\beta_0=0.12$.

A schematic of the coaxial half-wave resonator appears in Fig. 3. The inner and outer conductors were formed from 0.16-cm-thick and 0.32-cm-thick sheet niobium, respectively, of high RRR value (200-250). The bore-hole diameter was selected to be approximately 2.5 cm, and the length of each gap was approximately 2.5 cm. All welds were made with an electron-beam welder. There were no demountable plates in this cavity,

and thus the closure weld could not be inspected in detail. Accordingly, fabrication of this geometry is riskier than that of the coaxial quarter-wave geometry. This cavity is the first coaxial half-wave structure ever made.

The niobium resonator components were chemically polished at various stages during the fabrication process. The preliminary polishings were designed to remove damaged niobium surfaces resulting from mechanical stress introduced during the piece-forming steps. After the closure welds were completed a final chemical polish was performed to eliminate weld spatter and sharp edges which could not be identified by visual inspection. The chemical polishing procedure consisted of immersing the niobium piece in a 2:1:1 solution of phosphoric acid, nitric acid, and hydrofluoric acid, respectively, for 20 - 30 min. Approximately 60 microns of Nb are removed by this process. The piece was then rinsed in a 5% solution of H_2O_2 to remove insoluble niobium salts. This was followed by rinsing the piece with deionized water of semiconductor purity. After the final chemical polish the resonator was stored in a deionized water path for approximately 48 hrs. prior to mounting the rf pickup and drive coupling loops. The final step prior to rf testing of the cavity was to clean ultrasonically the structure in a high-purity methanol bath.

Table 2. Properties of the coaxial half-wave resonator.

Frequency	355 MHz
β_0	0.12
Energy gain[a)]	70.0 kV
Peak surface E field[a),b)]	3.2 MV/m
Peak surface B field[a),b)]	52 G
Energy content[a)]	12 mJ
Geometrical factor QR_s	53.3 Ω

[a)] at an accelerating gradient of 1 MV/m.
[b)] calculated from Ref.6

Early in the test several multipacting levels appeared as the power input to the cavity was increased. Critical coupling was established in the presence of this multipacting by varying the input line impedance. Once this was done, the multipacting processed out almost immediately to the point where no remaining multipacting levels were observed.

After multipactor processing was completed, a Q-curve was measured by monitoring the forward, reflected and pickup powers. As shown in Figure 4, Q varied from 7.7×10^8 at low rf field amplitude to 1.2×10^8 at the highest field achieved. In making these measurements, an average accelerating field of 10 MV/m was readily achieved. The cavity was then run overnight at moderate power (of order 10 W) to process out field-emission sites. An average cw accelerating gradient of 18.0 MV/m was then achieved with 40 W of rf power input to the cavity. X-ray radiation was monitored with a detector located external to the cryostat. The x-ray intensity at high rf fields was >200 mR/hr, indicating that electron loading in the form of field emission was present. Upon calibrating a NaI(Tl) photon detector and measuring the bremmstrahlung from the most energetic electrons, the average accelerating gradient was calculated.

The 18 MV/m gradient corresponds to an energy gain of 1.26 MV per unit charge. The associated peak surface electric and magnetic fields were approximately 58 MV/m and 936 G, respectively. Accelerating gradients as high as 10 MV/m could be generated with less than 2 W power input.

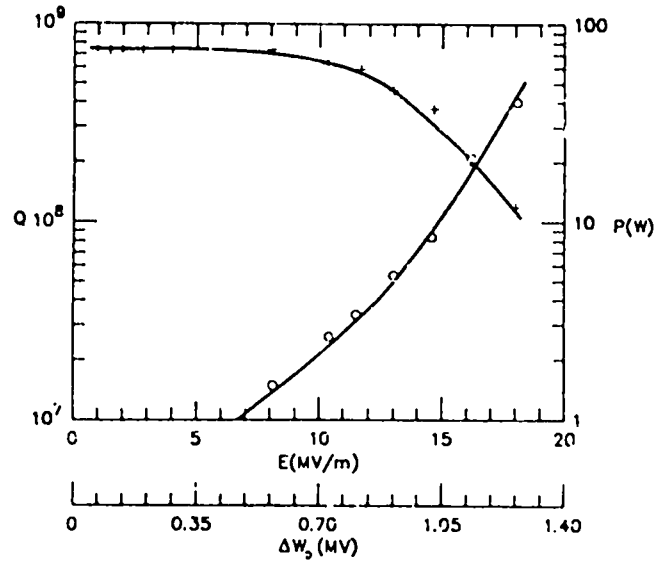

Fig. 3 Q-curve for the 355 MHz half-wave resonator.

IV. Conclusions

Niobium quarter-wave and half-wave structures have been constructed and operated. The half-wave structure achieved average cw accelerating gradients as high as 18 MV/m, which is a record for low-velocity superconducting resonators. The corresponding peak surface magnetic field was only 936 G, which is well below the rf critical field of niobium. Thus, these geometries provide the potential for even higher gradients.[10]

We are grateful to C. Batson for his assistance in the fabrication and testing of the resonators.

References

1. Proc. of the Second Workshop on rf Superconductivity; CERN, 1984; Editor: H. Lengeler.

2. Proc. of the Third Workshop on rf Superconductivity; Argonne, 1987; Editor: K. W. Shepard.

3. Proc. of the Fourth Workshop on rf Superconductivity; KEK, 1989; Editor: Y. Kojima.

4. J.R. Delayen, C.L. Bohn, and C.T. Roche, these Proceedings.

5. J.R. Delayen, Nucl. Instrum. and Meth., **B40-41**, 892 (1989).

6. J.R. Delayen, Nucl. Instrum. and Meth., **A259**, 341 (1987).

DESIGN OF A SUPERCONDUCTING INTERDIGITAL ACCELERATOR STRUCTURE FOR RADIOACTIVE HEAVY IONS

J.S. Fraser and H.R. Schneider
TRIUMF, 4004 Wesbrook Mall Vancouver, B.C. Canada V6T 2A3

Abstract

An on-line isotope separator (ISOL) has been installed on one of the beamlines at the TRIUMF cyclotron. Assuming a 60 keV/u, 50 MHz RFQ preaccelerator, a drift-tube linac design based on the superconducting interdigital structure developed at the Argonne National Laboratory, has been studied for acceleration of the ISOL radioactive beams. The linac consists of a first stage with 12 four-gap 50 MHz resonator tanks and 6 inter-tank superconducting solenoid lenses, followed by a second stage operating at 100 MHz, with 21 tanks and 7 inter-tank solenoids. This then can deliver a 1.6 MeV/u beam of ions with $q/A \geq .05$. Including solenoid lens space, the equivalent average acceleratiing gradient for singly charged ions is 1.9 MeV/m, about 60% higher than for a room temperature design reported earlier.[1]

The design was developed using a modified version of the PARMELA code, called PARMION, which dynamically varies the cell lengths to maintain a specified synchronous phase. The optimum synchronous phase was found to be -15°.

Introduction

Motivated primarily by a desire to study nuclear reaction cross sections involving short lived radioactive nuclei that are of astrophysical interest, a conceptual design of a post accelerator for a planned ISOL (isotope separator on line) facility at TRIUMF was developed about five years ago.[1] The accelerator considered at that time was a two stage linac, consisting of an RFQ to capture bunch, and accelerate the very low energy, singly charged ions from the ISOL to 60 keV/u, followed by a stripper to increase the ion charge to mass ratio (q/A) to a least 1/20, before being further accelerated in a Wideroe type drift-tube linac (DTL), to a final energy of 1 MeV/u. Conventional room temperature structures were considered in this case, and would have required more than 1 MW of cw rf power.

In recent years significant progress has been made in superconducting accelerator structure development. At ANL in particular, low beta interdigital structures have been built in which accelerating gradients greater than 6 MeV/m have been achieved[3]. It is possible that similar structures could be used in place of the Wideroe DTL to not only reduce the rf power requirement but perhaps also reduce the overall linac length. The study reported here was undertaken therefore to examine the use of superconducting structures in the ISOL post-accelerator application and in particular to examine the feasibility of providing adequate transverse focusing for the low velocity, low q/A beams. It will be assumed that the first stage of acceleration is a high gradient heavy ion RFQ such as that described by Chidley *et al.*[2]

The Design Approach

The ANL structure is inherently an $n\pi$ mode structure where n is an odd integer. Usually n=1 and the cell lengths (constant within a 4 gap tank, for mechanical simplicity), are equal to $\bar{\beta}\lambda/2$, where $\bar{\beta}$ is the design average ion velocity for the tank, and λ is the resonant rf wavelength for the tank. To accommodate the increasing β as the ion beam is accelerated through the linac, successive tanks should have correspondingly increased cell lengths. Indeed, in the ideal case successive cells within a tank should also increase in length to maintain a constant synchronous phase.

From a practical point of view it is desirable to keep the number of tank designs to a minimum. For this reason the ANL ATLAS injector will use only four tank designs,[3] and an earlier ISOL linac study used five basic tank geometries.[7] The penalty for this simplification is of course reduced accelerating efficiency because of phase slip of the ion bunches relative to the accelerating field for bunches with average velocities that differ from the design value for the tank.

For the current study, a fixed value of the entrance phase at each cell was adopted - as is usually the case in designing drift tube linacs. With a specified value for the field strength in the cell, the cell length is adjusted to equal $\beta\lambda/2$ where β is the average β in the cell.

A negative synchronous phase angle is necessary to maintain longitudinal focusing of the beam. This of course leads to a radial rf defocusing force which, in conventional drift-tube linacs, is compensated with quadrupole magnets in some or all of the drift-tubes. Because neither the superconducting surfaces nor the interdigital structure sizes are compatible with an integral magnetic lenses, gaps between tanks must be provided to allow installation of transverse focusing elements, such as superconducting solenoids. It is the maximum achievable transverse focusing that establishes the maximum accelerating field in this case, rather than the intrinsic superconducting surface characteristics.

The solenoid lenses used throughout are assumed to be similar to those described by Jaffey *et al.*[1] They are

iron-shielded Nb-Ti wire-wound solenoids operated with not more than 7 T magnetic field. The solenoid lengths used varied from [illegible] cm to 45 cm.

The linac design was carried out using a modified version of the particle tracking code PARMELA.[5] PARMELA incorporates an option to integrate the motion of a group of electrons through the tabulated rf fields of several types of cavities. Relativistic kinematics are used. The modified code, PARMION, handles the kinematics in the same fashion as PARMELA but accepts an arbitrary particle mass (in MeV) with an arbitrary charge state. In addition, a group of four contiguous cells can be designated as a tank with a specified entrance phase that will apply to each of the four cells for the reference particle of the bunch. Each of the four cells in the tank has the same value of the rf field strength. Execution of the code with a small number of particles is sufficient to generate a table of cavity lengths which can be used in later runs without the "tank" card. For cells that are not identical to those for which the rf field is tabulated in two dimensions, the code scales the interpolated intervals radially and longitudinally. In this way a given cell geometry can be used over a wide range of cell length with the understanding that the cell used in the simulation is a scaled replica, both radially and longitudinally, of the original cell for which the rf field was tabulated.

The basic accelerating cell, sketched in Fig. 1, was modelled in the SUPERFISH[6] code in the form of a simple $\lambda/4$ resonator, the right hand side of the figure representing the part connected to the $\lambda/4$ stub. The rf field in the accelerating gap was tabulated in a two-dimensional array for use in PARMION. Typical four-cell tanks are shown in Fig. 1 of Ref.[3]

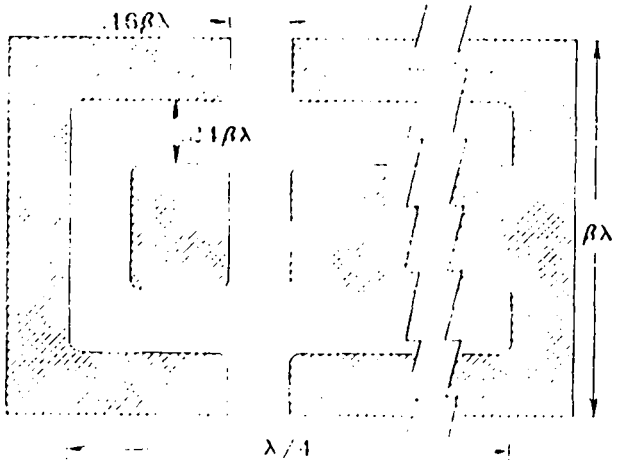

Fig. 1. Sketch of the accelerating cells as modelled in SUPERFISH.[6] In the linac simulation runs the cell dimensions (with the exception of the stub length) are scaled with β.

The Superconducting Linac

The frequency of the ISOL linac is not tied to the frequency of the URILAC [illegible] the pulsed structure of the primary proton beam is lost in the final production of an ionized beam of secondary heavy ions emerging from the ISOL. For the present study it was assumed that a high gradient, room temperature RFQ would be built to operate at 50 MHz. A beam of singly ionized ions would be accelerated to 60 keV/u with a normalized transverse emittance of $\epsilon_n = 0.035\pi$ mm mrad and in the longitudinal plane $\epsilon = 15 \times 50$ keV degree.[2]

Following the RFQ a stripper raises the charge state from 1^+ to 3^+ for ions of mass number up to 60. The quadrupole symmetry of the beam from the RFQ is transformed in a matching section[7] to deliver a converging beam of circular cross section to the SC linac. The acceptance of the SC linac is illustrated in Fig. 2. The beam delivered from the stripper fits well within the acceptance in all phase space coordinates.

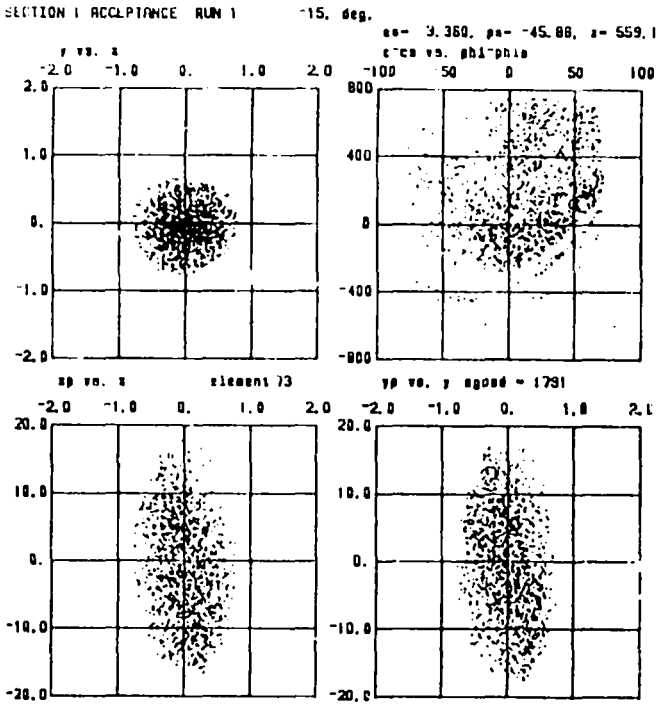

Fig. 2. Scatter plot of the linac acceptance. The plots show the initial phase space coordinates of particles surviving at the end of the 50 MHz section out of an initial population of 10,000.

Computations were made for synchronous phases in the range -40° to -10° for the initial few tanks of the 50 MHz section of the linac. At the -40° extreme the bunching force is large as is the radial defocusing force. Moreover, the average acceleration is relatively low. At the other extreme, the acceleration is higher and the bunching and defocusing forces are smaller. The bunching force is adequate over the whole range; the best balance between acceleration and defocusing was found at -15 degrees. For radial focusing, a solenoid is placed after every second tank.

Not surprisingly, it was found that emittance growth was held to a minimum when the focusing was

strong enough to hold the beam radius below 1 cm. Under these conditions the transmission was 100 percent and the emittance growth was of the order of 20%.

The initial cell length for a beam of $\beta = .01$ is about 3.4 cm. At a beam energy of 0.5 MeV/u, the cell length is about 2.2 cm, sufficiently long to permit a frequency doubling to 100 MHz. In the 100 MHz section of the linac, solenoids were placed after every third tank. This density of solenoids was found to be necessary to contain the beam for low emittance growth, not to prevent beam loss on the walls.

The complete SC DTL then consists of twelve 50 MHz tanks with six inter-tank solenoids, contained in two cryostats each about two metres long, followed by twenty-one 100 MHz tanks with seven solenoids in four 2 metre cryostats. The overall length of the DTL is 16.3 m and has an output energy of 1.6 MeV/u. This can be compared to the room temperature DTL of the earlier study[1] which had a similar length but an output energy of only 1 MeV/u.

The scatter plots of Fig. 3 show that at the exit from the linac, the longitudinal phase space is sufficiently correlated to allow a substantial reduction of the energy spread by rotating the phase space diagram in an energy compressor.

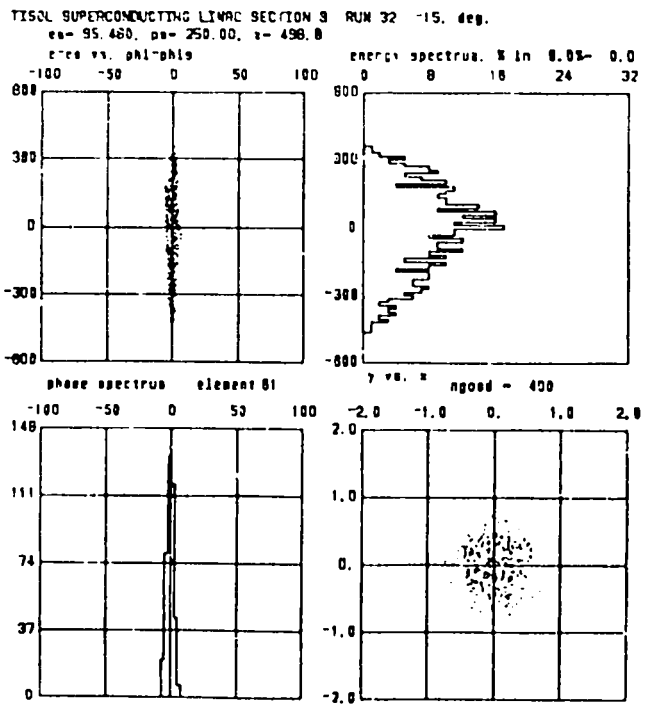

Fig. 3. Scatter plots and profiles of the beam delivered at the linac output.

Discussion of the Design

The continuously varying cell length used in this design has resulted in a large overall accelerating gradient (about 1.9 MeV/m for a [illegible] ion). Variation in the beam energy up to ±7% can be obtained by varying the rf phase in the last tank. Larger beam energy variations will require changes in the operating conditions for more than one tank.

In general, the tuning of the linac for a given output energy and ion q/A requires the adjustment of the phase and amplitude of the rf drive to every tank.

In the later stages of both the 50 MHz and the 100 MHz sections, the length of the four cells in the tank becomes a significant fraction of the $\lambda/4$ stub. For four cells the total length of structure in the beam direction on the end of the $\lambda/4$ stub is approximately $5\beta\lambda/2$ or a fraction 1.25β of the stub length. At the linac output this amounts to 6.25% of the stub length. In the design and construction of the tanks tuning and field flattening devices will therfore be required in the high-field regions to achieve a uniform field.

In the construction of such a linac, the continuous variation of the cell length may have to be compromised. For example the cell lengths in a given tank could be made equal to the average cell length as given by the PARMEO[5] code. This would reduce the multiplicity of cell designs by a factor of four although the tank lengths would still all be different, viz. $2\beta\lambda$.

References

1. H.R. Schneider, G.E. McMichael, B.G. Chidley, and R.M. Hutcheon, "A conceptual design study of a linear accelerator for radioactive ions at TRIUMF", Proc. of Accel. Rad. Beams Workshop, TRIUMF Report TRI-85-1, p. 189 (1985)
2. B.G. Chidley, R.M. Hutcheon, and G.E. McMichael, "A heavy ion RFQ with high accelerating gradient", Proc. 1986 Linac Conf., SLAC-303, p.361, (1986)
3. K.W. Shepard, "Development of a very low velocity superconducting linac" Proc. 1987 Part. Accel. Conf. p 1812, (1987)
4. A.H. Jaffey, R. Benaroya, and T.K. Khoe, "A hybrid superconducting solenoid as a focusing element in a superconducting heavy ion accelerator", Proc. 1976 Linac Conf., AECL-5677, p.102, (1976)
5. PARMELA, a time dependent, electron dynamics code for linear accelerators, Los Alamos National Laboratory, circa 1979.
6. K. Halbach, R.F. Holsinger, W.E. Jule, and D.A. Swensen, " Properties of the cylindrical RF cavity evaluation code SUPERFISH" Proc. 1976 Linac Conf., AECL-5677, p.122, (1976)
7. J.S. Fraser, J. D'Auria, L. Buchmann, and H.R. Schneider, "Dynamics of heavy ion beams in an interdigital superconducting accelerator structure", Proc. First Int'l Conf. on Radioactive Beams, p.553, (1989)

RADIO FREQUENCY SUPERCONDUCTING STRUCTURES DEVELOPMENT LABORATORY CAPABILITY AT LOS ALAMOS NATIONAL LABORATORY*

B. R. Rusnak, E. R. Gray, R. J. Houlton, G. Lawrence, E. A. Meyer, D. L. Schrage, A. Klapetzky, A. H. Shapiro, G. Spalek, J. E. Stovall, and P. Wright
Los Alamos National Laboratory, Los Alamos, NM 87545

Abstract

Los Alamos National Laboratory has established an in-house capability to pursue development of superconducting rf structures. Facilities including test pits, shielded cryostats, an ultrapure 500-gal. water system, a 600-ft^2 clean assembly area, and a helium pumping system have been installed and are now operational. High-field testing on cavities at 810 and 3000 MHz is progressing. This paper presents a facility description and recent cavity measurement results.

Introduction

Over the past three years, the Accelerator Technology Division of the Los Alamos National Laboratory has established a capability to work with superconducting accelerating structures. This capability includes designing, forming, and welding niobium cavities, chemically polishing and cleanly assembling the structures on cryogenic test fixtures, and testing the cavities at power with temperatures from 3.97 K to 1.7 K.

To date, we have designed and constructed cavities resonant at 810 MHz and 3000-MHz. The cavity type is the so-called elliptical cavity. We have fabricated 11 cavities at 3000 MHz. The tests conducted at this frequency use temperatures around 1.7 K, which are achieved by pumping on a bath of liquid helium. We have built two cavities at 810 MHz and have performed tests at this frequency at 3.97 K. All cavities are made of high RRR niobium (RRR > 250).

Measurements

Present testing at 3000 MHz is devoted to developing a distribution of field measurements to establish a base line of performance. To date, we have performed 7 high-field tests, of which 3 have had rf processing. A value representative of the highest levels achieved so far is 42 MV/m peak electric field at a $Q_0 = 1.6 \times 10^9$. Fig. 1 shows the behavior of the cavity Q_0 over the electric field range.

We have performed fewer tests at 810 MHz, because of the increased helium consumption and handling complexity. So far, 4 tests have yielded field levels as high as 25.4 MV/m peak electric field at a $Q_0 = 2.4 \times 10^9$. We have performed these tests at 3.97 K and have intentions to run them at around 2 K in the future. Fig. 2 shows a Q_0 versus peak electric field result for the 810-MHz cavity.

*Work supported by Los Alamos National Laboratory Institutional Supporting Research under auspices of the United States Department of Energy.

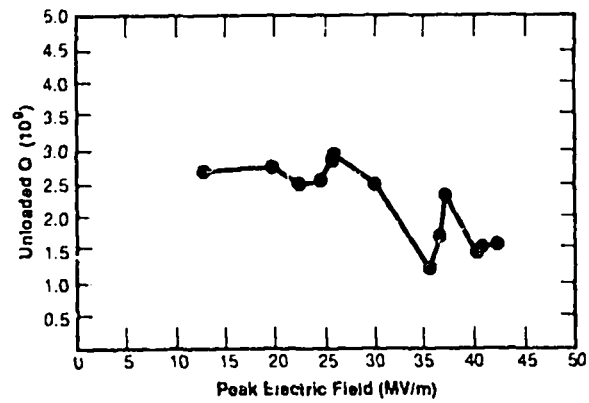

FIG. 1. Plot of Q_0 vs peak electric field, 3000 MHz single cell cavity.

For both cavity types, we have placed emphasis on refining the chemical polish, rinse, and clean assembling. With processing of this kind, that is no heat treatment, the values obtained thus far are commensurate with those achieved by the international superconducting cavity community using similar techniques[1,2].

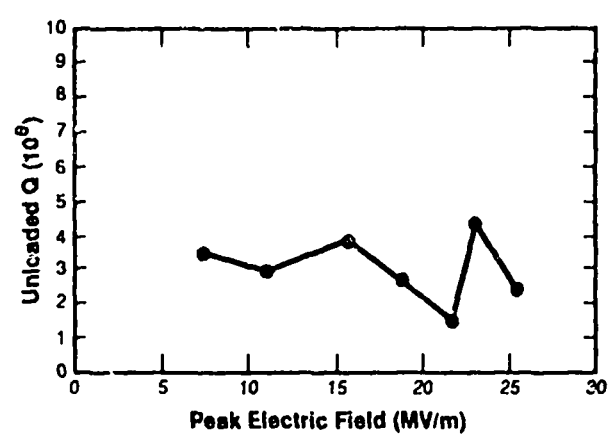

FIG. 2. Plot of Q_0 vs peak electric field, 810-MHz single cell cavity.

Facility

Facilities for cavity processing are in place that allow the cavities to be chemically polished, rinsed with ultrapure water, assembled in a clean room, and tested under high vacuum in shielded cryostats. The present setup can only polish,

assemble, and test up to a single-cell 810 MHz cavity, for a single-cell 400-MHz cavity, the setup provides clean assembly and testing.

Chemical polishing is done off site, using with a dip method that is applicable for up to single-cell 810-MHz cavities. The polishing solution is an equal mixture of concentrated nitric, hydrofluoric, and phosphoric acids. After the cavities are polished, they undergo four immersion rinses in deionized water. The cavities are weighed between polishes to determine material removal.

In the interest of working with larger cavities, We have designed and specified a piped chemical polishing system such that it is ready to be released on bid. The system uses teflon lined steel pipes and tanks to insure purity and containment, as well as a full sensing and status capability for programmable process control. The system will be capable of handling 50 gallons of acid, 150 gallons of clean water, and 250 gallons of waste water.

After chemical polishing, the cavity is rinsed with ultrapure water inside the clean room. The water system has a 500 gallon capacity, with a 2200 gallon-per-day makeup ability. The water quality has been measured as better than ASTM Electronics Grade E-1, as shown in Table 1.

TABLE 1.
Specified and measured values for the ultrapure water system.

Water Quality:	Specifications	Measurements
Resistivity (MΩ-cm)	18	18.2
Silica (μg/l)	5	2.0
Particulate (1μ m/ml)	2	0
Micro-organisms (per ml)	1	<1
TOC (μg/l)	50	6.9
Copper (μg/l)	1	0.5
Chloride (μg/l)	2	0.8
Potassium (μg/l)	2	2.0
Sodium (μg/l)	1	1.0
Residual solids (μg/l)	10	<5
Zinc (μg/l)	5	2.0
Additional Requirements:		
Resistivity	>18 MΩ-cm	18.2
Total Organic Carbon	<50 ppb	6.9
Particulate	<25 Particles >0.1μm per liter	0 >.5μm / 100 ml
Bacteria	<1 CFU/100 ml	<1
Total Residue	<0.1 ppm	<.005
Dissolved SiO_2	<5 ppb	2.0
Iron	<2 ppb	1.0

The clean assembly facility covers approximately 600 square feet, which includes the clean room laminar downflow unit, the anteroom, and the gowning area with its own downflow unit. Measurements on the different areas of the clean room were carried out with a laser particle counter in accordance with Federal Standard 209D. The bona fide clean room covers 100 square feet and was measured to meet the acceptance criteria for class 10 at rest. Additionally, the anteroom and the gowning area also met the acceptance criteria for class 10 at rest.

The operational value for the clean area (with personnel present) is more a matter of interpretation. Particulates off the gowns can push measured values for the lower part of the room, below the gown, to values meeting the criteria for class 100. But, above the gown, values are still consistent with class 10. These values indicate that good technique and care can go far in giving better results. We take advantage of the situation by working on the cavity from below and not entering the entrance plane above the cavity without rinsing the cavity afterwards. Future upgrades will include a gown more consistent with class 10 operation.

Additional facilities include 4 vertical test cryostats, which range in liquid helium capacity from 75 liters to 1700 liters. These cryostats are serviced by a 100-cfm roots blower package, which pumps on the liquid helium bath and reduces the operating temperature of the cavities.

Conclusion and Discussion

The Accelerator Technology Division at Los Alamos National Laboratory is developing a capability to build superconducting accelerating structures. To date, niobium cavities have been fabricated and run to levels comparable to values achieved at other established superconducting labs using similar processing steps.

Present efforts are focused on performing a sufficient number of tests to establish a statistically valid distribution of the field levels achieved. In addition, development is continuing on a high-pressure rinse system and a high-temperature vacuum oven to extend the possible combinations for cavity processing.

Acknowledgments

The establishment of a superconducting capability at Los Alamos was possible only through the help of a number of people. Specifically, the authors would first like to thank Helmut Piel and his group at Wuppertal for their assistance and guidance. In addition, Hasan Padamsee, Joe Kirchgessner, and the staff and students at Institute of Nuclear Studies at Cornell University provided valuable technical advice and direction. The support of other labs in the community, specifically Argonne, CEBAF, and CERN, has been also invaluable. Finally, the authors would like to recognize the contributions of groups WX-3 and MST-6 for the large cavity deep drawing, cavity electron beam welding, and chemical polishing.

References

1. H. Padamsee, et. al., Proceedings of the 4th Workshop on Rf Superconductivity, Tsukuba, KEK Report 89-21 (National Laboratory for High Energy Physics, KEK, Tsukuba, Japan, 1989, Y. Kojima, Ed.).

2. H. Piel, private communication

A NUMERICAL STUDY OF SUPERCONDUCTING CAVITY COMPONENTS*

B. C. Yunn and J. J. Bisognano
Continuous Electron Beam Accelerator Facility
12000 Jefferson Avenue, Newport News, VA 23606

Abstract

Computer programs which solve Maxwell's equations in three dimensions are becoming an invaluable tool in the design of RF structures for particle accelerators. In particular, the lack of cylindrical symmetry of superconducting cavities with waveguide couplers demands a 3-D analysis for a reasonable description of a number of important phenomena. A set of codes, collectively known as MAFIA, developed by Weiland and his collaborators, has been used at CEBAF to study its five-cell superconducting accelerating cavities. The magnitude of RF crosstalk between cavities is found to depend critically on the breaking of cylindrical symmetry by the fundamental power couplers. A model of the higher order mode coupler exhibits an unexpected mode which is in good agreement with measurement.

1. Introduction

The waveguide couplers necessary to damp higher order modes of superconducting cavities break the cylindrical symmetry of these accelerating structures in an essential way. Numerical modeling requires three-dimensional computations for both a qualitative and a quantitative description of a number of significant electromagnetic effects. In this paper studies of cavity-to-cavity cross talk and coupler modes are presented which are based on the 3-D code MAFIA of Weiland and his collaborators[1] which is available on NERSC.

2. Resonant Mode of HOM Couplers

Higher order modes (HOMs) of a superconducting cavity, which have intrinsically high Q values of order of 10^9, can be detrimental to beam quality if left undamped. In particular, multipass regenerative beam breakup studies of the CEBAF linac have shown that these HOM Qs must be reduced to the levels $< 10^7$ for stable operation at currents of hundreds of microampere. For a CEBAF cavity (Figure 1), a waveguide type HOM coupler was developed for efficient damping of higher order modes, especially those with high $\frac{R}{Q}$ values. Extensive measurements have shown that all important HOMs including quadrupole and sextupole modes are reduced successfully to $5 \times 10^2 \leq Q \leq 1.7 \times 10^5$. The CEBAF HOM coupler is sketched in Figure 2 with coordinate systems defined on a cross sectional area of the coupler. The two waveguide arms of the coupler, designed to couple effectively to both polarizations of deflecting modes, extend further to HOM loads through bent elbow segments made of niobium.[2]

It had been assumed that the HOM couplers do not support any resonant mode. However, a recent careful analysis of cavity mode measurements compared with URMEL[3] calculations and previously measured HOMs data suggested the existence of a trapped mode in the structure. Resonant modes below the lowest TE_{10} waveguide mode cutoff frequency, if they exist, are good candidates for trapped modes. All waveguide modes are evanescent in this case. Consequently, if the arms are long enough, the structure can effectively be regarded as closed for these modes. We note that the dimension of the rectangular waveguides is 7.899 cm × 3.81 cm. Therefore, the lowest TE_{10} mode is cut off at 1898 MHz.

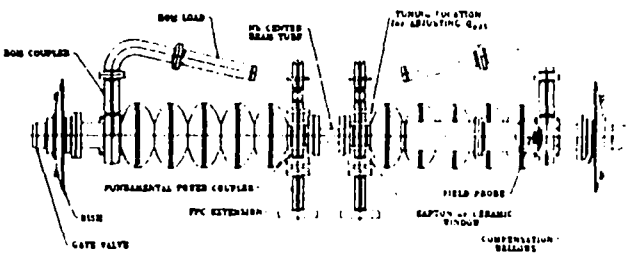

Figure 1. A CEBAF cavity pair.

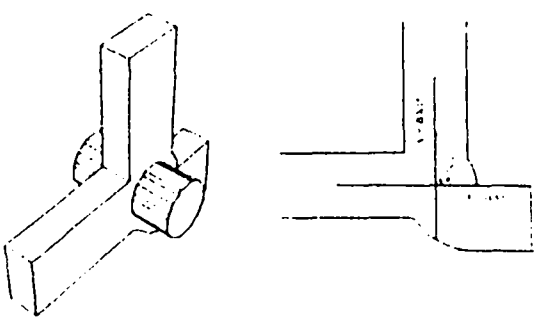

Figure 2. CEBAF HOM coupler.

The lowest five modes found by the MAFIA code for the coupler structure shown in Figure 2 are summarized in the following Table 1. Two waveguide arms are shorted at 19.95 cm from the pipe center; the beam pipe is cylindrical with $r = 3.5$ cm.

TABLE 1
Summary of Modes

Mode	Frequency (MHz)	Maxwell's Laws		
		$\langle \mathrm{div}(D) \rangle$	$\langle \mathrm{curl}\,\mathrm{curl}(E) \rangle$	$\langle \mathrm{div}(B) \rangle$
1	1782.193	0.1×10^{-11}	0.2×10^{-7}	-0.9×10^{-13}
2	2042.745	0.9×10^{-12}	0.1×10^{-8}	0.8×10^{-13}
3	2048.346	0.3×10^{-12}	0.5×10^{-10}	0.1×10^{-12}
4	2239.128	0.5×10^{-13}	0.8×10^{-10}	-0.1×10^{-12}
5	2430.439	0.3×10^{-12}	0.3×10^{-10}	0.3×10^{-13}

It is clear from Table 1 that only the lowest mode at 1782.193 MHz will survive as a resonant mode for the actual structure since the higher modes are above the 1898 MHz

* This work was supported by the U.S. Department of Energy under contract DE-AC05-84ER40150.

cutoff. We note that the ends of the waveguides and beam pipe are open. If a different boundary condition applied to the open end side of the structure makes a significant change in parameters which characterize a mode, the mode may not exist as a resonance. We find that the 1782 MHz mode indeed is well confined within the region near the stub and beam pipe center, and would stay resonant in the open structure as a result. The frequency agrees quite well with the cavity mode measurements. Experimentally, the Q of this mode is less than 10^5. Field plots for this mode at the midplane of the HOM coupler are shown in Figure 3. Despite a substantial change to the field patterns due to the fully three dimensional nature of the structure, the mode has a significant TM_{010} component. The mode, however, with all six components of electromagnetic fields nonvanishing, does not allow any simple characterization. We also notice that the position of maximum E_z has moved from the usual beam pipe center to the pipe edge along the waveguides.

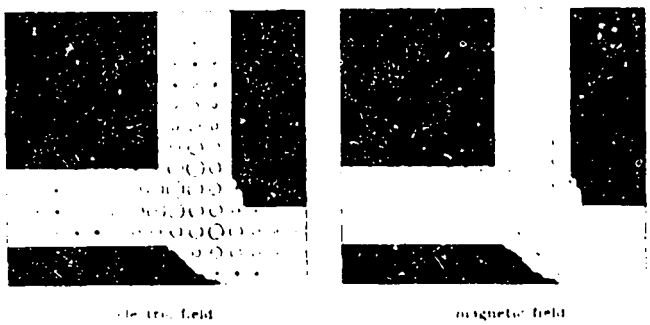

Figure 3. Electric and magnetic field plots of 1782 mode.

As a consequence of the non-vanishing transverse gradient of E_z at the beam pipe axis, the mode can deflect the beam passing the structure as well as cause an energy loss. As the mode can couple with the total charge of the bunch, the beam does not have to enter the structure off axis to excite the mode in contrast to deflecting modes commonly discussed in relation to beam breakup. Let us define the longitudinal (transverse) impedance by $R_{\parallel(\perp)} = |V_{\parallel(\perp)}|^2/P$, where P is the power dissipated in the structure walls. $V_{\parallel(\perp)}$ is the maximum longitudinal (transverse) voltage gained by a traversing charged particle. The impedances generally depend on both coordinates, r and θ. We find that the following expressions provide a reasonable first order approximation to the impedances in the region $r \leq 1.5$ cm:

$$\frac{R_\parallel}{Q} = 53.0(1 - \frac{0.066r}{1\ \text{cm}}\cos(\theta + \frac{\pi}{6}))^2\Omega\ ,$$

$$\frac{R_\perp}{Q} = 1.5\Omega\ .$$

This is consistent with the description of the mode as a superposition of the TM_{010}-like mode and the deflecting TM_{110}-like modes. The magnitude of the coupling, defined as the ratio of the maximum longitudinal voltage gain due to the dipole component to that of the TM_{010} mode assuming the relation to be valid in the whole beam pipe region, is about 0.23.

The main concern with the transverse impedance is its ability to cause beam breakup above a certain threshold current. At CEBAF extensive computer studies have been carried out to predict beam breakup threshold currents caused by various deflecting modes of superconducting cavity.[4] Compared to most dangerous dipole modes of the cavity, the transverse impedance, $\frac{R_\perp}{Q}$, of 1.5 Ω appears about a factor of 30 to 40 smaller. Therefore, since its Q is comparable to the strongest modes, this 1782 MHz mode is not expected to be a significant factor in limiting the current handling capability of the linac.

3. Coupling Between Cavities in a Cryounit

The linac RF system at CEBAF is required to have the ability to control the accelerating field gradient and phase of each cavity individually. Individual cavity controls will provide maximum flexibility in the operation of the RF system, which will allow maximum utilization of the individual cavity gradient performance. A CEBAF cryounit consists of two five cell superconducting cavities each equipped with its own fundamental power coupler (FPC) and HOM couplers connected through a 9.393 cm-long niobium adapter. The cavity beam pipe radius is 3.5 cm. The distance between the two nearest end-cells of the two cavities is one and a quarter λ, the wavelength of accelerating mode at 1497.0 MHz. (See Figure 4, where a CEBAF cavity pair with FPCs is illustrated. Only a single cell of the superconducting cavity is shown.) To ease the task of building individually controlled RF system which meet CEBAF design requirements, it is imperative to avoid significant cross talk between the two superconducting cavities at the design operating frequency of 1497.0 MHz.

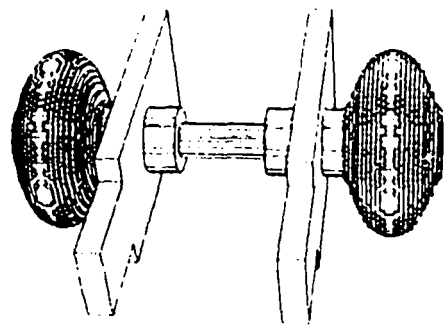

Figure 4. A CEBAF cavity pair with fundamental power couplers.

A few simplifications have been made to keep computing time and memory space under control. The cryounit with the full two elliptical 5-cell superconducting cavities along with couplers demands many mesh points, which is presently not practical to model, even with a Cray-2. For the study of cross coupling, we should be able to obtain a fairly accurate estimate by substituting a properly adjusted pill-box cavity for an elliptical 5-cell cavity. We note that the 1497.0 MHz mode is the π mode. The pill-box cavity chosen has a radius of 7.88 cm and is 10.0 cm long and turns out to be a quite adequate substitute for a single-cell elliptical CEBAF cavity given in Figure 4. As we will see later, the TM_{010} mode frequency, which is our only interest

in this section, is in excellent agreement with the operating frequency. We also neglect the presence of higher order mode couplers for this study. It is assumed that their effect on this coupling is minor compared to that of fundamental power couplers as the HOM couplers are located outside – not in between – the cavities. On the other hand, a realistic modeling of the FPCs has been provided with precisely dimensioned short stubs. The open end of the FPC, which consists of a 13.44 cm × 2.50 cm rectangular wave guide, has to be shortened to a convenient length.

The following Table 2 summarizes the results of MAFIA runs, which are to determine the eigenfrequencies of the coupled system and the degree of a cross talk.

TABLE 2
Eigenmodes of Coupled Cavities

Without FPC

r_{inner} = 3.5 cm	1498.659534
	1498.659542
	8

With FPC

	Boundary conditions on FPC	
Case	E	M
r_{inner} = 3.5 cm	1498.878301	1498.884335
	1498.878170	1498.884260
	131	75
r_{inner} = 2.5 cm	1498.879664	1498.885098
	1498.879655	1498.885093
	9	5
r_{inner} = 1.5 cm	1498.880697	1498.885660
	1498.880697	1498.885660
	0	0

The parameter r_{inner} is the radius of the niobium inner adapter placed between the FPCs to reduce crosstalk. In Table 2, the top line in each case lists frequencies for the symmetric mode and the second line frequencies for the antisymmetric mode in MHz. The difference Δf is given in the third line in hertz.

When there are no FPCs, the coupling of the cavity fields through the TE_{11} waveguide mode is not possible at 1497.0 MHz due to the axial symmetry. However, once the symmetry is broken by the introduction of FPCs, this is no longer the case. Indeed, one can easily check that there can be two orders of magnitude difference in field strengths transferred from one cavity to another depending on whether the coupling to the TE_{11} waveguide mode is allowed or not. Even though this fact alone does not translate directly to the magnitude of Δf, the MAFIA result is certainly consistent with this picture.

We may discuss the problem of a cross coupling by considering the motion of two identical harmonic oscillators of angular frequency ω, linearly coupled symmetrically and with a damping. As is well known, in the case of a free oscillation, the system has two eigenmodes: a symmetric and an antisymmetric modes. The difference in their frequencies is proportional to the coupling constant.

We need to look at the case of a stationary state of a forced oscillation when the driving frequency is one of the normal modes of the coupled system. Let us assume a force in the form $f(t) = \frac{\omega^2}{Q}\cos(\omega t + \phi)$ is applied only on the left cavity. One then obtains a steady state solution after transients die out:

$$V_{left}(t) = \frac{\sqrt{1+K^2}}{\sqrt{1+4K^2}}\sin(\omega t + \phi - \phi_\ell),$$

and

$$V_{right}(t) = -\frac{K}{\sqrt{1+4K^2}}\sin(\omega t + \phi + \phi_r),$$

where $\phi_\ell = \arctan\frac{K}{1+2K^2}$, $\phi_r = \arctan\frac{1}{2K}$, and $K = Q\frac{\Delta\omega}{\omega}$.

Now the ratio of the amplitude of the fields in the right cavity to that of the left one is given by:

$$\frac{K}{\sqrt{1+K^2}}.$$

Let us now apply the above results to the CEBAF cryounit with a 3.5 cm adapter. We have f = 1497 MHz, Δf = 150 Hz, and $Q = 6.6 \times 10^8$. f and Q are design values. Δf is an estimate based on results from MAFIA runs summarized in the above Table 2. We have $K = 0.66$ and 55% in the right cavity due to the coupling.

In steady state, one expects about 3% in the right cavity with the design Q and Δf = 7 Hz. To reduce the beating to a less than 1% level in the stationary case, $\Delta f \leq 2.3$ Hz is required. From Table 2, we may conclude that this seems clearly possible with $r_{inner} \leq 2.0$ cm. An adapter radius of 1.74 cm has been chosen and was found experimentally to meet the 1% criterion.

4. Conclusions

The studies presented demonstrate the importance of three-dimensional considerations in understanding the operation of superconducting cavities with waveguide couplers. Previously, the design of such accelerating structures has required painstaking bench measurements of hardware and considerable developmental time. The good agreement of the MAFIA modeling presented here with laboratory measurements clearly indicates that 3-D computations can provide considerable support for the design of the next generation of superconducting cavities.

References

1. R. Klatt et al., "MAFIA – A Three-Dimensional Electromagnetic CAD System for Magnets, RF Structures, and Transient Wake-Field Calculation", Proc. 1986 Linear Accelerator Conference, pp. 276, 1986.
2. For more details, see CEBAF Design Report, May 1986.
3. T. Weiland, "On the Computation of Resonant Modes in Cylindrically Symmetric Cavities", Nucl. Inst. Meth., Vol. 216, pp. 329, 1983.
4. G. A. Krafft and J. J. Bisognano, "Two Dimensional Simulations of Multipass Beam Breakup", Proc. 1987 IEEE Particle Accelerator Conference, Vol. 2, pp. 1356, 1987.

FIELD STABILIZATION IN THE QUASI-ALVAREZ STRUCTURE

M.Vretenar and D.J.Warner
PS Division, CERN, CH-1211 Geneva 23, Switzerland

Abstract

The Quasi-Alvarez accelerating structure, proposed for the Linac injector of the CERN heavy ion complex, has a super period consisting of drift tubes in 2.3λ and 3λ cells supported within a cylindrical cavity of diameter 0.7λ (f_0 = 202.5 MHz). Between 0.25 MeV/u and 2.0 MeV/u the design accelerating field increases by 95%, ideally with stabilization by post-couplers. As this is known to be difficult both as regards β and cavity diameter, a 500 MHz scale model of the 0.25 MeV/u to 0.65 MeV/u part has been used to study a comprehensive range of post coupler dispositions and geometries.

Introduction

The quasi-Alvarez structure is being studied at CERN as one of the injector Linac options for the heavy ion programme [1,2]. Its advantages as an accelerating structure between 0.25 MeV/u and 1.2 MeV/u have been detailed elsewhere with emphasis on the way the focusing periodicity leads to significant reductions in numbers and gradients of the focusing quadrupoles [3]. Another paper deals with the dynamics aspects of the structure showing that tight electric field tolerances are not necessary for good quality beams at 1.2 MeV/u [4].

The Need for Field Stabilization

Post couplers were initially developed a) to make the steady state accelerating field more stable against manufacturing errors and variations during operation, and b) to increase the group velocity of power flow especially under transient conditions. Note that the field errors in the unstabilised Alvarez structure scale as (cavity length/λ)^2. This was not a problem for CERN Linac 1 at low currents (maximum L/λ = 8.1). For Linac 2, with high currents (150 mA) and strict requirements on the field, post coupler stabilization was necessary on all three tanks. The novelty was to have post couplers on the first tank (L/λ = 4.7) and to set them asymmetrically relative to the drift tubes to obtain a stabilized field which increases by 21% along the cavity [5]. For the quasi-Alvarez the desirability of stabilization is more linked to field adjustment in the first cavity (where it increases by nearly 100%) than to field errors or transients (L/λ = 5.2 and low beam currents).

Previous experience with the stabilization of large diameter Alvarez cavities suggests that the stabilization with standard post couplers is very difficult or even impossible [6]. A comparison of accelerators where standard post couplers have been used (or tried) demonstrates that the limiting cavity wall to drift tube distance for stabilization being possible is about λ/4 [7]. The reason is that for a post coupled system to work two conditions must be satisfied: the couplers must be tuned to the correct frequency and they must couple to the TM01 band. For large diameter cavities, the tuned condition leads to large gaps between the post and the drift tube, but at the same time this distance determines the coupling between the two systems, which in such cases falls below the limit for effective stabilization. The particular geometry of the Quasi-Alvarez, where the critical distance is 1.23λ/4, led us to expect difficulties in the stabilization.

The Quasi-Alvarez Model

The aim with the model was to try configurations of posts with different periodicities and different geometries, for λ/4 types and if necessary the 3λ/4 type with a coaxial structure outside the cavity. In addition the field adjustment in the difficult region at low energy should be tested. The 0.414 scale cavity was machined from a solid cylinder of aluminium and has 11 drift tubes supported from a removable girder (Figs 1,2). It represents the 0.25 MeV/u to 0.65 MeV/u part of a high gradient version, and parameters are given in Table 1.

Inside Length		1021	mm
Inside Diameter		123	mm
Design Freq.(no stems)		193	MHz
Gaps		2.5→4.8	mm
	"Large" DTs	"Small" DTs	
Number	13+2x(1/2)	28	
Length	26.5→10.6	11.6→18.5	mm
Diameter	61.6	32.9	mm
Aperture Dia.	5.0	5.0	mm
Stem dia.	10.0	6.0	mm

Table 1: Parameters of the Quasi Alvarez Model

The Quasi-Alvarez model has movable end half drift-tubes to detune the end cells during field tilt measurements. In the cavity wall opposite the 13 large drift-tubes, 39 threaded holes of 30 mm diameter allow several varieties of post- coupler to be mounted with nearly regular arrangements possible for 13, 7, 6 and 4 couplers.

Measurements were made on frequency, Q, end tuner calibrations and frequency perturbation due to support stems. The TM010 frequency was 191.12 MHz but corrections for holes (+267kHz), support stems (+820 kHz) and air dielectric (+132 kHz) brings this to 192.4 MHz, close to the SUPERFISH computation (193.1 Mhz). The Q of the TM010 mode was 19300 i.e about 69% of theoretical for aluminium (and brass stems).

As a preliminary measurement to stabilization studies, dispersion curves for the lower bands of the cavity have been established (Fig. 3), identifying the different modes by exploring their field symmetry with dielectric or metallic perturbators. The band structure is that typical of an Alvarez cavity, where the TE11 band is separated by the presence of the stems into two polarities. For the one with the E-field parallel to the stems (TE11n||), the frequency is heavily loaded and falls below 300 MHz. The other with E-field perpendicular to the stems (TE11n⊥) is only slightly affected and starts below the TM01 band. The major effect of the stems on the TM01n band is to decrease the frequency of the modes with $n \geq 1$, causing the two bands to cross.

At the TM010 mode, the "Alvarez" mode, the electric field on axis was measured by moving a 2.5 mm diameter metallic bead along the cavity and recording the corresponding phase shift on a HP8753C Network Analyzer, to get the field distribution of Fig. 4. The particular drift tube arrangement of the quasi Alvarez structure produces a higher field level in the gaps between

two small drift tubes, and the measured ratio between the peaks in a cell agrees with the SUPERFISH computations. The tilt sensitivity of the model was then measured using the standard technique of inducing a longitudinal tilt by pushing in and out respectively the first and last half drift tubes, changing the frequency by 250 kHz (corresponding to a change in the gap of about 1 mm) and then coming back to the original value; the resulting tilted field on axis was measured, and then the measurement was repeated inverting the drift tube movements and therefore the tilt. For each of the 11 "central" gaps, the ratio of the difference between the two measured gap fields and their average value is calculated and plotted. The result is the curve of Fig. 5, whose slope represents the sensitivity of the cavity to perturbations involving components of the first longitudinal mode (TM011), and is the parameter to reduce to improve the cavity stability.

Stabilization with Stepped Post-Couplers

Special post couplers have been installed, having a step in the diameter from 28 mm to 10 mm, in order to decrease the post inductance and to have correspondingly smaller gaps between the posts and the drift tube, hoping in this way to increase the effective coupling to the Alvarez mode and make stabilization possible. Thirteen such post couplers were inserted, one in front of each large drift tube on alternate sides (Fig. 2). Fig. 6 shows the measured behaviour of the post couplers band for different gaps (S) between the post coupler and the drift tube. Comparing the curves of Fig. 3 and Fig. 6, one sees that effect of the post couplers is to capacitively load the modes of the TE11 band, characterized by a strong E-field on the plane of the posts, thus decreasing their frequency proportionally to the order of the mode. Moreover, the open TE11 band becomes the closed pass band of a periodically loaded structure. The mode at the highest frequency on this band has the same longitudinal period as the post couplers arrangement, and is therefore strongly affected by the posts. They change its field distribution drastically, as for all the modes on the top of the band, in such a way that those modes can couple with the TM01 band, making a confluence between the two bands possible.

In spite of the fact that the post coupler band crossed the confluence position, for none of the post lengths analyzed has a stabilizing effect been observed. The crossing between the two bands happens for S≃30 mm, and this distance is not short enough to assure a sufficient coupling for stabilization. Actually, the consequence of the low coupling is to reduce drastically the range of post coupler frequencies, and therefore post coupler lengths, where the confluence takes place, and where the tilt sensitivity is affected [8]. In fact, with the steps of a few mm of our measurement, nothing could be observed, but repeating the measurement with a reduced number of post couplers (7), it has been possible to find a single post coupler length where the tilt sensitivity was affected, but in a totally irregular way. This showed that a confluence was taking place, but the system in that case was so sensitive that no improvement was possible.

Stabilization with 3/4λ Post-Couplers

To increase the coupling yet keep the possibility of tuning the post to the required frequency, an arrangement of six 3/4λ post couplers (Fig. 7), has been installed, one in front of each second large drift tube. Here the post frequency is mainly determined by the external coaxial cavity, and it can be tuned by changing the length of the short-circuiting brass cylinder, thus changing the effective coaxial length. Several effective coaxial lengths have been tried, each one leading to a different distance between the post tab and the drift tube, and an optimum from the point of view of stabilization has been found for an external coaxial length of 95 mm, leading to gaps of about 22.5 mm. Shorter gaps make the system very sensitive to errors in the capacitance between the post and the drift tube, and therefore difficult to tune, while larger gaps retain the problems related to the low coupling coefficient.

With this arrangement of post couplers, stabilization was achieved relatively easily. The tilt sensitivity was first measured for different lengths of the post coupler arms (all at the same length). The sensitivities were not linear, because the increasing cell length in the model required different tuning states for the different post couplers. Therefore, all the post couplers have been adjusted to the length giving the flattest tilt sensitivity in the first half of the cavity, and then the length of the three post couplers in the second half of the cavity has been changed in order to flatten the tilt sensitivity there too. Residual small asymmetries have then been eliminated by changing slightly the length of the post coupler near to where the asymmetry was, to get finally the tilt sensitivity of Fig. 8, corresponding to an average S=22.5 mm, with 1.5 mm difference in length between the first and the last post coupler. In Fig. 8 one can observe that the first and the last gaps remain unstable, as the post couplers start only at the second drift tube. In the rest of the cavity the tilt sensitivity presents the typical saw-tooth pattern due to the fact that the post couplers stabilize the system only at each second drift tube. The overall increase in the stability for this configuration with respect to the unstabilized case (Fig. 5) is about a factor of 10.

When the tabs on the posts were rotated by ±90° from their central position, the induced tilt ranged from −3% to +35%. However, the tilt sensitivity did not change appreciably, indicating that the cavity remained stable.

Conclusions

As expected when this model of the input part of the Quasi-Alvarez structure was proposed, the stabilization proved very difficult with traditional λ/4 post couplers but with 6 of the nominal 3λ/4 (actually 1.81λ/4 !) couplers, it was possible to improve the tilt sensitivity by a factor 10. In addition this tilt sensitivity remained low for fields tilted by rotation of the coupler tabs, a strong reason for using post couplers on short tanks (5.2λ). Thus we conclude that for the full-sized Quasi-Alvarez structure it is worth developing post couplers with an external circuit especially as this external part is only 0.8λ/4 long.

Acknowledgements

The authors would like to acknowledge the ready help provided by the CERN main workshop during the design and construction of the model. We were also fortunate to be able to draw on the long experience of Dr. P. Lapostolle.

References

1. H.Haseroth (Ed.), "Concept for a Lead-Ion Accelerating Facility at CERN", CERN 90-01 (1990)

2. H.Haseroth, "A Heavy Ion Injector at CERN", This Conference.

3. D J Warner, "Heavy Ion Acceleration Using Drift-Tube Structures with Optimised Focusing", 1988 Linac Conference Proceedings, CEBAF Report-89-001, pp109 (1989)

4. P Lapostolle, E Tanke, M Vretenar, D J Warner and S Valero "Computer Design and Dynamics of the Quasi-Alvarez Linac", This Conference

5. D J Warner, "Calibration During Installation and During Initial Operation of the CERN 50 MeV Linac", Proc. 1979 Linac Conference, BNL-51134, p301, (1979)

6. L Earley, J Potter and A Thomas, "Tuning Experience with the EMIT Scale Model Drift-Tube Linac", 1981 Linac Conference Proceedings, LA-9234-C, p71 (1982)

7. J Billen, private communication

8. J Billen, G Spalek and L A Shapiro, "Field Stability in Two-Stem Drift-Tube Linacs", 1988 Linac Conference Proceedings, CEBAF-Report-89-001, pp125 (1989) LA-UR-88-3262 (1988)

Figure 1: Drift-Tube Arrangement in the Model

Figure 2: Quasi-Alvarez Model with Stepped Couplers

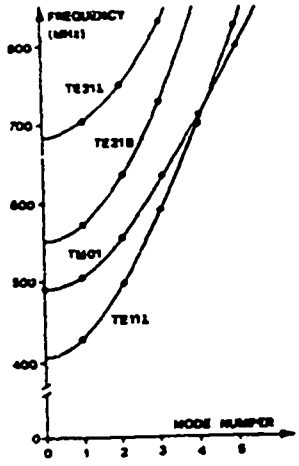

Figure 3: Dispersion Curves of the Unstabilized Model

Figure 4: Bead-Pull Measurement of the Field on Axis

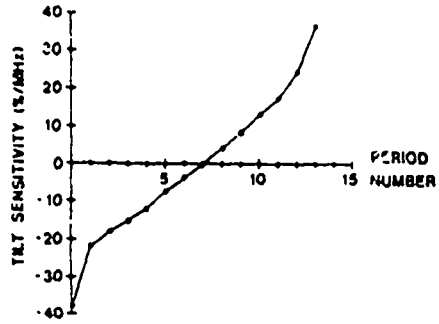

Figure 5: Tilt Sensitivity of the Unstabilized Model

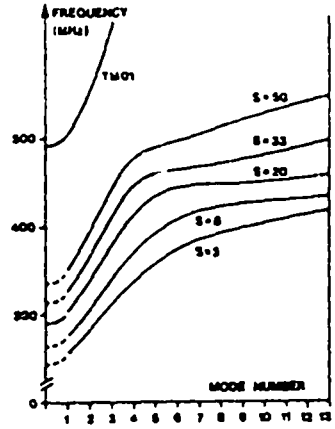

Figure 6: Dispersion Curves with Stepped Post Couplers

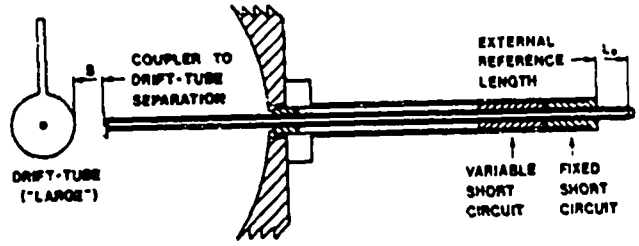

Figure 7: The $3\lambda/4$ Post Coupler

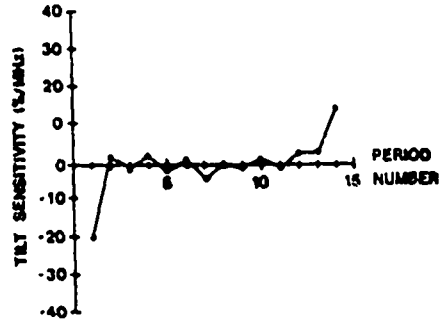

Figure 8: Tilt Sensitivity of the Model stabilized with $3\lambda/4$ Post Couplers

COMPUTER DESIGN AND DYNAMICS OF THE QUASI-ALVAREZ LINAC

P.Lapostolle*, E.Tanke, M.Vretenar, D.J.Warner
PS Division, CERN, CH-1211 Geneva 23, Switzerland
S.Valero
LNS, CEN-Saclay,F-91191 Gif-sur Yvette Cedex France

Abstract

A possible structure for the Linac of the CERN heavy ion complex is the quasi-Alvarez. This has superperiods including $2\beta\lambda$ cells and $\beta\lambda$ cells with focusing quadrupoles only in the longer cells. We have applied a new fully relativistic general formalism to three stages of the design. Firstly the longitudinal dimensions are defined via prescribed synchronous phase and electric field laws, using cavity computations to derive the axial fields. Then the transverse matching and quadrupole parameters are checked. Finally, multiparticle dynamics computations are used to investigate coupling and emittance variation between 0.25 MeV/u and 1.2 MeV/u.

Introduction

For the heavy ion programme at CERN [1,2], several distinct options for the injector linac are being developed, in particular the "quasi-Alvarez" drift-tube structure to accelerate lead ions (Pb25+) between 0.25 MeV/u and 1.2 MeV/u [3].

For low energy ions with small q/A (≈ 0.1) impracticably high quadrupole gradients are required in a $\beta\lambda$ accelerating structure, so the quasi-Alvarez minimises the number and strength of the quadrupoles by a) using an optimum quadrupole separation and a betatron phase advance of about 80°/focussing period and b) making the quadrupole length about $1.5\beta\lambda$ i.e. using a $2\beta\lambda$ period locally. To maximise the acceleration rate, $\beta\lambda$ periods are used between quadrupoles with smaller "empty" drift-tubes for RF power economy and mechanical simplicity. Thus each focusing period between 0.25 MeV/u and 2 Mev/u is $8\beta\lambda$ long (N=8) and has two long cells ($2\beta\lambda$) and 4 normal cells ($\beta\lambda$). Between 2 MeV/u and 1.2 MeV/u an N=16 focusing period is used.

Design Methods for Feasibility Study

The initial design was developed using simple programs for the beam dynamics. To study the transverse motion, and quadrupole strengths and dispositions, an analytical approach and a precise matrix formalism were applied to the critical region at 0.25 Mev/u [3]. With the selected period layout (N=8), the allowable RF defocusing and limits for tolerable surface fields, the first structure designs, could be tested using the RF cavity program, SUPERFISH to compute cells between 0.25 Mev/u and 2 MeV/u. Electric field results were interpolated at intermediate energies to give a first linac design e.g. cell lengths, numbers of cells and quadrupoles, and RF power. As the increase in β/accelerating gap is only 1.5% in most of the first section, the analytical formulae give good indications of acceptance in the longitudinal phase plane for comparison with computational results.

Beyond the feasibility stage, a more systematic approach is necessary, to cover the stages between the cavity computations and multiparticle optics. This was done for CERN Linac2 [4] but the programs used cannot treat the superperiodicity and local asymmetries of the quasi-Alvarez.

Design with a New Formalism

It was decided to apply the gap acceleration treatment of Lapostolle and Valero [5] to the three logical stages viz. longitudinal design (for precise cell dimensions), transverse design (to confirm the quadrupole settings) and multiparticle dynamics (to study coupling and emittance evolution). These new fully relativistic codes allow accurate trajectory computations through long rotationally symmetric accelerating elements for a wide range of particles e.g. protons and electrons as well as heavy ions. No particular symmetry is required for the longitudinal electric field.

For a bunch of particles, the speed of computation is substantially increased by developing the dynamics variables as a Taylor expansion around the bunch centre. In the longitudinal motion, the phase and energy dependant terms are such that the Jacobian is close to unity so the treatment satisfies Liouville's Theorem. Although the 4 x 4 matrix formalism applied to the transverse motion ignores third order abberations, all the chromatic terms are included as well as phase dependant effects and again the Jacobian is very close to one. This allows observation of transverse-longitudinal couplings and vice-versa, filamentation effects and emittance transfers. Comparisons with a very accurate but much slower step-by-step integration routine show no significant differences with the Taylor expansion method.

Particle Type: Lead Ions with A=208, q=25+	
Tank 1:	W_i = 0.24 MeV/u W_f = 2.0 MeV/u
Tank 2:	W_i = 2.0 MeV/u W_f = 1.2 MeV/u
Frequency	202.56 MHz
Effective Synchronous Phase ($\phi_{s,eff}$):	
Tank 1:	$\phi_{s,eff} = 4\beta^{-0.27} = -40°$ at 0.24 MeV/u
Tank 2:	$\phi_{s,eff} = -30°$
Mean Electric Field (MV/m):	
Tank 1:	E = 2.09 + 0.278z
Tank 2:	E const., W' continuous between tanks
Acceleration Periodicity:	
Tank 1:	3 gaps/$4\beta\lambda$
Tank 2:	4 gaps/$5\beta\lambda$

Table 1: Starting Conditions for Linac Design

Computations of Cell Dimensions

This section concerns the development of a program which will compute the sequence of cell lengths, given the starting conditions of Table 1 and interpolating between cavity field computations corresponding to a small number of different cell lengths to obtain axial field distributions.

* Consultant

Eleven cases corresponding to nine cell lengths between 0.25 MeV/u and 2.0 MeV/u (with two increases in aperture diameter) were computed for half RF supercells i.e. for a length of $2\beta\lambda$. Good resolution in the axial field results with an adequate representation of the drift-tube profile, could be obtained with 60 or more mesh points on the axis. The program HARMNY processes the field data by making a spline fit to 33 equally spaced points in each $\beta\lambda$ interval centred on the three gaps per superperiod. Then for other period lengths, the axial fields are derived from the two nearest cases computed by SUPERFISH. Best results were obtained by logarithmic interpolation (versus cell length) between actual fields rather than Fourier coefficients. Then a Fourier analysis over the $\beta\lambda$ interval provides up to 20 coefficients for HARMNY.

The condition $\phi_{s,eff} = A\beta^{-0.27}$ cannot be applied directly as a) the particle phase is only computed at the input and output of an accelerating interval and b) $\phi_{s,eff}$ will be some average value over three gaps (four for Tank 2). For the tank input at 0.24 Mev/u the unknowns are, the (exact) cell length and the particle input phase. These are adjusted iteratively using a simple algorithm so that $\phi_{s,eff} = -40^0$ and the ratio of input to output phase varies as β^{-x}. In subsequent cells the input phase is known so only the cell length need be adjusted to satisfy the phase relation. At each iteration the accelerating field distribution and average accelerating field must also be reset. The starting value for the cell length is an extrapolation from the two preceding cells and the linac cavity ends after the superperiod nearest to the prescribed energy. The design parameters produced by HARMNY (Table 2) correspond to the largest surface electric fields considered feasible at present.

	TANK 1	TANK 2
Energy (MeV/u)	.240→2.129	2.129→4.238
Length (m)	7.684	6.631
RF superperiods	31	12
Mean E field (MV/m)	2.090→4.152	3.960
Aperture dia. (mm)	12→16	18→20
Quad.length (mm)	51→125	115
Quad. Grad. (T/m)	170→61	16→41

Table 2: High Gradient Quasi-Alvarez Linac

First Order Transverse Dynamics

The transverse envelope matching, quadrupole strengths and batching are tested with the program TRANSPORTVA which has input data as a sequence of beam transport elements (c.f. TRANSPORT). In particular the accelerating regions use the above mentioned formalism. Cell lengths, electric fields and input conditions are as derived in HARMNY thus giving identical longitudinal dynamics. Transversely, the evolution of the beam envelope is computed using the RF defocusing term for the synchronous particle and the given quadrupole gradients. The usual matching and quadrupole optimisation features were unnecessary as the gradients derived by the matrix treatment gave sufficiently good beam envelopes. There was a slight worsening of the results when the quadrupoles were grouped into threes with identical gradients. Transverse matching features may be needed between the linac tanks, but here the difficulty may be to control the longitudinal phase increase.

TRANSPORTVA gives ideal first order dynamics results with no emittance increase or distortion and so provides a bench-mark for the multiparticle simulations.

	Tank 1	Tank 2	
Input Ellipse Semi-Axes			
x,x′ plane	5.10 x 8.6	2.17 x 6.9	mm mrad
y,y′ plane	1.99 x 22.1	5.66 x 2.61	mm mrad
W,ϕ plane	5.77x20.0	15.63 x 7.39	keV/u°
Output Ellipse Semi-Axes			
x,x′ plane	1.91 x 7.6	5.12 x 1.95	mm mrad
y,y′ plane	1.90 x 3.12	2.22 x 1.78	mm mrad
W,ϕ plane	15.0 x 7.7	18.5 x 6.13	keV/u°

Table 3: Nominal Input and Output Matching

Multiparticle Dynamics with SIMUL

This program uses the the Taylor expansion approach to advantage when it is applied to a bunched beam (represented here by 200 particles). With the dimensions and fields from (HARMNY), and the quadrupole and matching parameters as confirmed by TRANSPORTVA this program, SIMUL, checks the behaviour of the quasi-Alvarez linac. In particular, the way the emittance varies for changes in beam and machine parameters can be studied. The structure of the program follows the TRANSPORT model with additional subprograms concerning the accelerating regions, the filling of the input emittances with particles, and statistical analyses and graphs of the output beam .

The main optics problem at low energy concerns couplings between the phase planes. Qualitatively these are due to the variation of acceleration with radial position essentially as $I_0(2\pi r/(\beta\lambda))$ and the variation of RF defocusing with phase, essentially as $r \sin\phi$. In fact the standard input data uses an upper limit for normalised input emittance $E_n = 1\pi$ mm mrad, and the corresponding longitudinal emittance of $1.6\pi\ 10^{-6}$ eVs/u [1]. The (1 rms) emittances given in Table 3 are right ellipses with axes defined by the matrix treatment (transverse) and the linac acceptance formulae [3]. Two distinct ways of assigning particle initial co-ordinates were used.

Initially particles were chosen at 13 positions in the transverse planes so that the linear region near the axis and the limit of the emittance were represented. Then for each of these transverse positions, 13 co-ordinates in the longitudinal phase plane were assigned, (8 on the emittance boundary), giving sets of co-ordinates for 169 particles in total. The results at 2 MeV/u in fig. 1 show that particles initially at the same position in the longitudinal plane spread out depending on their initial transverse positions. However the net effect does not appear to be an increase in the longitudinal emittance because the limiting particles fall inside and outside the emittance ellipse fitted to the paraxial particles. In the transverse planes the dominant effect seems to be a spread in betatron phase for particles with differing initial longitudinal co-ordinates , but no net movement to outside the ideal emittance.

These coupling effects are rather smaller than might be expected at 0.24 MeV/u, as with a maximum radial excursion of 5mm, $I_0(2\pi r/(\beta\lambda)) = 1.23$. In fact the beam envelope in the accelerating gaps is less than 85% of the maximum, the envelope is not representative of the motion of individual particles and this coupling reduces with increase in beta.

For other beam simulations, random selections of particle co-ordinates were made so as to fill the 4-dimensional transverse phase space uniformly and simultaneously, to fill the longitudinal ellipse uniformly. These distributions were adjusted so that the first and second moments as computed by the standard statistical formulae, are exactly as prescribed despite the relatively small number of particles selected (200). Except where otherwise specified the standard input conditions of Table 3 were used. Surprisingly , for the majority of cases the emittance changes between 0.24 MeV/u and 2 MeV/u were barely significant. Thus for the normal case (Table 3) two results corresponding to distinct sets of random numbers differ by about 3% whereas the nominal emittance increases are less than 5%. A similar, comforting result was obtained when batching the quadrupoles in threes (to reduce the number of power supplies). The output projections on the three normal phase planes and the x,y plane are given in Fig. 2.

Attempts to demonstrate significant coupling between the phase planes were not conclusive. The method used was to make, in turn, one of the 3 emittances either twice the normal value or 10% of the normal value. The only significant emittance increases occurred in the longitudinal plane, by 10 to 15% when the transverse emittances were increased and then by 50% when the longitudinal input emittance was 10% of normal. Results where large increases in transverse dimensions could occur, are somewhat hypothetical as there might also be beam losses. Other tests were made using mismatched beams as would occur if the normal beam passed through a drift space until its length increased by 22%. These mismatches persisted throughout the acceleration to 2 Mev/u with a significant emittance increase, 18%, only for the longitudinal plane when it was mismatched.

One advantage of the quasi-Alvarez structure is its large longitudinal acceptance, which should allow efficient acceleration for several charge states around q=25+. Two complementary approaches were tried. Firstly the RF field level was varied by ±10% about the nominal level with the nominal input beam, which will evidently be mismatched both in input phase (by -6° and +8°) and in ellipse dimensions. These fields would be ideal for fictitious particles with q=22.5+ and q=27.5+ respectively! Another test used the normal accelerating conditions but for a beam with mixed charge states viz. q=24+, 25+ and 26+ in ratios 25%, 50% and 25% respectively. When varying the RF level there was a 10% longitudinal emittance increase at the -10% setting whereas for the nominally smaller effect (dq=± 1 cf dq=± 2.5) the superposition of three beams each making coherent oscillations gives a longitudinal emittance increase of 16%.

The results obtained between 2 and 1.2 MeV/u confirmed the above findings with negligible emittance increases except for the longitudinal plane with large input mismatch (18%).

Conclusions

This package of programs has been used to design a Quasi-Alvarez linac as far as its beam dynamics is concerned. Further iterations on the design e.g. to optimise cavity lengths for RF or post-coupler reasons [6], should be straightforward. With the relatively small rate of increase in β and the absence of space charge the close agreement with the simpler matrix and analytical approaches was not unexpected, but the negligible emittance increase, even with rather drastic mismatches, was an agreeable surprise.

References

1. H.Haseroth (Ed.), "Concept for a Lead-Ion Accelerating Facility at CERN", CERN 90-01 (1990)
2. H.Haseroth (Ed.), "A Heavy Ion Injector at CERN", This Conference
3. D.J.Warner, "Heavy Ion Acceleration Using Drift-Tube Structures with Optimised Focusing", 1988 Linac Conference Proceedings, CEBAF-Report-89-001, p109 (1989)
4. D.J.Warner, "Accelerating Structure of the CERN New 50 MeV Linac", Proc. 1976 Proton Linear Acc. Conf., AECL-5677, p49 (1976)
5. P.Lapostolle, F.Meot, S.Valero and E.Tanke, "A New Dynamics Code for Electrons, Protons and Heavy Ions", This Conference
6. M.Vretenar and D.J.Warner, "Field Stabilization in the Quasi-Alvarez Structure", This Conference

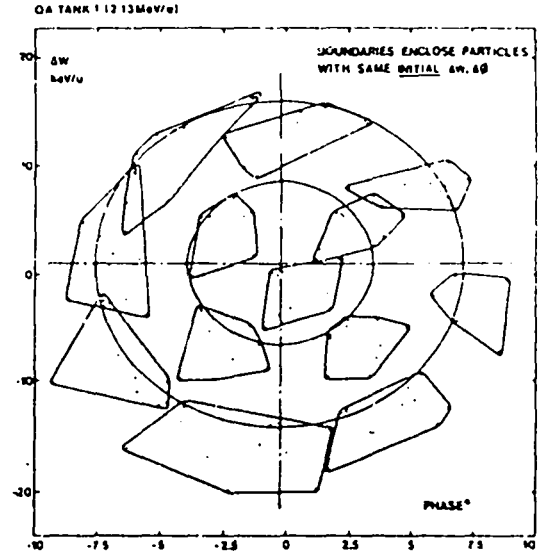

Figure 1: Coupling from Transverse to Longitudinal Phase Plane

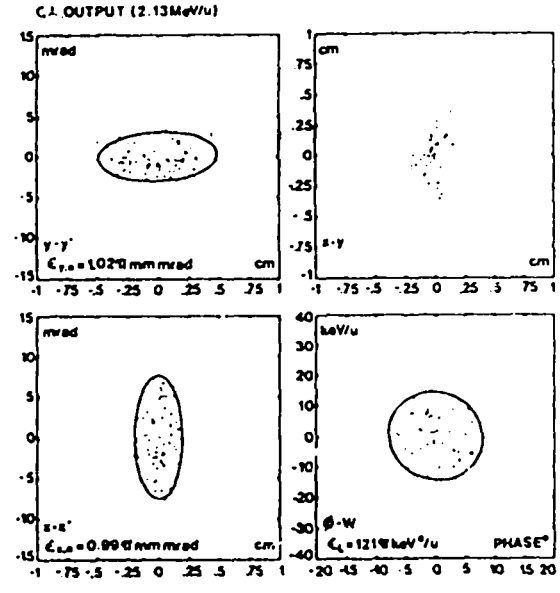

Figure 2: Phase Plane Projections at 2.13 MeV/u

Conditioning of High Gradient H^- Accelerating Cavities

T. Kroc & A. Moretti
Fermi National Accelerator Laboratory *
Batavia, Illinois 60510

Abstract

Three prototype cavities for the side-coupled accelerating structure of Fermilab's Linac Upgrade have been powered. The cavities operate at a nominal maximum surface electric field of 37-42 MV/m and have been run at close to 60 MV/m at 805 MHz. This paper will present the experience accumulated on x-ray production and RF breakdown frequency. We will try to compare our data with others' experiences with high surface electric fields.

Introduction

The Fermilab Linac Upgrade involves the replacement of the second half of the Alvarez drift-tube linac with a side-coupled structure similar to that used at Los Alamos. Because the Los Alamos structure was developed twenty years ago, a large R&D effort has been undertaken to take advantage of advances in technology and to develop local expertise. Included in this effort have been studies to understand the frequency of RF breakdown (sparking) and bremsstrahlung x-ray production to be sure that they fall within acceptable limits. RF breakdown inhibits the propagation of the beam through the linac, degrading the efficiency of the system and increasing activation levels. The amount of x-ray production determines the lifetime of organic materials in the vicinity and affects the shielding and therefore the civil construction requirements of the project.

The Fermilab structure will be operated at 805 MHz, have a maximum surface field of 37 MV/m, and a pulse length of 120 μsec. These parameters provide the opportunity to explore a relatively unexplored area of high surface electric fields and long pulse lengths and therefore may assist in the understanding of RF breakdown phenomena.

Physical Description

The side-coupled structure is based on the design of LAMPF shown in figure 1. Because of the high curvature on the nose piece, the surface electric field is approximately 5 times the accelerating field. The shunt impedance is 30% higher than LAMPF's and the the accelerating gradient is 5 times that of LAMPF[1].

The copper pieces are first annealed and then machined using a water soluable cutting lubricant. The coupling slots are machined in and a section is stacked and tuned. Then the whole structure (up to 16 cells) is brazed together in 3 steps in a hydrogen furnace at temperatures reaching 1910° F.

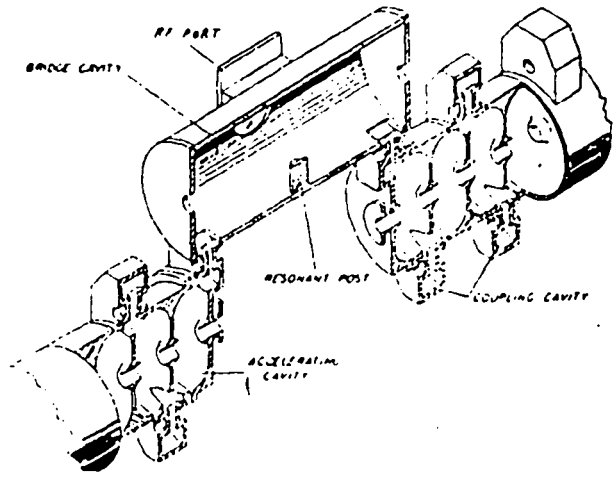

Fig. 1. View of LAMPF style side coupled accelerating structure. Prototypes 1, 2, and R-4 had 6, 6, and 16 cells respectively connected to a power cell. Prototype 1-A had 6 and 2 cells connected by a bridge coupler.

In order to guide the design of the production cavities, three prototype cavities were built and tested. Each had a different nose cone geometry. Prototype 1 (1-A) was a six cell structure (six plus two with a bridge coupler) that was given a sharper nose cone profile to enhance sparking for these studies. Prototype 2 was a six cell structure with a gentler nose profile. An even gentler nose cone profile was developed which was used in the sixteen cell Prototype R-4. (Prototype R-4 is actually one section of four that will make up a full prototype module which will be powered by a single klystron.) The average axial fields for Prototypes 1, 2, and R-4 were 7.67, 7.67, and 8.04 MV/m respectively. The ratio of the peak voltages on the nose cone to the average axial fields (E_{peak}/E_0) were 5.189, 5.001, and 4.547.

For these tests, the cavities were powered by a Litton L-5120 Klystron. It produced 1.5 MW (peak) in 120 μsec pulses at 15 Hz. For Prototype R-4 it was run at 2.9 MW with a pulse length of 50 μsec.

Sparks were recorded by a gated comparator that looked at the diode rectified signal from a directional coupler on the waveguide. The counter only counted pulses in which there was a spark even though there could be more than one spark within a single pulse

*Operated by the Universities Research Association, Inc. under contract No. DE-AC02-76H03000 with the U.S. Department of Energy.

(see fig. 2). The pulse length was nominally 120 μsec although the modules were sometimes run at 40 and 65 μsec. The gate for the comparator reduced the sensitive time to 75% of the pulse length.

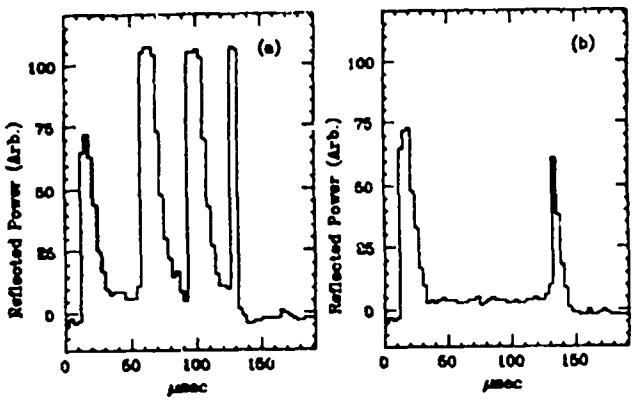

Fig. 2. Reflected power for a spark (a) and a normal pulse (b). The comparator was active for the time interval between t= 40 and 120 microseconds. If the reverse power was above a threshold, the comparator signaled that a spark had occurred. (a) illustrates that the sparks can be short lived phenomena, as short as ~ 10 μsec, and that more than one can occur within a pulse. The peaks in (b) occur due to the impedance mismatch during filling the cavity and the emptying of the cavity at the end of the pulse.

Figure 2 shows the results of a second spark monitoring system. The signal from the directional coupler was digitized and available for storage by a Sun workstation. If the comparator signaled that a spark had occurred the signal was stored. This permitted scanning of the reputed sparks to eliminate "false" sparks such as occurred when the comparator gate was not set correctly or the amplitude feedback loop on the signal generator had ranged out. A number of devices were used to measure the x-ray production of the cavities. All cavities were monitored by a Fermilab-built "Scarecrow". Prototypes 1 and 1-A also had a Victoreen-555 while Prototypes 2 and R-4 had a Nuclear Chicago 2592. The measurements from these were found to agree to within 10%.

Experimental Results

The data for Prototype 2 demonstrate best how the conditioning of these cavities occurs and are shown in figure 3. For this report, the chronological history of a cavity is measured by the number of RF pulses that have been applied. The counting was reset for Prototype 1, when the bridge coupler and the other two cells were added, which we then refer to as Prototype 1-A. Over the course of this investigation, Prototypes 1, 1-A, 2, and R-4 accumulated 8.53, 11.33, 18.87, and 17.81 million pulses respectively. In figure 3, the diamonds present the history of the sparking conditioning, the crosses show the x-ray production conditioning, and the ticks along the lower portion of the figure show when the cavity was energized to a higher level for the first time.

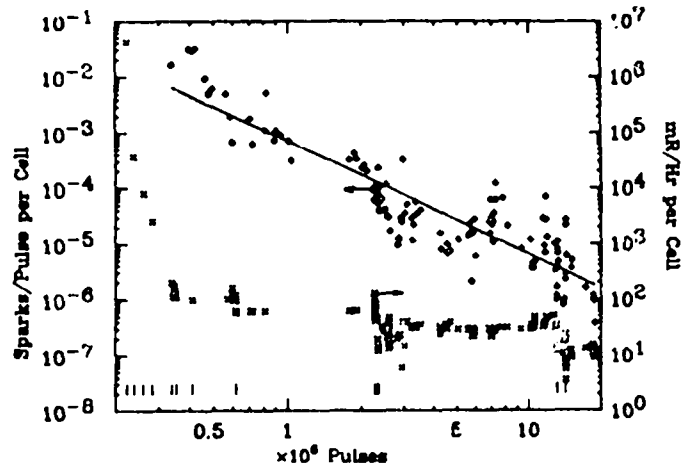

Fig. 3. Sparking rate (◇) and x-ray production (×) as a function of conditioning time as measured by the number of pulses in Prototype 2. Each have been corrected for pulse length and normalized to 37.1 MV/m. The ticks along the bottom indicate when a new electric field was achieved for the first time. The line is fit to the sparking rate for the interval between 500,000 and 19 million pulses and has a slope of -2.

Sparking

It was noticed that the sparking rate varied as the surface voltage to the ~19.5 power for fields between 33 and 60 MV/m. Since the cells are operated at various levels (X) for various lengths of time we assume the power law to be true and project all the rates (R) to the operating gradient of 37.1 MV/m.

$$R_{proj.}(37.1\frac{MV}{m}) = R(X\frac{MV}{m}) \times (\frac{X}{37.1})^{19.5} \qquad (1)$$

We have also observed that the sparking rate is directly proportional to the pulse length, so the rates are normalized to a full 120 μsec pulse length. The diamonds in figure 3 show how the sparking rate decreased as the cavity was conditioned. The line has a slope of -2 indicating that once 500,000 pulses have been accumulated, the sparking rate falls off as $1/(\#_{pulses})^2$. There is no indication of an asymptotic leveling off to a constant rate.

X rays

The x-ray production is governed by field emission as described by the Fowler-Nordheim equation. Over the range of operation explored here, the F-N equation

can be represented by a power law of order 11 - 14. The x-ray production is scaled in a manner similar to the sparking as in equation 1. The x-ray production was also corrected for pulse width. It would be preferable to use absolute values of the F-N equation but we have no way of measuring either the field-emitted current nor the area of the emitters. Notice that while the reduction in sparking is continuous, the change in x-ray production is not. The drops in x-ray production seem to be correlated with attaining higher electric fields within the cavity.

Discussion

Historically much work on RF breakdown (sparking) has been related to the "Kilpatrick Limit"[2] although today truly catastrophic breakdown seems to occur at a level about seven times this limit[3]. For Prototype R-4 careful attention was made to measure the sparking rate as soon as the gradient was high enough for the comparator to function. This occurred as soon as multipacting was passed. Sparks were recorded beginning at 0.2 times the Kilpatrick limit. We have gone as high as 1.7 times the Kilpatrick limit and others have gone up to the catastrophic breakdown threshold. Sparking occurs all through this region as a random statistical process. It appears that within this range, one needs only to condition long enough until the breakdown rate subsides to acceptable levels. Our results so far indicate that this is easy to achieve and that there is no indication of an asymptotic leveling off.

As mentioned above, field emission is described by the Fowler-Nordheim equation, however, most measurements of the field emitted current require a multiplicative enhancement factor, β, for the electric field. This factor is assumed to be due to geometric or dielectric characteristics of the metal surface which increase the electric field in localized areas. Wang and Loew have investigated the possibility of RF "scrubbing"[4] to try to process to high gradient without causing physical damage to the surface in order to reduce β. If one is not going to run near the catastrophic breakdown limit, it seems that "brute force" processing is perfectly adequate. Presumably this burns off emitting sites and the reduction in the emitting area offsets any increase in β due to damage from sparking, at least at our operating levels.

The x-ray spectrum is produced by bremsstrahlung from the impact of field-emitted electrons onto the copper surface and should be directly proportional to the field-emitted current. The fact that the x-ray dose can be reduced by high-gradient processing suggests that the field-emitted current can be reduced, possibly by deactivating field emission sites.

As discussed above we see different behavior of the sparking rate and the x-ray production rate as a function of the conditioning time. The sparking improves continuously while the x-ray production improves in a stepwise manner whenever higher gradients are achieved. This suggests to us that different mechanisms govern the two processes. The x-ray production mechanism seems firmly tied to bremsstrahlung and field emission. Most RF breakdown mechanisms are also based on field emission. Latham also talks about microparticle based processes[5] but it would seem that these processes would also lead to high field emitted currents. These currents would suggest that the x-ray production and the sparking behave similarly.

Conclusion

The Fermilab Linac Upgrade project requires that the losses due to sparking to be less than 1%. For each of the prototypes tested, this level has been attained after 5 - 10 million pulses of conditioning. At the linac's 15 Hz repetition rate this will occur in 4 to 8 days. We have not seen any evidence yet of the conditioning ceasing to improve. After the cavities have been let up to air, the previous sparking rate is recovered within a few minutes to hours. The x-ray production does not seem to be affected by the nose cone geometry and therefor the peak fields as one might have expected. However, it does seem possible to condition the cavities for lowest x-ray production by running the cavity to the highest fields available. These results are acceptable for the Fermilab Linac Upgrade.

In terms of understanding the dynamics of the two processes, the results are not as clear as each do not follow the same conditioning pattern as theories describing their origin would suggest.

References

1. R. J. Noble, "Fermilab Linac Upgrade," proceedings, this conference.
2. W. D. Kilpatrick, Rev. of Sci. Instrum., 28, 824,(1957).
3. J. W. Wang and G. A. Loew, presented at the 1987 Particle Accelerator Conference, SLAC-PUB-4247.
4. G. A. Loew and J. W. Wang, presented at the XIV International Conference on High Energy Accelerators, SLAC-PUB-5059.
5. R.V. Latham, High Voltage Vacuum Insulation: The Physical Basis,(Academic Press, London, 1981).

MECHANICAL CONSTRUCTION OF THE 805 MHz SIDE COUPLE CAVITIES FOR THE FERMILAB LINAC UPGRADE

Michael P. May, James R. Fritz, Thomas G. Jurgens, Harold W. Miller, James Olson, and Daniel Snee
Fermi National Accelerator Laboratory
Post Office Box 500, Batavia, Illinois 60510

Abstract

The manufacturing processes for the Side Coupled Structures (SCS) are intimately connected with their tuning requirements. Present Computer Numerical Controlled machining allows very repeatable accuracies of dimensions. This has led to a manufacturing sequence which reduces the need for repeated machining steps. Surface tolerances in the high field region of the accelerating cells were assured. Tuning steps were reduced at all stages of construction. This paper will describe the mechanical steps used to fabricate the SCS structure at Fermilab.

Introduction

The construction of the Fermilab Side Coupled Structure has evolved through years of experience from people who have worked on linac structures. The SCS was pioneered at Los Alamos in the 1960's for the construction of LAMPF. Based on beam dynamics and power considerations, the Fermilab SCS was segmented into 28 sixteen cell sections. In 1988 Fermilab began a research and development program which would lead to the design and construction of a side-coupled linac for the 400 Mev Linac Upgrade. Information about design, tuning, and construction techniques used for side-coupled cavity linacs was gathered from Los Alamos, SLAC, and other sources. After sifting through all the information, and digging into our own bag of tricks, we came up with the Fermilab version of the SCS.

Side Coupled Cavity Construction

The Fermilab SCS is similar in appearance to the LAMPF SCS, but that is about as far as the similarities go. The construction of the Fermilab SCS is significantly different.

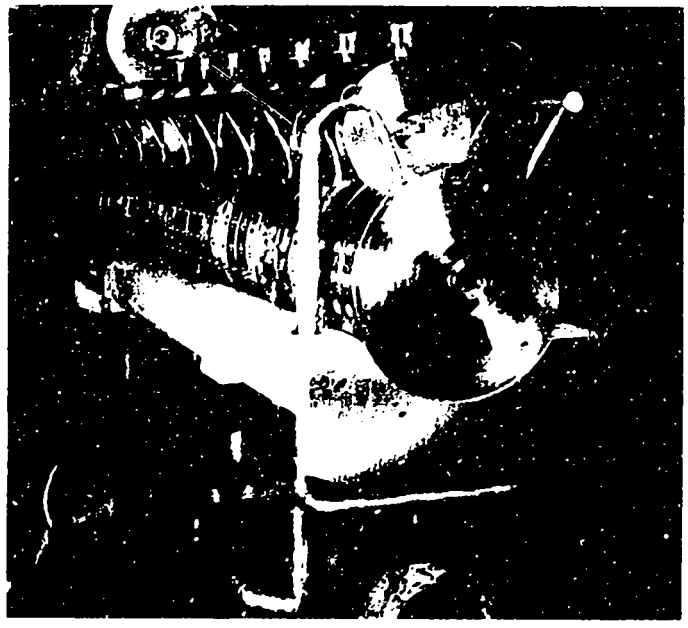

The biggest factor which dictated the design of the SCS was the availability of repeatable CNC machining. Superfish was used to calculate the exact shape of the main cavity sections. [1] The cavity shapes were transferred to CAD drawings and CNC programs. Models were machined using aluminum to check the predicted frequency in relation to the actual frequency. Adequate correlation and good repeatability of frequencies were achieved. CNC machining controlled tolerances to within .001" over a set of 17 segments. [2]

The first major decision which was made was to buy all our copper for the project from Hitachi. (Class 101 OFE) This decision was based on advice and past experiences of SLAC. The copper was purchased in a cross-grain forged condition. Hitachi also agreed to

rough machine the copper to within .050" of our final dimensions. The rough machining turned out to be a real bonus in that the parts had one machining operation completed when delivered, and we didn't have to pay to ship the extra weight from Japan to the USA. The copper was delivered from Hitachi to Copper & Brass Sales in Oakland, Cal.. From there, we had the Main Cavity section shipped to Pyromet Industries in San Carlos, Cal. for annealing. The Side Couples were shipped to Fermilab without being annealed.

Upon arrival at Fermilab, the copper parts were inspected and then shipped to the CNC machine shops for the next phase of machining. The accelerating and coupling cavity components were machined to pre-calculated dimensions determined by experimental models and Superfish calculations.

The Main Cavity sections were brought to the tuning lab at Fermilab after machining and each half cell was inspected, labeled, and the frequency measured. From there the Main Cavities went to our machine shop for an initial coupling slot cut.

While the Main Cavities were going through these steps, the Side Couples were being inspected after their first machining. They were then packaged in specially made foam shipping containers and shipped to Pyromet for the brazing of the two halves. This braze was accomplished using 35-65 braze alloy. A .002" foil was placed between the halves, and a .030" diameter wire was placed in the groove on the outside. The Side Couples were then returned to Fermilab where they were leak checked and sent to an outside machine shop to have the vacuum port hole machined in the top of the Side Couple and the scallop machined by EDM in the bottom. The tolerance on the arc was held to +/- .001".

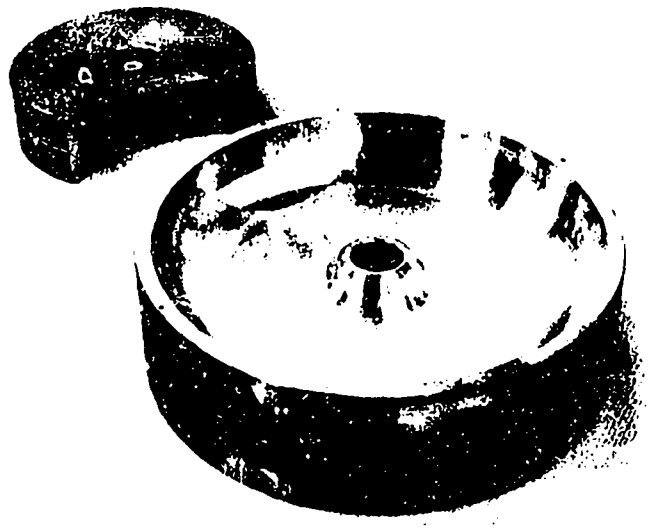

Five Main Cavities and Side Couples were staked on a special fixture and the Pi/2 frequency was measured. One to two additional cuts were needed to achieve the final slot depth. All the remaining cavity sections and bridge ends were machined to this depth.

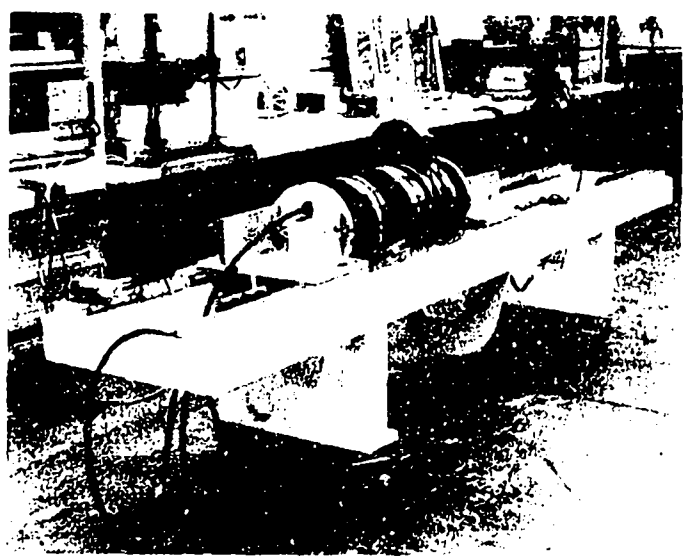

The Bridge Ends, Terminating Ends, and Bridge Side Couples needed special attention. Because of their non-repeating geometry, they require a different frequency than an interior cell. The frequency change was accomplished by removing material from the side wall. The exact frequency was determined when the stack of five is checked for slot depth.

The Bridge Side Couple is unique to Fermilab in its design. The flange which joins the Bridge Couple to the Bridge Side Couple is placed just above the tuning stub in the Bridge Side Couple. This was done for several reasons. It allowed the flange which couples the two parts to become very simple in geometry, thus, permitting us to use a rather standard type of copper gasket which acts as a vacuum seal and as a current carrying device. Another reason why the flange was located in this position, was to allow the tuning stubs to have a similar shape as those in the Side Couples. Thus, the Bridge Side Couples can be finely tuned after the Cavities are assembled to the Bridge Couples by simply pushing or pulling on the stubs.

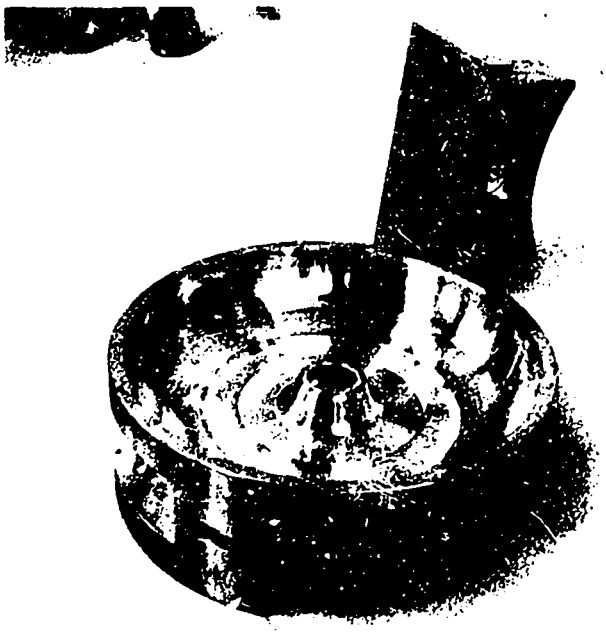

After all the tuning steps are completed in the specially designed stacking fixture, the parts are packed into an air ride cushioned box and shipped by an air ride van to Pyromet Industries in San Carlos, California where they are hydrogen furnace brazed.

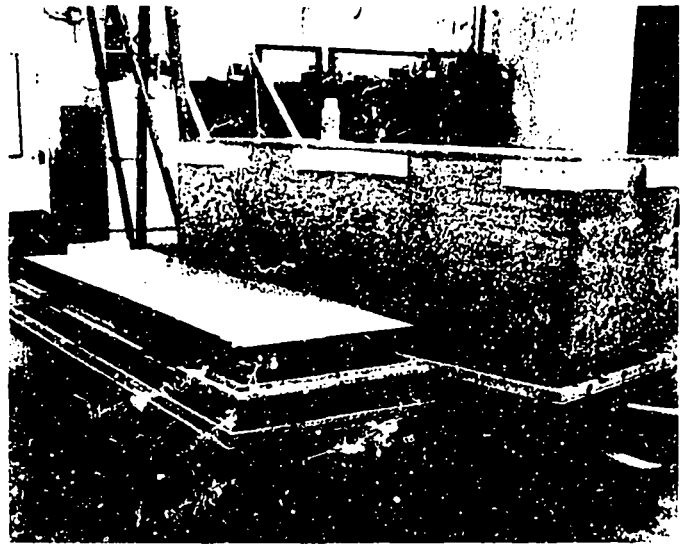

The Bridge Side Couples, and the Side Couples have previously been brazed with 35-65 braze alloy at this time. The first brazing step was to braze the Side Couples to the Main Cavities at the saddle joint, and to braze the stainless steel vacuum port to the Side Couple. This was accomplished using 50-50 braze foil, .002" thick and a 50-50 powder mixture fillet. After brazing, the joints were visually check for vacuum integrity. If there were any questionable areas, the joints were filled with 72-28 CuSil powder mixture. The Main Cavity joints were lapped to mak sure that they were absolutely flat for the next brazing step. After lapping, the joints were brush silver plated. The cavity was now stacked to a specific stacking order which was determined by matching the frequencies of the half cells. Having stacked the entire cavity, a .030" dia. braze wire of 72-28 CuSil wire was wrapped around each joint between cavity sections. The cavity was placed in the hydrogen retort and brazed. After the brazing operation, the entire structure was vacuum leak checked, packed into the same shipping crate that it came to Pyromet, and returned to Fermilab.

References

1 The Determination of the 805 MHz Side Coupled Structure Dimensions for the Fermilab Linac Upgrade. T. G. Jurgens. 1990 Linac Conf.. These proceedings.

2. Tuning Methods for the 805 MHz Side Coupled Structure in the Fermilab Upgrade. H. W. Miller. ibid.

THE DETERMINATION OF THE 805 MHZ SIDE COUPLED CAVITY DIMENSIONS FOR THE FERMILAB LINAC UPGRADE

Thomas G. Jurgens, Harold W. Miller, Alfred Moretti, and Ping Zhou
Fermi National Accelerator Laboratory *
POB 500 Batavia, Illinois 60510

Abstract

In order to achieve the proper frequencies and coupling in Side Coupled Accelerator Structures, it is often necessary to model the cavities. In order to reduce the number of modeling steps and hence reduce machine shop time and cost, we have drawn heavily upon previous LAMPF experience and present day numerical calculation programs. Using a few aluminum cavity models at selected machine energies, we have been able to predict the frequency and coupling of our structures with good accuracy. This paper will describe the steps used to determine the cavity dimensions that meet our structure requirements.

Introduction

The Fermilab Linac Upgrade Project[1] will increase the energy of the existing 200 MeV Linac to 400 MeV by replacing the last four drift tube cavities of the original Linac with higher gradient side coupled (SC) cavity accelerating structures. The determination of cavity dimensions required the synthesis of numerical simulation data and aluminum model measurements. Mechanical fabrication issues also played a role in the structure's design.

Design Constraints

The overall constraints placed on the design of the LINAC cavities derives from the power, beam dynamics and initial accelerating cavity analyses. These constraints result in a machine which accelerates the beam from 116 MeV to 400 Mev with seven independently powered SC modules. Beam dynamics considerations leads to the separation of the modules into sections separated by quadrupoles. Each of the sections has 16 identical accelerating cavities (of length $\beta\lambda/2$), and the SC Linac sections are designed at 28 different energies. The program SUPERFISH was used to optimize the shape of the accelerating cavities for high ZT^2 and reduced surface electric field.[2] The unslotted accelerating cavity frequencies, f_{SF}, used in these SUPERFISH runs were determined as outlined below. The major cavity radius of the accelerating cells was held constant at 13.455 cm to simplify their manufacturing.

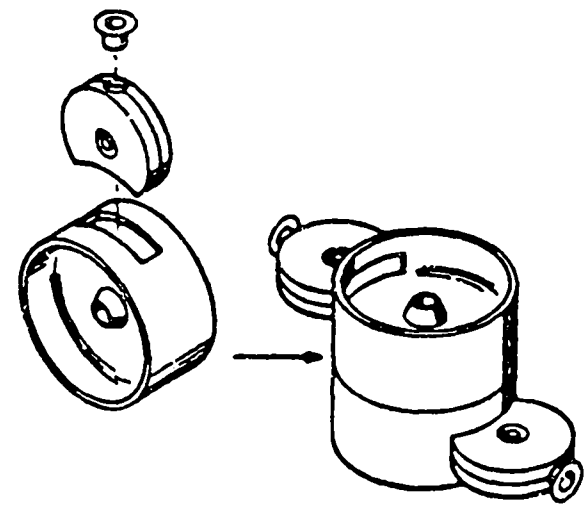

Figure 1: Segmented SC Cavity Design

Design Choices

Fermilab has chosen the LAMPF segmented construction for the new SC Linac. In the segmented design, two half accelerating cavities are machined from roughed-out copper cylinders of length $\beta\lambda/2$. The side cavities are also made from roughed-out cylindrical pieces. These two half accelerating cavities along with one full side cavity consitute a basic segment for the Fermilab design. This design permits higher speed lathe operations due to the symmetry of the

*Operated by the Universities Research Association under contract with the U. S. Department of Energy

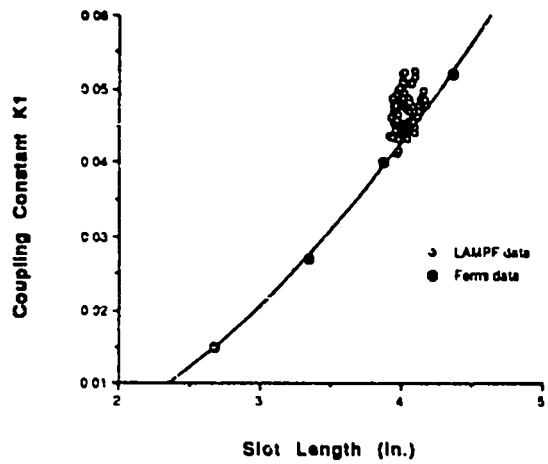

Figure 2. SCC Slot Length vs Nearest Neighbor Coupling Constant, k_1

cavity parts.[3] The Fermilab segmented design is illustrated in Figure 1.

The next goal of the design is an SC structure which has a constant nearest neighbor coupling constant k_1, a flat electric field from cell to cell on the beam axis and is simple to manufacture. Since the accelerating cavity shape is now fixed, the side cavity shape and location with respect to the accelerating cavities can be used to ensure a constant k_1.

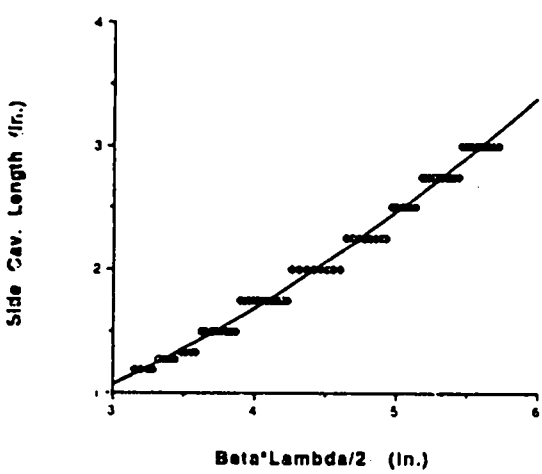

Figure 3: LAMPF Side Cavity Length vs Accelerating Cavity Length

In order to better understand the design of side cavity structures, a study of the design of LAMPF[4]

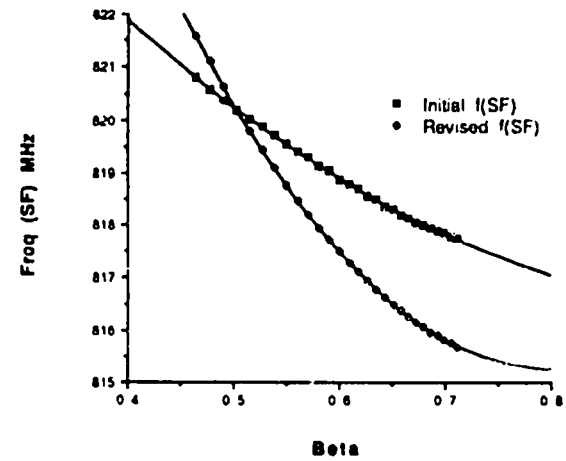

Figure 4: f_{SF} vs β for the Fermilab SCC

was carried out and aluminum SC cavity models were constructed and measured. Combining LAMPF data with the aluminum model data reveals that the geometric parameter which correlates closest to k_1 is the slot length, shown in Figure 2. The LAMPF data, illustrated in Figure 3, shows that the side cavity length increases with increasing accelerating cavity length (and energy) in a step-like manner. The step-like changes in the LAMPF side cavity length cause the slot length and hence k_1 to vary with β. In the Fermilab SC cavity design these variations in k_1 are eliminated by continuously changing the side cavity length with β in such a way as to keep the slot length constant. The center to center distance between the accelerating and side cavities and the side cavity radius are held constant for all βs.

Accelerating Cavity f_{SF} and Slotting

In SC cavity structures the side cavities are inductively coupled to the accelerating cavities via a slot. The resonant frequency of the unslotted accelerating cavity, f_{SF}, drops when it is slotted. The attachment of a side cavity to the slotted accelerating cavity pieces creates a basic segment. After stacking the basic segments and tuning them, the resulting SC module resonates at a mode[5] frequency $f_{\pi/2}$ equalling 805 MHz.[6] Therefore, f_{SF} needs to be known before slotting and stacking takes place. Initially, the f_{SF} was determined by taking the f_{SF} vs β graph for LAMPF and shifting the curve for dimensional differences between the Fermilab aluminum cavity models and LAMPF. Subsequently, prototype copper cavity sections were fabricated and measured. This new data led to a revision of the initial f_{SF} curve. Figure

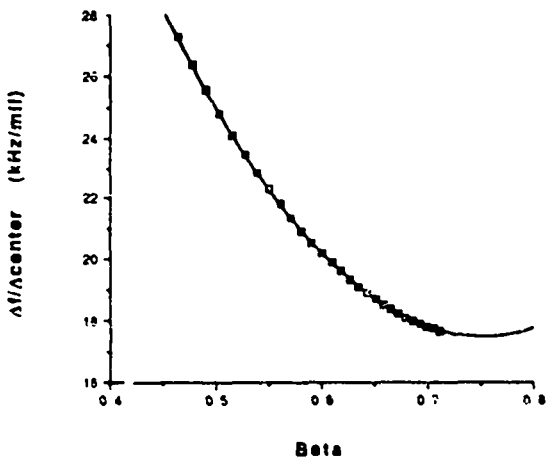

Figure 5: $\Delta f / \Delta center$ vs β for the Fermilab SCC

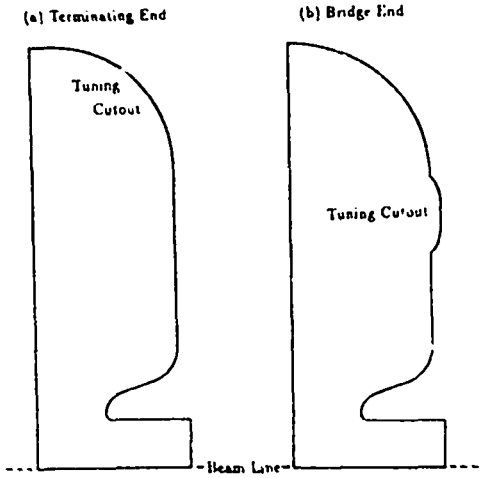

Figure 6: End Accelerating Cavity Cutouts, (a) Terminating (b) Bridge

4 shows the initial and modified curves.

The frequencies f_{SF} were chosen so that for a slot length of 10.516 cm k_1 equals 0.05. In practice the slot is not cut to the full length, rather it is cut to approximately 10.433 cm. This slot length corresponds to a slot depth[6] of 7.264 inches. Fine tuning of $f_{\pi/2}$ is accomplished by slightly varying the slot length. This results in $k_1 = 0.048 \pm 0.001$ (see Figure 5). The variation in k_1 for LAMPPF was 0.042 to 0.052.

The accelerating cavity sections are terminated with end cavities whose electromagnetic properies are different from interior cavities.[6] This difference arises from the fact that they either posses only one coupling slot, in the case of terminatig ends, or one of the two slots couple into a bridge coupler with a $k_1 \approx 0.1$. During tuning[6] material is removed from the outer wall of the terminating ends and just below the slot of the bridge ends. Figure 6 shows these cutouts.

Summary

The combination of numerical electromagnetic simulation programs, a few key measurements of prototype cavity structures and numerically controlled machining has allowed us to fabricate SCC cavity modules in an accurate, repeatable manner. This paper has outlined the rationale behind the dimensions of the Fermilab SC Linac.

References

1. R. J. Noble, The Fermilab Linac Upgrade, *1990 Linear Accelerator Conference*, (September 1990).

2. P. Zhou, Geometry Optimization Study of the Side Coupled Structure Using SUPERFISH, *Fermilab LINAC Upgrade Note*, (February 1989).

3. M. P. May, J. R. Fritz, T. G. Jurgens, H. W. Miller, J. Olsen, and D. Snee, Mechanical Construction of the 805 MHz Side Couple Cavities for the Fermilab Linac Upgrade, *1990 Linear Accelerator Conference*, (September 1990).

4. G. R. Swain, LAMPF 805-MHz Accelerator Structure Tuning and Its Relation to Fabrication and Installation, *Los Alamos Scientific Laboratory*, **LA-7915-MS**, 112 (July 1979).

5. D. E. Nagle, E. A. Knapp, and B. C. Knapp, Coupled Resonator Model for Standing Wave Accelerator Tanks *Rev. Sci. Instr.*, **3:11**, p.1583 (1967).

6. H. W. Miller, T. G. Jurgens, Q. A. Kerns, R. Padilla, and Z. Qian, Tuning Methods for the 805 MHz Side Coupled Cavities in the Fermilab LINAC Upgrade, *1990 Linear Accelerator Conference*, (September 1990).

TUNING METHODS FOR THE 805 MHZ SIDE-COUPLED CAVITIES IN THE FERMILAB LINAC UPGRADE

Harold W. Miller, Thomas G. Jurgens, Quentin A. Kerns,
Rene Padilla, Zubao Qian
Fermi National Accelerator Laboratory *
Batavia, Illinois 60510

Abstract

The fabrication and tuning of Side-Coupled Accelerator Structures (SCS) are strongly inter-related. Consideration of mechanical tolerances and fabrication sequences can reduce tuning steps that require repeated machining. With available CNC machines and numerical calculation programs, it is possible to machine cavities to a calculated shape. Accelerating cells are tuned by control of the depth of coupling slots rather than trimming the nose of accelerating cells. Predicting the correct frequency off-sets to use at each manufacturing stage produces a brazed structure of proper coupling with a minimum amount of tuning.

Introduction

Our structure consists of sixteen accelerating cells and fifteen coupling cells brazed into an accelerating section. There are twenty-eight sections in seven rf modules of the Linac upgrade. Construction schedules require that one section be completed every two weeks. Structure tuning and assembly must progress rapidly. Reducing repeated tuning steps was one goal. An automated measurement system is being implemented. [1]

Optimization of the structure was the result of many contributors. Nose cones were carefully shaped to insure minimal sparking. We decided that we would machine the noses once, including ends, and not trim them to adjust the cell frequency. This reduces the chance of scratching the high field region. End frequency adjustments are made in the "inductive" regions (cavity wall) of the cells. Field variation along the structure due to nose cone differences are eliminated.

Our SCS consists of a stack of 15 "interior" segments terminated with a bridge coupler cell at both ends or a bridge coupler cell and terminating cell at each end. For initial tuning, ends are terminated with flat plates. Basic interior segments consist of two accelerating half cells joined through a coupling slot with a coupling cell. This half terminated assembly supports a $\pi/2$ mode. The mode is higher than for a fully terminated interior cell and as cells are stacked the $\pi/2$ frequency is reduced. A plot of the $\pi/2$ frequency vs 1/n (the number of half cells) will project the correct $\pi/2$ frequency for an infinite stack. This frequency of the structure is maintained when fully terminated.

A coupling slot is cut into the accelerating cell body after machining the half cells to a SUPERFISH(SF) calculated frequency, f(SF). The depth of the slot is adjusted for the desired $\pi/2$ frequency. Increased depth of the slot lowers the frequency and increases coupling between accelerating and side cells. The length of the coupling slot is estimated for 5% coupling with full slot depth as β varies for each section. LAMPF data was used to estimate early values of f(SF) and coupling slot dimensions. Subsequent construction of R1 through R4 (sections of a prototype module), and aluminum models have allowed us to refine the values for f(SF) and given us reliable Δf values as the slot depth is changed. [2]

A standard five parameter model is used to describe the dispersion of the field modes in the passband. An adequate description is given in ref 1. Final tuning of the structure makes use of the fact that all accelerating cells are tuned to a frequency $\omega 1$ and all side coupling cells are tuned to a frequency $\omega 2$. When actually measuring the cells, the frequencies are not the same as the values calculated by the dispersion equation. Any method of shorting adjacent cells shifts their frequency. Probes inserted consistently provide controlled offsets in each cell. With cells at the same frequency tuning is straight forward. We start with the $\pi/2$ frequency low and just move all the accelerating cells up the amount of

*Operated by the Universities Research Association under contract with the U.S. Department of Energy

the error. If the stop band is off we move all the coupling cells the appropriate amount.

Individual cells are all identified and numbered. Frequencies are measured using an HP 8753C network analyzer and recorded on an Excel spread sheet. Temperature, barometric pressure and humidity are recorded for each measurement. Excel is used to correct frequencies to vacuum at 25 C. and for statistical data.

SUPERFISH Measurements

The CNC program is verified both mechanically and electrically on a sample part. Seventeen (two spares) accelerating interior cells without coupling slots are machined to final SF calculated dimensions and delivered to the tuning lab. They are inspected for mechanical defects, and cell length is measured and recorded. The rim is lightly lapped with 15 micron aluminum oxide coated mylar on a granite surface plate to verify flatness and remove copper oxide from the contact surface. Mechanical tolerances are met within 1 mil. Cells are clamped in a special fixture with flat copper terminating plates. We directly measure the SF frequency and Q of the half cells. Our goal is for an average and spread of frequencies within ± 300 KHz of calculated SF values. Table 1 shows our Prototype R machining experience. (frequencies are in MHz.)

Table 1
Prototype R Superfish Machining

Section	R4	R3	R2	R1
Target SF	820.20	820.39	820.59	820.80
Mach. Avg.	820.32	820.21	820.50	820.62
Off-set	+0.12	-0.18	-0.090	-0.18
Spread	0.657	0.535	0.398	0.365
Std. Dev.	0.193	0.108	0.102	0.086

Stacking Order

High and low frequency half cells are paired in a stacking order to best equalize the interior accelerating cells. The goal is to have frequencies within ± 30 KHz. High and low frequency half cells are placed at the ends where their frequency errors are incorporated into the terminating end tuning. Cells midway between highest and lowest are reserved as spares and can replace any cell in the stack. The paired results of selective stacking are shown in Table1.

Slotting

The slot depth is made using a cutter arc identical to the inside radius of the coupling cell. The cutter center is spaced relative to the center of the accelerating cell. A 7.2441 inch center spacing between the coupling and accelerating cells gives full penetration for the slot. We adjust target SF values, which range from 821.59 to 815.71 MHz with ß so that the pre-brazed stack is at 804.900 MHz when the center spacing is 7.264 inches. Typically, the frequency change, $\Delta f/\Delta$center ranges from 27 to 17 KHz per 0.001". A minimum of ±340 KHz frequency adjustment and associated coupling k1 of 4.7±0.1 % over a ±0.020" center spacing variation is expected. If the SF frequency drifts out of the adjustment range, we have three options. 1) Continuously correct Target SF values as sections are fabricated. 2) If cells are too low the slot can be backed out at with small reduction in coupling k1. 3) High cells can be remachined to correct their frequency. We have succesfully used option 1 for most sections. In section R2 where an unintended .002 inch taper of the web thickness from outer to inner radius caused six half cells to be 600 KHz low, we used step 3) to bring them back into range.

We determine the exact slot depth by a sequence of three cuts in the first five accelerating cells of the stack. The paired average SF frequency of the cells is compared to the target SF value and the slot center spacing is adjusted to the expected value for 804.900 MHz. We increase the expected center spacing by .020" and cut the first slot depth. The five cells are stacked in order and the $\pi/2$ frequencies measured and plotted vs the number of half cells to establish the infinite stack $\pi/2$ frequency. A second cut made half way between the measured and final expected value establishes a verification of the $\Delta f/\Delta$center for the cell. We calculate, cut and verify the third and final slot depth cut. Finally bridge end cells, followed by the accelerating cells, are slotted to the final depth.

End Terminations

End cells are tuned lower than interior cells. Material is removed at the outside radius of terminating ends and below the slot in bridge ends. Cut-out dimensions are determined by clamping the ends on the stack of five completed cells while the machining of the remaining cells proceeds. End cell

frequencies are lowered to the projected $\pi/2$ frequency by capacitive loading of the gaps. Balance is established by tuning for minimum energy in the adjacent side cells. Loop pickups inserted through the vacuum ports verify that there is little energy in all side cells. Cells adjacent to the ends are shorted and the end cell frequency is measured. The capacitive loading is removed and the resultant Δf is determined. A SF graph of Δf vs cut-out is made ahead of time for each section. Dimensions are simply taken from the graph and parts taken to the machine shop.

Pre-Braze Measurements.

After final machining the full structure is clamped together on the stacking fixture. Each accelerating cell and the $\pi/2$ frequency are measured and recorded in a spreadsheet. For individual cell measurement shorts are placed in adjacent cells. Shorts in side cells have appropriate spacers so that when the cells are re-measured after brazing on vacuum ports they are re-inserted to exactly the same position. Shorts on adjacent accelerating cells is accomplished by a centerless ground rod .002 inches under the bore size slid across the gap. This capacitively shorts out the desired cells. There are no fingers to scratch or fall off in the bore.

Post-Braze Measurements

After final brazing, welding on flanges and mounting the structure on a permanent cradle the frequency of accelerating cells and the $\pi/2$ mode are checked and compared to the pre-brazed condition. An assessment is made of the amount each accelerating cell must be increased to bring the structure up to the desired $\pi/2$ frequency. Checks here are intended to determine shifts in brazing and handling and to guide us in determining if 804.900 MHz. is low enough to insure all cells will need to be raised.

Section Tuning

Accelerating cells are tuned in a first pass to the same frequency and for a $\pi/2$ frequency of about 804.970 MHz. Indentations machined into the cell walls are pushed in with a punch to raise the cell frequency. Side cells are equalized to 805.030 MHz. Threaded studs brazed on the side cells allow their gap to be pushed in either direction. With our probe designs, cell frequencies can be equalized to ±5 KHz. End cells are adjusted by moving the end wall. A snap ring type groove in the end wall and special tool allow gap adjustment in or out. The frequency shift is about 100 KHz. per .001 inch. Ends are adjusted for minimum energy in the adjacent side cells. A "tuning cell" with adjustable nose pieces is mounted at the flange of the bridge coupling cell. The tuning cell and the end accelerating cell are tuned together until there is minimum energy in both the adjacent side cell and bridge coupling cell. Next the bridge coupling cell is shorted with a band of copper wrapped around the nose. The cell frequency is raised about 160 KHz with this configuration. We load the gap capacitively and measure all thirty-one modes in this configuration. A dispersion program is run and the frequencies, couplings and stopband are determined.

Vacuum Measurements

The section is put under vacuum and the modes are measured. The $\pi/2$ frequency and the stop band are determined and compared to the first pass tuning. From experience we find that the $\pi/2$ mode measured under vacuum is about 18 KHz lower than when it is corrected from atmospheric conditions. The stopband moves down 280 KHz due to deflection of the side cell walls. With measured offsets we retune the structure to 804.966 ± 0.01 MHz with a stopband of +150 KHz under vacuum at 25 C. Each section will have an independently controlled water loop and differential tuning between sections will be adjusted thermally.

Conclusion

We have developed tuning techniques that, in concert with mechanical fabricators, has lead to an efficient fabrication process and allowed the major machine work to be done by industry.

References

1. P.S. Prieto, T. Jurgens, T. Savord and J. Crisp, Side Coupled Accelerating Structure Automated Measurement System, 1990 Linear Accel. Conf. (Sept. 1990)

2 T. Jurgens, H.W. Miller, A. Moretti and P. Zhou, 1990 Linear Accelerator Conference, (September 1990)

SIDE COUPLED ACCELERATING STRUCTURE AUTOMATED MEASUREMENT SYSTEM

Peter Steven Prieto, Jim Crisp, Tom Jurgens and Tim Savord
*Fermi National Accelerator Laboratory**
Batavia, Illinois 60510

Abstract

A computer controlled, network analyser based measurement system was developed for evaluating the side coupled accelerating structure (SCS), which will replace part of the FermiLab linear accelerator. The SCS will boost the Linac energy from 200 MeV to 400 MeV, contributing to the reduction of beam emittance providing a higher intensity beam. The measured parameters include shunt impedance(Z_s), electric field($\vec{E}_0$) the total voltage(V), and transit-time factor(T) of the accelerating structure. Also, the stopband, frequency, and Q value of the $\pi/2$ mode are determined.

The first set of parameters (Z_s, $\vec{E}_0$, V, T) are measured using a bead-pull perturbation technique. The automated measuring system was designed around an IBM-AT compatible computer, (AST 286), controlling an Hewlett-Packard (HP8510B) network analyser and a Galil (DMC-400) motor controller, with the National Instruments GPIB interface card. Programs were developed under TurboC (version 2.0) assembler debugger environment. The dispersion measurements are carried out using a sub-set of the above mentioned instruments.

Introduction

The upgrade to the Linac will bring about an increase in beam kinetic energy from 200 MeV to 400 MeV. This will be accomplished by replacing the last four drift tube tanks in the existing Linac with seven modules of the side-coupled structure design. The seven modules break down into four sections of sixteen accelerating cells and fifteen side coupling cells. The sections are connected through bridge couplers[1]. These structures will operate at 805 Mhz, four times the present operating frequency. An automated system was developed for tuning verification and parameter characterisation of the structures. The measurements are divided into two classes, dispersion curve and bead-pull.

*Operated by the Universities Research Association, Inc. under contract with the U. S. Department of Energy.

Dispersion

The goal of this measurement is to assess the stopband of the $\pi/2$ mode. A chain of N coupled cavities will have N cavity chain modes. The resonance, or mode, occurs at the frequency which provides a total phase shift along the chain of $n\pi$ radians, where n is limited to 0,1,...,N-1. The mode which has $\pi/2$ radians of phase shift per cavity, or cell, is chosen because of the coupling efficiency of the biperiodic structure to the beam and its unique field stability with variations of beam loading and manufacturing inaccuracies.

A sufficient model for analysing the SCS assumes all accelerating cells and coupling cells are identical. The dispersion relation relates the N mode frequencies with the phase shift per cell. Using ω_1 as the resonant frequency of the accelerating cells, ω_2 that of the coupling cells, κ_1 the coupling coefficient between accelerating and coupling cells, κ_2 that between accelerating cells, and κ_3 that between coupling cells. The dispersion relation can be written as shown below [5].

$$\kappa_1^2 \cos^2\varphi = (1 - \frac{\omega_1^2}{\omega^2} + \kappa_2 \cos 2\varphi)(1 - \frac{\omega_2^2}{\omega^2} + \kappa_3 \cos 2\varphi) \quad (1)$$

In the above equation ω represents each of the N mode frequencies and φ the phase shift per cell. The dispersion equation has two solutions at $\varphi = \pi/2$, $\omega = \frac{\omega_1}{\sqrt{1-\kappa_2}}$, and $\omega = \frac{\omega_2}{\sqrt{1-\kappa_3}}$. The difference in frequency between these two solutions is called the stopband. A sufficiently small stopband insures field and phase uniformity along the SCS. In order to determine the stopband, the frequencies of the 31 modes are measured, then the ω, φ pairs are fit to the dispersion equation(1) using the least squares method[4]. Figure 1 is an example with a typical stopband of

21Khz. Measurements are performed using full cell terminations which provide a phase shift of $N\pi\frac{n+1}{N+1}$ where n=0,1,...,N-1.

Bead-Pull Perturbation Technique

The goal of the perturbation measurement is to characterise the field distribution along the beam axis of a module. The phase shift caused by the bead is measured and the fractional detuning computed (eq.2). Then the square of the Electric field per total energy(U) along the beam axis is obtained from the fractional detuning and bead volume (eq. 3).

$$\frac{\delta\omega}{\omega_0} = \frac{\tan\Delta\varphi}{2Q} \tag{2}$$

$$\frac{\vec{E}_0^2}{U} = -\frac{\delta\omega/\omega_0}{3\omega_0\epsilon_0 Vol_{bead}} \tag{3}$$

From this, the voltage across the complete structure can be calculated.

$$\frac{V}{\sqrt{U}} = -\int_0^z \vec{E}_0 \cdot \vartheta z \tag{4}$$

Finally, the shunt impedance per unit length per total energy is computed,

$$\frac{Z_s}{UL} = \frac{V^2 Q}{\omega_0} \tag{5}$$

where L is the length of the tank in meters.

Hardware

The automated measuring system was designed around an IBM-AT compatible computer, (AST 286), controlling an Hewlett-Packard (HP8510B) network analyser and a Galil (DMC-400) motor controller with the National Instruments GPIB interface card. For both dispersion and bead-pull measurements the transmission coefficient (S_{21}) is measured between magnetic field probes placed in the terminating cells of the cavity chain. The signal picked up from the cavity is amplified by 22dB to improve the measurement accuracy.

For the bead-pull, a mechanical gantry was made which attaches to the end of the cavity support cradle. Positioning arms can control the bead position along the beam axis with an accuracy of one-one thousandths of an inch. A kevlar thread, holding a brass bead, is run through and over the structure. The bead diameter used for the test is 0.166 inches and is pulled with a DC motor controlled from the AST 286 through a GALIL motor controller (DMC 400). The bead position is provided by a quadrature shaft encoder, 4000 pulses per revolution, mounted on the DC motor. Limit switches are mounted on the positioning arms to provide home reference and travel limits.

Software

The software was developed with the TurboC compiler, version 2.0. Both dispersion and bead-pull tasks were developed in two separate modules with a third module holding functions common to both. Two complete, stand-alone applications were created. The common module supports functions such as an input data parser, Q value function, 3dB point measurement function, network analyser parameter update function, GPIB communication functions and system error functions. All major variables and parameters are organised under appropriate structures in the common module and the task-specific applications.

For the dispersion curve measurement, the operator identifies the center frequency of each mode by placing the marker on the peak and then presing enter. Once all peaks are identified, the system optimises the frequency and amplitude scale to accurately obtain the frequency and Q of each mode. With these measurements, accelerating cell and side coupled cell frequencies (ω_1, ω_2), coupling coefficients ($\kappa_1,\kappa_2,\kappa_3$), and $\pi/2$ stopband are determined using a least squares fit to the dispersion curve. The results are corrected for temperature, humidity and pressure to predict the behavior of the structure with vacuum.

The bead-pull bases its results on two measured values, phase and bead position. The speed profile of the bead is dependent on the number of sections being measured and the step resolution chosen. After the set-up parameters are entered, the Q value is measured and the structure is driven at the $\pi/2$ frequency of 805 MHz. During the pull, the system reads the phase shift from the analyser and the bead position from the shaft encoder. Once the bead is out of the structure, $\delta\omega/\omega_0$, $\frac{V}{\sqrt{U}}$, E_0^2 and Z_s are computed. The raw data and the results are displayed using EXCEL version 3.0, a commercially available spread sheet.

Discussion

The hardware is completely in place and tested, except for automated reading of temperature, humidity and pressure. The software has been tested on Section 3, of Module 1, of the SC Linac upgrade. Data validation has been done against manual measurements and results are within 10 KHz for stopband measurement.

The results obtained during a bead-pull follow closely with those obtained from other analysers and

shunt impedance values correspond to those predicted with Superfish. The value computed for section 3 is 35 MΩ/m compared with 38 MΩ/m based on Superfish (derated by 15 percent).

The software was not designed to account for mis-identified peaks or baseline drifts due to temperature changes during the measurement. A second version of the software could incorporate error-correcting algorithms. Further tests must be carried out with a full module to evaluate the performace of the system.

References

1. R. Noble. "The FermiLab Linac Upgrade," Linac Conference (1990), These Proceedings.

2. P.M. Lapostolle, A.L. Septier. "Linear Accelerators," North Holland Publishing Company, (1970).

3. G.R. Swain. "Lampf 805-MHz Accelerator Structure Tuning and its Relation to Fabrication and Installation," Informal Report LA-7915-MS, (July 1979).

4. P.R. Bevington. "Data Reduction and Error Analysis for the Physical Sciences," McGraw-Hill N.Y.,(1980).

5. E.A. Knapp, B.C. Knapp, and J.M. Potter. "Standing Wave High Energy Linear Accelerator Structures," The Review Of Scientific Instruments. Vol.39, No.7. (July 1968).

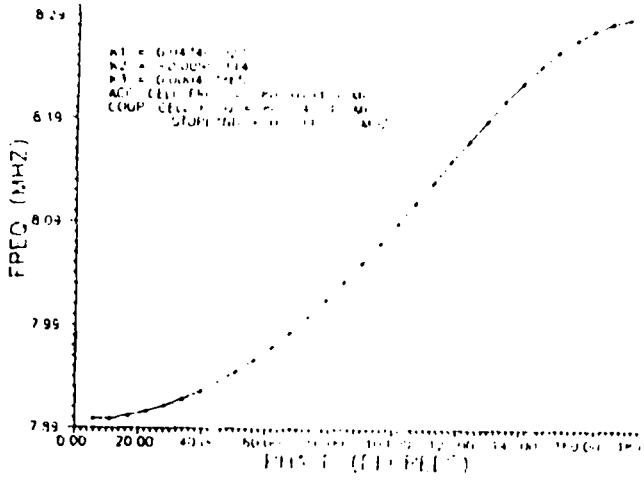

Figure 1: Dispersion curve of section 3. This shows the distribution of the modes about the $\pi/2$ mode, values for the κ's, stopband and corrected fundamental frequency for accelerating cell and side coupled cell.

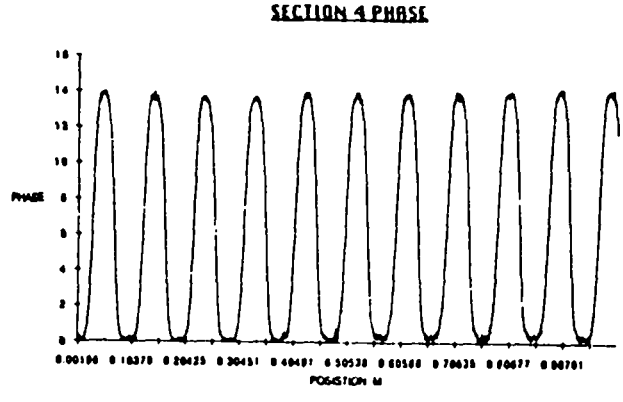

Figure 2: Phase shift produced with a 0.217inch diameter bead, sampled in 2.50 mm step increments

STABILITY OF FIELD DISTRIBUTION IN COUPLED CAVITY STRUCTURES

L.V.Kravchuk, G.V.Romanov
Institute for Nuclear Research, Moscow, USSR

Abstract

The general properties of coupled cavities structures are studied and the conditions of maximal stability of accelerating field distribution in respect to the random errors of manufacturing and tuning are determined. To describe the biperiodic structures with strong coupling such as DAW structure a coupled oscillator model with couplings of two types - elastic and inertial - is used. It is shown that the field distribution stability in the multicoupled cavity structures depends not only on the frequency separation between modes of structure's spectrum, but also on the field distribution and amplitudes of these modes.

Introduction

In order to increase the field distribution stability in the high energy proton linac the biperiodic structures operated in $\pi/2$ standing wave mode were developed[1,2]. The main instrument for investigation of the field distribution stability in such structures is a coupled oscillator model. The biperiodic chain of oscillators with nearest and next neigabor couplings was succesfully used in many cases [1,3 for example] . But this model does not give a good agreement between calculated spectrum of mode frequencies and experimental spectrum of the multicoupled biperiodic structure (DAW structure for example) and does not adequately describe the field distribution in such structures in full[4] . The chain of the oscillators with the two types of couplings - elastic and inertial - is the solution of this problem. The conditions of the maximal field distribution stability in the accelerating structures were specified using the developed oscillator model. The results were used and proved experimentally during the linac accelerator structure of Moscow meson factory (MMF) tuning procedure.

Coupled oscillator model

The small free oscillations of conservative system of coupled harmonic oscillators are described by a system of equations:

$$\sum_{j=1}^{N} (g_{ij} - \lambda m_{ij}) x_j = 0, \quad i = 1, \dots, N \qquad (1)$$

or in a matrix form:

$$G\vec{x} - \lambda M\vec{x} = 0, \qquad (2)$$

This matrix equation is considered here as a model describing the standing wave structure - a chain of multiply-coupled resonators. The rigity g_{ii} and the mass m_{ii} of the i-th oscillator determine the eigenfrequency of the i-th resonator $\omega_{ii}^2 = g_{ii}/m_{ii}$. The elastic couplings and the inertial ones (nondiagonal elements of G and M) characterize the couplings between magnetic and electrical fields of the resonators. The amplitude x_{ik} (the i-th component of the vector $\vec{x}_k$) is some integral characteristic of the field in the i-th resonator in the k-th mode of the chain. It together with g_{ii} and m_{ii} determines the stored energies of the magnetic and electrical components of the field in the i-th resonator. The solution of the equation (2) is N eigenfrequencies of the oscillator system $\Omega_k^2 = \lambda_k$, representing the frequency spectrum of the accelerating structure and N M-orthogonal eigenvectors $\vec{x}_k$, describing the field distribution at frequency Ω_k .

The model parameters (the elements of matrixes G and M) may be always determined if the full spectrum of the accelerating structure and the field distributions of all modes are known. Usually only the accelerator spectrum is used for the model parameter determination. But basing on the spectral theorem [5] and using any orthogonal system of vectors we can always find a matrix which has a given frequency spectrum. In such approach we have uncertainty in the describing of the field distribution and loose the physical meaning of the model parameters. To avoid this disadvantage the proper structure of the coupled oscillator system must be choosed. For periodic accelerating structures with half-cell termination there is a simple and reliable sign of the proper choice of the model structure - the eigenfrequencies of the model with number of oscillators (N+1) must be equal to odd eigenfrequencies of the model with number of oscillators (2N+1). The known model [1] is a canonical form of the equation (2) and doesn't satisfy this condition in every case because of the properties of the matrix $M^{-1/2} \cdot G \cdot M^{-1/2}$ or matrix $M^{-1} \cdot G$.

For DAW structure the coupled oscillator system shown in Fig.1 had been suggested. The oscillators "a" and "c" have

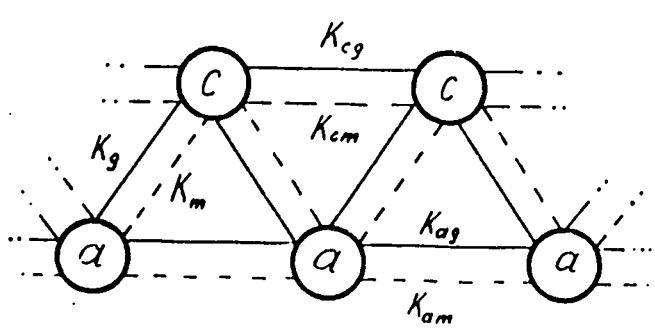

Fig.1

the eigenfrequencies $\omega_a^2 = g_a/m_a$ and $\omega_c^2 = g_c/m_c$ respectively. The subscript "g" signs the elastic coupling coefficient and the subscript "m" - the inertial ones. In the case of half-cell termination the end oscillators "a" have the rigity $g_a/2$ and mass $m_a/2$. The neighbouring oscillators "c" - ($g_c + K_{cg}$) and ($m_c + K_{cm}$) respectively. The numerical values of the model parameters are determined in general case by means of a fitting procedure so that the rms difference between the experimental spectrum and the calculated one (or between the parts of them) is minimal. The procedures of the parameter determination for the different models, including nonperiodic ones, are given in detail in [6] . The eigenvalues and the eigenvectors of the oscillator model are found by means of the numerical solution of the equation (2). The differencies between the calculated and experimental frequencies don't exceed 0.05%.

It is convinient to represent the spectrum of the biperiodic structure model as the solution of the sequence or the equations [7] :

$$\det[\lambda^{\pm} \cdot M(\theta) - G(\theta)] = 0 \qquad (3)$$

for every intresting $\theta_k = 0 - \pi/2$. The eigenvalues λ_k^+ and λ_k^- are above and below the operating frequency respectively. At the operating point a phase shift of a spatial harmonic between the oscillators is equal to π and between the oscillators "a" - $\pi/2$.

In the equation (3) the matrix

$$M(\theta) = \begin{pmatrix} m_a + 2K_{am}\cdot\cos 2\theta_k & 2K_m \cos\theta_k \\ 2K_m \cdot \cos\theta_k & m_c + 2K_{cm}\cdot\cos 2\theta_k \end{pmatrix}$$

and the matrix

$$G(\theta) = \begin{pmatrix} g_a + 2K_{ag}\cdot\cos 2\theta_k & 2K_g \cos\theta_k \\ 2K_m \cos\theta_k & g_c + 2K_{cg}\cos 2\theta_k \end{pmatrix}$$

In other words the biperiodic chain of oscillators for every θ_k is considered as two oscillators with the eigenvalues

$\mu_k = M(\theta)_{11}/M(\theta)_{22}$; $\nu_k = G(\theta)_{11}/G(\theta)_{22}$

and coupled with the coefficients $2K_g \cos\theta_k$ and $2K_m \cos\theta_k$ The Fig.2 shows the frequency spectrum with a stopband of one variant of the DAW structure.

The proper model structure is more important for adequate description of the

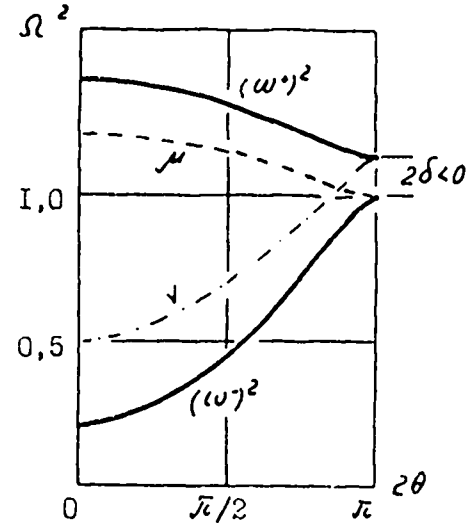

Fig.2

field distribution then for the exact reproducing of the experimental spectrum. In this sense the developed model gives an intresting result. Let the eigenvectors of the model is expressed in form $\vec{x}_k^{\pm} = a_k^{\pm} \cdot \vec{v}_k^{\pm}$. For an ideal structure with half-cell termination $\vec{x}_k^{\pm} = a_k^{\pm} \cdot \cos 2(j-1)\theta_k$ for the oscillators "a" (j is odd). In general case of the multicoupled biperiodic structure the model shows that $a_k^+ \neq a_k^-$ and $\vec{v}_k^+ \neq \vec{v}_k^-$ and there is no complete compensation of the nonoperating modes in the perturbated accelerating structure [7].

Field distribution stability

Basing on the small perturbation theorem it may be shown that in the case of the frequency detuning of the accelerator structure resonators the perturbed field distribution of the operating mode $\tilde{\vec{x}}_k$ is expressed in the terms of the unperturbated structure as

$$(\tilde{\vec{x}}_o - \vec{x}_o) = \sum_{\lambda_o \neq \lambda_k} \lambda_o a_o \left[\frac{(\Delta \vec{v}_o, \vec{a}_k)(a_k^+)^2}{\lambda_o - \lambda_k^+} \vec{v}_k^+ + \frac{(\Delta \vec{v}_o, \vec{v}_k^-)(a_k^-)^2}{\lambda_o - \lambda^-} \vec{v}_k^- \right] \qquad (4)$$

where Δ is the matrix small perturbations. The expression (4) characterizes a level of mutual compensation of the upper and lower (with respect to λ_o) nonoperating modes in perturbated accelerator structure. It is clear from (4) that the worsening of the compensation is possible a) because of an assymetry of spectrum - $|\lambda_o - \lambda_k^+| \neq |\lambda_o - \lambda_k^-|$; b) because of a dis-

balance of the nonoperating mode amplitudes - $a_k^+ \neq a_k^-$; c) because of an inequality of the field distribution shapes - $\vec{v}_k^+ \neq \vec{v}_k^-$.

For the periodic and biperiodic structures without the mixed and nextneighbouring couplings a stopband and a separation of mode frequencies play a main role in the field distribution stability. The increasing of the coupling between the resonators of an accelerating structure in order to increase the stability leads to an appearence of the mixed couplings and the nextneighbouring couplings. They cause the amplitude disbalance and the asymmetry of the spectrum (simultaneosly or separately). For instance, in the DAW structure tanks of MMF linac the amplitude disbalance reaches the value $a^+/a^- \approx 1.4$ and the width of the upper part of spectrum is smaller then the width of the lower part approximately by a factor 4. So, the DAW structure basically hasn't the complete mutual compensation of the nonoperating modes in the first order approximation.

An influence that or another factor on the stability depends also on an accelerating structure length. For the long structures a stopband is a main factor because the value $|\lambda_0 - \lambda_k|$ is very small and $a^+ \approx a^-$ for the nearest to λ_0 mode frequencies. For the short structures the asymmetry and the amplitude disbalance may be important. In some case the stopband may play a positive role compensating the disbalance and the asymmetry. In the real structures the inequality of the field distribution shapes $\vec{v}_k^+ \neq \vec{v}_k^-$ because of the local perturbations (detuned end half-cells, for example) may worse the stability. For the systems, consisting of small number of resonators, the resonant frequencies of which are different (four--tank accelerating module of MMF) this factor may be important [8] .

Conclusions

The considered factors effecting upon the accelerating field distribution stability were observed experimentally and taken into account during the accelerator system tuning at MMF. Inspite of the absence of the complete compensation in the DAW structure, this structure is much less sensitive to the tuning and fabrication errors then other biperiodic structures [9]. The strong couplings of the DAW structure provided good frequency separation of the spectrum of the 4-tank modules. But in order to avoid the instability due to the ineqality of the field distribution the special tuning procedure was developed [10] .

References

1. E.A.Knapp, B.C.Knapp and J.M.Potter, "Standing Wave High Energy Linear Accelerator Structures", Rev.Sci.Instrum. 39, 1968.
2. V.G.Andreev. J.Tech.Phys., v.41, p.788, 1971 (in Russian).
3. G.R.Swain, "Tuning Error Sensitivity of Stabilized Linear Accelerator Tanks With Full Cell Terminations", Nucl. Instrum.Methods 68,1969.
4. L.V.Kravchuk,G.V.Romanov. Preprint INR USSR AS P-0304, 1983 (in Russian).
5. B.N.Parlett, "The Symmetric Eigenvalue Problem",Prentice-Hall,Inc.,Englwood Cliffs, N.J. 07632, 1980.
6. G.V.Romanov. Preprint INR USSR AS P-0563, 1987 (in Russian).
7. G.V.Romanov. Preprint INR USSR AS P-0461, 1986 (in Russian).
8. G.V.Romanov. Preprint INR USSR AS P-0561, 1987 (in Russian).
9. S.K.Esin et all, "The Disk and Washer Structure for Moscow Meson Factory Linac", Proc. of the 1988 Lin.Ac. Conf., Williamsburg, 1988.
10. J.V.Bylinsky et all, "Meson Factory Accelerating Structure Tuning", Proc. of the European Particle Accelerator Conf., Rome, 1988.

A SYSTEMATIC ERRORS STUDY FOR THE BEAD PULL MEASUREMENTS

Yu.V.Bylinsky, I.V.Gonin, L.V.Kravchuk, P.N.Ostroumov,
V.V.Paramonov, V.A.Puntus

Institute for Nuclear Research of the AS of the USSR,
60-th October Anniversary Prospect, 7a, 117312, Moscow

ABSTRACT

The systematic error for the bead pull measurements in drift tube cavities and disk and washer structure is analyzed. The error is caused by the nonuniformity of the RF field distribution and mirror effect of the spherical bead. The method for error determination is provided which was verified for accelerating system of the Moscow Meson Factory Linear Accelerator (LA MMF). It is shown that the error must be taken into account for the RF field flattering procedure in drift tube cavities. Also this kind of errors is important in coupled cell structures.

INTRODUCTION

The stringent requirements are imposed for accelerating field E_z distribution for a high current proton linac like meson factory. The field distribution needed is achieved by an accelerating cavity tuning. It is known a several techniques for the field distribution measurements. For high quality ($Q = 10^4$) cavities the bead pull measurement [1], which use a small perturbing object, is preferable . For the field measurements in LA MMF tanks spherical perturbing objects are used . Both technique random and systematic errors, and systematic errors, caused by a discrepancy between a real accelerating field distributions and assumptions of a small perturbation method, effects on measurement accuracy. In order to decrease technique errors it is needed to increase the perturbing object - so increasing the shift in cavity resonant frequency δf, but this way give rise to a systematic error effect.

DETERMINATION OF THE SYSTEMATIC ERROR

At the field E_z distribution measurement in multy-gap accelerating structures (drift tube cavity, disk and washer or side coupled tank) the spherical bead size d, which is needed for a stable δf measurement, may be - first of all for a low β - comparable with the length of accelerating gap. It is known that the field distribution in an accelerating gap is nonuniform, and therefore the bead is placed in a nonhomogeneous field. This is first source of the systematic error. The second one - the mirror effect - is displaed when the bead diameter is comparable with distance to drift tube. The string sag - the bead displacement from axis - we taken't into account because usually special supports are used to avoid it. The error is displaed in fall of the relationship $\delta f(d)$ from cube for different values d. We propose the following procedure for the determinations of error:

a) let us calculate changes in frequency for n values of bead radii $R_1, R_i, \quad R_n$,

b) changes in frequency we represent as:

$$\delta f_i = \sum_{j=1}^{n} a_j R_i^j \qquad (1)$$

c) from system of equations

$$\begin{aligned} \delta f_1 &= \sum_{j=1}^{n} a_j R_1^j \\ &\ldots\ldots\ldots\ldots \\ \delta f_n &= \sum_{j=1}^{n} a_j R_n^j \end{aligned} \qquad (2)$$

we find a value of a_3 coefficient and estimate methodical error as:

$$\frac{\delta E}{E} = \sqrt{\frac{\delta f_i}{a_3 R_i^3}} - 1 \qquad (3)$$

Realisability of the procedure proposed depends critically on the accuracy of frequency f_n calculations. After consideration, modern numerical code MULTIMODE [2] was choosen.

ESTIMATION OF THE FREQUENCY CALCULATION ACCURACY

The code MULTIMODE was developed with using finite elements method and is intended for frequency calculations at axiallysymmetric cavities. Construction elements, disturbing an axial symmetry, for example, supports in drift tube cavity, are presented in an accelerating structures. Nevertheless these elements are choosed such that

THE ERROR FOR DRIFT TUBE CAVITY

Lengths of periods and accelerating gaps in the drift tube cavity are extending. For example, in first DTL tank of LA MMF length of the gap rises from 15 at the beginning to 133 mm at the end. The field distribution measurement error depends on the gap length critically. From Fig. 4 for first DTL tank LA MMF one can see, that for gaps in the beginning of the tank the error a highly great, because it is need to use spheries with a large radius (> 5 mm). It is known, that for accelerating gaps with large length (at high β) accelerating field distribution along the axis has two maxima, placed symmetrically from the gap center. In this case the $\delta E/E$ error changes sign as the radius of perturbing sphere increases, see Fig. 5. This dependence permits to recommend for field unflatness measurements in cavities with a high length of gaps a large enough spheres in order to minimize both random and systematic field measurements errors. More detail information about $\delta E/E$ dependencies on size and placement of perturbing sphere for LA MMF accelerating tanks is given in Ref. [3].

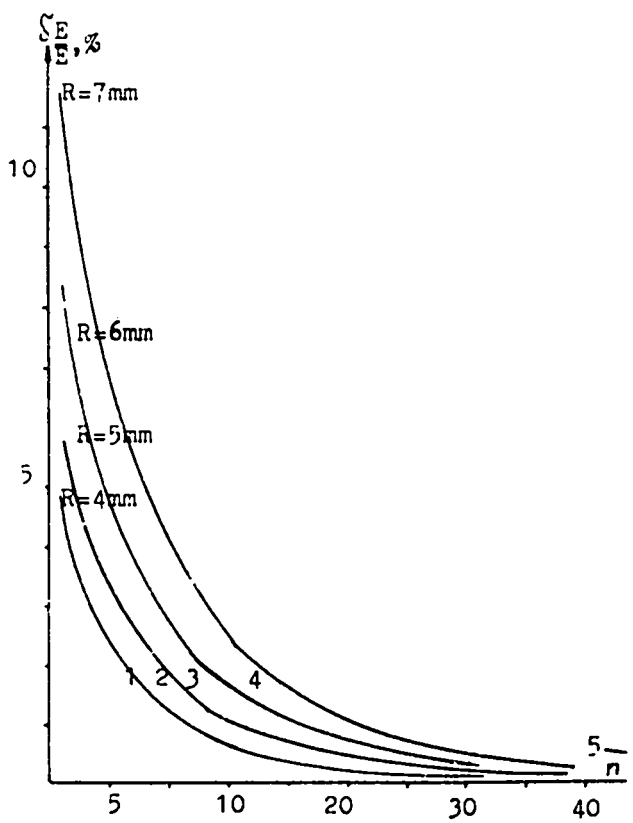

Fig. 4. Systemacic error of the field distribution measurements in first DTL tank. n - number of the accelerating gap.

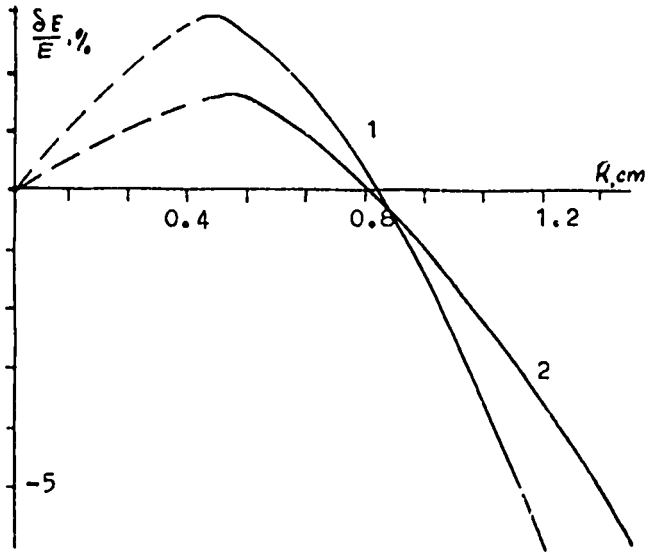

Fig. 5. Dependence of $\delta E/E$ vs sphere radius in fifth DTL tank for displacements from the center 1 - G/6, 2 - G/3.

CONCLUSION

The procedure of the systematic error estimation of the accelerating field distribution measurements with using a perturbing sphere for bead pull technique is proposed. It is shown, that is need to take into account the systematic error for drift tube linac cavity tuning if an accelerating gap length is comparable with a bead size. At large accelerating gap lengththe systematic error changes the sign as radius of a perturbing sphere is increased. It permits to choose a large sufficiently size of the perturbing sphere, thus decreasing both random and systematic errors. Results of this work are suitable for different linac accelerating structures with geometrically similar elements near the beam axis.

REFERENCES

1. L.C.Maier, J.C.Slatter. Journal of Applied Physics, v.23, n.1, p.68, 1952
2. I.V.Gonin et al. 2D codes set for RF cavities design. EPAC, Nice, France, 1990
3. I.V.Gonin et al. Preprint INR AS USSR, P-0523, Moscow, 1987, (in Russian)

not disturb the field distribution for an operating mode. Testing calculations were done because there isn't possibility to obtain analytical estimations for the calculation accuracy. We consider the spherical cavity with small metallic sphere in the center. An analytical solution for frequency and electromagnetic field distribution in spherical cavity is known. Considering a small sphere as rad and calculating the frequency change we can estimate the accuracy of the proposed prosedure. Calculation show, that in range of spheres radii relation from 0.006 to 0.036 product of relative frequency shift due to small sphere on error of this shift calculation is equal $(0.5-1.0)*10^{-7}$. In order to obtain reliable data about δE it is need to have the absolute error of $\delta E/E$ determination not worse then 10^{-8} and, therefore, the perturbing sphere must give the relative frequency change not less then $5.0*10^{-4}$, that is limitation from below on the perturbing sphere diameter. To obtain a high accuracy, the special procedure of calculations and data process was developed, which is described in detail in Ref.[3]. Leaning on testing results, we considered for calculations a perturbing sphere with such size, that provides accuracy of $\delta E/E$ determination about 0.1% for DAW structure and 0.3% for drift tube tank. Comparison of calculated systematic error with experimental results (Fig. 1) for several first gaps of first DTL tank LA MMF shows a good agreement for such precise measurements and calculations.

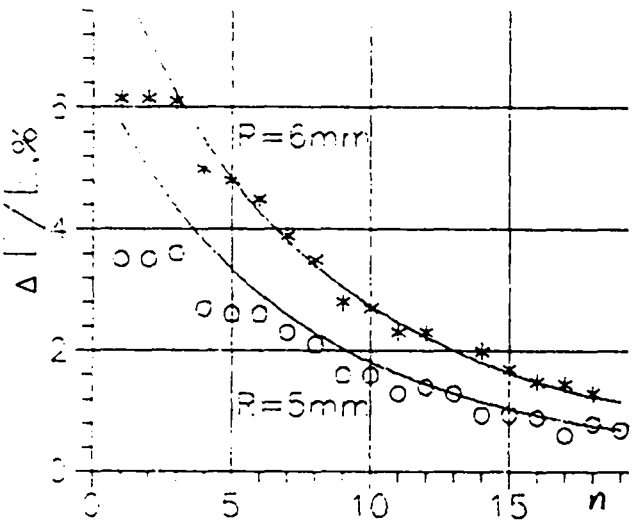

Fig. 1. Calculated (solid lines) and experimentally estimated (points) systematic error of the field distribution measurements in first DTL tank. n - number of the accelerating gap.

THE ERROR OF FIELD DISTRIBUTION MEASUREMENTS FOR THE DAW STRUCTURE

With using of the procedure described, the error of field measurement in cell was calculated both for the bead sphere position at the center of an accelerating gap and for sphere displacement along the beam axis. E_z field distribution becomes more quietly as β increases and therefore the error decreases. Decreasing of $\delta E/E$ is a most notice for large R>0.5a, (R - radius of the perturbing sphere, a - radius of aperture), see Fig. 2 . The error is

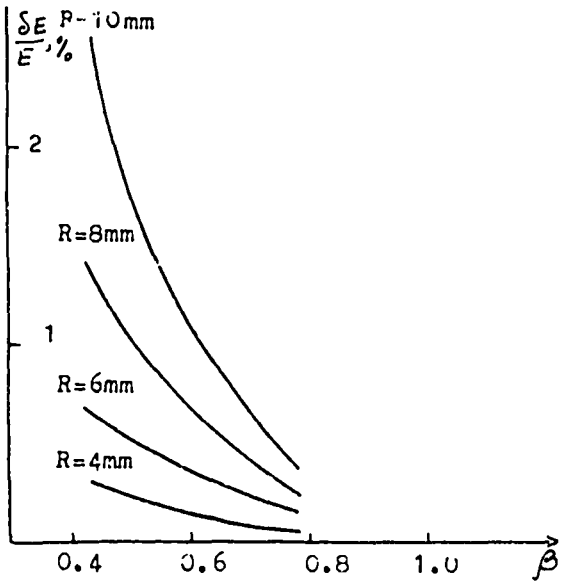

Fig. 2. Dependence of $\delta E/E$ vs β for measurements in the DAW structure. Perturbing sphere is in the center of the accelerating gap.

minimal at the center of an accelerating gap and is maximal at the edge, see Fig. 3. Usually tanks of accelerating structures on high β consist of cells with the same β. If so, the error is the same for all cells and not effect substantially on results of RMS and tilt accelerating field determination. The dependence $\delta E/E$ from sphere placement can exert an indirect effect for finding of the accelerating gap center. It is obvious that $\delta E/E$ is determined by a relationship between the sphere size and dimensions of accelerating structure elements near beam axis, which are choosed for achievement of maximal shunt impedance. Therefore, at the same frequency dimensions of elements near the beam axis for the DAW structure are the same as for another high -β structures and results of $\delta E/E$ calculation are suitable for them.

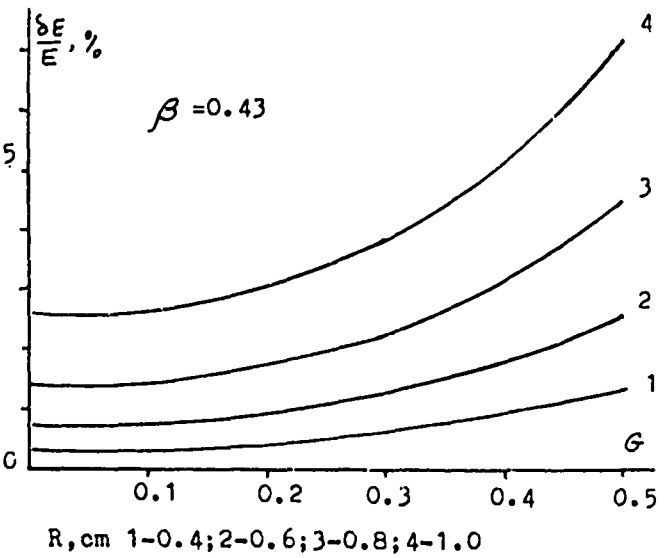

Fig. 3. Dependence of $\delta E/E$ vs displacement of the bead sphere from the center of the accelerating gap in the DAW structure. G is the length of the gap.

FABRICATION TECHNIQUE OF DRIFT TUBE WITH PERMANENT QUADRUPOLE MAGNET FOR THE LINAC OF THE JHP

Y. Iino, T. Adachi, T. Kawasumi and M. Ozaki
Mitsubishi Heavy Industries, Ltd. (MHI)
Nagoya Aerospace System Works

T. Kato, F. Naito, E. Takasaki and Y. Yamazaki
KEK-National Labolatory for High Energy Physics

Abstract

A compact drift tube will be used for the drift-tube linac (DTL) which is under development for the Japanese Hadron Project (JHP). The methods are briefly described for holding the permanent quadrupole magnet fixed into the drift-tube cell and for assembling the drift tube onto the DTL cavity tank.

Introduction

The 432-MHz drift-tube linac (DTL) for the Japanese Hadron Project (JHP)[1] is about half as small as conventional 200-MHz DTL's; the inner diameter of the tank is 441 mm, the outer diameter of the drift tube 80 mm, and the bore diameter for a beam 10 mm. This requires the developments of more precise machining of their components and more precise alignment of their quadrupole magnets (Fig. 1). Among various technical developments for this purpose we briefly describe the following three interesting techniques:

(1) Fixation of the permanent quadrupole magnet into the drift-tube inner cell.
(2) Insertion of the inner cell into the drift-tube outer cell.
(3) Assembly of the drift tube onto the DTL tank.

Since strong permanent magnets, such as SmCo and NdFeB are used for the DTL, special care is necessary to take into account effects of the strong magnetic field and property of the magnets.

Assembling procedures of Drift Tube

The drift tube comprising a permanent quadrupole magnet, an inner cell and an outer cell with a stem is assembled as follows. First, the permanent magnet is held fixed into the inner cell. Second, this inner cell is inserted into the outer cell and made vacuum-tight by the cold-shrinking method. Finally, the drift tube thus completed is assembled in the DTL tank, by inserting its stem into a tapered hole in the tank. In order to maintain the high quality of products it is important to eliminate any application of machining or surface finish after assembling. In other words, the plan of the assembling procedure should be formed so as to complete all the machining and surface finish on each part prior to the assembling.

Mounting Procedures of Permanent Quadrupole Magnet

A permanent quadrupole magnet comprises sixteen pieces with the same dimension, whose magnetized axes are respectively oriented to their specified directions (Fig. 2). All the pieces are mechanically assembled together with eight shims to form the quadrupole magnet, and held tight by a couple of spot-welded bands against the magnetic force. For the precise alignment of the magnet pieces into a drift-tube cell, it is important to measure the dimensions of the pieces as precise as possible which are used to determine the shim thickness. Also, special care is necessary in order to take into account complicated effect of the magnetic force in each assembling process.

The mounting procedure thus devised is as follows:

(1) The magnet pieces are classified into two groups (Fig. 2). The first group comprises four pieces whose magnetized axes are in the radial direction. Each piece of this group will be referred to as a single-piece unit. The other twelve pieces belong to the second group, characterized by an attractive force between three neighboring magnet pieces. Taking advantage of the attractive force, we adhere three neighboring pieces together into a three-piece unit with epoxy resin.
(2) A jig, a holding device illustrated at the right in Fig. 2, clamps the four single-piece units and four three-piece unit.
(3) A jack in the jig drives each unit toward the center of the jig, until the tip of the unit touches the surface of a central jig part which simulates the inner drift-tube cell. This is a place where the unit should be held fixed. Each unit was machined so that a gap should appear between any two neighboring units when all the units are thus placed.

Since the gap was prepared for being filled by a shim, the next step is to measure the size of the gap in order to determine the appropriate shim thickness.

(4) For this purpose, two single-piece units facing across each other are pushed further inwards, where openings are prepared in the central jig part. Measuring how far the two units can be pushed inwards, we can calculate the appropriate thickness of the shim, assuming that the angle of the arc of each single-piece unit is correctly machined. This method of the measurement of the gap should be very accurate.

(5) Two shims with the thickness thus determined are attached to each single-piece unit with an adhesive.

(6) All the units are reassembled in an inner drift-tube cell, by use of the same jig as used in (3), and tightly banded to secure.

The completed inner cell is illustrated at the center in Fig. 2.

Insertion of the Inner cell into the Drift-Tube Outer Cell

We have been developing the cold-shrinking method in order to fit the inner cell into the drift-tube outer cell for the following reasons. First, a silver-brazing method cannot be used, since permanent magnets cannot stand high temperature during the silver brazing. Second, an electron-beam welding (EBW) is difficult, since the strong magnetic field of the magnets bends the electron beam. Third, an electroforming method requires very elaborate care to prevent the electroplating fluid from leaking into a drift-tube cell during electroplating process. Otherwise, the leaked fluid would erode the permanent magnets. Finally, both the EBW and the electroforming method require machining and/or surface finishing after the assembly. This is a very painstaking process, since the magnet contained in the drift tube easily attracts magnetic microdust, giving rise to scratches on the surface. Thus, the cold-shrinking method being free from any of these troubles seems to be most suitable for mass production of quality drift tubes.

In the cold-shrinking method the inner cell is cooled down prior to the fitting. The condition of the cooling, the surface roughness, and the optimum fitting allowance and the fitting shape have been determined through a series of experiments. In particular, it is proved that the vacuum seal functions satisfactorily well.

In order to apply the cold-shrinking method to the assembly of drift tubes the inner cell should be positioned accurately with respect to the outer cell and quickly inserted into the outer cell. During the process, dewing should be eliminated and good heat balance should be ensured. In order to meet these requirements we fabricated a prototype of an assembling device shown in Fig. 3. The device is a case filled with dry nitrogen gas in order to prevent the inner cell from being dewed. A liquid-nitrogen vessel is used for cooling the inner cell, a holding rod for holding the inner cell, and a vertical rail for guiding the rod. A base plate made of ceramics is equipped with holes in order to vent the evaporated nitrogen.

Although we have obtained quite satisfactory results for the cold-shrinking method, there remains a problem to be solved: the inner cell was shifted in the axial direction with respect to the outer cell by a few microns to a few ten microns. At present we are attempting to solve this problem, supposing that this phenomenon is closely related to an effect of the thermal conduction and transfer in the holding rod and/or the base plate.

Assembling Procedures of the Drift Tube onto the DTL Tank

Another important item to be developed is how to mount drift tubes to a DTL tank, ensuring both vacuum-tight RF contact and precise alignment of the drift tubes that can stand long-term operation. If necessary, the drift tubes should be replaceable. In order to meet these requirements, attempts have been made to use a taper fitting by tapering both the stem of a drift tube and the hole of a tank. Needless to say, it is very important to keep the accuracy of the taper in micron order, requiring a ultra-precision numerically controlled turning machine. For the tapered hole in the tank, we are developing the method of roller-burnish finishing.

If we use the same material for both the stem and the hole in the taper fitting, mutual wedgelike slips between the tapered surfaces will arise from seizure and adhesion due to the securing pressure, resulting in vacuum leak. Thus, we are attempting to electroplate the upper part of the tapered stem with hard metal such as chromium and the lower part with soft metal; the hard metal will prevent the surface from seizing due to the friction, while the soft metal will help quality of vacuum seal.

REFERENCES

1. Y. Yamazaki and M. Kihara, "Development of the High-Intensity Proton Linac for the Japanese Hadron Project", this conference.

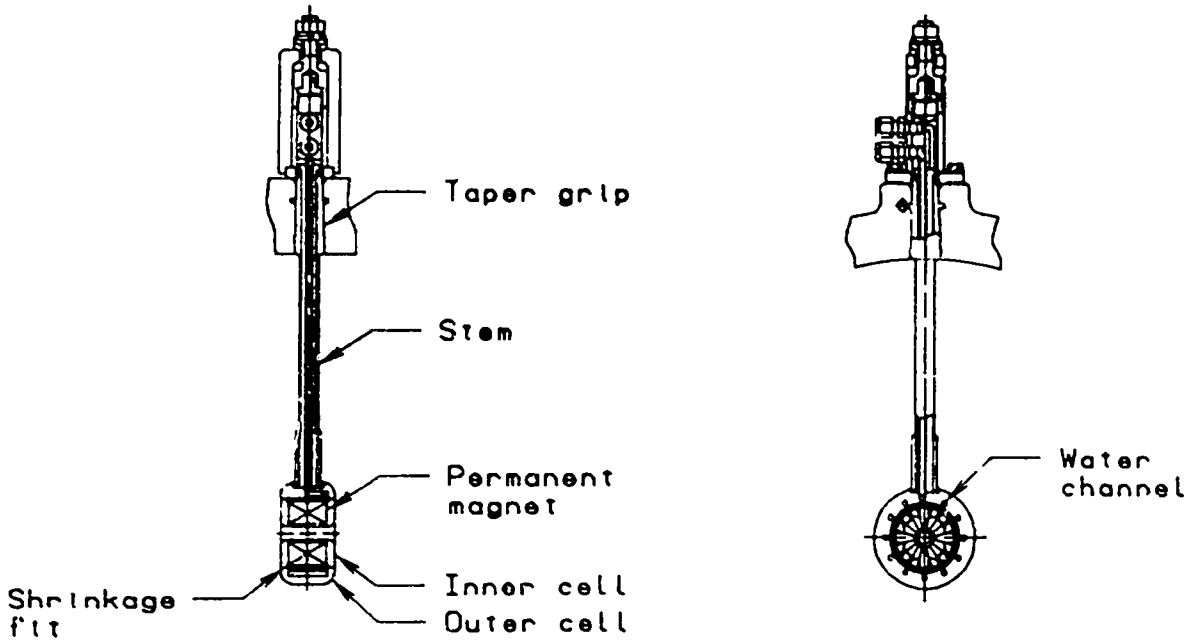

Fig. 1. Assembled drift tube

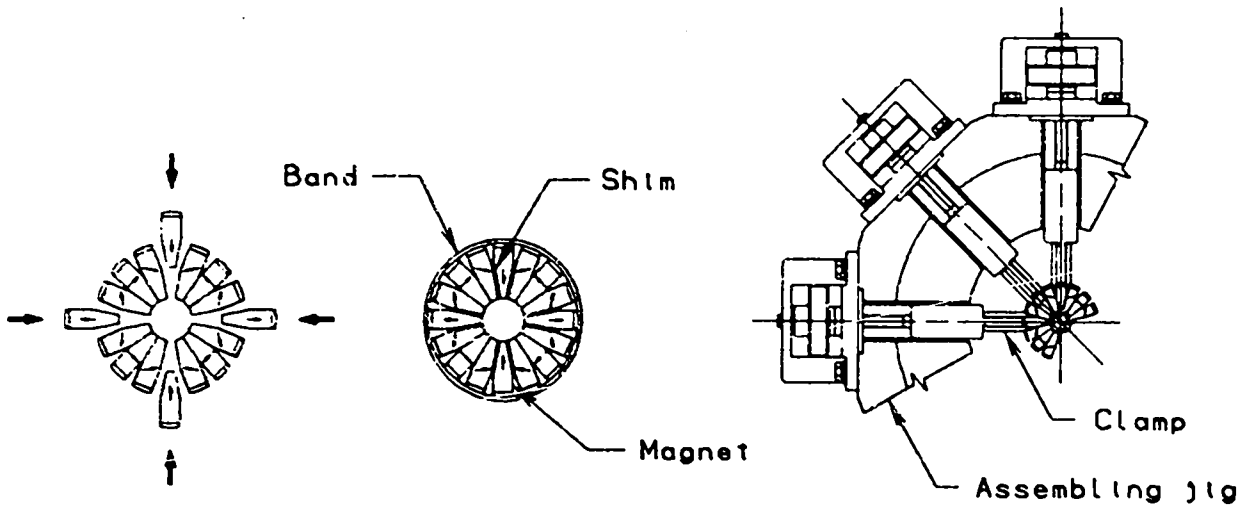

Fig. 2. Permanent quadrupole magnet

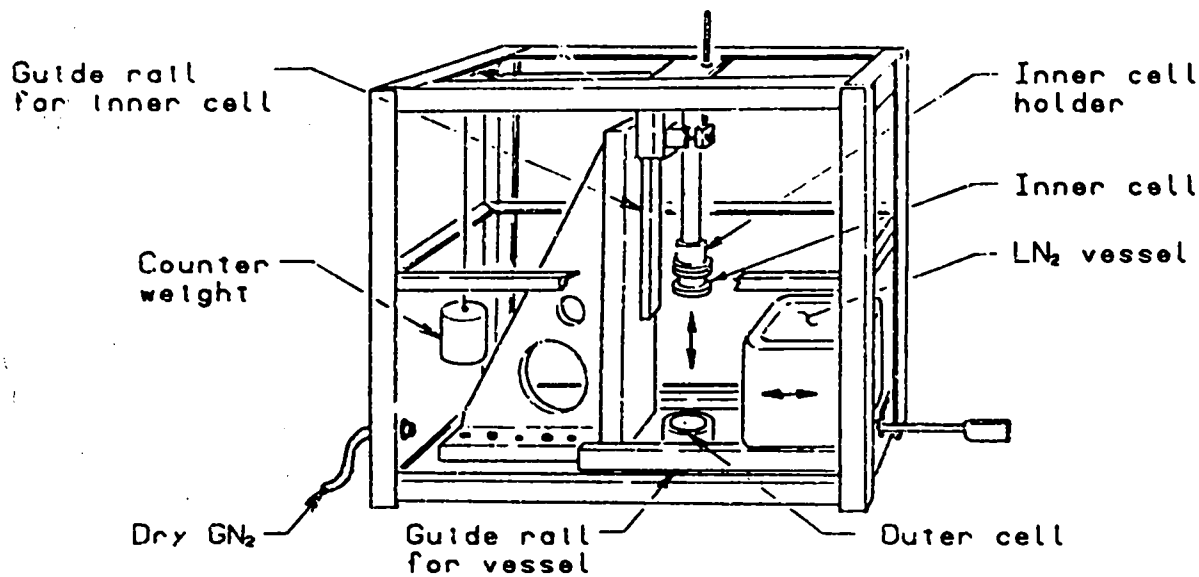

Fig. 3. Drift tube assembling jig

FABRICATION TECHNIQUE OF ACS CAVITY FOR THE JHP

K. Yamasu, T. Iwata and M. Hamaoka
Mitsubishi Heavy Industries, Ltd. Mihara Machinery Works
Itozaki-cho 5007, Mihara-shi, Hiroshima-ken, 729-03, Japan

T. Kageyama, Y. Yamazaki, Y. Morozumi and K. Yoshino
KEK, National Laboratory for High Energy Physics
Oho 1-1, Tsukuba-shi, Ibaragi-ken, 305, Japan

Abstract

A high power model of the annular-coupled structure (ACS) was fabricated and tuned to an operating frequency of 1296 MHz for the Japanese Hadron Project (JHP). The nose cone region is cooled by water channels in the unit in order to make possible the high-duty operation. Some details are described for machining high Q, ultra precision cavity segments including coupling slots. Detailed tuning procedures and brazing techniques are also presented.

Introduction

We have been developing a high-β coupled-cavity structure for the Japanese Hadron Project (JHP). Recent extensive studies on the annular coupled structure (ACS) have improved its quality factor extremely by understanding its RF characteristics: the quality factor of the ACS is only by 5 or 10 % smaller than that of the side coupled structure with the same condition. In this way the ACS becomes one of the most attractive candidates for the JHP linac, owing to the high stability and ease of fabrication inherent in the axially symmetric structure of the ACS. Thus, we have fabricated a high-power model of 1296 MHz ACS comprising two accelerator tanks (each 0.5 m long with a diameter of 0.4 m) and a bridge coupler connecting the two tanks shown in Fig. 1. Each tank is a five-cell ACS cavity. Although some techniques developed for the side-coupled structure were effectively applied to the ACS, considerable development was necessary in order to establish economical and efficient fabrication procedure owing to the difference in structure.

Design, Fabrication, and Tuning

Design

Both a half-accelerating cell and half-coupling cell are formed by machining an oxygen free copper

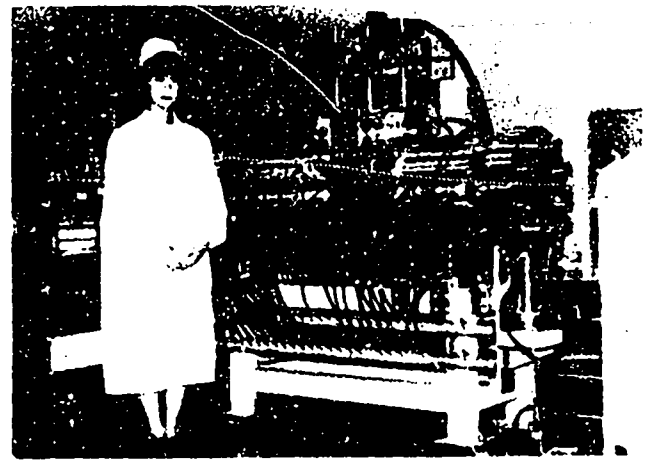

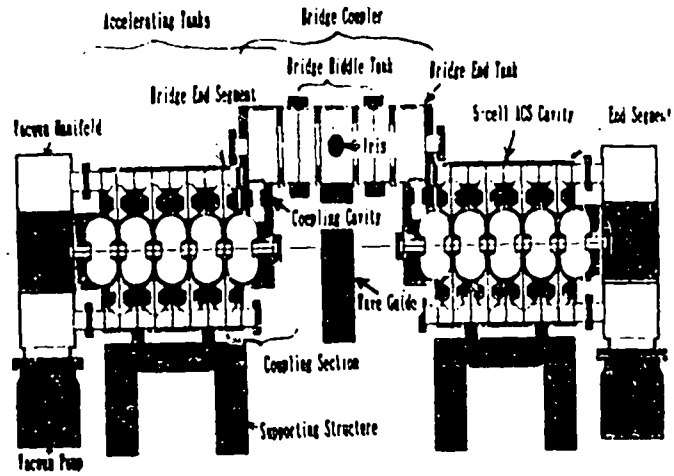

Fig. 1 Annular coupled structure

(OFC) block (Fig. 2). The block will be referred to as a half-cell unit in this paper. Water-cooling channels and vacuum-pumping channels are also machined into the half-cell unit in order to minimize the number of brazing processes.

A water-cooling system (5 ℓ/min./cell) removes the heat of 1 kW/cell, controlling the average cavity temperature within ± 0.4 ℃. The parallel path channels are carefully designed in order to minimize the pressure drop and the number of tube fittings, maintaining vacuum tightness and cavity shape.

For the high-duty operation of the JHP linac it is inevitable to cool the nose-cone by conducting cooling water to the nose-cone region. Then, we must drill the water-cooling channels in the wall between the accelerating cell and the coupling cell, requiring some thickness of the wall. However, as the wall becomes thicker the RF coupling between the accelerating and coupling cell decreases. In order to compensate the decrease of the coupling, we taper-bored the edges of the coupling arc from the coupling -cell side.

Machining

At first, an OFC ingot is forged into the required half-cell profile. The forged block is then rough-machined : one side into an accelerating half-cell, while the other into a coupling half-cell, incorporating vacuum-pumping channels. The block, thus rough-machined, is annealed in order to remove the residual stresses which would otherwise be released during finish-machining. This process is important for obtaining the accurate finish-machining. The anneal : block is then finish-machined, including the water-cooling channels in both sides, four coupling slots and dimpling holes. The internal surface and the brazing surface are finished with an ultra-precision numerically controlled turning machine (see Fig.2).

Since annealed OFC copper blocks are extremely soft and easily deformed, special care is necessary for accurate finish-machining. First, we require

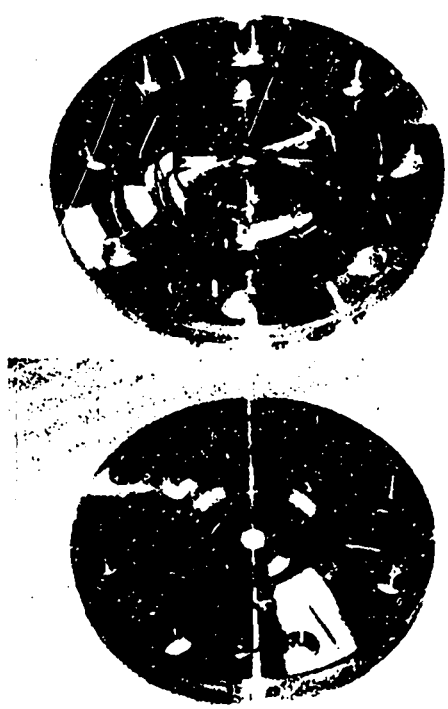

Fig. 2 ACS half-cell showing both sides of the final machined cavity.

very hard cutting tool : we use natural diamond bites for the finish-machining. Second, we developed a special fixture tool for machining in order to prevent cells from being deformed when clamped. We could machine profiles with a surface roughness of 0.1 to 0.2μm R_{max} (peak to peak) and dimensional tolerances of $\pm$ 5μm. (Plane surface to brazed requires flatness less than 10 μm after pre-braze tuning.) Quality of the surface finish can be evaluated by measuring the quality factor of a cavity. The measured Q-valve was 96 % of the thoeretical value, indicating that the present surface finish was sufficiently good. Here, a single cell was used without coupling slots for comparison with the calculated value.

Pre-braze tuning

Before the brazing process, all cavities are machined by using a ultra-precision lathe, until their resonant frequencies are tuned within 100 kHz of the designed value. If the measured frequency of a half-accelerating cell is lower than designed, the nose contour is machined. If higher, the ridge circumferentially prepared in the inner surface of a cavity is machined. Similarly, the coupling half-cells are tuned by removing material from the cell-center gap.

Brazing

The half-cell units are stacked and brazed in a vacuum furnace as shown in Fig.4. The brazing procedure is schematically shown in Fig. 3. It is seen that the assembling process is divided into three steps. Each brazing step is followed by the check of brazing-joint quality using helium-leak detector.

It is important to optimize the brazing condition, since the braze-joint quality regarding the vacuum tightness is dependent upon the brazing condition. In order to minimize the running-off of the filler metal on the interior surface of a cavity or to the inside of water-cooling channels, the joint clearance should be kept as small and as uniform as possible. Also, it is important to prevent the parts from being overheated and to keep the brazing time as short as possible.

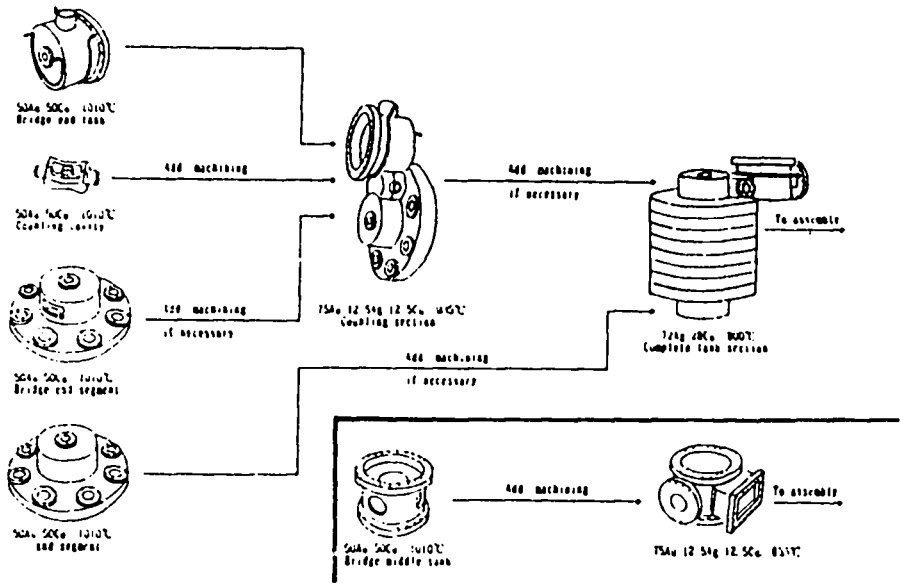

Fig. 3 Brazing assembly steps

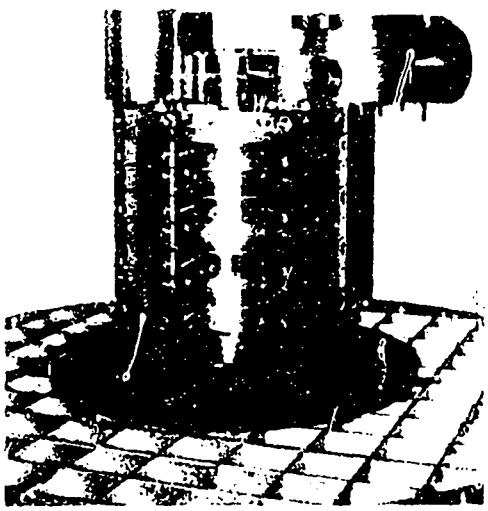

Fig 4 ACS stack arranged for the brazing process

Final tuning

After the final brazing, the frequencies of accelerating and coupling cells are measured. If necessary, it is possible to tune either of cells by dimpling the outer cavity wall : the thin copper wall at the bottom of a hole is pushed inwards to a depth near the interior surface of the cavity.

The iris size of the bridge coupler determines the waveguide coupling coefficient to the accelerator structure. The iris size is adjusted to obtain the good agreement between the measured and designed coupling coefficients.

Conclusions

A hot model of the ACS has been successfully fabricated for the first time. During the course of development, we have obtained many reliable production techniques which will be also useful for fabricating other types of structure.

In order to save the time of tuning procedure, we must develop appropriate tuning fixtures, with which the RF measurement of half-cell units is possible on a machining fixture.

References

1. Y. Yamazaki and M. Kihara, "Development of the High-Intensity Proton Linac for the Japanese Hadron Project", this conference.
2. T. Kageyama et al., Part. Accel. 32, 33 (1990)
3. T. Kageyama et al., "A High Power Model of the ACS Cavity," this conference.

EVALUATION OF RF SEALS FOR RESONANT CAVITY APPLICATIONS*

B. Rusnak, J. Rose, G. Spalek, G. O. Bolme, N. Bultman, A. Klapetkzy, E. L. Kemp, and J. E. Stovall**
Los Alamos National Laboratory, Los Alamos, NM 87545

Abstract

In radio-frequency quadrupoles (RFQ) and drift-tube linacs (DTL), electrical seals are required at mechanical interfaces to preserve the cavity quality factor (Q). Studies determined the response of copper-plated C-seals to continuous wave (cw), high-field operating conditions. In addition, low-power evaluations of machined-surface, knife-edge, indium wire, C-type, and multilam seals were done at room temperature and cryogenic (25 K) temperatures. For the high-field tests, the Q as well as seal temperature, was measured with power. For the low-power test, the Q was measured as a function of temperature.

Introduction

Resonant-cavity acceleration structures that require mechanical assembly often have physical separations in electrical current paths. Two structures of this type are the drift-tube linac (DTL) and the radio-frequency quadrupole (RFQ). Physical separations have a deleterious effect on the operational characteristics of the cavity. Specifically, interruptions in the current path cause structural power loss, which results in a low cavity quality factor (Q), poor efficiency, and high heating in the area of the joint.

Various forms of rf seals can prevent power loss by to providing a good current path, as well as mechanical detachability. Some common types are the C-seal for spring-loaded compression in the joint, and the indium wire seal and the knife-edge seal for deformation flow to fill the joint. In either of these approaches, the effectiveness of the joint is a function of the physical properties of the mating surfaces, the degree of real compression, and the electrical characteristics of the seal.

The effectiveness of a seal as a function of numerous variables, prompted a study of certain seals in selected applications. The goal of the study was to establish that the seals would perform as expected in their respective applications. Specifically, two types of tests were done. The first was a test of a copper-plated C-seal at cw field levels at and above that of present day RFQ applications. This test provided information about several topics: the effect on Q of putting a seal in a cavity, the heating of the seal up to 7500 A/m, and the electrical properties of the seal as a function of power.

The second test was a low-power evaluation of a number of different seals as a function of temperature (20 K to 298 K). Because it was done at low power in a coaxial test cavity, this test was a more "generic" study of power loss in the seal than the first test.

Experimental Configuration

The high-power C-seal test was done in a rectangular cavity (Fig. 1), resonant in a TE-011 mode at 502 MHz. The approach was to make a fully brazed structure first and measure its parameters at power. Next, the bottom was cut off and modified to accept the rf and vacuum seals. Finally, the cavity was run again and measured. Taking advantage of the rectangular geometry of the cavity allowed the modifications of the cavity to be accounted for in the Q_0 analytically and direct comparisons to be made. The cavity was driven to 110 kW cw with an unloaded Q (Q_0) of approximately 28 000.

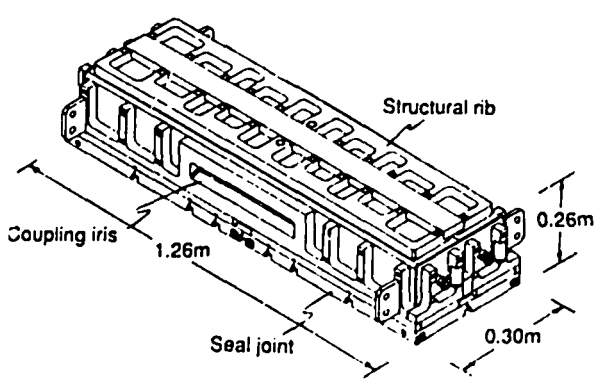

Fig. 1. Sketch of the high-power seal test cavity.

The low-power cryogenic seal test was done in a coaxial cavity, resonant at 425 MHz for the f-001

*Work supported and funded by the US Department of Defense, Army Strategic Defense Command, under the auspices of the US Department of Energy.
**Grumman Aerospace Corporation

mode. This mode has the currents crossing the midplane of the center conductor, where the seal was located. Measurements were done with a network analyzer, and the system was cooled with a modified cryopump cold head. The test seals were the machined-surface, knife-edge, indium wire, C-type, and multilam seals (Fig. 2).

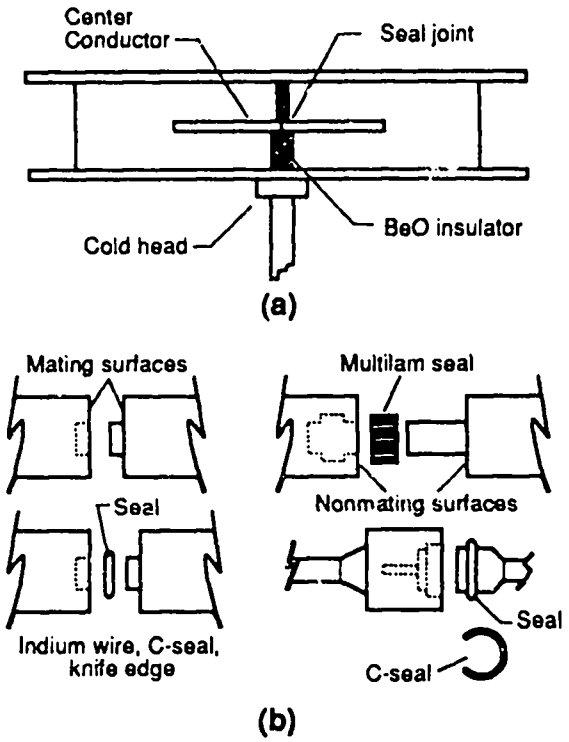

Fig. 2. a) Coaxial cavity configuration. b) Various seal set-ups.

Results

In the high-power seal test, it was necessary first to determine how the seal affected the cavity Q_0 at low power. The Q_0 of the brazed structure was measured and compared the theoretical value. Then a coupling iris was machined into the cavity, and a loss term for the iris was unfolded from the unloaded Qs for the cavity before and after the coupling iris was in place. Combining the loss term with the new theoretical Q_0, calculated from the changed dimensions, gave an overall theoretical Q_0 for the modified cavity. The overall value presumably represented the cavity Q_0 with no seals present. Comparing this value with the measured value for the unloaded Q gave a difference of 1.1%, which indicated that the seals at low power did not introduce a greater loss in the cavity than the wall itself.

Running the cavity at power then determined the response of the seal to higher wall currents. Measurements were made of the loaded Q, the coupling coefficient, and the temperature of the wall and the seal at the cavity midplane. These data were used to calculate the unloaded Q related to power in the cavity (Fig. 3) and to calculate the wall and seal temperatures related to the magnetic field at the wall (Fig. 4).

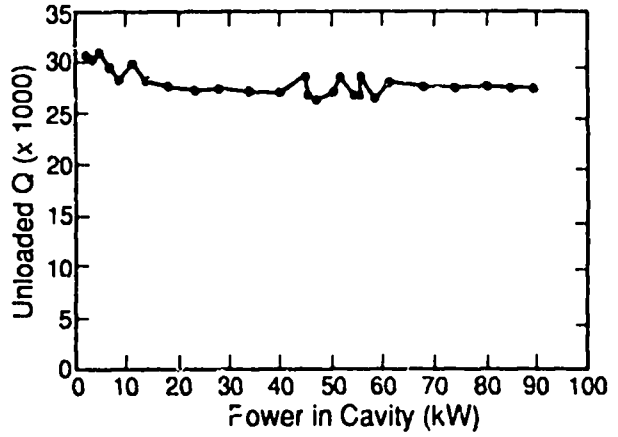

Fig. 3. Average unloaded Q as a function of power in the cavity.

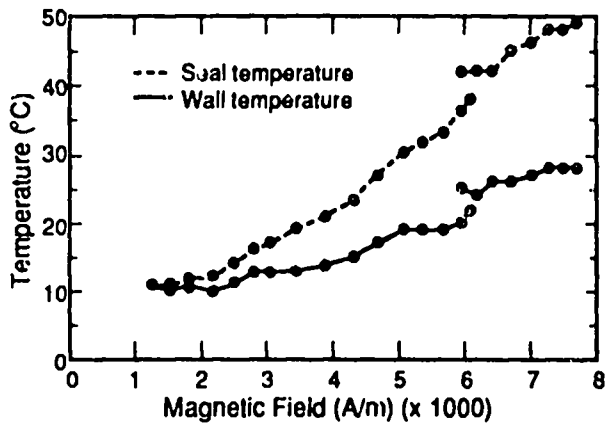

Fig. 4. Seal and wall temperature related to magnetic field at the wall.

The cavity Q_0 dropped by 9.2% from low to high power, a loss accounted for by the corresponding rise in the cavity temperature. This finding indicates that up to 7600 A/m (89-kW cw) at the wall, the seal's electrical performance deteriorated only in the form of ohmic heating a condition increased resistivity. There was no indication of mating surfaces changing and contributing to the electrical loss.

The temperature of the seal rose steadily with increased power, as did the wall temperature. Applying linear regression to the data obtains the following relation:

$$T_{seal} = 0.00662\, H_x - 1.749^\circ C \qquad (1)$$

TABLE I
Unloaded Q Data for Seals and Ratios[a]

Test[b]	Q_0 (298 K)	Q_0 (25 K)	Q_0 @ 298K / Q_0 SF	Q_0 @ 25K / Q_0 SF	P_{seal} @ 25K / $P_{bar + seal}$ @ 25K (%)
Plain Bar					
Solid	7452	27170	0.949	3.46	–
Machined	7418	25030	0.944	3.19	7.9
Knife edge	7512	25330	0.956	3.22	6.8
Indium	7655	27325	0.974	3.48	–0.6
C-seal	7346	24802	0.935	3.16	8.7
Multilam	6212	20791	0.791	2.65	23.5
Stepped bar					
Solid	7268	24875	0.987	3.38	–
C-seal	6691	23189	0.909	3.15	6.8

[a] f_0 = 424 MHz (fundamental mode); plain-bar SUPERFISH Q_0 SF = 7857; plain-bar SUPERFISH Q_0 cf SF = 7857; stepped-bar SUPERFISH Q_0 (SF) = 7362; cold-temperature values taken at T = 25 K.

[b] $$\frac{P_{seal}@25K}{P_{bar\ +\ seal}@25K} = \frac{(Q_0)_{seal}}{Q_{seal}} = 1 - \frac{(Q_0)_{seal}}{(Q_0)_{bar}} \quad ; \qquad Q_{seal} = \left[\frac{1}{(Q_0)_{seal}} - \frac{1}{(Q_0)_{bar}}\right]^{-1}$$

The tests run at power indicated no degradation of the seal physically to the field levels indicated at cw power levels on the time scale of hours.

In the cryogenic seal test, various seals were installed at the midplane of a coaxial resonator, and the Q was measured as a function of temperature.

Various ratios were used to determine the performance of the seal under test. Specifically, to establish the effectiveness of the seal, the room temperature Q_0 was compared with the value obtained from SUPERFISH with no seal. Determining the characteristics of the seal at cryogenic temperatures (25 K) required the following comparisons: comparing the cold Q_0 with the SUPERFISH value gave a Q_0 enhancement factor. Comparing enhancement factor with the value for the solid bar gave a measure of how well the seal maintained electrical contact down to low temperature. Finally, a value was obtained of what percent of loss in the bar assembly is due to the seal. Table I shows the Q data and ratios for the test seal.

Conclusion

For the copper-plated C-seal at cw power to 7500 A/m, the only observed degradation of the electrical performance of the seal from its low power value could be accounted for by normal ohmic heating of the seal. Further, there was only a small (less than 2%) difference in the wall loss of the cavity caused by the presence of the seal, compared to a solid wall.

For the cryogenic, low-power seal test, the machined-face, knife-edge, indium wire and C-type seals all had seal loss values of less than 9%. The multilam seal, likely resulting from a poor configuration geometry, gave a loss of 23.5%.

The indium wire seal gave exceptionally good results, equaling the solid bar within experimental error. This could be accounted for by slight surface differences between the copper bars. Generally, all the seals tested, except the multilam, maintained good electrical properties down to cryogenic temperatures at low power (less than 1 mW).

The indium wire seal gave exceptionally good results, equaling the solid bar within experimental error. This could be accounted for by slight surface differences between the copper bars. Generally, all the seals tested, except the multilam, maintained good electrical properties down to cryogenic temperatures at low power (less than 1 mW).

DAMPED AND DETUNED ACCELERATOR STRUCTURES*

H. Deruyter, Z. D. Farkas, H. A. Hoag, K. Ko, N. Kroll, G. A. Loew, R. Miller, R. B. Palmer, J. M. Paterson, K. A. Thompson, J. W. Wang, P. B. Wilson
Stanford Linear Accelerator Center, Stanford University, Stanford, CA 94309

Abstract and Introduction

This paper reports continuing work on accelerator structures for future TeV linear colliders. These structures, in addition to having to operate at high gradients, must minimize the effects of wakefield modes which are induced by $e^{\pm}$ bunch trains. Two types of modified disk-loaded waveguides are under investigation: damped structures[1] in which the wakefield power is coupled out to lossy regions through radial slots in the disks and/or azimuthal rectangular waveguides, whereby the external Q of the undesirable HEM_{11} mode is lowered to values below 20, and detuned structures in which the frequencies of these modes are modified from one end to the other of each section by ~10%, thereby scrambling their effects on the beam. Beam dynamics calculations indicate that these two approaches are roughly equivalent. MAFIA, ARGUS and URMEL codes have been used extensively in conjunction with low-power tests on S- and X- band models to identify mode patterns, dispersion curves and Q values, and to demonstrate damping or detuning of the HEM modes. Results of calculations and measurements on the various structures are presented and evaluated.

Damped Structures

a) Radially slotted disks with rectangular waveguides. The first structure investigated is best thought of as a conventional disk-loaded cylindrical waveguide in which the disks are divided into four quadrants by four orthogonal radial slots. The slotted disk quadrants continue radially outward past the walls of the cavities, transforming into double-ridged waveguides. These waveguides are dimensioned so their TE_{10} mode cutoff is below the frequencies of all resonances of the accelerator cavities. The fundamental accelerating mode of the structure is nevertheless undamped because its symmetry is such that it does not couple to the TE_{10} mode of the waveguide.

An exploded view of a single-cavity version is shown in Figure 1. This simplified structure is able to support only the 0 and π modes, which facilitates understanding its behavior. Figures 2 and 4 show network analyzer S_{21} plots obtained with coaxial E probes inserted in the designated end-plate holes (Figure 1).

With probes in C and D, the 0 and π resonances for the first two branches of the dispersion diagram (TM_{01} and HEM_{11}) are shown in Figure 2. The fields are oriented so so that they do not couple to the ridged waveguides. When probes are inserted in A and B, the fields for the dipole

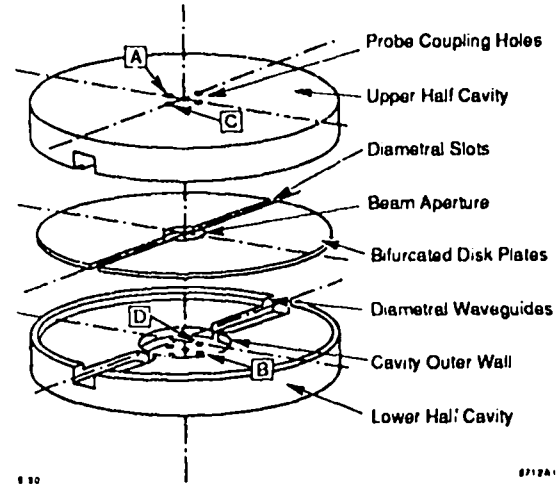

Figure 1. Single-cavity (two halves) model of damped S-band structure with two radial slots and waveguides.

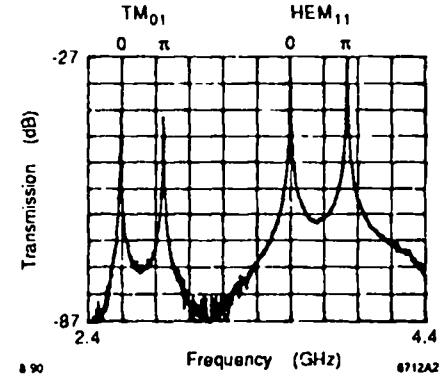

Figure 2. Single-cavity resonances excited through probes C or D so that they cannot couple through the ridged waveguides.

π-mode couple to the waveguides which, when shorted at equal radial distances from the structure axis, form a coupled-cavity system with multiple resonances above and below the fixed dipole 0-mode resonance. As the waveguide lengths (D) to shorts are decreased or increased, the resonances move up or down in frequency, respectively. The external Q (Q_e) and resonant frequency (f_r) of a cavity connected to matched waveguides can be determined from the frequency dependence of the system as a function of D, as shown in Figure 3. The calculation yields a value of Q_e of 8.1 ± 18% and a value of f_r of 3939 MHz ± 0.5% (see Reference 1). When the waveguides are left open at their outer ends, some power radiates outward, lowering the Q of the resonances. When the waveguides are terminated, the resonances cannot be seen on the display (Figure 4).

A similar experiment was performed at X-band with two full cavities and two half-ones in which 0, $\pi/3$, $2\pi/3$ and π-modes could be excited. Basically, the same general

* Work supported by the Department of Energy, contract DE-AC03-76SF00515.

results were obtained. Thus, it can be concluded that this structure can effectively damp the undesirable dipole modes.

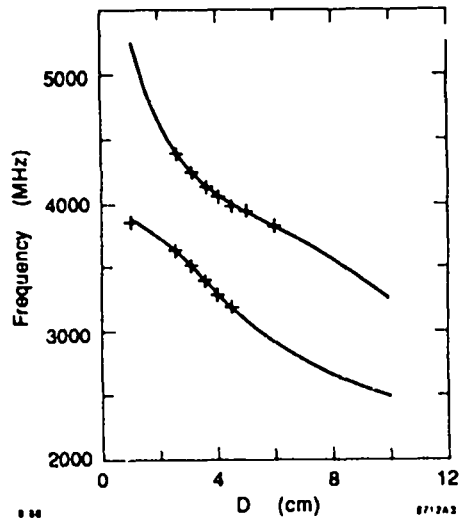

Figure 3. Measured single-cavity waveguide resonance frequencies (designated by +) as a function of waveguide length D. Solid lines are obtained by calculation.

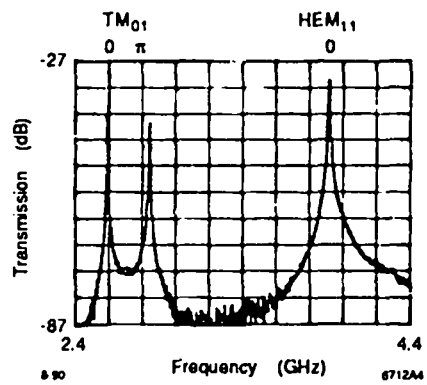

Figure 4. Single-cavity resonances excited through probe A or B so that the dipole π mode can couple to terminated ridged waveguides, but the 0-mode is trapped.

In parallel with these low power tests, a four-cavity S-band model was built with four slots (without radial waveguide outputs) to examine the effect of the disk slots at high power (See Figure 5). After gradual RF processing, the breakdown-limited gradient that was obtained and the corresponding experimental conditions are summarized in Table 1. It was determined from MAFIA that the ratio of the surface field (E_S) to the axial accelerating field (E_{acc}) was increased 8% by the presence of the slots.

For the corresponding traveling-wave structure, E_S/E_{acc} would be equal to 2.55, yielding a maximum accelerating gradient limit of 124 MV/m.

b) Azimuthal waveguide structures. The second structure that has been tested is the azimuthal waveguide structure which can trap the fundamental mode while

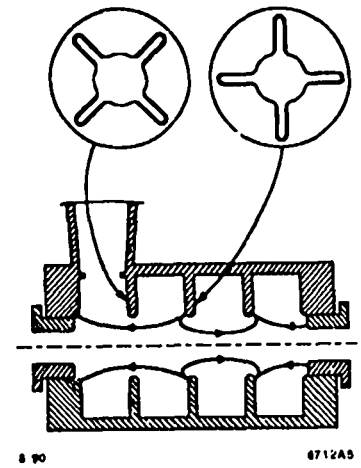

Figure 5. High power slotted-disk structure.

Table 1. Breakdown-limited gradient for $2\pi/3$ slotted-disk structure

Frequency	MHz	2857
Iris diameter	cm	3.6
Total length	cm	21
Filling time*	μs	0.87
Pulse length	μs	1.5-2.5
Peak power input	MW	21.5
E_S	MV/m	315
$E_S/\bar{E}_{acc}$ for SW structure		5.10†

* Assuming critical coupling

† The value obtained from MAFIA was 4.86. However, SUPERFISH being more accurate, we multiplied this value by a factor of 1.047, the ratio of the values calculated for an unslotted-disk structure (4.73 with SUPERFISH and 4.516 with MAFIA).

coupling out dipole and higher-order modes. The structure shown in Figure 6 has four guides forming a cross but another variation of this design with three outputs at 120 degrees is also under consideration. The three-output structure has the advantage that a greater fraction of the cavity wall is available for tuning.

The geometry of this structure possibly has the advantage over the radially slotted structure that it is easier to fabricate. The waveguide width and the diameter of the small remaining segments of the central cylindrical cavity must be chosen carefully so that the waveguide TE_{10} mode cutoff lies above the frequency of the fundamental accelerating mode and below the frequency of the undesirable HEM_{11} modes. Figure 7 shows the resonances obtained with a single cavity, with the outer ends of the rectangular waveguides shorted. The resonance patterns are independent of coupling probe positions in the end-plates because the crossed waveguides couple to all mode orientations. Again, a multiplicity of resonances above the fundamental 0 and π-modes are observed because of coupling between the shorted waveguides and the central cavity. With longer guides, the number of resonances increases. When the guides are terminated, first-order dipole resonances above the fundamental pair are heavily damped, as shown in Figure 8.

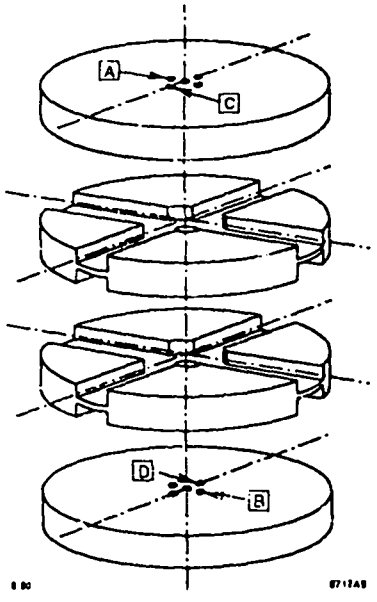

Figure 6. Azimuthal waveguide structure.

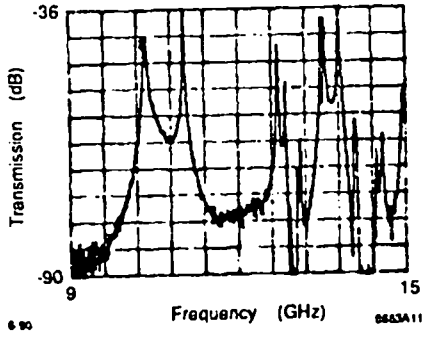

Figure 7. Single X-band cavity resonances with four azimuthal waveguides shorted.

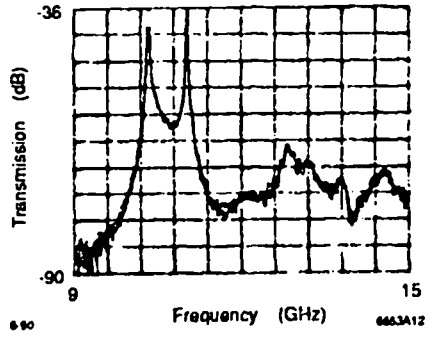

Figure 8. Single X-band cavity resonances with four azimuthal waveguides terminated.

Detuned Structures

Another approach to minimizing the effect of the HEM_{11} dipole mode is to design and build a disk-loaded waveguide structure in which the frequencies of these modes vary over the length of each section by some percentage. Calculations (see Figure 9) show that a frequency spread of about 10% from input to output of each section is sufficient to allow multibunch operation for a bunch spacing of 42 cm with essentially no transverse displacement from bunch-to-bunch at the end of a 3 km machine. A simple example of such a structure with a linear group velocity variation (similar to the constant-gradient design of the SLAC S-band structure) has been calculated with the characteristics shown in Figure 10. The results look very promising and would of course lead to a structure with a much simpler geometry than the damped designs described earlier. It remains to be seen if the longitudinal modes which cause bunch-to-bunch energy differences can also be sufficiently scrambled to make this approach entirely satisfactory.

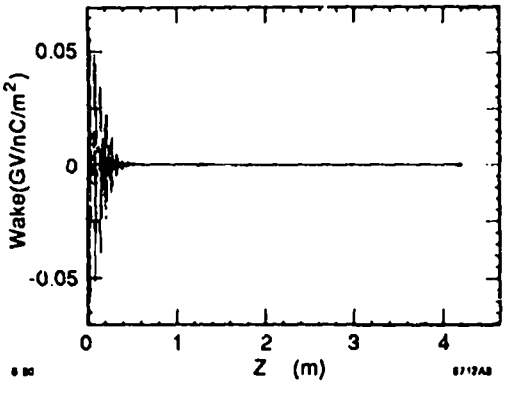

Figure 9. Wakefield behind a bunch, as a function of longitudinal distance z. The frequency of the fundamental transverse mode is detuned to 25 different values along each section. The weights of the different frequencies are given a truncated Gaussian distribution with total width = 5 σ and σ = 2%.

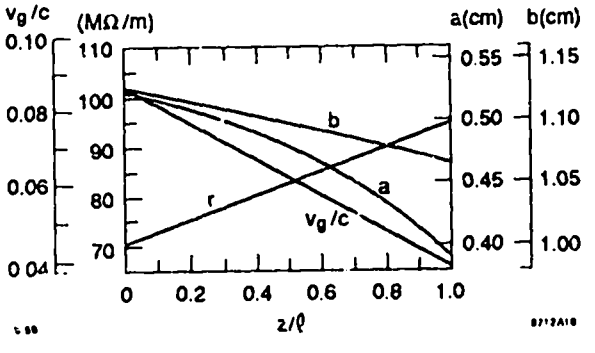

Figure 10. Design example of an X-band 1.5 m accelerator section showing the variations of normalized group velocity v_g/c, b, a and shunt impedance r as a function of nonnalized length z/l.

References:

1. "Damped Accelerator Structures," H. Deruyter et al, Proc. 2nd European Particle Accelerator Conference, SLAC-PUB-5263.

HEM_{11} MODES REVISITED*

J. W. Wang and G. A. Loew
Stanford Linear Accelerator Center,
Stanford University Stanford, CA 94309

Abstract

Concern with emittance growth in future multi-bunch linear colliders has rekindled interest in HEM_{11} dipole modes (sometimes also called "TM_{11}-like" or "TE_{11}-like") in disk-loaded waveguides. The availability of modern computer codes (URMEL, MAFIA) makes it possible to gain a deeper understanding of these modes and their properties. This paper presents ω-β dispersion diagrams, field configurations and transverse shunt impedances for the HEM_{11} modes as a function of iris aperture. The transition between forward and backward waves of the various branches is explored. This information serves as background material for another paper at this conference which reports recent work on linac structures in which these modes are damped or detuned.[1]

Introduction

In the early 1960's, following the formulation of the Panofsky-Wenzel theorem[2] in 1956, the properties of HEM_{11} dipole modes (sometimes called "TM_{11}-like" and/or "TE_{11}-like") in cylindrical disk-loaded waveguides became a subject of intense research in high energy physics laboratories all over the world. This flurry of interest was triggered by the useful applications of these modes to RF separators, RF deflectors and microwave beam position monitors, as well as by their deleterious beam-induced effects resulting in emittance growth and beam breakup instabilities. Authors such as H. Hahn at BNL, Y. Garault at Orsay, France, I. Aleksandrov, V. Kotov and V. Vagin at Serpukhov, USSR and others attempted to calculate the properties of these HEM_{11} modes by various analytic techniques. A fairly complete bibliography of the early work up to 1963 can be found in Reference 3.

Interest in HEM_{11} modes has recently been rekindled by concern with emittance growth in multi-bunch electron-positron linear colliders. In these machines, two transverse effects take place, one short-range, the other long-range. In the short-range effect, the head of a single bunch of finite length, if slightly offset with respect to the accelerator axis, excites HEM_{11} deflecting wakefields which cause the particles in its tail to experience emittance growth. In the long-range effect, the deflecting wakefields left behind by the first electron bunch produce increasing deflections of later electron bunches which cannot be corrected. Ultimately, these deflections result in losses in the luminosity at the interaction point because the electron bunches and their positron counterparts do not properly overlap. In the short range effect the time constants are very short and only focussing can counteract the RF deflecting forces. In the long-range effect, it is possible to damp or detune the HEM_{11} modes so as to reduce their cumulative transverse force.[4] However, before we attempt to damp or detune these modes, it is important that we first improve our understanding of their properties. This is the purpose of this paper. Modern computer codes such as URMEL and MAFIA are used to calculate the ω-β dispersion diagrams of these modes, their field configurations and transverse shunt impedances in regular unperturbed disk-loaded waveguides. The iris diameter (2a) is varied to explore the gradual transition from forward to backward wave.

Transversely Deflecting Modes

From the Panofsky-Wenzel formulation[2], it is apparent that transverse deflections can result only from cumulative interactions with RF modes in which the longitudinal E-field has a transverse gradient. Then, over a length l, the transverse momentum $p_\perp$ imparted in the x-direction to a synchronous particle of charge q by a mode of frequency ω is

$$p_\perp = \frac{q}{\omega}\int_0^l \left(\frac{\partial E_z}{\partial x}\right) dz$$

and one can define a transverse shunt impedance r_T as

$$r_T = \frac{\left|\left(\frac{\lambda}{2\pi}\right)\left(\frac{\partial E_z}{\partial x}\right)\right|^2}{-\,dP/dz}$$

where λ is the free space wavelength and the denominator is the RF power lost per unit length.

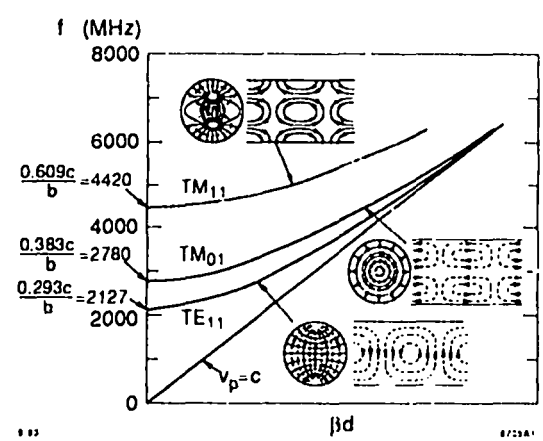

Figure 1. Dispersion diagrams of TE_{11}, TM_{01} and TM_{11} modes in smooth cylindrical waveguide. The length d in this case is arbitrary. For comparison with the example shown in Figure 2, f is given for the case where b = 4.13 cm.

* Work supported by the Department of Energy, contract DE-AC03-76SF00515.

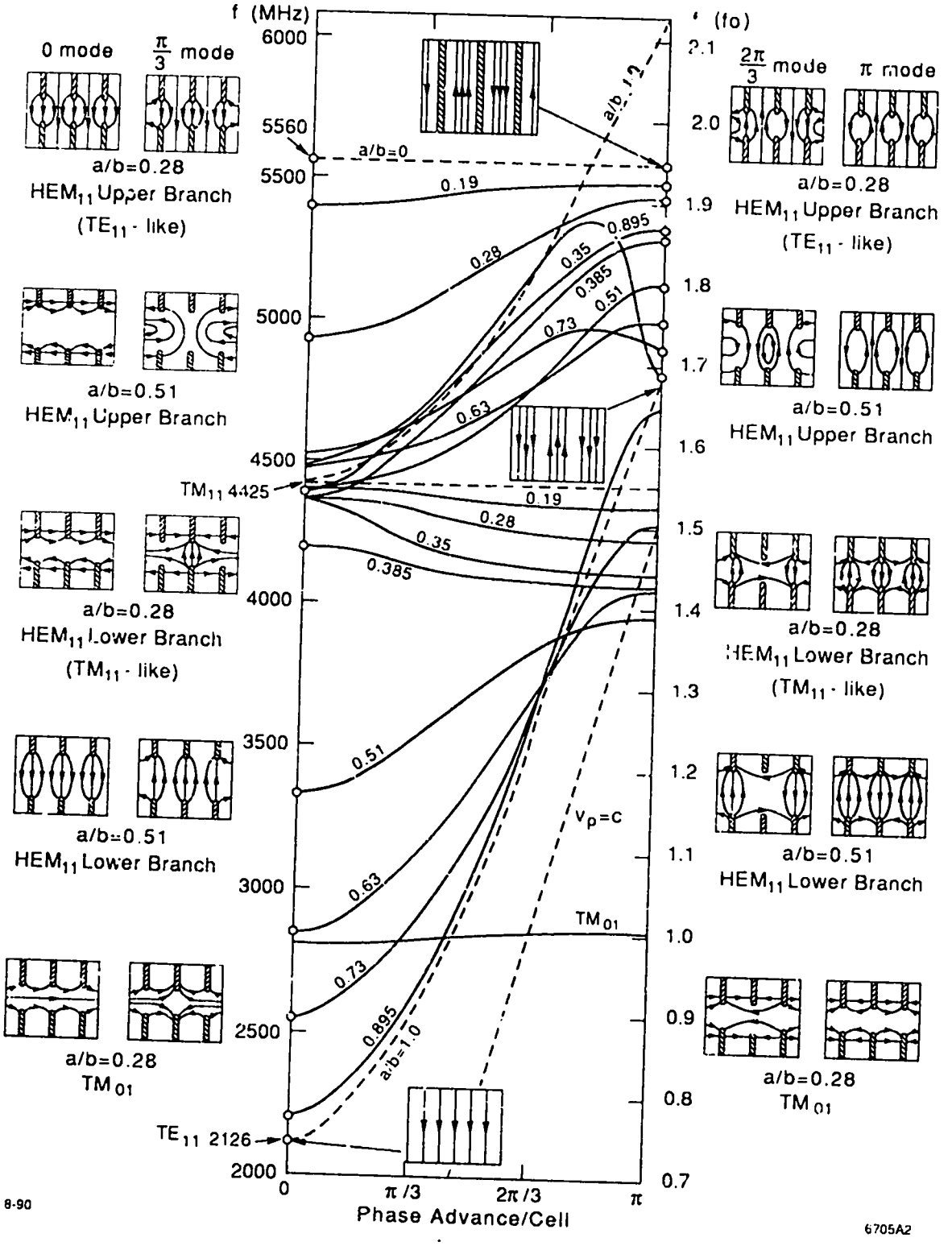

Figure 2. Dispersion diagrams and E-field configurations of TM_{01} and HEM_{11} modes as the b-dimension is kept fixed (4.13 cm) and the ratio a/b varies between 0 and 1.

Now consider first a smooth cylindrical waveguide of radius b in which the lowest modes of interest are the TE_{11} ($f_c = 0.293c/b$), the TM_{01} ($f_c = 0.383c/b$) and the TM_{11} ($f_c = 0.609c/b$). Their dispersion diagrams are shown in Figure 1. It can be shown easily that for all these modes, the quantities in the above equations are zero. However, as the cylindrical guides are made into disk-loaded waveguides of periodic length d and iris radius a, these modes become perturbed. It can be seen intuitively that as the disks are added, some E-lines terminate on the disk edges (a) rather than on the waveguide walls (b), TE_{11} and TM_{11} modes mix and a "hybrid" HEM_{11} mode is born. The patterns are no longer pure and the configurations change as one moves from the 0 to the π–mode frequency.

To facilitate understanding of this process, Figure 2 shows the entire evolution of the ω–β diagrams and E-field configurations as the b-dimension is kept fixed (4.13 cm) and the ratio a/b varies between 0 and 1. We see that the upper HEM_{11} branch keeps its TE_{11}-like identity throughout the band from 0 to π-mode in the range of a/b from 0 up to 0.35, and similarly, the lower HEM_{11} branch keeps its TM_{11}-like identity in this range even though it is a backward-wave mode in which phase and group velocity are of opposite sign. It is particularly interesting to examine the region which is shown in further detail in Figure 3. Note that for a/b between 0.38 and 0.41, the ω–β diagram has a minimum in mid-band and the net power flow through the iris changes direction. The original CERN RF separator structure[5] used dimensions very close to these and resulted in a ω–β diagram with a minimum in the middle which seemed puzzling at the time. The URMEL program is now capable of sorting out all these details. Also, note a similar reversal in the upper HEM_{11} branch when a/b exceeds 0.7.

The reason it is useful to understand this pattern evolution is that most linear accelerator and RF separator structures are designed to operate close to the transition zone of Figure 3. On the other hand, the structure designs for linear colliders tend towards larger a/b values (~0.45) than for example the SLAC constant-gradient design (0.235 to 0.314) because of the need, for single high-intensity bunches, to minimize longitudinal and transverse wakefields which vary approximately as $(a/b)^{-2}$ and $(a/b)^{-3}$ respectively.

Table 1 gives a summary of calculated transverse shunt impedances as a function of a/b using theoretical Q-values. For reference, note that the original SLAC RF separator operating at 2856 MHz (with a/b = 0.386 and 2π/3 mode) had a transverse shunt impedance of 16MΩ/m, and the transverse shunt impedance of the beam-breakup mode at the input of the SLAC 3-m long section (a/b = 0.314, close to π-mode) at 4139.4 MHz was also about 16 MΩ/m, assuming an experimental Q-value of 8000.

The information presented in this paper has been used to work out some of the design details needed in Reference 1. In the future, it will also be useful in the design of new RF separators planned for so-called "crab-crossing" schemes for linear colliders or B-factories.

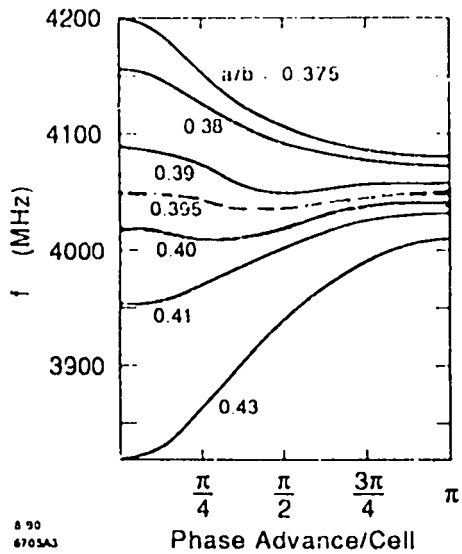

Figure 3. Dispersion diagrams of HEM_{11} modes in transition zone.

a/b	r_T (MΩ/m) LOWER BRANCH	UPPER BRANCH
0.28	29.3(π–mode)	1.58(3π/4-mode)
0.35	21.4(π–mode)	0.54(4π/5-mode)
0.375	18.9(π–mode)	0.29(4π/5-mode)
0.51	8.3(π–mode)	0.28(5π/6-mode)

Table 1. Transverse shunt impedance for HEM_{11} modes with $v_p = c$ as a function of a/b.

References

1. H. Deruyter, et al, "Damped and Detuned Accelerator Structures," This Conference.

2. W. K. H. Panofsky and W. Wenzel, "Some Considerations Concerning the Transverse Deflection of Charged Particles in Radio-Frequency Fields," Rev. Sci. Instr., 27. 967, 1956.

3. O. H. Altenmueller, R. R. Larsen and G. A. Loew, "Investigations of Traveling-Wave Separators for the Stanford Two-Mile Linear Accelerator," SLAC Report No. 17, August 1963.

4. Actually, to control the short-range effect there exists another method called BNS damping, which is similar to structure damping or detuning, whereby the tail particles are given lower energy than the head particles and thereby oscillate at an incoherent betatron frequency. "BNS" stands for the names of the inventors of this technique, V. E. Balakin, A. V. Novokhatskii and V. P. Smirnov, from INP, Novosibirsk, USSR.

5. M. Bell, P. Bramham, R. D. Fortuna, E. Keil and B. M. Montague, "RF Particle Separators," AR/Int. PSep/63-7, June 1963.

Structure Design for a 500 GeV S-Band Linear Collider

P. Hahne, N. Holtkamp, R. Klatt, T. Weiland

Technische Hochschule
Fachgebiet Theorie Elektromagnetischer Felder
Schloßgartenstr. 8, 6100 Darmstadt

Abstract

Constant gradient structures with an accelerating gradient of 20 MeV per meter are commonly used with S-band frequency. The well known features of these travelling wave tubes provide a dedicated design for their use in the next generation linear collider. Some of the required design parameters for this tubes are presented within the whole concept of this collider with an active length of about 30 km. The choice of these parameters is explained and calculations concerning the structure are presented.

Introduction

In order to have a realistic design for a 500 GeV e^+e^--collider for the near future, almost conventional rf-technology has to be used. This leads to an overall list of parameters for this type of collider, which is presented in another paper [1]. Multi-bunch operation with current pulses much longer than one filling time of the accelerating tubes, peak power limitations from the klystrons and *beam breakup* considerations are the strongest restrictions, which have a great influence on the design of these travelling wave tubes (**twt**).

The bunch population is $7 \cdot 10^9$ particles per bunch with approximately 170 bunches per pulse (≈ 100 mA) and a rf-pulse length of $\approx 3\,\mu$sec. With a low repetition rate of 50 Hz a luminosity of $\mathcal{L} = 2.4 \cdot 10^{33}\,\mathrm{cm}^{-2}\,\mathrm{sec}^{-1}$ will be reached. With these values the boundary conditions which come from the general list of parameters [1] are summarized.

General Layout

Several reasons lead to our decision to choose S-band frequency for the Linear Collider design. Wake fields impose strong limitations on the number of particles that can be accelerated. Transverse wake fields are scaling with ω^3 and longitudinal wake forces are proportional to ω^2. This accomplishes the design of a very high frequency accelerating structure, because for every cavity in the tube transverse mode damping is unavoidable [2] due to the scaling laws given above. Preliminary calculations have been done with a geometry identical to the SLAC cell nr. 45. For a $\sigma = 0.1$ mm long bunch the longitudinal wake potential has been computed [3] and is shown in Fig. 1. The maximum wake potential within the bunch is 260.74 V/pC/m leading to a single bunch energy spread of 1.7 % [4], which stays within the acceptance of the final focus. Due to the small bunch- to wavelength ratio, the energy spread can not be reduced by acceleration on the slope of the wave.

Having fixed the operating frequency of ≈ 3 GHz, due to scaling, a set of parameters can be derived within an accuracy of a few percent. For example, the shunt impedance per meter will be $\approx 53\,\mathrm{M\Omega/m}$ and the Q-value of the copper

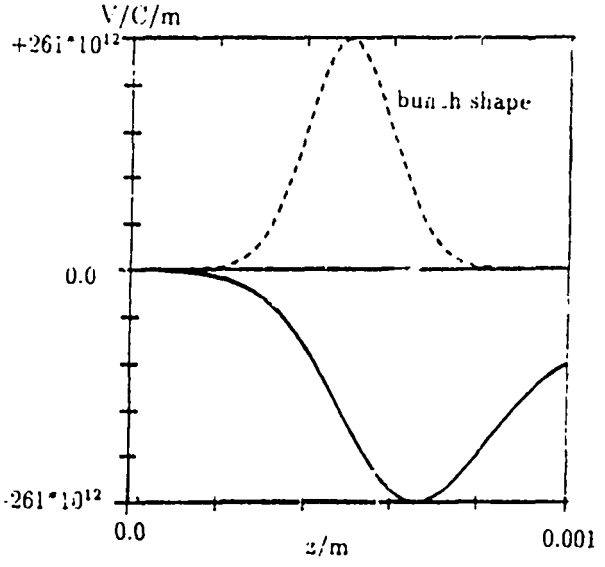

Figure 1: *Wake potential for a $\sigma = 0.1$ mm long bunch.*

cavities is $\approx 13\,000$. The maximum length of one **twt** which can be fed by one klystron is 12 m and given by the peak power limit. This technical limit today seems to be ≈ 130 MW per klystron with a rf-pulse length of $\approx 3\,\mu$sec provided by the modulator and the Pulse Forming Network (PFN).

Actually a structure length of 6 m is chosen to increase the average shunt impedance due to the smaller iris holes and as a consequence, the smaller required group velocity. At least only the attenuation parameter τ, defined in the following way:

$$\frac{P_{out}}{P_{in}} = e^{-2\tau} \qquad (1)$$

is variable. τ relates the input peak power for one **twt** to the outgoing power and as well determines most of the properties of the accelerating structure.

Peak Power Requirements

Obviously, for a given gradient in the structure, the required electric energy which has to be provided by the klystrons per pulse should be lowered in order to minimize operational costs.

The energy per pulse can be devided into the energy which has to be delivered during the filling time (T_f) and the energy required during the current pulse of length T_1. The first part is wasted in the sense that it can not be used for acceleration of particles. Therefore a low repetition rate and long current pulses are preferred. In terms of the

attenuation parameter τ this is shown for a constant gradient structure in equation (2):

$$W_\Sigma = W_f + W_l \qquad (2)$$

with:

$$W_f = P_0 \cdot T_f = P_0 \cdot \frac{2Q}{\omega} \cdot \tau$$
$$W_l = P_0 \cdot T_l$$

The meaning of other symbols is:

P_0	=	klystron peak power	=	$\alpha \cdot (1 - e^{-2\tau})^{-1}$
				$\alpha = G^2 L / R'_s$
G	=	unloaded gradient	≈	18.5 MeV/m
L	=	structure length	=	6 m
R'_s	=	shunt impedance	=	53 MΩ/m
T_l	=	current pulse length	=	2μsec

Calculation of the minimum leads to an implicit equation:

$$\tau = \frac{1}{2} \cdot \ln\left(1 + 2 \cdot \tau + \frac{\omega}{Q} \cdot T_l\right) \qquad (3)$$

The minimum is found to be $\tau = 0.855$ and, as can be seen from equation (3), in this approximation is independent of α.

Due to transient beam loading (≈ 7-10% in our case), which depends on τ itself, the required peak power per meter, to reach a fixed loaded gradient of 17 MeV/m, is increased and therefore τ will be lowered. In Fig. 2 the required energy per pulse and per meter is shown as a function of τ (beam loading included). From this picture the minimum energy per pulse for the loaded structure is given with $\tau = 0.7$. Because of the flat minimum of the curve, the required energy is not very sensitive to modifications of values between 0.5-0.8.

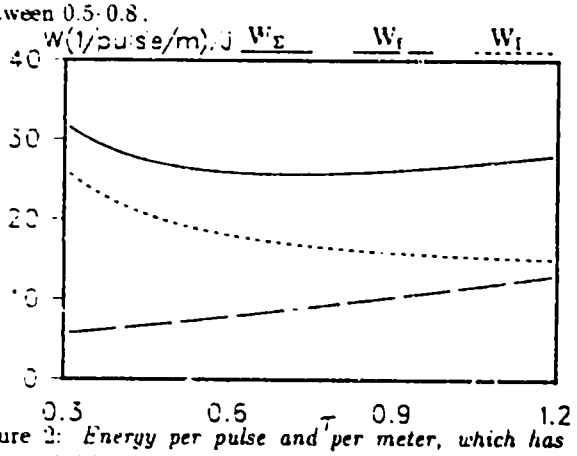

Figure 2: *Energy per pulse and per meter, which has to be provided by the klystron as a function of the attenuation parameter τ for a S-band structure with a loaded gradient of* 17 MeV/m.

For other proposed schemes (e.g.: **JLC, NLC, VLEPP** etc.) the current pulses are much shorter than one filling time which is one reason for the smaller envisaged attenuation parameters of $\tau \leq 0.5$. Short accelerating structures and high peak power levels for the klystrons are some of the consequences. For a loaded gradient of 100 MeV/m, typical current pulse length's of 10 nsec, a pulse current of ≈ 1.3 A and a 0.7 m long structure with a frequency of 11.424 GHz the same calculation is shown in Fig. 3 (current injection before the structure is completely filled to reduce the bunch to bunch energy spread, is taken into account).

The minimum is obtained for $\tau \approx 0.25$, which would require a peak power of ≈ 270 MW/m for this type of structure. In contrast to the S-band linac with long current pulses during operation, most of the energy is dissipated while the structure is filled (see W_f in the figures) and only the minor part is used to accelerate the beam.

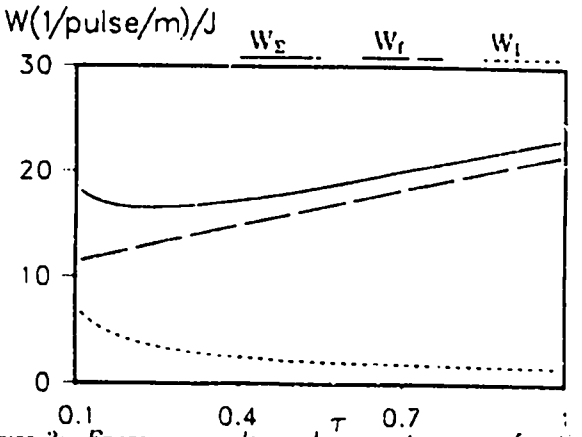

Figure 3: *Energy per pulse and per meter, as a function of the attenuation parameter τ for a short high-gradient, high-frequency X-band structure with a loaded gradient of* 100 MeV/m.

Structure Layout

Starting with the parameters listed in equation (2) and with an attenuation of 0.7 neper, some more general characteristics for the linac and the structure can be deducted. They are presented in table 1.

One type of structure we used for the calculations is shown in Fig. 4, but first without the banana like coupling holes above the iris. A **twt** with a $2\pi/3$ accelerating mode and a length of 6 m will consist of ≈ 180 cells, with a variation in iris diameter of d = 3.07-2.09 cm to provide the required decrease in group velocity along the structure.

Start Parameters		
tot. RF input power/pulse	250500	MW
active length	29411	m
average shunt impedance	53	MΩ/m
average gradient (unloaded)	18.4	MeV/m
average Q	13000	
current	100	mA
average RF power	≈ 38	MW
Structure and Beam Parameters		
0 current energy	543	GeV
loaded energy (100 mA)	500	GeV
trans. beam loading	43	GeV
peak power per twt	52	MW
power loss → load	13	MW
rf-pulse length	3.0	μsec
attenuation	0.7	neper
length of one twt	6	m
group velocity	3.7-0.9	% of c
filling time	1.0	μsec

Table 1: *List of parameters for the S-band Collider*

In order to save one input coupler per klystron, the possibility of using a combined forward- and backward-wave structure is investigated as well. Filling from both sides through one coupling cell avoids phase- and amplitude asymmetries and can also be done with less couplers in this scheme. The input coupler is placed in the middle of the structure, to provide filling towards both ends of the tube. In the backward wave **twt** the energy flow is up-stream.

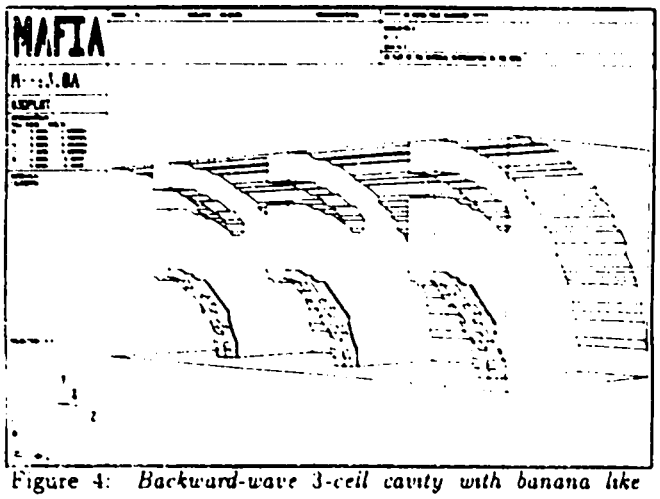

Figure 4: *Backward-wave 3-cell cavity with banana like shaped holes above the iris in order to provide strong magnetic coupling from cell to cell.*

while the phase of the wave is synchronous with the bunch. Therefore a negative group velocity is necessary and e.g. provided by banana like holes above the irises (compare Fig.4). The hole is placed near the maximum of the magnetic field, in order to increase the magnetic coupling from cell to cell which inverts the slope of the dispersion relation in the Brillouin diagram especially for the accelerating mode (compare Fig.5).

Modes which are not azimuthal symmetric split up into two or more curves depending on their symmetry and on the direction of polarization of these modes. For the HEM (or dipole-) modes this can be seen in Fig. 5 as well.

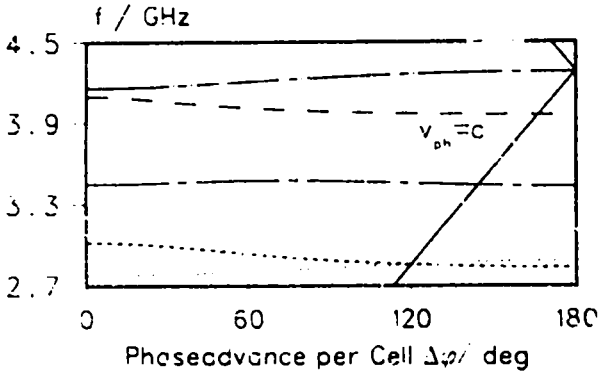

Figure 5: *Brillouin diagram for a forward- and a backward-wave cavity with dispersion relations for the accelerating and the first HEM modes.(acc. forward: · · · , acc. backward: ·····, HEM forward: – – –, HEM backward ||: -·—·, HEM backward ⊥: -·—·)*

Beam Breakup Considerations

One obvious method against cumulative *beam breakup* is, to randomly distribute the HEM mode frequencies in different sections of the linac over the entire length. In a backward-wave structure, part of this is done due to the splitting of the curves in the Brillouin diagram. In order to really randomize the HEM frequencies, a simple method for detuning them is required. The disk thickness has been varied in a forward-wave structure by 1 mm, which changes the frequency of the first HEM mode by ≈10 MHz. Because the accelerating mode is shifted as well, the group velocity has to be readjusted in order stay with the constant gradient

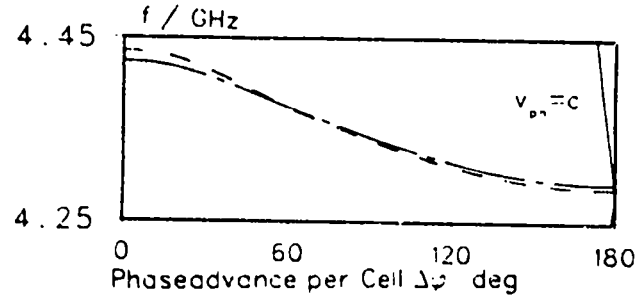

Figure 6: *Brillouin diagram for the first HEM mode. Due to variation of the disk thickness (1 mm) the curves are splitted.*

conditions. The splitting is shown in Fig. 6

Preliminary *beam breakup* simulations have been done regarding only one HEM mode frequency driving the transverse amplitude of the bunch train. For the calculation a simple FODO focussing scheme with a phase advance of 90° per FODO-cell has been chosen. One 6 m long structure is thought to be one cavity. The bunches are injected with an energy of 3.1 GeV (the damping ring energy) into a perfectly aligned linac with a transverse injection jitter of 0.1 mm. The dynamic has been simulated over a length of 1 km. With a random distribution of the first HEM mode frequency of ± 5 MHZ, the breakup disappears, as shown in fig. 7.

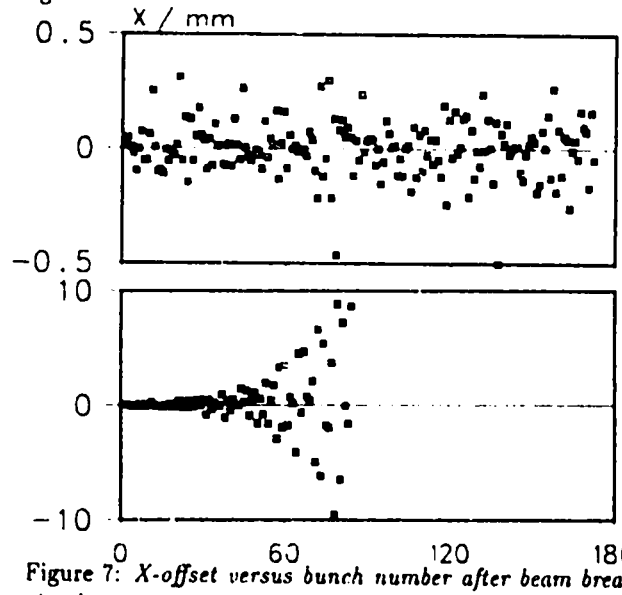

Figure 7: *X-offset versus bunch number after beam breakup simulation over a length of 1 km with (above) and without (below) random distribution of the HEM mode frequencies.*

Summary

Calculations made up to now, have shown, that S-band twt's can be used to build the proposed linear collider. The severest problem, the *beam breakup*, seems to be controllable.

References

[1] *Design Study for a 500 GeV Linear Collider*, T. Weiland, Deutsches Elektronensynchrotron DESY, Hamburg- and Technische Hochschule Darmstadt- Study Group, this conference.

[2] *Damped Acceleration Cavities*, R.B. Palmer, SLAC-PUB-4542, 1988.

[3] T. Weiland, *Transverse beam cavity interaction part I: short range forces*, NIM 212 (1983),p. 13-21.

[4] R. Klatt, R. Wanzenberg, private communication.

MACSE : ACCELERATING ELECTRONS AT SACLAY WITH SUPERCONDUCTING CAVITIES

Ph. Leconte, B. Aune, S. Bühler*, L. Cardman, J.M. Cavedon, J. Fagot, J. Gastebois, J.F. Gournay, J.M. Hisleur, M. Jablonka, M. Juillard, T. Junquera*, E. Klein, A. Mosnier, M. Promé, A. Veyssière**

Département de Physique Nucléaire
Service des Techniques d'Accélération Supraconductrices
DPhN/STAS CEN Saclay, 91191 Gif sur Yvette, France

Abstract

In order to master all the technological aspects of superconducting RF acceleration, a test facility for fully equipped accelerator modules is under completion at Saclay. First accelerated electron beam is expected by the end of this year.

Introduction

Since 1986, the Département de Physique Nucléaire at Saclay has started an R&D program on superconducting RF cavities. State of the art cavities have been produced[1]. Fundamental research is also being done on superconducting surface RF properties such as field emission, surface resistance[2], thin layer sputtering techniques[3], heat transfer models, and physico-chemistry of Nb oxides. The understanding of the physics of RF superconductivity and the know-how on cavity making, however essential, must be complemented by many other technological skills, before one is able to build and operate a superconducting accelerator.

This is the aim of the MACSE facility. Three cryomodules, with different types of cavities, will successively be built and submitted to full test with beam, so as to gain expertise, to have operation experience and to improve cost effectiveness. The design values for the 5-cell cavities of the first step are an accelerating field E_{acc} = 8 MV/m and a quality factor Q = 6.10^9 at 1.8 K.

The project has started on early 1989. The MACSE facility is being set up in the tunnel of the Saclay ALS 700 MeV electron accelerator, which has been shut down on June 10th 1990 and partly disassembled. First beam is expected by the end of 1990. One year will then be dedicated to successive tests of different prototype cavities and cryomodules.

General set-up, beam injector and diagnostics

Figure 1 shows the complete beam line : the 100 kV, 100 µA electron beam injector, the superconducting capture section, the intermediate tuning point and beam analysis, the 4-cavity cryomodule and the high resolution (10^{-4}) beam analysis.

The electron injector[4,5] has been lent by University of Illinois. It consists of a low emittance electron gun, two chopping cavities and one bunching cavity. These copper cavities have been made by Los Alamos Accelerator Technology Division.

The capture section accelerates 100 keV electrons to about 2 MeV. This cannot be done by a standard, β = 1, cavity. A shorter (β = 0.84), 5-cell superconducting cavity has been designed for this purpose. It is housed in a specific cryomodule.

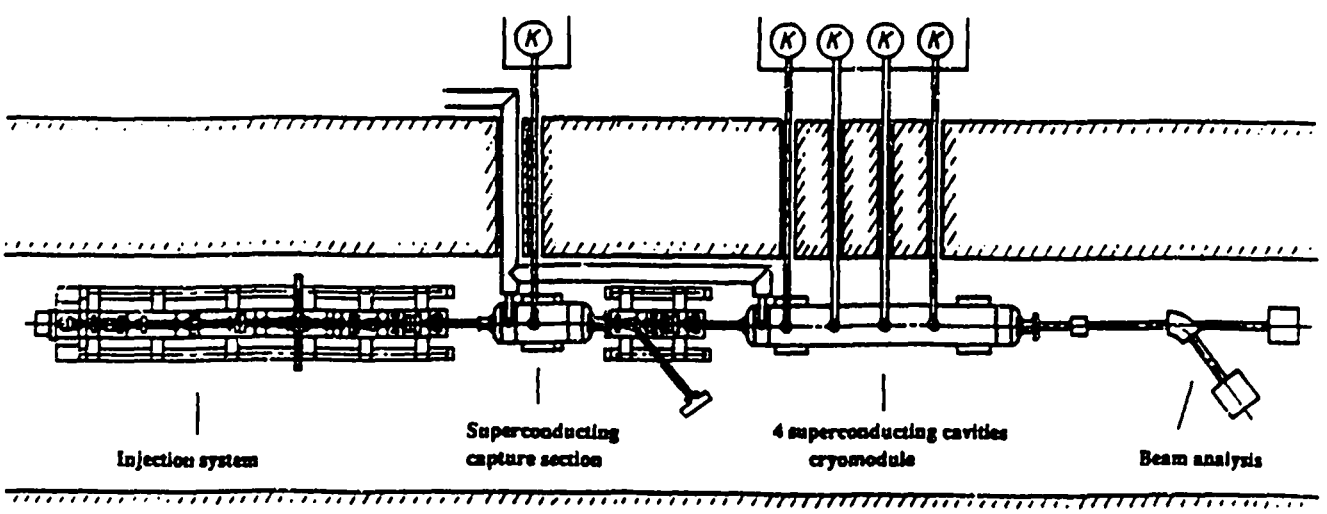

Figure 1 : Layout of MACSE.

Cavities

The design of the 5-cell cavities (figure 2) is derived from the CERN profile. The main coupler port is a pipe with a vacuum seal flange. Two Nb HOM couplers[6], specifically designed for 1.5 GHz, are welded on the beam pipe.

The cavities are fabricated by ATEA (France). They are hydroformed out of 2 mm sheets of Nb (RRR = 200 to 300). The chemical etching is done at Saclay, as well as the final RF surface preparation in a class 100 clean room.

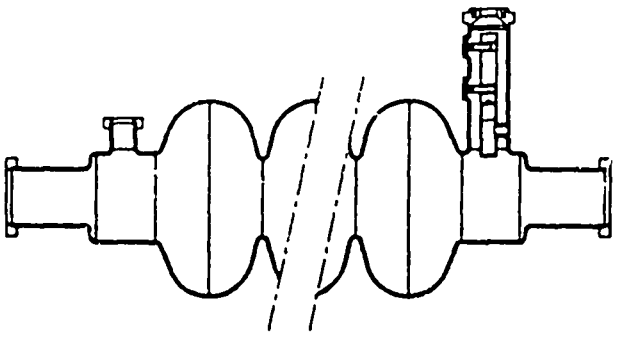

Figure 2 : 5-cell cavity profile.

Six 5-cell cavities have already been built and individually tested in vertical position. The final results are shown on figure 3. Previous erratic results have been discarded. They have all been traced back to inadequate cooling conditions : the cooling speed in the 200 K - 100 K range was too slow. This is now known[7] to increase the surface resistance by a factor 50 in the worst cases.

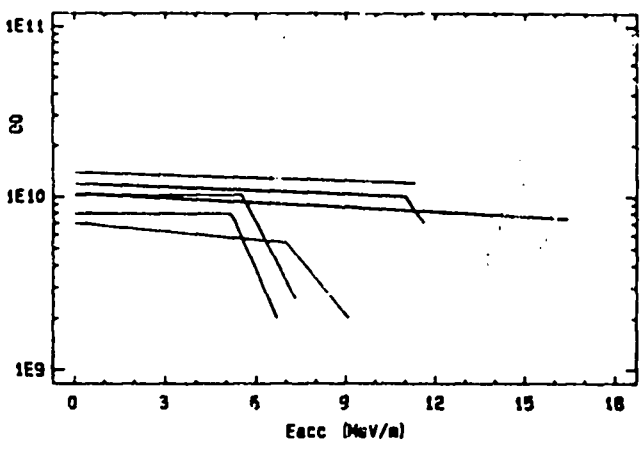

Figure 3 : Q(E) for the first six 5-cell cavities for MACSE.

Other types of cavities are under development. Two 3-cell cavities with much simpler HOM couplers have been tested. They withstand accelerating fields as high as 16 MV/m ; this already gives the same energy gain *per cavity* as the 5-cell prototypes.

Developments are under way for coating copper cavities with a thin layer of a superconductor of higher T_c and of low surface resistance.

Cryomodules

Cryomodule # 1 (Fig. 4) contains four 1.5 GHz, 5-cell niobium cavities. It is fabricated by ATEA (France). The set of four cavities is prepared by pairs in the clean room. The final assembly is done in a clean tent. Each cavity is then equipped with two frequency tuners : a mechanical one, actuated by a stepping motor, and a magnetostrictive rod. Both are immersed in the helium bath. The frequency tuning range is 1.5 MHz, with a resolution of 1 Hz. The 4 cavities assembly is then slid into the helium tank on a pair of aligned shafts. The helium tank is rigid enough to ensure alignment.

There is no feedthrough between cold helium and vacuum. All cavity gaskets are of Helicoflex type, made by Cefilac (France).

The main coupling lines are of coaxial type. A coaxial quarter-wave choke provides the proper RF continuity and an excellent thermal separation between the cold and warm parts.

Cryomodules # 2 and # 3 will be designed to house other types of cavities.

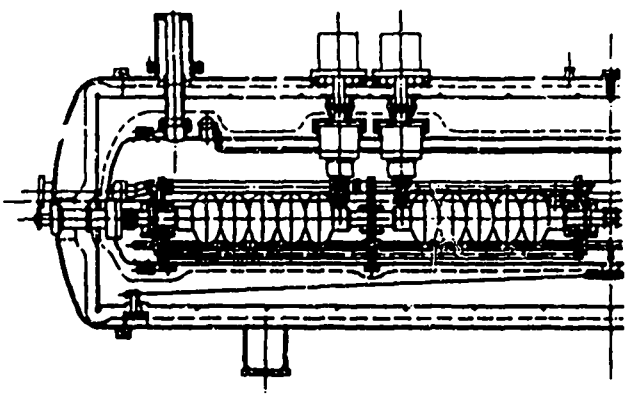

Figure 4 : Cross-section of half a cryomodule

RF power sources

The power sources are 5 kW klystrons resonating at 1497 MHz. Their efficiency is 35%. They are made by Thomson-TE (France). Rectangular L-band wave guides with circulators and 5 kW loads connect the klystrons to the

cryomodules. There are three feedback loops[6]: the two faster ones lock the phase and the amplitude of the cavity; the slow one detects the phase shift between klystron and cavity and tunes the cavity frequency.

Helium refrigerator

A commercial Helium liquefier has been purchased from Air Liquide (France). Together with a pumping unit and a 4.2 K/1.8 K heat exchanger, the system is expected to provide a cooling power of 60 W at 1.8 K. In a second step, a cold compressor and heat exchangers will double the cooling power. This set-up is designed and assembled by Saclay/DSM/DPhPE/STIPE.

Conclusion

All the main parts are presently built, and most of them are under assembly and qualification. This technical effort brings together the experience of 20 years of operation of the ALS linac, the expertise gained by successful construction and operation of 50 superconducting cavities for the heavy ion booster of Saclay, and recent efforts in R & D on cavities for electron acceleration. When successful, the present development will add one stone to pave the way for modern accelerator facilities of the future.

Acknowledgements

This work is being supported by the technical staff of DPhN/STAS. We thank the staff of Institut de Physique Nucléaire (Orsay, France) for its collaboration.

References

1. B. Aune et al., "Superconducting RF activities at Saclay : status report", in Proceedings of the 4th Workshop on RF Superconductivity, Tsukuba, Japan (1989).

2. M. Juillard et al., "SC surface resistance measurements with a TE011 cavity", 2nd European Accelerator Conference (EPAC), Nice, France (1990).

3. P. Bosland and F. Guémas, contribution to the ICMAS conference, Grenoble, France (1990), to be published.

4. L. Cardman et al., Nuclear Physics Research with 450 MeV microtron, Urbana, University of Illinois NPL, March 1986 Report, Chap IV.

5. B. Aune, M. Jablonka and E. Klein, "The MACSE injector", 2nd European Accelerator Conference (EPAC), Nice, France (1990).

6. A. Mosnier et al., "MACSE superconducting cavity RF drive system", 2nd European Accelerator Conference (EPAC), Nice, France (1990).

7. B. Aune et al., "Degradation of Niobium superconducting RF cavities during cooling time", contribution to this conference.

* Institut de Physique Nucléaire, 91406 Orsay, France
** Nuclear Physics Laboratory, University of Illinois, Urbana, Ill. 61820, USA.

HIGH GRADIENT EXPERIMENT BY ACCELERATOR TEST FACILITY FOR JAPAN LINEAR COLLIDER

Seishi Takeda, Mitsuo Akemoto, Hitoshi Hayano, Takashi Naito and Hiroshi Matsumoto

National Laboratory for High Energy Physics
Oho 1-1, Tsukuba, Ibaraki 350, Japan

Abstract

High gradient experiment by using a traveling wave structure in S-band frequencies is presented. Discussions are given about the dependence of dark current and structure length. As one of the parameters indicating the quality of the structure, the multiplication factor η has been proposed.

Introduction

For the e^+e^- linear colliders in TeV energy region such as the Japan Linear Collider (JLC), the accelerating gradient will be one of the important parameters affecting the over all design of main linacs. The gradient determines the accelerating structures, RF frequencies, peak power, AC power, total length and cost. The gradient of 100 MV/m is desirable to construct a 1 TeV linear collider with the reasonable length of 10 km. For the existing high energy linacs, the gradients are 10 to 20 MV/m, and 2.856 GHz is utilized as the standard RF frequency. The experimental studies on the maximum attainable accelerating gradients in standing-wave structures have been performed by several authors.[1-2] The experimental results show that the measured maximum surface electric field E_{smax} is a function of frequency for 1.5 to 4 μs RF pulse length,

$$E_{smax} \cong 195 \, f(\mathrm{GHz})^{1/2}.$$

For the traveling wave structures, the ratio of the surface field and accelerating field is 1.9 to 2.2. The maximum accelerating gradient E_{amax} at the RF breakdown limit is estimated to be 150 MV/m at 2.856 GHz. The higher RF frequencies are preferable to obtain high gradient. The frequencies of 11.424 GHz in X-band have been chosen for main linacs for the JLC project. The peak power of 120 MW is required to produce the gradient of 100 MeV/m in 0.7 m-long X-band traveling structure for the JLC main linacs. A prototype X-band klystron has been developing to generate 30 MW peak power with 1 μs pulse duration[3]

RF Sources for High Gradient Experiment

Experiments reported several authors[1-2] utilize the standing wave structures of one or a few cavities since the extremely high power RF sources are unavailable. However, the understanding of dark current phenomenon in long traveling structures is necessary to determine the maximum gradient that can be obtained and used realistically. In order to produce the gradient of 100 MV/m, the required peak power per unit length is 300 to 350 MW/m at S-band frequencies and 150 to 175 MW/m at X-band frequencies. At present, such extremely high peak power can be obtained at S-band frequencies.

Experimental Set-up

Figure 1 shows the experimental set-up. The peak power of 100 MW can be produced by a 67 MW SLAC-5045 klystron or 85 MW Toshiba-E3712 klystron at 450 kV cathode voltage and 1 μs pulse duration. The peak power of 200 MW can be produced by means of a 3 db coupler combining the rf power from two klystrons. The accelerating gradient of 100 MV/m can be obtained in 0.6 m-long traveling structures at 200 MW rf input.

The 0.6 m long constant gradient disk-loaded structure with 17 cells and 2 couplers. The diameter of disk aperture 2a is decreased from 19.0 to 15.9 mm along the structure. The average shunt impedance is 61.2 MΩ/m and figure of merit Q is 11,600. The attenuation constant τ is 0.37 and the filling time t_f is 0.47 μs. The material of the structure is 1st class OFHC. The surface roughness of both the disks and cylinders are 0.02 μm except the rounded irises where the surface roughness is 0.2 μm. The gradient of 100 MeV/m can be obtained at 200 MW RF input. The result of simulation by SUPERFISH shows that the peak surface electric field around the rounded iris is about 2.0 times higher than the average accelerating gradient. The klystron modulators are operated at 50 Hz repetition rate and the average power dissipation in the structure is estimated to be 5.2 kW. The cooling water flow through the pipe drilled in the cylindrical wall. The structure without water jacket gives rise to precise alignment of the structure. The axis of disk apertures can be estimated by measuring the position of the outer wall of the structure.

Faraday cups and current transformers are utilized for measuring the dark current at both the

downstream and upstream of the structure. The energy spectrum of the dark current is measured by an analyzer magnet.

The X-ray bursts due to the dark current are measured by ten plastic scintillators installed on the surface of the structure and photo multipliers and a 8 channel oscilloscope.

RF Processing

The gradient was increased by rf processing controlled the rf power to maintain the vacuum pressure below 1×10^{-7} Torr by a computer system. The accelerating gradient was achieved to 35 MeV/m after 60 hours of rf processing. The field emitted current except low energy region decreased after 90 hours, and gradient of 50 MeV/m could be attained after 200 hours. The total dark current generated in the structure is measured by the Faraday cup. The field enhancement factor β estimated from modified Fowler-Nordheim plots decreases from 90 to 66 by the rf processing of 300 hours. The accelerating gradient of 90 MV/m could be obtained at 160 MW rf input after 800 hours of rf processing.

Dark Current Measurement

The transient analysis of the dark current has been reported.[4] The experimental results show that the bursts of both the current waveform and X-ray are detected simultaneously with the RF from arrival to the output coupler. It seems to be considered that the RF breakdown due to multipactoring is produced near the coupler iris.

Figure 2 shows the energy spectrum of total dark current. The main portion of the total dark current is generated in the output coupler. However, the dark current from the structure can be obtained by eliminating the low energy components of the energy spectrum.

Figure 3 shows the field enhancement factor β estimated from modified Fowler-Nordheim plots. For the total dark current, enhancement factors (β = 66) agree with the measurement by means of Faraday cup. The field enhancement factor in the structure except output coupler is evaluated to be 39.

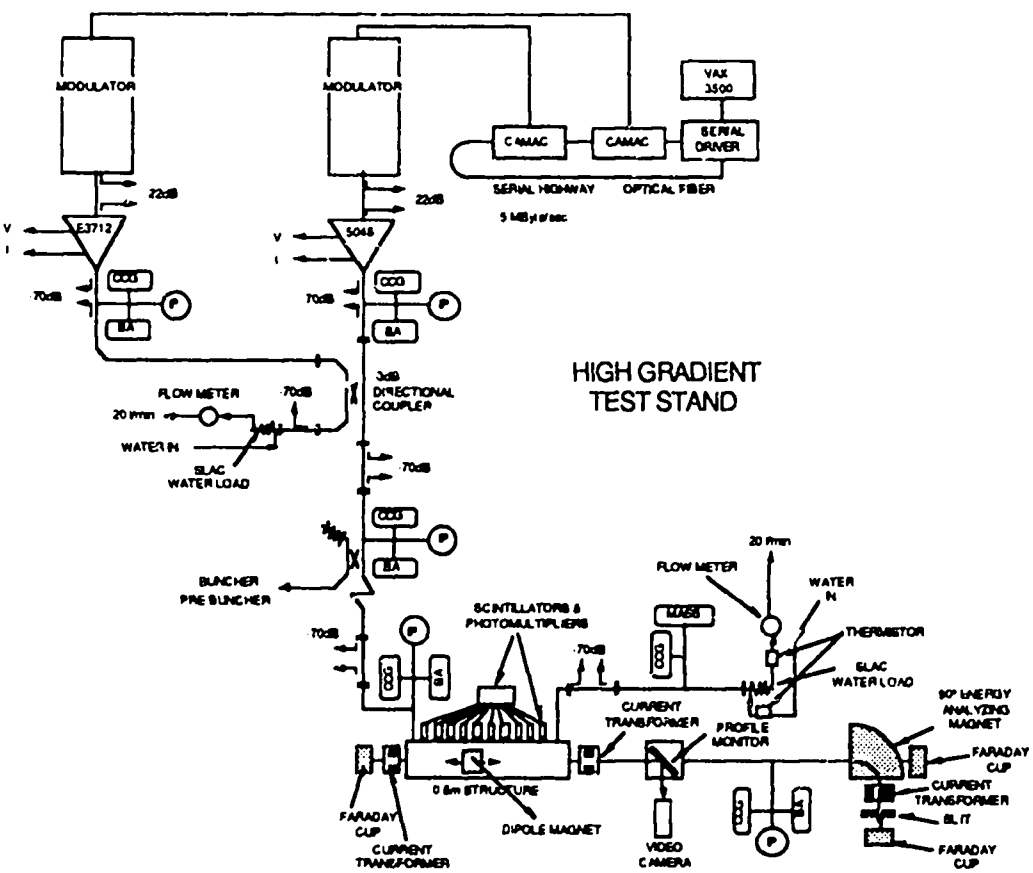

Figure 1. Diagram of the experimental set-up.

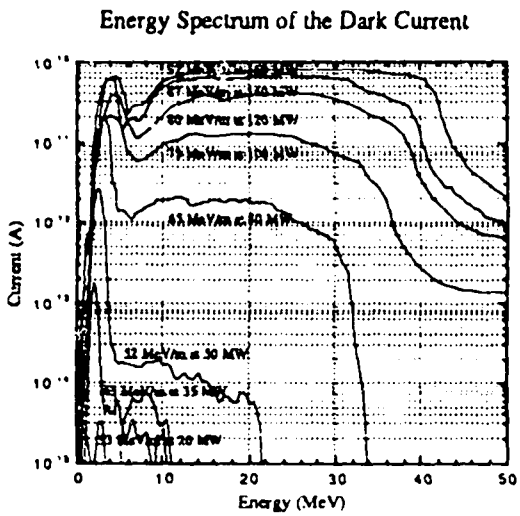

Figure 2. Energy spectrum of the total dark current.

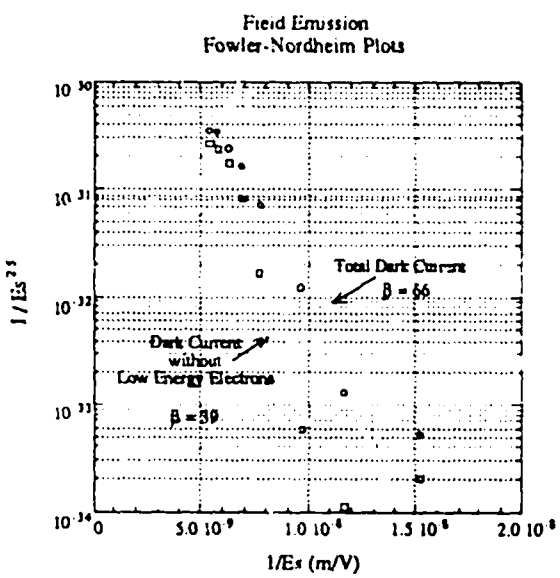

Figure 3 Fowler-Nordheim plots and the field enhancementfactor β.

Multiplication Factor η of the Dark Current

There has been an interest in the relations between the dark current and structure length. A permanent dipole magnet is set on the outside of the structure to trap the field emitted electrons from the upstream and to eliminate the downstream current at the magnet. For the dark current, the structure length can be decreased by moving the dipole magnet to the output coupler along the structure. The dark current except the low energy electrons generated in the output coupler is obtained from the energy spectrum. Figure 4 shows the logarithm of dark current against number of cells between dipole and output coupler. The figure 4 shows that the dark current Id will increase as η^N, where N is the number of cells in the structure. It is reasonable to consider that the field emitted electrons from the upstream cells are multiplied in a cell and the multiplication factor (η = 1.63/cell) is constant along the structure. It is predicted that the total dark current Id will be decreased, if the structures of low η can be realized.

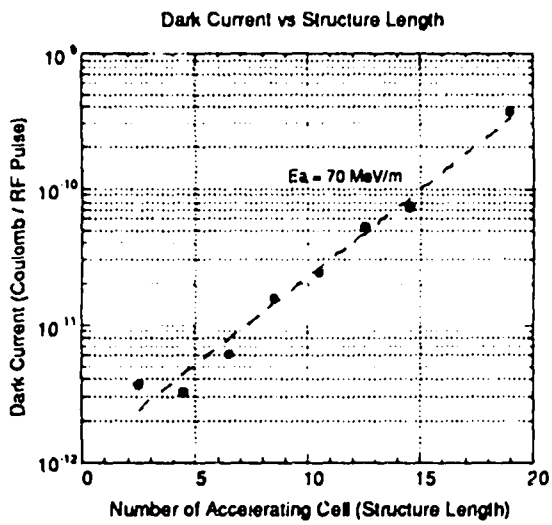

Figure 4. Dark current against the number of cells (structure length).

Acknowledgment

The authors wish to express their gratitude for the encouragement and financial support received from director general, H. Sugawara and directors Y. Kimura and S. Iwata. They also wish to express their thanks to Prof. K. Takata for the useful discussions. The experiment has been carried out by using the ATF Phase-I Linac constructed by the ATF sub-group of the JLC Study Group.

References

1. J. W. Wang and G. A. Loew, "Progress Report on New RF Breakdown Studies in an S-band Structure at SLAC," SLAC-PUB-4247, February 1987.

2. E. Tanabe, J. W. Wang and G. A Loew, "Voltage Breakdown at X-band and C-band Frequencies," Proc. 1986 Linear Accelerator Conference, Stanford, June 1986.

3. H. Mizuno, J. Odagiri, T. Higo, M. Akemoto and H Sakai, "X-band Klystron for Japan Linear Collider," Proceedings of this conference.

4. H. Matsumoto, M. Akemoto, H. Hayano, T. Higo, Y. Kimura, H. Mizuno, T. Shidara, K. Takata, S. Takeda, Y. Takeuchi, J. Urakawa, Y. Yamaoka and M. Yoshioka, "RF High Gradient Experiment of an S-band 0.6 m Disk-loaded Structure," Particle Accelerator 30, 231 (1990).

X-BAND ACCELERATING STRUCTURE FOR JAPAN LINEAR COLLIDER

T. Higo, M. Takao, M. Suetake, K. Kubo and K. Takata
KEK, National Laboratory for High Energy Physics
Oho 1-1, Tsukuba-shi, Ibaraki-ken 305, Japan

Abstract

The main linac for the Japan Linear Collider adopts X-band accelerating structures. This high frequency and therefore, a small accelerating structure for a long linac causes severe wake field problems against emittance preservation. To overcome the problems especially in multi-bunch operation, a damped structure with two slots in each disk is designed whose external Q value of the severest mode (TM110-π) is damped down below 25. The evaluation of the other higher modes are also described.

Introduction

The key issue of a high energy linear collider such as the Japan Linear Collider (JLC)[1,2] is to get a high energy beam with very low emittance using a reasonable amount of wall plug power. The JLC adopted 11.424GHz X-band accelerating structure operated at a gradient of 100MV/m for the main linac to get a 500GeV beam per a linac within several kilometers using a wall plug power of less than 200MW. This high operating frequency and the resulting small beam aperture were chosen to reduce a wall plug power. However, the wake field becomes very large for the structure with such a small beam aperture. Therefore, special cares should be taken to maintain the longitudinal and transverse emittance along the linac. To increase the luminosity without increasing total wall plug power much, 10 bunches are accelerated in an RF period in the JLC. Then, the longitudinal and transverse emittance of each bunch should be preserved by reducing the effect of the long-range wake fields.

In this paper, the basic parameters of the disk-loaded structure are first presented as the starting point to study an actual accelerating structure. Then the present paper describes a method to cure the multi-bunch wake field problems while details of the design consideration of a single bunch wake field are treated elsewhere.[3]

Basic parameters

Typical parameters[4] related to the accelerating structure of the main linac for JLC are listed in Table 1. If certain functional expressions[5] of the wake field are assumed, the energy spread of ±0.3% necessary for the BNS damping to reduce the single bunch transverse emittance growth can be obtained for the structure with a/λ =0.14 in the case of JLC.[3] The disk thickness of 2mm was chosen to locate the ratio of the surface field to the accelerating one near broad minimum.[4] The parameters related to the wall loss were assumed to be the same as those calculated.

Table 1 Parameters of JLC linac

Accelerating gradient	G	100 MeV/m
Particles in a bunch	N	$1.0 \cdot 10^{10}$
Bunches in a train	b	10
Bunch spacing	T_b	1.4 nsec
RF frequency	F_{rf}	11.424 GHz
2π/3 mode, Constant impedance, Travelling wave		
Beam aperture	a/λ	0.14
Disk thickness	t	2 mm
Total attenuation	τ	0.5
Shunt impedance	r	93 MΩ/m
Group velocity	v_g/c	0.02525
Elastance	s	1010V/pC/m
Structure length	Ls	0.697 m
Filling time	T_f	92 nsec
Power for a structure	Ps	121MW

All the structure-related parameters are those calculated by SUPERFISH.[6]

Evaluation of wake field

The dispersion curves of the structure with a/λ=0.14 were calculated using a frequency domain code URMEL[7] and shown in Fig. 1. The passbands in the following discussion are named following those in the figure. Because a component above the cutoff frequency of the beam pipe escapes out of the structure at a speed of its group velocity, the actual wake field should be evaluated taking this effect into account. The amounts of the wake fields were actually evaluated for a realistic multi-cell structure with a beam pipe radius the same as the beam hole radius of the accelerating cell using a time-domain code TBCI,[8] because it is difficult to evaluate them using URMEL for a long structure. Obtained wake fileds were fourier-transformed to discuss wake field problems by dealing with the wake field from the viewpoint of the higher modes of the structure. It was found that the wake field below cutoff frequency of the beam pipe is saturated as the number of the cells increases above 16. Fig. 2 shows the fourier transform of the wake fields for the 64-cell structure. The amplitudes of the typical higher modes thus obtained are presented in Table 2.

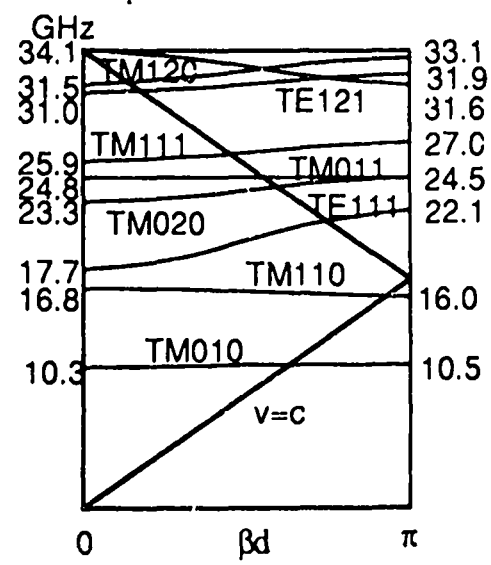

Fig. 1 Dispersion curves for disk-loaded structure for JLC.

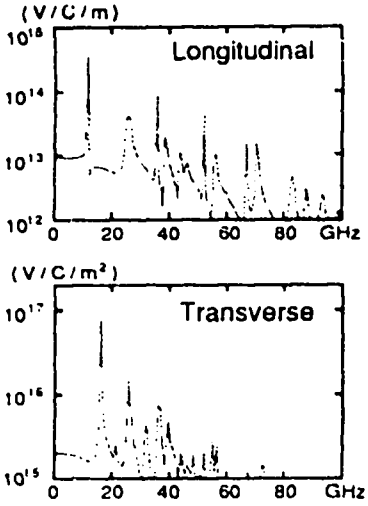

Fig. 2 Fourier transform of wake fields in structures for JLC.

Table 2 Wake field in the structure for JLC.

Mode	Frequency (GHz)	Long. Wake 10^{15}V/C/m	Qm	Q0	Qπ
TM010	11	0.5			
TM020&011	26	0.05			
TM021	36	0.09	270		
TM030	38	0.03			

Mode	Frequency (GHz)	Transv. wake 10^{17}V/C/m^2	Qm	Q0	Qπ
TM110	16	1.1	15	~0.2	20~25
TE111	21	0.03	70	16~30	~0.8
TM111	26	0.18	38		
TM120	32	0.06	72		
TM121	36	0.12	61		
TM130	39	0.05	96		

Qm: Maximum allowable Q values.

Q0,Qπ: Q values for the optimized structure.

Criteria on Q values

As shown in Fig. 2, the transverse wake field is mainly composed of the TM110 mode. By the arrival of the following bunch, the amplitude of the component decays by a factor $\mathrm{Exp}(-\omega_t T_b/2Q)$, where ω_t is the angular frequency of the mode. Therefore, if the Q value of the mode is less than 15, the emittance growth originated from the injection error is limited within a factor of $\sqrt{2}$ and also the cavity misalignment tolerance increases up to 80μm for the case of JLC.[3] Maximum allowable Q values estimated in the same criterion as above are listed for the other higher modes in Table 2. If the frequency of some mode is tuned somehow, the tolerance for the mode becomes loose. However, tuning of all the components of the wake fields is actually impossible. Therefore, the reduction of the Q values for the transverse higher modes down to the values listed in table 2 is necessary.

The energy spread among 10 bunches due to the beam loading induced in the accelerating mode can be reduced by an order of magnitude compared to a single bunch beam loading and also a single bunch energy spread, while sacrificing a net accelerating gradient by about 7%. Those due to the other longitudinal higher modes can also be reduced to the same level if the amplitude of the wake field at the next bunch driven by the preceeding bunch is an order of magnitude smaller than that of the fundamental accelerating one. Among the mode listed in Table 2, the Q value of only the TM021 mode should be reduced down to 270 to satisfy the condition.

Q values of damped structure

The severest higher mode in the JLC accelerating structure against transverse emittance preservation is the component of the wake field which locates in TM110 passband. The phase difference between the cells of the mode is very close to π. Therefore, the optimization of the geometry was performed to reduce the Q value of the TM110-π mode for the slotted disk-loaded structure, which is thought to be very effective to damp the mode.[9,10,11] The structure geometry and the parameters cited for the calculation are shown in Fig. 3. The cavity consists of two full cells with a slotted disk and two damping waveguides at the center of the cavity. The width of the waveguide wg is fixed to 11.1mm in both directions and the slot is ended at the interception of the waveguide and the accelerating cell. In an actual structure, these slots should be arranged at right angle from disk to disk as shown in Fig. 4 to make the slots effective to damp the transverse modes of both polarizations.

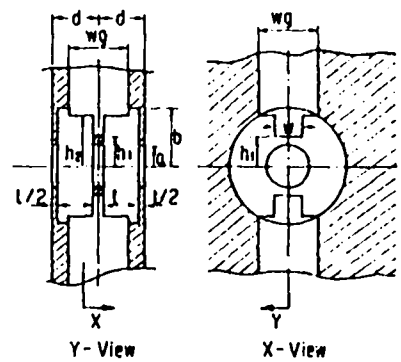

Fig. 3 Slotted structure geometry. Dimensions are as follows; a=3.6, b=10.6, t=2, d=8.75, wg=11.1 (units in mm).

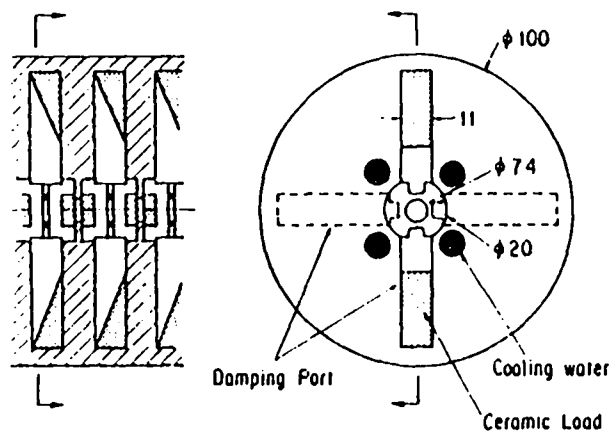

Fig. 4 Conceptual drawing of an actual damped structure.

The Q_{ex}'s were estimated using Slater's tuning curve method[12,13] where the resonant frequencies for various waveguide lengths were calculated by the code MAFIA.[14] As seen from the dispersion curves in Fig. 1, the nearest mode is TE111-0 mode, which appears in the boundary condition to

calculate the TM110-π mode. This mode is separated from the TM110-π mode more than the width of the Q value if the Q value is larger than 10. Therefore, the Q_{ex} of the TM110-π mode was estimated from the steepest point of the tuning curve assuming that the Q_{ex}'s of both modes are larger than 10.

As shown in Fig. 5, the dependence of the Q_{ex}'s on the slot geometry shows a broad minimum at the slot height h=5.5 and slot width w=5.0. In this optimum geometry, the Q_{ex} is as low as 14. Even if any further modification was introduced such as slotting the disk through the beam hole or extending a disk as a ridged waveguide into some point in the damping port with or without a taper structure, the Q_{ex} was found only to increase. If the width of the damping waveguide wg is reduced from 11.1mm to 10.3mm, the minimum Q_{ex} increases to about 18. Therefore, we can expect lower Q_{ex} for wider damping waveguide port. However, the cutoff frequency of the waveguide with wg=11.1mm is already 13.5GHz and the width of the port cannot be simply widened to make the accelerating mode well confined within the accelerating cell. Therefore, this geometry is thought an optimum one at present as far as this kind of slotted structure is concerned.

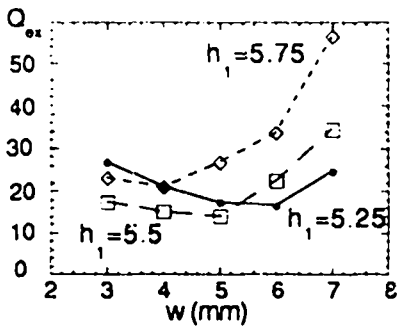

Fig. 5 Dependence of Q_{ex} of TM110-π mode on slot width w.

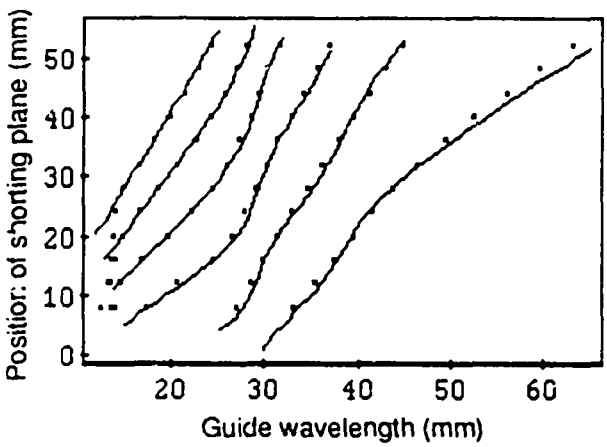

Fig. 6 Typical tuning curves. Solid curves are the results of fitting with two resonances.

For the optimized structure, the Q_{ex}'s of the higher modes were tried to evaluate. Because low Q resonances coexist in a small region of frequency, it was found important to apply the Slater's formulus

$$d = \frac{\lambda_g}{2\pi} \tan^{-1} \sum \frac{1/Q_{ex}}{(\omega/\omega a)-(\omega a/\omega)} + \frac{n}{2}\lambda g$$

directly and to fit many branches of the tuning curves at once, where ω_a is a resonant frequency, d a distance from the reference plane to the shorting one, λ_g the guide wavelength and n a number of the nodes in the wave guide. Fig. 6. shows the tuning curves for the case including TM110-π mode. Solid curves are the results of the fitting with the parameters of Q_{ex}'s and ω_a's of two resonances, TE110-0 and TM110-π, and the position of a reference plane common to all branches. The disagreement at high frequency side is because of the neglect of the TM111-0 mode in the fitting. The Q_{ex}'s thus obtained are listed in Table 2.

Discussion

The Q_{ex} of less than 25 for the TM110-π mode in an optimum structure is rather high for the JLC. Therefore, other structures such as those with four slots in a disk or those of crossed guide structure[15] should probably be examined. However, it is also important to study how to analyze the tuning curves to obtain the Q_{ex} reliably enough to discuss the optimization of the geometry for the case of low Q modes with frequencies close with each other. The evaluation of the Q_{ex} of such modes as TM111, TM011 or TM020 is also needed and can be performed by a better fitting and more accurate tuning curves up to higher frequency.

The passband width of the accelerating mode for the optimized structure was found 1.2% from the calculation by MAFIA. This value was smaller than that of 2.7% for the structure without damping slots and ports. This reduction is due to a magmetic coupling through the slots. The Q values of 0 and π mode in the fundamental accelerating passband were also calculated to be 0.91 and 0.76 of those without the slots and ports. This reduction of v_g and Q value considerably changes the parameters of the simple disk-loaded structure in Table 1 to the worse directions. Optimization of the geometry on the parameters of the accelerating mode should also be performed.

References

[1] S. Takeda et al., Particle Accelerators, 30(1990)1101.
[2] K. Takata, Proc. First Workshop on Japan Linear Collider (JLC), KEK, Oct. 24-25,1989, 2.
[3] K. Yokoya, Proc. First Workshop on Japan Linear Collider (JLC), KEK, Oct. 24-25,1989, p26.
[4] T. Higo, Proc. First Workshop on Japan Linear Collider (JLC) KEK, Oct. 24-25,1989, p91.
[5] R. B. Palmer, SLAC-PUB-4295 (1987).
[6] K. Halbach and R. F. Holsinger, Particle Accelerator, 7 (1976) 213.
[7] T. Weiland, NIM 216(1983)329.
[8] T. Weiland, DESY 82-015(1982) and NIM 212(1983)13.
[9] R. B. Palmer, SLAC-PUB-4542 (1989).
[10] T. Higo et al., Particle Accelerators, 30(1990)1119.
[11] M. Suetake et al., Proc. of the 7th Symp. on Accel. Scince and Technology, Osaka, Japan(1989), KEK-Preprint 89-164.
[12] J. C. Slater, "Microwave Electronics", Van Nostrand, 1950.
[13] T. Kageyama, KEK-Report 89-4.
[14] K. Klatt et al., Proc. of the 1986 Linear Accelerator Conf., SLAC-Report-303,1986, p276-278.
[15] H. Deruyter et al., SLAC-PUB-5263(1990)

A HIGH-POWER MODEL OF THE ACS CAVITY

T. Kageyama, Y. Morozumi, Y. Yamazaki, and K. Yoshino
KEK, National Laboratory for High Energy Physics, Oho 1-1, Tsukuba-shi, Ibaraki-ken 305, Japan

Abstract

During the last two years, we have developed the four-slot Annular Coupled Structure (ACS) for the high-β coupled-cell linac used for the 1-GeV proton linac of the Japanese Hadron Project (JHP). In order to study the performance in high-power operation, a 1296-MHz high-power model of the four-slot ACS cavity has been designed and constructed. The cavity has been successfully conditioned up to the designed value. This report presents the cavity design, thermal analysis for optimizing the cooling-water circuits, the RF properties, and the results of the high-power test.

Introduction

The standing-wave π/2-mode operation of a chain of coupled cavities has advantages over the π-mode operation; 1) a high degree of cell-to-cell uniformity in the accelerating field against cell-to-cell frequency errors, 2) a high degree of stability in the accelerating field between cells against turbulence by heavy beam loading.

For a π/2-mode coupled-cell structure, accelerating cells are located alternately with non-excited coupling cells. A disk-load structure operated in the π/2 mode[1] is a simple example; it is referr to as On-axis Coupled Structure (OCS). However, for the OCS, t shunt impedance is reduced owing to the coupling cells located on t beam axis. The side-coupled structure[2] was invented in order to avc this loss by placing the coupling cell at the side of the accelerating cc that is, off from the beam axis. Another possibility is the Annu Coupled Structure (ACS), which has an annular coupling cell arou the accelerating cell instead of a pillbox-type cell.

Although several studies[3,4,5] using cold models have been mac no ACS cavities have been developed up to the level for practical us Difficulties in developing ACS cavities arise from RF properties the annular coupling cell; the annular cell has the higher order mod of TM_{110} and TM_{210} in the neighborhood above the coupling mode TM_{010}.

The previous studies[4,5] on the ACS (with two coupling slo between the accelerating and annular coupling cells) can be summarized as follows. 1) When the slots face each other with respect to the central symmetrical plane of the annular cell (cell-to-cell slot orientation = 0°), the TM_{110} mode intrudes into the accelerating passband as the coupling factor increases. 2) When the cell-to-cell slot orientation is 90°, the accelerating mode excites a TM_{210}-like mode in the annular cell, resulting in the reduction in the shunt impedance.

Development of Multi-slot ACS

We have studied on the two-slo ACS by using the computer code MAFIA[6], and obtained the following results[7]. 1) The difficulties regarding the two-slot ACS arises from the breakdown in the axial symmetry by opening two slots. Compared with the mode spacings among the TM_{010}, TM_{110}, and TM_{210} modes, the degree of breakdown is not small, resulting in perturbative effects such as mode mixing. 2) The difficulties can be cured by increasing the number of slots (multi-slot configuration) and reducing the size of each slot, that is, by recovering the axial symmetry.

In order to study the possibility of the multi-slot ACS, we have made 4-slot and 8-slot cold models and measured their RF properties. From the measurements, we have obtained the following results[7]: 1) the difficulties regarding 2-slot ACS are cured by 4-slot configurations with cell-to-cell orientation = 0° and 45°; 2) no improvements were observed by increasing the number of slots from 4 to 8. As the number of coupling slots increases, the structural strength of the cavity becomes inferior. Therefore, the 4-slot ACS is probably one of the most practical choices.

According to the measurement of a 4-slot ACS model cavity with a coupling factor of 0.05, the effective shunt impedance has been reduced by 20% owing to the effect of coupling slots and by 5% owing to the surface imperfection. Since the 4-slot ACS is more advantageous than the SCS regarding its axial symmetry, we start the design and construction of a high-power model of the 4-slot ACS (cell-to-cell orientation = 45°) in the summer of 1989.

High-Power Model

Overall Design

As shown in Fig. 1 and 2, the high-power model comprises a pair of ACS cavities coupled via a bridge coupler. It is designed as a prototype for the coupled-cell accelerating structure at β=0.78 of the

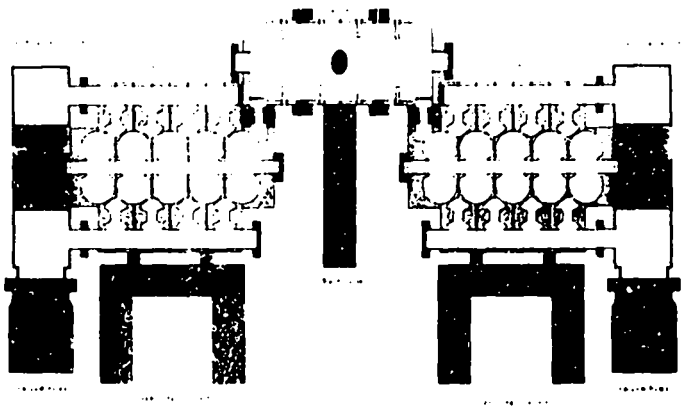

Fig. 1. A schematic drawing of the high-power model.

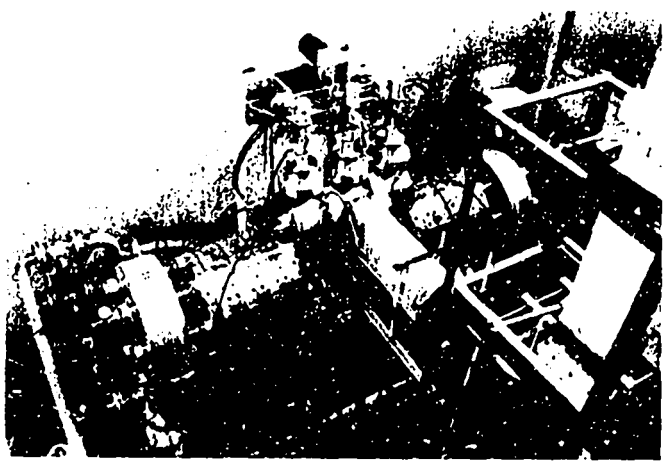

Fig. 2. The high-power model with waveguide in the test bench.

JHP 1-GeV proton linac. Design parameters for the high-power model are listed in Table 1. The shunt impedance and Q values in Table 1 are those calculated by SUPERFISH[8], which does not include the effect of coupling slots. For each ACS cavity-unit, five accelerating cells are arranged alternately with four annular coupling cells. For the bridge coupler, it was designed to be a 5-cell disk-loaded structure in order to avoid the mode-mixing between the TM_{01} and TE_{11} modes in a long cylindrical cavity. The ACS cavity and the bridge coupler is electromagnetically coupled via a side-coupled pillbox cavity. The RF power is fed through the iris at the central cell of the bridge coupler. Details on the disk-loaded bridge coupler are described in Ref. 9.

In order to generate the designed accelerating gradient of 4.5 MV/m, a peak RF power of 27 kW is required, considering the reduction of 20~25% in the shunt impedance compared with the theoretical value. Including the wall loss in the bridge coupler, the high-power model requires a peak RF power of 300 kW in total.

TABLE 1
Design Parameters for the ACS High-Power Model (β=0.78)

frequency	1296	MHz
accelerating gradient	4.5	MV/m
shunt impedance	54	MΩ/m
transit time factor	0.80	
Q value of accelerating cell	2.4×10^4	
Q value of coupling cell	9.6×10^3	
peak RF power per cell *	27	kW

* using the effective shunt impedance (80% of the theoretical value)

Structure of the ACS Cavity

The ACS cavity is a brazed assembly of eight middle segments and two end segments (Fig. 1). All the segments were machined from oxygen-free copper (OFC) by a super-precision lathe, and assembled by vacuum-furnace brazing. Further particulars on the fabrication techniques are found in Ref. 10.

Figure 3 shows the middle segment. The shape of the accelerating cell was optimized for the shunt impedance by using the computer code SUPERFISH[8]. The annular coupling cell is like a resonant ring of ridged-waveguide. The cross-sectional shape of ridged-waveguide was adjusted in order to make the diameter of the annular cell as small as possible. Four coupling slots are bored through the septum between the accelerating and annular coupling cells. According to the thermal analysis described later, a minimum septum thickness of 10 mm is required in order to drill cooling-water channels in it. Therefore, we refined the design of the coupling slot bored through the 10-mm-thick septum. In order to make both the magnetic coupling efficient and the arc-length of the slot as small as possible, both radial sides of the slot were taper-edged. The slot size was determined to be 32.5° in arc length and 26 mm in radial length by measurement of half-scale models.

The middle-segment have eight circular holes around the annular cell (Fig. 3). When all the segments are stacked and brazed, these holes form pumping-out ports running through the ACS cavity in the longitudinal direction. An annular vacuum manifold is attached to the end of each ACS cavity (Fig. 1 and 2).

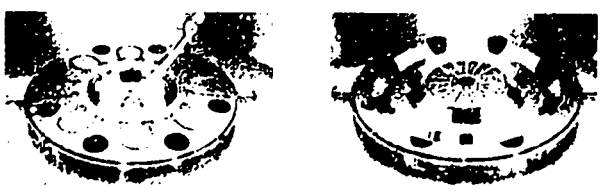

Fig. 3. Middle segment of the high-power model of the ACS cavity. The accelerating-cell side is shown in the left and the annular coupling-cell side in the right.

Thermal Analysis

The time-averaged power dissipation amounts to about 1 kW per accelerating cell as can been seen in Table 1. In order to make the thermal detuning as small as possible under high-duty operation, we have optimized the arrangement of cooling-water circuits by carrying out both thermal and structural finite element analyses for two-dimensional and three-dimensional structures by the computer code of Integrated Structure Analysis System (ISAS2)[11]. The thermal analysis indicates that the temperature rise at the nose cone amounts to 35°C with circumferential cooling circuits only, giving rise to a too large frequency detuning of about -510 kHz. This is due to the poor thermal conductivity at the septum between the accelerating and annular coupling cells, where four coupling slots are bored. Therefore, the nose cone region must be cooled directly by water flowing in the disk. Figure 4 shows the final design of cooling circuits, which requires channels drilled in the septum for water inlets and outlets. The temperature rise at the nose cone was drastically reduced to 3.1°C with 5 l/min of cooling water per disk, resulting in a detuning of -110 kHz.

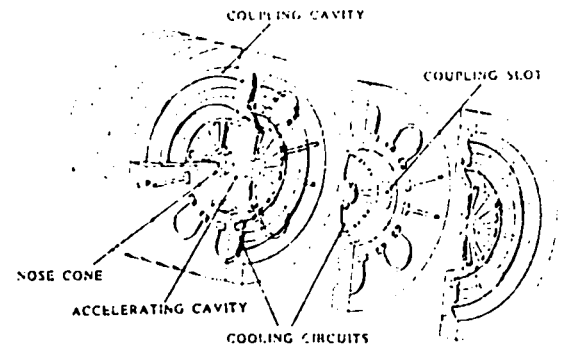

Fig. 4. Cooling-Water Circuits for the high-power model.

RF Properties

Prior to brazing, individual cells were tuned to the design frequency within ±100 kHz by fine machining. For the accelerating cell, either the nose cone or the inner surface along the line of latitude was machined. For the annular coupling cell, the height of the ridge was adjusted by fine machining. After brazing, if necessary, individual cells can be tuned by dimpling the thin-wall parts from outside.

Since the segments made of OFC are soft and easily deformed, we can not press stacked cavity-segments until its Q value is saturated, without causing considerable deformation. Therefore, the reduction in the Q value due to the surface imperfection was estimated from the result of a half-scale single-cell cavity (f = 2600 MHz), the inner surface of which was machined under the same condition as the high-

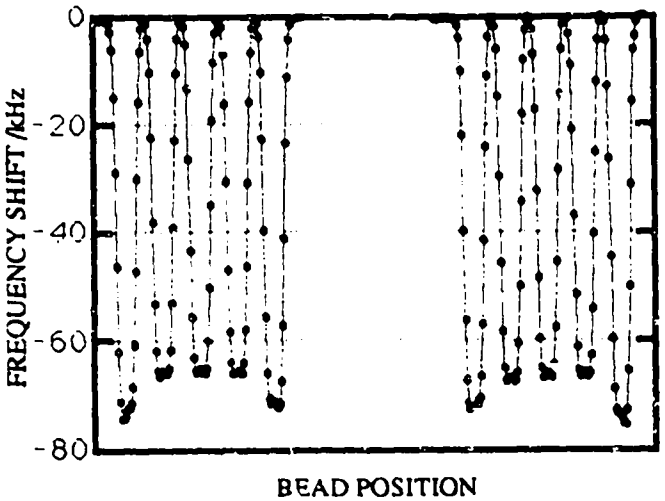

Fig. 5. A distribution of the accelerating field on the beam axis obtained by bead-perturbation measurement.

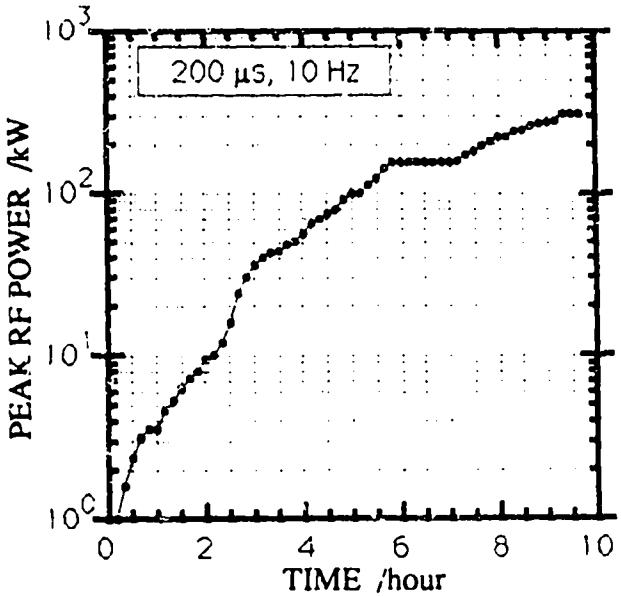

Fig. 6. The history of the first conditioning at a duty factor of 0.2% (200 μs, 10 Hz).

power model. The measured Q value was small by 4% compared with the theoretical value. Considering the skin-depth dependence on the RF frequency, the reduction for the high-power model (f = 1296 MHz) should be less than 4%.

The coupling factor was measured for all the middle-segment pairs stacked with cell-to-cell orientation = 45°. The result of k = 0.0551 ± 0.0002 indicates that the high accuracy was kept with a numerically controlled cutter during machining all the coupling slots.

After the construction at the MHI Mihara Works[10] completed, several low-level measurements were carried out at the high-power test bench in KEK. With a waveguide duct and an RF window, the loaded Q value and the coupling β of the high-power model were measured [illegible] 9.8x10³ and 0.98, respectively, indicating that the unloaded [illegible] was 1.9x10⁴. The stored energy in the bridge coupler is 7.1% of the total[7], and its theoretical Q value is 2.5x10⁴. Therefore, within an error of 1%, the Q value of the ACS cavity itself should be 1.9x10⁴, which is small by 21% compared with the theoretical value. Supposing a reduction of 4% arises from the surface imperfection, the rest of 17% should be due to the effect of the coupling slots.

The accelerating-field distribution on the beam axis was measured by using the bead-perturbation technique. It can been seen from Fig. 5 that the obtained field distribution was sufficiently uniform. Thus, we decided to make no tuning of individual cells by dimpling the thin-wall parts. Since the gap length of the middle-cell was enlarged by 5% compared with that of the end-cell in order to compensate a frequency decrease by the coupling slots, the electric field in the end-cell is larger than that in the middle cell by 4~5%.

From the field distribution data for a middle-cell, the R/Q value was calculated to be 201 Ω/cell. This value is in good agreement with the theoretical value of 205 Ω/cell by SUPERFISH[8]. Using the Q and R/Q values obtained from the measurements, the effective shunt impedance was estimated to be 42 MΩ/m. The reduction in the shunt impedance is 22% compared with the theoretical value, reflecting only the reduction in the Q value.

High-Power Test

The first RF conditioning was carried out at a low duty factor of 0.2%, where RF pulses were 200-μs duration at 10 Hz. The cavity was evacuated by two 300-l/s turbo-molecular pumps attached to the vacuum manifolds at both ends. The base pressure was 1.5x10⁻⁷ Torr when the RF off. Keeping the vacuum level below 2x10⁻⁶ Torr, the conditioning was progressed continuously. Through a pumping-out port, the annular coupling cells were monitored by a TV camera. During conditioning, no light emissions due to electric discharge or arcing were observed. Figure 6 shows the history of the first conditioning. The plateau of the history curve at 170 kW is probably the conditioning of the RF window. In proceeding on the plateau, blue light emissions were often observed around the RF window through a TV camera. The cavity was conditioned up to the design RF power level of 300 kW in 10 hours. After the conditioning, the base pressure was improved down to 1.2x10⁻⁷ Torr.

Conclusions

The high-power model of the 4-slot ACS cavity has been developed. The effective shunt impedance was 78% of the theoretical value. Without tuning of individual cells after brazing, a sufficiently uniform accelerating-field distribution has been obtained. The model has been successfully conditioned up to the design RF power level of 300 kW.

The RF conditioning will be carried out at the full duty factor of 3% in the near future, where the RF pulses are 600-μs duration at 50 Hz. The design of a ACS cavity for a low β of 0.5 is also in progress.

References

1. T. Nishikawa, S. Giordano, and D. Carter, Rev. Sci. Instr. 37, 652 (1966).
2. E.A. Knapp, B.C. Knapp, and J.M. Potter, Rev. Sci. Instr. 39, 979 (1968)
3. V.G. Andreev et al., Proc. Proton Linac Conf., 114 (1972)
4. R.K. Cooper et al., Preprint LA-UR-83-95 (Los Alamos National Laboratory) (1983)
5. R.A. Hoffswell and R.M. Laszewski, IEEE Trans. on Nucl. Sci. 30, 3588 (1983)
6. T. Weiland, Part. Accel. 17, 227 (1985)
7. T. Kageyama et al., Part. Accel. 32, 33 (1990)
8. K. Halbach and R.F. Holsinger, Part. Accel. 7, 213 (1976)
9. Y. Morozumi et al., "Multi-Cavity Bridge Coupler," this conference
10. K. Yamasu et al., "Fabrication Technique of ACS Cavity," this conference
11. ISAS2 is a software by Hitachi, Ltd.

MULTI-CAVITY BRIDGE COUPLER

Y. Morozumi, T. Kageyama and Y. Yamazaki
National Laboratory for High Energy Physics, Tsukuba 305, Japan

Abstract

A multi-cavity bridge coupler was designed for power feed to coupled-cavity accelerating tanks of the Japanese Hadron Project linac. A high power model of the coupler, together with a pair of accelerating tanks, was fabricated and was successfully conditioned up to a rated power of 300 kW.

Bridging of Accelerating Structures

The final accelerating section of the Japanese Hadron Project (JHP) linac[1] is planned to consist of newly developed 1296 MHz annular coupled structure (ACS) cavity tanks[2] with focusing magnets in between. A bridge coupler is a useful device for power feed and transfer among such a train of accelerating tanks. It is composed of a pair of coupling cavities side-coupled to two adjacent accelerating tanks and a bridging cavity also side-coupled to the coupling cavities, looking as if it were a bridge over the magnets. Power is fed through a vacuum-tight WR-650 waveguide window into a bridge coupler and transferred to a train of accelerating tanks coupled with bridge couplers. The bridging method not only saves microwave circuit parts but also promises automatic phase matching and conserves the symmetry of the accelerating fields. A power source and a group of accelerating tanks are connected by a single branchless waveguide system. The couplers and the accelerating structures make a $\pi/2$-mode coupled-resonator chain and keep a consecutive phase relation. The accelerating cavity is free from field deformation due to a large input coupling geometry which is in charge of the bridge coupler.

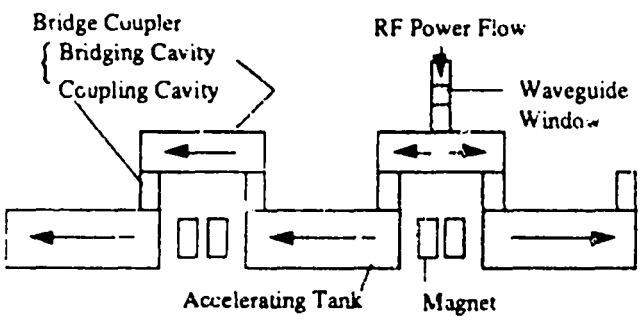

Fig. 1 Bridged accelerating tank chain

Design

The original example of the bridge coupler is found in the LAMPF coupled-cavity linac, where a long cylindrical single cavity was used as the bridging cavity and operated in the TM_{010} mode. Firstly the feasibility of a higher-order mode, for example the TM_{012} mode, operation for higher stability was investigated on this simplest structure. A simulation of the bridge coupler by the code MAFIA was attempted but led to the conclusion that a stable and controllable operation of this conventional bridging cavity cannot be expected in any mode because of a modal mixing with the neighboring modes[3]. The eigenmodes in such a long cavity are degenerately close in frequency (Fig.2) and the presence of the coupling to another cavity (like the coupling cavity) easily induces modal coupling resulting in complicated field patterns of mixed modes (Fig 3). The modal mixing is suppressed by bored disks partioning the bridging cavity into cells. A similar structure was already applied[4] for another purpose in order to ensure a stable operation by the $TM010$ $\pi/2$ mode with a large inter-cell coupling.

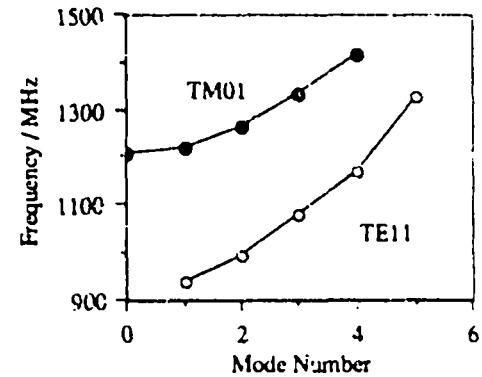

Fig. 2 Modes in a long cylindrical cavity with the diameter 19 cm and the axial length 80 cm.

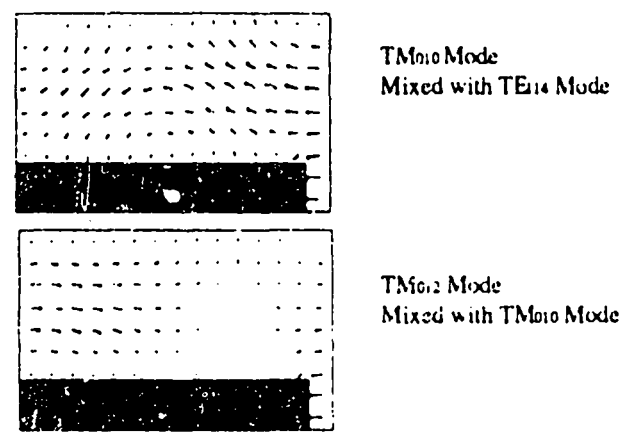

Fig. 3 Electric fields simulated with a half geometry of a single cavity bridge coupler under the electric short condition on the center symmetric plane. The actual system shows a more confusing pattern because of additional mixing with even modes such as TM_{011}, TM_{013}, TE_{115} which appear under the open condition.

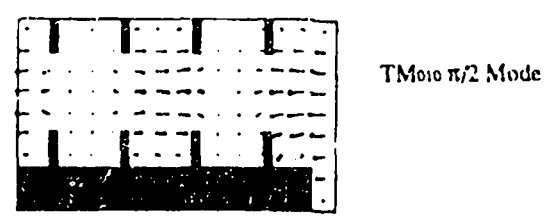

Fig. 4 Electric fields in a multi-cavity bridge coupler free from modal mixing. The bridging cavity is divided into short subcavities (cells).

The bridge coupler for the JHP was designed in this multi-cavity structure on the following principles.

1) The operation mode is separated far from the other modes in frequency, being free from mixing with any other mode.
2) The inter-cell coupling is strong enough to gain a large group velocity for stabilization.
3) The power loss in the bridge coupler is possibly small.
4) The frequency shift arising from dimensional error in design and fabrication and also from thermal deformation during operation is compensated by a tuning system.

The cavity radius is roughly determined (~ 9.3 cm) from the driving frequency although modified by the disk loading condition. A short disk spacing less than the radius gives a sufficient mode separation better than a frequency ratio of 1.5 (Fig. 5). The disk spacing was chosen to be 8 cm. A large disk bore makes a large inter-cell coupling but too large a bore allows a modal mixing again. The upper limit of the bore radius is about 55 % of the cavity radius, that is 5 cm, and the corresponding coupling coefficient amounts to 12 % (Fig. 6). The power loss in the bridging cavity is reduced with its large coupling coefficient to the coupling cavity compared with that of the accelerating

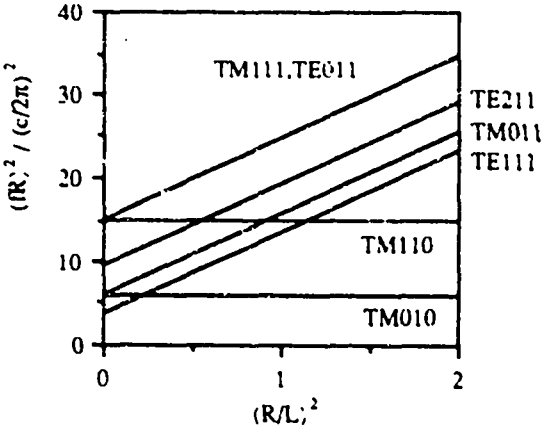

Fig. 5 Dependence of mode separation on cavity shape. Eigenmodes in a cylindrical cavity with the radius R and the length L are presented.

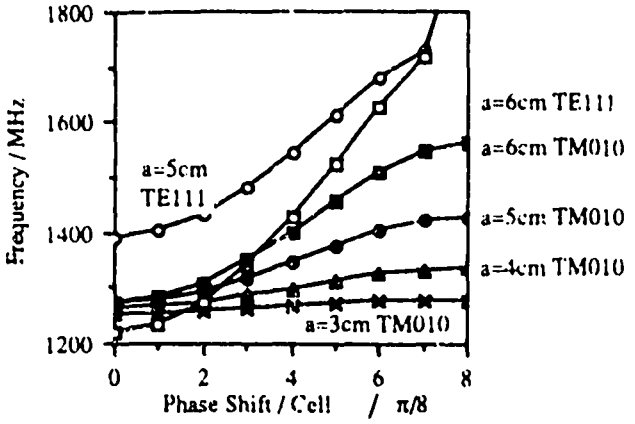

Fig. 6 Dependence of dispersion on disk bore radius a of an 8-cell cylindrical cavity with the radius 9.25 cm, the length 80 cm, and the disk thickness 1 cm.

cavity. Assuming the equivalence of a bridging cavity cell and an accelerating cavity the ratio of their stored energy is the inverse square ratio of their coupling coefficients to the coupling cavity. The ratio of coupling coefficients was set 2 : 1 and thus the ratio of power 1 : 4. Since the number of excited cavities is 3 for the bridge coupler and 10 for the ACS tanks, input power is shared between them in the ratio 3 : 43. For the present purpose of an off-beam experiment the waveguide should be in the critical coupling with the bridge coupler and ACS tank system, namely, the coupling factor is unity. The coupling factor to the bridge coupler alone should be 43/3 on the above assumption. The required iris radius was calculated at 6.5 cm on the basis of the preparatory experiment. The largest available tuning plungers 5 cm in diameter were prepared in order to acquire the widest possible tunable range. The tuner covers a frequency range of at least 20 MHz for the bridging cavity alone and 1.4 MHz for the total system. The coupling cavities were also equipped with tuners for adjustment.

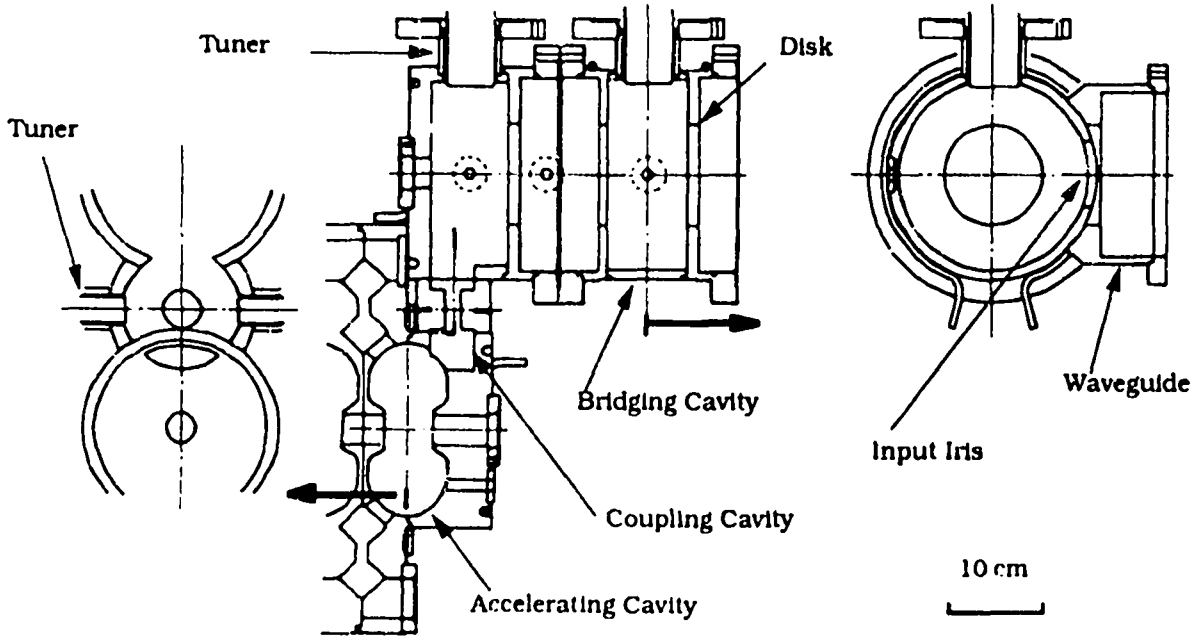

Fig.7 RF Structure of bridge coupler with 5-cell structure bridging cavity.

The designed values characterizing the RF structure are as follows.

Component Cavity Frequency	1296 MHz ± 5 MHz
Intra-Bridging Cavity Coupling Coefficient	12 %
Bridging-Coupling Cavity Coupling Coefficient	11 %
Coupling-Accelerating Cavity Coupling Coefficient	5.5 %
Input Coupling Factor	1.0 ± 0.1

The slightly loose allowance covers the difficulty in defining the frequencies of the mutually side-coupled cavities. Such a strongly coupled non-periodic asymmetric cavity structure lacks well-defined electromagnetic boundaries, which gives rise to the ambiguity in frequency. On the other hand the large coupling also allows a considerable tolerance. The cavity dimensions were determined from the computation with the codes SUPERFISH and MAFIA. The essential part of RF structure of the test 5-cell coupler is presented in Fig. 7.

The bridge coupler was divided into 3 sections by center planes of the 2 unexcited cells. Both end sections are joined to ACS tanks. They were connected with double-bite vacuum-sealing and RF-contacting flanges. The heat generation in the bridge coupler is quite small, which is less than that in an accelerating cavity of the ACS tank. It is enough to cool the periphery of each disk by a single turn of cooling tube. The parts were cut out of specially processed high-grade oxygen-free copper and precisely finished. They were brazed in a vacuum furnace with gold and silver filling alloys. Details are described elsewhere[5]. Photo shows the assembled whole system of bridge coupler and accelerating tanks.

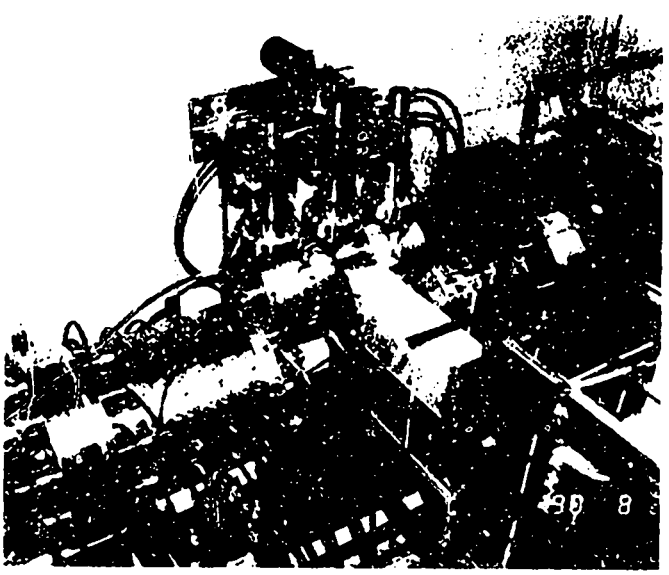

PHOTO Assembled bridge coupler and accelerating tank system

Measurement and Tuning

During and after fabrication the frequency of each component cavity was measured to tune to its design values. The detuning plunger method was applied to the frequency measurement. The frequency of the component cavity was measured detuning the neighboring cavities by conductive plungers with some correction based on computer simulation. The acquired frequencies agreed within the allowance and the coupling coefficients differed by no more than a few percent. The tuner effect on frequency shift was reduced to 7.1% when the ACS tanks were coupled. Accordingly the bridge coupler and ACS tanks share power in the ratio 7 : 93 almost equal to the ratio 3 : 43 estimated previously, which justifies the assumption that a cell of the bridging cavity is almost equivalent to an accelerating cavity. The dispersion relation of the bridging cavity is shown in Fig. 8. The theoretical dispersion equation was fitted to the data, yielding a coupling coefficient of 11.8 % in agreement with the designed and the separately measured values. The coupling factor of wave guide to the whole cavity system was measured to be 0.99 and the quality factor of the system was 9.9×10^3 when the system was tuned to the driving frequency by the tuners under the operation condition. The unloaded quality factor is, therefore, 2.0×10^4, which is consistent with the quality factor 1.5×10^3 of the bridge coupler itself loaded with the waveguide accounting the above power sharing ratio.

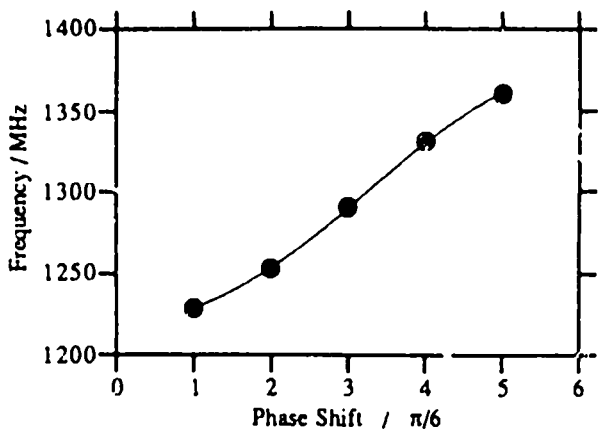

Fig. 8 Dispersion of the 5-cell bridging cavity with a fitted curve.

Power Test

The bridge coupler and ACS tank system was mounted in a test bench surrounded by a radiation-shield. It was equipped with evacuation pumps and a cooling system, and was linked to the waveguide from a klystron. Turbomolecular pumps evacuated the cavity system to an ultimate pressure of 1×10^{-7} Torr. The temperature was set 25.4 °C and controlled within ± 0.1 °C by a refrigerator-aided water circulation cooling system. The cavity system was driven by pulsed 1296 MHz RF power with a 200 μs width and a 10 Hz repetition and was conditioned up to 300 kW in about 10 hours. Frequent breakdown took place at 10 kW and 170 kW. Both cases were accompanied with rapid rise in pressure. They are assumed to be due to local discharge. Particularly in the latter case lightning was observed in the waveguide between the RF window and the input iris from the viewing window. There was nothing wrong elsewhere. The result is encouraging.

References

1 Y. Yamazaki and M. Kihara, in these proceedings.
2 T. Kageyama et al., in these proceedings.
3 Y. Morozumi et al., Proc. 14th Linear Accelerator Meeting in Japan, 202 (1989).
4 L. Young, private communication.
5 T. Iwata et al., in these proceedings.

DESIGN FEATURES OF THE INPUT COUPLER FOR THE DTL

F. Naito, T. Kato, Y. Morozumi, E. Takasaki, Y. Takeuchi and Y. Yamazaki
National laboratory for High Energy Physics, KEK
1-1 Oho, Tsukuba-shi, Ibaraki-ken, 305 Japan

Abstract

An rf input coupler for a drift-tube linac was designed and studied with the computer codes and the low-power models. It comprises four parts; a door-knob transition, an rf window of the ceramic disk, a short transformer of the coaxial waveguide and an rf loop coupler. The reliability of the design aided with computer codes was confirmed with the model test.

Introduction

A 432-MHz drift-tube linac (DTL) that accelerates the H^- ions to 150 MeV will be constructed as a part of 1-GeV injector linac for a ring accelerator of the Japanese Hadron Project (JHP)[1]. The tank of the DTL is driven with an rf power of 0.92 MW and a duty factor of 3% (600-msec pulse length and 50 Hz repetition rate). As a high-power 5.4-MeV DTL for a low energy beam test is under construction, an input coupler for the DTL is prepared for the high-power and beam tests.

An rf input coupler is one of the most important parts of a linac for the stable operation. Since a number of troubles during the operation of a linac have been related to an input coupler, the reliability of a linac system is largely dependent on that of an input coupler.

The output coupler of the 508-MHz klystron that feeds an rf power into the cavity of the TRISTAN works with high stability under the operation of 1.2 MW and 100% duty factor[2], being 1.3 times and 33 times as large as those of the DTL, respectively. Its design should be useful for an input coupler of the 432-MHz DTL.

Figure 1 shows the cross section of the output coupler of the 508-MHz klystron[2]. It is composed of three transition sections.

(1) The first section is the transformer between the coaxial wave guide of the WX77D and that of the WX152D. This junction also works as a shield of the rf window and a supporting disk from an irradiation caused with the beam in the cavity.

(2) The second section is a coaxial wave guide of WX152D with a ceramic-disk window. Inside- and outside-diameters of the rf window are 166 and 38 mm, respectively; the thickness is 10 mm. A relative dielectric constant of the ceramic disk is about 9. The impedance is matched with the choke structure.

(3) The third section is the door-knob transition between the coaxial wave guides of the WX152D and the rectangular wave guide of the WR1500.

Since the operational frequency 432 MHz for the DTL is different from the TRISTAN, the dimensions of each transformer must be readjusted in order to match the impedance at 432 MHz. When it is not easy to make a reliable equivalent circuit for a transformer, the transition section is designed with a number of "cut and try" in the models. In this paper, the computer codes, SUPERFISH[3] and MAFIA[4], are applied to the design of the transition section owing to the following advantages.

(1) The application saves the number of the "cut and try."

(2) Since the field distribution is illustrated, it is possible to improve the design in order to avoid a local strong electric field that gives rise to the break down.

The design principle for the application of the computer codes is summarized in the next section. The details of the design for each transition section are described thereafter.

The design principle of the transformer section on the basis of the computer codes

With the computer codes, SUPERFISH and MAFIA, we can obtain the standing-wave solution of a cavity under a given boundary condition. Since the traveling wave can be described in terms of a linear combination of two independent standing waves, these computer codes can also be applied to the traveling wave problems, as follows.[3,6]

1) Introduce the boundary planes S_1 and S_2 in the port-1 and port-2, respectively, as shown in Fig. 2. Calculate the resonant frequencies of the transformer bounded with S_1 and S_2 under two independent cases C_1 and C_2 of the boundary conditions; denote the resonant frequencies of the cases C_1 and C_2 by f_1 and f_2, respectively. For example, the case C_1 may imply short boundary conditions for both the S_1 and S_2, while the case C_2 may imply open conditions for both. It is noted that other cases can be chosen as far as the two cases are independent of each other.

2) Adjust one of the positions of the S_1 and S_2, for example S_1, until f_1 becomes equal to the operational frequency f_0 and denotes the adjusted position by P_{11}. Also, readjust the position of the S_1, until $f_2=f_0$ is obtained and denote it by P_{12}.

3) If the transformer is matched, the position P_{11} is the same as P_{12}.

4) In the mismatched case, the reflection coefficient can be estimated for the difference between P_{11} and P_{12}.

The procedure described above is applied to the design of a transformer. The input geometry of the transformer is optimized so that it meets the requirement of situation 3). The procedure will be particularly useful in the case that no reliable equivalent circuit exists. The code SUPERFISH is applied to the axially symmetric case and the code MAFIA for the asymmetric case.

The transformer between the coaxial wave guides

A short transformer is sufficient to match the two coaxial lines that have the same impedance but different diameters[7]. Since it is difficult to calculate the matched condition of the transformer with an equivalent circuit, the above-mentioned procedure with the code SUPERFISH was applied to the design of the transformer between the coaxial waveguide of WX77D and that of WX152D. Figure 3 shows the configuration of the transformer. The total length of the transformer is held fixed to 44.7 mm during calculation. A variable parameter is the length L_1 of the taper section of an inside cylinder shown in Fig. 3. Figure 4 shows the electric field patterns calculated with SUPERFISH for two boundary conditions. In Fig. 4-a both planes of S_1 and S_2 have the open boundary condition, while the short boundary condition in Fig. 4-b. The former corresponds to the condition of the C_1 and the latter corresponds to that of the C_2. The position of S_1 and S_2 are optimized in order to adjust a resonant frequency to the f_0.

The condition $f_1=f_2=f_0$(=432 MHz) was obtained with the L_1 of 30.7 mm. Figure 5 shows the dependences of the resonant frequencies' f_1 and f_2 on the parameter L_1. The measured VSWR of the model transformer designed on the basis of this calculation was less than 1.05 at 432 MHz, supporting the reliability of the design method.

The rf window of the ceramic disk

An rf window of the ceramic disk is installed in the coaxial waveguide in order to hold the vacuum in the DTL. At first, we have studied the rf window with the same size as that of 508 MHz klystron. The electric field pattern of the rf window with the choke structure was calculated with SUPERFISH and is shown in Fig. 6. Since it has a mirror symmetry on the center of the rf window, half of the structure was used for the calculation, holding virtual boundary plane S1 fixed in the middle of the rf window. The boundary condition of the plane S1 is open, while that of S_2 short, for the case of C_1 as seen in Fig. 6-a. The C_2 has the opposite boundary condition to the C_1 as shown in Fig. 6-b.

Variable parameters are the thickness t_c of the inside choke and the depth l_c of the inside and the outside chokes. There are two solutions. One is given with t_c=6 mm and l_c=43 mm. The other is given with t_c=5 mm and l_c=40 mm. The electric field pattern of the latter case is shown in Fig. 6. The frequencies were adjusted with changing the t_c keeping l_c constant. The frequency f_1 on the boundary condition C_1 is independent of the length l_c because the electric field does not exist in the choke.

One of the advantages of the choke coupling is that outlets of cooling air are located in the choke where no electric field exists.

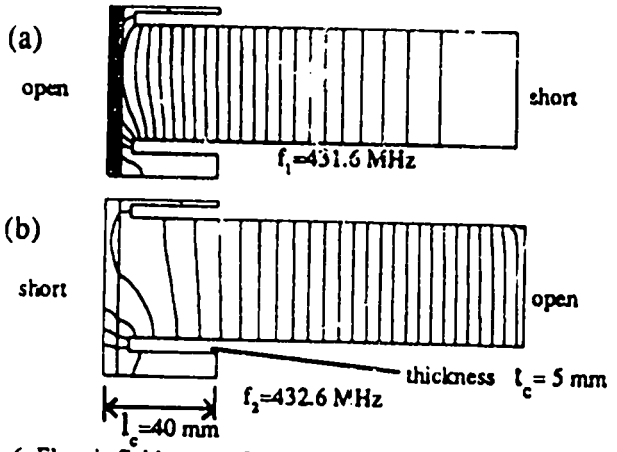

Fig. 6. Electric field pattern for the rf window of the choke type calculated with SUPERFISH.

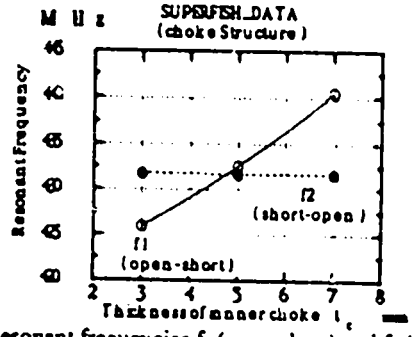

Fig. 7. Resonant frequencies f_1 (open-short) and f_2 (short-open) of the rf window of the choke type.

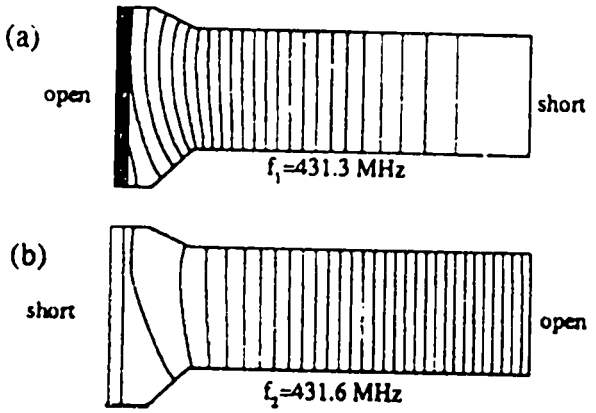

Fig. 8. Electric field pattern of the rf window of under/over cut type calculated with SUPERFISH.

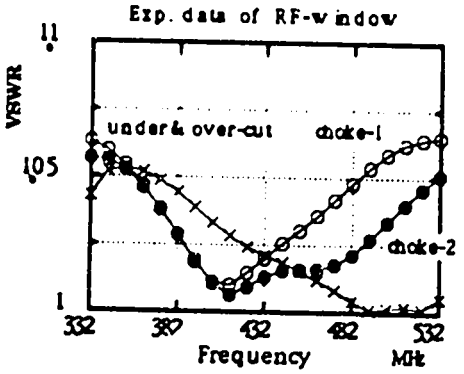

Fig. 9. Experimental data of VSWR for a low power model of the rf windows.

choke-1; t_c=6 mm, l_c=43 mm
choke-2; t_c=5 mm, l_c=40 mm

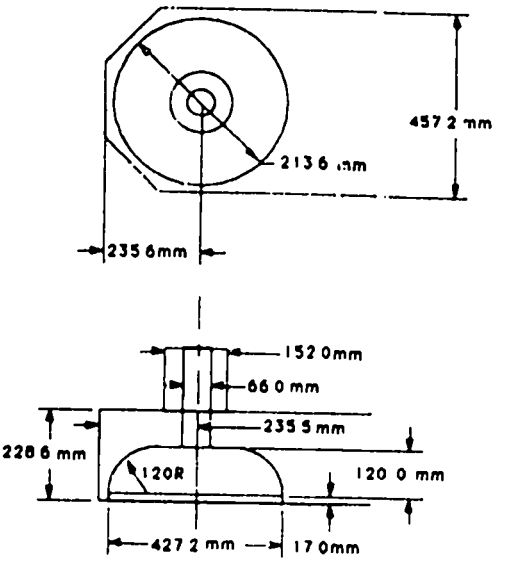

Fig. 10. Dimension of the 432 MHz door-knob transition.

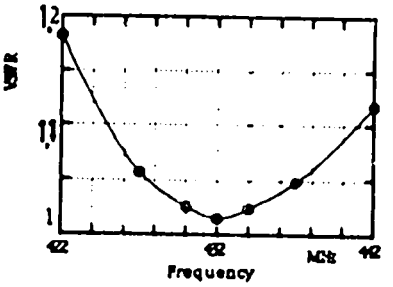

Fig. 11. Experimental data of VSWR for a low power model of the door-knob transition.

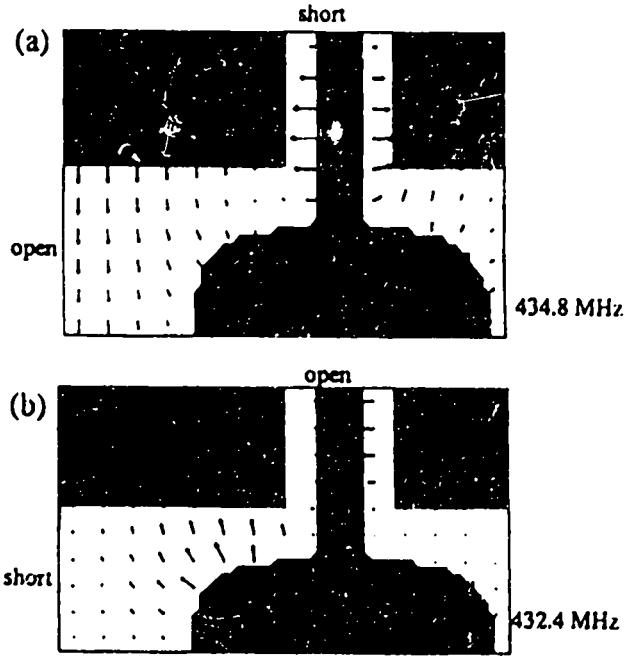

Fig. 12. Electric field patterns of the door-knob transition calculated with MAFIA.

Therefore, the size and shape of the air outlet can be easily designed. The disadvantages are that the structure becomes complicate and that the electric field normal to the rf window is induced. The electric field normal to the rf window gives rise to the multipactoring that results in the break down. Thus, the gap size between the ceramic and the head of the choke should be determined carefully in order to avoid the break down.

The impedance matching of an rf window can also be obtained with the structure of an under- and/or an over-cut of the waveguide. The rf window of the under-cut structure is in operation for the higher-mode damper of the accelerating cavity of TRISTAN[8]. The rf window with both over- and under-cuttings was designed by referring to the shape of the higher-order mode damper. It can be seen from the electric field pattern shown in Fig. 8 that the direction of the electric field is almost parallel to the rf window. This is more advantageous than the choke structure regarding the suppression of multipactoring and a local heating. However, the air outlets are located on the slope of under- and over-cutting area where the electric field exists. Thus, special care will be necessary to determine the size and the shape of the outlet, considering the cooling of the rf window and a field disturbance.

Figure 9 shows the experimental data of VSWR of the models for the rf window, designed with the present procedure. The VSWR for the frequency ranging from 382 to 482 MHz is less than 1.05 for all the structures studied. This data also supports the reliability of the design with the present procedure.

The door-knob transformer

The door-knob transformer was designed with the standard "cut and try" method. In principle the computer code MAFIA can be applied to the design of the door-knob transformer. However, the available mesh number of MAFIA was not sufficiently large for the design.

The basic dimension was determined with a scaling of the size of the coupler of 508-MHz klystron. The tuning parameters were the position of the moving short plane and the thickness of the spacer between the door-knob and the wave guide. Figure 10 shows the dimension of the door knob. The measured VSWR of the door-knob model is shown in Fig. 11.

Since the maximum number of the meshes in MAFIA has recently been increased to 10^6 in KEK, we applied MAFIA to the door-knob study. The electric field pattern is shown in Fig. 12. It can be seen that the field pattern changes from a rectangular waveguide mode (TE_{01}) to a coaxial waveguide mode (TEM) smoothly, leaving no strong electric field localized.

Conclusions

The input coupler of the 432 MHz DTL for the Japanese Hadron Project was designed. It is confirmed that the impedance matching of the transformer could be obtained with the SUPERFISH-aided design. The door-knob transition was designed with the model study. Its field pattern was checked with the code MAFIA.

Acknowledgment

The authors are extremely grateful for the advice offered by Prof. H. Baba.

References

1. T. Kato, Y. Yamazaki and M. Kihara, Proc. 2nd Int. Sym. on Advanced Nucl. Energy Research, JAERI, Japan, (1990), 177.
2. S. Isagawa, et al., Proc. IEEE Part. Accel. Conf., Washington D.C., (1987) 16
3. K. Halbach and R. F. Holsinger, Part. Accel. 7 (1976) 213
4. T. Weiland, Part. Accel., 15 (1984) 245
5. J. C. Slater, "Microwave Electronics", D. Van Norstrand, (1950)
6. Y. Yamazaki, a note of the "Proton Linac seminar," in KEK, unpublished, 1990
7. G. L. Ragan, "Microwave Transmission Circuit," MIT, Rad. Lab. Ser.9 (1948) 305
8. Y. Morozumi, T. Higo and Y. Yamazaki, Part. Accel., 29 (1990) 85

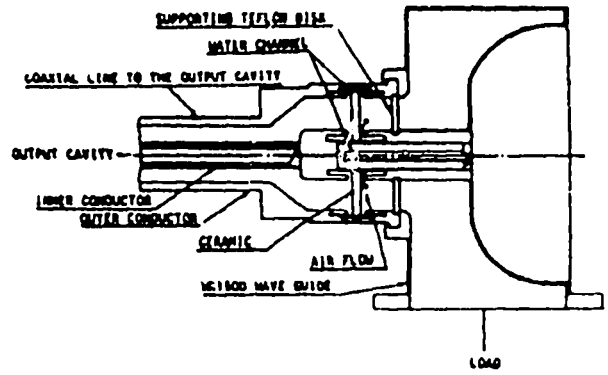

Fig. 1. Cross section of the output coupler of 508 MHz klystron[2].

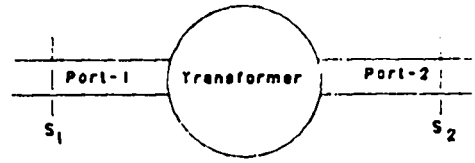

Fig. 2. Model of two ports transformer.

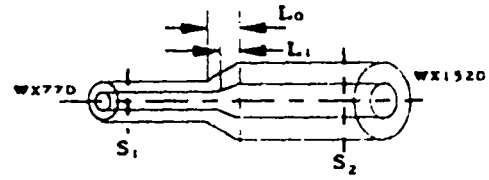

Fig. 3. Configuration of transformer for joining two coaxial lines.

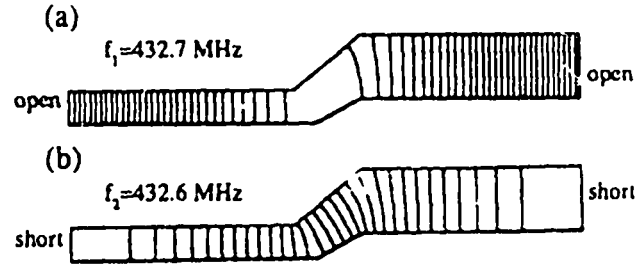

Fig. 4. Electric field patterns of the transformer calculated with SUPERFISH. (L_0=44.7 mm, L_1=30.7 mm)

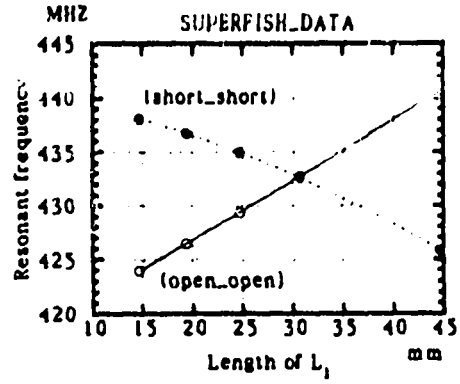

Fig. 5. Resonant frequencies f_1 (open-open) and f_2 (short-short) of the coaxial line transformer.

HIGH-POWER HYBRID ATTENUATOR&PHASE-SHIFTER SYSTEMS

S. Ohsawa, I. Abe, M. Yokota, Y. Ogawa,
S. Anami, I. Sato and A. Asami
National Laboratory for High Energy Physics
Oho, Tsukuba-shi, Ibaraki-ken, 305, Japan

Abstract

Two kinds of waveguide systems which can change the attenuation and phase independently have been newly designed utilizing 3-dB hybrids, and manufactured for the prebuncher and buncher of the 2.5-GeV Photon Factory Injector Linac. Measured data show the expected characteristics. The principles, structures and characteristics are described.

Introduction

In an electron linac, beam bunches are produced by a prebuncher and a buncher. Since the shape of the bunches greatly affects the beam characteristic, it is very important to optimize the microwave powers and phases in these devices. For the optimizing process, a system comprising an attenuator and a phase shifter is necessary for each of these devices. However, the former high-power variable attenuators have a problem in that a phase shift is introduced as the attenuation is varied. This feature made it complicated to search for the optimum parameters of the prebuncher and buncher. Accordingly, new systems were designed in order to solve this problem.

The old system for the buncher was pressurized with SF_6, so that it required windows which separate the gas from the vacuum. Bored holes with small cracks were found on the vacuum sides of the windows in the Spring of last year. Fortunately, the holes still did not reach to the other side. In order to avoid this kind of problem, the new systems were designed to be used under vacuum

Principle of new systems

Although the new systems have the same functions, they look quite different at first glance. It might therefore be better to explain them separately.

System for the prebuncher

We firstly discuss the attenuator & phase-shifter system for the prebuncher. The microwave power required in the prebuncher is usually less than 10 kW. Within this power range a dielectric substance is usually used for varying the power or phase. Therefore the microwave phase is inevitably shifted as the attenuator is changed.

On the other hand, the new system has the configuration illustrated schematically in Fig. 1. It comprises a 20-dB directional coupler as a power divider, a 3-dB directional coupler with two short plungers which move independently and a dummy load for termination. The power for the prebuncher is provided from the main line for the buncher by the 20-dB power divider. Then, the power is divided again by a 3-dB directional coupler into two parts, each of which is reflected by a short plunger at a different position; the two fields are then mixed by the same 3-dB coupler.

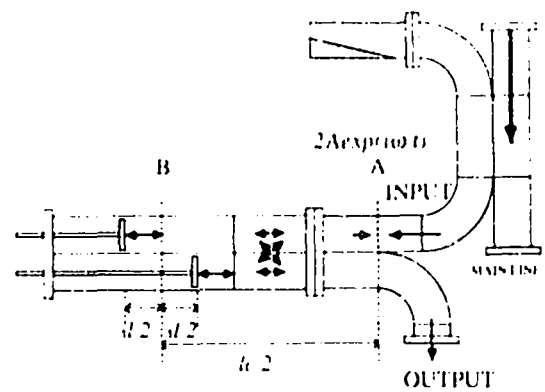

Fig. 1. Attenuator & phase-shifter for the prebuncher

We now consider the output power and the phase of the system. For simplicity, power losses and reflections due to imperfections of the devices are neglected in the discussions below. When the input microwave field is $A\exp(i\omega t)$ at plane A in Fig. 1, the output field E_o is given by[1]

$$E_o = A\cos\phi \sin(\omega t + \theta) \qquad (1)$$

where

$$\theta = lc / \lambda_g,$$

and

$$\phi = \Delta l / \lambda_g. \qquad (2)$$

Here, λ_g is the wavelength in the waveguide.

It can be seen from Eq. (2) that both θ and ϕ depend only on lc and Δl, respectively. This means that the output power or phase can be adjusted independently by moving the plungers in the opposite or same direction by equal amounts, respectively. The output power is changed without a phase shift over the full range from zero to the input power according to ϕ; on the other hand, the output phase, θ, is given by the average phase of the two

fields before being added. Thus, the new system has functions both of an attenuator and a phase shifter, as mentioned before.

The backward power returned to the input port is mainly absorbed by a dummy load connected at a port of the 20-dB directional coupler. The part of the power turns back to the source through the 20-dB directional coupler. This is, however, less than - 40 dB of the main line power, because the returning power to the source passes through the 20-dB coupler two times. Hence, this becomes negligibly small in practical use.

Although the plunger control becomes complex, because it is necessary to shift two plungers independently and simultaneously, the new system is both simpler and more compact.

System for the buncher

We next consider the attenuator & phase-shifter system for the buncher. Though the system for the prebuncher mentioned above has a simple configuration, it is not suitable for the buncher. This is because in the buncher system it might usually be impossible to use a very weakly coupled power divider as the 20-dB coupler in the prebuncher system. Without a weak coupler, high power might turn back to the source and destroy it. Even if a circulator is inserted in the circuit, the transient parts of a pulse might be turned back to the source.

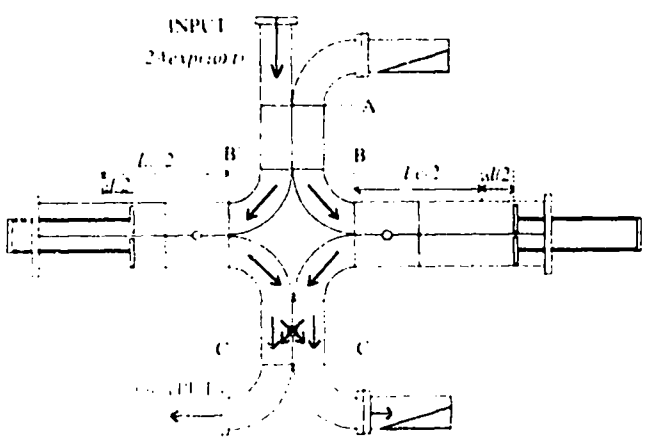

Fig. 2. Attenuator & phase-shifter for the buncher

Accordingly, another type of attenuator & phase-shifter system was newly designed for high power, so that any excessive power is perfectly absorbed by a dummy load and does not turn back to the source.[1] The new system is illustrated schematically in Fig. 2. It consists of four 3-dB directional couplers combined in a body, two sets of jointed short plungers, and two dummy loads. Each of the joined plungers can be moved independently. The system, comprising a 3-dB coupler and joined short plungers, is a well-known type phase shifter.

We now look at how the new system works. Let the input field be $Aexp(iwt)$ at the plane A in Fig. 2, same as in the previous case. The input power is divided at the first 3-dB coupler into two parts. After passing through the corresponding phase shifter, the fields are mixed by the next 3-dB directional coupler. Then, the final field, E_o, in the output port is given at plane C' as

$$E_o = A\sin\phi \sin(\omega t+\theta), \qquad (3)$$

where

$$\theta = lc / \lambda_g + \delta + \delta',$$

and

$$\phi = \Delta l / \lambda_g . \qquad (4)$$

The phases, δ and δ', correspond to the electrical lengths between planes A and B and planes B and C (or B' and C'), respectively.

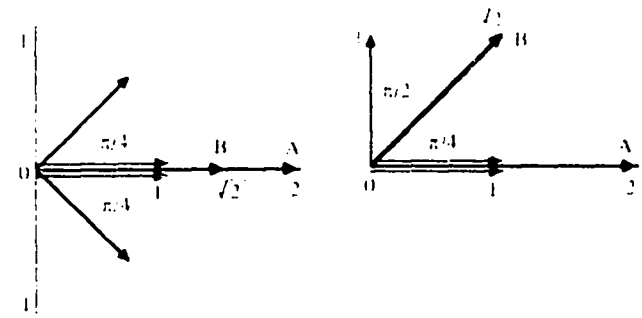

Fig. 3. Field addition in the new and old systems

We now compare the characteristics of the new system with those of the old one. Figure 3a clearly shows the features of the new system when the power is reduced to half. The added fields before and after being attenuated are shown by arrows A and B, respectively. The resultant amplitude is changed from 2 to $\sqrt{2}$ without any phase shift. On the other hand, in the old system, not only the resultant amplitude is changed from 2 to $\sqrt{2}$, but the phase also shifts by as much as $\pi/4$.

Characteristics of manufactured systems

Finally, we describe the characteristics of attenuator & phase-shifter systems which were manufactured according to the principles mentioned above. Figure 4 shows the microwave characteristics for the buncher system. It exhibits phase shifts over a frequency range when attenuations are changed: the phase shifts are shown in the upper part, and attenuations in lower part. Figure 4 shows that the phase shifts are small over a power range of 0 ~ -20 dB. At a frequency of 2856 MHz, the phase shifts are less than 1.2°, as shown in Fig. 5.

The output of this system should obey Eq. (3). Figure 6 shows this relation between ϕ and

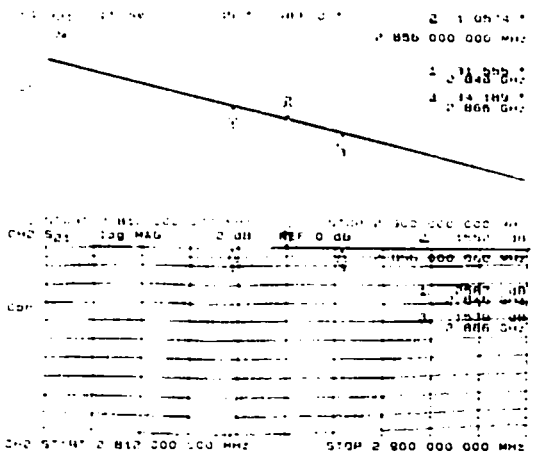

Fig. 4. Characteristics used as an attenuator

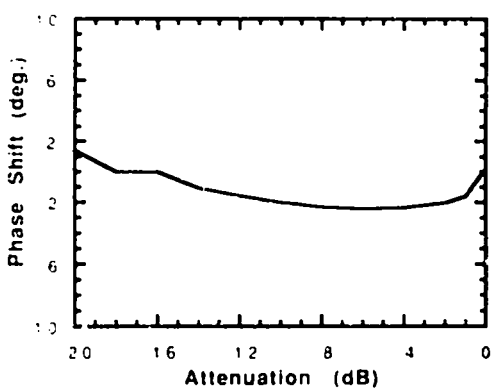

Fig. 5. Phase shift vs. attenuation at 2856 MHz

attenuation: A solid line indicating measured data and a dotted line given by Eq. (3) agree with each other, except in the range of larger attenuation. This disagreement comes from device imperfections: The power divide ratio of 3 dB directional couplers were carefully adjusted by tuning buttons; as the result, the directivity [illegible] degraded to about - 25 dB. According [illegible] field contains elements which have nothing to do with the plunger positions, although they are very small. Fortunately, it is possible to make the elements [illegible] each other by means of choosing the input port (Fig. 2) ; the performance of the system is not very impaired. Although there will be no problems in practical use, since the buncher is never used with a power level decreased as low as - 20 dB, the characteristics of the system are expected to be much improved by slightly changing the size of the 3-dB directional couplers in order to raise directivity. We did not, however, do it because of a lack of time.

Figure 7 shows the characteristics of this system when it is used as a phase shifter. It indicates that the power change is as small as - 0.2 dB when the phase is changed by 2π. The data were obtained under small attenuation.

The system for the prebuncher has similar characteristics. A micro computer controls the short plungers by using pulse motors, and measures their positions accurately with linear scales. The system for the buncher has had no problems under high-power testing.

Summary

Two waveguide systems which can change the attenuation and phase independently were newly designed and manufactured. The measured data indicate that they have the expected characteristics. The entire systems are scheduled to be used from this September. Both of the two systems have the distinctive feature that they do not introduce an rf phase shift as the attenuation is varied. Hence, it is expected that the process of converging on the optimum phase and power settings for the prebuncher and buncher will be greatly speeded up by the new systems.

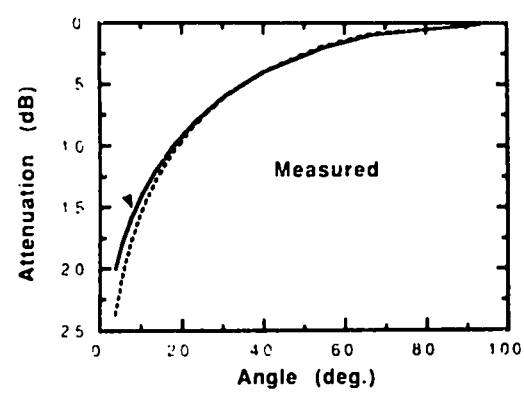

Fig. 6. Attenuation vs. ϕ of the system for buncher

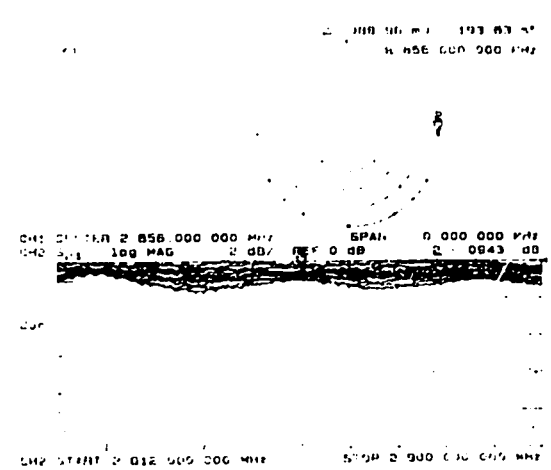

Fig. 7. Characteristics used as a phase shifter

References

1. S. Ohsawa et al. " New High Power Variable-Attenuator/Phase-Shifter Systems," 7th Symp. on Accelerator Science and Tech., Dec. (1989)

R&D ON AN X-BAND KLYSTRON MODULATOR FOR JAPAN LINEAR COLLIDER

Tetsuo Shidara, Mitsuo Akemoto, Masato Yoshida, Seishi Takeda, Koji Takata and Linear Collider Study Group
KEK, National Laboratory for High Energy Physics
1-1 Oho, Tsukuba-shi, Ibaraki-ken, 305 Japan

Abstract

Design considerations of an X-band klystron modulator for the future JLC (Japan Linear Collider) project are presented. This modulator has been designed to produce pulses that are 200-ns wide, 600-kV, 1200-A peak current and a short rise time of ~90 ns; it is based on magnetic-pulse-compression techniques with a very high peak-power capability and a repetition rate exceeding 200 Hz. R&D on amorphous core materials for magnetic compressors and solid-state devices (such as GTO and MAGT) for a discharging switch to realize an efficient and reliable modulator are currently being undertaken.

Introduction

As a post-TRISTAN project, an $e^+ e^-$ linear collider in the TeV region (JLC: Japan Linear Collider) has been proposed to reach energies beyond that of LEP.[1,2] It requires an accelerating gradient on the order of at least 100 MV/m for the facility to be of reasonable scale. Achieving this high field gradient requires high-power microwave sources with a peak output power of about 150 MW at a frequency of 11.4 GHz (see Fig. 1).[3]

To realize this high-power microwave source the development of high-power X-band klystrons using conventional technology was started.[4] Although the studies of a two-beam accelerator (TBA) scheme using free-electron laser technology were also started at KEK,[5] X-band klystrons could be in use at the first phase of the JLC.

For a prototype X-band klystron we expect an output power of 30 MW at the maximum design voltage of 450 kV. The diode model of this tube was high-voltage conditioned using one of the modulators prepared for the KEK test accelerator facility (TAF), which was established in 1987 to pursue R&D technology for future linear colliders.[6] Processing with 1-μs and 2-Hz pulses has increased to a voltage of 450 kV, which corresponds to a beam power of 81 MW.[7] Although this processing was successful, development of an X-band klystron modulator using magnetic-pulse-compression techniques[8] was initiated in order to supply very short pulses (~200 ns), since the required pulse flat-

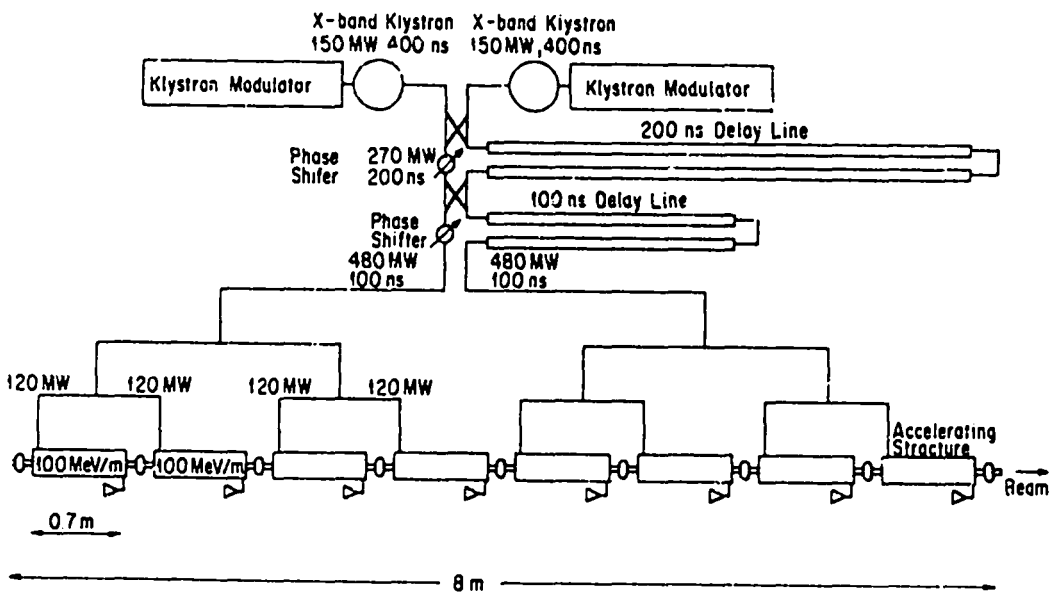

Fig. 1. Conceptual drawing of the JLC microwave distribution system.

top is on the order of 100 ns. Details of this X-band klystron modulator are described.

Modulator Specification

Specifications of the X-band klystron modulator are listed in Table I. Although the impedance of the prototype X-band klystron is on the order of several kΩ, the impedance of the modulator was designed to be 500 Ω for the following reasons: 1) Since we are in the very first R&D stage of using the X-band klystron, we have to prepare for any change of its design. Therefore, the lowest probable value of the klystron impedance should be taken into account for the modulator design. 2) Since a rather high impedance (several kΩ) results in a longer rise time (more than 500 ns) due to the estimated stray capacitance (~150 pF) around the output circuit and klystron socket, a lower impedance is preferable for the efficient production of short pulses (~200 ns). 3) Simultaneous power feeding to several klystrons by a single modulator is being considered for the future linear collider in order to reduce construction costs, resulting in a relatively low impedance.

TABLE I
Specifications of the X-band Klystron Modulator

Output pulse voltage range	400 ~ 600 kV
Output pulse current (max.)	1200 A
Output impedance	500 Ω
Rise time	< 100 ns
Pulse length (flat top)	> 100 ns
Pulse height deviation from flatness	±1.0 %
Pulse amplitude drift	< 2 %
Jitter	< 5 ns
Pulse repetition rate	200 pps

The requirement for an acceptable phase modulation (~5 °) of the microwave source limits the pulse-height deviation and pulse-amplitude drift of the modulator. Although, the microwave circuit design of the X-band klystron is tentative, a relativistic beam voltage of ~600 kV lessens the requirements on the pulse-top flatness and amplitude stability.

Circuits of the X-band Klystron Modulator

Two types of modulator designs using magnetic-pulse-compression techniques are considered because of their very short rise-time capability and high reliability, since they consist of only passive components, such as saturable inductors, capacitors and Blumlein.

Semi-conventional Type Modulator

A semi-conventional-type modulator (a combination of a pulse-forming network (PFN), pulse transformer and magnetic switches) has been intensively studied because of its ease in adjusting pulse-top flatness (see Fig. 2). The stored energy of capacitor C_0 is transferred into another capacitor (C_1) through a thyratron, then successively to the PFN capacitors by increasing the voltage through a 1:15 step-up transformer, and finally to a klystron through a 1:4 step-up transformer. The compression factor of each stage is 1/4. Assuming a stray capacitance of ~145 pF at the secondary circuit of the final step-up transformer, the output voltage of this circuit was simulated (see Fig. 3).[9] A rise time of ~90 ns is expected. The result of the simulation is very encouraging regarding the use of the X-band klystron modulators.

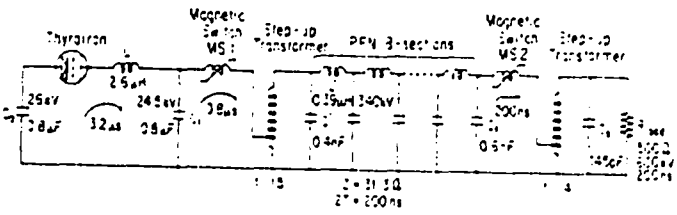

Fig. 2. Simplified diagram of the X-band klystron modulator using PFN, pulse transformer and magnetic switches.

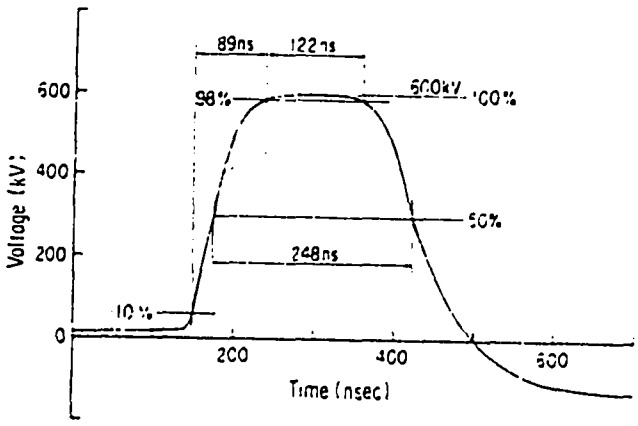

Fig. 3. Simulated output voltage of the X-band klystron modulator.

Blumlein Type Modulator

A Blumlein-type modulator (see Fig. 4) seems to have some advantage, since the impedance of the Blumlein is half that of the klystron load. The location of the magnetic switch and the charging reactor is important in order to eliminate any undesirable voltage during the charging process.[10]

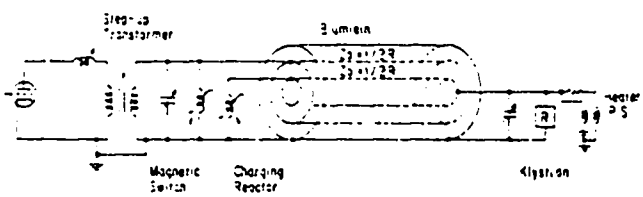

Fig. 4. Simplified diagram of the Blumlein-type modulator.

R&D Items

Although the simulated result is very hopeful, there are several R&D items required in order to put into use this type of modulator for the future linear collider.

Amorphous Core

Since the required pulse-repetition rate is 200 Hz, a temperature increase caused by power loss at the inductor core is a key issue regarding this type of magnetic compressor. Although a low-loss Co amorphous core is sufficient for our modulator use from a technical point of view, the price is a problem. Since more than 2000 X-band klystrons are used in the JLC, R&D on a low-cost amorphous core (for example; Fe amorphous core with a very thin thickness[11]) suitable for our use is inevitable.

Switch Device

If we endure the replacement of failed switch devices for the future JLC modulators several times per month the lifetime of each switch device should be on the order of 10^{12} shots, which is much beyond the present technology. Therefore, R&D on a switching device with a longer lifetime is a key point in realizing the JLC project. Solid sate devices, such as GTO (Gate Turn Off) thyristers, IGBT (Insulated Gate Bipolar Transistor) and MAGT (MOS-Assisted Gate Turn Off) thyristers, are good candidates.[12] We have started R&D on solid-state switching devices (MAGT) capable of large di/dt (5000 ~ 10000 A/μs).

Acknowledgement

The authors wish to express their gratitude for the encouragement and financial support received from director general, H. Sugawara as well as directors Y. Kimura and S. Iwata. They also wish to express their thanks to FEL R&D Group members (especially Profs. S. Hiramatsu and J. Kishiro) and X-band klystron R&D Group members for the fruitful discussions.

This paper is much indebted to the works of N. Ninomiya and A. Tokuchi of Nichicon Co., Drs. S. Yanabu and T. Teranishi of Toshiba Co.

References

1. Y. Kimura, Proc. European Particle Accelerator Conf., Rome, 1, 22 (1988).
2. K. Takata and Y. Kimura, "TRISTAN and High Energy Accelerator Plans at KEK", Particle Accelerators, **26**, 87 (1990)
3. S. Takeda, "Japan Linear Collider (JLC)", Particle Accelerators, **30**, 143 (1990).
4. H. Mizuno et al., "X-band Klystron Diode Test for Japan Linear Collider (JLC)", Particle Accelerators, **30**, 167 (1990).
5. S. Hiramatsu et al., "Conceptual Design of a Linear Collider in the TBA/FEL Regime", Particle Accelerator, **31**, 75 (1990).
6. S. Takeda et al., "Electron Linac of Test Accelerator Facility for Linear Collider", Particle Accelerators, **30**, 153 (1990).
7. H. Mizuno et al., Talk Presented at the Second International Workshop on the Next Generation of Linear Colliders (LC90), KEK, March 28 - April 5. 1990.
8. D.L. Birx et al., "Technology of Magnetically Driven Accelerators", IEEE Trans. Nucl. Sci. **32** (5), 2743 (1985)
9. A. Tokuchi (Nichicon Co.), private communication.
10. T. Teranishi (Toshiba Co.), private communication.
11. S. Nakajima (Hitachi Metals), private communication.
12. K. Okamura et al., Proc. 7th Int. Pulsed Power Conf., Feb. 1989.

MICROWAVE SOURCE UPGRADE OF THE KEK 2.5-GEV LINAC RELEVANT TO B-FACTORY PROJECT

Tetsuo Shidara, Hiroyuki Honma, Katsumi Nakao, Shozo Anami and Akira Asami
1-1 Oho, Tsukuba-shi, Ibaraki-ken, 305 Japan

Abstract

The KEK 2.5-GeV linac is planning to upgrade its microwave source relevant to a B-factory project. The B-factory will use 8-GeV electrons and 3.5-GeV positrons where each injection energy from the linac is 2.5 and 3.5 GeV, respectively. The increase in the injector linac energy from the present 2.5 GeV necessitates the replacement of existing 30-MW klystrons with new 60-MW units. A doubling of the klystron output power requires a modification of the modulator system. The 60-MW klystron requires a 350-kV beam voltage pulse. A new pulse transformer with a step-up ratio of 1:15 will be necessary to deliver the increased voltage. The modulator, with the exception of its pulse-forming network, will be unchanged while producing the required power increase. The discussion will cover the upgraded modulator specifications and its test station using the 60-MW klystron.

Introduction

TRISTAN at KEK has entered a new phase (phase-II: luminosity run by employing superconducting quadrupole magnets[1]) in order to achieve an integrated luminosity of 300 pb^{-1} until 1995. What comes next? An asymmetric B-factory two-ring collider is considered to be phase-III of the TRISTAN project. The required beam energy and design luminosity are 8 × 3.5 GeV^2 and 1 × 10^{34} /cm^2/sec from physics experiments.[2] Beam currents of 2.6 A for the 3.5-GeV positron ring and 1.1 A for 8-GeV electron ring are necessary in order to attain the design luminosity. The existing two injectors for the TRISTAN main ring, the KEK 2.5-GeV linac (see Fig. 1)[3] and the accumulation ring (AR), are also used for the injectors of the new B-factory rings.

The requirements from the B-factory project to the linac and its present status are summarized in Table I. Since the required injection energy of positron and electron beams for the B-factory are 3.5 and 2.5 GeV, respectively, the energy of the linac should be increased from the present 2.5 GeV to 3.5 GeV. Since the particle loss rate of B-factory rings is rather high, the intensity of the linac should also be increased in order to compensate for particle loss.

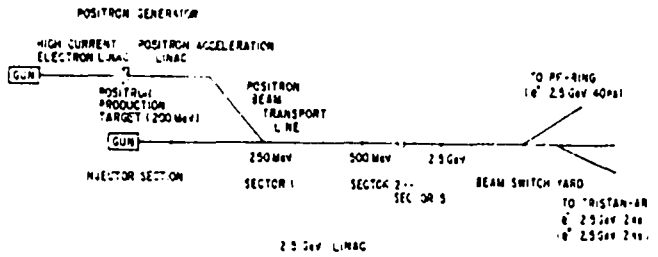

Fig. 1. Conceptual diagram of the present KEK 2.5-GeV linac.

TABLE I
Present Status of the Linac and Requirements from the B-factory

	present			B-factory	
	for AR		for PF	for AR	
	e^- 2ns	e^+ 2ns	e^+ 40ns	e^-	e^+
Energy (GeV)	2.5	2.5	2.5	2.5	3.5
Charge accumulation rate (× 10^{-8} C/min)	22.5	1.5	1.2	30 (75)	25 (75)
Pulse width (ns)	1	1	40	50	50
Peak current (mA)	150	10	2	2 (5)	1.6 (5)
Pulse repetition rate (pps)	25	25	25	50	50
Energy spread (%)	0.5	0.5	~1	~1	~1

This paper describes the upgrading of the KEK 2.5-GeV linac, especially its microwave system, in order to meet the demands from the B-factory project.

Linac Upgrade

A working group of the linac upgrade was organized in June of 1989 and has laid out several linac upgrade designs.[4] The following plan was tentatively adopted in order to satisfy the requirements from the B-factory project: I) In order to increase the positron intensity (1) positron beams with pulse width of 50 ns are accelerated; (2) the location of the positron production target is moved down to the 750-MeV point of the linac (see Fig. 2) since the positron-

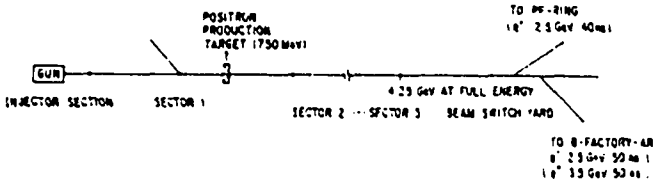

Fig. 2. Location of the positron production target in the upgraded linac.

production efficiency is proportional to the injection energy of the electron beams; and (3) the positron capture efficiency is improved by enlarging the acceptance of the focusing system. II) In order to increase the energy of the linac to 4.25 GeV (750-MeV electron beams + 3.5-GeV positron beams) all of the present 30-MW klystrons are being replaced with 65-MW high-power klystrons. The resultant accelerating gradient is 14.4 MV/m (see Fig. 3), which is sufficient for the linac with a total accelerating structure length of 300 m.

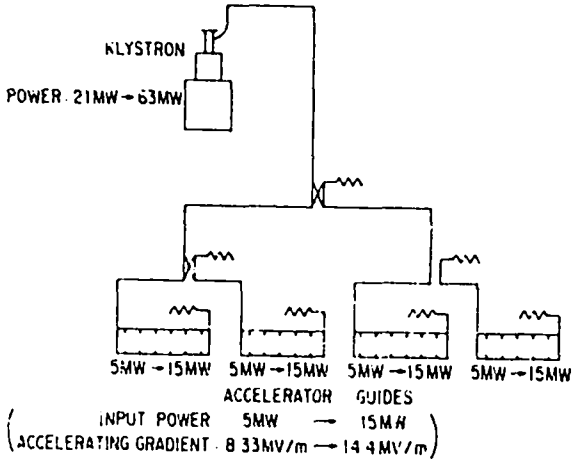

Fig. 3. Upgrade scheme of the power feed system to an acceleration unit.

Upgrade of the Microwave Source

Klystron

According to the SLC operation, 5045-type klystrons[5] are quite successfully supplying 65 MW of rf power. Therefore, we are planning to introduce this type of klystron as our new microwave source. Table II shows the specifications of the original and 5045-type klystrons.

Modulator

The doubling of the klystron output power requires a modification of the modulator system.

TABLE II
Comparison of the Original and Upgraded Klystron Specifications

	Original	Upgraded
Model designation	Mitsubishi PV-3030	SLAC 5045
RF peak output power (MW)	3.0	6.5
Beam voltage (kV)	270	350
RF pulse width (μs)	3.5	2.2
Repetition rates (pps)	50	50
RF gain	51	50
Micro-perveance	2	2
Efficiency (%)	40	45

Since the total modification of the modulator costs too much, the output voltage and average power of the modulator have remained unchanged. Consequently the 80 kV increase in klystron beam voltage could only be obtained by increasing the pulse transformer step-up ratio from the present 1:12 to 1:15. Accordingly, our new modulator is required to generate pulses with a 23.5-kV peak voltage, 6150-A peak current and 145-MW peak power. Table III shows the specifications of both the original and upgraded modulators.

TABLE III
Comparison of the Original[6] and Upgraded Modulator Specifications

	Original	Upgraded
Maximum peak power (MW)	84	145
Maximum average power (kW)	14.7	14.7
Transformer step-up ratio	1:12	1:15
Output pulse voltage (kV)	23.5	23.5
Output pulse current (A)	3600	6150
PFN impedance (Ω)	6.0	3.6
PFN total capacitance (μF)	0.3	0.3
Pulse width (μs)	3.5	2.2
Rise time (μs)	0.7	0.8
Fall time (μs)	1.2	1.5
Pulse repetition rate (pps)	50	50
Maximum pulse height deviation from flatness (%)	0.3 (peak to peak)	0.5
Maximum pulse amplitude drift (%/hour)	0.3	0.5
Thyratron anode voltage (kV)	47	47

Since the output impedance of the pulse-forming network (PFN) has been reduced from the original 6.0 Ω to 3.6 Ω, the PFN pulse width has also been reduced from 3.5 to 2.2 μs. Taking into account the pulse rise time of 0.8 μs and fall time of 1.5 μs for 65-MW rf pulses, a pulse flat-top of 0.7 μs is expected after the modification. Since the rf filling time of the accelerator guide is 0.5 μs, a 200-ns beam will be the longest case. This is the main reason why we have adopted the 50-ns beam for the B-factory project. A significant increase in the PFN discharge current is compensated using two PFN capacitors in parallel (see Fig. 4).

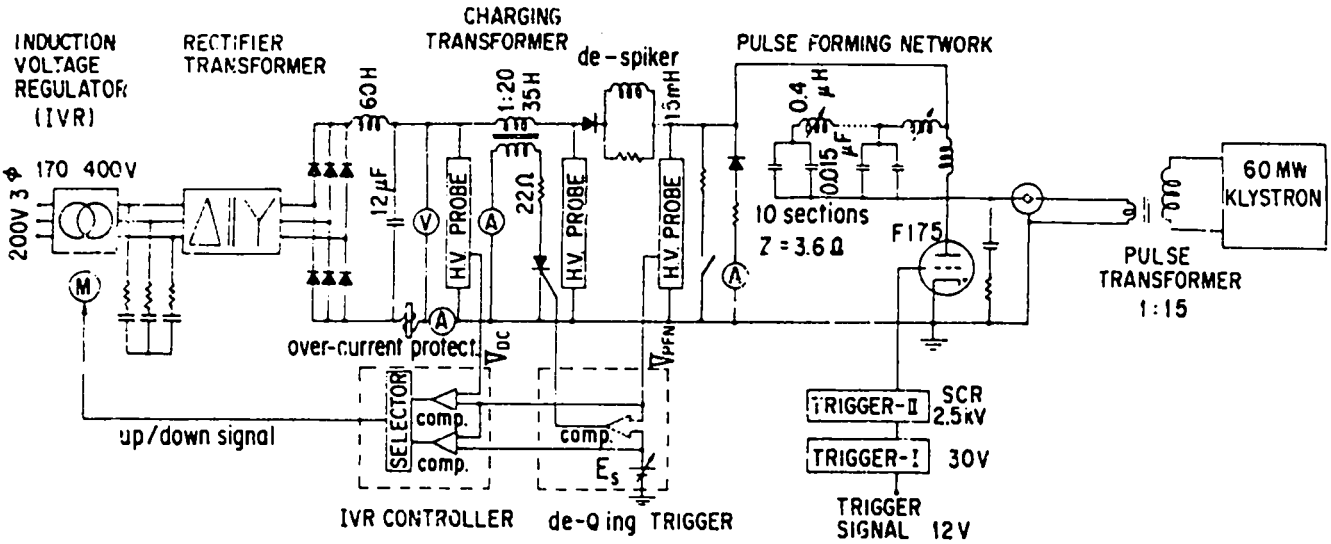

Fig. 4. Simplified diagram of the upgraded modulator.

Test Station

A new test station using a 5045-type klystron was established in order to confirm the above-mentioned modifications. This klystron is one of nine 5045-type klystrons which have been delivered from SLAC to the test accelerator facility[7] of the Japan Linear Collider (JLC) study group under the US-Japan collaboration program. The klystron has already been set at our test station (Fig. 5). A high-power test of this klystron using modified klystron modulator will start soon.

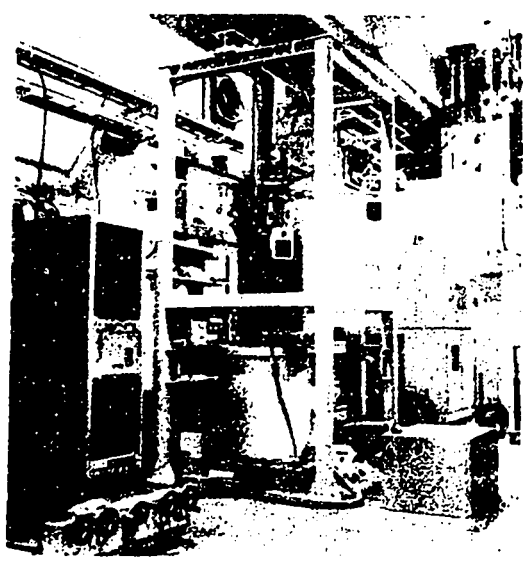

Fig. 5. 5045 klystron and tank assemblies set at a new test station.

Acknowledgements

The authors would like to express their thanks to Profs. K. Takata, and S. Takeda for their delivery of a 5045 klystron. One of the authors (T. Shidara) would like to acknowledge valuable discussions with Drs. M. Allen and A. Vlieks concerning the operation status of the 5045 klystrons at SLAC.

References

1. K. Tsuchiya et al., "Superconducting Magnet System for the TRISTAN Low Beta Insertion", KEK-preprint-90-56, June 1990.
2. ed. by H. Ozaki and Y. Yoshimura, "Feasibility Study for an Asymmetric B-factory at KEK", KEK-Report-90-7, June 1990.
3. J. Tanaka, "Construction of the Photon Factory 2.5 GeV Injector Linac", Nucle. Instr. Meth., **177**, 101 (1980).
4. A. Asami et al., "Linac Upgrade", Proc. of the Workshop on Asymmetric B Factory at KEK", KEK-Report-89-17, 252 (1989).
5. T. G. Lee et al., "A 50-megawatt Klystron for the Stanford Linear Collider", SLAC-PUB-3214.
6. T. Shidara et al., "Klystron Modulator for the KEK 2.5 GeV Linac", Nucle. Instr. Meth., **A279**, 423 (1989).
7. S. Takeda et al., "Electron Linac of Test Accelerator Facility for Linear Collider", Particle Accelerators, **30**, 153 (1990).

X-BAND KLYSTRON FOR JAPAN LINEAR COLLIDER

Hajime Mizuno, Jun'ichi Odagiri, Toshiyasu Higo
Mitsuo Akemoto and Hiroshi Sakai
National Laboratory for High Energy Physics, KEK
1-1, Oho, Tsukuba, Ibaraki 305, JAPAN

ABSTRACT

To achieve the acceleration gradient of 100 MeV/m necessary for Japan Linear Collider (JLC), an RF power source of more than 100 MW will be needed. As a first step for the development of 100 MW class X-band(11.424 GHz) klystrons, a 30 MW klystron named XB-50K was designeed and fabricated. The first RF power test was carried out at the end of last August, up to the cathode voltage of 350 kV. 11 MW RF power of 70 nsec pulse was achieved at the rep-rate of 2 pps. and the efficiency was measured as 28 %. Up to this power the test results showed a good agreement with the simulation results obtained by the FCI-code. An RF window ceramic was fatally damaged while conditioning around 11 MW RF output.

INTRODUCTION

As the main linacs for JAPAN LINEAR COLLIDER(JLC), X-band linacs in 11.424 GHz with the accelerating gradient of 100 MeV/m or more are the most probable candidate(1). To achieve this accelerating gradient, RF power sources which can produce the peak output power of more than 100 MW will be necessary. As a first step of the R&D to 100 MW-class klystrons, 30 MW-class klystron, named XB-50K, was designed, fabricated and tested.

KLYSTRON DESIGN

Prior to the design of the XB-50K, a Pierce type electron gun, named XB-50D was already fabricated and tested up to the cathode voltage of 480 kV and the test results showed good agreement with the computer simulation by the use of E-GUN code by W.B.Herrmannsfeldt(2). The design and some test results were reported in REF(3). The gun parameters are summarized in Table-1).

TABLE-1)

Cathode Voltage	450 kV
Beam Current	170 A
Maximum Surface Field	260kV/cm
Perveance	0.57 micro
Cathode Diameter	50 mm
Cathode Spherical Radius	60 mm

To reduce the maximum surface field strength compared to that of the XB-50D, the geometry of the cathode and anode were slightly changed and the maximum surface field strength is reduced down to 260 kV/cm at the cathode voltage of 450 kV(3). Fig-1) shows the focusing magnetic field distribution along the beam axis. The maximum field strength is 4.6 kgauss and on the cathode, 37.6 gauss was used in the beam trajectory simulation by the use of E-GUN code.

Fig-1)

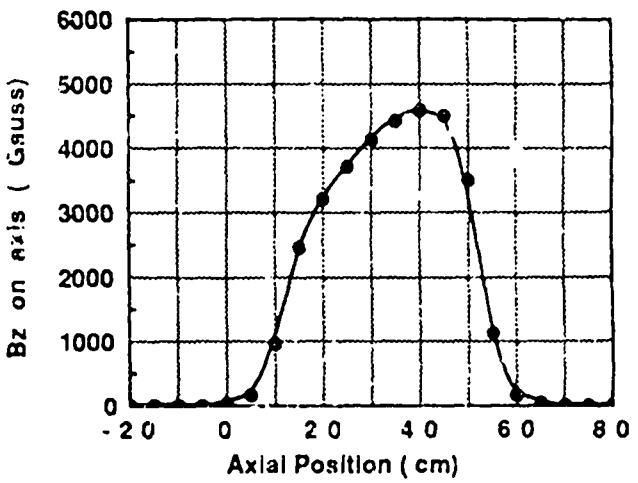

The beam trajectory obtained by E-GUN code is shown in Fig-2), and the focused beam revealing some scalloping could travel through the drift tube of 8 mm in diameter to the downstream of the output cavity which is located at 488 mm from the cathode center.

Fig-2)

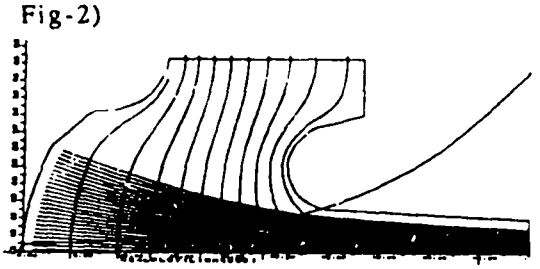

The RF simulations were performed by the use of FCI-code(Field Charge Interaction) developed by T.Shintake(4), and the results are summarized in Table-2). At the cathode voltage of 450 kV with the beam current of 170 A, RF output power of 36.2 MW with the efficiency of 47.3 % was obtained. The beam snap-shot picture of this simulation is also shown in Fig-3).

Fig-3)

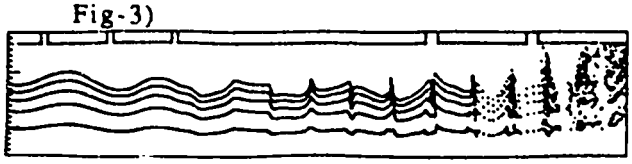

This result shows that the beam could travel through the output cavity with the beam aperture of 8 mm in diameter.

TABLE-2)

Beam Voltage	450kV
Beam current	170 A
Drift Tube Diameter	8 mm
Cathode Diameter	50 mm
Magnet Field(Bz,MAX)	4600 Gauss
(Bz,Cathode)	37.6 Gauss
Number of Cavities	5
Frequency	11.424 GHz
RF Power	36.2 MW
Gap Voltage(Output Cavity)	531 kV
Maximum surface Field (output Cavity)	102 MV/m
Efficiency	47.3%
Gain	53.5 dB

FABLICATION OF XB-50K

The first XB-50K was fabricated by TOSHIBA Corporation in accordance with the ordinary fabrication method of the pulsed klystrons. The cathode material is an Ir-coated dispenser cathode supplied by TOSHIBA Corporation(5), and the normal operating temperature is around 1000-degree Celsius. An overall view of XB-50K is shown in Fig-4). At the down stream end of the WRJ-10 wave guide, half-wavelength alminum ceramics is brazed inside of the rectangular wave guide flanges.

Fig-4)

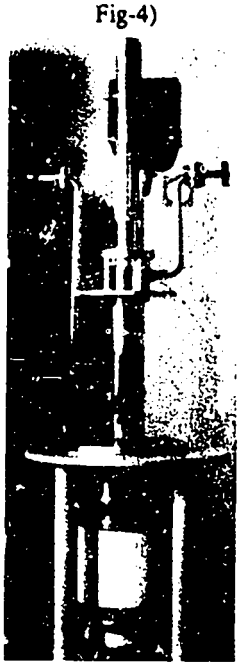

The cross sectional dimensions of this ceramics are the same as the WRJ-10 wave-guide, with the thickness of 4.55 mm. For the input window, the same window is also used. As shown in Fig-4), the gun structure and the materials are almost the same as those of XB-50D which is alresdy tested and reported(3).

TEST RESULTS

Prior to the RF processing, DC conditioning was performed at the repetition rate of 2 pps, until rather stable diode operation was achieved at the cathode voltage of 250 kV. After this preliminary processing, RF processing was started with the input RF pulse length of 500 nsec. Output RF power was monitored through the 63.2-dB directional coupler located at the upstream of the dummy load. After 20 hours of processing at the repetition rate of 2 pps, saturated RF power of 9.2 MW with the pulse duration of 140 nsec was reached at the cathode voltage of 338 kV. During this processing the input RF pulse length was shortened down to this value. Above this level, the input RF pulse was shortened down to 70 nsec, and the processing was continued up to the cathode voltage of 350 kV with the saturated RF power of 11MW. At this RF power level, due to the serious window discharge which emits a bright white and yellow light, the processing could not be completed until the stable opration of the tube was achieved.

The diode characteristics of XB-50K up to the cathode voltage of 350 kV are shown in Fig-5). Up to this voltage no serious break down or trouble were observed as long as the diode characteristics are concerned. The pulse wave-forms of a cathode voltage, beam current and RF output power observed during the RF conditioning, are shown in Fig-6).

Fig-5)

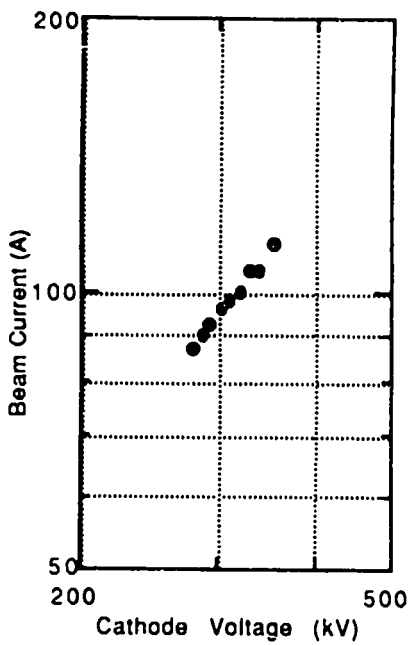

The RF output pulse duration and peak power were 140 nsec and 9.2 MW, respectively.

Fig-6)

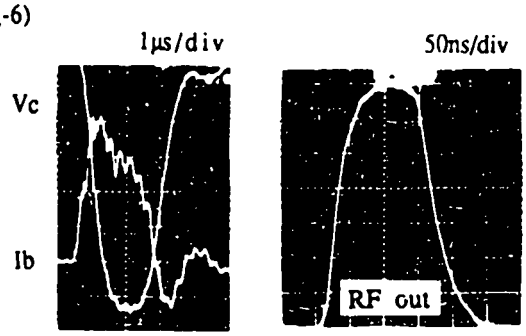

Fig-7) shows the relations of cathode voltage vs. saturated output RF power and efficiencies up to 350 kV of the cathode voltage.

Fig-7)

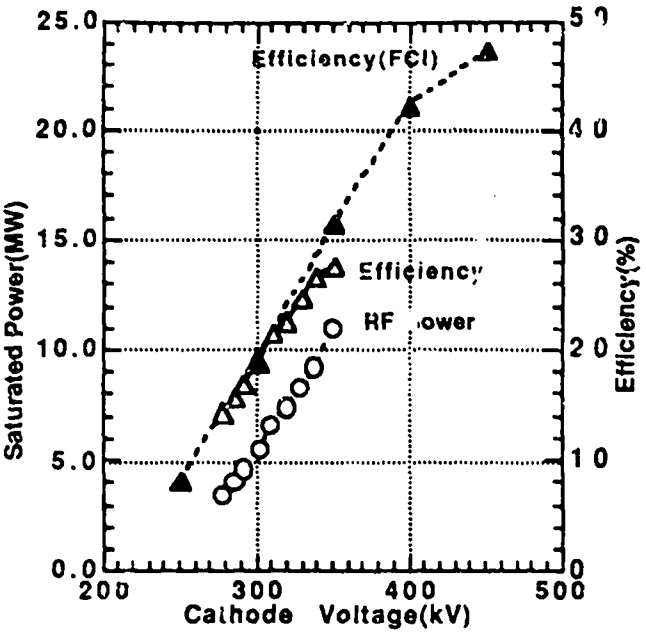

The efficiency and the simulation result by the use of FCI-code are also shown in Fig-7). The measured RF power and the efficiencies showed a good agreement with the FCI simulation results up to 350 kV cathode voltage and 11 MW RF output. The measured input vs. output performance with FCI simulation results are shown in Fig-8). At the cathode voltage of 250kV and 300kV, each measured curves are fairly good agreement with the FCI simulations.

Fig-8)

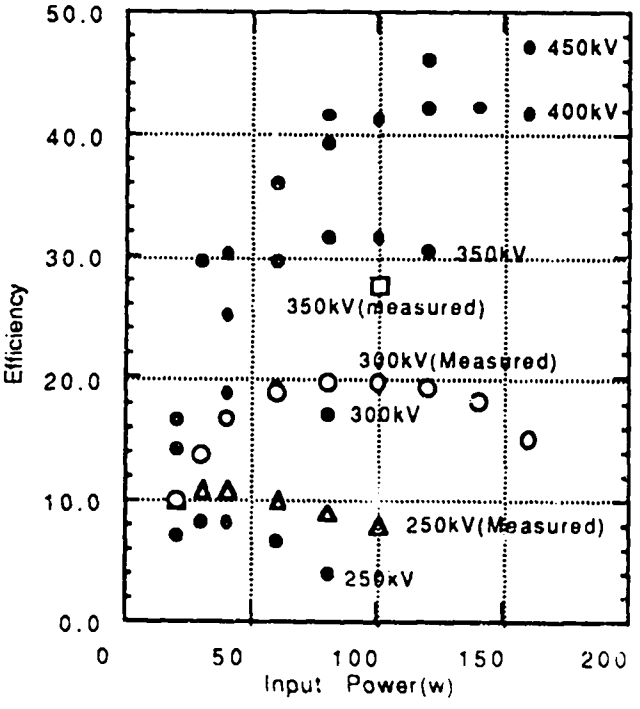

While conditioning the tube around or over 11 MW with the RF pulse duration of 70 nsec, the light emission from the window ceramics became brighter than before and the pressure burst in the wave guide increased up close to 1*10-6 Torr. At almost the same time RF output wave form became unstable and RF power level had to be decreased. On the ceramics surface of the atmospheric side of the RF window, a serious damage, which is apparently caused by the RF discharge, was observed and the window had an air leak fatal for a vacuum tube through the ceramics. On the surface of the ceramics, discharge marks of sputtered metal film was observed and inside of the waveguide, fine powder of the chipped ceramics was found.

SUMMARY

A X-band 30 MW klystron was built and tested. Saturated RF output and efficiencies between 250kV to 350 kV of cathode voltage were in good agreement with the FCI simulation results. As long as the diode operation is concerned, no significant trouble was observed. While processing at 11 MW with the 70 nsec pulse duration, the half wave-length aluminum ceramics output window was fatally damaged.

ACKNOWLEDGEMENTS

We thank Drs. M.A.Allen, T.Lee R.H.Miller and A.E.Vlieks for helpful suggestions on the design and technological features. We thank to Drs. H.Yonezawa and Y.Okazaki for the fabrication of the test tube.

REFERENCES

1)K.Takata and K.Kimura; "TRISTAN AND HIGH ENERGY ACCELERATOR PLANS AT KEK" Proc. 14th International conference on high energy accelerators PART4. Aug. 1989. P87.

2)W.B.Herrmannsfeldt;"ELECTRON TRAJECTORY PROGRAM" SLAC-226 UC-28(A).

3)H.Mizuno, J.Odagiri and T.Higo; "X-BAND KLYSTRON DIODE TEST FOR JAPAN LINEAR COLLIDER" Proc. 14th International conference on high energy accelarators PART4. Aug. 1989 P1125.

4)T.Shintake;"High-Power Klystron Simulations using FCI-Field Charge Interaction Code" KEK Report 90-3 May 1990 A/D.

5)S.Kimura et al.;"Long-life High-reliability Ir-coated Dispenser Cathode",Tech. Digest, IEDM.Washington D.C. P689.(1987)

KLYSTRON MODULATORS WITH HV COMMON-BUS FOR THE JLC

M. Akemoto, H. Hayano, T. Kawamoto, T. Shidara, J. Urakawa and S. Takeda

KEK, National Laboratory for High Energy Physics
Oho 1-1, Tsukuba, Ibaraki 305, Japan

Abstract

The Klystron Modulators with HV common-bus for the JLC (Japan Linear Collider) have been designed and constructed. The system consists of two modulators with a 10 or 18 section pulse forming network and a 45 kV DC power supply capable of driving 8 modulators. The modulators are operated for SLAC-5045 or TOSHIBA-E3712 klystrons at a maximum pulse repetition rate of 50 pulses/sec and the following two modes; 1) 67 MW in a pulse duration of 7.0 μs with a flat top of 4.5 μs and 2) 100 MW in a pulse duration of 3.5 μs with a flat top of 1.0 μs. The design, specifications and results of performance tests of the system are described in this paper.

Introduction

A TeV electron-positron linear Collider JLC (Japan Linear Collider) has been proposed in KEK[1]. It requires the S-band linacs as 1.54 GeV damping ring injectors[2], 4 GeV electron and positron pre-accelerators for the bunch length compression and 10-30 GeV electron linac for a positron production. The rf system of these linacs requires several hundred klystrons with a peak power of 100 MW at a frequency of 2856 MHz. Therefore, also a large number of klystron modulators are necessary. It is crucial to develop klystron modulators with a small size by a low cost modulator system of that a large power supply provide dc to many modulators with HV common-bus is one of the some methods to reduce a cost and size. In order to study the system of modulator system, we have designed and constructed a system which consists of two modulators with a pulse forming network (PFN) and a high voltage dc power supply which provide dc to 8 modulators, in the Accelerator Test Facility (ATF) for the JLC.

Design and modulator specifications

SLAC-5045[3] and TOSHIBA-E3712 klystrons are used as the S-band RF sources of ATF. SLAC-5045 klystrons used at SLC are operated at 67 MW peak power and 4.5 μs flat topped pulse duration. The peak power can be increased up to 100 MW peak power if the pulse duration is decreased to 1 μs. TOSHIBA-E3712 klystrons can produce the peak power of 100 MW at 1 μs. Table 1 shows the specifications of E3712 klystron.

Table 1. Specifications of E3712 klystron

Operation mode	Long Pulse	Short pulse
Peak RF power	80 MW	100 MW
RF pulse width	4.0 μs	1.0 μs
Beam voltage	375 kV	450 kV
Beam current	460 A	604 A
Peak beam power	173 MW	272 MW
Efficiency	46 %	39 %
Perveance	2.0 $\mu AV^{-3/2}$	2.0 $\mu AV^{-3/2}$
Average beam power	56 kW	48 kW
Repetition rates	50 pps	50 pps
Drive RF power	300 W	375 W
Gain	54.3 dB	54.3 dB
Frequency	2856 MHz	2856 MHz

These klystrons are operated at the following two modes; (1) 67 MW in a pulse duration of 7.0 μs with a flat top of 4.5 μs (long pulse mode for a RF pulse compression), (2) 100 MW in a pulse duration of 3.5 μs with a flat top of 1.0 μs (short pulse mode). The klystron modulators with HV common-bus consist of two modulators with a 18 section pulse forming network (PFN) and a 45 kV DC power supply capable of driving 8 modulators as shown in Fig. 1. Two klystron modulators are provided with power by means of 20D cables from a dc power supply. These modulators connected with HV common-bus receive the same voltage. Each modulator is of a line-type with a 18 section PFN. Regulation of the output pulse voltage is performed by the de-Qing circuit which controls the charging voltage of the PFN. Its output pulse voltage is stepped up to 15 times by a pulse transformer. The power supply and klystron modulators are remotely controlled from the main control room. The details are described in the following sections. Specifications of the modulator are listed in Table 2.

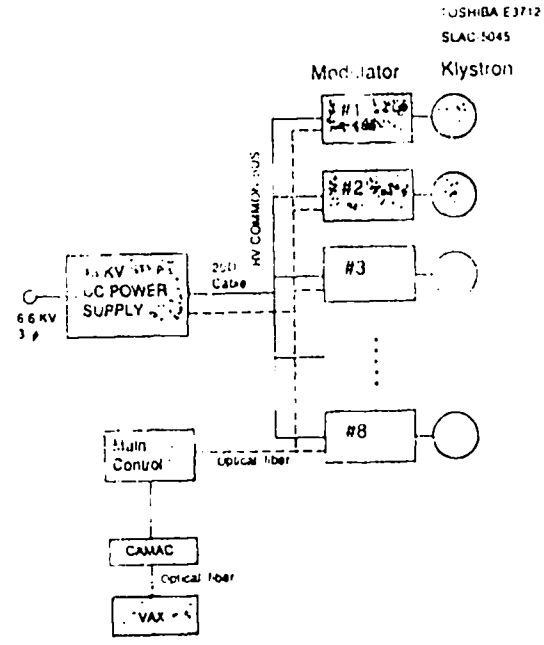

Fig. 1. Klystron modulators with HV common-bus
Modulators #3~#8 will be constructed in near future.

Table 2. Specifications of the modulator

Operation mode	Long Pulse (80MW)	Short Pulse (100 MW)
Peak power output	174 MW	272 MW
Average power output	60 kW	44 kW
Transformer ratio	1:15	1:15
Output pulse voltage	25.0 kV	29 kV
Output pulse current	6930 A	8625 A
Output impedance	3.6 Ω	3.4 Ω
Pulse flat top	4.5 μs	1.0 μs
Rise time	0.8 μs	0.8 μs
Pulse height deviation from flatness	1.0%(p-p)	1.0%(p-p)
Pulse amplitude drift		
Short term	<0.5 %	<0.5 %
Long term	<1.0 %	<1.0 %
Repetition rates	50 pps	50 pps

45 kV dc power supply

A simplified diagram of the dc power supply is shown in Fig. 2.

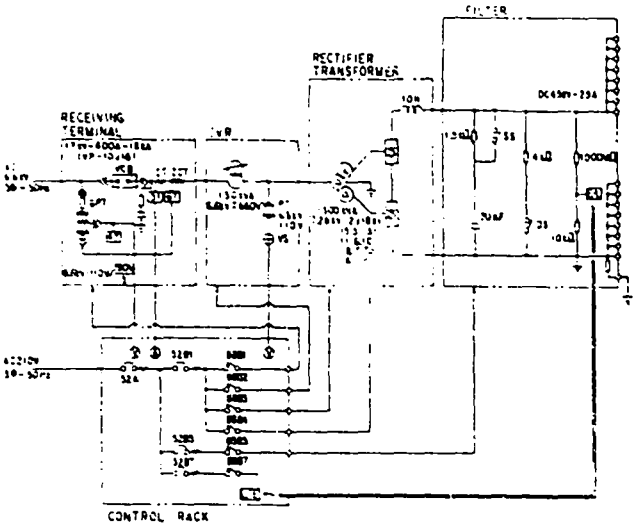

Fig. 2. A simplified diagram of the dc power supply

The line input is 6.6 kV ac, three-phase and 50 Hz and fed to receiving terminal board. A vacuum circuit breaker (VCB) is equipped to disconnect from the line for maintenance purpose as well as interlocks of over current and voltage of the common-bus. The VCB disconnects the line within one cycle of ac voltage (20 msec) when the interlock is worked. An induction voltage regulator (IVR) is used to regulate the ac line voltage in a range of ± 10%. The output voltage of the IVR is controlled with an accuracy of ± 1% by a feedback loop to the ac input line. The stepped-up ac is rectified to dc in 12-phase full wave scheme. The voltage level can be changed by selecting a primary tap of the rectifier transformer. The LC filter decreases the voltage ripple and determines the voltage drop due to the pulse load. A capacitance of 20 μF make this drop 7.5 % for the operation of two modulators. In order to reduce rush current in charging the capacitance, a limiter of 1.5 kΩ resister is prepared, which is by-passed after suitable charging time. A discharging-switch which is closed when the high voltage is off is installed as well as above mentioned limiter-switch in the filter cabinet. The specifications of the dc power supply are listed in table 3. The rectifier transformer, rectifier and choke are housed in the same oil tank.

Table 3. Specifications of 45 kV dc power supply

Rectification method	12 phase full-wave rectifier
Regulating range of IVR	± 10%
Maximum output voltage	45 kV
Maximum output current	25 A
Choice of rated output voltage	16,19,22,25,29,34,39,45 kV

Klystron modulator

The klystron modulator is composed of a charging unit with a de-Qing circuit and a discharging unit with the PFN, a trigger circuit, thyratron and an inverse-clipping shunt circuit as shown in Fig. 3. Each modulator connects with HV common-bus and receives the HV from the dc power supply through to 20D cables. The PFN capacitors are resonantly charged through a charging transformer. The inductance of the charging transformer was determined by the resonant charging frequency and total capacitance of the PFN (0.9 μF). The repetition rates is 50 pps and charging time is chosen to be 10 msec (half of the maximum repetition time). A de-Qing circuit in secondary of the charging transformer regulates the voltage applied to the PFN. A step down ratio of 25:1 was chosen to employ a silicon-controlled rectifier (SCR) switch. A simple series connection of the resistor and SCR switch was adopted. In this system, the common voltage is supplied to the modulators. The klystrons should be operated at different voltage to obtain the same rf power from each klystron since the perveance is slightly differnt. The regulation of the de-Qing circuit is chosen to be 15 % to realize the flexibility of adjustment of the klystron voltage.

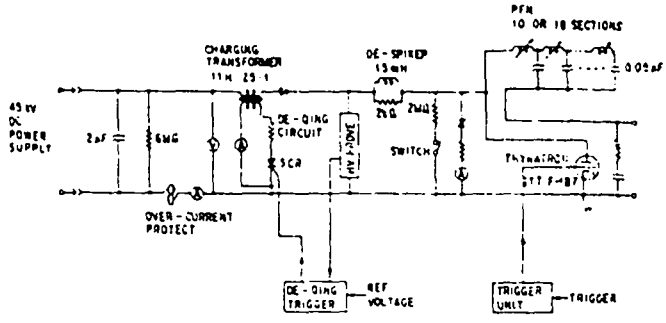

Fig. 3. A simplified diagram of the modulator

The PFN consists of 18 sections with fixed capacitors and tunable inductors. The capacitors are specified to be 0.05 μF and 70 kV operating voltage. The capacitors are composed by condenser paper, polypropylene film and aromatic hydrocarbon. As the inductance of each PFN coil is small, it is necessary to minimize the residual inductance of the capacitor. A special low inductance capacitor[5] was developed for the PFN. The residual inductance of each section is less than 100 nH. The tunable inductors are mounted on the capacitor's high voltage bushing stub. Fine adjustment is made by varying the insertion depth of an aluminum cylinder in the coil. The inductor consists of 7.5 turns of copper rectangular wire (2 mm X 45 mm) wound on the epoxy bobbin (97 mm diameter) of variable length with an aluminum insertion cylinder (89 mm diameter, 520 mm length). The inductance of this PFN coil is variable in a range from 0.4 to 1.4 μH, corresponding to a range of the characteristic impedance of the PFN between 2.8 Ω and 5.3 Ω.

Control and monitor system

The distance between the dc power supply and klystron modulators is about 100 m and each control equipment is distributed in a wide range. In order to operate this modulator system, the intensive control and monitoring system is indispensable. The modulator control system is schematically shown in Fig. 4.

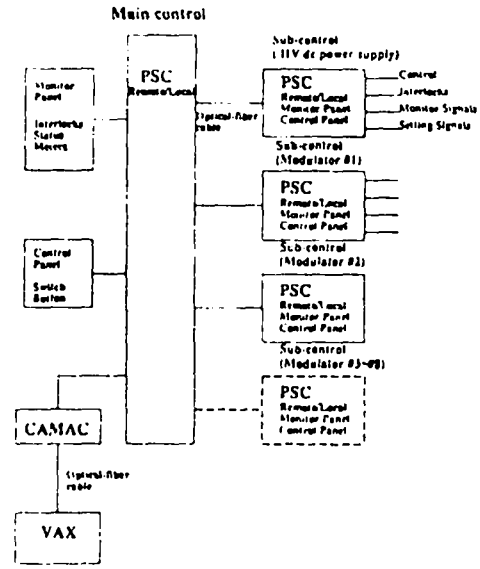

Fig. 4. Block diagram of the modulator control system.

It consists of a main control and sub-control equipments. The main control equipment remotely controls the dc power supply and all of eight modulators. It is necessary to operate the modulator system as a unit for a maintenance and test operation, and make it easy. The sub-control equipment manually controls each modulator in the local mode. It is located near the modulator and has the control panel which contains all the necessary controls, meters, and interlock displays to operate the modulator. The remote control and data collection are performed by a programmable sequence controller (PSC), which have a CPU, digital input/output, ADC, DAC and so on and act with reliability. The PSCs of the sub-control are connected to main control with optical-fiber cables. The PSC of the main control is also connected to the ATF control system consisting of CAMAC and two microVAXs which are connected to the KEK network.

Performances

Prior to the practical use of the modulator for klystrons, it is tested by feeding the output power to a dummy load (4Ω) using 32 ceramic resistors[7]. After adjusting the PFN inductances, the output pulse waveform is shown in Fig. 5, which is picked up by a current transformer in the dummy load. Its expanded trace of the pulse top is also shown in Fig. 6. The pulse top is flat within ± 0.5 %.

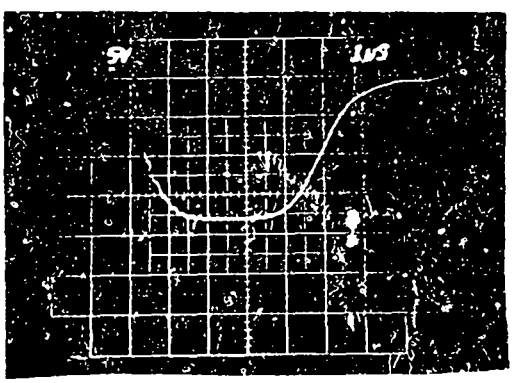

Fig. 5. Output pulse current (peak ~ 7200 A) at dummy load (1 μs/div)

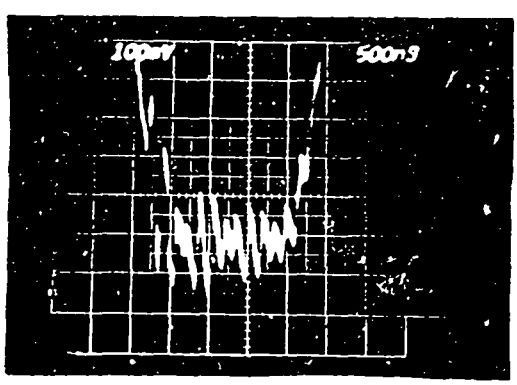

Fig. 6. Expanded pulse top trace of the output pulse current at the dummy load (500 ns/div).

For the high-gradient study[8,9] of S-band disk-loaded structures, this modulator system is used to operate SLAC-5045 and TOSHIBA-E3712 in short pulse mode to obtain a peak power of 200 MW, using a -3 db directional coupler. The output pulse waveforms of E3712 klystron in the operating are shown in Fig. 7.

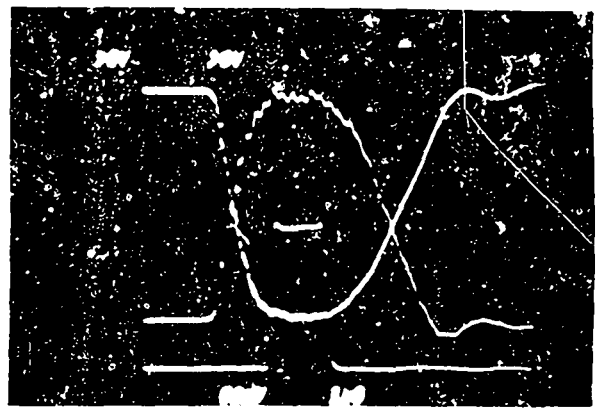

Fig. 7. Output waveform of E3712 klystron at 100 MW
H: 1 μs/div
Upper trace: Beam voltage (444 kV)
Middle trace: Beam current (535 A)
Lower trace: Output power (100MW)

Summary

In order to study the modulator system of a large dc power supply feeding many modulators, we have designed the modulator system consisting of a HV dc power supply and eight modulators. The HV dc power supply and two modulators have been constructed and used to operate SLAC-5045 and TOSHIBA-E3712 klystrons successfully to obtain 100 MW for each klystron.

References

1. K. Takata, "The Japan Linear Collider," contributed paper to this conference.
2. J. Urakawa et al., "Preliminary Design of 1.5 GeV Damping Ring and Bunch Compressor," contributed paper to this conference.
3. T. Lee et al.,"A Fifty Megawatt Klystron for the Stanford Linear Collider," 1983 International Devices Meeting, Washington, D.C., 1983.
4. H. Yonezawa et al.,"Development of a 100 MW S-band Pulse Klystron," Particle Accelerators, 1990, Vol. 30, pp. 219-224.
5. H. Sakaguchi (Nichicon Co.), private communication.
6. H. Hayano et al., "Control system of ATF," contributed paper to this conference
7. M. Yoshida et al.,"Fabrication of the 12 kW Dummy Load for the modulator," Proceedings of the 14th Linear Accelerator Meeting in Japan, 1989 (in Japanese).
8. H. Matsumoto et al.,"Experimental Study of the S-band High Gradient Electron Linac," contributed paper to this conference.
9. S. Takeda et al.,"High gradient Experiment by Accelerating Test Facility for Japan Linear Collider," contributed paper to this conference.

A LONG-PULSE THYRISTOR-SWITCHED MODULATOR FOR THE JHP PROTON LINAC

S. Anami, M. Kawamura, T. Kubo, K. Kudo, M. Ono, E. Takasaki and T. Takenaka
KEK, National Laboratory for High Energy Physics
1-1 Oho, Tsukuba-shi, Ibaraki-ken, 305, Japan

S. Ogawa and S. Koseki
Hitachi Works, Hitachi, Ltd.
Saiwaicho, Hitachi-shi, Ibaraki-ken, 317, Japan

Abstract

A long-pulse, high-duty klystron modulator which was fabricated as a prototype for the JHP 1-GeV proton linac has been operated at 15 MW peak power, 400 μs pulse width and 50 Hz repetition rate[1-3]. This modulator is of a line type which has a pulse forming network switched by two thyratrons in parallel. From a viewpoint of reliable operation and long lifetime it seems that thyratrons are unsuitable for our use of long-pulse and high-average currents (now, 15 A at 400 μs pulse width and, final, 23 A at 600 μs); therefore we must develop the use of SCR or GTO thyristors in place of the thyratrons. Prior to the construction of the full rate thyristor switch, the SCR-stack and GTO-stack modules with a 10 kV hold-off voltage were built and tested in the modulator with a klystron load through a pulse transformer. The design considerations and the test results are reported.

Introduction

The 1-GeV proton linac for the Japanese Hadron Project, which is now under development at KEK, requires 36 L-band klystrons and modulators in its high-β section. Although the klystrons will be operated at an rf output power of 4 MW at unsaturated level, the power capability is required to be about 6 MW in order to achieve the reliable operation; the first-fabricated prototype modulator, which is needed for testing the developed klystrons, must produce maximum 15 MW pulses.

The performance of modulators is a key point for successful operation of the rf system. We had decided to adopt a line type for the prototype from a standpoint of our great experience in operation. The main switch used for discharging a pulse forming network (pfn) is the most important device of a line type modulator. For its operational reliability and maintainability, it is apparent that solid state devices such as SCR and GTO are suitable rather than thyratrons for extremely high-duty factor and long-pulse operation.

Prototype Modulator

A 6-MW klystron requires a modulator with a 15 MW pulsed power and a 140 kV anode voltage, where the rf conversion efficiency and the perveance are estimated to be 40 % and 2×10^{-6} A/V$^{3/2}$, respectively[2]. Taking account of the characteristics of thyratrons, which is tentatively used as switching devices, we determined the modulator output voltage to be 20 kV; it means a pfn charging voltage of 40 kV, so that the step-up ratio of a pulse transformer is 1:7[3]. When the pulse width is 600 μs and repetition rate 50 Hz, the average output power becomes 450 kW[1].

The design value required for the prototype modulator is summarized in table 1. Widening in pulse width increases the pfn size and cost, and a very high duty factor makes it difficult to perform stable operation. Thus, at the first construction we had decreased the pfn pulse width to 200 μs, and then, after the various test operations, increased it up to 400 μs. This prototype modulator was designed so that the output pulse width can easily be increased up to the 600 μs only by adding a pfn section.

A circuit diagram of the fabricated and upgraded modulator is shown in Fig. 1. The output voltage is continuously variable from 20 % to 100 % by rotating the

TABLE 1
Basic Parameters of the Prototype Modulator

Peak Power	15 MW
Average Power	300 kW (* 450 kW)
Pulse Voltage	20 kV
Pulse Current	750 A
Pulse Width	400 μs (* 600 μs)
Pulse Rise Time	< 20 μs
Pulse Repetition Rate	50 Hz

(Symbol * indicates the final objective)

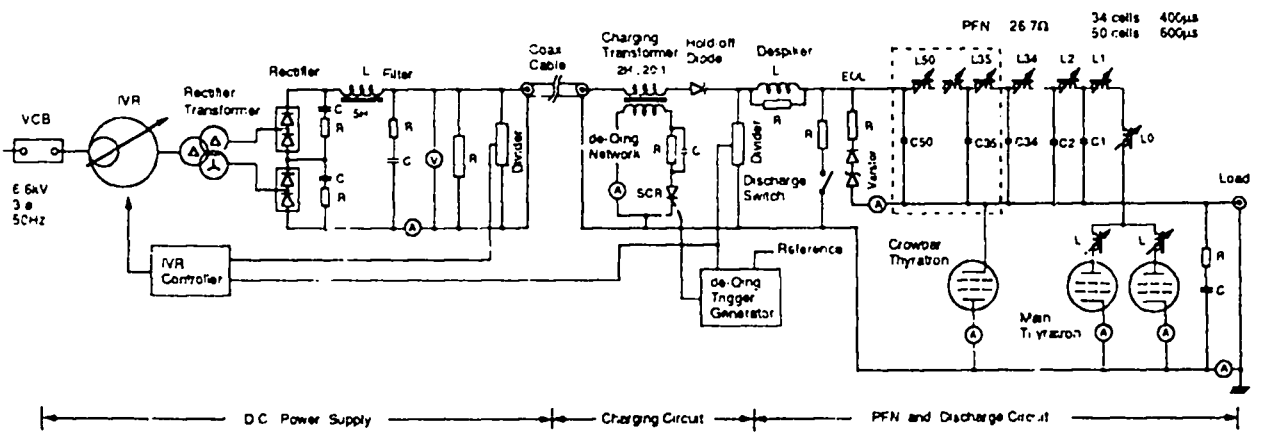

Fig.1 Circuit diagram of the prototype modulator. A dashed box indicates pfn components added at final phase.

rectifier transformer taps and the IVR, and regulated by a de-Q'ing circuit. A short circuit current in the event of a main thyratron faut or HV circuit arcing is limited to no more than 10 times the normal full load current by the IVR and transformer inductance of 10 %.

At first we used two ITT F-175 thyratrons in parallel as the main switch for 200 μs pulse width operation, but it was found that they could not withstand the charging voltage above 30 kV under our operation conditions. Immediately after that, we replaced two F-175's with one F-259, which was recently developed by ITT for very high duty use (50 kV, 10 kA peak and 25 A average). When increasing the pulse width up to 400 μs one more tube was added in parallel in order to be ready for the 600 μs operation.

Turn-off of Switches

In very high-duty line-type modulators it becomes impossible to turn off the main switch, because the time necessary to recover it after conduction is insufficient. The following methods can be considered to overcome this problem:

1. Short-circuiting the output for producing negative pulses.
2. Triggered charging (command charging) for delaying the charging of the pfn.
3. Using GTO thyristors for turning off the anode current.

The output short-circuiting method is adopted into our prototype modulator, in which a crowbar thyratron clips or short-circuits part of the first pulse tail or the positive mismatched pulse to ground by proper timing of its firing. However, since the reverse voltage pulse does not appear at the anode until the shorted pulse transmits between the pfn front and end, the charging current from the dc power supply is bypassed by the main thyratrons during more than one pulse output, resulting in lowering the circuit efficiency.

The command charging is the most conventional and useful method. By replacing a charging diode with some device which can be triggered, it becomes possible to control the charging start, and therefore to use even such SCR's with long recovery times as main switches.

SCR Switch

High hold-off voltage SCR's generally have high current handling capability and high critical rate of rise of anode current (di/dt). However, the allowable value of the di/dt for repetitive operation is not opened by device suppliers. If the initial rate of the anode current exceeds a certain value, the SCR may be either destroyed or permanently damaged owing to the excessive localized overheating.

In order to obtain the di/dt capability and to predict the lifetime under our required operating condition, we tested general-use type of SCR's (Hitachi CSP300AG35; 300 A, 3.5 kV). As a result of the test it was found that the di/dt value allowable for the long term use was estimated to be 100 A/μs at the repetitive pulse operation with 750 A peak current, 600 μs pulse width and 50 Hz repetition rate.

A circuit diagram of the SCR switch designed for the prototype modulator is shown in Fig. 2. The SCR switch consists of the 5 SCR-stack modules connected in series through each anode inductor for suppressing the rapid di/dt. As shown in Fig. 2, one SCR module is composed of a 6-SCR's stack with the circuits of RC snubbers and balance resistors, a gate-drive circuit and transformer, and an insulating transformer for supplying ac power. Characteristics of each SCR, turn-on time, off-state leak current and turn-off stored charge, are ranged within certain values by selection. The circuit parameters were determined according to the

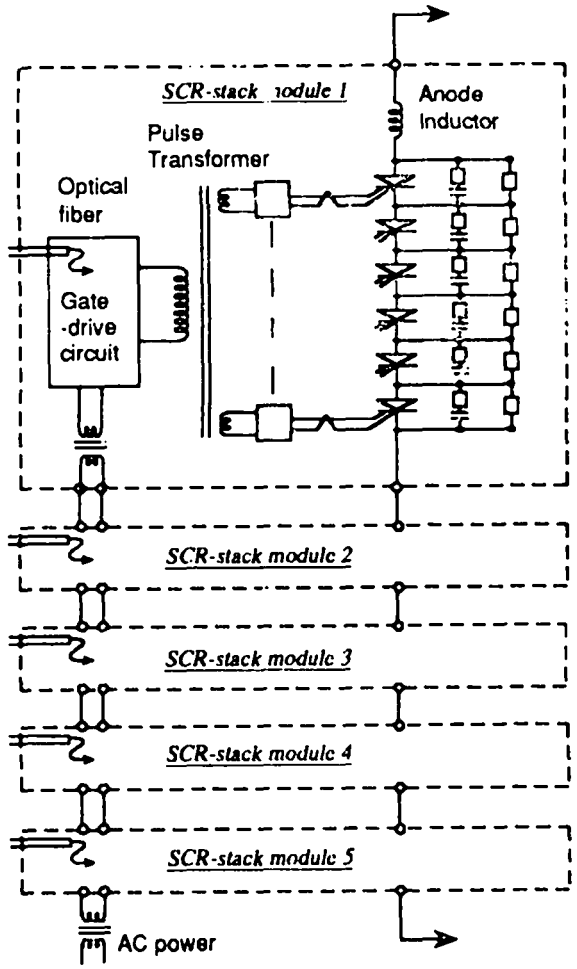

Fig. 2 Circuit diagram of the SCR switch designed for the prototype modulator (45 kV max. forward voltage, 750 A peak current).

conventional technology established in the industrial field of the high voltage electric power. These SCR modules will be operated at a maximum forward voltage of 9 kV, which means an applied voltage of 1.5 kV per SCR, corresponding to 43 % of the maximum allowable device voltage. The whole circuit is now being constructed and the first test will be done without a command charging circuit.

Test of SCR Stack Module

The 6-SCR's stack module was fabricated and tested to make sure of the switching performance in an actual high-power level. The SCR module incorporated into the prototype modulator was operated at a pfn charging voltage of 10 kV, and produced output pulses with 6.3 kV peak voltage and 130 A peak current. The modulator output was terminated with a klystron load through a step-up transformer. The observed waveforms are shown in Fig. 3(b), together with the ones obtained by the thyratron switch for comparison (Fig. 3(a)). In these waveformes, there is no difference between output pulses obtained by the SCR and the thyratron, but there are slight differences in the anode currents and voltages: a little reverse current appearance and lower forward voltage drop of

the SCR

GTO Switch and its Test

As mentioned above in the case of high duty it comes to be advantage that GTO thyristors capable of self-turning off are used even for line-type modulators; however, it is dangerous to turn off a high current flowing through circuit components with residual or lumped inductances. Since high power GTO's generally have very high, but uncontrollable, rate of fall of the anode current (−1000 A/μs) and result in inducing very high voltage at the falling time, very careful considerations must be given to the circuit design and the gate timing control.

A GTO stack switch was also tested in the prototype modulator to observe the turn-off transient. The GTO used has following characteristics: 8kV repetitive off-state voltage, 1000 A controllable on-state current, 300 A/μs critical rate of rise of on-state current and 300 A turn-off gate current (MEIDENSHA G10D80YNH). A circuit diagram of the tested GTO switch is shown in Fig. 4. Resistor and diode series circuits, called the flywheel circuit, were equipped in parallel with the first pfn inductor and the filter inductor for absorbing and suppressing overvoltages induced during rapid current falling. The observed waveforms are shown in Fig. 3(c). The test conditions were the same as those of the SCR module: 10 kV charging voltage and turn-off triggered at the same timing as the crowbar trigger.

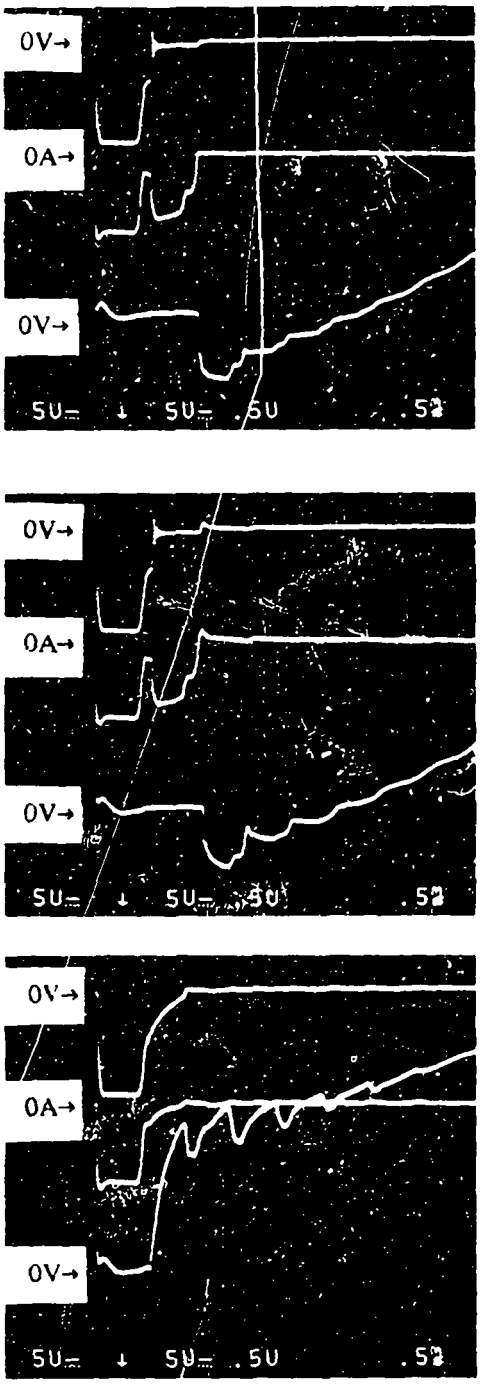

Fig. 3 Waveforms. Upper traces are klystron cathode voltage (25 kV/div), middle traces device cathode current (100 A/div) and lower traces device anode voltage (1 kV/div): Horizontal sales 0.5 ms/div.

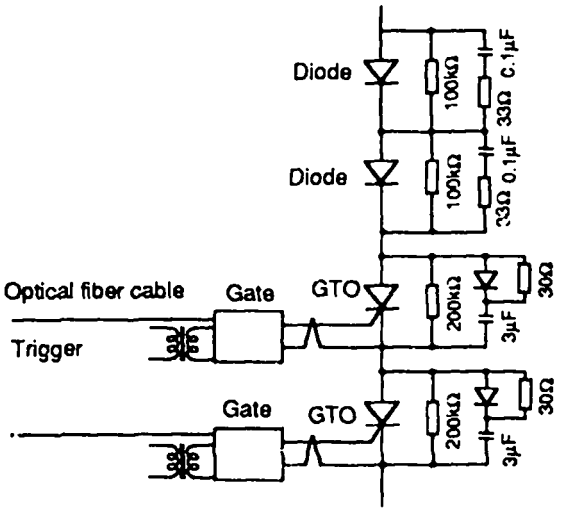

Fig.4 Circuit diagram of the GTO stack module.

Reference

1) S. Anami et al.,"Design and Construction of a Long-Pulse Modulator", submitted to Proc. 1989 Particle Accelerator Conf., 1989, Chicago.
2) M. Ono et al.,"Development of L-band High Power RF Source for the Japanese Hadron Project Proton Linear Accelerator", Proc. of the 14 Inter. Conf. on High Energy Accel. 1989, Japan, Part. Accel. 32 (1990) 51.
3) T. Kubo et al.,"Design and Construction of a Pulse Transformer for a Long pulse Klystron", ibid., Part. Accel. 32 (1990) 45.

RELATIVISTIC KLYSTRON SIMULATIONS USING RKTW2D*

Robert D. Ryne and Simon S. Yu
Lawrence Livermore National Laboratory, Livermore, CA 94550

Abstract

We are developing a two-dimensional, time-dependent computer code for the simulation of relativistic klystrons. We will discuss the main features of our code. We will also present an example simulation of a relativistic klystron with both a standing wave output cavity and a traveling wave output structure.

Introduction

Relativistic klystrons (RKs) that operate at high energy and with multiple extraction cavities are expected to be able to achieve high efficiencies. We are initiating experiments at the Advanced Test Accelerator at Lawrence Livermore National Laboratory to access this regime. The goal of this research is to develop induction linac-based RKs that produce around 1 GW of peak power for high gradient accelerator applications. We are developing a two-dimensional, time-dependent simulation code call RKTW2D to support this research.

Description of RKTW2D

RKTW2D follows a train of RF bunches, one at a time, through a klystron. The code has the following features:

1. 2D (r,z) azimuthally symmetric fields
2. self-consistent space charge (radial and longitudinal)
3. self-consistent beam-cavity interaction
4. treatment of standing wave (SW) cavities and traveling wave (TW) structures
5. time-dependent cavity excitation modelled using coupled circuit equations
6. cavity fields obtained from the RF cavity code SUPERFISH[1]

The basic equations used by RKTW2D are the single particle equations of motion and the coupled circuit equations governing cavity excitation. The single particle equations of motion are paraxial approximations to the Lorentz force equations using the longitudinal coordinate, z, as the independent variable:

$$\begin{aligned}
\frac{dx}{dz} &= v_x/v_z, \\
\frac{dy}{dz} &= v_y/v_z, \\
\frac{d\psi}{dz} &= \omega/v_z, \\
\frac{dv_x}{dz} &= \frac{q}{\gamma m}\left(\vec{E} + \vec{v}\times\vec{B}\right)_x, \\
\frac{dv_y}{dz} &= \frac{q}{\gamma m}\left(\vec{E} + \vec{v}\times\vec{B}\right)_y, \\
\frac{d\gamma}{dz} &= \frac{q}{mc^2}E_z,
\end{aligned} \tag{1}$$

where $\psi = \omega t$. Beam induced cavity excitation is based on a circuit equation (or coupled equations for TW structures). Assuming a single cavity mode is dominant, let the electric field in the nth cell of a traveling wave structure be given by

$$\vec{E}_n(\vec{r},t) = f_n\,\vec{\mathcal{E}}_n(\vec{r})\,e^{-i\omega t}, \tag{2}$$

where $\mathcal{E}_n$ denotes an eigenmode with eigenfrequency ω_n. Also, let ω denote the drive frequency of the klystron. Then it is possible to show that the excitations f_n are governed by the following coupled equations

$$\begin{aligned}
&\ddot{f}_n + \left(\frac{\omega_n}{Q_n} - 2i\omega\right)\dot{f}_n + \left(\omega_n^2 - \omega^2 - \frac{i\omega\omega_n}{Q_n}\right)f_n \\
&-\left(K_n^{n-1}f_{n-1} + K_n^{n+1}f_{n+1}\right) = \frac{i\omega}{\epsilon_o}\int dV_n\,\vec{\mathcal{E}}_n^*\cdot\vec{J}_1,
\end{aligned} \tag{3}$$

where Q_n denotes the quality factor of the nth cell, K_n^{n-1} and K_n^{n+1} denote coupling of the cell n to cell $n-1$ and cell $n+1$, respectively, and $\vec{J}_1$ denotes the RF current associated with the beam.

Simulation of the MOK-2 Relativistic Klystron

The MOK-2 is a Multiple Output Klystron that consists of an input cavity, three gain cavities, a SW output cavity and a TW output structure.[2] The klystron operates at 11.4 GHz. It was developed as part of a joint LLNL/SLAC/LBL collaboration in RK research. The MOK-2 achieved a maximum output power of 330 MW (30 MW from the SW output cavity and 300 MW from the TW structure) using a 1.3 MeV, 600 amp beam. The RKTW2D results shown below are not meant to show a careful comparison of the code with experiment, but are simply illustrative of the code's capabilities. A precise comparison of RKTW2D with experiment is being carried out at this time as an ongoing part of our RK research effort.

* Work performed under the auspices of the US Department of Energy by the Lawrence Livermore National Laboratory under W-7405-ENG-48

Figure 1 shows the input beam energy and current for the MOK-2 simulation. The 40 ns pulse has a 5 ns rise time , and 30 ns flat top, and a 5 ns fall time. The input cavity was driven at 1 kW and was assumed to have reached a steady state prior to the arrival of the beam. Figure 2 shows the voltage in the input cavity as a function of time and exhibits typical beam loading effects. Figure 3 shows the power produced by the SW cavity and Figure 4 shows the power produced by the TW structure. The SW cavity produces much less power because the RF current is lower there. Figure 5 shows that RF current as a function of distance along the klystron associated with an RF bucket 25 ns into the beam pulse. Though the SW output produces little power, it provides bunching so the RF current is large at the TW structure. The external magnetic field used in this simulation is shown in Figure 6; it is not the same as that used in the experiment but it does illustrate the code's ability to treat a variable magnetic field. Figure 7 shows the rms beam radius as a function of distance at 25 ns into the beam pulse.

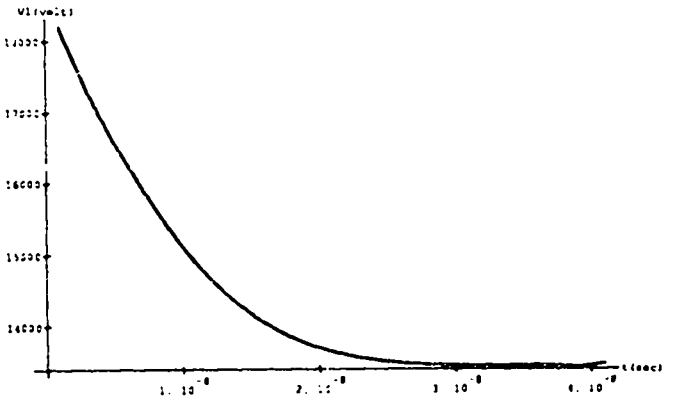

Figure 2 V_1 versus time

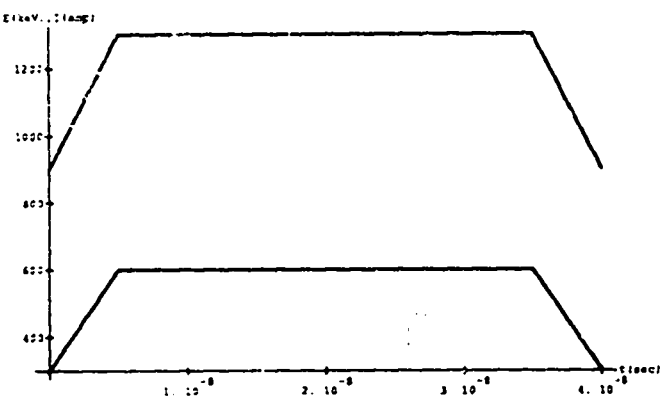

Figure 1 Beam energy (upper curve) and current (lower curve) versus time

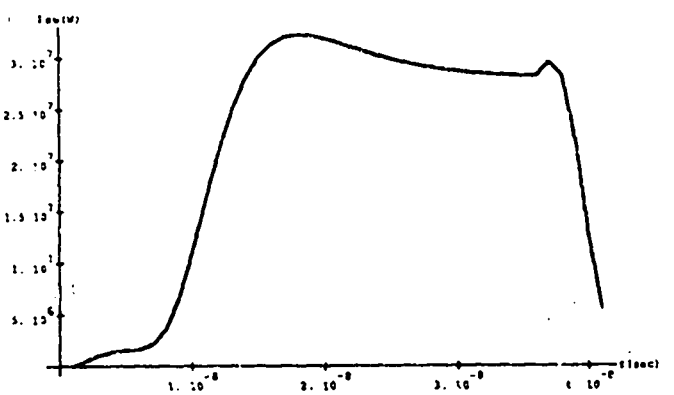

Figure 3 P_{sw} versus time

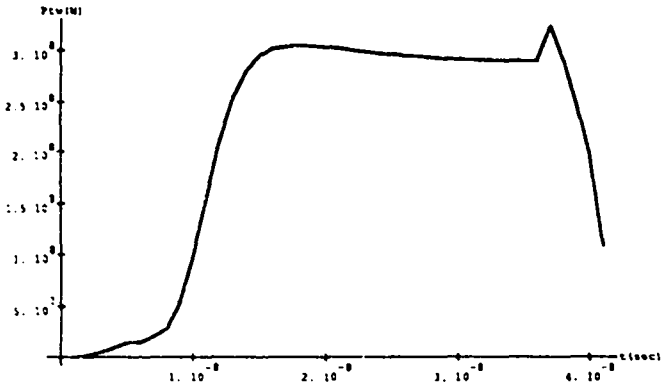

Figure 4 P_{tw} versus time

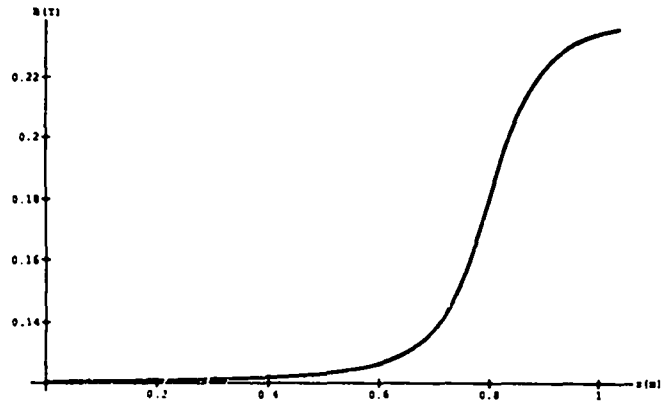

Figure 6 $B_z(r = 0)$ versus distance

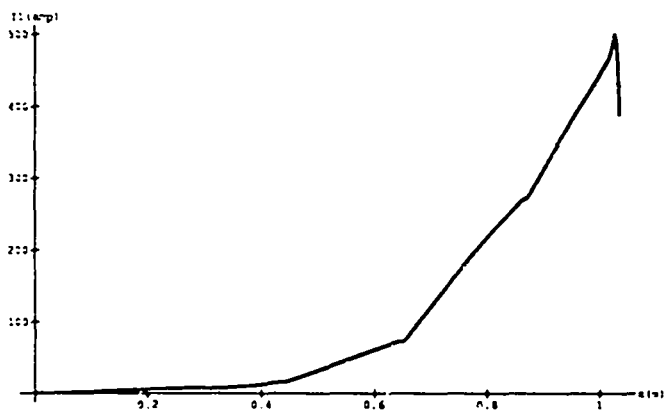

Figure 5 RF current versus distance (at t=25ns)

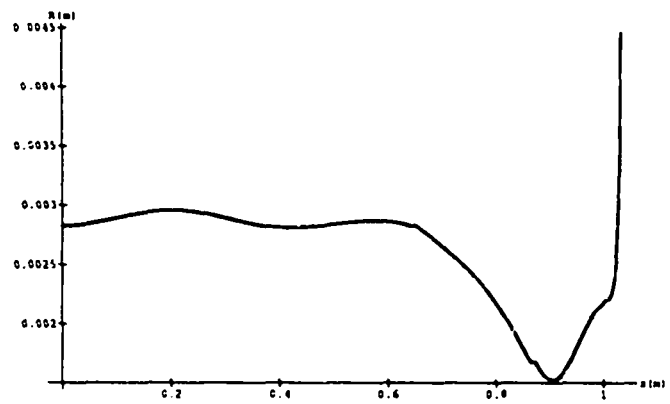

Figure 7 r_{rms} versus distance (at t=25ns)

Summary

We are developing a two-dimensional, time-dependent simulation code call RKTW2D to support relativistic klystron research at LLNL. Initial studies show that the code gives results that are similar to experimental results. We are carrying out careful comparisons of the code with experiment at this time.

References

1. K. Halbach and R. F. Holsinger, "SUPERFISH—A Computer Program for Evaluation of RF Cavities with Cylindrical Symmetry," Particle Accelerators 7, pp. 213–222 (1976)

2. M. A. Allen et al., "Recent Progress in Relativistic Klystron Research," Particle Accelerators 30, pp. 189–196 (1990)

USING TRAVELING WAVE STRUCTURES TO EXTRACT POWER FROM RELATIVISTIC KLYSTRONS*

Robert D. Ryne and Simon S. Yu
Lawrence Livermore National Laboratory, Livermore, CA 94550

Abstract

The purpose of this note is to analyze the excitation of traveling wave (TW) output structures by an RF current. Such structures are being used in relativistic klystron experiments at Lawrence Livermore National Laboratory. First we will present a set of difference equations that describes the excitation of the cells of a TW structure. Next we will restrict our attention to structures that have identical cells, except possibly for the first and last cells. Under these circumstances one can obtain difference equations that have constant coefficients, and we will present the general solution of these equations. Lastly we will apply our results to the analysis of a TW output structure. We will show that, by appropriate choice of the quality factors (Qs) and eigenfrequencies of the first and last cells, it is possible to obtain a traveling wave solution for which there is no reflected wave and where the excitation grows linearly with cell number.

Difference Equation Formulation

Consider a TW structure consisting of N cells. Let the electric field in the nth cell of the structure be given by

$$\vec{E}_n(\vec{r},t) = a_n(t)\vec{\mathcal{E}}_n(\vec{r})e^{-im\omega t}, \tag{1}$$

where $\vec{\mathcal{E}}_n$ denotes the eigenmode of the nth cell with eigenfrequency ω_n, and where we have assumed that $\omega_n \approx m\omega$. It is possible to show that, in the steady state, the excitations a_n are governed by the following difference equations:

$$\left(\omega_n^2 - m^2\omega^2 - i\frac{m\omega\omega_n}{Q_n}\right)a_n - \left(K_n^{n-1}a_{n-1} + K_n^{n+1}a_{n+1}\right) = \frac{im\omega}{\epsilon_o}\int dV_n \vec{\mathcal{E}}_n^* \cdot \vec{J}_m, \tag{2}$$

where $n = 1,\ldots,N$, and where $y_0 = y_{N+1} = 0$. In the above equations, K_n^{n-1} and K_n^{n+1} describe the coupling of cell n to cell $n-1$ and cell $n+1$, respectively. The quantity Q_n denotes the quality factor the nth cell. For a klystron output cavity, $\vec{J}_m$ denotes a component of the RF current associated with the bunched beam. It is important to note that the power extracted from the TW structure is proportional to $|a_N|^2$.

Below we will show that, by appropriate choice of Q_1, Q_N, ω_1 and ω_N, it is possible to obtain a solution of the difference equations that represents a traveling wave whose amplitude grows linearly with cell number.

To simplify our analysis, we will suppose that

$$K_n^{n-1} = K_n^{n+1} \stackrel{def}{=} K. \tag{3}$$

Then the difference equations have the following form:

$$\left(\omega_n^2 - m^2\omega^2 - i\frac{m\omega\omega_n}{Q_n}\right)y_n - K(y_{n-1} + y_{n+1}) = I_n, \tag{4}$$

where $n = 1,\ldots,N$ and where

$$y_0 = y_{N+1} = 0. \tag{5}$$

Now suppose that, except for the first and last cells, the quantities Q_n and ω_n are the same for all cells:

$$\begin{aligned} Q_n &= Q_\nu \quad (n = 2,\ldots,N-1), \\ \omega_n &= \omega_\nu \quad (n = 2,\ldots,N-1). \end{aligned} \tag{6}$$

We will allow for the possibility that Q_1 and ω_1 may be different; this would be the case if, for example, there were a coupling hole for power input. Also, we will allow for the possibility that Q_N and ω_N may be different; this would be the case if, for example, there were a coupling hole for power output. It follows that the difference equations can be written in the following form:

$$y_{n+1} - 2y_n\cos\alpha + y_{n-1} = f_n \quad (n = 1,\ldots,N), \tag{7}$$

where

$$\cos\alpha = \frac{1}{2K}\left(\omega_\nu^2 - m^2\omega^2 - i\frac{m\omega\omega_\nu}{Q_\nu}\right), \tag{8}$$

$$f_n = -I_n/K, \tag{9}$$

and with boundary conditions

$$\begin{aligned} y_0 &= \mu y_1, \\ y_{N+1} &= \eta y_N, \end{aligned} \tag{10}$$

where

$$\begin{aligned} \mu &= \frac{1}{K}\left[\left(\omega_\nu^2 - i\frac{m\omega\omega_\nu}{Q_\nu}\right) - \left(\omega_1^2 - i\frac{m\omega\omega_1}{Q_1}\right)\right], \\ \eta &= \frac{1}{K}\left[\left(\omega_\nu^2 - i\frac{m\omega\omega_\nu}{Q_\nu}\right) - \left(\omega_N^2 - i\frac{m\omega\omega_1}{Q_N}\right)\right]. \end{aligned} \tag{11}$$

(We usually deal with structures that have $Q_\nu \gg 1$. In this case α has a small imaginary part that can be neglected

* Work performed under the auspices of the US Department of Energy by the Lawrence Livermore National Laboratory under W-7405-ENG-48

if the total number of cells is not too large. In view of equation (8), the quantity ω_ν is the frequency for which the phase shift per cell equals $\pi/2$.)

The important point is that we have obtained difference equations with *constant coefficients* (at the expense of more complicated boundary conditions). These equations can be easily solved. The general solution of (7) is given by[1]

$$y_n = e^{i\alpha n}\left[\frac{-i}{2\sin\alpha}\sum_{r=1}^{n} f_r e^{-i\alpha r} + c_1\right] + e^{-i\alpha n}\left[\frac{i}{2\sin\alpha}\sum_{r=1}^{n} f_r e^{i\alpha r} + c_2\right], \tag{12}$$

where c_1 and c_2 are constants. In the above expression, the following is assumed:

$$\sum_{r=1}^{n} f_r e^{\pm i\alpha r} = 0. \tag{13}$$

Also, we assume that α is not equal to an integral multiple of π.

Application to a Traveling Wave Output Structure

Now we will apply these results to a TW output structure. Suppose the drive terms, f_n, have constant amplitude, but that the phase of f_n increases by α from cell to cell:

$$f_n = f e^{i\alpha n}. \tag{14}$$

It follows that

$$\sum_{r=1}^{n} f_r e^{-i\alpha r} = nf, \qquad \sum_{r=1}^{n} f_r e^{i\alpha r} = f e^{2i\alpha}\frac{1-e^{2i\alpha n}}{1-e^{2i\alpha}}. \tag{15}$$

It is easy to show that the solution of the difference equations is now given by

$$y_n = e^{i\alpha n}\left[\left(\frac{-i}{2\sin\alpha}\right)nf + \frac{fe^{i\alpha}}{4\sin^2\alpha} + c_1\right] + e^{-i\alpha n}\left[-\frac{fe^{i\alpha}}{4\sin^2\alpha} + c_2\right]. \tag{16}$$

Since we have assumed that the fields vary as $e^{-im\omega t}$, the first term above represents a wave traveling in the forward direction (from $n = 1$ to $n = N$), and the second term represents a wave traveling in the backward direction.

Now we must apply the boundary conditions given by (10) and (11). After some manipulation, the condition relating y_0 and y_1 leads to the following:

$$\mu = \frac{c_1 + c_2}{c_1 e^{i\alpha} + c_2 e^{-i\alpha}}. \tag{17}$$

The condition relating y_N and $y_N + 1$ is more complicated. However, we shall assume that

$$\cos N\alpha = 1, \qquad \sin N\alpha = 0. \tag{18}$$

In this case we obtain

$$\eta = \frac{\frac{Nf}{2i\sin\alpha}e^{i\alpha} + c_1 e^{i\alpha} + c_2 e^{-i\alpha}}{\frac{Nf}{2i\sin\alpha} + c_1 + c_2}. \tag{19}$$

Equations (17) and (19) are simultaneous equations in c_1 and c_2. Their solution is given by

$$c_1 = \left(\frac{-Nf}{4\sin^2\alpha}\right)\frac{(1-\mu e^{-i\alpha})(\eta - e^{i\alpha})}{1-\mu\eta}, \qquad c_2 = \left(\frac{Nf}{4\sin^2\alpha}\right)\frac{(1-\mu e^{i\alpha})(\eta - e^{i\alpha})}{1-\mu\eta}. \tag{20}$$

Summarizing, the solution to our problem is given by equation (16), where c_1 and c_2 are given by (20). The solution depends on the quantities μ and η. Assuming that Q_ν and ω_ν are given, the quantities μ and η are determined by the choice of Q_1, Q_N, ω_1 and ω_N through (11).

Matching Condition

By appropriate choice of μ and η it is possible to obtain a solution which consists of just a forward traveling wave. (This is what we mean by a "matched" structure). Referring to (16), the backward traveling wave will vanish when

$$c_2 = \frac{fe^{i\alpha}}{4\sin^2\alpha}. \tag{21}$$

Substituting equation (20) for c_2, we obtain the following matching condition:

$$N(1-\mu e^{i\alpha})(\eta - e^{i\alpha}) = (1-\mu\eta)e^{i\alpha}, \tag{22}$$

or

$$\mu e^{i\alpha} - \mu\eta\left(\frac{N-1}{N}\right) + \eta e^{-i\alpha} = \frac{N+1}{N}. \tag{23}$$

It follows that the solution of the difference equations is given by

$$y_n = \frac{fe^{i\alpha n}}{2i\sin\alpha}\left[n + \frac{\mu e^{i\alpha}}{1-\mu e^{i\alpha}}\right]. \tag{24}$$

The above equation shows that the excitation grows linearly with cell number in a matched TW structure.

Now consider the amplitude of the excitation in two extreme cases, $\mu = 0$ and $\mu \to \infty$:

$\mu = 0$

This corresponds to the case where the first cell has the same Q and ω as cells 2 through N. In this case, the matching condition reduces to

$$\eta = \left(\frac{N+1}{N}\right)e^{i\alpha}. \tag{25}$$

When $\mu = 0$, the constant term in square brackets in equation (24) (that is, the term that is independent of n) equals zero. In other words, the quantity in square brackets is equal to n.

$|\mu| \to \infty$

This corresponds to the case where $Q_1 \ll 1$. In this case, the matching condition reduces to

$$\eta = \left(\frac{N}{N-1}\right)e^{i\alpha}. \tag{26}$$

When $|\mu| \to \infty$, the constant term in (24) approaches -1, and the resulting quantity in square brackets approaches $n - 1$. Therefore the excitation of the nth cell is reduced from the $\mu = 0$ value by a factor $(n-1)/n$.

Obviously the true value of μ will lie between the extremes discussed above. Since the power produced by the structure is proportional to $|y_N|^2$, lowering the Q of the first cell will reduce the power output by a factor of at most $[(N-1)/N]^2$ from the maximum obtainable ($\mu = 0$) value.

Summary

The purpose of this note has been to analyze the excitation of TW output structures for use in relativistic klystrons. First we presented a set of difference equations that describes the excitation of the cells of a TW structure. Next we restricted our attention to structures that have identical cells, except possibly for the first and last cells. Under these circumstances, we were able to obtain difference equations that have constant coefficients, and we presented the general solution of these equations. Lastly we applied our results to the analysis of a TW output structure. We showed that, by appropriate choice of the quality factors and eigenfrequencies of the first and last cells, it is possible to obtain a traveling wave solution for which there is no reflected wave and where the excitation grows linearly with cell number.

References

1. F. Hildebrand, Finite-Difference Equations and Simulations, Prentice-Hall (1968), pp. 33–35.

STUDY OF HIGH EFFICIENCY LINEAR ACCELERATOR STRUCTURE

I. Sato and Y. L. Wang

National Laboratory for High Energy Physics
1-1 OHO, TSUKUBA-SHI, IBARAKI-KEN, 305 JAPAN

Abstract

A new type of traveling wave linear accelerator structure has been studied. This accelerator structure is based on the disk loaded structure increasing coupling slots on the disk. It has high shunt impedance, high Q value, high group velocity and low attenuation. Therefore this accelerator structure with the traveling wave resonant ring has high efficiency. Specially, for CW linacs or for the large beam current linacs, using this accelerator structure its efficiency can be reached as high as 90%.

The study was performed by means of computer codes SUPERFISH and MAFIA. The theoretical and experimental results of this study are presented.

Structure and Calculation

It is well known that for a disk-loaded accelerator structure parameters of shunt impedance R, group velocity Vg, Q value and attenuation α are functions of apeature 2a. They are shown on Fig. 1. If one wants to reduce apeature very small to get high R, it is impossible because of Vg and α changing rapidly that the energy can not propagate from one cell to the next cell. Our idea is that we punch some coupling slits on disks to increase the coupling. It makes the structure have the high shunt impedance R, high Q value, high group velocity Vg and low attenuation α. Its structures are shown on the Fig. 2. At first we calculate the type (a) using SUPERFISH code. The symbols a, b, D and t are as usual. rc is the radius of the center of the coupling slit and Δr is the width of the coupling slit. The Fig. 3, Fig. 4, Fig. 5 and Fig. 6 show the results of calculation.

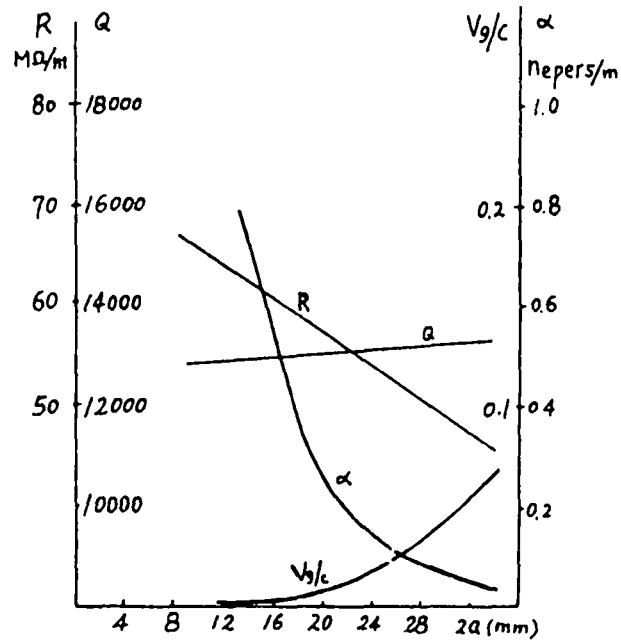

Fig. 1 Parameters of disk loaded

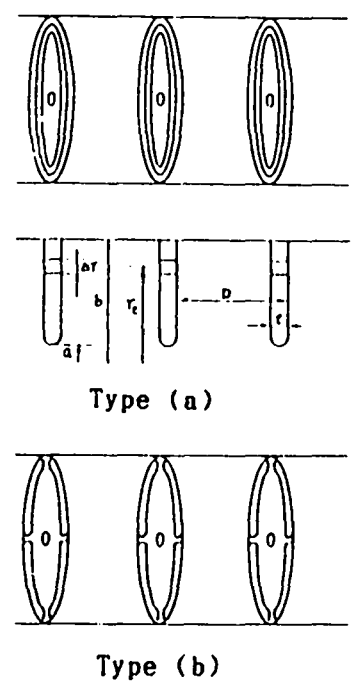

Fig. 2 Structure of test cavities

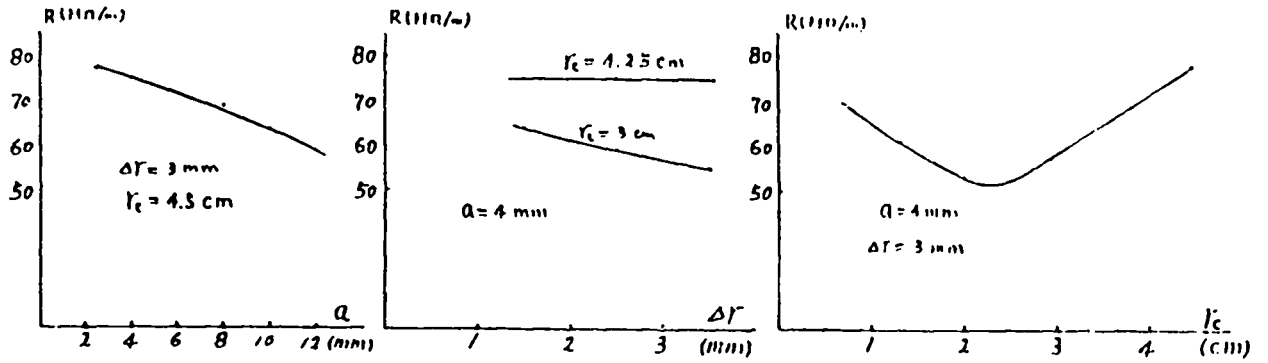

Fig. 3 Shunt impedance as functions of a, Δr and rc

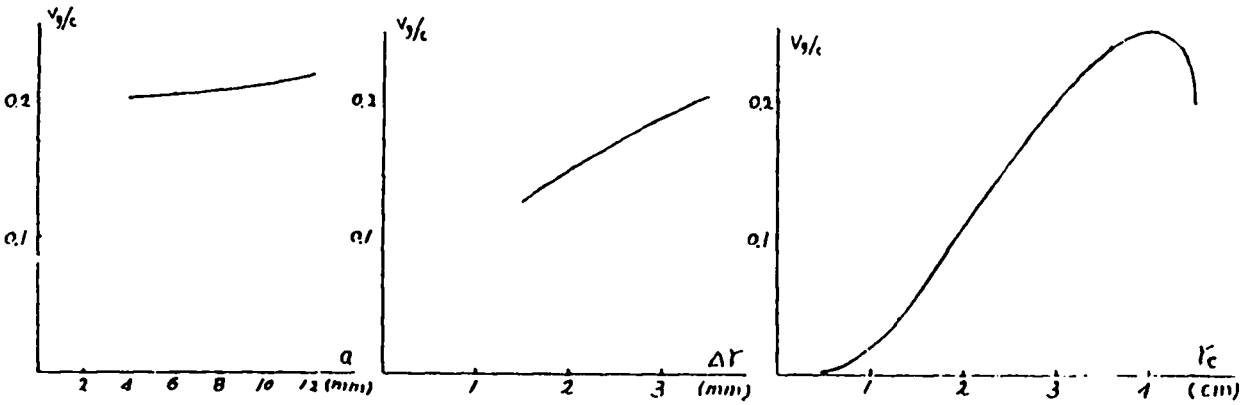

Fig. 4 Group velocity as functions of a, Δr and rc

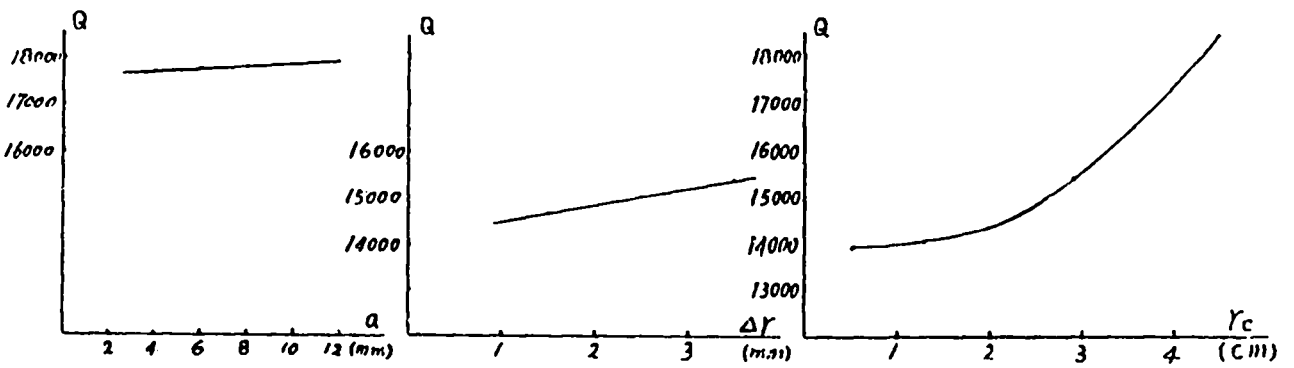

Fig. 5 Q value as functions of a, Δr and rc

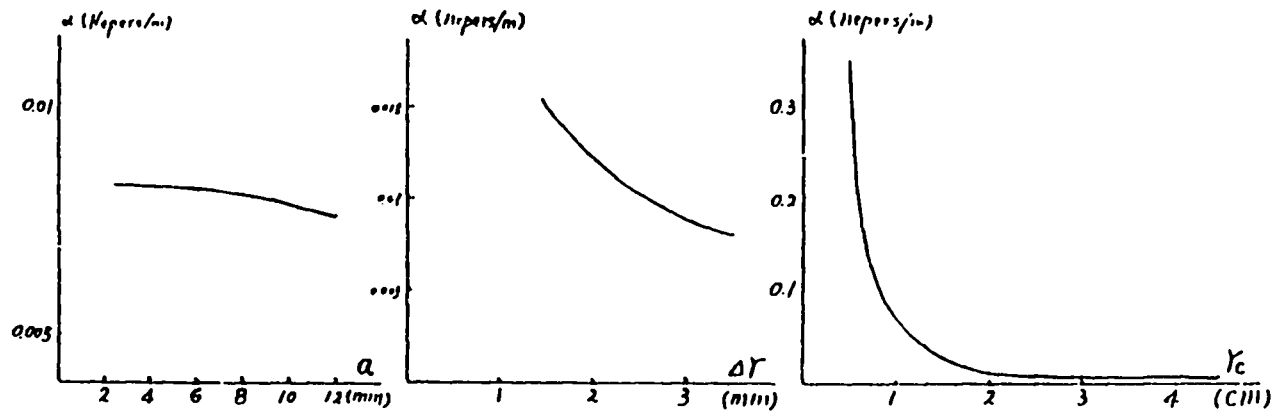

Fig. 6 Attenuation as functions of a, Δr and rc

Fig. 3 shows the shunt impedance R as functions of a, Δr and rc. R increases with decreasing a; R has a minimum when the coupling slit located at the middle of the disk and a maximum when the slit located at the side of the disk; when Δr increasing R decreases except that R is a constant nearly when the slit located at the side of the disk.

From above results we found that the structure in which the coupling slit located at the side of cavity ($rc=b-\Delta r/2$) is the best. It has high shunt impedance, high group velocity, high Q value and low attenuation. The accelerator using this structure has high efficiency. So we call it HELAS (High Efficiency Linear Accelerator Structure). The parameters of HELAS are shown on the Table 1.

Table 1. Parameters of HELAS

a mm	Δr mm	R MΩ/m	Vg C	α neper/m	Q
2.5	3.0	77.32	0.2040	0.00824	17760
4.0	3.0	75.10	0.2040	0.00821	17760
6.0	3.0	71.32	0.2058	0.00818	17790
8.0	3.0	66.60	0.2083	0.00806	17820
10.0	3.0	61.30	0.2126	0.00787	17860
12.0	3.0	56.08	0.2198	0.00763	17910

Because SUPERFISH can not calculate the three-dimension cavity shown on Fig. 2 type (b). We use MAFIA code to calculate it. In order to compare we calculate three types cavities (including type (c)-disk loaded). The results are shown on the Table 2.

Table 2. Results of Calculation

Type	(a)	(b)	(c)	Code
Vg. C	0.2348		0.0078	SUPER
	0.1904	0.2400	0.0035	MAFIA
R	75.10		62.2	SUPER
	51.30	33.5	51.5	MAFIA
Q	18510		13900	SUPER
	12200	12340	9990	MAFIA
α	0.0069		0.23	SUPER
	0.0124	0.0103	0.86	MAFIA

From Table 2 we can see that there are some difference results between by MAFIA and SUPERFISH calculation. According to MAFIA calculation the shunt impedance R, group velocity Vg and Q value are lower than that by SUPERFISH calculation.

Results of the experiment

A set of test cavities (type (a), disks supported by dielectric poles, Δr = 4mm, a = 4mm) has been manufactured. The ratio of the shunt impedance R to Q, Q value and frequencies of various modes are measured. The results are shown on Fig. 7 and Table 3. We can see that R/Q, Q value and frequencies measured are agreeable to that calculated by SUPERFISH code. Only Q value is lower than calculated. There are some dielectric losses. It is reasonable.

If we use the HELAS with traveling wave resonant ring to design a CW linac, the efficiency of the accelerator can get as high as 90%. It is very useful.

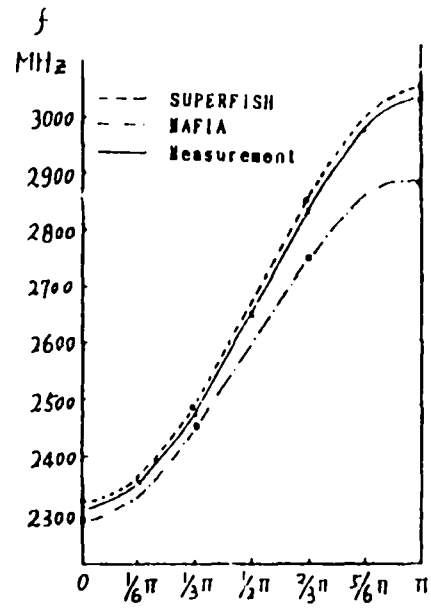

Fig. 7 Brillouin diagram of HELAS

Table 3. Results of experiment

	Ro/Q	Vg/C	Q
SUPERFISH	4057.2	0.2348	18510
MAFIA	4204.9	0.1924	12200
Measurement	3982.9	0.2300	13250

OPERATION OF A 473MHZ PULSED KLYSTRODE POWER SOURCE

W. W. MacKay, F. R. Huson, C. Kronke, D. Sun, and J. Zeigler
Texas Accelerator Center†, 4802 Research Forest Dr.,
Bldg. 2, The Woodlands, TX 77381.

Abstract

A 100kW peak rf power source was built using an Eimac 2KDW60LA klystrode at 473MHz. The klystrode has been operated at a peak power level of 104kW with 50μs pulses at a duty factor of 0.5%. The measured efficiency of the tube operating in this mode was 56%, with a gain of 23dB. This system is to be used as a power source for both a sparking cavity and a 500keV RFQ for H^- ions.

Introduction

The inductive output tube [1] or klystrode [2] (see Fig. 1) uses a combination of a cathode and grid to produce a density modulated electron beam which is accelerated with a high voltage and passed through an output cavity as in a klystron. Recently the klystrode has been revived as a compact and very efficient UHF power source for TV transmission [3].

In this paper, we describe a pulsed rf system using a TV klystrode, the Eimac 2KDW60LA, which was designed to provide a peak-of-synch output power of 60kW. The klystrode is to be used for two purposes: 1) to power a sparking cavity [4] for testing voltage breakdown of materials, and 2) to power a small RFQ [5] for accelerating H^- ions to 500keV. This klystrode has produced 5μs to 100μs pulses in excess of 100kW into a 50Ω load with a repetition rate of 100Hz.

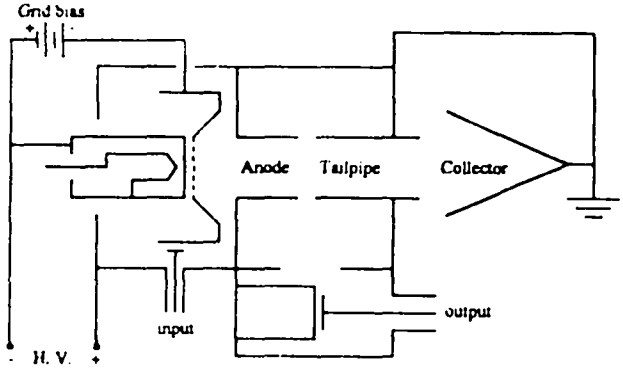

Fig. 1 Schematic of a klystrode with capacitive coupling for both input and output. The klystrode uses a grid to modulate the electron beam density but uses a cavity similarly to a klystron for the output.

Description of Apparatus

A pair of Eimac 3CX8007A planar triodes, operated in tuned cavities, are connected in series to drive the klystrode (see Fig. 2.) A small solid state amplifier (50dB, 10W) is used to amplify the signal from a Wavetek 2520 signal generator to a level sufficient to drive the triodes. The cw rf signal from the solid state amplifier is modulated in the triodes by pulsing the cathode to grid bias level between 35V and 4V. By pulsing the bias level, we are able to use a low current power supply for the anode to cathode voltage; a few milliamperes versus one to two amperes for cw operation. The second triode is capable of producing over 1400W in pulsed operation; however, only about 500W are required to drive the klystrode to a 100kW level. An isolator has been inserted before the klystrode to provide a constant load for the output of the second triode, since the input impedance of the klystrode varies with power level.

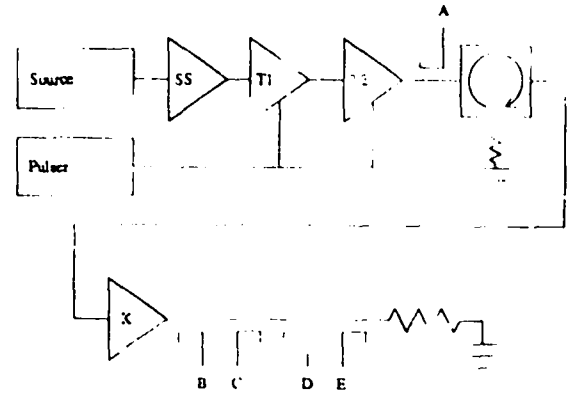

Fig. 2 A schematic of the amplifier chain. The symbols SS, T1, T2, and K respectively correspond to the solid state amplifier, the first triode, the second triode, and the klystrode. The modulation is done by pulsing the grid bias voltage of the triodes. The input to and output from the klystrode, as well as power reflected back to the klystrode, are monitored from the directional couplers labeled A through E. Here a 50Ω load is shown for the output device.

In addition to the klystrode, Varian/Eimac supplied the input fixture, output cavity, focusing magnet, Vacion pump, grid bias supply, and arc detection circuitry. The input fixture consists of four tuning stubs feeding a capacitively coupled resonant cavity with tuned connections for the grid and cathode. The output cavity is really a pair of tunable cavities coupled through a tunable iris. One section of cavity surrounds the ceramic output window of the tube, and the other section is capacitively coupled to an EIA $4\frac{1}{16}$" coaxial transmission line. The solenoid magnet of 250 to 300G is placed around the top of the klystrode, above the output cavity, to focus the beam into the collector.

The grid bias and heater power supplies for the klystrode are placed in a high voltage coffin and powered through an isolation transformer. The beam voltage is supplied to the cathode of the klystrode by a 4kW dc power supply with a maximum current of 65mA at 0 to 60kV. The peak current required for the beam is several amperes, so a high voltage 0.7μF capacitor was connected

in parallel with the supply to provide energy storage. At the 60kW level the klystrode may be operated with a beam voltage of only 32kV. For operation up to 100kW the voltage must be increased to 38kV.

For protection, an arc sense transformer couples the cathode current to a crowbar control circuit which can fire a spark gap in case of a fault. The crowbar can be fired also by a high vacuum reading in the klystrode or a high light level in the output cavity. The vacuum level is measured by a Vacion pump controller, and the light level is sensed by a photo resistor.

A small water pump and heat exchanger cool the collector, anode, and tailpipe. Additional cooling and ion clearing is provided by fans blowing air through both the input and output cavities of the klystrode. The entire rf power source including the klystrode and all required support equipment is housed in a movable 3-bay rack assembly measuring 32"×82"×80".

The output transmission line was stepped down to EIA $1\frac{5}{8}$" line and four directional coupling loops (two forward and two reverse) were installed for measurements and diagnostics. After passing through the top of the rack enclosure a connection is made to either a water cooled 20kW Bird load or to a flexible $1\frac{5}{8}$" coaxial line (Andrews Heliax 50Ω with air dielectric). The flexible line is then connected to the output device to be tested.

Measurements

Average power levels are measured with a Hewlett Packard HP438A power meter connected to one of the directional couplers, and pulsed measurements are analysed with a Tektronix DSA602 digitising signal analyser. The frequency generator, power meter, and signal analyser are connected to a Hewlett Packard 200 series computer with an IEEE-488 bus. The output power level is controlled mainly by varying the signal level from the frequency generator. Additional control is possible by varying the cathode to anode voltage of the triodes. When operating the triodes way below saturation, they are susceptible to an overshoot of the bias voltage at the beginning of a pulse. This causes a power spike at the beginning of the pulse. By lowering the triode anode voltage, the triodes will run closer to saturation, and the output pulse is much flatter. Typical settings are between 2kV and 3kV.

Figure 3 shows the klystrode output power vs the input power, measured from directional coupler A of Figure 2, with a beam voltage of 38kV. The gain versus output power is shown in Figure 4. The efficiency (see Figure 5) was calulated for 50μs long pulses with a duty factor of 0.5% by dividing the average output power by the dc power provided by the beam power supply during the rf pulse. A typical 50μs pulse is shown in Figure 6.

The x ray radiation from the klystrode near the anode at 32kV was measured to be less than 0.1mR/hr. At 38kV the level increased to about 6mR/hr. With the cabinet doors closed the radiation is less than 0.1mR/hr.

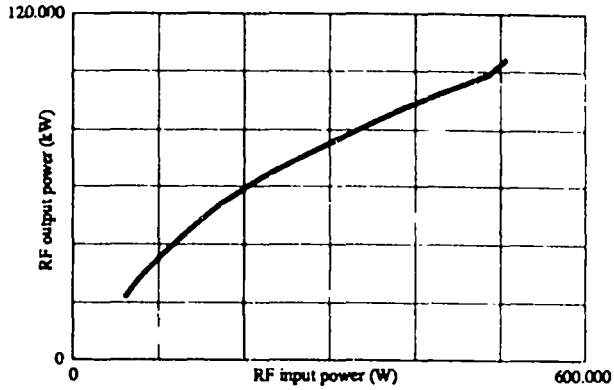

Fig. 3 The output rf power vs input rf power for the klystrode with an anode to cathode voltage of 38kV.

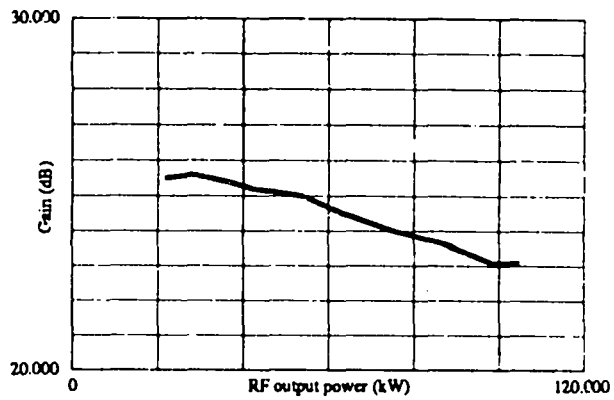

Fig. 4 The gain vs output rf power for the klystrode with an anode to cathode voltage of 38kV.

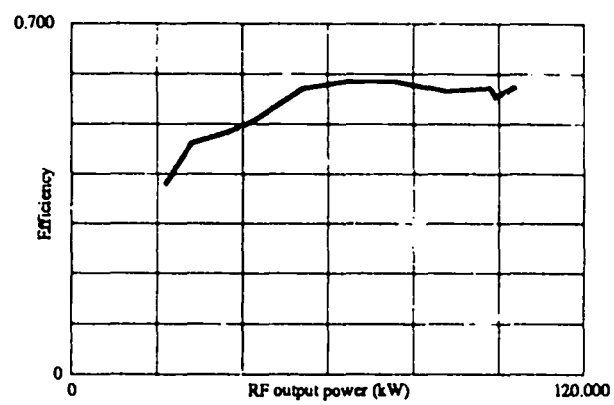

Fig. 5 The efficiency vs input rf power for the klystrode with an anode to cathode voltage of 38kV.

Future Modifications

A feedback circuit is being designed to sense the output power level and adjust the input to the solid state amplifier so that the output power remains constant. The signal from one of the forward directional couplers (B in Figure 2) will be converted to a dc voltage with a crystal detector. This voltage will be filtered and compared with a reference voltage to produce a difference voltage which will adjust a voltage-controlled attenuator placed in front of the solid state amplifier.

Additional instrumentation will be added to measure the tube's performance parameters. The feedback control, high voltage supplies, and instrumentation will

be connected to a supervisory control computer for automated operation.

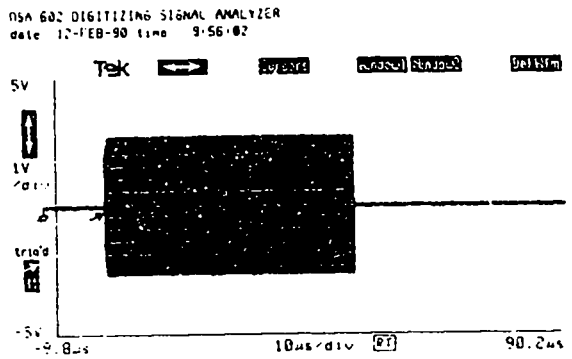

Fig. 6 A typical 50μs long rf pulse at 100kW level.

Conclusion

The klystrode is an excellent compact source of pulsed rf power for use in small accelerator systems operating in the UHF band. It is compact, and does not require a pulsed high voltage supply for the anode. Varian/Eimac has developed [6] a prototype 0.5MW tube at 425MHz which is physically only a little larger than the 2KDW60LA.

This work was supported in part by the SSC.

References

† TAC at HARC is a consortium of Rice University, Texas A&M University, the University of Houston, the University of Texas, Prairie View A&M University, Sam Houston State University, and the Baylor College of Medicine MR Center.

[1] A. V. Haeff, "An UHF power amplifier of novel design," *Electronics*, p. 32, Feb, 1939.

[2] D. H. Preist and M. B. Shrader, "The Klystrode-An unusual Transmitting Tube with Potential for UHF-TV,", IEEE, Vol. 70, No. 11, 1318(1982).

[3] Merrald B.Shrader, "Klystrode Technology Update", *Proceedings of the National Association of Broadcasters 66th Annual International Exposition*, Las Vegas (1988).

[4] D. Sun et al., "Voltage Breakdown Tests at 473MHz," This conference (1990).

[5] R. Kasimi et al., "Test of a 473MHz Four-Rod RFQ", This conference (1990).

[6] M. Shrader, Proceedings of the "SSC Linac Workshop", Dallas, 7-9 June 1989.

MODE COMPETITION IN HIGH POWER GYROKLYSTRON AMPLIFIERS*

P.E. Latham, W. Main, S. Tantawi, W. Lawson, C.D. Striffler, J. Calame,
S.M. Miller, and V.L. Granatstein

Laboratory for Plasma Research
University of Maryland, College Park, MD 20742

Abstract

Stability of multi-cavity gyroklystron amplifiers against parasitic modes is studied. The insertion of lossy dielectrics into the cavities and drift sections played a primary role in mode suppression in our two cavity system. Comparison between the theory and experiment of this method of mode control is presented. In addition, a three cavity design that incorporates large amounts of lossy dielectric is presented with its predicted nonlinear efficiency and gain.

I. Introduction

A serious problem facing the development of high power, multi-cavity gyroklystron amplifiers is the excitation of unwanted modes. The modes with the lowest start oscillation currents, and thus the hardest ones to suppress, are the whole-circuit modes. These arise when radiation is partially reflected by the discontinuities associated with the cavities, the nonlinear tapers, and the output window. These modes often extend over the whole circuit (thus their name), leading to an efficient linear interaction (linear efficiency scales as the third power of the interaction length).

There are two methods of suppressing unwanted modes: load the cavities or decrease the reflections. In the two-cavity gyroklystron under development at the University of Maryland (see the paper in these proceedings by W. Lawson et al.), we have employed both methods: lossy dielectrics have been placed in the drift sections and the output section has been modified to reduce the reflections off the nonlinear uptaper, as shown in Fig. 1. In this paper we compare the theory and experiment of various schemes for loading the cavities and drift sections with lossy dielectric. We also present a three cavity design with its predicted nonlinear efficiency and gain, and we calculate the required amounts of suppression needed for stable operation.

II. Suppression of Unwanted Modes–Lossy Dielectrics

The use of lossy dielectrics to suppress unwanted modes appears simple. There are, however, a number of considerations. The two most important are choosing the real and imaginary parts of the dielectric constant and deciding on a configuration, e.g., alternating rings of dielectric and metal versus solid dielectric. For high power tubes, the knowledge of the dielectric properties over a rather large frequency band, in our case 6-20 GHz, is essential. Thus, the issues of measuring both the real and imaginary parts of the dielectric constants and modeling the system numerically are important.

To model the dielectric loaded complex circuit, we have developed a code based on the scattering matrix method.[1] Our code, "CASCADE", assumes cylindrical symmetry and allows one region of lossy dielectric material (e.g., vacuum for $r < r_0$ and dielectric for $r_0 < r < r_w$ where r_w is the outer wall radius). In addition, we have a particle pushing code that allows us to calculate the start oscillation current in a complex dielectric loaded circuit.

Early mode suppression strategies for the drift regions used alternating dielectric and metal rings, see Fig. 2a. The dielectric rings turned out to be only slightly lossy ($\epsilon \simeq 9.7 + .05i$) and thus we had to rely on resonant effects to achieve attenuation. These alternating structures worked well near resonance but had limited bandwidth (~300 MHz). Preliminary beam tests on the two-cavity system revealed that unwanted oscillation occurred from 6 to 20 GHz. Steps to improve the suppression of modes for the two cavity system are described in the accompanying paper [W. Lawson et al].

To achieve attenuation over the range 6 to 20 GHz we are considering a nonresonant absorbing system for the three cavity circuit. Figure 2 shows the difference between a resonant, Fig. 2a, and nonresonant, Fig. 2b, absorbing system. By using a single piece of high loss material we form an absorber for which the attenuation per unit length is less frequency dependent. Figures 3a and 3b compare the measured and computed TE_{11} attenuation versus frequency for a resonant and nonresonant system. Figure 3a shows the attenuation of the 6-ring resonant absorber of Fig. 2a, both from experimental measurement and from CASCADE. The difference in the location of the resonance between the two curves can be removed by changing the dielectric constant used in the calculation by less than 5%. This difference is either due to an error in the measurement of ϵ, batch to batch variations in the dielectric material, and or the frequency dependence of the material.

In our gyroklystron the operating mode in all three cavities is the TE_{011} cavity mode. To isolate the cavities, the TE_{01} mode attenuation in the drift section between cavities must be greater than the intercavity gain, which is

40 dB between the input and buncher cavities and 20 dB between the buncher and output cavities. To achieve this attenuation in the nonresonant system we place a smooth metal drift section 1.5 cm long on each side of the input and buncher cavities and on the upstream side of the output cavity, see Fig. 4. These regions also isolate the TE_{01} mode at 9.85 GHz in the cavities from the absorbing structures, which could alter the Q of the cavities. At 9.85 GHz the TE_{01} mode is evanescent in these regions and is isolated by 12 dB/cm. Thus, in the first drift region the necessary isolation of 40 dB plus a 10 dB safety margin can be achieved if the 4.25 cm dielectric region has attenuation greater than 3.3 dB/cm. In the resonant system of Fig. 2a the metal rings used to adjust the resonance also cutoff the TE_{01} mode and thus this system achieves very good isolation in the operating mode.

For other than the operating mode, the absorbing structure is designed by optimizing the attenuation in the least attenuated mode. Depending on the frequency and kind of dielectric used, the least attenuated mode can be one of a number of hybrid modes which exist in a lossy dielectric lired tube. The regions in frequency or liner geometry where these modes cross generally give the best attenuation. Experience with the two cavity system has shown that attenuation of 1-2 dB/cm for the least attenuated mode is acceptable. In practice we measure the attenuation in the least attenuated mode by injecting the TE_{11} mode.

We used our scattering matrix code CASCADE to test different combinations of ϵ and thickness. We found that for low loss dielectrics such as $\epsilon = 4.6 + 0.66i$ the TE_{01} mode is sufficiently isolated only if the thickness is less than 2mm. whereas the least attenuated mode is sufficiently attenuated for thicknesses above 4.5 mm. For a lossy dielectric such as $\epsilon = 42 + 18i$ the TE_{01} is sufficiently isolated for any thickness; however, there is no thickness where the least attenuated mode is sufficiently attenuated. Between these extremes there is a combination that satisfies the requirements for both modes; this is $\epsilon = 6.2 + 2i$ and a thickness of 3 mm. This ϵ is close to the values attainable with carbonized aluminum silicate.[2] The carbonization process yields a nonuniform ϵ, so it is difficult to model our samples, however, the attenuation achieved by these samples is close to that predicted by CASCADE.

III. Three Cavity Design

Figure 4 shows the three-cavity system and Table I shows the operating parameters predicted by our nonlinear amplifier code. This code optimizes system operation by varying geometries and magnetic field. The quality factors are set relative to start oscillation current in the operating mode, assuming the field profiles for an all metal wall structure. The input and buncher cavities have dielectric loading and have similar design. The quality factor of the output cavity is almost completely diffractive. The drift tube is loaded with a nonresonant absorber as described in Section II.

Table 1: Beam parameters and operating parameters predicted by our nonlinear amplifier code.

Beam:	Power	80 MW
	Voltage	500 kV
	Velocity Ratio (α)	1.5
	Velocity Spread	6.8%
	Center Radius	0.79 cm
	Guiding Center Spread	0.268 cm
	Axial Magnetic Field	0.5-0.6 T
System:	Frequency	9.85 GHz
	Input Cavity Q	225
	Buncher Cavity Q	225
	Output Cavity Q	170
	Theoretical Efficiency	42%
	Theoretical Gain	60 dB

We used a start oscillation current code to design the cavity loading. The code shows that the finite quality factor of the cavity due to wall losses will not be enough to suppress oscillations for both the TE_{011} and TE_{021} modes. All other cavity modes are stable for magnetic fields around the operating point of 5.69 kG. Thus, the dielectric loading of the cavity should discriminate against the TE_{021} mode. This will reduce the Q of that mode considerably while leaving the Q of the TE_{011} mode high enough for efficient bunching of the beam. The structure which we found that works the best is a simple ring of lossy dielectric placed on the radial wall of the cavity. To operate at 70% of the start oscillation current with a beam of 160 A requires a cavity Q of 320. Figure 5 shows the computed start oscillation current of different modes after loading the cavities with dielectrics. As shown, the start oscillation current is well above 200 A for the operating mode.

We are in the process of computing the start oscillation currents for whole tube modes. The three cavity circuit will be cold tested in the near future and installed in the GKL system to study its amplification properties in the next few months.

References

1. J.M. Neilson, P.E. Latham, M. Caplan, and W.G. Lawson. IEEE Trans. on Microwave Theory and Techniques **37**, 1165 (1989).

2. J.P. Calame and W. Lawson, submitted to IEEE Trans. Electron Devices Part II (1990).

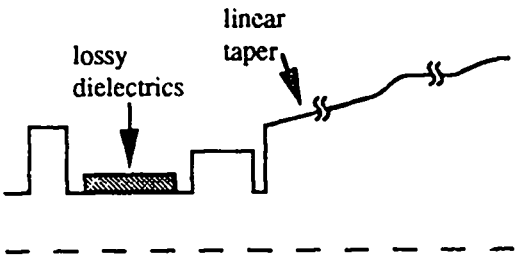

Figure 1. Two cavity design with lossy dielectrics in the drift region and a linear taper following the output cavity.

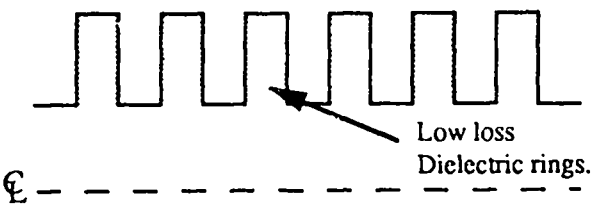

Figure 2a. Resonant absorber circuit attenuates strongly at certain desired frequencies. Metal rings adjust resonant frequency and cutoff operating mode.

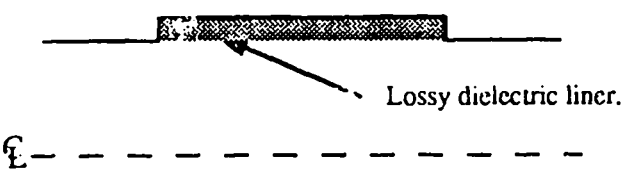

Figure 2b. Nonresonant absorber circuit attenuates over wide frequency range. Lossy dielectric attenuates operating mode and other undesired modes.

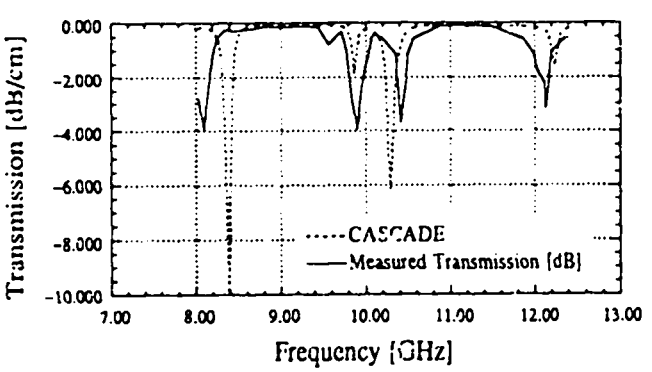

Figure 3a. Comparison of scattering matrix code "CASCADE" with measurement, for resonant microwave absorber circuit of Fig. 2a.

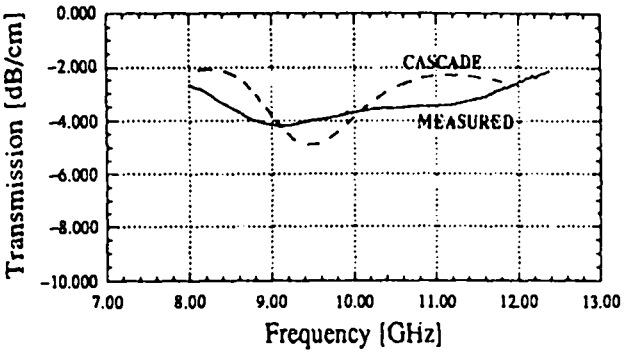

Figure 3b. Comparison of scattering matrix code "CASCADE" with measurement, for the nonresonant absorber circuit of Fig 2b.

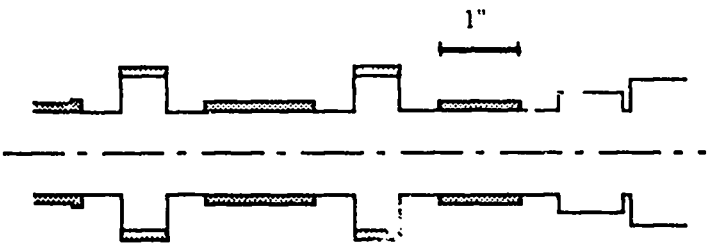

Figure 4. Scale drawing of three-cavity circuit design.

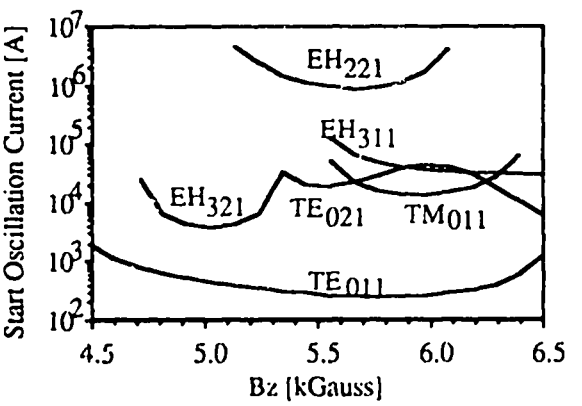

Figure 5. Results of SOC for the input and buncher cavity design. The TM_{010} mode is not unstable in this region of magnetic field. The operating current is 160 A.

RELATIVISTIC KLYSTRONS FOR HIGH-GRADIENT ACCELERATORS*

G. A. Westenskow[(a)], D.P. Aalberts[(a)], M. A. Allen[(b)], J. K. Boyd[(a)], R. S. Callin[(b)], G. A. Deis[(a)], H. Deruyter[(b)], K.R. Eppley[(b)], K. S. Fant[(b)], W. R. Fowkes[(b)], J. Haimson[(d)], H. A. Hoag[(b)], D. B. Hopkins[(c)], T.L. Houck[(a)], R. F. Koontz[(b)], T. L. Lavine[(b)], G. A. Loew[(b)], B. Mecklenburg[(d)], R. H. Miller[(b)], T.J. Orzechowski[(a)], R. D. Ruth[(b)], R.D. Ryne[(a)], A. M. Sessler[(c)], A. E. Vlieks[(b)], J. W. Wang[(b)], S. S. Yu[(a)]

Abstract

Experimental work is being performed by collaborators at LLNL, SLAC, and LBL to investigate relativistic klystrons as a possible rf power source for future high-gradient accelerators. We have learned how to overcome our previously reported problem of high power rf pulse shortening and have achieved peak rf power levels of 330 MW using an 11.4-GHz high-gain tube with multiple output structures. In these experiments the rf pulse is of the same duration as the beam current pulse. In addition, experiments have been performed on two short sections of a high-gradient accelerator using the rf power from a relativistic klystron. An average accelerating gradient of 84 MV/m has been achieved with 80-MW of rf power.

Introduction

During the past year researchers at Stanford Linear Accelerator Center and Lawrence Berkeley Laboratory have continued a collaborative effort with investigators at Lawrence Livermore National Laboratory to study some basic physics issues involved in combining linear induction accelerators with relativistic klystrons. In previous papers[1,2] we have reported results obtained with three experimental relativistic klystrons: a subharmonic buncher relativistic klystron ("SHARK"); a multicavity klystron at 11.4 GHz ("SL4"); and a multi-output klystron ("MOK-2"). These experiments were performed using beams with ≈1.2 MeV of kinetic energy and ≈700 A of current with a ≈50-ns duration.

SHARK is a low-gain, two-cavity tube driven by a 4-MW, 5.7-GHz source and has output power at 11.4 GHz. The maximum rf output level obtained from SHARK is 100 MW from a 1.1-MV, 400-A beam. SL4 is an 11.4-GHz, six-cavity, high-gain klystron. Use of a traveling-wave output structure[7] increased the flat pulse to 170 MW. This configuration had three intermediate gain cavities, a gain of ≈52 dB, and about 30% efficiency.

A feedback system is being studied to help reduce the nonrandom rf phase and amplitude variations for induction driven rf sources . We have also been working[6] on computer modeling of the TW output structures used in these sources.

MOK-2 Klystron

MOK-2 is a multi-output klystron with two outputs operating with high-gain klystron at 11.4 GHz. The tube was designed for a 1.3-MV beam. The first four cavities are the same as those used in SL4. The first output is a single standing-wave (SW) resonant cavity. This output cavity serves two purposes: it extracts power from the beam, and it further bunches the beam. The second output is a traveling-wave (TW) structure and is located 14 cm beyond the SW output cavity. The 11.4-GHz TW structure[3] is comprised of six $2\pi/3$-mode cells with an rf filling time of 1 ns, and a phase velocity ≈0.92c. The TW circuit was designed to generate 250 MW of output power when operating under synchronous conditions at an rf current of 520 A. At this power level the average electric field in the the output coupler is 40 MV/m, and the peak loss of beam energy in traversing the circuit is approximately 0.9 MeV.

The highest total power measured from both structures is 330 MW (30 MW from the SW cavity and 300 MW from the TW structure). The current through the klystron was 600 A and the beam voltage was 1.3 MV.

High-Gradient Accelerator

To study high-gradient acceleration, we built two 26-cm-long sections of 11.4-GHz accelerator structures operating in the $2\pi/3$ traveling wave

* Work supported in part by the DOE, contract numbers W-7405-ENG-48 (LLNL), DE-AC03-76SF00515(SLAC), and DE-AC03-76SF00098 (LBL).

(a) Lawrence Livermore National Laboratory, Livermore,,CA 94550

(b) Stanford Linear Accelerator Center, Stanford, CA 94309

(c) Lawrence Berkeley Laboratory, Berkeley, CA 94720

(d) Haimson Research Corporation, Palo Alto, CA 94303

mode. The constant-impedance structures consist of 30 cells and have r/Q = 14 kΩ/m. The filling time of the structure is 28 ns and the group velocity is 0.031c. The accelerating field on axis, for klystron power P, is 100 MV/m × $[P/(100MW)]^{1/2}$. Power through the structure is attenuated by 24%. The iris diameter was chosen to be 7.5 mm. Early experiments were done with a single section of HGA, and without an electron gun attached, using rf power from the SL4 klystron. The next experiments were performed using an electron gun. Finally experiments with both sections were performed using the MOK-2 klystron. The drift length between the two HGAs could be adjusted to achieve proper phasing of the two sections.

Field emission in the high-gradient structure (HGS) was measured in the absence of any injected beam. Figure 1 shows the field emission current for the second HGS. The measurements were taken after 500,000 rf pulses. The pulse shapes were triangular with about 10 ns FWHM. Levels were appreciably higher than earlier reported levels[2]. Although the surfaces of the first HGS might have had lower field emission currents the new values are in better agreement with several other measurements made on the first section.

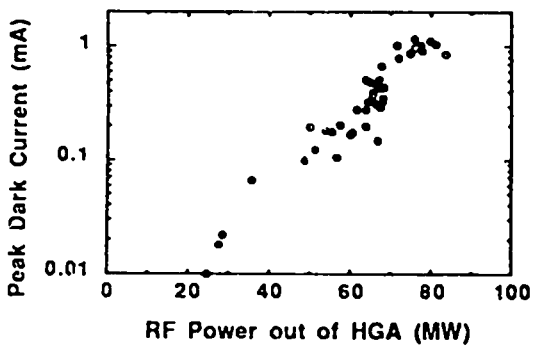

Figure 1. Peak field emission current from HGS

Electrons from a thermionic cathode were injected into the accelerator using a 80-kV gun pulsed for 5 ns. Prior to installation of the gun, persistent arcing was not apparent in the HGS at power levels as high as 160 MW. After installation arcing became persistent at klystron power levels in excess of 100 MW. There was evidence of barium on the surfaces of the HGA after running with the electron gun. In large colliders, where contamination from the cathode should not limit the maximum surface electric field levels, perhaps higher accelerating fields can be achieved.

The beam emerging from the accelerator was momentum-analyzed using a spectrometer consisting of a 40° horizontal bend, a 2.5-cm diameter collimator and a Faraday cup. The momentum resolution of the spectrometer was dominated by the window at the end of the accelerator.

In the single section test the measured momentum spectrum of the accelerated electron beam was nearly Gaussian with peak p = 17 MeV/c. Computer modeling of the accelerator beam dynamics using the particle tracking code PARMELA indicates that the injected electrons slip in phase relative to the rf wave, and that for 80-MW of klystron power, as measured, the total energy gain expected is 16 MeV, consistent with that observed. The maximum energy gain for synchronous particles, calculated from the 80-MW power level, is 23 MeV, corresponding to an average accelerating gradient of 84 MV/m in the 26-cm-long accelerator.

Results of the dual section test are shown in Figure 2. It was difficult to operate both HGA structures near their maximum holdoff values while operating MOK-2 at beam voltage which would yield useable phase stability during the pulse. For a comparable power level to the test shown in Figure 2 the first HGA earlier (during the single section test) yielded 11 MeV electrons. Assuming similar behavior the second HGA added about 19 MeV of energy; corresponding to a gradient of 70 MV/m in the second structure.

Two unanticipated features of the observed rf output pulses from the HGAs were their shape (significantly narrower and triangular compared to the input) and the output peak power levels (only weakly correlated with and sometimes greater than the input peak powers). Studies[4] of transient effects for short pulses (comparable to the filling time of the HGA) lead to an explanation of these features. Understanding the

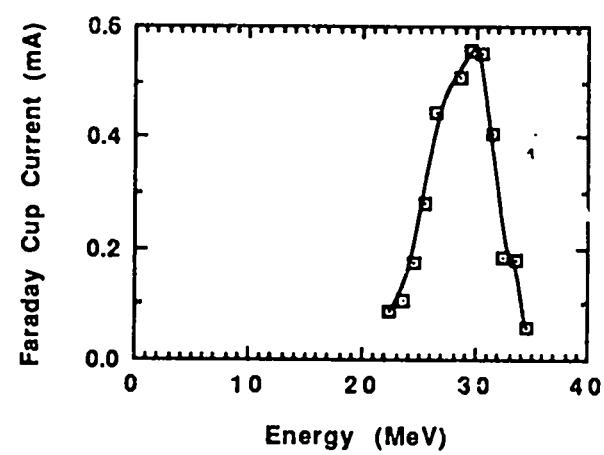

Figure 2. Analyzed momentum spectrum from the dual section HGA experiment.

transient behavior of the pulsed rf power in the type of high gradient accelerator planned for linear colliders will be important.

Future work

We are starting a new set of experiments to look at rf power sources at the Microwave Source Facility. For the initial studies we will be using the existing injector (3 MeV, up to 10 kA) at the Advanced Test Accelerator. The facility will provide a place to study high-frequency high-power microwave sources such as relativistic klystron, FELs[5], CARMs, TWT amplifiers and two-beam accelerators. Researchers from other institutions will be able to test their devices and structures without the duplication of the major effort involved with providing the drive beam. Its major objectives are:

1. To develop induction-linac-based relativistic klystrons and FELs into economically viable power sources.
2. To test key physics issues of two-beam accelerators schemes.
3. To provide a user facility for studying novel microwave sources and structures.

The first rf experiment[3] planned at the Microwave Source Facility is the Choppertron (shown in Figure 3). The first section is a 5.7-GHz chopping system designed to produce a train of short beam pulses with a period corresponding to 11.4 GHz from the initial uniform beam. The chopper design has reduced sensitivity to beam-energy sweep of the induction beam. Emittance growth in the chopper is reduced by operation with an axial magnetic field matched to the beam emittance and the betatron resonance.

The next section of the rf generator consist of two 11.4-GHz traveling-wave output structures. The use of high-group-velocity structures with short interaction regions provides a broadband, phase and temperature insensitive circuit. The chopper is designed to generate about 500 MW of pulsed rf power at 11.4 GHz when driven by a 1-kA, 3-MeV induction beam.

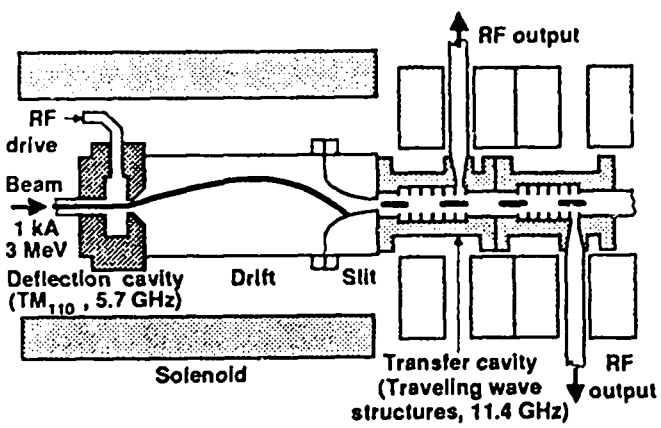

Figure 3. Schematic of the Choppertron.

The chopper will also be used to generate high-energy 11.4-GHz rf current for latter experiments. We want to study the key physics issues involved with reacceleration of a bunched beam by induction cells. We also wish to build a multiple output section to follow the chopper which utilizes inductively detuned output cavities to increase the efficiency.

Acknowledgements

For helping to make this work possible, we thank J. M. Paterson, D. Prosnitz, and M. Sheaffer. For helpful discussions, we thank G. J. Caporaso, M. Chodorow, Y. Goren, W. B. Herrmannsfeldt, E. W. Hoyt, T. G. Lee, P. L. Morton, V. K. Neil, R. B. Palmer, A. C. Paul, L. L. Reginato, H. Shay, G. Spalek, P. B. Wilson, D. Yu, and L. Zitelli. for engineering and technical assistance, we thank F. Allen, R. A. Early, S. A. Hawkins, C. Pearson, H. D. Schwarz, and D. O. Trimble.

References

1. M.A. Allen et al., "High Gradient Electron Accelerators Powered by a Relativistic Klystron," Physical Review Letters, 63 22, pp. 2472, Nov. 27,1989.
2. M.A. Allen et al., "Recent Progress in Relativistic Klystron Research," Particle Accelerators, 30 pp.189-196, 1990
3. J. Haimson and B. Mecklenburg, "Design and Construction of a Chopper Driven 11.4 GHz Traveling Wave RF Generator," Proceedings of the 1989 IEEE Particle Accel. Conf., pp. 243-245.
4. T.L. Houck, "Dispersion and Interbunch Energy Variation For an e+e- Linear Collider", to be presented at 1990 LINAC Conference, Albuquerque, NM, Sept. 10-14, 1990.
5. R. A. Jong , et. al., "17.1 GHz Free-Electron Laser as a Microwave Source for TeV Colliders", presented at the 1989 FEL Conference, Naples, Florida Aug. 28-Sept.1, 1989
6. R.D. Ryne, S.S. Yu, "Relativistic Klystron Simulations Using RKTW2D", and "Time-Dependent Simulation of Relativistic Klystron," to be presented at 1990 LINAC Conference, Albuquerque, NM, Sept. 10-14, 1990.
7. J. Haimson and B. Mecklenburg, "Use of TW Output Structures for High Peak Power RF Generators," to be presented at 1990 LINAC Conference, Albuquerque, NM, Sept. 10-14, 1990.

OPERATING CHARACTERISTICS OF A TWO-CAVITY X-BAND GYROKLYSTRON EXPERIMENT*

W. Lawson, J. Calame, D. Welsh, M.E. Read[†] B. Hogan, M. Naiman,
P.E. Latham, M. Skopec, C.D. Striffler, M. Reiser, and V.L. Granatstein

Laboratory for Plasma Research
University of Maryland, College Park, MD 20742 USA

Abstract

At the University of Maryland we have designed and are operating a high power two-cavity TE_{01} gyroklystron in the 9.7-10.0 GHz range. The target beam power is derived from a 500 kV beam with a current ranging from 120-240 A in 1 μs pulses. The target microwave parameters for this tube include a power level of 15-30 MW with a gain of 25-30 dB. In this paper we summarize the initial characterization of the electron gun performance and detail preliminary tube stability and microwave amplification experiments.

Introduction

At the University of Maryland we are evaluating the suitability of gyroklystron amplifiers as RF power sources for linear colliders. The initial sequence of experiments involves characterizing a two cavity system to address questions of tube stability and amplifier efficiency. We have completed investigations of our first three configurations and are currently examining our fourth. A schematic of the major subsystems of the two-cavity gyroklystron[1] is shown in Fig. 1. A line-type modulator supplies the main voltage pulse and an intermediate voltage to a double anode Magnetron Injection Gun (MIG).[2] The beam is adiabatically compressed in an increasing magnetic field as it passes from the cathode (0.047 T) to the circuit (0.565 T). At a current of 160 A, the beam theoretically achieves a perpendicular-to-parallel velocity ratio of $\alpha = 1.5$ with an axial velocity spread of 7%. The beam's phase-space distribution is modulated in the first cavity by a signal from a 100 kW, 2 μs magnetron. Energy is extracted axially through a coupling aperture in the second cavity and travels through two non-linear tapers and the beam dump to a half-wavelength output window.

*Work supported by the U.S. Department of Energy.

[†]Physical Sciences, Inc., Alexandria, VA

Beam Characterization

Our electron gun is the first thermionic MIG to operate at 500 kV with a cathode loading of 30-60% of the predicted space-charge limit. While the steady-state simulations predict a high quality beam, various approximations involving self-fields are questionable and electrostatic instabilities are not addressed. Consequently, we constructed a beam diagnostic chamber in an attempt to measure several key parameters. In the beam quality experiment, the chamber replaced the microwave circuit in the overall configuration. Air core Rogowski coils at the entrance and exit measured beam current and interception. Capacitive probes measured line charge density, which together with the current yielded the average axial velocity. For small velocity spreads, the beam voltage could then be used to obtain the average α. The capacitive probes were split into four sectors to provide alignment information. A diamagnetic loop signal could be unfolded to indicate average transverse energy which was used as a check on α.

A comparison of theoretical and experimental space-charge limiting current is given in Table 1. Numerical simulations converged poorly below 250 kV due to non-laminar flow and experimental values above 350 kV could not be obtained due to modulator impedance limitations. The agreement is impressive, especially since the simulations predict a limit significantly exceeding idealized analytic estimates. A typical comparison between simulated and measured values of average α is given in Table 2. The agreement is quite good for higher currents. At low currents a low signal-to-noise ratio yields large error bounds. Furthermore, the velocity spread is quite large and the numerical assumption of uniform cathode loading is poor. An unexpected result, obtained by examining the time dependence of the probe signals, is that the average α is approximately 10% larger at the beginning of the pulse.

Table 1: Comparison of experimental and numerical space-charge limiting currents.

Voltage (kV)	Experimental Current (A)	Theoretical Current (A)
200	84	—
250	116	116
300	152	153
350	192	201
400	—	240
450	—	300
500	—	360

The diagnostic chamber was extremely susceptible to microwave oscillations. Below 175 kV, oscillations at $\sim$ 12.2 GHz occurred for $\alpha \approx 0.5$ (it was function of current). Above 175 kV, oscillations at $\sim$ 10.0 GHz disrupted the system at comparable velocity ratios. Attempts to avoid these resonances by adjusting the circuit magnetic field were unsuccessful, so the parameter space available for study was quite limited.

Microwave Tube Characterization

A schematic of the first two-cavity circuit is shown in Fig. 2. Microwaves are injected through a slit in the sidewall of the first cavity. The coupling loss was about 3 dB. The required input cavity Q (170) was obtained by placing carbon-impregnated ceramic rings on the side walls. Computer simulations[1] indicated that "whole tube" modes existing between the two cavities would disrupt amplifier operation. An attempt to stabilize these oscillations was made by constructing the drift tube with alternating rings of copper and silicon-carbide impregnated magnesia. The output cavity frequency and Q were 9.85 GHz and 175, respectively.

The main microwave diagnostic for the initial experiment was an anechoic chamber after the output window. Calibrated crystal detectors gave power estimates and an HP8566B spectrum analyzer gave frequency information. Positioning of the horn gave some mode information. Microwaves could also be sampled in the input cavity via the coupling slot and through a J-band horn looking at the back of the electron gun. Combined with local gas pressure measurements, the relative origin of spurious oscillations could be determined.

Tube operation was hampered by four types of microwave oscillations. Many modes existed in the output waveguide in regions where the output window is a good reflector. These modes are often eliminated by amplifier operation and are of little concern. Near the operating frequency of 9.85 GHz, there is a predominantly TE_{12} mode operating near cutoff in the output waveguide section between the second cavity and the first non-linear uptaper. This mode interferes with amplifier operation, but can be eliminated by slightly tapering the waveguide radius in that region. The third type of mode is the "whole tube" mode. These occurred at several frequencies with a particularly disruptive one slightly above 9 GHz. These oscillations were of concern because they existed at current levels significantly below theoretical start-oscillation predictions. The final mode class involved oscillations in the beam tunnel downtaper before the input cavity. The oscillations depended on beam voltage and current and circuit magnetic field, but would always appear when the velocity ratio exceeded ≈ 0.6. The modes tended to severely disrupt the beam and occurred in two bands: 7.0 – 7.5 GHz and 8.1 – 8.4 GHz (also $m = 1$ modes). The downtaper was loaded with lossy absorbers, but there was an all metal region between a gate valve and the taper which is susceptible to oscillations.

Table 2: Comparison of experimental and numerical average velocity ratios for a 150 kV beam.

Beam Current (A)	Experimental α	Theoretical α
7	0.98	0.38
12	0.58	—
22	0.32	0.33
37	0.25	—
44	0.19	0.22

A stable region for amplifier experiments was found at 80% of the nominal magnetic field at a beam voltage of 175 kV and a current of 55 A. Numerical simulations estimate the velocity ratio to be $\alpha \approx 0.45$ and the axial velocity spread to be about 4%. Our computer simulations of amplifier operation indicated that the gain would be about 0 dB under these restricted beam parameters. The experiment confirmed this prediction and output power was thus limited by the input source. Typical input and output crystal detector responses are shown in Fig. 3. The lower trace is the output signal and its reduced width corresponds to the duration of the voltage pulse.

At the completion of the initial experiment, the

tube was disassembled and the downtaper and drift tubes were cold-tested. The basic measurement involved transmission of the TE_{11} mode through these regions. It was found that while the drift tube was quite lossy at the design frequency, there were two broad regions in X-band alone where the ceramic rings exhibited virtually no loss. The downtaper attenuation varied from a high of 9.5 dB at 7.5 GHz to a low of 4.0 dB at 10.3 GHz. We believe that these low attenuations and the problems that reflections at the gate valve could introduce account for the more serious of the spurious oscillations.

For our second and third tubes, we made two major modifications to the two cavity experiment. First, the drift tube ceramics were replaced with silicon-carbide impregnated beryllia which had been arranged in a configuration so that the single-pass attenuation was always greater than 10 dB for the TE_{11} mode. Second, a new, longer downtaper was constructed. Its loss exceeded 20 dB from 7 to 8 GHz and was nowhere less than 11 dB through X-band. Furthermore, it covered the gate valve opening, thereby removing problems from reflections. These changes eliminated the troublesome 9 GHz whole tube mode and drastically reduced the effect of the beam tunnel modes. The enhanced stability resulting from the modifications allowed amplification studies up to 350 kV. Output powers in excess of 1.5 MW were achieved at 300 kV and $\approx$ 90 A. The optimum magnetic field and input frequency were 0.452 T and 9.866 Ghz, respectively. The gain was approximately 15 dB and the efficiency was roughly 5%. Operation was limited by the TE_{12} mode near 9.85 GHz and the remaining beam tunnel modes.

The fourth tube has a 2° taper of the output waveguide radius after the output cavity. This taper has eliminated the TE_{12} mode and has reduced the effect of several others. We are currently examining amplifier operation.

References

1. Lawson, W., et al., 1988 IEDM Tech. Digest, p. 162.

2. Lawson, W., et al., Int. J. Electron. 61, 969 (1986).

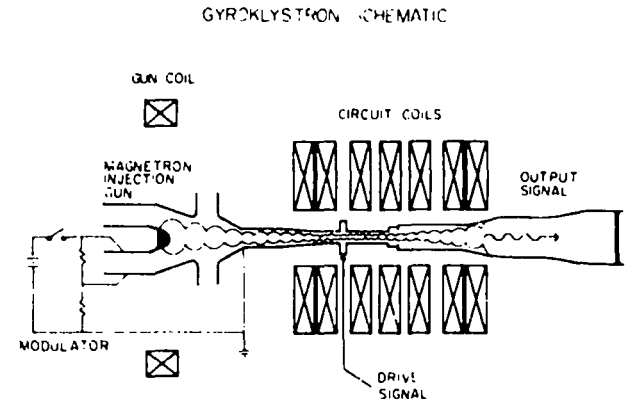

Figure 1: A simplified schematic of the two-cavity gyroklystron experiment.

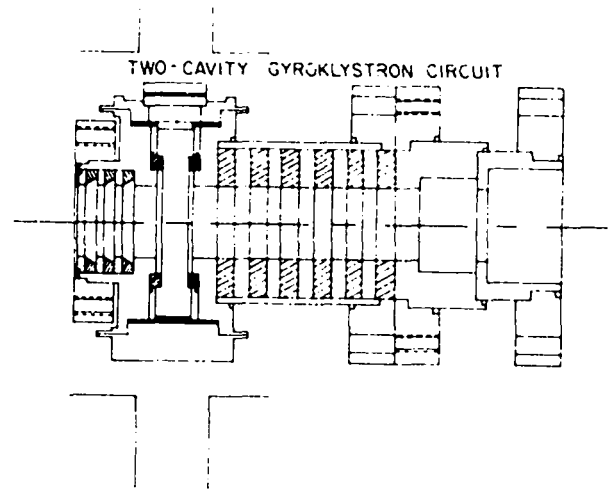

Figure 2: The initial two-cavity circuit.

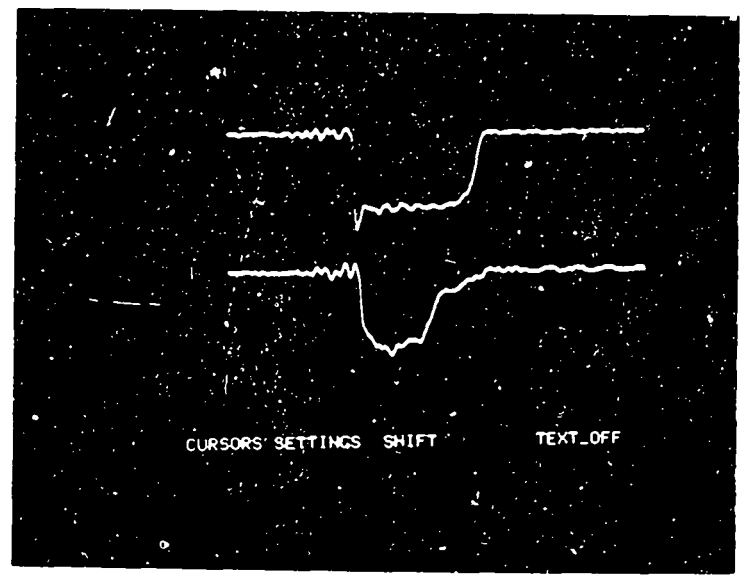

Figure 3: Crystal detector response of typical input and output microwave pulses. Lower pulse duration is $\sim 1\mu s$.

HIGH POWER RF AMPLIFIERS FOR ACCELERATOR APPLICATIONS: THE LARGE ORBIT GYROTRON AND THE HIGH CURRENT, SPACE CHARGE ENHANCED RELATIVISTIC KLYSTRON

R. M. Stringfield, M. V. Fazio, D. G. Rickel, T. J. T. Kwan, A. L. Peratt, J. Kinross-Wright, F. W. Van Haaften, R. F. Hoeberling, R. Faehl, B. Carlsten, W. W. Destler*, and L. B. Warner
Los Alamos National Laboratory,
Accelerator Technology Division,
MS H851, Los Alamos, New Mexico, 87545

ABSTRACT

Los Alamos is investigating a number of high power microwave (HPM) sources for their potential to power advanced accelerators. Included in this investigation are the large orbit gyrotron amplifier and oscillator (LOG) and the relativistic klystron amplifier (RKA). LOG amplifier development is newly underway. Electron beam power levels of 3 GW, 70 ns duration, are planned, with anticipated conversion efficiencies into RF on the order of 20 percent. Ongoing investigations on this device include experimental improvement of the electron beam optics (to allow injection of a suitable fraction of the electron beam born in the gun into the amplifier structure), and computational studies of resonator design and RF extraction. Recent RKA studies have operated at electron beam powers into the device of 1.35 GW in microsecond duration pulses. The device has yielded modulated electron beam power approaching 300 MW using 3-5 kW of RF input drive. RF powers extracted into waveguide have been up to 70 MW, suggesting that more power is available from the device than we have converted to-date in the extractor.

Introduction

Los Alamos has been investigating novel high power RF sources for the past eight years. Included in this research have been various vircator designs, magnetron-like designs (including the large orbit gyrotron (LOG), and the magnetically insulated line oscillator), and most recently, the relativistic klystron amplifier (RKA). Of these, the large orbit gyrotron, operated as an amplifier, and the RKA appear to us to offer the most promise as RF drivers for future improvements in particle accelerator design.

The Large Orbit Gyrotron

During the past three years we have investigated the large orbit gyrotron experimentally as an oscillator operated at a frequency of 2 GHz[1,2]. These results have encouraged us to begin, during the ongoing year, the initial work we hope will lead to an amplifier based upon the LOG's basic operating principles. The LOG amplifier is attractive for linear collider applications, since it requires relatively modest applied magnetic field requirements, only a few hundred gauss, since it operates at a harmonic of the cyclotron frequency. It can operate at frequencies of 15 GHz or more with these small magnetic fields. RF breakdown problems should be relatively small, as well, since the electrons move to smaller orbits, away from the walls of the device, as they convert their energy into microwaves. Hence electron bombardment of the walls, which can lead to breakdown, is relatively modest.

The oscillator we recently investigated is depicted in Figure 1. The device is powered by a

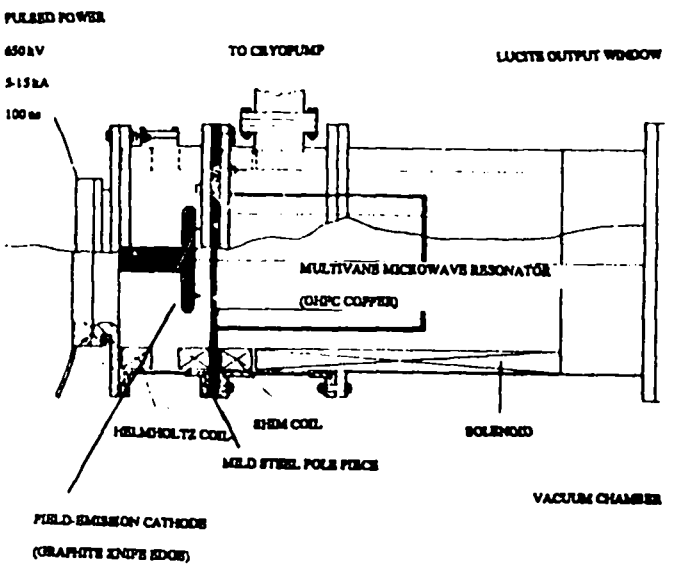

Figure 1. Cutaway drawing of the LOG oscillator experiment.

Marx-Blumlein pulser operated at 650-700 kV, 6 kA, for pulse lengths of 70 ns FWHM duration. RF power was radiated out of the device axially into a chamber lined with microwave absorber. RF radiated into the chamber was monitored with waveguide receivers, either standard gain horns or waveguide stubs. The signals were then coupled to coaxial cable and RF power was measured with crystal detectors. Heterodyning circuits monitored the frequency.

The device operates as follows. A 12.5 cm diameter annular electron beam is formed in an axial magnetic field having a magnitude of 500-800 gauss. An axis encircling, rotating beam is formed by passing the electron beam through a cusp magnetic field at the anode

plane. For these experiments, the ratio of rotational velocity to axial velocity downstream of the cusp (designated α) had a value in the range of 1.5 to 1.7.

Azimuthal bunching of the electron beam occurs through the negative mass instability. A periodically varying boundary along the circumference of the resonator serves to bunch the beam with a periodicity such that it interacts with the resonator, converting beam energy to RF standing wave energy in the cavity.

A representative RF output pulse from the device operating at 2 GHz is shown in Figure 2. A spatial mapping was performed of the power radiated from the device as a function of radial position off-axis. Of the total electron beam power available, 500 MW was injected into the resonator. The total power radiated from the device, within the solid angle monitored by this measurement, was 35 MW. This result corresponds to a conversion efficiency from electron beam power to microwave power of 7 percent. Only a portion of the total power radiated by the device was measured by this spatial scan, since the power was not zero in the wings of the measurement, far off axis. We were prevented from moving the receiving antenna to larger radial positions by physical barriers in the chamber. Hence the true efficiency in this experiment may be larger than that cited here. Further efficiency improvement may be achieved by increasing the ratio of rotational electron beam energy to axial beam energy in the resonator region. Measuring all of the currently generated RF, combined with increases in the fraction of rotational beam energy, should increase the efficiency to as much as 20 percent.

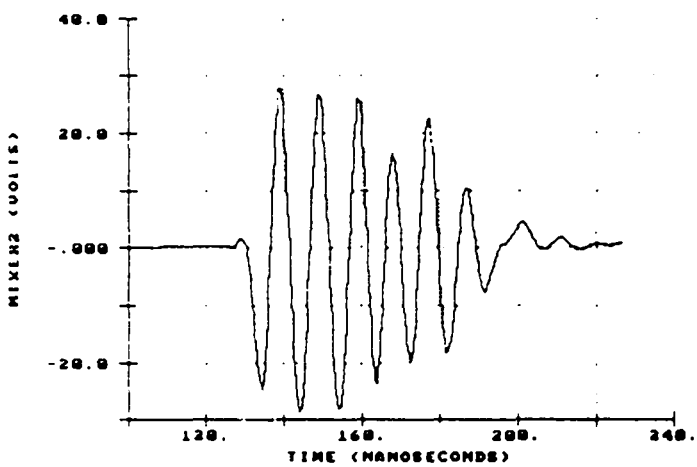

Figure 2. Sample downconverted RF for the LOG oscillator. The local oscillator signal for this measurement was 1.90 GHz, indicating a LOG frequency of 2.0 GHz.

Our initial step in developing an amplifier has been to examine methods of increasing the current fraction injected into the resonator from the diode, and to properly position the higher current in the interaction space. Computational modelling has been performed with the particle-in-cell code ISIS. Modelling has indicated that increasing the fraction of diode current injected into the resonator as a rotating beam and establishing a final rotating beam diameter of 12.5 cm can be achieved by launching the beam from a 2 mm thick annular cathode having a diameter of 14 cm. Such a condition was found computationally to be achieved by placing the emission annulus on a conical equipotential surface, having an angle of 22.5^{o} with respect to the direction normal to the axis of symmetry. Experiments are now underway to test these computational predictions.

We also are computationally investigating approaches to the design of the LOG amplifier. One approach, a two stage device, is shown in Figure 3. The device consists of a preliminary RF input stage which initiates electron beam bunching, and a final RF output stage in which the fully bunched electron beam generates a strong RF standing wave in an output resonant cavity. These stages constitute discrete, separate entities, separated by a beam transport section in which the bunching of the rotating electron beam develops to a maximum prior to entering the RF output section. The two stage design offers the flexibility to separately optimize the RF input and output sections of the device.

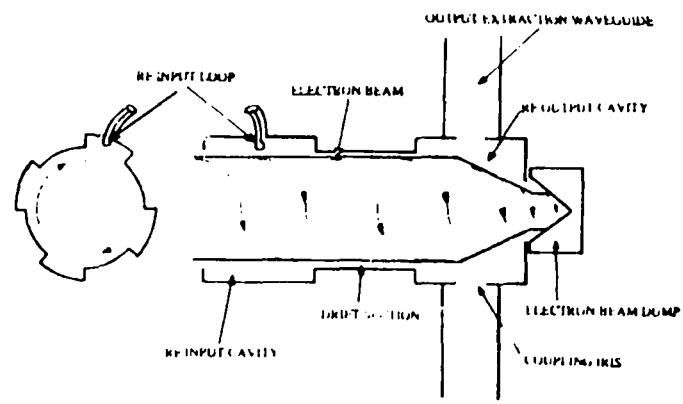

Figure 3. Conceptual arrangement of a LOG amplifier configuration.

The Relativistic Klystron Amplifier

One of the most promising concepts that we have begun to investigate experimentally at Los Alamos is the high current relativistic klystron amplifier (RKA) pioneered by M. Friedman and co-workers at the Naval Research Laboratory[3]. This RKA, as tested by Friedman, has produced several gigawatts of power with 40% efficiency at 1.3 GHz in a 100 ns long pulse on a single shot basis. Peak electron beam currents of 13 kA at 1.3 GHz have been produced. We have identified the high current relativistic klystron as a very promising source with great potential, that has exhibited very good performance in a very limited parameter space. We currently are engaged in a modest

effort to extend the performance envelope of this device from a 100 ns to a 1 μs pulse length, and eventually to repetitively pulsed operation at these very high power levels. The attraction of this device for accelerator applications, aside from amplifier operation, is its demonstrated high efficiency of 40%, even without energy recovery schemes being applied.

The present work has progressed well and the relativistic klystron amplifier shown in Figure 4 is being tested.

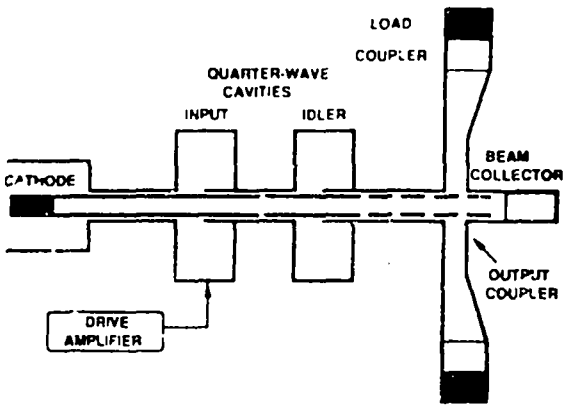

Figure 4. Los Alamos relativistic amplifier.

This device consists of a field emission diode producing a hollow beam that passes through the coaxial quarter-wave input cavity and idler cavity, and on to the rectangular waveguide output coupler. For RF beam modulation measurements the output coupler is replaced on the beam line with a beam pipe containing a linear array of B-dot loops. So far we have produced a modulated electron beam for one microsecond with a voltage of 350 kV, and a peak RF current of 0.9 kA after the second cavity. In some cases we have observed beam modulation in excess of 2 microseconds. The dc beam current is about 3 kA giving approximately a 30% beam modulation. The component of beam power at the microwave drive frequency (1.3 GHz) is approximately 350 MW. Pulse widths of modulated beam power range from 500 ns to 2,400 ns, with the highest gains at the shorter pulse widths. The RF drive level is 5 kW which will result in a gain of 42 dB if one can extract this power with an efficiency of 25% (a conservative estimate). Efforts to extract this power into the waveguide coupler are underway.

Pulsed Power

The availability of the BANSHEE pulsed power modulator currently driving the RKA makes possible high power microwave source development in a relatively unexplored pulse length regime. BANSHEE, which is described in detail elsewhere[4], is designed to deliver a 1 μs pulse at 1 MV and 10 kA at a 5 Hz repetition rate. The rep-rate capability is essential over the long term, because RF conditioning of the microwave tubes will be necessary to achieve reliable high power operation on the microsecond time scale. RF conditioning has historically been proven to be a necessity for reliable operation of high power microwave tubes and RF cavity accelerating structures

Summary

Work on a large orbit gyrotron amplifier has recently begun. Computational modelling of improved electron gun designs has been performed to increase the fraction of the diode current entering the microwave tube, and to achieve improved beam placement in the tube as well. The relativistic klystron amplifier is in the initial stages of experimentation, and has achieved to date 900 ns of bunched beam with a peak current of 0.9 kA. Efforts to extract this power into rectangular waveguide are in progress. The RKA has been designed with future repetitive operation in mind, when the BANSHEE pulser has been fully qualified for rep-rate operation.

ACKNOWLEDGEMENTS

This work was supported by Los Alamos National Laboratory Program Development and Internally Sponsored Research, under the auspices of the United States Department of Energy.

REFERENCES

1. W. W. Destler, et al, "High-power microwave generation from large-orbit devices," IEEE Trans on Plasma Science **16** (2), April 1988, p.71.

2. Y. Y. Lau and L. R. Barnett, "Theory of a low magnetic field gyrotron (gyromagnetron)," Int. J. of Infrared and Millimeter Waves **3**(5), 1982, p.619.

3. M. Friedman, et al, "Externally modulated intense relativistic electron beams," J. Appl. Phys. **64** (2), 1 Oct. 1988, p. 3353.

4. F. W. Van Haaften, et al, " A high-voltage, high-current electron beam modulator for microwave source development," presented at the Fifth National Conf. on High Power Microwave Technology, West Point, New York, May, 1990, to be published.

* Electrical Engineering Department, University of Maryland, College Park, MD.

L-BAND HIGH POWER AMPLIFIERS FOR CEBAF LINAC *

R. Nelson, R. Killion, and J. Fugitt
Continuous Electron Beam Accelerator Facility
12000 Jefferson Avenue, Newport News, VA 23606

Abstract

The high power portion of the CEBAF RF system utilizes 340 5kW klystrons providing 339 separately controlled outputs. Modulating anodes have been included in the klystron design to provide for economically efficient operation. The design includes shunt regulator-type modulating anode power supplies running from the cathode power supply, and switching filament power supplies. Remotely programmable filament voltage allows maximum cathode life to be realized. Klystron operating setpoint and fast klystron protection logic are provided by individual external CEBAF RF control modules. A single cathode power supply powers a block of eight klystrons. The design includes circulators and custom extrusion and hybrid waveguide components which have allowed reduced physical size and lower cost in the design of the WR-650 waveguide transmission system.

Introduction

The accelerator requires multiple high power RF sources for injector and linacs. A design providing a single klystron for each superconducting cavity was selected so that required phase and amplitude adjustment could be accomplished at low power levels.

Configuration

CEBAF's two linacs consist of 20 cryomodules, each with eight superconducting cavities. Individual cavities receive up to 5 kW of CW RF at 1.497 GHz. Including the injector, a total of 340 klystrons are required. Because of the basic linac design of eight cavities per cryomodule, an eight klystron HPA (High Power Amplifier) was appropriate.

In operation, varying amounts of RF power will be required. While a klystron's output power is directly dependant on drive, one disadvantage is that DC input power remains constant regardless of the output power. In a system with 340 klystrons, each with a maximum DC input power of 15 kW, some method of reducing power consumption when less th maximum RF power is required becomes very desirable. It is for this reason that a modulating anode was included in the klystron design. This allows us to reduce klystron beam current to the minimum required for the required RF power.

* This work is supported by U.S. Department of Energy under contract DE-AC05-84-ER40150.

Offers for production of a klystron built to our specifications were submitted by several manufacturers, with the Varian VKL-7811W ultimately being selected.[5] Once the klystron was defined, power supply requirements were also defined. Ripple requirements for the various supplies[6] were largely mandated by the klystron's phase stability with respect to supply variations and the ability of the RF control module to track these perturbations.

TABLE 1. POWER SUPPLY SPECIFICATIONS.

Cathode	
Input	480 V AC 3Ø
Output V	-11.6 kV DC, taps at 11.0, 10.4, 7 kV
Output I	10.6 A max.
Ripple	0.1% P-P
Filament	
Input	208 V AC 3Ø
Output V	programmable, 0-9 V DC
Output I	9 A max.
Isolation	20 kV
Ripple	2% P-P
Modulating Anode	
Input	-11.6 kV DC
Output V	programmable, 0-(-6) kV
Output I	5 mA source, 15 mA sink
Ripple	0.1% P-P

Controls

Drive to each klystron is provided by an RF control module, consisting of RF, analog, digital, and I/O portions. The heart of the module is an 80186 microprocessor. While the module was not part of the HPA procurement, its interaction with the HPA had to be coordinated. The HPA had to provide and accept signals that the module would generate or require.

Early in the design, it had been decided that "per klystron" parameters would be controlled and monitored by the module, while "per HPA" signals would connect to CAMAC. The module is responsible for protecting the klystron from excessive beam and body current and reflected power, and also for monitoring and setting modulating anode and filament voltages. The HPA's power supplies and klystron monitoring directly interface with the module.

Each system includes eight klystrons along with associated waveguide components (coaxial to waveguide transition, circulator, directional coupler) and auxiliary power

supplies, so eight modules, located in racks adjacent to the HPA, are required. The CAMAC interface is also located in these same racks, and takes care of status monitoring and main on-off functions.

Figure 1. Overall view of the HPA during installation.

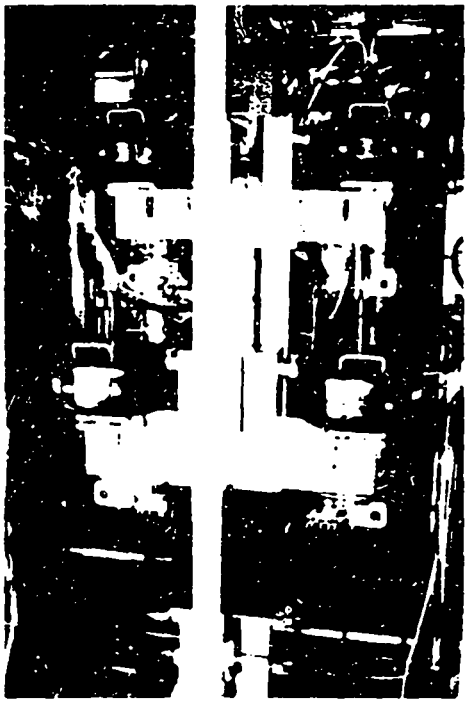

Figure 2. Four of eight klystrons installed along with associated waveguide.

Power Supplies

With the exception of cathode voltage, which is tap settable only, voltages are remotely programmed. The modulating anode setpoint determines a basic operating point and power consumption for the klystron. As life expectancy of the cathode is closely tied to cathode temperature[5], a remotely programmable filament power supply was included.

The filament supply is a resonant mode switcher.[3] Because the klystron filament supply must float atop the - 11.6 kV cathode voltage, its ferrite switching transformer does double duty, providing both step-down and high voltage isolation in one compact, lightweight design. Eight such power supplies are included, each a separate plug-in printed circuit board. The basic design was suggested in our specifications, though ETM Electromatic developed the final design. The board provides remote read-back of actual set voltage and local monitoring of individual filament currents. The power supply initially operates in a current limited mode, then converts to voltage regulated when the cathode nears operating temperature.

Eight klystrons are powered by a single cathode power supply.[2] The original design included no crowbar, so each klystron is connected through a 50 ohm isolating resistor to provide some protection in the event of klystron arcing. We have since designed our own crowbar circuit and have begun adding it to each of the cathode supplies.

High voltage relays to allow remotely isolating bad klystrons were not included in the design of either the HPA or the eight outputs of the cathode power supply. In the event of a defective klystron, this makes it impossible to remotely isolate a single unit from high voltage. Assuming a klystron still holds off high voltage but is otherwise defective (say with high body current), the modulating anode can be adjusted for lower beam current, and most likely lower body current. In worse cases the filament can be turned off, and in the most severe case all eight klystrons would go off-line until planned maintenance.

Rather than a separate power supply, the modulating anode supply is a shunt regulator card operating off a feed from the cathode power supply. The design consists of a series string of MOSFETS. Again the basic design was suggested by our specifications, with ETM developing the final design. While initial klystron tests had used a standard switching supply with some success, a major requirement of the supply was that it be capable of sinking the modulating anode intercept current. For a standard supply this required a fairly low resistance bleeder resistor hung on the output. A shunt regulator was the ideal choice for our requirements since it effectively provided a very low bleeder resistance.

An instrumentation interface board that, in addition to the filament and modulating anode parameters, also provides samples of body current and cathode current for each klystron is included. All "per klystron" signals including waveguide directional coupler samples, are fed to the RF control module. In the event a klystron problem cannot be corrected through manipulation of drive or beam current,

the module can kill high voltage, shutting down all eight klystrons in the HPA.

Mechanical

The HPA is almost 133" x 94" x 36", and in spite of that, it is about as small as it can be made and still be somewhat convenient to work on. It was necessary to maintain the required magnetic separation[5] while mounting eight klystrons along with waveguide components, filament and modulating anode power supplies in a single package. The design was further complicated by the requirement that each assembly of four klystrons and waveguide pieces be movable ± 1" in the x and z-axes, and ± 2.5" in the y-axis. This requirement is necessitated by potential misalignments in penetration spacing and floor height variations.[4]

The klystron's 1-5/8" coaxial output is immediately transformed to WR-650 waveguide. The straight waveguide pieces were produced from aluminum extrusion, cut to length, flanges welded, surfaced, and then iridited for corrosion resistance. CEBAF opted for this route for two main reasons. Estimates for traditional welded waveguide came in at about $30/foot, versus $10/foot for extrusion. Secondly, traditional waveguide houses were, at best, reluctant to produce lengths over 12 feet, which would then require inaccessible flanges inside the penetrations. Gas and RF tight gaskets are included at all flanges, and pressurizing the waveguide gives an indication of potential RF leakage through a drop in pressure. To reduce cabinet height, increase system integrity by eliminating flanges wherever possible, and reduce costs, the coaxial to waveguide transition was specified with an integral 40 dB mono directional coupler.

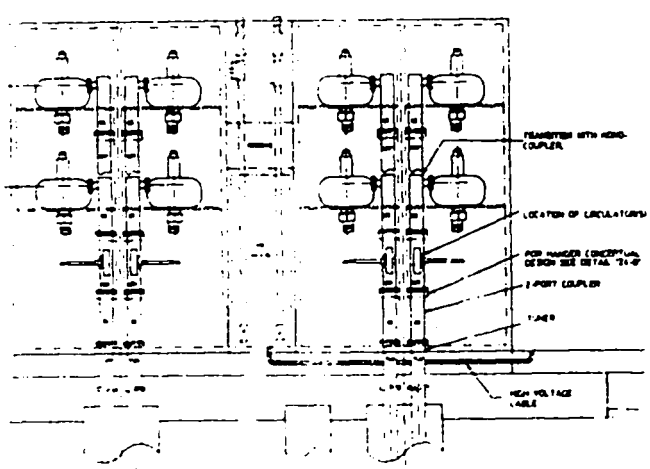

Figure 3. Location of klystrons and waveguide components.

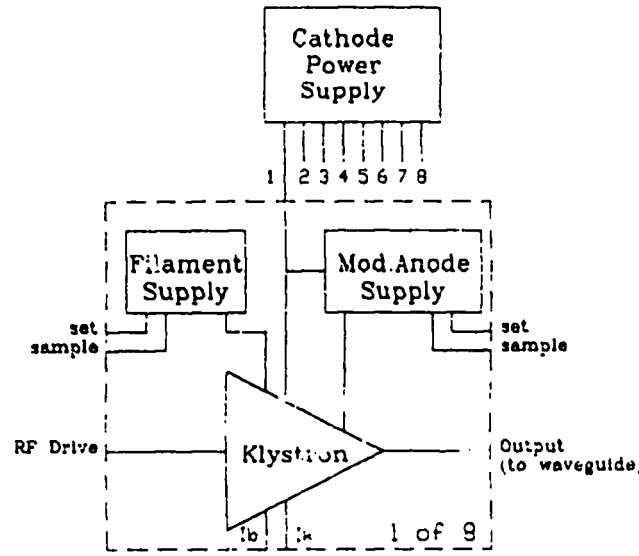

Figure 4. Simplified block diagram of power sections of HPA.

Final Comments

One other major constraint on this procurement was that the first units be delivered in a relatively short time. Some proposals had given 1.5 years as the design/delivery time, but the contract was awarded in July, with the first pair due by July 31. Even with this short time period, both vendors completed their designs and the finished products according to schedule. CEBAF has received the first two units and is now in the process of installing and performing final tests on them.

References

1. A. S. Gilmour, Jr., *Microwave Tubes*, Artech House, 1986.
2. Hipotronics, Inc., Brewster, NY 10509, type 811.6-16.3A/S.
3. ETM Electromatic, Inc., Newark, CA 94560, contract SURA90-C1736SD.
4. G. Curnow, *Initial Survey and Traverse*, CEBAF, 1990.
5. Varian, Microwave Tube Division, Palo Alto, CA, type VKL-7811W.
6. R. Nelson, CEBAF specifications EE25, EE26, EE27, EE28, CEBAF, 1989.

SLED II: A NEW METHOD OF RF PULSE COMPRESSION*

P. B. Wilson, Z. D. Farkas, and R. D. Ruth
Stanford Linear Accelerator Center, Stanford University, Stanford, CA 94309

Introduction

In the SLED[1] method of RF pulse compression, two high Q resonators store energy from an RF source for a relatively long time interval (typically 3 to 5 μsec). Triggered by a reversal in RF phase, this stored energy is then released during a much shorter interval equal to the filling time of the accelerating structure. A peak power gain on the order of three and a compression efficiency on the order of 60% are typically attained. The shape of the output pulse is, however, a sharply decaying exponential. In SLED-II the two cavities are replaced by two lengths of resonant line, forming a Resonant Line SLED (RELS) and resulting in a flat output pulse. Therefore, RELS stages can be cascaded to give a greater peak power gain. Using two stages, a peak power gain greater than ten can be achieved with a reasonable compression efficiency. Unlike the BEC,[2] the RELS compression factor per stage is not limited to two, albeit at the expense of intrinsic efficiency. Like the BEC, it uses long lines rather than short cavities.

Theory

A resonant line is a transmission line terminated in a short circuit and connected to an input transmission line via a coupling network as illustrated in Fig. 1. The distance between the coupling network and the short must be an integral multiple of half guide wavelengths. For the RELS, the losses are characterized by the line attenuation τ (rather than by Q_o) and the coupling is characterized by s, the reflection coefficient when the line is infinitely long (rather than by Q_e).

The RELS theory has been discussed.[3,4] Here we expand on the theory using a somewhat different approach. Let s be the reflection coefficient of the coupling network when the line is terminated in a matched load, $D/2$ its time delay and τ its attenuation in nepers. After turning on an incident field of amplitude E_i, the emitted field after nD time intervals is given by[5]

$$E_e(0) = 0 ,$$

$$E_e(n) = E_i(1-s^2)e^{-2\tau} \times \left[1 + se^{-2\tau} + s^2e^{-4\tau} + \ldots + s^{(n-1)}e^{-(n-1)2\tau}\right] ,$$

$$n = 1, 2, 3, \ldots . \qquad (1)$$

$$E_e(n) = E_i \frac{(1-s^2)e^{-2\tau}}{1-se^{-2\tau}} \left[1 - s^n e^{-n2\tau}\right] ,$$

$$n = 0, 1, 2, 3, \ldots . \qquad (2)$$

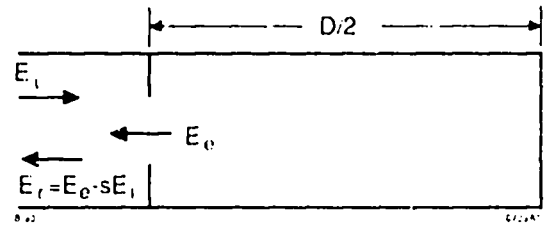

Fig. 1. Resonant line fields.

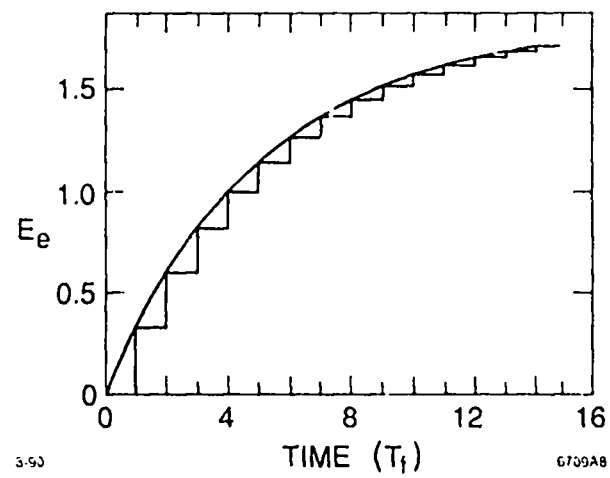

Fig. 2. Discrete and continuous emitted field vs time.

The steady state emitted field is

$$E_e(n = \infty) \equiv E_{ef} = E_i \frac{(1-s^2)e^{-2\tau}}{1-se^{-2\tau}} . \qquad (3)$$

If $\tau = 0$ then $E_{ef} = 1 + s$. As the maximum possible value of s is 1, the maximum emitted field is 2, the same as for SLED.

Let t_n be the beginning of each D interval, $t_n = nD$. Substituting $n \equiv t_n/D$ and $s \equiv e^{\ln s}$,

$$E_e(t_n) = E_{ef}\left[1 - s^{t_n/D}\exp\left(-\frac{t_n 2\tau}{D}\right)\right]$$
$$= E_{ef}\left[1 - \exp\left(-\frac{t_n}{D}(2\tau - \ln s)\right)\right] . \qquad (4)$$

Typical continuous and discrete emitted fields are plotted in Fig. 2.

The continuous emitted field of a resonant cavity is

$$E_e(t) = \alpha\left[1 - \exp\left[-\frac{\omega t}{2}\left(\frac{1}{Q_o} + \frac{1}{Q_e}\right)\right]\right] . \qquad (5)$$

Comparing the above two expressions, we obtain the relationship between attenuation and unloaded Q, and between reflection coefficient and external Q:

$$E_{ef} = \alpha , \qquad \frac{\tau}{D} = \frac{\omega}{4Q_o} , \qquad \frac{-\ln s}{D} = \frac{\omega}{2Q_e} . \qquad (6)$$

*Work supported by Department of Energy contract DE-AC03-76SF00515.

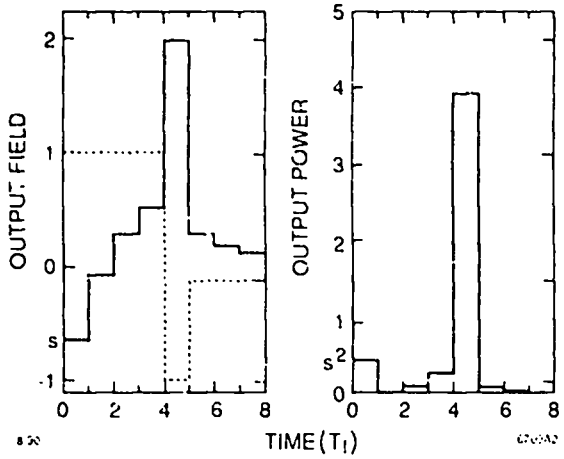

Fig. 3. RELS Single-stage output field and output power vs time in units of T_f. Dashed line shows input phase modulation.

For any piecewise variable input function E_i, as long as the changes in E_i occur at nD intervals, where n is an integer, the emitted field during each nD time interval, by analogy with a resonant cavity, is

$$E_e(n) = E_{ef} - [E_{ef} - E_{ei}]s^n e^{-n2\tau}, \quad n = 0, 1, 2, 3 \ldots . \tag{7}$$

Here, E_{ei} is the emitted field at the start of each interval. For the first interval E_{ei} is zero, and for the subsequent intervals it is the same as the value at the end of the previous interval. Using superposition, the reverse field is

$$E_r(n) = E_e(n) - E_i s . \tag{8}$$

The normalized reverse power during each time interval is

$$P_r(n) = E_r^2(n) . \tag{9}$$

The amplitude of the first step of E_r is $E_i s$. We can obtain the steady state value of the emitted field by measuring E_r the instant after turning off the RF, after it has been on long enough to reach steady state, and obtain τ by solving Eq. (3).

Single-Stage RELS

We can separate the incident from the reflected field by placing two resonant lines at the two isolated outputs of a 3 dB coupler, or by making it a part of a resonant ring. We then have a single stage RELS. Let the incident pulse width $T_k = n_o D$. At time $t = (n_o - 1)D$—as with SLED—we change the phase of the incident field by π, the incident field $E_i = -1$ from zero to $(n_o - 1)D$, and $E_i = 1$ from $(n_o - 1)D$ to $n_o D$. E_i changes sign instantaneously but—unlike with SLED—the emitted field remains constant for a duration D. The reverse field during this interval is

$$E_r(n_o - 1) \equiv E_p = E_e(n_o - 1) + E_i s . \tag{10}$$

Here, E_p is constant for a duration D and is the output pulse. We choose D to equal the accelerator section fill time, T_f. Here also, as with SLED, the maximum value of E_p is three.

TABLE I
One-Stage RELS Power Gain and Efficiency as a Function of Compression Factors and REL Attenuation.

		$\tau = 0.00$		$\tau = 0.01$	
n_o	s	P_g	η	P_g	η
3	0.549	2.66	89	2.57	86
4	0.610	3.44	86	3.29	82
5	0.651	4.02	80	3.81	76
6	0.685	4.49	75	4.21	70

The power gain, compression factor, and compression efficiency are

$$P_g = E_p^2 , \quad C_f \equiv T_k/D = n_o , \quad \eta = P_g/n_o . \tag{11}$$

The power gain and compression efficiency as a function of compression factor, with optimized s, are listed in Table I. The values agree with those given in Table 1 in Ref. 3. The output field and output power of a single stage RELS as a function of time in units of D for $n_o = 5$, are plotted in Figs. 3.

Two-Stage RELS

Unlike SLED where the exponential output pulse shape makes cascading of SLED stages impractical, the RELS output pulse is rectangular and therefore RELSs can be cascaded.

Definitions of parameters for a two-stage RELS:

D	Last stage RL round-trip delay
n_o	Last stage input pulse length in units of D
D_1	First stage RL round-trip delay
n_1	First stage input pulse length in units of D_1
T_k	Length of RELS input pulse
C_f	Overall compression factor

The input pulse to the last stage has to be the output pulse of the first stage. Hence,

$$D_1 = n_o D . \tag{12}$$

The length of the input pulse (to the first stage) and the compression factor are

$$T_k = n_1 D_1 = n_1 n_o D , \quad C_f = T_k/D = n_1 n_o . \tag{13}$$

The modulation for a two-stage RELS can be obtained as follows. Divide the input pulse T_k into C_f intervals of duration D. Let $E_{i1} = -1$ from zero to $(C_f - n_o)D$ and let $E_{i1} = 1$ from $(C_f - n_o)D$ to $C_f D$. Let $E_{io} = 1$ when n is not an integral multiple of n_o and $E_{io} = -1$ when n is an integral multiple of n_o. The incident field amplitude at each interval is

$$E_i(n) = E_{i1}(n)\, E_{io}(n) . \tag{14}$$

We calculate the power gain and compression efficiency as a function of C_f as follows. First we obtain the first stage output field—assuming single stage modulation—for a RELS with a line of length D_1. We then divide

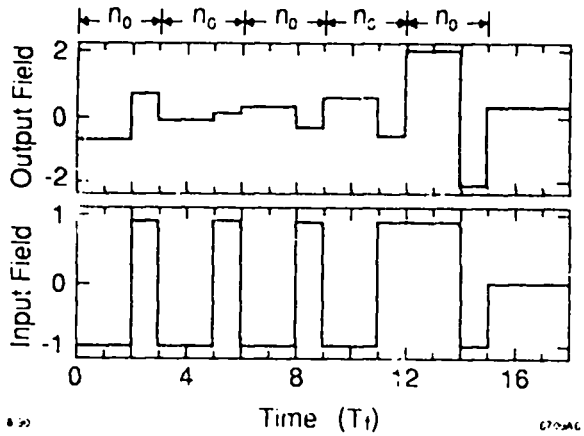

Fig. 4. First stage RELS input and output fields.

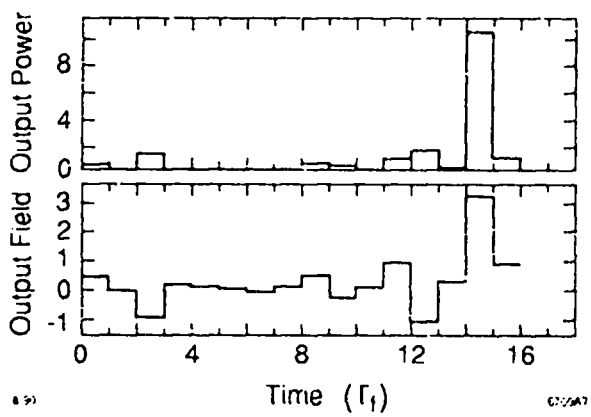

Fig. 5. RELS Second-Stage output field and power.

each constant amplitude interval D_1 of the first stage output wave into n_o intervals and modulate each interval D_1. We apply Eqs. (7),(8) to each of the n_o intervals in succession and obtain the reverse field as a function of n. The first stage input and output field waveforms for $n_1 = 5$ and $n_o = 3$ are plotted in Fig. 4. The second stage input field amplitude (first stage output), the output field, and the output power are plotted in Fig. 5.

The power gain and compression efficiency are:

$$P_g = E_r^2(C_f - 1)\,, \qquad \eta = \frac{P_g(C_f - 1)}{C_f}\,. \qquad (15)$$

The values of power gain end efficiency for several combinations of n_1 and n_o are tabulated in Table II.

The compression factor is the product $n_1 n_c$, and does not depend on the relative values of n_1 and n_o. The power gain and compression efficiency also depend only on the product of $n_1 n_o$. Therefore, if $n_1 \neq n_o$, then n_1 should be chosen to be greater than n_o if we wish to minimize line length, and less than n_o if we wish to minimize switching transitions.

Practical RELS

A two-stage RELS is shown in Fig. 6. Assume for the NLC a two-stage RELS with $n_1 = 5$ and $n_o = 3$. The pulse length required by the NLC is 80 ns; thus

TABLE II
Two-Stage RELS Power Gain and Efficiency as a Function of Compression Factors and Line Attenuation.

n_o	s_o	n_1	s_1	C_f	τ	P_g	η
3	0.549	3	0.549	9	0.000	7.05	78
3	0.549	3	0.549	9	0.005	6.53	73
5	0.651	3	0.549	15	0.005	9.60	64
3	0.549	6	0.685	18	0.000	11.0	61
3	0.549	6	0.685	18	0.005	10.4	58
6	0.685	3	0.549	18	0.005	9.69	54
5	0.651	5	0.651	25	0.005	14.0	56
6	0.685	6	0.685	36	0.005	16.5	46

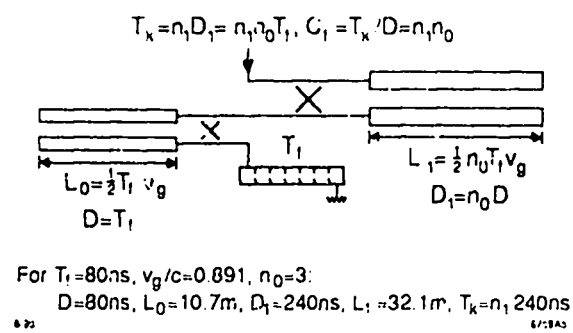

Fig. 6. Two-stage RELS.

$D = 80$ ns. Use a WC281 guide operating at 11.4 GHz in the TE_{01} mode with an attenuation of 0.1 nepers/μs. Because the short is not perfect, the attenuation must include the power absorbed by the short. The length of the first stage line is $D_1 = n_o D = 3D = 240$ ns. To obtain the length in meters multiply by the RL length by the group velocity which is, in this case, 0.267 m/ns. The RL lengths are 32.1 m for stage one, and 10.7 m for stage two. The klystron pulse length $T_k = 5(240) = 1.2$ μs. We expect a gain of about nine (line three of Table 2).

References

1. Z. D. Farkas et al., "SLED: A Method of Doubling SLAC's Energy," Proc. of 9th Int. Conf. on High Energy Accelerators, 1976, p. 576.
2. Z. D. Farkas, "Binary Peak Power Multiplier and its Application to Linear Accelerator Design," IEEE Tran. MTT-34, 1036 (1986).
3. A. Fiebig and C. Schieblich, "A Radio Frequency Pulse Compressor for Square Output Pulses," Proc. of EPAC, Rome, 1988, p. 1075.
4. V. E. Balakin and I. V. Syrachev, "A New Approach in RF Power Multiplication," VLEPP-Note-06/1990 (1990).
5. P. B. Wilson, "Theory and Design of Super Conducting Linear Accelerators," Proc. Linear Accelerator Conf. (North Holland, 1970) p. 1107.

RF TESTS ON THE INS 25.5-MHZ SPLIT COAXIAL RFQ

S. Shibuya*, S. Arai, A. Imanishi, T. Morimoto, E. Tojyo, and N. Tokuda

Institute for Nuclear Study, University of Tokyo
Tanashi, Tokyo 188, Japan

Abstract

A 25.5-MHz split coaxial RFQ with modulated vanes has been constructed. This RFQ will accelerate heavy ions with a charge-to-mass ratio greater than 1/30. We have finished field measurements and obtained the following results: the field strengths between neighboring vanes are same within ±0.6% over the vane length; the distribution of the intervane voltage in the axial direction is almost flat. Through high power tests so far conducted, we have attained an intervane voltage of 110 kV under a pulse operation with a peak power of 70 kW and a duty factor of 0.9%. The cavity is thus almost ready for acceleration tests.

Introduction

We have constructed a 25.5-MHz split coaxial RFQ with modulated vanes, and will accelerate heavy ions with a charge-to-mass ratio (q/A) greater than 1/30. The whole cavity consists of three module cavities. The cavity structure and its design procedure were reported elsewhere,[1,2] and main parameters of the RFQ are summarized in Table I. The RFQ presented here is a prototype of a real machine for the Japanese Hadron Project. The operating frequency and the length of a real machine under design are respectively 25.5 MHz and 22 m. This real machine will accelerate unstable nuclei ($q/A \geq 1/60$) up to 170 keV/u.[1]

Soon after the completion of the cavity construction in October, 1989, the resonant frequency was roughly tuned to 25.45 MHz.[2] Further fine tuning to 25.5 MHz was afterward accomplished by using three inductive tuners: a cylindrical aluminum block (188 mm in diameter) was inserted into each module cavity. We obtained experimentally the relation between the tuner length and the resonant frequency, and determined finally the length so that one tuner increases the frequency by 17 kHz. The distance between the beam axis and the tuner end is now 170 mm. The resulting resonant frequency is 25.5 MHz, and the unloaded Q-value is 6400. Through field measurements we obtained satisfactory results, as will be discussed below.

We are now conducting high-power tests by using a power supply with the following specifications: 100 kW in the maximum peak power, 10% in the maximum duty factor, 50 μs ~ 3 ms in pulse width. The rf power is fed into the cavity through a coaxial wave guide (WX-120D) and a loop coupler cooled with water. We have so far attained a intervane voltage of 110 kV under a pulse operation with a peak power of 70 kW and a duty factor of 0.9%.

This paper describes measurements of field distributions along the vanes and presents preliminary results of high-power tests.

TABLE I

Main Parameters of the Prototype RFQ

Frequency (f)	25.5 MHz
Charge-to-mass ratio (q/A)	$\geq$ 1/30
Input energy (T_{in})	1 keV/u
Output energy (T_{out})	45.4 keV/u
Normalized emittance (ε_n)	0.6 π mm·mrad
Vane length (L)	2.135 m
Kilpatrick factor (f_K)	2.2
Intervane voltage (V_v)	109.3 kV*
Mean bore radius (r_0)	0.946 cm
Minimum bore radius (a_{min})	0.521 cm
Margin of bore radius (a_{min}/a_{beam})	1.20
Focusing strength (B)	6.0
Limiting current (I_{lim})	2.5 mA*

* for q/A = 1/30 ions.

Field Measurements

We measured distributions of electric field strengths in the cavity by means of a perturbation method. When a perturbator comes into a cavity, the resonant frequency (f_0) changes (by Δf). Furthermore, the difference between the phase of the input wave and that of the transmitting wave shifts (by θ). These are expressed as:

$$-\tan\theta \simeq 2Q_0 \frac{\Delta f}{f_0} \propto E^2 , \qquad (1)$$

where Q_0 is the unloaded Q-value, and E the electric field strength at the perturbator position. We measured the above θ for the evaluation of field strengths.

We examined the filed balance among the quadrants

*The Graduate University for Advanced Studies, KEK, Tsukuba, Ibaraki 305, Japan

by measuring field strengths between vanes. A teflon perturbator (20 mm in diameter and 10 mm in length) was set between vanes, as shown in Fig. 1, and moved in the axial direction (the perturbator always touched two vanes). The measured θ's are shown in Fig. 1, where four curves, corresponding to the four perturbator positions between vanes, are drawn. At any axial position, each of four field strengths deviates from their average value by less than ±0.6%.

Field strengths in the beam aperture were measured with a teflon perturbator, 9.5 mm in diameter and 7.5 mm in length. The thick line in Fig. 2 is the result. The observed oscillation is due to the modulation of the vanes, as can be explained by a numerical calculation. From Eq. (1), we see that the phase shift θ is related to the energy of the electric field in the perturbator region. The field energy was computed by using electric field components derived from the Kapchinskij-Teplyakov potential function[3] and design values of vane parameters at each cell. The intervane voltage was assumed to be constant over the vane length, as is in the design. For comparison with the above

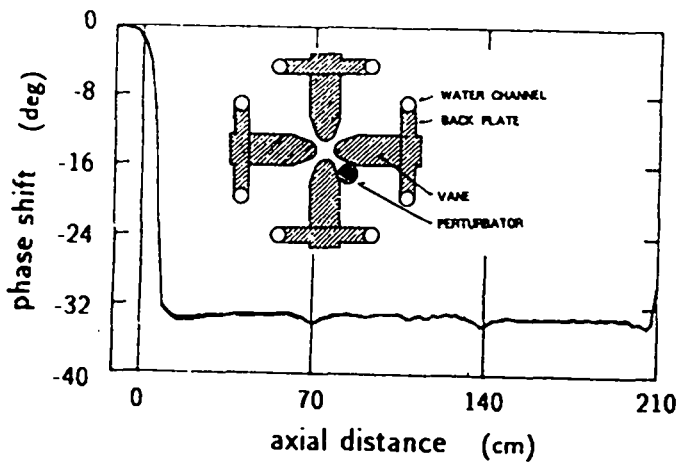

Fig. 1. Measured field strengths between neighboring vanes (four curves are drawn) and the perturbator position.

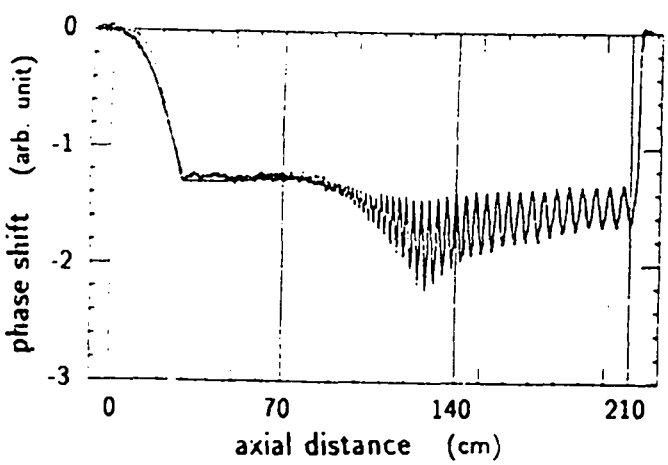

Fig. 2. Measured (thick line) and computed (thin line) electric field strengths in the beam aperture.

experimental data, the computed values of θ were normalized so that the measured and the computed θ's are equal at the exit of the radial matching section, 30 cm down from the cavity entrance. The thin line in Fig. 2 is the result of the computation. From the good agreement between the two curves, we infer that the intervane voltage is almost flat over the vane length, and that the electric field in the beam aperture is close to the ideal one.

High Power Tests

Measurements of intervane voltage

During high-power operations we should be able to measure intervane voltage. Two measurement techniques have been tried, and they yielded results consistent to each other.

One of the techniques is to measure a voltage of a signal from a monitor loop attached to the cavity side wall. The size of the loop and its angle to the magnetic flux were adjusted so that the picked-up signal might have a voltage about 1/10000 of the intervane voltage. For the calibration, we applied directly voltage between two neighboring vanes by connecting them to a signal generator with a cable and measured the output voltage of the monitor loop.[4] The resulting monitor-loop voltage against an intervane voltage of 1V was 0.1225 mV.

The other technique is to measure an input power P_{in} supplied to the cavity and calculate an intervane voltage V_v from the following relation:

$$V_v = \sqrt{2 R_p P_{in}} , \tag{2}$$

where R_p is the resonant resistance of the cavity. The value of R_p was experimentally obtained. We applied a certain voltage V_v to vanes in the manner same as at the calibration of the monitor loop, and measured a voltage V_c across a 50-Ω resistor terminating the loop coupler for high-power rf feed. We found thereby

$$R_p = 50 \left(\frac{V_v}{V_c}\right)^2 \tag{3}$$

$$= 86.8 \text{ k}\Omega .$$

The resonant resistance can be derived from another relation. Using measured values of the unloaded Q-value (Q_0 = 6400), the resonant frequency (f_0 = 25.5 MHz), and the capacitance (C = 453 pF) of the inner electrode, we obtained

$$R_p = \frac{Q_0}{2 \pi f_0 C} , \tag{4}$$

$$= 88.2 \text{ k}\Omega .$$

Substituting these R_p-values into Eq. (2), we obtained intervane voltages as functions of input power; the two curves in Fig. 3 are the results.

In the figure the curves are compared with open circles. The circles were plotted by using input powers indicated on a meter of the power supply and intervane voltages obtained from monitor-loop outputs. The three

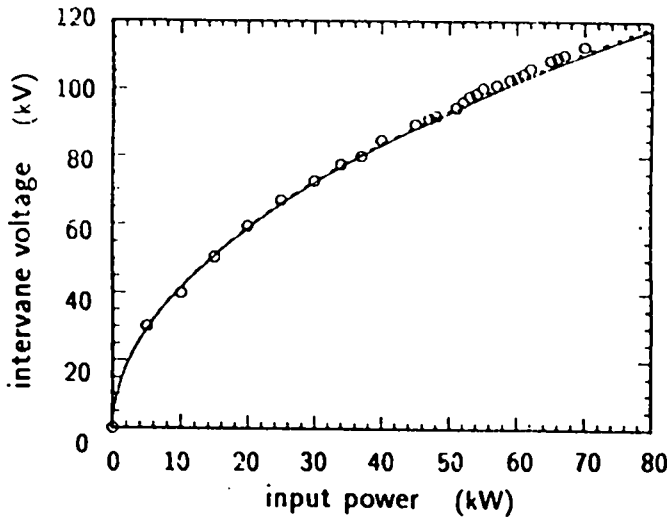

Fig. 3. Relation between intervane voltage and input power. The solid line is derived from Eq. (2) with $R_p = 86.8$ kΩ, and the dashed line with $R_p = 88.2$ kΩ. The open circles denote intervane voltages derived from monitor-loop signals as functions of the input power measured with a power meter.

results *i.e.*, the two curves and the set of open circles, are same within ±1.1%.

Cavity conditioning for high-power operations

We have attained an intervane voltage of 110 kV under a pulse operation with a duty factor of 0.9% and a peak power of 70 kW. This voltage is high enough to accelerate ions with a charge-to-mass ratio of 1/30; 109 kV is necessary for the ions. The high intervane voltage was attained after a conditioning, where we trained the cavity under operations with duty factors of 3% ~ 0.6% and increased the input power step by step so that the vacuum in the cavity might be kept less than 7×10^{-6} Torr.

Figure 4 shows the progress in attained intervane voltage during the conditioning. At the beginning we increased gradually the input power at lower levels, but could not stabilize the operation. After such a state lasting, the intervane voltage jumped abruptly to 6 kV, and the cavity came into a stable operation at this level. As the input power was increased further, the shape of the signal from the monitor loop warped and the vacuum got worth rapidly. These phenomena, caused by multipactoring, were observed at certain ranges of the intervane voltage. The multipactoring was severer at lower voltages, as indicated by the three plateaus in Fig. 4. From the observed multipactoring levels, we found that the applicable intervane voltages are at present between 6 kV and 110 kV, and that the RFQ can accelerate ions with a charge-to-mass ratio between 1/2 and 1/30.

Concluding Remarks

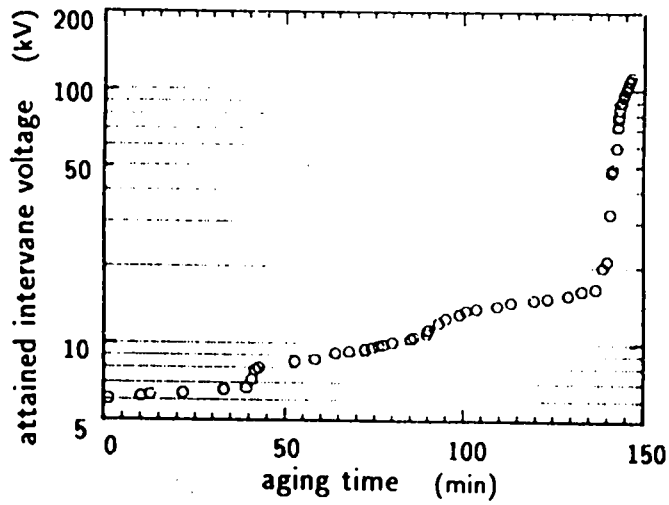

Fig. 4. Attained intervane voltage as a function of aging time, *i.e.*, operation time × duty factor.

The field measurements have verified that a good electric field is generated in the beam aperture. From our experience with other RFQ's at INS, we consider that the obtained field balance among the quadrants and the flat voltage distribution in the axial direction promise well for acceleration tests to be conducted soon. The issues of high-power tests from now on are 1) increase of the duty factor up to 10%, 2) examination of temperature increase and frequency shift under high-duty operations, and 3) measurement of the voltage break-down level. After constructing a test stand, we will accelerate N_2^+ ions.

Acknowledgments

The authors express their thanks to M. Kihara for his encouradgement. The RFQ work is supported by the Accelerator Research Division, High Energy Physics Division, and Nuclear Physics Division of the INS. The prototype model was constructed at Sumitomo Heavy Industries, Ltd. The computer works were carried out on FACOM M780 in the INS Computer Room. This project is supported by the Grant for Scientific Research of the Ministry Education, Science and Culture.

References

1. S. Arai, *Design Study of a 25.5-MHz Split Coaxial RFQ*, 14th Int. Conf. on H. E. Accelerators, KEK, Tsukuba, Aug., 1989.
2. N. Tokuda, *Structure and RF Characteristics of the INS 25.5-MHz Split Coaxial RFQ*, 7th Symp. on Accelerator Science and Technology, Osaka Univ., Dec., 1989.
3. I. M. Kapchinskij and V. A. Teplyakov, *Linear Ion Accelerator with Spatially Homogeneous Strong Focusing*, Prib. Tekh. Eksp., No. 2, 1970.
4. R. W. Müller, Private Communication, GSI, 1983.

CLOSE-COUPLED RF POWER SYSTEMS FOR LINACS

W. J. Hoffert, S. R. Schmidt, and D. A. Swenson
Science Applications International Corporation
San Diego, California 92121

Abstract

Close-coupled rf (CCRF) power systems for accelerator applications have been developed and tested. Prototypes, based on Eimac Planar Triodes (Y-690 and YU-176) in grounded-grid configurations, exhibit outstanding performance, efficiency, gain and simplicity. These units mount directly on the side of the accelerator and operate in an extension of the accelerator vacuum, thus eliminating many components of conventional rf power systems such as rf output resonators, transmission lines, and vacuum windows. Rf power is coupled to the accelerator through a loop operating at the anode potential. Cooling for the anode is provided through the coupling loop. After passing through the loop, the rf currents are shunted to ground through an integral rf-bypass capacitor. This same approach is relevant to larger tubes, offering peak powers in the 0.5-1.0 MW region, with all the same advantages, including substantial weight savings.

Introduction

High-strength, radio frequency, electromagnetic fields, bounded by resonant cavities, are commonly used in particle accelerator systems to accelerate, deflect and/or focus charged particle beams. The rf power required to create and sustain these fields is traditionally obtained from external rf power sources connected to the resonant cavities through some sort of rf power transmission lines and rf power coupling devices. These conventional distributed systems for powering rf devices in accelerator systems are unnecessarily complex and expensive.

A reduction in the cost and complexity of these systems would have a substantial effect on the viability of accelerator systems for medical, industrial, scientific and defense applications. One approach to this goal would be to develop a close-coupled rf power source where the active element of the rf power source mounts directly on the resonant cavity and interacts directly on the rf fields within the cavity. This could eliminate many components and functional interfaces of conventional rf power systems, resulting in simpler, less expensive, more compact, and more reliable accelerator systems for a variety of applications.

Close-Coupled RF Power Systems

Close-coupled rf power (CCRF) systems for accelerator applications are under development at SAIC. Prototypes of these systems, based on the Varian/Eimac planar triodes in grounded-grid, cathode-driven configurations, exhibit outstanding performance, efficiency, gain and simplicity. These units are designed to mount directly on the side of an RFQ linac, in an extension of the linac vacuum, and coupledpower directly to the linac fields through a loop operating at the anode potential. Cooling for the anode is provided through the coupling loop. After passing through the loop, the rf currents are shunted to ground through a rf-bypass capacitor, which is an integral part of the design. These CCRF power systems promise to eliminate many components of conventional rf power systems such as rf output resonators, rf output couplers, rf power transmission lines, and rf power windows.

Schematics for both conventional rf power systems and close-coupled rf power systems are shown in Fig. 1. In the conventional arrangement, power amplifier optimization and impedance matching to the resonant load are based on measurements of the forward and reflected power in the transmission line and the efficiency of the power transfer from the transmission line to the accelerator. They do not, however, indicate the amount of rf power actually generated by the power amplifier or the amount of power lost in the amplifier output circuits.

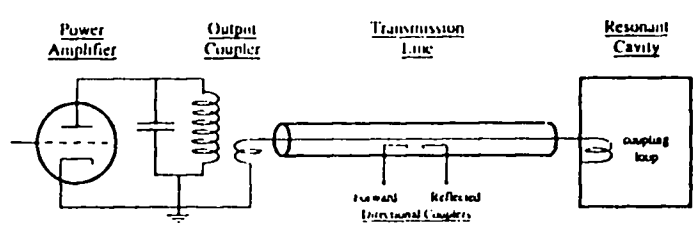

Fig. 1a. Conventional RF Power System.

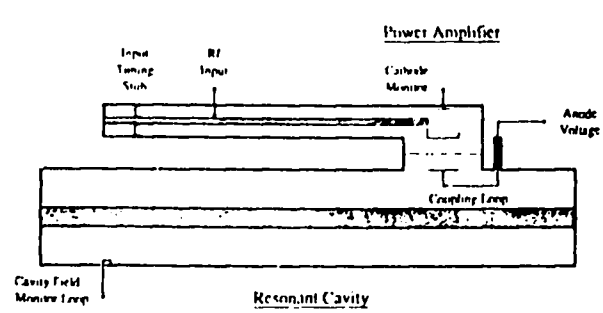

Fig. 1b. Close-coupled RF Power System.

In the close-coupled arrangement, there is no direct way to separate the performance of the power amplifier from the performance of the power coupling device. The concept of forward and reflected power, between the power amplifier and the resonant load, is not applicable. Hence, alternate techniques have been developed for system optimization. The only relevant measure of the system performance is the magnitude of the resonant fields, which, after all, is the principal reason for the system.

In order to optimize the performance of a close-coupled rf power system, there are several portions of the system that must be properly tuned and/or matched. The data available for these operations include the forward and reflected power of the rf input drive line, the cathode excitation, the cathode bias, the anode voltage and current, and the magnitude of the fields in the output resonator. The variables effecting these data are the position of the input resonator tuning stub, the position of the input resonator drive tap, the cathode bias (determined by selection of zener diode), and the size, shape and orientation of the coupling loop that couples the anode current to the magnetic fields of the resonant load.

The procedure for adjusting these variables to effect the optimum performance includes: 1) adjusting the rf drive frequency to the resonant frequency of the resonant load (or alternatively, adjusting the resonant frequency of the load to the drive frequency), 2) adjusting the position of the input resonator tuning stub and input resonator drive tap to achieve a minimum reflected power on the rf input drive line while maintaining a significant cathode plate excitation, and 3) adjusting the size, shape, and orientation of the coupling loop to achieve high efficiency ($\geq$70%) power transfer to the resonant load and a high power gain ($\geq$13 db) across the power amplifier as indicated by a measure of the magnitude of the resonant fields.

The Eimac planar triodes (Y-690, YU-141, YU-176) can produce peak rf power in excess of 20-30 kW with duty factors in the range of a few percent. They are rated for performance up to 2 GHz. They are small in size (one inch in diameter and two inches long) and reasonable in cost. They can be deployed in clusters for higher power requirements. A single cluster of 12 of these small tubes have produced as much as 360 kW of rf power for linac applications.

Planar triodes operate well, either singly or in clusters, in the grounded-grid, cathode-driven configuration. This implies that the anode and the coupling loop operate at elevated potential (6-10 kV) and should have considerable capacitance to ground (200 pf or more) for the rf currents. Using the required electrical insulation as the dielectric of the required rf bypass capacitor results in the compact and rigid configuration shown in Fig. 2. The anode cooling water enters the anode bypass capacitor ring, passes through the coupling loop to the anode cap, and then back to the capacitor ring on the way out.

Figures 3 and 4 suggest 4- and 8-tube configurations for powering RFQ linacs. The 8-tube configuration employs a pair of triodes in each CCRF module.

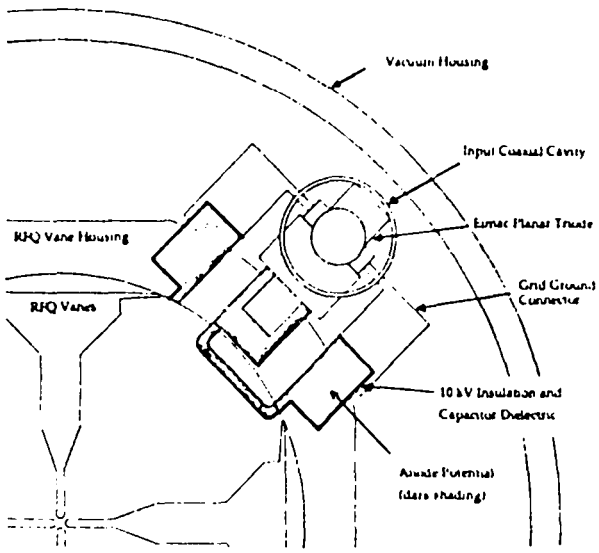

Fig. 2. Anode Loop Insulation and RF Bypass Capacitor.

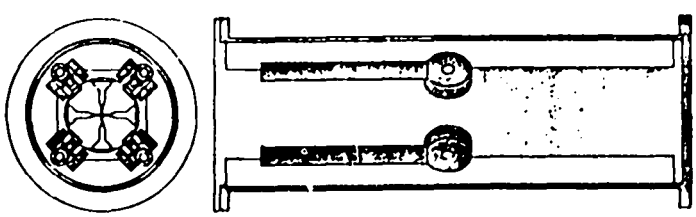

Fig. 3. Four-tube RFQ Configuration

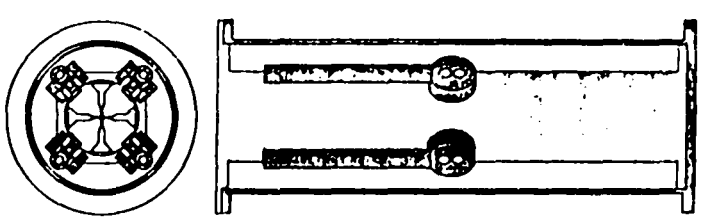

Fig. 4. Eight-tube RFQ Configuration.

Each triode or cluster of triodes (2 or more) requires a cathode excitation circuit, typically involving a resonant cavity or an impedance transformer. The configurations, shown in Figs. 3–5, involves a three-quarter wavelength coaxial cavity with the outer conductor grounded, a tuning stub at the far end, an adjustable tap for input coupling, and the open end of the center conductor connected to the cathode. The filament leads are routed through the center conductor of the input resonator so as to be at the same rf potential as the cathode.

Fig. 5 shows a two-tube, close-coupled rf power system coupled to a 425 MHz RFQ linac. The pair of planar triodes (YU-176) can produce in excess of 60 kW of peak rf power for 2% duty factor.

With many different input cavities, care must be taken to drive them in the proper phase so that their output powers will combine constructively They can either be driven as a plurality of coupled strip lines, a resonantly coupled chain, or through a power splitter and equal length lines. The preferred scheme will depend on the details of the configuration.

Applications

There are distinct advantages in power ing linacs with a multiplicity of smaller power units, namely, it is relatively easy to survive the failure of any one unit by calling on some reserve power from the remaining units, and the system hardware, being small in size and large in number, results in favorable design and fabrication costs. Most analyses suggest high reliability and substantial cost saving for the close-coupled scheme over the conventional rf power systems.

For an RFQ linac requiring 100 kW of peak rf power, one planar triode in each quadrant, as shown in Fig. 3, represents a conservative and symmetrical configuration having ample rf power for normal operation, with sufficient reserve to survive the failure of any single power unit.

For an RFQ linac requiring 200 kW of peak rf power, a pair of planer triodes in each quadrant, as shown in Fig. 4, would provide ample power for normal operation, with sufficient reserve to survive the failure of several units. Each pair of triodes would be clustered together as a unit with their outputs combined into a single rf drive loop.

Drift tube linacs (DTLs), requiring many megawatts of power, could be driven by clusters of four planar triodes connected to each drive loop. These clusters need only be 4 inches in diameter. Ter such clusters could produce more than a megawatt. One cluster every 4 inches represents a linear power density in excess of 1 MW/m.

An array of small planar triodes could be used to power coupled cavity linacs (CCLs), even at frequencies that are typically higher than that of RFQs and DTLs.

Conclusions

Close-coupled, loop-driven, rf power sources, using the linac resonator itself as their output resonator and power combiner, offer substantial savings in the cost, complexity, weight, and efficiency of the rf power sources for linac applications. By integrating the rf power sources with the linac, much of the mystery of both entities is removed. All problems associated with the extraction of the rf power from the power source, transmission of the rf power to the linac, and injection of the power into the linac are solved, in the simplest way, by the close-coupled configuration. The system control is simplified by eliminating any concern over reflected power and standing waves in the non-existant transmission lines. Such rf power sources are no longer a constraint on the linac frequency, since the major element of the rf system is the linac itself. The power source itself is essentially broad-band, delivering its power directly to the resonant load. The power efficiency is improved by eliminating the power dissipated in the conventional rf power output resonators, couplers and transmission lines. System reliability is improved by the general simplification of the system, the significant reduction in part count, and the ability to survive the failure of some power units (graceful degradation).

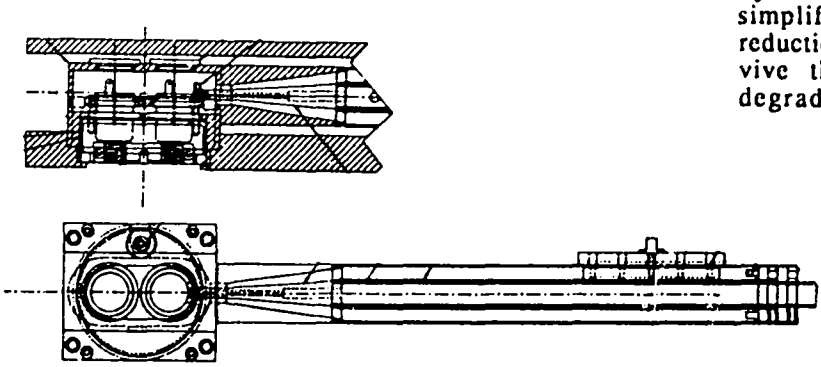

Fig. 5. Two-Tube, Close-Coupled RF Power System – Mark III.

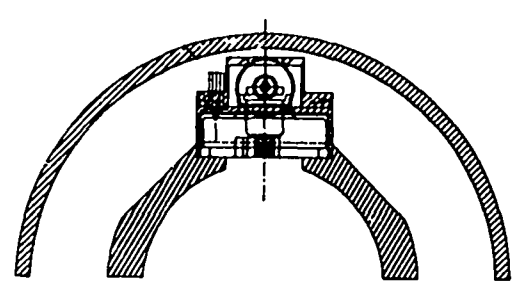

MEASUREMENT OF RF SURFACE EFFICIENCY AT CRYOGENIC TEMPERATURES USING A COAXIAL RESONANT CAVITY

G. O. Bolme, G. P. Boicourt, L. Booth, N. K. Bultman, E. Foley, D. J. Liska, R. A. Lohsen, J. B. Niesen, J. Rose,† B. Rusnak, G. Spalek, and N. G. Wilson
Los Alamos National Laboratory, Los Alamos, NM 87545

Abstract

Exploiting the potential efficiency gain of a normal conducting rf accelerator operated at cryogenic temperatures requires careful preparation of the rf conducting surface. Experimental apparatus has been assembled to study the surface conductivity to rf currents at 425 MHz and 850 MHz through a temperature range from room temperature to 14 K. The apparatus is built around an open-ended coaxial cavity with the cavity tubular ends below the cutoff frequency at resonance. The center conductor in the coaxial cavity is the test sample, and the use of a dielectric stand-off for the center conductor precludes the need for an rf contact joint and facilitates sample changes. The rf testing is conducted under vacuum with low-power rf. A CTI-Cryogenics cryopump coldhead is used for cryogenic temperature cycling of the test cavity. A detailed description of the apparatus and measurement procedures are presented.

Introduction

The H^- accelerator for the Ground Test Accelerator (GTA) has the purpose of verifying much of the space-traceable technology for the Neutral Particle Beam (NPB) program. Included in the space-traceability is the demonstration of increased efficiency and stability of operating normal-conducting, rf accelerating structures at cryogenic temperatures. The many different rf components in the GTA accelerator require varied fabrication processes, and the understanding of the fabrication processes and their effect on efficiency were not well known. The Cryogenic Test Fixture (CTF) was designed and assembled to provide a dedicated experimental facility for testing the rf structure efficiency of test surfaces and other cryogenic components. The CTF combines an rf coaxial cavity, a vacuum system, a cryogenic cooling system, temperature monitors, and the support diagnostics for measurements directed at this very specific technology issue.

Design Objectives of the CTF

A limitation of many of the surface efficiency experiments is associated with the expediency of testing and the capacity to limit the test to a specific uniform surface finish. The expediency of testing requires that the surface sample preparation be simple and uncomplicated, and that installation into the apparatus and subsequent testing be easy and rapid. Obtaining and testing a representative, uniform surface finish precludes the use of rf seals and the testing of an interior surface where machining, abrasive polishing, plating, and electropolishing give inconsistent results. These design requirements generated our decision to use an open-ended coaxial cavity for our testing program. Using the open-ended cavity and dielectric standoffs for supporting the center conductor results in a test cavity with no rf seals and in which the center conductor is easily replaced. By using only the center conductor as the sample, the test surface is mechanically simple and all processes are applied to an outside surface where uniformity is easier to achieve. Furthermore, the current densities are highest across the central region of the center conductor where the surface uniformity is best, and the current diminishes rapidly near the ends where the fabrication processes may change. A drawback to using a common outer conductor for all testing is that this conductor, necessarily, has a different conductivity, and only relative results for comparison of processes can be directly measured.

CTF Apparatus

The coaxial resonant cavity outer conductor is a 24-in. long cylinder fabricated from a 4-in. o.d. by 0.5-in. wall OFE-HIT copper tube. The tube length was selected from calculations and measurements, which guarantee that power leakage out of the cavity ends is far below 1%. The inside of the tube was turned down to an inside diameter of 3.530 in. as a compromise between reducing mass, removal of the sacrificial metal, maintaining cavity strength, and leaving sufficient material for mounting the diagnostic hardware. The inside machining was done with conventional techniques to rough dimensions, and the final three finishing cuts of less than 0.003 in. were made with a diamond tool at slow speed and feed. Two outer conductors have been prepared. Each outer conductor has been machined in a similar fashion, but one includes a final 500 C anneal and chemical polish for additional conductivity enhancement.

The center conductor samples are 0.971-in. diameter cylinders which result in a 77 ohm (maximum Q) configuration for the cavity. A smaller diameter would have resulted in greater domination of the measured data by the test sample; however, the selected diameter has greater rigidity for consistent machining. Each end of the cylinder has a 0.25-in. radius to diminish sharp edge effects during plating or electropolishing. Each end also has a 1/4-20 tapped hole as point of attachment for plating, electropolishing, and other processing as necessary. The sample lengths are 32.852 cm, 32.159 cm, and 15.160 cm resulting in resonance frequencies of 425 MHz, 433 MHz, and 850 MHz, respectively.

*Work supported and funded by the US Department of Defense, Army Strategic Defense Command, under the auspices of the US Department of Energy.
†Work supported under Industrial Partnership Agreement with Grumman Aerospace Corporation, Bethpage, NY.

The center conductor is supported at its center by a 0.5-in. thick, wedge-shaped beryllium oxide (BeO) dielectric standoff. BeO was selected for this application over boron nitride, alumina, polyethylene, and teflon because it retains both high electrical resistivity and high thermal conductivity across the entire temperature span of testing. The center conductor is held in place on the standoff by a spring-loaded BeO post. The spring loading is maintained by five Belleville washers mounted in series to accommodate the expansions and contractions of thermal cycling.

RF diagnostics connection to the resonant cavity is provided by two magnetic coupling probes located opposite each other around the circumference at the cavity longitudinal center.

A stainless steel, cylindrical vacuum vessel provides a clean vacuum environment for rf testing and cryogenic operation. Inside dimensions of 17-in. diameter by 44-in. length provide ample room for the cavity and other equipment. Access to the interior at each end of the vessel is provided by hinged, o-ring sealed flanges which are held closed under high vacuum by atmospheric pressure. These doors give access to the entire inside diameter when opened. The vacuum vessel is mounted on a moveable stand along with the following support equipment:

1. A Leybold-Heraeus Turbomolecular vacuum pumping system.
2. A CTI-CRYOGENICS gaseous helium refrigerator.
3. A Lake Shore Cryotronics diode thermometer system.
4. An AC heater system for cavity temperature control.

RF Cavity Modeling

For an rf resonant structure, the cavity Q is a scaled factor of the stored field energy divided by the required power, thus Q is directly related to efficiency.

$$Q_U = \omega \frac{E_{stored}}{P_{total}} \qquad (1)$$

The computed Q from an rf cavity modeling code provides the theoretical value for data comparison

An analytic solution of the coaxial cavity can be done if the boundary conditions for the cavity ends are clipped at the end of the center conductor. The analytic solution is informative; however, the end effects are extensive and require more detailed modeling. The SUPERFISH family of codes provides theoretical predictions for the resonant frequency, the cavity Q, and the power distribution between the center and outer conductors. The resonant frequency and field distributions are first-order calculations in SUPERFISH and have estimated accuracies of better than 1%. Cavity Q and power distributions are second-order calculations and, as such, have been assigned estimated accuracies of 2%, accordingly. Laboratory measurements of the cavity frequency for all three center conductors agree to well within 1% of the SUPERFISH prediction based on careful measurements of the component dimensions. Although end effects for the 433-MHz cavity result in an 8% difference in frequency between the SUPERFISH prediction and the analytic solution, the Qs for the two calculations agree to within 1%.[1]

Because most rf structures are built to specifications based on SUPERFISH modeling, power estimates for operation are scaled by the measured Q versus the SUPERFISH Q. For this reason any CTF Q measurements, which are scaled against the SUPERFISH Q, have value in predicting the performance of accelerator rf structures.

Testing Procedure

The unloaded Q is the quality factor of the rf structure alone with no external perturbations; however, the measurement of Q requires coupling the cavity to an external system. Our laboratory measurements, therefore, measure the cavity loaded Q, Q_L, and the unloaded Q must be extracted by also measuring the coupling of the field-sampling loops, β_1 and β_2. Q_U can then be calculated from Q_L using equation 2.[2]

$$Q_U = (1 + \beta_1 + \beta_2)Q_L \qquad (2)$$

For our test program, Q_L is measured by the bandwidth method, and β_1 and β_2 are calculated from a reflected power measurement of each port.

All measurements are made using a Hewlett Packard 8753B Network Analyzer. Because lengthy cables are used inside the vacuum to reduce thermal losses, it is impossible to calibrate the Network Analyzer to accommodate the cable losses at the field-sampling loops. As a result, it is necessary to determine the field-sampling loop coupling by measuring the ratio of resonance reflected power to the nominal, off-resonance reflected power for that port.

An assembled coaxial cavity with a test sample is installed in the CTF and is under high vacuum for all rf testing. Q measurements are made of the first- and third-cavity resonance modes for the 425-MHz and 433-MHz cavities; however, only the first mode of the 850-MHz cavity is measured because of power leakage out of the cavity ends for the third mode. Q measurements are taken at room temperature prior to turning on the refrigeration system. The cavity is then cooled to cryogenic temperatures using the CTI gaseous helium refrigerator. Q measurements are then taken at three cryogenic temperatures (the coldest operating temperature, ~20 K, and ~35 K) by using the heaters for selecting the given temperatures. For each of the above four temperatures, the network analyzer system is calibrated at the connection port to the vacuum feedthrough connector, thus assuring some degree of measurement consistency. After completing these four calibrated measurements, the coaxial cavity is again cooled to its lowest temperature. A sequence of Q measurements is then started for the duration of the warm-up cycle with the network

analyzer now under the control of a Hewlett Packard Computer. Because the region between 15 K and 40 K is especially interesting, approximately ten temperature points are set and stabilized using the heaters up to 40 K, and Q data collection is initiated by the computer. Without temperature control below 40 K, the temperature rises too rapidly for meaningful measurements. Above this temperature region, both the heaters and the refrigeration are turned off, and data is collected on a timed cycle for the remainder (approximately 2 days) of the warmup to room temperature. The network analyzer system is uncalibrated for the measurements made during the automated warm-up cycle.

Copper Surface Preparation Studies

The CTF has been most effective in accomplishing a surface efficiency study for identifying the best cavity fabrication processes for the GTA 850 MHz DTLs. This study used 17 different samples to compare various surface preparation techniques and the sequence of the preparation steps. Figure 1 displays the Q enhancement values relative to the SUPERFISH room-temperature, predicted Q for these samples. Each row is a different sample for a fabrication technique. Across each row is a check mark if a process was done on the sample or a numerical value for the Q enhancement if the sample was measured at that particular step. This study assisted the design engineers in selecting optimal sequences for the DTL fabrication and verified the safe application of some processes for the cryogenic structures.

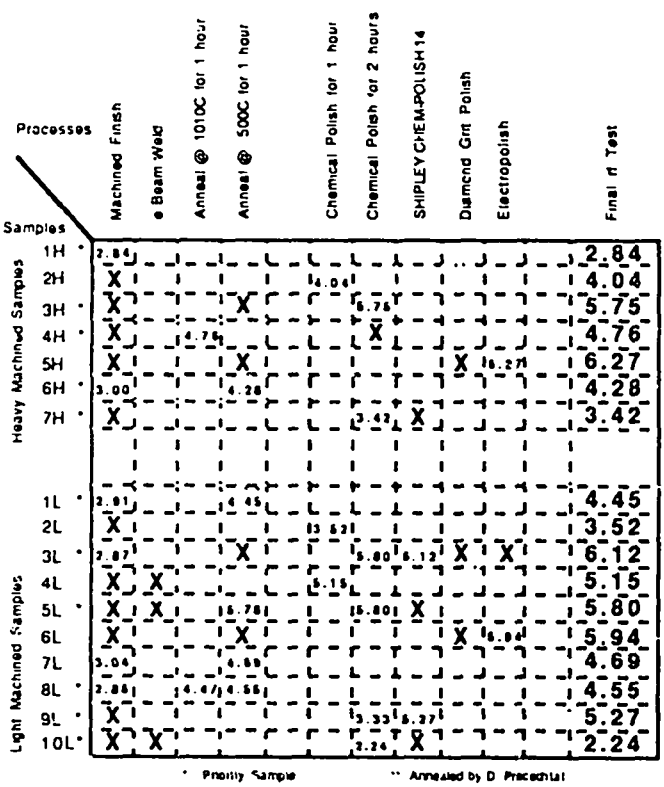

Fig. 1. Q enhancement of the GTA 850 MHz DTL Copper Surface fabrication processes.

Conclusions

The understanding of the affect of the near-surface conductive region on surface conductivity and rf structure efficiency has been used to design the features of the CTF. As a result, the CTF generates data directed specifically at technology issues for the NPB program.

The CTF has been a useful facility for the rf surface testing already completed for the GTA program. It has been used to verify the suitability of the rf surface for the GTA RFQ, to accomplish an extensive program of evaluating copper surface preparations for the GTA 850-MHz DTLs, and to evaluate the effect of single rf contacts at cryogenic temperatures. In the future, data from the CTF should be applied directly during the rf structure design phase to more accurately predict power and cooling requirements.

References

1. C. Geisik and G. O. Bolme, AT-2 Technical Note: 89-06, (1989).

2. E. L. Ginzton, Microwave Measurements, McGraw-Hill Book Company, Inc., New York (1957), pp 391-434.

VOLTAGE BREAKDOWN TEST AT 473 MHZ*

D.Sun, F.R.Huson and W.W.MacKay
Texas Accelerator Center†, 4802 Research Forest Drive,
The Woodlands, TX 77381

Abstract

RF breakdown test results with copper, titanium, stainless steel and SiO_2 coated copper are presented. The results show that SiO_2 coating may depress field emission.

Introduction

Voltage breakdown is one of the major factors to be considered in designing a high gradient accelerator structure. Since Kilpatrick proposed his semi-emperical criterion for rf breakdown in 1950's[1], several experiments have been conducted by various research groups. Figure 1 shows some of these results[2]-[8] and Kilpatrick's criterion curve. Obviously, these experimental data are widely dispersed and more data are needed, especially in the region of 425 - 2280 MHz.

In theoretical aspect, many models were proposed to explain dc breakdown, but few for rf breakdown. Up to now the mechanism of rf breakdown is still not clear. This fact not only limits the understanding of rf breakdown, but also affects the effort to achieve and maintain higher field gradients. More experimental information is also needed for theoretical modeling.

Motivated by the above mentioned needs, the research to be described in this paper is aimed to provide rf breakdown data at 473 MHz and to test the effect of thin films deposited onto a Cu surface, especially the possibility of SiO_2 coating to depress field emission.

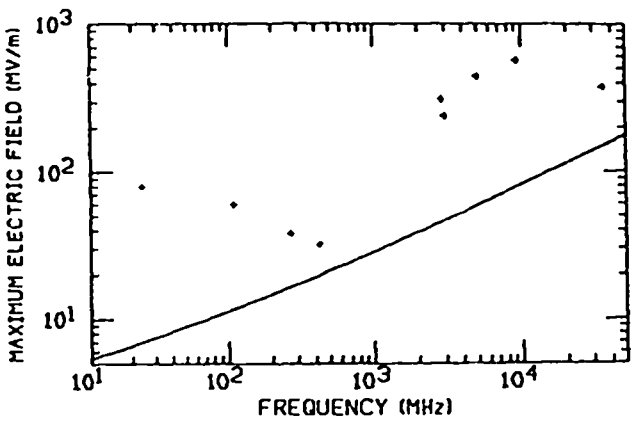

Fig.1. Experimental data and Kilpatrick criterion curve (solid line).

*Work supported in part by the SSC

Experimental Setup

The test setup is shown in Figure 2. The rf breakdown test cavity is a reentrant type resonant cavity which is in a vacuum chamber. The copper cavity consists of two demountable halves. The gap and resonant frequency can be changed easily by moving two electrodes. The electrodes are composed of two parts: body and end cap. The end caps which are made from various materials to be tested are screwed onto the bodies. A small area of each end plate of the cavity was coated with Ti to depress multipactoring. The cavity is water cooled. Table 1 shows some parameters of the cavity with different gap lengths which are results of SUPERFISH.

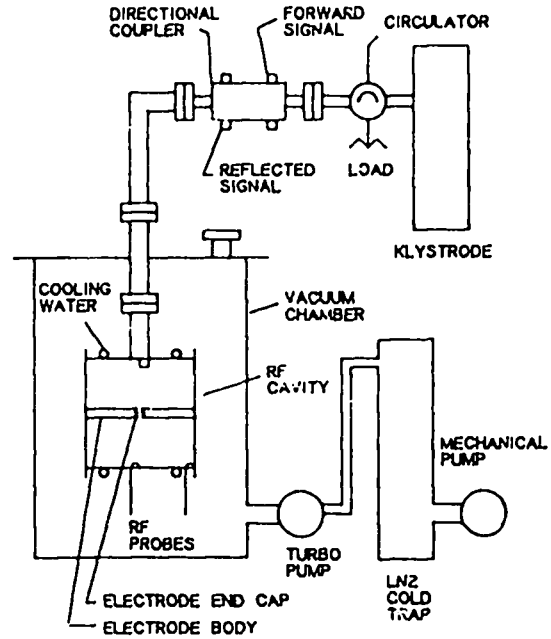

Fig.2. Experimental setup

Two rf probes are mounted at different positions to monitor rf power transmitted into the cavity. Also, the ratio of the two probes' measurements is used to detect other possible modes which may be excited at higher power levels. Seven thermocouples monitor cavity temperature at various positions.

An EIMAC 2KDW60LA klystrode was used as an rf power source providing 50 μs long pulses with a repetition rate of 100 Hz[9]. The forward and reflected power are

monitored with a calibrated four port directional coupler.

The vacuum system consists of a vacuum chamber, a 500 L/sec turbo pump, a liquid nitrogen cold trap and a mechanical pump. The vacuum feedthrough for the main rf coaxial transmission line is made using a Teflon insulator and a Viton O-ring.

X-ray radiation is monitored with a Ludlum model 177 radiation detector at 2 meters away from vacuum chamber.

TABLE 1
Cavity Parameters

Gap length (mm)	1.80	1.85
Q	10997	11059
Resonant frequency (MHz)	473.512	477.138
Emax (MV/m)	57.3	55.8
Power dissipated (W)	3365	3315

Experimental Procedure

All electrode end caps were carefully polished to less than 3 μm finish and ultrosonically cleaned . Two end caps were made from Ti and two from stainless steel. Four copper end caps were coated with Ti thin films of 100 - 120 nm by sublimation. Eight copper end caps were coated with SiO_2 thin films by electron beam evaporation. The thickness of SiO_2 is 200, 300 and 400 nm. The index of SiO_2 is 1.543.

The length of the gap was measured by two methods. First, a gauge was inserted into the gap to get accurate data of gap length and the resonant frequency was measured to make a frequency-gap length curve. Second, every time after changing electrodes and retuning the cavity, the gap length was measured by calliper and checked with the frequency-gap length curve.

Before every test, the Q of the cavity, SWR and attenuation of rf probes were measured several times with an HP8753B network analyzer. During tests, the signals from the rf probes were measured with a DSA602 digitizing signal analyzer. The forward and reflected power were measured with an HP438A power meter. The maximum electric field in the cavity was determined by the expression:

$$E_{max,exp} = E_{max,theo}\left[\frac{Q_{exp}P_{exp}}{Q_{theo}P_{theo}}\right]^{1/2} \qquad (1)$$

where $E_{max,theo}$, Q_{theo} and P_{theo} are the theoretical maximum electric field, Q factor and corresponding dissipated power as calculated by SUPERFISH, and Q_{exp} and P_{exp} are experimental ones.

Experimental Results

1. Copper, Titanium and Stainless steel

The maximum field for these 3 materials can be maintained at as high as 120 MV/m, although spark spots were found on electrode surfaces after tests. Although these three materials can reach the same field level, there are differences among them. It is more difficult to maintain stable operation with copper electrodes than titanium and stainless steel. There are more and bigger spark spots on the surface of the copper than on the surface of titanium or stainless steel. The stainless steel had just one spark spot after a total of 8 hours operation. Sparks actually started at a lower electric field of 60-90 MV/m irregulaly when power was increased. The indication of such breakdown is sudden a large power reflection, an X-ray burst and a change of vacuum. Since reflected power was very high at the field level of 120 MV/m, an alternative method to measure electric field in the cavity such as X-ray measurement is needed and is planned to establish these results.

2. Ti coated copper

Ti coating did not improve performance. At the electric field of 80-90 MV/m, clear breakdown signals were observed. At such a level, whenever power was increased, the breakdown occured irregularly (every several minutes) within a pulse for 10-20 minutes. After then, high field can still be maintained for a long time. The shape of spark spots are very similar to those on the surface of pure copper. At every spark spot, the Ti film was broken.

3. SiO_2 coated copper

The purpose of dielectric coating is to isolate the microprotrusions on the metal surface from vacuum[10]. However, space charge accumulation may become a serious problem. To our knowlege, there has been no publication about testing SiO_2 coating. At this initial stage, the 400 nm SiO_2 coated copper end caps were tested . The maximum electric field used up to now is 81 MV/m. Since the SiO_2 films are only 400 nm, as a first order approximation the formula (1) is still used to estimate the maximum electric field in the cavity. Up to this level, there was neither indication of breakdown during the test nor trace of breakdown on the surface after the test. The Q of the cavity was 6915. The ratio of signals from the two rf probes was similar to that of pure copper cavity. X-rays were negligible which may indicate that SiO_2 depressed field emission. Further X-ray measurement is being planned.

Discussion

1. Although the electrodes of those three different metals can work at the electric field level of the same order of magnitude, the results show that rf breakdown and high field performance of electrodes are still related with material characteristics which may include the latent heat of fusion.

2. SiO_2 can at least survive an electric field of 81 MV/m. It may reduce field emission from the copper surface, and therefore may be applied to protect copper electrodes in high gradient rf fields.

3. Since the secondary electron emission of Ti is less than that of SiO_2, the above results imply that the secondary electron emission may not play an important role

to initiate breakdown in high gradient rf fields.

References

† TAC at HARC is a consortium of Rice University, Texas A&M University, the University of Texas, Prairie View A&M University, Sam Houston State University and the Baylor College of Medicine MR Center.

1. W. P. Kilpatrick, "Criterion for Vacuum Sparking Desinged to Include Both rf and dc," Review of Scientific Instruments, **28** (10), 824 (1957).
2. Y. N. Nikolaev, "Investigation of High Voltage Vacuum Discharge at 25 Mc," Sov. Phys. **8** (4), 354 (1963).
3. A. Gerhard, *et al.*, "RF Sparking Experiments at 108.5 and 216 MHz," IEEE Trans. Electrical Insulation **24** (6), 1033 (1989).
4. R. M. Hutcheon, *et al.*, "Operation of a CW High Power RFQ Test Cavity," Proceedings of the 1984 Linear Accelerator Conference, pp74
5. S. W. Williams, *et al.*, "Voltage Breakdown Testing for the Radio Frequency Quadrupole Accelerator," Proceedings of the 1979 Linear Accelerator Conference, pp144.
6. J. W. Wang and G. A. Loew, "Measurements of Ultimate Accelerating Gradients in the SLAC Disk-Loaded Structure," IEEE Trans. Nucl. Sci. **32** (5), 2915 (1985).
7. E. Tanabe, "Voltage Breakdown in S-band Linear Accelerator Cavities," IEEE Trans. Nucl. Sci. **30** (4), 3351 (1983).
8. E. Tanabe, *et al.*, "Voltage Breakdown at X-Band and C-band Frequencies," Proceedings of the 1986 Linear Accelerator Conference, pp458.
9. W. W. MacKay, *et al.*, "Operaion of a 473MHz Pulsed Klystrode Power Source," this Conference.
10. W. Peter, "Vacuum Breakdown and Surface Coating of rf Cavities," J. Appl. Phys. **56** (5), 1546 (1984).

MEASUREMENT OF RF ACCELERATOR CAVITY FIELD LEVELS AT HIGH POWER FROM X-RAY EMISSIONS*

G. O. Bolme, G. P. Boicourt, K. F. Johnson, R. A. Lohsen, O. R. Sander, and L. S. Walling
Los Alamos National Laboratory, Los Alamos, NM 87545

Abstract

Energy spectroscopy measurements of x-rays from rf structures at high power provide an independent method of finding accelerating-gap voltages in the multiple-cell accelerating structures. An x-ray detector is used to measure the energy of the emitted x-rays; and the high-energy endpoint of the energy spectrum histogram corresponds with the peak-gap voltage in the rf structure. The x-ray measurements are used to provide a calibration relating peak-gap voltage to rf structure field sampling probes. The analyzed x-ray data has been compared to theoretical SUPERFISH and MAFIA3D predictions and to beam-dynamics data for the multiple-cell structures. Information about this diagnostic technique and its value for verifying accelerator modeling codes is presented.

Introduction

A primary objective of the GTA program is verification of the accelerator modeling codes. Codes such as the SUPERFISH family of codes and MAFIA3D model the performance of the rf structures; and particle-dynamics codes such as PARMTEQ and PARMILA predict beam parameters based on rf structure simulations. RF power and measured Q have been used to predict the field levels by means of the rf structure modeling codes; and these predicted field levels are applied as an input to the particle dynamics codes to generate the expected beam characteristics Thus, experimental verification of code performance has bridged both sets of codes by correlating measured beam parameters to the rf structure power consumption. Our rf cavity gap-voltage measurements using the x-ray emissions, determine the accelerating structure electric field levels—the interconnecting parameter of these two sets of accelerator modeling codes.

A direct measurement of the rf structure fields cannot be accomplished because any probe capable of measuring the full-field level would significantly perturb the cavity. A measurement of the rf structure x-ray emissions is nonintrusive on the cavity and its operation; therefore, an x-ray diagnostic system does not perturb or modify the rf structure. Our diagnostic apparatus is based on an x-ray spectroscopy system, which measures the energies of individual x-rays outside the accelerator cavity vacuum vessel. The upper end-point energy of the x-ray energy spectrum corresponds to the peak-gap voltage from which the electric field levels can be extrapolated. Sets of these data provide the scaling relation between cavity power and field level, and this scaling relation provides the field level correlation for beam data relating cavity power to beam parameters.

RF Structure X-ray Emissions

High-voltage gaps in a vacuum environment are well-known sources of x-rays. The rf accelerator sections are fabricated assemblies of one or more resonant electromagnetic cells, creating high-voltage gaps that the beam particles transit. These oscillating, high-voltage gaps are necessarily contained within a high-vacuum vessel; therefore, the accelerator sections are prolific sources of x-ray emissions under normal operation.

The source of these x-rays is a multistep process depicted in Fig. 1. The high voltage across any gap is associated with electric fields throughout the physical region of the gap. At the negatively-charged surface of the gap, the electric fields result in the field emission of electrons into the

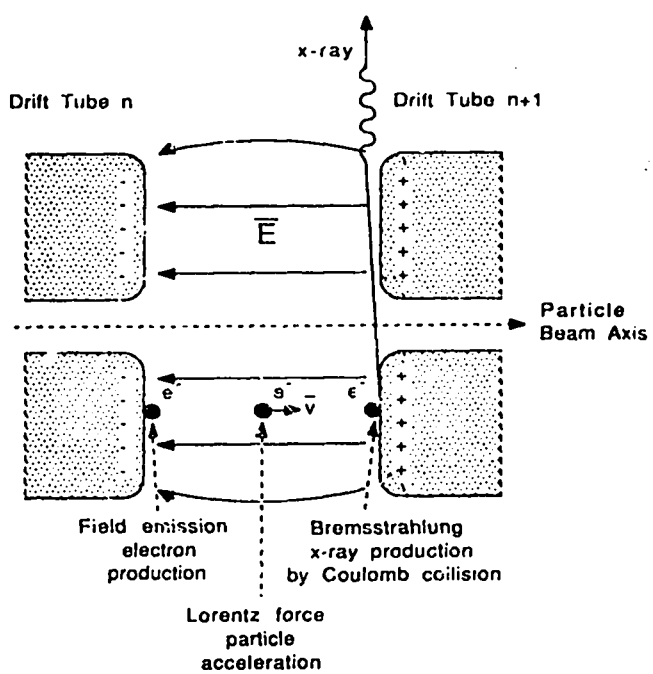

Fig. 1. Source of the rf structure x-ray emissions at high-power.

*Work supported and funded by the Department of Defense, US Army Strategic Defense Command, under the auspices of the Department of Energy.

vacuum gap. These electrons are accelerated within the gap by the fields present; and in transiting the gap, each electron attains a kinetic energy associated with almost all of the gap voltage, V_g.[1]

$$T \equiv \text{Electron kinetic energy} \approx eV_g \quad (1)$$

At the positively-charged surface, these accelerated electrons lose their energy in Coulomb collisions, thus, emitting Bremsstrahlung x rays. The x-rays have a full distribution of energies up to the full kinetic energy of the accelerated electrons. The angular distribution of these x-rays is strongly peaked in the forward direction of the incident electron; however, a finite number of x-rays are emitted throughout the full solid angle.[2] It is these emitted x-rays that carry the signature of the gap voltage, and their penetration outside the vacuum confinement wall provides us with an indirect means of measuring the gap voltage without perturbing the cavity structure or the fields within.

Apparatus

The x-ray detection system is based on a Canberra HPGe detector with a measured FWHM resolution ≤1% across the energies of interest. The detector analog signal is shaped by a spectroscopy amplifier and converted to digital data by a voltage-sensitive ADC. In order to reduce background and to limit x-ray data collection to the rf pulse, logic electronics are used to gate ADC conversion for x-rays occurring only during the rf pulse. All analog and logic signal processing, as well as digital conversions, are done by NIM electronic modules.

The data collection, display, and storage have been done by two different computer systems—a DEC microVAX and an IBM-PC. For both computer systems, the interface to the ADCs is controlled through CAMAC hardware.

Because many of the rf structures are multiple-cell rf cavities, it is necessary to limit the detector view to one cell of the accelerator structure. It is desirable to have an unobstructed view of the acceleration cell (voltage gap) of interest through a glass vacuum window. The glass vacuum window aids in the alignment of the x-ray detector, assists in verifying that the detector view is restricted to a single cell, and allows ≈100% transmission of x-rays above 20 keV. The HPGe detector is placed in a lead shield from 0.5-in. to 2-in. thick (measurement dependent) in order to block detection of x-rays from other structure cells, the rf amplifiers, or surrounding material that can scatter x-rays. The detector and lead shield are positioned as far back from the accelerating structure as geometry permits in order to further reduce count rate and background rate. Lead collimators with apertures of 0.040 in. to 0.250 in. are used to restrict the detector view to a single voltage gap and to control the x-ray counting rate. Tin, copper, aluminum, and lead sheets are placed over the collimator aperture to further control the x-ray counting rate as required. The planview of the detector apparatus is shown in Fig. 2.

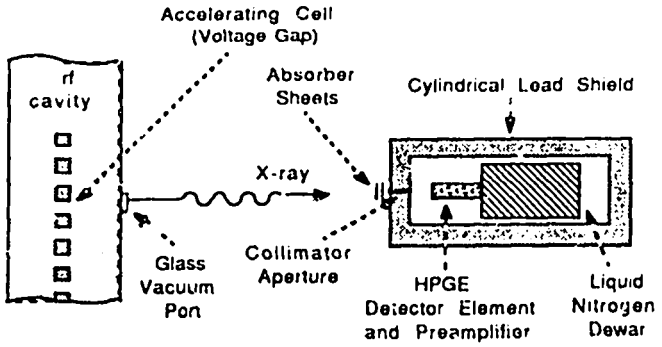

Fig. 2 Experimental planview for the x-ray emission apparatus.

Measurement Procedures

After configuring the apparatus according to Fig. 2, a ^{133}Ba x-ray source is positioned in front of the detector element for energy calibration of the detector system. The calibration data are collected without the rf timing gate until statistics are sufficient for good resolution of the x-ray lines. Occasionally, a second calibration data set is taken with the required rf timing gate and operating rf amplifiers to ensure that rf noise pick-up is not affecting the x-ray signals. The calibration is not normally taken in this mode due to the excessive time required for good statistics at the low rf duty factor.

The rf power is turned on to the desired level and the rf timing logic gate is set to window the center of the rf pulse. By restricting x-ray data collection to a time window at the center of the rf pulse, excess background and x-ray data associated with the transients of rf turn-on and turn-off are eliminated. The absorber foils and collimator aperture are then adjusted to limit the counting rate to 0.25 to 1.0 x-ray for each 500 μsec of rf pulse duration. Limiting the x-ray counting rate in this manner significantly reduces the pulse pile-up at the high-energy end of the data spectrum.

With the data rate adjusted, an x-ray data spectrum is collected at the fixed rf level until sufficient statistics are collected to permit fitting to the energy endpoint. An additional x-ray spectrum is taken with the collimator aperture blocked and the remaining configuration identical to data collection. This spectrum represents the background within the data spectrum. If the background counting rate is insignificant, a very short measurement is made; however, if the background rate is sizable, a longer measurement is made to permit a time-weighted subtraction of the background from the x-ray data prior to doing the energy endpoint fit.

Data Analysis

The x-ray data from the ADC is stored in the form of a histogram of counts versus ADC channel number. The

^{133}Ba x-ray source is used to energy scale the ADC channel number, because it has several, well-resolved x-ray lines and the two dominant x-ray lines (81.0 keV and 356.0 keV) bracket the energy endpoints of most of the rf structures. A least-squares fit with a Gaussian peak is made of the two dominant x-ray lines in the spectrum using the code, CURFIT.[3] A straight-line scale of x-ray energy versus ADC channel number is calculated from the peak centers of the 81.0 keV and the 356.0 keV x-ray lines.

With an energy calibration for the x-ray spectrum, the rf structure data can be fitted for the energy endpoint. If significant background radiation was detected, a time-weighted background spectrum is subtracted from the x-ray spectrum. A straight-line, least-squares fit is made of the x-ray spectrum with the code, CURFIT,[3] in order to project the largest possible x-ray energy. Since pulse pile-up creates a turn up at the high-energy end of the spectrum, a fitting window is set across a linear region of the energetic x-rays to most accurately project the spectrum endpoint. A sample of an rf structure x-ray spectrum and endpoint fit are displayed in Fig. 3.

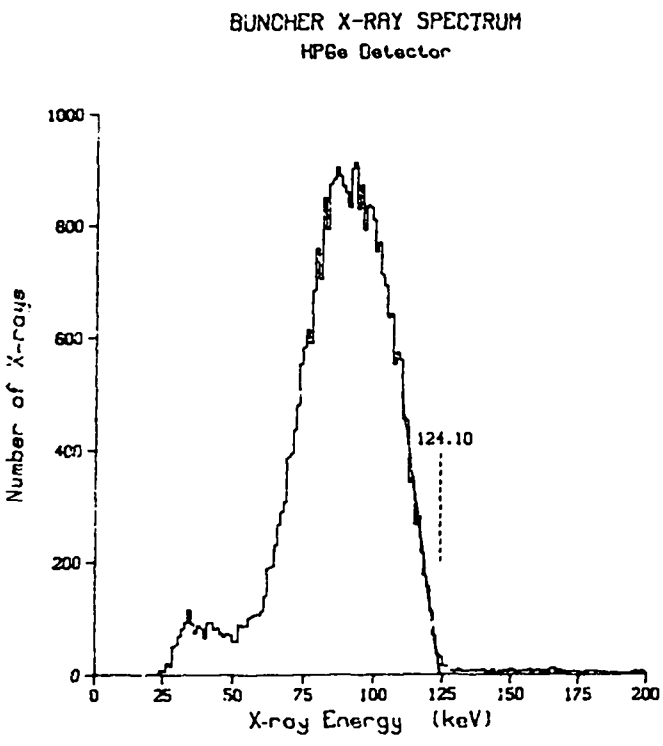

Fig. 3. Rf structures x-ray emission data spectrum.

A single x-ray energy endpoint does not provide an accurate prediction of peak-gap voltage as a function of rf power. For this reason, it is desirable to determine the energy endpoints for a minimum of 5 rf power levels. With multiple energy endpoints, a least-squares fit is made of endpoints versus power using the known $\sqrt{x}$ dependence. The fit is again made using the code, CURFIT.[3] The $\sqrt{x}$ dependence scale of this fit is now useful in correlating to the accelerator beam data. An example of a voltage-power fit is shown in Fig. 4.

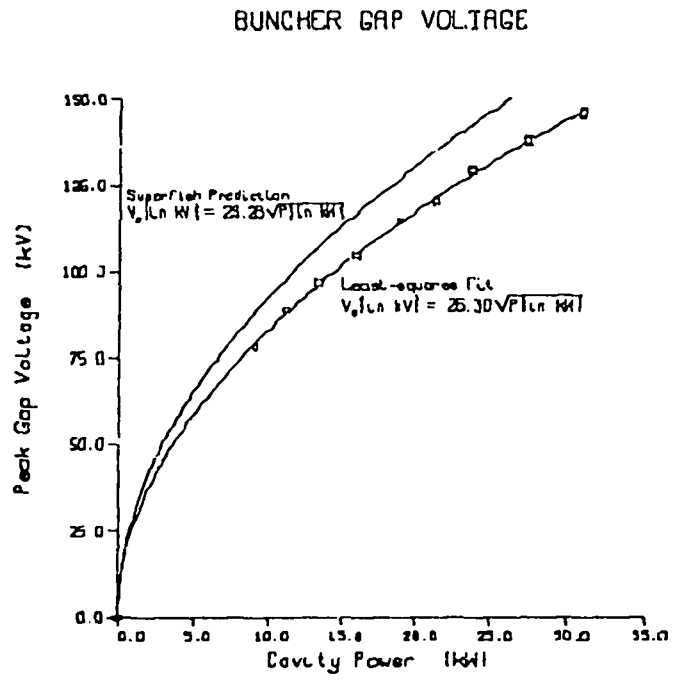

Fig. 4. Gap voltage versus rf structure power.

Discussions

Because the correlation between beam parameters and field level for the multiple-cell structures is primarily in beam quality and largely independent of the beam energy, the field amplitude measurement accuracy cannot be determined from the beam parameters of the multiple-cell structures. The best-accuracy estimate of the ATS diagnostic system is made from the beam energy gain/loss measurements of single- and double-cell structures. For single- and double-cell structures, the correlation of the energy measurements to the gap voltage is dependent only on the transit time factor for the beam in the structure and the accuracy of the energy measurements. The Cryo-DTL sparker and the four rebuncher cavities of the ATS funnel experiment have given us five independent beam energy correlations for the gap-voltage measurements. The comparisons for these structures are given in Table 1. The absolute beam energy error of the LINDA[4] data is 4 to 5 keV and the beam energy error of Phase-Scan[5,6] is unknown. The large discrepancy for the R3 and R4 data is unknown but is likely due to poor geometry between the voltage gap and the x-ray detector. Based on this information and the previous discussions, we have assigned an estimated accuracy of ±5% to the accuracy of the x-ray emission diagnostic system.

TABLE 1
Beam Energy Gain/loss Measurement for Single and Double Cell rf Structures

Cavity	X-Ray Prediction (keV)	Measured (keV)	Difference %	Diagnostic
CDTL	535	565	-6	Phase-Scan
R1	197.9	197	<1	LINDA
R2	157.1	151	+4	LINDA
R3	76.2	88	-15	LINDA
R4	142.3	161	-13	LINDA

Conclusions

The x-ray measurement of peak-gap voltages and field levels has been applied to all of the structures used in the ATS program, all ATS support sparker experiments, the rf Seal Test Cavity, and the BEAR RFQ. For every structure, it has benchmarked the cavity field levels relative to rf power levels.

The field levels measured by the characteristic x-ray emissions have also provided an important reference for much of the ATS beam data. These measured field levels have provided a check on rf structure stability, verified that sufficient fields were achieved during conditioning for operation, and provided a measured field value for comparison of beam parameters to code predictions. As it exists, this diagnostic has reached the maturity to provide useful information for accelerator operations on GTA.

References

1. R. Hawley, "Electron Emission from Metallic Surfaces," High-Voltage Technology, Oxford University Press, London (1968), pp 95-110.

2. J. D. Jackson, Classical Electrodynamics, John Wiley and Sons, Inc., New York (1975), pp 701-15.

3. P. R. Bevington, Data Reduction and Error Analysis for the Physical Sciences, McGraw-Hill, Inc., New York (1969), pp 237-9.

4. W. B. Cottingame, G. P. Boicourt, J. H. Cortez, W. W. Higgins, O. R. Sander, and D. P. Sandoval, "Nonintercepiive Technique for the Measurement of Longitudinal Parameters of Intense H^- Beams," Proc. 1985 Particle Accelerator Conference, *IEEE Trans. Nucl. Sci.* 32 (5), (1985) 1871.

5. J. D. Gilpatrick, R. E. Meyer, F. D. Wells, J. F. Power, and R. E. Shafer, "Synchronous Phase and Energy Measurement System for a 6.7 MeV H^- Beam," 1988 Linear Accelerator Conference, Williamsburg, Virginia, October 1988, Continuous Electron Beam Accelerator Facility CEBAF-Report-89-001 (June 1989), 134.

6. J. D Gilpatrick, L. Burczyk, C. Fite, B. Gunther, R. Meyer, J. Power, R. B. Shurter, and F. D. Wells, "Overview of the Microstrip Beam Diagnostics," 1989 Neutral Particle Beam Technology Symposium, Monterey, CA, July 1989.

THEORY AND 3-D SIMULATIONS OF AN RF ACCELERATING CAVITY WITH ASYMMETRIC POWER FEED*

Thomas P. Hughes, Thomas C. Genoni, and Robert E. Clark
Mission Research Corporation, 1720 Randolph Road SE, Albuquerque, NM 87106-4245

Abstract

We investigate the transverse wake potential of a side-coupled RF accelerating cavity both analytically and using a 3-D gridded code. We find that the asymmetry leads to a transverse wakefield which is not 90° out of phase with the accelerating potential. As a result, there is a net deflection, as well as a transverse tilt, of a micropulse whose center is in phase with the peak of the accelerating potential. The transverse tilt can be reduced to zero using a dummy compensating stub. The net deflection, however, is not affected by such a stub, and depends only on the average power flow into the cavity. The analytic model predicts values of the cavity Q and the amplitude and phase of the transverse wakefield which agree well with the 3-D simulations. Results for a 1 MV accelerating cavity are given.

Introduction

Single-cell RF cavities are being investigated for beam acceleration in high-power free-electron lasers.[1,2] Among the advantages of such cavities over conventional multi-cell designs are that they match well to existing power supplies, and damping of beam-induced modes is easier to apply.[1] Like multi-cell designs, the proposed single-cell cavities are fed from one side, producing a dipole asymmetry.[3,4] We have made a detailed study of the nature of this asymmetry, and its effect on beam pulses. In the following, we present the results of 3-D numerical wakefield calculations and an analytic model derived using matched eigenmode expansions.

3-D Wakefield Calculations

The gridded 3-D code SOS was used to model the single-cell RF accelerating cavity shown in Fig. 1. The geometry consists of a 25 cm radius cylindrical accelerating cavity, which is side-coupled to a rectangular (40 cm × 20 cm) waveguide through a rectangular (10 cm × 20 cm) slot. Opposite to the waveguide, we have a compensating stub of 0–10 cm in length. The stub has the same transverse dimensions as the waveguide, and is terminated with

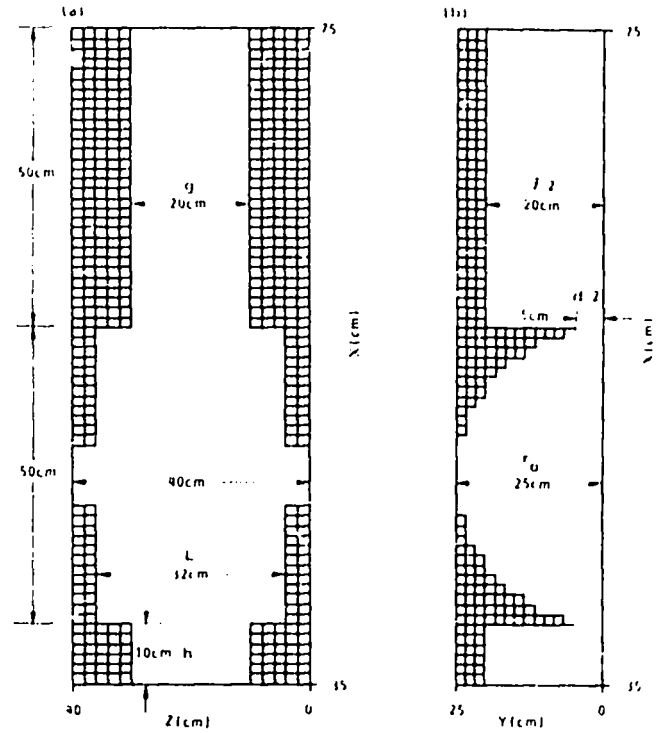

Fig. 1. Geometry of 3-D SOS cavity simulation in (a) the y = 0 midplane, and (b) the z = 20 cm midplane.

a conducting boundary. The grid sizes used are $\Delta x = \Delta y = 1.666$ cm, $\Delta z = 2$ cm. The timestep is $\Delta t = 3 \times 10^{-11}$ s, which is just less than the Courant limit. We make use of the symmetry of the cavity and the fields of interest about the y = 0 plane to cut the mesh size in half. Along the top boundary in Fig. 1, wave-transmitting boundary conditions are applied.

To measure the cavity Q, an ingoing TE_{10} wave with frequency equal to the fundamental TM mode of the cavity was launched from the top boundary in Fig. 1, and built up the cavity energy over many cycles. The TE wave was then turned off, and from the decay rate of the cavity energy, we measured to external Q to be $Q_e \approx 3,980$. This agrees well with the analytic estimate in Eq. (7).

Asymmetry of Undriven Cavity

Initial simulations were performed to measure the wakefields in an undriven cavity, since this is the

*Work supported by SDIO, monitored by W. J Schafer Associates.

case treated by our analytic model. The transverse and longitudinal wakefields are defined by

$$W_\perp(t) = \int_0^L \left[E_\perp\left(t + \frac{z-L}{v}\right) + v\hat{z} \times B_\perp\left(t + \frac{z-L}{v}\right)\right] dz \quad (1)$$

$$W_\parallel = \int_0^L E_z\left(t + \frac{z-L}{v}\right) dz \quad (2)$$

where L is the length of the cavity, and v is the particle z-velocity. The coupling slot produces only a non-zero x-component of $W_\perp$. We will denote the amplitudes of W_x, $W_\parallel$ by $\overline{W}_x$, $\overline{W}_\parallel$, respectively. Plots of W_x, $W_\parallel$ without and with a 10 cm compensating stub are shown in Fig. 2. Scaling the results to a 1 MV value for $\overline{W}_\parallel$, we find that without the stub, W_x has amplitude 6.8×10^3 V, and leads $W_\parallel$ by $\Delta\phi \approx 1.51$, which is close to $\pi/2$. When the 10 cm stub is present, the amplitude of W_x drops by a factor of 11.5 to 5.9×10^2 V, but $\Delta\phi$ is now 1.06, a large shift from $\pi/2$. We can understand this result by writing

$$W_x(t) = W_x^{(1)} \sin\omega_0 t + W_x^{(2)} \cos\omega_0 t \quad (3)$$

where $W_x^{(1)} = \overline{W}_x \cos\Delta\phi$, $W_x^{(2)} = \overline{W}_x \sin\Delta\phi$, and we assume $W_\parallel(t)$ varies as $\sin\omega_0 t$. The term $W_x^{(1)} \sin\omega_0 t$ is obtained from the component of the deflecting field B_y which is in phase with the accelerating electric field E_z. Therefore, the expression $W_x^{(1)}\overline{W}_\parallel$ is proportional to the time-averaged Poynting flux through the coupling slot, which is insensitive to the presence of the compensating stub. Thus, $W_x^{(1)}$ = const. for a given accelerating potential. The term $W_x^{(2)} \cos\omega_0 t$, on the other hand, is obtained from the component of B_y which is $\pi/2$ out of phase with E_z, i.e., the standing-wave component of B_y. From this one expects that $W_x^{(2)}$ depends on the length of the compensating stub, and can be made to vanish by terminating the stub at a position which is symmetric with the first zero of E_z in the waveguide. This implies a quarter-wavelength stub,[5] which is 27 cm for the present parameters.

The results in Fig. 2 are consistent with this picture. The 10 cm stub causes a large drop in $W_x^{(2)}$, but leaves $W_x^{(1)}$ unchanged, so that $\Delta\phi$ must depart from $\pi/2$.

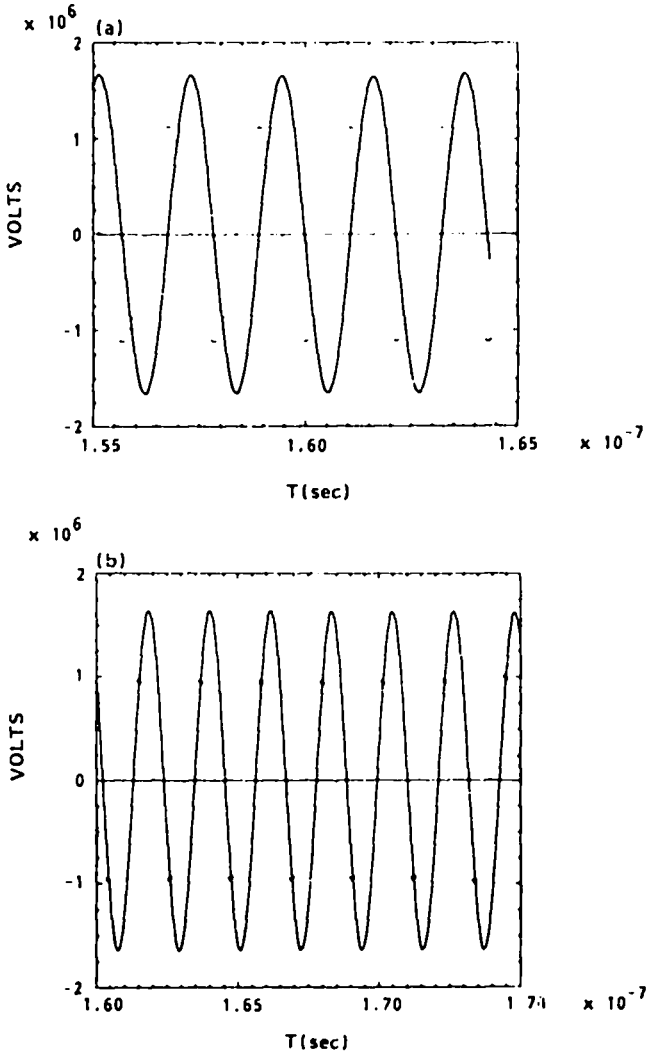

Fig. 2. Time histories of the longitudinal (solid lines) and transverse (dotted lines) wake potentials for cavities (a) without and (b) with a 10 cm compensating stub. W_x has been multiplied by 10^2 in (a) and by 10^3 in (b). Note that the time scale is different for (a) and (b).

Asymmetry of Driven Cavity

When the effect of driving fields entering from the waveguide are included, Eq. (3) becomes modified to

$$W_x(t) = \left(W_x^{(1)} - W_x^{(3)}\right) \sin\omega_0 t + W_x^{(2)} \cos\omega_0 t \quad (4)$$

where $W_x^{(3)}$ is obtained from the component of B_y produced by the incoming fields. The case $W_x^{(1)} = W_x^{(3)}$ corresponds to the case where the power entering the cavity equals the power leaving through the coupling slot. Due to beam loading, there must be a net power influx to maintain the accelerating field. If the total

Q of the cavity is Q_{tot} then, assuming a steady-state accelerating amplitude, we can write

$$W_x^{(1)} - W_x^{(3)} = W_x^{(1)}(1 - Q_e/Q_{tot}) = -W_x^{(1)} Q_e/Q_b \quad (5)$$

where Q_b is the effective Q due to beam loading. In terms of $W_x^{(1),(2)}$, the deflection and shear (defined as the difference in deflection between head and tail) of the pulse of duration τ_p whose center is in phase with the peak of the accelerating potential are given by

$$\theta_d = eW_x^{(1)} Q_e/Q_b \gamma mc^2$$
$$\theta_s = eW_x^{(2)} \omega_0 \tau_p/\gamma mc^2 \quad (6)$$

Analytic Model of Undriven Cavity

To obtain an analytic dispersion relation for the geometry in Fig. 1, we match eigenmode expansions of the electric and magnetic fields in the three regions (waveguide, cylinder and stub). An outgoing-wave boundary condition is applied in the waveguide. The curvature of the cylindrical eigenfunctions is neglected over the width of the matching regions. The fields E_z and B_y are used to do the matching (see Ref. 5 for details). The expression obtained for the cavity Q is

$$Q_e \approx \frac{(L/g)\pi^5}{8k_x\ell}\left(\frac{r_0\ell}{d^2}\right)^2 S^2 \quad (7)$$

where $k_x = \sqrt{\omega_0^2/c^2 - \pi^2/\ell^2}$ is the wavenumber of the outgoing wave in the waveguide, and $S \approx 1.2$. For the parameters in Fig. 1, this gives $Q_e \approx 4{,}000$, in good agreement with SOS. Without the compensating stub, we find

$$\overline{W}_x \approx \frac{\beta(\omega_0 r_0/c)(d/r_0)^2}{S\pi^3(L/g)}\overline{W}_{\|} \quad (8)$$

$$\Delta\phi \approx \frac{\pi}{2} - \frac{k_x\ell}{S}\left(\frac{2d}{\pi\ell}\right)^2 \quad (9)$$

where $\beta = v/c$. With a stub which is more than a few cm long, we find

$$\overline{W}_x \approx \frac{4\beta(\omega_0 r_0/c)(d^2/r_0\ell)^2(k_x\ell)}{S^2\pi^5(L/g)\sin(k_x h)}\overline{W}_{\|} \quad (10)$$

$$\Delta\phi \approx \frac{\pi}{2} - k_x h \quad (11)$$

For the parameters in Fig. 1, these expressions give $\overline{W}_x \approx 6.5 \times 10^3$ V, $\Delta\phi \approx 1.52$ for the case with no stub, and $\overline{W}_x \approx 580$ V, $\Delta\phi \approx 1.0$ for a 10 cm stub, in good agreement with the numerical results in Fig. 2. The above expressions also predict that $W_x^{(1)} \equiv \overline{W}_x \cos(\Delta\phi)$ is independent of the length of the stub, in agreement with the numerical observations.

Effect of Asymmetry on a Micropulse

For $\overline{W}_{\|} = 1$ MV, with beam loading such that $Q_b = 5{,}400$, the predicted deflection and shear for a $\gamma = 30$, 25 psec micropulse passing through the cavity in Fig. 1 are

	Deflection (μrad)		Shear (μrad)	
No Stub	13.3	(14.6)	33	(31)
10 cm stub	14.2	(14.7)	2.1	(2.3)

where the numbers in parentheses are from the analytic model.

References

1. H. A. Schwettman, et al., "Electron Acceleration Using High-Gradient Single-Cell Resonators," IEEE Trans. Nuc. Sci. **NS-32**, 2927 (1985).
2. A. M. Vetter, et al., "High-Power RF Tests of 433 MHz Single-Cell Accelerator Cavities and Associated Feed System," Proc. of 1989 IEEE Part. Accel. Conf., p. 183.
3. K.C.D. Chan, L. E. Thode, and R. K. Cooper, private communication.
4. A. Vetter, "Asymmetric Accelerating Cavity Fields—Measurement and Interpretation," 1988 Linear Accelerator Conf., Williamsburg, VA.
5. T. P. Hughes, et al., "Asymmetry of Waveguide-Coupled RF Accelerating Cavity," MRC/ABQ-R-1195, Mission Research Corporation, 1989 (available from the authors).

THE USE OF A SPREADSHEET IN THE DESIGN OF ACCELERATOR COMPONENTS*

S.K. Brown and E.A. Wadlinger
AT Division, Los Alamos National Laboratory, Los Alamos, NM 87545

Abstract

This work was undertaken to explore the capabilities of user-friendly technology in building an easy-to-use tool that could be applied to formulate quickly a workable design for a radio-frequency quadrupole (RFQ). The tool will be extended to include additional components. This paper outlines the derivation of scaling laws from which we obtained a set of self-consistent equations that describe the behavior of an RFQ. These equations are relations between accelerator parameters (electric field, rf frequency, zero-current transverse and longitudinal phase advances per period) and beam parameters (current, energy, and emittance) that act as guides for designing RFQs. These equations show the various tradeoffs involved in choosing RFQ designs and help to choose starting points in parameter space for optimizing an RFQ for a particular requirement. By entering values in a simple spreadsheet, the design parameters of an RFQ can be calculated. The spreadsheet is fully described.

Introduction

The design of complex devices, such as an RFQ accelerator module, has depended on the use of large design programs that are dependent for input on files of data that are treated like card files. This input method is the result of programming in the era of batch oriented computer processing. These tools continue to serve their purpose well for detailed design. However, setting-up these "decks" of input can be tedious and prone to error because the user is not given help as to what information should be supplied on what "card." Also, the information that is supplied is usually position sensitive. The initial impetus for this work grew out of discussions concerning the need for a design tool that addressed the problem of the difficulty of data entry as well as a tool that could be used by someone, physically removed from the person who normally "runs" the design tool. This led to the consideration of creating a tool that could be based on a PC-class machine, possibly portable, that could provide some ball-park estimates of the design and cost for an accelerator, and that would be user-friendly enough that its use would be intuitive. To examine these requirements an RFQ structure was chosen as a model because a new formulation of a set a scaling laws had been derived[1][2] and a spreadsheet format was chosen because of the availability of the spreadsheet software and its inherent user-friendly features. The particular spreadsheet software used is Lotus 1-2-3** based just on its availability on an IBM PC/AT.***

This paper presents the formulation of the scaling laws from the electrical field properties of the RFQ. Space-charge is included in the formulation. The formulation leads to a set of equations, four, which describe the RFQ. There is freedom to chose which of the many variables in these equations are fixed and which four are left free to vary as the four equations are simultaneously solved. There are some variables that would have little meaning to fix and some, such as beam current or emittance that a designer might be forced or at least want to fix. Finally the spreadsheet itself is described.

*Work supported and funded by U.S. Department of Energy.
**Lotus 1-2-3 is a trademark of Lotus Development Corp.
***IBM and PC/AT are trademarks of International Business Machines

Overview of Scaling Law Derivation

The RFQ[3][4] is a device that provides transverse focusing, longitudinal bunching, and acceleration of beam particles. The RFQ's electrical properties are determined by using an electrostatic potential function which is used to calculate the electric field for beam-dynamics modeling and gives the shape of the RFQ vanes. The transverse particle motion in the RFQ is modeled by the Mathieu equation and the longitudinal motion by a harmonic oscillator equation. The Mathieu equation is (X represents both transverse coordinates)

$$\frac{d^2X}{ds^2} + [\Delta_T + B\sin(2\pi s)]X = 0 ,$$

where s is a normalized length along the structure ($s = l$ = one period) and Δ_T and B are constants. The parameter B is calculated from the equation for the external alternating gradient force of the RFQ and Δ_T is calculated from the transverse external and space-charge (Coulomb) defocusing forces. These parameters depend on the RFQ vane potential (V), the vane radius (a), the vane modulation (m), the average beam bunch velocity (β_s), and the synchronous phase (ϕ_s) (relative phase between the beam bunch centroid and the cavity rf phase). When $\phi_s = 0$, there is maximum acceleration with no bunching and when $\phi_s = -90°$, there is maximum bunching with no acceleration. An approximate solution of the Mathieu equation is[5]

$$X(s) = X_0 \sin(\sigma_T s)[1 + \frac{B}{4\pi^2}\sin(2\pi s)] \text{ where}$$

$$\sigma_T = [\Delta_T + \frac{B^2}{(8\pi^2)}]^{\frac{1}{2}}. \qquad (1)$$

σ_T is the phase advance per period (represents the average focusing force) and X_0 is a constant set by initial conditions.

The longitudinal motion is modeled by the harmonic oscillator equation

$$\frac{d^2Z}{ds^2} + \Delta_L Z = 0$$

which has the solution $Z = Z_0 \sin(\sigma_L Z)$ where

$$\sigma_L = \sqrt{\Delta_L} . \qquad (2)$$

Linear space-charge defocusing terms are calculated from the electric-field components for a uniformly charged ellipsoid[6][7] to give Δ_{L-sc} and Δ_{T-sc} which add to the constant terms, Δ_L and Δ_T in the Mathieu equation and the harmonic oscillator equation. These space-charge terms depend on the dimensions of the ellipsoid (X_{ave}, Z_{Max}), the beam current (I), the charge-to-mass ratio [$Qe/(m_0c^2)$], and the rf wavelength (λ) that acts as a normalization factor. The Mathieu equation contains a periodic oscillating force term that is not present in the harmonic oscillator equation and that gives "flutter" to the beam. This is why we use X_{ave} instead of X_{Max}. The ratio of the transverse to longitudinal space-charge forces depends on the ratio of the transverse to longitudinal beam sizes (X/Z) through a form factor f[7]. Although $f(Z/X) = X/3Z$ is a good approximation, we use the exact equation.

Relationships between the beam parameters I, ϵ_T, ϵ_L (beam current, and transverse and longitudinal emittances defined below), and the external-force-determined parameters, σ_{T0} and σ_{L0}, which are zero-current phase advances generated by the RFQ, c.f., eqs. (1) and (2), are obtained by defining the space-charge parameters μ_L and μ_T (which are the negative of the ratio of the space-charge forces to the external focusing forces). These space-charge parameters relate the longitudinal and transverse phase advances, σ_T and σ_L, for a finite current beam with space-charge (Coulomb repulsion) forces to the transverse and longitudinal phase advances, σ_{T0} and σ_{L0}, for a zero current beam (no Coulomb repulsion). The phase advances σ_T and σ_L can be written as

$$\sigma_L^2 = \sigma_{L0}^2(1-\mu_L) = \sigma_{L0}^2 - \Delta_{L-sc} \quad \text{and}$$
$$\sigma_T^2 = \sigma_{T0}^2(1-\mu_T) = \sigma_{T0}^2 - \Delta_{T-sc}. \qquad (3)$$

If we want stable focusing, the values for μ_L and μ_T must be less than 1, otherwise the space-charge forces will overpower the external forces. Simulations have shown that the μ values should be kept less than 0.8 to minimize emittance growth.

The normalized emittances, ϵ_T and ϵ_L, are the areas/π of the beam, enclosed by phase-space ellipses having semimajor axes (X_{ave}, X'_{ave}) or (Z_{Max}, Z'_{Max}) [where $X' = (1/\lambda)dX/ds$ etc.] and are $\epsilon_T = X_{ave}X'_{ave}$, $\epsilon_L = Z_{Max}Z'_{Max}$. The significance of the emittance is that it describes the volume of phase space (position and divergence) occupied by the beam particles and is a conserved quantity for linear systems (where X, Y, and Z are decoupled) which we are modeling.

The equipartitioning theorem[8][9], which states that the thermal free energy is the same for each dimension (transverse and longitudinal), and the virial theorem, which states that the average kinetic energy equals the average potential energy for linear systems, are used to obtain $\epsilon_T\sigma_T = \epsilon_L\sigma_L$, which relates the transverse emittance and effective focusing force to the corresponding longitudinal quantities. All of the relationships defined above are used to calculate the scaling-law equations.

RFQ Functions

Using the above parameters and relationships, four equations must be satisfied by any RFQ that will transmit a beam in equilibrium with the linear forces.

$$f_1 : 0 = 2f\frac{\mu_T}{\mu_L} - (1-f)\frac{\sigma_{L0}^2}{\sigma_{T0}^2}$$

$$f_2 : 0 = \lambda - \epsilon_T \cdot \left[\frac{4\pi\epsilon_0 c}{3} \cdot \frac{\sigma_{L0}}{f\sigma_{T0}^{\frac{1}{2}}} \cdot \frac{m_0c^2}{e} \cdot \frac{\mu_L}{(1-\mu_L)^{\frac{1}{2}}} \cdot \frac{1}{QI(1-\mu_T)^{\frac{1}{4}}}\right]^{\frac{2}{3}}$$

$$f_3 : 0 = \frac{\pi(2\sigma_{T0}^2 + \sigma_{L0}^2)^{\frac{1}{2}}}{\sigma_{T0}^2} \cdot \sin\phi_s A R_r^2 \phi_r^2 \psi + 2\chi\left(\frac{1-\mu_T}{1-\mu_L}\right)$$

$$f_4 : 0 = \lambda - \left[\frac{4\pi^2(2\sigma_{T0}^2 + \sigma_{L0}^2)\psi}{\chi\sigma_{T0}(1-\mu_T)^{\frac{1}{2}}} \cdot \epsilon\left(\frac{R_r\frac{m_0c^2}{e}}{QE_0}\right)^2\right]^{\frac{1}{3}}$$

where χ and A depend on a, β_s, and λ through Bessel functions, ψ is the flutter factor that depends on the B term in the Mathieu equation and R_r is the ratio of the minimum RFQ vane radius divided by the maximum beam radius.

With four equations, four unknowns can be determined. It is up to the designer to pick just which four unknowns he wants to be determined. Another way of saying this is that the job of the designer at this point is to pick which parameters he wants to hold at a particular value. He must have a value for all but four of the parameters. There are three parameters for which one typically has no intuitive feel and can take whatever value is dictated by the rest of the model. The vane modulation factor, m, is one of these. The other two are the two sigmas, σ_{T0} and σ_{L0}. Allowing these three to be free to vary, one needs to pick yet another to be free to vary. This can be done by eliminating those variables that must be fixed. For example, one would not allow the particle mass or charge to vary. One would want to fix the ratio of the electric field to the Kilpatrick factor to get as much acceleration as possible. The synchronous phase is fixed because the designer knows how much acceleration he wants out of the structure. Continuing in this manner, we eliminate all variables except beam current, rf frequency and emittance. Picking one of these and allowing it to vary means the other two can be fixed to whatever value the designer wants. Thus, by deciding on values for beam current and emittance, for example, the equations will determine the frequency that the RFQ must have.

Reasons for Using Spreadsheet

Aside from the perception that spreadsheets are easy to use, there are several more subtle reasons that this particular technology was chosen and why it turned out to be a good choice. In programming languages such as Fortran, execution takes place in a linear fashion, that is the program steps are executed one at a time, working from first to last. One of the difficulties with this, especially when considering maintenance of the program, is finding dependencies. A variable, in the program, may depend on another variable which obtains a value several pages away from the point of interest. With a spreadsheet each step of the calculation is a simulated parallel computation of the whole sheet. Because of this, it doesn't matter where computation is placed on the sheet and thus the calculation of a particular variable can be localized to where the variable appears. By adopting some simple rules, such as all dependencies appear in the row corresponding to the variable in question, the organization of the computation can overcome the non-localization problem.

Spreadsheets were designed as a high-level tool to be applied to many problems that address themselves to the relatively computer-illiterate. Because of this, tools are provided for the spreadsheet designer that allow the building of menu-driven, fill-in forms that people find intuitive and easy to use. Also provided are tools that allow the designer, with relative ease, to put together graphs. Using a traditional programming language, most of a program is built around the user-interface and the display of the final answers. The spreadsheet has already taken care of these two problems. Of course, the draw-back here is that if you don't like the style of menu or what a graph looks like, that's too bad. You get what is provided. This has seemed to us a trivial point because the user-interface looks good and the graphics are flexible enough to do what we need. Also, in a traditional approach, one finds that for an iterative solution, the user is usually required to input all data on each iteration, although most of it remains the same. A programmer frequently corrects for this annoying input requirement by saving this "previously-input" data on the computer system's file system. This requires the addition of a number of program steps that are not directly related to solving the problem at hand. The menu that the spreadsheet provides keeps track of and displays the last values changed on the form, even between sessions.

The spreadsheet approach is not completely satisfactory, however. The PC/AT, the machine that the spreadsheet is implemented on, is fairly slow and because of this, the calculation

is not as fast as it might be. Using a spreadsheet for a lengthy calculation has its own set of problems of which an implementor must be aware. In a straight-forward implementation, the whole spreadsheet is recalculated each time a value in the spreadsheet is changed. This can cause huge delays, a real problem especially when maybe one doesn't care, at a particular point, whether there are up-to-date values in the spreadsheet. The capability has been provided to disallow recomputation or to cause recomputation over only limited portions of the spreadsheet. Judicious use of this facility can greatly enhance the speed of calculation. The use of this facility requires some sophistication in determining just how it works and implementing it properly. Another problem is the lack of true indirect addressing (as used in a Fortran subroutine). This makes reuse of code somewhat cumbersome.

Another rather specialized problem was inherent to this particular study. As was noted above, there are four complicated functions that require an iterative method to extract the four unknowns. The Newton-Raphson method was used to solve for the four unknowns and was implemented as a spreadsheet "macro." This worked relatively well and addressed the problem of preventing recalculation of the whole spreadsheet at each step since recalculation is disabled during macro execution. The Newton-Raphson method has a few peculiarities of its own. In his book, *The Mathematical Tourist*[10], Ivars Peterson describes an area of instability in the solution space of the Newton-Raphson method that will not produce a solution at all. We found it necessary to take a small fraction of the full correction step to guarantee stability in the method.

The maximum electric field that can be achieved on the RFQ vanes without sparking is determined by a fixed multiple of the Kilpatrick relationship[11] (with present vacuum and surface preparation techniques, we can generally design for electric fields that are twice this criterion). This relationship is such that a straight-forward solution is not possible. A specialized macro was built to compute the value of the Kilpatrick field given the frequency. The relationship between the two variables, frequency and Kilpatrick field (E_{KP}) is as follows:

$$freq = 1.643 E_{KP}^{2} e^{\frac{-8.5}{E_{KP}}}$$

Knowing the largest field and the smallest field that is possible and the frequencies that correspond to these fields, it is a rather straight-forward use of the method of bisection to find the field, given the frequency. A macro was implemented to use the bisection method to solve this problem.

Figure 1. shows the user interface to the spreadsheet. Each of the items at the top is a command to the spreadsheet. The first item, *DATA*, is highlighted as indicated by the heavy box around it. On the spreadsheet, this means that this item is selected. When a command is selected an explanitory line appears just below. In this case it says, "Enter New Data" indicating that we are in a data entry mode. This form of instruction is also part of the standard spreadsheet capability. The other commands indicate what the spreadsheet will do. For example, *I/S/S/M* indicates that a calculation allowing beam current (I), the two sigmas (S/S), and the vane modulation factor (M) to be the freely varying parameters is selected. *Look* allows the user to examine the spreadsheet at any location to which he wants to move, *Print* provides for printing the third column of the spreadsheet that contains all the useful numbers, and *Quit* terminates the spreadsheet. Selection is made by use of the arrow keys.

Conclusions

The use of a spreadsheet for the kind of calculation that is described above seems to have more advantages than disadvantages. We have demonstrated that rather complex calculations can be performed in this environment. The spreadsheet provides facilities that allow the implementor to put together quickly user-friendly screens that are intuitive to use. Facilities to gather and plot data are also provided and easy to use. This allows one to do studies of parameter interactions. Thus, design calculations can be done on inexpensive hardware that is, at least in principle, portable. The calculations are accurate enough also to provide real cost figures. One can come very close to the true price of an RFQ that will perform to given specifications using an easy-to-use, inexpensive platform. The down-side of this is, of course, speed. One has to be patient while the calculation is being performed.

DATA I/S/S/M F/S/S/M E/S/S/M Look Print Quit

Enter New Data

DATA ENTRY FORM

Mass(ev)	9.38E+08
Charge No. (=1 for P)	1
Current(amps)	0.125
Emit(tot norm pi-m-rad)	1.00E-06
Emax/K field ratio	2
F Enhance fac (1.3-1.4)	1.3
Sync Phase(deg)	-85
Frequency(Hz)	5.05e+08
mu-t	0.8
mu-l	0.8
min vane/max beam	1.2

Figure 1. Spreadsheet Data Entry Screen

References

[1] E.A. Wadlinger, "Scaling Laws for RFQ Design Procedures," Proc. 1985 Particle Accelerator Conf., IEEE Trans., Nucl. Sci. 32 (5), (1985), 2596.

[2] E.A. Wadlinger, "RFQ Scaling-Law Implications and Examples," 1986 Linear Accelerator Conference Proceedings, SLAC-303, CONF-860629, UC-28, (1986), 346.

[3] I.M.Kapchinskiii and V.A.Teplyakov, Prib. Tekl. Eksp. No. 2, (1970), 19 and No. 4, (1970), 17.

[4] K.R. Crandall, R.H. Stokes, and T.P. Wangler, "RF Quadrupole Beam Dynamics Design Studies," Proc. 1979 Linear Accelerator Conf., Brookhaven National Laboratory report BNL-51134, (1980), 205.

[5] Henri Bruck, *Circular Particle Accelerators*, Los Alamos National Laboratory translation LA-TR-72-10 Rev.

[6] R.L. Gluckstern, *Linear Accelerators*, R.M. Lapostolle and A.L. Septier, Eds., (North-Holland Press, Amsterdam, 1970), 827.

[7] Many of the equations that are stated in this paper can be found in the report by T.P. Wangler, "Space-Charge Limits in Linear Accelerators," Los Alamos National Laboratory report LA-8388.

[8] P.J. Channell, "Equipartitioning in Charged Particle Beams," Los Alamos National Laboratory report LA-9927-MS, November 1983.

[9] R.A. Jameson, "Equipartitioning in Linear Accelerators," Proc. 1981 Linear Accelerator Conf., Los Alamos National Laboratory report, LA-9234-C, (1982), 125.

[10] Ivars Peterson, *The Mathematical Tourist*, W.H. Freeeman and Company, New York

[11] W.D. Kilpatrick, Rev. Sci Instrum., 28 (10) (1957), 824.

DUAL KLYSTRON MODULATOR*

W. Joel D. Johnson and William E. Stein
Los Alamos National Laboratory, Los Alamos, NM 87545

Abstract

The first phase of a 40 MeV upgrade at the Los Alamos Free Electron Laser (FEL) experimental hall was completed during the summer of 1989. The second phase of this upgrade will be completed in November 1990. Because it was necessary to conserve facility space and expense, the concept of a dual klystron modulator was conceived. The novelty of this design is that a single switch tube and a single high voltage electronic circuit are used to simultaneously pulse two modulating-anode klystrons. In addition, this design configuration is amenable to extending the number of klystrons that are to be concurrently pulsed. In this short paper we report on this modulator design.

Introduction

A new 40 MeV high-brightness accelerator free-electron laser (HIBAF) facility is now nearing completion at the Los Alamos National Laboratory (LANL). The source for electrons is a laser driven photocathode injector.[1,2] The RF power necessary for this accelerator is supplied by four 6.5 MW modulating-anode klystrons. Although some of the previous components from the old single klystron modulator were utilized, this dual-klystron modulator represents a new and novel design. Because the cost of building a new klystron gallery was prohibitive, a two-klystron per one-grided switch-tube system was developed. A photograph of this modulator is shown in Fig. 1. Lead glass windows were installed to facilitate high-voltage arc location. Note the symmetry in mechanical design. The modulator tanks are 130 in. long x 49 in. tall x 53 in wide and requires approximately 18 — 55 gallon barrels of insulating oil.

Modulator Design

Referring to Fig. 2, resistors R2 and R13 protect against modulating-anode to ground discharges as well as modulating-anode to cathode discharges. In addition the resistors limit the current flow to the modulating-anode during klystron pulse-on conditions. Resistors R5 and R6 protect against cathode to ground arcs and are necessitated by the duality of the modulator design. Resistors R1 and R14 provide initial protection during cathode to ground and cathode to modulating-anode arcs until the crowbar fires as well as dissipate any residual energy stored in the high-voltage coaxial cables after the crowbar has been fired.

The 1.4 kV secondary output of the klystron filament transformer is boosted via a voltage doubler circuit to 2.8 kV. This voltage provides the back bias necessary to keep the klystron dark current below acceptable levels. With a non-isolated collector klystron, this cw background current could not be measured directly but only inferred from the outgassing as measured by the acuum-ion pump. With the increase in bias (up from 600 V) the vacuum ion pump measurement decreased an order of magnitude.

One common klystron filament transformer was used, i.e., one input, three secondary outputs–all on a common iron core. This design presents another difficulty; when one tube arcs, there is a large potential difference between the three collinearly wound secondaries. Miniature spark gaps (~2.5 kV) were placed across all transformer outputs, thereby minimizing these differences and protecting the transformer. The klystron filament transformer has been redesigned so that each secondary is physically separated from the other by insulating oil, i.e., non collinearly wound on a common core. This second generation dual filament transformer has been placed on order and will be used as a spare when needed.

The four klystrons are powered by one high voltage system. The system is comprised of a power supply, transformer, crowbar, capacitor bank, energy detector, and high voltage transport. Because physical space and reliability is a premium, the original 8 μF capacitor bank, made out of 40 kV capacitors, was augmented with 16 200 kV, 0.5 μF capacitors whose total volume is 112 in. long x 42 in. high x 26 in. wide. These capacitors were placed on a wooden table immediately adjacent to the original capacitor bank.

Conclusions

The HIBAF modulators have worked continuously since June 1989 without any problems. During klystron conditioning and once in a while throughout the year, the tubes have arced, but energy deposition was always mitigated and the klystrons have proven to be well protected.

References

1. P. G. O'Shea, et al. "Performance of the Los Alamos HIBAF Photoinjector Linac," these proceedings.
2. R. L. Sheffield, "Progress in Photoinjectors for Linacs," these proceedings.

*Work supported and funded by the US Department of Defense, Army Strategic Defense Command, under the auspices of the US Department of Energy.

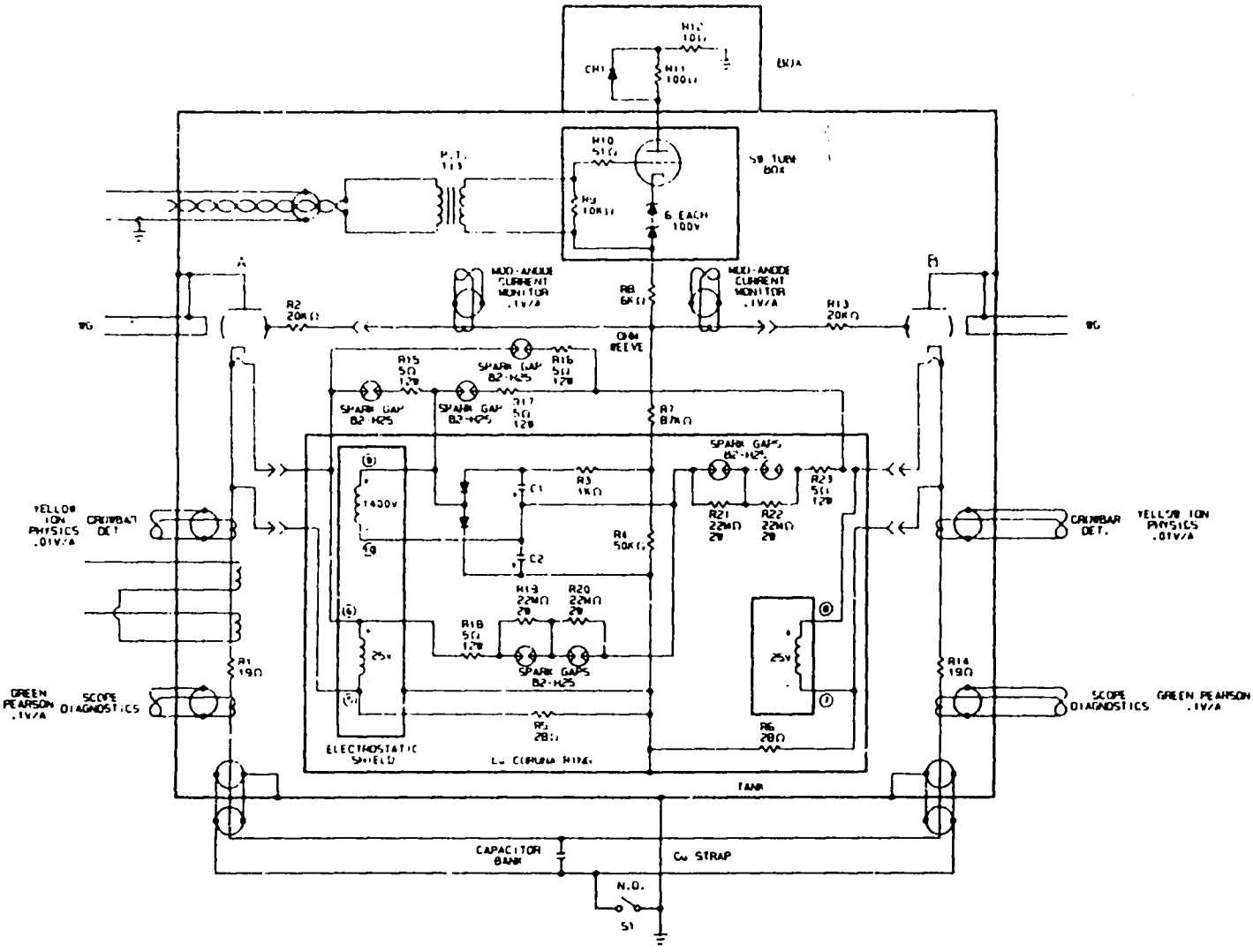

Fig. 2. Modulator schematic.

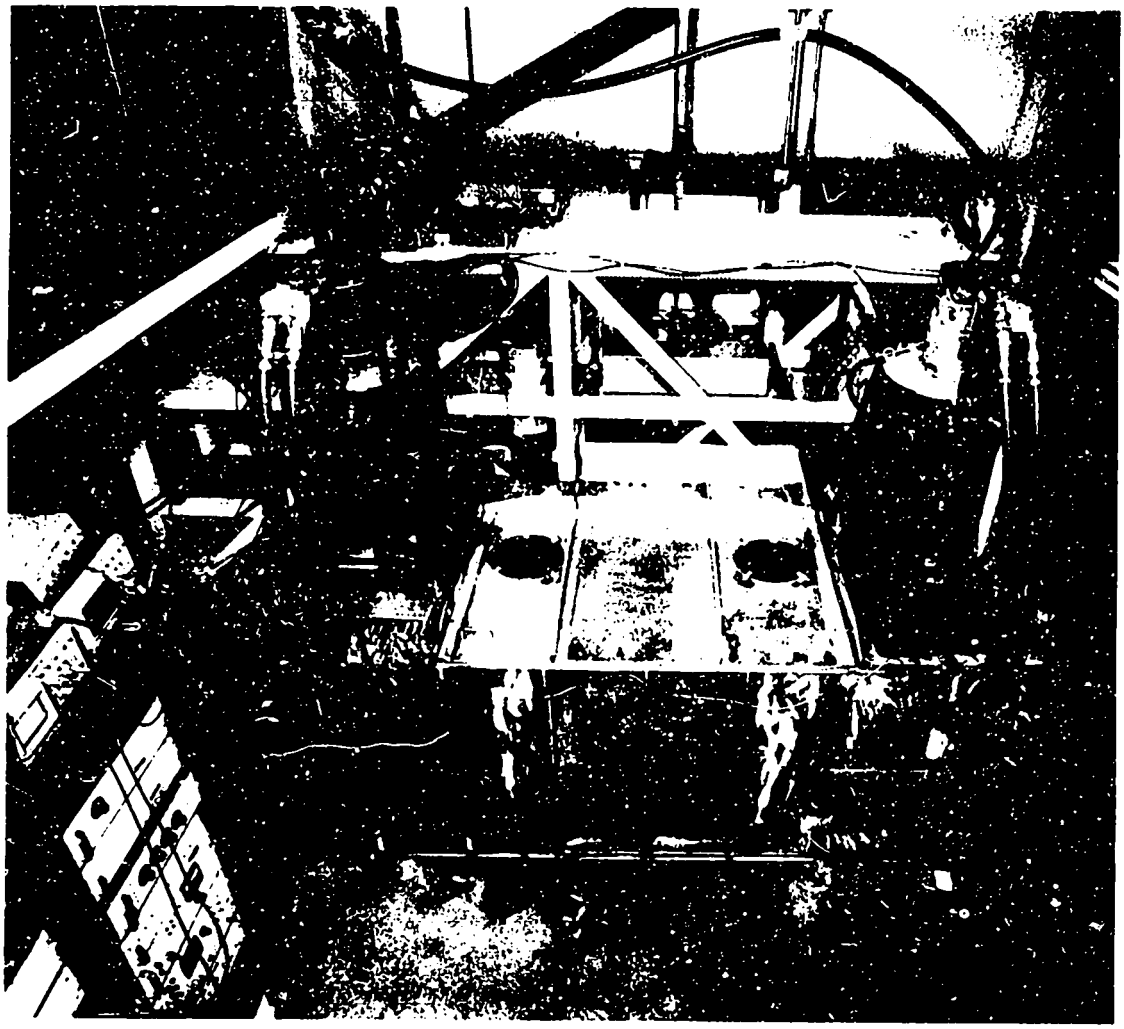

Fig. 1. Dual klystron modulator.

A HIGHLY EFFECTIVE DEFLECTING STRUCTURE*

C. Leemann and C. G. Yao
Continuous Electron Beam Accelerator Facility
12000 Jefferson Avenue, Newport News, VA 23606

Abstract

A structure is presented that combines high transverse shunt impedance ($\approx$ 500 MΩ/m at 500 MHz) with outside dimensions that are small in relation to the desired mode's resonant frequency. The basic idea was to find a practical way to resonate a small gap, two conductor, $\lambda/4$ transmission line with a field pattern that is locally very close to a TEM dipole mode (apart from important and essential modifications at the gap end). Two possible applications stand out: use as an RF separator (discussed here) or use as a high sensitivity microwave beam position monitor.

Introduction

The basic structure, a 1/4 wavelength resonator, is shown in Figure 1.[1] Two rods are placed along the z direction, with gaps between the rods and the cavity wall on one side. The desired mode is a dipole mode, field patterns of which are shown in Figures 2 and 3. The gaps are essential to excite this mode.

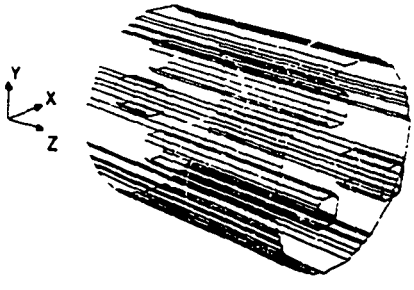

Figure 1. A 3-D picture of a 1/4 wavelength resonator.

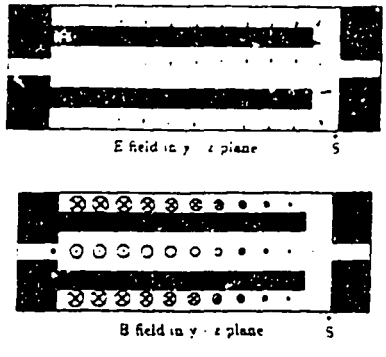

Figure 2. Field patterns in y - z plane.

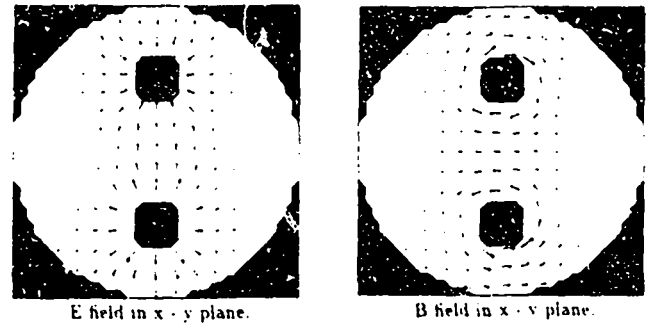

Figure 3. Field patterns in x - y plane.

The rods play an important role in two aspects. First, they cut down the outside cavity diameter. For example, the outside diameter of a disk loaded waveguide for a 500 MHz deflecting cavity is about 800 mm, but with the proposed cavity, it can be as small as 120 mm. It allows the effective RF separators used for bunch-to-bunch extractions at CEBAF to run at a frequency of 500 MHz, which will reduce emittance dilution caused by differential head-to-tail steering of RF separators. Second, they compress the field into the central region of the cavity, so that the fields in the central region of the cavity are very high which leads to very high transverse shunt impedance $R_\perp$. For example, for a square box deflecting cavity such as the CEBAF injector chopper, effective transverse shunt impedance $R_\perp \approx 6.8$ MΩ/m, and for a biperiodic structure of current CEBAF RF separator design $R_\perp \approx 15$ MΩ/m, but for the described structure the shunt impedance $R_\perp$ ranges from 200 to 500 MΩ/m depending on detailed choice of geometry.

Analytical Study

The cavity under study can be viewed approximately as a 1/4 wavelength transmission line, and is analyzed in this section following a discussion of Lambertson.[2] Its left end is short, and its right is open. Voltage and current distributions along z are, respectively:

$$V = V_0 \sin \frac{2\pi z}{\lambda} \tag{1}$$

$$I = \frac{V_0}{Z_c} \cos \frac{2\pi z}{\lambda} \tag{2}$$

where V_0 is a voltage across gaps. Z_c is characteristic impedance.

At resonance, the stored energy in the cavity is:

$$U = \int_0^{\lambda/4} L I^2 \, dz \tag{3}$$

where $L = \frac{Z_c}{c}$ is the inductance per unit length and c is the velocity of light. Using equation (2, this becomes:

* This work was supported by the U.S. Department of Energy under contract DE-AC05-84ER40150.

$$U = \frac{V_0^2}{Z_c^c}\int_0^{\lambda/4}\cos^2\frac{2\pi z}{\lambda}\,dz = \frac{V_0^2}{8Z_c}\cdot\frac{\lambda}{c}. \tag{4}$$

The effective transverse shunt impedance $R_\perp$ is[3] (for $\beta = 1$):

$$R_\perp = \frac{Q}{\omega U}\left(\frac{\nabla_\perp V}{k}\right)^2 \tag{5}$$

where Q is quality factor, ω is angular frequency, and

$$k = \frac{2\pi}{\lambda}$$

$$V = \int_0^\ell E_z e^{jkz}dz$$

$$\nabla_\perp^2 V = 0.$$

Using equations (4) and (5), we find

$$\frac{R_\perp}{Q} = \frac{8Z_c}{\pi k^2}\left(\frac{\nabla_\perp V}{V_0}\right)^2. \tag{6}$$

Z_c and $\nabla_\perp V$ are obtained from 2-D calculations. V is the solution of the boundary value problem having $V = 0$ on the outer shell and $V = \pm V_0$ on the rod's surface of diameter d_0 and rod space d_c. We are interested in the area near the origin. It can be approximately treated as electrostatic problem of two parallel conducting cylinders. On the line joining the centers of two rods (x direction) we would have

$$V = \frac{V_0}{\ln\frac{b+a}{b-a}}\left[\ln(b-x) - \ln(b+x)\right] \tag{7}$$

where

$$b = \frac{1}{2}\sqrt{d_c^2 - d_0^2}\quad,\quad a = \frac{1}{2}(d_c - d_0).$$

From equation (7) we obtain

$$\left.\frac{dV}{dx}\right|_{x=0} = -\frac{2V_0}{b\ln\frac{b+a}{b-a}}.$$

Also, we have

$$Z_c = \frac{Z_0}{2\pi}\ln\frac{d_c}{d_0}\quad (Z_0 = 120\pi\Omega) \tag{8}$$

where Z_0 is free space wave impedance. Using equations (7) and (8), we obtain

$$\frac{R_\perp}{Q} = \frac{1920}{\pi k^2}\,\frac{\ln\frac{d_c}{d_0}}{b^2\ln^2\frac{b+a}{b-a}} \tag{9}$$

and

$$\frac{R_\perp}{\ell Q} = \frac{7680}{\pi k^2\lambda}\,\frac{\ln\frac{d_c}{d_0}}{b^2\ln^2\frac{b+a}{b-a}}. \tag{10}$$

where $\ell = \lambda/4$.

It is interesting to see the $\frac{R_\perp}{\ell Q}$ dependence upon rod space d_c (as shown in Figure 4). When the two rods get closer to each other, the transverse shunt impedance rapidly increases.

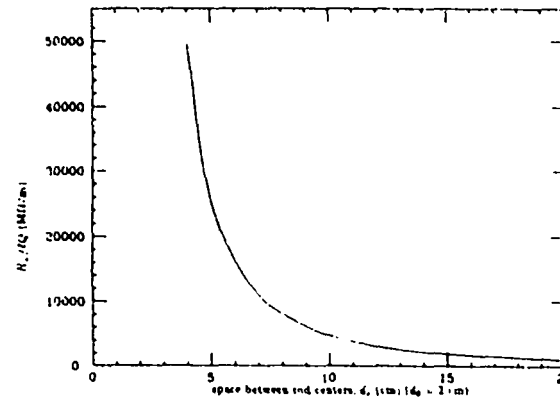

Figure 4. $R_\perp/\ell Q$ vs. d_c.

Numerical Study

We use MAFIA to calculate the properties of this type of cavity. The dimensions of the cavity under study are the following:

cavity length l = 150 mm

beam aperture d_{in} = 20 mm

rod diameter d_0 = 20 mm

Figure 5 shows the relationship between the frequency and gap width. As the gap gets larger, the frequencies of the modes go higher for all three modes.

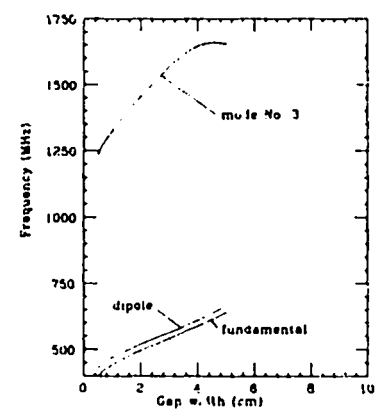

Figure 5. Frequency vs. gap width.

As gap width is decreased, Q goes down. Since this is a 1/4 wavelength resonator, it is expected that the frequency of the mode strongly depends on the rod length (or gap width) rather than the outside diameter of the cavity.

In some applications only one single cavity need be used. However, to make this type of cavity useful for the CEBAF RF separators that require a very strong deflection effect, it may be desirable to find a way to couple them together.

The field patterns in Figure 2 show that the electric field is perpendicular to the plane S and the magnetic field is very weak in the region close to the plane S. If the two 1/4 wavelength cells are put together facing each other as shown in Figure 6, and the plane S is taken away to form a 1/2 wavelength cavity (π mode), the field pattern will almost be unaffected, and its performances (frequency, $R_\perp$, etc.) will remain the same as a single 1/4 wavelength cell. Furthermore, we are able to couple several of these cavities together through slots in the webs to constitute a structure. This is a structure with magnetic coupling. It has a backward wave property. An increase in slot size will enlarge the separation of the modes.

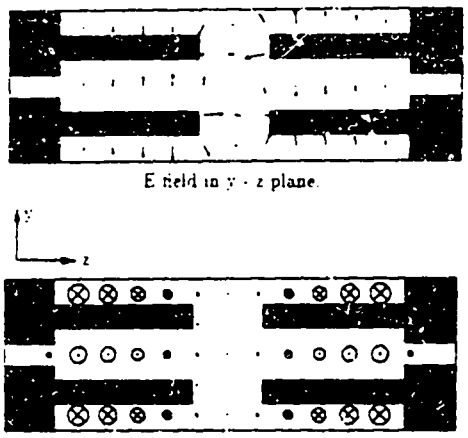

Figure 6. Field patterns in a half-wavelength cavity.

After careful optimization of cavity geometry the effective transverse shunt impedance $R_\perp$ over the whole structure, which is 60 cm long and operated at 500 MHz, is around 500 MΩ/m. The Q value of the structure is ≈ 10000. If this structure is used as an RF separator for the highest energy (5 GeV), the required RF power is:

$$p = \frac{(5\ \mathrm{GeV} \times 10^{-4} \times 1.16)^2}{R_\perp L} = 1.1\ \mathrm{kW}.$$

By comparison, the current design RF separator for the highest energy is ≈ 3 m long and requires 10 kW of RF power.

It can be seen from the field pattern that a large part of power dissipation is on the surface of the rods and the web, and special attention should be paid to cooling these parts of the structure.

Figure 7 shows the field uniformity in the central region of the structure. As can be seen the fields in the central region are more uniform with bigger rods. The phase space distortion caused by the deflecting structure is less than 1% if the beam size is about 1 mm in diameter. On the one hand, the field pattern is sextupole-like; any phase space distortion caused by the structure may presumably be corrected by a sextupole magnet placed with an appropriate phase advance downstream of the separator. On the other hand, field aberration could be minimized by choosing the proper shape of the rods.

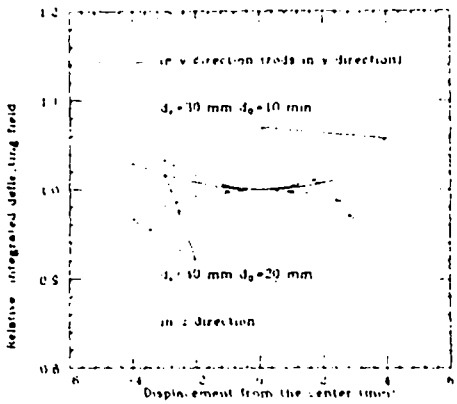

Figure 7. Field uniformity in central region.

Acknowledgement

We wish to thank R. Miller at SLAC, G. Lambertson at LBL, and W. Barry for valuable discussions.

References

1. C. Leemann, C. G. Yao, CEBAF TN-90-217, April 25, 1990.
2. G. Lambertson, Short Note to Ref. 1, August 6, 1990.
3. W. K. H. Panofsky, et. al., R.S.I. 1956, **27**, No. 11, p. 967.

IMPROVEMENTS TO THE PFN CAPACITORS FOR THE KLYSTRON MODULATORS OF THE KEK 2.5-GeV LINAC

Hiroyuki Honma, Tetsuo Shidara, Shozo Anami, Akira Asami and Hirokazu Sakaguchi*
KEK, National Laboratory for High Energy Physics
1-1 Oho, Tsukuba-shi, Ibaraki-ken, 305, Japan
*Nichikon Co. Ltd., 3-1, Yagura 2-chome, Kusatsu, Shiga-ken, 525, Japan

Abstract

Some of the capacitors in the pulse-forming network (PFN: 20 sections) of 48 klystrons in the KEK 2.5-GeV linac had begun to break down since 1986. Since there is no difference regarding the operating conditions between breakdown and normal capacitors, the breakdown seems to be due to individual capacitors. Careful investigations of the breakdown are continuing. Along with these investigations, life-span tests have been performed in order to evaluate newly designed capacitors. From these results, about 700 new-type capacitors have already been fabricated and installed in the klystron modulators.

Introduction

In the KEK 2.5-GeV linac, 48 klystron modulators are supplying pulses of 22.5 kV peak voltage, 3600 A peak current and 3.5 μs pulse width for 30-MW klystrons. The output pulse waveform contains a wide frequency band ranging from dc to ~10 MHz. The pulsed power is formed by a pulse-forming network (PFN) which comprises 20 LC sections.

Since the PFN capacitors are used under severe conditions, compared with normal power capacitors, careful attention has been paid to the long-term variation of their characteristics: tanδ as well as the insulation resistance and capacitance of all the PFN capacitors have been measured periodically every year since 1982 when the PF linac operation started.

Figure 1 shows the tanδ data (the maximum,minimum,and average values of twenty capacitors of each modulator) measured in 1987. We can divide all of the capacitors into two groups in terms of the large difference in the measured values. In one group (group 1 in Table I), they exhibit a great increment of tanδ. The intial value of tanδ was 0.01 % on the average. In the other group (group 2 in Table I), they exhibit no deterioration. Some capacitors in the former group had begun to break down since 1986. No latter group capacitors have broken down up to now. Since all capacitors were fabricated to satisfy the same specifications and there is no difference among the applied voltages for the two groups, the breakdown seemed to be due to individual capacitors.

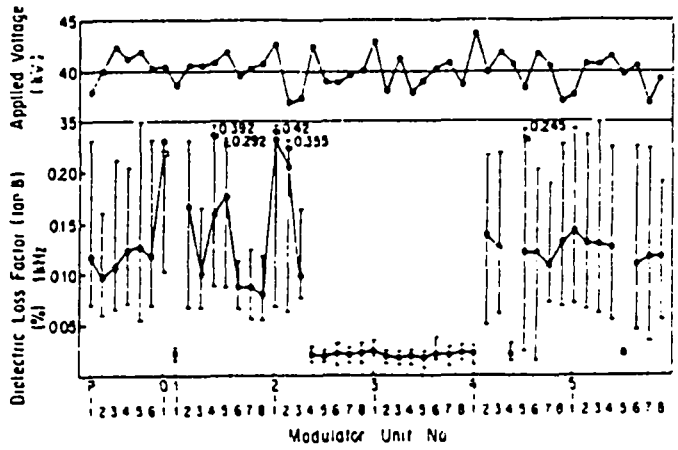

Fig. 1. The maximum, minimum and average tanδ values of twenty capacitors and the applied voltage for each modulator.

The number of breakdowns corresponds to 2.5 % of all capacitors. Once a breakdown occurs, it has great effect on linac operation. It was therefore necessary to solve this problem as soon as possible. In this report, outlines of the investigation of the breakdown and development of a new-type capacitor are described.

The Results of An Investigation Regarding Breakdown

The PFN capacitor has the following structure:[1] fifteen capacitor elements in series are oil immersed in a porcelain cylindrical insulator (see Fig. 2(a)). The dielectric of each element consists of a sheet of mica and two polypropylene films which are located just next to the electrodes (see Fig. 2(b)). To clarify the cause of breakdown, the same number of capacitors from both groups mentioned above were opened and investigated. Table I shows the characteristics of the samples. The following facts were found for both groups:

1. The insulating oil was not fully aromatic. (It is said that olefinic polymer (polypropylene) can

easily swell and hydrogen gas due to a corona discharge is not easy to be absorbed unless it is used in fully aromatic oil.)

2. The corona starting voltage (CSV) of elements is very close to the rated maximum voltage.
3. The value of the clamp ratio defined in Fig. 2(c) is very close to 100 %. This means that the insulating oil space between an electrode and the dielectric is very thin.
4. Line scratching along the electrode edge, resulting from corona discharge, was observed on the dielectric film , as shown in Fig.3.

Judging from these facts, it was found that the electrode-edge region of the dielectric had deteriorated owing to corona discharge in both groups. It also seems that swelling of polypropylene decreased the clamp ratio and consequently , the CSV of the capacitor elements.[2] It is not known whether this deterioration of the dielectric is related to the breakdown , since no group-2 capacitors have broken down.

Although the cause of the breakdown is not clear, all of the capacitors in the KEK 2.5-GeV linac should be replaced with improved capacitors in order to prevent any further breakdowns from occurring.

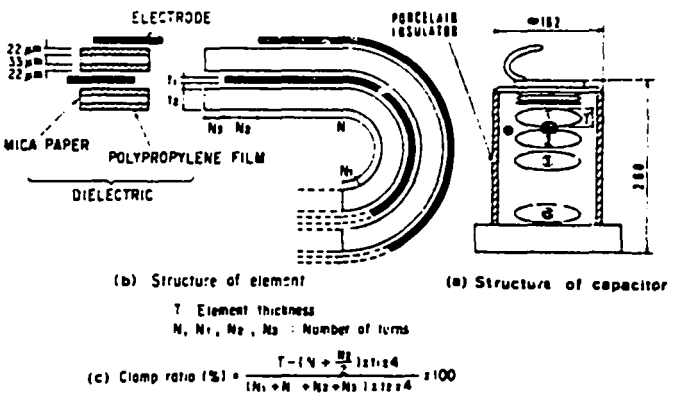

Fig. 2. The structure of capacitor and element,and the clamp ratio.

Fig. 3. Microphotograph (×65) of the dielectric film.Line scraching is marked along the electrode edge.

Life-Span Tests for A Newly Designed Capacitor

Life-span tests, in which a voltage higher than the rated maximum voltage (47 kV) was applied (but, of course, it was lower than the breakdown voltage), were performed at klystron modulators in the KEK 2.5-GeV linac in order to confirm new capacitor design. Two types of tests were designed. The first type (type-A) used mica as dielectric material and the second type (type-B) used low-density paper and polypropylene. For the type-A test capacitors (mica), three levels of electric-field strength (70, 110 and 140 V/μm) were applied, since mica has a large dielectric strength and is expensive compared with the dielectric of the type-B capacitors. For the type-B test capacitors (paper and polypropylene), three level fields around 60V/μm were applied according to the result of a preliminary test.

Table I
Characteristics of Sample Capacitors and Elements.

Group		1					2				
Sample NO.		1	2	3	4	5	6	7	8	9	10
Operation time ×1000 (hours)		14	14	13	21	21	16	25	25	25	25
Capacitor 1kHz tanδ (%)		0.57	0.18	0.19	0.11	0.09	0.03	0.02	0.02	0.03	0.03
Capacitor element	1kHz tanδ (%)	---	---	---	---	0.21	---	0.06	---	0.09	---
	60 Hz "	0.52	0.19	0.20	0.31	0.48	0.04	0.05	0.05	0.13	0.08
	CSV /Rating Voltage	1.1	1.2	1.2	1.1	1.0	0.9	1.2	1.1	1.2	1.1
	Clamp ratio (%)	---	---	---	97.5 ~102	97.2 ~101.5	---	98.9 ~103.5	98.1 ~106.6	100.9 ~103.3	96.7 ~105.6
	Average (%)	---	---	---	100.4	99.5	---	101.6	104.3	102	101.3
Insulating oil Tanδ (%)		0.28	0.94	1.29	0.84	0.58	2.5	2.2	1.5	1.2	1.3

In general, the shortest life-span(T) of practical operation can be estimated in terms of E, n, and T_0 by the euation:

$$T = T_0 \times E^n \quad . \qquad (1)$$

E: the ratio of the applied electric field strength of the test to the designed value.

n: the voltage acceleration coefficient.

T_0 : the shortest life span obtained by the test.

Figure 4 shows the dependence of the life-span for type-A test capacitors regarding the applied electric field strength. From this curve, an n of 13.1 was obtained by substituting E=1.57(the ratio of field level,110v/μm to 70v/μm), T_0=1.35 (life-span at field level,110v/μm), T=500(life-span at field level,70v/μm) in the eq.(1). The life-span test for the type-B test capacitors gave the shortest life-span of more than 2500 hours.

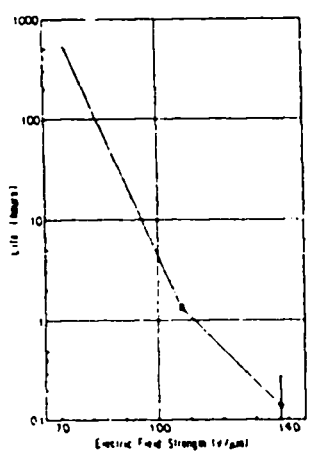

Fig.4. Life-span dependence of type-A capacitors on the applied electric-field strength.

The type-B capacitor was adopted as a new PFN capacitor. It was difficult to estimate the shortest life span of type-A capacitors owing to a lack of sufficient test data.

Though the tanδ value of the type-B capacitor is larger than that of old-type capacitor, there is no problem under our low-duty operating condition. By substituting E=1.5, n=15, T_0=2500 in eq. (1), the shortest life- span of a new PFN capacitor becomes more than one million hours. This value is sufficiently long to use them in the KEK 2.5-GeV linac.

From the result of this test, the new- type capacitors were fabricated and installed in the klystron modulators. Over 70 % of the PFN capacitors have been replaced by the new-type and successfully operated. Figure 5 shows the long-term variation of tanδ of both the new- and old-type capacitors. No deterioration of tanδ has been observed up to now.

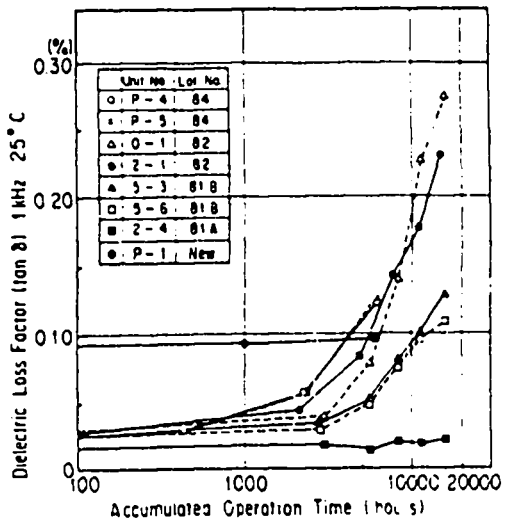

Fig. 5. Long-term variation of tanδ of both the new- and old-type capacitors.

Acknowledgement

The authors wish to express their thanks to Mr. T. Matuoka and other members of Soshin Electric Co. Ltd. for their periodical measurements of capacitor characteristics. They also express their thanks to all members of the KEK 2.5-GeV linac and Mitsubishi Electric Service Co. Ltd. for their help.

References

1. T. Shidara et al., "A pulse Forming Network with Specially Designed Capacitors for Klystron Modulators of The KEK 2.5-GeV Electron Linac", KEK Preprint 85-49, 1985.
2. R. J. Hopkins et al., "Development of Corona Measurements and Their Relation to the Dielectric Strength of Capacitors", AIEE Trans. Volume 70, 1643 (1951).

COMPUTER DETERMINATIONS OF THE PROPERTIES OF WAVEGUIDE LOADED CAVITIES*

Norman M. Kroll and Xin-Tian Lin
University of California, San Diego, La Jolla, CA 92093
and
Stanford Linear Accelerator Center, Stanford University, Stanford, CA 94309

Abstract

Two recently developed computer methods to determine the resonant frequency and Q_{ext} of waveguide loaded cavities are described. We present an application of these methods to a cavity of simple form with a range of coupling apertures. The methods are found to be in good agreement with each other and also with experiment.

1. Introduction

In this paper we describe methods to determine the properties of accelerator cavities which are loaded by external waveguides designed to damp higher order beam induced modes. The methods use MAFIA or ARGUS computations of the properties of the resonant modes of the combination of shorted sections of the loading waveguides coupled via apertures to the accelerator cavities. We begin with a review of the method of Kroll and Yu,[1] which makes use of the relation between the frequencies of the modes and the lengths of the shorted waveguide sections. A useful extension of this method[2] (which reduces the number of lengths required by a factor two) will be described. It makes use of the fact that the derivative of the frequency with respect to the shorted waveguide length can be computed from stored energy and field strength data provided by these computer codes. Some comparison of the method with experimental determinations will also be given. As will be shown by examples, the Kroll-Yu method is also well suited to experimental determinations of cavity properties, especially in situations where more standard methods are difficult to apply.

2. Basic Approach

We consider a cavity coupled to a waveguide through an aperture. We wish to determine the resonant frequencies and decay constants of various modes when the waveguide is terminated by a matched load. We neglect all internal losses so that the decay constant is directly related to the external Q of the cavity (referred to as Q henceforth). These quantities can be directly related to the mode spectrum of the coupled cavity-waveguide system formed by shorting the waveguide at a distance D from the output plane, by studying the dependence of the mode spectrum upon the distance D. A typical example of this dependence is illustrated in Fig. 1, where the frequency f is normalized to the frequency of the uncoupled cavity mode and the abcissa r refers to D normalized to one-half the cutoff wavelength of the waveguide. Since all of the curves refer to a single cavity resonance, we refer to them as branches. The following formula provides an excellent four-parameter representation of these curves in the vicinity of the resonant frequency of the cavity.

$$\tan\left[k(\omega)D + \chi(u) + \chi'(u)(\omega - u)\right] = \frac{u}{2Q(\omega - u)} , \quad (1)$$

Here $k(\omega)$ is equal to $2\pi/\lambda_g$ as usual. The parameter u represents the resonant frequency of the cavity coupled through the output and waveguide to a matched load, while the parameter Q represents the associated external Q. The remaining two parameters, $\chi(u)$ and $\chi'(u)$, parameterize the effect of distant cavity resonances. Theoretical background for Eq. (1.1) is provided in the Appendix. As noted by Kroll and Yu, the four parameters may be determined by computing four frequency-length pairs in the vicinity of the cavity resonance (as identified by inspection of field plots) and requiring that Eq. (1.1) be satisfied for each pair. A minimum

*Work supported by Department of Energy contracts DE-AS03-89ER40527 and DE-AC03-76SF00515.

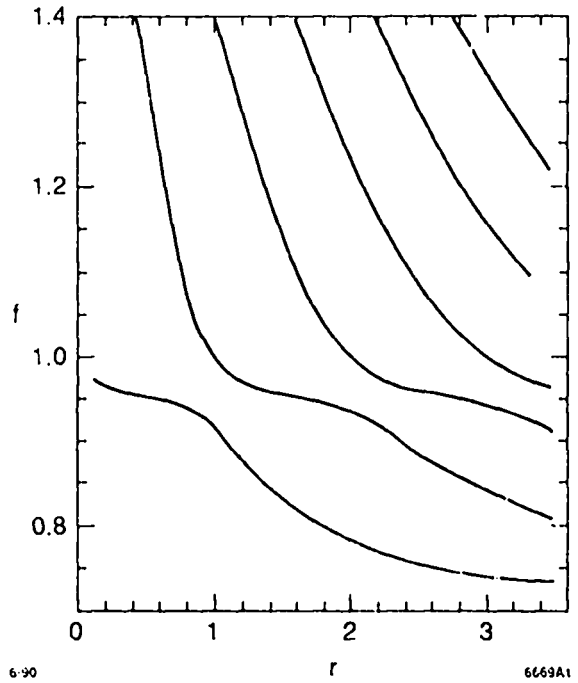

Fig. 1. Mode frequencies versus waveguide length.

of four computer runs at four different lengths is required to produce four reasonably placed points on a single branch. On the other hand, if the lengths are chosen in the vicinity of an avoided crossing region, where two branches are adequately close to the resonance, only two lengths are required and two frequency-length pairs are taken from each of the two branches. This reduces the amount of computing required by a factor two, since the computer run typically yields all the modes of interest at a specified length in a single run.

The extension of their method which we report here replaces two of the frequency-length pairs with a determination of the derivative of frequency with respect to length at the remaining two frequency-length pairs. By differentiating Eq. (1.1), we obtain

$$\frac{d\omega}{dD} = -k(\omega)\left[\frac{\omega D}{kc^2} + \chi'(u) + \frac{2Qu}{4Q^2(\omega - u)^2 + u^2}\right]^{-1} \quad (2)$$

where c represents the velocity of light. The four parameters are now determined by requiring that both Eqs. (1.1) and (1.2) be satisfied for the two frequency length pairs. The derivative which appears in Eq. (1.2) is obtained from the computer runs via the formula

$$\frac{d\omega}{dD} = -\frac{\omega \int \left(\mu_0 H^2 - \epsilon_0 E^2\right) dS}{2\int \mu_0 H^2 dV} , \quad (3)$$

which follows from cavity resonator perturbation theory. The volume integral in Eq. (1.3) is proportional to the stored energy of the mode, which is one of the standard outputs of a typical computer run. The surface integral is carried out over the shorting plane at the end of the waveguide. Since the field values are also available as output, it can be readily computed. In the case of standard waveguides, the surface integral can be determined from field values at single points; there is, of course, no electric field contribution in the case of TE waveguide modes.

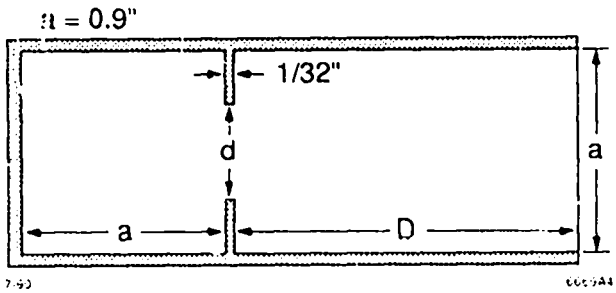

Fig. 2. Test cavity with iris and waveguide output.

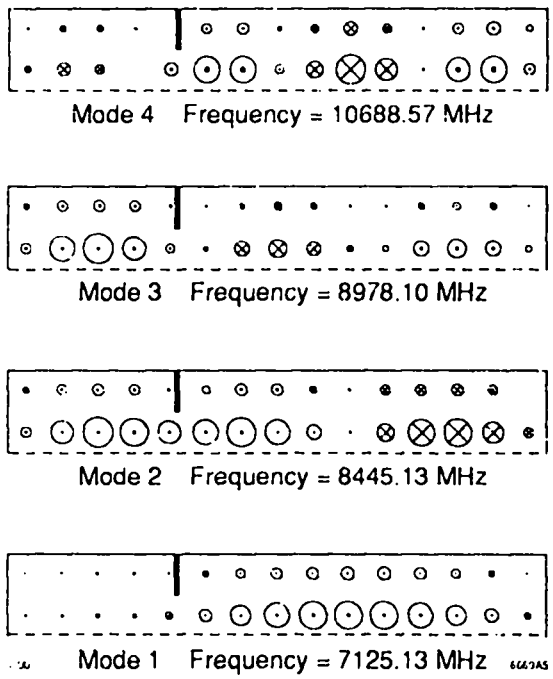

Fig. 3. Electric field plots for first four modes.

If it is clear from an examination of the field plots associated with a single computer run that two branches from the same cavity mode are present (as is often the case), then that run is sufficient to determine the properties of the resonance. If only one branch is recognizable, then a second run at a different length will provide a second point on the same branch, and the determination of cavity properties can be made from the two runs. This latter procedure may also be preferable when the frequency separation of the points on the two branches is too large.

3. Example

We illustrate the procedure for the simple cavity shown in cross section in Fig. 2. The cavity height is chosen to be small as the modes of interest to us here have frequencies independent of cavity height. In Fig. 3 we show electric field plots of the first four modes for the case $d/a = 0.5$ at $D = 2.0$ inches. Since we are studying the lowest cavity mode, which is symmetric with respect to the center of the iris, only half of the cavity-waveguide combination is shown. The curves of Fig. 1 imply that no matter what value is chosen for D, at least one mode will be close to a cavity resonance. Examination of the field plots shows that it is the third mode which is closest to the cavity resonance, that modes 2 and 4 are different branches of the same resonance, and that mode 2 is clearly the closer of the two. Since the two branches nearest resonance are clearly identified, a single length determination of cavity properties using modes 2 and 3 can proceed. The result obtained is frequency = 8769.07 MHz and $Q = 34.542$.

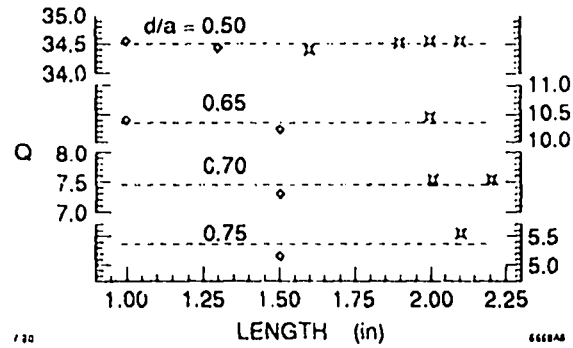

Fig. 4. Computed Q values for test cavity.

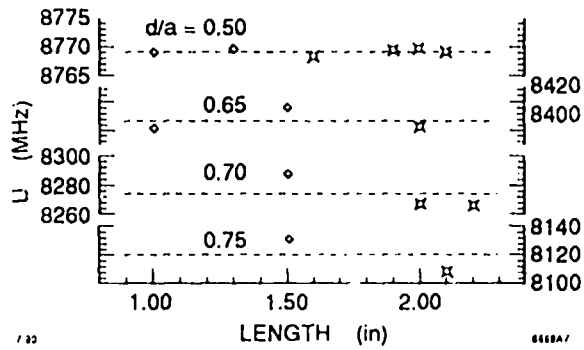

Fig. 5. Computed frequency values for test cavity.

In order to investigate the stability of results with respect to the waveguide length D chosen, we carried out computations at a number of different values. We also investigated a number of different iris openings d/a. The results for Q and frequency are shown in Figs. 4 and 5. Note that the points arising from the first two modes are displayed with a different symbol than those arising from modes 2 and 3. The horizontal lines represent arithmetic averages of the determinations for each d/a value, and are inserted to assist an assessment of the variation. A more thorough investigation of the dependence of results upon values for D and d/a has been carried out for an analytic approximation to the cavity of Fig. 2 with zero iris thickness. The analytic approximation also permits exact evaluations of the resonant frequency and Q to be compared with the single length determinations. Excellent agreement was found.[2]

Although single length, two-branch determinations proved to be satisfactory for this model at all lengths tested, there may be circumstances in which a two-length single branch determination is preferable. Accordingly, we used the data obtained to investigate the length dependence of the above results, to also test their consistency with two-length single-branch determinations. We were also able to compare results with those obtained from the Kroll-Yu method. A representative set of comparisons is shown in Table I. The method employed for each case should be clear from the branch and length lists.

4. Comparison with Experiment

In order to compare the results from Table I with experimentally determined values, a cavity conforming to the configuration of Fig. 2 was constructed from standard 0.9 in by 0.4 in waveguide and provided with a set of interchangeable irises with the d/a values listed in Table I. Measurements were carried out with the assistance of a Hewlett-Packard network analyzer. The standard detuned short

Table I

d/a	Frequency (MHz)	Q	Branches	Lengths (inches)
0.5	8769.07	34.54	2,3	2.0
	8769.09	34.52	2	1.3,1.9
	8768.93	34.63	2,3	2.0,2.1
	8768.84	34.59	2	1.3,1.6,1.9,2.0
0.65	8405.01	10.41	2,3	2.0
	8407.99	10.39	2	1.5,2.0
	8403.95	10.34	2,3	1.5,2.0
0.70	8266.35	7.54	2,3	2.0
	8270.48	7.48	2	1.5,2.0
	8263.87	7.48	2,3	1.5,2.0
0.75	8109.44	5.57	2,3	2.1
	8114.20	5.47	2	1.5,2.1
	8109.52	5.55	2,3	1.5,2.1

method of Q and frequency measurement was attempted, using a $0.26 \times 0.90 \times 0.72$ inch aluminum insert attached to the rear cavity wall to detune the cavity. Unfortunately, it produced adequate detuning to carry out the measurement only for the case $d/a = 0.5$, so that we are able to report detuned short method results for this case only. As an alternative, we carried out measurements for all four d/a values using the Kroll-Yu method. That is to say, we measured the phase of the reflection coefficient referred to the iris plane and used the Kroll-Yu four-parameter formula. The results obtained are shown in Table II and should be compared to Table I and Figs. 4 and 5.

Table II

d/a	Frequency (MHz)	Q	Method
0.50	8739	33.9	Detuned Short
	8750 ± 1	35.3 ± 1	Kroll-Yu
0.65	8375 ± 20	10.1 ± 0.8	Kroll-Yu
0.70	8210 ± 40	7.7 ± 0.7	Kroll-Yu
0.75	8040 ± 30	5.5 ± 0.2	Kroll-Yu

The uncertainties shown in Table II are crudely based upon variation observed with different selections of the four frequency phase pairs, and do not include an estimate of other sources of error. These variations are larger than those shown with different selections among the MAFIA computed pairs, and may reflect a lack of precision in the measurements.

5. Current Applications and Future Work

The methods described in this paper are being applied to the design and experimental analysis of accelerator cavities with heavily damped higher order modes. The experimental application of the method to the SLAC radial slot structure is described elsewhere in these proceedings[3] and will therefore not be repeated here. Application to the circumferential slot designs described there are in progress.

Preliminary work directed towards the design of accelerator cavities for a $B\bar{B}$ factory storage ring has indicated a need to deal with the problem of close resonances. We have recently developed an implementation procedure for the two-resonance representation[see Eq. (A5)] mentioned in the Appendix. It requires computer runs for at least two waveguide lengths. Initial results have been encouraging, and we hope to report in detail after we have more experience with the method. There is also a need for dealing with multiple nonsymmetric outputs and with multimode waveguide loading.

Appendix
Theoretical Background and Derivation of Eq. (1.1)

Following Kroll and Yu, we consider the boundary value problem presented by the cavity with its waveguide output, which we now consider to be infinitely long. We assume perfect conductor boundary conditions on all of the walls. As one proceeds along the waveguide towards infinity, the fields are required to approach those of the principal mode (assumed here to be the only one which can propagate without attenuation), propagating towards infinity. The eigenmodes of such a system are complex, with positive imaginary part, corresponding to oscillations which are exponentially damped in time. Writing this eigenvalue as $u + jv$, we identify u with the resonant frequency of the waveguide loaded cavity and $u/2v$ with the cavity Q.

The z dependence of the electric field between the waveguide origin and the shorting plane is of the form

$$e^{jkz} + Re^{-jkz}$$

where $k = 2\pi/\lambda_g$, z is distance along the waveguide axis, and R is the reflection coefficient referred to the waveguide origin plane. Since it must vanish at $z = D$, the shorting plane position, it must also be proportional to

$$2j\sin(kz - \psi - n\pi) = (e^{jkz} - e^{2j\psi}e^{-jkz})e^{-j\psi},$$

where $\psi = k(\omega)D$. Comparing the two forms, we see that $R = -\exp(2j\psi)$. We now observe that because the eigenfrequency corresponds to a situation in which there is an outgoing wave but no incoming wave, the reflection coefficient must have a pole there. This, combined with the fact that R must have absolute value one for real values of ω, means that it may be written

$$R(\omega) = -\frac{\omega - u + jv}{\omega - u - jv}\, e^{-2j\chi(\omega)} = -e^{2j\psi}, \qquad (A1)$$

where $\chi(\omega)$ is a real function, analytic at $\omega = u + jv$. It represents nonresonant effects, effects of distant resonances, and effects associated with the mode structure of the waveguide. Taking the logarithm of both sides of Eq. (A1) we find

$$\psi(\omega) = \tan^{-1}\left(\frac{v}{\omega - v}\right) - \chi(\omega) + n\pi \quad . \qquad (A2)$$

We shall assume that $\chi(\omega)$ can be adequately represented for real values of its argument in the vicinity of the resonance by the first two terms of its power series expansion about u. Thus, we write

$$\chi(\omega) \cong \chi(u) + \chi'(u)(\omega - u) \quad . \qquad (A3)$$

Equation (A3) is the basic approximation upon which the method is based. Taking the tangent of Eq. (A2), using Eq. (A3), and the expressions for ψ and Q yields Eq. (1.1).

The choice of representation of $R(\omega)$ by Eq. (A1) is not unique. There may be situations in which it is useful, for instance, to exhibit two resonances. The resonances may be too close to the frequency of interest to make the approximate Eq. (A3) adequate in itself. Taking account of the fact that $R(\omega)$ has a pole in the complex plane at both resonances, we replace Eq. (A1) with

$$R(\omega) = -\frac{\omega - u_1 + jv_1}{\omega - u_1 - jv_1}\,\frac{\omega - u_2 + jv_2}{\omega - u_2 - jv_2}\, e^{-2j\chi(\omega)} = -e^{2j\psi}. \qquad (A4)$$

Correspondingly, Eq. (A2) becomes

$$\psi(\omega) = \tan^{-1}\left(\frac{v_1}{\omega - u_1}\right) + \tan^{-1}\left(\frac{v_2}{\omega - u_2}\right) - \chi(\omega) + n\pi. \qquad (A5)$$

The function $\chi(\omega)$ is now analytic at both poles, and a linear approximation analogous to Eq. (A3) would normally be employed.

The guidance and assistance of W. R. Fowkes and T. Lee in carrying out the experiment is gratefully acknowledged.

References

1. N. M. Kroll and D. U. L. Yu, Part. Accel. **34**, 231 (1990).
2. N. M. Kroll and X.-T. Lin, SLAC-PUB-5296 (1990).
3. H. Deruyter et al., "Damped and Detuned Accelerator Structures," these proceedings.

DESIGN STUDY OF A HEAVY ION RF LINAC FOR MEV IMPLANTER

Hiroshi Fujisawa*, Yoshihisa Iwashita, Makoto Inoue, and Hidekuni Takekoshi
Institute for Chemical Research, Accelerator Laboratory, Kyoto University, Uji, Kyoto 611 Japan
*Ion Equipment Div. Nissin Electric Co., Ltd. 575 Kuze Tonoshiro-cho, Minamiku, Kyoto 601 Japan

Abstract

A preliminary design study is done for the design of a 4-rod RFQ linac. A modified PARMTEQ code is able to predict the transmission of an multiply charged ion beam and also to see what happens when injection energy is varied from the design value. Space-charge limited current is also checked, though our linac is not intended to be used for accelerating more than few mA of an ion beam. A 1/3 scale cold-model is constructed for the RFQ to check the resonant frequency, Q-value, and the field distribution. The number of electrode-supporting structure is six and the length of the electrodes is 793 mm. Our target is to optimize the dimension of the RFQ structure and operate the resonator in 100 MHz inside a 200 mm diameter tank. A 1/3 scale cold-model of spiral resonator is also build and its resonant frequency, Q-value, and on-axis field distribution are measured. This resonator is going to be placed downstream of the RFQ and operated as a post accel./decelerator in the same resonant frequency as the RFQ but in different phase condition.

Introduction

RFQ has its several appealing points to be recognized by industrial accelerator users as a high current and high energy accelerator in ion implantation application. Compared with conventional electrostatic accelerators, implanter's weight is going to be less heavier and radiation shield is much easier in RFQ linac design. Those points should be greatly appreciated and be carefully studied for the design of a successful commercial RFQ machine. We have been working on 4-rod RFQ for several years and accumulated quite a deal of experiences as we developed a proton accelerator.[1] Rod type structure has been selected because the diameter of the vacuum tank of the RFQ can be made smaller and the maintenance and tuning of this RFQ is expected to be much simpler than vane-type RFQ.

Rough Design Work

Unlike high-intensity light-ion RFQ , a particular attention is needed when doing the parameter search of a heavy ion RFQ in low beta regime. Transmission efficiency of the RFQ is restricted mainly by the acceptance of the linac not by the space-charge limits. Users are happy at moment if we could offer beam current at order of one mA and RFQ does not present much difficulty handling this amount of current load. Other important considerations are associated with mechanical and engineering difficulties and consequently the manufacturing costs. The length of the electrodes and the operating frequency must be optimized to guarantee the mechanical rigidity of rod-RFQ structure within the tolerance of assembly requirements.

Ion Source Emittance

An effective intrinsic normalized emittance, e_n is found as follows,

$$e_n = 2\, r_s\, (kT / Mc^2)^{1/2} \quad [\text{m-rad}] , \qquad (1)$$

where r_s is the beam radius at the emitter surface, kT is the source temperature - typical value is 3 eV - and M is the mass of ions.[2] e_n is roughly 1 mm-mrad for boron when r_s is 3 mm. An unnormalized emittance at energy 25 KeV is then approximately 0.045 cm-rad for this case. The acceptance of RFQ must then be larger or at least comparable to this value to accommodate a large portion of incoming ion particles. In PARMTEQ simulation, 10 % larger value of the above estimate is used for the input emittance.

PARMTEQ Simulation

RFQ parameters are listed in table 1. We intended to get most efficient parameters considering the length of RFQ, power requirement, and beam transmission. At moment this involves a long and repetitive work on computer and requires some experience to reach at satisfactory results.

Table 1
Design RFQ Parameters

Frequency	33.3 MHZ
Characteristic bore radius	0.8 cm
Focusing strength	6.79
Inter-electrode voltage	54.9 kV
Mass of ion	11 AMU
Charge state	1
Injection energy	25 keV
Output energy	1 MeV
Total length	310 cm
Number of cells	144

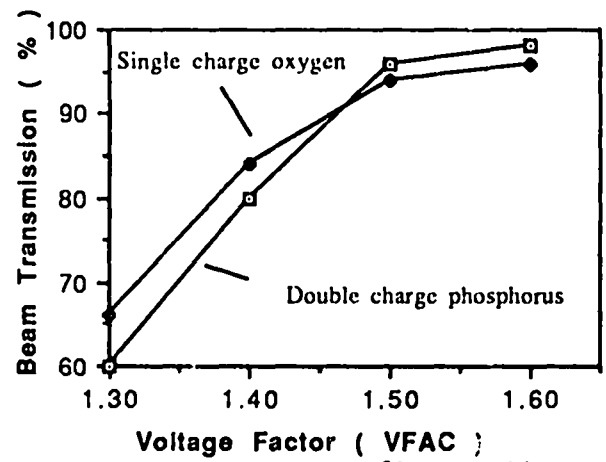

Fig. 1. Beam transmission of $^{31}P^{++}$ and $^{16}O^{+}$ in fixed structure and fixed operation frequency of a RFQ.

The beam transmission of $^{11}B^{+}$ is 92 % when the inter-electrode voltage is increased by 10 % of the design value in the dynamics calculations. Fig. 1 shows the beam transmission of $^{31}P^{++}$ and $^{16}O^{+}$ beam in the same RFQ. The results are that if we tolerate the transmission efficiency, a range of ion species can be accelerated by adjusting the input power. Fig. 2 is the transmission efficiency of $^{11}B^{+}$ beam as a function of injection energy. The results shows that our RFQ has a rather broad acceptance with regard to the variation of injection energies.

Space Charge Limits

The current limits are checked with LINACS.[3] The parameters are from the 110 th cell - supposedly at the end of the gentle buncher section - of the RFQ : the aperture, a =0.527 cm; the modulation, m=1.962; the output energy at the end of the cell, W_0=0.282 MeV; and the maximum field=10.47 MV/m. Fig. 3 shows both longitudinal and transverse current limits as a function of modulation parameter.

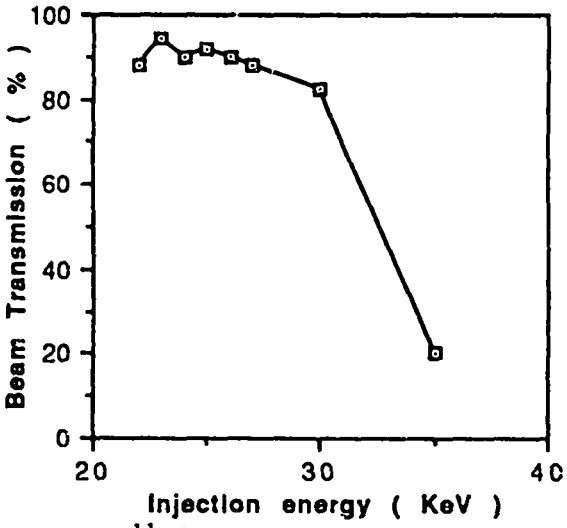

Fig. 2. $^{11}B^+$ beam transmission as a function of injection energy. The design injection energy is 25 keV.

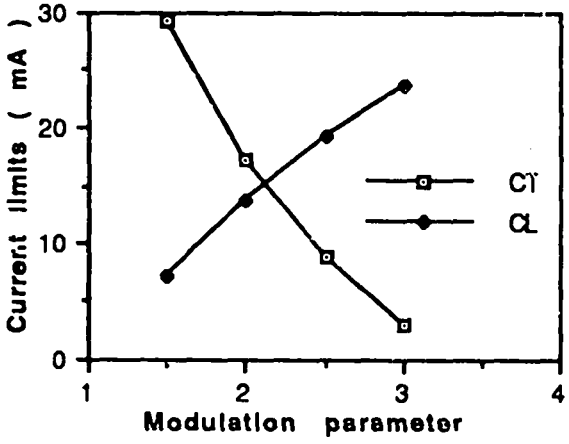

Fig. 3. Transverse (CT) and longitudinal (CL) space charge current limits as a function of modulation parameter.

Model Study of RFQ

4-rod RFQ presents relatively less rigorous engineering difficulties compared with 4-vane RFQ, nevertheless still there are important subjects we have to work and improve on . Those are structural rigidness and cost performance. Our 100 MHz 4-rod proton RFQ was only 75 cm long so it was not too heavy and sufficiently rigid with just 4 supporting structures. For a heavy ion RFQ with output energy reaching 100 KeV/nucleon, the resonator must be operated much lower frequency and its length becomes around 200 cm. If the structure is made with just 4-supporting posts, the droop of an cantilevered electrode will not be negligible and cannot be kept under machining and assembly tolerances. On the other hand, with 6-supporting post, the height of the post must be made much larger than that with 4-supporting post structure. The results are increase in the construction cost of the vacuum tank due to its larger diameter. The purpose of this model study is to search for the final dimension of the RFQ in reasonable size and to check its RF characteristics.

Droop of Electrode

The maximum displacement of electrode droop, Y can be estimated from the following equation,

$$Y = w L^4 / (8 E I) \qquad (2)$$

, where w is weight distribution, L is length, E is Young's modulus, and I is the second moment of system.[4] The cross-section of a RFQ is approximated by a rectangle of 24 by 60 mm, and its orientation is tilted 45 degree. Material is C1020-1/2H copper. The result is that when one end of an 50 cm long electrode-rod is fixed to the post, the maximum displacement becomes approximately 30 microns. This is less than but unfortunately comparable to what we expect for machining or assembly tolerances, 50 microns.

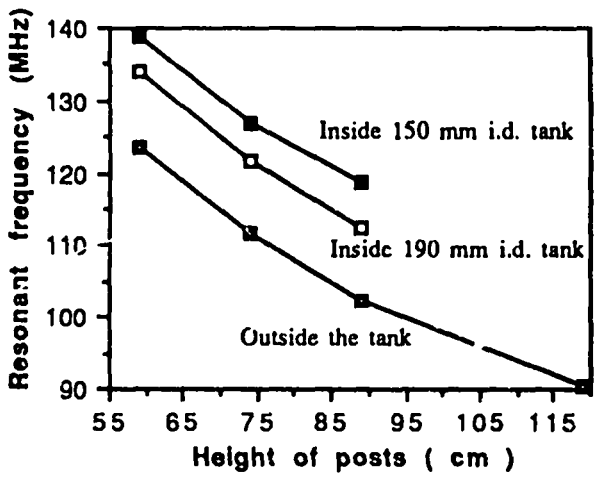

Fig. 4. Resonant frequency of 4-rod RFQ as a function of the height of the posts.

RF Characteristics

Fig. 4 shows the resonant frequencies of our 4-rod RFQ as a function of the height of the post in three different surrounding conditions: inside 190 mm diameter tank, inside 150 mm diameter tank, and outside the tank. The number of the post is six - this means a pair of RFQ electrode is supported by three posts. The width and thickness of the post are 80 mm and 15 mm, respectively. The posts are evenly spaced at 150 mm from each other. The electrode is un-modulated and its length is 793 mm. The aperture radius is 2.7 mm. RF contact between the tank and the base-plate of the RFQ assembly is made by commercially available "RF shield fingers". Note that the center of the aperture coincides with the center of the tank only in the case where post height is 59 mm and the diameter of the tank is 150 mm, otherwise they are eccentric.

We have developed an automated field measurement system which comprises of a HP-4195A, a workstation, and a stepping motor system. The principle is usual Slater's bead-pull method but our system is much simplified taking advantage of HP-4195A's high resolution performance. Fig. 5 is a typical

on-axis longitudinal electric-field distribution obtained from the experiments. The perturber's length is 10 mm and it is made just to fit in the aperture of the RFQ model. The results are that the variation of field along the axis is within 5 %. To achieve this degree of flatness, the electrode alignment tolerance must be as good as 0.05 mm.

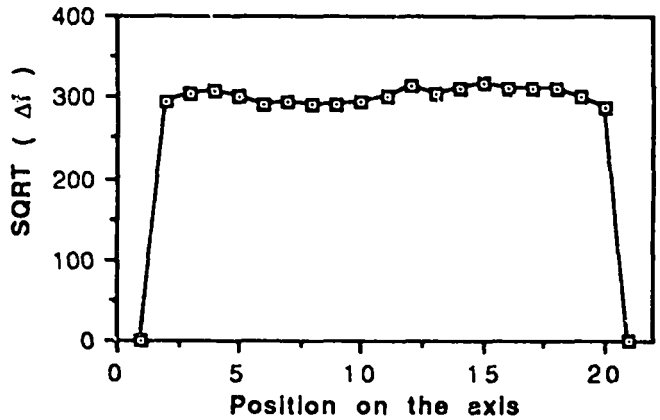

Fig. 5. Typical on-axis electric field distribution of 4-rod RFQ 1/3 scale cold-model. The resonant frequency is 94.72 MHz.

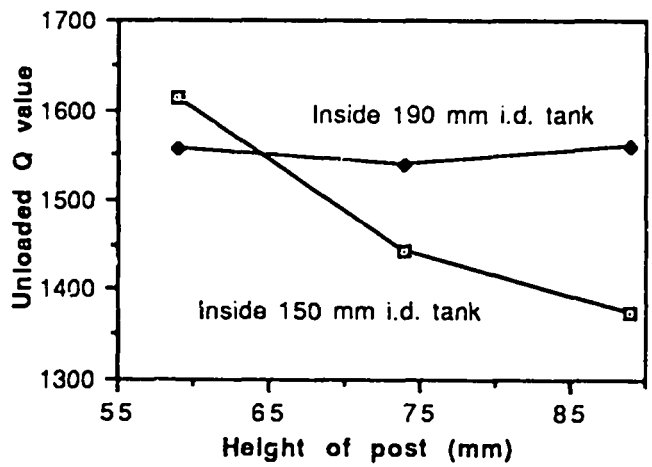

Fig.6. Unloaded Q-value as a function of post height.

Fig. 6 shows the unloaded Q-values as a function of the post height in 150 mm and 190 mm diameter tank. The size of posts, the distance between the posts, and the other conditions are the same as described above. The tendency is that the Q-value is basically irrespective to the height of the post, but will deteriorate as the electrodes come close to the wall of the tank.

Model Study of Spiral Resonator

Properties of spiral resonators have been studied elsewhere and we just followed their guidelines for building of our model.[5,6] A schematic drawing of a 1/3 scale spiral resonator is shown in fig. 7. The dimension of each parameter is defined and the experiment results are listed in table 2. On-axis field distribution is not presented here due to space limitation.

Concluding Remarks

There are still many other considerations to be given before the construction of a full scale machine. The RFQ's acceptance and its length, for instance, are probably the most important parameters to be optimized. The cooling of the RFQ structure presents the another engineering challenge for a stable operation of the accelerator.

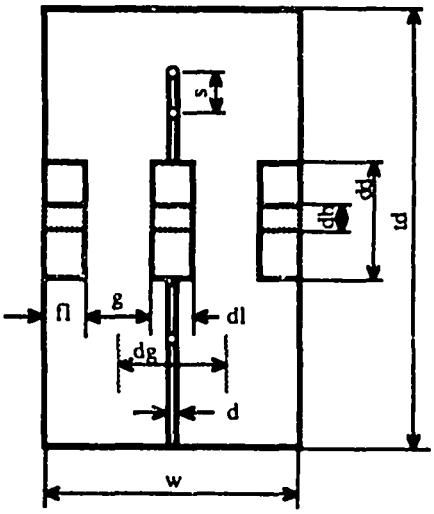

Fig. 7. Schematic drawing of 1/3 scale spiral resonator.

Table 2
Dimensions (in mm) and The Properties of 1/3 Scale Spiral Resonator.

	#1	#2	#3	#4
Gap length, g	7.0	7.0	7.0	7.0
Diameter of drift tube, dd	24.	32.0	24.0	32.0
Bore diameter, db	8.0	8.0	8.0	8.0
Gap-gap length, dg	18.0	18.0	18.0	18.0
Length of drift tube, dl	11.0	11.0	11.0	11.0
Length of field cutoff tube, fl	7.5	7.5	0.0	0.0
Separation pitch, s	18	18	18	18
Diameter of tube, d	7.0	7.0	7.0	7.0
Width of resonator, w	40	40	25	25
Diameter of tank, td	200	200	200	200
Length of spiral	660	660	660	660
Resonant frequency (MHz)	106.10	100.70	105.15	101.15
Unloaded Q value	1240	1260	880	920

Acknowledgments

The authors thank Toshihiko Katagiri for developing an automated field measurement system and also working on a spiral resonator.

References

1. H.Fujisawa and M.Naito," Research on RF Accelerators for MeV Ion Implantation System ", Nissin Electric Co., Ltd. Technical Journal Vol.35, No.2 (March1990).
2. M. Reiser, 1989 U.S. Particle Accelerator School.
3. A program developed by R. A. Jameson, LASL, USA.
4. " Kikai Sekkei Binran ", p712, Maruzen (1972).
5. A.Schempp, W.Rohrbach and H.Klein, "Measurements on Spiral Resonators at High Field Levels", NIM 140 (1977) 1-7.
6. A. Schempp and H. Klein, " Properties of Spiral Loaded Cavities ", NIM 135 (1976) 409-414.

USE OF TW OUTPUT STRUCTURES FOR HIGH PEAK POWER RF GENERATORS

J. Haimson and B. Mecklenburg

Haimson Research Corporation
4151 Middlefield Road • Palo Alto, CA 94303-4793

Abstract

The beam optics and electric field characteristics of several recently constructed TW structures are presented. These structures were designed to extract high levels of peak power from 11.4 GHz modulated, 500 to 1000A electron beams using three different RF amplifier configurations having nominal beam energies of 3.0, 1.2 and 0.5 MeV, respectively. The adoption of multicell, high phase velocity TW output circuits with unusually large beam apertures ($>\lambda_0/2$) has been instrumental in avoiding electric field breakdown and beam interception in these short wavelength, high current RF generators. For beam energies in the range of 0.45 to 1.3 MeV and RF output peak power levels of 100 to 300 MW, varying impedance and tapered phase velocity structures were used to minimize debunching and to maintain near synchronous conditions during beam traversal of the continuous interaction output circuit.

A concluding section discusses the design characteristics and performance of a new style 100 MW TW klystron specifically configured to operate in a small warm bore superconducting solenoid or a 4"ID water-cooled solenoid.

Introduction

The rationale for using TW output structures (a) to avoid RF breakdown at high levels of peak RF power, (b) to prevent beam interception when transporting large emittance, high current beams through short wavelength structures, and (c) to provide temperature and frequency insensitive, very fast response circuits (1 ns), has been presented elsewhere,[1] and this paper describes the reduction to practice of several high power TW output circuits designed for operation with three different combinations of beam energy and current, as listed in Table I below.

TABLE I. 11.4 GHz TW OUTPUT STRUCTURE APPLICATIONS

Application	Electron Source		I_{RF} (A)	Peak RF Output Power (MW)
	V_0 (MeV)	I_0 (A)		
TW Kly (X-791)	0.45-0.5	450-500	450-500	100
SL4/SHARK[2]	1.1-1.3	600-700	550-600	250-300
Choppertron[1]	2.7-3.0	1000	420-520	250†

†Design objective from each arm of a dual output system awaiting test.

All of the above RF generator applications make use of induction linac driven beams having nominal pulse widths of only 40 ns; however, the relatively low peak E-fields associated with these TW structures (as discussed in a later Section) imply that higher levels of peak RF power could be tolerated, or substantially longer pulse widths could be sustained.

TW output structures can be designed with beam apertures greater than $\lambda_0/2$ and are, therefore, particularly adaptable for operation with high current, large edge emittance beams ($\beta\gamma\varepsilon$ > 1000mm-mrad) having broad cross sections ($2a/\lambda_0$=0.4). Although large aperture designs result in a considerable loss of unit length shunt impedance, increasing the circuit length to compensate for this loss provides an added benefit because the beam induced fields can then be established over an extended distance substantially reducing the circuit maximum E-field.

When maximum power extraction is desired, the multicell TW structure can be designed to maintain near-optimum interaction conditions over the full length of the circuit by tapering the phase velocity to control de-bunching forces and maintain synchronism as the charge centroid is continuously de-accelerated. (Although this interaction is the inverse of that which occurs in externally driven high field gradient, high current TW buncher structures,[3] the same analytical design procedure can be applied.) Yet another technique for maintaining the RF current amplitude during traversal of the output structure is the use of a TW circuit and solenoid combination designed to allow the beam diameter to expand appreciably during growth of the circuit field gradient and extraction of RF power. (Refer to the TW klystron X-791 discussion in a following Section.)

Offsetting the advantages of TW output structures for high current applications is the risk of encountering pulse shortening and other beam induced high order mode instabilities caused by extending the circuit interaction length or by using multiple circuit arrays.

Choppertron TW Output Structures

The choppertron is a TW RF generator designed to operate with a 3MeV 1000A induction linac in support of the TBA[4] and Relativistic Klystron High Gradient Accelerator test programs at LLNL.[5] This RF generator comprises a 5.7 GHz chopper driver stage immersed in an axial magnetic field, and an 11.4 GHz TW dual output stage with each TW circuit designed to extract 250 MW of power at an RF current of approximately 450A. The principle of operation, design philosophy, and fabrication of the RF generator have been presented elsewhere,[1] and only the TW output structure characteristics will be discussed in this paper.

Each TW output structure has an overall length of $2\lambda_0$ and comprises five (three SST and two copper) velocity of light cells and a sidewall coupled, offset output cavity connected to a tapered WR90 RWG output arm via a special RF/vacuum flange designed as an integral part of the output cavity body. This configuration allowed short radial RWG feeds to be run directly from the centerline through the narrow spaces between the solenoid windings, instead of along the inside of the solenoid. Thus the solenoid bobbin diameters, as well as the size, weight and dissipation of the solenoid windings were significantly reduced.

Figure 1 shows views of the dual output structures, including the WR90 RWG and water-cooling connections, during installation of the solenoid modules.

A circuit beam aperture of 14 mm was chosen for this 11.4 GHz application as a design compromise between accommodating the relatively high beam emittance, and limiting the length of the structure without exceeding a maximum surface E-field design goal of 1600 kV/cm. This short pulse operation design goal was consistent with not exceeding an average E-field of 500 kV/cm in the output cavity.

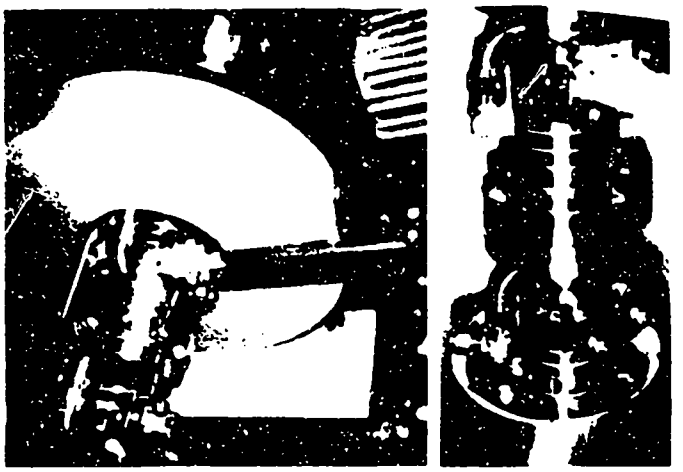

Figure 1. Dual TW Output Structures Shown during Assembly of the Choppertron.

The middle graph in Figure 2 shows the buildup of maximum surface E-field with distance along a choppertron TW output structure for a peak RF output power of 250 MW.

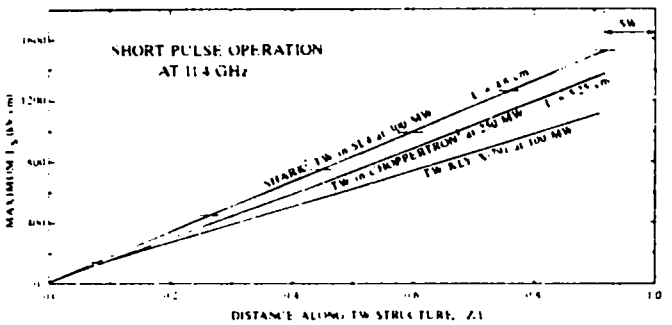

Figure 2. Maximum Surface E-Field Buildup in TW Output Structures.

Each choppertron output structure has an RF filling time of 1.05 ns, and a TW shunt impedance of 1.4 MΩ, giving a theoretical peak voltage reduction for synchronous on crest particles of approximately 1200 keV at an RF output power of 250 MW, with circuit total skin losses of less than 1 percent, and an output cavity average E-field of 450 kV/cm.

No specific precautions were taken to suppress the buildup of HOM instabilities[1] (the two prototype structures have identical frequency characteristics) so that it will be possible to evaluate this potential problem, especially in relation to the use of additional structures, during the early stages of the test program. Also, initial tests will be performed without the benefit of an HOM cut-off collimator in the drift region between the two circuits. Plans for the initial beam and RF tests are discussed in a companion paper.[5]

SL4/SHARK TW Output Structure

Since the beam energy specified for the SHARK (and SL/4) tests was considerably less than the Choppertron (refer Table I) and because of a desire for maximum power extraction, the SHARK TW structure was designed as a tapered phase velocity circuit comprising two stainless steel and four copper, $2\pi/3$ mode, cavities including a side wall coupled, offset output cavity. The circuit phase velocity was tapered from 0.94c to 0.90c over a 4.8 cm length; and the 1.01 ns RF filling time resulted in an extremely phase stable structure, insensitive to normal temperature and frequency variations, e.g., $\partial\phi/\partial f$ = 3.6 deg/10MHz and $\partial\phi/\partial T$ = 0.7 deg/10°C. This structure has a TW shunt impedance of 1.2 MΩ and was designed for an output cavity average E-field of 400 kV/cm at an output power of 250 MW. The SHARK TW circuit maximum surface E-field distribution is shown in Figure 2 for operation at a peak RF output power of 300 MW.

Figure 3 is a view of the SHARK output circuit assembly showing the bulkhead supports, water connections and RF output coupler, after final tuning and prior to attaching the WR90 output waveguide.

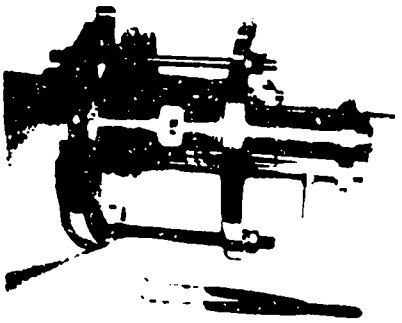

Figure 3. 11.4 GHz, 300 MW Tapered Phase Velocity Output Structure. Beam Aperture = 14 mmϕ

X-791 100 MW TW Klystron

This 11.4 GHz prototype RF generator was constructed as a five-section, high vacuum demountable assembly with the microwave cavities, RWG feeds, water-cooling connections, flanges and centering fixtures specially configured to allow the tube to be installed in a beam confining axial magnetic field system having a bobbin ID of only 4". The operating parameters are listed in Table II and an overall view of the tube is shown in Figure 4.

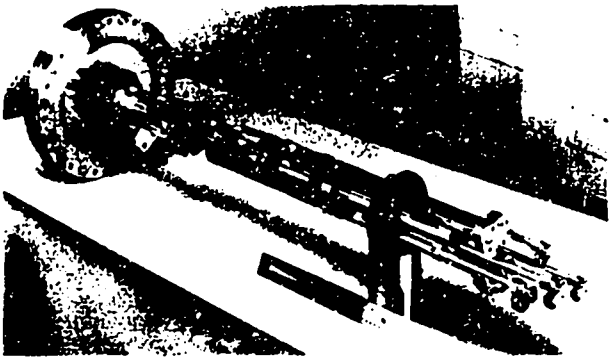

Figure 4. X-791 100MW TW Klystron with Independently Accessible Water Flow Paths for All Five Demountable Sections (Anode, Compression, Gain, Bunching and RF Extraction, and Collector).

Operating with a relatively high centerline pressure of $\approx 5\times10^{-7}$ Torr, the X-791 tube was run up to the 100 MW output power level without any evidence of RF arcing, pulse shortening, or cavity loading due to photoelectric, field, or secondary emission. (An RF output waveform is shown in Figure 8.) Key elements in the troublefree RF performance of the tube were conservative microwave circuit designs, progressively increasing beam apertures, an efficient TW output structure, and a well-matched, precision aligned, high quality axial magnetic field system.

TABLE II. X791 TW KLYSTRON OPERATING PARAMETERS

Beam Energy	500 kV
Electron Source	
Operational Microperveance	≈1.3
Normalized RMS Emittance	150π mm-mrad
RF Pulse Length (FWHM)	50 ns
Pressure at Anode Centerline	$\approx 5\times10^{-7}$ Torr
Nominal Beam Diameter in Gain Section	8-9 mm
Nominal Beam Diameter in TW Section	11-12 mm
Frequency	11.4 GHz
Gain	50 dB
Peak RF Output Power (full spectrum)	100 MW
Output Cavity Average Electric Field at 100 MW	230 kV/cm
Filling Time of TW Output Circuit	1.06 ns
Klystron Overall Length	48 in
Solenoid Bobbin ID	4.0 in
Solenoid Axial Magnetic Field	6 kG(max)
Solenoid Dissipation, less than	20 kW

Figure 5 shows final brazed assemblies of the tunable gain section, the tunable buncher and TW power extraction section, and the beam collector; and the 6" rule lying at right angles across the top of the TW output structure reveals the very compact nature of these high power components. With ongoing X-band interest in longer pulse widths and RF power levels >100MW,[8] the X-791 TW output circuit was designed as a very low impedance, tapered velocity structure with an output coupler average E-field of only 230 kV/cm at a peak RF output power of 100 MW. The associated maximum surface E-field distribution is shown in Figure 2. Precautions were taken to avoid pulse shortening caused by the forward propagating[1] (and then reflecting) HEM_{11}-like modes having resonances over an 800 MHz pass band centered at 13.5 GHz.

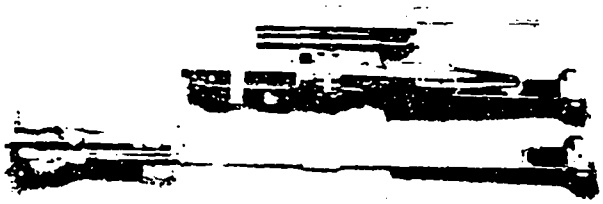

Figure 5. The Gain, TW Output and Beam Collector Sections of the X-791 Klystron.

A high electrostatic compression technique similar to that described by Lee,[7] was used for the electron source, followed by additional, near adiabatic, magnetic compression. To optimize output power, the axial magnetic field was graded along the TW output structure from 4.5 to 3 kG (as indicated in Figure 6) to give a 2:1 increase in beam cross-sectional area under saturated drive conditions.

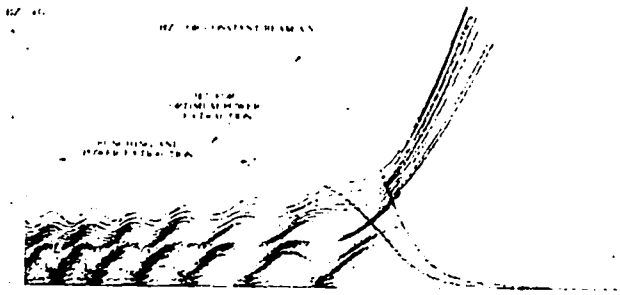

Figure 6. EGUN simulation of DC Beam with Graded Reduction of Axial Magnetic Field over the Output Structure.

Features of the X-791 beam confining magnetic field system include a 4" ID main solenoid having a dissipation of 16kW for 100MW RF operation; pancake winding transitions and a stacking technique to give full cancellation of internal axial current vectors; concentricity and collinearity of the klystron body and magnet assembly to 1/4 mm accuracy over the length of the tube; a large diameter, shaped iron, shielded bucking lens; and a precision alignment fixture that enables both the bucking lens and the main solenoid to be independently positioned axially with respect to the electron source. A view of the magnet system is shown in Figure 7.

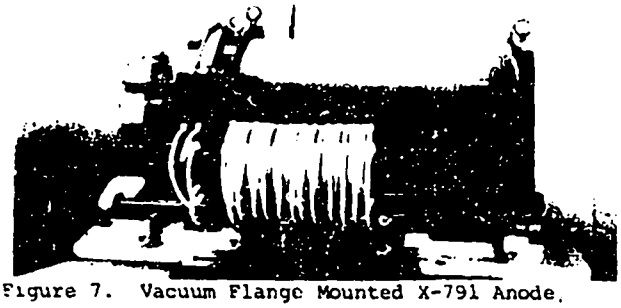

Figure 7. Vacuum Flange Mounted X-791 Anode, Independently Movable Large Bucking Lens System, and the Main Solenoid Assembly.

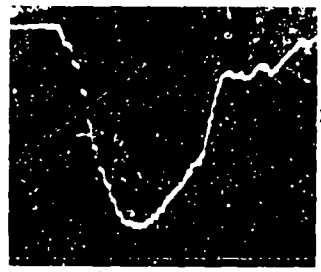

Beam Voltage = 500 kV
Frequency = 11.4 GHz
Peak RF Power = 100 MW
Gain = 50 dB
Diode Signal = 20 mV/div
Time Base = 20 ns/div

Figure 8. RF Output Waveform of X-791 TW Klystron Driven by an Induction Linac Beam. (The authors wish to thank the SRL/MIT Plasma Lab staff for providing this test data.)

The essential design features incorporated in the compact microwave structures discussed above, as well as the assembly, brazing and tuning procedures, and the offset coupler geometry and special RF packaging techniques, were derived from X-band TW resonant ring linac technology[9] developed over the past decade for well-logging applications.

References

1. J. Haimson and B. Mecklenburg, "Design and Construction of a Chopper Driven 11.4 GHz Traveling Wave RF Generator," 1989 PAC IEEE Conf. 89CH2669-0, p. 243.
2. M.A. Allen, et al., "High Gradient Electron Accelerator Powered by a Relativistic Klystron," Phys. Rev. Lett., 63, p. 2472, 1989.
3. J. Haimson, "Electron Bunching in Traveling Wave Linear Accelerators," Nucl. Instr. and Meth. 39 p. 13, 1966.
4. A.M. Sessler and S.S. Yu, "Relativistic Klystron Two-Beam Accelerator," Phys. Rev. Lett. 58, p. 2439, 1987.
5. G.A. Westenskow, et al., "Relativistic Klystrons for High Gradient Accelerators," Proc. Linear Accelerator Conference, Albuquerque, 1990.
6. "Electron Accelerator Techniques," Proceedings of the 6th Conf. on Electron Scattering, NIKHEF, Amsterdam, November 1989.
7. T.G. Lee, International Workshop on Next Generation Linear Colliders, SLAC, December 1988.
8. US Patent No. 4,713,581.

The Precise Measurement of Electric And Magnetic Fields in a Resonant Cavity

J. GAO
Laboratoire de L'Accélérateur Linéaire
91405 Orsay cedex, France

Abstract

In the area of microwave measurement, perturbation method is widely used, but the perturbation formulas which are often used will not stay correct when the perturbing object approaches the wall of the resonant cavity, which is the result from the effect of the induced charges on the cavity wall when the object approaches it.

This paper takes this effect into account, and gives modified perturbation formulas which were proved by some experimental results. These modified perturbation formulas could be widely used in the measurement of the electromagnetic fields in linear accelerator and other microwave devices.

Introduction

To demonstrate the effect of the charges induced on the cavity wall when a perturbing object approaches it[1,2], it is reasonable to measure the field in a resonant cavity in which the field distribution is well known. Now let's measure the electric field along the axis of a pill box resonant cavity in TM_{010} mode by using a small metal ball. The uncorrected perturbation formula[3] is

$$(f_o^2 - f^2)/f_o^2 = (4/3)3\pi E_o^2 A^3 \qquad (1)$$

where f_o is the unperturbed resonant frequency of the cavity, f is the perturbed resonant frequency of the cavity, E_o is the magnitude of the electric field where the small ball is located and A is the radius of the ball.

It's known that the magnitude of the electric field along the axis of a pill box cavity in TM_{010} mode is a constant. The measured result, however, turns out to be not the same as we have expected. In practice, the nearer the ball is to the wall, the greater $f_o^2 - f^2$ will be, and the conclusion we get from eq.(1) will be that the field along the axis is not constant. It is obvious now that eq.(1) has to be modified in order to be used for precise measurement of field.

The reason why $f_o^2 - f^2$ become larger when the ball is near the wall is that charges are induced on the cavity wall when the perturbing object is introduced into the cavity, and the contribution of the induced charges to the field becomes appreciably large when the object is near the wall, so that the field measured by eq.(1) is the combination of the field to be measured and the field produced by the induced charges on the wall. What we should do now is to pick the original field out, and establish a straight forward relationship between the unperturbed fields and the two frequencies f_o and f.

It is well known that electric field could be perturbed by dielectric and metal materials, magnetic field, however, could only be perturbed by metal material. In the following sections we will give directly the modified perturbation formulas to measure the electric, magnetic fields by using metal sphere perturbing objects. Experiments have been done to show the effectiveness of the modified perturbation formula. In the Appendixes the mathematic details have been given to show the way how these formulas are reached. As for the formula for dielectric purterbing sphere one could consult ref.[2].

Formula for Electric Field With Metal Sphere

According to perturbation theory[4] we have

$$f^2 = f_o^2(1 + \int_v (H_a^2 - E_a^2)dv) \qquad (2)$$

Starting from eq.(2) we distinguished two cases. The first of which will concentrate on the electric field and will be discussed in this section. Another will be discussed in the next section on the magnetic field and the combination of the two cases.

When there is no magnetic field where the sphere is located, eq.(2) could be changed into

$$(f_o^2 - f^2)/f_o^2 = \int_v E_a^2 dv \qquad (3)$$

After some mathematic derivations[Appendix 1], we get the modified perturbation formula

$$(f_o^2 - f^2)/f_o^2 = (4\pi/3)3E_o^2 A^3(1+\alpha) \qquad (E)$$

where E_o is the field to be measured without being perturbed by the ball, A is the radius of metal sphere and α is expressed as follows

$$\alpha = 4(A/C)^3 + 16(A/C)^6 + 55.6(A/C)^8 + 32(A/C)^9 \qquad (4)$$

where C is twice the distance from the centre of the ball to the wall. When the ball is far from the wall eq.(E) will return to eq.(1). Eq.(E) is well proved by the experiment, as shown in Fig.(1).

Formula for Magnetic field with Metal Sphere

When there is no electric field where the sphere is located, eq.(2) could be changed into

$$(f_o^2 - f^2)/f_o^2 = -\int_v H_a^2 dv \qquad (5)$$

After Appendix 2, we get the modified perturbation formula for magnetic field.

$$(f_o^2 - f^2)/f_o^2 = (4\pi/3)(3/2)A^3 H_o^2(1+\beta) \qquad (M)$$

*The work was done in Tsinghua University, Beijing and in IHEP.(Institute of High Energy Physics, Academia Sinica, Beijing).

Now we express E_r by letting n equal only 0,1,2. Therefore,

$$E_r = (2a_1^l A^{-3} + \sum_{i=1}^{l} \frac{2^i a_i^{l-1}(i+1)}{i! C^{i+2}} + E_o) P_1(cos\theta)$$

$$+(3a_2^l A^{-4} + \sum_{i=1}^{l} \frac{2^i a_i^{l-1}(2+i)!}{i! C^{3+i}} A) P_2(cos\theta) \qquad (A10)$$

The integral in eq.(3) should be performed in the following way

$$\int_v E_a^2 dv = \int_v E_r^2 dv = \int_0^A dA \int_v^{v+dv} E_r^2 dv \qquad (A11)$$

Now let $E_r = UP_1 + UP_2$ where

$$U = (2a_1^l A^{-3} + \sum_{i=1}^{l} \frac{2^i a_i^{l-1}(2+i)!}{i! C^{2+i}} + E_o) \qquad (A12)$$

$$Q = (3a_2^l A^{-4} + \sum_{i=1}^{l} \frac{2^i a_i^{l-1}(2+i)!}{i! C^{3+i}} A) \qquad (A13)$$

$$\int_v E_a^2 dv = \int_o^A (\frac{4\pi}{3} U^2 A^2 dA + \frac{4\pi}{5} Q^2 A^2 dA) \qquad (A14)$$

From this equation we could get modified formulas for different order of approximation by chosing l to be different numbers, for example when we chose $l = 0$, we could get the unmodified formula expressed in eq.(1). When we chose $l = 2$, after some tedious calculation we will get

$$(f_o^2 - f^2)/f_0^2 = \frac{4\pi}{3} 3E_o^2 A^3 (1 + \alpha) \qquad (A15)$$

where

$$\alpha = 4(A/C)^3 + 16(A/C)^6 + 55.636(A/C)^8 + 32(A/C)^9 \qquad (A16)$$

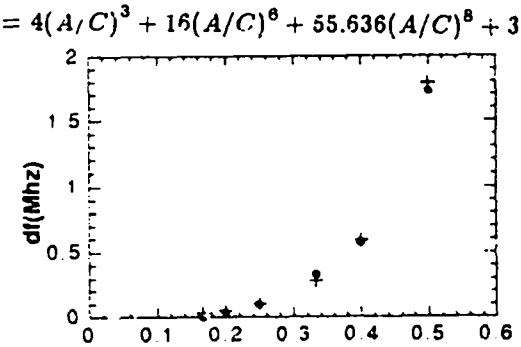

Fig.(1)

Appendix 2

In the same way as for the electric field, we consider the perturbation to the magnetic field by a small metallic ball. To start with we noted that Φ_m^l is the magnetic potential produced by the sphere introduced in the cavity. φ_m^{l-1} is the magnetic potential generated by the charges on the wall. Φ_{m1}^l is the magnetic potential inside the sphere by the magnetic field to be measured.

Therefore, to satisfy the boundary conditions on the surface of the sphere, that is R=A, and on the cavity wall $\Phi_m^{l-1} + \varphi_m^{l-1} = 0$ we have

$$\Phi_m^l - H_o R cos\theta + \varphi_m^{l-1} = \Phi_{m1}^l \qquad (A17)$$

$$\frac{\partial}{\partial R}(\Phi_m^l - H_o R cos\theta + \varphi_m^{l-1}) = 0 \qquad (A18)$$

where

$$\Phi^l = \sum_{n=0}^{\infty} b_n^l P_n(cos\theta) R^n \qquad (A19)$$

$$\Phi_{m1}^l = \sum_{n=0}^{\infty} a_n^l P_n(cos\theta) R^{-(n+1)} \qquad (A20)$$

$$\varphi_m^{l-1} = -\sum_{i=1}^{l} \frac{2^i a_i^{l-1}}{i!} \sum_{k=0}^{\infty} \frac{(k+i)!}{k!} P_k(cos\theta) \frac{R^k}{C^{k+1+i}} \qquad (A21)$$

From eqs.(A17) and (A18) we have

$$a_m^l = -\frac{A^{m+2}}{m+1}(H_o d_m 1 + \sum_{i=1}^{l} \frac{2^i a_i^{l-1}(m+i)! A^{m-1}}{i!(m-1)! C^{m+i+1}}) \qquad (A22)$$

When the sphere is far from the wall, Φ_m^l reduces to Φ_m^0[5], and

$$\Phi_m^0 = -H_o R cos\theta - \frac{H_o A^3 cos\theta}{2R^2} \qquad (A23)$$

By comparison between eqs.(A20) and (A23) we got

$$a_1^o = -\frac{H_o A^3}{2} \qquad (A24)$$

As for the magnetic field on the surface of the sphere, it only has component in θ direction, therefore we have

$$\int_v H_a^2 dv = \int_v H_\theta^2 dv \qquad (A25)$$

By asking approximation order $l = 1$ we got

$$H_\theta = -\frac{3}{2} H_o sin\theta + 3H_o sin\theta (A/C)^3$$

$$+(15cos^2\theta sin\theta - 3sin\theta)(A/C)^4 \frac{5}{2} H_o \qquad (A26)$$

$$\frac{(f_o^2 - f^2)}{f_o^2} = -\int_v H_\theta^2 dv = 2\pi \int_0^A \int_0^\pi H_\theta^2 A^2 sin\theta d\theta dA$$

$$= -\frac{4\pi}{3} \frac{3}{2} A^3 H_o^2 (1 + \beta) \qquad (A26)$$

where

$$\beta = -2(A/C)^3 + \frac{4}{3}(A/C)^6 + 16.9(A/C)^8 \qquad (A27)$$

where

$$\beta = -2(A/C)^3 + (4/3)(A/C)^6 + 16.9(A/C)^8 \qquad (6)$$

When the ball is far from the wall, eq.(M) will return to unmodified one[3]

$$(f_o^2 - f^2)/f_o^2 = -(3/2)H_o^2(4\pi/3)A^3 \qquad (7)$$

When there are both electric and magnetic fields at the same time where the ball is located, according to the theory expressed in eq.(2), combined perturbation formula is easily obtained

$$(f_o^2 - f^2)/f_o^2 = (4\pi/3)A^3 3(E_o^2(1+\alpha) - (1/2)H_o^2(1+\beta)) \qquad (C)$$

When the ball is far away from the wall, eq.(C) will be reduced to unmodified perturbation formula[3] as expressed

$$(f_o^2 - f^2)/f_o^2 = (4\pi/3)A^3 3(E_o^2 - (1/2)H_o^2) \qquad (8)$$

Till now we have given all the modified perturbation formulas of metal sphere.

Experiments

In the experiments we have used metal ball perturbing object to measure the electric field on the axis of the a pill box cavity. Before giving some experimental results we give some definitions to make the comparison between theory and experiment easier. We noted f_c to be the resonant frequency when the ball is in the center of the cavity.$\delta f_{th} = f_c - f_{th}(A/C)$ is the theoretical result, and $\delta f_{ex} = f_c - f_{ex}(A/C)$ is the experimental results. In the following Fig.(1) we will use only the notation δf but use + as theoretical value and · as experimental one. In Fig.(1) we used $A = 3mm$ copper ball to test Eq.(E). The result shows that theoretical modified perturbation formulas agree very well with the experimental results.

Conclusion

In this paper modified perturbation formulas concerning sphere metal perturbing object have been established and proved by the experiments. These formulas could be used in any kind of resonant cavity measurements.

Acknowledgements

The topic of this paper was introduced by Dr. Zhou Linong, IHEP, Beijing. The author benefited a lot from his guidance. Mr. Zhang Chuen-Sheng did the experiments with the author.

References

[1]Zhou Linong, Nuclear Energy Science and Technology, no. 3, 1981.
[2]William K. Saunders, IRE Convention Record, Part 8, P.81, 1955.
[3]L. C. Maier and J. C. Slater, J. Appl. Phys., Vol.23, no. 1, P.68, 1952.
[4]J. C. Slater, Microwave Electronics (D. Van Nostrand Company,Inc., New York, 1950), P.81
[5]W. K. H. Panofsky, Classical Electricity and Magnetism.

Appendix 1

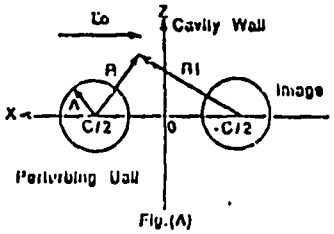

Fig.(A)

We treated this problem as a static one because the dimension of the perturbing object compared with the dimension of the wavelength of the microwave is very small. Therefore we have

$$\Phi_e^l = \sum_{n=0}^{\infty} a_n^l P_n(cos\theta) R^{-(n+1)} \qquad (A1)$$

$$\varphi_e^{l-1} = -\sum_{i=1}^{\infty} \frac{2^i a_i^{l-1}}{i!} \sum_{k=0}^{\infty} \frac{(k+i)!}{k!} P_k(cos\theta) \frac{R^k}{C^{k+1+i}} \qquad (A2)$$

where Φ_e^l is the potential produced by the sphere in the cavity. φ_e^{l-1} is the potential generated by the charges induced on the wall and l is the order of approximation.Both these potentials satisfy the boundary conditions on the wall

$$\Phi_e^{l-1} + \varphi_e^{l-1} = 0 \qquad (A3)$$

When the sphere is far from the wall, Φ_e^l will be reduced to Φ_e^o [6].

$$\Phi_e^o = -E_o R cos\theta + \frac{E_o A^3}{R^2} cos\theta \qquad (A4)$$

By comparing the two equations (A1) and (A4), we concluded that

$$a_1^o = A^3 E_o, a_n^o = 0, (n \neq 1), a_n^o = 0 \qquad (A5)$$

To satisfy the boundary conditions on the surface of the ball, that is $R = A$ we get

$$\Phi_e^l + \varphi_e^{l-1} - E_o R cos\theta = constant \qquad (A6)$$

$$\int\int_s \frac{\partial}{\partial R}(\Phi_e^l + \varphi_e^{l-1} - E_o R cos\theta) ds = 0 \qquad (A7)$$

and consequently we get

$$a_m^l = E_o A^3 d_{m1} + \sum_{i=1}^{l} \frac{2^i a_i^{l-1}(m+i)! A^{2m+1}}{i! m! C^{m+1+i}} \qquad (A8)$$

For the field on the surface of the ball in the direction of R, we have

$$E_r = \sum_{n=0}^{\infty}(n+1) a_n^l P_n(cos\theta) A^{-(n+2)}$$

$$\sum_{i=1}^{l} \frac{2^i a_i^{l-1}}{i!} \sum_{k=0}^{\infty} \frac{(k+i)!}{k!} P_k(cos\theta) + E_o P_1(cos\theta) \qquad (A9)$$

MEQALAC: A 1 MeV MULTICHANNEL RF ACCELERATOR FOR NITROGEN IONS

J.G. Bannenberg[1], W.H. Urbanus[1,3], R.G.C. Wojke[1,2], H. Klein[2], R.W. Thomae[2], A. Schempp[2], T. Weis[2], P.W. van Amersfoort[3]

1. FOM-Institute for Atomic and Molecular Physics, Association EURATOM-FOM, Kruislaan 407, 1098 SJ Amsterdam, The Netherlands
2. Institute for Applied Physics, J.W. Goethe-University, Robert-Mayer Strasse 2-4, 6000 Frankfurt/Main 1, Federal Republic of Germany
3. FOM Institute for Plasma Physics "Rijnhuizen", Association EURATOM-FOM, Edisonbaan 14, 3439 MN Nieuwegein, The Netherlands

Abstract

In the MEQALAC (Multiple Electrostatic Quadrupole Linear Accelerator) multiple N^+ ion beams are accelerated in 32 gaps which carry a rf voltage. The transverse focusing of the intense ion beams is achieved by means of sets of miniaturized electrostatic quadrupoles. Results are presented which show that the ion beams are accelerated to 1 MeV with an energy spread of less than 8%. The maximum time averaged beam current in a single channel is 0.2 mA; in four channels it is 0.56 mA. This is considerably less than the theoretically predicted current. It is shown that the smaller transmission is due mainly to misalignment of the quadrupole lenses.

Introduction

At the FOM-Institute in Amsterdam a MEQALAC for the acceleration of four intense N^+ ion beams has been built and is now in operation. In this type of rf accelerator, which is originally proposed by Maschke [1], the ions are accelerated in rf gaps while the transversely-directed space charge forces of the intense ion beams are opposed by the focusing forces of miniaturized electrostatic quadrupole lenses. These quadrupoles are mounted in the field-free drift spaces in between the rf gaps and arranged such that a large number of beams can be stacked into a small area, thus resulting in a high accelerated current. A further advantage of the MEQALAC set-up is that the rf power is used for acceleration only and not for transverse focusing, as in RFQ accelerators. Therefore, the acceleration efficiency of a MEQALAC is generally higher than for a RFQ [2].

A schematic set-up of the FOM-MEQALAC experiment is schematically shown in fig. 1. The experiment consists of a bucket-type plasma ion source with a four-grid, four-channel extraction system, a matching section, a Low Energy Beam Transport (LEBT) section with a buncher, and the rf accelerator section. The ion source produces both N^+ and N_2^+ ions, in a ratio of 3:2. With an extraction aperture of 4.5 mm a total ion current of 4.8 mA per channel is transported through the LEBT. Each of the four quadrupole channels has a radius of 3 mm.

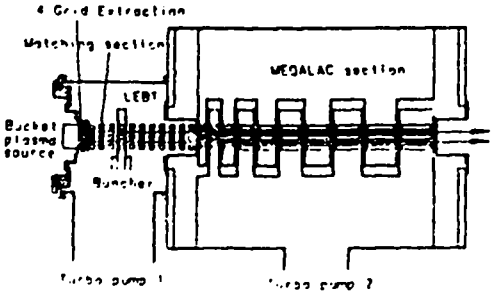

Fig. 1. Set-up of the FOM-MEQALAC experiment.

Acceleration from 40 keV to 1 MeV of the N^+ ion beams takes place in the 32 rf gaps of the accelerator section. The distance between the gaps is such that ions pass this distance in half a rf period and experience an accelerating field in all gaps. A MEQALAC is thus a fixed velocity maschine. The rf gaps are part of a modified interdigital-H-resonator, which is excited in the TE_{111} mode [6,7]. The resonance frequency is 25.4 MHz. The length, width and height of the resonator are 1.7, 0.5 and 1.0 m, respectively, and the length of the acceleration structure is 1.4 m. The rectangular cross-section of the resonator offers the possibility to vary the resonator width. This way, the inductance and thus the resonance frequency can be varied such that the ion energy can be varied.

Theoretical Background

In a rf accelerator the ion beam current is limited either transversely or longitudinally. The transverse current limit is determined by, amongst others, the space charge forces of the ion beam, the external transverse focusing forces of the electrostatic quadrupole lenses, and the channel acceptance which is a function of the channel dimensions and the quadrupole voltage [8]. A measure for the external transverse focusing forces is the so-called zero-current phase advance per cell, μ_{0T}, which is proportional to the quadrupole voltage. The transverse current limit, I_T, for our MEQALAC is shown in fig. 2. First I_T increases with μ_{0T} because the external focusing forces increase allowing a higher space charge density in the beam, and for $\mu_{0T} > 90^o$ I_T decreases due to the decreasing acceptance.

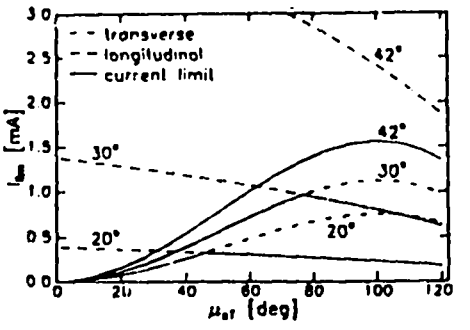

Fig. 2. The transverse, the longitudinal and the resulting total current limit for the MEQALAC 1-MeV N^+ accelerator, according to equations as given by Reiser [8]. For $\phi_s = -42^o$ the current is always transversely limited.

The longitudinal current limit is a function of, amongst others, the synchronous phase, ϕ_s [8]. For a large gap voltage and thus for a large rf power coupled into the resonator $|\phi_s|$ is high, which results in a large longitudinal current limit. This is also illustrated in fig. 2, which gives the longitudinal current limit for $\phi_s = -20^o$, -30° and -42°. This figure shows that for typical

operating values, e.g. $\phi_s = -42^o$ and $\mu_{oT} = 60^o$, the current is transversely limited.

Multiparticle simulations with PARMILA for the transmission of MEQALAC, both with and without the use of a buncher, are given in fig. 3. The simulations show that with increasing space charge the bunching becomes less efficient.

The energy and the energy spread of the accelerated ion beam have been simulated by means of PARMILA multi-particle simulations. In fig. 4 energy spectra are given for various values of the maximum gap voltage.

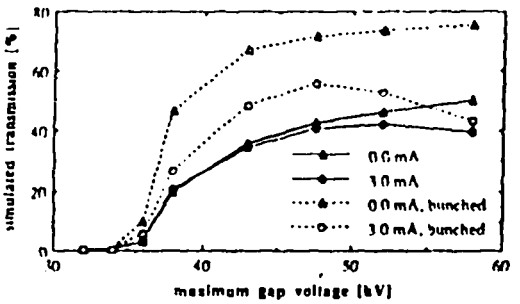

Fig. 3. The transmission of a zero current and a 3 mA N^+ ion beam through the MEQALAC section as a function of the maximum gap voltage, according to PARMILA multi particle simulations. The data refer to a single channel. For ε and μ_{0T} the values 30 π mm mrad and 84° are taken, respectively.

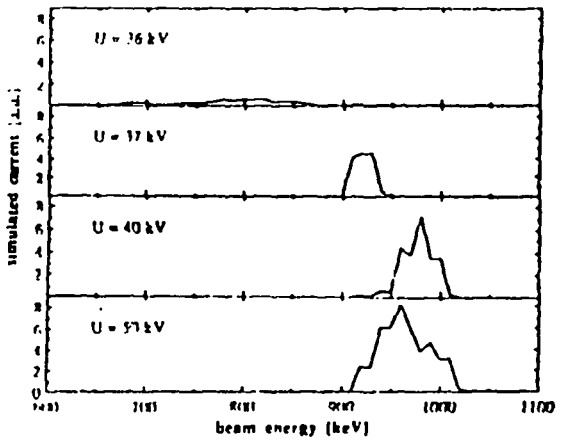

Fig. 4. Energy spectra of the accelerated beam as simulated by means of the three-dimensional code PARMILA. The injected N^+ current is 3 mA and the unnormalized rms emittance of the injected beam is 20 π mm mrad.

Experimental Results

The time averaged beam current and the ion energy are measured by a water-cooled Faraday cup, which can handle four 1.5-mA, 1-MeV ion beams, and an electrostatic energy analyzer, respectively. The energy analyzer can accept an ion beam with an energy width ΔE/E of 20%, measured with 21 detector channels behind the cylindrical analyser.

For most measurements only a single beam channel is used and the beam is not bunched prior to injection into the accelerator. The accelerated single beam current is shown in fig. 5, for an injected current of 4.8 mA, which contains N^+ and N_2^+ ions. The unnormalized rms emittance of the injected beam is some 20 π mm mrad. The current is shown as a function of the quadrupole voltage of the last 16 cells of the MEQALAC section. In the first 15 cells the quadrupole voltage is kept around 4 kV since measurements showed that this voltage gives the highest transmission through the first 15 cells. Results are given for normal polarity, which means that the first quadrupole is focusing in the x-direction, and for inverse polarity, when the first quadrupole is focusing in the y-direction.

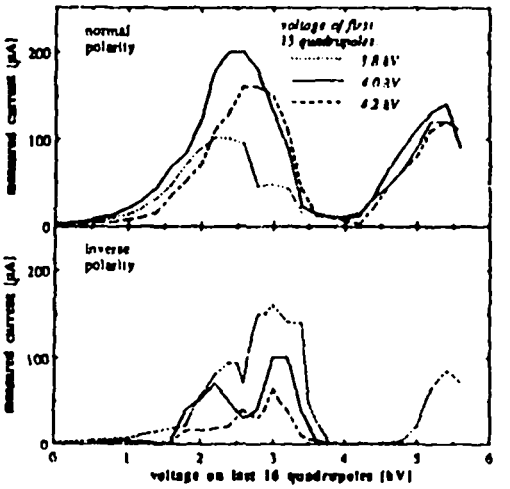

Fig. 5. The measured N^+ ion current of a single accelerated beam as a function of the quadrupole voltage in the last 16 cells of the MEQALAC. The quadrupole voltage in the first 15 cells is indicated. The total ion current (60% N^+, 40% N_2^+) is 4.8 mA per channel and the unnormalized rms emittance of an injected beam is some 20 π mm mrad.

In fig. 6 the accelerated current is shown as a function of the rf power coupled into the resonator. This measurement is done for the same injected current as given at fig. 5 and for optimum setting of the MEQALAC quadrupole voltages.

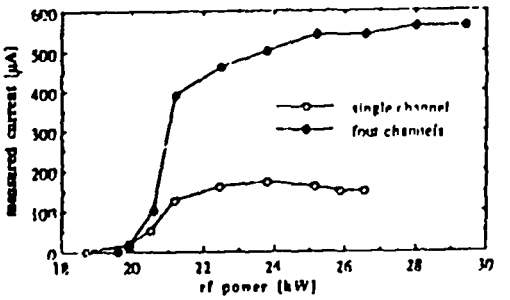

Fig. 6. The measured accelerated N^+ ion current for a single beam and for four beams as a function of the rf power coupled into the resonator. The beam properties are as given in fig. 5.

Time resolved current measurements with a fast 50 ohm Faraday cup show the microstructure of the current consisting of pulses with 10 nanosec halfwidth at 40 nanosec interval.

Fig. 7 shows energy spectra of the accelerated beam for various values of the rf power coupled into the resonator. The injected beam current is 4.8 mA.

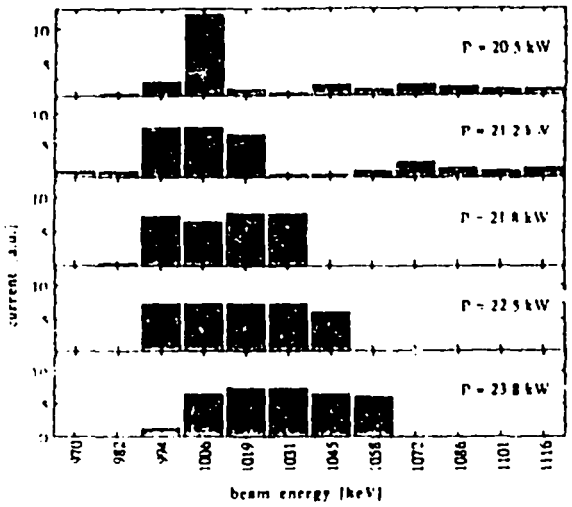

Fig. 7. Measured energy spectra as a function of the rf power coupled into the resonator. The resolution of the detector is 13 keV/channel. The beam properties are as given in fig. 5.

Discussion and Conclusion

We have demonstrated that our MEQALAC accelerates N^+ ions to 1 MeV. The energy spread corresponds well with values predicted by PARMILA simulations, see fig. 4 and fig. 7. With respect to the accelerated current we mention that the measured current is less than the current as predicted by a theoretical model and by PARMILA simulations which are performed for a perfectly aligned system. Further, we mention that optimum beam current was reached when the quadrupole voltages are higher (4 kV) in the first half of the accelerator section than in the second half (2.4 kV), which can be explained as follows.

In the MEQALAC both N^+ and N_2^+ ions are injected but only the N^+ ions are accelerated in successive rf gaps. These N_2^+ ions are lost during transport. Furthermore, also the N^+ ions outside the longitudinal acceptance are lost rapidly. Therefore, the space charge density of the beam strongly decreases within a few cells. As a result, the space charge depressed phase advance per cell, μ, changes during transport, which causes mismatch. However, by adjusting the external focusing forces, i.e. the quadrupole voltages, the phase advance per cell can be kept roughly constant.

The dependency of the transmitted current on the misalignment of the quadrupoles has been investigated by a simple simulation model which treats the quadrupole lenses as thin lenses and does not take space charge into account. In fig. 8 the transmission as a function of the quadrupole voltage is shown for an average mis-alignment, $\sqrt{\langle x^2 \rangle}$, $\sqrt{\langle y^2 \rangle}$, of 0.1 mm and 0.2 mm. Without misalignment the radial transmission is 100 % for quadrupole voltages between 2 kV and 5 kV; for lower voltages the focusing forces are too weak, and for higher voltages overfocusing occurs. For a misalignment of 0.1 mm the transmission in the optimum focusing region reaches values between 60 % and 100 %. For a misalignment with twice that value the transmission in the same voltage region is considerably less and changes drastically from 0 % to 80 % for only small differences in quadrupole voltage. The strong dependency of the transmitted current on the polarity indicates that misalignment plays an important role.

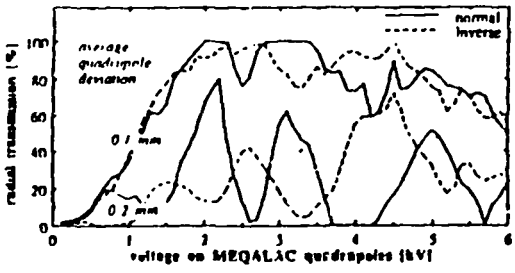

Fig. 8. The simulated transmission of a N^+ ion beam taking misalignment into account, as a function of the quadrupole voltage of the MEQALAC. The average misalignment in x and y-direction, $\sqrt{\langle x^2 \rangle}$ and $\sqrt{\langle y^2 \rangle}$, respectively, is indicated. The solid and dotted curves refer to various polarities of the quadrupole lenses, see text.

Comparison of the simulated beam current and the measured current (see fig. 5) shows that in spite of the limitations of the model the measured beam current as a function of the quadrupole voltages is properly explained as being a result of imperfect alignment. It is therefore reasonable to assume that a higher current can be obtained once the alignment of the system is improved.

Acknowledgements

This work is part of the research program of the association agreement between the *Stichting voor Fundamenteel Onderzoek der Materie (FOM)* and EURATOM, with financial support from the *Nederlandse Organisatie voor Wetenschappelijk Onderzoek (NWO)*, the *Nederlandse Ministerie van Onderwijs en Wetenschappen* and EURATOM.

References

[1] A.W. Maschke, Brookhaven Natl. Lab. rep. BNL-51209 (1979).

[2] W.H. Urbanus, R.G.C. Wojke, R.J.J.M. Steenvoorden, J.G. Bannenberg, H. Klein, A. Schempp, R.W. Thomae, T. Weis and P.W. van Amersfoort, Nucl. Instr. and Meth. A290 (1990) 1.

[3] R.G.C. Wojke, W.H. Urbanus, J.G. Bannenberg, H. Klein, A. Schempp, R.W. Thomae, T. Weis and P.W. van Amersfoort, Nucl. Instr. and Meth. A288 (1990) 329.

[4] W.H. Urbanus, R.G.C. Wojke, R.J.J.M. Steenvoorden, J.G. Bannenberg, H. Klein, A. Schempp, R.W. Thomae, T. Weis and P.W. van Amersfoort, Nucl. Instr. and Meth. A276 (1989) 433.

[5] F. Siebenlist, R.W. Thomae, P.W. van Amersfoort, F.G. Schonewille, E.H.A. Granneman, H. Klein, A. Schempp, T. Weis, Nucl. Instr. and Meth. A256 (1987) 207.

[6] R.G.C. Wojke, W.H. Urbanus, R.J.J.M. Steenvoorden, J.G. Bannenberg, H. Klein, A. Schempp, R.W. Thomae, T. Weis and P.W. van Amersfoort, Nucl. Instr. and Meth. A278 (1989) 318.

[7] W.H. Urbanus, R.G.C. Wojke, J.G. Bannenberg, H. Klein, A. Schempp, R.W. Thomae, T. Weis and P.W. van Amersfoort, in Proc. 1st European Part. Accel. Conf., ed. T. Tazzari, Rome (1988), World Scientific, Singapore (1989) 427.

[8] M. Reiser, J. Appl. Phys. 52 (1981) 555.

DEGRADATION OF NIOBIUM SUPERCONDUCTING RF CAVITIES DURING COOLING TIME

B. Aune, B. Bonin, J.M. Cavedon, M. Juillard, A. Godin,
C. Henriot, Ph. Leconte, H. Safa, A. Veyssière, C. Zylberajch
Département de Physique Nucléaire
Service des Techniques d'Accélération Supraconductrices
Centre d'Etudes Nucléaires de Saclay, 91191 Gif sur Yvette
FRANCE

Abstract

We report evidence that Niobium cavities that spend hours at temperatures between 100 K and 200 K, before completion of cooling, build up systematically an additional resistance on their RF surfaces, destroying their quality factor. They recover totally by a warm up to room temperature. Fast cooling prevents this phenomenon to develop. An attempt is done to characterize and modelize it.

Introduction

Continuous efforts in RF superconductivity technology have given enough confidence to start building large particle accelerators using Niobium cavities.

The design values commonly accepted are an accelerating field : E_{acc} = 5 MeV/m and a quality factor : $Q_0 = 2$ to 3.10^9.

Much higher performances have been obtained in laboratory tests (10 to 20 MeV/m with Q above 10^{10}). However, bad reproducibility has plagued them. Recently, erratic degradations of vacuum sealed cavities have been reported by different laboratories.[1,2,3,4] All laboratories present at a recent meeting at Cornell have shown concern on this subject.[5]

Investigations on this phenomenon have been initiated at Wuppertal.[2]

We report here on systematic experiments undertaken at Saclay that prove the existence of a reproducible phenomenon. We report also on the re-analysis of previous Saclay experiments that confirm it. We finally attempt to interpret the data on the basis of a simple model, assuming the formation of a uniform layer of a weak superconductor on top of Niobium surface.

Experimental evidence

Dedicated experiments were performed during summer 1990 on a 1.5 GHz single cell accelerating cavity, and on a pill-box cavity resonating at 4 GHz and 5.6 GHz (TE_{011} and TE_{012} modes).

a) Fabrication and preparation of cavities

A systematic procedure, mostly inherited from CERN, has always been followed for fabricating and preparing the cavities at Saclay. They are made by hydroforming and electron beam welding of high purity Niobium sheets (thickness : 2 mm, RRR 200 to 300). The surface preparation consists of a buffered chemical polishing (50 µm) in a 1:1:2 solution of $HF:HNO_3:H_3PO_4$ followed by rinsing in ultrapure water. Drying and assembly take place under laminar air flow in a class 100 clean room. The final mounting on the cryostat vacuum system is made in front of a dust free laminar flow. The cavity is evacuated by a turbomolecular pump, then by an ion pump down to 10^{-7} to 10^{-8} mb, before inserting in a cryostat and cooling down.

b) Dedicated tests

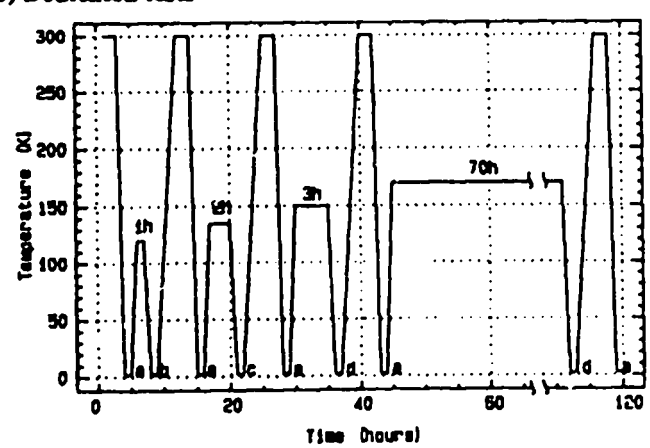

Fig. 1. Thermal cycles on the 1.5 GHz cavity

We have observed strong variations of the quality factor Q of the two cavities after particular thermal cycles. Figure 1 shows all the thermal cycles done on the 1.5 GHz cavity. During all cycles, the cavities remained under sealed ultra-high vacuum. The results can be summarized as follows :

1 - A fast cool down from 300 K to 1.6 K (in about 1 hour) gives always the same Q characteristics : Q value is larger than 10^{10} and does not vary significantly upon the

applied RF field up to a limit (quench or electron loading) : see figure 2, curve a.

2 - A partial warm up from 1.6 K to some intermediate temperature for a variable time duration followed by a new cool down to 1.6 K gives always degraded characteristics. Temperature plateaus were controlled by coarse manual regulation. They lasted from 1 hour to 70 hours at temperature levels ranging from 120 K to 170 K. The 70 hours long plateau did not result in a larger Q degradation than the 3 hours one. Shorter plateaus lead to smaller Q degradations. Curves b, c and d on figure 2 show different levels of Q degradation.

In such cases, one always notices a particular characteristic of the Q behaviour : starting at low field from an already low Q, it steps down to a still much lower level for a surface magnetic field of about 6 mT at 1.6 K and remains then approximately constant.

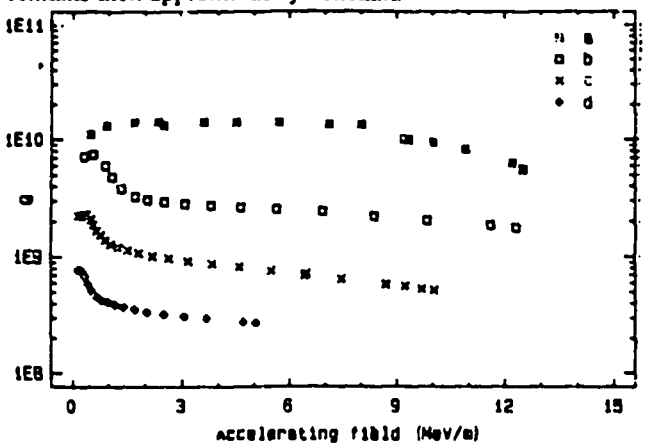

Fig. 2. Q(E) after thermal cycles. Labels refer to fig. 1.

Table 1 shows the corresponding surface resistances for 2 cavities tested at three different frequencies. R0 stands for no degradation, R1 for degradation at low field and R2 for degradation at high field.

TABLE 1
Measured surface resistances

F GHz	R_0 nΩ	R_1 nΩ	R_2 nΩ
1.5	20	350	1000
4	75	7100	13800
5.6	130	16600	24000

3 - A complete recovery of the original characteristics is always observed after a room temperature warm up. An extremely good reproducibility of the Q characteristics is observed.

c) A weak superconductor ?

In order to get better insight on the phenomenon, the surface resistances have been measured as a function of temperature between 4.2 K and 1.6 K. An "additional resistance" is calculated by subtracting the Niobium resistance (as measured in the non-degraded case) from the resistance measured in the degraded case.

Figure 3 shows the "additional resistance" as a function of temperature. The change of slope at 2.8 K and the field dependence (fig. 2) suggest the presence of a weak superconductor with a critical temperature of about 2.8 K and a critical magnetic field of about 9 mT.

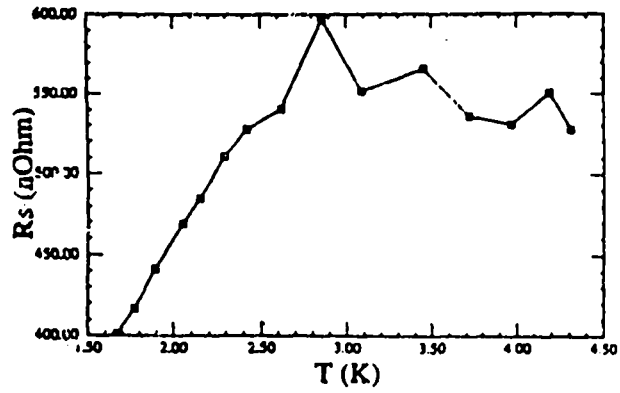

Fig. 3. Additional resistance for test d of figs. 1 and 2.

Analysis of previous experiments

Erratic results on the Q behaviours, common in many laboratories, were more frequent at Saclay. Some of the Q degradations were traced back to accidental pollutions, but many of them remained unexplained. Most of the puzzling results were obtained in a particular cryostat, having two possible cooling speeds. Its slow cooling procedure (LN_2 precooling) brings the cavities to the very conditions that degrade the Q.

A scan through the records of the 37 tests in this cryostat shows that :

- 11 fast cooldowns lead to 100 % success,
- 16 slow cooldowns lead to 25 % success,
- 10 unidentified tests lead to 10 % success.

A complete scan of 105 cold tests performed at Saclay with 3 cryostats confirms the disastrous effect of too long a cooling time, except for a few cases.

Discussion

We have established that some large additional resistance appears reproducibly whenever a cavity stays long enough at temperatures around 150 K. This resistance disappears totally after warm up at 300 K.

One can think of a particular resistive component appearing either in the Niobium or in the Niobium oxide

outer layer. This component should be unstable at 300 K and should build up around 150 K and stop growing at lower temperatures. It is present over all the surface, as shown by the quasi-uniform heating of such degraded cavities. The additional resistance has a frequency-squared dependence. This component behaves like a weak superconductor.

In order to derive parameters of this hypothetical component, we have used a model[6] which calculates the surface resistance of Niobium on which a thin uniform layer of a weak superconductor is superimposed. Figure 4 shows the experimental surface resistance at 4 GHz as a function of temperature together with computed values for a layer of a thickness of 28 nm and a conductivity at 4 K of $1.6\ 10^8\ \Omega^{-1}m^{-1}$.

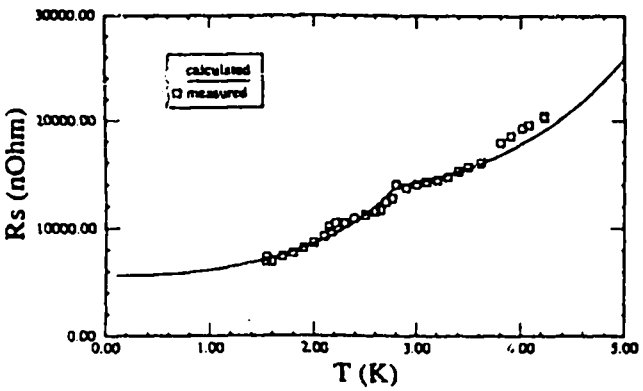

Fig. 4. Surface resistance measured at 4 GHz, and fit by a thin layer model.

The Sommerfeld constant of a superconductor deduced from the relation :

$$H_C = (\gamma/2\mu_0)^{1/2}\, T_C$$

gives in our case a value : $\gamma = 0.17$ mJ.mole^{-1}.K^{-2}

This value is much smaller than the one of Nb ($\gamma = 7.82$). This leads us to the idea of a polluted state of Niobium.

Röth et al[2] have proposed, as a candidate for the weak superconductor, a Nb_4H_3 phase, which they quote to be unstable above 220 K. This is a very interesting possibility in spite of a quoted critical temperature of only 1.2 K.

Questions

Many questions remain to answer :

Are the elements entering in the formation of the postulated component coming from the other parts of the vacuum system or are they present permanently in the Niobium surface ?

What is the exact temperature range where this component builds up ? At what speed does it form ?

Why did some cavities give good results in spite of a slow cooldown ? What are the initial conditions that play a key role in the apparition of the phenomenon ?

Why has this effect never been observed at CERN[7] or KEK ? Would it be because of the frequency scaling ?

Conclusion

A much better control on Q characteristics of superconducting cavities is to be expected from the knowledge of this effect. An immediate application to existing cavities and accelerators can improve their performances. Cryogenics costs can be dramatically reduced for future facilities, either by including constraints on the cooling speed of the cavities, or by preventing the effect to show up.

Finding an antidote to this poison will need a thorough understanding of surface physics at low temperatures.

Acknowledgements

We thank all the members of the Groupe d'Etudes des Cavités Supraconductrices for their enthusiastic support, especially during these summer tests.

References

1. D. Gräf (Private communication).
2. R. Röth et al. "Suppression of field emission in superconducting S-band accelerating structures". 2nd European Accelerator Conference Nice (1990).
3. B. Aune et al. "Superconducting RF activities at Saclay : status report". 4th Workshop on RF superconductivity. Tsukuba, Japan (1989).
4. D. Proch (Private communication).
5. TESLA meeting, Cornell, July 1990.
6. H. Safa, to be published.
7. H. Lengeler (Private communication).

Tuesday

Session TU1
Chairman: Y. Hirao
Invited Papers

REVIEW OF NEGATIVE HYDROGEN ION SOURCES

Charles W. Schmidt
Fermi National Accelerator Laboratory*
Batavia, Illinois 60540

Abstract

In the early seventies, significant discoveries for H^- ion sources were made at Novosibirsk. These and many improvements which followed have led to useful accelerator sources. With these sources charge-exchange injection into circular accelerators has become desirable and routine. This paper reviews the major developments leading to practical H^- sources. Different types and variations of these sources with some basic physics and operation will be described. The operating parameters and beam characteristics of these sources will be given.

Introduction

The usefulness of negative hydrogen ions has been recognized for several decades for a variety of purposes. Early Tandem Van de Graaff Accelerators used proton sources followed by an attachment canal to produce several hundred microamps of H^- ions.[1] The H^- ions were accelerated to a high potential, stripped to protons and accelerated to ground, gaining an energy of twice the potential.[2] Soon after, H^- ions were used with cyclotrons so extraction could be achieved by stripping to neutrals or protons. Penning type sources which fit within the Dees produced five milliamps of H^- current.[3]

Linear accelerators have long been used as proton injectors to synchrotrons. It was recognized early that H^- ions would be useful for charge-exchange injection into circular accelerators.[2] Intensity and reliability of H^- sources limited this possibility until the seventies when H^- injection was accomplished at the Argonne ZGS.[4] At that time H^- ions were achieved using a proton source with a charge-exchange cell.[5]

The next major step in H^- source development occurred in the Soviet Union at Novosibirsk. There, improved geometries and the addition of cesium produced intense sources with an output of several Amperes per square centimeter of aperture.[6] Geometries of both the Penning and magnetron forms were studied. These sources have become known as surface-plasma sources (SPS).

The Soviet work was adopted in the U.S. at Brookhaven to produce high current sources for neutral beam injectors for the confinement fusion program.[7] At Los Alamos the Penning geometry was studied to produce an accelerator source [illegible] current and duty factor.[8] At Fermilab the research magnetron of the Brookhaven group was redesigned into an operational source for pulsed applications with good current and low duty factor.[9] Significant improvements to this source design at Fermilab[10] and Brookhaven[11] have made the magnetron a highly useful H^- source for many [illegible] synchrotron injectors.[10-13] The Penning sources have been useful in high-duty and high-brightness applications.[14,15]

While the magnetron and Penning sources were being pursued for accelerators, a large potentially d.c. multicusp surface-plasma source originated at Berkeley for the fusion program.[16] Modified versions of this source were studied and used for accelerators.[17,18]

Parallel to the SPS effort, a French group at Ecole Polytechnique near Paris vigorously pursued obtaining H^- ions from a hydrogen plasma.[19] This effort, which has led to the volume source, is being studied at several laboratories.[20,21]

* Operated by the Universities Research Association under contract with the U.S. Department of Energy

This paper will deal primarily with the modern surface-plasma and volume-process sources useful or anticipated for accelerators such as linacs. These sources can produce reliable pulsed H^- beams from ≈10 to 100 mA with normalized emittances of 0.2 to 2 π mm-mr for 90% of the beam.

Where emittances are in other than 90% values, the given emittance will be quoted and a value for 90%, assuming a Gaussian distribution will be given in brackets for reference to other sources. [$\varepsilon_{(90)} / \varepsilon_{(rms)} = 4.6$, $\varepsilon_{(90)} / \varepsilon_{(95)} = 0.77$].

Basic Principles

Surface-Plasma Sources

The surface-plasma sources all produce H^- ions by the interaction of energetic plasma particles with a surface (Fig. 1). These particles, having energies of several tens to several hundred eV, are produced in a plasma near the surface. This surface is typically a cathode electrode. The incident particles may be protons, ionized hydrogen molecules, heaver positive ions, such as cesium, or energetic neutral atoms or molecules that may occur in the plasma. Upon striking the surface they may desorb hydrogen atoms which can leave the surface in several states, occasionally as an H^- ion. Also, protons or neutral hydrogen may reflect from the surface and acquire sufficient electrons to become an H^- ion. To improve the possibility that H^- ions will leave the surface and not lose electrons, cesium is added to the source to partially cover the surface and lower its work-function. As cesium covers the surface, typically tungsten or molybdenum, the work-function decreases from above 4.5 eV to ≈1.8 eV at 0.6 of a monolayer of cesium and then rises to about 2 eV for one monolayer or greater of cesium. To minimize the work-function and maximize the H^- yield the cesium feed is controlled. Cesium also ionizes easily to produce electrons and ions in the plasma improving the source stability. After formation the H^- ions pass through the plasma to the anode aperture and are extracted. Some ions incur collisions in the plasma and are lost or destroyed. Others may charge-exchange with neutral hydrogen atoms to form thermal H^- ions. These thermal ions are the basis for [illegible] source. Since [illegible] extract negative ions, electrons are [illegible] source and [illegible] dealt with.

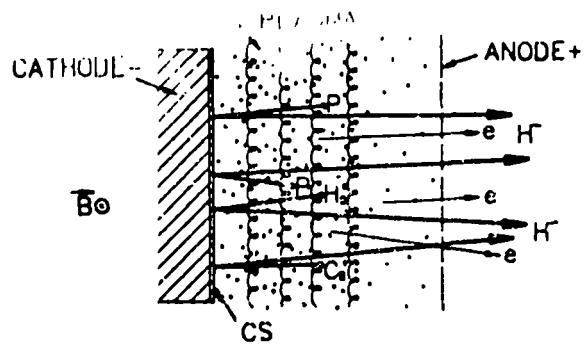

Fig. 1. Surface-plasma production of H^- ions.

Volume Sources

In volume sources, H^- ion formation relies on the greatly increased cross-section for the dissociative-attachment reaction when molecules are excited to high vibrational states. During collisions with walls or energetic electrons (>5 eV), hydrogen

molecules are excited to high vibrational states (v">6). For such molecules the cross-section for the dissociative-attachment reaction, $e + H_2(v") \rightarrow H^- + H$, $e \leq 1$ eV, increases more than five decades for v"=6 and continues to rise for higher states.[22] Although the destruction reactions: neutralization ($H^- + H^+ \rightarrow H + H$), associative detachment ($H^- + H \rightarrow H_2 + e$), etc.; can be serious, the increased production due to high vibrational states can give a significant population of H^- ions in the plasma.

The source therefore takes on the geometry of a two region chamber [22] (Fig. 2). The first region contains a broad range of electrons emitted from hot cathodes or filaments. Here energetic electrons and wall collisions create high molecular vibrational states: $e + H_2(v"=0) \rightarrow e + H_2(v")$, $e > 5$ eV. The second region is separated from the first by a magnetic filter so only low energy electrons (≤ 1 eV) can pass along with molecular hydrogen in various states. In the second region H^- ions are more readily created than destroyed forming a significant fraction of the plasma from which they are extracted. To extract the H^- ions with minimum electrons, a magnetic filter is again used at the extraction region.

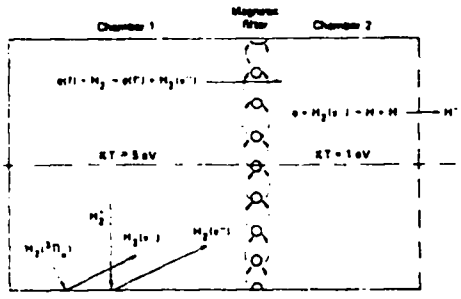

Fig. 2. Volume production of H^- ions.

Surface-Plasma Sources

Three basic geometries of H^- surface-plasma sources have been built for accelerators: magnetron, Penning and multicusp sources. The magnetron tends to be a low-duty-factor source and has been used with several linacs as injectors to synchrotrons. The Penning source can operate at much higher duty, possibly d.c. and tends to produce the brightest beam. It has been used on high duty-factor linacs and for stringent beam requirements. The multicusp source has its best application as a high-current, large-aperture d.c. source useful for neutral beam fusion injectors. It has been used on high duty-factor linacs. A discussion of these sources will show their typical operating characteristics and differences.

Magnetron H^- Source

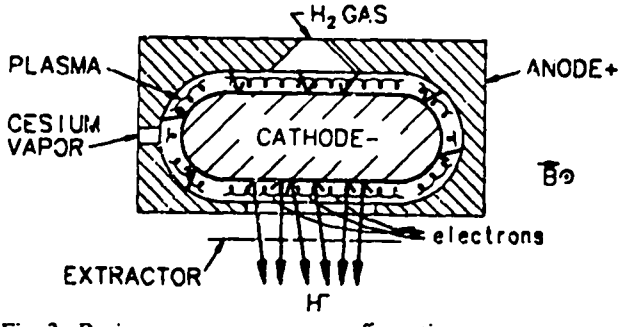

Fig. 3. Basic magnetron source configuration.

The magnetron source (Fig. 3) consists of a central oval cathode, the active surface, surrounded by an anode. A magnetic field passes through the source parallel to the cathode axis, perpendicular to the anode-cathode electrical field. This ExB configuration is highly efficient at confining electrons and producing dense plasmas. Ions and energetic particles from the plasma strike the cathode and reflect or desorb hydrogen atoms producing H^- ions. The H^- ions go through the plasma to the anode gaining energy and where possible pass through the anode aperture to be accelerated through the extractor. In this source the anode-cathode gap is small, typically 1 mm, to avoid significant destruction of the H^- ions while traveling through the plasma. Nevertheless, some ions are lost or charge-exchange with neutral thermal atoms: $H^-(fast) + H(slow) \rightarrow H(fast) + H^-(slow)$. These thermal ions can be extracted to form a beam of greater brightness. In the magnetron, energetic ions are extracted at low pressure (≈400 mTorr) where the source normally operates. At high pressure, low-energy ions dominate, but the gas consumption is large.

Hydrogen gas is introduced in the rear of the source by a closely connected pulsed gas valve. Since these sources are small and operate at low duty factor, the small volume allows the gas to be pulsed into the source to minimize vacuum requirements.[23] Cesium is obtained by heating metallic cesium in an oven at 150-200°C.[23] All parts of the cesium supply system must be maintained above the oven temperature to prevent condensation of the cesium. The vapors enter the source and coat the cathode surface. The cesium usage is <1 mg/hr. In operation the source operates at 350 to 450°C for good surface conditioning and sufficient cesium ions in the plasma. Heating of the source comes from the plasma arc power plus a small external heater if needed.[10] The plasma power, passive cooling and permissible source temperature limit this source to low-duty operation.

To increase the ions passing through the anode aperture, the cathode is curved to give focusing from the cathode to the anode.[24] With slit apertures the curving is a groove on the cathode parallel to the aperture. In the newer magnetrons circular apertures and extraction geometries are used and the cathode is dimpled behind the anode aperture.[11] These changes have reduced the arc current, increased the beam current and improved the beam optics.

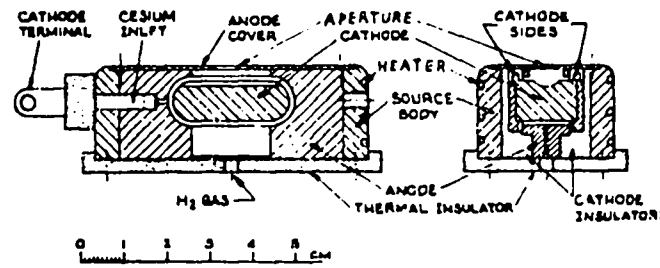

Fig. 4 The Fermilab H^- magnetron source.

Operating magnetron sources produce a beam current of ≥50 mA. In the Fermilab source [9] (Fig. 4) the beam is extracted at an energy of 18 keV from a 1-mm x 10-mm aperture. This large asymmetry creates a stronger space charge force in the narrow or perpendicular direction to the slit than in the parallel direction. To compensate for this difference and obtain a nearly circular beam, a 90°-bending magnet with a radius of 8 cm and a gradient index, $n = -rdB/Bdr \approx 1$, is used after the extractor. This magnet has pole extensions to provide the source field. Following the bending magnet, the beam enters the primary accelerating column and is accelerated to 750 keV (Fig. 5). At 750 keV the normalized emittance for 90% of the beam is $\varepsilon_{n\,horz\,(90)} = 0.9\,\pi$ mm-mr, $\varepsilon_{n\,vert\,(90)} = 1.5\,\pi$ mm-mr.

The Brookhaven source operates with a circular extraction geometry sized to produce >50 mA and extracts at 35 keV.[11] There is no bending magnet following the source. This arrangement produces a circular beam with emittance in both planes of $\varepsilon_{n\,(90)} = 1.1\,\pi$ mm-mr. The circular beam is matched to an RFQ by a 2-meter magnetic-focusing line (Fig. 6). The RFQ accelerates the beam to 750 keV.

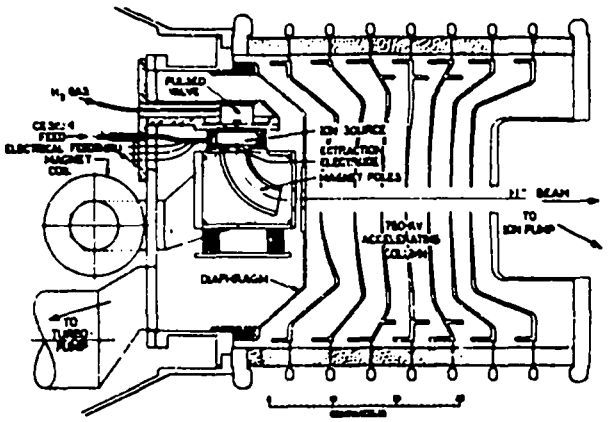

Fig. 5. The Fermilab H^- 750-keV preaccelerator.

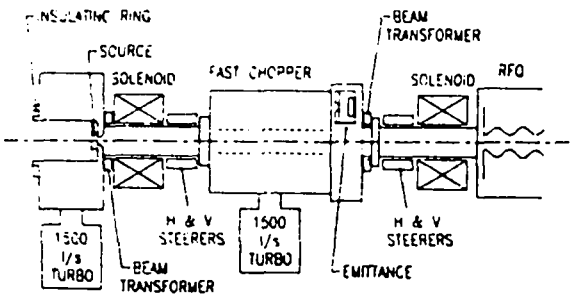

Fig. 6. The Brookhaven H^- source and transport line.

The magnetron source has been only used for pulsed operation at low duty factor. At Fermilab the beam-pulse width is up to 66 μs at a repetition rate of 15 Hz.[10] Brookhaven uses a 600-μs beam pulsed at 5 Hz [25] and Argonne operates at 30 Hz with 90-μs pulse width.[12] DESY uses even lower duty for the HERA injector [13] and pulses the source are between beam pulses to maintain source temperature.

Lifetimes for the source range from four to six months at Fermilab to about one year between changes at Argonne. Failures occur due to erosion of the cathode and the buildup of erosion products in the source. The piezoelectric pulsed gas valve is an occasional cause of early breakdown. Auto fuel injectors have recently been used for gas valves with good success.[26]

The magnetron, originally developed by the Novosibirsk group, is referred to as the planotron source in Soviet literature. A modification has produced the semiplanotron. The semiplanotron [27] (Fig. 7) is similar to the planotron but uses only the front portion where the plasma is produced.

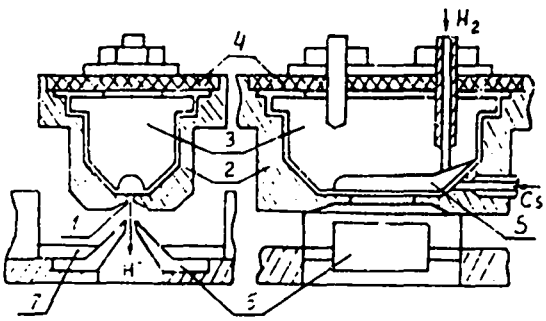

Fig. 7. The semiplanotron source. 1. emission slit, 2. anode, 3. cathode, 4. insulator, 5. groove, 6. extractor, 7. steel inserts.

Penning H^- Source

The Penning source geometry (Fig. 8) resembles a right circular cylinder as an anode with isolated caps at each end of the cylinder which are the cathodes. A magnetic field passes through the source parallel to the anode axis. In this arrangement the electric and magnetic fields are parallel. Electrons created in the source oscillate from cathode to cathode, trapped in the magnetic field lines, to produce a dense plasma. Positive ions from the plasma are accelerated into the cathode and, as in the magnetron, produce primary H^- ions coming from the cathode surfaces. Cesium is added to the source to lower the surface work-function and increase the H^- yield.

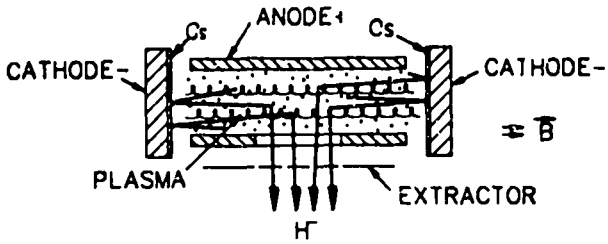

Fig. 8. Basic Penning source geometry.

In the Penning source, ions are extracted from an opening in the anode wall. Because of the aperture orientation it is difficult for the primary H^- ions to pass favorably through the opening. To obtain a useful beam, primary H^- ions must charge-exchange with thermal hydrogen atoms, $H^-(\text{fast}) + H(\text{slow}) \rightarrow H(\text{fast}) + H^-(\text{slow})$, to form slow H^- ions which can migrate to the aperture and be extracted. As in the magnetron, slit apertures of large asymmetry are used for the Penning source and strong-focusing bending magnets are used to handle the beam forces. Circular apertures are also being used with minimum bending to give higher quality beams.[28]

Beam currents of 50 to 100 mA is typical for Penning sources in operation or under study. Since the cathodes are accessible they can be cooled or rotated to produce sources of high duty factor and possibly d.c. operation. Because the ions leaving the source originate from thermal atoms their transverse energy is low and small emittance is typical of the Penning source. The Los Alamos sources [28] (Fig. 9) produce bright beams to 100 mA with a normalized rms emittance at ≈29 keV of $\varepsilon_{n\,(rms)} \approx 0.05\,\pi$ mm-mr, [$\varepsilon_{n\,(99)} \approx 0.23\,\pi$ mm-mr].

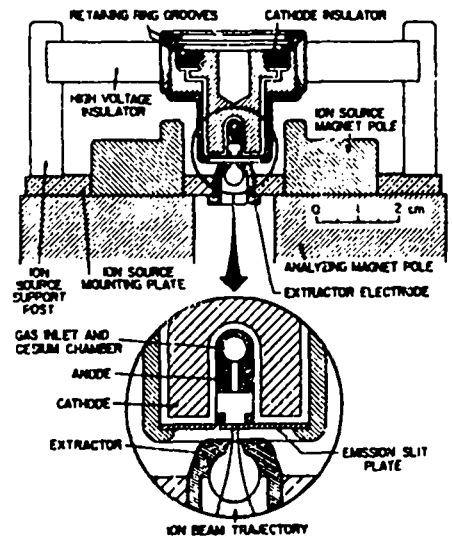

Fig. 9. A Los Alamos H^- Penning source.

Multicusp Surface-plasma Source

The multicusp surface-plasma source [16] (Fig. 10) is a large-volume low-pressure source that can operate at high duty factor. The source chamber is typically a cylinder of large diameter (≈20 cm) with alternating polarity magnetic dipoles on the outer surface to produce cusp magnetic fields inside. The chamber, usually the end plates, contain feedthrus for filaments in the source. Near the center of the chamber is the H^- production surface or converter. Opposite the converter surface is an opening in the chamber wall for extracting the H^- ions. In operation the filaments supply electrons to ionize the gas (pressure ≈1 mTorr) and create a plasma. The cusp field minimizes the electron loss to the walls and confines the plasma to the center of the chamber near the converter. Ions created in the plasma strike the converter surface which is biased negative with respect to the plasma. H^- ions formed on the converter surface are accelerated through the plasma region and into the extractor. As in other SPS, cesium is injected into the source to lower the converter surface work-function and increase the H^- yield. Negative ions reaching the extractor leave the source for further acceleration. Most electrons which would accompany the ions through the extractor are repelled by a magnetic filter made of dipole permanent magnets at the extraction aperture.

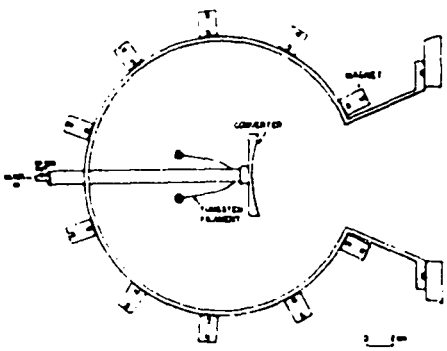

Fig. 10. Basic multicusp surface-plasma source.

Multicusp accelerator sources (Fig. 11) have been built at LAMPF and KEK. LAMPF developed a 20-mA source that is capable of long term operation at 10% duty factor (800-μs pulses at 120 Hz).[17] The normalized emittance for 95% of the beam is $\varepsilon_{n\,(95)} = 0.8\ \pi$ mm-mr. [$\varepsilon_{n\,(90)} \approx 0.6\ \pi$ mm-mr]. At KEK a multicusp source has operated on the 12-GeV synchrotron.[18] The source produced 15-20 mA of H^- beam with pulses of 200 μs at 20 Hz. The normalized emittance after acceleration to 750 keV is $\varepsilon_{n\,(90)} = 1.8 - 2.1\ \pi$ mm-mr. This source used lanthanum hexaboride (LaB_6) cathodes that ran cooler and survived longer than tungsten filaments. As a result the cesium consumption was lower, operation was more stable and lifetime much longer (>2500 hours) than previous sources.

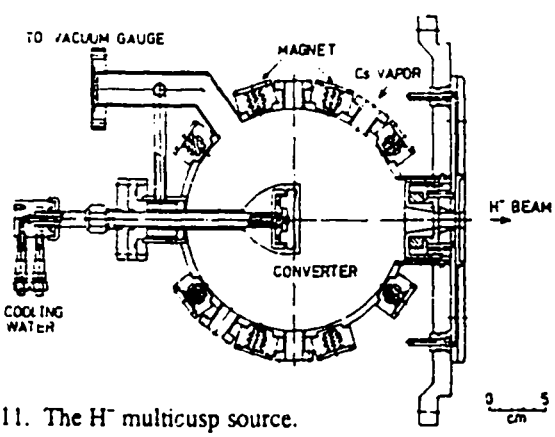

Fig. 11. The H^- multicusp source.

Volume Source

The volume source (Fig. 12) is another "large" source similar to the multicusp. The plasma is usually contained in a cylindrical chamber surrounded with permanent dipole magnets that form cusps and fields to confine the electrons of different energies. The rear or outer regions of the chamber contain filaments biased to create electrons of sufficient energy (E>5 ev) to excite hydrogen molecules to high vibrational states. The second region, separated from the first by a magnetic field, is located near the extraction aperture. This field prevents energetic electrons (E>1 ev) from entering the second region and destroying the H^- ions once produced. In this region the collision of slow electrons with excited hydrogen molecules produces H^- ions. Good operation is very sensitive to the dimensions and conditions in this region. At the extraction aperture another magnetic filter passes the H^- ions and hopefully excludes the electrons.

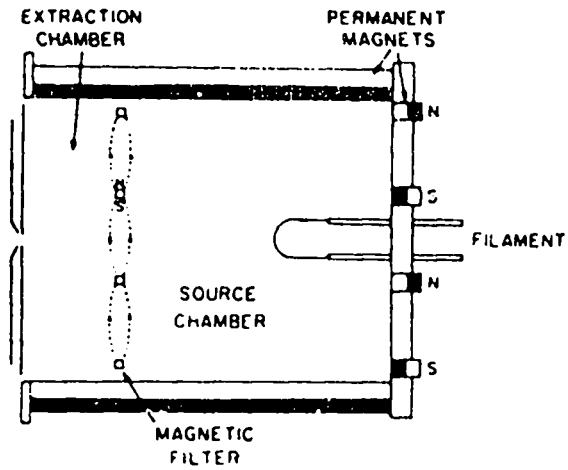

Fig. 12. Basic H^- volume source.

Several volume sources are in use or under study. TRIUMF uses a low-current (≈1 mA) volume source.[29] The normalized emittance is $\varepsilon_{n\,(90)} = 0.15\ \pi$ mm-mr. The source has good electron suppression with e/H^- as low as one.

Brookhaven has achieved 30 mA of H^- with 750 mA of electrons from a 1-cm^2-aperture volume source [30] (Fig. 13). With higher arc current the source pressure increases from 5 to 15 mTorr for optimum output. For a 21-mA beam the normalized emittance at 90% is $\varepsilon_{n\,(90)} = 0.94\ \pi$ mm-mr. Considerable work is still being done on the source.

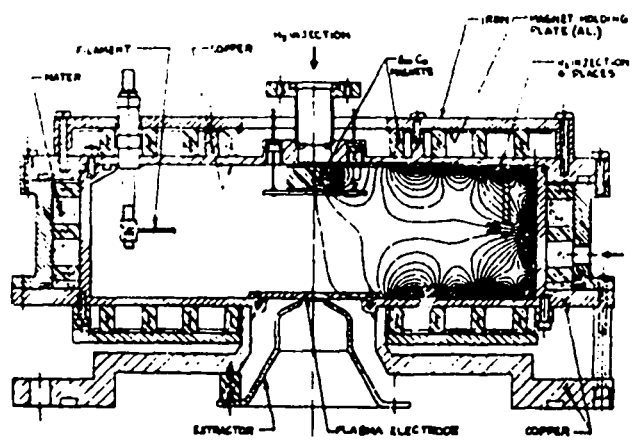

Fig. 13. The Brookhaven H^- volume source.

At Los Alamos, a volume source [20] has produced 10 mA with a normalized rms emittance of $\epsilon_{n\,(rms)} = 0.08\ \pi$ mm-mr, [$\epsilon_{n\,(90)} = 0.37\ \pi$ mm-mr]. The aperture was 6.3-mm diameter and the source operated at pressures of 2 to 20 mTorr.

At Berkeley, cesium has been added to a volume source with significant improvement.[31] At high currents the H^- output increased fivefold exceeding current densities of 250 mA/cm^2 with reduced e/H^- ratios. At high cesium levels, where extraction breakdowns occurred, the output exceeded 1 A/cm^2. Using an extractor of seven apertures (each 0.7 mm diam inside a 2.26 mm diam circle), 33 mA of H^- was extracted with an e/H^- of 20. At present the tungsten filaments limit the source lifetime. LaB_6 filaments should be a great improvement. To remove the filaments and improve the lifetime, the Berkeley group has been developing an rf driven volume source.[32]

Summary

H^- ion sources are still very new and there is much research and improvement to be done in this area. Each application has a unique set of requirements for the source and among the existing sources a great many applications can be met. Typically the accelerator usage has stressed duty factor, reliability, lifetime, gas consumption, intensity and emittance. Most modern sources have the intensity for linear accelerators (20 to 100 mA). For emittance or brightness the Penning or possibly the volume source is best with the magnetron being acceptable for general uses. The magnetron is presently good only for low duty-factor operation (<0.3%) in contrast to the other sources which have high duty factor capability and may achieve continuous operation. Lifetime is often dependent on the duty factor of the source and for low-duty usage the lifetime can be many months to a year as witnessed by operating magnetrons. The multicusp SPS has achieved many thousand hours running at high duty-factor operation using LaB_6 cathodes. The Penning source does operate many days at high duty factor and may do better with cathode improvements. Presently the largest operational experience has been with the magnetron and its reliability is very good. The multicusp SPS has also shown reliable operation. The other sources have not had the same operational experience.

For small sources the gas consumption depends on the operation. At low duty-factor operation the gas can be pulsed into the source so the consumption per a pulse is simply the volume times the pressure. Fortunately in these sources the volume is small since the pressure is relatively high (<2 cc, >100 mTorr). For larger and high duty factor or d.c. operation the pressure and anode aperture determine the gas flow. For the multicusp SPS and the volume source the aperture is large but the pressure is low (≈1 cm^2, 0.1-10 mTorr).

Cesium usage is typically about one milligram per hour or less for the cesium sources. Even though these sources may exist just before high voltage-gradient devices, additional sparking has not been a problem. In some cases refrigerated surfaces have been used before the accelerator while in others there has been little more than a meter or less transport line to minimize cesium contamination.

Many ideas look good and work fine on the test bench even under simulated operational conditions but the real operational proof for lifetime, reliability and other qualities can be determined only under running conditions. In operation, the daily fine adjustments done on a test bench are often not possible, and less then experienced operators must be able to keep it running. This is the real test of an ion source. Of course, the reliability of a source is not just the device from which the ions emerge. There are many support devices - vacuum, gas, cesium and cooling systems, power supplies, monitoring, controls, etc.- all which must operate reliably in the source environment.

References

In addition to the references cited, the Proceedings of the International Symposium on the Production and Neutralization of Negative Hydrogen Ions and Beams contain much detailed information on H^- ion sources. Five symposia have been held at Brookhaven. These Proceedings are published as:
First Symposium (1977) BNL 50727,
Second Symposium (1980) BNL 51304,
Third Symposium (1983) AIP Conf. Proc. 111,
Fourth Symposium (1986) AIP Conf. Proc. 158,
Fifth Symposium (1989) AIP Conf. Proc. 210, in print.
Likewise the book by A. T. Forrester, *Large Ion Beams*, (Wiley-Interscience, New York, 1988) has an excellent chapter on H^- sources.

1. R. P. Bastide, N. B. Brooks, A. B. Wittkower, P. H. Rose, K.H. Purser, IEEE Trans. Nuc. Sci. NS-12 V.3 (1965) 775.
2. Luis W. Alvarez, Rev. Sci. Inst. 22 (1951) 705.
3. K. W. Ehlers, Nuc. Inst. Meth. 32 (1965) 309
4. C. W. Potts, IEEE Trans. Nuc. Sci. NS-24 (1977) 1385.
5. John A. Fasolo, IEEE Trans. Nuc. Sci. NS-24 (1977) 1597.
6. Yu. I. Belchenko, G. I. Dimov, V. G. Dudnikov, Proc. 2nd Sym. on Ion Sources and Formation of Ion Beams, Berkeley, LBL-3399 (1974) VIII-1.
7. K. Prelec, Th. Sluyters, M. Grossman, IEEE Trans. Nuc. Sci. NS-24 (1977) 1521.
8. Paul W. Allison, IEEE Trans. Nuc. Sci. NS-24 (1977) 1594.
9. Charles W. Schmidt, Cyril D. Curtis, IEEE Trans. Nuc. Sci. NS-26 (1979) 4120.
10. C. W. Schmidt, C. D. Curtis, AIP Conf. Proc. 158 p. 425.
11. James G. Alessi, AIP Conf. Proc. 158 p. 419.
12. V Stipp, A. DeWitt, J. Madsen, IEEE Trans. Nucl. Sci. NS-30 (1983) 2743.
13. H. S. Zhang, G.-G. Winter, H. Krause, N. Shirm, I. Tessmann, DESY HERA 87-04, February, 1987.
14. Paul Allison, Joseph D. Sherman, AIP Conf. Proc. 111 p. 511.
15. P. E. Gear, R. Sidlow, Proc. 2nd Int. Conf. Low-Energy Ion Beams, Bath 1980: Inst. Phys. Conf. 54 (1980) 284.
16. K. N. Leung, K. W. Ehlers, Rev. Sci. Instr. 53(6), (1982) 30.
17. Ralph R. Stevens,Jr., Rob L. York, John McConnell, Robert Kandarian, 1984 Linear Accel. Conf., Seeheim, Germany, GSI-84-11, (1984) 226.
18. Y. Mori, A. Takagi, K. Ikegami, S. Fukumoto, AIP Conf. Proc. 158 p. 378.
19. M. Bacal, E. Nicolopoulou, H. J. Doucet, BNL 50727 p.26
20. Ralph R. Stevens,Jr., R. L. York, K. N. Leung, K. W. Ehlers, AIP Conf. Proc. 158 p. 271.
21. K. Prelec, IEEE Particle Accelerator Conference, 89CH2669-0, Chicago, (1989), 340.
22. J. R. Hiskes, AIP Conf. Proc. 158 p. 2.
23. C. W. Schmidt, C. D. Curtis, BNL 50727, p. 123.
24. J. G. Alessi, Th. Sluyters, Rev. Sci. Instr. 51(12), (1980) 1630.
25. Richard L. Witkover, AIP Conf. Proc. 111 p. 398.
26. J. G. Alessi, J. M. Brennan, A. Kponou, Rev. Sci. Instr. 61(1), (1990) 625.
27. Yu. I. Belchenko, V. I. Davydenko, G. E. Derevyankin, G. I. Dimov, V. G. Dudnikov, I. I. Morosov, G.V. Roslyakov, A. L. Schabalin, Rev. Sci. Instr. 61(1), (1990) 378.
28. H. Vernon Smith,Jr., Joseph D. Sherman, Paul Allison, 1988 Linear Accel. Conf., Newport News, Va., CEBAF-Report-89-001, (June, 1989) 164.
29. D. H. Yuan, R. Baartman, K. R. Kendall, M. McDonald, D. R. Mosscrop, P. W. Schmor, AIP Conf. Proc. 158 p. 346.
30. K. Prelec, J. G. Alessi, Rev. Sci. Instr. 61(1), (1990) 415.
31. K. N. Leung, C. A. Hauck, W. B. Kunkel, S. R. Walther, Rev. Sci. Instr. 60(4), (1989) 531.
32. K. Leung, LBL, Private communication. Soon to be published.

ECR Ion Sources and Applications with Heavy-Ion Linacs*

R. C. Pardo
Argonne National Laboratory, Argonne, IL 60439

Abstract

The electron cyclotron resonance(ECR) ion source has been developed in the last few years into a reliable source of high charge-state heavy ions. The availability of heavy ions with relatively large charge-to-mass ratios (0.1 - 0.5) has made it possible to contemplate essentially new classes of heavy-ion linear accelerators. In this talk, I shall review the state-of-the-art in ECR source performance and describe some of the implications this performance level has for heavy-ion linear accelerator design. The present linear accelerator projects using ECR ion sources will be noted and the performance requirements of the ECR source for these projects will be reviewed.

Introduction

In the past twenty years, the research efforts in the field of nuclear and atomic physics have moved strongly into experimental programs which require the use of 'heavy ions' - beams of particles heavier than helium. More recently the high energy physics community has begun to emphasize research with heavy ions. Industrial uses of heavy ions are also increasing dramatically, driven by fields such as semiconductor implantation, metallurgical surface treatments (tribology), and medical applications. This switch in the particle mix emphasis required from ion sources has placed before the ion source development community a difficult challenge to develop ion sources with sufficient reliability, beam current, and charge state performance to make delivery of heavy-ion beams economically feasible.

The first application of the electron cyclotron resonance principal was in a H^+ ion source by Geller in 1968(1). The first heavy-ion, high charge-state electron cyclotron resonance ion source (ECRIS) was Geller's MAFIOS in 1972(2). By 1974 SUPERMAFIOS(3) demonstrated most of the features which are identifiable in most modern ECRIS. Those features include a 'minimum B' magnetic field for good plasma confinement, two identifiable plasma regions ('stages'), and a multimode RF cavity. Although the performance of SUPERMAFIOS was good the electrical power consumed exceeded 3MW. Over the next 16 years, ECRIS source performance for high charge-state heavy-ions has continued to improve, the power for the source has decreased, the physical source size has become smaller, and the experience and reliability of the sources for essentially any element has significantly increased.

The first application of ECR ion sources in accelerator-based research was their use at cyclotrons. This application allowed cyclotrons for heavy ions to replace their PIG ion sources, and dramatically increase the energies available for an existing cyclotron due to the availability of large currents of high charge-state heavy ions from the ECRIS.

The applications of ECR ion sources with linacs quickly followed. The first actual use was the acceleration in the CERN linacs of oxygen and sulphur beams with further acceleration in the CERN synchrotrons. The first stand-alone heavy-ion linac project relying on an ECRIS was the Argonne Positive-Ion Injector(4). The high charge-to-mass ratio available from an ECRIS, combined with super-conducting technology, allowed the design of a new class of low-velocity linac using independently-phased resonant cavities even in low-velocity region of the linac(5,6). This proposal was followed quickly by the GSI low -intensity injector project(7) and the most recent plans for an ECR-linac injector, the ALPI(8) project.

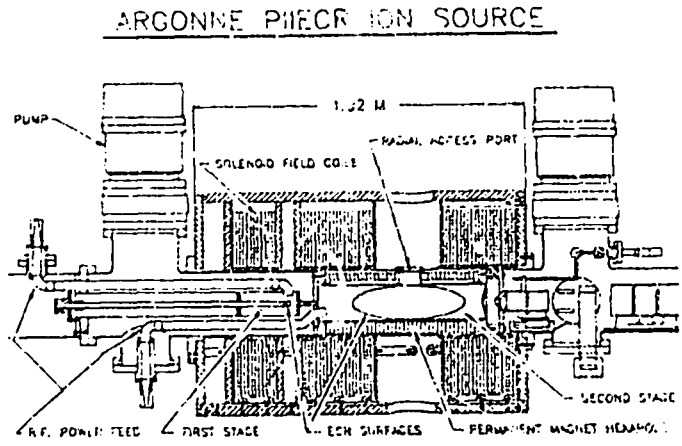

Fig. 1. The major components of the Argonne 10 GHz ECR ion source.

Each of these projects has a goal of accelerating virtually any stable isotope. The design of a linac must assume an initial injection velocity and a minimum charge-to-mass ratio (q/A) for the ion species to be accelerated. In 1985 the first of these projects, the ATLAS PII, chose a q/A≈20/238 for uranium as a reasonably safe design choice. In 1988 the GSI injector design team felt that a uranium q/A≈28/238

*This work was supported by the U.S. Department of Energy, Nuclear Physics Division, under contract W-31-109-ENG-38.

should be a good choice. Finally the ALPI ECRIS design at Legnaro expects to achieve a q/A≈32/238 for uranium. Of course each increase in the reliably achievable charge-to-mass ratio has a significant impact on the cost-performance ratio for such projects. For these projects, the planned beam currents are a few microamps. No significant difficulties with space charge in the linac injection region are expected.

The Present ECR Ion Source

The major features of a high-charge state ECR ion source are shown in Figure 1. An ion begins its journey through the source by introduction of gas into a small 'igniter' region - the first stage. This region usually contains a 'line' region across which the cyclotron resonance condition for electrons exists at the frequency of RF microwave power in use (2.5 - 18 GHz, up to now). Such a condition provides an efficient coupling of power from the microwave source to the electrons. These relatively low-energy electrons provide an initial ionization of the injected gas at high total pressure ($<10^{-4}$ Torr). This low charge-state, high-density plasma diffuses into the larger main region of the source - the 'second stage'. In this stage, a mirror magnetic field configuration is generated by electromagnetic solenoid coils. The magnetic field is shaped into an increasing-field geometry in all directions ('minimum-B') by a hexapolar field usually produced by a permanent magnet configuration. This minimum-B field configuration provides improved magnetic confinement of the hot electrons and produces an ellipsoidal surface on which the ECR resonance condition exists. These two effects allow the electron temperature and density to increase significantly ($T_e \approx 10$ keV, $n_e \approx 10^{12}$ cm^{-3}). The hot electrons further strip the ions, which are confined in an electrostatic trap created by the electrons, to high charge states. Finally the plasma is sampled by the extractor electrode and the ions are extracted from the plasma region.

The the high charge states are reached by sequential ionization. The cross-section for single electron ionization is much larger than any two-electron processes. The charge state of ions from an ECR plasma is a result of the competition between stripping and recombination cross-sections, the confinement time of electrons and ions, and the electron energy distribution temperature. In addition plasma-wall interactions and the elemental distribution of the plasma play an important role in the performance of the ECRIS.

The level of performance of ECR ion sources has increased dramatically over the past decade. The best performance of ECR ion sources for a few selected ion species and charge states is shown in Figure 2 as a function of time. Not only has the maximum ion current increased markedly, but the peak in the ion charge-state distribution available from ECR sources has also continued to increase. Source performance considered 'state-of-the-art' five years ago is now just 'average'. These improvements are the result of new sources incorporating known scaling factors and of improvements in the operating regime of existing sources to better utilise the competing processes mentioned above. The beam currents which are now being reported by new sources with operating frequencies of 14 GHz and greater are within a factor of 2-10 of the beam currents of low charge-state species available from other types of ion source(9).

The ions in an ECRIS plasma are weakly coupled to the RF power. This feature allows the ions to remain unheated by the RF power. The energy spread of ions from the source appears to be dominated by the source plasma potential, voltage stability of the extraction power supply, and energy coupling to the ions from electron-ion scattering. The result is ions which have an energy spread corresponding to an equivalent voltage variation of 7-15 ev(10). At the Argonne PII-ECR source, the energy spread of a beam of $^{11}B^{+3}$ was measured to be 7 volts using doppler-broadened line shapes by laser techniques. Such small energy spreads for high charge-state ions make it possible to deliver beams through linacs with a longitudinal phase-space volume of unprecedented small value. Measurements of the longitudinal emittance of beams from the new Argonne Positive Ion Injector for ATLAS indicate the system emittance is less than one third the corresponding emittance from the tandem injector. This allows the on-target energy spread and time spread to be very small, opening new possibilities in the design of experiments: a capability being used extensively at ATLAS.

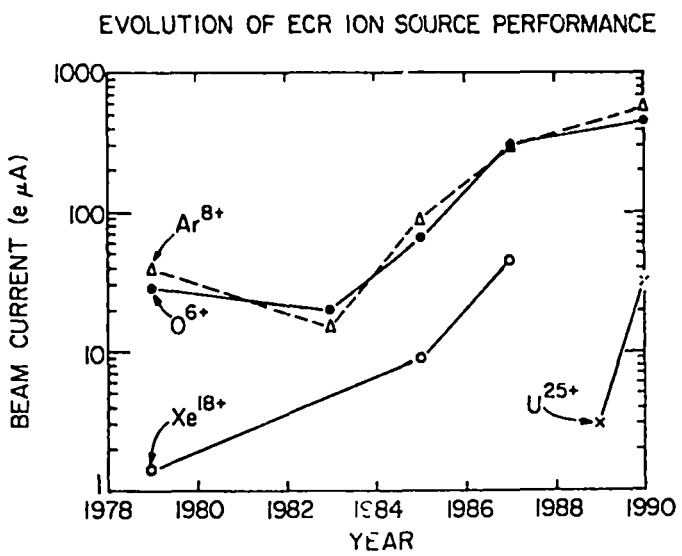

Fig. 2. Evolution of the reported maximum beam currents available from ECR ion sources. The dramatic increase in beam currents in the last decade shows no indication of stopping. (Data from Ref. #3, 17, 25, 27, 28, 29, 30).

The transverse emittance of ECR ion sources has been measured by a number of laboratories(11,12,13). The overall result is that the normalised emittance $\gamma\beta\epsilon$=0.1-0.2π mm-mr at approximately the 80% intensity contour. Such a value is significantly higher than the transverse emittance of other high quality heavy-ion sources such as negative-ion cesium sputter sources(14) which is generally 0.02-0.06π mm-mr, but when compared to the typical transverse emittance after stripping in a tandem accelerator terminal of ~0.09π mm-mr for A≃58, the ECRIS transverse emittance is similar. For extremely heavy ions, this comparison favors ECRIS beams as multiple scattering in stripper foils dominates the transverse emittance for tandem accelerators.

The measured values agree qualitatively with the assumption that the transverse emittance is dominated by the angular momentum conservation required for particles formed in a magnetic field. This model predicts that the transverse normalized emittance from an ECRIS will be

$$\gamma\beta\epsilon \propto (q/A)r^2B,$$

where q, A are the charge and mass of the ion of interest, r is the radius of the effective emitting surface, and B is the magnetic field at the effective emitting surface. A surprising result of this effect is that one expects the transverse emittance to decrease for heavier beams because the ratio (q/A) will be smaller for those beams than for lighter ions. Another surprise is that the actual measured emittances of beams from ECRIS's are smaller than would be expected from simple calculations with this model. Such an effect may imply that high charge state ions are emitted from a region smaller than that defined by the radius of the extraction hole.

The angular momentum model for emittance also predicts that the transverse emittance from high frequency sources will be greater than that from lower frequency sources. No data at present shows this effect. But it will be interesting to see if this feature is observed in the next generation of high frequency sources.

Since the ECRIS evolved from a plasma physics background the first operation of these devices was with gaseous materials. When using gases, an ECRIS demonstrates essentially infinite lifetime; that is the lifetime is limited only by the reliability of external components. But the desirable properties of beams from these sources soon caused demand for beams of heavy ions which could only be produces by using materials in solid form. These sources have demonstrated their ability to use solid material as primary feed material for a number of years. A variety of methods have been employed such as external electrically-heated ovens, plasma heated 'boats', the insertion of the desired material directly into the plasma region for evaporation by direct plasma heating, and the use of gaseous compounds for normally solid materials(15,16,17). An example spectrum for uranium ions from the Argonne ECRIS is shown in Figure 3.

Generally the solid material is injected directly into the 'second stage' in all these approaches. The source performance for these types of materials varies much more than for gases, but in general the performance in terms of beam currents and average charge states is somewhat lower compared to that for nearby elements which are gases. The overall operation of the source is maintained by a continued feeding of a gas such as oxygen or nitrogen which forms the dominate component of the plasma and the material of interest is only a small 'contaminating' portion of the total plasma. One of the negative aspects of using a solid is that the performance of the source may degrade with time, especially with regard to the production of the highest charge states. This effect appears to be related to the wall-plasma interaction noted above. Operating the source with SiH_4 and O_2 will generally recoat the source walls with a beneficial coating which is assumed to be SiO_2 and the source performance is restored.

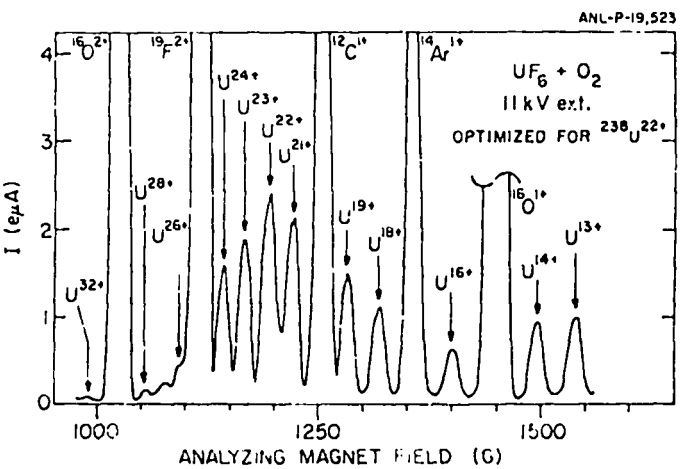

Fig. 3. Example of the charge state distribution for the Argonne ECR ion source for uranium.

The amount of material consumed in an ion source is an extremely important parameter with regard to the use of isotopically enriched material, special experimental applications such as accelerator mass spectrometry, and the long-term reliability of the source for solid material operation. The material consumption for the primary plasma gas can be quite high (tens of mg/h) and strongly depends on the details of the source design as well as operating mode. Material consumption can generally be minimized by feeding material into the 'second stage' region where the total gas flow is lowest. Under these conditions usage rates of approximately 1 mg/h for most materials can be obtained. At Argonne we have achieved usage rates of

approximately 0.2 mg/h for krypton. A long run with natural molybdenum consumed the material at a surprising 0.04 mg/h rate while producing approximately 1 electrical microamp of $^{92}Mo^{16+}$ from natural abundance material. This result corresponds to an ionisation efficiency of 0.38% for that isotope into the 16+ charge state. Such efficiency for high charge-state production is quite respectable. The value quoted above is similar to typical operating efficiencies for negative-ion cesium sputter sources(18).

A number of ECR sources have been built for low charge-state high-efficiency applications(19,20,21). These sources have demonstrated total ionisation efficiencies for 1+, 2+, and 3+ ions in material as heavy as neon with efficiencies ranging from 15% to over 50%. Such high efficiencies make a variety of accelerator applications appealing including the acceleration of radioactive beams(20,21). Literally a whole new world of applications may be in the offing for accelerator physics with performances of this class.

The Future for ECR Ion Sources

The technology of ECR ion sources continues to progress as graphically demonstrated in Figure 1. Some of the progress follows scaling guidelines which are derivable from reasonable plasma physics models of the ECRIS operating regime. These scaling assumptions have been described by Geller(22). The most important results from these considerations is the prediction that the peak in the charge-state distribution should increase rather slowly following a logarithmic relation with frequency:

$$\langle q \rangle \propto \log (\omega^{3.5}),$$

where ω is the RF power frequency. A second relationship predicts that the beam current for a particular charge should be expected to scale as:

$$I_q \propto \omega^2/A.$$

Both of these relationships have been experimentally supported in comparisons between sources operating over a frequency range of 6.4 to 16.6 GHz. It is these two relationships which are driving the construction of the next generation of high frequency ECR ion sources. The frequency dependence will be tested much further during the next five years as the 30 GHz superconducting ECR ion source project at Michigan State University(23) comes into operation at varying frequencies, culminating in 30 GHz operation later.

Following the predictions of these simple relations given above is made difficult because of the costs involved. Those costs derive from the high cost of high frequency RF power in the regime above 14 GHz, the increased RF power expected to be required in these regimes, and the added costs of the magnetic fields which must scale linearly with the increasing RF frequency in order to maintain confinement and the ECR resonance condition. Therefore, for many application, lower frequency ECRIS applications will continue to deliver the best cost/benefit ratio.

The simple scaling laws outlined above are not the only effects making important contributions to ECR ion source performance. In the last five years, a number of empirical results have changed the performance of existing sources and revised the way new sources are being designed. One of the first surprises was that the average charge state of one plasma species could be improved by introducing a second, lighter gas into the plasma. This gas mixing role is still not well understood, but may be due to energy transfer by elastic scattering of ions between the two species. An effect which may be similar has been observed in ion traps(24).

A second performance improvement came in the redesign of the compact source CAPRICE by Jacquot(25) in Grenoble. In this case, the average charge state did not change significantly from other 10GHz sources, but the total ion current increased by nearly a factor of 10 from the original design. Again exactly what causes the improvement is not fully understood, but may have to do with plasma wall interactions, secondary electrons streaming from an iron electrode, and the detailed shape of the magnetic field in the extraction region.

A third important area effecting ECRIS performance is the plasma wall interactions. The importance of this interaction has long been known. Even the earliest tests of solids in ECRIS's reported 'poisoning' of the source after these tests and minimizing the material usage was known to be beneficial. The first reported improvement in source performance by wall treatment came from the 6.4 GHz Berkeley ECRIS where Lyneis(26) clearly demonstrated improved performance from his source was correlated with previous use of SiH_4 and O_2. Lyneis has surmised that the formation of a SiO_2 layer on the wall provides a source of cold electrons because of the high secondary electron yield of SiO_2. This effect has been demonstrated at other laboratories and recoating the walls of the Argonne ECRIS after long solid material runs is a normal procedure.

Effects of the types described above are much more difficult to predict and understand. It is these types of developments that still keep the 'black magic' in ion source development and give hope of continued improvement for these sources without extreme financial expenditures.

References

1. J. Consolino, R. Geller, and C. Leroy, Proc. of 1st Inter. Conf. Ion Sources, Ed. I.N.S.T.N. Saclay, 537(1988).
2. R. Geller, Nucl. Sci., **23**(2), 904(1976).
3. R. Geller, IEEE Trans. Nucl. Sci. **26**(2), 2120(1979).
4. K.W. Shepard, these proceedings.

5. K.W. Shepard, IEEE Nucl. Sci., **32**(5), 3574(1985).
6. R.C. Pardo, K.W. Shepard, and M. Karls, IEEE Cat No. 87CH2387-9, 1228(1987).
7. J. Klabunde, 1988 Linear Accelerator Conference Proceedings, (to be published).
8. M. Cavenago and G. Bisoff, to be published in Nucl. Instrum. and Methods A.
9. B.H. Wolf, et al, Rev. Sci. Instrum. **61**(1), 406(1990).
10. F.W. Meyer and J.W. Hale, Rev. Sci. Inst., **61**(1), 324(1989).
11. N. Angert, et al, Proc. 1984 Linear Accel. Conf., GSI-84-11, 374(1985).
12. C.M. Lyneis and D.J. Clark, IEEE Trans. Nucl. Sci. **32**(5), 1745(1985).
13. Z.Q. Xie and T.A. Antaya, Rev. Sci. Inst., **61**(2), 793(1990).
14. G.D. Alton, Rev. Sci. Inst., **61**(1), 505(1990).
15. D.J. Clark and C.M. Lyneis, Jour. de Phys. C1, **50**(1), 759(1989).
16. P. Sortais, et al, Jour. de Phys. C1, **50**(1), 855(1989).
17. R.C. Pardo and P.J. Billquist, Rev. Sci. Inst , **61**(1), 239(1990).
18. David Elmore and Fred M. Phillips, Science, **236**, 543(1987).
19. V. Bechtold, H. Bohrmann, and S.A. Schiek, 7th Inter. Workshop on ECR Ion Sources, Ed. H. Beucher, Julick, 248(1986) (unpublished).
20. P. McNeely, et al, Rev. Sci. Instrum., **61**(1), 273(1990).
21. P. Decrock, et al, Rev. Sci. Instrum., **61**(1), 279(1990).
22. R. Geller, et al, in International Conference on ECR Ion Sources, NSCL Conf. Proc., #MSUCP-47, J. Parker ed., Michigan State Univ. 1(1987).
23. T.A. Antaya, Jour. de Phys. C1, **50**(1), 707(1989).
24. M.A. Levine and M.B. Schneider, in International Conference on ECR Ion Sources Proc., J. Parker ed., Michigan State Univ., #MSUCP-47, 1(1987).
25. B. Jacquot, et al Nucl. Inst. & Meth. in Phys. Res., **A269**, 1(1988).
26. C.M. Lyneis, Jour. de Phys. C1, **50**(1), 689(1989).
27. R. Geller and B. Jacquot, Physica Scripta, **T3**, 19(1983).
28. F. Bourg, et al, Workshop on the Sixth International ECR Ion Source, Jan. 17-18, 1985, Lawrence Berkeley Laboratory, Berkeley, CA, PUB-5143, 1(1985).
29. M.P. Bourgarel, Proc. 2nd European Particle Accel. Conf., Nice, Italy, June 12-14, 1990, (to be published).
30. C. Lyneis, private communication.

PROGRESS IN PHOTOINJECTORS FOR LINACS*

Richard L. Sheffield
Los Alamos National Laboratory, Los Alamos, NM 87545

Abstract

Several programs have started which are based on the photoinjector as the electron source. Some reasons for using a laser to produce an electron beam are improved beam brightness, high-charge single-bunch pulses (>50 nC), and several high-current pulses closely spaced in time.

This presentation will cover present and planned activities in photoinjector development. Topics will include materials, gun designs, and present experimental results.

Introduction

Free-electron lasers and collider machines require electron accelerators capable of delivering pulse trains of electron bunches of high charge density. A high electron density implies high peak current (100 A to 2000 A) and a low transverse beam emittance (<40 π·mm·mrad). This paper describes the present and planned research in photoinjectors.[1,2] A photoinjector is a laser-switched photoemissive source located in the first accelerator cell. By placing the photoemitter in a high-gradient rf cavity (Fig. 1), the space charge effects due high-electron densities can be substantially reduced.

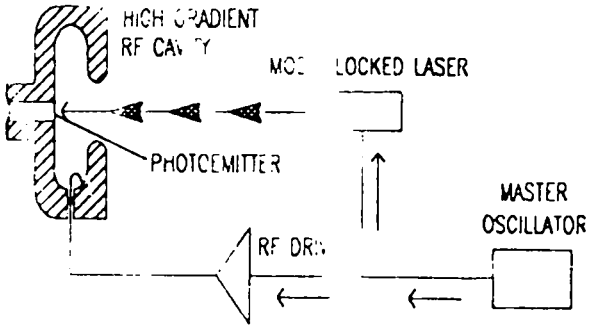

Fig. 1. Schematic of a photoinjector.

A laser-switched electron source gives precise control over all aspects of the electron distribution: peak current, spatial profile, and temporal profiles. This type of source also has a large flexibility in interpulse spacing; the interpulse spacing can range from picosecond pulse separations to a single pulse. The number of photoinjectors which are either operating or planned for operation has increased dramatically over the last several years. Figure 2 shows the increase in the number of projects which are based on this type of source.

*Work supported by Los Alamos National Laboratory Institutional Supporting Research, under the auspices of the United States Department of Energy

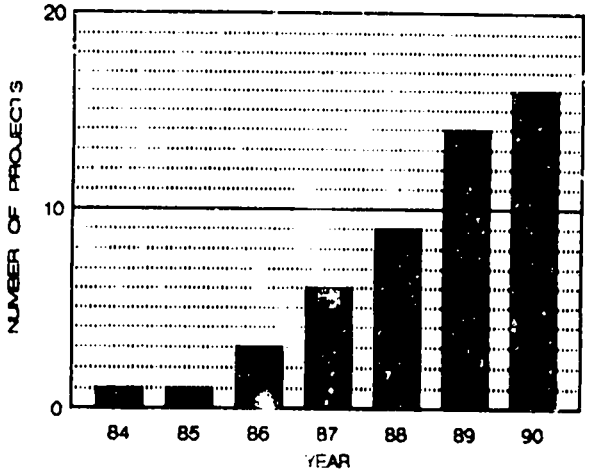

Fig. 2. Photoinjectors operating and planned.

This paper is divided into three sections following the introduction. The first section covers presently operating photoinjectors, the second section covers planned systems, and the third section covers some of the physics and engineering considerations.

Present research programs using photoinjectors electron sources

Upgrade of Los Alamos FEL Accelerator

The Los Alamos FEL (High Brightness Accelerator Facility or HIBAF) has been upgraded to provide electron beams of the quality and intensity required by shorter wavelength (<3 microns) FELs.[3,4] The improved electron beam is primarily the result of adding a photoinjector to the accelerator. However, the entire device is being modified to demonstrate that the beam quality can be transported to the FEL without degradation. The facility has produced initial data at 17 MeV. The results are a 300 A peak current, 12 ps pulse width and an emittance of 40 π·mm·mrad (90%, normalized). The photocathode was CsK_2Sb.

The purpose of HIBAF is to provide a benchmark of the computational models used to design advanced FELs. The final design goals of HIBAF are 40 MeV of electron energy, peak currents of 300 A, and a normalized emittance less than 35 π·mm·mrad (90%). An experiment layout is given in Fig. 3.

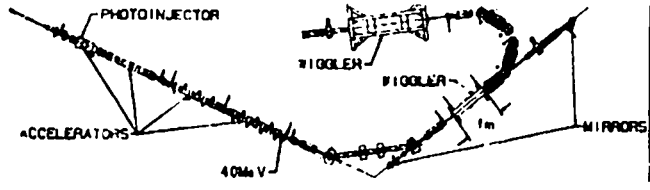

Fig. 3. Upgrade of Los Alamos FEL accelerator with photoinjector HIBAF

Duke-Rocketdyne Experiment

The construction of the Mark III accelerator has been described in detail elsewhere.[5] The layout of the experiment is shown in Fig. 4.

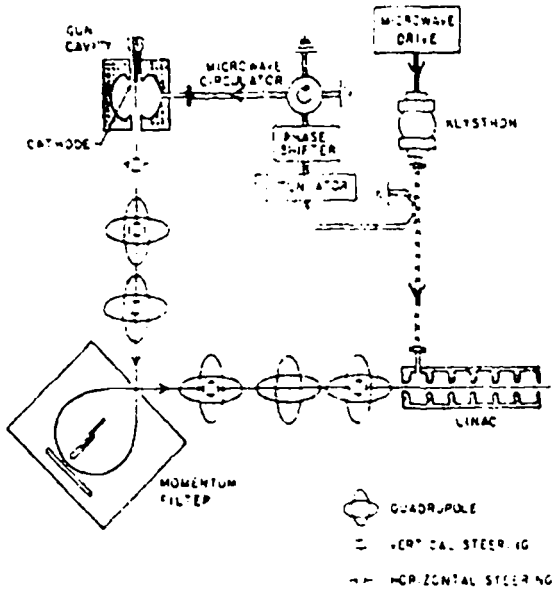

Fig. 4. Schematic of Mark III accelerator.

The machine parameters are as follows: macropulse length of 2-5 μs, micropulse length of 2.2 ps after obtaining an increase of 10 in peak current from the alpha magnet, and a gun energy of 1 MeV. The alpha magnet is a momentum filter and is able to limit the electron energy spread to less than 0.5%. The electron source is a LaB_6 cathode. Originally the cathode produced electrons by pure thermal emission. However, because the electrons are emitted at all phases of the rf, many of the electrons are accelerated at phases which enable the electrons to back-stream into the cathode. Since current emission from the cathode is limited by average-power heating, then by using the laser to limit the emission to the correct rf phase, higher peak currents can be obtained.[6] In this mode the LaB_6 was operated just below its normal emission temperature, and a laser was used to pulse the cathode. Operation with the laser resulted in an increase in peak current from 33 to 75 A with no observable loss in beam emittance. The beam emittance was estimated to be 4-8 π·mm·mrad. During operation, the gun pressure was about 5×10^9. Not enough operation time has been available to study the cathode lifetime; but based on previous performance, the expected lifetime should be much greater than 1000 hours.

LEL-HF in Bruyeres-le-Chatel

This photoinjector design[7,8] has a cavity frequency of 144 MHz. The lower frequency was chosen to reduce the rf effects by using larger cavity apertures and by having the rf fields approximate DC conditions during the electron transit. The design parameters are a beam with 10 to 20 nC, a 1 to 1.5 MeV exit energy from the first cavity, bunch lengths of 50 to 100 ps, an accelerator gap of 7 cm, and a surface field at the cathode of 15-20 MV/m. A schematic of the experiment is shown in Fig. 5. They have measured emittances of 80 π·mm·mrad at 10 nC.

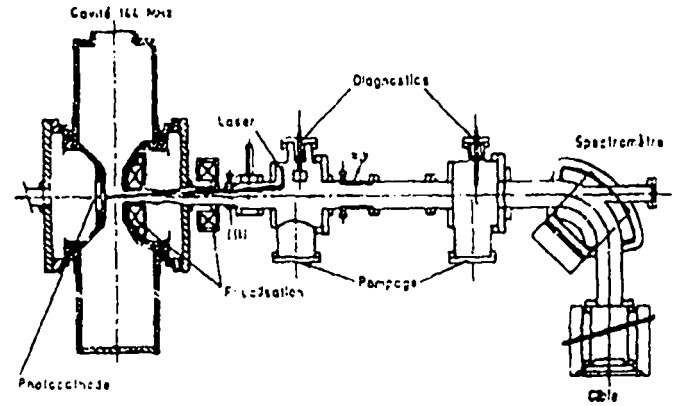

Fig. 5. Photoinjector designed at LEL-HF Bruyeres-le-Chatel

Accelerator Test Facility at Brookhaven National Laboratory

The Accelerator Test Facility at Brookhaven National Laboratory (BNL) is being developed into a research facility for laser acceleration and FELs. The design goal for the accelerator is a final energy of 50 MeV and an emittance of 15 π·mm·mrad at 1 nC. They are building a 2.856-GHz photoinjector to drive the linac.[9] The S band, standing wave, disk-loaded structure will operate in the short rf pulse regime (6 μs). The schematic of the photoinjector is shown in Fig. 6.

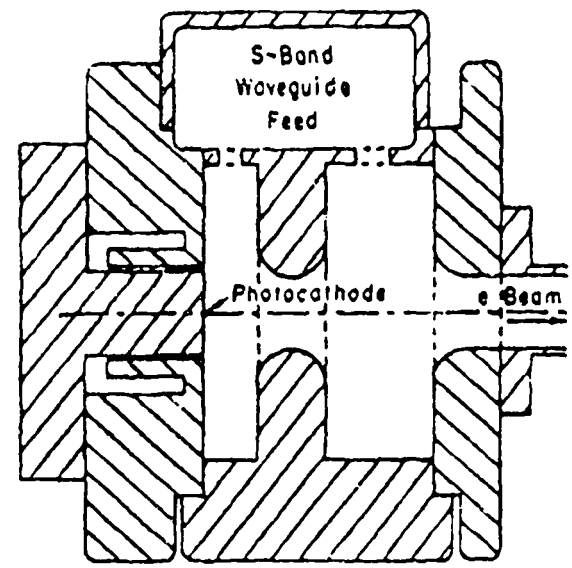

Fig. 6. Schematic of BNL photoinjector.

The photocathode is made of yttrium metal. They have operated the photoinjector at the design gradients which corresponds to a peak cathode field of 102 MV/m and peak surface fields of 120 MV/m.[10]

Summary of present experimental results

A compilation of the present experimental measurements of emittance from the preceeding experiments is given in Fig. 7.

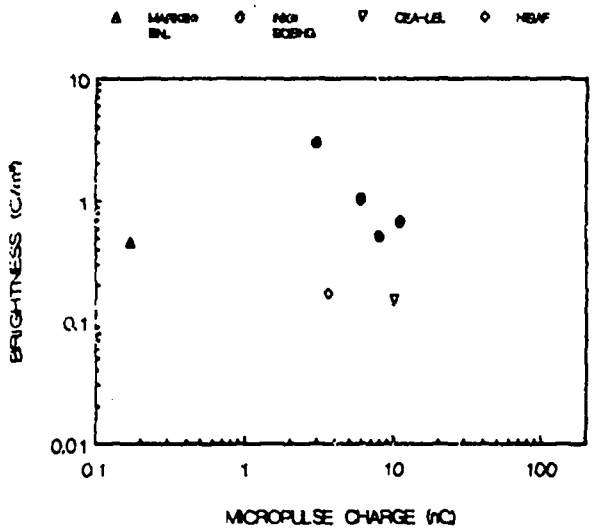

Fig. 7. Photoinjectors - experiment results.

The experimental results from the Mark III accelerator and the photoinjector program at Los Alamos National Laboratory (LNEX) relied upon scraping the electron beam. The CEA-LEO and HIBAF experimental results are rms emittance numbers for the entire electron beam distribution.

Planned research facilities using photoinjectors sources

A number of experiments are planned for operation in the next few years (Fig. 8).

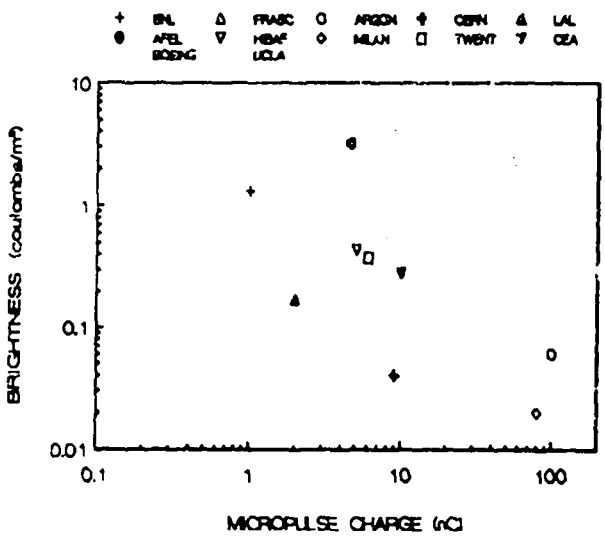

Fig. 8. Photoinjetors - planned experiments.

The following text briefly describes differences in the planned experiments. Experiments which are similar to the BNL design of an S-band accelerator and metallic photocathodes are UCLA and CERN[11] (also investigating multialkali photocathodes). Experiments which are similar to the HIBAF design at 1300 MHz and multialkali photocathodes are the AFEL at Los Alamos National Laboratory and the FEL project at the University of Twente.[12] The Laboratoire de l'Accelerateur Lineaire in Orsay[13] is building a S-band two cavity gun with independent rf control for the two cavities and a laser-driven dispenser cathode. The ELFA FEL project[14] in Milan will use two 352 MHz cavities and a multialkali photocathode. The Frascati ARES project[15] and the Bergische Universitat-Gesamthoschule Wuppertal[16] project will use two superconducting 500 MHz cavities and multialkali photocathodes. Argonne National Laboratory's wakefield accelerator facility[17] will use two 1300 MHz cavities and a metal photocathode. Boeing[18] will use a two cavity 433 MHz injector with a 25% duty factor and a multialkali photocathode.

AFEL

At Los Alamos the design of a new 20 MeV compact linac based on the photoinjector has been completed. The linac will be approximately 1.2 m long and will be operated with a 10 μs macropulse at up to 10 Hz with a 0.5 A average during the macropulse. The final electron beam characteristics, from PARMELA simulations, are a beam emittance of less than 12 π·mm·mrad, an energy spread of 0.2%, and peak currents in excess of 350 A. At these performance parameters and the use of a microwiggler with a period of 3 mm operating on the third harmonic, the calculated gain at 400 nm is greater than 50% at 20 MeV.

Physics and engineering considerations

By definition, a photoinjector relies on a light source to turn on and off the photoemitter. In almost every instance the light source is a laser. As a consequence, this type of electron source falls out of the typical experience of a source designer and could be viewed as a serious complication. However, laser development is also being driven by the development of photoinjectors and laser systems which match the requirements of some of the photoinjector designs can be bought from laser vendors.

The type of laser system depends on the choice of photocathode material. Photocathodes, such as GaAs and multialkali, can be manufactured to have a high quantum efficiency in the visible wavelength band. The laser for these types of cathodes can be built by existing laser vendors. The drawback of this type of photocathode is that it requires an UHV environment. Some photocathodes, such as LaB_6 and yttrium, have a response in the ultraviolet (<350 nm) but have much less stringent vacuum requirements. However, the laser system required to drive this type of cathode is more difficult to build and not readily supplied by vendors. Another consideration is the uniformity of the laser illumination and of the cathode quantum efficiency.

A possible problem in the higher quantum efficiency, high-gradient guns is field emission. The reduction in the work function at the cathode surface due to the presence of high fields can produce a measurable dark current. Dark currents have been observed at the HIBAF experiment. The dark current levels in that experiment did not adversely impact the operation of the accelerator but did produce a background signal on the beam diagnostics.

The remaining issue of the high quantum efficiency photocathodes is lifetime. Up to now, high quantum efficiency cathodes do not survive beyond a few days of operation in a rf cavity. However, the same cathodes have comparably long lifetimes when just rf is present or just the laser is present. Also, hundreds of coulombs have been extracted in DC gun experiments. The only observable difference when running a photoinjector is the presence of a large

pressure rise in the cavity when an electron beam is present. Ed Garwin of SLAC suggested that the lifetime problem might be similar to the problem experienced in storage rings. In storage rings, beam lifetime is limited by electron stimulated desorption (ESD) of gases from the walls of the ring. We know that some of the same gases produce by ESD can contaminate a cathode when present in small amounts (for instance, CO_2 or H_2O). ESD releases the gases trapped in the grain boundaries of the wall of the cavity. These gases are bound with several tens of eV energy. Therefore, a standard bake at 250 to 350 C would not drive out these gases. One way to clean up a system is to run beam. Figure 8 is photodesorption during beam conditioning for aluminum at the NSLS VUV storage ring.[19]

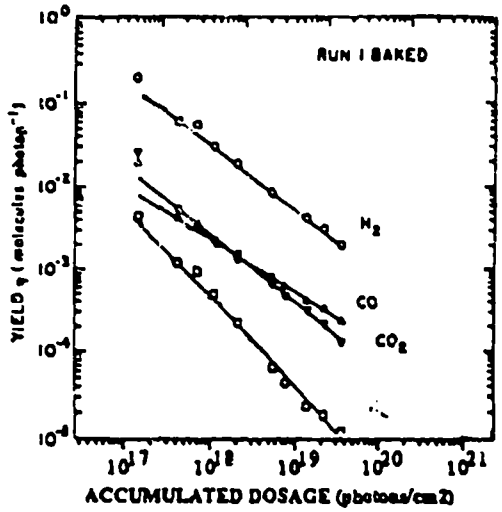

Fig. 9. Photodesorption yield during beam conditioning for Al at NSLS VUV storage ring.

For a low duty cycle experiment, this type of conditioning would take years and is therefore not practical. Another approach is to use glow discharge cleaning of the walls. Figures 10 and 11 demonstrate the effect on the rings at Brookhaven[20] and CERN,[21] respectively. This type of cleaning will be tried at HIBAF and the results known by the end of the calendar year.

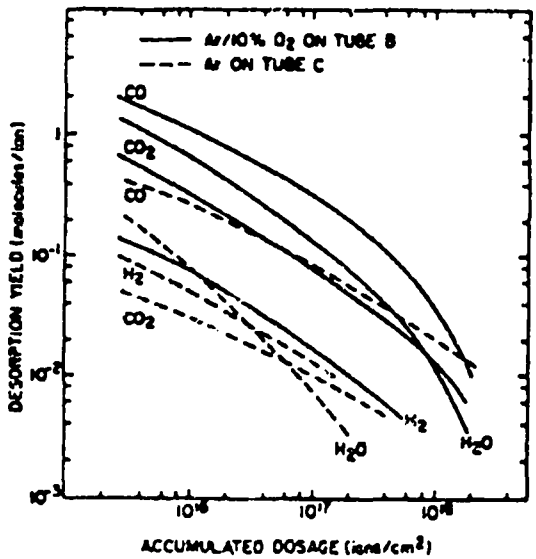

Fig. 10. Glow discharge cleaning of stainless steel tubes at Brookhaven ring.

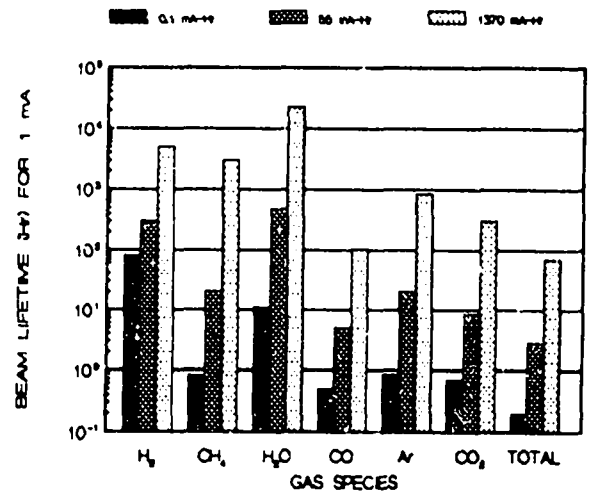

Fig. 11. Data from the electron positron accumulator ring at CERN.

Conclusions

The production of high-current high-brightness electron beams has enjoyed considerable progress over the last several years, mainly because of changes in the requirements imposed by free electron lasers. The photoinjector has demonstrated the ability to produce very bright electron beams. Several groups around the world are designing bright beams based on this technology and continued improvement in photoinjector design and engineering is expected. The real limit of electron brightness using a photoinjector is still to be determined.

I thank Chris Travier for recent information on present photoinjector projects. I also thank the following individuals for private communications on their projects: Bruce Carlsten, Ken Batchelor, Steve Benson, and Renato Dei-Cas.

References

1. R. L. Sheffield, "Photocathode RF Guns," Physics of Particle Accelrators, Vol. 2, American Institute of Physics Conference Proceedings NO. 184, pgs. 1500-1531.
2. C. Travier, Workshop on Short Pulse High Current Cathodes, Bendor, France, June 18-22 (1990).
3. D. W. Feldman, "Los Alamos High-Brightness Accelerator FEL (HIBAF) Facility," LASE '90, Los Angeles, CA, Jan. 18-19, 1990.
4. P. G. O'Shea, these proceedings (1990).
5. S. V. Benson, J. Schultz, B. A. Hooper, R. Crane, and J. M. J. Madey, *Nucl. Instr. and Meth.*, A272, 22-28 (1988).
6. M. Curtin, G. Bennett, A. Bhowmik, R Burke, P. Metty, S. V. Benson, and J. M. J. Madey, FEL conf (1989).
7. S. Joly, EPAC88.
8. R. Dei-Cas et al., Workshop on Short Pulse High Current Cathodes, Bendor, France, June 18-22 (1990).
9. K. Batchelor, J. Sheehan, and M. Woodle, Brookhaven Internal Report, BNL-41766 (1988).
10. K. Batchelor, these proceedings (1990).
11. Y. Baconnier, R. Bossart, K. K. Geissler, J. C. Godot, K. Huber, H. Kugler, J. H. B. Moadsen, A. J. Riche, J. Strode, and G. Suberlucq, these proceedings (1990).
12. G. J. Ernst et al. FEL89.
13. C. Travier, these proceedings (1990).
14. R. Bonifacio et al., NIM A289, 1 (1990).
15. L. Serafini et al., to be published EPAC (1990).
16. H. Chaloupka et al., EPAC 1986.
17. J. Simpson, these proceedings (1990).
18. J. L. Warren et al., PAC89.
19. T. Kobari and H. J. Halama, J. Vac. Soc. Tech., A5, 2355 (1987).
20. H. C. Hseuh et al., J. Vac. Sci. Tech. A, 3, No. 3, 518 (1985).
21. A. Poncet, CERN

Linacs for Free Electron Lasers

C. Pellegrini
Department of Physics
405 Hilgard Av., Los Angeles, CA 90024

Abstract

In this paper we discuss the use of a RF linac as a FEL driver. We first review the basic FEL physics and discuss the beam characteristics needed for a good FEL driver. We then compare these requirements with the present state of the art in RF linacs, and discuss some possible R&D lines.

Introduction

The interest in Free electron Laser is due to: its large wavelength range, which at present extends from about one centimeter to 0.24 micrometer; its tunability; its high peak power, ranging up to the GW level. Because of its flexibility the FEL can find applications in many areas, such as particle acceleration, heating of fusion plasmas, material sciences, biological, medical and solid state research. A review of the FEL operation and experiments can be found in reference 1, and in a recent paper by Roberson and Sprangle[2].

There are two main wavelength regions of interest for FELs applications, where they can be superior to other sources: one is the IR and millimeter to centimeter region; the second is the short wavelength region, below 0.1 micrometer. The first has been widely explored; many systems are in operation at these wavelengths in several laboratories. The second is the new frontier for FELs; its development requires electron beams with a six dimensional phase space density larger than that available today.

FELs use different types of electron accelerators, from induction linac to storage rings, depending on the radiation wavelength required, the beam energy and pulse duration. The RF linac can provide high quality beams of energies from a few MeV to Gev, to drive FEL in the infrared, visible or UV spectral regions. They could also be used in the future as drivers for Soft X-ray FELs. The short pulse duration, from picoseconds to tens of picoseconds, is a desirable property for many research applications, although it limits the operation at wavelength shorter than about 50 μm because of the slippage.

The Stanford superconducting RF linac was the accelerator used for the first FEL in 1976-77[3,4], and is still being used now by a Stanford-TRW group. This group has reported the operation of the first visible FEL, with a power of 21 KW at 0.52 μm[5]. Room temperature linacs have been used in the following years at Stanford[6,7,8], Los Alamos[9,10], Boeing[11] to drive FELs from 35 μm to the visible, with peak powers up to 40 MW, and pulse length as short as one picosecond. Both oscillators and master oscillator power amplifier [12] configurations have been used. Optical guiding, sidebands and harmonic generation have been observed.

Basic FEL Physics

To describe the basic FEL physics we use a model based on the 1-D theory[13,14], in which we include effects like diffraction, beam energy spread and optical guiding; other effects, as for instance undulator imperfections, are not and will have to be considered in a real design. The notations we use are those of reference[15] and are: beam energy (units mc^2), γ; particle density, n_e; radiation wavelength, λ; undulator period, λ_u; undulator field, B_u; undulator parameter, $K = eB_u\lambda_u/2\pi mc^2$; undulator frequency, $\omega_0 = 2\pi c/\lambda_u$; beam plasma frequency $\Omega_p = (4\pi r_e c^2 n_e/\gamma)^{1/2}$.

With these notations, and considering for simplicity a helical undulator, we can write the FEL synchronism condition as

$$\lambda = \frac{\lambda_u}{2\gamma^2}(1 + K^2) \tag{1}$$

In the 1-D FEL theory , and for a cold beam, the radiation field in the undulator grows exponentially until it saturates; the exponential gain length, L_G, and the saturation power are determined by one parameter[13,15],

$$\rho = \left(\frac{K}{4\gamma}\frac{\Omega_p}{\omega_0}\right)^{2/3} \tag{2}$$

The gain length is

$$L_G = \frac{\lambda_u}{2(3)^{(1/2)}\pi\rho} \tag{3}$$

Work done under DOE Grant DE-FG03-90ER-40565

the laser power at saturation is related to the beam power, P_L, by

$$P_L \sim \rho P_{beam} \tag{4}$$

and the saturation length is

$$L_s \cong \frac{\lambda_u}{\rho} \tag{5}$$

When the gain length is shorter than the undulator length it is convenient to use the Small Signal Gain, G, to characterize the FEL. This quantity can also be expressed in terms of ρ [13]

$$G = \frac{1}{2}(4\pi\rho N_u)^3 f(4\pi N_u \Delta) \tag{6}$$

where N_u is the number of undulator periods, Δ is the "detuning", i.e. the relative difference between the resonant and the actual beam energy, and $f(x) = (1-\cos x-(x/2)\sin x)/(x/2)^3$ is a function with a maximum value of about 0.6.

The gain and the gain length are reduced, by effects like energy spread, diffraction effects, and by how much we focus the beam through the undulator. This reduction is small if some additional beam conditions are satisfied:

a) limit on energy spread: $\sigma_e < \rho$;

b) limit on emittance: $\epsilon < \frac{\lambda}{2\pi}$;

c) optical guiding: $\frac{Z_R}{L_G} > 1$;

where $Z_R = \pi\sigma_r^2/\lambda$, is the Rayleigh range, σ_r the beam radius, and σ_E the relative energy spread. The gain length is a very important quantity: all effects which take place over a distance larger than the gain length will have little effect on the FEL performance.

One way to increase ρ, and decrease the gain length, is to strongly focus the beam through the undulator. This, however, can produce a reduction of the gain[16], except when the betatron oscillation wavelength, is that given by the transverse focusing produced by the undulator field,

$$\lambda_\beta = \frac{2^{1/2}\gamma\lambda_u}{K} \tag{7}$$

This reduction is small if we focus to a betatron wavelength smaller than (7) but larger than the gain length. The additional focusing can be obtained with external focusing elements, like quadrupoles[15], or, as proposed by Barletta and Sessler[17], with ion focusing.

The FEL wavelength is defined by (1), hence by the beam energy. The minimum linewidth is given by the inverse of the number of wavelength in a bunch length. For most application it is important to achieve this linewidth and keep the wavelength stable within the linewidth; this requires for the beam energy fluctuation $\Delta\gamma/\gamma < \Delta\lambda/2\lambda$.

FEL Scaling Laws

In the design of a FEL we maximize ρ for a given wavelength and beam characteristics. To this end we rewrite it using the beam invariants ϵ_N, transverse normalized rms emittance (we assume for simplicity a cylindrically symmetric beam), the longitudinal brilliance[14,15], and the charge per bunch eN, as

$$B_L = \frac{eNc}{(2\pi)^{1/2}\epsilon_L} \tag{8}$$

Using these quantities and condition "a" to write $\sigma_e = \eta\rho$, we obtain

$$\rho = \frac{\lambda}{4\pi}\frac{K}{1+K^2}\left(\frac{4\pi B_L \eta}{\lambda_\beta \epsilon_N I_A}\right)^{1/2}\gamma^{3/2} \tag{9}$$

where $I_A = ec/r_e$.

It is interesting to notice that the dependence of ρ on λ is not too strong, so that a FEL at short wavelength seems feasible; in addition (11) shows that it is convenient to use a large beam energy.

The value of the FEL parameter depends now on very few beam related quantities, the energy and the beam invariants, and is thus well suited for a discussion of the accelerator driving the FEL.

As an example we consider now a FEL operating in the Soft X-ray wavelength. A possible set of parameters can be obtained from the model discussed above and is given in Table 1. This FEL can be operated in an oscillator configuration, with an optical cavity[19], or in the Self Amplified Spontaneous Emission (SASE) mode[20]; a discussion and comparison of the two modes can be found for instance in reference[19,20].

The combination of small emittance and large longitudinal brilliance given in Table 1 is not obtainable today, and using existing accelerators one can only produce FEL radiation in the visible or near UV. Several groups are working to produce beams with the characteristics similar to that of Table 1, following two routes: storage

rings at Duke and Dortmund University; linacs at Los Alamos, Brookhaven and UCLA. These have been reviewed at a Workshop held at Brookhaven in 1987[21]. In the following section we will discuss the RF linac approach.

TABLE 1.

Example of Soft X-ray FEL

Wavelength, nm	5
Normalized emittance (rms), mm mrad	1
Electron energy, GeV	1.0
Longitudinal Brilliance, A	5000
Energy spread, %	0.1
Peak current, A	600
λ_β, m	3.3
ρ	0.0024
Undulator Period, cm	2
Gain Length, m	1.8
Rayleigh Length, m	1.7
Beam Power, GW	600
Laser Power, GW	1.4

The Linac

In this section we want to discuss the main characteristics of the beam produced by RF linacs. We will start with a discussion of the electron source and its limitation and will continue with the main accelerator.

The Electron Gun

The electron gun for an FEL driver linac is of very great importance. It must produce a beam with high peak current and small emittance and energy spread, with all these conditions being met simultaneously. The minimum normalized, rms emittance for a gun with a circular cathode of radius a and temperature T, neglecting space-charge and other effects like non-linear and time dependent forces, is

$$\epsilon_N = \frac{a}{2}\left(\frac{kT}{mc^2}\right)^{1/2} \qquad (10)$$

where the temperature is related to the transverse electron momentum, p_T, by $kT = p_T/2m$. The cathode radius is defined by the total current, I, that we need and the current density J; we can rewrite

$$\epsilon = \{(kT/mc^2)(I/4\pi J)\}^{1/2} \qquad (11)$$

For a thermionic cathode the current density is lower than about 40 A/cm^2, and kT is about 1 eV, leading to a normalized emittance of $0.6(I(A))^{1/2}$ mm mrad. For a photocathode one can have kT about 0.2 eV and a current density of about 1000 A/cm^2 or larger, leading to an emittance of about $0.055\ (I(A))^{1/2}$ mm mrad.

Space-charge and non-linear effects will substantially increase this values of the emittance, and much work has been done to minimize this blow-up. There are two main ways to approach the problem: DC or pulsed guns, followed by a bunching/compression system to produce high peak current and match the beam to the linac; RF guns, with the cathode inside a high field cavity and fast initial acceleration. In both ways one can produce peak currents of about 100 A or larger and emittances of about 10 mm mrad.

In the case of DC or pulsed cathodes one needs to bunch the beam using one or more bunching cavities, to produce the bunch length needed for subsequent acceleration in the linac, and the peak current in the 100 A range needed for the FEL gain. During this process the emittance increases substantially.

A recent design of an IR FEL driver at LBL[22] consists of a 100 KV gun producing a peak current of 2.5 A for 1 ns, followed by two bunching cavities at 146 and 511 MHz and one bunching L-band standing wave structure. The beam energy at the system exit is about 6 Mev, with a peak current of about 100 A, pulse duration of 10 ps, normalized rms emittance of 10 to 20 mm mrad, energy spread less than 0.5 %.The longitudinal brilliance is about 400 A.

In the case of RF guns[23,24,25] one can use either thermoionic cathodes or photocathodes. The space charge effects are reduced by applying large electric fields on the cathode surface, of the order of 50 to 100 MV/m, so that the electrons become relativistic in a distance from the cathode of the order of one centimeter. The best results have been obtained with photocathodes, at the cost of adding to the system a high power laser. In this case the beam is bunched by the laser pulse at the cathode, phased to produce electrons only when they are accelerated, and one can use the large current density to produce high peak current with a small cathode radius. For thermoionic cathodes the current is mainly limited by the heating of the cathode due to the backstreaming electrons.

As an example, the Los Alamos gun, operating at about 1.3 GHz, with a Cs_3Sb cathode, and a field on it of 60 MV/m, has produced a beam with a normalized rms emittance of about 10 mm mrad, and a longitudinal brilliance of 2000A[26].

The limitations on the beam emittance produced by a RF gun have been analyzed[27]; the main effects are: space charge, non linear and time dependent RF fields, cathode temperature and current density. For present systems the main contribution to the emittance is produced by space charge effects near the cathode, which depends on the longitudinal charge density, and makes it vary from the center to the tails of the bunch. This effect can be at least partly controlled by increasing the accelerating field, or shaping the laser pulse, to produce a step like density distribution, or by selecting the core of the bunch out of a longer one, or by introducing non-linear or time dependent focusing elements[28]. Similar limitations apply to the buncher section when using a thermionic low voltage gun. We expect that using these techniques we will able in the future to produce a beam as given in Table 1.

Beam Loading and Fluctuations.

To maintain the FEL wavelength and intensity within the limits required for many applications we must impose stringent tolerances on the beam energy and intensity, in addition to those on the emittance, energy spread, and peak current. There are two main type of effects which can change the beam characteristics during acceleration. Fluctuations in RF voltage and phase and in beam intensity can produce a bunch to bunch energy deviation. Wakefields induced by the beam can produce energy spread and emittance blowup within a bunch and multibunch effects (beam breakup).

The fluctuation in the beam energy must be limited to a value smaller than the energy spread, which we expect to be of the order of a few tenth of a percent. In addition, for a FEL oscillator we must control the arrival time of the bunches to the undulator to a fraction of the bunch length.

Klystron voltage fluctuations produce both a field and a phase fluctuation thus changing the output beam energy. These effects can be reduced by passive regulation in the modulator to about 0.5%. For further improvements one can use feed-back control. For pulses longer than the filling time, one can use feedback during the macropulse; for shorter pulses one can use a feedback system from pulse to pulse. For CW or almost CW operation, like one can have in a superconducting linac, it is possible to have better reproducibility of the beam characteristics. In the Stanford superconducting linac the total time averaged energy spread is less than 0.1%. Similar or better results can also be obtained in a race track microtron.

Fluctuations in the bunch arrival time must also be controlled to picosecond or sub picosecond level. In the case of a laser-gun this means also to control the time of arrival of the laser pulse on the cathode, using a single master oscillator for the RF system and the mode-locked laser.

For large average current and long pulses the beam break-up effect is a concern. Several techniques have been developed to control this effect, like increasing the accelerating gradient, reducing the higher mode impedance, and staggering the tune of the dangerous modes.

At the other extreme of a FEL operating as an amplifier or in the SASE mode, only one electron bunch is needed in a macropulse. In this case effects like the ripple of the klystron output are less important as long as the bunch is synchronized to the trigger system, and what matters is only the reproducibility of the RF waveform from pulse to pulse. Also in this case we expect to be able to have the bunch energy reproducible to about 0.1%.

For high gain, high peak current system wakefields become the dominant effect; the longitudinal wakefield can produce an energy spread and the transverse wakefield can blow-up the transverse emittance[29]. For a single bunch the energy variation along its length due to the longitudinal wakefield can be partly compensated using the sinusoidal form of the accelerating field. The compensation however cannot be perfect and a residual energy spread will remain. For bunch currents in the 100A region and an S-band linac this residue can be of the order of 0.2%. The wake field effects depend strongly on the linac RF frequency. The longitudinal wakefield scales like the inverse square of the wavelength and the transverse like the inverse cube. This favors low frequency linacs, where also the multibunch beam loading can be smaller because of the larger energy stored in the cavities, for the same accelerating field. Transverse wake field effects can be controlled using the BNS damping[30], i.e. introducing a controlled energy spread in the bunch and removing it at the linac output.

To reduce the effect of wakefields on a single bunch and achieve a large peak current and a small energy spread we can use the bunch compression technique at several stages during the acceleration process. For the example of Table 1 we assumed $\epsilon_L = 2.10^{-5}$ m at 5 MeV, corresponding to a charge in the bunch of 1 nC, a 0.3 % energy spread and a rms bunch length of 0.6 mm; at 100 MeV we assume that the emittance is $2.4.10^{-4}$, for an energy spread of 0.2%, determined by beam loading, and

the same pulse length; at this energy we can compress the bunch increasing the energy spread by 3 and reducing the pulse length to 0.2 mm; subsequent acceleration to 1 GeV would reduce the energy spread to less than 0.1%; in effect the energy spread is determined again by beam loading, and for this very short bunch length we expect this to remain at 0.1%. Using this beam manipulation the final peak current is 600 A a value consistent with results obtained in the SLC at SLAC, where the peak current is 400 A with an energy spread of 0.1%.

Conclusions

The RF linac is the driver of choice for the infrared to visible wavelength region. Compact high gradient linacs and RF guns now being developed can reduce the FEL cost and make it more attractive. Progress in increasing the beam peak current and its brightness, and reducing energy and intensity fluctuations, will allow to produce FELs with larger gain and more reproducible characteristics, making them more useful research tools. The work being carried out on electron sources to reduce the beam emittance while keeping the high peak current and small energy spread is very promising and can lead in the near future to the possibility of pushing the FEL wavelength in the Soft-X-ray region.

References

1. Free Electron Laser Handbook, W. Colson, C. Pellegrini, and A. Renieri eds., North Holland, Amsterdam, in press.
2. C. W. Roberson and P. Sprangle, Phys. Of Fluids B 1, 3 (1989).
3. L. R. Elias and Al., Phys. Rev. Lett. 36, 717 (1976)
4. D.A.G. Deacon et Al., Phys. Rev. Lett., 38, 892 (1977).
5. J. A. Edighoffer et al.,Appl. Phys. Lett. 52, 1569 (1988).
6. S. V. Benson and J. M. J. Madey, Nucl. Instr. and Meth. A32, 55 (1984).
7. S. V. Benson and al., Nucl. Instr. and Meth. A272, 22 (1988).
8. J. E. La Sala, D. A. G. Deacon, and J. M. J. Madey, Phys. Rev. Lett. 59, 2047 (1988).
9. B. E. Newnam et Al., IEEE J. Quantum Elec. QE-21, 867 (1985)
10. D. W. Feldman nd Al., IEEE J. Quantum Elec. QE-23, 1476 (1987).
11. K.E. Robinson et al., Nucl. Instr. and Meth. A259, 49 (1987).
12. L. Vintro et al., Phys. Rev. Lett. 64, 1662 (1990).
13. R. Bonifacio, C. Pellegrini, and L. Narducci, Opt. Commun. 50, 373 (1984).
14. P. Sprangle and R. A. Smith, Phys. Rev. A21,293 (1980).
15. C. Pellegrini, Nucl. Instr. and Meth , A272, 364 (1988).
16. W. M. Fawley, D. Prosnitz, and E. T. Scharlemann, Phys. Rev. A30, 2472 (1984).
17. W.A. Barletta and A. M. Sessler, Radiation from fine intense Self Focused Beams at High energy, LLNL Report UCRL-98767 (1989).
18. C. W. Roberson, IEEE J. Quantum Electr., QE-21, 860 (1985).
19. J.C. Goldstein, B. D. Mc Vey and C. J. Elliott, Nucl. Instr. and Meth. A272, 177 (1988).
20. J. B. Murphy and C. Pellegrini, J. Optic. Soc. Am. B2,259 (1985).
21. Proc. Of the ICFA Workshop on Low Emittance Electron Beams, J. B. Murphy and C. Pellegrini eds., Brookhaven National Laboratory Report BNL-52090 (1987).
22. Chemical Dynamics Research Laboratory Coceptual Design Summary, Lawrence Berkeley Laboratory Report PUB-5266 (1990).
23. R. L. Sheffield, E.R. Gray, and J. S. Fraser. Nucl. Instr. and Meth. A272, 222 (1988).
24. S. V. Benson and al., Nucl. Instr. and Methods A250, 39 (1986).
25. K. Batchelor and Al., Development of a High Brightness Electron Gun for the Accelerator Test Facility at Brookhaven, Proc. European Particle Accelerator Conf., p. 954, Rome 1988.
26. R.L. Sheffield et al., RF Photoelectron Gun Experimental Performance, Proc. Linac Conf., CEBAF Rep. 89-001, p. 520 (1989).
27. K.J. Kim and Y.J. Chen, RF and Space-Charge Induced Emittances in Laser-Driven RF Guns, Proc. Linac Conf., CEBAF Rep. 89-001, p. 322 (1989).
28. J. G. Gallardo and R.B. Palmer, Preliminary Study of Gun Emittance Correction, Brookhaven National Laboratory Report BNL-43862 (1990).
29. See for instance P. B. Wilson and J. E. Griffin, High Energy Electron Linacs; Application to Storage ring RF System and Linear Colliders, in Physics of High Energy Particle Accelerators, R.A. Carrigan et al. eds., AIP Confg. Proc. 87, p. 450 (1982).
30. V.E. Balakin et al., VLEPP: Transverse Beam Dynamics, Proc. 12th Int. Conf. on High Energy Accelerators, Fermilab, p. 119 (1984).

Tuesday

Session TU2
Chairman: J. Leiss
Invited Papers

DESIGN OF LONG INDUCTION LINACS*

G. J. Caporaso and A. G. Cole
Lawrence Livermore National Laboratory, Livermore, Ca. 94550

Abstract

A self-consistent design strategy for induction linacs is presented which addresses the issues of brightness preservation against space charge induced emittance growth, minimization of the beam breakup instability and the suppression of beam centroid motion due to chromatic effects (corkscrew) and misaligned focusing elements. A simple steering algorithm is described that widens the effective energy bandwidth of the transport system.

Introduction

In this paper we will discuss the various requirements imposed on the output beam of electron induction accelerators and the principal known mechanisms which make it difficult to satisfy these requirements. This will lead us to a self-consistent design strategy which overcomes these mechanisms and should make it possible to simultaneously achieve all the requirments discussed.

Output Beam Requirements

Electron induction linacs can be used for many purposes such as drivers for FEL's and relativistic klystrons, flash x-ray radiography and for propagation experiments in various gases. Most of these applications require a high beam brightness, especially the FEL. In addition, all the applications require a "quiet" output beam in the sense that the transverse motion of the beam's centroid should be small compared to its radius. Lastly, most applications require the energy variation over the usable portion of the pulse to be on the order of one percent to avoid violating the resonance condition in an FEL, or to avoid chromatic effects in the final focusing lens, etc.

Obstacles to Achieving Beam Requirements

Space Charge Induced Emittance Growth

For intense beams the most serious threat to beam brightness is from the effects of nonlinear space charge forces[1]. By now it is well known that "excess" non-linear field energy can be interchanged with transverse thermal kinetic energy causing emittance to vary in a beam which is propagating at its matched radius in a focusing channel. Profile oscillations of the beam can lead to oscillations in the emittance and a finite growth in the emittance which depends on the difference in non-linear field energy between the initial and asymptotic states of the beam spatial profile. This can be seen by integrating the equation for growth of the normalized rms emittance.

$$\frac{\partial E_n^2}{\partial z} = -\frac{2IR^2}{\gamma\beta I_0}\frac{\partial\Omega}{\partial z} \quad . \tag{1}$$

Here R is the rms radius, $I_0 \equiv 17$ kA and Ω is a dimensionless quantity that characterizes the field energy in the beam and is dependent upon the spatial profile[1]. Integration of this equation for constant R and γ yields

$$E_n^2(\infty) = E_n^2(0) + \frac{2IR^2}{\gamma\beta I_0}\left[\Omega(0) - \Omega(\infty)\right] \quad . \tag{2}$$

However, it is also possible to have additional emittance growth if a beam is mismatched in a focusing channel where a portion of the kinetic energy associated with the beam's envelope motion can be converted into transverse themal kinetic energy. Consider an oscillation of the beam rms radius so that $R=R_0+\Delta R \cos kz$. Profile oscillations will usually be associated with the envelope oscillations. It can be shown that the frequency of the profile oscillations is twice that of the envelope oscillations so that we may put $\Omega=\Omega_0+\Delta\Omega\cos(2kz+\theta)$ where θ is an unknown phase angle. If we substitute these forms for R and Ω into equation (1), average over an oscillation period and retain only lowest order terms we obtain

$$\frac{\overline{\partial E_n^2}}{\partial z} = \frac{1}{\gamma\beta I_0}(\Delta R)^2 k\, \Delta\Omega \sin\theta \tag{3}$$

where a horizontal bar denotes a time average over an oscillation period. This result admits a growing emittance for a proper value of the phase angle. The rate of emittance growth is proportional to the beam current, the focusing strength and to the square of the radial mismatch. At present there is no first principles' calculation that can describe the evolution of this angle so that we must rely on simulations for insight into this mechanism.

Beam Breakup Instability (BBU)

This instability dominates the design of the focusing system for the induction linac. The accelerating cells have dipole cavity modes which are driven by any beam transverse displacements. Usually one mode dominates the process. The magnetic field of the dipole mode interacts with the beam impressing a modulated transverse momentum on the beam at the frequency of the dominant mode and so exicites that mode in downstream cells to even greater amplitude. The evolution of the instability may be described by two modal equations which govern the excitation of the mode by the beam and the response of the beam to the cavity fields[2]:

$$\left(\frac{\partial^2}{\partial\tau^2} + \frac{\omega_0}{Q}\frac{\partial}{\partial\tau} + \omega_0^2\right)\Delta = \frac{\omega_0^3}{L_g}\frac{Z_\perp I\,\xi}{Q\,\gamma I_0} \tag{4}$$

$$\frac{\partial^2\xi}{\partial z^2} + \frac{1}{\gamma}\frac{\partial\gamma}{\partial z}\frac{\partial\xi}{\partial z} + k_\beta^2\,\xi = \Delta \quad . \tag{5}$$

Here ω_0, Q and $Z_\perp/Q$ are respectively the angular frequency, quality factor and transverse shunt impedance of the cavity mode and L_g is the average distance between cells. ξ represents either the phasor x+iy for solenoidal guiding (with $k_\beta=k_c/2$) or x or y for alternating gradient quadrupole focusing. Under worst case conditions for "strong" focusing we have

$$\xi \sim \xi_0 \exp\left(\frac{\omega_0\left(\frac{Z_\perp}{Q}\right) Q\, I}{2L_g I_0}\int_0^z \frac{dz'}{\gamma k_\beta}\right) . \qquad (6)$$

The quantity $\omega_0(Z_\perp/Q)Q$ appears in the exponent and may be shown to scale as[2]

$$\omega_0\left(\frac{Z_\perp}{Q}\right)Q = \frac{4w}{b^2}\eta \qquad (7)$$

where w is the axial width of the accelerating gap, b is the beam pipe radius and η is a dimensionless quantity that describes how well the cavity modes are damped. Typical values for η range from 1 to 3. It is currently thought that the minimum possible value for η is about 0.7[2].

"Corkscrew" (Chromatic Aberration)

This mechanism leads to the development of a time varying displacement of the beam centroid. The apparent frequency of the motion increases as the beam propagates further along the machine. Any focusing system that provides an energy dependent betatron wavelength will be subject to this difficulty since all beams have some variation of energy across the pulse[3,4,5]. The mechanism is illustrated in figure 1 where the motion of three beam "slices" labelled A, B and C, initially offset from the center line of the accelerator are followed through a focusing system. At each accelerating gap the particles receive a slightly different energy. Since the betatron wavelengths of the particles depend on their energies the particles will eventually fall out of step with one another and will lead to a displacement which varies with time across the pulse. The apparent local frequency of the time varying displacement or "corkscrew" is roughly given by

$$\omega = \frac{1}{\gamma}\frac{\partial\gamma}{\partial\tau}\int_0^z k_\beta\, dz' . \qquad (8)$$

For a system with solenoidal focusing k_β should be replaced by k_c in equation (8). It is clear from the above expression that the frequency of this motion will upshift as the beam propagates down the accelerator. Note that increasing the focusing causes the frequency to increase. It is important that the frequency of this motion be sufficiently small that the differential phase or integral of the frequency over time across the desired portion of the pulse be small compared to 1. The amplitude of the corkscrew is proportional to the orbit amplitude of a reference particle (say in the middle of the pulse). If the differential phase across the pulse is very large then the corkscrew amplitude will be on the order of the orbit amplitude of the reference partilcle. However, if the differential phase is small then the corkscrew amplitude is of order the orbit amplitude of the reference particle multiplied by the sine of the differential phase. Thus in this regime it is important to keep the differential phase as small as possible.

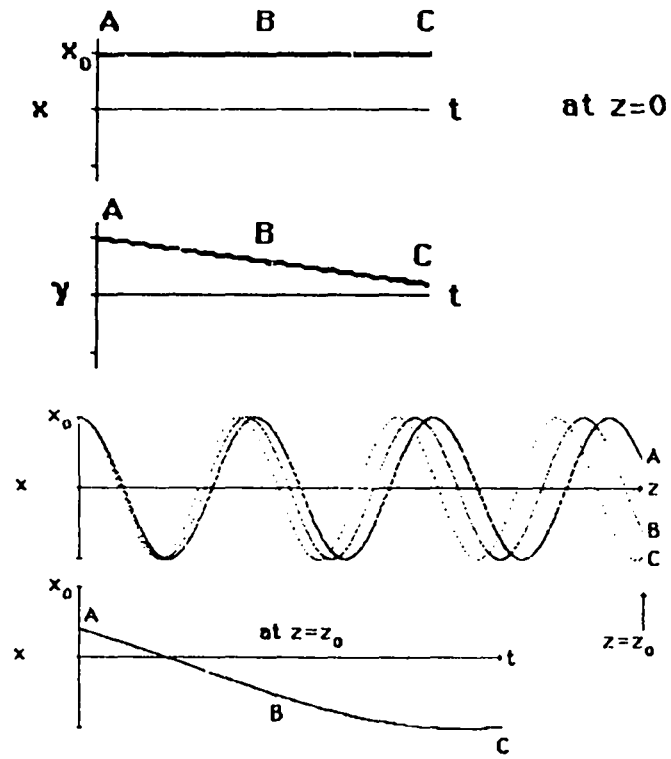

Fig. 1. Illustration of the corkscrew mechanism.

Sources of Energy Variation Across the Pulse

Figure 2 shows a circuit model of an accelerating gap. The pulse power unit is represented by the voltage source and the transmission line to the cell by the resistor Z_0. R_c is a compensation load resistor, C_g represents the capacitance of the cell, the current source represents the beam current and Z_c represents the ferromagnetic or ferrimagnetic core impedance.

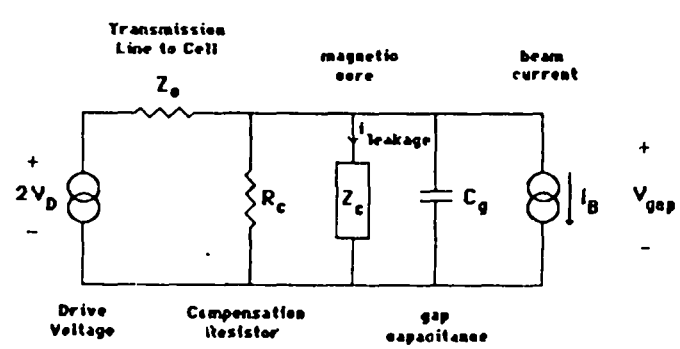

Fig. 2. Cell equivalent circuit model.

Considerable effort is usually expended to insure that the drive voltage waveform delivered to the cell is flat. Likewise a relatively constant voltage on the anode of the injector usually produces a current pulse with a flat top. Practically speaking there will be variations of both of these quantities on the order of several percent even in a well designed system. A feature which can cause an even larger variation in the cell voltage is

the fact that the leakage current which flows around the core of the cell is time dependent. In accelerators which are designed for high electrical efficiency this leakage current may be on the order of 50% of the beam current and so exerts a significant influence on the cell voltage.

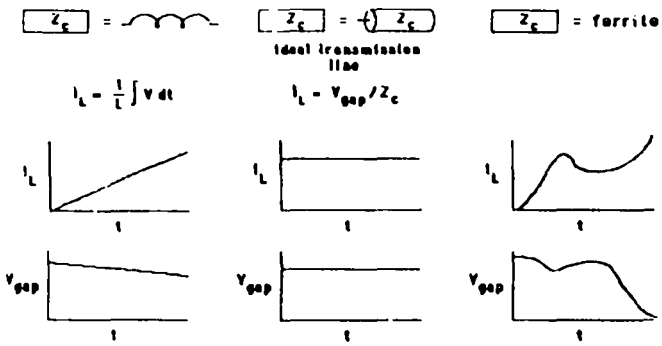

Fig. 3. Accelerator core models.

Various simplified models have been used to calculate the time dependence of the leakage current of ferrite cores and these are illustrated in figure 3. The actual behavior of the leakage current in a realistic core is much more complicated than any of the simple models and is only now beginning to be understood[6].

Another problem which occurs especially for highly efficient accelerators is the variation of cell voltage due to timing jitter of the injected current. Several cases are illustrated in figure 4. In the case of nominal timing a relatively flat voltage across the bulk of the pulse can be achieved. However if the beam current arrives earlier than expected at the cell it will load the voltage down too early and the duration of the "flat top" will be reduced. Likewise if the current arrives too late the cell voltage will overshoot and then decay also reducing the flat top. The voltage errors are proportional to the jitter time and decay with an exponential time constant on the order of Z_0C_g which may be roughly 10 nsecs. for an efficient accelerator. High efficiency generally translates into a high value of Z_0 thus making beam loading very important and causing the time constant to be increased.

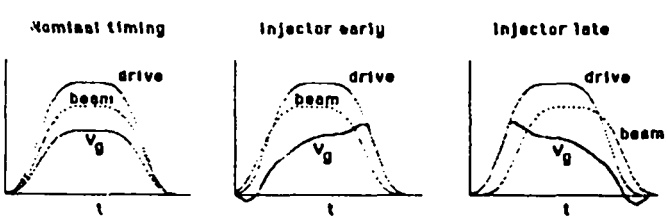

Fig. 4. Effects of current timing jitter.

Specific Solutions

Reduction of Emittance Growth by Rapid Acceleration

Simulations and equations (2) and (3) suggest that the scale length over which emittance grows due to envelope oscillations is inversely proportional to the focusing strength. In addition equation (1) suggests that if γ is increased rapidly enough the emittance growth can be quenched. By reducing the focusing field and increasing the average accelerating gradient significant reductions in emittance growth can be seen in simulations. Figure 5 shows the results of a simulation in which a high brightness beam is accelerated through a structure with an average gradient of 1.0 MV/meter with virtually no increase in rms normalized emittance. Figure 6 shows the change in the square of the normalized emittance for the same problem as a function of the accelerating gradient. This result suggests we seek a transport strategy that minimizes focusing and maximizes accelerating gradient as a way to preserve brightness against space charge induced emittance growth.

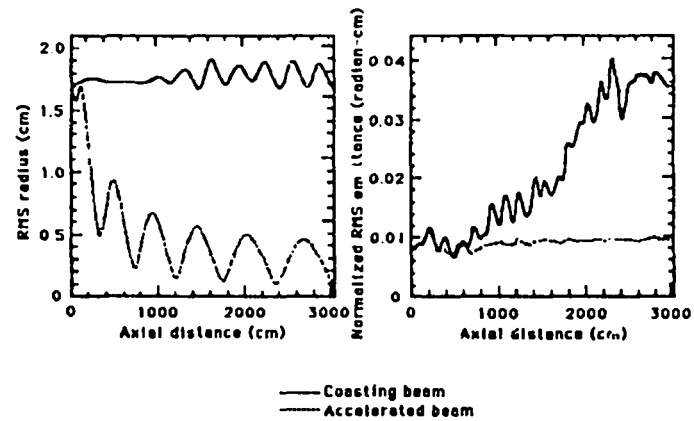

Fig. 5 Effects of acceleration on emittance.

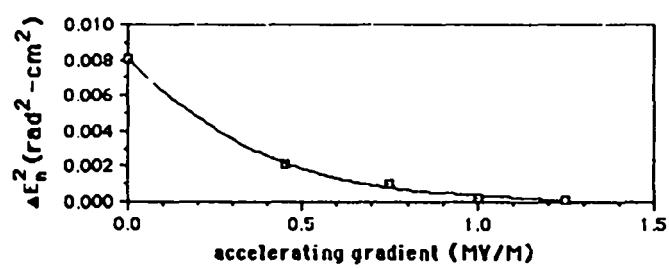

Fig. 6. Emittance growth vs. gradient.

Optimization of BBU and Corkscrew

We have considered two mechanisms which cause transverse beam motion, BBU and corkscrew. From equation (6) we see that BBU growth is reduced by increased focusing yet we see from equation (8) that the corkscrew amplitude is reduced by minimizing the phase advance. These two conditions can be used to find an optimum tune or focusing strategy for the accelerator. Specifically if we define Γ as the log of the BBU gain and ϕ_β as the betatron phase advance:

$$\Gamma = \frac{\omega_b Z_\perp}{2L_g}\frac{I}{I_0}\int_0^z \frac{dz'}{\gamma k_\beta} \tag{9}$$

$$\phi_\beta = \int_0^z k_\beta \, dz' \tag{10}$$

then if we minimize the phase advance with a fixed BBU gain we find that

$$k_\beta = \frac{\omega_0 Z_1}{L_g \lambda} \frac{1}{I_0} \frac{(\sqrt{\gamma_-} - \sqrt{\gamma_0})}{\Gamma \sqrt{\gamma}} \quad . \tag{11}$$

We find that k_β is proportional to $1/\sqrt{\gamma}$ so that the focusing field varies as $\sqrt{\gamma}$. Using this result we may define a figure of merit for an accelerator transport system[7]:

$$\Gamma \phi_\beta = \frac{2\,\omega_0 Z_1}{L_g \lambda^2} \frac{1}{I_0} (\sqrt{\gamma_-} - \sqrt{\gamma_0})^2 \quad . \tag{12}$$

Here λ is the gradient of the accelerator ($\gamma = \gamma_0 + \lambda z$). Reasonable numbers for a high performance design are $\Gamma = 3$ and $\phi_\beta = 100$ radians.

Techniques to Improve Focusing Field Alignment

The present discussion will be confined to the case of solenoidal focusing. Magnetic field errors can arise from several sources. First there may be undesirable components of fields due to the design. Current flowing in the coil leads for example may lead to residual transverse fields on axis. Even if the design is such as to generate no error fields there will be some error in laying down the windings which may cause significant error fields. Finally, even if the coil is perfectly designed and constructed there will be some error in its placement in the accelerator; the coil may be tilted or displaced with respect to the machine axis.

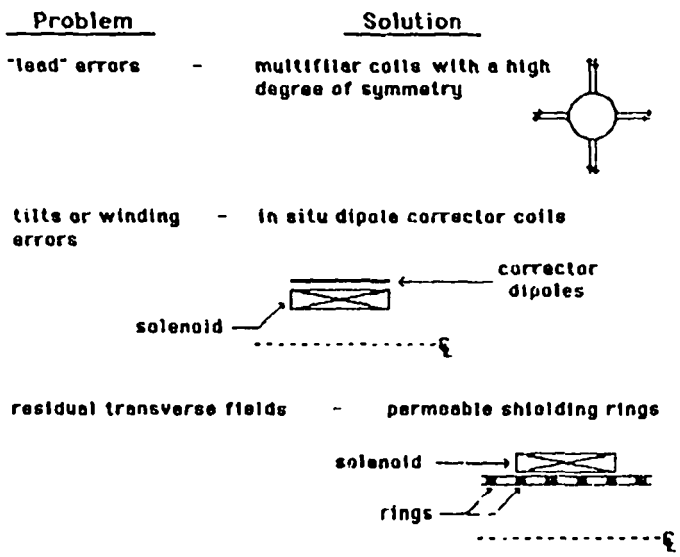

Fig. 7. Magnetic field alignment techniques.

A variety of approaches have evolved to treat the various types of errors. Providing a coil with a high degree of symmetry in the windings is a way to eliminate the transverse fields associated with the leads. Using multifilar coils such as a quadrufilar coil with eight leads packed in bundles of two spaced at 90 degrees around the coil reduces transverse fields on the axis[8]. Tilts and displacements may be minimized by taking care in the placement and alignment of coils within the accelerator cells. To correct for any residual dipole fields on axis a thin, flexible printed circuit set of dipoles may be wrapped around each solenoid for later adjustment. Such an arrangement is in use on several of the accelerators at LLNL[9].

Finally, to reduce any residual transverse fields magnetically permeable rings may be installed inside the coil assemblies. These rings present a low reluctance to any transverse fields and effectively "short" them out while the reluctance in the axial direction is only slightly affected[10]. Figure 7 illustrates these approaches. A pair of accelerators incorporating all of these measures simultaneously is planned for construction at LANL[11].

Delayed Feedback Steering

Even if well designed magnets are precisely installed in the accelerator there will still be residual transverse fields. These fields may be sufficient to cause large transverse beam motion in a long linac (for example if the requirement on transverse beam motion is 200 microns then a beam motion of 1 mm is "large"). In that case some additonal measures must be taken to correct the transverse motion of the beam.

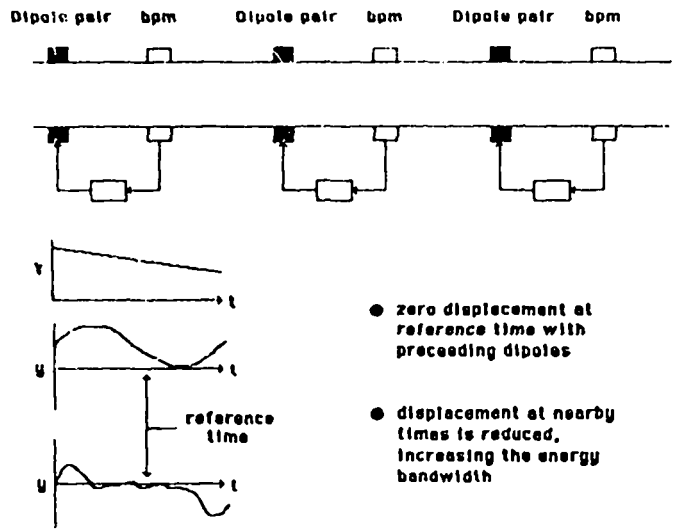

Fig. 8. Delayed feedback steering scheme.

A simple solution in moderate to high repetition rate machines is the use of a delayed feedback steering system. *The accelerator pulses must be sufficiently repeatable in order for this technique to work.* Beam position monitors (bpm's) are placed along the beamline so that there is less than 180 degrees of cyclotron phase advance between them. A point on the pulse (at the middle for example) is chosen as a reference point. A dipole corrector pair upstream of a bpm is then used to zero out the displacement of the reference point at that bpm. The correction is made after observing some number of pulses in order to determine an average correction. One then proceeds to the next bpm downstream and makes similar corrections. A resident computer system could make the corrections very rapidly. The bpm's have some resolution limit and accuracy and these will determine the minimum beam displacement that can be attained for the reference point if the monitors are sufficiently close together (i.e. on the order of 1 radian betatron phase advance between monitors).
An interesting effect occurs as a result of using delayed feedback steering of the reference point. Parts of the beam adjacent to the reference point are also corrected to a high degree if the their energy does not vary too much from that of the reference point. *This leads to a widening of the effective energy bandwidth of the transport system and a dramatic reduction in the corkscrew amplitude.* This is illustrated in

figures 8 and 9. There is a 5% energy variation from 20-65 ns. in figure 9.

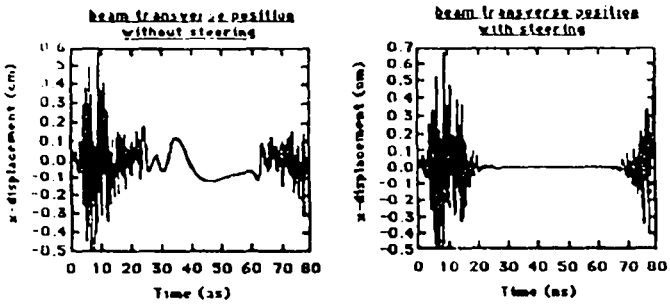

Fig. 9.Steering dramatically improves bandwidth.

Delayed Feedback Energy Regulation

A similar technique can be used to correct the final energy of the beam across the "flat top". The system for accomplishing this is shown in figure 10. An on-line energy analyzer is used to measure the pulse energy as a function of time throughout the pulse over subsequent pulses.

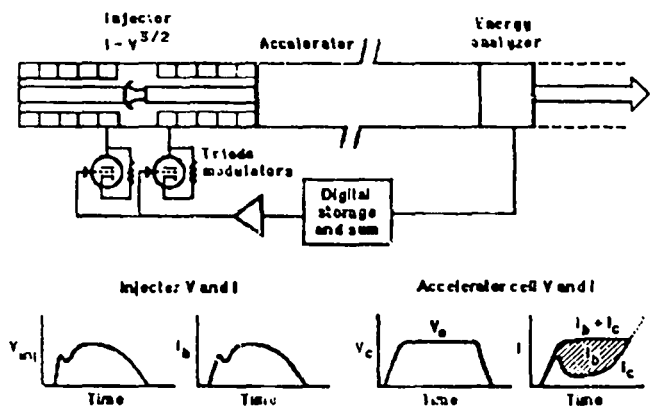

Fig.10. Delayed feedback current control .

This information is used to drive modulators which can apply time varying voltage corrections to the anode of the injector causing the current to vary in a prescribed manner as a function of time through the pulse. The modified beam current will cause cell voltage changes through beam loading and will result in a change in the final energy of the pulse. If the pulses are sufficiently repeatable the feedback system will cause the final energy to be flat limited only by the resolution of the energy analyzer and by the pulse to pulse variations in the final energy[12].

Design Strategy

All of the elements are now in place to formulate a self-consistent design strategy that addresses all the obstacles discussed thus far. The steps in the design are as follows. First determine Γ , the allowable BBU gain, from the output beam requirements. Next set the pipe radius to the maximum practical value and the accelerating gap width to the lowest practical value for the gap voltage and pulse width chosen. Design the cell with a code such as AMOS[13] to obtain a low value of η. Use the highest energy injector possible to minimize the phase advance required in the accelerator and to preserve brightness. These values will then specify the phase advance $\phi\beta$ through equation (12). Use multifilar coils with corrector dipoles and/or permeable rings to provide a relatively error free guide field. Space bpm's at approximately 1 radian betatron phase advance apart for use in delayed feedback steering (if the requirements are not too stringent or the accelerator too long one may be able to dispense with delayed feedback steering and operate the accelerator "open loop"). Use delayed feedback current control to regulate the final beam energy if required.

Conclusions

A number of problems have been discussed which limit the performance of induction linacs. These problems can be overcome by the use of a strategy which incorporates a low phase advance, and high accelerating gradient along with a focusing field that is ramped up proportional to $\sqrt{\gamma}$. The transport line should have the largest bore practical to reduce the BBU growth and thus permit reduction of the focusing field. This should facilitate brightness preservation and result in acceptable BBU gain. The corkscrew problem is then further reduced for a long linac by using delayed feedback to control the energy variations over the pulse and delayed feedback steering to correct the orbit of a reference point on the beam.

References

1. G. J. Caporaso, "Kiloamp High Brightness Beams", Proc. 1987 IEEE Particle Accelerator Conf., 1987,p. 1001.
2. G. J. Caporaso, "The Control of Beam Dynamics in High Energy Induction Linacs", Proc. 1986 Linear Accelerator Conf., 1986, p.17.
3. G. J. Caporaso, et. al., "Beam Dynamics in the Advanced Test Accelerator (ATA)", Proc. 5th Int Conf on High Power Beams (BEAMS'83).
4. G. J. Caporaso and R. J. Briggs, "High Current Electron-Beam Transport in Induction Linacs", Proc. Beijing FEL Seminar, World Scientific 1989.
5. Y.J. Chen, "Corkscrew Modes in Linear Accelerators", Nuc. Instr. and Meths. in Phys. Res. A292 (1990) 455-464
6. R.K. Avery, J.F. DeFord, G. Kamin, W.C. Turner and J.M. Zentler, "A Simple Model of Flux Reversal in Ferrites", J. Appl. Phys. 67 (9), 1 May 1990 p. 5562.
7. This was first pointed out to the authors by Ian Smith.
8. W.E. Nexsen, Jr., "Characterization of Field Errors of Layer Wound Short Solenoids", presented at these proceedings.
9. J. Clark et al., "Design and Initial Operation of the FTA-II Induction Accelerator", Proc. 1988 Lin. Acc. Conf., p. 19.
10. B. Feinberg, I.G. Brown, K. Halbach and W.B. Kunkel, "A Method for Improving the Quality of the Magnetic Field in a Solenoid", Nuc. Instr. and Meth. 203 (1982) 81-85.
11. M. Burns, LANL, private communication.
12. E.E. Bowles and W.C. Turner, "50 MHz 12 MW Induction Linac Current Modulator", Proc. 7th IEEE Pulsed Power Conf., Monterey, Ca. 1989.
13. J.F. DeFord, G.D. Craig and R.R. McLeod, "The AMOS Wakefield Code", Proc. Wkshp. on Acc. Codes, Los Alamos, NM, Jan. 22-25, 1990.

*Performed jointly under the auspices of the US DOE by LLNL under W.7405-ENG-48 and for the DOD under SDIO/SDC-ATC MIPR No. W31RPD-8-D5005.

HEAVY ION INDUCTION LINACS FOR FUSION

Roger O. Bangerter,
Lawrence Berkeley Laboratory, University of California, Berkeley, CA 94720;

Darwin D-M. Ho
Lawrence Livermore National Laboratory, Livermore, CA 94550

Abstract

In 1976 Denis Keefe proposed the heavy ion induction linac as a driver for inertial confinement fusion (ICF) power plants. Subsequent research has established that heavy ion fusion (HIF) is potentially an attractive energy source and has identified the issues that must be resolved to make HIF a reality. The principal accelerator issues are achieving adequately low transverse and longitudinal emittance and acceptable cost. Results from the single and multiple beam experiments at LBL on transverse emittance are encouraging. A predicted high-current longitudinal instability that can affect longitudinal emittance is currently being studied.

This paper presents an overview of economics and ICF target requirements and their relationship to accelerator design. It also presents a summary of the status of heavy ion induction linac research. It concludes with a discussion of research plans, including plans for the proposed Induction Linac Systems Experiments (ILSE).

Introduction

In 1974 A.W. Maschke proposed heavy ion accelerators as drivers for inertial confinement fusion (ICF) power plants. Synchrotrons and r.f. linacs were the first types of accelerators studied for this application. In the r.f. linac systems, the linac is followed by storage rings to accumulate enough energy and to produce enough power to drive the ICF targets. In 1976 Denis Keefe proposed using induction linacs rather than r.f. linacs. He recognized that the high current capability of inductions linacs might eliminate the need of storage rings. Subsequent research on both r.f. and inductions linac systems has continued to show that both remain promising ICF drivers.

Economics and Target Requirements

To be economically competitive with future fission or coal power plants, a fusion plant must cost less than about $2/watt. Thus, a typical 1 GW(electric) power plant must cost less than about $2B. This cost must cover the reactor, turbines, generators, target factory, and the driver. Detailed systems studies show that about $600M may be allocated to the driver.[1] The allowable driver cost is roughly proportional to the power plant capacity. Thus, the driver for a 2-GW power plant could cost about $1.2B and so on. In the U.S. power utilities prefer plants with capacities less than about 1 GW so that $600M is a desirable goal for a driver.

* This work was supported by the Director, Office of Energy Research, Office of Basic Energy Sciences, Advanced Energy Projects Division, U.S. Dept. of Energy, under Contract No. DE-AC03-76SF00098 and by the Lawrence Livermore Laboratory under Contract No. W7405 ENG-48.

In addition to cost there is also a requirement on the product of driver efficiency η and target gain G. For power plants using conventional thermal-to-electric energy conversion with an efficiency of 35-45%, ηG must be larger than about 10.[1] If ηG is low the power required to drive the driver becomes an unacceptably large fraction of the gross power output of the plant, leaving too little power available to be sold at a competitive price. Calculated efficiencies of heavy ion induction linacs are about 25% so that target gain must be larger than 40. Nearly all targets designed for ICF power production use deuterium and tritium as fuel. Target gain depends on total beam energy, ion range, and focal spot radius. Calculated target gain as a function of these variables is shown in Fig. 1.[2] Note that the gain decreases rapidly with increasing focal spot radius so that achieving adequate beam quality to allow a small focal spot is an important consideration in accelerator design. In order to achieve the target gain shown in Fig. 1, the beam pulse must be shaped. The beam power must initially be low, increasing to its peak value for about the last 20% of the pulse. Usually 60-80% of the total beam energy is delivered at peak power. The peak power requirement as a function of beam energy, ion range, and focal spot size is shown in Fig. 2.

For illustrative purposes we consider a single specific case, namely a 3.5-MJ pulse of 10-GeV heavy ions (A = 200 amu). These ions have a range of approximately 0.1 g/cm^2 in the hot matter of the fusion target. If the beams are focused to a radius of 2.5 mm, Figures 1 and 2 give a target gain of 50 and a peak power requirement of 300 TW. At 10 GeV, 300 TW corresponds to a particle current of 30 kA. Typical quadrupole focusing systems for heavy ion fusion (HIF) power plants produce a beam convergence angle of 10-20 mr so that the beam emittance must be less than 25-50π mm·mr. Since the particle velocity parameter β is about 0.3, the normalized emittance ϵ_N must be $\lesssim 10\ \pi$ mm·mr. In addition, chromatic aberrations in uncorrected systems limit the longitudinal momentum spread $\delta p/p$ to less than 0.5-1%.[3] A summary of the target and economic requirements is given in Table I. It must be emphasized that these requirements are only one example. Other plant capacities, ion kinetic energies, ion masses, and focal spot sizes would give other requirements.

Table I.
Example economic and target requirements for heavy ion fusion

• Total beam energy	3.5 MJ
• Ion kinetic energy	10 GeV
• Beam power	300 TW (particle current = 30 kA)
• Ion mass	~200 amu
• Focal radius	2.5 mm ($\epsilon_N \lesssim 10\pi$ mm·mr, $\delta p/p \lesssim 0.5\%$)
• Driver cost	$\lesssim$0.6 G$

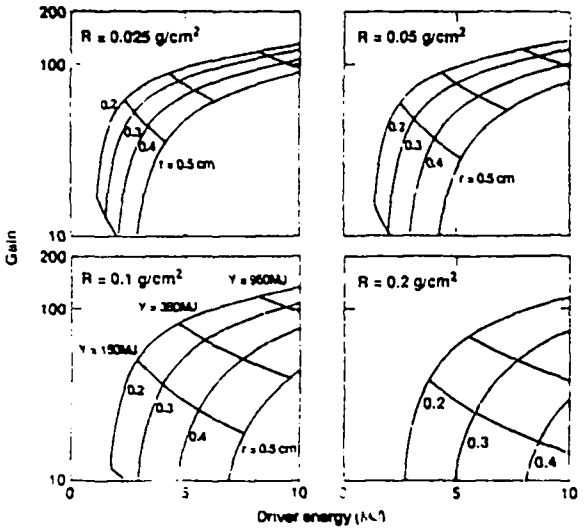

Fig. 1. Target gain as a function of driver energy, focal spot radius (r), and ion range (R). Curves of constant energy yield (Y) are also shown.

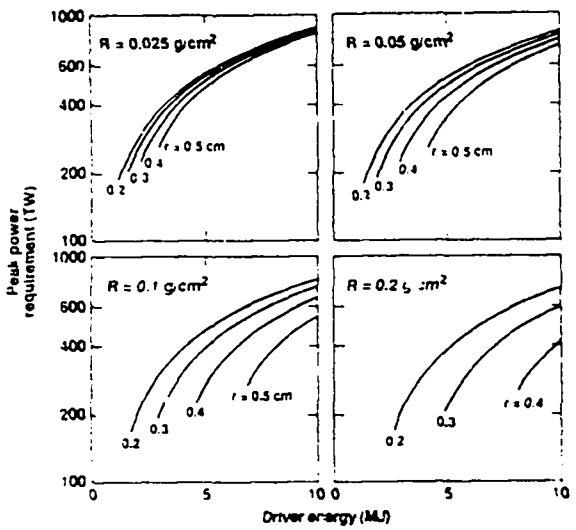

Fig. 2. Peak power requirements for the gain curves shown in Fig. 1.

Induction Linacs for Heavy Ion Fusion

An example of an induction linac designed to meet the requirements listed in Table I is shown in Fig. 3. This example uses charge state +3 which for 200-amu ions gives a shorter, less expensive linac than charge state +1. In terms of emittance and economics it is advantageous to accelerate multiple beams though common induction cores. The example shown employs 64 beams for ion energies less than 100 MeV. At 100 MeV the 64 beams are transversely merged into 16 beams. The ions in the 16 beams are then accelerated to 10 GeV. Since heavy ions at 10 GeV are not very relativistic, their velocity changes nearly a factor of 10 as they are accelerated from 100 MeV to 10 GeV. Thus, if the beam length were constant, the 225A electrical (not

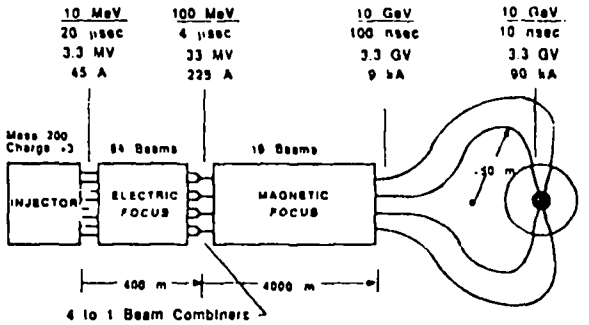

Fig. 3. Example induction linac concept.

particle) current at 100 MeV would increase to 2.25 kA at 10 GeV. In the example shown there is an additional 4-fold increase in current obtained by longitudinal bunch compression. The longitudinal bunch compression is obtained by accelerating the tail of the beam to a slightly higher speed than the head of the beam. The final current at the end of the accelerator is 9 kA or 3 kA of particle current. A current of 9 kA is well within the demonstrated capability of induction linacs, but it is an order of magnitude less than the 90 kA (30 kA of particles) required for target ignition. Therefore, the acceleration schedule is arranged so that the velocity difference along the beam gives an additional factor of 10 compression as the beam drifts toward the target. Numerical simulations suggest that the velocity profile may also be programmed to give the appropriate pulse shape.[4]

The scenario just described raises several important issues: Low emittance, high current, reliable heavy ion sources must be developed, preferably with the ability to produce ions in a specified charge state. The complexity of the accelerator and its alignment system are greater for 16 or 64 beams than for the standard 1 or 2 beams in most accelerators or colliders. The emittance growth associated with the acceleration, transport, merging, bunching, bending and focusing of high current beams must be studied. High current beams are also subject to the well known longitudinal instability that arises from the interaction of the beam with the impedance of the accelerating structure. This instability is discussed in the paper by Edward P. Lee and Lloyd Smith given at this conference. It is also discussed in the paper by J.R. Freeman and J.S. Wagner. The longitudinal instability is potentially important because it may give rise to excessive $\delta p/p$. Some calculations show that the instability is quenched by a momentum spread of about 1%; however, for the scenario described here, a 1% momentum spread in the accelerator corresponds to a 10% spread at the final focusing elements because of the longitudinal beam compression after the beam leaves the accelerator. In the opinion of the author some active feedback may be required to suppress this instability. Finally, cost is an issue. Studies show marginally acceptable costs ($500-1000M) for a 1-GWe power plant.[5]

Since the inception of the HIF program in 1976 a number of theoretical and numerical studies and a number of experiments have addressed the issues outlined above. In the late seventies Lawrence Berkeley Laboratory built a 1-ampere cesium source with a normalized emittance of the order of 0.1 π mm·mr or about two orders of magnitude lower than needed at the end of the machine.[6] A grid was used to increase the emittance of this source to 2π mm·mr[7] because of concerns about the stability of low-emittance beams. These concerns have now been alleviated. A single beam transport experiment using 86 electrostatic quadrupoles demonstrated stable beam transport without significant emittance growth for low-emittance space-charge-dominated beams.[8] The space charge forces in these experiments were strong enough to depress the betatron

frequency about an order of magnitude below its single particle value. Such strong depression means that the space charge forces are very nearly equal to the applied focusing forces. The Multiple Beam Experiment with 4 beams (MBE-4) started operation at LBL in 1987. It has demonstrated acceleration and bunching of multiple beams. Some details of this experiment are given in the paper by T. Garvey et al. at this conference.

New development and experiments are needed to resolve the remaining issues. Development of sources of ions other than cesium is needed. Transport of heavily space-charge-dominated beams has been demonstrated in electrostatic quadrupole systems but requires demonstration in magnetic systems. Bending, merging, bunching, and focusing have been studied analytically and numerically but experiments are needed. Characterization of large induction cavities and their associated circuitry is necessary to understand and control longitudinal dynamics. Finally, technology development is needed to achieve low cost.

Lawrence Berkeley Laboratory has proposed an integrated series of experiments, the Induction Linac Systems Experiments (ILSE)[9] to address many of the remaining issues. The present preliminary design of ILSE is shown in Fig. 4. The total length from injector to focus is roughly 100m. ILSE, at small scale, tests many of the features of a full-scale driver. ILSE has been favorably reviewed by DOE and Congressional review committees. A high voltage injector for ILSE is now being assembled at LBL. If funding is available, assembly of the remainder of ILSE will begin in about a year. One feature that ILSE cannot test well is the longitudinal instability. A large induction cavity is currently being built to provide an experimental determination of the longitudinal coupling impedance. The AMOS code is being used to simulate induction cavities for HIF. At this conference the papers by J.F. DeFord, C.C. Shang, G.D. Craig, and G. Kamin describe simulation of induction cavities and the AMOS code.

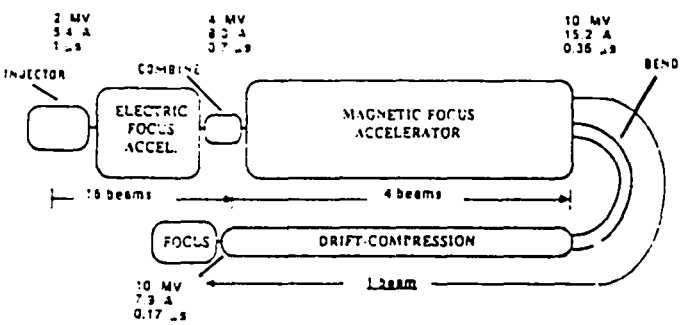

Figure 4. Diagram of the preliminary design of the Induction Linac Systems Experiments (ILSE).

Cost remains an important issue. Lawrence Livermore National Laboratory and Lawrence Berkeley Laboratory are evaluating recirculating induction linacs as a potential way to reduce cost. If this evaluation is favorable, it may be possible to test recirculation on ILSE by providing an additional 180° bend.

If the ILSE experiments are successful we hope to construct a larger intermediate facility in the latter half of the decade so that we can be in a position to construct a full-scale ICF driver early in the next century.

In conclusion, theoretical and experimental results to date are encouraging. It appears that HIF is potentially an attractive commercial energy source; however, significantly larger experiments such as ILSE are required to resolve remaining issues.

The authors thank the HIF staff at Berkeley and Livermore for their help and support in preparing this paper and for tireless efforts in behalf of the HIF program.

References

1. William J. Hogan and Wayne R. Meier, "Economic Requirements for Competitive Laser Fusion Power Plants," *Proc. 11th Symp. Fusion Engineering*, Austin, Texas, November 18-22, 1985. IEEE Cat. CH2251-7, p. 139, Institute of Electrical and Electronics Engineers (1986).

2. These results are based on recent work by D. D-M. Ho and R.O. Bangerter. They are revisions of results previously published. See R.O. Bangerter, "Targets for Heavy Ion Fusion," *Fusion Technology* 13, 348, (1988).

3. H. Wollnik, J. Brezina, and M. Berz, "Space Charge Effects in Final Focusing Systems," *Proc. INS Int. Symp. Heavy Ion Accelerators and Their Applications to Inertial Fusion*, Tokyo, Japan, January 23-27, 1984, p. 433, Institute for Nuclear Study, University of Tokyo (1984).

4. J. W-K. Mark, D. D-M. Ho, S.T. Brandon, C-L. Chang, A.T. Drobot, A. Faltens, E.P. Lee and G.A. Krafft, "Studies on Longitudinal Beam Compression in Induction Accelerator Drivers," *Proc. Int. Symp. Heavy Ion Fusion*, Washington, D.C., May 26-29, 1986, AIP Conference Proceedings 152, p. 227, American Institute of Physics (1986).

5. Jack Hovingh, Victor O. Brady, Andris Faltens, Denis Keefe, and Edward P. Lee, "Heavy Ion Linear Induction Accelerators as Drivers for Inertial Fusion Power Plants," *Fusion Technology*, 13, 255 (1988).

6. S. Abbott, W. Chupp, D. Clark, A. Faltens, E. Hoyer, D. Keefe, C. Kim, R. Richter, S. Rosenblum, J. Shiloh, J. Staples, E. Zajec, "Part III: The Experimental Program on Heavy Ion Fusion at Lawrence Berkeley Laboratory," *Proc. Heavy Ion Fusion Workshop*, Argonne, Illinois, September 19-26, 1978, ANL-79-41, p. 50, Argonne National Laboratory (1979).

7. W. Chupp, A. Faltens, E. Hartwig, E. Hoyer, D. Keefe, C. Kim, M. Lampel, E. Lofgren, R. Nemetz, S.S. Rosenblum, J. Shiloh, M. Tiefenback, D. Vanecek, and W. Herrmannsfeldt, "Operating Experience with a High Current Cs^{+1} Injector for Heavy Ion Fusion," *IEEE Trans.Nucl. Sci.* NS-28, 3, 3389 (1981).

8. M.G. Tiefenback and D. Keefe, "Measurements of Stability Limits for a Space-Charge-Dominated Ion Beam in a Long A.G. Transport Channel," *IEEE Trans. Nucl. Sci.*, NS-32, 5, 2483, (1985).

9. "Induction Linac Systems Experiments, Conceptual Engineering Design Study," PUB-5219, Lawrence Berkeley Laboratory, March 1989.

RECENT DEVELOPMENT IN INERTIAL FUSION BASED ON RF ACCELERATION

Ingo Hofmann
GSI Darmstadt, 6100 Darmstadt, Germany

Abstract

Heavy ions continue to be a challenging driver option for inertial confinement fusion. Completion of the GSI facility in 1990 provides an ideal testing ground for most of the accelerator issues for the rf linac/ storage ring approach to HIF. The status of this work is presented as well as the performance of an advanced driver scheme using non-Liouvillean stacking by photoionization of single charged ions. This scheme is expected to fulfil the increased power requirements of indirectly driven targets.

Introduction

The HIBALL study [1] has been the first overall system study for HIF. It has shown that the requirements for directly driven targets can in principle be met by conventional accelerator technology using an rf linac, several storage rings and buncher rings for final bunch compression. In that study it was, however, recognized that there are severe limitations due to the space charge of the intense beams and the associated emittance growth at various stages of the acceleration, stacking, storage and final bunch compression. The uncertainty of the HIBALL design would be serious, if several large emittance growth factors had to be accepted. It is accepted that the design of a consistent driver scenario has the highest priority among the various issues of inertial fusion (driver, target, reactor) [2]. The new GSI accelerator facility SIS/ESR - going fully into operation in 1990 - is suitable to answer most of these problems [3],[4],[5].

Recently Rubbia [6] has pointed out that the confidence in realizing a heavy ion fusion driver can be greatly increased by introducing a non- Liouvillean stacking from the linac into the accumulator ring. A related suggestion was made earlier by a group at Argonne National Laboratory who proposed to use photodissociation of molecular ions for non- Liouvillean injection from a synchrotron into a storage ring[7]. The most efficient use of the non- Liouvillean technique is, however, not at injection from the linac into the accumulator ring, but from the storage ring to the final bunch compression ring. This follows essentially an idea described in Ref. [5], where foil stripping was suggested for lighter ions. The main advantage of this new scheme is that the beam remains only a relatively small number of revolutions in the compression ring. Thus the phase space density can go far beyond the thresholds valid for usual storage times and power requirements of indirect drive can be fulfilled.

Status of SIS/ESR

The SIS/ESR (see Fig.1) is suitable as a testing ground for HIF machine and beam dynamics studies mainly for the following reasons:
(a) the UNILAC provides ions up to the highest masses.
(b) injection and re-injection from the SIS into the ESR gives a high flexibility in modes of operation.
(c) electron cooling allows to achieve maximum phase space densities for bunched and unbunched beams near the thresholds of instabilities.

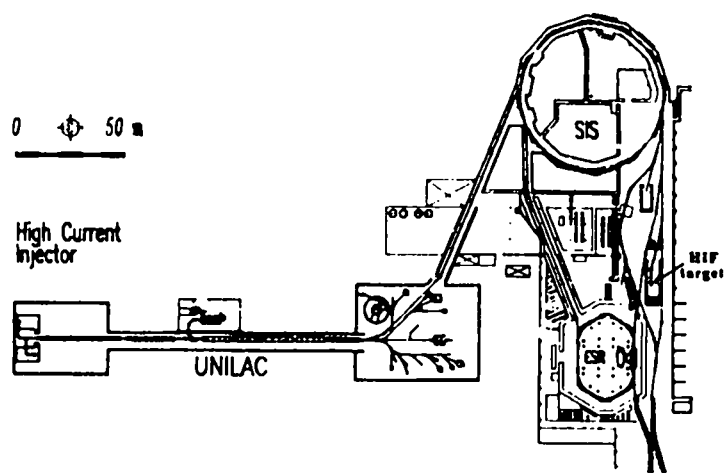

Fig.1. The SIS/ESR accelerator system.

Running-in Experiments

After beginning of operation of the ESR in April 1990 the main effort went into closed orbit, tune and chromaticity measurements and corrections. Electron cooling has been successfully demonstrated for beams of relatively low intensities (typically $< 10^8$ particles) with the Schottky diagnosis system, which indicates a decrease of $\Delta p/p$ from $\pm 2 \cdot 10^{-4}$ to almost $\pm 10^{-5}$. An increase of the intensity by an order of magnitude due to a more efficient transfer of beam from the SIS into the ESR is the goal of the next machine development periods end of 1990. This will bring the cooled beam into the space charge dominated regime with all phenomena of collective behaviour, in particular instabilities and nonlinear space charge forces.

High-Current Injector

A high-current injector into the UNILAC is planned for completion by the end of 1992. It will provide a beam of 1.4 MeV/u of charge state 2+ up to the heaviest ions. A prototype of the first section of the 27 MHz RFQ is presently built in a collaboration with the University of Frankfurt. Together with electron

cooling we expect to yield maximum intensities in a single bunch of up to 10^{11} particles and 2.5 kJ energy. In Table I we show the expected performance for a cooled Xe beam with the SIS filled by a high-current injector.

TABLE I
Expected Performance of Target Experiments at SIS/ESR

Ion	Xe^{44+}
N	$1.2 \cdot 10^{11}$
energy MeV/u	1100
Δt nsec	70
total energy J	2500
power density TW/cm^2 (peak)	200
average range g/cm^2	25
specific power TW/g	8

This will permit new experiments on beam plasma interaction, generation of plasmas near solid state density and dense plasma hydrodynamics [8].

Beam Dynamics Investigations

Longitudinal Microwave Instabilities

A heavy ion storage ring must operate at intensities, which are above the conventional Keil-Schnell threshold for the onset of the longitudinal (resistively driven) microwave instability, otherwise it would be impossible to satisfy the requirements on beam phase space density. An important result has been obtained in the Heidelberg TSR electron cooling storage ring. In Fig.2 we show the Schottky noise spectrum of a coasting beam of 2.5 mA of C^{6+} at 11.7 MeV/u before and after cooling [9].

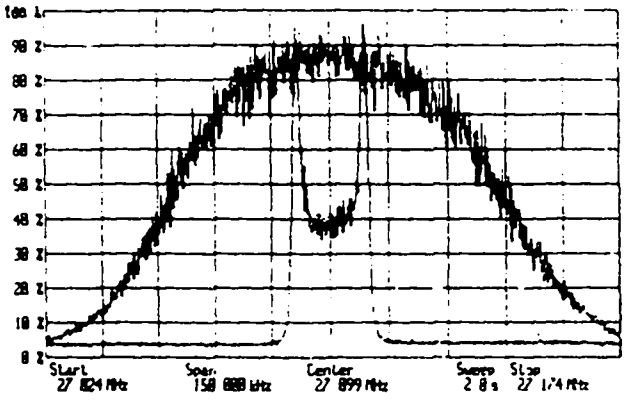

Fig.2. Schottky noise spectrum of uncooled and cooled beam in the TSR.

The uncooled beam noise spectrum reflects the Gaussian momentum distribution. The cooled beam spectrum (still with a Gaussian momentum distribution) shows two strong peaks, which are due to the excitation of collective oscillations. A theoretical evaluation of this noise spectrum has shown that it is equivalent to a current, which is a factor of 5.7 above the Keil-Schnell threshold [10]. The latter is usually defined for an assumed parabolic distribution; the cooling experiment has obviously resulted in a Gaussian distribution, which has extended tails that provide Landau damping and thus permit a higher current than a parabolic distribution.

This is an important basis for the design of the storage rings described below, where we can thus rely on a factor of 6 above the Keil-Schnell threshold. In the near future experiments can be performed in the ESR, which allow to study the resistive instability of bunched beams in the time domain. By stripping of a Ne^{3+} beam to Ne^{10+} we could exceed the threshold by an additional factor of 11 and investigate theoretical predictions on a nonlinearly evolving stabilizing tail [11] for beams far above the Keil-Schnell threshold.

Longitudinal Bunch Compression

In the ESR such experiments can be performed precisely under the conditions of final bunching in HIF, where the crossing of one or two integer resonances due to space charge forces is required. Cooling of a Ne^{3+} beam in an rf bucket of 0.16 kV amplitude to a space charge tune shift of $\Delta Q = 0.01$, stripping to 10+ in the re-injection line to the SIS and subsequent rf bunching by rising the amplitude to 16 kV can lead to $\Delta Q \approx 1$. This results in crossing of an integer and two half-integer resonances. Moreover, the effect of nonlinear space charge forces can be studied by measuring the longitudinal beam current profile at different instants of the bunch compression.

Advanced Concept for a Driver with Photoionization

Phase Space Compression Factor

Starting from the HIBALL accelerator as a reference we estimate the desired "compression-factor" in phase space volume by the following considerations:

1. The higher beam power for indirect drive must be delivered. We are aiming for a power density of 10^{16} W/g.

2. The safety margin for stable operation (in the sense of beam dynamics) must be increased, in particular with respect to the longitudinal microwave instability.

The main change is the smaller spot area by a factor 9. This requires an appropriate reduction in the product emittance times momentum spread, if we use as a first order estimate the following scaling relationship for chromatic aberrations [15]

$$\epsilon \Delta p/p \propto r_0^2/L \qquad (1)$$

where L is the focal length (i.e. reactor chamber radius).

In addition we want to increase the momentum spread in the storage rings from the HIBALL value of 10^{-4} to $3 \cdot 10^{-4}$ to bring the current in agreement with the above discussed experimental threshold for longitudinal stability. In this case the asumption of a stabilizing tail [11] in the momentum distribution as assumed for the HIBALL storage rings becomes unnecessary.

The reduced spot area and stability of storage rings thus require a reduction in the product $\epsilon \Delta p/p$ by a typical factor 27. This can be achieved, for instance, by a non- Liouvillean "compression-factor" of 16 (i.e. 16-fold stacking) and an increase of the total number of beam lines to the target from 20 to 40. We remark that the beam overlap at the focal spot has a similar effect as the non- Liouvillean stacking in the sense that it helps save phase space volume.

Photoionization Scheme

In the following we discuss some general features of the proposed non- Liouvillean "compression" scheme. We assume that the required $3 \cdot 10^{15}$ particles are filled into 10 storage rings similar as in HIBALL. For this purpose one could use as an injector the HIBALL linac, but now with the much more comfortable momentum spread of $3 \cdot 10^{-4}$ rather than 10^{-4}.

For Bi^{+1} and an emittance of 16π mm mrad we obtain a Laslett tune shift in the storage rings of $\Delta Q = 0.21$ for the coasting beam. This should be tolerable for the assumed maximum storage time during filling of all the rings within 5...10 milliseconds.

The next step is the transfer of the coasting beams into the compression rings by photoionization stacking in a common section of the two rings. The photon beam from a free electron laser is turned on for an interaction time Δt, (which is a small fraction of the revolution time), during which the charge state is changed from 1+ to 2+ in a single transit. The simplest scheme (Fig.4) is using two strong dipole magnets to separate the orbits. Due to the doubled magnetic rigidity and by using superconducting magnets it is possible to introduce an angle of the order of 100 mrad between the two beams and thus guide the doubly charged ion into the adjacent compression ring.

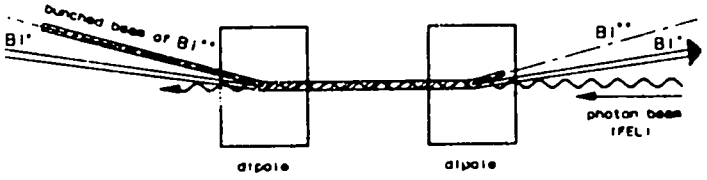

Fig.4. Scheme of photoionization bunch stacking

This method of using the laser in a combined function as "razor" to cut off chops of beam of finite duration, and as a tool for non- Liouvillean stacking allows to work with a coasting beam in the storage rings, rather than a bunched beam. The timing of the photon beam is such that the content of each storage ring is converted into 4 bunches of 100 nsec duration in the compression ring. This process takes 16 revolutions, after which an rf bunching voltage must be applied to compress the bunches from 100 nsec to 10 nsec by a fast bunch rotation. The final part of this rotation occurs within the beam lines to the target. The lattice of the beam lines must be sufficiently dense to transport the maximum current of 2.5 kA. For the above parameters we have calculated that this is consistent with a tune depression from $\sigma_0 = 60^0$ to $\sigma = 4.7^0$ for a pole-tip field of 3 Teslas.

The general scenario is shown in Fig. 5, where a stack of 10 storage and compression rings is required. We assume that the storage rings are filled one after the other by horizontal betatron stacking from the large accumulator ring, into which the linac beam is injected by vertical betatron stacking. A 8x8 stacking is required in order to step up a linac current of 122 mA to the storage ring current of 7.8 A. After transfer into the compression rings the final bunch rotation requires a coherent momentum spread of $\pm 1\%$ to overcome space charge, which can be provided by rf cavities in the compression rings. 20 beam lines should deliver beam on each target absorber disk.

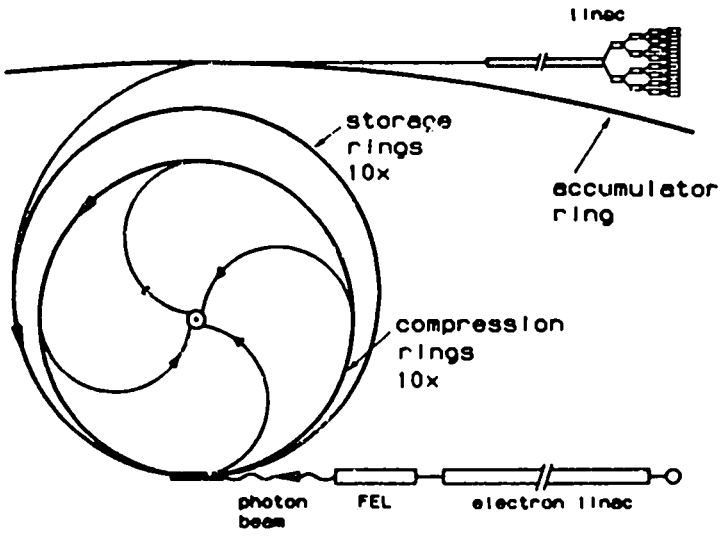

Fig.5. Advanced driver scenario.

High Current Beam Dynamics

Emittance growth in connection with the photon-ion beam interaction region is a crucial issue of the photoionization compression scheme, which leads to a step-wise increase of beam current to a maximum value of 250 A. As we consider only 16 revolutions for this process, we do not expect any problems with

single bunch stability, even though the final current is far above the Keil-Schnell threshold for the longitudinal microwave instability. Also, we expect that there is no serious bunch lengthening due to space charge during the time considered.

Emittance growth in the transverse phase planes during current increase has to be examined more carefully. The problem here is that the lattice of the compression ring must accommodate the zero-current bunch ends as well as the high-current bunch center, which is increased by 15.8 A every revolution (in our example). The betatron tune in our case is depressed to about half of its initial value due to space charge, hence the beam dynamics of these bunches is more related to a linac than to a storage ring. In a numerical simulation the effect of dipole errors during crossing of an integer resonance for the incoherent betatron tune has been found to be small [16], unless the coherent tune also crosses the integer. For the nonrelativistic energies considered here the coherent tune shift depends only on electrostatic images on the beam pipe, hence it can be made small by taking a sufficiently large beam pipe. We conclude that integer crossing is not a problem and that the lattice behaves more like a linear system. Hence, the remaining problem is to study the beam dynamics in a lattice composed of 16 periodically repeating interaction sections, with transport sections in between that correspond to the length of the ring circumference.

We have studied the effect of space charge by computer simulation of a coasting beam by increasing the current in steps of 8 A every time the beam goes through the interaction region. The code we have used is a two-dimensional tracking code with space charge calculated by means of a Poisson solver. In most cases we have used 500 simulation particles and modeled the current increase by increasing the charge per simulation particle.

For the lattice of the interaction region one can consider either a "mini-beta" waist or a periodic transport section with dense focusing. A small size of the beam in the interaction region is crucial in order to reduce the required laser power. Here we report about results for the mini-beta solution. With the relatively large emittance we have found that a 0.3 cm radius waist can be used effectively over 1 m length. We have defined such a mini-beta system with matching quadrupoles to match to the periodic transport under zero current conditions. The results can be summarized as follows:

(1) With increasing current the waist has moved away from its original position. This mismatch has to be compensated by resetting the matching quadrupoles every time the current is increased.
(2) The stacking of the phase space distribution within the original emittance works in principle, but a small fraction of the particles develop into a ring halo in transverse phase space (see Fig.6)

This preliminary result is encouraging as it shows that with acceptance of a small loss of intensity one can indeed stack in transverse phase space, even under extreme space charge conditions.

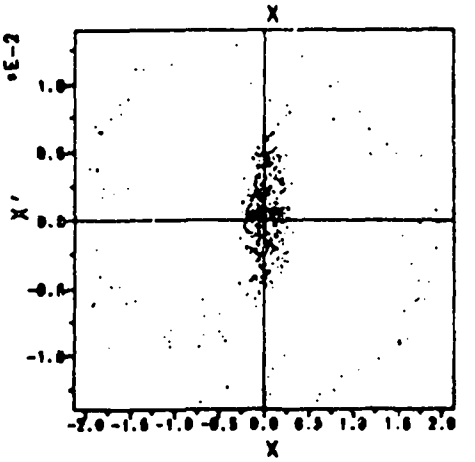

Fig.6. Transverse phase space after stacking.

FEL Requirements

We first consider the process $Bi^{1+} \rightarrow Bi^{2+}$ (see Ref.[6]) and assume a cross section σ_{ph}, a density of photons, n_{ph}, and a conversion path length Δl. With $\Delta N = N n_{ph} \sigma_{ph} \Delta l$ we find for 90% conversion that

$$n_{ph}\sigma_{ph}\Delta l \approx 2.3 \qquad (2)$$

Since we are interested in pulses of doubly charged ions of 100 ns duration we can only allow for typically 10 ns of interaction for the stripping process. This is equivalent to traveling over a distance of 93 cm for $\beta = 0.31$. We thus assume an interaction length of 1 m and obtain for the light beam of photons with energy E (eV) and a beam cross section F:

$$P = 2.3 \frac{FceE}{\Delta l \sigma_{ph}} \quad Watts \qquad (3)$$

For our example with F=0.28 cm^2 we find:

$$P \approx 0.3 \cdot 10^{-10} E/\sigma_{ph} \quad Watts \qquad (4)$$

In the moving frame we require a Doppler shifted photon energy of 20 eV for $Bi^{1+} \rightarrow Bi^{2+}$ and in the laboratory frame a Doppler shifted energy of 14.5 eV. If we assume a cross section of $3 \cdot 10^{-17}$ cm^2 this results in a laser power of 16 Megawatts to be delivered in pulses of 100 ns duration.

This might be more than technically feasible, even with advanced FEL schemes. We have therefore looked at other ions with possibly more favourable cross sections. Measured cross sections exist for Ba^+ ions[17]. For energies above the ionization threshold, namely at about 21.2 eV, these cross sections are as large as $2.8 \cdot 10^{-15}$ cm^2. They are sharply peaked due to resonant autoionization effects. Simple estimates show

that the energy and angular resolution of our beams is roughly compatible with the resonance width, which is about 0.025 eV. For this case there could be a reduction of the required laser beam power by almost two orders of magnitude, hence 0.2 Megawatt would be sufficient. This is the average laser power, which can be delivered by a train of short pulses. The requirements on electron beam performance for a high-gain FEL at 80 nm wavelength are demanding. Bonifacio [18] has suggested a double undulator, where the first one is resonant at the more comfortable wavelength of 240 nm wavelength and generates a third harmonic bunching of the beam, which is amplified in the second undulator. Thus one obtains several Megawatts of light at 80 nm wavelength, which can be generated periodically by an electron linac.

References

1. B. Badger et al., Karlsruhe Report KfK-3480 (1984)
2. R.O. Bangerter, Nucl. Instr. and Meth. A278 (1989) 35
3. D. Boehne, Proc. of the INS Int. Symp. on Heavy Ion Acelerators, Tokyo, January 23-27 (1984) 173
4. I. Hofmann, Proc. of the INS Int. Symp. on Heavy Ion Acelerators, Tokyo, January 23-27 (1984) 184
5. I. Hofmann, Nucl. Instr. and Meth. A278 (1989) 271
6. C. Rubbia, Nucl. Instr. and Meth. A278 (1989) 253
7. R.Arnold et al., IEEE Trans. Nucl. Sci. NS-24 (1977) 1428
8. D.H.H. Hoffmann, "Heavy Ion Beams for Inertial Confinement Fusions", Proc. European Particle Accelerator Conference, Nice, June 12-16, 1990
9. D. Kraemer et al., "One Year of Operation at the Heidelberg TSR", Nucl. Inst. Meth. A287 (1990) 287
10. I. Hofmann et al., "Diagnostics and Instability Studies of Cooled Ion Beams", Proc. European Particle Accelerator Conference, Nice, June 12-16, 1990
11. I. Hofmann, "Suppression of Microwave Instabilities", Laser and Particle Beams 3 (1984) 1
12. J. Meyer-ter-Vehn, Nucl. Instr. and Meth. A278 (1989) 25
13. J. Meyer-ter-Vehn, Proc. 16th European Conf. on Controlled Fusion and Plasma Physics, Venice, March 13-17, 1989
14. G. Buchwaldt et al., "Irradiation Symmetry of Heavy Ion Driven Inertial Confinement Fusion Targets", Laser and Particle Beams 1 (1983) 335
15. I. Hofmann, Adv. Electron. Electron Phys., Suppl. 13C (1983) 49
16. I. Hofmann and K. Beckert, IEEE Trans. Nucl. Sci. NS-32, (1984) 2264
17. I.C. Lyon et al., J. Phys. B, At. Mol. Phys. 19 (1986) 4137
18. R. Bonifacio et al., Proc. 11th FEL Conference, Naples, 1989

Tuesday

Session TU4
Chairman: J. Staples
Contributed Papers

A SCHEME TO COMPENSATE THE TRANSIENT BEAM LOADING IN TW ELECTRON LINACS

Jialin Xie* and Renshan Zhang*

ATF, Brookhaven National Laboratory, Upton, NY 11973

Abstract

A scheme to compensate the transient beam loading of the TW electron linac operated in multi-bunch mode is described. The proposed method is to excite an auxiliary cavity located at the end of the accelerator section with the residual rf power, which comes out of the section after one filling time, with properly adjusted phase and amplitude of the field. The transient energy gain of the electron beam in passing through the cavity will compensate the transient energy loss due to beam loading in the accelerator section. The parameters of ATF of Brookhaven National Laboratory are used for calculation as an example to illustrate the result of computation.

Introduction

Many scientific applications of the electron beam produced by linac require low energy spread and the subject of energy spread reduction has been studied by many authors. Among the various factors causing energy spread in a multi-bunch linac beam, such as space charge, rf phase spread, wake-field, modulator voltage ripple and jitter, tempture variation, etc., the transient beam loading which lasts one fill time before arriving at steady state is generally the most serious one. A well known method to alleviate it is to turn on the beam before the accelerator section is completely filled[1]. But, it should be noted that from the beam point of view, it still takes about one fill time to settle down. The transient beam loading is not important if the beam pulse is of several fill time long. However, in practice, most electron linacs operate in short beam pulse mode because of BBU, klystron and gun pulse width limit. Therefore, it seems worthwhile to explore some way that could compensate the transient beam loading of the linac and improve the energy spectrum for short pulse operation. Even though it is not always possible to find a scheme that gives perfect compensation, any method that could significantly reduce the energy fluctuation of the output electron beam will facilitate further compensation by other means.

Scheme of Compensation

The essence of the proposed scheme is to excite an auxiliary cavity (or cavities) located at the end of the linac with the residual rf power which comes out of the linac (or with another rf power source driven by the same oscillator) after one filling time. The transient energy gain of the electron beam passing through a cavity with the amplitude and the phase of the field properly adjusted by the coupling waveguide, will tend to compensate the transient energy loss due to beam loading in the linac. Fig.1 shows the schematical arrangement of the system. Fig.2 shows a typical transient beam loading in the linac and the build-up process in the cavity to illustrate the principle of operation. Actually, it can be envisioned that the auxiliary cavity be made as an integrated part of the accelerator section. The electric field variation with time at the end of accelerator wave guide and the energy gain of the electrons injected exactly after one filling time are given by the following expressions[2]:

$$E_a(l,t) = \left[E_0 - \frac{\omega r i_0}{2Q}(t-t_f)\right] U(t-t_f) + \frac{\omega r i_0}{2Q}(t-2t_f)\, U(t-2t_f) \tag{1}$$

$$\begin{aligned} U_a(t) = {} & \frac{E_0 l}{1-e^{-2\tau}}\left\{\left(1-e^{-\frac{\omega_0}{Q}t}\right)U(t) - e^{-2\tau}\left(1-e^{-\frac{\omega_0}{Q}(t-t_f)}\right)U(t-t_f)\right\} \\ & - \frac{r i_0 l}{2(1-e^{-2\tau})}\left\{\left(1-e^{-\frac{\omega_0}{Q}(t-t_f)}\right) - \frac{\omega_0}{Q}e^{-2\tau}(t-t_f)\right\}U(t-t_f) \\ & + \frac{r i_0 l e^{-2\tau}}{2(1-e^{-2\tau})}\left\{\left(1-e^{-\frac{\omega_0}{Q}(t-2t_f)}\right) - \frac{\omega_0}{Q}(t-2t_f)\right\}U(t-2t_f) \end{aligned} \tag{2}$$

where $E_0 l = (1-e^{-2\tau})^{1/2}(P_{0l} r l)^{1/2}$, E_0 is the average electric field amplitude along the accelerator axis, l, the linac length, P_{0l} is the rf power at the entrance of the linac, r, shunt impedence of the accelerator wave guide, i_0, the average accelerated current, $\tau = \omega_0 t_f/(2Q)$, the attenuation factor, t_f, the filling time of the linac, and U(t), the unit step function. These expressions are for the constant gradient structrue which will be taken in our calculation example while similar results hold for constant impedence case. The exit power from the linac is also a function of time and is given by:

$$P_e(t) = \frac{E_a(l,t)^2}{r(e^{2\tau}-1)} \tag{3}$$

*Permenant address: Institute of High Energy Physics, Academia Sinica, P.O. Box 918, Beijing, P.R. China.

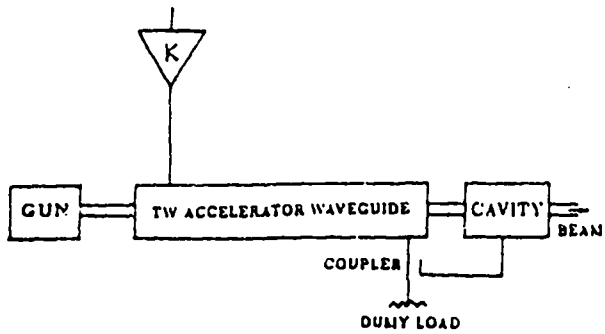

Figure 1: Schematic Diagram of the proposed scheme.

The energy gain of the electrons passing through the auxiliary cavity which is building up with a time varying driven power is given from Appendix A:

$$
\begin{aligned}
U_c(t) = U_{c0}\Bigg\{ & \left(1 - i\sqrt{\frac{RQ_e}{Q_0 P_0}}e^{\tau}\right)\left(1 - e^{\frac{-\omega_0}{2Q_L}t}\right)U(t) \\
& + \frac{Q_L r i_0}{Q E_0}\left(1 - e^{\frac{-\omega_0}{2Q_L}t}\right)U(t) \\
& - \frac{\omega_0 r i_0}{2Q E_0}\left[tU(t) - (t - t_f)U(t - t_f)\right] \\
& - \frac{r i_0 Q_L}{Q E_0}\left(1 - e^{-\frac{\omega_0}{2Q_L}(t - t_f)}\right)U(t - t_f)\Bigg\}
\end{aligned}
\tag{4}
$$

where $U_{c0} = 2Q_L\sqrt{\frac{P_{0l}R}{Q_0 Q_e}}e^{-\tau}$, Q_0, Q_L, the unloaded and loaded Q-value of the cavity separately, R, the effective shunt impedence, and i, the average beam current passing through the cavity.

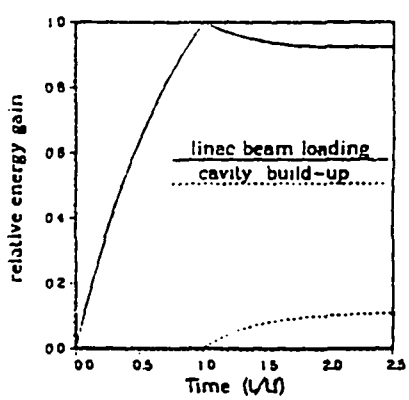

Figure 2: Diagram showing the transient beam loading in a linac and the build-up processes in the auxiliary cavity.

In order to have the energy loss of the accelerated beam due to beam loading completely compensated by the extra acceleration from the auxiliary cavity, the requirement is obvious:

$$U_a(t) + U_c(t) = const \tag{5}$$

Because the time dependence of $U_a(t)$ and $U_c(t)$ are not the same, this condition can hardly be realized in practice. However, we can use the following equations as a guide in the choice of cavity parameters.

$$U_c(\infty) + U_a(\infty) = U_a(0) \tag{6}$$

$$\left.\frac{dU_c(t)}{dt}\right|_{t=0} = -\left.\frac{dU_a(t)}{dt}\right|_{t=0} \tag{7}$$

which gives:

$$U_{c0}\left(1 - i\sqrt{\frac{RQ_e}{Q_0 P_{0l}}}e^{2\tau}\right) = \frac{r i_0 l}{2}\left(1 - \frac{2\tau e^{-2\tau}}{1 - e^{-2\tau}}\right) \tag{8}$$

and

$$Q_L = \frac{Q}{2}\left(1 - \frac{2\tau e^{-2\tau}}{1 - e^{-2\tau}}\right) \tag{9}$$

It should be mentioned here that eq.(8) and eq.(9) give good compensation for light beam loading only. Practically, the choice of cavity parameters should be proceeded by making the energy variation less than the allowable energy spread and using least square method for fitting.

Numerical Results

In order to illustrate how the proposed scheme works out, we take the parameters of the Accelerator Test Facility (ATF) of Center of Accelerator Physics (CAP), Brookhaven National Laboratory[3] and perform numerical computation. The ATF consists of two $3.05m$ SLAC constant gradient accelerator sections with $5MW$ rf power input to each section and $48mA$ accelerated current generated from a photo-cathode microwave gun. The beam pulse length is $1.25\mu s$, the shunt impedence of the accelerator section $r = 58M\Omega/m$ and attenuation factor $\tau = 0.57$.

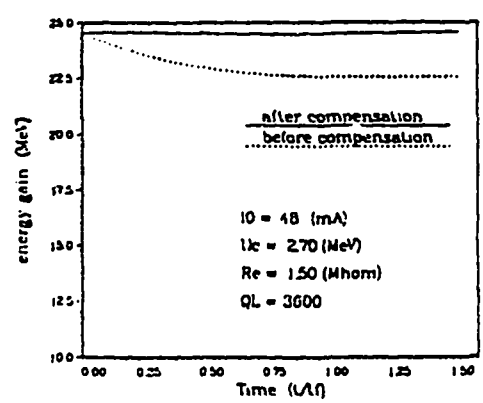

Figure 3: The energy gain variation with time after compensation for the ATF case.

Fig.3 gives the numerical result of exit electron energy gain of the ATF case after compensation. The cavity loaded Q-value Q_L is assumed to be 3060, which can be controled by adjusting the coupling. It can be seen the maximum energy spread $(U_{max} - U_{min})$ during the macroscope pulse is reduced from about 8% to about 0.4%. A 20 times reduction could be achieved in principle.

Acknowledgement

Authors wish to thank Ilan Ben-Zvi and Harold Kirk for their encourgement and support in this work. This project is supported by U.S. Department of Energy.

Appendix A:

Energy Gain of Electrons in Passing Through a Cavity Driven by Time Varying Power

The energy conservation law in a cavity can be expressed as[4]:

$$P_{in} = \frac{dW}{dt} + P_s + P_b \qquad (A.1)$$

where P_{in} is the power into the cavity, W, the energy stored in the cavity, P_s, the power dissipated in the cavity walls, and P_b, the power carried away by the beam.

$$P_s = \frac{\omega_0 W}{Q_0} \qquad (A.2)$$

$$P_b = i(P_s R)^{1/2} \qquad (A.3)$$

where Q_0 is the unloaded Q-value, R, the effective shunt impedence of the cavity, and i, the average beam current. In eq.(A.3), proper phasing has been assumed.

When the transient building up process is considered, the input admittance at resonance is:

$$\frac{Y_{in}}{Y_0} = \frac{Q_e}{Q_0'} + \frac{Q_e}{\omega_0 W}\frac{dW}{dt} \qquad (A.4)$$

where Q_0' is defined as:

$$Q_0' = \frac{\omega_0 W}{P_s + P_b} \qquad (A.5)$$

Therefore, the ratio of power fed into the cavity P_{in} to the incident power P_0 is:

$$\frac{P_{in}}{P_0} = \frac{4(Y_{in}/Y_0)}{[1 + (Y_{in}/Y_0)]^2} \qquad (A.6)$$

Substituting the eq.(A.2) — eq.(A.6) into eq.(A.1), one has:

$$\frac{dW}{dt} + \frac{\omega_0 W}{Q_L} = 2\sqrt{\frac{P_0\omega_0 W}{Q_e}} - i\sqrt{\frac{R\omega_0 W}{Q_0}} \qquad (A.7)$$

For the sake of convenience, letting $W = y^2$ and taking the Laplace transform with respect to time, we obtain:

$$sY(s) + \frac{\omega_0}{2Q_L}Y(s) = \sqrt{\frac{\omega_0}{Q_e}}\sqrt{P_0(s)} - \frac{i}{2}\sqrt{\frac{R\omega_0}{Q_0}} \qquad (A.8)$$

where $Y(s)$ is the Laplace transform of $y(t)$, and $\sqrt{P_0(s)}$ is the Laplace transform of the rf power fed into the cavity, $\sqrt{P_0(t)}$. Assuming the beam is injected into the linac exactly after one filling time and choosing the time at which the beam is tured on as zero, $\sqrt{P_0(s)}$ can, from eq.(3), be expressed as:

$$\sqrt{P_0(s)} = \sqrt{\frac{P_{0l}e^{-\tau}}{s}}\left[1 - \frac{C}{s} + C\frac{e^{-t_f s}}{s}\right] \qquad (A.9)$$

where $P_{0l} = \frac{E_0 e^{-2\tau}}{r(1-e^{-2\tau})}$ and $C = \frac{\omega_0 r i_0}{2QE_0}$. Substituting eq.(A.10) into eq.(A.8), taking the inverse transform and using eq.(A.3), we obtain the energy gain of electrons in passing through the cavity as follows:

$$\begin{aligned} U_c(t) = U_{c0}\Bigg\{ & \left(1 - i\sqrt{\frac{RQ_e}{Q_0 P_0}}e^{\tau}\right)\left(1 - e^{\frac{-\omega_0}{2Q_L}t}\right)U(t) \\ & + \frac{Q_L r i_0}{QE_0}\left(1 - e^{\frac{-\omega_0}{2Q_L}t}\right)U(t) \\ & - \frac{\omega_0 r i_0}{2QE_0}\left[tU(t) - (t - t_f)U(t - t_f)\right] \\ & - \frac{r i_0 Q_L}{QE_0}\left(1 - e^{-\frac{\omega_0}{2Q_L}(t-t_f)}\right)U(t - t_f)\Bigg\} \end{aligned} \qquad (A.10)$$

where $U_{c0} = 2Q_L\sqrt{\frac{P_{0l}R}{Q_0 Q_e}}e^{-\tau}$.

References

1. J. E. Leiss, Beam Loading and Transient Behavior in Traveling Wave Electron Linear Accelerators, Linear Accelerators, edi. P.M. Lapostolle and A.L. Septier, North-Holland publ. Co. (1970).
2. J. W. Wang, RF Properties of Periodic Accelerating Structures for Linear Colliders, SLAC-Report-339, (1989).
3. H. G. Kirk, edi, The Accelerator Test Facility (ATF) User's Meeting, BNL-43702, Nov. (1989).
4. Koichi Irie, et.al., A compact Electron Linac Using Side-Coupled Structure, Jan. J. Apl. Phys. 12 (1973) 277.

BEAM LOADING STUDIES AT CEBAF*

G. A. Krafft, S. N. Simrock, and K. L. Mahoney
Continuous Electron Beam Accelerator Facility
12000 Jefferson Avenue
Newport News, VA 23606

Abstract

When the CEBAF accelerator operates at 200 μA beam current, the superconducting cavities run with high beam loading. The CEBAF RF system (including the cavities, klystrons, and control systems) has been measured to obtain the response to low frequency current fluctuations and to obtain the transient response to rapid changes in the beam current. The data were collected both through RF tests where beam pulses are simulated by RF pulses and through beam tests. Both closed loop and open loop measurements were made, and the results are compared to detailed SPICE numerical simulations. It is concluded that CEBAF will operate with high control under a wide variety of loads.

Introduction

One source of phase and amplitude noise in the field of a superconducting cavity is created by beam current noise. Since the cavity may operate when highly beam loaded, substantial voltage fluctuations could result if the cavity field was not controlled. The RF controls reduce the noise by the closed-loop gain of the control system, but since the cavities and control loops are nearly identical throughout the linacs, errors in the control system generated by beam noise are likely to be correlated throughout the linacs. Therefore, the fluctuations due to beam noise must be suppressed to $\Delta V/V < 2 \times 10^{-5}$ in amplitude and $\Delta\phi < 0.1°$ in phase in order to be consistent with the CEBAF design specifications[1]. Our measurements indicate that for the gains to be found in the controls, the beam current fluctuations are small enough that the specifications are achieved.

To begin, the voltage fluctuation induced by a given current fluctuation is calculated when the control system is unlocked. When all the reflected power is absorbed by a circulator, the differential equation for the accelerating cavity voltage V_c is

$$\frac{d^2V_c}{dt^2} + \frac{\omega_c}{Q_L}\frac{dV_c}{dt} + \omega_c^2 V_c = \frac{\omega_c}{Q_c}\frac{dV_+}{dt} - \frac{\omega_c}{Q_c}\frac{dV_B}{dt}$$

where $\omega_c = 2\pi f_c$ is the cavity angular frequency, Q_c is the unloaded quality factor of the cavity, Q_L is the loaded quality factor of the cavity

$$Q_L = \frac{Q_c}{1+\beta},$$

β is the coupling factor,

$$V_+ = 2\sqrt{\beta}\sqrt{2Z_cP(t)}\cos(\omega_c t - \phi(t))$$

is the voltage induced in the cavity by the RF generator multiplied by $1+\beta$, Z_c is the cavity shunt impedance, $P(t)$ is the power from the generator, $\phi(t)$ gives the phase of the voltage, and $V_B(t) = Z_cI(t)$ is the beam loading voltage where $I(t)$ is the beam current. It is convenient to use $R = 2Z_c$, the accelerator shunt impedance[2], in the subsequent formulas.

For $P(t)$ and $\phi(t)$ constant, consider the voltage spread induced by a beam fluctuation at a given modulation frequency. If

$$\delta I(t) = \sum_{l=-\infty}^{\infty} q\cos(\omega_m t)\delta(t - l\tau),$$

the fluctuation in the voltage, δV_c, is

$$\delta V_c(t) = -\frac{\omega_c Rq}{2Q}\frac{e^{-\omega_c(t-n'\tau)/2Q_L}}{2}\times$$

$$\left\{\frac{e^{2x}\cos[\dot\omega t - n'\dot\omega\tau + n'\omega_m\tau]}{1 - 2\cos(-\dot\omega\tau + \omega_m\tau)e^{x} + e^{2x}}\right.$$

$$\left. - \frac{e^{x}\cos[\dot\omega t - (n'+1)\dot\omega\tau + (n'+1)\omega_m\tau]}{1 - 2\cos(-\dot\omega\tau + \omega_m\tau)e^{x} + e^{2x}} + \omega_m \leftrightarrow -\omega_m\right\} \quad (1)$$

where $x = \omega_c\tau/2Q_L$, $\dot\omega = \omega_c\sqrt{1 - 1/4Q_L^2}$, and n' is the greatest integer less than $f_c t$. If $1 \gg \omega_m\tau \gg \omega_c\tau/2Q_L$, Eqn. (1) may be expanded to yield

$$\delta V_c(t) \doteq -\frac{q}{2\tau}\frac{R}{Q}\frac{\omega_c}{\omega_m}\cos(\dot\omega t)[\omega_m\tau/2 + \sin(n'\omega_m\tau)], \quad (2)$$

a result independent of the cavity bandwidth $\omega_c/2Q_L$.

An energy argument clarifies this result. The total charge passing the cavity on the positive part of the modulation is

$$\Delta q = \sum_{n=-\pi/2\omega_m\tau}^{\pi/2\omega_m\tau} q\cos(n\omega_m\tau) \doteq \frac{2q}{\omega_m\tau}.$$

The total energy removed from the cavity by this charge is

$$\Delta U = \frac{2qV}{\omega_m\tau}.$$

Since the energy fluctuation is related to the voltage fluctuation by

$$\Delta U = 2\frac{QV}{R\omega_c}\Delta V,$$

the full width voltage fluctuation is

$$\Delta V = \frac{q}{\tau}\frac{R}{Q}\frac{\omega_c}{\omega_m} = I_{mod}\frac{R}{Q}\frac{\omega_c}{\omega_m},$$

consistent with Eqn. (2).

*This work was supported by the United States Department of Energy under contract DE-AC05-84ER40150.

For $1 \gg \omega_c\tau/2Q_L \gg \omega_m\tau$, i. e., the frequency of the fluctuation is well within the cavity bandwidth, the cavity has time to respond to the changed beam load. The voltage adjusts so that the same incident power goes into the beam

$$\delta V_c(t) \doteq -Q_L I_{mod}\frac{R}{Q}\cos(\omega t)\cos(n'\omega_m\tau).$$

For CEBAF, $R/Q = 480\ \Omega$, $V_c = 2.5$ MV, $f_c = 1500$ MHz, $Q_L = 6.6 \times 10^6$, and $\beta = 364$. Therefore, the cavity bandwidth is 110 Hz. For frequencies of this order, the more general expression in Eqn. 1 must be used. The general case is well approximated by the single pole result

$$|\Delta V_c| \doteq \frac{2Q_L I_{mod} R/Q}{(1 + 4Q_L^2\omega_m^2/\omega_c^2)^{1/2}}.$$

Given this estimate of the voltage fluctuation in the unlocked mode, it remains to note that ideally the fluctuation is reduced by the gain of the control system at the modulation frequency in the locked mode. The control system does this by properly adjusting $P(t)$ and $\phi(t)$ to cancel most of the induced error.

SPICE Model

An analysis of the control system has been performed using the computer code SPICE. A schematic diagram of the RF controls for a superconducting cavity appears in Fig. 1[3]. The block diagram of the SPICE gradient loop is shown in Fig. 2. The calculation employs simple models for major control loop components and error sources. Where possible, the transfer function of a model is defined numerically. Models for the loop amplifier and klystron amplifier include frequency roll off and saturation characteristics. Examples of possible error sources are beam transients, interloop coupling, and noise sources such as microphonic noise, beam noise, klystron noise, and detector noise. Of particular interest in this paper is the response of the control system to beam induced transients.

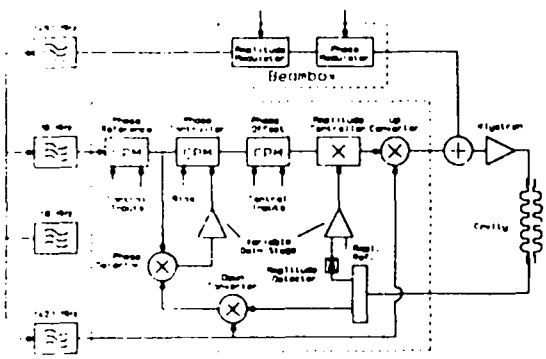

Fig. 1 RF System Schematic

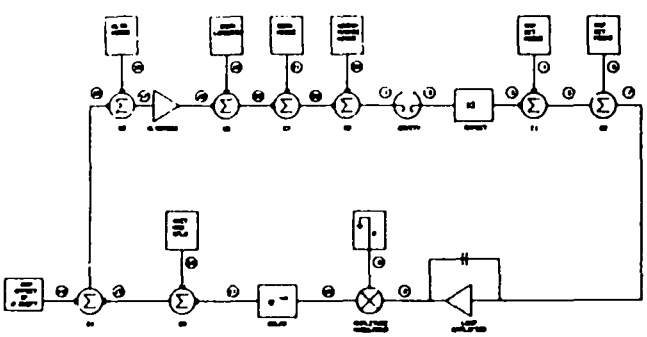

Fig. 2 SPICE Block Diagram

Beam Box Measurements

Transfer function data were obtained using a so-called beam box, which injects low-level RF power into the control loop before the klystron as in Fig. 1. If an amplitude modulated signal is fed into the control loop, by comparing the cavity voltage fluctuation levels with and without phase and amplitude lock, the overall gain of the control system is determined. For example, a square wave modulation at 10 Hz yielded the data in Fig. 3. The two curves are spectra of the amplitude error signal. For the top spectrum the amplitude lock was off and for the bottom spectrum the amplitude lock was on. Such measurements have verified the high gain ($\sim$ 80 dB) of the controls at low modulation frequencies. Given the measured gains, one can expect the CEBAF beam to be within specifications provided the current fluctuations at low frequency are less than 25 μA. By independent measurement of the beam current on apertures, it is known that the current fluctuations are in fact under 1 μA.

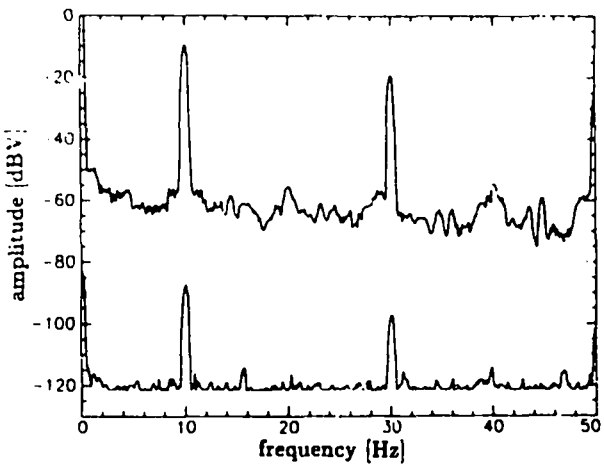

Fig. 3 Spectrum of Amplitude Error Signal in Open and Closed Loop Cases

The transient response of the control system is obtained by pulsing the RF power from the beam box on and off. A transient obtained by this technique is shown in Fig. 4, which gives the relative amplitude error vs. time after the beam box is first turned on. Overshoot oscillations were observed that were traced to the occurence of a 100 kHz pole in the control system, something eliminated in tests the with beam later on. The slow falloff evident in the trace shows the effect of low frequency gain in the system. The transient power corresponds to 800 μA of beam current, and the full range of the amplitude error was $\delta V_c/V_c = 1.7 \times 10^{-3}$. Given

the acceptance of the recirculation arcs at CEBAF of 2×10^{-3}, one can expect complete transmission of the beam up to transients of 1 mA.

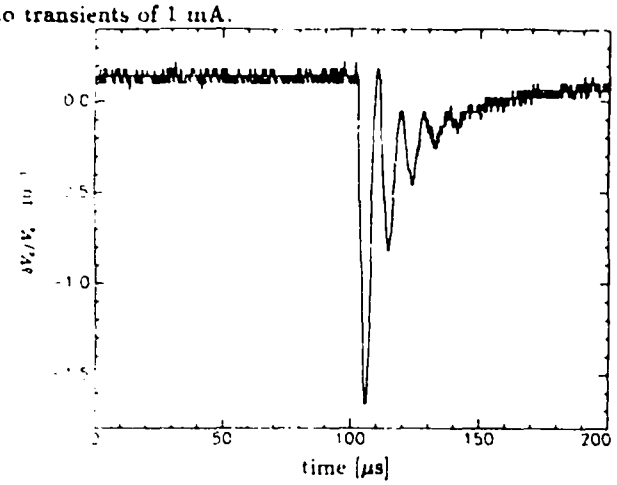

Fig. 4 Transient Amplitude Error Signal from Beam Box

Beam Measurements

An example of a beam induced amplitude transient in the superconducting cavity is shown in Fig. 5. The beam current was in 400 μA pulses of duration 1 msec. Removing the 100 kHz pole in the feedback loop has eliminated the overshoot previously observed, and the recovery time is 0.05 msec. The peak amplitude deviation is $\delta V_c/V_c = 1.9 \times 10^{-3}$.

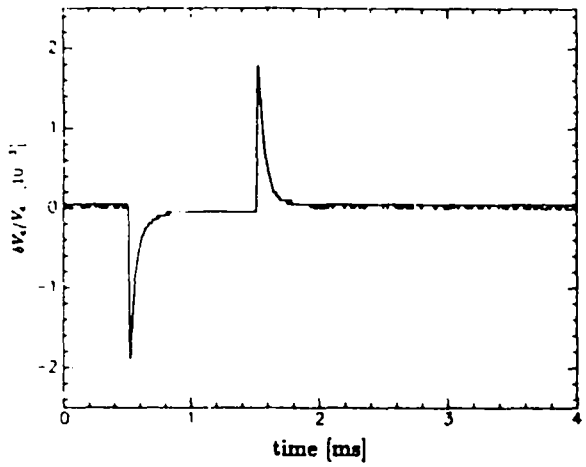

Fig. 5 Transient Amplitude Error Signal from Beam

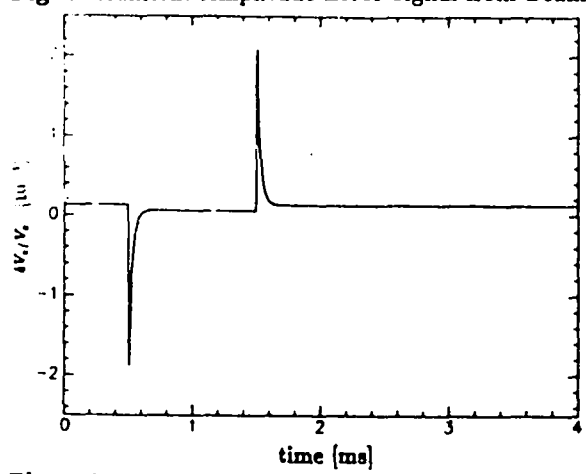

Fig. 6 Transient Amplitude Error Signal from SPICE

The level shift of 5×10^{-5} when the beam is on corresponds to a low frequency gain of 80 dB, consistent with the beam box measurements. Fig. 6 shows the results of SPICE calculations of the response of the amplitude control loop. The loop gains are the same as those for the measured response shown in Fig. 5. The agreement with the measured data is good. If transients in the system are limited to 2×10^{-3}, then rapid beam current changes must be limited to 400 μA.

The final beam measurement to be discussed was taken with a 400 μA CW beam passing through the first superconducting cavity. Very little difference was observed between the noise level when the beam was off and the noise level when the beam was on. This result is consistent with low beam induced fluctuations in the cavity, and one concludes that beam induced noise is not significant at the 2×10^{-4} level, the noise floor of the measurement. Unfortunately, the noise floor is higher than the 2×10^{-5} level that must be achieved. Thus, the beam box measurements still provide the stronger limit on the beam current fluctuations. It should be noted that at 200 μA extracted current, the current in a superconducting cavity is 1 mA.

Conclusions

In this paper, the results of studies of beam loading in the CEBAF superconducting cavities are given. Using beam box measurements, the overall gain by which the RF control system suppresses beam generated voltage fluctuations has been determined. Given the observed beam current fluctuations, the voltage fluctuations should be suppressed to acceptable levels by the controls. The measurements of noise levels in the RF controls with and without high current beam, where no appreciable difference in the noise level was observed, support this assertion. It remains to measure the transfer function directly by modulating the beam current itself, but this measurement is expected to confirm the beam box measurement. When the beam box measurements are confirmed, it can be concluded that beam loading effects will not be a significant contributor to the energy spread in the final CEBAF beam, at least in CW operation.

Data important for evaluating pulsed mode operating schemes have been obtained by our transient beam loading studies. The SPICE simulation reproduces the experimental data. It remains to use this information to evaluate individual pulsed beam schemes.

Acknowledgements

The authors wish to thank C. K. Sinclair for his help in obtaining the data with beam. J. C. Hovater and M. Crofford developed the beam box and D. Ferris set up the data aquisition software used in the experiments.

References

[1] CEBAF Design Report (May 1986)

[2] P. B. Wilson, AIP Conference Proceedings No. 87, 450 (1981)

[3] S. N. Simrock, J. A. Fugitt, J. C. Hovater, G. A. Krafft, and C. K. Sinclair, "Operation of the RF Controls in the CEBAF Injector", *Proceedings of the 1990 European Part. Acc. Conf.*

FEED-FORWARD COMPENSATION FOR TRANSIENT BEAM LOADING OF THE 805 MHZ DEBUNCHER FOR THE FERMILAB LINAC UPGRADE

J. A. MacLachlan, F. E. Mills, and T. Owens
*Fermi National Accelerator Laboratory,*Box 500, Batavia IL 60510*

Abstract

The expected momentum spread from the 400 MeV upgrade of the Fermilab linac is ±0.19% growing to about ±0.25% in 63 m of beam transport to the booster synchrotron. The desired injection value is about ±0.05%. An 805 MHz (h=1) debuncher is located 47 m downstream of the linac to reduce the momentum spread and the differences in mean energy between bunches. The beam pulse to the booster will vary from about 2 – 15 μs at average current of 30 – 50 mA depending on program need. During 15 μs the beam excitation of the debuncher can reach 2.2 MV/m for a three-cell cavity. This gradient is comparable to, but 90° out of phase with, the 3.85 MV/m required to minimise the momentum spread. We choose to use feed-forward compensation to control the cavity field for the entire beam pulse. We discuss some general features of transient beam loading as well as the design and detailed simulation of the compensation scheme.

Introduction

Fermilab is building an 805 MHz, 400 MeV, side-coupled H^- linac to replace the 116 to 200 MeV tanks of the present 200 MHz drift-tube linac used as an injector for the booster synchrotron.[1] Both the central energy and energy spread of the beam can vary unacceptably because of beam-induced shift of the debuncher phase. The beam parameters are summarized in Table I.

The basic scheme for the debuncher is to drift the beam so that the bunches cover somewhere between 60° – 90° of 805 MHz phase. Then the bunches pass through a cavity phased to decelerate the leading particles and accelerate trailing particles closer to the central momentum.

Beam Excitation of Debuncher

A first order calculation of the bunch lengthening along the 400 MeV transport has been made with TRACE-3D,[2] which accounts for the variations in longitudinal space charge force resulting from the changes in the transverse beam envelope using linearised envelope equations. The result in Fig. 1 shows both a 50 mA and a 0 mA solution which minimise momentum spread and match booster lattice functions at the injection point. The data for the debunching calculation are summarized in Table I. The solutions require $V_{eff} = E_0 Tl = 1.54$ MV for 50 mA beam and 1.41 MV for $\bar{I}_b = 0$.

The 400 MeV transport design assumes a 2 cm radius minimum aperture at the debuncher. Table II gives the expected electrical properties of a 400 MeV side-coupled structure with this bore.[3] The shunt impedance and Q have been reduced from the SUPERFISH result by a conventional 15%. A 50 kW TV klystron has been chosen as a suitable rf generator providing 200 kW in pulsed service. The minimum length of structure follows from the available power. For three $\beta\lambda/2$ cells the dissipation is 143 kW.

Ideal debunching requires that the cavity phase be −90° at the bunch centers. Passing bunches excite the cavity to produce a transient decelerating field shifting the phase progressively more negative. The induced voltage can be estimated by the bunch charge appearing across the gap capacity. From the stored energy given in Table II the gap capacity is 1.15 pF. Assuming the electrical energy is stored in the gap region, each bunch of 0.248 nC will generate a quadrature voltage of $\hat{V}_{beam} = q/C = 216$ V on each gap. In an extreme impulse approximation the entire beam pulse is short compared to τ_{RH}; the beam-induced voltage would be over 2 MV.

To permit modeling the effects of the compensation scheme, detailed calculations have been carried out with time domain simulation of the beam-cavity interaction applying a code used for synchrotrons.[4] Fig. 2 shows the quadrature voltage on the cavity as a function of time calculated by exciting an LCR cavity model with beam current pulses produced by evolution of a nominal linac bunch in the linac-to-booster drift with space charge included. The ratio of average beam radius to beampipe radius was estimated from the envelope result shown in Fig. 1. The calculated bunch length at the debuncher agreed reasonably with the TRACE-3D result. The effect of this quadrature voltage and a fixed generator voltage on the debunching is plotted in the next two figures. Fig. 3 shows the time dependence of the mean bunch energy; the plot is offset so that the initial beam energy is in the upper lefthand corner. Fig. 4 shows how the rms energy spread increases as the phase shifts leaving the bunch outside the linear portion of the potential. The phase error after 3000

*Work supported by the U. S. Department of Energy under contract No. DE-AC02-76CH0300.

bunches at 50 mA is 19°. Fig. 5 shows superposition of an early and a late bunch. The dotted lines demark the design tolerance of 0.1% FW on $\Delta p/p$. There is some short-term fluctuation in linac beam energy: a significant benefit of the debuncher is that it reduces the range of mean energy fluctuation by the same ratio it reduces the spread within the bunch. Note, however, that the Figs. 4 and 5 results do not include spread resulting from variation in the linac energy.

Beam Loading Compensation

Beam loading degrades the debuncher performance beyond the design tolerance. A system controlling cavity phase by feedback to the rf drive can not respond fast enough. However, the timing and intensity of linac beam batches are known rather well in advance. Introducing into the rf drive an appropriate level of quadrature drive just as the beam is to arrive will cancel the effects of the beam-induced voltage during most of the pulse. The rise time on the beam current due to chopper switching is ~ 20 - 50 ns, whereas the klystron bandwidth is about 5 MHz. Therefore the generator rf will be incorrect for ~ 200 ns or one tenth of a booster turn. The error could be reduced by using a structure with lower R/Q. Greater stored energy or more rf power means that the beam-induced voltage is relatively a smaller perturbation. Unfortunately, a major improvement in Q is not possible, and high power is not economical. However, it is possible to make a major improvement by giving the correcting drive an optimum lead time on the beam pulse. The model of the feed-forward scheme is shown in Fig. 6. Only the real branches of the complex envelope representation of the correction system are shown because the small phase correction to the feed-forward pulse is negligible. The output from the model is calculated with the ACSL (Advanced Computer Simulation Language); the results in Fig. 7 are normalized to $V_{out} = 1$. Fig. 7a shows an error of 0.2% in the quadrature component when the timing of the feed-forward pulse has the optimum 35 ns lead on the beam pulse. Figs. 7b and 7c show the error when the beam arrival is off respectively by plus and minus 20 ns, the present amount of jitter on the chopper that sends the linac beam down the booster transport. Note that the scale is per mil in Fig. 7a and percent in Figs. 7b and c. One sees a maximum of 0.7% error for feed-forward of the correct amplitude within ± 20 ns of optimum timing. The time variation of mean energy and energy spread was calculated for the case where the beam is 20 ns early: the calcultion was simplified slightly by replacing the curve in Fig. 7c with a simple decaying exponential with the same peak value and time constant. On the scale of Figs. 3 and 4 the results are indistiguishable from zero.

Conclusions

Although an ideal debuncher neither delivers energy to the beam nor receives energy from it, transient beam loading shifts the debuncher phase, decelerating the beam and increasing the momentum spread. When the energy distribution must be controlled throughout the pulse, phase feedback to the klystron drive is not adequate because delays in the feedback path and bandwidth limits result in phase and amplitude errors in the debuncher field. Furthermore, beam-induced fields are comparable to those generated by the klystron; therefore, regulation factors are impractically high for the required bandwidth. However, beam timing and intensity from a linac are generally stable so that a feed-forward correction can practically eliminate phase sluing. It has been shown that the error in correction resulting from finite klystron bandwidth can be reduced substantially, a factor of three for our case, by optimally timing the correcting drive ahead of the beam pulse.

References

1. R. J. Noble, "The Fermilab Linac Upgrade", this conference
2. K. Crandall "Trace 3-D Documentation", LA-110054-MS, Los Alamos report (Aug. 87)
3. T. Jurgens, priv. comm., SUPERFISH calculation
4. S. Stahl and J. A. MacLachlan, "A User's Guide to ESME v. 7.1", Fermilab TM-1650 (26 Feb. 90), unpublished

TABLE I
Properties of the 400 MeV Linac Beam

Beam energy (kinetic)	401.46	MeV
Average beam current (I_b)	50.	mA
Typical beam pulse	2 - 22	μs
Bunch frequency	201.25	MHz
Frequency of rf (f)	805.0	MHz
Repetition rate	15.0	Hz
H⁻/bunch	1.55	$\times 10^9$
Charge/bunch (q)	0.248	nC
Bunch area (5σ)	8.17 $\times 10^{-5}$	eVs
ϵ_{trans}(5σ, normalized)	6.88 π mm mrad	
Δ p/p at linac (FW)	0.00373	
$\Delta\varphi$ at linac (FW)	11.8	deg
Δ p/p at booster (FW)	0.005	
Debunched Δ p/p (FW)	0.001	

TABLE II
Properties of 400 MeV SCS Cell at 805 MHz

Cell length ($\beta\lambda/2$)	0.1329	m
Cavity bore radius (r_b)	2.0	cm
Effective shunt impedance (ZT^2)	41.4	MΩ/m
Transit time factor (T)	0.831	
Quality factor (Q)	2.352 $\times 10^4$	
Filling time (τ_{fill})	9.3	μs
R/Q characteristic ratio	117.0	Ω(true)
Stored energy (W)	0.0101	J

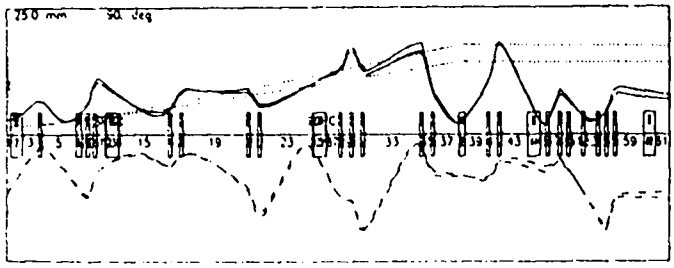

Figure 1: Beam envelope for the 400 MeV transport at $I_{beam} = 0$ and 50 mA

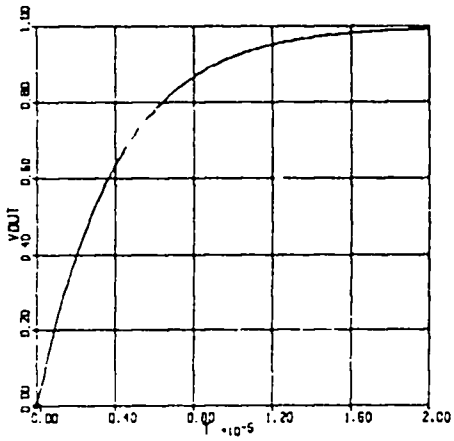

Figure 2: Quadrature voltage *vs.* time for un-corrected debuncher

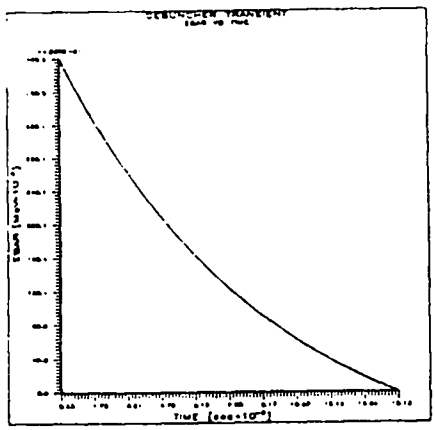

Figure 3: Mean bunch energy after debunching *vs.* time

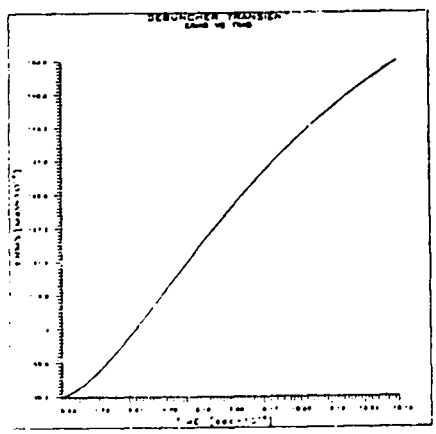

Figure 4: RMS spread of bunch energy after debunching *vs.* time

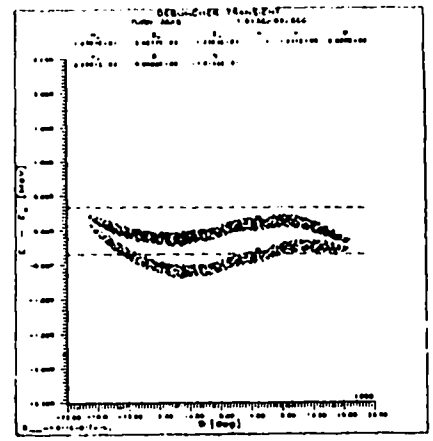

Figure 5: Bunches from 50 mA beam after debuncher — initial and 15 μs later

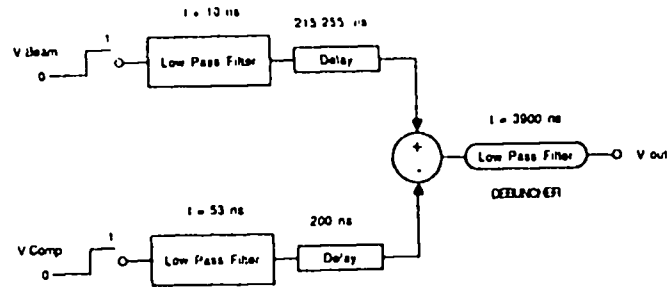

Figure 6: Model of feed-forward system — real part of complex envelope representation

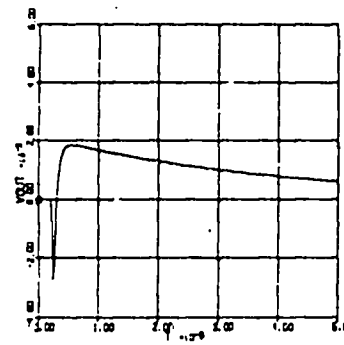

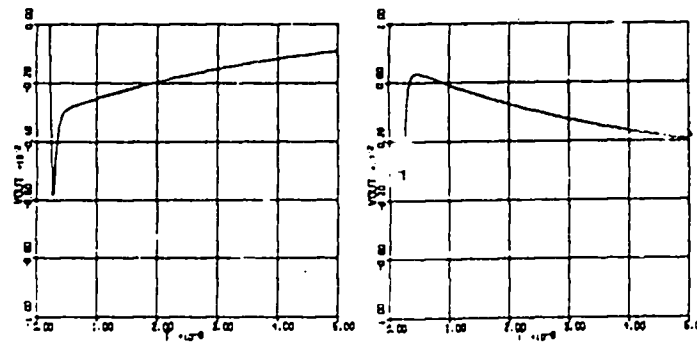

Figure 7: Fractional error in compensation *vs.* time for (a) 35 ns, (b) 55 ns, and (c) 15 ns beam anticipation

CUMULATIVE BEAM BREAKUP IN RADIO-FREQUENCY LINACS*

C.L. Bohn and J.R. Delayen
Argonne National Laboratory, Engineering Physics Division
9700 South Cass Avenue, Argonne, IL 60439

Abstract

An analytic model of cumulative beam breakup has been developed which is applicable to both low-velocity ion and high-energy electron linear accelerators. The model includes arbitrary velocity, acceleration, focusing, initial conditions, beam-cavity resonances, and variable cavity geometry and spacing along the accelerator. The model involves a "continuum approximation" in which the transverse kicks in momentum imparted by the cavities are smoothed over the length of the linac. The resulting equation of transverse motion is solved via the WKBJ method. Specific examples are discussed which correspond to limiting cases of the solution.

Introduction

In the usual treatment of cumulative beam breakup (BBU), the cavities which comprise the linac are considered to have negligible length and to be the only source of deflecting fields. In addition, a "continuum approximation" is also commonly invoked in which the discrete kicks in transverse momentum imparted by the cavities are considered to be smoothed along the linac. With this approximation, the equation of transverse motion of the beam is:

$$\left[\frac{1}{\beta\gamma}\frac{d}{d\sigma}\left(\beta\gamma\frac{d}{d\sigma}\right) + (k_T\mathcal{L})^2\right]\xi(\sigma,\zeta) = \epsilon(\sigma)\int_0^{\zeta} d\zeta' w(\zeta-\zeta')F(\zeta')\xi(\sigma,\zeta') . \tag{1}$$

Here, β and γ have their usual meanings; $\sigma=s/\mathcal{L}$ is a dimensionless spatial variable defined in terms of position along the linac, s, and the total length of the linac, $\mathcal{L}$; $\zeta=\omega(t-\int ds/\beta c)$ is the time, made dimensionless by use of the angular frequency ω of the deflecting mode, measured after the arrival of the head of the beam at s; k_T is the net transverse focusing wavenumber; ξ is the transverse displacement of the beam centroid from the axis; and $F(\zeta)=I(\zeta)/\langle I\rangle$ is the form factor for the current defined in terms of the beam current $I(\zeta)$ and average beam current $\langle I\rangle$. $\epsilon(\sigma)$, a dimensionless quantity which represents the strength of the BBU interaction, is given by

$$\epsilon(\sigma) = \frac{1}{2}\frac{\langle I\rangle Ze}{p}\frac{\Gamma}{\omega}\frac{\mathcal{L}^2}{L}, \tag{2}$$

a product of quantities describing the beam, cavities, and linac in which Ze and p are the charge and momentum, respectively, of a constituent particle of the beam, and L is the spacing between neighboring cavities. $w(\zeta)$ is a dimensionless "wake function" given by

$$w(\zeta) = e^{-\zeta/2Q}\sin\zeta \quad \text{for } \zeta\geq 0, \qquad = 0 \quad \text{otherwise}, \tag{3}$$

in which Q is the quality factor of the deflecting mode under consideration. Γ, a geometry factor, is given by

$$\Gamma = \frac{2}{\epsilon_0\omega}\frac{\left|\int_0^L e^{-i\omega z/\beta c}\frac{\partial E_z(0,0,z)}{\partial x}dz\right|^2}{\int_V E^2(\mathbf{x})\,d\mathbf{x}}, \tag{4}$$

in which the integrals are over the rf electric field of the deflecting mode, and ϵ_0 is the permittivity of free space.

Equation (1) is the foundation of the theory of cumulative beam breakup. Various forms of it have been solved analytically. Early investigators treated the case of a dc beam with no net transverse focusing both for $\beta=1$[1] and for $\beta\neq 1$[2], as well as the case of a focused relativistic dc beam.[3] These investigators developed approximate analytic solutions derived from a technique in which a Fourier or Laplace transform is applied to the equation of transverse motion, the transformed equation is integrated via the WKBJ method, and the transformation is inverted using the method of steepest descent. Later investigators applied this technique to the problem of relativistic, bunched electron beams. Both single-bunch[4] and multi-bunch[5-8] BBU have been considered, and the technique has been shown to give analytic results which agree very well with numerical integration where BBU is significant.[7,8] The analytic solution can be decomposed into a steady-state term valid after times long compared to Q/ω, and a transient term describing the approach to steady state. These features also apply to the case of a dc beam,[1,3,9] for which the exponential growth characterizing the transient behavior can also be predicted by assuming at the outset an oscillatory solution of the form $\exp(i\omega t-ikz)$.[10]

The principal qualitative distinction of the solution for a bunched beam versus that of a dc beam is the possibility for resonance between the deflecting-mode frequency and the bunch frequency. This resonance will determine whether the steady-state displacement grows exponentially along the linac. While the transient solution sets the most stringent constraint in high energy, short pulse length linacs such as linear colliders,[11] in cw linacs transient growth can be controlled,[12] and BBU behavior will then be set by the steady-state solution.

Beam breakup has yet to be investigated for a bunched beam of arbitrary β. This problem is important in the context of

*Work supported by the U.S. Department of Energy under contract W-31-109-ENG-38 and by the U.S. Army Strategic Defense Command.

the development of cw, high-current ion linacs. An effort is underway to apply rf superconductivity to the development of these accelerators.[13] Because their constituent cavities will be short and independently phased cumulative BBU is expected to be the dominant transverse instability, and it needs to be considered prior to the design of these linacs.

In this paper, we calculate the transverse behavior of a beam of arbitrary $\beta(\sigma)$ consisting of delta-function bunches in a linac with smoothly varying parameters. Two limiting cases are considered, one with no focusing and no acceleration, and the other with strong solenoidal focusing and a linear acceleration profile. The results for these cases are applied elsewhere to two conceptual low-β superconducting linacs.[13]

Beam Breakup with Delta-Function Bunches

With $x(\sigma,\zeta) \equiv \sqrt{\beta\gamma}\,\xi(\sigma,\zeta)$, eq. (1) becomes

$$\frac{d^2x(\sigma,\zeta)}{d\sigma^2} - [\phi(\sigma) - (k_T\mathcal{L})^2]x(\sigma,\zeta) = \epsilon(\sigma)\int_0^{\zeta} d\zeta' w(\zeta-\zeta')\,F(\zeta')\,x(\sigma,\zeta'), \tag{5}$$

where

$$\phi(\sigma) = \frac{2\gamma(\beta\gamma)^2(d^2\gamma/d\sigma^2) - (\gamma^2+2)(d\gamma/d\sigma)^2}{4(\beta\gamma)^4}. \tag{6}$$

We consider a beam consisting of delta-function bunches of identical charge separated by period τ. According to eq. (5), the displacement x_M of bunch M is governed by

$$\frac{d^2x_M(\sigma)}{d\sigma^2} - [\phi(\sigma) - (k_T\mathcal{L})^2]\,x_M(\sigma) = \epsilon(\sigma)\,\omega\tau\sum_{m=0}^{M-1} w_{N-m}\,x_m, \tag{7}$$

where $w_k = e^{-k\omega\tau/2Q}\sin k\omega\tau$. We solve this equation using the following Fourier series:[5]

$$X(\sigma,\theta) \equiv \sum_{m=0}^{\infty} x_m(\sigma)\,e^{im\theta};\quad x_M(\sigma) = \frac{1}{2\pi}\int_{-\pi}^{\pi} d\theta\, e^{-iM\theta}X(\sigma,\theta). \tag{8}$$

After transformation, eq. (7) governs $X(\sigma,\theta)$ in the manner:

$$\frac{d^2X(\sigma,\theta')}{d\sigma^2} - q^2(\sigma,\theta')\,X(\sigma,\theta') = 0, \tag{9}$$

where $\theta' \equiv \theta + i(\omega\tau/2Q)$, and

$$q^2(\sigma,\theta') = \frac{1}{2}\epsilon(\sigma)\frac{\omega\tau\sin\omega\tau}{\cos\theta' - \cos\omega\tau} + \phi(\sigma) - [k_T\mathcal{L}]^2. \tag{10}$$

In terms of the functions

$$\begin{Bmatrix} C(\sigma,\theta') \\ S(\sigma,\theta') \end{Bmatrix} = \sqrt{\frac{q(0,\theta')}{q(\sigma,\theta')}}\begin{Bmatrix}\cosh\\ \sinh\end{Bmatrix}\int_0^{\sigma} q(\sigma',\theta')\,d\sigma', \tag{11}$$

the WKBJ solution of eq. (9) is

$$X(\sigma,\theta) = C(\sigma,\theta')\sum_{m=0}^{\infty} x_m(0)\,e^{im\theta} + \frac{S(\sigma,\theta')}{q(0,\theta')}\sum_{m=0}^{\infty}\frac{dx_m(0)}{d\sigma}e^{im\theta}. \tag{12}$$

In turn, after some manipulation which is aided by noting that the Fourier series for $C(\sigma,\theta')$ and $S(\sigma,\theta')/q(0,\theta')$ contain only non-negative indices m, $x_M(\sigma)$ can be written in the form[14]

$$x_M(\sigma) = \frac{1}{2\pi}\sum_{m=0}^{M} e^{\frac{-m\omega\tau}{2Q}}\int_{-\pi}^{\pi} d\theta\, e^{-im\theta} \cdot\left[x_{M-m}(0)\,C(\sigma,\theta) + \frac{dx_{M-m}(0)}{d\sigma}\,\frac{S(\sigma,\theta)}{q(0,\theta)}\right]. \tag{13}$$

Equation (13) allows for the incorporation of arbitrary initial conditions for the transverse motion of each beam bunch upon entry into the linac. In what follows, we shall consider only the case of a "misaligned beam" in which $\xi_M(0,0) = \xi_o$ and $d\xi_M(0,0)/d\sigma = 0$ for every M. For this case, eq. (13) yields for the steady-state behavior ($M \to \infty$)

$$\xi_\infty(\sigma) = \xi_o\,\Xi(\sigma, i\omega\tau/2Q), \tag{14}$$

and for the approach to steady state ($M < \infty$),

$$\xi_M(\sigma) - \xi_\infty(\sigma) = -\frac{\xi_o}{2\pi}e^{-(M+1)\frac{\omega\tau}{2Q}}\int_{-\pi}^{\pi} d\theta\,\frac{e^{-iM\theta}\Xi(\sigma,\theta)}{e^{i\theta} - e^{-\omega\tau/2Q}}, \tag{15}$$

where

$$\Xi(\sigma,\theta) = \sqrt{\frac{\beta(0)\gamma(0)}{\beta(\sigma)\gamma(\sigma)}}\left[C(\sigma,\theta) + \frac{d\gamma(0)/d\sigma}{2\beta^2(0)\gamma(0)}\,\frac{S(\sigma,\theta)}{q(0,\theta)}\right]. \tag{16}$$

The integral in eq. (15) can be estimated by steepest descent. Two cases, the coasting beam with no focusing and the nonrelativistic accelerated beam with strong solenoidal focusing, will be considered. We now calculate the transverse displacement at the end of the linac ($\sigma=1$) for these cases.

Coasting Beam, No Focusing. For this case, β and γ are constants, and both ϕ and k_T are zero. If the linac is comprised of N identical, equally spaced cavities, then $\epsilon(\sigma)$ is also a constant. From eq. (14), the steady-state displacement is

$$\xi_\infty(N) = \xi_o\cosh\left[N\sqrt{\frac{\epsilon\omega\tau}{4}\left(\frac{L}{\mathcal{L}}\right)^2 p(\omega\tau)}\right], \tag{17}$$

in which $p(\omega\tau)$ includes the resonances between the frequencies $1/\tau$ of the accelerating mode and $\omega/2\pi$ of the deflecting mode:[6]

$$p(\omega\tau) = \frac{\sin\omega\tau}{\sinh^2\left(\frac{\omega\tau}{4Q}\right) + \sin^2\left(\frac{\omega\tau}{2}\right)}. \tag{18}$$

From eq. (15), steepest descent gives for the approach to steady state

$$\xi_M(N) - \xi_\infty(N) = -\xi_o \frac{\sqrt{E}\exp\left(\frac{3\sqrt{3}}{4}E - \frac{M\omega\tau}{2Q}\right)}{4M\sqrt{6\pi}\left[\sinh^2\left(\frac{\omega\tau}{4Q}\right) + \sin^2\left(\frac{\omega\tau}{2}\right)\right]} \quad (19)$$

$$* [(\cos\omega\tau - e^{\frac{\omega\tau}{2Q}})\cos\psi + \sin\omega\tau\sin\psi],$$

where

$$E = \sqrt[3]{\epsilon\omega\tau\left(\frac{L}{\mathcal{G}}\right)^2 N^2 M}, \text{ and } \psi = \frac{3}{4}E + \frac{\pi}{12} - M\omega\tau.$$

Accelerated Beam, Strong Solenoidal Focusing. For an accelerated beam with solenoidal focusing, the net focusing is, including radial defocusing from the accelerating gradient but ignoring defocusing due to space charge,

$$k_T^2 = \left(\frac{Ze\,B}{2p}\right)^2 + \frac{\pi\, Ze\, E_o T \sin\Phi}{pc\,\lambda_o(\beta\gamma)^2} = k_B^2 + k_R^2, \quad (20)$$

where B is the magnetic field in the solenoids, $E_oT\cos\phi$ is the real-estate accelerating gradient, and λ_o is the rf wavelength of the accelerating mode. We shall consider a nonrelativistic beam for which $\gamma = 1$ and which is being accelerated slowly enough and focused strongly enough that the first term in eq. (20) predominates. If B is sufficiently large and is uniform along the linac, then $k_T^2 = k_B^2 \gg \phi/\mathcal{G}^2$, and $k_T \propto 1/\beta$. Assuming the cavities have longitudinal dimensions scaling linearly with β and are spaced in the manner $L = L_o[\beta/\beta(0)] = 2\beta\lambda_o$, the geometry factor Γ is the same for each cavity, and therefore $\epsilon \propto 1/\beta^2$. With those assumptions, the steady-state displacement is

$$\xi_\infty(N) = \xi_o \cos[N k_B(0) L_o], \quad (21)$$

and the approach to steady state is

$$\xi_M(N) - \xi_\infty(N) = -\xi_o \frac{\sqrt{E}\exp\left(E - \frac{M\omega\tau}{2Q}\right)}{8M\sqrt{2\pi}\left[\sinh^2\left(\frac{\omega\tau}{4Q}\right) + \sin^2\left(\frac{\omega\tau}{2}\right)\right]} \quad (22)$$

$$* [(\cos\omega\tau - e^{\frac{\omega\tau}{2Q}})\cos\psi + \sin\omega\tau\sin\psi],$$

where

$$E = \sqrt{e(0)\,\omega\tau\frac{L_o}{k_B(0)\,\mathcal{G}^2}NM}, \text{ and } \psi = N k_B(0) L_o - M\omega\tau.$$

Summary and Conclusions

Cumulative beam breakup in radio-frequency ion accelerators has been calculated using, as a model, a beam of delta-function bunches. As examples, the limiting cases of a coasting beam with no focusing and a nonrelativistic, slowly accelerated beam with strong solenoidal focusing were delineated. These cases are used in Ref. 13 for applications to conceptual designs of high-current ion accelerators.

Limits on the Q of the deflecting mode required to control BBU would be larger than that inferred from these calculations if a more realistic set of assumptions were used. For example, the cavities will carry a distribution of deflecting-mode frequencies due to construction tolerances, and this suppresses BBU.[15,16] In addition, the transient growth of BBU can be controlled by smoothly varying the charge per bunch.[12]

Beams in low-velocity linacs are comprised of bunches of nonzero length, a property not included here. Bunch length will be most important in the consideration of high-frequency cavity modes because a given bunch will then fill a large fraction of the rf period of the mode. This will, for example, modify the beam-cavity resonance. Using Fourier transforms rather than Fourier series to solve eq. (1), we have developed a formalism both to include nonzero bunch length and to calculate the behavior of test particles constituting a longitudinal halo between bunches. It will be discussed in future papers. The results reported here are accurate for deflecting modes of low frequency in which a given bunch fills a small fraction of the rf period of the mode.

References

1. W.K.H. Panofsky and M. Bander, Rev. Sci. Instrum., **39**, 206 (1968).
2. V.K. Neil and R.K. Cooper, Part. Accel., **1**, 111 (1970).
3. R.H. Helm and G.A. Loew, Linear Accelerators, edited by P.M. Lapostolle and A.L. Septier (North Holland, Amsterdam, 1970), p. 173.
4. A.W. Chao, B. Richter, and C.Y. Yao, Nucl. Instrum. Methods, **178**, 1 (1980).
5. G. Decker and J.M. Wang, in Proc. 1987 Part. Accel. Conf., 1210 (1987).
6. R.L. Gluckstern, R.K. Cooper, and P.J. Channell, Part. Accel., **16**, 125 (1985).
7. K. Yokoya, DESY Report No. 86-084, 1986 (unpublished).
8. R.L. Gluckstern, F. Neri, and R.K. Cooper, Part. Accel., **23**, 53 (1988).
9. V.K. Neil, L.S. Hall, and R.K. Cooper, Part. Accel., **9**, 213 (1979).
10. Y.Y. Lau, Phys. Rev. Lett., **63**, 1141 (1989).
11. K.A. Thompson and R.D. Ruth, Phys. Rev. D, **41**, 964 (1990).
12. R.L. Gluckstern, F. Neri, and R.K. Cooper, Part. Accel., **23**, 53 (1988).
13. J.R. Delayen, C.L. Bohn, and C.T. Roche, these Proceedings.
14. This calculation involves a procedure similar to that of G. Decker and J.M. Wang, Phys.Rev. D, **38**, 980 (1988).
15. R.L. Gluckstern, F. Neri, and R.K. Cooper, Part. Accel., **23**, 37 (1988).
16. D.G. Colombant and Y.Y. Lau, Appl. Phys. Lett., **55**, 27 (1989).

SUPPRESSION OF SINGLE BUNCH BEAM BREAKUP BY BNS DAMPING*

R.L. Gluckstern, F. Neri†, and J.B.J. van Zeijts
Physics Department, University of Maryland, College Park, MD 20742

Introduction

The intense narrow beams now used or planned in linear colliders lead to strong wake fields which are capable of increasing the transverse emittance to unacceptable values. A brief analysis of this phenomenon, known as single bunch beam breakup[1], was outlined by Neri and Gluckstern[2] for a coasting beam, using the cumulative beam breakup formalism of Gluckstern, Cooper and Channell[3].

Balakin, Novokhatsky and Smirnov[4] suggested that, by decreasing the energy of the tail of a bunch relative to its head, the resulting increased focusing force on the tail of the bunch could offset the effect of single bunch beam breakup. This method (a form of Landau damping now known as BNS damping) has been implemented at SLAC[1] and is being incorporated into the CLIC design[5]. Recently Balakin[6] suggested a variant of BNS damping in which all particles in the bunch oscillate with the same transverse frequency, amplitude and phase. A possible implementation of this suggestion has been analyzed by Seeman and Merminga[7] for the SLC.

The recent work[1,5,7] is primarily an application to specific accelerators (SLC and CLIC) and depends on the details of bunch shape, structure, and acceleration history. We here instead analyze single bunch beam breakup with BNS damping for a uniform coasting beam in order to explore the dependence on parameters. We use an earlier formulation for cumulative beam breakup[3] and finally express the transverse beam growth in terms of two universal parameters.

Single Bunch Beam Breakup

In order to use the formalism for cumulative beam breakup[3], we divide the single bunch into M_0 equally charged macroparticles. The equations governing ξ_M^N, the displacement of the M'th macroparticle in a coasting beam as it enters the N'th cavity are

$$\xi_M^{N+1} - 2\cos\mu\,\xi_M^N + \xi_M^{N-1} = z_M^N \,. \qquad (1)$$

$$z_M^N = r\sum_{l=1}^{M-1} e^{-\frac{\omega\tau}{2Q}(M-l)}\sin(\omega\tau(M-l))\xi_l^N \,, \qquad (2)$$

where z_M^N is proportional to the excitation of the N'th cavity as the M'th particle enters. Here μ is the phase advance of the transverse oscillation between cavities, ω and Q are the frequency and quality factor of the transverse deflecting mode, and τ is the time interval between macroparticles. The parameter

$$r = \frac{N_p e^2}{2M_0 W}\frac{Z_\perp T^2}{Q}L \qquad (3)$$

is a measure of the charge of each macroparticle and its influence on the transverse motion. The bunch has energy W and total charge $N_p e$, and the cavities, separated from each other by a distance L, have a shunt impedance parameter $\frac{Z_\perp T^2}{Q}$, where T is the transit time factor.

In our analysis for a single bunch, we shall assume that $M_0\omega\tau$ is sufficiently small so that $\sin((M-l)\omega\tau)$ can be replaced by $(M-l)\omega\tau$ in Eq. (2). In addition, we assume a weak focusing approximation and treat the large parameters N and M as continuous variables. This permits us to rewrite Eqs. (1) and (2) as

$$\frac{\partial^2\xi_M^N}{\partial N^2} + \mu^2\xi_M^N = z_M^N \,, \qquad (4)$$

$$z_M^N = r\omega\tau\int_0^M dl(M-l)\xi_l^N \,. \qquad (5)$$

Two derivatives of Eq. (5) with respect to M lead to

$$\frac{\partial^2 z}{\partial M^2} = r\omega\tau\xi \,, \qquad (6)$$

where $r\omega$ should really be taken to be the sum $\sum_j r_j\omega_j$, over all transverse modes which are capable of deflecting the beam.

The dominant dependence on N suggested by Eq. (1) is $e^{i\mu N}$. By redefining ξ_M^N and z_M^N so as to remove this factor and assuming that the remaining factors are slowly varying with respect to N, we obtain

$$\frac{\partial\xi}{\partial N} = \frac{z}{2i\mu} \,. \qquad (7)$$

*Work supported by the Department of Energy.
†present address: AT Division, Los Alamos National Lab.

Equations (6) and (7) govern the asymptotic behavior of the displacement and cavity excitation for large N and M.

It is a simple matter to demonstrate that

$$\begin{aligned} \xi, z &\sim e^{ue^{-i\pi/6}} \\ u &= \tfrac{3}{2}\left(\tfrac{r\omega\tau}{\mu}\right)^{1/3} M^{2/3} N^{1/3} \end{aligned} \tag{8}$$

contains the dominant dependence for large N and M. In fact, an alternate calculation starting with the integral representation for the solution of Eqs. (1), (2), which uses a saddle point calculation for large N and M, leads to

$$\frac{\xi}{\xi_0} = \frac{1}{\sqrt{4\pi}} \Re \left(\frac{e^{i\mu N + ue^{-i\pi/6}}}{\sqrt{ue^{-i\pi/6}}} \right) . \tag{9}$$

Assuming that the dominant dependence on N is contained in the factor $e^{i\mu N}$ we can check the validity of Eq. (9) for large u by forming

$$\Lambda = \ln \frac{|\xi - \frac{i}{\mu}\frac{\partial \xi}{\partial N}|}{\xi_0} \tag{10}$$

from direct numerical simulations of Eqs (1) and (2). A plot of

$$\lambda_1 = \Lambda - \frac{\sqrt{3}u}{2} + \frac{1}{2}\ln 4\pi u \tag{11}$$

vs. u, is shown in Fig. 1 for $M_0 = 100$, $\omega\tau = 0.01$, $rM_0 = 0.06$, $\mu = \frac{\pi}{50}$. Since the value of λ_1 corresponding to Eq. (9) is zero, the figure shows that Eq. (9) is valid to an accuracy of about 10% for $u \geq 2.5$.

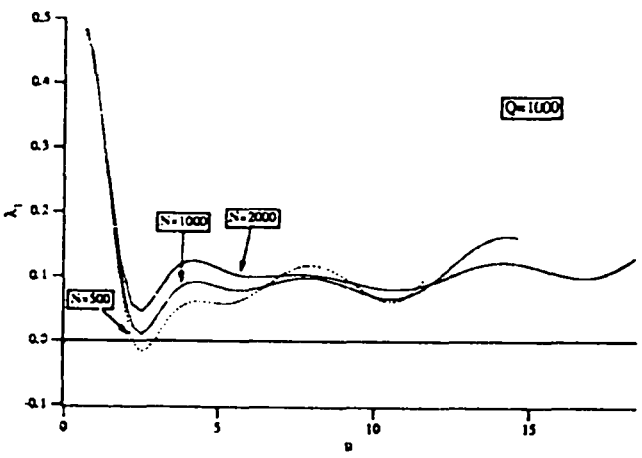

Figure 1: Check of Eq. 11 with simulation for $N = 500$, 1000, and 2000 .

BNS Damping

We shall now assume that the energy decreases linearly from the head to the tail of the bunch. Specifically, we replace μ^2 in Eq. (4) by

$$\mu^2 \rightarrow (\mu + \alpha M)^2 \cong \mu^2 + 2\alpha M \mu, \tag{12}$$

where $\frac{\alpha M_0}{\mu} \ll 1$ is the fractional increase in the phase advance per cavity during the pulse, and where μ is now independent of M. Removal of the factor $e^{i\mu N}$ from ξ and z in Eq. (4) then leads to an additional term in Eq. (7):

$$\frac{\partial \xi}{\partial N} + \frac{\alpha M \xi}{i} = \frac{z}{2i\mu} . \tag{13}$$

It is now convenient to change variables from N and M to u and v where u is given in Eq. (8) and where

$$v = \alpha\left(\frac{\mu}{r\omega\tau}\right)^{1/3} M^{1/3} N^{2/3} . \tag{14}$$

After considerable algebra, we find that, for large u, the solution of Eqs. (6) and (13) for $\frac{\xi}{\xi_0}$ can be written in terms of the universal parameters u and v, as

$$\frac{\xi}{\xi_0} = \frac{1}{\sqrt{4\pi u}} \Re \left(e^{uf(v) + g(v) + i\frac{\pi}{12} + i\mu N} \right) , \tag{15}$$

where $f(v)$ and $g(v) = \int_0^v \frac{N}{D} dv$ satisfy the following equations:

$$\begin{aligned} i + f^3 + 3vf^2 f' + \frac{9}{4}v^2 f f'^2 + \frac{1}{2}v^3 f'^3 = \\ iv\left(2f^2 + 2vff' + \frac{1}{2}v^2 f'^2\right) , \end{aligned} \tag{16}$$

$$\begin{aligned} N &= 24i(f + vf') - 9f'(4f + 3vf') \\ &\quad - 2v(-2iv + 9f + 6vf')f''(v) , \end{aligned} \tag{17}$$

$$D = 4(2f + vf')(-2iv + 3f + 3vf') . \tag{18}$$

The solution of Eq. (16) corresponding to $f(0) = e^{-i\pi/6}$ has been obtained by numerical integration and is shown in Fig. 2. Fig. 3 shows the result for $g(v)$, obtained by a subsequent numerical integration using $\frac{N}{D}$.

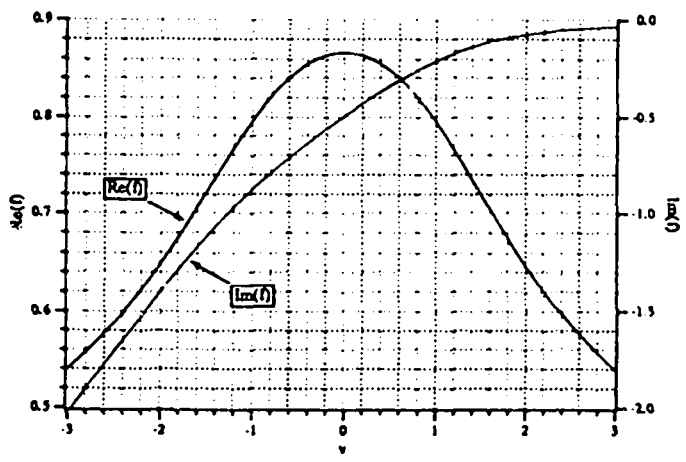

Figure 2: $f(v)$ vs. v.

The validity of Eq. (15) can be checked by forming Λ defined in Eq. (10), and

$$\lambda_2 = \Lambda + \frac{1}{2}\ln 4\pi u - u\Re f(v) . \tag{19}$$

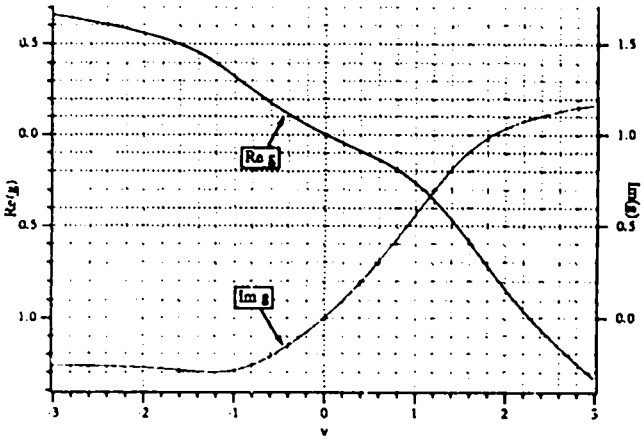

Figure 3: $g(v)$ vs. v.

The plot of λ_2 vs v in Fig. 4 for u = 14.57, 17.65, 20.35, adjusted s.t. $\lambda_2 = 0$ for $v = 0$, shows that the results are independent of u in this range, as predicted by Eq. (15). Furthermore, the agreement between λ_2 and $\Re g(v)$, shown as the dashed line in Fig. 4, clearly confirms the parametrization predicted in Eq. (15).

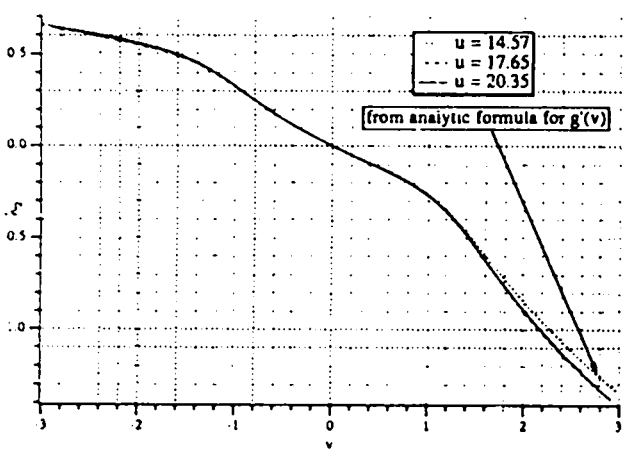

Figure 4: λ_2 and $g(v)$ vs. v for 3 values of u.

Discussion and Summary

The main result of this paper is the parametrization in terms of u and v in Eq. (15). In suppressing single bunch beam breakup one therefore determines the growth of the tail displacement in the absence of BNS damping ($v = 0$) and the value of v necessary to reduce this growth to an acceptable value.

An interesting result is obtained if one assumes that v is large and that $uf(v)$ is the dominant part of the exponent. It can be shown for large v that $f(v) \rightarrow \sqrt{\frac{8}{9v}}$, in which case

$$uf(v) \cong \sqrt{\frac{2Mr\omega\tau}{\alpha\mu}} \tag{20}$$

independent of N. If one now looks for a solution to Eq. (6) which is independent of M, this can be achieved by requiring in Eq. (4) that

$$\xi^N \Delta\mu^2 \cong \xi^N 2\alpha M\mu = z_M^N = \frac{M^2}{2} r\omega\tau\xi^N, \tag{21}$$

or $Mr\omega\tau = 4\alpha\mu$. The condition that the increase in focusing completely compensates for beam breakup is therefore similar to placing a numerical limit on the exponent in Eq. (15).

Finally, although our analysis is for a uniformly charged beam, the parameter $M_0 r\omega\tau/\alpha\mu$ can be written in a form independent of the bunch microstructure:

$$\frac{M_0 r\omega\tau}{\alpha\mu} = \frac{(M_0 r)(M_0 c\tau)}{(\alpha M_0/\mu)(\mu^2 c/\omega)}, \tag{22}$$

where $M_0 r$ is proportional to the total bunch charge, $M_0 c\tau$ is the equivalent bunch length, and $\alpha M_0/\mu$ is the fractional increase in the transverse phase advance. In order to suppress single bunch beam breakup this parameter should be of the order of 1 or less.

References

[1] K.L. Bane, IEEE Transactions on Nuclear Science, Vol. NS-32, No. 5, October 1985, p. 2389.

[2] F. Neri and R.L. Gluckstern, Proceedings of the Particle Accelerator Conference, Chicago, IL (1989), p. 812.

[3] R.L. Gluckstern, R.K. Cooper, and P.J. Channell, Particle Accelerators 16, 125 (1985).

[4] V.E. Balakin, A.V. Novokhatsky and V.P. Smirnov, Proceedings of the 12th International Conference on High Energy Accelerators, Fermilab, 1983, p. 119.

[5] H. Henke, Proceedings of the Particle Accelerator Conference, Washington DC, March 1987, p. 1346 ; also *A Two-Stage RF Linac for CLIC*, CERN-LEP-RF/87-57, April 1987.

[6] V.E. Balakin, Proceedings of the 1988 Workshop on Linear Colliders, SLAC, p. 55.

[7] J.T. Seeman and N. Merminga, *Mutual Compensation of Wakefield and Chromatic Effects of Intense Linac Bunches*, SLAC-PUB-5220, March 1990.

PARMTEQ CALCULATIONS ON BEAM DYNAMICS IN A FREQUENCY VARIABLE RFQ*

H. Deitinghoff and A. Schempp
Institut für Angewandte Physik der Johann Wolfgang Goethe Universität
Postfach 111 932, D-6000 Frankfurt am Main, FRG

Abstract

An RFQ is built for postacceleration of clusters at the accelerator facility of IPN, Lyon. The frequency of the RFQ is between 80 and 110 MHz, which allows the acceleration of clusters in a wide range of masses and energies. Beam dynamics calculations are presented and their results are discussed for few specific examples.

Introduction

During the last years the use of variable energy Radio Frequency Quadrupole (RFQ) accelerators has been proposed for various applications in ion implantation, postacceleration of light and heavy ions or clusters[1,2,3,4]. One project near completion is the upgrading of the Lyon cluster accelerator facility, which is carried out in cooperation between IPN, Lyon, KFK Karlsruhe and IAP Frankfurt/Main[5]. An energy variable RFQ serves for postacceleration of clusters with masses up to 55 to a maximum energy of 3 MeV, thus offering new possibilities for studies in cluster physics. Here a more detailed description of the beam dynamics properties of such an RFQ is given, whereas design criteria and the status of the project will be discussed elsewhere on this conference[6].

RFQ Beam Dynamics

The RFQ accelerator is a structure, which provides both acceleration and strong rf electrical focussing at the same time. From the RFQ potential linear equations of motion can be derived mostly for the case of ideal electrode profile[7,8]. A scheme of this profile is shown in fig. 1. These equations of motion

$$\frac{d^2 x_y}{d\tau^2} + (a \pm 2q\cos\tau)\,x_y = 0$$

$$\frac{d^2 u}{d\tau^2} - 2au = 0, \quad \tau = \frac{1}{2}(\omega t - \varphi_s) \qquad (1)$$

are of Mathieu type, the coefficients given by

$$a = -\frac{\xi e V A_{10} \sin\varphi_s}{2Amv^2}, \quad q = \frac{2\xi e V A_{01}}{Amv^2 k^2 r^2} \qquad (2)$$

with ξ/A = charge to mass ratio, v = particle velocity, k = wave number, r = apertureradius and the RFQ parameters describing acceleration and focusing respectively.

$$A_{10} = \frac{M^2 - 1}{M^2 I_0(kr) + I_0(kr)}, \quad A_{01} = 1 - A_{10} I_0(kr) \qquad (3)$$

For each kr the modulation M determines the ratio of acceleration to transverse focusing. Using smooth approximation as e.g. in [9] analytical expressions for longitudinal and transverse phase advances σ_{0l} and σ_{0t} resp., emittances and current limits, characteristic quantities in beam dynamics theory can be deduced:

$$\sigma_{0l}^2/\pi^2 = -2a$$

$$\sigma_{0t}^2/\pi^2 = q^2/2 + a \qquad (4)$$

$$\varepsilon = \bar{r}^2\sigma/\pi$$

RFQ design means to fix all these parameters along the RFQ, good beam quality being only one point of consideration besides rf properties, costs, power consumption, adjustment and fabrication tolerances. For a fixed design all parameters and mechanical dimensions are frozen, then (2), (3) and (4) give immediately the scaling rules for an energy variable RFQ

1.) $Amv^2 = \text{const} \rightarrow Am \sim v^{-2} \sim f^{-2}$

2.) $Am = \text{const} \rightarrow v^2 \sim f^2 \sim V$

In both cases the beam dynamics stays completely unchanged the values of (4) are not changed, i.e. the unnormalized acceptances, emittances and the transmission do not change with energy or cluster species. In case 2.) the electrode voltage can be varied in addition, but then (2), (3) and (4) are no longer constant.

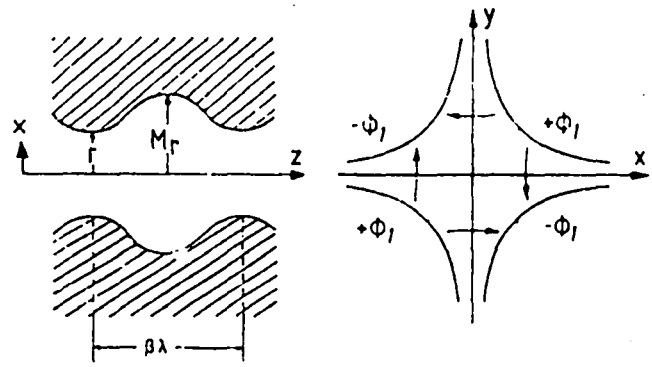

Fig. 1 Scheme of ideal RFQ electrode profile

VE-RFQ Parameters

The Lyon cluster postaccelerator RFQ was designed for high energy gain and compact dimensions. Table I summarizes main parameters, some of them being plotted in fig. 2. Maximum electrode voltage is 80kV, a shaper was omitted. Fig. 3 gives the range of masses and energies covered by the RFQ.

* Work supported by BMFT under contract no. 06 OF 186 I

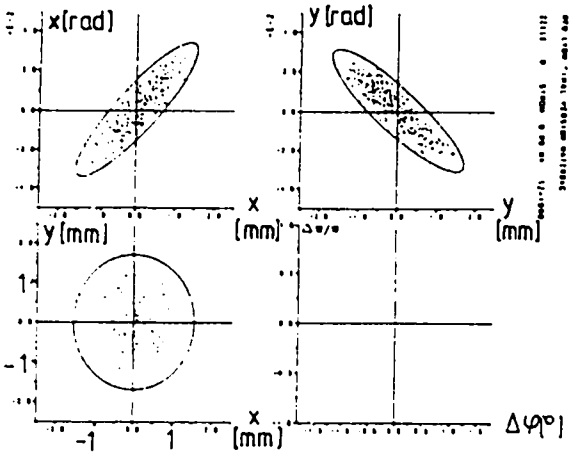

Fig. 4 a) Input emittance, ε^{tr} = 25 mm mrad

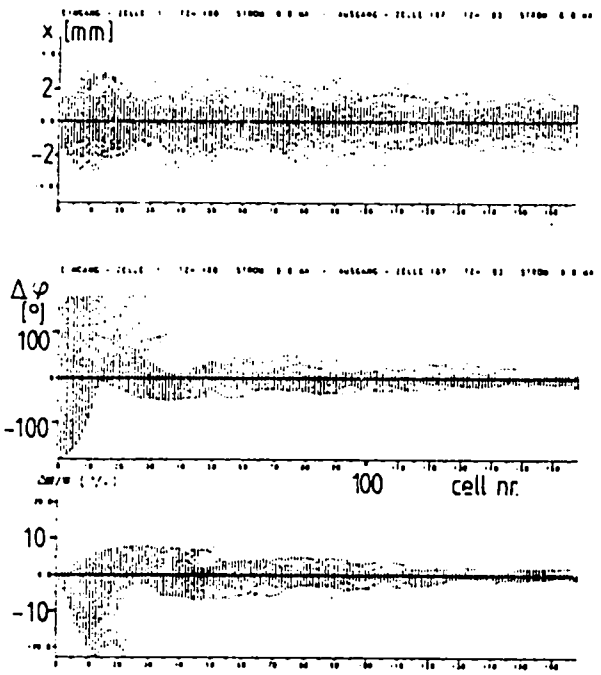

b) Transverse and longitudinal beam behaviour

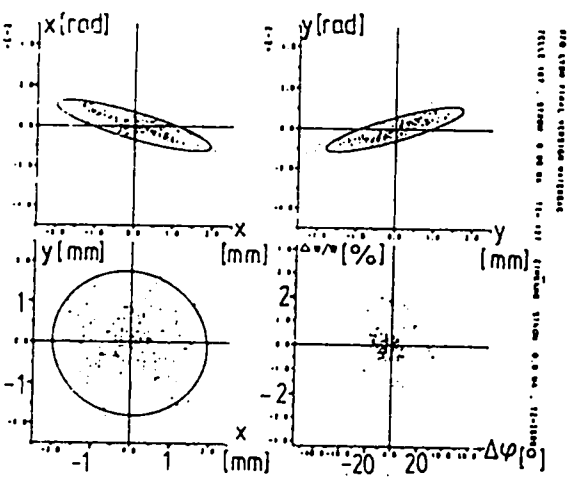

c) Corresponding output emittances

f = 110 MHz, A = 30, T_{in} = 300 keV, U = 80 kV

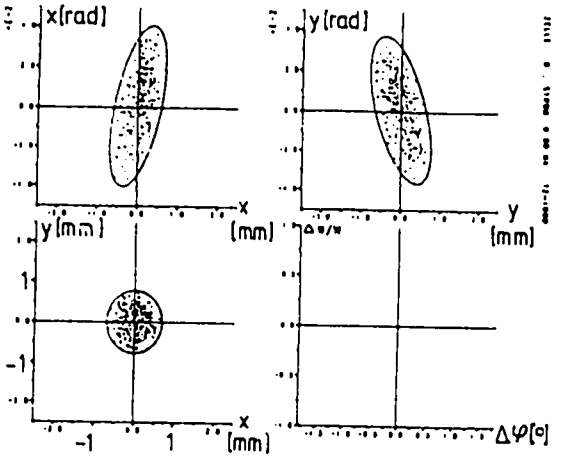

Fig. 6 a) Input emittance, ε^{tr} = 25 mm mrad

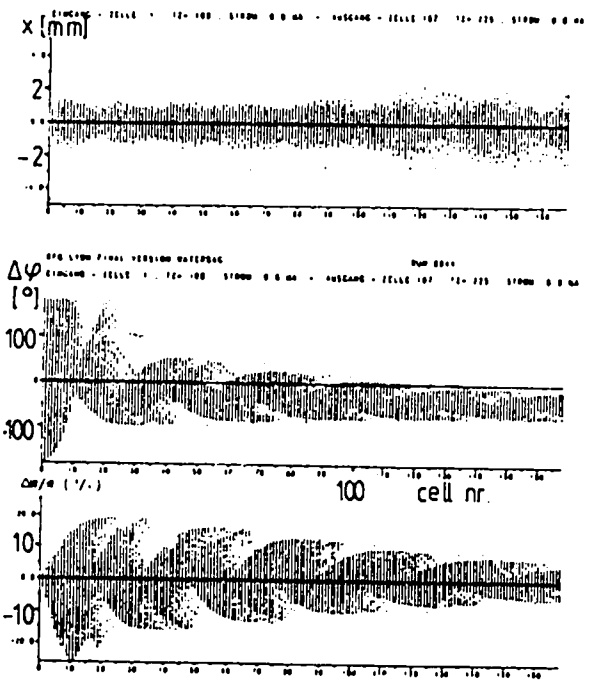

b) Transverse and longitudinal beam behaviour

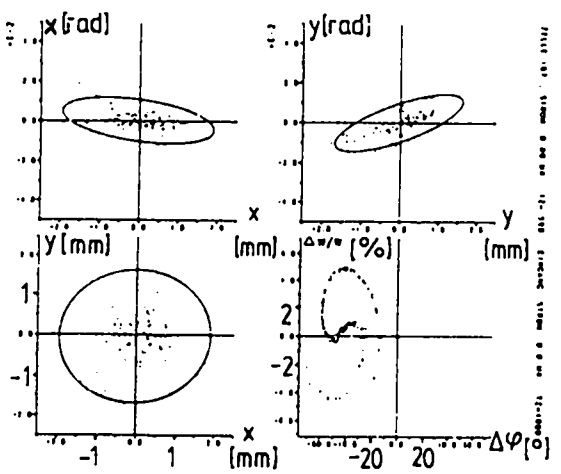

c) Corresponding output emittances

f = 80 MHz, A = 30, T_{in} = 160 keV, U = 80 kV

Table I RFQ parameters

f [MHz]	80 - 110
U [kV]	80
T_{in} [keV]	≤ 300
T_{out} [keV]	≤ 3000
charge state/mass	≥ 1/56
l [m]	1,96
cell number	167
modulation	1.1 - 2
φ_s [°]	50 - 15.5
a [mm]	3.1 - 2.5
σ_{ot}^{min} [°]	8.2 - 7.2

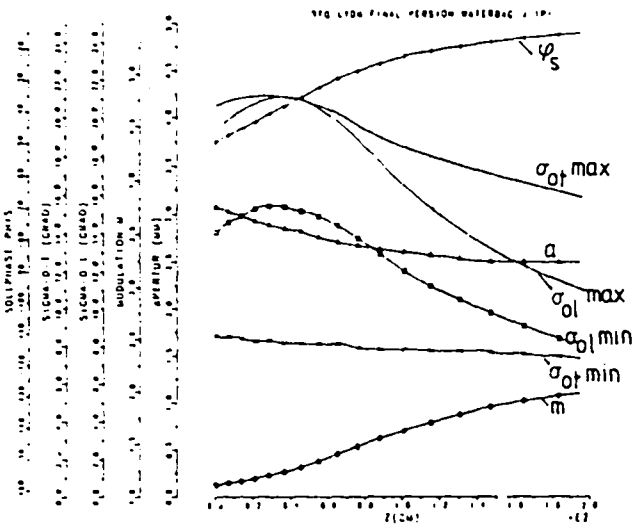

Fig. 2 VE-RFQ parameters vs. length

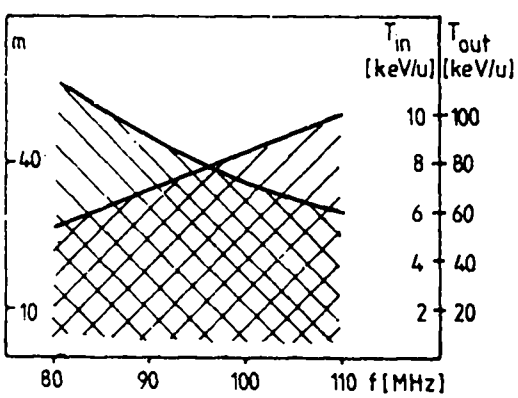

Fig. 3 Range of cluster masses and energies

Results of PARMTEQ Calculations

From (4) follows that for the heaviest particle at the highest frequency and velocioty phase advances are at minimum. Here mass 30 at 110 MHz and 10 keV/N input energy and all other masses scaled corresponding to rules 1) and 2) gives a transverse phase advance of ~7.5° and a synchronous acceptance of 52 mm·mrad (not norm.).

For an injected dc beam with this transverse emittance the transmission is ~ 17 % due to the omitted shaper and the rather low focusing strength. Emittance growth is about 25 %, the longitudinal output emittance is very small with < 2° keV/u (rms). The transmission is increasing to ~ 22 % for 25 mm mrad. figs. 4 a-c show input and output emittances and the beam behaviour along the RFQ. Fig. 5 illustrates for mass 30 the gain in focusing and transmission as function of electrode voltage for a lower frequency of 80 MHz, corresponding to an input energy of 160 keV. Figs. 6 a-c show input and output emittances for mass 30, U = 80 kV and f = 80MHz and the transverse and longitudinal beam behaviour.

As can be seen, particles are changing the synchronous phase along the RFQ, some additional emittance growth up to an factor of 2 seems to follow from this effect. The transverse input ellipse parameters were adjusted to maximum transmission, some flexible transverse matching should be provided[10].

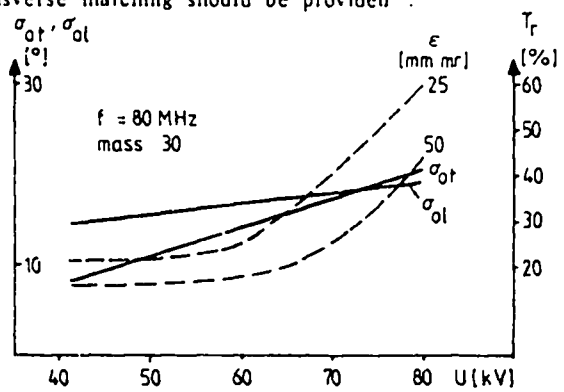

Fig. 5 Phase advances and transmission vs. electrode voltage, parameter transverse emittance ε.

Conclusion

An effective postaccelerator for cluster masses up to 56 has been designed and built, providing a high energy gain. PARMTEQ calculations proved scaling rules from linearized equations of motion. Work on optimization of beam optics and overall transmission from cluster source to the experimental area is in progress[11].

References

1. H.D. Moser, A. Schempp, NIM, B 24/25 (1987) 759
2. R. Hamm, Linac 1986, SLAC-Rep. 303 (1986) 33
3. A. Schempp, Nucl. Instr. Meth. B 40/41 (1989) 937
4. D. Hofmann et al., Nucl. Instr. Meth. B 50 (1989) 487
5. A. Schempp et al., Proc. EPAC 1990, to be published
6. A. Schempp, Variable Energy and Heavy Ion RFQs, this conference
7. I.M. Kapchinskiy, V. Teplyakov, Prib. Tek. Eksp. 119 No. 2 (1970) 17,19
8. K.R. Crandall et al., BNL-51143 (1980) 20
9. P. Junior, Part. Acc. Vol. 13 (1983) 231
10. H. Deitinghoff, IAP, Int. Rep. 90-21 (1990)
11. G. Hadinger, private communication

A NEW DYNAMICS CODE DYNAC FOR ELECTRONS, PROTONS AND HEAVY IONS IN LINACS WITH LONG ACCELERATING ELEMENTS

P. Lapostolle[1], F. Méot, S. Valero
Laboratoire National Saturne, CEN Saclay, 91191 Gif-sur-Yvette Cedex, France

E. Tanke
PS, CERN, CH-1211 Genève 23, Switzerland

Abstract

A new simulation program has been made for linacs, applicable to heavy ion machines with independent long cavities (including the possibility of entering in the same bunch, ions of different charge state). This program applies also to superconducting multicell cavities for electrons and, with the inclusion of space charge, will apply to proton linacs. Apart from the introduction of a matrix formalism, it follows the same approach as proposed in 1965 by one of the authors and used in standard codes like PARMILA and MAPRO. Its range of validity, however, has been extended to long accelerating elements where, instead of second order corrections, as suggested in 1986[1], other simpler averaging methods are used. In addition, for the transverse motion, the introduction of reduced canonical variables simplified the expressions and increased the accuracy. The precision over one accelerating element has been shown to be appreciably better than 1 % with the help of a complementary step by step integration routine of Hamiltonian form, always accessible in the code.

Introduction

The derivation of beam dynamics equations commonly used now was presented in 1966[2][3]. It applies to symmetrical accelerating gaps and has been used for the design of Alvarez-type accelerators.

The field distribution in each gap, known usually from computation, is supposed to be expressed around its centre of symmetry in the form of a Fourier integral. Assuming straight trajectory and constant velocity and introducing a thin lens formalism, the changes in energy W, phase φ, radius r and slope r', when crossing the median plane, are given by expressions where the field distribution only appears through the so-called transit time coefficient T(k) with $k = \frac{\omega}{v}$ (angular frequency over longitudinal velocity) and its derivatives with respect to k. Energy, phase, radius and slope must however be the actual values at this median plane and they have to be computed through a second set of equations via iterations using the so-called S coefficients, which are to be treated with some care due to analytical discontinuities in the derivations [4]. Second order terms, taking into account the change in velocity across the gap, were roughly computed to obtain their order of magnitude, but were not used.

In 1986 the method was extended for the treatment of long and complicated independent structures (helix type) with no exact symmetry, to be used with various ions of quite different velocities [1]. The structures are now characterized by their axial field distribution, given in the form of a set of Fourier coefficients, which can be used to compute the usual transit time coefficients. The treatment was modified using the input plane with a thin lens formalism (avoiding the difficulty mentioned concerning the S coefficients and avoiding the use of a median plane, no longer significant in the absence of symmetry). In order to increase the accuracy for long structures, second order terms were accurately computed in the form of a double series of transit time coefficients. Such second order terms, though complicated, gave very satisfactory results for the longitudinal motion (W,φ). For the transverse motion the method lacked precision, for a reason not understood at that time, and was therefore discarded.

In 1988 an attempt was made to use such a formalism for electron machines of the superconducting type with 5 cell cavities and accelerating gradients up to 10 MeV/m. For relativistic particles (more than 2 to 5 MeV injection energy), the formalism gave correct results for the longitudinal motion. Results for the transverse motion proved to be wrong, necessitating the development of a new formalism.

1) Consultant; private address:

3 rue Victor Daix, F-92200 Neuilly-sur-Seine, France

New Treatment for Transverse Motion

One drawback of the above method in the transverse motion is that the variables r and r' are not canonically conjugate. After having computed a change in transverse momentum across an accelerating gap, the corresponding change in r' has to include an additional term due to the change in longitudinal velocity. The emittance in r r' is not constant: it has to be multiplied by $\beta\gamma$ to become "normalized" and invariant.

In the field of electrostatic electron optics Cotte [5] makes use of a "reduced radius" R defined by the so-called Pitch transformation as :

$$R = r\sqrt{\beta\gamma} \tag{1}$$

With such a variable, the equation :

$$m_0 c\, d(r'\beta\gamma) = -qr\left(\frac{\partial E_r}{\partial r} + \beta c\frac{\partial B_\varphi}{\partial r}\right)dt \tag{2}$$

becomes in the paraxial approximation, using Maxwell's equation :

$$\frac{d^2R}{dz^2} - \left[\frac{1}{(\gamma^2-1)^{1.5}}\frac{q}{2m_0c^3}\frac{\partial E_z}{\partial t} - \frac{\gamma^2+2}{(\gamma^2-1)^2}\frac{q^2}{4(m_0c^2)^2}E_z^2\right]R = 0 \tag{3}$$

The first of the two terms within brackets in equation (3) is in fact equal to the one generally used in the equation for r. The second term is nothing else than the electrostatic lens expression as given by Cotte and is of second order in field. It is always larger than any second order correction to the first term (see previous section) and in some cases it is even larger than the first term as such (see fig 1 and 2).

The most important remark to be made however, is that the form of eq (3) implies, according to Liouville's theorem, that the emittance in RR' is an invariant as it has no R' term.

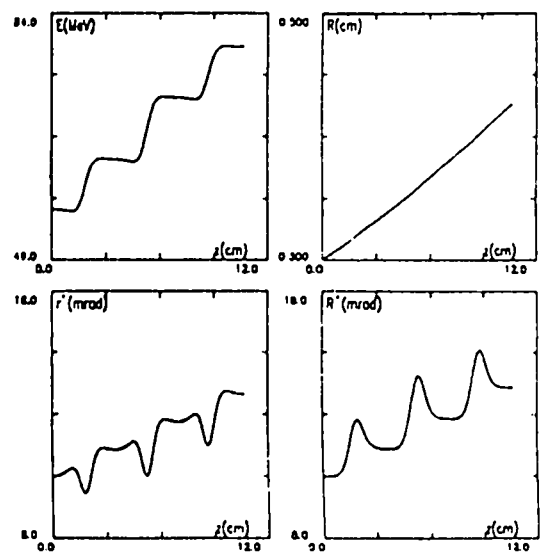

Fig.1. Evolution of energy, R, r' and R' for the acceleration of Pb^{13+} through 3 gaps of a Quasi-Alvarez period. The phase of the particle considered is at -20 deg from the crest. One observes the difference between R' and r'. While r' is of a complicated form, the R' curve clearly shows the effect of the first term of eq 3, which is the prominent one here.

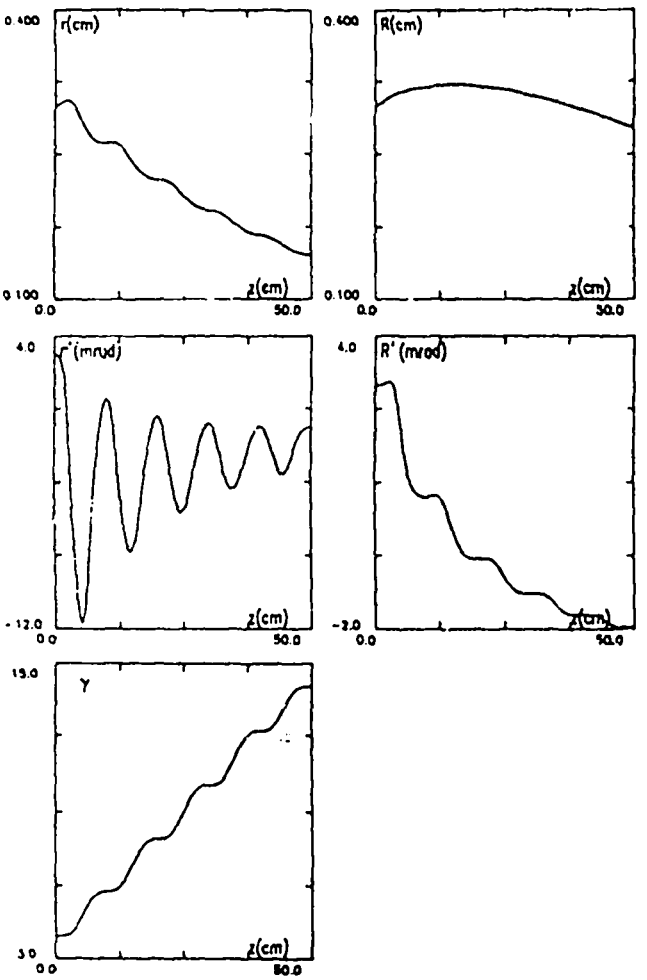

Fig.2. Same as fig 1 but for a 5 cell electron structure with an input energy of 1.5 MeV (6.5 MeV at the output). The phase is close to the crest. In eq 3 it is now the second term which is the largest; R' has a stepwise evolution, essentially converging.

New Computer Codes

With eq (3) for the transverse motion, a new 'suite' of codes to replace PARMILA and similar type codes has been developed. Such codes are now applicable to a great variety of linacs from ion machines (Quasi-Alvarez structure or independent long cavities) to electron machines of the CEBAF type (5 superconducting cells). Integration of the equations of longitudinal and transverse motions over long structures where β may change by 5% (or more for shorter structures) and γ by a factor of up to 3 or 4 requires, in order to get accurate results with the standard formalism, either additional higher order corrections or the use of some averaging procedure. This last method has been chosen. For instance, the $k=\frac{\omega}{v}$ of the transit time factor is computed via iterations with a beta which corresponds to the velocity defined by input and output phases in the accelerating element. In eq (3) the γ terms are taken as an average over the element, assuming a linear γ variation with z. Phase and radius are also corrected. Detailed derivations will be given in another paper in preparation.

A complementary step by step integration routine of Hamiltonian form allows a check of the direct expressions as well for transverse as for longitudinal motions. Such expressions have been found to be satisfactory for several accelerating structures (see figs 3, 4, 5, 6 and 7). Nevertheless, calculations with this step by step integration routine take almost 100 times longer than the analytical procedure.

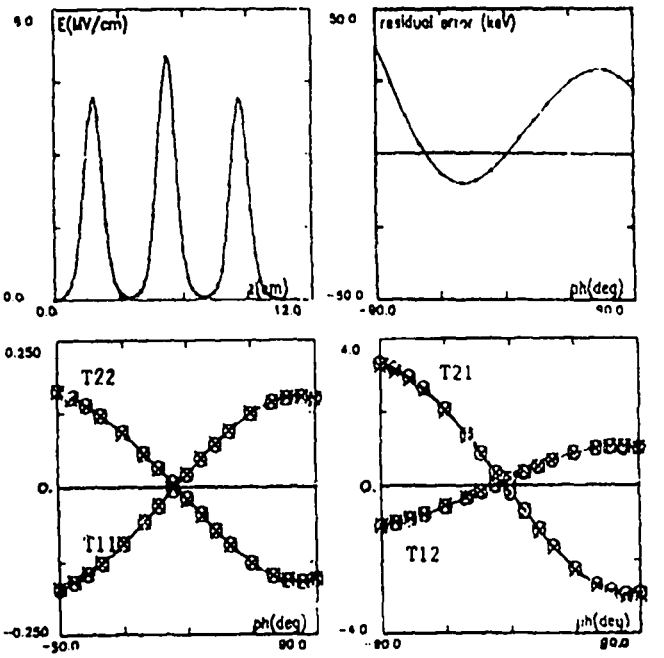

Fig.3. Comparison of the accurate step by step integration with the direct expressions used in the new codes, shown here for the acceleration of Pb^{25+} through a Quasi-Alvarez cell at around 0.24 MeV/nucleon (50 MeV kinetic energy). One can see the axial electric field distribution of the cell and the residual error in acceleration for phases in the range of -90 deg to +90 deg (at 200 MHz) around peak acceleration (here 3.4 MeV). The other two graphs show the evolution of the matrix coefficients T (T21 in mrd/mm, T12 in arbitrary units), used for the calculation of the reduced variables in the thin lens formalism (the circles correspond to the direct expressions, the crosses to the step by step integration).

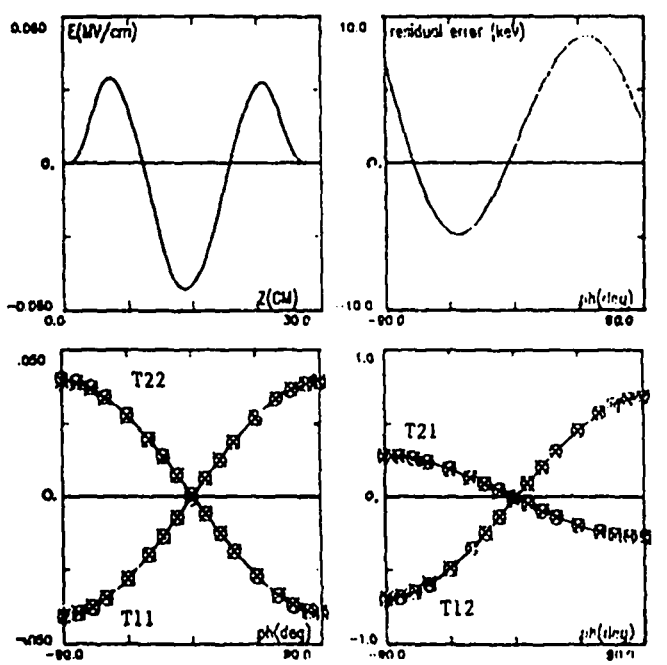

Fig.4. Same as fig 3, but for Ge^{19+} through a βλ helix for a β corresponding to optimal acceleration (close to 10 MeV, frequency 135 MHz).

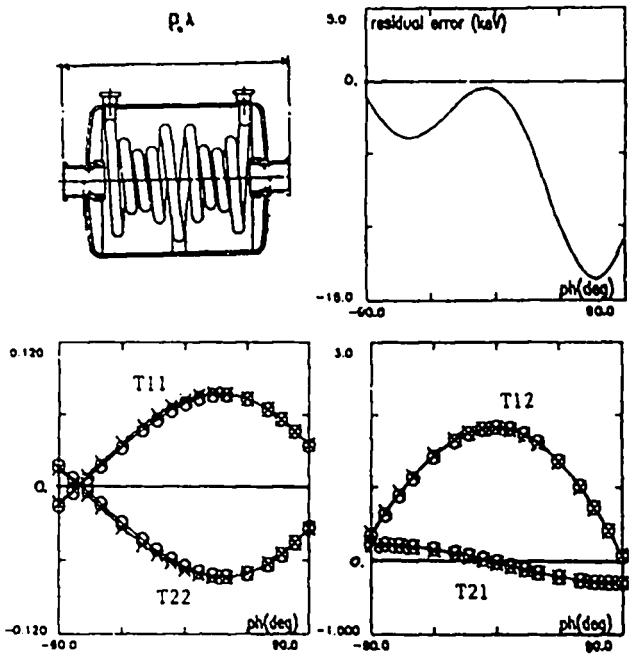

Fig.5. Same as fig 4, but at the edge of the velocity pass band (only 1.5 MeV peak acceleration). The shape of the helix is shown rather than the field distribution.

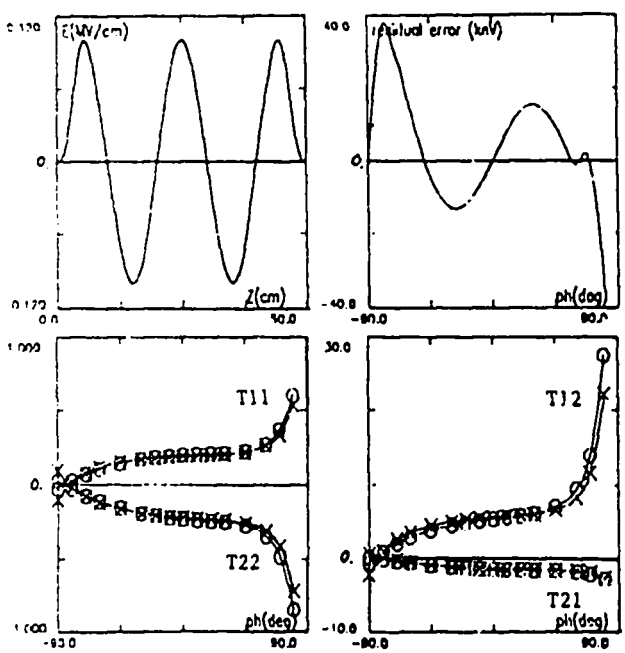

Fig.6. Same as fig 3, but for electrons injected at 1.5 MeV into a 5 cell cavity (frequency 1500 MHz, 5 MeV peak acceleration).

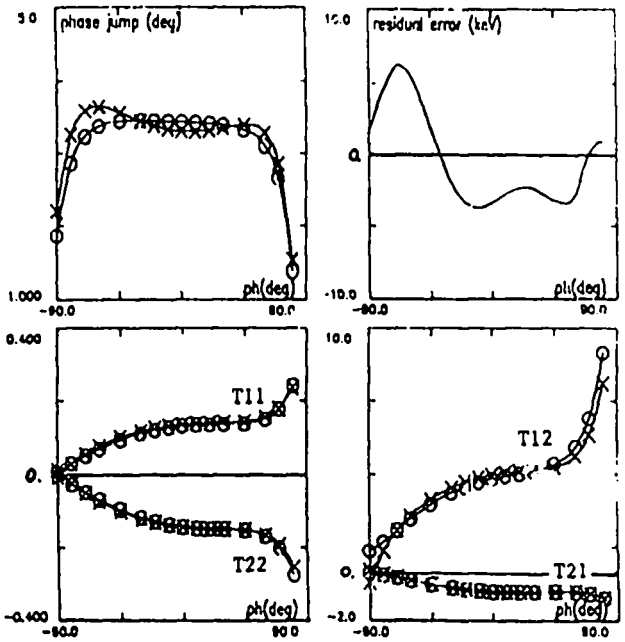

Fig.7. Same as fig 6, but for electrons injected at 2.5 MeV. Rather than the field distribution, the phase jump is shown (the phase variation across the cavity is around 1000 deg). The circles correspond to the direct expressions, the crosses to the step by step integration; the maximum difference between these two is of the order of a few tens of a degree. The errors found at higher injection energies are even smaller.

Conclusion

These codes, initially developed for the computation of a heavy ion booster at Saclay, and also installed and partially developed at CERN, now also include the possibilty of computing recirculating electron machines with the effect of synchrotron radiation in bending magnets [6]. At CERN, they form an integral part of a suite of programs for the design of a Quasi-Alvarez lead linac [7]. For present applications, space charge has not yet been included, but the logic used in the programs allows for such an addition. An extension for the simulation of an RFQ could also be foreseen.

Acknowledgements

The authors feel very indebted to G.Leleux from Saclay who suggested the use of the "reduced radius" and to D.J.Warner from CERN for all his suggestions from which many improvements result. We also want to thank H.Haseroth from CERN and A.Tkatchenko from Saclay for their continuous interest and support.

References

[1] P.Lapostolle and S.Valero, "Beam Dynamics in Long Transit Time Linac Cavities for Heavy Ion Boosters," Linac Conf.1986 SLAC, vol. 303, p. 315, 1986.

[2] A.Carne, P.Lapostolle, and M.Prome, "Accurate Beam Dynamics Equations in Proton Linacs," Vth Intern. Conf. on High Energy Acc., Frascati (CNEN, Roma), pp. 656-662, 1965.

[3] A.Carne and P.Lapostolle, "Design Equations in an Alvarez Type Proton Linac," Linac Conference, Los Alamos, vol. 3609, p. 201, 1966.

[4] B.Schnizer, A.Carne, P.Lapostolle, and M.Prome, *Linear Accelerators* Amsterdam: North Holland, p. 747, 1970.

[5] M.Cotte, Achromatisation des Systèmes Centrés de l'Optique, Académie des Sciences, Paris, 204, p. 170. 1937.

[6] E.Klein, Prise en Compte du Rayonnement Synchrotron dans un Code de Transport, Saclay, Gif-sur-Yvette, France, 1989.

[7] P.Lapostolle, E.Tanke, S.Valero, M.Vretenar, and D.J.Warner, "Computer Design and Dynamics of the Quasi-Alvarez Linac," This Conference, 1990.

DAMPING OF HIGHER-ORDER MODES IN ELECTRON LINACS*

P. Hülsmann, M. Kurz, H. Klein, A. Schempp
Institut für Angewandte Physik
Robert-Mayer-Straße 2-4, D-6000 Frankfurt am Main, Fed. Rep. of Germany

Abstract

Future linear e^+-e^-- colliders will operate at frequencies up to ten times higher than existing machines (e.g. CLIC [1] is being designed for 30GHz operating frequency). Therefore beam induced effects like long range- and short range wakes cannot be neglected. They are capable of severely deteriorating beam quality. The most dangerous modes existing in an iris structure will be evaluated and it will be shown to which extent they can be suppressed. Experimental work has been done determining low Q-values using a simple and precise measurement technique. First results will be presented.

Introduction

Existing electron linacs (e.g. SLAC, LIL) operating at S-band frequencies are scarcely affected by wake-effects. As the wake-potentials scale with ω^2 for longitudinal wakes and with ω^3 for transversal wakes their influence on the beam has to be taken into account for future colliders [2].

All proposed e^--linacs are for colliders are iris structures. To get rid of beam perturbing higher order modes slotted irises have proved to be an effective method of coupling those modes into a load [3].

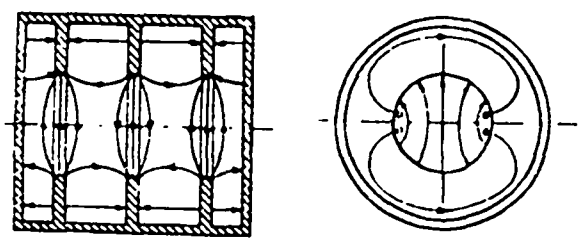

Fig. 1 TM_{110} π-mode, E- and H- field plot

Shape, orientation and number of coupling slots remain subject of investigations. According to Panofsky's theoreme [4, 7] TM-type dipole and quadrupole modes prove to be harmful to the beam. Therefore the TM_{110} π-mode is of special interest due to its phase velocity close to the one of the accelerating mode (see Fig. 1).

* work supported by BMFT under contract no. 055FM111

To judge the effectiveness of the coupling slots, the coupling factors for the perturbing modes have to be measured. To do this, Chipman's method (measuring the reflection coefficient of a complex load using a resonant line) [5] was used.

Experimental setup

In the experiments a three-cell iris structure ($2\pi/3$-mode TM_{010} at 2.45 GHz tuned to $v_{ph}=c$) was used. The middle iris of the structure was slotted and a rectangular waveguide (60mm width, 20mm height) was attached and terminated by a load. For the measurement of the coupling factors the load was replaced by a sliding short (see Fig. 2).

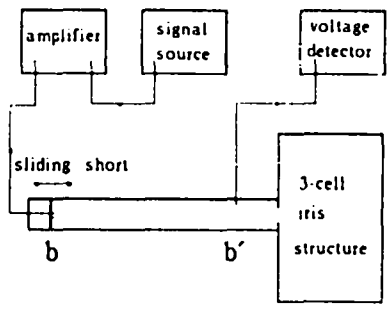

Fig. 2 Measurement setup

The rf-signal was fed from the signal source into a microwave amplifier and then inductively coupled to the waveguide exciting a TE_{10} wave. The amplitude of the rf in the waveguide was observed using a voltage detector.

The coupling slot to the waveguide was of 10mm height and 60mm width, the slot height in the iris varied from 1mm to 10mm (see Fig. 3).

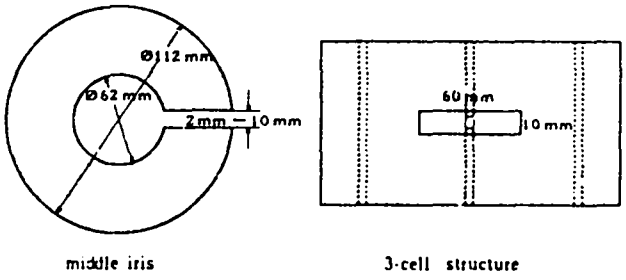

Fig.3 Coupling slot geometry

Theoretical aspects of the measuring method

We consider the signal-flow plot (sfp) of a transmission line terminated with a short on one side and with the attached cavity on the other, the cavity itself being represented by the reflection coefficient ρ_l. b and b′ are complex wave amplitudes (see Fig. 4).

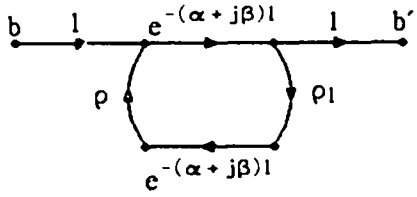

Fig. 4 Signal flow plot of the experimental setup $(\alpha + j\beta)$ = propagation constant of the line

It can be shown that the measured signal is proportional to the magnitude of the transmission factor $t_{bb'}=b'/b$. Hence we have to calculate $t_{bb'}$. Solving the sfp for $t_{bb'}$ we find

$$t_{bb'} = \frac{e^{-(\alpha+j\beta)l}}{1-\rho\rho_l\, e^{-2(\alpha+j\beta)l}} \quad . \qquad (1)$$

The reflection coefficient ρ is chosen -1 (sliding short) and introducing $\Gamma=\rho\rho_l=\exp(-2(\sigma+j\varkappa))$ we finally get:

$$|t_{bb'}| = \left(2\sqrt{|\Gamma|\,\{\sinh^2(\alpha l+\sigma)+\sin^2(\beta l+\varkappa)\}}\,\right)^{-1} . \qquad (2)$$

At a certain $\beta l_0+\varkappa=n\pi$, n being an integer, a maximum of the transmission factor will be observed. From this we get the phase information (modulo π).

The height of the maximum is proportional to the sinh term. To find σ, the line length l is varied by $\delta l_{1,2}$ to each side of the maximum until the signal has dropped to g times its value at l_0, $0<g<1$. We find from (2) that

$$\sinh\,(\alpha(l_0+\delta l_1)+\sigma)+\sin\,(\beta(l_0+\delta l_1)+\varkappa) = \sinh^2(\alpha l_0+\sigma)/g \ , \qquad (3)$$

$$\sinh^2(\alpha(l_0-\delta l_2)+\sigma)+\sin^2(\beta(l_0-\delta l_2)+\varkappa) = \sinh^2(\alpha l_0+\sigma)/g \ .$$

These equations now can be solved for σ. Often the damping coefficient α is very small in comparison with σ and can be neglected. In this case the two equations reduce to one. Now magnitude and phase of Γ are determined. If the sliding short cannot be thougt ideal one first has to measure its properties in order to get a correction for the value of ρ_l.

The coupling factors for the undercoupled and overcoupled case can be written as follows (at the minimum of ρ_l versus frequency):

$$k_u = \frac{1-\rho_l}{1+\rho_l} \ , \qquad k_o = \frac{1+\rho_l}{1-\rho_l} \qquad (4)$$

Which of these equations is applicable can be decided regarding the Smith chart affiliated with the problem.

Experimental results

For the purpose of identifying the eigenmodes of a resonator MAFIA [6] calculations for a three-cell iris structure were compared to perturbation ball measurements. The next neighbouring modes above the TM_{010} π-mode were identified and examined for their coupling properties [7] (see Fig. 1 and Fig. 5).

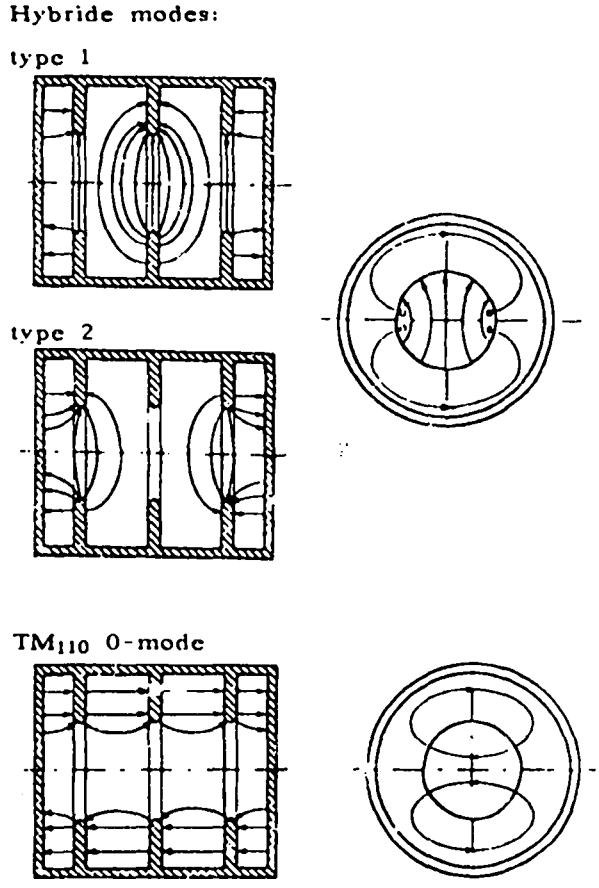

Fig. 5 Field plot of perturbing modes, E-field and H-field

The coupling factors of the modes to the waveguide were measured using slotted irises of various sizes.

Only one polarisation for each dipole mode would couple, the other is stongly suppressed by the slot. The following figures show reflection coefficients for several slot dimensions. All following figures refer to the TM_{110} π-mode.

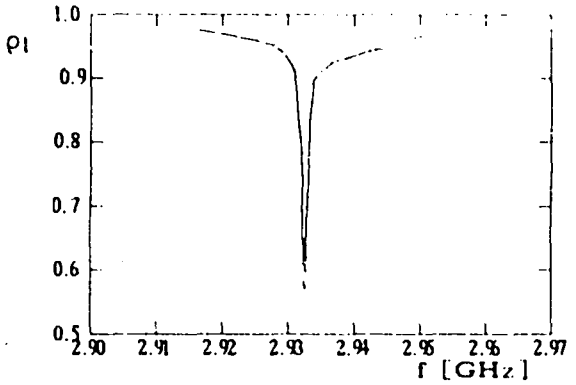

Fig. 6 Reflection coefficient versus frequency for a 5mm slot

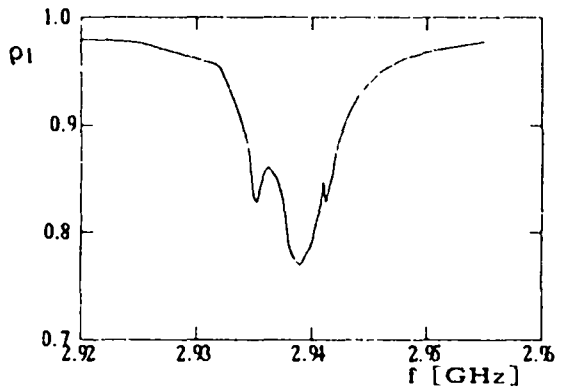

Fig. 7 Reflection coefficient versus frequency for a 2mm slot

The minimum left of the main minimum in Fig. 7 could be identified to be the second polarisation of the mode, the one to the right belongs to a resonance in the coupling system.

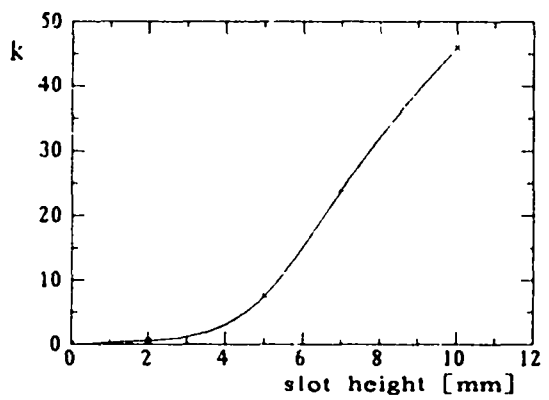

Fig. 8. Coupling factor versus slot height

The measurements were made with an uncalibrated sliding short, therefore all Q_l values are too high. This is true especially for the lowest values (assuming $\rho \approx -0.992$ corresponds to $Q_l \approx 70$ only for a 10mm slot).

Coupling coefficients were also measured for type 1 mode (see Fig. 5), results are given in Table I.

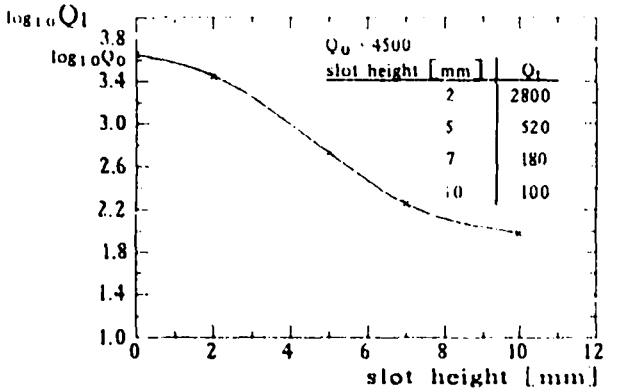

Fig. 9 Q_l versus slot height, $(Q_l = Q_0/(1+k))$

TABLE I
Coupling Factor k for Type 1 Mode
$Q_0 = 5000$

Slot height [mm]	k [1]
0	0.06
2	11
5	42

The TM_{110} 0-mode showed very weak coupling. Only for slots greater than 7mm slight coupling could be detected. The type 2 mode showed no coupling at all, due to the absence of fields in the middle iris. (see Fig. 5.).

Conclusions

Work on the structure described above has shown which amount of power of a certain mode (e.g. TM_{110} π-mode) can be brought out of a slotted iris structure. It could also be shown that the necessary low Q values of the disturbing modes can almost be achieved with one slot, a second slot should be sufficient. The problem of measuring very low Q values could be solved by using Chipman's method. This method does not require precise machining except for a calibration short.

References

[1] W. Schnell, EPAC, Vol. I (285), 1988

[2] H. Henke, CLIC Note 100, 1989

[3] R.B. Palmer, SLAC-PUB-4542, 1988

[4] W.K.H. Panofsky, W.A. Wenzel, Rev. Sci. Instr. 27 (967), 1956

[5] R.A. Chipman, Phys. Rev., Vol. 10 (27), 1939

[6] T. Weiland et al., DESY Report M-86-07, 1986

[7] P. Hülsmann, M. Kurz, Int.-Rep. 90-20, IAP-Frankfurt, 1990

EFFECT OF TANK SEQUENCING ON CCL ACCELERATORS†

C. C. Paulson, R. A. Hartley

Grumman Space Systems Division, 4 Independence Way, Princeton, N.J. 08540

ABSTRACT

For some high energy accelerator applications, coupled cavity structures provide the most efficient means of ion acceleration. This paper describes the results of a beam dynamics study into the effects of the use of various tanking sequence schemes on beam dynamics. The study was performed using two recently developed codes; a central particle pre-processor code and a multi-particle PIC CCL design code "PARMCCL". Particular attention is paid to transverse and longitudinal emittance growth. For a portion of the study, a particle distribution derived from PARMILA was used to prevent a free energy driven (changing of beam distribution) emittance growth. Additionally TRACE-3D has been modified to provide a matched beam for the CCL tanks.

Introduction

This paper presents brief descriptions of a Central Particle pre-processor CCL code (CPCCL) and a Particle-in-Cell (PIC) design code (PARMCCL) that have recently been developed. At present, only Side Coupled CCL structures have been included in these codes. PARMCCL is based on PARMILA and provides a logical extension of the ion accelerator design process.

Linear accelerator tanks are composed of a series of N coupled resonant cavities. Each set of boundary conditions defines N Electric and Magnetic field configurations (modes) which will resonate within the tank. The standard DTL configuration corresponds to the 0 Mode solution in which the Electric fields in all of the cavities are in phase. The synchronous condition for such an in-phase set is that the ions must travel the distance (L) from the center of one cell to the center of the next in one RF period ($L = \beta\lambda$). The π-mode configuration corresponds to a system with a 180° phase change between adjacent cells. In this case, the synchronous condition is $L = \beta\lambda/2$. The standard CCL configuration is the $\pi/2$ mode. In this configuration ion acceleration is obtained from every other cell. (Every other cavity has amplitude ± 1, intermediate cavities are empty.) The intermediate (unexcited) cells are termed "coupling cavities" and used for power transfer down the tank. The most common method of designing CCL structures is to remove the coupling cavities from the beamline entirely (for example; Annular, Slot, and Side Coupled CCLs). The cells remaining on the beamline then resemble a $\pi/2$ mode structure and the synchronous condition remains $L = \beta\lambda/2$. Although not a requirement, due to cost considerations, most CCLs are designed with each cell within a tank being identical.

The following two sections describe the multi-particle PIC code PARMCCL and the central particle code CPCCL. The final sections describe results obtained and items that remain to be done.

Parmccl

The code PARMCCL is broken into two sections: a central particle section that provides the cell table; and a particle dynamics section. The cell tables are calculated in the central particle section and are based entirely on the axial field component. They employ a central particle concept in which the beam is characterized by the parameters of the particle at the bunch center, rather than the more standard synchronous particle concept. The largest effect of this changed viewpoint is found in the phase. Since each cell in a CCL tank is geometrically identical, the phase that the central particle in a bunch sees in the tank varies from cell to cell. Allowing the term "synchronous phase" to refer to a particle having the tank design beta, the relationship between the central phase and the synchronous phase in cell i is given by:

$$\phi_i = \phi_s - \pi(1 - \beta_o/\beta_i).$$

The energy gain in CCL cell i can be written[1]:

$$\delta W_i = \int E_z^{(i)}(r,z,t)\,dz$$

$$= \int \left\{2E_oT\, I_o(kr)\cos\left(\frac{2\pi z}{L_2}\right)\right\}\cos(\omega t_i + \phi_i)\,dz\ .$$

In the above equation, the length L_2 refers to $\beta_o\lambda$ ($= 2L_0$) and the variable T refers to the standard Transit Time Factor defined in SUPERFISH. The Modified Bessel Function I_o has been included in the equation since it enters into the determination of the radial Electric field and circumferential Magnetic field for tracking the particles through the CCL. However, all equations are linearized ($I_o(kr) \approx 1$ and $I_1(kr) \approx kr/2$) in the code.

Defining the ratio of the design beta of the tank and the central beta of the bunch in cell i to be $\beta_i = \beta_o/(1+\Gamma_i)$ and expanding the functions proportional to the beta ratio, the energy gain equation can be rewritten as:

$$\delta W_i = \int 2E_oT\,dz\{f_i\cos(\phi)_i - g_i\sin(\phi)_i\}\ ,$$

where: $f_i = \cos^2(x) - \Gamma_i x\cos(x)\sin(x) - \frac{\Gamma_i^2}{2}x^2\cos^2(x)$,

$g_i = \cos(x)\sin(x) + \Gamma_i x\cos^2(x) - \frac{\Gamma_i^2}{2}x^2\cos(x)\sin(x)$,

and $x = 2\pi z/L_2$.

The cell tables are generated by dividing each cell into two halves, using average values in each cell half for each of the trigonometric terms above, and iterating for a self-consistent

† This work supported by Grumman Space Systems Division.

solution to the energy gain equation and the cell phase equation. To allow for examining "as built" configurations in which the set of tank design betas $\{\beta_0\}$ is known, it may be input at run time. Alternatively, the code will perform an additional iteration to determine the set, or any combination of the cases may be employed.

In describing the motion of the particles through the CCL, the three field components derived from Maxwell's Equations are used. These are:

$$E_z(r,z,t) = \left\{2E_0T\cos\left(\frac{2\pi z}{L_2}\right)\right\}\cos(\omega t_i + \phi_i)$$

$$E_r(r,z,t) = 2E_0T\frac{\pi r}{2L_0}\sin\left(\frac{2\pi z}{L_2}\right)\cos(\omega t_i + \phi_i)$$

$$B_\vartheta(r,z,t) = -2E_0T\frac{\omega r}{2c^2}\cos\left(\frac{2\pi z}{L_2}\right)\sin(\omega t_i + \phi_i)$$

In this portion of the code, each cell is broken into a predetermined (selectable at run time) number of sections, and each particle is followed using the drift - momentum kick - drift method described below. A space charge impulse is applied to each particle at the center of each cell.

For each cell section, all particles are allowed to drift to the center of the section by iterating for the average velocity for each particle in the section. After reaching the center of the sections, each particle receives a transverse impulse (equal time of flight is used for each particle):

$$\delta P_x^{(i)} = \frac{W_0}{c}\,\delta(\beta\gamma)_x^{(i)} = \int \overline{F_{(i)}}\cdot dt \;\bullet\; \overline{F}_{(i)}\cdot\frac{\lambda}{4c}$$

with $\overline{F}_x^{(i)} = \overline{E}_x - \overline{\beta}_i c\overline{B}_\vartheta$.

The average radial Electric field and circumferential Magnetic fields are found in the same manner as the average axial field

$$\overline{E}_r = A\frac{\pi r}{2\cdot L_0}\left\{\overline{T}^{(i)}\cdot\cos\vartheta_i - \overline{S}^{(i)}\cdot\sin\vartheta_i\right\} \quad \text{and}$$

$$\overline{B}_\vartheta = A\frac{\beta_0}{c}\frac{\pi\cdot r}{2\cdot L_0}\left\{\overline{V}^{(i)}\cdot\cos\vartheta_i - \overline{U}^{(i)}\cdot\sin\vartheta_i\right\}.$$

The sequence followed by the particles in traversing a cell with N sections (N must be even) is therefore given by :

$$[DMD]_1\,[DMD]_2 \cdots [DMD]_{N/2}\,[SC]\,[DMD]_{N/2+1}\,[DMD]_{N/2+2} \cdots [DMD]_N$$

In this relation, $[DMD]_i$ refers to Drift-Momentum kick-Drift sequence described above, and [SC] refers to the Space Charge momentum kick. In this code an equal "time of flight" concept is employed rather than that of "equal distance traveled". The space charge calculator has been rewritten to reflect this. Additionally, the routine has been rewritten to transform all particle coordinates to the particles' frame of reference prior to performing its calculations, to avoid any possible relativistic problems.

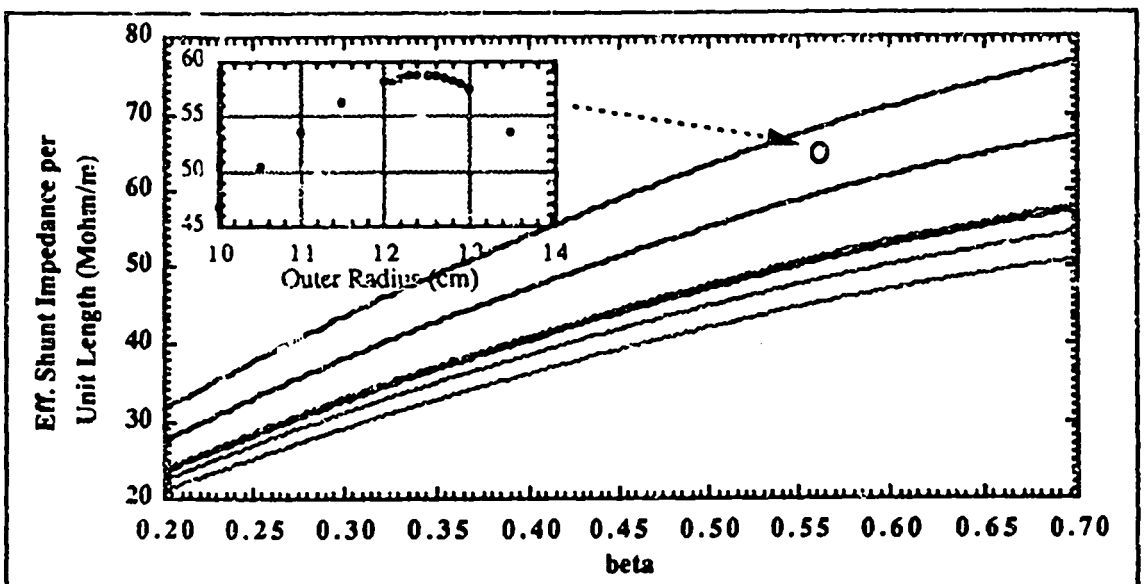

FIGURE 1 - ZTT verses Cavity Geometry

Central Particle Code

The major limitation of multi-particle PIC simulation codes is the time required to run them. Using a PIC code for trade studies is an arduous time-consuming process. In all types of accelerators, beam dynamics design requires the determination of many interacting parameters. CCLs have a particular problem - - a "best" design technique has not been prescribed to date. Providing the examination of the CCL parameter space to determine acceptable compromises between parameters almost necessitates the use of a preprocessor code.

In the present instance, this ability to rapidly scan the CCL operating space to determine parameter values is being

provided by the code CPCCL. In this code, the energy gain in each cell is given by:

$$\delta W_i = \frac{E_o T L_o}{2}\left(1 - \frac{\Gamma_i}{2}(1 + 0.322467\cdot\Gamma_i)\right)\cos\phi_i \quad .$$

with the cell phase and cell beta ratio (Γ_i) given by the same equations as in section 2. Since the accuracy found in PARMCCL is not required in this instance, the cell central beta is defined to be:

$$\beta_i = \beta\left(W + \frac{\delta W}{2}\right) \quad .$$

As before, self-consistent iterations are used to determine the tank and cell tables. Some of the inputs required for this code are:

E_o	:	Average accelerating field , or
σ_{Lo}	:	zero current longitudinal phase advance,
B'	:	Magnetic Field Gradient, or
σ_{To}	:	zero current transverse phase advance,
r_b	:	bore radius,
R	:	Cell outer radius,
I	:	Current,
f	:	frequency,
W_{in}	:	Input Energy,
W_{out}	:	Input Energy,
A	:	particle species,
φ	:	phase (absolute value),
N,M	:	no. of cells per tank, and cell lengths per magnet.

Items such as the shunt impedance, transit time factor, maximum surface field, quality, and gap length (along with the quantities derived from them such as the power consumed) are obtained from scaling from curves. These curves have been generated using data obtained from multiple SUPERFISH runs, and from references 2, 3 and 4. Additional quantities such as the current limit are obtained in the standard manner[5].

Figure 1 shows the Shunt Impedance per unit length as a function of beta, frequency, bore radius, and outer radius. The three solid curves are for an outer radius (R) of 12.6 cm, a frequency of 850MHz, and bore radii (r_b) of 0.5, 1.0 and 1.5 cm. The three dashed curves are for the same radii (R and r_b) at a frequency of 425MHz. (The two cases [f=425 MHz, r_b=0.5 cm] and [f=850 MHz, r_b=1.5 cm] lie on top of one another.) The insert shows the effect of the cavity outer radius.

Results

To provide a test of the code a series of runs were made to look at the effect of tank sequencing on the beam dynamics. Similar tanks were generated by varying the number of cells in the tank, the Magnetic focussing strength, and the accelerating field strength. For these tanks similarity was defined as maintaining the transverse focussing strength per unit length and accelerating field per unit length constant. In each tank, the transverse focussing element was a single (constant length) PMQ that was centered in a length $\beta_o\lambda/2$. The initial CCL used was one in which each tank consisted of one cell and a PMQ. For the one-cell tank, the values chosen were:

$B' = (B')_1 = 50$ Ts/m and

$E_oT = (E_oT)_1 = 7.5$ MV/m.

The parameters for the other tanks are then given by:

$(B')_n = \{(n+1)/2\}(B')_1$ and

$(E_oT)_n = \{(n+1)/2n\}(E_oT)_1$.

TRACE-3D was used to determine the matched beams for each case considered. Table 1 lists the phase advances found for the zero current and full current (100mA) cases for each configuration where a matched beam could be determined. Although the configurations were designed to be similar, they can be seen to cover a reasonably wide operational range.

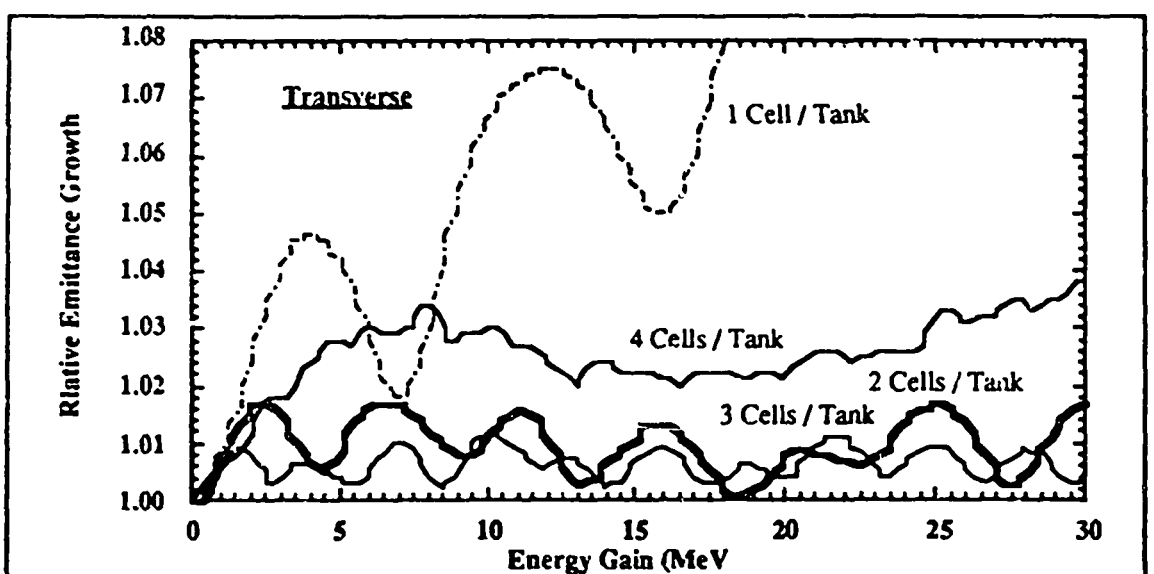

FIGURE 2 - Relative Transverse Emittance Growth

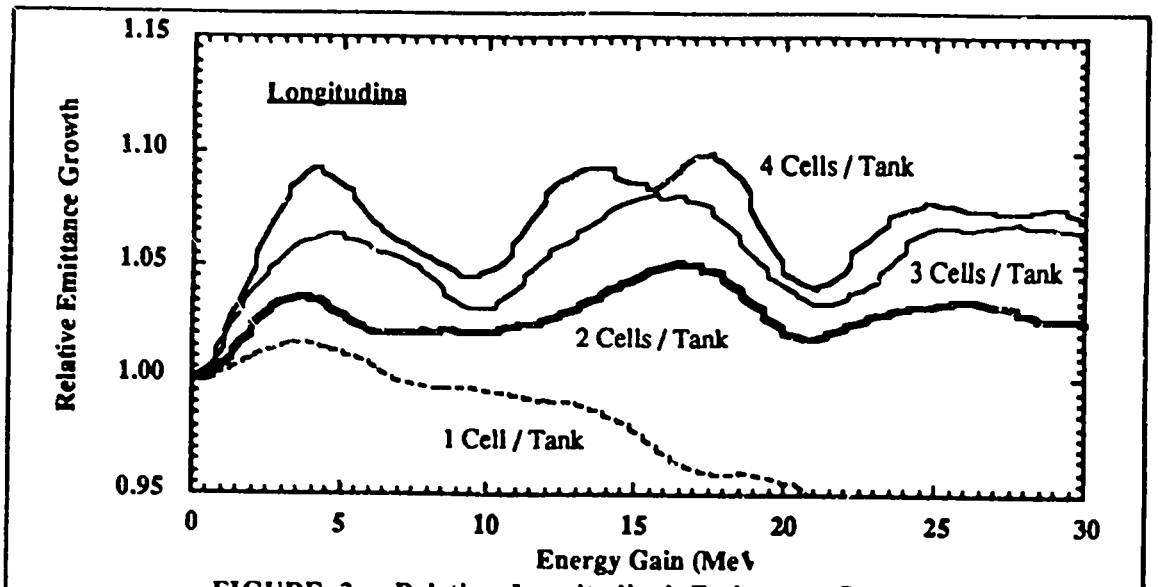

FIGURE 3 - Relative Longitudinal Emittance Growth

TABLE 1 - Phase Advances (per tank length)

Configuration	σ_{To} (deg)	σ_{Lo} (deg)	σ_T (deg)	σ_L (deg)
1 Cell / Tank	12.8	10.3	4.5	5.3
2 Cells/Tank	34.6	15.4	18.0	6.0
3 Cells/Tank	68.2	20.5	43.5	6.9
4 Cells/Tank	(no match found)		93.1	7.9
5 Cells/Tank	(no match found)		(no match found)	

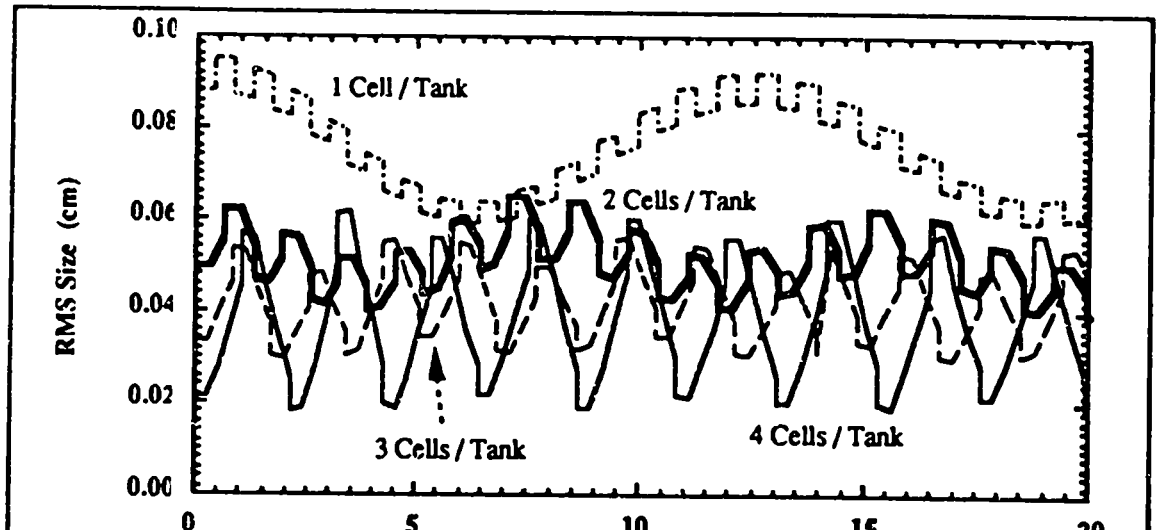

FIGURE 4 - RMS Beam Size

Figures 2 and 3 show the relative Transverse and Longitudinal emittance growths over a 30 MeV energy range for the full current cases. It can clearly be seen that case 1 corresponds to an under-focussed system and case 4 to an over-focussed system. In case 4, it is the space charge that is maintaining the stability of the system. Cases 2 and 3 are

relatively stable. Figure 4 shows the beam radius for the four cases. The relatively flat sections are the magnet locations.

Conclusions

A set of codes has been presented to help design CCL accelerators. The two codes are complementary in method and result type. The central particle code CPCCL allows the designer to rapidly scan the operating space to obtain acceptable compromises between design parameters. The PIC code PARMCCL provides a much more accurate assessment of the operating characteristics of a side coupled CCL. However, it requires relatively long run times.

The designer has available two variables to alter the run time of PARMCCL. These are the number of macro particles used and the number of sections in which to divide each cell. The code is presently running on two different computers: a μ-Vax, and an Stardent Titan (3 CPUs). On the μ-Vax, the code requires approximately 2 hours to calculate results over a 100 MeV range using two sections per cell in a 1000 particle simulation. Using eight sections per cell, this increases to approximately 5 hours. On the Titan, the two section per cell case runs in approximately 30 minutes and the eight section per cell to a little over 2 hours. To date, no attempt was made to make the code vectorizable.

A preliminary assessment has been made of the effect of number of cell section on emittance values. Eleven runs were made using 2 sections per cell and 12 runs were made using eight sections per cell. Each run was made using a different seed for the initial distribution random number generator. The mean transverse emittance and the standard deviation of the transverse emittance results for the the different cases were identical. The results for the longitudinal emittance differed slightly with the means differing by 0.4% and the standard deviations by ~3% (of a very small number). Since this evaluation was completed, most runs have used two sections per cell.

A second major limitation of the code, at present, is its restriction to a particular type of CCL. Work will be ongoing to expand this capability.

Acknowledgement

The authors would like to extend their appreciation to Jeanette Kania for her support, helpful discussions, and criticisms in the preparation of this manuscript.

References

1. K. R. Crandall; "TRACE-3D Documentation", LA-11054-MS, pages 74-81, Los Alamos National Laboratory, Los Alamos NM, August 1987.

2. J. J. Manca, E. A. Knapp; "TM_{01} Mode Accelerating Cavity Optimization", LA-7323, Los Alamos National Laboratory, Los Alamos NM, August 1978.

3. Dr. R. W. Hamm (Princ. Investigator); "Final Technical Report - Space-Based Neutral Particle Beam Linear Accelerator Scaling Study", AccSys Technology, Inc., Pleasanton Ca., September 1987.

4. "FERMILAB LINAC Upgrade - Conceptual Design", Fermi National Accelerator Laboratory, Batavia Ill, November 1989.

5. T. P. Wangler; "Space-Charge Limits in Linear Accelerators", LA-8388, UC-28, Los Alamos National Laboratory, Los Alamos NM, December 1980.

RFQ BEAM DYNAMICS MODEL DEVELOPMENT†

A. M. M. Todd and M. F. Reusch
Grumman Space Systems Division, 4 Independence Way, Princeton, NJ 08540, U. S. A.

Abstract

A generalized electric multipole coefficient fitting code, VFIT, that has been developed to match arbitrary RFQ vane profiles to high accuracy is described. These coefficients of a generalized potential are then passed to a modified version of PARMTEQ which performs the RFQ beam dynamics in the presence of arbitrary vane errors. For a particular high brightness mass 2 RFQ design, the results of both symmetric and asymmetric vane displacement errors are presented. The resultant performance degradation due to the induced dipole mode is found to be small at conventional tolerance levels (1 mil) and above. The effect of machining the vanes according to a two term potential or constant transverse radius prescription is also examined. Only an n=1, m=4 octopole, and to a lesser extent an n=0, m=6 dodecapole term, are found to lead to serious transmission performance degradation at high values of the cell modulation factor combined with small values of $\beta\lambda/2r_o$ and ρ/r_o. For the mass 2, $\rho = 3/4\ r_o$, RFQ considered, the transmission drops an additional 13% with the constant transverse radius cut. Further, the additional losses are in the high energy accelerating section of the device.

1. Introduction

High brightness accelerator design requires improved attention to details of the beam dynamics design of the components. To that end, we have developed improved RFQ beam dynamics models that address these issues.

A code, VFIT, that calculates the various multipole components corresponding to arbitrary vane geometry has been developed. We have also modified our standard version of PARMTEQ to accommodate axially varying arbitrary input multipole components.

These codes are then applied to the beam dynamics study of a high brightness, 352 MHz mass 2 RFQ design. This 430 cell RFQ accelerates the ion beam from 200 KeV to 2 MeV in a distance of 4.6 wavelengths. The peak modulation factor is 1.6, $r_o \sim 0.328$ cm, a constant transverse radius $\rho = 3/4\ r_o$ vane design is used and the peak surface electric field is 1.8 Kilpatrick.

Initial results indicate that attention needs to be paid to high order multipole terms since there are conditions under which significant performance degradation can result from their inclusion. However, minor design modifications can generally recover close to the basic two term potential performance.

† This work was supported by Grumman Space Systems Division.

2. RFQ Vane and Beam Dynamics Models

A generalized electric multipole coefficient fitting code, VFIT, has been developed to match arbitrary RFQ vane profiles to high accuracy. However, unlike the image charge model of Crandall[1] and the finite element solution technique of Diserens[2], the potential coefficients are determined by a relatively simple least-squares fitting technique to a given vane geometry, which is tolerant of the large problem condition number. This is accomplished by using a single value decomposition (SVD) numerical scheme applied with regularization techniques[3] to stabilize the solution.

The potential is expanded as,

$$U(r,\theta,z) = V \Big\{ \sum_{m=0}^{\infty} A_{om}\, r^m \cos(m\theta) + \sum_{m=0}^{\infty} B_{om}\, r^m \sin(m\theta)$$
$$+ \sum_{m=0}^{\infty}\sum_{n=1}^{\infty} A_{nm}\, I_m(nkr) \cos(m\theta) \cos(nkz)$$
$$+ \sum_{m=0}^{\infty}\sum_{n=1}^{\infty} A'_{nm}\, I_m(nkr) \cos(m\theta) \sin(nkz)$$
$$+ \sum_{m=0}^{\infty}\sum_{n=1}^{\infty} B'_{nm}\, I_m(nkr) \sin(m\theta) \cos(nkz)$$
$$+ \sum_{m=0}^{\infty}\sum_{n=1}^{\infty} B_{nm}\, I_m(nkr) \sin(m\theta) \sin(nkz) \Big\} / 2 \qquad (1).$$

VFIT calculates the coefficients A_{nm}, A'_{nm}, B_{nm}, B'_{nm} of Eq.[1], which can be used to represent both dipole and other non-quadrupole terms of arbitrary azimuthal and longitudinal symmetry. Specific features of the VFIT calculation include the automatic generation of geometry for Crandall's vane types, the ability to study asymmetric vane geometries, and a multi-cell fitting algorithm for longitudinal variation. An important aspect is that we have demonstrated the ability to accurately resolve moment coefficient variation for vane displacements of less than ± 1 mil (0.001 inch), which is the order of the engineering vane tolerance level for high brightness RFQs. Figure 1 shows a comparison between VFIT and Ref. [1] results for the accelerating efficiency, A_{10}, of a type 1 vane at three different values of $l = \beta\lambda / 2 r_o$, as a function of the vane modulation factor, m. Good agreement is evident for these disparate solution procedures.

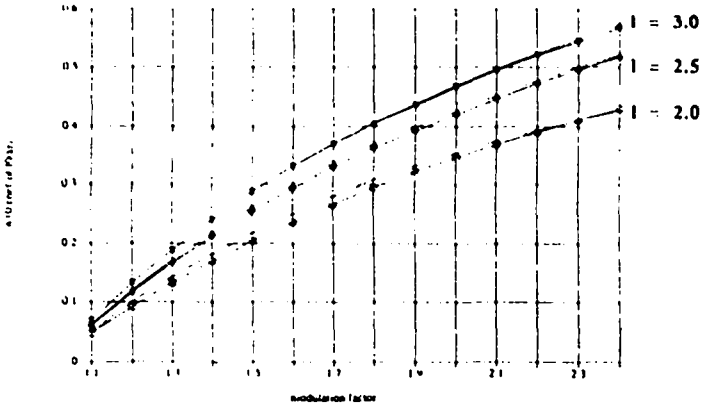

Figure 1. Comparison of the Accelerating Efficiency, A_{10}, Calculated by Crandall[1] and VFIT

3. Beam Dynamics Results

We have used VFIT to pass the various potential multipole coefficients to a modified version of PARMTEQ in order to perform RFQ beam dynamics in the presence of arbitrary vane errors. The results for a high brightness mass 2 RFQ design of both symmetric and asymmetric vane displacement errors show no significant performance degradation within a ± 1 mil engineering tolerance for vane machining and alignment.

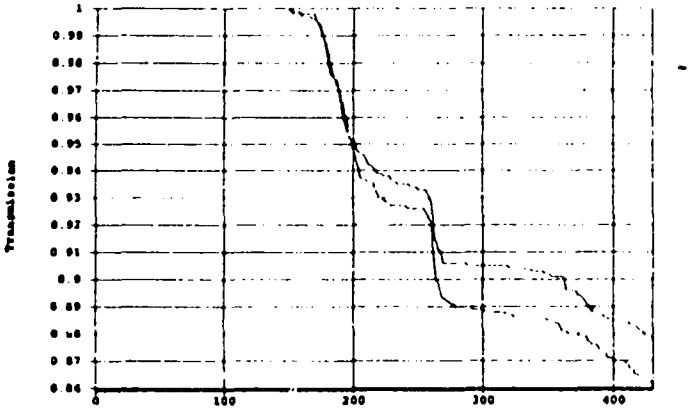

Figure 2. Transmission Profile for the Baseline Case and a 5 mil Off-Set "Y" Vane

Figure 2 shows the resultant axial transmission profile for the baseline case and one in which one "Y" vane is off-set by -5 mils along the entire length of the RFQ. This extreme case, as compared to the engineering tolerance level, introduces a dipole electric field component which leads to insignificant longitudinal (not shown) and transverse emittance growth, figure 3, and to the illustrated minor transmission loss (~ 1.5 %) with respect to the design point value. There is however an offset of the output beam axis due to the presence of the dipole field component which is shown in figure 4. The magnitude of this offset would however be readily correctable and is not significant.

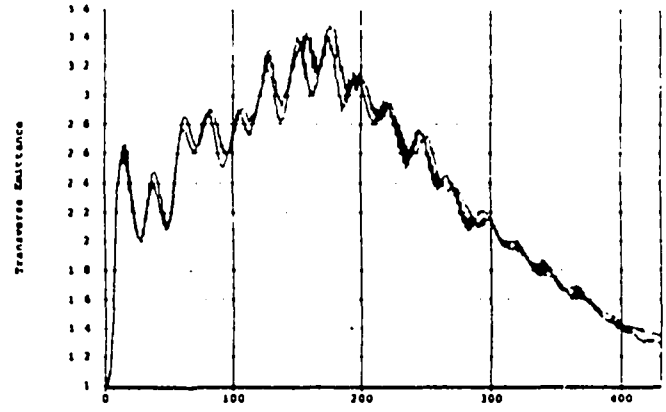

Figure 3. Axial Transverse Emittance Growth for the Baseline Case and a 5 mil Off-Set "Y" Vane

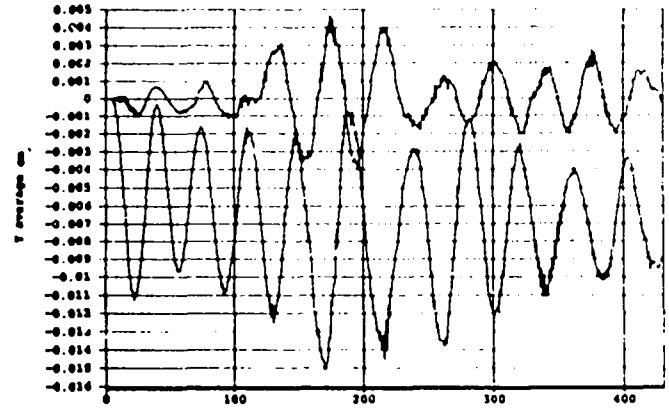

Figure 4. Axial Beam Axis Variation for the Baseline Case and a 5 mil Off-Set "Y" Vane

Next, we considered the effect of the specific vane tip geometry on output performance. For this study we compared the beam dynamics performance of a constant transverse radius ($\rho = 3/4\ r_0 \rightarrow$ Type III Vane) RFQ vane geometry with an equivalent two term potential cut. A comparison of the various multipole coefficients at a modulation factor, m=1.5, for two values of $l = \beta\lambda/2r_0$ is illustrated in Table 1. The VFIT values yield an rms voltage error of less than 0.003. When we apply these coefficients to our mass 2 RFQ design, as shown in figure 5, we find that this can lead to significant degradation in transmission performance (~13% reduction). By considering the effect of various coefficients we have identified the n=1, m=4 octopole term as the culprit. The n=0, m=6 dodecapole mode can also plays a significant role in the resultant beam dynamics performance. Table 2, illustrates the impact on transmission of these various multipole components.

These results agrees with those of Chidley[4], who found similar behavior at high modulation (m ~ 2) in a mass 1 RFQ design. Increasing ρ with respect to r_0 leads to improved

transmission because the octopole coefficient decreases rapidly as $\rho \rightarrow r_0$. The correlation of the transmission loss with the rise of the octopole coefficient along the RFQ length can be seen by comparing figures 5 and 6. Figure 6 shows that our mass 2 RFQ has a rapid rise of the octopole term in the accelerating section due to the rapidly increasing modulation factor, although $l \sim 5.7$ for m=1.6 at the 2 MeV exit energy. Regrettably, the additional loss consists of high energy particles in the RFQ accelerating section.

Table 1a Multipole Coefficient Comparison

m = 1.5, l = 2.0				
n	m	Two Term	VFIT ρ=3/4	Crandall ρ=3/4
0	2	1.000	1.003	0.992
0	6	0.000	0.036	0.037
1	0	0.395	0.295	0.324
3	0	0.000	0.001	0.002
1	4	0.000	0.134	0.099
2	2	0.000	0.033	0.023
2	6	0.000	0.002	0.005
3	4	0.000	0.001	0.002

Table 1b. Multipole Coefficient Comparison

m = 1.5, l = 4.0				
n	m	Two Term	VFIT ρ=3/4	Crandall ρ=3/4
0	2	1.000	0.983	0.983
0	6	0.000	0.037	0.033
1	0	0.392	0.361	0.363
3	0	0.000	0.002	0.001
1	4	0.000	0.066	0.060
2	2	0.000	0.017	0.016
2	6	0.000	-0.001	-0.001
3	4	0.000	-0.001	0.002

Table 2. Transmission Dependence on Multipole Coefficients

Transmission(%)	n=1, m=4	n=0, m=6	Other Terms
87 (Two Term)	No	No	No
76 (Eight Term)	Yes	Yes	Yes
84	No	No	Yes

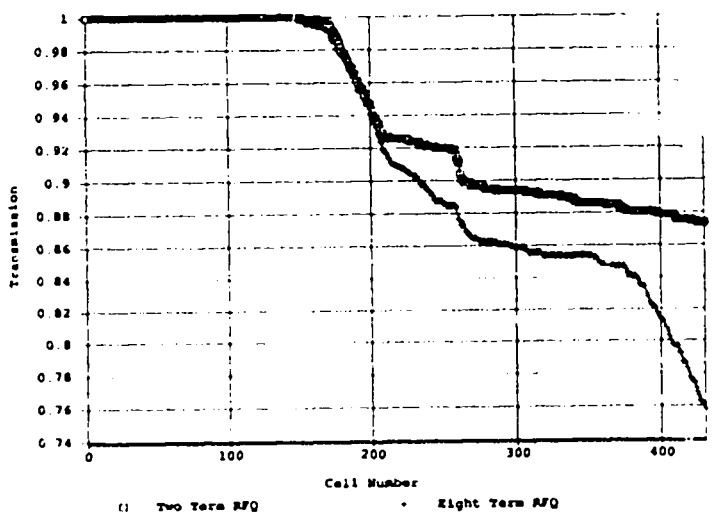

Figure 5. Axial Transmission Variation of Two Term and Eight Term (Type III) RFQ Vane Geometries.

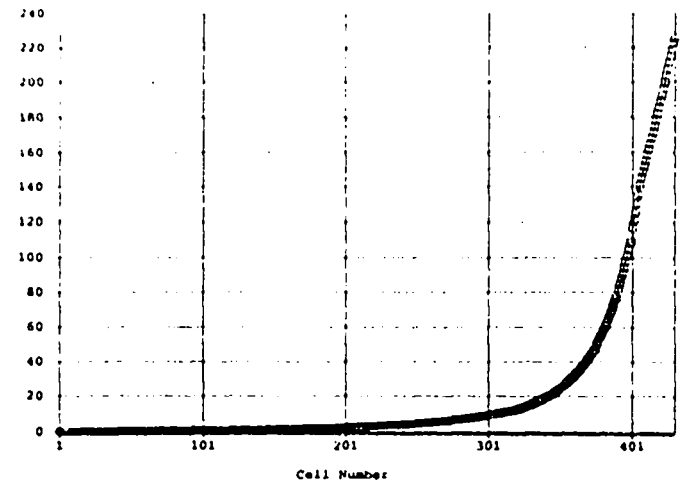

Figure 6. Axial Variation of the n=1, m=4 Octopole Term

4. Conclusions

Recent model development for high brightness RFQ beam dynamics analysis has been described. Specific applications that illustrate the utility of these models have been presented. We conclude from the dipole results that the principal driver for high accuracy vane machining appears to be the RF cavity characteristics (frequency sensitivity) rather than the beam dynamics performance. However, the high order multipole beam dynamics performance should be checked since particularly the n=1, m=4 octopole and the n=0, m=6 dodecapole mode can lead to beam dynamics performance degradation when the modulation factor is high ($m \geq 1.5$) while either ρ/r_0 is small ($\rho/r_0 \leq 0.75$) or $\beta\lambda/2r_0$ is small ($l \leq 4$). Relatively minor vane design modifications should circumvent this problem and recover close to the two term potential beam dynamics performance. Further studies are required to confirm and understand this behavior and to more clearly map out the regions of parameters space that lead to performance degradation problems.

5. References

1 K. R. Crandall, "Effects of Vane-Tip Geometry on the Electric Fields in Radio-Frequency Quadrupole Linacs", *Los Alamos Report* LA-9695-MS, April 1983.

2 N. J. Diserens, "Investigation of the Effects of Space Charge and Image Charge Forces on Beam Loss in an RF Quadrupole", *Proceedings of the 1984 Linear Accelerator Conference*, Santa Fe, New Mexico, page 91.

3 A. N. Tikanov, *Dokl. Akad. Nauk SSSR* **151** (1963) 501.

4 B. Chidley and G. McMichael, *Priv. comm.*

NEW BEAM-DYNAMICS DESIGN PROCEDURE FOR RFQs

A. Ueno and Y. Yamazaki
National Laboratory for High Energy Physics
1-1 Oho, Tsukuba-shi, Ibaraki-ken, 305, Japan

Abstract

So far, two computer programs have typically been used for the beam-dynamics design of radio-frequency quadrupole (RFQ) linacs. One is RFQUIK developed for high-current proton linacs. The other is GENRFQ developed for low-current heavy-ion linacs. In order to optimize the design of RFQs, especially intermediate-beam current RFQs, a new guideline is proposed by keeping the longitudinal acceptance constant for the design current in the gentle buncher. The acceleration efficiency in the acceleration section is also improved by gradually increasing the modulation factor under the condition of a constant transverse acceptance. An RFQ linac designed with these guidelines was simulated by using the code PARMTEQ. A good transmission efficiency and a small longitudinal emittance for a relatively short cavity length were obtained with this design procedure.

Introduction

Various computer programs[1-4] have been developed for designing the beam-dynamics of radio-frequency quadrupole (RFQ) linacs. We attemoted to use these programs in order to design the RFQ linac for the Japanese Hadron Project (JHP).[5] However, further improvements in the programs were necessary for the present purpose. The reasons for the improvements are presented by briefly describing the beam-dynamics designs of two typical programs, namely RFQUIK [1] and GENRFQ.[2] The former was developed at LANL (Los Alamos National Laboratory) for high-current proton RFQs and the latter was developed at INS (Institute for Nuclear Study, University of Tokyo) for low-current heavy-ion RFQs.

In the RFQUIK, an RFQ is divided into four longitudinal regions: a radial matching section, a shaper, a gentle buncher and an acceleration section. In the radial matching section, the bore aperture is tapered off in order to adjust the focusing strength from almost zero to its full value in the first several cells. This allows the injected DC beam to match into the time-dependent focusing of the RFQ. In the shaper, the modulation factor, m, and the synchronous phase, ϕ_s, increase linearly in order to shape the beam bunch. In the gentle buncher, m and ϕ_s are increased in order to keep constant the longitudinal infinitesimal oscillation frequency and the spatial length of the separatrix at zero current. The beam is gradually bunched as it is accelerated. In the acceleration section, m and ϕ_s are held fixed.

Two shortcomings of this design procedure come to mind. First, space-charge effects are not taken into account in the calculation of the bunch length. Second, it is hard to find any strong reasons for keeping both m and ϕ_s constant in the acceleration section. It is noted that the acceleration efficiency (accelerating energy per unit length) can be improved by making m and/or ϕ_s variable. The acceleration efficiency is important, particularly for a high-energy RFQ like the JHP linac, since the low acceleration efficiency results in a long RFQ which is, in general, difficult to fabricate. Thus, Kapania [3] proposed a new guideline for the acceleration section in which m is gradually increased so as to keep constant the transverse space-charge limited current defined by Wangler.[6] However, the nonlinearity of the longitudinal focusing force and the space-charge effects of other bunches are not considered in the calculation of the transverse and longitudinal space-charge limited currents defined by Wangler.

In the GENRFQ, the gentle buncher is further divided into two regions (the pre-buncher and the buncher), as is the acceleration section (the booster and the accelerator), in order to optimize the design more flexibly. In the pre-buncher and the buncher, m and ϕ_s are increased under the condition of constant longitudinal acceptance at zero current. The rf defocusing parameter, Δ_{rf}, is linearly changed in the pre-buncher and is kept constant in the buncher. In the booster and the accelerator, ϕ_s is held fixed. The modulation factor, m, is varied for keeping constant Δ_{rf} in the booster and the minimum bore radius, a, in the accelerator.

The space-charge effects are ignored in this design procedure, since the GENRFQ was developed for the design of low-current heavy-ion RFQs. Thus, the GENRFQ is not suitable for the design of RFQs with significant space-charge effects. The constraint of constant a and ϕ_s in the accelerator is not efficient for acceleration. However, the constraint of a constant longitudinal acceptance in the bunching procedure is a useful guiding principle.

In this paper, a new beam-dynamics design procedure is proposed in order to optimize the design of RFQs, especially for the intermediate-beam current RFQs. First, we estimate the longitudinal and transverse acceptances more realistically. Second, an attempt is made to improve the acceleration efficiency in the acceleration section by varying the modulation factor, m, while keeping a constant transverse acceptance. Third, the longitudinal acceptance is held fixed in order to determine the parameters in the gentle buncher, following the method of the GENRFQ. The new design procedure, thus developed, was programmed in the computer code package KEKRFQ. In the next section, methods to estimate the longitudinal and transverse acceptances in RFQs are described. Then, a new beam-dynamics design procedure is described. Finally, the acceleration efficiency and the beam qualities of the design are compared with those of the RFQUIK and GENRFQ on the basis of simulation results using the computer code PARMTEQ.[7]

Estimation of RFQ Acceptances

Estimations of the longitudinal and transverse acceptances are essential in order to optimize the RFQ design. The estimation method, in which the nonlinearity of the longitudinal focusing force and the space-charge effects are taken into account by numerical calculations, is described in this section.

The longitudinal acceptance, A_l, is estimated by solving the following differential equation system numerically with an assumption of the constant synchronous particle energy and by finding the area of a stable region:

$$\frac{d\Delta\phi}{dz} \cong -\frac{2\pi\Delta W}{\lambda m_0 c^2 \beta^3 \gamma^3}, \qquad (1\text{-a})$$

$$\frac{d\Delta W}{dz} = qAV\frac{\pi}{4}I_0(kr)(\cos(\phi_s+\Delta\phi) - \cos\phi_s) - qE_{SC}. \qquad (1\text{-b})$$

Here, $\Delta\phi$ and ΔW are the phase and energy differences between the reference particle and the synchronous particle, respectively; λ is the rf wavelength; m_0 is the rest mass; c is the velocity of light; β and γ are the relativistic parameters; q is the electric charge of the particle; A is the acceleration parameter; V is the intervane voltage; I_0 is the modified Bessel function; r is the distance from the beam axis, and $k=2\pi/\beta\lambda$. The electric field, E_{SC}, produced by the space charge in eq. (1-b) is given by

$$E_{SC} = \frac{\rho_{SC} f \beta \lambda}{2\pi\varepsilon_0}\Delta\phi + \frac{\lambda I}{c\beta^2\lambda^2}\sum_{i=1}^{n}\left[\frac{1}{(\phi_s+\Delta\phi-\phi_c+2\pi i)|\phi_s+\Delta\phi-\phi_c+2\pi i|} + \frac{1}{(\phi_s+\Delta\phi-\phi_c-2\pi i)|\phi_s+\Delta\phi-\phi_c-2\pi i|}\right], \qquad (2)$$

where ρ_{SC} is the charge density in the bunch and ε_0 is the permittivity of the vacuum. The space-charge effects from the other bunches, which we approximate by point electric charges, is represented in the second term of this equation.

The phase of the bunch centroid ϕ_c is approximated by

$$\phi_c = \phi_f - \sqrt{\frac{(\phi_f - \phi_i)(\phi_f - \phi_s)}{2}} \qquad (3)$$

by using the phases of the bunch head, ϕ_i, and the bunch tail, ϕ_f. Since none of the values of ϕ_i, ϕ_f or ϕ_c was known prior to the estimation of the longitudinal acceptance, an iteration procedure is necessary in determining these values.

It is noted that the field E_{sc} includes the effect of the other bunches which was neglected by Wangler. This effect is significant at the beginning of the bunching process, where the constraint of the constant longitudinal acceptance plays an important role. We also define the longitudinal space-charge limited current, I_l, as the minimum beam current which makes the longitudinal acceptance vanish. This value is more accurate than the value defined by Wangler, since the nonlinearity of the longitudinal focusing force and the space-charge effects of the other bunches are taken into account.

The transverse acceptance is estimated by

$$A_t = \frac{a^2\sqrt{\frac{B^2}{8\pi^2}+\Delta_{rf}+\Delta_{sc}}}{\beta\lambda\left(1+\frac{B}{4\pi^2}\right)^2}\beta\gamma, \qquad (4)$$

which was derived by Wangler[6] using a smooth approximation; B is a focusing parameter. For the space-charge defocusing parameter Δ_{sc}, we use the expression

$$\Delta_{sc} = \frac{3Z_0 q I \lambda^3 (1-f)}{8\pi m_0 c^2 \gamma^3 r_b^2 b}, \qquad (5)$$

assuming an ellipsoidal beam bunch with a uniform space-charge distribution. Here, Z_0 is the free-space impedance, I the beam current, r_b the radius of the beam and b the half-bunch length. The ellipsoid form factor, f, is a function of r_b and b. It can be seen that the bunch length is necessary in order to estimate the transverse acceptance. We use the bunch length calculated from the values of ϕ_i and ϕ_f, which were obtained in estimating the longitudinal acceptance.

New Design Procedure for RFQs

In the KEKRFQ, an RFQ is divided into four longitudinal regions in the same way as the RFQUIK. Each region is referred to by the same name as that in the RFQUIK. However, the guidelines for the gentle buncher and the acceleration section are different. We hold the average bore radius, a_0, fixed and use the guidelines to determine two independent variables of m and ϕ_s from which all of the cell parameters are derived.

In the gentle buncher, the longitudinal acceptance is kept constant and the rf defocusing parameter, Δ_{rf}, is determined as a function of β by

$$\Delta_{rf} = \Delta_{rfi} + (\Delta_{rfG} - \Delta_{rfi})\left(1 - \left|\frac{\beta - \beta_G}{\beta_G - \beta_i}\right|^n\right)^{1/n}, \qquad (6)$$

where Δ_{rfi} and β_i are the rf defocusing parameter and the relativistic parameter at the beginning of the gentle buncher, respectively, Δ_{rfG} and β_G are those at the end of the gentle buncher, and n is a free coefficient. Since eq. (6) varies Δ_{rf} gradually as the energy is increased, the transverse motion never suffers from an abrupt change of the focusing parameters.

The constraint of the constant longitudinal acceptance is imposed for the following reason. Since the injected DC beams almost fill out the longitudinal acceptance at the beginning of the gentle buncher, the longitudinal acceptance should always be smaller than or equal to those of the following cells in order to obtain a high transmission rate. On the other hand, at the first cell of the gentle buncher, where the beam energy is near the injection energy and the synchronous phase is slightly larger than -90 deg, the larger acceleration field ,that is, the larger Δ_{rf} implies the larger longitudinal acceptance. Therefore, the constraint of the constant longitudinal acceptance is a way to ensure a high transmission rate in the longitudinal motion, keeping a high acceleration efficiency.

In the acceleration section, the synchronous phase is fixed at a value of around -30 deg, following the other design procedures, since the acceleration efficiency can be improved slightly by varying ϕ_s. On the other hand, it is effective regarding acceleration efficiency to make the modulation factor, m, variable; m is increased as the beam is accelerated, while keeping the transverse acceptance constant. This is possible, since the defocusing parameters Δ_{rf} and Δ_{sc} in eq. (4) decrease for constant modulation factor as the energy is increased.

The beam-dynamics design based upon the above guidelines was made almost in the same way as the RFQUIK. The beam energy, W_G, and the cell parameters at the end of the gentle buncher, where both of the longitudinal and transverse acceptances have the minimum values, were determined first. For this purpose the code KEKRFQ1 was used in order to calculate the transverse acceptance and the longitudinal current limit for certain values of m, ϕ_s, a, W_G, and the bravery factor. The bravery factor is the maximum surface electric field divided by the Kilpatrick limit. In the KEKRFQ1 the maximum field was assumed to be 1.38*V/a_0. After the determination of the cell parameters at the end of the gentle buncher, the parameters of each cell were determined by the code KEKRFQ2 on the basis of the guidelines described above. The input data for the KEKRFQ2 were the cell parameters at the end of the gentle buncher, the shaper length L_{SH}, the synchronous phase of the end of the shaper ϕ_{SH}, and n of eq.(6). The cell parameters, thus obtained, were used in order to simulate the beam motion with the program PARMTEQ. The shaper length was adjusted in order to optimize the transmission and the longitudinal emittance of the simulation results.

Comparison of Designs

Three designs of the RFQ for the JHP, referred to as KEKRFQ-D, RFQUIK-D or GENRFQ-D, were made by using the programs KEKRFQ, RFQUIK and GENRFQ, respectively, and were compared on the basis of the simulation results with the PARMTEQ. The principal requirements for the RFQ are as follows: the resonant frequency is 432 MHz, the peak beam current is 20 mA, the 90% normalized transverse emittance is 1.0 π mm mrad, the injection energy is 50 keV and the final energy is 3 MeV. The GENRFQ-D was the first design for the JHP made by Tokuda.[8] In order to make a fair comparison, the same average bore radius (a_0=3.4 mm) was used for all of the designs. In the KEKRFQ-D, L_{SH}, ϕ_{SH}, and n of eq.(6) were chosen as 0.395 m, -88 deg and 3, respectively.

The cell parameters of the KEKRFQ-D, RFQUIK-D and GENRFQ-D are shown as functions of the longitudinal position in Figs. 1a), 1b) and 1c), respectively. As can be seen from these figures, the high acceleration efficiencies with relatively short cavities are obtained by rapid bunching in the cases of KEKRFQ-D and GENRFQ-D. The acceptances for the design current (20 mA) and the current limit of each design at the end of the gentle buncher estimated with the KEKRFQ1 are listed in Table I. These values almost determine the beam quality and limited current of the design based upon the KEKRFQ or RFQUIK, since both of the longitudinal and transverse acceptances have minimum values at the end of the gentle buncher in these design procedures. It can be seen from Table I that the longitudinal acceptances of the KEKRFQ-D and GENRFQ-D are smaller than that of the RFQUIK-D, but the limited currents do not decrease in proportion to the acceptances. Since the longitudinal acceptance restricts the longitudinal emittance of the accelerated beam, the smaller longitudinal emittance is expected for the KEKRFQ-D and GENRFQ-D than for the RFQUIK-D at the design current. The higher beam current can be accelerated with the KEKRFQ-D than GENRFQ-D, as can be seen from the limited currents in Table I. The estimated acceptances, the limited current and the half-bunch length of the KEKRFQ-

D are shown in Fig. 2 as functions of the longitudinal position.

In order to study the margin for the beam current, simulations were carried out for the following three different injected beams: (1) the design beam (the beam current I=20 mA and the 90% normalized transverse emittance ε_t=1.0 π mm mrad), (2) I=25 mA and ε_t=1.0×$\sqrt{(25/20)}$=1.12 π mm mrad which mean the same brightness as the design beam, (3) I=50 mA and ε_t=1.0 π mm mrad. The results of the simulation are summarized in Table II. It is seen that with the KEKRFQ-D we obtained the smallest transverse and longitudinal emittances of the accelerated beam for all cases. With the RFQUIK-D though a slightly higher transmission can be obtained, the longitudinal emittance is about 50% larger than that of the KEKRFQ-D at the design current. The transmission of the KEKRFQ-D is about the same as that of the GENRFQ-D at the design beam current, but higher at the higher injected current (50 mA).

Conclusion

The new design procedure is proposed and compared with two typical ones. For the intermediate-beam current RFQ we obtain the smallest emittances, both longitudinally and transversely, keeping almost the same transmission as those of the others. It is expected that this procedure is useful in order to optimize lower or higher beam current RFQs, since the nonlinearity of the longitudinal focusing force and the space-charge effects of the other bunches are take into account.

TABLE I
The acceptances and the limited current of each design at the end of the gentle buncher estimated with KEKRFQ1.

	KEKRFQ-D	RFQUIK-D	GENRFQ-D
Energy W_G (keV)	250	550	250
Longitudinal limited current I_l (mA)	34.8	46.5	29.7
Longitudinal acceptance (π deg MeV)	0.546	2.390	0.482
Normalized transverse acceptance (π mm mrad)	2.26	2.04	2.99

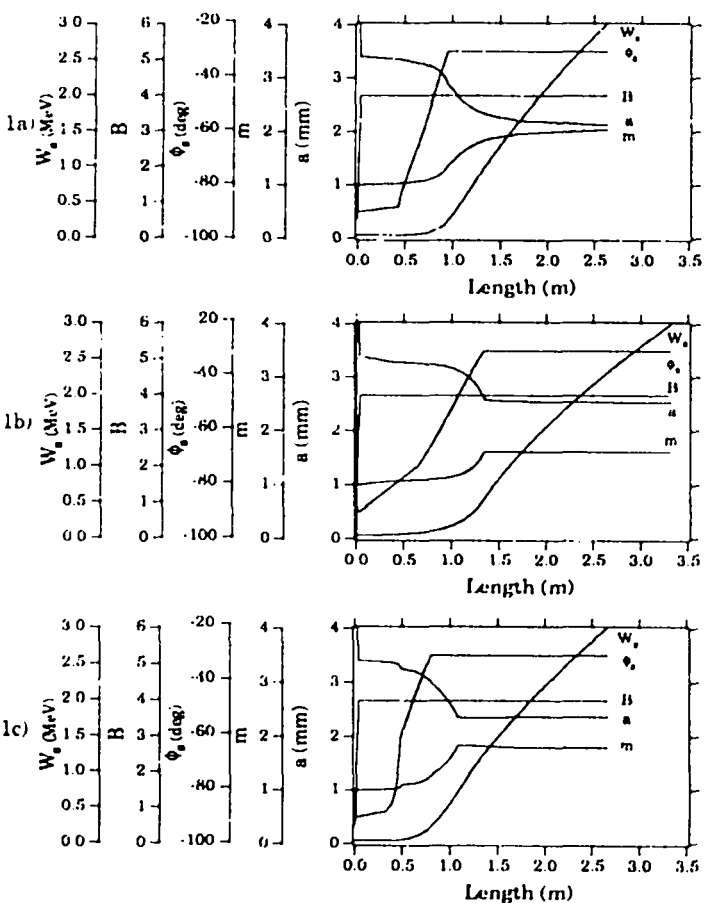

Fig. 1. The cell parameters of each design shown as functions of the longitudinal position: (a) KEKRFQ-D, (b) RFQUIK-D, (c) GENRFQ-D.

Acknowledgement

The authors are indebted to Prof. R. A. Jameson for his encouragement.

References

1. K. R. Crandall et al., IEEE Trans. Nucl. Sci., Vol. NS-26, 3469 (1979).
2. T. Nakanishi et al., Part. Accel. 20, 183 (1987).
3. D. Raparia, Proc. 1988 Linear Accel. Conf., 61 (1988).
4. A. Schempp et al., Proc. 1988 Linear Accel. Conf., 70 (1988).
5. Y. Yamazaki, "Development of a High-intensity Proton Linac for the JHP", this conference.
6. T. P. Wangler, LANL Report LA-8388, Dec. 1980.
7. K. R. Crandall and T. P. Wangler, AIP Conf. Proc. 177, 22 (1988).
8. N. Tokuda, "Report of the Design Study on the Proton Linac of the Japanese Hadron Project [1]", JHP-10, KEK Internal 88-8 (in Japanese), 38 (1988).

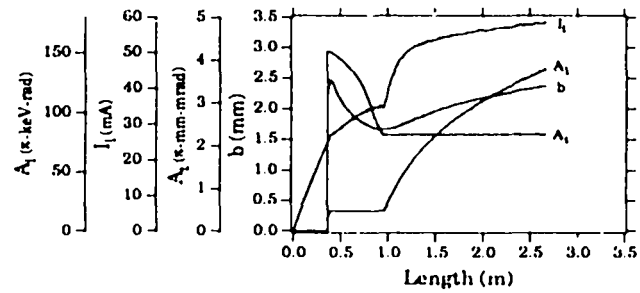

Fig. 2. The estimated acceptances, the limited current and the half-bunch length of KEKRFQ-D shown as the functions of the longitudinal position.

TABLE II
The principal parameters and the simulation results of each design (the number of injected particles is 5000).

	KEKRFQ-D	RFQUIK-D	GENRFQ-D
Kinetic energy (MeV)	0.05-3	0.05-3	0.05-3
Average bore radius a_0(mm)	3.4	3.4	3.4
Focusing parameter B	4.0	4.0	4.0
Inter-vane Voltage V(kV)	90.0	90.0	90.0
Cavity Length (m)	2.64	3.32	2.66
(1) Injected Beam: ε_t(90%)=1.0 π mm mrad, I=20 mA (DC)			
Transmission (%)	94.0	95.2	93.5
90% transverse emittance(π mm mrad)	1.10	1.18	1.15
90% longitudinal emittance(π deg MeV)	0.333	0.550	0.370
(2) Injected Beam: ε_t(90%)=$\sqrt{(25/20)}$π mm mrad, I=25 mA (DC)			
Transmission (%)	90.8	93.2	90.9
90% transverse emittance(π mm mrad)	1.19	1.25	1.29
90% longitudinal emittance(π deg MeV)	0.358	0.549	0.387
(3) Injected Beam: ε_t(90%)=1.0 π mm mrad, I=50 mA (DC)			
Transmission (%)	72.4	85.6	66.9
90% transverse emittance(π mm mrad)	1.06	1.16	1.25
90% longitudinal emittance(π deg MeV)	0.445	0.520	0.540

NUMERICAL MODELS OF BEAM DYNAMICS IN ION INDUCTION LINACS*

John R. Freeman and John S. Wagner
Sandia National Laboratories, Albuquerque, New Mexico 87185

Abstract

We have written a numerical simulation code to study beam dynamics in ion induction linear accelerators. The code is used to study axial beam expansion for a particular example. Voltage ramping of the gap reduces the expansion. The code is also used to study the longitudinal instability. The instability grows and saturates after increasing the axial divergence.

Introduction

High current linear induction accelerators have been proposed for many applications, including heavy ion fusion. Axial beam expansion and the longitudinal instability are two important issues for these accelerators. We have written a simulation code named FASTINS to study these problems.

Analytical scaling estimates and computational models of the longitudinal instability have been published by Stanley Humphries.[1] Humphries' simulation code, named LIDIA, used a 1-D multiple small radius disc dynamics model. The discs' space charge was used to compute an E_z that modified the discs' velocities. The gaps were described by a circuit equation. A laboratory frame periodic simulation box with a single gap was employed.

The FASTINS code discussed here was based heavily on the BUCKSHOT code.[2] BUCKSHOT is a gridless particle simulation code written to study relativistic electron beam propagation in the low pressure ion focused regime. The basic beam element (particle) in BUCKSHOT is a finite length cylinder. In BUCKSHOT, beam particles are constrained to stay in the same axial (z) beam slice they were born in. In FASTINS, beam particles are allowed to overtake each other. Both codes treat transverse motion identically. A 2-D Poisson solver is used to compute the E_z electric field. FASTINS thus generalizes the models of Humphries Lidia code.

For the first application studied, namely space charge driven expansion of the ends of the beam, the code was written in the beam frame. Accelerating gaps approach from the positive-z direction and pass through the beam. As they pass, the E_z of adjacent particles is instantaneously increased consistent with the gap voltage.

The second application was the study of the longitudinal instability. Both beam frame and lab frame simulations were carried out. The Humphries gap model was used, in which the gap was modeled by a simple resistance. For the lab frame periodic simulations, the average or dc voltage was subtracted from the total circuit based voltage.

*Work supported by the U.S. Navy, DARPA, and U.S.D.O.E.

Numerical Model

The transverse force model used in FASTINS is a generalization of the gridless BUCKSHOT model. The force between two cylinders moving paraxially is given by,

$$F = \frac{2Q_1Q_2}{r}\,(1 - \beta_1\beta_2)\,\left(1 - \frac{|z_1 - z_2|}{ds}\right) \qquad (1)$$

which includes both the electric and magnetic forces. In Eq. 1, Q is the charge, β is the velocity normalized to the speed of light, and ds is the cylinder length. The z-dependent factor allows the force between two cylinders to be proportional to the amount that they overlap. If $|z_1 - z_2|$ is greater than ds, then F is set to zero, since remote cylinders should not be included in the local force.

FASTINS uses an axial mesh with a cell-size equal to the cylinder length. This mesh is needed to accumulate the currents required as input to the gap model. It also provides axial resolution of diagnostics, such as the beam radius, divergence, and rotation. Another use of the mesh is pre-sorting of the cylinders before computing the self-consistent transverse force. The pre-sorting compiles a list for each mesh of cylinders within $\pm$ds of any of its own cylinders. The transverse force calculation scales with N^2, where N is the number of interacting particles. Sorting reduces N by excluding particles too far apart to interact. The overhead associated with sorting is small compared to the time saved by reducing N on the interaction list. This technique, which is vectorized on the Cray XMP, about doubled the speed of the transverse force computation.

The use of an analytic transverse force law and finite length cylinders requires that their length be much longer than the beam radius. In addition, they also must be much shorter than the gap spacing and the wavelengths to be resolved for the longitudinal instability. Typical values were 3-5 times the beam radius.

FASTINS requires an axial electric field $E_z(r)$ to allow the ends of the beam to expand axially. It is also needed to allow the beam to respond to gap-induced charge bunching. The radial electric field is already included in the gridless BUCKSHOT model.

The LIDIA E_z model used an axial mesh and an FFT solution. It was basically 1-D and had no radial resolution. For many accelerators, where the beam radius is only slightly less than the drift tube radius, this approximation is not adequate.

A 2-D iterative Poisson solver is used in FASTINS to compute the axially and radially resolved E_z. The individual beam cylinders are linearly weighted onto an axisymmetric r-z mesh at each time step. A finite difference solution for the electrostatic potential is differentiated to give E_z.

The initial beam transverse profile assumed was a uniform current density cylinder of radius 10 cm contained in a 16 cm radius vacuum drift tube. The transverse focusing force was assumed to be produced by a simple 35 kG uniform solenoid. A 10 MeV, 2.4 kA proton beam was injected into the linac. The current linear rise and fall

times were 50 ns. Typical beam lengths were assumed to be 40 m. Since the diode was assumed to be non-immersed, the beam had an average rms rotation velocity, normalized to the speed of light, of 0.037. An additional transverse thermal $\beta_{th} = 0.032$ was added to achieve an approximate transverse radial equilibrium.

The axial velocity distribution was computed by assuming that all of the protons had the same total energy γ_0, so that

$$\beta_z = \sqrt{1 - \frac{1}{\gamma_0^2} - \beta_\perp^2} \; . \qquad (2)$$

This produces the initial thermal spread in β_z shown in Fig. 1.

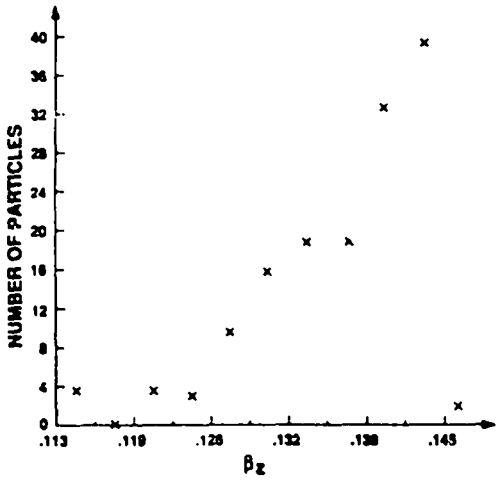

FIG. 1. Initial axial β_z distribution for a 144 particle-slice loading.

Longitudinal Instability

The longitudinal instability is triggered by beam loading of the gaps. High current perturbations receive less than the average acceleration. This portion of the beam slows, increasing the perturbation in an unstable manner.

One possible circuit equation describing the gap loading is given by[1]

$$V_g = \frac{2V_0(1 + \alpha)}{(2 + \alpha)} - \frac{I_B R_0 \alpha}{(2 + \alpha)} \; , \qquad (3)$$

where V_0 is the voltage applied by the pulsed power, V_g is the actual accelerating voltage, R_0 is the cavity impedance, I_B is the instantaneous beam current, and αR_0 is the shunt impedance. If the pulsed power is matched to the beam, $R_0 = V_0/I_0$, where I_0 is the average beam current in an unperturbed system.

The growth distance for an initially cold beam is given by[1]

$$L_g = 2 \left[\frac{T_0 D I_B (2 + \alpha)}{2\pi e V_0 \alpha} \right]^{1/2} \; , \qquad (4)$$

where L_g is the beam length, T_0 is its initial energy, and D is the gap spacing.

Initial axial velocity spreads have been predicted to stabilize the instability. The required velocity spread in terms of the normalized rms divergence is given by

$$\frac{\Delta\beta_z}{\beta_0} = \left[\frac{\alpha V_0}{(2 + \alpha)\; 2DT_0 k_0} \right]^{1/2} \; . \qquad (5)$$

Space charge electric fields have been predicted to provide a stabilizing factor, causing the beam clumps to re-expand. A measure of the importance of space charge effects is given by[1]

$$A = 2 \left(\frac{T_0}{eV_0} \right) \ln \frac{r_{wall}}{r_B} \, k_0 D K \, \frac{(\alpha + 2)}{\alpha} \; , \qquad (6)$$

$$\text{where } K = \frac{eI_0}{2\pi\varepsilon_0 m_p (\gamma\beta c)^3}$$

Space charge effects should be important if A is greater than unity.

For α = infinity, the present test case parameters yield $A = 2\,k_0$. For the shortest wavelengths, $\lambda = 2.0$ m and $A = 6.3$. For the full beam length of 40 m, $A = .31$.

The growth distance should be increased by $L_g/FI(A)$, where $FI(A) = 2(1 + A^2)^{1/4} \sin[\tan^{-1}(1/A)/2]$. For $A = .32$, $FI(A) = 0.86$, but for $A = 1.5$, $FI(A) = 0.52$. Space charge should be effective at damping short wavelengths, but should have a smaller effect on the longer wavelengths that would characterize full beam transport.

A series of runs used a periodic box of 40 m, a length equal to typical beam lengths. This allowed the simulation of the longest wavelengths that would be of concern. Figs. 2 shows the initial conditions. At z = 190 m, Fig. 3, the growth has reached non-linear levels, but the instability is still growing strongly. At z = 570 m, the phase space is beginning to become isotropic. This isotropic distribution then persists until the end of the accelerator with no re-growth. The final configuration is shown in Fig. 4 at z = 1140 m.

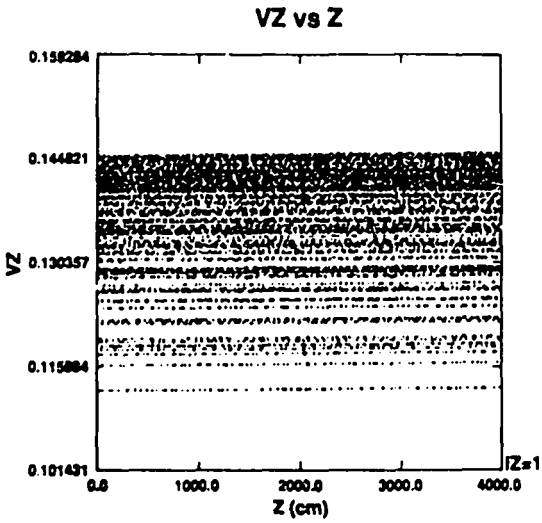

FIG. 2. Initial axial phase space distribution for 40 m beam length example.

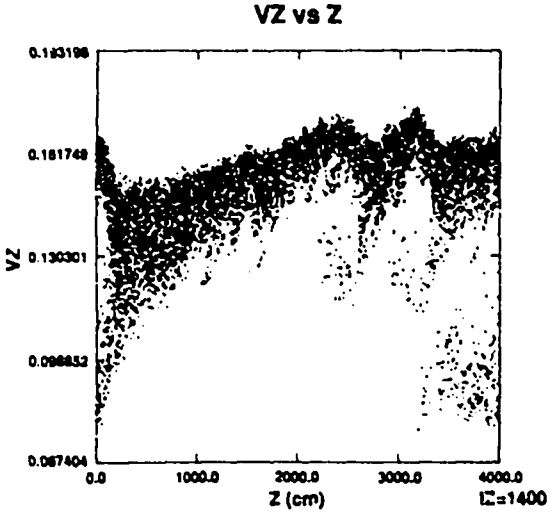

FIG. 3. Axial phase space after beam front has traveled 190 m. Initial loading from Fig. 2.

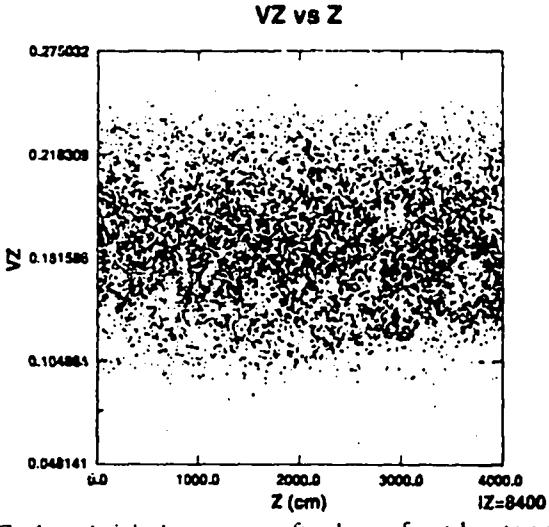

FIG. 4. Axial phase space after beam front has traveled 1140 m. Initial loading from Fig. 2.

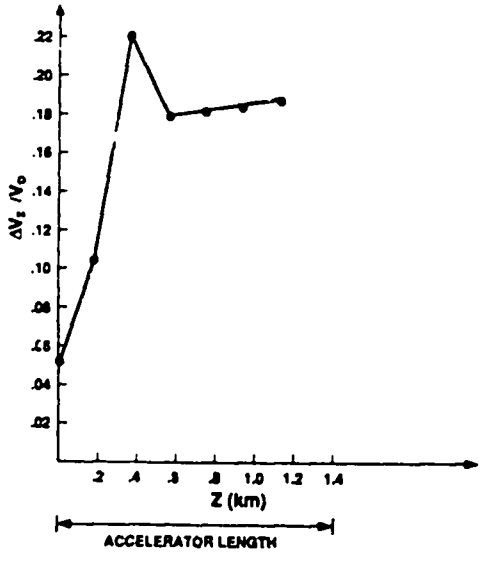

FIG. 5. Evolution of normalized axial divergence.

The growth and saturation of the instability for the full beam case can be quantified by the evolution of the normalize axial divergence, plotted in Fig. 5. The final value of the divergence has grown three to four times greater than the initial value. For some ion linac applications, this is allowable, but for others it would be excessive. The divergence required to stabilize the beam, given by Eq. 5 modified for space charge, is 0.32 for this example. It is interesting to note that the final saturated divergence is only 0.19. The computed results for this example are thus more optimistic about final saturation levels and what constitutes a stable equilibrium than the analytic theory.

Summary

A code for simulating beam transport in ion linear induction accelerators has been written. The code, named FASTINS, is based on the BUCKSHOT beam propagation code. The basic physical element in FASTINS is a long cylinder of charge. FASTINS couples the accelerating gaps to the beam cylinders by means of a circuit equation.

FASTINS has been used to investigate two problems of interest for ion induction linacs. The first was space charge driven expansion of the ends of the beams. The effect is quite strong at the 2.4 kA, 50 ns risetime level for an example using protons. Voltage ramping of the gaps helps, but large ramp rates would be required. (A discussion of this problem is contained in Ref. 3.)

The second problem studied was the longitudinal instability. Analytic linear growth rates are only available for cold beams. The natural initial beam axial divergence, combined with the stabilizing effect of space charge, significantly reduced the growth in the simulations. The instability grew to moderate amplitudes and saturated.

Preliminary beam frame simulations showed that the instability grew up at a rate similar to the lab frame simulations. This occurred even though the beam average energy was allowed to increase in the beam frame simulations.

References

1. "Simulations of Longitudinal Instabilities in Ion Induction Linear Accelerators," Stanley Humphries, Jr., Report ACCON-88-04. Also submitted to Physical Review.
2. "Analysis and Benchmarking Calculations for the BUCKSHOT Code," I. R. Shokair and J. S. Wagner, Sandia Laboratories Report SAND87-2015, 1988.
3. "Numerical Models of Beam Dynamics in Ion Induction Linacs," John R. Freeman and John S. Wagner, submitted to J. Appl. Phys., 1990.

THE FERMILAB UPGRADE LINAC: DYNAMICS DESIGN PROCESS

L. Oleksiuk, J. MacLachlan, F. Mills
Accelerator Division, Fermilab, Batavia Illinois.

Abstract

The Fermilab Coupled Cavity Linac requires dynamics design procedures that predict 805 MHz rf synchronization, non-linear emittance dilution and system error aspects of the device. Full 3-D beam simulations using three separate codes have shown the need for a central orbit monitor to detect desynchronization implicit in the longitudinal dynamics of coupled cavity devices. The new linac section accepts a 116 Mev (200MHz) DTL beam, requiring a transition matching section, before actual 805Mhz acceleration begins.This requirement places significant constraints on phase space acceptances of the side coupled structure.

We describe special aspects of the design codes used to verify these system attributes,with particular attention to the effect of system errors and RF noise on the beam performance. Results of beam loss simulations, using a PIC model of beam halo based on current knowledge of the 200 Mev beam is discussed.

Introduction

To raise the Fermilab Booster space charge limited beam(50ma) brightness an increase in injected beam energy is being implemented. [1] An optimized upgrade of the existing 200 Mev DTL linac indicated that a side coupled CCL with operating frequency at 805 Mhz, and average axial fields of 7.5 Mev/meter would interface with the upstream DTL at 116 Mev. Replacing the last 4 DTL structures with a CCL system consisting of a longitudinal bucket matching section, for bunch size matching,and a 28 cavity accelerating section could provide a 400 Mev injected beam for the Booster.

Project goals for the 400 Mev beam required both the ability to be debunched with a tolerable energy spread and little emittance dilution in all planes,and an axial allotment of 67 meters to keep the original Booster transport line length constant. These goals required careful attention to the bunch compression (transition) section, where space charge equipartition effects were expected to appear.

A tight radial dimension (1.50 cm.) for the cavity bore radius required beam loss simulations with all construction and drive errors in included, using realistic beam halo simulations. The choice of 805 Mhz vs. 1307.5 Mhz was made to lower the risk of beam emittance dilution(1) predicted for abrupt changes in structure parameters.

The dynamics design required a 3 stage effort. First a trial segmentation of the cavity array was generated with a 'genlin' code that used SUPERFISH (2) data (ZT**2,T,Emax/Eo) to constrain the selection of cavity average fields (Eo) consistent with rf drive power choices (12 MegWatt klystrons) and peak cavity fields.(37 MV/m)

The second stage required finding the matched Twiss parameters for the maximum space charge (50 ma.) beam conditions using the linear space charge beam matrix methods of TRACE3D. A known limitation in TRACE3D is its inability to recognize CCL travelling wave synchronization conditions implicit in the bridge coupler elements.For rf drive error studies in which several cavities are linked together in a single rf pathway, synchronous particle definitions require the ability to recognize the desynchronizing effects that may occur within a given drive module.

The third stage of the design involved a CCL specific PIC code that has a 2 1/2 D space charge (elliptical transverse charged rings) capability with many error simulating functions. This code (CAVDYN) utilized the same TRACE3D data sets used in stage 2 to assemble a CCL system and incorporated the same longitudinal linear dynamics, but included non-linear terms as well. In addition , a central orbit monitor developed for this code (3) was able to

[1] Work supported by the US Dept. of Energy

recognize any desynchronization within a complete CCL system, including all contributing errors. The key ingredient was the recognition of the rf drive boundaries by the PIC code. An extra 'tank' parameter has been imbedded in the TRACE3D code (TRACEX at Fermilab) to implement the z-plane central orbit data transfer to CAVDYN. This parameter provides check data for the internal consistency of the CCL tank,in TRACEX,and the downstream bridge coupler, in CAVDYN.It also provides the structure defined synchronous energy used to form the central orbit monitor in CAVDYN. CAVDYN will detect improper drive boundaries,and flag these as data failures before system simulation can be run.

System Overview

The synthesis of the new high gradient CCL started with defining the space charge matched beam Twiss parameters predicted from the operating DLT tank 5 design parameters. This beam matrix would be then transformed by a matching section to reduce the bunch size by 1/2,a result of the tighter rf focusing in the CCL dynamics, and expand the transverse beta functions up by a factor of 2.3, corresponding to the a 50ma. space charged matched conditions entering the CCL quadrupole FODO channel. The 7 module (28 tank) acceleration segment of the CCL design was chosen ,satisfying the 37 MV/m field maxima and uniform rf power distribution. By selecting 16 cell cavities, with 3-cell bridge couplers a uniform tank array was produced that simplified the quadrupole tune design. Larger (5-cell) bridge couplers produced significant bunch shape oscillation from the debunching.

The transition section design(4) uses 7 quadrupoles (3DTL, 4 CCL) to provide the FODO matching. Bunch compression is accomplished by two bunching cavities, sized to allow a 200 Kw klystron for rf drive.The transition section, because of the magnification of input energy swings, together with a 10 degree phase slippage off the travelling wave in the low energy cavities, produces a tighter input acceptance for DTL beam energy swings. A smaller initial cell segmentation (ie 11 cell cavities) would alleviate this constraint, but was not deemed necessary.

Error Studies

The simulation of CCL system errors has been layered at 3 levels. Level 1 allows major detunes of the TRACE3D data set to simulate major detunes or crashes for loss analysis.Level 2 allows correlated random alignment and drive errors to be inserted into the dynamics to assess emittance degradation, and beam centroid swings. Level 3, not reported here, is simulation of cavity phasors disturbances arising from real cavity conditions such as stopbands, power droops and coupling errors. This requires phase and amplitude errors resolved in individual cells.

The level 2, random correlated errors, have been simulated for 2 independent correlation groups, corresponding to rf drives, for z-plane dynamics, and transverse displacements for correlated groups of quadrupoles and cavities, for the transverse plane. The rf drive errors (phase and amplitude) were run for the 7 drives, using independent random errors in each drive. Because a central-orbit is established for a given TRACE3d file, rf drive error disturbances are superimposed on any central orbit swing,and give realistic assessment of non- linear dynamics. Level 3 disturbances to the central orbit,will eventually be taken into account, to produce a working central orbit.

Figure 1 shows the 400 Mev longitudinal phase space for a nominal CCL with ideal DTL input beam and with a random error in the 7 accelerating drives of +/-1.0 percent amplitude,1.0 deg phase ,uniformly distributed. At twice this tolerance band, significant non-linear dilutions occur in the phase -energy space. Figure 2 shows the effect of the same drive errors when the DTL beam is 0.5 Mev off the CCL synchronous input energy.This sensitivity to input energy error is related to the dynamics of the bunch compression (transition) section, which doubles the central orbit energy swing. Here, the central orbit swing produced by the DTL energy offset, is added to the klystron random errors,producing a significant non-linear z-plane disturbance, at the design tolerance band.

Transverse beam centroid swings had been simulated for the CCL girder design,which carries 4 cavity-quad pairs. Correlated displacement tolerances for girders and indiviual quadrupoles were set at 0.25 and .10 mm.(5)respectively, correspond-

ing to rms centroid swings of 4.5 and 2.7 mm respectively. These require 1.5 mrad dipole steering for each girder.Quadrupole field harmonics have also been simulated to check the harmonic tolerance band.

Loss Studies

The beam loss simulations were carried at both level 1 and level 2 error modes. The operating knowledge of current DTL 200 Mev transverse emittance permitted a realistic transverse halo model to be employed, which was described by a 4D- gaussian whose 95% limits were well established.. The crash modes investigated were loss of trim steering, single quadrupole crash, and a single rf drive modulator crash.Single rf drive losses were catastrophic in the low energy modules, as expected from phase slip arguments. Loss simulations were useful in providing strategies for interlock and alarm (6) provisions for initial safety system designs.

Summary and Conclusions

The design of the new CCL system at Fermilab has been studied using linear and non-linear dynamics. Simulations have predicted no significant emittance dilutions for the space charge 50 ma average beam current. 400 Mev beam centroid motion resulting from construction and rf drive errors appear to be acceptable to the Booster requirements. Required DTL stability in energy is estimated to be 0.2 Mev, to control z-plane emittance dilution from non-linear bucket excursions in the CCL.

Further studies ,using level 3 errors (intra-cavity phasor error distributions) will show realistic working central orbits.This will aid in the commissioning strategies for finding the working points of the klystron drive controls, typically for such methods as the delta-t process.

References

1. R.A. Jameson, Proc.1983 Linac Conf."New Linac Technology" p. 497.
2. P. Zhou, Upgrade note LU 139, Superfish calculations of CCL structure dependencies on Beta, Feb.1990.
3. L. Oleksiuk,Los Alamos Conf on Codes,Jan.1990, p. 233.
4. J. MacLachlan, Upgrade note LU 155, "Transition Section Design Rationale", April 1990.
5. F.Mills, Upgrade note LU 126, "Quad and Cavity Position Tolerances", November,1988.
6. J. MacLachlan,Upgrade note LU 161, "Expectations on Beam Loss in the 400 Mev Linac:", July 1990.

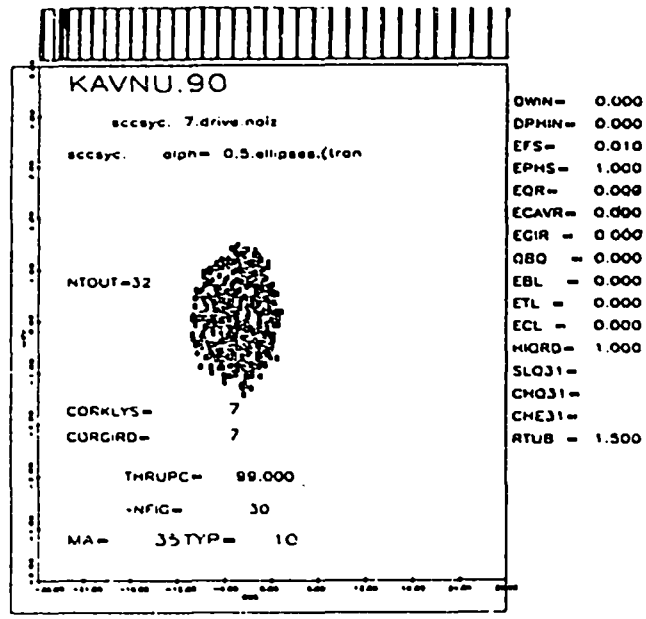

Figure 1: 400 Mev z-plane dw-dphi for 1 deg/% drive noise

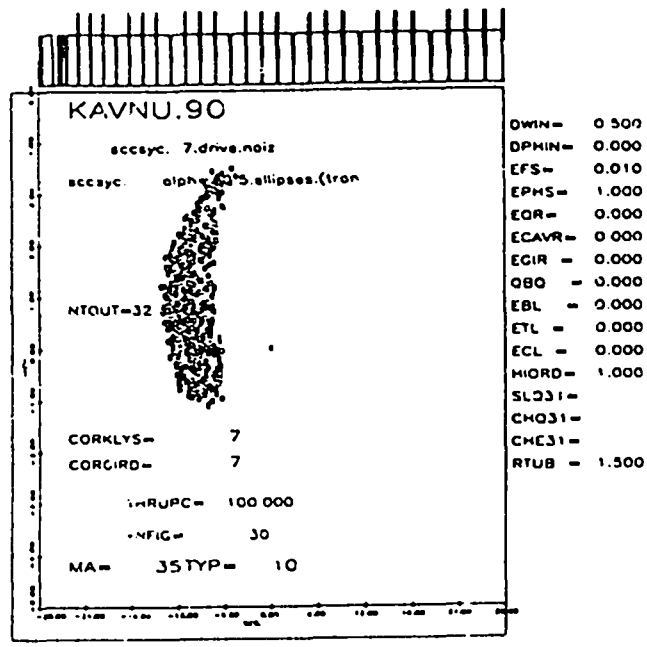

Figure 2: 400 Mev z-plane dilution from 0.5 Mev DTL error

BEAM DYNAMICS DESIGN OF A PION LINAC*

S. Nath, G. Swain, R. Garnett, and T. P. Wangler
Los Alamos National Laboratory, Los Alamos, NM 87545

Abstract

We have conducted a study of a superconducting linac to accelerate pions produced at LAMPF from 400 or 500 MeV to 925 MeV kinetic energy. For such a linac, it is necessary 1) to keep the machine as short as practical in order to minimize the loss of beam due to particle decay, and 2) to tailor the beam to achieve the maximum flux within the desired momentum bite at the exit. The interplay of these and other considerations with the transverse and longitudinal beam dynamics is discussed, and is illustrated with the simulated performance of reference pion-linac designs.

Introduction

A proposed linear accelerator for pions ("Pilac") would extend the capabilities of the Los Alamos Meson Physics Facility (LAMPF). Pilac would accelerate pions from the A2 target in the 800 MeV proton line. The pions would be accelerated from 400 or 500 MeV to 920 MeV kinetic energy, corresponding to a momentum of 1050 Mev/c. This project has the goal of providing a flux of 10^9 pions per second. The linac would use superconducting rf cavities in order to provide large apertures and transverse acceptance, and produce high accelerating gradients without a large cost in rf power.

In order to evaluate different design concepts for this linac, we have used a figure of merit which is the product of two factors: (a) momentum fraction and (b) survival fraction. The momentum fraction is the fraction of particles entering the linac that are within the desired momentum bite (2% full width, for example) at the linac exit. In order to maximize this factor, we may tailor the beam dynamics in the linac to produce a bunch that is wide in phase spread and narrow in energy spread at the linac exit.

The survival fraction is the fraction of particles entering the linac that have not been lost to decay by the time they reach the linac exit. For particles of rest mass E_{rest} (139.567 MeV for pions), kinetic energy W, mean life parameter $c\tau$ (7.803 m for pions), and traveling a distance L, the survival fraction is

$$F_{surv} = e^{-\frac{L}{c\tau\beta\gamma}},$$

where

$$\beta\gamma = \sqrt{\left(\frac{W}{E_{rest}}\right)\left(\frac{W}{E_{rest}} + 2\right)}.$$

For an accelerating section to take the beam from kinetic energy W_1 to W_2, the survival fraction is given by

$$F_{surv} = \left(\frac{E_2 + \sqrt{E_2^2 + E_{rest}^2}}{E_1 + \sqrt{E_1^2 + E_{rest}^2}}\right)^{-\frac{E_{rest}}{c\tau G}}$$

where E is the total energy of a pion

$$E_n = W_n + E_{rest}$$

at the start (E_1) or end (E_2) of the section, and G is the accelerating gradient

$$G = \frac{W_2 - W_1}{L}.$$

Strategies for Linac Design

We have used two design strategies in looking at possible Pilac designs. In the first strategy, designated as the fast-synchrotron-oscillation approach, we attempt to capture and accelerate the whole input bunch, but adjust the design phases along the linac to make the bunch rotate counterclockwise so that it is narrow in energy-phase space at the end (see Fig.1). For the energy gain we need for Pilac, the bunch rotates from the initial tilt at the start of the linac (Mod. 2) to where it is narrow in energy spread (Mod. 6), and then continues to rotate another half turn until it is narrow again at the linac exit. This approach emphasizes the momentum fraction at the expense of the survival fraction.

In the second strategy, designated as the slow-synchrotron-oscillation approach, the initial bunch is rotated slightly, but most of the design phases are chosen near the peak of the accelerating wave, so that the particles are shot through the linac as quickly as possible. This approach emphasizes the survival fraction at the expense of the momentum fraction. (See Fig. 2.)

---

*Work supported by Los Alamos National Lab. Institutional Supporting Research, under the auspices of the U.S. Department of Energy.

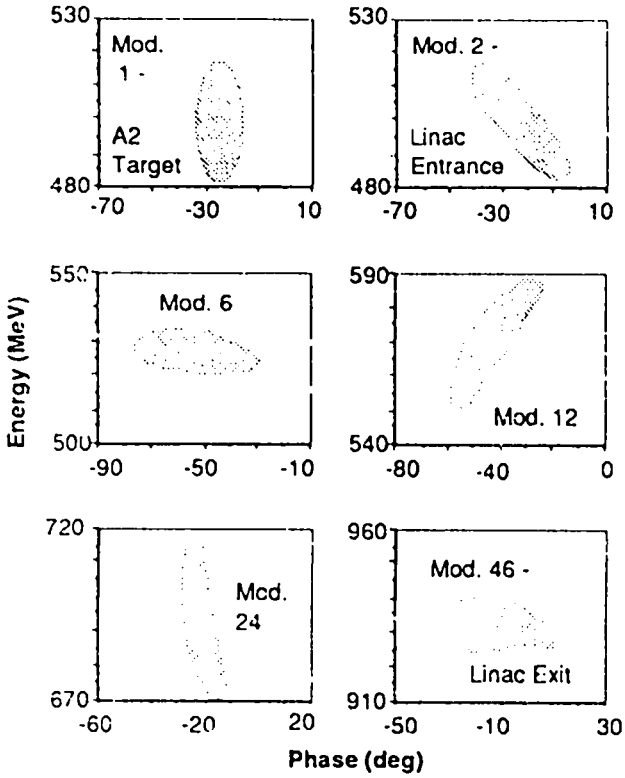

Fig. 1. Evolution of the bunch in energy-phase space for the fast-synchrotron-oscillation approach.

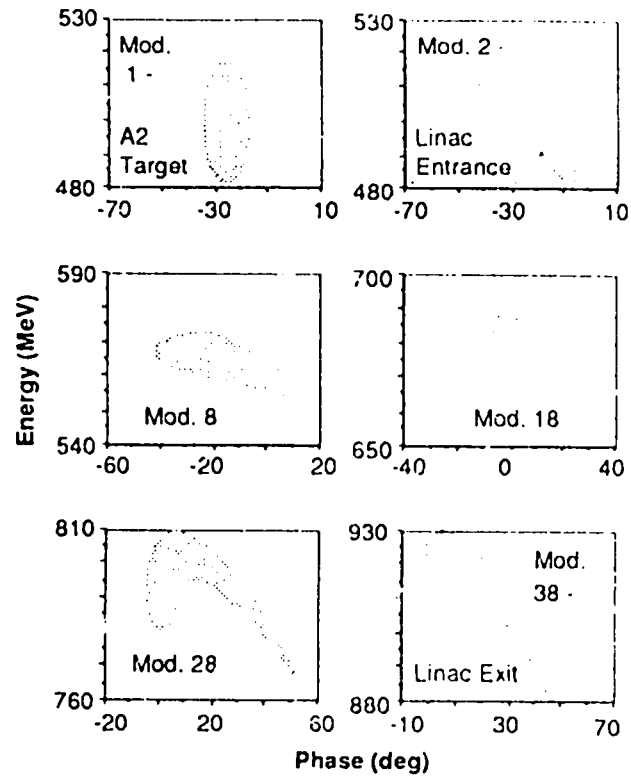

Fig. 2. Evolution of the bunch in energy-phase space for the slow-synchrotron-oscillation approach.

In either of these approaches, we attempt to choose the design phases of the rf cavities to maximize the number of particles in the desired dp/p bite at the linac exit. We have used the following approximate procedure to find these rf phases. We choose the design phases such that the trailing edge of the phase spread lies on a straight line in a plot of phase vs cavity number, as shown in Fig. 3. This allows the optimization to be done with only two parameters, the phases at the start and end of the straight line. In fact, the optimization is reduced to a one-parameter search for a given number of cavities, since after one end of the line is specified, the value at the other end must be set to give the desired output energy for the linac. Putting the trailing edge of the phase width on the straight line tends to move the design phase (at the middle of the bunch) away from the peak when the bunch is wide in phase, thus putting the bunch on a more linear part of

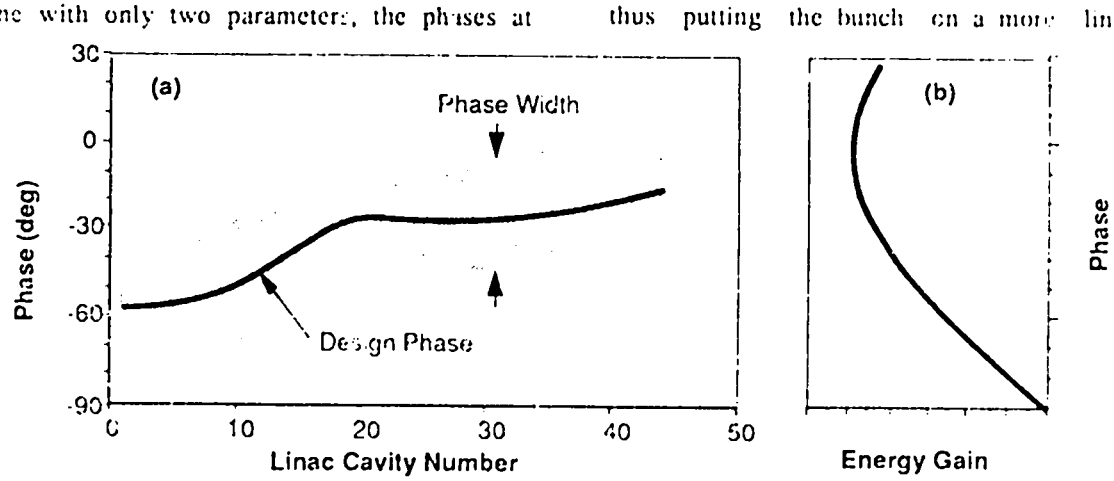

Fig. 3. The design phases are such that the trailing edge of the phase width is on a specified line, as shown for a representative case in (a). The accelerating wave is shown in (b).

the wave. When the bunch is narrow, it is allowed to ride higher toward the crest, as nonlinear effects are less important then.

Comparison of 402.5 and 805 MHz Linacs

We have looked at reference designs for both 402.5 and 805 MHz rf cavities. In order to compare these designs, we made the following assumptions. The initial beam at the A2 target was assumed to have a time spread of 60 ps, a momentum spread of 2.8 or 5.6% FW, a transverse emittance of 150 pi mm-mrad, and be transported 12.5 m before entering the linac. The rf cavities were assumed to have 5 cells each, and the linac to use quad doublets for focusing. Space was allowed between cavities for couplers, flanges, and bellows. At points where focusing magnets were needed, space was allowed for transitions to room temperature and miscellaneous vacuum and diagnostic equipment. The space for these was a function of the beam aperture size. The maximum accelerating gradient E_0T was assumed to vary as the surface area of the cavity to the -0.2 power (an empirical relation). This gives E_0T=13.2 MV/m for 805 Mhz cavities, corresponding to 10 MV/m for the 402.5 Mhz cavities.

The procedure for each frequency was as follows: First the number of cavities per quad doublet was chosen to make the beam fill the aperture for a 0.5 T pole tip field. Then the cavity design phases were optimized for minimum dp/p at the linac exit. This was then repeated for larger apertures until the spacing between cavities needed to keep the cavity-to-cavity coupling small dominated the survival fraction.

Calculated Performance

The calculated results for the 402.5 MHz and 805 MHz Pilacs for acceleration from 500 to 920 MeV are given in the tables below. The beam had an initial dp/p of 5.6% FW. The survival fraction (S.F.), momentum fraction (M.F.) for 2% FW dp/p at the linac exit, and combined figure of merit (SF*MF) are given for each design. The 402.5 MHz Pilac listed in Table I had to be quite long in order to obtain a bunch that was rotated enough to be narrow in energy spread at the exit. Hence the survival fraction for this case was small. For the 805 MHz cases, the constraints on cavity-to-cavity spacing made the survival fraction start to fall off as the beam aperture diameter was increased above 10 cm. The optimum design based on the combined figure of merit SF*MF for these cases has an aperture of about 13 cm.

TABLE I
Fast-Synchrotron-Oscillation Cases

Freq. (MHz)	Num. Cavs.	Aperture Dia. (cm)	S.F. (%)	M.F. (%)	SF*MF (%)
402.5	36	20	12.5	100.	12.5
805.0	43	10	20.3	100	20.3
805.0	42	10	21.9	94.8	20.8
805.0	44	13	21.2	100	21.2
805.0	42	15	21.0		

The difference in performance is much less pronounced between the 402.5 and 805 MHz slow-synchrotron-oscillation designs listed in Table II. The optimum aperture diameter for a 402.5 MHz Pilac is about 22 cm; for an 805 MHz Pilac, it is about 12 cm.

TABLE II
Slow-Synchrotron-Oscillation Cases

Freq. (MHz)	Num. Cavs.	Aperture Dia. (cm)	S.F. (%)	M.F. (%)	SF*MF (%)
402.5	24	20	26.1	97.8	25.5
402.5	24	22	25.6	96.8	24.8
805.0	36	10	26.9	82.1	22.1
805.0	36	11	29.0	82.3	23.9
805.0	36	13	29.2	82.3	24.0
805.0	36	15	(<27.3)		

Conclusions

For short linacs to accelerate unstable particles, it may be advantageous to sacrifice accelerating bucket area to gain in the number of beam particles surviving. For the linac designs we have examined, the slow-synchrotron-oscillation approach is slightly better than the fast-synchrotron-oscillation method. The slow-synchrotron-oscillation approach is also less dependent on the initial orientation of the beam ellipse in energy-phase space.

A recent re-examination of the linac requirements suggests that the optimum initial energy is around 400 MeV. Future work will include studies to check if the same conclusions apply for acceleration from 400 to 920 MeV.

A COMPARISON OF BEAM-DYNAMICS SOLUTIONS FOR THE SSC 1284-MHz COUPLED-CAVITY LINAC*

R.W. Garnett, G.H. Neuschaefer, T.S. Bhatia,
Los Alamos National Laboratory
and
J. M. Watson
Superconducting Super Collider Laboratory

Abstract

Two beam dynamics design examples for the SSC 1284-MHz, 70-600 MeV coupled-cavity linac (CCL), are described. The first of these examples consists of singlet quadrupole focussing with a constant accelerating gradient while the second example uses doublet focussing. Ramping the field gradients cell by cell in the first two tanks, for both the singlet and the doublet focussing examples, leads to a smooth transition from the DTL into the CCL. Comparison shows that the doublet focussing scheme offers some advantages.

Introduction

The proposed SSC linac is shown in the block diagram in Fig. 1. A 30-mA beam of H^- ions is accelerated to 2.5 MeV in a 428-MHz radio-frequency quadrupole (RFQ). Using a suitable matching section (MS1), the beam is then injected into a 428 MHz drift-tube linac (DTL), which accelerates it to 70 MeV. The proposed beam-dynamics design of the DTL is discussed in a companion paper.[1] Following a second matching section (MS2), the beam is accelerated to 600 MeV in a 1284-MHz coupled-cavity linac (CCL). In this paper we describe and compare two example beam-dynamics solutions for the CCL that meet the desired performance requirements for injection into the low-energy booster ring (LEB) of the SSC.

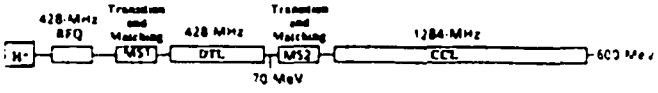

Fig. 1. Block diagram of the proposed SSC Linear Accelerator.

Singlet Design Example

The CCL design example included in the 1989 Site Specific Conceptual Design Report (SCDR)[2] consisted of a 70 to 600 MeV linac with constant accelerating gradient determined by $E_0T = 6.5$ MV/m; it employed a singlet quadrupole focusing lattice (FODO). This design was based on a tank geometry of 20 cells per tank with 5/2 $\beta\lambda$ intertank spacing. The parameters for this example are given in column 1 of Table 1 and are discussed in detail in the SCDR.

A slight variation of this design is obtained by ramping the field gradient in the first two tanks, cell-by-cell, from $E_0T = 1.0$ MV/m to 6.5 MV/m. All subsequent tanks are held constant at $E_0T = 6.5$ MV/m. The parameters for this two-tank ramped singlet design are given in column 2 of Table 1. A nearly current independent matching section between the DTL and the CCL (MS2) can be designed as a result of the ramping. Beam-dynamics simulation studies of the two singlet designs shown in Table 1 indicate that a linac built to these specifications could meet the desired performance requirements of the LEB.

Doublet Design Example

In an attempt to improve the beam dynamics performance and perhaps to reduce the cost of the SSC linac, we have considered a solution for the CCL design based on a doublet-focusing lattice (FDO). The general parameters for this design example are given in column 3 of Table 1. In this example, the field gradient was ramped, cell-by-cell, from 1.3 MV/m to 6.5 MV/m over the first two tanks. All subsequent tanks were held constant at $E_0T = 6.5$ MV/m, as in the singlet example. Furthermore, we have held the phase-advance per period constant at 70° throughout the CCL. The transverse focusing period is reduced by a factor of 2 if doublet focusing is used, thus increasing the phase-advance per unit length. This results in a smaller rms beam size throughout the linac. Preliminary error studies, where random quadrupole rotations and displacements are distributed along the linac, indicate that the bore radius of the CCL can be reduced by 20% to 30% if doublet focusing is used. By reducing the bore radius to 1 cm, the resulting increase in shunt-impedance leads to a smaller total power requirement. We have forced the tank geometry to be 24 cells per tank, which allows a reduction in the total number of accelerating tanks required. For example, it may be possible to eliminate 12 accelerating tanks and their two associated klystrons.

In order to preserve the overall footprint of the CCL, the intertank spacing could be varied over different sections of the linac (See Table 1). We determined that a minimum distance between tanks of 11/2 $\beta\lambda$ is required at 70 MeV in order to conservatively provide adequate space for the quadrupole doublet, vacuum flanges, bellows, and beam diagnostics. The effective length of the quadrupoles was chosen so that a identical electromagnetic quadrupole could be used throughout the CCL. The pole-tip field chosen for this example is conservative. Our study shows that a future upgrade of the CCL to an output energy of 1 GeV is feasible.

Comparison of Singlet and Doublet Designs

Beam-dynamics simulations were run for both the singlet and doublet design examples using as input an rms-matched uniform distribution (uniform ellipsoid in real space and approximately uniform in velocity space) of 1000 pseudoparticles. The coupled-cavity code, CCLDYN,[3] was used for the simulations. This code is a particle-in-cell code incorporating both linear and nonlinear rf defocusing and two dimensional space-charge forces. Figure 2 shows the 3σ beam size as a function of tank number along the CCL for both cases. No error conditions were used in these simulations. Clearly, doublet focusing achieves a smaller beam size, as was to be expected. Figure 2 also shows the phase and energy spread of the beam as a function of tank number. Figure 3 shows phase-space plots at 600 MeV for both designs. Table 2 shows input and output emittances for the two cases. The doublet design example results in a factor of 3.3 (2.9) reduction in transverse (longitudinal) emittance growth when compared with the singlet design. A comparison of the structure parameters for the singlet and doublet design examples appears in Table 3. In addition to providing slightly better beam dynamics performance, the doublet example seems to have potential cost savings through a reduction in the total power, number of accelerating tanks, and number of bridge-couplers required.

Effects of Gradient Ramping on Longitudinal Matching

There will be a factor of three increase in rf frequency between the 428-MHz DTL and the 1284-MHz CCL. The longitudinal focusing forces will therefore be greater in the CCL. Mills, et al.[4] have shown that nearly current independent rms matching between accelerating structures can be achieved if both the transverse and longitudinal focusing strengths are held constant during the transition. The transverse focusing strength can be maintained by keeping the phase-advance per unit length similar in both the DTL and the CCL. Because the length of the doublet focusing period more closely equals the DTL period than

*Work supported and funded by the U.S. Department of Energy, Office of the Superconducting Super Collider.

TABLE 1

General Parameters for the 70-600 MeV, 1284 MHz Coupled-Cavity Linac Design Examples

Focusing Lattice:	Singlet FODO	Singlet FODO	Doublet FDO
Phase-advance/period:	70°	70°	70°
Effective Quad Length:	6 cm	6 cm	15.3 cm
Interquad Spacing	N/A	N/A	6 cm
Quad Gradient:	37.5-38.2 T/m (600 MeV) 38.2-44.5 T/m (1 GeV upgrade)	28.4-38.2 T/m (600 MeV) 38.2-44.5 T/m (1 GeV upgrade)	27.0-49.4 T/m (600 MeV) 49.4-66.0 T/m (1 GeV upgrade) ($B_{pole,max}$ = 0.85T)
Number of Cells/tank:	20	20	24
Starting Energy:	70 MeV	70 MeV	70 MeV
E_0T	6.5 MV/m (no ramp)	1.0-6.5 MV/m (2-tank ramp)	1.3-6.5 MV/m (2-tank ramp)
Total Number of Tanks:	66 (600 MeV) 101 (1 GeV)	66 (600 MeV) 101 (1 GeV)	54 (600 MeV) 83 (1 GeV)
Tank Lengths:	86.8-185.1 cm (600 MeV) 185.8-204.2 cm (1 GeV)	85.8-185.1 cm (600 MeV) 185.8-204.2 cm (1 GeV)	104.5-222.0 cm (600 MeV) 223.0-245.3 cm (1 GeV)
Synchronous phase (ϕ_S):	-30°	-30°	-28°
Bore Radius:	1.27 cm	1.27 cm	1.0 cm
Linac Length:	120 m (up to 600 MeV) 207 m (1 GeV upgrade)	120 m (up to 600 MeV) 207 m (1 GeV upgrade)	130 m (up to 600 MeV) 210 m (1 GeV upgrade)
Bridge Coupler Length:	5/2 βλ	5/2 βλ	11/2 βλ, 70 to 117 MeV 9/2 βλ, 117 to 219 MeV 7/2 βλ, 219 to 608 MeV (7/2 βλ, 608 to 673 MeV, 5/2 βλ, 673 to 1000 MeV)

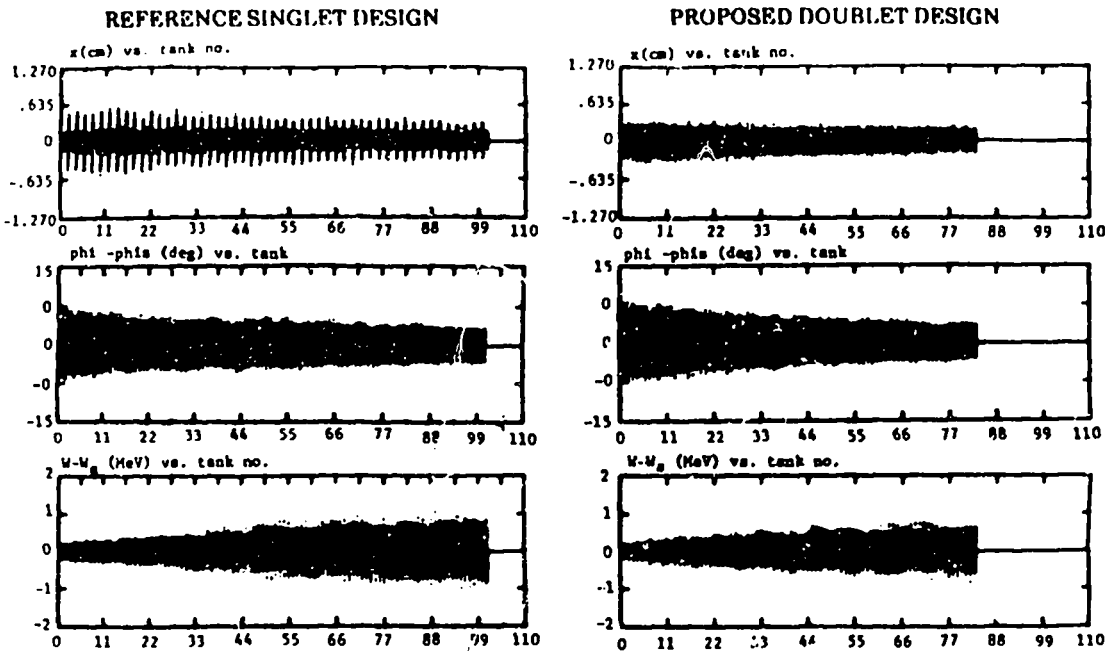

Fig. 2. Plots of beam size, phase and energy spread as a function of tank number along two proposed linacs.

does the singlet CCL, the doublet provides a smoother transverse envelope transition.

We determined that ramping the accelerating gradient cell-by-cell over two tanks is not adiabatic on the beam, but is gentle enough to provide a smooth longitudinal transition for the beam. To study how independently of current the beam could be matched from the DTL into the doublet CCL, we used TRACE 3-D[5] to simulate a matching region consisting of the last few DTL cells, an electromagnetic quadrupole, a five-cell buncher cavity (1284-MHz), an electromagnetic quadrupole doublet (with

TABLE 2

Input and Output Emittances from Simulation for the 1284-MHz CCL Examples using a Uniform Input Distribution

	Singlet Example	Doublet Example
70 MeV ε_x	0.0185 π·cm·mrad	0.0185 π·cm·mrad
600 MeV ε_x	0.022 π·cm·mrad	0.020 π·cm·mrad
70 MeV ε_L	0.305 π·deg·MeV	0.305 π·deg·MeV
600 MeV ε_L	0.335 π·deg·MeV	0.315 π·deg·MeV
Emittance Growth ε_x	18%	5.5%
Emittance Growth ε_z	10%	3.5%
Current (mA)	75	75
Transmission	100%	100%

TABLE 3

Comparison of the Structure Parameter for the Two Design Examples. Both are at 1284-MHz for 70-600 MeV Energy Gain

	Singlet	Doublet
E_0T	6.5 MV/m	6.5 MV/m
Phase advance/period	70°	70°
Length of the CCL	120 m	130 m
Tank geometry	20 cells/tank	24 cells/tank
# of tanks	66	54
# of modules	11	9
# of cells	1320	1296
# of bridge couplers	55	45
Bore radius	1.27 cm	1.0 cm

gradients independently adjustable), a second buncher cavity, another independently adjustable doublet, and the first three accelerating tanks of the CCL. This matching region is shown in Fig. 4. The buncher voltages provide two knobs for longitudinal matching, and the one single quadrupole and two doublet quadrupoles provide five knobs for transverse matching. The beam was rms matched, for a current of 25-mA at 428-MHz, from the DTL output to tank 3 of the CCL for various ramp rates (no ramping, and 0.1-6.5 MV/m to 1.3-6.5 MV/m) in the first two CCL tanks. The matching section parameters were then held constant as the DTL beam current was varied from 50% to 150% of the nominal 25-mA value. Twiss parameters resulting from this matching section were nearly the same as those wanted by CCL Tank 3. The matching section is largely current independent. Although not ramping any tanks of the doublet CCL gave good current independence, the non-ramped matching section exhibited rapid rf phase envelope size changes throughout the matching section. Additionally, the field gradient required in one of the bunchers was prohibitively high (7.2 MV/m); using 10-cell bunchers would allow operation at lower gradients. The longitudinal transition of the beam occurs most smoothly when the ramp rate is from 1.3 MV/m to 6.5 MV/m over two CCL tanks (see

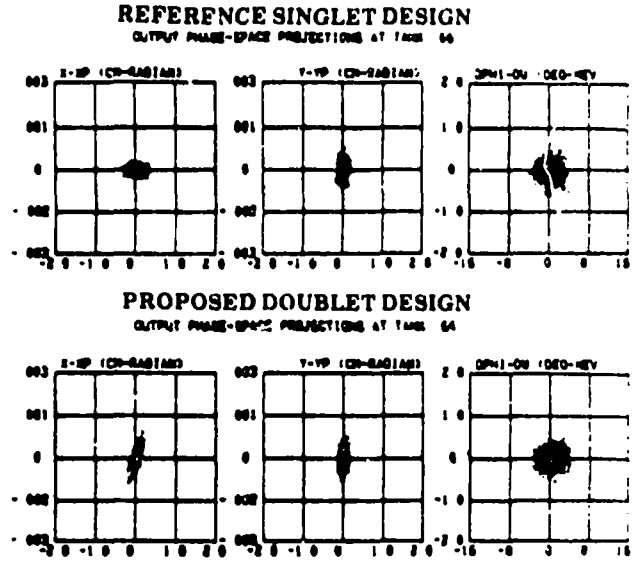

Fig. 3. Output phase-space plots at 600 MeV for the reference singlet design and the proposed doublet design.

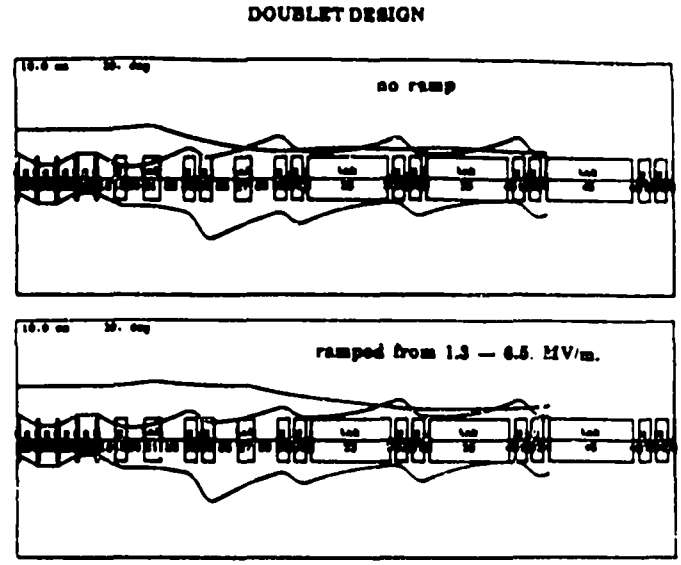

Fig. 4. Beam envelopes through the matching region for both the unramped and ramped doublet design examples. A smoother longitudinal transition is observed for the ramped case.

Fig. 4), thus achieving a nearly current-independent match. This matching section also performs very well for the singlet CCL.

Acknowledgments

We would like to thank D. Liska, L. Young, and T. Wangler at Los Alamos National Laboratory, and R. Bhandari and C. R. Chang at the Superconducting Super Collider Laboratory, for their useful discussions.

References

1. G. H. Neuschaefer, S. Nath, J. H. Billen, T. S. Bhatia, and J. M. Watson, "SSC Drift Tube Linac Physics Design", Proceedings of the 1990 Linac Conference, LA-UR-90-3098, September 1990.
2. Site Specific Conceptual Design of the Superconducting Super Collider, SSC Central Design Group, SSC-SR-1051, 108-114, June 1990.
3. R. W. Garnett, AT-1, "CCL Design and Dynamics Codes," Los Alamos National Laboratory memorandum AT-1:89-303, November 1989.
4. R. S. Mills, E. R. Crandall, and J. A. Farrell, "Designing Set Matching Lenses," Proceedings of the 1984 Linear Accelerator Conference, GSI-84-11, 112, September 1984.
5. E. Crandall, AT-1, "TRACE 3-D Documentation," Los Alamos National Laboratory report LA-11054-MS, August 1987.

ERROR AND TOLERANCE ESTIMATES FOR THE SSC CCL*

T.S. Bhatia, R.W. Garnett, and G.H. Neuschaefer,
Los Alamos National Laboratory
and
K. R. Crandall
AccSys Technology Inc., 1177 Quarry Lane, Pleasanton, CA 94566

Abstract

We have used a new code, CCLTRACE, to estimate error and tolerance limits for two possible examples of a 1284-MHz, 70- to 600-MeV coupled-cavity linac (CCL) for the SSC linac. By calculating the dynamics of the beam center as well as the beam ellipsoid, CCLTRACE can efficiently perform error studies using Monte Carlo techniques.

The Code CCLTRACE

After a CCL is designed, its performance is usually checked by a multiparticle simulation code, such as CCLDYN, which can estimate beam loss and emittance growth and display beam profiles and phase-space projections at points along the length of the CCL. The code CCLTRACE replaces the multiparticle dynamics of CCLDYN with the beam ellipsoid dynamics of TRACE 3-D.[1] CCLTRACE is related to CCLDYN in the same way that PARTRACE[2] is related to PARMILA.

Ken Crandall developed CCLTRACE to estimate the effects that are due to the presence of various error conditions, singly or in combinations, for CCLs. When tolerance limits on one or more types of errors in alignment or field adjustment (random over a uniform distribution of ± specified limit) are specified, CCLTRACE can calculate probability distribution functions for various effects on the beam. For example, for a specified set of tolerances, the user can determine the probability that the beam center will not be displaced from the axis by more than a certain distance or that the outer edge of the beam will not go beyond a certain fraction of the available bore. Using information generated by CCLTRACE, the CCL designer can set reasonable tolerances on the various types of unavoidable errors. Alternatively, CCLTRACE can help establish the need for corrective action along the structure in order to compensate for the effects of errors within specified tolerance limits.

To glenerate the probability distributions, the code runs a large number of "traces" for a specified set of tolerance limits. At each element, random values within the tolerance limits are chosen for the errors. Maximum values for the beam parameters and emittances are saved for each trace. At the end of a run, these values are sorted and a probability distribution is obtained.

CCLTRACE can be used for error estimates for CCLs with either singlet or doublet focusing lattices. The types of error conditions that can be handled by CCLTRACE, singly or in combinations, are

a. quadrupole displacements
b. quadrupole rotations (roll)
c. quadrupole tilts (pitch and yaw)
d. quadrupole gradient errors
e. doublet displacements
f. doublet tilts
g. doublet rotations
h. doublet gradient errors
i. tank displacement
j. accelerating field amplitude errors
k. accelerating field phase errors
l. initial beam mismatch errors

Error and Tolerance Estimates for SSC CCL Design Example

The effects that are caused by some errors are more serious than effects caused by other errors. We shall, in what follows, illustrate the results obtained using CCLTRACE for two CCL design examples. One of these is a CCL with a singlet focusing lattice. The other design example is based on a doublet lattice. Both design examples, described in a companion paper[3], accelerate 25 mA of H^- ions from 70 to 600 MeV. $E_0T = 6.5$ MV/m, and the phase advance per period is 70° for both of the 1284-MHz CCLs being considered. Probability distributions were generated from a set of 100 traces for each error condition described. The beam edge was assumed to extend to a distance of three times the rms width, (3σ).

Error Estimates for CCL with a Singlet Focusing Lattice

Each of the 66 tanks consists of 20 cells. The 6-cm-long quadrupole (quad) singlets are centered in the 5 $\beta\lambda/2$ space between tanks, and the gradients range from 3.41 to 4.45 kG/cm to maintain the 70° zero-current phase advance. Bore diameter is 2.54 cm.

The types of errors included in this study were magnetic quadrupole displacements, quad tilts (pitch and yaw), quad rotations (roll), quad gradient errors, and tank displacements. The gradient errors cause the beam to become mismatched and hence to oscillate in size. Quad rotations mix the x and y motions and cause an effective emittance growth in the x-x' and y-y' phase-space projections. The other types of errors cause the beam to oscillate about the CCL axis with an amplitude that depends on the random errors chosen for the misalignments. All of these errors cause the beam to come closer to the tank bore and can result in particle loss.

One measure of the effect of these errors is the bore filling factor. For a given set of random errors, at some point along the CCL (at 3σ for example) the beam edge will come closest to the tank bore. The distance from the CCL axis to this point on the beam edge will be denoted by r_{max}. The maximum filling factor, f_{max}, is defined to be r_{max} divided by the bore radius. A value of 1 for f_{max} therefore denotes beam scraping at the 3σ level.

The probability distributions of f_{max} obtained when the error tolerances on quad displacements were 0.002", 0.004", and 0.006" are shown in Fig. 1. Displacement errors of 0.002" seem to have an insignificant effect on f_{max}. Even with a 0.004" tolerance, there is a 90% probability that f_{max} will be less than 0.6. The beam is very insensitive to quadrupole pitch and yaw errors. A tolerance of

*Work supported and funded by the U.S. Department of Energy, Office of the Superconducting Super Collider.

50 mrad caused no effect on f_{max}. Also, tank displacement errors with a tolerance of 0.010" caused an insignificant effect on f_{max}.

The probability distributions of f_{max} produced by error tolerances of 1%, 2% and 5% in the quad gradients are shown in Fig. 2. A 1% tolerance has no effect on f_{max}; a 2% tolerance gives a 90% probability that f_{max} will be less than 0.6; a 5% tolerance is unacceptable.

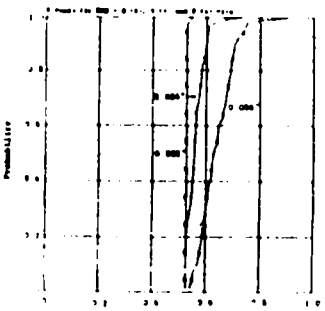

Fig. 1. Probability distribution of f_{max} (r_{max} = bore radius) for random quad displacement errors within ±0.002", 0.004", and 0.006" for the singlet design example.

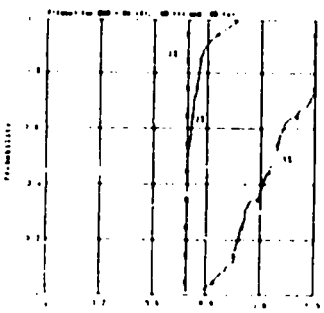

Fig. 2. Probability distribution of f_{max} (r_{max} = bore radius) for random ±1, 2, and 5% quad gradient errors for the singlet example.

The probability distribution for f_{max} produced by a combination of errors ± (0.004" quad displacements, 5-mrad quad tilts, 1° quad rotations, 2% quad gradient errors, and 0.010" tank displacements) is shown in Fig. 3. For this combination, there is a 95% probability that f_{max} will be less than 0.8.

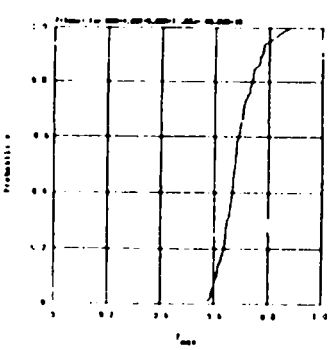

Fig. 3. Probability distribution of f_{max} (r_{max} = bore radius) for a combination of random errors for the singlet lattice, as described in the text.

Figures 4 and 5 show the projections of the equivalent uniform beam (total width is equal to $\sqrt{5}$ times the rms width) on the x, phase and energy axis when there are no errors (Fig. 4) and when there is a particular set of random errors (Fig. 5). Figure 4 shows that the beam is well matched and on axis. Figure 5 shows the beam oscillating about the axis and becoming somewhat mismatched (on the x axis). The error tolerances used in producing Fig. 5 were 0.004" quad displacements, 0.010" tank displacements, 2% quad gradient errors, and 1° phase errors.

Error Estimates for CCL with Doublets Between Tanks

Each of the 54 tanks consists of 24 cells having a bore diameter of 2.0 cm. Quadrupole doublets are centered in the space between tanks. Each doublet

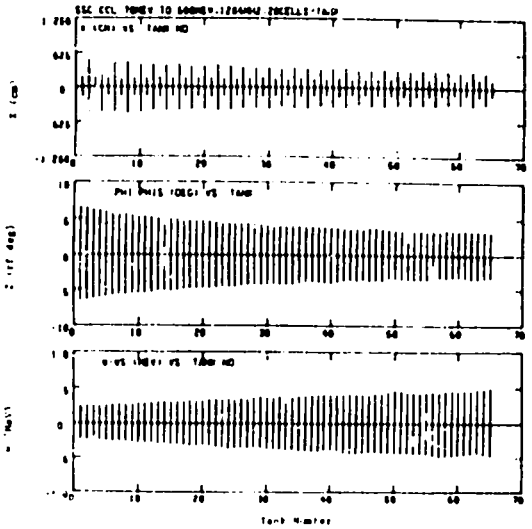

Fig 4. Beam size of singlet lattice with no errors.

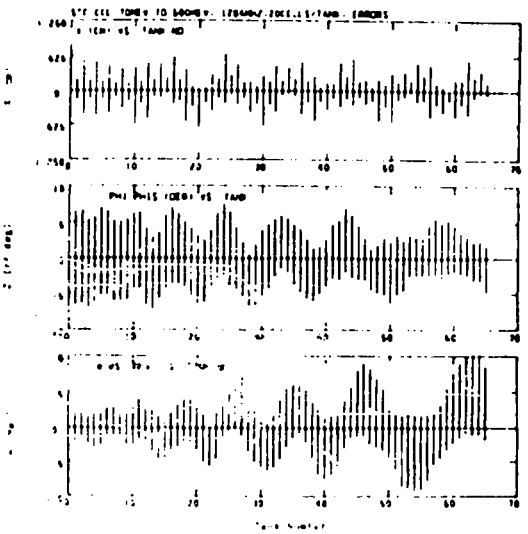

Fig. 5. Beam size of singlet lattice with a combination of random errors within ± 0.004" quad displacements, 0.010" tank displacements, 2% quad gradient errors and 1° phase errors.

consists of two 15.3-cm-long quadrupoles with 21.3 cm between quad centers. The quad gradients range from 2.67 to 4.94 kG/cm to maintain the 70° zero-current phase advance per period.

The types of errors included were doublet displacements, doublet tilt (pitch and yaw), doublet rotation (roll), and doublet gradient errors. In general, systems of doublets are less sensitive to displacements and rotations, but much more sensitive to tilts. The axis of the doublet is defined to be the straight line passing through the center of each of the two quadrupoles. Each quadrupole pair for a given doublet is assumed to have perfect relative alignment. The tilt angle is the angle between the doublet axis and the reference axis.

The probability distributions for f_{max} produced by 0.005", 0.010", and 0.015" doublet displacements are shown in Fig. 6. Error tolerances between 0.005" and 0.010" appear to be acceptable. The sensitivity of f_{max} to doublet tilt errors is given by the probability distributions shown in Fig. 7 for tilts of 0.25, 0.50, and 0.75 mrad. The tolerance on doublet tilt errors should be less than 0.50 mrad. Similarly, Figs. 8 and 9 show that doublet gradient errors of 2% and doublet

rotation errors of 2° should be acceptable. These latter two tolerances should be easy to meet.

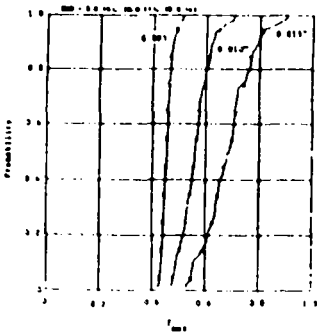

Fig. 6. Probability distribution of f_{max} for ±0.005", 0.010", and 0.015" random doublet displacement errors.

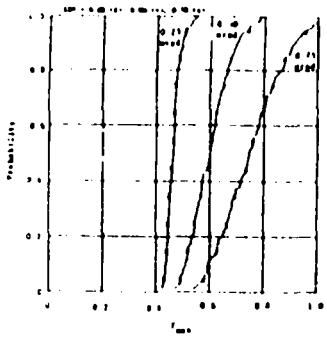

Fig. 7. Probability distribution of f_{max} for random doublet tilt errors of ±0.25, 0.50, and 0.75 mrad.

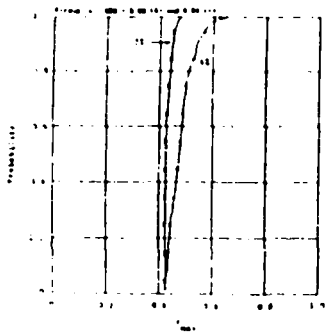

Fig. 8. Probability distribution of f_{max} for random doublet gradient errors of ±2% and 4%.

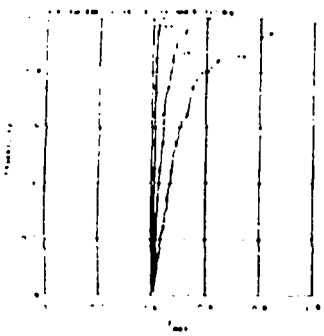

Fig. 9. Probability distribution of f_{max} for random doublet rotation errors of ±1°, 3°, and 5°.

A probability distribution for f_{max} produced by a combination of doublet errors (0.010" displacement, 0.5-mrad tilt, 3° rotation, and 2% gradient errors) is shown in Fig. 10. All of these tolerances are probably higher than would be accepted or could be achieved.

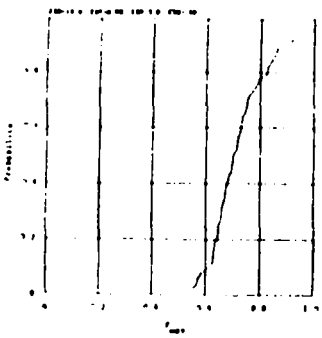

Fig. 10. Combination of doublet random errors within ± -- 0.010" displacement, 0.5-mrad tilt, 3° rotation, and 2% gradient errors.

Figures 11 and 12 show the x, phase and energy projections along the CCL for no errors (Fig. 11) and for a combination of errors (Fig. 12). The error tolerances used in producing Fig. 12 were 0.010" doublet displacements, 0.5-mrad tilt, 0.010" tank displacements, and 1° phase errors.

Conclusion and Recommendations

The CCLTRACE program is a useful tool for estimating the effects of various alignment and field

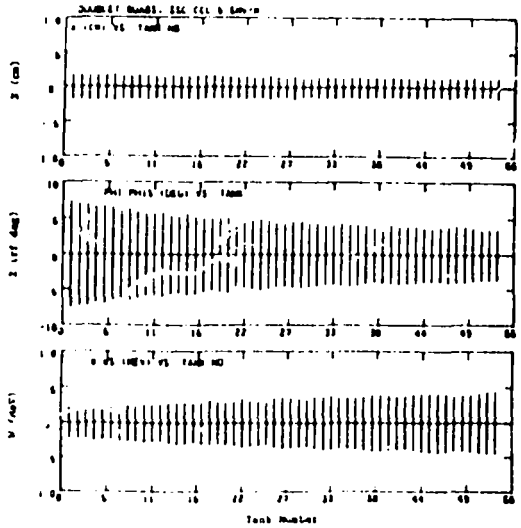

Fig. 11. Beam size of doublet lattice -- no errors.

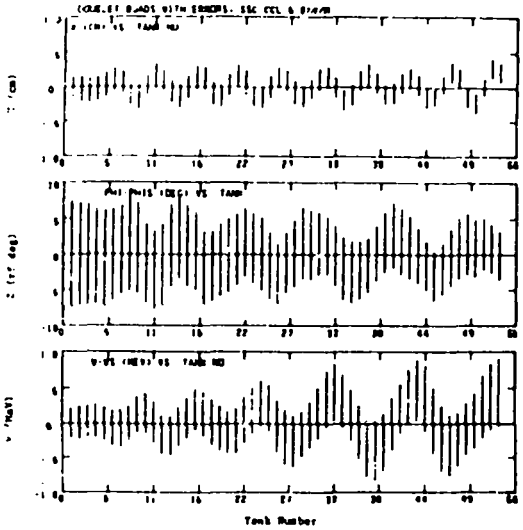

Fig. 12. Beam size of doublet lattice with combination of random error conditions within ± -- 0.010" doublet displacements, 0.5-mrad tilt, 0.010" tank displacements and 1° phase errors.

strength errors in a CCL. Tank displacements of 0.010" should be relatively easy to achieve and should have no significant effect on the beam. Quadrupole displacements should be less than 0.004". Quadrupole gradient errors should be less than 2%, and quad rotations should be less than 0.5°. If doublets are used instead of singlets, the acceptable displacements can be between 0.005" and 0.010", and doublet rotations of 2° would not be serious. The tightest tolerance is on the doublet tilt, which should not be much larger than 0.50 mrad.

References

1. K. R. Crandall, "TRACE 3-D Documentation," Los Alamos National Laboratory report LA-11054-MS.
2. K. R. Crandall, "Error Studies Using PARTRACE, a New Program that Combines PARMILA and TRACE 3-D," Linear Accelerator Conference, Williamsburg, VA, October 3-7, 1988.
3. R. W. Garnett et al., "A Comparison of Beam Dynamics Solutions for the SSC 1284-MHz CCL," Linear Accelerator Conference, Albuquerque, NM, September 10-14, 1990.

BEAM DYNAMICS SIMULATION OF THE LAMPF LINEAR ACCELERATOR

R. W. Garnett, R. S. Mills, and T. P. Wangler
Los Alamos National Laboratory, Los Alamos, NM 87545*

Abstract

We performed an end-to-end simulation of the LAMPF linac to test the capability of our codes to predict the actual performance of an accelerator system. We attempted to reproduce the measured H^- beam transverse emittances, and wire-scan, phase-scan and beam-loss data for a typical LAMPF operating cycle by using the known operating parameters of the linac. The simulations were also useful in understanding the beam dynamics of LAMPF and for explaining the sources of linac emittance growth and particle losses in the side-coupled linac.

Simulation Techniques

The LAMPF accelerator consists of a 0.75-MeV injector, with a low-energy beam transport (LEBT) line, a 0.75 to 100-MeV drift-tube linac (DTL), a 100-MeV transport line called the transition region (TR), and a 100 to 800-MeV side-coupled linac (SCL). The DTL incorporates singlet FODO focusing. The focusing period is doubled in the last two of four tanks by placing a quadrupole only in every other drift-tube. Doublet FDO focusing is used in the SCL. The number of particles per bunch is about 5 x 10^8, which gives a peak current of 15 mA at 201.25 MHz in the DTL. Because the physics of the LEBT is not well understood (the amount of beam neutralization is unknown and no measurements of the longitudinal beam structure are made), we decided to start the simulation at the entrance to tank 1 of the DTL, using longitudinal input distributions that represent different assumptions about the LEBT physics.

We simulated the DTL and TR using the PARMILA code. Two longitudinal input distributions were used. We obtained these distributions by propagating a beam in the LEBT, beginning with a truncated beam ($\pm 120°$) at the second of two bunchers, and ending at the entrance to the first tank of the DTL. The space-charge in PARMILA was set to zero for the first case to represent 100% neutralization and to a current of 17-mA for the second case. The first case was designated ZSC for zero space-charge in the LEBT and the second, SCD for space-charge dominated in the LEBT. In both cases, the transverse beam was regenerated at the DTL entrance as an rms matched Gaussian distribution (truncated at 3σ), which is consistent with the measured beam, and simulated at full current in the linac.

We believe that the longitudinal beam distribution is bracketed by these two extremes. Figure 1 shows longitudinal phase-space plots for these two distributions at both the entrance to the DTL (0.75-MeV) and the exit of the TR (100-MeV).

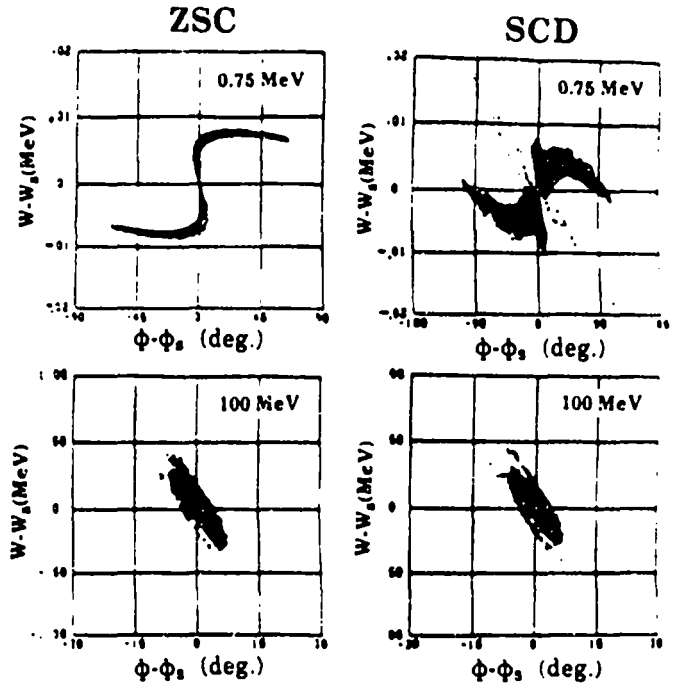

Fig. 1. Longitudinal phase-space plots for the two input distributions.

All simulations began with 10,000 pseudoparticles. The DTL r.f. amplitude in tank 1 is not accurately known and is purposely set below the maximum value for typical linac operation. In the simulations, the amplitude was set to 94% of the design value. This resulted in realistic transmissions through the DTL in the range of 72% to 80% for the various cases studied. We ran DTL simulations with both "design" and measured ("production") r.f. field gradients, quadrupole strengths, and cell lengths.

Output distributions from the PARMILA code simulations were used as input for the coupled-cavity code, CCLDYN. We used the SCL design values for r.f. field gradients and quadrupole strengths. Actual experimental settings for the last five quadrupoles in the DTL were used in all the DTL simulations to provide the experimental match to the CCL. Measured misalignments for tanks and magnets were not used.

At LAMPF, phase-scans done at 121-MeV in the SCL are used to determine the phase-width of the beam. An absorber-collector method is used. A copper absorber, placed in the beam with its thickness chosen so as to stop protons with kinetic energy (W) less than 117.42-MeV but to pass those with W > 122.58-MeV, places a lower-limit energy cut-off on the phase-space to be scanned. In the phase-scan simulations, particles with energy less than 5-MeV below the synchronous energy were rejected in order to mock up the effect of the

*Work supported by Los Alamos National Laboratory Institutional Supporting Research, under auspices of the United States Department of Energy

absorber. We ran particle-loss simulations with both the SCD and ZSC input distributions. No energy cut was made as the particles propagated, consistent with actual accelerator operation.

Comparison of Simulation and Measurement

The results of experimental measurements for LAMPF operating cycle 52[1] are given in Table 1. All emittances are rms-normalized values but do not include the factor of four that is sometimes used. The table shows a difference between wire-scan and slit and collector data at 100-MeV; experimental measurement uncertainties, however, were not available. Table 2 shows the results of the simulations for comparison. The 100-MeV phase-space plots in Fig. 1 and the results in Table 2, show that the beam becomes conditioned in the DTL regardless of its initial longitudinal distribution and that the properties of the core beam particles are mostly determined by the DTL. By contrast, the outer parts of the distribution (the tails) appear to be sensitive to the input longitudinal distribution.

TABLE 1
LAMPF Cycle 52 Experimental Results

Measurement	Value	
Particle Loss	~0.1%	
Phase-Scan at 121 MeV (just after module 6)	FWHM ≈ 15.9°	
Wire-Scan at 800 MeV for rms beam size	FWHM ≈ 0.54 cm	
Emittance Measurements		
100 MeV	Slit & Collector	$\bar{\varepsilon}_t$ = 0.026 π-cm-mrad
	Wire Scan	$\bar{\varepsilon}_t$ = 0.053 π-cm-mrad
800 MeV	Wire Scan	$\bar{\varepsilon}_t$ = 0.071 π-cm-mrad

The simulations predict all measured quantities to within 10% to 15%, except the total SCL beam losses, which we expect to be sensitive to the population of the tails. At 100-MeV, the simulations agree best with the slit and collector measurements. The SCL beam losses are best predicted, to within a factor of 3, by using the "design" SCD distribution. Use of the "production" distributions overestimates the losses by about an order of magnitude. Additionally, the locations along the SCL where most of the activation occurs were correctly predicted by any of the input distributions. Figure 2a shows a typical beam loss profile from the simulations. Figure 2b sshows the estimated beam losses in the SCL from activation measurements.

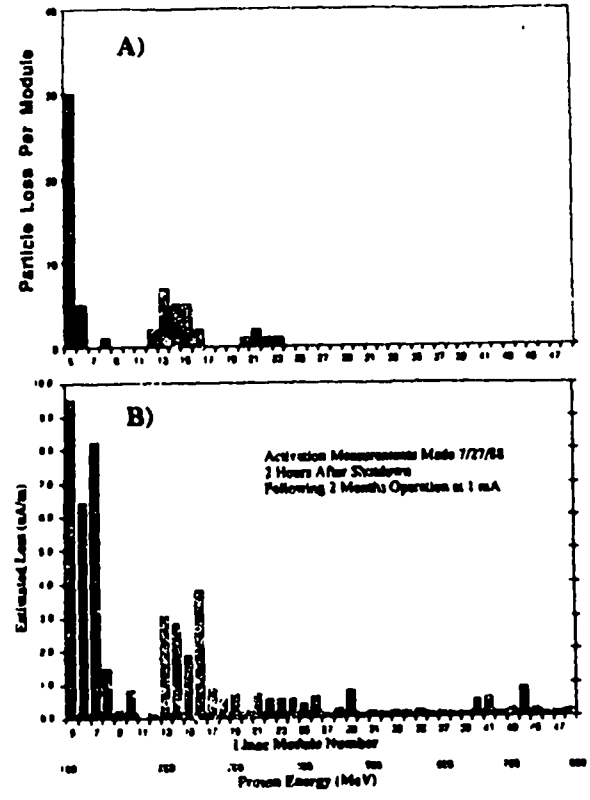

Fig. 2. Typical SCL beam-loss profile fromthe simulations. b) Estimated beam losses in the SCL from activation measurements.

TABLE 2
Results of LAMPF Simulation

Distribution Type	$\bar{\varepsilon}_t$ π-cm-mrad 100 MeV	$\bar{\varepsilon}_t$ π-cm mrad 800 MeV	$\bar{\varepsilon}_\ell$ π-cm-mrad 100 MeV	$\bar{\varepsilon}_\ell$ π-cm-mrad 800 MeV	121 MeV Phase FWHM (deg.)	800 MeV Size FWHM (cm)	Losses (%)
"DESIGN" SCD	0.026	0.065	0.575	1.090	17.03	0.60	0.35
"DESIGN" ZSC	0.028	0.067	0.637	1.175	24.69	0.78	0.41
"PRODUCTION" SCD	0.030	0.065	0.659	1.240	17.41	0.67	0.98
"PRODUCTION" ZSC	0.032	0.063	0.725	1.091	22.26	0.75	1.76

LAMPF Losses and Longitudinal Emittance

While longitudinal emittance is not directly measured at LAMPF, phase-scans give a one-dimensional phase projection of two-dimensional longitudinal phase-space. When LAMPF is being tuned, the operators attempt to minimize particle losses by narrowing the phase-width. It is impossible to determine from the accelerator tuning procedures used by the LAMPF operators whether this narrowing is accomplished by their decreasing the longitudinal emittance of the beam or by rotating it in phase-space to give a minimum projection.

To study the correlation between longitudinal emittance (or phase-width) and losses, we transformed the "design" SCD distribution at 100 MeV to change the rms longitudinal emittance and thereby alter the phase-width. We found that the SCL losses are indeed a function of the longitudinal emittance with a sharp minimum at $\epsilon_L = 0.497$ π-deg-MeV. This value of phase-width ($\Delta\phi = 15.7°$) is within 0.3° of the measured operating value, which gave minimum accelerator activation. The simulations showed that particles lost near tank 1 of the SCL (module 5) lie in the tails of the y-y' distribution but are close to the synchronous phase. Those particles that are eventually lost radially near tank 33 (module 13) have small initial transverse coordinates but are at the edge of the longitudinal acceptance.

Emittance Growth in the Linac

We compared PARMILA simulations of the DTL with and without the effect of space-charge forces. We determined that the transverse emittance growth in the DTL is caused by the non-linear space-charge forces acting on the beam. The longitudinal emittance growth was essentially unaffected. We believe that the longitudinal emittance growth is caused by the non-linear r.f. focusing forces encountered in the DTL. Figure 3 shows both the average transverse and longitudinal emittances along the DTL. Asymmetries in x-x' and y-y' emittances were encountered in both the DTL and SCL simulations. This feature, although it is also observed in the measured emittance data, is not understood and therefore we make comparisons of the average of x-x' and y-y' emittances. Figure 3 shows that rapid transverse emittance growth is seen to occur in tank 2 and tank 3 (where the focusing period changes). The simulation shows particle losses throughout the DTL, which tends to cause some reduction in the emittances.

It is commonly believed that most emittance growth occurs in the low-energy end of a linac. The measured slit and collector data at 100-MeV indicate that the transverse emittance grows by a factor of 2.7 between 100 and 800-MeV at LAMPF. Our simulations gave values in the range 2.0-2.5.

We believe that the emittance growth in the SCL is primarily due to mismatch (mostly longitudinal) of the beam and is caused by the nonlinear space-charge forces acting on it. To verify our belief, we turned off the effect of r.f. defocus in the simulations. We observed no change in emittance growth. For comparison, the SCL emittance growth became negligible when the space-charge forces were turned off. Table 3 gives mismatch factors at 100

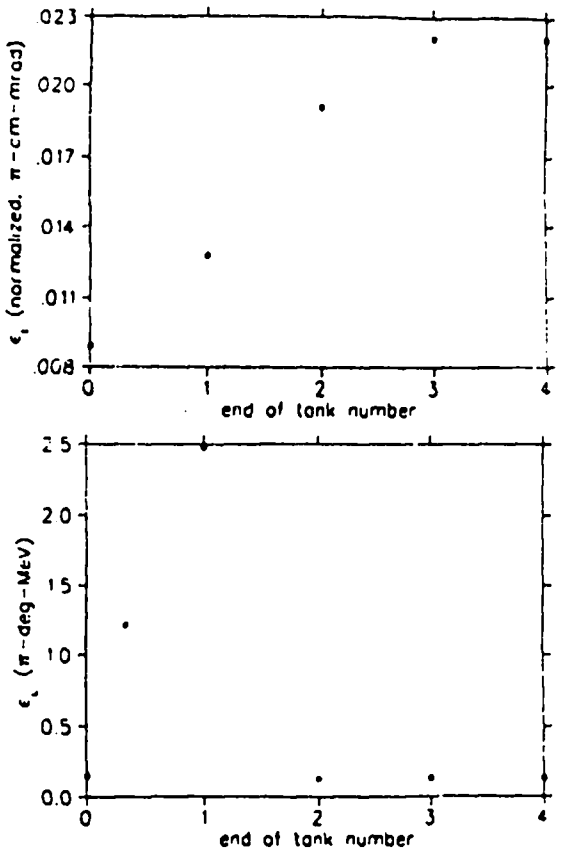

Fig. 3. Emittances as a function of tank number in the DTL from the simulations for the SCD beam. Longitudinal emittance is in units of π-deg-MeV at 201.25 MHz.

MeV calculated for both the SCD beam and the actual beam using the slit and collector data. The mismatch factor[2] is defined by

$$M = \left[\frac{1}{2} R + \frac{1}{2} \sqrt{R^2 - 4} \right]^{\frac{1}{2}} - 1$$

where $R = \beta_1 \gamma_2 + \beta_2 \gamma_1 - 2\alpha_1\alpha_2$ and $\alpha_i, \beta_i, \gamma_i$ ($i = 1,2$) are the Twiss parameters for the matched and unmatched ellipses. For a matched beam, $M = 0$.

TABLE 3
Mismatch Factors at 100 MeV

Distribution	M_x	M_y	M_L
"Design" SCD	0.155	0.896	1.381
Measured Slit and Collector	0.388	0.587	–

Figure 4 shows both the average-transverse and longitudinal emittances as functions of tank number along the SCL for the "design" SCD

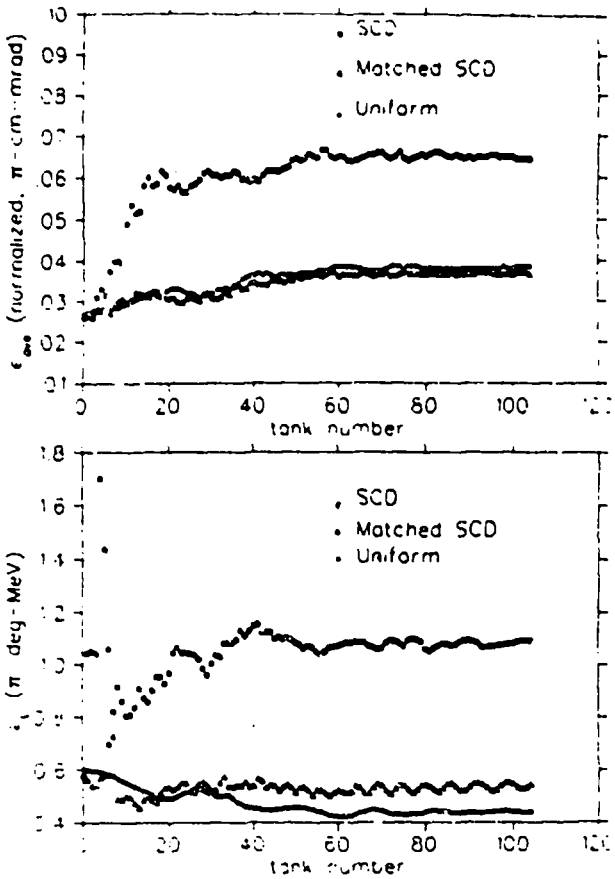

Fig. 4. SCL emittances for unmatched SCD, matched SCD, and uniform input distributions. Longitudinal emittance is in units of π–deg–MeV at 805 MHz.

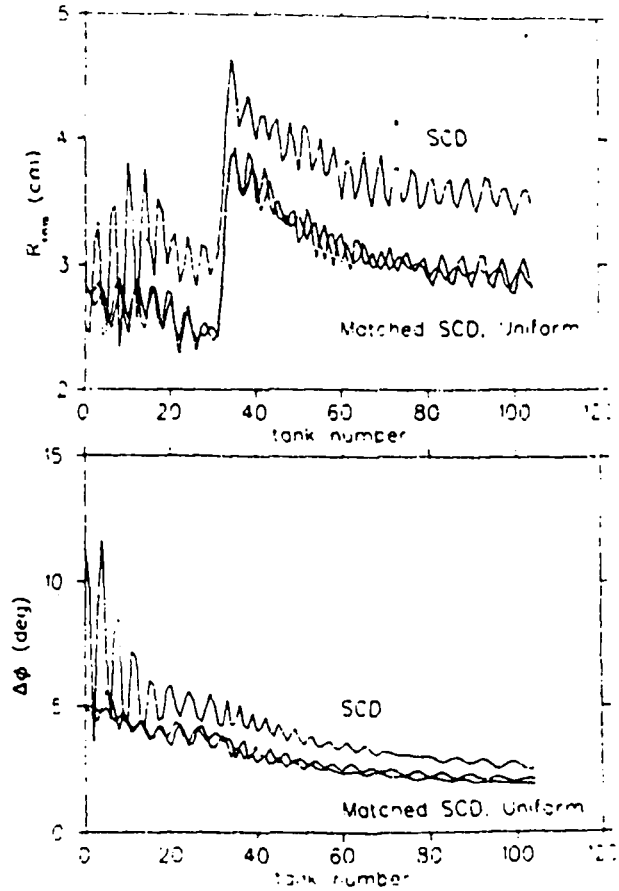

Fig. 5. Transverse and longitudinal rms beam sizes for the SCD and uniform beam in the SCL ($R_{rms} = \sqrt{X3 + Y2rms}$).

distribution. Also shown are curves for an rms-matched SCD distribution and a matched uniform distribution (uniform ellipsoid in real space and approximately uniform in velocity space).

We created a matched SCD distribution by transforming the coordinates of each particle of the "design" SCD distribution at 100 MeV such that the new distribution had Twiss parameters identical to those obtained from TRACE-3D[3] for an rms match at the input to the SCL. The initial emittances of the distribution were preserved.

Figure 4 shows that there is a drastic reduction in emittance growth, both transversely and longitudinally, if the beam is rms-matched to the linac. The matched beam behaves very much like the uniform beam, which is evident in both the emittances and rms beam sizes (Fig. 5). The observed increase in transverse rms beam size near tank 33 (module 13) is due to a reduction in quadrupole focusing strength at this point in the linac. The average quadrupole gradients and lengths remain constant at about 25 T/m and 0.1 m, respectively, but the tank lengths, and therefore the quadrupole spacings, approximately double. A factor-of-5 reduction in beam losses was also observed in the simulations for the matched beam. This is probably due to the reduction in synchrotron oscillation amplitude at the entrance to the SCL. This energy would otherwise later couple to the transverse degrees of freedom and cause particle losses further downstream in the linac.

Both longitudinal and transverse emittance growth are still observed for the ideal matched SCD and uniform beams. Figure 4 clearly indicates a coupling between transverse and longitudinal degrees of freedom. The longitudinal emittance decreases as the transverse emittance grows. We believe that this relationship is due to a lack of equipartitioning of the matched beam in the SCL. RMS matching and equipartitioning should result in a beam that more closely resembles an internally matched beam and should therefore reduce the space-charge-induced emittance growth.

Acknowledgments

We would like to thank J. Hurd and A. Browman of the LAMPF operations group for their interest and for providing us with the experimental data. Also, we would like to thank K. R. Crandall, G. P. Lawrence, S. Nath, and G. H. Neuschaefer for their help in this study.

References

1. J. Hurd, "Report on End of Cycle 52 Documentation," Los Alamos National Laboratory internal report (October 1988).
2. J. Guyard and M. Weiss, "Use of Beam Emittance Measurement in Matching Problems," in Proceedings of the 1976 Proton Linear Accelerator Conference, Atomic Energy of Canada Limited report, AECL-5677 (November 1976), p. 255.
3. K. Crandall, "TRACE 3-D Documentation," Los Alamos National Laboratory report LA-11054-MS (August 1987).

SSC DRIFT TUBE LINAC PHYSICS DESIGN*

G. Neuschaefer, S. Nath, J. Billen, and T. Bhatia
Los Alamos National Laboratory, Los Alamos, NM 87545
J. Watson
Superconducting SuperCollider Laboratory, Dallas, TX

Abstract

This paper describes the present status of the beam-dynamics design for the SSC drift-tube linac (DTL). The DTL is designed to accelerate a H^- beam from 2.5 MeV to 70 MeV. The design beam current is 25 mA at 428 MHz. The DTL consists of four tanks stabilized by post couplers. Transverse focusing is provided by permanent magnet quadrupoles (PMQs). Intertank longitudinal matching is provided by displaced end-cell rf gaps. The rf field is ramped in Tank 1 but is held constant through the remainder of the DTL. A brief description of the beam dynamics and structures issues is presented here. Details on these aspects will be available in a forthcoming report.

Physics Issues

A radio frequency quadrupole (RFQ) is expected to provide the DTL with a 25 mA, H^- beam of rms normalized emittance $\varepsilon = 0.02\ \pi$ cm-mrad in both the transverse and longitudinal phase spaces. The zero current longitudinal and transverse focusing strengths per unit physical length at the entrance of the 428-MHz DTL are chosen to be similar to those at the 428-MHz RFQ exit. This makes a nearly current independent "RFQ to DTL" matching section feasible. Accordingly the transverse and longitudinal phase advance per $\beta\lambda$ at zero current are kept approximately at 20° and 13.5° respectively throughout Tank 1. Although ramping[1] the rf field (E_0T) throughout the DTL will shorten the linac, power and peak surface field requirements limit this approach. In the present design, we choose to ramp E_0T and the synchronous phase (ϕ_s) only in Tank 1. This rf ramp prescription was first used in the Los Alamos proof-of-principal RFQ gentle buncher section.

The DTL starts with $\phi_s = -35°$ which is the same as at the RFQ exit. It is then ramped to $-30°$ for more efficient acceleration using

$$\psi^\circ = \psi^\circ_{\ldots}(\beta_{\text{last}}/\beta), \qquad (1)$$

where ψ° is the zero current longitudinal separatrix width in units of rf degrees, and β is the particle velocity divided by the speed of light; ϕ_s and ψ° are related by

$$\cos\phi_s = (\sin\psi^\circ - \psi^\circ)/(1 - \cos\psi^\circ). \qquad (2)$$

This ψ° ramp holds ψ°, the width of ψ in units of length, constant. After ϕ_s attains the value of $-30°$ in Tank 1, it is held constant, allowing ψ° to increase. E_0T is ramped from 1.5 MV/m (same as at the RFQ exit) to 4.0 MV/m. The final E_0T, 4.0 MV/m, is set by the limit on the peak surface electric field. A linear ramp approximates the E_0T ramp defined by the following equation:

$$E_0T \sin\phi_s / (\beta\gamma^2) = \text{Constant}, \qquad (3)$$

where

E_0 is the average accelerating field over a cell,
T is the transit time factor, and
$\gamma = (1-\beta^2)^{-1/2}$.

The above prescription keeps the longitudinal beam size (in units of length) in Tank 1 approximately constant. Keeping the beam size approximately constant throughout the DTL prevents emittance growth from energy exchange between the longitudinal and transverse phase spaces. In Tanks 2, 3, and 4, E_0T is held constant at 4.0 MV/m and $\phi_s = -30°$. This results in a slow longitudinal expansion of the beam size in real space.

Transverse focusing is provided by PMQs. Two focusing lattices, FODO and FOFODODO were examined. We simulated, in addition to the design beam of 25 mA, a high- and low-emittance 75 mA beam to observe the DTL's sensitivity to current and emittance. Table 1 shows very little emittance growth in all cases. Both transverse focusing schemes yield similar beam sizes when random quadrupole misalignments are included. Tank 1 PARTRACE[2] calculations[3] were done for both the schemes with ±0.005 inch random (uniform distribution) quadrupole transverse misalignments.

Table 1
Normalized rms emittance in π cm-mrad
(simulated as one tank from 2.5 to 70 MeV)

Focusing Scheme	Current mA	2.5 MeV Input Beam		70 MeV Output Beam		Zero Current Transverse Phase Advance per Cell degrees
		ε_t	ε_ℓ	ε_t	ε_ℓ	
fodo	25	0.020	0.020	0.020	0.022	23
fodo	75	0.060	0.060	0.060	0.063	23
fodo	75	0.010	0.010	0.010	0.024	23
fofododo	25	0.020	0.020	0.020	0.023	20
fofododo	75	0.060	0.060	0.065	0.064	20
fofododo	75	0.010	0.010	0.011	0.020	20

*Work supported and funded by the US Department of Energy. Other [illegible]

For a FOFODODO lattice there is a 99% probability that the beam outer edge will not exceed 0.63 cm (centroid displacement = 0.33 cm) when the beam enters in the geometric tank center. A FODO lattice has a 99% probability maximum beam edge radius of 0.64 cm. PMQ constraints limit the FODO bore radius to ~0.65 cm, however, the FOFODODO radius can be 1.1 cm. This led to the choice of a FOFODODO lattice. The beam (0.02 π cm-mrad, 25 mA) width in these calculations was taken to be 3 times the rms size. Tanks 2, 3, and 4 have fewer cells and therefore are less sensitive to magnet misalignments.

Drift Tubes

The design of individual cells in a tank was carried out using SUPERFISH[4]. A typical drift-tube shape is shown in Figure 1. Parameters are given in Table 2. The design of these drift-tubes was constrained by several interrelated factors: (a) the desirability of a large bore size, (b) a peak surface field (E_p) not to exceed 1.4 Kilpatrick field (E_k), (c) tank power not to exceed 3 MW, and (d) PMQs of required strength. The 'rf gap length' to 'cell length' was varied from cell to cell to attain the resonating frequency of 428 MHz. The DTL parameters for Tanks 1 through 4 are shown in Table 3.

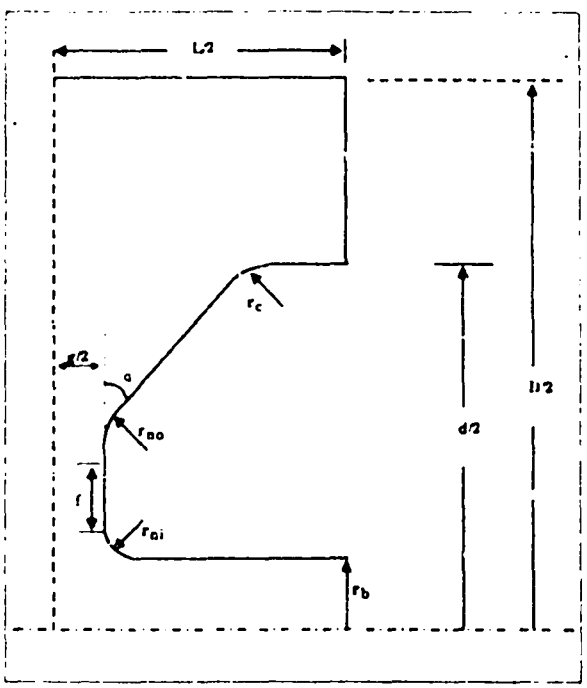

Fig. 1. Schematic cross-section of a drift tube. L: cell length, D: tank diam., d: drift-tube diam., r_b: bore radius, g: gap length, f: flat face length, r_{ni}: inner nose radius, r_{no}: outer nose radius, and r_c: corner radius, and α: face angle.

Permanent Magnet Quadrupoles (PMQs)

Typical shapes for PMQs, to be made out of Sm_2Co_{17}, are shown in Fig. 2. The pertinent parameters are given in Table 4. Data for the variation[5] of the magnetic field gradient along the axis of a real (soft edge) quadrupole are used as input to TRACE3D[6] to calculate the beam phase advance, including overlapping magnetic fields and rf defocusing. The quadrupole gradients must be varied to maintain $\sigma_{0t} \approx 80°$ as the energy goes up from 2.5 MeV to 70 MeV. The variation must be smooth to prevent beam mismatch. The DTL transverse and longitudinal tune depressions σ/σ_0 are 0.75 and 0.61, where σ_0 is the phase advance per focussing period at 25 mA. In between the tanks there is a 3βλ drift space. In order to maintain a smooth variation in longitudinal beam size through this 3βλ drift space the tank exit rf-gaps and

Table 2
Drift Tube Parameters

	Tank 1	Tank 2 & 3	Tank 4
L (cm)	5.1-12.2	12.2-22.4	22.4-25.6
D (cm)	44.0	42.0	42.0
g (cm)	1.2-4.6	2.6-8.2	8.1-10.2
d (cm)	14.0	8.0	8.4
r_c (cm)	1.0	1.0	1.0
r_{no} (cm)	1.0	0.75	0.75
r_{ni} (cm)	0.50	0.50	0.50
r_b (cm)	1.10	0.9	0.9
α (deg)	11.0	15.0	18.0
f (cm)	0.2	0.2	0.1

Table 3
DTL Design Parameters

[illegible]	[illegible]	[illegible]	[illegible]	[illegible]	[illegible]	[illegible]	[illegible]	[illegible]
1	[illegible]	[illegible]	[illegible]	[illegible]	[illegible]	[illegible]	[illegible]	[illegible]
2	[illegible]	[illegible]	[illegible]	[illegible]	[illegible]	[illegible]	[illegible]	[illegible]
3	[illegible]	[illegible]	[illegible]	[illegible]	[illegible]	[illegible]	[illegible]	[illegible]
4	[illegible]	[illegible]	[illegible]	[illegible]	[illegible]	[illegible]	[illegible]	[illegible]

*Includes 25 mA beam + 1.3 × SUPERFISH + tank endwalls

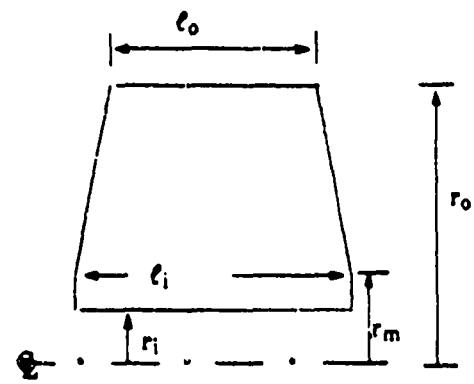

Fig. 2. Schematic cross-section of a PMQ. r_i = inner radius, r_o = outer radius, r_m = mid radius, ℓ_i = inner length, and ℓ_o = outer length

Table 4

FOFODODO MAGNETS

	Tank 1	Tank 2 thru 4
r_1 (cm)	1.30	1.10
r_2 (cm)	6.00	2.50
r_{ap} (cm)	2.00	1.70
ℓ_1 (cm)	2.80	3.10
ℓ_2 (cm)	1.30	2.40
$\langle B_r \rangle$ (KG)*	10.60	10.00
$\int G\,dl$ (KG)	28.7	28.6
Pole Tip Field (KG)	10.97	9.72

* $\langle Br \rangle = (B_r + H_c)/2$

entrance rf-gaps are shifted w.r.t the PMQs to provide additional focusing.

Two mechanically adjustable gradient PMQ's between the tanks provide transverse focusing and also provide 2 knobs to match the beam's transverse Twiss parameters to the next tank. These quadrupoles will also be transversely movable to provide beam steering. Each tank end may also need to be independently movable to provide position adjustment into the next tank's displaced (in the presence of drift tube misalignments) acceptance.

Simulation Results

With the DTL geometry and field configuration discussed above, the linac simulation code PARMILA[7] was run with 1000 macroparticles to examine the beam dynamics at 25 mA. The input phase-space distribution was that of a uniformly filled six-dimensional hyperellipsoid. Figure 3 shows the beam's horizontal and longitudinal dimensions as it traverses the DTL, along with its energy spread. As can be seen, the beam transverse and longitudinal dimension is approximately constant at all points in the accelerator and exhibits the size oscillation typical of an alternating gradient focusing system. The bunch length in rf degrees decreases from $\pm 16°$ to about $\pm 4°$ at the end of linac and energy spread increases to about $\pm$ 150 keV. Emittance (4 tank) results are shown in Table 5. There is very little growth in both ε_t and ε_ℓ with $\sigma_{0t} = 80°$.

Simulation (one tank to 70 MeV) results with $\sigma_{0t} = 60°$, 70°, and 85° (4βλ FOFODODO period) are approximately the same as with $\sigma_{0t} = 80°$. But at $\sigma_{0t} = 90°$ the envelope instability[8] appears resulting in a transverse beam halo and increased emittance growth.

Post Couplers

The DTL fields will be stabilized by resonant post couplers. Excellent stability can be provided by placing post couplers adjacent to every other full drift tube. The post couplers protrude into the tank at

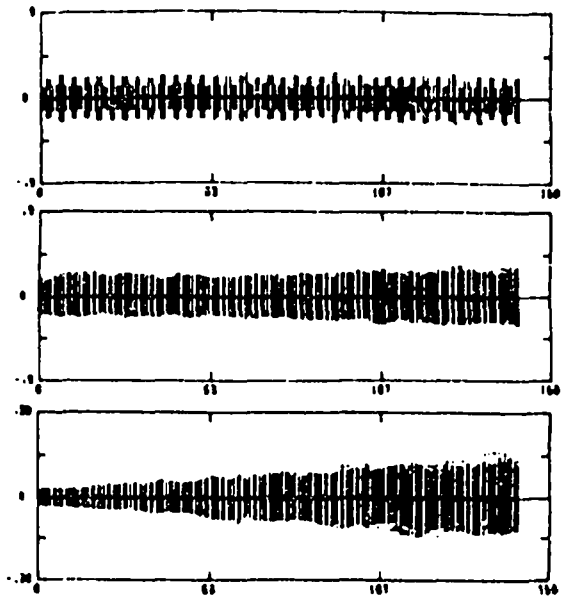

Fig. 3. Simulated DTL beam properties vs cell number.
Top: Horizontal Dimension (cm)
Middle: Bunch Length (cm)
Bottom: Energy Spread (MeV)

Table 5

Normalized rms Emittance in π cm-mrad (Four Tank Simulation)

Focusing Scheme	Current (mA)	2.5MeV Input Beam		70MeV Output Beam		Zero current transverse phase advance per cell (degree)
		ε_t	ε_ℓ	ε_t	ε_ℓ	
fofododo	25	0.0204	0.0210	0.0198	0.0214	20

right angles to the drift-tube stems alternating from side to side. Each tank has an even number of cells to facilitate this placement scheme. In traditional post-coupler-stabilized DTLs, the tank diameter D and the drift-tube diameter d are constrained to a narrow range by the relation[9]

$$0.9\,(\lambda/4) < (D-d)/2 < 1.03\,(\lambda/4)\,, \qquad (4)$$

where λ is the free-space wavelength corresponding to the cavity operating mode frequency.

Tanks 2, 3, and 4 of the DTL were designed with (D-d)/2 within the range given in Eq. 4. Tank 1 has (D-d)/2 = 0.86 (λ/4), which is just below the range in Eq. 4. Because the post couplers in Tank 1 will be shorter than those in the other tanks they are likely to be too high in frequency if the same tip design for the post is used. A slightly larger tab can be used on Tank 1 post couplers to lower the tuning range.

Frequency Shifts and Frequency Errors

The drift-tube stems, post couplers, dynamic tuners, and static tuning bars all tend to raise the cavity frequency. The coupling iris and any holes for pumping have the opposite effect. After the basic geometry has been determined, a small adjustment of the tank radius corrects for net frequency shift to ensure operation at 428 MHz.

We distinguish between these frequency shifts and frequency errors, which result from differences within machining tolerances between the as-built cavity geometry and the design geometry. Two static tuning bars will be provided in each tank to correct for the largest frequency errors expected. More than half of the potential frequency error results from the mechanical tolerance of ±.002 inches on the drift tube length. Other major contributions come from the ±.010-inch tolerance on the tank diameter (~22%) and the ±0.003 inch tolerance on the drift tube diameter (~17%). Both frequency shifts and frequency errors are derived using the Slater perturbation theorem[10].

Longitudinal Field Distribution

The beam-dynamics design provides for a ramped field distribution in Tank 1 and for a constant or "flat" field in Tanks 2, 3, and 4. For graded-β DTLs, the stem frequency effect on individual cells is larger on the low-energy (LE) end of the tank than on the high-energy (HE) end. This continuous detuning of cells along the cavity length produces a naturally ramped longitudinal field distribution, increasing in field strength toward the HE end. A calculation of the stem-produced cell-frequency differences combined with a measurement of the tank's tilt sensitivity gives an estimate of the resulting end-to-end field ramp.

To achieve the design field in each tank, the end cells will be detuned by slightly varying the drift-tube face angle of the end-wall half drift tube from the design face angle used throughout the tank. This procedure helps to simplify low-power tuning of the structure by reducing the level of excitation of the post couplers necessary to stabilize the design field distribution. With a high level of post-coupler excitation, the post couplers' dual functions of stabilization and field trimming tend to interfere with one another. Thus, in Tanks 2, 3, and 4, the stem-produced ramp will be removed by the end-cell detuning procedure, and in Tank 1, the end cells will be detuned to make up the difference between the design ramp and the stem-produced ramp.

Summary

The DTL physics design outlined above provides an excellent scheme for acceleration from 2.5 to 70 MeV with an output-beam of high quality. There is essentially zero growth (in the absence of fabrication errors) in emittance for the design beam, and the particles occupy less than one-third of the bore size for a uniform input beam. The design power requirement for each tank is less than 75% of the available power of 4MW. The design and materials for the drift tubes and magnet structures are all within the scope of available technology. The 4 tank DTL is 23.48 m long. The following considerations, among others, demand careful attention.

Careful measurements on the PMQs must be made in order to insure $75° \leq \sigma_{0t} \leq 80°$ before drift tubes are welded around them. In designing the drift tubes with SUPERFISH, the mesh size used ranged from 0.025 cm to 0.045 cm. Regeneration of cell sizes with a finer mesh will be necessary before fabrication. Future studies are necessary to coordinate "engineering designs, fabrication specifications & control systems" with "beam dynamics performance, tune up and operation requirements". Adequate beam diagnostics between the tanks are vital for transverse matching and rf control during commissioning and routine operation. Although not planned for at this time, it is possible to split a drift tube quadrupole and put a microstrip probe in the middle of a drift tube. When the drift tube minus quadrupole length is large enough for microstrip probes, every 4th cell, for example, could be equipped with a probe to track the beam centroid through a tank. This tracking can serve as an alternate method for measuring the acceptance rather than steering the beam to observe a drop in transmission. Emittance growth and bore used can be significantly minimized by placing the beam in the center of a tank's displaced acceptance.

References

1. T. P. Wangler, "Physics Design of Linear Accelerators for Intense Ion Beams", Proceedings of the Linear Accelerator Conference, Williamsburg, VA, Oct 3-7,1988, Los Alamos National Laboratory document LA-UR-88-3231.
2. K. R. Crandall, "Error studies using Partrace, A new program that combines PARMILA and TRACE 3-D", 1988 Linear Accelerator Conference, Williamsburg, VA., October 3-7, 1988
3. S. Nath, G. Neuschaefer, "SSC DTL Tank 1 Design", Los Alamos National Laboratory memorandum AT-1:90-231.
4. K. Halbach and R. F. Holsinger, "SUPERFISH - A Computer Program for Evaluation of RF Cavities with Cylindrical Symmetry," Los Alamos National Laboratory memorandum AT-6-TM.89-37.
5. G. P. Boicourt, J. L. Merson, "Calculations on Permanent Magnet Quadrupoles with Nonrectangular Cross Sections," Los Alamos National Laboratory document LA-UR 88-3149.
6. K. R. Crandall, "TRACE 3-D Documentation," Los Alamos National Laboratory document LA-11054-MS.
7. G. P.Boicourt, "PARMILA - An Introduction Workshop on Linear Accelerators and Beam Optics Codes," AIP conference Proceedings, San Diego, CA, January 19-21, 1988, Los Alamos National Laboratory document LA-UR-88-1544.
8. L. Smith, L. J. Laslett, I. Hofmann, and I. Haber, "Stability of KV Distributions in Long Periodic Systems," Particle Accelerators 13 (1983) 145.
9. J.H. Billen, "Survey of Drift-Tube Linacs with Post Couplers," Los Alamos National Laboratory memorandum AT-1:84-74.
10. E. L. Ginzton, Microwave Measurements, McGraw-Hill, 1957, Chapter 10.

MOMENT METHODS FOR SIMULATION AND DESIGN*

Walter P. Lysenko
Los Alamos National Laboratory, Los Alamos, NM 87545

ABSTRACT

It is often advantageous to describe a particle beam by the moments of its phase-space distribution. This paper relates original work by Sacherer to presently-used linear design codes like TRACE3D and to some recent results.

INTRODUCTION

Beam behavior is often better described by the evolution of the phase-space distribution rather than by the single-particle motion. Consider a periodic beamline. It transports a matched beam with no change in the distribution. But the usual (single-particle) transfer maps contain a large number of entries (aberration coefficients) related to the complicated motion of the individual particles that obscure the simple nature of the evolution of the matched distribution. One way to describe a beam in terms of the phase-space distribution is by moments of this distribution. Such a description has two important features First, the moments are closely related to observables such as beam positions (first moments) and sizes (second moments). Second, the moment approach is useful in simulations because only a small number of moments is required to describe a beam accurately to high order, a feature especially important in 3-D situations.

In 1971, Sacherer[1] presented his results based on the second-order moment equations, extending previous work on envelope equations by Kapchinsky and Vladimirsky[2]. Linear design codes like TRACE3D[3] make use of these results. Later, Paul Channell[4] proposed using the moment equations to higher order as the basis of a simulation code. Such a code was developed at Los Alamos[5]. Recent work on the moment description has led to more useful design and simulation tools, including a new version of BEDLAM[6]. The new BEDLAM code promises to be an efficient way to do 3-D problems involving space charge, without sacrificing accuracy or consuming huge amounts of computer time computing the 3-D effects.

SACHERER'S RESULTS

The original work of Sacherer[1] on the rms envelope equation was a second-order moment calculation, which corresponds to the effects of first-order (linear) forces. Let us redo his calculation using our present moment notation. For simplicity, we will do this for one degree of freedom. There are three second-order moment equations.

$$\begin{aligned} \frac{d}{dt}\langle x^2\rangle &= \frac{2}{m}\langle xp\rangle \\ \frac{d}{dt}\langle xp\rangle &= \frac{1}{m}\langle p^2\rangle + \langle xF\rangle \\ \frac{d}{dt}\langle p^2\rangle &= 2\langle pF\rangle \end{aligned} \tag{1}$$

We can eliminate $\langle p^2\rangle$ in favor of ϵ_{rms}, the rms emittance, which is the following function of second moments

$$\epsilon_{rms} = \frac{1}{mc}(\langle x^2\rangle\langle p^2\rangle - \langle xp\rangle^2)^{1/2}. \tag{2}$$

Assume the rms emittance is a known function of time. This reduces the number of equations from three to two:

$$\begin{aligned} \frac{d}{dt}\langle x^2\rangle &= \frac{2}{m}\langle xp\rangle \\ \frac{d}{dt}\langle xp\rangle &= \frac{\langle xp\rangle^2}{m\langle x^2\rangle} + \frac{mc^2\epsilon_{rms}^2}{\langle x^2\rangle} + \langle xF\rangle. \end{aligned} \tag{3}$$

If we least-squares fit the force F to a linear function of x, $F = kx$, the force constant k turns out to be $\langle xF\rangle/\langle x^2\rangle$. Thus the last term in the second moment equation above can be written as $k\langle x^2\rangle$. Therefore, the evolution of the second moments depends only on the linear part of the force, determined by least-squares fitting.

Now assume that the force is composed of a linear external focusing force and an arbitrary space-charge force.

$$F = -k_{ext}x + F_{sc} \tag{4}$$

Then the moment equations become

$$\begin{aligned} \frac{d}{dt}\langle x^2\rangle &= \frac{2}{m}\langle xp\rangle \\ \frac{d}{dt}\langle xp\rangle &= \frac{\langle xp\rangle^2}{m\langle x^2\rangle} - k_{ext}\langle x^2\rangle \\ &\quad + \frac{mc^2\epsilon_{rms}^2}{\langle x^2\rangle} + k_{sc}\langle x^2\rangle \end{aligned} \tag{5}$$

where the space-charge force constant is given by

$$k_{sc} = \frac{\langle xF_{sc}\rangle}{\langle x^2\rangle}. \tag{6}$$

Equation 5, which is a system of two first-order equations, is equivalent to the single second-order equation for the rms envelope given in Sacherer's paper. Sacherer has shown that the space-charge force constant k_{sc} is given by

$$k_{sc} = \frac{\text{const.}}{\langle x^2\rangle^{1/2}}, \tag{7}$$

where the constant is almost independent of the shape of the charge distribution. He did this by computing the constant for uniform, parabolic, Gaussian, and hollow ($x^2\times$

*Work supported and funded by the U.S. Department of Defense, Army Strategic Defense Command, under the auspices of the US Department of Energy.

Gaussian) distributions. Thus we can use any convenient model to compute k_{sc}, without regard to the particular charge distribution under consideration.

THE TRACE3D CODE

The equations above assumed the rms emittance to be a known function of time; often we just assume it to be constant. This is a very reasonable assumption for the usual application of Sacherer's results, which is found in design codes like TRACE3D[3]. These codes are used to design beamlines. While emittance growth could in general be substantial, final designs, for which the beam is matched to the beamline, usually will not experience significant emittance growth and thus be accurately described by the Sacherer model.

Sacherer presented results also for three degrees of freedom[1]. For this situation, the rms emittances are not conserved, even for purely linear forces. The moment invariants, described below, are the conserved quantities. TRACE3D handles this situation correctly because it evolves the σ-matrix, which is a description in terms of the 21 second moments that exist for 3 degrees of freedom.

Since the space-charge force constant is nearly independent of the distribution details, we can use any "equivalent" beam to represent the actual beam. Here, "equivalent" means having the same second spatial moments It would be convenient to take some simple equivalent beam for which we can solve the equations of motion and watch the behavior of its second moments, which should be close to those of the beam we are trying to simulate. But there is no beam that we know how to solve. If we assume a beam initially uniform in (x,y,z), then after one time step, it is no longer uniform. There is no such thing as a TRACE3D model distribution. What happens is that, at each time step, the space-charge force constant is computed from the second spatial moments, assuming a uniform charge density in a (x,y,z) ellipsoid. Though we do not assume that an initially uniform beam stays uniform and though we do not know what the distribution is like in detail, because of Sacherer's result we do not care[†].

Given our present knowledge, it appears that the physics of TRACE3D is as good as it can be for a linear-force (second moments) model. Unfortunately, there is no way to directly compare TRACE3D or other similar linear code with a particle simulation.

OTHER MOMENT RESULTS

The rms emittance is a function of second moments that is conserved in systems with linear forces having one degree of freedom. Recently, a whole family of functions of moments were discovered to be invariant for linear motion in systems with one, two, and three degrees of freedom[7, 8, 9, 10]. These moment invariants are conserved for linear motion, even in the presense of coupling. For example, the following is an invariant that is a function of second moments and is valid for two degrees of freedom

$$\begin{aligned} I_{22} &= \langle x^2\rangle\langle p_x^2\rangle - \langle xp_x\rangle^2 \\ &\quad + \langle y^2\rangle\langle p_y^2\rangle - \langle yp_y\rangle^2 \\ &\quad + 2\langle xy\rangle\langle p_xp_y\rangle - 2\langle xp_y\rangle\langle yp_x\rangle \end{aligned} \tag{8}$$

This is the sum of the squares of the rms emittances in the two directions plus a coupling term. There is another independent invariant that is a function of second moments. For three degrees of freedom, there are three invariants. There are also invariants that are functions of higher moments. For example, the following invariant is a quadratic function of fourth moments for one degree of freedom.

$$I_{44} = \langle x^4\rangle\langle p_x^4\rangle - 4\langle x^3p_x\rangle\langle xp_x^3\rangle + 3\langle x^2p_x^2\rangle^2 \tag{9}$$

The moment invariants can be used as diagnostics in simulation codes. This is done by computing the invariants at each time step and observing where they begin to change. Changes indicate the presence of nonlinear effects. Rms emittances are not useful indicators of nonlinear effects in systems with bends, for example, because the emittances can change from from longitudinal-transverse coupling as well. We observe rms emittance growth inside the bend. The emittances are restored to nearly their initial values at the end of the bend, if the bend is achromatic. The source of any unrecoverable emittance growth can be readily seen by examining where the growth of the moment invariant occurred. This technique has been applied to PARMILA simulations for beamlines containing skew bends in which the coordinate rotations introduce rms emittance growth that is not present at the end of the beamline[11]. There exists a simple algorithm for numerically computing the second moment invariants[9], which is useful for such applications.

THE MOMENT CODE BEDLAM

The original BEDLAM code numerically integrated the moment equations, using a collection of initial moments as the initial conditions. This code suffered from an instability problem that prevented the simulation of systems more than a few focusing periods long. We could not use a symplectic integrator to achieve stability because the moment equations cannot be put into the form of Hamilton's equations. An important recent result was the discovery that the moment equations can be put into a Hamiltonian formulation[12] using a generalization of the Poisson-bracket formulation. This work led to the development of Lie-Poisson integrators[13, 14] that preserve the bracket structure exactly, achieving numerical stability analogous

[†]Appendix D of the TRACE3D manual discusses a 6-D distribution with ellipsoidal symmetry that is uniform in all 3-D projections. The rms emittances of this distribution are shown to be one-fifth of the total emittances. No such distribution exists. But this is not a problem as the existence of such a distribution is not used in any way by TRACE3D. All that matters is that $\langle x^2\rangle$ is one-fifth of the maximum x^2 value for an ellipsoidal distribution uniform in (x,y,z). So we must scale all rms coordinates by $\sqrt{5}$ when presenting data to TRACE3D, which is what the manual instructs.

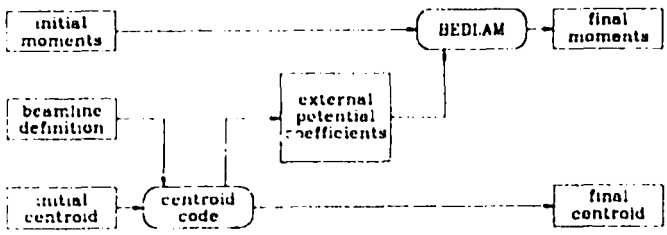

Fig. 1. Data flow at the top level for a BEDLAM simulation. Rectangular boxes indicate data files and boxes with rounded corners indicate processes that transform data.

to that provided by symplectic integration. The new BEDLAM code[6] uses Lie-Poisson integration. (Also, the new code has an improved space-charge model.)

Because of restrictions imposed by the Lie-Poisson integrator, the first moments (beam centroids) are handled separately in the new BEDLAM. Figure 1 shows the data flow for a BEDLAM simulation. We need a separate "centroid code" to compute the first moments and generate the external-force expansion used by the actual BEDLAM code. The centroid code provides the user interface. Various existing particle codes could be modified to be centroid codes for BEDLAM. Since the centroid motion is not affected by space charge (to good approximation) all we need of the centroid code is to trace a single particle, without space charge and evaluate the focusing forces at the centroid particle's location at each time step. BEDLAM will then do the difficult job of determining the high-order motion in the presence of 3-D space charge.

DISCUSSION

The moment approach is useful because moments are closely related to observable quantities and also simply because it deals with the distribution rather than the single-particle motion. Linear design codes are based on the moment work of Sacherer. New results are the discovery of moment invariants and the development of Lie-Poisson integrators. High-order moment codes are expected to provide accurate 3-D space-charge simulations. Furthermore, the efficiency of the moment method may mean we can have high-order design codes, using optimizers.

The new BEDLAM code is almost ready for testing on real problems. We will soon know if the promises of the new approach will be realized. There is work now in progress that promises even more improvements. Alternate Lie-Poisson integrators can handle more general Hamiltonians. A new scheme being investigated by P.J. Channell and J.C. Scovel should be able to handle the first moments directly in the moment code. Improved moment simulations could use moment invariants as the dynamical variables, thus factoring out the linear motion. By solving directly for the nonlinear effects, we should be able to improve numerical efficiency in a manner that action-angle or amplitude-phase methods do for single-particle motion.

The BEDLAM space-charge model contains nonlinearities to all orders that are truncated to the order appropriate to the order of the moments (linear forces for second-order moment simulations and cubic forces for fourth-order simulations). Therefore, a second-order BEDLAM simulation is not the same as a TRACE3D simulation. BEDLAM in its present form does not use Sacherer's idea of using least-squares fits to get the forces[4]. Testing of BEDLAM will quantify how useful Sacherer's idea really is. The high-order analog of this scheme would be (for fourth-order BEDLAM) to do a least-squares fit to fit the space-charge forces to a cubic polynomial. Some related work has already been done[15]. One question to answer is: How much improvement would the least-squares fit bring? And can we do better simply by running BEDLAM to a higher order?

REFERENCES

1. F. J. Sacherer, "RMS Envelope Equations with Space Charge," IEEE Trans. Nucl. Sci., **18** 1105 (1971).
2. I. M. Kapchinsky and V. V. Vladimirsky, " Proc. Int. Conf. on High-Energy Accelerators and Instrumentation," CERN 1959, 274.
3. K. R. Crandall, TRACE 3-D Documentation, Los Alamos National Laboratory report LA-11054-MS (August 1987).
4. P. J. Channell, "The Moment Approach to Charged Particle Beam Dynamics," IEEE Trans. Nucl. Sci., **30** 2607 (1983).
5. P. J. Channell, L. M. Healy, and W. P. Lysenko, "The Moment Code BEDLAM," IEEE Trans. Nucl. Sci., **32** 2565 (1985).
6. W. P. Lysenko and P. J. Channell, "New BEDLAM," Proceedings of the Conference on Computer Codes and the Linear Accelerator Community," Los Alamos, January 22–25, 1990 (to be published).
7. W. P. Lysenko and M. S. Overley, "Moment Invariants for Particle Beams," *Linear Accelerator and Beam Optics Codes, AIP Conference Proceeding 177*, ed. C. R. Eminhizer (American Institute of Physics, NY, 1988), 323.
8. A. J. Dragt, R. L. Gluckstern, F. Neri, and G. Rangarajan, "Theory of Emittance Invariants," *Frontiers of Particle Beams: Observation, Diagnosis, and Correction*, Proceedings, Anacapri, Isola di Capri, Italy, 1988, Lecture Notes in Physics 343, edited by M. Month and S. Turner (Springer-Verlag, Berlin, 1989), pp. 94.
9. [illegible] Rangarajan, "Kinematic Moment Invariants [illegible] Hamiltonian Systems," Phys. Rev. Letters [illegible] (1990).
10. D. D. Holm, W. P. Lysenko, and J. C. Scovel, "Moment Invariants for the Vlasov Equation," J. Math. Phys. **31** 1610 (1990).
11. C. C. Paulson, private communication (1990).
12. D. Holm, "Lie-Poisson Formulation of the Dynamics of Moments," unpublished (1988).
13. Z. Ge and J. Marsden, "Lie-Poisson Hamilton-Jacobi Theory and Lie-Poisson Integrators," Phys. Letters A, **133**:3 134 (1988).
14. P. J. Channell and J. C. Scovel, "Integrators for Lie-Poisson Dynamical Systems," Letters in Mathematical Physics (to be published).
15. W. P. Lysenko and H. Wollnik, "Representing Space-Charge Fields by Polynomials," Los Alamos National Laboratory report AT-3:TN-89-3 (January 1989).

[4] In TRACE3D, the space-charge model (uniformly charged ellipsoid) corresponds to linear forces so the least-squares fit is the same as taking the linear part. In BEDLAM, the situation is not so simple.

EMITTANCE GROWTH IN A MAGNETIC TRANSFER LINE CAUSED BY THE VARIATION OF BEAM NEUTRALIZATION*

T. Weis, J. Wiegand, R. Dölling, J. Pozimski, H. Klein
Institut für Angewandte Physik der Johann Wolfgang Goethe Universität
Postfach 111932, D-6000 Frankfurt am Main, FRG
I. Hofmann
GSI Darmstadt, Postfach 110541, D-6100 Darmstadt, FRG

Abstract

A beam transfer line has been set up to investigate the influence of varying space charge neutralization on transverse beam emittance. The system consists of a plasma beam ion source with triode extraction system (10 keV, He^+, 3 mA) followed by a solenoidal magnetic lens. The beam emittance could be measured in front and behind the magnetic lens. Using a series of independently biased cylindrical electrodes we were able to vary the beam space charge potential at different locations in the beam line. The total decompensation of the beam e. g. results in an emittance growth by at least a factor of two. The experimental results will be summarized and a comparison with numerical simulation and emittance growth theory will be given.

Introduction

Emittance degradation and particle losses in the low energy part of an accelerator system is a crucial point. Since the major emittance growth occurs in the accelerator injection system special attention is strongly recommended to keep the loss of beam quality small[1]. The rms emittance (for definition see below) is highly affected by all kinds of nonlinearities of applied external fields and self fields of the beam[2]. If we stick to the LEBT section a careful design of the LEBT elements and probably the use of only a fraction of the available aperture is requested. A source of transverse rms emittance increase due to beam self fields has been clearly identified[3,4]. A space charge density distribution which is not homogeneous necessarily produces a nonlinear space charge field causing the charge density to redistribute towards a more or less constant density profile, thus converting nonlinear field energy into transverse kinetic energy.

Charge density redistribution in partly space charge compensated beams means rearrangement of both ions and trapped electrons (for positive ion beams) to give a linear internal self field. The electron velocity distribution is heated by ion - electron collisions[5]. Therefore the electrons are not cold enough to be exactly pinned to the ion distribution easily causing "broader" distributions compared to the ion density distribution.

The rearrangement of ions under space charge compensation does not necessarily end up in a homogeneous distribution. Moreover the process is not adiabatic, because the creation and loss of electrons is a dynamic process and highly affected by energy exchange between external fields and the beam plasma. The variation of neutralization rate, caused by changing of residual gas pressure or only by varying beam radii is a continuous source for emittance increase. Measurements at GSI with a partly compensated Ar^+ beam indeed have shown significant increase of emittance[6].

Experimental Set Up

The properties of our magnetic transfer line have been reported previously[7]. The system (see fig. 1) contains a modified duoplasmatron ion source with a triode extraction system and a solenoidal lens and is equipped with two emittance measuring devices, two residual gas ion spectrometers (RGI 1, RGI 2) to evaluate the space charge potential depth inside the beam and four cylindrical electrodes (E1-E4). The electrodes can be biased independently to positive or negative potentials and allow for the variation of the degree of neutralization.

We were able to extract more than 3 mA of He^+ at 10 kV extraction voltage, which is equivalent to a beam perveance given by a 50 keV proton beam of 65 mA. The residual gas pressure at source operation was $2 \cdot 10^{-5}$ mbar.

Unfortunately we were not able to obtain full beam transmission throughout the system. After the insertion of a collimator in front of the diagnosis box, a 100% transmission of a 1.5 mA beam has been reached.

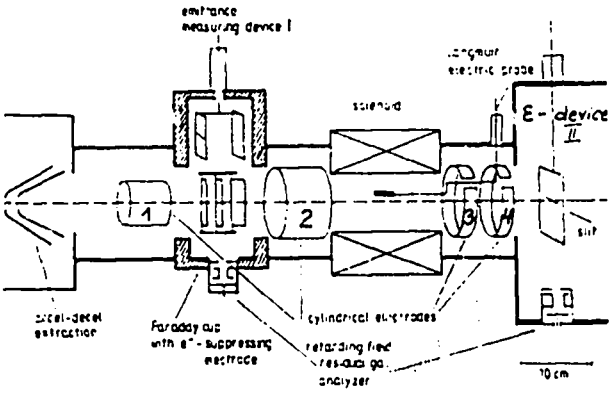

Fig. 1: Schematic layout of the experimental set up

Experimental Results

The evaluation of the beam emittance right after the collimator by inspection of the phase space pattern turned out to be difficult. The emittance is highly affected by some tens percent of neutral particles still present in the beam. Since most of these atoms have been neutralized in the region of high pressure in the first part of the extraction system, a few of them have slightly greater divergence angles compared to the beam ions, thus enlarging the measured phase space area behind the collimator. Moreover the distance between slit and grid of the emittance measuring device I allow only a few wires of the grid to be hit by the beam, leading to a reduced resolution of the system. Measurements of the ion source emittance with the large device II state that the normalized 90% rms emittance ($4 \cdot \sqrt{\langle x^2 \rangle \langle x'^2 \rangle - \langle xx' \rangle^2}$) is 0.35 $\pi \cdot$mm$\cdot$mrad. A reduction of the emittance pattern due to the geometry of the collimator gives a normalized emittance $\varepsilon_{n,rms}$(90%) of appr. 0.16 $\pi \cdot$mm$\cdot$mrad and 42 mrad divergence half angle.

The degree of compensation has been evaluated using the spectrometer RGI 1, giving 84% in the neutralized case, corresponding to 3.3 V potential depth in the beam (fig. 2). Roughly 80 V are necessary to decompensate the beam with

*Work supported by BMFT under contract no. 06 OF 186I

electrode E 1 (20 V total potential depth)[7]. The theoretical value for a beam with homogeneous density and 1.5 mA can be calculated to 19.4 V. This indicates that the ion beam density behind the collimator is almost constant.

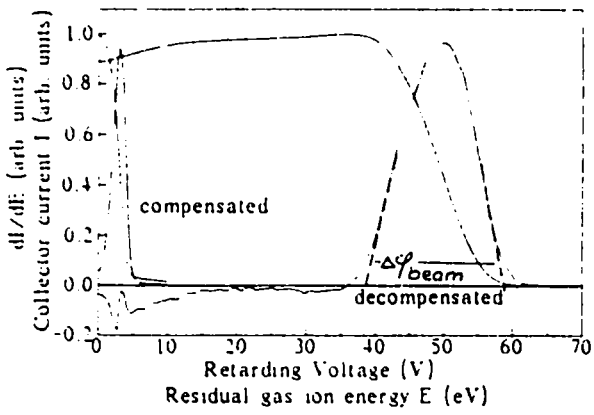

Fig. 2: Measured integral and differential residual gas ion currents versus retarding voltage V and ion energy E for the compensated and decompensated beam (1.5 mA, He^+, 10 keV)

The emittance and orientation of the beam has been measured behind the magnetic lens for different focusing strengths under space charge neutralized conditions. As an example fig. 3 shows the obtained transverse emittance pattern. The observed emittances for different lens strengths showed only slight deviations. Numerical enveloppe calculations gave a good agreement with the experimental results only, if a highly compensated beam is assumed[7].

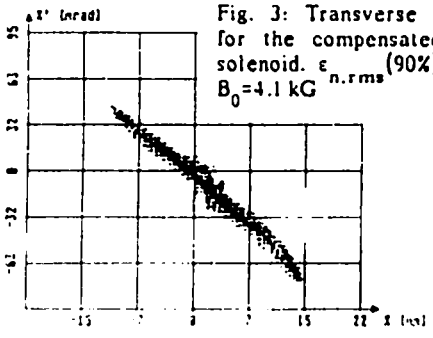

Fig. 3: Transverse emittance pattern for the compensated beam behind the solenoid. $\varepsilon_{n,rms}(90\%) = 0.18\ \pi \cdot mm \cdot mrad$, $B_0 = 4.1$ kG

[illegible] growth has been observed in the case of a partially and totally decompensated beam (see fig. 4 e g) Positive as well as negative voltages have been applied to the electrodes E 1-E 4 in this case. Fig. 5 shows a linear increase of the emittance ratio $\varepsilon_{final}/\varepsilon_{initial}$ (90% values) with the applied positive voltage. Here $\varepsilon_{initial}$ corresponds to the emittance for neutralized transport. The slope levels off at appr. 40 V electrode bias (maximum potential depth between beam axis and outer wall) and stays constant for increasing voltage. Calculations have shown that the electric fields of the electrodes have negligable influence on the particle trajectories, thus acting only via the decompensating process. Even high negative voltage bias showed increasing emittance, due to the fact that only a displacement of compensating electrons in and near the electrodes takes place. A slight reduction of the emittance as well as a reduction of small aberrations near the beam axis (see fig. 3) has been observed for small negative voltage bias. Enhanced trapping of electrons inside the magnetic lens together with a probably more linear space charge field could be an explanation.

Measurements with the spectrometers RGI 1 and 2 showed, that the degree of compensation in front of the solenoid is unchanged if electrode E 3 is set to 150 V and vice versa, indicating that the beam is still neutralized in the lens region.

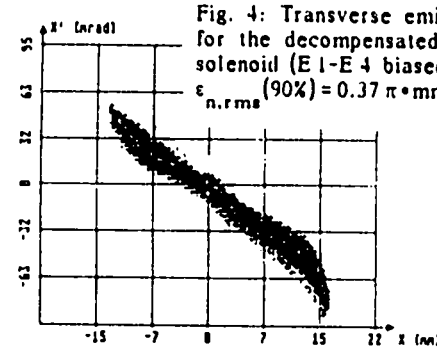

Fig. 4: Transverse emittance pattern for the decompensated beam behind the solenoid (E 1-E 4 biased to 150V). $B_0 = 4.1$ kG $\varepsilon_{n,rms}(90\%) = 0.37\ \pi \cdot mm \cdot mrad$

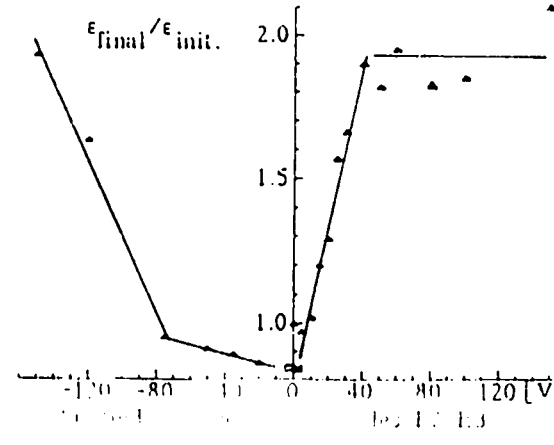

[illegible] emittance versus [illegible] plane [illegible]

Numerical and Theoretical Studies

As stated earlier in this paper emittance increase is caused by the nonlinearities of external and internal self fields. Therefore the nonlinearity of the acting space charge forces as well as existing sperical aberrations of the solenoid has to be taken into account to explain the observed results.

Measurements at the two-gap iron capsulated lens with 80 mm aperture diameter have been carried out with a pencil beam to evaluate the aberration properties[8]. The existing GSI-version of the particle code PARMILA TRANSPORT (Parmtra) has been extended to allow for the correct particle transformation in the solenoidal lens including spherical aberrations.

Numerical calculations with the code using peaked initial density distributions show emittance increase due to density redistribution under decompensated conditions (aberrations in the lens are neglected) and a drop of the emittance behind the lens, a result stated earlier by R. J. Noble[9].

Calculations with a constant initial density profile, as it is the case in our experiment, and different degrees of

compensation gave totally inconsistent results compared to the experiment. In these calculations the reduction of the acting space charge is considered only by the variation of the ion current in the space charge routine of the code.

As mentioned earlier even a constant ion density profile does not necessarily mean that the acting space charge forces are linear under partly neutralized conditions. For a thermal velocity distribution of compensating electrons, Holmes[5] has shown that a Gaussian density distribution of ions and electrons is a selfconsistent solution of the beam plasma, the electron distribution having a more "narrow" shape than the ion distribution:

$$n_i(r) = n_{i0} \cdot e^{-r^2/2\langle r^2\rangle}; \quad n_e(r) = n_{e0} \cdot e^{-1.33\, r^2/2\langle r^2\rangle}. \qquad \text{(1a,b)}$$

Here n_i, n_{i0}, n_e, n_{e0} are the density of ions and electrons as a function of the distance r from the beam axis and the values at the beam center respectively. $\langle r^2\rangle$ denotes the second moment of the ion distribution. For operating residual gas pressures lower than $5 \cdot 10^{-5}$ mbar the influence of the residual gas ions can be neglected and n_{i0} equals n_{e0}. Experiments carried out at Culham Laboratory were in good agreement with the theoretical assumptions[5].

Assumed that the consideration of a thermal electron velocity distribution is still valid in the case of a beam with constant density profile, the selfconsisting space charge potential can easily be derived by numerical methods from the Poisson equation including the Boltzmann distribution of thermal electrons (fig. 6). The electron temperature kT has been chosen to 4.2 eV. The resulting potential depth in the beam comes out to be 5 V, which is in the order of our experimental value of 3.3 V. According to equation (1b) the Gaussian density profile of the electrons is also shown in fig. 6, indicating that this solution is a good approximation also in the case of a beam with homogeneous density.

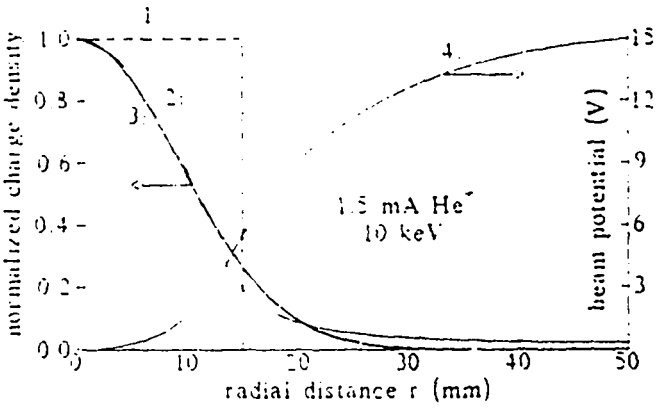

Fig. 6: Calculated normalized charge densities for the ions (line 1), the electrons (line 2 (calculated) and 3 (Gaussian shape)) and calculated beam potential (line 4) versus the radial distance r from the axis. For explanation see text.

The generation of a Gaussian shaped distribution of background electrons have been installed in the Parmtra code. The adaption to the varying beam radii and ion beam density profiles is done via the second moment $\langle r^2\rangle$ of the ion distribution equivalent to eq. (1b).

The numerical results obtained for various degrees of compensation explain qualitatively as well as quantitatively the experimental results obtained from experiment (see fig. 7a,b) and indicate that the more or less estimated input emittance of $\varepsilon_{n,rms}(90\%) = 0.16\ \pi \cdot$mm$\cdot$mrad is quite right.

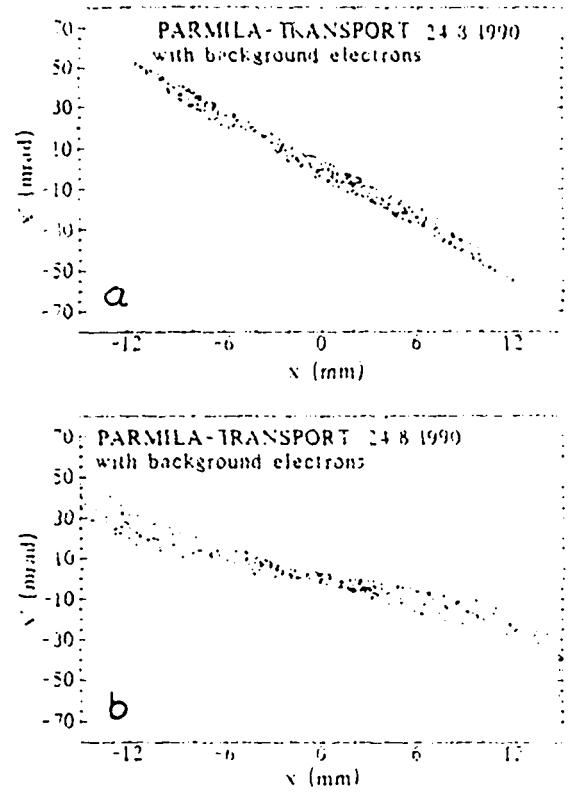

Fig. 7: Numerically derived emittance patterns for the compensated (a) and decompensated (b) beam according to fig. 3,4. $\varepsilon_{n,rms}(90\%)$ is 0.175 (a) and 0.350 $\pi \cdot$mm$\cdot$mrad (b).

The numerical derived evolution of the rms emittance along the beam path shows a slight increase during the initial drift, an enhanced increase in the lens due to the lens aberrations followed by a decrease of the emittance behind the lens.

Summary

We have shown that space charge neutralization is necessary to keep emittance degradation in a system with large lens aberrations small. This is in this case due to the reduced beam radii in the aberrative focusing element. The experimental, theoretical and numerical results however also indicate that after an initial density redistribution the uncompensated beam transport in the absence of aberrative elements is the only way to avoid further emittance degradation. Unfortunately the field nonlinearities in our magnetic transfer line are dominated mainly by the aberrations of the lens. The argumentation that emittance growth in partly compensated beams is due to the finite electron temperature and a Gaussian shape of the electron distribution causing field unlinearities can therefore only be preliminary.

References

1. T. Weis, Proc. 2nd EPAC, Nice (1990) to be published
2. T. Wangler et al., 1988 LINAC, Cebaf Report 89-001 p.211
3. I. Hofmann et al., Part. Acc. 21 (1987) 69
4. T. Wangler et al., IEEE Trans. Nucl. Sci. NS-32 (1985) 2196
5. A.J.T. Holmes, Phys. Rev. A19 (1979) 389
6. J. Klabunde et al., 1986 LINAC, SLAC-Report 303 (1986)
7. T. Weis et al., Proc. 2nd EPAC, Nice (1990) to be published
8. A. Müller-Renz, Institut für Angewandte Physik, Frankfurt University, diploma thesis (1985)
9. R.J. Noble, 1988 LINAC, Cebaf Rep. 89-001 (1989)

BEAM PARAMETERS OPTIMIZATION IN THE INITIAL PART OF LINAC

N.Edamenko, D.Ovsyannikov, A.Zhabko
Leningrad State University, 199034, Leningrad, USSR
V.Kabanov
Moscow Radiotechnical Institute,
USSR Academy of Science, 113519, Moscow, USSR

Recently the mathematical methods of optimization of various devices become of great interest in many branches of engineering.

Charged particles beams parameters optimization problems in linear accelerators are considered in report given. The tasks of focusing and acceleration of particles beams are treated from the mathematical point of view as a search of any extremums of some functionals, which were given in the particles trajectories and were depend on their initial data and controlling functions and parameters. In the capacity of one the parameters of electromagnetic field and beam -shaping channel are considered. A successful functional choice can reduce the optimization time essentially and give rise to new qualitative results.

The description of problem of charged particle control was developed in general case in monographies [1,2]. One can solve various tasks of beam dynamic optimization on the basis of mathematical models of control, in particular, the tasks in high intensity linear accelerators.

Write following equations, describing the evolution of particles beam [1,2]

$$dx/dt=f(t,x,u) \qquad (1)$$

$$\frac{\partial\rho}{\partial t} + \frac{\partial\rho}{\partial x} f(t,x,u) + \rho\,\mathrm{div}_x f(t,x,u) = 0 \qquad (2)$$

with initial conditions

$$x(0) = x_0 \in M0,\ \rho(0,x) = \rho_0(x) \qquad (3)$$

where

$$f(t,x,u) = f_1(t,x,u) + \int_m f_2(t,x,\theta)\,\rho(t,\theta)\,d\theta,$$

$t \in [0,T]$ - time, x - n-dimensional vector, describing particle position in phase space; $u=u(t,x)$ - r-dimentional vector-function of control to be choose in the procedure of optimization; $\rho=\rho(t,x)$ - particles distribution density in phase space at the moment t; f_1 - n-dimensional vector-function defined by external electromagnetic fields; f_2 - n-dimentional function modeling particle interaction, in particular, on the basis of computer simulation method [2,3]; M - cross section of beam trajectories originated from initial conditions array $M0 \in R^n$ and appropriated to control $u=u(t,x)$; $\rho_0(x)$ - particles distribution density in phase space at the initial moment.

It should be noted that the solution of system of equations (1)-(2) and initial conditions (3) exists and is single on [0,T] with sufficiently common suppositions on vector functions f1 and f2.

Introduce for equation (1) functional describing charged particles beam dynamics:

$$I(u)=\int_0^T\int_m \Omega(t,x_t,\rho(t,x_t))\,dx_t\,dt + \int_m g(x_t,\rho(T,x_t))\,dx_t \qquad (4)$$

Where Ω and g - some nonnegative functions. The goal of optimization is defined by choice of these functions.

In monography [2] were developed in detail mathematical methods of optimization on the basis of variation of functional (4).

In report presented was solved the problem of optimization of H+ and n- dynamic in the buncher of a linac. The buncher consists of accelerating gaps, solenoids and quadrupole lenses. The parameters of these elements of buncher should be optimized.

The dialoque computer program OPUS realized on IBM PC. The optimization of longitudinal motion is fulfilled by means of choice of functional providing maximum capture efficiency into separatrix. The optimization of transverse motion is connected with functional from ellipse in phase space provided that conditions of longitudinal motion were carried out.

References

1.D.Ovsyannikov. Mathematical methods of beams control. Leningrad, 1980.

2.D.Ovsyannikov. Modeling and optimization of charged particles beams dynamic. Leningrad, 1990.

3.V.Kabanov. Beam dynamic with Coulomb interaction. In: Ion linear accelerators. V.1 (Ed. by Murin). Moscow, 1973.

FIRST OPERATION OF THE 850 MEV C. W. ELECTRON ACCELERATOR "MAMI"*)

H. Herminghaus, H.H. Braun**), H. Euteneuer, F. Fiedler, A. Gauch**), G. Gruber**), A. Hager**), R. Herr, L. Jaekel**), P. Jennewein, K.H. Kaiser, R. Klein**), H.-J Kreidel, U. Ludwig-Mertin, K.W. Nilles, G. Patzner, H. Schöler, A. Streun, G. Stephan, T. Weis**), P. Zinnecker

Institut für Kernphysik der J.-Gutenberg-Universität
Becherweg 45, D-6500 Mainz, Germany

Abstract

The three stage normal conducting c.w. race track microtron "MAMI" (MAinz MIcrotron) of Mainz University has recently been operated for the first time at full energy. The parameters of the machine are briefly communicated. A preliminary report on its performance is given.

Introduction

At Mainz University a c.w. electron accelerator with output energy close to 1 GeV was demanded to allow coincidence experiments with electrons and photons in nuclear and medium energy physics. A maximum beam intensity of about 100 μA was considered to be ample for the experimental program envisaged. For the sake of ruggedness and reliability and to allow inhouse manufacture we decided to avoid the use of superconducting structure. Following these lines the concept of a cascade of three race track microtrons ("RTM") using normal conducting structure in c.w. operation was developed [1]. The first stage (14 MeV), using a van de Graaff at 2.1 MeV as an injector, was set into operation in 1979 [2], the second followed in 1983 [3]. This two stage version, called "MAMI A", was operated routinely for user experiments until fall of 1987 with output energies variable between 14 and 187 MeV [4], [5].

Setup of MAMI

The final setup of MAMI - sometimes called "MAMI B" - was carried out starting in 1986 in a new accelerator building on the site of the institute [6]. Its main parameters are compiled in Tab. 1. A plan view of the machine is shown in Fig. 1. In order to allow operation with polarized electrons

TABLE 1
Main Parameters of MAMI

General				
Stage No.		I	II	III
Input energy	MeV	3.46	14.39	179.8
Output energy	MeV	14.39	179.8	855
No. of recirculations		18	51	90
Magnet system				
Magnet distance	m	1.67	5.60	12.86
Flux density	T	0.1028	0.5553	1.2842
Max. orbit diam.	m	0.97	2.17	4.43
Weight per magn.	to	1.3	43	450
Gap width	cm	6	7	10
R.F. System				
No. of klystrons		1	2	5
Linac length (el.)	m	0.80	3.55	8.87
R.F. power dissip.	kW	8	48	103
R.F. beam power	kW	1.1	17	68
Energy gain	MeV	0.6	3.24	7.5
Beam (100 μA)				
Energy width	keV	±9	±18	±60
Emittance vert.	μm	$< .17\,\pi$	$< .014\,\pi$	$\leq .04\,\pi$
Emittance hori.	μm	$< .17\,\pi$	$< .014\,\pi$	$\leq .14\,\pi$
Injection:	100 keV gun and three linac sections, fed by another klystron			
Extraction:	from each even numbered return path of RTM 3, i.e. in steps of 15 MeV			
R.F.-structure:	on-axis-coupled biperiodic standing wave, vacuum brazed OFHC copper			
Klystrons:	Thomson TH 2075 50 kW c.w. max., 2449.6 MHz			

Fig. 1: Plan view of MAMI in the new accelerator halls.

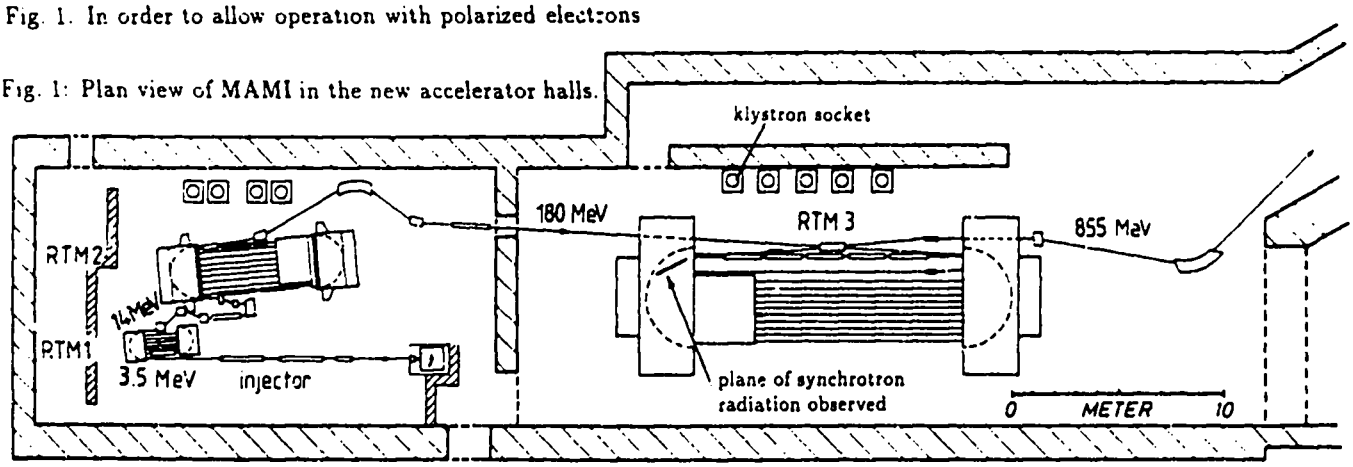

*) Work supported by HBFG and DFG, SFB 201

**) Affiliation changed meanwhile

[7] a 3.5 MeV linac is used now as an injector for the first microtron [8]. The first and second microtron are modified versions of the ones used with MAMI A. This new 180 MeV setup has been operated several times starting in June 1990, after considerable operational experience had been obtained earlier with the injector linac and the new 14 MeV stage. The general experience is that the new setup shows considerably better stability and reproducibility as compared to MAMI A. Most of this improvement is due to the new injector linac, whose performance is much better than that of the previously used van de Graaff. Further contributions are due to improved designs of several components like steerers, quadrupoles and monitoring devices, and a better understanding of the machine by use of computer simulations and computer aids in operation.

Yet further improvement is desireable if the new role of the 180 MeV assembly as a mere injector of the third stage is taken into account. There is some evidence that some of the reused components of the interface between stages one and two did not keep up with the new standards.

In the third stage, the beam has to be recirculated 90 times over a magnet distance of almost 13 meters and through a 12 mm diameter orifice (defined by a protection collimator in front of the linac). Therefore, we felt that in this stage careful homogenisation and adjustment of the reversing magnets would be particularly helpful to ensure sufficient operation comfort. Therefore, the method of field homogenisation by pole face correcting coils already used with the magnets of stages one and two was worked out further in several respects [9]. Also, great care was taken in calibration and presetting of the r.f. in the five accelerating sections.

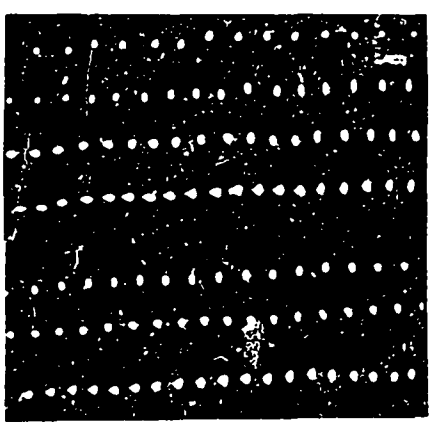

Fig. 2
Synchrotron radiation of the orbits in the left magnet of RTM3 as indicated in Fig. 1. Orbit number increasing from upper left to lower right.

On 10th of August 1990, when at the first time all parameters were set to their calibrated nominal values, the beam could be guided very easily within about half an hour through the 90 recirculations. During the procedure the beam was often ahead of the operator by up to about 10 turns. In fact, quite unexpectedly the first operation of the third stage was quicker and easier than that of the previous smaller ones and we assign this to the special precautions mentioned. Fig. 2 shows the synchrotron radiation of the recirculated beams, displayed in seven partially overlapping lines on two TV monitors. The size of the beam spots, as far as can be seen by a preliminary evaluation, is compatible with expectation. It is seen from the photograph that in this first, "historical" run there was still some mismatch, particularly in the vertical plane. Yet the beam transmission was 100 % as far as could be seen from the monitoring system. Beam intensity at this first run was below 1 μA c.w. However, the intensity during the 1.0 nsec marking pulses for beam monitoring [1] was about 100 μA. This demonstrates that beam intensity is at least not limited by emittance.

In a later run, the c.w. beam intensity was raised without any readjustment up to 12 μA by just increasing the gun current. For safety reasons we refrained from a further increase because part of the monitoring and beam interlock system is still in a preliminary state. Anyway, the excellent beam transmission was confirmed by the low radiation level after this run.

Acknowledgements

The list of authors of this paper contains only the scientific staff involved. However, undoubtedly the realization of MAMI could not have been carried out without the commitment of the entire technical staff of the institute. We would like to especially commend G. Meyer, who deserved well of the mechanical engineering of MAMI B, H. Mussel for his conscientious work all over the r.f. system and R. Böhm whose expert know-how contributed much to the good performance of the MAMI electronics.

References

1. H. Herminghaus et al., "The Design of a Cascaded 850 MeV Normal Conducting c.w. Race Track Microtron", Nucl. Instr. and Meth. 138 (1976) p. 1
2. H. Aufhaus et al., "Operating Experience with MAMI", Proc. of the 1981 Linear Acc. Conf., Santa Fe, N.M., LA-9234-c, p. 22
3. H. Herminghaus et al., "Status Report on the Normal Conducting c.w. Race Track Microtron Cascade "MAMI"", IEEE Transactions on Nuclear Sience, Vol. NS-30, No. 4, August 1983, p. 3274
4. K. H. Kaiser et al., "Four Years of Operation of the 180 MeV c.w. Electron Accelerator MAMI A", Proc. of the 1988 European Particle Acc. Conf. Rome, 1988, Vol. 1, p. 371
5. D. Drechsel and Th. Walcher edit., "Physics with MAMI A", Institut für Kernphysik Univ. Mainz, Internal Report May 1988
6. H. Herminghaus, "The Mainz Microtron - Operating experience and Upgrade Progress", Proc. of the 1988 Linear Acc. Conf., Williamsburg, VA, p. 247
7. W. Hartmann et al., "Source of Polarized Electrons", Proc. of the European Particle Acc. Conf., Rome, 1988, p. 1335
8. H. Euteneuer et al., "The Injector Linac for the Mainz Microtron", Proc. of the European Particle Acc. Conf., Rome, 1988, p. 550
9. H. Herminghaus et al., "The Reversing Magnet of the 850 MeV Stage of MAMI", Proc. of the European Particle Acc. Conf., Rome, 1988, p. 1151

Controlling Multi-Bunches by a Fast Phase Switching

F.-J. Decker, R.K. Jobe, N. Merminga, K.A. Thompson

Stanford Linear Accelerator Center, Stanford, California 94309, USA*

Abstract

In linear accelerators with two or more bunches the beam loading of one bunch will influence the energy and energy spread the following bunches. This can be corrected by quickly changing the phase of a travelling wave structure, so that each bunch recieves a slightly different net phase. At the SLAC Linear Collider (SLC) three bunches, two (e^+, e^-) for the high energy collisions and one (e^--scavenger) for producing positrons should sit at different phases, due to their different tasks. The two e^--bunches are extracted from the damping ring at the same cycle time about 50 ns apart. Fast phase switching of the RF to the bunch length compressor in the Ring-To-Linac (RTL) section can produce the necessary advance of the scavenger bunch (about 6° in phase). This allows a low energy spread of this third bunch at the e^+-production region at 2/3 of the linac length, while the other bunches are not influenced. The principles and possible other applications of this fast phase switching as using it for multi-bunches, as well as the experimental layout for the actual RTL compressor are presented.

1 Introduction

In current designs for future linear colliders each RF cycle accelerates several bunches in one pulse train to drop energy costs and to increase the luminosity (Fig. 1). This multi-bunch scheme can be disturbed by longitudinal and transverse wakefields of the high intensity bunches or by different purposes of the bunches, as in the SLC (Fig. 2). Here the two interaction bunches, e^+ and e^-, are followed by a scavenger bunch which produces the positrons for the next cycle at about 2/3 of the linac (Sector 19). At this point the scavenger beam should have a minimum energy spread, while the other two bunches are still decreasing their energy spread.

For the transverse stability of the beams an energy spread is introduced in the beginning of the linac, called BNS-damping or autophasing [1, 2, 3]. At the later part it is decreased so that the energy spread of the bunches is a minimum at the end of the linac. At Sector 19 the beams have about three times the final energy spread. By changing the longitudinal position of only the scavenger bunch by about 6° in phase (1.75 mm) the energy spread can be compensated there. This relative position shift can be either done at the beginning of the linac with a compressor phasing or by a fast phase switching of the RF drive to the linac after the first two bunches have passed through.

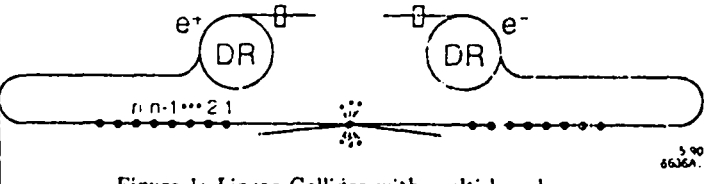

Figure 1: Linear Collider with multi-bunches.

A train of several bunches is extracted from a damping ring (DR) and accelerated. The energy of each bunch should be the same ($E_n = E_{n-1}$) and the energy spread minimized before colliding with the other bunch train.

*Work supported by the Department of Energy, contract DE-AC03-76SF00515.

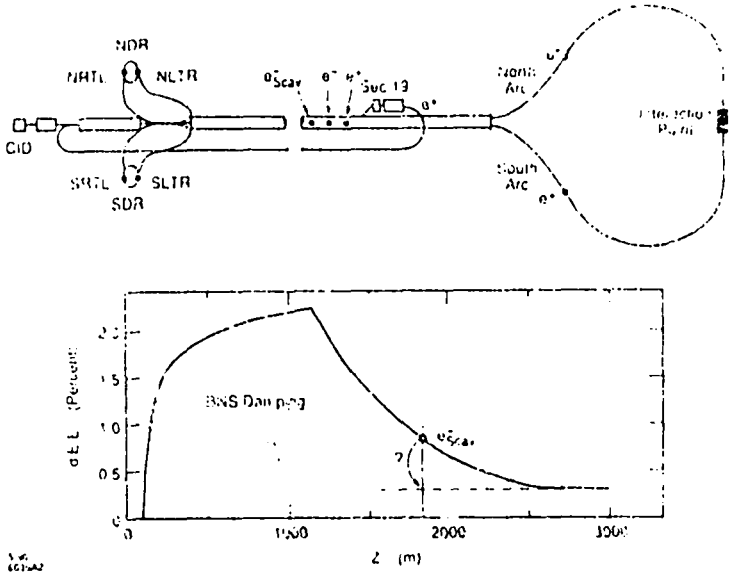

Figure 2: SLC energy profile.

The transverse motion of the particles is stabilized (BNS-damping) by increasing and afterwards decreasing the energy spread within the bunch. But the third bunch (scavenger) would get an intolerable big energy spread at the positron production area, if no fast phase adjustment would be done.

The principle and some details of this fast phase switching are presented first. Then the current set up for the scavenger beam with some experimental data are shown. At the end a possible scenario for a multi-bunch scheme even at the SLC demonstrates how powerful this fast phase switching can be.

2 Fast Phase Switching

A fast phase change introduces a phase gradient in an acceleration structure [4]. The spatially separated bunches can be influenced differently in integrated phase and amplitude.

2.1 Principle

A travelling wave accelerator structure is fed by an RF source which produces a sudden phase change from 0° to 90° (Fig. 3). A bunch of particles just prior to this change will see no difference. It will experience a phase of 0° and amplitude A_1. A second bunch, say the scavenger, arives a time t_b later, which corresponds to the bunch separation. When t_f is the filling time of the whole structure, t_b/t_f of its length is filled with the new phase. (No losses in a constant impedance structure are assumed.) For a 90° phase change the second bunch will see a net phase and amplitude of

$$\varphi_2 = \arctan\left(\frac{t_b}{t_f - t_b}\right), \quad A_2 = A_1 \frac{\sqrt{(t_f - t_b)^2 + t_b^2}}{t_f}$$

For $t_f = 600$ ns and $t_b = 60$ ns this gives $\varphi_2 = 6.3°$ and $A_2 \approx 0.9 A_1$. Figure 3c) shows the phasors of that change. Zero phase is horizontal, 90° is vertical and the length between the time steps

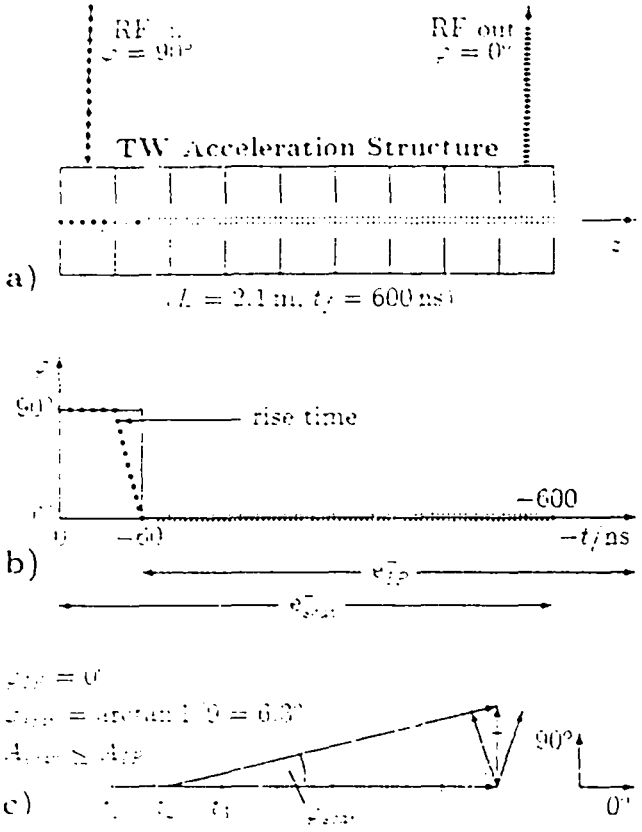

Figure 3: Principle of fast phase switching.

The phase of the RF to the input of a travelling wave structure is changed quickly (a) so a second bunch 60 ns later (b) will see a different net phase of about 6° (c).

corresponds to the amplitude of the averaged seen RF field. By changing the input phase a little bit around 90° the amplitude A_2 can be varied while the phase keeps mainly constant.

In general it is possible to change the phase φ_i and amplitude A_i for a bunch number i by a certain amount by changing the timing and the amount of the phase change.

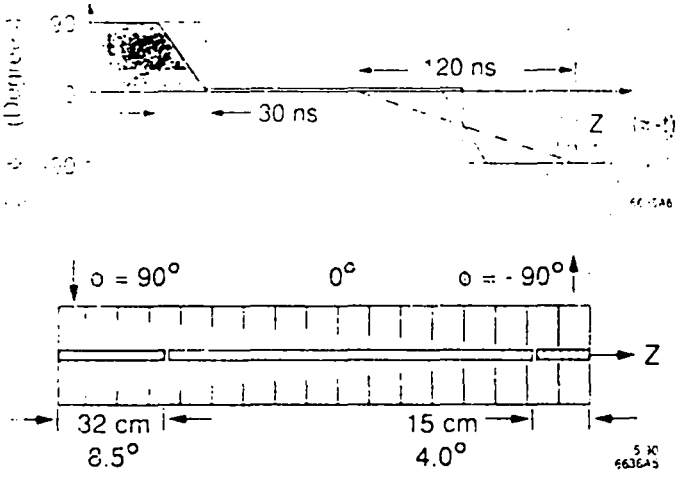

Figure 4: Phase changes in a constant gradient structure.

Due to the different group velocities at the input and output, about 32 cm or 15 cm can be filled with different phases within 60 ns. A finite risetime of the pulse decreases this value.

2.2 Actual RF Set Up

Two phase steps, which act at the input and the output, can provide twice the phase change. In the constant gradient structure of the SLC compressor the higher group velocity at the input rather than at the output changes the possible phase variation in 60 ns to about 8.5° (in) and 4.0° (out), see Fig. 4.

The risetime or transition time from one phase to the other is finite. This and the dispersion within the acceleration structure decreases the amount of a fast phase switching. For the input it is about 25 % less in 60 ns (Fig. 5).

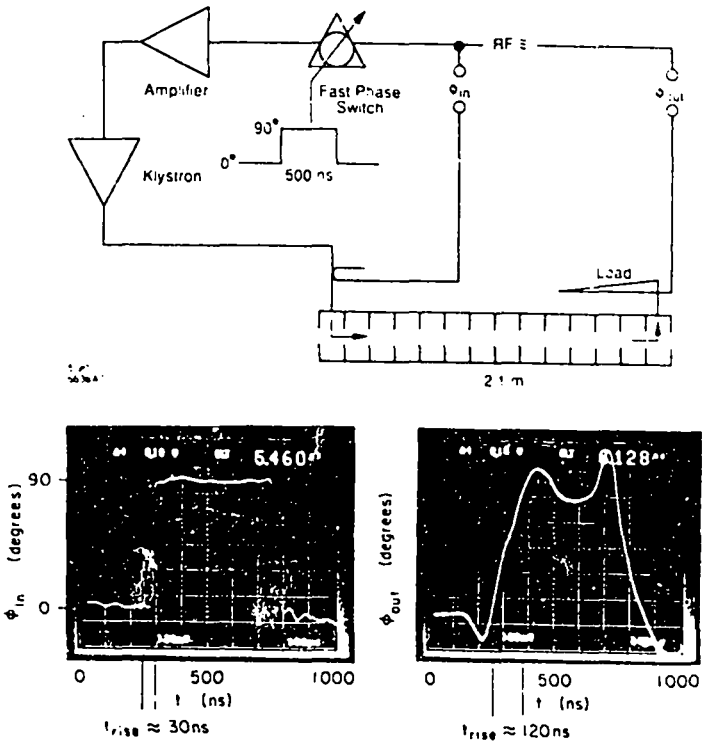

Figure 5: Set up of the fast phase switch.

Between the RF-source and the klystron, which feeds the compressor section, a fast phase switch has been installed. At the input coupler a fast phase risetime (30 ns) has been observed, while at the output the dispersion in the structure has strongly decreased the slope.

3 Experimental Result at the SLC

Figure 6 shows an experimental result with a beam. The bunch phase is normally set to the zero crossing of the compressor RF. A fast phase change of the RF provides a different mean energy of the beam and therefore an offset Δx in the high dispersion region of the RTL. So the second bunch will arrive earlier (or later) in the linac. The measured amount is in good agreement with the expected value of 3/4 of 8.5°. A more detailed discussion is given in [4], which can be summarized in the following way: Controlling the timing and also the amplitude of the RF phase change, changes the effective phase and amplitude for the second bunch in the compressor, which determinds the phase and bunch length in the linac resulting to a certain energy and energy spread at the end.

With the implementation of the fast phase switch the every day operation is simplified by the possible separate adjustment of the energy spread of the scavenger beam.

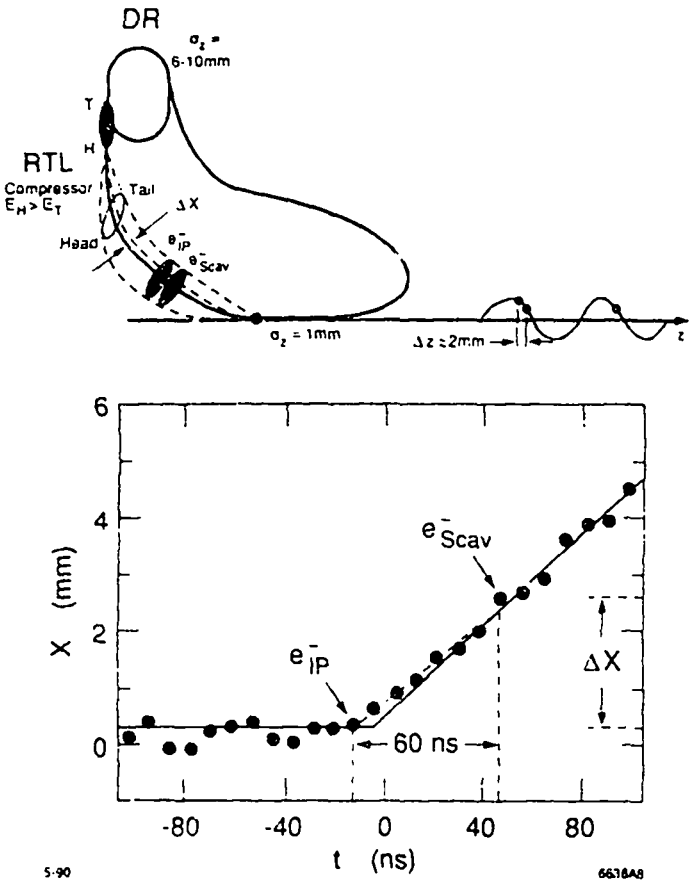

Figure 6: Beam respond to the phase switch.
The long bunches of the damping ring (DR) are compressed in the Ring-To-Linac (RTL) section. A fast phase change provides that the second bunch, about 60 ns later than the first one, is separated up to Δx = 2.2 mm in the RTL, which corresponds to a phase variation of 6.8° or to Δz = 2 mm earlier in the Linac.

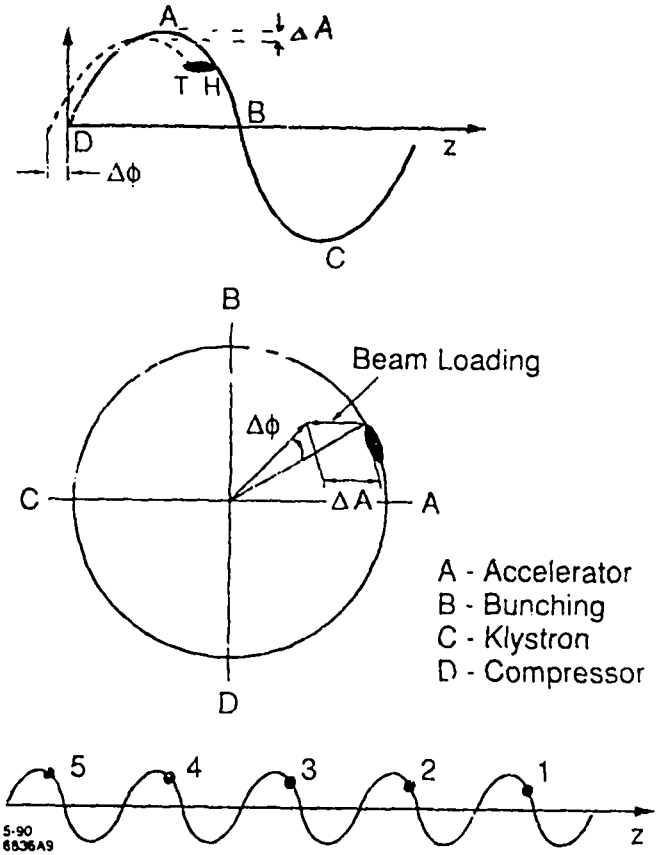

Figure 7: Compensating beam loading by different bunch phases.
In general the beam loading of one bunch introduces an amplitude and phase change (ΔA and $\Delta\phi$) to the next bunch. By putting the bunches to different phases, e.g. bunch 5 later than bunch 4 later . . . than bunch 1, the beam loading can be compensated. Besides a compensating amplitude variation, a fast phase switching helps, especially for the compensation of the $\Delta\phi$ beam loading in a compressor region.

4 Multi-Bunches

In a multi-bunch scheme with high currents the energy of each bunch would be different, if no compensation is used. Changing the amplitude of the RF by partially filling the structure for the first bunch [5], provides a good compensation, especially if the bunch is riding on the crest. Because of BNS-damping or longitudinal wakefield compensation, the beam sits off the crest. So beside the amplitude, a phase change is also necessary. Even a pure phase variation could adjust the invividual energies, if the bunch length from bunch to bunch is varied in an appropriate way (see Fig. 7).

The numerical evaluation of the effect shows [4], that even at the SLC three times five bunches of $5 \cdot 10^{10}$ particles could be controlled by a fast phase switching.

5 Summary

The fast phase switching has become an operational tool at the SLC. By varying the time and phase amount of the phase change the energy and energy spread of a bunch could be controlled. Beside the possibility of a multi-bunch scheme at the SLC, a fast phase switch has to compensate the big phase beam loading in a compressor region of future colliders.

Acknowledgement

We would like to thank K.L. Bane, M. Sands, J.T. Seeman and M. Ross for the inital discussions of the problem, J. Judkins for his personal eagerness during the test set up and the RF- and Electronic group for the final implementation.

References

[1] V. Balakin, A. Novokhatsky, V. Smirnov, *VLEPP: Tranverse Beam Dynamics* , Procedings of the 12th Int. Conf. on High Energy Accelerators, Fermilab, 1983, p. 119.

[2] Karl L. F. Bane, *Wakefield Effects in a Linear Collider*, SLAC-PUB-4169, December 1986.

[3] J.T. Seeman, N. Merminga, *Mutual Compensation of Wakefield and Chromatic Effects of Intense Linac Bunches*, SLAC-PUB-5220, April 1990.

[4] F.-J. Decker, R.K. Jobe, *Phase Gradients in Acceleration Structures*, 2nd European Accelerator Conference, Nice, France, June 12-16, 1990 or SLAC-PUB-5271, May 1990.

[5] R.D. Ruth, *Multi-Bunch Energy Compensation*, Workshop on Physics of Linear Collider, Capri, Italy, 1988.

FORMULAS FOR THE TWISS BEAM PARAMETERS FOR A MATCHED BEAM AT THE ENTRANCE TO A LINAC*

G. R. Swain
Los Alamos National Laboratory, Los Alamos, NM 87545

Abstract

Formulas for a transversely-matched beam are derived in terms of the r-matrix representation of accelerating and focusing elements in the first period of a linac structure. The formulas predict beam parameters close to the values actually used in tuning the LAMPF 805 MHz linac, and give reasonable-looking results in the other cases for which they have been applied.

Introduction

A beam occupying an ellipse in transverse phase-space may be said to be transversely matched into a linac when for a given emittance E, the Twiss parameters α and β at the start of the linac minimize the largest transverse widths of the beam in the first period or first few focusing periods of the linac. This results in a beam which is uniform (except for adiabatic damping) from one focusing period to the next: the width does not breathe in and out at twice the betatron frequency. We have found that we may obtain reasonably matched beams by finding α's and β's that are the same at the start and end of the first focusing period.

Transformation of α's and β's

The equation for the beam ellipse in one of the transverse phase spaces is of the form

$$\gamma x^2 + 2\alpha x x' + \beta x'^2 = E/\pi \,, \tag{1}$$

where x and x' are the position and divergence of a particle on the boundary of the ellipse, E is the emittance, and the Twiss parameters α, β, and γ are normalized such that

$$\beta\gamma - \alpha^2 = 1 \,. \tag{2}$$

The final coordinates x_f and x'_f at the end of a section of beam line may be related to the coordinates at the beginning using the R matrix:

$$\begin{bmatrix} x_f \\ x'_f \end{bmatrix} = \begin{bmatrix} r_{11} & r_{12} \\ r_{21} & r_{22} \end{bmatrix} \cdot \begin{bmatrix} x \\ x' \end{bmatrix} \,. \tag{3}$$

For representing linacs, we need the transformation for the Twiss parameters through the section when the determinant of the R matrix is not unity. Using Eq. (1) and the inverse relation corresponding to Eq. (3), we find[1] the parameters at the end of the section are given in terms of those at the beginning by

$$\begin{bmatrix} \beta_f \\ \alpha_f \\ \gamma_f \end{bmatrix} = T \cdot \begin{bmatrix} \beta \\ \alpha \\ \gamma \end{bmatrix} \,, \tag{4}$$

where

$$T = \frac{1}{d} \begin{bmatrix} r_{11}^2 & -2r_{11}r_{12} & r_{12}^2 \\ -r_{11}r_{21} & r_{11}r_{22}+r_{12}r_{21} & -r_{12}r_{22} \\ r_{21}^2 & -2r_{21}r_{22} & r_{22}^2 \end{bmatrix}$$

and $\quad d = r_{11}r_{22} - r_{12}r_{21} \,.$ (5)

Phase Advance

We may also generalize the concept of phase advance to apply for situations when the determinant of the R matrix is not unity. Any matrix whose determinant is unity may be represented in the form

$$R_1 = \begin{bmatrix} \cos\mu + \alpha\sin\mu & \beta\sin\mu \\ -\gamma\sin\mu & \cos\mu - \alpha\sin\mu \end{bmatrix} \tag{6}$$

for appropriate values of the parameters μ, α, β, and γ. The parameter μ is known as the phase advance. (We will come back to α, β, and γ in the following section.) If we have an R matrix for a focusing period of our structure for which the determinant d is not unity, the matrix

$$R_1 = \frac{1}{\sqrt{d}} \begin{bmatrix} r_{11} & r_{12} \\ r_{21} & r_{22} \end{bmatrix} \tag{7}$$

will have a unity determinant, and we can find μ from

$$\cos\mu = \frac{r_{11} + r_{22}}{2\sqrt{d}} \,. \tag{8}$$

For the types of linac that we have studied, μ increases as the focusing strength of the

---

*Work supported by Los Alamos National Lab. Institutional Supporting Research, under the auspices of the U.S. Department of Energy.

quadrupole doublets increases, and the focusing strength that gives the smallest beam size for a given emittance occurs near $\mu = 85$ degrees. Thus μ may be used as a guide to find the optimum focusing strength.

Formulas for Matched α and β

We take the matched condition to be when the Twiss parameters for the beam ellipse are the same at the exit of the first focusing period of a linac as at the start. We assume we can find a value of μ (with $0 < \mu < \pi$) that satisfies Eq. (8). Then using Eqs. (6) and (7) we may take

$$\beta = \frac{r_{12}}{\sqrt{d}\,\sin\mu}\,, \tag{9}$$

$$\alpha = \frac{r_{11} - r_{22}}{2\sqrt{d}\,\sin\mu}\,, \tag{10}$$

and

$$\gamma = -\frac{r_{21}}{\sqrt{d}\,\sin\mu}\,. \tag{11}$$

(These satisfy the normalization indicated in Eq. (2), and thus only α and β are sufficient to specify a matched beam.) If we substitute the α, β, and γ given above in the right side of Eq. (4), we find $\alpha_f = \alpha$ and $\beta_f = \beta$, and thus Eqs. (9) - (11) give the Twiss parameters for the matched condition.

Application of the Formulas to the LAMPF 805-MHz Linac and a Pilac Design

The horizontal and vertical Twiss parameter values as used for normal operation of LAMPF 805-MHz linac and the values given by Eqs. (9) and (10) are listed in Table I. The calculated values are quite close to the standard ones used in practice, and a plot of the beam widths for the calculated match is practically indistinguishable from such a plot for the standard match.[1]

TABLE I
Standard and Calculated Parameters For The LAMPF 805-MHz Linac

	α_x (-)	β_x (cm/rad)	α_y (-)	β_y (cm/rad)
Std.	0.337	329.	1.240	556.
Calc.	0.402	329.	1.39	573.

The first focusing period of this linac takes protons from 100 to 103.2 MeV kinetic energy, resulting in an R matrix whose determinant has the value d=0.9836.

The preceding example had an R matrix for the first focusing period whose determinant was not far from unity. Next, we look at a case for which this determinant is significantly different from unity: a reference design for a linac for pions (pilac). The first focusing period of this linac uses nine cavities, and takes the pions from 500 to 634.5 MeV kinetic energy, resulting in an R matrix whose determinant has the value d=0.8198. The entire pilac has three focusing periods and takes the pions to 920 MeV. The widths of the beam for calculated values of the Twiss parameters are shown in Fig. 1, and each plane is reasonably matched. (There are nine lines on this plot per focusing period.)

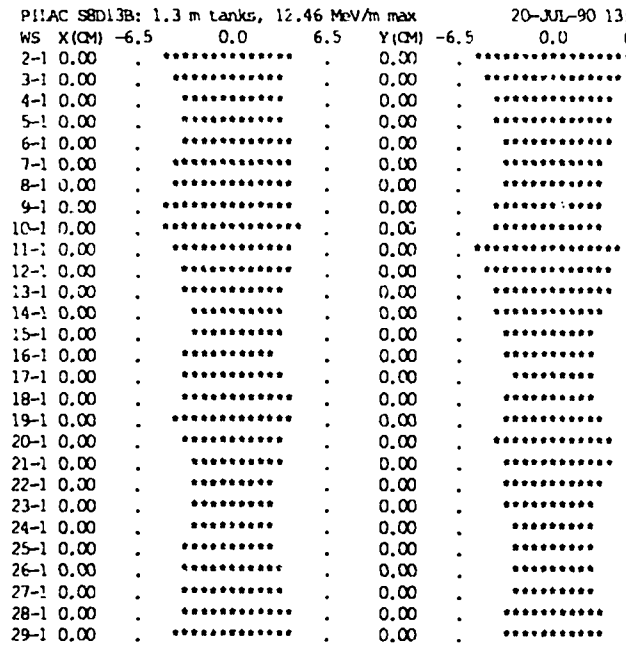

Fig. 1. Horizontal and vertical beam widths for a Pilac reference design, initial α's and β's from matching formulas.

Acknowledgements

The author is indebted to Peter Busch for assistance in the analysis and in running tests, and to Oscar Sander for helpful comments and suggestions.

Reference

1. G. Swain, "Formulas for the Transverse Phase-Space Twiss Beam Parameters for a Matched Beam at the Entrance to a Linac," AHF Tech. Note 90-001, Los Alamos National Laboratory, Los Alamos, NM (Aug. 1990).

SEMI-ANALYTICAL CALCULATION OF ACCELERATING BEAM IN A PHOTO-INJECTOR CAVITY*

Harunori Takeda
Los Alamos National Laboratory, Los Alamos, NM 87545

Abstract

The acceleration of electrons in an injector induces a beam emittance growth. To study the emittance growth in a photo-cathode injector, we model the acceleration process analytically. Then, the analytical model is compared with numerical simulations using the PARMELA[1] code. Although the analytical model cannot represent the correct beam behavior caused by the space charge, we model the normalized emittance in an environment of a magnetic field produced from axial coils as represented by a mechanical angular momentum. We derive analytical relations from a relativistic equation of motion of a particle (envelope equation). Using the envelope equation, we study the emittance growth in the acceleration by a numerical integration.

Equation of Motion

The rf cavities accelerate particles emitted from a ca[illegible]. Representing the equation of motion with the cylindr[illegible] coordinate system (r, θ, z), we interpret particle motion as the beam envelope propagation along the posit[illegible] axis. This assumption is valid only while a cylindr[illegible] symmetric beam maintains its coherence: the arti[illegible] envelope stays on the envelope and the parti[illegible] the beam stays in the beam along the propagation. For a [illegible]ly symmetric beam propagating in an axially symme[illegible] environment, the x emittance and the y emittance a[illegible] and they can be represented as $\pi r_{max} v_{\theta}$, where r_{max} [illegible] v_{θ} are the radius and the transverse velocity, respectiv[illegible] of the particle on the envelope. Later, we define the [illegible] emittance with the coordinates of the representative parti[illegible] on the envelope. This is similar to defining the emittance [illegible] the enclosing phase space ellipse. Denoting γ [illegible] the rel[illegible]stic energy factor, the equation of motion that is valid [illegible] to relativistic velocity is given as

$$\gamma\ddot{r} - r\gamma\dot{\theta}^2 + \gamma\dot{r} = \frac{\epsilon}{m_0 c}\left[r\dot{\theta}B_z - \dot{z}B_\theta\right] + \frac{\epsilon}{m_0}E_r(r) \quad , \qquad (1)$$

$$2\gamma\dot{r}\dot{\theta} + \gamma r\ddot{\theta} + \dot{\gamma}r\dot{\theta} = \frac{1}{r}\frac{d}{dt}\left[\gamma r^2\dot{\theta}\right] = \frac{\epsilon}{m_0 c}\left[\dot{r}B_z - \dot{z}B_r\right] \quad , \text{ and} \qquad (2)$$

$$\gamma\ddot{z} + \dot{\gamma}\dot{z} = \frac{\epsilon}{m_0}E_z + \frac{\epsilon}{m_0 c}\left[\dot{r}B_\theta - r\dot{\theta}B_r\right] \quad . \qquad (3)$$

In Eq. [illegible] the space charge electric field act[illegible] on a particle at beam envelope with radius r was represent[illegible] as $E_r(r)\dot{r} \equiv (2\dot{r}r)/(\gamma^2 r l)$, where the net charge q of particles is assumed to be uniformly distributed in a cylinder of radius r and length l $(l \gg r)$. The guiding coil may have radial, azimuthal, and z components of fields given as B_r, B_θ, and B_z, respectively. In an ideal accelerator cavity operating in the TM_{010} mode, the accelerating electric field is along the z axis, and the magnetic field 90° out of phase has only an azimuthal component on a transverse plane. However, in traversing each accelerating cell, the effect of the azimuthal magnetic field cancels. If the guiding coils are aligned to the axial center of the accelerator cavity, and if we can ignore the imperfection of the cavity field, the azimuthal magnetic field can be ignored. If the effect of azimuthal magnetic field does not cancel, the emittance can grow.

Integral of Motion

The azimuthal motion (Eq. [illegible]) can be readily integrated, and the conservation of angular momentum $m_0 K_1$ (Busch's theorem guarantees the conservation even if the B_z varies along the path) can be stated as

$$\gamma r^2\dot{\theta} + \frac{\epsilon}{2m_0 c}r^2 B_z - \frac{\epsilon}{m_0 c}\int_0^t \left[\frac{r^2}{2}\dot{B}_z + r\dot{z}B_r\right] dt = K_1 \quad . \qquad (4)$$

Normally, the canonical angular momentum is conserved if the space charge and other non-axially symmetric forces acting on the beam, which increase the emittance, can be ignored. If we measure the mechanical part of the canonical angular momentum in units of the rest momentum $m_0 c$, the mechanical angular momentum for a cylindrically symmetric beam is equal to the normalized beam emittance ϵ_n (in our argument, we consider the emittance ϵ_n defined only by the azimuthal motion of electrons).

In the integration of the mechanical angular momentum with time, we assume that the coil field is static in time and is nearly constant B_0 at position $z \geq z_0$. Defining t_0 as a time that takes to reach z_0, we divide the time integration into two domains, $t < t_0$ and $t_0 < t$. The mechanical angular momentum is expressed as

$$\gamma r^2\dot{\theta} = -\frac{\epsilon}{m_0 c}\left[\frac{r^2}{2}B_z(t) - \int_0^t \left(\frac{r^2}{2}\dot{B}_z + r\dot{z}B_r\right) dt\right] + K \quad , \qquad (5)$$

where the constant K is given with the quantities on the cathode (i subscripts):

$$K = \gamma_i r_i v_{\theta i} + \frac{\epsilon}{2m_0 c}r_i^2 B_{zi} \quad . \qquad (6)$$

With respect to the normalized emittance ϵ_n, Eq. 5 can be rewritten as

$$\epsilon_n(t) = \gamma r^2\frac{\dot{\theta}}{c} = \epsilon_n(0) - \frac{\epsilon}{m_0 c^2}\left[\frac{r^2}{2}B_z - \int_0^t \left(\frac{r^2}{2}\dot{B}_z + r\dot{z}B_r\right) dt\right] \quad , \qquad (7)$$

*Work su[illegible]ted and funded by the US Department of Defense, Army Strategic Defense Command, under the auspices of the US Department of Energy

where the normalized beam emittance at cathode was given as $\epsilon_n(0) = K/c$.

Equation 7 implies that we can reduce emittance, with these conditions. (1) if the particles are emitted normal to the surface of the cathode, $\epsilon_n(0) = 0$, (2) if the particles experience no magnetic field at the cathode, $B_{zi} = 0$, and (3) if the coil field is not present at the emittance measuring position, $B_z = 0$.

If the particles are emitted normal to the cathode, and a bucking coil behind the cathode is set to cancel the magnetic field on the cathode, the emittance observed downstream $z_0 < z$ is caused by the intrinsic emittance acquired during $0 < t < t_0$ and by the emittance enhancement [illegible] the coil field B_z. The intrinsic emittance acquired up to t_0 can be expressed as

$$\epsilon_n = \frac{e}{m_0 c^2} \int_0^{t_0} \left(\frac{r^2}{2} \dot{B}_z + r\dot{z} B_r \right) dt \quad . \tag{8}$$

Using Eq. 7 and the relation $\epsilon_n(0) = \gamma r_i^2 \dot{\theta}_i / c$, the angular momentum at time t ($> t_0$) can be expressed in terms of quantities at the cathode and the intrinsic emittance as

$$\gamma r^2 \dot{\theta} + \frac{e}{2m_0 c} r^2 B_z(t) = \gamma_i r_i^2 \dot{\theta}_i + \frac{e}{2m_0 c} r_i^2 B_{zi} + c\epsilon_n \quad . \tag{9}$$

To evaluate the model (Eq. 7), we compare the numerical simulation using the PARMELA code for the injector used in the HIBAF[2] facility at Los Alamos. Table 1 and Table 2 show the injector and beam parameters for a bunch with a Gaussian temporal profile. After the 4th cell, the same 4th cell structure repeats. Figure 1 shows the PARMELA-calculated normalized emittance after the 7th cell as a function of magnetic field at the cathode. The beam kinetic energy is about 7 MeV, and the bunch charge is 0.5 nC. The slope of the emittance near the minimum, calculated from the PARMELA simulation, is in the range 0.26 to 0.33 π mm-mr/G, and the analytical coefficient $-er_i^2/(2m_0c^2)$ equals 0.32 π mm-mr/G for a truncated Gaussian with the 0.34-cm FWHM beam. These slopes agree well.

Azimuthal Angles of Particles Emitted from a Masked Cathode

Solving Eq. 5 for $\dot{\theta}$ and integrating over time followed by a substitution of K with the emittance at cathode, we obtain an expression

$$\begin{aligned} \theta(t) = & -\frac{e}{2m_0 c} \int_0^t \frac{B(z(t))}{\gamma} dt + \left(\frac{e}{2m_0 c} \right) B_{zi} r_i^2 \int_0^t \frac{dt}{\gamma r^2} \\ & + \left(\frac{e}{m_0 c} \right) \int_0^t \frac{dt}{\gamma(t) r^2(t)} \int_0^{t'} \left(\frac{r^2}{2} \dot{B}_z + r\dot{z} B_r \right) dt' \\ & + c\epsilon_n(0) \int_0^t \frac{dt}{\gamma r^2} \quad . \end{aligned} \tag{10}$$

If the particles emerge normal to the photo cathode, $v_i = 0$, the beam starts with no emittance : $\epsilon_n(0) = 0$. The last term in Eq. 10 drops. For a smooth envelope, a part of radial dependence is canceled in the third term; the radial dependence also comes from the second term in Eq. 10.

If we set the magnetic field at the cathode to zero, the image at the cathode is preserved azimuthally through the varying magnetic field channel. To test the radial dependence of azimuthal angle from the second term, we set a vertical slit for a laser to produce electrons at the cathode. If the magnetic field is present at the cathode, the image at downstream could be deformed azimuthally according to the amount of change in the beam radial position. If the beam is transported with a constant radius, the azimuthal angle will show no radial dependence: the straight shape of the beam will be preserved.

Figure 2a shows the x-y profile of a beam produced with the PARMELA code at +100-G cathode field. The bunch charge is reduced for a negligible space charge effect at the narrow slit. The beam experiences a coil field change to a peak −476 G and then to a reduced −22 G at the profile point (z = 11.53 cm from the cathode). The beam is rotated counterclockwise. Because the coil field extends only up to 60 cm, the beam rotation is nearly preserved at z = 487 cm, but both ends of the profile are expanded counterclockwise. This is shown in Fig. 2b. If we apply an opposite magnetic field, we observe a clockwise beam rotation. The wings also extend clockwise. With no magnetic field on the cathode, the straight shape is preserved.

TABLE 1
Injector Parameters

Cell	Average E Field (MV/m)	Length (cm)
1	22.07	6.02
2	11.14	11.53
3	8.0	11.53
4	5.46	11.53

TABLE 2
Beam Parameters

Bunch Charge (nC)	Bunch Length (ps)	Spot Radius on Cathode (cm)
0.5	35 ($2\sigma_z$=12 ps)	0.42

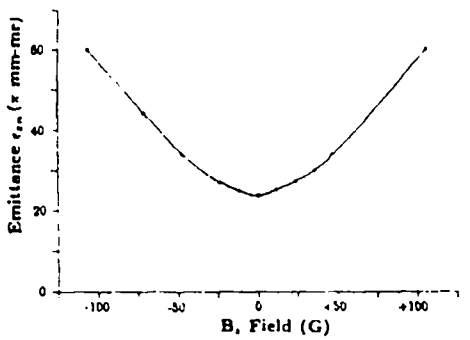

Fig. 1. The normalized emittance minimizes at zero cathode magnetic field.

Numerical Integration of Motion

In an actual photo-injector, the electric field acting on the particle varies according to each cavity gap voltage. Also the

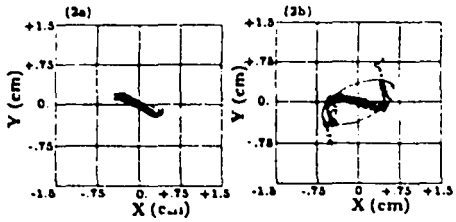

Fig. 2. The beam rotation by the coil field: observed at Z = 11.53 cm (2a), at Z = 487 cm (2b).

particles near the photo-cathode experience a large phase slip with respect to the rf wave. In our envelope model, we include the gap voltage at each cavity, but the transit time effect is averaged. Assuming that the reference particle is always on the beam envelope, we integrate the envelope equations Eqs. 1-3, without B_θ term.

For the HIBAF injector, as an example, Fig. 3 shows the profile of magnetic field $B(z)$ from field coil along the injector. The step-like accelerating electric field E_z, Fig. 4, is also shown similarly. We compare the results from test particle integration with the PARMELA simulation.

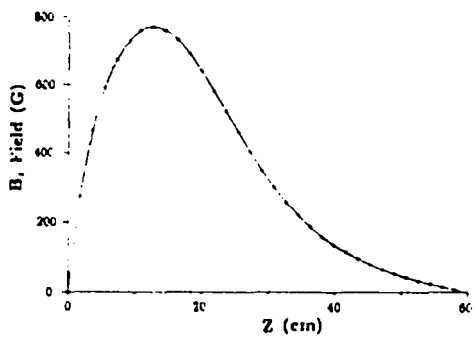

Fig. 3. The coil field, B_z, along the z axis.

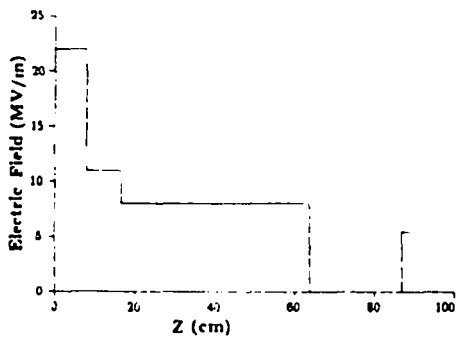

Fig. 4. The accelerating E field along the z axis.

We assume the coil field peaked at the same 769.1 G for the test particle calculation as was assumed in the PARMELA calculation. The radial profile for the test particle is shown in Fig. 5a. The corresponding PARMELA-calculated envelope (Fig. 5b) does not have a rapid initial expansion of envelope as shown in Fig. 5a. The normalized emittance from the test particle integration (Fig. 6a) has a profile similar to the PARMELA result, which calculated four times the RMS emittance (Fig. 6b). However, because of the conservation of canonical angular momentum, the assumed axial symmetry in the model produced zero emittance where the coil field is terminated. The magnitude is about two times larger than the emittance calculated with the PARMELA code. This is because the simplified space charge model does not represent well the profile of the bunch, which was Gaussian both in temporal and cross-sectional dimensions.

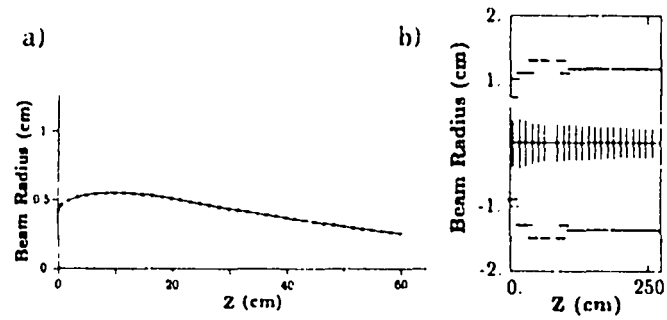

Fig. 5. The beam envelopes from the envelope model (5a) and from the PARMELA code (5b).

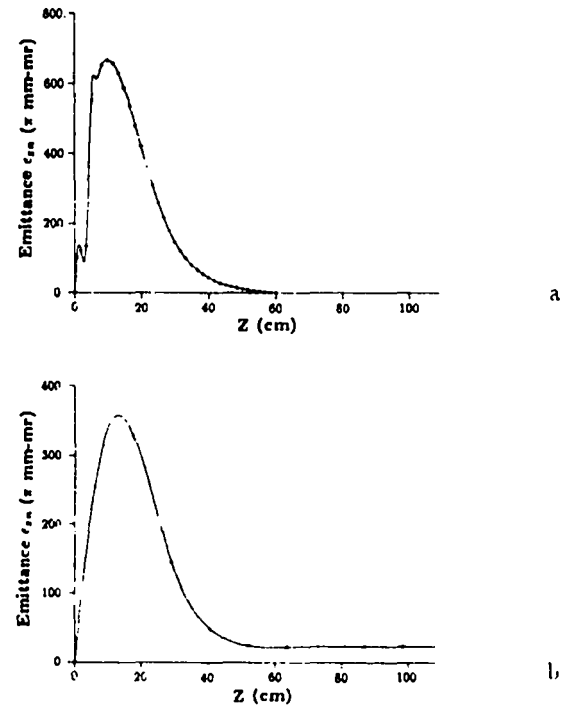

Fig. 6. Normalized emittances from the envelope model (6a) and from the PARMELA code (6b).

References

1. "Computer Codes for Particle Accelerator Design and Analysis: A Compendium," Los Alamos National Laboratory report LA-UR-90-1766 (May 1990), p.137.
2. W. D. Cornelius et al., "The Los Alamos High-Brightness Accelerator FEL Facility," 11th International Free Electron Laser Conference, Naples, Florida, August 28-September 1, 1989.

MAFIA RELEASE 3.X

M.Bartsch, M. Dehler, M. Dohlus, P. Hahne, R. Klatt, F. Krawcyzk, Z. Min, T. Pröpper ,P. Schütt, T. Weiland
(all at Technische Hochschule Darmstadt, FB 18, Schloßgartenstrasse 8, D-6100 Darmstadt, Germany)
S. Wipf, M. Marx ,F. Ebeling (all at DESY, D-2000 Hamburg,Germany)
B. Steffen (KFA Jülich, D-5170 Jülich,Germany)

Abstract

The new release of MAFIA is now available in version 3.1. The well-proven release 2.x version is now operational in 22 countries at over 120 locations. Over the recent years, the MAFIA codes have been completely overhauled. A new coherent user interface was designed which includes online help,.nacros, symbolic variables,do-loops,flexible file handling, built-in editor, mnemonic command names, and an easy-to-understand menu structure. The range of applicability has been extended by adding new solvers for electrostatics and magnetostatics, particle-in-cell simulation, and antenna radiation analysis. All two-dimensional solvers for frequency- and time-domain simulations (URMEL and TBCI) have been rewritten and incorporated into MAFIA. With this new version of MAFIA, which is now available, the user has a coherent computing tool for solving Maxwell's equations in 2D and 3D for a wide range of problems.

Introduction

The MAFIA family of codes which solve MAxwell's equations by the Finite Integration Algorithm is widely used in the computer-aided design of accelerator components. Rf cavities and vacuum junctions, collimators and magnets (to name but a few) have been successfully designed using these programs. The programs use Maxwell's equations in their integral form and produce a set of matrix grid equations which are then solved. A full description of the derivation of these equations can be found in the literature [1].
The allocation of the three dimensional field components is on a rectangular grid, using the Yee lattice [2]. The analytical properties of the matrix operators are preserved on the discrete grid [3]. Hence this method has the advantage that, after the eigenvalues of the problem are calculated, the numerical results can be tested for their physical correctness and any spurious solutions removed automatically.

The Programs

The 2D Programs

It is very useful to have 2D versions of the 3D programs for cylindrically symmetric structures and for exploratory tests before a large 3d model with many mesh points is calculated. The MAFIA package includes 2D versions of the 3D programs using the same user interface, mesh generator and post processor.

The Mesh Generator, M

The mesh is defined in cartesian coordinates and allows a non-equidistant grid. r-z coordinates will be available in release 3.1 for use with 2D versions of the programs and r-ϕ and r-ϕ-z will be added for release 3.2. Each rectangular cell may be divided in half along a diagonal to give a better approximation to the input geometry. Within this mesh of rectangular cells material fillings may be defined in various ways. Rectangular bricks may be filled with material. Cylinders of arbitrary cross-section with axis parallel to one of the coordinate directions and figures of revolution obtained by rotating an arbitrary plane shape through a given angle may be generated. Filaments represent line currents or wire electrodes and a large choice of pre-defined shapes is available.
At all stages *Diagnostics and Interactive Graphics Display* is provided to facilitate the visualisation of the geometry and to allow the user to check the input. Each input shape can be displayed superimposed on the approximated mesh model. Then mesh lines can be interactively added or deleted and the effect of the regenerated mesh on the mesh model is immediately displayed. Two dimensional cuts along any mesh plane can also be plotted. Finally the mesh model, with or without hidden lines, can be viewed in three dimensions and can be rotated.

The Static Solver, S

The Static code, S, solves Maxwell's Equations for electro- and magneto-static problems [4]. The electrostatic potential Φ, the field E, the flux D and the electrostatic charge distribution q can be calculated, or alternatively the magnetostatic field H and the flux B. An "open" boundary condition is included which uses an iterative method to analytically approximate the potential on the boundary, thus enabling a much smaller mesh to be used for the same problem. Ideally conducting or ideally permeable materials may be defined in all the 3D codes. In addition S allows materials with finite, non-zero and anisotropic ϵ and μ or with ϵ and μ dependent on the field strength and the non constant distribution may also be calculated. Filaments may carry linear currents or be defined as lines of constant potential. The solver uses an SOR over-relaxation method where the accuracy of the solution is an optional input parameter. A multigrid solver is also available for large problems.

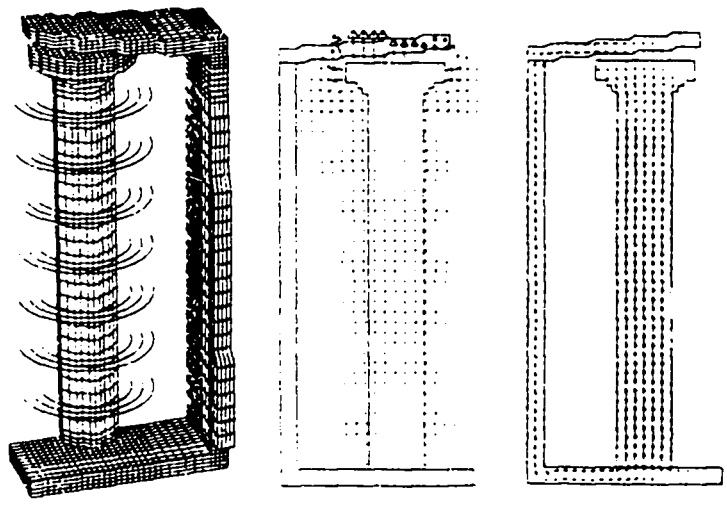

Figure 1: Modelled geometry of body and coil of a relais and arrow plots of the H- and B-field exited by a constant current and calculated with S.

The Frequency Domain Solver, R/E

The MAFIA codes R and E run in sequence, solve Maxwell's equations in the frequency domain. The material properties and the boundary conditions are defined in R where the matrices are set up. Periodic boundary conditions have been added in release 3.0. Then E calculates the fields E and B and the eigenfrequencies. As diagnostics, the accuracy of the frequencies is given and the quantities $div\mathbf{D}$, $div\mathbf{B}$ and $|curl\mathbf{E} - k^2\mathbf{E}|$. The Solver uses the SAP [7] eigenvalue solver, which has been much improved in both speed and accuracy using a method which combines iteration and modified polynomials. Several hundred modes can be calculated. *The 2D Version* of R/E (formerly called URMEL) can be used to obtain the frequencies of rotationally symmetric modes with azimuthal field variation and arbitrary angular mode numbers, (monopole, dipole etc.). The cutoff frequencies of waves in longitudinal waveguides can also be calculated using x-y geometry.
Figure 2 shows the modelled geometry of a multi-cell accelerating cavity with coupler and the E-field distribution of a $2\pi/3$-mode calculated calculated by E.

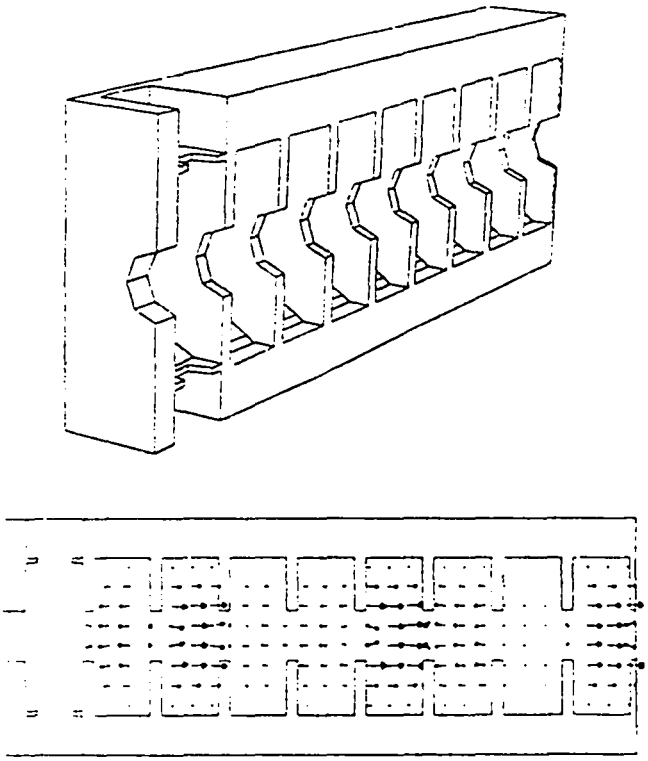

Figure 2: One half of a modelled nine-cell accelerating structure (above) and the arrow plot of a $2\pi/3$-mode calculated by E (below).

The Time Domain Solver, T3

T3 calculates the fields created by a moving, rigid bunch of particles [5] providing the E- and B-fields at user-specified time steps, the fields as a function of time at user specified positions and the longitudinal and transverse wake potentials. In addition the calculation of the propagation of transient electromagnetic waves has been add in release 3.1.
"Open" boundary conditions are available to simulate an infinite beam pipe or open space. The transverse bunch position, the charge distribution within the bunch, the particle speed and the number of time steps to be performed are all input parameters. A window option is also available for ultra-relativistic particles. The *2D Version* T2 (the former TBCI) calculates the diffraction of TM waves in addition to transient fields and transverse and longitudinal wake potentials.
Figure 3 illustrates the scattering of a plane wave by an electronic device consisting of a dielectric plate carrying some ICs surrounded by a partial metallic shielding. The exiting plane wave is propagating from above towards the top of the shielding. The arrow plots show the scattered time-harmonic E-field (real and imaginary part) surrounding this device.

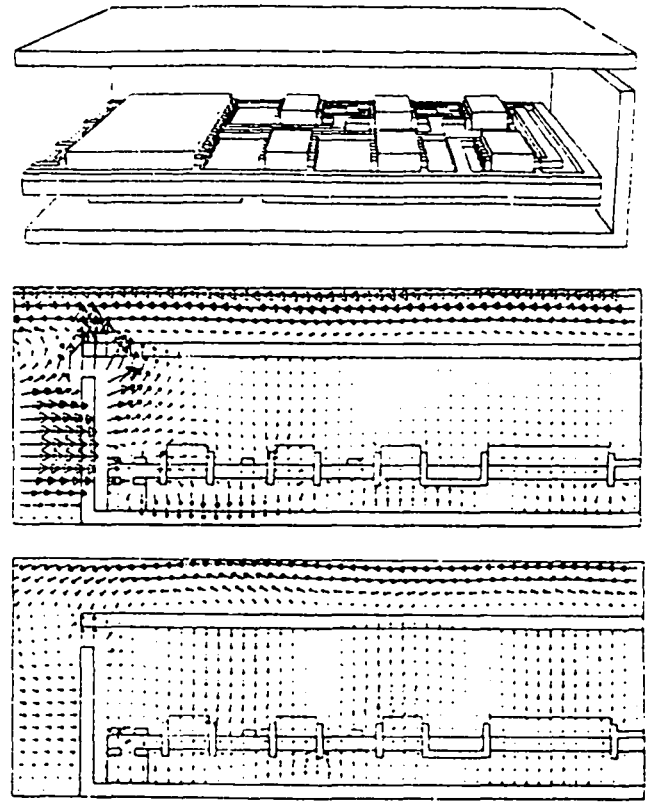

Figure 3: Modelled geometry of a dielectric plate carrying an array of ICs (above and middle) surrounded by a metallic shielding. Scattered time-harmonic E-field in a cutplane exited by a plane wave propagating from above and calculated by T3 (below).

The Self Consistent Time Domain Solver, TS3

TS3 is a particle-in-cell code, which enables the simulation of rf-klystrons, electron sources etc. Maxwell's equations and the equations of motion for the particles are solved self consistently, so that particle trajectories can be calculated taking space charge into account. The charge distribution within the bunch is also calculated. The initial conditions for the velocity, position and charge density of the particles are defined by the user. Static or resonant fields can be preset on the mesh.
In the *2 $\frac{1}{2}$D Version*, TS2 [6] both the initial field and the particle distributions have angular symmetry.

The Postprocessor, P

In the postprocessor, secondary results may be calculated from the fields, fluxes etc. which have been calculated. Field energy, power loss, shunt impedance and integrals over lines, areas and volumes can be obtained. The results can also be represented graphically.

Arrow plots are used to represent a 3D vector field in a mesh plane, isoline and contour plots show a scalar field or a vector component in a mesh plane and line plots show the variation of the same along a line. All plots and calculations can be restricted to windows.

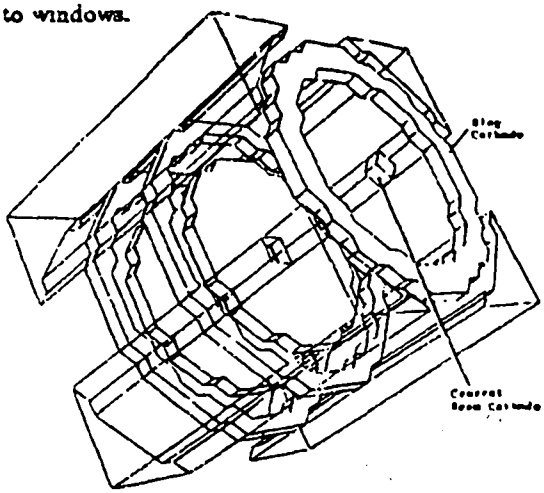

Figure 4: Two cell Wakefield Transformer, beam direction along the z axis,calculated by TS3. The central beam is accelerated by the wakefields which are produced by the ring beam which surrounds it.

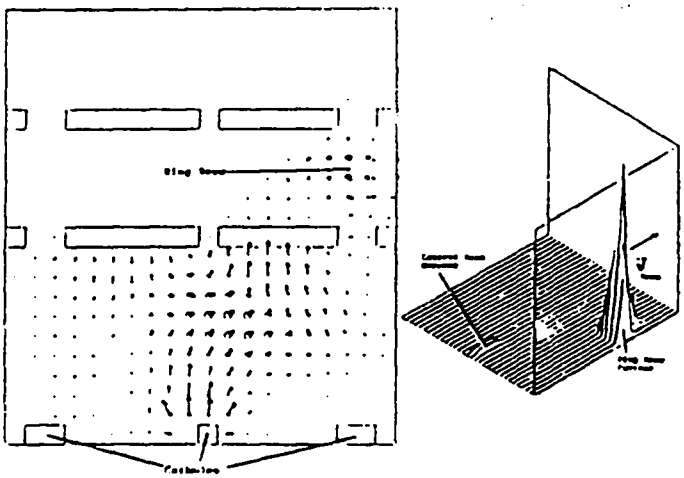

Figure 5: Arrow plot of the E-field and isoline plot of the current in a cut along the beam axis, a quarter of the ring beam current was generated.

MAFIA Release 3 - The Environement

Many new features are included in release 3. The powerful *Command Processor* includes a *Macro Facility* and *Symbolic Variables* and enables the construction of *Do Loops* over a range of commands. The *Command Error Checking* facility issues diagnostic messages. *Flexible File Handling* is a feature. Sequential files are used for print output, non-interactive command input and for recording the commands of an interactive session. *Profiles* can be created for particular modules, for individual users or for groups. There is a *Built-in Editor* both for these files and for command sequences which have been entered interactively, these may be edited and then immediately executed. The main MAFIA *Data Base* is a direct access file where all the results are stored. Up to twenty output devices are available for *Graphics Output*, e.g. metafile, terminal, plotter etc. *Mouse Input* is also provided for. The *Menu-controlled User Interface* includes an *On-line Help Facility*. The codes are *Completely Hardware Independent*.

Memory Requirements

The required memory for 32 bit accuracy using 100,000 nodes varies between 3 Mbyte for the mesh generator M and 14 Mbyte for both the eigenvalue solver E and the particle in cell code TS3 (for 100,000 particles). The other codes use 8 Mbytes or less. T3 includes a window option which enables 1,000,000 nodes with 100,000 nodes in the window for 11 Mbyte.

Hardware and Software Requirements

MAFIA Release 3.0 consists of separate source modules for each program and a utility library of routines common to all the programs. These are written in standard fortran77 and will run on any computer with an error-free ANSI-FORTRAN77 compiler. A built in facility will switch operation from single to double precision, avoiding the compatability problems of the standard. All installation dependant operations are called via a system interface and a graphics interface. These latter ensure that the programs are fully portable and installation independent.
Thus MAFIA runs on any machine, e.g. IBM 3090 and IBM Risc 16000, DEC SUN, APOLLO, EF. CRAY and many more. Similarly any graphics system may be used, e.g. GKS, PHIGS, DISSPLA.

Conclusion

A definite step forward in the computer aided design of accelerators has been achieved. The physical correctness and dependability of the Release 2 MAFIA is combined with the new modules S and TS3 and compatible 2D versions under one unified user interface. Release 3.0 is now ready for distribution, including the programs M, R, E, S, P. The 2D versions of R/E and S and the modules TS3, TS2, T3, T2 will be available towards the end of the year with release 3.1. Release 3.2 will include the eddy current module W3 and an automesh facility for M as well as r-ϕ-z coordinates.

References

[1] T.Weiland: "Numerical Solution of Maxwell's Equations For Static, Resonant and Transient Fields," Proceedings of the Int. URSI Symposium on Electromagnetic Theory, pp.537-542, Budapest, Aug. 1986

[2] K.S.Yee: "Numerical Solution of Initial Boundary Value Problems Involving Maxwell's Equations in Isotropic Media." IEEE, AP-14, 1966, pp.302-207.

[3] T.Weiland, "On the Numerical Solution of Maxwell's Equations and Applications in the Field of Accelerator Physics," Particle Accelerators 15 (1984), pp.245-292 and references therein.

[4] F.Krawczyk und Th.Weiland: "A New Static Solver with Open Boundary Conditions in the 3D-CAD-System MAFIA," IEEE, Trans.in Mag.22/1(1988) pp.55-57

[5] T.Weiland: "Transient Electromagnetic Fields Excited by Bunches of Charged Particles in Cavities of Arbitrary Shape," Proc. of the XI-th International Conf. on High Energy Accelerators Geneva 1980, Birkhauser Verlag, Basel pp 570.

[6] F.Ebeling, P.Schütt, T. Weiland, "Self-consistent Simulation of High Power Tubes with TBCI-SF," Proceedings of EPAC Conference, World Scientific Press 1989, pp.678-680

[7] J. Tückmantel, "Applications of SAP in URMEL", CERN/EF/RF 83-5, 11 July 1983 and 85-4.

THEORETICAL/NUMERICAL INVESTIGATION OF INDUCTION CAVITY IMPEDANCES FOR MODERATE TO LARGE GAP WIDTHS *

J. F. DeFord
L-626, LLNL, Livermore, CA 94550

Abstract

In order to understand the coupling of a charged particle beam to modes in induction cells with gap width to beampipe radius ratio $w/b > 1$, the variation of the transverse $Z_\perp/Q$ for both axially symmetric and axially asymmetric dipole modes in this regime is investigated. It is found that the gross behavior of the axially symmetric modes when $w/b > 1$ is at least consistent with the approximate analysis of Briggs, et al [1], although a thorough comparison has not been undertaken. The axially asymmetric modes are found to be unimportant until w/b approaches 2, and they generally exhibit lower values of $Z_\perp/Q$ than the axially symmetric modes.

Introduction

The coupling of a charged particle beam to cavity modes in linac induction modules can pose a significant threat to beam stability in high current accelerators [2]. In particular, the convective beam breakup (BBU) instability has been shown analytically and experimentally to put severe constraints on the cavity mode Qs and gap geometry. For low Q modes, the effects of the interaction between the beam and the induction cell may be characterized using the coupling impedance, and it may be shown that the asymptotic BBU growth rate is proportional to a positive power of the impedance [3]. For high Q modes, the relevant parameter is Z/Q. Briggs, et al. [1], have shown that for fixed b and small ratio of gap width to beampipe radius, w/b, the transverse dipole impedance scales linearly with w/b. This finding, coupled with a minimum gap width given by breakdown considerations, yields the requirement of relatively large diameter beampipes in high current accelerators. For a fixed volt-second requirement given by the gap voltage and the pulse length, the amount of ferrite or other magnetic material needed for inductive isolation in an induction cell scales linearly with the beampipe radius. To reduce the cost and weight of an induction machine, one would therefore like to make the beampipe radius smaller and increase w/b.

In this paper we analyze the scaling of the impedance with w/b of the modes in a "Briggs pillbox" when $w/b > 1$. To simplify the interpretation of the results we consider only undamped modes, and therefore focus on the value of $Z_\perp/Q$ instead of $Z_\perp$ itself. This effort is primarily a numerical code exercise, since analytic models for the modes either do not exist in this regime, or are only approximate. The AMOS wakefield code [4] is used to obtain the $Z_\perp/Q$ values for dipole modes in a variety of cases involving different w/b ratios. It is found that the impedances of the traditional BBU modes, i.e., those which are symmetric across the gap, all increase monotonically as w/b increases with b fixed, until $w \approx 2c/\omega$, when a rolloff occurs. Asymmetric gap modes are found to have a very different functional dependence on w/b, and they do not exhibit significant values of $Z_\perp/Q$ until w/b exceeds approximately 1.5.

Definitions

The radial component of the dipole wake potential in a rotationally symmetric structure has the form [4]

$$W_{r1}(s) = 2\left(\frac{r}{b}\right)\left(\frac{r_Q}{b}\right)\frac{w_{c1}(s)}{r}\cos(\phi), \qquad (1)$$

where ϕ is measured from the position of the source charge, r is the position of the test charge, and

$$w_{c1}(s) = \frac{1}{2q_s}\int_{s'=0}^{s}\int_{z=-\infty}^{\infty} E_{z1}(r=b,z,t)\Big|_{t=\frac{s+s'}{c}} dz\,ds'. \qquad (2)$$

q_s is the source charge, which moves axially at radius $r_Q = b$, and E_{z1} is the dipole moment of the axial electric field induced by the source charge [Ref. 4, Eqn. (27)].

The impedance that corresponds to the wake potential in Eqn. (1) is given by

$$Z_{r1} = \frac{-i}{c}\int_{-\infty}^{\infty} W_{r1}(s)e^{i\omega s/c}ds. \qquad (3)$$

It can be shown that the single-mode response of the rota-

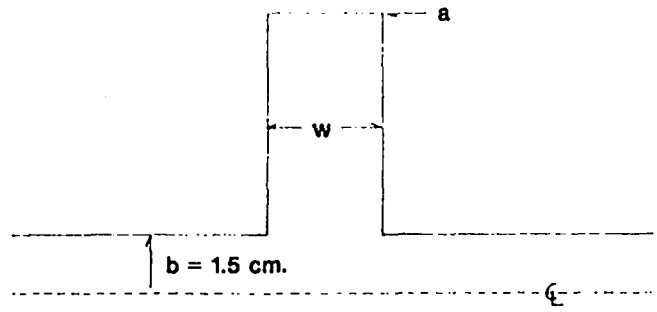

Fig. 1. Rotationally symmetric "Briggs pillbox" used in all calculations presented in this paper. Pillbox is terminated with a perfect conductor. Beampipe was long enough so that the beampipe terminations did not affect calculated results (considered only modes with resonant frequencies less than the beampipe cutoff). Pillbox radius $a = 6.7b = 10.05$ cm

* Work performed under the auspices of the U. S. Department of Energy by Lawrence Livermore National Laboratory under contract W-7405-ENG-48.

tionally symmetric geometry under consideration (Fig. 1) has the form [5]

$$W_{r1}^{(i)}(s) = \frac{\Re(Z_{r1}(\omega_i))}{Q_i}\omega_i e^{-\frac{\omega_i s}{2Q_i c}} \sin\left(\frac{\omega_i s}{c}\right), \qquad (4)$$

where ω_i and Q_i are the resonant frequency and quality factor of the ith mode, respectively. With reference to the impedance spectrum of the cavity as it would be computed by AMOS, the value of ω_i may be obtained from the position of the local maxima corresponding to the ith mode. When Q_i is small enough, the values of Q_i and $Z_{r1}(\omega_i)$ can also be obtained directly from the impedance spectrum. However, as $Q_i \longrightarrow \infty$, $\Re(Z_{r1}(\omega_i)) \longrightarrow \infty$, and the ratio $\Re(Z_{r1}(\omega_i))/Q_i$ must be evaluated independently. One method is to use an eigenmode solver such as URMEL-T [6], which will calculate the ratio directly. In the event that the impedance spectrum is available, and the modes are reasonably isolated from one another in frequency, a less computationally intensive approach may be used. For each mode of interest, the ratio can be computed by windowing the impedance function to remove the other resonances, then applying an inverse Fourier transform to the windowed impedance spectrum to obtain the component of the wake potential which is due to that mode. The value of $Z_\perp/Q$ is related to the amplitude of the derived wake potential using the expression

$$Z_\perp/Q = \frac{\Re(Z_{r1}(\omega_i))}{Q_i} = \frac{\left|W_{r1}^{(i)}\right|}{\omega_i}, \qquad (5)$$

where $\left|W_{r1}^{(i)}\right|$ is the amplitude of the sinusoidal oscillation in $W_{r1}^{(i)}$.

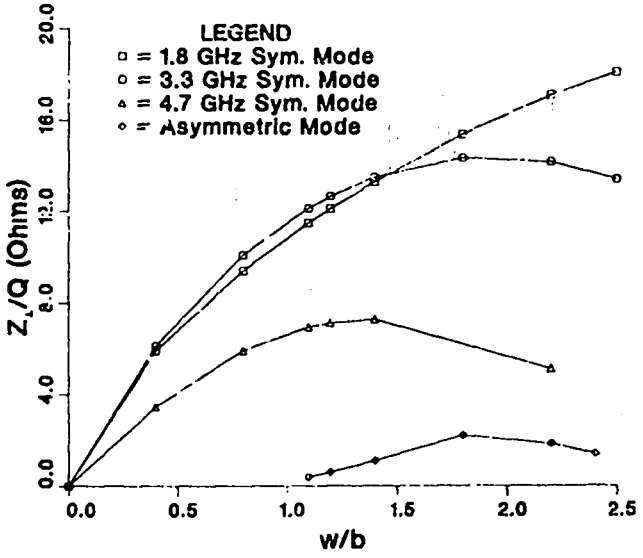

Fig. 2. Variation in $Z_\perp/Q$ with w for first (lowest frequency) three axially symmetric dipole modes and the first asymmetric dipole mode. Result is for $r = r_Q = b$, and $\phi = 0$.

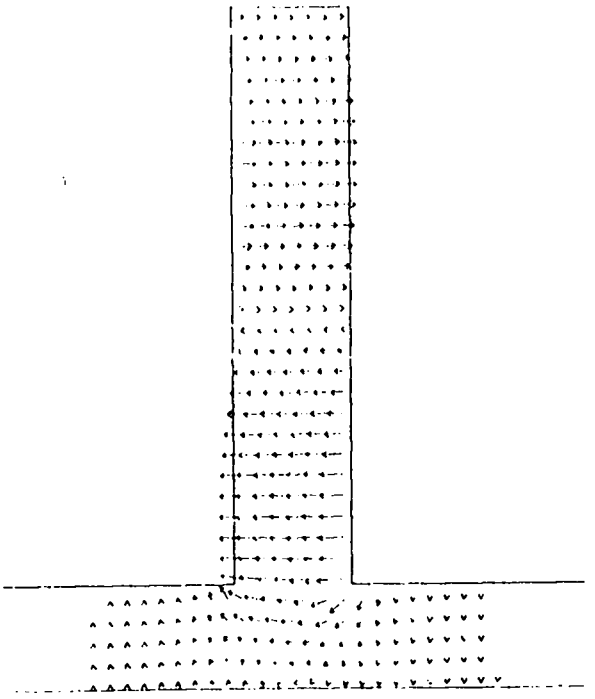

Fig. 3. Electric field pattern for 3.3 GHz axially symmetric mode when $w/b = 1.4$.

Simulation Results

The geometry under consideration is shown in Fig. 1. The series of calculations that will be shown all involve the dipole ($m = 1$) modes in the structure. The value of w/b was changed by altering w while leaving all other dimensions fixed. For each case we calculated the quantity $Z_\perp/Q$ for all resonances below the beampipe cutoff.

The results of this survey are depicted graphically in Fig. 2, which shows the calculated $Z_\perp/Q$ values for dipole modes in the Briggs pillbox when it is terminated by a short. In this configuration all of the modes below the beampipe cutoff are undamped, and Eqn. (5) is used to obtain the mode parameters. Shown are two types of modes: those which have a unidirectional axial electric field across the gap (axially symmetric modes) (Fig. 3), and one in which the axial electric field changes sign across the gap (axially asymmetric mode) (Fig. 4). For small values of w/b, the $Z_\perp/Q$ for the symmetric modes varies linearly with w/b, and the asymmetric mode is negligible. For larger values of w/b the impedances of the symmetric modes peak and fall off, while the asymmetric mode becomes evident for $w/b > 1$.

If it is assumed that the axial electric field doesn't vary across the gap for the symmetric mode, then the analysis of Briggs, et al., shows that the impedance should vary as $w\left(\frac{\omega w}{2c}\right)^{-2}\sin^2\left(\frac{\omega w}{2c}\right)$, which yields a maximum at $w \approx \frac{1.1c}{\pi f}$. For the three symmetric modes being considered, we find that $Z_\perp/Q$ should peak at $w/b \approx 4.0$, 2.2, and 1.5 for the 1.8 GHz mode, the 3.3 GHz mode, and the 4.7 GHz mode, respectively. These values are within 10% of those observed (see Fig. 2).

The character of the axially asymmetric modes in the

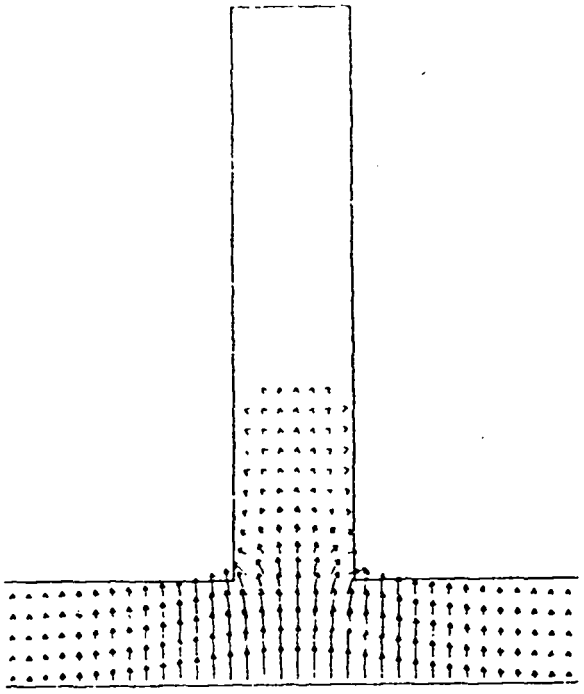

Fig. 4. Electric field pattern for lowest frequency axially asymmetric mode when $w/b = 1.4$. Note that the mode is evanescent into the beampipe and into the radial line. Resonant frequency of this mode is 5.42 GHz.

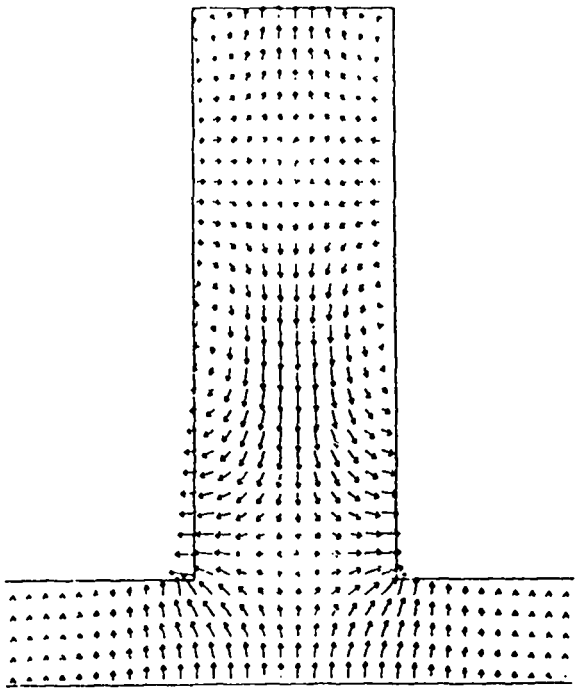

Fig. 5. Electric field pattern for axially asymmetric (p=1) pillbox mode when $w/b = 2.4$. Note that this mode is *not* evanescent into the radial line, but is evanescent into the beampipe. Resonant frequency of this mode is 5.13 GHz.

Briggs pillbox changes significantly when the frequency at which a half wavelength will fit in the radial line falls below the cutoff of the beampipe, which for dipole modes is when

$$\frac{w}{b} > \frac{\pi}{1.841}. \tag{6}$$

Below this limit the asymmetric modes must evanesce into the radial line (Fig. 4) and can only be damped by means applied in the vicinity of the gap. For $w/b > 1.7$ the impedance spectrum rapidly becomes more complex as the familiar $p = 1$ (1/2 wavelength axially) pillbox modes are supported. These modes extend to the pillbox termination (Fig. 5), and in principle are subject to absorption by the ferrite load in the cavity, or by other damping mechanisms not supported at the location of the gap. It is interesting to note, however, that the lowest frequency asymmetric mode persists, and remains weakly evanescent into the radial line, even when $w/b > 1.7$. This mode is neither a $p = 1$ or $p = 0$ pillbox mode, but rather a mode which exists only because there is a joint between the beampipe and the radial line. More detailed discussions of this mode have been made by by Godfrey [7], and by Craig [8].

Conclusions

In induction cavities with gap width – to – beampipe radius ratios that are greater than unity, both axially symmetric and asymmetric dipole modes may be expected. The values of $Z_\perp/Q$ for the axially symmetric modes are seen to peak at values of w/b near those suggested by the Briggs model. For the range of w/b investigated in this work the axially asymmetric modes generally have lower values of $Z_\perp/Q$, as expected, but they nevertheless may pose a BBU threat if the geometry is such that they are localized to the gap.

References

1. R. J. Briggs, D. L. Birx, G. J. Caporaso, V. K. Neil, and T. C. Genoni, "Theoretical and experimental investigation of the interaction impedances and Q values of the accelerating cells in the Advanced Test Accelerator," *Particle Accelerators*, **18**, Jan., 1985, pp. 41-62.
2. V. K. Neil, L. S. Hall, and R. K. Cooper, "Further theoretical studies of the beam breakup instability," *Particle Accelerators*, **9**, 1979, pp. 213-222.
3. G. J. Caporaso, personal communication.
4. J. F. DeFord, G. D. Craig, and R. R. McLeod, "The AMOS wakefield code," *Proceedings of the Conference on Computer Codes and the Linear Accelerator Community*, Los Alamos, NM, Jan. 22-25, 1990, pp. 265-289.
5. P. Wilson, "Introduction to wakefields and wake potentials," **SLAC PUB-4547**, SLAC, Stanford University, Stanford, CA, Jan., 1989.
6. U. van Rienen and T. Weiland, "Triangular discretization method for the evaluation of RF-fields in waveguides and cylindrically symmetric cavities," *IEEE Transactions on Magnetics*, **MAG-21**, 1985, pp. 2317-2320.
7. B. B. Godfrey, "Transverse wake potentials for wide radial lines," **MRC/ABQ-R-1046**, Mission Research Corporation, Albuquerque, NM, 1988.
8. G. D. Craig and J. F. DeFord, "Diagonal resonances and trapped 'TE' modes," **Beam Research Memo 88-44**, Beam Research Group, Lawrence Livermore Nat. Lab., Livermore, CA, July, 1988.

MODIFIED-YEE FIELD SOLUTIONS IN THE AMOS WAKEFIELD CODE *

C. C. Shang and J. F. DeFord
L-626, LLNL, Livermore, CA 94550

Abstract

A new numerical procedure by which field calculations in AMOS [1] are upgraded to model rotationally symmetric cavity structures in a more accurate fashion is described. The development work is aimed at implementing a modified finite difference update scheme on an irregular grid system. Elements of an irregular grid may be chosen to better fit object boundaries, resulting in increased solution accuracy. Our approach involves the placement of field components on a non-orthogonal body fitting grid and on a dual grid which is orthogonal to the first grid. It is found that this procedure retains several important computational advantages, including the ability to exploit the implied spatial relationships between nodes. Propagating fields on an irregular grid system have been observed and comparisons between finite difference AMOS and Modified-Yee AMOS field calculations are provided.

Introduction

Cavity cells with geometrical complexity are usually modeled with staircased approximations to the surfaces. Depending on the level of the cell complexity, the task of gridding the device may be either impossible or unsatisfying. The well-known time domain discretization of Maxwell's equations (Finite-Difference Time-Domain FDTD), which was originally proposed by Yee [2], is the standard field solver currently employed. However, the algorithm's primary limitation for modeling curved surfaces lies in the fact that the fields are distributed on a logically regular grid system.

Holland [3] demonstrates that staircased approximations to oblique surfaces cause large errors for the scattering problems encountered in radar cross section calculations. The work of Craig and Anderson [4] shows that careful representation of localized features inside a cavity yields significant improvements over idealized models. Thus, it is often important to increase the geometrical accuracy of the model.

The Modified Finite Volume (MFV) algorithm proposed in [5] shows how electric and magnetic field components may be distributed on a nonorthogonal grid system. This type of field update scheme allows better boundary modeling. However, for the particular problem of the cavity cells, one needs a combination of the computationally efficient FDTD calculations in the interior with more accurate geometrical MFV type modeling on the simulation boundaries. Hence, in order to perform these hybrid calculations, we pursue a field solving scheme which is, in essence, the limiting case of MFV or a Modified-Yee procedure.

Numerical Procedure

The FD-AMOS wakefield code computes fields in the rotationally symmetric cavity. Hence, the fields are of the form

$$F = f_p \cos(n\phi) + f_q \sin(n\phi) \tag{1}$$

To perform the corresponding Modified-Yee calculation in $2-1/2$ D, placement of six field components on an irregular grid is required. Fig. 1 shows how the field components are distributed on a sample dual grid system. The nonorthogonal solid line mesh is the electric field grid, and the dashed line mesh is the magnetic field mesh.

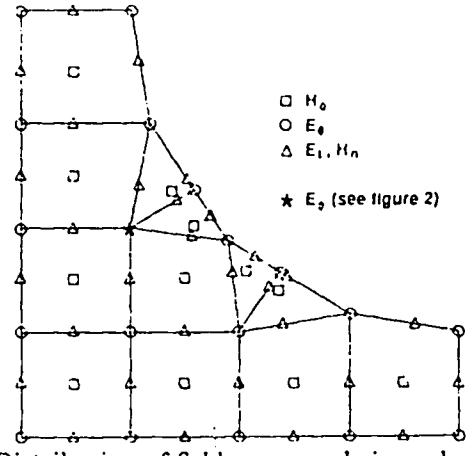

Fig. 1. Distribution of fields on sample irregular grid.

It can be readily seen that the two grids overlap in an orthogonal fashion. In cylindrical coordinates, E_ϕ nodes are distributed at intersections of solid lines and H_ϕ nodes are placed at intersections of dashed segments. The field components in the $r-z$ plane are located at the intersections of the two grids ($t \rightarrow$ 'tangential' and $n \rightarrow$ 'normal').

In order to describe the implications of this arrangement, we rewrite the EM time dependent curl equations

$$\nabla \times \vec{H} = \sigma \vec{E} + \epsilon \frac{\partial \vec{E}}{\partial t} + \vec{J}_s \tag{2}$$

$$\nabla \times \vec{E} = -\mu \frac{\partial \vec{H}}{\partial t} - \vec{K}_s \tag{3}$$

in the integral form

$$\oint \vec{H} \bullet d\vec{\ell} = \int\int \left(\sigma \vec{E} + \epsilon \frac{\partial \vec{E}}{\partial t} + \vec{J}_s\right) \bullet d\vec{A} \tag{4}$$

$$\oint \vec{E} \bullet d\vec{\ell} = -\int\int \left(\mu \frac{\partial \vec{H}}{\partial t} + \vec{K}_s\right) \bullet d\vec{A} \tag{5}$$

In Fig. 2, the graphical interpretation of Eqn. 4 - update of an E_ϕ node - is illustrated. This particular update

* Work performed under the auspices of the U. S. Department of Energy by LLNL under contract W-7405-ENG-48.

requires the values of the magnetic fields along the integration path with the contour integral being performed in the counterclockwise direction.

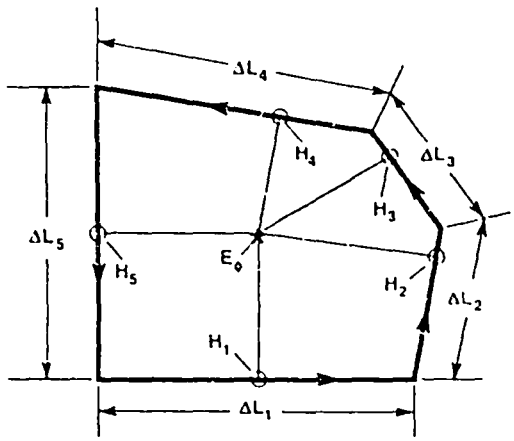

Fig. 2. Update diagram for E_ϕ node.

On the right hand side of Eqn. 4, the temporal derivative is performed by differencing the E_ϕ nodes at a time step k (previous time step) and $k+1$ (update time). The J conduction and source terms are assumed to be at the $k+1/2$ time step (current time). Hence, the explicit update equation for E_ϕ is given purely in terms of H fields and J_s. This update is precisely the same in both cylindrical and cartesian coordinates and may be written as

$$E_\phi^{k+1} = \frac{\frac{\{\sum_{i=1}^{m} H_i^{k+\frac{1}{2}} \Delta L_i\}}{A} - J_{s\phi}^{k+\frac{1}{2}} - E_\phi^k\{\frac{\sigma}{2} - \frac{\epsilon}{\Delta t}\}}{\left(\frac{\sigma}{2} + \frac{\epsilon}{\Delta t}\right)} \quad (6)$$

where A is the enclosed area, ϵ and σ are the permittivity and the conductivity, respectively, and Δt is the time increment.

To obtain the update equations for field components in the $r-z$ plane, the procedure is similar. However, the geometry of this case yields a contour path which requires integration of fields with a sinusoidal variation in ϕ. This ϕ dependence gives rise to a term with n as will be seen.

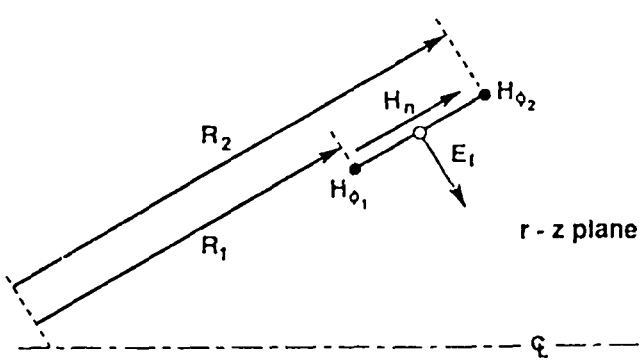

Fig. 3. Update for electric field node in the r-z plane.

For the general-oriented field component in the $r-z$ plane (Fig. 3), it can be seen that substituting Eqn. 1 into Eqn. 4 yields a discretized form given by

$$E_t^{k+1} = \frac{\frac{2.0\{r_2 H_{\phi_2}^{k+\frac{1}{2}} - r_1 H_{\phi_1}^{k+\frac{1}{2}} - n\ \Delta\ell H_n^{k+\frac{1}{2}}\}}{\{R_2^2 - R_1^2\}} - J_{st}^{k+\frac{1}{2}} - E_t^k\{\frac{\sigma}{2} - \frac{\epsilon}{\Delta t}\}}{\left(\frac{\sigma}{2} + \frac{\epsilon}{\Delta t}\right)} \quad (7)$$

where r_1 and r_2 are the radial distances to the H_{ϕ_1} and H_{ϕ_2} nodes, respectively, $\Delta\ell$ is the distance between ϕ nodes, and $R_2 > R_1$.

It should be noted that, if the field component is oriented with the field direction of positive slope (in $r-z$), the sign on n is switched to remain consistent with the convention of positive fields in the $+z$ direction. Next, we examine special cases involving E components which lie in the r and z direction. Referring to Fig. 3, one can see that as E_t becomes z-directed, $R_2 \rightarrow r_2$ and $R_1 \rightarrow r_1$. Hence, the update form for E_z follows immediately from Eqn. 7. The update of the E_r component is also similar in form to Eqn. 7. The primary difference is that the area enclosed by the integration path is $R\Delta\ell$, where R is the radial distance to the E_r node. Thus, one may write E_r as

$$E_r^{k+1} = \frac{\frac{\{R\ H_{\phi_2}^{k+\frac{1}{2}} - R\ H_{\phi_1}^{k+\frac{1}{2}} + n\ \Delta\ell\ H_n^{k+\frac{1}{2}}\}}{R\ \Delta\ell} - J_{sr}^{k+\frac{1}{2}} - E_\phi^k\{\frac{\sigma}{2} - \frac{\epsilon}{\Delta t}\}}{\left(\frac{\sigma}{2} + \frac{\epsilon}{\Delta t}\right)} \quad (8)$$

By duality, we obtain the discretized forms of the H field components which are

$$H_\phi^{k+1/2} = \frac{\frac{\{-\sum_{i=1}^{m} E_i^k\ \Delta L_i\}}{A} - K_{s\phi}^k + \frac{\mu}{\Delta t} H_\phi^{k-\frac{1}{2}}}{\frac{\mu}{\Delta t}} \quad (9)$$

$$H_n^{k+1/2} = \frac{\frac{2.0\{r_1 E_{\phi_1}^k - r_2 E_{\phi_2}^k + n\ \Delta\ell\ E_t^k\}}{\{R_2^2 - R_1^2\}} - K_{sn}^k + \frac{\mu}{\Delta t} H_n^{k-1/2}}{\frac{\mu}{\Delta t}} \quad (10)$$

$$H_r^{k+1/2} = \frac{\frac{\{R\ E_{\phi_1}^k - R\ E_{\phi_2}^k - n\ \Delta\ell\ E_t^k\}}{R\ \Delta\ell} - K_{sr}^k + \frac{\mu}{\Delta t} H_r^{k-1/2}}{\frac{\mu}{\Delta t}} \quad (11)$$

The principal reason for this approach in discretization is that one may easily match a FDTD grid to the nonorthogonal body fitting grid. In Fig. 1, the edges of the irregular piece fit exactly into an FD grid. As mentioned previously the irregular grid calculations require a large amount of information storage per node, primarily involving the spatial interrelationships between nodes. If

there are large interior free space regions, as in cavities, calculations are more efficiently performed on finite difference cells where spatial relationships between nodes are implicit, and thus, from a computational point of view, do not need to be stored.

Propagation Results

In this section we perform a calculation to illustrate the notion of mixed FDTD and irregular mesh calculations. Referring to Fig. 4, we perform a numerical propagation experiment involving a coaxial structure.

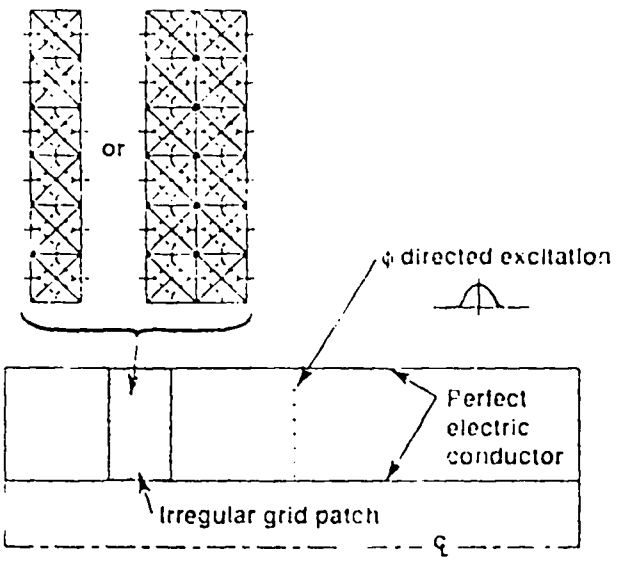

Fig. 4. Propagation in a coaxial structure.

A gaussian pulse with a $1/r$ dependence is driven in the center of the coax (in z). On the left hand side, we insert irregular grid patches that match exactly into the finite difference cells. At $t = 0$, we drive the nodes with a ϕ-directed excitation. Two identical TEM pulses are formed, with one traveling to right and the other to the left. It is found that the pulse, which must propagate through the irregular patch, emerged on the left of the patch with minimal reflection (Fig. 5).

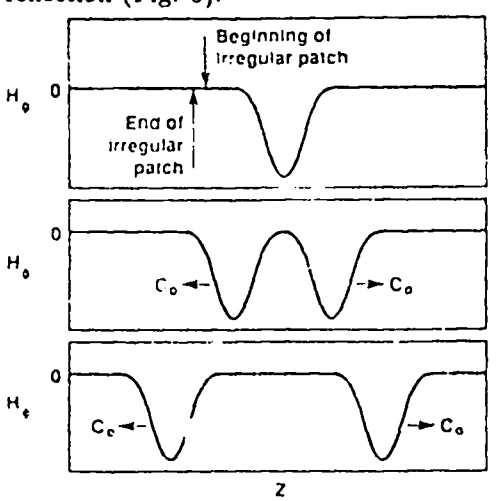

Fig. 5. Propagation of the TEM pulse through the irregular patch.

An effective reflection coefficient is computed by calculating the energy contained in the pulse after it emerges from the irregular patch (E_a) and then comparing it to the energy contained in the pulse just prior (E_b) to entering the irregular region, i.e.,

$$R_{eff} = \{1 - \frac{E_a}{E_b}\}. \tag{12}$$

The effective reflection coefficient (energy) for the patch of single cell thickness was found to be 3.280e-4. Calculations involving thicker irregular patches such as the two cell wide supergrid (Fig. 4) were performed, resulting in accuracies similar to those observed in the first case. The effective reflection coefficient for the two cell wide supergrid was approximately 5.303e-4.

When modeling curvilinear or oblique surfaces (in $r-z$), one would not, in most instances, use irregular patches much more than two cells thick. The results from the numerical propagation tests seem to indicate that at these patch thicknesses, the small numerical reflections may be to some extent typical. However, there could be instances where an irregular mesh of poor quality (i.e., nodes poorly distributed) might lead to problems in numerical reflections, phase velocity, and/or stability. We are investigating the effectiveness of the procedure in the different regimes in order to gauge the robustness of the algorithm.

Conclusions

We have demonstrated a field solver on an irregular dual grid system which will match into FD cells. The orthogonality between the overlapping dual grids permits simultaneous FD and irregular Modified-Yee calculations. This is useful since we may now model simulation boundaries with a greater degree of accuracy, and simultaneously, in regions away from the boundaries, update fields which remain distributed on finite difference cells.

References

1. J. F. DeFord, G. D. Craig, and R. R. McLeod, "The AMOS Wakefield Code," in *Proceedings of the Conference on Computer Codes and the Linear Accelerator Community*, Los Alamos, New Mexico, Jan. 22-25, 1990, pages 265-289.
2. K. S Yee, "Numerical Solution of Initial Boundary Value Problems Involving Maxwell's Equations in Isotropic Media," *IEEE Transactions on Antennas and Propagation*. Volume AP-14, May 1966, pages 302-307.
3. R. Holland, "The Case Against Staircasing," *Proceedings of the Sixth Annual Review of Progress in Applied Computational Electromagnetics*," 19-22 March 1990, pages 89-95.
4. G. D. Craig and B. Anderson, private communication, January 1990.
5. N. K. Madsen and R. W. Ziolkowski, "Numerical Solution of Maxwell's Equations in the Time Domain Using Irregular Nonorthogonal Grids," Wave Motion 10 (1988), pages 583-596.

WAKE POTENTIALS AND IMPEDANCES FOR THE ATA INDUCTION CELL *

George D. Craig
Lawrence Livermore National Laboratory, University of California
Livermore, California 94550

Abstract

The AMOS Wakefield Code is used to calculate the impedances of the induction cell used in the Advanced Test Accelerator (ATA) at Livermore. We present the wakefields and impedances for multipoles m=0, 1 and 2. The ATA cell is calculated to have a maximum transverse impedance of approximately 1000 Ω/m at 875 MHz with a quality factor Q = 5. The sensitivity of the impedance spectra to modeling variations is discussed.

Introduction

The ATA is an 80 meter long induction linac designed to accelerate a 10 kA electron beam to 50 MeV for a wide variety of applications. It consists of a 2.5 MeV injector and 190 induction cells of 250 kV each. The cells were designed to have low Q-values (Q < 10) in order to minimize spurious beam-cavity interactions. In practice the vacuum transport was limited to 6 kA by the onset of a beam breakup instability at 785 MHz. Early theoretical efforts identified the TM130 mode in the cell as the source of the instability.[1] In this paper we examine a more realistic model of the ATA cell using the AMOS Wakefield Code.[2] The AMOS code was developed to provide a more powerful method for designing low impedance cells for future high current induction linacs. The AMOS model of the ATA cell illustrates the power of this tool for evaluating induction cell designs. We present the wakefields and impedances for m=0, 1, and 2 as ATA benchmarks for improvement in future designs.

The Model

The AMOS model of the ATA induction cell is shown in Fig. 1. Beginning from the centerline at the bottom of the figure and moving upwards, the induction cell can be understood as a beam pipe with an accelerator gap connected to a radial transmission line which is terminated at its outer radius by a toroidal superstructure. This complex structure contains the vacuum-to-oil insulator, the oil, and the large ferrite toroid which provides the volt-seconds for the induction cell. The reflector at the top of the radial transmission line serves to direct beam-excited RF modes into a second thin ferrite toroid placed against the left wall of the cell where the modes are absorbed. The radius of the beam pipe is 6.725 cm and the width of accelerator gap is 2.70 cm. For modeling purposes, the cell is assumed to be cylindrically symmetric. The maximum radial extent is 41.5 cm and the end-to-end beam pipe length is 47.0 cm.

This model of the ATA cell is set up with the DRAGON geometric editor.[2] Zone sizes dr=2.24 mm and dz=2.25 mm provide a 30 zone resolution across the beam pipe and 12 zones across the radial transmission line. A few zone staircasing transition between the two is provided to reduce unrealistic diffraction scattering from the source charge. The DRAGON editor automatically zones up the cell interior, noting material changes. The typical ATA cell problem consists of about 20,000 zones. The insulator and oil have dielectric constants 5.6 and 2.3 respectively. The left and right ends of the beam pipe are terminated with a 377 ohm impedance boundary condition (IBC).

The ATA cell is actually three dimensional (3D) where it connects to high voltage feeds at the top and bottom of the cell. Beam excited RF can always propagate out these coaxial feeds as TEM waves and thereby affect the impedance of the cell. In an attempt to model this port, we use a 250 ohm IBC at the top of the cell, equal to the wave impedance of the oil, and insert a metal septum which should help couple out 2D TEM waves. Adding the septum reduces the frequency of the dominant BBU mode a few percent and moves it closer to the experimental value.

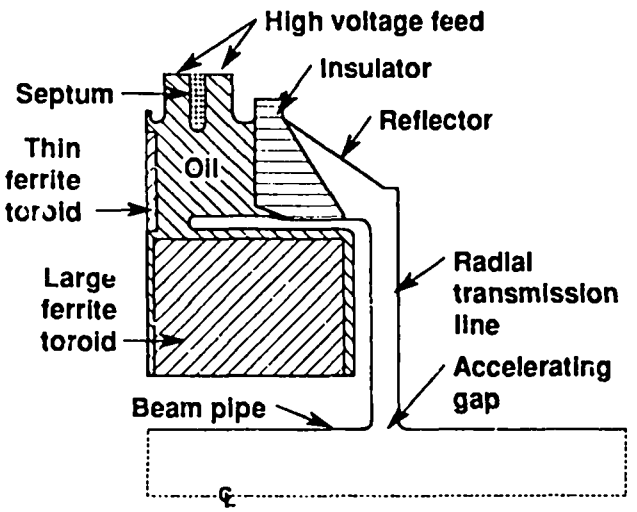

Fig. 1. DRAGON rendering of the ATA Induction Cell. The cell is rotationally symmetric about the axis, except for the power feeds.

We use a simple "get lost" model for the ferrite suggested by the experimental observation that the thin ferrite toroid readily absorbs microwaves with frequencies near 1 GHz. In this model, the two pieces of ferrite are replaced by respective 250 ohm IBC's which absorb normally incident RF modes. (Recently a more sophisticated magnetic loss model for the ferrite has been developed.[3] The main differences in the ATA impedances using the new ferrite model are noted below.)

Results

Wake potentials and impedances for the ATA cell described above are calculated with the AMOS Wakefield Code. AMOS uses finite difference time-domain techniques to calculate multipole moments of the wake potential. The impedance is then calculated from the Fourier transform of the wake potential. The wakes and impedances for the monopole (m=0), dipole (m=1), and quadrupole (m=2) moments of the ATA cell are summarized in Figs. 2-4.

* Work performed under the auspices of the US Department of Energy by the Lawrence Livermore National Laboratory under W-7405-ENG-48

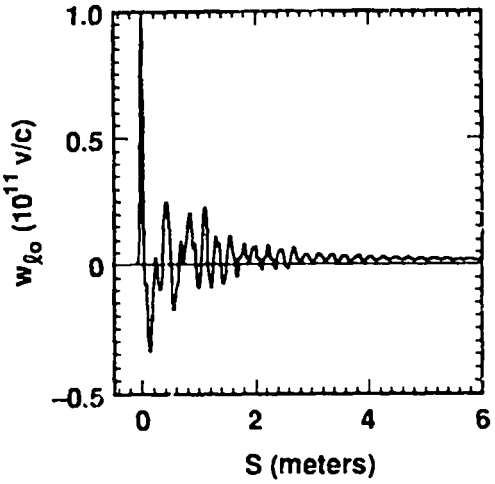

Fig. 2a. Longitudinal monopole wake potential $w_{\ell 0}(s)$ vs distance s for the ATA cell (m=0).

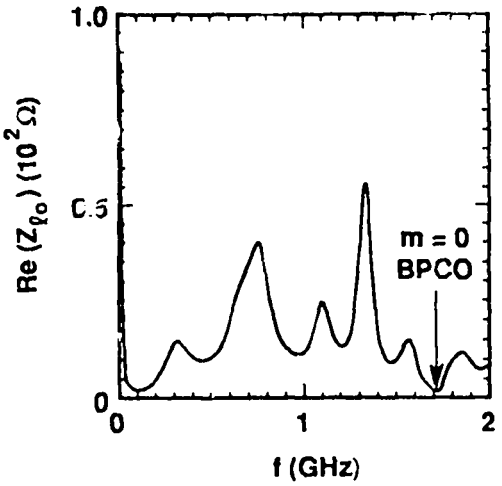

Fig. 2b. Longitudinal monopole impedance Re ($Z_{\ell 0}(f)$) vs frequency f for the ATA cell (m=0). The BPCO frequency f (TM_{01}) = 1.71 GHz.

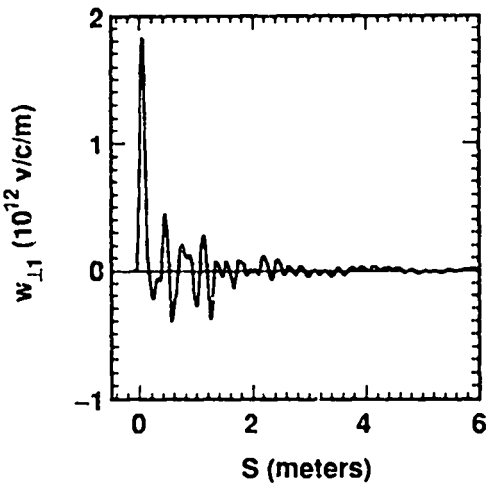

Fig. 3a. Transverse dipole wake potential $w_{\perp 1}(s)$ vs distance s for the ATA cell (m=1).

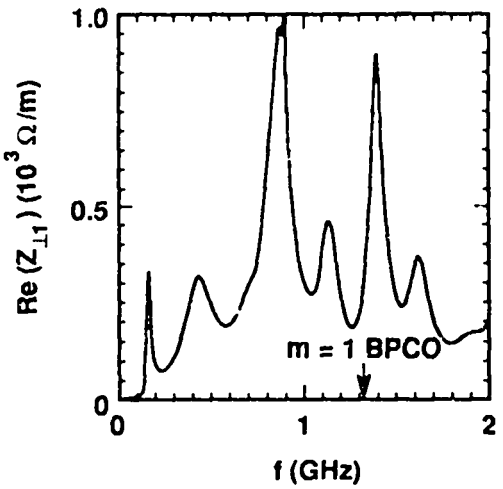

Fig. 3b. Transverse dipole impedance Re ($Z_{\perp 1}(f)$) vs frequency f for the ATA cell (m=1). The BPCO frequency f (TE_{11}) = 1.31 GHz.

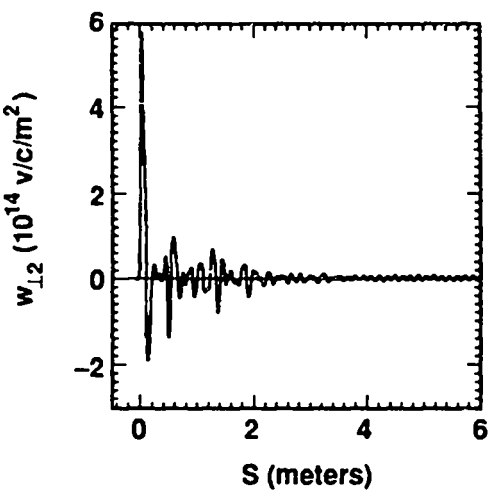

Fig. 4a. Transverse quadrupole wake potential $w_{\perp 2}(s)$ vs distance s for the ATA cell (m=2).

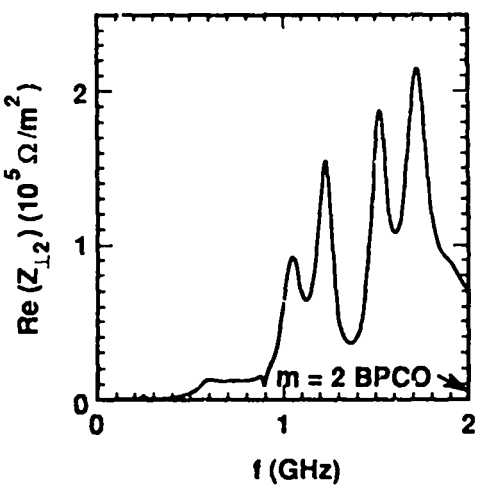

Fig. 4b. Transverse quadrupole impedance Re ($Z_{\perp 2}(f)$) vs frequency f for the ATA cell (m=2). The BPCO frequency f (TE_{21}) = 2.17 GHz.

Wake potentials extending 6 meters behind the test charge are plotted in Figs. 2a-4a. In each case the wake rapidly decays due to the energy loss out the high voltage cable and/or into the thin ferrite toroid. Ocassionally, as shown in Fig. 4a, the wake decays into a persistent oscillation. Such a situation may indicate the presence of one or more high-Q modes in an otherwise low-Q cell. These modes are undamped because their mode pattern is negligible where the damping materials are located.

The real part of the monopole, dipole, and quadrupole impedances up to 2 GHz are given in Figs. 2b-4b. It is clear from the multiple resonances in each plot that the test charge has excited many modes in the cell. An arrow in each plot indicates the frequency of the beam pipe cutoff (BPCO) for that multipole moment. Below that frequency the modes are localized in the vicinity of the cell and evanesce into the beam pipe. Above the BPCO modes can propagate in the pipe. The persistent wake potential oscillation in Fig. 4a generates a narrow spike in the impedance spectrum near the BPCO just off scale in Fig. 4b. Resonances near and above the BPCO may be sensitive to the IBC used to terminate the ends of the beam pipe and should be viewed with caution.

Discussion

The AMOS Wakefield Code and the Dragon Geometric Editor were originally benchmarked on the ATA induction cell because it was the subject of intensive theoretical and experimental work on the beam breakup (BBU) instability.[1] This work terminates the radial transmission line with a 754 ohm surface impedance and predicts a transverse impedance of 940 Ω/m for the ATA cell.[4,5] The present effort adds the large superstructure which is attached to the radial line and introduces different material properties into the cell. Model parameters are attributed to specific cell components. Finally, the simulation is carried out in the full space of possible 2D mode excitations and therefore allows for the appearance of new BBU modes and/or fine structure in the impedance spectra.

Physically, the m=1 BBU instability occurs when the beam enters a cell off-axis. The beam can excite RF modes in the cell which kick the beam further off-axis. From Fig. 3b we find that the well known "TM130" resonance for the ATA cell is calculated to be at 875 MHz and has a maximum transverse impedance of approximately 1000 Ω/m and a Q-value of 5 (FWHM). These values are essentially the same as derived from Ref. 1. On the other hand, the wake potential and impedance spectrum exhibit substantially more resonant structure than previously.

Numerous calculations have been made to test the sensitivity of the BBU spectrum to changes in the geometry, material properties, and boundary conditions of the large superstructure. It is possible, for example, to smooth out the satellite resonances around the "TM130" resonance. Other calculations suggest that this resonance may actually be a superposition of three resonances between 700-900 MHz. (Fig. 3b hints at this possibilty.) The different components can be seen more clearly by varying the impedance of the high voltage port. We also discovered a high-Q "insulator" resonance at 1.26 GHz. Though this resonance lies near the TE11 cutoff frequency of the ATA beam pipe, an extensive series of calculations with longer beam pipes prove that the mode is actually evanescing into the pipe and is not an artifact of its termination. This resonance is not present in Fig. 3b because it was surgically removed by placing a 159 ohm wave-matched impedance on top of the insulator. The same result is presumably accomplished in the actual accelerator by putting a ferrite impregnated "putty" ring around the insulator to absorb this mode.[6]

It is interesting to compare these results with those obtained by using the new magnetic loss model for the ferrite.[3] The IBC model used for Figs. 2 - 4 for the ferrite means we have replaced ferrite surfaces by wave-matched impedances which would absorb normally incident microwaves. The magnetic loss model, on the other hand, adds a magnetic conductivity term to Faraday's Law and applies to the whole ferrite volume. The real part of the relative permeability, the dielectric constant, and the magnetic conductivity are measured to be 1.0, 13, and 7.4 x 10^4 Ω/m at 875 mHz. AMOS simulations of the ATA cell with these values produced impedance spectra as complex as before. In general, the wakes and spectra are only somewhat larger than those shown in Figs. 2-4. However, the maximum transverse impedance of the "TM130" resonance has increased to 1400 Ω/m and Q = 10.

Conclusions

Monopole, dipole, and quadrupole wake potentials and impedances have been calculated for a 2D model of the ATA linear induction cell using the AMOS Wakefield Code. The microwave loss mechanisms in the cell are dominated by the high voltage feed and the strategically placed thin ferrite toroid. The massive ferrite toroid is too recessed to absorb microwaves effectively. New induction cell designs are exploring ways to reduce cell Q's even further by moving the large ferrite toroid into a more prominent position vis-a-vis the cavity modes.[2] Finally, we note that there is calculational evidence that the well known "TM130" BBU mode in the ATA accelerator may be a triplet of modes, the final resolution of which will depend on modeling the 3D transition to the high voltage feeds.

Acknowledgements

The author wishes to acknowledge the sustained support of J. F. DeFord and R. McLeod in making the AMOS Wakefield Code and the Dragon Geometric Editor into powerful tools for induction cell design and analysis. Discussions with G. J. Caporaso, A. G. Cole, and V. Kelvin Neil are gratefully acknowledged.

References

1. R. J. Briggs, D. L. Birx, G. J. Caporaso, V. K. Neil, and T. C. Genoni, "Theoretical and Experimental Investigation of the Interaction Impedances and Q Values of the Accelerating Cells in the Advanced Test Accelerator," Particle Accelerators, 18 (1985) 41.

2. J. F. DeFord, G. D. Craig, and R. R. McLeod, "The AMOS Wakefield Code," Proc. Conf.Computer Codes and the Linear Accelerator Community, p. 265, Los Alamos, New Mexico, Jan. 22-25, 1990.

3. J. F. DeFord and G. Kamin, "Application of Linear Magnetic Loss Model of Ferrite to Induction Cavity Simulation," this Proceedings.

4. The impedance in Ref. 1 assumes a 7.50 cm beam pipe radius and a 2.54 cm gap. In this note, it is rescaled to the ATA dimensions.

5. G. D. Craig and J. F. DeFord, "The Connection Between SLAC-DESY and LLNL Wakefield Formalisms," LLNL Report, UCID-21641, in preparation.

6. D. Birx and R. J. Briggs, "Corner Reflector for RF Mode Supression in the ATA/ETA Cells," LLNL Beam Research ATA Note #142, Feb. 1981.

APPLICATION OF LINEAR MAGNETIC LOSS MODEL OF FERRITE TO INDUCTION CAVITY SIMULATION *

J. F. DeFord and G. Kamin
L-626, LLNL, Livermore, CA 94550

Abstract

A linear, frequency independent model of the rf properties of unbiased, soft ferrite has been implemented in finite-difference, time-domain, electromagnetic simulation code AMOS for the purposes of studying linac induction cavities. The simple model consists of adding a magnetic conductivity term ($\sigma_m \vec{H}$) to Faraday's Law. The value of σ_m that is appropriate for a given ferrite at a particular frequency is obtained via an rf reflection experiment on a very thin ferrite toroid in a shorted coaxial line. It was found that in the frequency range 100 to 1000 MHz, the required value of σ_m varies only slightly ($<$ 10%), and so we approximated it as a frequency independent parameter in AMOS. A description of the experimental setup and the technique used to extract the complex μ from the measurements is described. The model has been used to study the impedances of the DARHT induction cavity, and comparisons between these experimental measurements and AMOS calculations is presented. Implementation of a frequency dependent version of this model in AMOS is being pursued, and a discussion of this effort is given.

Introduction

Ferrite can play an important role in damping RF modes in induction linac acceleration modules [1]. In the frequency range of interest for the induction cells of the Advanced Test Accelerator (ATA) and the Experimental Test Accelerator - II (ETA-II), which is 100 - 1000 MHz, skin depths in the (unbiased) soft ferrite typically used in induction cores are a few centimeters, and thus relatively thin slabs may be placed at strategic locations in a cell to effectively lower the Q's of troublesome modes. In order to quantify the effect that ferrite has on the impedances of cavity modes using a time-domain code such as AMOS [2], it is necessary to have an electromagnetic model of ferrite that accounts for the lossy nature of the material. For incident fields that result in large swings in the magnetization in the ferrite, the appropriate model is nonlinear and will in general depend on the history of the sample. However, for incident fields that produce only small perturbations on the magnetization, a linear, tensor permeability is appropriate [3]. When the sample has zero net magnetization (virgin sample), there is no preferred direction in the material, and the tensor collapses to a scalar. In the remanent state in soft ferrites there is a preferential direction that depends on the recent bias history of the sample, and this will lead to small off-diagonal elements in the tensor. For the purposes of this work we have *postulated* that the permeability may be characterized by a scalar in the absence of an applied field. Experimentally this appears justified for the samples we considered as there were negligible differences between the results for virgin ferrites and samples in a remanent state.

To represent the complex scalar permeability, $\mu = \mu' - i\mu''$, of unbiased ferrite in the time domain, we add a magnetic conductivity term to Faraday's Law, i.e.,

$$-\nabla \times \vec{E} = \sigma_m \vec{H} + \mu' \dot{\vec{H}}, \tag{1}$$

where σ_m is the magnetic conductivity, which is related to the imaginary part of μ by

$$\sigma_m = \omega\mu'' = \omega\mu_o\mu_r'', \tag{2}$$

where μ_o is the free-space permeability. In general, σ_m is a frequency dependent parameter, and to incorporate this characteristic into AMOS requires a significant extension to the standard finite-difference, time-domain algorithm. While this type of capability is the object of some interest in the simulation community [4], an efficient algorithm for general frequency dependencies is not yet available, and for this effort we assume that σ_m is independent of frequency. It was found experimentally that its value did not change significantly over the frequency range under investigation (100 MHz - 1 GHz), although outside this range the frequency dependence does become important. The variation in μ_r' is larger than the variation of σ_m over the frequency range, but as it is small as compared with either μ_r'' or ϵ_r over most of the range, its variation is relatively unimportant.

Experiments on Small Ferrite Cores

To obtain values of σ_m that are representative of the ferrites used as induction cores, reflection measurements were made on thin samples, from which the complex permeability and σ_m could be deduced. The experimental setup is illustrated in Fig. 1. The ferrite samples used in the experiments were thin toroids of rectangular cross section that had an outside diameter of 3.1 cm, an inside diameter of 1.9 cm, and had axial thicknesses of 1 mm and 2 mm. The samples were heated above the Curie temperature (130°C for the ETA-II ferrite, and 205°C for the ATA ferrite) and then cooled to room temperature prior to making the measurements to ensure that they were in an unmagnetized state.

The measured reflection coefficient (magnitude and phase) for the 1 mm thick samples of ETA-II and ATA ferrites are shown as functions of frequency in Fig. 2. The permeability is obtained by inverting the expression for the

* Work performed jointly under the auspices of the U. S. Department of Energy by LLNL under contract W-7405-ENG-48, for the SDIO and the U. S. Army Strategic Defense Command in support of SDIO/SDC-ATC MIPR No. W43-GBL-0-5007

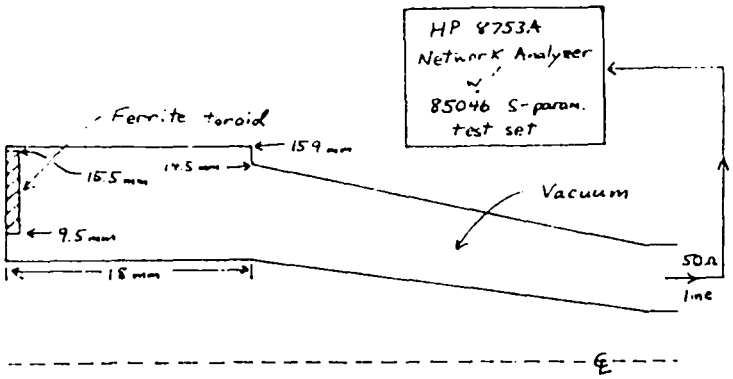

Fig. 1. Schematic of reflection experiment setup. Geometry is cylindrical, concentric about dashed centerline. 1 mm thick ferrite toroid is shown; experiments were also done on 2 mm thick samples. Effects of radial discontinuity and small impedance mismatch accounted for with calibration run.

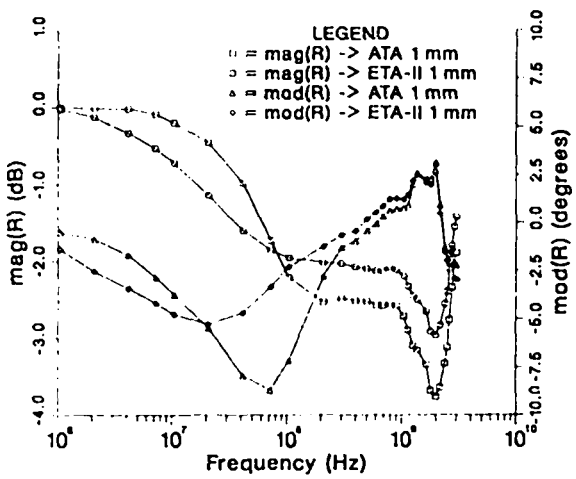

Fig. 2. Measured reflection coefficients, normalized by the reflection realized when no ferrite is present, for 1 mm thick samples of the ATA and ETA-II ferrites.

normalized reflection from a slab, of thickness $\Delta = 1$mm, backed by a short,

$$R = \frac{\left[\left(1+\exp^{-i2k\Delta}\right) - \eta_r\left(1-\exp^{-i2k\Delta}\right)\right]\exp^{i2k_o\Delta}}{\left(1+\exp^{-i2k\Delta}\right) + \eta_r\left(1-\exp^{-i2k\Delta}\right)}, \quad (3)$$

where $\eta_r = \sqrt{\mu_r/\epsilon_r}$ is the relative wave impedance of the ferrite, k is the wave number in the ferrite, and k_o is the free space wave number. R as shown in Eqn. (3) has been normalized by the reflection obtained when no material is present.

A first estimate of μ_r is obtained using the small argument ($|2k\Delta|^2 \ll 1$) expansion of Eqn. (3), i.e.,

$$\mu_r \approx 1 + \frac{1-R}{i2k_o\Delta}, \quad (4)$$

and then this value is refined using a numerical search. Values of μ_r for the ETA-II and ATA ferrites are shown in Fig. 3. The curves show a broad resonance or relaxation at low frequencies, and then a second resonance around 2 GHz. These two features have been attributed to domain wall motion and to spin rotation within domains, respectively [5]. Values of σ_m derived from the ferrite permeability are shown in Fig. 4. Note that they are relatively constant between 100 MHz and 1 GHz, and that there are only small differences between the values derived from the 1 mm samples and those taken from the 2 mm samples. These small differences may result from variations between samples, or from an inaccurate value for the permittivity. For both the ATA and ETA-II ferrites, the permittivity was taken to be $\epsilon_r = 13$, and assumed to be independent of frequency.

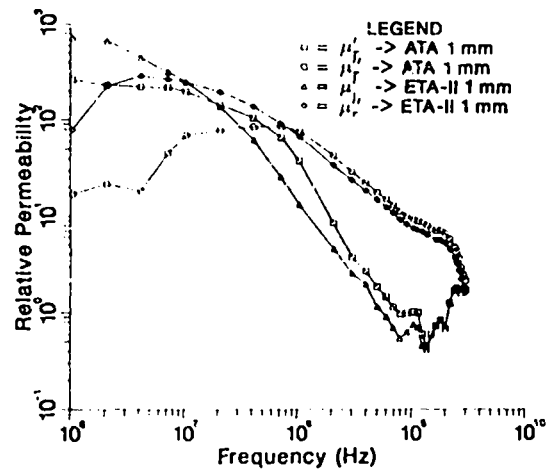

Fig. 3. Values of μ_r derived from the measured reflection data using Eqn. (3). Values shown have been modified (multiplied by the ratio of short area to core area = 1.3) to account for the incomplete coverage of the shorting plane by the ferrite.

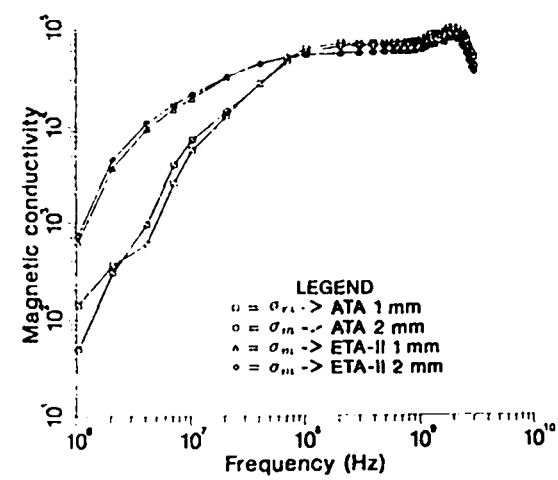

Fig. 4. Values of σ_m derived from the permeabilities shown in Fig. 3 using Eqn. (2).

Induction Cells: Simulation and Experiment

The first prototype induction module (called the Mod 0 cell) of the Dual Axis Radiographic Hydrodynamics Test Facility (DARHT) accelerator has recently been fabricated, and RF impedance measurements have been made on this cell with a partial ferrite load (see Fig. 5). The ferrite

used in the DARHT prototype is identical to the ferrite used in the ATA induction modules, and for this comparison the power feed lines have been removed from the cell and the remaining holes were plugged. These modifications have the effect of making the cell rotationally symmetric, which then allows a direct comparison between the experimentally measured impedances and the AMOS predictions. The ferrite properties that were used in the

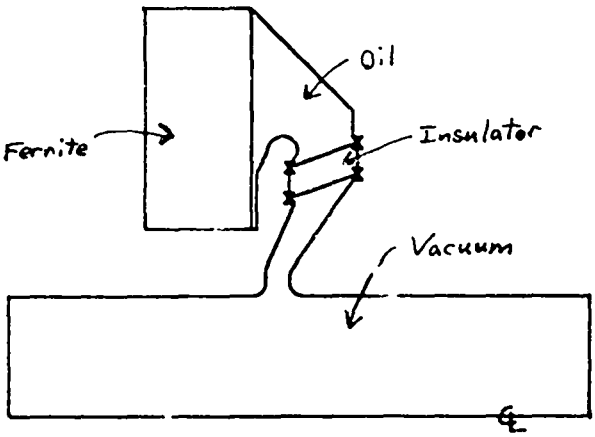

Fig. 5. Geometry of DARHT prototype cell with power feed lines removed. Cell is rotationally symmetric about centerline. Shown with partial ferrite load.

simulation were obtained from the small core experiment on the ATA ferrite, which yielded values of $\mu_r' = 1.0$ and $\sigma_m = 7.4 \cdot 10^4 \Omega/m$. The experimental and calculated values are in good agreement, as shown in Fig. 6. Additional measurements are currently being taken on the SNOMAD and ETA-II accelerator modules, and these data will be compared against AMOS simulations to provide additional information about the model.

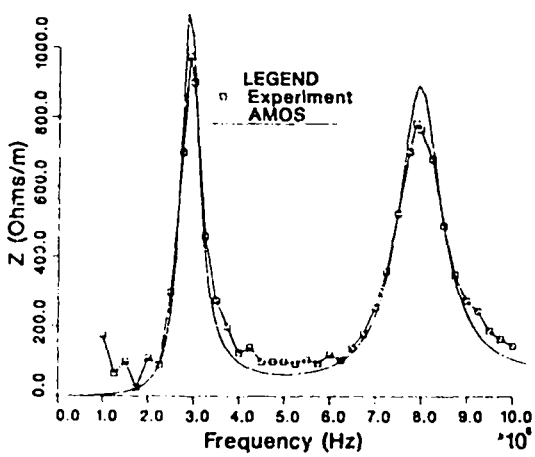

Fig. 6. Measured and calculated transverse (dipole) impedances vs. frequency for DARHT prototype cell.

If impedance data outside the given frequency range had been required, the values of σ_m would change significantly, and the material could no longer be treated as non-dispersive in a spread-spectrum calculation. In general, time-domain modeling of dispersive materials requires a convolution, which, in the case of a frequency dependent permeability, takes the form

$$\vec{B}(t) = \int_{\tau=0}^{t} \mu(t-\tau)\vec{H}(\tau)d\tau. \tag{5}$$

This equation is very expensive from a computational standpoint because it requires previous values of $\vec{H}$ for evaluation. Work is ongoing to alleviate the computational burden by representing σ_m in a form for which the convolution can be computed as a running sum, thereby eliminating the need to store previous values of $\vec{H}$.

Conclusions

A simple, linear model of the RF behavior of lossy soft ferrites has been implemented in the electromagnetic simulation code AMOS. The model represents the RF magnetic losses via a magnetic conductivity term in Faraday's Law. The value of σ_m that is appropriate for the ferrite of interest is obtained by making 1-D reflection measurements on thin samples. The model has been validated by using it to simulate the reflection experiments, and also by measurements made on the DARHT accelerator induction module. The current incarnation of the model is frequency independent; however, work is underway to incorporate the measured frequency dependence of the permeability to enhance the frequency range of applicability of the model.

Acknowledgements

The authors wish to acknowledge the efforts of Mike Burns and Don Liska of LANL for providing the geometric model of the DARHT cell, and for their work with AMOS that originally showed the deficiencies of using boundary conditions to mock up the effects of the ferrite. In addition, the authors acknowledge the efforts of Paul Allison, Linda Walling, and Alan Shapiro (LANL) in making the experimental measurements of the RF impedances of the DARHT cell.

References

1. R. J. Briggs, D. L. Birx, G. J. Caporaso, V. K. Neil, and T. C. Genoni, "Theoretical and experimental investigation of the interaction impedances and Q values of the accelerating cells in the Advanced Test Accelerator," *Particle Accelerators*, **18**, Jan., 1985, pp. 41-62.
2. J. F. DeFord, G. D. Craig, and R. R. McLeod, "The AMOS wakefield code," *Proceedings of the Conference on Computer Codes and the Linear Accelerator Community*, Los Alamos, New Mexico, Jan. 22-25, 1990, pp. 265-289.
3. R. F. Soohoo, *Theory and Application of Ferrites*, Prentice-Hall, New Jersey, 1960.
4. R. J. Luebbers, F. P. Hunsberger, and K. S. Kunz, "FDTD formulation for frequency dependent permittivity," *Proceedings of the 1989 IEEE AP-S International Symposium*, **1**, pp. 50-53.
5. G. T. Rado, R. W. Wright, and W. H. Emerson, "Ferromagnetism at very high frequencies. III. Two mechanisms of dispersion in a ferrite," *Physical Review*, **80**, Oct., 1950, pp. 273-280.

MUTUAL COMPENSATION OF WAKEFIELD AND CHROMATIC EFFECTS OF INTENSE LINAC BUNCHES*

J. T. Seeman and N. Merminga
Stanford Linear Accelerator Center, Stanford University, Stanford, CA 94309

Abstract

Mutual compensation of transverse and chromatic effects for intense electron bunches in a high-energy linac is a recent Novosibirsk idea which provides a new control of emittance enlargement. In this paper we elaborate on the principles and constraints for this new technique which requires careful matching of internal bunch parameters with external forces. With specific values of the bunch length, bunch intensity, and klystron phasing, the transverse-wakefield-induced forces within the bunch can be cancelled by energy-dependent forces from the quadrupole lattice at all positions along the linac. Under these conditions the tolerances for quadrupole alignment, dipole stability, and injection launch errors are significantly relaxed.

1. Introduction

The primary goal of linear colliders is to maximize the integrated luminosity for the experimental program. Small transverse emittances are a necessary condition for maximum luminosity. However, a number of single-particle and current-dependent effects cause emittance enlargement.[1] In particular, the spectrum of particle energies within the bunch allow chromatic phase-space mixing. Furthermore, current-dependent wakefield effects can result in emittance dilution. A technique[2,3] emanating from the Institute of Nuclear Physics in Novosibirsk called "autophasing" can be used to mutually cancel these chromatic and wakefield effects. A description of the physics principles of this technique, the method of application, and an example for the SLC will be discussed in this note.

In Section 2 the difference between autophasing and present practice is discussed. In Section 3 we start from the equation of motion of a particle in the presence of transverse wakefields and derive the condition for autophasing. Furthermore, we attempt an intuitive discussion of autophasing. In Section 4 we describe the procedure used to arrange the linear focusing of a lattice in order for autophasing conditions to hold. Finally, in Section 5 we apply the results of this analysis to the SLC linac.

2. Present Situation

Off-axis particles traversing an accelerating structure generate transverse wakefields which deflect all trailing particles. There are many causes for a bunch to be off-axis—betatron oscillations, local bumps, head-tail transverse offsets, or collimator deflections. These wakefield deflections accumulate along the linac and cause emittance enlargement of the beam. This beam blowup by wakefields can be reduced by BNS damping. The effect of BNS damping is to reduce the effective defocusing nature of the wakefield force by providing extra focusing for the core and tail particles. This is accomplished by lowering the energy of the trailing particles relative to the head so that the quadrupole lattice focuses them more strongly. The trailing particles are differentially lowered in energy by back-phasing klystrons early in the accelerator and forward-phasing downstream klystrons to keep the energy spectrum small at the maximum energy. The overall goal is to minimize the emittance at the end of the linac using as little extra acceleration as possible. The best configuration depends on many machine parameters and must be calculated for each case. However, with this adaptation of BNS damping the effective emittance is not controlled in the middle of the linac, and sensitivity to local errors is a result.

In this paper we present a new method of controlling transverse wakefields originally suggested by Balakin et al.[2,3] This method is based on the phenomenon of autophasing: all particles within the bunch—taking into account all forces acting on them—should oscillate with the same amplitude, phase and frequency. The significance of autophasing is that the bunch will remain coherent in its motion independently of any dipole-like perturbations to its trajectory at all locations, and hence the emittance will remain unchanged.

3. Autophasing

Let us assume a relativistic bunch whose transverse dimensions are zero. Let $x(z,s)$ denote the displacement of a particle in the bunch as a function of z, the longitudinal position relative to the center of the bunch (z is positive towards the head of the bunch), and s, the distance along the accelerator.

If we assume that the beam energy increases linearly with s as a result of acceleration and that the distance to double the energy is long compared to the betatron wavelength, then the equation of motion for $x(z,s)$ can be written:

$$\frac{d^2}{ds^2}\, x(z,s) + k^2(z,s)\, x(z,s) = \frac{r_0}{\gamma(z,s)} \int_z^\infty dz' \rho(z')\, W_\perp(z'-z)\, x(z',s) \quad , \tag{1}$$

where $\gamma(z,s)$ is the beam energy at position s in units of mc^2; ρ is the line density of the particles in the bunch normalized to the total number of particles in the bunch N; $eW_\perp x$ is the traverse field produced by a point charge displaced from the axis by x at a distance $z'-z$ behind that point charge; $k(z,s) = 2\pi/\lambda(z,s)$ where $\lambda(z,s)$ is the betatron wavelength; and $r_0 = e^2/mc^2$ is the classical radius of the electron. In writing this equation we have assumed that the betatron focusing is provided by a smooth function, rather than from a series of discrete quadrupole magnets.

To find the conditions for autophasing we attempt to find an identical solution for all particles independent of longitudinal position within the bunch. Let us consider an expression of the form

$$x(z,s) = x_0 \cos(k_0 s + \phi_0) \quad , \tag{2}$$

where ϕ_0 is an arbitrary initial phase, and derive the condition that needs to be satisfied in order for this expression to be a solution to Eq. (1). Inserting Eq. (2) into Eq. (1) and noting that Eq. (2) is independent of z, and hence that it can come out of the integral, we find

$$k^2(z,s) = k_0^2 + \frac{r_0}{\gamma(z,s)} \int_z^\infty dz' \rho(z')\, W_\perp(z'-z) \quad . \tag{3}$$

To gain some insight into the purpose of the previous mathematical manipulations, we first discuss the meaning of Eq. (3) and then we come to the solution of the equation of motion, Eq. (2). A particle at position z within the

*Work supported by Department of Energy contract DE-AC03-76SF00515.

bunch, subjected to wakefield forces from all the other particles ahead in the bunch, will experience a frequency shift given by the second term on the right-hand side of Eq. (3). The first term on the right-hand side is the square of the frequency with which all particles are required (by the form of the solution) to oscillate. For this condition to be possible, the external focusing forces must be such that when they act *alone* on the particle, its betatron oscillation frequency is given by $k(z,s)$. Hence, by carefully balancing the two frequencies—one coming from the chromatic effects, the other from the transverse wakefield effects—all particles in the bunch will oscillate with the same amplitude, phase, and frequency, as Eq. (2) suggests. It is important to note that the autophasing condition, Eq. (3), is independent of the transverse offset x_0 of the bunch. This condition is to be satisfied at all linac positions s.

To further realize the significance of this result, suppose that a dipole-like error perturbs the trajectory of a bunch along the linac, giving rise to a betatron oscillation. Since the autophasing condition is independent of the transverse displacement, it still holds true in the presence of betatron oscillations of arbitrary amplitude, and hence in the presence of any type of errors causing betatron oscillations in the machine! Dipole-like errors may come from injection errors in position and angle, from quadrupole displacements, RF kicks, or dipole strength changes. In the presence of any of these errors, the bunch will remain "compact," maintaining the beam emittance constant. Further, this technique is expected to work successfully for any charge density, as long as Eq. (3) is satisfied for each point in the linac, thus ensuring the emittance preservation throughout the whole machine! [It should be pointed out that chromatic effects can still occur when beam steering is done on a scale that is short when compared to $\lambda(s)$.]

Next we demonstrate how the lattice parameters can be adjusted so that the external energy-dependent forces compensate the internal wakefield forces, and the condition for autophasing is satisfied.

4. Lattice Adjustment: k_E

Let us define $k_W(z)$ as the right-hand side of the autophasing condition, Eq. (4). The subscript W serves as a reminder that this expression depends on the wakefields and on the internal parameters of the bunch. The goal now is to adjust the quadrupole lattice and klystron phasing so that the energy-dependent forces cancel the transverse wakefield forces at all points in the linac. Equivalently, we need to determine an energy-dependent function of z, $k_E(z)$, such that

$$k_W(z) = k_E(z) \quad . \tag{4}$$

In Fig. 1 we give a pictorial representation of Eq. (4). Figure 1(a) is a plot of the bunch density along the bunch. The Gaussian bunch length in this example is 1.75 mm and we assumed 3.5×10^{10} particles per bunch. Figure 1(b) displays the integrated transverse wakefield as a function of the longitudinal position z. By adding the frequency of the bunch head k_0 to the integral according to Eq. (4), we obtain Fig. 1(c) which is a plot of k_W as a function of z. Figure 1(d), on the other hand, shows the beam energy along the bunch. Longitudinal wakefields have been taken into account and the klystron phase has been chosen to be 8° in this particular example. Finally, Fig. 1(e) is a plot of the betatron frequency along the bunch as determined from lattice considerations and the bunch energy. The goal is to match

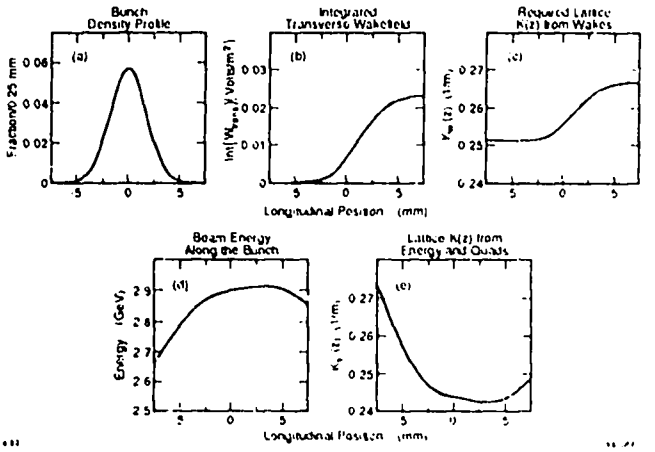

Fig. 1. Schematic representation of the mutual compensation of wakefield and chromatic effects of a bunch. This example is taken at the 100 m position in the linac.

the shape of Fig. 1(c) to the shape of Fig. 1(e) by varying the bunch length and the klystron phases.

From the definition of the chromaticity of a lattice ξ:

$$\frac{\delta\nu}{\nu} = \xi\frac{\delta E}{E} \quad , \tag{5}$$

k_E is given by

$$k_E(z) = k_0\left[\frac{E_0 + \xi(E(z) - E_0)}{E_0}\right] \quad , \tag{6}$$

where E_0 is the energy of the head of the bunch. The energy $E(z)$ corresponding to the betatron wave number $k_E(z)$ is given by

$$E(z) = E_{\rm inj} + \sum_{i=1}^{n}\left[\Delta E_i \cos(\phi_i + \phi(z)) + \Delta s_i \int_z^{\infty} W_{\parallel}(z'-z)\,\rho(z')dz'\right] \quad , \tag{7}$$

where $E_{\rm inj}$ is the injection energy; ϕ_i are the klystron phases (which are free parameters); $\phi(z) = 2\pi z/\lambda_{\rm RF}$, where $\lambda_{\rm RF}$ is the RF wavelength; ΔE_i is the maximum energy gain in the distance Δs_i; and the last term on the right-hand side of Eq. (7) is the longitudinal wakefield contribution to the particle energy.

Thus, the goal of lattice parameter adjustment is to determine the values of the bunch length and the klystron phases so that $k_E = k_W$ at every point along the bunch and the linac. In the following section we use the SLC linac as an example to demonstrate how this careful matching can be done in a realistic situation.

5. Autophasing Applied to the SLC

The applicability of autophasing to the SLC linac was studied with the goal of potentially improving the luminosity. A computer program was written to match the lattice and wakefield-determined spatial frequencies $k_E(z)$ and $k_W(z)$ over the length of a bunch at every longitudinal position along the linac. In parallel, a proposal to experimentally study this effect on the SLC has been made.[6]

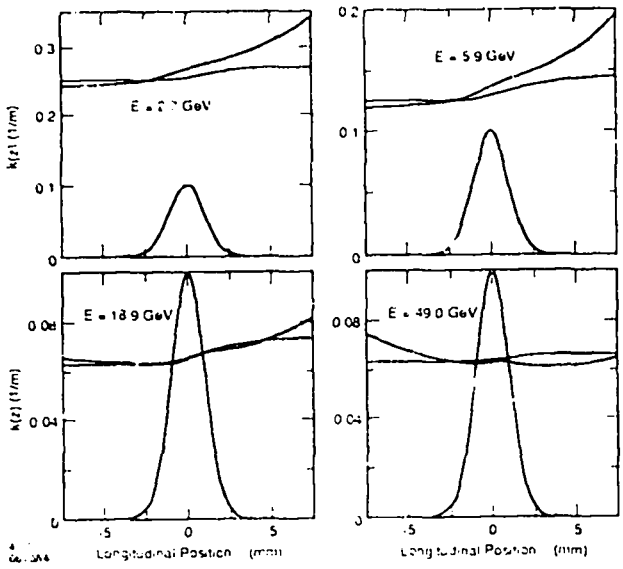

Fig. 2. Case 1. Klystron phases $\phi_i = -25°, -25°, -25°, 18°, 18°, 18°, 18°$, and $18°$; bunch length $\sigma_z = 1$ mm; and final energy spread $\sigma_E/E = 0.30\%$.

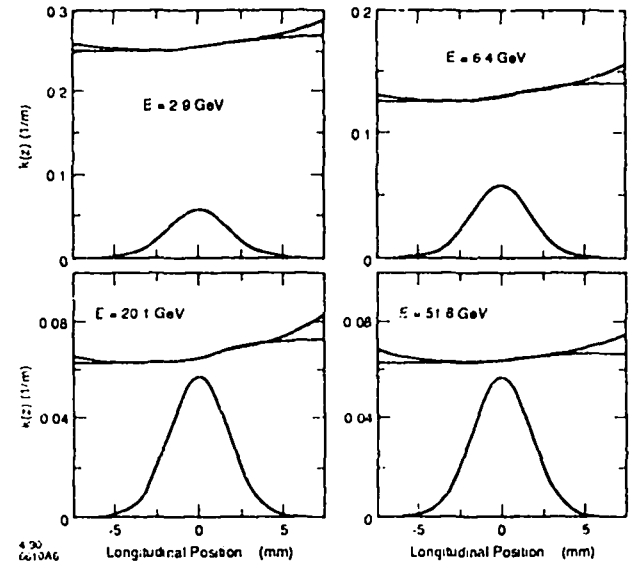

Fig. 3. Case 2. Klystron phases $\phi_i = -7°, -10°, -20°, -1°, -1°, 0°, 0°$, and $0°$; bunch length $\sigma_z = 1.75$ mm; and final energy spread $\sigma_E/E = 1.40\%$.

Computation inputs were made as realistic as possible. The transverse and longitudinal wakefields were those calculated for the SLAC linac.[7] The betatron focusing was assumed to be provided by a smooth function. A detailed description of the computer program can be found elsewhere.[8] The autophasing match was studied for 6 SLC linac conditions, assuming 3.5×10^{10} particles per bunch. Only two of the six cases studied are presented here. The rest can be found in Ref. 8. The functions shown in the following plots resulting from the calculations are for $k_E(z)$, $k_W(z)$, and $\rho(z)$ at four locations in the linac.

Case 1

Corresponds to the presently used BNS damping conditions and is shown in Fig. 2. The autophasing match is not good, as shown by the separation of k_E and k_W in the region of the bunch core.

Case 2

The bunch length was increased to 1.75 mm and the phases then were optimized. Results are shown in Fig. 3. A very good match is obtained over the entire bunch. The internal frequencies of the curves match very well.

Conclusions

In this paper we have studied the requirements of autophasing. By carefully matching the internal bunch parameters with external forces, mutual compensation of transverse and chromatic effects for intense electron bunches can be achieved. With this compensation it is expected that the alignment and launch tolerances can be significantly relaxed.

We started from the equation of motion of a particle in the presence of transverse wakefields and derived the condition for autophasing. We then discussed the physical meaning of the result and concluded that its significance lies in the fact that the bunch will remain coherent in its motion independently of any dipole-like perturbations to its trajectory, and hence the emittance ideally will remain unchanged.

These results were then applied to the SLC linac. In our numerical computations we used the transverse and longitudinal wakefields calculated for the SLAC linac, but assumed smooth focusing. We determined the appropriate klystron phases and bunch lengths for autophasing to hold in several positions in the linac. These initial studies indicate that autophasing is possible for the SLC, and that more studies and possibly beam experiments should be pursued. Additional studies of tolerances and applicability using FODO lattices are being made. The effects of non-Gaussian bunch shapes (e.g., those produced by the SLC bunch length compression system) will also be studied, and reported elsewhere.

References

1. J. T. Seeman, IEEE Proc. 89CH2669-0, Chicago, 1989, p. 1736, and SLAC-PUB-4886 (1989).
2. V. Balakin, A. Novokhatsky, and V. Smirnov, 12th Int. Conf. on High Energy Accel.; FNAL (1983).
3. V. Balakin, SLAC-Report-355, 55 (1988).
4. A. W. Chao, B. Richter, and C.-Y. Yao, Nucl. Instrum. Methods **178**, 1-8 (1980).
5. K. Bane, IEEE Trans. Nucl Sci. **NS-32**, 2398 (1985).
6. V. Balakin, V. Parkhomchuk, and V. Shiltsev, "The Experimental Examination of 'Autophasing for Transverse Oscillations' on the SLC at SLAC," Proposal from the Institute of Nuclear Physics, Novosibirsk, August 1989.
7. K. Bane and P. Wilson, Proc. 11th Int. Conf. on High Energy Accel. CERN (Birkhäuser Verlag, Basel, 1980) p. 592.
8. J. T. Seeman and N. Merminga, SLAC-PUB-5220 (May 1990).

NEW COMPENSATION OF TRANSVERSE WAKEFIELD EFFECTS IN A LINAC BY DISPLACING ACCELERATING STRUCTURES*

John T. Seeman
Stanford Linear Accelerator Center, Stanford, California 94305

Abstract

Beams accelerated in the linac of a linear collider experience transverse wakefield effects due to small residual misalignments of the accelerating structure. These wakefields lead to emittance growth. The traditional correction method is to add induced betatron oscillations to the trajectory of the beam to counteract the effects of the unknown actual errors and, thereby, reduce the emittance enlargement. However, practical considerations make this solution operationally difficult. In this note a second correction method is proposed where the positions of the accelerating structures are remotely controlled. By adding position offsets of the RF structure at the spatial frequency of betatron oscillations, direct wakefield reduction can be made. A hardware solution suitable for the SLC is presented which does not move the quadrupoles or position monitors.

History

The correction method for misaligned structures which is traditionally proposed [1,2] has three parts. (A) The beam is steered to the axis of the linac at low beam currents. (B) The beam intensity is then raised, exposing the effects of the misaligned structures in terms of trajectory errors and emittance growth. (C) The injection launch conditions into the linac (x,x',y,y') of the centroid of each beam are adjusted to minimize the emittance at the exit of the linac. Trajectory amplitudes comparable to the beam size are usually required. Experimentally, this correction has been shown to work [3]. However, the following practical considerations make this solution difficult to use. The optimization requires eight parameters to be adjusted simultaneously. This pushes the limit for human control, requiring computer feedback and complicated data analysis (spot shape determination). Furthermore, the reference trajectories for the launch feedback controllers need non-zero values which change with time. Finally, the requirement that both beams be steered at low currents then raised to high currents leads to beam loss problems (the trajectories change drastically), makes positron production problems (e.g. scavenger extraction energy changes and Sector 1 beam loading), and exasperates current dependant effects of the damping rings and bunch length compressors.

Effects of randomly misaligned accelerating structures

A two particle model of transverse wakefields will be used to calculate the effects of random displacements of accelerating structures. The only misalignments in the accelerator complex are the disk-loaded waveguide sections through which the beams pass. The head particle of charge N/2 traverses the entire linac in a straight line. The tail particle (charge N/2) follows the same trajectory as the head until a misaligned accelerator is reached as is shown in Fig. 1. The transverse wakefields produced by the head in this off-axis accelerator will deflect the tail which will subsequently execute a betatron oscillation. The betatron oscillation from all the misalignments will add linearly.

* Work supported by Department of Energy contract DE-AC03-76SF00515.

For these calculations we assume smooth focusing with constant betatron wavelength λ_β, no acceleration (can be added if needed), and lengths of offset accelerators that are short compared to λ_β. The transverse offset x_2 of the tail particle at the end of the linac is given by the standard transport equation downstream of the position (z_i) of the ith misaligned accelerator.

$$x_2(L) = \theta_i \beta_0 \sin[k(L - z_i)] \qquad (1)$$

where the deflection angle θ_i is given by

$$\theta_i = C d_i l_0 / E_0 \qquad (2)$$

and

$$C = (e^2 N W)/2. \qquad (3)$$

W is the value of the wakefield potential on the tail particle, d_i the transverse offset of the accelerator structure, l_c the length of a typical RF structure, e the electron charge, E_0 the beam energy, β_0 the average betatron function, and k the lattice spatial frequency. $L = n\, l_0$ where n is the number of structures. Each structure is assumed to have a uniform offset. Angles can easily be added but do not add anything new to the calculation.

An rms tail offset for an ensemble of machines can be calculated by summing the offsets over the entire linac assuming that the accelerator offsets are random with a normal distribution. Replacing the summation by an integral, the rms offset can be obtained.

$$< x_2(L) >_{rms} = C \beta_0 < d_{rms} > l_0 \sqrt{n/2} / E_0 \qquad (4)$$

For example, with $N=5 \times 10^{10}$, $< d_{rms} > = 400$ microns, $\beta_0 = 20$ m, $l_0 = 12$ m, $E_0 = 10$ GeV, $C=0.011$ GeV/m^2 (particle separation = 2 mm), and n =232, then $< x_2(L) >_{rms} = 1.1$ mm. This value significantly enlarges the emittance (X 20) and devastates the luminosity. However, if the beam is launched with a selected offset and angle, then wakefield effects due to the forced betatron oscillation can be made to reduce the accumulated effects from random misalignment on the tail [1] calculated from Eqn. (1).

Complications from BNS damping

A method to reduce the effects of injection launch jitter on emittance growth is to introduce an energy difference between the head and tail of the bunch [2,4]. This method works most effectively if the following condition is satisfied (from the two particle model).

$$e^2 N W / (4 E_0 k \delta k) = 1 \qquad (6)$$

Here $k = 2\pi / \lambda_\beta$. The difference in k between the head and tail is δk, with the tail having the lower energy and higher k. The difference in k is chosen to make the wakefield force and the additional quadrupole lattice focusing cancel. When Eqn. (6) is

satisfied,the tail follows the head exactly along the linac during a betatron oscillation and no growth occurs. Therefore, once BNS damping is used, the above correction scheme of induced injection launch oscillations to cancel misalignment errors is no longer effective. Another method must be used. (The BNS damping actually used in the SLC does not satisfy Eqn. (6) exactly and, thus, injection errors can be used to cancel structure offset effects. However, the magnitude of the required injection errors must be larger than without BNS damping.)

The effects of coherent structure misalignments

A control of the tail displacement can be obtained by deliberately displacing the RF structure at the betatron spatial frequency through external means. With mechanical displacements set at the betatron frequency of the bunch tail, all the deflections received by the tail add coherently and a large effect is obtained. Since the lattice is unchanged, the trajectory of the head particle remains a straight line. These driven offsets will be used to cancel random errors in the structure alignment. BNS damping will not affect the coherent addition of the displacement effects if the spatial frequency of the displacements is that of the tail of the bunch (not the head) including both the lattice and wakefields effects.

Given a structure offset along the linac with amplitude d_a and spatial frequency of the tail k_{tail}, the tail offset at the end of the linac (L) can be calculated using the two particle model (Eqn. 1).

$$x_2(L)_{driven} = \frac{C\, d_a\, n\, l_0}{2\, E_0\, k} \cos(k_{tail} L) \qquad (7)$$

The ratio of this driven tail growth (cosine = 1) to that produced by random offsets can be obtained from Eqns. (4) and (7).

$$\frac{x_2(L)_{driven}}{< x_2(L) >_{rms}} = \frac{\sqrt{n/2}\; d_a}{< d_{rms} >} \qquad (8)$$

where $k\,\beta_0 = 1$. For $n = 232$ and $< d_{rms} >$ about 400 microns, a coherent distortion d_a of about 37 microns on the average along the linac can be used to 'cancel' the average random build up. This is not a large mechanical movement. Algorithms using the position information along the linac as well as beam size information at the exit of the linac can be made to optimize this effect allowing local as well as global adjusts to be made.

With this new control the procedure for increasing the beam current would be to (1) steer the beam at low intensity, (2) raise the intensity, and (3) adjust the structure offsets until the low intensity trajectory and emittance are restored. It is believed that if the betatron spatial wavelength along the linac is maintained while the accelerator conditions drift, this correction will be stable with time.

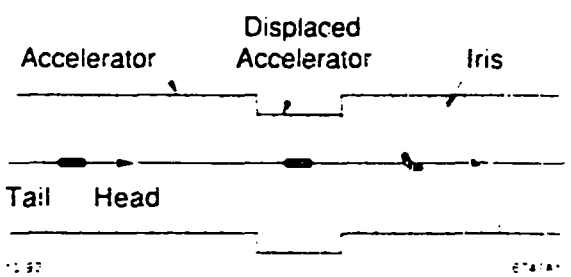

Fig. 1 Displaced accelerator structures produce wakefields effects.

Computer simulation

A computer tracking program WAKTRKACCEL was used to study the effects of random and driven structure offsets. A simulated beam with 24 longitudinal slices using acceleration and a corrected (0.3 %) energy spectrum at 47 GeV was studied. The as-used SLC lattice and energy profile were used with a beam of 5×10^{10} particles. The bunch length was 1.0 mm. Accelerator offsets for each 12 m girder had an rms value of 400 microns and were distributed as a gaussian to (+/-) three sigma.

The transverse displacements of the slices from the accelerator axis were used to compute the emittance for an ensemble of twenty distinct machines with offsets. Ten accelerators used no BNS damping with all klystron phases at +9 degrees to compensate longitudinal loading. The other ten simulated accelerators used BNS damping with the first 56 klystrons at -25 degrees and the remaining 176 klystrons at +18 degrees. Then, accelerator offsets at the betatron frequency were added to compensate the errors in each case. The phase and amplitude of the offsets were adjusted for minimum emittance. The emittance enlargements without BNS damping were reduced by a factor of 100 to 400 using coherent displacements with amplitudes of 50 to 400 microns. With BNS damping the initial emittance enlargements with random offsets but no compensation were about 50 to 100 times smaller than with no BNS. However, the use of coherent offsets at the betatron frequency with BNS damping did reduce the emittance enlargements by a factor of 1.5 to 8 with structure offset amplitudes of 70 to 400 microns. The resulting compensated emittances in both cases were approximately the same. These results confirm the expectation that the required coherent driven oscillations would be larger with BNS damping than without it for a given enlargement, but BNS damping allows less enlargement initially. The amplitudes of the moved structure were larger than predicted from the two particle model which indicates that a more complete calculation would have nonlinear terms and that acceleration plays a role.

Additional studies are underway to determine why the emittance reduction for all the random seeds are not equal and to determine the effects of a discrete focusing lattice (FODO).

Application to the SLC Linac

The SLAC Linac was fortuitously constructed in a way which allows independent adjustment of the transverse position of the disk loaded waveguide (DLWG) relative to the quadrupoles and beam position monitors [5,6]. The position monitors are mounted inside the quadrupoles which are in turn mounted on the thick aluminum girder end plates. Each girder end plate is supported directly from the tunnel floor and wall by rigid but adjustable jacks. A general layout is shown in Fig. 2. The accelerator structure is supported by a 40 foot, 24 inch diameter aluminum light pipe suspended between the girder end plates. The proposal here is to add remotely controlled horizontal and vertical jacks anchored to the floor and wall and attached to the center of the girder to force movements of up to +/- 1 mm. The center of the girder will move, but the girder ends including the quadrupoles and position monitors do not move as they are firmly held by the end jacks. The structure when bowed with an amplitude of up to 1 mm will give a net offset of about 0.5 mm to the entire girder, which is sufficient for wakefield correction given the spectrum of offset errors known for our accelerator. The accelerator with distortions adjusted to the betatron frequency would look like the schematic in Fig. 3.

The accelerator will not be damaged by these adjustments. Each girder supports four 10-foot sections. Each section has its own independent strongback which is supported at each end. The sections are welded together by a flexible islet. The flexing of the girder during the proposed control will occur at these islets. The worst angle is in the center islet where only 0.002 inch

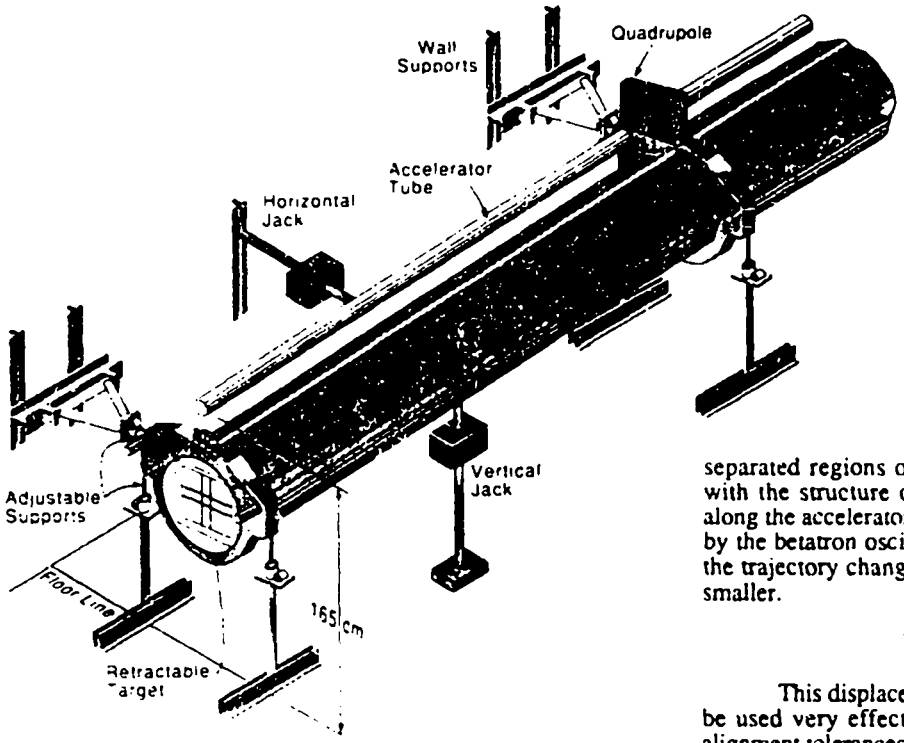

Fig. 2 Schematic view of position jacks to produce offsets in the center of the girders. The position of the end supports holding the quadrupoles remains fixed.

differential motion is expected over the islet diameter of 6 inches. This motion is not likely to be a problem. The present alignment procedure of the linac quarter points produces more flexing than this new control would make. However, the new procedure would be done more frequently.

There are several possible designs for the new jacks. The present plan calls for connecting arms on 'belly bands' attached to worm gear linear jacks driven by CAMAC. Since speed is not required, the CAMAC modules could drive the motors directly. Only one CAMAC module would be needed for several linac sectors if a simple fan-out chassis is built. The cost must be low as there are about 240 motor units to build and installed if half the linac is instrumented. Since the girders have known spring constants (500 lbs in the center bends a girder 1 mm horizontally and 0.7 mm vertically), load cells could be used to measure the applied force. Linear potentiometers could also be used to measure the position. The arms should be built such that any longitudinal motion of the girder is not resisted, such as for temperature cycling. Some adjustments in the connecting arms are needed when the girder end jacks are moved during normal quadrupole alignment. Finally, the movers must be earthquake resistant.

Some software support is needed to provide for online adjustment of these mechanical offsets and to calculate the sine and cosine spatial frequencies for both horizontal and vertical planes. Positrons and electrons experience the same corrections with slight differences given by their complementary betatron functions.

Structure displacements versus oscillating beams

If betatron oscillations starting at the entrance to the linac can be used to reduce the emittance growth, why should the effort and expense be used to make the accelerating structure movable? First, the structure alignment tolerance can be made less tight. Second, the structure movers can be used to cancel many error frequencies within the accelerator. Third, if the offset errors can be cancelled reasonably locally, then the displacement correction is likely to be stable over a long time. Both correction techniques suffer from changes in the energy profile along the accelerator which changes the betatron phase advance between separated regions of the accelerator containing errors. Fourth, with the structure displacement the head of the bunch travels along the accelerator on axis rather than oscillating off axis given by the betatron oscillation correction. Since the head is on axis, the trajectory changes with beam current changes will likely be smaller.

Future linear collider

This displacement technique of accelerating structures can be used very effectively in the next linear collider where the alignment tolerances are very tight. Since the misalignments at the betatron frequency are the main concern, this technique addresses this problem directly. Alignment errors over a very local region in the structure are not as important and can have much looser tolerances. An improvement of the structure tolerance of an order of magnitude is expected. New simulations will address this issue.

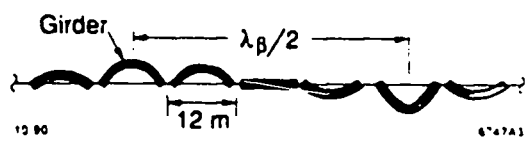

Fig. 3 Use of distorted accelerator girders to make structure offsets at the betatron spatial frequency.

References

[1] A. Chao, B. Richter, and C. Yau, "Beam Emittance Growth Caused by Transverse Deflecting Fields in a Linear Accelerator", NIM 178 (1980) pages 1-8.

[2] K. Bane, "Wakefield Effects in a Linear Collider", SLAC-PUB-4169.

[3] J. Seeman *et. al.*, "Observation and Control of Emittance Growth in the SLC Linac", XIV Int. Conf. on High Energy Accelerators, Tsukuba, Japan, 1989, Also SLAC-PUP-4889.

[4] V. Balakin, A. Novokhatsky, and V. Smirnov, "VLEPP: Transverse Beam Dynamics", 12th Int. Conference on High Energy Accelerators, FNAL, p. 119, 1983.

[5] R. Neal et al, The Stanford Two-Mile Accelerator, W. Benjamin, Inc., 1968.

[6] J. Seeman and J. Sheppard, 'Special Linac Developments', 1986 Linac Conference SLAC, p. 214.

STOCHASTIC ELECTRON BEAMS IN THE ION-FOCUSED REGIME[1]

K. J. O'Brien and J. R. Freeman
Plasma Theory Division 1241, Sandia National Laboratories
P. O. Box 5800, Albuquerque, NM 87185

Abstract

The ion-hose instability can catastrophically disrupt a classical electron beam propagating in the ion-focussed regime (IFR). Ion hose is driven by a resonant interaction between the smooth electron-betatron and ion-betatron orbits. In a classical beam phase correlations decay secularly in time $c(t)/c(t_0) \sim (t_0/t)^n$ $(0<n\leq 2)$. In a stochastic electron beam the electron orbits are chaotic. Such a beam can be immune to resonant instabilities because phase correlations decay exponentially fast $c(t)/c(0) \sim e^{-ht}$ thus destroying the coherence of the electron response on the growth time $1/\gamma_g$ if $h \sim \gamma_g$. Using the same principles we can also envsion a stochastic damping cell in which electron phase correlations damp exponentially $c(z)/c(0) \sim e^{-hz}$ thus centering and conditioning a beam more effectively than a classical phase-mixing cell in which $c(z)/c(z_0) \sim (z_0/z)^n$. A "triple-Bennett" IFR system and the analogous "triple-wire" damping cell are analyzed. The K-entropy is introduced as a figure-of-merit for such stochastic electron beam systems.

Introduction

IFR-guiding is a proven technique for transporting short-pulse-length ($\tau_p \sim 10$ nsec) 1-10 kA, 1-50 MeV classical electron beams in sub-Torr gas or plasma.[1-8] Long-pulse-length ($\tau_p \sim 1$ μsec) classical IFR beams are easily disrupted by ion-hose instability.[9-10] Offset or aiming errors in launching a beam onto an IFR channel typically provide the initial perturbations from which the instability develops. To reduce these errors the beam may be conditioned in a phase-mix damping cell prior to launch. Further phase mixing will occur in the IFR channel due to the radially anharmonic potential. In the conditioning and launch processes it is desirable to have strong phase mixing in order to quench any growing perturbations. In classical beams this decorrelation process is a sheared laminar flow in phase space in which phases "mix" ergodically (mixing rate a power law in time). For stochastic beams[11] the corresponding flow is a nonlaminar mixing flow called a K-flow (mixing rate exponential in time) (Figure 1).

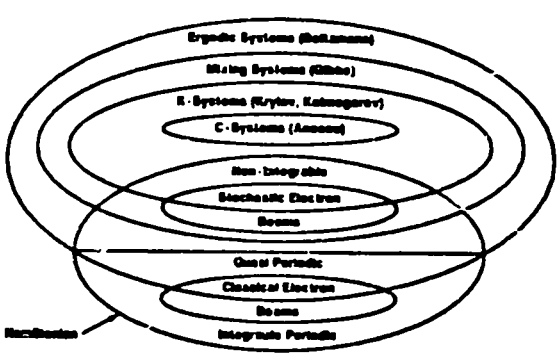

Fig. 1. Relation between classical and stochastic electron beams

In this paper we compare the phase-mixing properties of a classical IFR/wire system with those of the stochastic triple-IFR/wire system.

Stochastic triple-IFR/wire systems

For the IFR/wire systems depicted in Figure 2 the Hamiltonian for transverse electron motion is (in appropriate dimensionless variables)

$$H = p_r^2/2 + P_\theta^2/2\rho^2 + V(\rho,\theta;t) \tag{1}$$

where the potential $V(\rho,\theta;t)$ is

$$V(\rho,\theta;t) = \frac{2}{3}\log[\epsilon^3\rho^3\sin 3\theta + (1+\rho^2+\epsilon^2)^3 - 2\epsilon^2\rho^2(1+\rho^2+\epsilon^2)] \tag{2}$$

Here $\epsilon = d(t)/a$. The time dependent $d(t)$ enters because the IFR/wire separation is z-dependent (cf. Fig. 2) and for a fixed segment of beam we have $z = \beta ct \simeq ct$. The radius a is the IFR/wire radius and $\rho = r/a$ [the wire is treated by taking $a \to 0$ in the sense that a is much smaller than typical orbit radii].

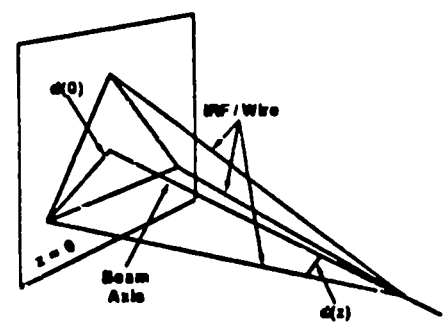

Fig. 2. Triple-IFR/wire system geometry

The corresponding classical IFR/wire systems are gotten by setting $\epsilon=0$ so $V \to V_0(\rho)$ where $V_0(\rho)$ is a Bennett potential. Self-field effects of order $1/\gamma^2$ are neglected as we consider highly relativistic beams. Figure 3 depicts typical orbits of Eqs. (1-2). The chaotic nature of the orbits for $d/a = 2$ is apparent.

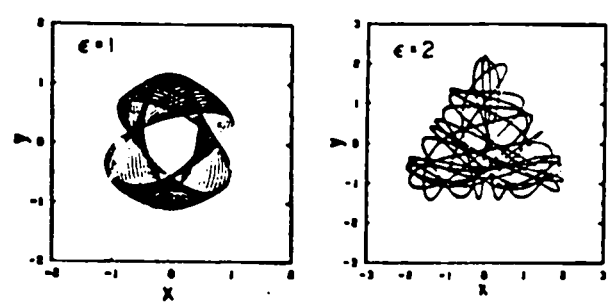

Fig. 3. Orbit of triple-IFR system (ϵ=1,2).

1. Work supported by the US Department of Energy and fully funded by the Strategic Defense Initiative Organization

K-entropy and phase decorrelation rates

In order to quantify the effectiveness of the stochastic IFR/wire systems we consider the global stability of orbits. Consider an orbit of H which we specify as $\eta(t) = [\rho(t),\theta(t),p_r(t),P_\theta(t)]$. At each point on this orbit the linearized version of Hamilton's equations for Eqs. (1-2) evolves according to

$$\Delta\dot{\rho} = \Delta p_r \quad . \tag{3a}$$

$$\Delta\dot{\theta} = (1/\rho^2)\Delta P_\theta - (2P_\theta/\rho^3)\Delta\rho \ , \tag{3b}$$

$$\Delta\dot{p}_r = -V_{\rho\rho}\Delta\rho - V_{\rho\theta}\Delta\theta + (2P_\theta/\rho^3)\Delta P_\theta - (3P_\theta^2/\rho^4)\Delta\rho \tag{3c}$$

$$\Delta\dot{P}_\theta = -V_{\rho\theta}\Delta\rho - V_{\theta\theta}\Delta\theta \tag{3d}$$

where subscripts on V indicate partial derivatives evaluated at $\eta(t)$. Here $\Delta\eta = (\Delta\rho,\Delta\theta,\Delta p_r,\Delta P_\theta)$ is a vector in the tangent space at $\eta(t)$ and the coefficients are also evaluated at that point. The eigenvalues $\lambda_\eta(t)$ of Eqs. (3) describe the local properties of the system at the point $\eta(t)$. Locally, we cannot properly distinguish between the stochastic and regular cases. For example, the axisymmetric Bennett potential has an inflection point at $\rho=1$ and thus has orbits which separate exponentially (but, do so only locally). For this reason, we proceed to look at the global properties, or the "tangent map" defined by these equations. The solutions of Eqs. (3) are of the form $\Delta\eta(t) \sim \exp(\lambda_\eta(t))\Delta\eta(0)$. Geometrically, the tangent map $\exp(\lambda_\eta(t))$ maps vectors from the tangent space at $\eta(0)$ into the tangent space at $\eta(t)$ and it is in this sense that it describes global properties of the orbit η.[14] The derivatives $d\lambda_\eta/dt = \Lambda_\eta(t)$ are determined as the roots of the quartic characteristic polynomial of Eqs. (3). The eigenvalues $\lambda_\eta(t)$ are then the time integrals

$$\lambda_\eta(t) = \int_0^t d\tau \ \Lambda_\eta(\tau) \quad . \tag{4}$$

Figure 4 depicts the positive real part of $\lambda_\eta(t)$ for a representative orbit $\eta(t)$. For this particular orbit the real part of $\lambda_\eta(t)$ is zero for all four eigenvalues unless $\epsilon > 1.3$ (approximately).

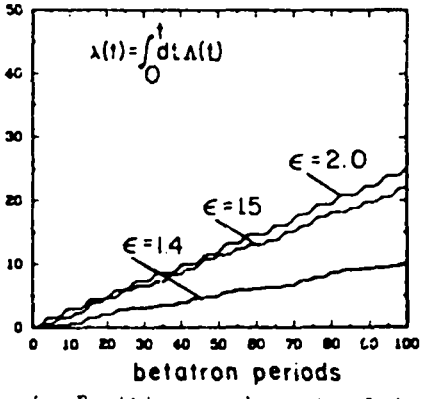

Fig. 4. Positive real part of $\lambda_\eta(t)$ for a representative orbit.

The quantity $|\Delta\eta(t)/\Delta\eta(0)|$ will grow exponentially during those times when at least one eigenvalue $\lambda_\eta(t)$ has a positive real part. To globalize we introduce the mean exponential growth rate $h(\eta)$

$$h(\eta) = \lim_{\Delta\eta(0)\to 0} \ \lim_{t\to\infty} \frac{1}{t} \log |\Delta\eta(t)/\Delta\eta(0)| \tag{5}$$

This quantity will certainly vanish (or be negative) unless one eigenvalue $\lambda_\eta(t)$ has a positive real part for a sufficiently large fraction of the time. Eigenvalues of autonomous two-degree-of-freedom Hamiltonian systems are always of the form $(-\lambda,0,0,\lambda)$ where λ may be pure real, pure imaginary, or complex. Thus, looking only at the one eigenvalue with a positive real part (if it exists) we may write

$$h(\eta) = \lim_{t\to\infty} \frac{1}{t} \mathrm{Re}[\lambda_\eta(t)] \quad . \tag{6}$$

When $h(\eta) > 0$ the orbit is "unstable in the global sense". Figure 5 is a plot of the ratio $\mathrm{Re}[\lambda_\eta(t)]/t$ for the orbit of Fig. 4. We see that the ratio converges to a positive constant, indicating strong orbit instability.

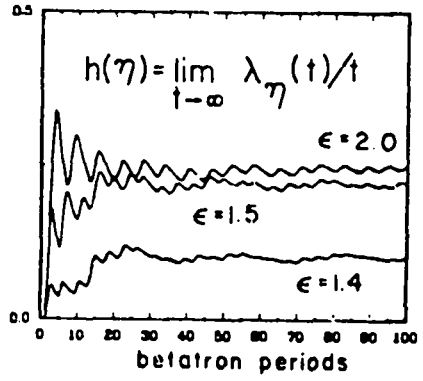

Fig. 5. Ratio $\mathrm{Re}[\lambda_\eta(t)/t] \to h(\eta)$ as $t\to\infty$.

A positive $h(\eta)$ indicates exponential instability of the orbit η. A related quantity is the Kolmogorov dynamical entropy or "K-entropy".[13] Strictly speaking, the K-entropy should be taken as an average of $h(\eta)$ over the triple-infinity of distinct orbits

$$h = \int d\mu(\eta) h(\eta) \quad . \tag{7}$$

This would account for the fact that different regions of phase-space can develop exponential instability at different rates (as a function of ϵ). For simplicity we have identified $h=h(\eta)$ assuming homogeneity.

Next, consider a pair of phase points (1,2) which are infinitesimally separated at z=0. In Figure 6 we plot x2(z)-x1(z) for the orbit of Fig. 4. For $\epsilon=2$ the exponential separation rate is apparent.

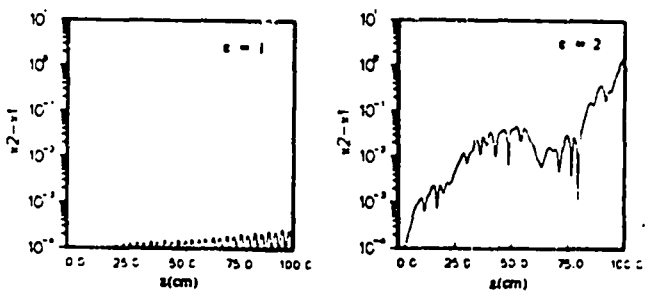

Fig. 6. Separation x2(z)-x1(z).

The autocorrelator c(z) describes how rapidly an orbit loses memory of its past. For an orbit $[x(n\Delta z),y(n\Delta z)]$ $n=1,\ldots,N$ we define an m-order correlator

$c_m = \Sigma_n \text{ sign}\{x(n\Delta z)x[(n+m)\Delta z]\}/(N-m)$ for $m=1,\ldots,N/2$. Note, $c_m = \pm 1$ is perfect correlation/anticorrelation. The further an orbit is from regular the closer c_m is to zero. In Fig. 7 we plot c_m versus m for $\epsilon=1$ and $\epsilon=2$ (same orbit as Fig. 4). Note the strong decorrelation for $\epsilon=2$.

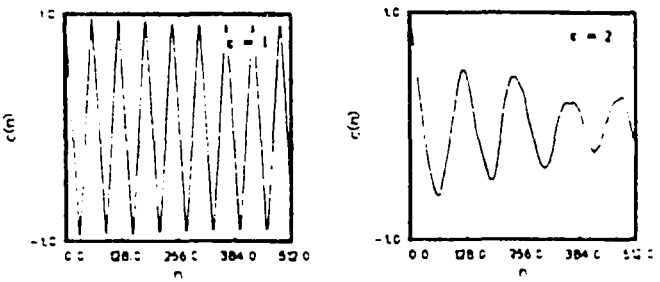

Fig. 7. Autocorrelator c_m versus m.

Conclusions

The K-entropy enables us to make statements about decorrelation rates.[14] In fact, when h=0, as for a classical beam, one obtains a power-law for correlation decay $c(t)/c(t_0) \sim (t_0/t)^n$ $(0<n\leq 2)$ [The Bennett potential is maximally anharmonic and has n=2.[15]] On the other hand, when h > 0 one obtains an exponential law for correlation decay $c(t)/c(0) \sim e^{-ht}$. In a fixed segment of beam the ion-hose instability grows exponentially with a growth rate γ_g scaling roughly as $\gamma_g \sim (2T_0/\gamma_b m_e a^2)^{1/2}$.[9-11] Growth requires a coherent response of the electrons within a given beam segment. Phase decorrelation results in a competition between the growth and decay of this coherence. To get an idea of the degree of stochasticity required to suppress growth we equate the growth and decorrelation rates. We thus find the requirement $h > 1/(2^{3/2}\pi)$. As indicated in Fig. 5 this is a value of h which is not difficult to achieve. Thus, we have a possible mechanism to suppress hose growth. Likewise, by employing a triple-wire (or some other array of wires) we may be able to condition a beam more efficiently than with a single wire. A converging wire array has another advantage (unrelated to stochasticity) in that it provides a more adiabatic transition of a badly centered beam to the single channel; thus, the emittance growth is less than with a single wire.[16]

Acknowledgements

We thank Dr. M. Lampe and Dr. R. Fernsler for their encouragement and interest in this work.

References

[1]J. R. Grieg, D. W. Koopman, R. F. Fernsler, R. E. Pechacek, L. M. Vitkovitsky, and A. W. Ali, Phys. Rev. Lett. 41, 174 (1978)

[2]A. N. Didenko, Ya. E. Krasik, A. V. Petrov, A. I. Ryabchikov, V. A. Tuzov, and Yu. P. Usov, Sov. J. Plasma Phys. 3, 624 (1978)

[3]D. S. Prono, G. J. Caporaso, A. G. Cole, R. J. Briggs, Y. R. Chong, J. C. Clark, R. E. Hester, E. J. Lauer, R. L Spoerlein, and K. W. Struve, Phys. Rev. Lett. 51, 723 (1983)

[4]W. E. Martin, G. J. Caporaso, W. M. Fawley, D. Prosnitz, and A. G. Cole, Phys. Rev. Lett. 54, 685 (1985)

[5]C. A. Frost, S. L. Shope, R. B. Miller, G. T. Leifeste, C. E. Christ, and W. W. Rienstra, IEEE Trans. Nucl. Sci. NS-32, 2754 (1985)

[6]G. J. Caporaso, R. Rainer, W. E. Martin, D. S. Prono, and A. G. Cole, Phys. Rev. Lett. 57, 1591 (1986)

[7]J. R. Smith, R. F. Schneider, M. J. Rhee, H. S. Uhm, and W. Namkung, J. Appl. Phys. 60, 4119 (1986)

[8]K. T. Nguyen, H. S. Uhm, R. F. Schneider, and J. R. Smith, in Proceedings of the Particle Accelerator Conference, Washington DC (IEEE, New York, 1987), p. 1096

[9]G. I. Budker, Sov. At. Energy 1, 673 (1956); D. Finkelstein and P. A. Sturrock, in Plasma Physics, edited by J. E. Drummond (McGraw-Hill, New York, 1961), p.224; B. V. Chirikov, J. Nucl. Energy C 8, 455 (1966); H. L. Buchanan, Phys. Fluids 30, 221 (1987); K. J. O'Brien, J. Appl. Phys. 65, 9 (1988)

[10]K. J. O'Brien, G. W. Kamin, T. R. Lockner, J. S. Wagner, I. R. Shokair, P. D. Keikel, I. Molina, D. J. Armistead, S. Hogeland, E. T. Powell, and R. J. Lipinski, Phys. Rev. Lett. 60, 1278 (1988)

[11]K. J. O'Brien, Phys. Fluids B 2(9), (1990)

[12]G. Benettin, L. Galgani, and J. Strelcyn, Phys. Rev. A 14, 2338 (1976)

[13]A. N. Kolmogorov, Dokl. Adad. Nauk SSSR 124, 754 (1959)

[14]G. M. Zaslavski and B. V. Chirikov, Sov. Phys. Uspekhi 14, 549 (1972)

[15]E. P. Lee, Phys. Fluids 21, 1327 (1978)

[16]J. R. Freeman and R. Fernsler, private communication

INTENSE ION BEAM TRANSPORT IN NEUTRAL GAS*

Craig L. Olson
Sandia National Laboratories, Albuquerque, NM 87185

Abstract

An analysis is made of the gas breakdown that occurs when an intense ion beam is injected into neutral gas and a high electrical conductivity is produced, providing charge and current neutralization for beam transport.

Introduction

Intense ion beam transport in neutral gas is used in several light ion fusion (LIF) transport schemes,[1-3] in some heavy ion fusion (HIF) transport schemes,[1,4] and between accelerating gaps in some multi-gap linear accelerator schemes. Here, the macroscopic properties of charge neutralization and current neutralization are examined. Then, as shown in Fig. 1, the microscopic properties of gas breakdown are examined, including ion impact ionization, secondary electron impact ionization, electron avalanching, and ohmic heating. These results are combined to give a physical picture of gas breakdown, including growth of the plasma electrical conductivity.

For LIF parameters for the light ion laboratory microfusion facility (LMF),[5] it is desirable to have the plasma conductivity reach a modest value ($\sim 10^{10}\ s^{-1}$) very quickly (< 1 ns), and then rise much higher ($\sim 10^{14}\ s^{-1}$) by the time of peak ion current to avoid the filamentation instability. Estimates for LMF parameters are given showing the desired growth in $\sigma(t)$.

Charge Neutralization

Charge neutralization is required for intense ion beam transport when the ion current I_i exceeds the space charge limiting current I_l.

$$I_l = \beta_i(\gamma_i-1)[M_p c^3/e](A/Z)[1 + 2\ln(R/r_b)]^{-1} \approx (\tfrac{1}{2})\beta_i^3(A/Z)(31\text{MA})[1 + 2\ln(R/r_b)]^{-1} \quad (1)$$

where the ion axial velocity is $\beta_i c$, $\gamma_i = (1 - \beta_i^2)^{1/2}$, c is the speed of light, M_p is the proton mass, A is the ion mass number, e is the electron charge, r_b is the beam radius (solid beam), and R is the metallic guide tube radius. The current I_l is the current that would create an electrostatic potential depression equal to $\varepsilon_i/(Ze)$, so that for $I_i \gtrsim I_l$ the beam would stop. Here ε_i is the ion energy and Z is the ion charge state in the gas. To permit beam propagation, a neutralizing electron background of density n_e must be present with an adequate value of the charge neutralization fraction $f_i = n_e/(Zn_i)$ where n_i is the ion beam density. For LMF type parameters (30 MeV Li^{+3}, $R \approx r_b$, particle current $I_b = 1$ MA, $I_i = ZI_b = 3$ MA), $I_i \approx 97\ I_l$ so $f_i > 0.99$ is required.

If no charge neutralization is provided, large space charge fields will be produced quickly that will draw electrons from nearby surfaces by field emission. For injection through a foil (that bounds the gas transport region), the electric field at the foil would be

$$E = 2\pi J_i t^2/t_r \qquad 0 \le t \le t_r \quad (2)$$

where J_i is the peak current density and t_r is the ion current risetime. For LMF parameters ($J_i = 3 \times 2$ kA/cm^2, $t_r \approx 10$ ns), this is

$$E = 3.4 \times 10^6\ [t(\text{ns})]^2\ \text{V/cm} . \quad (3)$$

This shows that on a nanosecond time scale, electric fields large enough to cause field emission would be created.

Given that electrons will be provided by gas ionization, field emission, or drawn from plasma surfaces, it is of interest to estimate how well charge-neutralized the beam front can become. Based on electron trapping arguments,[6] the potential well depth at the beam front will always be $\gtrsim \Delta\phi$ where

$$e\Delta\phi = 1/2\ m_e\beta_i^2c^2 \quad (4)$$

and m_e is the electron mass. For LMF parameters (30 MeV Li), this is $\Delta\phi \approx 2.3$ kV.

Current Neutralization

Current neutralization is required for intense ion beam transport when the ion current exceeds the Alfven magnetic limiting current

$$I_A = \beta_i\gamma_i(M_p c^3/e)\ (A/Z) \approx \beta_i\ (A/Z)\ (31\ \text{MA}) . \quad (5)$$

Generally it is desirable to have current neutralization so that the net current $I_{net} = I_i\ (1 - f_m) < I_A$, where $f_m = I_p/I_i$ is the fractional current neutralization and I_p is the plasma return current. For LMF parameters, $I_i \approx (0.4)I_A$ so the beam could propagate with betatron particle trajectories for $f_m = 0$. However, for certain LMF transport scenarios,[5] it is desirable to have essentially complete current neutralization ($f_m \approx 1$) so that the trajectories will be ballistic.

The evolution of the net current can be described as follows. For beam injection into neutral gas, the electrical conductivity σ starts at zero, but quickly rises as the gas is ionized and heated. The plasma current density evolves according to[7]

$$J_p/t_d + \partial J_p/\partial t = -\partial J_b/\partial t \quad (6)$$

where the magnetic diffusion time is $t_d = 4\pi\sigma r_b^2/c^2$ and J_b is the beam current density. The simplest picture of the evolution of J_p and J_{net} is shown in Fig. 2. Initially $\sigma = 0$, $t_d = 0$, $J_p = 0$, and $J_{net} \approx J_b$. If, at some later time τ the conductivity has suddenly increased so t_d is large ($t_d \gg t_b$ where t_b is the ion beam pulse length), then from then on, the magnetic field will be frozen at its value at $t = \tau$. Specifically, analysis of (6) shows

*Work supported by the U.S. Department of Energy.

$$J_{net} \approx J_b(t) \qquad 0 < t < \tau$$
$$J_{net} \approx J_b(\tau) \qquad \tau < t < t_r \,. \tag{7}$$

To have good current neutralization therefore requires that σ rise quickly so $t_d \gg t_b$.

Gas Breakdown

Ion beam induced gas breakdown occurs by several processes as follows.

(1) Ion impact ionization occurs throughout the whole ion beam pulse. Growth of the plasma electron density is given by

$$dn_e/dt = n_b(t)/t_i \tag{8}$$

where the ion impact ionization time is $t_i = (n_g\beta_i c\sigma_c)^{-1}$, n_g is the neutral gas density, and σ_c is the cross section. It can be shown that σ_c scales roughly as

$$\sigma_c \sim Z^2/(\varepsilon_b\beta_i^2) \tag{9}$$

where ε_b is the electron binding energy. For 1 MeV protons on hydrogen, $t_i \approx 0.55$ ns/p(Torr).[8] Using (9), it follows that for LMF parameters (30 MeV Li^{+3} on helium), $t_i \approx 0.23$ ns/p(Torr).

(2) Secondary electron ionization is caused as the newly created plasma electrons are accelerated toward the ion beam by the beam's space charge. The electrons may be trapped and continue to oscillate in the potential well near the beam head. These electrons ionize the gas by electron impact ionization.

$$dn_e/dt = n_e^f(t)/t_e \tag{10}$$

where n_e^f is the "fast" electron density and t_e is the electron impact ionization time. Typically $t_e < t_i$ for these energetic electrons.

(3) Electron avalanching occurs when an electric field E is present and the parameter E/p is in an optimal range ($10^2 \lesssim$ E/p (Volts/cm/Torr) $\lesssim 10^5$) where p is the neutral gas pressure. For higher E/p values, the electron may leave the system before it does substantial ionization. For lower E/p values, the electron may never gain enough energy to make ionizing collisions. The E fields that can drive avalanches are space charge fields (before $f_i = 1$), induced electric fields at the head of the beam (for $f_i = 1$ and $f_m < 1$), and the later time induced electric field that drives the plasma return current. When ion impact ionization and avalanching are the dominant processes,

$$dn_e/dt = n_b(t)/t_i + n_e(t)/\tau_a \tag{11}$$

where the electron avalanche time $\tau_a = \tau_{FP}/(8 \ln 10)$ and τ_{FP} is the formative time investigated by Felsenthal and Proud for many gases.[9] For example, for helium with E/p = 600 V/cm/Torr, $\tau_a \approx 1$ ns. Note that exponential growth in n_e will occur on the τ_a timescale.

For $f_i = 1$ and $f_m = 0$, the induced electric field at the beam head, on axis, will be

$$E_{in} = -[I_i/(c^2 t_r)]\,[1 + 2 \ln (R/r_b)] \,. \tag{12}$$

As the beam becomes current neutralized, E_{in} will be determined by dI_{net}/dt.

(4) Ohmic heating is the return current heating that occurs after breakdown and field freezing when the return current is described by

$$J_n = \sigma E \,. \tag{13}$$

Since for good current neutralization, $|J_n| = |J_i|$,

$$E = n_i e Z\beta_i c/\sigma \,. \tag{14}$$

The power dissipation (W/cm^3) for ohmic heating is

$$P = J_i^2/\sigma \tag{15}$$

and this goes into ionization and heating of the gas. It can be shown that the maximum energy gain of an electron in the E field given by (14) in one collision time is

$$\Delta\varepsilon = 1/2\, m_e\beta_i^2 c^2\, (Zn_b/n_e)^2 \,. \tag{16}$$

For LMF parameters (30 MeV Li) this shows $\Delta\varepsilon$ is large enough to cause ionizing collision until $n_e/(Zn_b)$ exceeds about 10.

A physical picture of how the above four ionizing and heating mechanisms combine to cause gas breakdown is as follows. (i) The charge neutralization phase begins with ion impact ionization and secondary electron impact ionization. The E fields are electrostatic and are large. (ii) The current neutralization phase includes ion impact ionization and electron avalanching. The E fields are inductive and are decreasing. (iii) The ohmic heating phase continues with ion impact ionization and ohmic heating. The E fields are small. Throughout the entire process, note the continual presence and importance of ion impact ionization.

Conductivity Growth

At each stage of the gas breakdown, the electrical conductivity σ is given by (for no magnetic field)

$$\sigma_0 = n_e e^2/(m_e \nu) \tag{17}$$

where the collision frequency $\nu = \nu_{en} + \nu_{ei}$, the electron neutral collision frequency is given by

$$\nu_{en} = (5.9 \times 10^7)\, [T_e(eV)]^{1/2}\, P_c p(\text{Torr}) \tag{18}$$

and the electron-ion collision frequency is given by

$$\nu_{ei} = (1.5 \times 10^{-6})\, n_e Z_g\, (\ln\Lambda)[T_e(eV)]^{-3/2} \,. \tag{19}$$

Here P_c is the "probability of collision,"[10] and Z_g is the gas atomic number. Combining (17)-(19) and using $\ln\Lambda \approx 10$,

$$\sigma_0 = (2.5\times10^8)\, n_e \Big[(5.9\times10^7)\, p(\text{Torr})\, P_c\, [T_e(eV)]^{1/2} + (1.5\times10^{-5})\, n_e Z_g\, [T_e(eV)]^{-3/2}\Big]^{-1} \tag{20}$$

Early in the ion beam pulse σ_0 is dominated by ν_{en}, whereas later in the pulse σ_0 is typically dominated by ν_{ei}.

If a transverse magnetic field is *present* (either a self magnetic field or an external magnetic field) then the relevant conductivities are $\sigma_{\parallel}$ along B and $\sigma_{\perp}$ perpendicular to B (Pedersen conductivity).

$$\sigma_{\parallel} = \sigma_0$$
$$\sigma_{\perp} = \sigma_0 \{1 + (\omega_{ce}/\nu)^2\}^{-1} \qquad (21)$$

where $\omega_{ce} = eB/(m_e c)$. For $\nu/\omega_{ce} \ll 1$, $\sigma_{\perp} \ll \sigma_0$, and current neutralization is impeded. For $\nu/\omega_{ce} \gg 1$, $\sigma_{\perp} \approx \sigma_0$ and current neutralization proceeds.

LMF Example

Transport scenarios for LMF include a ballistic lens scheme which uses ballistic transport in gas; and wall-confined channel transport and wire-guided transport, both of which use ballistic focused transport at their input. Therefore neutral gas transport is relevant to all approaches.

The parameters associated with one ion beam in LMF are: 30 MeV Li^{+1} at the diode, 30 MeV Li^{+1} after the gas cell foil, 1 MA peak particle current, $t_r = 10$ ns, $t_p = 30$ ns, $r_p = 18$ cm, $R \approx r_p$, and 1 Torr helium gas.

The first consideration for LMF ballistic lens transport is that the frozen net current be as small as possible. Ion impact ionization alone will make a plasma density equal to the ion beam density at the time $t = 2\,t_i \approx 0.46$ ns. At this time, (20) gives $\sigma_0 \approx 5 \times 10^{10}\ s^{-1}$ and $t_d = 225$ ns, so already $t_d \gg t_p$. In addition, the net current at this time should be less than the beam current because the charge neutralizing electrons will flow in a direction that aids current neutralization. Thus field freezing should occur easily in < 1 ns and the current neutralization should be very high.

The second consideration for LMF transport is that the plasma conductivity be high ($\sim 10^{1}\ s^{-1}$) when the full current is reached, to avoid the filamentation instability. Ion impact ionization alone will create a plasma density $n_e \approx 10^{14}\ cm^{-3}$ and $\sigma > 10^{13}\ s^{-1}$. Including electron avalanching and ohmic heating shows $n_e > 10^{15}\ cm^{-3}$ and $\sigma \approx 10^{14}\ s^{-1}$.

Conclusions

The basic mechanisms of gas breakdown have been examined, and examples for LMF have been given. The processes should now be examined with computer simulations and explicit experiments with extracted ion beams.

References

1. C. L. Olson, J. Fusion Energy 1, 309 (1982).
2. D. Mosher, D. D. Hinshelwood, J. M. Neri, P. F. Ottinger, J. J. Watrous, C. L. Olson, and T. A. Mehlhorn, Proc. 8th Int. Conf. High Power Particle Beams, Novosibirsk, USSR, July 2-5, 1990.
3. C. L. Olson, Proc. 1988 Linear Accelerator Conference, CEBAF Report 89-001 (1989), p. 34.
4. Heavy Ion Inertial Fusion, AIP Conf. Proc. 152, edited by T. Godlove and R. Bangerter (AIP, NY, 1986).
5. J. J. Ramirez et al, Fusion Technology 15 2A, 350 (1989).
6. C. L. Olson, ref. 4, p. 215
7. C. L. Olson, Phys. Fluids 16, 529 (1973).
8. C. L. Olson, Phys. Rev. A 11, 288 (1975).
9. P. Felsenthal and J. M. Proud, Phys. Rev. 139, A1796 (1965).
10. S. C. Brown, Basic Data of Plasma Physics (MIT Press, 1966), p. 13

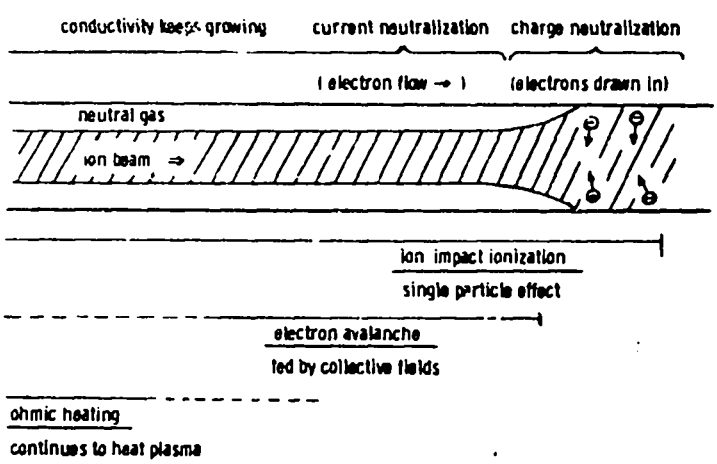

Fig. 1. Gas breakdown processes.

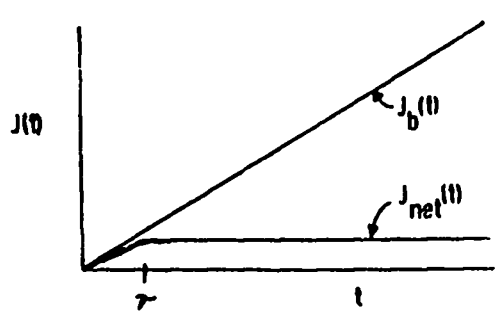

Fig. 2. Current neutralization.

DESIGN STUDIES OF SSC LOW-ENERGY-BEAM-TRANSPORT SYSTEM USING EINZEL LENSES

Chu Rui Chang
Superconducting Super Collider Laboratory
2550 Beckleymeade Avenue
Dallas, Tx 75237

Abstract

A 35 keV preinjector for matching a 30 mA H^- beam into the radio-frequency quadrupole (RFQ) section of the SSC linac has been designed using the SNOW code. The distinguishing feature of this injector is that the conventional gas-neutralized transport and matching units are replaced by two einzel lenses. Some advantages of this approach are discussed.

Introduction

This paper describes the design and simulation results of a dc H^- injector for a 428 MHz RFQ. The system consists of a magnetron H^- source, a single-gap source extraction system and a low energy beam transport (LEBT) system. Normalized rms emittance at the entrance of the RFQ should be kept approximately 0.2 π mm-mrad. In the LEBT system two electrostatic lenses are employed. They perform two major functions: (1) provide sufficient length (≥ 20 cm) for gas pumping; (2) provide proper focusing to match the beam into the RFQ. Major emphasis in the design is to minimize beam emittance and maximize the beam transmission through RFQ.

Electrostatic Focusing

Our new approach for transport of H^- beam uses electrostatic focusing instead of the usual combination of magnets and gas neutralization [1,2]. The benefits of using charge neutralization for focusing of the beam are well known. However, there are many disadvantages such as plasma instabilities, reproducibility and the problem of transition from the neutralized to unneutralized state. More importantly, the neutralization time must be very short compared to the pulse length; otherwise, a large fraction of the beam at the front of the pulse will be lost due to the inadequate focusing. The SSC linac requires a pulse length of 7-35 μs. For such short pulses, we believe it is better to use electric focusing, since it requires no neutralization time. The electric field provides sufficient focusing strength at the low energy. It also prevents the plasma buildup, thus eliminating the associated problems of varying charge neutralization.

* Operated by Universities Research Association, Inc. for the U.S. Department of Energy under Contract No. DE-AC02-89ER40486

Design and Simulation of the DC Pre-injector

Design Constraints

In our design studies, the minimum spacing d between any two electrodes with potential difference V must satisfy the electrostatic breakdown criterion[3]

$$d_{[cm]} \geq 1.4 \times 10^{-3}\, V^{3/2}_{[kv]}$$

Furthermore, in order to minimize the emittance growth, the maximum beam radius should not exceed about 50% of the lens radius.

Source Extraction System

The 35-kV beam voltage is low enough that a single-gap source extraction system is preferred. The parameters of the extraction system are optimized by SNOW and are listed in Table 1. The expected beam envelope is shown in Fig. 1

Table 1: Parameter Values of the Extraction System

Parameter	Value
$R_{source\ aperture}$	1.2mm
Current Density	6.63mA/mm^2
$R_{cone\ tip}$ mm	2.3 mm
Mim. Gap length	6.0 mm
$V_{breakdown}$	56.8 kV
Extraction Cone depth	35 mm

LEBT System

While there are at least four types of electric lenses that can be used in the LEBT system, the electrostatic einzel lens is the simplest candidate for 30 mA operating current. Since the beam is round both at the source and at the entrance of the RFQ, if axisymmetric lenses are used, only one lens is needed to provide two degrees of freedom to match the beam[4]. At least three lenses are needed if one uses electrostatic quadrupoles[5] or

helical electrostatic quadrupole lenses[6]. We use two einzel lenses to gain extra degrees of freedom and to provide enough spacing between the source and RFQ. We do not use classical thin-plate aperture lenses because we wish to avoid electric field concentrations. To reduce the spherical aberrations, we have carefully shaped all electrodes so that no sharp corners exist. The focusing electrodes in our final design look like rings (near the beam), similar to the "ring lens" at Lawrence Berkeley Laboratory[7]. Fig. 2 shows the physical layout of the two einzel lenses. Note that all insulators are hidden behind conductor electrodes and are shielded from the beam. The center electrode that separates the two einzel lenses is split into four pieces, a different voltage can be applied on each piece. This will create a dipole steering field to correct misalignment errors.

After a systematic search of parameters of the einzel lenses, the parameters of the optimal design given by SNOW are listed in Table 2:

Table 2: Parameter Values of the LEBT

Lens No.	Voltage	R_{lens}	Thickness	R_{beam}
1	-34.5 kV	20 mm	40 mm	8.0 mm
2	-33.7 kV	21 mm	40 mm	10.0 mm

The beam envelope vs distance in the LEBT system is shown in Fig. 3. The overlay of the acceptance ellipse of the RFQ and x-x' phase space distribution at the entrance of RFQ is shown in Fig. 4.

Transport Through RFQ

We have simulated the beam from the exit of the LEBT through the RFQ using PARMTEQ. The conceptual design parameters for the RFQ are listed in Table 3.

From Fig. 4 we see the phase space ellipse of the beam is not perfectly matched with the RFQ acceptance ellipse. This mismatch causes relatively large emittance growth in the RFQ. However, since the particle phase space distribution is contained almost entirely inside the acceptance ellipse, the transmission rate is high. Simulation results show over 93% transmission through the RFQ. The particle distributions in x-y, x-x, y-y' and W-ϕ after the RFQ are shown in Fig. 5.

Table 3: Parameter Values of the RFQ

Parameter	Value
W_i	35 keV
W_f	2.5 MeV
R_{bore}	3.0 mm
Length	2.2 m
E_{max}	1.73 Kilpatrick
I_{in}	30 ma
$\varepsilon_{n,rms,in}$	0.128 π mm-mrad
I_{out}	27.96 mA
$\varepsilon_{n,rms,out,x}$	0.237 π mm-mrad
$\varepsilon_{n,rms,out,y}$	0.211 π mm-mrad

Acknowledgements

The author greatly appreciates the encouragement and valuable suggestions from Jerry Watson in this work. Many thanks to Deepak Raparia for many helpful discussions. I also wish to thank Jack Boers for his help in running the SNOW code.

References

1] P. Allison and J.D. Sherman, "Operating Experience with a 100-keV,, 100-mA H^- injector", K. Prelec, Ed.; AIP Conf. Proc. 111,511 (1983)

2] J.G. Alessi, et al.,"AGS Preinjector Improvement", proc. of the 1987 Particle Accelerator Conference, Washington, DC, March 16-19, 1987.

3] R. Keller, "High-Brightness, High-current Ion Sources", AIP Conference Proceedings 139, 1985.

4] R.W. Hamm, D.W. Mueller, R.G.Sturgess, "A 30-kV Proton Injector for PIGMI", Proc. of the 1981 Linac Conf. Oct. 19-23, 1981 Santa Fe, NM.

5] C.Allen, C.R. Chang and M. Reiser, "Design studies of Low Energy Transport with Electrostatic Lenses", 1990 Linac Conference, Alburqurque, NM

6] D. Raparia, "HESQ, a Low Energy Beam Transport for the SSC Linac", ibid.

7] O.A. Anderson, L. Soroka, J.W. Kwan, and R.P. Wells, "Injector for RFQ using Electrostatically Focused Transport and Matching", LBL internal report No. 27953, Nov. 1989.

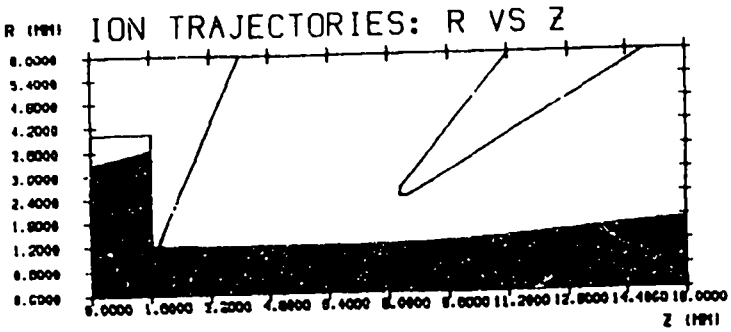

Fig. 1 Beam envelope vs distance in the source extraction system.

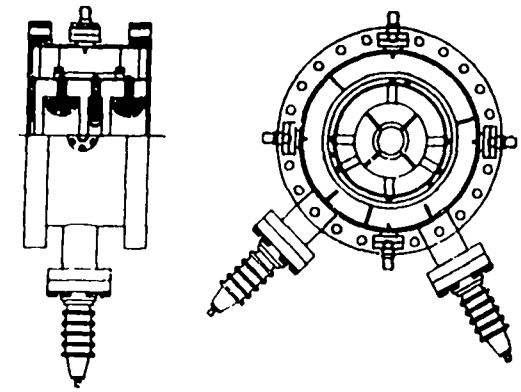

Fig. 2 Physical layout of the LEBT system. Left: y-z crossection at x=0 plane. Right: x-y crossection at the center electrode.

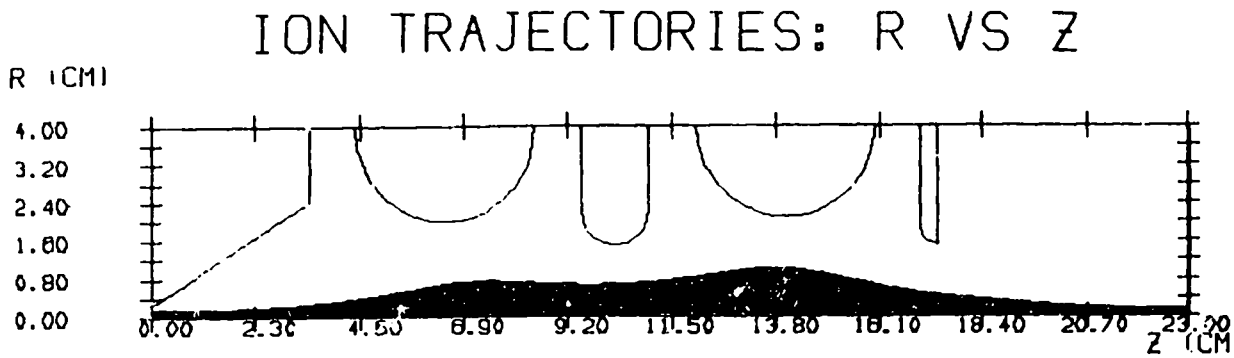

Fig. 3 Beam envelope vs distance inside the low energy beam transport system. The entrance of the RFQ (not shown) is located at z=22.2 cm.

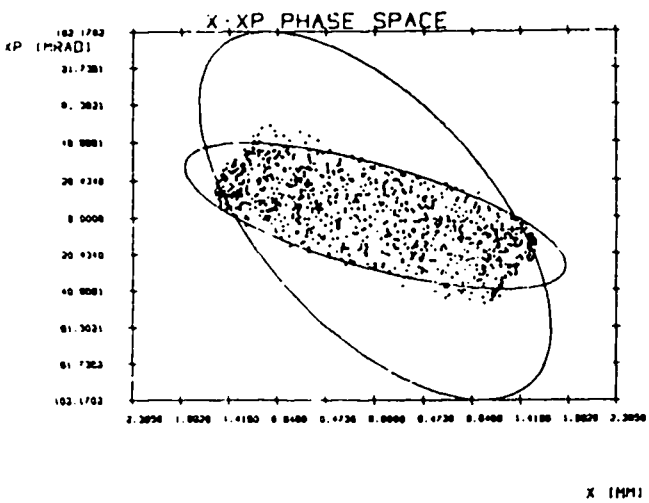

Fig. 4 Overlay of the RFQ acceptance ellipse and x-x' phase space distribution at the entrance of the RFQ. The smaller ellipse is the $4\epsilon_{rms}$ of the particle distribution.

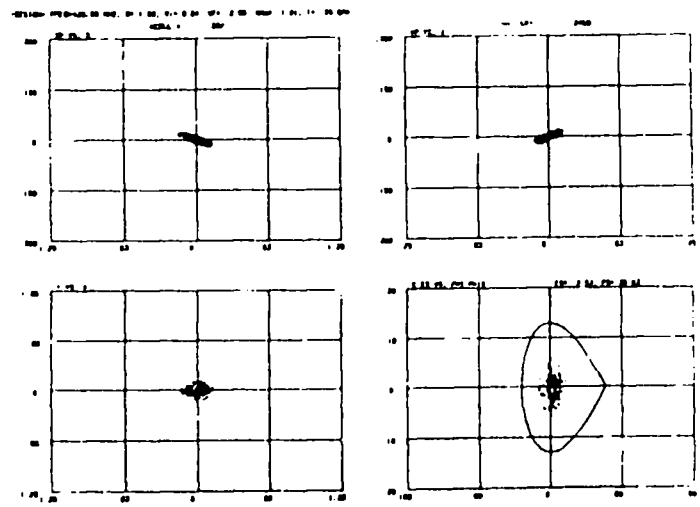

Fig. 5 The Particle distribution after the RFQ in x-x', y-y', x-y and W-ϕ plane.

DESIGN STUDIES OF LOW ENERGY H^- BEAM TRANSPORT WITH ELECTROSTATIC LENSES*

C. Allen, C.R. Chang† and M. Reiser

Laboratory for Plasma Research
University of Maryland, College Park, MD 20742

Abstract

We report the results of design studies for low-energy transport of a 35 kV, 30 mA H^- beam using electrostatic quadrupole (ESQ) and einzel lenses. Emittance growth is obtained from a modified PARMILA code for the ESQ configuration and from SNOW for the einzel-lens system. A comparison of important design considerations and parameters for the two electrostatic systems will be presented.

Introduction

In this paper we report the results of conceptual design studies for a 35 kV, 30 mA H^- LEBT system using either electrostatic quadrupole (ESQ) or einzel lenses for matching the beam into a Radio Frequency Quadrupole (RFQ) accelerator. The H^- beam is assumed to have an initial normalized rms emittance of 0.069π mm-mrad and an initial radius of approximately 1 mm. These numbers were chosen to achieve an emittance in the range of 0.1π to 0.2π mm-mrad at the entrance of the RFQ, which corresponds to the parameters of the BEAR project[1] and the SSC[2]. The spacing between source and RFQ was taken to be 30 cm for the ESQ design and 20 cm for the einzel lens system. To minimize nonlinear effects we limited the maximum beam radius, R_{max}, to about 10 mm.

There are several important differences between electrostatic quadrupole lenses and einzel lenses: (1) The ESQs provide strong, first-order focusing while the einzel lenses are weak, second-order focusing devices. Consequently, ESQs – in doublet or triplet configurations – operate with lower voltages than einzel lenses to achieve the same focusing strength per meter. (2) For matching purposes, one needs a minimum of only two einzel lenses, but at least four quads (two doublets) in the ESQ case. (3) Spherical aberrations are generally more severe in axisymmetric than in quadrupole field configurations. Consequently, the fraction of the lens aperture ("linear aperture") available for the beam is larger in ESQs than in einzel lenses. For our design studies we chose R_{max} to be about 75% of the aperture radius of the ESQs and 50% in the einzel lens system. (4) Since the electric field lines are predominantly in the transverse direction in ESQs and longitudinal in einzel lenses, chromatic aberrations tend to be more severe in ESQs than in einzel lenses. This effect limits the ESQ voltages to less than about 20% of the beam voltage while the einzel lens voltages can be almost as high as the beam voltage.

In our design studies, the minimum spacing d between any two electrodes with potential difference V must satisfy the voltage breakdown criterion[3]

$$d_{[cm]} \geq 1.4 \times 10^{-3}\, V_{[kV]}^{3/2}. \tag{1}$$

Electrostatic Quadrupole (ESQ) Design

The basic design studies for the ESQ system were performed with a linear beam optics code developed in house[1] that solves the coupled K-V envelope equations for $X(z)$ and $Y(z)$ given by

$$X'' + \kappa_x X - \frac{2K}{X+Y} - \frac{\epsilon^2}{X^3} = 0, \tag{2a}$$

$$Y'' + \kappa_y Y - \frac{2K}{X+Y} - \frac{\epsilon^2}{Y^3} = 0. \tag{2b}$$

κ_x and κ_y are assumed to be hard-edge focusing functions of length ℓ and separation L with values $|\kappa_x| = |\kappa_y| = (V_q/V_b)\left(1/R_q^2\right)$, where V_b is the beam voltage, V_q and R_q the quad voltage and radius, respectively. $K = (I/I_0)(2/\beta^3)$ is the generalized perveance, with $I_0 = 3.1 \times 10^7$ A, $\beta = v/c = (2qV_b/mc^2)^{1/2}$, and has the value of $K = 3 \times 10^{-3}$ for our 35 kV, 30 mA H^- beam. ϵ is the effective emittance given by $\epsilon = 4\bar{\epsilon} = 0.276$ mm-mrad, where $\bar{\epsilon} = \epsilon_{rms}$.

In order to minimize spherical and chromatic aberrations we tried to satisfy the constraints[4] $R_{max}/\ell \leq 0.10$, $R_{max}/R_q \leq 0.75$, $V_{max}/V_b \leq 0.05$, where $V_{max} = V(R_{max})$.

After many runs with the K-V envelope code we chose the six-lens design shown in Fig. 1, with the parameter values listed in Table 1. Note that the lenses 1 and 6, 2 and 5, and 3 and 4 are identical so that we have essentially two mirror-image triplets. This is a mere convenience for the computation, and in an experiment one may wish to vary all six voltages rather than pairing the lenses. The relative variation of the hard-edge focusing function κ_x/κ_0 is shown at the top and the two beam envelopes $X(z)$, $Y(z)$ at the bottom of Fig. 1. We note that the two lenses (3 and 4) at the center act like a cell of a FODO transport channel. The first and last lens doublets accomplish the actual matching of the diverging beam into a converging one. Thus, for matching alone one needs only about 20 cm. The 10-cm FODO cell at the center is only necessary to cover the total distance of 30 cm. We note from Table 1 that we were not quite successful in meeting the aberration constraints. However, our design is not yet optimized.

The second step of our study was to design an actual lens system equivalent to the hard-edge approximation and to calculate the realistic focusing function $\kappa(z)$ using a Laplace solver. This lens configuration is shown in Fig. 2 (top) and

*Research supported by ONR/SDIO and DOE.
†Present address: SSC, Dallas, TX 75237.

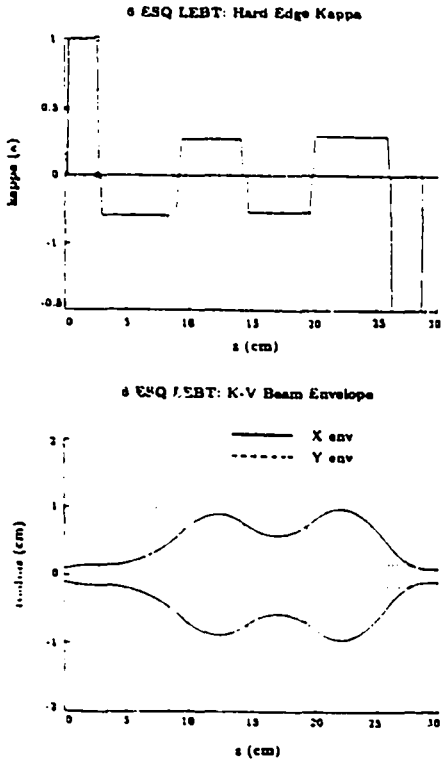

Figure 1: Hard-edge variation of the focusing function $\kappa(z)$ at top and beam envelopes $X(z), Y(z)$ at bottom.

Table 1: Parameter values for the ESQ Lens System

Quad No.	1/6	2/5	3/4
ℓ [mm]	25.00	60.00	50.00
L [mm]	2.50	2.50	5.00
R_{max} [mm]	4.00	9.83	8.86
R_q [mm]	6.00	15.00	15.00
V_q [kV]	3.53	6.47	6.00
V_{max}/V_b [in %]	4.5	7.9	6.0

the $\kappa(z)$ function at the bottom of the figure. A special computer code calculates the nonlinear force components up to third order with the aid of integral functions of $\kappa(z)$. The results, including chromatic aberrations, are then used as input – in the form of fringe-field matrices – for our modified PARMILA code, as described in Ref. 4. The results of our best PARMILA runs so far for the six-lens ESQ system are shown in Fig. 3. The two phase space plots at the beginning ($z = 0$) and after the last lens ($z = 29$ cm) illustrate the evolution of the particle distribution and the effects of nonlinear forces. We used lens voltages that differ somewhat from the values of Table 1 for this run to obtain better agreement with the K-V results. These voltages are shown in Table 2. The normalized rms emittances obtained from this PARMILA run are listed in Table 3. The average final rms emittance (normalized) between the x and y direction is 0.111 mm-mrad and the corresponding emittance growth is 1.60, or 60%, which is not excessive.

Einzel Lens Design

The einzel lens system is being studied as an option for the SSC, as reported elsewhere.[2] The design differs from that

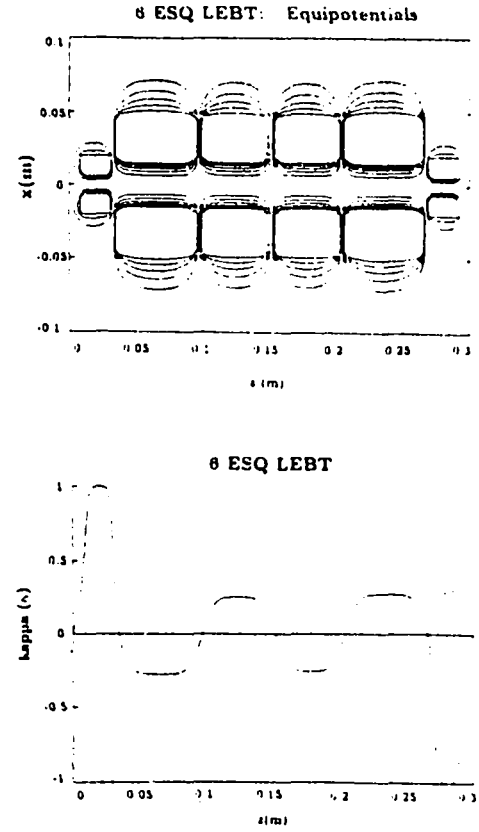

Figure 2: Geometry with potential distribution of ESQ system (top) and variation of $\kappa(z)$ along z-axis (bottom).

Table 2: Modified Quad Voltages for PARMILA Run.

Quad No.	1	2	3	4	5	6
V_q [kV]	3.460	6.395	5.700	5.750	6.010	3.360

Table 3: PARMILA Results for Normalized RMS Emittance

	$\bar{\epsilon}_n^{(i)}$	$\bar{\epsilon}_{n,x}^{(f)}$	$\bar{\epsilon}_{n,y}^{(f)}$	$\bar{\bar{\epsilon}}_n^{(f)}$	$\Delta\bar{\epsilon}_n$
mm-mrad	0.069	0.120	0.101	0.111	0.042

for the ESQ configuration in several respects. First, the total effective length of the matching section between ion source and RFQ entrance is only about 20 cm. This was dictated by the desire to use only two einzel lenses. (It is equivalent to leaving out quads 3 and 4 in the ESQ design.) Second, all of the design studies were done with the SNOW code. Third, the initial radius and slope of the beam emerging from the source were $R_i = 1.2$ mm, $R_i' = 0$, as compared to $R_i = 1.0$ mm, $R_i' = 0.020$ in the ESQ design. The larger radius and zero slope make it easier to match the beam in the einzel lens design.

The SNOW code in its present form can only handle a laminar beam. The corresponding distribution in phase space (r, r') is a line. The nonlinear forces due to the spherical aberrations of the lens fields deform the line into an S-shaped curve. From this curve an effective emittance can be calculated.

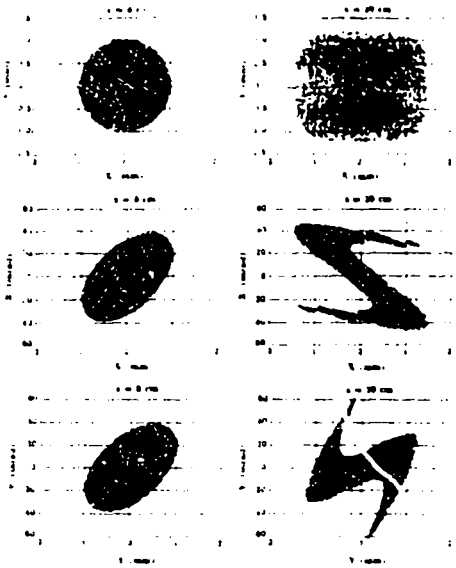

Figure 3: Phase-space plots of the particle distribution from the PARMILA code at the beginning and end of the six-quad ESQ system.

The results of the einzel-lens design with the SNOW code are shown in Figs. 4 and 5, with relevant parameters listed in Table 4.

The electrode configuration and the potential distribution are shown at the top, the ion trajectories at the bottom of Fig. 4. Note from Table 4 that very high negative potentials of −34.5 kV for the first lens and −33.7 kV for the second lens were required to achieve the desired matching conditions. The S-shaped curve representing the effects of aberrations on the laminar beam at z = 22.2 cm, is shown in Fig. 5. The corresponding normalized rms emittance projected in the x-x' plane is calculated to be $\Delta\tilde{\epsilon}_n^{(f)}$ = 0.102 mm-mrad. Adding the thermal emittance in uncorrelated form yields

$$\tilde{\epsilon}_n^{(f)} = [0.069^2 + 0.102^2]^{1/2} = 0.123 \text{ mm-mrad},$$

with a corresponding emittance growth of 1.78. Thus, to the

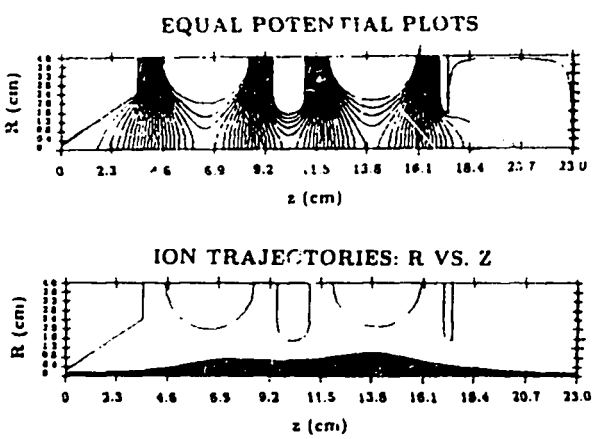

Figure 4: Electrode configuration of the einzel lens system with potential distribution (top) and beam profile (bottom) from the SNOW code.

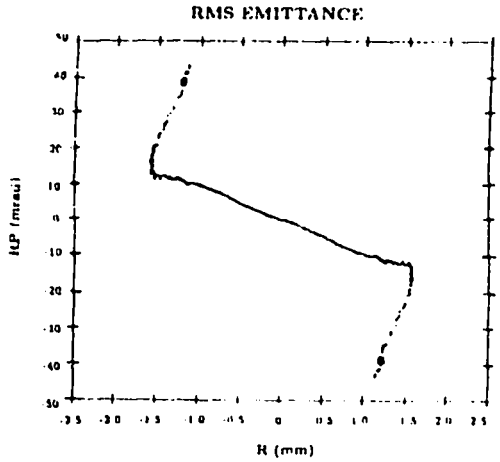

Figure 5: Phase space distribution of the laminar beam from the SNOW code at z = 22.2 cm.

Table 4: Parameter Values for the Einzel Lens System

Lens No.	Voltage	Aperture Radius	Electrode Thickness	Gap Width
1	-34.5 kV	20 mm	40 mm	10 mm
2	-33.7 kV	21 mm	40 mm	10 mm

extent that the two codes are accurate and can be compared, we find that the einzel lens system produces a slightly larger emittance growth than the ESQ system.

Comparison of the Two Systems

Our LEBT design studies for a 30 mA, 35 kV H^- beam with initial emittance of $\tilde{\epsilon}_n$ = 0.069 mm-mrad show that either electrostatic quadrupoles or einzel lenses can accomplish the desired matching task. The ESQ system requires relatively low voltages and a minimum of four quads (two doublets) to match the beam in both directions. However, we used six quads to cover the total LEBT length of 30 cm. The einzel lens system requires high potentials – comparable to the beam voltage – and two lenses for matching within the 20 cm distance. The emittance growth was found to be slightly lower in the ESQ design than in the einzel lens system (60% versus 78%). However, it is not clear whether the two codes (PARMILA and SNOW) are adequate tools to accurately evaluate the emittance growth. Further work and experiments are planned to fully assess the relative merits of the two schemes. In particular, one needs a better assessment of the capability and accuracy of the codes.

References

1. P.G. O'Shea et al, Nucl. Instr. and Meth. in Phys. Res. **40/41**, 945 (1989).

2. C.R. Chang, paper at this Conference.

3. M. Reiser, C.R. Chang, D. Chernin, and E. Horowitz, Proc. of SPIE, Vol. **873**, 172 (1988).

4. C.R. Chang, E.J. Horowitz, and M. Reiser, Proc. of SPIE, Vol. **1226**, (1990).

HESQ, A LOW ENERGY BEAM TRANSPORT FOR THE SSC LINAC

Deepak Raparia

Superconducting Super Collider Laboratory*
2550 Beckleyme... e Avenue
Dallas, Texas 75237

ABSTRACT

A Helical Electrostatic Quadrupole (HESQ) is an option for the low energy beam transport (LEBT) of the SSC linac to transport and match a 35 keV H^- beam from a circular symmetric Magnetron ion source to a 428 MHz RFQ. Being an electrostatic focusing lens, the HESQ avoids neutralization of the H^- beam due to the background gas. The HESQ lenses provide stronger first-order focusing in contrast to weak second-order focusing of einzel lenses and is also stronger than alternating gradient focusing. In this paper, we will present a design and results of a PIC code simulation with space charge.

INTRODUCTION

The low energy beam transport (LEBT) is the section of the linac that provides the matching between the ion source and the radio frequency quadrupole accelerator (RFQ). The LEBT consists of lenses that focus the beam into the RFQ. The beam from an ion source is relatively large in radius and divergence and must be matched to the RFQ.

Existing LEBT systems for H^- beams use magnetic focusing solenoids [1-3] or permanent magnetic quadrupoles[4]. These LEBT systems utilize charge neutralization in the background gas to minimize the required focusing strength. The neutralization time must be short compared to the pulse length; otherwise, much of the beam at the front of the pulse will be lost due to inadequate focusing. During this neutralization time the space charge force changes. Because of this the beam phase space ellipse rotates, making it difficult to match the beam to the RFQ acceptance. Additional problems arise due to beam-plasma instability and the fact that the beam becomes charged again, when it enters the electric field of the accelerating structure which sweeps away the charge neutralizing ions formed in the collisions. Improper matching in such transitions and emittance growth from sheath transitions into and out of gas neutralized regions may caused particle loss.

* Operated by the Universities Research Association, Inc., for the Department of Energy under contract No. DE-AC02-89ER40486.

The Superconducting Super Collider (SSC) linac requires 7-35 μsec pulse lengths. The neutralization time is of the order of 100 μsec with hydrogen as the residual gas. During the first 100 μsec the beam focusing would be changing. That means one would use a pulse length from the ion source of 107- 135 μsec and considerably reduce the lifetime on the ion source. The neutralization time can be reduced by introducing xenon in the LEBT; however, full neutralization will always considerably increase the pulse length required from the source. We have chosen to avoid neutralization by using focusing in the form of electric forces which can be provided by: (1) Einzel lenses, (2) Electrostatic quadrupole FODO channel (ESQ), (3) Helical electrostatic quadrupole (HESQ), or (4) Radio-frequency quadrupole (RFQ). The FODO channel typically uses very high voltage and have typically had significant reliability problems. The RFQ can probably transport higher currents with less aberration, but it is more complex ... adds another RF system. Einzel lenses [5] and HESQ[6-8] are the leading candidates for the SSC linac.

HELICAL ELECTROSTATIC QUADRUPOLE LEBT

The buildup of plasma and charge neutralization cannot occur in electrostatic lenses, as it does in magnetic lenses, since the electron-ion pairs produced in collisions between beam particles and background gas are swept out of the beam region by the electric field between the electrodes. Furthermore, magnetic focusing is particularly ineffective at low beta because of the velocity term in the force equation. Electric focusing, on the other hand, has no such velocity term in the force equation and should be a prime candidate for the focusing role at low velocities. The main problems in electrostatic focusing is breakdown and aberrations. The problem of the breakdown can be overcome by providing lower but spatially continuous focusing forces, as in a HESQ, instead of spatially discreet but higher focusing forces as in a FODO structure. The spatially continuous focusing forces also help keep the beam size smaller all the time, thus minimizing aberration.

Our new approach for transport of H^- beams uses HESQ focusing instead of usual combination of magnets and gas neutralization or the ESQ[9]. The HESQ is merely a continuously twisted electrostatic quadrupole (figure 1). The

HESQ lenses provide stronger first-order focusing in contrast to weak second-order focusing of einzel lenses, stronger focusing than the alternating gradient type and an axially symmetric beam which is necessary for the RFQ matching. The idea of a helical quadrupole is not new[10-14]. Past works were about 'magnetic helical quadrupoles' for different purposes. Some of the features of our plasma-free LEBT are: (1) gas independence permits beam with arbitrarily short pulse lengths, (2) gas independence improves reproducibility, and (3) emittance growth from plasma noise and from sheath transition into and out of gas neutralized regions is eliminated.

BEAM SIMULATION

The main parameters for the SSC HESQ are shown in table I. HESQ electrodes will be built by the nickel electroforming. Individual elements will have through - tapped holes near each end for installation of studs for ceramic standoff mounting. The beam cannot directly hit the ceramic and there should not be charge buildup (figure 2). The HESQ is longitudinally divided into four sections to provide four degrees of freedom for matching to the RFQ. Each section is 0.75 λ long. The first and third sections electrodes are powered individually so that steering can be provided.

Table I: HESQ Specification

Length	22.5	cm
Voltage	7.0	kV
Break down voltage	100.0	kV
Pitch of the Helix (λ)	15.0	cm
Electrode spacing	1.46	cm
Bore radius	1.5	cm

Beam dynamics and the constraints of the HESQ has been discussed previously [8]. Here we will present the PIC code simulation results only. This code is a two dimensional code which uses a 4 X 4 matrix representation for each component. The code also includes nonlinear space charge effects. Figure 3 shows the x and y profiles through the HESQ. Notice that the beam size is always lass then equal to 1 cm, i.e. 66 % of the aperture. Figure 4 shows the input and output phase space plots of the HESQ. Figure 5 shows the input and output phase space plots for a misaligned injected beam. Table II shows the input and output beam emittances for different currents for the waterbag input distributions.

Particle distributions obtained from the HESQ were used to simulate the RFQ performance using the code PARMTEQ.The transmission was more than 90% with 15 % transverse emittance growth. The main parameters of this RFQ are: bore radius=3mm,max field=1.73 x Kilpatrick, length 2.2 meter, freq=428 MHz, output energy 2.5 MeV.

Table II: Emittances (RMS)

Current	Input	Output
0 mA	0.18 π mm mrad	0.19 π mm mrad
30 mA	0.18 π mm mrad	0.22 π mm mrad
50 mA	0.18 π mm mrad	0.24 π mm mrad

CONCLUSIONS

The use of a HESQ in H^- LEBTs avoids neutralization problems for short pulses. It provides an axially symmetric beam which is necessary for the RFQ matching. The HESQ is presently being developed and may have superior performance and reliability than other LEBTs for short pulsed beam.

ACKNOWLEDGMENTS

We wish to thanks to C. R. Chang and R. Bhandari for useful discussions, R. Cutler for suggesting the electroforming techniques for manufacturing the electrodes, D. Evans for the engineering support, and J. Watson for his support and encouragement.

REFERENCES

[1]. J. Alessi, et al, Proc. of the European Particle Accelerator Conf., Rome, Italy. (June 1988)
[2]. S. H. Wang, DESY report, DESY 84-092. (Sept. 1984)
[3]. F. Cole et al., Proc. of the 1987 IEEE Particle Accelerator Conf., Washington D.C. p.1985 (1987)
[4]. P. G. O'Shea, et al., Proc. of the 1989 IEEE Particle Accelerator Conf., Chicago. p. 354 (1989)
[5]. C. R. Chang, This conference.
[6] D. Raparia and S. Machida, Proc. of the 1989 IEEE Particle Accelerator Conf., Chicago. p. 981 (1989)
[7] P. A. Tompkins, F. R. Huson and D. Raparia, Proc. of the IEEE Particle Accelerator Conf., Chicago. p.331 (1989)
[8] D. Raparia, to be published in the Proc. of the Fifth International Symposium on Production and Neutralization of Negative Ions and Beams, Brookhaven, NY. (1989)
[9] O. A. Anderson, et al., to be published in the Proc. of the Fifth International Symposium on Production and Neutralization of Negative Ions and Beams, Brookhaven, NY. (1989)
[10] L. C. Teng, Argonne National Lab. Report, ANLAD-55, (1959)
[11] S. Ohnuma. TRIUMF Report, TRI-69-10, (1969)
[12] G. Salardi, et al., Nuclear Instruments and Method in Physics Research 59, p.152 (1968)
[13] R. M. Pearce, Nuclear Instruments and Method in Physics Research 83, p. 101 (170)
[14] R. L. Gluckstrn, Proc. of the 1979 Linear Accelerator Conf., Montauk, p.245 (1979)

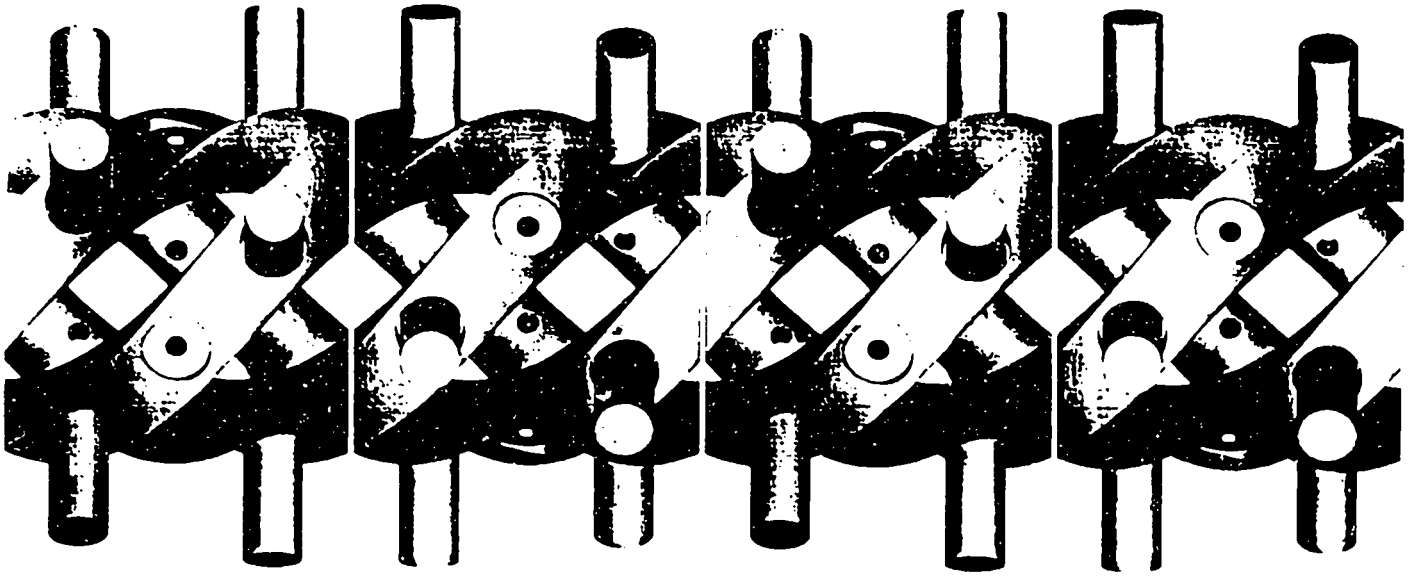

Figure 1. HESQ with electroformed nickel electrodes and ceramic insulators.

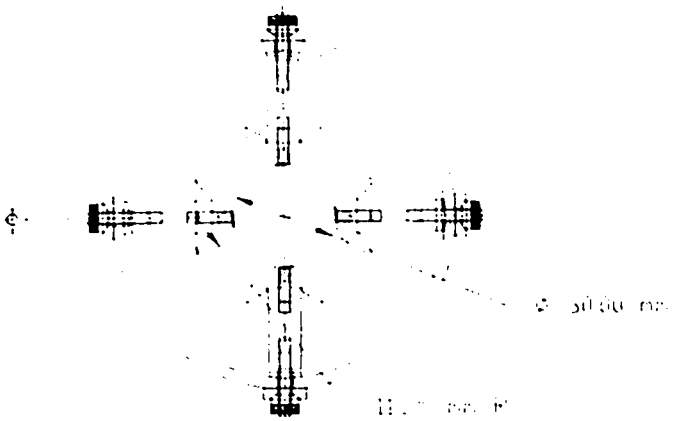

Figure 2. Planer section view of the HESQ.

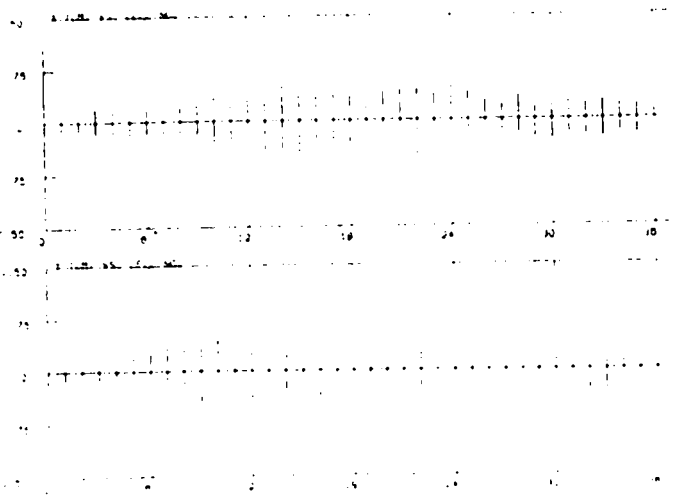

Figure 3. X and Y beam profile through the HESQ.

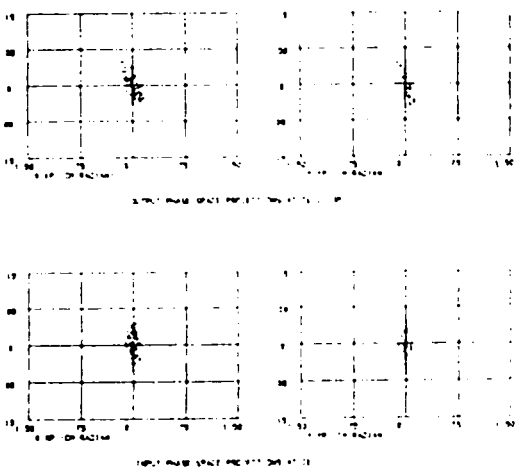

Figure 4. Input and Output phase space plots.

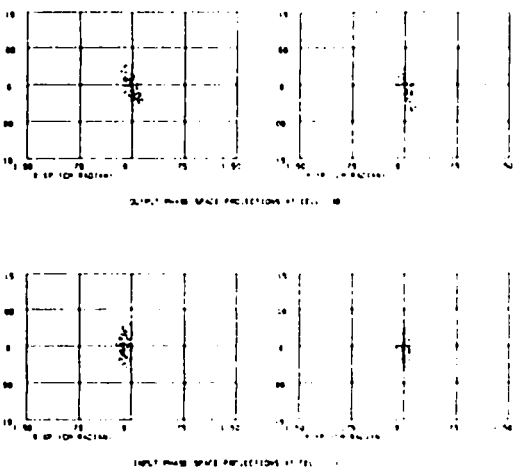

Figure 5. Input and output phase space plots of the HESQ for a misaligned injected beam

CONSTRUCTION OF A TEST MAGNET FOR JLC FINAL FOCUS

K. Fujii, M. Kikuchi, K. Kuno*, S. Kuroda, T. Matsui,
H. Nakayama, K. Oide, T. Tauchi and N. Yamamoto

National Laboratory For High Energy Physics(KEK),
1-1 Oho, Tsukuba-shi, Ibaraki-ken, 305 JAPAN
*Mitsubishi Electric Corporation, Kobe Works,
Wadasaki-cho, Hyogo-ku, 625 JAPAN

Abstract

A 10 cm long test quadrupole magnet having a bore radius of 2 mm has been constructed with vanadium permendur as an R&D model for the final focus system of the future e^+e^- linear collider, JLC (Japan Linear Collider). The bore of the magnet is 4 times larger than that of presently planned final doublet. Measurements by a small Hall probe show that the qradrupole magnet produces a 700 Tesla/m field gradient in the region where the radius <1/3 the half aperture without any serious field deformation due to saturation effects.

Introduction

A TeV e^+e^- linear collider, JLC (Japan Linear Collider), is one of the most promising candidates for KEK's high energy accelerator following the TRISTAN e^+e^- collider [1]. Since the annihilation cross sections drop as 1/s, where s is the squared center of mass energy, the luminosity required for the TeV collider is more than $10^{33}cm^{-2}sec^{-1}$. Therefore one of the most crucial questions to ask is whether we can realize a final focus system that focuses beams to a nano meter level.

In accordance with the present JLC parameters, design studies have been carried out for a final focus system that produces a 210 nm (H) x 1.7 nm (V) beam spot using conventional quadrupole magnets with a 1.4 Tesla pole tip field as a final doublet near the interaction point. The basic feature of the system is to use two families of sextupoles for correcting the chromaticities of the final doublet [2].

Following the conceptual design, experimental works are now under way to verify the design's feasibility within the scope of the present day technology.

In this paper we present the design, construction, and preliminary test results of our first R&D magnet.

Magnet Design

Design constraints for the final focus doublet near the interaction point are as follows: 1) The half aperture of the quadrupole is 0.5 mm with a pole tip field of 1.4 Tesla and the uniformity of gradients is better than 0.01% in the central region of 1/3 the half aperture. 2) The outer radius of the magnet is less than 50 mm. The inner radius is determined so as to let the 10-σ envelope of the beam go through without any disturbance from materials, and the outer radius is restricted by the detector acceptance for physics experiments.

We decided, however, to make a test magnet with a bore radius of 2 mm, since techniques at hand should be good enough to precisely measure fields in such a test model and also since the experimental verification of our field calculation for the test model should justify the extrapolation to the JLC final doublet.

To design the test quadrupole magnet, we used a computer program JMAG [3]. Prior to the detailed geometry design of the pole tip shape, we made a rough calculation with various B - H curves to select materials which can produce a 1.4 Tesla pole tip field that corresponds a field gradiant of 700 Tesla/m. The gradients at the highest excitation are sensitive to the choice of material parameters. The calculation showed that the required B - H property is characterized by B_{25} > 2.10 Tesla and B_{100} > 2.35 Tesla, where B_{25} and B_{100} are magnetic flux densities at H = 25 Oe and H = 100 Oe. This means that we need a saturation magnetization higher than that of conventional soft iron. We found the condition can be satisfied by vanadium permendur (49% Fe, 49% Co, 2% V).

Using the B - H data for a sample of vanadium permendur, we optimized the shape of the pole tip to keep the uniform gradient region as wide as possible. Fig. 1 sketches the geometry of the pole tip

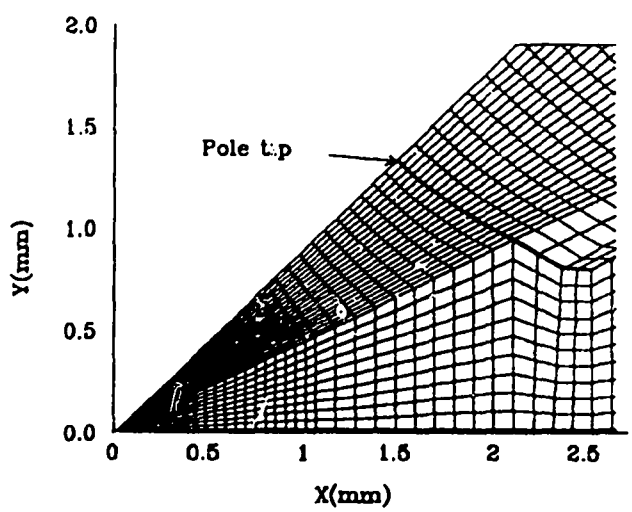

Fig. 1 Geometry of pole tip and mesh in JMAG.

together with the mesh used in the calculation. Fig. 2 shows the expected field gradient inside the magnet when we supply a current of 1500 AT. In the region r < 1/3 the half aperture, the uniformity is expected to be better than 0.01 %.

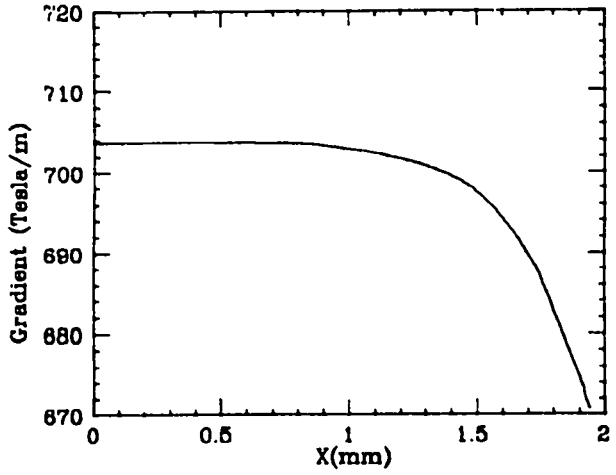

Fig. 2 Expected field gradient (1500 AT).

Construction and Testing

The quadrupole yoke was machined from a single piece block by a wire-EMD (wire electrical discharge machine) and the geometrical accuracy is better than 5 μm. The current is supplied by five turns of water-cooled conventional hollow conductors, 6 mm$^{\phi}$ (outer dia.) x 4 mm$^{\phi}$ (inner dia.). The maximum excitation requires the current of 300 A corresponding to 1500 AT in total. Fig. 3 is a photograph of the magnet whose parameters are summarized in Table 1.

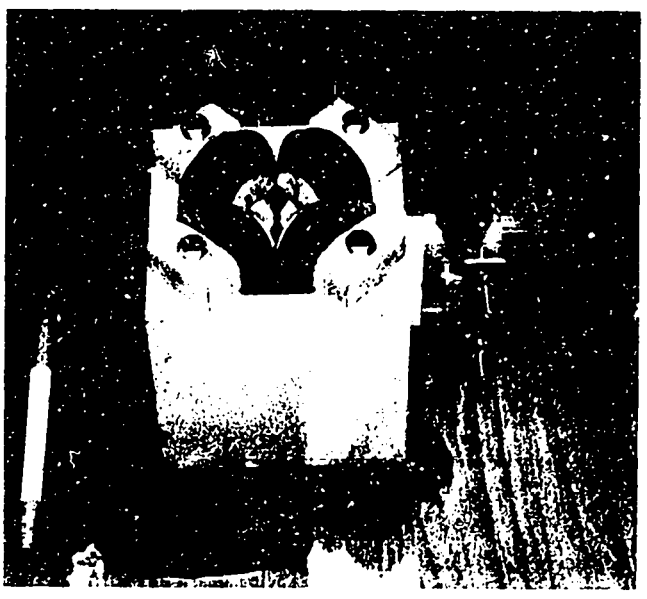

Fig. 3 Photograph of the R&D magnet.

Table 1
Parameters of The R&D Magnet

Bore diameter	4 mmϕ
Pole length	100.5 mm
Field gradient	700 T/m
AT	1500 AT/p
Current	300 A
Registance	7.92 mΩ
Voltage	2.4 V
Cooling water	
Flow	0.75 l/min
Pressure drop	0.34 kg/cm^2
Velocity	1 m/sec

We excited the magnet and performed preliminary measurements of the field quality using a small Hall probe (FC - 32, Siemens). The Hall generator has a 2 mm x 3 mm sensitive area and is placed in a ceramic box which has a dimension of 6 mm(W) x 12 mm(L) x 1.5 mm(H). The probe was calibrated by NMR in a dipole magnet. Coefficients of a 12th order polynomial were fitted to the data of the relationship between output voltage of the Hall probe and the field strength. The error in the calibration was estimated to be less than 0.5 Gauss.

Fig. 4 gives the excitation curve measured by the Hall probe placed at (x, y) = (0.8mm, 0.0). The results are almost consistent with the calculation and show a field gradient greater than 700 Tesla/m at the full excitation.

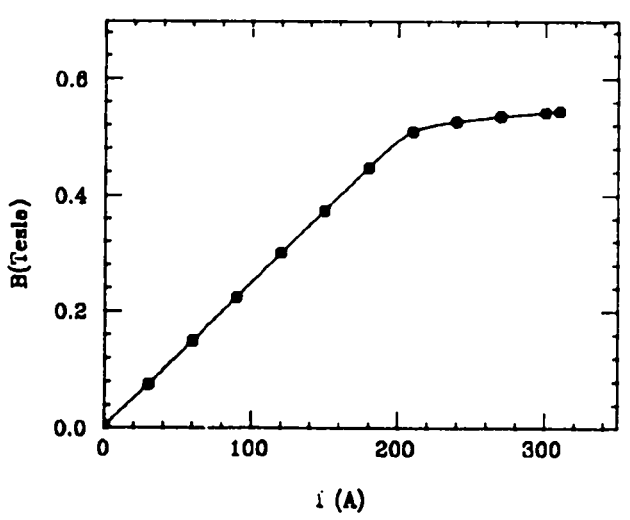

Fig. 4 Excitation curve measured by the Hall probe placed at (x, y) = (0.8mm, 0.0).

Fig. 5 plots the field strength on the median plane (y=0.0, -0.8 mm < x < 0.8 mm). The field gradient uniformity was confirmed to an accuracy of 1%, although the required accuracy was not achieved yet because of the positioning error of the Hall probe. Nevertheless the present results strongly supports the feasibility of constructing a 1.4 Tesla/m quadrupole magnet having a bore radius of 0.5mm.

We are now constructing a positioning device using techniques that have been developed in JLC alignment R&D [4]. The system can control the probe with an accuracy of 10 nm using piezo transducers as a drive unit and laser interferometers as a monitor unit. With this device, we expect to be able to measure the field to an accuracy of 0.01% in near future.

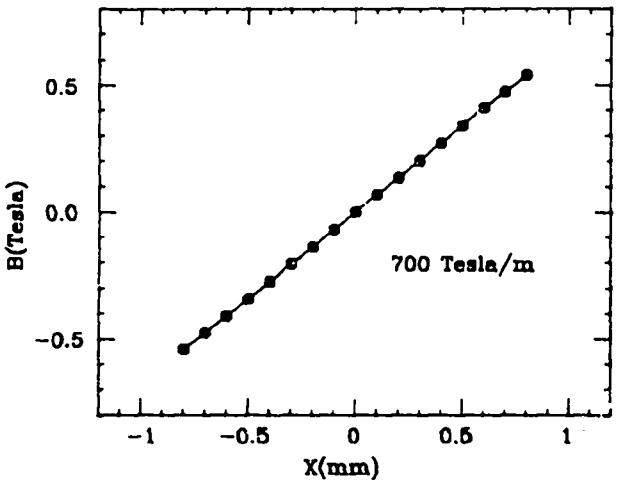

Fig. 5 Field strength on the median plane (y=0.0, -0.8 mm < x < 0.8 mm) at the full excitation of 700 Tesla/m.

Summary

We have constructed and tested a 10 cm long R&D quadrupole magnet, which has a bore radius of 2 mm, with vanadium permendur (49% Fe, 49% Co, 2% V). The magnet has a 4 times larger bore of the JLC final doublet. The magnet has produced a design field gradient of 700 Tesla/m without any serious field deformation due to saturation effects by using a material with high magnetization property. The results from preliminary field measurements strongly suggest the validity of the design calculation. We thus believe that the construction of the JLC final doublet is quite feasible using techniques at hand.

Acknowledgement

We would like to thank professors Y. Kimura and S. Iwata for their support and encouragement.

References

[1] K. Takata and Y. Kimura, KEK Preprint 89 -124 (1989). S. Takeda, Particle Accelerators, Vol. 31,143-152(1990), Proc. 14th International Conf. on High Energy Accelerators, Tsukuba, Japan, 1989.

[2] K. Oide, KEK Report 90 - 20, Proceedings of the First Workshop on Japan Linear Collider, KEK, 1989.

[3] Developed by Japan Information Service Ltd., Tokyo, Japan.

[4] N. Ishihara et al., Particle Accelerators, Vol. 31, 57-62(1990), Proc. 14th International Conf. on High Energy Accelerators, Tsukuba, Japan, 1989.

BEAM TRANSFER BETWEEN THE COUPLED CAVITY LINAC AND THE LOW ENERGY BOOSTER SYNCHROTRON FOR THE SSC

R. K. Bhandari and S. Penner
Superconducting Super Collider Laboratory*, Dallas, Texas 75237, USA

Abstract

Ion optical design of the transfer line, which will be used to inject H^- beam at 600 MeV from the Coupled Cavity Linac (CCL) into the Low Energy Booster (LEB) synchrotron, is described. Space charge effects of up to 50 mA average beam current have been taken into account.

Introduction

The transfer line must deliver a properly matched, stable and clean beam of small momentum spread and emittance to the stripper foil in the LEB. Nominal emittance at the linac exit is approximately 0.2 π mm-mrad (rms, normalized) in both transverse planes. Simulation studies[1,2] show that the phase space ellipses are almost upright here with β_x=3.13 m and β_y=9.97 m. The longitudinal emittance (rms) is about 268 π keV-deg and β_l=0.0066 deg/keV yielding an rms bunch size of 1.327 deg for the CCL frequency of 1284 MHz. The design average current for collider filling is 25 mA although the rated value for the CCL is 50 mA. The pulse rate is 428 MHz which is the Drift Tube Linac (DTL) frequency. The beam macropulse length is 6.6 μs for collider ring filling and up to 35 μs for the test beam operations.

The transfer line, figure 1, has been designed to perform various functions e.g. beam transport, achromatic bending, phase space matching, etc., with an emphasis on efficient measurement of the beam properties, stabilization and clean-up as well as dumping the beam during tuning. The calculations presented here correspond to matching an LEB beta function of 10 meters and normalized transverse emittance of 0.3 π mm-mrad (rms). An energy compressor RF tank will be used in the line to adjust the longitudinal phase space so that the beam is efficiently captured by the LEB RF system.

Description of the Transfer Line

The line was initially designed and optimized using the TRANSPORT code[3] ignoring space charge effects. Various segments of the line and their design considerations are briefly described in the following sections:

FODO Array

This segment is made up of 21 D and 20 F quadrupole magnets with interquad drift space of 2.38 meters. There are 20 identical unit cells in the array. The phase advance per cell is 90 degrees. These quadrupoles have an effective length of 70 mm and an aperture radius of 15 mm.

*Operated by the Universities Research Association, Inc. for the U.S. Department of Energy under Contract No. DE-AC02-89ER40486

Emittance Scraper Segment

The function of the scraper is to remove extreme tails from the beam profile - at most, a few percent of the beam current. Two apertures, separated by approximately 90 degrees of betatron phase, provide the desired emittance limit. First aperture will be placed at the exit of the last quadrupole of the FODO array. A quadrupole doublet Q1,Q2 provides the desired betatron phase advance. The second aperture is placed within a 28 meters drift following this doublet. At the end of this drift space, the doublet Q3,Q4 refocusses the beam into the following spectrometer. Quadrupoles Q1 and beyond have an effective length of 300 mm and an aperture of radius 37.5 mm.

Achromatic Spectrometer

This system is mirror symmetric about its center point where the energy stabilizing and scraper slits will be located. Optical aberrations in the spectrometer are minimized when there is a double waist at the symmetry plane. Energy resolution is maximized by minimizing the horizontal waist size. We achieve the desired waist conditions by adjusting the gradients of Q1 to Q4. Dispersion of the system at the symmetry plane is 1.534 meters and the momentum resolution is 0.04% (rms). Since there is only one constraint on the settings of Q5 and Q6, we chose to excite them to the same pole tip field but with opposite polarity. The dispersion (η) beyond the spectrometer can be adjusted by changing the ratio of fields in Q5 and Q6, while maintaining the condition R_{26}=0 at the symmetry plane. Angular dispersion can be changed by breaking the symmetry, i.e., by setting Q5' and/or Q6' differently from Q5 and/or Q6. Two sextupole magnets in the system are used to correct for the second order field inhomogeneity in the dipole magnets. They are symmetrically placed 35 cm upstream of D1 and 35 cm downstream D1'. The dipoles are rectangular, uniform field magnets, with an effective length of 2 meters.

Emittance Measurement Range

Following the spectrometer, the quadrupole doublet Q7,Q8 is used to produce a double waist near the mid point of a 20 meter long emittance measurement range. Three beam profile monitors will be used for this measurement, the central one being at the double waist location.

Matching Segment

This segment matches the beam on to the stripper in the LEB ring through the injection segment. Quadrupole doublets Q9, Q10 and Q11, Q12, separated by an 11 meters drift space, provide flexible capability to match to a variety of input and output conditions even for beams with high space charge effects. A 12 degrees dipole magnet midway between the two doublets is pulsed on to guide the beam to the second

beam dump, so that no beam enters the LEB ring during tune-up of the linac or between the LEB fills.

Injection Segment

About 2.8 meter downstream of Q12, the beam enters the injection septum magnet of length 1.407 meters and bending angle 5.66 degrees. The injection bump magnet, 10 cm downstream of the septum magnet, is 0.6 meter long and bends the beam by 2.46 degrees. The stripper is located 10 cm downstream of the exit of the bump magnet.

Second Order Effects

TRANSPORT calculations for the entire transfer line have been carried out to second order. Second order aberrations are found to be negligible, except for the effect of the sextupole component of the dipole fields.

Space Charge Calculations

Space charge effects have been estimated in a linear approximation and the beam line parameters reoptimized using TRACE 3-D interactive code[4]. In the zero beam current case, agreement with TRANSPORT is excellent. Beam envelopes for 5 times the rms emittance (90% beam), obtained using this code, are compared in figure 2, with and without space charge effects of 25 mA average beam current. In both cases, the phase space matching constraints at the stripper are same.

Due to rather long flight paths in the transfer line, space charge effects depend strongly on the energy spread in the beam. They are more pronounced in the case of short bunches like those emerging from the CCL. In view of this, location of the energy compressor cavity in the beam line is very important.

Location of the Energy Compressor RF Cavity

The energy compressor is a coupled cavity tank operating at 1284 MHz and consisting of 20 identical cavities each $\beta\lambda/2$ in length. Its total length is thus 1.85 meters for 600 MeV H^- beam. Synchronous phase, ϕ_s, of the reference particle is - 90 degrees. The rate of change of energy of the ions with charge q arriving at the cavity at phase ϕ is given by:

$$\frac{dw}{dz} = qE_0T\cos\phi$$

where, E_0T is the effective peak accelerating field in the cavity. Requirements on the tank are such that:

1) The rms energy spread (ΔE_{rms}) at the stripper in the LEB is compressed to about 100 keV for longitudinal matching.

2) The half bunch length for the rms beam ($\Delta\theta_{rms}$) at the tank entrance should be about 25 degrees so that most particles see the linear part of the RF waveform.

3) The value of E_0T is as low as possible.

This optimization has been carried out using the TRACE3-D code. First, the tank is placed in one of the drift spaces of the FODO array such that condition (2) is closely satisfied with space charge effects for the desired beam current turned on. Subsequently, E_0T is optimized to obtain the desired energy spread the stripper location.

Various cases corresponding to the average beam currents of 25 mA and 50 mA have been studied. Some of them are summarized in the table 1. While for the 25 mA case it is relatively easy to satisfy the abovementioned conditions, the 50 mA case offers some difficulty. In this case, in order to satisfy condition (2), the tank must be placed at 41.95 meters downstream of the linac exit. It was seen that in the subsequent flight path up to the stripper, space charge effects overcome the energy compression introduced by the tank and the desired energy spread could not be achieved. In view of this, the tank must be moved further downstream in order to satisfy the energy spread constraint at the stripper. This, however, is at the cost of longer bunch length than the desired 25 degrees at its entrance. Figures 3 and 4 show, respectively, variation of the rms energy spread and the half bunch length at the stripper as functions of E_0T for the tank at two different locations. These figures clearly indicate that minimum values of these parameters correspond to a unique value of E_0T which depends on the tank location and the beam current as discussed.

TABLE 1

			At the tank		At the stripper	
$I_{av.}$ (mA)	d (m)	E_0T (MV/m)	ΔE_{rms} (keV)	$\Delta\theta_{rms}$ (deg)	ΔE_{rms} (keV)	$\Delta\theta_{rms}$ (deg)
25	56.65	0.825	673.5	24.95	100.0	31.69
25	46.85	1.130	662.2	20.04	99.8	22.87
50	56.65	0.852	927.1	34.42	99.9	39.40
50	46.85	1.227	913.9	27.65	102.4	22.41
50	41.95	1.302	905.0	24.31	157.6	28.88

d : distance between the linac exit and the tank entrance

In the transverse directions, however, even with space charge effects of up to 50 mA, the beam remains well within acceptable magnet apertures. Desired phase space matching at the stripper is easily achievable by slight tuning of the matching quadrupoles. TRACE-3D readily finds new solutions for the matching quadrupole settings.

Conclusions

The CCL - LEB transfer line has a flexible optical design capable of handling almost twice the nominal linac emittance. Space charge effects of up to 50 mA average beam current have been determined to be tolerable. Longitudinal space charge effects strongly influence the position and excitation of the energy compressor RF tank. Phase space matching to the LEB requirements at the stripper are easy to achieve. Ray-tracing calculations[5] show that fabricational tolerances on all the magnets of the line can be easily met.

Acknowledgements

We greatly appreciate the deep interest and many useful suggestions from Jerry Watson in this work. Many thanks to Deepak Raparia for his help in running the TRACE-3D code.

References

1. SSC Site-specific Conceptual Design Report, December 20, 1989, Chapter 4, p.138.
2. T. S. Bhatia, Los Alamos National Laboratory, private communication.
3. K. L. Brown, F. Rothacker, D. C. Carey and Ch. Iselin, Report No. CERN 80-04, CERN, 1980 and D. C. Carey, Report No. 1546, Fermilab, September 1988.
4. K. R. Crandall, Report No. LA-11054-MS, Los Alamos National Laboratory, August, 1987.
5. R. K. Bhandari and S. Penner, an SSC report (to be published).

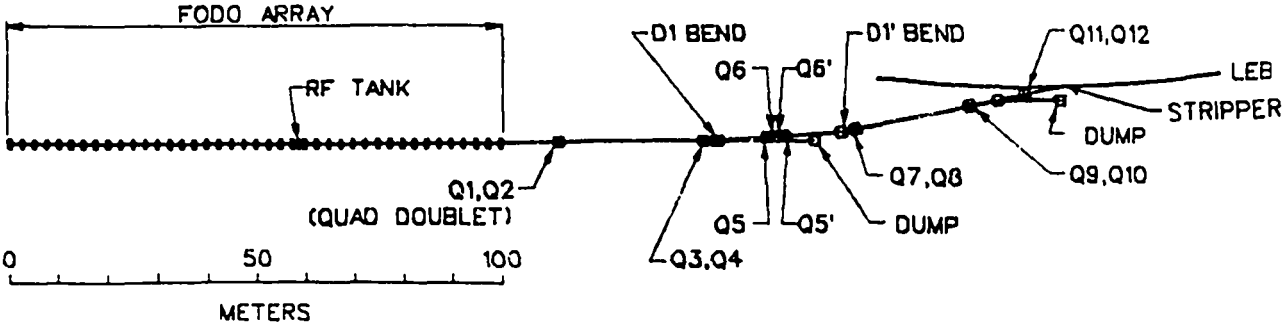

Figure 1: Layout of the beam transfer line between the coupled cavity linac and the low energy booster synchrotron. Q: Quadrupole magnets, and D: Dipole magnets. Total length of the line is about 207 meters.

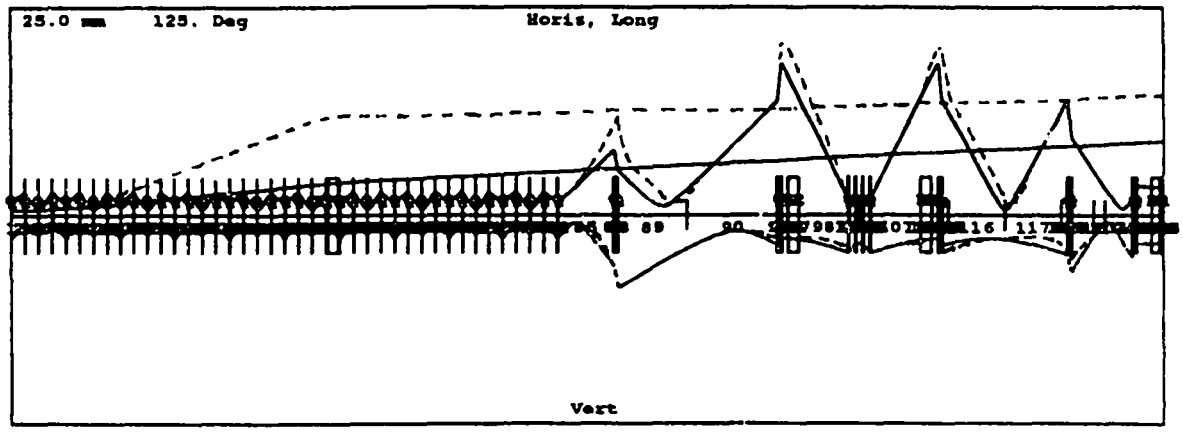

Figure 2: Beam envelopes for 5 times the rms emittance in the transfer line from linac exit up to the stripper in the LEB ring; Full line: Zero beam current; Dotted line: 25 mA beam current. E_0T for the RF tank was set at 0.366 MV/m for the zero beam current and 0.825 MV/m for the 25 mA beam current case.

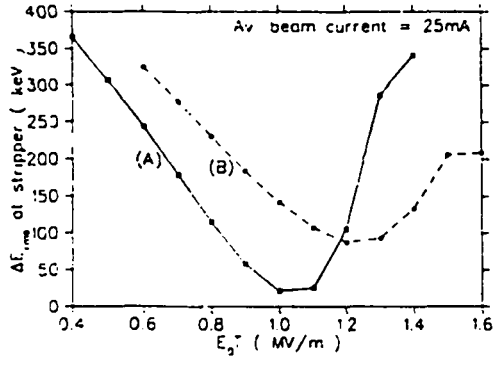

Figure 3: Effect of variation of E_0T on the rms energy spread at the stripper. RF tank is located at, (A) : 56.65 m and (B) : 46.85 m from the linac exit.

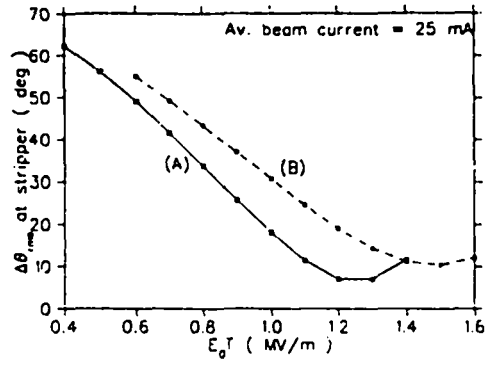

Figure 4: Variation of the rms half bunch length at stripper with E_0T for the cases of fig. 3. Value of $\Delta\theta_{rms}$ at tank entrance for case (A): 24.95° and (B): 20.04°.

MEASUREMENT AND SIMULATION OF WHOLE BEAM BRIGHTNESS ON THE ETA-II LINEAR INDUCTION ACCELERATOR *

Y.-J. Chen, J. C. Clark, A. C. Paul, W. E. Nexsen, and W. C. Turner
Lawrence Livermore National Laboratory, University of California
Livermore, California 94550

Abstract

Measurement of beam radius as a function of focusing strength of an upstream solenoidal field allows simultaneous determination of the beam energy, brightness and tilt of the phase space ellipse. On ETA-II beam radius has been measured by analyzing foil emitted Cherenkov light with a gated (5 ns) image intensified CCD camera. The beam energy measurement is corroborated with a spectrometer magnet and core brightness with a two hole emittance diagnostic. For a 6 MeV, 1.6 kA beam, the whole beam brightness was measured to be 4.0×10^8 A/(m-rad)^2 with an inner core (few percent) brightness of 1.2×10^9 A/(m-rad)^2. The data was simulated with a particle transport code that includes the effects of energy sweep and magnetic misalignment. The code predicts a halo produced by an orbital resonace that is also observed experimentally.

Introduction

The Experimental Test Accelerator-II (ETA-II)[1] is the first induction linac designed specially to be used as a driver for a 140 GHz microwave FEL. The nominal beam parameters for these experiments are 6 MeV energy, 2 kA current, 1×10^8 A/(m-rad)^2 brightness, 20 ns pulse flat top at the wiggler with a pulse repition frequency of 0.5 Hz. In this paper we present the results of measurements and simulation of beam brightness on ETA-II. The 2-hole brightness measurement, the Cherenkov measurement and the energy measurement were all made in a single run for each injector configuration in order to get a reasonable comparison of the data. The Cherenkov data are simulated with two particle simulation codes. Good agreement is found between the computer simulation results and the experiment.

Experiments

ETA-II consists of an injector and six 10-cell blocks. Two injector configurations, the D-1 diode and the T-3 triode, with a 12.7 cm diameter cathode were used. The D-1 diode was designed to achieve 3 kA at 1 MV from the injector for the microwave FEL experiments. It was expected that the diode would have an inherent brightness less than the T-3 triode that was designed for high brightness for up to 2 kA of beam current. The brightness measurements at 2.5 MeV with the T-3 triode was reported in Ref. 2. No previous brightness measurements had been made with the D-1 diode.

The beamline configuration of ETA-II is shown in Fig. 1. The energy analyzer and the 2-hole brightness diagnostic rely on quadrupole focusing for imaging the beam. The solenoid lens F1 is also used for the 2-hole brightness measurements in order to obtain the needed focus at the first aperature. The energy analyzer measures the beam energy by measuring the deflection of the beam in a known dipole magnetic field.

* Work performed jointly under the auspices of the U.S. Department of Energy by Lawrence Livermore National Laboratory under contract W-7405-ENG-48, for the Strategic Defense Initiative Organization and the U.S. Army Strategic Defense Command in support of SDIO/SDC MIPR No. W43-GBL-0-5007

The magnetic field in the bending magnet is calibrated using a rotating coil gaussmeter that is accurate to better than 0.1%. The entrance angle to the bending magnet is determined from the offsets of the current monitors T2 and T3 which are in a field free drift space. Likewise, the exit angle is determined from the offsets of EA1 and EA2. The offset and the bending magnet data is combined to get the energy as a function of time.

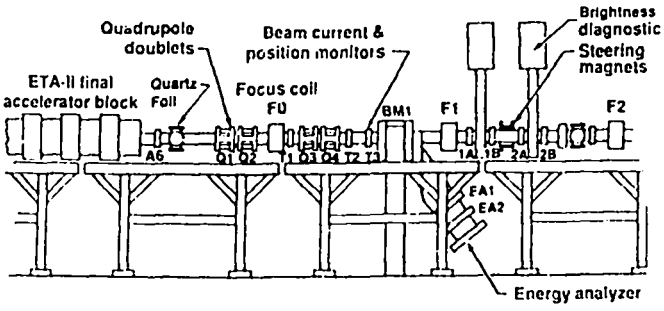

Fig. 1 ETA-II beamline configuration

The field-free, 2-hole emittance selector consists of two aperatures with 3 mm holes separated by 67.5 cm. The impinging current is I_1. The current tasnsmitted through the first aperture is I_2, and that through current through the second aperature is I_3. The configuration is the same as that used in energy measurements except that the apertures have been modified to be installed and removed remotely so that the beam can be characterized and then transported into the FEL wiggler. The normalized brightness is

$$J = \frac{I_3}{(\beta\gamma)^2 V_4 \delta} \quad , \tag{1}$$

where $\beta\gamma$ is the usual relativistic factor, V_4 is the acceptance of the collimator and δ is a space charge correction factor. The brightness measurements are made by focusing the beam current I_1 to obtain a waist at the center of the two apertures. About 125-150 A of current I_2 is transmitted through the first aperture. Steering and focusing of the beam onto the first aperture is aided by a fast-gated TV camera that views the beam image at the first graphite aperture. The sine/cosine steering coil set located between the two apertures is used to steer the beam onto the second aperture, and current I_3 is maximized with this steering.

The radial distribution of beam brightness was made at the same time by measuring the beam generated light intensity profile at the end of the accelerator as a function of the upstream solenoid magnetic field in the last 10-cell block. This allowed the beam energy, brightness and tilt of the phase space ellipse to be extracted from a self consistent fit to the focusing data. The excitation of the solenoid focusing field of the sixth ten cell block was varied from 30 to 280A. The beam profile was measured using a fast-gated image intensified CCD camera viewing the Cherenkov light generated in a thin quartz foil which is located 32.3 cm away from the end of the accelerator

Energy Analyzer results

The energy measured 5.9 to 6.4 MeV over the main part of the pulse for the D1 diode configuration. The energy used for the brightness calculation is 6.2 MeV. This is the best match for the energy during the 5 ns gate-width of the TV camera and corresponds to a time near the peak of the I_3 current, though it is not possible to precisely measure the relative timing because of unknown propagation delays through different instruments such as the oscilloscopes and the TV cameras. The relative timing in the pulse is probably known to within 5 ns.

The T-3 configuration requires a higher injector volatge to obtain a 1.6 kA beam current. The individual accelerator gap voltages were reduced to compensate for the increase in injector voltage, however, the total beam energy is slightly higher. In this case the energy measured 6.4 to 6.7 MeV. The energy used in the 2-hole brightness calculation was 6.5 MeV. The energy from the Cherenkov data is 6.4 MeV for both the D-1 and T-3 configurations.

2-hole brightness measurement results

The results of the brightness meaurements for the D-1 diode and the T-3 triode are summarized in Table I. The beam energy used in the calculation of brightness is taken from the energy analyzer measurements. In both the D-1 and the T-3 sets of data the I_3 current is considerably narrower in time than the I_2 current. This is a result of the beam sweep induced by the corkscrew instability[3,4].

Table I. 2-Hole Brightness

Date	I_2(A)	I_3(A)	J(A/(m-rad)^2)	$1/\delta$	E(MeV)
D-1 injector					
12/06/89	148.7	14.9	9.0×10^8	1.15	6.2
12/06/89	129.2	14.3	8.4×10^8	1.14	6.2
12/06/89	140.7	14.0	8.4×10^8	1.14	6.2
T-3 injector					
12/18/89	144.4	24.5	1.40×10^9	1.18	6.5
12/18/89	138.0	21.3	1.20×10^9	1.16	6.5
12/18/89	135.0	21.0	1.17×10^9	1.16	6.5
12/21/89	129.8	15.3	8.30×10^8	1.13	6.5
12/21/89	129.2	14.7	8.00×10^8	1.13	6.5

Cherenkov measurement results

Analysis of the Cherenkov data (beam size versus upstream focusing solenoid field) at different light intensity contours unfolds the beam emittance, phase space tilt and energy as functions of radius. In the data analysis the beam is reconstructed at the beginning of the sixth cell block. The whole beam energy used in the analysis is 6.24 MeV for both configurations.

The whole beam brightness is

$$J = \frac{2I_1}{\pi^2\beta^2\gamma^2\epsilon^2} \quad . \tag{2}$$

where ϵ is the whole beam emittance. The Cherenkov light intensity is at its maximum on the beam axis. The light intensity within the 90% light contour represents the very inner core of the beam. If we assume that the beam has a parabolic four-volume distributrion function. then 97% of the beam is enclosed by the 10% light intensity contour. The 10% light intensity contour defines the beam edge. The beam current $I_4(r)$ is the current enclosed by a radius r. The core current I_c within the sub-ellipsoidal phase space associated with a betatron amplitude r is roughly the same as the current passing through the two slit emittance selector of aperture radius r The core brightness J_c, core current I_c, and I_4 as functions of radius obtained from the analysis for the D-1 and T-3 configurations are given in Fig. 2. The brightness of the D-1 beam varies from 3.83×10^8 A/(m-rad)^2 at the beam edge to 1.14×10^9 A/(m-rad)^2 at the core to be compared with a value of 8.6×10^8 A/(m-rad)^2 measured by 2-hole emittance selector (Table I). The brightness of the T-3 beam varies from 5.68×10^8 A/(m-rad)^2 at the beam edge to 1.71×10^9 A/(m-rad)^2 at the core. The core brightness measured by the 2-hole brightness diagnostic on the same day is 8.2×10^8 A/(m-rad)^2.

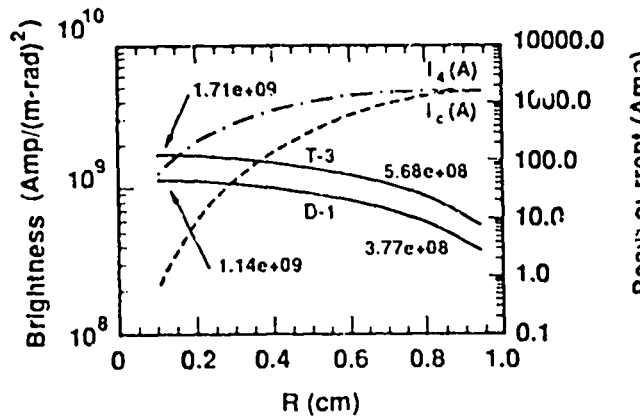

Fig. 2 Core brightness, core current I_c and I_4 as functions of radius obtained from Cherenkov analysis for the D-1 and the T-3 configurations

Simulations

The experimental conditions of the T-3 configuration on 12/21/89 were simulated with the DPC[5] and WIRE[6] codes. DPC was used to simulate the beam from the cathode to 20cm into the anode pipe. The WIRE code was then used to follow the beam through the six ten-cell blocks to the Cherenkov foil. In the simulations, we used the measured tilts of the cell block solenoids. The tilts of the intercell magnets were chosen such that the corkscrew amplitudes of a 1200 A, 4.6MeV beam calculated by the BREAKUP[7] code matched the experimental corkscrew amplitude[1] at all beam bug locations. The Cherenkov light was gathered over a 5 ns time slice. Typically, the beam energy changes 3% within a 5 nsec period[1]. In order to simulate the effects of corkscrew oscillations on the Cherenkov measurements, the WIRE code was run three times with 2000 particles with slightly different accelerating gap voltages for each given solenoid focusing current. The accelerating gap voltages were chosen such that the beam energy of each run differents by 1.5% with an average energy of 6.2 MeV. The particle data generated by these three runs are analyzed together in order to obtain the beam radius and brightness.

Simulation results

The WIRE code calculations indicate that some particle orbits are in resonance with the periodic magnetic structure in the first two 10-cell blocks. This resonance leads 20-25% of particles to walk away from the bulk of the beam and form a halo. The normalized beam emittance tripled within the first two 10-cell blocks. There is a large corkscrew motion for the 5 nsec beam segment. The large corkscrew motion and beam halo cause some current loss when the beam is defocused. The beam current at the Cherekov foil varies from 1350A to 1650A over the 50-280A focusing current range of the last 10-cell block. The images of the T-3 beam and the simulated beam agree very well.

Comparison between the beam sizes obtained from the simulations (dashed curves) and Cherenkov analysis (solid curves) is shown in Fig. 3. The locations of the minimum and maximum beam radius at the various intenisty levels agree between simulations and experiment. The simulated beam sizes are somewhat larger than that fitted from the Cherenkov light data. Only the light intensity data measured within ±3 cm from the center of the beam in both the x and y directions were recorded in the experiments. When the beam is large and fills the image frame, the backgroud subtraction during the data processing will lead to an underestimated beam size. By applying this procedure to the simulation data, we found that the beam sizes at the 10% intensity contour were reduced by roughly 10%.

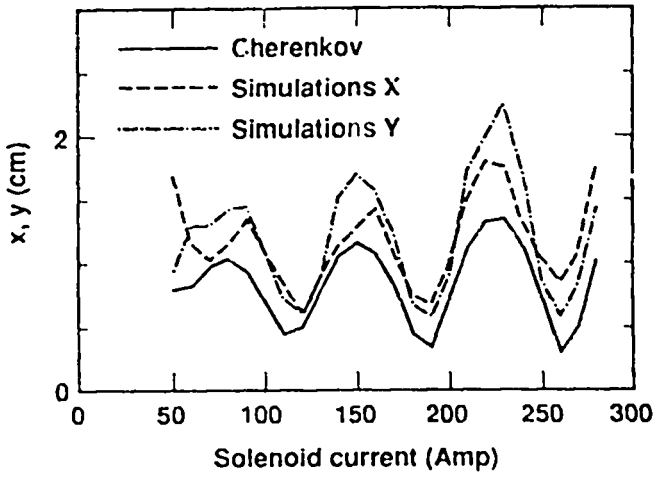

Fig. 3 Comparison between the simulated (dashed) and Cherenkov analysis (solid) beam sizes for the 10% beam intensity contours.

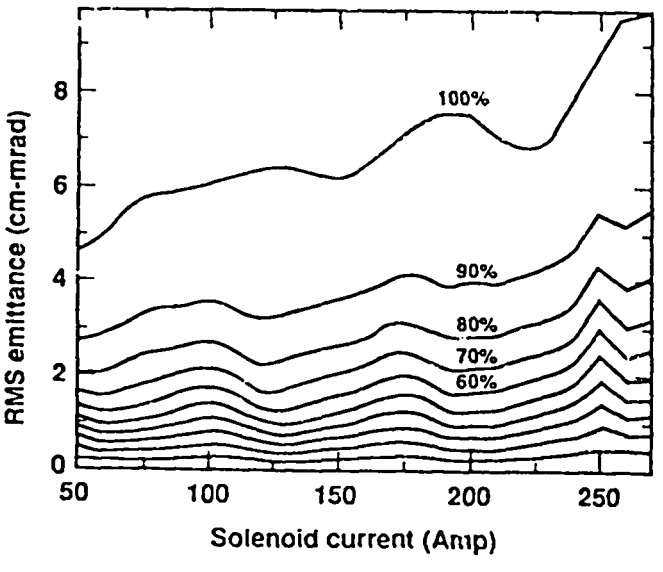

Fig. 4 Effective emittance versus focusing current for 10, 20, ... 90% of the beam current. The effective emittance increases as the focusing current in the last cell block moves away from 80 A.

The effective emittance[4] of the beam within a 5 ns slice is larger than the "instantaneous" beam emittance due to the presence of the corkscrew oscillations. The effective emittance increases when the corkscrew amplitude increases. If the solenoid focusing current in the last 10-cell block is very different from that in the fifth 10-cell block, the corkscrew amplitude increases due to the large transverse magnetic field at the intercell region. In the experiment the focusing current in the fifth 10-cell block is 81.93A. The simulations show that the effective emittance increases (see Fig. 4) and the effective brightness decreases as the focusing current in the last 10-cell block moves away from 80A. Ten curves of effective RMS emittance versus focusing current are plotted for 10, 20, ... 100% of the beam current. For the 80 A focusing solenoid current case, the calculated effective RMS emittance is 2.5 cm mrad for 80% of the beam (enclosed by the 10% light intensity contour) and 5.7 cm-mrad for the whole beam. The edge emittance is four times of the RMS emittance for a parabolic beam. The Cherenkov analysis gives a value of 1.53 cm-mrad for the RMS emittance within the 10% light intensity contour. The brightness averaged over the 50-280A range of focusing solenoid current for 80% of the beam current (1280 A) is 1.37×10^8 A/(m-rad)^2 which is to be compared with a value of 5.75×10^8 A/(m-rad)^2 obtained from the Cherenkov analysis. The inner core brightness is 1.81×10^9 A/(m-rad)^2 from the simulations, 1.71×10^9 A/(m-rad)^2 from the Cherenkov technique, and 8.15×10^8 A/(m-rad)^2 from the 2-hole brightness diagnostic. By subtracting the beam halo of 20% current, the adjusted Cherenkov value becomes 4.60×10^8 A/(m-rad)^2 for 80% of the beam and 1.37×10^9 A/(m-rad)^2 for the inner core

Conclusions

The whole beam brightness measured by the Cherenkov technique on ETA-II ranges from 3.8×10^8 to 6.8×10^8 A/(m-rad)^2 for both injector configurations operating at about a beam current of 1600 A. The beam core brightness from the Cherenkov analysis ranges from 1.1×10^9 to 2.0×10^9 A/(m-rad)^2 to be compared with the 2-hole brightness diagnostic values of 8.15×10^8 and 1.4×10^9 A/(m-rad)^2. The WIRE code predicts a halo caused by a parametric instability of particle orbits that is also observed experimentally. Simulations show the ETA-II beam experienced large corkscrew oscillations within the 5 ns time slice of the experiment. In general, parametric instabilities are relatively easy to avoid simply by adjusting the parameters of the machine such as the magnetic tune and beam energy. Studing the ETA-II tune theorectically before running the experiments will allow us to avoid parametric instabilities[8].

References

1. W. E. Nexsen, et al., *Proc. of the 11th Int. FEL Conf.*, Naples, Florida (August 28-Sept. 1, 1989).
2. W. C. Turner, et al., *Proc. 1989 Part. Accel. Conf.*, Chicago, Illinois (March 20-23, 1989), p. 996 .
3. G. J. Caporaso, et al., *Proc. of the 5th High Power Part. Beams Conf.*, San Francisco, Ca., Sept. 12-14 (1983).
4. Yu-Jiuan Chen, *Nucl. Instr. and Meth.*, **A292**, 455 (1990).
5. D. W. Hewett and J. K. Boyd, *J. Comp. Phys.* **70**, 166 (1987).
6. G. J. Caporaso and A. G. Cole, *IEEE Trans. Nucl. Sci.*, **Ns-30**, 2618 (1983).
7. G. J. Caporaso, A. G. Cole, and K. W. Struve, *IEEE Trans. Nucl. Sci.*, **Ns-30**, 2507 (1983).
8. W. C. Turner, et al., "Reduction of Beam Corkscrew Motion on the ETA-II Linear Induction Accelerator", this conference.

ENERGY SWEEP COMPENSATION OF INDUCTION ACCELERATORS

S. E. Sampayan, G. J. Caporaso, Y-J Chen, T. A. Decker, and W. C. Turner
University of California, Lawrence Livermore National Laboratory
P. O. Box 808, Livermore, CA 94550

Abstract

The ETA-II linear induction accelerator (LIA) is designed to drive a microwave free electron laser (FEL). Beam energy sweep must be limited to ± 1% for 50 ns to limit beam corkscrew motion and ensure high power FEL output over the full duration of the beam flattop. To achieve this energy sweep requirement, we have implemented a pulse distribution system and are planning implementation of a tapered pulse forming line (PFL) in the pulse generators driving acceleration gaps. The pulse distribution system assures proper phasing of the high voltage pulse to the electron beam. Additionally, cell-to-cell coupling of beam induced transients is reduced. The tapered PFL compensates for accelerator cell and loading non-linearities. Circuit simulations show good agreement with preliminary data and predict the required energy sweep requirement can be met.

Introduction

Linear induction accelerators (LIAs) are used for the production of high average power charge particle beams. These accelerators have been operated at high current (greater than 1 kA), moderate energy (order 10 MeV) and at high repetition rates (order 5 kHz) [1-3].

An LIA consists of an injector used to generate the initial charge particle beam pulse, multiple accelerator cells, and a pulse generator with a pulse distribution system [4]. The injector normally consists of multiple accelerator cells with an internal conductive structure, which in the case of ETA-II, contains an electron source on a "cathode shank" and a re-entrant anode structure. This injector geometry sums the energy gain of individual cells and allows achievement of the required beam qualities.

Energy sweep is defined as the quantity dE/E, and represents the variation of the beam energy about some mean value. In the LIA, non-linear loading at the accelerator cell is inherent. Consider a simplified model of the pulse generator and accelerator cell (Fig. 1). The energy gain at the accelerator cell, proportional to V_b, is a function of the cell current, i. e., current through C_{gap}, the ferrite current, and the beam current. As ferrite current is a function of the integral of the voltage at the cell, a non-linear accelerator cell response results [5].

From the circuit equations, the effect of the ferrite non-linerity takes the form:

$$\frac{dV_b}{V_b} = \left[\frac{Z_0}{Z_f}\right]\left[\frac{dZ_f}{Z_f}\right] \qquad (1)$$

As an example, ETA-II uses PE-11B NiZn ferrite and a cell source impedance of Z_0=40 ohm. From previous data [5], dV_b/V_b, which is proportional to the energy sweep, is calculated to be 6% when 75% of the volt-second product of the ferrite cores is used.

For the simplest case, compensation of the energy sweep contribution at an accelerator cell, on the s-plane, requires:

$$\frac{V(s)}{H(s)} = \frac{V_0}{s}\left(1 - e^{sT}\right) \qquad (2)$$

where H(s) is the pulse distribution system and cell response, V(s) is the applied pulse, T is the pulse width, and V_0 is the accelerator gap voltage.

To compensate the energy sweep contribution at an accelerator cell, H(s) and V(s) may be adjusted. For an ideal V(s), i. e. $V(s) \propto s^{-1}$ and a non-perturbing pulse distribution system, H(s) can be made to approach a constant by modifying the total cell current to eliminate non-linearities. This modification of H(s) can be done by adjusting the beam current profile or by introducing additional components at the accelerator cell, i. e. non-linear components [6], RLC filters, etc. Modification of V(s) for a defined H(s) requires modification of the pulse generator.

Minimum total accelerator energy sweep requires minimum energy sweep at the injector or the use of compensating accelerator cells. The latter assumes the energy sweep associated with the injector is fixed and the initial accelerator cells are used for compensation. That is, the sum of the injector and these accelerator cells result in a minimum total energy sweep. Although slightly less than ideal for minimum corkscrew motion [7], this technique is considered here.

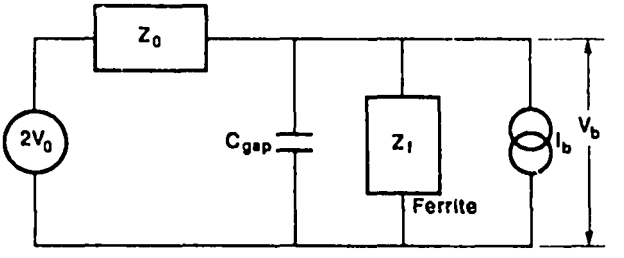

V_b = beam voltage
$= 2V_0 - (I_c + I_f + I_b) Z_0$

Figure 1. Simplified Pulse Generator and Accelerator Cell Model.

Energy Sweep Compensation on ETA-II

The predominant factors on ETA-II which influence H(s) are: beam and applied high voltage pulse phasing, accelerator cell feed structures, and the non-linear effects of the cell ferrite. In the initial stages of development on ETA-II, the accelerator cell feed structures were dominant in the determination of H(s).

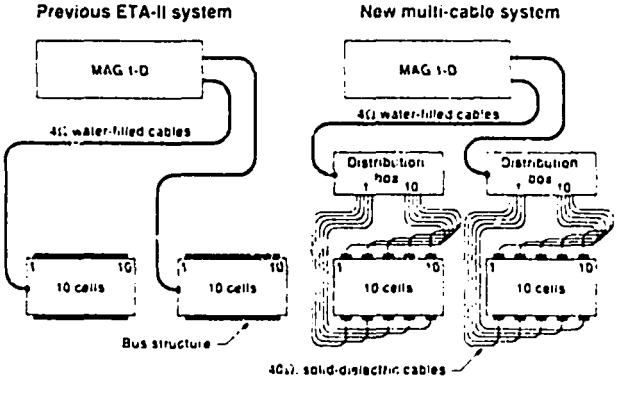

Figure 2. ETA-II Modifications. Previous ETA-II bus structure (left). Modified ETA-II "two cell" bus structure (right).

The high voltage pulse on ETA-II was previously applied to the accelerator cell through two bus structures on each side of a module of ten accelerator cells (Fig. 2). The pulse generator, i. e. MAG1-D [8], was connected to the 10 cell module through a single cable. Two effects were associated with this struc-

ture. First, the capacitance associated with each accelerator cell combined with the bus structures to form a slow wave structure. Second, the beam return current introduced transients on this slow wave bus structure with a polarity opposite to the applied high voltage pulse. Improper phasing of the high voltage pulse with the beam and severe distortion of the MAG1-D pulse resulted. Compensation was much more difficult since the total response of the feeds, cells, and their interaction needed to be considered.

A new accelerator cell feed was developed and implemented. The slow wave bus structure was replaced with a bus connecting two accelerator cells. This "two-cell" feed structure placed the cell capacitance across the bus termination. Slow wave transit time effects were eliminated. Distribution to each two cell structure was done with individual transmission lines properly timed to the beam transit. Thus, this new system only introduced a time delay and nearly isolated the response of a single cell.

In this new system, compensation can be accomplished by adjustment of V(s). This compensation may be done in two ways. The first method relies on the output characteristics of the MAG1-D at various voltages, i. e., the output pulse shape varies with output voltage [9]. By properly adjusting the output voltage pulse amplitude, a minimum energy sweep may be obtained. This technique, however, confines the accelerator to a single operating point in our energy range of interest. We present the modeling, sensitivities and preliminary test results in the section Single Operating Point Compensation.

The second method requires the use of a variable taper PFL [10], i. e., a PFL with an adjustable impedance variation along its length. The impedance variation results in an output pulse shape required to meet the cell impedance non-linearities with minimum energy loss. This method allows energy sweep compensation at any accelerator operating point. We present our initial analysis and sensitivity calculations in the section Multiple Operating Point Compensation.

Single Operating Point Compensation

Cell response modeling using SCEPTRE [11] and prototype verification were performed to determine the performance of the two cell structure. The model included the non-linear effects of the ferrite and was implemented by a function derived from experimental data. Typical performance of the model compared with measurement is shown in Figure 3.

The combined effect of the bus structure connecting the two independent cells was taken into account by directly measuring the voltage across a two cell structure. Agreement between the measured and calculated two cell voltage pulse shape was within 1% in an area surrounding the peak. Absolute amplitude was in agreement within 10%.

Analysis of the accelerator performance was similarly performed using MAG1-D output pulse and previous beam current data (Fig. 4). Significant energy sweep, however, associated with the injector is present in the ETA-II system. Elimination of this energy sweep required intentionally introducing additional sweep at the accelerator cells which countered that of the injector.

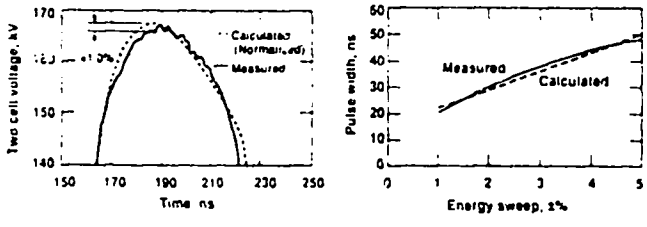

Figure 3. Circuit Model and Prototype Measurement

The parameters of Injector Timing (injector pulse to accelerator cell voltage pulse arrival timing) and MAG1-D input Charge Voltage, V_0, were varied to obtain a maximum pulse width (total accelerator energy sweep) of 38 ns, ± 1% energy sweep (Fig. 5). The optimization curve exhibits the property of being relatively insensitive to both parameters.

In our present experiment of 20 accelerator cells, the minimum total energy sweep occurred at an accelerator cell gap voltage of 80 kV. We are presently planning a 60 cell experiment. The sensitivity of the energy sweep at individual cells to timing jitter at this voltage, however, was found to be unacceptable. Further analysis showed that this sensitivity was significantly less at 90 kV without degradation in the total energy sweep. Thus, consistent with the objective of maximum pulse width at the cell and minimum sensitivity, we plan to operate the remaining 40 accelerator cells at this gap voltage of 90 kV.

Simulations were also performed using the BREAKUP code [12] to predict the resultant corkscrew amplitude. Results from the calculation indicated an amplitude on the order of ± 250 microns. Comparison with simulations developed for the previous ETA-II bus structure (Fig. 6) indicate that the corkscrew amplitude will be reduced by at least an order of magnitude.

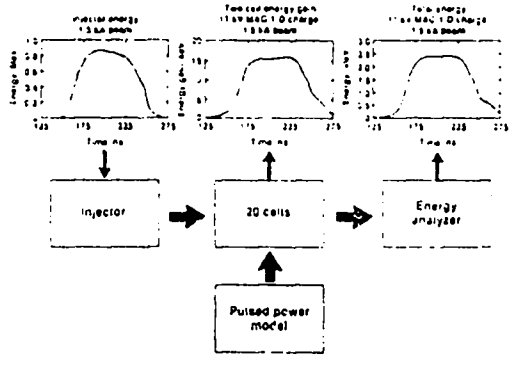

Figure 4. Compensation of the ETA-II 20 cell experiment.

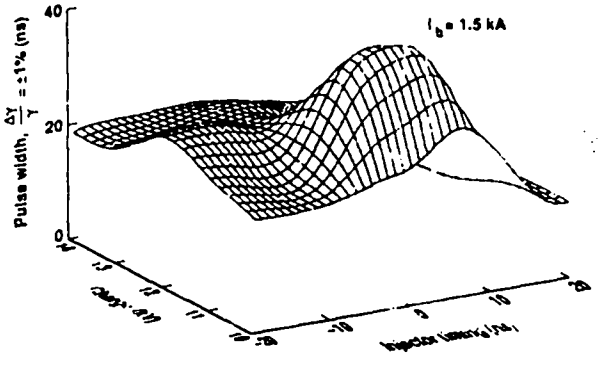

Figure 5. ETA-II 20 Cell Experiment Pulse Width Optimization Surface. Pulse width values are for dE/E= ± 1%, I_{beam}=1.5 kA.

Multiple Operating Point Compensation

Additional calculations were performed to evaluate the performance of a variable taper PFL in the MAG1-D pulse generator. Physically, the device is a tri-plate transmission line. This configuration allows two objectives to be met. First a more uniform constant impedance transition can be made from the PFL to the coaxial output switch, and second, mechanical actuators necessary to control the impedance taper can be easily implemented.

Optimum impedance tapers were calculated for two experimental beam currents (Fig. 7). A resultant pulse for the matched cell case, i. e., Z_{cell}=40 ohm is shown in Figure 8. It was determined that

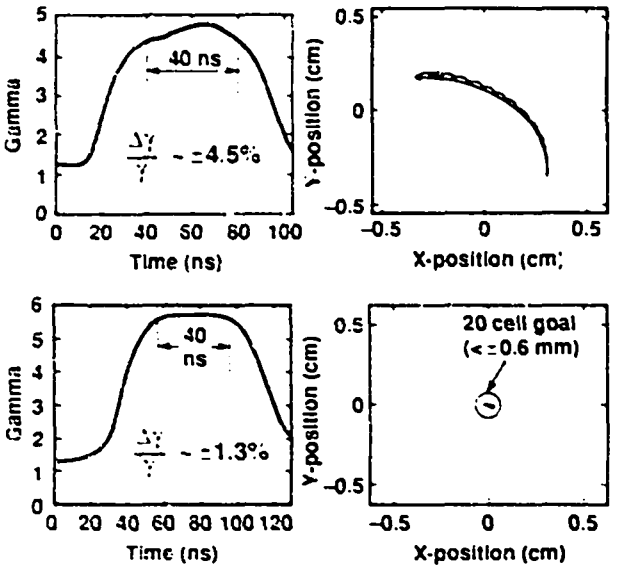

Figure 6. BREAKUP Simulations. Corkscrew motion is plotted for 40 ns as shown in each accompanying plot. ETA-II simulations for previous bus (top). Simulations of expected results (bottom), dE E= ±1.3%.

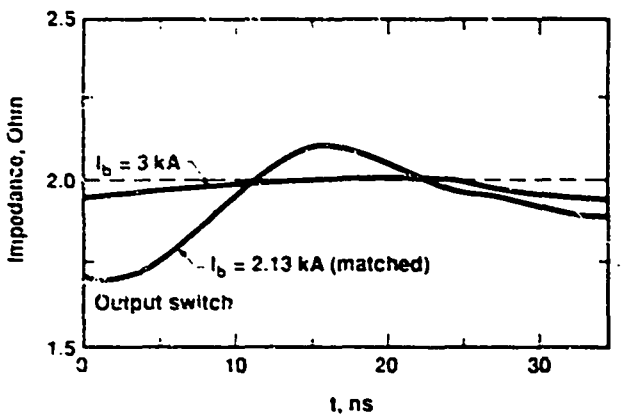

Figure 7. Optimum impedance tapers for specified beam currents.

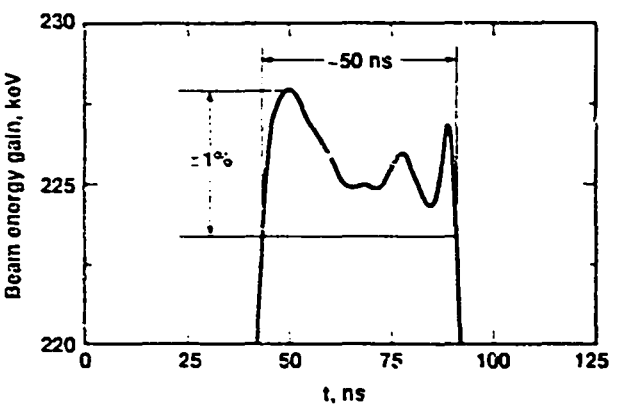

Figure 8. ETA-II "Two-cell" Acceleration Gap Voltage Pulse. I_{beam}=2.13 kA.

increased beam currents required less impedance taper. Reduced pulse width resulted, however. We speculate that the reduced impedance taper results from the self compensating effects of the beam current profile toward the peak and trailing edge of the pulse.

Development

Further refinements in the modeling effort are required. In addition to refinements in modeling magnetic materials, i. e. accelerator cell ferrite and the MAGI-D output switch, investigation into design centering of the PFL taper is required. We are pursuing each of these areas.

We are also considering the alternate implementation of the tapered PFL in the MAGI-D driving the injector on ETA-II. This implementation would allow compensation of the cell response by adjusting the beam current profile.

Acknowledgments

This work was performed jointly under the auspices of the U. S. Department of Energy by Lawrence Livermore National Laboratory under contract W-7405-ENG-48, for the Strategic Defense Initiative Organization and the U. S. Army Strategic Defense Command support of SDIO/SDC MIPR No. W43-GBL-0-5007.

The authors acknowledge the assistance of B. Poole with the SCEPTRE calculations; and C. Ollis and D. Pendleton for their assistance with the prototype experiments.

References

1. R. J. Briggs, D. L. Birx, D. S. Prono, D. Prozzitz, and L. L. Reginato, "Induction Linac Based FELs," in Proceedings of the IEEE Particle Accelerator Conference, Washington D. C., pp. 178-182, 1987.
2. L. L. Reginato, "The Advanced Test Accelerator (ATA) a 50 MeV, 10 kA Induction Linac," presented at the 198[illegible] Particle Accelerator Conference, Santa Fe, New Mexico, March 1983.
3. W. A. Barletta, "Accelerating Intense Electron Beams," in Energy and Technology Review, Lawrence Livermore National Laboratory, Livermore, CA, UCRL-52000-79, September, 1979.
4. S. Humphries, Principals of Charged Particle Acceleration, John Wiley and Sons, New York, 1986.
5. W. C. Turner, G. J. Caporaso, G. D. Craig, J. F. DeFord, L. L. Reginato, S. E. Sampayan, R. W. Kuenning, and I. D. Smith, "Impedance Characteristics of Induction Accelerator Cells," presented at the 7th International Conference on High-Power Particle Beams, Karlsruhe, Germany, July 4-8, 1988.
6. W. M. Parsons and M. L. Hodgdon, "Voltage Regulation in a Linear Induction Accelerator Using Metal Oxide Varistors," in the Proceedings of the 19th Power Modulator Symposium, San Diego, CA, June 26-28, 1990.
7. Y. Chen, "Corkscrew modes in Linear Accelerators," Nucl. Instrum. and Meth. in Physics Research, A292, pp. 455-464 (1990).
8. see for example: D. M. Barrett, "Modeling the Characteristics of a Magnetically Switched Pulse Forming Line," in the Digest of Technical Papers, 7th IEEE Pulsed Power Conference, Monterey, CA, June 11-14, 1989.
9. W. C. Turner, D. M. Barrett, and S. E. Sampayan, "Critical System Issues and Modeling Requirements-the Problem of Beam Energy Sweep in an Electron Linear Induction Accelerator," presented at the International Magnetic Pulse Compression Workshop, Lake Tahoe, CA, February 12-14, 1990.
10. I. A. D. Lewis and F. H. Wells, Millimicrosecond Pulse Techniques, Pergamon Press, New York, 1959.
11. D. Becker, Extended SCEPTRE, Vol. 1, Air Force Weapons Laboratory, Kirtland Air Force Base, NM, AFWL-TR-73-75, Vol. 1, December 1974.
12. G. J. Caporaso, A. G. Cole, and K. W. Struve, "Beam Breakup (BBU) Instability Experiments on the Experimental Test Accelerator (ETA) and Predictions for the Advanced Test Accelerator (ATA)," IEEE Trans. Nucl. Sci., NS-30, pp. 2507, (1983).

CHARACTERIZATION OF FIELD ERRORS OF LAYER WOUND SHORT SOLENOIDS*

William E. Nexsen, Jr.
Lawrence Livermore National Laboratory
P. O. Box 808, L-626, Livermore, CA 94550

Abstract

We report on a study of the error fields of a set of layer-wound short solenoids of the type used in high-current electron linacs. These error fields are mainly caused by the azimuthal variation of the winding pitch angle. The conventional winding pattern design tends to concentrate the error fields in a dipole component perpendicular to the solenoid axis. Compounding the problem are smaller contributions due to the asymmetric coil feeds and conductor crossovers from one layer to the next. We have constructed and tested a prototype quadrufilar solenoidal magnet which utilizes symmetry to cancel the effects of current leads and crossovers and, in the absence of winding errors, should have an intrinsically straight magnetic axis. This design tends to concentrate the error field in the much less harmful octupole component. Measurements of the dipole error field yield a value of the order of one milliradian for the quadrufilar magnet as compared with about six milliradians for the conventional ETA-II magnets and twelve milliradians for the ATA magnets. The improved cooling of the quadrufilar design allows DC operation at fields almost three times higher than the conventional magnets.

Introduction

High-current linacs require magnetic focusing to avoid space-charge-induced beam loss. For achromatic beam transport and high average acceleration gradient, the magnetic field is usually generated by an array of closely spaced short solenoids, most of which are built into the induction cells. For satisfactory beam injection into extraction devices such as wigglers, the magnetic axis of the individual magnets must be aligned to a small fraction of a milliradian with respect to the mechanical axis. Problems with magnetic misalignment have been encountered in two linacs at LLNL, the 50-MeV ATA and the 6-MeV ETA-II; as a consequence, a program was undertaken to determine the source of these errors.

Solenoid design considerations

Fabrication

Maximum fields of the order of several kilogauss may be required for beam transport, making necessary the forced cooling of the magnet windings. The ETA-II magnets, for example, use a 0.25-in.^{2} hollow copper conductor covered by a ~6 mil glass-dacron insulation layer heat-bonded to its surface. The magnet has four layers of about 33 turns each; a single conductor length (or filar) is used to wind two layers, so two conductor lengths, electrically in series but with parallel water cooling paths, form each magnet. The magnets are vacuum impregnated with an epoxy formulation that provides mechanical strength and dimensional stability.

Perpendicular dipole field windings (sin/cos coils) were incorporated in the newer ETA-II design to compensate for misalignments and error fields. The winding pattern is photoetched on circuit board which is then wrapped around the magnet prior to impregnation. These trim windings are limited in the field they can produce and are not effective in correcting the higher-order multipoles that may cause emittance growth. Thus, even when trim coils are used, there is a premium in producing as error-free a magnet as possible.

Sources of error

A perfect axially symmetric short solenoid will show no azimuthal variation of its field components around its mechanical axis. I define "error fields"as deviations of the measured field from that expected from a "perfect" short solenoid. Such deviations may be due either to the choice of winding pattern or to errors in attempting to reproduce that winding pattern. The conventional single filar winding pattern described above even if accurately reproduced does not have a straight magnetic axis. Asymmetries at the ends caused by the current leads and crossovers (the region at the end of a winding layer where the conductor makes a transition to a larger winding radius in preparation for the return winding) cause all of the field lines to bend in these regions. These effects are small, but they are not random; consequently, in an accelerator the total error introduced is linear with the total number of magnets in series and can lead to loss of the beam in the absence of correction fields.

These end effects can be eliminated by the use of a multifilar winding pattern. If the symmetry number s is the number of indistinguishable positions to which the winding pattern can be turned in one complete rigid rotation around the winding axis, then $s = 1$ for the conventional single filar winding pattern. Winding patterns with $s > 1$ have no perpendicular field component along their winding axis and the magnetic axis coincides with the winding axis. Any deviation of the axis from straightness in an actual magnet with a $s > 1$ winding pattern is only due to symmetry-breaking winding errors which make $s = 1$.

Winding errors can arise in two ways, as variations either of the winding radius or of the winding pitch angle. Of these two the latter is the much more important for layer wound solenoids.The winding pattern for an error-free conductor layer is given by

$$x = R\cos\theta,\ y = R\sin\theta,$$
$$z_{io} = [(n\theta/2\pi)-i+1]\,w, \qquad (1)$$

for $i-1 < (n\theta/2\pi) < (L/w)+i-1$. Here n is the total number of filars, $i = 1\ldots n$, w is the separation center to center between adjacent conductors, L is the axial length of the winding, and R is the mean radius of the winding layer. Axial winding errors modify the pattern to

$$z_i = z_{io} + \delta z_i(\theta) \qquad (2)$$

*Work performed jointly under the auspices of the U. S. Department of Energy by Lawrence Livermore National Laboratory under contract W-7405-ENG-48, for the Strategic Defense Initiative Organization and the U.S. Army Strategic Defense Command in support of SDIO/SDC MIPR No. W31RPD-0-D4074

Commonly, layer-wound-magnet conductors are packed as closely as possible to maximize the number of turns. Close packing forces the conductors to be nested with the axial coherence length of perturbations long compared with the length of the magnet. Thus the perturbation is cyclical to lowest order and can be represented by a Fourier series,

$$\delta z(\theta) = \Sigma_m (\delta z)_m \cos(m\theta - \Phi_m) \quad (3)$$

For small mean pitch angle the axial surface current density is given by

$$k_z = (I/w)[(nw/2\pi R) - (1/R) \Sigma_m (\delta z)_m m \sin(m\theta - \Phi_m)] \quad (4)$$

where I is the conductor current. The azimuthal variation of the axial surface current is a source of multipole radial error fields. The dipole contribution (m = 1) produces the only asymmetric field component with a non zero value on the mechanical axis. Along this axis the normalized error field is

$$B_1/B_z = (\delta z)_1/2R. \quad (5)$$

which is independent of z. To illustrate the sensitivity to this type of error, a single layer winding of radius 100 mm will need a $(\delta z)_1 < 200$ μm for a dipole error field less than a milliradian.

Eqn. 5 should be compared with the expression for the variation of perpendicular field along an axis tilted a small angle α with respect to the magnetic axis of a perfect solenoid

$$B_1/B_z = \alpha(1+(z/2B_z)dB_z/dz) \quad (6)$$

Measurement of the axial variation of B_1/B_z should aid in identifying the source of error fields.

Measurement of error fields

Solenoid error fields were measured with a system similar to that described in Ref. 1. A F.W. Bell Model #811AB meter with an HTJ8-0608 transverse Hall probe, capable on its highest gain setting of covering the range of 0.01 to 100 gauss, was used. The sensor area is of the order of 1 mm^2. The instrument uses a precision-machined 2-in.-diam., 24-in.-long rotating horizontal brass shaft with a coaxial 60° tapered hole at each end. Axial thrust centers the shaft between 61° fixed brass dead centers, which are supported by precision x,y adjustment stages. The shaft is rotated by a stepping motor through a drive belt coupling. The Hall probe, oriented to measure the radial field component, is inset in a milled slot in the shaft and can be set at a number of axial positions and two radial positions in the slot. The instrument axis of rotation is aligned either to the mechanical axis defined by alignment rings on the magnet or to the coil i.d. (if there are no alignment rings on the magnet under test). The accuracy with which this can be done sets the experimental resolution, which we estimate to be of the order of a few tenths of a milliradian.

For each set of magnet measurements, the value of the coil current and the Hall probe signal were read out after every 5° step of azimuthal rotation for one revolution, after which the axial position was shifted. Separate measurements of the axial field profile were used to normalize the data

At each axial position the data of the radial field measurements were Fourier analyzed to obtain the amplitude and phase angle of the first five terms, $B_0 ... B_4$, of the multipole fit to the data. The azimuthally independent term B_0 is not an error field but is present if the plane of the sensor is not exactly parallel to the axial field and/or is displaced with respect to the axis of rotation. The dipole and higher-order multipole terms are the error field components. The sum of the five term Fourier series matched our measured data to a small fraction of 1%.

Experimental results

Data from eighteen ATA-type and three ETA-II type magnets have been reduced. In addition we have built and tested a quadrufilar magnet (s = 4). For the set of ATA type magnets, the average value of the dipole field, normalized to the local value of the axial field and the average phase angle is shown in Fig. 1. The error bars show the standard deviation of the data.

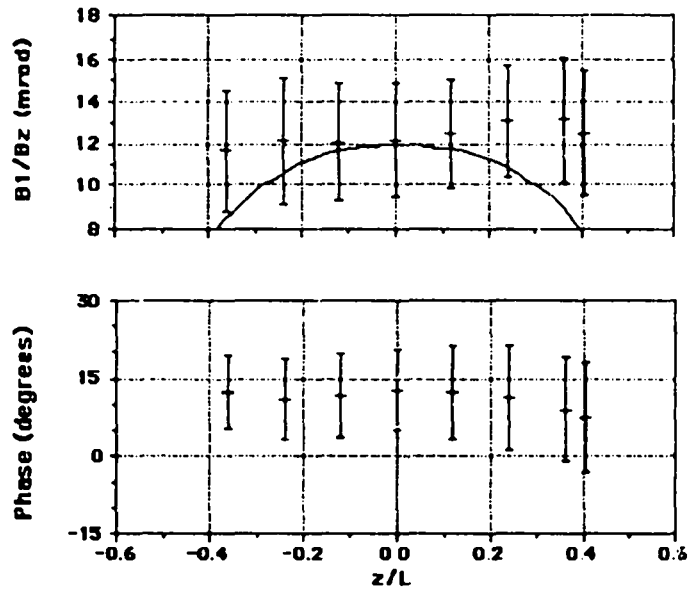

Fig.1 Average dipole field normalized to local axial field and average phase angle of set of eighteen ATA magnets. (a/R=0.39, R=91mm, L=211mm) Solid curve is from Eqn. 6 for a tilted magnet.

The set of three ETA-II magnets all have dipole strengths in the same range with a mean value of six mrad, about one half the mean ATA value.

The quadrufilar magnet was designed to replace a conventional ETA-II induction cell solenoid with only minor modifications to the cell; it uses the same size conductor and has the same dimensions and number of turns(Fig. 2).

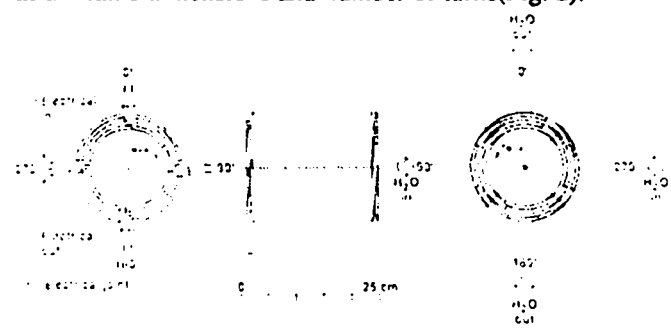

Fig.2 Prototype quadrufilar magnet.

A number of separate runs were made on this magnet to check the reproducibility of results. Figure 3 shows the average values and standard deviation of the multipole strengths obtained from the reduction of four runs with the sensor at a

normalized radius a/R=0.44. The measurements of the normalized multipole strength are reproducible within a few tenths of a milliradian, in agreement with our previous estimates. This data shows that the quadrufilar has much smaller error field than the others tested. In Fig. 4 we compare a

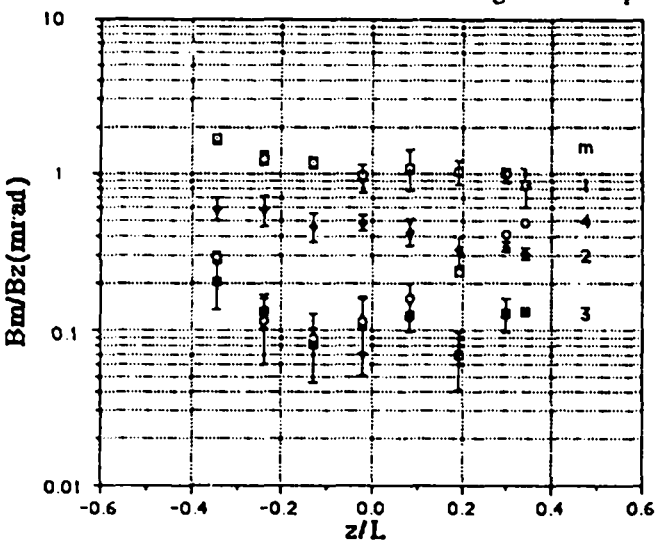

Fig. 3. Strengths of first four poles of the error field of the prototype quadrufilar magnet normalized to the local value of the axial field. (a/R=0.44, R=81mm, L=237mm)

field line calculated from the ETA-II magnet data with one calculated from the quadrufilar data. For these data we have found the set of Eulerian angles to transform from the initial x,y,z coordinate system to the tilted x',y',z' system, in which the z' axis is parallel to the magnetic axis and the field line lies

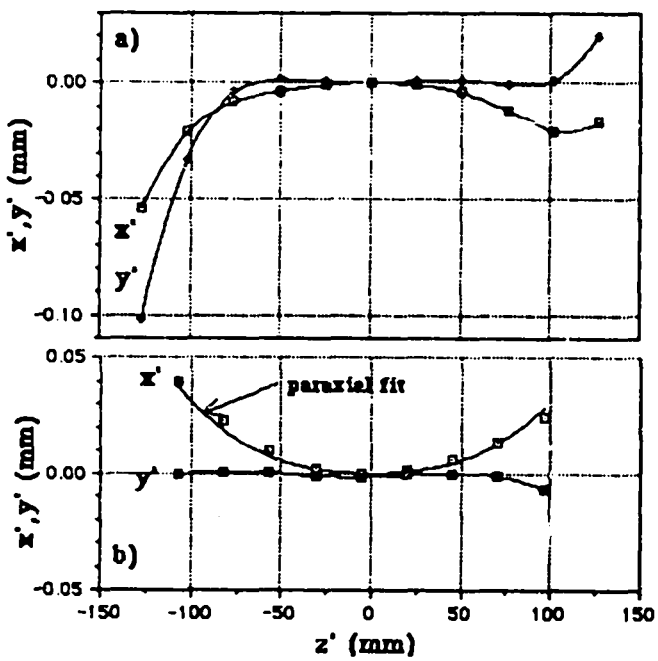

Fig.4 a) Field line calculated from ETA-II magnet data.
b) Field line calculated from quadrufilar data

in the x',z' plane near the origin which is located at the field maxima. The ETA-II magnet line has large displacements from the x',z' plane and changes of slope near the ends, which we ascribe as due to the asymmetries of the feed and crossovers. The quadrufilar magnet line is much better behaved and lies in the x',z' plane over almost its entire length. In Fig 4 b) we compare these data to the paraxial expression for a field line

$$x' = -(x'_0/2)\ln(B_z/B_{zmax}) \qquad (7)$$

Here x'_0, the displacement of the origin from the magnetic axis is a fit parameter equal in this case to 146 μm. The fact that the data points lie within a maximum distance of a few microns from the x',z' plane and within a maximum deviation of 6 μm from the paraxial field line fit indicates that the symmetry of the quadrufilar winding has eliminated the problems connected with the feeds and crossovers. The fit also implies the existence of a magnetic axis displaced from the origin by about 150 μm and straight to less than 10 μm.

Discussion

We expect the same magnitude error fields in both conventional and multifilar windings for a given pitch variation. In the conventional magnets which we have measured, the dipole field is large and shows a degree of repeatability of magnitude and phase that suggests a systematic winding error introduced by the design. The conventional magnet winding pattern with a single wedge establishing the winding pitch is prone to emphasize dipole errors if the wedge angle is not exactly right. Because these wedges have a fixed relationship to the leads and crossovers, their effect would be repeatable in magnets of the same design. The four wedges used in establishing the quadrufilar pattern, even if they are not right but are alike, should emphasize the much less harmful, octupole component. This hypothesis is supported by the data of Fig. 3 where we see that the dipole error has been greatly reduced from that of the conventional magnets while the octupole field is only exceeded by the dipole. Note that the octupole component drops rapidly away from the ends; this may be evidence that the coherence length for the shorter wavelength winding errors is short compared with the coil length.

The alignment of quadrufilar magnets with errors of the order measured in the prototype could be improved by indexing the alignment rings to the measured magnetic axis. For the existing magnet we would need to shift the ring position only by about 100 μm at each end to accomplish this.

A dividend of the use of a multifilar winding pattern is the improved cooling due to multiple, shorter cooling channels. The field measurements of the quadrufilar were made at 800 A magnet current, the limit of the available power supply. (Data from the ETA-II magnets were taken at 100 A and from the ATA magnets at 450 A). With a cooling-water pressure drop across the magnet of 90 psi, the temperature rise was ~20°C. From these values, we estimate that for this same pressure drop a limit of 60°C rise would allow operation at a maximum magnet current of over 1.4 kA producing a maximum axial field of ~8.5 kG, almost three times that obtainable from the ETA-II design for the same pressure drop and temperature rise.

Reference

1. H. Nishihara and M. Terada, J. Appl. Phys. 39, 4573(1968).

PROGRESS IN ETA-II MAGNETIC FIELD ALIGNMENT USING STRETCHED WIRE AND LOW ENERGY ELECTRON BEAM TECHNIQUES*

Lee V. Griffith and Fred J. Deadrick
Lawrence Livermore National Laboratory, Livermore, CA 94550

Abstract

Flux line alignment of the solenoidal focus magnets used on the ETA-II linear induction accelerator is a key element leading to a reduction of beam corkscrew motion. Two techniques have been used on the ETA-II accelerator to measure and establish magnet alignment. A low energy electron beam has been used to directly map magnetic field lines, and recent work has utilized a pulsed stretched wire technique to measure magnet tilts and offsets with respect to a reference axis. This paper reports on the techniques used in the ETA-II accelerator alignment, and presents results from those measurements which show that accelerator is magnetically aligned to within ~±200 microns.

Introduction

Alignment is a critical step in the assembly of any linac. Mechanical/optical alignment of accelerator hardware is only a part of the total process. It is equally important to assure that the magnetic flux lines produced by focus solenoids also be aligned to high accuracy. The magnetic axis of a magnet may not always be coincident with the mechanical axis, and thus it is important that the magnetic axis be used in the alignment criteria.

The ETA-II, as presently configured, is a 9.4m long accelerator, consisting of a total of 28 solenoidal magnets. Four solenoids are in the injector, and the accelerator sections are configured into two 10-solenoid cell blocks. The remaining four solenoids are used as intercell magnets in the transport regions between the cell blocks. Each of the solenoid magnets are fabricated with separate horizontal and vertical trim coils. The trim coils are used to correct for magnet tilts, but not for magnet offsets.

To minimize the buildup of beam corkscrew motion, we attempted to align the magnetic flux lines of ETA-II solenoids to a straight line. To accomplish this, a straight line reference axis on the mechanical center was first established between the injector and the end of the accelerator. Each solenoid's magnetic axis was then measured with respect to this reference, and where feasible, the magnets were physically moved to make their magnetic axis coincide with the reference axis. Additionally, for each magnet, a horizontal and vertical trim correction current was established to compensate for any inherent magnetic tilt. The manner in which the magnetic alignment was performed is described in more detail below.

* Performed jointly under the auspices of the US DOE by LLNL under W-7405-ENG-48 and for the DOD under SDIO/SDC-ATC MIPR No. W31RPD-8-D5005.

Magnet Alignment Techniques

Low Energy Electron Beam Alignment Technique

Since magnetic flux lines cannot be viewed directly, it is necessary that one resort to measuring the influence that a magnetic field has upon a measurable quantity. For instance, one way to map magnetic flux lines is to use a low energy electron beam. The low energy e-beam will closely follow a given magnetic field line, and a phosphor screen can be used to convert the e-beams energy to light. The light spot can then be digitized with a computer and TV camera to map the position of the field lines as a function of distance down the accelerator. This technique has already been successfully used during the initial assembly of ETA-II, and was reported earlier by Clark, et al.[1]. The difficulty with using this technique is that the entire accelerator assembly must be under vacuum, and all solenoids must be energized to properly transport the e-beam. Additionally, magnet offsets and tilts are not directly obtainable using this technique.

Stretched Wire Alignment Technique

An alternative technique for measuring magnet alignment is to sense the force produced on a current carrying conductor placed in a magnetic field. With this technique, a wire is stretched along the center reference of the accelerator through all the solenoidal magnets. A short current pulse, I, is then applied the wire, and if any transverse magnetic fields are present, the Lorentz force $d\mathbf{F}$ produced on an element $d\mathbf{l}$ of a conductor is given by equation (1) as:

$$d\mathbf{F} = I\, d\mathbf{l} \times \mathbf{B}_{\perp}. \qquad (1)$$

The force on the wire will cause the wire to deflect an amount proportional to the magnitude of the transverse field errors. This deflection propagates as a travelling wave along the stretched wire, and one can sense this deflection as a measure of magnet misalignment. Since a perfectly aligned solenoid will have no transverse fields on its axis, one attempts to null out the deflections of the stretched wire, and when the deflected signal is nulled, the wire then lies along the magnetic axis.

The stretched wire alignment technique has been used successfully at LANL by Warren and Elliot[2] in the fabrication and testing of wigglers, and by Liska, et al.,[3] in the precision alignment of permanent-magnet drift tubes. The inherent simplicity of the stretched wire alignment technique is an attractive feature. No high vacuum conditions are required as with the e-beam technique, and both the offset and tilts can be obtained for each individual magnet.

Stretched Wire Implementation We use a thin (4-mil) BeCu wire stretched through the bore of the linac and positioned on the mechanical center reference axis at the two ends of the accelerator. The wire is attached to a X-Y translation stage at each end so that the wire can be moved by measurable amounts off the reference axis to determine how far the magnetic axis of a given solenoid is off the mechanical axis. While the wire is tensioned near its tensile strength to minimize the catenary droop from the vertical axis, we calculate the amount of catenary offset at each solenoid, and include this as a correction to the vertical offset data.

Two photo-optical sensors positioned 12.8 cm away from the termination point are used to sense the minute wire deflections. One of the sensors is used to measure vertical motions, and the other sensor measures horizontal deflections. The sensor itself is a very simple, low cost, and a readily available component used in industries as diverse as computers to textiles. It consists of a GaAs infrared emitting diode illuminating a silicon phototransistor across a 0.1 inch gap. The detector senses the deflection of the wire in the gap by the wire's affect on the light transmission. Figure 1 shows typical detector sensitivity curves obtained for 4 and 8 mil wires. We position the wire at a point of maximum slope on the detector curve to give the greatest sensitivity, which in the case of a 4 mil wire is on the order of 25 millivolts per micron of motion.

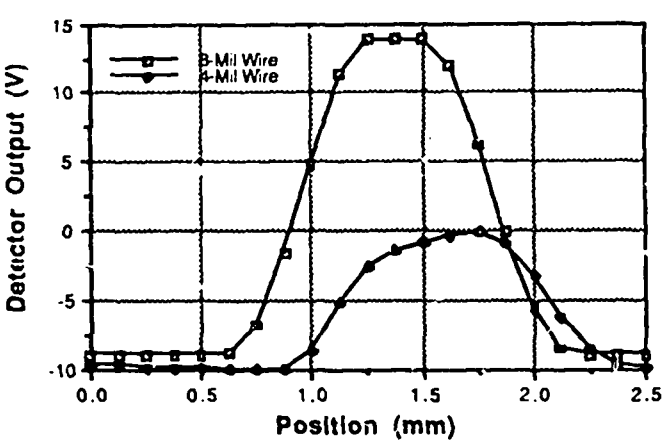

Figure 1. Detector output response for 4mil and 8mil wire.

Figure 2 shows a block diagram of electronics used in the data acquisition system. The horizontal and vertical detector circuits are simple opamps to increase the sensitivity, and the oscilloscope is a digital storage unit with signal averaging to improve signal to noise ratios. A single solenoid is energized at one time, and a 1 millisecond long current pulse of 1-2 amperes is typically applied to the stretched wire. Any transverse magnetic fields due to magnet misalignments will cause the wire to be perturbed off axis by the Lorentz force on the wire during the time that the current pulse is applied. This deflection pulse propagates down the wire at the acoustic velocity in the wire and passes the photo-optical position sensors.

By viewing the wire deflection waveforms it is possible to distinguish magnet tilts from offsets, since tilts and offsets have different waveform signatures as shown in figure 3.

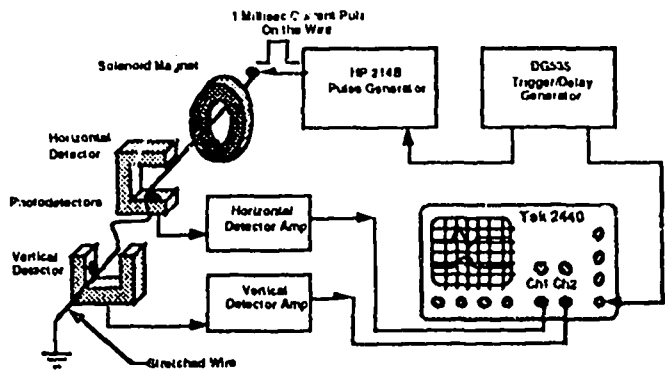

Figure 2. Block diagram of detector circuit.

To quantify magnet offsets, the wire end points are moved in unison until a null occurs in the offset waveform signature. To determine magnet tilt angles, we apply current to the trim coils, and we convert trim current to an equivalent tilt angle by using equation 2 below:

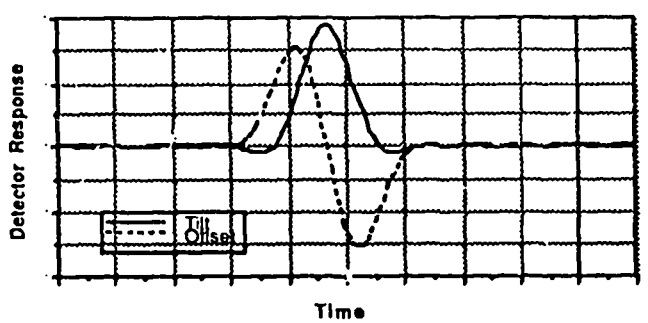

Figure 3. Response signatures for magnet tilts and offsets.

Magnet tilt angle can then be calculated as

$$\alpha = -2\frac{\int_{-\infty}^{\infty} B_{\perp}\,dz}{\int_{-\infty}^{\infty} B_{z}\,dz} \qquad (2)$$

where we have measured the relationship between trim current and the perpendicular magnetic field, $B_{\perp}$ produced by the trim coils, and measured B_z as a function of solenoid current.

ETA-II Alignment Results

This section summarizes the alignment data on ETA-II. All alignment work was performed for a Bz field of 1.3kG in the accelerator and 540G in the injector. We believe the injector, intercells and accelerator 10-cell blocks are aligned to within ±400μm with an rms misalignment of 270μm in the horizontal direction and 120μm in the vertical direction. Figures 4a and 4b show the measured offset values for each of the solenoids. The alignment measurements were repeated a number of times in order to obtain confidence in the repeatability of the measurements. Magnets in the

injector and 10-cell blocks are not individually adjustable mechanically, since the assemblies are pin aligned at the time of assembly. Therefore, we adjusted the position of the entire cell block to the best linear fit through the measured data. We accounted for the catenary deflection of the wire by calculating the catenary value for each cell, and raised the wire end points an appropriate amount to compensate for the droop. Individual magnets in the intercells were moveable, and we positioned these coils by locating the wire on the reference axis at the coil, and then moved the solenoids so as to null the stretched wire response. This adjustment was not completely successful, however, because of difficulties arising from over-constraints in the mechanical design.

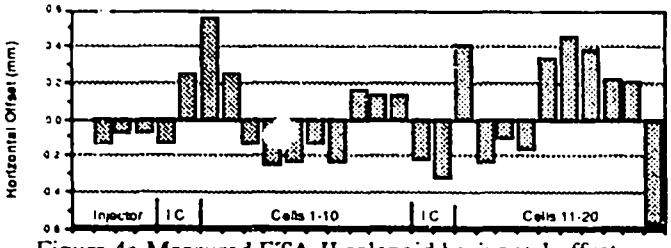

Figure 4a Measured ETA-II solenoid horizontal offsets.

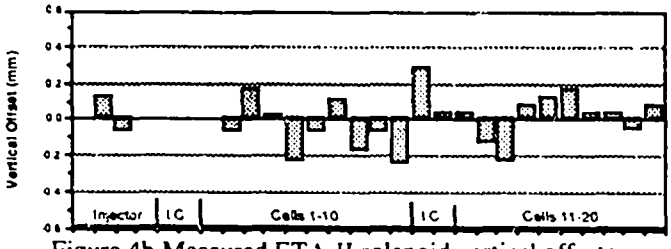

Figure 4b Measured ETA-II solenoid vertical offsets.

Figures 5a and 5b show the resulting magnet tilts found by evaluating equation 2. It should be noted that the tilts shown are for coils with no correction currents applied. When trims are applied, the field tilts are compensated to better than ±1 milliradian based upon our confidence in the repeatability of the measurements.

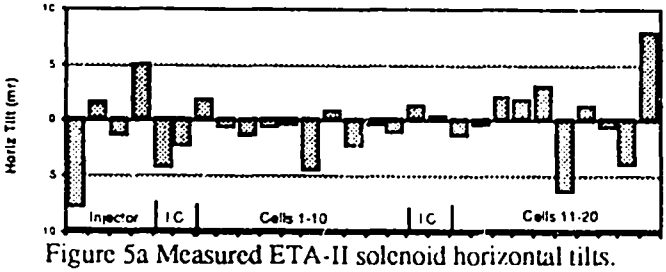

Figure 5a Measured ETA-II solenoid horizontal tilts.

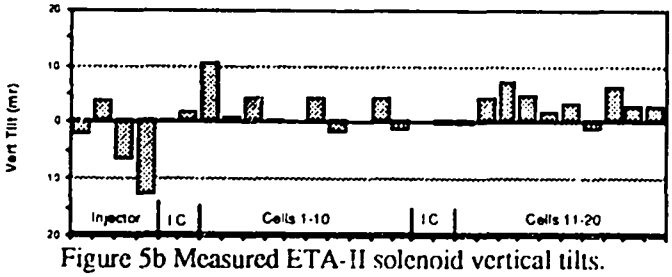

Figure 5b Measured ETA-II solenoid vertical tilts.

While the magnet offsets and tilts as determined by the stretched wire alignment technique do not directly provide us with a plot of the magnetic field lines through the accelerator, we have measured the field for each of the magnets used on ETA-II, and this data can be used along with the tilt and offset data to obtain an equivalent flux line pattern based upon a superposition of the individual field components. This plot is shown in figure 6.

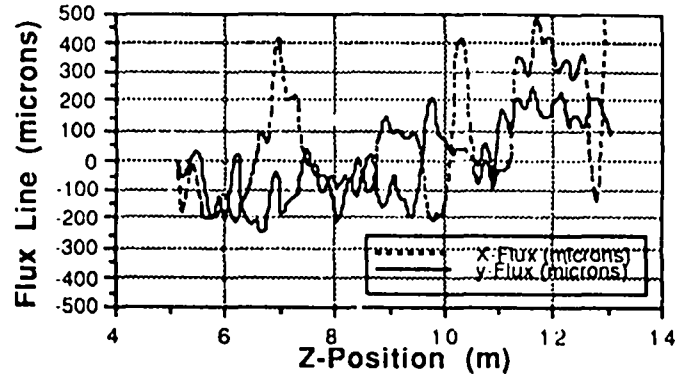

Figure 6 Calculated horizontal and vertical flux line based upon magnet tilts and offsets.

Conclusions

We have found the stretched wire alignment technique to be very useful in measuring the alignment of ETA-II. Measurement times for the 28 solenoids is on the order of 4 hours, with potential improvements requiring even less time. The technique lends itself well to establishing magnetic alignment during the fabrication and assembly stage of the accelerator cell blocks, and this will be implemented in the future.

Our interpretation of the tilt and offset waveforms has been based upon that of an experienced user. Work is currently underway to develop an on-line digital signal processing capability to extract offsets and tilts directly from the waveforms. When some of the operator's subjectivity is removed, it is believed that even greater accuracies will be obtained.

References

1. J. Clark, et al., "Aligning the Magnetic Field of a Linear Induction Accelerator with a Low-Energy Electron Beam", Lawrence Livermore National Laboratory, Livermore, CA, UCRL-99593, March 1989.

2. R. Warren and C. Elliot, "New System for Wiggler Fabrication and Testing", Los Alamos National Laboratory, Los Alamos NM, LA-UR 87-2981.

3. D. Liska, et al., "Precision Alignment of Permanent-Magnet Drift Tubes", Los Alamos National Laboratory, Los Alamos NM, LA-UR 86-1718.

PULSED TAUT-WIRE ALIGNMENT OF MULTIPLE PERMANENT MAGNET QUADRUPOLES*

C.M. Fortgang, L.B. Dauelsberg, C. Geisik, D.L. Liska, and R.E. Shafer
Los Alamos National Laboratory, Los Alamos, NM 87545

Abstract

A pulsed taut-wire system for aligning many collinear permanent magnet quadrupoles (PMQs) is described. Applications include aligning magnets in drift tube linac (DTL) tanks and linear transport lines. A short (<100-μs), rectangular current pulse accelerates the wire transversely at each PMQ by an amount proportional to the displacement of the wire from the magnetic center. The transverse waves propagate along the wire to a sensor where they are measured using a wide-band noninterceptive technique similar to that used for measuring beam position. Displacing the wire by known amounts using translation stages gives an accurate calibration of signal size versus misalignment. A technique for measuring the gradient-length product of a PMQ using the pulsed taut wire is also described.

Introduction

The technique of using a taut wire to align the quadrupoles in a DTL was developed at Lawrence Berkeley National Laboratory (LBL) around 1974. In the LBL technique all the magnets but one are turned off each time the wire is pulsed with current. The wire is deflected if it is not positioned at the magnetic center of the magnet under test. In this manner, the magnetic centers of all the magnets are measured, one at a time. The technique was further developed for finding the magnetic center of individual permanent magnet quadrupoles at Los Alamos.[1] Because these magnets could not be turned off the measurements had to be done on individual drift tube magnets before assembly of the DTL. Warren and Elliot [2] first applied the idea of using a short current pulse to give the wire an impulse, in the form of transverse momentum. The impulse varies along the length of the wire in proportion to the local magnetic field. This work was performed on magnetic dipoles used in wigglers. The transverse momentum splits into two equal amplitude waves that travel along the wire in opposite directions. Because the waves from each magnet are created by an impulse they are spaced along the wire and arrive at different times at a fixed sensor that measures wire position as a function of time. In this manner, multiple magnets can be measured with a single current pulse. We have extended the technique of using a short current pulse to align PMQs in DTL tanks. Techniques have been developed to obtain an absolute measurement of the position of each magnet with respect to the wire, and to subtract out wire sag when doing vertical alignment. In addition, we measure *in situ* the relative gradient-length product for all the magnets after they are assembled in the DTL tank.

Theory

If, at t = 0, a short current pulse (short being defined below) is applied to a wire displaced from the magnetic axis of a quadrupole by an amount ΔX_{mag} then the transverse impulse imparted to a length dz of wire is

$$\rho \, dz \, V_x = I \, \Delta t \, G(z) \, dz \, \Delta X_{mag} \qquad (1)$$

where I, Δt, G(z) ρ, V_x, and ΔX_{mag} are the current, pulse length, quadrupole gradient, wire linear mass density, transverse velocity, and magnet displacement from the wire, respectively. The transverse impulse splits in half and propagates along the wire at a speed given by $c = \sqrt{(T/\rho)}$ where T is the wire tension. After the transverse wave passes a given point along the wire, the displacement of the wire from its initial position is given by the time integral

$$\Delta X_{wire} = \int V_x \, dt$$

$$= (I \, \Delta t \, \Delta X_{mag} / (2 \rho)) \int G(z) \, dt$$

$$= (I \, \Delta t \, \Delta X_{mag} / (2 \rho c)) \int G(z) \, dz$$

$$= (I \, \Delta t \, G \, L_e / (2 \rho c)) \, \Delta X_{mag} \quad . \qquad (2)$$

where L_e is the effective length of the quadrupole and G is its average gradient.

The slope of the line that describes ΔX_{wire} versus ΔX_{mag} is proportional to GL_e the magnet gradient-length product, and a measurement of I, Δt, ρ, and c determines the gradient-length product absolutely.[3] We use translation stages to move the wire by known amounts relative to the magnet, thus varying ΔX_{mag}. For each position, the wire is pulsed with the same I and Δt and the wire deflection (ΔX_{wire}) is measured. Typical values for I, Δt, $G\text{-}L_e$, ρ and c are 20 A, 40 μs, 5 Tesla, 3.8×10^{-5} kg/m, and 130 m/s so that the proportionality constant relating ΔX_{wire} and ΔX_{mag} is of order unity; therefore, resolution for measuring magnet displacement is approximately equal to the resolution of the sensor and associated electronics for measuring wire position. Accurate measurements require satisfying the transverse impulse approximation, that is, that the wire moves a negligible amount transversely during the current pulse. Given two quadrupoles that are of opposite polarity but equally displaced from the wire, the measurement should, of course, indicate equal displacement. However, if the wire moves transversely before the current pulse is switched off, the focusing quad will move the wire into a weaker magnetic field and the defocusing quad into a stronger magnetic field, and the measurement will thus indicate that the defocusing magnet is a greater distance from the wire than the focusing magnet. Mathematically, the condition to be satisfied is

$$V_x \, \Delta t / \Delta X_{mag} = (I \, \Delta t^2 \, G)/\rho \ll 1 \quad . \qquad (3)$$

An easy check on this condition is as follows: a reversal of the sign of the current effectively changes the polarity of

*Work supported and funded by the US Department of Defense, Army Strategic Defense Command, under the auspices of the US Department of Energy

each magnet yielding an equal but opposite deflection of the wire due to each magnet. A second condition on the pulse is that the distance the waves propagate along the wire during the current pulse be small compared to the distance between magnets, so that waves from different magnets are not superimposed. If Δz is the distance between magnets, this condition is satisfied if $\Delta z > c\,\Delta t$.

Wire Position Measurement

The wire position measurement technique is based on the development of electronics for precision, real-time position measurement of bunched particle beams.[4] A ferrite-loaded, 20 MHz $\lambda/4$ coaxial cavity is driven with ~ 1 W of RF power. The wire passes through the inner conductor along the axis of the cavity and is coupled to the longitudinal RF electric field at the open gap between the center conductor and the cavity end-wall. In this manner an RF current is induced on the copper wire. The RF field from the wire is detected by four B_θ loops that are used with signal processing electronics to measure the x and y position of the wire. Presently, wire position is measured with a 10 micron resolution and 35 kHz bandwidth. The bandwidth required is determined by the distance between magnets and longitudinal wave speed. For applications that require lower bandwidth, the signal-to-noise ratio improves and thus resolution improves. Sensitivity of the wire position measurement is determined by moving the sensor relative to the wire with translation stages. Our apparatus with a 4-mm aperture has a sensitivity of 1.4 mV/micron.

Experimental Results

Figures 1 and 2 are examples of raw data for vertical and horizontal deflections respectively from a DTL tank, before alignment, with 40 PMQ magnets arranged in a FODO lattice. The parabolic shape of the envelope of the vertical data in Fig. 1 is due to wire sag over the 2.3 meter-long tank. The average signal gets larger (smaller) in the middle of the tank if the wire is suspended below (above) the center of the magnets. The first step of analysis involves finding the peaks in the data as indicated by the circles in Figs. 1 and 2. For each magnet the deflection of the wire caused by that magnet is calculated from the difference between neighboring peaks. This procedure is repeated after translating the wire a known distance (ΔX_{mag}) and again measuring the wire deflection caused by each magnet. The difference of the wire deflection for the two cases is taken, inverted, and multiplied by the amount the wire was moved to yield a calibration in microns/volt for each magnet without any explicit measurement of the current, pulse length, wave speed, etc. In practice, the wire is moved between two positions on the opposite sides of the magnetic center, and thus signals of opposite polarity are obtained, as shown in Figs. 1 and 2. Therefore, by simply adding the absolute values of the deflections we obtain a number proportional to the G-L_e product as indicated by Eq. (2).

An example of this result for horizontal data is shown in Fig. 3. The top curve of Fig. 3 is inverted and multiplied by the distance the wire is moved to obtain the microns/volt calibration for each magnet. With a calibration file established an absolute measurement of the magnet alignment

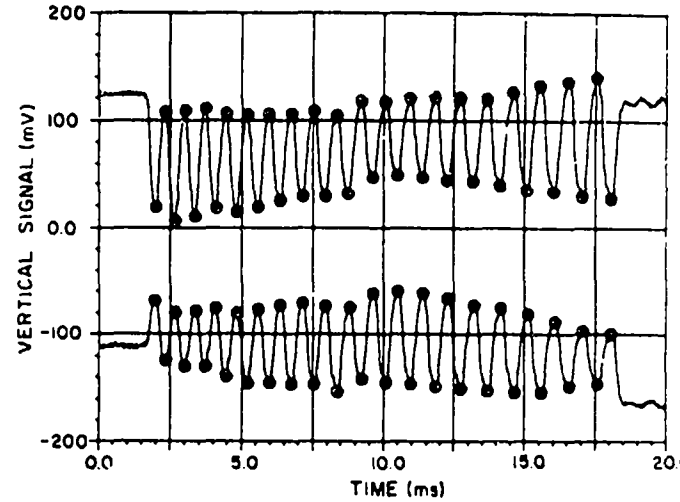

Fig. 1. Vertical position raw data for two different wire positions separated by 1.02 mm.

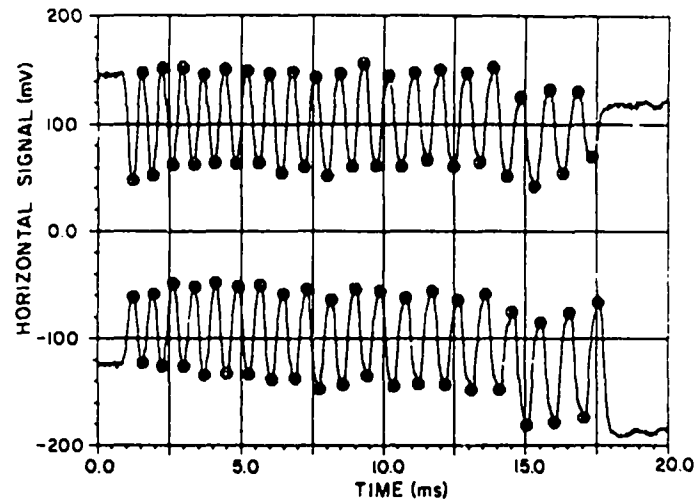

Fig. 2. Horizontal position raw data for two different wire positions separated by 1.14 mm.

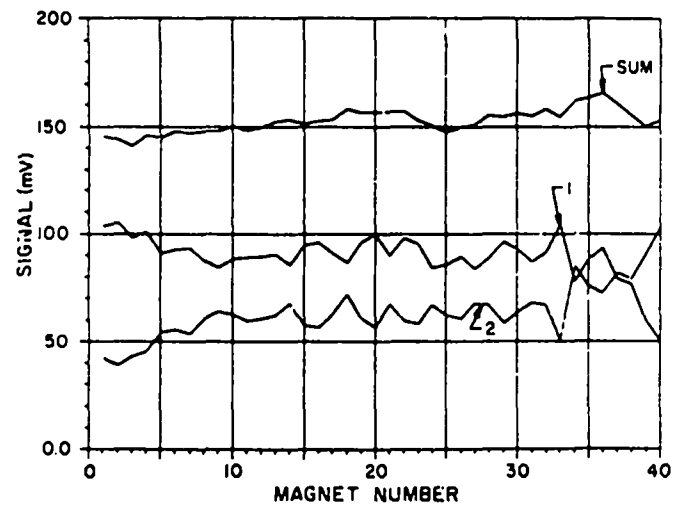

Fig. 3. Curves 1 and 2 are analyzed horizontal data for two different wire positions. SUM, the addition of curves 1 and 2 is proportional to the G-L product along the magnetic axis.

is obtained in the following manner. For data as shown in Figs. 1 and 2 the magnitude of the average deflection is calculated and then subtracted from the magnitude of the deflection due to each magnet. The magnitude of the average deflection is proportional to how far the wire is displaced from the magnets on average, whereas the difference from that average measures how far each magnet is displaced from the magnetic axis. Finally, this data is multiplied by the calibration factors to give a plot of the relative position of each magnet, in microns, with respect to the average displacement of the magnets from the wire.

Examples of these measurements in both planes are shown in Fig. 4. With analysis that yields plots such as Fig. 4 the magnets can be precisely aligned. Fig. 5 is a plot of the calibrated displacement after fine adjustments to the magnet positions have been made from the case shown in Fig. 4. The adjusuments are made to fit the vertical data to the parabola that describes the calculated sag of the taut wire, whereas the adjusuments fit the horizontal data to a straight line with zero slope so that the magnetic axis is parallel with the wire.

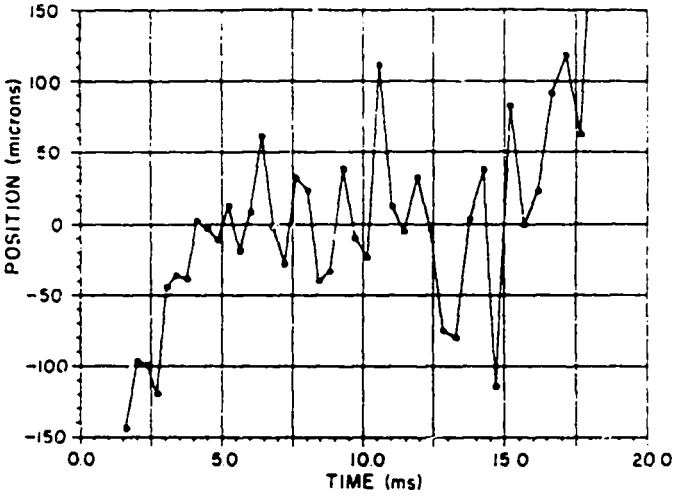

(a)

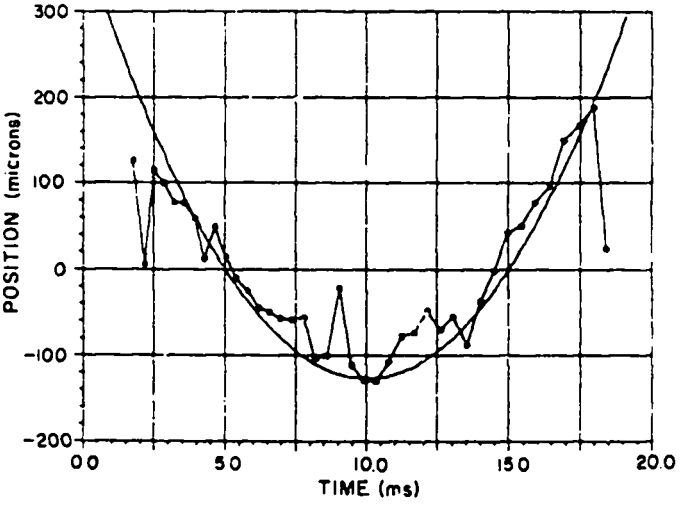

(b)

Fig. 4. Horizontal (a) and vertical (b) alignment before adjusting magnet positions.

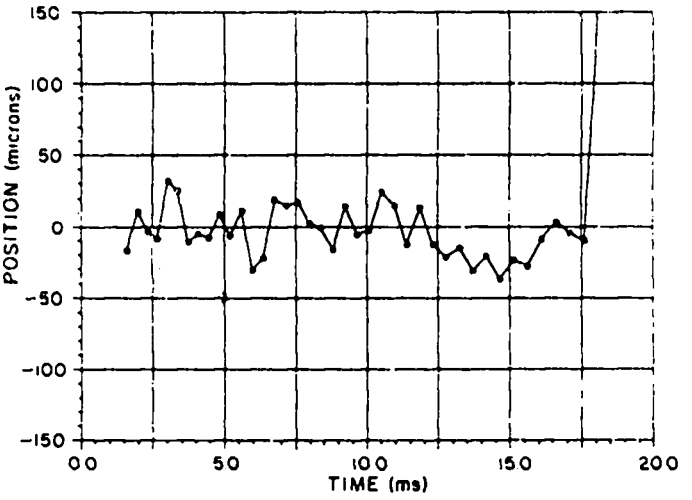

(a)

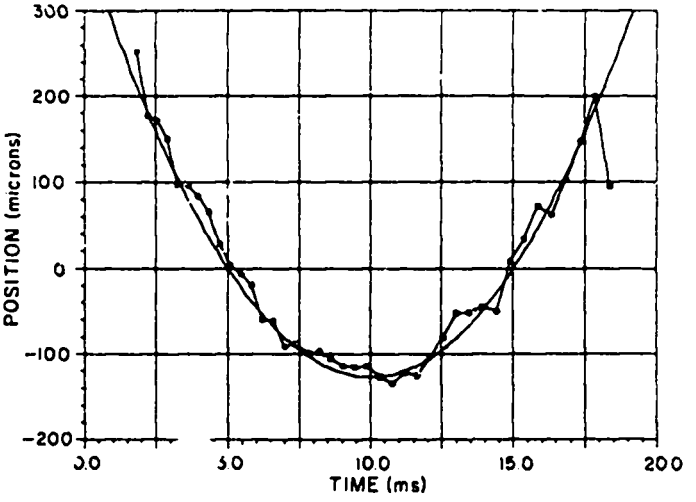

(b)

Fig. 5. Horizontal (a) and vertical (b) alignment after adjusting magnet positions.

References

1. D. Liska, L. Dauelsberg, and G. Spalek, "Precision Alignment of Permanent-Magnet Drift Tubes," in Proceedings of the 1986 Linear Accel. Conf.,Stanford,SLAC-303, p. 48 (1986).

2. R. Warren and C. Elliot,"New System for Wiggler Fabrication and Testing",Los Alamos National Laboratory,LA-UR 87-2981,(1987).

3. C. Fortgang, "Taut-Wire Measurement of Magnetic Quadrupole Gradient-Length Product," Los Alamos National Laboratory, AT-3 Technical Note:89-9 (1989).

4. F. Wells and S. Jachim, "A Technique for Improving the Accuracy and Dynamic Range of Beam Position Detection Equipment," in Proceedings of the 1989 IEEE Particle Accelerator Conference, Catalog No. 89CH2660-0, p. 1595 (1989).

A SMALL-BORE HIGH-FIELD SUPERCONDUCTING QUADRUPOLE MAGNET*

D. B. Barlow, R. H. Kraus, C. T. Lobb and M. T. Menzel
Los Alamos National Laboratory, Los Alamos, NM 87545

P. L. Walstrom
Grumman Space Systems at Los Alamos, NM 87545

Abstract

A prototype superconducting quadrupole magnet was designed and built for use in superconducting coupled-cavity linacs where the use of permanent magnets is ruled out by consideration of trapped-flux losses. The magnet has a clear bore diameter of 1.8 cm and outside diameter of 11 cm and length of 11 cm. The magnet was operated at a temperature of 4.2 K and obtained a peak quadrupole field gradient of 320 T/m.

Introduction

Small-bore, high-field quadrupole focusing magnets are required between cavities in superconducting coupled-cavity linacs. Stray magnetic fields of only a few gauss in cavity walls before cooldown can be trapped and cause excessive rf losses during cavity operation. Fields of a few-hundred gauss, when applied to cavities after cooldown, can also cause excessive rf losses. Accordingly, the focusing magnets must have a low fringe field during operation and be capable of being turned off during cavity cooldown. Superconducting quadrupole magnets are a natural choice for the focusing elements, since they can be turned off during cavity cooldown, be designed to occupy little space, and be kept at liquid helium temperature by the refrigeration system for the superconducting cavities. Compact superconducting quadrupole magnets wound from commercially available superconducting wire can operate with field gradients of hundreds of teslas per meter in a clear bore of a few centimeters. This performance meets the needs of most superconducting coupled-cavity linac designs.

Design and Construction

The 2-D magnet codes POISSON[1] and FLUX2D[2] were used to optimize the geometry and design of the magnet and to calculate the expected fields and operating currents. A schematic of the prototype magnet is shown in Figs. 1 and 2. The magnet was designed to fit between cavities in a typical array of small superconducting accelerating cavities, and includes field clamps to minimize fringe fields. The magnet has a clear bore diameter of 1.8 cm and can be assembled around a beam pipe and vacuum flange projecting from the end of a cavity without removing the flange or adding extra beam pipe between cavities. The outside dimensions of 11 cm long by 11 cm in diameter were kept as small as possible to minimize the spacing between cavities. The poles, flux-return yoke, and field clamps were all made of low-carbon steel. The 6-cm-long poles were made with flat instead of hyperbolic tips, since the poles are almost completely saturated at nominal operating fields.

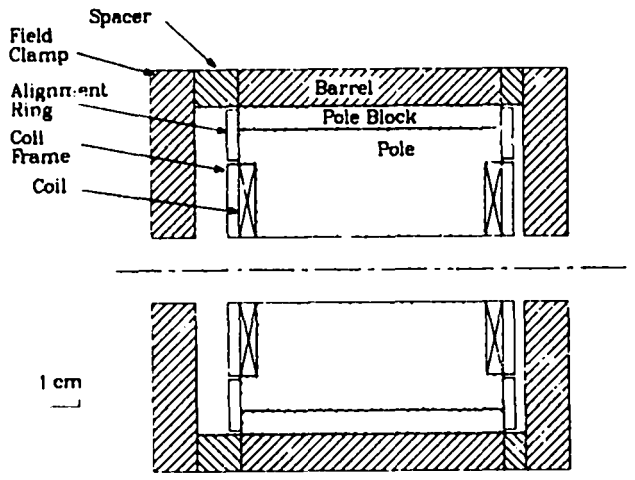

Fig. 1. Schematic of the magnet (side view).

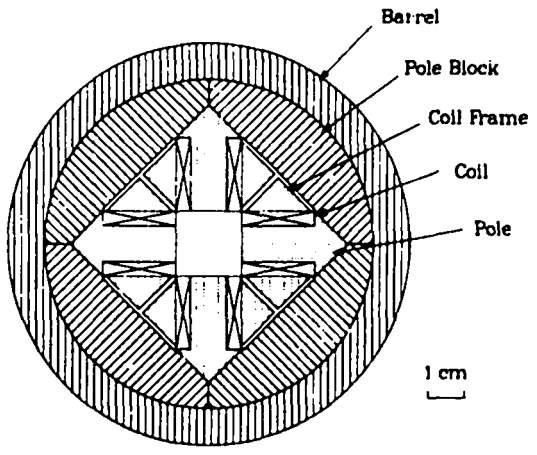

Fig. 2. Schematic of the magnet (end view).

*Work supported by the US Department of Energy, with Los Alamos National Laboratory Program Development funds.

POISSON was used to determine the width of the pole that would minimize the the first allowed (n=6) harmonic. A pole width of 1 cm was found to null out the n=6 harmonic and produce higher order fields of less than 0.02% of the quadrupole at a reference radius of 5 mm, at typical operating current densities. The 3-D code, TOSCA[3], was run for the final magnet design to estimate the gradient-length product and the magnitude of the stray field beyond the ends of the magnet. These results indicated that the 1-cm-thick field clamps, which were separated from the central part of the magnet by low-permeability stainless-steel spacers on both ends, reduced the stray fields everywhere outside the magnet to less than 100 G at nominal operating currents.

The coils for the magnet were made of commercially available 0.25-mm-diameter, 54-filament NbTi/Cu superconducting wire. The racetrack-shaped coils contain 762 turns of conductor and have a rectangular cross section measuring 2.00 by 0.35 cm. The coils were wet-wound with an aluminum-oxide-filled epoxy on a slightly oversized mandrel. After the epoxy had cured, the coils were pressed off the mandrel and the inside dimension relaxed slightly to form a snug fit when mounted on the poles. The cross section of several sample coils were inspected under a microscope to check for uniform packing of the windings. Each coil was checked for internal shorts using an impedance meter to measure the coil's Q as a function of frequency. (A short would have caused the coil to have a Q value less than the nominal.) The coils were then mounted on the poles and potted with epoxy into stainless-steel frames. The frames were needed to contain the outward Lorentz forces that would cause movement of the windings and premature coil quenches. After being potted, the coils were individually tested at 4 K to be sure they operated above 70 A without quenching; this current in the coil test configuration corresponds to ~95% of the short-sample critical current specified by the manufacturer. After testing, the coil and pole assemblies were mounted in the barrel of the magnet, aligned and held in place by the four pole blocks that were adjusted by set screws. The alignment of the poles was fixed by means of an alignment ring mounted on both ends of the magnet. The four coils were connected in series with superconducting bus bars made of heavy-gauge copper wire wrapped with several strands of superconducting wire. All joints were soldered with indium, and care was taken to insure that the coil leads had no sharp bends or unsupported sections between the coil and the bus bars. The bus bars were routed out the side of the magnet and indium-soldered to the ends of vapor-cooled current leads.

Results

The assembled magnet was tested in a bath of atmospheric pressure liquid helium (a temperature of ~4.2 K). At this temperature, the maximum current obtained was 62 A. Only a few training quenches were required to bring the magnet up to the maximum current. Fig. 3 shows a plot of the peak field in the windings, calculated by FLUX2D vs the current. Included in Fig. 3 is a plot of the short-sample critical current vs field for the superconducting wire. The intersection of the two

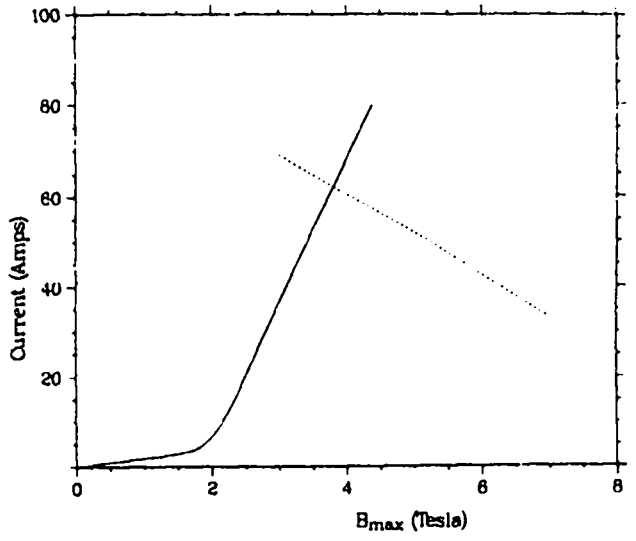

Fig. 3. Load line (solid curve) vs critical current (dashed curve) for the magnet. The calculations of the peak field in the coil windings were done using FLUX2D. The critical current vs field was provided by the manufacturer of the wire.

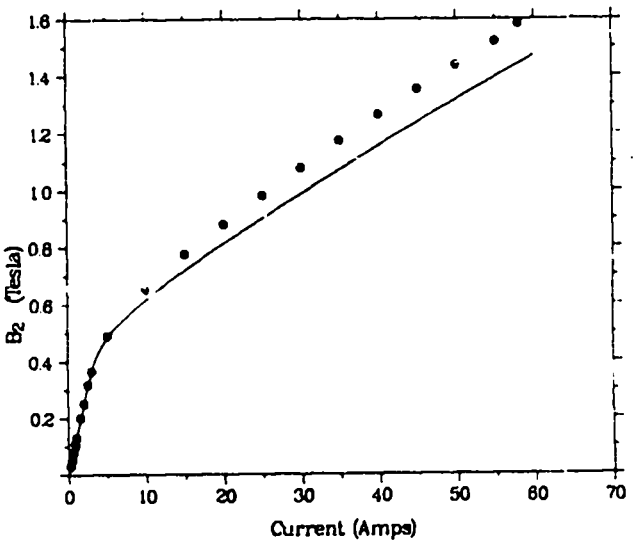

Fig. 4. The quadrupole field (B_2) at a reference radius of 5 mm measured by the Hall probe (solid points) and calculated by FLUX2D (solid curve) vs the magnet current.

curves indicates the maximum current achievable. A peak current of 62 A for the complete magnet corresponds to a field of ~3.7 T in the coil windings, which is ~95% of the short sample critical current.

The radial field near the center of the magnet was measured with a small Hall probe at a radius of 5 mm. The Hall probe could be rotated about the axis of the magnet and provided a map of the central field. The resolution of this measurement was limited by the finite size of the probe. In addition, a rotating coil was used to measure the integral field map and integral multipole strengths of the magnet. The coil consisted of 100 turns of wire wound around a rectangular form that was parallel to the magnet axis and extended beyond the fringe fields on both ends of the bore. The coil voltage was integrated by a voltage integrator and the coil angle was measured by a potentiometer to obtain the flux as a function of the angle. A plot of the quadrupole field measured by the Hall probe as a function of the magnet current is shown in Fig. 1, along with the field calculated by FLUX2D. The reason for the ~10% disagreement between the calculated and measured fields above 5 A is not understood. Saturation of the iron pole tips occurs at a current of 5 A, as indicated by the change in slope of this curve. At 60 A the pole-tip field was 2.88 T, corresponding to a quadrupole gradient of 320 T/m. The rotating coil measured a gradient-length product, normalized to 60 A, of 16.4 T. Fourier analysis of the rotating coil data at 55 A indicated that the integral dipole and sextupole contributions were 3% and 1%, respectively, of the quadrupole, at a radius of 7 mm. The dipole term is most likely the result of a ±0.1 mm offset in the alignment of the rotating coil, while the sextupole term is probably the result of a slight misalignment of one or more of the coils. After operating the magnet at 60 A, the remnant fields on the surface of the magnet measured less than 1 gauss.

Summary

A working prototype superconducting quadrupole has been built and tested. The magnet achieved ~95% of its calculated critical current limit. At maximum current, the magnet produced a quadrupole gradient of 320 T/m and gradient-length product of 16.4 T. The small stray and remnant fields of this magnet should not interfere with the performance of nearby superconducting cavities. An estimated 25% increase in the quadrupole strength of the magnet could be achieved by operating the magnet at a reduced temperature of 1.8 K. Calculations also indicate a 10% increase in the field strength could be realized by using the rare-earth metal, holmium, as a pole material, in place of low-carbon steel. Holmium saturates at 3.9 T, vs 2.2 T for iron, and has a slightly higher permeability at fields above 4 T. In addition, the Curie temperature of holmium is 20 K, making it possible to erase any remnant field in the poles by raising the temperature above this point.

References

1. User's Guide for the POISSON/SUPERFISH Group of Codes, LANL Report No. LA-UR-87-115, Los Alamos Accelerator Code Group, (1987).

2. Magsoft Corporation, Troy NY, USA, (1987).

3. Vector Fields Limited, Oxford England, (1988).

HIGH ORDER OPTICS OF MULTIPOLE MAGNETS *

Peter Walstrom, Filippo Neri & Tom Mottershead
Los Alamos National Laboratory, Los Alamos, NM 87545

ABSTRACT

We have developed a new capability to compute third and fifth order Lie algebraic transfer maps for a family of realistic multipole magnets, including dipoles. The general Hamiltonian is expanded symbolically to arbitrary order. The vector potential off axis, for a given multipole symmetry, is determined from the appropriate magnetic field gradients and their longitudinal derivatives on axis.

Subroutines to compute the required gradients are available for Halbach REC quadrupoles and for general multipoles, with the current distribution on a cylindrical surface specified by a shape function. This function can be supplied by the user, or selected from internal options.

Both the reference trajectory, and the map about it are calculated by numerical integration through the general magnetic field, using modular GENMAP software. This allows the calculation of curved reference trajectories in a general dipole magnet, as well as offset reference trajectories needed for misalignment tolerence studies. These new calculational capabilities have been added to the MARYLIE Lie Algebraic beam optics design code.

EQUATIONS OF MOTION

In magnetic optics, the particle coordinates commonly used are dimensionless deviations from a reference trajectory, defined as the path of a selected reference particle through the system. The longitudinal position s of the reference particle is taken as the independent variable in place of the time, and the deviations in time of flight ($\tau = c\Delta t$) and energy ($p_\tau = -\Delta E/p_0 c$) relative to the reference particle are taken as new longitudinal coordinates. The tranverse momenta are scaled with respect to the design particle momentum: $P_x = p_x/p_0$, $P_y = p_y/p_0$. For convenience, we will often denote the vector of these new phase space coordinates by $\vec{z} \equiv (x, P_x, y, P_y, \tau, p_\tau)$.

When expressd in these new beam coordinates, the Hamiltonian turns out to be essentially the old p_z [1]:

$$H = -\frac{A_z}{B\rho} - \sqrt{1 + p_\tau^2 - 2\frac{p_\tau}{\beta_0} - (P_x - \frac{A_x}{B\rho})^2 - (P_y - \frac{A_y}{B\rho})^2} \tag{1}$$

The special role of the z-component of the vector potential should be noted. In regions where the transverse components of the vector potential vanish, the Hamiltonian has the form of a kinetic term plus a potential $A_z/B\rho$.

Hamiltons equations of motion in beam coordinates may be written:

$$\frac{dz_a}{ds} = -\{H, z_a\} \equiv -:H: z_a, \tag{2}$$

where the new symbol $:H:$ denotes the "Lie operator" associated with the Hamiltonian. The action of this differential operator on any function $f(\vec{z})$ is defined by the Poisson bracket with the Hamiltonian: $\{H, f\}$.

LIE ALGEBRAIC REPRESENTATION OF TRANSFER MAPS

The idea of a transfer map is simply that the final state of a particle is some function of its initial state: $\vec{z}_f = \vec{F}(\vec{z}_i)$ The transfer map can also be viewed as an operator $\mathbf{M}(s)$ that converts initial phase space coordinates (at $s = 0$) into final ones: $\vec{z}(s) = \mathbf{M}(s)\vec{z}(0)$. Hamilton's equations of motion for $\vec{z}(s)$ imply corresponding formal equations of motion for this operator, with the initial conditions $\mathbf{M}(0) = \mathbf{I}$, the identity. The equations have the form

$$\frac{d\mathbf{M}(s)}{ds} = -:H: \mathbf{M}(s). \tag{3}$$

For a beamline element of length L in which the Hamiltonian H is constant, this equation may be formally integrated to yield a map of the form

$$M = e^{-L:H:} \tag{4}$$

The exponential of a Lie operator is called a "Lie Transformation", which may be defined (for arbitrary $f(\vec{z})$) by the usual power series for an exponential. The application of this Lie transform to a general function $g(\vec{z})$ thus takes the form

$$e^{:f:}g = g + \{f, g\} + \frac{1}{2}\{f, \{f, g\}\} + \cdots \tag{5}$$

The GENMAP [2,3] routines in MARYLIE 3.0 represent the map of an optical system in the "reverse factorized" form

$$M = e^{:f_4:}e^{:f_3:}e^{:f_2:}, \tag{6}$$

where the $f_m(\vec{z})$ are homogeneous polynomials of order m. Substitution of this explicit form into the equation of motion of the map reduces it to a set of coupled nonlinear differential equations for the Lie polynomials. The Hamiltonian itself, which depends on the vector potential,

*Work supported and funded by the U.S. Department of Defense, Army Strategic Defense Command, under the auspices of the US Department of Energy.

must also be Taylor expanded into a series of homogeneous polynomials:

$$H(\vec{z},s) = \sum_{n=1}^{\infty} H_n(\vec{z},s). \tag{7}$$

Finally, the first order behavior of the system is taken out by transforming to the "interaction representation" in which only deviations from first order motion are considered. The Interaction Representation of the nth order part of the Hamiltonian is:

$$H_n^I(z,s) \equiv H_n(R(s)z,s), \tag{8}$$

where $R(s)$ is the linear (matrix) part of the map $\mathbf{M}(s)$, whose motion is determined by $H_2(s)$ alone.

After all of this, the equations for f_3 and f_4 are:

$$\frac{\partial f_3(z,s)}{\partial s} = -H_3^I(z,s), \tag{9}$$

$$\frac{\partial f_4(z,s)}{\partial s} = -H_4^I(z,s) + \frac{1}{2}\left[f_3(z,s), \frac{\partial f_3(z,s)}{\partial s}\right]. \tag{10}$$

These equations are further separated power by power into coupled non-linear differential equations for the 209 polynomial coefficients (for m = 2, 3, and 4) that represent the transfer map to third order, as used by MARYLIE 3.0. The GENMAP routines numerically integrate these 209 differential equations.

The fifth order code MARYLIE 5.0 uses m = 2 through 6, for a total of 923 equations to be integrated. The additional equations of motion for the f_m are more complicated, involving multiple Poisson brackets.

REPRESENTATION OF THE VECTOR POTENTIAL

Given the Fourier expansion of the scalar potential

$$V(r,\theta,z) = \sum_{m=1}^{\infty} U_m(r,z) sin(m\theta), \tag{11}$$

a vector potential giving the same field is

$$\begin{aligned} A_z &= -\sum_{m=1}^{\infty} \frac{cos(m\theta)}{m} r\frac{\partial}{\partial r} U_m(r,z) \\ A_r &= \sum_{m=1}^{\infty} \frac{cos(m\theta)}{m} r\frac{\partial}{\partial z} U_m(r,z). \end{aligned} \tag{12}$$

Here we have choosen a gauge where $A_\theta = 0$. The scalar potential off-axis may be written

$$U_m(r,z) = r^m \sum_{l=1}^{\infty} \frac{(-1)^l (m-1)!}{l!(l+m)!} \left(\frac{r}{2}\right)^{2l} \left(\frac{\partial}{\partial z}\right)^{2l} g_m(z), \tag{13}$$

where

$$g_m(z) = \lim_{r\to 0} \frac{m U_m(r,z)}{r^m} \tag{14}$$

represents the profile of the mth multipole.

This is a general solution to Maxwell equations order by order, for arbitrary $g_m(z)$. The problem is thus reduced to computing the generalized field gradients on axis for realistic magnet models. We report here on the implementation of a family of magnet models representable by current sheets on a cylindrical surface.

CURRENT SHEET MAGNETS

Cylindrical current sheets can be used not only to represent radially thin windings on a cylinder, but also to calculate arbitracy fields in the source-free volume bounded by a cylindrical surface. In the latter case, fictitious surface currents that produce the same interior fields as complicated outside sources replace them for rapid field calculation. (For some simple volume field sources, it can be better to work directly with analytical expressions for the field from the source). Continuous currents on the surface of a cylinder of radius a can be represented by a stream function $\Psi(\phi,z)$ of the surface coordinates as follows [4]:

$$j_\phi = -NI\frac{\partial \Psi(\phi,z)}{\partial z}, \quad j_z = \frac{NI}{a}\frac{\partial \Psi(\phi,z)}{\partial \phi}. \tag{15}$$

The quantity NI is introduced to make Ψ dimensionless. The above prescription produces currents that are automatically divergence-free. The stream function can be used to find a set of discrete turns that approximate a continuous distribution, since current streamlines are contours of constant Ψ; to make spiral windings, successive closed turns are cut and transitions between them are inserted. The stream function can be written as a sum of Fourier components as follows:

$$\Psi(\phi,z) = \sum_{m=1}^{\infty} w_m(z) sin(m\phi). \tag{16}$$

The $w_m(z)$ are called shape functions. The $m = 0$ case is excluded here because it requires special treatment. If only a single m value is present in Eq.16 and the boundaries are rotationally symmetric, the resultant field has m-pole θ dependence everywhere. For open boundaries, the scalar potential produced by the currents of Eq.15 is

$$V(r,\theta,z) = \frac{\mu_0 NIa}{\pi} \sum_{m=1}^{\infty} sin(m\theta) \int_{-\infty}^{+\infty} w_m(x) G_m(r,z,x) dx. \tag{17}$$

The Green's function $G_m(r,z,x)$ has the form

$$G_m(r,z,x) = \frac{\partial}{\partial a}\left[\frac{1}{2\sqrt{ar}} Q_{m-\frac{1}{2}}\left(\frac{a^2+r^2+(z-x)^2}{2ar}\right)\right], \tag{18}$$

where $Q_{m-\frac{1}{2}}$ is a Legendre function of the second kind of half-integral order. (For the closed-boundary case of a surrounding cylinder of infinitely permeable material, hybrid series solutions containing both ordinary and hyperbolic

Bessel functions have been obtained). Expressions for the magnetic field and vector potential are easily derived from Eq.17. For calculation of fields, etc., the $Q_{m-\frac{1}{2}}$ are not directly used; instead, the $\frac{1}{2\sqrt{ar}}$ factor cancels a factor in the hypergeometric series expression for $Q_{m-\frac{1}{2}}$; the resultant expression is regular as $r \to 0$. The generalized on-axis gradient for a single multipole m was defined in Eq.14. This limit of Eq.17 is

$$g_m(z) = \frac{\mu_0 N I a (2m-1)!!}{(m-1)! 2^{m+1}} \int_{-\infty}^{+\infty} w_m(x) K_m(z,x) dx \quad (19)$$

where

$$K_m = \frac{\partial}{\partial a} \left\{ \frac{a^m}{[(z-x)^2 + a^2]^{m+1/2}} \right\} \quad (20)$$

If $w_m(x)$ is a piecewise continuous polynomial, exact analytic integration of Eq.19 can be done. An exact quadrature subroutine for polynomials of up to the 4th degree in Eq.19 is used to calculate g_m and its z derivatives to arbitrary order. This routine is called by routines for shape functions of several types, including flattops with square or rounded edges, a symmetric quartic, etc. Lambertson coils are represented by two shape functions, the first for the fundamental with a given m value for the angular dependence, and second for the first allowable harmonic, with an angular dependence of 3m. The two shape functions are represented by a series of parabolic arcs precomputed in an initialization call. Finally, a user may provide a shape function in the form of a set of points; these points are then interpolated by parabolic arcs. The above routines have been implemented in MARYLIE, along with a routine for Halbach REC quadrupoles. The implementation is quite flexible, allowing almost arbitrary sequences of overlapping elements, as well as fitting and optimization.

EXAMPLE

As an illustration of the new capabilities, we show some calculations on a point-to-parallel telescope consisting of a quadrupole doublet with a concentric bending dipole. After setting the quadrupoles to obtain a focal point 3.0 m upstream with the dipole off, we turn on the bending dipole, and refocus the quadrupoles to compensate for the fringe fields of the bend. This excercises the curved reference trajectory, overlapping fringe fields, and fitting capabilities of the new code. This is the description of the telescope in our program input language:

```
initp    mult
  0 0 0 0 0 0
stm      mult
  2 50000000000000     -1.000000000000000E-02   1.00000000000000
  0 200000000000000     1.00000000000000       -2 50000000000000
qm1      mult
  1 00000000000000     -0 378358314677254       2.00000000000000
  0 100000000000000     1.00000000000000        0 500000000000000
qm2      mult
  1 00000000000000      0 261552436692153       2.00000000000000
  0 100000000000000     1 00000000000000        3.00000000000000
int      int
  8 5  1 0 0 200 0
#lines
point
    1*initp      1*stm       1*qm1       1*qm2       1*int
```

Fig.1 shows the effect of the uncorrected second and third order aberrations on the beam divergence.

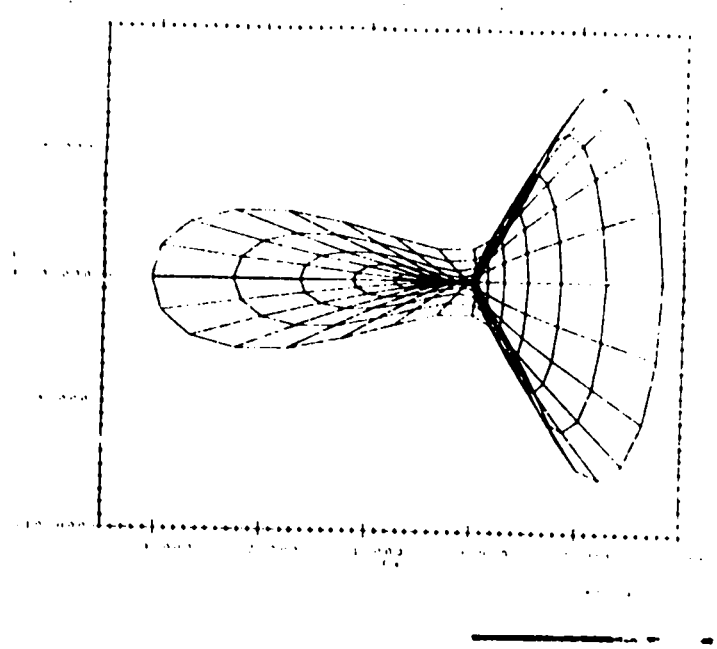

CONCLUSION

The significance of all this is that for the first time we can compute high order maps of realistic multipole elements with overlapping fringe fields. Since the routines have been written for arbitrary m, a basis has been laid for realistic calculations beyond fifth order. Since the reference trajectory, and the map about it are calculated by numerical integration through the general magnetic field, we can now calculate the curved reference trajectories in a general dipole magnet, as well as the offset reference trajectories needed for misalignment tolerance studies.

REFERENCES

1. A. J. Dragt, "Lectures on Nonlinear Orbit Dynamics," 1981 Fermilab Summer School on High Energy Particle Accelerators, AIP Conference Proceedings, vol. 87 (1982).
2. A. J. Dragt, F. Neri, G. Rangarajan, D. R. Douglas, L. M. Healy, and R. D. Ryne, "Lie Algebraic Treatment of Linear and Nonlinear Beam Dynamics," Ann. Rev. Nuc. Part. Sci. 38, 455 (1988).
3. R. D. Ryne, "Lie Algebraic Treatment of Space Charge," Ph.D. Thesis, University of Maryland (1987).
4. P. Walstrom, "Magnetic Fields and Inductances of Cylindrical Current Sheet Magnets", to be published as a Los Alamos National Laboratory Unclassified Report (1990).

REDUCTION OF BEAM CORKSCREW MOTION ON THE ETAII LINEAR INDUCTION ACCELERATOR*

W.C.Turner, S.L.Allen, H.R.Brand, G.J.Caporaso, F.W.Chambers, Y.-J.Chen, F.E.Coffield, F.J.Deadrick, T.A.Decker, L.V.Griffith, D.L.Lager, W.J.Mauer, W.E.Nexsen, A.C.Paul, V.L.Renbarger, S.Sampayan

Lawrence Livermore National Laboratory, Livermore,CA 94550

Abstract

The ETAII linear induction accelerator (6MeV,3kA,70ns) is designed to drive a microwave free electron laser (FEL) and demonstrate the front end accelerator technology for a shorter wavelength FEL. Performance to date has been limited by beam corkscrew motion that is driven by energy sweep and misalignment of the solenoidal focussing magnets. Modifications to the pulse power distribution system and magnetic alignment are expected to reduce the radius of corkscrew motion from its present value of 1 cm to less than 1mm. The modifications have so far been carried out on the first 2.7 MeV (injector plus 20 accelerator cells) and experiments are beginning. In this paper we will present calculations of central flux line alignment, beam corkscrew motion and beam brightness that are anticipated with the modified ETAII.

Introduction

Previously ETAII has successfully operated with 6 MeV beam energy, accelerated beam current up to 3 kA (70ns FWHM) and driven a 140 GHz FEL with peak power in the range 200-400 MW. [1,2] However the FEL output pulse width was generally much narrower (5-10ns) than the beam pulse due to the corkscrew motion of the electron beam. [3,4] The corkscrew motion is a differential rotation of the beam centroid between the center and leading and trailing edges of the pulse. It is driven by the combination of energy sweep and misalignment of the solenoidal focusing field and at a fixed axial location leads to a time dependent sweeping of the beam centroid that cannot be corrected with static steering coils. Consequently we have embarked on a program to reduce energy sweep and improve magnetic alignment before proceeding further with FEL experiments.

From the viewpoint of FEL operation beam quality is characterized by brightness (defined here as $J = I/(\beta\gamma)^2 V_4$), energy sweep and spatial sweep (or corkscrew amplitude which we will define below). Past performance and our near term goals for these parameters are given in Table 1 below. Brightness of the entire beam has been measured by analyzing beam radius as a function of focusing strength of upstream solenoids[5]. A brightness value of 1×10^8 A/m^2rad^2 is adequate for a microwave FEL and has already been exceeded with the measured value 6×10^8 A/m^2rad^2. However a brightness 2×10^9 A/m^2rad^2 is required for a micron wavelength FEL and this is our near term goal. Energy sweep of ±1% or less is desirable for limiting the phase of corkscrew motion and for satisfying FEL resonance. Previously an energy sweep of ±1% has been maintained for only 13 ns out of the 70 ns FWHM. Our near term goal is to extend this to 30 ns by modifications to the pulse power distribution system which improve the flatness of accelerating pulse applied to the cell gaps[6]. Ultimately we hope to extend the ±1% energy flattop to 50 ns by modifying the shape of the beam current pulse to compensate for impedance variation of the ferrite in the accelerating cells. Efficient FEL operation requires that the magnitude of beam spatial sweep be controlled to approximately ±1mm at the exit of the accelerator whereas previously the spatial sweep has been an order of magnitude higher - ±1 cm. Improvements in flux line alignment together with reduced energy sweep are expected to allow us to reach our goal of ±1mm.

Table 1: Beam quality parameters for ETAII

parameter	status (12/89)	goal
brightness (A/m^2rad^2)	6×10^8 @ I= 1.3 kA	2×10^9 @ I= 1.5 kA
energy sweep	±1%, 13ns	±1%,30ns
corkscrew amplitude	±1cm,50ns	±1mm,30ns

Flux Line Alignment

The electron beam in ETAII is focused by a continuous solenoidal channel interrupted only by gaps for acceleration, insertion of beam position monitors and vacuum pumping. The typical strength of solenoidal field is 100 to 500 G. A sin/cos coil pair is wrapped around each solenoid to correct for transverse dipole field errors described in the paper by W. Nexsen.[7] The magnitudes of transverse displacements and equivalent tilts of the magnetic axis relative to a straight line mechanical reference axis have been measured with the pulsed stretched wire technique.[8] The transverse displacement errors are ±.5mm horizontally and ±.25mm vertically. The magnitude of transverse displacement errors is minimized by adjusting the axis of an entire cell block of ten acceleration cells, however there is no provision for adjustment of the transverse displacement of individual cells once they have been assembled into cell blocks. Sin/cos coil currents correct the magnetic axis of each solenoid to approximately ±1mrad standard deviation error. The field solver portion of our expert control system MAESTRO[9] has been used to calculate the trajectory of the central magnetic flux line from the transverse displacements and winding errors measured with the stretched wire. Results are shown in Fig. 1(a) without and (b) with the sin/cos correction coils turned on. The magnitude of flux line wander is reduced an order of magnitude with the sin/cos coils, from ±3.5mm to ±200 microns. Residual errors with the sin/cos coil currents on are due to several effects; (1) the overlap of the sin/cos coils with the dipole winding errors is not perfect, (2) there are residual errors in the magnitudes of

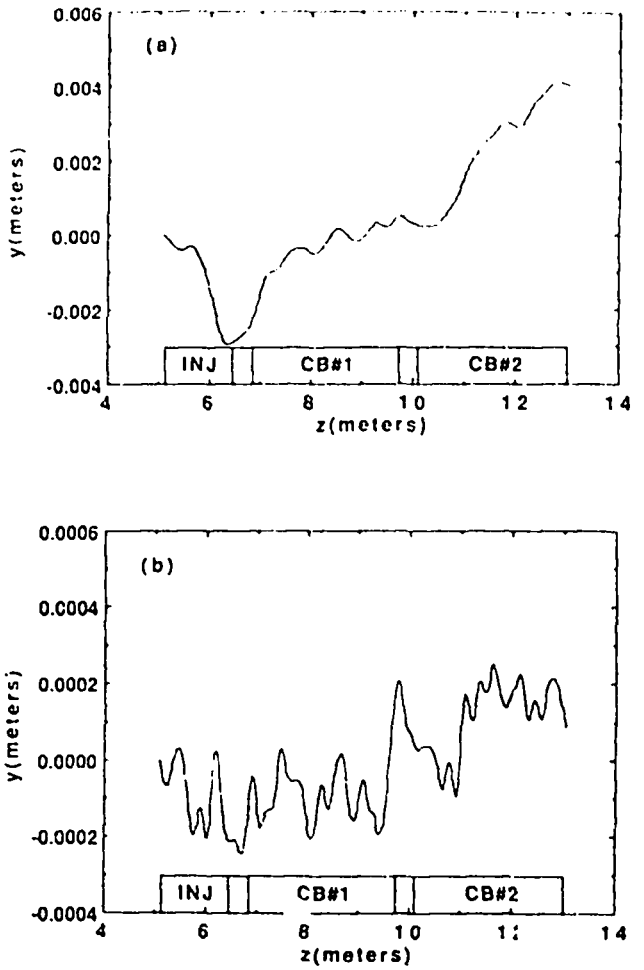

Fig. 1. Mapping the central flux line of ETAII, (a) without and (b) with sin/cos correction coils.

the sin/cos coil currents and (3) the sin/cos coils correct for angular misalignments of the magnetic axis but not for transverse displacements. Reduction of the transverse displacement errors could be facilitated by incorporating the stretched wire alignment technique into the assembly of the ten cell blocks.

Corkscrew Motion

The magnitudes of magnetic field errors described in the last section and the energy sweep anticipated with the new pulse distribution system have been used as input to the BREAKUP code[10] which then calculates the corkscrew motion of the beam centroid. Results are shown in Fig. 2. The energy sweep is ±1.3% for the 40 ns indicated in Fig. 2(a) and the corresponding corkscrew motions are indicated in Fig. 2(b) without and Fig. 2(c) with sin/cos correction coils. Without correction coils the corkscrew amplitude is ±4 mm and with correction coils is reduced to ±0.4 mm. The calculation was done for the present configuration of injector plus 20 cells. Calculation for the full sixty cells predicts a corkscrew amplitude of ±.5 mm with correction coils.

A field tuning algorithm is being incorporated into MAESTRO to minimize the corkscrew amplitude "A" defined at a given axial location by

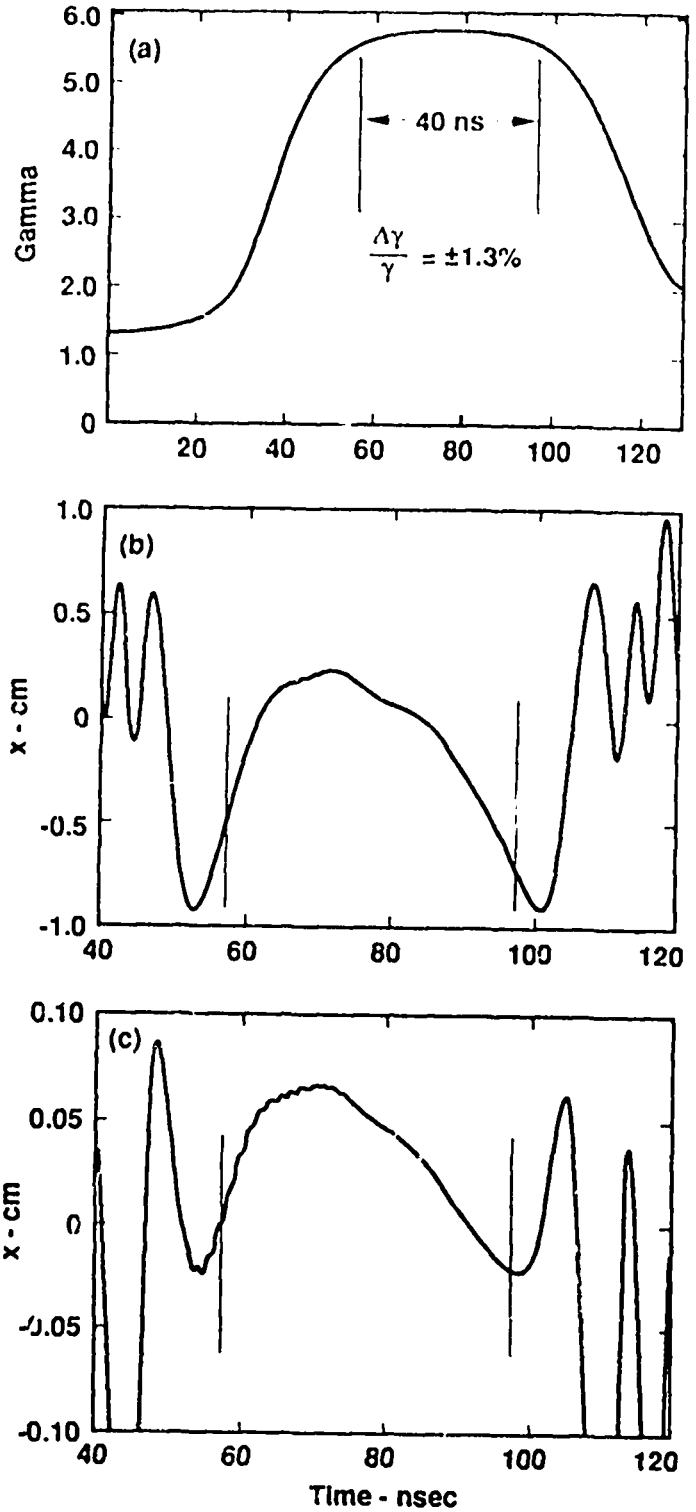

Fig. 2. Anticipated corkscrew motion of the ETAII electron beam. Gamma versus time (a), transverse x position versus time at the end of 20 cells (b)without and (c) with sin/cos coils.

$$\langle A^2 \rangle = \langle x^2 + y^2 \rangle$$

where x and y are the beam centroid coordinates measured by beam position monitors and < > denotes time averaging. Fig. 3 shows a BREAKUP calculation of "A" versus the

current in a single sin/cos correction coil with the optimum current at the minimum value of A.

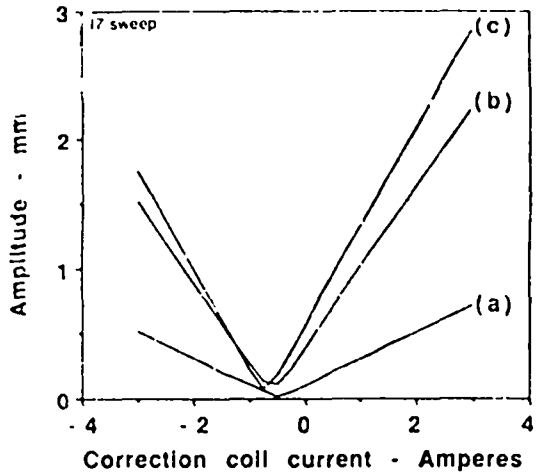

Fig. 3. Corkscrew amplitude (a) at the end of the injector, (b) at the end of 10 acceleration cells and (c) at the end of 20 acceleration cells versus current in a single sin/cos correction coil.

Accelerator Tune and Brightness

Whole beam brightness has previously been measured on ETAII at 6 MeV by measuring the beam radius as a function of focussing strength of upstream solenoids.[5] With the present injector plus twenty cell configuration the beam energy is reduced to 2.5-3.0 MeV, space charge forces totally dominate emittance, and this technique is no longer viable. Instead we will use the pepper pot technique. Analysis of our previous data has revealed a tune dependent generation of halo electrons which degrade beam brightness.[5] The degradation occurs when there is an approximate resonance condition between the cyclotron wavelength and an integer number of acceleration cells. Calculations of beam scatter plots at the end of twenty cells are shown in Fig. 4(a) for the old tune and (b) for a new tune which avoids resonances. The brightness of the beam is predicted to be improved by more than a factor of four.

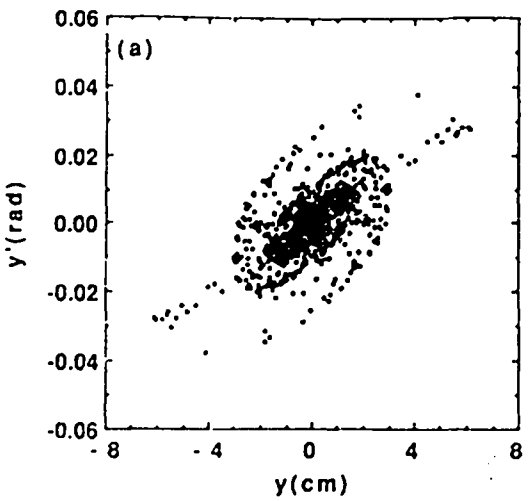

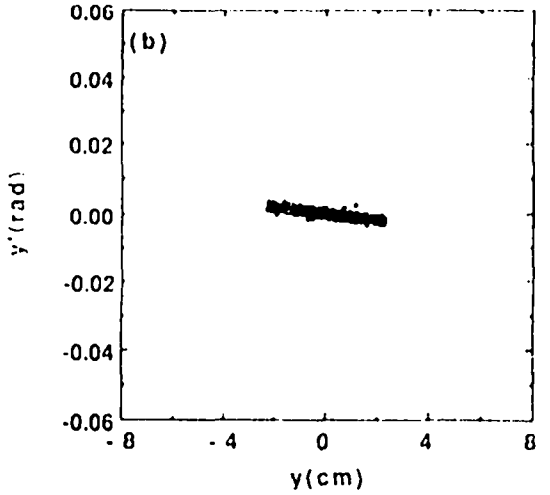

Fig. 4. Reduction of halo electron production with choice of accelerator tune, (a) resonant and (b) non-resonant tune.

References

1. W.E.Nexsen et. al.,"The ETAII Induction Linac as a High Average Power FEL Driver",Proc. of the 11th Intl. Conf. on Free Electron Lasers, Naples, FL., Aug.28-Sept.1,1989. Also UCRL-101154.
2. S.L. Allen, M.D. Brown, J.A. Byers et. al.,"Free Electron Laser Experiments in the Microwave Tokamak Experiment, MTX", to be published in Proc. of the Thirteenth Intl. Conf. on Plasma Physics and Cont. Fusion, Washington,D.C.,Oct. 3-8, 1990. IAEA, Vienna.
3. G.J. Caporaso, W.A. Barletta, D.L. Birx et. al.,"Beam Dynamics in the Advanced Test Accelerator (ATA)",Proc. of the 5th Intl. Conf. on High Power Particle Beams, San Francisco, CA.,Sept.12-14, 1983.pg.427.
4. Y.-J. Chen,"Corkscrew Modes in Linear Accelerators", Nucl. Inst. and Methods in Phys. Res. A292(1990)455.
5. Y.-J. Chen, J. C. Clark, A.C. Paul, W.E. Nexsen and W.C. Turner,"Measurement and Simulation of Whole Beam Brightness on the ETAII Linear Induction Accelerator", this conf..
6. S.Sampayan, G.J. Caporaso, Y.-J.Chen, T.A. Decker and W.C. Turner, "Pulsed Power Distribution and Tapered PFL Design for Achieving Low Energy Sweep in ETAII", this conf..
7. W.Nexsen, "Characterization of Field Errors of Layer Wound Short Solenoids", this conf..
8. L.Griffith and F. Deadrick, "Progress in ETAII Magnetic Field Alignment Using Stretched Wire and Low Energy Beam Techniques", this conf..
9. F.W. Chambers, F.E. Coffield, H.R. Brand, D.L. Lager and G.J.Caporaso, "Progress on an Expert Control System for ETAII",this conf..
10. G.J. Caporaso, A.G. Cole and K.W. Struve, "Beam Breakup (BBU) Instability Experiments on the Experimental Test Accelerator (ETA) and Predictions for the Advanced Test Accelerator(ATA)", IEEE Trans. Nucl. Sci., NS-30 (1983) 2502.

*Performed jointly under the auspices of the US DOE by LLNL under W-7405-ENG-48 and for the DOD under SDIO/SDC-ATC MIPR No. W31RPD-8-D5005.

"SMILE" A NEW VERSION FOR THE RADLAC II LINEAR ACCELERATOR*

M. G. Mazarakis, J. W. Poukey, S. L. Shope, C. A. Frost
P. J. Pankuch, B. N. Turman, J. J. Ramirez, K. R. Prestwich

Sandia National Laboratory
P. O. Box 5800
Albuquerque, NM 87185

Abstract

We present here the SMILE modification of the RADLAC II accelerator which enabled us to produce high quality 12-14 MV, 100 kA beams. The modification of replacing the 40-kA 4-MV beam injector, magnetic vacuum transport and accelerating gaps by a long cathode shank which adds up the voltages of the 8 pulse forming lines. The beam now is produced at the end of the accelerator and is free of all the possible instabilities associated with accelerating gaps and magnetic vacuum transport. Annular beams with $\beta_\perp \leq 0.1$ and radius $r_b \leq 2$ cm are routinely obtained and extracted from a small magnetically immersed foilless electron diode. Results of the experimental evaluation are presented and compared with design parameters and numerical simulation predictions.

Introduction

Following the successful operation of the four-feed, 8-MV magnetically insulated transmission line injector[1], an eight-feed Self Magnetically Insulated Transmission Line ("SMILE") for the RADLAC-II accelerator was designed and installed. The design is similar to that of the HERMES III[2] and HELIA[3] accelerators and was done using the Creedon formalism[4]. The basic idea is to replace all accelerating gaps by an MITL voltage adder which runs along the entire length of the device. The design was validated with the PIC MAGIC[5] code.

In the following sections we present the SMILE design, numerical simulations validating the design, and experimental results.

SMILE Design

The SMILE design is based on a pulse forming line-fed self-magnetically insulated transmission line (MITL) system which performs the series addition of voltage pulses from 8 source modules (feeds). The cathode geometry is shown in Figure 1, and it is preferred over a continuous taper for the following reasons: it is easier and cheaper to manufacture, the constant radius segments provide constant vacuum impedance along each MITL segment, and the impedance increases gradually at each successive voltage feed with a rate of increase which follows the voltage axial gradient along the feed. The latter assures constant current flow over the entire length of SMILE.

The vacuum impedance of each section i of SMILE depends only on the dimensions of Figure 1 and can be easily calculated from the following expression

$$Z_i = 60 \ln (R/r_i) \ [\Omega]; \ r_i = 1, 2, \ldots 8 \qquad (1)$$

where R = 21.5 cm is the anode inner radius and r_i is the radius of the i-th cathode segment. The selection of the radius r_i of each cylindrical section was done in a fashion to provide constant operating load impedance for all the pulse forming line feeds of RADLAC II. Some deviations were allowed at the beginning of the cathode shank where self-magnetic insulation is not that critical and also at the high voltage end for mechanical and construction reasons.

The point design is for 110 kA and assumes equal 2-MV voltages at each insulating stack feed. An MITL operating with conditions similar to SMILE is a "balanced" one. Because of the relatively short voltage pulse (40 ns fwhm) of each feed, the current flow is self limited and to a large extent independent of the diode impedance conditions. However in our design we stayed as close as possible to the constant current conditions all the way to the end of the cathode tip. At first we selected the radius of the cathode tip. The outside wall radius of the anode cylinder was defined by the existing RADLAC II insulating stacks, and the end voltage was assumed to be 16 MV. With these initial parameters and Creedon equations for minimum current flow I_ℓ to establish self limited magnetic insulation:

$$\begin{aligned} I_\ell &= 8500 \ g\gamma_\ell^3 \ \ln\left[\gamma_\ell + (\gamma_\ell^2 - 1)^{1/2}\right], \\ \gamma_o &= \gamma_\ell + (\gamma_\ell^2 - 1)^{3/2} \ln\left[\gamma_\ell + (\gamma_\ell^2 - 1)^{1/2}\right], \\ g &= [\ln R/r_i]^{-1} \text{ and } \gamma_o = V[MV]/mc^2 + 1, \end{aligned} \qquad (1)$$

we estimate the cathode radii and operating impedances of the entire SMILE line. Our main concern was to keep the current I_ℓ the same or at least not smaller than I_ℓ = 110 kA in all segments.

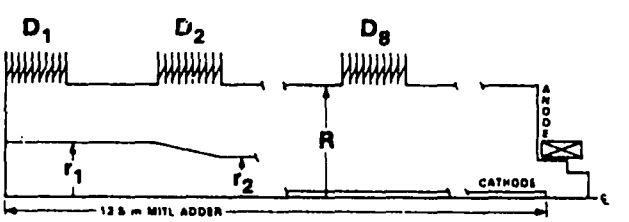

Fig. 1: Schematic cross section of the SMILE adder system

*Supported by the U. S. DOE contract DE-AC04-76DP00789 and DARPA/AFWL ARPA order No. 5789.

Table I summarizes SMILE dimensions and design parameters. The cathode electrode is 12.5 m long and is candilevered from the low voltage end of the accelerator. It starts with a 10-cm radius cylinder at the cathode end plate and tapers off to 1-cm radius at the A-K gap of a magnetically immersed foilless diode (Fig. 2). Seven conical tapers have been utilized along with seven cylindrical sections and an equal number of flex-adjusting, double washer sections. The outer shell (anode cylinder) is formed by eight 21.6-cm-inner-radius insulating stacks (feeds) alternating with seven stainless steel cylinders, plus the final anode extension cylinder. The cathode electrode (Fig. 3) is preloaded before insertion into the anode cylinder to compensate for gravitational droop. The final adjustment is made in situe. Because of the large difference in radius between anode and cathode shank, precise alignment and centering of the cathode stock inside the anode cylinder is not very critical since the electrical potential is a logarithmic function of the radii.

The magnetically-immersed foilless diode design (Fig. 4) is similar to that of the IBEX accelerator[6] and actually utilizes the same pancake coil assembly. The anode extension cylinder makes it possible to locate the diode outside of the water tank and greatly facilitates operations and produced beam parameters evaluation.

The design of Table I was validated with a number of MAGIC simulations. The calculated impedances agree with the minimum parapotential theory[4] within 10%. Figure 5 compares the voltage input of each feed with the MAGIC simulated voltage output applied at the A-K gap of the electron diode. Because of the lack of flat top wave forms at the input, the peak output voltage is not 16 MV but only ~ 14MV. This is due mainly to inductive losses and some impedance mismatch at the load end.

The main differences between HERMES III[1] and SMILE designs are the current or operating impedances and the length of the voltage feeds. The RADLAC II feeds are 50 cm long while HERMES III are only 3.8 cm. This makes SMILE almost a "continuous" adder, the first of its kind. Another first is that SMILE is the highest impedance 16 MV MITL voltage adder. The final operating impedance is 140 ohm versus 30 ohm of HERMES III. These differences made the design, construction and operation of the SMILE adder very challenging.

TABLE I
SMILE Self-Limit. & Minimum Current MITL Desigr.

MITL Segment i	Segment Voltage Vi (MV)	Optimum Cathode Radius ri (cm)	Actual Cathode Radius ri (cm)	Vacuum Impedance Zi (Ω)	Operating Impedance Zi (Ω)
1	2.0	13.33	10.2	45.3	30
2	4.0	8.05	7.6	55	40
3	6.0	6.10	5.7	80	61
4	8.0	3.86	3.5	96	80
5	10.0	2.69	2.5	121	97
6	12.0	1.90	1.8	149	122
7	14.0	1.35	1.3	152	135
8	16.0	0.92	1.0	180	151

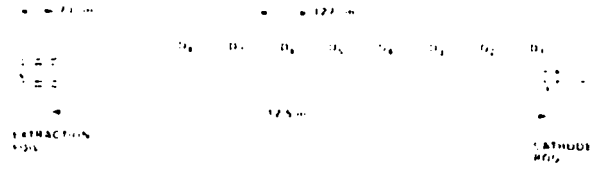

Fig. 2: SMILE configuration

Fig. 3: SMILE cathode electron before insertion into the anode cylinder

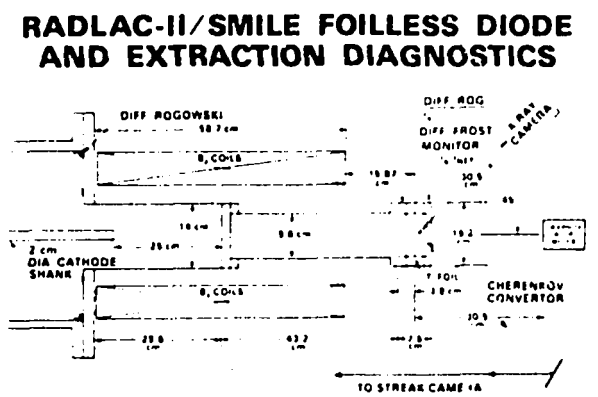

Fig. 4: Schematic diagram of the immersed foilless diode with beam diagnostics

Computer-generated movies of SMILE simulations clearly show that we have self-magnetic insulation for a large part of the input voltage wave form. There are some electron losses at the beginning and at the end of the voltage pulse. This is to be expected since self-limited magnetic insulation is established by driving some electron current at the anode wall during the rise time of the voltage pulse. The losses during the fall time are due to the fact that the following current drops below the minimum current I_ℓ and the line loses self-magnetic insulation. Figure 6 shows an electron map at 75 ns following the arrival of the voltage pulse at the first feed (t = o). The line is magnetically insulated. The losses near the cathode tip are due to the radial component B_r of the applied magnetic field of the immersed foilless diode. They occur at the point where the self field B_θ becomes equal to the B_r component of the applied field.

A number of electron diodes were studied to fit the end of SMILE. Among them the magnetically immersed foilless diode of Figure 4 was selected because it provides the canonical angular momentum to the extracted electron beam necessary for the B_θ wire conditioning cell.

Experimental Results

The SMILE operates very reliably, consistently producing high quality, high current electron beams with parameters repeating themselves from shot to shot. From the first shot we extracted from the diode magnetic field and into full pressure air thin annular beams with radius $r_b \leq$ 2 cm. The preliminary beam transverse velocity component estimates from the annulus thicknesses are less than 0.1. The voltage and current wave forms are similar to those of the first SMILE shot shown in Figure 7. We can vary the extracted beam current by changing the A-K of the diode (Fig. 4), the strength of the B_z field, or both. The observed beam radius and emittances are in good agreement with diode numerical simulations. One possible explanation for the obtained low temperature beam is that all the sheath electrons of large radius escape to the anode following the radial magnetic flux lines of the applied B_z field.

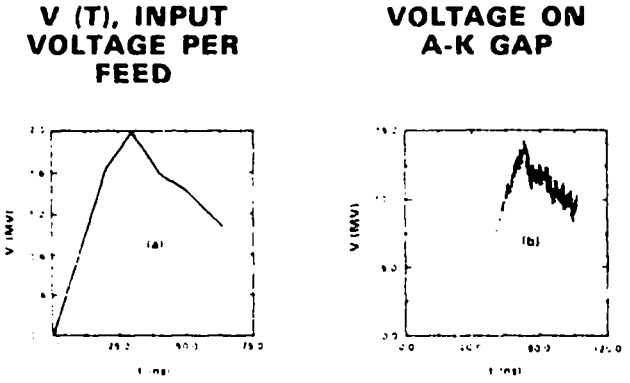

Fig. 5: Time dependance of RADLAC/SMILE input voltage (a) and combined 8-feed voltage output at the A-K gap of the foilless diode

Conclusions

We have designed and installed into the RADLAC II water tank a self-magnetically insulated transmission line SMILE. The coaxial transmission line replaces the original beam line with the solenoidal magnets and accelerating gaps and performs the voltage addition along the long cathode shank. The total voltage is applied at the A-K gap of a magnetically immersed foilless diode located at the end of the coaxial line outside the water tank.

SMILE operation is reliable and reproducible, consistently generates beams with low transverse velocities (~ 0.1) and small radii (~ 1 cm). The beam currents can be varied between 50 and 100 kA by changing diode parameters as predicted by MAGIC simulations.

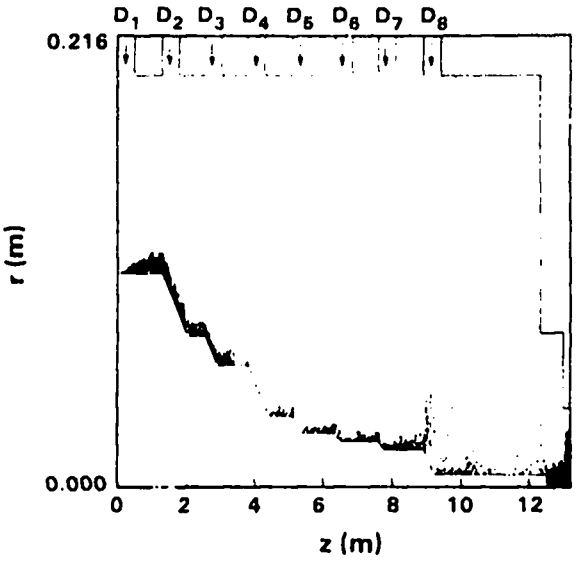

Fig. 6: Electron map for SMILE obtained with MAGIC PIC code at t ~ 75 ns from the energization of the first insulating Stack D_1

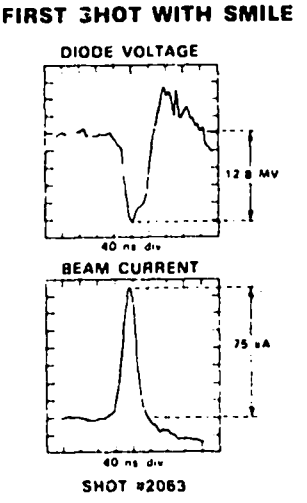

Fig. 7: Voltage and current wave forms of the SMILE magnetically insulated diode

References

1. M. G. Mazarakis, et al., Bull. Am. Phys. Soc. 35, No. 4, 931 (1990).
2. R. C. Pate, et al., Proc. 6th International IEEE Pulsed Power Conference, Arlington, VA, p. 478 (June 29-July 1, 1987).
3. J. J. Ramirez, et al., Proc. 5th International IEEE Pulsed Power Conference, Arlington, VA, p. 143 (June 10-12, 1985)
4. J. H. Creedon, J. Appl. Phys. 48, No. 3, pp. 1070-1077 (1977)
5. See paper "Numerical Models of Injectors for High-Current Electron Linacs," by J. W. Poukey and M. G. Mazarakis, this conference.
6. M. G. Mazarakis, et al., J. Appl. Phys. 62, 4024 (1987).

CALCULATION OF TIME DELAY LINES WITH H_{0n} MODES FOR RF - ENERGY UPGRADE SYSTEMS

S. Yu. Bogdanovich, Yu. A. Majorov, V. I. Kassadin, and V. A. Semenov

Moscow Engineering Physics Institute
Kashirskoe sh., 31, 115409, Moscow, USSR

Abstract

A calculation method for time delay lines based on circular iris - loaded waveguide with H_{0n} modes is discussed in present paper. The lines are intended for use in RF - energy upgrade systems as an energy storaging elements. Some practical results of delay lines calculation are represented and discussed also. This results show that a satisfactory parameters of delay lines can be obtained when using circular iris - loaded waveguides excited at H_{0n} modes.

Time delay lines intended for RF - energy storage are among the most important elements of certain RF - energy upgrade systems [1]. Upgrade systems characteristics, e. g. power multiplying coefficient and and efficiency, are in strong correlation with the time delay lines used parameters. The main requirements for this lines parameters are as following: minimum possible RF - energy losses and dimensions. Rather small losses one can achieve using a superconducting device. But superconductivity usage is unconvenient in most cases because of considerable growing of the device cost. Also this concerned the delay line dimensions (aspecially its length) that shouldn't be extremely big. That's why an actual problem is a compact time delay line with small energy losses construction. Calculations show that an acceptable value of energy losses is not higher than 1 dB.

RF - energy losses in delay lines can be decreased by using a circular waveguides with H_{0n} modes. Because of their anomally small losses they are widely used in RF - communication lines. Existance of some parasitic modes is perhaps the only but essential disadvantage of this modes using. In particular singularity of H_{0n} and E_{1n} modes takes place for all frequencies. It leads for additional energy losses. The main goal of this paper is to show that low enough values of energy losses can be achieved in circular iris - loaded waveguides - CIW - excited at H modes for relatively small values of group velocity β_{gr} (about 0.01 - 0.03). This gives a possibility to construct a compact delay line at submicrosecond puls width band. Moreover in CIW the E_{1n} and H_{0n} modes natural frequencies are separated and so their singularity eliminated [2].

A partial regions method was used to calculate a CIW electromagnetic characteristics for H_{0n} modes. A not big memory volume and not high operation speed computer is acceptable for this method using.

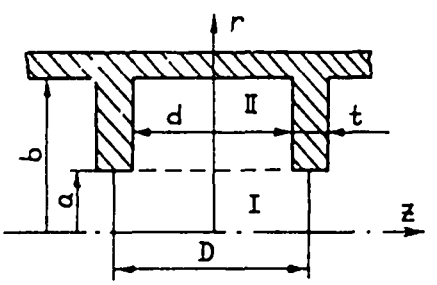

Fig. 1. Iris - loaded waveguide cell.

To carry out the calculations a waveguide is devided by a cylinder surface with radius r = a into two parts as it is shown at fig. 1. For magnetic - type modes discription here magnetic vectror Π_μ consistent with a Helmholtz equation can be used [1]

$$\frac{\partial^2 \Pi_\mu}{\partial r^2} + \frac{1}{r}\frac{\partial \Pi_\mu}{\partial r} + \frac{\partial^2 \Pi_\mu}{\partial z^2} + \kappa^2 \Pi_\mu = 0 \qquad (1)$$

Solution of this equation can be represented as following for both partial regions:

$$\Pi_\mu^{I} = -\sum_{n=-\infty}^{+\infty} A_n \frac{I_0(p_n r)}{p_n^2 I_0(p_n a)} e^{ih_n z}$$

$$\Pi_\mu^{II} = \sum_{s=1}^{\infty} B_s \frac{\Phi_0(æ_s r)}{æ_s^2 a} \sin\frac{\pi s}{2}\left(1 - \frac{2z}{d}\right) \qquad (2)$$

Here $I_0(x)$ is a modified Bessel function.

$$\Phi_0(æ_s r) = \frac{J_1(æ_s b) N_0(æ_s r) - N_1(æ_s b) J_0(æ_s r)}{N_1(æ_s b) J_1(æ_s a) - J_1(æ_s b) N_1(æ_s a)};$$

$$h_n = \frac{\vartheta + 2\pi n}{D}; \quad p_n = \sqrt{h_n^2 - \kappa^2}; \quad æ_s = \sqrt{\kappa^2 - \eta_s^2}; \quad \eta_s = \frac{\pi}{d} s;$$

ϑ is a phase shift for the period.

Equations for fields in partial regions as a sums of space harmonics (I region) and standing waves (II region) one can get using a definition for Π_μ.

$$E_\varphi^{I} = \sum_{n=-\infty}^{+\infty} A_n \frac{\kappa}{p_n} \frac{I_1(p_n r)}{I_0(p_n r)} e^{ih_n z};$$

$$E_\varphi^{II} = -i \sum_{s=1}^{+\infty} B_s \frac{\kappa}{æ_s^2 a} \Phi_0'(æ_s r) \sin\frac{\pi s}{2}\left(1 - \frac{2z}{d}\right);$$

$$H_r^{I} = -i \sum_{n=-\infty}^{+\infty} A_n \frac{h_n}{p_n} \frac{I_1(p_n r)}{I_0(p_n a)} e^{ih_n z};$$

$$H_r^{II} = -\sum_{s=1}^{+\infty} B_s \frac{r_i s}{æ_s^2 a} \Phi_0'(æ_s r) \cos\frac{\pi s}{2}\left(1 - \frac{2z}{d}\right); \qquad (3)$$

$$H_z^{I} = \sum_{n=-\infty}^{+\infty} A_n \frac{I_0(p_n r)}{I_0(p_n a)} e^{ih_n z};$$

$$H_z^{II} = \sum_{s=1}^{+\infty} B_s \frac{\Phi_0(æ_s r)}{æ_s a} \sin\frac{\pi s}{2}\left(1 - \frac{2z}{d}\right).$$

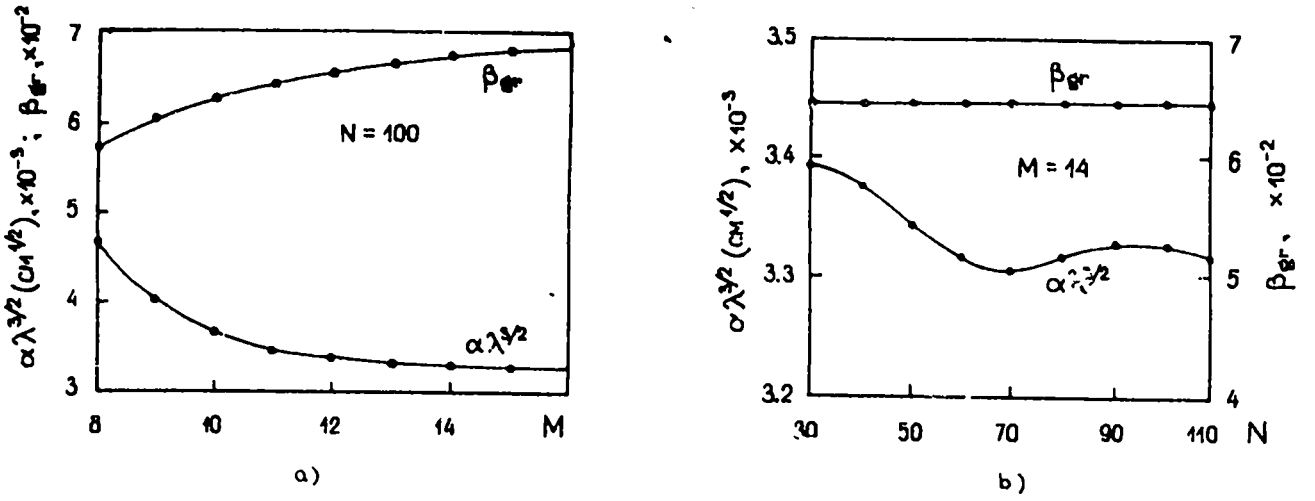

Fig.2. Group velocity and damping convergency against parameters M (a) and N (b) for H_{01} mode.

Here marked function Φ_0' is the derivative with respect to argument.

Such a representation satisfied a boundary conditions in resonant region and Floke conditions in axial region. To satisfy a boundary condition at its walls and a tangential components continuity condition at a regions boundary one may represent field E_φ for $r = a$ as following [3]:

$$E_\varphi\Big|_{r=a} = \sum_{m=-\infty}^{+\infty} F_m \sqrt{1-\left(\frac{2z}{d}\right)^2}\, e^{ih_m z} \times \begin{cases} 1, & |z| < d/2 \\ 0, & d/2 < |z| < D/2 \end{cases} \qquad (4)$$

Expressed fields amplitudes in partial regions by F_m and used the magnetic field tangential components continuity at regions boundary a system of simultaneous linear algebraic homogeneous equation in unknown F_m can be set up. To set a dispersion equation one should equate the systems determinant to zero. When equation roots are found out it is possible to determine unknown F_m and serpently a field decomposition components for partial regions. Then a CIW characteristics (group velocity β_{gr} and a wave damping coefficient $\alpha\lambda^{3/2}$ where λ is a free - space wavelength) can be determined.

Frequency comparison was used for equation solving program precision control. When H_{01} mode is excited in CIW which parameters are close to a smooth circular waveguide (r = 4.038 cm ; ϑ = 0.3 rad ; a/b = 0.991) relative calculation error is about 1.54 % and for a cylinder cavity with H_{011} mode (r = 4.038 cm and its length l = 3.69 cm) this error drops to 0.05 %.

Solution convergence investigation is very important for a partial regions method use. A special investigations were carried out to determine an optimal values of parameters M (according to (3) and (4) m = ±1; ±2,...,±M; s = 1, 2, ...,2M) that defines the combined equations order and N (according to (3) n = 0, ±1, ±2,...,±N) that defines a sum terms number in the determinant elements. Values of this parameters should be chosen in such a way that one can obtain a satisfactory precision with acceptable calculating time. A convergence of β_{gr} and $\alpha\lambda^{3/2}$ can be illustrated by fig. 2 where this parameters are given as a functions of M (a) and N (b) for copper CIW with following parameters : a/λ = 0.402 ; t/λ = 0.0927 ; $\vartheta = \pi/2$; β_{ph} = 3.66 ; a/b = 0.4729. All further calculations are carried out for M = 13...15 and N = 80...100.

Calculation results of damping coefficient $\alpha\lambda^{3/4}$ and group velocity β_{gr} for time delay line based on CIW with E_{01} modes are plotted. Normalized damping $A\lambda^{3/2}/\tau$ as a function of phase velocity β_{ph} for H_{01} mode is shown at fig. 3. Normalized damping $A\lambda^{3/2}/\tau$ is the whole damping in the line with length L and delay time τ (and so $A = 20L\alpha(\lg e)$). A plot of group velocity β_{gr} vs β_{ph} is given at fig. 3 also. Within considered phase velocities band a minimum energy losses are for $\beta_{ph} \simeq 3.6$. For example at 10 - cm wavelength band a lowest value of damping is about 1.5 dB/μs and so less than 0.6μs delay time is permitted in order not to exceed 1 dB damping value. At this point $\beta_{gr} \simeq 0.065$ and the delay line would be 12 m long.

Much more interesting results can be obtained for H_{02} mode in CIW. Plots of $A\lambda^{3/2}/\tau$ and β_{gr} against β_{ph} and a/λ for H_{02} mode are shown at fig. 4 and fig. 5 respectively. A group velocity sign changing is observed within considered values of β_{ph} and a/λ . In the sign change point a $A\lambda^{3/2}/\tau$ function has a singularity. At the

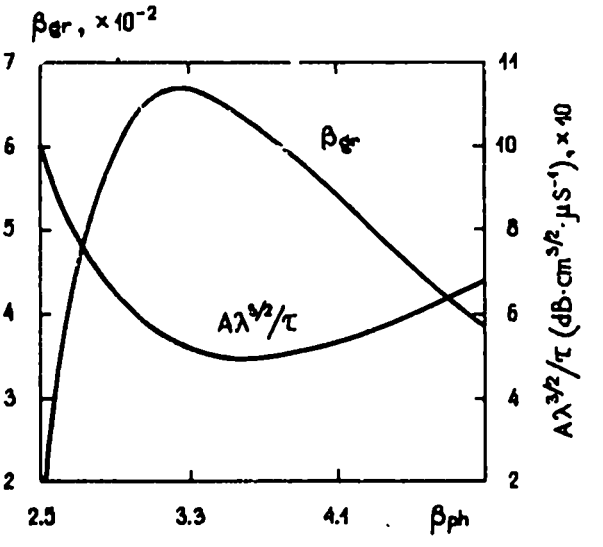

Fig.3. Normalized damping $A\lambda^{3/2}/\tau$ and group velocity β_{gr} as a function of phase velocity β_{ph} for H_{01} mode.

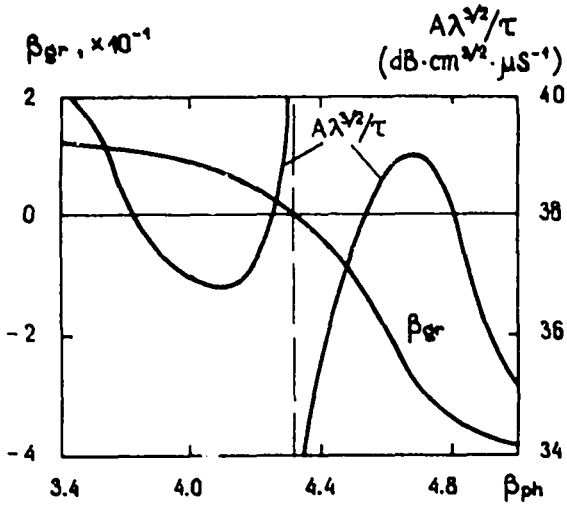

Fig.4. Normalized damping and group velocity as a function of phase velocity for H_{01} mode.

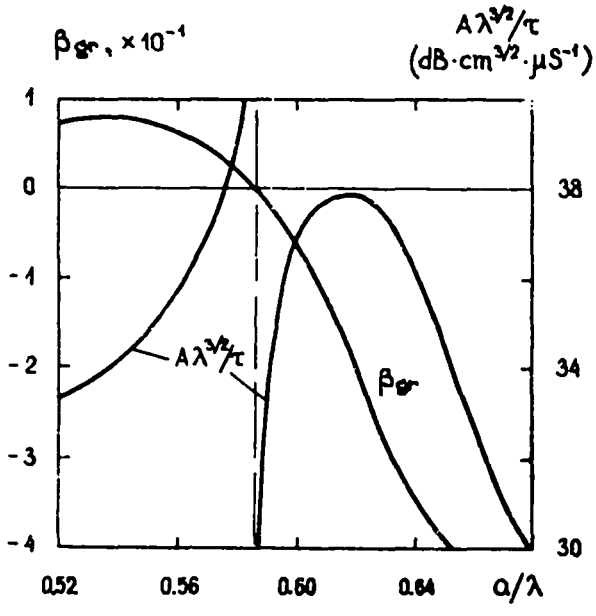

Fig.5. The plots of normalized damping and group velocity against parameter a/λ for H_{01} mode.

right side from this point (see fig. 4 and fig. 5) damping is tended to zero. A small enough values of normolized damping and group velocity both can be achieved in this region. For example when a/λ = 0.585 (β_{ph} = 4.4) we are having β_{gr} = 0.0182 and $A\lambda^{3/2}/\tau \simeq 2\cdot 10^{-2}$ $dB\cdot cm^{3/2}\cdot \mu s^{-1}$. Delay line energy losses would be about 0.7 dB/ at 10 - cm wavelength band and about 7.5 dB/μs at 2 - cm band. So in this case a compact time delay line with 1 dB energy losses and about 0.5 ..1.0 m long (it s depended on the t/λ parameter) can be constructed for 1.5 μs delay time at 10 - cm wavelength band.

However it's impotant to note that given calculated results dont take account of the CIW inner surface conditions (surface treatment clearniess, impurities ets.). Real values of energy losses are about 10 % to 70 % higher.

The results obtained show that the time delay line for RF - energy storage can be constructed based on CIW with H_{01} modes. An acceptable values of energy losses and line dimensions can be obtained for wavelength bands from 10 - cm to 2 - cm. The lines parameters can be determined by the method described.

References

1. P.B.Wilson, " Linear Accelerator for TeV Colliders ". SLAC-PUB-3674, May 1985.
2. A.S.Ilinsky, G.Ya.Slepyan, " Kolebaniya i volni v electrodinamicheskich systemach s poteryami ", M.: Isd. MGU, 1983 (Russian).
3. E.L.Burshtein, G.V.Voskresenskiy, " Lineynie uskoriteli electronov s intensivnimy pachkami ", M.: Atomisdat, 1977 (Russian).

ORBIT CORRECTION TECHNIQUES FOR A MULTIPASS LINAC*

A. Barry, B. Bowling, J. Kewisch, and J. Tang
Continuous Electron Beam Accelerator Facility
12000 Jefferson Avenue, Newport News, VA 23606

Abstract

The CEBAF accelerator includes a linac section which accelerates multiple beams with different energies. Problems arise when performing orbit correction, due to the fact that correction of higher energy passes disturb lower energy trajectories. Therefore, a perfect orbit correction cannot be obtained for all energy beams at the same time.

We present methods and performance (using simulation results) for performing orbit corrections in such a system. Limitations to the correction methods are also addressed.

Introduction

The electron beam in the CEBAF accelerator is recirculated five times in order to make the most efficient use of the accelerating structure in the linac. Therefore, the orbit correction in the linacs is distinguished from other existing high energy linear accelerators by the fact that five beams, each with different energies, travel at the same time through the linac.

The linacs are equipped with beam position monitors, which have the ability to differentiate between the five beams, and correction dipoles adjacent to each quadrupole. The orbit correction of the lowest energy beam can therefore be done simply by making the beam offset in each monitor zero, using the correctors attached to the previous quadrupole. However, these corrector settings are not necessarily the optimum settings for the higher energy passes. Therefore, a perfect orbit correction cannot be obtained simultaneously for all beams.

Most of the orbit distortions are caused by misplacement of quadrupoles ($\sigma = 0.2$ mm) and misalignment (pitch and yaw) of the linac cavities ($\sigma = 2$ mrad). Other smaller contributions come from steering due to the asymmetric RF feeds and residual magnetic fields of the earth's magnetic field. In addition to these active distortions, we assume that the beam position monitors have an accuracy of 0.1 mm and a misplacement relative to the quadrupole of 0.2 mm.

All orbit correction schemes predict the effect of a corrector kick at one point on the beam position in a monitor at a second point from the strength of the quadrupoles between the two points. In our simulation we assumed a strength error of $\frac{\Delta k}{k} = 10^{-3}$ for all quadrupoles.

All correction procedures described in this paper have been simulated using the computer code PETROS.[1]

* This work was supported by the U.S. Department of Energy under contract DE-AC05-84ER40150.

First Pass Correction

The idea of the first pass correction is very simple: Since the simulated linac design uses an alternating beam position monitor and corrector pattern, we compute the upstream corrector value required to make a downstream monitor reading zero. The kick $\Delta x'_k$ needed in the correction coil is calculated from the beta functions and phase advance:

$$\Delta x'_k = -\frac{\Delta x_m}{\sqrt{\beta_k \beta_m}\,\sin(\phi_m - \phi_k)\sqrt{\frac{p_k}{p_m}}} \qquad (1)$$

In this expression, p_k and p_m are the momenta of the electron beams in the corrector and the monitor, respectively. This factor must be included due to the energy gain in the cavities. For the same reason the beta functions have to be calculated according to reference 2. Figure 1 shows the corrected low energy beam together with the higher energy passes.

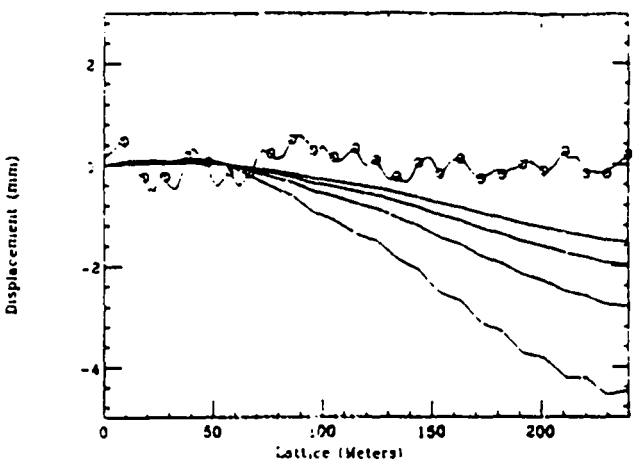

Figure 1. Low energy corrected orbit with higher energy passes.

Correction of the Higher Passes

Further correction of the higher passes through the use of correction coils is limited because any change applied to a corrector will disturb the low energy beam. The following methods can be implemented for the correction of the higher energies: (1) Optimization of injection angle and displacement, (2) the use of beam bumps in the low energy line, which act as a kick for the higher energies, (3) a combination of the above methods, (4) a least-squares fit to 26 variables (26 corrector dipoles with 26 monitor readings), and (5) 36 variables (26 correctors and 10 initial conditions).

Optimisation of the Initial Beam Coordinates

The first correction step for the higher passes is the optimisation of the angle and displacement for the injection of the beams into the linac. This is done with two correction coils immediately preceding the linac. While any displacement within the aperture can be produced in theory with these coils, the injection angle is limited by the beam pipe aperture. Figure 2 is the result of this correction.

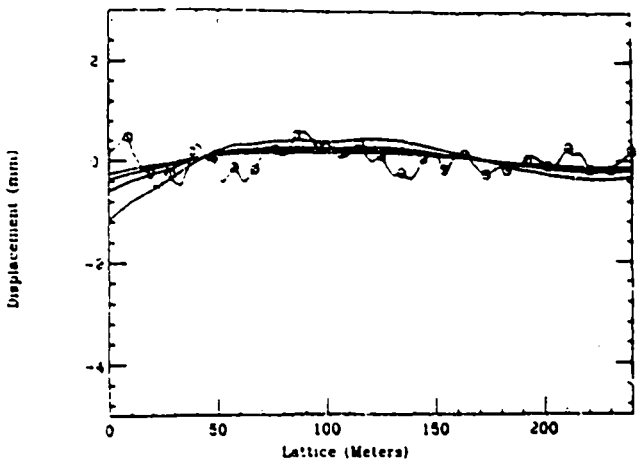

Figure 2. Optimization of injection parameters.

Correction Using Beam Bumps

The idea of this correction method is to produce a beam bump in the lowest energy beam in order to produce a deflection of the higher energies that propagate down the linac. This has the effect of improving higher passes by sacrificing the orbit in a limited region of the lowest pass. With a bump of 2.5 mm in the low energy beam, this method corrects the higher passes as effectively as the previous method.

Least-Squares Fit Method

This method determines values for all of the correctors simultaneously in an attempt to find the optimum orbits for all of the energy lines. The method is equivalent to applying simultaneously all possible beam bumps. The result is better than the single beam bump method and also avoids the large excursion in the first energy line.

Combination of Methods

The combination of the beam bump method with simultaneous adjustment of the initial conditions gave a larger displacement of the first beam than in the case of the beam bump only.

The extension of the matrix method to include the initial conditions for each energy line in this method failed due to an ill-conditioned matrix. The failure with both attempts to combine correction methods indicates that this concept of method integration has inherent difficulties.

We have seen previously that each of the methods by themselves is comparably effective. When used in combination, however, the methods tend to work against each other, resulting in a small improvement in orbit. The other correction schemes are therefore preferred.

Systematic Misalignment Errors

Systematic misalignment errors arise from the lower accuracy in measuring larger distances. We have simulated this case and have assumed a maximum sagitta of 5 mm. The orbits after correction of the initial conditions are shown in Figure 3 for two fiducials.

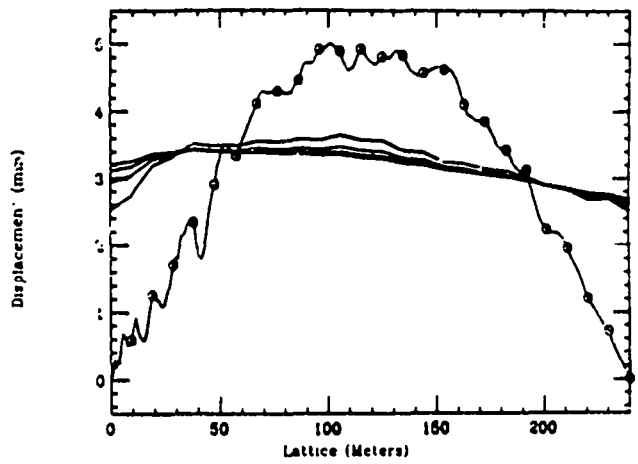

Figure 3. Systematic error with two fiducials.

We see that the highest energy beam is a "straight" line within 0.4 mm. The high energy beam can therefore be used in both linacs to establish a reference line for the alignment of the linac. From the viewpoint of the beam position monitors, the high energy beam oscillates around the center of the quadrupoles. A good rule of thumb is that we can expect deviations of the high energy beams from the center of the quadrupoles of approximately half the linac sagitta.

Limitations

Three effects which provide an influence on the performance of the preceding orbit correction methods were investigated: (1) Changes in linac lattice lengths, (2) cavity operating gradient, and (3) betatron phase advance.

The above simulation results were obtained using a model of the CEBAF lattice. This linac has a designed length of 240 meters. In the future, it may be desirable to construct recirculating accelerating linacs of longer physical lengths. Therefore, to further test the abilities of the correction methods, a simulated linac was created with a length of 960 meters, 4 times the length of the CEBAF unit. The maximum orbit excursion exhibited when apply-

ing beam entrance corrections is approximately the same as for the shorter linac. From this result it is apparent that longer accelerating sections are correctable using this method.

Cavity gradient clearly plays a role in the correction methods. Using the long linac model, cavity gradients were varied, and the maximum orbit deviations were noted. Figure 4 is a plot of these deviations as a function of gradient. From this, the predictable result is that the correction method is more effective for higher cavity gradients.

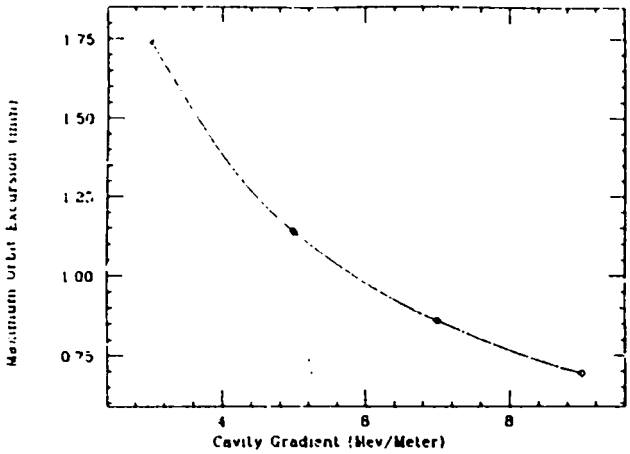

Figure 4. Cavity gradient effects on orbit deviations.

A similar analysis was done for betatron phase advance (Figure 5). Here we see a small trend in orbit deviation with increasing phase advance. This effect is due mainly to the effect of quadrupole influences discussed earlier.

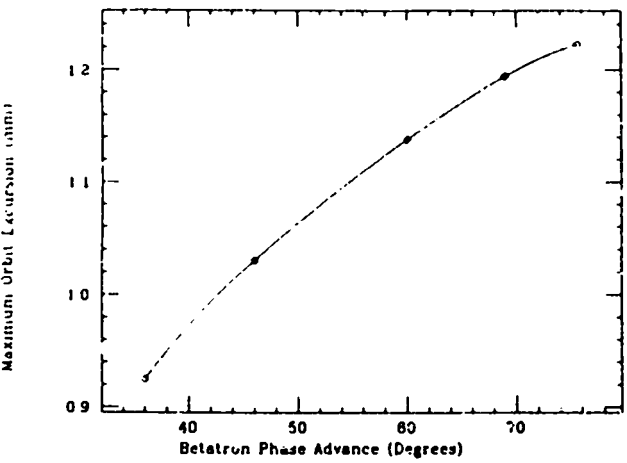

Figure 5. Betatron phase advance effects on orbit deviations.

References

1. K. Steffen, J. Kewisch: *Study of Integer Difference Resonance in Distorted PETRA Optics*, DESY Internal Report (1976).
2. D. Douglas, J. Kewisch, R. York: *Betatron Function Parameterization of Beam Optics Including Acceleration*, CEBAF-PR-89-001, Proc. 1988 Linac Conference.

Accelerator Deflection-Mode Dampening Experiments at Argonne

E. Chojnacki, W. Gai, C. Ho, R. Konecny, S. Mtingwa,
J. Norem, M. Rosing, P. Schoessow, and J. Simpson

Argonne National Laboratory, Argonne, IL, 60439, USA

Introduction

As the dimensions of accelerating structures become smaller and beam intensities higher, the non-axisymmetric wake fields driven by the beam become quite large even with slight misalignments of the beam from the geometrical axis. These deflection modes then cause bunch-to-bunch beam breakup and intra-bunch head-tail instabilities. An rf slow-wave structure that has very low Q for the deflection modes while maintaining a high Q for the accelerating modes would then be desirable since the unwanted modes can be selectively damped.[1] Such a device utilizing dielectric-lined waveguide is shown in Fig. 1 where the uniform outer conductor is replaced by axial, closely spaced, insulated wires which allow only axial wall currents to flow at that boundary. This dielectric-based configuration is of specific interest to the Čerenkov wake-field accelerator program under development at Argonne.[2] A configuration consistent with traditional iris-loaded waveguide is shown in Fig. 2 where the outer conductor is segmented to allow only axial currents and the irises are segmented to allow only radial currents. Severe enough damping in either configuration to eliminate the head-tail instability could be difficult to obtain depending on the bunch length considered, but strong enough damping to combat bunch-to-bunch beam breakup using these schemes appears quite feasible. Presented here will be experimental results of the dielectric-lined waveguide case.

Mode Considerations

The desired accelerating modes in slow-wave structures are TM_{01} in nature, consisting of many axial harmonics in iris-loaded waveguide or consisting of one pure mode in dielectric-lined waveguide. These axisymmetric TM_{0n} modes exert negligible deflecting force on a relativistic particle, the force having amplitude proportional to $1/\gamma^2$, where γ is the relativistic mass factor of the particle. Deflection modes are non-axisymmetric hybrids containing both axial electric and magnetic fields. The hybrid modes are labeled HEM_{mn} where m refers to the azimuthal harmonic and n is an ordering index not necessarily referring to radial harmonics. At cutoff, the dispersion relation for these hybrids degenerates to the conventional TM_{mn} and TE_{mn} waveguide modes, although the field amplitudes for TE modes are identically zero at cutoff. Of interest here, deflection modes for dielectric-lined waveguide, are the HEM_{11}, HEM_{21}, and HEM_{12} modes which correspond to the TE_{11}, TE_{21}, and TM_{11} modes at cutoff, respectively.

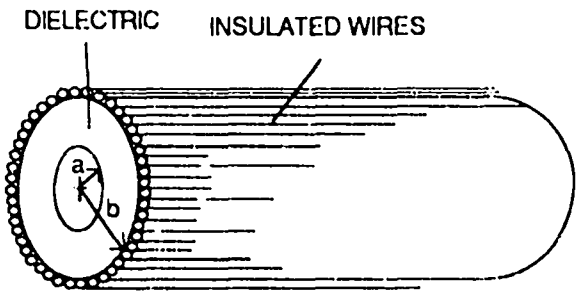

Figure 1: Dielectric-lined waveguide with segmented outer conductor.

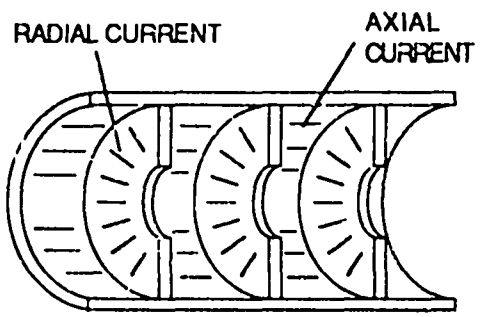

Figure 2: Iris-loaded waveguide with segmented outer conductor and segmented irises.

The rf field components of TM_{0n} modes are E_r, B_θ, and E_z. The surface currents on an outer conducting boundary necessary to support these modes are strictly axial and surface currents on irises, if any, are strictly radial. The segmented conductors on the waveguides shown in Figs. 1 and 2 will then contain these modes unperturbed, just as though the conductors were uniform.

The non-axisymmetric deflection modes, however, are comprised of all six cylindrical field components and will require azimuthal surface currents on various regions of the conductors in addition to axial and radial surface currents. If the conductors are segmented to allow only axial surface currents, the deflection modes will not be confined and will radiate beyond the outer wall, establishing a surface wave or trapped mode within a subsequent uniformly conducting boundary (vacuum vessel). This outer region can then be filled with rf absorbing material and the deflecting modes will be severely attenuated.

Bench Measurements

All bench measurements and direct wake-field measurements were performed on dielectric-lined waveguide with

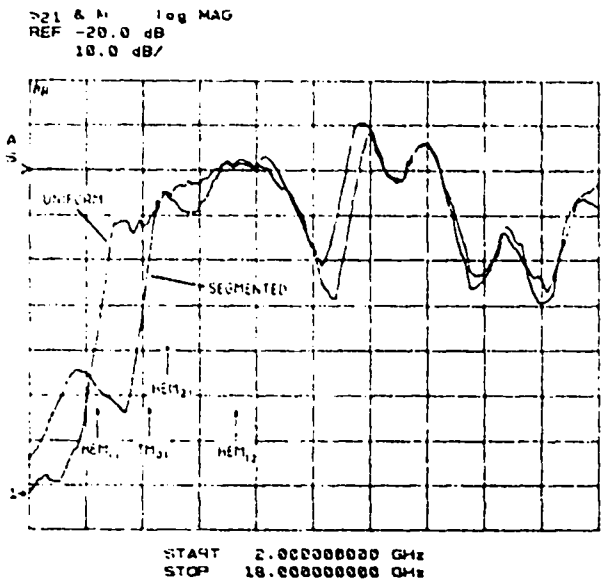

Figure 3: Network analyzer transmission measurements of dielectric-lined waveguide with and without segmented outer conductor.

dimensions $a = 1.270$ cm, $b = 1.905$ cm, and relative permittivity $\epsilon_r = 2.55$. The modes and frequencies of interest are listed in Table I. As illustrated in Fig. 1, the segmented outer conductor consisted of 173 epoxy-insulated #21 copper magnet wires strung axially in intimate contact. The parameter measured with the network analyzer was transmission coefficient S_{21} using small coupling loops at each end of a 17 cm long sample waveguide. Shown in Fig. 3 are S_{21} measurements as a function of frequency for the two cases of dielectric-lined waveguide with uniform outer conductor and with segmented outer conductor wrapped with rf absorber. The measurements should be viewed relative to each other due to coupling probe mismatches. Various mode cutoffs are indicated on the figure and the attenuation of the HEM_{11} mode is obvious. The attenuation of the HEM_{21} and HEM_{12} modes is obscured, however, by the propagation of the TM_{01} mode above cutoff.

Table I. Mode cutoffs and frequencies synchronous with a 20 MeV electron for dielectric-lined waveguide having $a = 1.27$ cm, $b = 1.905$ cm, and $\epsilon_r = 2.55$.

Mode	Cutoff (GHz)	Synchronous (GHz)
HEM_{11}	3.96	6.76
TM_{01}	5.44	7.64
HEM_{21}	5.85	8.40
HEM_{12}	7.82	12.18

From the measurements shown in Fig. 3, which again, are relative to probe coupling mismatches, the damped HEM_{11} mode has an additional attenuation of $\alpha_{dB} \sim 235$ dB/m above that of normal resistive wall losses. Ignoring resistive wall losses, the attenuation e-folding time and cavity Q for this mode can then be found from

$$\tau = \frac{1}{\alpha_t} = \frac{8.686}{\alpha_{dB}\, v_g} \quad \text{and} \qquad (1)$$

$$Q = \frac{\omega}{2\,\alpha_t\, v_g}, \qquad (2)$$

where α_t is the attenuation in units of [nepers/sec], α_{dB} is the attenuation in units of [dB/m], v_g is the group velocity of the particular mode, 8.686 is a dB-neper conversion factor, and ω is the angular frequency of the mode. For all of the modes in question, $v_g \sim c/2$ to within 10%, thus for the HEM_{11} mode $\tau \sim 246$ ps and $Q \sim 5.2$.

Direct Wake-Field Measurements

Direct measurements of beam induced wake fields in the above described dielectric-lined waveguide were performed at the Advanced Accelerator Test Facility (AATF) at Argonne.[3] In this facility a 20 MeV, 30 ps, 5 nC drive bunch excites wake fields in any test structure and the fields are then sampled by a much less intense 15 MeV witness bunch which has a variable-delay behind the drive bunch. The wake fields are quantified by viewing the witness in an energy spectrometer.

The two dielectric-lined waveguide structures tested had parameters as listed in Table 1 and were 52 cm in length. One had a uniform aluminum outer conductor while the other had the segmented conductor described previously. Shown in Fig. 4 are the measured *longitudinal* wake functions for the two structures normalized to 1 m of axial length and 1 nC of drive charge. The enhanced wake amplitude during the first cycle, $\lesssim 120$ ps, is due to several higher order TM_{0n} modes being nearly in phase at that time. The slow, linear decrease of longitudinal wake thereafter is due to rf power exiting the interaction region at the mode's group velocity. Shown in Fig. 5 are the Fourier transforms of the longitudinal wakes and the principle mode seen for both structures is the TM_{01}, agreeing with the calculated frequency of 7.64 GHz. Within measurement uncertainty there is negligible difference between the two structures in longitudinal wake amplitude or frequency.

The deflection modes have field amplitudes proportional to $I_m(\omega\, r_0/c\beta\gamma)$, where I_m is the modified Bessel function, ω is the mode's angular frequency, r_0 is the drive bunch radial coordinate, c is the speed of light, $\beta\gamma$ are normalized velocity and relativistic mass factor associated with the wave phase velocity, and $m \geq 1$ is the mode's azimuthal harmonic. In the limit of phase velocity approaching the speed of light, the argument of I_m approaches zero and the deflection modes then have field amplitudes proportional to r_0^m. The fields seen by the witness, however, have functional dependence on witness radial position given by r^{m-1}. The deflecting force on the witness bunch is then proportional to $r_0^m\, r^{m-1}$ and for dipole modes ($m = 1$) this is simply linearly proportional to the drive bunch radial position. Thus, the transverse wake function for the dominant deflection mode (dipole) can be determined by measuring the transverse deflection of the witness for several drive bunch radial positions, checking for

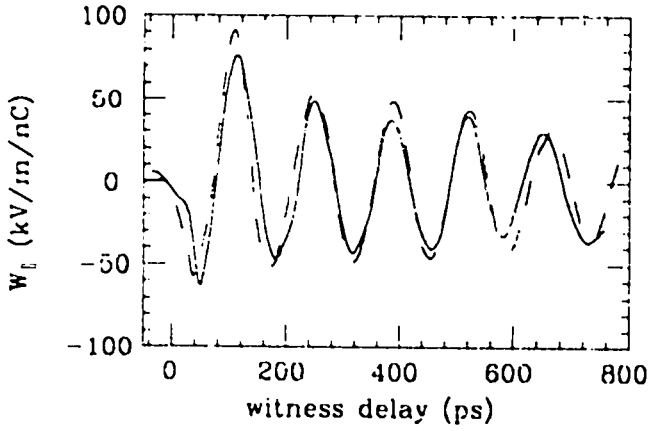

Figure 4: Measured longitudinal wake functions for segmented (dashed) and uniform (solid) outer conductor.

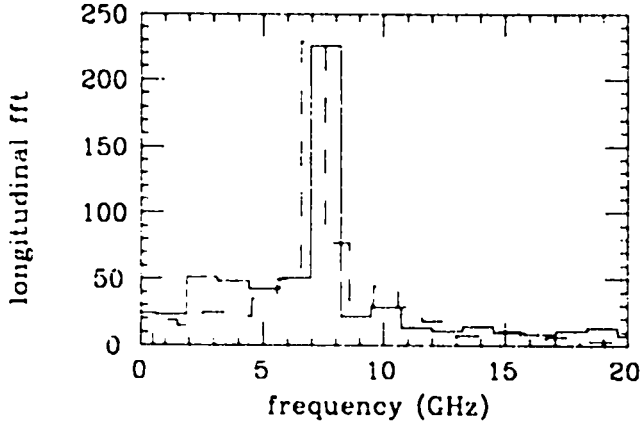

Figure 5: Fourier transforms of longitudinal wake functions shown in Fig. 4.

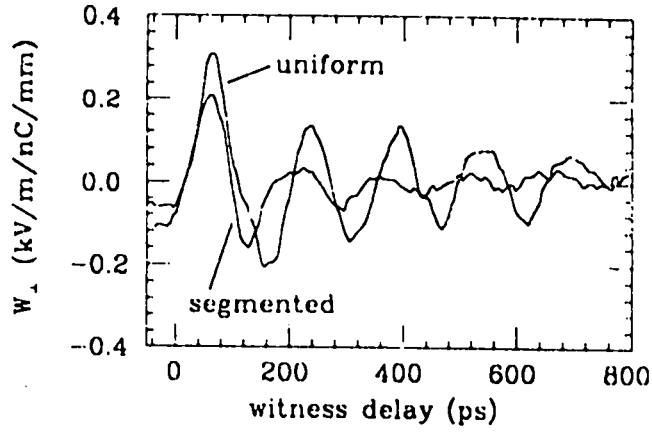

Figure 6: Measured transverse wake functions for segmented and uniform outer conductor.

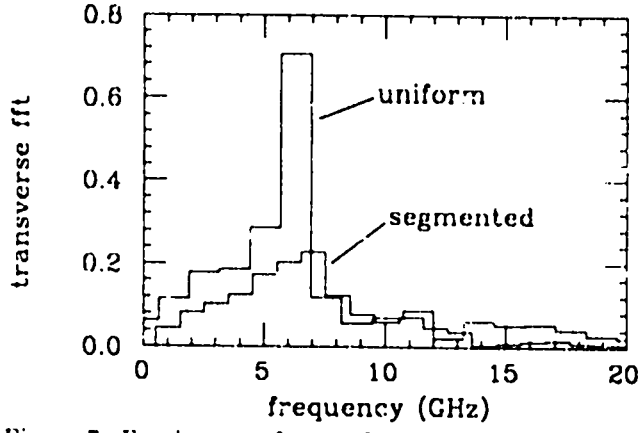

Figure 7: Fourier transforms of transverse wake functions shown in Fig. 6.

linearity, and then normalizing to 1 m of axial length, 1 nC of drive charge, and 1 mm of drive bunch radial offset. In Fig. 6 are then shown these normalized *transverse* wake functions for the two Čerenkov wake-field structures with the Fourier transforms shown in Fig. 7. The principle mode in Fig. 7 for the uniform outer conductor is the HEM_{11}, agreeing with the calculated frequency of 6.76 GHz. For the segmented outer conductor, however, the frequency composition is broad band due to the strong attenuation seen in Fig. 6. The attenuation is consistent with the 246 ps e-folding time bench measurement. This demonstration of strong deflection-mode damping thus indicates that bunch-to-bunch beam breakup instabilities can be greatly reduced in Čerenkov wake-field accelerating configurations via use of segmented conducting boundaries followed by rf absorber.

Discussion

We have demonstrated a technique for attenuating deflection-mode wake fields in dielectric slow wave structures using appropriately segmented conductors and rf absorber. The accelerating modes were negligibly affected within resolution of the measurements. A test that remains to be performed is that of voltage standoff between the segmented conductors due to E_θ fields which are continuous there rather than zero. This test will require smaller waveguide dimensions and the much more intense beam that will be available from the Argonne Wake-field Accelerator linac.[2] The dielectric-lined waveguide should not be susceptible to such rf break down since the conductor is at a large radius, low field density location. The iris-loaded guide will be most vulnerable at the inner edge of the aperture but this can be cured by not segmenting the iris until larger radial positions.

This work supported by the U. S. Department of Energy, Division of High Energy Physics.

References

[1] R.B. Palmer, DPF Summer Study: Snowmass 1988, Colorado; SLAC-PUB-4542.

[2] P. Schoessow, E. Chojnacki, W. Gai, C. Ho, R. Konecny, S. Mtingwa, J. Norem, M. Rosing and J. Simpson, Proc. 1990 EPAC Conf., Nice, France (June 11-15, 1990).

[3] H. Figueroa, W. Gai, R. Konecny, J. Norem, A. Ruggiero, P. Schoessow, and J. Simpson, Phys. Rev. Lett. 60, 2144 (1988).

SECONDARY ELECTRON METHODS FOR ION PHASE MOTION RESEARCH

A.M.Tron
Moscow Engineering Physics Institute, Kashirskoe shosse 31, 115409, Moscow, USSR

ABSTRACT

Methods for phase spectrum and longitudinal emittance research of ion beam are considered. They has been grounded upon a secondary electron detectors (IFS) which isochroniously transform a primary ion beam into secondary electron and then collect it in accordance with its particles phase relatively to RF chopper of detector. The IFS has small size along accelerating channel up to 10 cm and high phase resolution nearly 1 degree calculated according to bunch repetition frequency. The results of IFS testing under 100 MeV proton beam have been described. For meson facility linacs IFS with longitudinal modulation must be used.

INTRODUCTION

A problem of bunches' phase length measurement and beam boundary determination in longitudinal phase space in real accelerating and focusing channels of linacs is practically important for longitudinal phase space matching. Two methods of measurement are known recently. First one is based on elliptical phase boundary restoration by three bunches' lengths measurements. Second consists of phase spectrum detection for a number of momentum values and computor restoration of elliptical beam phase boundary. First method has been described in details in [1,2] and more generally for five parameter phase ellipse restoration in one of papers presented on this conference. In this paper second method is discussed.

PHASE-SPECTRUM DETECTOR REQUIREMENTS

A major device for experimental research of ion phase motion is a phase-spectrum detector (IFS). Applied to medium energy and high average current ion accelerators IFS have to satisfy a number of strong requirements.

For ion bunches with phase extent about 10° IFS phase resolution must be not more than 1°...2° according to pulse repetition freq. A detector's length along accelerator axis have to be not more than 20 cm, a beam perturbation by it must be small. IFS construction have to ensure its serviceability check without equipment disassembling in accelerating channel. Major IFS parameters are to be independent of ion energy what makes posssible its single type applying for entire accelerator.

According to Kotelnikov's theorem [3] phase resolution of 1...2 degree at .2 GHz corresponds to detector's bandwidth 36...48 GHz or time resolution of 14...28 ns.

RF secondary electron phase-spectrum detectors [4,5,6,7,8] most completely satisfy mentioned above requirements. In this devices secondary electrons transfer ion beam's phase spectrum from high to low energy domain.

One of the first detectors of this type was a device for secondary electrons outlet time dispersion measurement [4]. The dispersion is not more than 6 ps and it determines a limit on secondary electron methods of phase spectrum measurement.

DETECTOR OF PHASE SPECTRUM

IFS consists of primary converter (PC), RF chopper, collector of secondary electrons and corresponding hardware.

PC is used for isochronous transformation of primary beam into secondary electron and for electron beam focusing on RF chopper income, an axis of which is perpendicular to ion beam. PC must be installed within ion channel aperture to minimise an influence of primary and secondary beams' own fields upon IFS resolution. PC represents a target unit with threadlike focusing electrodes a plot of which is given in fig.1. Target sizes and mutual layout becomes clear from this figure. When a proton beam with an energy 100-600 MeV is analysed, potentials of target and A electrode are equal to U, while B electrodes are under .3·U.

Beam's finite transverse sizes in PC and electron initial velocity spread results in electron dephasing $\Delta\varphi_1, \Delta\varphi_2$ respectively. By choosing PC parameters for corresponding proton energy a value $\Delta\varphi_1$ may be reduced to negligibly small compared with $\Delta\varphi_2$. Dependences $\Delta\varphi_1(W_e)$, $\Delta\varphi_2(W_e)$ on electrons' energy W_e which are connected with target potential by $W_e=eU$ for given target configuration and 100 MeV proton energy are displayed in fig.2. According to this figure the isocronism breakdown in PC at W =4keV is less than 1° at .2 GHz.

Supplement error mainly originates from electron and ion bunches own fields. Dependences of secondary electron beam divergence $\Delta x'$ on PC outcome, its momentum spectrum width δ and electron dephasing $\Delta\varphi_q$ upon ion own field influence are displayed in figs 3,4. Proton beam parameters were: energy 100 MeV, diameter 5 mm, bunch phase length 10° at .2 GHz and pulsed current .05 A. PC parameters were: for fig.3-target potential U=-4kV, distance from target and ion beam axis to rf cavity wall is equal to 20 mm; for fig.4 distance x_1 from target to the wall was changing, other parameters were the same as for fig.3.

It has been shown that to obtain phase resolution in the range 1°...2° values δ, $\Delta x'$, $\Delta\varphi_q$ must be not more than 1%, .01 rad,

.5°...1° respectively. Then as it follows from figs 3,4 an equivalent target radius R_t must be not less than 2 mm and the target have to be in ion current density maximum.

Simulation of secondary-electron own fields' influence or their dephasing has shown that target voltage must be less than -4 kV, electron beam width -minimum and RF cavity capasitive gap has to be installed on longuide boundary. That's why a target as a thin 4 mm strip has been chosen, and cavity had transit hole of 1mm width.

RF CHOPPER OF IFS

Choppers of longitudinal [5,6] and transverse [4,7,8] types have been used. In first one electrons have been modulated on momentum component parallel to beam axis (with regard to their initial phase) are spatially separated by spectrometer. In second RF modulation perpendicular to beam axis is used and electrons are separated in free of fields interval.

Chopper operation must be indenendent of particles' position on its income. It can be more easely realised in longitudinal type of devices. For example by choosing a thoroidal cavity with a 5...6 mm gap one can ensure essential uniform RF field in electron transit 1...2 mm slot and in the same time suppres multipactoring in meter wavelength range.

Chopper's phase resolution may be defined as relation of electron momentum spread or their divergence on chopper's inlet to this values maximum gain on the outlet. Then as it follows from figs 3,4 bunches own fields influence on phase resolution will be minimum for longitudinal chopper.

A choice of this chopper type and this cavity position on longuide boundary provide IFS high resolution. It must be noted that one should never install capasitive gap in ion beam space because electrons are modulated by resulting field of generator and beam in this case.

In terms of matrix formalism one can easily determine choppers phase resolution under condition of spatial separation of two beams' outlet phase portraits depending from each other by inlet phase $\Delta\varphi_3$.

Dependences $\Delta\varphi_1, \Delta\varphi_2, \Delta\varphi_3$ and IFS space resolution $\Delta\varphi$ with an account of W_0 for two chopper cavity gap voltages 1 kV and 3 kV are displayed in fig 2. Dependence $\Delta\varphi_3(W_0)$ is given for next chopper parameters at twofold accelerator bunch repetition frequency for I-100 linac: 5.5 mm gap, angle and bending radius of magnetic spectrometer 180° and 90 mm respectively. In fig 5 the chopper phase resolution dependences on inlet phase φ_0 for 4 keV electrons were shown when moduling amplitude has been 1 kV (solid line) or 3 kV (broken line). Adduced dependences show that this choper ensures high resolution in wide range of inlet phases. Thus with an installation of multichannel secondary electron current collector on spectrometer outlet one can realise an IFS with phase spectrum detection time less than duration of current pulse. When U_1 =1kV a dependence $\Delta\varphi(W_0)$ has an optimum for U =4kV and it has been realised in IFS tested under I-100 beam.

MEASUREMENT OF PHASE-ENERGY DISTRIBUTION IN ION BUNCH

Ion phase-energy distribution in a bunch on linac outlet has been measured by two-slot method in longitudinal phase space. This distrbution represented a number of phase spectra obtained by means of IFS described above in the form of bar charts for beam particles momentum that have been picked out by magnetic spectrometer. Spectrometer's value of relative resolution by particles' momentum was equal to .0011 . To eliminate phase distribution measurement error of particles in a bunch as a result of coherent longitudinal oscillations a power of IFS has been phase-locked with an accelerated current second harmonic by feed of its detector (see fig.6) signal on IFS' RF amplifier input.

Steps of phase spectra sampling and spectrometer re-tuning in relative momentum units were equal to resp. 2.2° at 297 MHz and .0011 . Given intervals were taken as scale units in fig 7.

In longitudinal phase space φ, δ (δ = $\Delta p/p$) points of particles' equal density (see fig.7) are distinguished. They have been determined on .1 and .5 levels from maximum of phase-energy distributions for beam close-to-axis particles (points near curves 1,2) and particles at a distance .5 cm. This particles' situation have been determined by intersection of respecting level line with phase-spectra functions.

Phase trajectories were determined by least-square technique as ellipses an equation of which was taken

$$M \equiv A\varphi^2 + 2B\varphi\delta + C\delta^2 + 2D\varphi + 2E\delta + F = 0$$

where $A=\cos^2\alpha/R+R\sin^2\alpha$, $2B=\sin 2\alpha\,(R-1/R)$, $C=\sin^2\alpha/R+R\cos^2\alpha$.

Ratio R is a relation of ellipse's axii. As it is known from linear theory of synchrotron oscillations by measuring this ratio one can determine their frequency and average axial field.

It follows from an above consideration that software development for phase-energy spectra measurement produces new additional information on longitudinal phase motion parameters with a required high precision.

It must be mentioned in conclusion that by substituting spectrometer of this type in IFS on spectrometer with crossed electric and magnetic fields IFS' sizes along accelerating channel may be reduced up to 10 cm.

REFERENCES

1. P.Strehl, IEEE Trans. Nucl. Sci. ,NS-30 (1983),No 4,2198
2. Tron A.M.,Feschenko A.V., Voprosy atomnoy nauki i tehniki. Ser.Tehnika fisicheskogo experimenta. 1983, Vyp 3(15), 51
3. Gonorovsky I.S. Radiotehnicheskie tscepi i signaly.Moscow,Sovetskoe radio,1971
4. Ernst E.W.,Von Foerster H.,J. Appl. Phys.

Vol 26(1955),No 6, 781
5.Witkover R.L.,Nucl.Instrum.& Meth., V 137 (1976), 203
6.Tron A.M.,Feschenko A.V. Trudy 7 vsesouznogo soveschania po uskoritelyam zaryazhennyh tchastic. Dubna,1981,V 2,125
7.Tron A.M.,Metody raschota i experimentalnye issledovanyia sistem lineinyh uskoritelei. Moscow, Energoatomisdat,1987,35
8.Feschenko A.V. ,Ostroumov F.N. Proc. 1986 Linac Conf. (Stanford, June?-6,1986),323

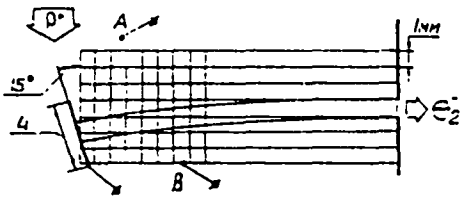

Fig.1 Plot of primary converter

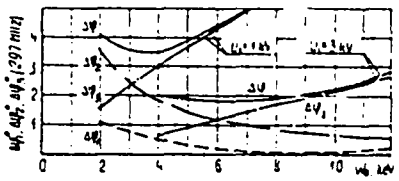

Fig.2 Dependences of chopper resolution $\Delta\varphi_3$, IFS resolution $\Delta\varphi$ and dephasing $\Delta\varphi_1$, $\Delta\varphi_2$, on electrons' energy W_0.

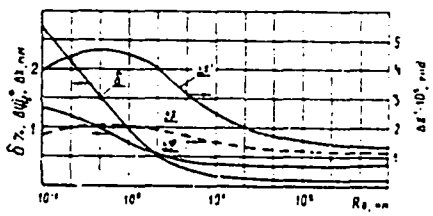

Fig.3 Values δ, $\Delta\varphi_3$, $\Delta x'$, Δx dependences on target equivalent radius R_0.

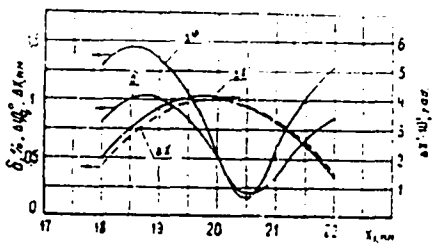

Fig.4 Values δ, $\Delta\varphi_3$, $\Delta x'$, Δx dependences on target position in relation to ion beam axix x_f.

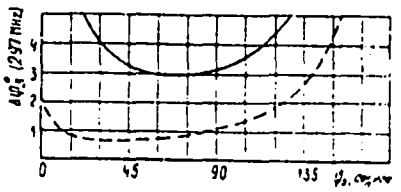

Fig.5 Chopper phase resolution on electrons inlet phase ω_2. Upper curve for gap voltage 1kV, lower 3kV.

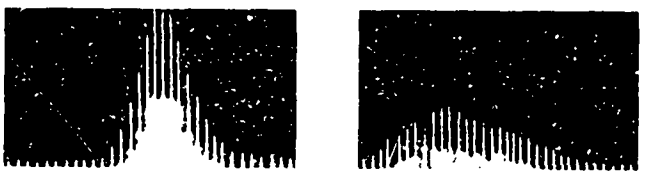

Fig.6 Proton beam's phase spectra under IFS syncronization with current second harmonic and linac's RF field. Device for compensating field decrease due beam loading is switched off.

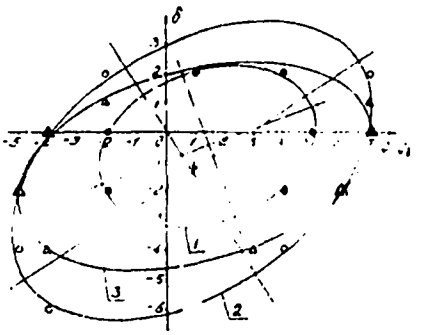

Fig.7 Equal phase density lines for 100 MeV proton beam on the I-100 linac outlet.

GENERATION OF A RECTANGULAR BEAM DISTRIBUTION FOR IRRADIATION OF THE ACCELERATOR PRODUCTION OF TRITIUM TARGET*

Barbara Blind
MS H811, Los Alamos National Laboratory, Los Alamos, NM 87545

Abstract

A scheme has been developed to produce, without beam scraping, a well-confined, rectangular beam-intensity distribution of greatly enhanced uniformity from an initially peaked intensity distribution such as a Gaussian or a parabolic distribution. This scheme employs a system of linear and nonlinear transport-line elements. The linear elements prepare the beam for the nonlinear focusing and govern the beam size at a downstream target. Uniformity is achieved with octupoles, and beam confinement is assured with duodecapoles. The scheme was applied to the target focus for the Accelerator Production of Tritium (APT) system. An initially Gaussian-distributed beam of 1.6-GeV protons was shaped into a rectangular 4-m by 2-m beam spot of acceptably uniform intensity at the tritium-production target. The scheme eliminates the need for sweeping the beam in a raster pattern to produce uniform target illumination. Details of the scheme are discussed.

Introduction

Uniform target illumination, either static or in a time-average sense, prevents target damage and optimizes target efficiency in high-intensity accelerator systems such as the APT system.[1] In this system, tritium production is achieved by interaction of energetic protons with a target composed of Pb pins and Li-Al pins. Neutrons are produced by spallation in the lead and interact with the lithium to produce tritium. The APT beam, with 250 mA of 1.6-GeV protons, has 400 MW of beam power. The maximum power density allowed in the production target is 100 W/cm^2. This dictates a beam at the target of approximately uniform intensity covering an area of 8 m^2. The desired beam footprint is a rectangle 4-m wide by 2-m high. Due to the high beam intensity, no significant fraction of the beam can be tolerated on the structural materials outside the target area, nor can the beam fringes be scraped.

Uniform target illumination in a time-average sense is achieved with sweep magnets, while static beam redistribution is accomplished with a beamline containing a combination of linear and nonlinear transport-line elements, henceforth called a beam expander.[2,3] For the APT geometry, a two-dimensional raster scan requires sweep magnets with unfeasible specifications for power and size. An alternative approach, a ribbon beam of uniform intensity swept across the target in the direction orthogonal to the ribbon, requires a sweep magnet with achievable performance specifications, but with a peak reactive power of [illegible] MW. No sweep magnets are needed to run the two-dimensional beam expander.

Beam-Redistribution Method

The method for producing a ribbon beam is explained in detail elsewhere.[4] With an octupole one can affect the beam phase-space area in one transverse plane in such a way that, during subsequent transport, the beam fringes are folded into the core of the beam and the originally peaked projections of the beam-intensity distribution, in that plane, are transformed into projections of greatly enhanced uniformity. With the proper focus the other transverse plane is not affected and the projections of the distribution in that transverse plane remain peaked.

The method can be applied to both transverse planes. With the appropriate linear transport, this results in a folded horizontal and a folded vertical beam phase-space area at the target. Now the projections in all transverse coordinates, and in particular the x and y projections, are relatively uniform and the contour lines of the x-y intensity distribution are rectangles.

An acceptable beam distribution at the target cannot be produced with a single octupole. Due to the x-y coupling caused by the octupole, such attempts result in beams with distorted contour lines that display big lobes in the corners of the distributions, as illustrated in Fig. 1 for a Gaussian input distribution. Here, as for all figures of this type, an input distribution containing 10^5 particles was transported through the beam expander using the beam-transport code PATH,[5] and the resulting distribution was characterized by its x and y projections and by its 10%, 50%, and 90% contour lines.

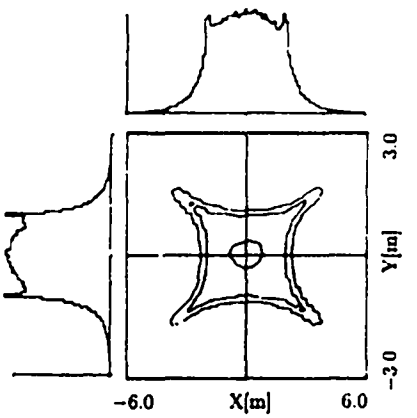

Fig. 1. Beam-intensity distribution obtained from a Gaussian input beam and a beam expander with a single octupole.

The following beam-expander components are needed to successfully produce a uniform rectangular beam distribution: a section to prepare the beam for the first octupole [illegible] horizontally and small vertically to manipulate the horizontal beam phase-space area without distorting the vertical beam phase-space area; a section to prepare the beam for the second octupole; a second octupole, where the beam is large vertically and small horizontally to manipulate the vertical beam phase-space area without further distorting the horizontal beam phase-space area; and a section to prepare the beam for the target.

The simplest beam expander for producing an acceptable beam distribution consists of two octupoles separated by a drift. Depending on the desired beam footprint at the target, more magnetic elements may be required. Adding a quadrupole between the two octupoles serves, at the second octupole, both to decrease the beam size in the transverse plane manipulated by

*Work supported by the US Department of Energy, with Los Alamos National Laboratory Program Development funds.

the first octupole and to increase the beam size in the transverse plane manipulated by the second octupole. Adding a quadrupole after the octupoles serves to reduce the length of the final drift. Care must be taken when placing quadrupoles. Depending on position and polarity, a quadrupole will enhance, negate, or not affect beam folding.

APT Beam Expander

Table I lists the elements of the APT beam expander, designed to produce a sufficiently uniform rectangular beam with the required 4-m by 2-m footprint. This beam expander represents one of many possible combinations of magnetic elements and drifts to achieve this goal. The pole-tip fields of all magnets are kept at or below 1.5 T, and the drifts are kept short. The design is not unique and further optimization is desirable before building the system.

TABLE I

APT beam expander to produce a uniform rectangular beam with a 4-m by 2-m footprint. The drift lengths between elements, and the element effective lengths, bore radii, and pole-tip fields are given.

type of element	length (m)	r_o (m)	B_p (T)
first octupole	0.50	0.020	0.768
drift	6.50		
focusing quadrupole	0.50	0.100	0.712
drift	2.19		
second octupole	1.00	0.134	0.914
drift	15.50		
defocusing quadrupole	2.00	0.356	1.499
drift	10.50		

The first octupole in the line manipulates the horizontal beam phase-space area. Once the beam is folded, the focusing quadrupole decreases the horizontal beam size and increases the vertical beam size at the second octupole while not affecting beam folding. The second octupole manipulates the vertical beam phase-space area. The defocusing quadrupole achieves the large footprint at the target, a very short distance away.

For the high-intensity APT beam, magnets with large apertures are desirable to avoid beam scraping. The magnets also must provide the fields dictated by the beam-transport calculations, and these fields are strong because the beam rigidity is large. It is thus impossible to dimension nonlinear beamline elements to have a substantial effect on the beam in the significantly populated beam fringes and not scrape the insignificantly populated far fringes of the beam. The APT beam expander was designed to clear 7σ (where σ is the rms beam size) of a Gaussian-distributed input beam. The radii given in Table I are those necessary to accept this beam.

Beam Distributions at the Target

The dimensions of the beam footprint at the target are fixed by the beam-expander configuration and the input-beam rms sizes and divergences, but the beam distribution at the target depends on the input beam distribution. For each input beam distribution there is a different nominal input beam, resulting in an acceptable beam distribution at the target.

Non-nominal input beams can result in unacceptable beam distributions. Non-nominal input beams caused by failures of accelerator quadrupoles or accelerator rf modules result in non-nominal but acceptable beam distributions. Varying the strengths of the beam-expander octupoles changes the beam distributions at the target as discussed below.

Nominal Beam Distributions

A Gaussian beam distribution provides the most realistic simple model for the distribution from the Coupled-Cavity Linac (CCL) planned for APT. A parabolic distribution, although often considered in beam-transport calculations, is not a good model for the CCL output beam. With an initially parabolic distribution one can achieve essentially uniform beams, while with an initially Gaussian distribution one cannot. Figures 2 and 3 show the beam distributions at the target for the nominal Gaussian and the nominal parabolic input beam, respectively.

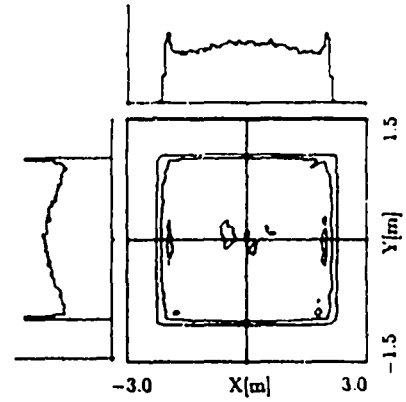

Fig. 2. Beam-intensity distribution at the target obtained from the APT beam expander and the nominal Gaussian input beam.

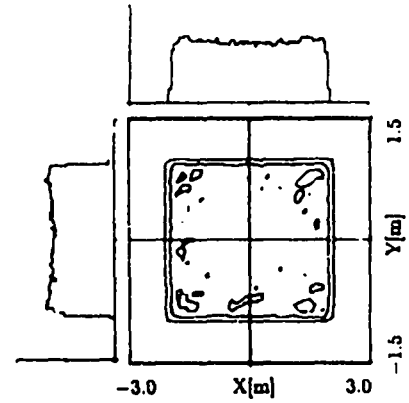

Fig. 3. Beam-intensity distribution at the target obtained from the APT beam expander and the nominal parabolic input beam.

Distribution Dependence on Octupole Strength

The dependence of the x projection of the beam-intensity distribution at the target on the strength of the first octupole in the APT beam expander is shown in Fig. 4, both for the nominal Gaussian and the nominal parabolic input beam. Only half of each symmetric projection is shown. Very weak octupoles influence only the far fringes of the beam, resulting in a beam that is similar to the input beam except for the tails of the distribution. Excessively strong octupoles fold the beam near the core, producing a beam with large spikes at the distribution edges.

Acceptable Non-Nominal Beam Distributions

Failure of an accelerator quadrupole causes a doubling of the transverse emittances of the CCL output beam. Instead of the nominal beam, a larger beam passes through the beam expander, and therefore the distribution at the target exhibits large spikes at the edges, characteristic of a beam subjected

to excessively strong octupoles. The footprint dimensions are unchanged, and the distribution remains acceptable. Increased beam loss in the beam expander occurs.

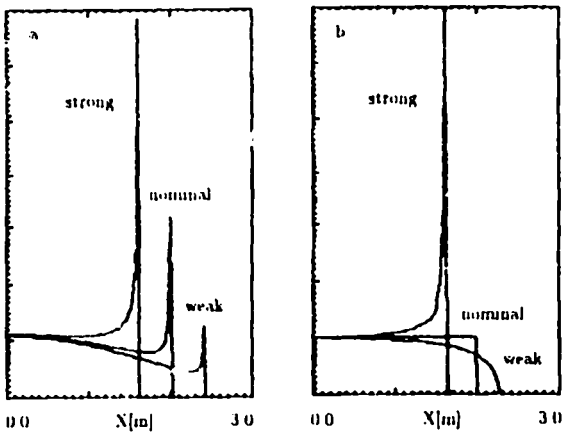

Fig. 4. Horizontal projection of the beam-intensity distribution obtained from the APT beam expander with a weak, nominal, and strong first octupole and (a) the nominal Gaussian and (b) the nominal parabolic input beam.

Failure of an rf module at or above 320 MeV causes a shift in the energy of the CCL output beam by up to ±10 MeV. The resulting non-nominal input beams yield different but acceptable target beam distributions and footprint dimensions.

Beam Jitter

For the APT beam expander, the rms beam sizes and divergences at the target are orders of magnitude larger than those at the exit of the CCL. Jitter of the beam centroid by one rms at the exit of the CCL would result in jitter by one rms at the target without octupoles and thus in only slightly less than one rms with octupoles, because these are dimensioned to have little effect on the core of the beam. Unless severe, jitter does not affect the footprint dimensions. On the other hand, jitter does have noticeable effects on the beam-intensity distribution.

Jitter control to 0.1 rms is feasible, and 0.1 rms of jitter can be tolerated for APT, as is illustrated in Fig. 5. For Fig. 2, a Gaussian-distributed input beam traversed the beam expander with its centroid on axis. For Fig. 5, the same beam traverses the beam expander with its centroid shifted by 0.1 rms. The previously symmetric contour lines and projections of the beam-intensity distribution at the target have become skew[illegible]

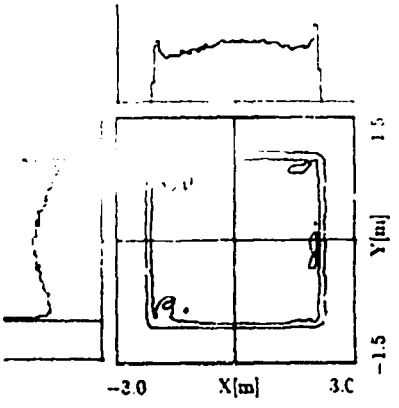

Fig. 5. Beam-intensity distribution at the target obtained from the APT beam expander and the nominal Gaussian input beam with a 0.1-rms centroid shift.

Beam-Fringe Control With Duodecapoles

Octupoles dimensioned to cause beam redistribution have the desired effect on the particles in the near beam fringes but an undesirably large effect on the particles in the far beam fringes. This results in intolerable beam loss downstream of the octupoles. Addition of appropriately dimensioned duodecapoles to the octupoles counteracts this effect.

The duodecapoles to be added to each of the two APT beam-expander octupoles are specified in Table II.

TABLE II

Duodecapoles to be added to the APT beam-expander octupoles for beam-fringe control.

type of element	length (m)	r_o (m)	B_p (T)
first duodecapole	0.50	0.020	0.538
second duodecapole	1.00	0.134	0.678

In Fig. 6 the beam footprint at the target of a Gaussian-distributed input beam populated to 7σ is shown for the APT beam expander without and with duodecapoles. Without duodecapoles, the far fringes of the original distribution have been folded into the core and actually protrude from the opposite distribution edges. With duodecapoles, the fringe particles to 7σ are totally contained in the core of the beam.

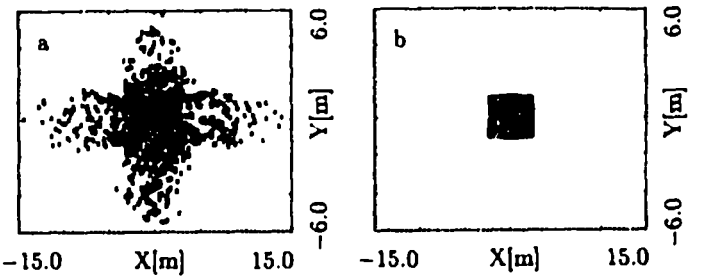

Fig. 6. Beam footprint obtained with the nominal Gaussian input beam populated to 7σ and the APT beam expander (a) without duodecapoles and (b) with duodecapoles.

References

1. G. P. Lawrence, "New Applications for High-Power Proton Linacs," to be publi[illegible] in *1990 Linear Accelerator Conference* [illegible]

[illegible] Beam," IEEE [illegible]

3. H. [illegible] Bailey [illegible] Kashy, and C. Leakeas, "Use of Multipole Magnetic Fields for Making Uniform Irradiations," Nucl. Instr. and Meth. B40/41, 1004 (1989).

4. A. J. Jason, B. Blind, and E. M. Svaton, "Uniform Ribbon-Beam Generation for Accelerator Production of Tritium," 1988 Linear Accelerator Conference Proceedings, CEBAF Report 89-001, 192 (1989).

5. J. A. Farrell, "PATH – A Lumped Element Beam Transport Simulation Program with Space Charge," Proc. of Berlin Conf. on Computing in Accel. Design and Operation, W. Busse and R. Zelany, Eds., Springer Verlag, Berlin, 267 (1984).

DIAGNOSTICS FOR THE 400 MEV FNAL LINAC

Elliott S. McCrory and Glenn Lee
Fermi National Accelerator Laboratory*, Batavia, IL 60510
Robert C. Webber
SSC Laboratory*, Dallas, TX 75237

Introduction

The last four 201 MHz alvarez tanks of the twenty-year-old, 200 MeV Fermilab Linac are being replaced by seven high-gradient (7 KV/m), high-frequency (805 MHz) side-coupled-cavity structures to produce a 400 MeV beam for injection into the Booster[1]. Good, reliable beam diagnostics are an important factor in the success of this project.

The commissioning and operation of the new linac present several interesting challenges which the beam diagnostics system will address.

✓ In order to increase the efficiency of the cavities (raising the shunt impedance), the aperture of the new linac is only 3 cm; the aperture of the old linac is 4 cm, so good beam steering will be very important.

✓ To increase the achievable gradient in the side-coupled linac, the fourth harmonic of the alvarez linac, 805 MHz, has been chosen as the resonant frequency. The smaller longitudinal phase-space will make matching into the new structure difficult. Therefore, measuring and understanding the longitudinal match between the two structures also will be very important.

✓ The space available for diagnostics is limited. There is only the four-meter transition section and $3\beta\lambda/2$ drifts between each accelerating section for the diagnostics. Therefore, the diagnostics elements must be small. (Terminology: sixteen side-coupled cavities are braised together to make a *section*, four sections are connected together to make a *module*, a module is powered by a klystron.)

✓ Our linac, as reliable as it is, has yielded precious little information about the nature of its beam, especially in its middle where injection to the new linac is to occur. Thus, many plans and designs for the new linac, the transition section in particular, rely on the existence of excellent diagnostics to identify and correct unexpected features of the beam revealed during commissioning.

✓And, finally, we will need to commission the new linac as quickly as possible, so it will be important to have reliable diagnostics as soon as commissioning begins.

Beam position/steering, wire scanners, a new-style bunch length monitor, beam loss monitors and special beam-phase pick-ups are being incorporated into the new linac. Figure 1 shows the mechanical layout of the inter-section regions for the first accelerating module, the tightest overall fit.

Diagnostics systems

Beam Position Monitors and Steering Correction

A quadrupole-stripline, non-intercepting beam position monitor (BPM) has been designed and prototyped, see Figure 2. The four plates each subtend 20°. The inside diameter of the monitor is 3.25 cm. The overall length is 4.0 cm; this small dimension is chosen as a compromise between minimum space and smaller signal from a shorter monitor.

Compact, picture-frame iron dipole magnets of the type used currently are to be used in the new linac. These magnets can be made quite short, and we plan to make them as short as 4 cm. A problem presently under investigation is if the proximity of these magnets to the quadrupole focusing magnets in each inter-section drift causes any problems.

Correcting the steering in the new linac is going to be easier than it has been in the old linac. The procedure for correcting the trajectory of the beam in the old linac has included the measurement of the beam trajectory followed by the physical realignment the drift tubes. This laborious process requires opening the linac tanks and, with a surveying crew present, moving the drift tubes. In the new linac, we plan to have two BPMs in every module, producing four position readings per 2π phase advance (79° per FODO cell), enough readings to accurately measure the steering and the betatron amplitude. In particular, we will put several BPMs and correction elements in the transition section to insure

*Operated by the Universities Research Association under contract with the U.S. Department of Energy.

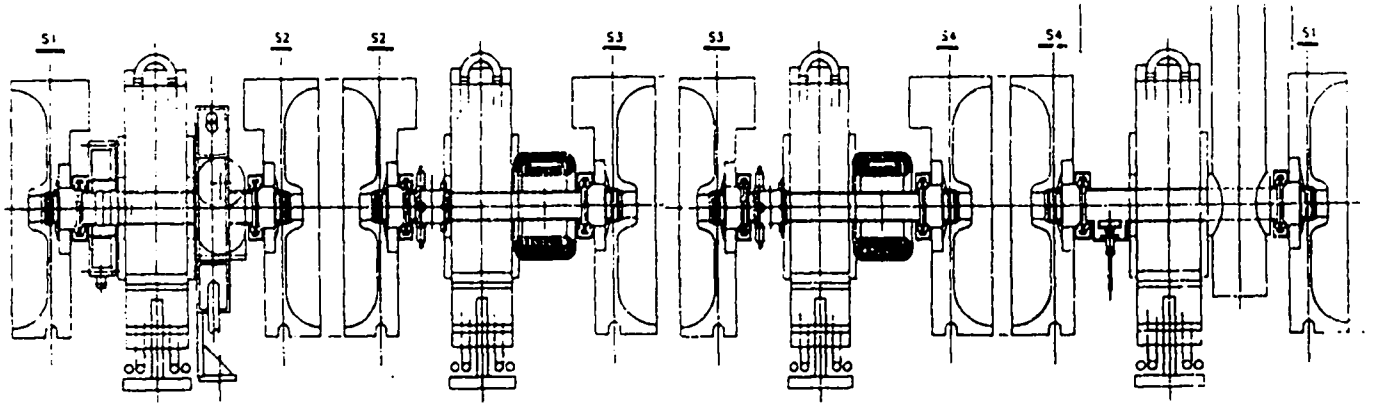

Figure 1. Mechanical layout of the beam diagnostics within the first accelerating module of the new 400 MeV Fermilab Linac.

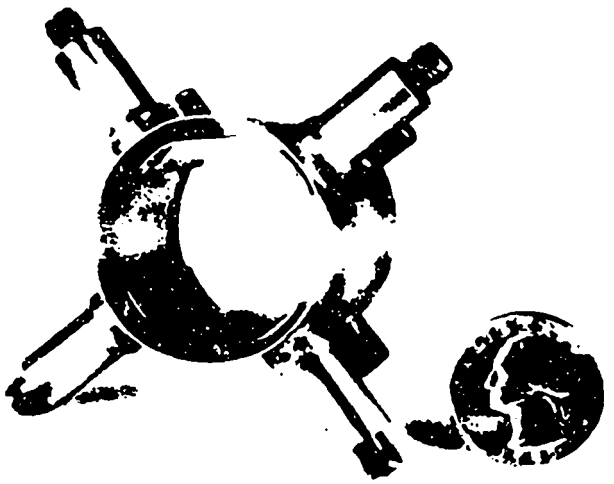

Figure 2. a Beam Position Monitor for the new 400 MeV Fermilab Linac

that the steering starts off right. Alignment of the four sections and four quadrupoles on a "strongback" will lead to alignment accuracies of better than 0.01 cm through the module; careful module-to-module alignment will produce alignment errors of about 0.025 cm. [2]. The steering correction needed for this level of alignment is 0.5 cm, 0.15 mrad maximum at the end of the linac. A deflection field of around 100 gauss-cm is needed to correct for this. 600 gauss on a 4 cm picture-frame magnet is not difficult.

The BPMs are read out by an RF module/decoder similar to the one presently in use [3]. The old design has been modified to increase the bandwidth to approximately 20 MHz (from 1 MHz).

A linac control system local control station [4] will run a local application program to actively correct the steering of the entire (new) linac on a pulse-by-pulse basis.

Wire Scanners

A new, compact two-plane wire scanner has been designed, see Figure 3. Its overall length is 6.5 cm; its length along the beam is 5 cm. Three wire scanners will be placed in the transition section and at the beginning and end of the new linac. They are to be located at a transverse waist so that the emittance in that vicinity can be measured.

We have built the first wire scanner and are preparing to install it at the exit of tank five of the present linac. This is the injection point into the new linac, so we hope to determine the Twiss parameters at that point[5].

Bunch Length Monitor

A technique exists to accurately measure the phase extent (*a.k.a.* bunch length) and the phase density of a linac beam [6]. This idea was invented by R. Witkover [7] and refined by A. V. Feschenko [6]. We have consulted with Feschenko and have built two prototypes.

Referring to the reference [8] and to Figure 4, the bunch length monitor, or BLM, works as follows. The primary ion beam impinges on a wire, 1, which is at high voltage, V. The passage of the beam through the wire causes secondary electrons to be liberated from the atoms in the wire. Free secondary electrons near the surface migrate out of the wire and are accelerated

Figure 3. a wire scanner for the new 400 MeV Fermilab Linac

radially away from it by the voltage, V, to the slit, 2. The electrons which get through the slit then pass between a pair of deflector plates, 3, which are excited at opposite phase by a voltage equal to

$$A_0 \cos(\omega t + \varphi)$$

where ω is the bunching frequency of the beam and φ is an arbitrary and adjustable phase angle. (Our deflector will probably be a cavity excited in a deflecting mode.) The electron beam is focused by an electro-static einsel lens, 4, onto a slit, 5, and the particles which pass through the slit are detected by an electron detector, 6. Plotting the phase angle of the deflecting voltage, φ, versus the signal on the detector produces a distribution which is proportional to the longitudinal density of the ion beam.

The resolution of this device is determined by three kinds of factors: limits set by Nature, assembly/alignment precision and the choices made for the optics of the secondary electron beam, see Table 1. Their predicted effect on the resolution of the device is listed in Table 2 and compared with the results obtained by

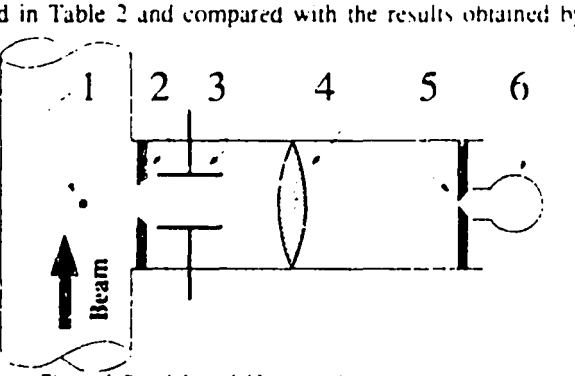

Figure 4. Bunch Length Monitor schematic

Table 1

Limits on the Resolution of a Bunch Length Monitor

① *Natural Limits*

a. Energy and Angle spread of Secondary Electrons

b. Ejection time spread of Secondary Electrons

② *Geometric Precision*

a. Alignment of wire, lens and electron detector

b. Deminsions of wire and final slit

③ *Optics of Secondary Electron Beam*

➸ Einsel lens optics:

a. Path length differences

b. Lens dimensions, aberrations

c. Magnification

➸ Deflector plates:

d. Strength of deflection

e. Fringe fields

f. Max deflection within deflector (related to transit time)

Feschenko [9]. The most severe effect at 805 MHz is the time it takes for the secondary electron to actually be ejected from the wire. The best measurement to date indicates this time is no greater than 6 picoseconds [10]. The other major effect worth noting is the drift-time differences among electrons within the secondary electron beam. The monitor is time sensitive only in the region from the wire to the deflector, so velocity differences or path-length differences in the secondary electron beam to the deflector should be reduced. Velocity differences arise from the thermal velocity variations in the secondary electron beam (expected to be around 3 eV, but with tails out to several tens of eV [7]); increasing the voltage on the wire reduces the effect of the velocity spread. Path length differences are reduced by either reducing the aperture of the device, by placing the deflector as close to the wire as possible or by both.

My improvements should come from: higher secondary electron beam energy, better alignment, and reducing the effective path lengths of the secondary electrons by placing the deflector in front of the lens. Our goal is to obtain a resolution of approximately 1° at 805 MHz, a factor of 3 improvement over Feschenko's 0.8° at 198 MHz. Non-linear effects (3b, e and f) are not addressed at this time.

Our design, with the deflector in front of the lens, requires a rather high gradients, around 2KV/cm, to achieve adequate resolution. We are working on a design for a suitable deflector.

We have tested the optics of the secondary electron beam, without a deflector, in the lab and had good results. We have obtained an image on a thick phosphorus screen approximately 0.030 cm wide using a 0.013 cm wire thermionically emitting electrons. A prototype is being built to put in the 200 MeV beam, again without a deflector, to test if primary electrons from the H-beam significantly affect the device.

We want to install three BLMs in the transition section, two in the 400 MeV transfer line and one near the end of the linac.

The Δt procedure

A procedure has been established at several laboratories, most notably LAMPF, to accurately set the phase and gradient of a series of linac accelerating modules. This procedure, referred to as the "Δt procedure," is described elsewhere at this conference [11]. We are installing a resistive wall monitor [12] at the entrance to each accelerating module to facilitate this measurement. The resistive wall monitor, developed for use in the Tevatron, has a bandwidth of 6 GHz, so some bunch length information can be obtained.

Table 2

Resolution of Proposed and Existing BLMs

BLM Type \ Resolution Effect	1.a	1.b	2.a	2.b 3.d	3 a,c	Total
Fermilab	**0.04**	**<1.74**	**0.3**	**0.7** (3KV/cm, 15 cm)	**0.1**	**0.77 (1.90)**
Feschenko	**0.29**	**<0.43**	**0.2**	**0.4?**	**0.21**	**0.57 (0.72)** (200 MHz)

Other Devices

We will also include standard beam toroids, one per module, and beam loss monitors in the new linac.

Conclusions

In order to commission the new 805 MHz/400 MeV Fermilab Linac in the allotted time, extensive and accurate beam diagnostics are to be used. In addition to fairly standard beam position monitoring and correcting, we plan to include in the new linac: wire scanners for emittance measurement, Δt pickups to aid in setting the phase and gradient of the high-power klystrons, and bunch length monitoring devices throughout the linac.

References

[1] Robert Noble, "The Fermilab Linac Upgrade Project," this conference, Talk number MO1-01.

[2] "Fermilab Upgrade Conceptual Design, Revision 3."

[3] E. S. McCrory, G. Lee, R. C. Webber, "Observations of Transverse Instabilities in the FNAL 200 MeV Linac," 1988 Linear Accelerator Conference proceedings, Williamsburg, VA, pp 182-184; and R. Webber, *et al.*, "A Beam Position Monitoring System for the Fermilab Booster," Proceedings of the 1987 IEEE Particle Accelerator Conference, IEEE Catalog 87CH2387-9, pp 541-543.

[4] E. S. McCrory, R. W. Goodwin and M. S. Shea, "Upgrading the Controls for the Fermilab Linac," this conference, talk number TU4-63.

[5] We are also installing a resistive-wall monitor, similar to the ones in the Tevatron [12], to give us some clue on the longitudinal nature of the beam at that point.

[6] A. V. Feschenko and P. N. Ostroumov, "Bunch Shape Measuring Technique and its Application for an Ion Linac Tuning," 1986 Linac Conference Proceedings, pp 323-327.

[7] R.L. Witkover, "A Non-destructive Bunch Length Monitor for a Proton Linear Accelerator," NIM 137 (1976), #2, pp 203-211.

[8] "Design Considerations for a Bunch Length Monitor for the Fermilab Linac" by E. McCrory; FNAL Linac Upgrade note number 161.

[9] Alexander V. Feschenko, personal communications, June, 1990.

[10] A.V. Feschenko told me of a Soviet Atomic Physics paper which quotes this result.

[11] T. Owens and E. McCrory, "The Δt Experiment at Fermilab," this conference, talk number TH4-51.

[12] C.D. Moore, *et al.*, "Single Bunch Intensity Monitoring System Using an Improved Wall Current Monitor," proceedings of the 1989 IEEE Particle Accelerator Conference, Vol 3, pp 1513-1515.

RFQ1 DIAGNOSTIC DEVICES†

B.G. Chidley, G.M. Arbique, M.S. de Jong,
G.E. McMichael, W.L Michel, B.H. Smith
AECL Research, Chalk River Laboratories
Chalk River, Ontario, Canada, K0J 1J0

Abstract

The diagnostic devices in use on RFQ1 will be described. They consist of a double-slit emittance-measuring unit, a 45° deflection energy-analysis magnet, parametric current transformers, optical beam sensors, beam-stop current monitors, and an x-ray end-point analyzer. All of these devices are able to operate up to the full output current of RFQ1 (75 mA cw at 0.6 MeV).

Introduction

The RFQ1 accelerator system is a test bed for a wide range of high-power RFQ accelerator experiments. It is built to accelerate up to 75 mA of protons to 600 keV at 100% duty factor. It comprises a 50 keV injector, a 60° bending magnet for ion species selection, and a 600 keV 267 MHz RFQ.[1] This paper describes the diagnostic devices used to measure the beam at the output of the ion source, and at the input and output of the RFQ.

RFQ1 Diagnostic Devices

The diagnostic devices on RFQ1 are the following:

1. Emittance-measuring Unit (EMU),
2. Beam-stop Current Monitors,
3. Parametric Current Transformer (Bergoz meter),
4. Energy-analysis Magnet,
5. Optical Beam Sensors (Reticons), and
6. X-ray End-point Apparatus.

Emittance-measuring Unit

The Emittance-measuring Unit (EMU) is used to measure the output beam quality of the RFQ. The beam strikes a water-cooled beam stop containing a slit. This slit lets a slice of the beam through to a second slit Faraday cup assembly, so that the beam can be analyzed as a function of position and angle. Two beam stops have been built, one with the swirl tubes vertical to allow a vertical slit for (X,X') emittance measurements, and the second with the swirl tubes horizontal to allow a horizontal slit for (Y,Y') emittance measurements. The Faraday cup can be rotated to place its slit in the appropriate direction.

The primary slit is 0.127 mm wide by 50.8 mm high and can be scanned horizontally and vertically over a total range of 100 mm. The slit on the Faraday cup is 0.152 mm wide and the Faraday cup assembly may be scanned over a total range of 75 mm with respect to the main slit.

The main slit has water-cooled swirl tubes and is capable of absorbing the full output beam of RFQ1. It is not necessary to cool the second slit and Faraday cup assembly, because of the low fraction of the beam that is transmitted to it.

The positioning motors are controlled by an IBM PC and the Faraday cup current is read by a Keithley low-current amplifier and recorded in the PC. A computer program allows a complete beam scan to be done automatically.

A number of problems originally limited the usefulness of the system but these are being resolved. The system was originally very slow, being limited by the speed of an autoranging pico-ammeter used to read the Faraday cup current. Replacing the meter with a current amplifier allowed a continuous scan, rather than moving the cup to a discrete position and remaining there while the reading was determined. A related problem was that position was determined by counting pulses sent to the stepping motors, but this became unreliable as motor speed was increased. The motor controllers were in a separate unit and had unnecessary limitations, so the motors were replaced by new ones, with the position controlled directly by the PC. The position is now read by a linear potentiometer position indicator.

Measurements can be made either of horizontal emittance (X,X') or of vertical emittance (Y,Y'), although switching from one to the other requires that the unit be opened to replace the primary beam stop.

Recent (X,X') measurements transformed back to a waist are shown in Figs. 1 and 2.

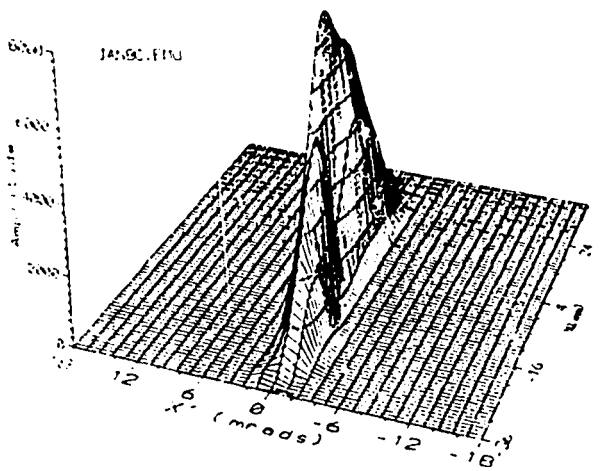

Fig. 1. RFQ1 EMU contour plot.

The data shown in Fig. 1 was obtained using a 3-aperture source operating at 45 mA. The EMU was 1 m from the RFQ and the data was collected using 12 primary slit positions and approximately 250 secondary slit positions. Some processing of the data is needed to allow the plotting program to work correctly. The analysis program can derive an rms emittance as shown in Fig. 2. Development work is continuing on the most suitable way to display the results.

Beam-stop Current Measuring Devices

Most of the beam-intercepting surfaces in RFQ1 are isolated from ground, so that the beam current falling on them can be measured. Surfaces and beam stops monitored are:

1. Entrance port solenoid,
2. Entrance port solenoid beam plate,

†This work was partially supported by Los Alamos National Laboratory under contract no. 9-X5H-0578G-1.

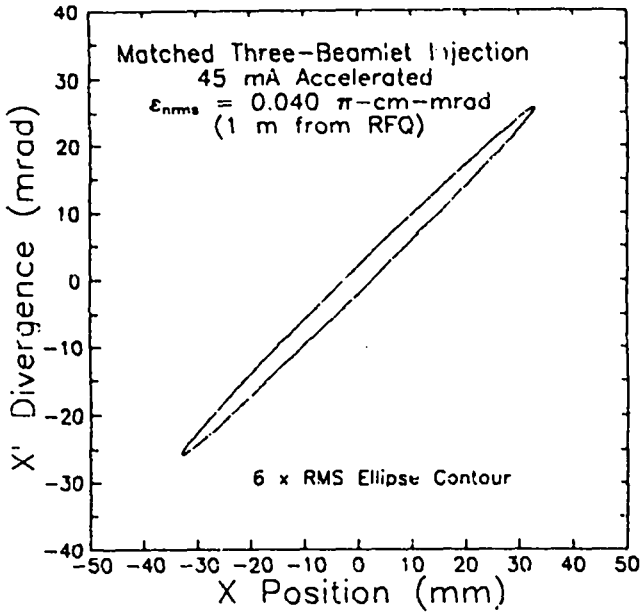

Fig. 2. RFQ1 rms emittance.

3. Straight-through beam stop,
4. H_2H_3 beam stop,
5. Fractional-energy beam stop,
6. Exit port beam plate,
7. Plunging beam stop,
8. Collimator top,
9. Collimator bottom,
10. Collimator left,
11. Collimator right, and
12. Main beam stop.

These devices are grounded with 1, 10, or 100 ohm resistors and typically will have a voltage of between 0 and 100 mV. Intercepted currents are accurate to about 10%. Errors are due mainly to secondary emission, so some inconsistencies are present, but they do provide a useful guide for adjustments of the system. These signals are monitored by the Taurus data logging system and numbers 1, 7, and 12 are also displayed on a digital panel meter.

Parametric Current Transformer

Bergoz DC beam-current monitors of the type developed at CERN by K. Unser[2] were used. These devices are non-intercepting and have a current range of -250 mA to +250 mA, with a frequency range of dc to 20 kHz. Absolute accuracy is about ± 0.1%.

Each monitor has two main toroidal cores with a primary ac signal that drives the cores to saturation in both directions. Two secondary coils are wired in opposition so that in the balanced condition no output signal results. The beam current passes through the toroid and unbalances the saturation so that a second harmonic component appears in the secondary windings. A feedback circuit adjusts the current in a single-turn feedback line to restore the balance, and this current is equal to the beam current.

The toroids have magnetic shields, but still are sensitive to stray magnetic fields, such as from the bending magnet. A zero offset is established after all magnets have been turned on. The device reads current flowing through the aperture of the toroid, so although a metal beam tube may be used, it must have an insulating break to prevent ground currents from flowing on the tube wall.

Electrons from secondary emissions can influence the measurements, so the monitors must be located away from surfaces that may intercept beam.

Two of these units are installed--one at the entrance to the RFQ and the other at the exit. They are connected to the Taurus data logging system.

Energy Analysis Magnet

The RFQ will transmit beam of all energies, so the presence of an output beam is no guarantee that beam is being accelerated by the RFQ. A 45° magnetic analyzer is used to measure the output beam energy. A typical measurement is shown in Fig. 3. The analyzer has a resolution of about 0.2% but no energy calibration has been done; the energy scale on the figure is based on field maps, giving an uncertainty that could be as great as 10%.

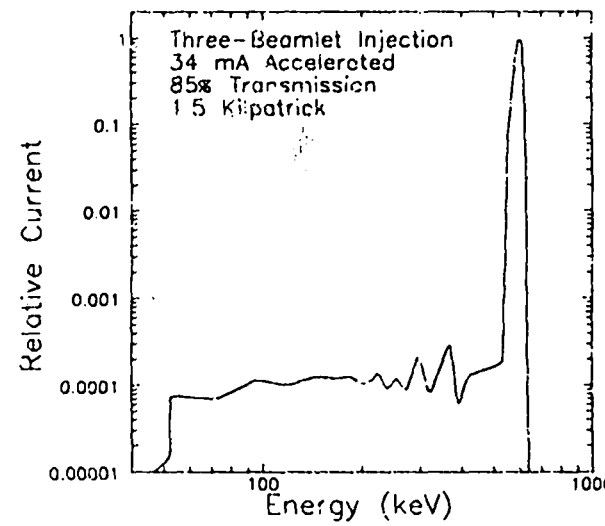

Fig. 3. RFQ1 energy spectrum.

Optical Beam Sensors (Reticons)

Ionization of the residual gas by the beam allows the beam to be observed visually. The light intensity is affected by residual gas composition and pressure. Therefore, optical measurements are not a reliable measure of beam current, but they are a useful measure of beam size and position.

The light intensity depends on the beam energy. It is a maximum in the 50 to 100 keV range, which makes it very suitable for injector diagnostics. For 50 keV protons the intensity is sufficient to give a good signal-to-noise ratio at currents ≥ 5 mA and gas pressures ≥ 10^{-5} torr.

The system uses two Reticon LC1902 line scan cameras to view the beam, one looking at the horizontal profile, the other looking at the vertical profile. The present configuration has a pair of cameras viewing the beam at the exit of solenoid #1. A diagnostics box was built to hold a second pair of cameras in the beam line before the plunging beam stop, but that position is now occupied by one of the Bergoz current monitors. An alternate position for a second pair of cameras is between the end of the dc column and the entrance to solenoid #1.

The present Reticon system has amplifiers optimized for speed as opposed to resolution. As a result, the circuit has poor

offset compensation and poor gain stability. Improvements are planned.

In the present installation, the cameras are connected to an IBM PC and each produces a line scan of the beam that is converted to a table of intensity at 256 positions. This can be displayed as linear intensity plots or saved for later analysis.

The results of a scan using the top port on a 3-aperture beam are shown in Fig. 4. An analysis program has been written which decomposes the trace into three components with equal intensity. The peak height and width of the components are estimated manually, and the program adjusts their positions to produce a composite curve that best fits the data.

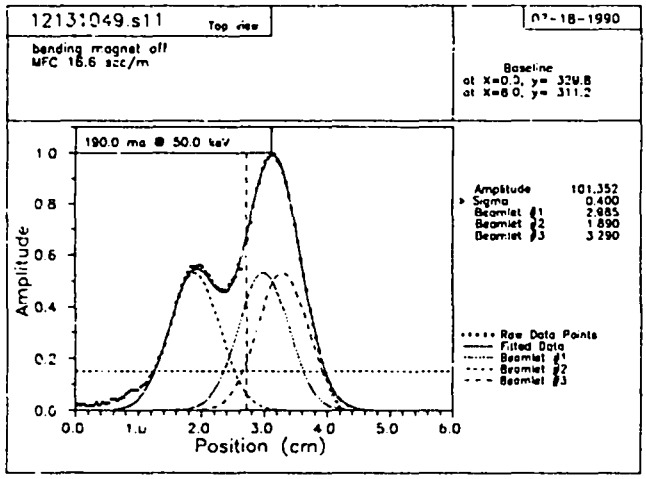

Fig. 4. Three-beamlet top view.

Figure 5 shows a similar scan using the side port with a 4-aperture beam.

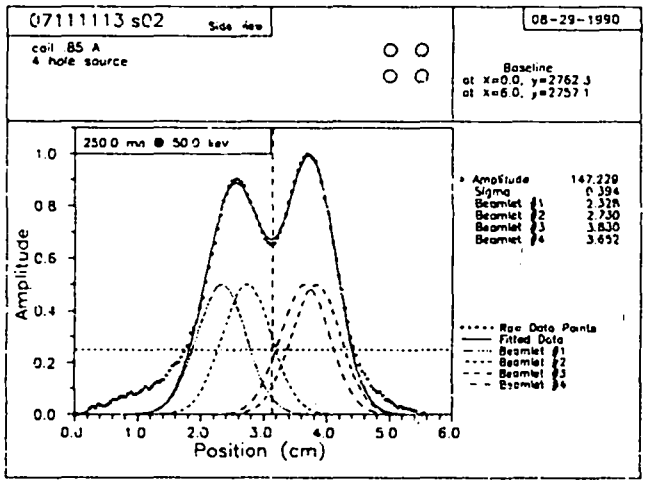

Fig. 5. Four-beamlet side view.

X-ray End-point Apparatus

X-rays are generated by electrons accelerated between surfaces at different potentials in the RFQ. The most energetic of these will occur in the region of the highest electric potential difference, across the intervane gap. This will give rise to Bremsstrahlung radiation, with an end point equal to the peak intervane voltage.

The x-rays are measured with an intrinsic germanium detector located to the side of the RFQ. To limit the counting rate, it is necessary to use an aluminum attenuator and place the detector about 5 meters away from the RFQ. End-point energy can be determined within ± 0.5 kV and the measurement is local enough to be able to detect longitudinal field tilts in the RFQ.

The design intervane voltage is 78 kV, and the spectrometer is calibrated using the 60 keV gamma of Am^{241} and the 122 keV gamma of Co^{57}. Fig. 6 shows a typical spectrum. The resolution is 140 eV/channel and the end point is 78 ± 0.7 kV.

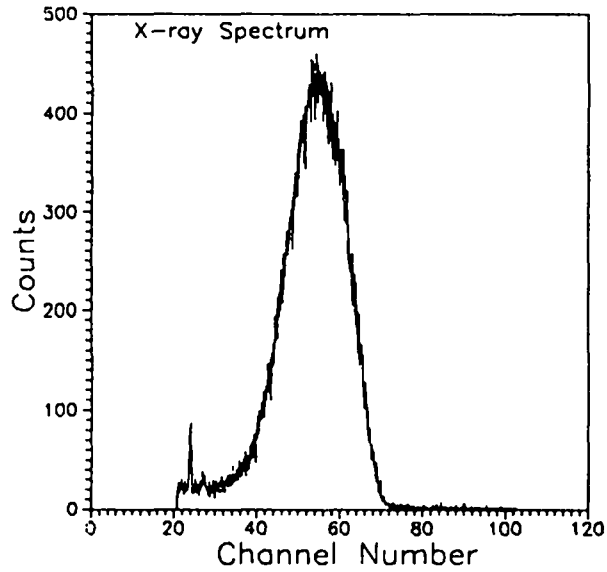

Fig. 6. X-ray spectrum for vane voltage determination.

Conclusions

A number of diagnostic devices have been developed and refined on RFQ1. A companion paper[3] gives results of the measurements made with them.

References

1. G.M. Arbique, B.G. Chidley, G.E. McMichael and J.Y. Sheikh, "CW Operation and Initial Beam Experiments with the RFQ1 Accelerator", Proc. 1988 LINAC conf., Continuous Electron Beam Accelerator Facility report CEBAF-Report-89-001 (1989) 91.

2. K. Unser, "A Torrodial D.C. Beam Current Transformer with High Resolution", IEEE Transactions on Nuclear Science, Vol. NS-28, No.3, (1981), 2344.

3. G.M. Arbique, B.G. Chidley, M.S. de Jong, G.E. McMichael and J.Y. Sheikh, "Beam Performance and Measurements on the RFQ1 Accelerator", these proceedings.

A FLUOR AND WIRE-SHADOW DIAGNOSTIC FOR LOW-ENERGY ION BEAMS*

K. Saadatmand,** J. D. Schneider, C. Geisik, and R. R. Stevens, Jr.
Los Alamos National Laboratory
Los Alamos, NM 87545

Abstract

A video diagnostic technique utilizing a fluorescent screen and a video camera has been developed to monitor the two-dimensional beam-intensity profile and angular divergence of low-energy (25-35 keV) ion beams. Detailed off-line analysis is used to compare and augment standard beam emittance data. Experimental results on 2-D beam profiles will be presented.

Introduction

A fluor screen is placed in the low-energy beam transport (LEBT) line between two solenoid magnets, where the observed beam is nearly parallel and of maximum diameter. Fluor material is Aluminum-Oxide that is plasma-jet sprayed onto the surface of an aluminum or a water-cooled copper substrate. When the beam hits the surface of the fluor, it fluoresces in the visible with a bluish-white color. Over a wide range, the light intensity is directly proportional to the beam intensity at that location. Use of an optional, upstream shadowing wire allows the determination of local beam divergence. The digitized image from a CCD camera is stored and subjected to off-line data analysis. This diagnostic is capable of providing:

1. A measure of real-time beam size and shape on a pulse-to-pulse basis
2. Beam profiles in both transverse directions
3. A measure of the convergence (or divergence) of the beam
4. Beam local divergence (emittance)

Beam Profile Measurements

Figure 1 shows the digitized image of a single 30-keV beam pulse when the LEBT's first solenoid current was set for converging beam. An unexpected beam structure is immediately apparent. The following real-time observations can be made:

1. The beam is nearly circular (the oval shape is caused by the camera angle distortion and can be corrected) with a diameter of 3.5 cm.
2. There is a hot spot at the center of the beam.
3. There is a bright halo on the outside of the beam.

*Work supported and funded by the US Department of Defense, US Army Strategic Defense Command, under the auspices of the Department of Energy.
**Grumman Corporate Research Center

Figure 2 is a 3-D reconstruction of this beam pulse which reveals an enhanced view of the beam structure. This real-time diagnostic capability enabled us to perform a series of experiments to determine if the beam structure is preserved under varying extractor voltages and LEBT focus conditions.

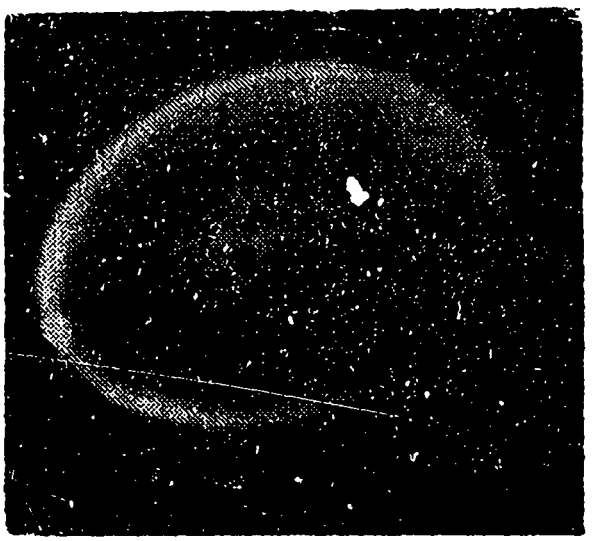

Fig. 1. 30 keV beam intensity profile.

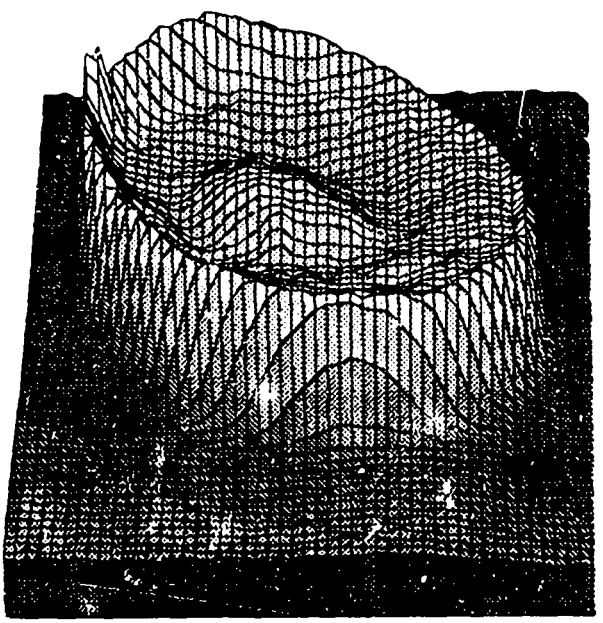

Fig. 2. 3-D reconstruction of the beam intensity profile shown in Fig. 1.

This beam structure was not readily apparent from the standard emittance profiles. The beam structure was present only for the under-focused beams with energies lower than the design energy of 35 keV, for which the beam perveance is not properly matched in the injector. For comparison, Fig. 3 shows the digitized beam image when the beam perveance is properly matched (2 cm diameter, Vext = 35 keV, solenoid current was set for converging beam).

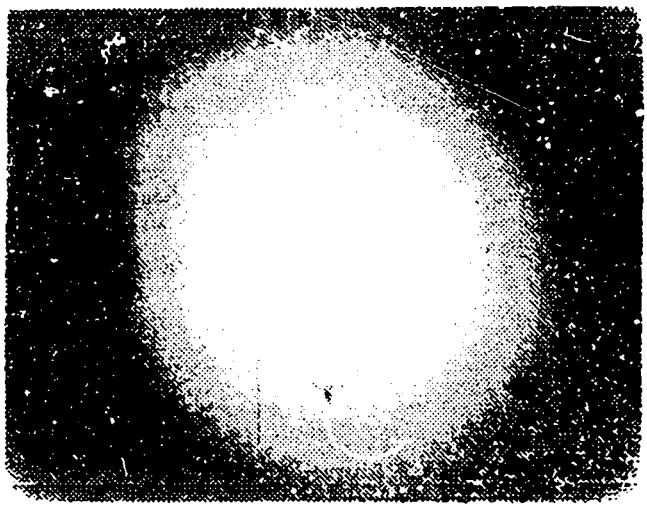

Fig. 3. 35 keV beam intensity profile.

Beam Divergence Measurements

A wire placed in the beam path (upstream of the fluor) will cast a shadow on the fluor. Analysis of the shadow profile leads to the determine of beam divergence. For a beam with a flat spatial distribution and Gaussian transverse velocity (angular) distribution

$$f(\theta) = K \exp\left[-\frac{\theta^2}{2\sigma^2}\right],$$

one can show that the ratio of the downstream current density to the initial on axis current density is given by[1]

$$J(x,z)/J(0) = 1 - 1/2\left[\mathrm{Erf}\left[\frac{x+a}{\sqrt{2}\,Z\,\sigma}\right] - \mathrm{Erf}\left[\frac{x-a}{\sqrt{2}\,Z\,\sigma}\right]\right]$$

where

- $a \equiv$ wire radius
- $z \equiv$ distance between the wire and the fluor
- $\sigma \equiv$ beam divergence
- $x \equiv$ transverse distance along the fluor

In the case of the beam with a small divergence, it is easily shown that the depth of the shadow given by

$$\mathrm{Depth} = \mathrm{Erf}\left[\frac{a}{\sqrt{2}\,Z\,\sigma}\right]$$

can be used to determine the divergence of the beam.

Experiment

A wire grid consisting of three Nichrome wires (0.13-cm wire diameter) in each direction, was placed 10 cm upstream of the fluor. Grid wires were positioned 1.27 cm apart. Figure 4 shows the shadow depth as a function of beam divergence for this setup.

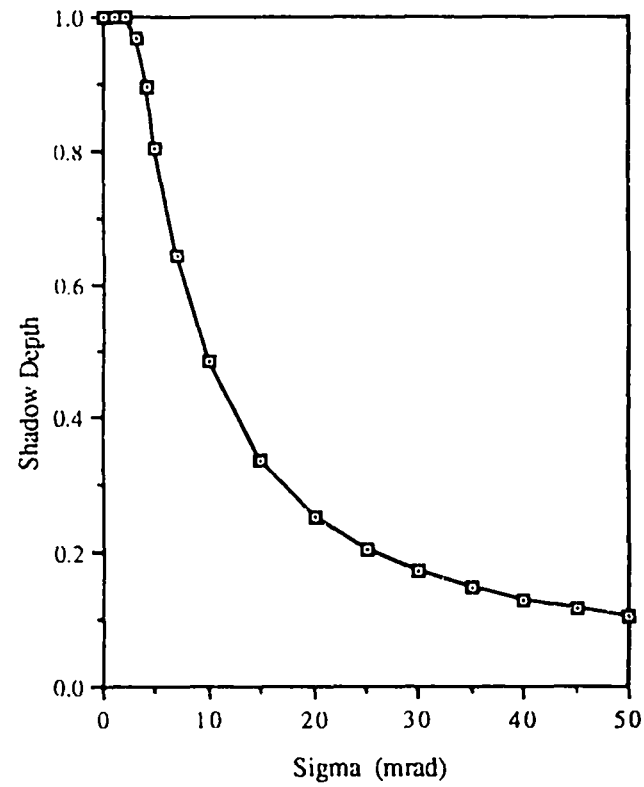

Fig. 4. Shadow depth as a function of beam divergence.

Figure 5 is the digitized image of a 25 keV beam pulse (first solenoid current was set for converging beam). The beam is 3.5 cm in diameter and the distance between the markers on the fluor screen is 1 cm. Beam envelope divergence can be calculated by measuring the shadow spacing on the fluor and comparing it with the grid spacing upstream. This will give the tilt of the phase space ellipse. This beam is converging and the measured portion of the phase space ellipse of the horizontal plane is shown in Fig. 6.

Using figure 4, the local beam divergence can be estimated by measuring the depth of the wire shadows in the various regions of the beam. Figure 7 is a horizontal cut of the beam pulse of Fig. 5. This beam has a localized one sigma divergence angle of 3-5 mrad throughout (Fig. 6). This

value of local divergence is similar to values measured for the similar beam using the emittance-scanner diagnostic.

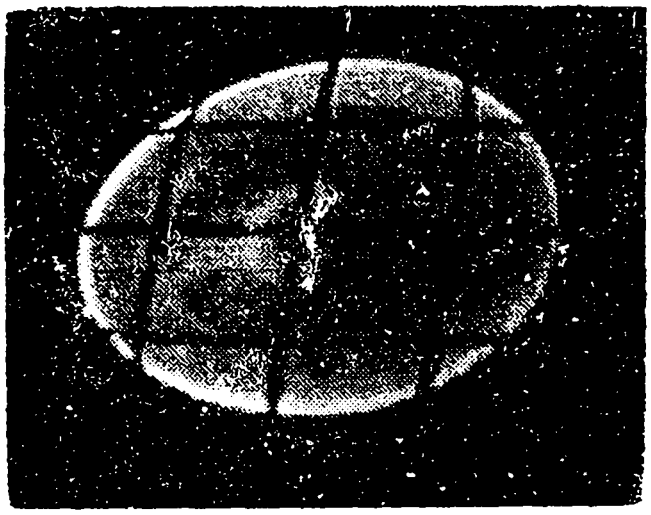

Fig. 5. 25 keV beam intensity profile. Shadows shown are cast by the wire grid upstream.

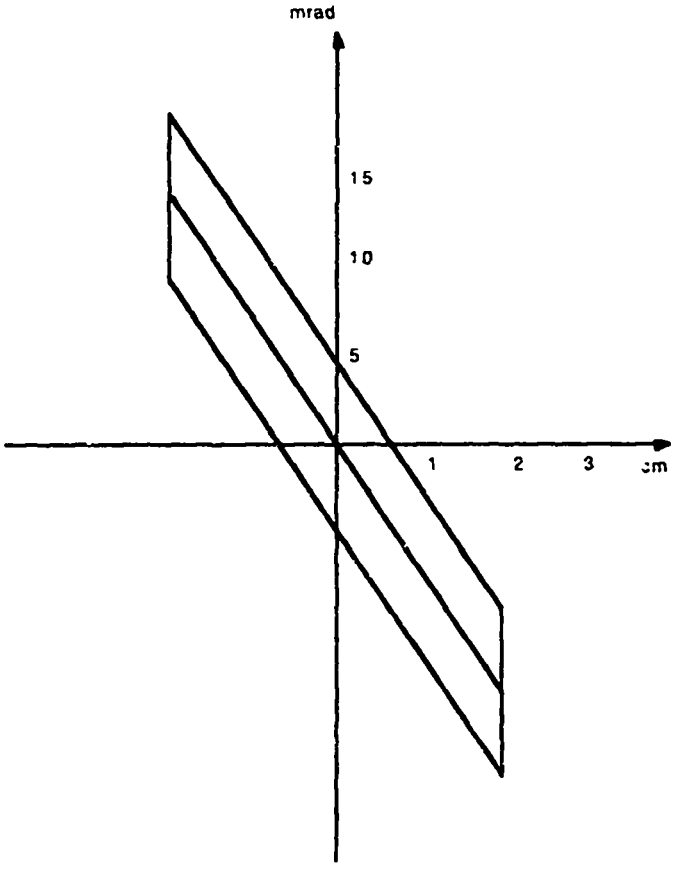

Fig. 6. Phase space distribution of the beam shown in Fig. 5.

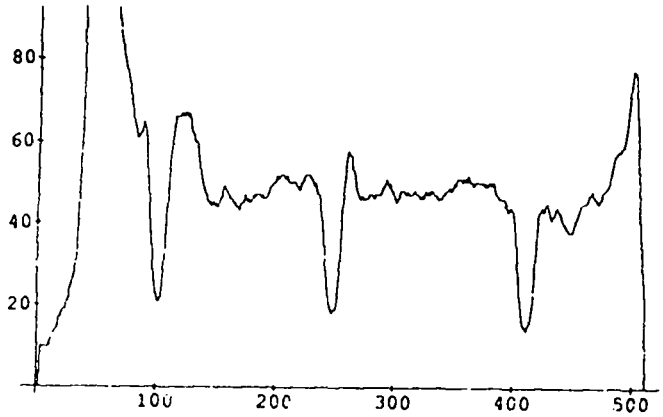

Fig. 7. A horizontal cut near the center of the beam shown in Fig. 5.

Conclusion

The real-time visual knowledge of the beam structure, shape and size, alone, emphasizes the importance and effectiveness of this diagnostic. Prior to this experiment, only emittance scanner beam profile information (which is averaged over hundreds of beam pulses) was available. This technique can be a very useful aid to the experimentalists in providing the desired beam by real-time observation of the beam response to parameter changes. Quantitative information, such as beam local divergence, make this diagnostic a primary candidate for any particle beam system.

Acknowledgements

We would like to thank J. H. Marquardt, N. Nereson and M. T. Smith for their assistance in the experimental set up. We would also like to thank W. B. Ingalls for the operation of the injector.

References

1. J. H. Head, 'private communication.'

A VERY WIDE BANDWIDTH FARADAY CUP SUITABLE FOR MEASURING GIGAHERTZ STRUCTURE ON ION BEAMS WITH VELOCITIES DOWN to $\beta < 0.01$*

J. M. Bogaty, R. C. Pardo and B. E. Clifft
Physics Division, Argonne National Laboratory, Argonne, IL 60439

Abstract

A stripline Faraday Cup of exceptional bandwidth (DC to 6.1 gigahertz) has been developed. An electrostatic shield in the ground-plane geometry prevents electric-field coupling of incoming ions so that the time distribution of low-velocity ($\beta \gtrsim .01c$) particles can be measured. The cup is very rugged compared to other detectors used for ion-bunch timing measurements. We have measured bunch widths of 400 picoseconds on 3.9 MeV $^{84}Kr^{+15}$ beams (200 nanoampere average). Bunch widths down to 100 picoseconds should be observable with a sampling oscilloscope. Beam bunch shapes have been monitored at current levels of 1.0 nanoampere to 10 microampere average.

Introduction

The ATLAS Positive-Ion Injector[1] upgrade has significantly increased beam current and the ion-mass regime available for research. The next upgrade will complete this cycle with the added capability of accelerating uranium beams. These advances have focussed attention on the issue of suitable RF timing and energy measurement diagnostics, especially for low-velocity ($\beta \approx .01c$) particles. A diagnostic was desired that could function over a large range of beam currents, be rugged, and economical. In addition, we wished to avoid detectors that would be marginal for certain ion-mass ranges, exhibit a limited lifetime, or have intrinsically unstable calibration parameters. The Wide Bandwidth Faraday Cup satisfies our criteria for RF timing measurements and will also function as a time-of-flight detector for energy determination.

Bandwidth Considerations

Accurate bunching information is dependant on sufficient frequency response from the overall measuring system. That is, the combined response of Faraday cup, amplifiers, oscilloscope, and interconnecting cables must be sufficient for the narrowest beam bunch anticipated. A good estimate of the bandwidth requirement is given by

$$f = \frac{0.35}{T_r} \qquad (1)$$

where: f = upper(-3DB) frequency response and
T_r = risetime of bunch measured from the 10% to 90% points.

For example, 1.0 ns wide (FWHM) bunches require a system response of approximately 875 MHz for accurate timing measurements. The low end frequency response should be sufficient to avoid differentiation of bunching signals.

*This research was supported by the U.S. Department of Energy, Nuclear Physics Division, under Contract W-31-109-ENG-38.

Transmission Line Faraday Cups

The bandwidth indicated can be achieved by utilizing either coaxial or stripline construction techniques.

Equation 2 estimates the fundamental cut-off frequency of a 50Ω coaxial Faraday cup of 0.5 in.^{2} target area.

$$\lambda_c = \pi(R+r)\sqrt{\epsilon_r} \qquad (2)$$

here: λ_c = Cut-off Wavelength
R = Inner radius of outer conductor - 0.0467 M
r = Radius of inner conductor - 0.0202 M
ϵ_r = Dielectric constant relative to air - 1.0

The cut-off wavelength for this example is 0.105 meters or 2.86 GHz. This limit can be improved. However, bandwidths beyond a few gigahertz would be difficult to achieve with large diameter coaxial Faraday cups.

Striplines

Striplines have much the same frequency limitations as coaxial lines, however, their flat geometry allows greater flexibility in accommodating Faraday cups of acceptable target area. This advantage permits the use of thin dielectrics which are necessary for high-frequency operation. The fundamental cut-off frequency for a stripline is given by

$$f_c = \frac{1}{2H\sqrt{\mu\epsilon}} \qquad (3)$$

where: f_c = Cut-off frequency (Hz)
H = Dielectric Thickness (m)
μ = Permeability of Dielectric (H/m)
ϵ = Permittivity of Dielectric (F/m)

The extremely uniform dimensions of a printed circuit board yields precision striplines at low cost. High-frequency performance is enhanced because of this uniformity and without the expense of precision machining operations. We have had no trouble manufacturing 6 → 10.0 GHz bandwidth striplines without resorting to mode suppression techniques.

Electrostatic Shielding

Electric fields from moving ions extend in all directions and will couple to an unshielded Faraday cup. As a result, current will be induced in the Faraday cup prior to the ion's arrival. This effect

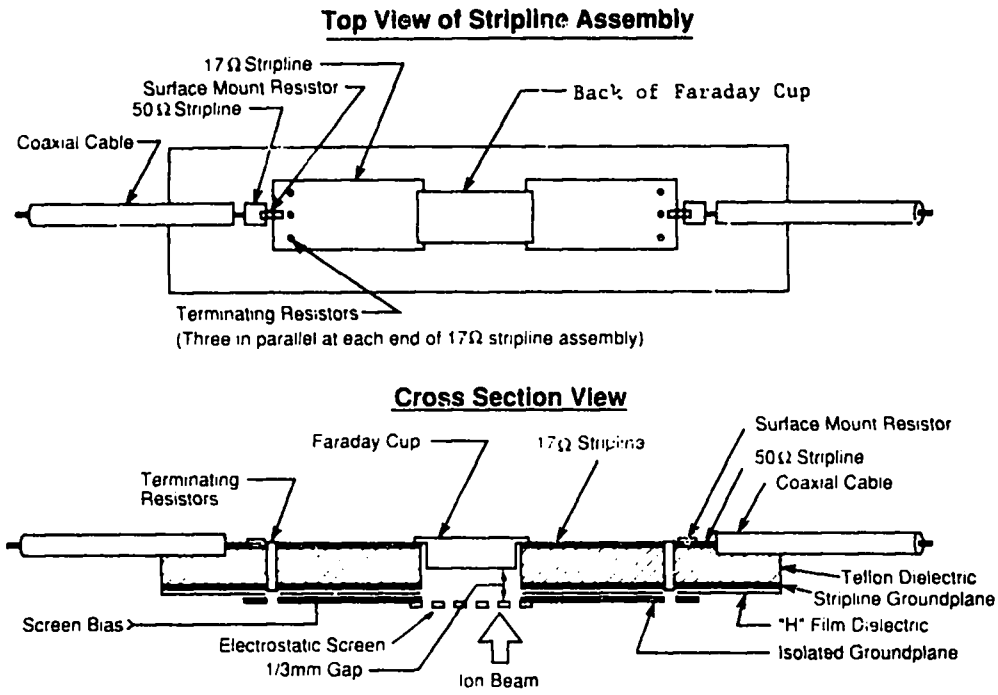

Figure 1

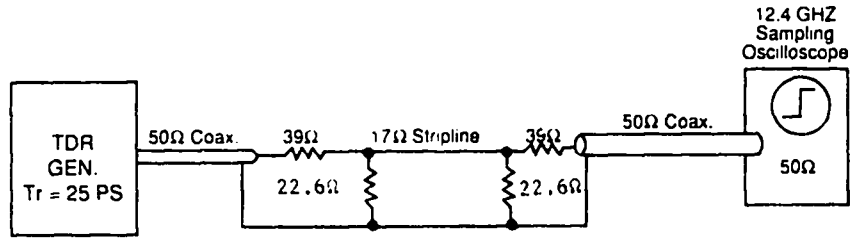

Figure 2

Faraday Cup Output Response
Input pulse rise time = 52 picoseconds
Output pulse rise time = 64 picoseconds

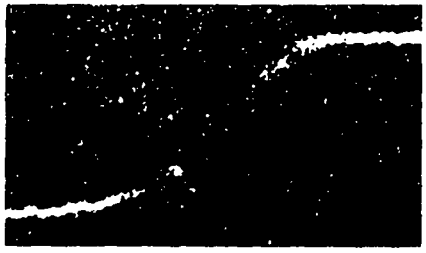

Output pulse at 20 picoseconds/cm

Figure 3

Bunching Analysis
Inside Alpha Cryostat

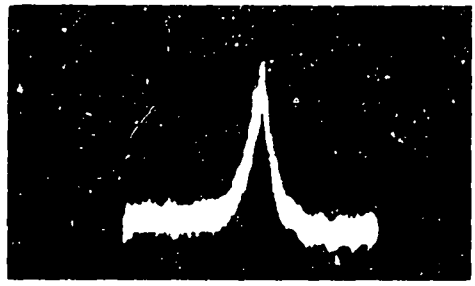

3.9 MeV Kr_{84}^{+15} 400 picoseconds (FWHM)

Figure 4

reduces the high-frequency performance to an extent that depends on the ion's velocity.

Effective electrostatic shielding is accomplished by the placement of a metallic screen in close proximity of the Faraday cup's surface. The screen is capacitively coupled to the stripline assembly and functions as part of the RF ground plane. We used a commercially photo-etched Molybdenum screen 0.005 in. thick, with a grid pattern comprised of 0.005 in. wires at 0.026 in. intervals. This geometry provides 80% particle transmission and effective electrostatic shielding. The spacing between the screen and Faraday cup face must be chosen for acceptably low precursor field induction with the lowest velocity ions, as determined by

$$D = TV \qquad (4)$$

where: D = Screen to Faraday Cup spacing
T = Precursor field time limit
V = Ion velocity

We chose a precursor field time limit of 1.1×10^{-10} sec as acceptable for $\beta = 0.01$ velocity ions. Equation 4, with these parameters, was used to determine the screen spacing at 0.013 in. (1/3 mm).

Stripline Faraday Cup Design

Figure 1 shows a cross section view of the stripline Faraday cup assembly. The printed circuit board is cut away to receive the machined copper Faraday cup. Striplines adjacent to the cutout are etched to match the Faraday cup impedance and carry signal currents to end terminations. Spacing of the electrostatic shield has been set at 0.013 in. which, in conjunction with the cups width, determines characteristic impedance. Equation 5 was used to estimate characteristic impedances of both the Faraday cup and printed circuit striplines.

$$Z_0 = 377 \left[\frac{H}{W}\right] \left(\frac{1}{\epsilon_r}\right)^{1/2} \qquad (5)$$

where: Z_0 = Characteristic impedance
W = Strip width
ϵr = Dielectric constant

These calculations are only approximate because edge effects are not accounted for. Time Domain Reflectometry (TDR) Techniques were used to evaluate all sections of the stripline Faraday cup. The complete assembly is checked using TDR response analysis. Impedance matching to a few percent was relatively easy to achieve. The TDR generator we used has an output risetime of 25 picoseconds, which in conjunction with a 12.4 GHz sampling oscillo- scope, yields impedance profiles out to 9.0 GHz bandwidth. Figure 1 shows a top view of the stripline segments which provide attachment points for surface mount resistors, and connection to 50Ω coaxial cables. Figure 2 shows an electrical equivalent of the stripline Faraday cup. The coaxial cables are used to inject test pulses for TDR and risetime measurements. As the drawing shows, either end can be driven and the resulting signals monitored with the other coaxial cable. One of the coaxial cables is replaced with a terminating resistor when testing is finished. The remaining cable is used to transmit beam signals for evaluation. Frequency response is checked by two methods. TDR pulses are injected into one of the 50Ω coaxial cables and the resulting output viewed on a sampling oscilloscope. This provides a record of risetime and pulse response characteristics. We also used a RF sweep generator to drive the cup from 10 MHz to 8.0 GHz, the resulting output confirmed the bandwidth implied by risetime measurements. Figure 3 shows the pulse response characteristics when a 52 picosecond risetime pulse is injected into one end of the stripline Faraday cup. This unit exhibited a bandwidth of over 9.0 GHz with no apparent ringing.

Faraday Cup Bias and Operation

As shown in Fig. 1, the electrostatic screen is isolated for DC voltages. This permits the application of bias on the screen, to suppress electrons, when accurate peak beam-current measurements are desired. If a positive bias is applied, the overall beam current sensitivity is enhanced by a a factor of 3.9. This is an advantage when measuring low beam-current bunching and has no apparent effect on bunch-width measurements according to our testing. We apply a standard bias of plus or minus 180 VDC, with the polarity primarily dependant on beam intensity.

For most beams, we simply use a broad bandwidth 60 DB amplifier to boost the Faraday cup signals and display them on a 12.4 GHz sampling oscilloscope. The signal to noise ratio of the overall system is sufficiently high to allow direct visual interpretation of the oscilloscope signals with no other processing. When weak beams are measured we use digital processing techniques to enhance signal-to-noise ratios and store the results in a Nicolet Digital oscilloscope. This process allows beams as weak as 1.0 nanoampere (electrical) to be analyzed.

Faraday Cup Uses

The Wide Bandwidth Faraday Cup has been in use at ATLAS for one year now. Several versions of this design are permanently installed and routinely used. A low beta ($\beta = 0.01c$), close screen, version is installed in our Positive Ion Injector line where RF bunching is monitored for beam bunch initialization. A miniaturized version is installed in the first Positive Ion Injector cryostat and operates at liquid helium temperatures. This cup has 10.1 GHz bandwidth and is used to set up bunching into the first accelerating cavity. Here, the bunches are a few hundred picoseconds wide as shown in Fig. 4. A high-velocity version of the Faraday cup has been developed and is installed at the end of ATLAS where ion velocities are up to 20% the speed of light. This design has five times more sensitivity than the low beta version due to a wider cup-to-screen spacing and 50Ω impedance. This Faraday cup has been used to monitor stripping foil energy loss of a 1.0 nanoampere silicon beam and will be used to monitor beam timing for timing sensitive experiments.

References

1) P. K. Den Hartog, et al., Nucl. Instrum. Methods in Phys. Res. B40/41, 900 (1989).

CONTROL SYSTEM OF ATF

H. Hayano, J. Urakawa, M.Akemoto and T. Naito
KEK, National Laboratory for High Energy Physics
1-1 Oho, Tsukuba-shi, Ibaraki-ken, 305 Japan

Abstract

A computer control system of Accelerator Test Facility(ATF) is described in detail. The ATF presently consists of 60MeV electron injector linac and two klystron test stands, and is controlled by a workstation computer with CAMAC interfaces. For its nature of R&D accelerator aimed to realize TeV region linear collider, the control system also should have a flexibility in both hardware and software. Programmable sequence controllers are introduced in the electron gun system and klystron modulator systems and their performances are tested. The control software which is coded using FORTRAN consists in many independent programs. Each program can access to full functions of a specified device or can control the function which is common to many devices.

Introduction

The ATF has been constructed to stimulate R&D work for the linear collider in TeV region.[1] We completed the first stage of the construction and can proceed R&D programs by using their 60MeV injector linac and two klystron test stands. The injector linac is composed of a 240keV thermionic electron gun, three stage subharmonic bunchers(SHBs), prebunchers and a buncher followed by high gradient accelerating structures. The main control computer is a VAXstation 3500 workstation and the backup and development machine is a VAXstation II/GPX. The interface is a CAMAC system using a serial highway of optical fiber cables, and their interface modules are the same ones used in TRISTAN control system (see Fig. 1).

Control Hardware

Computer

The VAXstation 3500 and the VAXstation II/GPX are 32-bit workstation computers with 3MIPS and 1MIPS performance respectively.[2] The VAXstation 3500 includes a 19" high resolution(1024x864) color monitor, three-button mouse, keyboard, and is equipped with 16Mbytes of memory, a 280Mbytes hard disk and Ethernet. The selection of computer was made because of its useful VMS operating system, efficient program development environment, powerful networking(DECNET) ability and easy installation to the existing KEK network system. The main computer is VAXstation 3500 which controls all equipments of the ATF using CAMAC interfaces. VAXstation II/GPX also has a 19" color monitor, three-button mouse, keyboard, and is equipped with 13Mbytes of memory, a 318Mbytes hard disk. Because of lower CPU performance compared with VAXstation 3500, we use it for program development, test of CAMAC modules and supplemental console for main computer.

CAMAC Interface

We decided to adopt CAMAC system as interface standard. The reasons are

1) We can use many CAMAC modules developed for the TRISTAN control and experience obtained in the TRISTAN control.
2) Wide varieties of CAMAC modules are commercially available, reducing a risk to develop a fully new system.[3]

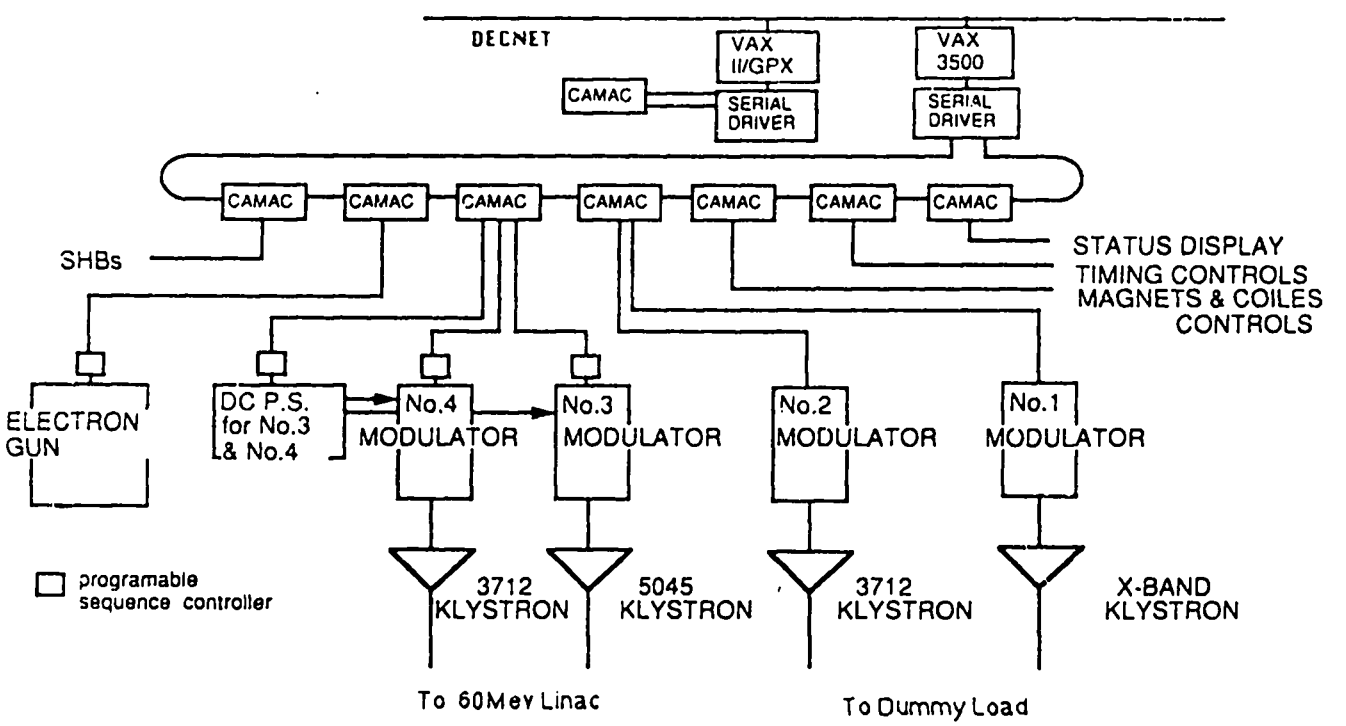

Fig. 1 Computer control scheme of the ATF

The CAMAC system uses 5Mbytes/sec serial highway. Each crate is connected by optical fiber U-port adopters with bypass and loop-collapse functions. Using this optical fiber communication, we can easily extend its distance between the computer and the CAMAC crates without picking up any induced electromagnetic noise. An enhanced serial highway driver(2160-z1f,Kinetic System corp.) is used in the VAX's Q-bus and provides 1.7Mbytes/sec DMA throughput. 7 CAMAC crates are used respectively for klystron modulators No.1 & No.2, klystron modulators No.3 & No.4, electron gun, focusing and steering coils, trigger timing controls, SHBs and various monitors. Each crate is installed in the most nearest place to the device. The CAMAC modules for device control are status input gate(SIG), status output register(SOR), scanning A/D converter(SAD), D/A converter(DAC) and pulse train generator(PTG) which are designed for general purpose use in the TRISTAN control. Several kinds of CAMAC modules from venders are also used in this system.

The basic philosophy of our device control is to keep continuity of control between remote computer control and local manual control. In other words, we must easily take back a control from computer without any discontinuity of operation. In order to accomplish this philosophy, the interface of newly designed device is changed to keep continuity of operation. For example, current setting of a helmholtz coils is usually made by D/A converter from CAMAC and potentiometer from device panel. It has discontinuity of current setting for turning local/remote switch. Then we adopted a single reference current setting generator in the power supply which is controlled upward or downward by pulse from CAMAC module or by pulse from buttons of device panel.

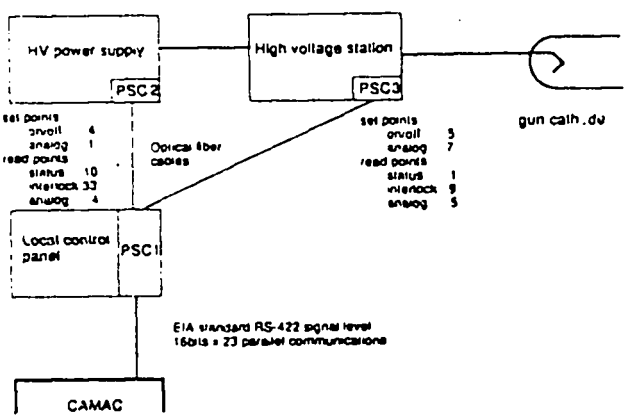

Fig. 2 Programmable sequence controller for electron gun

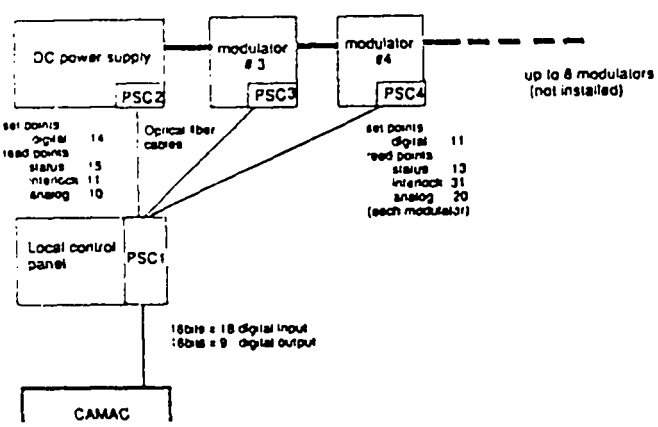

Fig. 3 Programmable sequence controller for klystron modulator

Programmable Sequence Controller

A distributed control system needs to construct a huge and complex control system like the linear collider. Programmable sequence controllers(PSC) are one of the candidate of the distributed control devices. They have CPU, digital input/output, ADC, DAC, etc. and act with high reliability. We adopted these devices to klystron modulators and electron gun system (see Fig.2,3).[4,5] The electron gun system has the modulator of which the behavior is same as klystron modulator. In the figures, when main PSC(PSC1) get commands from CAMAC interfaces or local control switches, the PSC send the commands to target PSC(PSC2,PSC3, . .), located in the hardware, after all PSC's conditions are checked. Conversely when interlocking signals arise in target PSC, the PSC turn concerned devices off and send the status and the kind of interlocking signal to main PSC. Therefore PSC can reduce software load of host computer and simplify the program. In the aspect of hardware, the wires are reduced by target PSC located in the hardware.

These PSC act with high reliability in the hardware. But following two points must be improved mainly.

1)Working speed: about 10 sec. is required for varying 10kv of the de-Qing voltage of Klystron modulators. In this case, the reasons are we don't care about software optimization and the PSC haven't adequate working speed of this purpose.

2)Trouble-shooting: when hardware troubles arise, it is difficult to know the failure source of device, because the signals from the PSC can't be verified by host computer directly.

CATV System

Various informations for operation(operation status, scope signal, beam plofile, local instruments information, etc..) can be viewed everywhere in the experimental hall and control room using the CATV system. At the control room, there are eight 10" TV monitors and one 25" TV monitor which can select and monitor the informations of 11 TV channels allocated in the range of 70 to 250MHz frequency presently.

Control Software

The software has three generation shown in Fig. 4. The lowest generation routines are 2160 VMS CAMAC driver(Kinetic System Corp.). They are strongly device dependent routines which interface to CAMAC serial driver hardware. In order to interface generally to higher routines, we adopted IEEE std 758-1979 routines which can provide us general interface to CAMAC and put it over 2160 VMS CAMAC driver, so that we can easily change interface hardware or computer itself. The next higher level routines are device handlers which control a function of a device such as LV switch, HV switch, trigger switch of a klystron modulator etc.. These routines are FORTRAN Function type programs. There are two types of function for each hardware device. One is a controllable function, we can read its status and write control to the device. The other is a only readable function, for example reading cathode voltage, beam current of a klystron etc.. We use FORTRAN Function routines for controllable functions, and for readable functions. Also Subroutine routines are used for group reading at one time for readable functions. The higher level programs interface to operators are constructed by device handlers. Their programs generally display the status of devices repeatedly. Operator can interrupt displaying and can issue an command that controls the device. The use of VT-type

character display screen is for aiming of the use of various kind of terminals such as workstations, VT-series terminals, personal computers, portable computers. We also used bit-map color display of the workstation as a graphic terminal for data plots and visualization of status. These device control programs are made for electron gun, klystron modulators, focusing coils, trigger timings and phase/amplitudes of prebunchers and buncher, klystrons and SHEs. Status display programs are also in the same level. They can display the klystron status repeatedly on monitor TVs. We can operate each control program watching the monitor TV.

Operation

In the ATF, various experiments are performed, such as electron gun test and conditioning, klystron test and conditioning, test of high power devices, high gradient experiments and injector study with beam.[6] In order to cope with these experiments, we need a simple control program rather than smart, complicated and automated operation program. So we made programs which control a device or some kinds of function separately. Those programs perform each test and conditioning of device individually at same time. When we use those programs together with, we can operate a accelerator as a whole. A workstation is adequate terminal for that purpose by using its multi-window ability. By this program construction method, we can use these programs not only from VT-terminals near devices but from terminals via network without any expensive console.

Summary

This control system has worked without delay after the installation of hardware devices and contributed greatly to the ATF R&D. Especially it's effective at continuous, controlled operation(cavity conditioning, electron gun's cathode activation, etc.). The PSC are useful in this system. But more careful design and trouble-shooting tool(for example PSC behavior monitor) are required. At next step, we would like to research new interfaces(VME, etc.), network system and others.

Acknowledgments

We would like to express our thanks to Professor Y.Kimura and Professor K.Takata for their encouragement in constructing the system. We would also thank other members of JLC R&D group for their support.

References

1. J.Urakawa, "JLC control system", Proc. of First Workshop on Japan Linear collider, KEK Report 90-2 April A/1-1 121(1990)
2. J.Urakawa et al.,"Control System of the Test Accelerator Facility for linear collider", the XIV International conference on High Energy Particle Accelerators vol. 30 183 (1990)
3. J.Urakawa et al.,"The Status and Prospects of the Control System of an Accelerator Test Facility for Linear colliders", NIM A293,23(1990)
4. M.Akemoto et al.,"Electron Gun of the Accelerator Test Facility for the JLC", contributed paper to this conference.
5. M.Akemoto et al.,"Klystron Modulators with HV common-bus for the JLC", contributed paper to this conference.
6. H.Hayano et al., "Automatic Aging System for Pulsed Klystron", Proc. of 14th Linear Accelerators Meeting in Japan held at the Institute of Scientific and Industrial Research, Osaka Univ., Sep. 313 (1989)

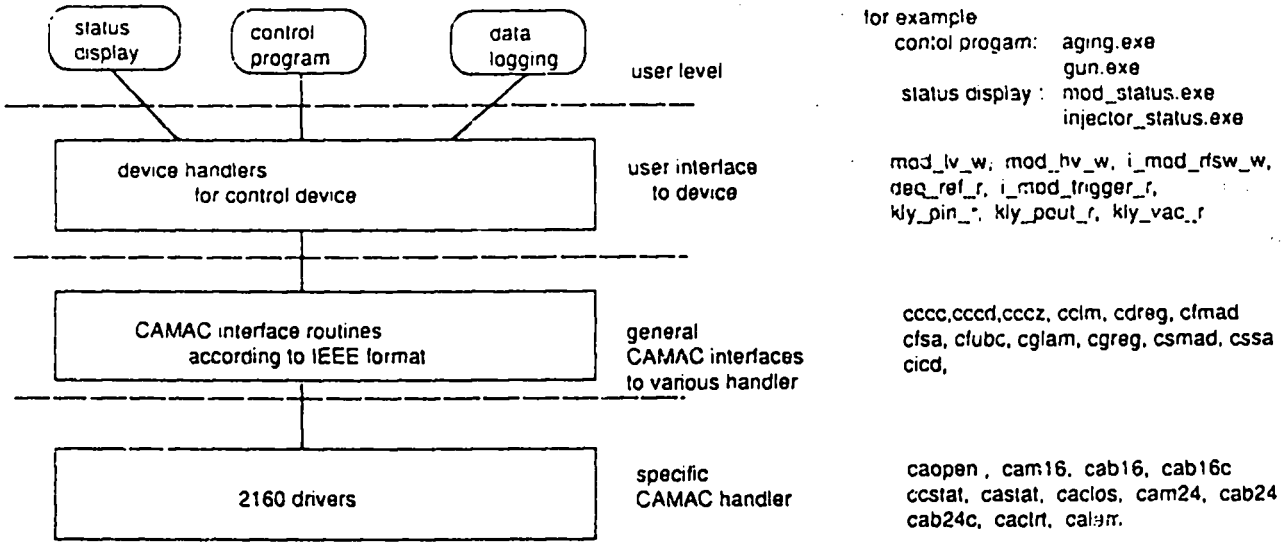

Fig.4 ATF Control Software Structure

EXPERT SYSTEM FOR DIAGNOSIS OF KLYSTRON MODULATOR(KMTS)

I.Abe, H.Hanaki, S.Anami, K.Nakahara, M.Kitamura*, and A.Asami

Photon Factory, National Laboratory for High Energy Physics
1-1 Oho, Tsukuba-shi, Ibaraki-ken 305, Japan
*Department of Nuclear Engineering, Tohoku university
Aramaki-Aza-Aoba, Sendai, Miyagi 980, Japan

Abstract

A diagnostic expert system, KMTS (Klystron Modulator Trouble Shooting system), was developed for the Photon Factory 2.5GeV electron/positron linac and was connected to the linac computer network for receiving real data from the linac.

The klystron RF modulator is a 84MW pulse(4.5us) power supply operated at 25pps. There are 47 modulators along the 500m linac.

This project has been undertaken in an attempt to reduce linac operator's diagnosis duties and to explore AI technologies.

Introduction

The Photon Factory(PF) Linac[1-3] is operated 24 hours a day, a total of 5000 hours a year, making injections to the PF storage ring and the TRISTAN e+/e- collider.

When any trouble occur in the Klystron Modulator, although the operator is usually not an expert to diagnose modulator trouble, he is required to do it, even at night.

Any assistance given to the linac operator regarding operation and diagnosis is extremely desirable. A knowledge-based expert system(ES) seems to be appropriate in order to optimize the operation environment.

We have been looking for appropriate expert system shells and tools with which to build up an expert system easily and rapidly.

For several years, a small ES based on a personal computer was initiated to be used for exploring the applications of AI techniques to the accelerator field. A prototype system, KMTS, had been build on a workstation by May 1989, and connected to the computer network of the PF Linac.

In KMTS, knowledge representation was very interesting; it was tried in order to determine whether or not the problems can generally be solved using an ES. The KMTS started to run, using hundreds of rules, for diagnosis from October 1989.

Basic Approach

At present, each klystron modulator has several microprocessor units(MPUs) which are connected to the local network(LOOP-2) using optical fiber.

The LOOP-2 has a HDLC-like protocol developed in the PF Linac. When a fault occurs in a klystron modulator, the MPU picks up the first reason, FCS(First Change Status), for the trip down and sends a message to the minicomputer, MELCOM 70, in the subcontrol room through LOOP-3, LOOP-2, and CAMAC. There are 50 interlocks and analog data displays at the local klystron modulator panel. Of course, ES requires more information for complete diagnosis. Most of the same data which is available to check locally is transfered to the main computer and to the expert system.

The KMTS is triggered to start diagnosis upon receiving an FCS message through the network.

Hardware Configuration

Figure 1 illustrates the hardware configuration of the KMTS and the network of klystron modulators. The KMTS has the following configuration: HP9000/370 (development station), 375(linac operator's console), HP-UX, C, NEXPERT-OBJECT (HYBRID-tool), Data-View (graphic tool), equipped with a 16MB RAM, 300MB(600MB) hard disk, and 3.5 floppy disks. There is a pre-process station (FMR-50 personal computer) which has a 600MB magnetic compact disk (CD).

The KMTS involves a human interface for interviewing in multiwindows. The interface supports graphic multiwindows and a mouse. The KMTS is connected to the Linac computer network through the ethernet and RS232C. Though there is important waveform information concerning various analog signals, these have not yet been taken into the KMTS.

Fault rate

Under usual operation, the fault rate of the klystron modulators is 720 times/month. In some fault cases, the modulator can not be recovered immediately without treatment by the operator.

Since the system receives real-time data concerning shutdown informations from the klystron modulator, it can usually be restarted very soon. This used to be done at the linac operator's discretion.

Software configurations

The KMTS expert system has a debugging mode for diagnosis which makes it easy for users to carry out simulation at any time. The KMTS can operate in two modes (AUTO or MANUAL) at the operator's discretion. In the AUTO mode, when the KMTS receives serial shutdown data from pre/post processor through the network, it automatically starts diagnosis periodically. In the debugging mode, inference is fired manually by the knowledge engineer. Each rule should be simulated in this MANUAL mode both before and after running using empirical knowledge.
Knowledge or result integration is carry out by C language.

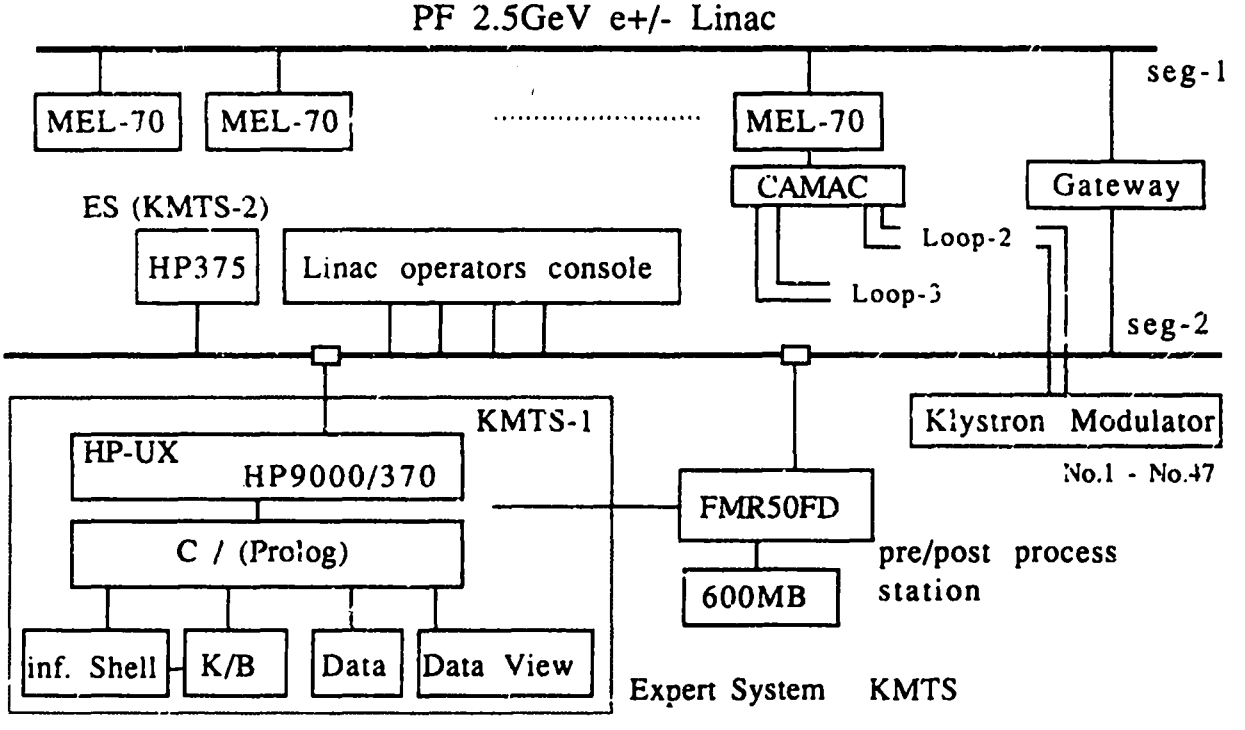

Knowledge Acquisition

Generally, knowledge acquisition can not be based on any model in this kind of diagnosis; KE(Knowledge Engineers) must build knowledge-base extracting rules and procedures in an empirical approach through interviewing experienced field experts regarding both operation and repairing.

One of the methods is to stimulate an expert who remembers by asking what operations and diagnosis must be carried out when facing troubles. Two months have been spent on interviewing and knowledge engineering during the first stage. After that, we determined that diagnosis concerning the klystron modulator would result in shallow targeted diagnostics, still a big help to linac operators.

It is also necessary to have other methods to obtain more knowledge by making sure after the system(KMTS) done.
A hundred expressions concerning production rule, frame, and object were handled by KE in the KMTS.

Results

The expert system environment was constructed using easy user interfaces and a knowledge base concerning a shallow target.
Though the diagnostic capability is still primitive and limited, it is necessary to start with a small knowledge base in an expert system. Though the execution time of the expert system does not need to be very short, it is sufficiently fast and hundreds of times faster than human(operators) diagnosis. Therefore, the speed is not of primary importance at this stage.

Just after completing the expert system, the fault rate of klystron modulator became very low; consequently, we have started to change our goal to not only diagnosis, but also to offer an operation support expert system without big changes. The New K/B(Knowledge Base) including pictures and graphics are now being added and tested for expected phenomena in order to obtain more reliability. Moreover, we are studying CASE-BASED REASONING as well as how to gain transparency of the K/B. We are going to change the KMTS in order to be able to control the klystron modulator to turn it on by the KMTS. At the same time, an attempt is being made to construct an operation support expert system for the electron gun system of the linac. The new system will be different from the previous system.

References

[1] K. Nakahara, I. Abe, R.P. Bissonnette, A.Enomoto, Y.Otake, T.Urano, and J.Tanaka, Nucl. Instr. and Meth.A251(1986) 327-336

[2] K.Nakahara, I. Abe, A.Enomoto, Y.Otake, and T.Urano
Nucl. Instr. and Meth.A247(1986) 153-158

[3] Isamu ABE, Masasi Fujieda
Proceeding of the 6th symposium on Accelerator Science and Technology(1987)

UPGRADING THE FERMILAB LINAC LOCAL CONTROL SYSTEM

Elliott S. McCrory, Robert W. Goodwin and Michael F. Shea
Fermi National Accelerator Laboratory, Batavia, IL 60510†

Introduction

A new control system for the Fermilab Linac is being designed, built and implemented. First, the nine-year-old linac control system [1] is being replaced. Second, a control system for the new 805 MHz part of the linac [2] is being built. The two systems are essentially identical, so that when the installations are complete, we will still have a single Linac Control System.

Replacing the Old Control System

The old control system, commissioned in 1982 and detailed in reference [1], is incompatible with our controls plans for the upgraded linac. The old system, based on locally designed and built components using Multibus-I, an 8MHz MC68000 cpu board and the SDLC network, is difficult to expand, to maintain and to integrate into the more modern system envisioned for the new linac.

The design criteria of the replacement control system are:

1. Retain the desirable features of the old system, including local access to the equipment and the monitoring and reporting of of the local information at the repetition rate of the accelerator, 15 Hz. (In particular, if a reading goes out of tolerance, the control system can disable beam on the next pulse.)

2. Minimize the software effort,

3. Use commercial hardware as much as possible,

4. Limit the amount of downtime necessary for the changeover.

In order to minimize the software effort, the same system used in the DØ high-energy physics experiment at Fermilab [3], which itself is based on the existing linac control system, is being used. Essentially nothing needs to be changed to use this system, although some features have been added. The DØ control system is quite large, so the relatively small linac control system will not require very much additional effort, except during commissioning.

The replacement system for the existing linac is shown schematically in Figure 1. Its major features are outlined here. The IEEE 802.5 Token Ring network connects a series of VMEbus

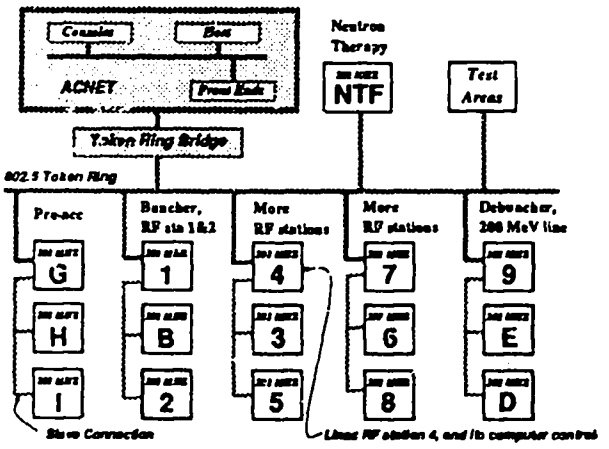

Figure 1, Upgraded controls for the existing Fermilab Linac.

† Operated by the Universities Research Association under contract for the Department of Energy.

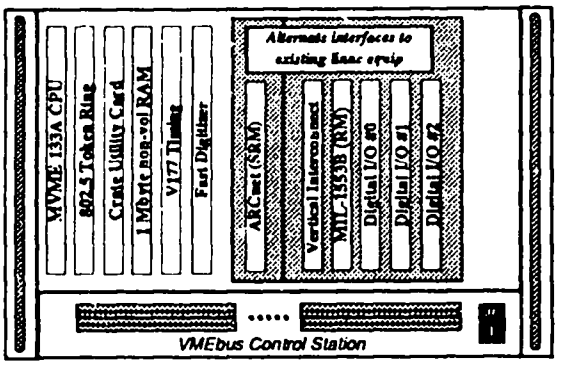

Figure 2, Typical VME station in the Upgraded Controls for the Linac

crates to each other and, through a bridge, to the rest of the Fermilab accelerator complex. The VME crates contain the hardware necessary to connect to each other (token ring) and to control the existing linac hardware, see Figure 2. Contained in each crate are the following core set of VME cards: a cpu card, the MVME133A; a token ring card; a crate utility card; and non-volatile RAM. Other I/O will also be used. Because the new system has been designed to handle up to 2000 analog channels, it is not necessary to have a new system for each old RF station. A ratio of one computer control station for every three RF stations has been adopted.

We are considering two ways to interface to the old linac hardware, as suggested in the grey box of Figure 2. The first way, Figure 3a, is to use three commercial, six-byte digital I/O cards configured to match exactly the old system's eighteen-byte I/O scheme. This scheme requires that a VME crate be located near the digitizing hardware. Two of the crates would be slaved to the first by linking the VME memories. A VME card has been developed to give limited memory access to several remote VME crates from a master crate. This card is called a "vertical interconnect" or VI. It maps 16 Mbyte blocks of VME memory (24-bit addressing) into each of four digital crates. As many as 24 slave crates are served from six VI master cards in a single local station. For each control station there are two additional VME crates. Each of the three VME crates contains the digital I/O cards necessary to interface with the old hardware.

This method has been successfully tested on the extra 201 MHz RF station in the linac. The RF stations which now have a Multibus-based 12-bit D/A board (used for dipole magnet set-

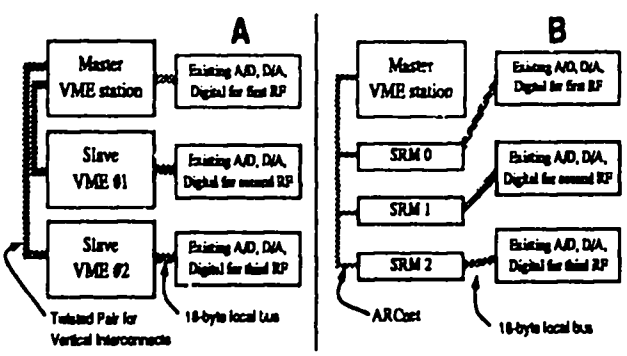

Figure 3, two ways to connect to the old linac hardware

tings) would be equipped with a Rack Monitor (RM). The rack monitor, as built for DØ, contains eight twelve-bit D/A channels, 64 (unheld) twelve-bit A/D channels, four 16-bit words of digital I/O and a MIL-STD-1553B interface. A 32-channel sample-and-hold chassis would be needed to use the digitizer on the RM. The rack monitor gets its name from the fact that the interface to all the equipment in a 19-inch rack can usually be made through one RM.

The second method, Figure 3b, uses a new Motorola chip designed to control a modern automobile engine, the MC68332 microcontroller. This 68020-based chip includes sixteen counter/timer channels, a serial communications interface, two kbytes of RAM and a system integration module. This processor is available as a small subsystem called a Business Card Computer (BCC), a 2.25 by 3.5 inch circuit board that has the MC68332, 128 kbytes of PROM, 64 kbytes of RAM and an RS-232 serial interface.

We would incorporate this BCC into a new type of rack monitor creating a Smart Rack Monitor (SRM, [4]). The BCC would attach to the motherboard of the SRM through its two 64-pin DIN connectors. All the address, data, control and I/O pins of the MC68332 are available on these two connectors. Included on the silicon of the chip is an extensive system integration module—a collection of interface features normally provided by peripheral chips. A SRM would add the following functions: Tevatron-style clock decoder, ARCnet local-area network interface to the VME master, eight bytes of digital I/O, sixteen-channel D/A, twelve-bit S&H A/D and a 64-channel analog multiplexor. We have designed new nine-byte digital I/O daughter cards to communicate with the old linac equipment. Two would be needed for each SRM.

The control system alternative with SRM's would be less expensive, more powerful and faster than the other alternative. Unfortunately, we do not yet have a clear idea of how to write the software to drive the SRM.

Changeover Plans

The decision as to which type of interface to use is imminent. When the decision is made, we will order the hardware necessary to convert completely the old linac control system to the system described above. We will assemble the new stations at their final locations, load the appropriate local data base and perform thorough testing off-line before the actual changeover. We anticipate it will take less than a week to perform the switch, but, naturally, we expect a somewhat longer unstable period. We hope to have the new system for the old linac installed by the summer of 1991. This new system will remain in place, controlling the old linac, for about a year. The last four tanks of the old linac, along with that part of the control system, will be removed as the new linac is rolled in.

Control System for the New Linac

The new linac addition at Fermilab is detailed elsewhere at this conference [1]. The major aspects of that system are as follows. The H- beam exiting tank five, at 116 MeV, is captured by an 805 MHz transition section and injected into a seven-module side-coupled-cavity accelerating structure. The 805 MHz modules fit in the space vacated by our old tanks six through nine which now accelerate the beam to 204 MeV. The beam in the new structure is accelerated to a final energy of 401 MeV. This higher-energy beam is easier for the next accelerator, the Booster, to handle because of a 75% reduction in the space-charge tune shift there. The two small transition section cavities, the seven large accelerating modules and the debuncher cavity are powered by 805 MHz klystrons. The seven accelerating modules each use a 12 MW klystron under development by Litton; the other three smaller cavities are driven by a pulsed-version of a UHF-TV channel 69 80-kW-cw klystron.

The following control system is being built for the 805-MHz part of the new linac, see Figures 4 and 5. The control stations are connected to each other and to the rest of the world by token ring. The system interfaces with hardware subsystems either through a VI to a slave VME subsystem or through rack monitors (smart or dumb). Each control station manages two major systems, usually two klystron RF systems. A color console is located at each control station to give local access to the information.

There are several distinct subsystems in each RF station. Modulator and low-level RF computer-controlled subsystems are being developed. Conventional water systems, beam diagnostics and safety systems are also being built. How each of these interfaces to the control system is described here [5].

The modulator and low-level RF subsystems both contain a smart controller in, respectively, VME and VXI environments. Communications occur through VME memory over a VI. Each smart subsystem will perform its own A/D and D/A conversions. The local intelligence of these systems will provide the pertinent digitized readouts in a contiguous block of VME memory which the master control station can read, over the VIs, at 15 Hz. A similar block of contiguous memory will be provided by each

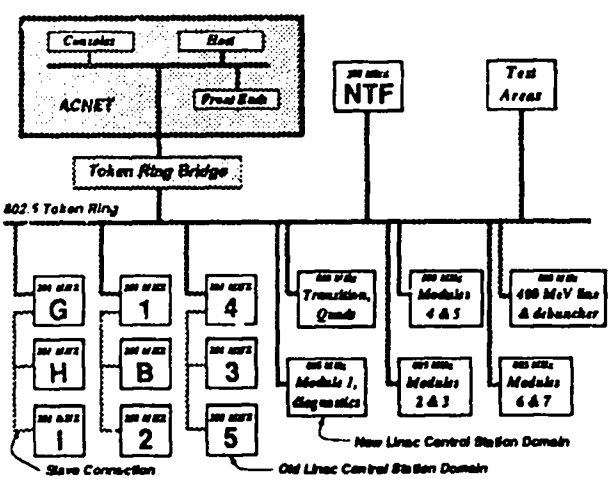

Figure 4, The controls system for the Upgraded Linac

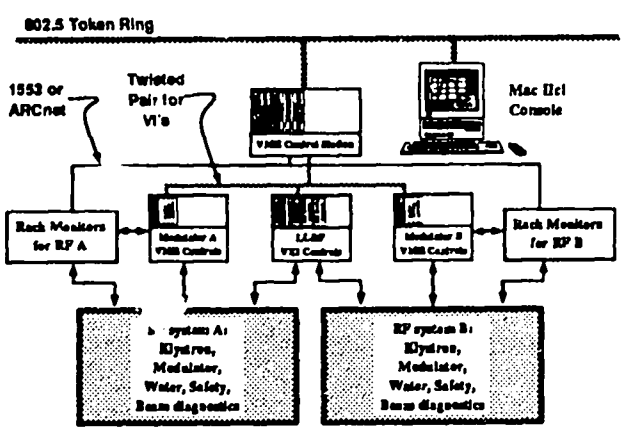

Figure 5, Detail of a single control station for the new Linac.

system for making settings.

The modulator provides a 180 KV, 141 ampere, 128 μs pulse to the klystron. It appears to a Linac control station as, simply, a self-regulating, self-protecting high-voltage power supply. The control station generates a 16-bit voltage setting for the modulator system. Several analog and digital readbacks are provided. The local intelligence for the modulator is responsible for:

1. 15 Hz closed-loop control in the modulator;

2. 15 Hz readout of local analog and digital information;

3. transient recording of pertinent waveforms within the hardware;

4. fast closed-loop/feed-forward control to insure that the proper level of voltage regulation (0.1%) is obtained.

One VME crate per modulator, two per control station, are necessary for noise suppression. The transient waveforms are sorted according to the condition of the modulator—most are recorded as "good" waveforms, but the real purpose of this capability is to access the waveforms generated during a failure of the modulator. These waveforms can be accessed in the VME memory of the modulator crate over the VI. Although the amount of data stored for these transient waveforms is large (several MBytes), it is thought that the frequency they are viewed will be small.

The low-level RF hardware runs in the VXIbus environment. This system is responsible for providing an RF signal of the correct phase and amplitude to the 500-watt klystron-driver amplifier so that beam is properly accelerated through the cavity. The local VXI microprocessor will generate and adaptively change that waveform according to phase and amplitude information obtained from recent beam pulses: "adaptive feed-forward." Two klystrons will be fed from a single VXI crate containing two low-level RF hardware modules. As discussed above, readings and settings to this system from the master control station will be done through VME/VXI memory over a VI.

The beam diagnostics [6] provide several analog signals which are read through a sample-and-hold/RM. Since the aperture of the new linac is significantly smaller than the old linac (3 cm vs 4 cm), we are going to implement a local application (see below) to actively keep the beam in the center of the beam pipe. It is likely that a local application will also be needed to assist with the measurements for the "Δt" experiment [7].

The interface to the klystron interlocks/safety system is through several (twenty) bits in a RM at each RF station. A computer-reset and a computer-ready bit are provided. (Naturally, the primary safety aspects of the accelerator are contained in the hardware. The computer controls system is not part of the safety system.) The water system interface is through a RM.

Also present at each control station is a color computer console. This console uses the Macintosh IIci computer with an Apple TokenTalk Nubus card. The applications presently available are a color parameter page, a parameter plotting package and a VME memory-dump page. These programs are quite mature and reflect the standard Macintosh "look-and-feel." Additionally, we have a token ring driver to the LabView package[8].

Software Features

Several aspects of the local controls software need to be mentioned explicitly. The software is being developed to have each local station respond directly to data requests generated from the consoles in the Main Control Room, thus eliminating the need for a protocol-translating front-end computer. These consoles communicate via the Accelerator Controls Network (ACNET) protocol which the other accelerator controls subsystems at Fermilab use. Each Linac control station is to recognize two sorts of network message protocols, the original ("classic") protocol, used in communication between control stations, and the ACNET protocol.

A critical part of the control station software is supporting multiple, simultaneous, local control procedures. Each local station now has the ability to run many "Local Applications," or LAs. The LAs being implemented now include:

1. 201-MHz system recovery, *e.g.*, from a modulator crowbar;

2. DTL quad reset;

3. 805-MHz system water temperature stabilization (note: there will be four cavity water systems and a klystron water system for each RF system: that's ten water loops per control station),

4. beam steering;

5. 805-MHz turn-on and turn-off;

6. low-energy emittance scan.

The software for the smart rack monitor is not settled yet. The MC68332 is based on the MC68020, so most, but not all, of the instructions of the '020 are in the '332. The hope is that we can implement simple but extensible software on the '332 which allows, initially, the SRM to behave like a dumb RM. Then, features could be added to support SRM local applications.

Conclusions

The control system for the Fermilab linac has been redesigned. The old linac control system is to be replaced in the summer of 1991 by one similar to that required to operate the 805 MHz/400 MeV linac. The old D/A and A/D hardware is retained on the old RF systems. The control system for the new linac requires some new techniques, in particular, interfacing with several smart subsystems. The two types of local control are designed to work together to control the whole new linac in a coherent, integrated and efficient fashion

References

[1] R. Goodwin and M. Shea, "The Distributed Control System for the Fermilab 200 MeV Linac," Proceedings of the 1981 Linac Conference, pp 277-280.

[2] R. Noble, "The Fermilab Linac Upgrade," this conference, talk MO2-02.

[3] R. Goodwin, *et al.*, "Initial Operation and Current Status of the Fermilab DZero VMEBUS-Based Hardware Control and Monitoring System," proceedings of the 1989 International Conference on Accelerator and Large Experimental Physics Control Systems, Vancouver, BC, Canada.

[4] M. Shea, "Smart Rack Monitor," internal note, available from the authors.

[5] The modulator, low-level RF and safety systems are in the design phase. The best reference so far on these systems is found in the design report for the 400 MeV Fermilab Linac.

[6] "Diagnostics for the 400 MeV Fermilab Linac," Elliott S. McCrory, Glenn Lee and Robert Webber, this conference, talk number TU4-1

[7] T. Owens and E. McCrory, "The Delta-t procedure at Fermilab," at this conference, paper TH4-51.

[8] This product is available from National Instruments in Austin, TX. Additionally, a Unix interface to the token ring VME data has been written and a parameter page, plot package and a token ring driver to the DataViews package, available from VI Corporation in Amherst, MA, have been written. The Unix software is somewhat more capable, but a lot less mature than the Macintosh software.

A NEW TECHNIQUE FOR TRANSVERSE PHASE ELLIPSE MEASUREMENT

P.B. Vasilev, A.M. Tron
Moscow Engineering Physics Institute Kashirskoe shosse 31, 115409, Moscow,USSR

ABSTRACT

To reconstruct transverse beam's emittance as a 5 parameter ellipse using the results of its three profile measurements a new technique is presented. Compared with known before the new one gives an additional information on ellipse's position in phase space and its relative contents of particles. An emittance determination precision as a function of detector parameters and profile measurement errors has also been submitted. For beam particles' paraboloidal or Gaussian transverse phase space density distribution an error of technique has been determined. Means of improving of theese technique precision are under discussion.

INTRODUCTION

Measurement of beam's boundary in transverse or longitudinal phase space in existing accelerators is of particular interest for computor control of accelerating process.

As a rapid, practically nonperturbing a primary beam, a three cross-section method (CS-method) is intended to be used for that purpose (see [1],[2],[3]). The method deals with reconstruction of elliptical phase boundaries by measuring of three beam widths in three points or transverse planes along accelerator axis. It is assumed that transforming matrix of an accelerator's section is known and an emittance is invariant. Therefore, a measurement of transverse (or longitudinal) beam sizes is a base for determination of its phase boundaries. The sizes' measurement error depends on profilometer parameters. To simplify analysis let's consern that beam width is measured along one of coordinates (x), which is perpendicular to its axis, and a profilometer is a set of thin wires, having been stringed equidistancly and orthogonally to beam axis in one same plane.

Inspite of rather large number of papers, devoted to beam's emittance measurement, a method's error problem is studied unsatisfactory. That's why assuming beam phase boundary have been elliptical and concerning profile and beam width (for given density level of particles' distribution) measurement error negligibly small, let's see a correlation between measured and true values of emittance and beam relative content of particles within phase ellipse. As a model of particles' two dimensional distribution in transverse phase space a Gaussian and elliptic paraboloidal ones were taken. This choice is ensured by facts that the lines of equal density of both distributions are ellipses and both of them are in good correspondance (for a large number of cases) with experimentally obtained distributions.

DEFINITIONS

To ease further consideration a number of definitions and terms must be done. Let $j(x,x')$ be a density of particles' distribution in transverse phase space (x,x'), where x and x' are respectively distance from an accelerator's axis and angle between it and particle trajectory. Than we mean as a beam profile that is directly measured experimentally a function

$$j_e(x)=\int_{[x']} j(x,x')dx'$$

where $[x']$ -domain of a function and it is called an experimental profile. A true, real profile of $j(x,x')$ function is its orthogonal progection in (j,x) plane and it has been signed as $j_\mu(x)$ (see fig.1). A cross section on relative level h from $j_\mu(x)$ or $j_e(x)$ maximum defines beam width on h level $(0<h<1)$ and it has been signed $D_\mu(h)$ or $D_e(h)$. This way a cross section of two dimensional distribution $j(x,x')$ on h level is a square, that is in this case limited by elliptical curve G. This section having been msasured experimentally or having been defined from model of phase spase distribution is named an experimental $S_e(h)$ or true (real) $S_\mu(h)$ beam emittance or simply beam emittance on h level. Than relative content values of beam particles $m_e(h)$, $m_\mu(h)$, $n_e(h)$, $n_\mu(h)$ for corresponding sections of distributions $j_e(x)$, $j_\mu(x)$, $j_e(x,x')$ and $j_\mu(x,x')$ on h level are defined in following way

$$m_e(h)=\int_{x_{e1}}^{x_{e2}} j_e(x)dx \Big/ \int_{[x]} j_e(x)dx \qquad (1)$$

$$m_\mu(h)=\int_{x_{\mu1}}^{x_{\mu2}} j_\mu(x)dx \Big/ \int_{[x]} j_\mu(x)dx \qquad (2)$$

$$n_e(h)=m_e(h) \qquad (3)$$

$$n_\mu(h)=\iint_G j(x,x')dxdx' \Big/ \int_{[x]} dx \int_{[x']} j(x,x')dx' = \qquad (4)$$
$$= V_\mu(h)/V_\mu ,$$

where $x_{e1}, x_{e2}, x_{\mu1}, x_{\mu2}$ are coordinates that limit beam width on h level. $[x_\mu],[x_e]$ -domains of $j_\mu(x)$ or $j_e(x)$ functions, $V_\mu(h)$ -volume that is limited by (x,x') plane, by elliptical cylinder that contains G curve and by $j(x,x')$ distribution, V_μ -volume that is limited by (x,x') plane and by $j(x,x')$ function and its value is proportional to full number of beam particles or beam current I_0.

CS METHOD ERROR

A CS method error problem in determining emittance and relative beam content of par-

ticles which depends on h level is discussed here for two types of $j(x,x')$ distribution. Given errors can be written in a next way:

$$\Delta S(h)/S(h)=|S_e(h)-S_\nu(h)|/S_\nu(h)= \quad (5)$$
$$=2|D_e(h)-D_\nu(h)|/D_\nu(h)$$
$$\Delta I(h)/I_\nu=|n_e(h)-n_\nu(h)|/n_\nu(h)= \quad (6)$$
$$=|m_e(h)V_e-V_\nu(h)|/V_\nu(h)$$

First a transverse phase distribution $j(x,x')$ as an elliptical paraboloid was taken. In some point z along accelerator's axis it is

$$j(x,x')=1-x^2/a^2-x'^2/b^2 \quad (7)$$
$$-a\leq x\leq a,\ -b\leq x'\leq b.$$

In point z a measured beam profile is given

$$j_e(x)=4b/(1-x^2/a^2)^{3/2}/3 \quad (8)$$

It can be shown for every $z_i\neq z$ that measured profile has more general formulation

$$j_e(x)=j_{em}(1-x^2/x_m^2)^{3/2} \quad (9)$$

where j_{em} is profile maximum and x_m is its width. Measured profile (9) and real one $j_\nu(x)$ that were obtained from the same distribution $j(x,x')$ are displayed in fig.1b, here are also beam widths on h level

$$D_e(h)=2x_{e2}=2a\sqrt{1-h^{2/3}} \quad (10)$$
$$D_\nu(h)=2x_{\nu2}=2a\sqrt{1-h} \quad (11)$$

Relative beam content of particles $m_e(h)$ within emittance $S_e(h)$ can be calcelated with a use of next equation

$$m_e(h)=I(h)/I_o=4(3h^{1/3}/2+h)\sqrt{1-h^{2/3}}/3\pi+ \quad (12)$$
$$+2\arcsin\sqrt{1-h^{2/3}}/\pi,$$

where full volume $I_o=I_\nu=ab/2$ is limited by surface (7). Eq.(12) was obtained by integrating (9) within interval (10).

Relative beam content of particles $n_\nu(h)$ within emittance $S_\nu(h)$ is determined by common volume of cylinder $x^2/a^2+x'^2/b^2=q^2=1-h$, surface $j=1-x^2/a^2-x'^2/b^2$ and plane $j=0$, it is equal

$$n_\nu(h)=1-h^2 \quad (13)$$

Dependences $n_\nu(h)$ (12) and $m_e(h)$ (13) are displayed in fig.2, a difference between them (6), which determines an error of methoo, is in fig.3. A needable emittance measurement error dependence on h level value for given $j(x,x')$ may be found out of (5), (10), (11) as

$$\Delta S(h)/S(h)=2(\sqrt{(1-h^{2/3})/(1-h)}-1) \quad (14)$$

this equation is displayed in fig.3.

Let's see the same dependences for Gaussian $j(x,x')$ distribution

$$j(x,x')=\frac{1}{2\pi\sigma_x\sigma_{x'}\sqrt{1-\rho^2}}\exp\left[\frac{-1}{2(1-\rho^2)}\left(\frac{x^2}{\sigma_x^2}-2\rho\frac{xx'}{\sigma_x\sigma_{x'}}-\frac{x'^2}{\sigma_{x'}^2}\right)\right] \quad (15)$$

where $\sigma_x,\sigma_{x'}$-dispersion, ρ-correlation ratio. A measured profile $j_e(x)$ will be

$$j_e(x)=j_{em}\exp(-x^2/2\sigma_x^2) \quad (16)$$

A true profile can be given by the same way

$$j_\nu(x)/j_{\nu m}=\exp(-x^2/2\sigma_x^2) \quad (17)$$

Hence Gaussian distribution profiles $j_\nu(x)/j_{\nu m}$ and $j_e(x)/j_{em}$ are equal and according to (5) an error of emittance measurement method is zero. But relative content of particles within real emittance differs from that in measured one. A bound of section q on $j(x,x')$ h level was fonded to be (while $\rho=0$)

$$h=j(x,x')/j_m=\exp(-q^2/2)= \quad (18)$$
$$=\exp(-x^2/2\sigma_x^2-x'^2/2\sigma_{x'}^2)$$

From (18) $q=\sqrt{-2\ln(h)}$ and x or x' variates in interval from $-q\sigma_{x,x'}$ to $q\sigma_{x,x'}$. An amount of particles into a volume limited by plane $j=0$, cylinder $x^2/\sigma_x^2+x'^2/\sigma_{x'}^2=q^2$ and by surface (15) is

$$I_\nu(h)=I_o[2\Phi_o(\sqrt{-2\ln(h)})]^2 \quad (19)$$

Here I_o is a full amount of beam particles,

$$\Phi_o(w)=\frac{1}{\sqrt{2\pi}}\int_0^w e^{z(-t^2/2)}dt$$

Eq. (19) shows a real emittance content, while experimental number of particles have to be obtained by integrating an experimental profile (16) by x from $-q\sigma_x$ up to $q\sigma_x$:

$$I(h)=2I_o\Phi(\sqrt{-2\ln(h)}) \quad (20)$$

Dependences $m_e=I_e(h)/I_o$ and $n_e=I_e(h)/I_o$ are displayed in fig.2, curves 3,4 respectively, an absolute difference between them related to real $I_\nu(h)/I_o$ is shown in fig.3 with broken line.

Adduced examples has made clear "sources" of errors in determining relative particles content within emittances, in measuring beam boundary and thus calculating the very emittances. Meamwhile it becomes clear that beam sizes measured on the same h level of profile belongs to the same section of $j(x,x')$ distribution. Next procedure of determining beam emittance with particle contents close to 100% may have been submitted: to measure profile with $h\geq.1$, then to reconstruct it for lower levels $h\leq.1$ and finally to calculate beam sizes and emittance in terms of equations written before.

Determination of function $j(x,x')$ section's bound for $h\geq.1$ may be possible after process of iteration had been realised and it can be described in further publication.

RESTORATION OF PHASE BOUND

To reconstruct beam phase boundary as a five parameter ellipse by measuring three beam widths in three z_1,z_2,z_3 accelerator's axis points a next procedure is presented. Z axis is assumed to coinside with accelerator axis, $z_1<z_2<z_3$. General inlet ellipse equation in z_1 is

$$Ax^2+2Bxx'+Cx'^2+2Dx+2Ex'=F, \quad (21)$$

and here $AC-B^2=1$. It is known that ellipse's centre has coordinates

$$x_o=BE-CD \quad (22)$$
$$x_o'=BD-AE \quad (23)$$

Let x_{max} and x_{min} denote coordinates of most and least, respectively, distant points on ellipse's bound measured along x axis from zero point. Subject to (22),(23), from (21) this values are

$$x_{max,min}=x_o\pm\sqrt{x_o+FC+E^2} \quad (24)$$

where

$$x_o=(x_{max}+x_{min})/2. \quad (25)$$

The product of x_{max} and x_{min} in z_1 point is

$$(-x_{max}x_{min})=FC+E^2 \quad (26)$$

Let $\|t_{ij}\|$ be radius vector reverse transformation matrix from z_2 to z_1, i.e.

$$\begin{bmatrix}x_1\\x_1'\end{bmatrix}=\begin{bmatrix}t_{11} & t_{12}\\t_{21} & t_{22}\end{bmatrix}\begin{bmatrix}x_2\\x_2'\end{bmatrix} \quad (27)$$

The ellipses ratii in z_2 section (distinguished oy line) may be expressed in terms of $\|t_{ij}\|$ matrix and ratii in z_1 as

$$\bar{C}=At_{22}^2+2Bt_{12}t_{22}+Ct_{21}^2 \quad (28a)$$
$$\bar{E}=Dt_{12}+Et_{22} \quad (28b)$$

By substituting (28) into right (26) a connection between product $\bar{x}_{max}\ \bar{x}_{min}$ having been measuring in z_2 point and ellipse's ratii in z_1 can be found out of

$$-(\bar{x}_{m,i}, \bar{x}'_{m,i}) = t_{12}^2(AF+D^2) + 2t_{12}t_{22}(BF+DE) + t_{22}^2(CF+E^2) \quad (29)$$

Naturally, when beam boundary $x_{max,i}, x'_{max,i}$, $i=1,2,3,\ldots$ are known, one can write a set of equations

$$-(\bar{x}_{max}, \bar{x}'_{max}) = u_1 a_{i1} + u_2 a_{i2} + u_3 a_{i3} \quad (30)$$

with unkknown u_1, u_2, u_3 and solve it for them. Here $a_{i1} = (t_{12}^2)_i$, $a_{i2} = 2(t_{12}t_{22})_i$, $a_{i3} = (t_{22}^2)_i$. To obtain ellipse's (21) ratii by known u_1, u_2, u_3 its centre coordinates must have bee known. But according to (25) only x coordinate can be measured in each of three points and while transformation matrixes T_1 from second to first point and T_2 from third to first are known, one can calculate

$$x_{0i} = (x_{max,i} + x_{max,i+1})/2 \quad (31a)$$

$$x'_{0i} = [(t_{22})_1 x_{0i3} - (t_{22})_2 x_{0i2}] / [(t_{12})_1 (t_{22})_2 - (t_{12})_2 (t_{22})_1] \quad (31b)$$

where $x_{0i1,2,3}$ -centre coordinates along x axis in 1 or 2 or 3 point z, x'_{0i1} -an angle coordinate in first (basic) point, $(t_{ij})_{12}$ a ratii of transfer matrix from z_2 to z_1 (subscript 1) and from z_3 to z_1 (subscript 2). Meanwhile, one can obtain from the set (30) with regard to (31)

$$A = (u_1 + x_0'^2)/Q, \quad B = (u_2 - x_0 x_0')/Q,$$
$$C = (u_3 + x_0^2)/Q, \quad F = (u_1 u_3 - u_2^2)/Q,$$
$$Q = \sqrt{(u_3 + x_0^2)(u_1 + x_0'^2) - (u_2 - x_0 x_0')^2} \quad (32)$$
$$D = -Ax_0 - Bx_0', \quad E = Bx_0 - Cx_0'$$

It follows from an adduced consideration that algorythm having been described allows to reconstruct a five parameter ellipse employing results of measuring beam width in three points along accelerator's channel, i.e. by three profilometers.

CHOICE OF PROFILOMETER PARAMETERS

Even if three profilometers are identical, a beam emittance measurement error depends on beam phase portrait on measurement system inlet, on profilometers' mutual disposition and accelerating channel's optical qualities, on profile digitization number N which is equal to relation of beam width to spatial step of profilometer grid Δx, on grid's period $k = \Delta x/\Delta x_0$, where Δx_0 is a single wire diameter, and on wire signal measurement error ε. Hence obtaining of general analytical dependence of this type is impossible because of large number of factors. That's why when a measuring system having been under designing a mathematical simulation of measuring procedure is suggested.

Results of simulation for 600 MeV proton beam with incoming canonic phase ellipse of 18 mm* 2.8 mrad are displayed in fig. 4. Dependences were calculated when profilometers have been situated into free of field intervals with equal distance between them and profiles were assumed to be Gaussian. As it follows from fig.4, when number of digitization N=20 includes 95% of beam current, an error not more 1% can be ahieved in a free of field length equal to 5 meters.

It should be mentioned in conclusion that x variable may be not only distanse between particle's trajectory and axis, but also its phase along accelerating wave. Hence results can be extended to measuring phase spectrum, phase length and beam longitudinal emittance.

REFERENCES

1. I.H.Chiang, J.A.Smith, A.Soulias, IEEE Trans.Nucl.Sci., NS-30(1983),2331.
2. K.Ebihara, M.Jumma, T.Kawakubo, Nucl. Instrum. & Meth.,A202(1982),403.
3. V.I.Artyomov, S.A.Dobromirov, F.A.Peev, D.A.Styopin,Pribory i Tehnika Experimenta, 1989, No4,42.

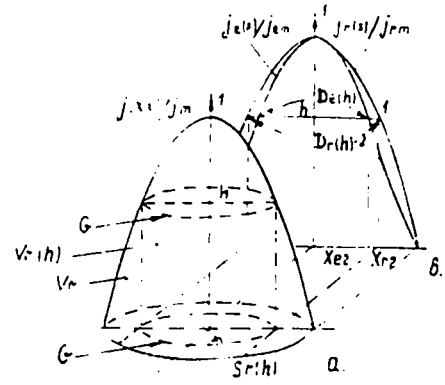

Fig.1 A model of paraboloidal $j(x,x')$ distribution (a) and its profiles in (j,x) plane.

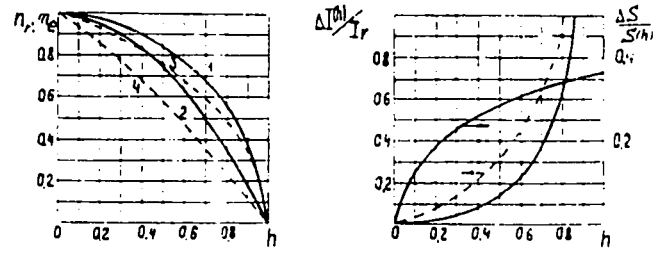

Fig.2 Relative content m_e, n_r of particles within cross-sections for two types of $j(x,x')$ distribution. Solid line--elliptical paraboloid, broken line--Gaussian; 1,3 experimental, 2,4 real.

Fig.3 Relative error of emittance measurement $\Delta S/S$ and its content of particles $\Delta I/I$. Solid line-paraboloid, broken line -Gaussian distribution.

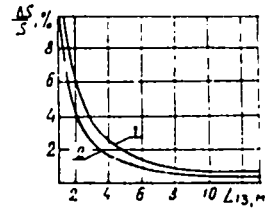

Fig.4 A CS method relative error. $L_{13}=z_3-z_1$
curve 1: N=20, k=10, ε =.1
curve 2: N=40, k=10, ε =.1

CALIBRATION AND OPERATION SCHEMES FOR CEBAF RF CONTROL*

S.N. Simrock, J.C. Hovater, I. Ashkenasi
G.E. Lahti, K.L. Mahoney, and J.A. Fugitt
Continuous Electron Beam Accelerator Facility
12000 Jefferson Avenue
Newport News, Virginia 23606

Abstract

The RF control system for the CEBAF accelerator uses calibration tables to calibrate and linearize critical components in the RF control modules. This includes compensation for temperature drifts. Calibration data are stored in nonvolatile RAM on the CPU board in the control module. Algorithms for calibration of components like the vector modulator for the phase reference and the gradient detector are described. The calibration will be performed in a dedicated test stand which will be completely automated. The microprocessor in the control modules allows running of complex algorithms to achieve phase lock and optimize system gains for minimum residual errors for different gradients and beam loading.

Introduction

The CEBAF RF control system[1-5] has to control the gradient and phase in the 338 superconducting cavities of the CEBAF accelerator. In addition RF control for the two chopper cavities, the buncher cavity, the capture section, and up to five separators has to be provided. In the machine control center (MCC) 3 supervisory computer (SC) are available to control the injector with its 22 cavities and the north and south linac with 160 cavities each. The supervisory computers access the RF controls modules through 10 local computers (LCL) in the north and south linac and one LCL in the injector as shown in figure 1. Each LCL controls 16 RF control modules through CAMAC interface cards and the two high power amplifiers (HPA) associated with two cryomodules, each of which contains 8 cavities. The system hierarchy is displayed in figure 1. The microprocessor in the RF control module provides the local intelligence for calibration, control of loop parameters, data aquisition, interlock functions, and HPA control.

Signals Used for RF Control

The microprocessor in the RF control module controls 20 analog outputs, 40 analog inputs, 32 digital inputs, 32 digital outputs, and 7 interrupt inputs. Those are used to control and read parameters in the RF feedback loop, the HPA and interlocks. Figure 2 contains a partial list of the available signals.

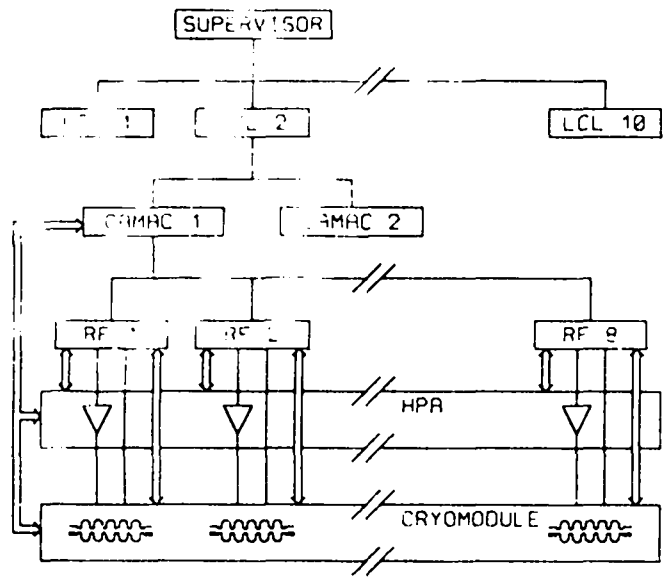

Figure 1. Computer controls for the CEBAF RF system.

Calibration Schemes

The calibration of the signals require characterization of the components in the RF module, HPA, coaxial cables and cavities. Components in the RF module are calibrated in a dedicated test stand, and calibration coefficients are stored in nonvolatile RAM on the CPU board. The calibration data for all other equipment and components will be downloaded from a database which can be accessed by the supervisory computer.

The two most important signals to be calibrated are the field gradient and the phase of the accelerating field in the cavities. Other signals to be calibrated are waveguide forward and reflected power, the detuning angle, and the frequency dependent system gains in the amplitude and phase feedback loop. Measured signals are compared with setpoint values. Critical signals will be monitored in 50 ms intervals, less critical signals every 500 ms. Interlock procedures, alarms, or warnings will be initiated if signals are out of range. The signals are also compared with predicted values to indicate fault or improper operating conditions. The forward power, for example, will be calculated as a function of beam current and detuning angle. A rapid (< 50 ms) decrease in the gradient or a high ratio of forward power to transmitted power indicates a quench and shuts down beam and RF drive.

* Supported by U.S. Department of Energy under contract DE-AC05-84ER40150.

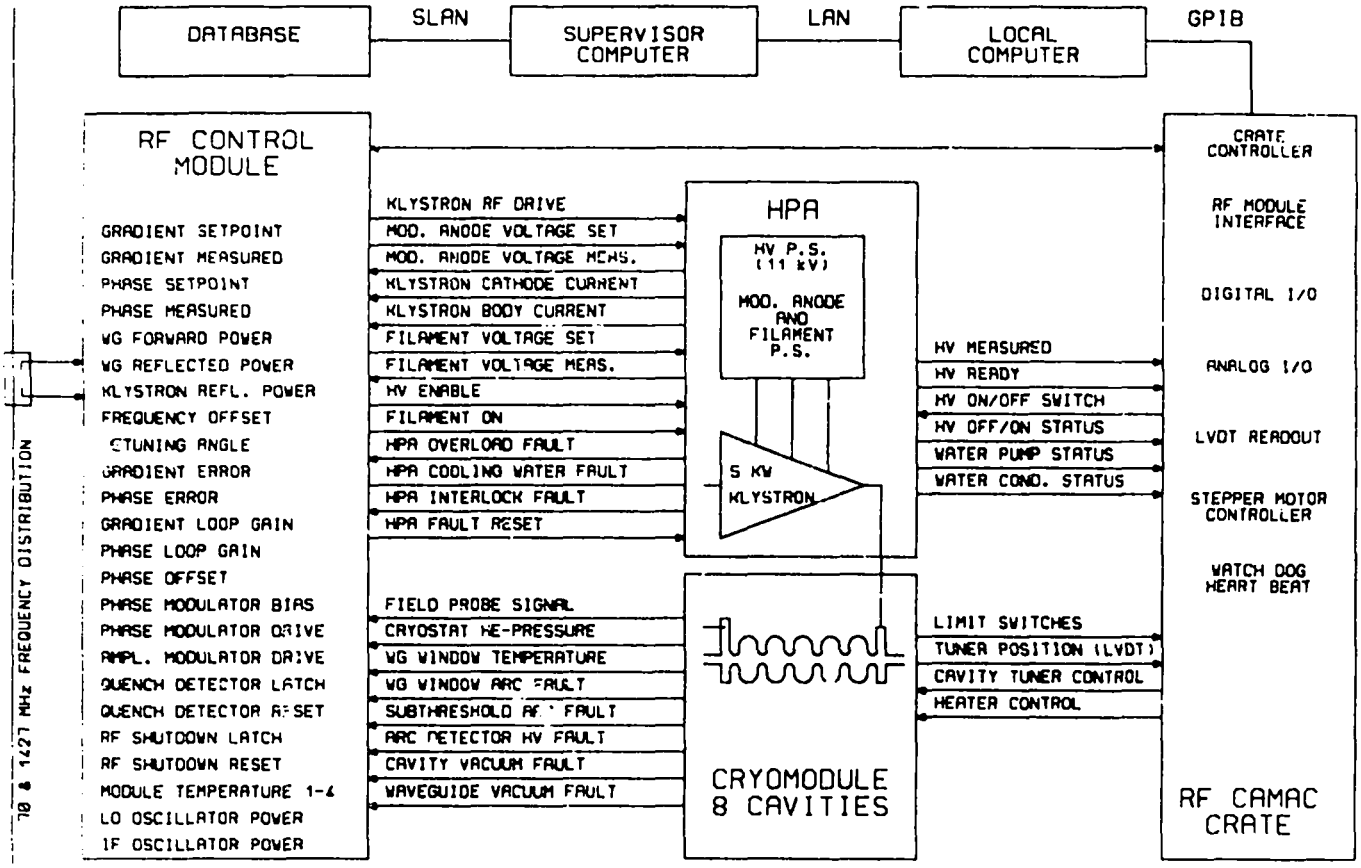

Figure 2. Signals used in CEBAF RF control system.

Gradient Calibration

The gradient detector is a schottky diode located on the converter board. It will be driven in its linear range at about 13 dBm at 5 MV/m. The calibration of the detector output voltage versus input power to the RF control module will be performed in the RF module test stand. Cable attenuation and field calibration coefficients will be downloaded from the database to the nonvolatile RAM. The field gradient is calculated as

$$E_{acc} = \alpha \cdot \sqrt{P_t}$$

with

$$P_t = \frac{1}{\sqrt{\gamma_1(t) \cdot \gamma_2(t)}} \cdot f(a_i, V_d)$$

with the field calibration constant α, cable attenuation γ_1, HOM filter attenuation γ_2 and the detector voltage V_d. Absolute accuracy is about 20% determined mainly by the precision of the field calibration. A better field calibration can be achieved by a measurement of the change in beam energy when varying the gradient. The calibration will be affected by temperature changes of the cables and the HOM filter in the converter. These are measured and used for correction of the gradient setpoint.[6] The detector diodes are oven stabilized to (71 ± 1)°C to avoid complicated compensation algorithms for temperature changes. The temperature stability of gradient detection will be $\approx \pm 2 \cdot 10^{-5}$/°C. Remaining drifts will be regulated by a vernier system which measures the beam energy at the end of each linac and corrects the gradient setpoint in selected cavities.

Phase calibration

Phase detection takes place at 70 MHz by use of analog multipliers[7]. The phase setpoint is controlled by a vector modulator consisting of a 90° hybrid, two analog multipliers, and a combiner. The two control voltages are set to $V_x = V_0 \cdot \sin(\phi)$ and $V_y = V_0 \cdot \cos(\phi)$ respectively. Differences in gains in the multipliers, nonlinearity effects, and finite isolation between inputs and output give us an intrinsic accuracy of about $\pm 2°$. With calibration algorithms a relative accuracy of $\pm 0.15°$ can be achieved. The control signals have to be modified to

$$V_x' = \sum_{i,j=0}^{N} a_{ij}(t) \cdot V_x^i \cdot V_y^j$$

$$V_y' = \sum_{i,j=0}^{N} b_{ij}(t) \cdot V_x^i \cdot V_y^j$$

a_{00} and b_{00} compensate for offsets due to finite isolation between input and output, a_{10} and b_{01} for different gains of the orthogonal signals. Higher order terms correct for nonlinearities. Systematic errors in the calibration process with the network analyzer are eliminated by two measurements with different cable length and therefore different phase offsets in the measurements. For the measurement, the control inputs of the vector modulator are stepped through from -1.0 V to +1.0 V in 0.1V steps. The resulting phase errors are up to $\pm 2°$ as shown in figure 3a. With the corrected values for V_x and V_y the error is reduced by one order of magnitude as shown in figure 3b. Typical temperature sensitivity of the vector modulator is 0.14°/°C. Temperature sensors monitor the temperature of the multipliers and will be used to correct the calibration coefficients for temperature changes. An environmental oven in the test stand will be used for for all temperature dependent calibrations.

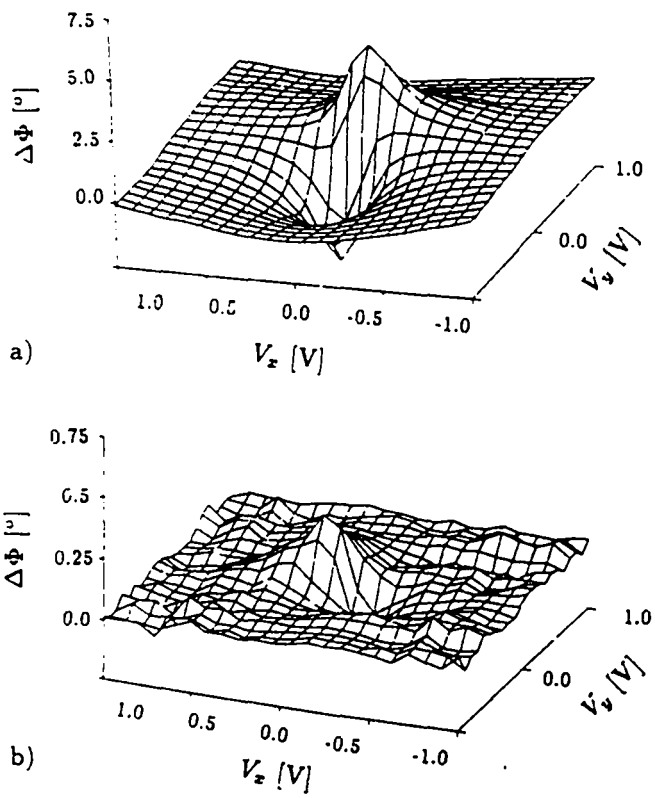

Figure 3. Phase error of vectormodulator. a) uncalibrated and b) calibrated. The calibration coefficients are optimized for $\sqrt{V_x^2 + V_y^2} > 0.4V$

Operation Schemes

The 160 cavities in the injector and the two linacs will be operated from 3 RF supervisory computers in the MCC. The SC for the linac will use two monitors, one for the actual control, the second as a status display and for alarm and warning messages.

The control logic treats the the RF control for the 8 cavities in one cryomodule as a state machine with the following states:

- Idle Mode
- Filament Mode
- HV Mode
- RF Mode

The main control screen for one linac displays push buttons for each 8 seater HPA, displaying 20 HPA's (8 klystrons per HPA) at one control screen. The operator has to go manually through the whole sequence to turn the RF on.

In "idle mode" all hardware will be running, the RF modules will perform continuous checks of all RF system associated hardware and bring any fault to the attention of the operator. In this mode down loading of external calibration parameters will be enabled. Those parameters are stored in the nonvolatile RAM on the CPU board. They describe cavity parameters, HPA characteristics, and cable losses. Downloading will be necessary if parameters change or an RF control module is replaced. In "filament mode" the filaments of the 8 klystrons in an HPA will be turned on giving a HV ready after a warmup time of 5 minutes. If the interlocks show no fault, "HV mode" is used to turn on the klystron cathode voltage for 8 klystrons. At this stage the RF can be turned on by pressing "RF mode". In case of an interlock trip the machine will go back to a safe state. The fault indicators display the HPA and the RF control channel that showed a fault.

In "RF mode" the operator has the choice between "two knob" operation or "expert" mode. In "two knob" operation the operator has only access to phase and gradient setpoint but can control the eight cavities in a cryomodule from one screen. In "expert" mode the operator can access all parameters in the RF control module. This mode allows control of only one cavity from a screen.

Expert Mode

This mode is used for debugging purposes, allowing extensive diagnostics of one of the RF control channels. In this mode the operator has access to about 30 parameters in the RF control loop. The parameters are phase and gradient setpoints, measured values and error signals, loop gain parameters, phase offset, error window setpoints, open and closed mode switches, gradient clamp voltage, several bias voltages, the RF attenuation, RF shutdown switch, and readings for 70 MHz and 1427 MHz local oscillator (LO) power.

Two Knob Mode

This mode will be the normal operating mode. Since the operator has control only over the gradient and phase setpoint, all other parameters have to be preset or automatically derived from other machine parameters. The loop gains will have standard preset values but can be permanently modified in the "expert" mode. An example for automated procedures is the offset phase, which adjusts the optimum operating point of the phase controller. The averaged modulator drive signal is measured continuously and should be zero if the cavity is on resonance. Deviations from the expected value are used to correct the offset phase. Another example is the gradient clamp voltage which limits the maximum possible RF drive to avoid excessive forward power to the cavity. This setpoint is calculated from power requirements which depend on beam current, detuning angle, and microphonic noise levels.

Interlocks

Interlocks are used to prevent damage to the RF control system including the superconducting cavities. Fast interlock circuits such as waveguide arc detector, beam pipe vacuum, and cavity quench detector are implemented in hardware, while slow varying or less critical parameters such as waveguide window temperature, ratio of transmitted to incident power or detuning angle are software controlled interlocks. The hardware generated trip signals use the fast (beam) shut down system and the RF kill input to interrupt beam and/or RF. Software interlocks use the available signals in the RF control module. For example, the detuning angle is monitored in 50 ms intervals. If it exceeds 20°, the motor tuner will be activated to bring the cavity to its home position.

Conclusion

In this paper the basic ideas of calibration and operation procedures for the CEBAF RF control system are discussed. The RF control modules are calibrated in a dedicated test stand and calibration parameters are stored in nonvolatile RAM in the RF control module. Other calibration data will be downloaded to the RF control module during operation and updated if necessary. The calibration scheme uses algorithms which include temperature dependency of calibration coefficients. Each module contains four temperature sensors to monitor the critical elements and uses the temperature information of the feedback cable to correct phase and gradient setpoint to compensate for temperature changes. The algorithms will be extensively tested in the front end test (FET) which involves all 18 superconducting cavities of the injector.

From an operational standpoint, the RF controls will be treated as state machine with four different modes for each HPA. The highest level is the "RF mode" in which the "two knob" operation will be normally used for phase and amplitude control. In "expert" mode all 30 parameters of the RF control modules are accessible for debugging and diagnostic purposes. The "expert" mode has been a powerful tool during the 5 MeV injector test but is too cumbersome if 340 cavities have to be controlled simultaneously.

Acknowledgement

The authors wish to express their thanks to R. Nelson, B. Vignato, B. Morgan and C. West who provided enormous help in documentation and software development.

References

1. S.N. Simrock, J.A. Fugitt, J.C. Hovater, G.A. Krafft and C.K. Sinclair, "Operation of the RF Controls in the CEBAF Injector", *2nd European Particle Accelerator Conference*, (Nice, France, June 12-16, in print.
2. S. Simrock, C. Hovater, S. Jones and J. Fugitt, "RF Control System Development at CEBAF", *Proceedings of the 1989 Particle Accelerator Conference*, (Chicago, March 20-23, p. 1885.
3. R. Bork, C. Grubb,G. Lathi, E. Navarro and J. Sage, "CEBAF Control System", *1988 Linear Accelerator Conference Proceedings*, Newport News, Virginia, October 3-7, 1988, p. 415.
4. I. Ashkenazi and G. Lahti, "Microprocessor Control for the CEBAF RF Control Module", *Proceedings of the 1989 Particle Accelerator Conference*, (Chicago, March 20-23, 1989, p. 1861.
5. R. Bork, "The CEBAF Control System Architecture", *1987 IEEE Particle Accelerator Conference*, (Washington, D.C., March 16-19, 1987, p. 523.
6. C. Hovater, R. Abbott and S. Simrock, "Elimination of Temperature Drifts in the CEBAF RF Control System", Proceedings of this conference
7. C. Hovater and J. Fugitt, "Analog Techniques in CEBAF's RF Control System", *1988 Linear Accelerator Conference Proceedings*, Newport News, Virginia, October 3-7, 1988, p. 412.

THE CEBAF FAST SHUTDOWN SYSTEM*

J. Perry and E. Woodworth
Continuous Electron Beam Accelerator Facility
12000 Jefferson Avenue, Newport News, VA 23606

Abstract

Because of the high power in the CEBAF beam, equipment must be protected in the event of beam loss. The policy that has been adopted is to require a positive permissive signal from each of several inputs in order to operate the gun that starts the beam. If the permissive is removed, the gun shuts off within 20 μs.

The inputs that are now monitored include (1) radiation monitors that detect beam loss directly, (2) vacuum monitors (which also observe the status of various in-line valves), and (3) general input from the rf system, which combines detection of klystron failure, arcs, and rf window high temperature. The system is expandable, so other fault detectors can be added if experience shows their necessity.

I. Introduction

The CEBAF beam carries great destructive power, and the accelerator must be protected from it. The CEBAF fast shutdown system (FSD) must provide critical services to the accelerator control system:

- Primarily, the system must shut a stray beam off before it can puncture the vacuum wall (≈ 50 μs).
- Secondarily, the system must provide:
  - a watchdog timer to ascertain that the control system is in constant communication with every part of the accelerator
  - readback registers for system integrity checks at system startup
  - first fault trace in case of a shutdown
  - current fault traces after a shutdown trace.

The system is explicitly designed for highly reliable shutdown, easy expandability, and fast fault tracing.

II. Architecture

The high power (800 KW) and small diameter (200 μm) of the CEBAF beam imply that a stray beam will burn through the vacuum wall in an estimated 50 μs – 100 μs. Since there are already up to 21 μs of beam stored in the accelerator, the time limit for shutdown is actually about 30 μs. We chose to design to a 24 μs limit, apportioning 10 μs to alarm detection functions, 10 μs to logic functions, and 4 μs to signal propagation time.

Preliminary estimates of required inputs to the FSD system were of the order of 400–600 alarm sources, among which were

- beam loss monitors
- vacuum loss monitors
- fast vacuum valves
- arc detectors of various kinds.

Since the needs were not well defined when it was necessary to start the design of the fast shutdown system, a substantial overcapacity is available to be sure of avoiding an overloaded system at the end of construction.

To ensure both adequate capacity and adequate speed, the FSD incorporates a tree structured system (Figure 1), which allows both a hierarchical organization and liberal expandability. Since a tree structure allows exponential increases in input capacity with more levels, we were able to trade off input capacity for shutdown speed and gain a logical organization. Figure 1 shows the structure for initial accelerator testing. As more segments of the accelerator come on line, their FSD branches will be attached at the indicated points, and their inputs unmasked.

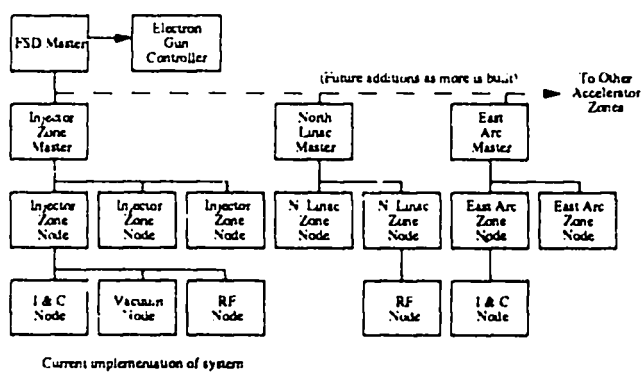

Figure 1. Fast Shutdown Tree Structure.

The requirement for high reliability demanded a permission signal that would fail, if it must, in a safe manner. We took a two-pronged approach to the fail-safe problem:

- First, we require the presence of a permission signal to run, rather than the absence of an inhibit signal.
- Second, we use a 5 MHz trapezoidal waveform as the permission signal to eliminate unsafe "stuck at ..." failures.

Figure 2 shows the permission signal and its characteristics. A normal fault is defined as a low state; it will be detected by the permission decoder within three cycles (600 ns). Only FSD system failures will cause the permission signal to remain high, and the permission decoder will detect this and remove permission within about 1.8 μs.

* This work was supported by the U S. Department of Energy under contract DE-AC05-84ER40150.

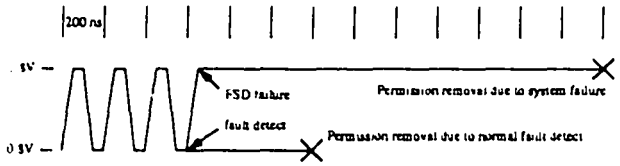

Figure 2. FSD Permission Signal - One Level of Tree.

Shutdowns must be checked out, and the FSD system provides for two types of fault traces:

- a first fault trace, if there has been a shutdown;
- a current fault trace, if there has been no shutdown since the last reset.

Figure 3 illustrates a fault trace. Upon shutdown, each FSD node module in the shutdown chain holds the state of its inputs at the instant of shutdown, allowing determination of first loss of permission within about 2 μs. The control system may at any time query any module about its permission status, and the module will provide the state of every permission input either at the time of shutdown, or at the last time of reset if there was no intervening shutdown.

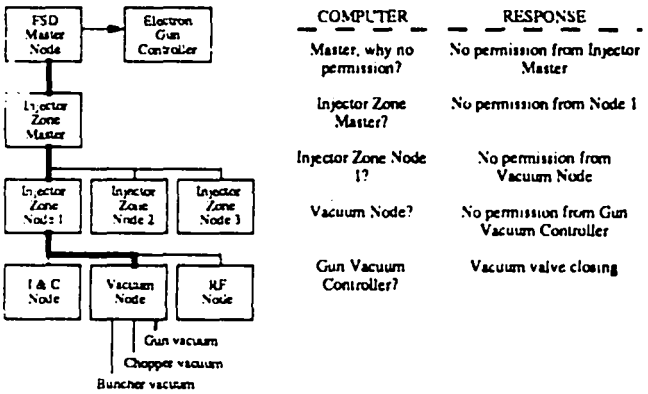

Figure 3. Fast Shutdown Fault Trace.

III. Node Module

The FSD node module (Figure 4) is a single-width CAMAC module which incorporates the functions listed above. There are 16 input fault sources in four groups:

- seven fiber optic permission inputs for tree expansion
- seven optically isolated permission inputs for fault detection sources
- watchdog timer for communications integrity monitoring
- bussed P1 line connection for intra-crate signals.

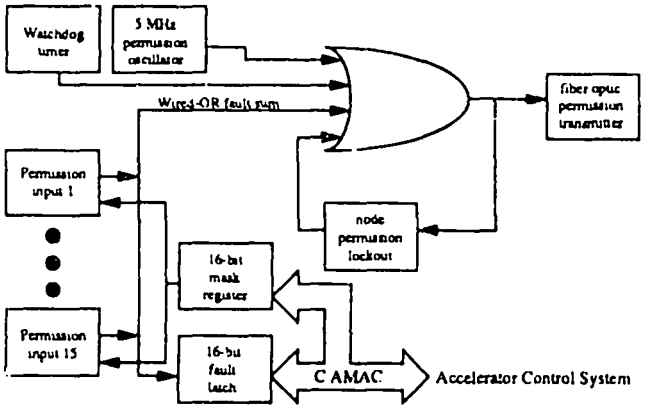

Figure 4. FSD Node Module Block Diagram.

We were able to design a highly reliable permission signal decoder (Figure 5) that would remove permission to the next level of the tree within 600 ns of a fault, and that permitted us to define a convenient number of seven fault inputs and seven structural (tree) inputs. This kept the cost of a module reasonable and allowed a small number of levels to keep the logic propagation time down. The present organization of five levels allows $7^5 + 7^4 + 7^3 + 7^2 + 7 = 19,607$ fault inputs at a worst case normal delay of $5 \times .6 = 3$ μs, plus propagation time.

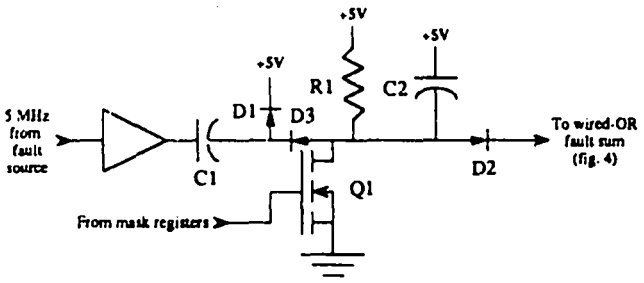

Figure 5. FSD Permission Signal Decoder - One of 15 Per Node.

The watchdog timer in the FSD node module supplies a system integrity need for the control system. The highly distributed control system at CEBAF incorporates a number of relatively independent control functions. It is possible that certain functions could continue to operate in the event of a failure in communications with the control system, resulting in segments of the system working at cross purposes. The watchdog timer offers a switch-programmable check on control scan interval from 13 ms to 426 s in 16 binary steps (.013, .026, ..., 215, 430). If the control system takes more than the programmed time limit to send a CAMAC command to the module, the watchdog timer times out and removes permission.

The last of the 16 permission inputs is the P1 line, which is a dual purpose input/output line for fault sensors that are either alone in a CAMAC crate with the FSD node module, or for which the order of faulting is unimportant. The node module drives the P1 line with a slow transition time 5 MHz permission signal, and a fault detector must short the P1 line to ground to remove permission from the system. If a source on another input removes permission from the node module, the node module also removes the signal from the P1 line, so that other users may monitor local fault conditions.

There is a fault latch and a mask register for each permission source. The fault latches hold the state of each permission source at the instant a fault is detected, and the mask registers keep unused inputs from interfering with the system. The fault latches and the mask registers correspond bit for bit with each of the 16 permission sources.

The fault latches have two functions:

- They latch if a fault is received by a previously clear module.
- They latch all current faults if a reset command is received after a fault.

The fault latches may be read at any time via CAMAC commands, and writing to their address resets the latches and updates them to the current input fault status (the specific datum written has no significance or effect). New faults cannot be latched until a previous fault has been reset; therefore resetting latches any new faults. If there are no existing faults, the node is armed to detect future faults.

Masks may be set at any time from the control system. A masked input will neither remove permission from the system, nor set its fault latch. We have taken the approach that only rigorously enforced administrative procedures are effective in preventing undisciplined maintenance violations of system integrity, and therefore only password protection in the control system software in combination with enlightened operating procedures will be used to prevent unauthorized masking of critical inputs.

IV. Reliability

Since a vacuum accident in the superconducting linacs would cause severe damage, reliability must be very high; therefore the design emphasized reliability both from the point of view of part by part integrity and redundancy of critical paths. The critical paths were carefully analyzed and optimized; however, noncritical paths were designed according to ordinary industrial design standards to reduce cost of the system.

Within a node module, the only critical components, those that can cause a failure to remove permission, are R1, D1, and Q1 in Figure 5. These have been made redundant, and have been specified at a sufficiently high reliability level that we expect no critical failures during the life of the accelerator. Furthermore, we are incorporating into the control system software regular automated integrity checks to identify any failures that might occur in spite of our efforts.

Finally, certain extremely sensitive inputs are being considered for full system-level redundancy to avoid the possibility of poisoning the expensive superconducting cavities in case of a beam loss in the vicinity of an undetected failed beam loss monitor or vacuum fault.

ROBUST RF CONTROL OF ACCELERATORS

W. Joel D. Johnson
Los Alamos National Laboratory, Los Alamos, N.M., 87545

Chacuki T. Abdallah
University of New Mexico, ECE Dept., Albuquerque, N.M., 87131

Abstract

The problem of controlling the variations in the rf power system can be effectively cast as an application of modern control theory. Two components of this theory are obtaining a model and a feedback structure. The model inaccuracies influence the choice of a particular controller structure. One can design either a variable, adaptive controller or a fixed, robust controller to achieve the desired objective. The adaptive control scheme usually results in very complex hardware; and, therefore, shall not be pursued. In contrast, the robust control method leads to simpler hardware. However, robust control requires a more accurate mathematical model of the physical process than is required by adaptive control. Our research at the Los Alamos National Laboratory (LANL) and the University of New Mexico (UNM) has led to the development and implementation of a new rf power feedback system. In this paper, we report on our research progress. In section one, the robust control problem for the rf power system and the philosophy adopted for the beginning phase of our research is presented. In section two, the results of our proof-of-principle experiments are presented. In section three, we describe the actual controller configuration that is used in LANL FEL physics experiments. The novelty of our approach is that the control hardware is implemented directly in rf without demodulating, compensating, and then remodulating.

Philosophy of Robustness

In order to synthesize a control architecture for rf systems, a mathematical model must be developed. This requires measuring the gain- bandwidth characteristics of the rf amplifiers and the accelerators. Accompanying each of these measurements is a degree of uncertainty. The causes of these errors are the nonlinearities in the device under test and the lack of precision in the measurement. However, calibrating the diagnostic equipment and then carefully characterizing all the individual subsystems in the amplifier chain can be a time consuming and nonrewarding task. Indeed, you could spend more time explaining errors between different measurements rather then designing a feedback system with the imperfect knowledge you already possess.

An additional uncertainty exists for control designers of particle accelerators - the beam. If you view the accelerator as a resonant structure with a definable 'Q', and view the beam as an impedance, from beam-loading to no beam-loading (or from beam-loading variations), there will be a perturbation in the 'Q'. Therefore, during operation the "poles" of the accelerator move around in the complex plane. The traditional theory of control deals with precise mathematical models and maintains that with good gain and phase margins the physical system will also be stable. Unfortunately, the result of these uncertainties is that although the mathematical feedback system has good phase and gain margins, the physical control system could be unstable. In fact, it is well known that having good gain and phase margins is insufficient to prove physical stability.[1]

During the past decade, the theory of robust control has emerged to deal with the incongruence between the mathematical and physical feedback stability problem. This new theory is an extension to the foundations laid by Bode and Nyquist. That is, by definition, the task of robust control is to analyze and design a stable, high performance control system despite having models with significant uncertainties[1]. It is possible to determine a priori the maximum uncertainty bound beyond which no controller can be synthesized to stabilize the given system.

Robust control is subdivided into two concepts; robust stability and robust performance. Optimal state-feedback is one tool by which to achieve robust stability, there are also output-feedback stability robustness methods[1,2]. No complete synthesize technique currently exists for the robust performance problem and is an open research topic. We decided to pursue the state-feedback concept because of its theoretical results of infinite forward gain margin, -6db reverse gain margin, 60° phase margin, and nonlinear stability margin.

State Feedback

Experimental selection of a state follows from its basic definition: the state of a dynamic system is the smallest set of physical variables such that the knowledge of these variables, together with the input, determine the system's behavior. Since we wish to control the electric fields in the accelerator, which are produced by the rf power flowing into the accelerator, the minimal set is formed by the output of each of the amplifiers and the accelerator. Including internal amplifier physical variables would be more than sufficient, and hence would form a nonminimal set. These outputs or states then determine the behavior of the system.

The methods investigated were a pole placement design and an optimal state-feedback design with its stability robustness properties. In addition, all dynamic control devices were discarded, leaving only the amplifier chain (Fig. 1). Both the amplifiers and the accelerator were modeled as first-order low-pass equivalent filters.

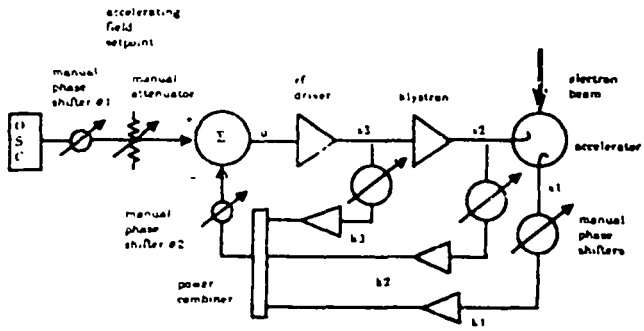

Fig. 1 State Feedback Controller.

The uncertainty enters the model when measuring the -3db bandwidth points and trying to fit this data to a first-order filter. This was done in order to research the simplest model achievable that would still retain feedback system accuracy. The low-pass equivalency retains generality because the control system bandwidth arises from the demodulated version of each signal. The rf driver and the accelerator have normal, smooth frequency transfer functions. However, the klystron does not. Its gain-frequency curve is asymmetric. Below the center frequency, the gain roll-off rate is less than it is above the center frequency. For frequencies close to the center (1.3 GHz ± 4 MHz) the gain curve is flat. The resultant nominal model without beam-loading disturbance is given by

$$dx/dt = \begin{bmatrix} -1.1 & 1 & 0 \\ 0 & -40.25 & 1 \\ 0 & 0 & -7.7 \end{bmatrix} x + \begin{bmatrix} 0 \\ 0 \\ 5.7 \times 10^5 \end{bmatrix} u ,$$

$$y = [1 \quad 0 \quad 0]\, x ,$$

with uncertainty entering the A matrix and b vector as

$$\delta A = \begin{bmatrix} \pm 14 & 1 & 0 \\ 0 & \pm 1.5 & 1 \\ 0 & 0 & \pm 2.1 \end{bmatrix} , \quad \delta b = \begin{bmatrix} 0 \\ 0 \\ \pm 1.7 \times 10^5 \end{bmatrix} .$$

*Work supported by the Los Alamos National Laboratory Institutional Supporting Research under the auspices of the United States Department of Energy and University of Twente, Netherlands.

Beam loading is a disturbance which induces plant parameter variations in the nominal model.

With simple eigenvalue assignment to {−6.28, −40.2, −7.7} the feedback gains were −77 db, −97 db, and −116 db for k_1, k_2, and k_3 respectively. These gains include the coupling coefficients from the accelerator and the directional couplers. Pole placement does not try to optimize the feedback system. Therefore, eigenmode assignment resulted in some states with no feedback. The residual accelerator field fluctuations were less than 0.03%, but droop across the pulse was significant. Figures 2 through 5 depict open-loopversus closed-loop with beam-loading disturbance

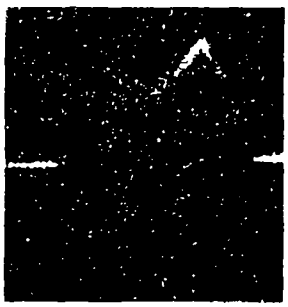

Fig. 2. Open-loop phase variation with beamloading. 2° and 20 μsec per division.

Fig. 3. Open-loop amplitude variation with beamloading. 100 mV and 20 μsec per division.

Fig. 4. Closed-loop phase variation with beamloading. 2° and 20 μsec per division.

Fig. 5. Closed loop amplitude variation with beamloading. 100 mV and 20 μsec per division.

Next a Linear Quadratic Regulator (LQR) optimal control approach was used with the following performance index:

$$J = \frac{1}{2} \int_0^\infty \left(x^T Q x + u^T r u \right) dt .$$

In the above equation, Q minimizes deviations in the states and r minimizes the control input energy. That is, a small r implies a large power reserve and a large entry in Q implies small deviations in that state.

The optimal control feedback gains were −73 db, −69db, and −40 db for k1, k2, and k3, respectively. Figures 6 and 7 show these results without beamloading. The phase margin was measured to be 75°. The infinite gain margin of an ideal LQR design is destroyed by the fact that every loop has some finite time delay associated with it. One disadvantage with optimal control is that different Q's and r's will result in different feedback gains. The designer must still apply his knowledge of the system in order to determine if the gains make sense. Once you determine the boundary of sensible gains; however, the algorithm will automatically determine what gains are "best" for a given constraint.

Fig. 6. Closed-loop (phase) optimal control without beamloading. 1° and 10 μsec per division.

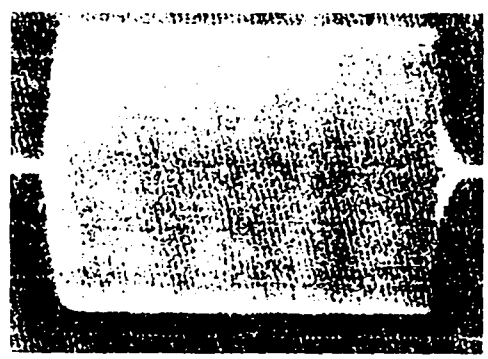

Fig. 7. Closed-loop (amplitude) optimal control without beamloading. 100 mV and 10 μsec per division.

In fig. 1 the three phase shifters in the feedback loops are used to negate the various line lengths at 1.3 GHz. The gains are actually fixed microwave attenuators. The manual phase shifter #2 is used in order to ensure negative feedback. The summer is a passive, 180°, hybrid combiner. The manual phase shifter #1 and variable attenuator are used to experimentally set the correct reference input.

Frequency-shaped State-feedback

The normal state-feedback cannot frequency shape the control system. As seen in the above results, the "proportional-derivitive" control did not produce a high enough gain controller to correct for low frequency disturbances. However, this negative result was not without its merits. There was a significant reduction in the medium to high frequency noise and a large unity-gain bandwidth (~550 khz). The task now became to design a controller which would preserve this noise performance yet improve the low frequency disturbance rejection.

The explanation for how the optimal controller works is easily seen in the frequency domain. It synthesizes a closed-loop system that possesses a proper, (relative degree identically equal to one) "1/s"-like loop transfer function. This is why the controller yields such large stability margins. In order to improve low frequency response, proportional gain must be increased. However, eventually time delay and klystron saturation preclude any further increase in gain. Because power and bandwidth are related, the unity-gain bandwidth is ultimately limited by the klytron's reserve power.

If the original physical system does not possess an integrator in the loop transfer function then, as in the traditional

feedback method, an integral state must be augmented to the system. Physically this configuration is shown in Fig. 8. The high Q pillbox cavity in the outer loop approximates an integrator directly at rf. An alternative to the cavity is a resonant SAW device. The equations which describe this "P.I.D." controller is given by

$$\begin{bmatrix} dx/dt \\ dz/dt \end{bmatrix} = \begin{bmatrix} A & 0 \\ E^T & 0 \end{bmatrix} X + \begin{bmatrix} b \\ 0 \end{bmatrix} a$$

$$y = FX$$

where dz/dt defines the integrator state.

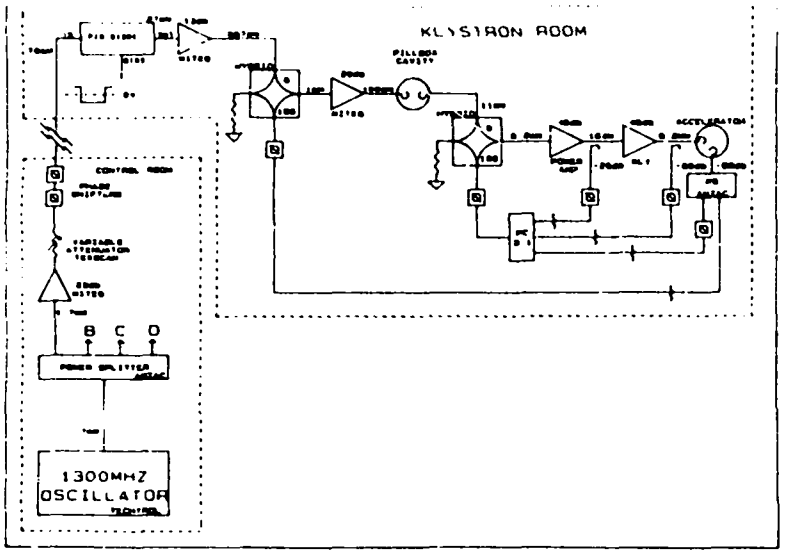

Fig. 8. "P.I.D" State Feedback design.

Figures 9 through 12 depict open- loop versus closed-loop performance. Optimization proceeds precisely the same way as before. With this new feedback system, the results todate are 0.25% amplitude droop, 0.03% amplitude noise, 0.5° phase droop, and 0.05° phase noise.

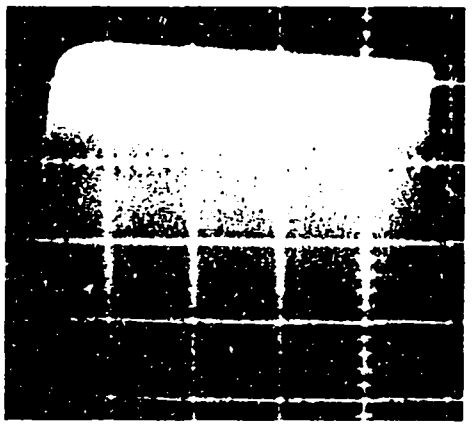

Fig. 9. Open-loop phase variation without beamloading. 2° and 20 μsec per division.

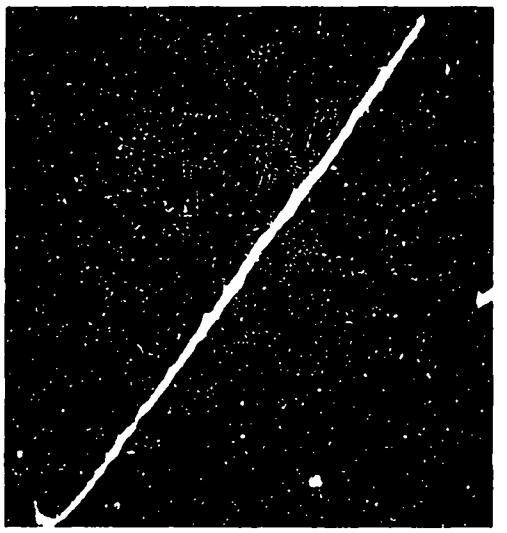

Fig. 10. Open-loop amplitude variation without beamloading. 12% and 20 μsec per division.

Fig. 11. Closed-loop phase variation without beamloading. 1° and 20 μsec per division.

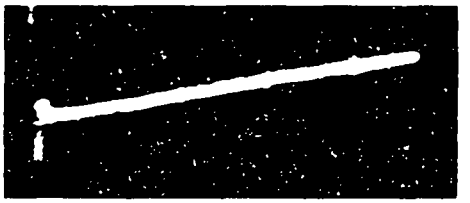

Fig. 12. Closed-loop amplitude variation without beamloading. 0.25% and 20 μsec per division

Conclusion

The first phase of our control research at LANL and UNM has been completed. Our effort has yielded a new controller with very low noise properties and large bandwidths. The beam-loading at the FEL is 50% and with a gain of 25 this results in a 2% steady-state error. For FEL operation it is far more important for the noise properties and transient error to be well controlled and to tolerate a small steady-state error. Future research will be directed at reducing this error. It is expected that with a pillbox cavity Q greater than 30,000, the steady-state error will be further reduced.

There are three major advantages of this new approach. The first is significant reduction in energy spread and energy slew. The second is the greatly reduced hardware. The third is that the feedback gains are implemented using only passive elements.

With the emphasis of robust control guiding the design of the feedback system, the synthesise technique yielded stable control systems. Robust stability and robust performance output feedback methods will be the subject of future experiments.

Reference

1. "Robust Control", Ed. P. Dorato, IEEE Press, 1987.
2. "Recent Advances on Robust Control", Ed. P. Dorato, IEEE Press, 1990.

PRECISION, 32 CHANNEL POWER SUPPLY SYSTEM*

N. Dobeck, J. Beaufait, E. Boettcher, G. Burtner, P. Francis,
R. LaMora, M. O'Sullivan, C. Settles, and C. Sharp
Continuous Electron Beam Accelerator Facility
12000 Jefferson Avenue, Newport News, VA 23606

Abstract

A modular, multichannel current regulator system has been developed to power the low current correction and focusing magnets used for beam transport. The basic module consists of a relay rack housing four card crates with eight regulators per crate. The rack also contains a utility chassis and common power supplies. Each regulator card includes a communications microprocessor and a temperature controlled analog circuit block containing precision reference, serial DAC, shunt resistor and error amplifier. The regulators are linear, bipolar units capable of furnishing up to 10 amps at 20 volts with less than 0.01% ripple and drift.

Introduction

The block diagram of a typical system is shown in Figure 1. Although all 32 channels are shown in the diagram, initially some of the regulator slots in the rack will be left open for future additions due to more magnets or higher power requirements.

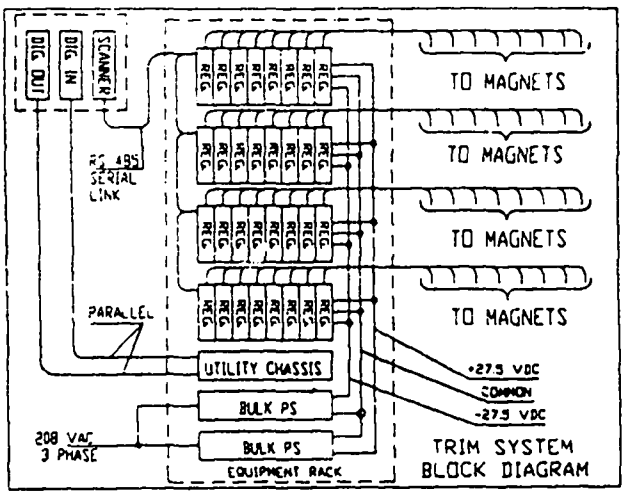

Figure 1. Trim System Block Diagram.

Although only the corrector dipoles require a bipolar output, all of the regulators have this capability. This allows all of the current regulation needs to be handled by one design. Having only one regulator design kept the initial development effort down, made the configuration of the systems very versatile, made a more economical buy possible and will make maintenance easier.

Because of the relatively tight packaging requirements, a large blower was added on top of the rack. The blower pulls filtered, ambient air through louvres in the back door and up through four levels of regulator modules. A drawing of the mechanical rack is shown in Figure 2.

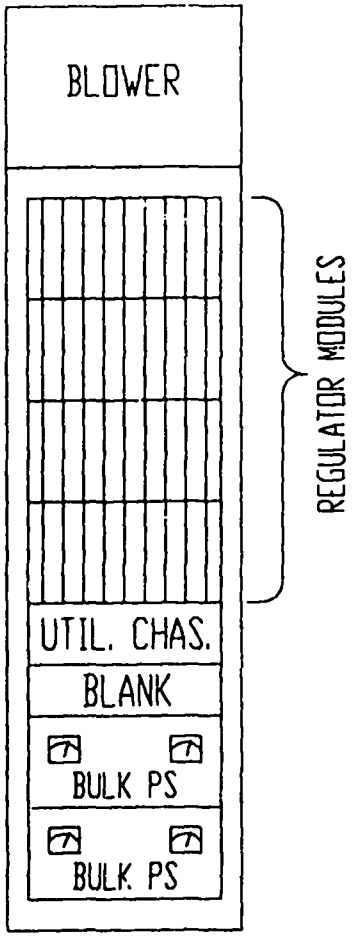

Figure 2. Mechanical Rack Drawing.

* This work is supported by U.S. Department of Energy under contract DE-AC05-84-ER40150.

Three-phase 208 VAC power enters at the top of the rack through a line filter located in the blower housing. Because of concerns about coupling stray AC fields through the regulators, the AC feed wires going down to the bulk power supplies are run in steel conduit as far as possible.

DC power from the bulk power supplies is distributed through bus bars, fuses and #8 wires to the custom backplanes. Each branch circuit handles four regulators and is capable of furnishing 40 amps.

The #10 wires from the regulator outputs terminate at the bottom of the rack on terminal blocks mounted on a DIN rail. The magnets are fed from these terminal blocks with paired #10 wires.

A utility chassis houses a PLC (Programmable Logic Controller) which provides rack thermal monitoring, interlock control and interface logic. The PLC interfaces with the main control system through CAMAC digital input and output modules. The utility chassis also houses several miscellaneous power supplies needed for bias and control.

Monitor and control of a rack system is handled by a 32 node, RS-485, multidrop serial link. One master scanner located in a CAMAC crate is linked to all 32 regulators through connectors on the back planes. Each regulator has an on-board microprocessor to handle communications as well as do local diagnostics.

Detailed Descriptions

Card Cage

As much as possible standard Eurocard components were used for the card cage. The primary deviations from standard are a greater depth and side panels that form the main supports for all four of the cages and result in one large assembly instead of four independent card cages.

Bulk Power Supply

Two bulk power supplies are used in each rack, with one of the units furnishing up to +320 amps and the other furnishing as much as −320 amps. The power supplies are commercially available 10 kW, high frequency switchers requiring 3 phase, 208 VAC input power. By using switching rather than thyristor technology, the size and weight of the power supplies was reduced significantly.

Utility Chassis

A utility chassis is used to house the miscellaneous power supplies and control functions that are needed to make a fully functioning rack. A 5 volt logic supply, two small bias supplies and a 24 VDC control power supply are located here. A small PLC provides local control logic and rack monitoring. This PLC monitors rack temperatures, airflow and door interlock status. Digital monitor and control signals are exchanged with the main control system through digital input and output CAMAC modules.

Regulator Module

A simple circuit diagram of the 200 watt regulator module is shown in Figure 3. The output stage uses complementary darlingtons to keep the drive requirements down. Base drive for the output stage is furnished by amplifier U1. The crucial current sensing and amplification is done by the analog block. This is a temperature regulated, surface mount device which includes a serial DAC, precision voltage reference, precision shunt resistor, shunt pre-amp and error amplifier. All critical analog functions are handled here. A simple schematic of the analog block is shown in Figure 4.

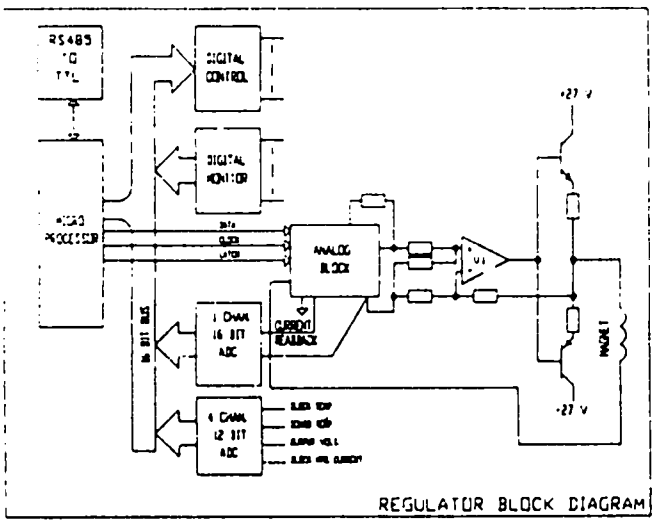

Figure 3. Regulator Block Diagram.

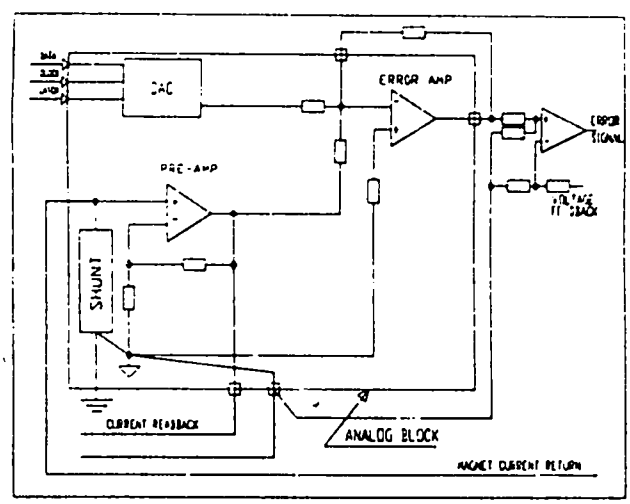

Figure 4. Precision Analog Block.

Monitor and Control

Because of the relatively stringent 100 ppm output noise and drift specification, the monitor and control of the regulator is handled entirely by a full duplex serial communications link. This greatly reduces the chance of coupling ground loop or other noise into the input stages of the regulator.

An on-board communications microprocessor drives the 16 bit serial DAC located on the analog block, monitors the 16 bit current readback ADC, monitors a 12 bit, 4 channel, general purpose ADC and handles digital I/O functions on the printed circuit board. Both of the ADC's are slow, dual slope integrating devices.

The serial link is designed to achieve a scan cycle time of 50 milliseconds or less with 32 nodes on the network. Because the microprocessor is used for communications only 1/32 of the available time, there is considerable time open to do on-board diagnostics and control. Possible examples are controlled ramping of the output current and monitoring of the output voltage allowing calculation of the magnet coil resistance.

The microprocessor is an 8 bit Motorola device with 4K of on-chip ROM. About 2K of the ROM is used for the basic communications and control tasks, leaving 2K for further diagnostics and control. The code was written in assembly language.

The 32 node, RS-485 serial link is driven by a 32 channel scanner module. The scanner is a commercially available, double wide CAMAC module that functions entirely as a communications controller. The communications microprocessor interfaces with the CAMAC system through dual ported memory.

Performance

These current regulators were able to meet a 24 hour, 100 ppm noise and drift specification over an ambient temperature swing of 40°C during tests in an environmental chamber. The temperature coefficient over the 40°C swing was 1 ppm per degree C The 100 ppm specification includes power line ripple as well as low frequency noise. It is unlikely that any of the service buildings will see a 40°C temperature swing over any 24 hour period after warm up, so the installed systems should be able to match the performance shown in the regulator board tests.

Summary

A straightforward and versatile power supply system has been designed to drive the low power corrector and focusing magnets in the accelerator beam transport system. A simple bipolar regulator module furnishes 10 amps at 20 volts. Common bulk power supplies furnish pre-regulated power for the regulator cards. Current low frequency noise, drift and ripple are within a 100 ppm envelope. Monitor and control of the regulator modules is handled with an RS-485 compatible serial link driven by a 32 channel CAMAC scanner module.

HIGH STABILITY SWITCHING MODE POWER CONVERTERS FOR MAGNET LOADS

Oscar Calvo, Coles Sibley and Tomas Russ

Massachusetts Institute of Technology

Bates Accelerator Center
PO Box 846, Middleton, MA 01949

ABSTRACT

The availability of general purpose switching mode power supplies in the KW range has prompted the possibility of using them for powering optical elements in linear accelerators. They are, however, not designed specifically to be operated as high stability current sources into inductive loads.

We have modified and conditioned commercial, off the shelf switching mode power supplies for use in powering multipole magnets. Temperature stability in the constant current mode has been upgraded to 15 ppm/C. Other stability parameters have been similarly improved. We modeled power supply operation using the program Spice, and verified its results experimentally. An analog controller was designed to compensate for instabilities in the feedback loop. This circuit was incorporated into a Bitbus power supply controller which is used as interface to the control system. Analysis of shielding techniques and tests results for a 2.5 KW power supply are provided.

Introduction

The South Hall Ring (SHR) under construction at the MIT Bates Linear Accelerator center will provide high duty factor (CW) electron beams and an internal target capability for nuclear research. This project is the culmination of Bates developments over the last decade aimed at providing coincidence capability throughout the important energy range up to 1 GeV. Proper operation of the proposed pulse strecher ring places stringent criteria on the operation of all magnetic elements such as dipoles, quadrupoles, sextupoles, etc. A large number of power supplies, with power capabilities ranging up to 10 kW and stabilities better than 15 ppm full scale, are needed to power up all the multipole magnets.

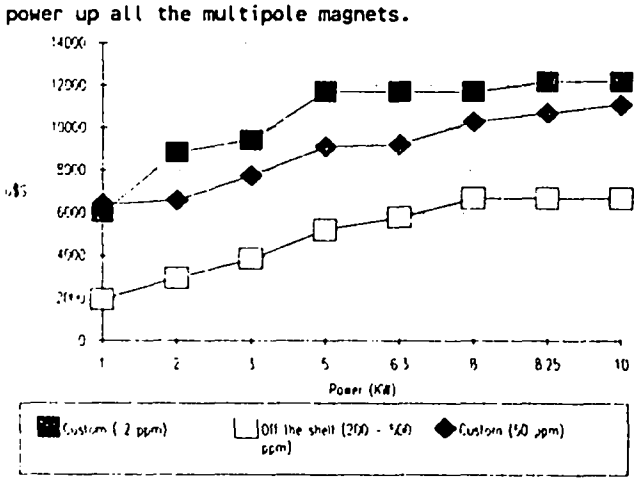

Figure 1. Power supply costs (with controller)

These requirements are normally satisfied with custom designed power supplies. However, in the Pulse Strecher, large number of these supplies are needed and cost factors rule out this approach (figure 1).

The well known advantages of switched mode power supplies, such as high efficiency, low weight and cost, make them very attractive for medium and high power levels This popularity resulted in availability of off the shelf products at very reasonable prices. However, they are not optimized to work as current controlled power supplies. They are usually built to operate in voltage controlled mode and powering resistive loads.

The solution adopted here was to analyze the performance of various commercial power supplies and modify them to suit our needs. The internal controller was upgraded to enhance performance and stability with inductive loads. The current shunt was replaced by an external one with low temperature drift characteristics. In addition, a digital interface was provided for remote operation from a personal computer.

Operation

After a preliminary selection of different vendors we opted for the EMS 40-60-2 power supply. This particular unit delivers 2.5 kW but its circuitry is very similar for all the models ranging from one to five kilowatts. The supply operates in current and voltage modes and is suited for resistive loads. It exhibits a long term stability of 500 ppm with a temperature coefficient of 300 ppm in current mode. It regulates within a 0.1 % with load or input voltage changes and has a ripple of 30 mV at 40 V/ 60 Amps. A block diagram of the switched mode power converter is shown in figure 2.

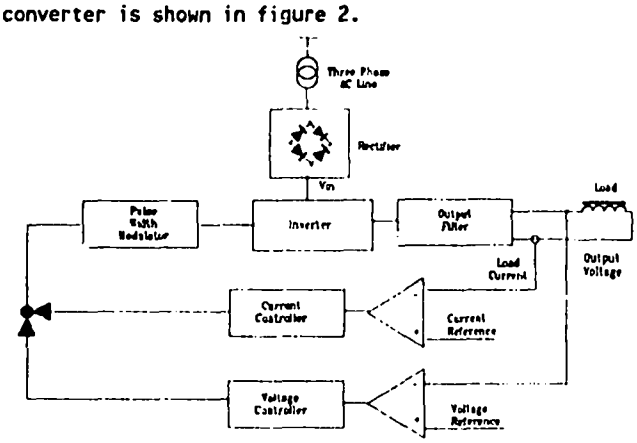

Figure 2. SMPS block diagram

The three phase input AC is rectified and filtered to provide an unregulated voltage (265V - 350V) DC bus, which is converted into a high frequency square wave through a high frequency power transformer. This AC is then rectified and filtered to provide a low level DC output. Control of the output voltage or current levels is achieved by modifying the duty cycle of the high frequency AC voltage.

In the current controlled mode, the output current must be sampled and compared with a reference. The error signal is sent to integrated PWM controllers (UC3524), operating in the master slave mode. They control the duty cycle of the drivers, which are magnetically coupled to the output stage.

In order to operate the Power Supply with the desired long and short term stability of fifteen parts per million, some critical components must be improved. It can be easily proven that in a feedback loop, if enough gain is provided in the direct loop, the elements that determine the accuracy and stability of the system are the transductor, the reference and the error amplifier.

The internal shunt, made of Manganin, with a temperature coefficient of 150 ppm was unsatisfactory. A zero flux transductor would be appropiate to monitor the high output current but its cost becomes prohibitive when large number of them are required. Instead, a more inexpensive unit, a resistive shunt made of Zeranin, was utilized. These shunts exhibit a temperature coefficient better than five parts per million per degree Celsius over the range of 0° C to +60° C. The shunt is water cooled and the temperature of the water is kept within one degree Celsius. The unit tested dissipated up to 100 Watts, delivering one volt at 100 Amps. This signal is amplified by a low noise instrumentation amplifier.

The internal reference was also replaced by an external one, with very low drift (0.6 ppm)/ and excellent line regulation (2ppm/V). The reference feeds a sixteen bit Digital to Analog converter that can be set remotely from a computer. The output of the DAC is used to provide the current reference to the power supply.

The error amplifier was upgraded to a low drift instrumentation amplifier providing very high gain (140db) at low frequencies, thereby reducing the errors in the stationary state. The original current and voltage regulators were coupled with diodes to the Pulse Width Modulator, and by using the same method to incorporate our upgraded controller to the loop we avoided the need to modify the power supply motherboard.

Modelling and compensation

The supply used in our tests operates in a full bridge configuration as a Buck converter. A simplified diagram of this type of converter is shown in figure 3. The inductor is energized when the transistors are conducting, with a slope given by Vi-VO/L, and discharges across the capacitor and load when the transistors are off, with a slope given by -VO/L.

Using two state averaged differential equations, a simplified model for the PWM can be easily derived [ref 3 and 4]. This model replaces the PWM with a Voltage source that depends on the duty cycle "d" and a filter as shown in figure 4.

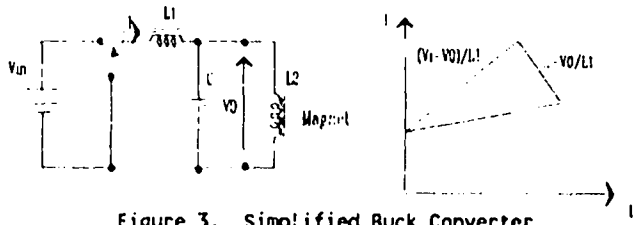

Figure 3. Simplified Buck Converter

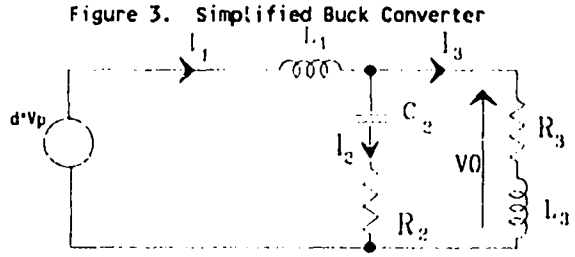

Figure 4. Simplified model for the PWM

The internal shunt was originally placed before the output filter capacitor and, even though the average current across the capacitor should be zero, a temperature dependent leakage current was measured which affected the regulation. Placing the shunt resistor in series with the load solves this problem but increases the order of the transfer function and the internal compensators were no longer appropriate.

Solving the current and voltage expressions for the circuit in figure 4, the transfer function between the output current and the control signal is:

$$G(s) = \frac{(1 + s\,C2\,R2)}{(s^2\,L1\,C2 + s\,R2\,C2 + 1)(s\,L3/R3 + 1)}$$

By inspecting the previous equation, it can be seen that the PWM presents a zero introduced by the capacitor with its ESR, it has a complex poles produced by the filter LC and extra pole introduced by the load. Replacing the components by its numeric values the roots are as follows:

poles:

p1,2 = -362.7 +/- 664.52i (fn = 121 Hz)
p3 = -10.114 (f3 = 1.6 Hz)

zero:
Z1 = -800 (f1 = 127 Hz)

An external compensator was designed with three lead and one lag circuit. The first lead has a zero to cancel the pole introduced by the load. The second lead has it zero cancelling one of the complex poles. The third lead was placed at high frequencies to improve the phase margin, and the lag circuit introduces a pole at the origin to integrate any possible dc error. The gain was chosen to obtained a closed loop response with a frequency bandwidth of two kilohertz.

The design was verified with a model developed in Spice (Figure 5). Figure 6 is a Bode Plot that compares the models (Spice and Mathematica) with the values measured experimentally with 4 mH Magnet load.

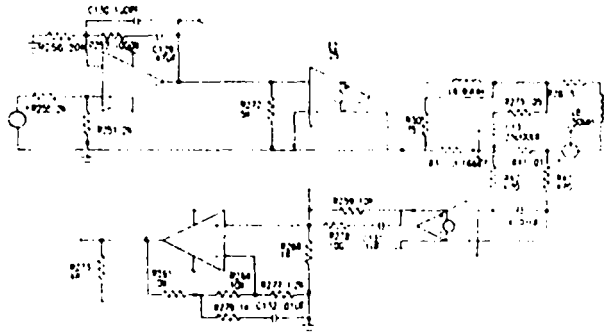

Figure 5. Spice model of the upgraded power supply

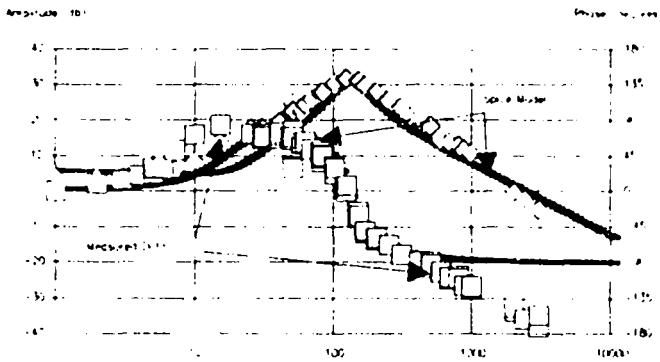

Figure 6. Open Loop Frequency Response of the PWM

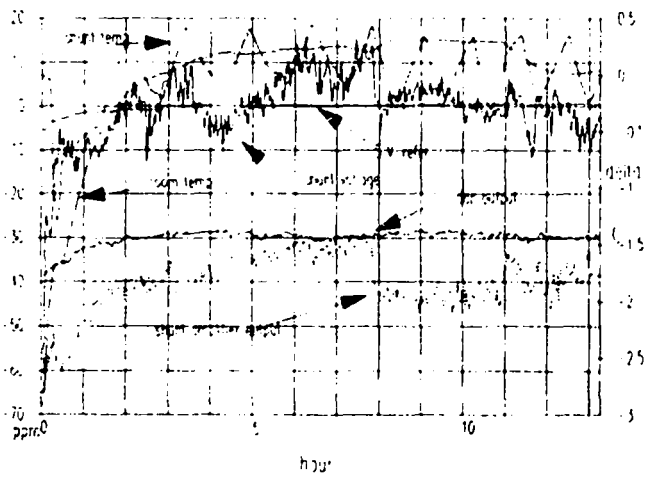

Figure 7. Experimental results

Shielding

The shielding techniques for the controller are critical to the succesful operation of the power supply. This is obvious for any high gain, low signal amplifier. Three basic rules for shielding techniques were followed (see ref.6). First, all shields and enclosures must be tied to a zero reference to be effective. The enclosures for the power supply, analog controller and power shields are all tied to earth ground. The shields for the signals and the analog ground plane are all tied to the controller zero reference in the power supply. Since the output of the supply must be floating, the analog shield and the earth shields are capacitively coupled. The analog shields must drain current away amplifier inputs, i.e. toward the source. They should also be configured to avoid ground loops from shield to shield so no daisey chaining of the shields is allowed. Each shield is connected at the same point in the controller, which is also connected to the signal common in the power supply. Separate shields for each independant signal into or out of the controller box and an additional shield for the power entrance was provided.

Several configurations of the ground and shield connections were tried. The setup in figure 8 has had the best results. A Ferrite core was needed in the shunt cable to reduce the high frequency common mode noise entering the controller from that point.

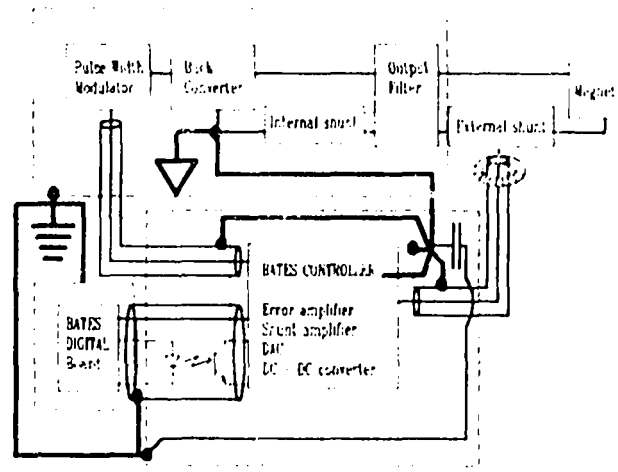

Figure 8. Shielding techniques

Conclusions

Power units from different manufacturers where tried out and the circuit developed was modified only sligthly to regulate properly. Power levels ranged from 1 to 2.5 kWatts. Some noise is still measured in the prototype version and the shielding needs to be improved. Some of the problems observed in the prototype will be solved when a pc board is developed with proper ground planes for digital and analog signals. Analysis is been developed to build a state variable feedback type of controller. By using feedback from the internal shunt and also from the output voltage, we believe that the compensator can be reduced to simple coefficients, improving the dynamic response and simplifying the design.

References

1. T. Russ, C. Sibley, ``A distributed Power-Supply Controller using the Bitbus interface'', Nuclear Instruments and Methods in Physics Research'', A293, 1990.

2. D. Mitchell, ``Switching Regulator Analysis'', McGraw Hill Book Company, ISBN 0-07-042597-3

3. R. Middlebrook and S. Cuk, ``A general Unified Approach to Modelling Switching Converter Power Stages'', IEEE Power Electronics Specialists Conference Record, June 1976, pp. 18-34.

4. Switched Mode Power Supply Transfer Determination using Spice'', IEEE Power Electronics Specialists Conference Record june 1984, pp. 297-303.

5. Instruction manual for EMS power supply 40-60-2, Electronic measurements, Neptune, NJ.

6. R. Morrison, "grounding and shielding Techniques in instrumentation",John Wiley & Sons, 1977.

APPLICATION OF A RELATIONAL DATA BASE FOR DOCUMENTING THE GROUND TEST ACCELERATOR CABLE ROUTING AND WIRING INTERCONNECTIONS*

D. B. Blackwell, W. L. Rogers, V. W. Brown, G. A. Ekeroth, and T. O. McGill
Los Alamos National Laboratory, Los Alamos, NM 87545

Abstract

The Ground Test Accelerator (GTA) has many different types of equipment and interconnections to support the operation. Various functions are performed by these equipments such as signal generation, instrument control, and diagnostics. All of the thousands of signals must be routed from the protected tunnel area into the operational control area of the building. Tabulating the routing of these cables, interconnections, terminations, and even the installation status, results in an enormous amount of data collection and maintenance. A relational data base program called Wireflex was written to allow real-time storage, instant recall, and reporting of this information. The operational environment is the VAX network with password security to protect the integrity of the stored data. The format of the program data bases, with the relationships and interchange of information, will be described. Examples of input forms will show the type of information being stored and the indexing for searching specific entries. Reports will also be included displaying the flexibility of types as well as the ability to recover specific entries or ranges of information.

Introduction

The Ground Test Accelerator (GTA) is situated in a tunnel to provide personnel and sensitive equipment protection from the effects of radiation. All of the necessary control signals for initiating functions, electro-mechanical actuator, and drive-signal control, as well as signal sampling and diagnostics, must be routed between the tunnel and the adjacent control building. Diagnostic signals are typically low level compared to control signals, and this requires routing cables in different conduits and cable trays for physical separation to reduce the potential for interference. Many junction boxes and connectors are utilized for interconnecting these cables. All of the cable identifications, interconnections, signal paths, and signal types must be documented. The completed, operating GTA will have upwards of 100,000 cable pairs, triads, co-ax's, etc., with probably 1,000,000 connections handling dozens of signal types. The Wireflex program was written to provide the data bases for documenting all of this diverse information and to allow on-screen searches as well as many printed reports.

Information Requirements

The first requirement in setting up any data base program is to outline the kinds of information that will be stored with their categories. This allows an overview of the various types of information and how they are related. For example, signals are directly related to the wires that they connect to, and wires are directly related to the cable in which they are grouped. This cable is then directly related to its termination points in the facility. Having this knowledge and understanding is vital to the proper set up of a data base. Tabulating and storing this information in a relational data base is then easier, because similiar information is not duplicated throughout the data storage. For example, there are many cables of the same type from the same manufacturer in the cable file, but the manufacturer's part number and specifications do not need to be stored with every cable of that type. Only a cable-type number needs to be stored in the cable file to identify what type of cable it is and relate it to all of the cable specifications that are stored in the cable-type file. By the same token, the manufacturer's name, address, etc., do not need to be stored with all of his cable information, because it is stored once in the vendors file.

The second consideration is the interrelationship of this information between files. All files can be "related to," providing access between them when searching or reporting, and allowing the required information to be presented. To give an example, each block of information about a specific cable is a "record" and each bit of information about that specific cable is in a "field." Cable number, type, number of conductors, length, etc., are each a field in the record about this cable. Fields that need to be related to other files can be set up. Additionally, fields that require finding a specific cable record by a particular bit of information in a field can be indexed. Indexing is the directory for finding a particular record. For example, cables can be searched in "cable-type" order to find all cables of a certain type. Information that must be pulled from another file for a specific report, such as the manufacturer's part number of a cable to be in a cable report, can be matched to each cable as it is printed in the report.

The third most important thing that needs to be defined in the beginning is the types of on-screen searches and printed reports that will be desired. This is vital to clarify the grouping of information that will be required in the particular searches and reports. The key to finding information is the indexing that is set up. This must be carefully considered because more indexes and more fields that are indexed will take more data storage space. Setting out report requirements also points out the additional relations between data bases that will be required to provide the necessary information for the report. Any information can be found in any record once a relationship is established.

The Wireflex Program

The Wireflex program was written in the Dataflex database format from Data Access Corp., operating on the VAX network in the facility. It is made up of several sections with the "cable" and "wire" as the two main data files. The other five are for the "cable types," "connector types," "system

*Work supported and funded by the US Department of Defense, Army Strategic Defense Command, under the auspices of the US Department of Energy.

types," "device types," and "vendors." The cable file data base input form is shown in Fig. 1. On-screen searching can be done on the indexed fields that are shown bracketed by the < >. Printed reports also use these indexed fields.

```
>>>>>PROGRAM NAME= CAB.FRM<<<<<
Ground Test Accelerator Wire Plant
WIREFLEX V1.1

****CABLE ENTRY FORM****

Cable Number:<______>    Route:<____.>
Type:<__.>  Number of Conductors: ___.  Length:____. feet
Source:<_____________>   Connector Type:___.
Destination:_____________   Connector Type:___.
Remarks:____________________________________________
Installed (Y/N)?._   Revised: __/__/__   Init:___

Search can be done on fields with  <  >  at each end.
Copyright 1989 by Los Alamos National Laboratories
```

Fig. 1. Sample of the Cable Entry Form.

The wire input form is shown in Fig. 2. Again, the indexed fields are shown. Note the "cable number" field. This field is related to the same field in the cable data base, and, in fact, the information that is in the "Source" and "Destination" fields for the "Device/Rack Name:" is in the same fields in the "cable" file. The relationship allows displaying this information in the wire file rather than saving it with every wire stored, because it is the same for every wire in that cable.

The relationships for the wire and cable data bases for the various screen searches and printed reports are shown in simplified form in Fig. 3. Notice the extensive sharing of information from both files that, depending on the report's intended use, is from several different fields in the data bases.

An example of a report from the cable and wire file is shown in Fig. 4. A cover page (not shown) identifies the title, date, time, and the starting and ending cables in the report. In the report, the cable number, source, and destination name are all from the cable file, whereas, the wire number, color, source, and destination pins are from the wire file. This is a perfect example of related data being combined in a report.

```
>>>>>PROGRAM NAME= WIRE.FRM<<<<<
Ground Test Accelerator Wire Plant
WIREFLEX v1.1

****WIRE ENTRY FORM****

Cable Number:<_____>  Wire Number:<___.>  Path:<______>--Seq (A to Z):
                                          (Seq A starts at the beamline-'
                 Color: _______
               Device:<_________>
                       SOURCE            DESTINATION
   Device/Rack Name: ____________   ____________
               Pins: _____          _____
Note : ________________________________________
Installed (Y/N)? _   Revised: __/__/__   Initials:___
Search can be done on fields with  <   >  at each end.
Copyright 1989 by Los Alamos National Laboratories
```

Fig. 2. Sample of the Wire Entry Form.

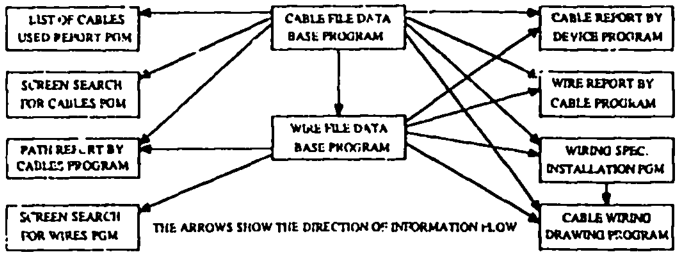

Fig. 3. Simplified Data Base Relationships.

ACCELERATOR TECHNOLOGY 4 LOS ALAMOS NATIONAL LABS

****WIRE REPORT BY CABLE****

DATE= 06/ /90   TIME= 14:12   PAGE: 1

CABLE NUMBER	WIRE NUMB	SOURCE NAME	SOURCE PIN	COLOR	DESTINATION PIN	DESTINATION NAME
RQ-121	1	RQ1-FQT-004-P54	P54-G	brown	J02-K	RQ1-PORT A-J02
RQ-121	2	RQ1-FQT-004-P54	P54-H	red	J02-L	RQ1-PORT A-J02
RQ-121	3	RQ1-FQT-004-P54	P54-J	orange	J02-N	RQ1-PORT A-J02
RQ-121	4	RQ1-FQT-004-P54	P54-K	yellow	J02-P	RQ1-PORT A-J02
RQ-121	5	RQ1-FQT-004-P54	N/C	shield	J02-R	RQ1-PORT A-J02
RQ-122	1	RQ1-POS-001-P61	P61-G	brown	J02-Y	RQ1-PORT A-J02
RQ-122	2	RQ1-POS-001-P61	P61-H	red	J02-Z	RQ1-PORT A-J02
RQ-122	3	RQ1-POS-001-P61	P61-J	orange	J02-b	RQ1-PORT A J02
RQ-122	4	RQ1-POS-001-P61	P61-K	yellow	J02-c	RQ1-PORT A-J02
RQ-122	5	RQ1-POS-001-P61	N/C	shield	J02-d	RQ1-PORT A-J02

RECORDS PRINTED = 10

Fig. 4. Sample of the Cable Report.

An additional report called the Cable Wiring Report will allow selecting cables and producing a cable wiring drawing. This is a standard page-size drawing as shown in Fig. 5.

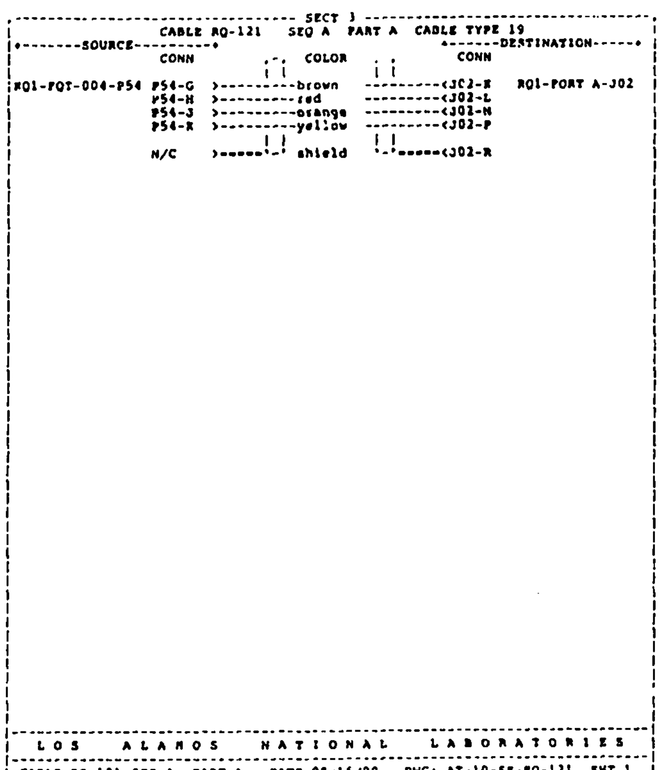

Fig. 5. Sample of the Cable Wiring Drawing.

Summary

The Wireflex relational data base for documenting the necessary information about the GTA has been invaluable. As soon as the wiring requirements are identified, the cable, wire, and connector assignments are made and entered into the data bases. Then, a Wiring Installation Specification is printed that gives the Scope Of The Job, other building drawings to be referenced, General Notes applicable to all wiring installations, and Special Notes that are pertinent to this particular task. This is followed by a full listing of the cables to be installed and the type, length, source, destination, and total footage of each type of cable. The final pages are a computer printout that is a drawing of the cable (Fig. 5) showing conductors, pin connections, source, destination, wire color, and shield connections and is identified with a drawing number that includes the cable number. This program has not only simplified the record keeping of vast amounts of data but also meets the requirements of full documentation. Anyone can access the data base for information retrieval, but only authorized people have the password to get into the portions of the program where data is entered or changed, thus, maintaining secure data storage.

RF PULSE SHAPE CONTROL USING A RECCURENT ALGORITHM FOR A FEL RF-GUN CAVITY

P. Balleyguier, R. Del-Cas

Commissariat à l'Energie Atomique
Service de Physique et Techniques Nucléaires
B.P. n° 12, 91680 Bruyères-le-Châtel, FRANCE

Abstract

FEL application requires a very constant RF accelerating field during the pulse. A classical feedback regulation loop cannot be very efficient when pulse duration is just a few times longer than the filling time of the cavity as the loop gain cannot be high enough.

For that reason, we decided to control the RF shape along the macropulse in a reccurent way : the pulse profile is corrected step by step by computation from the measurement of previous pulses and the desired shape.

The control algorithm is given and its performances will be presented.

Introduction

In the FEL-ELSA injector cavity[1], a very stable accelerating field is required during the macropulse, to achieve an energy spread in the 10^{-3} range. Moreover, in order to reduce the reflected power during the rising and the falling edges, the RF pulse should be trapezoid in shape. Since the frequency cavity is 144 MHz, and the unloaded Q value is 28000, the field raise/fall time constant is about 60 µs. Compared with the electron pulse duration (200 µs), that time is not small enough to allow a classical analog feedback system (fig.1) to be efficient during the pulse[2].

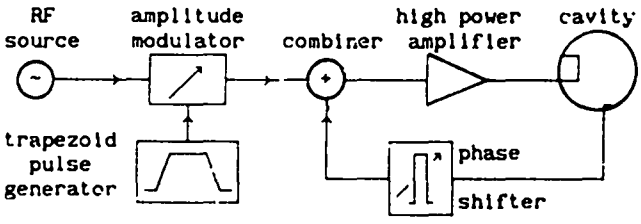

Fig.1. Analog RF feeback loop.

However, if a trapezoid shaped pulse is injected in the RF amplitude modulator, the electric field inside the cavity will not have this ideal time profile because of effects like: transient response of the amplifier, cavity filling time, beam loading and other non-linear effects. The used feedforward technique consists in synthesizing a particular shaped pulse and in injecting it into the low level RF modulator, in such a way that the measured time profile of the field inside the cavity fits the ideal trapezoidal curve.

Function feedback principle

The question is now how to guess what this particular shape should look like. This can be done by a "training" technique: in a typical feedback loop, the demanded output value of a transformer (in broad sense) is compared with its actual output value. The difference is then filtered and sent back to the transformer (fig.2). Studying the feedback system consists then in choosing the filter. In the linear modelization, the filter is fully characterized by its complex transmission coefficient, at each excitation frequency. In direct current (zero frequency), this coefficient is just a real number, usually called *loop gain*. In digital loops, the most simple and usual way is to use an infinite impulse response filter (IIRF), defined by:

$$\text{output}(i) = \alpha\ \text{output}(i-1) + \beta\ \text{input}(i-1),$$

where i is the reccurent indice.

Fig.2. Typical feedback loop.

In our case, the principle is the same, apart from that the signal to be regulated is not a simple scalar but a function representing the pulse shape. This function can be seen as a mathematical vector, either in time or frequency domain; (from that point of view, the classical scalar feedback loop can be called a 1-D loop). Thus, the loop gain is no more characterized by a simple coefficient but by an operator $\mathcal{G}$ which will be chosen as linear.

The filter type will be the IIRF mentionned above. In other words, at each step, the pulse shape injected in the RF modulator, represented by te vector $\mathbf{e}(i)$, will be computed from the previous one $\mathbf{e}(i-1)$, the demanded shape $\mathbf{c}$, and the previous pulse profile $\mathbf{s}(i-1)$ measured inside the cavity, by the following formula:

$$\mathbf{e}(i) = \mathbf{e}(i-1) + \mathcal{G}\,[\mathbf{c} - \mathbf{s}(i-1)]. \qquad (1)$$

Stability

Classical stability criteria (Nyquist, for example) are helpless here because they deal with 1-D feedback loops. So, we have to find out another criterion.

Let us call $\mathcal{F}$ the transfer function of the RF chain, i.e.: modulator, power amplifier, cavity and detector. $\mathcal{F}$ transforms the vector **e** into the vector **s**. We will assume $\mathcal{F}$ to be linear. Eq.(1) can be written as:

$$\mathbf{e}(i) = (\mathcal{I}-\mathcal{G}\mathcal{F})\,[\mathbf{e}(i-1)] + \mathcal{G}\,[\mathbf{c}], \qquad (2)$$

where $\mathcal{I}$ is the identy operator.

The classical *fixed point theorem*[3] of topology, says that the vectorial sequence $\mathbf{e}(i)$ will converge if the operator $(\mathcal{I}-\mathcal{G}\mathcal{F})$ is a contraction, i.e. it reduces distances:

$$\forall \mathbf{x}, \forall \mathbf{y}, \quad \|(\mathcal{I}-\mathcal{G}\mathcal{F})[\mathbf{x}] - (\mathcal{I}-\mathcal{G}\mathcal{F})[\mathbf{y}]\| < \|\mathbf{x}-\mathbf{y}\|, \qquad (3)$$

or, simply: $$\|\mathcal{I}-\mathcal{G}\mathcal{F}\| < 1. \qquad (4)$$

Since the operator $\mathcal{G}\mathcal{F}$ is fully characterized by its complex transmission coefficient $\gamma(\omega)$, the stability criterion (4) may be stated in the frequency domain as: for any angular frequency ω, $\gamma(\omega)$ has to be inside a disc of radius 1 and centered on 1 (fig.3).

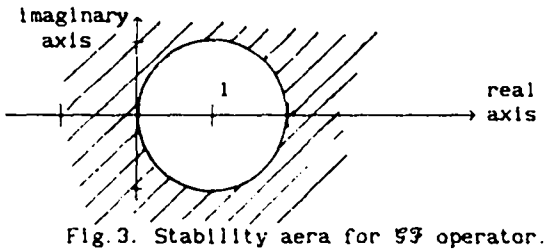

Fig.3. Stability aera for $\mathcal{G}\mathcal{F}$ operator.

So, the operator $\mathcal{G}$ has to be chosen correlated with $\mathcal{F}^{-1}$. In case of convergence, the limit vector $\mathbf{s}(\infty)$ will satisfy the following equation derived from eq.(1):

$$\mathbf{s}(\infty) = \mathbf{c} + \mathbf{r}, \qquad \text{where} \quad \mathcal{G}[\mathbf{r}]=0.$$

The operator $\mathcal{G}$ should ideally be inversible, to insure the error output vector **r** to be nul. In any case, $\mathcal{G}$ has not to loose too much information.

Beam loading can be taken into acount by the addition of a constant term **f** in the transfer function $\mathcal{F}$, representing the RF signal induced by the beam inside the cavity:

$$\mathbf{s} = \mathcal{F}[\mathbf{e}] + \mathbf{f} = \mathcal{F}_1[\mathbf{e}].$$

It has to be noticed that substituting $\mathcal{F}_1$ into $\mathcal{F}$ in eq.(3) would not change it: beam loading should not perturb the loop stability, as long as the electron macropulses are repetitive.

Choice for operator $\mathcal{G}$

Since $\mathcal{F}$ is not exactly known, one cannot just decide to take $\mathcal{G} = \mathcal{F}^{-1}$. Let us call $\tilde{\mathcal{F}}$ the expected value for $\mathcal{F}$. With $\mathcal{G} = \tilde{\mathcal{F}}^{-1}$, the stability condition (4) would become:

$$\| \mathcal{I} - \tilde{\mathcal{F}}^{-1}\,\mathcal{F} \| < 1,$$

which would probably not be verified for every vector. As a matter of fact, if **x** is a vector for which $\|\mathcal{F}[\mathbf{x}]\|/\|\mathbf{x}\|$ is very small, $\|\tilde{\mathcal{F}}^{-1}[\mathbf{x}]\|/\|\mathbf{x}\|$ would probably be very large, and a small error on $\tilde{\mathcal{F}}$ would certainly lead to a value of $\|\tilde{\mathcal{F}}^{-1}\mathcal{F}\|$ much larger than unity.

A more suitable choice for $\mathcal{G}$ seems to be ${}^t\tilde{\mathcal{F}}$ (${}^t\tilde{\mathcal{F}}$ transposed) which is somewhat correlated with $\mathcal{F}^{-1}$, but has not the same drawback. The limit vector $\mathbf{s}(\infty)$ will then differ from **c** by a vector **r** for which ${}^t\tilde{\mathcal{F}}[\mathbf{r}]=0$ and then, $\mathcal{F}[\mathbf{r}]=0$. Then, a small error on the valuation of $\mathcal{F}$ would not have major consequence.

Since the RF chain transfer function is dominated by the filling time of the cavity τ, $\mathcal{F}$ will be represented by a simple low-pass filter $\tilde{\mathcal{F}}$, which gives, in the time domain:

$$s_j = \sum_{k=0}^{\infty} \exp(-k\,\Delta t/\tau)\; e_{j-k}\,,$$

where s_j and e_j are the samples of **e** and **s**, respectively, and Δt is the sampling period. Then, the assumed matrix of the RF chain transfer function is, in the time domain:

$$\tilde{\mathcal{F}} = \begin{bmatrix} \alpha^0 & 0 & \cdot & \cdot & \cdot & 0 \\ \alpha^1 & \alpha^0 & 0 & & & \cdot \\ \cdot & & \cdot & & & \cdot \\ \cdot & & & \cdot & & \cdot \\ \cdot & & & & \cdot & 0 \\ \alpha^n & \cdot & \cdot & \cdot & \alpha^1 & \alpha^0 \end{bmatrix},$$

with $\alpha = \exp(-\Delta t/\tau)$.

Upper right zeros are due to causality: s_j cannot be influenced by e_k if $k > j$. If a pure delay T occurs between **e** and **s**, all the coefficients of $\tilde{\mathcal{F}}$ are translated $m=T/\Delta t$ times in lower-left corner direction, giving $\tilde{\mathcal{F}}'$. So, the operator $\mathcal{G}$ may be choosen as $\lambda\,{}^t\tilde{\mathcal{F}}'$, where λ is a coefficient to be adjusted experimentally.

Finally, three parameters have to be adjusted in $\mathcal{G}$. They may be interpreted as: feedback coefficient (λ), low-pass filter with negative time response (α), and negative pure delay (m). The application software described later allows the system user to change any of these parameters at any time, without stopping the reccurent algorithm.

Practical realization and results

The scheme of the actual feedback system is given in fig.4. The high power amplifier consists of a chain of amplifiers ended by a 2 MW tetrode. Both acquisition and restitution systems work at 0.5 MHz sampling frequency, with about four hundred 12-bits samples.

A convergence check-out algorithm has been implemented to avoid divergence in case of sudden RF chain cut-off: the residual output error (characterized by **s**-**c**) is computed at each step; if it grows, the feedback algorithm is automatically suspended.

In order to save time, calculations (feedback algorithm, convergence check-out, data curve display) are made on single precision integers, and the software was written in assembly language. This allowed the computer (PC AT 286 with a 10 MHz clock) to carry out its task in less than 30 ms.

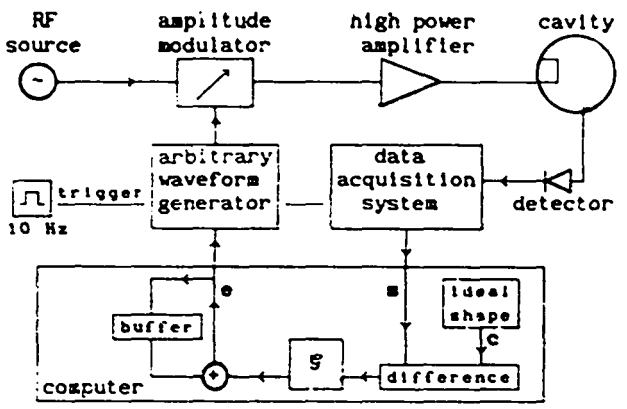

Fig.4. Function feedback loop.

Experiments showed that first and second order discontinuities on the demanded shape could generate instabilities: slowly growing ondulations on the pulse. For that reason, the demanded shape was smoothly designed (fig.5a), and the output data (s) was smoothed after each reccurence with a 1-2-1 pattern. Fig.5 shows experimental results after a few seconds, when a steady state has been achieved, without electron beam. The field amplitude stability ($\Delta P/2P$) is about 0.3% in the flat part of the pulse. Fig.6 shows a preliminary result with 30% beam loading. The field stability was about 2.5%; this value should be improved in the future.

Conclusion

A quite constant RF amplitude field has been obtained during the pulse. Including an analog feedback loop for regulating the amplifier alone (which has a much shorter time response than the cavity) could improve the system performance. For the moment, the limitation seems to come from the reproductibility of the electron macropulse itself.

The next step will be to improve this regulation system in a way to stabilize also the RF the phase whithin the pulse.

The authors would like to thank M.P.Tardy and his team (from Thomson TTE) for hardware implementation of the system.

References

1. S.Joly et al., "Progress report on the BRC photo-injector", EPAC, Nice, 1990.

2. P.Boussard, "Beam Loading", CERN Accelerating School, Oxford, 1985.

3. L.Schwartz, in "Cours d'analyse", Edition Hermann, Paris, 1967, p.101.

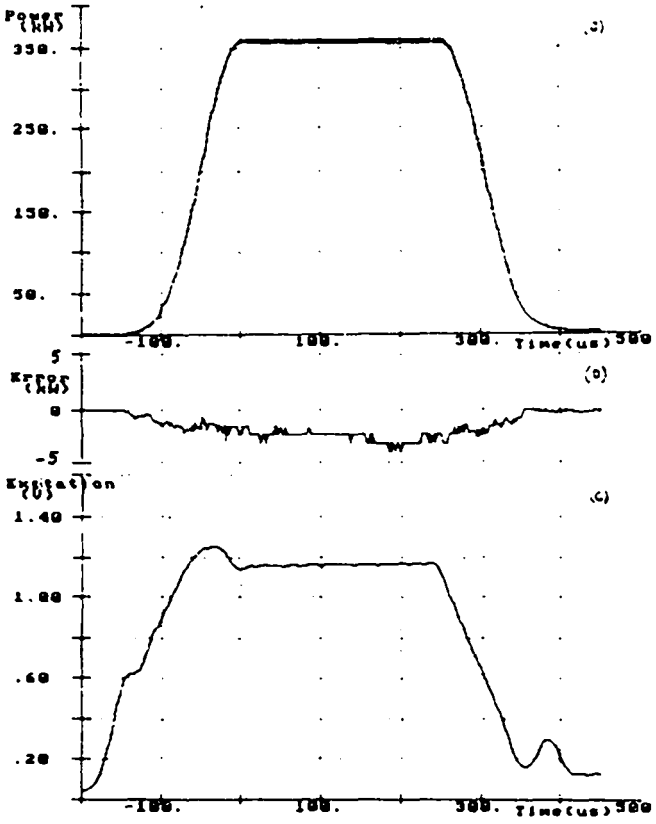

Fig.5. Results without beam.
(a) Demanded and actual power pulses (overlaping).
(b) Difference. (c) Corresponding input pulse.

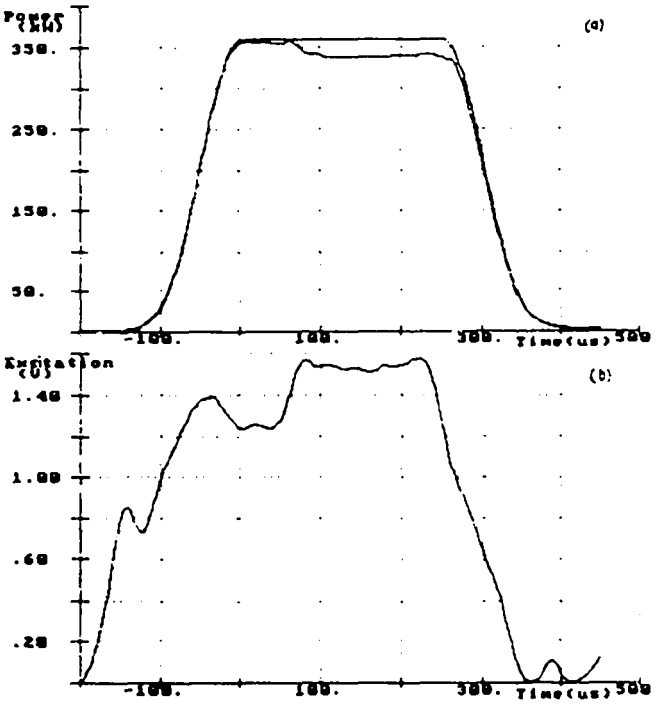

Fig.6. Results with 30% beam loading.
(a) Demanded and actual power pulses.
(b) Corresponding input pulse.

Wednesday

Session WE1
Chairman: L. Bollinger
Invited Papers

SUPERCONDUCTING RF CAVITY TECHNOLOGY*

H. Padamsee
Laboratory of Nuclear Studies, Cornell University, Ithaca, NY 14853

Abstract

Large-scale application of superconducting rf (SRF) cavities to electron and ion accelerators is in progress at many laboratories around the world [1]. In the last few years over 70 meters of niobium cavities have been built for high energy physics storage rings and nuclear physics recirculating linacs. In acceptance tests, these structures reach an average accelerating field of 9 MeV/m with Q values over 2×10^9. Attractive future application possibilities to high luminosity storage rings (B-factories) and free-electron lasers are discussed. Research towards higher gradients continues. With a new, furnace based preparation technique, several single cell cavities (10 cm active length) now reach surface fields corresponding to accelerating fields of 25 MeV/m, with the record value of 30 MeV/m at Q's of 2×10^9. This performance level is attractive for future application to a TeV Energy Superconducting Linear Accelerator (TESLA). An SRF TeV linac eliminates the need for ultra high peak power sources, allows a low rf frequency (1-3 GHz), long (msec) RF pulse lengths, and substantially reduces the long and short range wakefield problems that exact tight tolerances for alignment and jitter. We also briefly review the status of materials other than bulk Nb.

Operating SRF Systems

Linac Boosters for Heavy Ions

To provide precision beams of heavy ions for nuclear physics research, SRF linacs have been one of the most successful applicatons of SRF technology. 5 facilites are operating, utilizing over 180 resonators (~60 meters). The first facility (ATLAS) started operation in 1978. Completed heavy-ion accelerator facilities now provide beams with mass up to 100 atomic units and energies up to 25 MeV/nucleon. These are ATLAS, SUNYLAC, Saclay, U. of Washington and Florida State U.

Split ring, modified helix and, recently, quarter wave resonators are used. The on-line gradient average is 2 - 3 MeV/m. Apart from economy, the SRF linac preserves the excellent beam quality from the tandem because of the stable cw operation, in addition to the general desirability of a cw beam for experiments.

Storage rings

To increase the energy of e^+e^- storage ring colliders, accelerating systems must provide voltages that increase as the 4th power of the beam energy to make up for energy losses from synchrotron radiation. In this application, SRF cavities pose many advantages over normal conducting copper structures. They can be economically operated at accelerating voltages of ~5-10 MeV/m compared to 1 - 2 MeV/m for copper structures. With copper systems, a large fraction of the available rf power is dissipated in the walls of the structure, whereas with SRF cavities, most of the rf power can be available for the beam, allowing higher beam energies.

The presence of an accelerating structure has a disruptive effect on the beam, and the associated impedance limits the maximum current for high luminosity. With the higher voltage capability, SRF systems can be shorter, reducing the overall impedance, allowing higher beam currents. In copper cavities, the need to provide the maximum accelerating voltage for minimum rf dissipation leads to structure geometries with small beam holes and re-entrant irises, i.e high impedances. SRF cavities can have large beam holes and smoother iris geometries which are more suitable for higher beam currents. Both single and multi-bunch instability problems are greatly reduced through use of SRF cavities.

* Supported by the National Science Foundation with supplementary support from the US-Japan Collaboraboration

Prototype structures for storage rings have been developed by CERN, Cornell, DESY and KEK. Between 1982 and the present these structures have been tested extensively in the storage rings CESR, PETRA, SPS, and the accumulation ring TAR at KEK with steady progress. The maximum current stored was 69 mA.

A full scale accelerating system of 32, 5-cell, 500 MHz niobium cavities (~50 meters) is now operating in TRISTAN at KEK, raising the beam energy from 27.5 to 32 GeV [2]. It uses a 6.5 Kwatt helium refrigeration system. The average accelerating gradient achieved in the horizontal cryostat tests without beam was 7.5 MeV/m. Routine measurements on the performance in the ring over 600 days showed no degradation in all but 4 cavities. The structures were operated cold at ~5 MeV/m for over 7000 hours, and with over 5000 hours of physics runs. The maximum current stored was 13 mA.

At CERN [3], a 6.8 meter active length SRF system has been operated in LEP using an 800 watt refrigerator. The accelerating structure consists of 4 x 4-cell 350 MHz Nb cavities, connected to a single 1 Mwatt Klystron. Tested individually, the cavities reach > 5 MeV/m, and together were operated at 4.7 MeV/m, storing 2.5 mA beam current (LEP design current = 2x3 mA). 20 more cavities are ordered.

To increase the energy of the SPS injector for LEP from 20 to 21.8 GeV, an SRF system of 2 x 4-cell, 350 Mhz, Nb/Cu cavities has been installed. Off-line tests reached 6.7 MeV/m and the on-line average gradient achieved was 4.9 MeV/m [4].

SRF Systems Under Construction

Heavy Ion Boosters

Argonne [5] is presently replacing the tandem by a new injector based on Nb quarter-wave resonators, specially designed to accelerate very low velocity ions, provide a higher beam current and extend the mass range up to uranium ions. Argonne is also providing Nb split-ring resonators for a booster at Sao Paolo, Brazil. JAERI in Japan in constructing 40 Nb quarter-wave structures. Several other laboratories are planning and protyping resonators for future boosters.

Storage Rings

Based on successful storage ring beam tests and installations in TRISTAN and LEP, plans are underway to install a complete SRF system to raise the LEP energy to 100 GeV using more than 320 meters. At DESY, construction is in progress to install 16 cavities (4 cells, 500 MHz) in HERA to raise the energy of the electron ring and reduce the polarization time [6].

Recirculating Linacs

Nb cavities are replacing normal conducting systems in medium energy (4 GeV) electron accelerators for nuclear physics. When completed in 1994, CEBAF will use 180 meters of Nb cavities [7]. In addition to lower overall power consumption, SRF cavities offer special advantages for nuclear physics electron accelerators in the form of high average currents (1-2x100 μA), continuous beams (100 % duty cycle) and excellent beam quality. In a cw superconducting machine, the rf phase and amplitude can be controlled very precisely, resulting in an energy spread of 2×10^{-5}, vs 2×10^{-3} typical for a competitive normal conducting linac with a pulse stretcher. A low transverse emittance is also essential to minimize the background events due to beam halo. For a given desired average current, a cw machine can have lower peak currents which reduces the emittance degrading interaction of the beam with the cavity and vacuum chamber. For CEBAF, the expected emittance is 10^{-9} m-rad at 1 GeV, as compared to 2×10^{-7} m-rad for a normal conducting option.

The Cornell cavity design was chosen for CEBAF because it exceeded the performance and higher mode damping requirements, and was proven in a beam at CESR. In the industrial prototyping stage, 10 cavities were produced by various companies and tested at Cornell U and Wuppertal U. In acceptance tests, the average gradient was 10 MeV/m and the average Q was 7×10^9 at 2 K, far exceeding the machine design specifications of 5 MeV/m and Q = 2.4×10^9. Industrial and in-house (CEBAF) production of cavities has started. The average of first 10 cavites is Eacc = 9 MeV/m [7]. A full scale cryo-module comprising 8 cavities was tested, reaching an average gradient of 7.5 MeV/m and acceptable Q.

Progress continues on the installation of a 130 MeV recirculating linac by a Darmstadt/Wuppertal collaboration. In Saclay, France, a machine (ALS II) [8] similar to CEBAF is under planning. SRF facilities have been installed, 1.5 GHz 1-cell and multi-cell cavities tested, and a pilot accelerator section is underway.

Future Applications.

B-Factories

Recently SRF cavities are under consideration for advanced storage ring colliders in the B-quark energy range (5 GeV + 5 GeV) with a target luminosity of 50 - 100 times CESR's world record of 10^{32} per cm^2 per sec. Such machines call for very high beam currents (amps). Therefore low impedances are a must. To provide tighter focussing needed for higher luminosity, another feature exploited is the use of very short bunches, e.g. $\sigma_l < 1$ cm, calling for even higher voltages. As for other storage ring applications, SRF cavities offer high accelerating voltage with low impedance at substantially reduced wall plug power.

There are major development challenges ahead to advance the capability of the present generation of storage ring SRF cavities to carry the needed amps of current. New fundamental and higher mode couplers with higher power capability have to be developed. Higher modes need to be damped heavily ($Q_l < 100$). An attractive approach to meet these needs is to distribute the input and output powers over a large number of single cell cavities each equipped with couplers. A possible B-factory parameter list calls for an input power/cell of 500 Kwatts, a total HOM power loss of 15 Kwatts/cell.

Free Electron Lasers

The first free electron laser (FEL) at 3 micron wavelength was demonstrated with the electron beam from the superconducting linac (SCA) at Stanford University [9].

Among the many candidate drivers considered for FELs, the rf linac is in principle suitable for a broad range of laser wavelengths from infra-red to visible to ultraviolet. For short wavelength FELs, good beam quality and high peak currents are essential features. For reasons discussed in connection with nuclear physics accelerators, SRF linacs excel in both beam emittance and energy spread. For example at 90 MeV, an emittance of 10^{-8} πm-rad and an energy spread of 3×10^{-4} were achieved in the SCA.

A linac driver offers high extraction efficiency and therefore higher average power. In the SCA experiment at 1.6 microns, more than 1% of the beam energy was converted to laser energy as compared to 0.001% [10] in storage rings. For high efficiency, energy recovery in a SRF linac has been demonstrated in principle at the SCA [11]. The overall system efficiency, defined as photon power out/rf power supplied to the beam was increased by a factor of 10.

At INFN (Italy) [12] as well as at JAERI (Japan) [13], infra-red FELs are under construction using 500 MHz HERA and TRISTAN storage ring cavities. Modern SRF structures can handle much higher peak currents than the SCA as shown in storage ring beam tests (> 1000 amps).

Pilac

Los Alamos is considering adding 500 - 920 MeV to its pion linac using SRF cavities. Because the pion deacys rapidly, higher gradients are desirable. The laboratory has acquired SRF technology, and is testing Nb cavities at 3 GHz and 805 MHz. A momentum compactor cavity (402.5 MHz) for the low energy pion beam was ordered from industry and a gradient of 6 MeV/m was achieved. A PILAC technical workshop will be held at Los Alamos following this conference. Nb cavity applications are also forseen in upgrades to LAMPF and compact FELs.

Superconducting Linear Colliders

The most promising technique for producing e+e- interactions in the TeV energy range is the linear collider. In contrast to existing applications discussed above, the rf must necessarily be pulsed to keep the refrigerator associated capital and operating cost of such a large machine affordable. Although pulsed, a high duty cycle (few %) retains many of the inherent advantages of the superconducting approach discussed below.

TESLA Workshop A 4-day Workshop on a TeV Energy Superconducting Linear Accelerator (TESLA) was held at Cornell University on July 23 - 26, 1990. The purpose of the meeting was to work on an improved parameter list for TESLA, discuss related accelerator physics issues, explore ideas on improving gradients and on developing accelerating structures/cryostats suitable for TESLA, review costs, advance ideas for cost reduction, and arrange collaborations for work on TESLA issues. About 70 scientists participated from the laboratories at Argonne, BNL, CEBAF, CERN, Cornell, Darmstadt, DESY, Fermilab, IHEP Protvino, INFN (Frascatti, Genova, Milano), KEK, Lawrence Livermore, Los Alamos, Saclay, SLAC, Stony-Brook, and Wuppertal. Several cavity manufacturing firms were also present.

A staged approach to TESLA was considered reasonable (Table 1). However the starting energy is a function of High Energy Physics (HEP) interest and of progress in developing higher gradients in SRF cavities. Linear colliders have the advantage that, if a suitable site is selected, the length can be extended periodically.

TABLE 1
Possible TESLA Machines Depending on HEP Interest

Energy (GeV) Linac	Lumin. (cm^{-2} sec^{-2}) $\times 10^{33}$	Length (km Linac)	Gradient (MeV/m)	Beamstr-ahlung δ	Physics
50	2.6	3.3	15	.006	Z-Factory
150	1.8	7.5	20	.003	Top Fac.
250	2	10	25	.006	≈ NLC
500	5.1	16.7	30	.09	≈ JLC,TLC
750	10	18.8	40	.62	≈ TLC-1.5

Parameter Philosophies In the past, several different approaches have been used to develop a parameter set for a superconducting TeV linear collider. In one approach, Sundelin [14] adopted beam parameters for the final focus and the source as in the SLC, with the philosophy that these are demonstrated. A design luminosity $\sim 10^{33}$ $cm^{-2}sec^{-2}$ was achieved in a 2 TeV CM SRF linac without calling for major developmental efforts in areas such as very small spot size at the interaction point and accompanying very low emittance at the source. In another approach, Rubin et al [15] considered a 1 TeV CM machine with L $\sim 8 \times 10^{33}$ $cm^{-2}sec^{-2}$, and adopted all the advances in source and final focus that a normal conducting TLC would count on, such as flat beams of aspect ratio 100, final vertical spot size of $\sigma_y = 2.2$ nm, source emittances $\epsilon_y = 0.05$ μm, and very short bunch length, $\sigma_y = 70$ μm. A low frequency SRF linac was substituted for the high frequency, high gradient normal conducting linac.

At the TESLA workshop, a middle road was followed to take further advantages offered by an SRF linac which allows higher beam powers by virtue of its higher efficiency. Thus it was possible to reach L = 5×10^{33} $cm^{-2}sec^{-2}$ in a 1 TeV CM machine and relieve the final focus spot size to $\sigma_y \sim 100$ nm, use smaller aspect ratios (~25) and larger source emittances with SLC like bunch length. In

Table 2, we present one of the TESLA parameter sets generated and compare it with the corresponding normal conducting machine (NLC), as well as with the SLC.

TABLE 2
Comparison of Possible Parameters Between TESLA-1/2 and Normal Conducting (NLC & SLC) Linear Colliders.

	TESLA-1/2 1990	NLC	SLC	Units
General				
CM Energy	1	1	0.1	TeV
Luminosity 10^{33}	2	2	.002	$cm^{-2}sec^{-1}$
Length/linac	10	2.6-5.2	3.0	kmeters
Source				
Particles/bunch	4.2	0.7-1.2	5	10^{10}
Bunch Length	2	.07-.1	1	mm
emittance x/y	25	100	1	
emittance y(ϵ_n)	1	.0185	15	μm
Final Focus				
β_x	19.5	28	7.5	mm
β_y	5	0.087	7.5	mm
σ_y	101	2.4-3.6	1463	nm
σ_x	998	162-420	1463	nm
D_y	8.65	17	0.7	
H	1.79	2	2	
Beamstr. energy spread δ	0.006	.11	.001	
Beamstr. parameter Υ	0.02	0.2		
Linac				
RF Frequency	1.5	11.4	2.86	GHz
Accel. Gradient	25	50-100	17	MV/m
Q	8×10^9	10^4	10^4	
Q_L(HOM)	10^5-10^6	20	10^4	
Rep Rate	20	120-360	120	Hz
RF Pulse Width	1598	0.06-.08	9	μsecs
Bunches Per Pulse	400	10	1	
Bunch Spacing	1200	1.8	(18)	meters
Tolerance		26	100	μm
Peak Power/length	0.04	120-240	60	Mwatts/m
Total peak power	400	6.2×10^5		Mwatts
Beam Power/linac	13.4	0.6-1	0.05	Mwatts
Wall Power	75	50-100	26	Mwatts
Efficiency(%)	18	1	0.2	

Attractive Features of TESLA The TESLA parameters provide a significantly smaller beamstrahlung induced energy spread, δ, (by a factor of 18 for Table 2) improving the physics potential, especially in cases such as a Toponium factory. The beamstrahlung parameter Υ is substantially lower, drastically reducing backgrounds due to the electron-positron pairs generated by beamstrahlung photons. A larger beam size σ_y makes it easier to bring the beams into collision. The large bunch length, σ_z, eliminates the need for bunch compression. The smaller ratio of horizontal /vertical emittance reduces coupling between the two planes which can dilute emittance.

Peak RF Power Because losses are so low, SRF cavities can be filled slowly, drastically reducing the peak rf power demand over a copper linac, for e.g., from 240 Mwatts/meter to 40 Kwatts/meter as in the above example.

Higher efficiency Because the energy can be stored for long pulse lengths, many hundreds of bunches can be accelerated, increasing the overall conversion efficiency from ac power to beam power.

Low rf frequency The inclination towards higher rf frequencies in normal conducting linacs makes the wakefield effects very serious, the number of power feed points per unit structure length very large and the rf pulse lengths very short. Because of low losses, SRF cavities can store energy efficiently, allowing the use of low rf frequency (1.5 - 3 GHz). At these frequencies, transverse wakefield effects are substantially reduced, relaxing requirements on alignment tolerances and injection jitter. With reduced longitudinal wakefields, the energy spread after acceleration is smaller, so that the energy bandwidth of the final focus can be made narrower, permitting larger final quadrupole apertures, and precluding the need for crossing angles and related complications.

Rf pulse length and bunch spacing Because SRF cavities can store energy efficiently, the rf pulse length can be many thousand times longer than for copper cavities. A large number (several hundred) of bunches can then be spaced far apart from each other (km), eliminating the possibility of wrong bunches running into each other at the collision point. With the large bunch spacing and lower wakefields, the damping requirements on the higher modes are considerable relaxed. To avoid multibunch instabilities, normal conducting colliders require very heavy damping (Q_L < 10) for the transverse higher modes of the accelerating structure because of the close spacing (3 meters) of the bunches within the short rf pulse length. With this close a spacing, many bunches are present at the same time in the interaction region, making a crossing angle necessary, which complicates the final focus system, and places severe requirements on the final focus quadrupoles.

For the TESLA workshop, the program LINACBBU was used to calculate the transverse blow-up factor for each bunch in 200 bunch train with 1 μsec between bunches (1.4×10^{10} population). For 1.5 GHz Cornell/CEBAF SRF cavities, it was found that Qext < 10^6 yields a transverse blowup factor of only 1.2 [16]. SRF cavities for storage rings need $Q_L \sim 10^4$. The reduced damping requirement can be advantageously used to lower structure costs by increasing the number of cells per structure and by reducing the number of couplers per module.

Challenges for TESLA The capital cost of TESLA is dominated by the structure. Thus the major challenges are to increase the gradients and lower the costs. Progress towards the first is discussed in the next section. Substantial progress has been registered towards lowering structure costs [17]. Polarized cells have been developed to orient deflecting modes so that a single coupler can damp both polarizations of transverse modes. Nb polarized cavites at 1.5 and 3 GHz have been built and tested to show that no multipacting occurs from the polarizing shape distortions. Cavity fabrication procedures have been simplified. Machined steps are eliminated at cavity weld joints and new parameters developed that allow all cylindrically symmetric welds to be performed in one pump-down of the weld chamber. Calculational tools have been developed to predict the Qext achievable by a coupler placed on the beam-pipe past the end cell. Predictions are that in the highest impedance mode families, increasing the number of cells to 10 still allows tolerable Qext values.

Towards Higher Gradients

The present state of the art of gradients achieved with structures for electrons is shown in Fig. 1. Achieved gradients in off-line tests on more than 70 meters of structures average close to 9 MeV/m. Key aspects responsible for this outstanding performance are the anti-multipactor cell shape, high thermal conductivity Nb to stabilize against premature breakdown of superconductivity and clean surface preparation to ensure low field emission.

At 1.5 - 3 GHz, the best 5-cell and 6-cell accelerating structures from four different labs reached surface electric fields between 33 and 40 MV/m (Fig. 2) with the standard chemical surface treatment. In structures with reduced Esp/Eacc = 2.1, of which the Cornell structure in Fig. 2 is one example, these results correspond to Eacc = 16 - 19 MeV/m. Thus several labs have now provided existence proofs for Eacc > 15 MeV/m in full scale accelerating structures.

Field emission is recognized to be the dominant obstacle to reaching higher fields. Efforts to reduce field emission by using a UHV furnace treatment in the final stages of surface preparation

have made steady progress. Using solid state gettering with Ti, techniques have been developed that simultaneously improve the Nb thermal conductivity and provide a cleaner RF surface. With heat treatment at 1400 - 1500 C, 1.5 GHz single cells tested at Cornell, now reach much higher fields that cavities with standard preparaton (Fig. 3) The average surface field is 50 MV/m at Q values above 10^9, with 60 MV/m as the record best value (Fig. 4) With the new heat treatment at Wuppertal, 3 GHz single cells have reached Esp = 70 MV/m, and a 5-cell, 3 GHz structure reached Esp = 67 MV/m These values correspond to Eacc = 24 - 32 MeV/m (Fig. 4).

Exploration has started on an alternate technique to overcome field emission using pulsed high power for processing emitters. With

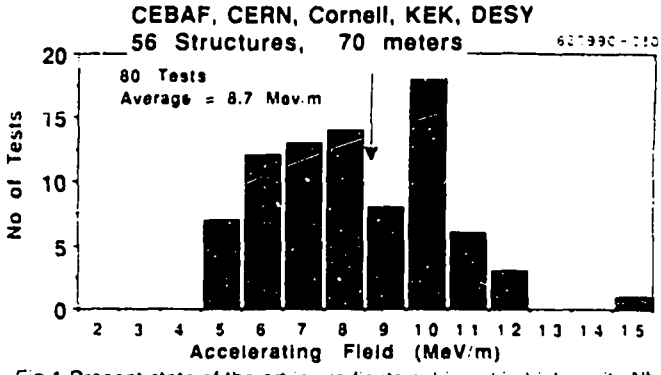

Fig.1 Present state of the art in gradients achieved in high purity Nb structures.

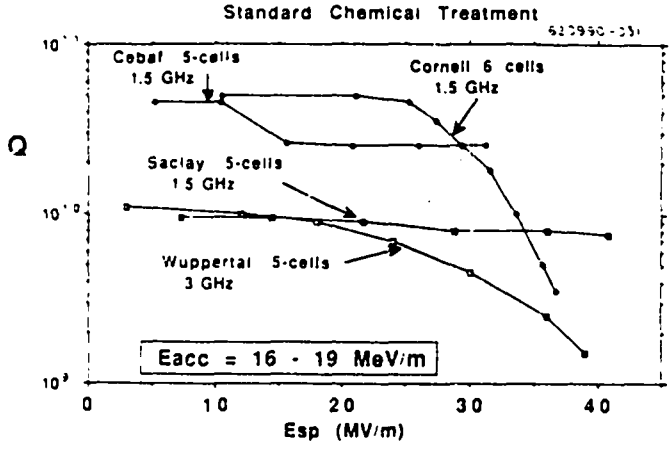

Fig.2 Existence proof provided by several labs in multi-cell structures for Eacc > 15 MeV/m.

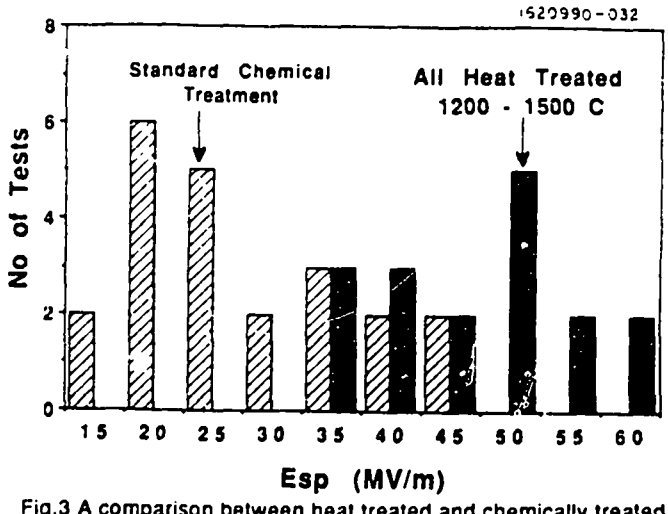

Fig.3 A comparison between heat treated and chemically treated (standard) 1-cell, 1.5 GHz cavities prepared by Cornell

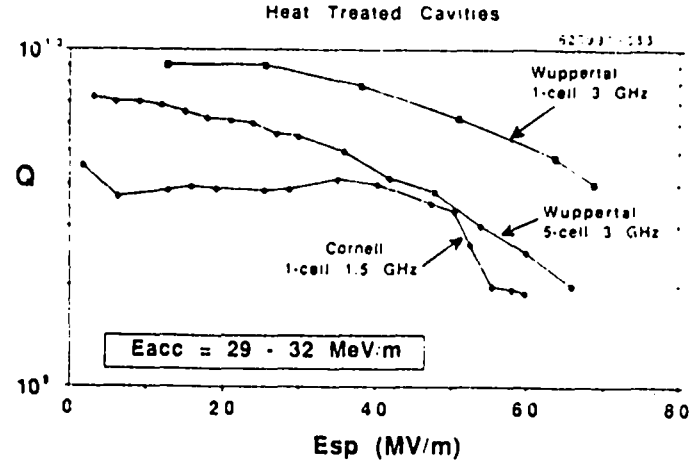

Fig.4 Best Q vs. T on heat treated 1-cell and multi-cell structures.

pulses up to 1 msec long and power between 2 and 50 Kwatts, the onset of field emission in 1-cell, 3 GHz cavities was moved up from Esp = 20 - 30 MV/m to fields of Esp = 36 - 40 MV/m Recently, in a 9-cell, 3 GHz accelerating structure, pulsed processing was used to process emission from Eacc = 10 MeV/m, Q = 10^9 to Eacc = 15 MeV/m Q = 5×10^9.

Basic Studies in RF Superconductivity

With the newest heat treatment techniques, average surface magnetic fields of 1200 Oe, with a maximum of 1500 Oe have been reached in 1.5 GHz, 1-cell cavities. A Nb cavity operating near the theoretical limit set by the critical magnetic field (2000 Oe) needs to support an rf surface electric field ~100 MV/m. A basic question is whether a Nb surface under any condition will tolerate this value. In a specially designed "mushroom" shaped cavity at Cornell [18] and in an "RFQ-type" cavity at Argonne [19], cw surface rf electric fields of 145 MV/m were demonstrated without breakdown, while a pulsed (1 msec) field of 210 MV/m was reached in the RFQ.

Using a high speed temperature mapping system, extensive studies have been carried out on the nature of emitters in rf cavities, under various surface treatments. Results show that, like emitters studied with dc fields, emissive areas are randomly distributed between 10^{-8} to 10^{-12} cm^2, and β values fall between 100 and 400, with a distribution increasing sharply for lower β values. The density of emitters is about 0.2/cm^2 at 40 MV/m with standard surface treatment, falling by a factor of 10 with heat treatment, which also shifts the distribution of β down by a factor of 2. Clean air, water and methanol are proved not to bring emitters in cavities. Chemical residues or minute impurity inclusions remain as possibilities to be investigated, other than debris introduced by improper cleaning or assembly procedures. Condensed gases are shown to enhance emission from potential sites, and He processing is shown to be effective against the associated emission.

Alternate Materials to Bulk Nb

Nb/Cu [20] The chief motivation in developing Nb/Cu cavities is to provide increased stability against thermal magnetic breakdown. Other advantages are Nb material cost savings and the elimination of magnetic shielding allowed by the lower sensitivity to the earth's magnetic field. The possibility of hydroforming the base copper cavities for further cost reduction is also under exploration.

Several full scale LEP style cavities have been tested. Early coatings gave disappointing performance attributed to the presence of foreign particles, which when buried under the Nb, produce blisters in the film. Weld areas were also found to be trouble spots. Improved cleanliness before coating and improved welds with an internal e-b gun were found to ameliorate coating quality reproducibility problems. Strict adherence to an elaborate sequence of procedures is essential.

At low field, Q values of 10^{10} and, at 5 MV/m, Q values of 5 - 7 x 10^9 were obtained in the best of the Nb/Cu cavities. Unlike bulk Nb, losses are observed to increase with increased field even before field emission losses start. The best cavity reached 9.4 MV/m after 10 hours of rf processing. Sputter coated cavities have also been studied at 500 and 1500 Mhz. The residual resistance was found to scale with f^2, increasing from 4 nΩ at 0.35 GHz to 100 - 200 nΩ at 1.5 GHz [8].

Nb_3Sn [21] Nb_3Sn is a promising material because of its higher Tc and higher theoretical rf critical magnetic field (~4000 Oe). Compared to Nb cavities, Q improvement factors of ~200 are achieved at 4.2 K. Q values close to 10^{10} have been measured at 4.2 K over 1 - 3 GHz cavities. The residual resistance is observed to scale as f^2 [8].

Cavity Q values are sensivite to the cool down rate because of trapped magnetic flux generated by thermoelectric currents. Q values are also observed to drop permanently if there is a local breakdown, again attributed to thermoelectric currents. Residual losses increase with increasing field, for e.g. at 3 GHz, 140 to 470 nano Ω was observed between low fields and Eacc = 10 MeV/m. Typical accelerating fields for low purity base Nb are 5 MV/m, while best accelerating field values at 4.2 K and 3 GHz are ~10 MeV/m using medium purity Nb (RRR = 160).

High Temperature Superconductors [22]. The new superconductors offer important potential advantages: the rf critical field is likely to be more than 4 times higher than for Nb, suggesting the future possibility of gradients as high as 200 MeV/m and operating temperatures as high as 77 K.

To be competitive with Nb for accelerator application at the same rf frequency, the surface resistance of a high temperature superconductor (HTS) may be as high as 10^{-5} Ω (as compared to 10^{-7} Ω for Nb) because of the increased overall refrigerator efficiency.

Observed properties of bulk sintered ceramics fall far short of the minimum desirable values. For example, at 500 MHz, best values are 10^{-4} ohms at 77 K, increasing with frequency as f^2. Moreover, the resistance increases rapidly with increasing rf surface magnetic field, to 10^{-3} Ω at few Oe and to 10^{-2} Ω at 20 Oe. Oriented bulk ceramics show lower losses at low fields in the good orientation.

High quality crystals and thin films show significantly lower resistance and better behavior with increasing field. At 6 GHz and 90 Oe, the resistance of the crystals remained below 5×10^{-4} Ω at 20 K, showing that the high resistance of the bulk ceramics at high fields is also not an intrinsic property of HTS.

At this performance level, HTS films are attractive for passive electronic applications, such as multipole band-pass filters, but not for accelerators.

CONCLUSIONS

RF superconductivity has become an important technology for particle accelerators. Practical structures with attractive performance levels have been developed for a variety of applications. Over 100 MVolts have been installed in accelerators for heavy ions and over 300 MVolts for electron accelerators [23]. Experience in these machines shows that high accelerating fields with low rf losses can be maintained for operationally significant lengths of time. Substantial progress has been made in understanding field limitations and in inventing cures through better cavity geometries, materials and processes. The technical and economic potential of RF superconductivity makes it an important candidate for future advanced accelerators at both the luminosity as well as the energy frontiers.

References

1. For detail reviews on laboratory projects and on the many sub-fields of SRF, proceedings of the recent workshops on RF superconductivity cited below are highly recommended
   a. Proceedings of the Third Workshop on RF Superconductivity, Argonne, Illinois, ANL-PHY-88-1, Argonne National Lab, Ed. K. Shepard (1988).
   b. Proceedings of the Fourth Workshop on RF Superconductivity, KEK, Tsukuba, Japan, Ed. Y. Kojima, KEK Report No. 89-21 (1990)
2. Y. Kojima, Proc. of the 1989 Particle Accelerator Conference, IEEE Cat. No. 89CH2669-0, p. 1789 (1989) and in refs. 1b, p. 85.
3. C. Arnaud et al, CERN/AT-RF/90-06 & 07
4. C. Benvenuti et al, CERN/AT-RF/90-08
5. K. Shepard, this conference
6. D. Proch, Proc. of the 1988 Linear Accelerator Conf., CEBAF Report 89-001, p. 216 (1989).
7. B. Hartline, this conference
8. B. Aune et al, Proc. of the 1988 Linear Accelerator Conf., CEBAF Report 89-001, p. 432 (1989)
   B. Aune et al, in refs. 1b, p.97.
9. D. A. G. Deacon et al., Phys. Rev. Lett. 38, 892 (1977).
10. J. State, AIP Conf. Proc. No. 130, Ed. C. Joshi and T. Katsouleas, p. 505 (1985)
11. T. I. Smith et al, HEPL 977 (1986)
12. A. Aragona et al, Proc. of the 1988 Linear Accelerator Conf., CEBAF Report 89-001, p. 680 (1989)
    R. Boni et al in refs. 1b, p. 75
13. S. Takeuchi in refs. 1b, p. 151.
14. R. Sundelin, Proc. of the 1987 Particle Accelerator Conference, p. 68, Cat. No. 87CH2387-9 (1987).
15. D. Rubin et al, Proc. of the 1989 Particle Accelerator Conference, IEEE Cat. No. 89CH2669-0, p. 721 (1989).
    D. Rubin in refs. 1b, p. 413.
16. K. Thomson, priv. comm (1st TESLA Workshop)
17. J. Kirchgessner et al, Proc. of the 1989 Particle Accelerator Conference, IEEE Cat. No. 89CH2669-0, p. 479 (1989)
18. D. Moffat et al, in refs. 1b, p. 445.
19. K. Shepard, priv. comm. (1st TESLA Workshop)
20. C. Benvenuti et al, in refs. 1a, p145
21. M. Becks et al in refs. 1b, p. 109.
    M. Peiniger et al, p. 503 in refs. 1a.
22. G. Mueller, p. 267 in refs. 1b.
    H. Padamsee, Proc. of the 1988 Linear Accelerator Conf., CEBAF Report 89-001, p. 227 (1989)
23. K. W. Shepard, Proc. of the 1989 Particle Accelerator Conference, IEEE Cat. No. 89CH2669-0, p.1764 (1989)

THE ATLAS POSITIVE ION INJECTOR

K. W. Shepard, L. M. Bollinger, and R. C. Pardo
Argonne National Laboratory, Argonne, IL 60439

Abstract

This paper reviews the design, construction status, and beam tests to date of the positive ion injector (PII) which is replacing the tandem injector for the ATLAS heavy-ion facility. PII consists of an ECR ion source on a 350 KV platform injecting a very low velocity superconducting linac. The linac is composed of an independently-phased array of superconducting four-gap interdigital resonators which accelerate over a velocity range of .007 to .06c. In finished form, PII will be able to inject ions as heavy as uranium into the existing ATLAS linac. Although at the present time little more than 50% of the linac is operational, the independently-phased array is sufficiently flexible that ions in the lower half of the periodic table can be accelerated and injected into ATLAS. Results of recent operational experience will be discussed.

Introduction

Since the first operation of a superconducting heavy-ion linac in 1978 [1], the number and size of this class of accelerator has steadily increased [2]. Until the present project, all these machines have served as post-accelerators, increasing the energy of beams from tandem electrostatic accelerators. The largest of the post-accelerators is the ATLAS linac, completed in 1985 [3]. Performance of the ATLAS facility has been limited by characteristics of the 9 MV tandem injector to mass A < 127 and to beam currents of typically a few particle nanoamperes for the heavier ions.

Several years ago, we undertook to replace the tandem portion of ATLAS with a new injector which would provide greatly increased beam current, and extend the mass range of ATLAS to uranium[4,5]. The positive ion injector (PII) project was motivated by the availability of electron-cyclotron resonant (ECR) ion sources which can provide highly- positively-charged ion beams with good transverse and longitudinal emittance. The technical goal has been to incorporate an ECR source into a superconducting linac injector which maintains and exceeds tandem-like beam quality while matching the beam into ATLAS.

Construction has proceeded in several phases. First, the technology for a very-low-velocity superconducting linac was developed [6,7,8]. At the same time an ECR source was designed and built on a high voltage platform [9,10]. The source, beam transport and bunching system, and a small (3.5 MV) portion of the linac were com-

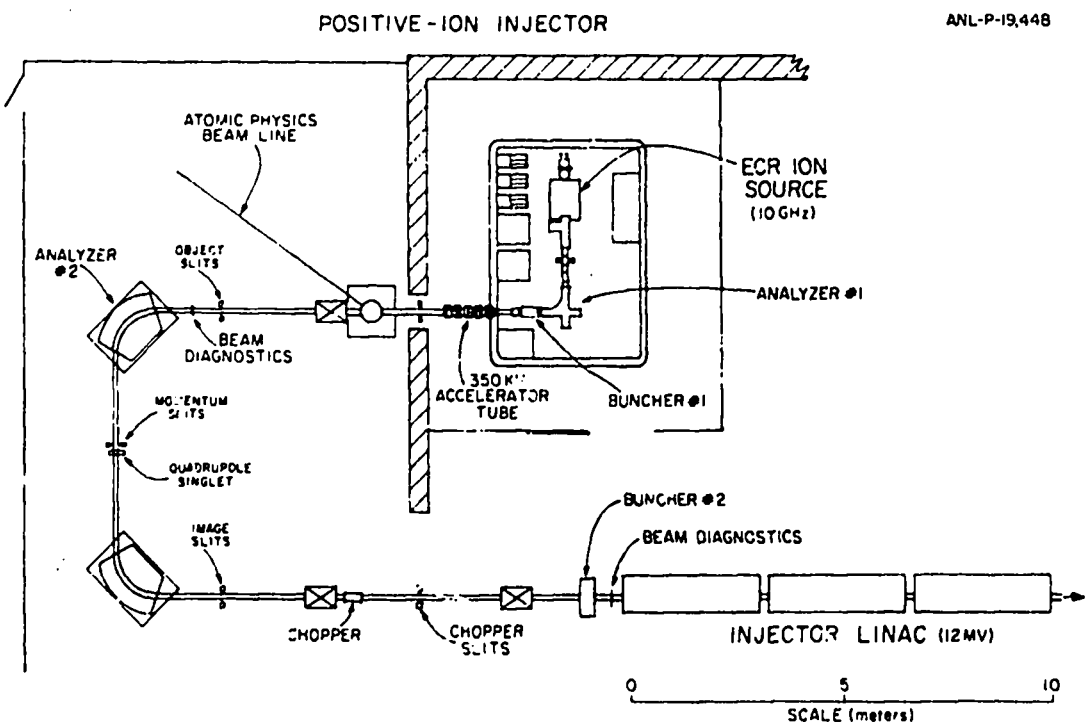

Fig. 1. Layout and major elements of the positive ion injector (PII).

pleted and first tested with beam in early 1989 [11]. Early this year, the system was operated with 7 MV of linac installed. PII will be fully completed in early 1991 when the linac is enlarged to 12 MV. This final injector will accelerate uranium ions up to more than 1 MeV/A, enough for ATLAS to accept the beam and further accelerate to ≈ 8 Mev/A.

In what follows, the design and status of the several elements of PII are reviewed, then results of operational tests are discussed.

Elements of the PII System

The elements and layout of PII are shown in Fig. 1. The primary features, reviewed in detail below, are:
1. An ECR source on an open-air, 350 KV high-voltage platform, designed to produce beams up to uranium at velocities of .008c.
2. A two-stage harmonic bunching system which produces bunches of less than 300 psec time width at the linac entrance.
3. A very-low-velocity superconducting linac, which accelerates over the range $.007 < \beta < .06$, and which produces very little emittance growth.

ECR Source and Voltage Platform

The ECR source is in most respects a typical 10 GHz source. Unique features are operation on a 350 KV platform and provision for radial access to the plasma region. This latter feature is to facilitate introducing solid source materials (in the form of wire, for example) into the plasma. To provide good beam bunching and longitudinal beam quality, the platform voltage must be stable to better than 1 part in 10^4.

Construction of the ECR source and high-voltage platform was completed in 1987. The source has been used since then both for beam tests and for several atomic physics experiments: much of this work has been reported elsewhere [9,10]. Some important results are that: 1) a variety of beams have been produced from solid samples with very high efficiency, 2) more than 1 eμA of $^{238}U^{24+}$ has been produced, and 3) the voltage on the high voltage platform is sufficiently stable for excellent beam quality.

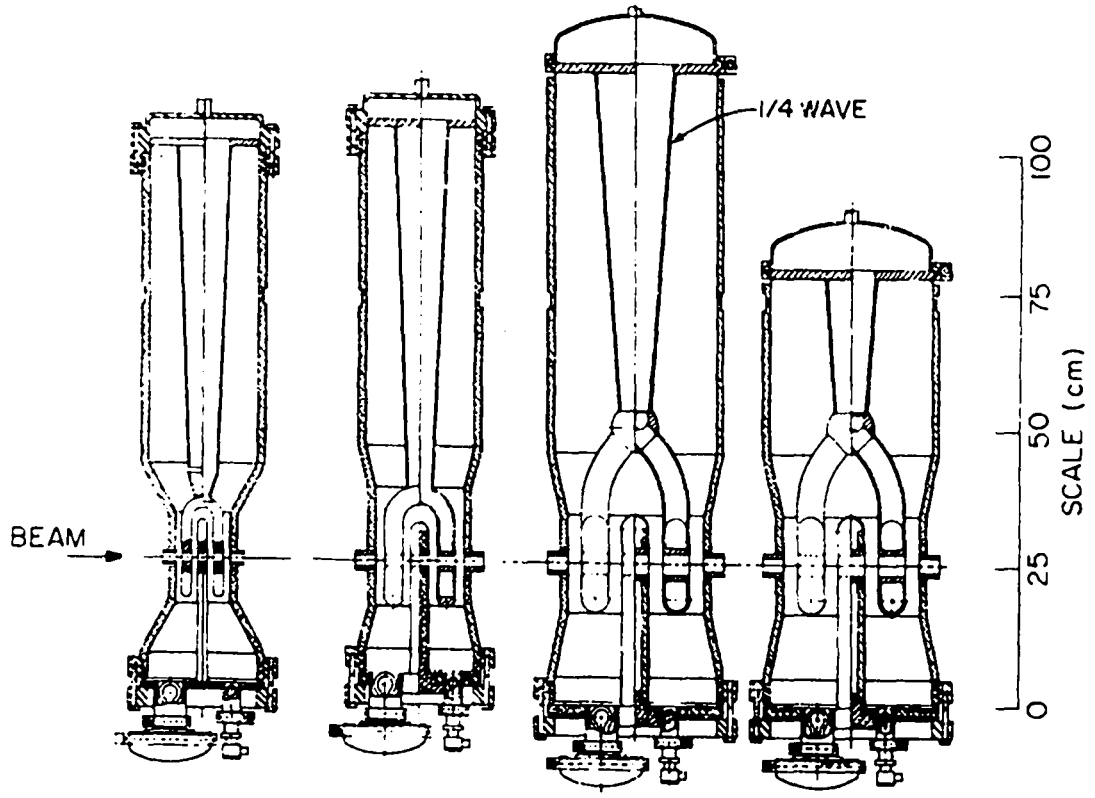

β	0.009	0.016	0.025	0.037
L_a (cm)	10.2	16.5	25.4	25.4
f (MHz)	48.5	48.5	48.5	72.75

Fig. 2. Four resonant geometries used for the injector linac.

Beam Bunching and Mass Analysis

Mass analysis is performed in two stages: first with a 90° magnet on the high voltage platform with a resolution of ≈ 1%, and second with a larger 90° magnet at ground potential with a resolution of ≈ .2%

The two-stage bunching system is similar to that used for ATLAS. The first stage is a gridded-gap using a four-harmonic approximation to a saw-tooth voltage with a fundamental frequency of 12.125 MHz. The amplitude of the first stage is adjusted to form a time waist about 35 m downstream, at the second stage buncher. The second stage is a two-gap, normally-conducting spiral-loaded resonator, operating at 24.25 MHz, which forms a time waist ≈ 1 m downstream, at the entrance to the linac.

Beam pulse widths are measured with a fast detector in which incident ions strike a 10 μ tungsten wire and the resulting electrons are accelerated to a channel-plate detector. For example, with a $^{40}Ar^{12+}$ beam, the pulse formed by the first stage buncher was 1.2 nsec, and the second stage buncher could form a 130 psec bunch at a detector 55 cm downstream. This time spread is remarkably small for such a low energy beam (0.061 MeV/A).

The Injector Linac

The injector linac is formed from four types of independently-phased, four-gap accelerating structures (shown in Fig. 2.) The linac is based on the fact that short, high-gradient superconducting accelerating structures can be closely interspersed with short, powerfully focusing superconducting solenoids. The rapid alternation of radial and longitudinal focusing elements maintains the beam in much the same way as does a Wideroe-type rf structure with magnetic lenses in the drift-tubes, but with the simplicity and versatility of independently controlled, modular elements.

The construction sequence for PII has been based on this versatility. Fig. 3 shows the velocity acceptance characteristics of the four resonator types of PII. The discrete points represent the single-resonator velocity increments for a $^{238}U^{24+}$ beam, and the whole string of points show the passage of such a beam through the 18 resonant cavities that will form the final configuration of the PII linac.

Beams of lower mass, however, enter the linac typically with much higher charge to mass ratios: the velocity increments are correspondingly larger and the linac requires fewer resonant cavities of each type to bring such beams up to β=.05 for injection into ATLAS. In fact, the linac can be configured to provide a useful capability with as few as five resonant cavities, as was shown in the first series of beam tests [11]. To realize such inherent flexibility, the linac cryostats were designed to permit the spacing and sequence of focusing and accelerating structures to be easily changed.

At present 10 of 18 resonant cavities have been completed and are operational. Accelerating field levels obtained in off-line tests average above 4 MV/m. The average on-line level is 3 MV/m, the original design goal, but is presently limited by characteristics of the fast-tuning system and is not believed to be a fundamental limit. The lowest velocity resonator (β = .008), has over the past 18 months repeatedly operated, with beam, at gradients above 6 MV/m.

Beam Tests and Operation

The highly adaptable nature of the linac has permitted a series of beam tests as construction of the low-velocity linac has proceeded. This has included several periods of actual operation of ATLAS injected with the PII system.

First beam through PII was obtained in February 1989, with a 3.5 MV configuration of the linac. A 1μA beam of $^{40}Ar^{12+}$ was accelerated to as much as 36 MeV. In the course of these tests the beam was injected into ATLAS, accelerated to 1[illegible] MeV, and used for a brief (6 hr) experiment. In spring of 1990, with a 10-resonator , 7 MV configuration of the linac, another series of tests was performed.

A variety of beams have been accelerated, including $^{3}He^{1+}$, $^{13}C^{4+}$, $^{16}O^{6+}$, $^{40}Ar^{12+,13+}$, $^{86}Kr^{15+}$, and $^{92}Mo^{16+}$. In addition to tests for shakedown and development of PII, the system has been used to inject ATLAS

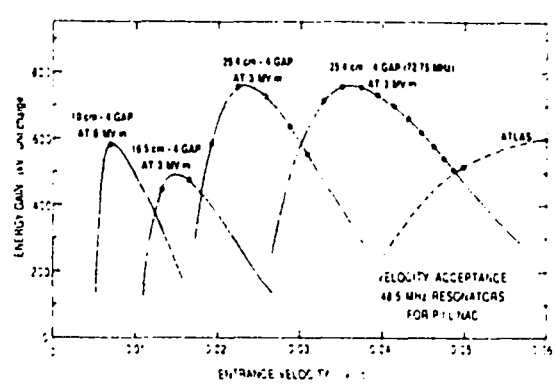

Fig. 3. Velocity acceptance profile for the resonators forming the low velocity linac. The discrete points show the single-resonator velocity increments for a $^{238}U^{24+}$ beam.

and deliver beam for several experiments for a time period totaling more than four weeks.

Operation of the PII system has been characterized by excellent reliability and stability. Even in these early tests, all elements of the system typically run for extended periods, several days, with little or no operator intervention.

A primary goal for the new injector has been to achieve beam quality competitive with that of the tandem, especially in longitudinal phase space. We have measured longitudinal emittance at the output of PII in a direct and unambiguous way by measuring the width of two time distributions: 1) the time spread at the rebuncher between PII and the ATLAS linac, and 2) the width of a time waist formed by the rebuncher.

Measured longitudinal emittance of several beams is shown in Table I. It should be noted that the observed beam quality by no means represents a limit for PII, as the machine is in several respects not in optimum configuration. It is already clear, however, that the beams have substantially smaller longitudinal emittance than similar tandem beams, and that PII sets a new standard of quality for heavy-ion beams.

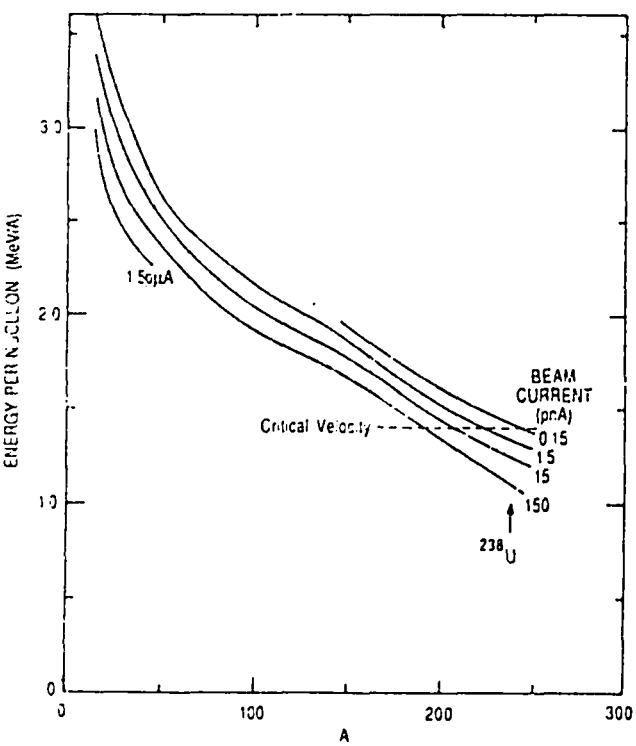

Fig. 4. PII output energy as a function of mass and beam current. The critical velocity shown is the minimum velocity for acceptance and further acceleration by the ATLAS linac.

TABLE I
Measured Longitudinal Emittance

Projectile	Post-injector Stripping	ϵ_z (KeV - nsec) Tandem	PII
$^{3}He^{2+}$	no		<1.0π
$^{16}O^{6+}$	no	15π	
$^{16}O^{8+}$	yes	20π	
$^{40}Ar^{12+}$	no		5π
$^{58}Ni^{10+}$	no	30π	
$^{58}Ni^{19+}$	yes	40π	
$^{86}Kr^{15+}$	no		19π

Conclusions

The results of beam tests to date indicate that all design goals for the PII system will be met. Fig. 4. shows, as a function of ion mass, the beam currents and output energies that will be available from PII in its final, 18 resonator configuration, expected to be complete in early 1991.

Tests of the partially completed system already demonstrate that the combination of an ECR ion source with a low-velocity superconducting linac provides an alternative to tandem electrostatic accelerators that is not only cost-effective, but can also provide increased beam quality and increased beam current.

Acknowledgments

A number of ATLAS staff and Argonne support groups have contributed to this project. We acknowledge in particular the contributions of the following ATLAS staff: P. J. Billquist, B. E. Clifft, P. Markovich, F. H. Munson, and G. P. Zinkann.

This research was supported by the U. S. Department of Energy, Nuclear Physics Division, under contract W-31-109-ENG-38.

References

1. J. Aron, R. Benaroya, L. M. Bollinger, B. E. Clifft, W. Henning, K. W. Johnson, J. M. Nixon, P. Markovich, K. W. Shepard, Proceedings of the 1979 Linear Accelerator Conference, Mantauk, New York, 10-14 September 1979, Brookhaven National Laboratory Report BNL-51134, p. 104 (1979).

2. K. W. Shepard, Proceedings of the 1989 IEEE Particle Accelerator Conference, Chicago, Illinois, March 20-23, 1989 , p. 1764 (1989).

3. J. Aron, R. Benaroya, J. Bogaty, L. M. Bollinger, B. E. Clifft, P. DenHartog, K. W. Johnson, W. Kutschera, P. Markovich, J. M. Nixon, R. Pardo, K. W. Shepard, G. P. Zinkann, Proceedings of the 1984 Linear Accelerator Conference, Seeheim, W. Germany, 7-11 May 1984, GSI Report GSI-84-11, p. 132 (1984).

4. L. M. Bollinger and K. W. Shepard, Proceedings of the 1984 Linear Accelerator Conference, Seeheim, W. Germany, 7-11 May 1984, GSI Report GSI-84-11, p. 217 (1984).

5. R. C. Pardo, L. M. Bollinger, and K. W. Shepard, Nucl. Instrum. and Methods B24/25, p. 746 (1987).

6. K. W. Shepard, Proceedings of the 1986 Linear Accelerator Conference, Stanford, California, June 2-6, 1986, SLAC Report 303, p. 269 (1986).

7. K. W. Shepard, Proceedings of the 1987 IEEE Particle Accelerator Conference, Washington, D.C., March 16-19, 1987, p. 1812 (1987).

8. K. W. Shepard, P. K. Markovich, G. P. Zinkann, B. Clifft, R. Benaroya, Proceedings of the 1989 IEEE Particle Accelerator Conference, Chicago, Illinois, March 20-23, 1989, p. 974 (1989).

9. R. C. Pardo, P. J. Billquist, and J. E. Day, Journal de Physique C1 supp. #1, p. 695 (1989).

10. R. C. Pardo and P. J. Billquist, Rev. Sci. Instr. 61(1), p. 239 (1990).

11. L. M. Bollinger, P. K. Den Hartog, R. C. Pardo, K. W. Shepard, R. Benaroya, P.J. Billquist, B. E. Clifft, P. Markovich, F. H. Munson Jr., J. M. Nixon, G. P. Zinkann, Proceedings of the 1989 IEEE Particle Accelerator Conference, Chicago, Illinois, March 20-23, 1989, p. 1120 (1989).

THE PROS AND CONS OF CRYOGENIC ACCELERATORS: AN ENGINEERING POINT OF VIEW*

W. Fox
Los Alamos National Laboratory, Los Alamos, NM 87545

Abstract

The design of cryogenic linacs is a challenging engineering task; however, significant improvements in accelerator performance are possible. Resistive power losses may be reduced by a factor of four or greater. Greater flexibility is possible in thermal management as a result of substantial increases in thermal conductivity for certain materials. Radio frequency structures may be an order of magnitude more stable in terms of frequency shifts due to thermal transients resulting from very small coefficients of thermal expansion at cryogenic temperatures. Significant engineering problems must be addressed, such as the design of effective rf contacts that will not be affected by thermal cycling and the design of cryogenic mechanisms and dynamic components, such as frequency tuners, that operate reliably at cryogenic operating temperatures. The areas of high-power sparking and multipactoring have not yet been experimentally addressed. Both Los Alamos, Grumman Aerospace Corporation, and Boeing Corporation have built or are building and testing cryogenic accelerator structures. This paper will review the advances made in cryogenic technology applied to radio frequency quadrupole (RFQ) and drift tube linac (DTL) structures and will discuss the advantages and engineering challenges that these linacs present.

INTRODUCTION

Los Alamos National Laboratory and Grumman Aerospace Corporation are designing cryogenic accelerators for the Neutral Particle Beam (NPB) Program. Figure 1 is a photograph of the radio frequency quadrupole (RFQ) used in the Ground Test Accelerator (GTA) being designed by Los Alamos. The RFQ is designed to accelerate a proton beam from 35 KeV to 2.5 MeV and operates at 35 K. The GTA RFQ is but one element in a 24-MeV accelerator which has been designed for continuous wave (CW) operation but will only operate at a 2% duty factor to conserve rf power. The CW deuterium demonstrator (CWDD) being designed by Grumman is an accelerator that will accelerate a deuteron beam to 7.54 MeV under CW conditions at cryogenic temperatures. The design goal for these two cryogenic accelerators is to achieve higher levels of performance and efficiency in rf accelerators.

Cryogenic operation of rf accelerators offers the potential for higher rf efficiency and more stable operation in rf structures. The initial motivation for the design of cryogenic accelerators for the NPB program was the potential for lower rf power consumption resulting from smaller copper losses because of increased electrical conductivity of accelerator structures at cryogenic temperatures. Liquid oxygen and liquid hydrogen cryogens will be used on the NPB platform as an energy source to drive prime movers. The availability of refrigeration capacity in the form of cryogens provided the premise upon which to evaluate the potential gains of operating an NPB accelerator at cryogenic temperatures. Substantial gains in thermal conductivity, in addition to increased electrical conductivity, are possible at cryogenic temperatures and will allow much simpler cooling schemes to be employed in rf structures; in some cases, these cooling schemes provided the only viable means for handling the very high, local heat fluxes produced in these very compact high-power devices.

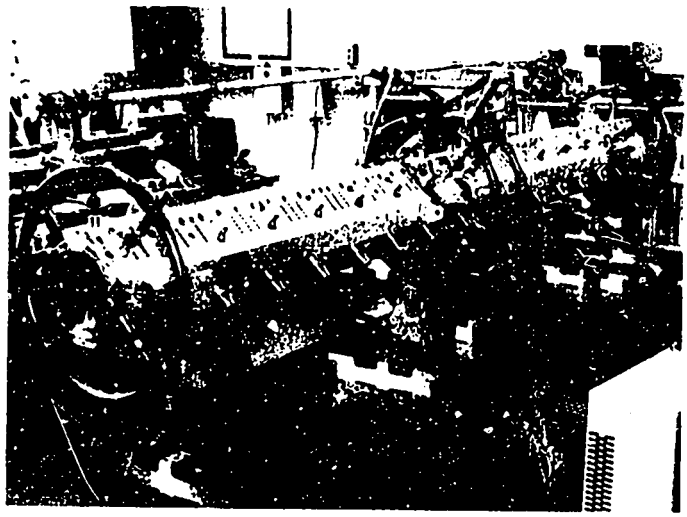

Figure 1 - Radio Frequency Quadrupole

Defining cryogenic operation for these accelerators is important. The operating temperature range of the accelerator is between 20 and 35 K. The rf structures are not superconducting; however, rf conductivity in the structures can increase by factors up to six at these temperatures. Because the structures are not superconducting, they are not subject to the phenomena of quenching, which can produce dramatic changes in resistive heat loads in superconducting structures. However, a significant nonlinearity in the temperature-dependent electrical conductivity of these cryogenic structures does exist and must be considered in the design. The GTA is designed to be cooled by either gaseous helium at a pressure of 16 bars for a 2% duty cycle or by supercritical hydrogen at a pressure of 22 bars for CW operation. The CWDD is designed to be cooled by neon.

*Work supported and funded by the US Department of Defense, Army Strategic Command, under the auspices of the US Department of Energy

PROS AND CONS OF CRYOGENIC OPERATION

Cryogenic operation of rf cavities offers the opportunity to take advantage of higher rf conductivity, higher thermal conductivity, and lower thermal expansion in the structure. The rf power loss that normally occurs as a result of resistive losses in the cavity can be reduced by 75%. The efficiency of an rf cavity is most easily measured in terms of its quality or Q. The ratio of Q for a cavity at cryogenic temperatures to the ratio of Q for a cavity at room temperature is known as the Q factor and can be as high as six in a pillbox rf cavity with no joints. In cavities that are representative of actual rf structures incorporating rf joints, Q factors of four have been achieved. The temperature dependence of the Q factor is clearly illustrated in Fig. 2. Testing of various materials and surface-material conditions has shown that the rf conductivity is strongly affected by the surface preparation of the cavity, as well as the surface-material condition at rf joints. Machining techniques, heat treatment, and surface impurities strongly influence the rf conductivity at cryogenic temperatures. Eliminating local work hardening of the surface to maintain high rf conductivity is extremely important, this can be accomplished by minimizing the depth of machining cuts in the surface of the cavity and by using chemical or electrochemical polishing techniques to remove surface-hardened material. The performance of rf joints is strongly dependent on the surface condition of the materials in the joints. We are currently evaluating the effect of various surface preparations on rf conductivity across rf joints as well as evaluating the long-term effects of thermal cycling at rf joints.

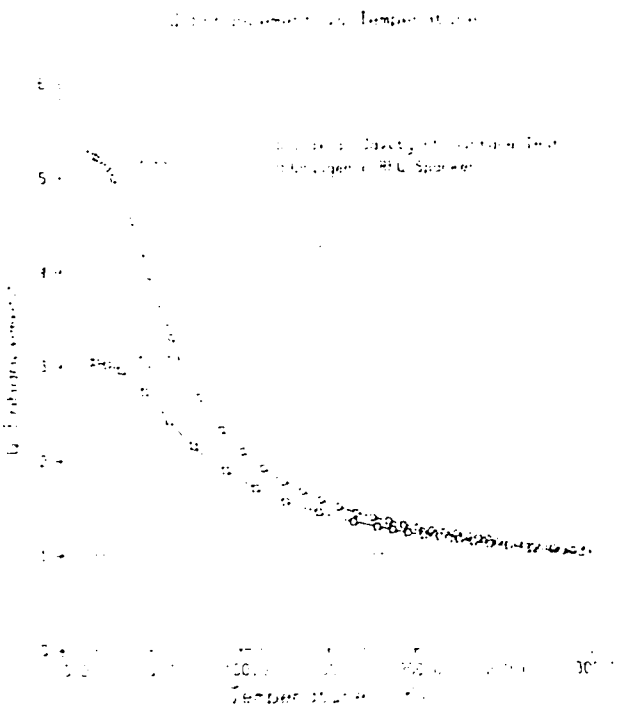

Figure 2 Cryogenic Cavity Q Enhancement

The stability of cryogenic structures can be increased by an order of magnitude at cryogenic temperature because of much smaller coefficients of thermal expansion at these temperatures. The temperature dependent effect of the coefficient of thermal expansion for AL 2219 and OFE copper can be seen in Fig. 3. Not only does the coefficient of thermal expansion become much smaller at lower temperatures, but also the slope of the coefficient of thermal expansion as a function of temperature becomes much flatter. These effects combine to produce much smaller thermal strains at cryogenic temperatures as a result of changes in power deposition on cavity surfaces. In turn, smaller cavity frequency shifts are produced, and a smaller cavity tuner range is required. The tuning rates of these tuners are also substantially lower because of the very flat slope of the temperature dependent coefficient of thermal expansion at cryogenic temperatures. This effect on rf cavity frequency response can be seen in Fig. 4: the flows are balanced in the major vane to produce a frequency response to thermal transients that results in the return of the cavity to its design frequency. This is accomplished by placing cooling channels in a manner to produce thermal gradients that result in off-setting changes in the inductance and capacitance of the cavity. The room temperature RFQ cavity produces a frequency shift ten times greater than the cavity operating at 35 K as a result of a step function thermal transient. The time constant for the cavity operating at 35 K is also much shorter than for the room temperature cavity. The RFQ cavity operating at 35 K requires a much smaller dynamic tuning range than a room temperature cavity and will return to its principal frequency more rapidly if dynamic tuners malfunction. When dynamic tuners are used to maintain the cavity on its design frequency during thermal transients, the rate at which the tuners must compensate for frequency shifts is much less in the cavity at 25 K. The maximum required tuning rate in the cryogenic cavity is 4 kH_z as compared with 30 kH_z in the room temperature cavity. This fact indicates that smaller, slower-moving tuners may be used in the cryogenic cavity.

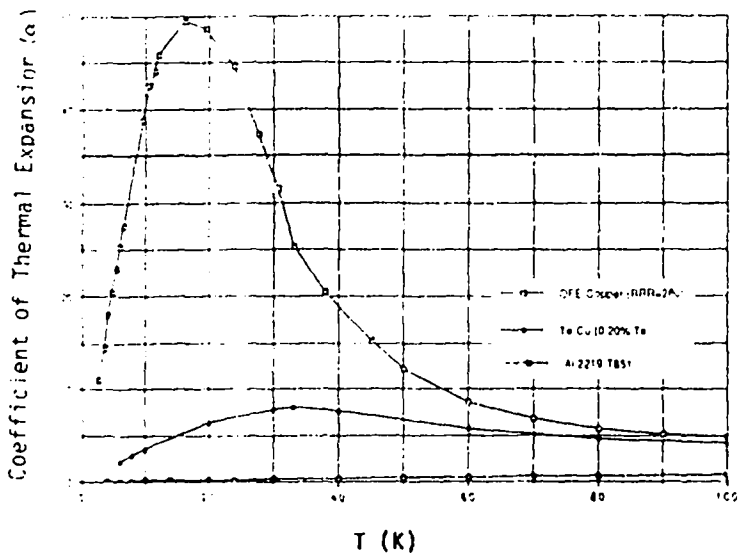

Figure 3 - Thermal Conductivity Comparison

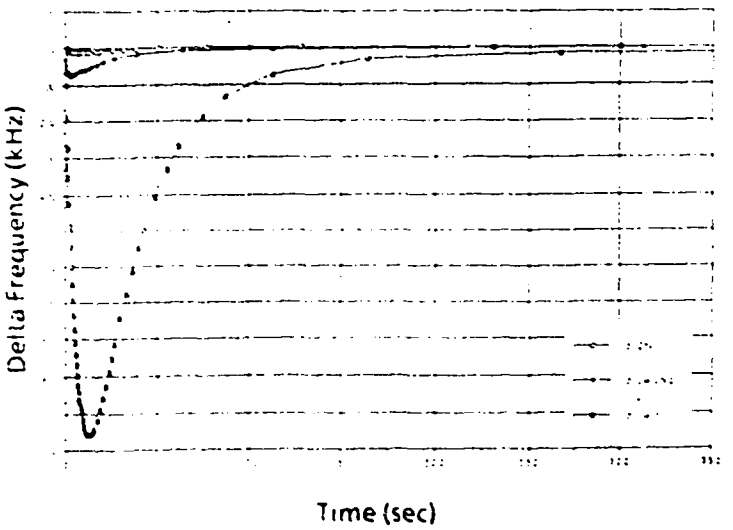

Figure 4 - Transient Frequency Response

The thermal conductivity of OFE copper increases by a factor of 60 at cryogenic operating temperatures. This substantial increase in thermal conductivity allows for increased flexibility in the design of cooling schemes for rf structures. Heat transfer by thermal conduction can play a predominant role in reducing the number of cooling channels and the size of cooling channels required within the structure. Increased thermal conductivity can also result in lower thermal gradients and a more uniform temperature distribution within the structure. High thermal conductivity provides a mechanism to dissipate locally high thermal fluxes to prevent thermal overloads and local melting of the structures.

Cryogenic operation of accelerator structures does result in significant problems. Refrigeration capacity is not an issue with NPB accelerators, because of the availability of cryogens on the platform; it is, however, clearly an important consideration in other applications. The decrease in rf power consumption does not offset the increase in power required for the refrigeration system. Other benefits to the performance of the structure, such as stability, cooling simplicity, and robustness, are difficult to compare in an absolute sense but will become obvious with operational experience. The alignment of cryogenically cooled structures is difficult to accomplish and predict a priori, because thermal gradients and temperature fields must be accurately understood ahead of time to predict the location of cryogenic components at operating temperatures. Direct measurements of component alignment at cryogenic temperatures is also very difficult because the vacuum insulating envelope must be penetrated to make these measurements, and the instruments used to make the measurement may be affected by the thermal gradients themselves. Cryogenic accelerators will be exposed to multiple thermal cycles as a result of operation and maintenance. The long term stability of materials used in rf structures and the performance of rf joints over a significant number of cycles are not well understood in these temperature regimes. Substantial stresses may be induced as a result of temperature cycles between dissimilar materials necessary in the design of rf structures. These combined effects are not well understood at this time and continued research in these areas are necessary.

Accelerators require mechanisms for tuning and component alignment, and in the case of cryogenic accelerators these mechanisms must frequently operate at cryogenic temperatures. Designing mechanisms to operate at cryogenic temperatures reliably is very difficult because of different coefficients of thermal expansion and thermal gradients in the many components that are required in the mechanism. These differences can produce interferences in bearings, rotating shafts, and gears, which, in turn, can result in binding and failure of the mechanism. Most mechanisms require lubricants in bearings and gears to operate reliably; the characterization and performance of lubricants in this temperature range is not well understood and continued research in this area is also necessary. Research is also necessary for some of the materials used in cryogenic accelerators. One example is the samarium cobalt in the permanent magnet quadrupoles (PMQs) used in the DTL portion of the accelerator. Preliminary research has indicated that the field strength of these magnets increases between 6 and 8% as a result of cryogenic cooling. Fully characterizing the reproducibility of this increase is necessary to accurately design the magnet. Other material properties such as the temperature-dependent conductivity of copper oxides that form at the interface of rf joints also need to be characterized. Little is known of the effect of cryogenic operation on the rf conditioning and multipactoring of cavities, as well as the maximum attainable fields in the cavities.

CONCLUSIONS

It is difficult to compare quantitatively the pros and cons of cryogenic acceleration until additional experience is gained in their operation. The design, construction, commissioning, and operation of cryogenic accelerators such as GTA and CWDD offer an important opportunity to evaluate both the pros and cons of cryogenic accelerator operation. We must document operation results and continue research in the areas of cryogenic accelerator design that are not well understood.

LOW BETA CW LINACS FOR INTENSE BEAMS

G.E. McMichael
AECL Research, Chalk River Laboratories
Chalk River, Ontario, Canada K0J 1J0

Abstract

Pushed by interest in intense charged particle beams for neutron sources and neutral beams for military applications, there have been tremendous technical advances in cw linac technology in recent years. Although no one has yet broken the record for high current in a cw linac set over 35 years ago by the MTA accelerator, RFQ accelerators small enough to fit within the beam bore-hole of an MTA Mark 1 drift tube are coming close, and produce orders-of-magnitude brighter beams. A brief history of cw hydrogen linacs will be given. CW experience with the presently operating 75 mA RFQ accelerator at Chalk River will be described. An overview of the cryogenically-cooled D^- RFQ and drift-tube linac due to be installed next year at Argonne will be included.

Introduction

The story of low-beta cw linacs for intense beams is really one of accelerator technology development. There have been numerous plans to use intense high-energy proton, H^-, or D^- beams, but only the low-energy sections or prototype cavities for the high-energy section have been or are being built.

Historical Summary

Livermore (MTA)

The MTA project[1] at Livermore was the first to involve high-current cw linacs. A series of prototype accelerators was built over the period from about 1950 to 1955. The eventual goal was to build a 350 MeV >100 mA deuteron accelerator to breed plutonium for nuclear weapons.

The first prototype, Mark-I, could not reach the operating gradient required for deuterons, but in 1952 it accelerated 225 mA of protons to 15 MeV at 20% duty factor and 100 mA in a cw operating mode. This accelerator was a 9-gap, 18 m long by 18 m diameter Alvarez linac with solenoidal magnets in the drift tubes. It operated at a resonant frequency of 12 MHz, and the beam bore-hole diameter in the higher-energy drift tubes was almost 1 m (large enough to completely enclose a modern RFQ accelerator).

The final MTA accelerator, A-48, comprised a quarter-wave accelerator and two 3.6 m diameter, 6 m long, 48.6 MHz Alvarez-type cavities. It accelerated more than 100 mA cw of protons to 3.75 MeV, and 30 mA of deuterons to 7.5 MeV. Despite the problems encountered with MTA (sparking and damage to drift tubes), three cw accelerators built and operating in 5 years stands as a record, as does the peak cw current of just over 100 mA. Legacies of MTA included a new generation of higher-frequency rf amplifiers used in many subsequent accelerators, and a supply of copper-clad steel plate, without which several later accelerators would not have been considered.

Los Alamos (FMIT, LANL/Culham RFQ)

Los Alamos, in conjunction with the Hanford Laboratory, proposed to build a Fusion Materials Irradiation Test (FMIT) facility, an 80 MHz 35 MeV 100 mA deuteron linac with a liquid lithium target, as an intense neutron source for materials studies for fusion reactors. Work on the FMIT accelerator began about 1980 with plans to build the first 5 MeV section as a prototype at Los Alamos prior to committing the full facility at Hanford. Only the first 2 MeV stage, dc injector and RFQ, had been operated and components for a 2 to 5 MeV Alvarez section fabricated when, five years later, plans for the facility were halted due to escalating costs and lack of agreement on the facility's mission.

Los Alamos physicists realized early in the program that it would be extremely difficult to achieve the injector beam current and quality requirements of FMIT with conventional dc accelerating columns. Although the Radio Frequency Quadrupole (RFQ) accelerator had been invented 10 years earlier[2] and RFQ development was taking place in the USSR, it was the FMIT requirement and the resulting development work on the POP (Proof-of-Principle) accelerator that introduced the RFQ to the world accelerator community outside the USSR. Most of the RFQ's now operating or being built were designed using computer codes and design recipes developed by the team working on FMIT — another example of how cw linacs, even when they never get beyond the prototype stage, have advanced accelerator technology.

Although there are many pulsed RFQ's around the world, the FMIT RFQ, shown in Fig. 1, was the first and until recently the only high-power cw RFQ. Data from FMIT strongly influenced cw thinking and design for Chalk River's cw program, and for the early stages of the US Neutral Particle Beam (NPB) program. The FMIT RFQ operated to design cw field (vane-tip fields of 1.68 Kilpatrick) and accelerated more than 50 mA of H_2^+ (50% of design current) to full energy (2 MeV). Deuteron acceleration was not attempted to avoid activation problems. H_2^+ as a substitute was not too successful because stripping and dissociation led to large neutral and H^+ beam halos which damaged output beamline components. As was the case with MTA and cw structures at Chalk River, the FMIT RFQ experienced numerous problems with rf heating[3] (surface damage and melting of rf seals). Multipactoring problems were solved by coating interior surfaces with titanium nitride. Field enhancement (and local heating) in the cut-back region at the end of the vanes in an RFQ was first reported on FMIT.

Subsequent to FMIT, Los Alamos began another cw RFQ project, a collaboration with the Culham Laboratory to demonstrate high current, high beam quality room-temperature cw capability for the neutral particle beam (NPB) program, a component of the Strategic Defense Initiative (SDI) program. The design for the 353 MHz 2 MeV proton RFQ had been completed, but no hardware had been built when this cw RFQ program was terminated in 1988 (because of budget limitations and the decision within SDI to concentrate resources on a cryogenic demonstration). The design

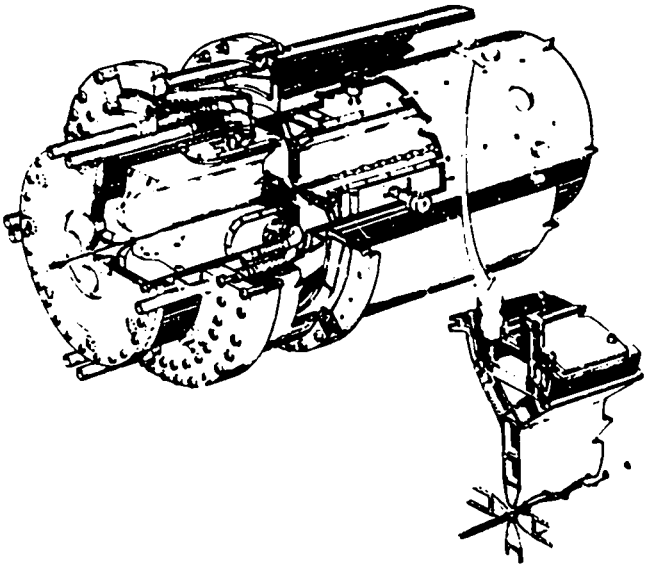

Fig. 1 Cutaway drawing showing details of the manifold-coupled FMIT cw RFQ.

broke new ground in the proposed use of high-strength copper alloys, fabrication techniques, and thermal management to control frequency shifts during rf power changes.

Chalk River (CWPL, RFQ1)

The Chalk River cw linac program started in the mid 1960's with a proposal to build a 65 mA, 1 GeV proton linac as an intense neutron source for physics research. Like MTA and FMIT, the full machine was never funded, but also like MTA and FMIT, prototype work was undertaken. This resulted in the first cw proton linac since MTA, a 750 keV dc accelerator and 3 MeV 269 MHz Alvarez Continuous Wave Proton Linac (CWPL).[4] Throughout its history, CWPL was plagued by a combination of physical and budgetary problems, and first beam was not accelerated in the Alvarez accelerator until 1981. The program was ended in 1983, having accelerated just over 5 mA (10% of design cw current). However, much was learned about the safe handling of cw beams, cooling for cw, minimizing currents in drift-tube stems[5] and design of components for cw linacs.

Interest in cw linacs at Chalk River was maintained over the 1970's and early 1980's by proposals for accelerators to breed fissile fuel for power reactors from thorium or uranium.[6] Optimization studies showed that ≈ 300 MW of proton beam power (at between 1 and 2 GeV energy) was required, and design of a prototype injector to demonstrate proof-of-principle of the first 10 MeV of such a breeder accelerator was begun in 1980. The 300 mA of cw protons was so beyond state-of-the-art (at that time the first RFQ at Los Alamos, POP, had demonstrated 30 mA in short pulse), that it was decided as an intermediate step to build a lower current cw RFQ using the existing 270 MHz cw rf amplifiers. At this frequency, and with conservative assumptions on what peak electric fields could be used, the design current limit for the RFQ was calculated to be 75 mA. This accelerator, RFQ1, accelerated first beam in 1988 and is at present the only operating high-current cw RFQ.[7]

CW Operating Experience with RFQ1

The RFQ1 accelerator comprises a 50 keV, 90 mA dc injector, a 600 keV 267 MHz RFQ and ancillary subsystems. A cutaway drawing of the RFQ is shown in Fig. 2. It is a copper-electroplated mild-steel weldment (following FMIT's lead), but with solid OFHC copper vane tips, so there is no risk of sparks between the tips damaging the plating and exposing mild steel to the rf fields. At design fields (78 kV intervane voltage, peak surface field 24.7 MV/m), structure power is 135 kW, roughly 1/3 of that for the FMIT RFQ. However, because of the higher frequency, the surface power density is 4 times that of FMIT (6.8 vs 1.6 W/cm^2). In the undercut region at the ends of the vanes, the MAFIA code predicts a surface power enhancement of more than a factor of 5 (to almost 40 W/cm^2) and temperatures of >200°C have been measured on the vane-to-tank racetrack seals in this area.[8] Other papers at this conference describe in detail the diagnostics devices,[9] and beam operations[10] on RFQ1.

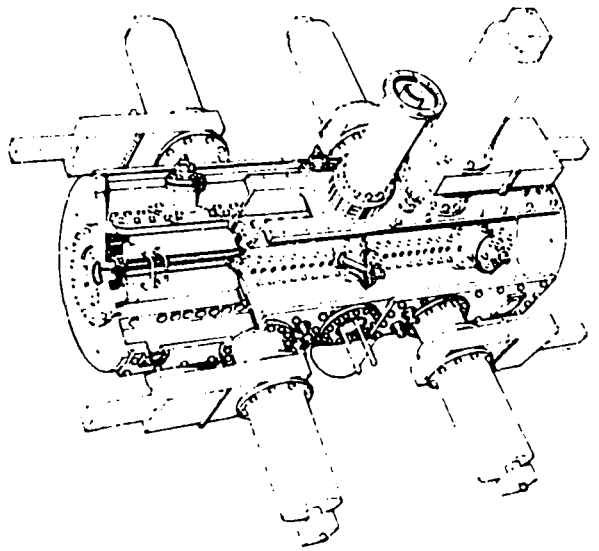

Fig. 2 Cutaway drawing of loop-coupled RFQ1 RFQ showing installation of vanes through slots in side of steel tank.

Highlights of the first two years operation on RFQ1 include:

- Acceleration of 67 mA cw, 90% of design.
- Solution of initial beam-matching problems to increase the multi-beamlet RFQ transmission from 35% to the design 85%.
- Operation with single and multi-beamlet sources.
- Motor-driven stub tuners that perform flawlessly at cw power levels approaching 8 W/cm^2.
- Arcing problems in an rf coupling loop. This loop handled up to 175 kW of cw power for two years, but now fails at less than 100 kW.
- RF loop analysis with a new code, SEAFISH, a SUPERFISH-like code able to compute complex-valued travelling-wave rf field distributions and VSWR's, and used to redesign the coupling loop.

Reliable cw operation of vane-coupling-rings (to suppress dipole fields in the RFQ) and of deformable "racetrack" vane-to-tank rf/vacuum seals.

New vanes designed to operate at higher electric field will be installed to upgrade the RFQ1 facility to 1.2 MeV.[11] These vanes are being fabricated from alumina dispersion-strengthened copper[12] (a high-strength, high conductivity copper alloy). The Los Alamos RFQ design recipes, developed for the BEAR accelerator[13] were used to maximize the energy gain over the 1.47 m long vane length that will fit in the RFQ1 tank.

CWDD, the "Next Generation" CW Linac

Grumman Aerospace Corp., assisted by the Culham Laboratory and Los Alamos National Laboratory, are presently building a cryogenically-cooled, 80 mA cw, 7.5 MeV D linac. The Continuous Wave Deuterium Demonstrator (CWDD) is to demonstrate proof-of-principle of the first stage of an accelerator suitable for a space-based NPB weapons system. High beam quality, space traceability, remote operation and high reliability are primary requirements. CWDD will be installed, and US Army acceptance tests performed, at Argonne National Laboratory, following which it is expected that the accelerator will be turned over to Argonne for further experiments. Installation of major components at ANL will begin in mid-1991, with demonstration of full cw beam scheduled for mid-1992.

The CWDD accelerator comprises a 0.2 MeV 92 mA dc D injector, a 352 MHz RFQ, to accelerate 80 mA to an output energy of 2 MeV, and a single tank 7.5 MeV output energy ramped-gradient drift-tube linac (RGDTL). A conceptual drawing of the accelerator is shown in Fig. 3. The RFQ is nearly 4 m long (4.63 λ at 352 MHz), made up of four, 1 m long units that bolt together. Each unit is fabricated from four tellurium-copper ingots, electroformed after machining to give a single monolithic structure, similar to that successfully used for the BEAR accelerator.[13]

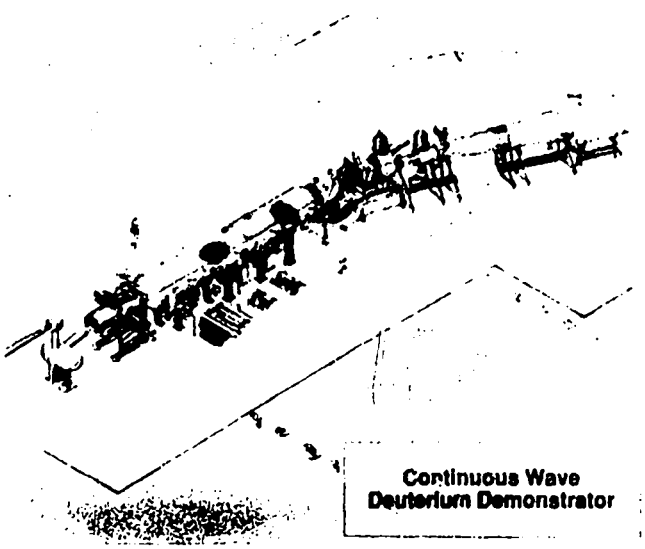

Fig. 3 Conceptual drawing of the CWDD 80 mA cw deuteron accelerator. From left: dc injector, RFQ, DTL, HEBT with bending magnet for beam analysis, beam stop.

High surface currents (typically of the order of 5000 A/m for a 300 MHz structure) flow on the interior of a 4-vane RFQ. The capacitance in an RFQ resonator is mostly between the vane tips, so the charging currents flow radially along the vane sides, and circumferentially along the connecting tank wall. As well as making a very strong, stress-free (and therefore stable) structure, electroforming gives a continuous interior surface. This means that the main rf-current path in the RFQ is free of mechanical joints, eliminating one of the most failure-prone features (joints in high rf-current regions) of all previous cw DTL and RFQ accelerators.

CWDD demands significantly higher beam quality than any previous RFQ, requiring an extensive computer analysis of effects of vane displacement errors, fringe fields and multipole fields.[14] Emittance and brightness predictions for CWDD have not been released. However, some indication of the improvements in beam quality from MTA to CWDD can be inferred from the fact that space-charge-limited beam radii in RFQ's are essentially inversely proportional to frequency. Similar scaling occurs for DTL's. By ignoring changes in focusing period, $\beta\lambda/2$, $\beta\lambda$, etc., between RFQ's and DTL's, and differences between protons and deuterons, one can use the quantity $I*f^2$ as an "indication" of relative beam brightness. Design and achieved currents (I_d and I_a), frequency (f) and "relative-brightness" factor (If^2, normalized to MTA Mark I = 1) for the linacs of this report are given in Table I. Beams have not yet got bigger, but they are very much brighter!

TABLE I
Approximate Relative Beam Brightness

Linac	f (MHz)	I_d (mA)	I_a (mA)	$I_d f^2$ (rel)	$I_a f^2$ (rel)
Mk-I**	12	200*	100	1	0.5
A-48**	48	250	100	20	8
FMIT	80	100	50	22	11
CWPL	269	50	5	126	13
RFQ1	267	75	67	186	166
CWDD	352	80		344	

* Estimate, based on pulsed performance.
** Solenoid focusing was used in the MTA DTL's, so relative brightness numbers for MTA are too generous. If the drift tube bore radius is used as the indicator of beam size, the increase from Mk-I to CWDD is over 2000, instead of the 344 suggested by the frequency ratios.

CWDD will break new ground in other areas besides effective length, fabrication methods and beam brightness. It will be the first cryogenically-cooled cw linac (supercritical neon will keep the structure temperature below 35 K) and the first RFQ to have multiple drive loops in the RFQ cavity. The cryogenic temperature simulates space operation, where liquid hydrogen would provide the cooling. The effective Q of the cavity is increased by nearly a factor of 5, decreasing the rf power required to excite the cavity.

The FMIT RFQ had multiple rf drives, but to an rf manifold. RFQ1 has provision for two drives to the RFQ cavity, but can be driven to full power with only one, and tests of a dual drive cannot begin until after delivery of a dual, klystrode-based rf amplifier, scheduled for delivery in late 1991. CWDD will, from the outset, have a 4-way split of the power from a 1 MW cw klystron to excite 4 drive loops in the RFQ.

A cryogenically-cooled Alvarez linac will accelerate the 2 MeV beam from the CWDD RFQ to a final energy of 7.54 MeV. The DTL will have a ramped-gradient, following the Los Alamos recipe,[15] to minimize longitudinal emittance growth. For the CWDD tank, this requires that the accelerating field increase linearly by 68% from the input to the output end. The ramp will be generated by detuning the two end gaps; post-couplers will be used for fine tuning and to stabilize the DTL fields. Transverse focusing in the DTL will be provided by samarium-cobalt quadrupole magnets in the drift tubes, employing a F-F-D-D lattice structure to reduce the required permanent-magnet quadrupole gradient to achievable levels. Calculated peak surface electric fields in the DTL are ≈ 26 MV/m (1.4 Kilpatrick), somewhat lower than the 1.8 Kilpatrick fields in the RFQ. At 35 K, rf power requirements are expected to be 175 kW to excite the cavity, and 440 to accelerate the beam, giving a beam loading factor $P_b/(P_b + P_c)$ of > 70%.

Conclusions

CW RFQ and DTL linac technology has matured to the point where average beam intensities, currents and brightness are within about a factor of two of peak values that are reached in low duty-factor linacs. Although no high-energy cw linac has yet been funded, the successes of the prototypes augurs well for the future. At present, cw linac development is being driven primarily by the NPB program of the US military, and critical parts of this program, particularly related to improvements in beam quality and control of beam emittance, are classified. However, it speaks volumes about the progress that is being made when experts in that community will now propose, and can then get favourable technical reviews for, a 250 mA high-energy cw proton linac on which one can do hands-on maintenance.[16]

Acknowledgements

The author wishes to thank M. Lorello, J. Rathke and A. Todd for reference material on CWDD, and W. Cornelius for helpful discussions on FMIT. Special thanks to G. Arbique and J. Ormrod for helpful discussions on the Chalk River program and assistance in preparing this manuscript.

References

1. P.V. Livdahl, "The Livermore MTA Project and Its Influence on Modern Linacs", Proc. 1981 LINAC Conf., Los Alamos National Laboratory report LA-9234-C (1982), 5.
2. I.M. Kapchinskij and V.A. Teplyakov, "Linear Ion Accelerator with Spatially Homogeneous Strong Focusing", Prib. Tekh. Eksp. 2(1970), 19.
3. W.D. Cornelius, "CW Operation of the FMIT RFQ Accelerator", Nucl. Instr. and Methods B10/11, (1985), 859.
4. J. Ungrin, B.G. Chidley, J.C. Brown, G.E. McMichael, D.W. Clements and H.F. Campbell, "Operating Experience with a 100% Duty Factor Alvarez Accelerator", Atomic Energy of Canada Ltd. report AECL-8952 (1985).
5. J. Ungrin, S.O. Schriber and R.A. Vokes, "Post-Coupler and Stem Current Measurements for High Current CW Drift-Tube Linacs", IEEE Trans. Nucl. Sci. NS-30 (4) (1983) 3013.
6. S.O. Schriber, "The ZEBRA Project - Past and Present", Proc. 1984 LINAC Conf., GSI report GSI-84-11 (1984) 501.
7. G.M. Arbique, B.G. Chidley, G.E. McMichael and J.Y. Sheikh, "CW Operation and Initial Beam Experiments with the RFQ1 Accelerator", Proc. 1988 LINAC conf., Continuous Electron Beam Accelerator Facility report CEBAF-Report-89-001 (1989) 91.
8. T. Tran Ngoc, G.E. McMichael and G.M. Arbique, "Components for CW RFQ's", these proceedings.
9. B.G. Chidley, G.M. Arbique, M.S. de Jong, G.E. McMichael, W.L. Michel and B.H. Smith, "RFQ1 Diagnostic Devices", these proceedings.
10. G.M. Arbique, B.G. Chidley, M.S. de Jong, G.E. McMichael and J.Y. Sheikh, "Beam Performance and Measurements on the RFQ1 Accelerator", these proceedings.
11. B.G. Chidley, F.P. Adams, G.E. McMichael, T.Tran Ngoc and T.S. Bhatia, "New Vanes for RFQ1", these proceedings.
12. T.Tran Ngoc and R.M. Hutcheon, "Study of High Strength Coppers for RFQ1's New Vanes", these proceedings.
13. D. Schrage, L. Young, B. Campbell, J.H. Billen, T. Wangler, J. Stovall, F. Martinez, W. Clark, S. Gibbs, G. Bolme, P. O'Shea, M. Lynch, J. Devenport, J. Rathke, R. Micich, J. Rose, R. Richter and G. Rosato, "A Flight-Qualified RFQ for the BEAR Project", Proc. 1988 LINAC conf., Continuous Electron Beam Accelerator Facility report CEBAF-Report-89-001 (1989) 54.
14. A.M.M. Todd, M.F. Reusch, C.C. Paulson and J.I. Mendelsohn, "Beam Dynamics Model Development", these proceedings.
15. T.P. Wangler, "Physics Design of Linear Accelerators for Intense Ion Beams", Proc. 1988 LINAC conf., Continuous Electron Beam Accelerator Facility report CEBAF-Report-89-001 (1989) 211.
16. T.P. Wangler, "Linac for Production of Tritium: Physics Design", these proceedings.

Wednesday

Session WE2
Chairman: H. Klein
Invited Papers

INTERDIGITAL RF STRUCTURES

U. Ratzinger
GSI, P.O. 11 05 52, D-6100 Darmstadt, FRG

Abstract

The main advantage of the interdigital rf-structure is its shunt impedance which is outstanding especially at low particle energies.
During the last 4 decades several investigations with rf models were done to study the shunt impedance of cavities with interdigital structures and their suitability for the acceleration of protons and heavy ions. The "SchweIN" at the Munich Tandem Laboratory was the first IH-type cavity in use. It has postaccelerated heavy ions with q/A>0.3 from 2.4 MeV/u to 4.3 MeV/u since 1975. It is a short structure and does not contain any focusing elements, the velocity profile can be changed, the duty cycle is 100 %.
After the development of a special kind of beam dynamics it is now possible to combine tanks of the SchweIN-type to form a long linac.
Two-cavity combinations are in use at the Tandem laboratories in Munich and Roskilde, Denmark; one cavity is used at Tsukuba, Japan.
Recently there is a growing number of applications, where the structure is used to accelerate low energy beams. The Tokyo Institute of Technology built an IH structure with W=0.24 MeV/u - 2.4 MeV/u, using conventional beam dynamics and magnetic quadrupole focusing.
For the new 1.4 MeV/u injector at UNILAC/GSI, an IH-type cavity is under construction with innovations in beam dynamics and rf-structure.

Introduction

This article describes interdigital drift tube structures mounted inside a cavity and operated in the H_{111} mode. So far only room temperature devices exist.
Early studies of this structure on rf models were done around 1950 at several laboratories.
In 1956 J.P. Blewett mentioned some characteristics of that structure during his talk at the CERN-Symposium.[1] Some more detailed studies are reported in the Sixties from groups in the Soviet Union[2,3] and France[4,5].
In 1976 the first IH structure came to routine operation at the Munich MP Tandem Laboratory[6].
In the Eighties the application of this structure was extended to the acceleration of low energy Tandem beams at the Tokyo Institute of Technology[7] and to He^+- and N^+-beams out of a 40 kV plasma source at the FOM-Institute Amsterdam[8].

Geometry and field distribution

Fig. 1a shows the distribution of the electric and magnetic field lines inside a cylindrical cavity operated in the H_{111}-mode. By mounting the $3\lambda/2$-drift tube structure the resonance frequency is typically reduced by about 60 % of the original value (in case of the Alvarez structure the corresponding value is only 10 % - 20 %).
These numbers demonstrate that the effective capacity in case of the IH structure is very well concentrated at the drift tubes.

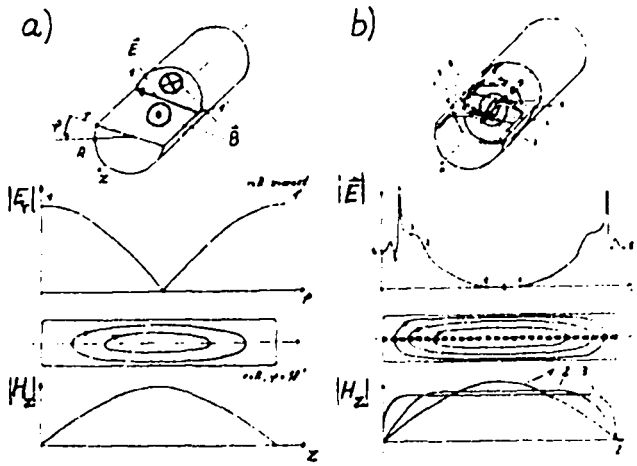

fig. 1a: Field distribution inside a cylindrical cavity, operated in the H_{111}-mode
b: Field distribution of the IH structure

One main problem to be solved was the flatness of the gap voltage distribution along the beam axis. It means to shift the magnetic field distribution from curve 1 of fig. 1b (capacity and inductivity per unit length of the cavity constant) to curve 3 (capacity and/or inductivity per unit length of the cavity increased towards the ends).
Figs. 2a and b show two ways of gap voltage flattening which provided good results and could stand cw operation:

- The Munich "f-SchweIN" cavity[6] consists of three parts. The middle part provides extended areas at the tank ends for the penetration of the magnetic field lines. The constant gap voltage distribution is additionally gained by variation of the gap length to cell length ratio g/L along the beam axis.
- The "second Tokyo tank" uses an optimized open end-type boundary to get a flat voltage distribution. By keeping the g/L-ratio constant the "E"-shaped magnetic-flux inducers at each side are matched to the velocity profile of the structure[7].

IH structures in operation

Table 1 shows a list of laboratories which use interdigital rf structures for the acceleration of heavy ions. The main characteristics of the different devices are mentioned in the last column. Figs. 3 and 4 give an impression of the variety of realized geometries.

Efficient beam dynamics

As described above the effective resonator capacity C_R of the IH cavity is very well concentrated at the drift tube structure. At constant rf frequency, constant particle velocity and flexible tank dimensions the shunt impedance scales with $C_R^{-3/2}$. At constant tank dimensions and constant particle

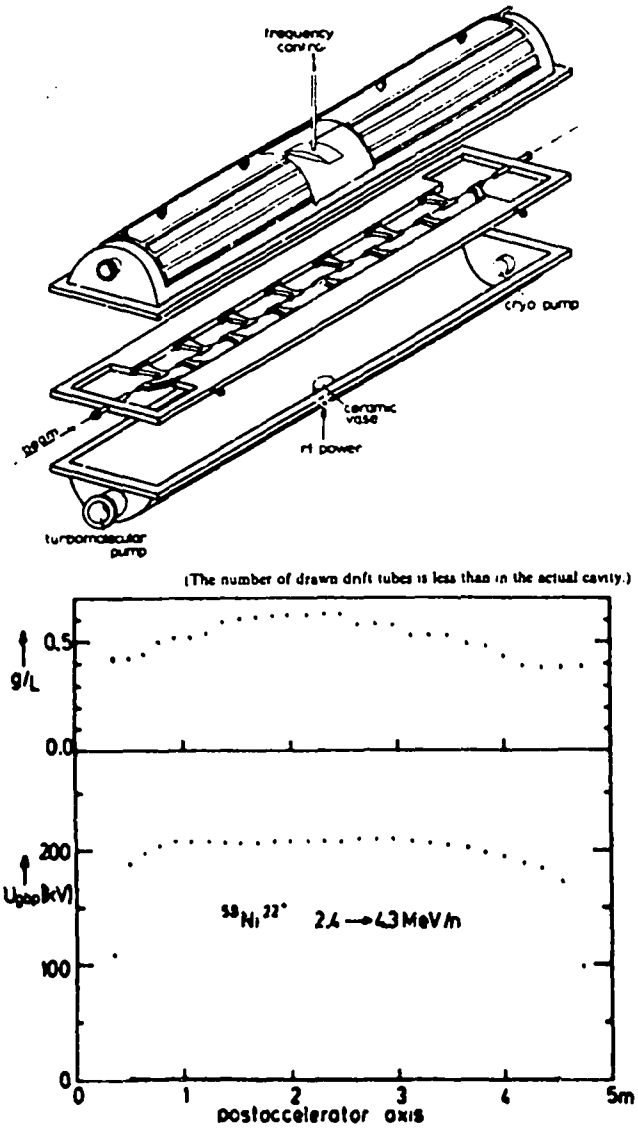

fig. 2a: Construction of the Munich "f-SchweIN" and flattening of the gap voltage distribution by variation of the g/L-ratio.

velocity the shunt impedance scales with $C_R^{-7/4}$ by varying the rf frequency.[8]
To achieve an optimum effective shunt impedance the drift tubes outer diameter should be as small as possible, that means construction of drift tubes without any quadrupoles or other space consuming focusing elements. This was the motivation to reduce the radial defocusing action of negative synchronous particle structures using ϕ_s=-30° typically.
A beam dynamics which accelerates the particle very close to the crest of the wave and has good transport capabilities in the 6-dim phase space was developed gradually in connection with the IH structure[9,10,11]. The theory was confirmed by experiment.
The main aspects of the "Beam dynamics of combined 0° synchronous particle structures" are summarized qualitatively below:

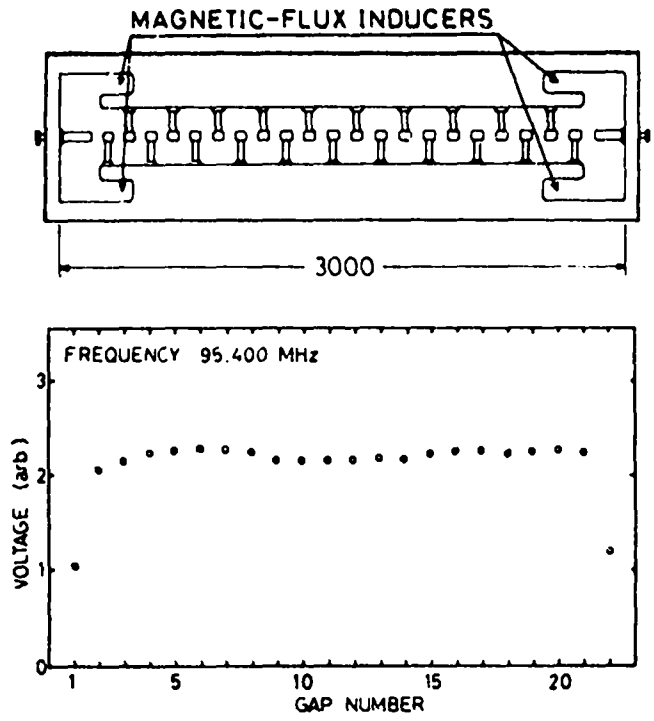

fig. 2b: The middle part of the Tokyo "2f-tank" and flattening of the gap voltage by "magnetic-flux inducers".

- Injection of the particle pulse at higher energy relative to the 0° synchronous particle (fig. 5). The excess energy Δ_0 of the pulse center at injection is related to the half axis δ_0 of the longitudinal beam emittance ($\Delta_0 = r \cdot \delta_0$: $1<r<1.5$ typically).
- In each 0° synchronous particle section the center particle of the pulse makes about one quarter phase oscillation around the synchronous particle. The energy-phase relation at the connection between neighbouring 0° synchronous particle sections can be seen from fig. 6. By that method it is possible to keep the position of the particle pulse mainly inside the second quadrant of the energy-phase plane providing a stable beam transport.
- The longitudinal focusing forces are concentrated near the end of each 0° synchronous particle section (position of the particles at negative rf phases). The motion of a single particle around the center particle of the pulse is shown qualitatively by fig. 7. Necessary conditions for cyclic motion are discussed in ref. 11.
- The transversal focusing of the beam is done at the end of each 0° synchronous particle section usually. This arrangement of longitudinal and transversal focusing provides a small beam diameter and allows for an accelerator construction with reduced apertures.

In case of low q/A-beams with big transversal emittance rebunching behind each lense by a short negative synchronous particle section may become necessary. An example is given in ref. 12, describing the IH structure for the new GSI injector[13].

Location		fr MHz	Ø m	L m	Z_{eff} MΩ/m	W_i MeV/u	W_f MeV/u	$(\frac{q}{A})_{min}$	characteristics
Munich									
Tandem	tank 1	78.5	1	5.0	150	2.4	4.3	0.34	φ_s = 0° Injector: 12 MV-Tandem;
Laboratory	tank 2	157	0.5*	3.0	150	4.3	6.0	0.40	- " - quadrupole doublet between cavities;
Techn. Univ.									
Roskilde									
Niels Bohr	tank 1	100	0.72	3.64	142	2.4	3.7	0.29	φ_s = 0° Injector: 9 MV-Tandem;
Institute	tank 2	100	0.72	3.64	105	3.7	4.9	0.29	- " - quadrupole triplet between cavities; high reliability of operation;
Tsukuba									
University	tank 1	100.5	0.75	3.03	134	3.14	4.0	0.42	φ_s = 0° Injector: 11 MV-Tandem; available rf power limited;
Tokyo									
Inst. of.	tank 1	48	1.4	7.0	132	0.24	2.4	0.25	φ_s =-30° Injector: 1.6 MV-Tandem;
Technology	tank 2	96	0.76	3.0	130	2.4	3.4	0.25	φ_s = 0° FODO quadrupole channel along tank 1;
Amsterdam									
FOM-Inst.	tank A	40	0.4	0.65	--	0.01	0.03	0.25	φ_s =-38° MEQALAC, $^4He^+$,
& IAP, Ffm.	tank B	25	0.8*	1.7	-30	0.0028	0.071	0.07	φ_s =-30°...-42°, 4 beam channels, N^+, 0,56 mA;

* := tank has no circular cross section

Table 1: IH structures used for heavy ion acceleration

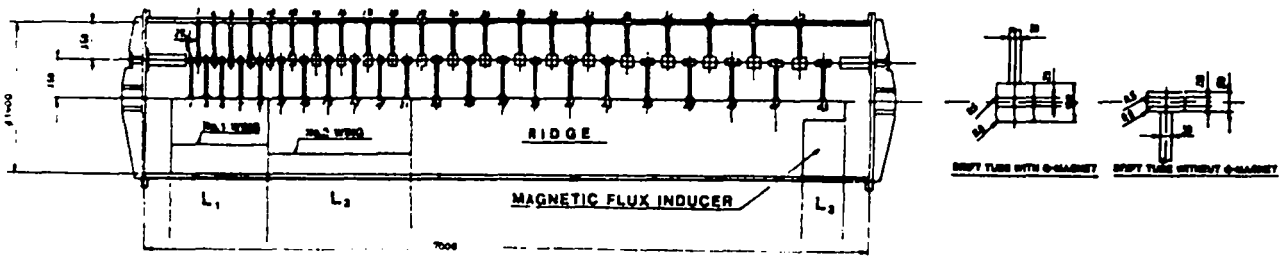

fig. 3: The Tokyo "f-tank".

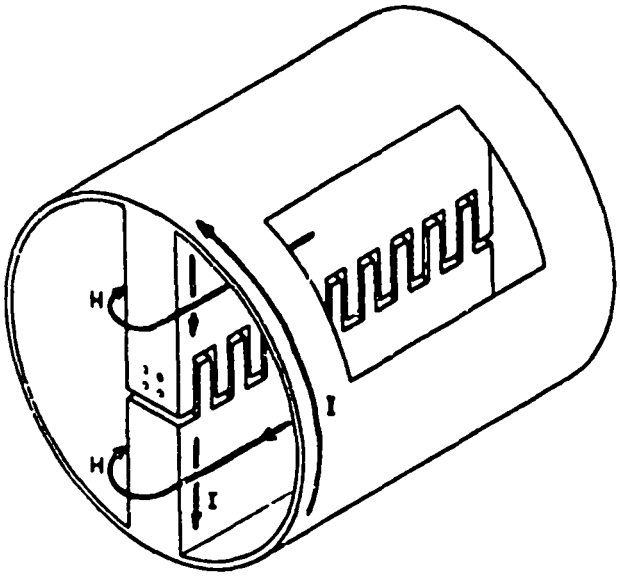

fig. 4: The Amsterdam "MEQALAC"-prototype, sketch[15].

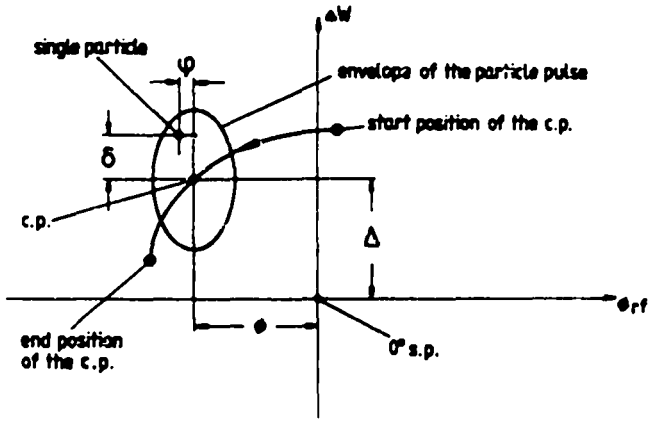

fig. 5: Motion of the particle pulse around the 0° synchronous particle in the longitudinal phase space.

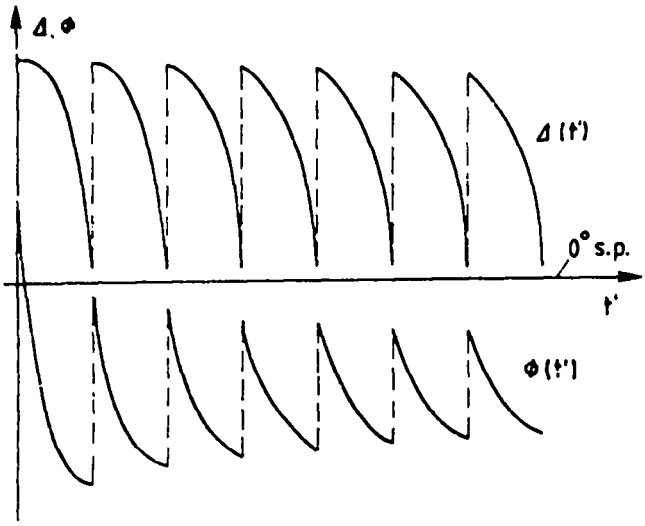

fig. 6: Position of the particle pulse center relative to the 0° synchronous particles of a long structure.

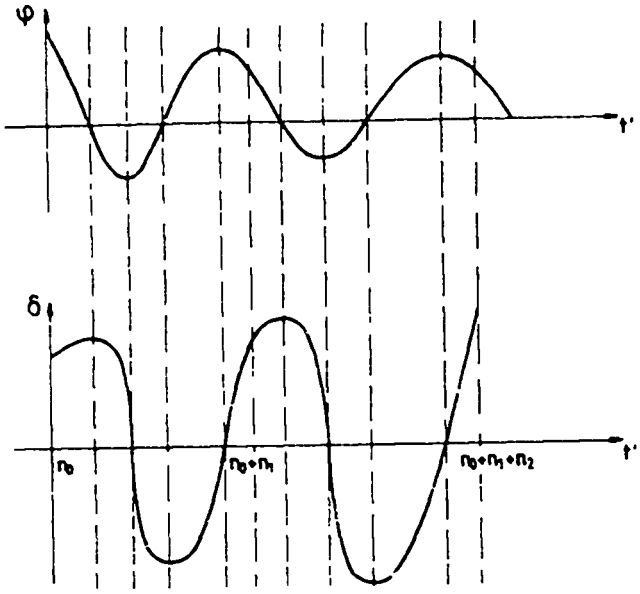

fig. 7: Oscillation of a single particle around the pulse center.

Improved drift tube geometry

To optimize the shunt impedance, the walls of the drift tubes and the capacitive ends of the stems should be thin; the inductive ends of the stems should be thick to get a low surface current density.
This procedure is limited by the electrical peak surface fields which are enhanced by reducing the outer diameter of the drift tubes. Another limit is the asymmetry of the gap field which is caused by the capacitive coupling between each drift tube and its neighboured stems (fig. 4 in ref. 10). This asymmetry grows when the capacitive coupling between the drift tubes is reduced.
By making use of thin walled drift tubes with a specific asymmetric shape (fig. 8), one can partly overcome the second limitation, which is serious especially for low energetic particles.

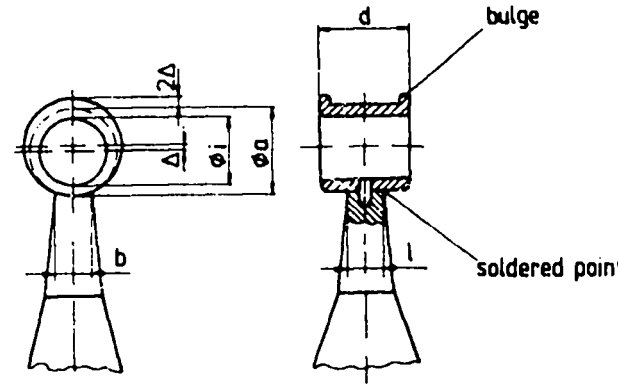

fig. 8: Dipole compensated drift tube geometry.

The advantage of the proposed geometry was confirmed qualitatively first by repeating the off axis perturbation measurements along some modified drift tubes at the GSI interdigital rf-model.
Quantitative numerical results were obtained by using the 3-dim computer code PBM3D[1].
This program is solving Maxwell's equation of continuity:

$$\mathrm{div}\,[(\kappa + i\omega_0\varepsilon_r)\cdot \mathrm{grad}\,V] = 0;$$

κ: = electrical conductivity
V: = electrical potential

The code is based on the "method of differences" and can be used to find the field distribution of the capacitive part of a cavity with complicated geometry.
The voltage distribution along the stems is defined by their geometry and by κ. This distribution can be varied in a wide range without significant influence on the gap field distribution.
The tank walls are kept on zero potential.
The geometry used for the new GSI IH structure is shown in fig. 8. It is optimized to eliminate the dipole component at the low energy side.
The reduction of the dipole component at higher energies is shown in fig. 9.

Shuntimpedance

The efficiency of interdigital rf structures is shown by fig. 10. However additonally the normalized transversal acceptances α_n/π•mm mrad and $(q/A)_{min}$ have to be taken into account to compare with the UNILAC-structures:

Index in fig. 11:	1	2 + 3	4	5
α_n/π mm mrad	1.5	0.3	1	10
$(\frac{q}{A})_{min}$	0.11	0.3	0.04	0.11

Conclusions

Though the advantages of small size and very high shuntimpedance are known since about 40 years it took a long time to construct IH structures which allow for stable operation and high service load.
This structure is a very efficient tool for the acceleration of low energy beams up to about 20 Mev/u and q/A-values below one.
The dependence of the optimum rf frequency on the beam velocity is rather strong.

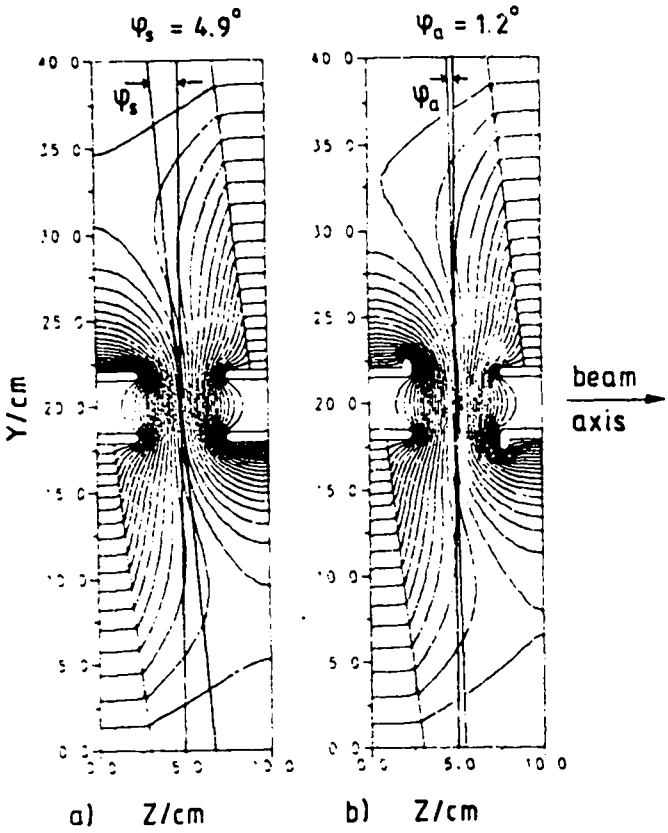

fig. 9: Influence of the bulges on the transverse electric field component.

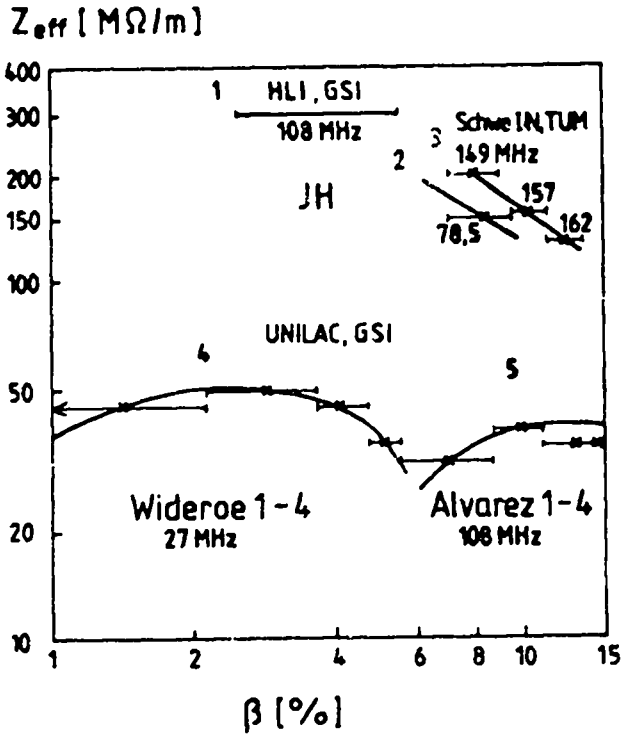

fig. 10: Comparison of shunt impedance and velocity range of several drift tube linacs

Acknowledgement

I like to thank Prof. H. Morinaga who was one of the very early pioneers to investigate the IH structure. He fortunately remembered to his former studies when he came to Munich and provided an interesting field of activity to many of his students.

References

[1] J.P. Blewett, Linear accelerator injector for proton synchrotrons, CERN symposium (1956), 162.
[2] P.M. Zeidlitz, V.A. Yamnitskii, Accelerating systems employing H-type waves, Plasma Physics (Journal of Nucl. Energy, Part C), Vol. 4 (1962), 121.
[3] V.A. Bomko, E.I. Revutskii, L.I. Bolotin, High frequency characteristics of a linear accelerator raising multicharge ions to energies of 1 MeV per nucleon in an H_{111} wave, Soviet Physics Techn. Physics, 9 (1965), 977.
[4] J. Pottier, A new structure for heavy ion linacs, IEEE Trans. Nucl. Sci. Vol. NS-16/3 (1969), 377.
[5] M. Bres, A. Chabert, J.-C. Gavet, D.T. Tron, B. Veyron, G. Voisin, Study on interdigital H-Type structure for heavy ion linear accelerator, IEEE Trans. Nucl. Sci., Vol. NS-16/3 (1969), 372.
[6] E. Nolte, G. Geschonke, K. Bendermann, R. Oberschmid, R. Zierl, M. Feil, A. Jahnke, M. Kress and H. Morinaga, The Munich heavy ion postaccelerator, Nucl. Instr. and Meth. 158 (1979), 311.
[7] K. Satoh, T. Mitsumoto and E. Arai, Construction and operating experience with the Tokyo Institute of Technology post accelerators, Nucl. Instr. and Meth. A 268 (1988), 538.
[8] E. Nolte, R. Geier, W. Schollmeier and S. Gustavsson, Improved performance of the Munich heavy ion postaccelerator. Nucl. Instsr. and Meth. A 201 (1982), 291.
[9] U. Ratzinger, R. Geier, W. Schollmeir, S. Gustavsson and E. Nolte, The three-harmonics double-drift buncher at the Munich heavy ion postaccelerator, Nucl. Instr. and Meth. 205 (1983), 381.
[10] U. Ratzinger, E. Nolte, R. Geier, N. Gärtner and H. Morinaga, The upgraded Munich heavy ion postaccelerator, Nucl. Instr. and Meth. A 263 (1988), 261.
[11] U. Ratzinger and U. Bleil, Acceleration of low energy heavy ion beams with the IH structure, to be published in Nucl. Instr. and Meth.
[12] U. Ratzinger, A low beta rf linac-structure of the IH-type with improved radial acceptance, proc. of 1988 Linac Conf., CEBAF-rep. 89-001 (1989), 185.
[13] N. Angert, L. Dahl, J. Glatz, J. Klabunde, M. Müller, U. Ratzinger, B. Wofl, H. Deitinghoff, J. Friedrich, H. Klein, A. Schempp, A new 1.4 MeV/u injector Linac for the UNILAC, these proceedings.
[14] Computer code PB M3D for the calculation of electrical fields with capacitive and ohmice components. Author U. Bleil
[15] J.G. Bannenberg, W.H. Urbanus, R.G.C. Wojke, H. Klein, R.W. Thomae, A. Schempp, T. Weis, P.W. van Amersfoort, MEQALAC: A1 MeV multichannel rf accelerator for nitrogen ions, these proceedings.

TUNING AND STABILIZATION OF RFQ'S*

Lloyd Young
Los Alamos National Laboratory, MS-H817
Los Alamos, NM 87545

Abstract

Recent advances in tuning and stabilization of Radio Frequency Quadrupoles (RFQ) will be presented. New designs of RFQs as long as four times the free-space wavelength and requiring field flatness of a few percent and less than a few percent dipole component can now be built and tuned. The tuning is performed by measuring the RFQ fields with a beadpull in each quadrant and using a computer program (RFQPERT) to analyze the beadpull data. The program calculates a set of perturbations to an ideal RFQ that would mix in nearby modes to give the measured fields. Slug tuners are then used to cancel the calculated perturbation in the real RFQ to get the desired pure RFQ mode. The pros and cons of several methods that have been used to stabilize the field in RFQs will also be discussed.

Introduction

A large number of Radio Frequency Quadrupole (RFQ) accelerators have been studied but there are relatively few operating RFQs in the world[1,2]. The two major types of RFQs are the 4-vane and the 4-rod; names that signify the construction technique used in each case. The 4-vane RFQs are generally higher frequency (80 - 425 MHz) and used for light ions; the 4-rod RFQs are generally lower frequency (6 - 220 MHz) and used for heavy ions. The 4-rod RFQs are, in general, short compared to the wavelength of their operating frequency and, therefore, are fairly easy to tune. Opposite rods are supported by common supports that eliminate problems with dipole modes in the 4-rod RFQ. The only long RFQs (i.e., RFQs that are greater in length than two wavelengths) currently in existence, are the 4-vane type.

The sensitivity to tuning errors has been expressed as proportional to $(L/\lambda)^2$, where L is the length of the RFQ and λ is the free-space wavelength[3]. This expression only applies to the longitudinal stability of the TE210 mode (the RFQ mode) and not to tuning sensitivity (with respect to dipole components mixing with the RFQ mode), which depends only on the difference between the frequency of the nearby dipole modes and the frequency of the RFQ mode. Because short RFQs are comparatively easy to tune and easy to stabilize, long RFQs that are all 4-vane RFQs will be emphasized in this paper. The stabilization techniques discussed in this paper will refer mostly to stabilizing the RFQ mode from the effects of the dipole modes. A technique of stabilizing RFQs longitudinally is discussed in a contributed paper to this conference titled Coupled Radio-Frequency Quadrupoles as Compensated Structures. [4]

The Ideal RFQ

The ideal RFQ is defined in this paper as a 4-vane RFQ with the end region tuned to the cutoff frequency of the RFQ in such a way that the frequency of the TE210 mode (the quadrupole mode) is equal to the cutoff frequency of the RFQ. The computer program SUPERFISH calculates the frequency of the TE210 mode for a cross section of the RFQ, and this calculation is shown in Fig. 1. The frequency of the TE21n mode is then given by

$$freq\{TE21n\} = \frac{c}{2\pi} \times \sqrt{\left[\frac{2\pi}{c} \times freq\{TE210\}\right]^2 + \left(\frac{n \times \pi}{L}\right)^2}, \quad (1)$$

where n is the number of nodes in the mode and L is the length of the RFQ.

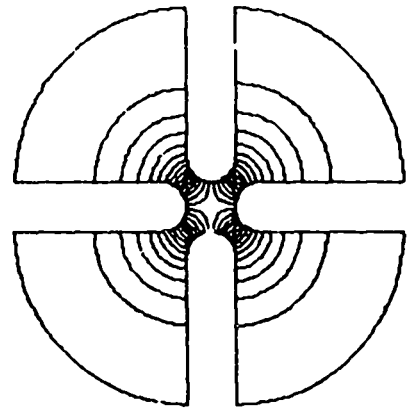

Fig. 1. The TE210, or Quadrupole Mode in a Simple RFQ as calculated by SUPERFISH.

This expression assumes that the end regions are also tuned correctly for the TE21*n* modes, which, for a long RFQ, is a very good approximation because the TE211 mode, for example, is very close to the frequency of the TE210 mode. For a RFQ that is 4 wavelengths long the TE211 mode is only 0.78% higher than the TE210 mode. If the ends of the RFQ were also tuned correctly for the TE11*n* modes (the dipole modes), the same form of the expression could be used for the TE11*n* modes. A SUPERFISH calculation of one orientation of the dipole mode is shown in Fig. 2. In the ideal RFQ the ends of the RFQ are also tuned correctly for the TE110 mode. The frequencies of the TE21*n* and the TE11*n* modes are shown in Fig. 3 for an ideal RFQ that has a length of 4.25 wavelengths. Figure 4 shows the longitudinal variation of the amplitude of the TE21*n* and TE11*n* modes from $n = 0$ to $n = 3$. The amplitude of the fields of the TE21*n* and TE11*n* in the ideal RFQ will have the form

$$cos\left(\frac{n \times z \times \pi}{L}\right), \quad (2)$$

where z is the position along the RFQ. A plot of the first 4 modes given by Eq. 2 is shown in Fig. 4. In a real RFQ

that is tuned well, the amplitude of the TE21n modes are described very well by Eq. 2. However, the TE11n modes can be significantly different.

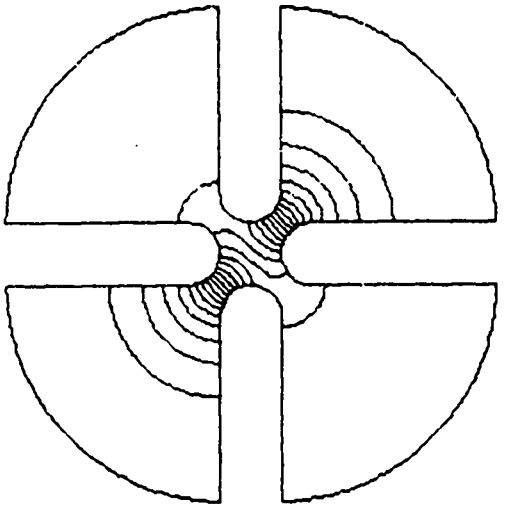

Fig. 2. One orientation of the TE110, or Dipole Mode in a Simple RFQ as calculated by SUPERFISH.

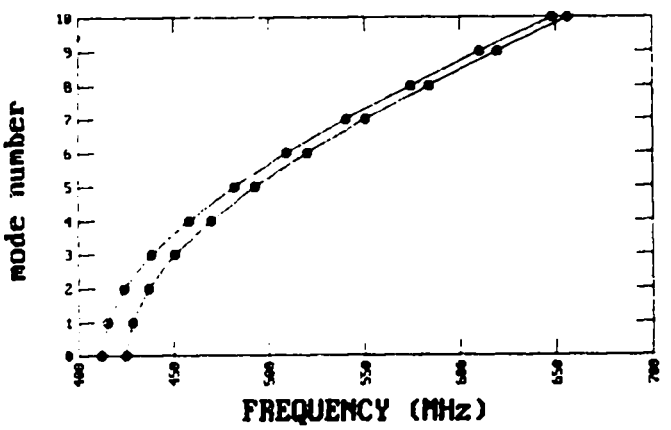

Fig. 3. The Frequencies of the TE21n and TE11n modes in an ideal RFQ with open boundary conditions for n=0 to 10. This ideal RFQ is 3m long and operates at 425 MHz.

Real RFQ

In a real RFQ the ends can be tuned so that the frequencies of the TE21n modes are given quite accurately by Eq. 1, but normally the ends of the RFQ are not tuned correctly for the TE11n modes. Therefore, Eq. 1 will not be accurate and the longitudinal variation of the amplitude will not be as shown in Fig. 4. For example, if the ends of the RFQ are tuned high for the TE11n modes, then the longitudinal variation of the amplitude of the TE11n modes will look more like that shown in Fig. 5. Because the ends are tuned high, the frequency of the first mode will be above cutoff and will approach the frequency of the TE111 mode in a RFQ with the ends shorted. Tuning the ends lower than the cutoff frequency is also possible, and then the fields may look like those shown in Fig. 6, where the modes are identified by the number of nodes.

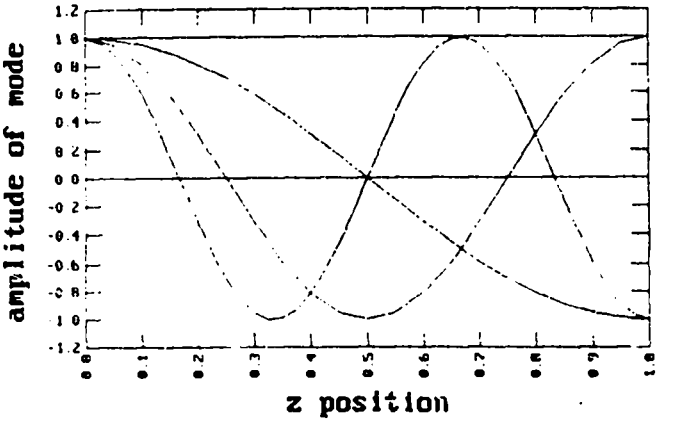

Fig. 4. The Amplitude of the First 4 Modes in an Ideal RFQ as a function of position with open boundary conditions on the ends.

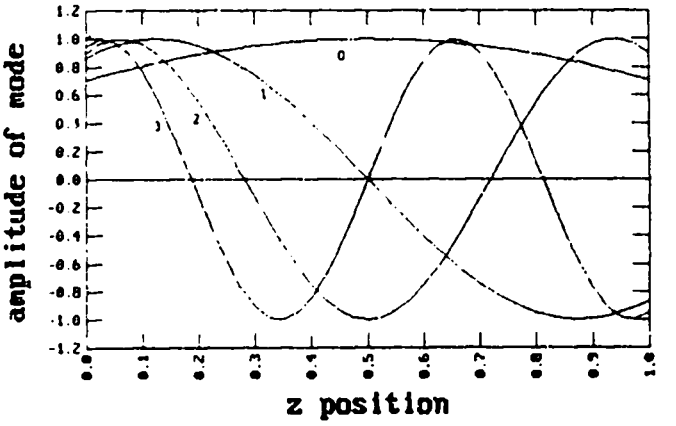

Fig. 5. The Amplitude of the First 4 Modes in an Ideal RFQ with ends that do not have open boundary conditions. In this case, the ends are tuned high in frequency.

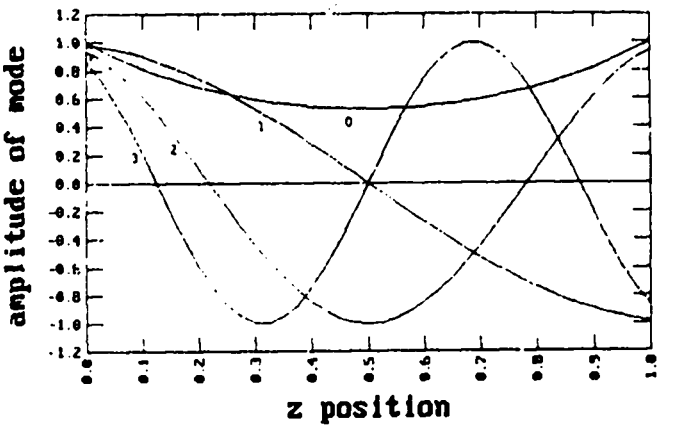

Fig. 6. The Amplitude of the First 4 Modes in an Ideal RFQ with ends that are tuned low in frequency.

In a waveguide, the wavelength λg is given by

$$\frac{1}{\lambda_g} = \frac{1}{c} \times \sqrt{\text{frequency}^2 - (\text{cutoff frequency})^2} \qquad (3)$$

If the frequencies of the modes are given by Eq. 1 the form of Eq. 2 can be changed to

$$\cos\left(\frac{2 \times z \times \pi}{\lambda_g(n)}\right) \tag{4}$$

where $\lambda_g(n)$ is the waveguide wavelength of the n'th mode. In a real RFQ the frequencies of the modes may not be given exactly by Eq. 1 and therefore L will not equal $n \times \lambda_g(n)/2$. Equation 4 must therefore be modified to accurately represent the actual modes in the RFQ. In an ideal RFQ where end regions are not tuned to the frequency of the cutoff frequency, the modes are given by:

$$\cos\left[\frac{(z - \text{offset}) \times 2 \times \pi}{\lambda_g(n)}\right] \text{for frequencies} > \text{cutoff frequency}$$

or

$$\cosh\left[\frac{(z - \text{offset}) \times 2 \times \pi}{i \times \lambda_g(n)}\right] \text{for frequencies} < \text{cutoff frequency} \tag{5}$$

where i is square root of -1 and offset is the factor that makes the expression symmetric or antisymmetric about the middle of the RFQ. If n is even, the expression is symmetric; if n is odd, the expression is antisymmetric. $Offset$ is given by $L/2 - \lambda_g(n) \times n/4$.

With the expression for the modes in an ideal RFQ with untuned ends, representing the actual measured field distribution in a RFQ as a combination of the ideal modes is now possible using Eq. 5. If $f(z,l)$ is the field in quadrant l (l is 1, 2, 3, or 4 representing the 4 quadrants) at position z, then

$$f(z,\ell) = \sum_{n=0}^{N}[A(n) \times Q(z,l,n) + B(n) \times D1(z,l,n) + C(n) \times D2(z,l,n)] \tag{6}$$

where
$Q(z,l,n)$ is $Qn(n) \times (-1)^{(l-1)} \times$ Eq. 5; $D1(z,l,n)$ is 0 for $l = 2$ or 4 and is $\pm D1n(n) \times$Eq. 5 for $l = 1$ or 3; and $D2(z,l,n)$ is 0 for $l = 1$ or 3 and is $\pm D2n(n) \times$ Eq. (5) for $l = 2$ or 4. $Qn(n)$, $D1n(n)$, and $D2n(n)$ are normalization factors that equalize the stored energy of of each mode. $Qn(0)$ is chosen to be equal to 1, and then the rest of the normalization factors are determined. $A(n)$, $B(n)$, and $C(n)$ are the coefficients that represent how much of each mode is mixed with the desired mode. N is the number of modes used to approximate the actual Field distribution. N is typically less than ten. A perfectly tuned RFQ will have $A(0) = 1$ and all other coefficients zero. However, if there is a small perturbation that raises the frequency by $P(k)$ in this perfectly tuned RFQ at position $Z(k)$, in quadrant $L(k)$ then the other coefficients will be given by

$$A(n) = \sum_k \frac{P(k) \times Q[Z(k), L(k), n)]}{[FQ(0) - FQ(n)]}, \tag{7}$$

$$B(n) = \sum_k \frac{P(k) \times D1[Z(k), L(k), n)]}{[FQ(0) - FD1(n)]}, \text{and} \tag{8}$$

$$C(n) = \sum_k \frac{P(k) \times D2[S(k), L(k), n)]}{[FQ(0) - FD2(n)]}, \tag{9}$$

where $FQ(n)$, $FD1(n)$, and $FD2(n)$ are the frequencies of the corresponding quadrupole or dipole mode.

These relationships suggest a method of tuning RFQs, because if the perturbations are assumed to be at the locations of the tuners and the value of the perturbations are known, then the tuners can be moved to remove the perturbations. The perturbations can be found by applying a least square fit of Eq. 6 to the beadpull data. The program RFQPERT implements this method for tuning RFQs. Ideally, this method should be able to tune a RFQ in one step, but in practice it has taken at least two or three iterations to tune a long RFQ, such as the Continuous Wave Deutron Demonstrator (CWDD) cold model or the Ground Test Accelerator (GTA) RFQ. With enough tuners the RFQ can be tuned so that the fields are flat to within 1% and with less then 1% dipole component. The reproducibility and accuracy of the beadpull data limits the tuning to this level.

The ends of the RFQ need to be undercut an appropriate amount so that the frequency of the TE210 mode equals the cutoff frequency of the RFQ. If there are tuners near the ends, the undercuts do not have to be exactly right, because the end tuners can be used to trim the end tuning. Capacitive end tuners that have been used in the past on RFQs (especially without undercuts) are inefficient, because they increase the stored energy in the RFQ unnecessarily.

Stabilization Of RFQs

Several methods of stabilizing RFQs have been used to reduce the susceptibility to dipole mode mixing with the desired quadrupole mode. Vane coupling rings (VCRs) have been used with good results in a number of RFQs. VCRs raise the dipole modes well above the frequency of the quadrupole mode and practically eliminate the dipole problem even in poorly aligned RFQs. VCRs do not affect the longitudinal stability. However, the disadvantage of VCRs is that they lower the frequency of the quadrupole mode substantially and cause scalloping of the fields on axis. Both the lowering of the frequency and the scalloping of the fields are caused by the extra intervane capacitance at the location of the VCRs. Because VCRs lower the frequency so much, a RFQ must be designed to use VCRs, and if it is designed to use the VCRs, they must be used or the frequency of the RFQ will be wrong. Another problem with VCRs is the difficulty of installing VCRs that could be actively cooled in high-duty-factor RFQs.

In very short RFQs, it is possible to use resonant circuits at the end of the RFQ that couple to the dipole modes and split the lowest dipole mode into two modes equally spaced above and below the quadrupole mode, thus stabilizing the RFQ from the effects of the dipole mode mixing. In short RFQs, the frequency of the dipole mode can be very close to the frequency of the quadrupole mode, because the ends of the RFQ are tuned for the quadrupole mode and not for the dipole modes. In general, the ends of the RFQ will raise the frequency of the dipole modes with respect to the quadrupole modes. The cutoff frequency of the TE11 modes is usually about 3% lower than the cutoff frequency of the TE21 mode. However, in a short RFQ the TE110 dipole mode can be nearly degenerate with the TE210 quadrupole mode, because the ends

of the RFQ raise the frequency of the TE11 modes. In a long RFQ the ends will not have as much effect on the frequency of the dipole modes, but the frequency of the TE111 or TE112 modes may come very close to the TE210 quadrupole mode. If the ends of the RFQ are tuned independently for the dipole modes with devices that do not affect the TE210 quadrupole modes, the frequency of the TE11n modes can be shifted so that none of the TE11n modes are near the frequency of the TE210 quadrupole mode. The Beam Experiment Aboard a Rocket (BEAR) RFQ used this method successfully to lower the frequency of the TE110 mode[5]. The GTA RFQ is using this method to lower the frequency of the TE112 mode, which was slightly above the frequency of the quadrupole mode to well below the quadrupole mode. The TE113 mode is still well above the quadrupole mode. In the CWDD cold model, similar results were obtained. These end tuners are compatible with the program RFQPERT.

The end tuners can be made in several forms. The BEAR RFQ used four simple L-shaped rods attached to the end plate of the RFQ on the center line, midway between the vanes. The end tuners were tuned by a hollow cylindrical tuner on the outer wall of the quadrant. The gap between the tuner and the L-shaped rod formed the capacitance of the LC circuit which could be tuned by adjusting this gap. Some of the magnetic field of the TE11 modes must pass through this (LC) circuit, and, therefore, the frequency of the TE11 modes can be changed by this end tuner. Because the L- shaped rods are on the center line between the vanes, the magnetic field of the TE21 modes do not pass through the loop of the end tuners and therefore are unaffected by them.

Azimuthal stabilizers, which are resonant coaxial lines that are loop coupled to opposite quadrants, were tried on the GTA cold model and on the CWDD cold model. (They were planned to be used on the GTA RFQ and on the CWDD RFQ.) They worked by splitting the dipole mode nearest the TE210 quadrupole mode. On these RFQs the TE112 mode was nearest the TE210 mode. The splitting of the TE112 mode was very unpredictable, and the split modes could not be simply described by equations similar to Eq. 5. Thus, the program RFQPERT could not be used to tune the RFQ once the azimuthal stabilizers were mounted which changed the field distribution enough to require further tuning. The effectiveness of the azimuthal stabilizers was attributed to splitting the dipole mode nearest to the quadrupole mode into two modes that had similar characteristics – one with frequency above the quadrupole and one below the quadrupole. Perturbations would tend to mix these modes equally with opposite polarity, thus canceling their effect. Another problem encountered with the azimuthal stabilizers was that mode splitting occurred, but the two modes did not always have the same characteristics and, therefore, the cancellation was ineffective. The end tuners worked better and have now been adopted on both the GTA RFQ and the CWDD RFQ.

RFQ Construction

RFQs must be fabricated with precision, because the gap between the vanes is small with respect to the overall dimensions of the cavity, and small changes in the gap cause large changes in the frequency. An RFQ can be thought of as a waveguide with open boundary conditions on the end. The desired mode operates at the cutoff frequency of the waveguide. If the gaps between the four vanes vary or are unequal, the fields of the quadrupole mode will not be flat, and the dipole modes will mix with the quadrupole mode. One method of tuning RFQs has been to move the vanes to equalize the gaps, which sometimes involved bending the vanes with positioners holding the vanes in the RFQ. After the vanes were aligned mechanically, improving the field distribution was only possible by trail and error, furthermore, this procedure left the RFQ with built-in stresses that would slowly release with time, which could change the field distribution. In addition, this tuning procedure was usually very time consuming.

A better method of constructing RFQs has been to machine the vanes so that they are straight, align them mechanically without bending the vanes, and assemble them in as stress-free condition as possible. Those designs that use C seals for the rf joint will necessarily have some stress associated with the compression of the C seals. The structure can then be tuned with slug tuners on the outer wall as described above. Moving vanes for tuning the RFQ in the precise way that slug tuners can be moved for tuning is impossible. Some of the RFQs that have been built with this philosophy include the BEAR RFQ, the CWDD RFQ, the GTA RFQ, and the CERN RFQ, called RFQ2[6].

When designing an RFQ, maintaining a constant capacitance per unit length along the length of the RFQ is important. New designs do not have a constant r_0, the average distance from the vane tip to the center line, along the RFQ. This average distance is increased when the modulation of the vane tips would otherwise decrease the aperture of the RFQ. Decreasing the aperture of the RFQ would decrease the current carrying capacity. If the RFQ cross section is not changed, a change in r_0 would result in a change in the capacitance and a change in the local cutoff frequency of the waveguide, which would cause a severe tilt in the fields. To keep a constant capacitance per unit length when r_0 is not kept constant, Los Alamos changes the radius of curvature (ρ) of the vane tip. As r_0 is increased, ρ is increased in such a way that the cutoff frequency remains constant as calculated by SUPERFISH. Keeping the cutoff frequency constant by maintaining a constant capacitance per unit length has an important advantage: measuring the magnetic field with a beadpull near the outer wall gives an accurate measure of the voltage across the gap. If the cutoff frequency was kept constant by changing the outer wall and allowing the capacitance to vary, the beadpull data would need to be corrected to measure the gap voltage, or a beadpull in the gap would need to be performed.

Summary

New methods of building and tuning RFQs have resulted in RFQs that have high quality fields and that are easy to tune.

References

1. A. Schempp, Recent Progress in RFQ's in Proceedings of the 1988 Linear Accelerator Conference, Continuous Electron Beam Accelerator Facility (CEBAF) report-89-001 (June 1989), p. 460.
2. S. O. Schriber, Present Status of RFQ's, IEEE Transactions on Nuclear Science 32 (5), 3134 (1985).
3. D. D. Armstrong, W. D. Cornelius, F. O. Purser,

R. A. Jameson, and T. P. Wangler, RFQ Development at Los Alamos, Los Alamos National Laboratory report LA-UR 84-498 (1984).

4. M. Jean Browman and Lloyd M. Young, Coupled Radio-Frequency Quadrupoles as Compensated Structures , 1990 Linac Conference, (September, 1990).

5. D. Schrage, L. Young, B. Campbell, J. H. Billen, T. Wangler, J. Stovall, F. Martinez, W. Clark, S. Gibbs, G. Bolme, P. O'Shea, M. Lynch, J. Devenport, J. Rathke, R. Micich, J. Rose, R. Richter, and G. Rosato, A Flight-Qualified RFQ for the BEAR Project, in Proceedings of the 1988 Linear Accelerator Conference, CEBAF-Report-89-001, (June 1989), p. 54.

6. J. L. Vallet, M. Vretenav, M. Weiss, Field Adjustment, Tuning, and Beam Analysis of the High-Intensity CERN RFQ, 1990 Linac Conference, (September, 1990).

VARIABLE ENERGY AND HEAVY ION RFQs*

Alwin Schempp

Institut für Angewandte Physik, J.W. Goethe Universität
D-6000 Frankfurt am Main, Postfach 111932, Germany

Abstract

RFQs are low energy rf accelerator structures which can efficiently transport and accelerate high current ion beams. RFQs have a fixed velocity profile and therefore fixed input and output energies per nucleon. The ion energy can be varied by changing the resonator frequency. This has been done for a 4-Rod-RFQ, i.e. the type of RFQ resonator developed in Frankfurt, which is well suited for such an application.

The status of two RFQ projects for cluster- and heavy ion acceleration with a possible variation of the output energy by a factor of two will be discussed together with work on fixed energy RFQs for heavy ions.

Introduction

In a Radio Frequency Quadrupole[1,2] (RFQ) structure acceleration is achieved by a geometrical modulation of quadrupole electrodes leading to axial components of the field. These electrodes are part of an rf resonator, excited in a TE_{210}- like mode to generate the necessary field distribution.

The mechanical modulation of the RFQ - quadrupole electrodes, as indicated in fig. 1, adds an accelerating field component to the focusing channel, resulting in a structure which accelerates and focuses with the same rf fields.

Electrical focusing forces are independent of the ion velocity v_p and if rf-fields are applied, higher voltages than in a dc quadrupole system can be reached, giving a very strong focusing with a large radial acceptance. Because the focusing structure is homogeneous the accelerating and focusing cells can be very short, which makes it possible to apply the concept of adiabatic bunching[3]. The phases φ_s between the particles and the rf- fields and the amplitude of the accelerating fields E_z are changed very slowly according to the increasing ion velocity v_p, transforming a dc beam from an ion source into a bunched beam with a minimum of emittance growth and particle losses.

The mechanical shape of the electrodes is characterized by the aperture radii a_i, the modulations m_i, and the modulation periods L_i, as shown in fig. 1. Together with the electrode voltage U_Q it determines the acceleration and focusing fields. Therefore a voltage as high as possible (close to the breakdown voltage) and an aperture as small as possible will be chosen for a high focusing strength $G \sim U_Q/a^2$ and a high ion current capability[3]: Limiting current $I_{lim} \sim U_Q^2 v_p |\varphi_s| / (a^2 f)$. For the same focusing strength the voltage U_Q which has to be applied to the quadrupole electrodes is proportional to the ratio of ion mass A to charge q: $U_Q A/q$.

Thus the choice of the frequency f and the electrode voltage U_Q are starting parameters for the particle dynamics design.

The rf power N required to provide the design quadrupole voltage U_Q on the electrodes is proportional to the length L_s of the structure and depends on the type and parameters of the structure and the operating frequency f. The shunt impedance R' which characterizes the rf efficiency of the accelerator structure is defined by: $R' = U_Q/N \cdot L_s$. R' is roughly proportional to $f^{-1.5}$ while the cavity length L_s will be inversely proportional to the frequency[4,5].

The various applications of RFQ accelerators can be distinguished by the ion beam species, the ion energy and current, the emittance, the duty factor, and the specific charge of the ions, which lead to the different techniques of beam dynamics and rf-structure design.

The velocity profile is fixed and can be changed by varying the length L_i or the phases between groups of cells by breaking the structure into several individually driven and phased subunits like in postaccelerators[6] or with a variable frequency keeping the electrode structure unchanged. The second way of changing the Wideroe[7] resonance condition $L_i = \beta_p \lambda_o/2 = v_p/2f$, is the way which has been used for compact ion RFQs with variable energy (VE-RFQ)[8].

The electrode and cavity design is based on the development of fixed frequency (energy) 4-Rod RFQs[9,10], which is well suited for low frequency heavy ion acceleration. Therefore, examples of recent developments of fixed energy heavy ion RFQ will be discussed at first.

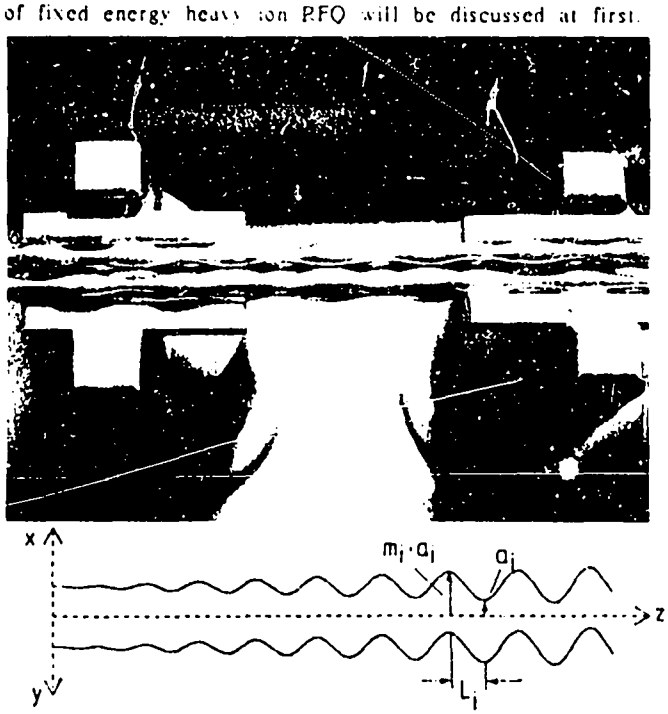

Fig. 1 Modulated RFQ electrodes

* Work supported by CEC under contract SC1 0333-C(EDB) and BMFT under contract 60F186I

RFQ design examples

The 4-Rod RFQ rf-structure consists of coupled $\lambda/2$ oscillators in a linear arrangement as indicated in fig. 2, and although the current densities at the electrode supports are relatively high the efficiency does not fall short compared with other RFQs. The resonator is very stable in respect to rf operation because neighboring modes are clearly separated and all major current conducting parts can easily be cooled, which is important especially for high duty cycle operation and possible application for superconducting RFQ resonators[11,12].

The RFQ structure should be as short as possible to save rf power and costs proportionally. When the structure frequency and electrode voltage have been chosen to give good focusing properties, the length L_s has to be optimized in respect e.g. to the beam emittance, the power consumption and the transmission, which is the ratio of d.c. input beam versus output beam.

Fig. 3 shows the design parameters a.m. and L_i along the RFQ structure for the new HLI injector for the GSI[13,14]. The RFQ with a length of 2.9 m and an electrode voltage of 80 kV operates at 108.5 MHz and requires approximately 120 kW rf power with a duty cycle of up to 50%. PARMTEQ calculations show a radial emittance growth[15] of only 10% and a small longitudinal emittance of 8 °keV/u (90%, r.m.s.) which comes even close to values achieved for more linear bunching schemes. The slow increase of the ion energy T as function of the RFQ cell number N is demonstrating the fact that a significant part of the RFQ structure is required for bunching.

Fig. 4 shows the cross section of the tank which is of a coffin like design which facilitates installation, alignment and maintenance as well as the burial. Fig. 5 shows the low energy end of the cavity, which incorporates also beam diagnostic devices. The tank has been manufactured and will soon be copper plated. First operation is scheduled for spring of 1991.

Another fixed energy 4-Rod RFQ has been built for heavy ions (specific charge q/A=0.25, energy 10 - 300keV/u) as injector for the storage ring CRYRING at the MSI Stockholm. The RFQ resonator has been designed, built, and tested in Frankfurt and is now installed at the injector beam line at MSI[16].

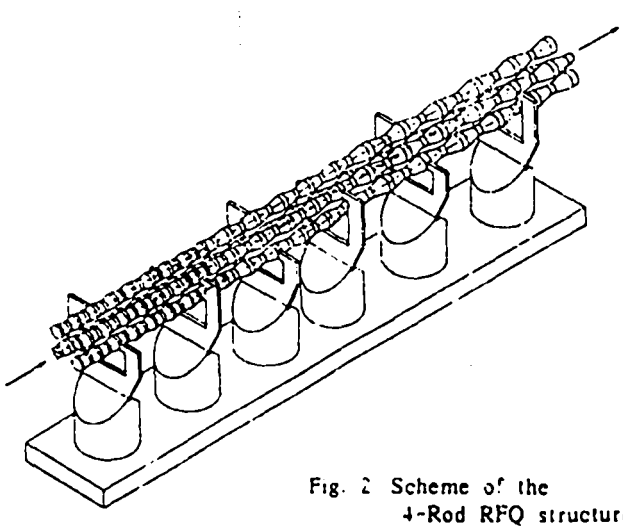

Fig. 2 Scheme of the 4-Rod RFQ structure

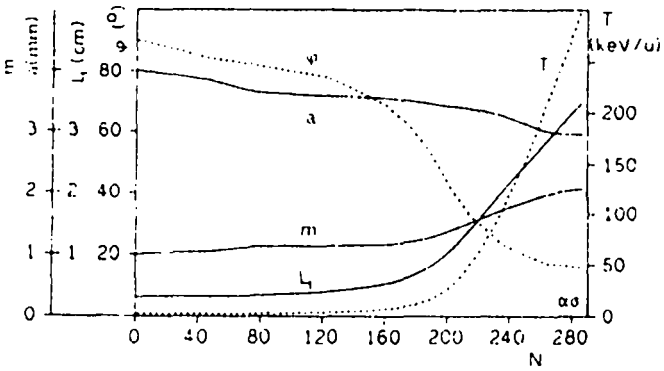

Fig. 3 Electrode design for the HLI-RFQ

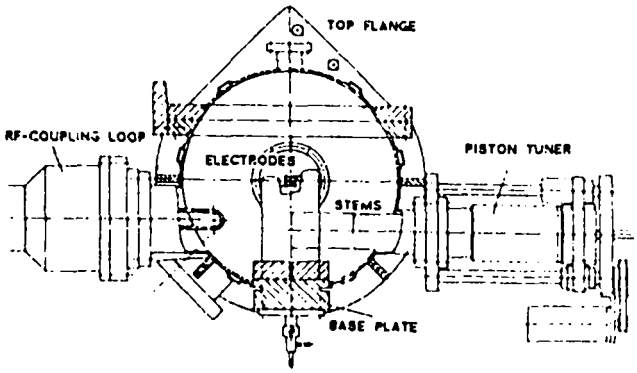

Fig. 4 Cross section of the HLI-RFQ

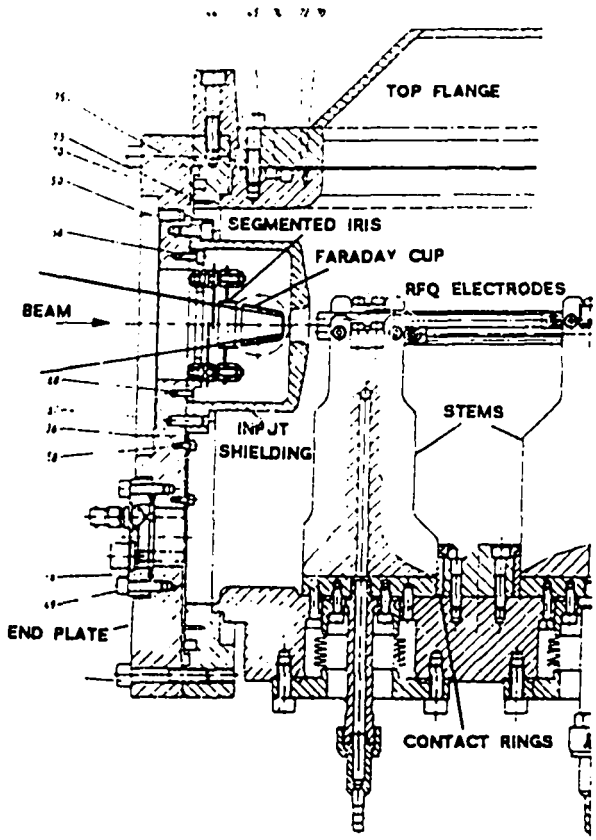

Fig. 5 Low energy end of the HLI-RFQ

Fig. 6 shows a view of this RFQ. Design features are a small size (tank diameter 35 cm at 108.5 MHz, length 1.54 m), a good rf efficiency and modest mechanical tolerances. The results of the beam tests were in very good agreement with PARMTEQ calculations. The rf-efficiency was better than expected so that also ions with smaller specific charge ξ/A can be accepted.

This experiments confirmed that the method of designing the electrode parameters along the RFQ without shaper, gentle buncher, and accelerator sections[4], can give shorter RFQ structures without drawbacks in beam quality .

Based on this results other heavy ion structures have been designed or will be built. There are plans for a new special injector for the TSR at the MPI Heidelberg[17] and for a new Lead-Linac RFQ for CERN[18], for which the HLI-RFQ and the CRYRING RFQ are valuable "prototypes". There is also a collaboration with GSI to built a prototype of a High current RFQ for U^{2+} (HSI) using the 4-Rod structure with spiral stems[19,20]. This HSI-RFQ is designed for the acceleration of up to 25mA U^{2+} ions from 2.5 to 20 keV/U. It will be 4 m long and operate at 27 MHz (1% df). First beam experiments are planed in the first half of 1991.

Variable Energy RFQs

The advantages of the RFQ structure are clear: low energy acceleration of ions from as low as 1 keV/amu up to approximately 1 MeV/amu with strong rf focusing and the possibility of high beam currents. The design of the RFQ has to be made for the heaviest particle to be accelerated and for fixed initial and final ion velocities v_p (or energy per mass unit u: T/u) A change of the output energy is possible by varying the resonance frequency of the cavity using the same electrode system: $v_p \sim f$.

Keeping the electrode voltage U_Q constant heavier particles with mass m = A×u and charge state q can be accelerated at a lower frequency with the same RFQ electrodes to the same final energy T_f : $T_f \sim A/q f^2$. To change the frequency of the 4-Rod RFQ the resonator can be tuned capacitively or inductively. For the first Variable-Energy- (VE-) RFQ structures to be built, the effective length of the driving conductor will be changed with movable shorts as indicated in Fig. 7, which results in a sufficiently large tuning range. Even though the problems with movable contacts exist, they are simpler to solve than for a comparable cavity resonator. In Frankfurt the VE-RFQ was developed at first for the application as a cluster postaccelerator at the 0.5 MV Cockroft Walton facility at the IPNL in Lyon (France).

The upgrading of the Cluster Facility is being performed in a collaboration between IPN Lyon, KfK Karlsruhe and IAP Frankfurt[21,22].

For the Lyon postaccelerator an upper frequency of 110 MHz could be used because of the relatively high preaccelerator voltage of 500 kV and the restriction to cluster masses of 30 u resp. 50 u. The RFQ for postacceleration of clusters is designed for 10 keV/u injection energy and up to 100 keV/u (3MeV for m=30u, 5MeV for m=50u) final energy. A layout of the cluster accelerator is shown in fig. 8.

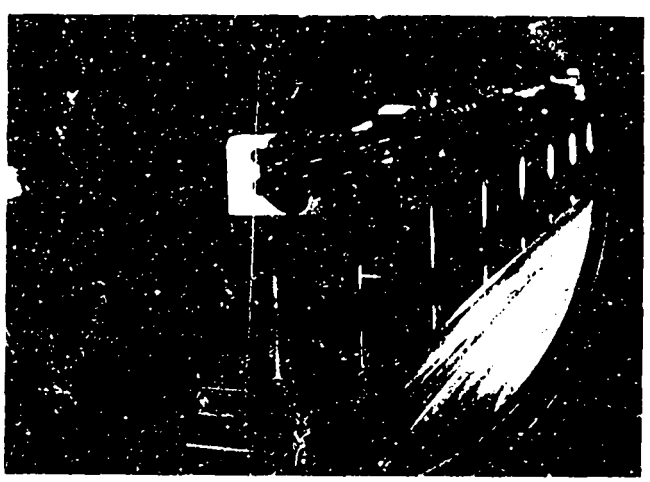

Fig. 6 View of the CRYRING RFQ resonator

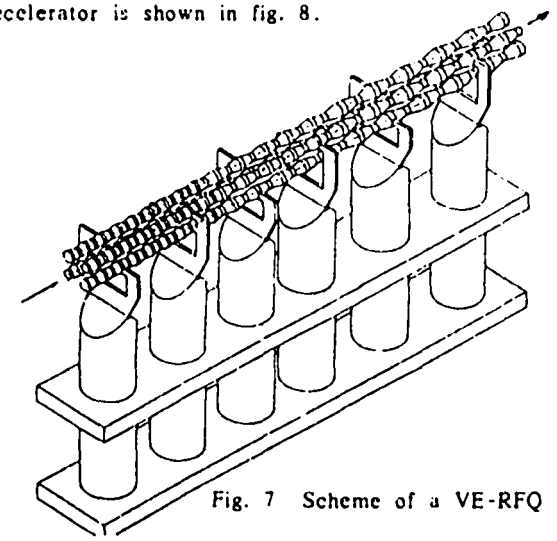

Fig. 7 Scheme of a VE-RFQ module

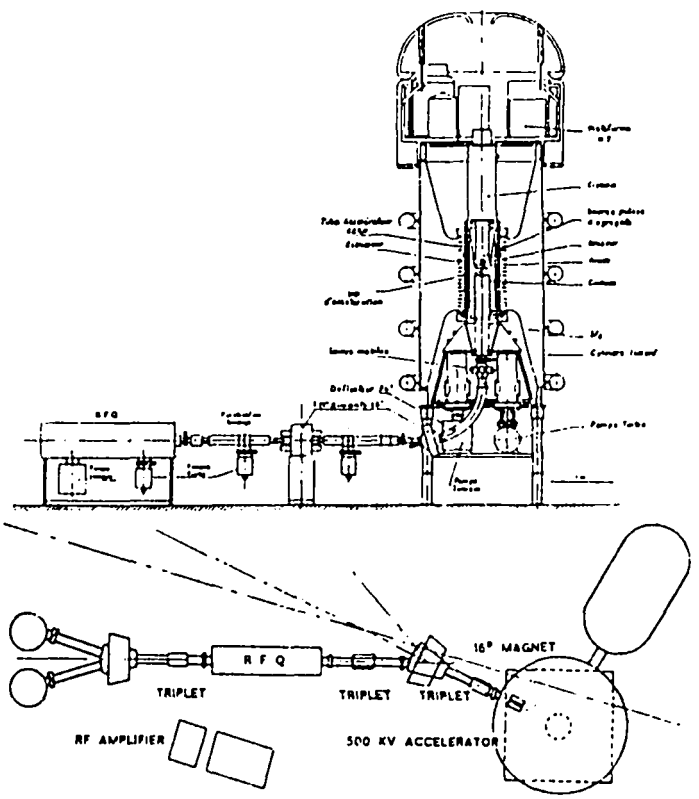

Fig. 8 Layout of the Lyon cluster accelerator

The beam is accelerated vertically, then bent into the horizontal direction by a cylindrical electrostatic deflector and a bending magnet which provides mass selection. The beam transport and matching into the RFQ is done by electrostatic quadrupole triplets, which are very effective at the low cluster velocities.

For energy variation the resonator can be tuned within an appreciable range to scan e.g. the FM range from about 80 MHz to 110 MHz corresponding to an energy change by a factor of approximately two.

The particle dynamics design for the heaviest particle resp. the minimum charge to mass ratio q/A necessary for acceleration is characterized by Fig. 9. Taking the "design particle" as reference, better q/A ratios or acceleration to lower energies requires only a lower voltage: $U \sim A/q \times f^2$. Compared to other RFQ designs[5] the buncher part has been skipped for a very effective acceleration, e.g. an average field strength of up to 2.5 MV/m, which is even higher than in classical ion accelerators. This is on cost of a relatively small transmission of appr. 25%.

The work on the Cluster injector and the beam lines is in progress. The RFQ is behind schedule, but has been successfully assembled and tuned and is beeing transported to Lyon for first beam experiments. The left part of fig.10 shows a view of the VE-RFQ.

The Lyon RFQ shows, that the design of variable frequency RFQs is not aiming at the highest beam currents and highest brilliance but on flexibility. A second system based on the 4-Rod principle, which has a larger frequency range resulting in an energy variation between 300 and 1500 keV is being developed by AccSys[23,24] as an ion implanter.

Another VE-RFQ is built for an ECR-RFQ combination at the IKF at the University of Frankfurt[25,26]. Interesting new experimental possibilities will be available for atomic physics as well as for ion implantation and materials characterization.

The basic parameters of this VE-RFQ are an output ion energy of T_f = 100 - 200 keV/u, the same frequency variation of f = 80-110 MHz, a minimum specific charge of q/A = 0.15, an electrode voltage of U_Q = 70 kV and a structure length of L_s = 1.5 m. The rf power consumption will be 60 kW (110 MHz).

The beam-dynamics design results in the energy/frequency plot of Fig.11. For a specific ion, the electrode voltage can be lowered for obtaining smaller frequencies and energies according to $U_Q \sim A/q \cdot f^2$. While the radial phase advance per cell σ and the focusing strengh B will stay constant, the acceptance ε and the maximum ion current I_f are smaller for lower frequencies because of the reduced voltage U_Q. Fig. 12 shows the possible range of improvement when the voltage U_Q is kept constant. Thus the focusing strengths can be improved resulting e.g. in a constant ion current for all frequencies. Fig.13 shows relative mass and energy ranges of a VE-RFQ and the extension for the constant voltage option. More detailed calculations about the beam dynamics properties are presented by Deitinghoff[27].

The tank of this RFQ has been manufactured and will be copper plated at GSI. The parts of the electrode insert are ordered, an existing transmitter will be modified. First beam tests are planed for 1991.

Conclusions

The results of the work on low-energy ion RFQs are showing that accelerators with fixed and variable energies can be built with properties matched for the specific application.

The fixed energy 4-Rod structure has shown convincing results. Operating experience with the VE-RFQ has to prove, if reliability and practicability belong also to its properties.

Table 1 Lyon cluster VE-RFQ parameters

Max. initial/final kinetic energy	10/100 keV/u
Min. initial/final kinetic energy	5/50keV/u
Maximum kinetic energy for m=30u	3.0 MeV
Length/diameter of the structure	2.0/0.5m
aperture	3.1-2.5 mm
Number of cells/modulation of electrodes	167/1.1-1.98
Frequency	80-110 MHz
Peak voltage/maximum field strength	80kV/42MV/m
Transverse phase advance per cell	8.2-7.2°
Synchronous phase	50-15.5°

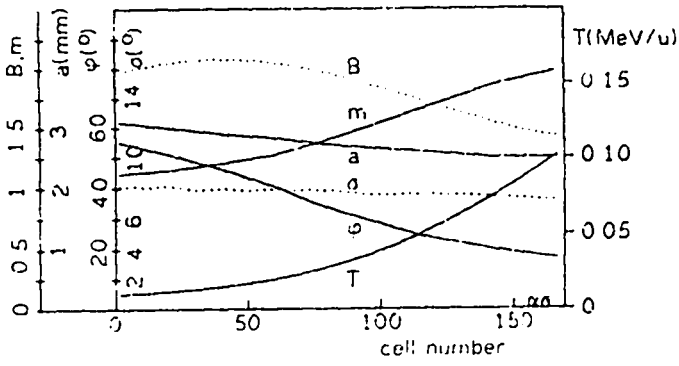

Fig. 9 Electrode parameters along the RFQ

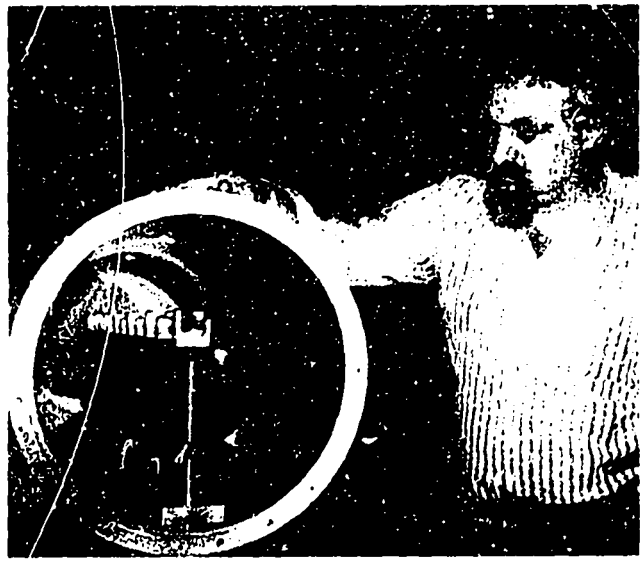

Fig 10 View of the Lyon VE-RFQ

Acknowledgements

I am grateful for many contributions made by collegues and friends. I especially want to thank H.Deitinghoff, T.Weis, G. Hadinger, J. Klabunde, H.O. Moser and the think-tank-plumbers J. Friedrich, A. Kipper, J. Madlung, U. Bessler and R. Veith

References

1. I.M. Kapchinskiy and V. Teplyakov, Prib. Tekh.Eksp. 119, No.2(1970) 17.19
2. R.H. Stokes, T.P. Wangler, Ann. Rev.Part.Sci.,38(1988)97
3. T.P. Wangler, LANL Rep. LA8388, 1980
4. A. Schempp, EPAC88, World Sci. (1989) 464
5. A. Schempp et al., Linac88, Cebaf 88-001 (1989) 460
6. E. Jaeschke, Linac84, GSI-84-11(1984)24
7. R. Wideroe, Archiv f. Elektrotechnik, 21 (1928)387
8. A. Schempp, NIM B40/41 (1989) 937
9. A. Schempp et al., NIM B10/11(1985) 831
10. A. Schempp, M. Ferch, H. Klein, PAC 87, IEEE 87CH2387-9 (1987) 267
11. J.R. Delayen, K.W. Shepard, Appl. Physics Letters, 1990
12. A. Schempp, J.R. Delayen, K. W. Shepard, this conf.
13. N. Angert et al., this conf.
14. A. Schempp, PAC89, IEEE 89CH2669-0(1989) 1093
15. H. Deitinghoff, IAP Int Rep. 16/8/90
16. A. Schempp et al., EPAC90, Nice France, June 1990
17. E. Jaeschke, EPAC90, Nice France, June 1990
18. R. Billinge et al., CERN 90-01, 1990
19. A. Schempp, H.Deitinghoff,A.Kipper, NIM A278(1989)169
20. A. Kipper et al, GSI Ann. Rep. 1989 (1990)
21. H.O. Moser, A.Schempp, NIM B24/25(1987)759
22. A. Schempp, H.O. Moser, J. Physique 50-C2 (1989) 205
23. R. Hamm, Linac86, SLAC Rep. 303 (1966) 33
24. R. Hamm, this conf.
25. D. Hofmann et al., NIM B50 (1990)478
26. A Schempp, NIM B50(1990)460
27. H. Deitinghoff et Al., this conf.

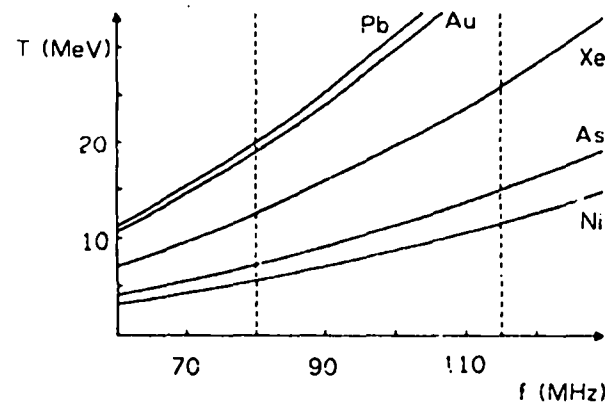

Fig. 11 Ion energy as function of RFQ frequency

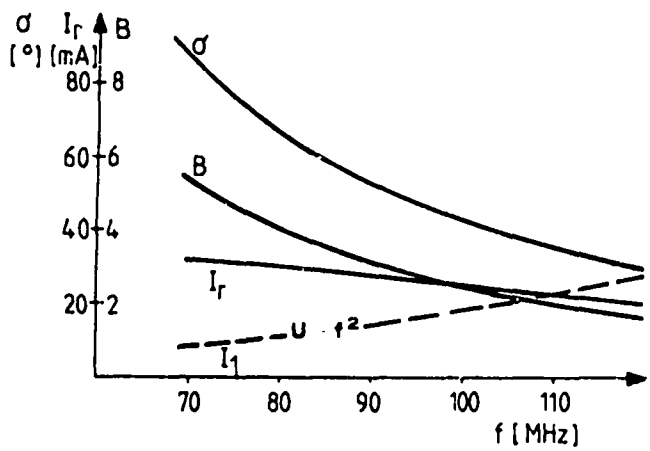

Fig. 12 Tune and current limit for constant electrode voltage

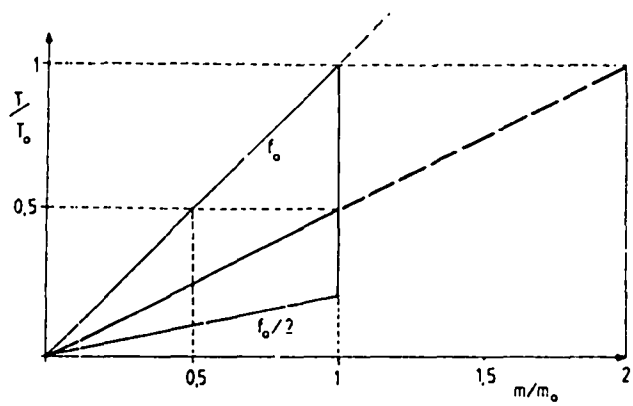

Fig 13 Energy mass plot for VE-RFQs

Thursday

Session TH1
Chairman: P. Grand
Invited Papers

DEVELOPMENT OF THE HIGH-INTENSITY PROTON LINAC FOR THE JAPANESE HADRON PROJECT

Y. Yamazaki and M. Kihara
National Laboratory for High Energy Physics (KEK)
1-1 Oho-machi, Tsukuba-shi, Ibaraki-ken 305, Japan

Abstract

The 1-GeV proton linac will be constructed for the Japanese Hadron Project (JHP). Our design concept and development program are based on the viewpoint of how to meet the requirements for the linac. The development includes the construction of a 10-MeV linac comprising a volume-production type ion source, a long RFQ (about four times as long as its wavelength) and a DTL with permanent quadrupole magnets. The test of an L-band high-power rf source had been successfully accomplished up to full power, and recently fed the power to a ten-cell cavity (annular-coupled structure) with a bridge coupler as designed. The present status of our development is described.

Introduction

A linac will be constructed to inject proton beams to the ring accelerator for the Japanese Hadron Project(JHP).[1-9] The optimum design of a specific linac is dependent upon required parameters as an injector. The requirements for the JHP linac are summarized in Table I. Low-emittance negative hydrogen beams are required for efficient injection to the ring. High energy is preferable in order to increase the space-charge limit of the current in the ring; our choice of 1 GeV is probably a reasonable one. A repetition rate not higher than 50 Hz is necessary for spallation neutron experiments. Keeping these constraints in mind we must design the proton linac that can accelerate a high-intensity beam of 400 μA. Here, the high integrated-type beam current that is actually useful for experiments is required rather than the record current. In other words, we must design and develop a linac that can be operated with extreme stability and reliability. Design parameters that are to meet the above-mentioned requirements are presented in the next section together with a rationale for the chosen parameters.

Conceptual Design and Development Program

A high-energy, high-intensity proton linac immediately requires very high rf power. In general it is advantageous to reduce the number of rf sources by increasing the rf power of a single rf source, regarding cost performance, stable operation and easy maintenance. This is, however, very difficult in the JHP for the following reasons. The peak current of the low-emittance, high-duty negative hydrogen beam is relatively limited and probably around 20 mA for a 90 % normalized emittance of 1 πmm mrad and a duty factor of a few percent. In order to obtain an average current of 400 μA we require a rather long beam pulse length of 400 μs for the repetition rate as low as 50 Hz. We must therefore prepare an rf pulse length of 600 μs including a margin. In Fig. 1 the rf powers of available klystrons are plotted versus their pulse lengths. It can be seen that the available power rapidly decreases with increasing pulse length, since the discharging or sparking limit is a decreasing function of the pulse length. (The increasing power dissipation also has some effect.) Furthermore, the cost of a single rf source on the highest-power line in the graph is increased as the pulse is lengthened. Consequently, the rf power becomes very expensive for the JHP linac in comparison with shorter-pulse

TABLE I
Requirements for the Linac

Beam	H^-	
Energy	1	GeV
Repetition rate	50	Hz
Average current (without chopper)	400	μA
Average current (with chopper)	> 200	μA
Normalized emittance (90%)	~ 2	πmm·mrad

TABLE II
Design Parameters of the Linac

Total length	500	m
Beam pulse length	400	μs
RF pulse length	600	μs
H^- ion source		
Type	Volume-production	
Peak beam current	20	mA
Normalized emittance	1	πmm·mrad
RFQ		
Input energy	50	keV
Output energy	3	MeV
Frequency	432	MHz
Vane length	2.7	m
Minimum bore radius	0.24	cm
RF power	0.8	MW
Transverse emittance (Normalized, 90%)	1.1	πmm·mrad
Energy spread (90%, full)	0.03	MeV
Phase spread (90%, full)	15	deg
DTL		
Output energy	148	MeV
Frequency	432	MHz
Total length	83	m
Bore radius	0.5	cm
Number of cells	342	
Number of tanks	13	
RF power	12	MW
Transverse acceptance (90%, normalized)	8.9	πmm·mrad
Acceptable energy spread (90%, full)	1.4	MeV
Acceptable phase spread (90%, full)	88	deg
High-β linac		
Output energy	1	GeV
Frequency	1296	MHz
Total length	411	m
Tank length	303	m
Bore radius	1.5	cm
Number of cells	3568	
Number of tanks	152	
RF power	99	MW
Klystron output power	3	MW
Number of klystrons	36	
Transverse acceptance (90%, normalized)	29	πmm·mrad
Acceptable energy spread (90%, full)	3	MeV
Acceptable phase spread (90%, full)	87	deg

machines and the optimum design of the linac is strongly dependent upon reliable information regarding the power of a single source which can be obtained stably and reliably. This is the main reason why we started our program by developing an rf power source for the high-β linac that takes a large part of the linac. For our conceptual design we estimated a highest power of 6 MW and have decided to use it at 4 MW for improving reliability.

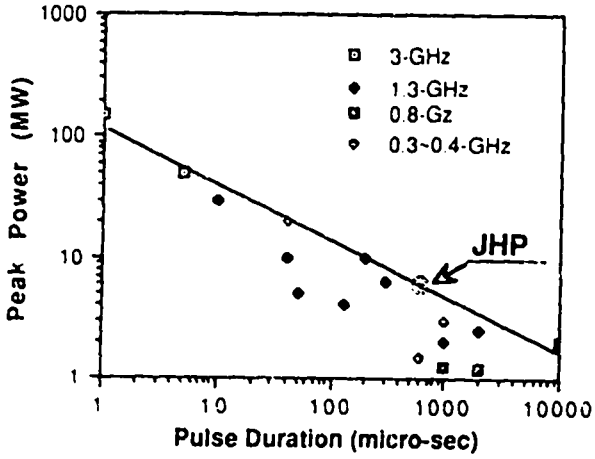

Fig.1. The rf powers of available klystrons versus their pulse lengths.

Since the total shunt impedance is proportional to the cavity length, the total rf power is inversely proportional to the length, if the beam loading effect can be neglected, while the costs of cavities and buildings are roughly proportional to the cavity length. Therefore, if the rf power is relatively expensive, as in the present case, the optimum length of a linac would tend to be increased in order to save rf power by improving the total shunt impedance. Although a total length of 500 m was primarily determined due to our available space, we believe that it is nearly the optimum length, taking into account various requirements for the linac.

In this context, the accelerating frequency is another important parameter. In order to save rf power a higher frequency is preferable, since the shunt impedance per unit length of a cavity with the same figure is proportional to the square root of the frequency. (The possible accelerating field is also proportional.) On the other hand, as the frequency increases, the size of the accelerating cavities and klystrons decreases, so that the cooling of these components become difficult and the beam acceptance of the accelerating cavities decreases. Therefore, the nearly highest frequency should be chosen, as far as the cooling of the rf components is feasible and the beam acceptance is sufficient. In this way we have chosen 1296 MHz for the frequency of the high-β linac, taking into account its relation to that of the drift-tube linac (DTL) and RFQ linac as follows.

In a high-intensity, high-energy proton linac beam losses should be eliminated at the high-energy region of the accelerator. Otherwise, radioactivity caused by beam loss would become a serious problem during long-term operation and limit the possible beam current. Thus, sufficiently large beam acceptances should be prepared both transversely and longitudinally for all accelerator tanks. In order to ensure a sufficiently large transverse acceptance we have chosen a rather large bore radius of 1.5 cm for the high-β linac, while sacrificing the shunt impedance to some extent.

In order to ensure a sufficiently large longitudinal acceptance we have chosen one third of the frequency of the high-β linac for both the DTL and RFQ linacs. For the same reason, we use rather high transition energies of 3 and 150 MeV for the RFQ to the DTL and for the DTL to the high-β linac, respectively, since the debunching effect in the drift space inevitable for the transition is smaller for higher energy. The design parameters, thus determined, are listed in Table II. More detailed parameters and rationale can be found in Ref. 3.

Further optimization of the design of a highly stable machine with easy maintenance and operation requires both technical data and experience that can be accumulated only through the construction and operation of major components of the machine. Thus, we have formed a development program for the major components as follows.

Since one of the most difficult components of the proton linac is a high-power rf source (several MW) with a long pulse length (600 μs),[10-14] it is crucial to test the possibility and performance of the rf source for success of the project. Thus, a high-power test station was prepared, as shown in Fig.2. Second, we began to study and develop the high-β linac, since it also represents a large part of the linac. The power station is used to feed power to the high β linac. Another important item in our development program is concerned with the front end of the linac. Obviously, the above-mentioned design was based upon various assumptions that must be confirmed empirically. The assumptions can be listed as follows:

1) The ion source can produce high-intensity, low-emittance beam as designed.
2) An RFQ can accelerate a 20 mA beam from 50 keV to 3 MeV.
3) An 432 MHz DTL of sufficient quality can be fabricated.
4) Emittance growth and generation of a halo can be properly suppressed from the ion source to the DTL, and the designed acceptances of the high energy section are sufficiently large to prevent the machine from being activated.

In order to confirm these assumptions and to develop the fabrication technique we are going to construct a 10 MeV proton linac for the high-intensity beam tests within a few years.

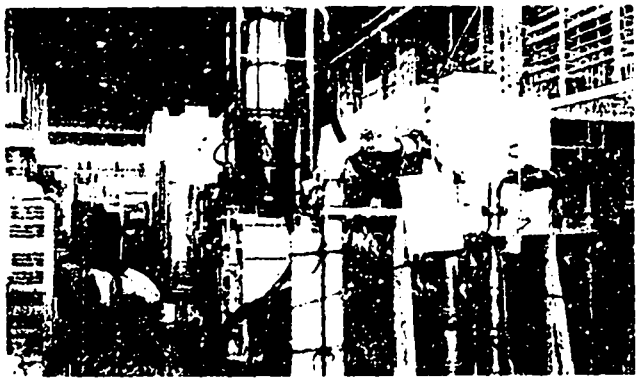

Fig.2 The high power test station showing the 5-MW klystron and the line-type modulator.

RF Power Source

A line-type modulator with an output power of 15 MW has been constructed. The line-type was chosen owing to its excellent stability with a de-Qing circuit and its high efficiency. At present, the pulse length of its pulse-forming network (PFN) is 400 μs. An L-band 5 MW klystron (THOMSON TH2104A) with a pulse transformer (step-up ratio of seven) were installed in the station. Testing of the complete system has

been successfully accomplished up to full power with a repetition rate of 30 Hz.[11-13] A test at the designed repetition rate of 50 Hz will be performed after the acceptable average power of a dummy load is doubled. The pulse of the modulator will be lengthened up to the full length in the near future.

High-β Linac

A standing-wave coupled-cell linac operated at the π/2 mode will be used[15] for the high-β linac rather than the 2π/3 mode.[16] Among the various possible candidates for the high-β structure, manufacturing techniques of an alternating periodic structure(APS)[17] or an on-axis coupled structure (OCS) and a side-coupled structure (SCS)[18] have been developed.[4] The axially symmetric APS has advantages over the axially asymmetric SCS with respect to both mechanical simplicity and beam stability. However, the shunt impedance of the APS is much lower than that of the SCS, particularly in the low-β section, since the coupling cells of the APS are located on the beam axis and consume space that could otherwise be used for acceleration. In this context, the annular-coupled structure (ACS)[19] became attractive, owing to its symmetric structure.

Although it had been reported[20] that a serious depression of the quality factor arises from the excitation of the coupling-cell quadrupole mode, we succeeded in improving the shunt impedance of the ACS by adopting four coupling slots.[21] In order to show the effect of the coupling slots on the quality factor, the measured quality factors were divided by that of a single cell without coupling slots, and plotted versus the coupling factor (Fig. 3). Another important feature of the four coupling slots is that the dipole and quadrupole modes in the coupling cells are situated at higher frequencies than the passband of the accelerating mode. Thus, we have fabricated an ACS cavity with two 5-cell tanks[22] connected by a 5-cell bridge coupler[23,24] (Figs.4 and 5) and tested it up to full RF power. (An effective accelerating field is 3.6 MV/m and a power dissipation per cell is 30 kW.) Details of the fabrication and high-power test are presented in Refs. 22, 24 and 25.

A disadvantage of the ACS, compared with the SCS, is its large size, or heavy weight, that is inevitable due to symmetrization of the structure. We appreciate the advantages of the axial symmetry of the ACS rather than its disadvantage.

Ion Source

When our development started, no ion source existed that met our requirements. It was, however, expected that a volume-production type H^- ion source could produce a high-intensity H^- beam with low emittance and high duty, an attractive feature being that it would be free of cesium vapor that could reduce the breakdown voltage of the following RFQ. Thus, a test volume source[26] was constructed in order to study the mechanism of volume production. We have obtained a beam current of 20 mA with an anode hole diameter of 7.5 mmφ, where the normalized 90 % emittance was 1 πmm·mrad at 30 keV and the pulse length is 400 μs. It is interesting to note that the introduction of a small amount of cesium vapor increases the current density, even in the volume source, by a factor of four or more. It should be emphasized that the amount of cesium used in the volume source is much less than that in the conventional surface source. This amount of cesium will probably not cause any harm to the RFQ. Further development of the volume source is in progress.

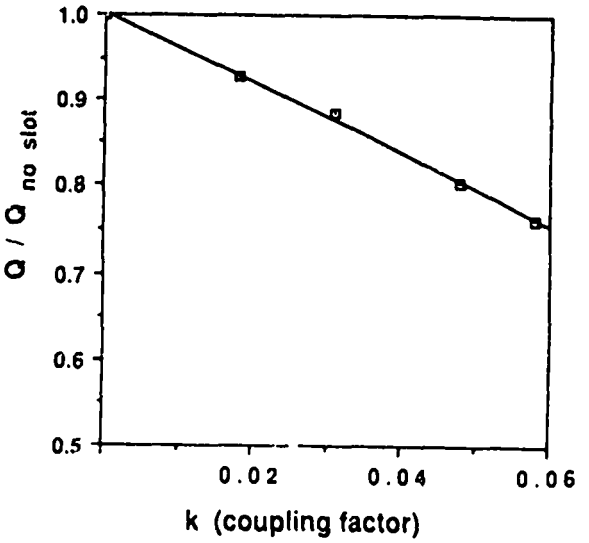

Fig.3 Measured coupling-factor dependence of the Q-value of the four-slot ACS divided by that of a single cell without slots. The 5 % coupling will be used.

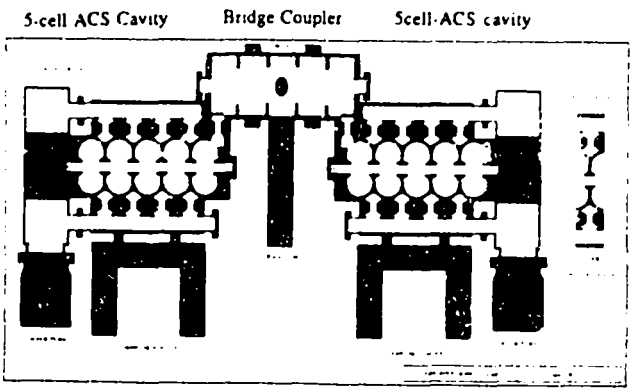

Fig.4 A high-power ACS model comprising two five-cell ACS cavities and a five-cell bridge coupler.

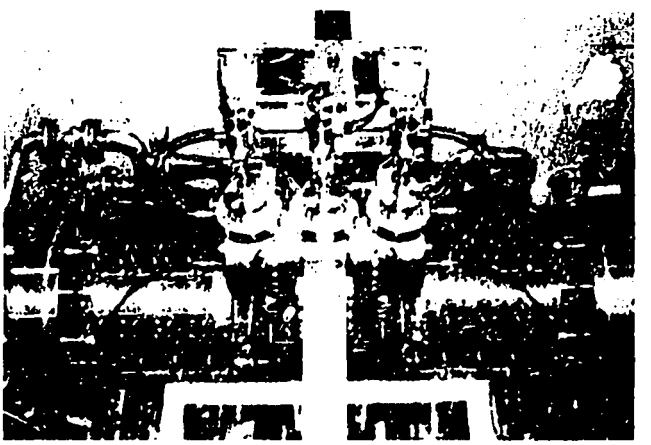

Fig.5 Photograph of the high-power ACS model.

RFQ Linac

A 432-MHz RFQ linac will accelerate a beam from 50 keV to 3 MeV. A design study for the beam dynamics has indicated that its vane length should be 2.7 m (about four times as long as the wavelength).[27,28] We have developed a new beam-dynamics design procedure,[28] taking into account the space-charge effect in the bunching process more realistically. It is, in general, difficult to fabricate a conventional four-vane RFQ linac that is long compared with the wavelength for the following reasons. First, a slight structure imperfection easily gives rise to field tilt in the long tank. Second, an RFQ linac consists of four cavities separated by the four vanes; these four cavities are coupled very weakly. Thus, a slight azimuthal asymmetry gives rise to a non-uniform distribution of the stored energy among the four cavities. (The effect is closely related to the mixing of the dipole modes with the quadrupole mode.) As a result severe specifications are required for the structural dimensions. It has been believed that the specifications become more severe for a longer RFQ. On the other hand accurate machining naturally becomes more difficult for longer vanes.

Neither a four-vane RFQ with vane coupling rings nor a four-rod RFQ for curing the above-mentioned problems can easily meet the present requirements of high duty and high frequency. On the other hand, the above-mentioned difficulty regarding the four-vane RFQ was not understood quantitatively enough to make a final decision for a choice of the RFQ parameters. Thus, a cold model[9,29] (Fig. 6) was fabricated in order to develop a machining method for the severe specifications and to study the effect of possibly harmful dipole modes. Silver was added (0.2 percent) to vacuum-melted oxygen-free copper in order to strengthen the material mechanically.

The results of the measurements on the cold model are described in detail in Refs. 9 and 29. The field distributions are uniform within ± 3.5%. Although the geometries of the vane ends and the end plates were adjusted in order to obtain this uniformity, no side tuners were used.

The measured dispersion curves of the dipole and quadrupole modes shown in Fig. 7 indicate that the accelerating quadrupole mode (TE210) is located just at the middle of the dipole modes (TE111, TE112). Separation is fairly large, implying a small mixing of the dipole modes. Also, good machining accuracy is seen from the small breaking of the degeneracy of the dipole modes. It is noted that more mixing of the dipole modes is expected for the shorter RFQ, since the frequency of the TE111 mode is increased and becomes closer to the TE210 quadrupole mode if the vane is shortened in this region of the length. In other words, a longer RFQ will be easier to fabricate than a shorter one.

During the course of development we devised a new field-stabilizing concept, referred to as a π-mode stabilizing loop (PISL)[30,31] (Fig. 8) that pushes up the dipole mode frequencies far from the quadrupole one. A three-dimensional calculation indicates that the loop is quite promising for stabilizing the RFQ field, increasing the dipole mode frequencies by an amount of several 10 MHz. We will thus substantiate the feasibility of the PISL empirically with the existing cold model and continue development, including studies of the effects of the matching section, vane modulation, input coupler and tuning plungers in order to obtain the necessary data for the final design of a high-power model of the RFQ.

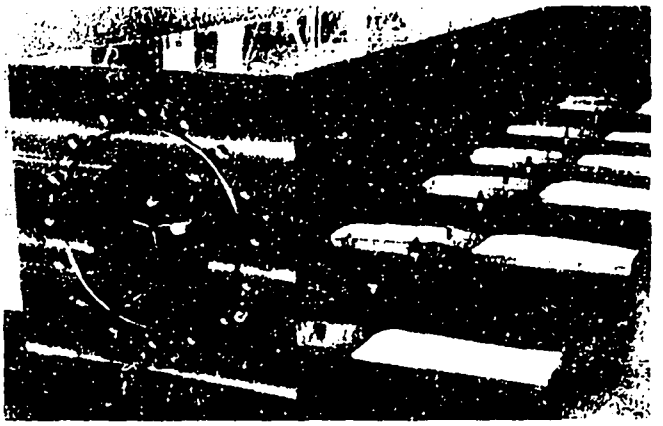

Fig.6 Cold model of the 432-MHz 3-MeV RFQ linac.

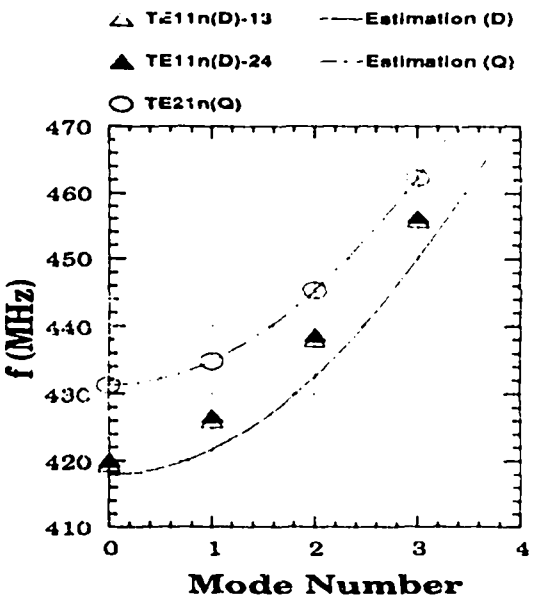

Fig.7 Measured dispersion curves of the quadrupole and dipole modes in the present RFQ.

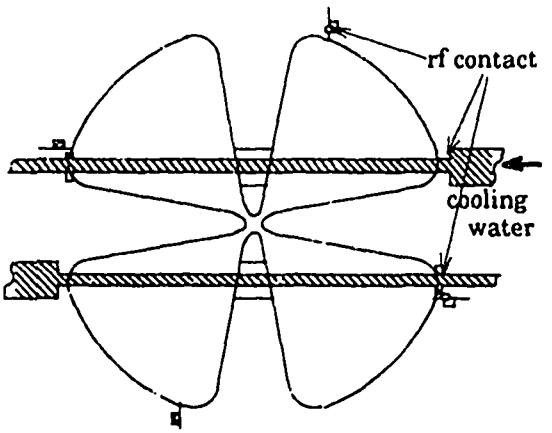

Fig.8 Example of π-mode stabilizing loops.

Drift-Tube Linac

For the 432-MHz drift-tube linac (DTL), permanent quadrupole magnets, such as SmCo and NdFeB, will be used since they require neither electrical wiring nor water-cooling and become maintenance-free. We have recently succeeded in fabricating NdFeB quadrupole magnets (Fig. 9) with a field center that coincides to their mechanical center within 20 μm. It should be emphasized that this was realized without any shuffling of magnet pieces, but with elaborate quality control in both machining and production. On the other hand, it is difficult to seal drift tubes containing these permanent magnets, since the magnets cannot stand high temperature during silver brazing; also, the strong magnetic field of the permanent magnets bends the electron beam for the electron-beam welding (EBW).

Thus, the electroforming method[5] has been applied to seal the drift tubes from vacuum, since electroplating is carried out at room temperature. A drift tube and a NdFeB permanent quadrupole magnet were assembled and successfully electroformed. The EBW of drift tubes with the permanent magnets was also successful by shielding the electron beam from the strong magnetic field. At present we are developing a method[32] using cold shrinking that will be more suitable for mass production.

A cold model (3 to 8 MeV, 35 cells, 2.6 m)[33,34] made of aluminum for half of the first DTL tank has been fabricated in order to obtain necessary data for the final detailed design.[35] Without post couplers, a field flatness within 1.2 percent was obtained throughout the tank. It is noted here that the β-dependence of the effect of stems was corrected by adjusting the gap lengths between the drift tubes in order to make the frequencies of all cells uniform. In order to test the effectiveness of the post coupler, a field tilt was intentionally produced by frequency tuners; it could be eliminated by adjusting the positions of the post couplers.[32] The effect of the number of post couplers was extensively studied regarding field stability.[33] Based upon these developments, the fabrication of the 5.3 MeV DTL is now under way, as shown in Fig.10.

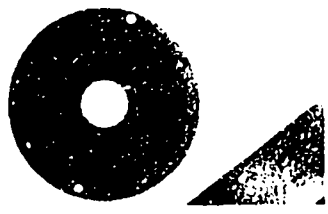

Fig.9 NdFeB quadrupole magnet.

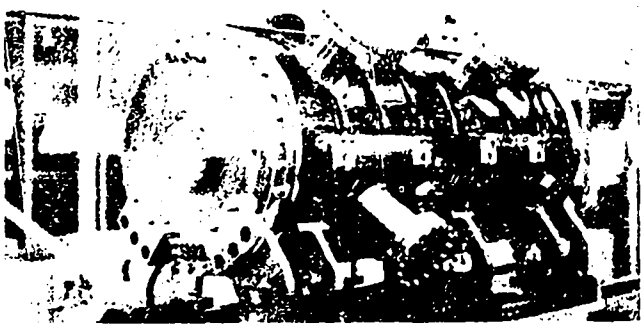

Fig 10. Hot model of the 5.3 MeV DTL.

REFERENCES

1. M. Kihara, LA-11130-C p.67; KEK Preprint 86-106.
2. M. Kihara, LA-11432-C p.4.
3. Y. Yamazaki et al., LA-11432-C p. 80 ; KEK Preprint 87-159.
4. Y. Yamazaki et al., Proc. 1988 Linear Accel. Conf. 79 (1988).
5. Y. Yamazaki et al., "Development of the 1 GeV Proton Linac for the Japanese Hadron Facility", submitted to 1989 Particle Accelerator Conf., Chicago.
6. M. Kihara, Part. Accel. 32, 1(1990).
7. T. Kato et al., KEK Preprint 89-187.
8. E. Takasaki et al., KEK Preprint 90-16.
9. Y. Yamazaki, KEK Preprint 90-15.
10. S. Anami et al., "Design and Construction of a Long-Pulse Modulator," submitted to Proc. 1989 Particle Accelerator Conf., 1989, Chicago.
11. M. Ono et al., Part. Accel. 32, 51(1990).
12. T. Kubo et al., Part. Accel. 32,45(1990).
13. M. Ono et al., "L-Band RF Source for the JHP Proton Linac," this conference.
14. S. Anami et al., "A Long-Pulse Thyristor-Switch Modulator for the JHP Proton Linac," this conference.
15. Y. Yamazaki, Part. Accel. 32, 39(1990).
16. B. Epsztein and Tran Duc Tien, Proc. 1968 Proton Linear Accel. Conf., 457 (1968).
17. T. Nishikawa S. Giordano, and D. Carter, Rev. Sci. Instr. 37, 652 (1966).
18. E. A. Knapp, B. C. Knapp, and J. M. Potter, Rev. Sci. Instr. 39, 979 (1968).
19. V. G. Andreev et al., Proc. 1972 Proton Linac Conf., 114 (1972).
20. R. K. Cooper et al., Preprint LA-UR-83-95 (Los Alamos National Laboratory).
21. T. Kageyama et al., Part. Accel. 32, 33(1990).
22. T. Kageyama et al., "A High Power Model of the ACS Cavity," this conference.
23. L. Young, private communication.
24. Y. Morozumi et al., "Multi-Cavity Bridge Coupler," this conference.
25. K. Yamasu et al., "Fabrication Technique of ACS Cavity for the JHP," this conference.
26. Y. Mori et al., KEK Preprint 90-64; submitted to Nucl. Instr. Meth.
27. N. Tokuda et al., Proc. 13th Linear Accelerator Meeting in Japan, 248 (1988).
28. A. Ueno and Y. Yamazaki, "New Beam Dynamics Design Procedure for RFQ," this conference.
29. A. Ueno et al., "RF Field Measurement of an RFQ Cold Model Cavity for the JHP," this conference.
30. A. Ueno and Y. Yamazaki, KEK Preprint 90-38; submitted to Nucl. Instr. Meth.
31. A. Ueno et al., "The p-Mode stabilizing Loop for Four-Vane Type RFQ," this conference.
32. T. Adachi et al., "Fabrication Technique of Drift Tube with Permanent Quadrupole Magnet for the Linac of the JHP," this conference.
33. F. Naito et al., Part. Accel. 32, 27(1990).
34. F. Naito et al., "Development of the DTL for the JHP," this conference.
35. F. Naito et al., "Design Features of the Input Coupler for the DTL," this conference.

LINEAR ACCELERATOR FOR PRODUCTION OF TRITIUM: PHYSICS DESIGN CHALLENGES*

T. P. Wangler, G. P. Lawrence, T. S. Bhatia, J. H. Billen, K.C.D. Chan, R. W. Garnett, F. W. Guy, D. Liska, S. Nath, G. H. Neuschaefer, and M. Shubaly,
Los Alamos National Laboratory, Los Alamos, NM 87545

Introduction

In the summer of 1989, a collaboration between Los Alamos National Laboratory and Brookhaven National Laboratory conducted a study to establish a reference design of a facility for accelerator production of tritium (APT). The APT concept is that of a neutron-spallation source, which is based on the use of high-energy protons to bombard lead nuclei, resulting in the production of large quantities of neutrons. Neutrons from the lead are captured by lithium to produce tritium. This paper describes the design of a 1.6-GeV, 250-mA proton cw linear accelerator for APT.

Reference Accelerator Configuration

The reference accelerator configuration (Fig. 1) consists of two low-energy, 350-MHz, 125-mA proton linacs, whose beams are funneled at 20 MeV and injected into a single 700-MHz, 250-mA linac for acceleration to 1600 MeV. Each dc injector consists of a duoPIGatron ion source and low-energy beam transport (LEBT) line, which produces a 140-mA beam for injection into a radiofrequency-quadrupole (RFQ) linac structure. The RFQ focuses and adiabatically bunches the injected beam, and with the same rf electric fields accelerates the beam to an energy of 2.5 MeV. At this energy the drift-tube linac (DTL), which provides more efficient acceleration and focusing from electromagnetic quadrupoles inside the drift tubes, increases the beam energy to 20 MeV. The two 20-MeV, 350-MHz beams arrive out of phase at an rf deflector element, which funnels them into a single colinear 700-MHz bunched beam for further acceleration in a high-energy, 700-MHz, 250-mA coupled-cavity linac (CCL) to the final energy of 1600 MeV.

The APT linac is designed with minimizing beam loss as first priority and efficiency as second priority. Radiation-hard electromagnetic quadrupoles are used in the drift tubes rather than permanent-magnet quadrupoles because of concerns about radiation damage. The size of electromagnetic quadrupoles imposes an upper limit on the choice of DTL frequency. A 2βλ-type DTL is chosen to accomodate the physical length of the quadrupoles. For performance reasons, a two-frequency linac design is employed: 350 MHz for the RFQ and DTL, and 700 MHz for the CCL. Beam funneling is employed because it results in improved beam quality and reduced particle losses in the CCL for the desired current level. The CCL is designed in a modular fashion with the lattice units identified as types 1 to 7. Type 1 is composed of 2-cell lattice units; the number increases to 10 cells per lattice unit for Type 7. Overall there are 1451 lattice units in the CCL, with a total of 10275 accelerating cells. If necessary, an emittance filter, a system of collimators to remove beam halo, can be installed at 40 MeV after the major accelerator transitions. Lengths, rf power to the structure, and beam power are shown in Fig. 1 for each type of accelerating structure. A table within the figure provides an estimate of the number of rf tubes: 470 at 700 MHz and 12 at 350 MHz. A second table gives transverse and longitudinal emittances for a nonideal beam case used in the simulations, in which the beam is

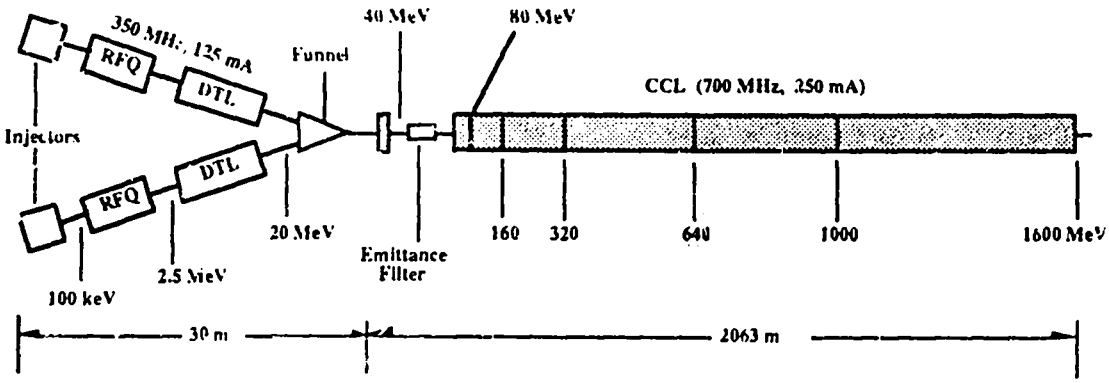

	Length (m)	RF Power (MW) Copper	Beam	Total	# RF Tubes
RFQ	3.4	0.4	0.3	0.7	2
DTL	11.3	1.3	2.2	3.5	10
CCL	2063	114.8	395.0	509.8	470
Total	2100	118.2	400.0	518.2	482

Total AC Power for Accelerator = 910 MW
(Assuming ac → beam efficiency = 0.49)

	Trans. Emittance* (π cm-mrad) Input	Output	Long. Emittance* (10^{-6}π eV-sec) Input	Output
RFQ	0.020	0.023	0.0	1.4
DTL	0.027	0.058	1.6	3.0
CCL	0.061	0.068	2.9	4.4

* Emittance values are for non-ideal beam.

Fig. 1. The APT reference accelerator configuration.

*Work supported by the US Department of Energy with Los Alamos National Laboratory Development funds.

deliberately mismatched to the DTL. Designing with a nonideal beam provides a safety margin, especially for considerations associated with beam loss.

We have chosen 350 MHz and 700 MHz for the APT reference design. The optimum choice of frequencies involves many issues, and we believe complete designs at different frequencies would be necessary to rigorously establish the best choice for APT. High frequencies distribute the total charge in more bunches and produce less space-charge-induced growth of emittance and halo. But at higher frequency the transverse dimensions decrease, and alignment and steering become more difficult. Furthermore, the apertures must decrease at higher frequency to avoid a high penalty in structure power efficiency, and at high frequency, nonlinear fields in the rf gaps reduce the usable apertures. On the basis of linac design experience, we believed that a choice of frequency much higher than 350/700 MHz would result in diminishing returns with respect to growth of emittance and halo and would probably significantly increase the problems associated with higher frequency. Low frequencies have the advantage of allowing larger apertures but generally result in larger beam size and more particles in fewer bunches, which translates into undesirable space-charge-induced growth of emittance and halo. Furthermore, lower frequencies require accelerating structures with larger transverse dimensions. The mechanical design and handling of very large and heavy components can make fabrication and precise alignment difficult. The German Spallations-Neutronenquelle (SNQ) design study[4] used frequencies of 100/200 MHz, which are the lowest values that we considered in the APT study. Comparison of SNQ with APT simulation results shows that SNQ had significantly more emittance growth than APT, which was not offset by the larger apertures (i.e., the aperture-to-rms ratios are larger for APT). For a definitive conclusion, a systematic study should be undertaken, using one linac-design approach. For the moment we believe the evidence suggests that our choice of 350/700 MHz for APT is not far from optimum.

Linac Design Approach

Linac Design Philosophy

The main design objective for the APT linac is to provide high beam transmission and low particle losses to minimize radioactivation of the accelerator. A twofold strategy is used in the design. First, we establish good beam quality in the low-energy accelerators to minimize beam emittances (phase-space area) and halo. This is accomplished by (1) operating in a cw mode to reduce the peak current and the related space-charge effects, (2) using the RFQ for low-velocity bunching and acceleration, (3) using ramped accelerating fields in the DTL to control the longitudinal distribution, (4) funneling to provide the desired current at lower emittance, and (5) using high frequency accelerating structures to reduce the charge per bunch and the undesirable nonlinear [illegible] that [illegible] halo growth. Second, in the high-energy linac we try to keep the beam away from round apertures and longitudinal bucket limits and to reduce beam losses that cause activation. This is accomplished by providing (1) a large aperture to rms beam size ratio, (2) a large bucket (separatrix) width to rms bunch length ratio, (3) good alignment and beam steering, and (4) good phase control of the accelerator structures. Activation and radiation damage effects from residual halo and beam losses can be limited by (1) using radiation-hard electromagnetic quadrupoles wherever possible, (2) restricting the major transitions (bunching and frequency doubling) to the lowest velocities, where the associated local beam losses have minimal activation effects, and (3) using emittance filters after the major transitions to remove halo that leads to particle losses.

It is important to control the growth of emittance and the associated beam halo to reduce beam losses. Although the causes of beam halo formation in phase space are not completely understood, we have observed in numerical simulation studies that nonlinear space charge forces act to produce halo. Nonlinear space charge forces at transitions in the accelerator, where parameters change, appear to increase the amount of halo. Transitions such as changes in the strength of the external focusing force, changes in periodicity of the focusing lattice, introduction of deflecting elements, or changes in rf frequency cause a change in the external focusing, and the beam must adapt. Given a sufficient number of beam-plasma periods after such a transition is introduced, the beam has evolved to a quasi-stationary state. During this evolution process, beam halo is produced. The time scale for halo production is not yet well established but appears to be in the range of a few to a few tens of beam-plasma periods. This time scale may be relevant to the design of emittance-filter systems. It does appear that accelerator transitions should be introduced only when necessary; for example, ion source extraction, bunching, and (in some cases) funneling require accelerator transitions. If these transitions are kept at the low-energy end of the accelerator, the activation effects of the associated local beam losses are minimized, and collimator systems that act as emittance filters to remove the halo will be more effective and easier to implement. Good beam matching across these transitions is very important to minimize the disruption to the beam. With regard to rms emittance, we believe this is a quantity whose growth should be controlled. Not only is rms-emittance growth often correlated with halo production, but the rms emittance affects the overall spatial size of a given beam distribution; the larger the rms emittance, the larger the beam size and the greater the extension in real space of the halo that already exists.

Radio-Frequency Quadrupole

The RFQ design parameters are shown in Table 1. The RFQ bunches the 140-mA input dc beam and accelerates it from 0.1 to 2.5 MeV. The output beam from the RFQ is then injected into the following DTL using a matching section, which consists of four electromagnetic quadrupole magnets and two rf buncher cavities. The beam transmission, output current, and output emittances for the RFQ are based on the results of numerical simulation with the PARMTEQ code. By using a vane geometry with constant transverse radius of curvature, we expect a maximum peak surface electric field of about 1.8

TABLE 1
APT RFQ Parameters

Frequency	350 MHz
Energy	0.1 to 2.5 MeV
Synchronous phase	-90° to -37°
Vane modulation	1.0 to 1.8
Radial aperture (a)	0.375 to 0.310 cm
Intervane voltage	95 kV
Peak surface field	33 MV/m
DC injection current	140 mA
Output current	128 mA
Beam transmission	0.91
Transverse rms emittance	0.020 to 0.023 π cm-mrad
Longitudinal rms emittance	0.0 to 1.4 x 10^{-6} π eV-s
RFQ length	3.4 m
Copper power	0.4 MW
Beam power	0.3 MW
Total power	0.7 MW

times the Kilpatrick value, which corresponds to 33-MV/m. The current limit is 250 mA, and we used a constant-current-limit accelerating section to reduce the RFQ length for easier tuning. The RFQ cavity can be driven with a single 350-MHz klystron.

Drift-Tube Linac

The DTL parameters are shown in Table 2. The DTL uses a FODO focusing lattice composed of radiation hard electromagnetic quadrupole magnets inside the drift tubes and a 2βλ cell to provide sufficient room for the magnets. The quadrupole magnets require a gradient of 46-T/m and an effective length of 6.4 cm, which results in a zero-current betatron phase advance per focusing period of σ_0 = 70°. The DTL can be configured in five separate rf tanks, each of which can be driven from a single 350-MHz klystron. The output emittances listed in Table 2 are conservative values, obtained from numerical simulation using the PARMILA code for a nonideal case where the beam is deliberately mismatched to the DTL.

Funnel

Table 3 shows the parameters of the funneling system for APT. The beams are focused transversely with electromagnetic quadrupole magnets and longitudinally with 350-MHz rf-buncher cavities. As

TABLE 2.
APT DTL Parameters

Structure	2βλ
Lattice	FODO
Frequency	350 MHz
Energy	2.5 to 20 MeV
Transverse rms emittance	0.027 to 0.058 π cm-mrad
Longitudinal rms emittance	1.6 to 3.0 x 10^{-6} π eV-s
Synchronous phase	-40°
Accelerating gradient (E_0T)	1.1 to 3.1 MV/m
Peak surface field	22 MV/m
Radial aperture	0.84 cm
Length	11.3 m
Number of cells	51
Copper power	1.3 MW
Beam power	2.2 MW
Total power	3.5 MW

TABLE 3.
APT Funnel Parameters

Energy	20 MeV
Number of quadrupoles	2 x 5 + 2 = 12
Number of dipoles	2 x 2 = 4
Number of bunchers	2 x 2 = 4
Number of rf deflectors	1
Length	1.5 m
Initial beam separation	60.5 cm
Aperture radius	0.8 cm
Input beam current	2 x 125 mA
Output beam current	250 mA
Transverse rms emittance	0.058 to 0.061 π cm-mrad
Longitudinal rms emittance	3.0 to 3.0 x 10^{-6} π eV-s
Copper rf power	0.25 MW

the beams approach the common final axis, the spacing becomes small, and more compact permanent-magnet quadrupoles and 700-MHz buncher cavities are required. Finally, the beams are merged in an electromagnetic quadrupole that is horizontally defocusing and passed into the 350-MHz rf deflector. The deflector phase is chosen so that the transverse rf fields act on the two out-of-phase bunched beams to produce the final beam, which is injected into the 700-MHz linac.

Coupled-Cavity Linac

The CCL parameters are summarized in Table 4. The longitudinal phase advance for zero current ranged from 15° at the CCL entrance to 3.4° at the end. The transverse phase advance for zero current was held constant at 70°.

TABLE 4.
APT CCL PARAMETERS

Structure	Side-Coupled
Lattice	FODO, 7 Sections
Frequency	700 MHz
Energy	20 - 1600 MeV
Current	250 mA
Transverse rms emittance	0.061 to 0.068 π cm-mrad
Longitudinal rms emittance	3.0 to 4.4 x 10^{-6} π eV-s
Number per bunch	2.2 x 10^9
Accelerating gradient (E_0T)	1 MV/m (lattice average)
Peak surface field	7.2 MV/m
Aperture radius	1.4 - 3.5 cm
Synchronous phase	-60° to -40°
Length	2063 m
Number of lattice Units	1451
Cells/tank	2,3,4,6,8,10
Copper power	115 MW
Beam power	395 MW
Total rf power	510 MW

To provide strongest focusing in the CCL, we have chosen to use relatively short tanks with a singlet FODO lattice, ensuring a high density of focusing elements. To guarantee a large transit-time factor and better stability against adverse effects from excitation of high-order modes, we have designed each tank length to correspond to the

correct local value of velocity (β). Having different sections in the CCL allows us to optimize the linac parameters for each velocity region. A relatively small number of sections results in fewer different component parameters (e.g., aperture size, quadrupole parameters, rf-module designs, etc.), which facilitates fabrication of the accelerator. This feature must be balanced against the advantage of keeping the parameter changes small from section to section to avoid introducing significant transitions that can disturb the beam equilibrium and cause growth of halo and additional beam spill. We chose seven CCL sections for the APT reference design. We chose a large radial aperture within each velocity region and limited the aperture to a value of about $\beta_i\lambda/2\pi$, where β_i is the initial velocity of the section, to avoid a large reduction in transit-time factor. Additional design studies may allow us to determine whether this criterion is necessary. We chose the number of cells per tank, and the corresponding focusing lattice period, in each section to ensure a large value of aperture to rms-beam-size ratio calculated from a 3-dimensional uniform ellipsoid model. Although the choice of short tanks is desirable to maintain strongest focusing, this requires a larger number of component tanks to achieve the full energy gain.

We examined the effects of high-order-mode excitation by the beam (beam breakup) for the CCL reference design. The most serious effect is generally associated with excitation of a cavity dipole mode, usually the TM_{110} mode, by an off-axis beam; this effect occurs above a certain threshold in beam current. When the cavity dipole mode is excited, it exerts a transverse force on the beam. The TM_{110}-mode frequency is not harmonically related to the accelerating-mode frequency, and after an initial transient buildup, the final beam is subject to a time-dependent deflection, which causes an effective jitter of the beam centroid. Consequently, the envelope of the output transverse phase-space distribution is enlarged, when averaged over time, and the effective emittance is increased. This problem has been of concern for high-current electron linacs, but we conclude that it is not serious for the APT CCL for two reasons: first, the proton is nearly 2000 times more massive than the electron, which reduces the deflection for a given cavity-excitation level. This greater inertia of the proton provides stabilization against deflection. Second, the design velocity of the cavities increases from tank to tank in the APT CCL (the proton dynamics are not in the extreme relativistic region, as are the electron dynamics in most electron linacs). Although the accelerating-mode frequency is the same for all tanks, the TM_{110}-dipole mode frequency differs from tank to tank. This difference makes the growth of a significant TM_{110} amplitude difficult because a TM_{110} deflection of the beam from a given tank is not able to drive a TM_{110} excitation in subsequent cavities. A TM_{110} frequency mismatch can be increased, if necessary, during tuning of the cavities to ensure that the TM_{110}-mode excitation causes no significant emittance growth.

APT Numerical Simulation Calculations

The numerical simulation codes used consist of PARMTEQ for the RFQ, PARMILA for the DTL and funnel, and CCLDYN for the CCL. These codes track particles through the accelerator, and most treat the space-charge forces using a fast 2-dimensional particle-in-cell approach. In each time step, the particles are allocated to cells of an r-z mesh, and space-charge fields are calculated and used together with the external forces to advance the particles for the next step. In the funnel, where the average x- and y-plane beam envelopes are not symmetrical, a 3-dimensional space-charge calculation is used. We carried out the simulation studies for APT with an initial matched Gaussian dc beam using 7500 particles into the RFQ. (The measured beam from relevant dc injectors is consistent with a Gaussian profile). The input beam is distributed uniformly in the longitudinal direction and is assigned zero initial energy spread (a good approximation for the 10-to 100-eV energy spread of a real beam). We did simulation studies for two cases: an ideal beam case and a nonideal beam case. For the ideal beam case, all linac fields were set to their design values, and the matching quadrupoles and rf cavities preceding the DTL and CCL were set to provide an ideal match as determined by the program TRACE3D. (Matching into the CCL is provided by beam elements of the funnel line, and matching into the DTL, by a special matching section composed of four quadrupole lenses and two rf cavities.) The nonideal APT beam differs from the ideal beam in that we changed parameters in the matching section before the DTL to produce a large mismatch. Although we believe the nonideal beam represents a more realistic representation of the typical beam quality that has been obtained in previous high-energy linacs, it may be possible to improve the performance from that of the nonideal case, especially by providing and using the information from high-performance beam diagnostics.

The simulation results for the nonideal beam are shown in Figure 2. The upper figures show transverse displacement versus angle (x versus x' and y versus y'). The lower right figure shows the energy versus phase relative to the design particle (longitudinal phase space). The stable longitudinal region is also shown in the lower right figure for

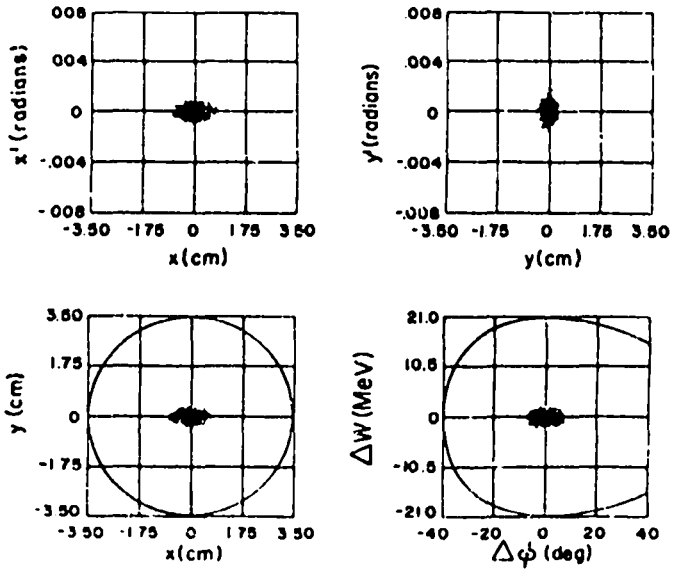

Fig. 2. Output beam at 1600 MeV from the numerical simulation for the nonideal beam case

TABLE 5.
Beam Loss Estimates in APT CCL Based on Extrapolation Procedure Using Simulation Results

Energy (MeV)	20	40	80	160	320	640	1000
Peak loss (nA/m)	3000	20	0.06	0.06	0.06	0.06	0.06
Distributed loss (nA/m)	80	0.4	0.001	0.001	0.001	0.001	0.001

TABLE 6.
Activation Estimates from the Simulation Results

Energy (MeV)	20	40	80	160	320	640	1000
Peak (mRem/h)	48	1.6	0.024	0.12	0.48	0.96	1.4
Distributed (mRem/h)	1.3	0.032	0.0004	0.002	0.008	0.016	0.024

comparison with the particles. The lower left figure shows the x-versus-y cross section and the circular output aperture for the final beam. The space occupied by the beam in the CCL is much smaller than the acceptance limits, which was a main objective of the design. Beam emittances for the nonideal beam simulation are given in Fig. 1 and Tables 2 through 4. The aperture to rms-beam-size ratio in the CCL ranged from 20 to 31 for the ideal beam and from 14 to 22 for the nonideal beam. Thus, above 20 MeV, the design procedure succeeded in obtaining large aperture to rms-beam-size ratios.

To arrive at an initial estimate of losses in the reference design, we have adopted an extrapolation procedure, which we have applied to the nonideal beam simulation. In this procedure, we obtained beam loss values in each section of the CCL for reduced values of the aperture. We extrapolated these loss values to an effective aperture that we chose to be two standard deviations (3.4 mm) less than the true aperture, to account for estimated beam mis-steering. In cases where the extrapolated numbers were too small to be significant, we used upper-limit values for the extrapolation to provide a conservative estimate. The results are shown in Table 5. We conservatively obtained the peak-loss estimates by reassigning all the losses of a section to the first four cells of the section, where the highest losses are observed in the simulation. We obtained the distributed-loss estimate by artificially distributing all lost particles of a section in a uniform loss distribution. Thus, in obtaining these estimates, we used the same extrapolated lost particles for both the peak and distributed losses. We believe our procedures should result in upper bounds of simulation code prediction for losses for each type. The corresponding activation levels can be estimated if (1) we take the rule-of-thumb from the Los Alamos Meson Physics Facility (LAMPF) that 1 nA/m loss results in 20 mrem/h activation at 800 MeV, and (2) we assume that the activation level as a function of energy is proportional to the yield of neutrons per incident proton in copper (which depends nearly linearly on proton energy above 500 MeV). The results, shown in Table 6, are that the most radioactive area is at the entrance to the CCL, which may require remote maintenance for certain jobs. Except for this one place, the activation levels would be no more than a few mrem/h, which is acceptable for hands-on maintenance.

Our goal has been to produce a conservative reference design with a compact, high-quality beam and low beam losses. We used numerical simulation studies, which included space charge, to confirm the good beam characteristics of this reference design.

Acknowledgments

The APT reference design was carried out by many people at Los Alamos, whose efforts and ideas we acknowledge. We thank M. Lynch and P. J. Tallerico, who are responsible for the rf-system design, and B. Blind and A. J. Jason, who are responsible for the high-energy optics design, neither of which was discussed in this paper. We acknowledge the critical evaluation of the design ideas by S. Schriber, A. Browman, and R. Jameson, and thank R. Burick for his support and encouragement.

References

1. M. T. Wilson, T. S. Bhatia, F. W. Guy, G. H. Neuschaefer, T. P. Wangler, and L. M. Young "Accelerator for the Production of Tritium (APT), Proc. of the 1989 Particle Accelerator Conference, 761 (1989).
2. "Accelerator Production of Tritium APT," Brookhaven National Laboratory report BNL/NPB-88-143 (1989).
3. Clemens Zettler,"The Linear Accelerator and Pulse Compressor of the SNQ Project," Proceedings of the 1984 Linear Accelerator Conference, Gesellschaft fur Schwerionenforschung, GSI Report-84-11, 480 (1984).

NEW APPLICATIONS FOR HIGH-POWER PROTON LINACS*

George P. Lawrence
MS H817, Los Alamos National Laboratory, Los Alamos, NM 87544

Abstract

Advances in high-current rf proton linac technology have made it possible to project credible designs for a new generation of very intense spallation neutron sources for nuclear process applications. Current intest is focused on transmutation of nuclear waste and tritium production. Accelerator production of tritium was proposed recently as a contingency backup to the reactor approach.[1] The concept is based on a 250-mA, 1.6-GeV cw proton beam incident on a matrix of lead (Pb) and lithium-aluminum (Li-Al) rods. Neutrons produced in the Pb are absorbed in lithium to produce tritium. A review by the Energy Research Advisory Board (ERAB) affirmed the technical feasibility of the accelerator concept. This finding stimulated investigation of alternate target/blanket concepts, leading to a separated-function scheme that produces tritium through neutron capture on ^{3}He in a thermal flux level > 10^{16} n/cm^2-s. The potential of such high thermal neutron intensities opens an exciting range of new approaches to accelerator transmutation of long-lived actinides and fission products, and to the possibility of reducing time scales for eliminating such wastes from >10^4 years to human lifespans.

Nuclear Process Applications

Light-ion accelerators have been considerd for more than 40 years for nuclear process applications, including fissile-fuel breeding, fuel-element regeneration, energy production from fertile materials, and transmutation of nuclear wastes. In 1947 a Livermore group proposed a 500-MeV, 320-mA D$^+$ cw (50-MHz) drift-tube-linac (DTL) for breeding ^{239}Pu and ^{233}U from ^{238}U and ^{232}Th, using a beryllium neutron-production target surrounded by a ^{238}U multiplier.[2] This project, named the Materials Test Accelerator, was not implemented because of the discovery of large uranium deposits in the western US, but a prototype 33.5-MeV, 12-MHz DTL was built and operated with proton beam currents up to 225 mA (20% duty factor).

In the early 1960s Chalk River Nuclear Laboratories (CRNL) proposed the Intense Neutron Generator (ING), a 65-mA, 1.0-GeV cw proton accelerator for nuclear physics, materials research, and for testing electronuclear fuel breeding concepts. A central motivation was the interest in converting ^{232}Th to ^{233}U to expand fuel resource for the CANDU reactors. Although ING was not funded, an accelerator R&D program evolved at CRNL in the late 70s and early 80s aimed at building a 300-mA, 1.0-GeV demonstration fuel breeder.[3] A high-current 10-MeV cw front end prototype (ZEBRA)[4] was planned, but postponed in 1984 because of the uncertain future of nuclear power in Canada and dropping uranium prices.

BNL also studied accelerator-driven nuclear process concepts during the late 1970s and early 80s.[5] They considered a 300-mA, 1.5-GeV proton linac bombarding a large-volume liquid lead-bismuth (Pb-Bi) eutectic target, surrounded by a blanket of reactor-like fuel elements. Their studies included subcritical assemblies for energy production, fissile fuel element regeneration, production of fissile fuel from fertile material, and also touched on waste transmutation and tritium production. As in the CRNL approach, these schemes employed a fast neutron spectrum (10^3 - 10^6 eV) in the conversion blanket, and a relatively low neutron flux distributed over a large volume.

The stagnated growth of nuclear power has eliminated near-term interest in electronuclear fuel production and enrichment. However, waste transmutation and tritium production have different economic and political drivers. There is increasing public concern about accumulating nuclear wastes, and growing disenchantment with the proposed geologic repository solutions. Transmutation using accelerator-driven neutron sources could play the key role in solving the nuclear waste problem, and may be the most promising application area for high-power proton linacs in the near future. Such facilities may also have the potential for electric power generation and tritium production.

APT Concept and ERAB Evaluation

Tritium decays at the rate of 5.5% per year to ^{3}He and must be continuously replenished to maintain the effectiveness of the US nuclear defense. The DOE is proceeding with plans to replace the aging production reactors at the Savannah River Plant (SRP) with two new production reactors (NPR). In 1988 LANL, BNL, and Westinghouse Hanford Company (WHC) proposed accelerator production of tritium (APT) as a backup or contingency production technology, and an initial concept was described in reference 6. A point design of the accelerator, beam transport system, and target/latttice was developed by LANL and BNL during 1989, and was evaluated by ERAB, a high-level technical review panel composed of accelerator, reactor, electric power, and project engineering experts.

The APT system, which is sized for the same tritium production capacity as the heavy-water NPR, is illustrated conceptually in Fig. 1. A cw rf linac delivers a 250-mA beam of 1.6-GeV protons to a large-volume target composed of a matrix of Pb and Li-Al pins. Each proton produces about 45 neutrons in the Pb by spallation and nuclear evaporation. The neutrons produce tritium via the ^{6}Li(n, α)T reaction, and the tritium is extracted at intervals by chemical processing of the Li-Al pins. The electric power required to generate the 400-MW proton beam is >900 MWe, and must be supplied externally since no fission power is produced (by design) in the target matrix.

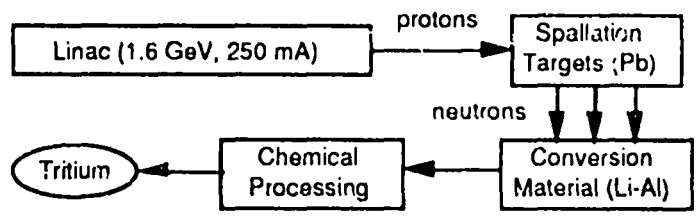

Fig. 1. APT System Concept

The APT has attractive environment, safety, and health features in comparison with a reactor. Since there is no fissile material in the target, there are no pathways to criticality. No transuranic waste is produced, and the radioactive waste stream is small. The process can be shut down rapidly by turning off the beam, and the the taget afterheat is very low. The ERAB Report[7] concluded that there were no serious flaws preventing implementation of the APT scheme, given a suitable development program. The report established the accelerator and beam-transport design concepts as technically sound, and described the target scheme as a conceptual first approach. A major concern was the availability and cost of the required electric power.

High-Power Accelerator

The APT linac can be taken as representative of the class of machines needed for nuclear process applications. Accelerator

* Work supported by the US Department of Energy with Los Alamos National Laboratory Program Development funds.

physics design challenges for such a high-power linac are discussed elsewhere[8] and only a summary of the main design points and parameters is presented here. Figure 2 shows the reference accelerator configuration, which consists of a 2-km-long, 700-MHz, coupled-cavity linac (CCL), injected at 20 MeV by a funneled beam-launching system. The launcher is made up of two 100-keV injectors each containing 140-mA proton sources, two 350-MHz radiofrequency quadrupoles (RFQs) providing 125-mA outputs at 2.5 MeV, and two 350-MHz (2βλ) DTLs accelerating beams to 20 MeV. A funnel similar to that tested recently at Los Alamos is used to combine the beams into a 250-mA, 700-MHz bunch train that is then accelerated to 1.6 GeV in the CCL. The

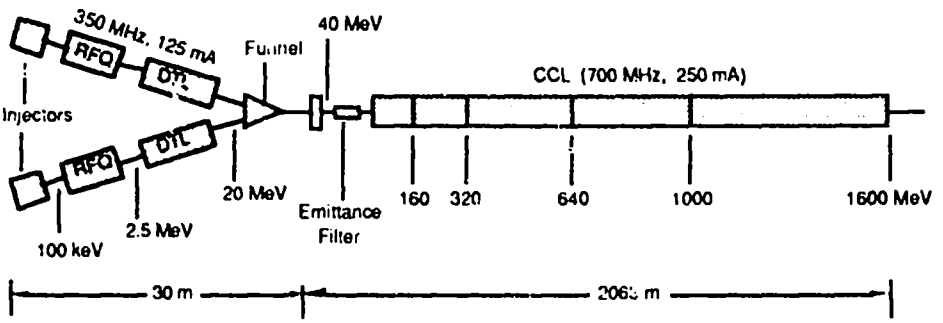

Fig. 2. Reference Accelerator Design for APT

CCL is subdivided into sequences of lattice units, each composed of an n-cell coupled-cavity accelerating module (with n increasing from 2 to 10 as the particle β increases from 0.2 to 0.93), a beam diagnostic and a quadrupole. Figure 3 shows an 8-cell unit. Cavity modules are bridged together in numbers requiring 1 MW of rf input power. The rf tube powering the RFQs and DTLs could be the 1-MW cw 350-MHz klystron developed for the CERN/LEP project. A new 1-MW cw 700-MHz klystron design is needed to power the CCL, which requires about 470 such tubes. Assuming a klystron dc-to-rf efficiency of 0.67, the overall ac-to-beam power efficiency is estimated as about 0.47. Table 1 summarizes the principal parameters of the accelerator; reference 8 provides details on parameter selection, beam dynamics considerations, and the simulations used to predict beam performance.

The overall philosphy governing the linac design is that the low-β beam launcher is optimized to prepare a low-emittance, high-current beam with little halo, and the CCL parameters are selected to assure very low beam loss while maintaining high rf efficiency.

The beam launcher design is very different from the front end of earlier-generation linacs (LAMPF), taking advantage of a decade's advances in the technology of high-current low-β proton linacs. These advances, stimulated partly by the neutral particle beam (NPB) program, include: 1) RFQs replacing high-voltage dc injectors to provide major beam handling improvements in the first accelerating stage; 2) funneling to obtain current doubling with no emittance penalty; 3) higher accelerating-structure frequencies and strong focusing for transverse emittance preservation; 4) ramped accelerating gradients for longitudinal emittance preservation; and 5) proton sources capable of producing high-brightness outputs in the 100-mA range.

Because of the potential for neutron-induced damage to permanent-magnet (PM) materials, the quadrupoles in the DTLs and CCL are radiation-hard electromagnets. Size constraints on the DTL quads then bound the upper frequency limit for the DTL at about 400 MHz. The frequency selection was influenced by the commercial availability of 1-MW cw 350-MHz klystrons. The choice of 20 MeV for the DTL-to-CCL transition is a compromise between the highest practical funneling energy and the lowest practical starting energy for a coupled-cell structure. The low shunt impedance of coupled-cell structures below 100 MeV is relatively unimportant for this design because of high beam loading, and the dominant cost impact of the high-β CCL.

The CCL geometrical layout is similar to LAMPF, with features borrowed from the design of the SNQ linac.[9] The side-coupled linac is in a tunnel buried below 10-15 m of earth shielding. Klystrons, magnet power supplies, and instrumentation are located in a gallery above the linac that is accessible during operation. A non-occupation auxiliary tunnel alongside the linac allows shielding of radiation-sensitive equipment that must be located near the accelerator. The average "real-estate" accelerating gradient is 1 MV/m, a value near a broad minimum in projected facility lifetime costs. The design is driven to this low gradient because of the dominating effects of rf system capital and operating costs. Thermal calculations show that the CCL structures can easily be cooled at this gradient in cw operation, even at the low-β end, where the structure-averaged gradient reaches 2.5 MV/m.

While the average current of the APT CCL is 250 times that of the highest power existing linac (LAMPF), the charge per bunch is actually only 4 to 5 times greater, because the duty factor is 1.0 and all the CCL rf buckets contain protons. Thus the charge-density increase in the bunches compared with demonstrated operating levels is only moderate, and is compensated by stronger transverse focusing. The APT CCL has 4 times the quadrupole linear density of LAMPF, and 50% larger apertures. Given the small beam emittance produced by the modern front end, the ratio of aperture to rms beam size for the APT CCL is 3 to 5 times larger than in LAMPF. This large ratio assures the extremely low fractional beam losses needed to preserve hands-on maintenance of the linac, and has little impact on overall rf efficiency

Table II
APT Linac Parameters

	RFQ	DTL	CCL
Frequency (MHz)	350	350	700
Energy (MeV)	0.1 to 2.5	[illegible]	[illegible]
Synchronous phase (degrees)	-90 to -37	-40	-60 to -40
Radial aperture (cm)	0.4 to 0.3	0.8	1.4 to 3.5
Beam current (mA)	140 to 128	125	250
Length (m)	3.4	11.3	2063
Peak surface field (MV/m)	33	22	7.2
Accelerating gradient (MV/m)		1.1 to 3.1	1.0 (lattice avg)
Copper power (MW)	0.4 (x2)	1.3 (x2)	115
Beam power (MW)	0.3 (x2)	2.2 (x2)	395
Total power (MW)	0.7 (x2)	3.5 (x2)	510
Beam loading	0.43	0.56	0.78
Number of klystrons	1 (x2)	5 (x2)	470
Accelerating structure	4-Vane	2βλ	Side-Coupled
Trans. emittance (π mm-mrad)	0.20 to 0.23	0.27 to 0.58	0.61 to 0.68
Long. emittance (10^{-6} eV-sec)	0.0 to 1.4	1.6 to 3.0	3.0 to 4.4

because of the high CCL beam-loading (0.77). An emittance filter may be desirable following the DTL/CCL structure transition to remove residual phase-space tails.

Technical Issues, LAMPF Experience, and Present Technology Base

In the late 1970s accelerator designers assessing the technology base for nuclear process applications had already identified the major technical issues for a high-power proton linac. These were (and still are): 1) beam-loss activation of machine components, which threatens hands-on maintainability; 2) machine damage from misdirection of the high-power beam; 3) improvement of rf system efficiency and reduction of rf-system unit capital costs; and 4) reliability and longevity of components needed to achieve a 75% plant factor. Some important performance parameters had been demonstrated (300-mA peak current in the FNAL injector linac), and some critical components were available or under development (1-MW cw klystrons). It was recognized that an integrated front end demonstration would be essential to establish the engineering basis for high-power cw operation.

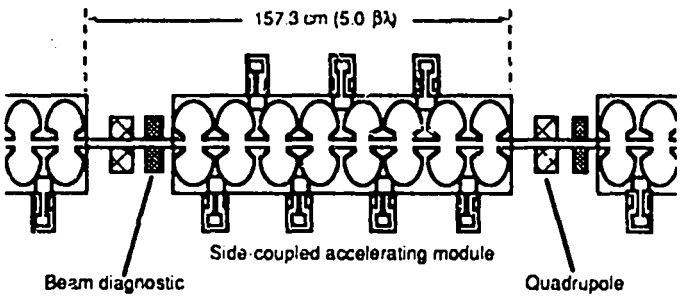

Fig. 3. CCL 8-Cell Lattice Unit

An integrated high-power cw demonstration is still necessary, but accelerator technology improvements and advances in understanding of high-current beam behavior now allow us to project considerably higher confidence that a machine of this class and power can be built and operated. The reference design for APT has taken us a significant step beyond earlier conceptual thinking, and addresses the technical issues point by point. The design includes end-to-end beam simulations with "realistic" matching errors, a machine configuration layout, preliminary engineering analysis of critical components (DTL quads), selection of components to match availability in the existing technology base (klystrons, ion sources), an analysis of off-normal accelerator conditions and beam/target safety arrangements, and a cost and optimization model to [illegible] design codes have been benchmarked in the relevant energy and charge-density regimes by simulation [illegible] high-current behavior on the NPB Accelerator Test Stand at Los Alamos, and by an end-to-end simulation of LAMPF[10] that confirms measured emittance values as well as beam loss locations and rough magnitudes.

Experience with existing linacs that have operated for years with high availability as multi-program research factories has provided a strong foundation for making extrapolations to the APT performance regime. Because of its high average current, operational experience at LAMPF, is especially relevent, particularly in addressing the important beam-loss issue. For most of the CCL length, LAMPF beam losses are estimated to be < 0.2 nA/m, and radiation levels after shutdown are compatible with unlimited-access hands-on maintenace at nearly all locations. Given the much larger aperture-to-beam-size ratio in the APT CCL and the higher quality input beam, we are able to project high confidence of contact maintainability even though average currents are two orders of magnitude higher. Simulations suggest that absolute losses could be lower than at LAMPF. Klystron longevity, although not in cw operation, has also been partly addressed by LAMPF statistics. Typical lifetime of the 1.25-MW peak-power 805-MHz klystrons (up to 12% duty factor) has been > 50,000 hours, with many tubes having operated for more than 80,000 hours. Another area in which LAMPF experience is relevant has been the demonstrated ability to protect accelerator structures from high peak beam power damage by rapid detection of abnormal beam conditions and fast shutdown (in a few μs).

The technology base for high-power linacs is significantly closer to APT requirements than it was in the late 1970s. The nominal ion source selection for APT is a multiaperture duoPIGatron similar to those being used in the CRNL high-power test program. Other promising candidates are the cusp-field source used for the FMIT prototype and an ECR source under development at CRNL. A 267-MHz proton RFQ at CRNL has operated at 67 mA, cw. Peak (H^-) currents of 100 mA have been demonstrated in a 7-MeV ramped-gradient 425-MHz DTL at Los Alamos, and an 80-mA cw D^- DTL is being built as part of the NPB program. Beam funneling in the relevant current and frequency range has been successfully demonstrated at Los Alamos. High power (0.5 - 1.0 MW) cw klystrons are available at several frequencies, including 352 MHz, 500 MHz, and 1000 MHz. Some have de-rf efficiencies close to 0.70, and manufacturers believe that further efficiency improvements are possible.

High Energy Beam Transport and Target

The APT linac output is directed to one of two alternate tritium production target assemblies by a high-energy beam transport (HEBT) system depicted in Fig. 4. The HEBT includes an achromatic bend whose δp/p bandwidth is ±2% and terminates in a nonlinear optical expander[11] that produces a nearly uniform 4m x 8m rectangular beam distribution at the target face. The expander, which includes two octupoles, eliminates the requirement for beam rastering or sweeping that was a problem in the initial APT concept.[6] The large momentum acceptance of the HEBT makes the APT system relatively tolerant to single klystron failures. The result of a single rf station failure above 320 MeV is that the beam is accelerated to full energy and is transported to the target, but with a momentum deviation up to ±1% of the nominal value. This design feature significantly improves overall machine availability, given an anticipated failure rate of 2 to 3 tubes (out of 470) per week; only 20% of the failures would force immediate shutdown.

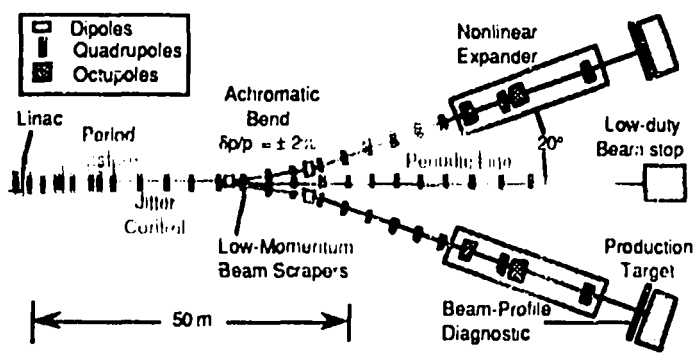

Fig. 4. APT High-Energy Beam Transport

The initial target concept proposed for APT consists of a 4m-high, 8m-wide, 2m-deep rectangular lattice (Fig. 5) of removable 30-cm diameter stainless-steel pressure tubes (7 rows), each of which contains an integral bundle of Pb and Li-Al rods in a 2:1 ratio. The lithium is enriched to 50% ^{6}Li. Light water flowing inside the steel tubes at relatively low temperature (<120 °C) and pressure (<150 PSI) provides cooling and neutron moderation. The entire assembly is designed, in this approach, to look and behave like the core of an SRF reactor, so that SRP fuel fabrication technology and tritium extraction technology would apply with only minor modifications. Neutron flux levels in the lattice are relatively low (< 5×10^{14} n/cm^2-s), and power densities inside the target are comparable to those in an SRP core. Tritium is recovered through processing involving bi-annual removal of the

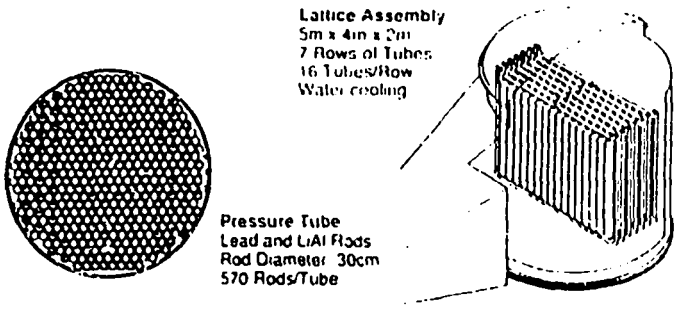

Fig. 5. Initial APT Target Concept

pressure tubes, followed by heating of the Li-Al rods after they are separated from the pin bundles. Neutron yields and spectral distributions in the lattice were calculated using the intra-nuclear cascade code HETC, and tritium production in the lattice was estimated using the point cross section code MCNP with an explicit representation of the lattice rod/tube geometry.

Principal concerns for this target concept are: 1) radiation damage to structural components from the proton beam, which penetrates the entire lattice; 2) formation of highly radioactive ^{24}Na from p,α reactions in the Li-Al, complicating the tritium extraction process; 3) disposal of the radioactive lead waste; and 4) pressure tube failure resulting from an overfocused beam.

^3He Target Concept

An alternate APT target concept has been suggested at Los Alamos that may have significant advantages in comparison with the Pb/Li-Al matrix. This new approach employs the reaction $^3He + n \rightarrow T + p$ (which has a 5300 barn thermal cross section) to recycle the existing ^3He inventory. In this scheme (sketched in Fig. 6) the 1.6-GeV, 250-mA proton beam is vertically incident on a 1-m-diameter liquid Pb-Bi eutectic target surrounded by a 4-m-diameter blanket of D_2O moderator. The eutectic flows in the form of a cylindrical fountain, with the liquid pumped upward at the wall (at 150-200 °C), falling through the beam interaction region, and exiting below at 350-400 °C. A NaK cooling loop can be used to remove the heat to a forced-air sink or to recover 25% of the beam power through a steam generator. In this target-blanket configuration the neutron production volume is separated from the conversion region, allowing somewhat higher neutron yield per proton (55 vs 45) than in the Pb/Li-Al lattice, greater design flexibility, and reduced proton radiation damage to structural components. Neutron induced damage in the high flux at the Pb-Bi containment wall may be a concern, but is within the experience range of existing fast fission reactors (EBR II), and is less than in planned fusion facilities. ^{210}Po production from proton capture on Bi would contribute significantly to target afterheat, but can be continuously removed from the liquid metal transport. Liquid Pb and Pb-Bi targets and transport systems have been studied and developed by a number of groups for application to high-power spallation sources[12], and there is a considerable technology base, although not at APT power levels.

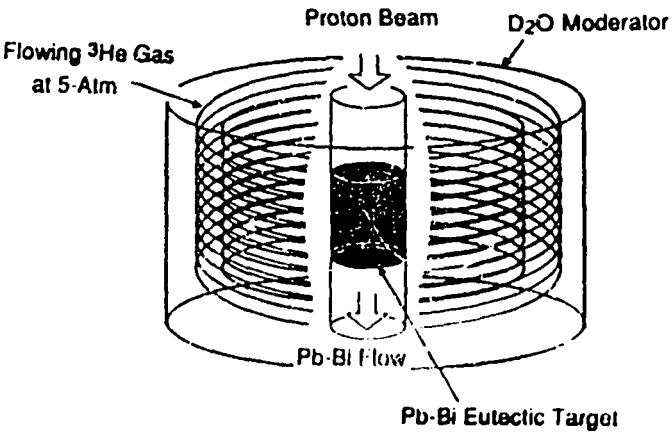

Fig. 6. High-Flux ^3He Target/Blanket

Neutron transport calculations show that thermal neutron flux levels $>2\times10^{16}$ n/cm^2-s can be achieved in the blanket region near the target wall. ^3He at about 75 PSI flows continuously through stainless-steel tubing immersed in the D_2O, and a fraction is converted to tritium on each pass through the neutron field. In a continuous external processing loop similar to that in the Los Alamos TSTA facility, the hydrogen isotopes are first removed by palladium filtering, and then tritium is separated from the other isotopes by fractional cryogenic distillation. The balance of plant for this scheme, which requires a tritium processing capability smaller than TSTA, would be much less costly to build and operate than the SRP process for tritium extraction from Li-Al. Additional advantages of the scheme are that 1) the mixed waste produced is negligible, since the lead target is recycled, and 2) the on-line extraction process greatly reduces the risk of tritium release in an accident.

Nuclear Waste Transmutation

Stimulated by the favorable ERAB evaluation of the APT accelerator concept, preliminary studies at Los Alamos are revealing exciting new nuclear process possibilities for a high-power linac combined with a high thermal-flux target/blanket. These concepts open previously unexplored parameter regimes for transmutation of nuclear waste. It is proposed that the initial application of these ideas would be to the partitioned wastes in the DOE defense complex, and later to the unprocessed used fuel rods currently stored at commercial power reactor sites. There also appears to be interesting potential for energy production without a waste stream, and for tritium production without burdening the electric power grid.

The key to these possibilities is the production of very high ($>10^{16}$ n/cm^2-s) fluxes of thermal neutrons in a useful working volume, which can be achieved with a separated-function target-blanket concept like that described in the previous section, in which a Pb-Bi spallation target is surrounded by a D_2O-moderated conversion volume. Previous accelerator transmutation schemes have required a fast neutron spectrum in the blanket. With the attainment of such high fluxes of low energy neutrons, 100 times greater than in standard reactor designs, significant technical advances are possible. The higher actinides (such as ^{237}Np) are converted by neutron capture to daughter products that are fissioned rapidly by a second neutron interaction before they can decay to non-fissile isotopes. High fluxes of neutrons at thermal energies, where cross sections are large, also permit rapid conversion (to stable isotopes) of long-lived fission products such as ^{99}Tc and ^{127}I. Shorter-lived species, such as ^{90}Sr and ^{137}Cs, can also be converted at rates faster than their natural decay, if the neutron flux is high enough. These processes are shown schematically in Fig. 7. The high flux also provides access to a new, very dilute operating regime that permits high transmutation rates using very low inventories of fissile materials in the blanket. System studies have shown that yearly amounts of transmuted material are similar to those in reactor-based or conventional accelerator-based concepts, but with 100-200 times less resident actinide materials. This leads to positive implications for safety as well as for nuclear safeguards and security.

It is becoming clear that the present plan for disposal of defense and commercial high-level nuclear waste, namely vitrification and very-long-term (10^4 to 10^5 years) storage in geologic repositories, is meeting increasing and deep-seated public skepticism and resistance. Transmutation, while not eliminating the

need for short-term storage sites, may offer a way out of this dilemma. Taken together with appropriate chemical processing, there appears to be good potential that a small number of accelerator-driven thermal-neutron transmuters could form the key ingredient in a waste-management system that can destroy accumulated high-level defense wastes within a human lifespan.

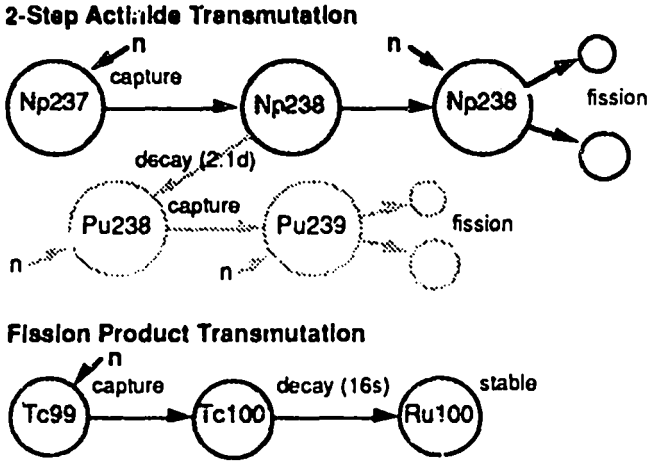

Fig. 7. Transmutation in Thermal Neutron Flux

Figure 8 provides an overview of a full-scale transmutation system currently being studied at Los Alamos, in which a 1.6-GeV, 250-mA proton beam falls on a Pb-Bi target surrounded by a D_2O moderated blanket in which the material to be transmuted is carried in a dilute solution of molten fluoride salts. The molten salt flows continuously in a loop at high temperature, using technology similar to that developed at ORNL years ago for the experimental molten salt reactor program.[13] Higher actinides or Pu in the salt multiply the spallation neutron flux, producing sufficient fission power to run the accelerator. Advanced continuous fluoride chemical partitioning and processing methods appear to be capable of separating stable products from material that is recycled through the transmuter.

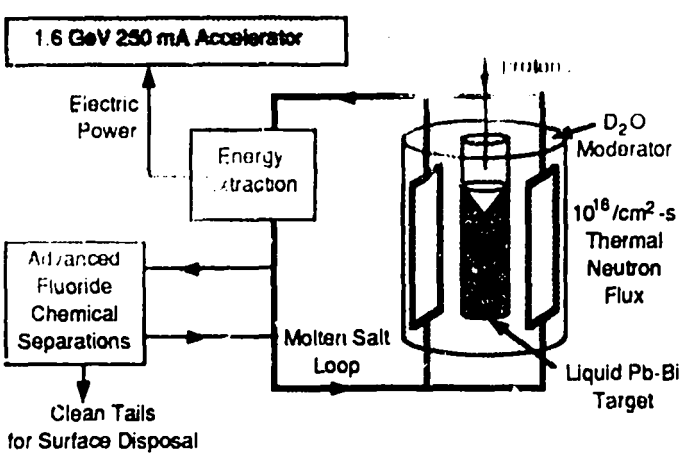

Fig. 8. Los Alamos Transmutation Scheme

Two-dimensional neutron transport calculations for an unoptimized target-blanket geometry show that a single APT-class (250-mA) facility could transmute waste actinides and fission products at a rate of 500 kg/year. Given present inventory levels, the accumulated defense wastes could be converted in 20 to 30 years. While these numbers show what can be done, this first calculational model is far from ideal, with about 50% of the accelerator-produced neutrons being absorbed in structural materials. Very general neutron economy arguments applied to similar systems show that the potential for performance optimization is large. If, for example, a 13% neutron loss is assumed (consistent with molten salt reactor experience), then the beam current required to attain similar performance is much lower, and we could expect 500 kg/yr transmutation rates with a 30-mA accelerator.

Using this neutron economy picture, we can show that one APT-class accelerator can burn the waste discharge of about eleven 1000 MWe light-water reactors (not including U and Pu to be recycled), while providing enough power to run itself. Using the high temperature molten salt concept, overall thermal-electric efficiencies of about 30% appear feasible, if the accelerator-driven system is used to generate power from Th or U fertile material feed, and enough neutrons would be left over to burn the fission products made in this process. This last concept could eventually lead to a new regime of nuclear energy production with minimal requirements for long-term radioactive waste disposal.

Acknowledgement

The material discussed in this paper represents the ideas, contributions and efforts of a large group of people at Los Alamos National Laboratory, drawn from several technical Divisions.

References

1. Accelerator Production of Tritium (APT), Executive Report, Brookhaven National Laboratory Report BNL/NPB-88-143, March, 1989.
2. C. M. Van Atta, "A Brief History of the MTA Project," Proceedings of an Information Meeting on Accelerator Breeding, CONF 770107, Brookhaven National Laboratory, Upton, NY, January 18-19, 1977.
3. P. R. Tunnicliffe, B. G. Chidley, and J. S. Fraser, "High Current Proton Linear Accelerators and Nuclear Power", Proceedings of 1976 Proton Linear Accelerator Conf., Chalk River Nuclear Laboratories Report AECL-5677, November 1976, 36-44.
4. S. O. Schriber, "The ZEBRA (Zero Energy Breeder Accelerator) Program at CRNL - 300-mA, 10-MeV Proton Linac," Proc. 1981 Linear Accelerator Conf., Los Alamos National Laboratory Report LA-9234-C, February 1982, 363-366.
5. M. Steinberg, "Accelerator Spallation Reactors for Breeding Fissile Fuel and Transmutation of Fission Products", Nuclear Technologies in a Sustainable Energy System, Eds. G. S. Bauer and A. McDonald, [illegible]
6. [illegible] S. Bhatia, [illegible] H. Neuschaefer, T. P. Wangler and [illegible] Young, "Accelerator for the Production of Tritium (APT)," [illegible] 1989 IEEE Particle Accelerator Conf., March 20-23, 1989, Chicago, IL, IEEE Cat. No. 89CH2669-0, 761-763.
7. Accelerator Production of Tritium (APT), A Report of the Energy Research Advisory Board to the United States Department of Energy, February 1990, Department of Energy Report DOE/S-0074.
8. T. P. Wangler, G. P. Lawrence, T. S. Bhatia, J. H. Billen, K. C. D. Chan, R. W. Garnett, F. W. Guy, D. J. Liska, M. R. Shubaly, S. Nath, and G. H. Neuschaefer, "Linear Accelerator for Production of Tritium: Physics Design Challenges," Proceedings of 1990 Linear Accelerator Conf., Albuquerque, NM, September 10-14, 1990, to be published.
9. G. S. Bauer and J. E. Vetter, "The FRG Project for a High-Power Spallation Neutron Source for Fundamental Research," Nuclear Technologies in a Sustainable Energy System, G. S Bauer and A. McDonald, Eds., Springer-Verlag (1983), 237-263.
10. R. W. Garnett, R. S. Mills, and T. P. Wangler, "Beam Dynamics Simulation of the LAMPF Linear Accelerator," Proceedings of 1990 Linear Accelerator Conf., Albuquerque, NM, September 10-14, 1990, to be published.
11. B. Blind, "Generation of a Rectangular Beam Distribution for Irradiation of the APT Target," Proceedings of 1990 Linear Accelerator Conf., Albuquerque, NM, September 10-14, 1990, to be published.
12. Realisierungsstudie zur Spallations-Neutronenquelle, Teil II, SNQ Report, KfA-Julich/KfZ-Karlsruhe, May 1981.
13. E. S. Bettis and R. C. Robertson, "The Design and Performance Features of a Single-Fluid Molten-Salt Breeder Reactor," Nuclear Applications and Technology, 8, February 1970, 190-207.

COMMERCIAL APPLICATIONS OF LINACS

Robert W. Hamm
AccSys Technology, Inc., 1177 Quarry Lane, Pleasanton, CA 94566

Abstract

Although research and development of new linear accelerators will continue, linac technology is already well accepted for commercial applications. Dedicated electron linacs have been used for almost 30 years to do cancer radiation therapy. Electron linacs are also being routinely used for high energy x-ray radiography, irradiation of products with x-rays or electrons, and free-electron lasers. The development of the Radio Frequency Quadrupole (RFQ) linac has now also made the ion linac a practical tool for commercial applications. Ion linacs are being commercially supplied for medical isotope production, particle radiation therapy, neutron activation analysis, high energy ion implantation, and neutron radiography. The demand for commercial linac systems is expected to significantly increase in this decade and well into the next century.

Introduction

Linear accelerators developed for physics research have resulted in practical systems for commercial applications. As the technology of these early linacs was improved by researchers, practical applications were developed using these machines. When the technology was proven, commercial companies began to build these linacs for specific markets. One example is the development of the standing-wave side-coupled-cavity linac. Soon after its demonstration at Los Alamos[1] in 1966, compact standing-wave electron linacs were designed for cancer radiation therapy.

The medical electron linac market has grown enormously since its beginning, as seen in Fig. 1. This success is due to these compact systems having no competition in operational reliability, size, cost and safety. Electron linacs now being developed for industrial applications in product irradiation and free electron lasers have similar advantages over competing technologies. Since electron linac applications have been thoroughly discussed in a previous review,[2] this paper emphasizes the more recent development of ion linacs for commercial applications.

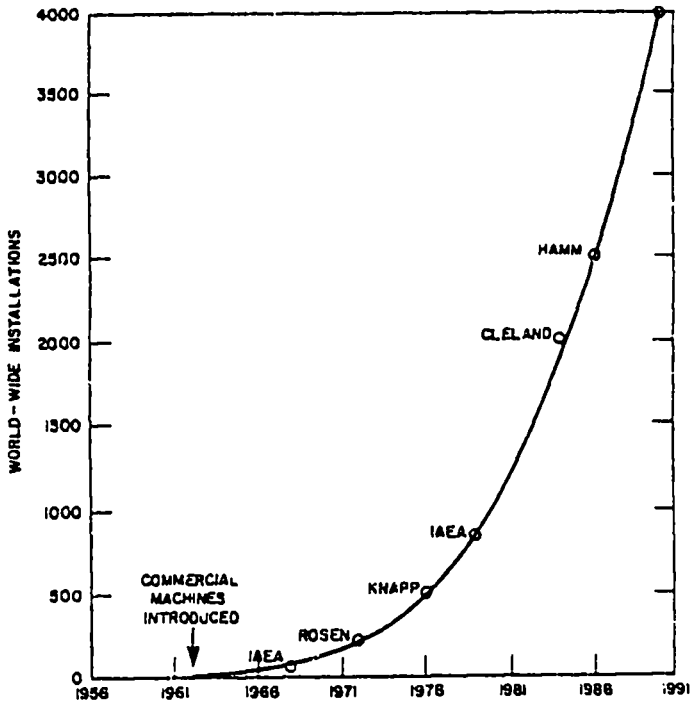

Fig. 1. Growth of electron linacs for radiation therapy.[2]

Just as the introduction of the side-coupled linac spurred the commercial development of electron linacs, the introduction of the RFQ has spawned commercial applications of ion linacs. The same attributes of compact size, operational reliability, cost and radiation safety have enabled the ion linac to become competitive for ion beam applications over a wide range of energies and currents. Low energy ion beam applications (up to several MeV) require only the RFQ, while higher energy beams require the use of a drift tube linac (DTL). Future applications of ion linacs at very high energies (>100 MeV) will even require the use of coupled-cavity linac structures

For this review, a "commercial application" is defined as any process for which an ion linac system is or will be

available from a commercial company. It, therefore, does not cover research linacs constructed by universities and government laboratories, except where the system is used for a practical application or fabricated by an industrial company.

Ion Linac Applications

The commercial applications of ion linacs can be divided into four separate areas: medical, industrial, military and research. The first three comprise the bulk of the commercial ion linac business, while the last one accounts for most of the ion linacs built to date. More than twenty large ion linacs have been constructed by universities and national laboratories worldwide for physics research and ten RFQs have been built as injectors for these linacs.[3]

Medical

The commercial applications of ion linacs in the medical field are cancer therapy and medical isotope production. Cancer therapy is performed with particle beams by bombarding the cancer directly with accelerated protons or heavy ions, or with secondary beams of neutrons or pi mesons created by bombarding a target with an accelerated particle beam. Such treatments have much better dose distributions than bremsstrahlung radiation as seen in Fig. 2, which is a comparison of the depth dose distributions of various radiation therapy treatments.[4] The sharp "Bragg peak" associated with charged particle therapy allows much better localization of the dose with less damage to the skin and healthy tissue surrounding a tumor.

Particle therapy is being performed at twelve research accelerators worldwide, but dedicated systems are now being developed at several facilities listed in Table I.[5] An ion linac will be the injector for many of these accelerators. An example is the 250 MeV proton synchrotron developed by Fermilab for Loma Linda University Medical Center, which is injected by a commercial 2 MeV RFQ linac.[6] In addition, a 250 MeV proton linac has now been proposed by AEA Industrial Technology of England as an alternative to the synchrotron for proton therapy.[7]

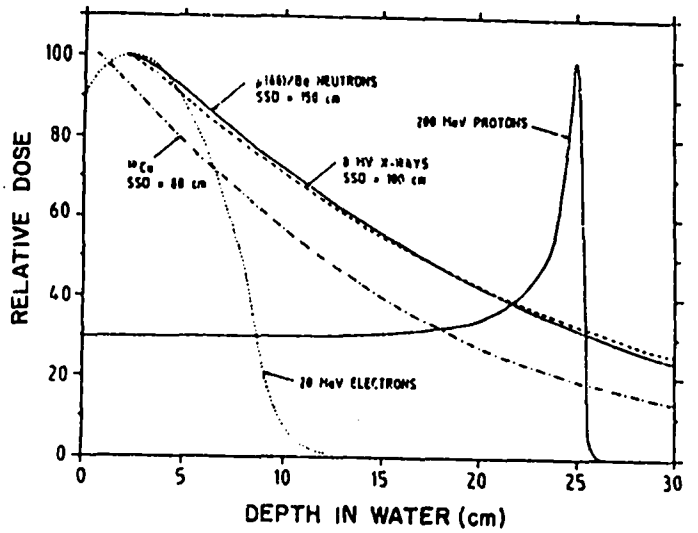

Fig. 2. Depth dose data from radiation therapy beams.[4]

TABLE I
Dedicated Particle Therapy Facilities

COMPANY	COUNTRY	ACCELERATOR	PARTICLE	DATE
Loma Linda	USA	Synchrotron	p	1990
Orsay	FRANCE	Synchrocyclotron	p,n	1991
Nice	FRANCE	Cyclotron	p,n	1991
Chiba	JAPAN	Synchrotron	HI	1994
Chicago	USA	Linac	n,p	1995
EULIMA	EUROPE	Cyclotron	HI	199?
Tsukuba	JAPAN	Synchrotron	p	1995
Novosibirsk	USSR	Linac	p	1995

Neutron therapy has also been performed for many years with existing research accelerators, including linacs, and is being done now with seven dedicated cyclotrons. A dedicated 70 MeV proton linac facility for neutron therapy is planned in Chicago.[8] Pion therapy was performed with the Los Alamos Meson Physics Facility linac and new technology was developed at Los Alamos for a practical 600 MeV, 100 μA proton linac to generate pions,[9] but the cost was prohibitive for commercial production.

Boron neutron capture therapy (BNCT) is a new mode of radiation therapy in which a tumor is loaded with a boron-doped compound and then irradiated by epithermal neutrons. The high capture cross-section of the boron results in a preferential energy deposition in the tumor over the surrounding healthy tissue. The high flux of epithermal neutrons requires a reactor or an accelerator with a high beam power. A 2.5 MeV proton RFQ bombarding a molten lithium target with a 10 mA beam has been

proposed in the USA,[10] while a 30 MeV proton cyclotron bombarding a beryllium target with a 100 μA beam has been suggested in Europe.[11]

The largest potential medical application for ion linacs is radionuclide production. This includes short-lived isotopes for Positron Emission Tomography and long-lived isotopes for nuclear medicine. Linacs at Los Alamos National Laboratory and Brookhaven National Laboratory have been used for many years to generate long-lived isotopes, but cyclotrons have been the work-horse of commercial isotope production, with approximately thirty-two machines in routine operation worldwide. With the development of the RFQ, ion linacs are now competitive with cyclotrons for this application. Three ion linacs for production of PET isotopes are being developed to compete with the small cyclotrons currently used. The parameters for these systems are given in Table II. A large linac for producing nuclear medicine isotopes has been proposed,[12] with an even larger linac for tritium production being presented at this conference.[13]

TABLE II
Proposed PET Isotope Production Linacs

	AccSys Model PL-11	AccSys Model DL-3	SAIC ^{3}He RFQ
RF structure	RFQ + DTL	RFQ	RFQ
Ion specie	H^+	D^+	^{3}He
Final energy (MeV)	11.0	3.5	8.0
Peak current (pmA)	25.0	15.0	7.5
Beam pulse length (μsec)	67	167	167
Average current (pμA)	100	300	150
Accelerator length (m)	4.6	3.0	3.4
Peak beam power (kW)	275	52	120
Peak rf power (kW)	1250	245	360
Average rf power (kW)	7.5	4.9	7.2

Industrial

The primary industrial applications of ion linacs are ion implantation and neutron activation analysis, with a smaller market being neutron radiography. The largest industrial application is high energy ion implantation, for which Fig. 3 shows the required beam energies and ion doses.[14] At the present time, at least five companies worldwide have high energy ion implantation systems available or under development, as listed in Table III. All are designed to accelerate singly or doubly charged heavy ions such as boron, nitrogen, phosphorus arsenic, and antimony. Most of these linacs are four-rod type RFQs with two exceptions, as detailed in Table III. Several of the RFQs are variable frequency so that variable energies and ions can be achieved. The Eaton linac is a phase and amplitude controlled independent-cavity system for this same reason. These variable frequency heavy ion RFQs are described by A. Schempp.[15]

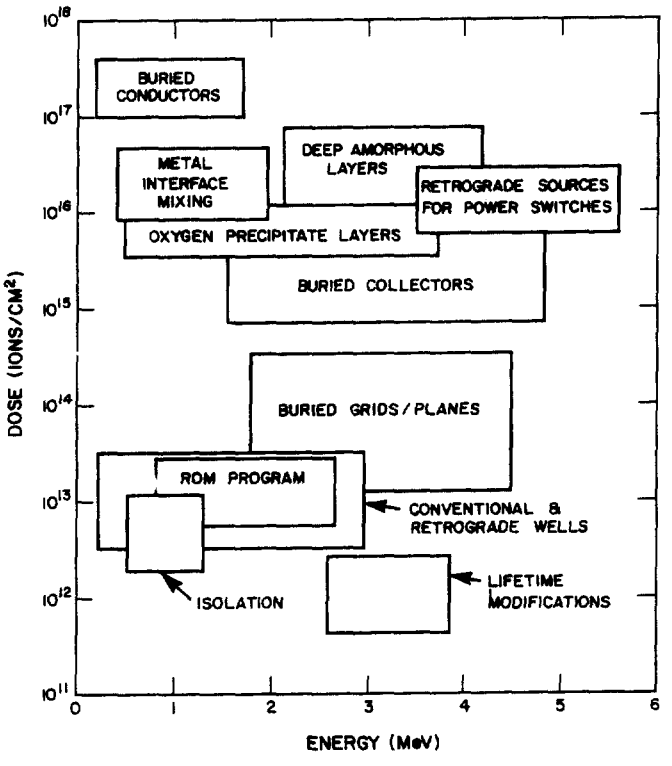

Fig. 3. Applications of High Energy Ion Implantation.

TABLE III
High Energy Ion Implantation Linacs

Company (Origin)	RF Structure	Length (m)	Frequency (MHz)	B^+ Energy (MeV)	Present Status
Eaton (US)	Ind. Cavity	2.4	6.8	1.0	Prod.
AccSys (US)	RFQ-Rod	2.4	15-100	1.5	Dev.
P.E.T. (Germany)	RFQ-Rod	1.2	81.4	1.0	Proto.
Shimadzu	RFQ-Vane	1.85	70	1.012	Proto.
Hitachi (Japan)	RFQ-Rod	N/A	var.	1.0	Dev.

The second industrial application of ion linacs is the production of neutrons for neutron activation analysis. The high beam current capability of the RFQ makes it a prolific source of neutrons from the

Be(d,n) reaction, which produces neutrons with energies of a few MeV. For most applications in neutron activation, thermal neutrons are required. Most existing sealed neutron tubes utilize the T(d,n) reaction which produces 14.1 MeV neutrons. These are much harder to shield and moderate to thermal energies than those from Be(d,n). An RFQ is much safer than radioactive sources that produce fission neutrons at approximately the same average energy, since it can be turned off. Since ion linacs span a wide range of ion energies and currents, ion linac neutron generators can cover a wide range of neutron outputs.[16]

Although neutron activation analysis has already been used for industrial analysis of contaminants, such as sulfur in coal,[17] the first application of an ion linac in this field is for the detection of explosives in aircraft passenger baggage. A small RFQ developed for this (shown in Fig. 4) produces a neutron flux of up to 10^{10} neutrons/sec from a thick beryllium target using a 0.9 MeV d^+ beam. It is pulsed at a high repetition rate (up to 1500 Hz) with an rf duty factor up to 0.0225, resulting in a quasi-continuous thermal neutron flux.

The detection of explosives in airline baggage can be accomplished by a number of nuclear techniques. As reviewed by L. Grodzin,[18] these include not only thermal neutron activation, but fast neutron activation, gamma ray resonance absorption, and neutron backscattering and absorption. Many of these techniques can employ ion linacs as neutron and gamma ray sources. At the present time, the only technique being deployed for actual airport use is the thermal neutron activation system, with the five first systems fielded containing ^{252}Cf fission neutron sources. The final choice of the technique to be used in production units must await the results from these and several new systems under development.

A smaller industrial market for ion linacs is neutron radiography. This nondestructive testing technique was proposed as a use of the RFQ soon after the testing of the first one at Los Alamos in 1979.[19] Linacs for this application are much more powerful than the neutron activation analysis systems. Typically, they accelerate proton or deuteron beams to energies of several MeV to tens of MeV, with beam currents from several hundred microamperes to one millampere or more. Neutron fluxes range from 10^{11} to more than 10^{13} neutrons/sec. The principal application for such systems is to replace radioactive sources and small reactors for neutron radiography of munitions and aircraft parts. For example, a 4 MeV proton RFQ is being developed for the U.S. Navy for realtime neutron radiography at China Lake Naval Weapons Center.[20]

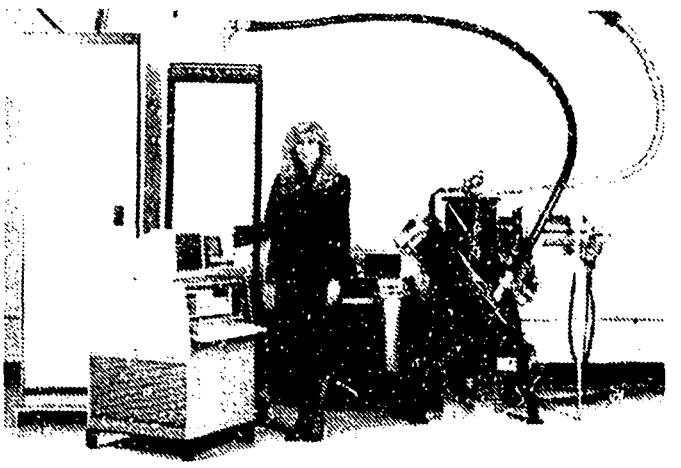

Fig. 4. Model DL-1 RFQ Linac neutron source for Explosive Detection.

Military

The principal military applications of commercial ion linacs are neutron radiography, as described above, and neutral particle beam (NPB) weapons. The latter is not presently a "commercial" application, since this program is still very much in the development phase. However, industrial participation in the NPB development program at Los Alamos has resulted in the commercial production of accelerators, such as the small 1 MeV RFQ linac flown aboard a test rocket last year.[21] This industrial participation is continuing in several more recent NPB programs, with complete linac systems now being built as demonstration units by commercial aerospace companies.[22]

Research

As described earlier, this application accounts for the bulk of the ion linacs built to date, but has involved

very little commercial participation with the university and laboratory groups who have built them. However, prior to the commercial availability of RFQ linacs (and even today in Europe), many of the RFQs in use at research laboratories worldwide originated from only a few research groups. Ten RFQs have been built for other research facilities completely by or in cooperation with Los Alamos and Lawrence Berkeley Laboratory in the U.S. and University of Frankfurt in Europe. Although ion linacs will continue to be developed for research applications by university and national laboratory groups around the world, an increasing number will be procured from commercial companies as the technology matures.

One example is the L3 Calorimeter Calibration RFQ shown in Fig. 5. This system will be mounted onto the large L3 detector in LEP at CERN. It will provide a pulsed H^0 beam (10mA at 1-3 μsec) to bombard a Li target at 1.85 MeV in order to provide intense pulses of radiative-capture gamma rays to calibrate 12,000 BGO crystals in the calorimeter. A new rf-driven H^- ion source has been developed to provide a 25 mA beam pulse for injection into the RFQ with a long source lifetime, even when operating at 150 Hz.[23] A gas neutralizer will strip the H^- beam to a neutral H^0 beam for injection through the magnetic field of the L3 solenoid.

Fig. 5. L3 Calorimeter Calibration RFQ.

REFERENCES

1. D.R. Copenhagen, E.A. Knapp and J.M. Potter, Proc. 1966 Linear Acc. Conf., Los Alamos, 137 (Oct. 1966).
2. R W. Hamm, Proc. 1986 Linear Acc. Conf., SLAC Report 303, 33 (Sept. 1986).
3. J.G. Alessi, Nucl. Inst. Meth Phys. Res. B40/41, 954 (1989).
4. J. Sisterson, ed, PARTICLES, No.3, 4 (June 1989).
5. J. Sisterson, ed, PARTICLES, No. 6, 8 (June 1990).
6. R. Hamm, J. Bower, K. Crandall, M. Hamm and J. Potter, Proc. 1988 European Part. Acc. Conf., Rome, 1462 (June 1988).
7. N. Griffiths, priv. comm. and London Times, 10 June 1990.
8. A.J. Lennox, Proc. 1988 Linear Acc. Conf., CEBAF Report 89-001, 86 (Oct. 1988).
9. L. Hansborough (compiler), Los Alamos Report LA-8880 (1981).
10. T. Wangler, et. al., Proc. 1989 Part. Acc. Conf., IEEE 89CH 2669-0, 678, (March 1989).
11. B. Larsson, Proc., 1990 European Part. Acc. Conf., Nice (June 1990), to be published.
12. J. Stovall, L. Hansborough and H. O'Brien, Proc. 1981 Linear Acc. Conf., Los Alamos Report LA-9234-C, 344 (1981).
13. T. Wangler, "Linac for Production of Tritium: Physics Design", this conf.
14. N. Turner, K. Purser and M. Sieradzki, Nucl. Inst. Meth. Phys. Res. B21, 285 (1987).
15. A. Schempp, "Variable Energy and Heavy Ion RFQs", this conference.
16. R. Hamm, Proc. Third World Conf. on Neutron Radiography, Kluwer Publ., 231 (May 1989).
17. G. Vourvopoulos, D. Humphrey, P. Setters and K. Lamkin, Nucl. Inst. Meth. Phys. Res. B40/41, 852 (1989).
18. L. Grodzins, Symposium on Technological Measures for Airport Security, Cambridge, MA, April 1990, presentation summary (June 1990).
19. J. Stokes, L. Parks, C. Preskitt and J. John, IEEE Trans. Nucl. Sci NS-30, No. 2, 1623 (1983).
20. U S. Navy SBIR Contract to AccSys Technology, Inc., N60530-90-C-0226.
21. D. Schrage et.al., Nucl. Instr. Meth. Phys. Res. B40/41, 949 (1989).
22. Grumman Space Systems, Continuous-Wave Deuterium Demonstrator data sheets PA0065-900, 1990.
23. K. Leung et.al., Lawrence Berkeley Laboratory Report LBL-29315, 1990.

Thursday

Session TH2
Chairman: R. Gluckstern
Invited Papers

SUMMARY OF 1990 CODE CONFERENCE *

Richard K. Cooper and Kwok-Chi D. Chan
Los Alamos National Laboratory, Los Alamos, NM 87545

Abstract

The Conference on Codes and the Linear Accelerator Community was held in Los Alamos in January 1990, and had approximately 100 participants. This conference was the second in a series which has as its goal the exchange of information about codes and code practices among those writing and actually using these codes for the design and analysis of linear accelerators and their components. The first conference was held in San Diego in January 1988, and concentrated on beam dynamics codes and Maxwell solvers. This most recent conference concentrated on 3-D codes and techniques to handle the large amounts of data required for three-dimensional problems. In addition to descriptions of codes, their algorithms and implementations, there were a number of paper describing the use of many of the codes. Proceedings of both these conferences are available[1,2].

Introduction

Finding a coherent scheme of classification for the many codes discussed at the conference is tricky at best. The 3D/2D breakdown is insufficient, so we have broken the codes into two broad categories, namely codes that solve for electromagnetic fields and push particles in those fields, and codes that we will call beam optics codes. The latter category includes codes that are based on some model of beam interactions with their surroundings. We present the codes discussed in the conference in these two broad categories in two tables, Table I and Table II, respectively.

Field and Particle Solvers

In the design of accelerators we are interested in moving charged particles through electromagnetic fields. The ordering of the codes in Table I has roughly to do with whether the principal emphasis of the code is on the fields or the particles. Thus the codes MAGNUS-3D, TOSCA, HFSS, and MSC/EMAS deal almost exclusively with electromagnetic fields, while the particle-in-cell (PIC) codes such as ARGUS, SOS, and QUICKSILVER are equally concerned with particles and fields, and finally codes such as DPC, WARP, and ELBA, used in the analysis of very high current beams, are principally concerned with the motion of the particles. In Tables I and II all those code names set in boldface type are to be found in the new compendium[3] of codes published by the Los Alamos Accelerator Code Group for the DOE Office of High Energy and Nuclear Physics. Inclusion in Ref. 3 does not necessarily constitute a recommendation or endorsement of a given code. However, additional details on each code are available in the compendium; details include code function, purpose, history, author, references, status, individual maintaining the code, and individual distributing the code.

*Work supported and funded by the U.S. Department of Energy, Office of High Energy and Nuclear Physics.

The column labeled $\partial/\partial t$ in Table I is meant to indicate whether the code is a static solver (entry 0), a sinusoidal state solver (entry ω_0), or a general time dependence solver (entry x). An entry in the column labeled ω_λ means that an eigenvalue problem can be solved by the code. The FD/FE column indicates whether finite differences or finite elements are being used, respectively. An entry in the column labeled m_{PIC} indicates that particle motion is tracked; if the entry is ∞, then the motion is non-self consistent, i.e., the motion is prescribed.

The three-dimensional codes presently in use by our community have typically come from either the accelerator community or from the plasma physics community. Though the codes arose initially from differing computational requirements, as accelerator currents become more intense and plasma effects become more important, we see a convergence in the capabilities of these codes. Now emerging are codes from commercial sources, again arising from differing computational needs, but holding some promise for the accelerator community. The code MSC/EMAS is a commercial 3-D time- and frequency-domain solver from the MacNeal-Schwendler Corporation, arising from the desire to solve three-dimensional time-dependent problems involving solid-state materials. The HFSS code (not in fact presented to the conference) was written by the Ansoft Corporation for sale by the Hewlett-Packard Corporation, and is intended to solve three-dimensional scattering matrix problems.

Beam Optics Codes

The beam optics field has seen quite a revolution in the past decade, branching out from linear matrix transformations and from numerical ray tracing. In this time interval we have seen the introduction of Lie-algebraic methods into the field, and more recently the differential-algebra approach has been introduced. Also introduced in this decade has been the use of moments to high order to describe beam behavior.

Emphasis these days is on higher-order effects, not just the dependence on the first power of position and momentum. All of the codes listed in Table II have some higher-order capability, and all have some space-charge model incorporated. As in Table I, a code name set in boldface means that it is listed in the code compendium, Ref. 3.

Miscellaneous

There is always some item that just won't fit into a tidy classification scheme, and in the codes discussed at the conference the code FELPPC was a good example. FELPPC stands for Free-Electron Laser Physical Process Code and is a code which incorporates models of the component parts of a free-electron laser into a code which can perform a great many simple calculations to determine mass, cost, and size of system with specified performance. Additionally, the suite of codes CAVGEN, TRACEX, and CAVDYN being used at FNAL for linac tolerance simulations do not fall neatly into the Table I, Table II scheme. Reference 2 contains the details of these codes.

Table I. Field and Particle Codes

Code Name	3D	2D	$\partial/\partial t$	ω_λ	FD/FE	m_{PIC}	Notes
GFUN	x		0				Magnet design, volume integral
PE2D		x	ω_0		FE		Eddy current
CARMEN	x		ω_0		FE		Eddy current
TOSCA	x	x	0		FE		Magnet design
MAGNUS-3D	x		ω_0		FE		Magnet design, eddy current
HFSS	x		ω_0		FE		S parameters
MSC/EMAS	x	x	x	x	FE		
ARCHON		x	γ		FD	∞	Wakefield, parallel, dielectrics
ARRAKIS		x	x		FD	∞	Wakefield, parallel, dielectrics
AMOS		x	x		FD	∞	Wakefield, losses, dielectrics
MAFIA 3.0	x			x	FD	∞	
MAFIA 3.1	x	x	x	x	FD	x	
MASK		x	x		FD	x	
CONDOR		x	x		FD	x	
MAGIC		x	x		FD		
ARGUS	x		x	x	FD	x	
SOS	x		x	x	FD	x	
QUICKSILVER	x		x		FD	x	
DPC/ST/ENV	x		x			x	Intense electron beam motion
ELBA	x		x			x	Intense beam motion
WARP	x		x			x	High current ion beams

Table II. Beam Optics Codes

Code Name	Notes
PATH	3D space charge.
MARYLIE	Lie-algebra based, 3rd order optics, higher order for some elements.
BEDLAM	Moment based, Lie-Poisson integration for numerical stability, 3D space charge model.
COSY INFINITY	Differential algebra based, arbitrary order possible.
TRIBO	Beam optics to high order including 2D and 3D space charge.

Conclusion

A paper summarizing a conference involving discussions of a multitude of codes cannot do justice to even a handful of them. The proceedings are the best summary of the conference providing the interested individual with detailed information and references. As a guide to those interested in this subject, We include here a list of the papers to be found in the Proceedings of the Conference on Codes and the Linear Accelerator Community, Ref. 2.

- Solving Maxwell's Equations in 3D and 2D by means of MAFIA
- Three-Dimensional Modeling of Accelerators
- MAGIC User's Group Software
- Magnet Design Using Finite Element Software
- MAGNUS-3D: Improvements in Three-Dimensional Magnet Calculations
- Study of Separators Using Numerical Simulations
- ELBA: A Three-Dimensional Particle Simulation Code
- Extraction Induced Emittance Growth for Negative Ion Sources
- WARP: A 3D (+) PIC Code for HIF Simulations
- COSY INFINITY, A New Arbitrary Order Optics Code
- New BEDLAM
- Analytic Transfer Maps for Lie Algebraic Design Codes
- Integrated Numerical Experiments (INEX) and the Free-Electron Laser Physical Process code FELPPC
- Accelerator Code Simulation of FXR Transport
- Coupled Cavity 3-D Codes for Linac Tolerance Simulations
- Applications of 3-D Maxwell Solvers to Accelerator Design
- The AMOS Wakefield Code
- Some Initial Results from the New SLAC Permeameter
- Numerical Simulation of Cross Field Amplifiers
- Simulation of IFR Transport in the Sandia Recirculating Linear Accelerator Using ELBA
- Architecture and Computing Philosophy of the QUICKSILVER, 3D, Electromagnetic, Particle-In-Cell Code
- Numerical Simulations of Beam Dynamics in the Spiral Line Induction Accelerator Using ELBA
- Three Dimensional TOSCA Calculations on the TRIUMF Second Arm Spectrometer Magnet
- Comparison of Results Between Different Precision MAFIA Codes
- Space Charge Models and "PATH"
- Wakefield Calculations on Parallel Computers
- Analysis of Electromagnetic Resonant Cavities and Waveguides Using MSC/EMAS
- PARMILA Documentation
- Aberrations of Electrostatic Lenses Consisting of Rotationally Symmetric Electrodes
- Codes Maintained by the LAACG at the NMFECC
- TRIBO, a Program to Determine High-Order Properties of Intense Ion Beams
- Fifth-Order Aberrations in Magnetic Quadrupole-Octupole Systems

References

1. Charles R. Eminhizer, Ed., *AIP Conference Proceedings 177: Linear Accelerator and Beam Optics Codes, La Jolla Institute 1988*, (American Institute of Physics, New York, 1988).
2. Richard K. Cooper, Compiler, *Proceedings of the Conference on Computer Codes and the Linear Accelerator Community*, Los Alamos National Laboratory, January 22-25, 1990, LA-11857-C.
3. H. K. Deaven and K. C. D. Chan, Eds., *Computer Codes for Particle Accelerator Design and Analysis: A Compendium*, LA-UR-90-1766, May 1990.

A HEAVY ION INJECTOR AT CERN

H. Haseroth
CERN, CH-1211 Geneva 23, Switzerland

Abstract

The request of the nuclear and high energy physics community for high energy heavy ions at CERN has lead to a proposal to upgrade the present facilities for this purpose. This scheme uses the (improved) existing accelerators: the Proton Synchrotron Booster (PSB), the Proton Synchrotron (PS) and the Super Proton Synchrotron (SPS). The Linac, however needs a complete rebuild.

This paper reviews the early "ion history" at CERN, where Linac 1 was used to accelerate deuterons and alpha particles. The experience gained during these exercises resulted in the more spectacular production of oxygen and sulphur ions over recent years. This work is to be continued up till 1992.

The future goal of heavy ion acceleration requires a new linac and substantial improvements to the ion source and also to the down-stream accelerators. Details of the procedure for arriving at the linac specifications and special features, particular to the CERN accelerator complex, will be described.

Introduction

Ions, or more precisely heavy ions play a rather special part in the accelerator and also in the linear accelerator world. Though it is well known that the linear accelerator proposed by Ising in 1924 was to accelerate ions, and that also the experimental work by Wideröe used sodium and potassium ions, no further particular interest arose for the acceleration of heavy ions. The classical (Alvarez) linac is a proton machine. The very few exceptions (Hilac, Unilac ...) are rather the confirmation of this rule. Only in the last few years electron linacs made a major impact. What are the reasons for this? Of course, as in every free market system the "clients" determine what will be built for them. In the past protons dominated the floor and electrons only caught up because of the increased physics interest (studies of Z_0 e.g. in LEP, to name but one example) and also to a lesser degree because of industrial applications. Apart from some nuclear physicists, for whom some fairly special machines were built, there was no wide-spread interest for heavy ions, in particular at higher energies. It is only now that after some preliminary work with light ions interest is large enough to pursue the issue at CERN and also at BNL (RHIC).

Past Experience with Ions at CERN

Though the CERN machines (i.e. originally only the 50 MeV Linac and the Proton Synchrotron) were built for protons, trials were made in 1964 to accelerate deuterons with the Linac. They were repeated in later years with higher intensity, longer pulses and followed by acceleration in the PS. It must be stressed in this context that these experiments were pushed by the machine people to widen their understanding of beam dynamics in the accelerators and not requested by high energy physicists. Nevertheless as it happened that deuterons were available at high energy and (fairly) high intensities, they were also stacked (and accelerated) in the Intersecting Storage Rings (ISR)[1] and the experiments set up there for protons were also used to look at the collision of deuterons. The results prompted a request for the production of alpha particle beams, which are somewhat heavier ions and presumed to be cheap. Originally it was hoped to produce them with the normal proton source, which used to be a standard duoplasmatron. It was quickly understood that this way the intensity would be fairly low, probably too low for further acceleration in the PS. Therefore it was preferred to produce a He^{1+} beam with the full pre-injector voltage, applying subsequent stripping (with about 30% efficiency) to He^{2+} and then injection into the Linac - with the correct β–value for the $2\beta\lambda$ mode. Stripping was achieved with a pulsed gas jet stripper requiring no expensive additional pumping. The intensities obtained this way were practically identical to those of the deuterons[2] , especially as the PSB was used[3] (for the first time) for this purpose. It should be mentioned that all these modifications were substantially eased by the availability of Linac 2, which served as the "proton factory" leaving Linac 1 (the original one) for more sophisticated experiments. The $2\beta\lambda$ mode required RF levels similar to the proton RF levels and some change of the "tilt" of the first cavity.

Incidentally the $2\beta\lambda$ mode was an essential condition for the exercise: due to the fact that the deuterons move with half the proton velocity, the momentum (except for some minor relativistic effects) stays the same as that of the protons. As the charge is identical, the magnetic rigidity remains the same too. This means that all the quadrupole settings in the linac remain essentially untouched (or rather slightly lowered because of the reduced space charge effects).The same statement holds for the magnetic elements of the injection line and the emittance and spectrometer lines. At the time it would not have been feasible to upgrade all this expensive equipment including the kickers and bending magnets for splitting the Linac beam into the four PSB rings. Maybe there would be no ion programme at CERN without these particular properties of the $2\beta\lambda$ mode on Linac 1.

Light Ions

There was never, even in the case of the α-particle beams, a strong demand by the physicists for ions but rather the interest from certain individuals expressed with different arguments. The idea of achieving high energy densities with nuclear collisions was already expressed earlier but there was not a strong consensus, partially because there was still enough to do with protons, partially because the experiments were thought to be too difficult with ions.

The situation changed around 1980[4], when a strong group of nuclear physicists put forward a request for ions at PS energies demonstrating that they would be able to digest the expected "mess". Some work had been done already on the machine side in anticipation and some studies about the different possibilities were made[5]. CERN was not able - against the strong proton lobby - to invest a substantial amount of money into providing somewhat heavier ions, and it was also felt that there was a lack of experience to deal with the problem.

The way out of this situation was to set up a collaboration between CERN, Gesellschaft für Schwerionenforschung and Lawrence Berkeley Laboratory (GSI and LBL), the latter ones not only having the interest in the final experiments but also having the particular know-how. To minimize the overall cost - it was planned at that time to run experiments with O-ions for about two times 10 days - it was thought to use the existing Linac 1 and just modify the front end. This new front end (Fig. 1) was composed of an Electron Cyclotron Resonance (ECR) source and a special Radio Frequency Quadrupole (RFQ), designed to inject again into the Linac in the $2\beta\lambda$ mode.This new equipment was provided for by GSI (with the source subcontracted to C.E.N. Grenoble) and LBL. CERN had to care about its existing

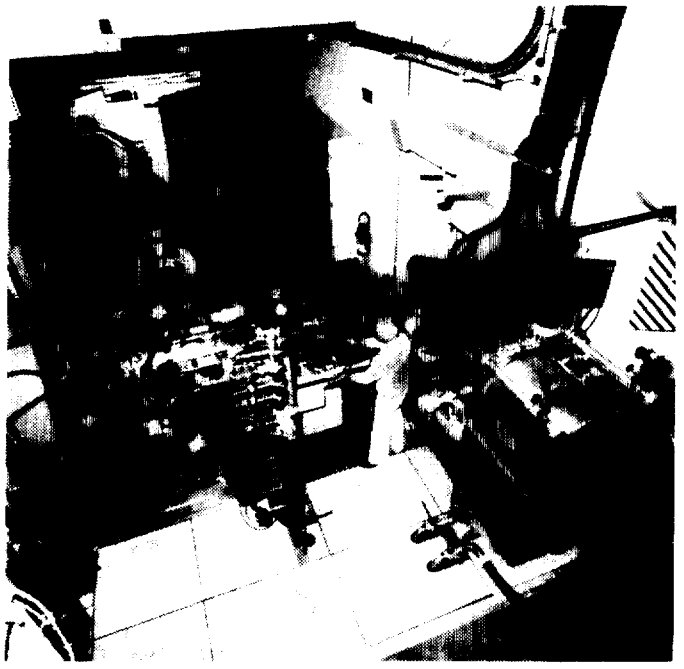

Fig.1. Front end of Linac 1.
Left: End of 1st cavity. Right: O-ion source.
Left center: O-ion RFQ; Left background: proton source and RFQ

accelerators and their "upgrading" to low intensities and had in particular to deal with the somewhat risky and ambitious plan to increase the focusing and accelerating fields of Linac 1 by some 33%. This increase was necessary to cope with O^{6+} ions expected from the source. Obviously O^{8+} ions could have been accelerated as easily as deuterons or α-particles but the intensity from the source would have been by far too low. O^{6+} seemed to be the correct compromise[6]. The increase of the RF fields required, apart from more RF power, an improved vacuum on the first cavity (obtained with a cryo pump) and computer-controlled RF conditioning.The latter proved to be of vital importance for the successful completion of the programme[7,8].

Because Linac 1 had to serve also as injector to the Low Energy Antiproton Ring (LEAR), it was necessary to keep this facility and continue to inject protons or H^- beams into the Linac if required by LEAR.

The experimental programme has gained by now considerable momentum and has been extended to the acceleration of S^{12+} ions[9]. Both O^{6+} and S^{12+} are accelerated by the Linac to 12 MeV/u and subsequently fully stripped by means of a carbon foil, hence for PSB, PS and SPS they look essentially like deuterons. As in the case of S^{12+} production the source produces also O^{6+}. Both of them are accelerated in the Linac in the same way. Even after stripping to 0^{8+} and S^{16+}, they are almost indistinguishable. This feature helps PSB and PS for their monitoring, especially for the RF beam control. Both species are only separated at PS transition. For source adjustments it is of course important to measure the relative intensities: this is done after the Linac by differential energy degradation, making use of the Z^2 dependence of dE/dx and allowing analysis in the spectrometer line after passage through a somewhat thicker "stripping foil" of 1.35 mg/cm^2).

Beam Quality and Measurements

As already mentioned, apart from the complications of 33% higher fields in the Linac and the special RF gymnastics (due to the lower β value) in the circular machines, the beam intensity - or rather the lack of intensity - is one of the major problems. Most of the measurements around the Linac and in the transfer line towards the PSB are made with current transformers and secondary emission monitors ("SEM"-grids and -wires). Depending on the environment, the resolution of the beam transformers goes down to the 1 μA level. The sensitivity of the SEM-grids is around 20 nA/strip, i.e. the profile of a beam well below 1 μA can be measured easily. After calibration these monitors have a very good long-term stability and are therefore also used for intensity measurements. As of course the sensitivity goes up with the Z of the ions, calibration must be made with the appropriate ion.

Future Plans for Lead Ion Acceleration

The present CERN Linac 1 has been pushed to its real limits with the acceleration of O^{6+} and S^{12+} ions. Any possible additional gain in terms of charge to mass ratio would remain very marginal without a substantial rebuild. As quite a few of the interesting phenomena in heavy ion physics are proportional to $A^{1/3}$ (A is the atomic mass number), it is also clear that another small factor gained for A would not help tremendously to discover the quark gluon plasma. The next step should be to accelerate really heavy ions like e.g. lead. Of course, if there would be ion sources available that could supply sufficiently high intensities of lead ions with a charge to mass ratio similar to O^{6+} on S^{12+}, Linac 1 would still be useful, provided some upgrading of the vacuum could be achieved. Unfortunately, this requirement means almost fully stripped ions for Pb: no ion source is available which can provide the required intensity. Therefore, a new Linac has to be built and some upgrading of the existing machines has to be done[10]. A schematic layout is shown in Fig. 2.

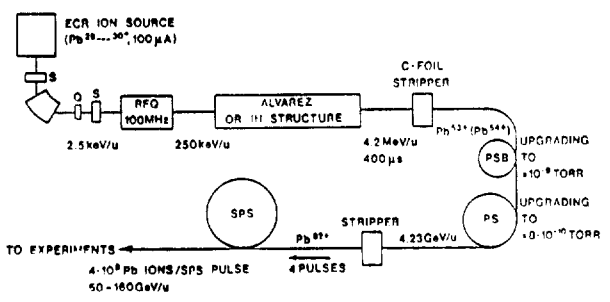

Fig. 2. Schematic layout of CERN's accelerator complex for Pb-ions

Specifications for a New Lead Ion Accelerating Facility

As mentioned already A must be of the order of 200. Lead has originally been chosen because it has a round nucleus - in contrast e.g. to uranium - but there is of course nothing magic in it. Au or Bi would be equally good, in a way even better, because in the case of Pb one would have to go to artificially enriched ^{208}Pb if one does not want to lose a factor of 2 by using natural lead.

The next important parameter is the required intensity. For fixed target experiments at the SPS this intensity originally has been specified as 5×10^7 ions per SPS pulse, i.e. per 10 ... 15 seconds with four pulses injected from the PS. Of course, very quickly afterwards different requests came up asking for more and this trend may continue.

Basically, two options are open:

i) a very low charge-to-mass ratio at fairly high current from the ion source, subsequently very long accelerators, and possibly (to reduce the excessive length) intermediate stripping

ii) a charge-to-mass ratio larger than 0.1 at an intensity that can still satisfy the users. A fairly short linear accelerator is then sufficient, but intermediate stripping must be kept to a minimum to limit intensity losses.

With the progress of modern high charge-state ion sources the second option is the more interesting one, the first option suffers anyhow from the fact that each intermediate stripping foil reduces the intensity by almost one order of magnitude. The next important parameter is the output energy of the Linac. A priori one would like it to be as high as possible, e.g. to do a 100% efficient stripping to Pb^{82+}. Unfortunately, the Linac would be a monster and the PSB would not be needed at all. For cost effectiveness the Linac energy has to be considerably lower. Which are the parameters of importance to determine how low the energy should be?

The future lead ion linac has to be integrated into the CERN accelerator complex. Both the charge-state and the velocity of the ions are important for the subsequent accelerators. The velocity of the ions determines the duration of injection and ejection into the synchrotrons and the required pulse length for all pulsed elements. The velocity range in the circular machines determines the necessary frequency swing of the RF or requires special RF gymnastics.

The obtainable velocity is of course linked to the charge-state. A higher charge-state (for the same β) results in a smaller magnetic rigidity and in a more efficient acceleration.

On the low energy end it is the ion source that determines the charge-state. With reasonable intensities it is possible to aim for 25+ to 30+ in the case of Pb ions. To keep maximum intensity it would be highly desirable to have no intermediate stripping. This would mean that the original charge-state would have to be kept through the PSB and the PS. The vacuum improvements needed in this case are prohibitive for both machines and the output energy of the PS would be rather on the low side for further acceleration in the SPS. One intermediate stripping is therefore needed and to avoid too difficult conditions for the PSB, the intermediate stripping should be after the Linac. To make life easy for the PSB, to get the maximum energy from PSB and PS and to reduce the stringent vacuum requirements in both machines, the conclusion is again that the charge-state after stripping and hence the energy of the Linac should be as high as possible. As for cost reasons it would be desirable to put the lead ion Linac into the buildings of the present Linac 1 and to use the same injection line into the PSB, which is also used for the 50 MeV protons from Linac 2. This fairly complicated line puts some limiting conditions on the ion energy.

As a final compromise we have chosen a Linac energy of 4.2 MeV/u yielding after stripping a charge-state of 53+. This corresponds to a magnetic rigidity which is about 13% higher than for 50 MeV protons and can be achieved with a fairly modest improvement of the present injection line. Due to the low velocity of the ions, pulses of about 400 µs (instead of 150 µs for protons) will be used for efficient injection into the PSB. This will require a more substantial upgrading of several pulsed elements. In spite of this "high" energy and high charge-state an improvement for the vacuum of PSB and PS by more than one order of magnitude will be necessary.

Vacuum Requirements

Amongst the losses specific to heavy ions the dominant mechanism is charge-exchange between molecules of the residual gas and the passing ion, which captures or loses one or more electrons. Any of these events causes immediate loss of the ion concerned in a circular machine. In order to evaluate the probability of loss during the acceleration cycle we need to know the cross-sections for these processes as a function of the energies in the range of interest. Besides numerous theoretical calculations there are only a few experimental fixed points to verify the former. We have used an empirical formula fitted to GSI data[11] backed up by as yet unpublished calculations and measurements from LBL[12,13].

Vacuum improvements in PSB and PS will be needed to reach pressures below 10^{-9} mbar (Fig. 3).

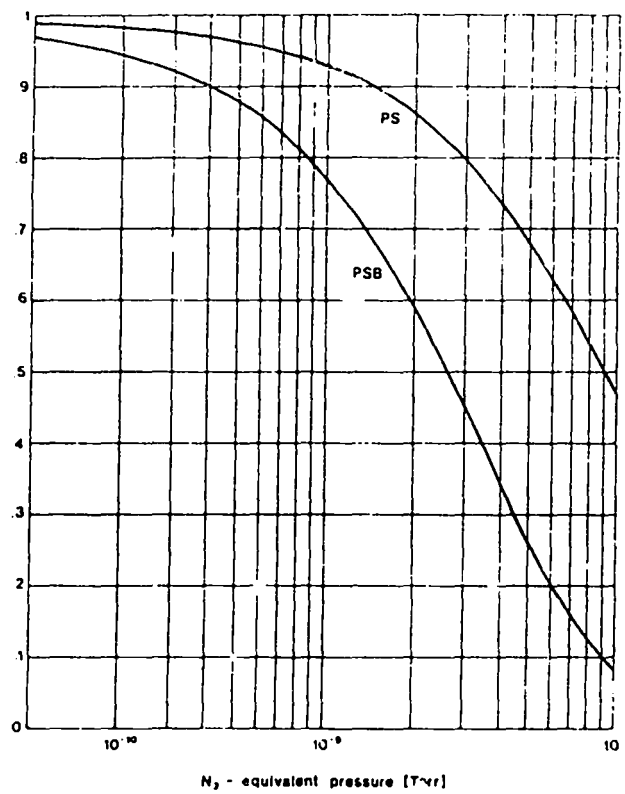

Fig. 3. Transmission losses of Pb^{53+} in PSB and PS as a function of pressure

Options for the Lead-Ion Linac

The lead-ion Linac complex would comprise the following main components :

i) ion-source, including the electrostatic preaccelerator,
ii) low-energy accelerator (RFQ),
iii) high-energy accelerator (Alvarez or interdigital H).

Ion Source. Apart from the ECR source, already used at CERN for the oxygen and sulphur ion production, the EBIS has been envisaged as well as laser ion sources. For the moment these last two are not competitive when aiming for high intensities and heavy ions. Laser ion-sources have been studied e.g. at Munich and have been used at Dubna for light ions, where

encouraging results were obtained for Mg ions. Studies are continuing, also at CERN, to try to answer the question whether they are also interesting for heavy ions. EBIS-sources still lack intensity but development is going on in several laboratories.

Low Energy Acceleration. The RFQ is here the only choice. The only options here are the frequency and the mechanical design: 4-rod or 4-vane structure.

High Energy Acceleration. Neglecting superconducting-, spiral- or other more exotic structures, it seems that there are only two promising alternatives: an Alvarez or an Interdigital H (IH) structure.

A possible option is a normal Alvarez structure operated in the $2\beta\lambda$ mode[14] at least at the low energy end. Unfortunately the number of quadrupole lenses implied in this solution is large. Another proposal[15,16] which reduces the number of quadrupoles and increases the acceleration rate, is the "quasi-Alvarez", a hybrid between a $2\beta\lambda$ and a $\beta\lambda$ structure. A model is shown in Fig. 4

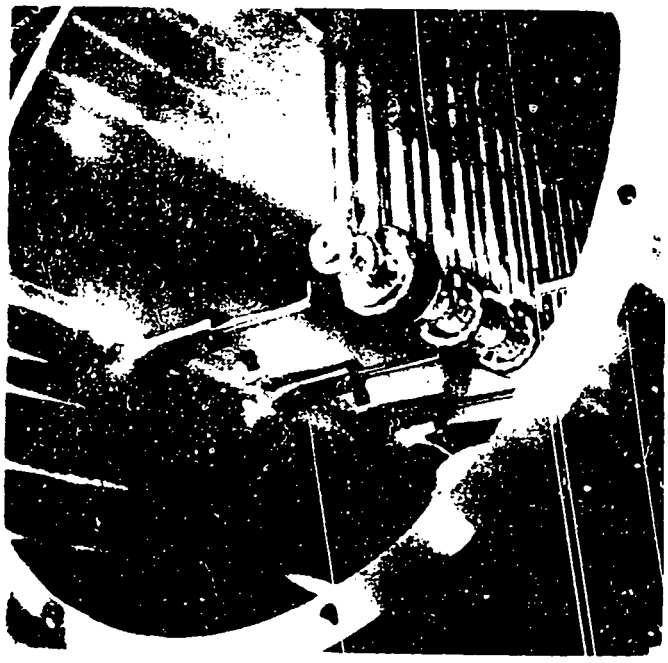

Fig. 4. Model of quasi-Alvarez with post-couplers

Interdigital H structures have been used successfully above 2 MeV/u as Tandem Van de Graaff post-accelerators[17]. Their attraction lies in the high shunt impedances that can be obtained (about four times that of the Alvarez structure) and comes from three main sources, the field mode (H vs E), the acceleration mode ($\beta\lambda/2$ vs $\beta\lambda$), and the low capacitive loading arising from the very small diameter drift tubes (no quadrupoles). It has been proposed to apply this principle at 0.25 MeV/u and 100 MHz operating frequency. The operation of this structure relies at present on the sequence: acceleration at or near the RF peak, i.e. with no phase stability and no external focusing, followed by a focusing section (doublet or triplet) to provide a convergent beam, and finally a longitudinal matching section (several drift tubes) to prepare the beam for the next "standard" accelerating section. These problems are being actively studied at CERN and GSI[18,19]. GSI is building an IH cavity that could be used for the CERN facility if it was followed by another two cavities to boost the energy from 1.4 MeV/u to 4.2 MeV/u.

The Present Linac Scheme

Ion Source. The source will be an ECR source with the following characteristics:

ion :	Pb^{28+}
current :	100 μA (electrical)
extraction voltage :	25 kV
normalized emittance :	0.6 π mm mrad (for 80% of the beam)
repetition rate :	10 Hz (≈1 Hz used initially)
pulse length :	≥ 400 μs

A preliminary design has the following parameters :

Low energy acceleration (RFQ):

Acceleration factor :	0.34
Focusing factor :	4.25
Voltage (kV) :	60.5
Aperture (mm) :	3
σ_{0T} (°) :	23
σ_{0L} (°) :	21
Length (m) :	5.30
Transmission (%) :	93.6
E_s/E_{KP} :	1.85

Required RF power : 100 kW at 101.28 MHz
Pulse duration : 500 μs

Another possible design would be very similar to one developed by IAP/Frankfurt for GSI/Darmstadt for use at the Unilac.[21]

Since Linac 1 and Linac 2 run with 202.56 MHz it would of course be of advantage to keep this frequency.However, in order to have a large enough acceptance[14], the frequency of the low energy part of the accelerator has to be lower. As the whole Alvarez and at least the high energy end of an IH structure can run at 202.56 MHz, the RFQ should operate at half this frequency.

High energy acceleration: For the Linac itself there are two competitive designs: for a quasi-Alvarez[15,16] and for an IH structure[18]. A final decision as to which one should be built, will be made by March next year.

The Basic Parameters of the Alvarez Design are :

Particle type : Lead Ions with A=208, q=25+
Frequency 202.56 MHz
Effective Synchronous Phase ($\phi_{s,eff}$) :
Tank 1 : $\phi_{s,eff}=A\ \beta^{(-0.27)}$ = -40 deg at 0.24 MeV/u
Tank 2 : $\phi_{s,eff}$= -30 deg
Mean Electric Field (MV/m) :
Tank 1 : E = 2.09 + 0.278 z
Tank 2 : E const. with W' continuous between tanks
Acceleration Periodicity :
Tank 1 : 3 gaps/4 $\beta\lambda$
Tank 2 : 4 gaps/5 $\beta\lambda$

	TANK 1	TANK 2
Energy	0.240 to 2.129	2.129 to 4.238 MeV/u
Length	7.684	6.634 m
No. RF Superperiods	31	12
Mean E Field	2.090 to 4.152	3.960 MV/m
Aperture Dia.	12 to 16	18 to 20 mm
Quadrupole Length	51 to 125	145 mm
Quadrupole Grad.	170 to 61	46 to 41 T/m

In the case of the IH structure 3 cavities would be used, with the first one operating at 101.28 MHz and the others at 202.56 MHz.A detailed design is being worked out at GSI[18]. In case of the Alvarez solution simultaneous acceleration of several (three) charge-states and hence an increase in intensity seems to be possible.

The beam line after the Linac will contain the carbon stripper foil and a three magnet filter system to select the desired charge-state(53+). Emittance and energy measurements will be possible for the original as well as for the stripped beam.

Conclusion

It is perfectly feasible to upgrade the CERN accelerator complex for heavy ion acceleration. Further increases in intensity are possible which satisfy also LHC requirements[20]. The whole scheme is not yet in a project stage and it will not become a CERN project in the traditional sense but major contributions will come from other laboratories with which a collaboration will be set up in the near future.

Acknowledgements

The paper presented here is based on a thorough study presented in a report [10]. I would like to thank the authors of this report and also the numerous colleagues from other laboratories, especially from GSI (Darmstadt), LBL (Berkeley), IAP (Frankfurt), GANIL (Caen), C.E.N. (Grenoble), C.E.N. (Saclay) and MPI (Heidelberg). Their contribution to this project has been essential.

References

1. P. Asboe-Hansen, O. Barbalat, D. Boussard, M. Boutheon, J. Gareyte, H. Haseroth, J. Jamsek and S. Myers, "Acceleration and stacking of deuterons in the CERN PS and ISR", Proc. 7th Particle Accelerator Conf., Chicago, 1977 [IEEE Trans. Nucl. Sci. NS-24,1557 (1977)].

2. M. Boutheon, R. Cappi, H. Haseroth, C.E. Hill and J.P. Koutchouk, "Acceleration and stackingof α-particles in the CERN Linac, PS and ISR", Proc. 9th Particle Accelerator Conf., Washington, 1981 [IEEE Trans. Nucl. Sci. NS-28, 2049 (1981)].

3. K.H. Schindl, "Light ions via the PS Booster", PS/BR/Note 81-10 (1981).

4. R. Stock et al., "Study of particle production and target fragmentation in central ^{20}Ne on Pb reactions, at 12 GeV per nucleon energy at the CERN PS external beam", Letter of Intent to the PSCC, PSCC/80-129/I 56 (1980).

5. H. Haseroth, "Light ions at CERN", Proc. Workshop on Quark Matter Formation and Heavy Ion Collisions, Bielefeld, 1982, Eds. M. Jacob and H. Satz (World Scientific, Singapore, 1982), p. 557.

6. B.H. Wolf et al., "Heavy ion injector for the CERN Linac 1", Nucl. Instrum Methods A258, 1 (1987).

7. N. Angert, J. Klabunde, B. Langenbeck, K. Leible, P. Spädtke, J. Struckmeier, B.H. Wolf, S. Abbott, D. Brodzik, R. Gough, D. Howard, H. Lancaster, J. Staples, H. Haseroth, C. Hill, P. Têtu, M. Weiss and R. Geller, "A heavy-ion injector for CERN Linac. 1", Proc. Linear Accelerator Conf., Seeheim, 1984, Ed. N. Angert (Report GSI-84-11, Darmstadt, 1984), p. 374.

8. H. Haseroth, C. Hill, P. Têtu, M. Weiss, B.H. Wolf, K. Leible, P. Spädtke, J. Klabunde, B. Langenbeck, N. Angert, R.A. Gough, J Staples, R. Caylor, D. Howard, R. MacGill, and J. Tanabe, "Ion acceleration in the CERN Linac 1", Linear Accelerator Conf., Stanford, Calif., 1986 (SLAC-Report-303, Stanford, Calif., 1986), p. 355.

9. N. Angert, E. Brouzet, R. Garoby, S. Hancock, H. Haseroth, C.E. Hill, K. Schindl and P. Têtu "Accelerating and separating mixed beams of ions with similar charge to mass ratio in the CERN PS complex", Proc. European Particle Accelerator Conf., Rome, 1988, Ed. S. Tazzari (World Scientific, Singapore, 1988), vol. 2, p. 1367.

10. H. Haseroth (Ed.), "Concept for a lead-ion accelerating facility at CERN", CERN 90-01 (1990).

11. B. Franzke, IEE Trans. Nucl. Sci. NS-28, 2116 (1981).

12. H. Gould and B. Feinberg, LBL, private communication, 1988.

13. W. G. Graham et al., Phys. Rev. A30, 722 (1984).

14. H. Haseroth, A. Lombardi and M. Weiss, "Feasibility study concerning a possible layout for a lead-ion injector for the CERN accelerator complex", Particle Accelerator Conf., Washington, DC, 1987 (IEEE Catalog No. 87CH2387-9), vol. 1, p. 296.

15. D. J. Warner, "Heavy ion acceleration using drif-tube structures with optimized focusing", Proc. Linear Accelerator Conf., Newport News, Va., 1988 (CEBAF-Report-89-001, Nat. Techn. Information Service, Springfield, Va., 1989), p. 109.

16. P. Lapostolle, E. Tanke, M. Vretenar, D. J. Warner, "Computer design and dynamics of the quasi-Alvarez Linac", This conference.

17. U. Ratzinger et al., "The upgraded Munich linear heavy ion post accelerator", Proc. Washington Conf. as in Ref. 14, vol. 1, p.367.

18. U. Ratzinger, Minutes of the 2nd Lead Linac Meeting, CERN Int. Rep. PS/DI/DS/Min. 88-2 (1988).

19. U. Ratzinger, "Interdigital RF Structures", This conference.

20. D. Brandt, E. Brouzet, R. Cappi, J. Gareyte, H. Haseroth, P. Lefèvre, S. Maury, D. Möhl, F. Pedersen, K. Schindl, T.R. Sherwood, L. Thorndahl, D. Warner, "High intensity options for the CERN heavy ion programme", To be published in the proceedings of the 2nd European Particle Acc. Conf. EPAC90, Nice, 1990.

21. Variable Energy and Heavy Ion RFQ's, A. Schempp, this conference.

SOME NEW METHODS OF RF CONTROL*

S. P. Jachim
Los Alamos National Laboratory, Los Alamos, NM 87545

Abstract

This presentation will focus on several recent developments at Los Alamos in the area of RF control for accelerators. Included in the discussion will be in-phase/quadrature (I/Q) field control, the application of six-port reflectometers for cavity instrumentation and resonance control, a technique for phase stabilization of critical RF cables, an application of state-variable feedback for field control, and the direct integration of RF and computer-interface hardware using the VXIbus standard.

Introduction

The advent of accelerators intended for defense applications has driven research and development in many areas of technology. The important field of RF control is one of these areas. In order to reliably meet the unique objectives of these machines, such as remote operation and automatic startup, the need for a thorough, analytically-based system approach to the RF controls was perceived. This paper is an attempt to share some results of the engineering efforts applied at Los Alamos to this end. This is not intended to be an exhaustive study of RF control methods in the accelerator community at large, and thus unfortunately excludes much important work outside of its focus.

The first sections of this paper will describe two distinct approaches to feedback control of cavity fields, namely I/Q control and state-variable feedback. Then a new approach to cavity resonance control and instrumentation, using a six-port reflectometer, will be outlined. A technique for precise phase stabilization of transmission lines will follow. Finally, the direct integration of the RF controls with the associated computer control hardware, using the VXIbus standard, will be discussed.

I/Q Feedback Control

A new method for feedback control of RF cavity fields is under investigation. Rather than operating on the amplitude and phase (A/P) of the cavity field, this approach controls the in-phase and quadrature (I/Q) components of the cavity field. This technique, as illustrated in figure 1, measures and regulates the I and Q components of the field with respect to an RF reference signal, thereby regulating the field parameters. Some related work can be found in [1-3].

* Work supported and funded by the US Department of Defense, Army Strategic Defense Command, under the auspices of the US Department of Energy.

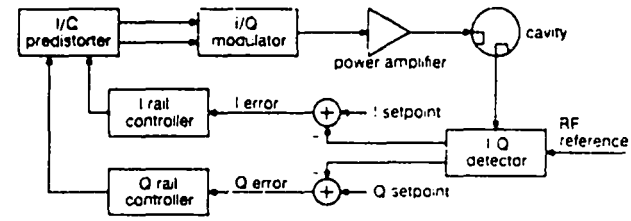

Figure 1. Block diagram of I/Q field control system.

Several important considerations drove the need for I/Q control. The signal processing components required for a typical A/P control system, such as phase shifters and modulators, are usually expensive, bulky and have difficulty achieving the requisite performance. On the other hand, the corresponding processes in an I/Q system can be realized with standard integrated circuits. The precision phase shifter usually required to set the cavity phase in an A/P control system can be eliminated in an I/Q system, as any desired field vector can be selected with the I and Q control setpoints. These tradeoffs are made all the more significant by the requirement for computer-controlled remote operation of the system. The technology used to implement an I/Q system is inherently better adapted to this need. I/Q control also offers a clear path to large-scale integration, with the concomitant benefits in cost and weight.

The response function of an accelerating cavity [4,5] is best described in rectangular (i.e., I/Q) coordinates [6]. The subsequent analysis is also simplified by taking advantage of the isomorphism (i.e., analog) between the real-signal and complex envelope domains [7]. A real-valued bandpass signal, $s(t)$, can be expressed as a linear combination of two orthogonal carriers at the center frequency (ω_c) of the bandpass signal, each amplitude-modulated by a real-valued baseband envelope, as shown in (1).

$$s(t) = m_i(t)\cos(\omega_c t) - m_q(t)\sin(\omega_c t) \qquad (1)$$

$m_i(t)$ = in-phase envelope
$m_q(t)$ = quadrature envelope

The complex envelope, $\tilde{s}(t)$, of the bandpass signal is thus described in the time domain as

$$\tilde{s}(t) = m_i(t) + jm_q(t) \qquad (2)$$

The complex envelope retains all of the features of the temporal modulation of the original bandpass signal, but with the center-frequency variation suppressed. This transformation permits the RF system to be accurately modelled at baseband, obviating the need to use a sampling rate based on the RF frequency. It also gives direct insight into the behavior of the RF system and forms the analytical basis for the I/Q control system.

The equivalent baseband voltage response ($[\tilde{V}(s)]$) of a bandpass circuit to an arbitrary current distribution ($[\tilde{I}(s)]$) is determined from

$$[\tilde{V}(s)] = \begin{bmatrix} \tilde{V}_r(s) \\ \tilde{V}_i(s) \end{bmatrix} = \begin{bmatrix} Z_r(s) & Z_i(s) \\ -Z_i(s) & Z_r(s) \end{bmatrix} \begin{bmatrix} I_r(s) \\ I_i(s) \end{bmatrix} = [\tilde{Z}(s)][\tilde{I}(s)] \qquad (3)$$

The components of $[\tilde{Z}(s)]$ for a parallel-resonant circuit detuned from the drive frequency are[1]

$$Z_r(s) = \left(\frac{R_s}{\tau}\right)\left(\frac{s + a_{11}}{s^2 + b_1 s + b_2}\right)$$
$$Z_i(s) = \left(\frac{R_s}{2Q\tau}\right)\left(\frac{s + a_{12}}{s^2 + b_1 s + b_2}\right) \qquad (4)$$

$$a_{11} = \left(\frac{1}{\tau} - \frac{\Delta\omega}{2Q}\right) \qquad b_1 = \left(\frac{2}{\tau}\right)$$
$$a_{12} = \left(\frac{1}{\tau} + 2Q\Delta\omega\right) \qquad b_2 = \left(\frac{1}{\tau^2} + \Delta\omega^2\right)$$

τ = cavity damping time constant (sec)
R_s = cavity shunt resistance (ohms)
Q = cavity unloaded quality factor
$\Delta\omega = \omega_0 - \omega_d$ = cavity detuning frequency (rad/sec)
ω_d = cavity drive frequency (rad/sec)
ω_0 = cavity resonant frequency (rad/sec).

Taking into account the boundary conditions at the drive port junction and beam loading [8,9], the equivalent baseband operational scattering model for a cavity detuned from the drive frequency is as shown in figure 2.

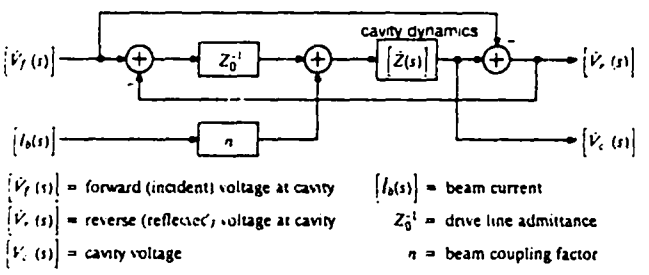

Figure 2. Operational scattering model of a cavity.

The transfer function of figure 2, $[\tilde{H}(s)]$, from forward voltage to cavity voltage is

$$[\tilde{H}(s)] = 2(Z_0^{-1})[I + Z_0^{-1}[\tilde{Z}(s)]]^{-1}[\tilde{Z}(s)] \qquad (5)$$

This transfer function has the same structure and order as does $[\tilde{Z}(s)]$, but with the pole and zero locations shifted as functions of Z_0. With I/Q control, the dynamic crosscoupling of the cavity can be completely removed with rudimentary linear circuits at baseband. Decoupling can also be achieved with A/P control, albeit with greater difficulty [10]. This function is incorporated as the I/Q predistorter in figure 1. In essence, the predistorter deliberately crosscouples the drive signals to the cavity and the cavity then "unscrambles" them, with the overall effect of orthogonal control; thus the term predistorter. When the proper predistortion function $[\tilde{P}(s)]$ is concatenated with $[\tilde{H}(s)]$ as shown in (6), the result is a compound response $[\tilde{F}(s)]$ which is decoupled. The required I/Q predistortion functions are simple, linear and realizable.

$$\begin{bmatrix} H_r(s) & H_i(s) \\ -H_i(s) & H_r(s) \end{bmatrix} \begin{bmatrix} P_r(s) & P_i(s) \\ -P_i(s) & P_r(s) \end{bmatrix} = \begin{bmatrix} F_r(s) & 0 \\ 0 & F_r(s) \end{bmatrix} \; ; \qquad (6)$$

$$P_r(s) = 1 \text{ , and } P_i(s) = -\left(\frac{H_i(s)}{H_r(s)}\right)$$

A significant difference between the I/Q and A/P control methods lies in their relative tolerance of time-varying phase shift (i.e., droop) in the power amplifier. In an A/P control loop, phase droop represents a phase rate perturbation. Integral feedback gain in an A/P loop will reduce this to a constant phase tracking error of the cavity field. The same droop in an I/Q system induces a rotation of the control vector, the effect of which, for small phase shift variations, is to slightly crosscouple the I and Q loops. If not held within limits, this phase shift can lead to destabilization of the loops. This can be avoided by direct feedforward compensation of or local feedback around the amplifier, and thus is usually not a serious practical problem.

State-Variable Feedback

An intriguing approach to RF control using state-variable feedback is under investigation by J. Johnson [11]. Readers are referred to the cited reference for more detailed information; only a brief overview will be given here. A block diagram of this scheme is shown in figure 3. In this implementation, samples of three system states are scaled in magnitude (a_i) and phase ($\Delta\phi_i$) and applied as feedback functions. The sum of these weighted feedback functions is compared to an RF reference signal, and their difference is used to drive the RF system.

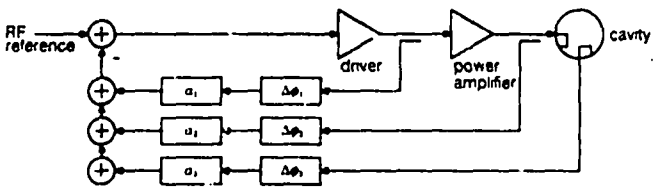

Figure 3. Block diagram of state-variable control system.

Two significant benefits accrue from this approach. A state-variable feedback system [12,13] which utilizes direct, proportional observations of system states can be shown to have a high degree of stability and performance robustness with respect to variations of the plant. Thus gain and bandwidth variations in the power amplifier, for instance, do not have a strong effect on the behavior of the closed-loop system. Also, as seen in figure 3, all feedback and signal processing functions are performed directly at the RF frequency. The elimination of conversion, detection, and modulation equipment can have a substantial impact on the system cost. Related analysis of RF feedback can be found in [14,15].

1. The equations given in [6,8] differ inadvertently from those shown here by a factor of two. The functions shown here are indeed correct.

However, restricting the feedback functions to proportional gain limits the ability of the feedback loop to suppress external disturbances, such as beam loading. The lack of Nyquist-type gain shaping of the feedback functions, particularly integral gain, does not allow the available loop gain to be customized for disturbance suppression. Similar to the I/Q approach, the state variable control system also exhibits sensitivity to such things as power amplifier phase droop, in that large phase shift variations can destabilize the loop. Within these constraints the state-variable control system works well and has been demonstrated on a FEL cavity.

Resonance Control

This section describes a system with which to measure and tune the properties of resonant accelerating structures at high power levels. With the addition of a few passive components, a standard dual directional coupler can be transformed into a six-port reflectometer [16,17], as shown in figure 4. This device can be used to determine the vector reflection coefficient of a cavity attached to the coupler simply by measuring the RF power at each of the four sidearm ports.

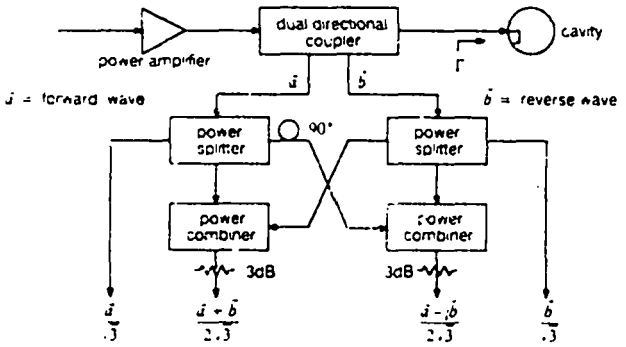

Figure 4. Block diagram of a six-port coupler.

There is no need for vector ratio processing, and any phase shift induced in the sidearm signals, say by cables, is irrelevant. The vector nature of the measurement is inferred from the correlations among the sidearm signal levels, as shown in (7) [18]. For noncritical applications, the calibration constants can be determined by inspection of the network in figure 4. For applications requiring greater precision, a calibration procedure can be used to implement vector error correction in software. Many useful calibration procedures are in existence, but an approach tailored to high-power applications has been developed [19]. Experimentally, reflection measurements made with a calibrated six-port reflectometer, operating at 1kW, matched those made with a calibrated automatic network analyzer to less than 1%.

$$\Gamma = \frac{\sum_{i=1}^{4}(F_i + jG_i)P_i}{\sum_{i=1}^{4} H_i P_i} \tag{7}$$

Γ = reflection coefficient of cavity
F_i, G_i, H_i = real calibration constants of six-port coupler
P_i = power measured at i^{th} sidearm port

By sampling and digitizing the measured data from a six-port reflectometer, resonance control of a cavity in a pulsed RF system has been demonstrated. This was achieved in software by applying a feedback control algorithm, via a slug tuner, to minimize the susceptance observed at the plane of the detuned short [20]. Figure 5 illustrates a typical computer display of this tuning process, wherein a cavity which is initially detuned is brought into resonance along a constant-conductance contour of the Smith chart.

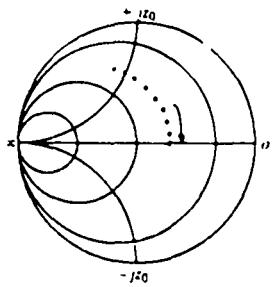

Figure 5. Reflection coefficient locus displayed during resonance control.

This device can also be used to instrument an accelerator RF system. By making susceptance slope measurements [21] at appropriate times during the RF pulse, the unloaded Q, beam-loaded Q and beam loading factor can be determined. These measurements can be made without disturbing the normal operation of the accelerator. Good agreement has been found between high-power and low-power Q measurements on a cryogenic DTL [22].

RF Transport Stabilization

A common requirement in accelerators is a phase-stable means of delivering RF signals to their appropriate points of use. A successful solution to this problem [23] is shown in figure 6, wherein a signal from a reference oscillator is transported to a remote load. The circuit shown operates as follows. An RF calibration signal at a frequency equal to one and one-half times the frequency of the signal to be delivered to the load is split and applied both to a phase detector and another splitter/combiner where it is then transmitted through a diplexer onto a single coaxial line. Upon arrival at a second diplexer, this calibration signal is reflected, via a short-circuit termination, back toward the first diplexer where it is extracted from the coaxial line and applied to the phase detector. The output of the phase detector is filtered and proportional and integral control actions are developed from this information. The output of the feedback controller

is used to drive the phase shifter via the DC motor in such a way as to hold the electrical length of the transport path constant. The RF reference signal is superimposed and transmitted on this same stabilized path. A similar technique for optical signals is described in [24].

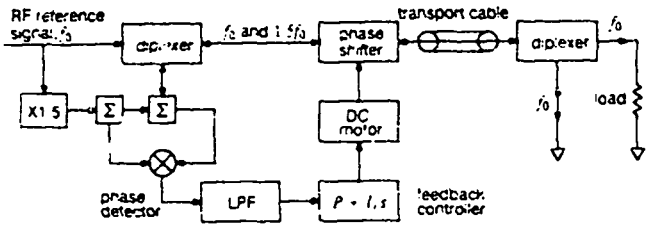

Figure 6. Phase-stable RF transport block diagram.

A diplexer is a device which is used to combine or separate two signals of different frequency. Space does not allow a full description of the diplexer that was used, but suffice it to say that it exhibited the required high degree of phase stability. The results of a 68 hour test of this system are shown in figure 7. A 150 foot coax was used for the transport cable. The output phase was held constant to within ± 0.036° at 435MHz.

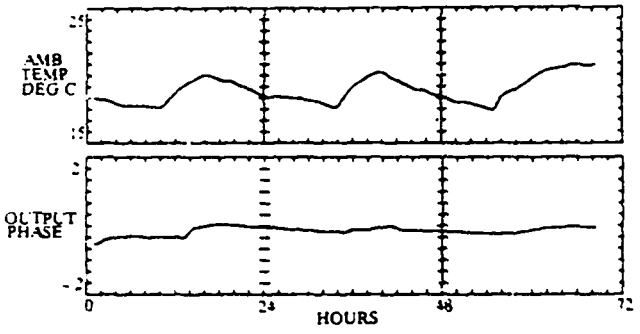

Figure 7. Phase-stable RF transport test results.

System Integration

A new approach to the implementation and integration of RF controls has been undertaken. The I/Q field control, six-port resonance control, and the phase-stable transport systems are being realized in card-modular form using the VXI standard [25]. This emerging standard was developed by a consortium of major instrument manufacturers, and extends the ubiquitous VME standard to support precision instrumentation and RF applications. A typical layout for a VXI module that is used for RF control is shown in figure 8.

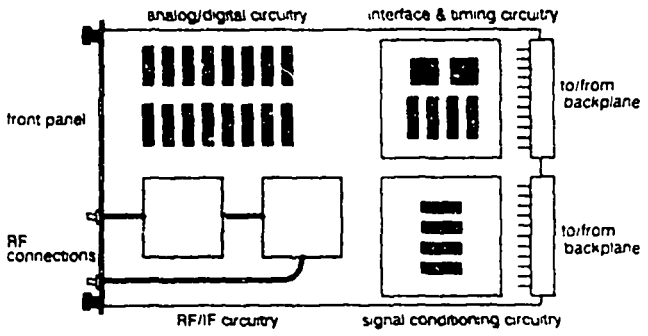

Figure 8. Typical layout of a VXI module for RF control.

The integration, setup and operation of the RF control system is greatly simplified by this modular approach. The functions of timing, analog I/O, and digital I/O are directly accessed over the VXI backplane to/from each individual module, thus vastly reducing cabling and interconnects. The system clock and master trigger are broadcast across the VXI backplane, and timing pulses are then generated on each card by addressable countdown registers. The interface is a straightforward VME-style register-based design with minimal software requirements. Because all of the RF signal processing is done electronically, troublesome RF components, such as trombone lines, have been eliminated. The benefits to system reliability and maintainability are clear.

By design, the RF control system is fully operable from a remote location. All control parameters, for instance integral feedback gain, drive phase adjustment, and fast-protect thresholds, are remotely programmable. This approach also enables the RF control system to be easily adapted to a wide variety of accelerators simply by loading the appropriate control parameters. What has been achieved to a large extent is a generic, modular RF control system.

Acknowledgements

The developments that have been presented here are a product of team effort. The following people are recognized for their considerable contributions in this regard: C. Boyd, T. Brooks, P. Carrier, A. Cheo, B. Cheo, T. Cote, M. Curtin, I. Debaca, P. Denney, C. Eaton, L. Eaton, C. Fortgang, D. Gutscher, E. Hansberry, J. Hornkohl, T. Jones, C. Little, M. Lynch, J. Martinez, E. Natter, R. Przeklasa, A. Regan, S. Scarlott, A. Young, and C. Ziomek.

References

1. J. R. Delayen, et. al., "A Microprocessor-Based Feedback System for Phase and Amplitude Control of Superconducting Resonators," IEEE Trans. Nucl. Sci., vol. NS-24, pp. 1759-1761, June 1977.

2. H. D. Gräf and A. Richter, "The Darmstadt Superconducting LINAC," Proc. Linear Accel. Conf., pp. 231-236, 1988.

3. D. Boussard, "Control of Cavities with High Beam Loading," IEEE Trans. Nucl. Sci., vol. NS-32, pp.1852-1856, October 1985.

4. P. B. Wilson, "High-Energy Electron LINACs: Application to Storage Ring RF Systems and Linear Colliders," SLAC-PUB-2884, February 1982.

5. J. E. Griffin, "RF Cavity Primer for Cyclic Proton Accelerators," FNAL Tech. Memo #TM-1519, April 1988.

6. S. P. Jachim and E. F. Natter, "Beam Loading and Cavity Compensation for the Ground Test Accelerator," Proc. IEEE Particle Accelerator Conf., pp. 1870-1873, 1989.

7. S. Haykin, Communication Systems. New York: John Wiley & Sons, 1983, pp. 80-108.

8. E. Natter, et. al., "An Improved Cavity Model and Dynamic Simulation of the GTA Accelerator RF System," Proc. Neutral Particle Beam Tech. Symp., 1989.

9. B. R. Cheo and S. P. Jachim, "Dynamic Interactions Between RF Sources and LINAC Cavities with Beam Loading," submitted to IEEE Trans. Elec. Dev.

10. F. Pedersen, "Beam Loading Effects in the CERN PS Booster," IEEE Trans. Nucl. Sci., vol. NS-22, pp. 1906-1909, June 1975.

11. J. Johnson, "Robust RF Control of Accelerators", Proc. Linear Accel. Conf., this issue, 1990.

12. W. L. Brogan, *Modern Control Theory*, Englewood Cliffs, NJ.: Prentice-Hall, inc., 1985.

13. J. M. Maciejowski, *Multivariable Feedback Design*, Addison-Wesley Publishing Co., 1989.

14. F. Pedersen, "Beam Loading Aspects of TRIUMF Kaon Factory RF Systems," TRIUMF tech. note #TRI-DN-85-15.

15. S. T. Craig and R. J. West, "Beam Loading Compensation for 52MHz RF Systems," Proc. European Particle Accel. Conf., June 1988.

16. C. A. Hoer, "The Six-Port Coupler: A New Approach to Measuring Voltage, Current, Power, Impedance, and Phase," IEEE Trans. Instrum. Meas., vol. IM-21, pp. 466-469, November 1972.

17. C. A. Hoer and K. C. Roe, "Using an Arbitrary Six-Port Junction to Measure Complex Voltage Ratios," IEEE Trans. Microwave Theory Tech., vol. MTT-23, pp. 978-984, 1975.

18. C. A. Hoer, "Using Six-Port and Eight-Port Junctions To Measure Active and Passive Circuit Parameters," NBS Tech. Note 673, September 1975.

19. S. P. Jachim and W. D. Gutscher, "A Statistical Method for Calibrating the Six-Port Reflectometer Using Nonideal Standards," IEEE Trans. Microwave Theory Tech., vol. 37, no. 11, pp. 1825-1828, November 1989.

20. S. P. Jachim, et. al., "High-Power Measurement and Tuning of Accelerator Cavities Using a Six-Port Reflectometer," Proc. Neutral Particle Beam Tech. Symp., 1989.

21. G. L. Matthei, et. al., *Microwave Filters, Impedance-Matching Networks and Coupling Structures*, Dedham, MA.: Artech House, 1980, pp. 430-434.

22. C. M. Fortgang, et. al., "Heavy Beam Loading Measurements of an RF Accelerating Cavity Under Amplitude and Phase Control," accepted for publication, Rev. Scientific Instrum.

23. S. P. Jachim, et. al., "A Phase-Stable Transport System," Proc. Neutral Particle Beam Tech. Symp., 1990.

24. E. Peschardt and J. P. H. Sladen, "Phase Compensated Fiber-Optic Links for the LEP RF Reference Distribution," Proc. IEEE Particle Accelerator Conf., pp. 1960-1962, 1989.

25. C. D. Ziomek, "Interfacing RF Control Electronics to the VXIbus for the Ground Test Accelerator," Proc. Neutral Particle Beam Tech. Symp., 1990.

Thursday

Session TH4
Chairman: A. Vlieks
Contributed Papers

LINEAR ACCELERATOR FOR BURNER-REACTOR

G.I.Batskikh, B.P.Murin, A.P.Fedotov
Moscow Radiotechnical Institute
USSR Academy of Sciences, Moscow, USSR

General Consideration

Future development of nuclear power engineering depends on the successful solution of two key problems of safety and utilization of high level radioactive wastes (HLRW) of atomic power plants (APP) .

Modern methods of HLRW treatment involve solidification , preliminary storing for a period of 30 - 50 years necessary for the decay of long-living nuclids and final burial in geological formations several hundred meters below the ground surface. The depth burial of the radioactive wastes requires complicated under ground constructions. It's very expensive and doesn't meet modern ecological requirements.

Alternative modern and more reasonable methods of APP HLRW treatment are under consideration now. One of the methods involves separation of APP waste radionuclids for use in economy with subsequent transmutation of the long-living isotopes into the short-living ones by high-intensity neutron fluxes generated by proton accelerators [1 - 3].

The installation intended for the long-living radionuclides transmutation into the short-living ones is called burner-reactor. It can be based on the continuous regime proton accelerator with 1.5 GeV energy, 0.3 A current and beam mean power of 450 MW. The preferable type of the proton accelerator with the aforementioned parameters is the linear accelerator [4 - 5].

Accelerator layout and parameters

Experience and new ideas in linear proton accelerator design lead to the accelerator scheme presented in Fig. 1.. The following basic concepts were taken into account in burner-reactor linear accelerator (BRLA) design.

- Simultaneous acceleration of H^+ and H^- beams is specified to provide for a number of output beams. Therefore the frequency increase factor (the ratio of the operating frequencies in different parts of accelerator) has to be odd. It was chosen to be equal to 3. Larger values lead to fact that phase spread of the bunch at the output of the first part of accelerator due to space charge effect and accelerator parameters errors surpasses the phase width of the accelerator second part separatrix.

- At the present design stage two pairs of operating frequencies for the accelerator parts are considered : 330 and 990 MHz (990 MHz is the operating frequency of the second part of meson physics facility linear accelerator at the INR of the USSR Academy of Sciences); 200 and 600 MHz. The first frequency pair is preferable. It enables the RF generator size and cost to be decreased. At the same time the beam dynamics still remains favorable with regard to the particle losses.

- Specific acceleration in both accelerator parts was chosen to be equal to 1 MeV/m.

- According to the world achievements in RF high-power generator design the output power of a single generator in both parts of accelerator was chosen to be equal to 5 MW. The numbers of cavities and generators in accelerator parts are equal to 8 and 100 respectively (with due allowance for 10 per cent reserve and feeder losses).

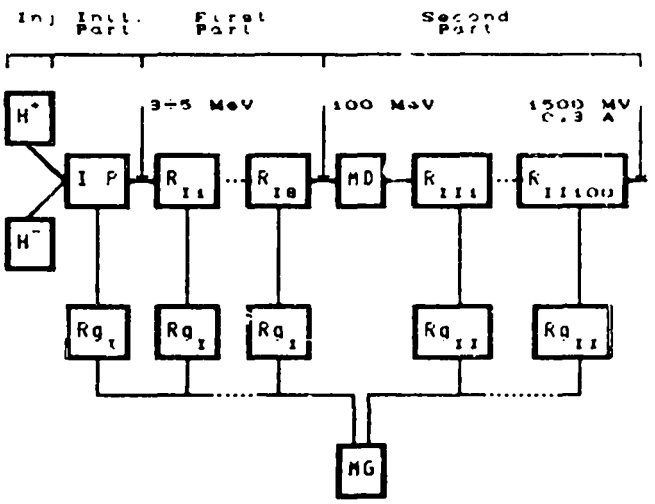

Fig. 1. The diagram of the burner-reactor linear accelerator

Consider the BRLA layout (Fig. 1). The accelerator involves two injectors of H^+ and H^- beams, initial part (IP), first and second parts.

The IP proposed in MRTI is based on the 5 - 8 T superconducting solenoid focusing. The solenoid contains a resonator with opposed vibrators providing for high accelerating wave amplitude E_m. The 1 A value of limiting current corresponds to E_m = 15 kV/cm with equilibrium phase of 70° and injection energy of 200 keV [6,7].

The resonators with drift tubes are used in the first part of the accelerator. Initial energy is 3 - 5 MeV. The main second accelerator part is based on the resonators with washers and diaphragms developed in MRTI for the USSR Academy of Sciences Meson Generator (MEGAN) [8].

An appropriate focusing system for both accelerator parts is that with permanent quadrupole lenses. The option provides for high reliability along with the simplified and unexpensive maintenance. In both accelerator parts a FODO focusing period structure is used which is less sensitive to the magnetic field errors then the FDO structure.

High degree of injected beam current stability (about 1 per cent) is necessary to meet the strict RF field amplitude and phase stability requirements (1 per cent and 1 respectively) of the 500 MW RF power supply system with due allowance for cavity beam loading and desirable system high efficiency.

Regotron - high power RF amplifier

The implementation of RF power supply systems for continuous mode accelerators with total RF power of several hundred MW requires RF generators with at least 5 - 10 MW output power, 70 - 80 per cent efficiency and 20 dB gain. Proposed in MRTI regotron, i.e. a relativistic electron beam generator with distributed RF power extraction system meets the aforementioned requirements [9,10].

One of the generator's peculiar features is the utilization of a certain number N of uncoupled cavities in the power take-off system. The technique provides for the microwave power take-off which is N times that of a single resonator with the given ultimate dielectric strength.

To increase the device efficiency $\eta = 1 - W_f/W_i$, where W_i and W_f are the beam initial and final energies respectively, one has to organize the particle dynamics so as to preserve the bunch configuration and hence the current harmonic at the entrance of the power take-off system through the whole deceleration process till the minimum possible final energy W_f. The well-known principle of the accelerator theory - that of autophasing - is used in the device to solve the problem. The most effective method of the autophasing implementation in a distributed power take-off system is based on the use of cavity pairs. The first cavity of each pair is passive. It is detuned to the higher frequencies with regard to the operating frequency and serves as a beam buncher, whilst the second cavity , which is active, is tuned in to the resonant frequency. It is coupled with the load and takes off the beam power. The typical current first harmonic I_1 variations are plotted in Fig. 2 against the bunch relative energy W/W_o in the power take-off system with (curve 2) and without (curve 1) the autophasing. The autophasing clearly provides for the longer beam energy take-off feasibility and thus for the higher efficiency. Investigations show that regotron is capable of generating 5 - 10 MW HF power in continuous mode with 70 - 80 per cent efficiency.

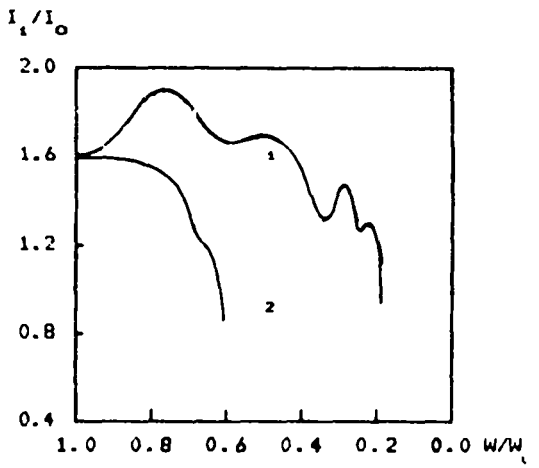

Fig. 2. The dependence of beam current first harmonic on the bunch energy

Initial part of accelerator

The proposal of the radiofrequency quadrupole focusing (RFQ) in the initial part of accelerator is the real basis of the linear proton continuous mode accelerators implementation [11]. However the limiting current of the RFQ initial part of accelerator is less than 1 A.

The next stage of the linear ion accelerators is the development of strong axial magnetic field focusing accelerators with 5 - 8 T superconducting solenoids. In the accelerator the main problem of the initial part - that of focusing - was thus removed. The increase of the synchronous phase in the strong azimuthal magnetic field focusing (SAMFF) accelerators enables the limiting current to be enhanced up to several Amps.

An accelerator based on the SAMFF was proposed in MRTI [6,7]. Experimental proton accelerator with the following parameters was also built.

Output energy	1.5 MeV
Injection energy	100 - 130 keV
Accelerated proton beam current	0.4 A
Operating frequency	196.8 MHz
Beam pulse length	30 - 70 s
Pulse repetition rate	1 pulse/sec
Accelerating-wave amplitude	3.7 MV/m
Focusing magnetic field	7.6 T

The idea of SAMFF was used in the initial part of BRLA. The input and output energies are 100 KeV and 3 - 5 MeV respectively.

Problems

Among the integral problems of accelerator design as a whole name the three main problems - that of economical efficiency, reliability and radiation purity.

<u>Efficiency and reliability problems</u> [12,13]

The total accelerator efficiency is basically

defined by that of RF resonator energy transformation into the beam kinetic energy (resonator efficiency η_r) and electric power transformation into the RF generator energy (generator efficiency η_g). The total efficiency is equal to the product of the two components $\eta=\eta_r\eta_g$.

The resonator efficiency estimate has a form of

$$\eta_r = 1/\left[1+(E_a/I_b ZT^2\cos^2\Phi_a)\right]$$

where I_b is the beam current, E_a is the voltage corresponding to the proton energy gain per unit length (its value is equal to the energy gain per 1 m of accelerator), ZT^2 is the effective shunt resistance of resonators per unit length. If ZT^2 = 40 MOhm/m, φ_a = 30° and I_b = 0.3 A then the resonator efficiency amounts to 0.9.

The accelerator efficiency problem should be solved by the construction of regotron with at least efficiency of 0.8. Then $\eta_r\eta_g \approx 0.7$ and the total accelerator efficiency estimate is 0.6.

Consider the reliability problem. The reliability of the accelerator can characterized by beam availability, which is equal for LAMPF accelerator - 0.85 and for " I-100 " accelerator - 0.99.

The following problems are crucial for solution of the BRLA reliability problem : creation of reliable high-power regotron type generators with service life of at least 10 thousand hours, provision for the reservation scheme, use of passive elements such as permanent magnets in quadrupole lenses, development of the failure prediction system.

Radiation purity problem.

A linear accelerator is considered to be radiation pure if the induced γ-activity doesn't exceed the occupational radiation dose of 28 μGy/hour at the distance of 1 m from the axis of accelerator after 1 hour upon its shut down. The corresponding permissible beam loss in the energy range W = 0.1 - 1 Gev amounts to [4]

$$W\,q \approx 0.05 \text{ GeV nA/m} \qquad (1)$$

The problem is essentially that of limiting the beam loss at the level given by the eq.(1). Under the condition the accelerator maintenance does not require manipulators and can be performed manually. Since the time of direct accelerator engineering service is limited, the manual service is permissible even with the dose power of 0.5 mGy/hour. The corresponding level of beam losses amounts to

$$W\,q \approx 1 \text{ GeV nA/m} \qquad (2)$$

Under the condition (2) and with specific acceleration of 1 Mev/m in the second part of accelerator (i.e. 0.1 - 1.5 GeV) the total permissible beam current losses amount to 3 μA. With the beam current of 300 mA it leads to the permissible relative losses of about 10^{-5}.

Several methods were proposed and developed in MRTI to solve the radiation purity problem. Some of them were applied, in particular, in MEGAN accelerator. Among the methods are the following: beam phase volume filtering, suppression of coherent longitudinal and transverse beam oscillations, contactless beam parameters measurement, beam distortion diagnostics through the beam loss measurement, and residual gas pressure limitation in the H^- beam channel.

The analysis of linear proton accelerator science and technology development and current status along with the modern problems shows that the design and construction of continuous mode 1.5 GeV - 0.3 A linear proton accelerator is feasible and does not encounter with unsolvable science and technology problems.

References

1. S.Schriber,J.Fraser,P.Tunnicliffe, " Future of High Intensity Accelerators in Nuclear Energy ". Proc. X Int. Conf. High Energy Accelerators, v.2, p.408, Protvino, 1977
2. B.Murin,A.Fedotov, "Main Aspects of Proton Linear Accelerators for Nuclear Fuel Breeding". Proc. 6-th All-Union Conf. on Part. Accelerators, v.1, p.241, Dubna, 1978 (in Russian)
3. G.Batskikh, O.Lupandin, B.Murin, A.Fedotov, " On the Way to High Power Linear Accelerators for Long-living Nuclides Transmutation " Preprint 9001, MRTI, Moscow, 1990 (in Russian)
4. B.Murin, B.Bondarev, V.Kushin, A.Fedotov. Ion Linear Accelerators, v.1, Problems and Theory, Moscow, Atomizdat, 1978
5. B.Murin, V.Kulman, L.Lomize, B.Polyakov, A.Fedotov. Ion Linear Accelerators, v.2, Basic Systems, Moscow, Atomizdat, 1978
6. B.Bondarev, A.Kuzmin, B.Murin, V.Pirozhenko, L.Solovyov," The Use of a Superconducting Focusing Solenoid for the Limiting Linear Accelerator Current Enhancement ". Proc. 6-th All-Union Conf. Particle Accelerators, v.1, p.260, Dubna, 1978 (in Russian)
7. B.Bondarev et al. " Experimental RF Proton Accelerator with Superconducting Solenoid Beam Focusing ". Preprint 8901, MRTI, Moscow, 1989, (in Russian)
8. V.Andreev, Zh.Techn.Fiz. ,v.41, No.4, p. 788 , 1971 (in Russian)
9. F.Vodopyanov, B.Murin, " The Method of RF Oscillations Generation with the Use of Relativities Electron Beam ".Proc. RTI, No.22, p. 20, 1975 (in Russian)
10. B.Murin, A.Durkin, O.Shlygin, I.Shumakov, " Superhigh-Power RF Regotron-Type Generator for Linear Accelerators with High Mean Power ", this Conference
11. I.Kapchinsky, B.Teplyakov, Pribory i Tekhnika Eksperimenta, No.2, p.19, 1970 (in Russian)
12. B.Murin, A.Fedotov, " Radiation Purity and Efficiency Problem in Modern Linear Proton and H Ion Accelerators with High Mean Currents ", Atomnaya Energiya, v.38, No.3, p.146, 1975 (in Russian)
13. A.Fedotov, B.Murin," Towards a Radiation-Free Linac of Meson or Neutron Generator ", Proc. 1976 Proton Linear Accelerator Conf., Chalck-River Nucl.Lab., p.377, 1976

SUPERHIGH-POWER RF REGOTRON-TYPE GENERATOR FOR LINEAR ACCELERATOR WITH HIGH MEAN CURRENTS

B.P.Murin, A.P.Durkin, O.Yu.Shlygin, I.V.Shumakov
Moscow Radiotechnical Institute USSR Academy of Sciences,
113519 Moscow, USSR

Theoretical principles and construction scheme of new-type super-power microwave relativistic electron-beam (REB) generator (Regotron) are discussed. Unlike other type of REB-generator, Regotron includes distributed power take-off system. To increase device efficiency the autophasing-principle is used. Such principles of device construction eliminate output power generator limitations. Theoretical basis of general generator construction principles is proposed; the results of mathematical simulations are presented; the different versions of construction scheme are discussed. It is shown that regotron efficiency can reach 70...80 % at output power levels up to 10 MW CW.

Due to recent development of large accelerating complexes (LEP, UNK, SSC, etc.), the RF amplifiers with high mean power become of ever increasing interest [1]. Reliability and efficiency requirements of such RF devices are increasing as well. This is specifically the case with the RF power-supply generators of proton linear accelerators which now under consideration for use in the burner-reactors. A total mean power of about 1 GW is necessary to accelerate a continuous beam in such accelerator. As preliminary investigation shows, the implementation of the devices has to be based on RF generators with at least 5...10 MW output power, 70 per cent efficiency and 20 dB gain. It stands to reason that the most powerful up-to-date devices, namely klystron amplifiers, are unable to meet the aforementioned power and efficiency requirements. An alternative RF system implementation with relatively modest generator parameters results in significant size and weight growth and increased maintenance problems.

A possible way out was outlined in the paper [2], where a new method of microwave generation was proposed. The method makes use of a bunched relativistic electron beam passing through a chain of N cavities and thus enables high efficiency to be obtained in the device with distributed RF power extraction system.

The peculiar feature of the device called "regotron" is the utilization of a number of uncoupled cavities in the power take-off system. The technique provides for the microwave power take-of which is N times that of a single cavity (which is the case with a klystron where the power taken off of the beam is limited by the ultimate dielectric strength). Implementation of the method enables one to place the output cavities in the vicinity of the load (e.g. near the accelerating sections of a particle accelerator) thus both simplifying the microwave system and decreasing its power loss.

The installation diagram is presente in Fig. 1. The generator involves high voltage injector (I), buncher (B), distributed power take-off system (PS) and collector (C).

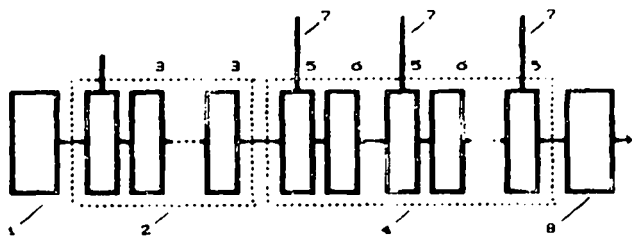

Fig.1. RF installation diagram.
1 - high-voltage injector (I) 2 - buncher (B)
3 - passive cavities of the buncher
4 - distributed power take-off system (PS)
5 - active cavities power take-off system
6 - bunching cavities of the power take-off system 7 - output cavities 8 - beam collector

The preferable design scheme of the electrostatic accelerator is that of Cockroft-Walton. In the continuous-beam accelerator one can also use an alternative high-voltage source in the form of dc high voltage transmission line (U > 500 kV). The latter simplifies both the generator design and accelerator RF system as a whole.

Quite a novel design approach is needed in the resonator part of the generator. The stretch of the power take-off system is limiting the perveance of the beam which has to reach the finite minimal energy after the deceleration in spite of the destructive action of the Coulomb forces. The perveance has to fall into the (0.1 0.5) * 10 $A/V^{3/2}$ range where effective beam deceleration is possible. This requirement is easily met with the 10 - 30 A relativistic beams.

If the generator design is based upon the klystron bunching then the initial beam energy has to be less than 700 keV - the limiting value for the klystron bunching to be still effective. If the initial energy W_o exceeds 1 MeV then the magnetic bunching is preferable.

The distributed nature of the power take-of system complicates the bunched beam dynamics problems. The device efficiency $\eta = 1 - W_k/W_o$, where W_k is the beam finite energy at the collector. To increase the efficiency and to decrease the collector power one has to organize the particle beam dynamics so as to preserve bunch configuration

and hence the current harmonic through the whole deceleration process and to provide for the minimum possible value of W_k. The well-known principle of the acceleration theory - that of the autophasing - is used in the device to solve the problem. The most effective method of the autophasing implementation in the distributed power take-off system is based on the use of cavity pairs [3]. One of the two cavities (see (5) in Fig. 1) is passive. It's detuned to the higher frequencies with regard to the signal frequency while the anotner cavity (which is the active one, see (5) in Fig. 1) is tuned in to the resonant frequency and coupled with the load. Thus the voltage U_a which is excited in the active cavity, is in-phase with the first harmonic of the beam current I_1 whilst the phase lead of the voltage U_p in the passive cavity with regard to the first harmonic of the current is about $\pi/2$ (see Fig. 2). The beam is affected by the net voltage U_Σ with the phase lead with regard to the current first harmonic. This phase lead plays the role of the equilibrium phase and the bunches fall into the autophasing regime. If R_1 and R_2 are the shunt resistances of the cavity pair then the net effect of the pair on the beam is equal to that of a signal cavity with the shunt resistance $R_\Theta = \sqrt{R_1^2 + R_2^2}$ and the detuning angle φ_Θ ($\cos\varphi_\Theta = R_1/R_\Theta$). Thus the autophasing regime with the desired equilibrium phase is realizable through the proper choice of the cavity parameters.

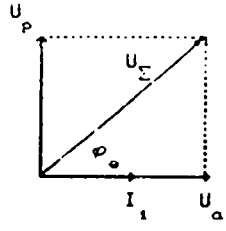

Fig.2.

Klystron bunching in the regotron has its specific features. Since the particles in the power take-off system are oscillating with regard to the equilibrium phase, the main problem of the bunching is to provide for the maximum capture into the stable oscillation domain. The boundaries of the domain are usually defined by the following inequalities $|\varphi - \varphi_\Theta| \leq 60^\circ$, $|\Delta W/W| \leq 10\ \%$. In the case current harmonic at the entrance of the power take-off system doesn't define unambiguously the device efficiency. During the deceleration the value of current harmonic increases and the mean current harmonic over the whole take-off system exceeds the input value.

A computer simulations of bunching and power take-off processes was performed with the aim to investigate the beam dynamics to optimize the generator parameters over the wide frequency range [3-7]. The generator efficiency increase due to the autophasing was confirmed by the computer simulation results. A typical example is presented in Fig. 3. The calculated current harmonic variation is plotted against the relative bunch energy in the energy take-off system with (curve 1) and without (curve 2) the autophasing. The parameters were as follows : W_o = 700 keV, $\Delta W/W$ = 0.08 per cavity, Equilibrium phase of the autophasing $\varphi_\Theta = 60^\circ$. The autophasing clearly provides for the longer beam energy take-off feasibility and thus for the efficiency up to 80 per cent. The efficiency of the power take-off system without the autophasing is about 40 per cent.

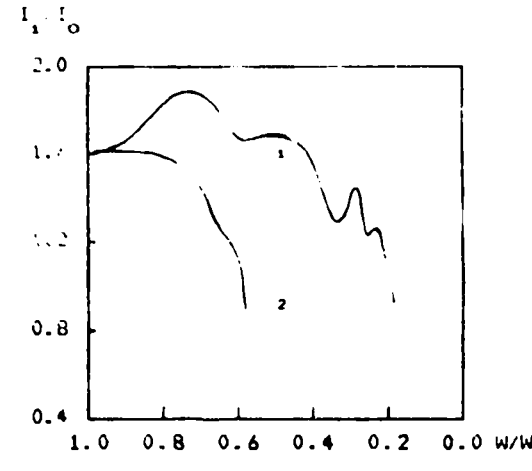

Fig.3.

The higher is the value of W_o, the higher are both the efficiency and the output power of the system.

The calculated performances of regotron with different operating frequencies are presented in Table I. The efficiency, dimensions of buncher L_b and power take-off system L_{ps} as well as the number of active cavities L_a were obtained through the optimization based on the calculation results of papers [3-6]. At present a pulsed regotron model with 3000 MHz operating frequency is being built in the Moscow Radiotechnical Institute of the USSR Academy of Sciences.

TABLE I

Calculated Performances of Regotron

f[MHz]	P[MW]	η[%]	I_o[A]	W_o[MeV]	L_b[m]	L_{ps}[m]	N_a
350	5÷10	70÷80	10÷30	0.5÷0.7	9÷12	4÷5	5÷10
600	5÷10	70÷80	10÷30	0.5÷0.7	6÷8	3÷4	6÷12
900	5÷10	70÷80	10÷30	0.5÷0.7	4÷4.5	1.5÷2	6÷12
3000*	3.5	70	10	0.5	2	1	7

* - pulsed regotron model

Main computer simulation results will be checked against the experiments with the model and different system will be tried out. The calculated performances of the regotron which is intended for the energy supply system of the burner-reactor's linear proton accelerator are given in Table II.

TABLE II
Calculated Performances of Regotron for burner-reactor's linac

Beam parameters	
Current, A	10
Initial energy, keV	500
Beam radius, cm	1.5
Buncher parameters	
Number of cavities	3
Input power, kW	2
Operating frequen , MHz	600
Cavity characteristic wave impedance, Ohm	130
Cavity Q-factor	10500
Length of the buncher, m	7
Power take-off system parameters	
Number of cavities	7
Cavity characteristic wave impedance, Ohm	206
Cavity Q-factors : active	22
passive	14000
Equilibrium phase, deg	60
Output power, MW	5.8
Efficiency, per cent	77
Length, m	3

The choice of the beam initial energy W_o = 500 keV enables the well developed dc energy supply system to be used. In Fig. 4 the beam current first harmonic variation along the device is presented (B - buncher, PS - power take-off system).

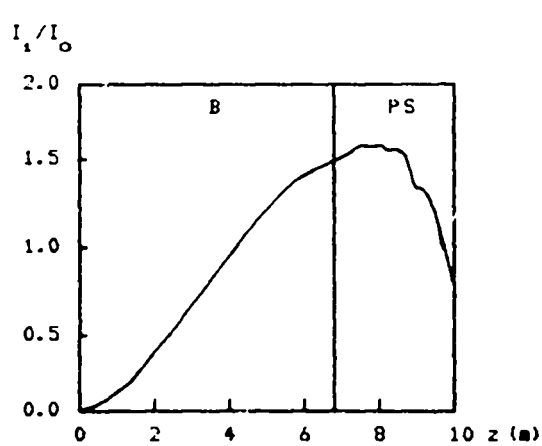

Fig.4.

The resonant part of the generator consists of the toroidal cavities with the TM_{010} wave. The focusing system involves a number of solenoidal lenses with magnetic induction which is less then 0.1 T. A constant magnet design is under consideration now.

This investigation shows that the proposed superhigh-power RF regotron-type generator is to produce 5 - 10 MW RF power in continuous mode with the 70 -80 per cent efficiency. The regotron-type generators should also be used in the energy supply systems of high-energy particle accelerators with high mean currents.

References

1. B.P.Murin. High power RF supply systems for particle accelerators Preprint 833, RTI, USSR Academy of Sciences, 1983 (in Russian)
2. F.A.Vodopyanov, B.P.Murin. RF generation method based on the use of relativistic electron beam. In : "Accelerator technology", RTI, USSR Academy of Sciences, 1975, p. 20 - 33 (in Russian)
3. B.P.Murin, L.G.Lomize, A.E.Sominski. Deceleration of relativistic electron bunches in stretched cavity system. In : "Relativistic microwave generators. Theory and technology", RTI, USSR Academy of Sciences, 1988, p. 96 - 100 (in Russian)
4. B.P.Murin, A.P.Durkin, O.Yu.Shlygin. Electron beam bunching in a microwave quasicontinuous-mode generator. Ibid., p. 76 - 84 (in Russian)
5. B.I.Bondarev, A.P.Durkin, O.Yu.Shligin. Klystron bunching of charge particle in linear accelerator. In : "Particle accelerators", MRTI, USSR Academy of Sciences, 1989, p. 44 - 48 (in Russian)
6. B.I.Bondarev, A.P.Durkin, O.Yu.Shligin. Particle dynamics in the multicavity bunched beam power take-off system. In : "Physical principles of the plasmochemical reactors with REB", MRTI, USSR Academy of Sciences, 1989, p. 113 - 122 (in Russian)
7. V.N.Litvinov, A.P.Durkin, O.Yu.Shligin. Electron beam dynamics in the multicavity energy transformation system. Electron Technology, "Microwave electronics", 1987, No. 4 (398), p. 66-67 (in Russian)

OPERATING EXPERIENCE WITH THE IMPELA-10/50 INDUSTRIAL LINAC

J. Ungrin, S.B. Alexander, S.T. Craig, G. Frketich, V.A. Mason,
I.L. McIntyre, M.P. Simpson, D.L. Smyth, R.J. West, and B.F. White
AECL RESEARCH, Chalk River Laboratories
Chalk River, Ontario, Canada, K0J 1J0

ABSTRACT

AECL is building and marketing the IMPELA family of high-power linear electron accelerators designed specifically for the industrial market. The accelerators are built around an L-band on-axis coupled structure that is assembled in a modular fashion and is driven in the long-pulse mode with a modulating anode klystron. A wide range of average power is achieved with the same basic accelerator components by simply changing the beam duty factor and the size of the power supply. The control system for the IMPELA family is built around a simplified operator interface that incorporates automatic sequences, fast control loops, self-diagnostics and the instrumentation that is key to reliable, simple operation and rapid maintenance. The first member of the IMPELA family, the 10 MeV, 50 kW, IMPELA-10/50, is a highly instrumented industrial prototype that has been operating at full power since 1989 November. It is now undergoing prolonged testing at Chalk River Laboratories.

INTRODUCTION

AECL is building and marketing the IMPELA family of high-power electron linacs that has been designed specifically for the industrial irradiation market.[1] These accelerators are designed conservatively around an L-band standing-wave, on-axis coupled accelerating structure and are driven in the long-pulse mode by a modulated anode klystron. High beam loading (typically 60-65%) is achieved with a modest output current (typically 100 mA). This high beam loading, combined with an optimized rf cavity design, ensures good rf efficiency for the accelerator. A wide range of average power can be achieved with the same accelerator components by varying the duty factor while retaining the conservative energy gradients and beam current. The single-resonator, 1300 MHz structure is an assembly of modules that has been designed with adequate cooling for operation at duty factors up to 100%. The 10 MeV, 50 kW, IMPELA-10/50 (Fig. 1) under test at Chalk River operates at a 5% duty factor (typically 200 μs pulse lengths at 250 pps). This accelerator has been built as an industrial prototype and is being used as a fully instrumented test bed where a detailed characterization of the existing hardware and of several additional variants under development is possible. The prototype is equipped with a wide range of diagnostics to allow rigorous testing of both the physics and the engineering design aspects. It is in the process of undergoing extended lifetime testing to ensure that all systems can meet the high reliability required by industry.

Details of the IMPELA accelerating structure,[1] rf system[2] and the control system design[3] have been previously reported. This paper reports the operation at full power.

AUTOMATED CONTROL

The IMPELA family of accelerators have been designed for industrial use. The control system is built around a GE-FANUC Series-6 industrial programmable logic controller (PLC) and uses a simplified operator interface with automatic sequences, hardware and software-based control loops and self-diagnostic instrumentation that is largely transparent to the industrial user, who will generally lack the specialized skills or knowledge normally required to operate a high-power rf linac. The control system has been designed with the capability to operate with two redundant processors for those applications that require very high reliability. In addition to the PLC system, a set of high-speed hardware loops has been developed to provide the machine protection actions required to act on a microsecond timescale.[3] These high speed loops which act to trigger the high-voltage power supply crowbar or to disable the rf drive or the electron gun current are supervised and monitored by the PLC.

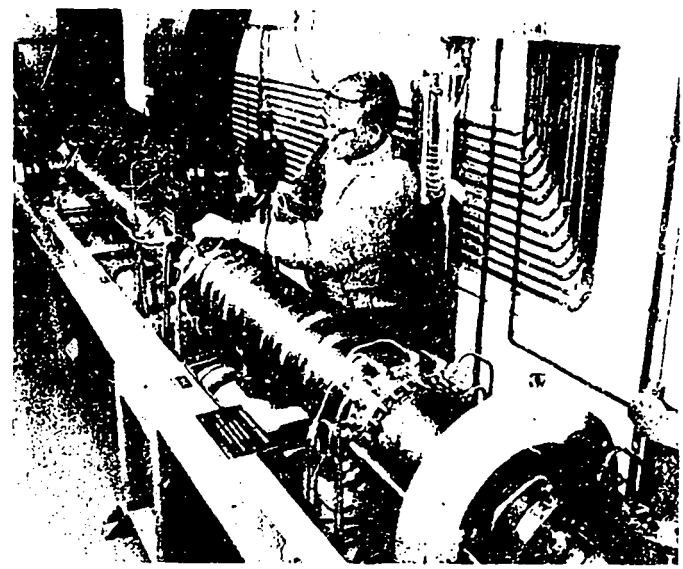

Fig. 1 View of IMPELA-10/50 from the injector end.

A set of automatic sequences controlled by the PLC have been developed to provide an industrial operator with a reliable and convenient means of starting and stopping the irradiator operation. These sequences have been based on the commissioning and operating experience gained with the prototype accelerator. They provide an orderly path through turn-on of cooling systems, warm-up of the filaments and other devices that require time to stabilize, application of high voltage to the electron gun and rf systems and finally the turn-on of all the accelerator systems at low beam power with all the applicable control loops closed. The set points for the control loops and all the controlled devices are derived from a set of parameters previously saved in the PLC memory. The sequences have reverse paths to control shutdown through to a full power-off condition.

All the normal interlocks and alarms are active during the execution of the automatic sequences. A sequence action that is inhibited by an interlock or alarm causes the sequence timer to fail and to abort the sequence. An aborted sequence generates an alarm

to the operator. In addition to the alarm, the sequence state is indicated on the operator display, which shows the state of each sequence: inactive, executing, complete or aborted.

The automatic sequences have become a routine means of operating the accelerator and subsets of the full sequence are regularly used to control operation during tests of various procedures or of equipment performance.

CONTROL LOOPS

The operation of IMPELA is greatly simplified by the use of a number of automated feedback control loops. Seven independent loops have been developed to control key accelerator parameters. These include the conventionally-controlled accelerator parameters, beam energy (structure field amplitude), output beam current, rf drive frequency, klystron high voltage and temperature control of the cooling circuits both for the water-cooled accelerator and for the oil-cooled rf modulator. In addition, a control loop has been developed to regulate the filament heating in the electron gun to compensate for power deposited in the cathode by off-phase electrons reflected to the electron gun by the accelerator. This latter effect, normally absent on most research linacs, is significant on IMPELA, which uses a simple low-voltage electron gun that is closely coupled to the accelerator and does not use an independent buncher with its associated rf drive and control requirements. The filament control loop maintains a constant cathode temperature by adjusting the filament power to maintain a fixed filament resistance.

Dedicated high-speed electronics have been developed to control the field amplitude to ± 2% of setpoint on an intra-pulse timescale. Intra-pulse control has been introduced to reduce the energy spectrum and to provide a more uniform dose distribution from the accelerator. Control of the structure rf field on this timescale is particularly significant for a long-pulse accelerator where significant gain change will occur in the klystron due to power supply droop. Additional important factors affecting the design of the loop are the wide variation in duty factor (pulse lengths of 50-500 μs at repetition rates from 1 to 500 pulses per second), long loop lengths at relatively high Q (≈4000) and a wide range of operating temperature.

The block diagram shown in Fig. 2 illustrates the amplitude control feedback circuit. Temperature controlled crystal detectors convert structure rf signals into an average amplitude envelope that is compared with a setpoint supplied by the PLC. A gated Proportional-Integral (PI) controller processes this amplitude error signal to produce the required attenuation for a PIN modulator which is in-line with the drive chain. Thus, the drive power is automatically adjusted to bring the structure fields to the desired amplitude independent of beam current, pulse length or frequency tuning errors.

The gated PI controller forms the heart of the loop. Wideband, 6 MHz, proportional control provides rapid correction for small disturbances while, over a microsecond timeframe, a gated integrator corrects larger disturbances and drift. Bandwidth constraints imposed by the rf drive chain and by the loop transit time prohibit use of a large proportional gain. The controller employs inter-pulse memory and sequential deployment of controller terms to achieve the necessary integral gain without overshoot. A portion of the mid-term pulse integral term is stored for use as the initial value with the next pulse. Fast yet smooth pulse turn-on is accomplished by first applying the drive power as stored in the integrator memory and engaging the proportional control action. After a delay of ≈4 μs the integral term is engaged. Thus the integrator acts only when the field is close to the desired strength and upsets at the leading edge of each pulse are avoided.

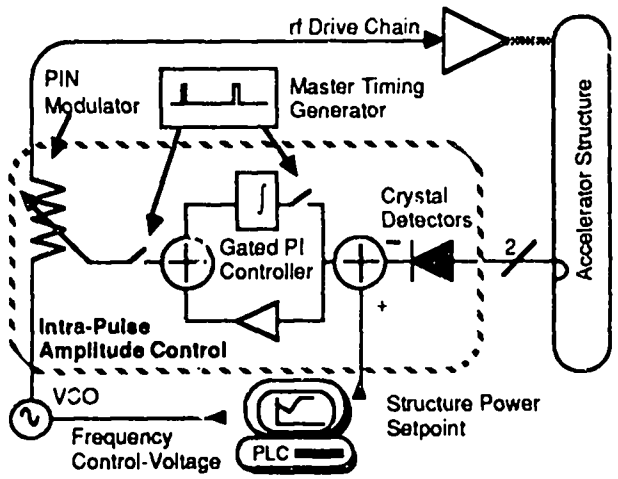

Fig. 2 Block diagram of the field amplitude control circuit.

A comparison of intra-pulse performance with and without feedback control is shown in Fig. 3. Operating experience has shown that the controller can be readily tuned to regulate the field within ± 0.5% (voltage) following a 6 μs pulse rise and settling time.

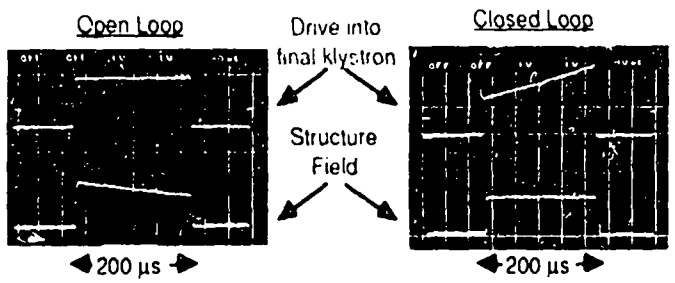

Fig. 3 Structure field level control.

The remaining six control loops are implemented by Proportional-Integral-Differential (PID) controllers via the software in the PLC. The beam current, drive frequency and klystron voltage loops employ zero-droop sample and hold circuits which sample the process variable at a predetermined time in the pulse and hold this value for asynchronous input to the PLC. Conventional PLC algorithms are then used to control these pulsed variables on a timeframe of a few seconds. Coolant temperatures and electron gun filament power are not pulsed variables and the PLC PID controller is applied directly to these loops. The operation of the six PID loops are summarized in Table I.

EXPOSURE DOSE UNIFORMITY AND ASSURANCE

The industrial application of radiation from a high-power electron linac requires distributing the beam power through a product volume. In most cases the beam power is spread over an exposure area and the product is conveyed in a direction normal to the major axis of the exposure pattern at a carefully controlled rate.

Table I
Software-Based Control Loops

Loop	Control Variable	Response Time	Regulation
Current	Wehnelt Voltage	2 s	±0.1%
Frequency	VCO	2 s	±0.5°
Klystron HV	SCR Firing Angle	10 s	±0.3%
Cathode Temperature	Filament Current	10 s	±0.3%
Water Cooling	Secondary Flow	20 s	±0.3°C
Oil Cooling	Secondary Flow	60 s	±0.3°C

The processing of a specific product requires a uniformity of dose delivered throughout the product volume. To obtain the volume uniformity with good electron economy a variety of measures may be applied, including the use of "tailored" beam exposure distributions, external scattering surfaces or the use of a dose build-up layer.

The IMPELA prototype employs a low frequency (5 Hz) magnetic spot scanner that deflects the electron beam to produce a pattern of overlapping spots, each 8-10 cm in diameter, at the exposure plane[4]. The scanner uses a simple iron magnetic circuit for the magnet. To overcome the non-uniform distribution that results with such a magnet due to eddy-current and hysteresis effects when driven with a simple triangle-wave drive current, the scan magnet drive system applies an appropriately corrected, deformed current excitation, which produces a linear deflection of the beam. A dose uniformity within ± 5% across an 80 cm wide distribution has been achieved using this method (Fig. 4). This method can equally be used to tailor an appropriate non-uniform exposure dose that will result in improved beam usage and dose uniformity for specific products.

The performance of the beam scanner is dependent on the stability of the beam energy and the scan drive electronics. Probes positioned at the ends of the scan pattern sense the maximum deflection for each scan cycle. A control loop that regulates scanner operation on the basis of these signals is being developed. This loop will regulate both the position of the centroid of the beam and the scan width.

Many industrial applications require continuous monitoring of a number of key accelerator parameters to demonstrate the stability of the radiation pattern delivered at the end of the accelerator. All the parameters essential to characterize the stability of the delivered beam are logged and archived by the PLC via a dedicated data logger and a Cimstar computer (an industrial IBM-AT compatible) with a FIX software package.

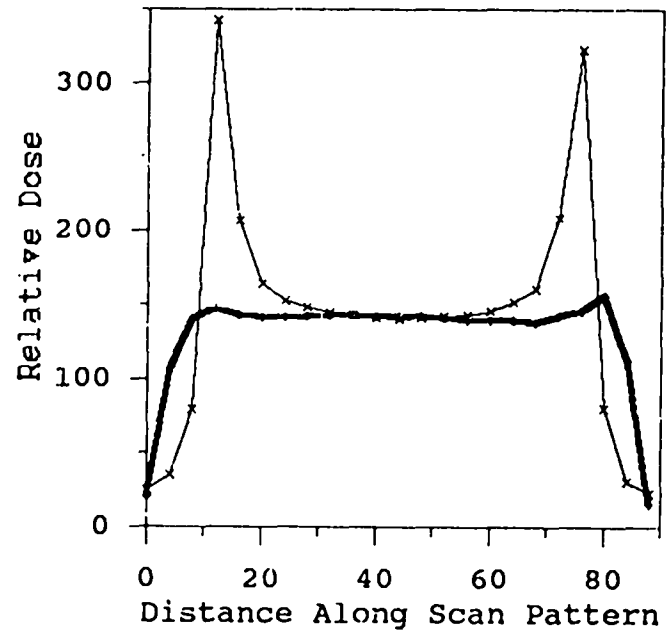

Fig. 4 Exposure dose distribution 15 cm beyond the linac with triangular (light line) and shaped (dark line) wave form.

ACCELERATOR PERFORMANCE

The IMPELA-10/50 prototype has been operating at full power at Chalk River since 1989 November. Extensive testing has been carried out with the automatic sequences, feedback control loops and exposure dose control system and significant operating experience has been gained. Several minor improvements have been incorporated to further simplify operation. The degree of automated control has reached a point where the accelerator will routinely operate uninterrupted at full specifications for periods of up to 10 h with no operator intervention. This operating simplicity combined with the excellent regulation of the energy and current loops and the ability to tailor the exposure dose at the exit of the linac make IMPELA a powerful, user-friendly accelerator for the non-expert industrial user. Extended lifetime-testing of the machine hardware and software systems continue on this unique industrial prototype.

REFERENCES

1. J-P. Labrie et al., Nucl. Instr. and Meth. B40/41(1989)1153.
2. J-P. Labrie et al., Proc. 1989 IEEE Part. Accel. Conf. Vol.1 (1989), 153.
3. C.B. Lawrence et al., Proc. Eur. Part. Accel. Conf. EPAC (1988), 1237.
4. V.A. Mason and R.W. Davis, 1988 Lin. Accel. Conf. Proc., CEBAF-Report-89-001, 553.

AN ELECTRON LINAC FOR INTRAOPERATIVE RADIATION THERAPY

Gerhard T. Konrad
Siemens Medical Laboratories, Inc., Concord, CA 94520

Abstract

Several medical linear accelerators for intraoperative electron therapy have been built by Siemens. The first one, at the University of Texas M.D. Anderson Cancer Center, has been in clinical use for more than one year. The linac is isocentrically mounted in a gantry that can rotate ±115° from the vertical. The energy of the electron beam is defined and controlled through the use of a 270° achromatic bending magnet. The source to rotation axis distance is 100cm. The radiation field size is controlled by the inserted size of the annulus fixture and the applicator cone. Dose rate settings of 300, 600, and 900 cGY/min are available. Power is normally supplied by a 2.9 MW magnetron. Currently a machine is being commissioned that is powered by a klystron amplifier system capable of as much as 7.5 MW. The latter will permit operation from 6 MeV to 21 MeV. On the other hand, the magnetron driven machines can operate up to 18 MeV.

Introduction

The number of institutions performing intraoperative therapy has been increasing in recent years.[1] Usually such procedures are performed by doing the surgery in the operating room and then transporting the patient to the radiation therapy room where the irradiation is performed. It can be done in this way because many radiation therapy machines have both X-ray and electron treatment modes for improved flexibility. The machine to be described here is permanently located in the operating room, thus eliminating the need for transporting the patient back and forth between two rooms. Siemens has developed an accelerator system with only electron beams to fill the above need. The electron mode is appropriate and adequate for this application because surface treatment is usually desired due to the fact that the tumor is exposed during the operation.

The machine is wall mounted so as not to waste space in the operating room. All components requiring service, such as the RF power, cooling, and control systems, are outside of the operating room. RF power is fed through the wall and then through a rotary joint, into the gantry and into the accelerator. Thus no cooling fans and high voltage electrical systems are located in the operating room.

In many instances, intraoperative procedures are performed with electron energies of less than 18 MeV. This need was met by Siemens with the Mevatron ME, which makes use of an RF system containing a magnetron. Recently, a machine was built and designated the KE. This machine is capable of electron energy up to 21 MeV using the same accelerator but a klystron driven RF system.

RF System

The heart of the Mevatron is the electron linac and its associated RF system. A block diagram of the major components used is shown in Fig. 1.

As in all Siemens Mevatrons, and in fact as in most commercial radiation therapy machines, the accelerator consists of a side-coupled cavity structure. The foundations for this technology were laid at Los Alamos during the 1960s.[2] The accelerator operates in the standing wave mode at a frequency of 2998.5 MHz. Table I lists operating parameters at the maximum energy available from the system.

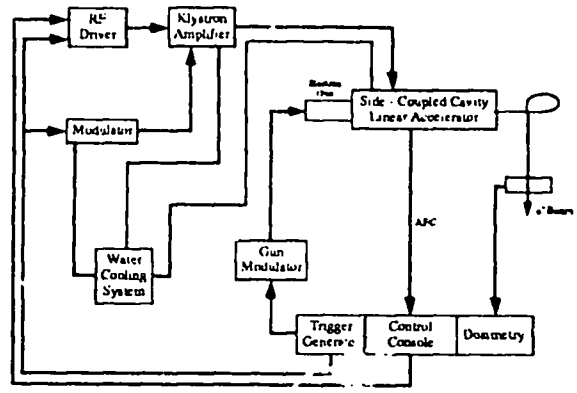

Fig. 1. Functional block diagram

TABLE I
Representative Operating Parameters

Operating Frequency	2998.5 MHz
Electron Energy	21 MeV
RF Power	4 MW
Accelerating Gradient	15 MV/m
Peak Surface Gradient	~30 MV/m
Kilpatrick Gradient	45 MV/m
Peak Injected Current	10 mA
Capture Ratio	<10%
Beam Loading	~1%
Beam Pulse Length	3 microsec
Beam PRF	135 Hz
Radiation Output	900cGy/min

A photograph of the accelerator is shown in Fig. 2.

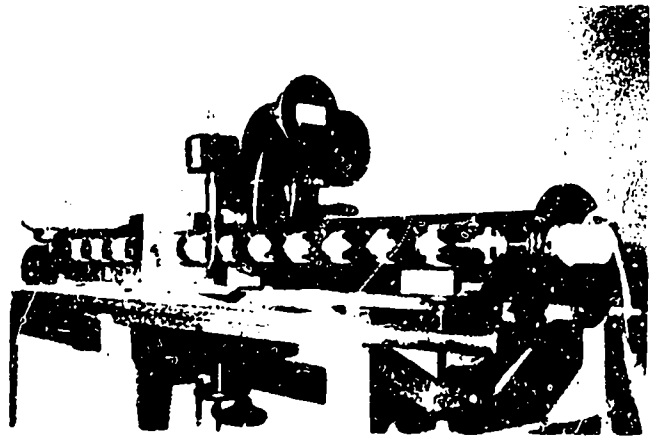

Fig. 2. Side-coupled cavity linear accelerator

A 2 l/s ion pump is provided for monitoring vacuum quality in the accelerator. Figure 3 shows many of the RF components in the gantry and in the rotating structure.

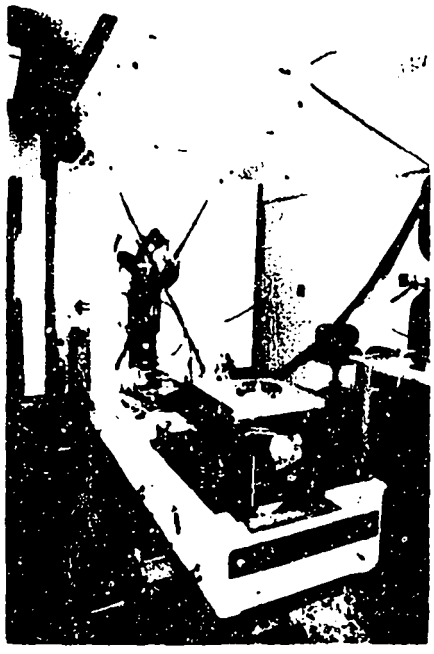

Fig. 3. Intraoperative radiation therapy machine assembly

Note that the current needed for this application (900cGy/min max.) is only 10mA, resulting in very light beam loading. A relatively low capture efficiency is also acceptable. The dose rate required for treatment is obtained by adjusting the repetition frequency.

When the beam leaves the accelerator it passes through a 270° achromatic bending magnet. This magnet serves as an energy filter and as a beam focusing element. Primary and secondary dose chambers monitor the beam, as well as flatness and symmetry, dose rate and dose per pulse for beam control purposes.

RF power is supplied by a Thomson CSF TH2066U klystron capable of 7.5 MW peak power. A circulator in the waveguide run insures that the tube always works into a well-matched load. The operating frequency of the accelerator is tracked by an AFC loop which controls the RF driver. The klystron modulator is a conventional line-type modulator[3] with a pulse transformer. The maximum operating voltage required by the tube is 160KV. Individual pulse energy is controlled by a command charging system consisting of a pass tube. In that way the length of time during which the thyratron has to hold off high voltage is minimized. Also, the energy per pulse can be maintained constant over a wide range of repetition frequency. A photograph of the modulator and klystron is shown in Fig. 4. Component cooling is provided by a closed loop water circulation system containing a heat exchanger to industrial water. The cooling system operates at ~40° C.

Description of Machine

The electron source to the rotation axis distance is 100cm, which is common in the industry. The isocenter height above the floor is adjusted at installation between 112 and 135cm. The gantry rotation range is ±115° from the vertical. For simplicity, and to insure reliability, all adjustments needed in the gantry to set up the system for treatment, except gantry rotation, are manually made. The primary scattering foils that must be in place for each energy setup are manually inserted by rotating a carousel. An interlock prevents a mismatch between the energy selected at the console and the foil chosen. A shaped secondary scattering foil is used to flatten the beam.[4]

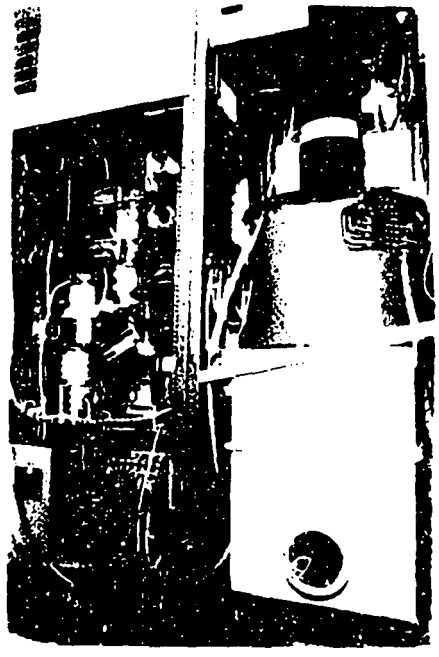

Fig. 4. RF system showing klystron and modulator.

Figure 5 shows a cross-sectional view of the entire machine including the gantry.

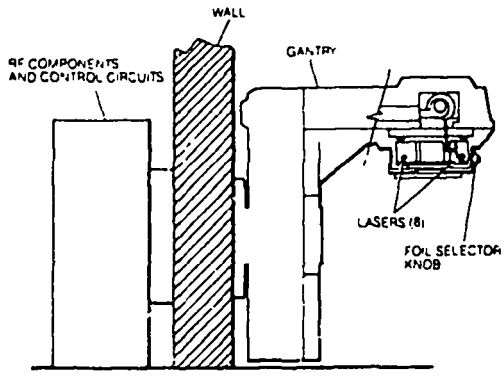

Fig. 5. Mevatron ME and control cabinets as installed

In Fig. 6, a view of the treatment head and the applicator cone may be seen.

The beam is collimated in two steps by round collimators attached to the annuli fixture and inserted into the accessory holder. The size of the precollimators selected depends on the field size needed for treatment. This machine uses a laser light alignment system so that there is no electrical or mechanical contact to the patient. This minimizes the chance for patient injury. The electron applicator cone is attached to the table side rails and can be prepositioned when the operating

table is away from the machine or under it. The eight laser lights project dots to the surface of a round plate mounted on the applicator cone. When the tip of the cone is at isocenter and the electron beam axis and cone axis coincide, the eight dots coalesce to four dots equally spaced on a ring engraved on the surface of the alignment plate.

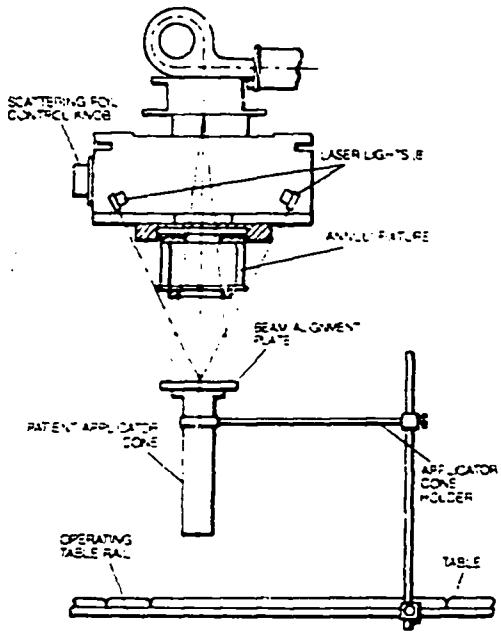

Fig. 6. Cross section of treatment head and patient applicator cone system

Operation of Machine

The operating conditions for the machine are shown in Fig. 7, where electron energy is plotted as a function of RF power. Note that the required energy range of 6 to 21 MeV is covered by varying the klystron output power from 1MW to 4MW. The klystron output power is adjusted by controlling the klystron beam voltage and current. The bending magnet current setting automatically corresponds to the energy selected.

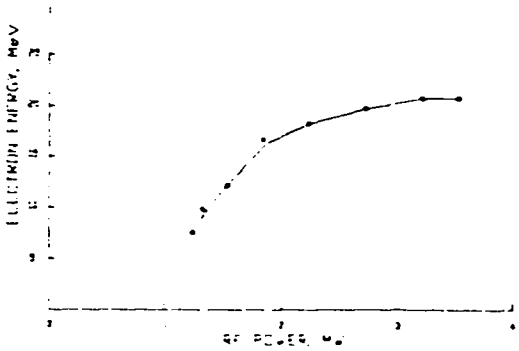

Fig. 7. Accelerator energy vs. RF power

For intraoperative radiation therapy procedures, smaller fields than are used in regular applications are sufficient. The maximum fields needed can be obtained from a beam flattened in a 20cm diameter field. Because the field requirements are smaller for this machine, thinner scattering foils can be used. The thinner scattering foils produce less X-ray contamination and contribute less energy spread in the beam at isocenter compared to thicker foils. The small energy spread results in a steeper drop-off of the depth dose curve. Figure 8 shows typical depth dose curves.

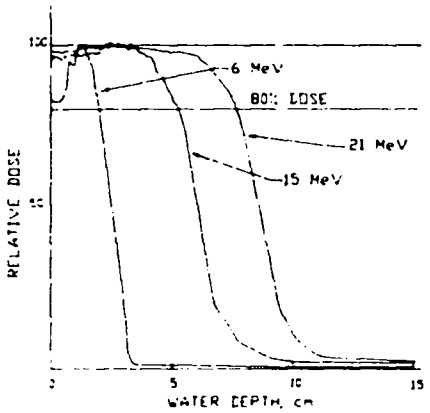

Fig. 8. Depth dose curves from water phantom

Some dose profiles for 15 MeV at a depth where the maximum dose occurs are shown in Fig. 9. These data were taken in a solid phantom and cylindrical applicator cones of the size indicated were used.

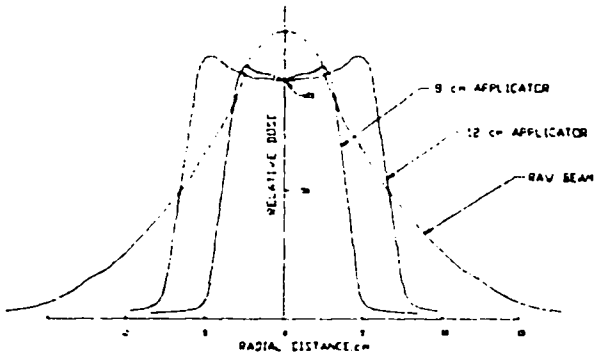

Fig. 9. Dose distribution with 15 MeV beam

References

1. T. A. Rich, "Intraoperative Radiotherapy," Radiotherapy and Oncology, vol. 6, 207 (1986)

2. E. A. Knapp, B. C. Knapp and J. M. Potter, "Standing Wave High Energy Linear Accelerator Structures," Rev. Sci. Instr., vol. 39, 979 (1968)

3. G. W. Ewell, "Radar Transmitters," McGraw-Hill (1981)

4. A. Green, K. Hogstrom, A. Shin and D. Oline, "Methodology for Design of Dual Scattering Foil Systems For Flattening High Energy Electron Beams," Proc. 1990 AAPM Annual Meeting, St. Louis, MO (1990)

INJECTOR SYSTEM OF HIMAC

S. Yamada, T. Hattori*, A. Itano, M. Kanazawa, A. Kitagawa, T. Kohno, Y. Miyazawa†, O. Morishita‡, K. Noda, H. Ogawa, K. Sato, Y. Sato, K. Sawada‡, M. Sudou, E. Takada, T. Yamada and Y. Hirao

National Institute of Radiological Sciences
4-9-1 Anagawa, Chiba 260, Japan

Abstract

This paper describes a brief review of a design of an injector system of a synchrotron facility for heavy ion therapy, HIMAC. Some results of rf measurements of an Alvarez type acceleration cavity are also described. Construction of major components of the injector system started in 1987, and will be completed within 1992.

Introduction

As a direct expansion of our long experience with proton, neutron and photon radiotherapy, a heavy ion synchrotron has been adopted for the clinical treatment of tumors at NIRS.[1,2] The superiority of the heavy ion therapy is characterized by excellent dose localization. Another important feature of this type of therapy is a very high value of a linear energy transfer to tumor cells resulting in a low oxygen enhancement factor.

HIMAC is an accelerator facility dedicated to medical use especially for the clinical treatment of tumors. It will be the first heavy ion synchrotron complex in a hospital environment in Japan. The accelerator consists of a 100 MHz injector linac, two separated function type synchrotron rings and a beam delivery system.

The maximum output energy of HIMAC is 800 MeV/u for ions with $q/A = 1/2$. The ion species required for the clinical treatment range from ^{4}He to ^{40}Ar. A beam intensity from the HIMAC synchrotron is determined so that a dose rate as high as 5 Gy/min·ℓ is realized in a 14 (diameter)×10 (depth) cm^2 irradiation volume. The irradiation of heavy ions can be completed within a few minutes, and a set of more than ten times of such irradiation is required through about a one month to treat human cancers.

The facility has three treatment rooms two of which are equipped with vertical beam lines. The horizontal beam will be introduced to the two treatment rooms. The construction of the facility will continue until fiscal year 1993 when the clinical trials are expected to start.

Injector design

The injector system of HIMAC comprises a PIG source for light ions, an ECR source for heavier ions, an RFQ linac of 100 MHz and three Alvarez type linac tanks with the same frequency. A debuncher cavity is to be installed in an output beam transport line in order to reduce a momentum spread. The system has no charge stripper either between or before the linac tanks, and will accept heavy ions with a charge-to-mass ratio as small as 1/7.

*Research Laboratory for Nuclear Reactors, Tokyo Institute of Technology, Ohokayama, Meguro-ku, Tokyo 152

†The Institute of Physical and Chemical Research, RIKEN, Hirosawa, Wako-shi, Saitama 351-01

‡Sumitomo Heavy Industries LTD., Soubiraki-cho, Niihama-shi, Ehime 792

Table 1
Injector specification.

Ion species	^{4}He to ^{40}Ar
Charge to mass ratio	> 1/7
Ion source type	PIG & ECR
Frequency	100 MHz
Repetition rate	3 Hz Max.
Duty factor	0.3% Max.
Acceptance	0.6 πmm·mrad (normalized)
RFQ linac	
Input/Output energy	8 / 800 keV/u
Vane length	7.3 m
Cavity diameter	0.59 m
Max. surface field	205 kV/cm (1.8 Kilpatrick)
Alvarez linac	
Input/Output energy	0.8 / 6.0 MeV/u
Total length	24 m (3 rf cavities)
Cavity diameter	2.20 / 2.18 / 2.16 m
Average axial field	1.8 / 2.1 / 2.1 MV/m
Shunt impedance	31 - 46 MΩ/m (effective)
Max. surface field	130 kV/cm (1.1 Kilpatrick)
Focusing sequence	FODO (6.0 kG/cm Max.)
Output beam emittance	≤ 1.5 πmm·mrad (normalized)
Momentum spread	≤ $\pm 1 \times 10^{-3}$

The specifications and a layout of the overall injector system are presented in Table 1 and Fig. 2, respectively. Expected beam intensities of the injector linac are listed in Table 2 for typical ions.

Ion Source

Two types of ion sources are adopted: one is a hot cathode type PIG source for light ions up to around Ne, and another is an ECR source for heavier ions. Both sources are located independently on high voltage platforms with a maximum voltage of 60 kV.

Beam tests of the PIG source are now under way, and the obtained beam intensities exceed the required values given in Table 2 up to Ne for both DC and pulsed operation.[3] The source is equipped with a bombard electrode and will provide solid ion species.

The ECR source is expected to produce heavy ions up to xenon. A compact single stage structure is adopted for the source. The structure is similar to that of Caprice[4] developed at Grenoble. The microwave frequency and power are 10 GHz and 2 kW at maximum, respectively. The maximum strength of an axial magnetic field is about 1 T with seven solenoid coils excited by 45 kW in total. A transverse field generated by a NdFe permanent sextupole magnet reaches about 0.8 T at the chamber wall.

RFQ Linac

The ions pass through a low energy beam transport line about 7 m long before injection into an RFQ linac.

Table 2
Beam intensity schedule for typical ions.

Ion species	C^{6+}	Ne^{10+}	Ar^{16+}
Output current (eμA)	170	120	69
Transport transmission		0.75	
Stripper efficiency	0.93	0.67	0.18
Alvarez transmission		0.9	
RFQ transmission		0.8	
Transport transmission		0.7	
Source current (eμA)	160	140	340
Ions from source	C^{2+}	Ne^{3+}	Ar^{6+}

A rather low value of 100 MHz is chosen for the linac so as to give sufficient focusing strength. An acceptance of the linac is 0.6 πmm·mrad normalized (145 πmm·mrad unnormalized).

The linac is a conventional four vane type and separated longitudinally into four tanks. The four vanes are precisely set in each tank independently. A longitudinal and a transverse voltage distributions are tuned with about 40 side tuners. The tuners are fixed by welding after the voltage tuning. A vane coupling ring has not been adopted for this linac.

The entire linac tank is fed with a 300 kW peak rf power through a single loop coupler. The tank is made of copper plated mild steel, whereas the vanes are solid copper. The rf contact between the vanes and the tank wall is achieved with silver coated stainless steel spring-rings.

Alvarez Type Linac

The RFQ linac is followed by an Alvarez type linac operated at the same frequency. The linac tank is separated into three independent rf cavities and each cavity is fed with an rf power of 1.4 MW peak. The maximum surface field is chosen to be 128 kV/cm (1.13 Kilpatrick). The linac tank is 24 m long in total, and consists of 106 unit cells. The diameter of the cavity is about 2 m and changes with one tank to the next in order to obtain reasonable values for the transit time factors.

The tanks are made of copper-clad mild steel, and the drift tubes are copper-plated stainless steel. The thicknesses of the clad and plated copper are 8 mm (before machining) and 100 μm, respectively. A photograph of an inside view of the third Alvarez tank is given in Fig. 1. Each drift tube is supported by horizontal and vertical stems, the diameters of which are 3 and 5 cm, respectively. Every second drift tube is equipped with a quadrupole magnet. The magnets have laminated cores and are excited by pulse power sources with a very low flat-top-duty of 0.3% in order to reduce the heavy thermal loads.

RF System

An rf amplifier of the Alvarez linac is designed to deliver more than 1.4 MW and is equipped with a power tube of Siemens's RS 2074 SK. In the two driver stages of the amplifier system, RS 2058 CJ and RS 2032 CL vacuum tubes have been adopted and deliver rf powers of 100 and 5 kW, respectively. Three sets of 1.4 MW amplifiers with a single plate power supply will be used to excite the three Alvarez cavities. The construction of the amplifier for Alvarez tank no.3 is already finished, including high power tests.

In a 300 kW amplifier for the RFQ linac, the Eimac tubes have been adopted: 4CW 100,000 E for the final stage and 4CX 20,000 C for the driver stage. A 30 kW amplifier for the debuncher cavity is the same as the driver amplifier.

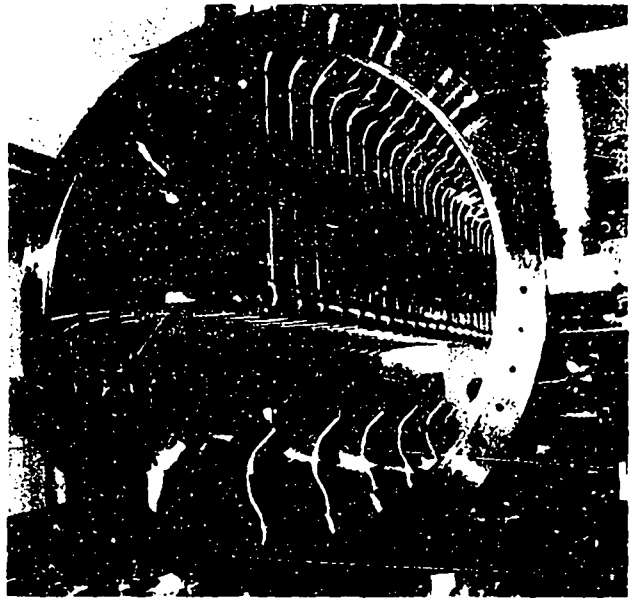

Fig. 1. An inside view of no. 3 Alvarez type linac tank.

Charge Stripper and Debuncher

At the output end of the Alvarez linac, a 100 $\mu g/cm^2$ carbon stripping foil is installed in order to improve a charge to mass ratio for further acceleration. Only one stripping section is used at a relatively high ion energy because of the reliability of the system and of future expansion to the acceleration of heavier ions.

A 100 MHz debuncher cavity is introduced in the output beam line to suppress the momentum spread of the accelerated beam. A distance between linac end and the debuncher cavity has been optimized to be about 9 m. An rf voltage of 300 kV (for $q/A = 1/4$) rotates the beam bunch in longitudinal phase space, and reduces the energy spread of the linac beam from $\Delta W/W = \pm 1.2\%$ to a satisfactorily good value of $\pm 0.11\%$. Some kind of tuning error of the Alvarez linac, however, tends to increase the energy spread up to more than $\pm 0.2\%$.

Control System

A computer system of the injector consists of three mini-computers: a system control unit (SCU) of μVAX 3500 and two group control units (GCU) of μVAX II. The SCU mainly covers the man-machine interface and controls the injector as a total system, whereas the GCU directly controls a peripheral device through a universal device controller (UDC), which is a 16-bit micro-computer installed within the device.

The SCU is connected to a central computer unit through an ethernet by which other control units for a synchrotron system and a high energy beam transport system etc. communicate with each other. A control computer for medical treatment will also be connected to the network. Another ethernet is used to ensure communication between the SCU and the GCUs. The GCU and a UDC are linked with an optical fiber line.

All devices in the injector system, including a timing unit, are controllable from an operator console with four touch panels and three rotary encoders.

RF Characteristics of Alvarez No.3 Tank

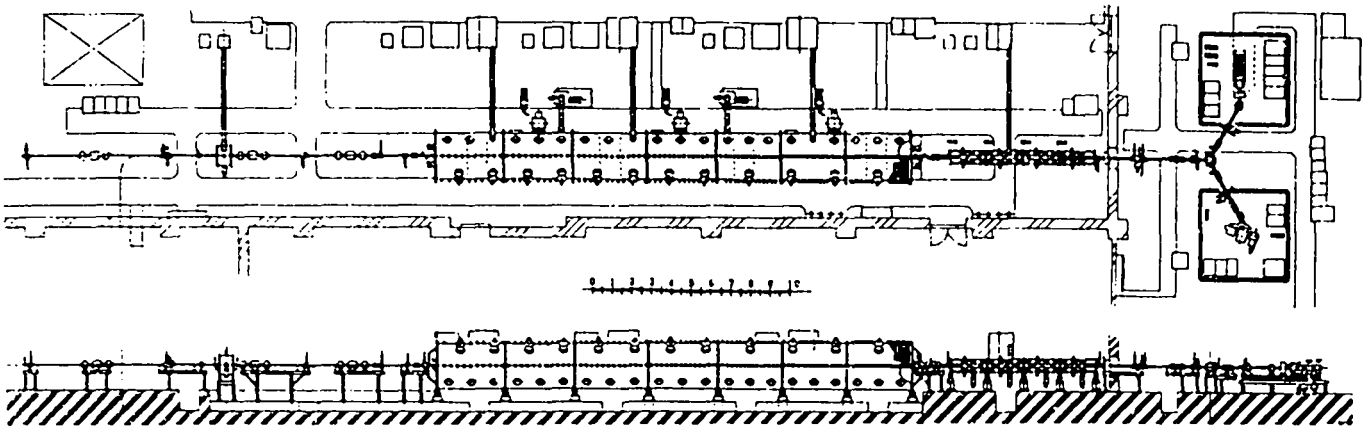

Fig. 2. A layout of the HIMAC injector.

An inside diameter of the tank was machined within an error of ±0.3 mm. After that, the copper surface was treated with a orbital sander to a surface roughness of 0.4a (1.2s). An alignment accuracy of better than ±0.1 mm has been achieved for the transverse position of a drift tube with an alignment telescope and an optical target inside a bore hole of the tube. The bore hole was machined with an accuracy of ±10μm after measurements of a center position of the quadrupole field. A longitudinal positioning error of the drift tube was measured to be better than ±0.2 mm.

Low Power Tests

A resonant frequency of the cavity exists very close to a desired value with calculated positions of a frequency tuner. The frequency is about 1 MHz apart from the nearest neighboring mode of TM_{011} (Q_0 is about 50,000). An unloaded Q-value, Q_0, of the fundamental TM_{010} mode was measured to be 88,000 for a virgin tank and about 70% of a calculated value including stem losses.

A tilt of the acceleration field was tuned with six side tuners within an error of 2%. The positions of the tuners were fixed after the low power measurements by welding. A small jump (about 2%) in the acceleration field appears at the end of the tank where a unit cell volume is a little bit reduced with a 2.5 cm thick copper wall separating the cavity from the next one.

Field and frequency measurements were carried out in order to obtain dependencies on a longitudinal position and a radius of an end drift tube. All efforts, however, resulted in little effects on the compensation of the field jump at the end cell.

A field distribution in the acceleration gaps was also measured with a bead pull method. The results were very well reproduced by the calculated values.

The resonant frequency changes with the cavity temperature by 1.2~1.4 kHz/deg and the value agrees well with a calculated one.

High Power Tests

A full design power was successfully injected into the virgin cavity after conditioning of about one whole day. There was no visible damage to the coupling loop and any other components. A maximum surface field of 150 kV/cm (1.3 Kilpatrick) is stably obtained.

A length of a coaxial line between the amplifier and the cavity is optimized with a trombone tuner so that coupling between the amplifier and the cavity takes its minimum value. A rise time (0 to 90% value) of the field level is about 500 μs without any feed back loop, and about 50% longer than a simply predicted value of 320 μs. The rise time, however, is reduced to about 400 μs with an automatic gain control loop. A flatness better than $\pm 1 \times 10^{-3}$ is obtained in the duration of more than 700 μs for an rf pulse width of 1.2 ms.

Phase stability was measured to be better than ±0.5°/8hr with an automatic phase controller, and well within the acceptable range. After a long run test of 24 hr, the unloaded Q-value of the cavity was improved to 102,000 (79% of Superfish value).

Construction Schedule

Mechanical construction of a debuncher cavity is already finished and rf measurements are now under way. Major part of the RFQ linac is machined and the fabrication will be finished soon. Machining of the Alvarez no.1 and 2 tanks has already started and will be completed early next year. Tests of parallel operation of the three Alvarez cavities is scheduled in the middle of the next year.

After characteristic measurements, all components will be carried into NIRS during the last part of 1991. The first beam from the synchrotron will be obtained in 1993.

Acknowledgements

Heartfelt thanks go to the members of Division of Accelerator Research of NIRS who have given continuous encouragement and fruitful discussions. The authors also express their sincere thanks to the engineers of Sumitomo Heavy Industries, LTD. for their great assistance and valuable discussions.

References

1. Y. Hirao, *et al*, Proc. of Europ. Part. Accel. Conf., Niece, France, 1990, to be published.
2. S. Yamada, *et al*, Proc. of 6th Symp. on Accel. Sci. & Technol., RCNP, Osaka, Japan, 1989, p45, and related papers in the symposium.
3. Y. Sato, *et al*, Rev. Sci. Instrum. **61(1)**, 466 (1990).
4. B. Jacquot & R. Geller, Proc. of Int. Conf. on ECRIS & Their Applications, MSU, USA, 1987, p254.

TEST LINAC FACILITY AT PHOTON FACTORY, KEK

H. Kobayashi, T. Urano, A. Enomoto, T. Oogoe, S. Ohsawa, N.Kamikubota, T.Kurihara, K. Nakamura, K. Furukawa, H. Honma, Y. Yamazaki and A. Asami
Photon Factory, National Laboratory for High Energy Physics
1-1 Oho, Tsukuba-shi, Ibaraki-ken, 305 Japan

Abstract

A test linac facility is progressing at National Laboratory for High Energy Physics (KEK), Photon Factory, Injector Division. The facility is used both for testing of components of the 2.5-GeV linac, which is the injector of PHOTON FACTORY and of TRISTAN, and for research on accelerator science and technology. The linac is to be the most suitable configuration for every experiment. Therefore, the linac doesn't have a fixed layout. A universal bed with a length of 13.5 meters is being prepared. The maximum beam output, restricted due to radiation safety, is 60 MeV and 10 μA. The design and manufacturing of both a conventional electron gun and a microwave electron gun are being carried out. The present status regarding the construction of the linac is presented.

Introduction

A new project to construct a test linac facility has started and is progressing. An increase in the total operation time of the 2.5-GeV linac makes it difficult to test its components, furthermore, the operation time for machine studies has not been sufficient under such busy machine operation. The basic motivations to develop this project has been to solve these problems. In addition to the testing of components of the linac, the following activities concerning accelerator science and technology are expected.

1. High-brightness beam acceleration experiments.
2. Improvement of the energy spectrum.
3. Experiments on a free-electron laser.
4. Testing high-gradient acceleration.
5. Development of a newly designed beam monitoring system.
6. Improvement of the production technique for a positron beam.
7. Experiments concerning large peak-current acceleration.
8. Testing microwave electron guns.
9. Others.

Site of linac

The site of this test linac is situated beside the electron-gun room of the 2.5-GeV Linac. One part of that room is partitioned by blocks with a thickness of 1 meter. The size of the room is 18 meters long by 4.5 meters wide and a universal bed for linac components with a length of 13.5 meters is installed in the room. The layout of this linac will be changed for every experiment, as mentioned above. A typical layout of the linac is shown in fig. 1.

Power source

The pulse modulator for the electron gun produces 17.0kV, 1300 amperes pulses with a width of 4.0 μs. A step-up transformer installed in the shield room connected by a low-impedance

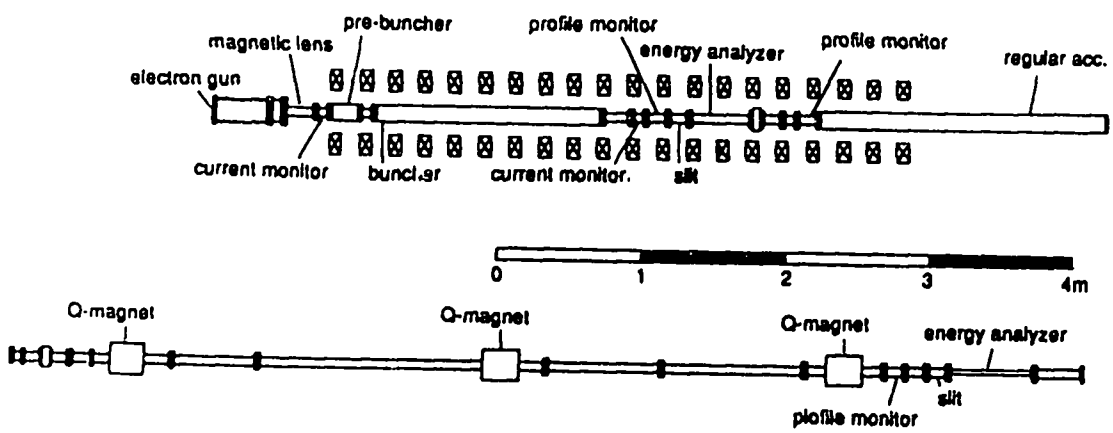

Fig.1 Typical layout of the test linac. The linac is assembled on a universal bed with a length of 13.5 meters.

cable with the pulse modulator can apply a 200 kV pulse to the electron gun under testing.

The pulse modulator for the klystron installed in the klystron gallery produces 84MW pulses with a width of 3.5 μs. The klystron, type PV-3030, generates microwaves of 30 MW. The microwave power is divided into two, and used for the buncher section and the regular section, respectively. The power for the pre-bunching cavity is picked up from the power for the buncher.

High-brightness beam acceleration

Preparation of experiments concerning the high-brightness beam acceleration has started. The production of a low-emittance beam is one of the main themes in this facility. Some users want to use synchrotron radiation generated by a micro-pole undulator installed in the linac complex to obtain a high time resolution. As is well known, the pulse width of the linac output is typically several picoseconds. A beam emittance similar to that of a storage ring is desirable for these purposes. Furthermore, some of the themes mentioned above can not be carried out without a low-emittance beam. For example, the beam quality is a crucial parameter for experiments on a free-electron laser oscillation. Research concerning the acceleration of a high-brightness beam is described below.

Conventional electron gun

The design of an electron gun with high quality represents the beginning of research on high-brightness beam acceleration. The brightness of a cathode is given by [1]

$$Bn=3.7\times10^{9}J \quad (\text{amps./m}^2\text{rad}^2) \text{ at } 1300K, \quad (1)$$

where J is the current density of the cathode in units of amps./cm^2.

The brightness is proportional to the current density of the cathode. We have tried to design an electron gun which has a emittance of ca. 1πm m mrad, 1/100 of that of the gun used in present 2.5-GeV linac. A high electric field is applied to the cathode surface, and the cathode area is reduced in order to obtain low emittance. An electron gun with a cathode diameter of 1 mm has been designed. The gun is operated at 180 kV. Calculations have been carried out using a computer code developed by Herrmannsfeldt.[2] The distance between the anode and the cathode is 31 mm and is fairly long compared with the diameter of the cathode (1 mm). The entire area in the gun is divided into 4 blocks along the z-axis. One mesh size is 0.1mm by 0.1 mm and 6400 points are calculated in each block. The first block contains the cathode, and the output of this area is input of the second block. Calculations are repeated successively and, finally, the output of the gun is obtained at the fourth block. The emittance at each block in the gun was compared and degradation of the emittance at the anode hole was large. An anode hole with a mesh grid will be effective to avoid any lens effect. Calculations with and without the mesh grid were carried out and the emittance without the mesh grid was two-times larger than that with it. The results described below are for the case with the anode mesh. A current of ca. 600 mA is obtainable. The brightness and emittance from calculations are 5.3×10^{10} amps./m^{2}rad^2 and 1.1πmm mrad, respectively. Then, the current density of the cathode is 80 amps./cm^2. The brightness of the cathode calculated from equation (1) is 3.1×10^{11} amps./m^2 rad^2. The cathode assembly for this gun is shown in fig. 2. and its calculated ray-trace is shown in fig. 3 respectively.

The diode described above is to be used at the beginning of experiments; a triode will also be

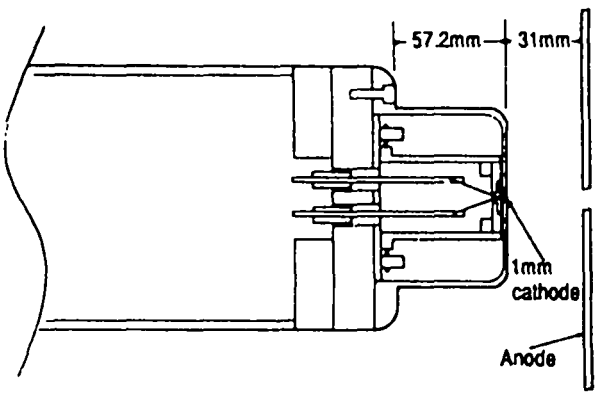

Fig.2 Cathode and anode assembly of the gun. The diameter the cathode is 1 mm.

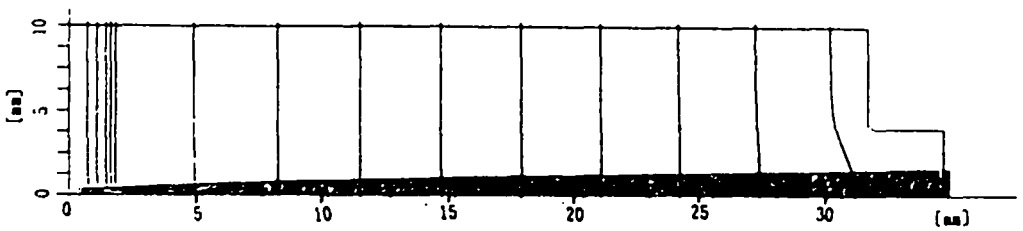

Fig.3 Ray-trace of the gun. The beam slightly diverges in the gun.

used in the linac for some experiments. The effect of the grid on emittance growth is also calculated. The emittance is increased by several times, depending on voltage of the grid.

Microwave electron gun

A microwave electron gun (RF-gun) is suitable for the production of a high-brightness beam. The design of a RF-gun with three electrodes (anode, cathode, grid) and testing it under low power have been carried out. When a photo-cathode is used, the pulse width can be controlled by the time duration of the laser pulse. In the present system, the pulse width is controlled by the energy selection. The single-cell RF-gun and the energy-analyzing system are shown in fig. 4. A multi-cell RF-gun is being investigated as a next step. A high-power test of it and beam acceleration will be carried out in the test linac facility.

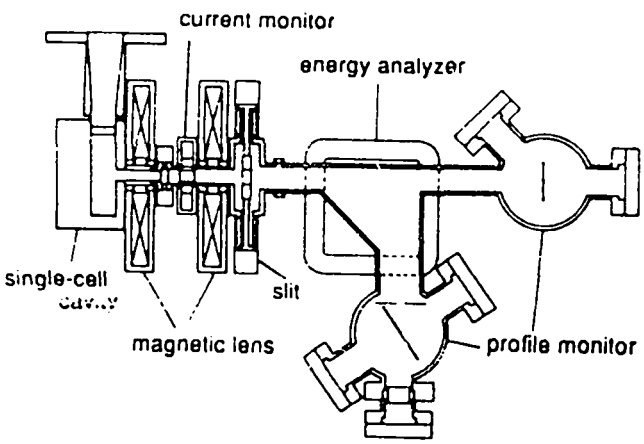

Fig.4 The layout of the RF-gun. The single-cell RF-gun, energy-analyzing magnet and the beam-monitoring system are shown.

Design of injector

The emittance growth in the buncher is serious problem for high-brightness beam acceleration. The cause of emittance growth is mainly lens action of microwaves excited in the cavity. T. Smith[3] et al. proposed mixing the fundamental and third harmonics in order to obtain a flat-top of acceleration field which would provide no phase-dependent effects. A small beam size is also effective to avoid emittance growth, since the radial force increases with a transverse displacement of the beam. A calculation of the emittance growth using PARMELA has been carried out. The emittance growth in a single-cell pre-buncher is described as one example. The phase space of the output of the electron gun described above is used as input data and is shown in Fig. 5(a). A magnetic lens converges the electron beam to a focus point at the center of the pre-buncher. The phase space at the output of the pre-buncher both with and without the magnetic lens are shown in figs.5(b) and 5(c), respectively. When the beam size is small at the pre-buncher, the effects of the radial force, depending on the microwave phase, are small. A focusing system used to minimize any emittance growth is being investigated.

Conclusion

The test linac facility is progressing. Construction of the shield room, installation of modulators and tests of the safety interlock system were completed. The design of the electron gun containing a very small cathode with a diameter of 1 mm was completed. Low- power tests of the RF gun were carried out and high-power tests will be performed after completion of the construction of waveguides for high-power microwaves.

References

1) J. S. Fraser and R. L. Sheffield,"High-Brightness Injectors for RF-Driven Free-Electron Lasers,"IEEE J. QUANTUM ELECTRONICS,QE-23(9),1497(1987)

2) W. B. Herrmannsfeldt,"Electron Trajectory Program," SLAC-226

3) T. I. Smith, "Intense Low Emittance Linac Beams for Free Electron Lasers," Proc. 1986 Linear Acc. Conf. p421

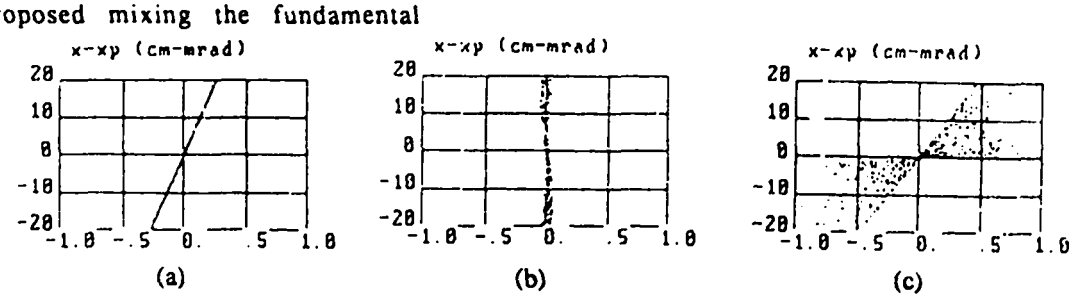

Fig.5 Phase space at the output of the gun, (a). Phase space at the output of the pre-buncher with focusing, (b) and without focusing, (c).

NUMERICAL MODELLING OF THE CEBAF ELECTRON GUN WITH EGUN*

P. Liger and G. A. Krafft
Continuous Electron Beam Accelerator Facility
12000 Jefferson Avenue, Newport News, VA 23606

Abstract

The electron source used in the injector for the CEBAF accelerator is a Hermosa electron gun with a 2 mm diameter cathode and a control electrode. It produces a 100 keV electron beam to be focussed on the first of two apertures which comprise an emittance filter. A normalized emittance of less than 1π mm mrad at 1.2 mA is set by the requirements of the final beam from the CEBAF linac, since downstream of the filter, a system of two choppers and a third aperture removes 5/6 of the current. In addition, for RF test purposes a higher current of about 5 mA is needed, possibly at higher emittance.

This paper presents a way of calculating the characteristics of the CEBAF electron gun with the gun design code EGUN, and the accuracy of the results is discussed. The transverse shape of the beam delivered by the gun has been observed, and its current measured. A halo around the beam has been seen, and our calculations can reproduce this effect.

Introduction

The nominal voltage of the gun is −100 kV. The electrons are emitted by a 2 mm diameter dispenser cathode; the gun current depends on the voltage of the control electrode, which has a 2 mm aperture. The control voltage (V_{ce}) is set between −70 and −400 V with respect to the cathode. The distances are 1.75 mm between the cathode and the control electrode, and 159 mm between the cathode and the exit through the anode hole.

Because the length of the gun is large compared with the size of the cathode, it is impossible to compute the gun properties in a single EGUN run. A complete calculation involves five EGUN runs; only the final three runs include beam space charge. The calculation procedure is outlined in the first part of this paper. Next, sensitivity of the results to changes in EGUN parameters is discussed. Finally, the calculated results, the beam profile and the delivered current versus V_{ce}, will be compared with measurements.

EGUN Calculation

The program is operated using cylindrical coordinates, the axis being through the centers of the cathode, the control electrode aperture, and the anode aperture. Since the cathode is so small relative to its distance from the anode and since the number of mesh points in the code is limited, a grid fine enough to resolve the cathode cannot be generated in a single EGUN run. EGUN allows one to define several regions of different mesh size and provides a way to connect results between adjacent regions. One can focus on cathode details in one set of runs, the region between the control electrode and a point 8 mm downstream in a second set of runs, and from there to the anode in a third set of runs. For our problem, we found that at least three regions were needed to eliminate unacceptable dependence of the results on the input parameters of the run.

Region 1 runs use 7,238 mesh points to model the region between the cathode and the control electrode. The left-hand boundary represents the cathode, where emission occurs along 32 mesh units of 0.03125 mm size. The control electrode occupies most of the right-hand boundary. A Neumann boundary condition is placed on the large radius open boundary, and a Dirichlet boundary condition is placed on the control electrode aperture. The boundary values are chosen as discussed below. Region 2 runs use 10,879 mesh points of 0.2 mm size to describe the cathode and the control electrode to the left, to 8 mm downstream from the control electrode on the right, and to the radius of a focussing electrode at large radius. The upper and right-hand limits are both Dirichlet boundaries; the potential along the upper boundary is set point by point, and the downstream boundary is an equipotential surface drawn nearly point by point as discussed below. Region 3 runs use 3853 mesh points of 2.0 mm size to describe the main body of the gun. The field is dominated by that given by the 100 kV.

Figure 1 shows EGUN generated boundary plot for Region 3. The figure also shows the equipotential surfaces when there is no beam.

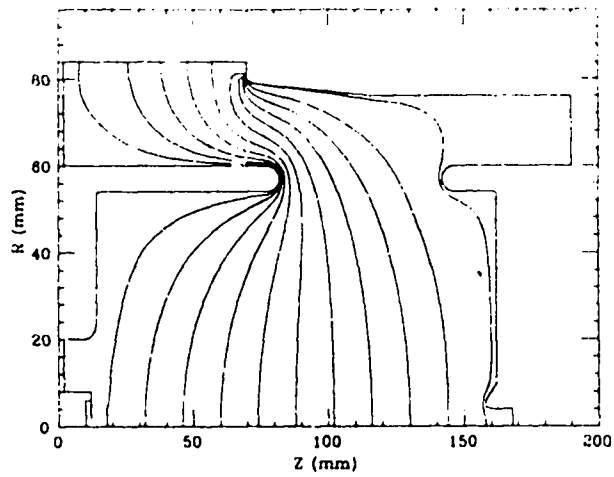

Figure 1. EGUN plotted calculation of Region 3 boundaries and equipotential lines.

As an example consider using EGUN with the following voltages: 0.0 V at the cathode, 322.0 V at the control electrode, and 100 kV at the anode. The Region 2 downstream equipotential values are found by solving the Laplace equation in Region 3, and by interpolating the coordinates of the solution's 1650.0 V points to fit the contracted coordinate scale of Region 2. This 1650.0 V equipotential surface is far enough from the control electrode to prevent the ray dynamics nearby the control electrode from any serious error due

* This work was supported by the U. S. Department of Energy under contract DE-AC05-84ER40150.

to the interpolation. It is close enough to the control electrode, however, to let Region 2 hold less than 11,000 mesh points, the maximum in our version of EGUN. The Region 2 upper boundary values are fixed to the potential computed from the Region 3 calculation. Once the Region 2 boundaries are specified, the Laplace equation is solved to find the potential on the Region 1 boundary. Now a Region 1 calculation is done with beam. The rays are stopped upstream of the boundary of Region 1 to avoid error introduced by the Dirichlet boundary condition imposed in the space charge calculation. These rays provide initial conditions for a Region 2 calculation with space charge. The cycle is repeated to go from Region 2 to Region 3, where the beam dynamics are again computed with space charge.

Thermal Effects

To model thermal effects at emission, EGUN splits each generated ray into 3 or 5 subrays which are given different perpendicular velocities. The initial radial velocities are

$$v_{-1} = 0, \qquad v_{-2} = \sqrt{\frac{2kT_c}{m}}, \qquad v_{-3} = -\sqrt{\frac{2kT_c}{m}},$$

in case of 3 subrays, and in addition

$$v_{-4} = 2\sqrt{\frac{2kT_c}{m}}, \qquad v_{-5} = -2\sqrt{\frac{2kT_c}{m}},$$

in the case of 5 subrays, where T_c is the cathode temperature. The splitting process conserves the current of each original ray. In the case of the 3 subray split, the non-deflected ray transports half of the current, and each deflected ray transports a quarter of the current (1-2-1 ratio). In the case of the 5 subray split, the non-deflected ray transports no current, the two less deflected rays transport 9/20 of the current, and the two more deflected rays transport 1/20 of the current (1-9-0-9-1 ratio).

Splitting the current in other distributions has given similar results except when the subrays which are not deflected (0 transverse velocity) carry more than 10% of the total current. Results of using different current distributions are presented in Table 1. The emittance figures include only the beam core, not the secondary halo discussed below. For 5 subray calculations, one observes that the emittance varies by a factor 2 depending on the model of current distribution used, but the total current delivered by the gun stays constant. The difference between 1, 3, and 5 subray calculations seems to provide the largest EGUN parametric dependence we observe in our problem, and the 5 subray calculations are probably most accurate. The 5 subray calculation of the gun current agrees with the measurement.

Beam Profile

The beam has been observed 63 cm downstream of the anode on a fluorescent viewscreen. Figure 2 is a picture of the beam produced by the gun with 125 V control voltage. One clearly distinguishes a halo of electrons surrounding the central beam.

One way to produce the beam halo is to assume that the control electrode emits secondaries on the edge parallel to the beam current, since at 120 V, secondary emission is the most probable result of electron bombardment of the surface[3]. An example of the EGUN rays calculated in Region 1 appears in Fig. 3. It was assumed that the secondaries are emitted with energies up to 15 eV and angles from normal to the surface to within 1° of the surface[4]. Figure 4 shows the rays when they are near the viewscreen. The halo rays occupy radii at about 6.6 mm, very close to that measured, and the beam core has a radius of 3.5 mm, again precisely as measured. The only conditions that we have found when the secondaries would actually stay in the core is if the secondaries are emitted along the emitting surface at angles less than 0.5°, a highly unlikely event.

TABLE 1
EGUN results for various emission models

Number of Subrays	Current Ratio	Current (mA)	Normalized Emittance (π mm mrad)
1	1	3.366	0.19
3	1-2-1	3.224	0.51
3	2-1-2	3.231	0.63
5	1-1-1-1-1	3.104	0.93
5	5-5-0-5-5	3.107	1.04
5	4-6-0-6-4	3.108	0.98
5	3-7-0-7-3	3.108	0.91
5	2-8-0-8-2	3.109	0.84
5	1-9-0-9-1	3.110	0.77
5	1-9-1-9-1	3.109	0.75
5	1-9-2-9-1	3.108	0.73
5	1-9-3-9-1	3.107	0.72
5	1-9-6-9-1	3.106	0.68
5	1-9-9-9-1	3.104	0.65

Figure 2. View of the beam delivered by the gun. The halo is 13 mm in diameter.

Current Versus Control Voltage

The control electrode intercepts a significant fraction of the current emitted by the cathode. There is complete transmission through the anode, even in the extreme case of 322 V on the control electrode, where the transmitted current and the beam dimensions are maximum. For 26 values of V_{ce}, between 70 V and 322 V, the procedure to calculate potentials on the downstream limit of Region 2 was repeated, by solving the Laplace equation in Region 3.

Next, two sets of calculations were done. Firstly, an EGUN run with Region 2 was used to compute the current emitted by the cathode. Secondly, EGUN was used to solve the Laplace equation in Region 2 to obtain boundary values for a Region 1 calculation. The code was then used to compute the current emitted by the cathode and the current transmitted through the control electrode. Figure 5 shows the results of these calculations of current versus the voltage of the control electrode, along with the measurements of the current from the CEBAF gun. In descending order, the curves are the current emitted by the cathode according to the Region 1 calculations, the current emitted by the cathode according to the Region 2 calculations, the current passing the control electrode from the Region 1 calculations, and the measurement. The current emitted by the cathode is about the same in the two calculations, giving an indication of the error expected from our procedure. Due to the agreement with the measurements, it is concluded that by subtracting the current carried by rays which are stopped at the control electrode from the total emitted current, one obtains the delivered current.

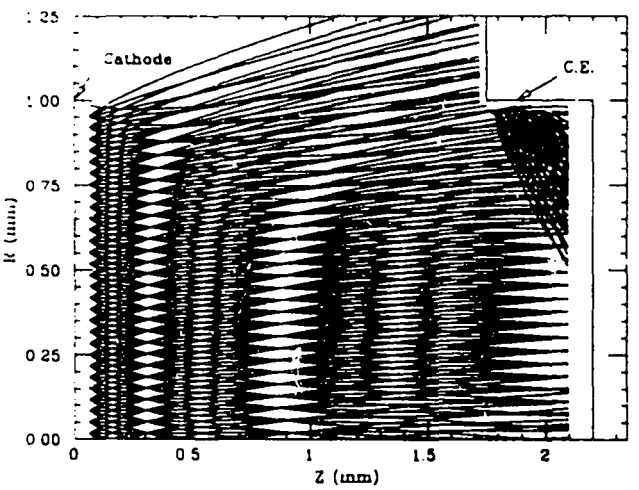

Figure 3. EGUN rays in Region 1, V_{ce} = 120 V.

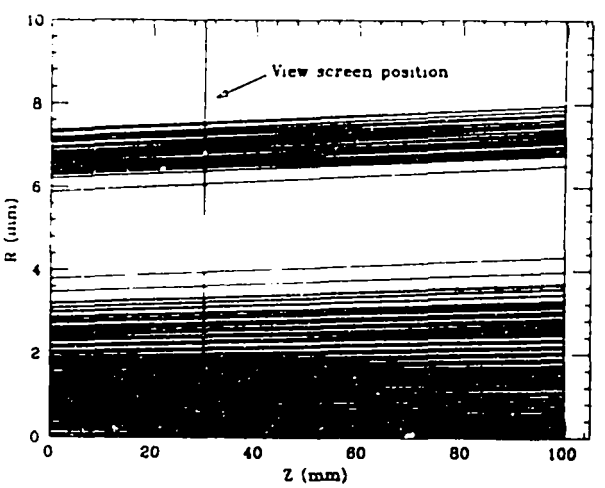

Figure 4. EGUN rays near viewer, V_{ce} = 120 V.

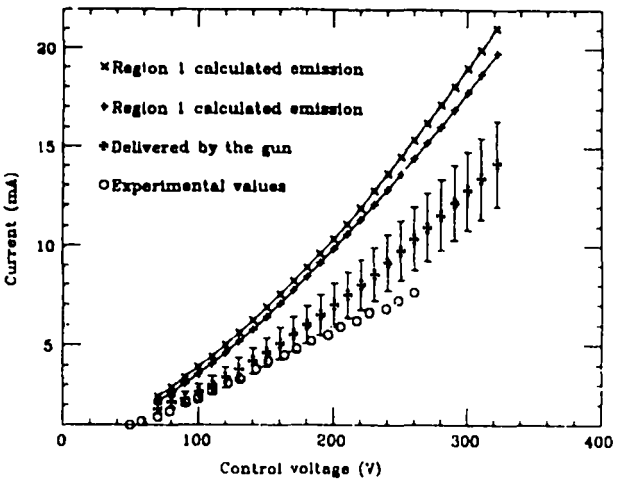

Figure 5. Current versus control voltage.

As expected, the emitted current varies as the 3/2 power of the control voltage. The control electrode stops 32% of the emitted current for V_{ce} from 90 to 320 V. The uncertainty of 10% indicated in Fig. 5 corresponds to the current carried by the outer ray passing through the control electrode. The calculations agree with measurements in the range of V_{ce} from 90 to 170 V. The difference at higher voltages arises from the neglect of thermal effects in the calculations. For example, when V_{ce} is 120 V the current transmitted through the control electrode decreases from 3.4 mA to 3.2 mA using 3 subrays with T_c = 1250 K, and to 3.1 mA using 5 subrays with T_c = 1250 K, while measurements give 3.1 mA when V_{ce} is 121.7 V.

Summary

Some properties of the CEBAF gun have been computed, despite a design which makes an EGUN calculation difficult. The results are consistent with measured beam properties. A beam halo is formed from secondary electrons emitted from the control electrode. Since the computed value of the normalized emittance of the core depends sensitively on the run parameters, we can only estimate its value to within a factor of two, 0.75 π mm mrad at the anode.

Acknowledgements

C. K. Sinclair and J. Jackson provided their encouragement, useful advice, and all experimental data included in this paper.

References

1. CEBAF design report, May 1986.
2. W. B. Herrmannsfeldt, "EGUN-an electron optics and gun design program", updated version of SLAC-226, Stanford.
3. Harrower, G. A., *Phys. Rev.* 104, 52 (1956)
4. Jonker, J. L. H., *Philips Res. Rep.* 12, 249 (1957)

LAL (ORSAY) RF GUN SIMULATIONS AND MODEL CAVITY DESIGN

C. Travier, J. Gao and H. Liu
Laboratoire de l'Accélérateur Linéaire
Bât. 200, Centre d'Orsay
91405 ORSAY Cedex, FRANCE

Abstract

The use of dispenser cathode for RF gun allows both thermionic and laser-driven operation. Simulations results for both cases and cavity design are presented. The status of the project is described.

Introduction

Over the last 5 years, a growing interest for very bright electron sources has been shown in different laboratories around the world. RF gun first developed in Stanford [1] and Los Alamos [2] has the potential of providing such very bright beams. More than twenty RF gun projects are now going on [3], in view of FEL and future accelerators.

At LAL Orsay, we are planning to develop a laser-driven RF gun [4], in order to gain some experience in this field and to provide a possible bright source for the high-gradient accelerator facility NEPAL [5]. A (W, Ba, Ca) dispenser cathode will be used, therefore allowing both thermionic and laser-driven operation [6]. Simulations for both operating conditions are presented here.

A low-level RF model cavity was launched to check some RF properties of the design and to evaluate the size of the coupling slots. Basic design characteristics are presented.

Laser-Driven Gun Simulations

The theoretical investigations that led to the chosen field profile shown in figure 1 are presented in reference 7.

For the simulations done with PARMELA [8] and PRIAM [9], the following assumptions are made. Since the bunch is quite long and the current not too high, the mesh grid method for space charge calculations is preferred to the point to point method [10] in order to save computer time. The effect of image charges in the cathode plane or cavity walls is not included. Electrons are assumed to leave the cathode with no energy and a zero emittance. The laser pulse is taken uniform in both transverse and longitudinal dimensions.

The PARMELA longitudinal random particle generation is changed to a deterministic one. This new generation gives consistent results for 100 particles as compared to 300 to 400 particles needed in the case of the random generation.

The emittance is taken as the normalized r.m.s. emittance defined as $\epsilon_N = 4\pi [< x^2 >< (p_x/mc)^2 > - < x(p_x/mc) >^2]^{1/2}$ where x is the coordinate of a particle in the beam, p_x is the particle's momentum component in the x direction and $< >$ indicates averaging over the entire beam. It corresponds to the "90 % emittance" for a beam which distribution is gaussian in each coordinate.

The optimization procedure and the results for different values of accelerating field are given in reference 4. Results are presented here for a maximum on-axis field of 70 MV/m corresponding to a maximum surface field of 112 MV/m which is just above two times the Kilpatrick limit. 30 ps laser pulse length is assumed. Figures 2 and

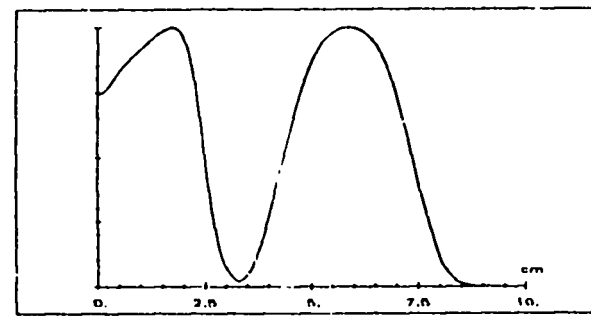

Fig. 1: Longitudinal on-axis electric field

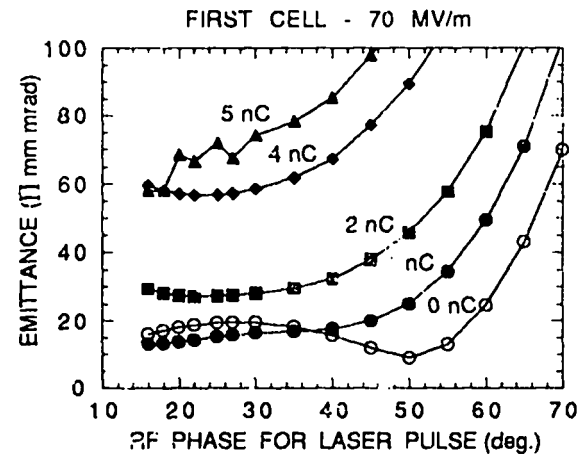

Fig. 2: Emittance vs. laser phase after first cell

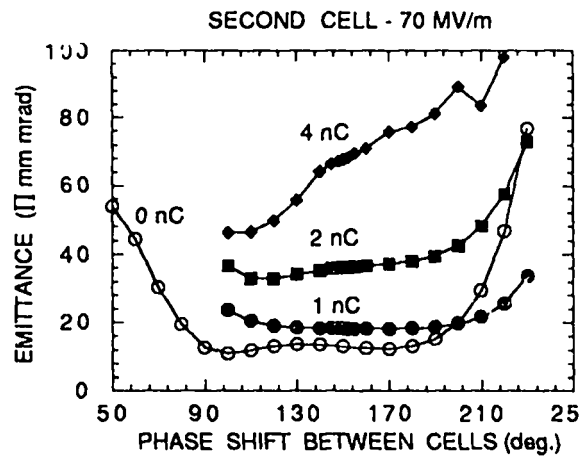

Fig. 3: Emittance vs. ϕ_{12} after second cell

3 show the emittance as function of the RF phase for laser pulse at the end of the two cells for different values of the bunch charge. For 4 nC, some particles are lost within the second cell, while for 5 nC, some are lost in the first cell. Table 1 gives the main parameters for a typical run.

Thermionic Gun Simulations

When running the gun in a thermionic way, the goal is to provide an electron beam to test the various measurement devices.

Since, in this case, the electron micropulse repetition rate is high, the cathode should work at a low temperature to limit the extracted current, in order to limit the beam loading. On the other hand, we should have an output energy roughly as high as for the laser-driven case. Based on these considerations, we have investigated the gun performances.

The thermionic emission of electron micropulses is assumed to obey the Richardson-Schottky equation. For a typical case, one has T = 1000 K, $\phi_0 = 1.9$ eV, $\bar{E}_1 = \bar{E}_2 = 35$ MV/m and $\phi_{12} = 156.5°$, where T and ϕ_0 represent the operating temperature and work function of the cathode, respectively; $\bar{E}_1$ and $\bar{E}_2$ represent the average on-axis electric field amplitudes in each cell; ϕ_{12} is the phase shift between the two cells. In this case, the beam loading is around 0.2 MW. The characteristics of the electron micropulse out of the second cell are shown in figure 4.

A transport line similar to that of BNL [11] is considered. Based on the beam parameters at the exit of the second cell obtained with PARMELA, the transport line parameters are calculated with TRANSPORT [12]. Then the beam dynamics along such a transport line is simulated again using PARMELA. The first results show that the normalized r.m.s. emittances are increased finally to about 20 π mm mrad for x dimension and to about 12 π mm mrad for y dimension, from an initial value of 6 π mm mrad for both dimensions; for such a case, the total energy spread and phase spread are 36 keV and 7° respectively, with the central energy at 2.866 MeV; the r.m.s. energy spread and r.m.s. phase spread are 9 keV and 2° respectively; the average current is about 4 mA. These values correspond to a small fraction of the beam that could be selected with momentum slits.

Cavity Design

The cavity design constraints are as follows: obtain a field profile as close as possible to the theoretical one, minimize the peak surface field, obtain decoupled cells separated by the shortest drift possible and with the lowest priority, maximize the shunt impedance. The cavity which contour is shown in figure 5 is designed with SUPERFISH [13]. Figure 6 shows a PRIAM 3-D view of the cavity as provided by G. Le Meur. Table 2 gives the RF parameters as obtained with SUPERFISH, PRIAM and MAFIA [14] codes. Following the work done in references 15 and 16, MAFIA calculations of the coupling slots size were performed: the results are shown in figure 7. Figure 8 shows a 3-D EUCLID [17] view of the model cavity recently manufactured. This model cavity will be used to check that the cells are decoupled, to determine the coupling slots size, to estimate the unsymmetrical field distortion due to these coupling slots and to check the efficiency of the $\lambda/2$ stub used for the cathode holder. Measurements will proceed soon.

Project Status

Simulations are continuing for both the laser driven and thermionic cases. Different parameters will be investigated. A two stage experiment is foreseen. First, the gun itself will be tested in both operating modes. At

Table 1: Parameters for a typical run

Laser pulse length (ps)		30.
Laser spot radius (mm)		3.
RF Frequency (GHz)		3.
First cell length (cm)		3.325
Second cell length (cm)		5.835
Cell aperture radius (mm)		5.
Emittance at cathode (π mm mrad)		0.
Magnetic field (T)		0.
Number of particles		100
Charge in a bunch (nC)		2.
RF phase for laser pulse (deg.)		22.
Phase shift between cells (deg.)		160.
	1st cell	2nd cell
Max. electric field (MV/m)	70.	70.
Kinetic energy (MeV)	1.326	2.867
Bunch length (ps)	17.	17.
Peak current (A)	118.	118.
Bunch radius (r_{max}) (mm)	3.1	3.9
Max. energy spread (keV)	186.	33.
Max. energy spread (%)	14	1.1
Emittance (π mm mrad)	27.3	34.2
Emittance (RF) (π mm mrad)	18.7	15.5
Angular divergence (mrad)	44.7	24.2

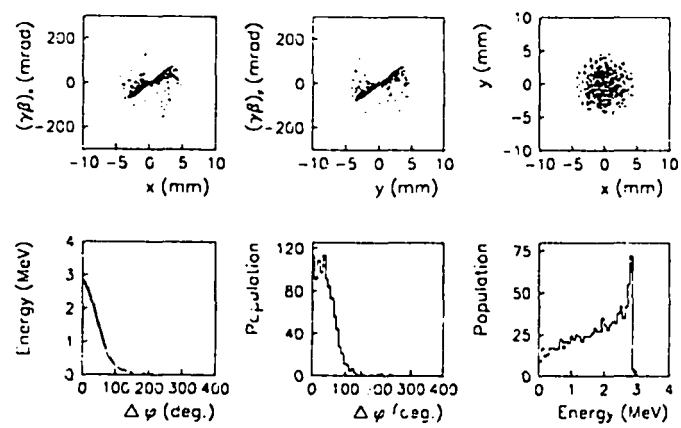

Fig. 4: Thermionic gun simulation

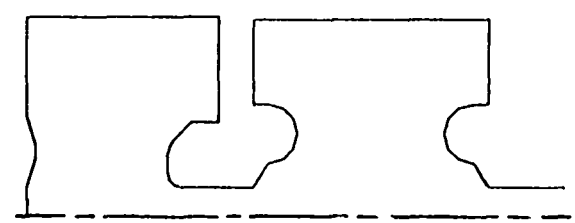

Fig. 5: Cavity contour (upper-half)

this stage, it will be followed by a transport line including measurement devices that could be either an "α-magnet" or a line similar to that of BNL [11]. At a second stage, it is planned to place the gun directly upstream from a high gradient accelerating structure. This small accelerator will then be followed by a magnetic bunching system. This configuration will allow us to experiment the method described by B. Carlsten [18] to reduce emittance. Simulations for this second stage of experiment will be performed very soon. A low-level RF model cavity was built. Measurements will start soon. The final prototype design should be completed by the end of 1990. The first beam is scheduled for the first semester of 1991.

Acknowledgements

We would like to thank Y. Thiery who performed all the lengthy simulation runs for the laser-driven case and B. Mouton who diligently modified PARMELA according to our wishes. We greatly appreciated the help of G. Le Meur when using PRIAM. We are pleased to thank H. Hanaki who performed the MAFIA calculations. M. Desmons is acknowledged for the mechanical design of the cavity. Many valuable advices from several colleagues were greatly appreciated. Finally, we wish to thank Dr. J. Le Duff for his constant support.

References

[1] G.A. Westenskow, J.M.J. Madey, Laser and Particle Beams (1984), Vol 2, Part 2, pp. 223-225.

[2] R.L. Sheffield et al., Proc. of the 1988 Linear Acc. Conf., Williamsburg, VA, October 3-7, 1988, pp. 520-522.

[3] C. Travier, Proc. of the Workshop on Short Pulse High Current Cathodes, Bendor, France, June 18-22, 1990.

[4] C. Travier, J. Gao, Proc. of the 2nd European Part. Acc. Conf., Nice, June 12-16, 1990.

[5] G. Bienvenu, Proc. of the 2nd European Part. Acc. Conf., Nice, June 12-16, 1990.

[6] H. Bergeret, M. Boussoukaya, R. Chehab, B. Leblond, J. LeDuff, Proc. of the Workshop on Short Pulse High Current Cathodes, Bendor, France, June 18-22, 1990.

[7] J. Gao, to be published in the Proc. of the 12th FEL Conf., Paris, Sept. 17-21, 1990.

[8] Version from R. Crandall and L. Young at LANL, with modifications from K.T. McDonald (BNL), B. Mouton (LAL) and H. Liu (IHEPB). User's manual from B. Mouton, LAL/SERA 89-356, 1989.

[9] G. Le Meur, Proc. of the 2nd European Part. Acc. Conf., Nice, June 12-16, 1990.

[10] K.T. McDonald, DOE/ER/3072-43, Princeton University, 1988.

[11] X.J. Wang et al., Proc. of the 1989 Part. Acc. Conf., Chicago, March 1989, p. 307.

[12] K.L. Brown et al., CERN 80-04, SPS Division, 1980.

[13] K. Halbach, R.F. Holsinger, Proc. of the 1976 Part. Acc. Conf., pp. 213-222

[14] e.g.: G. Fischerauer, T. Weiland, Proc. of the 2nd European Part. Acc. Conf., Nice, June 12-16, 1990.

[15] T.F. Wang et al., Proc. of the 1988 Linear Acc. Conf., Williamsburg VA, October 3-7, 1988, p. 373.

[16] H. Henke, W. Wuensch, CLIC note 108, 1990.

[17] 3-D mechanical design code from MATRA Datadivision.

[18] B.E. Carlsten, R.L. Sheffield, Proc. of the 1988 Linear Acc. Conf., Williamsburg VA, October 3-7, 1988, pp. 365-369.

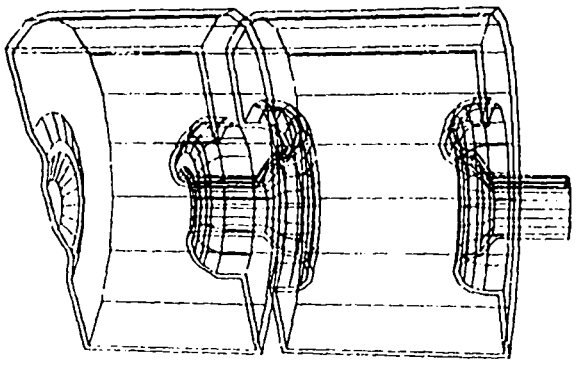

Fig. 6: PRIAM view of the cavity

Table 2: Cavity RF parameters

	1st cell	2nd cell
SUPERFISH (2-D)		
Frequency (MHz)	2993.8	2990.8
Shunt impedance Z_0 (MΩ)	3.26	3.39
Quality factor	11880	11353
Field ratio*	1.61	1.54
Mesh size (mm)	0.5	0.6
PRIAM (2-D)		
Frequency (MHz)	2989.5	2989.0
Field ratio*	1.3	1.3
Mesh size (mm)	1.-2.	1-1.5
MAFIA (3-D)		
Frequency (MHz)	2881.95	2832.3
Shunt impedance Z_0 (MΩ)	3.17	3.
Quality factor	11610	10420
Field ratio*	1.46	1.36
Mesh size (mm)	0.75-4.	0.6-2.5

*: Max. surface field / max. on-axis field

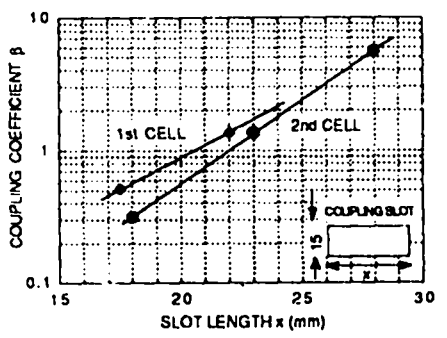

Fig. 7: MAFIA calculation of coupling slots

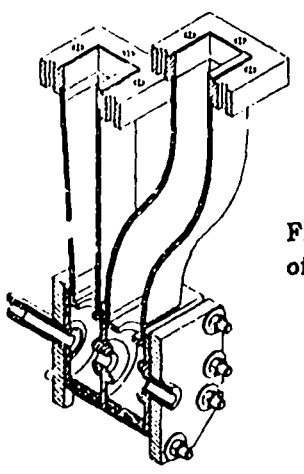

Fig. 8: EUCLID view of the model cavity

ELECTRON DIODES AND CAVITY DESIGN FOR THE NEW 4-MeV INJECTOR* OF THE RECIRCULATING LINEAR ACCELERATOR (RLA)

M. G. Mazarakis, D. L. Smith, J. W. Poukey, L. F. Bennett
W. R. Olson, and B. N. Turman
Sandia National Laboratory
P. O. Box 5800
Albuquerque, NM 87185

Abstract

We have designed and constructed four types of electron-beam diodes for the new 4-MV RLA injector: a non-immersed foilless diode, a magnetically immersed foilless diode, a foil diode and an ion-focused foilless diode. They are tailored to fit the new injector cavity. The design goals were to produce high quality 10-kA to 20-kA electron beams with a $\beta_\perp$ smaller than 0.2 and a beam radius of the order of 2 cm. These beams will be matched to the RLA IFR channel so $\beta_\perp$ must be equal to or smaller than the square root of the ratio of the beam current versus Alfven current for $f_e = 1$. A reentrant anode geometry was selected for the injector cavity design, because it offers substantial savings on the required amount of ferromagnetic cores. The inner radius of the outside shell, now only 30 cm, would have been twice as large (60 cm) if a coaxial non-reentrant geometry had been adopted. The shape of the anode and cathode electrodes were carefully selected to minimize the electric field stresses. The field stresses on the inner surface of the outer shell do not exceed 200 kV/cm.

Introduction

Figure 1 is a schematic diagram of the Sandia Laboratories recirculating linac (RLA). The focusing of the intense relativistic electron beam (IREB) is accomplished with the aid of an ion focusing channel (IFR). The plasma channel is generated by the ionization of 0.1 to 0.4 mTorr argon or xenon gas. The usual Sandia technique of low-energy electron-beam (LEEB) ionization(1) is utilized to form the plasma column. Figure 1 depicts a closed racetrack; however, an open-ended spiral configuration(2) is as easy to implement, and it is being studied in parallel with the racetrack.

In the recirculating experiments reported up to now we have utilized two IREB injectors; a 1.3-MV Radial Isolated Blumlein (RIB) and the 4-MV IBEX accelerator. Both injectors have the shortcoming of a triangular voltage wave form with a very small flat top (~ 10 ns). This makes the design and operation of the electron diode sources difficult and the matching of the produced beam to the transport and injection system inefficient(3). In addition, since the beam erosion in the IFR channel is dependent, the remaining beam pulse length following the first recirculation would be very short.

*Supported by the U. S. DOE contract DE-AC04-76DP00789 and DARPA/AFWL ARPA order No. 5789.

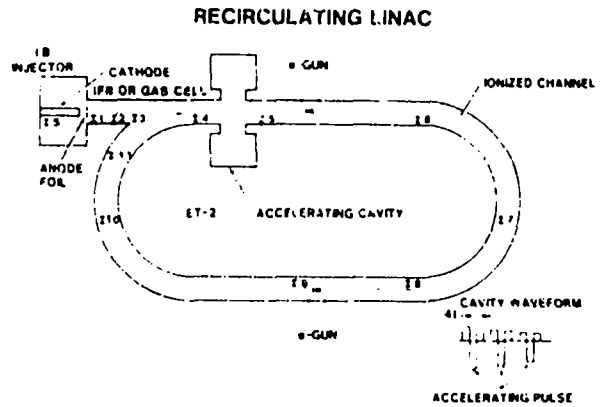

Fig. 1: Schematic diagram of the RLA. Closed racetrack channel configuration.

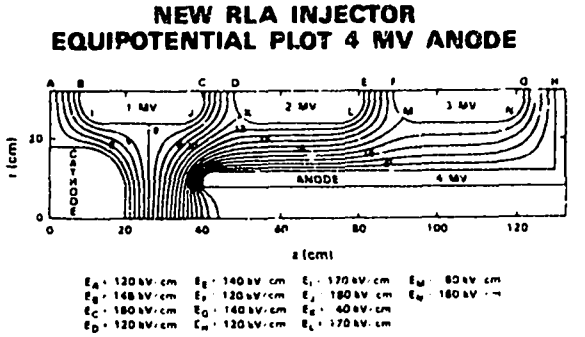

Fig. 2: The new 4-MV RLA injector cavity design and equipotential plots. The magnetically non-immersed foilless diode geometry is also shown.

A new 4-MV injector which produces a longer duration (40 ns FWHM) voltage pulse with almost rectangular shape (25 ns full width at 90% peak) is currently being constructed. Figure 2 shows a drawing of the new injector cavity. Four series-stacked, 1-MV ferro-magnetically isolated cavities provide the voltage waveform of Figure 3 at the A-K gap of the electron beam diode. MAGIC PIC CODE(4) was utilized to calculate the voltage waveform at the diode. The timing and voltage of each of the four feeds was estimated using several network solver code models. A number of 4-MV electron diodes were designed to fit the new injector and will be discussed in this paper.

Electron Diode Sources for the 4-MV Injector.

a. Non-Immersed Foilless Diode(3):

This diode is our best choice because it produces the lowest temperature electron beams

which can be magnetically transported in a vacuum channel with minimum losses or beam quality deterioration. It operates with minimum gas load release from the cathode and large (~ 20cm) A-K gap. However, in order to obtain good beam quality and transport, fine tuning of the solenoidal coils and voltage pulse with substantial flat top is required. Figure 2 shows the accelerating cavity fitted with the non-immersed foilless diode. The electrode surface shapes and the location of the A-K gap are selected in a way to minimize the field stresses on the electrodes and keep them below 200kV/cm.

The electron emitting area of the cathode surface is defined by a layer of felt cloth. The emitting threshold for felt is of the order of 60 kV/cm. Figure 4 shows the electron trajectories obtained with TRAJ[5] code.

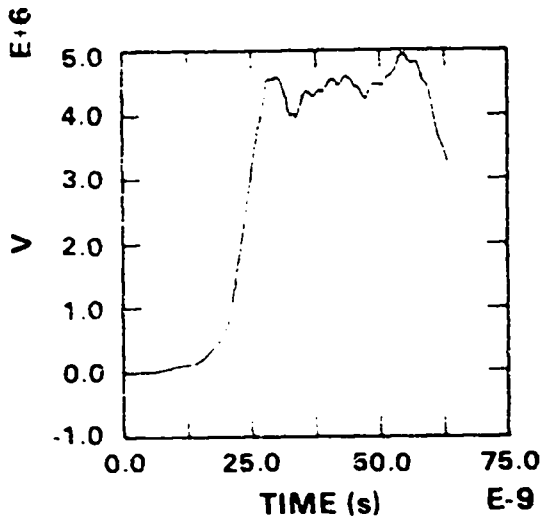

Fig. 3: MAGIC calculated output voltage wave form of the new injector.

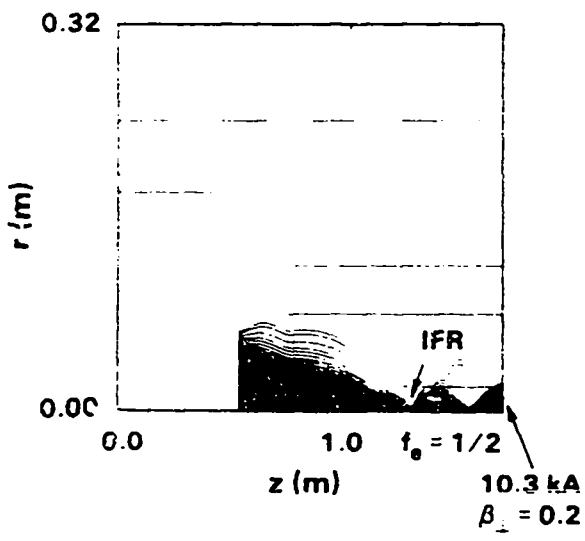

Fig 4: Electron trajectories for a 4-MV, 10-kA beam.

b. Magnetically Immersed Foilless Diode.

Figure 5 shows a schematic diagram of the hardware accommodating both an immersed foilless diode (solenoidal coil on) and a non-immersed foil diode (solenoid off). The magnetically immersed foilless diode produces (Figure 6) a relatively low temperature beam. The required large magnetic field makes it somewhat difficult to match the beam to the IFR channel. However, we have designed magnetic flux excluders which minimize plasma column deterioration at the injection point. Figure 6 shows an electron map of the magnetically immersed foilless diode A 1.6mm radius cathode tip produces 10-15 kA electron beams with similar emittances to the non-immersed foilless diode. Because of the small cathode radius the contribution after extraction from the magnetic field to the total beam transverse velocity $\beta_\perp$ of the canonial angular momentum is small.

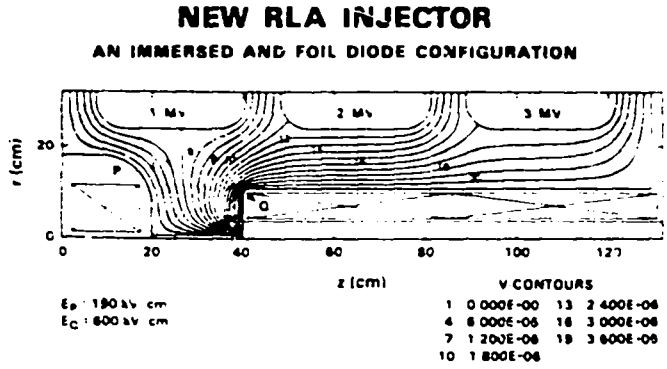

Fig. 5: Schematic diagram showing how the same hardware can accommodate two types of diodes: magnetically immersed and foil diodes.

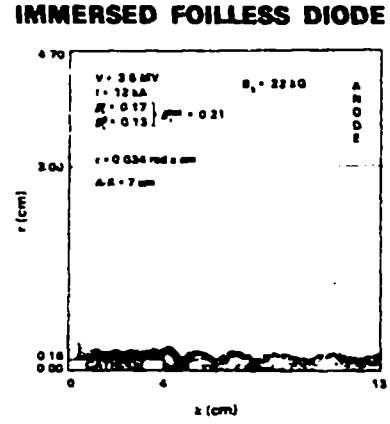

Fig. 6: The magnetically immersed foilless diode produces a low emittance beam.

c. Apertured Foil Diode.

By properly aperturing the anode foil (Figure 7) we can select a fairly cold, 10-15 kA beam. Fortunately the current coming from the shank does not mix with the central part of the beam which has a very low transverse velocity component and can be apertured easily.

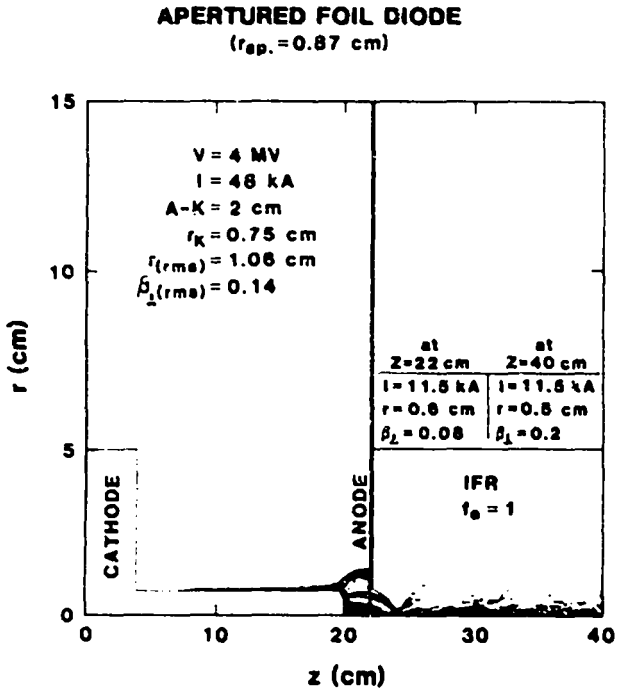

Fig. 7: 4-MV foil diode electron map.

d. Ion Focused Foilless Electron Diode[6]

This diode is similar to the apertured foil diode but without the anode foil, and it has a smaller bore aperture and larger A-K gap. We recently postulated the mechanism of operation of this diode and experimentally verified it with the IBEX accelerator. At the beginning of the pulse the electron beam diverges and hits the aperture, depositing enough energy to create a surface plasma sheathe. Positive ions from the sheathe are accelerated towards the cathode, providing space charge neutralization and focusing the electron beam into the aperture. A 700 A ion current (Figure 8) moving in the direction opposite to the beam can focus 15 kA of the electron beam into the 3 cm aperture.

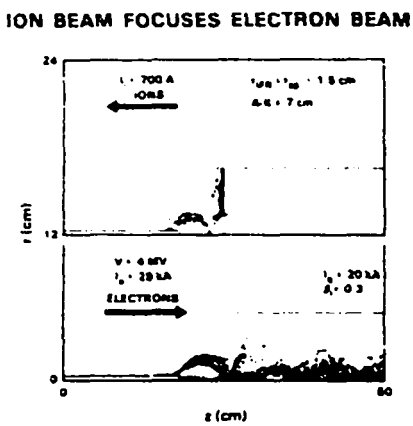

Fig. 8: Foilless apertured diode focused with the positive ions emitted from the anode plasma sheathe

Conclusions

Four types of electron diode sources have been designed and constructed to fit our new 4-MV injector. They produce low temperature and low emittance electron beams that can be injected and propagated inside the IFR channel with high transport efficiency. The injector assembly is approaching completion, and the first beam tests are projected for October 1990.

References

1. W. K. Tucker, et al., Proc. IEEE Part. Accel. Conf. Washington, DC, March 1987, IEEE No. 87CH2387-9, p. 957.

2. S. L. Shope, et al., Proc. IEEE Part. Accel. Conf. Washington, DC, March 1987, IEEE No. 87CH2387-9, p. 917.

3. M. G. Mazarakis, et al., Proc 1988 Linear Accelerator Conf., Williamsburg, VA, October 1988, CEBAF-Report-89-001 June 1989, p. 345.

4. B. Goplen, et al., Mission Research Corp. Report MRC/WDC-R-068, 1983.

5. J. W. Poukey, Proc. of the 12th Conf. on Numerical Simulations of Plasms, San Francisco, CA, Sept. 1987

6. J. W. Poukey, M. G. Mazarakis and R. C. Platt, "Experimental Verification of an Ion-Induced-Focus Model for the Recirculating-Electron-Beam Injector" Accepted for publication, Applied Physics Letters, August 1990.

NUMERICAL MODELS OF INJECTORS FOR HIGH-CURRENT ELECTRON LINACS*

J. W. Poukey and M. G. Mazarakis
Sandia National Laboratories, Albuquerque, NM 87185

Abstract

We have used four types of codes to aid in the design of injectors for our high-current linacs. The typical procedure begins with the electrostatic field code JASON to find a geometry with acceptable field stresses. Next, the 2-D electromagnetic PIC code MAGIC[1] is used to study the addition of voltage waves from the input feeds, and the resulting beam generation and dynamics in a space-charge-limited diode. Then, the 2-D trajectory code TRAJ[2] is used for parameter and optimization studies. Finally, in some cases 3-D effects may be examined with the PIC code QUICKSILVER.[3]

Introduction

The codes used in modeling injectors for our electron linacs are summarized in Table I. Here we include only codes used in designing an injector itself, not the circuit codes used to design the pulse power system feeding the injector.

TABLE I
Injector-Design Codes at Sandia

Code	Space Dimensions	Type	Running Time
JASON	2	e.s. fields	secs
MAGIC	2	e.m. PIC	hour
TRAJ	2	trajectory	min
QUICK-SILVER	3	e.m. PIC	many hours

In the Table, "e.m. PIC" refers to an electromagnetic field solver coupled with particle-in-cell algorithms.[4] "Trajectory" refers to a "ray-trace" method coupled to electrostatic and magnetostatic solvers. The run times are given only to indicate orders of magnitude on a Cray machine.

The codes in Table I have been used to study many facets of a variety of electron accelerators. In this paper we shall briefly describe some recent results for three particular injectors for the accelerators listed in Table II. Here the voltages and currents are nominal values, applying to the injectors only.

*Work supported by the U.S. Navy, DARPA, and U.S.D.O.E.

TABLE II
High-Current Linac Injectors at Sandia

Accelerator	Voltage	Current	B-Field, Cathode
RADLAC	12-14 MV	50-90 kA	immersed
RLA	4 MV	10 kA	non-immersed
CASSANDRA	1 MV	1 kA	non-immersed

RADLAC

Until recently, RADLAC[5] indeed qualified as an induction linac, using an injector as the source of a beam to be post-accelerated by 4-6 gaps. Recently, however, the machine has been re-configured in the Hermes III style.[6] This is illustrated by the MAGIC calculation in Fig. 1; note that the z-scale is very compressed relative to the r-scale (we work in cylindrical coordinates r, θ, z).

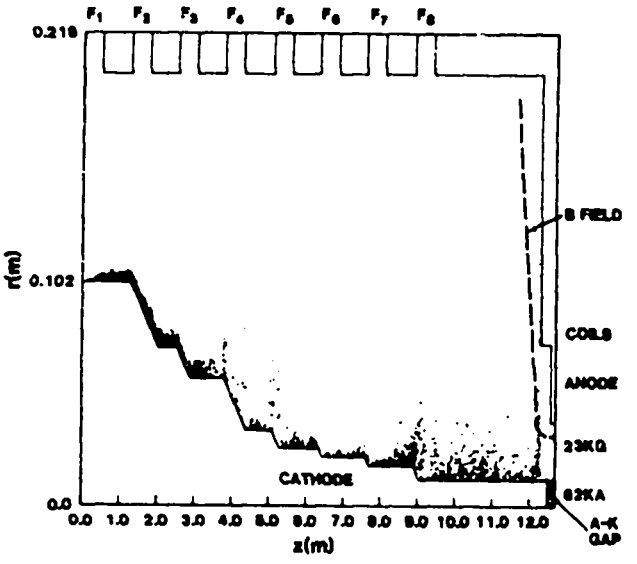

Fig. 1. The latest RADLAC injector ("SMILE") as simulated by MAGIC, shown at a time (60 ns) near peak total voltage on the A-K gap. The dots are electrons, and one B-field line is shown (cathode tip in 23 kG). In this example, a 62 kA beam is produced for about 12 MV on the A-K gap. The radial current loss occurs mostly along the fringing B lines. The F_i are the voltage feeds.

In Fig. 1, about 2 MV is fed into each radial line F_i, but the pulse shapes are somewhat triangular so there is some LI loss, and the sum voltage on the diode is about 12 MV, instead of 16 MV. The essence of the design is to use self-magnetic-insulation over most of the cathode shank. For strong applied fields (23 kG) on the diode, however, a substantial radial loss current develops along the fringing B-lines. Experiments with this new RADLAC configuration are now underway, and will be reported elsewhere at this conference.[7] Details of the diode design and the conditioning-cell behavior have also been simulated and will be discussed in future papers.

RLA

The Recirculating Linear Accelerator[8] has had a number of injectors designed for it, including laser diodes, immersed and non-immersed foilless diodes, and apertured diodes with or without anode foils. A JASON calculation of a diode at low voltage of 1.3 MV, with maximum stress 200 kV/cm, is shown in Fig. 2. Here, both anode and cathode surface shapes are optimized for minimum E-field stress: the bipolarity of the applied voltage pulse necessitates preventing emission from all surfaces except the inner $r \lesssim 5$ cm on the cathode.

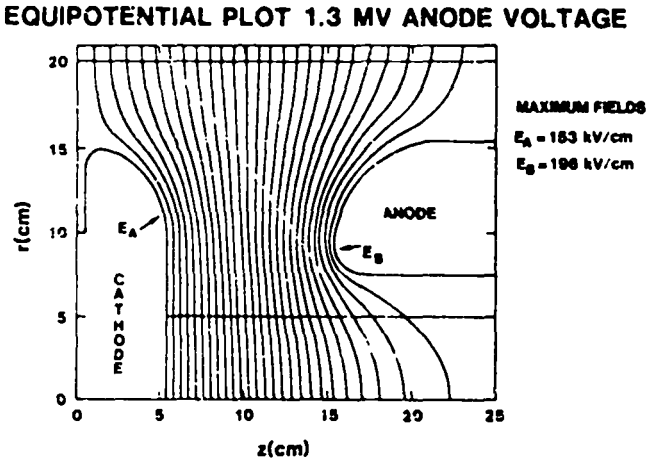

Fig. 2. A sample JASON run of an RLA diode, with surface shapes chosen to keep electric stress < 200 kV/cm.

A more recent design, at peak V = 4.6 MV on the diode (1.15 MV per feed), is shown in Fig. 3. Here the (equilibrium) trajectory code TRAJ was employed, although JASON was used in designing the feeds and electrode shapes. Also, MAGIC was run with realistic input time-dependent feed voltages, and at peak diode (total) voltage, the MAGIC result agreed very well with the TRAJ solution, justifying use of the much more economical TRAJ (see Table I) code to do parameter variations on this type of injector. The four-feed re-entrant injector in Fig. 3 is now being assembled.[9]

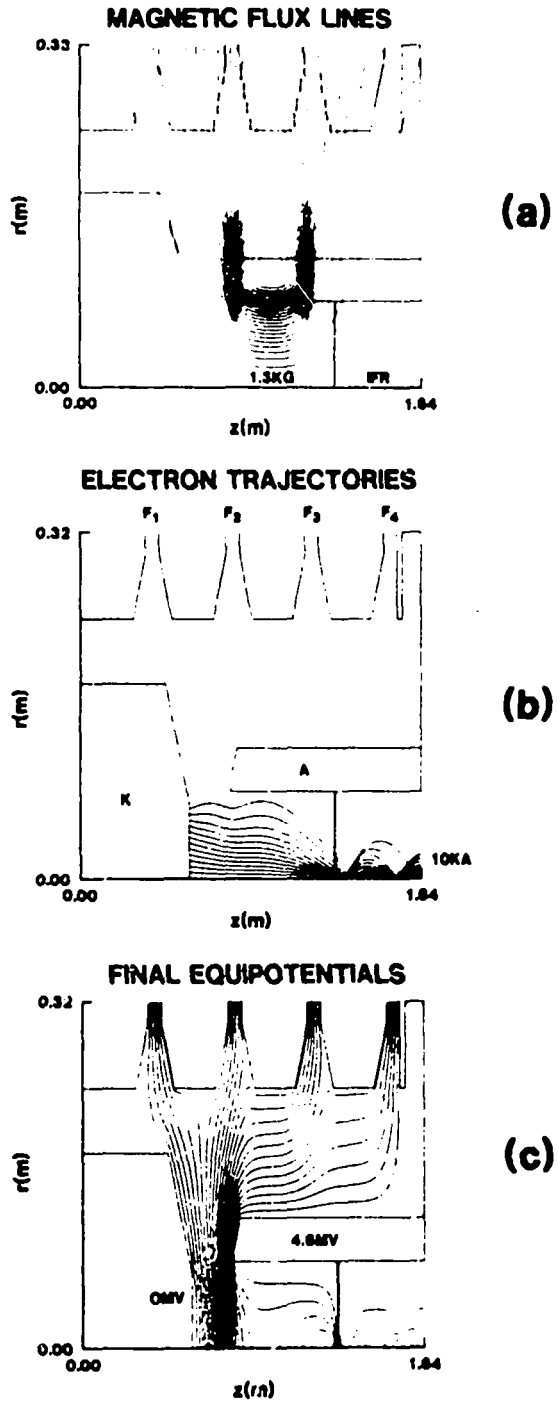

Fig. 3. The new RLA injector, as modeled with TRAJ. Top (a): applied B field. Middle (b): electron trajectories (every fifth is plotted). Bottom (c): equipotentials with beam space charge.

The physical result in Fig. 3 is straightforward. The 10 kA beam is focused by the applied B onto an IFR channel (f=0.5), which guides the beam to the "racetrack" for further acceleration. Based on further TRAJ runs, this design is not unduly sensitive to small variations in voltage amplitude, applied B, or IFR modeling details.

CASSANDRA

The 1 kA, 1 MV CASSANDRA[10] injector is shown in Fig. 4; again, TRAJ was used. The basic system design is similar to the RLA in Fig. 3, with two important differences. First, a Pierce geometry was employed for the cathode to help focus the lower-current beam. Second, no IFR channel is used, necessitating a more complicated applied B (Fig. 4a, b). The result, after some parameter variation, is a very well-focused beam (Fig. 4c) which will be further accelerated by gaps located downstream. Only the first two gaps have been simulated thus far; no problems are foreseen provided the applied B transport coils are designed carefully.

QUICKSILVER

It is not usually practical to simulate large systems with 3-D PIC codes, so work thus far has concentrated on relatively simple off-center beam effects. For example, an RLA beam (10 kA) in a vacuum wire conditioning cell with initial 1 cm offset is seen to evolve into a "corkscrew" mode with a 20% loss; a return current of 5 kA is induced in a 2 mm wire carrying 15 kA. Injector asymmetries could also be studied with this code, in principle.

Conclusions

The utility of the design codes MAGIC, TRAJ, and JASON has been demonstrated in the problem of injector design for electron linacs in the multi-kA range. Where comparisons with experiment can be made, the codes are found to agree well with reality. Besides design aid, the major value of the codes is found to be in making sensitivity and optimization studies.

References

1. B. Goplen et al., Mission Research Corp., report MRC/WDC-R-068, 1983.
2. R. B. Miller et al., J. Appl. Phys. 62, 3535 (1987). Also, J. W. Poukey, Proc. 12th Conf. Num. Sim. Plasma, San Francisco, 1987, PM10.
3. M. L. Kiefer et al., Bull. Am. Phys. Soc. 34, 2079, (1989).
4. C. K. Birdsall and A. B. Langdon, Plasma Physics via Computer Simulation (McGraw-Hill, 1985).
5. R. B. Miller et al., J. Appl. Phys. 52, 1184 (1981).
6. T.W.L. Sanford et al., J. Appl. Phys. 67, 1700 (1990).
7. See paper "Smile": A New Version for the RADLAC II Linear Accelerator, by M. G. Mazarakis et al., this conference.
8. M. G. Mazarakis et al., Proc. Linac Conf. Newport News, VA, Oct. 3-7, 1988, CEBAF-Report 89-001, p. 345.
9. See paper "Electron Diodes and Cavity Design for the New 4-MeV Injector of the RLA," by M. G. Mazarakis et al., this conference.
10. J. M. Wilson et al, Proc. 19th Power Modulator Symposium, June, 1990, paper 11.5.

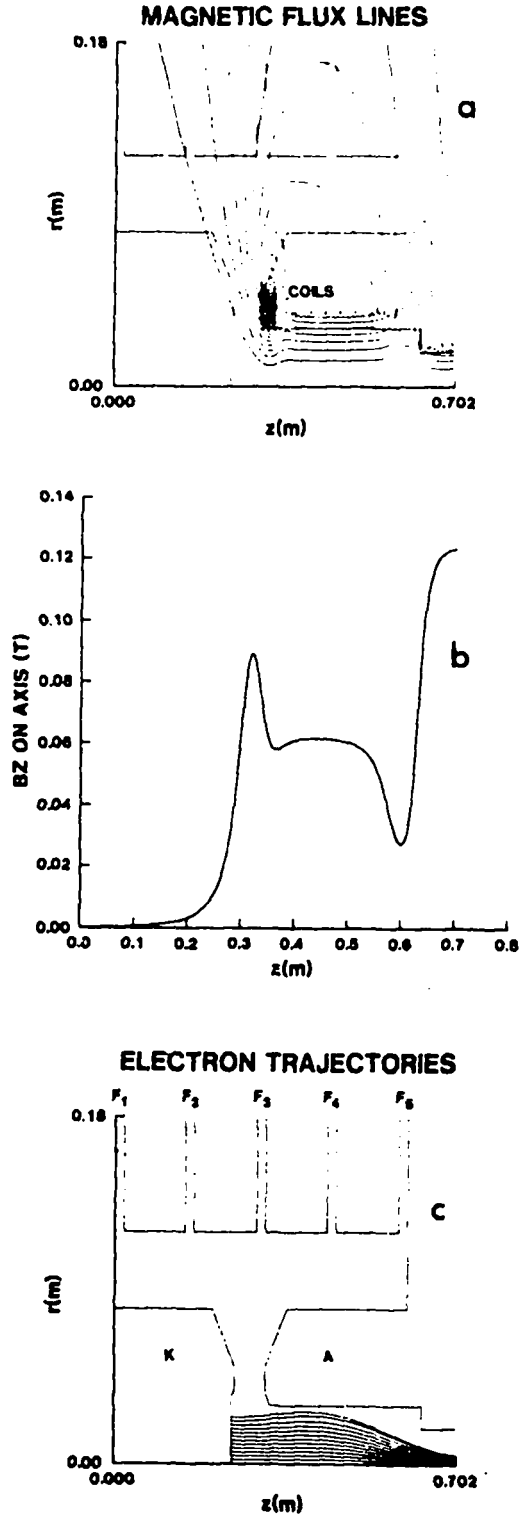

Fig. 4. TRAJ model of the CASSANDRA five-feed injector at 1 MV, 1 kA. Note the Pierce cathode design. Unlike Fig. 3, magnetic transport (not IFR) is used downstream.

THE LINAC INJECTOR FOR THE ANL 7 GeV ADVANCED PHOTON SOURCE*

A. Nassiri, W. Wesolowski, and G. Mavrogenes
Argonne National Laboratory
9700 South Cass Avenue
Argonne, IL 60439 USA

Abstract

The Argonne Advanced Photon Source (APS) linac system consists of a 200 MeV electron linac, a positron converter, and a 450 MeV positron linac. Design parameters and computer simulations of the two linac systems are presented.

Introduction

The Argonne Advanced Photon Source is a 7 GeV synchrotron X-Ray facility. The APS machine parameters have been described.[1] Here, we will focus on the design of the linac systems. We present the results of beam dynamics calculation and computer simulations of the two linac systems.

Electron Linac

General Description

The electron linac components are shown in Figure 1. An electron gun produces pulses of 30 nsec at a 60 Hz repetition rate with a nominal energy of 110 keV and a current of 2.5 A. Each 30 nsec macropulse traverses a standing wave single-gap, pre-buncher operating at 2856 MHz and is broken into approximately 86 micropulses via velocity modulation. After a 22 cm drift space, the micropulse of electrons has been longitudinally compressed to 60°. Further longitudinal compression to 12° is achieved by passing through a constant impedance $\beta = 0.75$ travelling waveguide main buncher consisting of six cavities. The reference particle energy at exit of the buncher is about 1.4 MeV. The bunched beam is then accepted and accelerated through five constant gradient travelling waveguides, each approximately 3 m long, to their final energy of more than 200 MeV.

Dynamics of Bunching

The dynamics of bunching have been described before by Slater.[2] In a gap-and-drift buncher, a beam of electrons passes through a single-gap cavity excited by a sinusoidal electric field. For uniform electron velocity, the higher order harmonic effects can be neglected. In the low space charge limit,[3] the change in energy of each electron as it traverses the gap is given as

$$\Delta\gamma(\theta) = -\alpha\,\xi_{gap}\sin\theta_o \qquad (1)$$

$$\theta_o = -\omega t$$

$$\alpha = \frac{eE\lambda}{m_o c^2} = \text{normalized electric field}$$

$$\xi_{gap} = \frac{\Delta z_{gap}}{\lambda} = \text{normalized length of gap}$$

Electrons which reach the gap when $\omega t<0$ are decelerated while electrons which arrive at the gap when $\omega t>0$ will gain energy. As the electrons traverse the drift space, they bunch around the electrons which crossed the gap at $\theta=0$. As the electrons travel the drift space, θ will change as

$$\frac{\Delta\theta(z)}{\Delta\xi} = \frac{2\pi z}{\lambda}\left(\frac{1}{\beta_o} - \frac{1}{\beta}\right) \qquad (2)$$

where β_o is the initial normalized velocity of the electrons.

Integration of the above equation gives θ as a function of ξ along the drift space. Figure 2 illustrates the bunching properties of the gap-and-drift prebuncher. Particles traversing the gap at $\theta_o=-90$ have the highest energy, while particles crossing the gap at +90 have the lowest. At $\xi=2.0$, electrons are bunched into about 60° of phase.

In the travelling waveguide buncher, assuming a uniform electron velocity, the longitudinal component of the field is written as

$$E_z = E\sin\omega(t-z/v_o) \qquad (3)$$

The equation of motion of an electron in this field is given by:

$$dp/dt = eE\sin\omega(t-z/v_o) \qquad (4)$$

*Work supported by the U.S. Department of Energy, Office of Basic Sciences, under Contract W-31-109-ENG-38.

In a reference frame, moving with velocity v_o of the travelling wave, the displacement z' with respect to the moving frame is $z'=z-vt$.

In this frame the Hamiltonian[2] is given by:

$$H = \sqrt{m_o^2 c^4 + p^2 c^2} - pv_c - eE \frac{v_o}{\omega} \cos \frac{\omega z'}{v_c} \qquad (5)$$

and the equations of motion are derived from the Hamiltonian

$$\frac{dp}{dt} = -\frac{\partial H}{\partial z'}, \quad \frac{dz'}{dt} = \frac{\partial H}{\partial p} \qquad (6)$$

Since the Hamiltonian is not an explicit function of time, it is a constant. Figure 3 shows the phase space plot. The bounded electrons follow a closed orbit about the point $\theta=0$, $p=p_o$. Electrons going slower than the wave lose energy until they fall behind the phase null. They then gain energy until they are synchronous with the wave and they continue to gain energy until they pass the phase null ($\theta=0$). Then they lose energy until they are slower than the synchronous velocity and the cycle repeats.

PARMELA Simulations

PARMELA has been used to design, study, and simulate the beam dynamics in the electron linac. About 65% of the particles can be bunched within approximately 12°. The energy spread at the end of the buncher is approximately 1 MeV. Velocity modulation and longitudinal space charge are the main factors contributing to the energy spread in the bunching system. The electrons next traverse five accelerating sections.

Figure 4 shows the results of beam simulations at the positron target. The reference particle has an energy of over 200 MeV with a current of approximately 1.7 A. A beam spot size of 3 mm and emmitance of $\epsilon \leq 1.2$ mm-mrad can be obtained at the target. It should be mentioned that PARMELA does not take into account the effect of beam loading. However, we have introduced a phase shift of about 15° at the beginning of the second waveguide to simulate the effects of beam loading. The overall energy spread is about ± 8%. This result is in agreement with beam loading calculations using TRANSPORT.

Beam Transport Focusing System

PARMELA and TRANSPORT have been used to design the focusing system for the electron linac. Simulations indicate that a set of three quadrupole triplets are adequate to provide focusing and transport properties.

Positron Production

Following the DESY design, the positrons are produced in a water-cooled, tungsten retractable target of thickness equal to two radiation lengths (7 mm). A double-layered pulsed solenoid located immediately after the target defines the solid-angle acceptance of the positrons. A field strength of 1.5 T is necessary. The accepted positron emittance is ϵ=330 mm-mrad (220 mrad x 1.5 mm) in each transverse plane when a beam size of 1.5 mm radius is used.

Positron Linac

Beam Focusing System

The positrons emerging from the pulsed solenoid are further focused by a solenoidal field of 0.4 T which encompasses the first two positron accelerating structures. The subsequent focusing system consists of a FODO array. COMFORT has been used for beam simulations. Figure 5 shows the beam envelope.

PARMELA Simulation

PARMELA has been adapted[4] to simulate the capture of the positrons from the target through the end of the positron accelerator. Results indicate that one could transport the positrons with a small phase spread, therefore the requirement of a 1% energy spread at 450 MeV can be met. See Figure 6. The normalized emittance of positrons at 450 MeV is 6.6 mm-mrad in each transverse plane.

Acknowledgement

The authors wish to thank R. Miller of SLAC, L. Young of LANL, and C. Kim of LBL for helpful discussions.

References

1. "7 GeV Advanced Photon Source Conceptual Design Report" ANL-87-15, April, 1987.

2. J. C. Slater, "Review of Modern Physics 20, p 473 (1948).

3. Mary Beth James, "Production of High Intensity Electron Buncher for the SLAC Linear Collier," PhD Thesis, SLAC Report 319 (1987).

4. A. Nassiri, Unpublished Report.

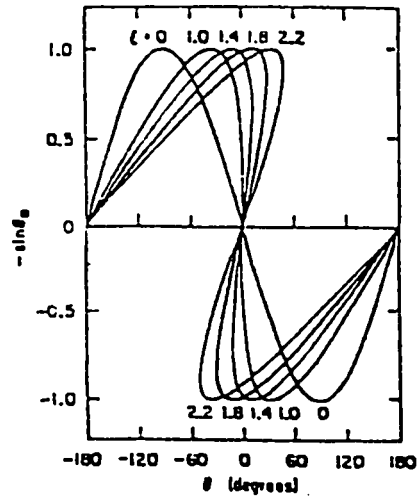

Figure 2 Constant ξ curves in phase space for a gap-and-drift prebuncher (from M. James)

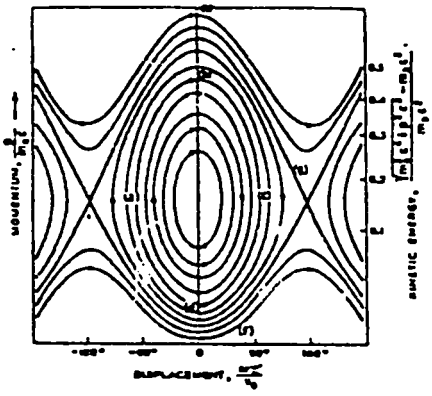

Figure 3 Constant phase velocity buncher phase space for $\beta_m < 1$ (from Slater)

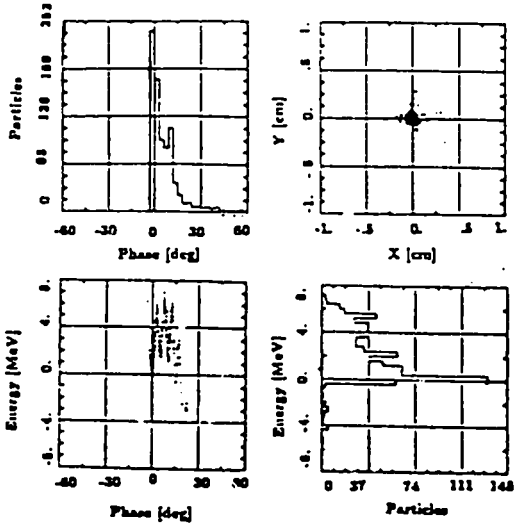

Figure 4 Beam simulation of electron bunch at the positron target

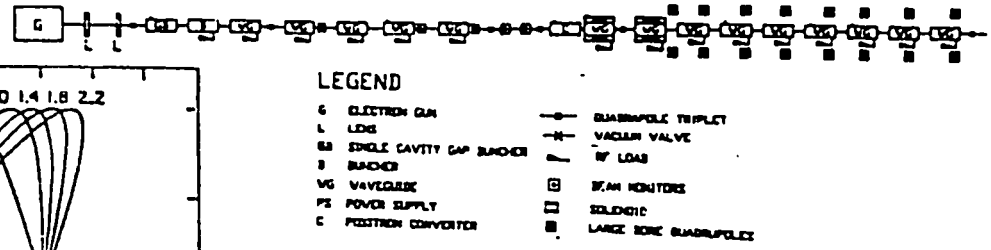

Figure 1 Linac Components

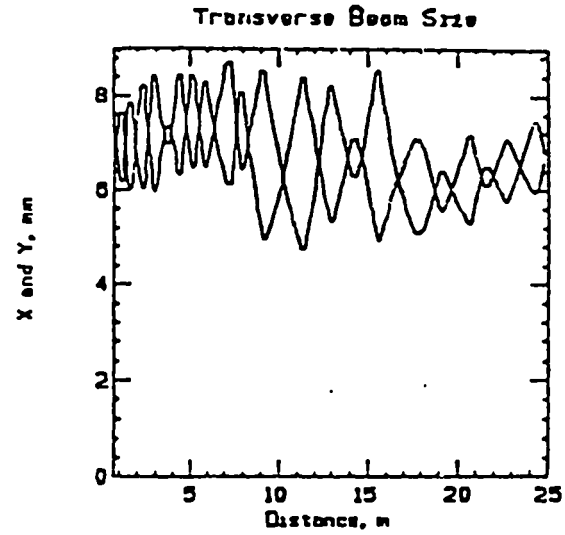

Figure 5 Beam envelope for positron accelerating sections

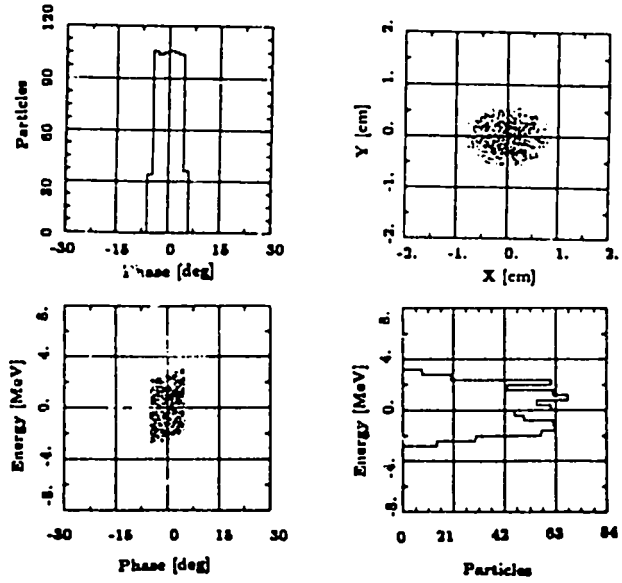

Figure 6 PARMELA simulation of positron beam at the end of the positron linac

THE LEP INJECTOR LINAC

R. Bossart, J.P. Delahaye, J.C. Godot, J.H.B. Madsen, P. Pearce, A. Riche, L. Rinolfi

CERN, CH-1211 Geneva 23

ABSTRACT

The LEP Injector Linac (LIL) has been working for two years of routine operation as the LEP injector. Performance limitations are discussed and typical beam measurements are presented. Measures to improve the reliability are explained and a scheme for possible improvements of the positron production is described.

INTRODUCTION

Operating since 1988 as the LEP source, three main objectives have been addressed:

- Measure and optimize the peak performances
- Improve the reliability
- Study an improved positron production scheme

Although the overall peak performance is above the nominal value, a consolidation programme has been set up to improve the long term reliability. In particular, a new gun modulator, a new bunching system, a change of accelerating section front-plates, a fixed target and an upgrading of the klystron modulators. In the light of future projects, the bottleneck of LIL would be the positron production and a study has been made to improve this parameter.

LIL PERFORMANCE

A detailed description of LIL is given in reference[1]. The design was optimized around its positron performance which is determined mainly by the characteristics of the electron beam on the target, the matching of the e^+ flux into the accelerating section, and further acceleration and transport downstream. Table 1 shows the beam performance of the linac providing the primary e^- beam:

Table 1
Peak Performance of Primary Beam at the Target

No-load energy:	225 MeV
Charge:	48 nC
Pulse length:	20 ns (at FWHH)
$\frac{\Delta p}{p} = \pm 8\%$	(full width at the base)
Horizontal beam size:	1 mm (FWHH)
Vertical beam size:	2.5 mm (FWHH)

The e^+ production is not very sensitive to spot size and position within [illegible] mm. Matching the e+ flux into the accelerating section is obtained with a pulsed solenoid (1.5 T) put right after the target.

With the bunching system optimized and LIL optics matched, several measurement sessions of the peak performance have been made. Results (for both beams) are reported in reference [2]. Table 2 gives a summary for e^+ production. Figure 1 presents a comparison of the peak performance reached and the design values.

Table 2
Positron Production Characteristics

Gun current:	5 A
Transmiss. efficiency in the buncher	80%
for primary beam:	80%
N^o of e^- on the target:	$2.9\ 10^{11}$
N^o of e^+ at the end of LIL total:	$17.4\ 10^8$
within $\frac{\Delta p}{p} = \pm 1\%$:	$12.9\ 10^8$
Unresolved conversion efficiency:	$6\ 10^{-3}$
Resolved conversion efficiency:	$4.4\ 10^{-3}$
Final energy:	500 MeV

RELIABILITY IMPROVEMENTS

A new gun modulator has been designed to improve the maintainability. The control of all parameters is made through fibre optic links. The platform reaches a maximum of 100 kV, and the working value is 80 kV. The amplitude of the pulse, applied to the grid of the gun, is adjusted according to the beam intensity for e^- and e^+ cycles. A facility which allows the pulse length to be varied is also implemented. A beam test line has been designed and installed to measure the performance in the laboratory.[3].

The present buncher was designed for a maximum beam current of 20 A and an input energy of 100 keV. It provides a no-load energy gain of 28 MeV with a bunching efficiency of 60 % within $\Delta\phi = 16°$ (80% of particles). However, after several RF break-downs occurred in the buncher, a series of machine studies were made [4], and the results obtained helped clarify the behavior of the bunching system. Presently, a project is going on to replace the buncher by another one seven times shorter. The output energy will be reduced to 4 MeV. Calculations have shown that the bunching efficiency could be kept similar to the present one in the range of a beam intensity of 10 A [5]. The mechanical assembly will be simplified, reduced in size, and the construction of a spare will be possible at a relatively low cost. The free space will be used to install a matching section between the buncher and the first accelerating sections and to add instrumentation. The new gun modulator and the new bunching system will be installed on LIL, at the end of 1990.

During the construction of LIL, the envelope end plates of the accelerating sections were corroded. With time, several vacuum leaks appeared. All sections were removed from the tunnel and the corroded welds redone [6].

The SLED type cavities, called LEP Injector Power Savers (LIPS) [7], used to increase the RF peak power, have their end flanges made of mild steel. This was a weak point for the vacuum in the LIPS tank. An improvement has been made with the construction of a new tank built completely in stainless steel with larger pumping holes and new types of gasket. In August 1990, a new set of cavities were successfully tested with an RF peak power of 32MW.

During 1989 two designs of target systems without any mechanical movement were investigated:

i) The required e^- intensity is made to pass through a 0.25 mm diameter hole on the axis of the target. The energy spread in the e^- beam is larger than before.

ii) Deflecting the electron beam (cycle e^-) through a 2.5 mm diameter hole beside the 5 mm diameter target [8]. Figure 2 gives a sketch of the layout. Behind the target, focusing is given by solenoids. The extended version of TRANSPORT [9] was used to calculate the new e^- trajectory. Both solutions were used in operation during LEP runs and the stability was good. In the first solution, the small central hole, reduces the e+ production by roughly 10% and the continuous high beam intensity gives a large activation in the target area. Hence the second method is currently being used [10].

Over the last two years the reliability of the klystron modulators has been increased [11]. Despite more than 5000 hours of beam requested yearly, the downtime, due to modulator faults has been reduced. As with the SLAC experience a regular adjustment of each thyratron reservoir voltage has been found necessary to minimize the faulty shot rate, and obtain long lifetimes. The present useful lifetime of these tubes looks to be in excess of 17000 hours at the 100 Hz rate with 35 kV, 3400 A and a voltage pulse width of 6.5 µs. The individual klystron power outputs have been adjusted to give between 13.5 and 24 MW with a 4.5 µs RF pulse width, depending on their position in the linear accelerator. The present indications are that the average lifetime of these devices does not exceed 15000 heater hours.

New PIN-switches have been installed in spring 1990, in order to work with a higher RF-power (up to 400 W) at the input of the klystrons. The reliability of the phasing system for the klystrons has been improved by a modular construction of the RF-phase detectors and a new design of the signal processing for phase correction by a new microprocessor system.

STUDY FOR IMPROVED POSITRON PRODUCTION

The positron production rate would have to be improved for two possible future CERN projects namely the LEP luminosity improvement programme[12] and a possible Beauty Factory (BFI)[13]. The positron rate including the capture and acceleration by LIL as well as the accumulation is given by: $\frac{dN^+}{dt} = \eta_a \eta_p N^- E^- f$; where η_a is the accumulation efficiency, η_p is the e^- to e^+ conversion efficiency, N^- is the number of particles in the primary beam, E^- is the energy of the primary beam, f is the linac repetition frequency. In principle all these different parameters can be improved. Schemes[12] based on the increase of the primary beam power are summarized in Table 3.

Moving the converter target downstream in the linac (Fig 3) and powering two adjacent accelerating sections with one modulator equipped with LIPS, allows to increase the mean acceleration from a conservative value of 12 MeV/m to 18 MeV/m. The primary beam energy is then enhanced from 220 MeV to 700 MeV. The remaining RF sections of LIL are then sufficient to accelerate the beam to the operational energy or up to 700 MeV, which would reduce the accumulator damping time by a factor 2.7 and therefore permit a LIL repetition frequency of 150 Hz which is possible with some improvement of the klystron modulators[11]. The primary beam intensity is presently limited by the momentum spread introduced by the beam loading in the accelerating sections. A higher field in the RF sections would allow the higher charge to be accelerated within the same momentum spread. Finally η_p would also be improved with a flux concentrator inspired by the SLC system and η_a could be raised by using a magnetic energy compressor at the end of LIL. As a preparation, high gradient tests will be performed with the spare LIL section.

CONCLUSIONS

The typical performance of the LEP Pre-Injector is now a factor 3 for e+, and a factor 5 for e-, above the nominal requirements assumed during the LEP design. The reliability of LIL is such that beam availability for the LEP machine is close to 96 % of the scheduled time. The scheme and the necessary LIL modifications will be implemented if and when an improved positron performance will be required.

Table 3

Parameters	Unit	Design performance	Present max. performance	Required for LEP 200	Required for BFI
e^+ accumulation rate	10^{10} e^+/s	1.8	6.5	20	45
Primary beam power	W	576	1056	3065	7380
Number of particles	10^{11}	1.8	3.0	4.3	4.6
Primary beam energy	MeV	200	220	440	660
Repetition frequency	Hz	100	100	100	150

ACKNOWLEDGEMENTS

We acknowledge the contributions made by all of the staff of the Lepton Group in the PS division and the Operation Team.

REFERENCES

[1] J.H.B. Madsen, CERN Divisional Report PS 89-56 (LP)

[2] J.P. Potier, L. Rinolfi, CERN Internal Note PS/LP 90-12

[3] A. Pisent, L. Rinolfi, CERN Internal Note PS/LP 90-14

[4] R. Bossart, J.P. Delahaye, L. Rinolfi, CERN Internal Note PS/LP 89-36

[5] A. Pisent, L. Rinolfi, CERN Division Report 90-.58 (LP)

[6] J.C. Godot, CERN Internal Note PS/LP 89-17

[7] A. Fiebig, C. Schieblich, EPAC, Nice (1990) and CERN Divisional Report PS 90-13 (RF)

[8] A. Riche, CERN Internal Note PS/LP 89-23

[9] A. Riche, EPAC, Nice (1990) and CERN Divisional Report PS 90-22 (LP)

[10] R. Bertolotto, J.H.B. Madsen, A. Riche, L. Rinolfi, Internal Notes PS/LP 89-24 and 89-27

[11] P. Pearce, S. Hutchins, 19th Power Modulator Symposium, San Diego (1990) and CERN Divisional Report PS 90-27 (LP)

[12] J.P. Delahaye, K. Hübner, CERN Internal Note PS/LP 89 - 32

[13] B. Autin et al., EPAC, Nice (1990) and CERN Divisional Report PS 90-25 (LP)

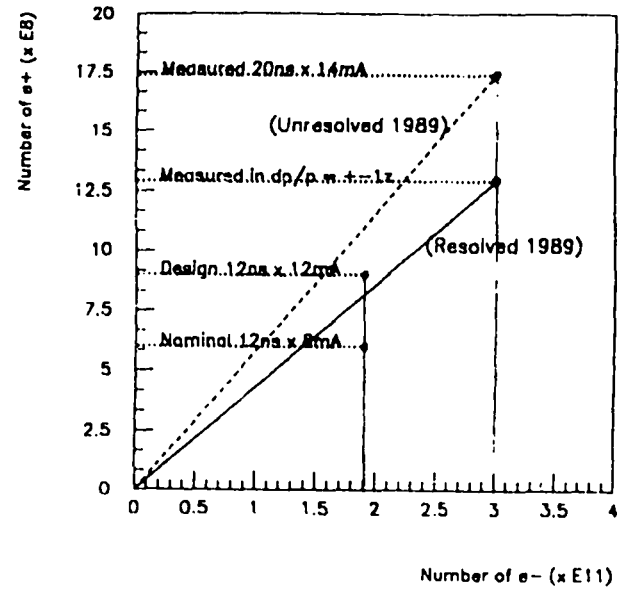

Figure 1: Comparison of peak performance to design performance

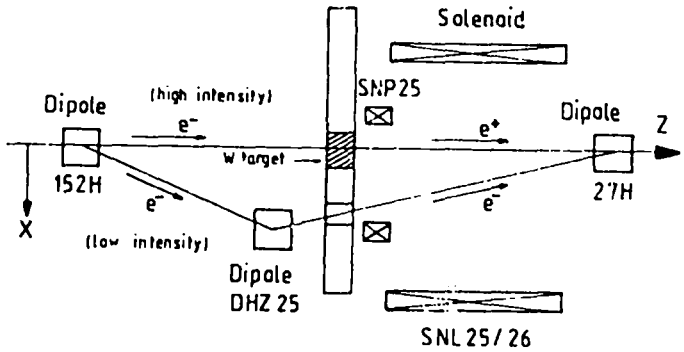

Figure 2: Layout with a fixed target for the e⁻ and e⁺ production

A) Present LIL configuration

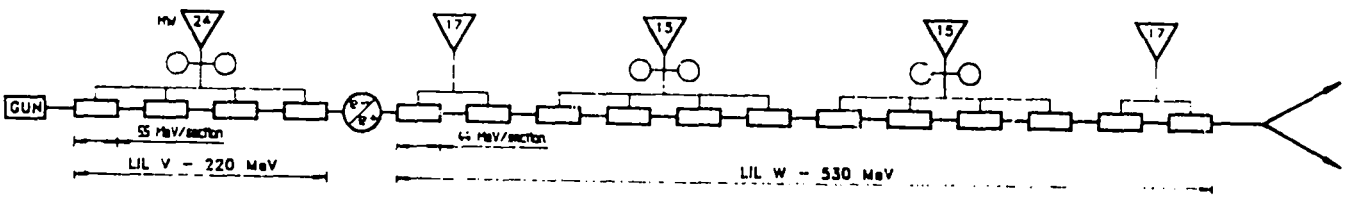

B) 8 Modulators/Klystrons with Lips

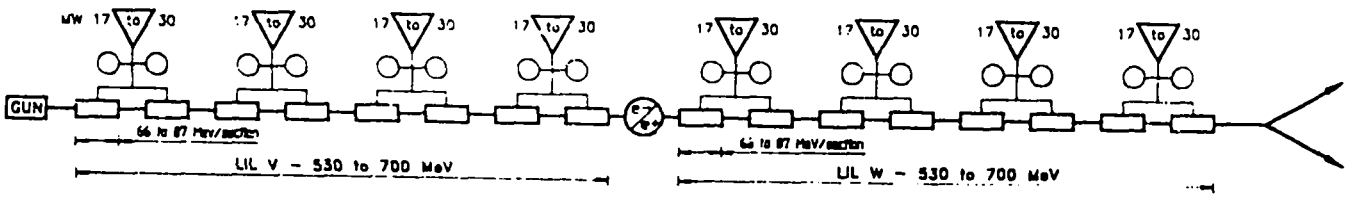

Figure 3: Proposed LIL configuration for an improved e⁺ production

THE INJECTOR LINAC FOR SPring-8

H.Yoshikawa, N.Nakamura, H.Suzuki,
M.Iizuka, T.Ishida, K.Yamada, A.Mizuno,
K.Mashiko and H.Yokomizo

Japan Atomic Energy Research Insitute,
Tokai-mura, Naka-gun, Ibaraki-ken, JAPAN.

Abstract

The Japanese project of the large synchrotron radiation source, named SPring-8(Super Photon ring 8GeV), is in progress now. SPring-8 consists of the injector linac, the synchrotron, and the storage ring. A creation of the site was started last year, and a part of the linac will be constructed from this year. This paper reports the design of the linac. The detail of the gun and the bunching system will be described elsewhere[1].

Introduction

The linac consists of major four parts(Fig.1); the high current linac(HL), the positron linac(PL), the electron linac(EL) and the main linac(ML). HL produces high current beams from a large cathode electron gun to bombard the target for positron production. PL has a converter target and a pulsed solenoid to focus and accelerate the positrons to 120MeV. EL lies on the side of PL, and accelerates the electrons to 120MeV. ML follows EL/PL and accelerates the electrons and the positrons to 1GeV. Two different linac lines, HL and EL, are provided due to the differences in the electron gun performance between EL and HL. The linac is about 200m long and three switch yards are provided in ML to supply beams for other fields of scientific research. Major parameters of the linac, the synchrotron[2] and the storage ring[3] of SPring-8 are listed in Table 1.

TABLE 1
Major Parameters of the Linac and the Synchrotron

Linac	
Energy	1.0 GeV
Repetition rate	60 Hz
Radio frequency	2856 MHz
emittance	1.5 πmm-mrad
(long pulse of positrons)	
current	10 mA
pulse width	10 ns
(long pulse of electrons)	
current	100 mA
pulse width	1us
(short pulse of positrons)	
current	10 mA
pulse width	1ns
(short pulse of electrons)	
current	300 mA
pulse width	1ns
Synchrotron	
Injection Energy	1.0 GeV
Maximum Energy	8.0 GeV
Circumference	396 m
Repetition time	1 sec
Natural emittance	192 nm-rad
Number of cells	40
Periodicity	2
Radio frequency	508.58 MHz
harmonic number	672
Radiation loss(8GeV)	11.55MeV/turn
Accelerating voltage(8GeV)	17.1MV
Quantum lifetime	over 10 sec
Storage ring	
Energy	8.0 GeV
Circumference	1436 m
Natural emittance	6.9 nm-rad
Number of cells	48
Periodicity	4
Radiofrequency	508.58 MHz
Harmonic number	2436
Radiation loss in bending magnet	9.04 MeV
RF voltage	12.7 MV
Quantum lifetime	over 1 day

The linac design is dictated by the requirements of the beam parameters which are established to insure acceptance by the booster synchrotron.

Four Components

EL

EL has a low emittance thermoionic electron gun which is driven in different two modes. One is a long pulse mode (100mA, 1us pulse width), and the other is a short pulse mode (300mA, 1ns pulse width) to adapt the synchrotron operation of a single bunch mode. The cathode assembly model Y646B supplied by EIMAC will be used and the electrodes are designed of a low perviance for the low emittance. The electron beam extracted from the gun is bunched into 50 degrees phase spread on the first-pass through two prebunchers which are reentrant resonant cavity type of 2856MHz. These 50 degree bunches enter the buncher when the RF phase is near null, and the bunch length becomes 5 degree width. Three accelerator sections accelerate the bunches to 120MeV.

HL

The electron gun of HL is required to be able to deliver of high current above 20 Ampere because of a low e+/e- conversion ratio and transport efficiency. This gun

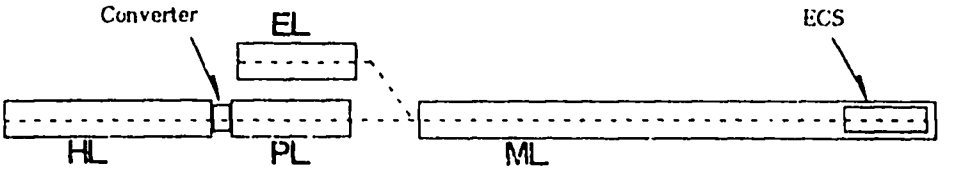

Fig.1 Conceptual view of the linac.

will be made of a large diameter cathode assembly Y796 of EIMAC. The preliminary calculated emittance is 181 mm-mrad at the point of 150 mm from the gun cathode. This value will become better as modifying the shape of the wehnelt and the anode. HL has a subharmonic buncher which is a quarter-wave reentrant resonant cavity with the frequency of 238MHz. This frequency and the drift space are discussed still now, and they will be optimized in the near future. Through HL, bunches of 10 Ampere, 1ns are accelerated up to 300 MeV. In this project, we suppose the positron use, and the efficiency of the positron yields is one of the most significant issue, because the positron yields ratio depends on the high current and the high energy on the target. Moreover, the beam must achieve a 3 mm-diameter spot size including the chromatic effects of the transport system.

PL

For the high density positron beam, it is important how many positrons are accelerated after the target. We are carrying out two experiments about the target structure to aim of a high conversion ratio. One is a conventional type of the combined pulsed solenoid, and the other is a RF gun type. High current beams from HL bombards the target, and the pulsed solenoid coil and the helmholtz coil are used to converge produced positrons. The collected positrons have a wide energy spread. Thus, the beam transport line must have a large acceptance. PL is set to accept positrons with an energy of 10±5 MeV, and the solid-angle acceptance of this line is defined by a pulsed solenoid, placed immediately downstream of the target, and by matching the positron-accelerator section with the dc solenoid. The pulsed solenoid has a field strength of 1-2 T and is 10 cm long. Positrons produced within the angle of 200 mrad in each transverse plane are captured in the acceptance aperture of the dc solenoid. The loss factor in the accelerating sections of PL is assumed to be 50 percent, and PL will finally provide a 10 mA positron beam to ML.

ML

ML receives either electron beams from EL or positron beams from PL at 120MeV. At first, there is a small angle bending section to separate the positron beam from electrons when the positron beam is used. The beams are focused by three quadrupole triplets placed between every other accelerator section. 23 accelerator sections accelerate beams from 120 MeV to 1 GeV. For the consideration of the energy spread of positron beams, the energy compression system is placed at the tail of ML. This energy compression system has a low compression factor because of a large acceptance for positron beams.

Accelerator section

The accelerator section of this linac has to achieve high performance. This performance is determined by the shunt impedance, the Q-value, the material, the operating vacuum level and so on. Anyhow, reliability is most important to the injector linac for many users of SPring-8. A conventional disk-loaded wave guide of 2856 MHz, $2\pi/3$ traveling-wave mode with a constant-field gradient was chosen. Each section is 2.835m long and containing 81 cells. Several kinds of the iris diameter of the disk are mixed to prevent from a cumulative beam break-up. we are now discussing about the modified type accelerator secitions. The cross sectional shape is modified, shown in Fig.2, for high shunt impedance 65 MOhm/m. These accelerator sections will be made by electric welding method. The first test tube was made already, and has been tested on JAERI-linac. The adoption of this modified type accelerator section depends on the results of the test.

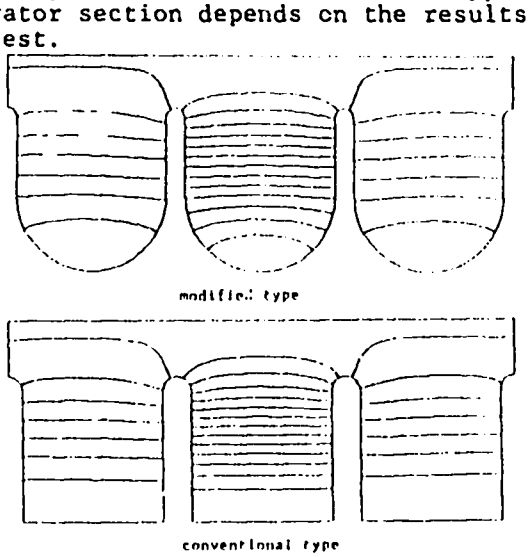

Fig.2 Cross sectional view of cells of a accelerator section.

TABLE 2
Characteristics of
the modified accelerator section

Frequency	2856 MHz
Structure	disk-loaded type
Accelerating mode	$2\pi/3$
Tube length	2.835 m
Number of cell	81
Range of iris dia.	26-20mm
Energy gain	40MeV
Input power	25MW
Shunt impedance	65 M-Ohm/m
Energy gain	40 MeV

RF system

Klystron and modulators

RF power is fed to each accelerator section from a single klystron. The maximum power of those klystrons is 35MW, and they are used around 30MW in average. Each klystron amplifier is provided with a line-type modulator rated at 85 MW peak and 20 kW average power, at a pulse length of 5us, and a maximum pulse repetition rate of 60pps. The pulse-forming network in the modulator is discharged through a hydrogen thyratron. Each modulator is provided with a de-Qing circuit which compares the charging voltage of the pulse network during each charging cycle to a reference voltage. When the charging voltage reaches the reference voltage, the energy stored in a charging transactor is dumped into a dissipative circuit by means of rectifier switch. If the stability of the power source, a motor generator will be used to exclude noise in the electric power provided to the modulators.

Phase control

The 2856MHz low-level output of a highly stable master oscillator will be distributed by coaxial cables and amplified by either newly developed solid state rf high power amplifiers or booster klystrons. Each amplifier provides a signal to a power klystron. The phase of the rf power is controlled by low-power phase shifters, which will be simple and reliable. The phase of the accelerator is initially adjusted by maximizing the energy of the linac and at the same time minimizing the energy spread. This phasing system uses the phase of the beam bunches as the reference phase. It is based on the principle that the phase of the beam-induced wave should be synchronized with the klystron rf phase. The relative phase difference is kept constant by a control computer.

Control system

This linac is designed to be reliable and to have minimal failures. The control system should contribute to minimizing down-time of the machine. However, it is necessary to adapt and modify devices and operating conditions. The block diagram of this control system is shown in Fig.3. There is a VME cage in each modulator and control signals are distributed to the modulator and magnet power sources near by, and monitor signals are gathered in this cage. In each component, these VME cages connect LAN by mini-MAP or ether-net. Furthermore, four LAN servers of each component are connected to the main computer of this linac by MAP or FDDI. The main computer will be used on UNIX. OS-9 or VxWorks will be used as a operating system of VME controllers.

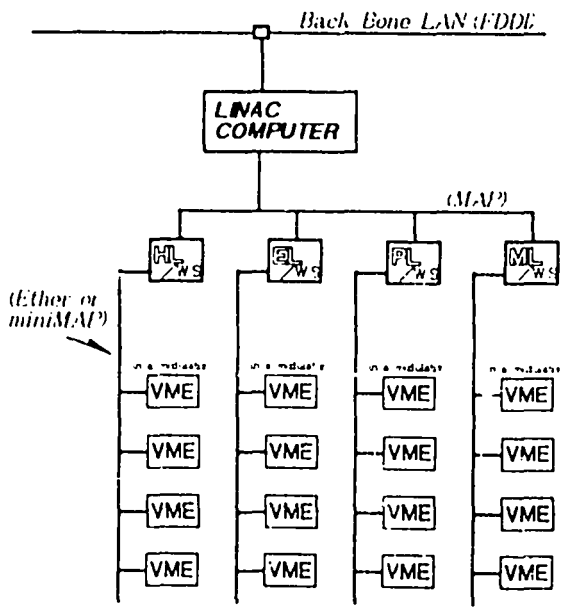

Fig.3 Block diagram of the control system.

Reference

[1]N.Nakamura, et. al. "DESIGN OF A BUNCHING SYSTEM FOR A HIGH CURRENT ELECTRON LINAC", This proceedings. (1990)

[2]T.Harami, et. al. "INJECTOR DESIGN FOR THE 8 GEV SYNCHROTRON RADIATION FACILITY IN JAPAN", Particle Accelerators,(33),63,(1990)

[3]M.Hara, et. al. "STORAGE RING DESIGN FOR THE 8 GEV SYNCROTRON RADIATION FACILITY IN JAPAN", Particle Accelerators,(33),51,(1990)

KEK 2.5-GEV ELECTRON/POSITRON LINAC STATUS AND RESEARCH ACTIVITIES

Akira Asami
National Laboratory for High Energy Physics
1-1 Oho, Tsukuba-Shi, Ibaraki-Ken, 305 Japan

Abstract

Even though the annual operation time has exceeded 4,500 hours for these three years, the operation rate reached more than 98 % in FY 1989 due to various improvements. A new attenuator & phase-shifter has been developed, and a considerable reinforcement of the positron focussing system is in progress. Construction of the Test Linac has begun, and research on the breakdown of alumina rf windows, multibunch instability in the linac, and plasma wakefield accelerators has begun.

Introduction

The KEK 2.5-GeV electron linear accelerator was completed in March, 1982, and was commissioned for synchrotron radiation research in June, 1982. TRISTAN AR tests began in September, 1983. Its first operational status is reported in ref. 1. The positron generator was under construction from 1982 to 1984; its construction and improvements are reported in refs. 2, 3.

In this report, recent operational status is first described, together with some of the improvements achieved. Second, two modifications presently taking place are described: one is the development of a new attenuator and phase shifter; the other is the reinforcement of the positron focusing system, aimed at increasing the positron intensity by a factor of two. Finally, some research programs, most of them undertaken recently, concerning the following subjects are mentioned: (1) construction of a small linac for advanced accelerator studies, (2) breakdown mechanism of high-power klystron rf windows, (3) multi-bunch instability caused by a transverse wakefield in the linac, and (4) plasma wakefield acceleration.

Operation status

The annual operation time during these eight years is summarized in Fig.1. The scheduled operation time expected in FY 1990 is also about 4,500 hours. In spite of such a long operation time, the operation rate has steadily improved, and reached more than 98 % in FY

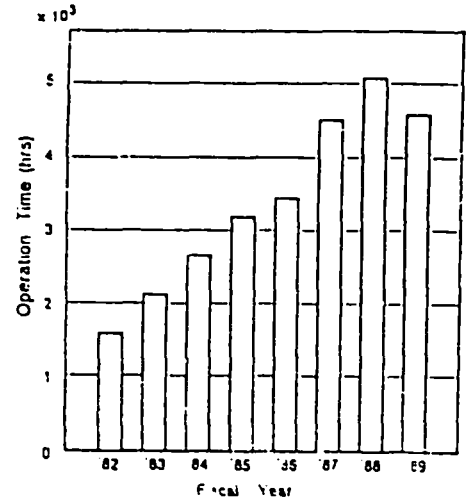

Fig. 1 Linac oeration time.

1989. This high rate is the result of continuous efforts made to improve various instruments of the linac. In the following, these recent improvements are described briefly.

Since the initial operation of the linac, one of the most serious problems has been related to the main high-power klystrons.[4] In 1987, a new-type klystron, which has a Barium-impregnated (BI) cathode, was test-used, showing excellent characteristics. Since then, the old-type klystrons with oxide-cathodes have rapidly been replaced by new ones; at present there are thirty-nine klystrons with BI cathodes among a total of fourty-eight. Most of the klystrons with BI cathodes have demonstrated excellent characteristics, resulting in a much lower failure rate.

The energy analyzing and monitoring systems of the beam have been considerably reinforced.[5] Energy analysis of the beam is now possible at four positions along the accelerator, and the beam currents and profiles are more easily to measure. The monitors of the rf system have been also improved, and variation is more easily and widely detected for the rf phase and power.

In addition to these items, significant improvements have also been made on the control system[6] of the linac by introducing a CAVT system and an additional network (Ethernet) for man-machine interface

enhancement. The DS-Link and beam-switching systems were also improved.

Development and Improvement

An attenuator and a phase shifter at high rf power are usually required in the injector section of the linac for optimum tuning of the accelerator. Though these two quantities should desirably be independent of each other, this is not the case, and the power variation is closely related to the phase change in the high-power attenuators currently used. This makes tuning of the machine very complicated and, therefore, the dependence of the beam characteristics on these quantities is often ambiguous.

To avoid this difficulty a new attenuator and phase shifter is being developed,[7] which enables us to vary the power or phase quite independently. This is a single device with a structure in which the usual attenuator and the phase shifter are combined as shown in Fig.2; it works both as an attenuator and a phase shifter. The details are described in ref. 7.

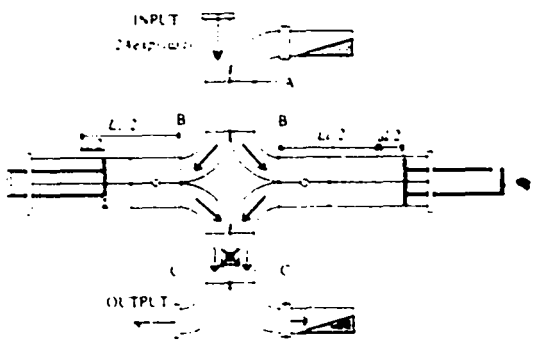

Fig. 2 Attenuator & phase-shifter for buncher.

As in TRISTAN, high-luminosity experiments started in 1990, and the TRISTAN group requested the linac group to supply more positrons. In order to meet this requirement, the positron source was examined and it was decided to reinforce the positron focussing system.[8] This system comprises a pulsed coil, a DC solenoid, and quadrupole magnets. Both the pulsed coil and the DC solenoid are to be replaced by components which are capable of producing a higher magnetic field than the present ones by almost twice. As for the quadrupoles, only those in the positron generator are to be altered at this time; and the remaing ones in the transport line and in the initial sectors of the 2.5 GeV linac will be altered the next FY. The present modification will be completed early next year. Details are given in ref. 8.

Research

In addition the work mentioned above to improve the accelerator, some research started recently, in the Linac Division. These are presented below.

For research concerning an advanced accelerator, it is important to have a suitable facility; and it was therefore decided to build a new small linac, the Test Linac.[9] The main parameters of the Test Linac are as follows: The maximum acceleration energy is to be 60 MeV at a 10 μa maximum average current; and its length is to be about 14 m. This linac is presently under construction and is expected to be completed soon. Some major subjects to be investigated are (1) high brightness beam production and acceleration, (2) RF gun, and (3) experiments on a free-electron laser.

In recent years the output rf power of klystrons has been steadily rising, while aiming at future advanced accelerators: for example, linear colliders. Breakdown of ceramic windows is still one of the major problems to be solved with those klystrons. An investigation of the breakdown mechanism has been intensively continued. It was recently shown that the puncture of an alumina disc is induced by localized surface melting which is caused by multipactor electron bombardment heating.[10] An example of simulation is shown in Fig. 3. It was also confirmed that a TiN coating is effective to suppress the multipactor.

In accelerating a high-current beam up to high energies in linear accelerators, it is

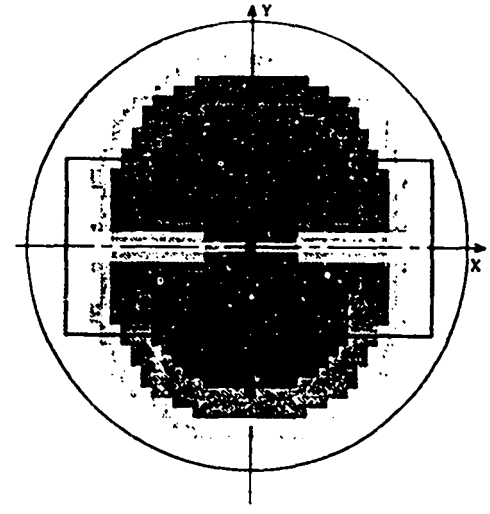

Fig. 3 Incident energy distribution weighted by impinging rate of multipactoring electrons on the alumina ceramic disk with an rf power of 30 MW.

important to know the properties involved and to suppress any wakefield effects caused by the beam. This problem will become more serious in future accelerators; the wakefield effect due to a multi-bunched beam is particularly important to such a collider as the Japan Linear Collider, since multi-bunched beam is to be used. In making use of the electron acceleration section of the positron generator, some preliminary

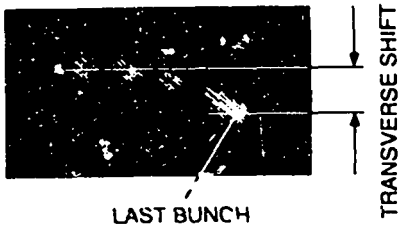

Fig. 4 Transverse (vertical) shift of the last bunch observed at a profile monitor.

measurements were performed,[11] since high-current, high-energy beams were available in the section. It was observed that the last bunch of the beam, comprising five bunches, was in fact appreciably deflected by a field caused by preceding bunches (Fig. 4). Details of preliminary results and analysis of the measurements are described in ref. 11.

In making use of similar electron beams as those mentioned above, another investigation has been progressing concering so-called plasma wakefield accelerators (PWFA).[12] A PWFA is one of the promising candidate for future high energy accelerators, since there is no insulator or wall material necessary, which usually imposes an upper limit to the accelerating gradient of conventional accelerators. It has been predicted

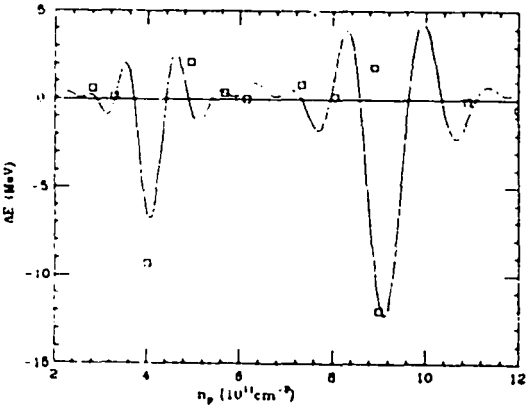

Fig. 5 Observed centroid energy shifts of the maximum bunch as a function of the plasma density.

in PWFA that it would be possible to obtain an extreemly high accelerating gradient.[13] At the end of the positron generator installed there was a chamber, in which 10^{11}-10^{13} cm^{-1} plasma was produced. Several electron bunches of 500 MeV energy with total charge of 5-10 nC were injected into the plasma; it was observed that the trailing bunch was shifted in energy by about 12 MeV.[12]

References

1. J. Tanaka, "Operation of the 2.5 GeV electron linac", Prof. of 1984 Linac Conf., Darmstadt, 1984, pp 475-479.
2. A. Asami et al., "Injector of the Positron Generator", Proc. of 1986 Linac Conf., SLAC, 1986, pp 496-498.
   I. Sato et al., "Accelerator Characteristics of Positron Generator Linac", ibid, pp 502-504.
3. A. Asami et al., "Progress of Positron Generator at KEK," Proc. of 1988 Linac Conf., Williamsburg, 1988, pp 577-579.
4. Photon Factory Activity Reports #6, 1988, #7, 1989.
5. S. Shidara et al., "Improvements to the Monitoring System of the KEK 2.5 GeV Linac and Its Performance Tests", Particle Accelerators, 29, 1990, pp 239-244.
6. K. Nakahara et al., "An Operator-Console System of the Photon Factory Injector Linac", NIM A293, 1990, pp 446-449.
7. S. Ohsawa et al., "High Power Hybrid Attenuator & Phase-shifter System", This Conference.
8. A. Enomoto et al., "Present Status and Reinforcement Plan of the KEK Positron Generator", This Conference.
9. H. Kobayashi et al., " Test Linac Facility at Photon Factory, KEK", This Conference.
10. Y. Saito et al., "Breakdown of Alumina RF Windows" IEEE Trans. on Electrical Insulation 24 6, 1989, pp 1029-1032.
    Y. Saito et al., "Breakdown of Alumina RF Windows", Int. Symp. on Discharge and Electrical Insulation in Vacuum, Santa Fe, 1990, to be published.
11. Y. Ogawa et al., "Experimental Investigations of Multi-Bunch Instability by Transverse Wake-Field", This Conference.
12. K. Nakajima et al., "Plasma Wake Field Accelerator Experiments at KEK", NIM A292 1990, pp 12-20.
    A. Enomoto et al., "KEK Plasma Wakefield Accelerator Experiments", Proc. of 2nd EPAC 90, Acropolis, 1990 to be published.
13. P. Chen et al., Phys. Rev. Lett., 54, 1985, 693.

PRESENT STATUS AND REINFORCEMENT PLAN OF THE KEK POSITRON GENERATOR

A. Enomoto, T. Oogoe, T. Kamitani, K. Kakihara, S. Ohsawa, I. Sato and A. Asami
National Laboratory for High Energy Physics (KEK), Oho, Tsukuba-shi, Ibaraki-ken, 305, Japan

Abstract

The KEK positron generator has successfully provided positron beams to both TRISTAN and the Photon Factory (PF). However, to meet increasing requirements regarding positron beam use, the focusing system of the KEK positron generator will be extensively reconstructed. This paper describes the present status, the reinforcement strategy and design of the positron generator focusing system.

Introduction

As a part of the TRISTAN project the KEK positron generator [1] was constructed on the south-west side of the PF 2.5-GeV electron linac during 1982-1985; it was then combined with the 2.5-GeV linac. In the autumn of 1986 it started routine-operation to inject a 2.5-GeV positron beam into the TRISTAN ring; in the autumn of 1988, the PF ring changed the storage beam from electrons to positrons in order to realize more stable operation. Figure 1 shows the composition of the KEK positron generator: a 250-MeV primary electron linac, a positron radiator with a quarter-wave-transformer (QWT)-type focusing system, a 250-MeV post-linac and a 30°-beam transport to transfer the positrons to the 2.5-GeV linac. A distinctive feature of the KEK positron generator is the conjunction of a compact focusing system with a high-current (>10 A), short pulse(<2 ns) linac as a primary electron linac. This choice enables low-power operation (<100 kW) of the focusing system and the direct injection of a single-bunch beam (<2 ns = 1/(500-MHz ring accelerating frequency)) to the TRISTAN ring, with the required positron current (>10 mA).

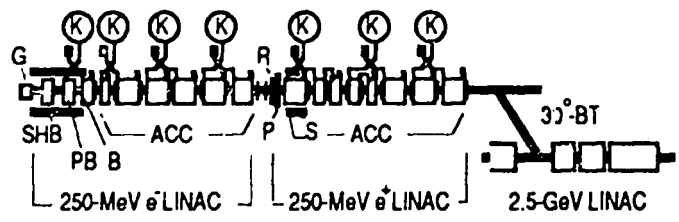

Fig. 1. Block diagram of the KEK positron generator: G is the electron gun; SHB, a subharmonic buncher; PB, a prebuncher; B, a buncher; ACC, a regular accelerator section; R, a positron radiator; P, a pulsed solenoid; S, a uniform solenoid; K, a klystron.

Instead of energy-front studies in the TRISTAN PHASE-I experiment, high-luminosity operation of the colliding ring is aimed at PHASE-II, which started this year. Furthermore, in a few years, a B-physics plan is eagerly expected to be realized as PHASE-III. In these experiments, additional positron beams are required in order to save injection time; especially, the B-Physics plan requires roughly ten times as many positrons as the present beam produces. To meet such requirements, an integrated upgrade is necessary for the injector linac (e.g., to increase the primary electron energy, etc.); improvements of the positron focusing system started first.

Present Status

The 2.5-GeV linac injects positrons to both TRISTAN and PF. For PF, a 40-ns beam is used instead of the 2-ns beam for TRISTAN, because a single-bunch beam is not required for PF at present and it is advantageous for both increasing the charge number and suppressing the space-charge effect. These two kinds of beams are accelerated by switching a gun-grid pulser and by turning on/off a 119-MHz subharmonic buncher (SHB). The operational parameters of the positron generator are summarized in Table 1.

TABLE 1
Operational Parameters of the Positron Generator

General		
Acceleration frequency	2856	MHz
Pulse repetition	25	Hz
Primary electron linac		
Energy	250	MeV
Peak current	10(2)	A
Pulse width	2(40)	ns
Emittance	0.05	πMeV/c cm
Electron-to-positron converter		
Radiator(thickness)	tantalum	8.2 mm
Pulsed solenoid	QWT	type
Conversion rate	0.3	%
Positron beams		
Peak current at 250 MeV	30(6)	mA
Peak current at 2.5 GeV	15(2)	mA
Energy spread at 2.5GeV	0.5(0.8)	% at FWHM
Emittance	0.15	πMeV/c cm

( ): positrons for PF

Figure 2 shows a typical display of the injection time for TRISTAN and PF, respectively. Under routine TRISTAN operation, every 2-2.5 hours the colliding beams are renewed. A current of 12 mA (e^+, e^- x 2 bunch, 3 mA each) is stored and accelerated in the colliding ring (main ring MR, circumstance c = 3016 m) through the accumulator ring (AR, c = 381 m). During the setup time (30-40 minutes) for the colliding beam, the linac spends 4-6 minutes for four injections of the positron beam and <1 minutes for an electron beam.

For the PF 2.5-GeV storage ring (c = 187 m), the linac injects a positron beam of up to 350 mA every 12 hours and, sometimes, every 24 hours. Because of the full-energy injection, only the loss current is quickly filled up. After a short adjustment of the linac beam, the linac completes the injection within 5-6 minutes. In the case of the initial fill from the vacancy, it takes < 20 minutes.

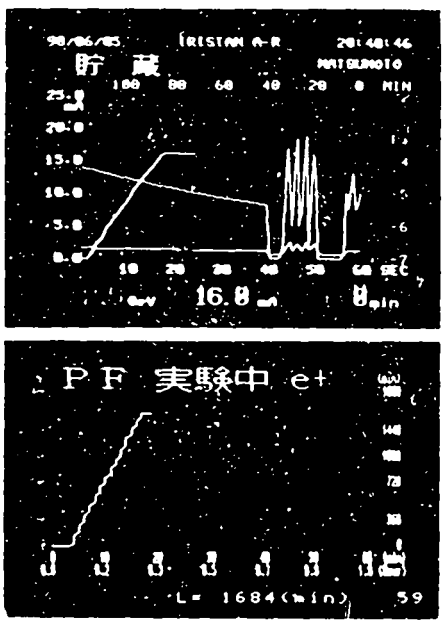

Fig. 2. Display for injections to TRISTAN and PF

Reinforcement Plan

General Feature of the QWT-type Focusing

The specific positron yield, n, for primary electrons striking a radiator with an energy E is approximately (for the forward angle) given by

$$n/E = (d^2n/Ed\Omega dP)\ \delta\Omega\ \delta P,$$

where $d^2n/Ed\Omega dP$ is the measured specific yield at 0° (e.g., $0.24\times10^{-3}(1-(25/E(MeV)))^{2}$; $\delta\Omega$ and δP are, respectively, the solid angle and the momentum width of the positrons acceptable by the focusing system. Hence, assuming that both E and $d^2n/Ed\Omega dP$ are constant, the positron yield depends on parameters $\delta\Omega$ and δP, which are determined by the positron focusing system.

The KEK positron generator adopts the QWT-type focusing system as shown in Fig. 3. A strong axial field, Bi(effective length L), just behind the radiator is produced by a pulsed solenoid; it is followed by a lower field, Bf, applied over the accelerator sections.

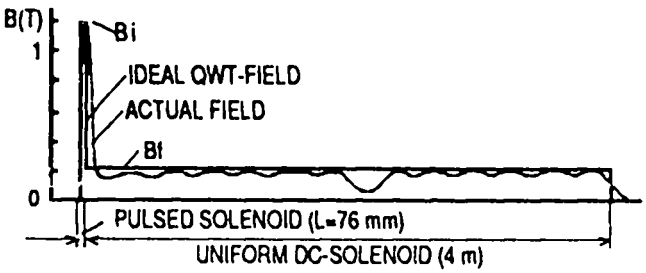

Fig. 3. Field distribution of the positron focusing system.

Using the analytical expression for the QWT system [3], and assuming that the accelerator aperture, a, is constant, the proportionality between the focusing system parameters and the field parameters are represented as follows:

(Admittance)		$U \propto Bf$
(Matched beam on the positron radiator)		
radius		$x \propto Bf/Bi$
transverse momentum	$p \propto$	$U/x \propto Bi$
longitudinal momentum		$P \propto BiL$
(Positron acceptance and yield)		
solid angle	$\delta\Omega \propto$	$(p/P)^2 \propto L^{-2}$
momentum acceptance	$\delta P \propto$	$PBf/Bi \propto BfL$
positron yield	$n \propto$	$\delta\Omega\delta P \propto Bf/L$

The above expressions make the problem clear:
(1) For a larger solid angle, it is necessary to fabricate a shorter pulsed solenoid. The strength, Bi (times L), determines the acceptable positron momentum, P. It is preferable that Bi is higher, since it suppresses any debunching effects due to speed and orbit differences of positrons.
(2) For a wider momentum acceptance, it is effective to make Bf stronger.
(3) The positron yield is proportional to Bf/L.
Adding to these features, the following should also be taken into account:
(4) As the solid angle becomes larger, the positron production cross section decreases with a rough dependence of exp(-θ/0.35), where θ is the positron production angle, p/P.
(5) A larger Bf increases the debunching effect of the orbit difference.

Reinforcement Schedule

A reinforcement of the KEK positron generator focusing system will be performed, dividing it into two stages (Table 2). At first, using the present pulsed solenoid, the solenoid field Bf will be reinforced from 0.2 to 0.4 T. In this condition, though the solid angle is not changed, the momentum acceptance increases. As for the matching condition of the beam on the radiator, the beam radius may be twice as large as the present radius; this means that the beam adjustment on the target becomes rather easy. One problem to be discussed is debunching due to orbit differences; assuming that the accelerator gradient, dP/dz, and Bf are constant, the phase slip is given by [3]

$$\delta\phi = (\pi/\lambda) \int (p/P)^2 \, dz = (\pi/\lambda)(p^2/(PdP/dz).$$

The maximum transverse momentum in a field Bf is calculated by U/πa. Substituting 0.43 MeV/c, 8.7 MeV/c, 10 MeV/c/m, and 0.105 m into p, P, dP/dz, λ, respectively, one finds that δφ is 0.02π, i.e., 3.6°. This phase slip may be within a tolerance.

TABLE 2
Parameter Change of the QWT System

	Present	Step 1	Step 2
Solenoidal field			
pulsed solenoid Bi(T)	1.2	----->	2.0
effective length L(mm)	76	----->	50
DC solenoid Bf(T)	0.2	0.4	0.4
Acceptance			
U(πMeV/c cm)	0.15	0.30	0.30
Matched beam on the radiator			
radius x(cm)	<0.12	<0.24	<0.14
momentum P(MeV/c)	8.7	----->	9.5
transverse momentum p(MeV/c)	1.25	----->	2.1
Positron yield (relative values)			
solid angle dW	1	----->	2.3
momentum acceptance dP	1	2	1.3
specific yield n/E	1	2	2.4

In the next stage the pulsed solenoid will be improved. The pulsed solenoid of the KEK positron generator was fabricated while considering that of DESY [1]: to avoid any accidents, it was modified so that the water-cooled coil is installed outside of the vacuum. Consequently, it has become more difficult to make a compact coil. Improvement of the pulsed coil will be carried out gradually.

Design of the Focusing System

By increasing Bf, the acceptance of the focusing system will become 0.3 πMeV/c.cm, twice as large as before; to obtain this acceptance over the entire accelerator length, not only a uniform solenoid for producing Bf, but the downstream quadrupole magnet system will also be reconstructed. Figure 4 shows an illustration of the new focusing system as well as an example of the calculated matched beam. In the new system, the uniform solenoid installed over the accelerator section is extended from 4 to 8 m. In order to monitor the positron current, an e^+/e^- separator comprising of an achromatic bending system is introduced at the exit of the solenoid, since electrons which also emerge from the radiator are transported as well as the positrons. Downstream of the solenoid system, first, a quadrupole-singlet system (FODO-system) is applied over the accelerator sections and then periodic quadrupole triplets are set between the accelerator sections.

References

1. A. Enomoto et al., "FOCUSING SYSTEM OF THE KEK POSITRON GENERATOR", NIM A281 (1989) 1-9.
2. T. L. Aggson and L. Burnod, "PRODUCTION DE POSITRONS A L'ACCELERATEUR D'ORSAY", LAL Report 27 (1962).
3. The Stanford Two-Mile Accelerator, Chap. 16, "THE POSITRON SOURCE", Benjamin, New York (1968).

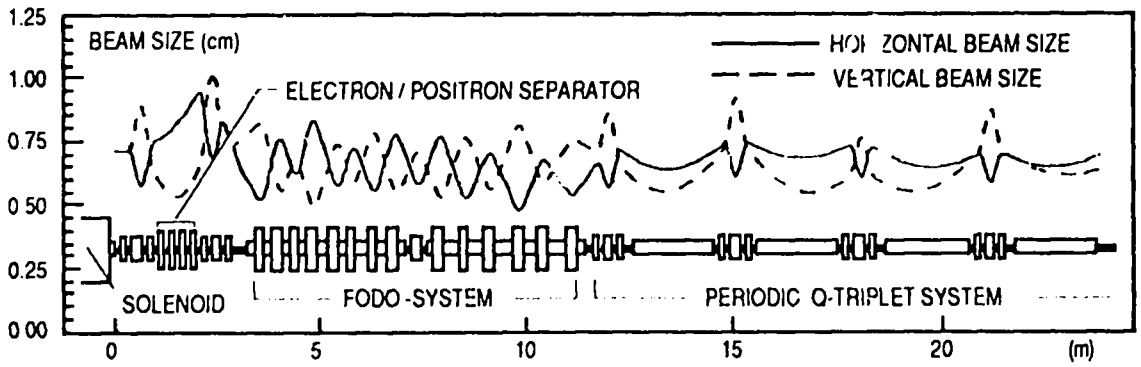

Fig. 4. The new configuration of the reinforced positron generator focusing system and calculation of the matched beam using the computer code TRANSPORT.

FIRST OPERATION OF THE SUPERCONDUCTING 130 MeV CW-ELECTRON-ACCELERATOR AT DARMSTADT*

K. Alrutz-Ziemssen, D. Flasche, H.-D. Gräf, V. Huck, K.D. Hummel, G. Kalisch, C. Lüttge, J. Pinkow, A. Richter, T. Rietdorf, P. Schardt, E. Spamer , A. Stascheck, A. Stiller, O. Titze, H. Weise, and W. Ziegler
Institut für Kernphysik, Technische Hochschule Darmstadt,
Schlossgartenstr.9, D-6100 Darmstadt,West-Germany

Abstract

The installation of the accelerator has been completed in January 1990 and its present status is reported. In the meantime all eleven superconducting structures and the normal conducting chopper and prebuncher resonators are operated by the new microprocessor controlled rf-system which had been tested extensively with the superconducting injection linac in fall 1989. The rf control system is integrated into the main computer control system of the accelerator. Operational experience with a newly developed mechanical coarse and fine tuning system is presented. The horizontal and vertical emittance of the injector beam have been measured systematically. First experience with the transport of the beam through the recirculating beamlines and to one of the spectrometers in the experimental area as well as phase measuresments of the recirculated beam with respect to the injected beam are discussed. Accelerating gradients of the superconducting cavities (including one post purified and three fabricated from 'RRR280' material) determined from beam energies are given.

Introduction and Present Status

Reports on the status of the Superconducting Darmstadt Linear Accelerator (S-DALINAC) have been given regularly. Therefore, we will focus on the progress which has been achieved since the most recent reports [1,2] in late summer last year. The design parameters of the S-DALINAC are summarized in Tab.I below.

TABLE I
Design parameters of the S-DALINAC

Beam Energy / MeV	10 – 130
Energy Spread / keV	±13
CW Current / μA	≥ 20
Operating Frequency / MHz	2997
Number of Structures (1 m)	10
Capture Section (0.25 m)	1

Most of the figures quoted above like energy, energy spread, and cw operation are requirements resulting from the fact, that the accelerator (besides being a driver for an FEL) will be used for inelastic electron scattering coincidence experiments.

The installation of the accelerator could be completed in January of this year. This is documented by Fig.1, a photograph of the accelerator taken from the side where the beam is extracted to the experimental area. In the upper right part the 270 keV injector can be seen, followed by the superconducting injector linac formed by a short cryomodule, housing the 5-cell capture section, and a standard cryomodule containing two 20-cell accelerating cavities. An isochronous beam transport system (180° bend) allows the beam from the injector to enter the main linac (center of Fig.1) which consists of four cryomodules, containing two 20-cell cavities each. The foreground of the photograph shows the two 180° bends of the recirculating beamlines. Their straight sections (left portion of Fig.1) lead to two identical bends (in the rear of the photograph), where the recirculated beams are reinjected into the main linac via a four magnet chicane. Extraction of the beam to the experimental area is performed in the lower right corner of Fig.1. The magnets sitting to the right of the straight section of the first recirculation form the beam handling system of the FEL project [3]. They will be installed during the next shutdown this summer.

Performance of the Superconducting Cavities

The present installation contains quite different cavities made from niobium of different purity ranging from RRR = 30 to RRR = 280. The average accelerating field of the RRR = 30 cavities (four 20-cell cavities) amounts to 2.7 MV/m, whereas the RRR = 100 cavities (two 20-cell cavities and the 5-cell capture section) yield 5 MV/m. The prototype of a series of six 20-cell cavities fabricated from RRR = 280 niobium achieved an accelerating gradient of 6.6 MV/m but showed a severe degradation in Q_0 after an intermediate warm up to 130 K due to a shutdown of the refrigerator. Since similiar effects have been observed also in other laboratories [4] with cavities made from high RRR niobium the next two cavities of this series were fired at 650°C for several hours in the UHV furnace at Wuppertal prior to installation in the accelerator cryostat. Both cavities reached 5 MV/m with $Q_0 = 1 \cdot 10^9$ and were limited at 6 MV/m with $Q_0 \approx 5 \cdot 10^8$and their performance was not affected by a temperature cycle from 2 K to 180 K and back to 2 K. The present installation also contains a 20-cell cavity originally made from RRR = 30 material which has been postpurified by high temperature titanium treatment [5] at the University at Wuppertal. This cavity achieved a gradient of 3.6 MV/m quite well in agreement with a value of 3.9 MV/m determined in a first test at Wuppertal. We therefore presently conclude that there are two possible ways to achieve the design gradient of 5 MV/m with our 3 GHz 20-cell cavities: i) postpurification by high temperature titanium treatment from the outside [5,6] which does not require a subsequent chemical polishing from the inside and ii) fabrication of cavities from high RRR niobium which apparently requires a heat

*Supported by the Bundesministerium für Forschung und Technologie under contract number 06 DA 184 I.

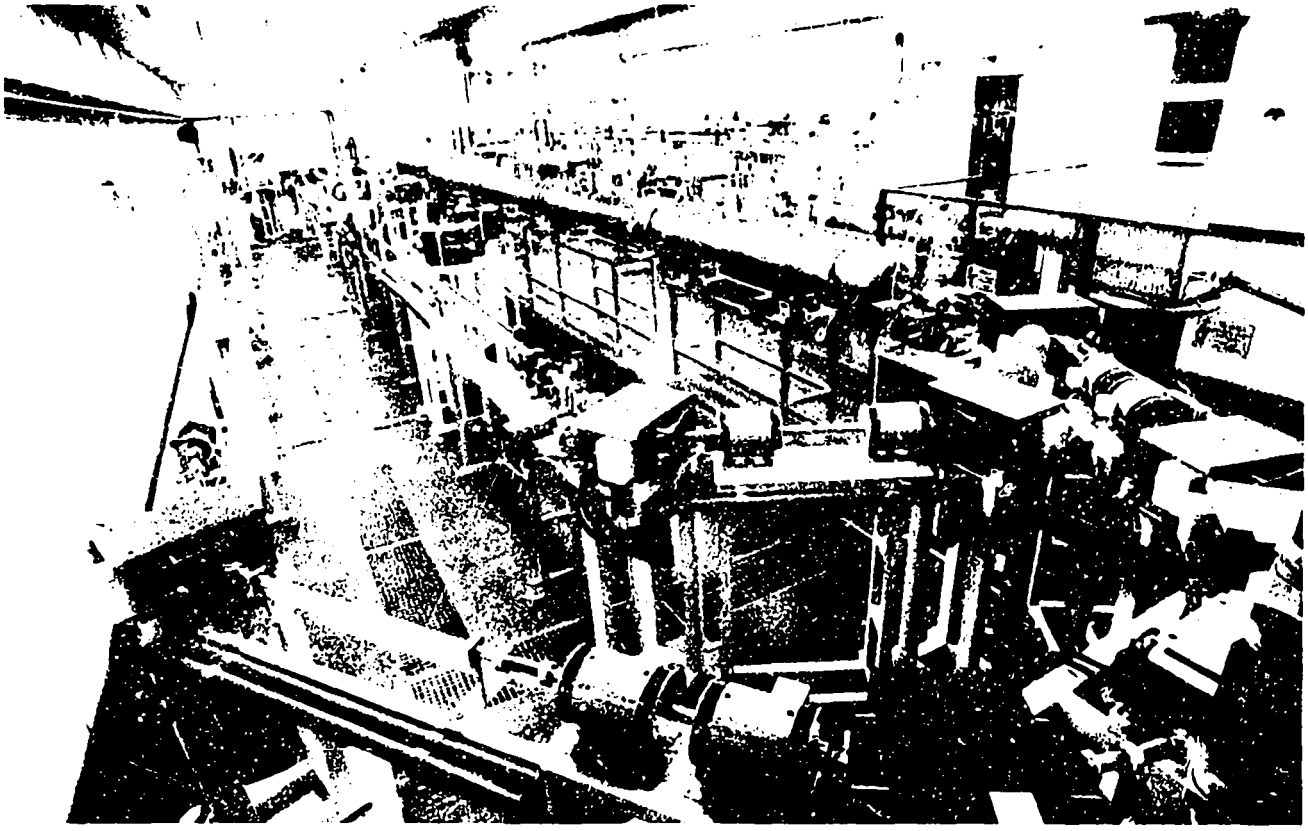

Fig.1 Photograph of the Darmstadt superconducting 130 MeV cw-electron-accelerator

treatment (very likely for outgassing of hydrogen) prior to the installation of the cavities.

Developments

Besides the properties of the cavities themselves the performance of the equipment directly associated with the cavities inside the cryostat is extremely important. We therefore developed a new mechanical coarse and fine tuner described in detail in Ref.[1].

In the present installation, the 5-cell capture section and three new 20-cell cavities are equipped with these tuners. Two of them operated extremely well since January whereas the other two got stuck because of too close tolerances in the series production.

Similiar considerations like in the case of the mechanical tuners led to the development of new rf input- and output couplers. The new design basically consists of a concentric tube inside the cutoff tube of the cavity, forming a coaxial line with an impedance of 21 Ohms, which is shorted at the end pointing away from the cavity. The 50 Ohms 7/8" coaxial input line is connected radially to this device via a $\lambda/4$ impedance transformer at a distance of $\lambda/4$ from the shorted end. Calculations using the computer code URMEL [7] predict that an external Q of $3 \cdot 10^7$ will be obtained with the distance between the open end of the center tube and the iris of the first cell of the cavity being as comfortable as 80 mm. The cylindrically symmetric construction ensures that the electron beam sees no transverse electrical field at all while entering or leaving the cavity. The coupler is mechanically very rigid, promising a good reproducibility of the external Q. Two prototypes have been built and are presently investigated at room temperature. Next steps will be the calculation of the coupling to cavity modes other than the fundamental TM_{010} passband and measurements using a variable coupling between the 7/8" input line and the coaxial line of the coupler.

In connection with the fabrication of the six new cavities a new method for the tuning of the field flatness has been developed. Following the ideas of ref.[8], a comparison was made between the Eigenfrequencies of the fundamental passband calculated with URMEL and via a lumped circuit model. The analysis shows, that in our cavities, which have a cell to cell coupling of 4.2%, coupling to the cells following the direct neigbours still amounts to $7 \cdot 10^{-4}$, decreasing by approximately a factor of 50 from cell to cell when looking at even more distant cells. We therefore developed a tuning method, which works as follows: In a first step the field profile of the π-mode is determined by a bead pull measurement. Then the most evident deviations from the ideal field profile are tuned to such an extent, that the phase of each cell can be expected to be correct. In a second step the frequencies and field profiles of all 20 modes of the fundamental passband are measured and from these data the complete matrix describing the Eigenvalue problem is calculated. This means, that coupling from each cell to any other cell is taken into account. Then in a numerical procedure the Eigenfrequencies of the individual cells are varied in such a way, that i) the desired frequency for the π-mode and ii) a flat field profile for the π-mode are achieved. The results of this calculation are the necessary corrections for the Eigenfrequency of each cell and mode frequencies as well as field profiles for each step of the correction procedure. This allows a quick check during the final tuning procedure by measuring the mode frequencies any time a cell has been tuned. The result of this procedure is a fieldflatness of $\leq 2\%$ in the π-mode.

Accelerator Tests and Utilization of Beam

In order to operate the eleven superconducting cavities of the completely installed S-DALINAC, the new microprocessor controlled rf system [9] had to be put into

operation in January of this year and has been working without major problems since then.

In order to recirculate the beam from the main linac and to accelerate it correctly two requirements have to be observed: i) the energy of the recirculated beam has to be five times the energy of the injector beam because the last magnet of the chicane for reinjection is identical with the last magnet of the 180° bend for the beam from the injector and ii) the phase of the recirculated beam has to match the phase of the beam from the injector. The energies of the injector beam as well as of the recirculated beam are easily determined from settings of the dipole magnets in the respective bends whereas for the measurement of the relative phases rf current monitors in front of and behind the main linac in conjunction with a pulsed beam are used. Beam pulses with a width of 70 ns (the round trip time in the first recirculation amounts to 135 ns) at a repetition rate of 1 kHz allow to distinguish between signals in the rf monitors induced by the injector beam or the recirculated beam respectively.

A phase lag of 10° of the 20 MeV recirculated beam with respect to the injector beam could be measured at the position of the rf monitor in front of the main linac. Taking into account the not yet completely relativistic beam energies, this means, that the path length of the first recirculation has to be increased by 2 cm. We will during the next period of operation continue these measurements and investigate to which extent the chicane will tolerate a deviation from the energy ratio of five to one.

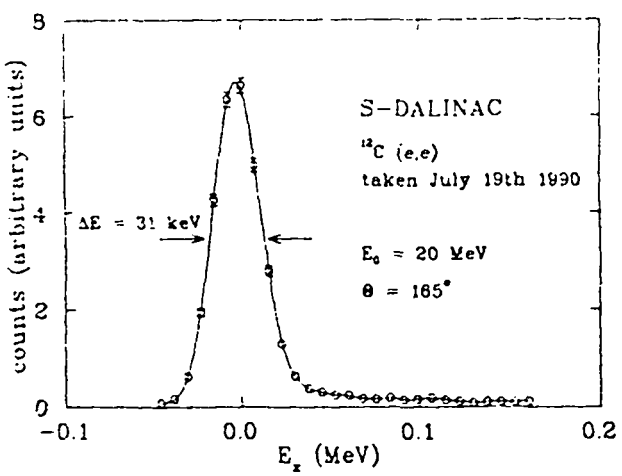

Fig.2 First spectrum of elastically scattered electrons obtained with a 20 MeV singles pass beam

Finally a 20 MeV single pass beam was extracted from the accelerator and reinjected into the existing beam transport system [10] to the 169° high resolution spectrometer. Figure 2 shows a first spectrum of elastically scattered electrons obtained there with the cw beam from the new S-DALINAC.

The properties of the injector beam were measured extensively at beam energies between 4 and 6.5 MeV and their dependence on the focussing of the 270 keV beam from the room temperature injection into the superconducting capture section was studied. It turned out, that the normalized emittance is always between 1 and 3 π mm mrad in the horizontal as well as in the vertical direction; no significant dependence on the beam energy was found. Best results were always obtained, when the 270 keV beam was focussed in such a way, that it had a waist at the entrance of the 5-cell capture section.

We also found that the orientation of the phase space ellipses do not agree with the predictions of simulation calculations. An additional quadrupole doublet behind the injector linac is therefore used to optimize the beam transport through the isochronous 180° bend, which by itself is not very tolerant with respect to different orientations of the phase space ellipses.

Outlook

Presently the accelerator is at room temperature and another two RRR = 280 cavities are being installed. At the same time the 5-cell capture section will be replaced by a cavity which is able to operate at higher gradients and the three inoperative tuners of the old version will be replaced by new ones.

The magnets of the beam transport system for the FEL have to be incorporated into the straight section of the first recirculation, because the delivery of the undulator is scheduled for December 1990. Also the modification of the room temperature part of the injection (installation of a high intensity gun and a subharmonic chopper- and prebuncher system) has to be performed during this shutdown period. We expect the accelerator to be operative again by the end of October.

Acknowledgement

The accelerator is the result of a very fruitful collaboration with H. Piel and his group from the physics department of the University at Wuppertal. The still continuing help of H. Heinrichs, R. Röth and J. Pouryamout, particularly in connection with the high temperature titanium treatment of existing and the firing of new cavities is greatfully acknowledged. We are much indebted to H. Lengeler for fruitful discussions and his continous support. Stimulating discussions with B. Aune, I. Ben-Zvi, J. Delayen, T. Grundey, E. Haebel, A. Mosnier, D. Proch, J. Sekutowicz, A. Schwettman, K. Shepard and T. Weiland have been very helpful in the course of the project. We are very grateful for the tremendous help provided by the technical staff at the S-DALINAC and the mechanical and electronics workshops.

References

[1] K. Alrutz-Ziemssen et al., Proc. 4th Workshop on RF Superconductivity, KEK 89-21, Tsukuba, Japan (1989) 53.

[2] K. Alrutz-Ziemssen et al., Proc. Part. Acc., Vol.29, (1990) 53.

[3] K. Alrutz-Ziemssen et al., Proc.1990 European Part.Acc.Conf., June 12-16, Nice, France, to be published.

[4] D. Proch, DESY, Hamburg, private communication.

[5] M. Becks et al., Proc. 4th Workshop on RF Superconductivity, KEK 89-21, Tsukuba, Japan (1989) 109.

[6] J. Kirchgessner et al., Proc. 4th Workshop on RF Superconductivity, KEK 89-21, Tsukuba, Japan (1989) 37.

[7] T. Weiland, Nucl.Instr.Meth. 216 (1983) 329.

[8] J. Sekutowicz et al., Proc. 4th Workshop on RF Superconductivity, KEK 89-21, Tsukuba, Japan (1989) 849.

[9] V.Aab et al., Proc.1988 European Part.Acc. Conf., 1988, Rome, Italy, 335.

[10] T. Walcher et al., Nucl.Instr.Meth. 153 (1978) 17.

HIGH-GRADIENT EXPERIMENT OF THE S-BAND ELECTRON LINAC

H. Matsumoto, M. Akemoto, H. Hayano, T. Naito and S.Takeda
KEK, National Laboratory for High Energy Physics
Oho 1-1, Tsukuba - shi, Ibaraki - ken 305, Japan

Abstract

The electron beam has been accelerated by the field gradient up to 85 MV/m with input peak current of 1 A and pulse width of 0.2 μsec successfully. The accelerating structure is a traveling wave 0.6 m-long constant gradient disk-loaded type at S-band. The output power of two klystrons was combined and fed into the structure. The output power of each klystron was 72 MW with 1μsec RF pulse duration at 50 Hz.

Introduction

The accelerating gradient of the Japan Linear Collider (JLC) is 100 MV/m for the X-band main linac and 50 MV/m for the S-band injector and the pre-accelerator[1]. In order to realize such a high gradient, we have started the construction of an accelerator test facility (ATF) in 1987, which is mainly composed of a 1.5 GeV S-band linac, a damping ring and a 1 GeV X-band linac[2]. As a first step, the construction of an injector part of the S-band linac has been already completed as shown in Fig. 1, which makes it possible to accelerate a single bunch beam of 5×10^{10} electrons and high current multi-bunches at high accelerating gradient.

Experimental studies on the upper limit of the electric field strength in conventional disk loaded structures and single cavities have been reported from several laboratories[3-8], though without the beam acceleration and mostly by standing wave structures. It was then decided to launch further studies on beam behavior under high accelerating fields in disk loaded structures.

General layout of the injector

The injector consists of a 240 kV thermionic electron gun[9], three subharmonic bunchers (119 MHz, 238 MHz and 476 MHz), single gap double prebunchers, a traveling wave buncher and an S-band constant gradient disk-loaded structure with length of 0.6 m as shown in Fig. 1. The SHB's are not used in this experiment. The SHB's, the prebunchers and the buncher are installed in the 25 Helmholtz coils whose current can be controled independently. The distribution of the axial magnetic field can be tapered from 150 Gauss to 700 Gauss so that the beam flows in Brillouin condition.

The support system of the injector consists of a 9 m long and 0.67 m wide table made of SUS316-L. The flatness of the table surface is 36 μm/9 m. All the components can be aligned easily within 100 μm accuracy.

In order to generate the maximum accelerating gradient of 100 MV/m, the output power of two 100 MW klystrons is combined and fed into the structure as shown in Fig. 2. RF output power of 200 MW with RF phase deviation and amplitude variation in the combined output was held to less than 2 degrees and 1% during any pulse, respectively. The klystron modulators[10] have been developed in KEK to drive the klystrons, SLAC 5045 and TOSHIBA E3712[11]. A small fraction of the combined power is used to feed the prebunchers and the buncher. The input RF power and the phase to the prebunchers, the buncher and the 0.6 m structure are controled by using a computer system[10].

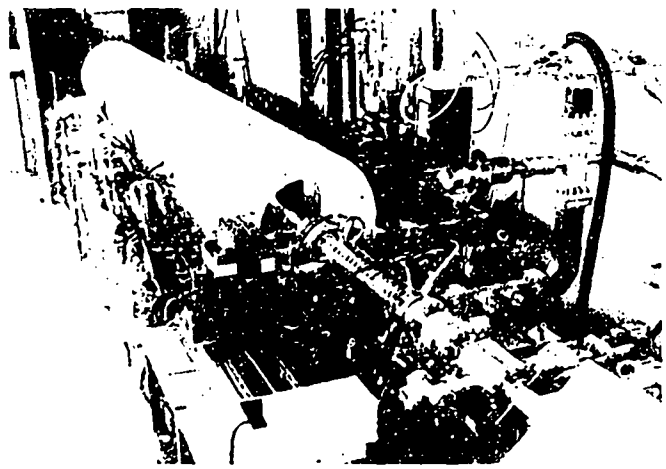

Figure 1 A photograph of the Accelerator Test Facility viewed from downstream.

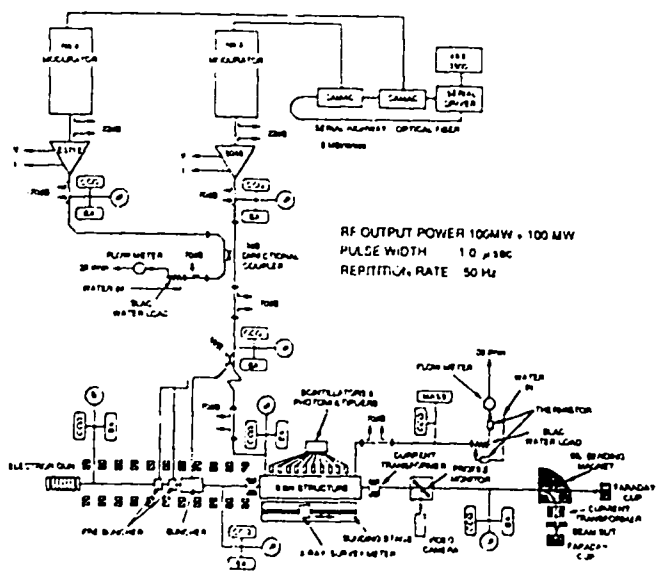

Figure 2 A schematic diagram of the experimental setup

Experimental Setup

The 0.6 m structure is a $2\pi/3$ traveling wave constant gradient type with 17-cells, input and output couplers. The disks and cylinders were machined from OFHC blocks with diamond bite. The surface roughness of the beam hole is less than 0.2 μm and that of the flat surface is less than 0.02 μm. The vacuum tightness and a good electrical contact are obtained by brazing process in hydrogen atmosphere.

The parameters of the structure to obtain the gradient of 100 MV/m at input RF power of 195 MW are given in Table 1. From these parameters, the accelerating field without beam can be calculated in the following way:

$$E_{acc}\,(MV/m) = 7.16 \times \sqrt{P_{in}\,(MW)} \qquad (1)$$

where P_{in} is the input RF power in MW.

TABLE 1
Parameters of the 0.6 m structure

Phase Shift/Cell	$2\pi/3$	Constant Gradient
Structure Length	60.5	cm
Iris Diameter 2a		
in	1.8938	cm
out	1.5900	cm
Cavity Diameter 2b		
in	8.172	cm
out	8.124	cm
Resonant Frequency f	2856	MHz at 36.5°C, VAC
Quality Factor Q	11600	
Shunt Impedance r	62	MΩ/m
Attenuation Constant α	0.48	Neper/m
Average Group Velocity vg/c	0.00445	
Filling Time Tf	0.475	μsec

The RF power of both the forward wave and reflected wave was monitored by dual Bethe-hole couplers with a coupling ratio of -70 dB. The transmitted power through the 0.6 m structure was monitored by also a Beth-hole coupler and terminated by the SLAC RF water load. The momentum of the accelerated beam is measured with a magnetic spectrometer. The peak current and pulse shape of the beam were monitored by two current transformers at the upstream and downstream of the 0.6 m structure. A beam profile monitor using a luminescent ceramic is mounted downstream of the 0.6 m structure.

Experimental procedure and result

The injector including the waveguides are pumped down to 5×10^{-9} Torr by five 60 l/s ion pumps and three 160 l/s ion pumps. The vacuum pressure is monitored by the cold cathode gauges (CCG) and the BA gauges. CCG's are used for the interlock system of the vacuum during the RF operation. The interlock level is set at 2×10^{-7} Torr. The vacuum pressure of the injector has been kept around 2×10^{-8} Torr.

After processing the accelerating structure up to 60 MV/m, the structure was exposed in atmosphere for one week to replace the experimental setup. Then it was evacuated again and reprocessed starting from several MV/m to 70 MV/m for 170 hours as shown in Fig. 3 before the beginning of the beam acceleration.

First beam acceleration was started at 50 MV/m and the accelerating gradient was increased up to 70 MV/m without any serious problem. However, it took considerably long period to reduced the rate of the breakdown and dark current at 70 MV/m since the structure was not processed above the level. The accelerated beam current was 0.9 A and pulse width was 0.2 μsec. Figure 4 (a) shows the pulse shape of RF and beam current. The second peak appearing in curve (2) of Fig.4 is due to the dark current. Figure 5 (a) is momentum spectrum of the accelerated beam. Since the emittance of the dark current is large, only a small peak is observed around 3 MeV/c in the Fig. 5 (a). The beam profile seen on the profile monitor is shown in Fig. 6. In this profile, the core part and the outer ring correspond to the accelerated beam and the dark current, respectively. Accelerating gradient was raised to 80 MV/m after one day processing. After futher RF processing for 120 hours, the beam was accelerated at 85 MV/m which is the maximum gradient in the present experiment. The current was 0.9 A and the pulse was 0.2 μsec. Figure 4 (b) and Fig. 5 (b) show the pulse shape of RF, beam current and momentum spectrum. At these gradients above 80 MV/m, dark current is very heavy and RF breakdown takes place frequently as is given elsewhere[13].

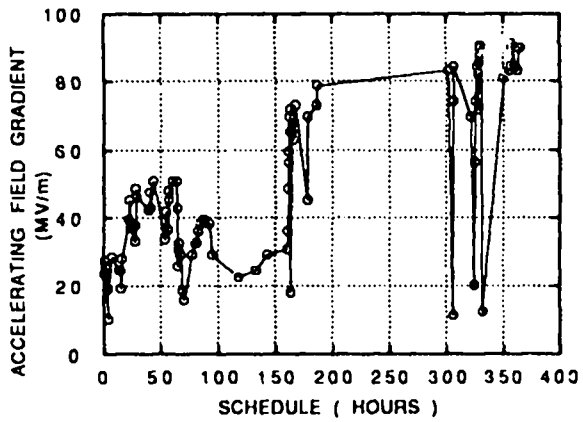

Figure 3 RF processing history for the 0.6 m structure.

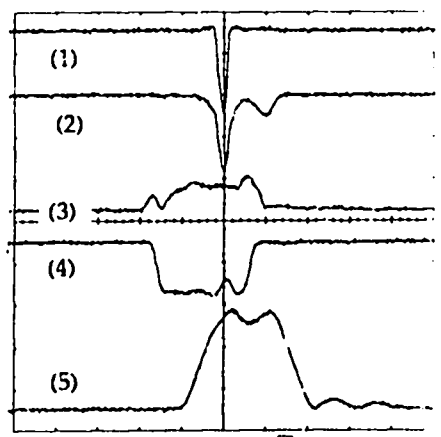

(a) Eacc = 70 MV/m,

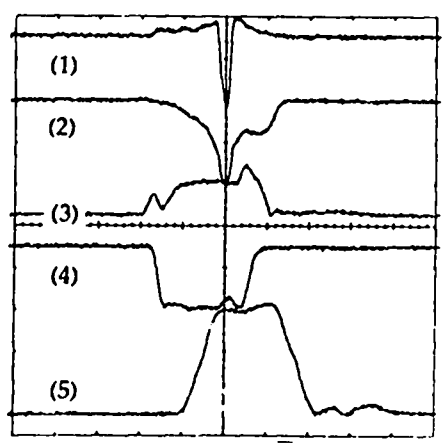

(b) Eacc = 80 MV/m

Figure 4 Pulse shape of RF and beam current.
1) Input and 2) output current of the 0.6 m structure, 3) reflected RF from the prebuncher, 4) transmitted RF of the buncher and 5) the 0.6 m structure.

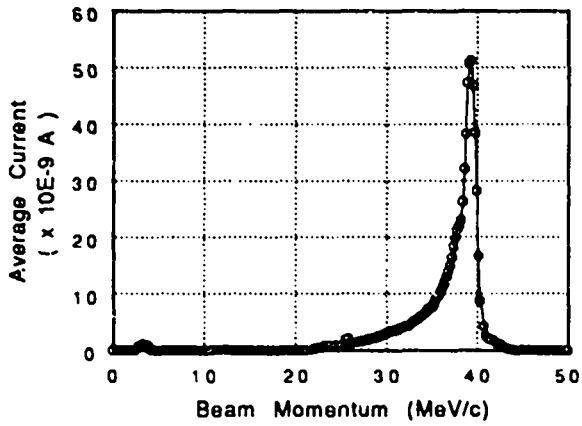

(a) Eacc = 70 MV/m,

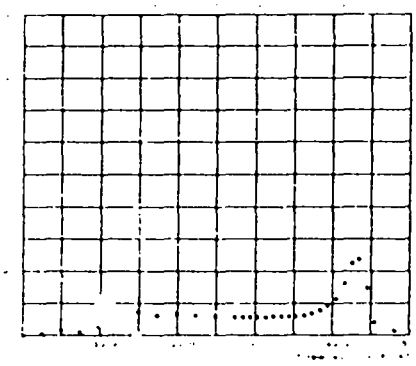

(b) Eacc = 80 MV/m

Figure 5 Momentum spectrum of the accelerated beam.

Figure 6 Beam profile

SUMMARY

We have achieved the acceleration of the electron beam of 0.9 A and pulse width of 0.2 μsec by the 0.6 m structure at the gradient of 85 MV/m. At this gradient, the dark current is very heavy and breakdown occurs frequently. However, at 70 MV/m, beam acceleration is fairly stable. It seems feasible to operate the accelerating structure at this gradient for the practical use after a reasonable processing period.

It is confirmed that the operation of 50 MV/m at S-band is quite promising. This level corresponds to 100 MV/m at X-band which meets requirement of the JLC.

REFERENCES

1. K.Takata, "The Japan Linear Collider",Proc. of the Linear Accelerator Conference (Albuquerque, USA), 1990.
2. S.Takeda, et al., "Jpan Linear Collider", Proc. of the Particle Accelerator Conference (Tsukuba,Japan) 1989.

3. G.A.Loew and J.W.Wang, "RF Break Down and Field Emission", SLAC-PUB-4845,Jan. 1989
4. E.Tnabe, "Voltage Breakdown in S-band Linear Accelerator Cavities", IEEE Trans.NS-30, No.4,(1983)3551
5. E.Tnabe, "Breakdown in High-Gradient Accelerator Cavities", Proceedings on 8th Linear Accelerator Meeting Held at Institute for Nuclear Study University of Tokyo,July 1983
6. A.H.Mceuen, et al., "High-Power Operation of Accelerator Structure at Liquid Nitrogen", IEEE Tarns. NS-32, No.5(1985)2972
7. H.Matsumoto et al.,"RF Breakdown Studies on an S-band Disk Loaded Structure", Proc. of the IEEE Particle Accelerator. Conference (WashingtonDC) 1654,1987
8. H.Matsumoto et al., "RF High Gradient of an S-band 0.6 m Disk Loaded Structure",Proc. of the Particle Accelerator Conference (Tsukuba,Japan) 1989.
9. M. Akemoto, "Electron Gun of the Accelerator Test Facility", Proc. of the Linear Accelerator Conference (Albuquerque, USA), 1990.

10. M.Akemoto et al., "Klystron Modulator with HV Common-Bus for the JLC", Proc. of the Linear Accelerator Conference (Albuquerque, USA), 1990.
11. H.Yonezawa, et al., "Development od A 100 MW S-band Klystron", Proc. of the Particle Accelerator Conference (Tsukuba,Japan) 1989.
12 H.Hayano, et al., "Control System of ATF", Proc. of the Linear Accelerator Conference (Albuquerque, USA), 1990.
13. S.Takeda et al., "High Gradient Experiment by Accelerating Test Facility for Japan Linear Collider", Proc. of the Linear Accelerator Conference (Albuquerque, USA), 1990.

THE INJECTOR OF THE SUPERCONDUCTING LINAC LISA

A.Aragona, C.Biscari, R.Boni, M.Castellano, N.Cavallo#, F.Cevenini#, V.Chimenti, G.P.Di Pirro, A.Gallo, A.Ghigo, F. Giacco#, S.Kulinski*, P.Patteri, B.Spataro, F.Tazzioli, M.Vescovi.

INFN, Laboratori Nazionali di Frascati, C.P.13, 00044 Frascati, Italy
* On leave of absence from Institute for Nuclear Studies, Swierk, Poland
#INFN, Sezione di Napoli and Dip. di Scienze Fisiche dell'Università di Napoli, pad.20, Mostra d'Oltremare, 80125 Napoli, Italy

Abstract

The injector of the LNF project LISA (LInear Superconducting Accelerator) is a room temperature system, consisting of a 100 keV gun, a transport line with chopper and prebuncher systems, a capture section (a graded-β 2.5 GHz structure) which accelerates the beam to 1.1 MeV, and an isochronous and achromatic transport line which injects the beam into the SC-Linac after a π-bending. The status of the project is presented.

Introduction

The superconducting (SC) electron linac LISA[1], in construction at Frascati INFN Laboratories, is a test-bench machine aimed at studying the larger SC linacs for colliders or CW machines for nuclear physics and at implementing a high efficiency FEL in the infrared wavelength region. In addition to the acquisition of the general techniques related to superconducting acceleration, LISA will allow to study such interesting topics as low emittance electron guns, beam recirculation and beam break-up that are fundamental in such machines.

In the first step of the project the beam parameters are mainly defined by the FEL application, which will require a 25 MeV beam and 5 A peak current. The bunch compression required to obtain this peak current from the 2 mA average current is performed in the injection system.

Injector Description

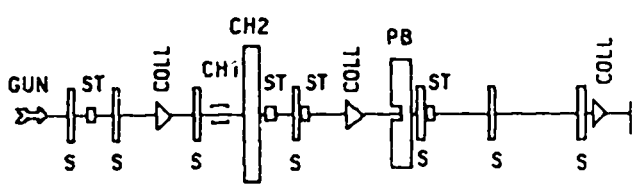

S - Solenoidal lenses; ST - Steerings; COLL - Collimator; CH1 - Chopper 1 (50MHz); CH2 - Chopper 2 (500MHz); PB - Prebuncher (500MHz).

Fig.1 - Sketch of the injector line at 100 keV.

The injector[2,3] consists of the following major parts:

- 100 keV thermionic gun;
- Double chopping system;
- 500 MHz prebuncher.;
- 1 MeV, 2.5 GHz capture section;
- Spectrometer channel;
- Achromatic and isochronous transport line between the capture section and the SC Linac.

The other elements of the injector are: solenoidal focusing lenses, steering coils, collimators, current monitors, fluorescent screens.

All RF elements in the injector have been constructed and successfully tested[4].

The block diagram of the 100 keV part of the injector is shown in Fig.1.

The Gun

As an injector of a SC Linac, the low energy line has been designed for working in a cw mode, but to keep the mean beam power within the limit posed by the Radiation Security Service (1 kW maximum), we decided to work in a pulsed mode. Thus the gun is a Pierce-geometry thermionic triode which nominally delivers 1 ms macropulses at a repetition rate of 10Hz, although macropulse length and frequency can be freely changed keeping the duty cycle constant.

The gun has been designed in our laboratory[5] using the Hermannsfeldt code SLAC-GUN and constructed by the Italian firm PROEL. The design parameters are: current I≥200 mA, normalized emittance $\varepsilon_n<10^{-5}$ m rad, energy W = 100 keV, energy dispersion $\Delta W/W = 10^{-3}$.

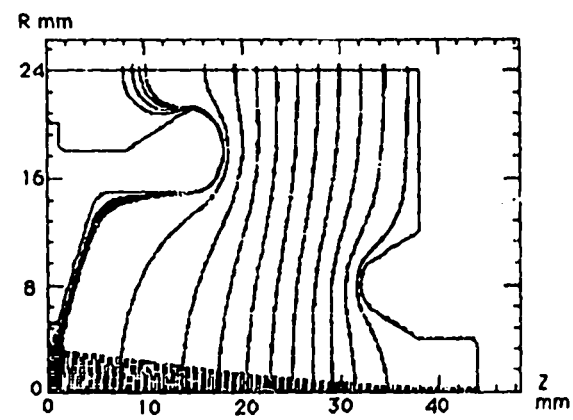

A sketch of the LISA gun together with electron rays and equipotential lines. Main gun parameters: V_a = 100 kV, V_g = 350 V, I = 0.2 A,calculated emittance (inv.) $\varepsilon = 1 * 10^{-6}$ mrad at the distance of 40mm from the cathode. cathode diameter (height) D_k=6.4mm, cathode (spherical) radius R_k = 40mm.

The gun is presently under test, as we want to measure its performances before the final installation on the LISA injector.

A dedicated channel has been constructed, composed of a solenoid lens, magnetic steering coils, a toroidal current monitor and a ceramic fluorescent screen seen by a high resolution CCD camera, as shown in fig. 2.

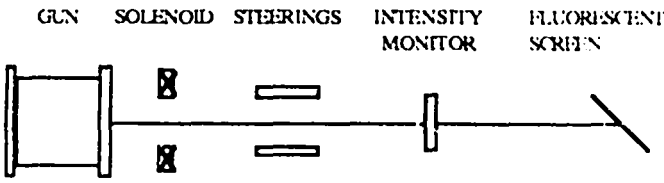

Fig. 2 - Test channel scheme.

The current vs grid voltage characteristics of the gun have been measured as function of the anode potential. A sample of the experimental data is shown in fig. 3.

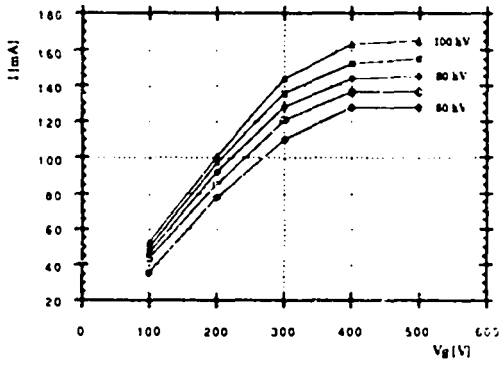

Fig. 3 - Gun current vs grid voltage as a function of the accelerating potential.

The maximum current value of 160 mA is lower than the 200 mA project value because the filament power supply resulted insufficient to heat the cathode up to the right temperature of 1020 °C.

The current vs anode voltage at the fixed grid value of 500 V, shown in fig. 4, has been fitted with the formula

$$I = G\left(500 + \frac{V}{\mu}\right)^{1.5}$$

giving μ = 350 and G = 6. 10^{-6}, in good agreement with the design values.

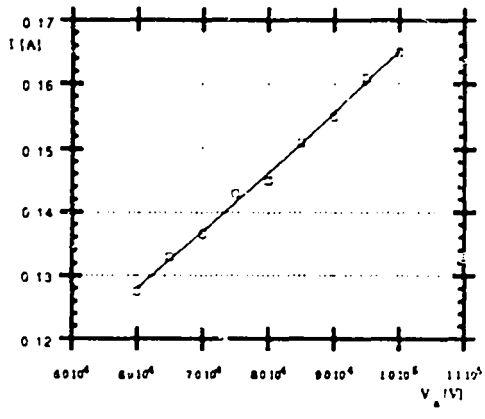

Fig. 4 - Gun current vs anode voltage at 500 V grid potential.

The beam transverse emittance can be evaluated measuring the spot dimension on the screen as function of the solenoid strength. The equations derived by the transport matrices of the beam envelope for at least three different solenoid current values can be inverted giving the optical functions and the emittance in each transverse plane if the space charge effects can be neglected.

In our preliminary measurements the beam dynamics suffered from two different drawbacks: the low current caused an early focussing in the gun, and consequently a large beam in the transport channel, sensitive to nonlinearities in solenoid and steering coil fields. The diffuse field of two small ion pumps positioned very near the gun output, that were required to lower the vacuum in the gun itself, clearly influenced in a nonlinear way the beam trajectory.

In these conditions the emittance measurements must be evaluated with great caution and considered only as very preliminary results.

Applying the described technique, with an accelerating field of 90 kV and a transported current of 100 mA, we obtain a normalized rms emittance of .9 10^{-5} m rad in the vertical plane and of 1.2 10^{-5} m rad in the horizontal one.

Chopping and Prebunching Systems

A double chopping system has been chosen in order to operate with lower average current without diminishing the peak current, relaxing so the shielding requirements. The first chopper CH1 operates at the subharmonic frequency f_1 = 50 MHz and consists of a pair of deflecting electrodes. It selects 10% of the total current so that the beam afterwards is composed of a succession of micropulses at the frequency of 50 MHz. The second chopper CH2 is a RF rectangular copper cavity oscillating at f = 500 MHz in the deflecting TE_{102} mode. It selects a phase spread $\Delta\Phi_{ch}$ ranging between 36° and 60° over the wavelength according to the accelerated percentage of the total current. Both choppers act deflecting vertically the beam; a pair of steerings corrects this deflection so that only the selected ~1% of the current passes through a collimator whose walls absorb the ~99% of the beam power.

The prebuncher is a klystron type microwave cavity oscillating in TM_{010} mode at the same frequency of the superconducting cavities, followed by the corresponding drift (D=1.44m). The gap length is one tenth of the wavelength; the voltage is of the order of 10 kV.

The capture section[6] is a normal conducting S-Band, standing wave, biperiodic $\pi/2$ graded-β accelerator, working at the fifth harmonic of the basic frequency, f_{cs} = 2500 MHz. It prepares the injection of the electron bunches into the SC Linac with sufficiently large β = 0.94, small phase bunch length $\Delta\phi \sim$ 1°-2° (@500MHz), and small energy dispersion $\Delta W/W \sim$ 1-2%. An axial magnetic field produced by superimposed solenoids counterbalances the radial defocusing forces due to either the space charge or to the radial component of the accelerating field.

The transport line between the capture section and the SC linac is achromatic to avoid dispersion in the horizontal phase plane and isochronous to avoid bunch lengthening. Since electrons are not fully relativistic at the injection energy, the spread in arrival time due to the energy spread has been taken into account and properly compensated with the trajectory length dependence on the dispersion function. The bending is obtained with three dipoles (45°, 90°, 45°) and two symmetric quadrupole doublets which adjust the dispersion function to the isochronism condition at the midpoint of the central dipole. Two triplets in front and after the arc take care of the matching between the linacs and the arc itself.

The Spectrometer

In the matching line between the capture section and the arc, a pulsed magnet deviates the beam to the spectrometer, the pulse timing is such that a single macropulse can be extracted, or the whole beam derived to the spectrometer arm. The spectrometer consists of two 60° sector bending magnets and two quadrupoles. The beam dimensions are analyzed on a fluorescent screen.

A bunch length measurement[7] is foreseen exploiting the spectrometer line: a vertically deflecting 2.5 GHz cavity, positioned before the pulsed magnet, gives an angular kick to the electrons depending on their position along the bunch, causing a vertical widening of the beam spot on the screen proportional to the bunch length. To increase the sensitivity of the measurement a different set of quadrupole gradients will be used in this configuration which will give the optimum vertical phase advance between the cavity and the screen, so that while the energy measurement will be on-line this last diagnostic tool will be used off-line.

Particle dynamics

Tracking of particles along the injector has been carried out with a modified version of the program PARMELA[8] simulating different currents, in order to determine the acceptance of the system in different working conditions.

The extremely high beam quality required asks for a careful adjustment of all the components of the line from the very beginning. In fact space charge problems influence the bunch transverse dimensions and the longitudinal phase space all along the transport. The nominal average current of 2 mA in the Linac can be obtained using an extracted beam from the gun of 200mA and a chopping angle of CH2, $\Delta\phi_{ch} = 36°$, or otherwise it is possible to decrease the initial current and to increase correspondingly $\Delta\phi_{ch}$. In fact the longitudinal space charge prevents the squeezing of the bunch to very short lengths at the input of the capture section. If the bunch length after the chopper system is longer the space charge effects are weaker for the same bunch charge; furthermore decreasing the beam current intensity between the gun and the choppers the emittance growth due to transverse space charge can be avoided. So I_{gun} = 120 mA and $\Delta\phi_{ch} = 60°$ have been chosen.

The increase of the beam emittance at low energies can be further reduced if the bunch length is not led to its possible minimum at the input of the capture section keeping the current density below critical values. The high peak current at higher energies can be obtained using the appropriate phase in the capture section, so that in the first cells of the section the beam is still under the bunching process. The longitudinal magnetic field produced by the solenoid around the section has been measured for different values of the current in the windings; the analytical expression obtained with a polynomial fit of the measured values has been introduced in the program PARMELA and used for particle tracking[6].

Tolerances

Tolerances of the line up to the capture section have been checked with PARMELA simulations: 10% errors in the field intensities of magnetic lenses do not change appreciably the line transmission, while 1% precision in the field of the capture section solenoid is needed. The prebuncher voltage must be fixed up to 0.5%. Element alignment precision of 0.5 mm are needed.

The quadrupole gradients along the line must be optimized depending on the optical functions at the capture section exit, which will be measured using the spectrometer line. Errors in the measurements of even 50% in the initial optical functions have been simulated and tracked with PARMELA resulting in an emittance degradation of the same order as in the case with no errors, a little more significant in the horizontal plane; the degradation of course is higher for lower initial emittances. The beam envelopes are perturbed but not in a significant way; the final betatron functions can still be matched to the SC Linac transport. The final bunch length is almost independent on the initial transverse conditions: only differences of some tenths of millimetres have been observed.

Errors of the order of 1% in the initial energy measurements have been also simulated and they do not affect much the final bunch length nor the transverse behaviour.

References

1 F.Tazzioli et al., 'Status of the LISA Superconducting Linac Project, EPAC 1990 Proceedings.

2 A.Aragona, C.Biscari, R.Boni, S.Kulinski, B.Spataro, F.Tazzioli, M.Vescovi, "Injector for LISA", Proceedings of the 1988 Linear Accelerator Conference - CEBAF, 1988, p.400.

3 C.Biscari et al., 'Status of the LISA Injector', EPAC 1990 Proceedings.

4 R.Boni, A.Gallo, F.Tazzioli, 'The RF System of the Frascati LISA 1 MeV Injector', EPAC 1990 Proceedings.

5 S.Kulinski,M.Vescovi, 'A Gun for LISA', Internal Report LNF-87/98(R).

6 J.Bigolas et al., 'Design and Construction of 1MeV S.W Accelerator Structure for LISA', EPAC 1990 Proceedings.

7 C.Biscari, R.Boni, M.Castellano, A.Gallo, B.Spataro, "Bunch length measurement system in the injector section of the SC Linac LISA", Internal Report LNF 90/024 (1990).

8 K.Crandall et al., Program PARMELA, Los Alamos National Laboratory.

THE LINEAR SUPERCONDUCTING ACCELERATOR (LISA) PROJECT AT FRASCATI INFN LABORATORIES

A. Aragona, S. Bartalucci, C. Biscari, R. Boni, M. Castellano, N. Cavallo*, F. Cevenini*, V. Chimenti, G. Di Pirro, S. Faini, A. Gallo, U. Gambardella, A. Ghigo, S. Kulinski°, C. Marchetti, C. Milardi, L. Palumbo**, P. Patteri, C. Sanelli, M. Serio, B. Spataro, S. Tazzari, F. Tazzioli, L. Trasatti, M. Vescovi

INFN, L.N.F., P.O. Box 13, 00044 Frascati (Roma), Italy
**INFN, Sezione di Napoli, Mostra d'Oltremare, Pad. 20, 80125 Napoli, Italy*
°On leave of absence from: Institute of Nuclear Studies, 05-400 Otwock-Swierk, Poland
***Dip.Energetica Univ. Roma 'La Sapienza', Via A. Scarpa 14, 00161 Roma, Italy*

Introduction

The construction of a 25 MeV superconducting (SC) radio-frequency (RF) electron linac is in progress at Frascati INFN Laboratories.

It will be a test machine for advanced technology oriented towards future linear colliders.

In a first phase of the project the machine will be applied to realize an infrared FEL.

In a second phase, in addition to the acquisition of general techniques related to SC RF acceleration, LISA will constitute the injector of a larger SC linac (ARES project).

A description and a status of LISA and a few words on future developments follow.

The machine

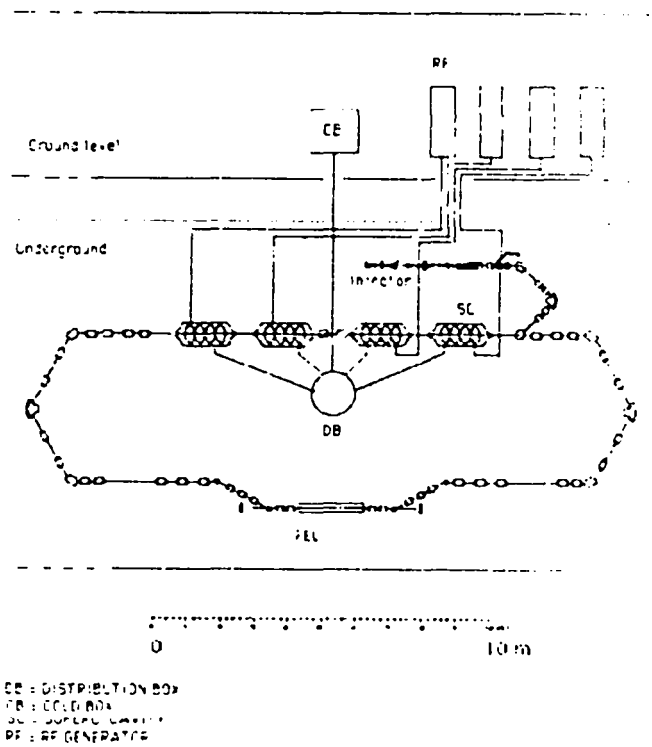

Fig. 1 - Schematic Layout of LISA Accelerator

The machine has been described in previous conferences [1], however, for the reader's convenience, the main parameters are summarized in Tab. I and a layout is shown in Fig. 1.

Table I - Main Parameters of LISA.

Energy (MeV)	25 + 49
Bunch length (mm)	2.5
Bunch charge (pC)	40
Peak current (A)	5
Duty cycle	≤ 2%
Average macropulse current (mA)	2
Invariant emittance (π m rad)	10^{-5}
Energy spread (@25 MeV)	$2 \cdot 10^{-3}$

The beam parameters are mainly defined by the FEL application whose characteristics are recalled in Tab. II. In the layout is shown a possible recirculation lattice, that has been studied [2,3], however, in a first phase a simpler direct transport line from the linac to the undulator may be implemented.

Table II - FEL: Main Parameters.

Beam energy (MeV)	25
Number of undulator periods	50
Undulator wavelength (cm)	4.4
Undulator parameter K_{rms}	0.5+ 1
Radiation wavelength (μm)	11 + 18
Optical cavity length (m)	6
Micropulse frequency	50 MHz
Macropulse frequency	10 Hz
Macropulse averaged power	500 W

In the first phase a normal room temperature injector will be used, consisting of a 100 KeV thermionic triode gun and a 1 MeV graded velocity buncher.

A detailed description of it can be found in this same conference [4]. It is envisaged to replace it later with a radio-frequency photocathode gun.

Downstream from the buncher the beam will be analyzed by means of a spectrometer and a special bunch length measuring system based on a deflecting cavity.

The beam is then deflected through a 180° achromatic and isochronous bend and injected into the four SC accelerating cavities.

Beam diagnostics consist of strip line position monitors placed in each quadrupole and fluorescent targets. On the quadrupoles will be also inserted additional windings that constitute correcting coils acting in both transverse directions. The SC cavities are made of bulk Nb and each one is placed in a separate cryostat, as shown in the sketch of Fig. 2. Their design characteristics are shown in Tab. III.

Table III - Parameters of the RF Cavities.

Frequency (MHz)	499.8
r/Q_0 (Ω/m)	380
Useful length (m)	1.2
Overall length (m)	2.5
Number of cells	4
Accelerating field (MV/m)	5
Q_0 (@ 4.2 K)	$2 \cdot 10^9$
Q_{ext}	$6.5 \cdot 10^6$

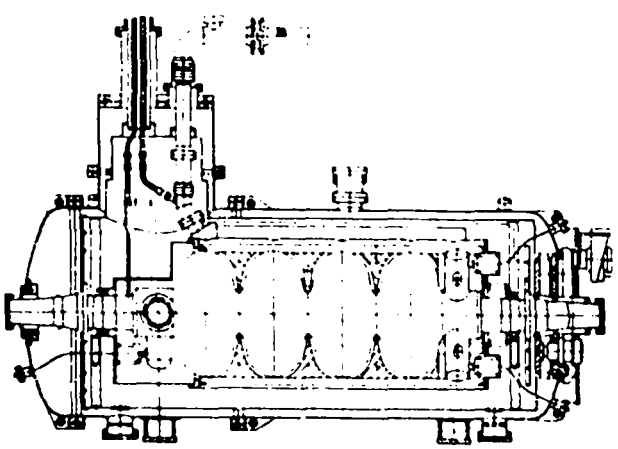

Fig. 2 - 500 MHz Accelerating Module.

The operation of the cavities requires the removal of about 200 W at liquid Helium temperature. To provide a reasonable safety factor a 300 W at 4.5 K refrigerator (Sulzer TCF-50) has been acquired. The refrigeration scheme features a distribution box between the cold box and the cryostats.

The RF system to power the cavities consists of four independent 15 KW klystrons, each separated from its cavity by a circulator.

The machine will be placed inside an underground vault while at ground level are situated the power generators, the refrigerator and the control room.

There is also a building dedicated to assembling, testing and development of SC cavities. It contains a dust free room, a clean water facility and a shielded zone for cavity tests.

Status of the project

The room temperature injector has been completed and its main parts tested.

Cold tests on one of the SC cavities have been performed at the manufacturing industry (Interatom). The cavity was completely assembled in its horizontal cryostat and it was powered through its main RF coupler.

The behaviour of the quality factor Q vs. the accelerating field E, determined by calorimetric measurements (boil off rate of LHe), is shown in Fig. 3. Measured stand by losses of the cryostat are 6 W.

The buildings are completed and installation of refrigerator, power generators and connecting cables is in progress.

The delivery of all four SC cavities is foreseen in November 1990 and completion of machine assembly is planned for the summer of 1991. Commissioning will follow immediately.

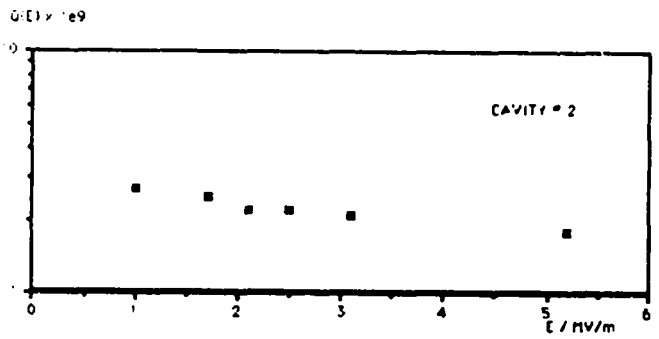

Fig. 3 - Behaviour of Quality Factor vs. Accelerating Field.

Future developments

The key to the realisation of high energy SC linear colliders is the achievement of high gradients with good quality factors in industrially produceable structures, and the generation and acceleration of very high peak current, low emittance electron beams.

Based on these considerations, a design study of an expanded SC linac, the ARES project [5], has been submitted to the management board of our Institution INFN, that has approved a program that will develop on a rather slow time scale (6 years), for compatibility with other programs in Frascati laboratories.

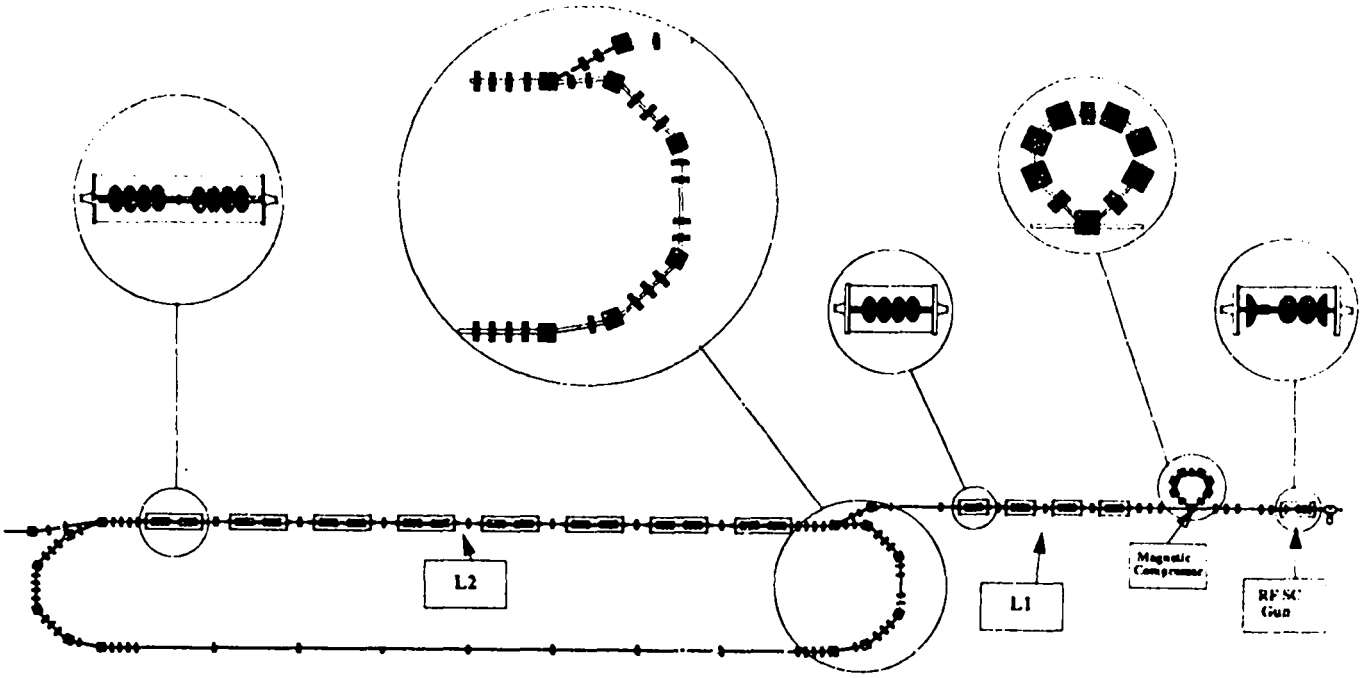

Fig. 4 - Sketch of the ARES Design Accelerator.

This program is intended as the natural continuation of the R&D work in progress on LISA and on SC-RF cavity design and construction techniques in collaboration with Italian industry, and will be developed by expanding the LISA buildings and facilities.

The final accelerator, as prospected in the ARES design study, will consist of twenty 500 MHz, four cells SC high performance cavities (the goal is E=10 MV/m at $Q=3x10^9$). Its nominal energy, 240 MeV, is high enough that recirculation without excessive deterioration of beam quality can be envisaged as a later upgrade. Such an energy would allow to extend the eventual FEL application to the X-VUV range. The beam will be generated by a RF gun with photocathode.

A sketch of the ARES design accelerator is shown in Fig. 4.

References

[1] A. Aragona et al.: "The Linear Superconducting Accelerator Project LISA", Proceedings of the 1988 EPAC, p. 52.

[2] Xu Janming: "The preliminary study of the whole lattice of LISA", Memo LIS-50. Aug. 1989.

[3] C. Biscari: "A new lattice for the 25 MeV transport line of LISA", Memo LIS-60. Oct. 1989.

[4] M. Castellano et al: "The injector of the superconducting linac LISA", (in this conference).

[5] "The ARES superconducting linac", LNF-90/035(R), May 1990.

DESIGN OF A BUNCHING SYSTEM FOR A HIGH-CURRENT ELECTRON LINAC

N.Nakamura, H.Yoshikawa, H.Suzuki,
M.Iizuka, T.Ishida, K.Yamada, A.Mizuno,
K.Mashiko and H.Yokomizo.

Japan Atomic Energy Research Insitute.
Tokai-mura, Naka-gun, Ibaraki-ken, JAPAN.

Abstract

The high-current electron linac for the positron generation operates in two modes: a single bunch mode of 1 nsec and a multibunch mode of 10-40 nsec. In order to generate 10 mA positron beam, the high-current electron linac is designed to provide 10 A electron beam onto the target. The high-current electron linac bunching system consists of a high-current gun, a following subharmonic buncher, two single cavity S-band prebunchers, and a S-band buncher. The gun is able to deliver 18 A beam at 200 kV. The subharmonic buncher is a quarter-wave reentrant resonant cavity with 1/12th the linac frequency 238 MHz. The prebunchers and the buncher are standing-wave structure with the linac frequency 2856 MHz.

Introduction

The injection system for the 8 GeV synchrotron radiation facility consists of a 1 GeV linac and a 8 GeV synchrotron [1,2,3]. The linac accelerates both the electron and positron beams up to 1 GeV.

The ultimate qualities of the electron and positron beams emerging from a linac depend on the design of the bunching system. It consists of two parts; the electron linac(EL) bunching system for the 120 MeV electron linac section and the high-current electron linac(HL) bunching system for the 300 MeV high-current electron linac section.

The principal differences between the two bunching systems are the specifications for the gun and the existence of a subharmonic buncher in the HL bunching system.

The electron beam experiences strong space-charge forces which affect longitudinal and transverse beam dynamics. Expected performance is analyzed with computer simulations.

We discuss the bunching system for the HL. The characteristics of the high-current linac are given in Table 1.

TABLE 1
Design Parameters of the High-current Electron Linac

Energy	300 MeV
Current	10 A
Pulse width	
short	1 nsec
long	10 nsec
Repetition rate	60 pps
Momentum spread	5 %
Emittance	12 π mm-mrad

Design of the HL Injector

A schematic diagram of the high-current electron linac(HL) bunching system is shown in Fig.1. It consists of a 200 kV electron gun, a 12th subharmonic buncher, two fundamental frequency prebunchers and a standing-wave buncher. The gun is placed out of radiation shield wall because of easy maintenance. The wall thickness is 100-150 mm. The beam from the gun is focused by magnetic lens so that we can adjust the radius and convergence of the beam at the entrance to Helmholtz coils. Solenoidal focusing by Helmholtz coils are used along the entire length of

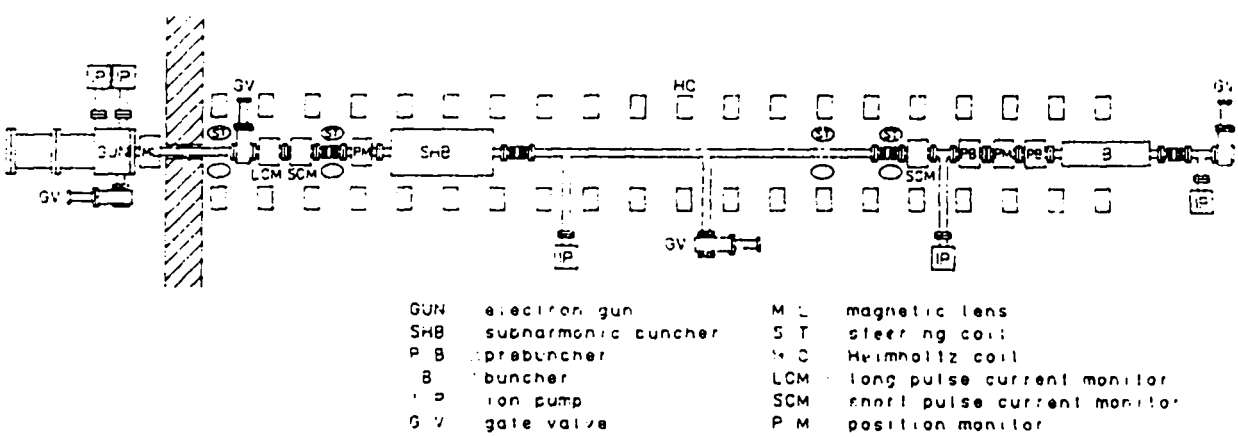

Fig. 1. The high-current electron linac bunching system.

the bunching system to provide radial confinement of the electron beam.

Beam diagnostic devices are arranged as shown in Fig.1 to control and measure the beam qualities. Two kinds of current monitors are used; core monitors (current transformers) are used for long pulses, and wall-current monitors are used for short pulses. We also make research and development on a short pulse monitor using amorphous metal. Beam profile monitors are fluorescent screen monitors using ceramic.

Electron Gun

The gun of the HL section require to have high intensity because of a low conversion(e+/e-) efficiency. The high-current thermionic gun is based on a dispenser cathode assembly (model Y796) developed by EIMAC. The gun is a triode type with a 2.0 cm^2 cathode. It will be able to deliver 18 A pulsed beam at 200 kV. The emission current can be pulsed for duration of 10 nsec and 2-3 nsec FWHM(full width at half maximum) by varying the grid voltage in the triode.

We have simulated the beam optics using the electron trajectory program[4]. Therefore the emittance is calculated with suitable weighting for the current of each ray. The magnetic lens is arranged just after the gun in order to converge the beam, because the gun is separated from the Helmholtz coils by the radiation shield wall. The Helmholtz coils are about 400 mm away from the cathode of the gun. Since the drift distance is long, we have designed to minimize the radial beam size and the transverse emittance. Beam optics to 150 mm for this gun are shown in Fig.2. The calculation predicts an output current of 18 A at 200 kV. We assume that the emission ability of the cathode is 10 A/cm^2 . The calculated overall emittance area is 181 π mm-mrad with the radial beam size of ϕ12 mm at the position of 150 mm from the cathode of the gun. Beam optics to 400 mm are shown in Fig.3. The magnetic lens is arranged at the position of 150 mm. The calculated overall emittance is 362π mm-mrad with the radial beam size of ϕ19 mm at the position of 400 mm from the cathode of the gun.

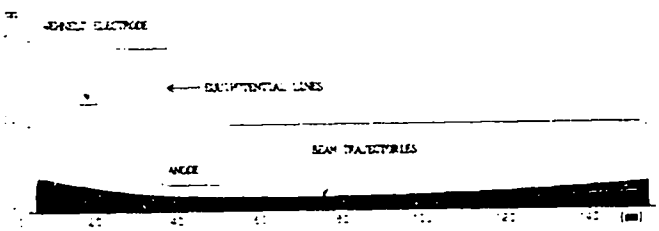

Fig. 2. Beam optics to 150 mm.

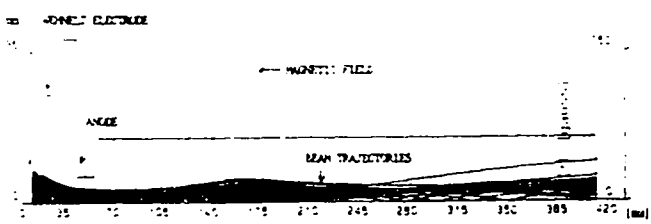

Fig. 3. Beam optics to 400 mm with magnetic field. The scale of vertical axis and horizontal axis is different.

Subharmonic Buncher

The subharmonic buncher is a quarter-wave reentrant resonant cavity. The subharmonic frequency is the 12th subharmonic (238 MHz) of the linac frequency(2856 MHz). The electron beam from the gun is bunched to within about half a cycle of the subharmonic. This allows the beam pulse from the gun to 2-3 nsec long. The subharmonic buncher will deliver the electron beam having a pulse width of approximately 1 nsec at 200 kV to the following 2856 MHz prebuncher. For the long pulse mode (10 nsec), the subharmonic buncher is not used.

We have simulated the bunching characteristic using the modified disk-model trajectory program[5]. In the simulation, we have assumed that the beam pulse from the gun is the 18A peak Gaussian shaped beam with 2 nsec FWHM. And further we have assumed the beam bore size of ϕ16 mm and the drift tube size of ϕ32 mm. We have modeled a beam as 51 infinitely thin disks of charge. Fig.4 represents the evolution of phase focusing, or bunching. The gap voltage of the subharmonic buncher cavity is 30 kV. The simulation results that 2 nsec (170 degrees) of the Gaussian shaped beam bunches to 0.75 nsec (65 degrees) at the position of 2500 mm from the entrance of the gap. It corresponds to 76% of the 18 A peak Gaussian shaped beam. The equivalent peak micropulse current is 37 A. The first prebuncher position (PB) is indicated in Fig.4.

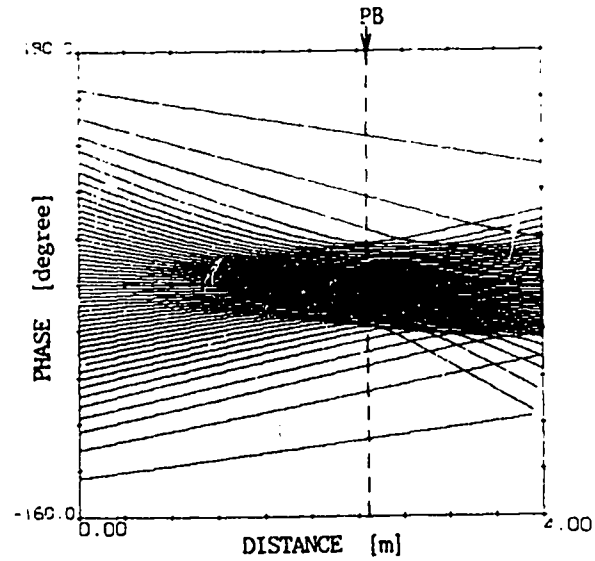

Fig. 4. The evolution of phase bunching in the subharmonic buncher.

Prebuncher

We use two prebunchers to get the high capture efficiency. The prebunchers are reentrant resonant cavity with same linac frequency 2856 MHz.

In the simulation, we have assumed that the beam pulse from the subharmonic buncher is the 37 A peak uniform charge density beam. And further we have assumed the beam bore size of Φ10 mm and the drift tube size of Φ32 mm. We modeled a beam as 51 infinitely thin disks of charge. Fig.5 represents the evolution of bunching. The gap voltage of the first prebuncher cavity is 30 kV, and that of the second prebuncher cavity is 60 kV. The drift distance between the gaps of two prebunchers is 200 mm, and the drift distance between the gap of second prebuncher and following standing-wave buncher is 95 mm. The buncher position (B) is indicated in Fig.5. The velocity modulation by the prebuncher causes 70% of the electrons to be bunched into a 50 degree phase spread at the entrance of the buncher.

The buncher is a standing-wave structure with varying phase velocity. The 50 degree bunches enter the buncher section when the phase field is near null. In the simulation without space charge effect, they become bunched to approximately 5 degrees and asymptotically approach the crest of the wave as they are accelerated in the buncher.

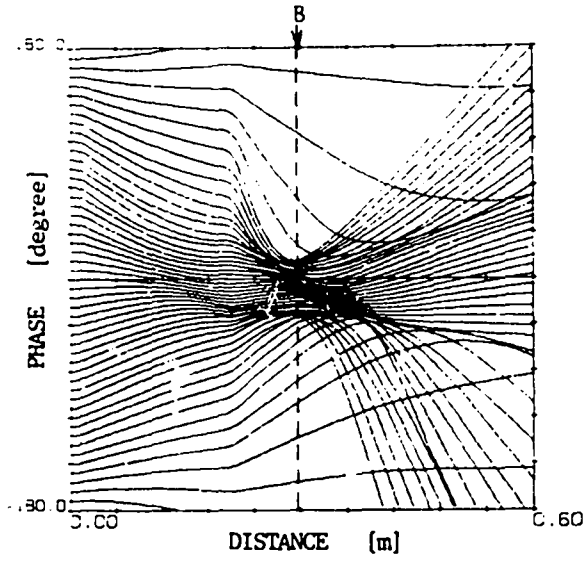

Fig. 5. The evolution of phase bunching in the two prebunchers.

Conclusion

We have designed the bunching system with the subharmonic buncher. Our simulation results that bunching efficiency of the subharmonic buncher is 76%, and that of a pair of bunchers is 70%. Consequently 1 nsec macro pulse width and 26 A peak current beam is obtained.

We are going to simulate the transverse beam dynamics in the bunching system and longitudinal beam dynamics in the buncher in consideration of space charge. We are also going to discuss the 24th subharmonic (119 MHz) buncher in order to accept longer beam pulse emitted from the gun.

References

1. H.Yokomizo et al., 'Injection System for the 8 GeV Synchrotron Radiation Facility in Japan', Proc. 1989 IEEE Particle Accelerator Conf., Chicago, IL March 20-23, 1245 (1989).
2. T.Harami at al., Proc. 14th International Conf. on High Energy Accelerators, Particle Accelerators, 33, 63 (1990).
3. H.Yoshikawa at al., 'The Injector Linac for SPring-8', proceedings of this conference.
4. W.B.Herrmannsfeldt, "Electron Trajectory Program", SLAC Report 226, November 1979.
5. S.Takeda at al., 'A Proposed High-current Injector for the Osaka University Single Bunch Electron Liner Accelerator', Proc. 4th Symposium on Accelerator Science and Technology in Japan, November 24-26, 275 (1982).

MAGNETIC BUNCHERS FOR THE GENERATION OF HIGH PEAK CURRENT, LOW EMITTANCE ELECTRON PULSES AT MEDIUM ENERGY*

B. E. Carlsten, B. D. McVey, and E. M. Svaton,**
G. R. Magelssen, and L. M. Young
MS H825, Los Alamos National Laboratory, Los Alamos, NM 87545

Introduction

A goal of many electron accelerator systems is high peak current, low emittance, and low energy spread. This is particularly useful for Free-Electron Laser (FEL) devices,[1] but is also beneficial for other uses.[2] In Fig. 1 we see typical FEL performance as a function of peak current, emittance, and energy spread. Unfortunately, these goals are basically contradictory. As the peak current is increased, the space charge forces also increase, and the emittance due to nonlinear space charge forces grows. There has been significant improvement in the design of photoelectric injectors which minimizes the emittance growth due to space-charge forces,[3] but in general the normalized 90% emittance scales as:

$$\epsilon_{90\%norm}^2 = r_o^4\left(1 + \tau_b^2 k_2^2\right)^2 + \left(\frac{k_3 eQ}{2m\epsilon_o \pi\sqrt{z^2 + 4r_o^2}}\right)^2$$

where

$$z = \frac{mc^2}{eE}\left(\sqrt{1 + \tau_b^2\frac{e^2E^2}{m^2c^2}} - 1\right)$$

and Q is the bunch charge, e is the electronic charge and m its mass, E is the accelerating gradient at the cathode, r_o is the initial beam radius, and τ_b is the duration of the laser pulse. The constants k_1, k_2, and k_3 depend on the exact design of the photoinjector, but typically lead to a dependence like

$$\epsilon_{90\%norm} = 10 + 5\frac{Q}{\sqrt{1 + \left(\frac{z}{2r_o}\right)^2}}$$

where Q is in nanoCoulombs and the units of emittance are π mm mrad.

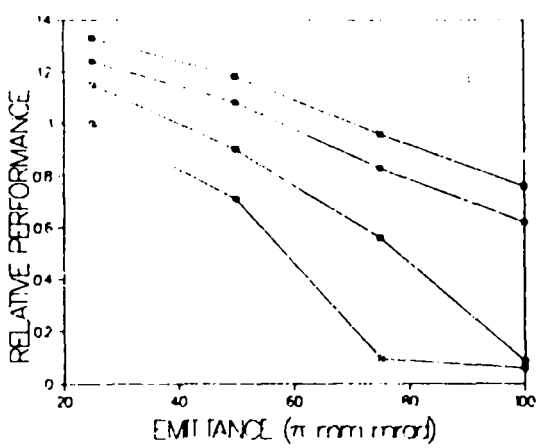

Fig. 1. FEL performance as a function of emittance. Squares are for 0.5% energy spread and circles are for 0.8% energy spread. Solid symbols are for 625 A and open symbols are for 375 A.

We see two effects from this scaling. First, for vanishingly short pulses, the emittance does not increase past a certain value for a given charge because the radial space charge force remains finite. Next we see that if the pulse length is increased, the emittance contribution due to the space charge drops.

*Work supported and funded by the US Department of Defense, Army Strategic Defense Command, under the auspices of the US Department of Energy.
**Rockwell International, Rocketdyne Division.

Sufficient motivation arises from this scaling to start with a long pulse length (until the rf effects cannot be ignored) and then bunch the beam to the desired peak current. If possible, this bunching should be done at a high enough energy so the reduced space charge forces will not lead to additional emittance growth. This bunching is provided by a transport section with magnetic dispersion. Bunching occurs if the correct energy-phase correlation is impressed on the bunch, typically by dephasing the rf fields slightly from the maximum energy gain of the beam.[4,5] The emittance growth of previous designs roughly obey

$$\Delta\epsilon_{90\%norm}(\pi \text{ mm mrad}) = 25\frac{I}{\gamma^2}$$

where the current I is in Amperes.[5] In this paper we will discuss new types of magnetic bunchers with one third the emittance growth, allowing bunching to 1KA at medium energy (20 to 40 MeV) with emittance increases of less than 10 π mm mrad, added in quadrature.

We will also consider in this paper the effects of limited rf power. In general, it is always preferable to bunch at as high an energy as possible, but under certain limitations[6] this cannot be done. In the next section, we will outline the various physical constraints and issues for magnetic buncher design. Discussion of achromatic design and dispersion and minimizing rf power will be presented.

In the following section we will provide generic designs for positive and negative dispersion. A short section will follow describing the effect of curvature in the energy-phase correlation due to the sinusoidal nature of the rf fields on the output pulse shape. Methods to remove the curvature will be examined. The final section will cover simple nonlinear dispersion which can compensate for the curvature.

General Considerations

In this section, the basic ideas for magnetic buncher design will be discussed. First, geometric and chromatic aberrations must be avoided. The concepts of linear and higher order dispersion are introduced. Next, the curvature in the energy slew will be discussed. Finally, the emittance growth in the bunchers due to space charge forces will be examined. After these items are introduced, we will discuss specific magnetic bunchers and comparisons of them. Space charge forces are ignored until the end of the section.

To second order, the magnetic field in a dipole can be expressed as[7]

$$B_y(x, 0, \Delta s) = B_y(0, 0, \Delta s)(1 - nhx + \beta_c h^2 x^2)$$

where h is the inverse bending radius $\frac{qB_y}{mc\beta\gamma}$, n is the field gradient, β_c is the field curvature term, and Δs is the path variable within the dipole, for a dipole with field in the transverse y direction. A general analysis of the electrons' behavior in the dipoles must include a description of the transfer matrix R with field gradient n and field curvature β_c. However, since we will look at the transport from a geometrical basis and there are several complete descriptions available,[7,8] it will not be included here. From this theory, multiple dipoles are required for any magnetic system to eliminate chromatic aberrations.

In Fig. 2 we see an example of a type of a magnetic buncher called the chicane, which provides geometrical and chromatic symmetry. This is true of a larger class of bunchers which has pairs of parallel pole faces. Any transverse displacement of the beam yields an equal final transverse displacement. Initial transverse velocities produce final displacements linear with the initial velocity (for small velocities), and the velocity is preserved. The buncher

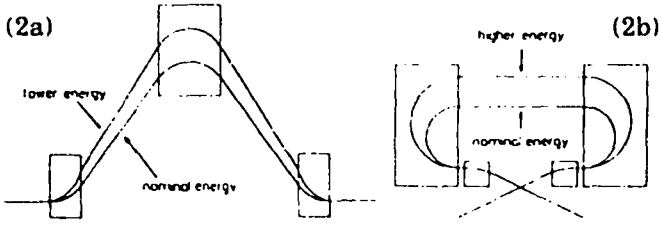

Fig. 2. Configuration of the chicane (a) and circular (b) bunchers.

essentially looks like a drift to the beam. The chicane buncher has some nonlinear dispersion, even with constant gradient dipoles.

These properties are inherent with symmetric designs with parallel pole faces,[9] and we will only discuss this class of bunchers. This allows us to neglect the R matrix analysis, until we use nonzero field gradients in a later section. Another variant of the parallel pole face idea is also shown in Fig. 2, called the circular buncher. This design has only linear dispersion with zero field gradients.

The cavities after the buncher must be phased to eliminate the energy slew required for bunching. Let W_1 and N_1 be the maximum energy gain per cavity and the number of cavities before the buncher, and W_2 and N_2 be them after the buncher. The angle ϕ_1 and ϕ_2 are the rf phases the center of the bunch sees before and after the buncher. If θ_1 is the pulse phase length before the buncher and θ_2 after the buncher, then the energy spread ΔW satisfies

$$\Delta W = 2N_1W_1\cos\phi_1\sin\frac{\theta_1}{2} \tag{1a}$$

$$\Delta W = -2N_2W_2\cos\phi_2\sin\frac{\theta_2}{2}. \tag{1b}$$

The curvature, or deviation from a straight line, for the energy slew is

$$\Delta W_c = N_1W_1\left(\cos\phi_1\left(\sin\theta_1 - \theta_1\right) - \cos\theta_1\sin\phi_1\right) \quad . \tag{2}$$

We see that this is increased with increased pulse length θ_1, and has a maximum for ϕ_1 near $\frac{\pi}{2}$. The curvature is greatest for the larger dispersion bunchers, and longer initial pulse lengths. Without compensating for the nonlinear dispersion in the buncher, this results in a skewed final current profile. Usually this is not desirable, and can lead to significant emittance growth during the rest of the transport.

Assuming that the emittance growth for nonlinear optics and the fringe fields are eliminated, the emittance growth from a buncher is due only to the space charge forces. In particular, there are axial and radial forces within the bend. The predominate effect is when the forces change the kinetic energy of a particle while it is still within the buncher, destroying the achromaticity of the buncher. The axial force changes the energy, inversely proportional to gamma. It can be made quite small by decreasing the path length or operating at a higher energy. The radial force creates a potential redistribution of the particles as the beam bunches, and the energy change is independent of gamma. Usually this is small, but can dominate if the other effect is reduced enough. These effects can be minimized by focusing the beam to a waist in the final dipole.[9]

In order to compare these effects, we should in principle compare the rms potential change of the beam. However, the resulting algebra and complicated expressions mask the underlying physics, and we will make scaling arguments from simple formulas. The voltage change from the axial space charge force is very dependent on the actual longitudinal density distribution. The initial distribution is somewhat parabolic. This allows for an axial force throughout the pulse; if the initial distribution is square, the voltage change is primarily located at the axial ends. The emittance growth scales as the energy change divided by the energy. The potential redistribution is also dependent on the longitudinal density distribution, although in all cases it is distributed along the entire length of the pulse.

The resulting emittance is of a different nature from the two effects. The emittance growth from the axial space charge force arises from a twist in phase space for different axial locations in the pulse; the emittance at a single axial location is quite small. On the other hand, the emittance from the potential redistribution effect appears as a radial twisting in the phase space for all axial slices.

The space charge field at a point from a transverse disk of charge Δz away, where r_o is the disk's radius, and ρ is the charge density, is

$$\Delta E_z = \frac{\rho}{2\epsilon_o}\left(1 - \sqrt{\frac{\Delta z^2}{\Delta z^2 + r_o^2}}\right) \tag{3}$$

It is easy to check that this expression reduces in the limit Δz is zero to the surface field from Gauss's law, and in the limit r_o is zero to Coulomb's formula for a point charge.

Integrating this expression for a uniform slug of charge, we find that the axial field at the ends of the slug is (to lowest order in $\frac{r_o}{z_o}$):

$$E_{z,rest} = \frac{Q}{4\pi\epsilon_o r_o z_o}, \tag{4}$$

for a pulse length of z_o. This axial field is in the beam's rest frame, and

$$z_o = \gamma\beta c\tau_b \quad .$$

Using

$$E_{z,lab} = E_{z,rest} \quad ,$$

the resulting voltage change for the ends of the pulse after a drift of length ΔS is then

$$\Delta V = \frac{Q\Delta S}{4\pi\epsilon r_o\tau_b\gamma\beta c} \quad . \tag{5}$$

For an accurate answer, we should integrate over the path ΔS in the buncher as τ_b decreases, but as an approximate answer, we can assume ΔS is roughly one quarter of the path length in the buncher and τ_b is the final pulse length. Since the voltage change is mostly at the axial ends, we will write for it

$$\Delta V = F\frac{Q(\Delta S/4)}{4\pi\epsilon r_o\tau_{b,final}\gamma\beta c} \tag{6}$$

where F is a form factor, less than one.

The relative voltage change from the potential redistribution of the center of the beam (for a uniform beam) is given by

$$\Delta V = \frac{Q}{4\pi\epsilon_o\beta c}\left(\frac{1}{\tau_{b,final}} - \frac{1}{\tau_{b,initial}}\right) \quad , \tag{7}$$

where $\tau_{b,final}$ and $\tau_{b,initial}$ are the final and initial pulse lengths. Assuming that the initial pulse is long, we equate Eqs. 6 and 7 to see at what buncher path length the two effects are of the same size

$$\Delta S = 4\gamma r_o\frac{1}{F} \quad .$$

For beam sizes around 2.5 mm, energies of 20 MeV, and using a form factor of 0.5, we see that the axial space charge effect becomes smaller than the potential redistribution for path lengths less than 80 cm. This is of course just a rough estimate, but it indicates that we should try to design bunchers with path lengths well under one meter.

Examples of Positive and Negative Dispersion Bunchers

In this section, we will compare the circular and chicane bunchers. For equal path lengths, the circular buncher has about three times the dispersion and that its dispersion is positive, while the chicane has negative dispersion. For geometrical reasons, positive dispersion bends usually have more dispersion.

The dispersion of the circular buncher is completely linear, but there is some nonlinear dispersion for the chicane. This is because the rotation angle caused by the first dipole is not linear with energy but instead satisfies the transcendental equation

$$L\theta = \Delta S\sin\theta$$

where L is the width of the dipole and ΔS is the path length in it. Because the particles' paths in the dipoles of the circular buncher are circles sliced into two and displaced, there is no nonlinearities in its transport. It looks like a drift to the beam.

In Fig. 3 we see the emittance increase as a function of energy for both bunchers. The smaller emittance introduced with the circular buncher is due to its larger dispersion and shorter path length. Emittance diagnostics indeed show that the emittance growth is dominated by the potential redistribution.

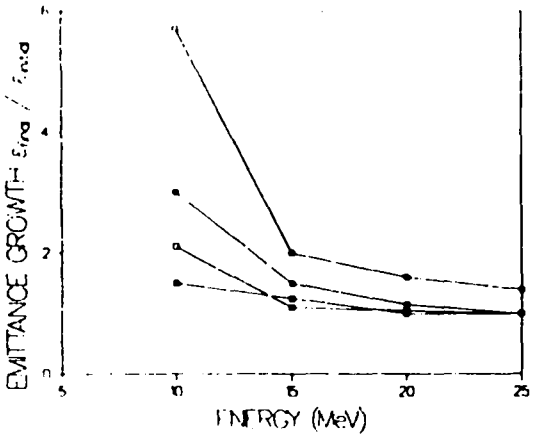

Fig. 3. Transverse emittance growth for bunching 8 nC from 160 to 500 A for the chicane (open symbols) and circular (solid symbols) bunchers at different energy. Squares are for horizontal emittance, and circles are for vertical emittance.

Effects of the Curvature of the RF

In Fig. 4 we see the initial parabolic and final skewed current profiles before and after the circular buncher. The units of phase are degrees at 433 MHz. The skewing is from the curvature in the energy phase slew, also shown in Fig. 4. This skewed output current profile is undesirable. The curvature can be removed before the start of the buncher. A conventional approach is to use a third harmonic rf cavity.[10] Another technique is to use a series of wake-field producing apertures or other disturbances. The initial current profile is typically cosine-like shaped from the initial axial space-charge forces in the first cavity. The wake potential lags somewhat behind the current profile, but if the lag is short relative to the length of the pulse, the energy-phase slew can be significantly straightened.

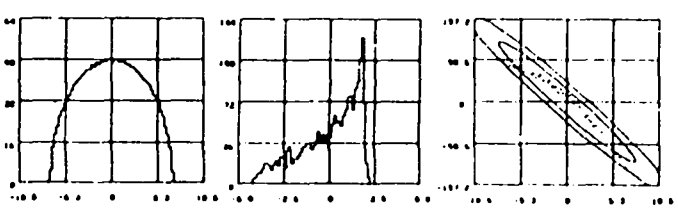

(4a) (4b) (4c)

Fig. 4. Initial current profile (a) and after bunching (b) for the circular buncher. Energy slew is shown in (c).

Alternatively, nonlinear dispersion in the dipoles from nonzero field gradients or field curvature can compensate for the energy slew curvature. In Fig. 5 we see an example generated by angling the pole faces apart. The path length in the dipoles is now a nonlinear function of a particle's energy.

Conclusion

We have presented a class of magnetic bunchers which have parallel pole faces. This symmetry reduces or eliminates

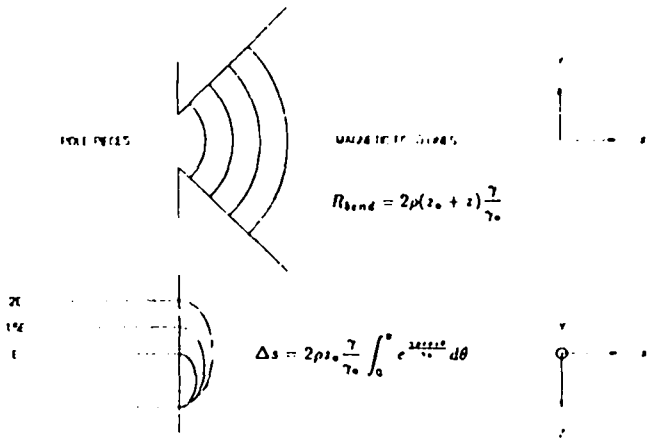

Fig. 5. Simple nonlinear dispersion in the circular buncher can be provided by separating the pole faces at an angle, reducing the magnetic field for the higher energy particles.

geometrical and chromatic aberrations, and leads to smaller emittance growth than with conventional designs. We have further divided this class into two subclasses, those with positive and those with negative dispersion. The positive dispersion designs have larger dispersion and smaller emittance growth, but the smaller energy spread results in a larger curvature in the energy-phase slew. This curvature results in a skewed output current profile. The curvature can be removed before the bend either by rf or by space charge forces. If it is not removed, nonlinear dispersion in the bend can be added, which corrects the pulse profile, but may introduce small geometrical aberrations.

References

1. J. C. Goldstein, B. E. Carlsten, and B. D. McVey, "INEX Simulations of the Los Alamos HIBAF Free-Electron Laser MOPA Experiment," Proc. 11th Int. Free-Electron Laser Conf., Naples, Florida, Aug. 1989, to be published.
2. J. B. Murphy and C. Pellegrini, Preface, Proc. ICFA Workshop on Low Emittance e^--e^+ Beams, Brookhaven Natl. Lab., March 1987, BNL report 52090.
3. B. E. Carlsten,"Photoelectric Injector Design Code," Proc. 1989 IEEE Particle Accelerator Conf., IEEE Catalog No. 89CH2669-0, 133 (1989).
4. B. E. Carlsten and K. C. D. Chan, "Preliminary Injector, Accelerator, and Beamline Design for RF-Linac-Driven XUV Free Electron Lasers," *Nucl. Instrum. Meth. Phys. Res.* **A272**, 208 (1988).
5. T. I. Smith,"Summary of the Working Group on Electron Linac Guns," Proc. ICFA Workshop on Low Emittance e^--e^+ Beams, BNL, March 1987, BNL report 52090.
6. B. E. Carlsten, R. L. Sheffield, and B. D. McVey, "Photoelectric Injector Designs at Los Alamos National Laboratory," Proc. ICFA Workshop on Short Pulse High Current Cathodes, Bendor, France, June 1990, to be published.
7. K. R. Crandall, "TRACE 3-D Documentation," Los Alamos Report LA-11054-MS.
8. D. C. Carey, R. V. Servranckx, and K. L. Brown, "Second-Order Path Length Terms for a General Bending Magnet," Particle Accelerators **13**, 199 (1983).
9. L. M. Young, Los Alamos National Laboratory, private communication.
10. K. C. D. Chan and J. S. Fraser, "Minimum Beam-Energy Spread of a High-Current RF Linac," Proc. 1987 IEEE Particle Accelerator Conf., IEEE Catalog No. 87CH2387-9, 1075 (1987).

ELECTRON GUN OF THE ACCELERATOR TEST FACILITY FOR THE JLC

M. Akemoto, H. Akiyama, H. Hayano, H. Kobayashi, T. Naito, H. Matsumoto, Y. Otake and S. Takeda

KEK, National Laboratory for High Energy Physics
Oho 1-1, Tsukuba, Ibaraki 305, Japan

Abstract

For the electron source of the JLC (Japan Linear Collider), the electron guns with a low emittance and high current are required. In order to realize these requirements, the thermionic electron gun capable of operating at 240 kV has been designed and constructed for the Accelerator Test Facility. A conventional EIMAC Y-796 cathode-grid assembly is used as the electron source. This paper describes the design, specifications and results of test of the gun system.

Introduction

High-current, low-emittance and multi-bunch beam is required to attain high-luminosity of 10^{33} $cm^{-2}s^{-1}$ for the JLC (Japan Linear Collider)[1]. The parameters of the beam are summarized in Table 1 and the structure of the bunch is schematically shown in Fig. 1. The number of particles per bunch is 1.0 x 10^{10}. The number of bunches per bunch train is 10 with the bunch spacing of 1.4 nsec and the repetition rate of 200 Hz. The fluctuation of each bunch in a bunch train should be less than ± 2% to obtain the required luminosity. The rms normalized emittance should be also less than 10^{-3} rad·m for the acceptance of damping ring[2]. Increasing the cathode voltage of the gun, the beam emittance is decreased as well as the longitudinal space-charge forces in the pre-buncher. Therefore, the higher voltage is preferable to obtain low emittance high current beam. A 240 kV gun has been designed and constructed for an electron source of the Accelerator Test Facility.

Table 1 Beam parameter of the JLC

Number of particles per bunch	1.0 x 10^{10}
Number of bunches per rf pulse	10
Repetition rate of rf pulse	200
Bunch spacing	1.4 nsec
Flatness	< ± 2 %

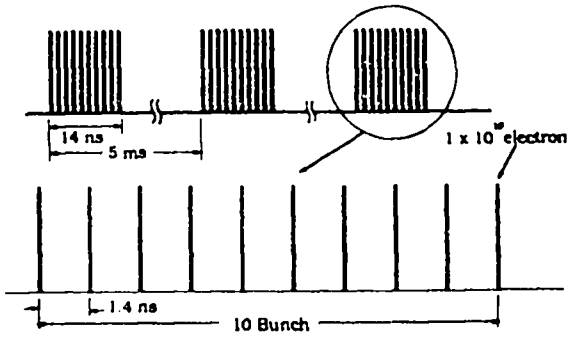

Fig. 1. Beam structure of the JLC

Electron Gun Design

The simulation of the beam trajectory was performed to design the electron gun with an applied voltage of 240 kV by using the electron trajectory program made by W. B. Herrmannsfeldt. The shape of the anode and cathode electrode are optimized in order to obtain a laminar flow and small beam size. The beam trajectory for the optimized geometry is shown in Fig. 2.

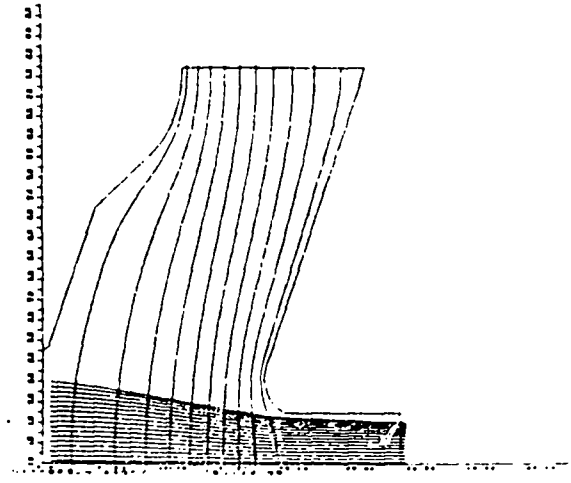

Fig. 2. Simulation of beam trajectory at 240 kV and beam current of 10 A

As shown in Fig. 3, EIMAC Y-796 cathode-grid assembly is utilized for the gun cathode. The electron gun consists of a cathode stem, HV insulator, vacuum chamber with anode and magnetic lenses. The diameter of the insulator is determined from the size of the flanges and the ICF253 flanges are used for the present gun. The length of the insulator is 360 mm, which is determined to avoid the HV breakdown in atmosphere along the outer surface of the insulator. The key issue of the gun design is the alignment of the cathode, anode, magnetic lenses, magnetic shield. Alignment of the axis both the cathode and anode is realized by precise machining of the flanges of the insulator. The axis of the cathode and anode can be aligned in 100 μm. The anode and magnetic lenses are fixed on the same SUS316L block which is also machined precisely to align the axis in 50 μm accuracy mechanically. The electron gun is installed on the support system where the linac components are set up. The support system is a 9 m long and 0.7 m wide L-block made of SUS316L. The flatness of the block surface is 36 μm/9 m. The components can automatically be aligned within 50 μm by setting on the support and alignment system. As the results, The electron gun, magnetic lenses and magnetic shield can be aligned within 100 μm

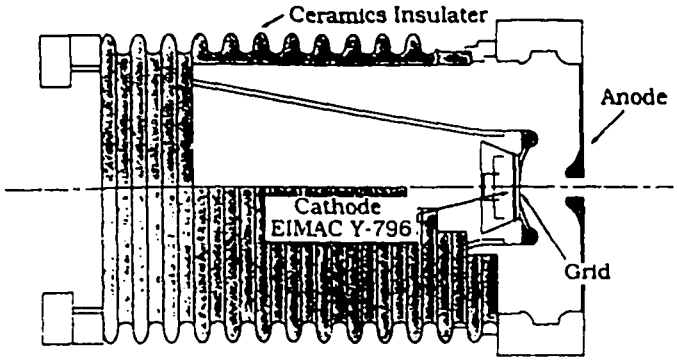

Fig. 3. ATF Electron gun assembly

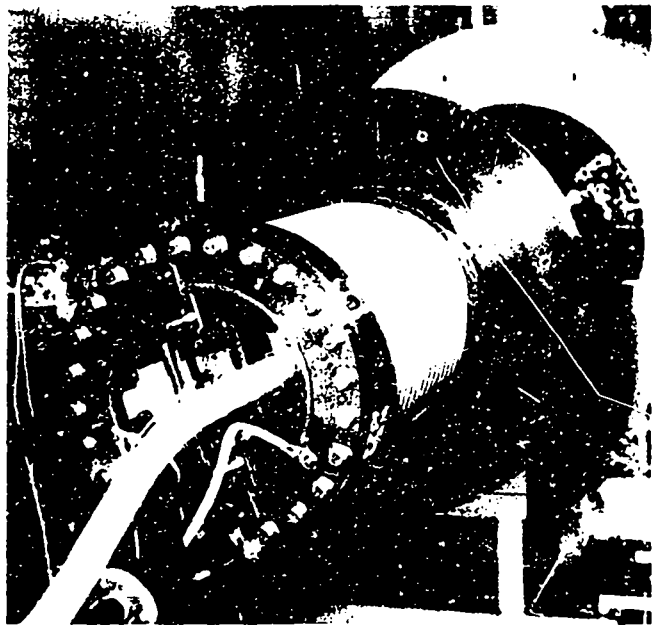

Fig. 4. A photograph of the gun

Gun modulator

The gun modulator consists of a 240 kV pulse modulator, a HV station with grid pulser and a control system. The high voltage pulse is generated by the HV modulator of a line-type with a 16 section pulse forming network and a de-Qing circuit stabilizes the output pulse. A high power dummy load is installed in a pulse transformer to decrease the impedance and to eliminate the sag of the output voltage. The gun pulsers are installed in the HV station set up near the electron gun. The gun pulser is designed to generate the following three modes: (1) long pulse mode (0.8 - 3 μsec), (2) semi-long pulse mode(10 - 100 nsec) and (3) short pulse mode (5 nsec). These modes can be switched easily by the computer control system as described below.

Table 2. Specifications of the HV modulator

Peak power output	24 MW
Average power output	8.4 kW
Output pulse voltage	240 kV
Output pulse current	100 A
Output impedance	2.4 kΩ
Load impedance	2.4 kΩ
Transformer ratio	1:15
Pulse width	7 μsec
Pulse flat top	3 μsec
Rise time	2 μsec
Repetition	50 pps
Pulse height deviation from flatness	<± 0.3 %
Pulse amplitude drift	
Short term	<0.2 %
Long term	<0.5 %

Control system for modulator and grid pulser

The schematic diagram of the control system is shown in Fig. 5. The local controllers are installed in both the modulator and HV station and they are connected with the main control console. These two local controllers provide the manual control of modulator and grid pulser individually. At the main control console, both the modulator and grid pulser can manually be controlled The controllers provide the controls and data acquisitions by programmable sequence controllers (PSC) with a CPU, DI, DO, ADC, DAC etc. The PSCs of the HV modulator and HV station are connected to the main control console with optical-fiber cables. The PSC of the main control console is also connected to the ATF control system[3] consisting of CAMAC and two microVAXs which are connected to the KEK network. The timing of the trigger pulses for the gun pulser and HV modulator can be controlled by VAX station through the CAMAC module.

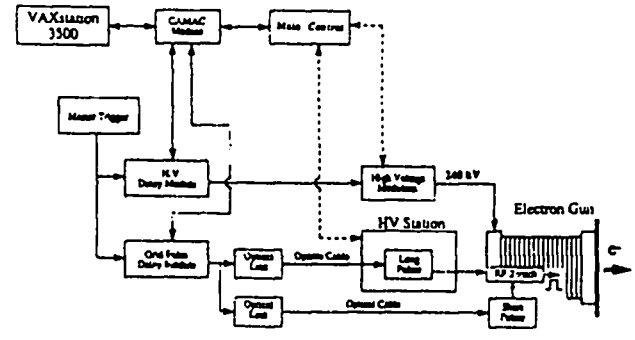

Fig. 5. Gun control system

Performances

The activation of the cathode after assembling whole system is made by a computer controlled automatic processing system under the condition that the vacuum pressure is kept less than 6×10^{-7} Torr.

The maximum voltage of 220 kV can be applied without using SF_6 tank outside the ceramic insulator at 5 pps. At the maximum voltage of 240 kV, the HV breakdown is generated inside the gun.

The beam current is observed with a wall current monitor and a core monitor. The beam profile is observed by a screen monitor made of a Cr doped Al_2O_3 plate and sets at 2 m downstream of the gun. The photograph as shown in Fig. 6 is the beam profile obtained at the accelerating voltage of 205 kV without using any steering magnet. As shown in Fig. 6, the dark part is the shadow of the support of the grid mesh and the pattern of the grid is clearly projected on the screen. This shows that the alignment of the gun has been made successfully.

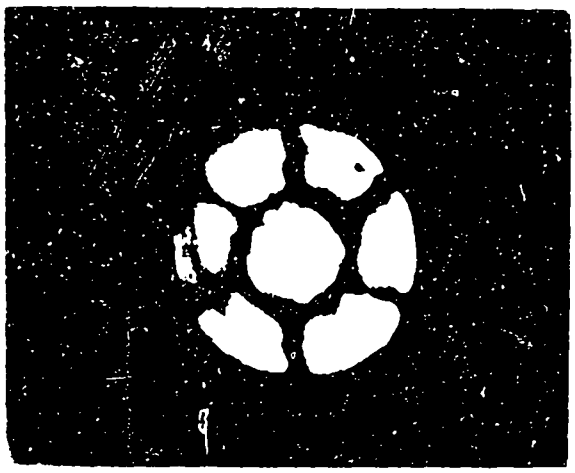

Fig. 6. Photograph of the beam profile at 2 m downstream of the gun.

Figure 7 shows the current waveform of the long pulse beam at the high voltage of 200 kV, the peak current of 2 A and beam width of 3 μsec.

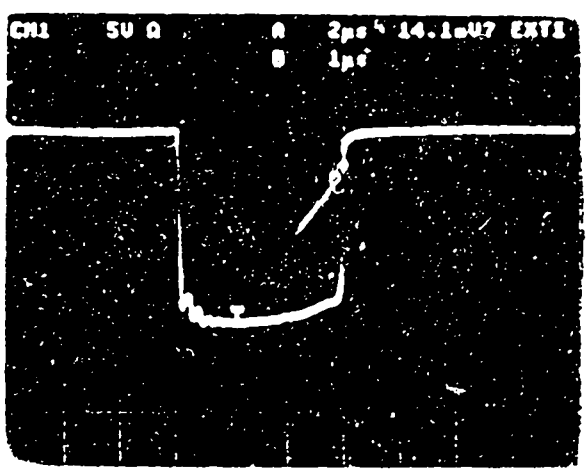

Fig. 7. Output waveform of the long pulse mode.

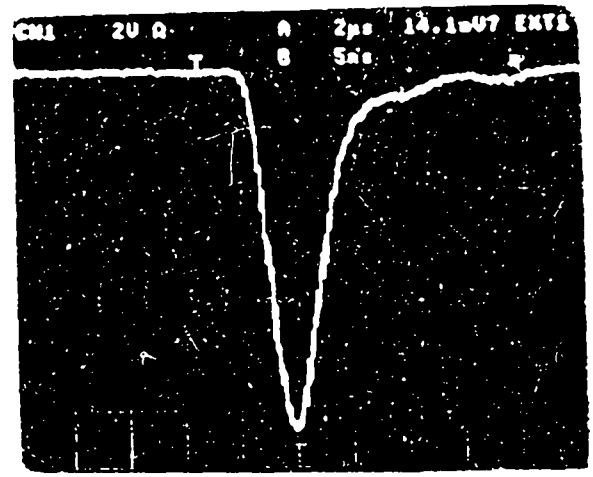

Fig. 8. Output waveform of the short pulse mode.

Figure 8 shows the current waveform of the short pulse mode at high voltage of 200 kV, the peak current of 4.8 A and the beam width of 5 nsec.

Summary

The construction of the electron gun has been completed and operated successfully[4]. The high voltage of 220 kV is applied without any serious problem. We expect to apply 240 kV without using SF_6 tank. The beam can be guided to the accelerating structures without using steering magnets since the accurate alignment system are effective. The whole system can be controlled easily with the computer control system through the network.

References

1. K. Takata, "The Japan Linear Collider," contribution paper to this conference.
2. J. Urakawa et al., "Preliminary Designs of 1.54 GeV Damping Ring and Bunch Compressor," contribution paper to this conference.
3. H. Hayano et al., "Control system of ATF," contribution paper to this conference.
4. H. Matsumoto et al., "Experimental Study of the S-band High Gradient Electron Linac," contribution paper to this conference.

DEVELOPMENT OF POLARIZED ELECTRON SOURCE USING GaAs-AlGaAs SUPERLATTICE

Y.Kurihara, T.Omori, Y.Takeuchi, M.Yoshioka, K.Itoga,
T.Nakanishi*,H.Aoyagi *,M.Tsubata *,
T.Baba **, and M.Mizuta **

KEK, National Laboratory for High Energy Physics,
Oho 1-1, Tsukuba 305, Japan
*Faculty of science, Nagoya University
Furo-cho, Chikusa-ku, Nagoya 406, Japan
**Fundamental Research Laboratories, NEC Corp.,
Miyukigaoka 34, Tsukuba 305, Japan

Abstract

We have measured a polarization of photoelectrons emitted from a GaAs-AlGaAs superlattice. The polarization of 52.5+0.3(stat.)+5.0(sys.)% was obtained at a photon wavelength of 775 to 800nm. This polarization is interpreted that electrons excited from [illegible] heavy hole state only.

A spin polarized electron beam is a very powerful tool to study the electroweak interaction by electron positron colliders at high energy.[1] In linear colliders, for example the JLC[2], polarized electrons can be introduced to a interaction point without depolarization during acceleration, therefore a development of the polarized electron source is very important.

The polarization of 49% was obtained by a photocathode of a bulk GaAs with negative electron affinity (NEA) surface excited by circulary polarized photons[3]. However the intrinsic upper limit is 50% because of a spin degeneracy of hole stats at G point. The degeneracy is separated in superlattice, the one can get then intrinsic upper limit of 100%. The photocathodes of GaAs-AlGaAs superlattice (SL) are developed by several groups[4,5,6] to get highly polarized electrons, however no one achieved the polarization greater than 50%. We have tested the photocathode of GaAs-AlGaAs superlattice of which parameters are optimized according to the method presented by Ref.7. The SL photocathode was made by Molecular Beam Epitaxy (MBE) method. The SL structure is shown in figuer 1. First a 50nm layer of a GaAs buffer was grown on a GaAs substrate to make a flat surface. On the GaAs buffer a 1μm layer of AlGaAs was inserted to avoid low polarized (less than

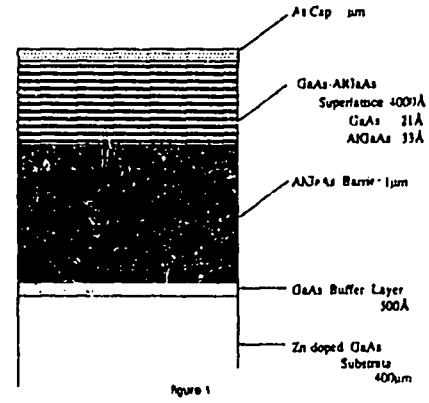

figure 1

50%) electrons coming from the GaAs substrate. Then, GaAs-AlGaAs SL layers were grown. The layer thickness of GaAs (AlGaAs) was 21Å(33Å), respectively. The final layer of the SL was GaAs. The surface of the SL is covered by Arsenic for protection against atmosphere. Band structures of the SL calculated by a method in ref.7 are summarized in figure 2.

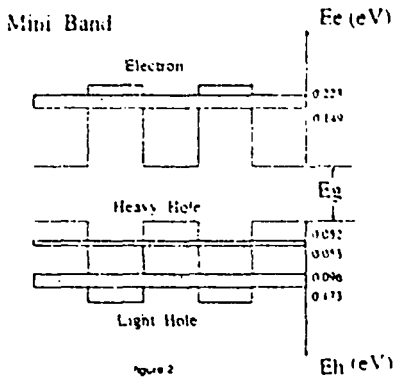

The electron spin polarization was measured by the Mott scattering using the apparatus[8] shown in figure 3. The Titanium:Sapphire tunable-laser, excited by Ar-Iron laser, with 1/4 λ plate supply circular-polarized monochromatic photons. The photoelectrons emitted from the superlattice are accelerated to 4 KeV. Up to here, electron beam is polarized longitudinally. Next the electrons were bedded 90o by a spherical static electrode, then those spin were rotated to have transverse polarization. Finally, the electron beam is accelerated to 90 KeV and introduced to the Mott Analyzer with the Au foils. Cesium and Oxigen were used to activate the SL surface in NEA. Before the NEA activation, the As cap was removed by heat cleaning at temperature of 400oC. It was confirmed that the heat cleaning process dose not destroy SL structure(7).

A figure 4 shows electron spin polarization as a function of laser wavelengths. One can see two flat regions on the electron polarization. It was interpreted that a flat region in λ=775-800nm with average polarization of 52.5+0.3+5.0% is a contribution from the electrons excited from the heavy hole band only, and that in λ=700-743nm with 33.0%+0.5+5.4% is from the electrons excited from the heavy hole band and the light hole band. The first error is statistical error and the second is systematical one. The quantum efficiency was measured to be 7.7×10^{-3}% (1.09×10^{-4}%) at 775 nm (800nm). In the region whose wavelength is longer than 800nm, we could not measure polarization because the quantum efficiency is too small. The width of the first flat region of 25nm (this

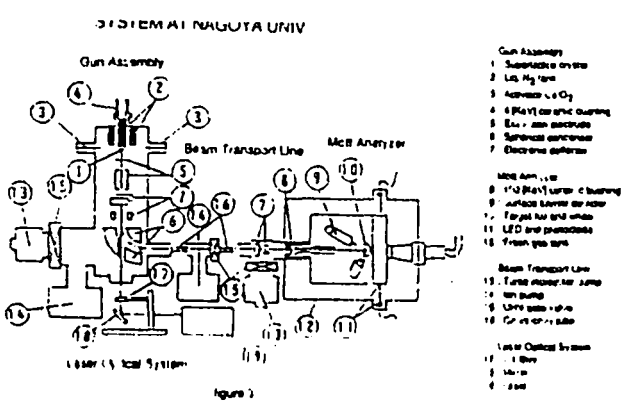

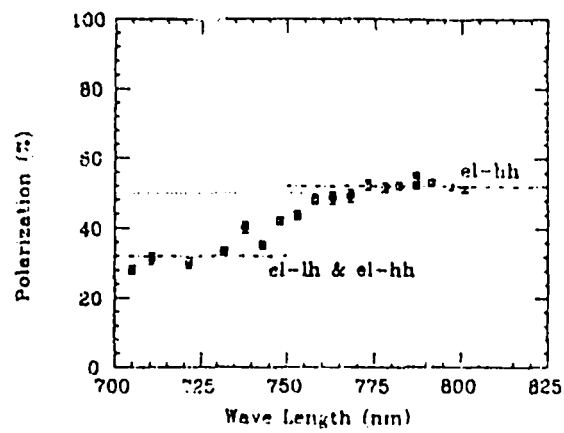

corresponds 50meV) agrees with the calculated energy gap between the top of heavy hole band and the top of the light hole band (43.4 meV) as shown in figure 2. There are no measured points below 700nm of wavelength because our laser dose not work there.

The result of photoluminescence at room temperature is shown in figure 5. The large peak at 750nm is those from the SL. The small peak at 675nm corresponds the photoluminescens come from AlGaAs barrier layer of 1mm which is located behind the SL. A endpoint at longer wavelength side (about 800nm) agrees well with a point at nearly zero quantum efficiency. That shows we actually extracted the electrons excited at the threshold energy.

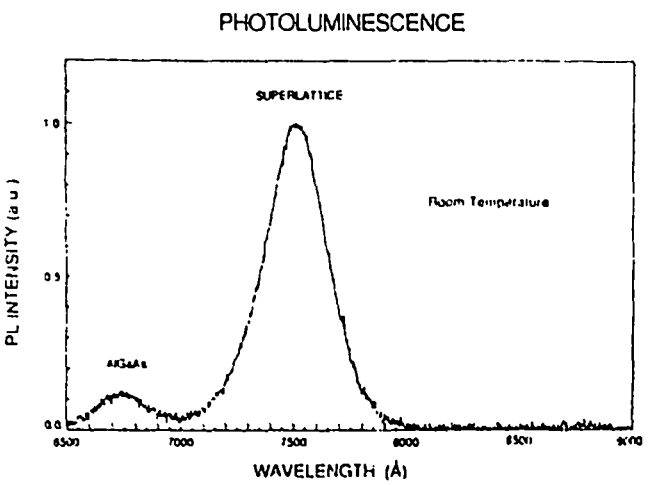

figure 5

References

(1) W.B.Atwood, I.Duniets and P.Grosse-wiesmann, SLAC PUB-4544
B.F.L.Ward, Phys. Rev. D40 1411(1989)

(2) proceedings of the first workshop on Japan Linear Collider, KEK Report 90-2, Editor:S.Kawabata.

(3) T.Maruyama, R.Prepost, E.L.Garwin, C.K.Sinclair, B.Dunham, and S.Kaiam, Appl. Phys. Lett. 55(16), 1686 (1989).

(4) S.F.Alvarado, F.Ciccacci, and M.Campagna, Appl. Phys. Lett. 39(8), 615 (1981).

(5) D.T.Pierce, R.J.Celotta, G.C.Wang, W.N.Unertl, A.Galejs, C.E.Kuyatt, and S.R.Mielczarek, Rev. Sci. Instrum. 51(C), 478 (1980).

(6) R.Houdre, C.Hermann, and G.Lampel, Phys. Rev. Lett. 55, 734 (1985).

(7) Y.Kurihara, T.Omori, Y.Takeuchi, M.Yoshioka, T.Baba and M.Mizuta, KEK Preprint 90-77.

DESIGN OF A 10-MeV PHOTOINJECTOR ACCELERATOR FOR ELFA*

A. Cucchetti** and L. Young
Los Alamos National Laboratory, Los Alamos, NM 87545

Abstract

This paper presents the design of an RF photoinjector that will provide the electron beam for the FEL project in Milan (ELFA). The goal of this project is to test the new regimes of superradiance with high gain. This FEL requires a pulsed beam with 80 nC per pulse; each pulse will be 200 ps long with a peak current of 400 A. The rms energy spread must be approximately 1% and the normalized transverse emittance less than 100 π $cm - mrad$. We have chosen the operating frequency to be 352 MHz so that the Lep2 superconducting accelerator structure can be used to accelerate the beam from the photoinjector to 10 MeV. This paper presents The main characteristics of this accelerator and the beam simulations obtained with PARMELA.

Introduction

The accelerator has been designed to generate, accelerate and transport a high-charge beam (80 nC), with pulses 200 ps long. The first part of this paper will briefly describe the different elements of the accelerator. The new technology of the photoinjector has been applied to this design to extract the 80 nC beam and a superconducting accelerator is used to accelerate the electrons up to 10 MeV. The second part of the paper will be dedicated to the most important aspects of the beam dynamics and to the solutions found for optimizing the emittance and the energy spread of the beam. Recent theoretical calculations have proved that the combined action of space charge forces and of focussing forces can reduce the transverse emittance [ref 1].

Numerical simulations show that with proper focussing the emittance increases in the first cell of the photoinjector and decreases in the drift region.

The Accelerator Design

As it has already been stated in the abstract, the FEL theory for this experiment requires a pulsed beam of 4 micropulses, each with 80 nC of charge which are 200 ps long and 2.8 ns apart [ref 2]. Generating and transporting this high-charge beam imposes strict conditions on the choice of the source and requires particular care in the design of the first accelerating section. Each bunch is generated by photoemission with a laser shot that determines the length and the charge of each electron pulse and the separation between pulses. With this type of source the beam is emitted directly inside the first cavity of the injector. Therefore, the design of the first cavity is very important for the dynamics of the particles. The final scheme consists of two accelerating sections having a resonant frequency of 352 MHz, that provide an energy gain of 3 MeV and 7 MeV respectively. Two drifts, the first between the accelerators and the second between the last accelerator and the wiggler, allow the installation of the diagnostic instruments, the injection of the photocathode laser beam, and the 3 mm radiation into the wiggler. Enough space remains for the cryostat. A focussing system on the injector reduces the effects of the space charge force and four quadrupoles, in the last drift, match the beam into the wiggler (fig 1).

The design of the injector and all the cavities parameters are chosen to minimize the emittance growth caused by the space charge and by the non linear

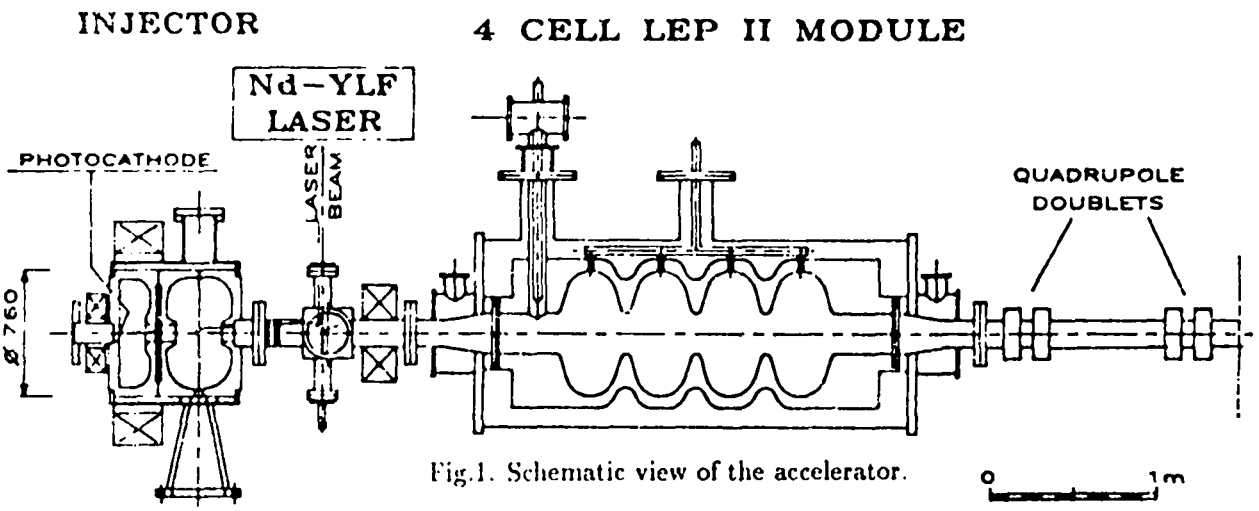

Fig.1. Schematic view of the accelerator.

*Work supported and funded by INFN, Italian Institute of Nuclear Physics, through a collaboration with Los Alamos National Laboratory under the auspicies of the US Department of Energy.

radial components of the rf accelerating field. The space charge forces are particulary strong when the particles are moving slowly. The injector consists of one short accelerating cell, one coupling cell ,and one full accelerating cell. We have compared two different shapes for the first cell. One has a flat wall which allows the highest accelerating gradient but no focussing forces. The other with a shaped wall provides rf focussing at the expense of the longitudinal component of the accelerating field. Beam dynamics simulations show that with the flat wall the values of energy spread and emittance are lower; we have made the final choice for this simpler shape. The coupling cell resonantly couples rf power from one accelerating cell to the other. With this configuration operating in $\pi/2$ mode, the relative amplitude of the rf fields in the two accelerating cells is fixed by the coupling constants between the coupling and the accelerating cells. A klystron having 1.6 MW of power can easily sustain a spatial average field gradient of 9.4 MV/m in the first cell and 5.6 MV/m in the second cell. Because the effects of the space charge forces are proportional to $1/\gamma^2$, it is advantageous to accelerate the beam to a high energy quickly; therefore, a higher accelerating gradient has been selected for the first cell of the photoinjector. A necessary aperture at the end of the first cavity forces the electric field lines to bend outward toward the nose, inducing a radial defocussing component of the rf field. The pattern of the field near the aperture is determined by the nose shape ,and the emittance is minimized when the forces are linear. A particular shape of the nose has been studied in which the radial component of the electromagnetic field satisfies this condition [ref 3]. Both the radial electric field and the space charge forces cause the beam to expand radially in the injector; therefore, a fundamental part in the design of the accelerator has been the focussing system. Two solenoidal focussing magnets placed over the first accelerating cell control the beam expansion and reduce the emittance growth. A third solenoid placed behind the cathode nulls the magnetic field on the photosensitive surface. These solenoids are adjusted to make the beam slightly convergent as it exits the injector. Another solenoid approximately halfway between the injector and the superconducting accelerator matches the beam into the superconducting cavities. The second accelerating section consists of 1 full niobium superconducting cavities of the Lep2 type resonating at the same frequency of 352 MHz [ref 4]. The structure is kept at 4.5 K°, at this temperature the power losses are almost negligible (40 W), so it is possible to achieve an accelerating gradient of 5 MV/m with a low power source. The total energy gain is 7 MeV.

A second drift of almost 3 m is necessary between the superconducting accelerator and the wiggler to place both the diagnostic instruments and the focussing system required to match the beam into the wiggler. Two quadrupoles doublets have been studied to provide a good match so that the beam parameters are conserved inside the wiggler.

The Beam Dynamics

In this section we will discuss the most important aspects of the beam dynamics. The results presented are for a single bunch and they have been obtained using the program PARMELA. In the simulations the charge distribution in the longitudinal direction is uniform, neglecting the raising time of 20 ps. However, two possible distributions of charge have been considered in the radial direction; the uniform and the gaussian distribution.

The transverse dimensions are determined by the laser spot and the cathode. The simulations showed that a cathode radius of 1.5 cm was optimum for both the gaussian and the uniform distribution. For the gaussian distribution, a σ_r of 1.2 cm was used. The total charge in the bunch is 80 nC, which means that a peak current of 400 A/cm^2 has to be extracted from the photocathode. With a photosensitive surface of 7 cm^2, the current density is lower than 60 A/cm^2 averaged over the photocathode.

The length of the beam at the generation has been selected to be 180 ps or 22° rf which gives a beam of 200 ps or 25° long at the end of the linac. The bunch lengthening occurs mainly in the injector and along the first drift where the space charge forces are strongest; however, more than 90% of the particles remain confined in 25° as required. The growth of the bunch length and of the energy spread have been further minimized by optimizing the injection phase of the beam in the first cell. The possibility of choosing the starting phase, however, is limited to a range of 10° because the length of the first cell and the accelerating gradients are fixed and the electrons have to reach the second accelerating cell in phase so they will not be decelerated. Just as the bunch is leaving the cathode, it forms a flat disk of charge next to a conducting surface (the cathode). The space charge produces an electric field that attracts the tail of the bunch back to the cathode whitout affecting the head of the bunch. The phase of the rf at injection is adjusted to partially cancel this effect by using the rising part of the rf field. The tail of the bunch sees a stronger accelerating field near the cathode than the head of the bunch. We have selected the injection phase at 53° for the reference particle. In the longitudinal phase space, though the beam is fairly long, the energy spread has been minimized by adjusting the relative phase of the rf in the different cells. The PARMELA simulations shows an rms energy spread of $\simeq$ 1% at the entrance to the wiggler. Furthermore, bunch lengthening only affects the head and the tail of the pulse so that most of the particles are confined in the required 25°.

The main problems in the first cell are the rf defocussing and the space charge effects, which cause the beam to enlarge in the radial direction. A large increase in beam size and emittance results. To minimize these effects, a higher accelerating gradient and a focussing system is used in the first cell. It has been analytically demonstrated that for a high current beam an appropriate magnetic field can help to remove the spatial correlation induced by the space charge forces [ref 1]. Numerical simulations show a progressive decrease of the transverse emittance along the first drift ,while a minimum is reached just before the entrance to the Lep2 cavities. However, in a previous design, the emittance value was doubled when the particles were accelerated in the four superconducting cells of the Lep2 type [ref 5]. This increase was probably due to the effect of the linear time-dependent rf fields that causes an emittance

growth proportional to r^2. The beam was made smaller when the strength of the lens between the photoinjector accelerator and the Lep2 cavities was increased and the lens position was adjusted .

These adjustments reduce the beam size and the emittance at the exit of the Lep2 cavities from 59.2 π *cm mrad* to 38.5 π *cm mrad* when a gaussian distribution is used on the photocathode and from 46.4 π *cm mrad* to 16.7 π *cm mrad* when a uniform distribution is used. Table I reports the values of normalized emittance ϵ_n and energy spread $\Delta\gamma/\gamma$ relative to the different elements for a beam with a uniform distribution of charge.

TABLE I

Uniform beam parameters along the beam line

Element	Position(cm)	ϵ_n(π cm-mrad)	$\Delta\gamma/\gamma$(%)
Ent. Injector	0.	0.	0.
Exit Injector	63.8	65.4	1.36
Drift	128.8	37.5	1.94
Solenoid	138.8	35.7	2.03
Ent Lep2	158.8	24.3	2.23
Exit Lep2	509.9	17.3	1.04
Drift	529.9	16.7	1.04

These values of emittance and energy spread remain approximately unaltered when the beam goes through the matching section. The computer code TRACE3D calculates the gradients of the quadrupoles magnetic field so that the dimensions of the beam are reduced ($x \simeq 0.5$ *cm* and $y \simeq 0.3$ *cm*) and the beam can enter the wiggler without changing the value of emittance and energy spread. Since the head and the tail of the beam have experienced different space charge forces from the center, some electrons are underfocussed or overfocussed by the quadrupoles doublets. At the end of the matching section a small halo of particles appears. This halo may have some effect on the FEL superradiance regime. A possible solution could be bending the beam line between the Lep2 [illegible] and the wiggler. The 3 *mm* [illegible] can then be injected easily into the wiggler for the FEL process. In addition, with the use of slits it is possible to [illegible] all the high and low energy tails of the electron beam. These tails occur at the head and at the tail of the beam and are responsible for the halo.

To investigate some of the possible variations on the proposed design we have analyzed the option of reducing the beam charge to 60 *nC*. In this case the emittance decreases $\simeq$ 20% and the energy spread goes from 1.05 % to 0.85 %, confirming that the space charge forces play a fundamental role in the evolution of the beam parameters. We have also considered the possibility of much higher gradients for the injector in order to achieve a lower value of emittance. Numerical results show that a quicker acceleration of the electrons reduces the emittance growth, particulary if the beam has a uniform distribution of charge. With high accelerating fields and the uniform distribution, a emittance of 11 π *cm mrad* can be obtained at the end of the accelerator.

The charge distribution seems to be a fundamental parameter in the physics design of this accelerator. In Table II the comparison between the final results obtained with the gaussian and the uniform beam, in the basic case, demonstrates the importance of generating the particles as uniformly as possible to avoid nonlinear space charge effects.

TABLE II

Beam parameters at the Lep2 exit

Beam parameters	Uniform	Gaussian
Bunch length(rf°)	25.9	27.2
Beam radius(cm)	0.9	0.8
Energy gain(MeV)	9.96	9.98
ϵ_n(π cm-mrad)	16.7	38.5
$\Delta\gamma/\gamma$	1.04	1.05

Conclusion

The physics design presented here shows that the theoretical requirements can be satisfied with both a gaussian and a uniform distribution of charge. However, the numerical results confirm the importance of a uniform distribution to get better values both of emittance and energy spread.

References

1. B. E. Carlsten, New Photoelectric Injector Design for the Los Alamos National Laboratory XUV FEL Accelerator , *Nucl. Instr. and Meth.*, A285 313-319 (1989).

2. R. Bonifacio, F. Casagrande, G. Cerchioni, L. De Salvo Souza and P. Pierini, *in Proceedings* [illegible]

3. M. E. Jones, W. K. Peter *IEEE Trans. Nucl. Sci.*, NS-32, 1794 (1985).

4. P. Bernard et al., *Proceedings EPAC Conf.*, Rome, June 1988.

5. LASA(INFN, Milan), AT-1 (Accelerator and tecnology division, Los Alamos), The Photocathode Injector and the Superconducting Linac for the Elfa Project , *in Proceedings EPAC Conf.*, Nice, June 1990

**On leave of absence by the university of Milan.

ENERGY FLOW AND HIGH REPETITION RATE ISSUES FOR THE ETA II MAGNETIC MODULATOR SYSTEM

M. Newton, D. Barrett, C. Ollis, D. Pendleton
Lawrence Livermore National Laboratory
Livermore, California 94550

Abstract

ETA II is a linear induction electron beam accelerator designed to operate at high repetition rates (<5 kHz) and high average powers (<3 MW). The 2 kA electron beam is accelerated with 70 ns, 100 kV pulses generated by a system of magnetic modulators. There are a number of critical issues associated with high repetition rate and high average power operation of the magnetic modulators in a linear induction accelerator power conditioning system. A discussion of the initial investigation into the high repetition reset issues is also presented.

Introduction

High average power operation of electron beam accelerators requires the ability to generate drive pulses efficiently and precisely at high repetition rates[1 2 3]. ETA II uses magnetic modulators (MAG 1-D s) to generate 100 kV, 70 ns drive pulses into 2 Ω at repetition rates up to 5 kHz. Magnetic modulator efficiency and reset become significant issues at high average powers and high repetition rates. Modulator inefficiencies which can be tolerated during low average power operation, result in major cooling problems in the magnetic core materials during high average power operation. In addition, this thermal load causes changes in the temperature dependent component characteristics throughout the modulator. The greater the temperature change the greater the component changes and the more difficult it becomes to generate a precise pulse train. Measurements were made to evaluate and understand the energy flow through the magnetic modulators on ETA II. The results of the investigation will be presented in this paper.

Reset also becomes an issue at high repetition rates because the magnetic cores in the magnetic modulators must be reset before each pulse. Stable and precise reset can be easily accomplished at low repetition rates but as the repetition rate increases and the time available for reset decreases, maintaining a precise reset condition becomes much more difficult. Precise reset is required because of the requirement to maintain a drive pulse jitter of less than 1 - 2 ns.[4] This paper will briefly describe the measurements that have been performed on the MAG 1-D to evaluate the reset issue.

System Description

The ETA II accelerator is driven by four magnetic modulators (MAG 1-D s)[5]. Each modulator drives twenty accelerator cells with a maximum output voltage of 100 kV. The MAG 1-D consists of three stages of magnetic pulse compression which compress a 3.8 μs charge pulse to a 70 ns output pulse with approximately a 20 ns risetime. The input voltage is also stepped-up from 25 kV at the input to 100 kV at the output with an auto-transformer in the MAG 1-D. A diagram of the MAG 1-D is shown in Figure 1.

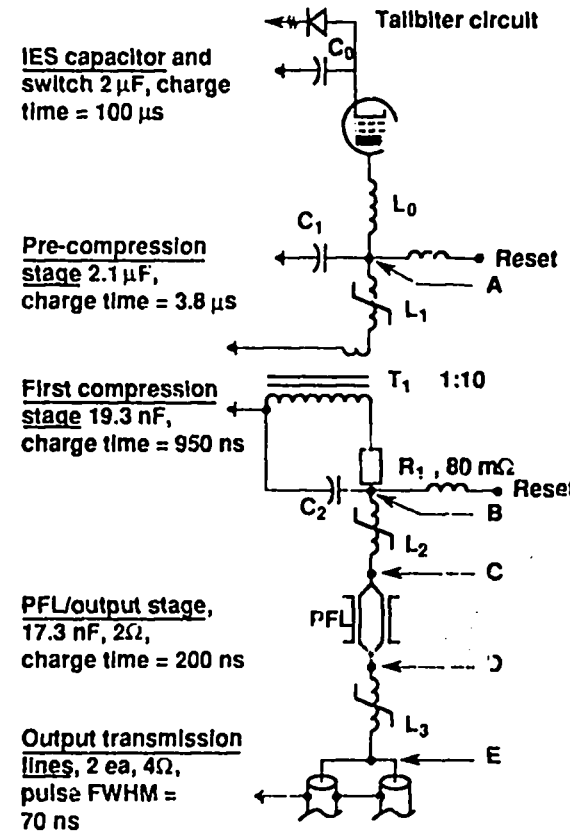

Fig. 1. Schematic of MAG 1-D magnetic pulse compression modulator.

The pre-compression stage of the MAG 1-D is charged from an intermediate energy storage (IES) capacitor C_0 through a thyratron switch. As the pre-compression stage capacitor reaches its peak voltage, the pre-compression stage reactor, L_1 saturates, discharging C_1, through the 10:1 step-up transformer, T_1, into the 1st stage water capacitor C_2. C_2 is charged in approximately 1 μs and discharges in about 200 ns when the 1st stage reactor, L_2, saturates. The PFL is charged in 200 ns and as the PFL voltage reaches its peak, the output switch, L_3, saturates and delivers the PFL energy to the load. The component values are listed in Table 1.

TABLE 1
Component values for MAG 1-D

Components	Values
C0	2.0 μF
C1	2.1 μF
L1 (sat)	87 nHy
T1	10 : 1 step-up
C2	19.3 nF
L2 (sat)	614 nHy
PFL	2 ohms, 35 ns
L3 (sat)	23 nHy

All cores in the MAG 1-D are wrapped with 2605 CO Metglas with the exception of the transformer which is 2605 SC. Mylar, .25 mil thick, is used for the interlaminar insulation in the cores.

Capacitive voltage dividers were installed on each of the capacitor stages in the MAG 1-D and on the output switch. Each of the capacitive voltage dividers were calibrated against a Tektronix P6015, 1000:1 high voltage probe. Each probe was calibrated in place in the MAG 1-D by inserting the high voltage probe through access ports at a symmetric locations on the modulator housing. The capacitive probes were then used to measure the voltages in the MAG 1-D under various circumstances to evaluate efficiency and reset.

Energy Flow Measurements

The voltage waveforms at each stage of the MAG 1-D were recorded at a constant input voltage but not simultaneously. The maximum energy stored in each stage was defined at the peak voltage of each stage. Table 2 shows a summary of these voltage measurements and the calculated maximum energy storage of each stage. From Table 2 it is easy to see that the losses increase dramatically near the output stage of the MAG 1-D. Approximately 236 joules are lost during the transfer of energy from the 1st stage water capacitor, C_2, to the PFL. This is not unexpected because the output switch [illegible] the highest $\partial B/\partial t$ (~15 T/μs) This is nearly 36% of the energy stored in the IES capacitor, C_0. The overall efficiency of the MAG 1-D was measured to be approximately 58%.

TABLE 2
Summary of measurements on MAG 1-D

Stage	Voltage	Energy
IES capacitor	25.5 kV	655 J
Pre-compression stage	23.7 kV	592 J
1 st stage capacitor	246 kV	583 J
PFL	200 kV	347 J
Output pulse	103 kV	380 J

Further experiments were performed to attempt to understand the loss mechanisms in the last two stages where the majority of the losses appear to be. These experiments focused specifically on the transfer of energy to the PFL stage and magnetic losses in the output switch. In one experiment, the output switch was removed and the energy in the MAG 1-D was allowed to oscillate through the MAG. The voltage on the PFL was measured at its peak to determine the amount of energy that was transfered to the PFL with no output switch in the circuit. This value was then compared with the measurements taken with an output switch shown in Table 2 to determine the losses due to the output switch. A summary of the distribution of the energy losses in the MAG 1-D resulting from these measurements is shown in Table 3.

TABLE 3
Energy Balance Summary

1. Energy dissipated in charging pre-compression stage	30 J
2. Energy dissipated in water capacitor (1st stage)	37 J
3. Energy dissipated in the PFL charge	32 J
4. Energy dissipated in output reactor	85 J
5. Energy dissipated in discharge of PFL	21 J
6. Energy reflected into MAG 1-D	70 J
7. Energy dissipated in load	380 J

The losses in Table 3 were further categorized as 120 joules in effective series resistance losses, 85 joules in the output reactor magnetic losses and 70 joules of energy reflected at the output stage back into the MAG 1-D.

Reset Losses

[illegible] the MAG 1-D magnetic [illegible] each [illegible] reset [illegible] amount of reset voltage, $v_r(t)$, across the core windings such that the integral of the reset voltage, $\int v_r(t)\,dt$, is equal to that of the integral of the main pulse voltage, $\int v_p(t)\,dt$. If these two integrals are not equal, then the core will not be fully reset before the next pulse. Timing variations in the output pulse will result from inadequate reset. It has been estimated that in order to maintain output pulse jitter of less than or equal to 1 ns, the core must be reset to within $1*10^{-3}$ Tesla[6]. Maintaining this type of accuracy becomes very difficult at high repetition rates where there is less time for reseting the cores. Presently dc reset is used to reset the cores.

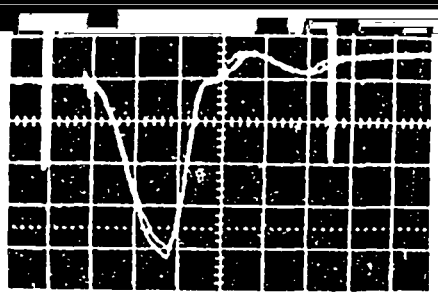

Fig. 2. Pre-compression stage voltage showing reflected energy that appears as reverse voltage on C_1.(Upper trace 50 µs/div, Lower trace 2 µs/div)

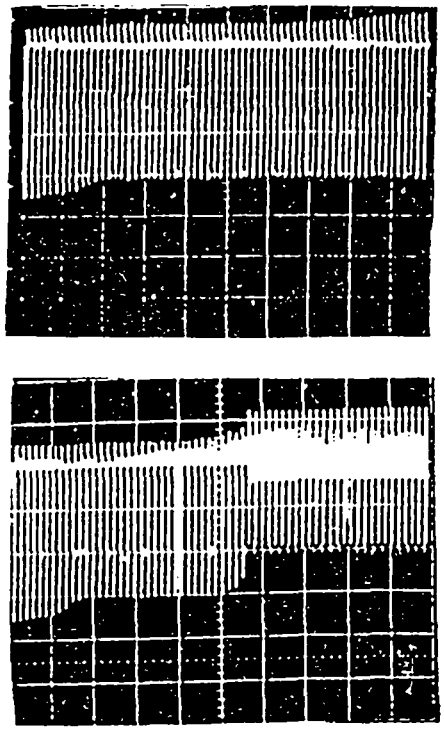

Fig. 3. Pre-compression stage voltage waveforms during bursts at 3 kHz in the top photo and 5 kHz in the bottom photo.

A preliminary investigation of high repetition rate reset was conducted on a MAG 1-D. One of the issues associated with the MAG 1-D that makes reset more difficult is the 70 joules of reflected energy that does not get delivered to the load. Figure 2 shows the reflected energy that appears at the pre-compression stage after the inital discharge pulse. This energy oscillates in the MAG 1-D for greater than 200 µs after the main pulse. These oscillations make it nearly impossible to maintain a stable reset condition at high repetition rates (3-5 kHz)

This reflected energy can easily be dissipated when it returns to the pre-compression stage of the MAG 1-D. The tailbiter circuit shown in Figure 1 was installed to dissipate this reflected energy in a few microseconds. Preliminary evaluations of the magnitude of the reset problem were made with the tailbiter installed. Figure 3 From Figure 3 it is obvious that the present reset scheme is inadequate for repetition rates of 3 - 5 kHz. The problem seems to be less severe at 3 kHz than at 5 kHz as indicated by less amplitude variations, but neither is acceptable. This preliminary investigation shows that considerably more effort will be needed to fully understand and solve the reset problems.

Conclusions

Investigations have been conducted to study the efficiency and reset issues of the MAG 1-D Voltage measurements on each stage indicate that although losses are distributed through out the entire MAG 1-D, a large fraction of the losses occur during the transfer of energy from the 1st stage water capacitor to the PFL. This can be partly explained by the losses in the output switch due to the high $\partial B/\partial t$ that the output switch sees.

A preliminary investigation of the reset problem was conducted in which significant variations of amplitude on the pre-compression stage capacitor were observed. The measurements indicate that the present system cannot produce stable pulses at repetition rates above 3 kHz. Additional work is needed to characterize the output pulse behavior at high repetition rates and to fully understand the reset dynamics.

Acknowledgements

All measurements described in this paper were conceived and executed by David Barrett.

References

[1] W. Nexsen, et al, "The ETA II Induction Linac as a High Average Power FEL Driver", Proceedings of the 11th International Conference on Free-Electron Lasers, Naples, Florida, August 1989.

[2] D. Prono, et al, "High Average -Power Induction Linacs", Proceedings for the 1989 Particle Accelerator Conference, Chicago, Illinois, March 1989.

[3] J. Clark, et al., "Design and Initial Operation of ETA-II Induction Accelerator", 1988 Linear Accelerator Conference Proceedings, Williamsburg, Virginia, October 3-7, 1988, pp. 19-23.

[4] M. Newton, J. Watson, "Timing and Voltage Control for Magnetic Modulators on ETA II", Proceeding for the 7th IEEE Pulsed Power Conference, p.175.

[5] M. Newton, et al., "Design and Testing of the 5 kHz, 3 MW Thyratron Modulators for ETA II", Proceedings for the Eighteenth Power Modulator Symposium, p. 71.

[6] Internal communications from D. Barrett.

*Performed jointly under the auspices of the U.S. DOE by LLNL under W-7405-Eng-48 and for the DOD under SDIO/SDC-AT MIPR No. W31RPD-0-D4074

SIMULATION OF A STANDING-WAVE FREE-ELECTRON LASER*

W. M. Sharp, A. M. Sessler[(a)], D. H. Whittum[(a)], and J. S. Wurtele[(b)]
Lawrence Livermore National Laboratory, University of California
Livermore, California 94550

Abstract

The standing-wave free-electron laser (FEL) differs from a conventional linear-wiggler microwave FEL in using irises along the wiggler to form a series of standing-wave cavities and in reaccelerating the beam between cavities to maintain the average energy. The device has been proposed for use in a two-beam accelerator (TBA) because microwave power can be extracted more effectively than from a traveling-wave FEL. The standing-wave FEL is modeled in the continuum limit by a set of equations describing the coupling of a one-dimensional beam to a TE_{01} rectangular-waveguide mode. Analytic calculations and numerical simulations are used to determine the time variation of the reacceleration field and the prebunching required so that the final microwave energy is the same in all cavities. The microwave energy and phase are found to be insensitive to modest spreads in the beam energy and phase and to errors in the reacceleration field and the beam current, but the output phase appears sensitive to beam-energy errors and to timing jitter.

Introduction

The next generation of linear colliders is expected to require accelerating gradients of 100 MeV/m or greater. For the high-gradient structures that have been tested, this field strength corresponds to a microwave power of about 100 MW/m, and the required frequency is typically in the range of 10-30 GHz. The microwave free-electron laser (FEL)[1] and the relativistic klystron (RK)[2] have both demonstrated the required power level in this frequency range, and they have been proposed as collider power sources in a configuration known as the "two-beam accelerator" (TBA)[3], in which a high-current "drive" beam generates microwave energy in a beamline that parallels the high-gradient structure. Both the RK/TBA and the FEL/TBA have practical problems. The RK operates best in the X-band (8.4-12 GHz) and so cannot be used with many high-gradient accelerator designs. Conventional FELs, in contrast, have no fundamental frequency limitation, but experiments have shown that microwave extraction is difficult.[4]

The cavity-coupled FEL/TBA[5] has been devised to sidestep the problems found with RKs and conventional FELs. This new device would replace the usual FEL waveguide by a series of short standing-wave cavities, each about a wiggler period in length. The cavities would be separated by irises that allow the beam to pass but reflect most of the microwave power, and between cavities there would be induction accelerating cells to maintain the beam energy. Microwave energy from these cavities would be connected to the high-gradient structure by couplers and would oscillate between the two beam lines with a period that is much longer than the beam time scale but much less than the resistive loss time. This coupling scheme was proposed by Henke[6] for a RK/TBA and is discussed elsewhere.[5]

In this paper, we present preliminary numerical simulations of the standing-wave FEL (SWFEL) used in the cavity-coupled FEL/TBA. The SWFEL has two important differences from conventional FEL amplifiers. One difference is that the standing wave phase ϕ develops in time only at each cavity location z, whereas the wave phase in conventional devices evolves in z along with the "particle phase" $\theta_j = (k_s + k_w)z - \omega_s t$, where the subsript j denotes the jth particle. This difference works against the preservation of a nearly constant average bucket phase $\langle\psi_j\rangle = \langle\theta_j + \phi\rangle$ that is needed for good bunching. As a consequence, the SWFEL requires an unusual form of prebunching, as we discuss later. A second difference is the use of frequent reacceleration to maintain a nearly constant beam energy. Reacceleration is used rather than tapering of the wiggler strength because it is more appropriate for the very long beamlines expected in linear colliders and because it in principal allows the beam energy to be adjusted in time as well as in z. Since the unusual phase evolution is a critical novel aspect of SWFEL physics, we choose a very simple simulation model that retains this feature but ignores other arguably important features, such as the discrete nature of the standing-wave cavities and the competition between waveguide modes. The next section describes this model briefly and is followed by a section on simulation results. We offer some tentative conclusions in a final section.

Model

Assumptions and Equations

Simulation particles are modeled by a pair of wiggle-averaged equations for the total energy γ_j in units of $m_e c^2$ and the particle phase θ_j. Radial motion and the effects of the transverse beam structure are neglected, and the beam is assumed to couple only with a TE_{01} waveguide mode, which is usually most strongly coupled mode. The signal wavenumber for this mode in a rectangular waveguide with height h and width w is $k_s = (\omega_s^2/c^2 - \pi^2/h^2)^{1/2}$. For the fields, we assume an idealized linear wiggler with a vector potential

$$\underset{\sim}{A}_w = \frac{m_e c^2}{e} a_w \cos(k_w z)\, \hat{\mathbf{x}} \tag{1}$$

and an appropriate form for the signal field

$$\underset{\sim}{A}_s = -\frac{m_e c^2}{e} a_s\, \underset{\sim}{g}_\perp(x,y) \cos(k_s z - \omega_s t + \phi), \tag{2}$$

where $\underset{\sim}{g}_\perp = -\sin(\pi y/h)\, \hat{\mathbf{x}}$ is the transverse structure for a TE_{01} mode. A number of other conventional assumptions are made that are suitable for most Compton-regime FELs and significantly simplify the equations. The energy is taken to be sufficiently high that $a_w/\gamma_j \ll 1$, and the energy spread is assumed small enough that all particles have effectively the same axial velocity V_b. We treat the signal amplitude a_s as small

* Work performed under the auspices of the U. S. Department of Energy by Lawrence Livermore National Laboratory and Lawrence Berkeley Laboratory under contract DE-AC03-76SFF00098 and by the U. S. Department of Energy Division of High-Energy Physics

a. Lawrence Berkeley Laboratory, Berkeley, CA 94720

b. Massachusetts Institute of Technology, Cambridge, MA 02139

compared with a_w, and the both a_s and ϕ are assumed to be slowly varying compared with $k_s z$ and $\omega_w t$. This last assumption makes the equations inappropriate for modeling waveguide modes near cutoff.

The wiggle-averaged particle equations are iden[illegible] those in a conventional single-mode microwave FEL. Taking z to be the independent variable, we write the equations as

$$\frac{d\theta_j}{dz} = k_u + k_s - \frac{\omega_s}{c} - \frac{\omega_s}{2c\gamma_j^2}\left[1 + \frac{a_u^2}{2} - 2D_x a_u\,(a_r\cos\theta_j - a_i\sin\theta_j)\right] \quad (3a)$$

$$\frac{d\gamma_j}{dz} = -D_x\frac{\omega_s}{c}\frac{a_u}{\gamma_j}\,(a_r\sin\theta_j + a_i\cos\theta_j) - \frac{eE_z}{m_e c^2}. \quad (3b)$$

Here, the coupling coefficient D_x is given for a TE_{01} mode by

$$D_x = \frac{1}{2}\left[J_0(\xi) - J_2(\xi)\right], \quad (4)$$

where $\xi = \omega_s a_u^2/(8ck_u\gamma_j^2) \approx (a_u/4)(1 + a_u^2/2)$. An equation for the complex signal amplitude $a \equiv a_r + ia_i = a_s\exp(i\phi)$ is obtained by assuming that a evolves only in time and requiring that the wiggle-averaged equations conserve energy. Taking the distance back from the beam head $s \equiv V_b z - t$ as the "time" coordinate, this procedure gives the field equation

$$\frac{\partial a}{\partial s} = i\eta\left\langle\frac{\exp(-i\theta_j)}{\gamma_j}\right\rangle, \quad (5)$$

where the coefficient η in general depends on s and is given by

$$\eta = \frac{4\pi}{hw}\frac{eI_b}{m_e c^3}\frac{c}{V_b}\frac{c}{\omega_s}D_x a_w. \quad (6)$$

While this equation implicitly assumes an infinitesimal cavity length and ignores field coupling through the cavity irises, it does model the novel signal evolution expected in a SWFEL.

"Single-Particle" Solution

Some understanding of the SWFEL equations is gained by looking at a z-independent "single-particle" solution, in which the full beam current is assigned to a single phase-space point. Linearizing the equations for small $\delta\gamma = \gamma - \gamma_r$, where $\gamma_r = \omega_s(1 + a_u^2/2)/2c(k_u + k_s - \omega_s/c)$ is the resonant energy, we obtain the approximate particle equations

$$\frac{d\theta}{dz} \approx 2\left(k_u + k_s - \frac{\omega_s}{c}\right)\frac{\delta\gamma}{\gamma_r} \quad (7a)$$

$$\frac{d\delta\gamma}{dz} \approx -D_x\frac{\omega_s}{c}\frac{a_u}{\gamma_r}\,(a_r\sin\theta + a_i\cos\theta) - \frac{eE_z}{m_e c^2}. \quad (7b)$$

Requiring $\delta\gamma$ to be z-independent gives the E_z required for equilibrium:

$$E \equiv -\frac{eE_z}{m_e c^2} \approx D_x\frac{\omega_s}{c}\frac{a_w}{\gamma_r}\,(a_r\sin\theta + a_i\cos\theta). \quad (8)$$

If $\delta\gamma$ is initially zero, then θ is likewise independent of z and equal to some arbitrary $\theta_0(s)$. The components of a in Eq. (8) are obtained by integrating the linearized field equation, which gives

$$a(s) = a(0) + \frac{i}{\gamma_r}\int_0^s ds'\eta(s')\exp[-i\theta_0(s')]. \quad (9)$$

As a practical special case, we consider a beam with constant η which is prebunched at a frequency $\omega_s + \Delta\omega$, so that $\theta_0(s) = \alpha - (\Delta\omega/V_b)s \equiv \alpha + \beta s$. The components of a are then given by

$$a_r(s) = a_r(0) + \frac{\eta}{\beta\gamma_r}\left[\cos(\alpha) - \cos(\alpha + \beta s)\right] \quad (10a)$$

$$a_i(s) = a_i(0) - \frac{\eta}{\beta\gamma_r}\left[\sin(\alpha) - \sin(\alpha + \beta s)\right], \quad (10b)$$

and the corresponding reacceleration field is

$$E = D_x\frac{\omega_s}{c}\frac{a_w}{\gamma_r}\left[a_r(0)\sin(\alpha + \beta s) + a_i(0)\cos(\alpha + \beta s) + \frac{\eta}{\beta\gamma_r}\sin(\beta s)\right]. \quad (11)$$

The bucket size shrinks with increasing $E/|a|$, and it is straightforward in this case to calculate the minimum extent of the bucket in θ and γ as the signal develops in s. These minimum values are approximately

$$\Delta\theta \approx 3.4\left(-\frac{\beta\gamma_r|a(0)|}{\eta}\right)^{1/2} \quad (12a)$$

$$\Delta\gamma \approx 3.3\left(\frac{\omega_s}{c}\frac{D_x a_w}{k_w + \delta k}\right)^{1/2}\left(-\frac{\beta\gamma_r}{\eta}\right)^{1/2}|a(0)|, \quad (12b)$$

where $\delta k = k_s - \omega_s/c$. This result shows that the bucket vanishes when β is zero or negative and that the longitudinal acceptance $\Delta\theta\,\Delta\gamma$ increases with a larger initial signal and larger $-\beta/\eta$. It is found that Eq. (12) underestimates the acceptance for distributions with spreads in θ and γ because the required reacceleration field in such cases is somewhat lower than for the single-particle case. There is also a weak dependence of the acceptance on the initial average particle phase α, with the largest acceptance occurring for $\alpha + \phi(0) = 0$.

Simulation

Parameters

The operating frequency ω_s and the final energy per unit length W_{out} left in the cavities are determined in practice by the TBA requirements. With these quantities given, the specification of the waveguide dimensions h and w, the wiggler wavelength $\lambda_w = 2\pi/k_w$, and the wiggler strength a_u sets the principle beam parameters. The beam energy is determined by the resonance condition, and the total beam charge, given by $I_b L_b$ when the current is constant, is set by W_{out}. Since the initial spreads in θ and γ are usually determined by the intrinsic emittance from the accelerator and the additional emittance introduced by prebunching, the values are not considered free parameters.

Two remaining beam quantities, the beam-current envelope $I_b(s)/\max I_b$ and the prebunching factor β can be chosen by practical considerations. Since the acceptance is found to be proportional to I_b^{-1}, it is preferable for the current to be low near the beam head, where the bucket reaches its minimum size. It is also found from the single-particle equations that a current that increases like s or faster leads to a monotonically increasing E_z for $s \le L_b$, which is an easier field to generate than a short pulse. For these reasons, we use a beam with a uniform current ramp as our standard case. The prebunching factor is chosen by considering the β-dependences of various beam quantities in the single-particle solution. We find that the

Table 1 Nominal standing-wave FEL parameters

peak beam current	I_b	2.17 kA
beam length	L_b	180.0 cm
initial energy	γ_r	27.6
initial θ-spread	$\Delta\theta_0/2\pi$	0.1
initial γ-spread	$\Delta\gamma_0/\gamma_r$	0.01
wiggler strength	a_w	8.86
wiggler wavelength	λ_w	25 cm
wiggler length	L_w	20 m
waveguide height	h	3 cm
waveguide width	w	10 cm
signal frequency	$\omega_s/2\pi$	17.1 GHz
cavity Q	Q	10^4
input power	P_{in}	50 kW / m
output energy	W_{out}	10 J / m

required beam charge and the longitudinal acceptance increase with βL_b, while the maximum reacceleration field decreases. Since the beam emittance is difficult to decrease in induction accelerators, we choose $\beta L_b = \pi$, although a lower value might be selected if the limited acceptance of the SWFEL is not found to be a problem.

The nominal parameters used in the simulations here are listed in Table 1. These values are appropriate for a generic TBA, and little effort has been made to optimize the waveguide size or the wiggler strength and wavelength.

Initialization

The simulation initialization parallels the single-particle solution. A distribution with prescribed spreads $\Delta\theta_0$ and $\Delta\gamma_0$ in θ_j and γ_j is loaded so that $\langle\theta_j\rangle = \alpha + \beta s$ and $\langle\gamma_j\rangle = \gamma_r$. Sinulation particles are uniformly distributed within this phase-space rectangle, and different random position are chosen for each beam slice. Such a distribution is not realistic, but it allows the longitudinal acceptance to be tested systematically.

The reacceleration field required to keep $\langle\gamma_j\rangle$ constant is given by

$$E = D_x \frac{\omega_s}{c} a_w \left(\hat{a}_r \left\langle \frac{\sin\theta_j}{\gamma_j} \right\rangle + \hat{a}_i \left\langle \frac{\cos\theta_j}{\gamma_j} \right\rangle \right) \qquad (13)$$

This field could be recalculated at each z and s value, but this algorithm introduces a high-frequency noise component in E that increases exponently with z. A more practical approach is to calculate $E(s)$ at $z = 0$ and to use it at all subsequent z positions. With this second technique, the calculated E is noise free and reduces to Eq. (11) in the limit that $\Delta\theta_0$ and $\Delta\gamma_0$ are zero.

We set the initial signal level $|\hat{a}(0)|$ by assuming some input microwave power per unit length P_{in} and balancing this with cavity-wall losses, specified by an assumed cavity Q.

Results

The output microwave energy W_{out} and phase ϕ for a beam with the nominal parameters and a linearly increasing I_b are shown in Fig. 1. The spreads $\Delta\theta_0 = 0.1$ and $\Delta\gamma_0 = 0.01$ used here are small enough that the distribution remains trapped and the output signal is reasonably insensitive to beam and field errors. The principle z dependence in this case is the initial ripple in W_{out} due to synchrotron motion. This ripple would probably be much reduced for a realistic distribution.

For the standard case, the greatest sensitivity to parameter errors is found for fluctuations in the initial energy. When the reacceleration field is calculated for a beam at the resonant energy and the simulation is run with an energy that is 2% higher, W_{out} is nearly unaffected, but ϕ has a ripple of about $\pi/2$ with a wavelength in z corresponding to the synchrotron wavelength in the initial field. This phase ripple can be reduced by choosing larger a_w or λ_w, which gives a higher resonant energy. In contrast to this energy sensitivity, a 2% error in I_b has a negligible effect on either W_{out} and ϕ. A change of 2% in the magnitude of E_r likewise has little effects on either the output energy or phase for the standard case, but introducing a 0.1 ns time lag in the reacceleration field again causes a long-wavelength ripple of about $\pi/2$ in ϕ due to beam-energy loss during the initial period when $E_r = 0$.

Studies with a constant-current beam show that the final wave phase is as stable as for a beam with a linear current ramp, but there is a 10% ripple in W_{out} that persists in z. A beam with constant I_b also begins to lose particles when errors in energy or current exceed about 1.5%, indicating the reduced acceptance for this current envelope.

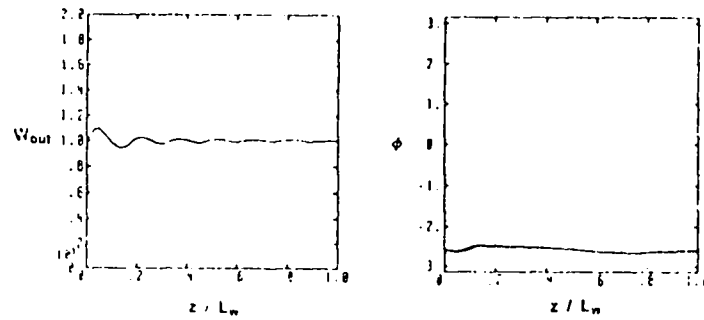

Fig. 1 Output energy per unit length W_{out} and wave phase ϕ as functions of z for the standard case.

Conclusions

From the 1-D simulations discussed here, a standing-wave FEL appears to be a possible microwave source for a two-beam accelerator. Using a beam with modest current and energy, we find that the final microwave energy in cavities is adequate to drive a high-gradient structure, and this energy remains effectively constant in z for fluctuations in energy, current, the reacceleration field, and timing of up to 2%. The final signal phase appears to be more sensitive, with 2% errors in energy or timing causing a phase variation in z of up to $\pi/2$. Work is underway to determine how such a phase error would affect the performance of the high-gradient structure. The need for tight prebunching is another potential shortcoming of the standing-wave FEL.

References

1. T. J. Orzechowski, *et al.*, Phys. Rev. Lett. **57**, 17 (1986).
2. M. A Allen, *et al.*, "Relativistic Klystrons" in *Proceedings of the 1989 IEEE Particle Accelerator Conference*, March 1989, Chicago, IL, edited by F. Bennett and J. Kopta (IEEE, New York, 1989), p. 1123.
3. A. M. Sessler, in *Laser Acceleration of Particles*, AIP Conf. Proc. 91, edited by P. J. Channell (AIP, New York, 1982), p. 154.
4. D. B. Hopkins, private communication
5. A. M. Sessler, D. H. Whittum, W. M. Sharp, M. A. Makowski, and J. S. Wurtele, to be published.
6. H. Henke, CLIC Note 59, March 1986.

TOWARDS A 12 GeV ELECTRON ACCELERATOR FOR NUCLEAR PHYSICS WITH A 100% DUTY CYCLE

B. Aune, J.L. Belmont, J.P. Didelez, G. Leleux, J.M. Loiseaux,
M. Gouttefangeas, M. Promé, A. Tkatchenko
Institut National de Physique Nucléaire et de Physique des Particules, Paris,
and Commissariat à l'Energie Atomique,
CEN Saclay, 91191 Gif-sur-Yvette Cedex, France

Abstract

For the future researches in nuclear physics it is widely believed that the electromagnetic probe is a very useful tool. Therefore in 1989 a preliminary study of a 4 GeV, 100% duty cycle accelerator was carried out. The accelerator consists essentially of a recirculating linac using the superconducting cavities being developed at Saclay. Two nuclear physics experimental rooms would be fed simultaneously at the 1.5 GHz RF frequency. Provisions could be made for a later upgrading of the accelerator up to 12 GeV, as recommanded by the French Academy of Sciences, although other approaches towards a 12 GeV electron accelerator are also under study.

Introduction

This 4 GeV project was made to obtain :

a 100 μA beam with a 100% duty cycle

an emittance (phase surface/π) = 10^{-8} m.rad for 95% of the electron beam

a relative energy spread = $3 * 10^{-4}$ FWHM

two beams being delivered at the same time on fixed targets, either at the same energy, or at different energies (one being chosen at random up to 4 GeV, the choice for the other one is restricted to a set of a few values corresponding to extraction at a previous turn)

The project is based on recirculating linacs. The general lay-out is shown on figure 1 and 2.

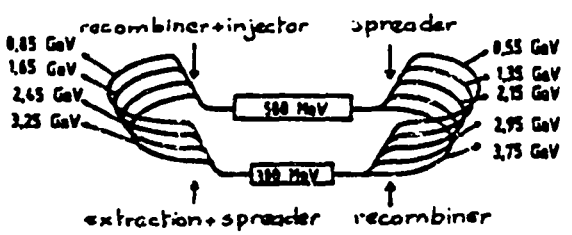

Fig 1.General layout of the 4 GeV recirculating accelerator.

Although it can be seen that this is a "CEBAF-like" design [1], with five turns in the linacs, the project differs from the CEBAF design on four main points :

1. The two beams delivered simultaneously on the experimental areas are energy separated instead of being time separated. The consequence is that each user sees bunches coming at 1.5 GHz (which is the RF frequency) instead of half of this frequency. This is obviously an advantage as far as the detectors electronics is able to catch events at the rate of 1.5 GHz.

2. Superconducting cavities are supposed to be operated at an effective accelerating field :

E_{acc} = 10 MV/m

with an unloaded quality factor :

$Q_0 = 6 * 10^9$ @ 1.8 Kelvin

3. The so-called HOM couplers, responsible for rejecting higher order modes in the cavities, are especially designed for recirculating linacs. It means that they are efficient primarily for the transverse modes. The concept results in a simpler coupler design [2].

4. The general design of the accelerator is a compact one. Of course the linacs are shorter since the accelerating field is large, but the radius of the arcs has been taken as small as possible taking into account the requirements stated above.

We will not give a general description of this project, since the concept of recirculating linacs is well known. We will rather focus on the points which are specific to this design. Detailed informations will be found in the so-called "blue book" proposal.

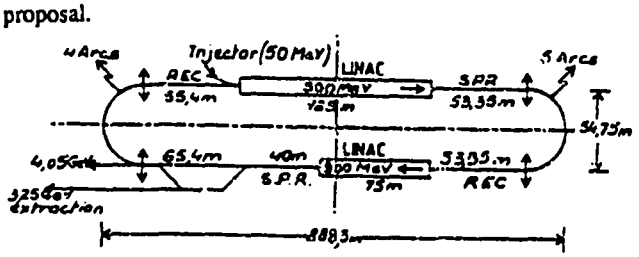

Fig 2.Main structures of the Linac.

Injection and extraction

A 50 MeV injection energy has been chosen for two reasons : first, the velocity of the electrons is close enough to c so that the phase shift in the first turn of the linac is acceptable ; second, focusing in the linac is not too difficult. This value guarantees that the threshold current for BBU should be much larger than the design value with the chosen cavities.

Actually, two beams are injected at the same time and the same place. Their energies differ by 4 MeV. This 4 MeV difference will be carried all the way to the final energy, and will be used to separate the two beams at the extraction level. Figure 3 shows schematically the injection system. It can be noted that provisions have been made for a polarized electron source.

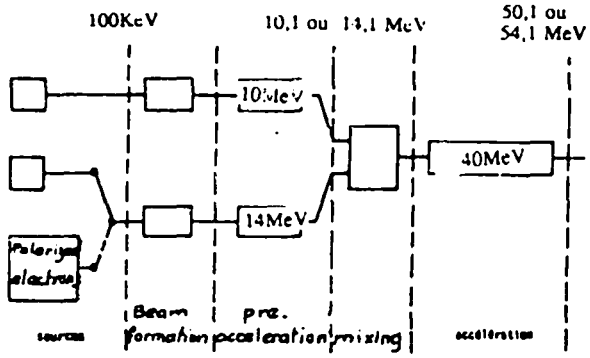

Fig 3.Injector design.

The two sets of bunches differing by 4 MeV are exactly superimposed in the linacs. They are slightly separated in the radial direction in the arcs. The choice of 4 MeV for the energy difference results from a compromise between an easy separation at extraction and a small enough radial spread in the first arc.

Superconducting cavities

A research and development program on superconducting cavities started at Saclay a few years ago. It includes basic research on RF superconductivity, studies on field emission, surface characterization, development of HOM couplers and statistics on industrially manufactured niobium cavities. This R/D program is beeing continued, but it already showed that a project can be based on cavities with an effective accelerating field of 10 MV/m and a quality factor of $6*10^9$ at 1.8 Kelvin.

Last year it was decided to build a test facility for superconducting electron linac, the so-called "MACSE" [3]. This is going to be a small CW linac with a current of a few hundreds of microamperes. Technological developments undertaken for this project have been applied to the design of the 4 GeV accelerator. One cryomule consists of 4 five-cell cavities. Its length is about 4 meters. There are 44 such cryomodules in the 4 GeV project. Each cavity is fed with a 5 kW klystron, which means 176 klystrons altogether. Only half of these 5 kW are needed for the beam. The other half is available for dynamic compensation of cavity detuning.

The cryogenic system power must be 2.5 kW at 1.8 Kelvin. The corresponding line power amounts to 5 MW.

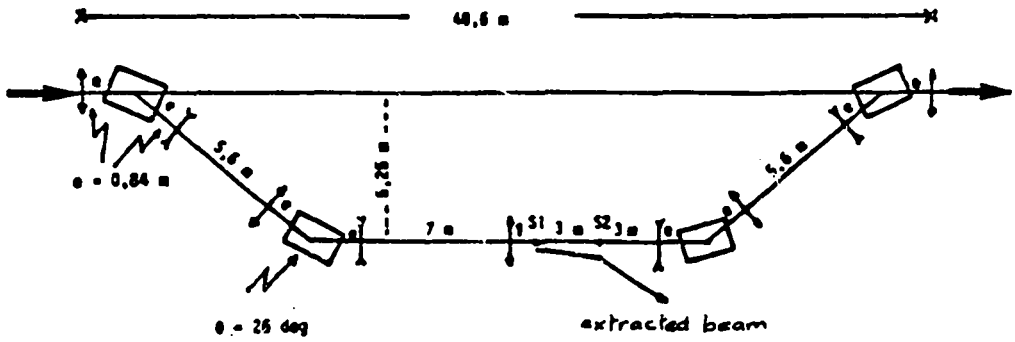

Fig 4.Design of the extraction system at 3.25 GeV and at 4 GeV.

Figures 4 and 5 show the extraction system and the bunch separation in the radial phase space.

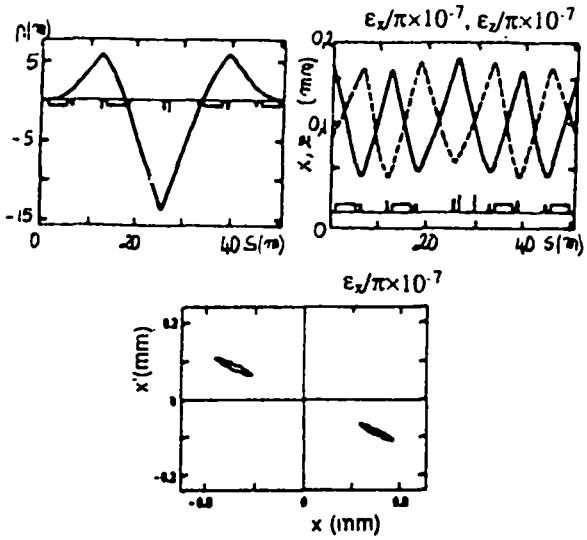

Fig 5.Optical characteristics of the extraction system at 3.25 GeV.

Focusing in the linacs

Focusing is chosen so that the beam is adapted for its first turn (with a $2\pi/3$ betatron phase advance). But it must still be good enough for the other turns. The 50 MeV beam entering the first linac reaches 850 MeV at its output. This large relative energy gain obliged to put a quadrupole every 5 meters, which means that there is always a quadrupole between two cryomodules. The β functions are displayed on figure 6 for the first and last turn.

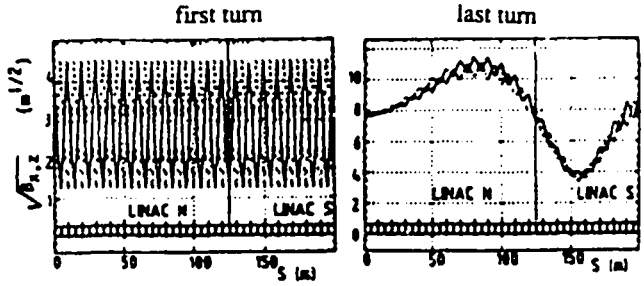

Fig 6. $\sqrt{\beta x,z}$ functions for the first and fifth turn.

The arcs

The arcs consist of 4 periods, each period consisting of 3 FODO cells and 4 magnets (missing magnets technique). The magnetic radius is 10 meters, while the physical radius of the arc is 27 meters. The arc is an achromat, and the structure provides isochronism from linac to linac.

With such arcs, it has been caculated that the $\langle \mathcal{H} \rangle$ function is equal to 0.45 meter, which is small enough to avoid large emittance growth in the arcs.

Figures 7 and 8 show respectively the β functions for one period and the dispersion coefficient for one arc.

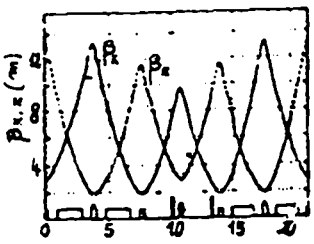

Fig 7.βx,z functions for one lattice.

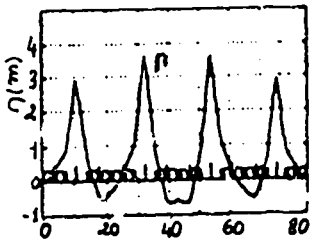

Fig 8.Dispersion function for one arc.

Spreaders and recombiners

They are still rather long, more than 50 meters. Obviously the principle of spreaders and recombiners must be modified in the case where one should wish to have a larger number of turns in the linacs (for instance use vertical and horizontal spread).

Upgrading up to 12 GeV

To follow recommandations issued by the French Academy of Sciences, a modified version of this project has been made. It consists in a two phase construction. As shown on figure 9, the two linacs (500 + 300 MeV) have been replaced by a single 800 MeV linac. During phase 1, the RF cavities are operated at 10 MV/m and the maximum energy is 4 GeV as before. Phase two consists in building additional arcs with a 100 m physical radius. In the meantime the development of RF superconducting cavities is expected to have reached the point where effective accelerating fields of 15 MV/m can be routinely obtained ; the existing 800 MeV linac would benefit of such improvement either by changing the cavities (worst case) or by a simple surface treatment of the cavities (best case) ; it would become a 1.2 GeV linac. Ten passes of the beam would deliver a 30 μa, 12 GeV beam, the total beam power being kept constant. The emittance would be 10^{-7} m.rad for 95% of the beam and the relative energy spread 10^{-5} FWHM.

Other approaches

At a time where the nuclear physics community is discussing on what is the most interesting research field in the long term, the specifications for the needed accelerator are not clearly stated. It seems that a first step at 4 GeV may be worthless, a higher energy being required at once ; a recirculating linac project would have to be optimized consequently. Moreover the desired maximum energy may be significantly higher than 12 GeV. In that case, a recirculating linac may not be the best choice. Discussions have started at a European level so as to be able to answer the needs when they are known.

References

1. C. Leeman, "CEBAF design overview and project status", CEBAF-PR-88-001.

2. A. Mosnier and al. "Damping of the HOM's in a multicell superconducting cavitiy", Proceedings of the European Particle Accelerator Conference, Rome 1988, p. 1287.

3. B. Aune and al. "MACSE : a superconducting test facility for superconducting electron linac", this conference.

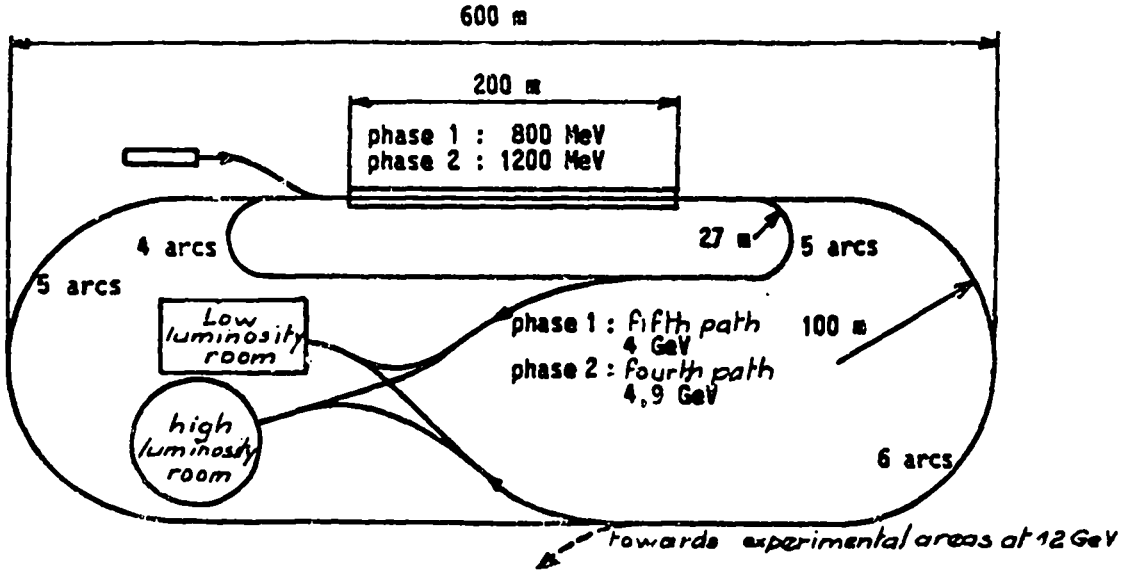

Fig 9.Layout of the 12 GeV recirculating Linac.

THE ENERGY STABILIZATION FOR THE SLC SCAVENGER BEAM*

Ian Hsu, M. Browne, T. Himel, R. Humphrey
K. Jobe, M. Ross, J.-L. Pellegrin, J. Seeman
Stanford Linear Accelerator Center
Satnford University, CA 94309

Abstract

The energy of the SLC scavenger beam which is used to produce positrons must be carefully maintained so that the beam can be transported through the collimators in the dispersive region of the extraction line which leads from the Linac to the positron target. A feedforward control loop has been developed to compensate the energy fluctuations due to the beam intensity fluctuations. The loop detects the beam intensities in the damping rings and then calculates how much energy needs to be compensated due to beam loading effects. The energy is corrected by adjusting the acceleration phases of two sets of klystrons right before the extraction. Because there is feedback loop using the same controls, their interaction needs to be carefully treated. This paper presents an overview of the feedforward algorithms.

Introduction

When operated at 120 Hz, in each beam pulse , there are three bunches in the SLC linac. These are, in order, collider positrons , collider electrons and the scavenger electrons. The last one, the scavenger electrons, is extracted at sector 19, the 2/3 point of the Linac, with energy 33 GeV to produce positrons for use later. The intensity variations of the two leading bunches and the scavenger bunch will cause an energy variation of the scavenger bunch due to the beam loading and the self-beam loading effects. A collimator, used to protect the extraction line, defines the energy acceptance to be ± 1.2 %. If, on some pulse, the scavenger beam energy is greater than 1.2 % above nominal, the collimator will scrape some of the scavenger beam and therefore reduce the intensity of the produced positrons, as shown in Fig. 1. As a consequence of that, the energy of the scavenger beam one subsequence pulse will be increased since it follows the lower intensity bunch of positrons. This energy variation will add up with the previous one and cause even more scavenger beam loss and reduce the positron beam intensity further and so on. The radiation due to the beam loss in the extraction line will trip off the whole machine by the MPS (Machine Protection System). This kind of rolling snow ball mechanism can trip off the machine within a couple beam pulses at moderate to high intensity. It is so fast that the existing extraction energy feedback loop can not prevent it. Therefore, a pulse by pulse feedforward loop has been developed to cure the problem.

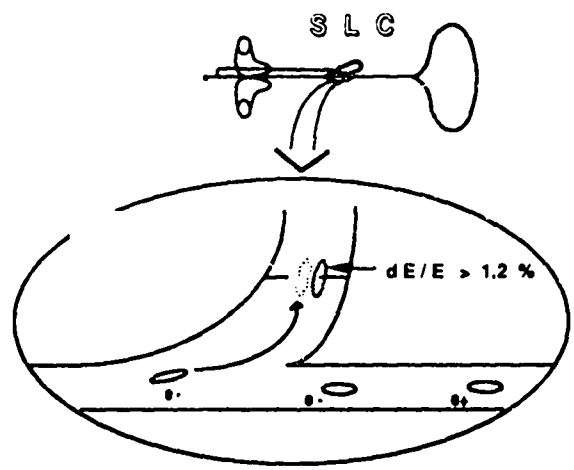

Fig. 1 The schematic drawing of the extraction line.

The Feedforward Loop

A schematic drawing of the feedforward loop is shown in Fig. 2. We pick up the three beam intensity signals in the damping rings at 5.3 msecs before they are extracted into the Linac. The intensity signals are converted into a scavenger beam energy change according to the known loss parameter k of the SLC linac structure. This is summarized in the next section. The signal for the required energy compensation is sent down the Linac to sector 17 and sector 18 which are the sectors right before the scavenger electrons extraction line. By changing the sub-booster phases of sector 17 and sector 18 in opposite direction we can accomplish the required energy compensation without changing the beam energy spread. If it takes 1 ms for the sub-booster phase to stabilize, data processing must be completed after 4.3 ms. Due to the short data processing time, the manageable algorithm and the cost of a software intensive solution, we decide to use hardware data processing techniques. The block diagram is shown on Fig. 3.

* Work supported by the Department of Energy, contract DE-AC03-76SF00515.

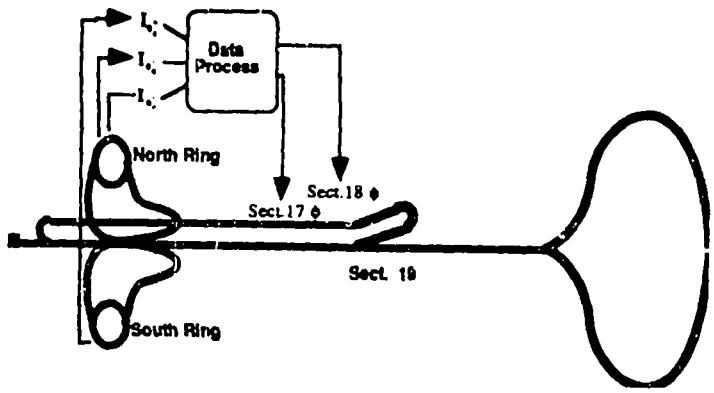

Fig. 2 The feedforward loop to stabilize the scavenger beam energy.

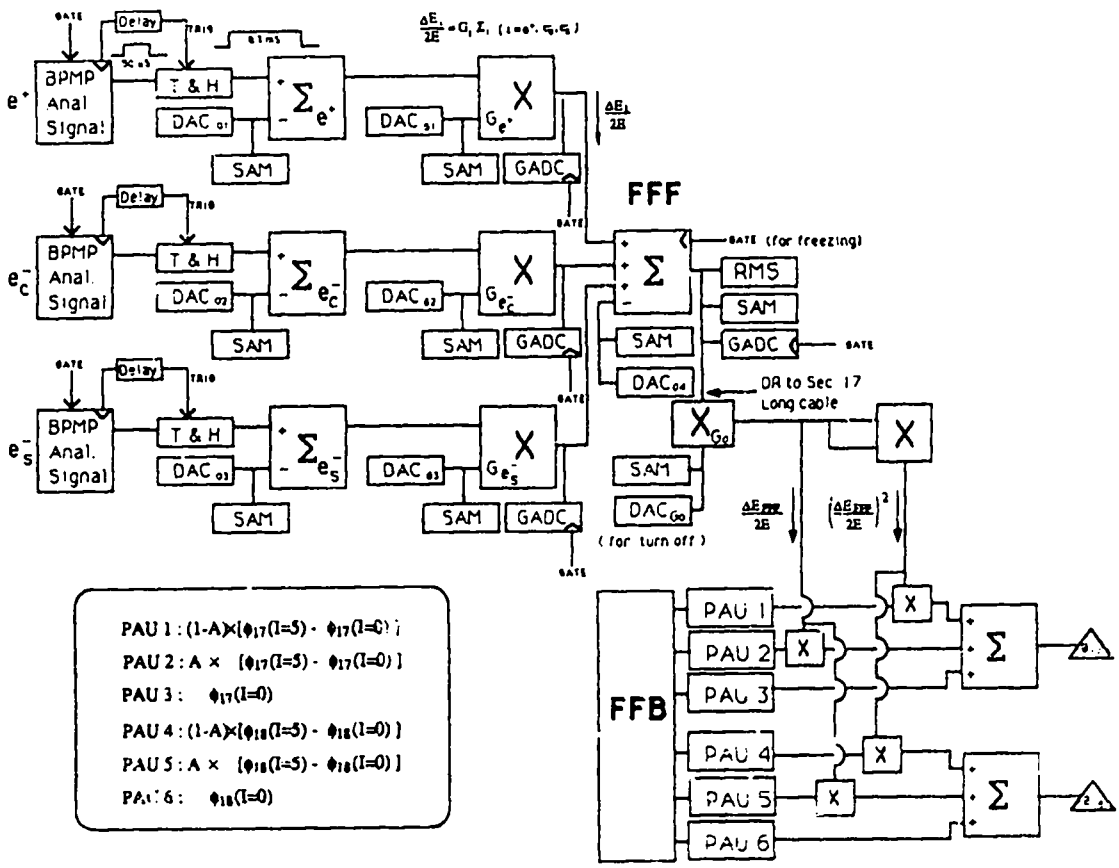

Fig. 3 The block diagram showing the overall loop structure.
Where

- **T & H : Track and Hold**
- **SAM : Smart Analog Monitor (ADC)**
- **GADC : Gated ADC**
- **PAU : Pulsed Amplitude Unit (DAC)**
  (The detail of PAU 1 - 6 is described at the end of the paper.)
- **FFF : (Fast) FeedForward loop**
- **FFB : (Fast) FeedBack loop**

The Summary for the Beam Loading Estimation

For SLC Linac :

Loss parameter : k = 19 V/pC/m

Beam loading enhancement factor : B = 3.1
(for bunch length = 1 mm)

The scavenger beam energy loss due to

1) The fundamental mode wake of :

e_c^+ : 94.6 N_{e^+} $\frac{MeV}{10^{10}}$

e_c^- : 102.8 $N_{e_c^-}$ $\frac{MeV}{10^{10}}$

e_s^- : 55.5 $N_{e_s^-}$ $\frac{MeV}{10^{10}}$

2) The [illegible] beam loading of the higher [illegible] mode wake :

ϵ [illegible] (B-1) ×55.5 $N_{e_s^-}$
[illegible] 116.5 $N_{e_s^-}$ $\frac{MeV}{10^{10}}$

[illegible] the loop is finished the above theoretical results will be confirmed by checking the correlation between the beam intensities and the scavenger beam energy at the extraction line.

The Interface Between the Feedforward Loop and the Feedback Loop

As we mentioned in the introduction, there is a feedback loop to stabilize the scavenger beam energy and the extraction position and angle. The control variables of the energy feedback loop are the sub-booster phases 17 and 18. The feedforward loop, for purposes of the simplicity, could use another pair of sub-booster phases as the control variables but would take about 1 GeV of energy for the head room. Therefore, we decided to use the same sub-booster phases for control. In this way, we can also utilize the existing control software and some of the hardware by merging two loops together.

After the analysis, we discovered that because the feedback loop energy measurement is in the extraction line, downstream of the two klystron sets, and the feedforward loop intensity monitor is upstream, these two loops will not fight each other and will not diverge. In fact, if there is a consist error of the feedforward loop, it will be corrected by the feedback loop.

Several methods for merging these two loops have been studied. Due to the non-linear (cosine) wave form of the RF field, an exact mergence circuit would need three arcosine operations and one square root operation which are in principle possible in hardware but may be somewhat complicated. Under some approximations, those operations can be reduced to a single arcosine operation. According to simulations, the maximum fractional energy error due to this approximation is 0.54% which is about the half of the tolerance. A different approach is to use the final feedforward signal to do the linear interpolation of the feedback output. In this way, complicated arcosine operation is not needed, but the maximum fractional energy error is 0.64%. The method which we will use for this project is that instead of using linear interpolation , we use quadratic interpolation . In this case the maximum fractional energy error is reduced to 0.20% which is well inside the tolerance. The equation for the quadratic interpolation is :

$$\phi_{17}(I) = [1-A(\phi_{17}^0,\phi_{18}^0)] \times [\phi_{17}^{max} - \phi_{17}^0] \times [\frac{\Delta E_{FFF}(I)}{2E}]^2 + A(\phi_{17}^0,\phi_{18}^0) \times [\phi_{17}^{max} - \phi_{17}^0] \times [\frac{\Delta E_{FFF}(I)}{2E}] + \phi_{17}^0$$

where

I : The current vector = [$I_{e_c^+}$, $I_{e_c^-}$, $I_{e_s^-}$].

$\phi_{17}(I)$: The phase is applied to the sub-booster 17 for the detected currents I.

ϕ_{17}^{max} : The phase would be applied in the case of maximum currents.

ϕ_{17}^0 : The phase would be applied in the case of zero currents.

$A(\phi_{17}^0,\phi_{18}^0)$: The interpolation coefficient which dependents on ϕ_{17}^0 and ϕ_{18}^0.

$\frac{\Delta E_{FFF}(I)}{2E}$: The fractional compensation energy of the feedforward loop at I.

The formula for the sub-booster 18 is similar the above equation.

THE PROBLEMS OF ION BEAMS MODELING IN INJECTORS AND RFQ LINACS

Yu.P. Vakhrushin, M.F. Vorogushin, Yu.A. Svistunov

D.V.Efremov Scientific Research Institute of Electrophysical Apparatus

Abstract

Problems of simulation of ion dynamics in injectors and RFQ linacs are discussed. Two methods of modeling of fields and particle dynamics in injection systems are considered. Ion optics as function of electrodes dimension in high gradient RFQ linacs are examined.

State-of-the-arts

Great progress made recently in Radio-frequency ion linacs have become possible due to the radio-frequency quadrupole focusing (RFQ), proposed by I.M.Kapchinsky and V.A.Teplyakov [Ref.1]. RFQ accelerators used as a low energy part of linac (LEBT) enable to provide a high ion trapping coefficient at a low injection energy and a small beam emittance at the inlet to the main part of an accelerator (HEBT). But to realise this it is necessary to fulfil quite exacting requirements for beam parameters at the inlet to the LEBT, especially at great phase current densities.The problems of matching a beam to the regular part of an accelerator were considered in a number of studies [e.g.Ref.2]. It has been revealed that the best matching of a beam to the regular channel will be obtained if the beam at the inlet to the bucher is convergent, symmetrical and with an optimal ratio of large and small semiaxes of phase ellipces in the planes XX^{I} and YY^{I}. The calculations of an ion injector with physical parameters providing the fulfilment of these conditions, is extremely labour-consuming and requires repeated modeling of the 3-dimensional ion dynamics in the injector chahhel. A standard scheme of a negative hydrogen ion injector with a plasma source is shown in Fig.1 (the same scheme may be used also to form a positive hydrogen ion beam).

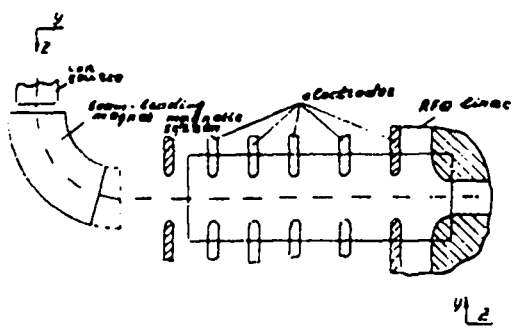

Fig1. Schematic configuration of ion injector of RFQ linac

The charged particle beam transport in such an injector is complicated by a considerable difference in the residual gas pressure (by 3 - 4 orders of magnitude) along the injector and the presence of a beam space-charge field. Near the source and in the bending magnet, which is used to remove heavy ions and caesium atoms from an H^- beam, the beam charge is compensated by ions arising during ionization of residual gas atoms or molecules. The density of the neutral atoms or molecules of residual gas and the density of a gas, entering the drift space from the source, is usually such that the density of an ion plasma formed as a result of the ionization may be compared to or even considerably exceed the density of particles in a beam. As the mobility of ions and electrons of plasma being different, there appears a plasma ambipolar electric field, equilizing the fluxes of opposite charged particles in the radially limited systems (the injector length considerably exceeds its lateral dimension). This field may drastically affect the particle dynamics in the injector regions, where external elestromagnetic fields are absent or negligible. The external fields are of great importance in that part of the injector before the accelerator, where a beam volume charge is not compensated, and to match the beam emittance with the accelerator acceptance there is used a preaccelerating focusing system consisting of several electrodes.

Attempts to model the fields and particle dynamics in ion injection systems were made by J.H.Whealton and co-workers during 1978-1989, the problems of not only the transport(the region to the right of the source slit) but the ion extraction (the region to the left of the slit) having been considered. But the problem was not solved completely though up-to-date computers were made use of. The plasma density to the right of the source was suggested to be always sufficiently small. The results of these studies are reviewed by J.H.Whealton in [Ref.3]. His approach, consisting in the modeling of the Poisson equation and three kinetic Vlasov equations, is at present the only serious program allowing to model the process of an ion extraction from plasma sources of different types and to obtain results consistent with the experiment. But as for the modeling of ion transport processes in the preacceleration systems of different complexity more economical calculation methods are possible, which allow to obtain good results.

2. The model of the given field

To calculate a field potential and phase characterastacs of a beam in the region of high-to-low-pressure transition the following system of equations must be solved: the equation for the potential φ

$$\Delta\varphi = -\frac{e}{\varepsilon_o}[n_i(\varphi)-n_b-n_e(\varphi)] \qquad (1)$$

plus the movement equations, that determine the distribution of the density of plasma ions and electrons, n_i and n_e, and beam ions, n_b.

But while carryng out prelliminary calculations, the problem may be simplified, considering the gas distribution in the injector as the given one, as it is mainly

determined by the vacuum pumping system and a source operation mode. The experiments of M.D.Gabovich [Ref.4] showed that the dependence of beam potential on the pressure $\varphi_B = \varphi(p)$ near the volume charge compensation point is of a logarithmic character. Thus, knowing the function $\varphi_B=\varphi(p)$ and pressure distribution $P = P(z)$ it is possible to calculation $\varphi_B = \tilde{\varphi}(z)$. Such an approach in modelling the 3-dimensional ion dynamics in an injector with large pressure difference has been realized in the PL-codes [Ref.5]. The calculation of the proper field of a beam, taking into account the dependence $\varphi_B=\tilde{\varphi}(z)$, permitted to avoid the solution of a self-consistent problem. The dynamics of beam ions in the field of given forces is considered along the whole injector channel. The field of axial-symmetric electrostatic systems are calculated numerically by solving the Laplace equation with corresponding boundary conditions. The processes of an ion extraction from the source and the formation of a plasma boundary are not considered. The form and size of the phase beam volume of "large" particles are given in the point immediately after the extracting electrodes. As a rule, the initial phase volume is known from the experiment. The calculations of a negative hydrogen ion injector for a RFQ-accelerator have been made, with the help of this code, and the axial-symmetric electrostatic system of preacceleration, the bending magnet parameters being properly selected, have been shown to provide small losses of H^- ions in the injector channel and good matching of the beam emittance to the RFQ-structure acceptance [Ref.6].

3.The hydrodynamic model

A more strict approach to the modeling of processes in the injector channel includes the calculation of a self-consistent field in the plasma-beam system and further the calculation of the ion dynamics in the given field. This approach is justified, as one of the tasks of the injector design is to provide a small emittance growth of an acceleratted beam. To describe the behavior of electron and ion plasma components the equations of the two-fluid hydrodinamics are used, i.e. movement and continuity ones, as well as the Poisson or Gauss equations for a self-consistent beam-plasma field. These equations for a symmetrical plasma source (external fields are absent) may be written in a one-dimentional form, taking into account that the injector length considerably exceeds its lateral sizes, and supposing a weak nonuniformity of plasma and gas parameters along the injector ($\partial E/\partial r \gg \partial E/\partial z$ and $E_r \gg E_z$). Assuming that a beam ionized the gas only once the gas ionization by secondary electrons is negligible and only elastic collisions occur in the plasma itself. Under these assumptions the plasma-beam system may be modelled by five integro-differential equations [Ref.7]:

$$\int_V \frac{dn_\alpha}{dt}\, dV = \int_V \nu_H n_b dV - \oint_S n_\alpha u_\alpha dS,$$

$$\oint E_r dS = 4\pi e \int_V (n_i - n_b - n_e) dV, \qquad (2)$$

$$\frac{\partial u_\alpha}{\partial t} = -u_\alpha \frac{\partial u_\alpha}{\partial r} \pm \frac{eE_r}{m_\alpha} - \nu_H \frac{n_b}{n_\alpha} u_\alpha - \frac{T_\alpha}{m_\alpha n_\alpha} \times \frac{\partial n_\alpha}{\partial r} - \nu_{\alpha o} \frac{m_o}{m_o + m_\alpha} u_\alpha .$$

Here, the index α takes on values i, e (ions, electrons); n_α and u_α are the densities and directed velocities of plasma ions and electrons; n_b and v_b are the density and velocity of beam particles; ν_H and $\nu_{\alpha o}$ are the collision frequencies equal to $\nu_H = n_g(z)\sigma_i v_b$ and $\nu_{\alpha o} = n_g(z)\sigma_{\alpha o} v_\alpha$, respectively; n_g is the gas atom density; σ_i is the cross-section of a gas atom ionization by beam ions; $\sigma_{\alpha o}$ is the cross-section of elastic collisions of plasma components with gas neutrals; T_α, v_α, m_α are the temperature, thermal velocity and plasma particle mass; m_o is the gas atom mass. In system (2) the directed velocity of neutral gas atoms is accepted to be equal to zero without violating the generality. The boundary conditions are of the form:

$$\left.\frac{\partial u_\alpha}{\partial r}\right|_{r=0} = 0; \quad \left.\frac{\partial n_\alpha}{\partial r}\right|_{r=0} = 0; \quad u_i\Big|_{r=R} = \text{const}\left(\frac{2T_e}{m_i}\right)^{\frac{1}{2}}. \qquad (3)$$

$$u_e\Big|_{r=R} = \left(\frac{3T_e}{m_e}\right)^{\frac{1}{2}}; \quad \frac{\partial}{\partial r}\left(\frac{\partial n_\alpha}{\partial r}\right)\Big|_{r=R} = 0; \quad \frac{\partial}{\partial r}\left(\frac{\partial u_\alpha}{\partial r}\right)\Big|_{r=R} = 0; \qquad (4)$$

They are discussed in detail in the paper of the same authors that in [Ref.7], which is to be published in JTP in the hearest future. Zero values of densities and directed velocities of plasma components correspond to the initial conditions of the problem. In case the space beam charge is not fully compensated by the plasma, when $n_i, n_e \ll n_b$, in order to calculate the field the beam movement equations ought to be added to equation system (2). With the external electrostatic fields the problem becomes the two-dimensional one. Fig.2 presents the curves of the resulting field in the plasma -beam system for three gas densities, $n_{g1} = 3{,}6 \times 10^{20}\ m^{-3}$, $n_{g2} = 3{,}6 \times 10^{19} m^{-3}$, $n_{g3} = 3{,}6 \times 10^{18} m^{-3}$, corresponding to three points of the injector along the longitudinal axis Z: $Z_1 < Z_2 < Z_3$. The maximum particle density on the system axis amounted to $n_b = 10^{13} m^{-3}$, the effective beam radius $r_b = 3$ cm, $T_e = 3$ eV, $T_i = 0{,}03$ eV, $v_b = 2 \times 10^8$ m/s. To avoid the influence of boundary effects on the field near the beam the radius of the system wall was chosen considerably larder than that of the beam (20 cm). The case $n_g =$

n_{g2} corresponded to the full beam charge compensation ($n_i, n_e \geq n_b$). Under these conditions the plasma-beam system is consistent, and the dependence of an electric field potential on radius in the region 0...0.15 m corresponds to the one observed experimentally [Ref.8] (see Fig.3).

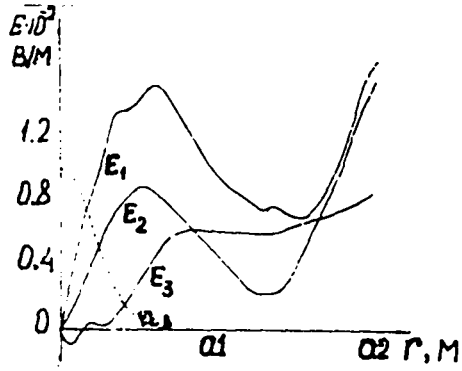

Fig2. A field distribution in the beam-plasma system
E_1-curve correspond to gas density n_{g1}; E_2- n_{g2}; E_3- n_{g3}.

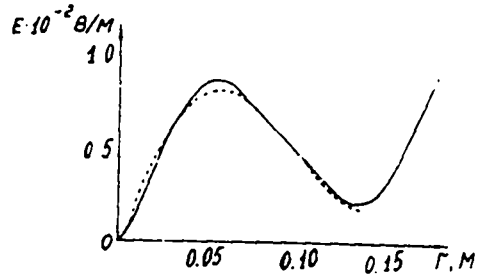

Fig3. Case of full charge compensation. Dependance of an electric field on the radius
——— Theory; ----- Experiment

4. Modeling of the ion dynamics in RFQ linacs

The calculation of the dynamics of charded particle beams with large density of a volume charge in RFQ accelerators is time-consuming, especially in carrying out multivariant calculations for optimization problems or in detecting the torerances for the manufacture of accelerating structures. Using different models of a particle beam considerably reduce the time for numerical modeling. There are another problems as taking into account the influence of heighbouring bunches on each other, the difference in calculation results for "ideal" and "real" electrodes of an RF resonator. In going from resonators with a 150 MHz operating frequency to those operating in a 400 - 500 MHz drequency range the number of bunches (eoxept the main one) to be taken into account in the model increases from two to four. Usually the account of only the terms of the first order, determining the acceleration and focusing effect, in the function of the potential dictribution corresponds to some ideal surface poles. In going to a real pole surface in resonators, operating with 400 MHz frequency and above, it results in considerable changes in the acceleration efficiency and ion trajectories, especially for the RFQ accelerating gradient($\Delta U/\Delta z$ > 1 MeV/m). The particle losses over the length for an accelerator with a 2 MeV finite energy for the "ideal"and "real"electrodes are shown in Fig.4. RFQ linac such as that must be built in D.V.Efremov Institute as LEBT for PET system, like one in [Ref.10].

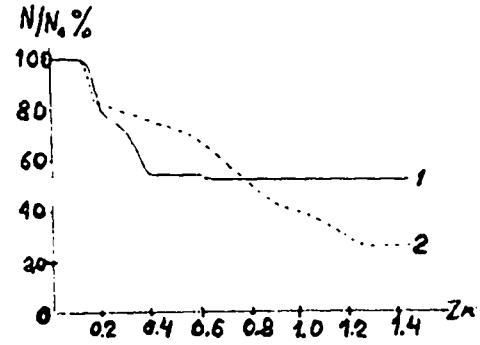

Fig4. The particle losses over the length for a accelerator
1- "ideal" electrodes;
2- "real" electrodes.

In going from the "ideal"to "real" electrodes current at the outlet is reduced by a factor of two. In this case the current was increased up to the former level by increasing the potential on the electrodes by 2 kV. But in generally case while calculating the particle dynamics in resonators with f>4[illegible] MHz the terms of higher orders of the potential expansion are to be taken into account.

Besides, for high-gradient structures the dependence of output beam characteristics on the parameters of initial phase ellipse becomes so sensitive that it is required to consider a common injector- accelerator system while modeling the ion dymamics.

References

1. I. M. Kapchinsky, V. A. Teplyakov. Lineinyi uskoritel ionov s prostranstvenno- odnorodnoj zhestkoj fokusirovkoj. PTE, issue 2, 1970, p. 19.
2. A. I. Balabin, V. S. Kabanov, V. V. Kushin, I. M. Lipkin. Chislennoe issledovanie soglasovaniya puchka s prostranstvenno odnorodnym kanalom.- M., 1984. Preprint/ITEP-28.
3. J. H. Whealton, M. A. Bell, R. J. Raridon, K. E. Rothe and P. M. Ryan. Computer Modeling of Negative Ion Beam Formation. J. Appl. Phys. 64(11) 1988, c 6210.
4. M. D. Gabovich, A. P. Naida, I. M. Protsenko, L. S. Simonenko. Gazovaya fokusirovka puchka otritsatelnykh ionov i eyo osobennosti.//ITP. 1974 vol 44, N 4, p. 861.
5. E. N. Vyuga, Yu. V. Zuev, Yu. A. Svistunov, A. P. Strokach. Chislennoe modelirovanie dinamiki chastits v inzhektore ionov s plazmennym istochnikom.-M., 1988. Preprint/NIIEFA-V-0797;TsNIIAtominform.
6. S. V. Grigorenko, Yu. V. Zuev, Yu. A. Svistunov, A. P. Strokach. Negative Ion Beam Forming in Linac Injector Proceedings of the II European Particle Accelerator Conference, Nice, June 12-16, 1990.
7. A. M. Astapkonich, Yu. V. Zuev, Yu. A. Svistunov, V. P. Sidorov, S. Yu. Udovichenko. Dinamika plazmy, polnostyu ili chastichno kompensiruyuszczej zaryad ionnogo puchka.-M., 1989. Preprint/NIIEFA-V-0839 TsNIIAtominform.
8. A. J. T. Holmes. A Theoretical and Experimental Study of Space charge in Intense Ion Beam - Preprint CLM-P539 Abingdon, Oxfordshire, 1978.
9. M. F. Vorogushin, Yu. A. Svistunov, A. E. Lukyanova, D. A. Ovsyannikov. Matematicheskoe modelirovanie dinamiki puchkov chastits s bolshoj plotnostyu obemnogo zaryada. VANT, seriya: yaderno-fizicheskie issledovaniya, issue 6 (6), 1989, p. 59.
10. R. W. Hamm, J. H. Bower, K. R. Crandall, M. E. Hamm and J. M. Potter. Commercial Ion Linacs. Proceeding of European Particle Accelerator Conference. Rome, Italy June 7-11, 1988.

Induction Acceleration Module for Maryland Pulse Compression Experiment*

J. G. Wang, D. X. Wang, E. Boggasch[a], D. Kehne, M. Reiser, and T. Shea[b]
Laboratory for Plasma Research and Department of Electrical Engineering
University of Maryland, College Park, MD 20742

Abstract

A compact induction acceleration module has been designed and constructed for the electron pulse compression experiment at the University of Maryland. The design parameters, operation principle and performance characteristics of this device are briefly reported in this paper.

Introduction

The Maryland Electron Pulse Compression Experiment[1] requires a fast electron beam pulse with quadratically time-dependent energy shear. This is achieved by an electron beam injector that consists of a variable-perveance gridded electron gun, three solenoidal matching lenses and an induction acceleration module. The electron gun[2] produces a beam with 50 ns pulse width, 40 mA current and 2.5 keV energy. The induction acceleration module produces a voltage that varies as a quadratic function with time from 0 to 5 kV across its gap. This voltage imparts an approximately linear head-to-tail velocity shear to the beam electrons to cause compression. In this report we present the induction acceleration module design, its operating principle, modulator circuit analysis, and some test results.

Induction acceleration module

A toroidal ring of magnetic material surrounded by a conducting loop is driven by a voltage pulse from a modulator, and the change in flux in the magnetic core induces an axial electric field[3,4]. The voltage appearing across a gap in a second loop during the flux change is expressed by

$$V_g(t) = \oint \mathbf{E} \cdot d\mathbf{l} = -\iint \frac{d\mathbf{B}}{dt} \cdot d\mathbf{s} \qquad (1)$$

where the accelerating particles perform the line integration and the surface integral is taken over the cross section of the ferromagnetic material. The gap voltage will drop dramatically if the toroidal core material reaches magnetic saturation. Assuming a t^2 gap voltage during operation, Eq. (1) yields

$$V_{g\,max}\,\tau = 3\,A\,\Delta B \qquad (2)$$

which relates the maximum gap voltage, the core cross-sectional area A, the total change in the magnetic flux density, ΔB, and the maximum operation time τ before the core saturation.

As illustrated in Fig. 1, the induction acceleration module consists of a single-turn primary around 2 soft ferrite cores (H material) with the beam completing the single-turn secondary. This arrangement forms an inductively isolated gap with a one-to-one voltage ratio. The primary is driven symmetrically from two opposite sides in a balanced mode to minimize deflections of the beam. The beam tube has a radius of 1.9 cm and the gap distance is 4 mm. The dimensions of each ferrite are 14.82 cm in outer diameter, 6.35 cm in inner diameter and 1.59 cm in width. The total cross-sectional area of the core is 13.45 cm^2. The saturation flux density B_s of the material is 0.34 Tesla. Taking the maximum gap voltage of 5 kV at τ=50 ns, Eq. (2) yields the maximum change of the magnetic flux density of ΔB=0.06 Tesla which is much smaller than the saturation flux density of the material. It is expected that the first quadrant of the B-H curve of the material is adequate for operation. Nevertheless, the gap voltage will swing up to a higher value after the 50 ns beam pulse period, that could drive the core into saturation. Since the material has a residual magnetism B_r of 0.15 Tesla, one needs a reversal current after each shot to restore the core approximately to the origin of its B-H curve.

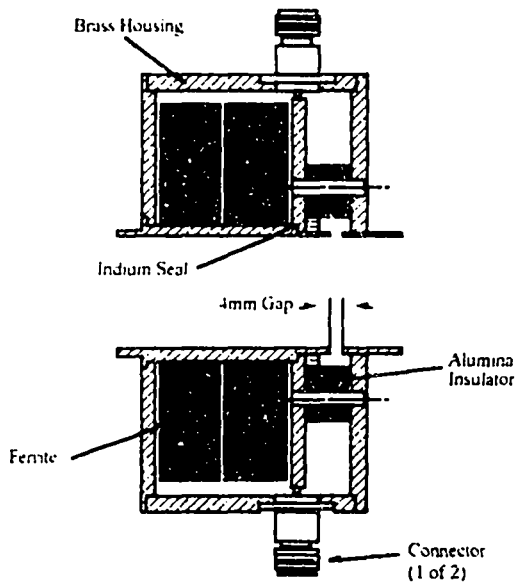

Fig. 1. Mechanical drawing of the induction acceleration module.

Since the gap voltage V_g is quadratically time-dependent, the gap physical characteristics will rely on this feature. For instance, the longitudinal impedance of the acceleration gap will vary in a large range during the beam pulse. The very low impedance at the beam front results in heavy load problem and waveform distortion. The acceleration gap acting on the beam as a focusing lens will also produce severe chromatic aberrations that cause problems with beam matching to the periodic focusing channel and may also lead to emittance growth.

Modulator

The schematic diagram of the induction acceleration module and its associated modulator circuits is shown in Fig. 2. The induction acceleration module itself is equivalent to a RLC parallel circuit where R accounts for the resistive loss in the core. With the external capacitance and inductance, the five components C_1, L_1, C_2, L_2, and R constitute a Pulse Forming Network (PFN).

The behavior of the PFN is governed by a fourth-order differential equation. In the complex frequency domain the

* Research Supported by the U.S. Department of Energy

[a] GSI Darmstadt, W. Germany

[b] Brookhaven National Laboratory

voltage on the induction module is related to the charging voltage V_0 on the capacitor C_1 by

$$V(s) = \frac{V_0 \omega_3^2 s}{s^4 + s^3 \omega_0 + s^2 \left(\omega_1^2 + \omega_2^2 + \omega_3^2\right) + s\omega_0 \omega_1^2 + \omega_1^2 \omega_2^2} \quad (3)$$

where the characteristic frequency constants ω_0 thru ω_3 are determined by the PNF parameters RC_2, L_1C_1, L_2C_2, and L_1C_2, respectively. Transforming Eq. (3) back to the time domain is straightforward, and one finds the induction gap voltage as

$$V(t) = V_0 \omega_3^2 p e^{-at} \left[\cos(bt) + \frac{q - ap}{bp} \sin(bt)\right] - V_0 \omega_3^2 p e^{-ct} \left[\cos(dt) + \frac{r - cp}{dp} \sin(dt)\right] \quad (4)$$

where the constants a, b, c, d, and p, q, r are determined by the PNF parameters. For a small time scale t, equation (4) can be approximated as

$$V(t) \approx \frac{1}{2} V_0 (\omega_3 t)^2 \quad (5)$$

This proves that under certain conditions the induction acceleration module with the driving modulator circuit does lead to a quadratically time-dependent voltage.

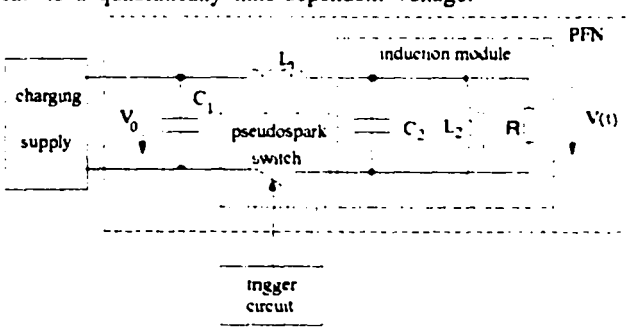

Fig. 2. Schematic diagram of the induction acceleration module and its modulator.

Ignoring the resistive loss of the core, the current through the induction acceleration module can be found as

$$i(t) = \frac{V_0 C_2 \omega_3^2}{\left(d^2 - b^2\right)} \left[\frac{\left(d^2 - \omega_2^2\right)}{d} \sin(dt) + \frac{\left(\omega_2^2 - b^2\right)}{b} \sin(bt)\right] \quad (6)$$

Equation (6) shows that the current through the induction acceleration module is sinusoidal. With the proper switch that allows current reversal, the cores will be degaussed after each shot and the induction acceleration could be operated without a separate reset circuit.

Pseudospark switch

A pseudospark switch is employed to control the PFN operation. The pseudospark discharge switch[5] is a fast, spark-like, low-pressure gas discharge that operates on the left side of the Paschen curve. A gap geometry that supports the pseudospark discharge consists of two insulated metal electrodes with a center hole. The discharge can be triggered at the cathode by a flashover initiated inside the bore hole across a thin mylar surface. Table 1 shows the typical operating parameters for this switch. This data set indicates superior performance of the switch in the aspects of fast risetime, small jitter, repetition rate and long lifetime. The tests show that the pseudospark switch has current reversal ability when the charging voltage V_0 is more than 6 kV.

Table 1
Operating Parameters of the Pseudospark Switch

Hold-off voltage	20 kV
Current	10 kA
Current rise (max.)	500 A/ns
Jitter	1 ns
Delay	30 ns
Repetition rate	100 Hz
Gas pressure	30 millitorr
Lifetime	> 1 million shots
Gas type	nitrogen

Test results

The induction acceleration module has been tested with respect to its gap voltage, module current, and circuit behavior. The modulator components used in this test are C_1=2400 pF, L_1=2.3 μH, C_2=2000 pF, and L_2=3.4 μH.

A typical gap voltage waveform taken at the charging voltage of V_0=18 kV is shown in Fig. 3. In the first 50 nanosecond or so, the gap voltage increases quadratically with time during which the electron beam will be synchronized and accelerated. This time dependence gradually disappears at larger time scales when the conditions for Eq. (5) are no longer satisfied. However, this has no effect on beam acceleration. Figure 4 fits the gap voltage data to the ideal t^2 curve, that shows reasonably good agreement between the theory and experimental data. The waveform of the t^2 dependence could be further improved by increasing C_1 or L_1, but that would require a higher charging voltage or lower repetition rate of operation. The measured gap voltage versus the charging voltage V_0 is plotted in Fig. 5 which shows reasonably good linearity of operation.

The current waveform passing through the induction module is shown in Fig. 6. The peak current is about 450 A when the charging voltage is 18 kV. The reverse current has a peak value of approximately 200 A and lasts about 300 ns. This results in a reasonable degauss effect on the core operation. In Fig. 7 the forward and reverse peak current of the induction module as a function of the charging voltage is also plotted. The linear behavior of the forward current indicates that the core is operated without getting into saturation. The nonlinearity of the reverse current explains the current reversibility of the pseudospark only at a higher charging voltage.

Summary

A compact induction acceleration module has been designed and constructed for the Longitudinal Compression Experiment at the University of Maryland. It generates an acceleration gap voltage that varies approximately as a quadratic function of time. This imparts a head-to-tail velocity spread to the electron beam pulse which is injected into a solenoidal focusing channel. The velocity spread will produce longitudinal compression of the electron pulse as it propagates down the 5 m long channel. The induction acceleration module employs a pseudospark switch to achieve good performance in synchronization and current reversibility. The induction acceleration module has been tested and the test results show satisfactory performance of this device. The interaction between the beam and the induction gap will be studied in detail with the new injector and the results will be reported in the near future.

References

1. T. Shea, E. Boggasch, Y. Chen, M. Reiser, "The University of Maryland Electron Pulse Compression Experiment", Proceedings of the IEEE Particle Accel. Conf., Chicago, p.1049, March 1989.
2. J. G. Wang, E. Boggasch, P. Haldman, D. Kehne, M Reiser, T. Shea, and D. X. Wang, "Performance characteristics of a variable-perveance gridded electron gun", to be published in IEEE Trans. ED.
3. N. C. Christofilos, R. E. Hester, W. A. S. Lamb, D. D. Reagan, W. A. Sherwood, and R. E. Wright, "High current linear induction accelerator for electrons", Rev. Sci. Instrum., 35(7), 886-890 (1964).
4. James E. Leiss, Neil J. Norris and Mark A. Wilson, "The design and performance of a long-pulse high-current linear induction accelerator at the National Bureau of Standards", Particle Accelerators, 10, 223-234 (1980).
5. J. Christiansen and C. Schultheiss, Z. Phys. A290, 35 (1979).

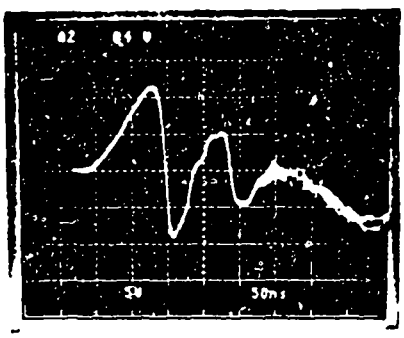

Fig. 3. Measured induction gap voltage waveform at V_0=18 kV which shows a quadratically rising gap voltage at the first 50 ns period (5 kV/div. vertically).

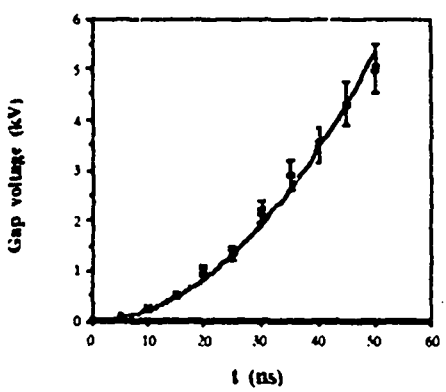

Fig. 4 Gap voltage in the first 50 ns where the smooth curve is a t-square form fitted to the experimental data by least square method.

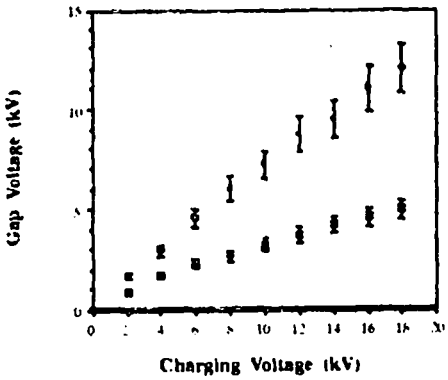

Fig. 5. Gap voltage versus charging voltage V_0 where the top points are the peak gap voltage and the bottom points are the gap voltage at τ=50 ns.

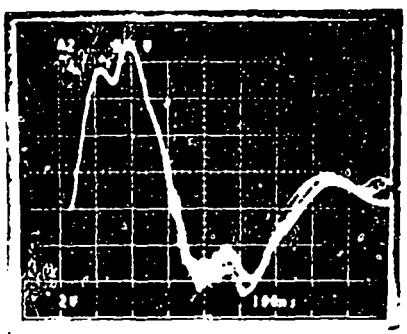

Fig. 6. Induction module current waveform (100 A/div. vertically) at V_0=18 kV which shows the reverse current through the pseudospark switch to reset the core.

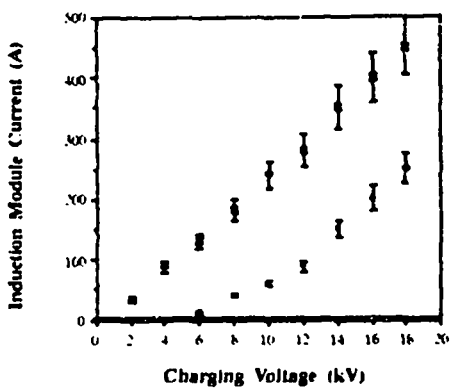

Fig. 7. Induction module current versus charging voltage V_0 where the top points are the peak forward current and the bottom points are the peak reverse current.

STATUS OF THE BNL TOROIDAL VOLUME H^- SOURCE*

J.G. Alessi and K. Prelec
AGS Department, Brookhaven National Laboratory
Upton, NY 11973

Abstract

A volume H^- source having a toroidal discharge chamber and conical filter field has been developed. Parametric studies of this source have been in progress for two years. Extraction apertures from 0.5 cm^2 to 1.87 cm^2 have been tried, and an H^- current of up to 48 mA has been extracted. The electron-to-H^- current ratio in the extracted beam can be as low as 10 for ≈ 25 mA H^-. The measured emittance (normalized, 90%) of a 19 mA beam was 0.44 π mm mrad. When operating with deuterium, the D^- output was 50-60% of the H^- current under the same discharge conditions. The addition of cesium to the discharge increased the H^- output and decreased the electron current so that at 30 mA of H^-, one obtained an electron-to-H^- ratio of 1. Using a two gap extractor, with a dipole field in the intermediate electrode, approximately 80% of the extracted electrons could be removed from the primary beam.

Introduction

Volume H^- ion sources have an advantage over surface production negative ion sources, which are more commonly used on accelerators, in that they don't need cesium for operation. Amoung the disadvantages, on the other hand, are the usually very large extracted electron current, and the relatively low extracted H^- current density. At Brookhaven, the design and study of a novel volume H^- source began in 1988.[1] The goal is to develop a source which will produce at least 50 mA of H^-, in 500 μs pulses and a 10 Hz repetition rate, to replace the magnetron surface-plasma source in operation on the 200 MeV linac. The source has a toroidal geometry, with the discharge region surrounding the central extraction region. A conical filter field separates the two regions. The idea of the toroidal geometry was to get the best utilization of the discharge, and to maintain a full rotational symmetry of the source.

While at this point we can reach the desired current by "pushing" the source, it is still just the first prototype, and would probably not be able to deliver 50 mA for weeks of continuous operation. Presently, reliable operation at 30 mA is more realistic. In the following sections, features of the source are first given, and then the results of some parametric studies are presented.

Features of the Source

Figure 1 shows a cross section of the source. The source chamber is cylindrical, 6 cm long and 20 cm ID. The walls of the chamber are lined with SmCo magnets, arranged to form ring cusps (typically 4 each on the front and back plates, and 3 rings around the side). A SmCo disc magnet opposite the extraction aperture produces the conical filter field. The calculated magnetic field lines are also shown in Fig. 1.[2] The cathode is a single loop of tungsten wire placed outside the filter field region. The gas and discharge were pulsed for the following measurements, typically at 0.5-1.3 Hz, with a 1.2 ms discharge width. A negative dc extraction voltage was applied to the source, and the extraction gap was typically 0.97 cm. Most of the data presented here was taken at 12-18 kV.

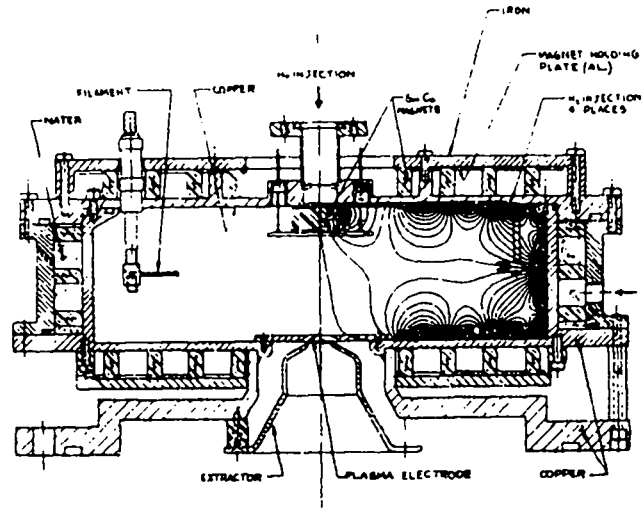

Fig. 1. Cross section of the volume source. The calculated magnetic field lines are also shown.

A Faraday cup and slit-and-collector type emittance head were located 10 cm from the source. A strong dipole field in front of the Faraday cup removed electrons from the beam, while deflecting the H^- only slightly. A current transformer on the output of the extractor power supply measured the total supply drain current. The difference between the H^- current measured on the Faraday cup and the total supply current was assumed to be electrons.

Results

The following subsections give brief summaries of the some of the source studies.

Conical vs. Dipole Filter Field

Normal volume H^- sources use a dipole filter field to separate the discharge region from the extraction region. The conical filter field was removed from the source, and a dipole filter field was placed near the extraction aperture. Figure 2 shows the H^- current vs. arc current for the two cases. The conical filter field increased the H^- current by ≈ 50%.

Dependence on Filament Parameters

Also shown in Fig. 2 is the dependence of the H^- current on the circular W filament diameter. A higher output was obtained with the smaller diameter filament loop, but the arc current was limited to < 150 A due to the smaller emitting area.

*Work performed under the auspices of the U.S. Department of Energy.

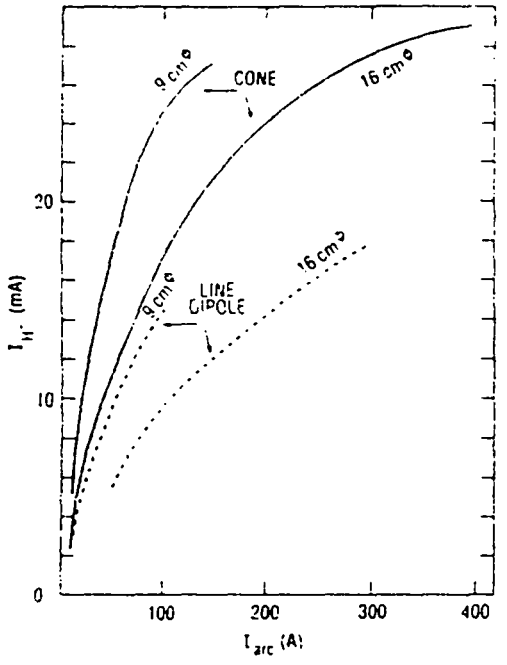

Fig. 2. H^- yield vs. arc current for the dipole and conical filter fields. Shown for each filter type are two different filament diameters.

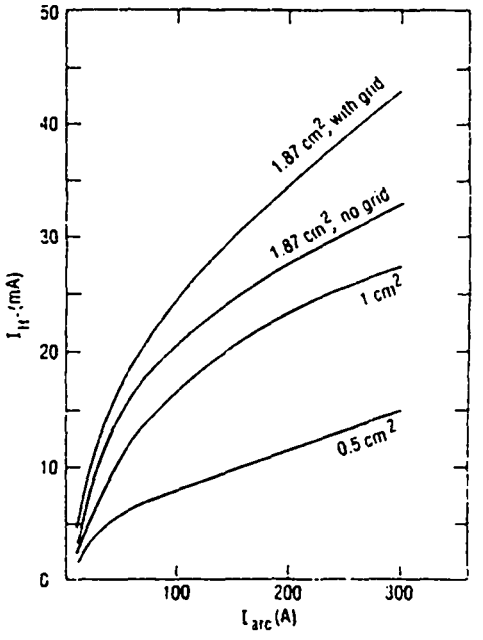

Fig. 3. H^- current vs. arc current for three different extraction apertures. The "grid" is a thin tungsten cross put over the aperture.

The output also depended on filament wire diameter (1 mm is approximately the optimum), axial position of the filament, and direction and magnitude of the instantaneous ac or dc filament current.[3] Normal operation is now with the filament current interrupted during the discharge pulse.

Plasma Electrode Bias

The plasma electrode is isolated from the discharge chamber. With this electrode floating, the output is usually slightly higher, but the electron current is much higher, compared to operation with it grounded. If the electrode is biased, going from a negative to a positive bias reduces the H^- slightly, but the electrons much faster.[4]

Source Pressure

As the source pressure is varied, one can go through a broad maximum in the H^- current, and at the same point one goes through a broad minimum in the electron current.[4] The pressure measured in the discharge chamber is typically 5-10 × 10^{-3} Torr.

Extraction Aperture Size

Figure 3 shows the H^- current vs. aperture area. With the largest aperture, the extracted current density dropped significantly. However, by putting a thin tungsten wire cross across the aperture the H^- current density returned to near that of the smaller apertures. Operating at a 400 A discharge with the 1.87 cm^2 aperture gave an H^- output of 48 mA.

Extracted Electron Current

The ratio of electron current to H^- current depends on many parameters. Figure 4 shows a scatter plot of the e^-/H^- ratio vs. H^- current for a variety of operating conditions. This

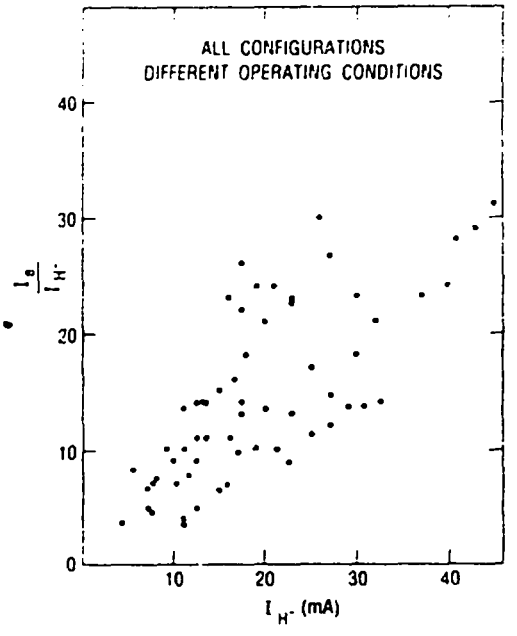

Fig. 4. The ratio of electron to H^- current as a function of arc current. The points are values taken under many different operating conditions, source geometries, etc.

includes different arc currents, aperture sizes, plasma electrode biases, filament geometries, etc. Details of the dependence on various parameters can be found in the references.

Emittance Measurements

Emittance measurements were taken with a 1 cm^2 extraction aperture, and a 0.97 cm extraction gap.[5] For a 13 mA beam, a normalized, 90% emittance of 0.32 π mm-mrad was measured, or an RMS value of 0.07 π mm mrad. This corre-

sponded to an effective ion temperature of 0.57 eV. At 19 mA the emittance was $\varepsilon_N(90\%) = 0.44\ \pi$ mm-mrad.

Double Gap Extractor

A two-gap extractor was tried, in an attempt to remove the electrons from the beam at less than the full energy. All three electrodes had apertures of 1.13 cm diameter. The intermediate electrode was 1 cm thick, and had permanents magnets imbedded in it in order to produce a dipole field to dump the electrons. We were able to dump more than 80% of the electrons on this intermediate electrode, operating at ≈ 5 kV relative to the source. There was a 10-20% loss of beam current due to an insufficient gradient in the first gap, and further optimization of the geometry is planned. Also, while the emittance area was the same as with the single gap extractor, the beam divergence could be reduced.

Isotope Effect

When the source was operated with deuterium, the D^- output was 50-60% of the H^- output obtained under the same arc conditions.[6] At a given D^- current, the extracted electron current was at least 4-5 times higher than that obtained when running with hydrogen.

Cesium Vapor Effect

A small cesium oven was installed inside the discharge chamber, and the effect of cesium on the source performance was studied.[6] Figure 5 shows the H^- output vs. arc current with

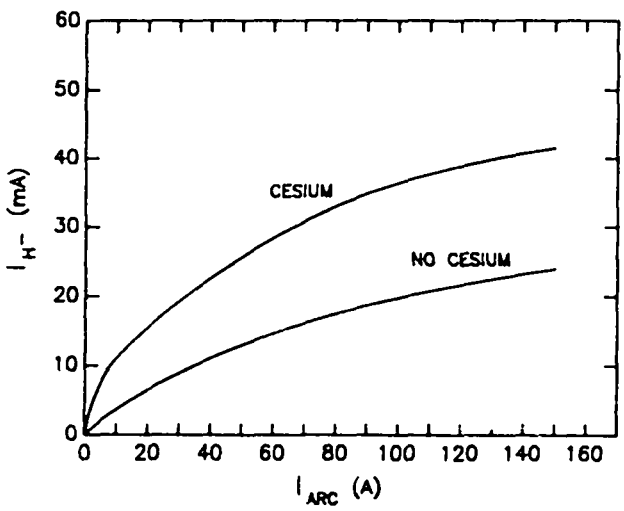

Fig. 5. H^- current vs. arc current with and without cesium in the source. The extraction aperture was 1.87 cm^2 and the voltage 16 kV.

and without cesium, for a 1.87 cm^2 aperture (single gap extractor). Generally, the output approximately doubled with cesium, while at the same time the electron current dropped. Figure 6 shows the H^- current and I_e/I_{H^-} ratio as a function of the plasma electrode bias. Note that with cesium added, one can adjust the electrode bias to get a very low I_e/I_{H^-} ratio without much loss of H^- current. We could obtain >30 mA of H^- with $I_e/I_{H^-} < 1$. In addition, the operating pressure could be reduced by approximately a factor of two with cesium. The effect of the cesium remained after the Cs supply was turned off, and even when the source was opened to air, some efffects of the Cs remained. While the H^- current went back to near the levels before Cs was introduced, the operating pressure remained low, and the I_e/I_{H^-} ratio remained near unity. The source had to be thoroughly cleaned to bring it back to its original "cesium-free" levels.

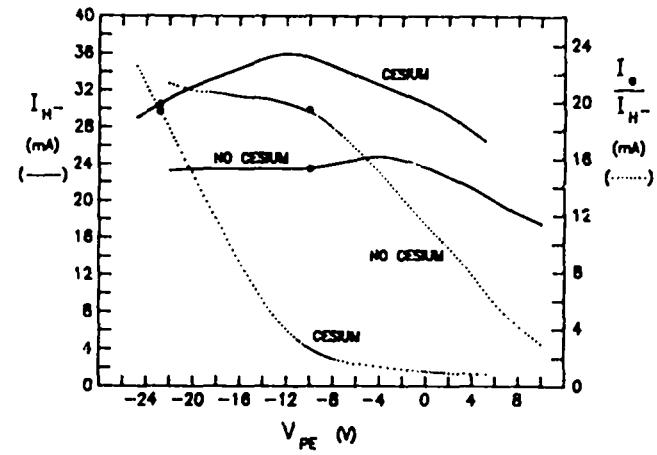

Fig. 6. H^- current and ratio of electrons to H^- as a function of the plasma electrode bias, with and without cesium. I_{arc} = 150 A, V_{arc} = 250 V, and V_{ext} = 16 kV. The dots indicate the floating potential.

Acknowledgements

We would like to thank D. McCafferty, who has tirelessly made the many modifications to the source and assisted in the measurements.

References

1. K. Prelec, Proc. 1988 European Part. Accel. Conf., Rome, 1327 (1988).
2. C.R. Meitzler, Proc. Fifth International Symp. on the Production and Neutralization of Negative Ions and Beams, to be published in AIP Conf. Proceedings (1990).
3. K. Prelec, Proc. Fifth International Symp. on the Production and Neutralization of Negative Ions and Beams, to be published in AIP Conf. Proceedings (1990).
4. K. Prelec, Proc. 1989 IEEE Part. Accel. Conf. (Catalog No. 89CH2669-0), 340.
5. J. Alessi, Proc. Fifth International Symp. on the Production and Neutralization of Negative Ions and Beams, to be published in AIP Conf. Proceedings (1990).
6. J.G. Alessi and K. Prelec, Proc. 1990 European Part. Accel. Conf., Nice, France, to be published.

THE BNL 200 MEV H^- LINAC – PERFORMANCE AND UPGRADES*

J.G. Alessi, J.M. Brennan, A. Kponou,
V. LoDestro, P.A. Montemurro
AGS Department, Brookhaven National Laboratory,
Upton, NY 11973

Abstract

For the past two years the linac has had reliable operation from the new RFQ preinjector. The performance of this preinjector is described. There is a fast beam chopper in the transport line between the ion source and RFQ. By injecting narrow pulses into the AGS we can obtain an accurate linac energy measurement, or the detailed shape of the linac beam energy distribution, on a single pulse. Some general comment on the linac operation are also presented.

Introduction

The BNL 200 MeV linac began operating as the proton injector for the AGS in 1971. In 1982, the linac was switched to H^- operation. In 1983 a polarized H^- source and 750 keV RFQ were added to the preinjector area, and polarized protons were accelerated in the AGS. In 1988, a second 750 keV RFQ was installed in place of the Cockcroft-Walton preinjector, for high intensity H^- operation, so we now have only the two RFQ's as preinjectors. The linac presently delivers ≈ 25 mA of H^- in 500 μs pulses, at a 5 Hz repetition rate. In this paper, we will first describe some features of the new RFQ preinjector, and discuss its performance. As part of this new beamline, a fast beam chopper was added. This chopper has allowed us to do several interesting linac studies, and we will describe accurate measurements of the linac energy and energy distribution, both obtained on a single pulse basis using the fast chopper. Finally, some general comments will be made on the linac reliability, and improvements being made.

RFQ Preinjector

We have now been operating for two years (approximately 7 months continuous per year) with the RFQ preinjector. Details of the beamline have been given previously.[1] Briefly, the line is as follows. H^- is produced in a magnetron surface-plasma source, with a circular extraction aperture. The beam is extracted at 35 keV, and transported 2 m to the RFQ. Focusing in the 35 keV line is provided by two pulsed solenoids, with a fast beam chopper located between the two solenoids. The 4-vane RFQ, designed and built at Lawrence Berkeley Laboratory,[2] accelerates the beam to 750 keV. There is then a 6 m transport line from the RFQ to the linac. (The line is long to allow room for the polarized H^- beam from the other RFQ to also be injected into the linac). Transverse focusing in the line is provided by three quadrupole triplets and a quadruplet. The bunch structure of the beam out of the RFQ is maintained by three buncher cavities in the transport line.

The operation of the RFQ has been trouble free, with only an occasional problem with its rf power supply. (An RCA 4616 tetrode is used as the final stage, delivering approximately 160 kW). Both maintenance requirements and downtime are much improved over previous operation with the Cockcroft-Walton. Under typical operation, we measure 50-60 mA on a current transformer 60 cm before the RFQ entrance, and get ≈ 80% transmission to the exit of the RFQ. Better transmission was observed in early tests in which the source extractor design was different, but the present extractor was chosen for its improved reliability. With ≈ 45 mA out of the RFQ, we lose 25-30% of this current in the 6 m transport to the linac. The exact source of this loss is not well understood, and discrepancies still exist as well between measured emittances and computer modelling of the optics in this 750 keV transport. Transmission through the linac is typically 80%, with ≈ 25 mA measured at 200 MeV. In comparisons of the emittance measured 76 cm upstream of the RFQ, and the emittance measured 173 cm downstream of the RFQ, there is an ≈ 50% emittance growth. Previous measurements on a test stand, taken closer to the RFQ entrance and exit, had shown only an ≈ 10% emittance growth.

Based on the design calculations, the proper voltages are obtained in the RFQ cavity at 121 kW. This is the power level maintained under normal operation. We observe, however, that the RFQ output drops off only slightly down to 80 kW. The transverse emittance of the beam at 30 kW is also essentially the same as at 121 kW. We have not measured the bunch structure of the beam at this lower power, but with no retuning of the bunchers from their normal values, we still accelerate ≈ 66% of the normal current to 200 MeV at 80 kW. We have also studied the dependence on injection energy. Under normal operation at 35 kV, the source output is space charge limited rather than emission limited. Therefore, as the source extraction voltage is decreased, the current out of the source drops as $V^{3/2}$. However, the fraction of the beam transmitted through the RFQ drops by only ≈ 10% at an energy of 29 keV. At this energy, the output emittance is also still constant. At an injection energy of 23 keV, however, the accelerated beam through the RFQ is essentially zero.

Linac Studies With the Fast Chopper

A fast beam chopper is included in the 35 keV transport line between the ion source and RFQ.[3] The purpose of this chopper is to allow bunch-to-bucket injection of beam into the AGS or Booster, in order to throw away at 35 keV those particles which would be lost at injection because they are outside the synchrotron rf bucket. Beam bunches can be produced with the width and delay of each bunch programmable to match the moving rf buckets during multiturn injection. In addition, when this chopper is used in conjunction with a sine wave chopper in the 750 keV transport line, one can accelerate single 200 MHz bunches through the linac, with periods ranging from 50 ns to once per macropulse. The < 1 ns wide pulses can be used for neutron time-of-flight experiments.[4]

*Work performed under the auspices of the U.S. Department of Energy.

The chopper is a pulsed electrostatic deflector, where voltages of approximately ±700 V are applied to plates above and below the beam to deflect the beam outside the RFQ entrance aperture. The chopper has a total length of 38 cm, and a separation between the upper and lower plates of 8 cm. The chopper is made up of 15 pairs of plates over the 38 cm length, which are connected as a slow-wave structure by coaxial cables, so that the voltage pulse travels plate-to-plate at the beam velocity. The chopper plates are powered by a pair of commercial solid state pulse generators having rise and fall times of less than 10 ns. Rise and fall times of 10 ns are measured on the beam pulses.

Under normal operation, the beam is space charge neutralized in the 35 keV transport line. However, when the chopper is used, the neutralizing ions are partially swept out of the beam by the plate voltage, and even though the voltage is off when the H^- beam passes through, the space charge neutralization does not build back up during the short pulses.[5] The effect of this loss of neutralization is a poorer match of the beam into the RFQ, and even when the line is retuned, approximately 20-60% of the instantaneous beam current is lost (the degree of neutralization depends on the duty factor of the chopper). Because of this loss, the chopper has so far been used only for machine studies, and a new chopper is now being built for the 750 keV line. It is a similar traveling wave structure, and in spite of the higher beam energy it will operate at essentially the same plate voltage. This is possible because the new chopper is approximately twice as long, with half the plate separation, and the rejection slits will be located at a more favorable position.

Several linac studies have been done using the 35 keV chopper, and the AGS as the diagnostic line. There is a momentum recombining bend between the linac and the AGS, and at the point of maximum dispersion are located a position monitor and profile monitor. Using this, and the magnet calibration, we are able to determine the linac energy. However, by injecting a ≈ 100 ns beam pulse into the AGS (with the accelerating voltage off), and watching the signal on a wall current monitor as the beam spirals, we are able to determine the absolute value of the linac energy in a very clean way on a single pulse. The radius of the AGS is accurately known (128.457 meters), so if the time is measured for the beam to spiral for 100 turns, one is doing a time of flight measurement over ≈ 80 km. Using a LeCroy 9400 digital oscilloscope, a 500 μs trace of the spiraling beam can be taken with 20 ns per point, and the center of the bunch on the first and 101 turn can be determined to within ±20 ns. From this, the absolute energy of the beam is known to within ±50 keV. Even a variation in the radius of the AGS by 1.0 cm (a large variation) only changes the determined energy by 41 keV.

We have used this method of energy measurement to periodically check the stability of the linac, and we occasionally noted unexpected changes in the energy. It was finally determined that these energy changes were coming from changes in the phase at which the bunched beam entered the linac. In Fig. 1, a measurement of the linac energy as a function of this phase is shown (the absolute value of the phase shown is arbitrary). Also shown is the linac transmission as a function of this phase. We see from this that the linac energy can change by ≈ 1 MeV without a significant change in transmission (this phase had typically been set by optimizing transmission). The shapes of the two curves could be reproduced fairly well with PARMILA. By optimizing the buncher phases relative to the RFQ, we can get transmission vs. input phase curves such as shown in Fig. 2.

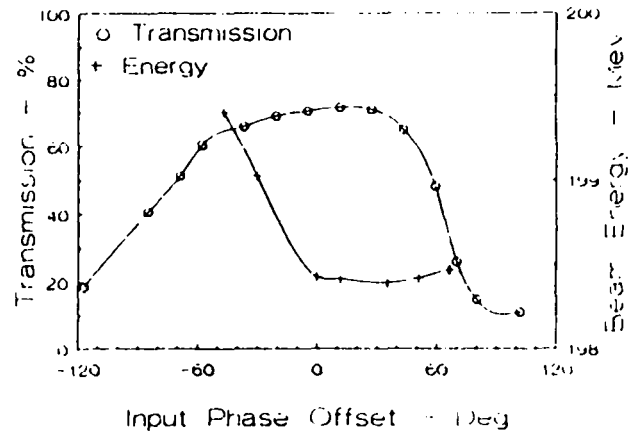

Fig. 1. The output energy of the linac, and linac transmission, as a function of the phase of the injected beam relative to the linac rf. The absolute value of the phase shown is arbitrary.

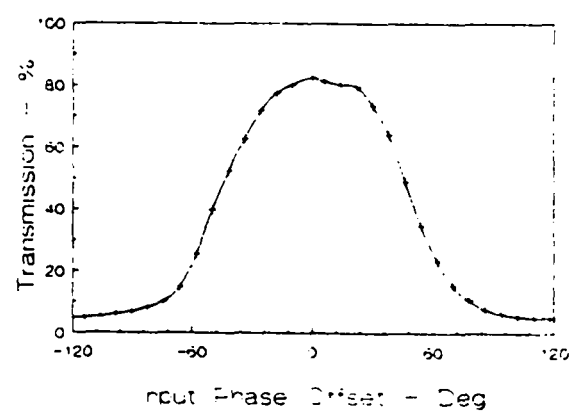

Fig. 2. Linac transmission vs. phase of the injected beam.

At the same time that the linac energy is measured with the spiraling beam, one can also observe the spreading of the pulse over the 100 revolutions, and estimate from that the energy spread of the beam. More interesting, however, is the case in which the single 100 ns bunch is injected into a high voltage bucket of the AGS. In this case, its synchrotron motion will rotate the energy coordinate into the time coordinate in 1/4 of a synchrotron period. If the bunch is ±45° the motion is essentially linear. Figure 3 is a single trace measurement of a bunch taken 1/4 synchrotron period after injection. This plot gives a detailed picture of the linac beam energy distribution. The horizontal axis is equivalent to 0.4 MeV/division, with low energy on the right. It was observed that the detailed shape of the energy distribution can be changed completely by changing the phase at which the bunched beam is injected into the linac, even moving the shoulder from one side to the other. With the relative ease of this measurement, we hope to study further its dependence on various linac and preinjector parameters, and improve the shape of the distribution.

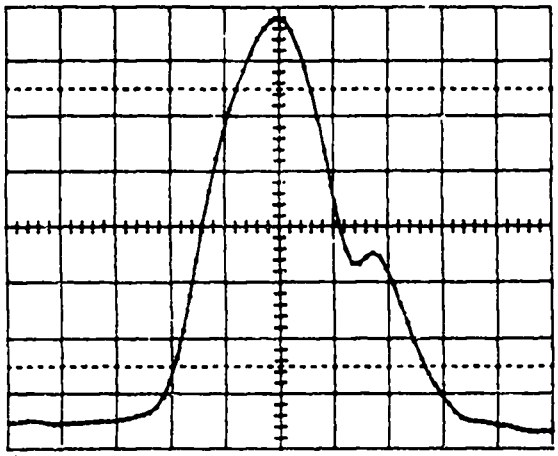

Fig. 3. The linac energy distribution, measured on a single pulse. The horizontal axis is 0.4 MeV/division, with low energy on the right.

Linac Operations

In recent years, the linac has operated ≈ 5000 hrs/yr for the physics program, with ≈ 95% availability. The rf systems are the largest contributor to the downtime, spread among the various components. Vacuum problems come next, followed by ion source downtime. The quadrupole systems typically cause only a few hours of downtime per year. In the past few years, we have begun to experience occasional pinhole leaks developing in the rf windows at several locations. (The feed loops are on the atmospheric side of the window, and ≈ 2 MW peak power is fed through each window). We do not yet understand the sudden occurrence of this problem after many years of trouble free operation.

Many of the 45 ion pumps on the 9 linac tanks have never been rebuilt (20 years old), and were beginning to trip off frequently or develop shorts. Therefore, approximately 20 ion pumps have been rebuilt by the AGS Vacuum Group over the past two years, and this program is continuing. In addition, vacuum valves are being installed on each tank to allow us to do an intermediate stage of pumping, after roughdown, with a cryopump. In tests, this reduced the pumpdown time of a tank from 8-12 hours to only 2-3 hours. In addition, less stress will be put on the ion pumps, since they will be turned on at a much lower pressure than is presently possible.

References

1. J.G. Alessi, J.M. Brennan, H.N. Brown, J. Brodowski, R. Gough, A. Kponou, K. Prelec, J. Staples, J. Tanabe, R. Witkover, and D. Yee, "AGS Preinjector Improvement", Proc. 1987 IEEE Part. Accel. Conf. (Catalog No. 87CH2387-9), 276.

2. R.A. Gough, J. Staples, J. Tanabe, D. Yee, D. Howard, C. Curtis, and K. Prelec, "Design of an RFQ-based H^- Injector for the BNL/FNAL 200 MeV Proton Linacs", Proc. 1986 Linear Accel. Conf., SLAC Report 303, 260 (1986).

3. J.M. Brennan, L. Ahrens, J. Alessi, J. Brodowski, J. Kats, and W. van Asselt, "A Fast Chopper for Programmed Population of the Longitudinal Phase Space of the AGS", Proc. 1989 IEEE Part. Accel. Conf. (Catalog No. 89CH2669-0), 1154.

4. T.E. Ward, J. Alessi, J. Brennan, P. Grand, R. Lankshear, P. Montemurro, C.L. Snead, Jr., and N. Tsoupas, "Pulsed-neutron Production at the Brookhaven 200 MeV Linac", Proc. ICANS X, Institue of Physics Conference Series No. 97, Institute of Physics, Bristol and New York, 565 (1989).

5. J.G. Alessi, J.M. Brennan, and A. Kponou, "H^- Source and Low Energy Transport for an RFQ Preinjector", Rev. Sci. Instrum. **61**, 625 (1990).

BEAM PERFORMANCE AND MEASUREMENTS ON THE RFQ1 ACCELERATOR*

G.M. Arbique, B.G. Chidley, M.S. de Jong,
G.E. McMichael and J.Y. Sheikh
AECL Research, Chalk River Laboratories
Chalk River, Ontario, Canada K0J 1J0

Abstract

RFQ1 comprises a 50 keV dc injector and a cw radiofrequency quadrupole (RFQ) accelerator. The structure, designed to accelerate 75 mA of protons to an energy of 0.6 MeV, is a test bed for a wide range of high-power RFQ experiments. The injector has delivered 100% of the design current to the RFQ. The RFQ has accelerated up to 90% of design current at 1.5 Kilpatrick. A summary of beam performance is presented and measurements are reported on the emittance and beam energy.

Introduction

RFQ1[1] is an accelerator research project at Chalk River to develop high-current cw RFQ's suitable for industrial applications such as neutron sources and fissile fuel breeding. RFQ1 comprises a 50 keV dc injector and a cw radiofrequency quadrupole accelerator. The injector is designed to provide a matched 50 keV multi-beamlet proton beam, variable up to 90 mA, to the RFQ. The RFQ is a 100% duty factor radiofrequency quadrupole, designed to accelerate 75 mA of protons to a final energy of 600 keV.

Since commissioning, in mid-1988, the RFQ1 has accelerated up to 90% of design current. Attempts to achieve the design RFQ injection current with a three-aperture source were unsuccessful. A higher current four-aperture source has replaced the three-aperture source and a modification has been made to a beam-limiting aperture in the injector to provide the design injection current.

After a brief description of the accelerator facility, efforts to achieve the design beam performance are summarized and emittance and energy measurements of the RFQ output beam are reported.

Description

Figure 1 shows a drawing of the injector and RFQ subsystems.

The major components of the injector are an ion source and low-energy beam-transport system (LEBT). The ion source, a duoPIGatron,[2] provides high currents with modest proton fractions (30%-40%). The LEBT includes a 60° dipole magnet to separate the unwanted molecular species from the beam. Solenoids, after the source and at the RFQ entrance, match the ion source beam to the RFQ acceptance.

*This work was partially supported by Los Alamos National Laboratory under contract No. 9-X5D-7842D-1.

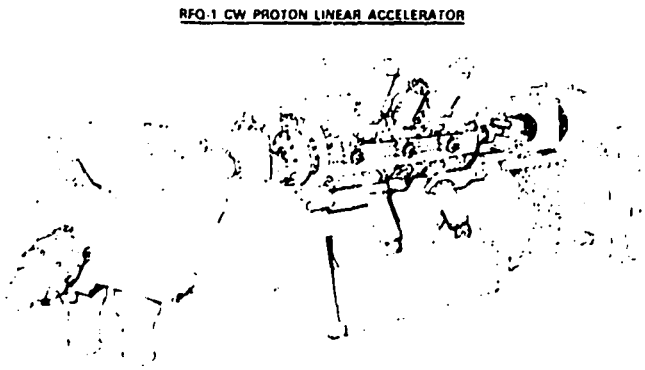

Fig. 1. RFQ1 Accelerator Components and Layout.

The accelerator is a cw four-vane loop-coupled RFQ, resonant at 267 MHz. It is constructed of mild steel, 1.5 m in length, with internal surfaces electroplated with about 100 microns of copper. Vane tips are of OFHC copper and are brazed to the vane bodies. The mean bore radius, R_0, is 4.13 mm. At the design peak electric fields of 1.5 Kilpatrick[3] (24.7 MV/m) the cavity power is 130 kW (90 kW/m) and heat fluxes on the tank walls and vane sides are ≈ 7 W/cm^2.

Beam Performance

The RFQ was designed using the code PARMTEQ.[4] At 1.5 Kilpatrick, a 90 mA 0.05 π-cm-mrad normalized rms emittance beam (design 3-beamlet injection) should have 85% transmission (75 mA output current). At injection currents less than 50 mA (i.e., lower space-charge) transmissions in excess of 90% are predicted.

Transmission levels measured during the initial low-current commissioning runs on RFQ1[5,6] were much lower than predicted (≈ 35% for three-beamlet injection). A deficiency in the RFQ entrance solenoid current, and misalignment of LEBT elements, prevented a good match to the RFQ acceptance. With improved focusing and better alignment, transmissions in excess of 90% were achieved for single beamlet injection, and cw currents of up to 15 mA were accelerated.

Attempts to achieve the design injection current with the three-aperture source were unsuccessful. Operating the source in the matched condition (minimum beam divergence, and hence minimum emittance), about 50 mA of proton beam could be transported to the RFQ, with 85% transmission through the accelerator. Figure 2 shows the injector and RFQ output currents (measured with non-intercepting beam current monitors) for a three-beamlet operation. An aperture on the plunging beam stop (PBS), at the exit of the

injector (past the injector beam current monitor), acts to limit the beam size. Since the beam is nearly parallel at this location, the aperture acts as an emittance scraper. Operated "over match", the source could produce proton current in excess of 90 mA, but the PBS aperture limited the current transported to the RFQ, and RFQ output current reached a plateau of about 55 mA.

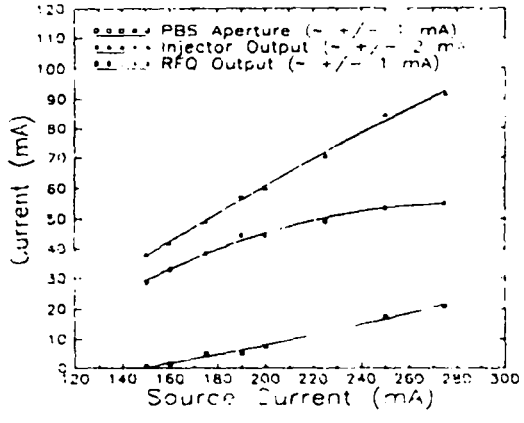

Fig. 2. Three-Beamlet Injection Transmission Currents.

Two main limitations prevented us from achieving the design injection current with the three-aperture source. It was originally planned to use an extraction column gap of 5 mm, but this gap is too small for reliable operation. At 6.4 mm, the smallest gap used to-date, the extraction column spark rate averages about one per hour, a rate considered maximum tolerable for reliable operation. The second limitation was in the plunging beam stop aperture, which intercepted about 15% of the proton current at match. Calculations with the code TRANSOPTR[7] indicate that it was undersized for a three-beamlet beam

To achieve higher current, a four-aperture extraction column was installed with an estimated emittance 15% larger than the three-beamlet source. To accommodate the larger beam, the PBS aperture diameter was increased by 25%. Four-beamlet operation results are preliminary, but, at match, about 70 mA of protons can be transported to the RFQ, with loss on the PBS of about 10%. Operating the source "over match", the design current of 90 mA can be exceeded. Under these conditions, up to 67 mA (90% design) was accelerated through the RFQ.

Figure 3 shows RFQ transmission for three-beamlet and four-beamlet operation as a function of relative matched source-current. Transmission is an optimum for matched source-current (i.e., minimum source emittance), and due to beam scraping on the PBS aperture, the transmission curves are fairly broad. The 85% peak transmission for three-beamlet injection is in good agreement with the PARMTEQ prediction. As expected, the transmission for four-beamlet injection (i.e., higher current, larger emittance) is decreased; the highest transmission measured to date is about 80%.

Figure 4 shows the RFQ transmission versus the vane-tip field for three-beamlet injection. At 1.2 Kilpatrick, transmission is down to 70% from 85% at the 1.5 Kilpatrick design field. PARMTEQ

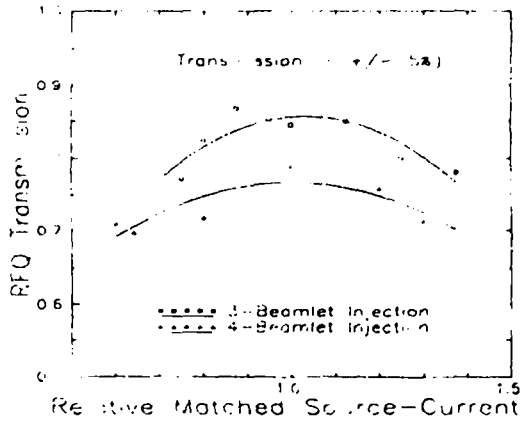

Fig 3 RFQ Multi-Beamlet Transmission.

predicts that transmission can be increased by operating at higher fields. However, an rf overheating problem at the ends of the vane-seal-gaskets prevents us from further increasing the fields at this time.

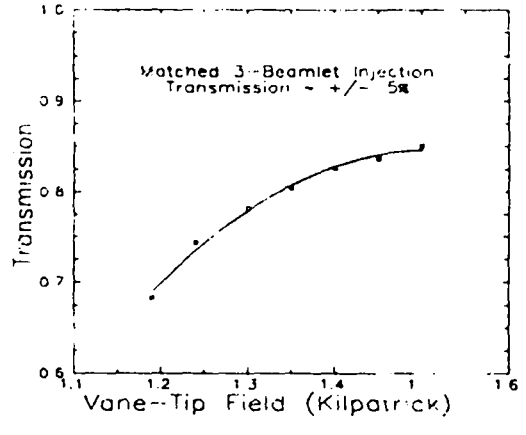

Fig. 4. RFQ Transmission vs. RF Vane-Tip Field.

RFQ Output Beam Measurements

Figure 5 shows the transverse phase-space of the RFQ output beam for matched three-beamlet injection, measured in the horizontal plane of the injector 60° bend magnet. The emittance is 0.04 π-cm-mrad, and the distribution shows no signs of the original three beamlets. We do not have a measurement of the injector output emittance, but, from ion source test stand measurements, and RETICON[8] measurements on the injector, we estimate our source emittance to be slightly less than 0.04 π-cm-mrad. The similarity of the source and RFQ output emittance does not necessarily indicate zero emittance growth in the LEBT and RFQ. We expect some growth in effective emittance in the LEBT, but the PBS aperture acts as a beam scraper, to limit the emittance of the injected beam.

Figure 6 shows the RFQ on-axis energy spectrum for matched three-beamlet injection at design and 1.2 Kilpatrick vane-tip fields. The measurements were made using a 45° bend, magnetic energy-

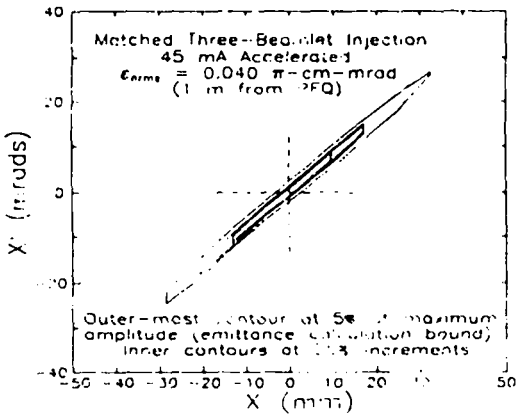

Fig. 5. RFQ Output Beam Transverse Phase Space for Matched Three-Beamlet Injection.

analysis system with an energy resolution of about 0.2%. With design field in the RFQ, the spectrum is characterized by a single peak at 600 keV with a width of about 50 keV. Lower energy peaks are present in the spectrum; however, they are reduced in intensity by over three orders of magnitude. At reduced fields, the transmission decreases and the energy spectrum shifts to lower energies. At 1.2 Kilpatrick, the main peak width at half-maximum is decreased by about 1/3 and the base is broadened on the low-energy side. Lower energy peaks in the spectrum are increased in magnitude; the most prominent at 360 keV has a height close to 70% of the 600 keV peak, although it is narrow, with a width of less than 10 keV.

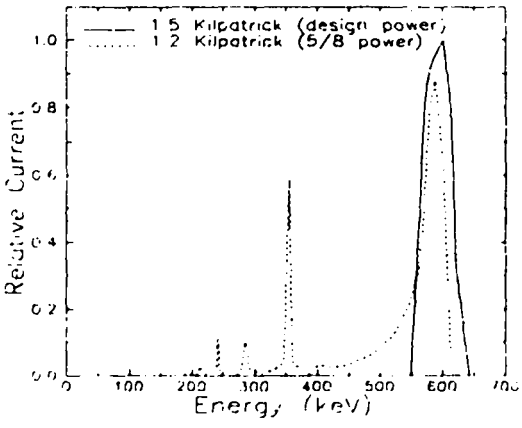

Fig. 6. RFQ Energy Spectrum.

Summary and Discussion

RFQ1 has accelerated up to 90% of the design current. A higher current four-beamlet source was installed on the injector when the design current could not be achieved with the three-aperture source. The four-beamlet emittance is larger than the design acceptance and beam transmission through the RFQ structure is about 5% less than the 85% target.

Emittance measurements have been made on the RFQ output beam for three-beamlet injection. The measured output emittance was in good agreement with the source emittance. Emittance growth in the system is limited by beam scraping on the PBS aperture.

The energy spectrum of the RFQ, at design power, is characterized by a single peak at 600 keV with a width of 50 keV. At low power the transmission decreases due to decreased longitudinal acceptance. The energy spectrum shifts to lower energy and lower energy peaks become more prominent.

Acknowledgements

The authors gratefully acknowledge the efforts of numerous persons involved in the RFQ1 project. In particular: L.F. Birney, A.D. Davidson, and M.H. Thrasher, who operate and maintain the accelerator and systems; A.B. Hood and B.H. Smith for electronics support; and W.L. Michel for work on the system diagnostics.

References

1. G.M. Arbique et al., "Commissioning of the RFQ1 Injector", Proc. IEEE Particle Accelerator Conference, Washington D.C., March 16-19, 1987.

2. M.R. Shubaly and M.S. de Jong, "High Current DC Ion Beams", IEEE Trans. Nucl. Sci. NS 30, No. 2, (1983).

3. W.D. Kilpatrick, "Criterion for Vacuum Sparking Designed to Include both RF and DC", Rev. Sci. Instr., Vol 28, No. 10, Oct 1957.

4. K.R. Crandall and T.P. Wagner, "PARMTEQ - A Beam Dynamics Code for the RFQ Linear Accelerator", Proc. Workshop on Linear Accelerator and Beam Optics Codes, San Diego, CA, Jan 19-21, 1988, AIP Conf. Proc. No. 177,22.

5. G.M. Arbique et al., "CW Operation and Initial Beam Experiments with the RFQ1 Accelerator", 1988 Linear Accelerator Conf. Proc., CEBAF, Newport News, Va, Oct 3-7, 1988.

6. G.E. McMichael et al.,"Exploring the Beam Parameter Space of a CW RFQ Proton Accelerator", Proc. 1989 Particle Accelerator Conf., Chicago, IL, Mar 20-23,1989.

7. E.A. Heighway and M.S. de Jong, "TRANSOPTR - A Beam Transport Design Code with Space Charge, Automated Internal Optimization and General Constraints", AECL-6975, Rev. A, June 1984, Atomic Energy of Canada Limited, Research Company, Chalk River, Ontario, K0J 1J0.

8. B.G. Chidley et al.,"RFQ1 Diagnostic Devices", these proceedings.

CESIUM EFFECT ON VOLUME H^- ION SOURCE

Yoshiharu Mori, Toshihisa Okuyama, Akira Takagi, Dick Yuan*
National Laboratory for High Energy Physics, Oho 1-1, Tsukuba,Ibaraki 305, JAPAN
*TRIUMF,4004 Wesbrook Mall,Vancouver, CANADA

[abstract]

Observation of the H^- beam intensity enhancement by introducing a very small amount of cesium vapor in the volume H^- ion source developed at KEK is shown in detail. The extracted H^- beam current of 20mA was obtained in the cesium-mode operation and the measured 90% normalized beam emittance was about 1πmm.mrad for 12 mA beam. It was found that the workfunction of the cesium covered surface of the beam extracting plasma electrode was important in increasing the H^- beam intensity.

Introduction

The volume H^- ion source has been devloped at KEK.[1] The surface-plasma type of H^- ion source, in which the H^- ions are generated on the cesiated low workfunction molybdenum surface placed in the hydrogen plasma, is being used in the 12 GeV proton synchrotron.[2] This ion source produces about 30mA H^- beam with a 90% normalized beam emittance(phase-space area x b x g) of 1.5πmm.mrad in pulse-mode operation. This ion source is rather delicate to keep its maximum intensity during the operation because the H^- beam intensity is very sensitive to the cesium coating on the molybdenum surface. If a small cesium consuming or cesium-free H^- ion source was realized, it would be very useful for the high intensity and high duty accelerators.

One of the potential candidates of such an ion source is a volume-production type of H^- ion source and at KEK, the pulse operated volume H^- ion source has been developed since 1988. It is aiming for a pulsed H^- beam of more than 20mA with a 90% normalized emittance of less than 1 π mm.mrad. One of the difficulties in operation of the volume H^- ion source is its poor efficiency. A relatively large arc current is required to obtain an intense beam current of more than 10mA. Moreover, the total electron drain current from the ion source reaches 100 times of that of the extracted H^- beam.

Kao Leung et al have recently found that the extracted H^- beam current could be increased by injecting cesium vapor into the ion source plasma chamber.[3] We have also observed this cesium effect in our volume H^- ion source. The extracted H^- ion beam current was increased more than four times of that before injecting cesium vapor and the extracted H^- ion current reached a maximum of 20 mA. The cesium consumption rate was surprisingly small compared with the surface H^- ion source and this may hence reduce the difficulties described above in operation of the ion source with cesium vapor.

Cesium-mode operation

A schematic diagram of the present test apparatus of the KEK volume H^- ion source is shown in Fig. 1. The ion source consists of a cylindrical plasma chamber which is surrounded by SmCo permanent magnets and a single hot filament cathode. A pair of SmCo permanent magnets, which make a dipole magnetic field, a so called virtual magnetic filter, are placed at the the outside of the plasma chamber and close to the plasma electrode. Through the experiment, a single hole of 7.5mm in diameter was used as the anode aperture. The anode material is molybdenum.

A helical coil shaped LaB_6 filament is used as a hot cathode and it is attached on the molybdenum supporting rods which are cooled by water. The operating temperature of the filament is about 1400°C and the lifetime is more than several hundred hours.

Cesium vapor is injected into the plasma chamber from the outside reservoir through a heated feedthrough. The high temperature valve, which can be closed to stop the cesium feeding immediately after the H^- ion beam current is increased, is located between the ion source and the reservoir. The reservoir temperature is normally 200-250°C.

At the end plate of the plasma chamber, a small glass window is mounted. By injecting an Ar laser beam(l=514.5nm) through this window, the workfunction changes of the anode electrode

can be estimated by measuring the photo-emission electron current from the anode electrode.

The H beam current is measured by a Faraday cup which is placed about 1 meter away from the anode electrode. Beam emittance can be also measured with an electrostatic deflection type of emittance monitor, which is located at the front of the Faraday cup.

Cesium effect

The extracted H^- beam intensity is dramatically changed by injecting cesium vapor into the plasma chamber. Figures 2-a and 2-b show the typical H^- beam waveforms before and after the cesium vapor is injected, respectively. In these figures, the total drain currents(H^- + electron) from the ion source are also shown. The H^- beam current is increased from 3mA to 12mA and on the other hand, the total drain current is decreased from 350mA to 100 mA. By optimizing the various parameters of the ion source after the cesium vapor is injected, the H^- ion beam current was increased to 20mA as shown in Fig. 3.

The cesium consumption rate was very small in operating the ion source. For example, once the beam intensity was increased after opening the valve for the cesium feed line, it kept almost constant for several ten of hours even when the valve was closed. This is a quite different situation from that of the ordinary surface type of H^- ion source and it helps a lot to eliminate sparkings in the extraction region during long period operation.

The beam emittance was also measured before and after the cesium injection. Figure 4 shows the typical value of the beam emittance after injecting the cesium vapor at beam intensity of 12mA.

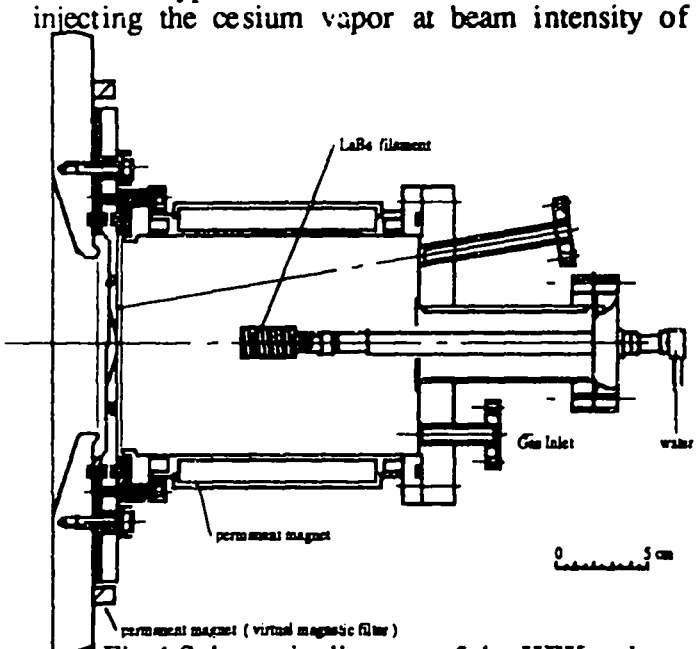

Fig. 1 Schematic diagram of the KEK volume H^- ion source.

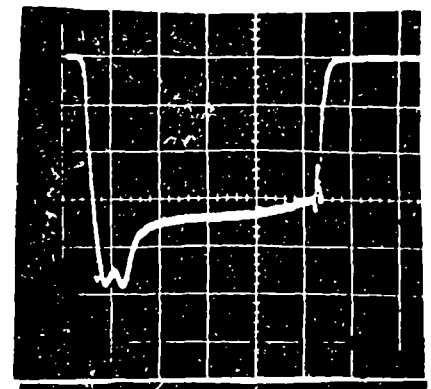

Fig.2-a H^- beam waveform before injecting cesium vapor. Vertical axis: 1 mA/div. Horizontal axis: 0.1 msec/div.

Fig.3-b H^- beam waveform after injecting cesium vapor. Vertical axis: 2 mA/div. Horizontal axis: 0.1 msec/div.

We have observed a dramatic beam current increase in the H^- ion source at the cesium-mode operation. There have been proposed several explanations of this effect. Among them, the following two processes concerning the surface condition of the ion source wall which is covered by cesium atoms are considered as the most likely candidates to account for the effect. One is that numbers of vibrational excited hydrogen molecules, which are considered to play an important role in the volume-production process of H^- ions, are produced from H_2^+ and/or H_3^+ ions by picking up electrons from the cesiated low workfunction surface of the ion source inner wall. [4] The other is that H^- ions can be formed directly on the cesiated surface from thermal hydrogen atoms.[5] Although this reaction probability is predicted to be very small,[6] the density of the atomic hydrogen contained in the ion source plasma is very large($n>10^{15}$ atoms/cm^2) and this may hence lead an enhancement of H^- ions. In both processes, the workfunction of the inner surface of the ion source is very important and it has to be reduced by injecting the cesium vapor into the ion source.

In order to check this, we have measured workfunction changes of the plasma electrode before and after the cesium injection. The workfunction change was measured by detecting the photo-emission electron current which is generated by a single mode Ar ion laser beam(l= 514.5nm).[7] While we made the measurements

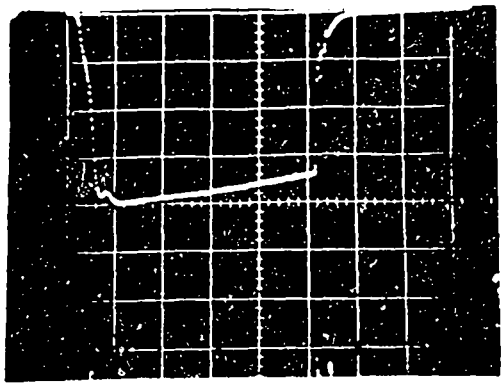

Fig.3 Optimized H^- ion beam current. Vertical axis: 5 mA/div. Horizontal axis: 0.1 msec/div.

several times, the results were always very reproducible. In Fig.5, photo-emission electron current changes are plotted as a function of time elasped after the valve of the cesium feedline was opened. Also we found that the workfunction kept decreasing for long time during the operation of the ion source even after the valve of the cesium feedline was closed. This may relate to the fact that the cesium consumption rate is very small.

In order to examine which surface, the plasma electrode surface or other wall surface, is most effective in generating H^- ions when the cesium vapor is injected, we cleaned the plasma electrode surface only by Ar ion sputtering. Before the Ar ion sputter cleaning, the H^- ion current was 12 mA, however, it decreased to about 3mA just as before the cesium injection and the photo-emission electron current was also disappeared after one hour cleaning. Thus the plasma electrode surface seems to affect very much on the enhancement of the H^- ion production in the cesium-mode operation. It is interesting that only the plasma electrode surface seemed to be important to enhance the H^- beam intensity.

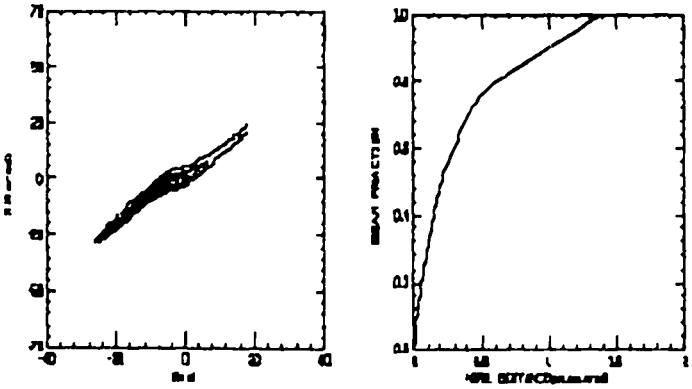

Fig.4 Emittance shape and normalized emittance vs percentage of total H^- ion beam after injecting cesium vapor. The total H^- ion beam current was 12 mA.

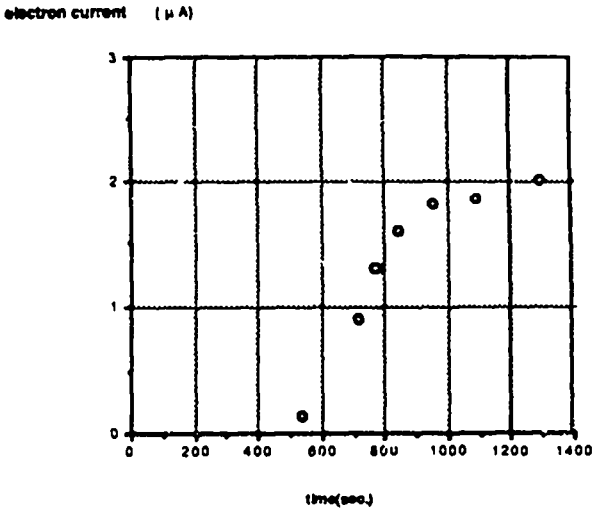

Fig.5 Photo-emission electron current changes as a function of time elapsed after the valve of the cesium feedline was opened.

Conclusion

The characteristics of the volume H^- ion source changed dramatically by injecting the cesium vapor into the ion source. More than four times more H^- ion beam current was extracted after the cesium injection and, nevertheless, the cesium consumption rate was very small. It was also observed that the surface condition of the plasma electrode played an important role in the cesium-mode operation by the workfunction measurement with a photo-emission electron technique, .

The authors appreciate Profs. H. Sugawara, Y. Kimura, S. Fukumoto and M. Kihara for their continuous encouragement. They are also indebted to Mr. K. Ikegami for his technical support.

(REFERENCES)

(1)Y.Mori, Y.Okuyama,A.Takagi,D.Yuan; submitted to Nucl. Instr. Meth.,
(2)Y.Mori,A.Takagi,K.Ikegami,S.Fukumoto; 4th Int. Symp. on Production of Neutralization of Negative Ions and Beams,BNL ,1986, AIP conf. series,page378.
(3)K.N.Leung et al;Rev.Sci.Instr.,60(1989)531.
(4)J.R.Hiskes; to be published in Proc. of 4th Int. Symp. on Production and Neutralization of Negative Ions and Beams,Brookhaven,1989.
(5)M. Seidl; ibid.
(6)W.G.Graham; Phys. Let., 73A(1979)186.
(7)H.Yamaoka et al.,Nucl.Instr.Meth.,B36, 227

DECELERATION OF ANTIPROTONS WITH A RFQ

A. Schempp, H. Deitinghoff, M. de Saint Simon[x], C. Thibault[x], F. Botlo-Pilat[xx]
Inst. für Angewandte Physik, Univ. Frankfurt, D-6000, FRG
[x]CSNSM, F-91406 Orsay, France,
[xx]CERN, CH-1211, Geneva, Switzerland and CSNSM, F91406 Orsay, France

Abstract

A 4-Rod-RFQ is being built for the deceleration of antiprotons which will be extracted from LEAR at 2.0 MeV and injected at 0.2 MeV into the rf-mass spectrometer built by CSNSM, Orsay for the high precision mass measurement of protons and antiprotons (PS189). The design of the RFQ system, which should improve the counting rate by a factor of up to 10^3 and the status of the project will be reported.

Introduction

The CSNSM Orsay experiment: "Antiproton - Proton mass comparison with a radio - frequency mass-spectrometer "(PS189)[1,2] aims at the reduction of the present upper limit on a hypothetical CPT theorem violation in baryon-antibaryon pairs. The experimental set-up is a specially designed radiofrequency mass spectrometer of L.G. Smith type. It has been installed at CERN at the LEAR (low energy antiproton ring) experimental area in order to make a comparison of the charge to mass ratio of an antiproton and a proton by measuring the cyclotron frequencies of antiprotons and H^- ions rotating in the same very homogenous magnetic field. The physical parameters are fitted to reach a mass resolving power of 5×10^5, enabling a mass comparison accuracy of 5×10^{-9}.

Several proposals for rf - deceleration to provide 0.2 MeV Antiprotons for the spectrometer e.g. with help of a small synchrotron, a cyclotron or a RFQ were not realized because of complexity and the costs involved[3,4,5], but the RFQ system proposed was the least complex one.

Deceleration is an new application for RFQs, which has been proposed for highly stripped heavy ions and for antiprotons, which have been stored and cooled in a synchrotron ring[3,6]. In this context LEAR is a bulky ion source.

RFQs are unique for low energy deceleration because of the strong electric focusing with rf quadrupole fields[7,8]. The low final energy in case of a decelerator at relatively high operating frequency is very important, because the structure is compact and the $\bar{p}$ are slowed down efficiently and with little emittance growth.

[x]now at SSC, Waxahachie, Tx

Design considerations

In a new effort work was concentrated on the reduction of costs e.g. by a pulsed mode RFQ deceleration with a less complex RFQ structure and simpler bunching schemes. Other important points were the change of the data taking mode at the experiment and success of the LEAR team in decelerating the $\bar{p}$ beam from 6.0 to 2.0 MeV with an ejection lasting 0.5 msec.

A layout of experiment PS189 is shown in Fig.1. The acceptance of the spectrometer is extremly low: ε_H = 1π mm mrad, ε_V = 2π mm mrad (not normalized), $\Delta T/T$ = ± 6 eV and the kinetic energy of the particle is not allowed to exceed 0.2 MeV.

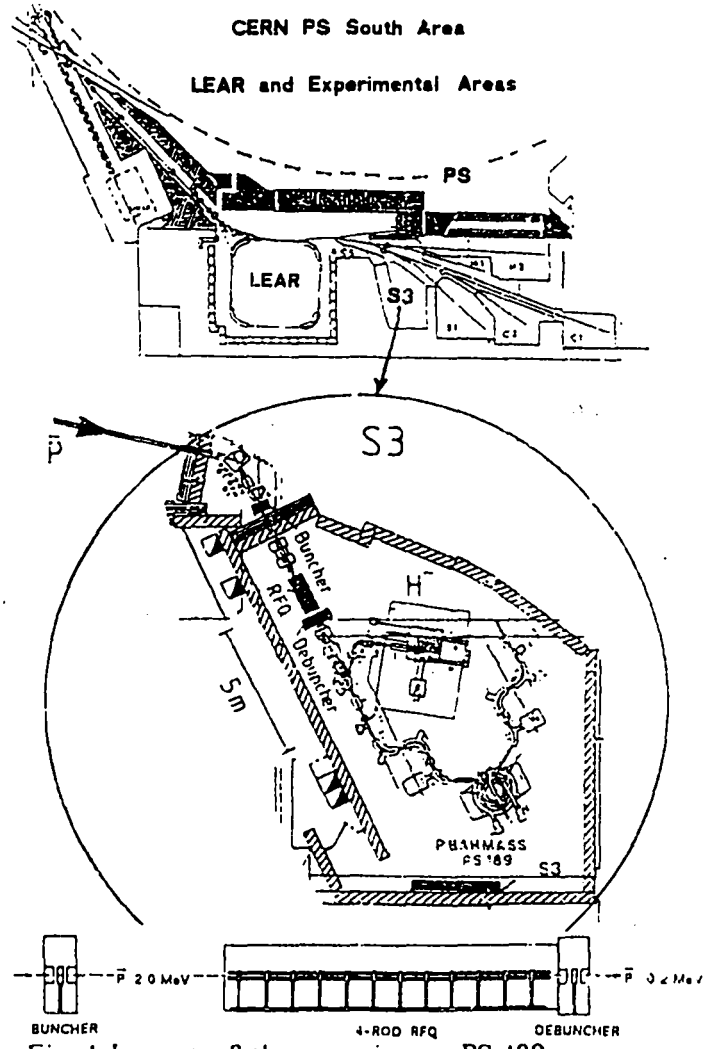

Fig. 1 Layout of the experiment PS 189

The deceleration with the RFQ has to be optimized for the transmission to the spectrometer. The overall transmission is planned to be 10^{-5} to gain at least 10^2 in comparison with an energy degrading process using a foil coupled with a bunching-debunching technique.

A RFQ decelerating system has to match the spectrometer and has to be compact and relatively simple. A short RFQ requires a high electrode voltage and therefore a high rf power, which is no problem for the CERN Linac frequency of 202.5 MHz, because a Linac transmitter will be used.

The spectrometer accepts only the core of the phase space of the beam. That means that usual RFQ design procedures aiming at high transmission have to be revised[9]. Adiabatic bunching for a decelerating RFQ would require a RFQ of appr. 20m length and would not increase the transmission of the system.

The output emittance is sensitive to the electrode voltage, the buncher voltage and possible energy variations of the beam. It will be fine tuned with the help of a debuncher cavity attached directly to the low energy end of the RFQ as shown in fig. 2. This additional degree of freedom allows both a precise orientation of the output ellipse and some energy variation.

Simplicity of the system restricts the length of the drift to about 3.5m because a buncher infront of the last bending magnet would introduce chromatic errors. The same argument works against a scheme with a prebunching at a frequency of 202.5 MHz in LEAR[10]. The gain in transmission does not pay off because the phase space dilution.

RFQ Design

The 4-Rod RFQ resonator design is based on the structure operated successfully at DESY[11,12]. It consists of an array of flat stems on a common base plate supporting the four electrodes which have a periodically changing diameter. Fig. 2 shows a scheme of the 4-Rod RFQ structure. Changes have been made for the improvement of alignment, vacuum, and rf-efficiency.

The resonant 4-Rod insert will be cooled efficiently by water tubes in the base plate. The structure has been operated already with much higher duty cycles e.g. rf-losses up to 20kW/m and electrode voltages up to 150 kV. These values are clearly higher than the design values for the decelerator which are summarized in Table I.

The beam dynamics design of the RFQ which determines the variation of modulation, aperture and cell length along the structure is characterized in fig. 3.

The bunchers will be spiral loaded cavities which are efficient and compact. They have been developed for application in post-accelerators[13] and have been built e.g. for GSI and DESY for use as linac bunchers[14].

Beam Transport

The small acceptance of the PS189 spectrometer requires a careful design of the antiproton beam transport in order to optimize the particle transmission through the system. The high energy beam line with a length of 30m transports the $\bar{p}$ beam from LEAR to the entrance of the RFQ. Practical aspects like

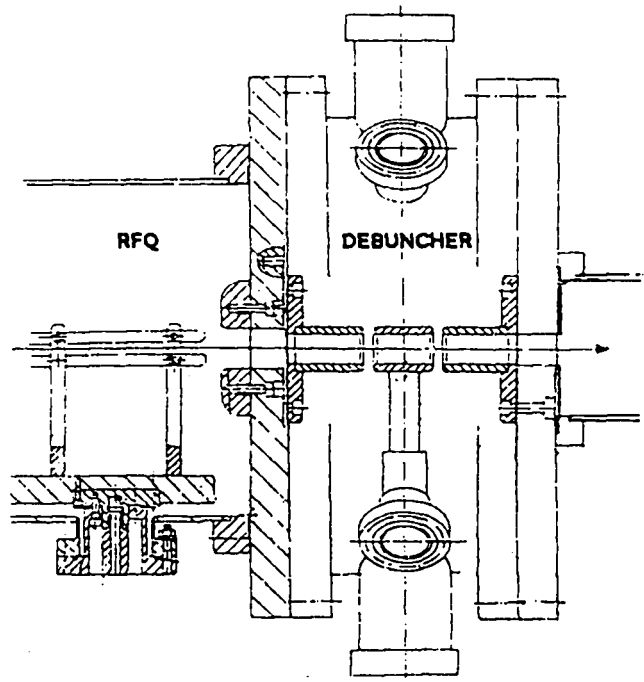

Fig. 2 Scheme of the low energy end of the RFQ

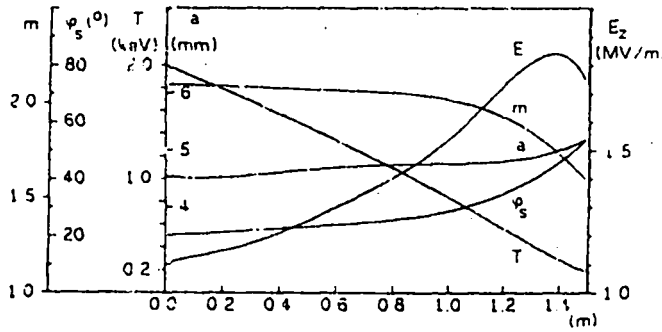

Fig. 3 Electrode design of the decelerating RFQ

Table I Parameters of the decelerating RFQ

Frequency	202.5 MHz.	Electrode voltage	111 kV
Input energy	2.0MeV.	Output energy	0.2MeV
Length	1.49 m.	number of cells	46
Phase	-160 - -126°.	Aperture	4.5-5.25 mm
Modulation	2.1-1.6.	Maximum field	35 MV/m
Impedance R_p	60kΩ.	Rf-power	210 kW
normalized transverse acceptance			5.0 πmmmrad

sharing the first part of the beam line with other experiments restrict changes to the part after the bending magnet. A design for a line able to match different RFQ input conditions is shown in Fig. 4.

The low energy beam line is about four meters long. The beam from the RFQ-Debuncher system has a large divergence which can be matched to the spectrometer with a set of two quadrupoles close to the RFQ and a central triplet . The design of the low energy beam line is more difficult because of the transverse (absolute) emittance increase of about a factor three caused by deceleration. This corresponds to a 10% increase in normalized emittance only. the final energy spread being rougly 4% including the debuncher.
Fig. 5 shows results of simulations with PARMTEQ for the deceleration of a $\bar{p}$ beam with LEAR parameters.

The present design of the lines is consistent with an estimated transmission of 1×10^{-5} for the overall system. Final optimisation of the transport beam lines and the whole system is in progress[15].

Status

The preparation of the experiment is now near completion. The RFQ delivery should take place by the end of the year in order to test the equipment during next spring and to run data taking in 1991 and 1992

Acknowledgements

We want to thank H. Bernas, P Lefevre, H. Haseroth and M. Weiss for encouraging support and useful discussions.

References

1. C. Thibault et al., Nucl. Phys. B8 (1989)454
2. M. de SaintSimon et al., LEAR-4. Villars (1987)633
3. P. Lefevre, D. Möhl, Cern PS Rep. 1984
4. J. Billen et al., LEAR-3. Ed. Frontieres (1985) 107
5. C. Biscari, F. Iazzourne, LEAR-3, Ed. Frontieres(1985)
6. A.Schempp et al., Linac 84. GSI 84-11 (1984)100
7. I.M. Kapchinskij, V.A. Teplyakov, Prib. Tekh. Eksp. (1970) 17,19
8. R.H.Stokes, T.P.Wangler, Rev.Part.Sci. 38 (1988) 97
9. A. Schempp, EPAC 88, World. Sci. (1989)464
10. D. Möhl, CERN/PS 85-38
11. A. Schempp et al., PAC'87, IEEE 87CH2387(1987)267
12. A.Schempp et al., Linac88, Cebaf 89001(1989)73
13. E.Jaeschke, Linac 84, GSI Rep. 84-11 (1984) 24
14. J. Häuser et al., EPAC'88, World Sci.(1889)1140
15. A.Coc et al., LEAP 90, Stockholm, July 1990

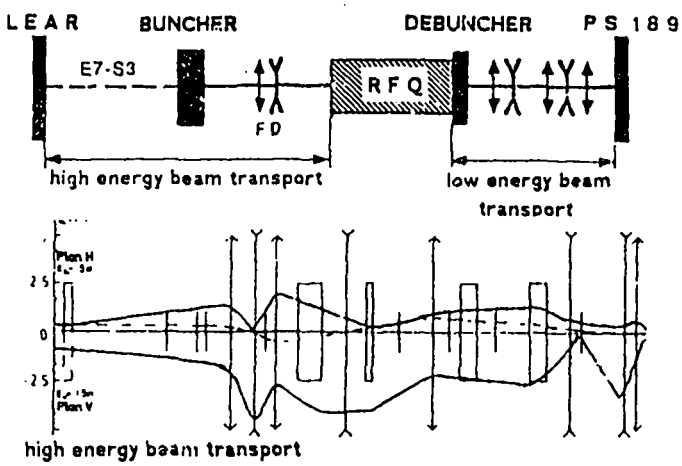

Fig. 4 HEBT for the PS189 experiment

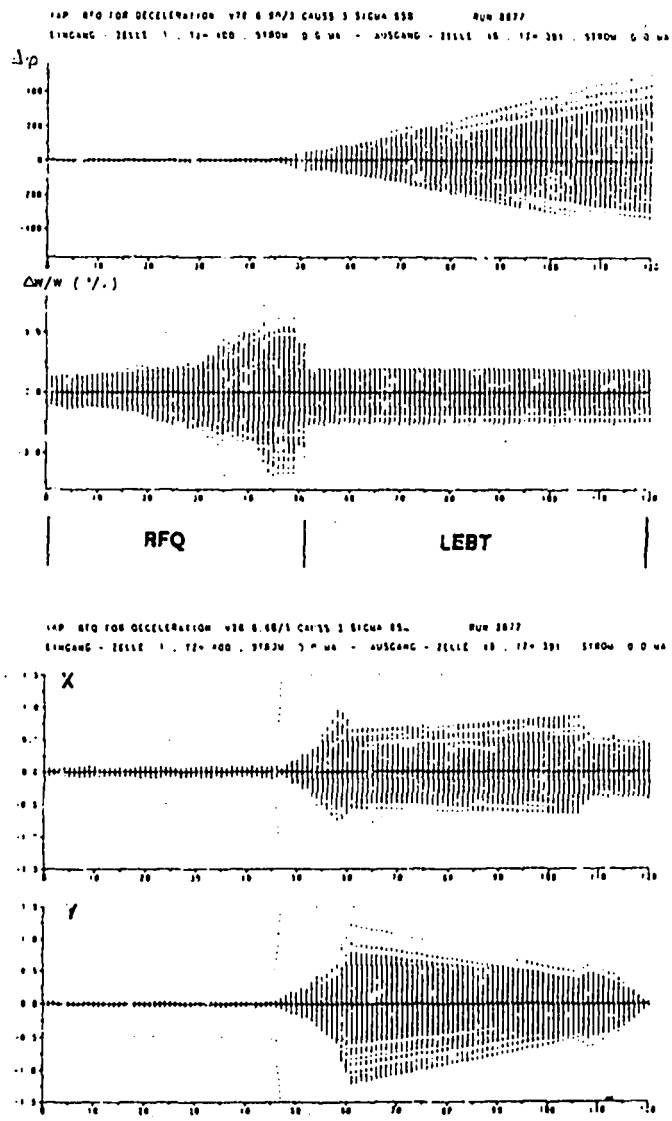

Fig. 5 Example of Parmteq simultation for RFQ and LEBT

PERFORMANCE OF THE CERN HIGH-INTENSITY RFQ

E. Tanke, M. Vretenar and M. Weiss
PS Division, CERN, CH-1211 Geneva 23, Switzerland

Abstract

The CERN RFQ2, designed to become the injector of the CERN Linac 2, has delivered its nominal proton current of 200 mA at 750 keV from the start of the beam tests. However, prior to its installation at Linac 2, extensive measurements on a test stand have to be carried out to assess the quality of the beam and the overall reliability of the accelerator.

Unfortunately, the measurements have been perturbed owing to accidental oil pollution of the RFQ2. The removal of the cracked oil from the vane tips, the reconditioning of the RFQ2, and the reduced measurement programme are reported.

Introduction

The RFQ2, after its very successful start, has been operating reliably on a test stand. The nominal proton beam of 200 mA at 750 keV could be easily obtained. By raising the vane voltage by about 10% and by increasing the input current, output intensities of 240 mA were registered. For the sake of completeness, the RFQ2 parameters are presented in Table I.

TABLE I: Main RFQ2 design parameters

RF frequency	f_0	202.56 MHz
Input energy	W_{in}	90 keV
Output energy	W_{out}	750 keV
Output current	I_{out}	200 mA
Trapping efficiency	η	~ 90%
Vane voltage	V_0	178 kV
Final synchronous phase	φ_s	-35°
Modulation factor	m_{max}	1.62
Mean aperture radius	r_0	7.87 mm
Cavity length	L_{RFQ}	178.5 cm
Vane length	l_v	175.2 cm
Cavity diameter	D	35.4 cm

When the system on the test stand was put into operation after a shutdown, breakdowns started to occur in the RFQ2 already at very low RF levels, and it was impossible to reach the nominal vane voltage. Inspecting various elements of the vacuum system, it was realized that a missing interlock of the vacuum valve between the turbomolecular pump and the RFQ2 could have caused, by accident, an oil pollution of the latter. We then tried to recondition the cavity by slowly increasing the RF level, thus progressively eliminating the oil from the vane tips. This allowed us to reach finally, after several days and at the price of many breakdowns, the nominal operating level. However, the RFQ2 was not very stable and, after a few days of interruption of the tests, the situation degraded again. It was then decided to open the RFQ2 and, once the end covers were removed, the typical damage to the vane tips (presence of cracked oil), caused by the breakdowns, together with the marks of excessive heating on the vanes above the turbomolecular pump, could be seen. The RFQ2 was then dismantled from its test stand and brought to the workshop for cleaning. At the same time, all elements of the beam line were cleaned, either *in situ* or elsewhere. When the experimental set-up was reinstalled, careful reconditioning of the RFQ2 permitted us again to reach and go above the nominal RF level. Similar output beam intensities and emittances to those before the accident were obtained.

The experience gained with the cleaning of the RFQ2 had to be paid for by a delay in beam measurements: only a part of our measurement programme has been carried out so far.

Cleaning of the RFQ2

To clean such a complicated structure as the RFQ2, containing a lot of weldings and brazings, is far from obvious. The oil deposited on various surfaces could have been removed, but the cracked oil on the vane tips was the real problem. It rendered any normal operation impossible, in particular in view of the high fields which are required for the RFQ2 (2.5 × Kilpatrick limit). To remove the cracked oil, chemical or mechanical cleaning has to be employed. Chemical cleaning requires subsequent rinsing with distilled water, which is incompatible with the tank being made of mild steel. Therefore, mechanical cleaning making use of inorganic abrasive paper with aluminium-oxyde grains deposited on a substrate was used. The danger is that, after the cleaning, the grains remain encrusted in the cleaned surface. Several papers were tried out and it was found that grains of at least 5 μm were necessary to remove the cracked oil. Before starting the cleaning, a sample of the vane material (Cu–Cr alloy) was gently cleaned with such a paper, rinsed with alcohol, and then analysed under a microscope: no encrusted grains were seen on the sample.

A strip of the abrasive paper was fixed on two Plexiglas rods, which permitted progressive cleaning of the vane tips, see Fig. 1. The progress of the cleaning was continually checked by an endoscope. A few hours were necessary to clean a vane. After all the vane tips were cleaned, the RFQ2 was placed in vertical position and rinsed with alcohol and freon, and then left to dry.

RF measurements and reconditioning

Once the experimental set-up had been put together again, the usual series of tests were performed. In particular, the RF field in the RFQ2 was carefully checked. The measurement showed a degradation in the field symmetry of the quadrants, which was ±1% previously and now raised to ±4%, owing to a decrease of the field in the quadrant where the turbo pump, responsible for the contamination, was mounted. The probable explanation for this asymmetry is the excessive heating in that quadrant due to the many breakdowns occurring exactly in front of the pump hole (where most of the oil was concentrated) and which could have caused mechanical shocks to the vanes. This asymmetry will eventually be corrected by installing a new fixed tuner. However, the asymmetry

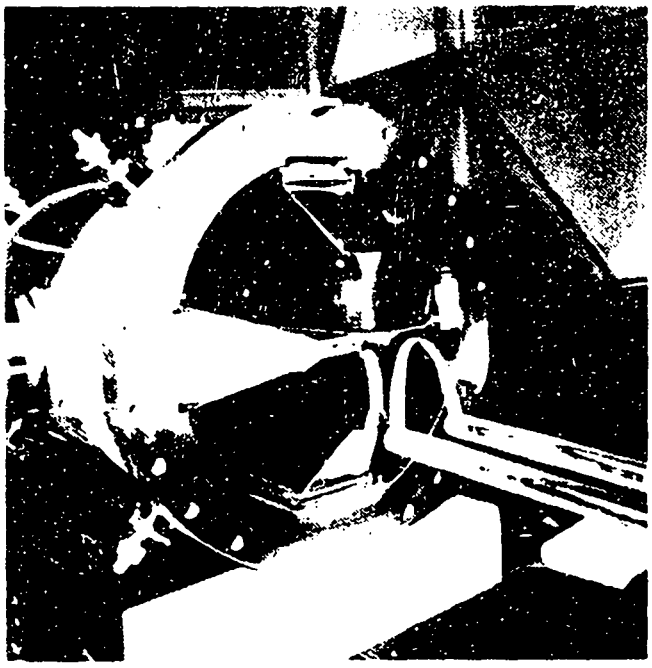

Figure 1: Mechanical cleaning of the vane tips

was present during the beam measurements reported in this paper.

Pumping has been applied for about a week before switching on the RF power. Careful and slow RF conditioning, which lasted also about a week (initially the RFQ2 was conditioned in about a day) brought us, finally, to the situation we had before the accident, with the nominal RF level kept stable. Note that the vanes of the RFQ2 had a gold deposit of about 1 μm, as a protection against oxidation during tuning and adjustment of the cavity, which was removed from the vane tips during the mechanical cleaning; nevertheless, no difference in voltage holding could be detected.

Beam measurements

Our experimental set-up is shown schematically in Fig. 2 When starting to do beam measurements, several tests, already performed before the accident, were repeated.

The duoplasmatron ion source was adjusted to yield a proton beam of about 220 mA. The matching solenoid

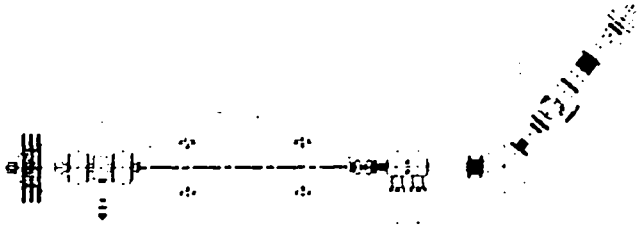

Figure 2: Experimental set-up of the RFQ2: (1) solenoid lenses, (2) emittance measurement device, (3) bending magnet and (4) detector grids (SEM grids)

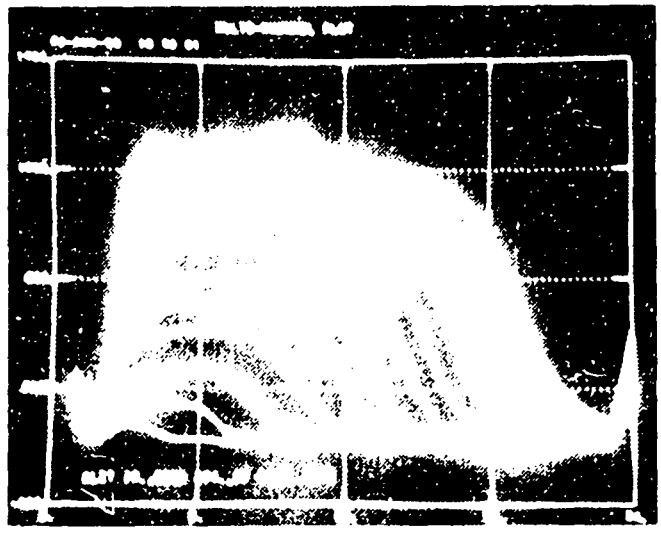

Figure 3: Energy spreads of the RFQ2 beam for different vane voltages. (Horiz. scale: 39 keV/div.)

lenses were given the same values as before. With these settings, the following results have been obtained:

Output beam intensity: for the nominal vane voltage, intensities of about 190 mA were measured The nominal 200 mA beam could be obtained with a 5% higher vane voltage. Increasing the vane voltage even more, and readjusting the ion source, resulted in an output beam of 215 mA. So far, we have not tried to go to a higher intensity.

Energy spread: about ±70 keV was measured, for an output beam of 200 mA and a 5% higher vane voltage (note that the space charge increases the energy spread by a factor of about 3 between the RFQ2 and the measurement device). In Fig. 3 one sees the energy spreads for different vane voltages, ranging from 70 to 105% of the nominal value.There are practically no particles in the right energy range for voltages below 70%. The areas under the various curves are proportional to the accelerated beam.

Output beam emittances: the measured output emittances are shown in Figs. 4 and 5. The normalized r.m.s. value, $\varepsilon_{rms,n}$, is about 0.6π mm·mrad. For comparison, we also show emittances measured before the accident, see Figs. 6 and 7. Their $\varepsilon_{rms,n}$ value is about 0.5π mm·mrad. The corresponding input emittance values are $\varepsilon_{rms,n} \approx 0.4\pi$ mm·mrad.

It seems that the impaired field symmetry slightly reduces the output beam and increases the output emittances.

Discussion and conclusion

The oil pollution of the RFQ2 prevented us from following up our previously established measurement plan. Intensity limits, bunch measurements, and the detailed analysis of emittance and energy spread still remain to be done. However, prior to this, we intend to re-establish the field symmetry in the quadrants, if possible at the previous value of ±1%.

The experience showing that cracked oil can be mechanically removed, without damaging the vane tips and without impairing the voltage holding, can be considered as a positive result.

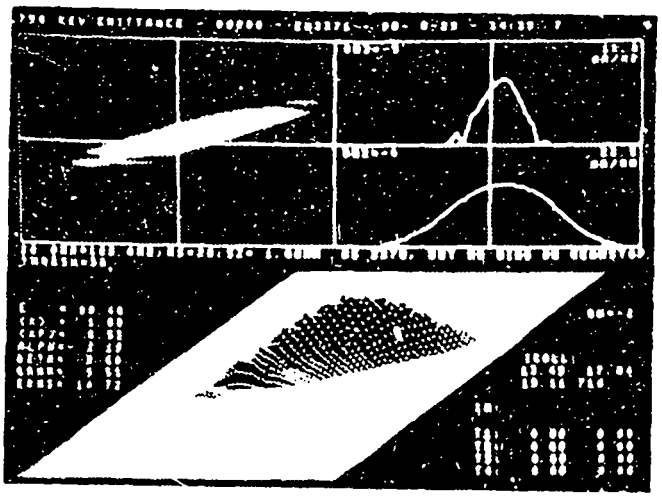

Figure 4: Horizontal output beam emittance

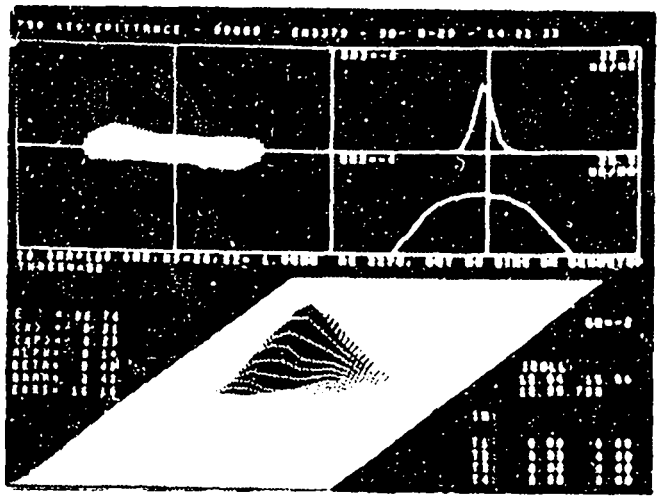

Figure 5: Vertical output beam emittance

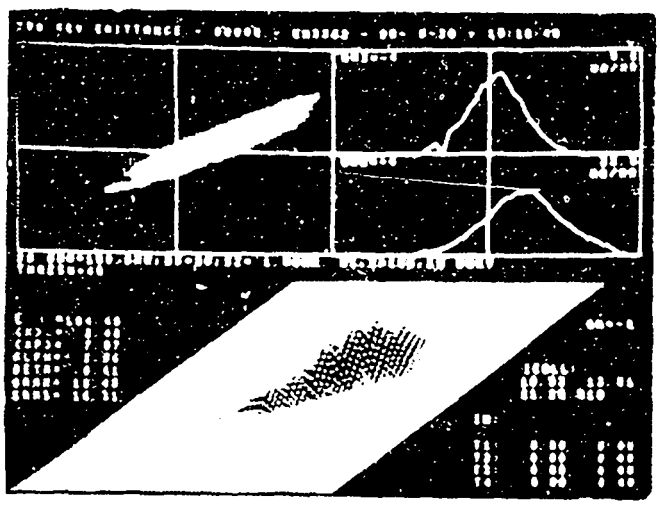

Figure 6: Horizontal output beam emittance, before accident

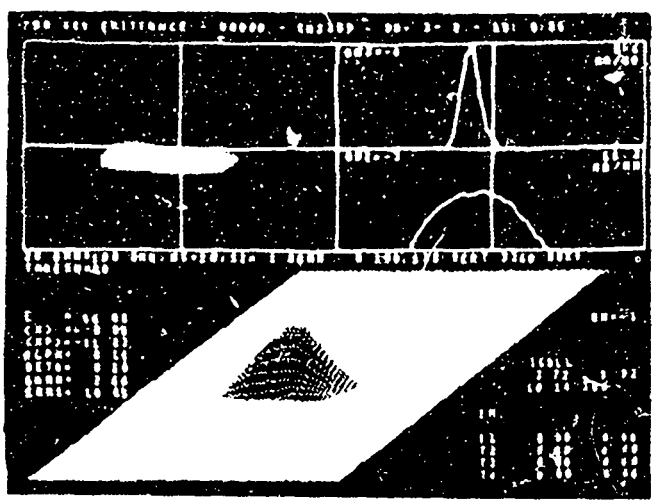

Figure 7: Vertical output beam emittance, before accident

Acknowledgements

C. Biscari, now with INFN Frascati and A. Lombardi, now with INFN Legnaro, have participated in the design study of the RFQ2. The beam measurements profited from the collaboration of J.L. Vallet and G. Amendola. G. Henchoz and J.P. Romero helped in cleaning the RFQ2 after the pollution. E. Boltezar has been asked for advice in several 'critical' situations. To all of them go our thanks.

Reference

1. J.L. Vallet, M. Vretenar and M. Weiss, Field adjustment, tuning, and beam analysis of the high intensity CERN RFQ, Proc. European Particle Accelerator Conf., EPAC90, Nice (France), 12-16 June 1990, to be published.

PRELIMINARY DESIGNS OF 1.54GeV DAMPING RING AND BUNCH COMPRESSOR FOR THE JLC

J.Urakawa,K.Egawa,T.Higo,T.Ieiri,K.Kanazawa,M.Kikuchi,
H.Kitamura,K.Kubo,S.Kuroda,Y.Mizumachi,H.Nakayama,K.Oide,
Y.Sakamoto,S.Sakanaka,M.Takao,S.Takeda,Y.Takeuchi,M.Tejima,
N.Yamamoto,S.Yamamoto,K.Yokoya and M.Yoshioka
KEK, National Laboratory for High Energy Physics
Oho 1-1, Tsukuba-shi, Ibaraki-ken 305, Japan

ABSTRACT

We describe preliminary designs of 1.54GeV damping ring and bunch compressor for the JLC(Japan Linear Collider). The design of the damping ring is changed into feasible one by introducing a pre-damping ring for the positron beam. Parameters of the bunch compressor are adapted to parameters of the damping ring and the JLC requirements. The normalized emittances of the extracted beam from the pre-damping ring are $\gamma\epsilon_x = 220\mu$radm horizontally and $\gamma\epsilon_y = 7.5\mu$radm vertically. The damping time of the pre-damping ring is τ =3.16msec. The main-damping ring has normalized emittance of $\gamma\epsilon_x = 2.9\mu$radm and $\gamma\epsilon_y = 28.9$nradm. The damping time is τ =6.23msec. The main parameters of the compressor as well as results of some simulations are presented. It produces bunch trains with a bunch length of the order of 60μm and a momentum spread of $\Delta p/p \sim 2\%$.

Introduction

In order to realize the JLC project, we have been discussing for several years on possible parameter sets of the JLC. We were requested to increase the normalized emittance of the injected positron beam into the DR(damping ring) about six months ago. So we designed a pre-damping ring(PDR) for the JLC because the normalized emittance more than 3.0×10^{-3}*radm* gives very severe requirements for the aperture, the jitter tolerance of the extraction kickers and the damping time. Fig.1 shows the layout of the JLC according to the parameter set so far obtained.[1,2,3]

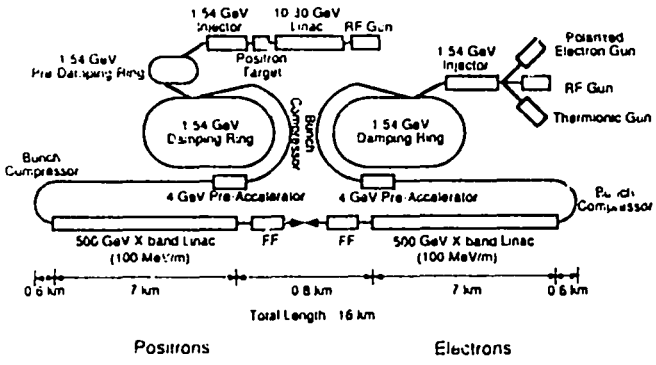

Fig.1 Layout of the JLC

The design parameters of the MDR(main-DR) and the BC(bunch compressor) which are required from the design of the JLC are as follows:

1) 1.0×10^{10}particles/bunch,

2) 10 bunches/train with the bunch spacing of 1.4 nsec.

3) repetition frequency 200Hz,

4) the normalized emittances of the extracted beam from the DR are less than

$\gamma\epsilon_x/\gamma\epsilon_y = 3.0 \times 10^{-6}/3.0 \times 10^{-8}$ radm,

5) the bunch length from the BC is less than 76μm.

One of the characteristics of the present design of the JLC is to operate in a multi-bunch mode. The linac accelerates bunch trains where the bunches contained in a train are separated by about 42cm and the number of particles per bunch is 1×10^{10}. We assume that the total time duration for the kickers to turn on, extract/inject a train, and turn off is less than 130nsec. Thus the trains must be separated by at least 60nsec. We have decided to introduce damping wigglers in zero-dispersion region and also selected a racetrack configuration as a ring style for the reduction of dispersion suppression and matching regions. The type of lattice in the arc is a separated fuction FODO since simple lattice are favored for operation simplicity.[4] In the following sections, we present preliminary designs of the PDR, the MDR and the BC. Also we discuss the merits of introducing the PDR and results of some simulations are presented.

Pre-Damping Ring

A lattice design of the PDR is illustrated in Fig.2. The ring has a circumference of 50.2m and a superperiodicity of two. The optical functions β_x and β_y and the dispersion function η_x for a quarter of the ring are plotted in Fig.3. Basic parameters of the PDR are as follows: beam energy 1.54GeV, Circumferrence 50.2m, damping time 3.16msec, equilibrium natural normalized emittance 2.18×10^{-4}radm.

The normalized emittance of the injected beam was increased from 1.0×10^{-3}radm to 3.0×10^{-3}radm. The energy acceptance was also increased from 0.7% to 1.0%. In order to accept the beam with 2.0% energy spread, energy compressor before the PDR is necessary. The PDR has mainly four merits.

1. Normalized emittance of the injected beam is easily increased because the PDR has not damping wigglers.

2. Jitter tolerance of the extraction kickers of the MDR is relaxed.

3. Requirement of the damping time for the MDR is loosened.

4. Requirement of the dynamic aperture for the MDR is relaxed.

Design of Damping Ring

A lattice design of the MDR is illustrated in Fig.4. The ring has a circumference of 172.8m. The optical functions β_x and β_y and the dispersion function η_x for the ring are plotted in Fig.5. Basic parameters of the MDR are as follows: beam energy 1.54GeV, Circumferrence 172.8m, damping time 6.2msec, equilibrium natural normalized emittance 2.92×10^{-6}radm, bunch length 5mm.

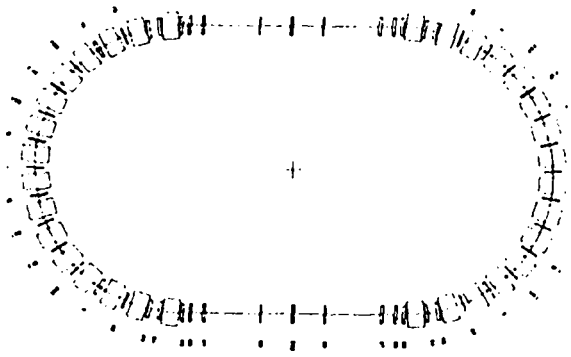

Fig.2 Schematic of the PDR.

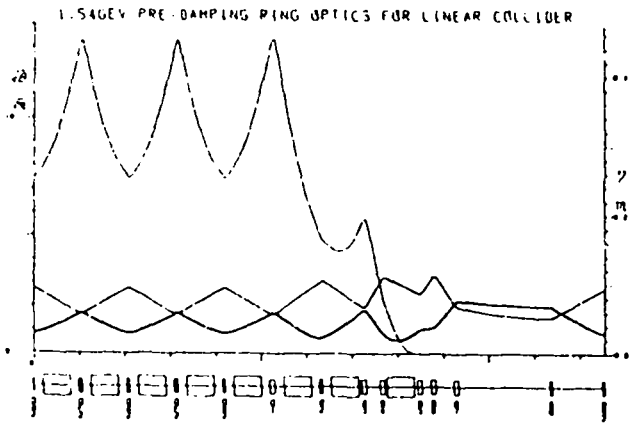

Fig.3 Optical functions for a quarter of the PDR

It is extremely important that the extraction kicker have very small jitter.[5,6] We would like to achieve a jitter tolerance of one tenth of the beam size $\sigma_{x,y}$ at the IP. This specifies a tolerance on the kicker.

$$\frac{\Delta\theta}{\theta} \leq \frac{\sigma_{jit}}{x_{kick}}$$

where

$$\sigma_{jit} \leq \frac{1}{10}\sigma_x$$

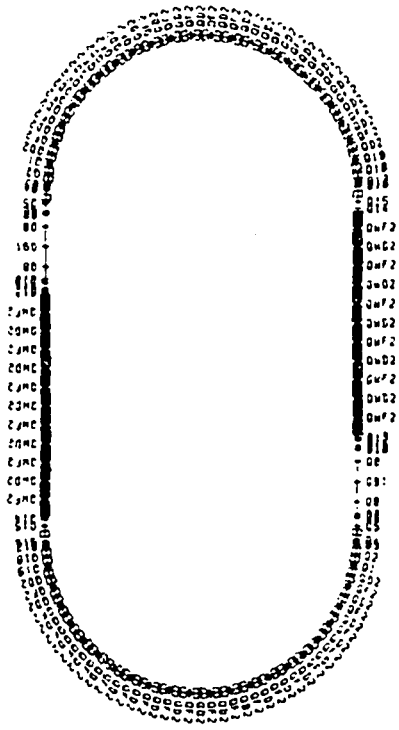

Fig.4 Schematic of the MDR.

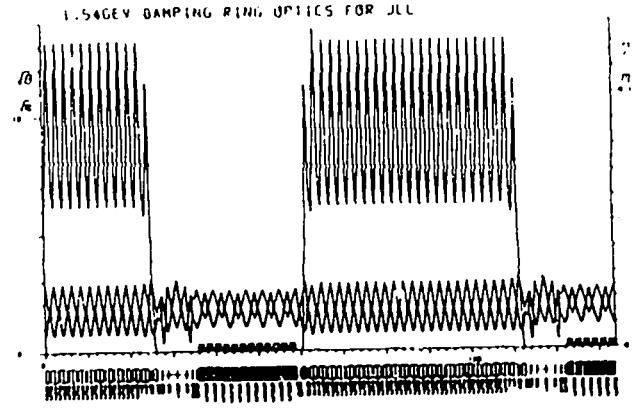

Fig.5 Optical functions for the MDR

, where x_{kick} is the transverse displacement of the kicked beam at the septum. This tolerance can be written in a more transparent form:

$$\frac{\Delta\theta}{\theta} \leq \frac{1}{10}\frac{\sqrt{\epsilon_{ext}\beta_{xsept}}}{x_{septplat} + 1mm + N_s\sqrt{\epsilon_{inj}\beta_{xsept}}}$$

where $\gamma\epsilon_{ext}$ and $\gamma\epsilon_{inj}$ are injected and extracted beam emittances. N_s is the distance between the closed orbit and the septum plate in units of the injected beam size. we assumed $N_s = 3$ and, since damping the bunch for $\sim 10msec$ reduces the emittance of the injected beam by two orders of magnitude, this value gives sufficient beam life time. The septum plate in a DC septum with strong fields cannot be made much thinner than 3mm. Assuming $\gamma\epsilon_{inj} = 3 \times 10^{-3}radm$ and $\beta_{xsept} = 7.5$m, the jitter tolerance on the kicker is

$$\frac{\Delta\theta}{\theta} \leq 7.08 \times 10^{-4}$$

The jitter tolerance of the extraction kickers $\frac{\Delta\theta}{\theta}$ is increased from 7.08×10^{-4} to 1.4×10^{-3} by using the PDR. The stored time of each train is reduced from 7τ to 5τ. This result reduces the number of the damping wigglers from 44 to 24. The required aperture of the MDR is reduced from $80\sigma_0$ to $40\sigma_0$, where σ_0 is maximum equilibrium beam size in the MDR. But the physical aperture is limited to the inner diameter more than $30mm$ because the condition of the vertical emittance growth rate due to the Rutherford scattering with residual gas requires the pressure less than $\sim 10^{-7} Pa$. The results of sumilation(SAD(KEK original code)) indicate that the dynamic aperture is more than $100\sigma_0$ and that the tolerances of the quadrupole misalignment and rotational misalignment, the sextupole misalignment, the magnetic field error and the monitor setting error are less than $30\mu m$ vertically, $60\mu m$ horizontally, 0.5mrad rotationally, 0.1% and 0.1mm to obtain the required emittance, respectively.

Design of Bunch Compressor

JLC requires the bunch length of $\sim 60\mu m$ for controlling the adverse effects caused by the transverse wake field and for obtaining high luminosity . A bunch of this length is not readily obtainable from a damping ring and, hence, a compressor will be needed to transform a long bunch with small momentum spread $\Delta p/p$ into a short bunch with a larger momentum spread. For the bunch extracted from the MDR the momentum spread will be typically $\Delta p/p \approx 0.08\%$ with a bunch length of $l \approx 5mm$. Compression of this bunch length to $\sim 60\mu m$ would then require increasing the momentum spread to 7%. That is clearly unacceptable when chromatic aberrations and practical aperture limitations are considered. Therefore, a two-stage compressor with an intermediate acceleration is assumed in the present design.[7] Fig.6 shows the layout of the BC for the JLC.[8]

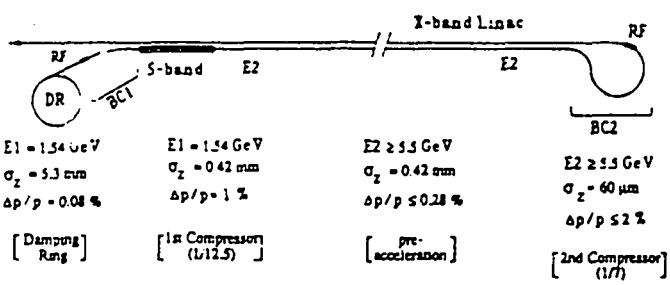

Fig.6 Layout of the BC for the JLC

The second compressor accomodates 180° bend before the injection to the main linac which make it easy to upgrade the energy and to handle the beam from control center. Transport line must have spin rotator without any degradation of spin polarization. Sextupoles were incorporated near the quadrupoles to form achromatic cells that relax the alignment tolerance as well as chromatic effects. The results of tracking simulation with 1000 particles input beam in the second BC are plotted in Fig.7. The second compressor with 2% energy spread does work and shrink the beam up to $66\mu m$ although 5% particles spread out beyond $2\sigma_z$.

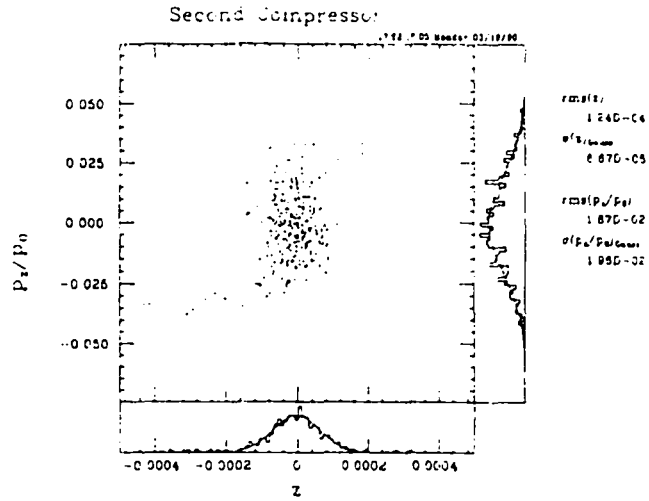

Fig.7 Results of tracking 1000 particles in the second BC

Acknowledgement

The authors would like to thank Professors Y.Kimura, K.Takata and S.Iwata for their encouregements during the work.

References

1. Y.Kimura, "The Performance of TRISTAN and Accelerator Development at KEK", Proc. European Particle Accelerator Conference (held at Nice, 1990).

2. K.Takata, "The Japan Linear Collider", contributed paper to this conference

3. S.Takeda,"Japan Linear Collider(JLC)", Proc. XIV International Conference on High Energy Accelerators, August 22-26, 1989, Tsukuba, Japan and Particle Accelerators, Vol.30, pp.143(1990).

4. J.Urakawa, "1.54GeV Damping Ring Design for Linear Collider" , Proc. of First Workshop on Japan Linear Collider, KEK Report 90-2 April A/H 33(1990).

5. Lenny Rivkin, Tor Raubenheimer," Summary of Damping Rings and Sources Group Discussions", Proc. of the International Workshop on Next Generation Linear Colliders, SLAC-335, UC-28(M)

6. T.O.Raubenheimer, L.Z.Rivkin, R.D.Ruth, "Damping Ring Designs for a TeV Linear Collider" SLAC-PUB-4808 (1988) and Proceedings of the DPF Summer Study, Snowmass '88

7. S.A.Kheifets et al., "Bunch Compression for the TLC", Proc. XIV International Conference on High Energy Accelerators, August 22-26, 1989, Tsukuba, Japan and Particle Accelerators, Vol.30, pp.79(1990).

8. M. Kikuchi and J. Urakawa, "The Design Study of Bunch Compressors for the JLC and the ATF", Proc. of 15th Linear Accelerators Meeting in Japan held at Faculty of Engineering, Hokkaido University, Sep. (1990)

ION SOURCE AND INJECTOR IMPROVEMENTS AT THE SUPERHILAC*

B. Feinberg, G. Behrsing, B. Gavin, S. Ryce, K. Sihler, and D. Syversrud
Lawrence Berkeley Laboratory, University of California, Berkeley, CA 94720

Abstract

Major improvements have been made on the Adam injector at the SuperHILAC heavy ion accelerator. Adam is a pressurized Cockcroft-Walton injector, typically run at voltages in excess of 2 MeV. The PIG ion source was redesigned to increase the length of the discharge column and the extraction slit, while remaining within the magnet poles of the source magnet. To maintain cooling, part of the thinner soft-iron end cap was replaced with a copper section, modifying the magnetic circuit. These modifications resulted in more than doubling the ion beam intensity. A large liquid nitrogen cryotrap within the pressure vessel was replaced by an RF shielded, commercial cryopump head with a custom pumping array. This reduced the pressure at the ground end of the injector by an order of magnitude and reduced that at the source by a factor of two, even with the additional gas load due to the longer slit. The pressure reduction was essential to minimize charge exchange loss of the highly charged ions, such as Fe^{1+}. Plans are underway to replace a 3 watt cryopump in the terminal end with a 10 watt pump which is expected to result in a 50% faster cooldown time, and greater than a 50% increase in running time before regeneration of the cryopump is necessary.

Introduction

The SuperHILAC is used primarily as the injector for relativistic heavy ion experiments at the Bevalac. The middle range of masses is provided by the Adam injector,[1] a pressurized Cockcroft-Walton injector run at voltages in the range of 2 MeV, shown in Fig. 1. Experiments at the Bevalac using secondary beams (radioactive beams produced by fragmentation of the primary beam in a thick target) often use ions from Adam for the primary beam. Since the secondary beam intensity is reduced by orders of magnitude compared to that of the primary beams, intensity improvements in the Adam injector are crucial to the experiments. In this paper we describe several recent improvements to the Adam injector which more than double the injected beam into the Bevalac, enhancing secondary beam production.

*This work was supported by the Director, Office of Energy Research, Office of High Energy and Nuclear Physics, Division of Nuclear Physics, of the US Department of Energy under Contract No. DE-AC03-76SF00098.

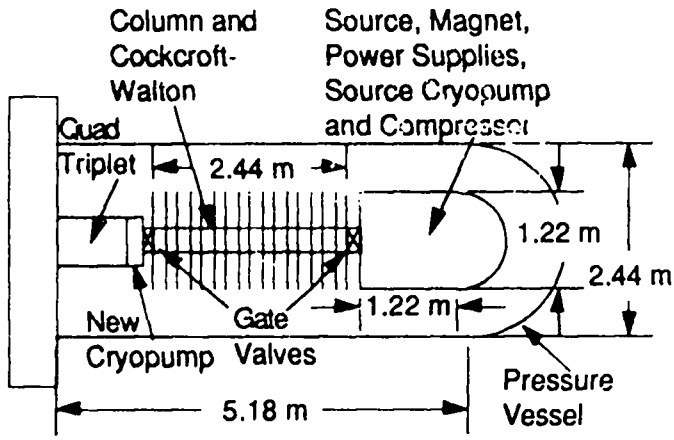

Fig. 1. Sketch of the Adam injector showing the limited space available.

Ion Source Improvements

As can be seen in Fig. 1, space in the Adam injector pressure vessel (165 psi nitrogen) is at a premium. All components, including the source magnet, the source itself, and the power supplies are optimized to fit in the smallest possible volume. The PIG ion source[2] was redesigned to accomplish several objectives without enlarging the overall size of the source. A schematic of the ion source is shown in Fig. 2. Not shown in the diagram is the sputter electrode (which provides the beam for solid elements), located opposite the slit.

The principle objective was to lengthen the ion source active region, providing a longer ionization region and extraction slit. It was hoped that this would increase the beam intensity while keeping the emittance within the acceptance of the accelerator. A second objective was to improve the mounting of the vanadium cathode, allowing it to be pressed into the holder.

To make these changes while remaining within the poles of the magnet, the soft-iron caps on the source needed to be made thinner, which presented two problems. First, making the iron thinner would reduce the heat transfer from the

cathodes to the cooling channels. Since the source works best at close to the maximum power, reducing the power-handling ability was not desired. Secondly, any change in the magnetic circuit which results in a non-uniform field in the active region of the source would likely degrade performance. As can be seen in Fig. 2, the changes increased the non-uniformity of the end caps in the vicinity of the active region of the source.

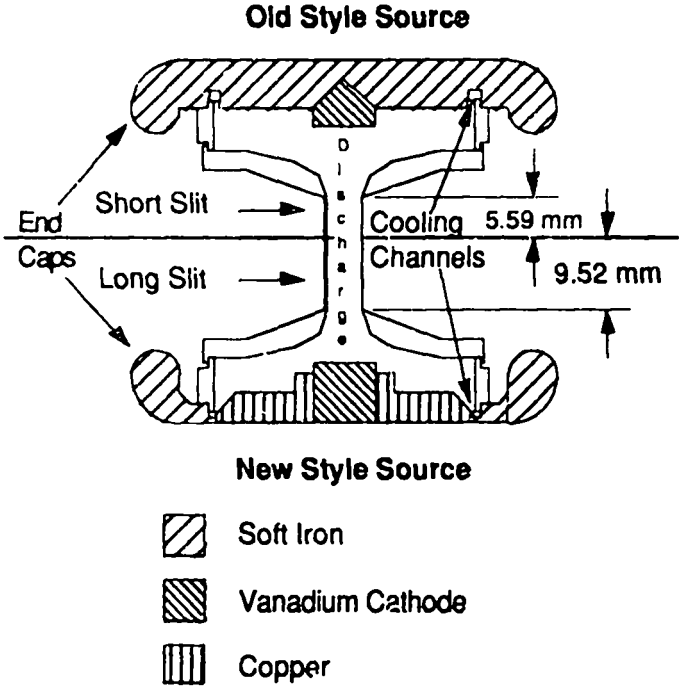

Fig. 2. Schematic of the Adam ion source. The top part of the schematic shows the previous version of the source, while the lower part of the diagram shows the new version of the source.

These problems were both solved by replacing the central section of the iron caps with copper. The copper conducts heat much more efficiently than the iron, allowing a much thinner section of copper to conduct the same heat flux as the thicker iron. In addition, the copper is not a high permeability section of the magnetic circuit, so any non-uniformities in its thickness do not result in a non-uniform field. The field is, of course, slightly reduced by removing the iron from above and below the active region, but it remains uniform.

A number of sources were built to test these hypotheses. Fig. 3 shows the performance of several sources. The sources were run at a number repetition rates to represent the various operating conditions.

The graph clearly shows that the new source, with the extended slit and the copper end cap, performs best at all repetition rates. These intensity increases were also verified at the exit of the linac, where the intensity increased by a factor of two for low pulse rate operation.

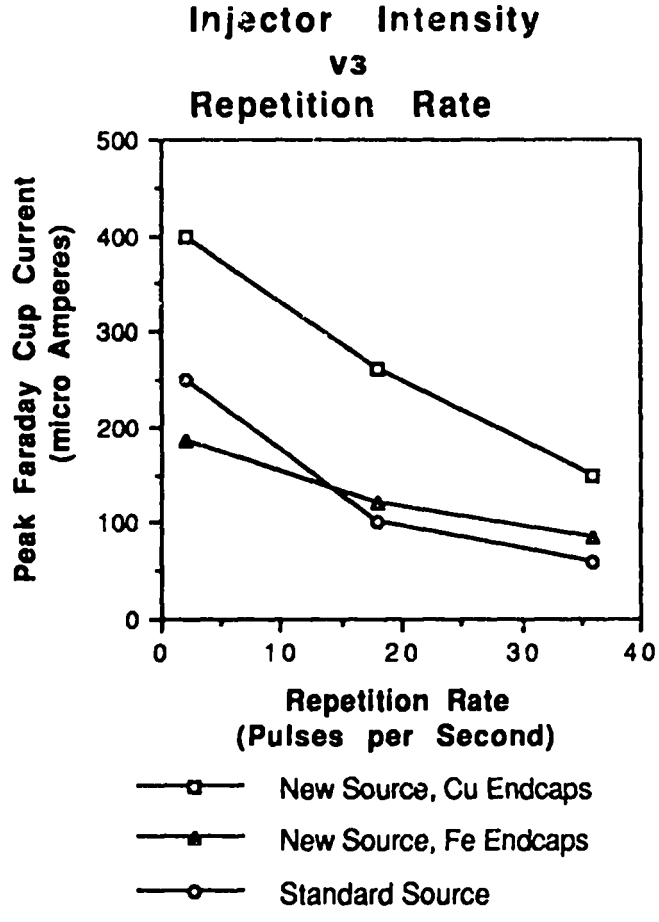

Fig. 3. Performance of various source models versus repetition rate. Intensity is measured at the entrance to the SuperHILAC Alvarez linac. The three curves represent two new versions, one with copper endcaps and the other with iron endcaps, both with a 19 mm long slit, and one older version with an 11 mm long slit.

Pumping Improvements

Introduction of the new source reinforced the need for improvements in the vacuum system. The longer slit allows more gas to leak out of the source, raising the background pressure. A high background pressure allows the high charge state ions (e.g. Fe^{4+}) to exchange electrons with the gas atoms, especially in the low velocity region at the upstream end of the accelerating column where the

charge exchange cross section is a maximum. Charge exchange will cause the ion to be lost, reducing the intensity.

One improvement was made at the ground end of the accelerating column shown in Fig. 1. A liquid nitrogen (LN) cryotrap, operating at 77° K, acted to freeze out gases, thus reducing the background pressure. This was replaced by a commercial cryopump refrigerator (CTI 350)[3] and a custom pumping array, shown in Fig. 4. The custom array, necessitated by the available space for the pump, cools down in approximately 90 minutes. For typical operating conditions the pressure at the ground end of the column improved by an order of magnitude, and the pressure just downstream of the source, at the upstream end of the column, improved by a factor of two, even with the additional gas load due to the longer slit in the new source. Since the fraction of beam undergoing charge exchange fraction is an exponential function of pressure, the factor of two improvement is significant.

The cryogenic refrigerator required shielding to enable it to function in the field of the Cockcroft-Walton. The C-W operates at an RF frequency of 100 kHz, with the actuating coils surrounding the cryopump assembly. A copper shield was constructed to shield the moving parts of the refrigerator from the RF field, thus removing a major cause of bearing and motor driveshaft failure.

A second vacuum improvement to be installed this fall is the installation of a larger compressor for the cryopumps at the source end of the column. The increased capacity should allow most Bevalac experiments to be completed without a source change. Changing the source in the Adam injector typically requires half a shift (4 hours), due to the time needed to regenerate the cryopumps and that needed to pressurize and de-pressurize the injector tank, so reducing the frequency of source changes will be a major improvement.

Conclusion

A number of improvements to the Adam injector at the SuperHILAC have been described. These improvements have as their principle goal increasing the intensity of the beam delivered to the Bevalac, especially for secondary beam experiments which are severely intensity limited. The improvements have, so far, more than doubled the beam intensity, increased the time between source changes (with plans for further increases), and have strengthened the construction of the source, allowing for more reliable operation.

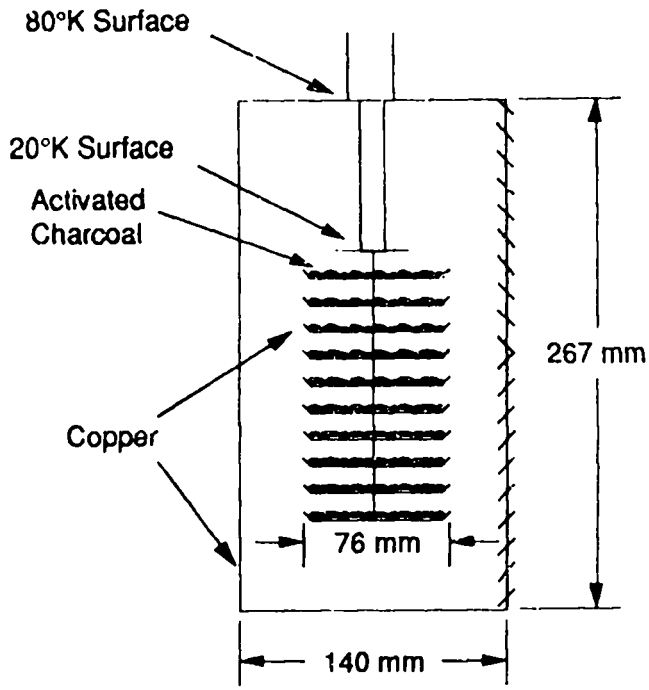

Fig. 4. Cryogenic pumping array, composed of copper with activated charcoal adsorbent.

Acknowledgements

This work could not have been accomplished without the dedicated support of the Bevalac operations and electronic maintenance staff, who worked to take the data presented and to maintain the operation of the injector during these tests.

References

1. D.A. Spence, B.F. Gavin, R. Peters, L.L. Reginato, B.H. Smith, and R.C. Wolgast, "A 3-MV Injector for the SuperHilac," IEEE Trans. Nuc. Sci. NS-18, 97 (1971).
2. B. Gavin, "Anode Sputtering Characteristics of the Berkeley 2.5 MV Source," IEEE Trans. Nuc. Sci. NS-32, 1008 (1976).
3. CTI-Cryogenics, Waltham, Mass.

DEVELOPMENT OF THE DTL FOR THE JHP

F. Naito, T. Kato, E. Takasaki and Y. Yamazaki
National Laboratory for High Energy Physics, KEK
1-1 Oho, Tsukuba-shi, Ibaraki-ken, 305 Japan

Abstract

Experimental investigation for the development of the 432-MHz DTL is in progress with the aid of new engineering techniques with high accuracy. The required fabrication accuracy was tested with the construction of the low-power model of the DTL. The rf properties of the model in the low-ß region were studied. The field stabilization with post coupler was also studied by using the model and by the field patterns calculated with MAFIA. On the basis of the study of the low-power model, the high-power model of the DTL is being constructed for beam tests. The quadrupole magnets of high quality were fabricated.

Introduction

A 1-GeV high-intensity proton linac will be constructed as an injector for a ring accelerator of the Japanese Hadron Project (JHP)[1]. The proton linac comprises a radio frequency quadrupole (RFQ), a drift tube linac (DTL) and a coupled cell linac (CCL). The DTL accelerates H^- ions from 3 MeV to 148 MeV. A frequency of 432 MHz was chosen in order to increase the shunt impedance and to use stable klystrons.

The increase in the frequency reduces the size of the DTL. Thus, the precision machining tools can be utilized for a new fabricating method of the DTL. Therefore, a low-power model of the DTL was fabricated in order to test the accuracy both of machining and of assembling of the drift tubes. We also studied the rf characteristics, in particular, a stabilization of the field with post couplers. An analysis of the field pattern with MAFIA was applied to a DTL with post couplers.

A high-power model of the DTL is being constructed on the basis of the study of the low-power model. A permanent quadrupole magnet (PQM) is chosen for a focusing magnet because it is strong and compact. It requires neither the cooling nor maintenance. Assembling tools of PQM are also developed.

The low-power model of the DTL

The low-power 35-cell model of the DTL, 2.6 m in length, is divided into four unit tanks, that makes it easy to use precision machining tools. The drift tubes were held in the tank as shown in Fig. 1. The end part of the stem is tapered and fitted to a tapered hole on the tank. The taper section has two important functions; keeping good rf contact and aligning the drift tubes on the beam axis.

Since the cell length varies rapidly in the low-ß region, so does the effect of the stem on the cell frequency. The distribution of the frequency shift due to the stem is reduced by changing the diameter of the stem near the drift tube as seen in Fig. 1. Then, it was taken into account in the SUPERFISH calculation of the cell frequencies in order to obtain a flat distribution of an accelerating field. The field flatness thus obtained without post couplers was within 1.2%, where the accelerating field on axis was measured by a standard bead perturbation method.

The transverse deviations of drift tubes from the beam axis were 93, 28, 22 and 75 µm for four unit tanks, respectively. We found that the amount of the deviation among unit tanks depended upon manufacturing machines that made the taper section. It means that we can achieve the final goal of 20 µm with the aid of more precise machines for the machining of high-power model of the DTL.

Field stabilization with post couplers

An accelerating field in a DTL is distorted by some perturbations because of the zero group velocity of an accelerating TM_{010} mode. The perturbations will arise from thermal detuning, beam loading and structure imperfection. Post couplers are used for stabilizing the field against the perturbations by increasing the group velocity[2]. In general, a reduced number of post couplers are desirable as far as it is possible to keep the field stability because post couplers decrease the Q value. Thus, we studied the dependence of the field stability on the number of post couplers[3,4,5].

For discussing the field stability qualitatively it is useful for defining a distortion parameter[4] D by

$$D = \sum_{i=1}^{15} |E_i - \langle E \rangle|$$

where E_i is an average electric field of the i-th cell on axis normalized by the maximum electric field and <E> is an average of E_i's. A distortion parameter of 1.1×10^{-3} was obtained for the unperturbed field. A perturbation was intentionally introduced by inserting four frequency tuners. It gave rise to a 15% tilt of the field ($D=3.6\times10^{-3}$). If post couplers stabilize the field, the value of D will be reduced against the perturbation.

At first, thirty-four post couplers were inserted into the model. A fine, individual tuning of the length of each post coupler was required for stabilization of the accelerating field. The details of the tuning are described in Ref. 3. The distortion parameter of 1.5×10^{-3} was obtained on the stabilized condition. In order to study the effect of the number of the post couplers on the field stability we attempted to reduce the number of post couplers (17, 12, 6, 4, and 3 post couplers). The field stabilization was observed except for the case of three post couplers.

A group velocity of the accelerating mode, defined as a derivative of the measured dispersion curve, is another measure of the stabilization effect[5]. It can be seen from Fig. 2 that the group velocity with 34 post couplers is approximately equal to that with 12 post couplers. The maximum group velocity was obtained with 17 post couplers. On the other hand, the Q value decreases with increasing the number of post couplers; about 7% decrease by inserting 34 post couplers, which is not negligibly small. It is thus concluded that the optimum number of post couplers for the model is 17, compromising between the obtained group velocity and the decrease in the Q value.

The analysis of field patterns with MAFIA

The stabilization with post couplers was introduced on the analogy of a π/2 mode CCL[2]. Properties of the stabilization were explained from calculations of an equivalent circuit[6,7]. The computer code MAFIA[8] was used in order to study field patterns of the TM and the post modes of a DTL with 7 cells and 6 post couplers. The input geometry with 1.8×10^5 meshes is prepared as shown in Fig. 3. Both accelerating gap and the size of the drift tube are kept constant for the simplicity. The calculated dispersion curve is shown in Fig. 4. Among these modes, both nearest neighboring modes of TM_{010}, the TM_{011} mode and the post mode PC_1, play an important role in the stabilization effect. Here the PC_1 is the highest among the post modes. The electric field Ez on the beam axis is shown in Fig. 5 both for the TM_{011} and for the PC_1 mode. It can be seen that the Ez of TM_{011} and PC_1 have a node in the center of the DTL. Figure 6 shows the E vector in the y-z plane including a beam axis. Figures 7 and 8 show the E and H vectors in the z-x plane below the drift tubes. The patterns of these vectors show the following facts. (1) The field of TM_{011} is distorted by the stems as seen in Fig. 6-a. It contains a TE-like field pattern because it has the loop of the magnetic field in the z-x plane as seen in Fig. 8-a. (2) The field pattern of TM_{011} below the drift tubes resembles that of the PC_1 as seen in Fig. 7. (3) The Ez of TM_{011} mode and PC_1 have an opposite sign of tilt if TM_{011} mode has the same phase as PC_1 mode in the lower half of the DTL.

The Ez of TM_{010} mode is stabilized mainly by the contribution from TM_{011} and PC_1. However, the result of MAFIA suggests that Ey's of both modes on the beam axis are not compensated. Instead, Ey's are enhanced when Ez's are compensated. The strength of Ey depends on the situation of the stabilization and the design of DTL. The maximum values of Ey both of TM_{011} mode and of PC_1 mode are about 5% of Ez. The maximum value of Ex of the TM_{011} mode is less than 1% of Ez, while that of PC_1 mode is about 3% of Ez in the above calculation.

The high-power model of the DTL

The high-power model of the DTL, 1.2 m in length and 0.44 m in diameter, is being constructed on the basis of the study of the low-power model. The DTL, made of an oxygen-free copper (OFC), accelerates the H^- beam from 3-MeV to 5.4-MeV. It has 18 cells and

2 unit tanks. The post couplers are installed in every other cell of the model.

The following new problems related with a new fabrication method should be solved before the construction of the high-power model; (1) assembling of adjacent two unit tanks, (2) assembling of drift tubes, (3) seal of drift tubes containing quadrupole magnets in the drift tube, (4) fabrication of compact and strong permanent magnets, and (5) development of an input coupler. The assembling method of the drift tube is shown in Fig. 1. It has three functions; an rf contact, a position alignment of the drift tube and a vacuum seal. There are three kinds of method of the seal of the drift tube. They are the electron beam welding (EBW), the electroforming (EF)[9] and the cold shrinking method[10]. The developments of EBW and EF have been done successfully. The cold shrinking method is now under development. An input coupler was designed[11] with the aid of the computer codes, SUPERFISH and MAFIA.

The permanent quadrupole magnet

Specifications of the quadrupole magnet required from the beam dynamics are as follows. (1) The integrated field is 5.5 T for 3-MeV H^- injection in order to obtain a transverse phase advance of about 60 degrees. It requires a gradient of the magnetic field of 184 T/m with a magnet length of 30 mm. (2) The deviation of the quadrupole field center from the beam axis is about 20 μm (r.m.s.). (3) The variation of the field gradient is within ±4.4%.

The Nd-Fe-B permanent magnet that satisfies the specification (1) was chosen for making the quadrupole magnet. Figure 9-a shows a cross section of the quadrupole magnet, that is composed of 16 segments with five kinds of directions of magnetization[12]. The segments with three kinds of axis of magnetization were made as shown in Fig. 9-b. The specification (2) requires the high accuracy of the fabrication for each segment. The calculation with the computer code PANDIRA[13] gave the displacement of the center of quadrupole field with two kinds of perturbation for three kinds of segment. Results are summarized in Table. I.

Table. I
Displacement of Quadrupole Field Center

Perturbation for a segment	PANDIRA Displacement of field center (μm)	Types of segments
Deviation of magnetization of 1%	3	0°
	< 5	45°
	5	90°
Deviation of direction of magnetization of 1°	5	0°
	2	45°
	8	90°

The deviations of the field strength and the direction of magnetization from the designed values must be less than ±0.4% and ±0.3° respectively in order to obtain the specification (2) mentioned above. The fabrication of the segments was carefully carried out in order to achieve the required accuracy. The accuracy thus obtained are shown in Table. II. The magnetic field of the two sets of PQM's was measured by using a rotary coil. The deviations of the quadrupole field centers from the mechanical center of the PQM were 25 and 8 μm respectively with the experimental error of about 10 μm. Since the segments of permanent magnet were assembled into the PQM without a shuffling, the measured deviations were small enough to meet the requirement within the error.

Table II
Accuracy of Test Segments of Magnet

Types of segments	Deviation from the designed value (degree)	Standard deviation of the field strength (%)
0°	0.2±0.2	0.3
45°	0.7±0.3	0.2
90°	0.2±0.2	0.2

Conclusions

The development of the DTL for the JHP is in progress with the aid of new engineering techniques with high accuracy. The accuracy of the fabrication was tested by means of the construction of the low-power model of the DTL. The rf properties of the model in the low-β region were also studied. The stabilization of an accelerating field by post couplers was confirmed. The number of post couplers was optimized. The field patterns of a DTL with post couplers were studied with MAFIA. The high-power model of the DTL is under construction. The quadrupole magnets of high quality were fabricated.

Acknowledgment

The authors would like to thank Prof. Kihara and the member of the 1 GeV Proton Linac group in KEK for their valuable discussions

References

1. T. Kato, Y. Yamazaki and M. Kihara, Proc. 2nd Int. Sym. on Advanced Nucl. Energy Research, JAERI, Japan, (1990) 177.
2. D. A. Swenson, et al., Sixth Int. Conf. on High Energy AcceleratorCambridge, Mass.,CEAL-2000, (1967) 167
3. F. Naito, et al., Particle Accelerators, 32 (1990) 27.
4. J. Ungrin, S. O. Schriber and R. A. Vokes, IEEE Trans. Nucl. Sci., 30 (1983) 3013.
5. M. Bell, Particle Accelerators 3 (1978) 71.
6. T. Nishikawa, (1967) unpubiished.
7. T. Kato, KEK Report, 86-5 (1986).
8. T. Weiland, Particle Accelerators, 17 (1985) 227.
9. E. Takasaki, et al., Proc. 2nd Int. Sym. on Advanced Nucl. Energy Research, JAERI, Japan, (1990) 184.
10. T. Adachi, et al., "Fabrication Technique of Drift Tube with Permanent Quadrupole Magnet for the Linac of the JHP," this conference.
11. F. Naito, et al., "Design Features of the Input coupler for the DTL," this conference.
12. K. Halbach, Nucl. Inst. and Meth., 169 (1980) 1.

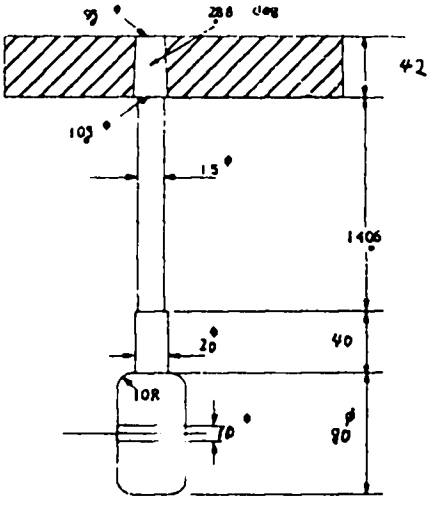

Fig. 1. Drift Tube and Stem.

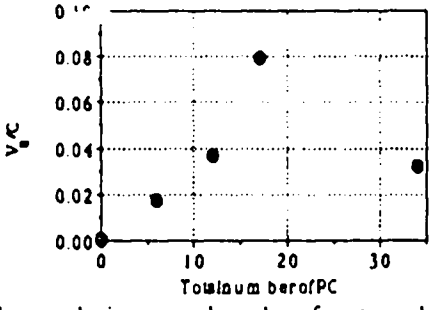

Fig. 2 Group velocity vs. total number of post couplers.

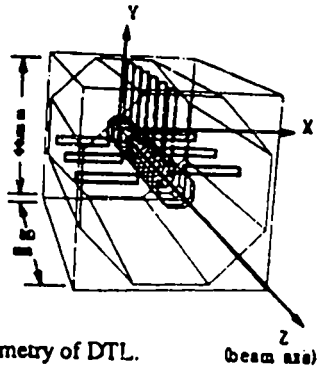

Fig. 3 Input geometry of DTL.

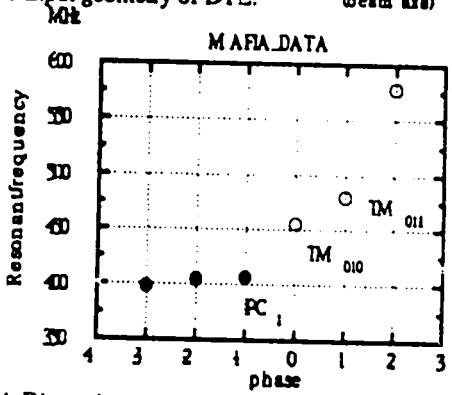

Fig. 4. Dispersion curve of TM_{01} and post modes calculated with MAFIA.

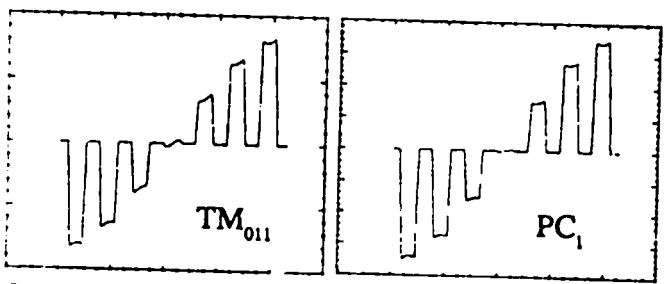

Fig. 5. z component of the electric vector on beam axis.

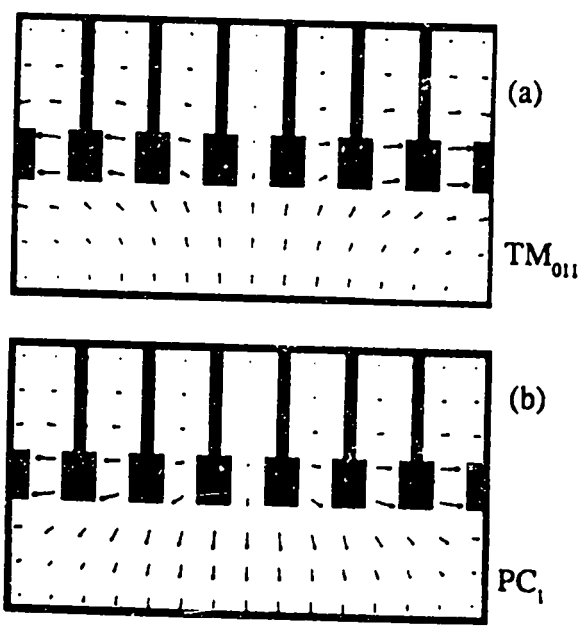

Fig. 6. Electric vectors in y-z plane included beam axis.

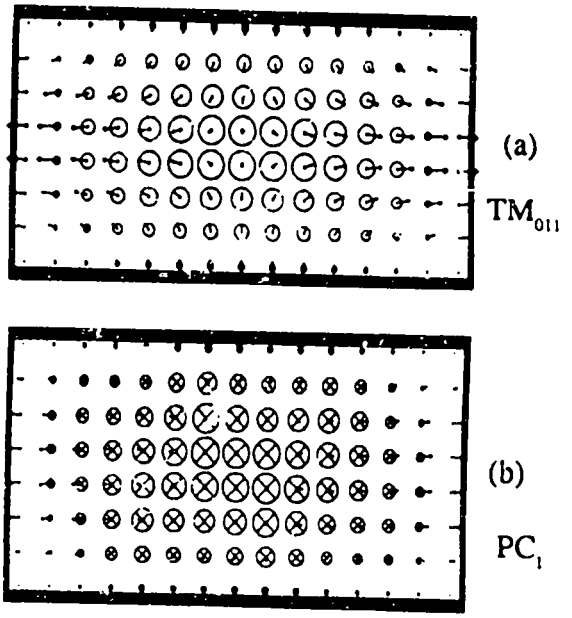

Fig. 7. Electric vectors in z-x plane below drift tubes.

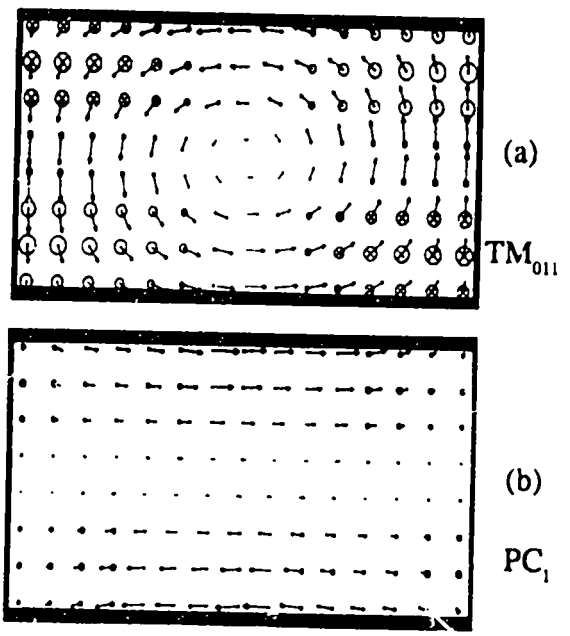

Fig. 8. Magntic vectors in z-x plane below drift tubes.

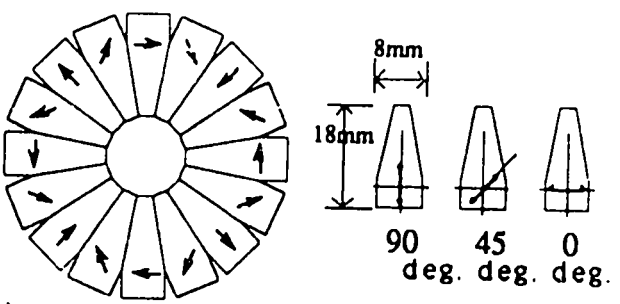

(a) Cross section of PQM. (b) Direction of magnetization.

Fig. 9. Parmnent Quadrupole Magnet.

TEST OF A 473 MHZ FOUR-ROD RFQ†

Reza Kasimi, F. R. Huson, and W. W. MacKay
Department of Physics, Texas A&M University and Texas Accelerator Center
TAC, 4802 Research Forest Dr., Building 2, The Woodlands, TX 77381

Abstract

A 500 keV 473 MHz RFQ using a new type of four-rod design has been fabricated at Texas Accelerator Center. Our purpose is to test the structure by accelerating a 10 mA beam of H^- ions through the RFQ. This paper presents the structural characteristics of the RFQ, the beam dynamics parameters, the tests of a cold model , and the results of the low power rf tests of the RFQ.

Introduction

The four-rod RFQ structure invented at Frankfurt[1] not only has been a viable alternative to the four-vane structure, but also offers many advantages such as simplicity of structure and elimination of the dipole mode. However, the four-rod design has not been studied extensively for frequencies much above 200 MHz. Higher frequencies (400 to 500 MHz) are desirable for pre-injectors of proton machines. By introducing a small variation to the Frankfurt geometry we have developed a four-rod type design for these higher frequencies.[2,3] After designing several simple test models, checking them using computer codes such as MAFIA[4], and obtaining desirable results from cold model measurements, we set out to make a test RFQ at 473 MHz and to accelerate a 10mA of H^- ion beam from 30 keV to 500 keV. (The reason for 473MHz is the rf power source.) We first made a short cold model of the structure to check our calculations and to discover and solve possible problems in construction and assembly. Next, we made a full beam dynamics design for a short low power RFQ. Pieces were machined and assembled and a cold test of the RFQ was done. This paper will discuss the design of the structure, the test results of the cold model, the beam dynamics design, and the cold test of the final RFQ.

† TAC at HARC is a consortium of Rice University, Texas A&M University, The University of Houston, The University of Texas, Prairie View A&M university, Sam Houston State University, and the Baylor College of Medicine MR Center. This work was also supported by the SSC laboratory.

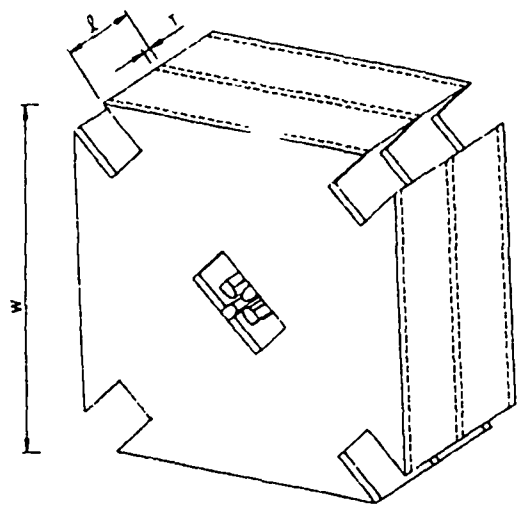

Figure 1. Two modules of the 473 MHz structure.

The structure

The structure is made of a series of modules. Figure 1 shows two modules next to each other. Each basic module of length ℓ consists of two square plates of thickness T and width W supporting the four rods. Each supporting plate is connected to two opposing rods. Four rectangular plates cover the sides of the structure with the corners of the structure being left open to give better vacuum quality. The corners can be left open for the following reasons: First, the diagonal planes going through the opposing corners are the symmetry planes of the structure. Therefore, there should be no currents crossing these planes. In other words, the $\vec{B}$ field is perpendicular to these planes. Second, the fields are weak at the corners, so leaving the corners open should not appreciably change the resonant frequency or the Q. Figure 2 shows the magnetic field for a cross section at the middle of a module ($z = \ell/2$), showing that $\vec{B}$ is negligible at the corners.

Since the two opposing rods are attached to the same plates at many points through the structure, the dipole mode, which appears when the two opposing rods oscillate at different voltages, is not a problem. In other words, there is no mixing of unwanted dipoles mode with the desired quadrupole mode. This is an advantage that all the four-rod type structures share over the four-vane types in which the mode mixing could be a serious problem.

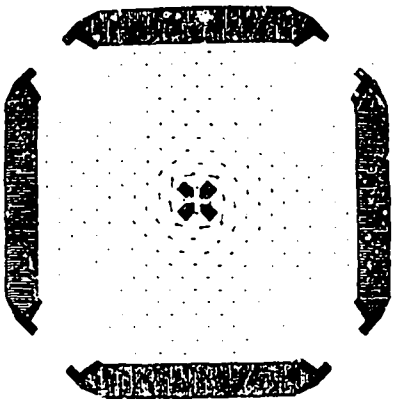

Figure 2. Plot of the magnetic field in the middle of a module. (MAFIA output)

All parts of the structure are bolted together, and as a result, it can be fully disassembled. To make it possible for the vanes to be positioned exactly in place and attached to the square plates, each plate is split diagonally into two halves. The rods are then held in place between these two halves and positioned using dowel pins. To make good rf contacts at the joints, thin annealed copper wires are squeezed in at the contact points between the plates and the sidewalls, and the rods and the plates. However, we need not worry about the quality of the joints between the two halves of the square plates; since they fall on one of the two diagonal symmetry planes which have no currents crossing them.

To design such a structure at a specific frequency, we only need to design a module using the MAFIA code. Since the structure is made of a series of identical modules it will have the same frequency, quality factor, power per unit length, etc., as a single module. Our RFQ structure is made of 10 module. Table 1 lists the dimensions of a module for the 473 MHz structure. It also lists the frequency and Q factor predicted by MAFIA and capacitance per unit length of the vanes calculated by the CAP program, a modification of POSSION for calculating capacitance. Note that the quality factor predicted by MAFIA is not a good prediction since the Q factor also depends on other factors such as small geometrical details, surface quality, and so on, which are not taken into account by the code.

The Cold Model

A cold model consisting of four modules was constructed. In this model the geometry of the vanes is the same as that the RFQ's except that they are shorter and the shapes of the tips of the vanes are different. However, using the CAP program we made sure that the intervane capacitance per unit length is the same in both cases. A resonant

TABLE 1

Dimensions of a 473 MHz module

Length of the module(ℓ)	5.48 cm
Width of square plates (W)	18.8 cm
Thickness of the plates (T)	1.27 cm
Intervane capacitance (C_T)	107 pf/m
MAFIA Results.	
Frequency	473 MHz
Q	8500

frequency of 471.5 MHz was measured for the quadrupole mode. this was less than half a percent away from the design frequency of 473 MHz. Then by slightly modifying the geometry of the back of the vanes, the resonant frequency was changed to 473.1 MHz. The unloaded quality factor for this model was 4400. More importantly, no neighboring mode was seen within 100 MHz of this mode, which confirms our prediction that there is no mode mixing to worry about. Fig 3 shows the reflection coefficient versus the frequency. The sharp absorbtion happens at the resonant frequency 473.1 MHz. The cold model can be fine tuned within about 1 MHz simply by inserting a copper rod into one of its four corners.

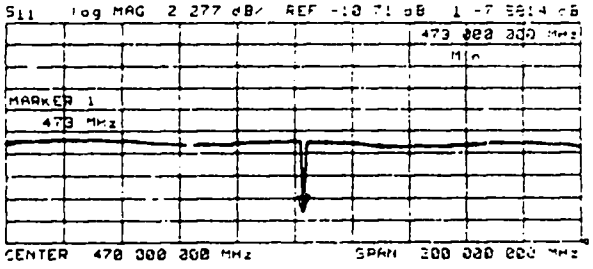

Figure 3. The reflection coefficient vs. frequency for the cold model.

The Beam Dynamics Design

The beam dynamics of the RFQ has been studied using the PARMTEQ program. In this design an effort has been made to keep the length of the RFQ short and the intervane voltage low, so that the total power required is below 100 kW. The input to the RFQ is 10 mA and .7 π mm-mrad (normalized 90%) emittance. The output beam should be about 9 mA with less than 10% emittance growth. Table 2 and figure 4 give the parameters of the RFQ.

The RFQ

The RFQ consists of 10 modules described above. At the low energy end of the RFQ, a small single gap cavity has been added to eliminate any axial electric field at the

TABLE 2

Ions	H^-
Target frequency	473 MHz
Initial energy	30 keV
Final energy	500 keV
Vane length	56.25 cm
Intervane voltage	37 kV
Aperture (r_0)	0.25 cm
The Cold Model:	
Frequency	473.1 MHz
Q	4400
The RFQ:	
Frequency	470.3 MHz
Q	4800
Power	90 kW

beginning of the RFQ. The two opposite corners of the wall between this extra cavity and the first module of the RFQ have been opened wider to let the magnetic field couple the cavity to the first module of the RFQ. The resonant frequency is kept constant by decreasing the length of the first module in the RFQ from 5.48 cm to 4.1 cm.

The coordinates for machining the RFQ vane tips were calculated based on the PARMTEQ results. The transverse radius of the vane tip is 0.188 cm ($0.75 \cdot r_0$) and is kept constant through the RFQ length. The machining of the vanes turned out to be a difficult job and great care was needed for two reasons. The first was to make sure that data points were smooth enough, since after machining, no polishing was allowed. This is because the vanes have to hold high surface electric fields and polishing would embed small particles to the surface and create possible sparking points. The second reason was that machining the vanes was to be done to high tolerances over their full length as required by the beam dynamics. This was successfully done on the MAZAK computerised numerically controlled milling machine. A high speed cobalt tool was used to machine the modulation on the vanes which are made of tellurium copper.

A resonant frequency of 470.3 MHz was measured for the RFQ. This is lower than the design frequency of 473 by about half a percent and will be fixed by tuning. The unloaded Q value is 4800, requiring a structure power of about 90 kW which is within the reach of our 100 kW rf source. Figure 5 shows the reflection coefficient versus the frequency for the RFQ and once again there are no neighboring modes.

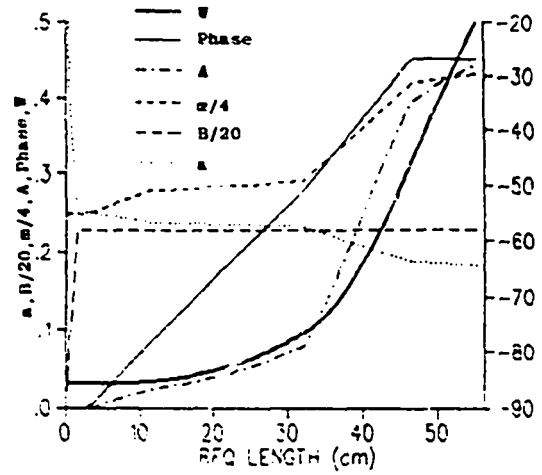

Figure 4. The RFQ parameters vs. RFQ length.

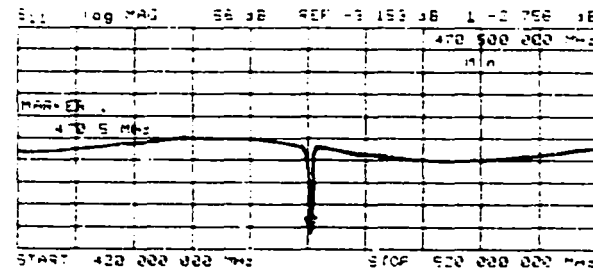

Figure 5. The reflection coefficient vs. frequency for the RFQ.

Conclusion

Thus far the cold model tests of our structure and low rf power measurements of the RFQ have been accomplished and results have had a good match with the calculations. The next step is to do the full power test of the RFQ. Finally, the RFQ will be attached to the ion source and The LEBT system.

References

1. A. Schempp et al., "Zero-Mode-RFQ Development in Frankfurt," in Proceedings of the 1984 Linear Accelerator Conference, 100 (1984).
2. R. Kasimi, "A Four-Rod Cavity RFQ," in Proceedings of the 1988 Linear Accelerator Conference, 140 (1988).
3. R. Kasimi et al., "Study Of A Four-Rod RFQ Structure At 470 MHz," in Proceedings of the 1989 IEEE Particle Accelerator Conference, 990 (1989).
4. R. Klatt et al., "MAFIA – A Three-Dimensional Electromagnetic CAD System for Magnets, RF Structures, and Transient Wake-Field Calculations," in Proceedings of the 1986 Linear Accelerator conference, 276 (1986).

THE SINGLE-BEAM FUNNEL DEMONSTRATION: EXPERIMENT AND SIMULATION *

K. F. Johnson, O. R. Sander, G. O. Bolme, J. D. Gilpatrick, F. W. Guy,
J. H. Marquardt, K. Saadatmand,** D. Sandoval, and V. Yuan
Los Alamos National Laboratory, Los Alamos, NM 87545

ABSTRACT

Accelerator concepts for heavy-ion fusion and for the transmutation of nuclear waste require small-emittance, high-current beams. Such applications include funnels in which high-current, like-charged particle beams are interlaced to double the beam current. The first experimental demonstration confirming the beam dynamics of the funnel principle (with contained emittance growth) was recently completed at Los Alamos National Laboratory. A single leg of a prototype 5-MeV, H^- funnel was successfully tested. This single-beam demonstration explored physics issues of a two-beam funnel. The experiment contained elements for emittance control, position control, and rf-deflection. Diagnostics allowed measurement of beam intensity, position and angle centroids, energy and phase centroids, transverse and longitudinal phase-space distributions. Results of the experiment will be presented along with comparisons to simulations.

INTRODUCTION

An experimental demonstration confirming the beam dynamics of beam funnelling was recently completed on the Accelerator Test Stand (ATS)[1] at Los Alamos National Laboratory. Although this experiment utilized a single-leg of a prototype 5-MeV H^- funnel, it addressed most of the physics issues concerned with a two-beam funnel. The only known beam dynamics issue that was not addressed was the beam-beam interaction. Objectives of this experiment were position control (with ~100% beam transmission), successful use of rf-deflection,[3] and control of emittance growth.

EXPERIMENTAL TECHNIQUE

The H^- input beam was from the ATS, 425-MHz, 5-MeV drift tube linac (DTL). The beamline is shown schematically in Fig. 1. Beam position control was achieved with four permanent-magnet dipoles (PMDs), four off-set permanent-magnet quadrupoles (PMQs), four movable PMQs for steering, and one rf deflector. Reference 2 contains component design specifications for the funnel beamline. Funnel transverse emittance control was maintained by 15 PMQs. The PMQ focusing was chosen to match the periodic focusing of the ATS DTL. Funnel longitudinal emittance control was done with four rf bunchers (two 425-MHz and two 850-MHz), whose amplitude and phase could be independently varied to change the longitudinal emittance shape.

Beamline diagnostics included three broad-band toroids and nine microstrip probes (MBPs). A large cylindrical vacuum vessel contained the beamline which was mounted on four separate plates (M1 through M4) to allow for staged installation (Fig. 1). The diagnostics for beam characterization were mounted on a diagnostics plate (D-plate), which was placed after each M-plate. The diagnostics consisted of two pairs of slit-collectors for transverse emittance measurements, the LINDA[3] (a longitudinal emittance measurement technique) intersection points and a sweeping magnet for longitudinal emittance measurements, three MBPs, one wide-band toroid, a beam stop, and a Faraday cup.

EXPERIMENTS AND RESULTS

The single-beam funnel experiment was performed in four stages. They were the characterizations of the output beams from the DTL, M1-, M3- and M4-plates.

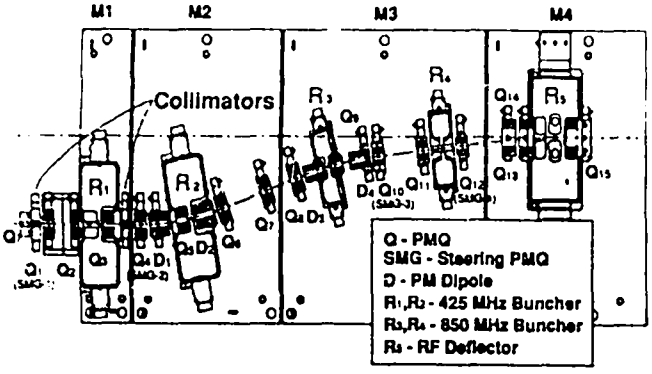

Fig. 1. Funnel beamline schematic. Shown are the locations of the optics elements. These included PMQs (fixed and movable), PMDs, collimators, and rf cavities.

Characterization of the DTL

The DTL rf amplitude and phase set-points were determined using the phase-scan technique.[4-5] This technique utilizes MBPs to measure the energy and phase centroids of the beam as a function of the DTL amplitude and phase. A comparison of data to single-particle simulations provides the signature for determining the DTL operating set-points. The phase-scan hardware-software system allows rapid determination of the DTL set-points (5 to 10 minutes). The rf amplitude was also determined by monitoring high-energy x-rays[6] from the DTL. Disagreement in the determination of the DTL gap voltage from phase-scan or x-ray data was ≤5%.

Longitudinal and transverse phase-space distributions were characterized as a function of DTL amplitude and phase. Comparisons between these measurements and those made previously indicated a problem with respect to the transverse phase-space. The transverse emittance in the horizontal and vertical planes had increased by a factor of 1.7 to 2.0 over the previously observed values. Extensive instrumental checks showed that the increase was real. Scheduling constraints limited the search for the cause of this emittance growth, so an alternative approach was used. Two collimators (movable vertically and horizontally) were installed on the M1-plate (at its entrance and exit). The collimators were designed to reduce the transverse emittance to an acceptable level to permit a meaningful physics test of the remainder of the funnel beam-line (i.e., the M2- through M4-plates).

Characterization of the M1-Plate

The M1-plate contained one 425-MHz buncher cavity (R1), one movable and two fixed PMQs, three MBPs, one toroid, and two movable collimators. The positions of the

*Work supported and funded by the US Department of Defense, Army Strategic Defense Command, under the auspices of the US Department of Energy
**Industrial partner, Grumman Corporate Research Center.

movable collimators and movable PMQ (SMG1) were optimized to prepare the beam for injection into the M2-plate. The final settings of the collimators and SMG1 were fixed for the duration of the funnel experiment. The M1-plate beam transmission was ~58%. Depending on ATS operation, the M1-plate output current varied from 25 to 40 mA.

Phase-scans were made to determine the R1 rf amplitude and phase set-points. With the collimators and R1 set, the transverse and longitudinal phase-spaces of the collimated beam were characterized. The expected transverse emittance was achieved (~0.021 π cm-mr in each plane).

Characterization of the M2- and M3-Plates

The M2- and M3-plates contained nine PMQs (three movable), three rf bunchers (one 425-MHz, R2, and two 850-MHz cavities, R3 and R4), four PMDs, six MBPs, and two broad-band toroids.

Good transmission (~100%) through the M2- and M3-plates was achieved with the steering PMQs (SMG2-SMG4). These PMQs were used to adjust the beam position and angle centroids for injection into the M4-plate. The error on the transmission measurement was dominated by beam noise and not toroid measurement precision. For quiet beams, a relative uncertainty of ~2% on beam transmission was possible.

The funnel steering model was checked by moving the SMGs one at a time, vertically or horizontally, and measuring the changes in beam position and angle centroids at the funnel exit. In general, the model and measurement agreed within the experimental errors of ±0.2 mm and ±1 mr.

The phase set-points for R2, R3, and R4 were determined by beam loading and the amplitude set-points were determined by using LINDA to measure beam energy gain. The phase-scan technique could not be used due to RFI (rf interference) in the MBPs. The RFI significantly reduced the accuracy of the microstrip measurements of position, angle, energy, and phase centroids. The principal source of the RFI was rf leakage from the R1 cavity and the beam itself.

Longitudinal and transverse phase-space distributions were measured for optimum settings of the four rf bunchers. To study phase-space distribution sensitivities to non-optimum conditions, the measurements were repeated as conditions were adjusted (all rf buncher amplitudes decreased by 20%, all rf bunchers off, etc.). The normalized horizontal (vertical) transverse emittance ε_x (ε_y) was unchanged when the buncher amplitudes were decreased by 20% from their optimum settings. For bunchers off, ε_x increased by ~33% (dispersion in the bend plane), but ε_y remained unchanged, as expected.

Characterization of the M4-Plate

The M4-plate contained three PMQs, the rf deflector (425-MHz), two MBPs, and one toroid. The D-plate was aligned with the deflector "on" beam axis. This choice prohibited certain types of measurements when the deflector was "off."

Good transmission (~100%, 2% relative uncertainty) was achieved through the rf deflector with rf power "on" or "off." To achieve this level of transmission, slight adjustments of SMG2, SMG3, and SMG4 were necessary.

RF deflector performance was critical to the success of the funnel experiment. The horizontal beam deflection, the relative ε_x and ε_y, and ε_L were measured as functions of deflector phase and cavity power. The rf power set-point was determined from x-ray monitor data. For 86 kW of cavity rf power, analysis of the x-ray data gave a gap voltage of 333 ± 17 kV (design value 333 kV). Figures 2 and 3 show the dependence of the relative horizontal beam deflection and relative ε_x on the relative deflector phase. Both the deflection and ε_x show extremums at the same input phase. This behavior is also observed for the Courant-Snyder parameters α, β, and γ. The extremums in β and γ are related to minimization of position and angle spreads. There is a clear signature for the rf phase set-point (~60° relative phase) of the deflector. This phase was shown to be independent of cavity power (Fig. 2), and ε_y was shown to be independent of the deflector phase. Both observations were as predicted. The behavior of ε_L with respect to deflector phase (Fig. 4) is similar to that of ε_x. Although broader, its minimum occurs at approximately the same phase, as it should.

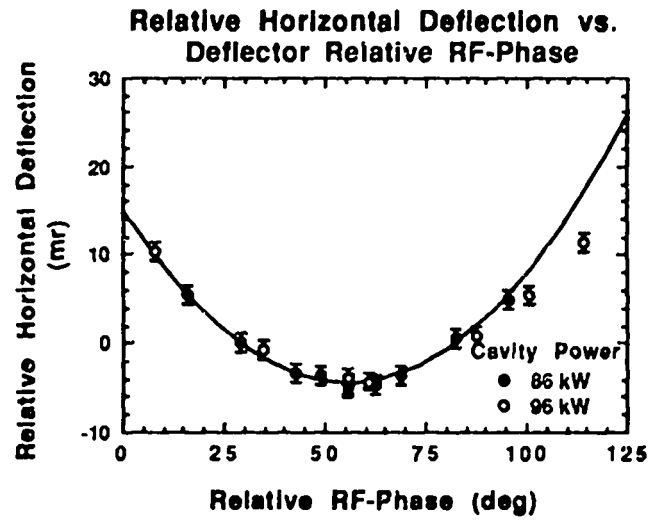

Fig. 2. Relative deflection angle of the deflector output beam in the horizontal (bend) plane vs. relative deflector phase. Data are shown for two deflector cavity power levels. The curve is to guide the eye.

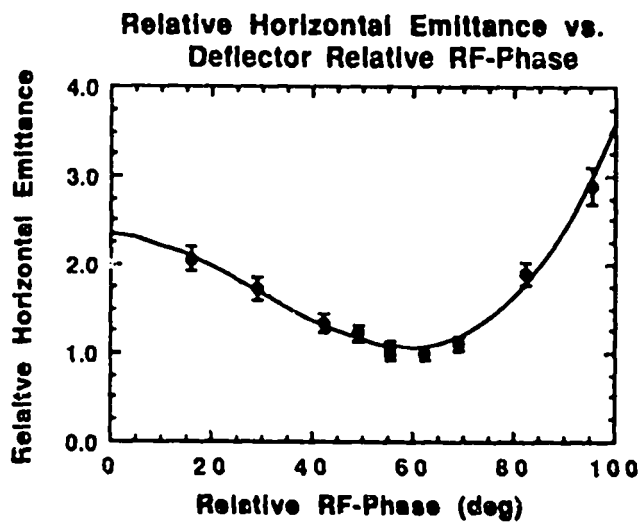

Fig. 3. Relative ε_x of the deflector output beam in the horizontal plane vs. relative deflector rf phase. Cavity power set at 86 kW. The curve is to guide the eye.

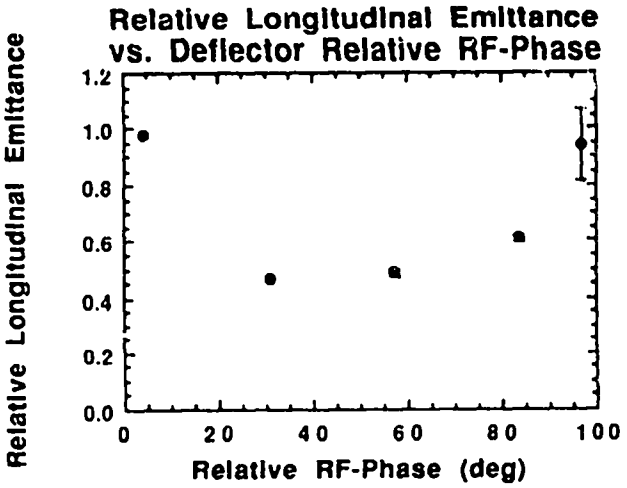

Fig. 4. Relative ε_L vs. relative deflector phase. Deflector cavity power set at 86 kW.

Relative ε_x, ε_y, ε_L, and the Courant-Snyder parameters (in x and y) were shown to be independent of deflector cavity power.

With the rf deflector set at its experimentally determined "best" power and phase set-points, the measured absolute horizontal deflection of the beam was 36 ± 2 mr. Simulations predicted a deflection of 38.4 mr. Within the experimental error (±2 mr) and the 5% uncertainty in gap voltage, there was excellent agreement between measurement and simulations. The beam deflection scaled with rf power as expected.

With the four bunchers and the rf deflector at their optimum phase and amplitude set-points, the transverse and longitudinal phase-space distributions were measured. When the observed emittances and currents at the exit of the M1-plate are used as input, simulations predict an upper limit of ~5% transverse emittance growth through the rest of the funnel beamline. Within experimental error, the data (ε_x = 0.022 π cm-mr or ε_y = 0.020 π cm-mr) are consistent with simulations and with no transverse emittance growth. The short-term and day-to-day reproducibility of the data is 2 to 3% and 8 to 10%, respectively. The error on the emittance measurements is 5 to 8% with background subtraction being the dominant component of the error.

The attempt to produce a measureable emittance growth with non-optimum operation of the rf bunchers (amplitudes 20% low) also produced a null result (consistent with simulations). With the four rf bunchers "off", ε_x increased by ~33%, at the M3-exit, and by a factor of 3 at the M4-exit (due to beam debunching). Large emittance growth (in ε_x and ε_L) was also observed for improper phasing of the deflector (Figs. 3 and 4).

Using the DTL design ε_L as input, simulations predict an upper limit of ~5% ε_L growth through the funnel. The observed growth was ~15 to 20%. The error on ε_L is a few percent (~5%) and reflects the scatter in the measured values. The results for non-optimum buncher operation were basically the same. The measured ε_L of the DTL output beam was ~4 times smaller than the design value of ε_L, so even a 20% emittance growth through the funnel was not detrimental to the funnel's performance.

SUMMARY OF THE FUNNEL PERFORMANCE

The major objectives of the ATS single-beam funnel were realized. Position (i.e., steering) control was achieved throughout the funnel with a ~100% beam transmission.

The use of rf-deflection was successful. The dependence of beam deflection, ε_x and ε_y, the horizontal Courant-Synder parameters, and ε_L on deflector amplitude and phase was as expected The desired amplitude and phase set-points were easily determined.

Transverse and longitudinal emittance growth through the ATS single-beam funnel were controlled. Within experimental precision no transverse emittance growth was observed as expected. Non-optimum operation of the rf bunchers also failed to produce any measureable transverse emittance growth.

Longitudinal emittance growth through the ATS single-beam funnel was controlled to a level which was not detrimental to the funnel's performance. A measurement of longitudinal emittance growth in a drift (~35 cm) showed large growth (60-80%). Transverse and longitudinal emittance control in the funnel beamline (length ~160 cm) has eliminated this large growth.

ACKNOWLEDGEMENTS

The successful completion of the ATS single-beam funnel experiment would not have been possible without the cooperation of many individuals throughout the Accelerator Technology Division of LANL.

REFERENCES

1. O. R. Sander, et al., "Review of the Accelerator Test Stand Performance and Expectations," 1989 Neutral Particle Beam Technology Symposium, Monterey, CA, July 1989.

2. R. J. Kashuba, et al., "Physics Design of the ATS Funnel Experiment," 1989 Neutral Particle Beam Technology Symposium, Monterey, CA, July 1989.

3. W. B. Cottingame, et al., "Noninterceptive Technique for the Measurement of Longitudinal Parameters of Intense H^- Beams," Proc. 1985 Particle Accelerator Conference, IEEE Trans. Nucl. Sci. 32 (5), 1871 (1985).

4. C. M. Fortgang, et al., "Londgitudinal Beam Dynamics of a 5-MeV DTL," 1988 Linear Accelerator Conference, Williamsburg, Virginia, October 1988, Continous Electron Beam Accelerator Facility CEBAF-Report-89-001 (June 1989), p. 167.

5. J. D. Cilpatrick, et al., "Synchronous Phase and Energy Measurement System for a 6. 7 MeV H^- Beam," 1988 Linear Accelerator Conference, Williamsburg, Virginia, October 1988, Continous Electron Beam Accelerator Facility CEBAF-Report-89-001 (June 1989), p. 134

6. G. O. Bolme, et al., "Measurement of RF Accelerator Cavity Field Levels at High Power from the Characteristic X-ray Emissions," this conference.

TRANSVERSE COUPLING IMPEDANCE MEASUREMENT STUDIES OF LOW-Q CAVITIES*

Linda Walling, Paul Allison, and Alan Shapiro
Los Alamos National Laboratory, Los Alamos, NM 87545

Abstract

We report studies using wire and beadpull measurement techniques to determine the accuracy of transverse coupling impedance measurements, particularly for the case of very low-Q cavities. The studies were performed on simple pillbox cavities in preparation for the measurement of Dual-Axis Radiographic Hydrotest Facility (DARHT) linac cavities, which require extremely low coupling impedances for the deflecting modes of the cavity.

Introduction

This report describes two methods of measuring the transverse impedance of TM_{1n0} modes of pillbox cavities. We measured pillbox cavities to determine the accuracy of the measurement techniques before attempting to measure the actual DARHT cavities, which are low-Q ($Q \leq 5$) ferrite-loaded cavities that accelerate beam by applying a dc-voltage across the cavity gap. In order to avoid beam instabilities the transverse impedance, Z_t, where Z_t represents the LLNL definition[1] of transverse impedance, may need to be measurably small ($\omega Z_t/c \leq$ 400 ohms/m).

Previous coupling impedance measurements[2] were for beam pipe structures and cavities having Q's on the order of 100 or greater; however, we had not considered whether there might be difficulties inherent in measuring cavities with very low Q's, nor did we have much knowledge of the accuracies of the measurements. The present work explored both wire and bead-pull measurement techniques on high-Q pillbox cavities (a geometry in which the coupling impedances are readily calculated by the 2-D code URMEL-T and the analytical model described in Ref. 1, hereafter called the Briggs model.)

The TM_{1n0} (or dipole) modes are deflecting modes of cavities, and the transverse coupling impedance is a measure of how efficiently the beam interacts with these modes. This paper will use two different definitions of coupling impedance: the LLNL definition,[1] which has been converted to the MKS system of units

$$\frac{Z_t}{Q} = \frac{c^2[\int B_y\, dz]^2}{2\omega_0 U}, \tag{1}$$

and the SLAC-DESY definition[3]

$$Z_\perp = \frac{j}{\beta I \Delta}\int_{-l/2}^{l/2} (E + v \times B)_T dz, \tag{2}$$

where $\beta = v/c$, I is the beam current, v is the beam velocity, l is the length of the cavity, and Δ is the transverse distance of the beam from the cavity axis. The two definitions of have the following relationship:[4,5]

$$Z_t = \frac{c}{\omega} Re\, Z_\perp . \tag{3}$$

*Work supported by the U.S. Department of Energy, Weapons Activities, GB01.

Beadpull and wire measurements were performed on the following configurations: an Al pillbox cavity, the Al cavity with a mu-metal insert to lower the Q, the Al cavity with large magnetically-coupled, terminated loops to lower the Q, and a steel cavity with and without the terminated loops. These couplers were conducting rods inserted at about mid-radius in the plane containing the maximum electric field. The couplers were shorted to one end of the cavity and were terminated by a resistor to the other end of the cavity. Figure 1 shows the couplers and the electric field patterns for the first three dipole modes of the cavity. Each of the cavities has a 12.7-cm radius. The Al cavity is 38 mm long: the steel cavity is 12.7 mm long. The beam pipe radius is 17.5 mm.

URMEL-T, a computer code that computes TM and TE modes in cylindrically symmetric structures, was used to calculate the transverse impedance:

$$\frac{Z_t}{Q} = \frac{1}{2\omega_0 r_0^2}\frac{|\int_{r_0} E_z\, dz|^2}{U} . \tag{4}$$

where r_0 is the radial distance from the axis. URMEL-T calculates the integral of E_z at the beam tube radius; then it calculates an equivalent value for any specified r_0 by using the known radial distribution (linear for TM_{1mn}, quadratic for TM_{2mn}, and so forth).

Measurement Methods

Figure 2 shows a diagram of the cavity and test environment for the wire measurements. The cavity is transformed into a shielded, balanced coaxial TEM line by adding a section of beam pipe on each end and placing two center conductors inside the pipe. Reference 2 gives complete detail on the wire method.

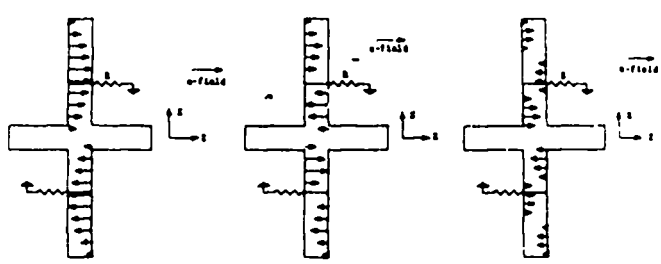

Fig. 1. Position of coupling rods with respect to electric field patterns of first three dipole modes of pillbox cavity.

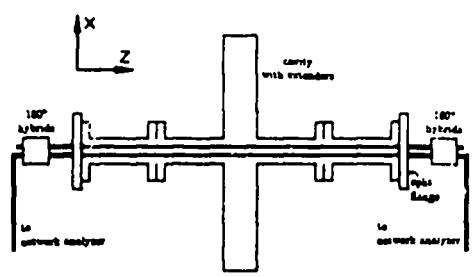

Fig. 2. Wire measurement of transverse coupling impedance of pillbox cavity.

A TSD calibration removes the effects of all mismatches and lengths of line from inside the network analyzer up to the the test cavity with its beam pipe extensions is inserted. Two 180° hybrids are used to excite the beam pipe and cavity with transverse currents. Because the cavities measured are short compared to a wavelength, the cavity is modeled as a lumped parallel resonant circuit imbedded between two sections of transmission line. The two equations that result permit the impedance to be calculated from the magnitude and phase of the measured transmission (after the transmission phase has been corrected to remove the effect of the length of the cavity):

$$re[T^2 Z_t] = \frac{2Z_0}{\Delta^2}\left(\frac{\cos\theta}{|S|} - 1\right) \tag{5}$$

$$im[T^2 Z_t] = \frac{2Z_0}{\Delta^2}\frac{\sin\theta}{|S|}, \tag{6}$$

where T is the transit time factor. In this paper, all of the following references to values for $Z_\perp$ or Z_t are referring to the real part only. The distance between the two wires is Δ, $|S|$ is the magnitude, and θ is the corrected phase of S_{21}, the transmission through the cavity. Typically, the calibration procedure can be performed with an accuracy of better than ±1% at 100% transmission, and involves measuring a through connection, applying the calibration, and then finding the magnitude of the transmission to be 1 ± 0.01 (calibration precision will be discussed more fully in the discussion of results). Therefore, if the pipe radius is equal to 17.5 mm, the wire radius equal to 1.6 mm, with the wires spaced 24 mm apart ($Z_0 = 200\,\Omega$), and the frequency of the TM_{110} mode approximately 1400 MHz, the minimum measurable impedance is $T^2 Z_\perp \geq 230\ \Omega/m$, or $Z_t \geq 8\ \Omega$. Errors due to field distortions caused by the wires can be minimized by the use of thin wires (calculations by Gluckstern[6] indicate that these field distortions would result in errors of 20% or less). Although we had not previously done extensive testing to determine the accuracy of these measurements, measurements on several devices had yielded results that were very close to calculated impedances.

Measurement of the coupling impedance using the beadpull method is based on the Slater perturbation theory[8], which states that the frequency shift in a cavity due to perturbation by a small, conducting sphere is

$$\frac{\delta f}{f} = \frac{(\frac{3}{2}\mu_0 H^2 - 3\epsilon_0 E^2)}{4U}\frac{4\pi a^3}{3}. \tag{7}$$

Alternatively, for a small, dielectric sphere,[9]

$$\frac{\delta f}{f} = -\frac{\pi a^3}{U}\left(\frac{\epsilon - 1}{\epsilon + 2}\right)\epsilon_0 E^2. \tag{8}$$

We calibrated our dielectric beads by pulling them and a metallic bead of known diameter on axis for the TM_{010} mode, noting the maximum frequency shift at the center of the cavity, and calculating a constant for the dielectric bead that represented the effects of its size and permittivity.

The transverse impedance of the dipole modes can be measured by beadpulls in two different ways. The electric field of these modes is nearly zero on axis; for a perfect pillbox, it is exactly zero, however the presence of the beam pipes causes fringe fields. The magnetic field is so strong on axis, however, that the frequency shift caused by a metal bead pull is almost entirely due to the displacement of magnetic field. Thus, for a dipole mode, one may pull a metal bead along the axis of the cavity, calculating the integral of the magnetic field. Errors in this measurement would be due to fringe electric and longitudinal magnetic fields; however, these errors should be small. Combining Eqs. 1 and 7,

$$\frac{Z_t}{Q} \simeq \frac{c^2\mu_0}{\omega_0 \pi a^3}\left|\int\sqrt{\frac{\delta\omega}{\omega_0}}\,dz\right|^2. \tag{9}$$

Alternatively, the measurement could be performed by pulling a dielectric bead off-axis and measuring the electric field. Because

$$B_y = \frac{1}{j\omega}\frac{\partial E_z}{\partial r} \tag{10}$$

and because, for the dipole modes,

$$E_z = r_0\frac{\partial E_z}{\partial r}, \tag{11}$$

combining Eqs. 1, 10, and 11,

$$\frac{Z_t}{Q} = \frac{c^2}{2\omega_0^3 r_0^2 U}\left|\int_{r_0} E_z\,dz\right|^2. \tag{12}$$

Results

Table I shows, for the TM_{110} mode, the measurement results for the Al pillbox cavity. The bead size was 1.59 mm both for the magnetic field measurement (metallic bead, on axis) and for the electric field measurement (dielectric bead, off-axis). The degenerate dipole mode (orthogonal to the one being measured) was moved by using shorting rods in the plane x=0. Also, because significant field extended into the beam pipes on both sides of the cavity, all measurements were performed with attached beam pipes long enough (the first three modes were below cutoff for the beam pipe) to provide attenuation at the ends of the pipes.

TABLE I. RESULTS OF Al CAVITY MEASUREMENTS
R = 12.7 cm, g = 3.8 cm, b = 1.75 cm and Δ = 2.4 cm

Q	Z_t/Q Briggs	Z_t/Q URMEL-T	Z_t/Q Beakpull	Z_t/Q Wires
7040	30.5	37	36.6[a]	
			30.9[b]	
2450				48
360[c]			34.8[b]	
490			26.5[b]	
300[d]				25
275			20.2[b]	
22[e]				22

[a]Off-axis electric field measurements. [b]On-axis magnetic field measurements. [c]Mu-metal-lined cavity. [d]One large coupler. [e]Two large couplers.

The discrepancies between URMEL-T and the wire measurement results are fairly large ($\simeq$ 30%) for the higher-Q measurement. This may be because as the cavity impedance gets very large, the magnitude of the transmission $|S|$ becomes very small. Calibrations on network analyzers tend to yield large errors in $|S|$ as $|S|$ becomes very small. The errors in impedance vary as $\Delta Z_\perp/Z_\perp = \Delta|S|/|S|$. Figure 3 shows data taken from specifications for three Hewlett Packard network analyzers. All data are for a full 12-term 2-port calibration using precision 7-mm calibration hardware. This particular measurement with Q = 2450 corresponds to $|S| \simeq -42$ dB, which is possibly beyond the small error region for this experiment. The wire measurement technique must be used with care when measuring medium-to-high-Q cavities (beadpull methods require a high Q in order to have measureable frequency shifts). Another source of error is that the cavity gap represents 18% of a wavelength at 1420 MHz, so the lumped approximation is not very good. The measured values for Z_t (both wire and beadpull) with the couplers in place are low because the coupling rods present a large perturbation to the fields (see Fig. 1) for this mode and thus actually lowers the impedance.

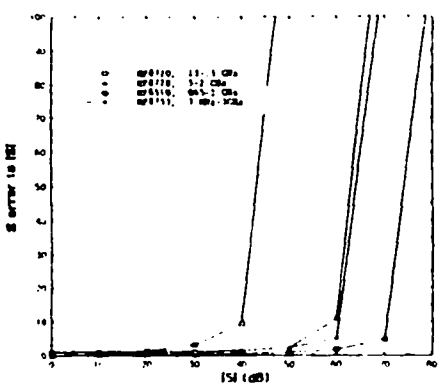

Fig. 3. Accuracy of transmission measurements.

Table II shows the results of the measurements of the steel cavity. We would expect that the beadpull measurements of this cavity may be less accurate than the Al cavity because the gap, being only 1.27 cm long, is not a lot greater than the size of a bead needed to produce measurable signal with low Q's. The bead is no longer a small perturbation to the field, and the Slater perturbation formulas do not describe the measurement as well as before. On the other hand, we would expect greater precision from the wire measurement because the shorter cavity gap will fit the lumped impedance model better than a longer one. The higher-Q measurements (ones with no couplers) were performed both with the wires close together (7.6 mm, Z_0 = 170 Ω) and with the wires placed far apart for greater sensitivity (24 mm, Z_0 = 200 Ω). The bead pull was performed using a metallic bead on axis and only for the lowest mode because we do not have a synthesizer above 2 GHz that can be phase-locked.

As expected, the wire measurements on the steel cavity agree more closely with calculations, probably because the cavity now has a lower Q and better represents a lumped impedance. With the couplers in place, the impedances again are lowered, as with the Al cavity.

TABLE II. RESULTS OF STEEL CAVITY MEASUREMENTS
(R = 12.7 cm, g = 1.27 cm, r = 1.75 cm)

Mode	f	Q	Z_t/Q Briggs	Z_t/Q URMEL-T	Z_t/Q Beadpull	Z_t/Q Wires
TM110	1410	180	16.3	16	11	21[a]
						16[b]
		12[c]				13[b]
TM120	2560	280	12.4	14		17[a]
						13[b]
		65[c]				16[b]
TM130	3730	430	7.6	10		9[a]
						7[b]
		170[c]				5[b]

[a]Close-spaced wires. [b]Wide-spaced wires. [c]Two large couplers.

Conclusions

The pillbox measurements indicate that the wire measurements can be performed with a sufficiently high degree of sensitivity and accuracy to measure the DARHT cavity models. The DARHT cavities have a gap that is short compared to the wavelength of the first two dipole modes, the wires will be small compared to the dimensions of the cavity, and the impedances will be low but well above the noise floor of the measurement. These measurements have also shown that impedance measurements of high-Q cavities may require beadpull methods and that low-Q cavities (especially ones with small gaps) require wire measurements.

References

1. R. J. Briggs, D. L. Birx, G. J. Caporaso, V. K. Neil, and T. C. Genoni, "Theoretical and Experimental Investigation of the Interaction Impedances and Q Values of the Accelerating Cells in the Advanced Test Accelerator," UCRL-92095, Lawrence Livermore National Laboratory, Livermore, CA.
2. L. S. Walling, D. E. McMurry, D. V. Neuffer, and H. A. Thiessen, "Transmission-Line Impedance Measurements for an Advanced Hadron Facility," *Nucl. Instrum. Methods Phys. Res.* **A281**, p. 433-447 (1989).
3. F. J. Sacherer, "*9th International Conference on High-Energy Accelerators*," (U.S. Atomic Energy Commission, Washington, 1974), p. 347.
4. G. Craig and J. DeFord, "The Connection Between SLAC-DESY and LLNL Wakefield Formalisms," Lawrence Livermore National Laboratory research memorandum UCRL-100623.
5. P. Wilson, "High Energy Electron Linacs: Applications to Storage Ring RF Systems and Linear Colliders," Stanford Linear Accelerator Center report SLAC-PUB-2884 (1980).
6. R. Gluckstern and R. Li, "Analysis of Coaxial Wire Measurement of Longitudinal Coupling Impedance," presented at the Fourteenth International Conference on High Energy Accelerators, Kek, Japan (1989).
7. L. Maier, "Field Strength Measurements in Resonant Cavities," MIT Research Laboratory of Electronics MIT-RLE-TR-143 (1949).
8. L. Mullett, "Perturbation of a Resonator," A.E.R.E. G/R.853, A.E.R.E. Harwell (1952).

HIGH-CURRENT, LOW-ENERGY RF ION ACCELERATOR

B.P.Murin, V.M.Pirozhenko, O.V.Plink
Moscow Radiotechnical Institute USSR Academy of Sciences,
113519 Moscow,USSR

Abstract

Theoretical and applied aspects of a beam current increase in ion linacs with superconducting solenoid focusing are considered.

Introduction

The main restriction of a beam current in low-energy RF ion accelerators is the coulomb particle repulsion. The simultaneous achievement of the accelerating and focusing fields high values is necessary to compensate for the high-current beam coulomb fields. That can be realized in the accelerating- focusing system with the resonator placed inside the focusing solenoid [1]. According to estimations, the beam current limit by the transverse coulomb repulsion may be increased up to several amperes and higher by using the superconducting solenoid with the induction of 7...8 T [1].

The accelerating system development with minimum transverse dimensions is necessary to achieve a high value of a beam current. The RF accelerating channel has to provide high values of the beam current limits by the longitudinal coulomb repulsion and the capture efficiency. It is necessary to realize the required accelerating field distribution along the accelerator axis under high resonator beam loading conditions.

The strong magnetic fields use for the beam focusing requires the solution of a number of specific problems. First one needs to solve the beam injection problem into the strong magnetic field. The resonator electrical insulation and the ion injector operation are influenced by the above mentioned magnetic field.

The main results of these investigations are briefly described below.

Beam Dynamics

In the accelerating structure of this type accelerator one should use the adiabatic beam bunching with carrying out of the bunch quasi-stationary conditions during the bunching. The bunch quasi-stationary conditions allow to safe the space-charge density distribution in the bunch and to simplify the beam matching with the accelerating-focusing system.

It can be shown that the expressions for the amplitude E_m of the accelerating wave and synchronous phase φ, providing the bunch quasi-stationary conditions, are the following

$$\cos\varphi_s = [1+\delta^{-1}\exp(-\xi)]^{-1};\ E_m/E_{mo} = 1+\delta(\exp\xi-1);$$

where $\delta = (\pi/2-|\varphi_{so}|) \ll 1$, $\xi = qE_{mo}z/2W_{so}$, q - the particle charge, z - the longitudinal coordinate, W_s - the synchronous particle energy. The variables with indexes "o" and "f" correspond to the bunch beginning and end accordingly. The large buncher length is necessary to achieve a high value of the capture efficiency k_c in the adiabatic buncher with the bunch quasi-stationary conditions correct carrying out. So, the buncher length is equal to 1.15 m for k_c= 95 %, when W_{so} = 100 keV, E_{mo} = 1 MV/m, $|\varphi_{sf}|$= 45°. It is necessary to refuse the bunch quasi-stationary invariants safe along the buncher axis to shorten the buncher length. The bunch quasi-stationary conditions approximate carrying out is possible for the buncher with the linear change of the wave amplitude and synchronous phase. The buncher length and the accelerating wave amplitude rising are calculated on the basis of the equality conditions of the small phase oscillations frequencies and the separatrixes geometric length for the buncher input and output :

$$\mathcal{L}_b = \frac{5.6\ W_{so}}{q\ E_{mo}},\quad \frac{E_{mf}}{E_{mo}} = \frac{\beta_{sf}}{\beta_{so}\sin|\varphi_s|}$$

where β_s - the reduced velocity of a synchronous particle. In general, the RF accelerating channel contains the adiabatic buncher and the acceleration section, where the amplitude of the accelerating wave and synchronous phase are constant. On the supposition of the beam current limit defined by the adiabatic buncher end and the bunch phase length is equal to $2|\varphi_{sf}|$, we have that the beam current limit by the longitudinal coulomb repulsion is equal to

$$I^* = 1.5\ (\beta_{sf}\ \varphi_{sf})^2 \frac{R_b}{\lambda}\left[\frac{\Omega_f}{\omega}\right]^2 I_o,$$

where R_b - the beam radius, λ - the operating wave length, $\omega = 2\pi c/\lambda$, Ω - the cyclic frequency of the longitudinal oscillations, I_o - the characteristic beam current , c - the velocity of light.

In the SIU-1 experimental proton accelerator the adiabatic beam bunching has been used in the accelerating field with linear rising and the bunch

quasi-stationary conditions approximate carrying out. The channel characteristics are following : the low injection energy (100 keV), the high accelerating rate (1.75 MeV/m). The channel general parameters are : E_{mo} = 1 MV/m, E_{mf} =3.7 MV/m, φ_{so}=-90°, φ_{sf}=-45°, R_b= 5 mm. For the above mentioned parameters it is found that $\mathcal{L}_b$= 0.56 m, W_{sf}= 0.7 MeV, I^*= 2.5 A for λ =1.5 m. The bunch quasi-stationary conditions disturbance is order 25 % in the SIU-1 buncher. Numerical simulations of a beam longitudinal dynamics indicate that the beam current limit is equal to 2.75 A, the capture efficiency achieves 96 % for the beam current of 1 A.

Magnetic fields of 5...7 T are necessary to focus the beam with the current density of about 1 A/cm^2 and the phase density of several A/cm mrad for λ = 1.5 m. During the beam injection into the magnetic field the particles longitudinal energy is decreased. For compensation that it is necessary to increase an injection energy up to 20 ÷ 30 %.

Accelerating structure

The combination of the small transverse sizes, the low sensitivity to the strong beam loading, capability of the uniting the large number of accelerating gaps and high value of an accelerating field can be reached in the opposed vibrator resonator (OVR) (see Fig.1.)

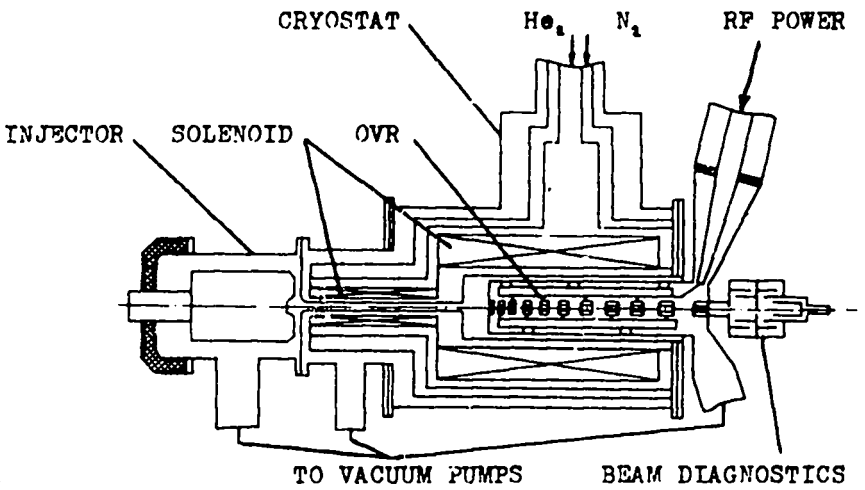

Fig. 1.

The OVR can be considered as a system of the coupled lines loaded by the lumped elements [2].

One can show that the structure dispersion equation is of the form

$$kl(1 + \sqrt{1 + x})/2 = \pi/2 + \alpha\cos\varphi - \beta\cos^2\varphi,$$

where k - the wave number in the free space, φ - the normal wave phase shift in the l length structure section. Here α and β are the distributed and lumped coupling coefficients, x is the capacitive load coefficient.

In the lowest passband the resonance condition of the OVR, consisting of N sections, is $\varphi = \pi m/N$, m = 0,1,...,N. Together with the large bandwidth , the small number of the modes for the resonator, consisting of the large number of the accelerating cells, defines good modes separation in the OVR, and, hence, the low sensitivity to the strong beam loading. By means of the resonator section detuning , the various accelerating wave amplitude distributions are possible in the OVR, in particular, the increasing law, which is needed to realize adiabatic beam bunching and to achieve the accelerating channel equal electric insulation.

The high value of the accelerating wave can be achieved in the OVR. At the channel axis the accelerating wave amplitude is coupled with the maximum electric field at the drift tubes surfaces E_m by the relation [3] :

$$E_m = \frac{E_m k_g \cos(\pi k_g/2)}{I_o[\pi a/h + \pi(1 - k_g)/2]},$$

where h - the accelerating cell length; k_g -the gap coefficient; I_o - the modified Bessel function.

The maximum accelerating gradient can be achieved with k_g = 0.6...0.7.The accelerating wave amplitude should increase along the channel axis for $\pi a/h$ > 0.5. E_m can achieve the value of about 5...10 MV/m with E_m= 20...30 MV/m. Thus, at the SIU-1 accelerator resonator the accelerating wave amplitude of about 8 MV/m has been achieved.

The OVR has a high value of the shunt impedance in the low-energy region. The SIU-1 accelerator resonator has the shunt impedance of about 30 MOhm/m.

The Prove of Principle Experiments

The RF ion acceleration has been realized at the SIU-1 RF experimental proton accelerator. The accelerator is described in short at [4] and in details at [2]. The accelerator scheme is presented at Fig.1. The SIU-1 accelerator design and investigation were carried out as follows :

1. The autonomous tests of the injector, the accelerating resonator and the focusing solenoid. All the calculating parameters have been obtained.
2. The test of the accelerating resonator with focusing solenoid. The test showed the resonator electric insulation decreases at the presence of a strong magnetic field.
3. The injector tests with the focusing solenoid. The tests indicated the magnetic field influence on plasma in the source. To decrease this influence the compensating coil has been installed in the discharge chamber section. The beam current at the resonator input has been risen up to 0.6 A.
4. The beam acceleration experiments. The typical forms of the voltage on measuring loop in the resonator and the beam current from the Faraday-cylinder are presented at the Fig.2a. It is obvious, that the strong RF voltage decrease takes place up to about the half of its value. A number of experiments were carried out using the automating amplitude tuning system to compensate this decrease. The beam current and the RF voltage pulses obtained with the operating automatic amplitude tuning system are presented at the Fig.2b. Experimental data are presented in Table I.

TABLE I
SIU-1 Experimental Accelerator Performances

Maximum particle energy (MeV)	1.5
Injection energy (keV)	100...130
Maximum accelerated beam current (A)	0.4
Operating frequency (MHz)	196.8
Beam pulse duration (μs)	30...70
Repetition rate (puls/s)	1

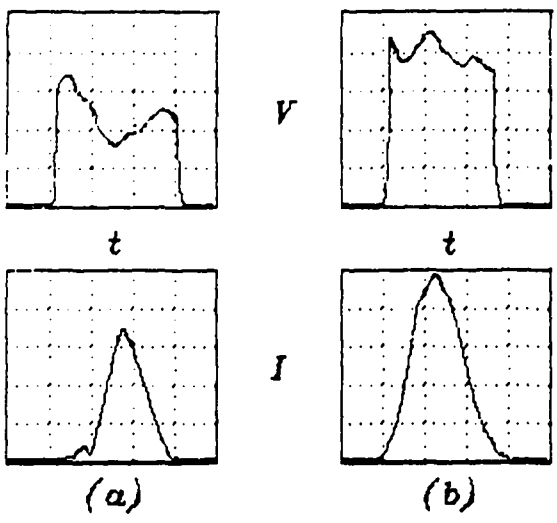

Fig.2.

Development and Application

The limiting calculated beam current possibilities of the SIU-1 accelerating-focusing system has not been achieved. The main reason of it is that the magnetic field distribution was not optimal because of the solenoid design. At present the SIU-1 accelerator is under development to increase the accelerated beam current. In the SIU-1 accelerator with the injection energy rise up to 200 keV and the simultaneous accelerating wave amplitude decrease to about 1.5 MV/m it is planned to get the proton beam with the energy of about 1.5 Mev and current up to 1.5 A.

This current value is not a limit to this type of the accelerator. Physical simulations of a beam dynamic using an electron probe indicate that the beam with the current up to 5 A may be accelerated at the frequency of about 200 MHz [5]. The further beam current increase can be achieved using the lower operation frequency. The beam dynamic calculations indicate that at the operating frequency of about 20 MHz the beam current may rise up to 15 A [4].

The accelerator with the superconducting solenoid focusing can be used as the initial part of the accelerator for the burner-reactor [6]. The beam with the average current of about 0.3 A can be accelerated using the accelerating wave amplitude of about 1.5...2 MV/m in the accelerator with the injection energy of about 100 keV.

References

1. B.Bondarev et al. " The Focusing Superconducting Solenoid Application for the Current Limit Increase in the Ion Linac " Proc. of the 6-th All-Union Conf. on the Charged Particles Accelerator, v.1, 260 (1979).
2. B.Bondarev et al. " The Experimental RF Proton Accelerator with the Superconducting Solenoid Beam Focusing ", Preprint of the Moscow Radiotechnical Institute USSR Academy of Sciences, N 8901 (1989 .
3. O.V.Plink, Journ. of Techn. Phys., 59, 196 (1989).
4. B.Bondarev et al. "High-current RF Ion Accelerators with Longitudinal Magnetic Field Focusing ", Proc. of the 8-th International Conf. on High-Power Particle Beams (1990).
5. U.Jiarcov et al." Issues of the Atomic Science and Technology " S. " Physical Experiment Technique " N.2 (37), 41 (1988).
6. G.Batskikh, B.Murin, A.Fedotov " The Linear Accelerator for the Burner-Reactor ", this Conference.

PROGRESS ON THE TAC ION SOURCE AND LEBT

C.R. Meitzler, P. Datte, F.R. Huson, and P. Tompkins
Texas Accelerator Center†
4802 Research Forest Dr.
The Woodlands, TX 77381

and

D. Raparia
SSC Laboratory
2550 Beckleymeade Ave., Dallas, TX

Abstract

A 500 keV RFQ accelerator is being developed at the Texas Accelerator Center. The ion source for this machine is a magnetron type ion source with a single extraction gap. The design current is 10 mA of H^- with an energy of 30 keV and $\epsilon_{n,90\%} = 0.2\ \pi$ mm-mrad. To date, peak currents in excess of 28 mA have been extracted from this ion source indicating that the current density at the extraction aperture is 2.1 A/cm^2. Preliminary emittances have been obtained 10 cm from the extraction aperture. The extracted beam is transported approximately 30 cm by a helical electrostatic quadrupole lens (HESQ). Initial low current tests of the HESQ have shown that 55 % of the focused beam lies within the RFQ acceptance.

Introduction

A 500 keV prototype RFQ accelerator is being developed at the Texas Accelerator Center. One of the prominent features of this accelerator is the inclusion of a short electrostatic low energy beam transport (LEBT) line between the ion source and the RFQ. This work is being performed as a part of a larger project to construct a 2.5 MeV RFQ linac.

The requirements on the ion source are derived from several sources: the current and pulse length requirements of the SSC, and longer pulses for other applications such as isotope production. The length of the beam pulse that is produced from the ion source and LEBT ranges from 8 μs to 200 μs, with a risetime of 100 ns. The desired current is 10 mA which is determined by the current limit of the 500 keV RFQ prototype. The present work describes the current state of the development of the ion source and LEBT for this project.

Ion Source

The ion source is a BNL[2] type magnetron H^- ion source with diode extraction optics. The basic mechanical design follows the work done at BNL: a cathode with a spherical dimple to provide geometrical focussing, a re-entrant source mount, an external cesium supply, and permanent magnets to provide the source's magnetic field. There have been, however, several changes made to the extraction geometry to adapt the source to the requirements presented above. First, the inner molybdenum anode cover plate and stainless steel extraction plate used at BNL has been joined into one stainless steel anode cover plate which provides both the gas seal for the magnetron source volume and the extraction aperture. This particular modification has been quite reliable and has not yet shown significant wear. The second design change has been to adjust the extraction optics to provide a 10 mA H^- beam whose normalised 90% emittance is 0.2 π mm-mrad. The initial anode aperture is 1.3 mm in diameter with a 4.5 mm gap between the electrodes. Figure 1 shows the extraction geometry used in these tests.

The test beams were extracted from the ion source by applying a constant −30 kV potential to the ion source and grounding the conical extraction electrode. The intensity of the extracted beam was measured by a 6.6 X 8.3 cm planar Faraday cup located 10 cm downstream from the extraction gap. The discharge was operated in 100 μs long pulses with an arc voltage of 147 V and an arc current of 20 A. The extracted H^- current measured by this cup was 28 mA, which indicated that the current density at the extraction aperture was 2.1 A/cm^2.

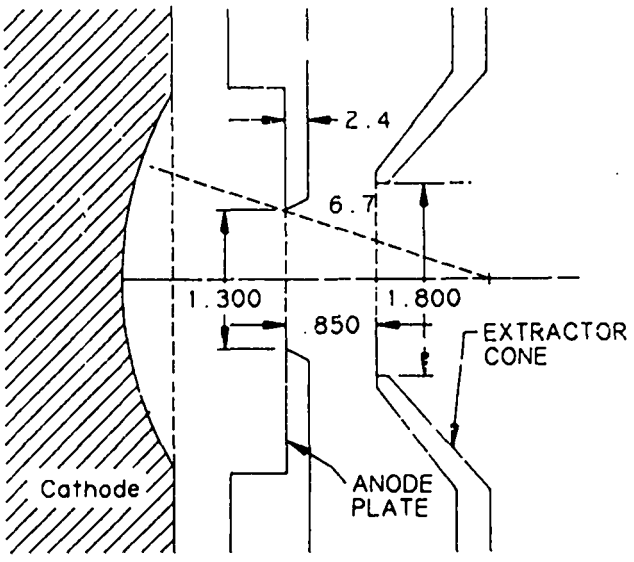

Fig. 1. Extraction geometry (not to scale) for 28 mA source. All dimensions are given in millimeters.

Using this density the area of the extraction aperture in the anode cover plate was scaled down to provide a 10 mA beam. This density is roughly equivalent to the the densities reported by BNL[3].

The ion source emittance was measured with an electrostatic emittance scanner[4] (EES) located 10 cm from the extraction gap. The current incident upon the face of the scanners was measured to provide pulse-to-pulse normalization of the data.[5] The current waveforms in each of the EES Faraday cups, located immediately after the second analysing slit, and the face current were recorded by a Hewlett-Packard Model 54501B digital oscilloscope. Due to the fact that the neutralisation time of an H^- beam in hydrogen is roughly as long as the pulse length, the EES was used in two different modes to see the behavior of the beam. The first mode placed the EES at a fixed radial position and had fixed deflection plate voltages permitting us to view the behavior of the beam at a fixed point in $x-x'$ or $y-y'$ space. Figure 2 shows the extracted H^- current measured on the scanner face and the analysed current when the scanner was located at -3 mm and the deflection voltage set for -18.7 mrad. Since the shape of the analysed current pulse is in good agreement with the shape of the extracted pulse, it would appear that the ellipse rotation due to neutralization is not a major problem. The second EES mode was to use it to obtain emittances in a manor described by Allison[4]. Preliminary values for the measured normalized, 90% emittances are 0.29 π mm-mrad for the horizontal axis, and 0.36 π mm-mrad for the vertical axis. It should be noted that there was an angular offset of 25 mrad in the vertical direction due to the presence of the magnetic field required to operate the source.

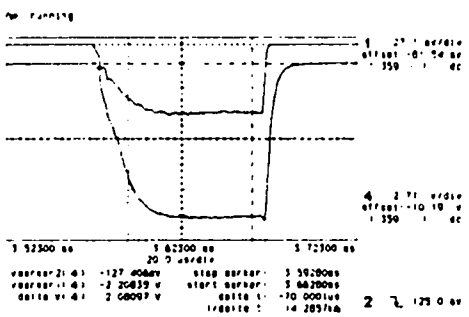

Fig. 2. Waveforms observed on the emittance scanner face and analysed beam Faraday cup. The upper trace is the scanner face current while the lower trace is the analysed current pulse shape.

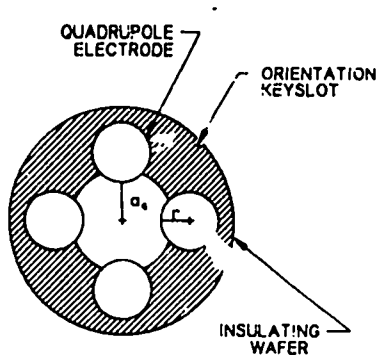

Fig. 3. End view of a HESQ cell. The radius of the electrodes, r, is 1.0 cm. The radius of the available aperture, a_q, is 1.3 cm.

Low Energy Beam Transport

The rotation of the emittance ellipse due to the build up of neutralising particles during the beam pulse may be countered by imposing an external electric field on the beam. Raparia[6] has developed a helical electrostatic quadrupole which is capable of focussing highly charged beams into a RFQ. A HESQ prototype capable of transporting currents up to 10 mA has been constructed at TAC and initial testing is underway.

The first HESQ prototype has been built using a discretised approximation of the helical pole pieces. The entire lens has been divided into four independent HESQ segments for flexibility during operation. Each HESQ segment has been built from a given number of identical unit cells, where each successive cell has been rotated 18 degrees from the previous cell to form the helical structure. Each segment is electrically isolated from the its adjacent cells to provide flexibility during operation. The first three segments have been constructed using 10 cells, and the final segment has been constructed using 8 cells. Figure 3 shows one unit cell. Each cell consists of four stainless steel disks held in place by a single G-10 insulator. A notch on the outside of the G-10 disk provides the rotational alignment. The diameter of the open aperture is 26 mm. The center of each of the cells in the structure was aligned to within ± 0.05 mm. G-10 end insulators are used to provide electrical isolation from support structure at the end of the lens and to provide enough compression to hold the cells firmly in place. The pole voltages for each segment are supplied by eight separate 10 kV, 0.4 mA power supplies. One positive and one negative supply are connected to the electrodes in each segment. The electrical connection between cells is accomplished by contact between the electrodes in adjacent cells. Each HESQ segment was tested without beam up to 10 kV.

The initial tuning of the HESQ pole voltages was accomplished by inserting a tandem Faraday cup into the beam 4.2 cm from the end of the HESQ. The front Faraday cup had a pair of 6 mm apertures to simulate the entrance acceptance to the RFQ: the first aperture was at the back face of the Faraday cup and the second was located 51 mm downstream from the first. Immediately

after the second aperture was a second Faraday cup to measure the current that would pass into the RFQ. The fraction of the beam within the RFQ acceptance, f, was obtained from the ratio $f = I_{back}/(I_{front} + I_{back})$, where I_{front} is the current into the first faraday cup and I_{back} is the current that successfully passes into the second faraday cup. Current striking the second aperture is included in I_{front}. The pole voltages were tuned to maximise both f and the total current.

A low current H^- beam was obtained by detuning the magnetron source and injecting the extracted beam into the HESQ. The current of the injected beam is not immediately known due to the close coupling of the ion source and HESQ. It was found that when a total transmitted current of 2.5 mA was transmitted through the HESQ, the fraction within the RFQ acceptance was 55%. When the transmitted current was increased to 5 mA, f decreased to 42%. The fact that this ratio decreased was due to the 10 kV limit to the pole voltages in the first segment where the beam emerging from the ion source is captured: we were unable to increase the voltage in the first segment far enough for the high current beam to go through a peak in the transmission.

Conclusions

The ion source produced 10 mA of H^- with preliminary normalized, 90% emittances of 0.29 π mm-mrad in the horizontal direction and 0.36 π mm-mrad in the vertical direction, which are in good agreement with computer simulations. The initial trials of the HESQ with low current, 2.5 mA beams have shown that the lens is focusing 55% of the transmitted beam into the RFQ acceptance, but decreased as the injected current increased. It is likely that this fraction will be improved with further improvements such as adding electrostatic or magnetic steering to the system and upgrading the high voltage power supplies on the first segment. This work represents an important first step towards making this lens a usable matching section on future RFQ accelerators.

Acknowledgements

One of the authors (C.R.M.) would like to thank Jim Alessi, Hovi Kponou, Tom Russo, and Ron Clipperton at BNL for many helpful discussions during this project.

This work supported in part by the SSC.

References

† TAC at HARC is a consortium of Rice University, Texas A&M University, the University of Houston, the University of Texas, Prairie View A&M University, Sam Houston State University, and the Baylor College of Medicine MR Center.

1. D. Raparia, "Beam Dynamics of the Low Energy Beam Transport and Radio Frequency Quadrupole", Ph.D. Dissertation, University of Houston, (1990).
2. J. G. Alessi, J. M. Brennan, J. Brodowski, H. N. Brown, A. Kponou, V. LoDestro, P. Montemurro, K. Prelec, and R. Witkover, Proc. of the 1989 Particle Accelerator Conference, Chicago, IL, March 1989.
3. J.G. Alessi, private communication.
4. P.W. Allison, J.D. Sherman, and D.B. Holtkamp, IEEE Trans. Nucl. Sci. NS-30, 2204 (1983).
5. T.W. Debiak, L. Solenstein, J.J. Sredniawskik, Y.C. Ng, and R. Heuer, Rev. Sci. Instrum. 61, 392 (1990).

PROPOSAL OF A PULSED ECR-SOURCE FOR SYNCHROTRON INJECTION

U. Ratzinger, W. Bleuel, B. Wolf and N. Angert
GSI, 6100 Darmstadt, Fed. Rep. of Germany
R. Geller
CENG, 38041 Grenoble, France

Summary

The ECR-source uses magnetic confinement of the plasma by a Minimum B configuration. The number of confined ions depends on the volume and on the density of the plasma.

If a large amount of stored ions could be extracted during about 100 µs the pulsed current would be increased considerably-compared with continuous operation. By installing a pulsed solenoidal coil inside an enlarged plasma chamber of a standard ECR source, the magnetic bottle can be opened and the charged particles - ions and electrons - are accelerated towards the extraction hole by the "Fermi force".

A test setup is under construction at GSI to check that idea.

It is confirmed by some calculations, that "high particle current" and "high charge state" is not necessarily a contradiction.

Dependence of current limits on q/A

The formulas for transversal and longitudinal beam current limits of RFQ structures are derived in ref. 1. It is assumed that the particle pulses have ellipsoidal shape and a homogeneous charge distribution.

This chapter summarizes results from investigations which are described in more detail in ref. 2. The main goal is to demonstrate that high q/A-values out of an ion source are also attractive to build up high current accelerators.

Assumptions about RFQ parameters used in the current limit formulas:

- Limits of longitudinal and transversal phase advances without space charge[1]:

  $\sigma_{0l}, \sigma_{0t} < 90°$

- Limits of longitudinal and transversal space charge parameters[1]:

  $\mu_l, \mu_t = 0.35$

- Choice of the structure parameters in such a way, that the sparking limit is approached; this gives maximum beam current. The dependence of the maximum field strength on the distance between the electrodes[3] is regarded in the calculations.

- The current limit of an RFQ is defined at the bunching section, where the synchronous phase is changed continuously from - 90° to the final value used in the accelerating section.

  For the calculation we use:

  $m = 1.3$, $\phi_s = -60°$, $a/8\lambda = 0.1$ resp. 0.12.
  m:= modulation parameter of the RFQ vanes;
  a:= aperture radius

- The kinetic energy of the ions at the investigated position depends on the charge state q, on the source potential V_s and on the effective rf voltage gain V_{rf} of the ions:

  $W = q \cdot (V_s + V_{rf})$

  In case of high q-values it is favourable to use a low value for $_s$ because it is more complicated to bring that type of ion sources up to high potential.
  Instead of V_s the rf voltage gain during the bunching process can be much higher for high q-values and high rf frequency, because the bunching section can consist of much more unit cells in that case as the length of the structure is not a serious problem.

Results

Table 1 shows the electrical current limits I_l and I_t and the resulting particle current limit I_p in dependence from q/A and rf frequency.

Fig. 1 shows the dependence of the current limits on the mass number of the particle beam. The graphs correspond to the parameter sets in line 1, 2, 6 and 7 of table 1.

q	ν MHz	a/8λ	$\beta \cdot 10^3$	a mm	$E_s \cdot 10^{-7}$ V/m	σ_{0t} deg	σ_{0l} deg	I_t emA	I_l emA	I_p µmA
28	108	0,1	10	3	2,8	39	28	117	150	4,2
28	54	0,12	8,7	5,8	2,3	66	44	212	218	7,6
20	54	0,12	7,4	4,9	2,5	60	42	156	173	7,8
10	54	0,1	5,2	2,9	2,8	59	34	76	67	6,7
10	27	0,12	5,2	6,95	2,2	76	47	152	142	14,2
2	27	0,1	2,3	2,6	2,8	52	32	28	28	14
2	13,5	0,12	2,3	6,1	2,2	67	45	59	59	29,5

Table 1: Dependence of the particle current limit I_p on the charge state q of ^{238}U and on the rf frequency ν.

Interpretation:

- The current limit is inverse proportional to the resonance frequency. At a given resonance frequency the current limit is independent from the q/A-value as long as σ_{0t}, σ_{0l} don't approach the stability limit of 90°.

- By using ion sources for high charge states one can adjust the q/A-ratio for the whole mass region to the optimum value - this means

operation of the RFQ at maximum electric field strength. This makes the dependence of the current limit on the mass number of the particle beam very weak (fig. 1).

- If an ion source for low charge states and one or more stripping processes along the Linac are used[4], the resulting current out of the Linac is lower than in the case of ions out of an ion source for high charge states.

- If ion sources for high particle current and high charge states are available the accelerator structures for heavy ions will become much more simple, compact and efficient.

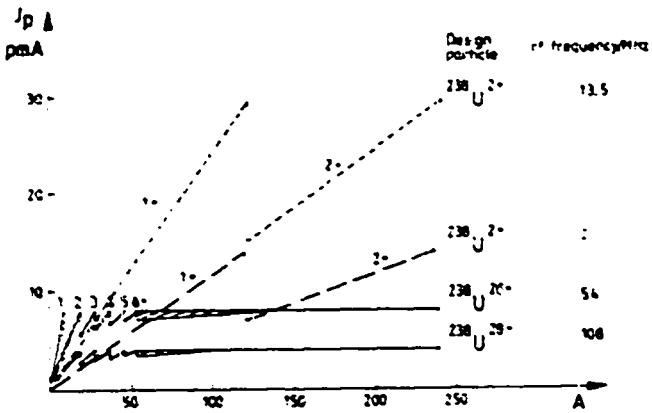

Fig. 1: Dependence of current limits in different RFQ-designs on the mass number of the particle beam.

Number of confined ions in an ECR-plasma

The ECR plasma is heated by the e^- in the zones where the condition for electron cyclotron resonance is fulfilled (eq. 1). Its maximum charge density is limited by resonance coincidence between rf frequency and plasma frequency (eq. 2).

$$B = 0.035 \cdot \nu \; [T/GHz] \qquad 1)$$

$$n_e = 1.85 \cdot 10^{13} \cdot \nu^2 \; \left[\frac{1}{cm^3 \cdot GHz^2}\right] \qquad 2)$$

The rf heating times to reach the equilibrium densities for high charge states lie in the interval:

$$10 \text{ ms} < \tau < 30 \text{ ms} \qquad 3)$$

The e^--gas is not in thermic equilibrium[7]. The e^--energy is in the [keV]-range while the ions during their lifetime in the plasma are heated up by the e^- to kinetic energies in the [eV]-range only.

Using the data of analysed ECR-beams one can calculate the total number of ions confined in the plasma by the formula:

$$N = \frac{n_e \cdot V_{eff} \cdot I_{an}}{I_{ex} \cdot q} \qquad 4)$$

n_e := plasma density (eq. 2)

I_{an} := analysed electric current of the required ion type

I_{ex} := total electric extraction current

q := charge state of the required ion type

N := total number of ions of the required type

V_{eff} := effective plasma volume

The number of confined ions seem to be sufficient to form particle pulses of about 100 µs duration with analysed beam currents in the [mA]-range up to mass numbers above 100.

To reach this goal, three main problems have to be solved:

- A great portion of the confined ions has to be extracted during about 100 µs.

- The extraction voltage has to be increased up to about 100 kV.

- One has to analyse a pulsed extraction current in the [A]-range.

Pulsed extraction of the plasma ions

The force acting on charged particles in a magnetic mirror with axial symmetry around the z axis can be approximated by the following equation:

$$F_z = -\frac{W_\perp}{B_z} \cdot \left(\frac{\partial B_z}{\partial z}\right)_{r=0} \qquad 5)$$

$W_\perp$:= kinetic energy of the charged particle perpendicular to z.

The formula is valid if the transversal distances from the z axis are not too big.

If the distribution of the magnetic field strength B_z in the ECR-source could be changed from curve 1 to curve 2 of fig. 2 the plasma would be moved towards the extraction hole.

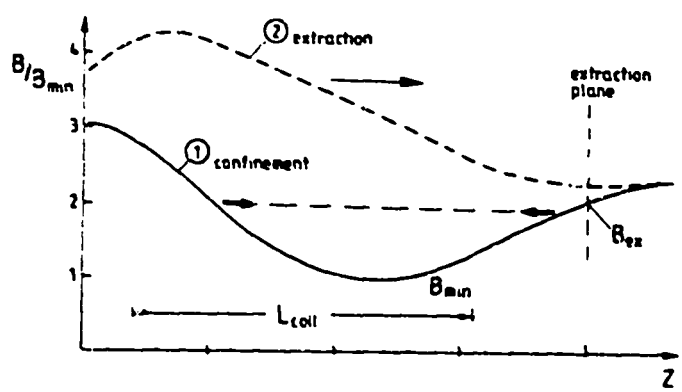

Fig. 2: Magnetic field strength B_z along the axis of the ECR-source:
1 := Distribution during heating and confinement of the plasma
2 := Distribution during ion extraction

To get an idea about the longitudinal energy which is gained by the particles during the extraction process we can use the following approximations in eq. 5):

$$W_z = W_{tot} \cdot \int_{z_1}^{z_{ex}} \frac{1}{B_z} \cdot \frac{\partial B_z}{\partial z} \cdot dz \leq 1 \; ;$$

$$\rightarrow \int_{z_1}^{z_{ex}} F_z \cdot dz \leq W_{tot}$$

W_{tot} := kinetic particle energy.
B_{ex} := magnetic field strength at the extraction plane z_{ex}.

This means that the gain in longitudinal energy during the magnetic extraction process ranges up to the original kinetic energy of a particle. As a consequence the e^- react much faster on the pulsed field.

If the extraction hole is big enough, a great amount of e^- are reflected back into the plasma by the extraction potential and neutralize the plasma till the ions are extracted.

Suggested test array

A 10 GHz Minimafios source, built by CEN Grenoble and recently installed at GSI will be modified to test this extraction principle.

A sketch of the geometry is shown by fig. 3.

The permanent multipole is placed inside the pulsed coil to get enough fieldstrength. A decapole geometry with its steep increase of field strength close to the plasma surface will be used because of the following reasons:

- The transversal magnetic field components, which hinder the pulsed extraction process are weak inside an extended region around the z axis.
- A transversal expansion of V_{eff} is expected. This effect would rise N (see eq. 4) and allow to feed bigger extraction holes with beam, compared to the present experience with sextupole devices.

Another advantage is the smaller outer diameter* of a permanent decapole which defines the inner diameter of the extraction coil (fig. 3).
The pulsed coil consists of two layers.
The end pointing towards the extraction is kept on source potential. At the opposite end the pulsed voltage is applied symmetrically between the inner and the outer coil layer. The permanent magnetic multipole will be enclosed in two housings, isolated from each other.
By that way, closed paths for the flow of eddy currents surrounding the plasma are suppressed.

The excitation of the pulsed coil has to be synchronized with the interrupt of the rf heating.

The magnetic pulse length will be flexible, the rise time is about 100 µs.

References:

1. T.P. Wangler, LA-8388, 12.1980, Los Alamos, Nat. Lab.
2. U. Ratzinger, GSI-UNILAC-INT/89-3
3. I. Hofmann, L.J. Laslett, L. Smith and I. Haber, Particle Accel. 13 (1983) 145
4. M. Reiser, Nucl. Instr. and Meth. A278 (1989) 138-142
5. A. Gerhard, Diss. Uni Frankfurt, 1989
6. J. Klabunde, N. Angert, L. Dahl, R. Keller, M. Müller, R.W. Müller, P. Spädtke, GSI, J. Häuser, H. Klein, A. Schempp, A. Schönlein, Uni Frankfurt, Proc. of the 1986 Linac Conf. Stanford, SLAC-303
7. G. Melin, F. Bourg, P. Briand and R. Geller, Journal de Physique, Jan. 1989 (1-727)
8. K. Halbach, Nucl. Instr. and Meth. 169 (1980) 1-10.

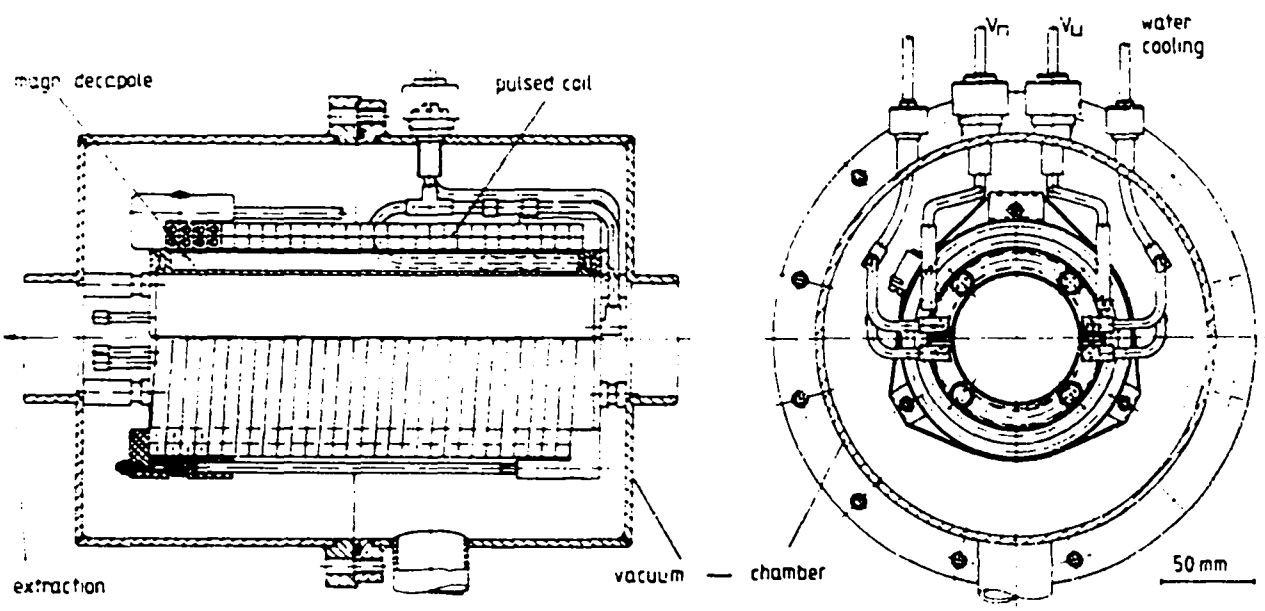

Fig. 3: Modified second stage chamber of a 10 GHz ECR source MININAFIOS.

ASYMPTOTIC ANALYSIS OF THE LONGITUDINAL INSTABILITY OF A HEAVY ION INDUCTION LINAC*

Edward P. Lee and Lloyd Smith
Lawrence Berkeley Laboratory, University of California, Berkeley, CA 94720

Abstract

An Induction Linac accelerating high ion currents at sub-relativistic energies is predicted to exhibit unstable growth of current fluctuations at low frequencies. The instability is driven by the interaction between the beam and complex impedance of the induction modules. In general, the detailed form of the growing disturbance depends on the initial perturbation and ratio of pulse length to accelerator length, as well as the specific form of the impedance. An asymptotic analysis of the several regimes of interest is presented.

Linac Model

We treat a cluster of beams drifting at velocity v, with line charge density λ and current $I = \lambda v$. It is assumed here that all the beamlets $(N \sim 16)$ effectively act in concert so that λ and I are the total values and v is the common velocity. The continuity equation, written in laboratory frame quantities (z,t) is:

$$\frac{\partial \lambda}{\partial t} + \frac{\partial I}{\partial z} = 0 \ . \tag{1}$$

A smoothed longitudinal field E, induced by interaction of I with the induction modules, acts on v:

$$\frac{\partial v}{\partial t} + v\frac{\partial v}{\partial z} = \frac{qe}{m} E \ . \tag{2}$$

In general E is related to I through an impedance

$$E(\omega) = -Z(\omega)\, I(\omega) \ . \tag{3}$$

However in the present study the low frequency interaction is modeled as that of a resistance R and capacity C in parallel. We may use the circuit representation:

$$\frac{E}{RC} + \frac{\partial E}{\partial t} = -\frac{I}{C} \tag{4}$$

Most previous related work[1] has neglected the capacity, but included a direct space-charge force proportional to $\partial\lambda/\partial z$ The present model appears to be more representative at low frequencies for the Heavy Ion Fusion application. In general the capacity reduces growth rates compared with the case of pure resistance by lowering the impedance as frequency increases.

A perturbation analysis is carried out for small variations from constant equilibrium values. For:

$$v = v_o + \delta v \ ,$$
$$\lambda = \lambda_o + \delta\lambda \ ,$$
$$I = I_o + \delta I \ ,$$
$$E = \delta E \ ,$$

the perturbed equations are:

$$\delta I = \lambda_o \delta v + v_o \delta\lambda \ , \tag{5}$$

$$\frac{\partial \delta\lambda}{\partial t} + \frac{\partial \delta I}{\partial z} = 0 \ , \tag{6}$$

$$\frac{\partial \delta v}{\partial t} + v\frac{\partial \delta v}{\partial z} = \frac{qe}{m}\delta E \ , \tag{7}$$

$$\frac{\delta E}{RC} + \frac{\partial \delta E}{\partial t} = -\frac{\delta I}{C} \ . \tag{8}$$

The values of R and C are related to beam parameters by considerations of system efficiency. For a good match of source to beam load, R must not be too different from the matched value $R_o = G/I_o$, where G is the average accelerating gradient. For the typical parameters $G = 10^6$ volts/m and $I_o = 1000$ amp, we have $R_o = 1000\ \Omega$/m. In this case R could be reduced to 300 Ω/m without serious loss of efficiency. The characteristic time $RC \equiv \alpha^{-1}$ should be a small fraction of the pulse length to avoid excessive energy flow in charging the accelerating gaps. For the typical value $C = 3\times10^{-10}$ F-m, we have $RC = 90$ ns, which is short compared with a typical 500 ns pulse length.

In this simple model, time scales with $RC = \alpha^{-1}$, where the "retarded time" variable $\tau = t - z/v_o$ is used. A second scale quantity

$$K = \sqrt{\frac{qe\lambda_o}{mv_o^2 C}}$$

appears in the theory and scales the variable z. That is, $\alpha\tau$ and Kz appear in a dimensionless formulation of Eqs. (5-8).

Perturbation Analysis

If we neglect the self-force from space charge, proportional to $\partial\lambda/\partial z$, the coupled equations for perturbed field and current are conveniently written using z and the retarded time $\tau = t - z/v_o$ as independent variables. We have

$$\frac{\partial^2 \delta I}{\partial z^2} = K^2 C \frac{\partial \delta E}{\partial \tau} \ , \tag{9}$$

$$\left(\alpha + \frac{\partial}{\partial \tau}\right)\delta E = -\frac{\delta I}{C} \ . \tag{10}$$

Initial conditions on δI are specified at $z = 0$ for $\tau \geq 0$; in this model no disturbance is able to propagate backwards into the zones, $\tau < 0$ or $z < 0$. If the initial perturbation is a time-dependent velocity error generated at $z = 0$, the initial conditions are:

$$\delta I(o,\tau) = 0 \ ,$$
$$\delta E(z,o) = 0 \ ,$$
$$\frac{\partial}{\partial z}\delta I(o,\tau) \equiv f(\tau) = \frac{\lambda_o}{v_o}\frac{\partial \delta v(o,\tau)}{\partial \tau} \ . \tag{11}$$

The solution is now found with the aid of a Laplace transformation in z:

$$\left(\tilde{\delta I}, \tilde{\delta E}\right) = \int_0^\infty dz \exp(i\Omega z)\,(\delta I, \delta E) \ . \tag{12}$$

* This work was supported by the Director, Office of Energy Research, Office of Basic Energy Sciences, Advanced Energy Projects Division, U.S. Dept. of Energy, under Contract No. DE-AC03-76SF00098.

Equations (9) and (10) yield

$$C\widetilde{\delta E} = \int_0^{\tau} d\tau' \frac{f(\tau')}{\Omega^2-K^2} \exp\left[\frac{\alpha\Omega^2}{\Omega^2-K^2}(\tau'-\tau)\right] , \qquad (13)$$

$$\delta\tilde{I} = -\left(\alpha + \frac{\partial}{\partial\tau}\right) C\widetilde{\delta E} , \qquad (14)$$

with inversion formula

$$(\delta I, \delta E) = \int_{-\infty}^{+\infty} \frac{d\Omega}{2\pi} \exp(-i\Omega z)\, (\delta\tilde{I}, \delta\widetilde{E}) . \qquad (15)$$

The inversion contour runs above any singularities in the complex Ω plane.

It is instructive to examine the case of an impulsive perturbation $f(\tau)$ resulting from a velocity step of amplitude $Av_0H(\tau-\tau_0)$; from Eq. (11):

$$f(\tau) = A(\tau_0)\lambda_0\delta(\tau-\tau_0) .$$

Then Eq. (13) gives

$$C\widetilde{\delta E} = \frac{A\lambda_0 H(\tau-\tau_0)}{\Omega^2-K^2} \exp\left[-\frac{\alpha\Omega^2}{\Omega^2-K^2}(\tau-\tau_0)\right] . \qquad (16)$$

The inversion may be written

$$C\delta E = A\lambda_0 H(\tau-\tau_0) \int_{-\infty}^{+\infty} \frac{d\Omega}{2\pi} \frac{\exp(g)}{\Omega^2-K^2} , \qquad (17)$$

where we have defined

$$g(\Omega,\tau,z) = -i\Omega z - \frac{\alpha\Omega^2(\tau-\tau_0)}{\Omega^2-K^2} . \qquad (18)$$

The function [Eq. (17)] has been evaluated analytically for positive (τ,z), and may be regarded as a Green's function for general $f(\tau_0)$. However, its complicated form does not give a qualitative description of the pattern of growth with z and τ. The saddle point analysis presented here, while inexact, does provide this picture in several regimes of (z,τ). We set $\tau_0 = 0$ in the following.

Note that there are poles in Eq. (17) on the real axis at $\Omega = \pm K$. These points are intrinsic singularities since the poles also appear in g. These singularities are associated with "mountain ranges" containing saddle points as displayed in Figs. 1 and 2. An asymptotic evaluation of δE may be performed by the standard path of steepest descent method applied around the these points.

Saddle Point Analysis

The stationary (saddle) points of $g(\Omega)$ are the four solutions (Ω_S) of the quartic equation

$$0 = \left(\frac{\partial g}{\partial\Omega}\right)_S = -iz + \frac{2\alpha\tau K^2\Omega_s}{(\Omega_s^2-K^2)^2} .$$

In general, two solutions lie in the lower half-plane and make little contribution to δI. The pair in the upper half-plane are found to be pure imaginary for $\Delta \equiv \alpha\tau/Kz > 8/(3\sqrt{3})$ and complex for $\Delta < 8/(3\sqrt{3})$ (see Figs. 1 and 2).

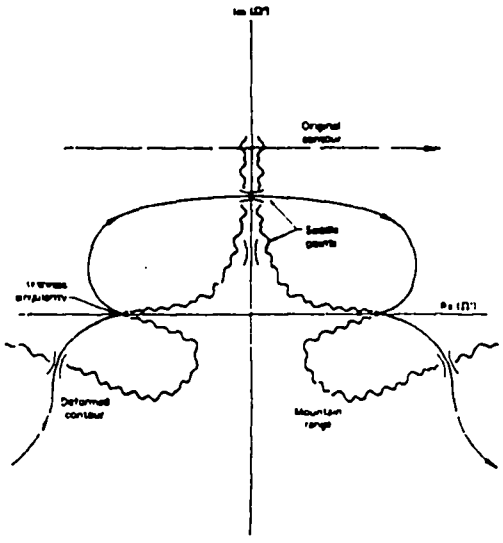

Fig 1. Topography of the Ω' plane ($\Omega' = \Omega/K$) for $\alpha\tau/Kz > 8/(3\sqrt{3})$.

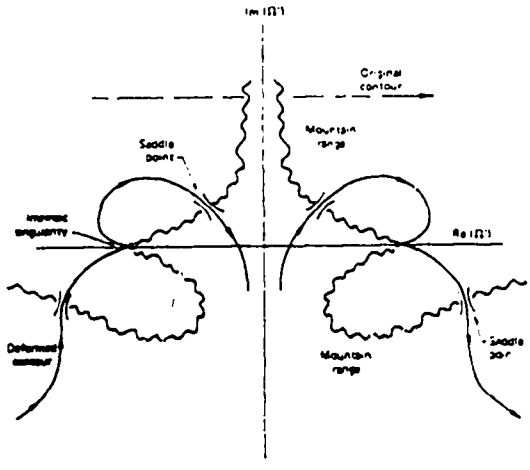

Fig 2. Topography of the Ω' plane for $\alpha\tau/Kz < 8/(3\sqrt{3})$.

Denoting $\Omega_S = K(\psi+i\mu)$, we have the parameterization in terms of μ:

Class 1

$$\Delta > 8/(3\sqrt{3}), \quad \mu > 1/\sqrt{3} ,$$

$$\Delta = (\mu^2+1)^2/2\mu , \qquad (20)$$

$$g_s = \mu Kz - \frac{\mu^2}{\mu^2+1}\alpha\tau .$$

Inversion contour is horizontal through the upper saddle.

Class 2

$$\Delta < 8/(3\sqrt{3}), \quad \mu < 1/\sqrt{3} \ ,$$

$$\Delta = 4\mu^2\sqrt{\mu^2+1} \ ,$$

$$\psi = \pm\left[\mu^2 + 1 - 2\mu\sqrt{\mu^2+1}\right]^{1/2} \ , \qquad (21)$$

$$\mathrm{Re}(g_s) = \mu Kz - \alpha\tau + \frac{\Delta\alpha\tau/2\mu}{(\Delta/2\mu)^2 + 4\mu^2\psi^2} \ .$$

Inversion contour is oblique through each saddle point.

The special case of $\Delta = 8/(3\sqrt{3})$ has the upper half plane saddles coalesce at $\mu = 1/\sqrt{3}$.

Case of $\Delta << 1$

Here the saddles lie close to the singularities $\Omega = \pm K$. Physically, z is large enough that resonant growth can dominate at small τ. The quartic for Ω_s is readily solved by iteration from these values to obtain

$$\Omega_s \approx \pm K\left(1 \pm \frac{1+i}{2}\sqrt{\Delta}\right)$$

$$g_s \approx \pm iKz\left(1-\sqrt{\Delta}\right) + \sqrt{Kz\alpha\tau} - \frac{3}{4}\alpha\tau \ . \qquad (22)$$

Case of $\Delta >> 1$

From Eq. (20) we have

$$\mu \approx (2\Delta)^{1/3} \ ,$$

$$g_s \approx \frac{3}{2}(2\Delta)^{1/3} Kz - \alpha\tau \qquad (23)$$

The expected result that the RC decay should dominate at large τ appears explicitly.

Maximum Growth with z

If z is fixed and the real part of g_s is maximum in τ we find a point of the class 2-type $\Delta = (\alpha\tau/Kz) < 8/(3\sqrt{3})$:

$$\mu = \frac{1}{\sqrt{8}} = .3535 \ ,$$

$$\psi = \pm\sqrt{\frac{3}{8}} = \pm .6124 \ ,$$

$$\frac{\alpha\tau}{Kz} = \frac{3}{4\sqrt{2}} = .5303 \ ,$$

$$R_e(g_s) = \frac{Kz}{2\sqrt{2}} = .3536\ Kz \ . \qquad (24)$$

This solution represents the peak of a wave packet moving backward in the pulse (increasing τ) and forward in z with trajectory $\alpha\tau/Kz = .5303$. The same result is obtained by perturbing the beam sinusoidally at $z = 0$ for a long duration (τ), with frequency $\omega_0 = \alpha/\sqrt{3}$.

Application to Heavy Ion Fusion Driver

The maximum growth is calculated here at a medium energy point in a fusion driver, with ion parameters (T = 1000 MeV, m = 200 amu, q = 1). We also adopt the previously given quantities ($C = 3 \times 10^{-10}$ F-m, $R = 300\Omega$/m, $I_0 = 10^3$ A, $\tau_p = 500$ ns). Then we have (non-relativistic calculation).

$$v_0 = .104\ c, \quad \lambda_0 = 32.2\ \mu C/m \ ,$$

$$\alpha^{-1} = 90.0\ \mathrm{ns}, \quad K = 7.33 \times 10^{-3}\ m^{-1} \ ,$$

$$\alpha\tau = 5.56\ \tau/\tau_p \ , \quad Kz = 7.33\ z_{km} \ ,$$

$$\Delta = \alpha\tau/Kz = .758\ \frac{\tau/\tau_p}{z_{km}} \ .$$

From eqs. (24) we have the maximum growth point for a perturbation initiated at the pulse head:

$$\frac{\tau/\tau_p}{z_{km}} = \frac{.5303}{.758} = .699 \ ,$$

$$\mathrm{Re}\ (g_s) = .3536\ Kz = 2.59\ z_{km} \ .$$

It is clear that this asymptotic limit is available within the 500 ns pulse length for z out to ~1.4 km, and several e-fold of growth can occur over this distance. The growth rate is small enough that it may be possible to control it with a feed-forward system. Note that this maximum growth rate, when associated with a perturbation of constant frequency at $z = 0$, occurs at

$$\nu_0 = \frac{\alpha}{2\pi\sqrt{3}} = 1.02\ \mathrm{MHz} \ ,$$

which is very low considering the 500 ns pulse length. For the more reasonable $\nu_0 = 10$ MHz we find the very low growth rate with distance of .636 km^{-1}.

References

1. Edward P. Lee, Proc. 1981 Linear Accelerator Conference, Los Alamos Report LA-9234-C, 263.

TECHNIQUE OF MEASURING BUNCH LENGTH BY PHASING AN RF CAVITY*

W. Barry, P. Kloeppel, and R. Rosamanith
Continuous Electron Beam Accelerator Facility
12000 Jefferson Avenue, Newport News, VA 23606

Introduction

The bunch length in the CEBAF electron beam, less than 1° in phase or 2 ps when fully relativistic, is too short to be measured by direct timing techniques. An indirect measurement that has been proposed is the well-known method of changing the phase of an accelerating cavity and observing the energy spread in the beam. The bunch usually rides at the crest of the rf wave in order to maximize the acceleration and to minimize the energy spread. By altering the phase of one or several cavities, the energy spread can be increased by an amount that is proportional to the bunch length. By measuring the energy spread for several phases, the bunch length can be determined.

The method has been applied in tests at the CEBAF injector. The aims of the trial were to see the limitations of the technique, and to understand how it could be improved to the point that it could be used as a regular diagnostic tool. Then the backphasing method can provide a rapid and inexpensive, if rather imprecise, measurement of the bunch length.

The cavities in the injector, shown in Figure 1, are driven by two klystrons. The first cavity raises the beam energy to about 2.7 MeV, which is nearly fully relativistic ($\beta = 0.98$). The phase of the second cavity can then be altered to increase the energy spread. Calculations have indicated that the phase length of the bunch at the entrance of the second cavity can be measured with 10% precision; this figure represents the limit of validity of the computation, and is further degraded by spectrometer errors.

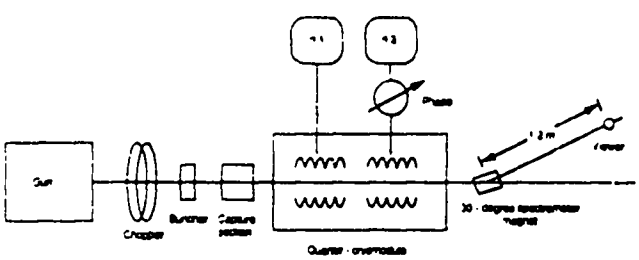

Figure 1. Schematic layout of CEBAF Injector

Energy Spread in the Beam

To a first approximation, the energy spread produced in the beam by the second rf cavity because of phase spread is given by

$$\delta E = E_0 \sin \phi \, \delta\phi, \tag{1}$$

where E_0 is the energy an electron would gain in traversing the cavity at optimum phase, ϕ is the phase difference of the bunch centroid from optimum, and $\delta\phi$ is the phase spread in the bunch. The bunch length l is related to the phase spread by

$$l = \lambda \beta \, \delta\phi/(2\pi), \tag{2}$$

where λ is the rf wavelength, and $\beta (= v/c)$ is very nearly equal to 1. A closer approximation for δE can be gained by using the beam transport code PARMELA, which includes the effects of phase drift that is present because β is not quite equal to 1. A PARMELA subroutine has been prepared by Geoffrey Krafft explicitly to model the CEBAF cavity.[1]

We can characterize the beam by its energy spread δE and its phase spread $\delta\phi$. Their values at the output of a cavity can be connected to their values at the input. Let the subscript i denote input, and o denote output. For small dispersions, we have the following linear relations:

$$\begin{aligned} \delta E_o &= \left(\frac{\partial E_o}{\partial E_i}\right) \delta E_i + \left(\frac{\partial E_o}{\partial \phi_i}\right) \delta\phi_i \\ \delta\phi_o &= \left(\frac{\partial \phi_o}{\partial E_i}\right) \delta E_i + \left(\frac{\partial \phi_o}{\partial \phi_i}\right) \delta\phi_i. \end{aligned} \tag{3}$$

The transfer coefficients $\partial E_o/\partial E_i$, $\partial E_o/\partial \phi_i$ are computed by PARMELA.

The energy spread is measured by the 5-MeV spectrometer, consisting of a rectangular magnet to bend the beam 30°, 1.20 m of drift space, and a viewer. The diameter of the working region of the viewer is 2.2 cm. The line after the cryomodule has no focusing magnets. The diameter of the observed spot is equal to the sum of $\sqrt{\beta e}$ and the dispersion. Since only the dispersion is interesting, the 'native' spot size represents an offset that must be subtracted away. We find δE_o for several different phases of the second rf cavity, holding everything upstream of the cavity fixed. The spot diameter is measured for several phases of the second cavity relative to optimum. The angular divergence $\delta\psi$ of the beam is then related to the momentum spread,

$$\delta\psi = 2 \tan\left(\frac{\psi}{2}\right) \frac{\delta p}{p} + C, \tag{4}$$

where $\psi = 30°$ is the bend angle, p is the momentum, and C is a constant (equal to $\sqrt{\beta e}/L$). We set $\delta p/p = \delta E/E$ and combine Equations 3 and 4 to give

$$\delta\psi = 2 \tan\left(\frac{\psi}{2}\right) \left[\left(\frac{\partial E_o}{\partial E_i}\right) \frac{\delta E_i}{E_o} + \left(\frac{\partial E_o}{\partial \phi_i}\right) \frac{\delta \phi_i}{E_o}\right] + C. \tag{5}$$

* This work was supported by the U.S. Department of Energy under contract DE-AC05-84ER40150.

Results

The results for the measurements are given in Table 1. The constant C, the input energy spread δE_i, and the input phase spread $\delta\phi_i$ can be found by least squares, yielding as the best fit the following values:

$$\begin{aligned} \delta E_i &= 0.0386 \text{ MeV}, \\ \delta\phi_i &= 0.247^\circ, \\ C &= 3.34 \times 10^{-3}. \end{aligned} \tag{6}$$

Bounds for the systematic error can be established by assuming extreme values for the constant C. It can be no less than 0, for an arbitrarily precise spectrometer, and it can be no larger than the smallest observed value of $\delta\psi$, 7.5 mrad. With these values for C, the corresponding values of $\delta\psi$ are 0 and 0.53°. Thus,

$$\delta\phi_i = 0.25^\circ \begin{pmatrix} +0.28^\circ \\ -0.25^\circ \end{pmatrix}. \tag{7}$$

TABLE 1
Results of Bunch Length Measurements

Phase	Final Energy (E_o)	Diameter	($\partial E_o/\partial E_i$)	($\partial E_o/\partial \phi_i$)
			(from PARMELA)	
°	MeV	radians		MeV/°
0.0	5.106	0.00796	1.0	0.0*
20.0	4.560	0.00749	1.0	0.0156
40.0	4.536	0.00870	1.0	0.0281
60.0	3.873	0.01022	1.0	0.0375
70.0	3.483	0.01088	1.0	0.0406

* ΔE_o is of second order in $\Delta\phi_i$ near optimum phase.

The diameter is shown as a function of phase in Figure 2, which also plots the function for the best-fit values of Equation 6.

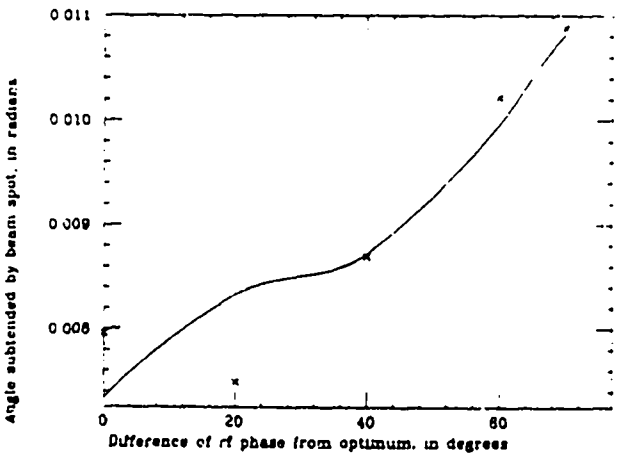

Figure 2. Spot size as a function of phase shift

Summary

In summary, we conclude that the method has proven to be practical for a quick measurement of the bunch length, suitable for preliminary beam setups. Further improvement can be achieved by installing a profile monitor in place of or in addition to the viewer, and by using more sophisticated optics in the spectrometer. With a profile monitor and with spectrometer resolution of 10^3, we will be able not only to find the bunch length but also to observe its structure.

Acknowledgements

Many persons have helped in obtaining the results reported here. We wish to express particular thanks to George Neil and Charlie Sinclair for their operation of the injector, and to Kelly Mahoney for running the rf controls.

Reference

1. Geoffrey Krafft, CEBAF-TN-0051.

THE DELTA-T TUNEUP PROCEDURE FOR THE FERMILAB LINAC

Thomas L. Owens and Elliott S. McCr ry
*Fermi National Accelerator Laboratory**
P. O. Box 500, Batavia, IL 60510

Abstract

The delta-t procedure provides a means of monitoring and setting to design values the phase and amplitude of fields within a linear accelerator. Deviations from design values of energy entering an accelerator module can also be determined. The procedure will be used to tune the upgraded linac under construction at Fermilab.[1] Results of preliminary tests of the technique on the existing 200 MeV linac show qualitative trends in agreement with analysis. Quantitative comparisons show some differences.

Introduction

The delta-t procedure was developed at the Los Alamos National Laboratory many years ago for the purpose of adjusting the phase and amplitude of the fields in each of 44 modules in the LAMPF linear accelerator.[2] Recently, workers in the USSR, at the Institute of Nuclear Research, extended the analysis and utility of the procedure by treating second order effects that become increasingly important as the longitudinal extent of the beam bunches increases.[3] Other recent work has examined use of the delta-t procedure on the linac of the Advanced Hadron Facility.[4]

The procedure entails measurements of the deviation from design of changes in the times of flight between points along the accelerator as the module fields are alternately turned on then off. Following the analysis presented in reference 2, module phase, $\Delta\phi_A$ and module input energy, ΔW_A, can be related in a linear fashion to the deviation from design of the difference in time of flight at a point just beyond the module being tuned (Δt_B) and at a point further down the accelerator (Δt_C) according to the relation,

$$\begin{bmatrix} \Delta\phi_A \\ \Delta W_A \end{bmatrix} = A \begin{bmatrix} \Delta t_B \\ \Delta t_C \end{bmatrix} \qquad (1)$$

The 2x2 matrix, A, is derived from the transformation matrix through the module. It is a function of the electric field in the accelerator gaps and the accelerator geometry. The electric field is determined using a variety of techniques. One way involves measuring the energy out of the module as input phase is changed. The ratio of energy change to phase change is equal to the (2,1) element of the transformation matrix. The known dependence of this element upon electric field then determines the electric field value. Another technique to estimate the electric field magnitude involves locating the peak in the energy change as phase is varied. The amplitude and phase location of this peak for a given electric field can be calculated using beam dynamics simulations, then compared to the measurements.

Once the electric field has been estimated and brought up to design levels, the phase and input energy displacements from design can be estimated from measurements of the delta-t values according to equation 1. Corrections to the module phase and input energy can then be made. The electric field and delta-t measurements are repeated and adjustments to field, phase and input energy are continued in an iterative fashion until the module is tuned to the desired accuracy.

Tests on the Fermilab Linac

Preliminary tests of the delta-t procedure have been performed on the 200 MeV drift tube linac at Fermilab in preparation for use on the 400 MeV accelerator upgrade. Tests have focussed on measurements of Δt_B and Δt_C as the phase is varied, as was done early on in the LANL tests, in order to understand some of the basic features of the procedure. Curves have been generated for many of the linac accelerator modules for a variety of electric fields and input energies. An example of the type of curves that are generated is given in figure 1 for the fifth accelerator module out of a total of nine

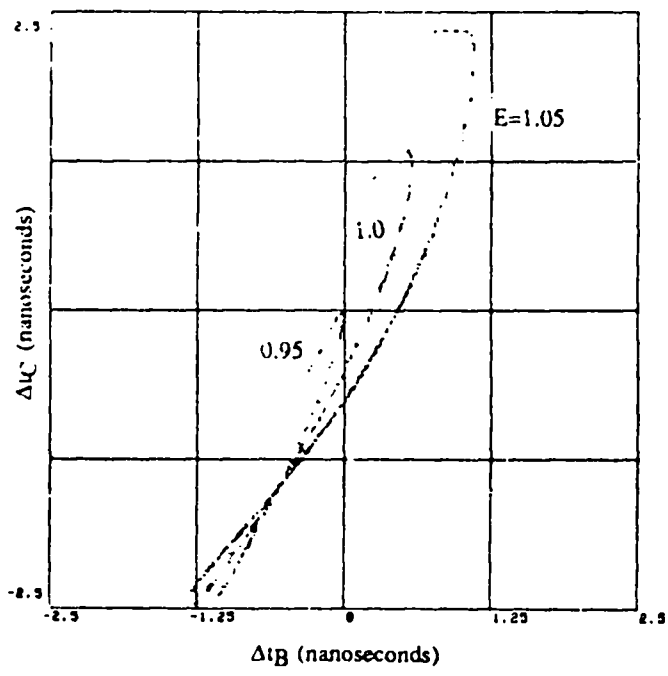

Figure 1. *Experimental measurements of delta-t values for module 5 as phase is varied. Electric field magnitude is varied ±5% about nominal (center curve).*

*Operated by the Universities Research Association under contract with the U.S. Department of Energy.

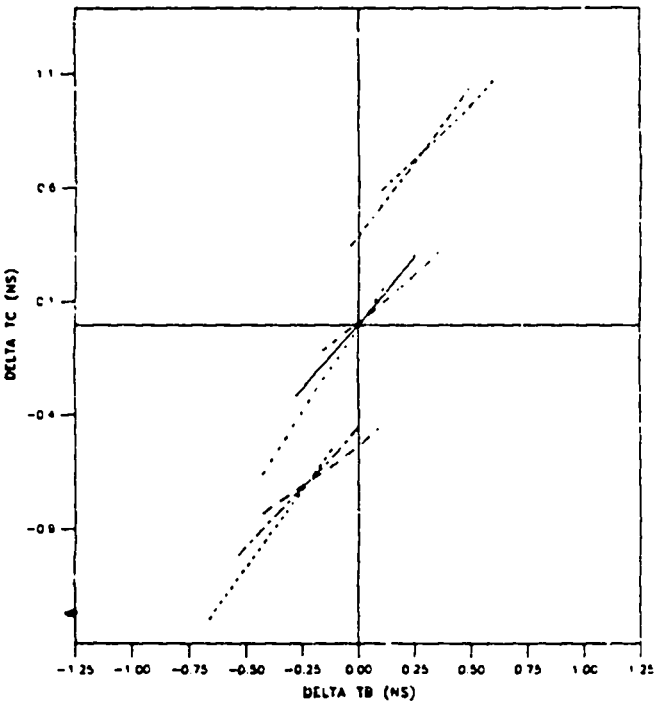

Figure 2. *Theoretical delta-t curves for module 5. For the upper curves, input beta=0.41331; for the center curves, input beta=0.41414; and for the lower curves, input beta=0.41497. Electric fields are varied ±5% about nominal within each cluster.*

modules which make up the Fermilab linac.

Computer simulations of the same type of curves for the conditions of module 5 are given in figure 2 for comparison with the experiment. We find good qualitative agreement. Basically, at a given input energy, all curves are clustered around and intersect with a single point in the delta-t plane. Separate clusters of curves occur for each input energy. As the electric field amplitude is varied, the slopes of the curves change. For a perfectly tuned module, the intersection point would lie at the origin in the delta-t plane and the curve generated by varying the phase would have a specific slope dictated by the design field setting. For module 5, the experimental curves in figure 1 indicate that the input energy into module 5 is high by a few tenths of a percent and the electric field is low by a few percent.

We have been able to vary the input energy into module 5 by adjusting the phase of module 4. A series of curves similar to the theoretical presentation in figure 2 is obtained. In figure 3, we have plotted the location in the delta-t plane of all of the points of intersection of these curves. Also plotted in figure 3 is the theoretical prediction. In agreement with theory, the points of intersection all lie on a straight line, but the slope of the line generated experimentally differs somewhat from theory, and it does not quite pass through the origin.

The source of the disagreement between theory and experiment is not known at present. Linac geometery is the only parameter that greatly affects the theoretical line generated in figure 3, according to the theory developed by Crandall.[2] The effect we are seeing is similar to what is predicted by the higher order theory described in reference 3. A careful comparison with the theory of reference 3 has not been made. Other possible reasons for the differences are currently under

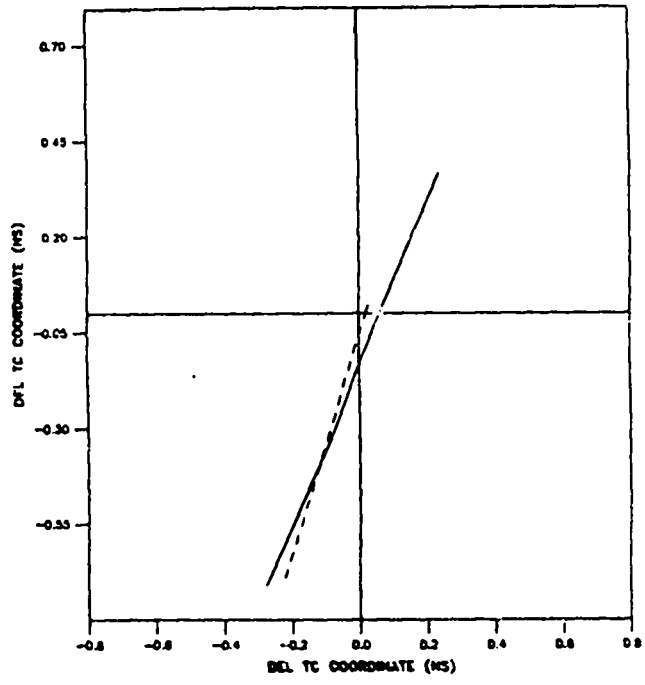

Figure 3. *Variation of the intersection points of curve clusters for module 5 as input energy is varied. Solid line - experiment, dashed line - theory.*

investigation.

We have tested the technique, mentioned in the introduction, for estimating the electric field using measurements of the peak energy out of the module. In this case, electric field is estimated by comparisons between simulation and experiment. Figure 4 shows measurements of

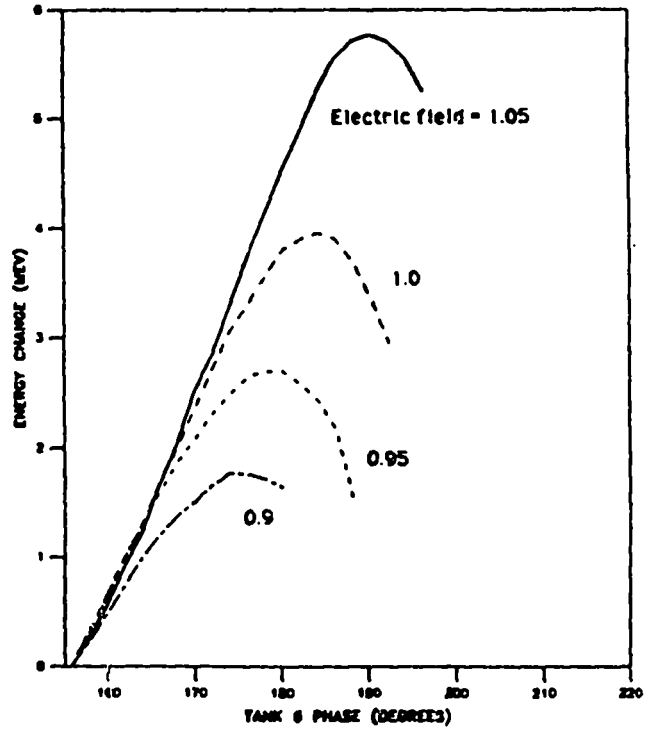

Figure 4. *Experimental measurement of particle energy increase in module 6 versus module 6 phase. Nominal phase setting is 155.7 degrees.*

the energy out of module 6 of the Fermilab linac as phase is varied. The figure demonstrates that the energy peak is highly sensitive to electric field magnitude, and should therefore provide a very accurate means of setting field magnitude within the context of the delta-t procedure. Surprisingly, we found substantial differences between the curves of figure 4 and computer simulations. Detailed comparisons indicate that the differences arise because the beam is not well centered in the rf bucket for this module.

In principle, all of the information necessary for tuning a given module is present in experimental plots like figure 1. However, we have found that the curves are all nearly parallel to one another by the seventh or eighth module in the Fermilab linac, and results become inaccurate. The procedure must be modified for these higher-energy modules, as discussed in reference 2 and in the next section.

Procedure for High-Energy Modules

Since inaccuracies in the higher-energy modules are due to the fact that the delta-t curves generated by varying the module phase are nearly parallel, we choose a procedure which seeks a target line that is perpendicular to the variable phase curves. We have reproduced the theory[2] necessary to simulate this procedure in order to determine its effectiveness on our linac. As discussed in reference 2, any procedure must be stable. The criterion for stability is that the percentage energy displacement at the output of the module must be less than the input percentage energy displacement. If this stability criterion fails, the beam will tend to walk out of the rf bucket.

Figure 5 shows the degree to which our linac is stable. Plotted here is the ratio of the output percentage energy error to input percentage energy error (the stability ratio) for modules 3-9. Any value below one in the figure is stable. We have found that the procedure is quite stable for modules 4-9, but is unstable for earlier modules.

Figure 6 is a plot of the uncertainty in the output energy for one picosecond error in the delta-t measurements for modules 3-9 of the Fermilab linac. We have assumed that errors in the measurements are random. Larger errors in output energy can be produced if there are systematic errors in the time difference

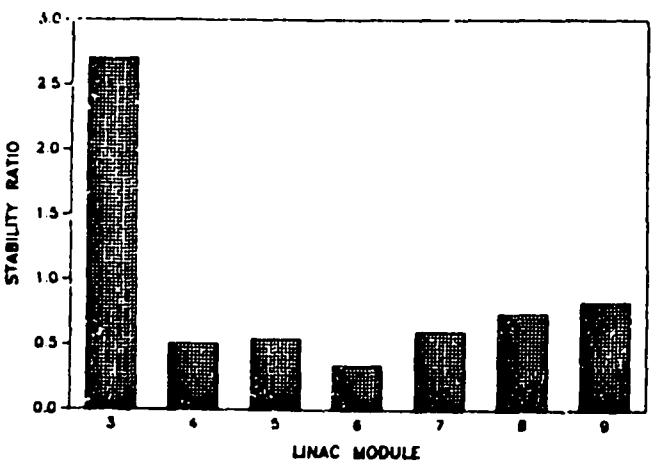

Figure 5. *Ratio of output percentage energy displacement to input percentage energy displacement (stability ratio) for the high-energy delta-t procedure in the Fermilab linac. Stability limit is unity.*

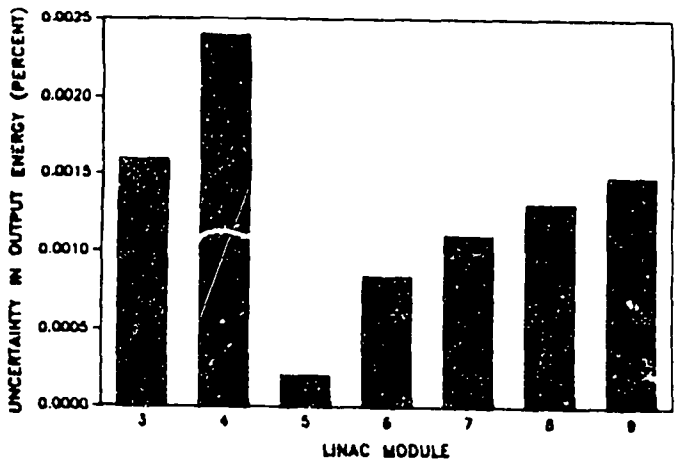

Figure 6. *Uncertainty in output energy for the high-energy delta-t procedure in the Fermilab linac. One picosecond random errors in delta-t measurements are assumed.*

measurements. We anticipate total random errors on the order of 13.8 picoseconds. From figure 6, uncertainties are expected to be less than approximately 0.02 % for each of modules 5-9 of the Fermilab linac, which should allow the beam to be well centered in the rf bucket using this procedure.

Summary

The delta-t procedure appears to be a potentially accurate and stable technique for setting the phase and electric field magnitude in the Fermilab linac. Some differences between theory and experiment have been found. Resolution of these differences would improve the accuracy of the technique.

References

1. R.J. Noble, " The Fermilab Linac Upgrade," this Proceedings.

2. K. R. Crandall, "The Delta-T Tuneup Procedure for the LAMPF 805 MHz Linac," LANL Report LA-6374-MS, June, 1976.

3. G. A. Dubinski, A. V. Reshetov, Y. U. Senichev and E. N. Shapashnikova, "New Features of the Delta-T Procedure For An Intensive Ion Linac," in *1988 Linear Accelerator Conference Proceedings*, Newport News, VA, Oct. 3-7, 1988 .

4. G. R. Swain, "Use of the Delta-T Method For Setting RF Phase and Amplitude in the AHF Linac," in *Proceedings of the Advanced Hadron Facility Accelerator Design Workshop*, Feb. 20-25, 1989 (Also LANL Report LA-11684-C).

SIMULATIONS OF HIGH DISRUPTION COLLIDING BEAMS *

J. R. Boyce, S. Heifets†, and G. A. Krafft
CEBAF, 12000 Jefferson Ave. , Newport News, VA 23606

Abstract

Recent B-factory proposals[1,2] that use a linac beam colliding with the beam from a storage ring to achieve high luminosities ($L > 10^{34}$ cm^{-2}sec^{-1}) result in very high disruption of the linac beam. The effects of such high disruption have been studied using the relativistic. 3-D code SWARM. We discuss the assumptions, parameters, and results of a series of runs that model such collisions. Regimes of high beam loss and methods to avoid them are also discussed.

Introduction

Colliding beam experiments using a positron beam stored in a storage ring require that the electrons do not destabilize the positrons because of the collision. This requirement is summarized in the constraint that the beam-beam tune shift of the stored positrons remains low. Most B-factory designs require the beam-beam tune shift to remain under ≤ 0.06.

In this study we investigated collisions where the positron bunch and the electron bunch have parameters typical of linac-storage ring B-factory designs. In the first section we discuss the assumptions of the model, the forces, and the luminosity calculations. In the second section we confirm the pinching discussed in Ref. 3. In the third section we discuss a matching procedure that reduces the pinching, and hence the beam-beam tune shift of the circulating positrons. These results show that large electron disruption may be consistent with small positron tune shift, a necessary condition to achieve high luminosity in "disruption assymetric" colliding beam B-Factories.

Basic Assumptions

There are six main assumptions made in this model:

1. The beams are relativistic.[4]
2. The bunches can be characterized by thin transverse slices randomly populated by groups of particles called macroparticles.
3. The force between two macroparticles is zero when the distance between them is zero, linearly increases to the "radius" of the macroparticle, and decreases as $1/r$ for distances greater than the radius.
4. When the bunches overlap, the force on any macroparticle in a given slice is the sum of forces from the macroparticles in the overlapping slice in the other bunch. That is, there are no interactions between macroparticles in non-overlapping slices because the beams are relativistic.
5. The total luminosity is the sum of the individual luminosities due to the collision of the individual macroparticles.
6. The charge distribution in the bunch is parabolic longitudinally and gaussian in both transverse dimensions.

Fig. 1 is a schematic of the model.

The impulse delivered between two relativistic point charges goes inversely as the impact parameter. If two relativistic distributions of charge interact, and they do not overlap spatially, likewise the total impulse delivered goes inversely with separation of the centers of the distributions. If the macroparticles represent distributions azimuthally symmetrical about their centers, by symmetry the impulse delivered vanishes linearly with the separation between the centers. Therefore, a force law between macroparticles consistent with both these limiting behaviors is:

$$F = \frac{ar}{(1 + br^2)} \tag{1}$$

where r is the distance between the centers of the macro particles, $b = 1/\sigma_M{}^2$, σ_M characterizes the radius of the macroparticle, and a is proportional to the macroparticle charge. The macroparticle radius σ_M provides a short distance cutoff, i. e., it reduces unphysical collisional diffusion due to short wave noise in the model, much as finite grids in more common PIC simulations smooth shortwave fluctuations. It is important that the results of a calculation be independent of σ_M for that calculation to be significant.

The total charge of the bunch is divided among the macroparticles in the following fashion: the longitudinal charge is parabolic about the center of the beam bunch and Gaussian in both transverse directions.

The initial coordinates of the macroparticles are random within each slice. At each step in the iteration, the position of each macroparticle is changed due to the integrated forces on that macroparticle.

* This work was supported by the U. S. Department of Energy under contract DE-AC05-84ER40150.

† Now at the Stanford Linear Accelerator Center, Stanford University, Stanford, CA 94305

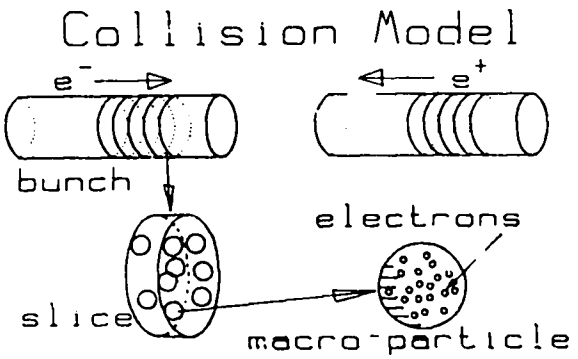

Fig. 1 The bunches are divided into slices, each slice has randomly distributed macroparticles containing the charged particles. The overall behavior of the particles in the bunch is approximated by the behavior of the macroparticles.

The luminosity is calculated by the evaluating the overlap integral:

$$L = f_c 2c \int n_1 n_2 dx dy dz dt \qquad (2)$$

f_c is the collision frequency, c is the speed of light, n_1 and n_2 are the particle densities in the two bunches, and the integration is over the collision region and over the time of collision. If

$$n_i(\mathbf{x}) = \sum_j q_i n_{macro}(\mathbf{x} - \mathbf{x}_j) \qquad (3)$$

where $n_{macro}(\mathbf{x})$ is the normalized macroparticle density function, and q_i is the number of particles per macroparticle. Eqn. 2 is evaluated by performing the sum:

$$L = \frac{f_c}{2\pi r_o} \sum_{ij} \sum_{nm} q_i q_j \frac{\alpha}{[1 + b(\mathbf{x}_n - \mathbf{x}_m)^2]^2} \qquad (4)$$

where

$$\alpha = \frac{-2r_o b(1 + \beta_e \beta_p)}{(\beta_e + \beta_p)} \qquad (5)$$

and r_o is the classical electron radius, β_e and β_p are v/c for the electrons and positrons, respectively, and the sum is over all macros in each overlapping slice and over all iteration steps as the bunches pass each other.

A relativistic collision code, SWARM, has been written to perform these calculations. The code models bunches in three dimensions, is vectorized, allows for large disruption parameters for the beams, and takes into account the finite length of the bunches. Particles in the bunches are tracked through the collision process. The code also calculates rms bunch sizes before, during, and after the collision along with the resulting luminosity. Although the code was written for asymmetric electron-positron colliding beams, it is applicable to any two relativistic colliding beams. A similar model has been used to discuss bunch dynamics at high disruption.[5]

Regimes of high beam loss

In an earlier 2-D model[3], individual electrons were tracked through a positron bunch. Here we report full 3-D calculations that track all the macroparticles in an electron bunch through the positron bunch.

These calculations confirm earlier results[3] that under certain conditions, the electron bunch pinches near the front of the positron bunch. Fig. 2 illustrates the effect. Positrons caught at the pinch point, which is stationary in the positron bunch, have a tune shift greater than 0.06. Therefore, if uncorrected, hard pinches would quickly destroy the positron bunch.

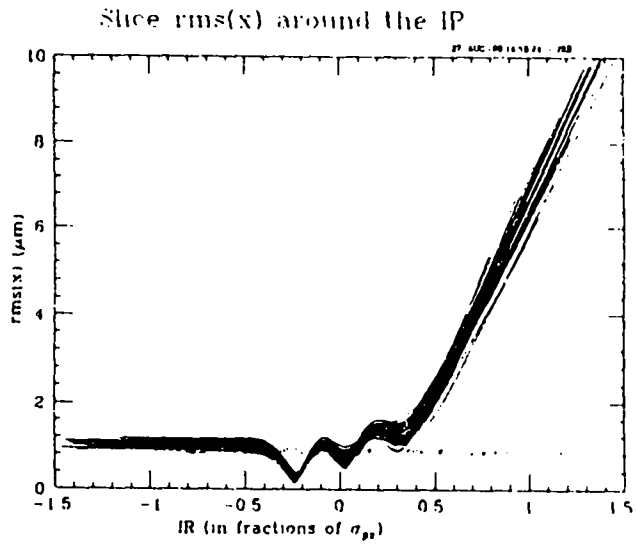

Fig. 2 The rms of the positions of all the macros in each slice is plotted relative to the center of the positron bunch. The solid lines are for electrons and the dotted lines are for the positrons (plotted relative to the center of the electron bunch). The narrow waist is the pinch discussed in the text.

Matching procedure to stabilize the beam

The matching procedure is the 3-D extension of the procedure used in Ref. 3. We assume that inside the central region of the collision process, electrons behave as if they are in a space charge lens. That is, the electrons are transported in the positron bunch in an adiabatic manner with a plasma frequency $k(s) = 1/\beta(s)$. The free parameter, z_{min}, marks the boundary of this central region. The matching requirement is that the bunch sizes of the two beams be the same at this z_{min}, i.e., that $\sigma_{ex} = \sigma_{px}$, $\sigma_{ey} = \sigma_{py}$.

Each slice in the electron bunch is populated at z_{min} with macroparticles that are then transported to "pre-collision" coordinates by free motion. In particular, the initial coordinates of each macroparticle are determined by:

$$x_e(-z_{min}) = \xi\sigma_{px}\left[\frac{D_{ex}}{2u}\sqrt{\frac{2}{\pi}}\right]^{\frac{1}{2}} \quad (6)$$

and

$$x'_e(-z_{min}) = \frac{\sigma_{px}}{\sigma_{pz}}\left[2uD_{ex}\sqrt{\frac{2}{\pi}}\right]^{\frac{1}{2}}(\eta - \xi/2) \quad (7)$$

where η and ξ are random numbers with a Gaussian distribution, the subscripts "px" and "pz" refer to the positron bunch coordinates x and z, z_{min} is the matching point, and $u = 2(z_{min}/\sigma_{pz})^2$. D_{ex} is the electron disruption in the x direction. Similar equations hold for the y direction.

Initial coordinates are found by applying free motion from the matching point to the starting point:

$$x_e(-L) = x(-z_{min}) - lx'_e(-z_{min}) \quad (8)$$

and

$$x'_e(-L) = x'_e(-z_{min}) \quad (9)$$

where we have defined $l = L - z_{min}$.

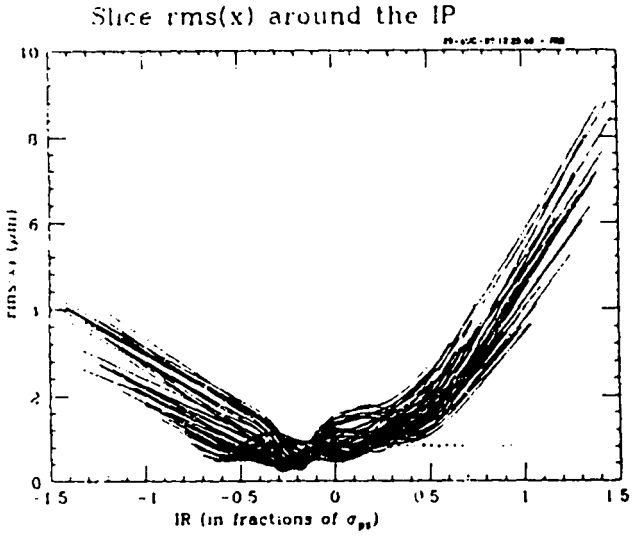

Fig. 3 The collision case shown in Fig. 2 was recalculated after applying the matching procedure discussed in the text. The nodes shown in Fig. 2 are smoothed out dramatically.

Results and Discussion

Results of applying the matching procedure to Fig. 2 are shown in Fig. 3. The nodes that were so clearly defined in Fig. 2 are smoothed out dramatically. The beam-beam tune shift on the positrons is reduced resulting in greater stability of the positron beam.

Figure 4 shows how the bunches appear just before collision. Note that the matching has effectively "pre-focused" the electron bunch, and that by so doing, the dissruptive pinch shown in Fig. 2, is reduced.

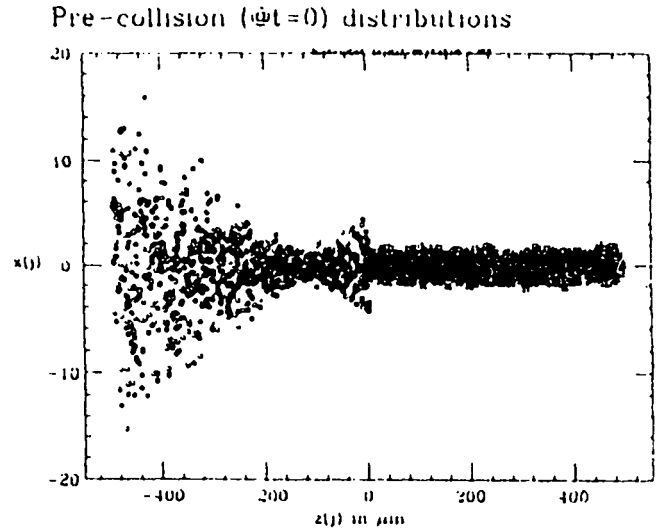

Fig. 4 The position of the negative macros (left of zero) and the positive macros (right of zero) just prior to the collision of the two bunches. The IP is at 0. Note the waist in the negative macro bunch. This "pre-focusing" is a result of the matching procedure.

Conclusion

We have studied colliding beams with high disruption using a "coulomb law" model. By matching, nodes in the disrupted electron bunch can be smoothed out if the electron bunch is properly shaped prior to the collision. Unfortunately, when matched, the enhancement factor is not large.

Further studies with better statistics, flat beams, and more realistic bunch parameters can now be undertaken.

Valuable discussions with R. Sah and J. S. Wurtele are acknowlegdged.

References

1. P. Grosse-Wisemann, "Colliding a Linear Electron Beam with a Storage Ring Beam", SLAC-PUB-4545, February 1988.

2. J. Bisognano, et. al., "A Beauty Factory Using an SRF Linac and a Storage Ring", 1988 Linac Conference, October 1988, Williamsburg, VA.

3. S. A. Heifets, G. A. Krafft, and M. Fripp, "On Asymmetric Collisions with Large Disruption Parameters", CEBAF PR-90-003, June, 1990.

4. R. C. Sah, "A Beam-Beam Simulation for the Single-Pass Collider", Proceedings of the 11th International Conference on High Energy Accelerators, pp. 736-740, 1980.

5. J. S. Wurtele, Private Communications.

DISPERSION AND INTERBUNCH ENERGY VARIATION FOR AN e^+e^- LINEAR COLLIDER

T.L. Houck
Lawrence Livermore National Laboratory, Livermore, CA 94550

Abstract

Recent studies concerning optimization parameters for e^+e^- super linear colliders use multiple particle bunches for each rf pulse to increase the luminosity and overall efficiency. Requirements for final focusing of the beams severely restrict the bunch to bunch energy variation during the rf pulse. To accurately determine the accelerating fields and energy variation, the dispersion related transient behavior of the rf drive pulse must be considered. A numerical study of dispersion effects on several different accelerating structures is presented.

Introduction

High-gradient accelerator (HGA) structures driven by relativistic klystrons (RK) are part of a collaborative experimental effort on high power microwave sources between the Lawrence Livermore National Laboratory (LLNL), Lawrence Berkeley Laboratory (LBL), and Stanford Linear Accelerator Center (SLAC).[1,2] As the duration of the rf drive pulses is about one fill time of the structure, the propagation of the rf pulse is dominated by transient effects related to dispersion. Several questions concerning the performance of these structures driven by the short RK generated pulses are posed:

1. How can transient fields be determined?
2. Where are the regions of high field stress?
3. What is the energy gain of the electrons?
4. Are there limits on the shape of the rf drive?
5. How does the energy vary between bunches?

These questions are important in the design of high energy e^+e^- linear colliders. Steady state conditions are not approached for several structure fill times. However, to minimize power requirements, high energy linacs are designed to operate with drive pulses approximately equal to one structure fill time. Methods for minimizing energy variation over a bunch train use a partially filled structure.[3]

Analysis of Dispersion

The structures used in the RK experiments are iris-loaded, cylindrical waveguides of constant geometry design. These structures were modeled as band pass filters and analyzed using Fourier analysis.[4] The axial field for the fundamental accelerating mode can be expressed as:

$$E_z(z,t) = \int_{-\infty}^{+\infty} E(\omega)\, e^{i(\omega t - kz)}\, d\omega \,, \qquad (1)$$

where

$$E(\omega) = \frac{1}{2\pi}\int_{-\infty}^{+\infty} E_z(0,t)\, e^{-i\omega t}\, dt. \qquad (2)$$

The wave number, $k = \beta + i\,\alpha/2$, is a function of frequency determined by the dispersion relationship of the structure. The attenuation coefficient, α, is due to wall losses and can be treated as constant for the narrow frequency pass bands typical of high-gradient structures. For constant geometry, the dispersion relationship is:[4]

$$\omega(\beta) = \omega_m - \frac{B}{2}\cos(\beta d)\,, \qquad (3)$$

where B is the bandwidth, ω_m is the mid-band frequency, and d is the structure cell length. Equation (3) assumes B/ω_m and the attenuation are both $<<1$.

Selecting the operating frequency, group velocity, v_g, operating mode, and structure efficiency, determines the dispersion relationship. Given the rf drive pulse incident on the structure, equations (1) and (2) can be used to calculate the accelerating fields for any position along the axis of the structure at any later time.

This analysis will also determine the energy gain of an electron transiting the structure. The total energy gain is:

$$U = e\int_0^L |E_z(z,t)|\cos(\theta(z,t))\, dz\,, \qquad (4)$$

where L is the structure length, and $t = t_0 + z/v_e$ where t_0 is the time the rf pulse was applied prior to injection, and v_e is the electron's velocity. $|E_z|$ and θ represent the magnitude and phase of the accelerating field at the electron's position.

Comparison to Experiment

The accuracy of the band pass filter theory was verified by predicting the rf pulse at the exit of the HGA structure in the RK experiments. The magnitude and phase of the incident rf pulse was measured and digitally recorded. A discrete FFT routine transformed the pulse, frequency components were adjusted for dispersion, and the adjusted pulse transformed back to the time

* This work performed under the auspices of the U.S. Department of Energy by Lawrence Livermore National Laboratory under contract No. W-7405-ENG-48.

domain. A comparison with the measured output is shown in Fig. 1.

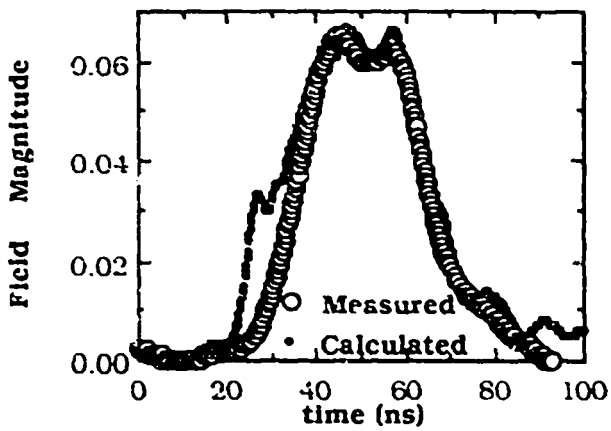

Fig. 1. Comparison of predicted to measure output pulse for the HGA in the RK experiments.

For the case shown in Fig. 1, the peak fields at the input were about 40 MV/m, and the peak fields of the output pulse were about 35 MV/m. At the moderate power level used, beam loading due to dark current was negligible.

Computer Simulations

The computer simulations used a square incident rf drive pulse. Beam loading was assumed negligible. Six different structures were studied (see Table I). The operating mode was $2\pi/3$ for all structures except number 2 which was $\pi/2$. The operating frequency was 11.424 GHz for all cases.

Regions of High Field Stress

An unanticipated finding of the simulations concerned regions of high field stress. The structures studied were constant impedance and have uniformly decreasing fields along the axis for steady state. This is not true while the rf pulse is initially filling the structure. Fig. 2 shows the accelerating field along the axis of structure 1 for two different propagation times. A vertical height of 1.0 corresponds to the incident pulse strength.

TABLE I
Simulated Acceleration Structures

Structure	Length (cm)	Fill Time (ns)	Structure Efficiency
1	26.25	27.57	0.74
2	26.25	27.57	0.62
3	52.5	55.14	0.54
4	100	55.6	0.76
5	150	68.0	0.71
6	200	111.2	0.57

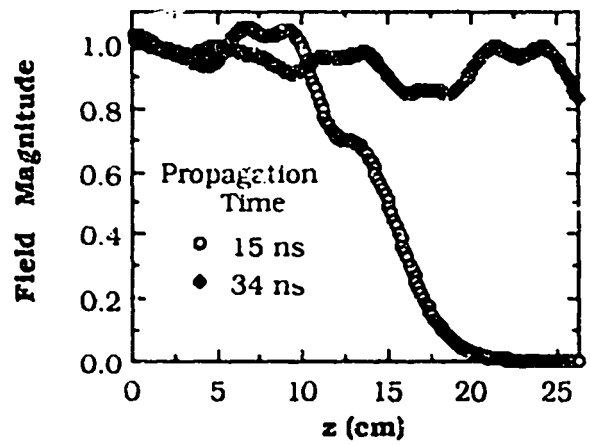

Fig. 2. Accelerating field along axis of a HGA.

The field can have peak values larger than the incident field. For times somewhat larger than one fill time, the fields at the end of a $2\pi/3$ operating mode structure are comparable to incident field strengths and are sustained for a significant portion of a fill time (~20%). For the $\pi/2$ mode, high field levels are experienced at the end of the structure, but for a shorter duration.

This is an interesting result as damage related to electrical breakdown was found at the end of the HGA used in the RK experiments. Electrical arcing at the end of an S-band, constant gradient structure has been reported.[5] As less rf conditioning is accomplished towards the end of an accelerating structure, this region would be more susceptible to breakdown.

Energy Gain Under Negligible Beam Loading

The energy gain of an electron for different injection times was calculated using equation (5) assuming an initial drive field of 100 MV/m and duration 30 ns. As can be seen in Fig. 3 for

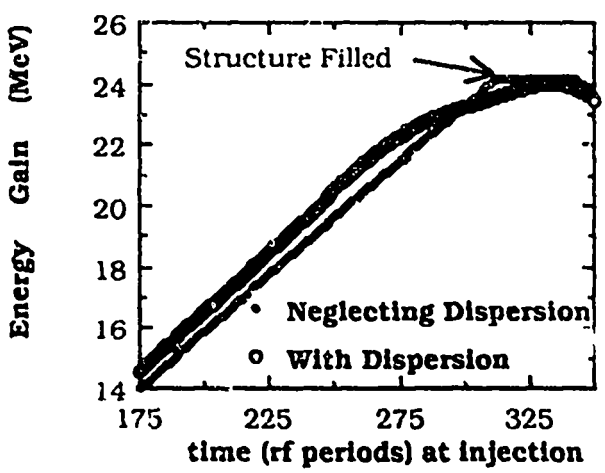

Fig. 3. Energy gain as a function of injection time.

structure 1, there is a noticeable difference between the gain when dispersion is included than when it is neglected.

The increase gain for earlier injection times with dispersion is due to the faster group velocity of the lower frequency components of the drive pulse. Although field levels are lower, the field propagates further . As the fill time is approached, the lower frequency components are exiting the structure and no longer contribute to acceleration/energy gain. Steady state is reached when the slower, high frequency components arrive at the end. Although the energy difference for injection after one fill time amounts to only a few percent of the total gain in the $2\pi/3$ operating mode (and is negligible in the $\pi/2$ mode),the rate of energy gain is different and impacts energy variation over a train of electron bunches.

Minimizing Energy Variation of a Train

For a train of bunches, the accelerating field is a superposition of the rf drive and beam loading. A numerical study of energy variation was performed by subtracting the effects of beam loading from the energy gain calculated from filter theory for a square drive pulse of 100 MV/m.

Beam Loading

For the fundamental accelerating mode, the wake field for a short bunch with charge q after propagating a distance L is given by:

$$E_{wake} = -2\ kq\ e^{-\alpha L/2}\ , \qquad (5)$$

where α is the attenuation coefficient and k is the loss parameter. The loss parameter can be related to the bunch efficiency factor, η, by:

$$\eta = 1 - \frac{(E_z - E_{wake})^2}{E_z^2} = \frac{4\ kq}{E_z}\ . \qquad (6)$$

The energy loss of the second bunch due to beam loading over the length, L, of the accelerating structure can be expressed as:

$$\Delta V_2 = \int_{\Delta s'}^{L} \left\{ -2\ kq\ e^{-\frac{\alpha}{2}\left(\frac{V_g}{V_e}[z - \Delta s'] + \Delta s'\right)} \right\} dz\ , \qquad (7)$$

where $\Delta s'$ is related to the bunch spacing, Δs, by:

$$\Delta s' = \Delta s \left(1 + \frac{V_g}{V_e - V_g}\right)\ . \qquad (8)$$

For subsequent bunches, the energy loss is a sum of integrals similar to equation (7), and for the Nth bunch can be expressed as:

$$\Delta V_N = -\frac{4kq}{\alpha} e^{-\gamma} \frac{V_e}{V_g} \left(e^{-\beta} \frac{1 - e^{-(N-1)(\beta+\gamma)}}{1 - e^{-(\beta+\gamma)}} - e^{-\delta} \frac{1 - e^{-(N-1)\gamma}}{1 - e^{-\gamma}} \right), \qquad (9)$$

$$\text{with } \gamma \equiv \frac{\alpha\ \Delta s}{2}\ ,\ \beta \equiv \frac{\alpha\ \Delta s'}{2} \frac{V_g}{V_e}\ ,\ \text{and } \delta \equiv \frac{\alpha L}{2} \frac{V_g}{V_e}\ . \qquad (10)$$

Results of the Numerical Study

For the six different structures listed earlier, equation (9) was used to calculate the energy loss for various bunch spacings and bunch efficiency factors for a train of 10 bunches. The values were subtracted from the energy gains corresponding to different injecting times into the partially filled structure. Minimum energy variation parameters for the different structures are listed in Table II.

Table II
Parameters for Minimizing Energy Variation

Structure	η (%)	spacing (# λ)	$\Delta V/V_{ave}$ (%)	V_{ave}/V_m (%)
1	2.0	3	0.093	80.5
2	1.6	3	0.054	88.3
2	2.2	4	0.078	86.2
3	1.7	6	0.084	70.4
4	1.9	6	0.072	75.3
5	1.8	7	0.096	77.4
6	2.0	14	0.153	79.6

The structure number refers to the structures listed in Table I, ΔV is one half of the energy range over the train, V_{ave} is the average energy of the train, and V_m is the maximum single bunch energy gain for a filled structure. For synchroneity, spacing must be an integral number of wavelengths, λ. Small changes in η or spacing will cause a large increase in energy variation.

Conclusions

The questions asked in the Introduction are adequately addressed with filter theory. Transient fields can be accurately calculated as well as the energy gain of accelerated electrons. High field stresses are expected at both entrances and exits of structures as noted experimentally. The leading edge "squareness" of a drive pulse will be limited by the frequency band of the structure. For multi-bunches , dispersion will lower the average energy of a bunch train for a desired energy variation.

Acknowledgements

I would like to thank W.R. Fowkes, R. Hawkins, K.A. Thompson, G.A. Westenskow, A.E. Vlieks, and S.S. Yu for their advice and encouragement.

References

1. M.A. Allen et al., "High Gradient Electron Accelerators Powered by a Relativistic Klystron", Phys. Rev. Lett., 63 22, pp. 2472, Nov. 27, 1989.
2. G.A. Westenskow et al., "Relativistic Klystrons for High-Gradient Accelerators", to be presented at 1990 LINAC Conference, Albuquerque, NM, Sept. 10-14, 1990
3. R.D. Ruth, "Multi-Bunch Energy Compensation", SLAC-PUB-4541 (1988)
4. J.E. Leiss, in *Linear Accelerators*, eds. P. Lapostolle and A. Septier (North Holland, 1970), 147.
5. H. Matsumoto, "RF High Gradient Experiment of an S-Band 0.6 m Disk Loaded Structure", Particle Accelerators,30, pp. 231-236, 1990

DESIGN CONSTRAINTS FOR ELECTRON-POSITRON LINEAR COLLIDERS*

Alfred Mondelli and David Chernin
SAIC, 1710 Goodridge Drive, McLean, VA 22102

Abstract

A prescription for examining the design constraints in the e^+-e^- linear collider will be presented. By specifying limits on certain key quantities, an allowed region of parameter space can be presented, hopefully clarifying some of the design options. The model starts with the parameters at the interaction point (IP), where the expressions for the luminosity, the disruption parameter, beamstrahlung, and average beam power constitute four relations among eleven IP parameters. By specifying the values of five of these quantities, and using these relationships, the unknown parameter space can be reduced to a two-dimensional space. Curves of constraint can be plotted in this space to define an allowed operating region. An accelerator model, based on a modified, scaled SLAC structure, can then be used to derive the corresponding parameter space including the constraints derived from power consumption and wake field effects. The results show that longer, lower gradient accelerators are advantageous.

Interaction Point

The interaction point may be characterized by eleven parameters: the number of particles per bunch (N), the particle energy (γmc^2), the bunch size (σ_x, σ_y, σ_z), the bunch repetition frequency (ν), the luminosity (L), the disruption parameter (D), the energy loss to beamstrahlung (δ_{BS}), the average beam power (P_b), and the Yokoya parameter ($A \equiv \sigma_z/\beta^*$). These parameters have been described by several authors.[1,2] Still more parameters are needed if the bunches have unequal intensities or if the collisions are offset. Such complications have been neglected here.

The four relationships between the IP parameters are as follows:

$$L = \frac{\nu N^2}{4\pi\sigma_y^2 R} H_D(D,R,A) \qquad (1)$$

$$D = \frac{2 r_e N \sigma_z}{\gamma \sigma_y^2 (1+R)} \qquad (2)$$

$$\delta_{BS} = \frac{2}{9}\frac{r_e^3 N^2 \gamma}{R\sigma_y^2\sigma_z} H_b(D,R,A) H_\delta(\Upsilon) \qquad (3)$$

$$P_b = \nu N \gamma mc^2 \qquad (4)$$

where $R \equiv \sigma_x/\sigma_y$, Υ is the quantum beamstrahlung parameter, and r_e is the classical electron radius. The special functions H_D, H_δ and H_b are described in Amaldi's paper.[1] The beam-beam simulations by Yokoya[3] have been used to describe the pinch-enhancement factor.

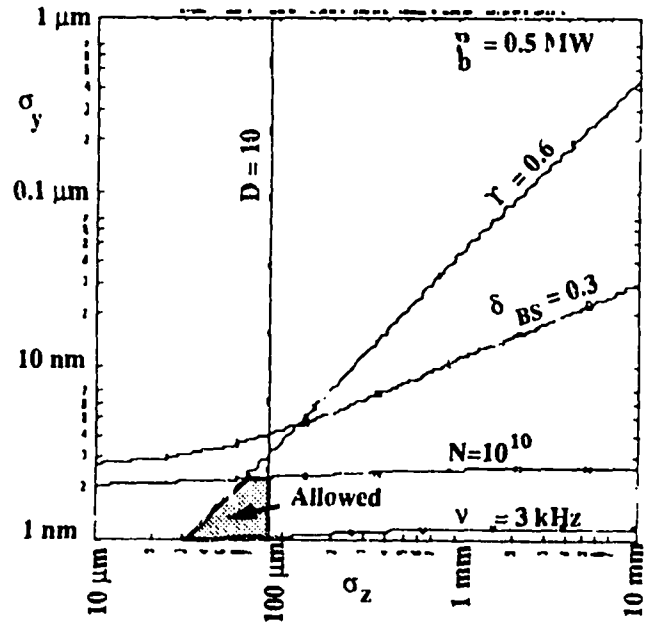

Fig. 1 Interaction Point Parameter Space for a 1 TeV (CM) Collider with $L=2\times10^{37}$ m^{-2}-s^{-1}.

If γ, R, L, P_b, and A are specified in advance, then with Eq. (1) - (4) the unknown IP parameter space is reduced to two parameters (e.g. σ_y and σ_z) which may be visualized as a two-dimensional space. Curves of constraint may be plotted on this plane, as shown in Figure 1. For this figure the collider is assumed to be 1 TeV(CM), with $L=2\times10^{37}$ m^{-2}-s^{-1}, A=0.2, R=100, and P_b=0.5 MW.

The constraint curves used in the figure represent "soft limits" on IP quantities. The allowed region on the figure corresponds to a parameter set where $N \le 10^{10}$, $D \le 10$, $\delta_{BS} \le 0.3$, $\nu \le 3$ kHz, and

$\Upsilon \leq 0.6$. The limit on D arises from the sensitivity of the luminosity to offset collisions at large D, while the need to limit coherent pair production sets the constraint on Υ.[4]

Accelerator Model

The accelerator model utilizes a SLAC-type RF linac with an enlarged iris, $a/\lambda=0.2$, to reduce wake-field effects. The structure is scaled linearly with the RF wavelength λ in all dimensions. SLAC wake fields, scaled in both iris aperture and RF frequency, are used. The transverse wake field is derated by up to a factor 4 from the scaled-SLAC value to take account of the effect of procedures to de-Q the long-range beam-breakup (BBU) instability. It is assumed that the BBU mode has been reduced to Q≈10-20, so that multi-bunch wake-field effects can be ignored.

The total AC-to-RF conversion efficiency, including pulse compression, has been assumed to be 29% at all RF frequencies. The structure efficiency, i.e. the ratio of incident RF energy per pulse to the energy stored in the structure, has been assumed to be 60%. The single-bunch beam efficiency, i.e. the ratio of the energy acquired by the beam to the stored RF energy, is $\eta_b = NeE_a/w_s$, where E_a is the average accelerating gradient, and $w_s = E_0^2/4k_1$ is the RF energy stored per unit length. E_0 is the electric field at the peak of the RF wave and k_1 is the longitudinal wake-field loss factor for the accelerating mode. The calculations presented below assume that there are 10 bunches per RF pulse.

If the center of the bunch is advanced from the peak of the RF wave, the longitudinal wake field can be used to offset the energy spread which results from the finite bunch length on the RF wave. This procedure leads to a minimum energy spread at some phase advance θ_0. With this procedure the average accelerating gradient and the energy spread are given by

$$E_a = E_0\left[e^{-\theta_z^2/2}\cos(\theta_0) - \frac{Nek_L}{E_0}\right] \qquad (5)$$

$$\left(\frac{\sigma_E}{E}\right)^2 = \left(\frac{E_0}{E_a}\right)^2 \left\{\frac{1}{2}\left[1+e^{-2\theta_z^2}\cos(2\theta_0)\right] + \left(\frac{Ne}{E_0}\right)^2 I_T \cdot \left(\frac{2Ne}{E_0}\right)\left[I_c\cos\theta_0 - I_s\sin\theta_0\right]\right\} - 1 \qquad (6)$$

where k_L is the total longitudinal loss factor and $\theta_z \equiv 2\pi\sigma_z/\lambda$. The coefficients, I_T, I_c and I_s have been defined in an earlier publication.[5]

Single-bunch transverse wake-field effects, including both energy spread and acceleration have been studied previously,[6] and expressions have been derived for the ratio of the transverse displacement to the initial displacement, x/x_0, as functions of distance s along the accelerator, distance ζ measured backward from the bunch head, head-to-tail energy spread ε, and a parameter

$$\alpha \equiv \left[\frac{Ne^2 W_1(\ell_b)}{\gamma_0 mc^2 k_{\beta 0}^2}\right]^{1/2} \qquad (7)$$

where $W_1(\ell_b)$ is the dipole wake field at the end of the bunch, and γ_0 is the beam energy at the location where the betatron wavenumber is $k_{\beta 0}$. For large s there is an asymptotic regime where the transverse displacement oscillates without growth as

$$\frac{x}{x_0} \approx \left[I_0(u) + \frac{2\varepsilon\zeta}{u} I_1(u)\right]\frac{\cos(r_\varepsilon s)}{(1+\varepsilon\zeta)} - \frac{1}{s}\left\{\frac{2\alpha}{\zeta^{1/2}(2\varepsilon)^{3/2}} J_1\left(\frac{u}{(1+\varepsilon\zeta)^{1/2}}\right)\sin(s) - \frac{\alpha^2 r_\varepsilon}{2\varepsilon^2}(1+\varepsilon\zeta)^2\left[I_0(u) + \frac{2\varepsilon\zeta}{u} I_1(u)\right]\sin(r_\varepsilon s)\right\} \qquad (8)$$

to order $O(1/s^2)$, where $r_\varepsilon \equiv [(1-\varepsilon\zeta)/(1+\varepsilon\zeta)]^{1/2}$ and $u \equiv 2\alpha[\zeta(1+\varepsilon\zeta)/2\varepsilon]^{1/2}$. The functions $I_0(x)$, $I_1(x)$ and $J_1(x)$ are Bessel Functions.

The accelerator model has been reduced to the parameter plane, (E_0,λ), where curves of constraint are plotted. Figures 2 and 3 show the results of these calculations for the collider having its IP parameters as shown in Figure 1. The IP parameters are specified at the largest (σ_y,σ_z) in the allowed region on Figure 1; $\sigma_y \approx 2.2$ nm and $\sigma_z \approx 90$ μm; $N=10^{10}$ and D=10. The allowed region in Figure 2 corresponds to an accelerator having $\sigma_E/E \leq 0.5\%$, $x/x_0 \leq 1.2$, average AC power less than 55 MW/linac, peak RF power per feed less than 400 MW, and accelerator length less than 6 km/linac. The x/x_0 constraint corresponds to approximately a 25% increase in the normalized beam emittance during acceleration. The transverse wake field in these calculations is one-quarter of the scaled SLAC value, corresponding to an assumed wake-field reduction due to measures to control the multi-bunch BBU mode. Without this assumption there is no allowed region (without using BNS damping[7]). These results indicate that BNS damping may not be needed in a structure which has been modified to reduce the long-range dipole modes.

Figure 2 shows that under these assumptions there is an operating window for RF frequencies in the range 11.5 GHz - 20 GHz. For higher frequencies the transverse wake fields will cause greater than 25% emittance growth. For lower frequencies the peak RF power will exceed 400 MW/feed for ≤6 km/linac. Of course, the frequency range can be expanded to lower frequencies by allowing longer linacs.

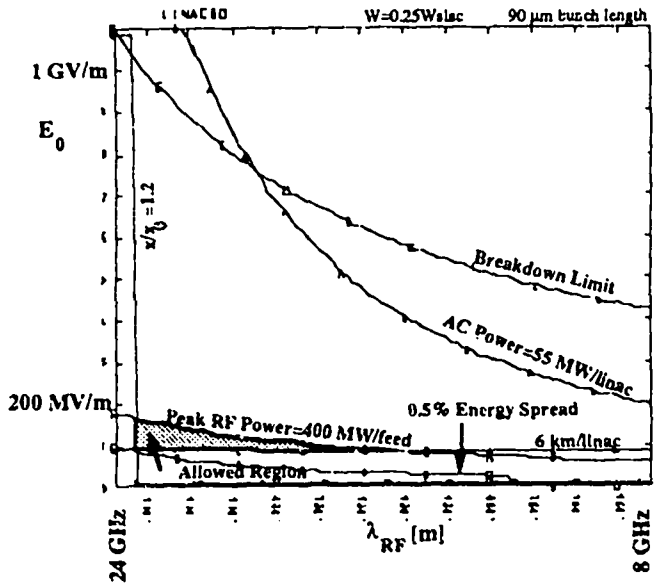

Fig. 2 Accelerator Parameter Space Using Largest Allowed (σ_y-σ_z) From Fig. 1.

Using twice σ_z (180 μm) leads to basically the same allowed range of frequencies, except that in this case the high frequency cut-off is set by the energy spread constraint ($\sigma_E/E \leq 0.5\%$) rather than by emittance growth.

It is interesting that as σ_z is decreased, the average transverse wake field over the bunch gets weaker while the average longitudinal wake field gets stronger. But, transverse wake-field effects are effectively damped by energy spread, and shorter bunches have far lower energy spread than long bunches. The net result, as seen in Figure 3, is that shorter bunches can suffer larger emittance growth due to transverse wake fields than long bunches.

Figure 3 shows the result obtained using half σ_z (45 μm), with all other parameters the same as those used for Figure 2. In this case the constraint curve for $x/x_0=1.2$ shifts to longer wavelengths, effectively shrinking the operating window in Figure 2 to a single point.

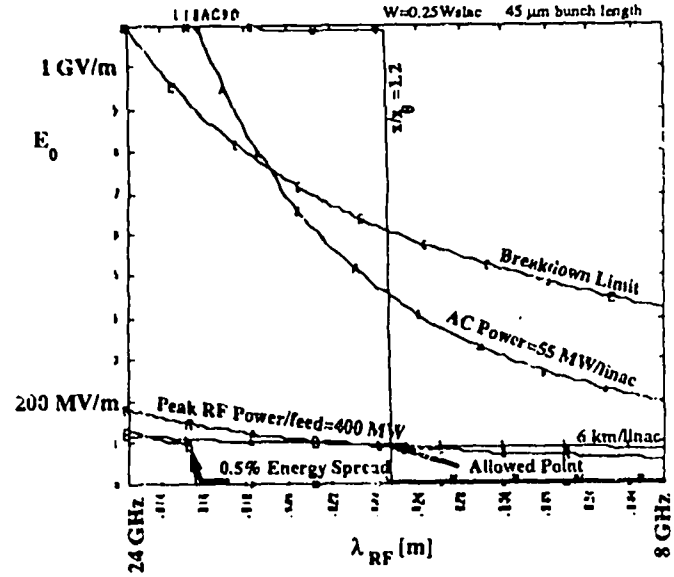

Fig. 3 Same Parameters As Fig. 2, Except σ_z Has Been Reduced By Half.

* Work supported by the U.S. Department of Energy, Office of High-Energy Physics.

References

1 U. Amaldi, *Introduction to the Next Generation of Linear Colliders*, in **Frontiers of Particle Beams**, Proc. South Padre Island, Texas, Oct. 23-29, 1986 (M. Month and S. Turner, eds., Springer-Verlag, Berlin), pp. 341-389.

2 P.B. Wilson, *RF-Driver Linear Colliders*, Proc. 1987 IEEE Part. Accel. Conf., Washington, DC, Mar. 16-19, 1987 (E.R. Lindstrom and L. Taylor, eds., IEEE Cat. No. 87CH2387-9), Vol. 1, p. 53.

3 P. Chen and K. Yokoya, SLAC-PUB-4339 (1987).

4 P. Chen, *Review of Beam-Beam Interaction*, Proc. Intl. Wkshp. on Next-Generation Linear Collider, SLAC, Nov. 29-Dec. 9, 1988 (SLAC-335, 1988), p. 335.

5 V.L. Granatstein and A. Mondelli, *Microwave Sources and Parameter Scaling for High-Frequency Linacs*, in **Physics of High Energy Particle Accelerators** (AIP Conf. Proc. No. 153, 1987), p. 1505.

6 D. Chemin and A. Mondelli, *Effect of Energy Spread on the Single-Bunch Beam Break-Up Instability In A High-Energy RF Linac*, Part. Accel. 24, 177 (1989).

7 V. Balakin, A. Novokhatsky, and V. Smirnov, Proc. 12th Intl. Conf. on High Energy Accelerators (Fermilab, 1983), p. 119.

The CERN Linear Collider Test Facility

Y. Baconnier, R. Bossart, K.K. Geissler, J.C. Godot, K. Hübner, H. Kugler,
J.H.B. Madsen, A.J. Riche, J. Ströde, G. Suberlucq
CERN, CH-1211 Geneva 23, Switzerland

ABSTRACT

In the CLIC scheme, the rf power at 30 GHz used for acceleration in the main linac is generated by a drive beam. This beam contains very short (1 mm) high-intensity (10^{12} e^-) bunches with 10 mm spacing. The generation of such a beam requires the development of electron sources and bunch compressors. For this work a test facility is under construction. This paper describes work on photocathodes, laser systems, the rf gun, beam analysis, and acceleration to 60 MeV. Preliminary results and the current status are reported.

1. Introduction

A study of a two-beam linear collider (CLIC) is in progress in CERN [1,2]. In this scheme, a high-intensity relativistic drive beam running along the whole linac produces the required 30 GHz rf power for the main linac by interaction of the drive beam with TW transfer structures. The drive beam is kept relativistic by periodic acceleration in superconducting cavities operating at 0.35 GHz.

The main objective of the CLIC Test Facility (CTF) is the study of the generation of the drive beam. The best method seems an injector combining an rf gun equipped with a laser-driven photocathode and a couple of magnetic bunch compressors, properly interleaved with accelerating sections. Given the 3 GHz equipment at hand, it was proposed to start with an rf gun at this frequency[3]. This gun operating at 10 cm wavelength is not able to produce the CLIC drive beam which will consist of 4 bunch trains having a spacing in the train of 1 cm corresponding to 30 GHz. However, it allows a study of the basic problems associated with the generation of high-intensity bunches having a typical length of the order of 10 ps. The second objective is to generate 30 GHz rf power for a variety of CLIC structure tests. This is done by accelerating the 4.5 MeV electron bunches from the gun by a spare accelerating section of the LEP Injector Linac (LIL) to more than 50 MeV. A small accelerating section adding 4 MeV and a bunch compressor might eventually precede the LIL section. This beam then interacts with a 26 cm long TW structure of the CLIC main linac used as a transfer structure which converts the energy extracted from the beam into rf power. For 40 nC in the pulse we expect 24 MW at the output. Coupling this power to a second, identical CLIC structure produces there the nominal gradient of 80 MV/m, which can be verified with a probing beam. The CLIC main linac structure is used as transfer structure in this experiment in order to compensate with its high shunt impedance the relatively low intensity of the experimental drive beam. However, this short beam pulse will also serve for testing the real low-impedance CLIC transfer structure and it can be used for tests of the position monitors and other instrumentation of CLIC.

In a first stage, the gun will be operated with an Y or CsI cathode because these materials can be exposed to air without adverse effects on their performance. A Nd:YAG laser providing a long pulse (8 ns), not synchronized with the rf, will illuminate the cathode. The first part of the beam line with instrumentation after the gun has been designed. It acts as a spectrometer to study and later to monitor the beam parameters. Then the beam line to the LIL accelerating section will be completed probably first without bunch compressor. In the second stage, a preparation chamber will be attached to the gun for in-situ preparation of Cs_3Sb and metallic cathodes. The laser will be replaced by an rf synchronized one producing either single pulses or a train of pulses spaced by a multiple of the rf period (10 cm). At this stage, controlled 30 GHz rf generation will become feasible. The first stage is planned for the end of 1990, the second stage for the middle of 1991. In the following a progress report on the key issues is given.

2. Photocathode development

In order to produce a few tens of nC in the rf gun, the cathode must have a quantum efficiency η of 0.1% and a good lifetime. Initial work [4] has concentrated on Y,Sm[5] and Cs_3Sb[6] after a start-off with CsI. The electron yield is measured with the cathodes inserted in a dc gun providing a gradient between 5 and 8 MV/m. The cathodes were illuminated first by a pulsed Nd:YAG (266 nm, 8 ns) laser; now an excimer laser (308 nm, 15 ns, about 0.1 mJ at cathode) is used. The cathodes can be transferred under vacuum from the preparation chamber to the dc gun by a translator. The beam instrumentation downstream of the gun (luminescent screen, current and charge monitor) completes the dc test stand[4].

Recently, Cs_3Sb cathodes have been produced under improved vacuum conditions, continuously monitoring the electron emission triggered by excimer laser light during the deposition of the materials. Evaporating Sb and then Cs onto the stainless steel substrate in a vacuum in the nTorr range resulted in a cathode with $\eta = 0.5\%$, very similar to the value previously obtained[4]. If the cathode is stored under vacuum at 0.5 nTorr, η slowly decreases, dropping to half the initial value within about 6 days. The cathode illuminated with low energy laser pulses (10 μJ) remained relatively stable; η dropped by 30% over 40 h. However, η decays faster if the laser energy is higher, e.g. to 50% in 7 h with a laser pulse of 350 μJ. All tests were conducted at 2.5 Hz repetition frequency. It appears that Cs_3Sb is a suitable cathode material to start with. Tests with Ar glow-discharge cleaned Y and multi-alcaline cathodes are the next steps envisaged.

3. The laser system

A number of these tests on the dc test stand will be repeated with shorter laser pulses produced by tail-quenching in a dye which is pumped by the excimer laser. A N_2 laser (337 nm, 0.5 ns, 0.1 mJ at cathode) is also in preparation for the dc tests. For the rf gun, a second Q-switched, frequency-quadrupled Nd:YAG laser (266 nm, 8 ns, 15 mJ) will be used in the first stage. Later on, a laser that can be synchronized with the rf will become available. This system produces either single pulses or the energy of

one pulse may be split into a train of sub-pulses produced by a mirror system. The train lasts about 2 filling times (2 x 11.4 ns) of the CLIC main linac structure, and the spacing of the pulses in the train is a multiple m of the 3 GHz rf period (m = 1,2,4,8..). The laser system consists of a mode-locked, diode-pumped Nd:YLF laser oscillator with phase and amplitude stabilization producing a pulse train at the 12th subharmonic of the rf, 250 MHz, and at 1047 nm with 0.4 nJ in these ≤ 20 ps (FWHH) pulses (timing stability ≤ 1 ps relative to rf). After a single-pulse selector, a Nd:YLF regenerative amplifier and two further Nd:YLF single-pass amplifiers raise the pulse energy to > 5 mJ, while a grating pulse compressor reduces the pulse length to 7 ps (FWHH); 10 ps, 30 ps, and 50 ps will also be available. Harmonic generators provide light at 524, 349 and 262 nm with the respective single pulse energy 2 mJ, 0.5 mJ and 0.2 mJ. The repetition rate of the laser, ≤ 10 Hz, defines the repetition rate of the CTF.

4. The rf Gun

The gun consists of a half-cell containing the cathode and a full cell (Fig. 1). The input waveguide is coupled to both cells in such a way that only the π-mode is excited[3,7]. In order to test fabrication techniques and to have a model for comparison between field calculations and low-power rf measurements in air, an OHFC copper model was built without cathode plug. The coupling slot to the waveguide was cut later. The dimensions had been scaled from the BNL design[3] to f_{LIL} = 2998.55 MHz, taking into account that the gun would operate at 30° C. The dimensions were adjusted until URMEL [8] gave the correct frequency of the π-mode f_π and the accelerating electric field in both cells was the same. The rf measurements on the model without slot showed that the measured f_π was within 0.16% of the calculated value. After making the eigenfrequencies f_i of the two cells equal by tuning the second (λ/2) cell, the frequency difference between π and 0 mode was 1.9 MHz, which is a measure for the coupling between the two cells. The unloaded Q was measured to be 10800.

Having demonstrated that the dimensions of the model were correct, "Gun 2" was produced. Its individual parts are brazed together and its main body is equipped with 3 water cooling circuits which are machined into the copper. Each cell is equipped with a radial piston tuner which is, for the moment, set manually. The tuning range is ± 2 MHz. An additional cell 1 tuning offset can be obtained by adjusting the length l of the cathode plug, the sensitivity being df_1/dl =-26 MHz/mm, which indicates tight tolerances on the cathode thickness. Each cell is equipped with a small, calibrated coupling loop. According to the calculations, 6.3 MW are sufficient to produce in both cells E(r = 0) = 100 MV/m provided the theoretical Q (11700) can be achieved. The gun can be baked to 150°C in order to obtain a vacuum in the lower 0.1 nTorr range. The low-power rf measurements are being made and the high-power tests will be performed soon.

Simulations[9] with TBCI-SF[10] up to 75 nC initial pulse charge were carried out assuming in most cases a parabolic distribution I(t) at the cathode having Δt =30 ps at the base. The results of TBCI-SF at 1 nC were cross-checked[9] with PARMELA and PRIAM[11]. When an optimistic cathode performance (r_c = 7 mm, j = 8A/mm²) is assumed, a pulse charge up to 32 nC with 6.5 ps rms could be expected provided 15% beam loss in the gun is accepted. However, more realistic parameters r_c = 5 mm, j = 4 A/mm² were adopted for the nominal case yielding 9.4 nC with the standard initial distribution. The results are summarized in the first line of table I. In this case no beam loss occurs in the gun and emittance as well as energy spread are much smaller. The phase Φ between the zero-crossing of the cathode field E_1 (dE_1/dt > 0) and the start of the laser pulse is very important and its choice is a compromise. Small or negative Φ leads to a welcome bunching in the gun but is always associated with particle loss. Table I is for Φ = 30° providing minimum momentum spread. The left part of the table gives the initial conditions, the right part the gun output parameters: average longitudinal momentum <p>, rms momentum spread δp/p, rms bunch length δz and the normalized emittance in the transverse plane using the usual definition[9]. Variation of the initial beam dimensions keeping the charge constant (Table I, 2nd and 3rd line) shows that space charge does not play a major rôle. Trading emittance against bunch length seems to be possible. Cases with E = 50 and 25 MV/m were also run showing a degraded performance.

Table I, Beam Simulation Results at Gun Exit for Q = 9.4 nC and E = 100 MV/m

Dt ps	r_c mm	j A/mm²	< p > MeV/c	dp/p %	dz mm	e_n rad.m
30	5	4	4.6	0.4	1.8	1.2×10^{-4}
30	5/√2	8	4.6	0.5	1.9	0.8×10^{-4}
15	5√2	4	4.5	0.2	0.9	1.5×10^{-4}

The simulations indicate that it might be difficult get the required 40 nC in a well-behaved bunch from the gun. In this case, a train of bunches with a time structure described under point 3 will be used. It can be shown that the power produced by such a bunch train generates virtually the same gradient in the second CLIC structure as a single bunch, provided that the total charge in the train per filling time and in the single bunch are the same; the bunch length must also be equal. The requirement on the gun can in this way be considerably reduced.

Initially, the laser synchronized with the rf will not be available. An 8 ns long pulse of a Nd:YAG laser will be used. Simulations with TBCI-SF, assuming constant current emission yielding at the cathode 3.2 nC during 166 ps, with E = 100 MV/m show 0.3 nC/bunch at the gun exit with 20 ps at the base in the ± 0.5% momentum bite at peak energy, consisting of particles having departed around Φ = 55°. The simulations further show that the particles emitted with an unfavorable phase are at first accelerated but then return to the cathode, depositing there almost 0.5 mJ/rf cycle, which is 2.5 times the laser power and which could lead to cathode damage.

5. Other components of CTF

A blockhouse constructed alongside LIL contains the beam line. It has inside dimensions l x w x h = 19.2 x 4.8 x 3.2 m, and the concrete shielding is laterally 2.4 and 1.6 m at the top. The equipment room at the top (17.5 x 8.0 x 3.6 m) houses the laser, instrumentation, controls and power supplies.

The 35 MW spare klystron of LIL provides the 3 GHz power for the rf gun, for the deflecting cavity foreseen for bunch length measurements, and for the spare LIL accelerating section. Power and phase for the first two items can be controlled independently. The non-load energy is 60 MeV (rf gun + LIL section).

The layout of the beam line based on first-order optics up to the LIL section follows the BNL/ATF solution: three straight sections and two 90° bends (Fig. 2). This solution is attractive because i) the spectrometer can be used permanently and the slits provide the appropriate cuts in longitudinal phase space producing the short pulses during the running-in with the 8 ns Nd:YAG laser; ii) the laser beam is centered on the gun axis. To cope with the large e^- beam divergence after the gun, a solenoid is positioned at the gun outlet followed by a quadrupole triplet. The momentum defining slit is in the horizontal beam waist at D_{xmax} between the two dipoles. The two quadrupoles in this straight section are adjusted to suppress the dispersion after the second dipole magnet. Further triplets focus the beam into the LIL accelerating section. Instrumentation is foreseen to measure beam charge and position with magnetic pick-ups. Beam size is measured with a secondary emission grid, transparent to the laser, in the first straight section and with screens in the rest of the line. Bunch length is measured with a 3 GHz vertically deflecting cavity sweeping the beam over a horizontal slit placed between the two dipoles, and by observing the transition or Cerenkov radiation emitted by a thin foil placed in the beam after the first dipole.

The CTF building including utilities is ready and the rf network is partially installed. Installation of the rf gun, the Nd:YAG laser and the first part of the beam line will be completed by the end of the year.

Acknowledgements

W. Pirkl has contributed to the field calculations in the rf gun and helped to define the rf measurements. We also thank M. Dykes for critical reading of the manuscript.

References

1. W. Schnell, Proc. Linac Conf.,Williamsburg, report CEBAF 89-001 (1988) 696
2. G. Guignard, this conference
3. K. Batchelor, H. Kirk, J. Sheehan, M. Woodle, K. McDonald, Europ. Part. Accel. Conf. (EPAC), Rome (1988) 954
4. Y. Baconnier, K.K. Geissler, J.H.B. Madsen, A. Pisent, G. Suberlucq, pres. at EPAC, Nice (1990); also CERN Divisional Report PS 90-24
5. J. Fischer et al., pres. at ICFA Workshop, Bendor (1990)
6. R.L. Sheffield et al., Proc. Lin. Accel. Conf. (1988) 520
7. K. Batchelor, J. Sheehan, M. Woodle, Internal Report BNL-41766
8. U. Lauströer, U. van Rienen, T. Weiland, Internal Report DESY M-87-03 (1987)
9. H. Kugler, A. Pisent, A.J. Riche, J. Ströde, presented at EPAC, Nice (1990); also CERN Divisional Report PS 90 -23
10. F. Ebeling, P. Schütt, T. Weiland, EPAC , Rome (1988) 678
11. G. Le Meur, F. Touze, presented at EPAC , Nice (1990)

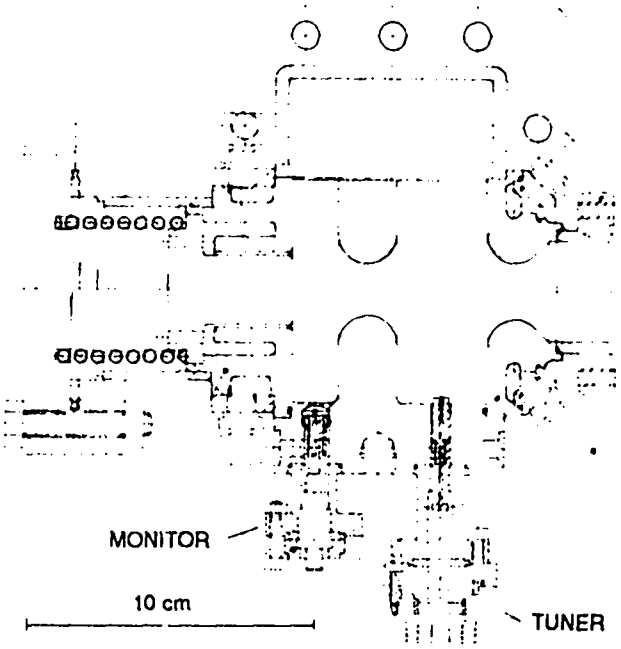

Fig. 1: Cross-section of 3 GHz rf gun (derived from BNL/ATF design [3])

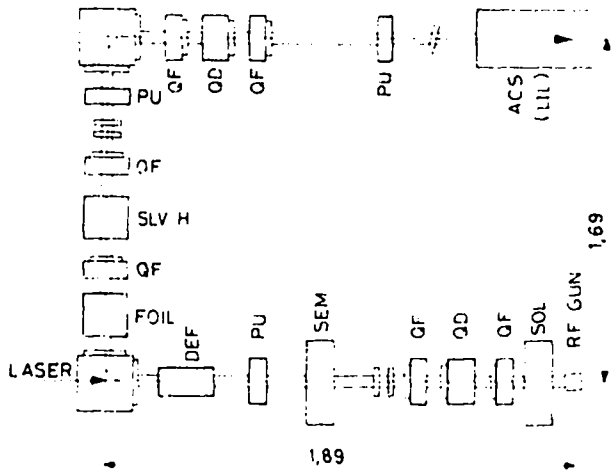

Fig. 2: Layout of beam line after gun; SEM-secondary emission grid; DEF-vertically deflecting cavity; FOIL-foil for streak camera; SLV-H-vertical and horizontal slits; PU-beam position and charge monitor; ACS-LIL accelerating section

COMPUTER SIMULATIONS OF NEW DIELECTRIC ACCELERATOR DEVICES*

K. C. D. Chan
Los Alamos National Laboratory, Los Alamos, NM 87545
P. Schoessow
Argonne National Laboratory, Argonne, IL 60439

Abstract Recently, dielectric wakefield accelerator structures have been successfully demonstrated at the Argonne Advanced Accelerator Test Facility. This paper describes computer simulations of these experiments, including schemes for damping transverse deflecting forces in these devices. These simulations were performed using the MAFIA and ARRAKIS codes. MAFIA is a set of electromagnetic solvers in three dimensions widely used for designing accelerator components. The ARRAKIS codes are time-domain electromagnetic solvers which have been recently developed and implemented on massively parallel computers such as the Connection Machine.

Introduction

Time-domain finite-difference (TDFD) codes have been useful tools for calculating wakefield effects, and have been extensively validated for structures involving metal and vacuum only [1]. Experiments performed recently at the Argonne Advanced Accelerator Test Facility (AATF) [2] to measure longitudinal and transverse wakefields induced by electron beams in dielectric structures offer an unique opportunity for validating these TDFD codes for applications that include dielectric materials.

In this paper, we report computer simulations of AATF experiments and related dielectric schemes using the MAFIA codes [3] and the ARRAKIS codes [4]. The MAFIA codes are a standard set of general purpose electromagnetic solvers in three dimensions widely used for designing accelerator components. The TDFD code in the MAFIA group is called T3. Although the geometries involved in the AATF experiments at this time have been mostly axisymmetric, T3 will allow us to extend our simulations to 3D dielectric device geometries in the future.

The ARRAKIS codes differ from the MAFIA package in having been designed specifically for problems involving dielectric devices. Although presently restricted to 2D problems, thus requiring each azimuthal mode to be computed individually, these codes permit some flexibility in specifying dielectric properties and boundary conditions. Rapid computational turnaround with large meshes is achieved through the implementation of the ARRAKIS codes on parallel computers, with the ARCHON subset (used for the simulations reported in this paper) developed for the Connection Machine. Recent work on ARRAKIS has emphasized studies of transverse wake suppression mechanisms and noncollinear drive-witness beam transformer geometries.

*Work supported by the US Department of Energy, Offices of High Energy and Nuclear Physics, including Contract W-31-109-ENG-38.

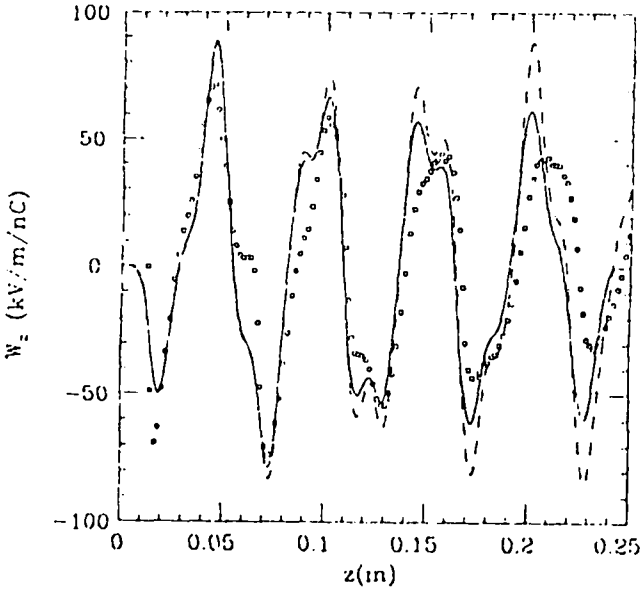

Figure 1: AATF measurement (o) of the longitudinal monopole wake with MAFIA (solid curve) and ARCHON (dashed curve) calculations.

Dielectric Device Simulations

Longitudinal (monopole) and transverse (dipole) wakes were computed for one of the AATF dielectric waveguide experiments [5]. The device geometry used here consisted of a dielectric tube of inner radius 1.27 cm, outer radius 2.22 cm, dielectric constant $\epsilon = 2.6$, and rms drive bunch length $\sigma_z = 3.0$ mm. The computed and measured wakes are shown in figures 1 and 2. Note that the ARCHON and T3 longitudinal wakes have each been convolved with a Gaussian ($\sigma_z = 3.0$ mm) to reflect the smearing of the measured wake by the finite length witness beam. No attempt was made to adjust the computed transverse wakes. The accuracy of the measurements is roughly ±5 kV/m/nC for the monopole wake and ±0.4 kV/m/nC/mm for the dipole wake.

The numerical and experimental results demonstrate reasonably good agreement over a long distance (24 cm) behind the drive bunch. The computed wakes reproduce well the overall shape of the measurement, with some discrepancies in detail on the amplitudes of the maxima and minima, and in the wavelength of the dipole wake.

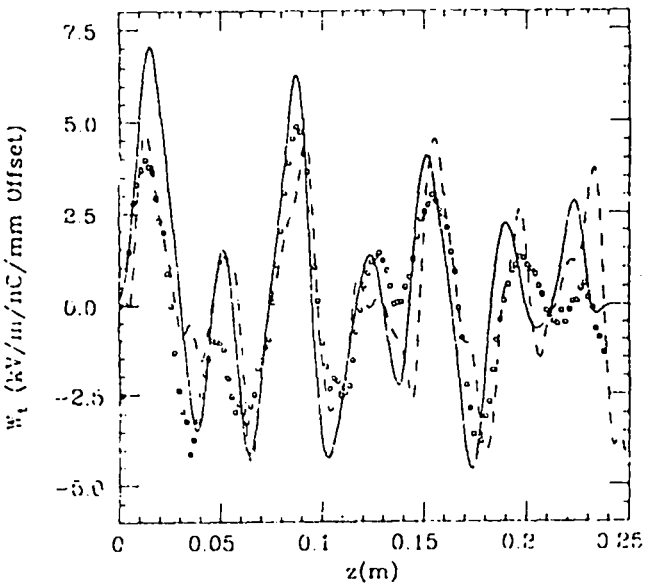

Figure 2: AATF measurement (o) of the transverse dipole wake with MAFIA (solid curve) and ARCHON (dashed curve) calculations.

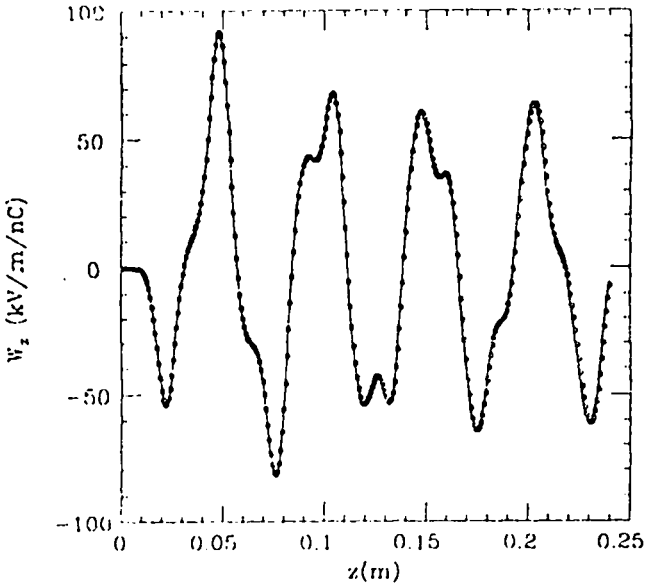

Figure 3: Comparison of longitudinal wakes in a dielectric structure with (o) and without (line curves) longitudinal cuts to interrupt azimuthal current flow in the outer boundary. (T3 simulation)

Another set of simulations were performed for dielectric structures with the thickness of the dielectric small compared to the radius of the structure. In this limit the longitudinal and transverse wakes have been shown analytically [6] to reduce respectively to a cosine and a sine function with the same wavelength. This asymptotic behavior has been reproduced in the MAFIA and ARCHON simulations. The amplitudes and wavelengths of these sinusoidal functions calculated using the two codes are compared with the analytic values in Table 1 for structures of inner radius 12.7 mm, $\epsilon = 2.25$, $\sigma_z = 4$ mm, and dielectric thicknesses of 1.6 and 2.4 mm.

For the most part, the codes are in good agreement with theory, with the largest discrepancies occuring in the transverse wake amplitudes. The origin of this disagreement is not understood and is currently being investigated.

The suppression of deflecting wakes is of some importance if dielectric wakefield structures are to be of use in high energy accelerators. A technique for effecting this [2] proceeds from the observation that while the accelerating modes in dielectric devices are pure TM_{0n}, the deflecting modes are all hybrids (HEM_{mn}). Interrupting the azimuthal current flow in the outer conducting jacket, either by introducing cuts or replacing it altogether by a longitudinal wire layer, should therefore not affect the monopole components of the wake but should allow the dipole and higher parasitic modes to leak through for damping by an external layer of lossy material.

T3 simulations were performed to show that longitudinal cuts at the outer metallic wall of a dielectric structure will modify the dipole but not the monopole wake. The geometry used was the same as for the calculation in figures 1-2, but with two longitudinal cuts in the outer jacket, taken in the plane normal to the plane of displacement of the drive beam. Both cuts were 2mm in height, and the beam length used was $\sigma_z = 4$ mm. Closure was provided by assuming a second cylindrical conducting shell at a radius of 3 cm.

Figures 3-4 show the computed wakes for this device with and without the longitudinal cuts. Differences between the monopole wakes are negligible, while the shape of the transverse wake is greatly distorted in the cut geometry.

ARCHON was used to model an experiment performed at the AATF which used a dielectric device in which the outer jacket was replaced by a longitudinal wire layer. The inner and outer radii of the dielectric tube were 1.27 and 1.905 cm respectively, and $\epsilon = 2.6$. Beam parameters were $\sigma_z = 3.5$ mm, charge/pulse= 4 nC, and offset= 6 mm. The device was enclosed in a solid conducting tube 2.54 cm in radius.

The longitudinal wire boundary was treated in ARCHON by assuming E_ϕ is continuous across it and neglecting any effects of the finite wire dimensions. The simulation (figure 5) is in qualitative agreement with the AATF data.

Conclusions

The MAFIA and ARRAKIS codes were used to model wakefields in dielectric loaded accelerator struc-

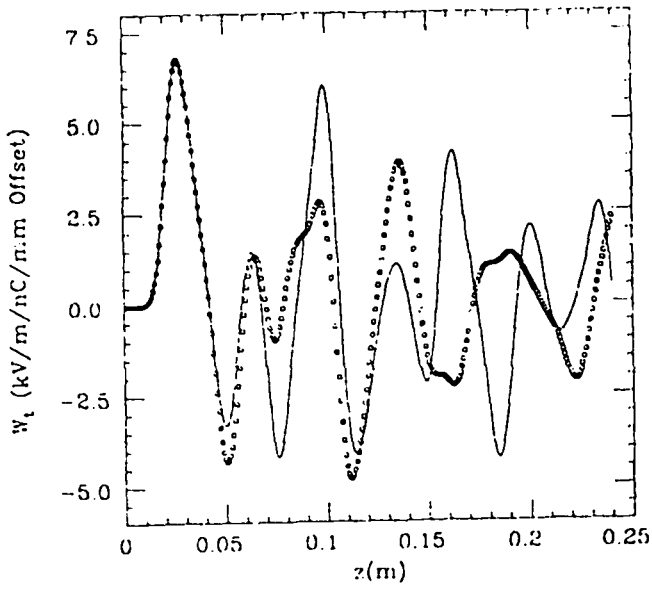

Figure 4: Transverse wakes for the same devices as figure 3. Note the distortion of the wake introduced by the longitudinal cuts.

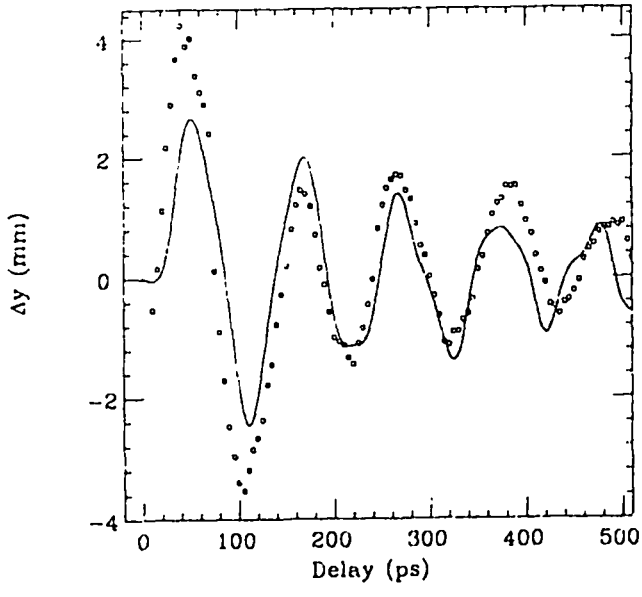

Figure 5: AATF data (o) and ARCHON simulation (solid curve) of the dielectric structure with longitudinal wire boundary described in the text. Witness beam transverse deflection is plotted as a function of relative driver-witness delay.

tures. With some exceptions reasonable agreement with measurements at the Argonne Advanced Accelerator Test Facility and with theory were obtained. The simulations also demonstrated that transverse wakes in dielectric devices may be controlled by interrupting the azimuthal current in the outer wall, without affecting the monopole wake.

Acknowledgements

MAFIA calculations were performed at the National Energy Research Supercomputer Center at The Lawrence Livermore National Laboratory. Connection Machine time for the ARCHON runs was provided by the ANL Mathematics and Computer Science Division's Advanced Computing Research Facility.

References

[1] K. C. D. Chan, Nucl Inst. Meth. in Phys. Res. **B40/41** (1989) 1076-1079.

[2] E. Chojnacki et al., these proceedings.

[3] T. Weiland, in Proceedings of the Conference on Computer Codes and the Linear Accelerator Community, Los Alamos National Laboratory, January 22-25, 1990, Los Alamos National Laboratory report LA-11857-C (1990), R. Cooper (ed.)

[4] P. Schoessow, in R. Cooper, op. cit.

[5] M. Rosing and W. Gai, to be published in Phys. Rev. D. See Fig. 4a and 4b in this paper.

[6] R. L. Gluckstern, Accelerator Theory Note AT-6:ATN-90-1, Accelerator Technology Division, Los Alamos National Laboratory, (1990).

Table 1. Comparison of MAFIA, ARCHON, and analytic results for the thin dielectric limit.

W_l (10^{13} eV/m/C) and λ_l (mm) are the amplitude and wavelength of the longitudinal wake; W_t (10^{15} eV/m^2/C) and λ_t (mm) are the amplitude and wavelength of the transverse wake.

	MAFIA	ARCHON	analytic
(1.6 mm dielectric)			
W_l	4.87	5.61	5.20
λ_l	16.2	17.5	15.4
W_t	2.27	1.56	1.40
λ_t	17.2	16.8	15.4
(2.4 mm dielectric)			
W_l	7.73	7.79	8.66
λ_l	20.4	20.5	18.3
W_t	4.46	2.30	3.12
λ_t	21.7	21.8	18.2

A LINEAR ACCELERATOR IN SPACE - THE BEAM EXPERIMENT ABOARD ROCKET

P. G. O'Shea, T. A. Butler, M. T. Lynch, K. F. McKenna, M. B. Pongratz, T. J. Zaugg
Los Alamos National Laboratory, Los Alamos, NM 87545

Abstract

On July 13, 1989 the BEAM experiment Aboard Rocket (BEAR) linear accelerator was successfully launched and operated in space. The flight demonstrated that a neutral hydrogen beam could be successfully propagated in an exoatmospheric environment. The accelerator, which was the result of an extensive collaboration between Los Alamos National Laboratory and industrial partners, was designed to produce a 10 mA (equivalent), 1 MeV neutral hydrogen beam in 50 μs pulses at 5 Hz. The major components were a 30 kev H^- injector a 1 MeV radio frequency quadrupole, two 425 Mhz RF amplifiers, a gas cell neutralizer, beam optics, vacuum system and controls. The design was strongly constrained by the need for a light-weight rugged system that would survive the rigors of launch and operate autonomously. Following the flight the accelerator was recovered and operated again on the laboratory.

Introduction

Neutral particle beam (NPB) technology is considered to be one of the most promising concepts under development for the United States Strategic Defense Initiative. The BEAR project was the first test in space of the critical low energy accelerator technology that will be built upon in future systems. The principal aims of the project were to successfully operate a particle accelerator in space and to study the propagation of a neutral hydrogen beam, and to examine the effects of spacecraft charging.

The three main sections of the spacecraft are (figure 1): a) the Telemetry and Physics section, containing communications equipment and a number of experimental packages to study spacecraft charging and the nearby plasma environment; b) the Accelerator section, where the H^- beam is generated accelerated and neutralized; c) the Beam Diagnostics section, which contains beam sensors, and cameras for beam tracking.

Accelerator

A conceptual view of the accelerator in shown in figure 2. The main components were as follows: an H^- ion source with 30-kV extraction, a low-energy beam transport (LEBT) quadrupole system; a radio frequency quadrupole (RFQ) and RF system to accelerate the beam to 1 MeV, a high-energy beam transport (HEBT) system to collimate the beam; and a xenon gas cell neutralizer The general design parameters are given in table 1.

The accelerator conceptual and physics design were carried out by Los Alamos National Laboratory. The major industrial partners involved in the accelerator engineering were: McDonnell Douglas (injector, HEBT and vacuum system); Grumman Aerospace (RFQ); and Westinghouse Electric (RF amplifiers).

The launch and flight environments required that all accelerator components be both rugged and light weight to a

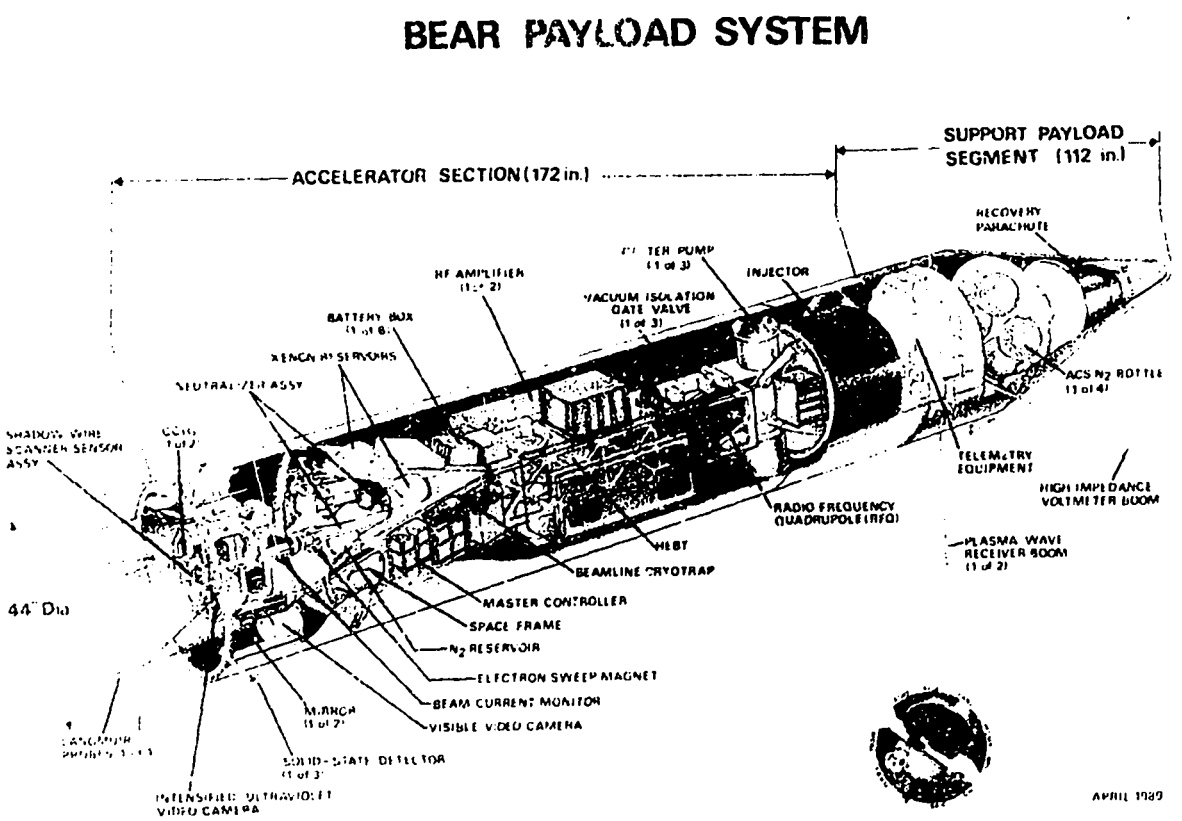

Fig. 1. The BEAR payload after booster separation.

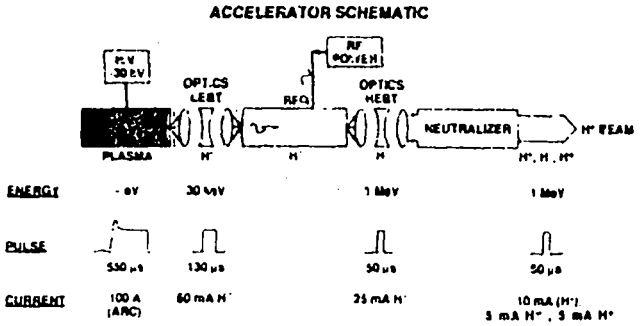

Fig. 2. A conceptual view of the accelerator.

Table 1. Bear Accelerator Performance.

	Design 1985	Test Stand** (10/88)	Payload (3/89)	PAD T 5 min	Flight
H⁻ Extraction Voltage (kV)	30	34	35	35	35
H⁻ Current from LEBT (mA)	40	60	55	54	40
Emittance at RFQ X (π cm mrad)	0.007	0.007	-	-	-
(RMS) Y (π cm mrad)	0.014	0.015	-	-	-
RMS Beam Diam into RFQ (mm)	1.5	2	-	-	-
Current out of RFQ (mA)	26	27	20	17	13
Rep Rate (Hz)	5	5	5	5	5
Beam Pulse from RFQ (μs)	50	50	50	50	50
Energy out of RFQ (MeV)	1	1	-	-	-
Emittance out of RFQ (π cm mrad)	0.011	0.012	-	-	-
Current out of HEBT (mA)	23	25	18	15	11
H⁰ Particle Current (mA)	10	12*	7	-	5
Beam Divergence (mrad, rms)	±1	±1	±1	-	±1
Beam Diameter (mm, rms)	11	10	10	-	10
H⁰ Beam Brightness (A/(π mrad)², rms)	1 x 10¹²	1.2 x 10¹²	0.7 x 10¹²	-	0.5 x 10¹²

- Not measured in flight configuration
- *Without shadow wire
- **Prototype injector

degree unnecessary for ground based systems. The payload capacity of the Aries booster limited the accelerator weight to 700 kg.

The H^- ion source is a modified Penning-Dudnikov source[1]. Cesium is contained in a plenum inside the source in the form of $Cs_2Cr_2O_7$ mixed with Ti powder. The cesium is delivered to the plasma region by thermal decomposition on heating the anode and cathode. The anode and cathode are a self aligning coaxial structure. The source housing is made of aluminum, the cathode solid molybdenum, and the anode is stainless steel with a molybdenum insert. Hydrogen gas is pulsed into the plasma region by a piezoelectric valve at in 350 μs long pulses at 5 Hz. The average flow rate is 0.04 torr l/s. Extraction of the H^- at 30 kV across a single gap through a 4 x 1 mm^2 slit.

The LEBT, which focuses the H^- beam from the source to the RFQ, consists of a quadrupole triplet made of NdFeB permanent magnet blocks. This was designed to be a fixed focus system with no on-line adjustment of quadrupole strength or position. The match in to the RFQ is adjusted by varying the extraction voltage from the ion source and by controlling the plasma neutralization in the LEBT region through the addition of Xenon gas[1]. This has resulted in a less than ideal but stable and reliable match in to the RFQ.[2,3]

The vacuum system for the source/LEBT region consists of two specially modified SORB-AC™[4] getter pumps, which have an effective pumping speed of 600 l/s for hydrogen and zero for Xenon. The only xenon pumping from the LEBT is 0.6 l/s through the RFQ orifice to a 2000 l/s helium cryo condensation pump located between the HEBT and the neutralizer. This provides a means of allowing a high partial pressure of xenon and a low partial pressure of hydrogen, which is desirable for optimum operation. The beam passes through the cryopump, which is a coaxial hollow Dewar containing super critical helium, with one of the vacuum walls being the condensation surface. All gases except H_2, He and Ne are pumped by the cryopump. The cryopump is assisted by a getter pump attached to the HEBT housing. Little electrical power is required by the vacuum system. For example, the getter pumps require less than 6 watts each to maintain a pumping temperature of 80°C.

The RFQ cavity, which weighs only 55 kg, is an electroformed aluminum-copper structure[5] with no RF or mechanical joints. The cavity walls are copper plated on aluminum, with the vane tips being bare aluminum. The minimum aperture diameter is 2.4 mm. The design intervane voltage is 44 kV (1.8 Kp). It is designed to accelerate 25 mA of H^- with a copper power requirement of 70 kW and 1 kW per mA of accelerated beam. The low duty factor of 0.025%, along with frequency control of the RF amplifier, precluded the need for cooling.

The RF power[6,7] is provided by two solid-state amplifiers, each capable of producing 60 kW pulses, 60 μs long, at 5 Hz with a frequency of 425 +/- 0.5 MHz. The resonant frequency of the RFQ is automatically tracked to within 0.02 MHz, which eliminates the need for temperature stabilization. The BEAR accelerator is the first to be operated exclusively with solid-state amplifiers.

The HEBT is a quadrupole triplet similar to the LEBT. It collimates the beam from the RFQ, giving a divergence of 1 mrad rms and a beam diameter of 11 mm rms.

The neutralizer is designed to be approximately 50% efficient. Xenon gas is the neutralizing agent which is injected into the beamline by a piezo-electric valve. The efficiency of the neutralizer and the net current produced can be varied by adjusting the amount of gas injected. For normal operation the one obtains approximately 50% H^0, and 25% each of H^- and H^+

After the neutralizer the beam exits the spacecraft via a gate valve. Beyond this is a shadow wire scanner which measures the beam profile and divergence.

Details of the performance of the accelerator during ground testing have been presented elsewhere,[8] and are summarized in table 1. The accelerator is shown in figure 3 in its flight configuration with the payload skins removed.

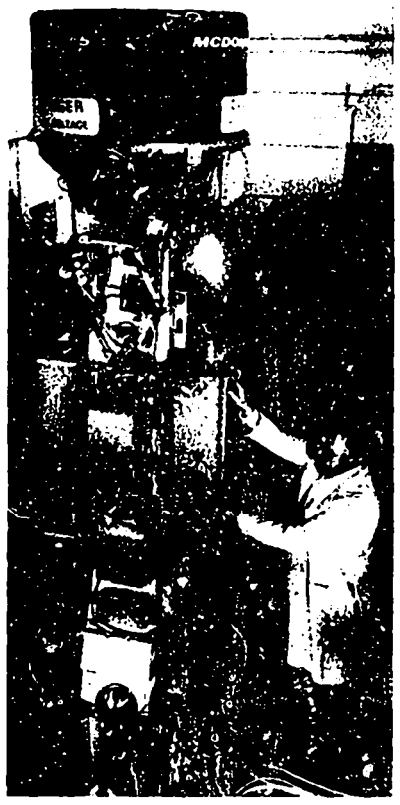

Fig. 3. The accelerator in its flight configuration. The injector is at the top of the picture.

Flight

The BEAR accelerator was launched into space on July 13, 1989. Details of the pre-programed accelerator and payload activities are given in table 2, and the nominal flight profile is shown in figure 4. The accelerator systems were maintained in a fully operational state until 155 seconds before launch. At this time the injector extraction high voltage and the RF power to the RFQ were switched off. The H^- ion source remained on through launch. By T+127 seconds all accelerator systems were operational. The beamline exit valve opened at T+128 s and the beam was injected into space. The neutralizer had been programed to produce a slightly net negative current of approximately 1 mA with individual species currents of $H^+ \approx 2$ mA, $H^0 \approx 5$ mA and $H^- \approx 3$ mA. During the two periods when the neutralizer was switched off a net negative current of -10 mA of H^- was emitted. Late in the flight excess xenon was injected into the beam producing a net positive beam current of + 1.4 mA. The three issues that were addressed by the BEAR flight were answered as follows:

Accelerator performance: Figure 5 shows the beam divergence as the beam left the payload for various ground tests and for the flight. The divergence of 1.05 mrad during flight was comparable to the best results obtained on the ground.

Table 2. Bear Flight Timeline

Time (seconds)	Event
T = 0	Launch (Ion source on)
T + 85	Booster separation
T + 91	Extractor high voltage on
T + 105	RF system on Beam out of RFQ
T + 127	Neutralizer on
T + 128	Beamline exit gate valve open Beam injected into space (Net current -0.8 mA)
T + 260 - 270 and 322 - 332	Neutralizer off (Net current -10 mA)
T + 360 - 390	Overneutralize (Net current + 1.4 mA)
T + 390	Beamline gatevalve closed Accelerator off

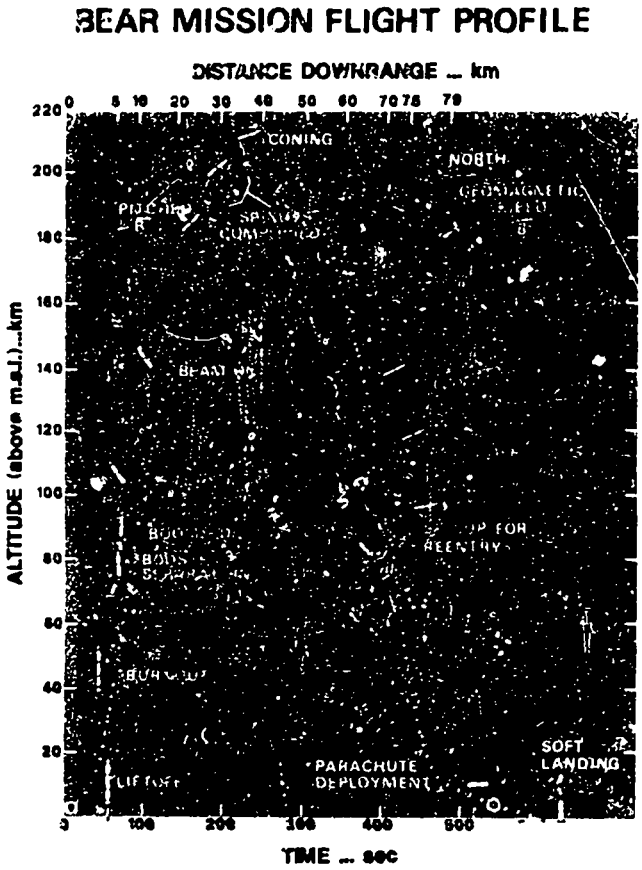

Fig. 4. Mission flight profile.

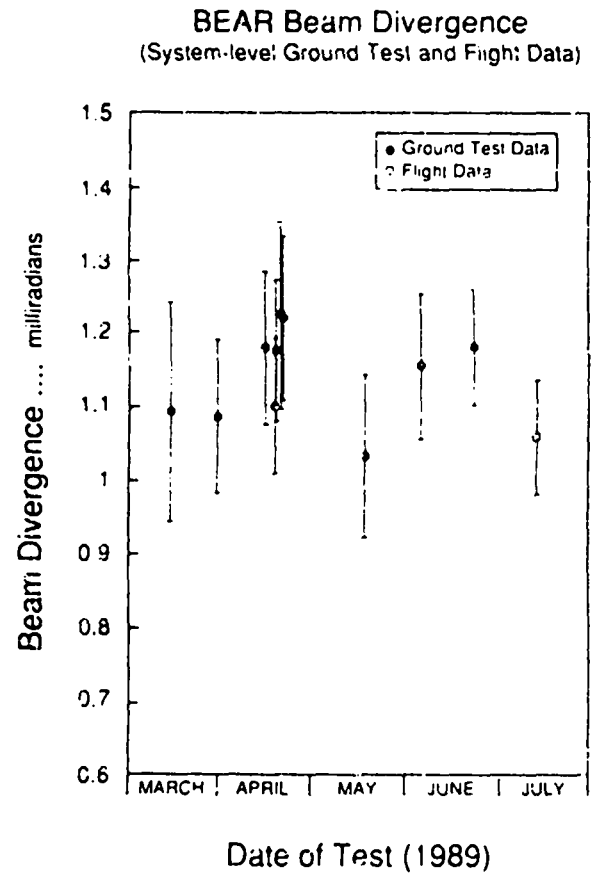

Fig. 5. Beam divergence history of the neutral beam.

NPB propagation: Figure 6 shows the beam propagating in space as seen by one of the onboard cameras. There was no evidence of any unexpected beam behavior such as

Fig. 6. Neutral beam (vertical line) propagating away from the spacecraft as viewed from an onboard wide-angle camera whose line of sight is almost parallel to the beam. The beam exits the accelerator at the bottom of the picture.

instabilities that could cause beam break-up, or of anomalous stripping of the neutral beam.

Spacecraft Charging: When the neutralizer was operating nominally no charging of the spacecraft was observed. When the neutralizer was switched off charging was observed as would be predicted by the emitted current and vacuum capacitance of the payload. However there was no effect on accelerator operation.

All of the accelerator subsystems with the exception of one performed flawlessly. The exception was the piezoelectric pulse valve which fed hydrogen gas to the H^- ion source. At T+85 s when the booster separated from the payload the valve experienced a shock of at least 22 g. This caused the valve to inject approximately 10% more hydrogen per pulse into the ion source than normal. The result was an unstable arc in the ion source and reduced output current from the accelerator.

The payload was recovered and returned to Los Alamos. Despite the severe shock of landing, the beamline was still under vacuum when examined the following day. In Los Alamos the payload was reconnected to its ground support equipment. The only repair necessary was the reconnection of a wire to the injector xenon valve which had come loose. On July 26th the accelerator was operated successfully at the same performance levels as before launch.

The BEAR flight has demonstrated that accelerator technology can be adapted to a space environment. This first operation of an NPB accelerator in space uncovered no unexpected physics.

REFERENCES

1. P. W. Allison and J. D. Sherman, "Operating experience with a 100-keV, 100 mA H^- injector," Proceedings of the 3rd symposium on Production and Neutralization of Negative ions and Beams, AIP Proc. 111, p. 511, 1983.
2. P. G. O'Shea, T. J. Zaugg, R. G. Maggs, P. Schafstall, and J. E. Dyson, "Variable Gradient Permanent Magnet Quadrupole Lenses", Proceedings of the 1989 IEEE Particle Accelerator Conference, Chicago, Illinois, p. 354, 1989.
3. P. G. O'Shea, D. L. Schrage, L. M. Young, T. J. Zaugg, K.F. McKenna, and L. D. Hansborough, "Laboratory Performance of the BEAR RFQ" Nucl. Instr. and Meth. B40/41, 946 (1989).
4. SAES Getters, Colorado Springs, Colorodo.
5. D. Schrage, L. Young, B. Campbell, J. H. Billen, J. Stovall, F. Martinez, W. Clark, G. Bolme, S. Gibbs, D. King, P. G. O'Shea, T. Butler, J. Rathke, R. Micich, J. Rose, R. Richter and G. Rosato, "Beam Experiment Aboard Rocket RFQ" Nucl. Instr. and Meth. B40/41, 949 (1989).
6. C. Davis, M. Lynch, D. Reid, "60 kW UHF, Solid State RF Power Supply", Proceedings of the 1989 IEEE Particle Accelerator Conference, Chicago, Illinois, p. 162,1989.
7. M. T. Lynch and J. Devenport, ibid. p. 1867.
8. P. G. O'Shea, T. A. Butler, L. D. Hansborough, M. T. Lynch, K. F. McKenna, D. L. Schrage, M. R. Shubaly, J. E. Stovall, and T. J. Zaugg, "The BEAR Accelerator," Proceedings of the 1989 IEEE Particle Accelerator Conference, Chicago, Illinois, page 354.

ABOUT FE ELECTRON LOADING OF THE CAVITY WITH HIGH LEVEL RF POWER

O.K.Belyaev, V.P.Gamarsky, A.V.Gladkov, R.Yu.Ivanov,
Yu.G.Malynin, A.B.Masaev, S.V.Pusanov, A.N.Semizarov,
V.B.Stepanov, V.A.Khmara, Yu.M.Yashnov

Institute of High Energy Physics, 142284 Protvino, Moscow Region, USSR

Abstract

The degradation of the radio-technical parameters of the cavities in the proton linear accelerator with RFQ focusing at a high level RF power has been investigated. The Faraday cup is used to show that this is caused by the FE electron loading of the cavities without discharge development. The dependencies obtained are in agreement with the results on measuring the intensity of the x-ray radiation at different levels of the RF power, fed to the cavity. The data characterising emission properties depending on the treatment of the electrode surfaces, are given. Possible ways to suppress the FE electron loading are discussed.

When operating the injector for the proton synchrotron booster [1] we have revealed the dependence of the tuning system with RF feedback on reflectional wave on the RF signal value, steepening of the pulse from the cavity and shortage of the generator power. The phenomena mentioned above deteriorate the beam parameters at the accelerator output and require to be studied and eliminated.

A possible reason for this may be the increase of the RF losses in the accelerator cavities. The measurements carried out at a low power level showed no Q decrease, therefore the conclusion was made that the aforementioned effects are characteristic to high RF power levels. Figure 1 shows the accelerator section connected with a powerful RF generator through a decoupling ferrite Y-circulator, which was done with the view to investigate the dependence of the cavity performances versus power level. The

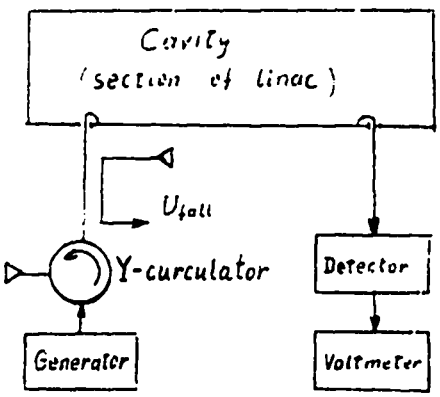

Fig.1. Block diagram of measurement system.

field level U_n in the cavity was recorded with the aid of the coupling loop and a block of pulse-height detector. The value for the power from the cavity corresponded to the U_{fall} readings from the reflectometer. Figure 2 presents the experimentally obtained dependences of the relational Q value (curve 1) and field level in the cavity (curve 2) versus the root of the relative power value in the cavity. The experimental results revealed the instability of the Q factor and nonlinear changes of the field level, it is worth mentioning that the deterioration rate of the Q factor increases more than three time within the range of curve 2 nonlinearity. FE electron loading without further development of the multipactor electron loading may be the reason for what was said above. By a capturing a fraction of

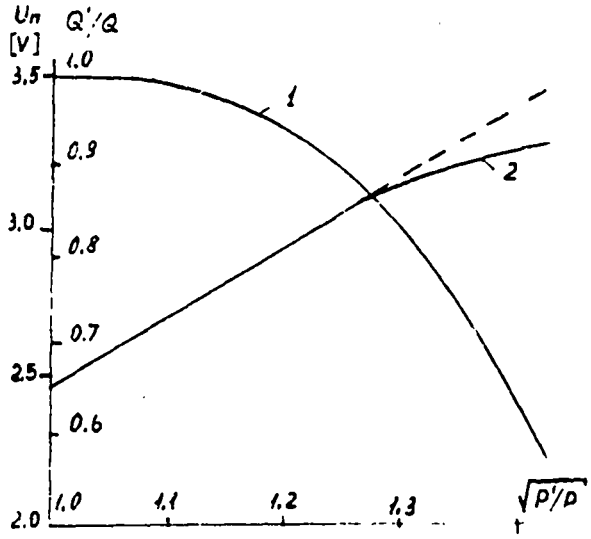

Fig.2. Dependences of the relational Q value (C-1) and field level in the cavity versus the root relational power.

the electron beam with the Faraday cup we tries to find confirmation of our assumptions. The construction of the cylinder installed on the accelerator section at a minimal distance from the accelerating beam line electrodes is schematically shown in figs.3a,b.

Figure 4 presents the FE electron loading dependence on the field in the accelerator section working without the beam. Curve 1 corresponds to the accelerator commissioning after a long shut down, when air leakages occurred. Curve 2 was obtained after the linac conditioning, curve 3 - commissioning the machine after one week shut down

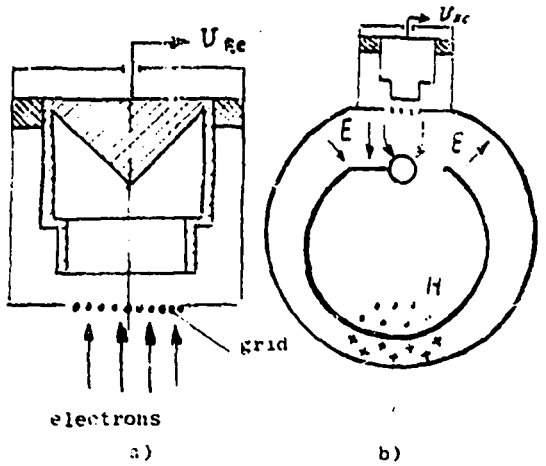

Figs.3a,b). a) Faraday cup; b) Faraday cup and H-cavity.

without air leakage. Curves 4 and 5 correspond to the measurements after 5 and 40 days after continuous operation of the machine. The x-ray intensity is described with curve 6. The correspondence in the forms of the FE electron loading dependence and Roentgen radiation points to the existence of the electron fluxes.

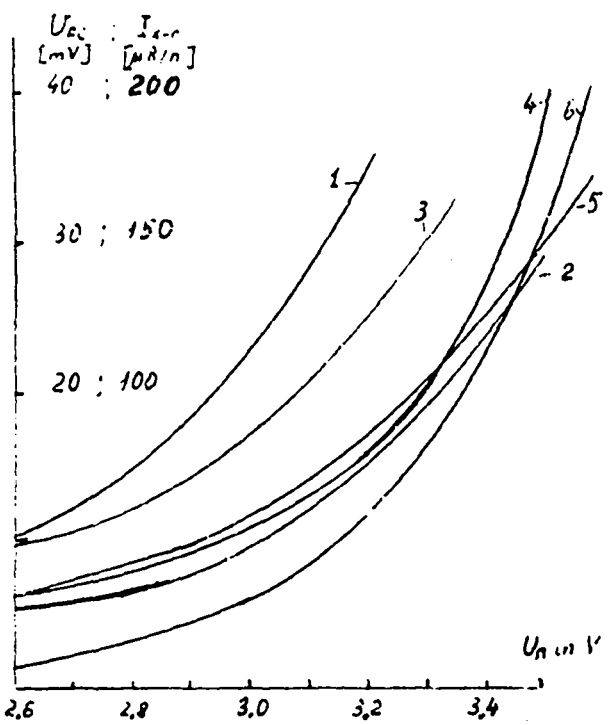

Fig.4. Dependences of the U_{FC} (curves 1÷5) and x-ray intensity -6 on the field in the accelerator section.

From the data quoted it follows that in the course of the machine conditioning the FE electron loading decreases 1.5-2 times and becomes stable at a constant field value U_n. With the growth of U_n the FE electron loading increases nonlinearly, in this case the nominal level of the RF field in the cavity U_n=(3.4-3.6) V corresponds to a sharp growth of the FE electron loading current. The current density of the loading is approximately equal to 60 μA/cm^2. Since the electrical field distribution in the cavity is rather inhomogeneous one can carry out only averaged calculations of the current growth over the surfaces of the cavity units because of the loading. Under constant energy stored in the cavity we obtain that $J'_{\tau i}/J_{\tau i} = \sqrt{Q/Q'}$ where $J'_{\tau i}$ and $J_{\tau i}$ is the current over the surface of the i-th element with and without loading, respectively.

From the data of fig.2 we have the current ratio of 1.3, which causes larger losses in the elements, and consequently their thermal deformation increases 1.7 times.

To eliminate those phenomena one should reduce electron emission. According to the data from [2] the values for the pre-breakdown currents at a constant voltage depend on the material and physical-mechanical properties of the electrode surface. In connection with this we studied the emission properties and limit electrical strength of the electrode samples made of OFHC copper depending on the their surface treatment. This particular material was chosen for the tests because the electrodes of the injector for the booster are made from OFHC copper. The electrodes work at the voltages very close to the breakdown ones [5]. In our investigations we used electrode-samples Ø 15 mm of the Rogovski profile installed in the flat-parallel gap of 0.3 mm. The electrodes were treated without any cooling lubricant and polished with tungsten wire until the surface clearance was 0.2 Ra and then electropolished at the current of 10 A/cm^2 at a depth of 10, 50, 100 μm . The vacuum in the facility was 10^{-7} Tor. The technique applied allowed one to take constant current-voltage characteristics after breakdown conditioning. Some of the samples were fired right in the test vacuum chamber at 600° C according to the well-known technique. The field amplification factor and emission area are calculated in agreement with the standard FE technique [2]. As it follows from the results of Table vacuum firing deteriorates practical voltage limits and leads to a considerable growth of electron currents. It seems that this phenomenon may be explained by the appearance of a solid oxide film produced during e.p.*), which hinders the emission (which makes the emission difficult). Under vacuum firing this layer is deteriorated. It has been shown that the samples with the electropolishing depth of 10 μm posses best characteristics. It seems that a large depth of polishing smears the lattice and isolates the grains in the structure, as it was observed in [6] , which in its turn increases the number of emission centers.

It should be noted that the results obtained at a constant voltage should be confirmed in the work with the RF power supply. According to the data from refs. [3,4], the suppression of the electron multipactoring in the cavity may achieved by covering the surface with a thin layer (10^{-6} m) of dielectric (TiN or carbon). Under certain assumptions about the influence of such a layer on the secondary emission coefficient as well as on the emission properties of electrodes, one make a conclusion about a *necessity to study possibly suppression* of electron RF loading by using different lay-

ers on the cavity surface.

Table

Variants of the treatment \ Parameters			E_{max} kV/mm	I mA	μ —	$A \cdot 10^{-14}$ cm^2	I, when U=20kV mA
without Vacuum-firing	w.e.p.**)		67	0,11	119	140	-
	electropol.*) μm	10	95	0,20	122	10	0,008
		50	91	0,35	202	0,8	0,025
		100	74	0,40	182	5	0,200
Vacuum-firing cathods	w.e.p.**)		86	0,25	128	12	-
	electropol.*) μm	10	86	0,40	93	500	0,032
		50	65	2,00	121	1000	4,0
		100	62	1,2	114	5000	5,0
Vacuum-firing anods	w.e.p.**)		85	0,25	128	12	-
	electropol.*) μm	10	73	0,3	360	0,16	0,18
		50	59	1,0	293	3,0	8,0
		100	46	2,5	243	6,0	>100

References

1. A.A.Egorov et al. URAL-30 Proton Linear Accelerator Start-up. Journal of Technical Physics, 1981, v. 51(8), p. 1643.
2. I.N.Slivkov. Processes in Vacuum at the High Voltage. Moscow, Energoatomizdat, 1986.
3. W.D.Cornelius. CW Operation of the FMIT RFQ Accelerator.//IEEE Transactions of Nuclear Science, v. NS-32, No 5, October 1985, p. 3139.
4. R.Lehmann. Experiments with an RFQ Sparker.// Particle Accelerators, 1987, v. 22, p. 161.
5. V.A.Zenin et al. The Operating Results of the Linac with RFQ-Focusing Proc. of XIII Internal Conf. on High Energy Accelerators, 1986, Novosibirsk, Nauka, v. 1, p. 312.
6. L.M.Sevrukova et al. Electrical Instability Phenomena at the Anodical Reduction of Metals. IHEP Preprint 85-191, Serpukhov 1985.

*) Electropolishing.

**) Without electropolishing.

7MeV-PROTON LINAC

Y.Iwashita, M. Inoue, H. Ego, H. Okamoto, S. Kakigi,
M. Sawamura*, T. Shirai, H. Fujita, K. Fukunaga
and H. Takekoshi
Nuclear Science Research Facility, Institute for Chemical Research, Kyoto University
*Japan Atomic Energy Research Institute

Abstract

The construction of a 7MeV-433MHz proton linac was started at 1986. The accelerator was installed in a new building at the Uji campus of Kyoto University in 1988. The accelerator system, the RF control system and the vacuum system are described.

Introduction

A new accelerator was constructed at a new accelerator laboratory building of Institute for Chemical research (ICR) in Uji campus of Kyoto University. It consists of a 2 MeV-RFQ linac[1,2] and a 7 MeV-Alvarez DTL[3]. The main specification is shown in Table 1. The operating frequency is 433.3 MHz throughout the system. The frequency is about twice higher than conventional DTLs and the size is about a half of them [4]. The higher frequency also permits the use of Klystrons. A higher energy accelerating tank is planned to be connected after the DTL in the future. The operating frequency of the high-ß structure should be 1.3 GHz, which is three times higher than the low energy part, and it allows the simultaneous acceleration of both positive and negative ions.

The area of new accelerator building space is 2650 m^2 in total, and the shielded area surrounded by 1 meter thickness wall is 600 m^2. The compact size of the accelerator structure makes enough area for a future development as shown in Fig.1. Fig.2 shows the layout of the accelerator system.

TABLE
Main specification of the linac

Ion source	
multicusp field type	proton 50keV
Accelerating structure	
four vane RFQ	50 keV~2 MeV
vane length	2195 mm
cavity inner diameter	170 mm
characteristic radius	3 mm
min. bore radius	2 mm
inter vane voltage	80kV
transmission efficiency	95% (at 30 mA)
DTL (Alvarez)	2MeV~7MeV
cavity length	1868 mm
number of drift tubes	28
focusing Q magnet	NdB iron permanent magnet
RF power source	
frequency	433.3 MHz
peak power (for each tube)	1 MW
repetition rate	<180Hz
duty factor	1%
Klystron	Litton L-5773

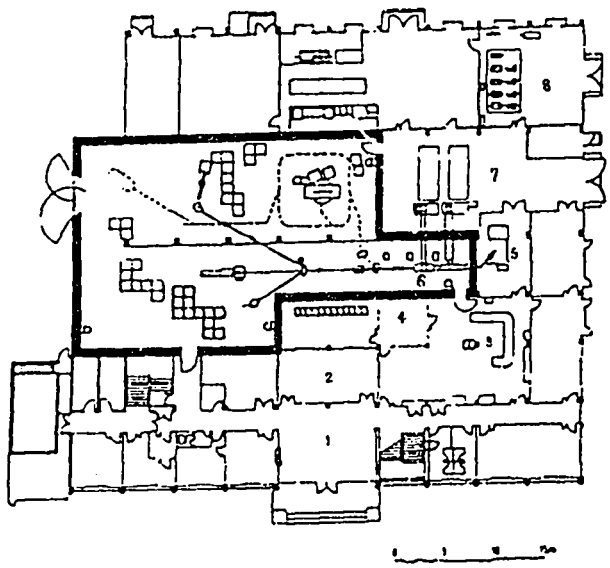

Fig. 1 Plan view of the Accelerator Laboratory (1F)
1 Entrance Hall 2 Court Yard
3 Control Room 4 Computer Room
5 Ion Source Room 6 Accelerator Room
7 Klystron Room 8 Cooling Pump Room

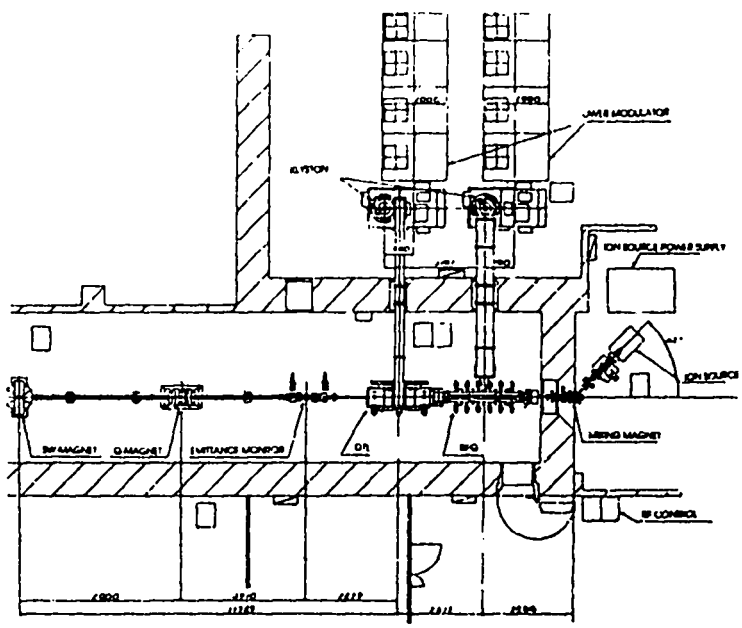

Fig. 2 Layout of the accelerator system.

Accelerator System

Injector

A multicusp-field ion source is used to produce 50 kV H^+ ion. The arc voltage of the ion source is switched for pulsed operation of up to 10% dutycycle. The designed peak beam current is 60 mA. There is an einzel-lens and a pair of x-y steering electrodes after a 50 kV accelerator column. For the future simultaneous acceleration of positive and negative ions, the low energy beam transport (LEBT) has a 45 degree mixing magnet. After the mixing magnet, a solenoidal focus coil is used to match the beam phase space configurations to the RFQ. (see photo 1)

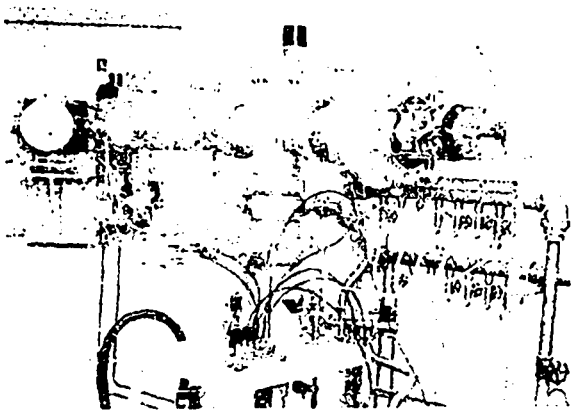

Photo 1 View of Ion Source

RFQ

The 4-vane RFQ is operated at the frequency of 433.3MHz.(see photo 2) The outer wall and the vanes are made of CrCu(Cr 0.75, Zr 0.08) which has 80% electric conductivity of Cu and 80% Young's modulus of stainless steel. The vane tips are cut by a concave cutter and have a constant curvature along the axial direction. (see photo 3) Each vane has a 20 mm diameter cooling channel in it. For field distribution tuning, 6-plug-tuners are installed in each quadrant. The designed intervane voltage is 80 kV. The RF power is generated by 1MW-peak-power Klystron L-5773, and coupled through WR-2100 waveguide by a loop into the RFQ cavity after a waveguide-to-coaxial line transition. The measured Q value is 5000, while SUPERFISH result is Q=6600.

Photo 2 View of the RFQ tank

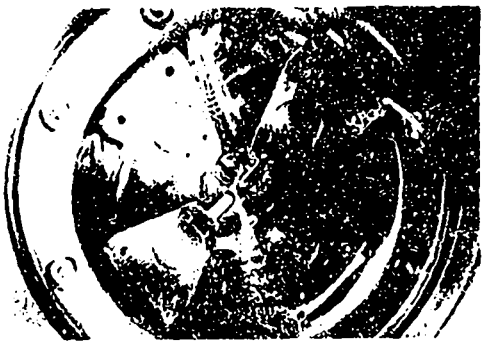

Photo 3 Inside view of the RFQ tank.

Beam Matching Section

Permanent quadrupole magnets are used to focus the output beams from RFQ. Four of them are installed before a buncher and another four quadrupole magnets are installed before the DTL cavity. The buncher is needed to match the beam to the longitudinal acceptance of the DTL. Beam monitors will be installed in this section to investigate the output beam from the RFQ.

DTL

The tank is made of standard Cu, and the drift tubes and the stems are made of CrCu. The drift tube diameter is 55 mm and the bore radius is 5 mm. Permanent quadrupole magnets are installed in the drift tubes to focus beams. Each drift tube is supported by a stem from the bottom plate which is demountable from the tank. (see photo 4) The 28 drift tubes was aligned on the plate before installation into the tank. The 5 tuners of 10 cm diameter are installed in the tank. Two of them are fixed, and three are tunable. The klystron L-5773 is also used as the power source and the power is coupled by a 5 cm width slot on the tank top. The slot length is about 15cm. The unloaded Q is about 38000. The average accelerating field is 3MV/m.

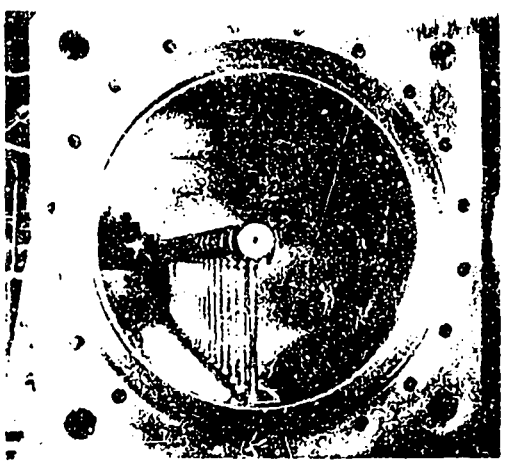

Photo 4 View of the DTL tank

RF Control System

A schematic block diagram of control system is shown in Fig. 3. The base RF is generated by a SSG HP8656B and the operating frequency is phase locked to the RFQ cavity resonant frequency. The RF phase of each cavity is also phase locked to the base SSG phase. For resonance control, the tuners of the buncher and the DTL tank can be adjusted by phase differences between the input RF and the RF in the cavities. The relative phase between the cavities is adjustable. Each klystron needs up to 300W RF input to generate 1MW RF, and the 300W RF power is generated by a FET amplifier respectively. To keep the RF voltage constant, the input power to the klystron is controlled by AGC circuit. ECL D-flipflops are used for the phase detectors, and the detecting range is ±180 degrees.

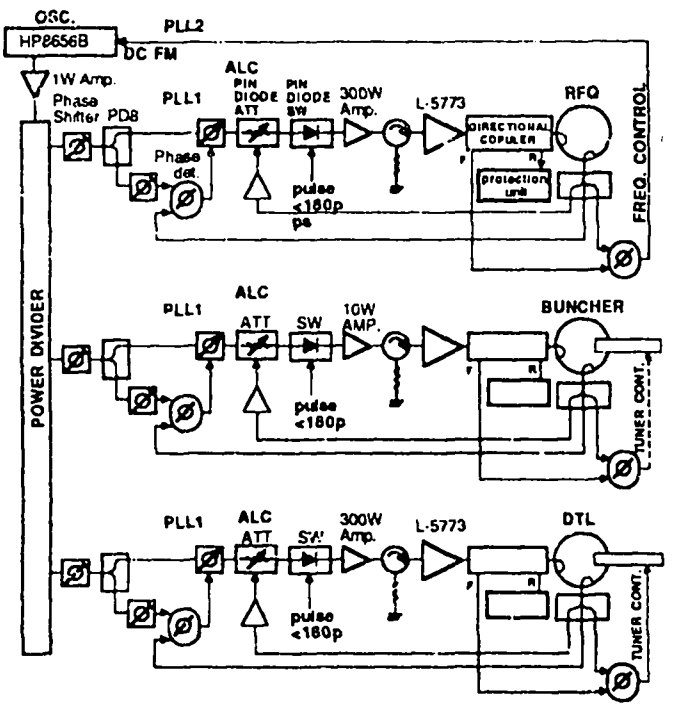

Fig. 3 RF control system

Vacuum System

Fig. 4 shows a block diagram of the vacuum system. A 500-liter/s turbo molecular pump (TMP) is used for the ion source, and a 150-liter/s TMP is installed at the LEBT section. Both turbo pumps have the ordinary bearing system.

Because of the poor vacuum conductance through the RFQ tank, the pumps are installed at both the entrance and exit side. To evacuate the RFQ tank, a 270 liter/s turbo molecular pump is installed at the entrance side, and a 700-liter/s cryo pump (2100-liter/s for H_2O) is also installed at the RFQ-DTL connecting section to evacuate from the RFQ exit side. At the DTL tank, a 400-liter/s TMP is installed. Both turbo pumps are oil free with magnetic floating rotars. A 160-liter/s Ion Pump is also installed at each RF feeder. One is at the bottom of the waveguide-coax transition of the RFQ, and another is at the coupling slot of the DTL. Since the vacuum in each tank seems not good, these ion pumps are planned to be replaced with a 500 liter/s TMP and 700 liter/s cryo pump respectively. The replaced ion pumps will be moved to the center ports of the RFQ tank, which is 60 mm diameter. It will improve the vacuum situation.

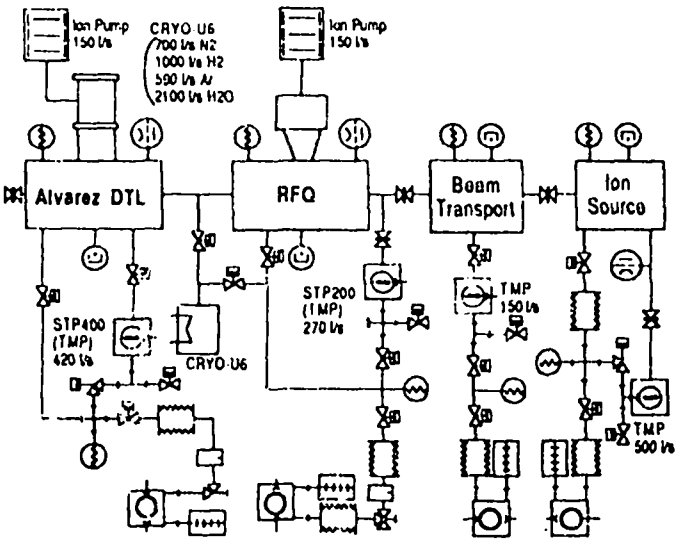

Fig. 4 Vacuum system

Acknowledgements

The authors would like to thank Dr. R.A.Jameson (Los Alamos) for his continuous encouragement and help.

The entire system was constructed by Sumitomo Heavy Industry, and the klystron pulse power supplies were manufactured by Nissin Electric Co.Ltd, RF control units by R&K Co. Ltd. The patient co-operation and skilled working of the staffs of these companies are especially acknowledged.

References

1) H.Okamoto, et al. : "Design of 433.3-MHz Proton RFQ Linac", Bull. Inst. Chem. Res. Kyoto Univ., 65, No.1 (1987)
2) M. Sawamura, et al. : "RF Characteristics of 433.3-MHz Proton RFQ Linac", Bull. Inst. Chem. Res. Kyoto Univ., 66, No.1 (1988)
3) M. Sawamura, et al. : "Design of 433.3-MHz Alvarez Drift Tube Linac and Beam Matching Section", Bull. Inst. Chem. Res. Kyoto Univ., 66, No.1 (1988)
4) L. D. Hansbrough, Compiler,"PIGMI:A Design Report for a Pion Generator for Medical Irradiation",LANL report LA-8880(1980).

A NEW 1.4 MEV/U INJECTOR LINAC FOR THE UNILAC

N. Angert, L. Dahl, J. Glatz, J. Klabunde, M. Müller, U. Ratzinger, B. Wolf
GSI, P.O. 11 05 52, D-6100 Darmstadt, FRG
H. Deitinghoff, J. Friedrich, H. Klein, A. Schempp
IAP, D-6000 Frankfurt, FRG
R. Geller
CEN, F-38041 Grenoble, France

Abstract

GSI has extended its accelerator facility by a heavy ion synchrotron and an experimental storage ring; the UNILAC has been upgraded to supply beams for these new machines while also serving the low energy physics experiments.

With the installation of two new injector linacs for the UNILAC - a high current and a high charge state injector - fast switching of ion species, beam energy and intensity will become available.

The high charge state injector, presently being assembled, will be described in this paper. It consists of an ECR ion source, a 108 MHz RFQ linac and an interdigital H-type accelerator structure. Highly charged ions (U^{28+}) from the ECR source are accelerated up to 1.4 MeV/u and injected into the Alvarez linac of the UNILAC without stripping. The status of the project will be reported.

Introduction

GSI has extended its accelerator facility by a heavy ion synchrotron (SIS) and an experimental storage ring (ESR). Fig. 1 shows the plan view of the whole accelerator facility. The preparation of the site started in November 1986, first beam was accelerated in the synchrotron at the end of 1988, storage of ions in the ESR started in April 1990. The UNILAC is used as injector for the synchrotron. It has been upgraded to deliver beams for these new machines while also serving low energy physics experiments.

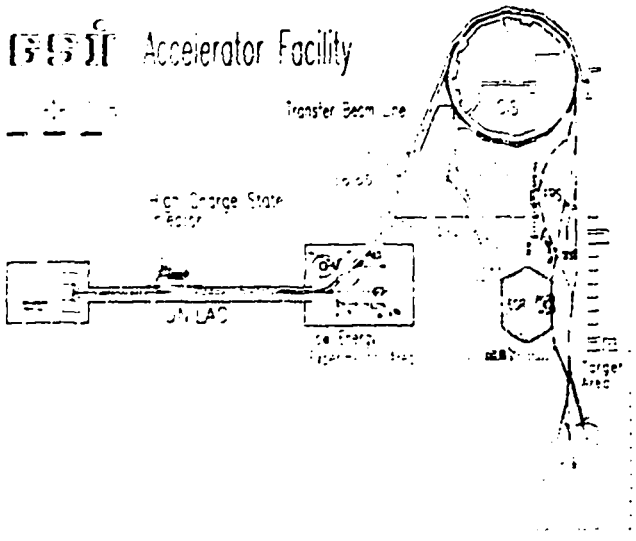

Fig. 1: Plan view of the extended GSI accelerator facility

For efficient operation of the GSI accelerator facility, the scheme of time-share operation has been adopted for the UNILAC: beams of different ion species and currents will be extracted from the injectors, accelerated to the desired energies and delivered into the UNILAC experiment areas or to SIS on a pulse-to-pulse basis.[1]

In a first step, the UNILAC poststripper accelerator was modified for time-share operation.[2,3] With the commissioning of SIS, energy switching was available for routine operation.

Fast switching of ion species will be possible with the installation of a new injector linac which will be described in this contribution.

The present injector linac consists of two DC preaccelerators with PIG ion sources. Four 27 MHz Wideröe tanks accelerate the ions to 1.4 MeV/u. After stripping and charge state selection, the beam (e.g. U^{28+}) is injected into the Alvarez linac operating at 108 MHz. The following intensities (typical peak electrical current) are available after stripping: $^{20}Ne^{7+}$ 100 eμA, $^{40}Ar^{10+}$ 100 eμA, $^{129}Xe^{21+}$ 10 μA, $^{208}Pb^{26+}$ 2 eμA, $^{197}Au^{25+}$ 5 eμA, $^{238}U^{28+}$ 5 eμA. It will be discussed below that the new injector linac will not deliver considerably higher intensities. Therefore, the intensities of both injectors do not allow to reach the space charge limit of the synchrotron for medium and heavy mass ions. An increase of intensity up to three orders of magnitude should to be achieved by a future high current injector. Present concepts favour the modification of the UNILAC prestripper linac. A new RFQ linac up to the energy of 216 keV/u is under discussion. The high charge state linac presently being assembled, will then be used for the continuation of the research program at UNILAC energies.

Design of the new injector

The new injector consists of an ECR (Electron-Cyclotron-Resonance) source followed by an RFQ and an IH accelerator tank. During the last years, ECR sources have been developed continuously. Now this source type can deliver the same charge states of heavy ions at low energy which have been generated so far by gas stripping at 1.4 MeV/u. The intensities are comparable or [illegible] the existing prestripper linac. [illegible] state ions [illegible] efficient acceleration up [illegible] MeV/u.

The layout of the new injector - called HLI linac (High Charge State Injector - Hoch-Ladungs-Injektor) - is shown in fig. 2, a summary of the major parameters are listed in Table 1.

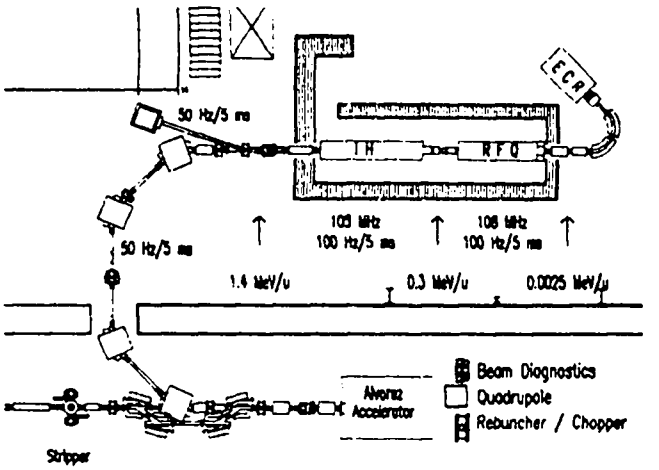

Fig. 2: Layout of the new 1.4 MeV/u injector (HLI)

Table 1: Summary of major injector parameters

Injection	
Ion source	ECR-type, 14.5 GHz
Charge-to-mass ratio	0.105 to 1
Extraction voltage	23.8 kV
Energy	2.5 keV/u (β=0.0023)
Radial emittance (norm.)	0.46 π·mm·mrad
Radial emittance (unnorm.)	200 π·mm·mrad
Mass resolution $\Delta m/m$	3×10^{-3}
RFQ accelerator	
Structure type	four rod
Energy, input	2.5 keV/u (β=0.0023)
Energy, final	300 keV/u (β=0.025)
Radio frequency	108 MHz
Repetition frequency	100 Hz
Duty cycle	50 %
Max. RF power (for U^{25+})	125 kW
Max. Voltage	78 kV
Length	[illegible] m
Tank diameter	[illegible]
Radial acceptance [illegible]	[illegible]
Longitudinal [illegible]	
Energy [illegible]	
Bunch width	[illegible]
IH accelerator	
Energy, input	300 keV/u (β=0.025)
[illegible], final	1.4 MeV/u (β=0.055)
[illegible] frequency	108 MHz
Repetition frequency	100 Hz
Duty cycle	50 %
Max. RF power (for U^{25+})	110 kW
Max. field strength	150 kV/cm
Length	3.55 m
Tank diameter	0.63 m
Shunt impedance	310 MΩ/m
Radial acceptance (norm.)	1.5 π·mm·mrad
Radial acceptance (unnorm.)	60 π·mm·mrad
Longitudinal acceptance	150 π·keV/u·deg

ECR-Source and Low Energy Beam Transport

The ECR source was developed and manufactured by the "Centre d'Etudes nucléaires" (CEN) in Grenoble. It is an upgraded version of the 10 GHz Caprice source. The excellent performance of ECR sources was reviewed by Geller at the 1986 Linac Conference.* The commissioning of the source for the GSI injector took place at Grenoble, the source will be delivered in September 1990. A photograph of the source is shown in Fig. 3.

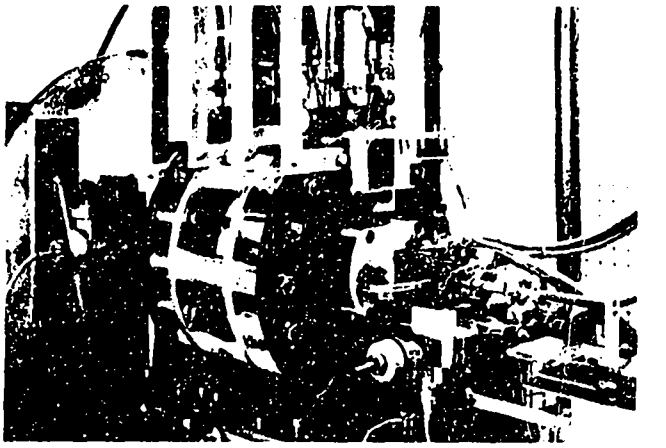

Fig. 3: Photograph of the ECR-Ion Source, taken during the commissioning at Grenoble.

In Table 2, the measured intensities of some ions are listed. A uranium charge state distribution is shown in Fig. 4.

Table 2: Measured ion currents of the ECR Source

U^{28+}	: 5 eμA (max. 10 eμA)
U^{25+}	: 15 eμA
Pb^{24+}	: 5 eμA (10 kV Extr. Volt.)
Pb^{25+}	: 6 eμA (20 kV Extr. Volt.)
Au^{24+}	: 14 eμA
Au^{26+}	: 5 eμA
Xe^{17+}	: 27 eμA
Xe^{21+}	: 15 eμA
[illegible]	[illegible] Extr. Volt.)

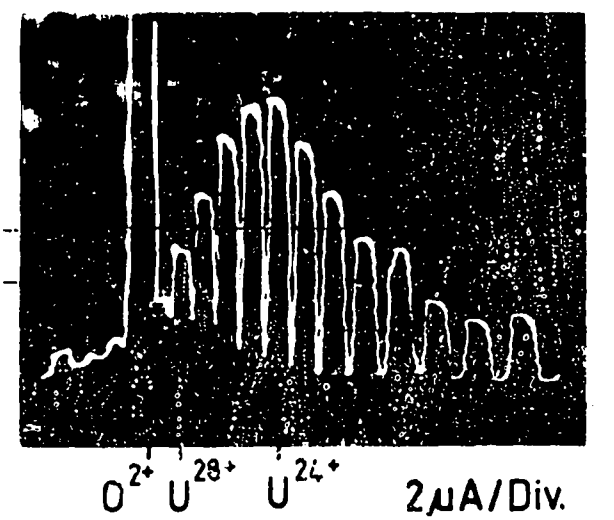

Fig. 4: Charge state distribution for uranium from the 14 GHz ECR source

The power of the klystron was varied in the range 300 - 600 Watt, the maximum hexapole field was 5800 Gauss. For better source operation, the output power of the 14 GHz klystron was stabilized. The long-term stability of the output current is

impressive: over 40 hours operation only small changes occurred. The noise modulation is less than 15 %. The measured output intensities listed in Table 2 fit the design values.

The low energy beam transport is designed for a beam with 200 π mm• mrad at 2.5 keV/u. A spectrometer has been assembled which allows charge state and mass separation. Even lead isotopes can be separated. The dipole magnet is splitted into two 67.5° magnets in order to minimize second order effects by curvatures of the inner pole faces. A triplet and a solenoid serve to transport and match the beam to the entrance of the RFQ accelerator.

RFQ Accelerator

The design and construction of the RFQ linac have been carried out at the Institut für Angewandte Physik, University of Frankfurt.[5] Acceleration from 2.5 keV/u to 300 keV/u is being done with a Four-Rod RFQ. A scheme of the structure is shown in Fig. 5.

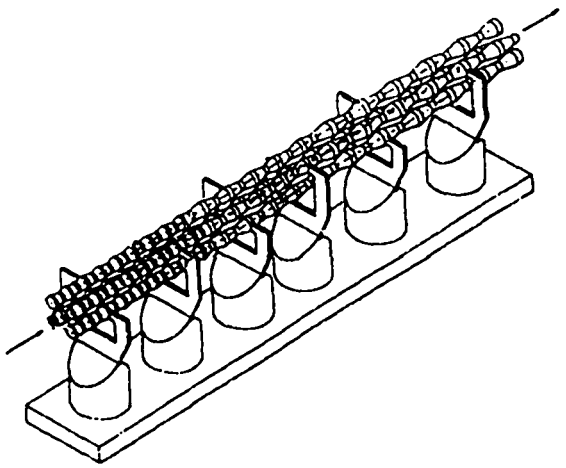

Fig. 5: Scheme of the Four-Rod RFQ

Circular rod electrodes are supported by a linear array of straight radial stems. The particle dynamics design was optimized for a minimum longitudinal and transverse emittance growth and good transmission. An RFQ was designed with a length of 2.9 m, electrode voltage 90 kV, a minimum aperture of 3.0 mm and a maximum modulation of 2.1.

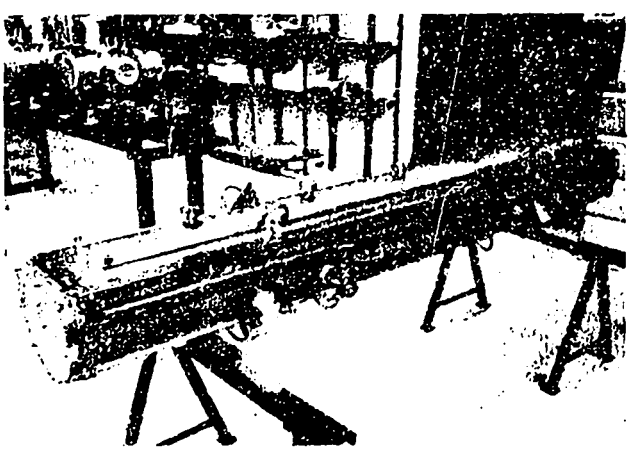

Fig. 6: Photograph of the RFQ tank. Length is 3 m.

The mechanical design had to take into account the high duty cycle of 50 %, e.g. direct cooling of the rod electrodes. The tank itself consists of two halves to facilitate installation and alignment. A photograph of the 3 m tank is shown in Fig. 6. The tank is made of stainless steel and is being prepared for copper plating at GSI.

IH-Accelerator

Details of the IH accelerator section are given at the Linac 88 and in a contribution to this conference.[1,6,7] Characteristic parameters are listed in Table 1. The efficient acceleration from 0.3 to 1.4 MeV/u is demonstrated by these parameters. All parts for the IH-structure were ordered. The 3.7 m long tank made of mild steel was delivered. The copper plating has been started.

Beam Transport at 1.4 MeV/u

A 180° beam transport system was designed for the injection of the 1.4 MeV/u beam into the UNILAC poststripper accelerator (see Fig. 2). An 11° fast kicker magnet behind the IH-tank will serve local experiments. For switching the beams from the new and "old" injector, a 30° kicker magnet will be installed. Five quadrupole lenses for pulsed operation in front of the Alvarez linac will form the two beams to match the transverse acceptance of the first Alvarez tank.

Status and Schedule

All components were ordered. But the delivery for some components has been delayed. Together with man power problems at GSI - the synchrotron and storage ring have been installed with high priority - the new injector project is behind the schedule. Cooling water, electrical supplies and cabling and other utilities are now being installed. The unforeseen repairs on the tanks in our copper plating workshop and the exchange of the electrolytic bath caused a late beginning of copper plating of the IH- and RFQ-structure - it will be finished in October this year. In the revised time schedule, the first beam is planned for the spring 1991.

References

1. J.Klabunde, "The UNILAC Upgrade Project", Proc. of 1988 Linear Accelerator Conf., CEBAF-Rep.-89-001, p.242, 1989.
2. J.Glatz, "The Unilac as a Fast-Switching, Variable Ion and Energy Accelerator", Proc. of the 1986 Linear Accelerator Conf., SLAC-Rep.303, p.302, 1986.
3. N.Angert, L.Dahl, J.Glatz, J.Klabunde, M.Müller, B.Wolf, "UNILAC Modifications for an Improved Synchrotron Injector Performance", Proc. of the European Particle Accelerator Conf., Nice, 1990.
4. R.Geller, P Briand, B.Jacquot, P.Ludwig, G.Melin, M.Pontonnier, "ECR Ion Sources for Accelerators", Proc. of 1988 Linear Accelerator Conf., CEBAF-Rep.-89-001, p.455, 1989
5. A.Schempp, "4-Rod RFQ Injectors for the GSI Linac", Proc. of the 1989 IEEE Particle Accelerator Conf., p.1093, 1989.
6. U.Ratzinger, "A Low Beta RF Linac-Structure of the IH-Type with Improved Radial Acceptance", Proc. of 1988 Linear Accelerator Conf., CEBAF-Rep.-89-001, p.185, 1989.
7. U.Ratzinger, "Interdigital RF Structures", these proceedings.

TRANSVERSE BEAM DYNAMICS STUDIES OF A HEAVY ION INDUCTION LINAC

T. Garvey, S. Eylon, T.J. Fessenden, K. Hahn, E. Henestroza and D. Keefe
Lawrence Berkeley Laboratory, University of California, CA 94720

Abstract

The multiple beam induction linac experiment (MBE-4) was built to study the accelerator physics of the low energy, electrostatically focussed end of a driver for heavy ion inertial confinement fusion. In this machine four beams of Cs^+ ions are accelerated through 24 common induction gaps while being focussed in separate AG focussing channels. Each channel consists of a syncopated FODO lattice of 30 periods.

We report results of the most recent studies of the transverse beam dynamics of a single drifting (180 keV) beam in this machine. The dependence of the emittance on the zero-current phase advance shows systematic variations which may be understood in the light of previous theoretical work on this topic. This result, unique to the beam parameters of a linac for heavy ion fusion, will be discussed in the context of its implications for a driver design. In addition we will discuss recent measurements of the motion of the beam centroid through the linac. These measurements, coupled with simulations, have proven to be a powerful tool in determining the presence of misalignment errors in the lattice of the accelerator.

Introduction

MBE-4 is an experimental induction linac in which four beams of Cs^+ propagate through 24 common induction gaps while being focussed by individual electrostatic quadrupole channels, each consisting of 30 FODO periods[1,2]. The linac is constructed from six sections (denoted A through to F) each comprising 5 "lattice periods (l.p.)". Each l.p. is followed by a gap the first four of which are accelerating gaps while the fifth is reserved for diagnostic access. The diagnostic ports allow measurements of the beam size, emittance, and position and angular offsets of the beam centroid with respect to the linac axis. These measurements can be made in both planes transverse to the direction of propagation. This paper describes recent studies of the transverse emittance of one of these beams as it drifts through the linac at its injection energy of 180 keV. This beam has a nominal current of 5 mA and enters the linac with a normalized r.m.s emittance, ε_n, of 0.03 π mm-mrad where the normalized emittance is defined as

$$\varepsilon_n = 4\beta\pi\,(\langle x^2\rangle\langle x'^2\rangle - \langle xx'\rangle^2)^{1/2}$$

with β equal to the ratio of the ion speed to the speed of light and x and x' are the usual phase space variables.

Theory

For the parameters of MBE-4 one can calculate that the ratio of the space-charge depressed tune, σ, to the zero-current tune, σ_0 is give by $\sigma/\sigma_0 = 0.1$. Simulations have shown that such strongly space charge depressed beams propagating in electrostatic focussing systems might exhibit oscillations and growth in emittance[3]. As part of this work it was found that a small dodecapole component in the quadrupoles is beneficial, and the MBE-4 quadrupoles are so constructed. More recent simulations pertinent to the MBE-4 lattice configuration and quadrupole geometry have confirmed this behavior and have shown the evolution of the emittance to be strongly dependent on the amplitude of the coherent betatron oscillation of the beam[4]. Emittance variations are due to the excitation of coherent beam modes driven by external non-linear fields and image forces, amplitude modulated by the beam's coherent oscillation[4].

Experiments

Measurements made at the discretely available diagnostic stations on MBE-4 have indeed shown that the emittance is not constant but decreases and increases while the beam drifts through the linac. As MBE-4 is configured to allow diagnostic access at the end of each section only, however, a method is required whereby one could effectively measure the emittance at points both up and downstream of a given diagnostic station. The total distance travelled by a beam drifting in a linac can be expressed equally well in terms of accumulated betatron phase advance (for any given phase advance per unit cell). The technique then was to measure the emittance at a given diagnostic station for varying values of the lattice focussing strength, i.e. varying σ_0. This is achieved by simply varying the voltages on the quadrupoles. That this method allows one to observe the oscillation over all phases can be seen by inspection of figure 1(b). This figure shows the variation of the beam centroid, $\langle x\rangle$, with changes in zero-current tune measured in the horizontal plane at l.p. 20 (end of section D). The finite amplitude of this betatron oscillation is due primarily to injection offsets. One can see that to obtain a phase excursion of 2π

This work was supported by the Director, Office of Energy Research, Office of Basic Energy Sciences, Advanced Energy Projects Division, U.S. Department of Energy, under Contract No. DE-AC03-76SF00098.

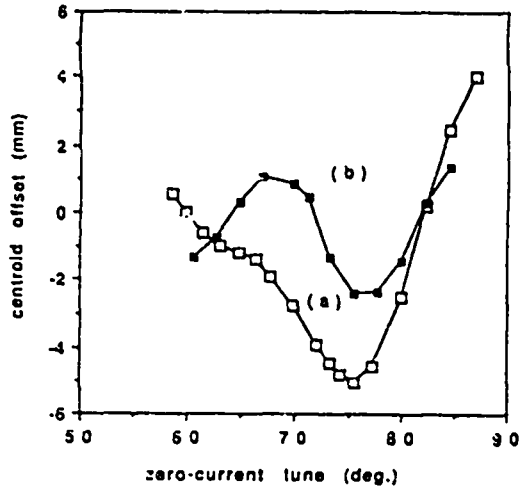

Fig. 1. Beam centroid position for kicked (a) and un-kicked (b) beam vs. zero-current tune.

one requires a change in σ_0 of 18°/cell for the 20 cells as expected. Similar variations in the offset of the angle of the beam centroid, <x'>, are also observed.

Emittance measurements

Initial emittance measurements were made in the horizontal plane at l.p. 25. As in the simulation, large variations were observed, up to 50%, in the emittance about the matched tune value of σ_0 = 70°, figure 2(a). The range of quadrupole voltage employed was restricted by the requirement not to lose beam due to radial expansion (low voltage end) or instability (high voltage end). Although we did not re-match the injector for each linac quadrupole setting we do not believe mis-match errors to be responsible for the large variations in emittance. Indeed many measured emittances are below the value measured for the matched beam.Similar variations in emittance were observed in the vertical plane at l.p. 25 and in the horizontal plane at l.p. 20, fig.3(a).

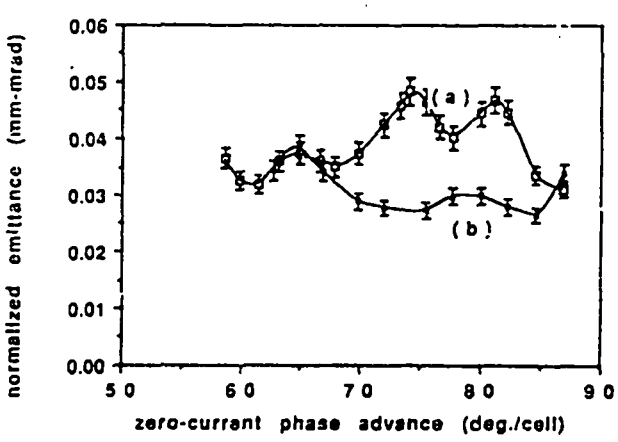

Fig. 2. Emittance measured at l.p. 25 for coherent amplitudes of (a) 4.5 mm and (b) 1.2 mm.

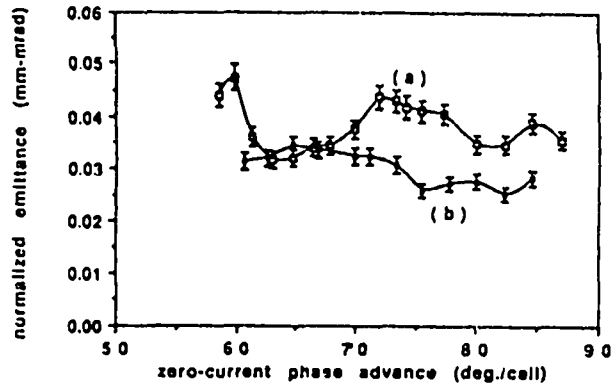

Fig. 3. Emittance measurements at l.p. 20 for coherent amplitudes of (a) 4.5 mm and (b) 1.9 mm.

The corresponding coherent amplitude in the horizontal plane was +/- 4.5mm (i.e. 9 mm peak to peak). One should bear in mind that the beam envelope has a maximum radius of 10 mm (nom.) and travels through a channel of 27 mm bore radius. Although this amplitude is good for driving the emittance changes it was too large to be accounted for in terms of injection offsets. In addition the variation of observed betatron phase was much less than expected on the basis of tune excursion. It was concluded that the horizontal motion of the beam was subject to a disturbance, perhaps due to a mechanical misalignment in one of the lattice quadrupoles. This subject is discussed further below.

To test the hypothesis that the emittance variations are the result of the large coherent amplitude we removed the offending disturbance to the beam and repeated the measurements at l.p. 20. This resulted in a coherent amplitude of +/- 1.9 mm determined by injection conditions and residual alignment errors. The variation in emittance also fell rather dramatically to 25%. A greater reduction in the coherent amplitude (1.2 mm) was achieved by using a steering array to reduce the initial offsets in the horizontal plane at the input to the linac. Subsequent measurements at l.p. 25 show little variation of emittance for tune values between 70°/cell and 85°/cell, fig. 2(b). This is in stark contrast to the variation found over the same tune range for the 4.5 mm coherent amplitude, fig. 2(a). The theory predicts that emittance growth in one plane may result from offsets in either plane. Therefore, some variation in the emittance may be accounted for as a result of offsets in the vertical plane which we have not attempted to correct.

Beam Centroid Measurements

As stated previously the amplitudes of the coherent oscillation measured at l.p. 20 and l.p. 25 were too large to be explained by the initial offsets of the position and angle of the beam centroid. Nevertheless the data for <x> and <x'> at l.p. 20, when mapped through 5 lattice periods, were found to be in good agreement with the data at l.p. 25. To investigate the possibility that the beam was suffering a kick in the linac we measured the

variation of <x> for the beam as a function of σ_0 at each diagnostic station. The amplitude observed at l.p. 10, 1.4 mm, was consistent with the initial injection conditions and the Twiss parameters appropriate to the lattice optics. However at l.p. 15 it was found that the coherent amplitude was no longer consistent with a well aligned linac. We conclude that the data taken at l.p. 20 is due to the superposition of two oscillations, one due to the initial offsets and a second due to the kick in section C[5]. In fact we were able to locate the position of the kick close to l.p. 11 by fitting the measured data to transport computations in which the beam was given a single kick at different locations in turn. In order to remove the disturbance to the beam (the cause of which is still unknown) we replaced section C of the machine with section F, having already established the integrity of section F by successfully mapping data from l.p. 25 onto data taken at l.p. 30. The variation of <x> with σ_0, measured at l.p. 20, before and after the exchange of section C for section F is shown in figures 1(a) and 1(b). The data clearly confirm that the disturbance was located in section C. The amplitude and period of the oscillation for figure 1(b) is consistent with injection offsets.

Discussion and Conclusions

As the preservation of alignment and beam emittance are both crucial to the HIF driver concept it is clear that emittance growth in the low energy electrostatic focussed section of the linac is highly undesirable. The experiments discussed above therefore may impact choices in the design of this part of a driver. It is clear that, if one wishes to keep emittance growth to a minimum, one must strive to keep the beam on axis. This may be achieved by specifying sufficient machining and alignment tolerances on the lattice elements and it is necessary to determine how stringent the alignment tolerances must be. Alternatively, the detection and subsequent correction of errors in the motion of the beam may be possible. Both of these alternatives will have their respective financial consequences. A third possibility, that might obviate strict alignment or frequent correction, would be to run the linac with less tune depression[6]. This however may require a more expensive focussing channel for a given beam current.

In conclusion we have obtained experimental evidence in support of the simulation work of references 3 and 4, i.e. that the transverse emittance of strongly space-charge dominated ion beams propagating in electrostatic focussing structures will be subject to oscillation if the beam is off-axis as it travels through the structure. In contrast, when the beam is on, or close to the axis, the degree of variation in the emittance is considerably smaller. In addition our measurements of the coherent betatron oscillation amplitude have revealed the presence of alignment errors in the linac. Our technique of measuring the position of the beam centroid while changing the total accumulated phase advance at a given diagnostic station has since proven to be a valuable means of determining whether or not misalignments are present in the linac.

Acknowledgements

We are indebted to A. Faltens and L. Smith for helpful discussions. One of us (T.G.) thanks A. Faltens for pointing out how the beam in a misaligned linac behaves.

References

1. A.I. Warwick et al, "Performance of MBE-4, an Experimental Induction Linear Accelerator for Heavy Ions", in Proceedings of the Linear Accelerator Conference, (Williamsburg) 1988.
2. T. Garvey et al, "Multiple Beam Induction Linac Research at LBL", to appear in the Proceedings of the 8th International Conference on High Power Beams,(Novosibirsk) 1990. Also LBL-28167.
3. C.M. Celata, "The Effect of Nonlinear Forces on Coherently Oscillating Space-Charge-Dominated Beams", Proceedings of the Particle Accelerator Conference, pp 996-1000, (Washington), 1987.
4. K. Hahn and L. Smith, "MBE-4 Simulations", in HIFAR Half-Year Report, LBL-29094, 1990.
5. A. Faltens, priv. comm.
6. At the time of writing we are performing experiments which appear to indicate that beams of higher initial emittance do not exhibit the emittance oscillations discussed above.

INVESTIGATION OF BEAM ABERRATIONS AND BEAM HALO BY 3-DIMENSIONAL EMITTANCE MEASUREMENTS*

G Riehl, J.Pozimski, W.Barth
Institut für Angewandte Physik der Johann Wolfgang Goethe Universität
Postfach 111932, D-6000 Frankfurt am Main, FRG

Abstract

We investigated the beam aberrations and beam halo caused by solenoids, Gabor lenses and Radio Frequency Quadrupoles. Thrfore we used a microprocessor controlled multifunctional profile- and emittance measurement system. Online profile measurements, 2-dimensional slit-to-slit and also 3-dimensional point-to-slit emittance measurements have been made[1,2]. Construction of the measurement system and experimental results will be presented.

Concept of the Device

Fig. 1 shows a schematic diagram of the measuring device. Up to 4 slit/profile harp combinations may be installed to 6 stepping motor driven UHV feedthroughs. The profile currents of one harp are switched by a multiplexer to the 60-channel current amplifier. Motor and amplifier electronics are controlled by an 8-bit microprocessor system with digital I/O boards. This microprocessor is connected to a 68000-PC which handles interactive dialogs, data measurement, and data evaluation. The independent movable slits and profile harps provide online profile measurements, emittance measurements and also point-to-slit emittance measurements with crossed slits: The slits filter a beam partition of the coordinates x,y. The profile harps determine the angles x' and y' of this partition, therefore obtaining the beams charge distributions I(x,y,x') and I(x,y,y'). Out of these 3-dimensional distributions calculation of all 2- and 1-dimensional subspaces of the beam distribution is possible[3,4].

Emittance Measurements behind a Solenoidal Lens

We used a plasma beam ion source[5] with a successive solenoidal lens[6] and extracted a 10 keV/3.6 mA He^+ beam. The ion beam occupies at least 75% of the lens aperture, causing aberrations of the beam phase space distribution. Fig.2 shows the measured x-emittance, the I(x,x') distribution of the beam, measured with slit and profile harp. The convergent He^+ beam and a divergent neutral beam can be clearly distinguished. The dark 80% partition of the He^+ beam shows an 'S' shaped contour, due to the effect of the nonlinear solenoidal field. In addition the phase space distribution has a 'butterfly' shape. The latter is caused by the radial symmetry of the nonlinear field, which twists different beam partitions I(x,x',y) dependent on their position y. Fig. 3 shows the 2-dimensional beam profile, I(x,y). We distinguish a high intense beam core, a homogenous middle part and increasing intensities at the edge of the

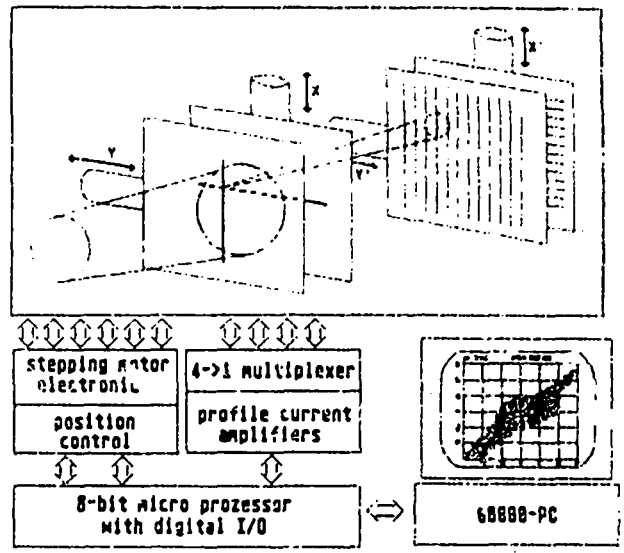

Fig. 1: schematic drawing of the diagnostic device. Crossed slits and crossed profile harps provide measurements of the I(x,x',y) and the I(y,y',x) charge distributions

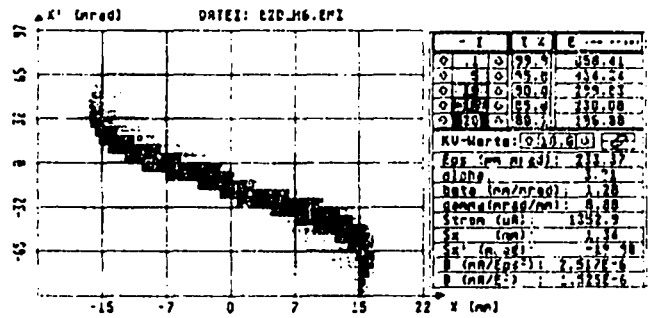

Fig. 2: The distribution I(x,x') of a 10 keV He^+ beam, measured with a slit/profile harp combination behind a solenoidal lens

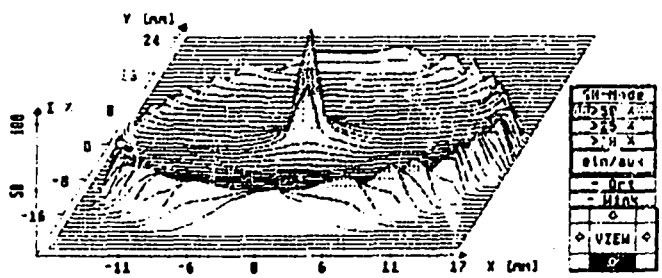

Fig. 3: Distribution I(x,y) of the He^+ beam, calculated from the measured distribution I(x,x',y)

beam. The distribution has a 'sombrero' like shape. The rim of this distribution is caused by strongly focused beam particles with shorter focal lengths than the inner part of the beam. Behind the beam focus these particles forms a wide halo. We measured the beam distribution I(x,x',y) with the point to slit method for the same beam parameters. Fig.4 shows different parts $I(x,x',y_i)$ of this measurement, with y=-14, -12, -10 and 0 mm. At the edge (y=-14mm) a small xx' distribution can be seen, showing less aberrations. The I(x,x',y=-12mm) distribution is characterized by an '8' shaped contour, which is caused by the nonlinear field in addition with the drift space inside the solenoid. The distributions next to the center of the beam show the same contour, but the '8' becomes wider. Therefore the 'butterfly' shape of the emittance and also the beam halo is composed out of different '8' shaped I(x,x',y) distributions. The marginal emittance is increased by the twisted 3-dimensional phase space distribution by a factor of 1.7 (90%) and 2.5 (99%). The RMS emittance is also affected by the 'S'-shaped filamentation, we calculate an RMS emittance growth of 1.5 (90%) and 2.2 (99%). Additional measurements with different beam and solenoid parameters and also computer simulations are in good agreement.

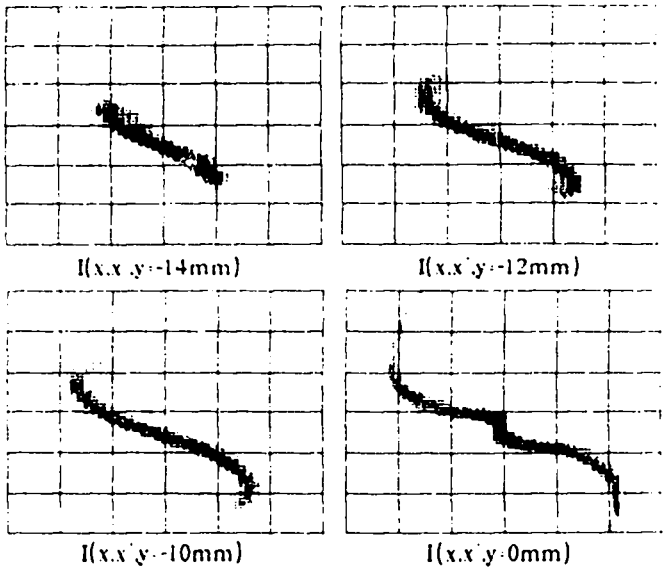

Fig. 4: He^+ beam distributions I(x,x',y) at different positions y, measured with two crossed slits and profile harp.

Emittance Measurements behind a Gabor Plasma Lens

For a second measurement series we replaced the solenoid by a Gabor plasma lens[8]. The figures show the phase space distributions of a 10 keV/ 125 μA Ar^+ beam behind the lens. Again the beam occupied a large fraction of the aperture. Fig. 5 shows the xx'- emittance of the beam measured with slit and profile harp, composed of an extreme high intense convergent 'butterfly', a second low intense convergent 'butterfly' and a divergent neutral beam. The 3-dimensional distributions I(x,x',y) (Fig. 6) give an explanation of the structure of the 2-dimensional emittance: The Ar^+ beam is divided by the lens in a high intense central part and a low intense outer part, both showing the contour of an inverse 'S'. Compared with the shape obtained from solenoid measurements, the focusing strength inside the solenoid increases with radius, the Gabor lens shows a decreasing with radius. At the beam center decreasing charge intensities can be observed. The 2-dimensional beam profile in space (Fig. 7) shows, that we get a hollow beam. This may be explained by the incomplete filling of the lens by electrons occupying only the region near the axis.

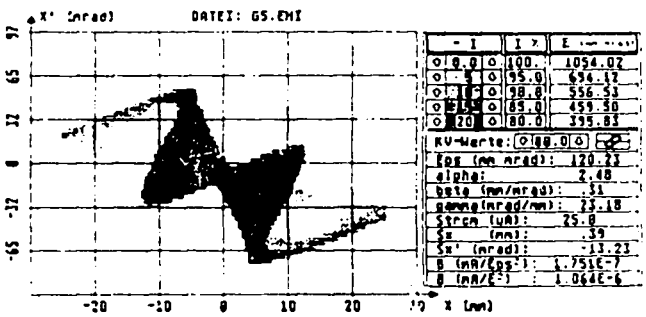

Fig.5 : Distribution I(x,x') of a 10 keV/125 μA Ar^+ beam, measured with slit and profile harp behind a Gabor plasma lens

Emittance Measurements behind a Split-Coaxial RFQ

For a third measurement series we connect ion source, solenoid and a split-coaxial RFQ[9]. The figures show the phase space distributions of a 50 keV/ 800 μA He^+ beam behind the accelerator. The perspective view to the beam emittance (Fig. 8) shows elliptical contours without any remarkable twist or filamentation. The 3-dimensional distributions $I(x,x',y_i)$ (Fig.9) show a filamentation of the ion beam and in all distributions two

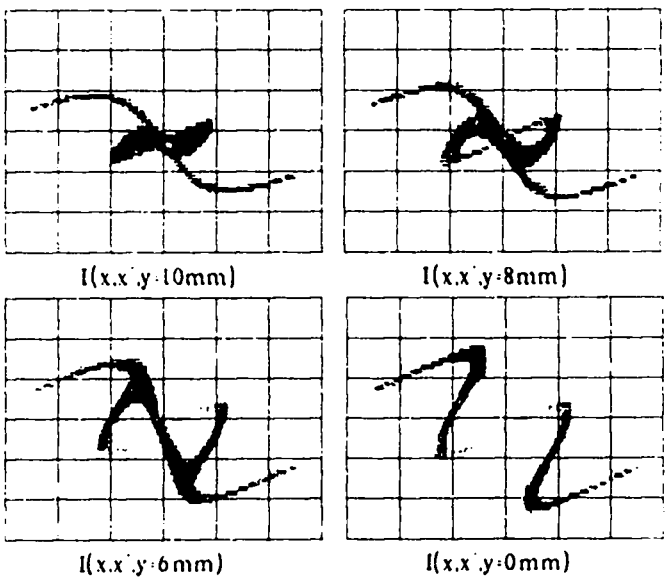

Fig.6: 3-dimensional distributions of the Ar^+ ion beam

beam centers can be clearly distinguished. The ion beam separates into two parts. This leads to an emittance growth of 1.4 (90%). The beam profile in space (Fig.10) shows a rectangle, nearly homogenous charge distribution.

Conclusion

The diagnostic device is a powerful tool to investigate 1-, 2- and 3-dimensional phase space distributions of ion beams. The analysis of the 3-dimensional distribution I(x,x',y) and I(y,y',x) gives important information about the genesis of beam halo, emittance aberrations and emittance growth. All experimental results show filamentation of the phase space distribution of the beam which increases the beam emittance. Further development of the device will include reconstruction of the 4-dimensional phase space distribution I(x,x',y,y').

*work supported by the BMFT under contract number 06OF1861

Reference

1. T.Weis et. al. "Emittance growth... ", this conference
2. A.Schempp, "The CRYRING RFQ", EPAC-90, Nice
3. G.Riehl, Internal Report 89-14, Institut für Angewandte Physik D-6000 Frankfurt/M. , Pstf. 111932, FRG
4. G.Riehl, Internal Report 89-16, mailing adress see [3]
5. K.Langbein, IEEE Catalog No. 87CH2387-9 1987, Vol.1, p.379
6. A. Müller-Rentz, diploma thesis 1985, mail. adr. see [3]
7. G. Riehl, J. Pozimski, W. Barth, Interner Report 90-14, mailing adress see [3]
8. J. Pozimski, diploma thesis 1990, mail. adr. see [3]
9. P.Leipe, diploma thesis 1985, mail. adr. see [3]

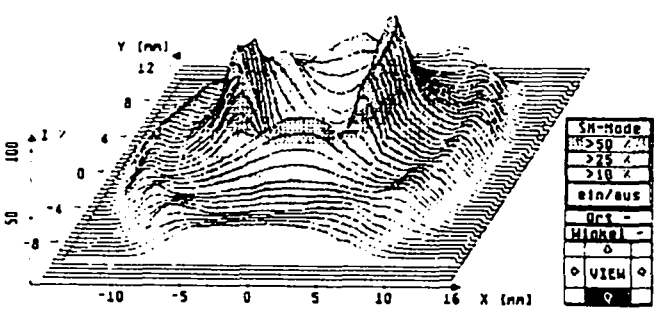

Fig. 7 : perspective view to the Ar^+ beam distribution I(x,y)

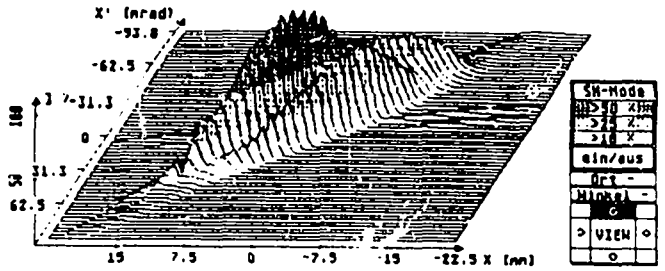

Fig. 8: perspective view to the He^+ beam emittance behind the split-coaxial RFQ

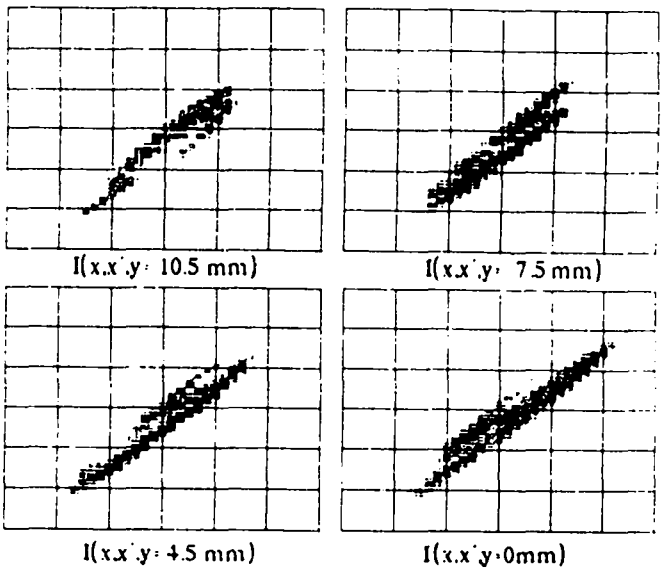

Fig. 9: He^+ beam distributions I(x,x',y) at different positions y.

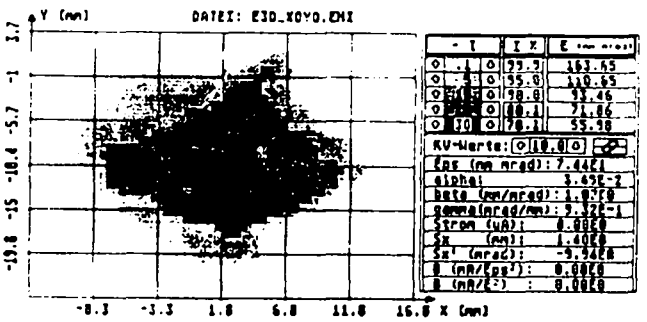

Fig. 10: The He^+ beam profile I(x,y)

EMITTANCE DETERMINATION OF ELECTRON GUNS BY ANALYSIS OF BEAM PROFILE MEASUREMENTS

B. Strorgin and A. Salop
Varian Associates Inc., 611 Hansen Way,
Palo Alto, CA 94303

Abstract

A method of analyzing beam profile data is used to determine the transverse emittance of electron guns used in microwave tubes and medical linacs. The emittance is obtained by fitting measured transverse beam profile data to a theoretical model which includes contributions from both emittance and space charge. The beam analyzer used for the measurements consists of a Faraday cup mounted on an XYZ translational stage, and allows both vertical and horizontal beam profiles to be measured as a function of the distance from the gun's anode. The data are then fit to a polynomial, and vertical and horizontal emittances are calculated.

Introduction

Knowledge of the gun emittance is important for optimizing accelerator performance as well as for realistic simulation of accelerators. Gun emittance measurements are usually accomplished by splitting the beam into many small "beamlets" with either pepper-pot targets or slits, and analyzing the angular divergence of the individual beamlets. In this paper we present a different method for the gun emittance measurements based on analyzing beam propagation in free space.

Method

Consider an electron beam propagating along the z-axis in a field-free drift region. The evolution of the beam envelope R as a function of z is described by the following differential equation[1]:

$$R''(z) = \frac{\varepsilon^2}{R^3(z)} + \frac{K}{R(z)}, \qquad (1)$$

where the derivative is with respect to z, ε is the transverse emittance, and K is the generalized perveance

$$K = \frac{I}{I_0}\frac{2}{\beta^3\gamma^3}. \qquad (2)$$

Here I is the beam current, I_0 is the critical current (I_0 = 17 kA for electrons), and β and γ are the usual relativistic parameters.

After one integration over z Eq. 1 becomes

$$R'(z) = [(R_0')^2 + 2K \ln\frac{R(z)}{R_0} + \varepsilon^2(\frac{1}{R_0^2} - \frac{1}{R(z)^2})]^{1/2} \qquad (3)$$

where $R_0 = R(z_0)$ and $R'_0 = R'(z_0)$ are the initial conditions at $z = z_0$. To simplify Eq. 3 one may choose z_0 to be the location of the beam waist in which case $R_0' = 0$. Then one obtains the following expression for the emittance:

$$\varepsilon^2(z) = \frac{(R'(z))^2 - 2K \ln\frac{R(z)}{R_0}}{\frac{1}{R_0^2} - \frac{1}{R^2(z)}} \qquad (4)$$

A second integration yields the following implicit relationship between R and z:

$$z - z_0 = \int_{R_0}^{R} [(R_0')^2 + \varepsilon^2(\frac{1}{R_0^2} - \frac{1}{R^2}) + 2K \ln\frac{R}{R_0}]^{-1/2}\, dR \qquad (5)$$

To obtain emittance values from Eq. 4 a polynomial function was fit to the experimental values R(z). This allowed R'(z) and R_0, and finally $\varepsilon(z)$ to be determined.

In the second approach a least squares minimization procedure was used to find the emittance value which gave the best fit of the theoretical relation of Eq. 5 to a polynomial function representing the beam profile data R(z). In both approaches the vertical and horizontal emittances were determined separately.

The beam profile data used in this analysis were provided to us by the Varian Microwave Tube Division[2]. The beam current was measured by a beam analyzer consisting of a Faraday cup mounted on an X-Y-Z translational stage. The cup diameter as well as positioning accuracy of the stages was about 0.05 mm. The system was evacuated to 10^{-8} Torr, and no magnetic field was present.

To derive the effective beam size from the current profile data $J(\xi,z)$ we used the following definition[1,3]:

$$R^2(z) = 4\frac{\int \xi^2 J(\xi,z)d\xi}{\int J(\xi,z)d\xi} \qquad (6)$$

Here ξ is either the horizontal or the vertical coordinate. This definition of $R(z)$ is consistent with the definition of effective emittance being four times the r.m.s. emittance.

Results

The emittances of two different guns were determined using the two approaches described above: one is a diode gun for microwave tubes, and the other is a gridded gun for medical accelerators. The two guns were tested under different operating conditions: the anode voltage for the diode gun was 20 kV with the cathode current of 127 mA: the voltage of the gridded gun was 6 kV, and the cathode current was 93 mA. In both cases we found that the Debye length $\lambda_D = (\varepsilon_0 kT/e^2 n)^{1/2} << R_{beam}$, and therefore the space charge effects are important. Figs. 1 and 2 show beam radii for the diode and the gridded gun respectively, points with errors represent data, and the smooth lines represent the fit polynomials. Fig. 3 and 4 show horizontal (unnormalized) emittances for the diode and the gridded gun respectively as functions of z, these emittances were calculated using Eq. 4. Fig. 5 shows the best fit of the theoretical relation of Eq. 5 to the polynomial representation of the beam radius data for the diode gun and lists the value of ε corresponding to the best fit. The two other curves show the deviations of the theory from the polynomial representation for an emittance value 20% higher and 20% smaller than the best fit value. Fig. 6 is a similar presentation for the gridded gun. These figures give an indication of the resolution of the matching technique.

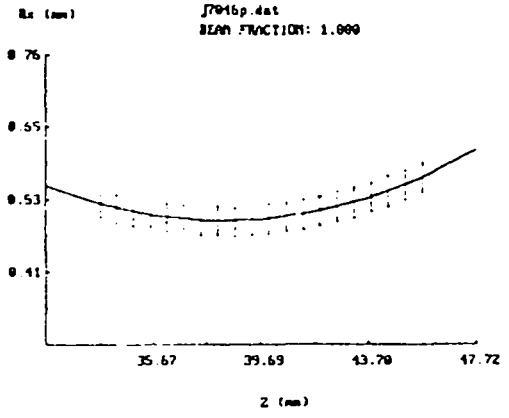

Fig. 1. Beam profiles for the diode gun. Points with error bars represent data, the solid line is the fit polynomial.

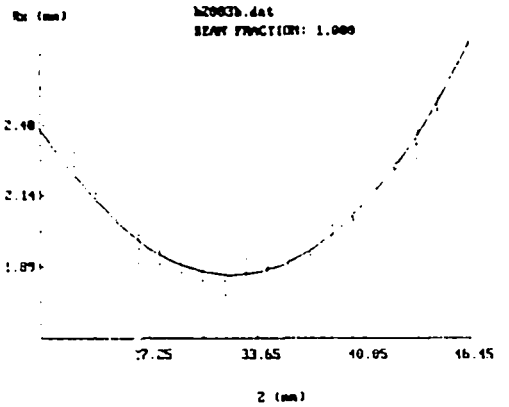

Fig. 2. Beam profiles for the gridded gun. Points with error bars represent data, the solid line is the fit polynomial.

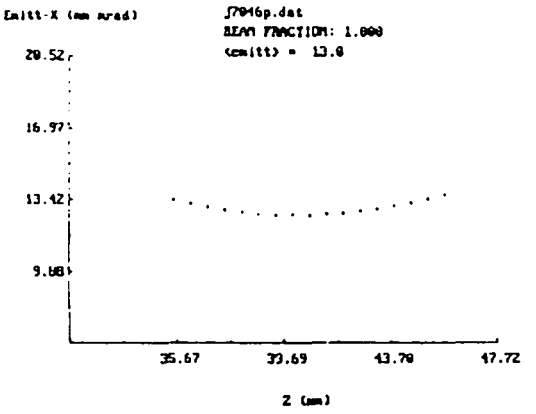

Fig. 3. Emittance of the diode gun as a function of z.

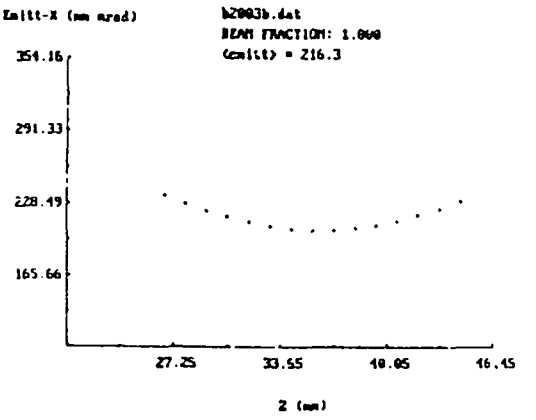

Fig. 4. Emittance of the gridded gun as a function of z.

The results obtained with the point-to-point calculation based on Eq.4, and the fit results from Eq. 5 are summarized in Table 1 which shows normalized emittances $\varepsilon_{norm} = \varepsilon\beta\gamma$ for both guns. For the point-to-point technique the average values are quoted. Also included in Table 1 are the calculated values of the normalized thermal emittance for each gun

en by $\varepsilon_{therm} = 2R_c \sqrt{\frac{kT}{m_0c^2}}$, where R_c is the cathode ius, and T is the temperature.

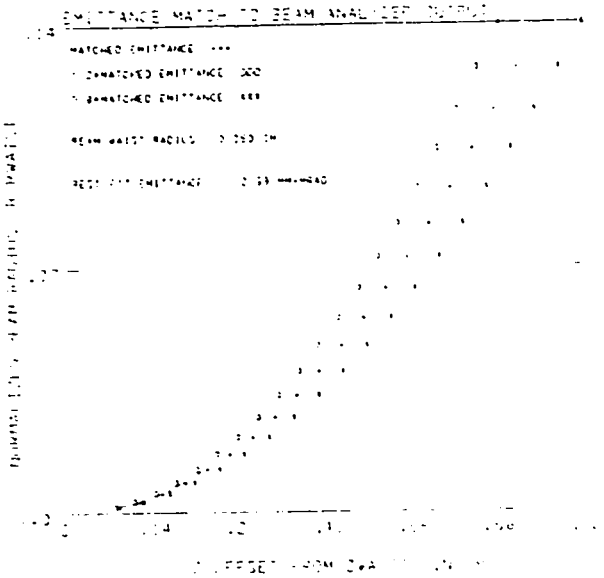

g. 5. Emittance determination by a match of theoretical relation (Eq. 5) to a polynomial representation of beam radius data (continuous curve) for the diode gun.

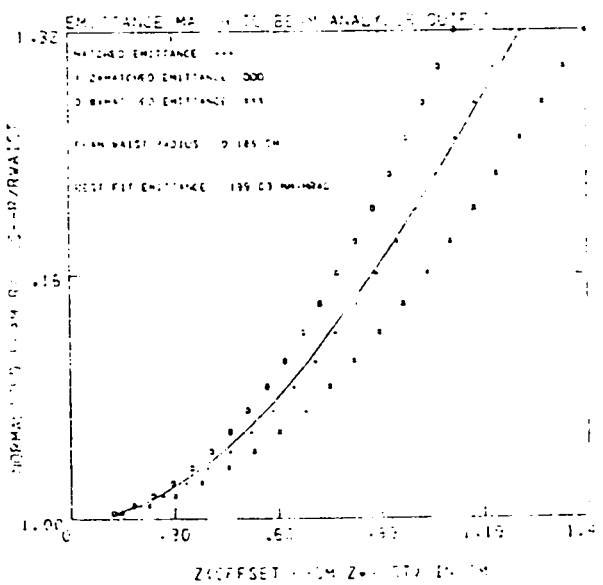

Fig.6 Emittance determination by a match of theoretical relation (Eq.5) to a polynomial representation of beam radius data (continuous curve) for the gridded gun.

TABLE 1.

Normalized emittance values.

	Diode Gun (mm mrad)		Gridded (mm mrad)	
	point	integr.	point	integr.
$\langle\varepsilon_x\rangle$	3.67	3.56	33.24	30.40
$\langle\varepsilon_y\rangle$	3.93	3.8[illegible]	34.75	32.23
ε_{therm}	2.4[illegible]		4.85	

Thes[illegible]lts suggest that the emittance of the diode gun is close to [illegible] theoretical lower limit, indicating a r[illegible]tively small emitt[illegible]ce growth in the beam as it traverses the drift regio[illegible] the anode. In contrast the emittance of the [illegible]d gun appears to be about a factor of six or seven [illegible]r than the thermal emittance, which may be attributed to [illegible]e field inhomogeneities and scattering effects introduced by the grid.

Conclusions

The method presented here allows relatively quick and easy measurements of electron gun emittance using existing conventional beam analyz[illegible] without any additional hardware.

Acknowledgements

The authors gratefully acknowledge Varian Electron Device Group members G. Merdinian, M. Cattelino, and J. Legarra for their generous help in obtaining the beam data and its analysis. We also thank G. Meddaugh, K. Crandall, and E. Seppi for informative discussions.

References

1. M. Reiser, "Theory and Design of Charged Particle Beams", to be published
2. J. Legarra, private communication.
3. P.M. Lapostolle, IEEE Trans. Nucl. Sci. NS-18, 1101 (1971).

PERFORMANCE OF THE 2 MeV MICROWAVE GUN FOR THE SSRL 150 MeV LINAC*

M. Borland,[I] M. C. Green,[d] R. H. Miller,[◇] L. V. Nelson,[d] E. Tanabe,[◇,d] J. N. Weaver,[I] and H.Wiedemann[I]

[◇] AET Associates, Cupertino, CA 95014

[I] Stanford Synchrotron Radiation Laboratory, Stanford University, Stanford, CA 94309

[◇] Stanford Linear Accelerator Center, Stanford University, Stanford, CA 94309

[d] Varian Associates, Palo Alto, CA 94303

Abstract

As described previously,[1] the p[illegible] injector linac for SSRL's 3 GeV synchrotron is fed b[illegible] MeV, 1.5 A, low-emittance microwave gun, consisting [illegible] thermionic cathode mounted in the first cell of a [illegible] cell S-band cavity. In this article, we report the successful operation of the gun, the longitudinally-bunching α-magnet, and the three-microbunch FET-pulsed beam-chopper. Simulations predict a normalized rms emittance at the gun exit of $< 10\,\pi \cdot m_e c \cdot \mu m$; chromatic effects in transport optics increase this to $\lesssim 30\,\pi \cdot m_e c \cdot \mu m$. The gun has a longitudinal phase-space suited to magnetic compression, as a result of which we predict that peak currents > 300 A in a 1 ps bunch are feasible.

Gun Design Overview

The SSRL RF gun was designed in collaboration by SSRL, AET Associates, and Varian Associates. The gun design had a number of goals, which were chosen not only with the needs of the SSRL Injector in mind, but also with the intention of producing a high-brightness electron source. These goals were: (1) For a cathode current density $J \leq 100\ A/cm^2$, each bunch injected into the linac should contain 10^9 usable electrons; i.e., electrons with momenta $\geq 80\%$ of the peak momentum. (2) Peak momentum of 2 to 3 MeV/c for peak, on-axis electric fields in the second cell < 120 MV/m. (3) Near-linear, monotonic dependence of momentum p(t) on exit-time for 20-40 ps during a bunch, in order to allow magnetic bunch compression. (4) Gently converging beam in the gun for a wide range of current densities ($J < 100 A/cm^2$). (5) Normalized rms emittance, $\epsilon_x \equiv \pi\left(\langle x^2\rangle\langle p_x^2\rangle - \langle x \cdot p_x\rangle^2\right)^{1/2}$ for the useful beam [as defined in goal (1)] of $< 15\pi \cdot m_e c \cdot \mu m$. (6) Manageable (i.e., < 5 W average at 10 pps for a 2 μs pulse) back-bomdardment power due to electrons returning to hit the cathode.

Figure 1 shows a cross-sectional view of the gun, which consists of a demountable, 6 mm diameter thermionic cathode in the first cell of a 1-1/2-cell S-band cavity. In order to thermally isolate the cathode from the metal walls of the cavity, the annular focusing structure around the cathode is also a thermal barrier made from metallized ceramic. RF electrical contact between this structure and the cathode is obtained using a toroidal tungsten-wire spring around the cathode stem.

The assumptions of design goal (1) turned out to be conservative in terms of the current density needed. The limiting factor was the RF power available to the gun. Obtaining beam momenta of the level desired implies cavity wall losses of about 1 MW. It was anticipated that about 4 MW total RF power would be available, implying 3 MW for the beam. For average kinetic energy 2 MeV, this implies that 1.5 A ($3.3 \times 10^9\ e^-$ per bunch) could be accelerated, requiring $J \approx 30\ A/cm^2$. In order to obtain a match to the RF source under these conditions, the normalized load impedance without beam was chosen to be $\beta = 4$.

To satisfy goals (2) and (3), it was necessary to alter the excitation ratio of the two cells from the usual one-to-one ratio. In particular, the excitation level of the second is ≈ 2.9 times that of the first. This permits the gun to be operated over a wide range of gradients without obtaining the sinusoidal p(t) curve that appears when particles arrive in the second cell ahead of the crest. If one characterizes the excitation level of the gun in terms of the peak, on-axis electric field at the RF crest in the second cell, E_{p2}, then operation in the range $50 MV/m < E_{p2} < 90 MV/m$ (giving maximum momentum between 1.3 MeV/c and 3.3 MeV/c) produces a beam compatible with magnetic compression. Higher excitation yields more efficient extraction of beam, resulting in higher currents for the same current density.

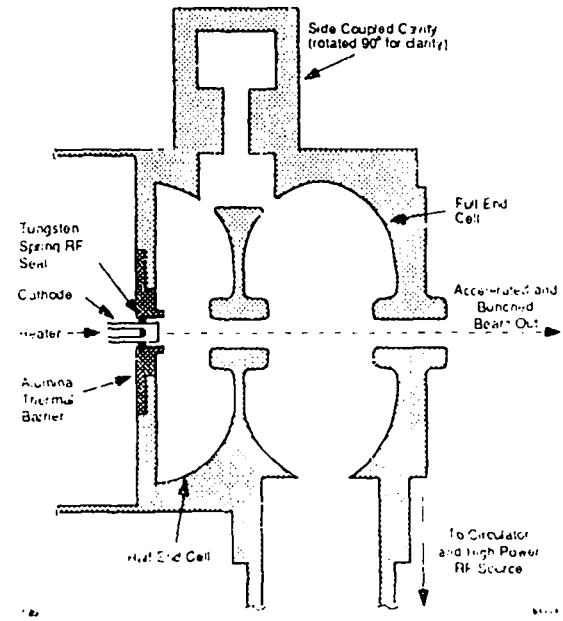

Fig. 1. Cross section of the gun cavity.

The shape of the focusing structure was arrived at using MASK[8] in order to satisfy design goals (4) and (5). The shape of the cavities themselves was not altered appreciably from that used for Varian medical linacs. Simulation details are reported elsewhere.[1,6]

As for goal (6), it was found that back-bombardment power would exceed 5 W average for $J \gtrsim 50\ A/cm^2$ for the nominal gradient of $E_{p2} = 75\ MV/m$. Fortunately, it is not necessary to use such high current densities in our application.

Operating experience with the gun to date indicates that the design goals have been largely met. Specifics of the longitudinal and transverse phase-space characterization are presented below. Here we offer a few general comments. Stable currents of up to 1.65 A have been obtained with ≈ 3.5 MW power, though the current installation does not provide sufficient RF power to exceed ≈ 900 mA. While back-bombardment is in evidence, it is a minor effect, permitting effective control of current via cathode filament power. The cathode currently in the gun has been run for about 300 hours with no sign of degradation.

*Work supported by Department of Energy contract DE-AC03-76SF00515.

Presented at the Linear Accelerator Conference, Albuquerque, New Mexico, September 10-14, 1990.

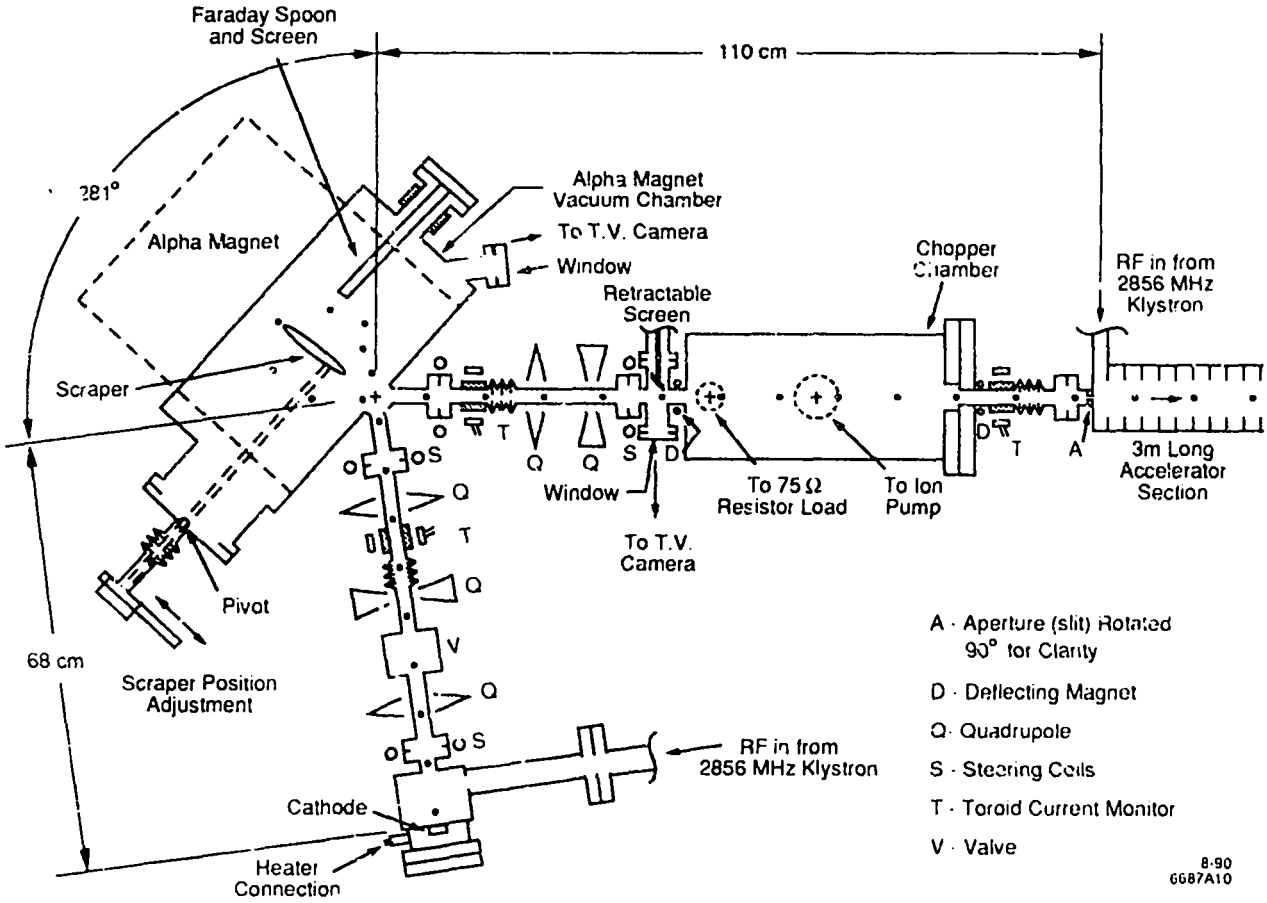

Fig. 2. Gun-to-linac layout.

Gun-to-Linac Transport Line

The Gun-to-Linac transport line ("GTL line"), shown schematically in Fig. 2 serves four main functions. The GTL line provides bunching of the beam in order to match to the longitudinal acceptance of the linear accelerator, and allows filtering out low-momentum particles. These functions are achieved using an α-magnet.[10] Quadrupoles and steering dipoles control the beam size and trajectory. The quadrupoles are required as part of the momentum filter (for good resolution), and to match the beam to the transverse acceptance of the accelerator, while providing a well-focused beam for proper operation of the chopper. The FET-pulsed beam-chopper permits the injection into the linac of only three S-band bunches of the several thousand that emerge from the gun during the RF pulse.

Magnetic Bunch Compression

The principle of magnetic bunching is to use a beamline with momentum-dependent path length. An additional requirement is zero dispersion at the end of the beamline, to avoid increasing the beam-size due to energy spread. Finally, momentum filtration requires nonzero dispersion at a location where an obstruction can be moved into the beam. All of these requirements can be satisfied with a system containing an α-magnet.[10]

The beam from the gun has a near-linear, monotonic dependence of exit time on momentum: $t_{exit}(p) \approx t_o + (dt_{exit}/dp)_o\ (p - p_o)$, where $p \equiv \beta\gamma$. To bunch the beam, all particles of interest must arrive at the linac at the same time. For reasonably small momentum spread, one can expand to first order in momentum deviation, and obtain the bunching condition:

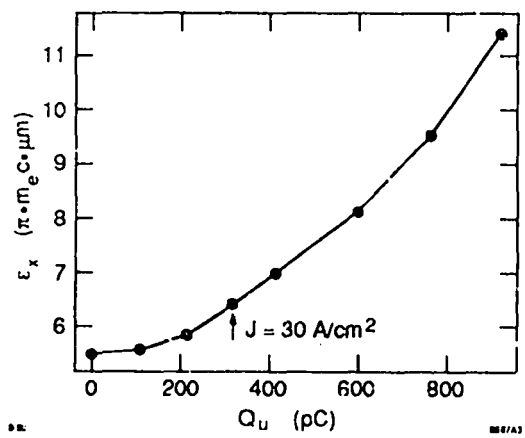

Fig. 3. Emittance versus charge per bunch.

$$\nabla B_\alpha = \frac{p_o K_\alpha^2 [\beta_o - 1/(2\beta_o)]^2}{\left\{c p_o (dt_{exit}/dp) + L_{drift} [\beta_o - (1/\beta_o)]\right\}^2},$$

where the constant $K_\alpha = 4.64210\ (m_e c/e)^{1/2}$ (MKS), was determined by numerical integration.[9]

Transverse Phase-Space

Figure 3 shows the predicted, normalized rms emittance in each plane for the "useful" beam (as defined above) at the gun exit, as a function of charge in the beam obtained through variation of the current density, from MASK simulations with $E_{p2} = 75$ MV/m. Note that the actual

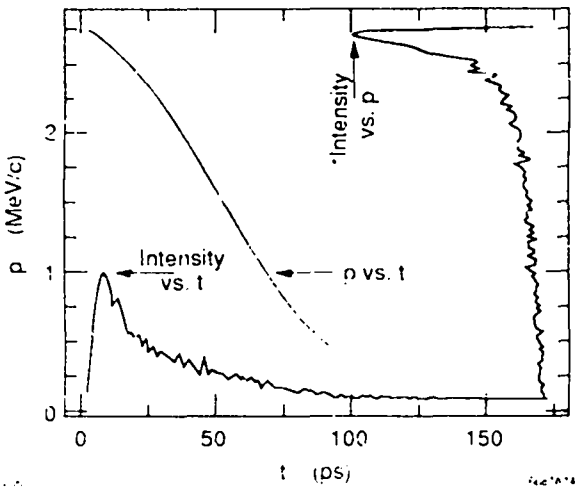

Fig. 4. Gun longitudinal phase-space.

emittance at the end of the GTL line is predicted to be significantly greater because of quadruople chromatic aberrations, and because we use ±10% momentum spread. In addition, since the beam is fully coupled, one can obtain significantly smaller emittance in one plane at the expense of the other plane. Hence, it is better to use the geometric mean, $\bar{\epsilon} = (\epsilon_x \epsilon_y)^{1/2}$ of the emittances in the two planes. Simulations predict that for $E_{p2} = 75$ MV/m, $\bar{\epsilon}$ at the end of the GTL is $\lesssim 30\ \pi \cdot m_e c \cdot \mu m$ for $J \leq 40$ A/cm^2, with only a weak dependence on current density, due in part to the overriding effect of chromatic abberations (compare Fig. 3).

The insertable screen before the beam-chopper can be used in conjunction with the quadrupole after the α-magnet to make measurements of the beam size versus the quadrupole strength. This data can be used to deduce the emittance. Measurements give horizontal emittances between 35 and 40 $\pi \cdot m_e c \cdot \mu m$. Future work will report on the emittances for both planes.

Longitudinal Phase-Space

Figure 4 shows MASK longitudinal phase-space results for $E_{p2} = 75$MV/m and $J = 10$A/cm^2. For a wide range of gradients, the longitudinal phase-space is characterized by a near-linear, monotonic dependence of momentum on exit-time. The momentum distribution is well-peaked near the maximum momentum and the particles are similarly bunched in time. In general, about 50% of the particles exiting the gun are within 20% of the maximum momentum, and these same particles extend over about 25 ps. For higher currents at the same gradient, the momentum peak is broader, as expected from the mutual repulsion of electrons in the beam; roughly speaking, one might find as much as a factor of two broadening in going from $J = 10$ to 40 A/cm^2.

Spectrum measurements can be made using a moveable scraper in the α-magnet, together with toroids before and after the α-magnet. Given such measurements, one can make various comparisons with simulations. For example, one can look at the dependence of the position of the momentum peak on the gradient. There are no field probes in the gun, so the gradient must be deduced from power conservation. The beam power can be inferred from the spectrum measurement with account taken of losses in the transport line. Following this procedure, one can obtain an experimental relationship between the position of the momentum peak and the gradient. For "low-current" (i.e., < 100 mA average), we obtain reasonable agreement with simulations.

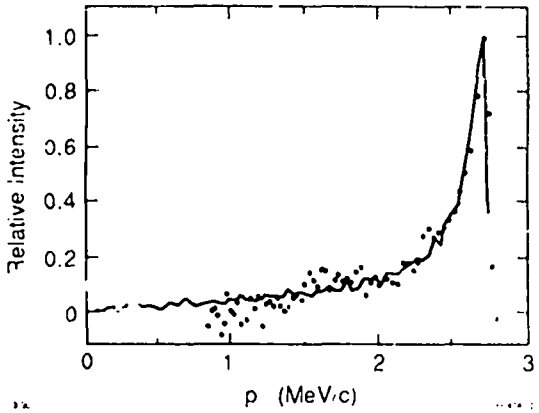

Fig. 5. Measured and simulated momentum spectra.

High-current (i.e., > 100 mA) experimental data seem to indicate that the actual power going into electrons is about twice what can be accounted for based on measurements of beam power transmitted through the α-magnet; possible explanations under investigation are secondary electrons,[11] detector diode calibration errors, stray magnetic fields, and transverse RF fields due to coupling slots.

One can also compare measured momentum distributions to calculated momentum distributions by matching the peaks of the distributions. Because of the space-charge effect mentioned just above, this is subject to the ambiguity of not knowing the current density. However, this does not become important until $J \lesssim 30$ A/cm^2. A comparison between measured and simulated spectra is shown in Fig. 5.

Simulations predict that it is possible to obtain bunch lengths of 1 ps. For a gradient of 75 MV/m and $J = 10$ A/cm^2, a peak-current of 125 A is predicted, with 6×10^8 e$^-$ per bunch and $\bar{\epsilon} \simeq 22\ \pi \cdot m_e c \cdot \mu m$. If J is increased to 40 A/cm^2, this becomes 347 A, with 2.3×10^9 e$^-$ per bunch and $\bar{\epsilon} = 23\ \pi \cdot m_e c \cdot \mu m$.

While this latter operating condition requires more RF power than currently available, the former operating condition has been achieved and exceeded, though the bunch length (and hence the peak current) has not been measured. Future experiments will measure the bunch length.

Acknowledgments

The authors wish to acknowledge the following people for design and engineering contributions: M. Baltay, B. Youngman (SSRL), R. McIntyre (VA). The following individuals provided technical and experimental support: C. Chavis, L. Emery, P. Golceff, J. Haydon, R. Hettel, B. Lavender, H. Morales, D. Mostowfi, J. Safranek, J. Sebek, D. Wang, C. Wermelskirchen (SSRL), W. Leong, S. Skellenger, and R. Tol (VA).

References

1. E. Tanabe *et al.*, SLAC-PUB-5054 (1989).
2. T. I. Smith, Proc. 1986 Linac Conf., pp. 421-426.
3. R. Miller *et al.*, Proc. 1986 Linac Conf., pp. 144-147
4. J. S. Fraser, Proc. 1986 Linac Conf., pp. 411-415.
5. G. A. Westenskow *et al.*, Laser and Particle Beams 2, Pt. 2, 223-5 (1984).
6. R. L. Sheffield *et al.*, NIM, 222-226 (1988).
7. K. T. McDonald, IEEE **QE-23**, 1489-96 (1987).
8. A. T. Drobot *et al.*, IEEE Trans. **NS-32**, 2733-7 (1985).
9. M. Borland, Ph.D thesis, Stanford Univ., to be published.
10. H. A. Enge, Rev. Sci. Instrum. **34**, No. 4, 385-389 (1963).
11. R. L. Sheffield, private communication.

AUTOMATION TOOLS FOR ACCELERATOR CONTROL
A NETWORK BASED SEQUENCER

Peter Clout, Mark Geib and Robert Westervelt

Vista Control Systems, Inc., 127 Eastgate Dr. #30800, Los Alamos, NM 87544

Abstract

In conjunction with a major client, Vista Control Systems has developed a sequencer for control systems which works in conjunction with its realtime, distributed Vsystem database. Vsystem is a network-based data acquisition, monitoring and control system which has been applied successfully to both accelerator projects and projects outside this realm of research. The network-based sequencer allows a user to simply define a thread of execution in any supported computer on the network. The script defining a sequence has a simple syntax designed for non-programmers, with facilities for selectively abbreviating the channel names for easy reference. The semantics of the script contains most of the familiar capabilities of conventional programming languages, including standard stream I/O and the ability to start other processes with parameters passed. The script is compiled to threaded code for execution efficiency. The implementation will be described in some detail and examples will be given of applications for which the sequencer has been used.

The Problem

Most control systems provide a conventional computer programming interface for the operators and users to aid in the automation of the system as the experience, understanding and confidence in the operation of the machine increases. The addition of these programs to the control system is vital to the continued development of understanding and performance up to and sometimes past the design goals. Several attempts have been made in the past [1,2] to make this process easier for the users and operators. These attempts have focussed on developing interactive languages with realtime and multi-processor enhancements. This has resulted in facilities that have been easy to use for debugging programs but where the source program has almost always been interpreted by the computer, resulting in slow execution, and involving the user in defining the I/O to the hardware and taking account of the networking between computers. Thus, the user has had to worry about more than the the basic problem at hand.

Ideally, the user should be able to express the trial solution to the problem in terms that are confined to the language of the problem and which exclude any aspects of the I/O subsystem, the computers, their operating systems and the networking of the computers that make up the whole control system. Together with a client, we have developed an automation tool that we believe advances the art in this area.

The Background for the Line Sequencer

The predecessor to Vsystem was developed at Los Alamos National Laboratory [3,4] and licensed to Vista Control Systems. We have developed and documented the control system, Vsystem, so that it is now a useful product in the marketplace. The backbone for Vsystem is the networked realtime database. This database is used initially to model the I/O connections to the control system. The contents of the database are defined by a regular ASCII file which can be generated directly with editors or with a traditional database. Database channel names can be freely chosen to be generally meaningful. Code then has to be developed to make the connection between the database and the I/O subsystem. This code could well come with the package, but the user is also given the documentation and help to write custom code so that almost any I/O system can be supported. Generally, this code is just a few lines for each type of I/O module. The system also supports any user written data conversion routine that can be expressed in a computer programming language and how to write and include these routines is documented.

The data in the database is accessed through a library of subroutines, Vaccess. The actual database in a system can be distributed among the computers of the system and each computer can have many individual databases installed. Each individual piece of the database is held in main memory as a global section to give good performance. Vaccess routines make the database appear to the user as one database taking care of the computer network access. The concept is that the user interacts directly with the database model of the machine. The code running between the database and the I/O subsystem ensures that the database reflects the state of the actual machine and that requested changes are written to the I/O subsystem.

The second component of Vsystem is the operator interface tool, Vdraw. This tool allows for the rapid development of a graphical interface between the user and the database. It is based on the computing concepts developed at Xerox Parc in the '70s and first popularized by Apple Computers. This tool allows the user to draw operator windows with a draw package and also put objects on the screen which are connected to the data in the database. This allows the operator to quickly see the state of the machine and make changes to settings. By clicking with the mouse in a defined area, the operator can also execute other programs or start another operation in the computer. Vdraw runs under Xwindows and with this tool, complex but intuitive windows can be defined in hours.

Vaccess and Vdraw together provide the tools necessary to build a supervisory control system. They also provide the basis for the extension of the system into automation.

The Line Sequencer

The requirement for the Line Sequencer was to provide a facility whereby scientists not familiar with conventional computer programming languages can define the automation of their experiments, including the analysis of the data, without the need to learn FORTRAN. This language was developed together with a client experienced with this requirement.

The Sequencer provides transparent network management of sequences of action. A powerful feature of the Line Sequencer lies in the fact that since no special programming knowledge

is necessary, the people most connected with the process, the engineers, operators and users, can write the script used to execute action. This eliminates the difficult communications/specifications step between the user and the programmer.

The three primary components of the Line Sequencer are the compiler, the command interface, and the engine. Commands are entered into the Line Sequencer with a simple English–like language. The **compiler** must translate this English–like script into an intermediate language for the sequence engine. The **command interface** controls and monitors all sequences of actions and communicates back and forth with the engines during user command execution. The **engines** execute source code generated by the compiler.

The Line Sequencer creates an environment which allows multiple servers to run multiple engines, each performing different sequences of actions. Sequences can be repetitive or conditional in nature. Each sequence runs in a separate engine. This allows one server to run multiple engines simultaneously, thus permitting several sequences of actions to execute at the same time. Figure 1 is a diagram of the Line Sequencer environment.

Compiler

The **compiler** is designed for easy use in writing Vsequence script by someone with little or no programming experience. Vsequence Script is based on a simple keyword/value syntax, with all extra text ignored. Because you can include text and keywords simultaneously, Vsequence script is even readable to someone unfamiliar with it. Vsequence script has some of the flexibility and generality of pseudo–code in that there are many ways to express the same action. Also, the sequence compiler generates helpful error messages and will flag conditions or statements that it finds ambiguous. This allows the user several ways of expressing functionality with the confidence that the compiler is interpreting the instructions correctly.

Vsequence Script

English–like constructs can be used in the Vsequence script with keywords used to generate the Vsequence source code. For example, lines of script such as

Turn VALVE12 ON to start the flow of water

or

Initialize by setting VALVE12 ON

are both acceptable. This will set the database channel VALVE12 to the ON state. The extra text allows the script to be self–documenting.

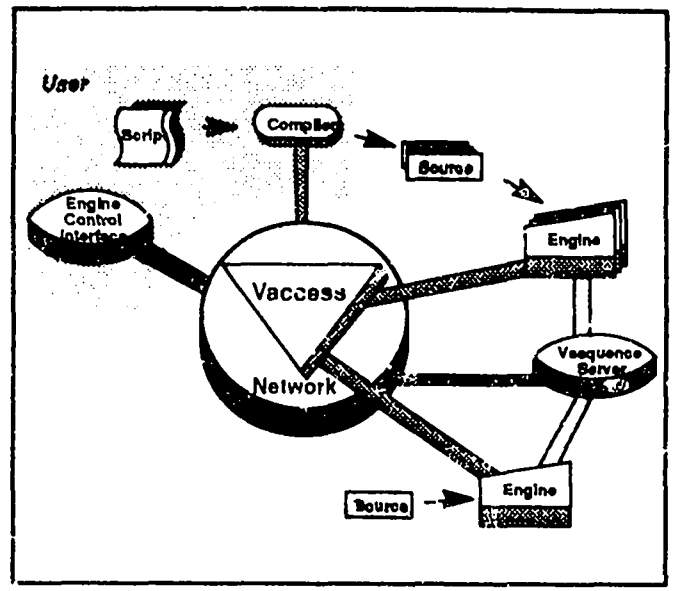

Figure 1: Line Sequencer Environment

The user enters English–like script, which is converted to source by the compiler. This source is then executed by the engine. The Vsequence server monitors and controls the sequence of actions being executed by the engine.

The Vsequence script language has a complete set of flow control constructs for looping and condition testing. In addition, it has a WAIT UNTIL control construct which is useful for holding execution until some condition is reached in the system under control. The WAIT UNTIL control function also has a TIMEOUT capability built–in so that it will not hang while waiting for some condition that may never occur. All of the functionality of a true programming language has been provided. The Line Sequencer's English–like script is a free form, context sensitive, programming language aimed at laboratory automation. It is tightly coupled to the rest of the Vsystem, which will greatly simplifies the command interface.

The Line Sequence Compiler has a rich set of logical operators (expressible in many different forms), mathematical functions, and file I/O capabilities. Additionally, the compiler understands the structure of the Vaccess database and handles setting values in the database transparently.

Command Interface/Vsequence Server

The **command interface** which controls the actions of sequences is based on a client/server model. The *client* is the user interface program which accepts commands from the user and sends them for execution to the appropriate server. The *server* provides and controls the resources necessary for sequence execution, i.e. the sequence engines. This approach allows the user to run sequences without having direct access to the computer on which the sequence is executing, while providing a clean mechanism for distributing the workload over the network.

Each sequence server can support up to 32 engines running on a node at one time. The actual number of sequence engines executing may be less because of the VMS system

configuration. With these 32 engines, the server can also support up to 32 links to users at the same time. Each user's commands are executed in the order in which they are received by the server.

The server also provides security protections for sequences. There are two levels of security for each sequence engine. The engines are run under VMS user accounts and users must have network proxy to access the a specified account. This means that only certain users can run sequences under a given account. Also, only these users can issue commands to the sequence engine. The ATTACH command further restricts access to an engine to one user at a time. Thus, two different users cannot issue conflicting commands to an engine at the same time.

The command interface allows complete control over the creation and execution of sequences. There are commands to create, set the parameters, and show the status of sequence execution. There are also facilities provided for rudimentary debugging of the sequence. The **DEBUG** mode displays the currently executing Vsequence source instruction on the user's terminal, while a single **STEP** mode executes single instructions at a time.

Engine

The **sequence engine** provides an environment which will execute **Vsequence source**. The instructions are intended to provide all the functionality required to write programs which will easily access Vsystem realtime database channels.

The instructions provide for conditional branching, time based operations, limited control of VMS processes, and transparent access to Vsystem database channels. The engine provides limited aid for debugging Vsequence source through a debug mode and single stepping through Vsequence source. C–style I/O is provided and supports any standard VMS stream device. In addition, support is provided for opening DECterm windows on workstations running DECwindows. The engine is stack based; thus, most Line Sequencer instructions take operands off the stack and leave results on the stack. Condition handling is provided by establishing condition handling branches which are taken when a condition occurs at run time.

The execution of Vsequence source is very efficient. The instructions are compiled, and a vector table of instruction entry points provides execution of instructions at run time.

The engine provides a number of utility commands to aid the user. For example, during the loading of Vsequence source the actual source lines for each instruction are stored and can be examined with the DUMP command. The status of the engine can be examined with the SHOW command, which provides the current program counter and status bits.

Example

Figure 2 shows an example Line Sequencer script. In this example, an oven is being ramped up to a given values and then allowed to cool. The "!" character is the comment delimiter and the "load" command causes the sequence engine to search the database defined and load the channel names that fit the search string. In this case, all channel names will match. The channels can now be referenced in the script using only the remainder of the name. In the third line, the words "make" and "degrees" are ignored and in the next to last line there are four words that are ignored.

```
!load all the database channel names
#load FDB::
make set_point 20.0 degrees
!ramp the furnace to 1000
until (set_point > 1000) then
 set_point = set_point + 50.0
 wait 5.0 seconds
end
!wait for sample to reach 1000.0 degrees
wait until ( temp > 1000.0 )
!hold at 1000.0 for 1 min.
wait 60.0 seconds
!go back to room temp
return the set_point to 20.0 degrees
wait until ( temp < 50.0 )
```

Figure 2: An Example Line Sequencer Script

The source will be loaded to the engine for running. Note that the parsed script forms the initial comments and that the engine is a stack–oriented device.

Conclusion

The Line Sequencer is currently in production use and has already demonstrated its power in several demonstrations and a production environment. As the source interface is defined in the documentation, users can develop their own custom interfaces should they wish. We will be developing the capability of the Line Sequencer and also using the engine as the basis for future automation tools.

Acknowledgements

We acknowledge the many interactions with John Thurtell, Greg Maier and Bill Lucas of Mobil Oil Central Research Laboratories in the definition stage of the Line Sequencer. Greg Maier and Bill Lucas also wrote the Script Compiler of the Line Sequencer.

References

1. M.C. Crowley–Milling and G.C. Shering, The Nodal System at the SPS, CERN 78–08
2. P. Haskell, GRACES Reference Manual Version–2, RL–84–043
3. M.A. Fuka P.N. Clout, A.P. Conley, J.O. Hill, R.B. Rothrock, L.L. Trease and M.E. Zander, Proc. 1987 Particle Accelerator Conf. IEEE 87CH2387–9, pp. 652–654
4. P. Clout, R. Rothrock, V. Martz, R. Westervelt and M. Geib, Past, Present and Future of a Commercial, Graphically Oriented Control System, Proc. Int. Conf. on Accelerator and Large Experimental Physics Control Systems, NIM A293 (1990) 456–9

INCREASING OUTPUT POWER OF A 850 MHZ TETRODE WITH A FLOATING-DECK MODULATOR*

Daniel Rees and Carl Friedrichs
Los Alamos National Laboratory, Los Alamos, NM 87545

Introduction

Designers of high-power amplifiers generally regard the region above 300 MHz as a domain dominated by velocity-modulated (klystron/TWT) devices. However, as the power requirements diminish, there are attractive alternatives. The high-power 850-MHz requirements of the ground test accelerator (GTA) program can be filled by 1-MW klystrons, but it would be more efficient to use a lower-power device for a 50-kW requirement. To meet the 850-MHz medium-power requirements, Los Alamos National Laboratory is developing an 850-MHz tetrode amplifier. These amplifiers will provide RF power to the momentum compactor and bunch rotator cavities of the GTA.

Available tubes provide only a limited safety margin for a low-risk design at the power levels and duty factor required for GTA cavities. At 850 MHz, the output power capability of available tubes is reduced because of transit time effects and limited anode voltage holdoff. Pulsing the anode of the output tetrode amplifier will allow higher output power with minimum design risk. A floating-deck modulator acts as a high-voltage/high-current switch, so voltage is applied to the anode of the gridded tube only during the rf pulse. The anode voltage holdoff capability of the tube is substantially enhanced by operating in this mode. This paper will describe the design of the floating deck modulator and its impact on the design risk of the 850-MHz tetrode amplifier.

Gridded Tube Limitations at 850-MHz

Gridded tubes at high frequencies are limited in power output for a number of specific reasons. For high-frequency operation, it is essential to minimize the output spacing (grid-to-plate spacing for a triode or screen-to-plate spacing for a tetrode) and the circumference. The circumference must be minimized to prevent the introduction of radial modes in the axially symmetric output cavity of the tube, and the output spacing must be decreased to minimize transit time effects. These factors result in a tube design that decreases in size with increasing frequency of operation. The decrease in size leads to a smaller emitting surface (reduced current capability) and a smaller anode (reduced dissipation capability). Also, the decrease in output spacing limits the anode voltage holdoff capability.

850-MHz Gridded -Tube Design

The tetrode amplifier currently under development at Los Alamos is being designed to satisfy a 50-kW requirement for the GTA. The design is for a 65-kW, 850-MHz, pulsed tetrode amplifier with a maximum pulsewidth of 2 ms and pulse repetition frequency of 10 Hz. The design power level is higher than required to provide for transport losses and control margin for the cavity phase and amplitude closed loop control system. The amplifier consists of four stages and will be operated class B.

The first three stages will consist of a solid-state driver and two tetrode amplifiers. The last stage uses a Burle 4632 tetrode amplifier. The output power from a gridded tube is the product of the fundamental component (850 MHz) of anode current and the anode voltage swing. The anode voltage swing is the product of the fundamental anode current and the rf resistance presented to the anode by the output resonant cavity. The midpoint of the swing is the bias voltage of the anode. As the electrons traverse from the screen to plate, they see a time-varying accelerating gradient (transit time effect). At lower frequencies the effect is negligible; however, at 850 MHz the transit time becomes a significant portion of a wavelength. The resulting time-varying accelerating gradient tends to debunch the electrons and results in decreased fundamental current, increased harmonic current content,[1] and reduced output power. To minimize this effect and boost the power capability of the gridded tube at 850 MHz, a floating-deck modulator has been designed. The modulator will pulse the voltage to the anode of the final stage of amplification for 2 ms, thereby increasing the anode voltage holdoff capability by 50% over the dc value. The increased voltage holdoff allows for a larger anode voltage swing and accelerating gradient resulting in increased output power and minimal transit time effects.

Burle 4632 Tetrode Amplifier

The 4632 tetrode will be used for the final stage of amplification. The 4632 has a continuous anode voltage rating of 10 kV which would limit the output power to 45 kW. In order to provide for a 65-kW design, a floating-deck modulator will pulse the anode voltage to 15 kV. The proposed operating conditions are listed in Table 1.

The currents, power, and rf resistances listed in the table are calculated from a Fourier analysis of the tube characteristics.[2] The circuit efficiency represents the resistive losses in the tube and cavity structure. The transit time efficiency is calculated by a one-dimensional simulation of electrons crossing the output gap of the 4632 tetrode under the bias conditions in the table in the presence of the time-varying rf voltage.[1] The modulator will provide a pulsed anode voltage to the 4632 of 15 kV at a minimum of 13.5 A anode current.

Modulator Design

Figure 1 contains a block diagram of the floating-deck modulator. The major components are a 20-kV power supply, two EIMAC 8960 switch tubes in parallel, hexfet cathode modulators, a 20-kV isolation transformer, a grid supply, a screen supply, an optical interface, a fault detection interface, a high-voltage insulated deck and a high-voltage enclosure.

*Work supported by the US Department of Energy, Office of High Energy and Nuclear Physics.

Table 1
4632 Tetrode Operating Conditions
Cathode Drive

Parameter	Design
DC Plate Voltage	15000 volts
DC Screen Voltage	1500 volts
DC Cathode Bias	50 volts
DC Plate Current	13.5 A
DC Screen Current	000 A
DC Grid Current	2.5 A
DC Cathode Current	16.0 A
Fund.PK.PLT.Current	20.1 A
2ND HAR.PK.PLT.Current	6.6 A
3RD HAR.PK.PLT.Current	1.3 A
FundPK.CATH.Current	25.0 A
Peak Plate Swing	8000 volts
Clircuit Efficiency	95. %
Transit Time Efficiency	86. %
Output Power	65. KW
RF Plate Load	399. Ohms
Peak Cathode Swing	170.0 volts
Drive Power	2.1 KW
RF Cath.Input Resistance	6.9 Ohms
Plate Dissipation (peak)	108 KW
Plate Dissipation (avg)	2.2 KW

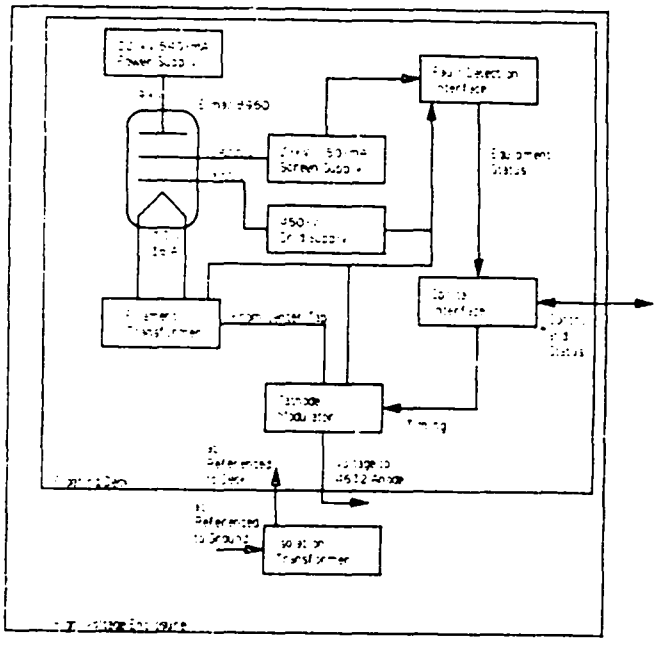

Fig. 1. Floating-deck modulator block diagram.

The EIMAC 8960 is a glass-envelope, air-cooled, power tetrode designed for pulse modulator or switch-tube service, operating at voltages to 50 kVdc or anode current as high as 12 A. The tube has a thoriated-tungsten filament, and the maximum average anode dissipation rating is 1200 W. Cooling is accomplished by radiation from the anode and by circulation of forced air through the base and around the envelope. The current required by the 4632 is in excess of the capability of a single 8960, so two 8960's are connected in parallel . The modulator operating point is calculated in Figure 2 based on a 270-Vdc grid bias. Figure 2 displays load lines for the 4632 and 8960 tetrodes. The curves have opposite slopes and the operating point is the intersection of the two curves. The curve for the 8960 tetrode is read from the EIMAC data sheet. The curve for the 4632 tetrode is calculated by varying dc anode voltage, with rf drive and screen voltage remaining constant. The horizontal axis in the figure represents the plate voltage drop across the EIMAC 8960. The voltage drop across the 4632 tetrode is 19 kV minus the drop across the 8960.

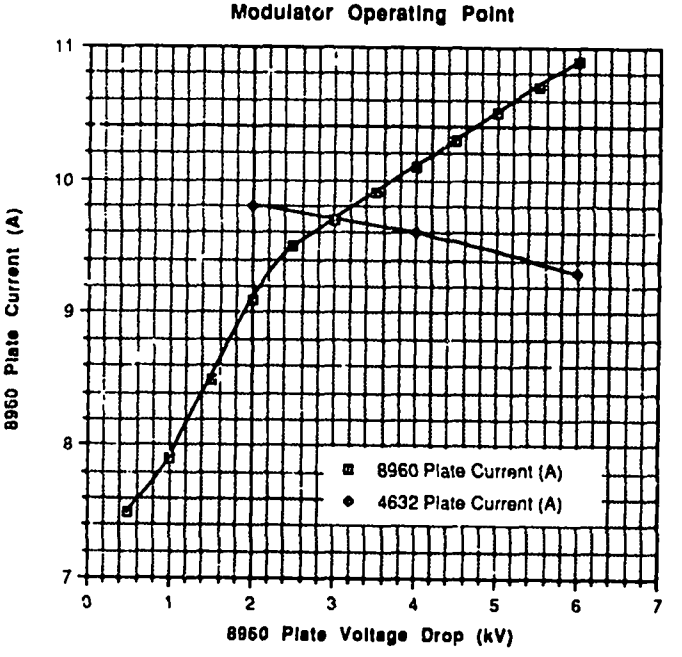

Fig. 2. Floating deck modulator operating point.

A 20-kVdc, 540-mA SCR controlled power supply will provide dc voltage to the anode of the 8960's. This supply provides a peak current of 27 A from an internal capacitor bank at the rated voltage and duty factor. The screen voltage for the 8960's is provided by a 2-kV, 150-mA high-voltage power supply, and the grid voltage is provided by a 450-Vdc unregulated power supply. An optical interface will receive a gating signal from the tetrode controller and pass back the status of the equipment. The gating signal will drive the hexfets connected between the cathodes of the 8960's and the deck. This will cause the tube to conduct and provide a pulsed voltage to the 4632 anode. From Figure 2 it can be seen that a 3-kV voltage drop will occur across the switch tube. Hence a supply voltage of 18 kV is needed to provide the 15-kV pulse to the anode of the 4632. A fault detection interface will monitor filament current, power supply voltages, and the cathode hexfet modulators for equipment faults. All equipment is contained within a metal enclosure called the floating deck. The potential of the floating deck is identical to the potential of the 4632 anode and will pulse from 0 Vdc to 15-kVdc with the rf pulse. The floating deck is contained within a high-voltage enclosure at ground potential. The floating deck and high-voltage enclosure are designed to minimize sharp corners or ridges that could lead to voltage breakdown. The 20-kV transformer provides ac power to the equipment

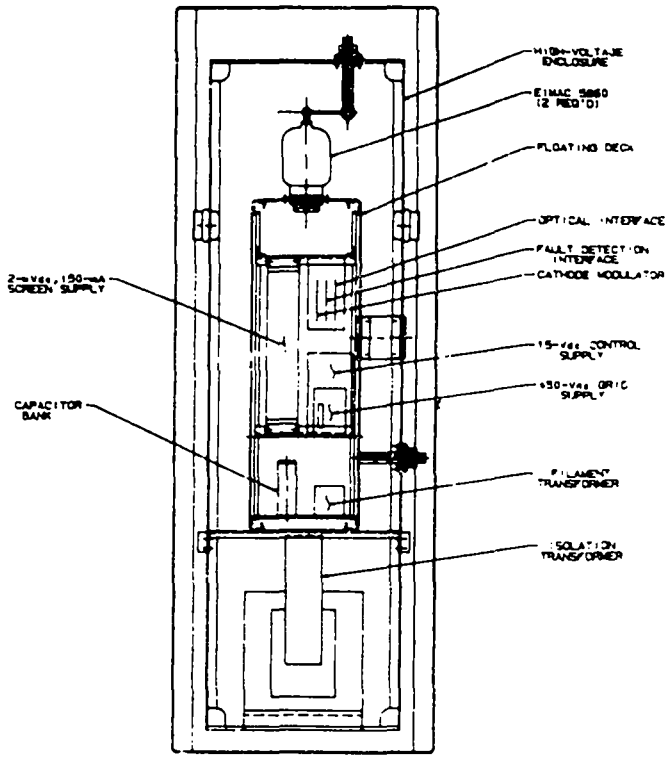

Fig. 3. Floating-deck modulator mechanmical layout.

within the floating deck. The secondary of the transformer is referenced to the deck potential Figure 3 contains a mechanical drawing of the floating deck, power supplies, and high-voltage enclosure.

Status

A floating-deck modulator has been designed and tested. Tests were conducted using a resistive load to simulate the load line of the 4632 tetrode. The floating-deck modulator performed as designed and provided a pulsed voltage of 15 kV and a pulsed current of 13.5 A to the resistive load. The peak value of the pulsed voltage is variable by adjusting the operating parameters of the switch tube. When the development is complete for the 4632 tetrode cavity, the modulator will be integrated with the final stage of amplification for rf testing.

References

1. Humphries, "Numerical Simulation of Transit Time Effects in Gridded Tubes, Numerical Simulation in Pascal", Los Alamos National Laboratory, January 15, 1989.
2. Varian EIMAC, Care and Feeding of Power Grid Tubes, San Carlos California, 1967.

LASER INTERFEROMETER FOR THE PRECISE ALIGNMENT OF A LINEAR ACCELERATOR

Yujiro Ogawa, Toshikazu Suzuki, Kazuro Furukawa,
Akira Asami, and Isamu Sato
KEK, National Laboratory for High Energy Physics
Tsukuba, Ibaraki 305, Japan

Abstract

Since the beam spot size reaches nanometers at a final focusing region in future linear colliders, vibration displacement must be suppressed to the order of nanometers, which we call dynamic alignment hereafter. A technique involving laser interferometers allows such precise measurements of the displacements of accelerator components. In the alignment of linear accelerators, the most important quantity to be measured is transverse to the laser direction, which defines a reference line. In order to realize it, the possibility of using phase-conjugate mirrors with a laser interferometer was investigated.

Introduction

Recent research and development concerning future linear colliders[1] suggest that the beam spot size at the collision point should be reduced to the order of nanometers in order to increase luminosity. To realize this, the dynamic alignment accuracies of such accelerator components as the quadrupole magnets at the final focusing region must be of the order of nanometers, or less. This requires technological innovations in both measuring and controlling the dynamic alignment precision. Although so-called nanometer-technology has been progressing in industries, there had been no need to obtain the same accuracy over such a very long distance as that found in linear accelerators. In the following, we introduce the technology of an ultra-precise laser interferometer[2] developed in gravitational-wave experiments, and examine its sensitivity. The possibility of transverse alignment peculiar to the alignment of a linear accelerator was also investigated using phase-conjugate mirrors.

Laser Interferometer

Principle

The laser interferometer is a Michelson-type, comprising a stable coherent light source (laser), a beam-splitter, and high-reflectivity mirrors at the end of each arm. One of the light beams separated by the beam-splitter enters the longer arm; there it is reflected by the end-mirror and returns to the beam-splitter. The other beam goes to the reference arm and is reflected by a mirror back to the same beamsplitter. By observing the interference pattern of both beams, a vibrational displacement separated by a long distance can be precisely measured relative to the length of the reference arm. The precision is usually determined by the order of the light wavelength, which is not sufficient in our case. We introduced a dark-fringe locking method which had been developed in gravitational-wave experiments, which assured the desired precision.

Sensitivity

The fundamental sensitivity limit is determined by an uncertainty relation based upon a quantum fluctuation of the mirror motion. This is realized when the photon-counting error and the radiation pressure to the mirror are balanced. Since the laser power for such a condition is extremely large, the sensitivity limit is given in terms of the photon-counting error (for instance, about 10^{-15} m/Hz$^{1/2}$ with a laser power of 10 mW(He-Ne).). This value is sufficiently small for our purpose, and is neglected here. The noise source for practical sensitivity is classified into the following items:

[1] Laser noise
[2] Seismic Noise
[3] Thermal Noise
[4] Residual Gas, etc.

[1] Laser noise There are two types of noise sources in a laser: frequency fluctuation and intensity noise. In the case of frequency fluctuation, the interferometer sensitivity is determined by the product of the frequency stability($\delta f / f$) and the absolute difference of the light path. A commercially available He-Ne laser, for instance, has a frequency stability of the order of 10^{-10}. Since the absolute difference of the light path may be long in the interferometer for the alignment of a linear accelerator, possibly reaching 100-1000 m, the sensitivity becomes more than 10 nm. To resolve this, one could stabilize the frequency by locking it to an ex-

ternal Fabry-Perot cavity, or decrease the path difference by using a multipath method for the reference arm. The product of the intensity fluctuation and the residual deviation from a dark fringe when locking limits the sensitivity. For dark-fringe locking, one needs a relatively high modulation frequency, since the intensity fluctuates, especially in a low-frequency region. In the example of the He-Ne laser, the stability of the intensity is about 10^{-4}, which is negligibly small.

[2] Seismic Noise Since the dynamic alignment precision must be high in the low-frequency region, the effects of seismic noise must be considered. The typical spectrum of seismic noise is known to be roughly $10^{-7}/f^2$ m/Hz$^{1/2}$, indicating the necessity of an effective vibration-isolation system for the accelerator components. There are two types of vibration-isolation methods: a passive method using a coil spring or a pneumatic spring, and an active method using feedback control.

[3] Thermal Noise All components of the system, such as accelerator components, mirrors and optical elements, have their own mechanical resonant modes, with which thermal noise is associated. It is also important to note that the vibration-isolation system for seismic noise accompanies thermal noise. In order to decrease thermal noise, one needs a low temperature for the mode, a large effective mass of vibration, an appropriate selection of the resonant frequency and a high mechanical quality factor. Thermal motion is generally very small when the temperature of the mode is 300 K, or the component is in thermal equilibrium with the environmental temperature. It is, however, taken account of in relation to the feedback system of vibration isolation.

[4] Residual Gas Fluctuation of the refractive index of residual gas causes a variation of the effective path length, and limits the sensitivity. A vacuum system is also necessary for suppressing acoustic coupling with environmental noise.

Preliminary Experiments

Preliminary experiments were carried out on a long-arm interferometer in air. Fig. 1 shows the experimental configuration. The arm length is about 80 m and the light source a frequency-stabilized 0.7 mW He-Ne laser. The beam size can be set to about 15 mmϕ by using a beam expander. A retroreflector reflects the beam parallel to the incoming beam, in such a way that the reflected beam into the laser does not disturb its stabilization system. We observed the interference pattern on a screen. The results showed both large coupling with the environmental acoustic noise and the effect of residual gas, suggesting that the vacuum system is essential in the current stage of experiment. We are now preparing a suitable vacuum system and the introduction of a dark-fringe locking method. Each type noise mentioned above will be identified using this system.

Transverse Alignment

The most necessary quantity to measure regarding linear-accelerator alignment, is the transverse one with respect to the laser direction, which defines a reference line. In order to realize this, one of the possibilities to use phase conjugate mirrors with a laser interferometer was investigated. A phase-conjugate mirror has a novel property in that reflected light always comes back in the direction of injection. Using this property, one could expect to achieve transverse measurements with an interferometer technique. Fig. 2 shows one possible example under experimental study. The light beam of a 15 mW Ar^+ laser enters the phase-conjugate mirror at an injection angle of 45 degrees with the crystal surface. The phase-conjugated light is reflected in the same direction as that of the incoming light. The incoming light is also reflected directly to the flat mirror. The ordinary light reflected at the flat mirror returns together with the phase-conjugated light and interferes. From a variation of the interference pattern, one can determine any transverse displacement, which is decoupled with the longitudinal one in this scheme. The experiment with phase-conjugate mirror is, however, very delicate and strongly depends on the power and stability of the laser. Although we have not obtained any definitive experimental results so far, we note our belief that the principle should be reconsidered.

Authors wish to thank the Japan Linear Collider study group for their warm encouragement and valuable discussions.

References

[1] G. Horikoshi, Y. Kimura, and T. Nishikawa, in *Proceedings of the 1988 Linear Accelerator Conference*, Williamsburg, VA, USA, 1988; R. B. Palmer, SLAC-AAS-36, 1988.

[2] D. Shoemaker, R. Schilling, L. Schnupp, K. Maischiberger, and A. Rudiger, Phys. Rev. **D38**, 423 (1988).

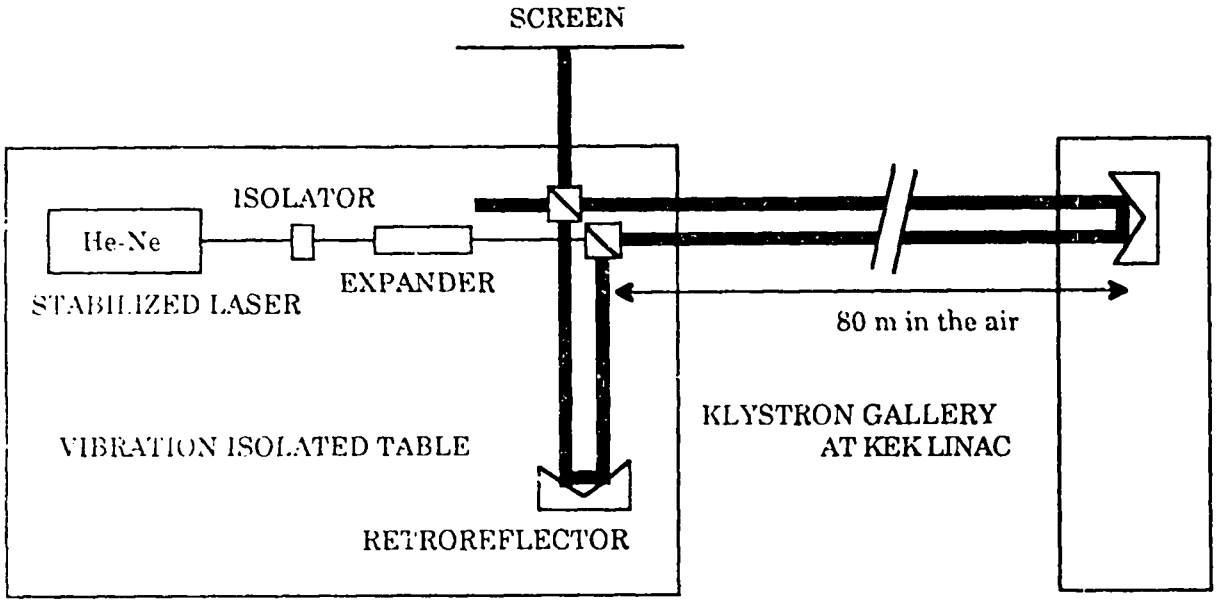

Fig. 1. Preliminary expeiments on a long-arm interferometer in air.

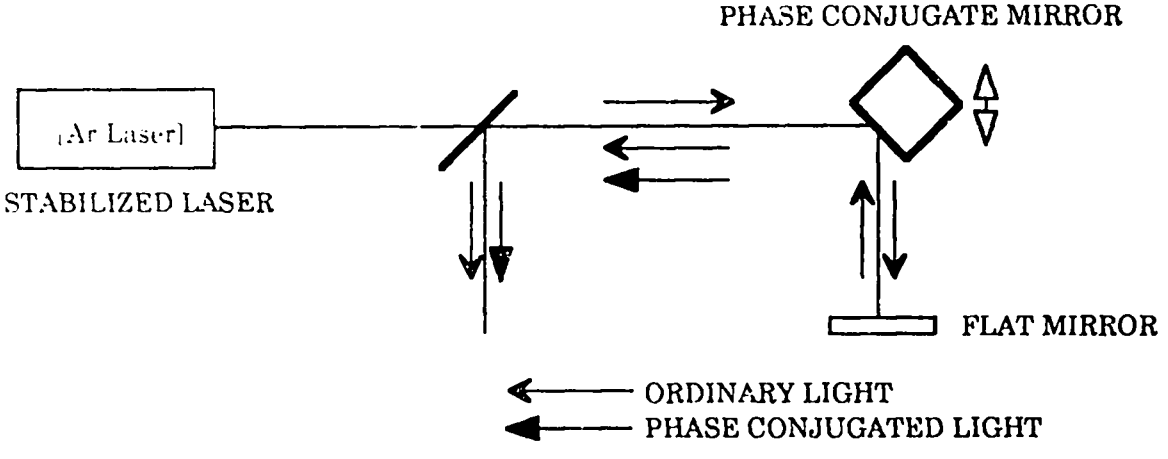

Fig. 2. Transverse alignment with a phase conjugate mirror.

EXPERIMENTAL INVESTIGATIONS OF MULTI-BUNCH INSTABILITY BY A TRANSVERSE WAKE FIELD

Yujiro Ogawa, Tetsuo Shidara and Akira Asami
KEK, National Laboratory for High Energy Physics
Tsukuba, Ibaraki 305, Japan

Abstract

A multi-bunch instability due to a transverse wake field relevant to future linear colliders was investigated at the primary electron section of the KEK positron generator linac. A transverse shift of the last bunch was observed by changing a transverse offset of the beam position at the entrance of the first accelerating cavity.

Introduction

Future linear colliders[1] will require multi-bunch operation for the attainment of large luminosity. Under multi-bunch operation, it is essential to overcome any beam instability induced by a transverse wake field, since it may result in both emittance growth and blow-up of the spot size at the collision point.[2] The problems related to the transverse wake field and its effects on a high-intensity, single-bunch electron beam have been already resolved both theoretically and experimentally by several researchers.[3] The multi-bunch instability, however, has so far been treated only theoretically;[4] results suggest several possible methods to reduce this instability. Only a few experimental studies[5] have taken place concerning high-intensity, multi-bunch electron beams; especially, no experiments have been reported on the multi-bunch instability caused by a transverse wake field (except for BBU[6] or pulse-shortening effects for a very long train of bunches, where only the beam loss was observed). We first observed a multi-bunch instability for a few bunches at the primary electron section of the KEK positron generator linac.

Experimental

The layout of the KEK positron generator linac[7] is shown in Fig. 1. It involves a 250-MeV primary electron section, starting from a 150-keV, high-intensity electron gun with a peak emission current of 10 A and a pulse width of 4.2 ns. The electron beam is longitudinally compressed to a 2-ns pulse with a peak current of about 15 A by a Sub-Harmonic Buncher(SHB) with a modulation frequency of 119 MHz and a subsequent drift space of about 3 m. It is then split into several bunches in a bunching section operating at 2856 MHz, and accelerated to 250 MeV in a regular accelerating section at the same frequency. Fig. 1 also shows parts of the focusing system related to the experiment: the steering coils and quadrupole magnets that are arranged so as to produce a betatron wavelength of about 40 m. An energy-analyzing station[8] in front of the positron conversion target comprises collimators, an energy-analyzing magnet, beam-profile monitors, a current monitor, a slit, and a bunch monitor of the strip-line type.[9] The measured energy spectrum of the beam indicated several peaks, which have been identified as being bunches using a bunch monitor. The electric charge on each bunch amounted to several nano-Coulomb; the total energy spread was about 9 %.

In order to observe at PRM-A how the transverse position of the beam moves, we changed the transverse (vertical) offset of the beam position at the entrance of the first accelerating cavity by flowing a current in a steering coil, ST-1(see Fig. 1) . A photograph of a typical case is shown in Fig. 2; the bunch structure appears and the last bunch (right-most side) moves very sensitively to the vertical offset at the entrance of the accelerating cavity. In Fig. 3, the transverse displacement of the last bunch is plotted as a function of the offset at the first accelerating cavity, which was measured at the profile monitor, PRM-1, immediately after steering coil, ST-1. It shows an almost linear dependence, which is reasonable from a theoretical point of view.

Several tests and analyses were performed to confirm that the observed effect is due to a transverse wake field. First, the beam trajectory for two typical cases in which the effect seems to appear, was checked. The result showed normal behavior of betatron oscillations (Fig. 4). The transverse beam positions at PRM-A with SHB both ON and OFF was then compared. No effects were observed when SHB was OFF (Fig. 5a). Since SHB being ON and OFF corresponded to five- and twelve-bunch operations with almost the same total charge, the same average energy, and the same total energy spread, we could verify in this way that the observed effects depend on the electric charge per

bunch, and that the effects are not caused by different possible orbits due to momentum differences. A semi-long beam with a peak current of 2.3 A and a pulse width of 40 ns was accelerated in order to determine whether the effects appear when the electric charge per bunch is smaller (the total electric charge was almost twice that of the 2-ns beam). No transverse blow-up was observed (Fig. 5b), verifying that the electric charge per bunch is essential for the effects. Finally, the z-dependence (here, z is again the length of the accelerator) of the effects was investigated. By changing the beam offset, at the second accelerating section (see Fig. 1), not at the first, reduced z by maintaining almost the same offset, we found that the effects became smaller (Fig. 5c). The reduction ratio of the transverse offset was about 3.5, obtained by applying a large initial offset, so as to produce the same transverse effect.

Discussion

The results are summarized as follows:

(1) The observed shift of the beam position at the output of the accelerator is proportional to the offset at the entrance of the accelerating cavity (Fig. 3).

(2) The observed effects depend on the electric charge per bunch, not on the total electric charge (Fig. 5a,b).

(3) The dependence of the effects on the length of the accelerator is sufficiently strong (Fig. 5c).

In order to quantitatively explain the results, we tried to make a very rough estimation by applying, for instance, a two-particle model by Wilson to our case. Wilson's formula[3] is

$$\frac{X_f}{X_i} \cong \frac{eN\beta W_d z}{8\pi V_0},$$

where X_f and X_i are the offsets at the entrance and output of the accelerating cavity, respectively; N the number of particles; β the betatron wavelength; W_d the dipole wake field at the separation between the model particles; z the length of accelerating sections; and V_0 the average energy. If we take eN=10 nC, β=40 m, $W_d \cong 10^{15}$ V/C/m^2, z=24 m, and eV_0=120 MeV,

$$\frac{X_f}{X_i} \cong 3,$$

which is roughly consistent with the experimental value of about 1 (Fig. 3). Here, the value obtained at SLAC[2] for a dipole wake field was assumed. The difference may be attributed, for instance, to the fact that it is of the cavity type; KEK's is a quasi-constant gradient type, while SLAC's is a constant-impedance type. As a result, the above (1) and (2) were verified semi-quantitatively. The z-dependence (above (3)) was also checked by using the same formula, where it is linear in z. In our experiment, the ratio of z in the two cases is about 22 m/16 m ≅ 1.4. Taking into account the energy dependence, this factor is reduced to about 1.7, which still seems to be too small to explain the experimental value (about 3.5).

The discrepancy may be explained by the multi-particle model by Suzuki.[10] According to his theory, the transverse shift in a multi-bunch scheme is proportional to z^{n-1}, where n is the bunch number. In our case, it gives about $(1.4)^{5-1} \cong 3.8$, after taking into account the energy dependence again, the ratio of the transverse shift becomes about 4.6. This value agrees roughly with the observation of about 3.5. In this connection, we will continue to analyze the observed data based on Suzuki's model as well as numerical simulations.

The authors wish to thank the members of Electron Linac Group at KEK for their help in operating the high-intensity electron linac in various ways. They have also greatly benefited from discussions with T. Suzuki and K. Oide.

References

[1] G. Horikoshi, Y. Kimura, and T. Nishikawa, in *Proceedings of the 1988 Linear Accelerator Conference*, Williamsburg, VA, USA, 1988; R. B. Palmer, SLAC-AAS-36, 1988.

[2] T. Shidara and J. Le Duff, LAL/PI, 86.09/T, Orsay, May 6, 1986 (unpublished).

[3] P. B. Wilson, SLAC-PUB-4547, SLAC/AP-66, January, 1989, and references therein; A. W. Chao, SLAC-PUB-2561,1980; H. Henke, and W. Schnell, CERN-LEP-RF/86-18: CLIC NOTE 22, 1986; J. T. Seeman, SLAC-PUB-4182, 1987.

[4] K. A. Thompson and R. D. Ruth, Phys. Rev. **D41**, 964 (1990).

[5] Y. Ogawa, T. Shidara, H. Kobayashi, Y. Otake, and G. Horikoshi, Particle Accelerators **27**, 133 (1990).

[6] R. B. Neal and W. H. Panofsky, Science **152**,1353 (1966).

[7] A. Asami, and the Electron Linac Group, in *Proceedings of the 1988 Linear Accelerator Conference*, Williamsburg, VA, USA, 1988 ; A. Enomoto, I. Sato, A. Asami, G. Horikoshi, and J. Tanaka, Nucl. Inst. and Meth. **A281**, 1 (1989).

[8] T. Shidara, T. Oogoe, Y. Ogawa, S. Ohsawa, Y. Otake, K. Kakihara, N. Kamikubota, H. Kobayashi, K. Furukawa, A. Enomoto, T. Urano, and G. Horikoshi, Particle Accelerators **29**, 239 (1990).

[9] Y. Otake, private communication.

[10] T. Suzuki, AIP, **156**, 480 (1987).

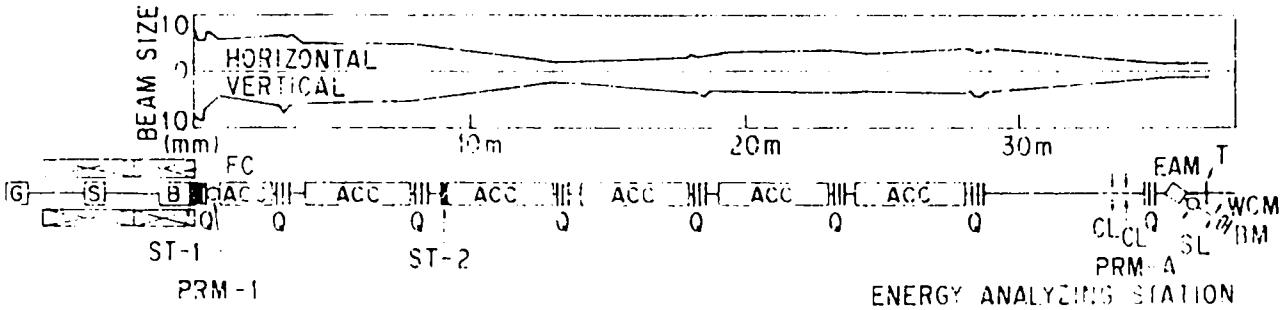

Fig. 1. Layout of the primary electron section of the KEK positron generator linac. The calculated beam size is also shown (see also Ref. 9). G is an electron gun; S, SHB; B, a prebuncher and a buncher; ACC, accelerating cavities; FC, focusing solenoids; Q, quadrupole magnets; ST, steering coils; EAM, an energy-analyzing magnet; PRM, profile monitors; CL, collimators; SL, a slit; WCM, a wall current monitor; BM, a bunch monitor; and T, a positron production target.

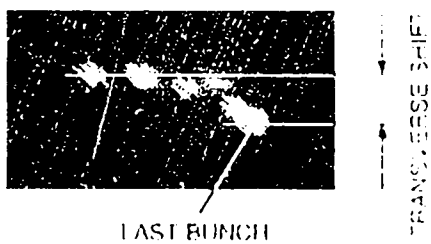

Fig. 2. Transverse(vertical) shift of the last bunch observed at the profile monitor PRM-A at the energy-analyzing station.

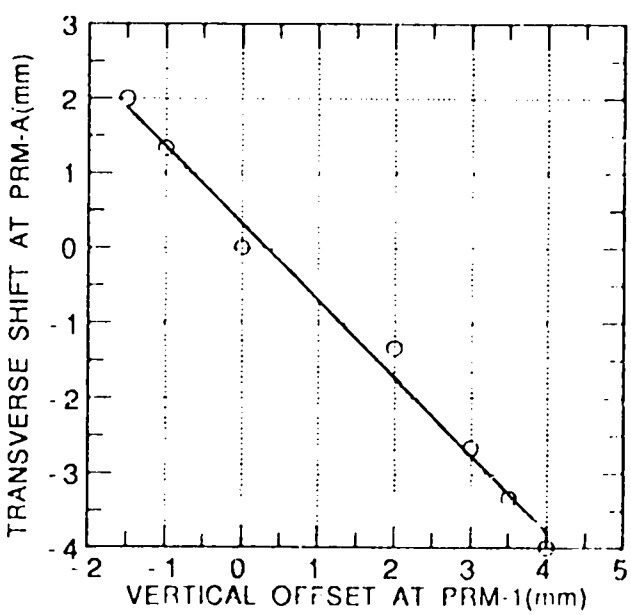

Fig. 3. Transverse shift at the end of the accelerator as a function of the initial offset. The solid line shows a least-squares fit.

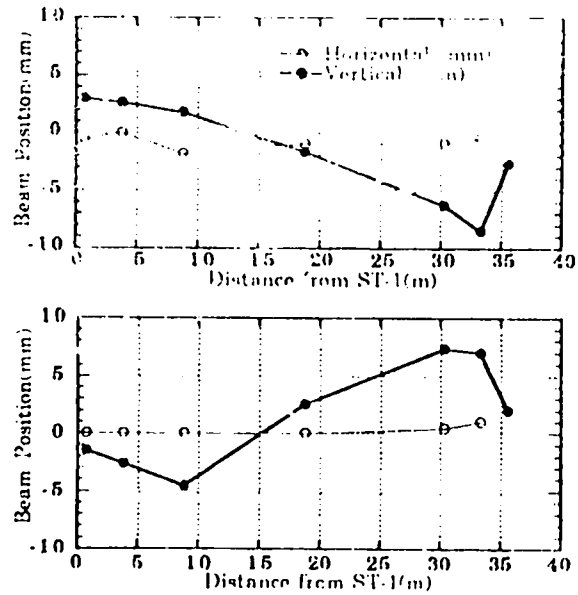

Fig. 4. Beam trajectory for two typical cases in which the effect seems to appear.

(a)

(b)

(c)

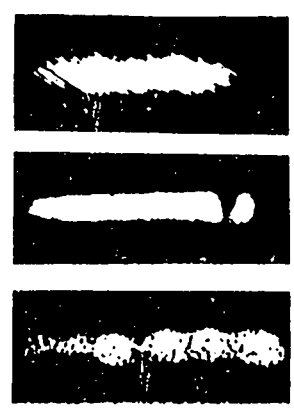

Fig. 5. No transverse blow-up was observed (a) with SHB OFF, and (b) with a semi-long pulse beam. The effect is smaller when the length of accelerator is diminished (c).

CHOICE OF THE BLOCK-SCHEME OF 1-1.5 GeV 300 mA LINEAR ACCELERATOR

I.M.Kapchinskiy

Institute for Theoretical and Experimental Physics, 117259, Moscow, USSR

The consideration of some questions related to design of 1-1.5 GeV proton linac is associated with the efforts to solve fuel cycle long-lived radioactive waste management problems.

The proposed linac consists of three parts:

1. Initial part comprising electrostatic injector and 3.5 MeV RFQ;
2. Middle part providing acceleration up to the energy of 100-150 MeV;
3. Main part, where protons reach the energy of 1-1.5 GeV.

Accelerating and focusing structures of each part are characterized by its own range of particle velocity changes, where the parameters of acceleration and focusing are optimized.

Initial part $\beta = 0.0080 - 0.10$
Middle part $\beta = 0.080 - 0.50$
Main part $\beta = 0.40 - 0.92$

In the initial part the electrostatic injector voltage must be sufficiently low in order to provide the necessary margin of electric strength of accelerating tube at 100% duty factor.

Historically the first main part of high energy proton accelerator was designed in Los Alamos for meson factory. The structure comprised the sequence of one-gap side-coupled resonators. But now many scientists consider the disc and washer structure proposed by V.G.Andreev (Moscow Radiotechnical Institute)[1] and designed for INR meson factory to be the best. This structure is characterized by the most wide dispersion and the most high shunt impedance. Disk and washer structure in some of its modifications is in fact being the only used today.

For the middle part of the linac three types of accelerating structures can be considered:

1. H-structure with alternate phase focusing;
2. H-structure with periodic RF quadrupoles;
3. E-structure (Alvarez tank) where the beam is focused by rare-earth magnet quadrupoles.

First type of structure was proposed in 1956 by Ya.B.Fainberg (Kharkov Institute)[2] and then subsequently modified by V.V.Kushin (Moscow Radiotechnical Institute)[3a] and N.A.Khizhnjac (Kharkov Institute)[3]. Such structures are being developed in ITEP[4,5] and Kharkov Institute. The second type of structure was proposed in 1956 by V.V.Vladimirskiy (ITEP)[6] and then subsequently modified and manufactured by V.A.Tepljakov (Serpukhov Institute); such structures are being developed and operated in Serpukhov Institute. As concerns the third type of structure, the focusing of particles by rare-earth magnet quadrupoles was proposed simultaneously and independently in 1979 by K.Halbach[8] and a group of ITEP scientists (I.M.Kapchinskiy, N.V.Lazarev and V.S.Skachkov)[9,10]. Rare-earth magnet quadrupoles are being developed in ITEP and in a number of scientific centers abroad.

Alternating phase focusing (APF) is obviously not suitable for high current linear accelerators. As is known, the main advantages of this structure are cheapness and technological simplicity that enables to use it successfully for applied linacs with low pulse currents and relatively low energy, especially when high acceleration rate is needed. Nevertheless such disadvantages as low capture, low current limit and the trend to decreasing of shunt impedance as the particles velocity increase prevent to use it for large linacs.

The structure with spatially periodic RF quadrupoles (with so called "horned" electrodes) is free from disadvantages typical for APF structures. This structure was successfully used in the injector to Serpukhov proton synchrotron booster[11]. Nevertheless, the use of the structure in 100% duty factor high current linac is not justified due to the difficulties in structure cooling, reduced margin of electric strength and impossibility to chose independently the parameters of longitudinal and transverse motions.

It seems to us that DTL with rare-earth magnet quadrupoles is the most suitable for the middle part of high current linac. The advantages of Alvarez linac such as constancy of acceleration rate along the structure, high mean acceleration rate, relative simplicity of cooling and practically constant value of shunt impedance along the structure are well known. Use of rare-earth magnet quadrupoles substantially increase the radiation resistance of the linac compared with the linac equipped with electromagnetic quadrupoles. Rare-earth magnets don't release heat and don't need stabilized power supply systems, this obstacle solves the same problem which initiated the development of RF focusing methods. It should be mentioned that use of rare-earth magnet lenses allows to decrease the drift tube dimentions and hence to reduce RF losses and in necessary cases to open the way for substantial increase of accelerating field frequency. The disadvantages of this structure are its relative expensiveness and technological complexity. However for large linear accelerators these disadvantages are not so important.

In the initial part of the linac it is necessary first of all to provide rather high rigidity of focusing at low

particle velocities. Compact RF structures with solenoidal focusing and RFQ structures satisfy this condition. Solenoidal focusing practically withdraw limitations on beam current caused by transversal Coulomb repulsion because the frequency of transversal oscillations can be infinitely increased. The magnetic field should be very high that is why only superconducting solenoids can be used. At given aperture the current limit is increasing by a factor of 10 at field strength of 5 T and by a factor of 40 at 10 T compared with alternating-sign focusing (the assesment was made not taking into consideration possible instability of beam envelope). In case of solenoidal focusing the limitations are associated mainly with longitudinal Coulomb repulsion. The effect of longitudinal repulsion can be mitigated if the equilibrium phase is rather high. It makes the use of superconducting solenoids in low energy high current accelerators very attractive. As concerns the use of solenoidal focusing in the initial part of large high current accelerator, in our opinion it is not justified because the substantial difference between the transversal oscillations frequencies in the initial and subsequent parts of the linac makes the matching very complicated or even practically impossible. Criogenic facility needed for superconducting solenoid of the initial part reduces the reliability of large linac as a whole and makes the operation very complicated.

The implementation of RFQ structure in the initial part allows to use rather low voltage electrostatic injector and provides practically full capture of particles produced by the ion source into acceleration. These two features are the most important for 100% duty factor high current accelerator. The methods of beam matching in case of RF focusing are well developed and proved at the operating facilities. In order to minimize beam losses the acceptance of 100% duty factor high current accelerator should have sufficient margin. This task can be solved in view of recent developments. The funneling scheme proposed in USA allows to sum the beams without the increase of phase volumes and peak currents[12,13]. In particular the initial part can have two accelerating channels, each of them being connected to its own ion source. The number of accelerating channels can be increased if necessary. Such a structure is called "tree-like". Thus, in our opinion the optimum block-scheme of 100% duty factor high current linear accelerator should comprise RFQ as the initial part, Alvarez tank with rare-earth magnet quadrupoles as the middle part and the Andreev's structure (DAW) as the main part. The main parameters of such 1.5 GeV linac are presented in another report submitted to this Conference[14].

Indirect confirmation of the validity of such a scheme is illustrated by the fact that many scientific centers (in USSR,USA,FRG and Japan) are widely use it as a whole or by parts[5-17].

The choice of radio frequency for each part is determined by three conditions: provision of enough acceptance margin for given emittance and beam current; provision of beam funneling; provision of beam overcapture without particle losses at beam transfer from one part to another.

References

1. D.E.Nagle, E.A.Knapp, B.C.Knapp, RSI, 1967, V.38, p.1583
2. V.G.Andreev, Jornal of Technical Physics, USSR, 1969, V.13, p.1070-1077.
3. Ja.B.Fainberg, a) Proc. of CERN Symp. on High Energy accelerators, Geneve, 1956, p.91; b) Jornal of Technical Physics, USSR, 1959, V.29, p.568
4. a) V.V.Kushin, Atomnaja Energija, 1970, v.29, issue 2, p.123; b) I.V.Chuvilo et al., CEBAF Report 89-001 Newport News, 1989, p.146
5. N.A.Khizhnjac et al., Voprosy Atomnoi Nauki i Techniki, series: Technika Fizicheskogo eksperimenta, 1981, issue 1(7), p.31
6. V.V.Vladimirskiy, Pribori i Technika Eksperimenta, 1956, No.3, p.35
7. a) V.A.Tepljakov, Proc. of V All-Union Conference on Charged Particles Accelerators, 1976, Moscow, Nauka, 1977, V.1, p.288; b) A.A.Egorov et al., Jornal of Technical Physics, USSR, 1981 V.51, issue 8, p.1643
8. K.Halbach, a) IEEE,NS-26,1979, p.3882; b) NIM, 1979, V.169, p.1; c) NIM, 1981,V.187, p.109
9. I.M.Kapchinskiy et al., Pribori i Technika Eksperimenta, 1977, No.5, p.42
10. a) V.S.Skachkov, Preprint ITEP-76, Moscow, 1979 b) N.V.Lasarev et al., Proc.of Conf.on Linear Accel.1979, BNL-51134, p.380
11. V.A.Zenin et al., Proc.of XIII Int.Conf.on High Energy Part.Accel., Novosibirsk, Nauka, 1987, V.1, p.312
12. K.Bongardt, Proc.of the 1984 Linac Conf., GSI, p.389
13. F.W.Guy, .N.Stokes, Proc. of the 1989 Part. Accel. Conf., Chicago, p.883
14. P.P.Blagovolin et al., Submitted on XV Conf. on Linear Accel., Albuquerque, 1990
15. a) G..Lawrence et al., 1989 Part. Accel. Conf., p.684; b) M.T.Wilson et al., ibid., p.761
16. B.Bager et al., KfK-3202/UWFDM-450 (1981) and KfK-380/FPA - 84 -4/UWFDM -625 (1985)
17. Y.Hirao, Proc. of the 1984 Linac Conf., GSI, p.490

HIGH CURRENT ION LINACS FOR TRANSMUTATION OF LONG-LIVED WASTES

P.P.Blagovolin, I.V.Chuvilo, I.M.Kapchinskiy, N.V.Lazarev

Institute for Theoretical and Experimental Physics, 117259, Moscow, USSR

Introduction

Nuclear power development not once has created the tasks that required the implementation of accelerator technology. Cross-sections and other nuclear constants needed for reactor calculations were determined using accelerators. In view of possible exhaustion of uranium ore deposits the accelerators-breeders were proposed. The present state of fuel resources economics and the aggravation of nuclear safety problems postponed the implementation of electronuclear breeding to future. However, the increasing attention to ecologic problems stimulated the development of the technology for transmutation of long-lived nuclides containing in wastes produced by NPP reactors.

Some actinides and neutron-scarce nuclei can be treated in special nuclear burner reactors. Unfissioning long-lived wastes and especially neutron-redundant nuclei can be transmuted into short-lived and stable nuclei only in accelerator targets. To such wastes along with some fission products as ^{90}Sr and ^{137}Cs one can consider products of neutron activation of reactor constructional elements (^{14}C, ^{59}Ni, etc.). After decomissioning of the reactor the question of reliable disposal of radioactive wastes becomes very important. In case of wide use of nuclear power plants and bearing in mind strict regulations for the disposal of very long-lived wastes ($T_{1/2} \geq 10^6$ years) the application of accelerators for transmutation becomes very attractive.

In the target of proton linear accelerator transmutations will undergo in hadron cascade. Hadron cascade will spread without significant losses for ionization of the matter at the energy of protons about 1-1.5 GeV. It means that the length of the accelerator will be about one kilometer and the facility will be very expensive. It should be also mentioned that in hadron cascade substantial share of transmutations happens due to forming of residual nuclei (so called "stars"). Secondary evaporated neutrons,in spite of their large number, are not very suitable for transmutations because their mean energy is about 3 MeV that in many cases is not enough for transmutations in (n,2n) type reactions.

In view of above mentioned the concept of intensive neutron generator comprising 50-150 MeV deutron accelerator and lithium target also looks very attractive.

In this case deutron stripping produces neutrons with the energy of several tens of MeV. It is the energy range where (n,xn); (n,p) and other reactions leading to transmutations are comparable with inelastic scattering (n,n'γ). The effectiveness of both transmutation options depends greatly on cross-sections of target nuclei that needs detailed experimental and theoretical studies. That why it is reasonable today to design both types of accelerators.

Intensive neutron generator.

The facility comprising deutron linear accelerator and liquid lithium target for deutron stripping and spallation can provide intensive neutron flux of high energy. The scheme of the facility was suggested in ITEP in 1977[1]. 100% duty factor linac should provide 35 MeV deutrons, beam current being 100 mA. The designed value of 15 MeV neutron flux was (6.6-9) 10^{13} n/sec.

However the present state of ion linac development allows to increase the intensity of neutron flux. The most important achievement in this field was the proposal to use funneling where the beams are combined without increase of phase volume and peak current[2,3]. It is possible to construct a linac with a large number of accelerating beam-lines. In the initial part of the linac each beam is produced by its own ion source that allows to obtain at the linac output the intensive beam and don't enhance requirements to the phase density of the beam at the output of the ion source. Funneling needs to double accelerating field frequency in each subsequent accelerating section. The block-scheme of 100% duty factor, 1A deutron linac is presented in Fig.1. Four parallel line RFQ's[5] can be used for the initial part and drift tube linacs with rare-earth magnet quadrupoles[6,7] for two subsequent parts.

The increase of deutron beam current by the order of ten leads to corresponding increase of integral neutron flux.

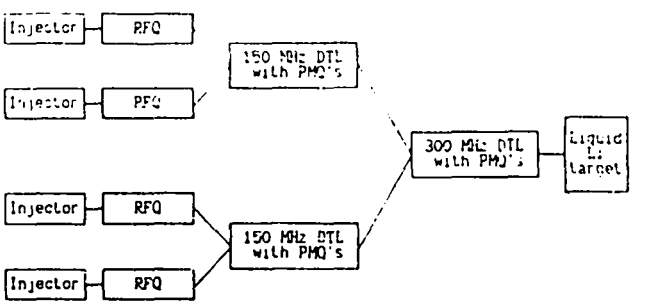

Fig.1. Block-diagram of the 1A deutron linac.

Another way to raise neutron flux intensity is to increase deutron energy. Ionization path is proportional to the square of deutron energy: spallation path in the first aproximation depends only on nucleus and deutron radii. Thus the probability of neutron production in lithium target is growing as the square of deutron energy. The data on emission of neutrons of mean energy E_n vs deutron energy are given in Table I. The size of lithium target area was chosen in the result of heat engineering calculations[1], providing the heat load on the unit area of the target is the same.

TABLE I

Neutron yields estimates

Deutron beam current	Deutron energy	Neutron energy E_n	Neutron yield	Section area of Li target
A	MeV	MeV	neutrons	cm^2
0.1	35	15	$(6.6\text{-}9.0)10^{15}$	10x10
1.0	50	20	$(1.3\text{-}1.8)10^{17}$	40x40
1.0	100	40	$(5.4\text{-}7.3)10^{17}$	55x55
1.0	150	70	$(1.2\text{-}1.6)10^{18}$	65x65

Such parameters as the linac length, RF power and the total power consumed by deutron linac for three energy levels (50,100, and 150 MeV) are given in Table II. Resonators efficiency (electronic) is about 85%. RF generator efficiency can be assumed to be 70%[8]. Thus the total linac efficiency would be about 60%.

TABLE II

Some parameters of deutron linac

Deutron energy	Linac length	RF power	Mains consumptions
MeV	m	MW	MW
50	40	60	100
100	68	115	190
150	96	170	285

Main designed parameters of accelerator sections are given in Table III.

Using of liquid lithium target enables to regenerate power and makes the neutron generator rather economic.

The choice of deutron energy will depend upon the assessments of transmutation efficiency and also on the results of feasibility studies.

TABLE III

Main design parameters of deutron linac

Parameters	Units	Initial part	Middle part	Main part
Operating frequency	MHz	75	150	300
Number of channels		4	2	1
Deutron energy				
input	MeV	0.1	6	20
output	MeV	6	20	50/100/150
Section length	m	10	12	18/46/72
Acceptance	cm mrad	1.9	5.6	3.0
Emittance (calc.)	cm mrad	0.4-0.6	1.0-1.5	1.5-2.0
Current per channel	mA	250	500	1000
Limit beam current	A	1.28	2.78	4.75
RF losses in Cu	MW	3.6	1.5	3.0/7.7/12.4

Choice of proton linac parameters.

Optimum output parameters of the linac can be chosen on the base of trade off decisions and after the assessment of technological systems capacities (ion source, RF power supply, cooling and so on) and possible beam losses. For this purpose let us assume the output energy of 100% duty factor linac to be 1.5 GeV, beam current - 300 mA. These figures are very close to those that were chosen in 50-70th for electronuclear breeders. However, if to base on modern and advanced developments the linac block-scheme, technical performance of main systems and hence the facility lay-out and the assessments of construction and operating costs would substantially differ from previously made. The block-scheme of the linac (target design is not discussed) is given in Fig.2. The details are discussed in another report[9] submitted to this conference. It is proposed to use two parallel 75 MHz RFQ's where each 150 mA beam is accelerated from 0.1 to 3.5 MeV. Bunched beams are funneled and injected into 150 MeV,150 MHz Alvarez tank and then after additional bunching (to decrease phase length) are accelerated up to the energy of 1.5 GeV in 900 MHz Andreev's (or disk and washer - DAW) structure.

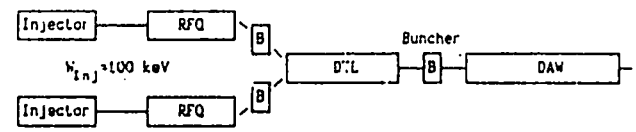

W_{output}	(MeV)	3,5	150	1500
f	(MHz)	75	150	900
I	(mA)	2x150	300	300
P_{Cu}	(MW)	2x0,66	14	58
P_{beam}	(MW)	2x0,525	44	405
P_{Σ}	(MW)	2,5	60	500
V_e	(cm mrad)	6,6-3	5,6-9,4	12,8-23
I_{lim}	(A)	0,93	4,4	42
l	(m)	8	69	550

Fig.2. Block-diagram of high-energy linac.

The parameters of proton linac are given in Table IV. The calculated data are presented in Tables V and VI correspondently.

Conclusion

The increased requirements to nuclear power safety initiated the concept of minimizing the total activity of

TABLE IV

Parameters of the high-energy proton linac

	Parameters	Units	RFQ	DTL	DAW
1	Operating frequency	f (MHz)	75	150	900
2	Number of channels		2	1	1
3	Input energy	W_{in} (MeV)	0.1	3.5	150
4	Output energy	W_{out} (MeV)	3.5	150	1500
5	Length	L (m)	8	70	550
6	Apertures	2a (cm)	1.8-3.32	5	5
7	Current per channel	I (mA)	2x150	300	300
8	Synchronous phase	φ_s (degree)	90°-30°	36°	35°
9	Accelerating structure		modulated vanes	drift tubes	Andreev's structure
10	Focusing		RFQ	PMQ's	PMQ's
11	Voltage between adjacent electrodes	U_t (kV)	255	-	-
12	Averege axis field	E_0 (kV)	-	30	35
13	RF power (losses)	P_{Cu} (MW)	2x0.66	14	58
14	RF power (beam)	P_b (MW)	2x0.55	44	405
15	RF power total)	P_Σ (MW)	2.5	60	500

TABLE V

Initial part (one channel)

	Parameters	Units	Bunching section		Regularly acceleration section	
			Input	Output	Input	Output
1	Average radius	R_0 (cm)	2.5	2.5	2.5	2.5
2	Phase width of separatrix	Φ°_{sep}	298°	91°	91°	91°
3	Momentum width of separatrix	$(\Delta P/P)_{sep}$	± 16.6%	± 5.46%	± 5.46%	± 3.17%
4	Phase length	φ°	298°	91°	91°	68°
5	Momentum spread	$(\Delta P/P)_a$	-	± 5.46%	± 5.46%	± 2.25%
6	Modulation	m	1.1	2.01	2.01	2.01
7	Transit time factor	T	0.01966	0.4215	0.4215	0.4569
8	Relative velocity	β	0.0146	0.0480	0.0480	0.0862
9	Phase advance of transverse osc. per period	μ	0.696	0.648	0.648	0.695
10	Min. velocity of phase advance	v_φ	0.470	0.448	0.448	0.487
11	Normalized emittance(adopted value)	ε(cm mrad)	0.2	0.4	0.4	0.5
12	Acceptance (calculated value)	A_t(cm mrad)	6.65	3.09	3.09	7.61
13	Relative frequency of longitudinal osc	Ω/ω	0.08916	0.08916	0.08916	0.05162
14	Current limit	I (mA)	2.64	0.93	0.93	3.37
15	Output energy	W (MeV)	0.1	1.08	1.08	3.50

TABLE VI

Main part of linac

	Parameters	Units	The first part DTL		The second part DAW	
			Input	Output	Input	Output
1	Phase width of separatrix	Φ°_{sep}	116°	116°	106°	106°
2	Momentum width of separatrix	$(\Delta P/P)_{sep}$	± 5.86%	2.72%	± 0.96%	± 1.15%
3	Phase length	φ°	68°	17°	52°	22°
4	Momentum spread	$(\Delta P/P)_a$	± 1.4%	± 0.42%	± 0.84%	± 0.20%
5	Gap length factor	g/λ	0.18	0.30	0.30	0.30
6	Transit time factor	T	0.777	0.853	0.698	0.805
7	Relative velocity	β	0.0862	0.5067	0.5067	0.9230
8	Phase advance of transverse osc. per period	μ	1.242	1.09	0.888	0.567
9	Min. velocity of phase advance	v_φ	0.562	0.601	0.588	0.465
10	Normalized emittance(adopted value)	E_t (cm mrad)	0.6	0.7	0.8	0.9
11	Acceptance	A_t (cm mrad)	5.62	9.39	12.8	23
12	Length of quadrupoles	l (cm)	10	50	20	20
13	Gradient of magnetic field	G (kGs/cm)	2.71	0.471	2.94	6.0
14	Relative frequency of longitudinal osc	Ω/ω	0.0748	0.0260	0.0100	0.00237
15	Current limit	I (mA)	4.43	3.54	24	48

nuclear fuel cycle radiactive wastes up to the level of the total activity of natural uranium involved. The detailed investigation of transmutation options and designing of the facility comprising high current linac and special target could help to solve one of the most important tasks the mankind being faced - to develop the nuclear power safely without possible ecological consequencies for future generations.

References

1. B.L.Ioffe, I.M.Kapchinskiy, N.V.Lazarev, A.D.Leongardt, I.V.Chuvilo, R.G.Vasilkov, Preprint ITEP-118, Moscow, 1977

2. K.Bongardt, Proc.of the 1984 Linac Conference, GSI, p.389.

3. R.H.Stokes, G.N.Minerbo, Proc. of the 1985 Particle Accelerator Conference, Vancouver, p.2593

4. F.W.Guy, R.N.Stokes, Proc. of the 1989 Particle Accelerator Conference, Chicago, p.833.

5. I.M.Kapchinskiy, Uspechi Fizicheskih Nauk, V.132, Part 4, 1980, p.640.

6. V.S.Skachkov, Pribory i Technika Eksperimenta, No.3, 1980, p.34.

7. I.M.Kapchinskiy, V.S.Skachkov et al., Proc. of the 1989 Particle Accelerator Conference, Chicago, p.1073.

8. B.P.Murin, Preprint Radiotechnical Institute of Academy Sci.USSR, No.833, Moscow, 1983.

9. I.M.Kapchinskiy, this Conference.

"ISTRA-10" LINEAR PROTON ACCELERATOR START-UP

V.A.Andreev, V.S.Artemov, I.V.Chuvilo, I.M.Kapchinskiy, A.M.Kozodaev, A.A.Kolomiets, V.S.Kosjak, Ju.N.Kuzmin, R.P.Kujbida, V.V.Kurakin, N.V.Lazarev, I.M.Lipkin, A.M.Raskopin, N.I.Rybakov, V.S.Skachkov, Ju.B.Stasevich, N.V.Shachraj, R.M.Vengrov, A.M.Vishnevskij

Institute for Theoretical and Experimental Physics, 117259, Moscow, USSR

ISTRA-10 linear proton accelerator was launched at ITEP. It consists of the initial part with RFQ sructure (see Fig.1) and the main part which is Alvarez tank with permanent magnet quadrupoles (PMQs) The Alvarez tank is excited at the frequency (297 MHz) double higher than the RFQ. Between the initial part and the main part the matching channel is mounted comprising the buncher and the drift part.

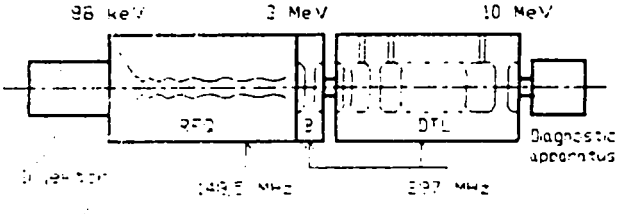

Fig.1 Block diagram of the linac Istra-10

ISTRA-10 linac is the first part of ISTRA-56 linac (56 MeV, 150-200 mA pulse current) [1-4] which will be used as the injector of ITEP proton synchrotron and also will serve as a pulse prototype of high current accelerators needed for radiopharmachemicals production, material irradiation tests and for solving of some nuclear power tasks. Main design parameters of ISTRA-56 linac are given in the Table. Bird's-eye view on the ISTRA-10 linac is presented in Fig.2.

In the RFQ launched a few years ago[5] the beam is accelerated from 88 keV to 3 MeV at the maximum current of 250 mA. In the output beam the share of particles accelerated to the energy of 3 MeV was 95%, in the current range of 0 - 100 mA the beam losses were negligible. The operating experience showed that the mechanical rigidity of the RFQ sructure was not enough. For ISTRA-56 linac the new RFQ section was manufactured. This RFQ is being under tests.

ISTRA-10 linac comprises the old RFQ, the matching channel with the buncher and 10 MeV Alvarez tank. The focusing channel of the linac has FODO structure and is formed by rare-earth magnet quadrupole lenses. Each lense consists of two layers of SmCo5 rod magnets[6] fixed in duralumin cylinders (see Fig.3). The lense doesn't contain materials which could deteriorate vacuum quality. This fact allowed to open the interior of the drift tubes, where the lenses are mounted, to high vacuum of the tank chamber. The interior of the drift tubes is pumped through special holes drilled in the drift tube body. Thus it is possible to avoid vacuum-tight welding of the drift tube, because the presence of strong magnetic field in the welding area makes the task very complicated.

Each of 33 drift tubes contains 50 mm long lense. At the input of channel the gradient is maximum and is equal to 60 T/m. The rms deviation of the gradient values

TABLE

ISTRA-56 DESIGN PARAMETERS

Parameter	Unit	Initial part	Main part: Tank 1	Main part: Tank 2	Main part: Tank 3
Input energy	MeV	0.089	3	10	36
Output energy	MeV	3.0	10	36	56
RF field wave length	m	2.02	1.01	1.01	1.01
Wave type	-	H_{211}	E_{010}	E_{010}	E_{010}
Focusing	-	RFQ	*rare - earth quadrupole magnet*		
Tank length	m	4.57	3.56	11.64	9.15
Tank diameter	cm	44.9	65.0	63.0	58.0
Drift tube diameter	cm	-	10.0	8.5	8.5
Number of drift tubes	-	-	1/2+33+1/2	1/2+53+1/2	1/2+29+1/2
Gap length factor	-	-	0.180-0.254	0.170-0.289	0.239-0.292
Modulation factor	-	1.00-1.74	-	-	-
Aperture diameter	cm	8.11-1.54	1.2	1.6	2.4
Quadrupole lense length	cm	-	5.0	10;15	15
Field gradient in quadrupole	kG/cm	-	6.0-5.6	3.23;2.56	2.36
Synchronous phase (absolute value)	degree	90-35	50-37	37-30	30
Time-of-flight factor	-	0-0.39	0.812-0.854	0.902-0.840	0.879-0.830
Momentum spread	%	2.32 output	4.00-1.86	1.86-0.84	0.84-0.65
Acceptance	cm mrad	1.28	0.63-0.83	1.48-1.73	3.91-4.00
Maximum pulse current at phase density of 1 A/cm mrad	mA	200	250	520	1490
Rated pulse RF power losses in copper	MW	0.44	0.43	1.11	1.07
Pulse RF power needed at beam current 150 mA	MW	0.44	1.09	3.90	3.00

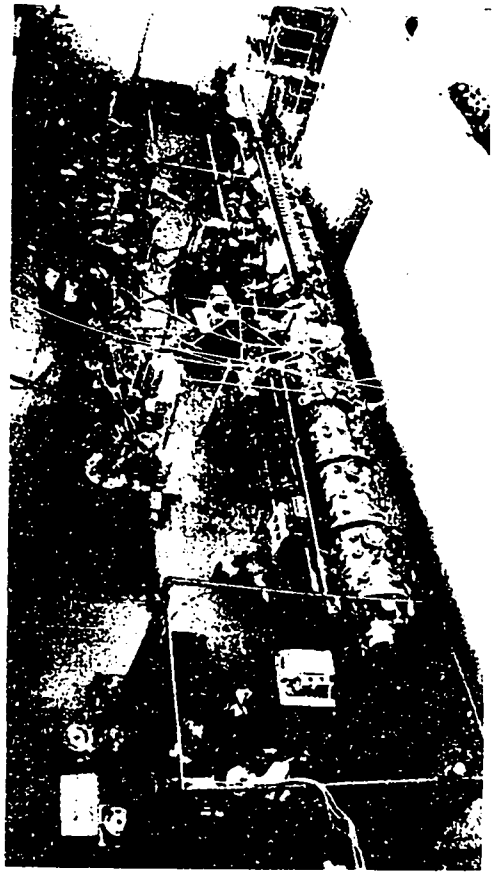

Fig.2 General view of the Istra-10 Linac

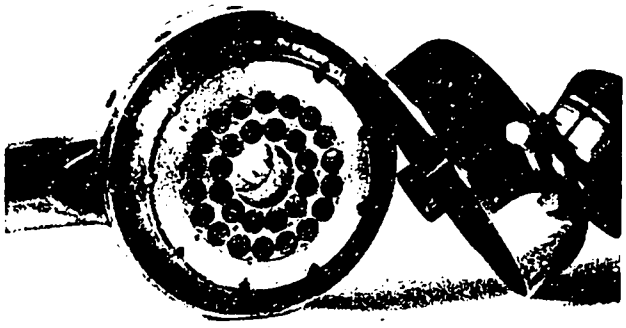

Fig.3 Open into vacuum the drift tube with PMQ (before assembling)

from the rated ones (over all lenses) is 0.6%, nonlinearity - 0.5%. Mean displacement between the geometric and magnetic axes over all lenses is 0.03 mm.

Increasing of frequency in the Alvarez tank allowed to decrease its dimensions that along with the decreasing of the drift tubes diameter permitted to reduce RF losses but didn't lead to beam current limitation. The Alvarez tank is fabricated of trimetal and at the same time is a vacuum chamber. The drift tubes were aligned with the rms displacement of 0.08 mm in transversal planes. The longitudinal alignment error is 0.05 mm. Quality factor of resonator is 33000. The difference between the operating mode and the nearest one is 1.8 MHz. Unflatness of the mean field level on the axis (the designed value E=30 kV/cm) is up to 5%. The cavity is excited by two loops, the loops being isolated from the vacuum chamber by quartz windows which have antimultipactor grooves. The training was carried out both at direct excitation and autoexcitation. As a result the field level achieved exceeds the designed value by 16%.

The one gap buncher is made as copper torus-like resonator, gap length is 22 mm and the aperture - 18 mm. Two rare-earth magnet quadrupoles mounted in its halftubes provide the gradient of 58.4 T/m. Intensive multipactor effects were observed during first excitation tests. Reliable operation of the buncher was achieved only after special antimultipactor measures were taken such as improving of contacts, cleaning of surfaces and so on. The gap voltage of 290 kV was achieved that exeeded the design value by 30%.

At the drift part of the matching channel (421 mm long) six electromagnetic quadrupoles are mounted, but by the moment of linac start-up this part of the channel wasn't optimized for maximum beam transmission.

The total volume of the linac vacuum chamber is 3.5 m^3, the operation pressure was 10^{-6} - $6 \cdot 10^{-6}$ Torr.

RF power of 1.3 MW at the frequency of 148.5 MHz is supplied to RFQ by two-cascade generator based on GI-27AM triode. The Alvarez tank is excited by three-cascade generator (two cascades on GI-27 and the third on GI-50A triode) providing 1.7 MW at the frequency of 297 MHz. The modulators connected to RF generators include step-up cable transformers, thyristor rectifiers, optical control lines, etc. Automatic control systems sustain resonant frequencies of the cavities with the accuracy of ± 200 Hz and the phase difference between them with the accuracy of 1.5 phase degree.

The assesement of the influence of the buncher on the accelerated by the RFQ particles movement (before the Alvarez tank was mounted) showed that in the case of proper established RF field level and phase in the buncher the momentum spread grew by a factor of two and the phase length at the output of the drift part (at the first gap of Alvarez structure) decreased up to 80 phase degree (for frequency 297 MHz) that corresponded the designed value.

During the start-up of ISTRA-10 linac the proton energy at the output was measured by the magnetic analyser. The calibration of RF fields in the cavities was carried out by determining their threshold levels. Enough acceptance of the focusing channel in the Alvarez tank provided transportation of 3 MeV beam from the RFQ to the measuring channel through the Alvarez tank in the absence of RF field in the tank.

In September 1989 10.3 MeV proton beam was registered at the output of the Alvarez tank, output current being 15 mA, pulse length - 5 μs, repetition rate

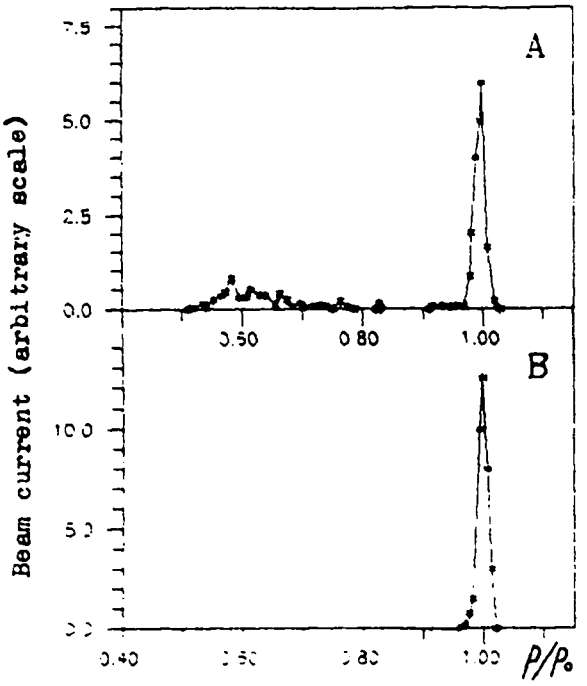

Fig.4. Spectrum of the output beam at the buncher off (A) and on (B)

- 1 Hz. Such a beam had no significant influence on the RF field level but provided enough intensity for reliable measurements.

Beam spectrum, measured at the designed level of RF field in the RFQ and the Alvarez tank at the optimum phase difference between them (the buncher was switched out), is presented in Fig.4a. Capture factor, defined as the ratio of accelerated to the designed energy protons current to the total output current, in this case was 68%. Protons of the designed energy were considered as those which momentum differs from the rated not more than by value of halfspan of the separatrix in the Alvarez tank.

In the case of switched on buncher it provided almost full overcapture of particles at their transfer from the RFQ to the Alvarez tank. Momentum spectrum for this case is presented in Fig.4b, capture factor being close to 1.

Now the efforts are aimed at the increase of beam current.

References

1. V.A.Andreev et al., The Construction of the Proton Linac ISTRA-56 in ITEP, Proc. of XI All-Union Conference on Charged Particles Accelerators, Dubna, 1989, Part I, p.245
2. A.I.Balabin et al., The Main Physical Parameters of the Proton Linac ISTRA-56, (Part 1), Moscow, 1989, Preprint ITEP 157-89
3. I.A.Vorobjev et al., The Main Physical Parameters of the Proton Linac ISTRA-56, (Part 2), Moscow, 1989, Preprint ITEP 158-89
4. A.A.Kolomiets et al., The Investigation of Proton RFQ linac in ITEP , Voprosy atomnoy nauki i techniki. Series: Technika fizicheskogo eksperimenta, Kharkov, 1985, V.2(23), p.20
5. A.I.Balabin et al., Transversal Matching of the Beam in RFQ Linac, Proc. of X All-Union Conference on Charged Particles Accelerators, Dubna 1987, Part I, p.403
6. R.M.Vengrov et al., REC Quadrupoles for Ion Linac, Proc. of XI All-Union Conference on Charged Particles Accelerators, Dubna, 1989, Part I, p.379

Friday

Session FR1
Chairman: G. Loew
Invited Papers

BEAM DYNAMICS IN LINEAR COLLIDERS*

Ronald D. Ruth
Stanford Linear Accelerator Center (SLAC)
Stanford University, Stanford, California 94309

Introduction

In this paper, we discuss some basic beam dynamics issues related to obtaining and preserving the luminosity of a next generation linear collider. In Figure 1 you see a diagram illustrating the main subsystems of one-half of the collider. The beams are extracted from a damping ring and compressed in length by the first bunch compressor. They are then accelerated in a preaccelerator linac up to an energy appropriate for injection into a high gradient linac. In many designs this pre-acceleration is followed by another bunch compression to reach a short bunch. After acceleration in the linac, the bunches are finally focused transversely to a small spot.

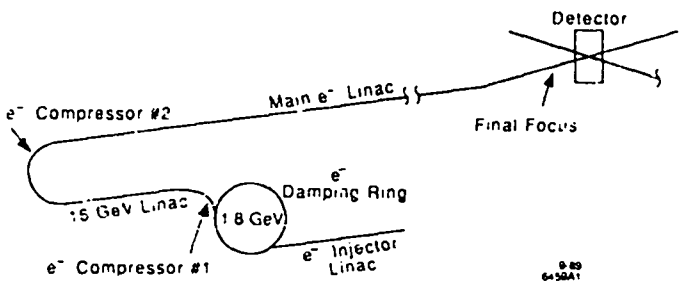

Fig. 1. Schematic of a Next Linear Collider

Before discussing each subsystem, it is useful to discuss the overall philosophy and parameters of this paper.[1,2] The energy range presently considered in various designs throughout the world varies from 1/2 TeV to 2 TeV in the center of mass while the desired luminosity varies from $10^{33} - 10^{34}\,\mathrm{cm}^{-2}\mathrm{sec}^{-1}$. The energy will be achieved by RF acceleration at acceleration gradient $\mathcal{E}_z$ for a certain length L. The acceleration gradients currently under consideration are in the 100 MV/m range while the RF frequencies range from 10–30 GHz. In this paper we only discuss the RF in so far as it affects the luminosity. Although obtaining the energy of a linear collider may be very expensive and require technical development, it is, in a sense, the easy part of the problem. The hard part is to obtain the luminosity.

The increase in luminosity over the SLC is obtained primarily in two ways. First, the spot cross-sectional area is decreased. Second, the energy extraction is improved by the use of multiple bunches per RF fill which effectively increases the repetition rate of the collider. Both of these techniques lead to many beam dynamics questions.

The proposed vertical beam sizes at the interaction point are the order of a few nanometers while the horizontal sizes are about a factor of 100 larger. This cross-sectional area is about a factor of 10^4 smaller than the SLC. However, the main question is: what are the tolerances to achieve such a small size, and how do they compare to present techniques for alignment and stability?

These tolerances are very design dependent. Alignment tolerances in the linac can vary from 1 μm to 100μm depending upon the basic approach. It is the premise of this paper that in order to achieve a next linear collider in this century, we must make design and correction choices which move most alignment tolerances into the 100 μm range. We begin the discussion with the damping rings.

Damping Rings

The SLC damping ring has achieved normalized emittances of $\gamma\epsilon_x = 3 \times 10^{-5}$ and $\gamma\epsilon_y = 5 \times 10^{-7}$. A next generation linear collider will need a horizontal emittance at least an order of magnitude smaller. In addition, most designs use $\epsilon_x/\epsilon_y \simeq 100$. This type of emittance ratio is naturally produced in an electron storage ring provided that the vertical dispersion and coupling are controlled. This sets tolerances for vertical alignment in the 50–100μm range which might be loosened by the addition of skew quadrupoles for compensation.

The ring designs typically include wigglers to decrease the radiation damping time. As mentioned earlier, most plans include the use of multiple bunches per RF fill. In order to efficiently use the circumference it is possible to damp several "batches" of bunches at once, each batch having the order of 10 bunches each. The batches must be separated by a distance which allows a kicker rise and fall time so that one batch can be extracted while allowing the remaining batches to continue damping.

Due to the small dispersion of the ring, the broad band impedance must be quite low ($Z/n \lesssim 0.5\Omega$) in order to avoid bunch lengthening. The long-range wakefield must also be controlled to avoid coupled-bunch instabilities. Because of the very close spacing of the bunches within a batch ($\sim$ 30 cm), inter-batch feedback would be quite difficult.

Example designs for a damping ring are given in Ref. 3. Aside from higher energy ($\sim$ 1.8 GeV) and larger circumference (155 m), this design uses combined function bends to enhance the horizontal damping at the expense of the longitudinal. Similar designs have been developed also at KEK, CERN and INP; therefore, it seems that damping rings which produce flat beams of the desired emittance are relatively straightforward.

* Work supported by the Department of Energy, contract DE AC03-76SF00515.

Bunch Compression & Preacceleration

In order to prepare the bunches for injection into a high-gradient structure, it is necessary to reduce their length by bunch compression. Actually, there are two primary reasons for bunch compression. First, the bunch length must be less than the β^* at the interaction point. Since in many designs $\beta^* \sim 100\mu m$, we must have $\sigma_z \lesssim 100\mu m$. In addition, we should reduce the bunch length to reduce transverse wakefields.

If the bunch length and the relative energy spread in the damping ring are 5 mm and 10^{-3} respectively, then two bunch compressions are needed to reach 50 μm bunch length. Each compression reduces the bunch length by a factor of 10, and they are separated by a preacceleration section which reduces the initial relative energy spread at the second compression back to about 10^{-3}.

The energy spread is kept to $\sim 1\%$ during each compression in order to avoid emittance dilution due to chromatic and dispersive effects in the compressors. After compression the bunch must be matched into the linac lattice. Studies of bunch compressors have been completed and tolerances are presently under study.[4]

Linac[5]

Injection Errors

As the beam enters the linac, it is necessary to match the lattice functions to those of the linac. In particular the dispersion must vanish. For typical flat beam parameters, the beam size is about $2 \times 20\mu m$ which yields a tolerance on dispersion D given by

$$\begin{aligned} D_y &< 0.2 \text{ mm} \\ D_x &< 2 \text{ mm} \quad . \end{aligned} \tag{1}$$

This is an additive effect. There are also multiplicative effects due to the mismatch of the lattice functions. If the beam were monoenergetic, these mismatches would not filament; however, since this is not the case, there will be some filamentation. Allowing for complete filamentation, the emittance dilution is given by[6]

$$\frac{\epsilon}{\epsilon_o} = \frac{1}{2}\left[\frac{\beta_o}{\beta}(1+\alpha^2) + \frac{\beta}{\beta_o}(1+\alpha_o^2) - 2\alpha\alpha_o\right] \quad , \tag{2}$$

where α_o and β_o are the matched values, and α and β are the mismatched values. For $\alpha = \alpha_o$ and $\beta = \beta_o + \Delta\beta$, this reduces to

$$\frac{\Delta\epsilon}{\epsilon_o} \simeq \frac{1}{2}\left(\frac{\Delta\beta}{\beta}\right)^2 \quad . \tag{3}$$

For incomplete filamentation, the emittance dilution will be somewhat less.

Wakefields and BNS Damping

Wakefields are a key problem not only for linear colliders, but for all accelerators and storage rings. The standard solution to this problem is to first reduce the wakefield forces until they are small compared to the applied external fields. Then compensation can be used in the form of feedback, or we can simply live within the limits by keeping the number of particles in the bunch sufficiently small.

For linear colliders the transverse wakefield within the bunch can be reduced first by keeping the RF frequency sufficiently small or by increasing the iris size. Secondly, the β-function in the linac must be kept sufficiently small. Then compensation can be applied by using BNS damping—the use of a correlated energy spread to cancel wakefield effects. The BNS correlated energy spread is given by[7]

$$\left(\frac{\Delta E}{E}\right)_{\text{BNS}} \equiv \delta_{\text{BNS}} = \frac{e^2 N W_\perp(\sigma_z)\beta_o^2}{4E_o} \quad , \tag{4}$$

where N is the number of particles, $W_\perp(\sigma_z)$ is the transverse wakefield evaluated at σ_z, and β_o is the β-function at energy E_o. For this paper I define a small wakefield by the condition

$$\left(\frac{\Delta E}{E}\right)_{\text{BNS}} \lesssim \frac{1}{\psi_{\text{tot}}} \lesssim 1\% \quad , \tag{5}$$

where ψ_{tot} is the total phase advance in the linac.

If the wakefield is large, then one can still satisfy Eq. (4) with a variation of focusing strength along the bunch rather than energy variation. In this case, however, coherent oscillations filament rapidly. To avoid emittance dilution with strong wakes, the alignment and trajectory tolerances are less than the beam size. This leads to 1 μm alignment tolerances.[8,9] As we shall see in the next sections, these tiny tolerances can be avoided by keeping the wakefields weak.

In the weak wakefield regime, BNS damping has been tested at the SLC linac.[10] In this case the tail growth due to a coherent oscillation was reduced by an order of magnitude. BNS damping has since been adopted as the normal running configuration for SLC.

Chromatic Effects

Upon injection into the linac, the compressed bunch has about a 1% uncorrelated energy spread. As the beam is accelerated, this relative spread decreases inversely with energy. At the same time a correlation between energy and bunch position is introduced due to the longitudinal wake and the curvature of the RF. Thus, the distribution in phase space becomes a wavy line which, when projected on the energy axis, yields an effective energy spread. At any location along the accelerator, the overall energy spread is a combination of the damping injected energy spread and the variation of energy along the bunch. After the bunch emittance is sufficiently damped, the relative energy

spread remains constant unless deliberately increased by phase changes. For this reason it is useful to consider two models; one with constant energy spread and one with damping energy spread.

The first chromatic effect to consider is that of a coherent betatron oscillation. If the variation of the phase advance with momentum (chromatic phase advance) is much greater than unity, the oscillation filaments. In this case the oscillation amplitude must be less than the beam size to avoid emittance dilution. If the chromatic phase advance is small ($\delta\psi_{tot} < 1$), then the tolerance on a coherent oscillation of size $\hat{x}_o$ is

$$\hat{x}_o < \frac{\sigma_\beta}{\delta_o \psi_{tot}} = \frac{\sigma_\beta}{\delta_o \psi_{cell}} \frac{2}{N_q} \quad . \qquad (6)$$
$$< 2\sigma_\beta \quad \text{(ILC)}$$

where $\delta_o = 2 \times 10^{-3}$ is the constant relative momentum, ψ_{cell} and ψ_{tot} are the phase advance per cell and total phase advance respectively, and N_q is the number of quadrupoles. In all cases we give not only the formula but also the value for an example design of an Intermediate Linear Collider (ILC) of energy 0.5 GeV in the center of mass.[1,2] For the case of a damping energy spread with initial value $\delta_i = 0.01$, the tolerance is

$$\hat{x}_o < \frac{\sigma_\beta}{\delta_i \psi_{cell}} \frac{2}{N_q} \left(\frac{\gamma_f}{\gamma_i}\right) \qquad (7)$$
$$< 5\sigma_\beta \quad .$$

For the case of a corrected trajectory let us consider the model of a sequence of random bumps. In this case the tolerance on the trajectory or alignment is

$$(\Delta x)_{rms} < \frac{\sigma_\beta}{\delta_o \psi_{cell}} \left(\frac{3}{N_q}\right)^{1/2} \qquad (8)$$
$$< 30\mu m \quad ,$$

for a constant energy spread δ_o. For an initial damped energy spread δ_i, we have

$$(\Delta x)_{rms} < \frac{\sigma_\beta}{\delta_i \psi_{cell}} \left(\frac{1}{N_q}\right)^{1/2} \left(\frac{\gamma_f}{\gamma_i}\right)^{3/4} \qquad (9)$$
$$< 30\mu m \quad .$$

Misaligned Accelerator Sections

BNS damping only cures the growth and filamentation of coherent oscillations in the linac; it is an average compensation rather than a local one. In an actual linac, the wakefield kicks are not cancelled locally by adjacent quadrupoles. This leads to an incoherent growth of wakefield tails due to a random sequence of misalignments between the trajectory and the accelerator structure. If we parameterize the strength of the wakefield kick by δ_{BNS} as defined in Eq. (4), the tolerance on random accelerator misalignments is given by

$$(\Delta x_{structure})_{rms} < \frac{\sigma_\beta}{\delta_{BNS} \psi_{cell}} \left(\frac{3}{N_q}\right)^{1/2} \qquad (10)$$
$$< 25\ \mu m \quad .$$

for $\delta_{BNS} = 2.5 \times 10^{-3}$. From Eqs.(8) and (10) above, we see that the structure tolerances and quadrupole alignment tolerances are comparable provided that $\delta_{BNS} \sim \delta_o$, that is, provided that the energy correlation needed for BNS damping is equal to the minimum energy spread in the linac.

Compensation of Chromatic/Wakefield Effects

The alignment tolerances shown above assume that the trajectory is a random sequence of bumps. There is no particular reason that it has to be random. Let us for the moment neglect wakefields. Then it is possible to measure the trajectories for particles of different energy and choose a trajectory which yields a small difference. Such a difference trajectory can be generated by scaling all the magnetic fields in the linac by a small amount so that the entire beam has an effective energy which is changed. By choosing the corrector sequence to minimize this difference trajectory (as well as the actual trajectory), the dispersion generated by misalignments is cancelled locally.

This technique is called dispersion free correction. Provided that the beam position monitors have precision the order of 1 μm, it is possible to essentially decouple the quadrupole misalignments from the dispersive effects.[11] This increases the tolerances given in Eqs. (8) and (9) by an order of magnitude.

When we include wakefields, the coherent motion is BNS-damped and the incoherent motion gives rise to a random tail growth which can be controlled by tight tolerances. All that really matters for this effect is the value of the offset of the bunch within the structure. The offsets can be caused by two effects: misalignments of structures and trajectory offsets in structures. The trajectory is under our control; therefore, it is possible to use a trajectory which cancels the wakefield effects locally. Recently, T. Raubenheimer at SLAC has shown that by modifying the dispersion-free trajection technique, he can obtain a trajectory which cancels both the wakefield effects and the energy variation of the trajectory.[12]

Finally, we are left with the misalignments of accelerating structures. The most straightforward technique is to simply align the structure to the beam by using a BPM which is geometrically linked to the structure center. Such a BPM could consist of simply measuring the transverse wakefields induced by the beam.[13] One can use this information to either move the structure or move the trajectory to minimize the wakefield effects. Alternatively, for weak wakes, it is

possible to deliberately move the beam or the structure to add a wakefield which cancels the effect of the rest of the accelerater.[14]

Beam Tilt

If there are RF kicks due to construction errors in the accelerator sections, the tail of the beam receives a different kick than the head. This can give a tilt to the beam. If we assume a random uncorrelated sequence of RF kicks, and compensate the center of the bunch with dipole correctors, the tilt tolerance is given by

$$(\Theta_{\rm rms})\left\{\beta_o < \sin\phi_o >_{\rm rms} \frac{2\pi}{\lambda_{\rm rf}} \sqrt{N} \left(\frac{\gamma_o}{\gamma_f}\right)^{1/2}\right\} < \frac{\sigma_y}{\sigma_z} \tag{11}$$

where $\Theta_{\rm rms}$ is the rms RF kick angle for a beam with energy γ_o, N is the number of accelerator sections and σ_z is the bunch length. For the ILC we have

$$\Theta_{\rm rms} < 2\mu{\rm rad} \quad . \tag{12}$$

If such a kick is caused entirely by the systematic tilting of irises in a section (the bookshelf effect), then the tilt angle of the iris must be restricted by

$$\Theta_{\rm iris} < 0.3 \text{ mrad} \quad . \tag{13}$$

Jitter and Vibration: Motion Pulse to Pulse

Feedback is essential to handle the "slow" drift of x, x', y, y', E. In practical cases it is possible to feedback at $f \lesssim \frac{f_{rep}}{5}$. This sets the scale for what we consider slow. Time variation has many sources in linear colliders, for example: damping ring kicker jitter, power supply variations and ground motion. The jitter of the kicker in the damping ring must be kept small compared to the natural divergence of the beam at the kicker. Tolerances in power supply variations are also set in many cases by the beam divergence. The effects of ground motion depend upon the design and assumptions for the motion. If the wakes are weak and chromatic effects are kept small, there is no filamentation, and the beam moves coherently from pulse to pulse. If wakes are strong, and there is a large spread of betatron wave number, there is filamentation so that the beam size varies from pulse to pulse with a smaller centroid motion.

If we assume coherent motion, then for random magnet-to-magnet jitter the tolerance is

$$(\Delta x)_{\rm rms} < \frac{\sigma_\gamma F}{\beta} \left(\frac{3}{N_q}\right)^{1/2} < (0.04)\sigma_\beta \quad \text{(ILC)} \quad , \tag{14}$$

where F is the focal length of a lens. If, on the other hand, there is magnet-to-magnet correlated motion, then the dominant effect occurs when the wavelength is equal to the betatron wavelength. However, since the betatron wavelength changes $\propto \gamma^{1/2}$, the resonance is only temporary. If $2\pi\beta_i < \lambda < 2\pi\beta_f$, then the tolerance is given by

$$\Delta x_\lambda < \sigma_\beta \frac{2}{(\pi\psi_{\rm cell})^{1/2}} \left(\frac{\gamma_f}{\gamma}\right)^{1/2} \left(\frac{2}{N_q}\right)^{1/2} < (.1 \text{ to } .4)\sigma_\beta \quad \text{(ILC)} \quad , \tag{15}$$

where γ is the energy at which $2\pi\beta = \lambda$.

Multibunch Effects

In order to efficiently extract energy from the RF, it is possible to accelerate many bunches per RF fill. This can increase the luminosity by an order of magnitude. To achieve the largest luminosity, we should put the maximum charge in a single bunch subject to restrictions on single bunch effects and beam-beam effects, then we should increase the number of bunches to extract as much energy from the RF as possible. This is not trivial in that the use of multiple bunches impacts every system.[15]

The most difficult problem, however, is the main linac, where the primary problems are bunch-to-bunch energy spread and transverse beam breakup. The basic tolerance for bunch-to-bunch energy spread is that it be less than the single bunch energy spread. This assures that the bunch-to-bunch chromatic effects will be no worse than single bunch ones.

Transverse beam breakup in the linac is a very difficult effect to control. For a normal traveling wave structure at 11.4 GHz, the 10th bunch blows up by many orders of magnitude by the end of the linac. Fortunately, there are solutions to this problem. The most useful approach seems to be the damping of the transverse modes in the structure to Q's $\sim$ 10-40 using external waveguides.[16] For the larger Q's, damping alone is not completely sufficient; however, if the frequency of the first higher mode is also adjusted with a tolerance $\sim$ 0.5%, the 2nd bunch can be placed near the zero crossing of the wake and the blowup vanishes.[17] This technique of damping high modes has also been shown to be useful for controlling coupled-bunch instabilities in the damping ring.[18] Recently, Q's as low as 8 have been measured in damped structures at SLAC.[19,20]

It is also possible to reduce the net wakefield by detuning the higher order modes in each cell of the structure. Provided that there is a large enough frequency spread, the net wakefield averages to zero by the time the second bunch arrives.[20] This technique might be much easier to implement if it proves to be successful.

Final Focus

Much progress has been made on the design of final focus systems.[21,22,23] As mentioned earlier, the final spot size desired is in the range 2-5 nm × 100-

300 nm. The limiting effect seems to be the radiation of the particles in the final quadrupoles which yields a minimum vertical spot size in the nanometer range.[24]

Once the design is specified, one is led to the question of the sensitivity of the design to different types of errors. The most serious vibration tolerance is in the final doublet, but there seem to be solutions to provide the required isolation.[25] Alignment tolerances in the absence of any correction are quite tight; however, it has recently been shown that one can recover from misalignments in the range 10–30 μm.[26] There is much more work to be done here, but the initial results indicate that tuning will be possible in the presence of errors.

A Final Focus Test Beam is presently being constructed at SLAC by a collaboration from SLAC, INP, KEK, Orsay, and DESY.[27] The purpose of this test is to study a flat beam final focus system which can demagnify the spot by a factor of about 300 in the vertical direction. This is precisely the demagnification necessary for the Next Linear Collider. For this experiment, due to the larger emittance of the SLC beam, the goal is to produce a spot with dimensions $\sigma_y \times \sigma_x = 0.06\ \mu\text{m} \times 1.0\mu\text{m}$.

Outlook

Before completing a realistic design of a next-generation linear collider, we must first learn the lessons taught by the first generation, the SLC. Given that, we must make designs fault tolerant by including correction and compensation in the basic design. We must also try to eliminate these faults by improved alignment and stability of components. When these two efforts cross, we have a realistic design. I believe this will not occur in the 1 μm alignment range. However, from the results presented here, I do believe that, with compensation, designs exist which move us into the 100 μm range and closer to a realistic design.

Acknowledgements

I would like to thank K. Bane, J. Irwin, S. Kheifets, N. Kroll, T. Raubenheimer, J. Seeman, and K. Thompson for their useful discussions, and T. Boysen for help in preparation of the manuscript.

References

1. *Linear Collider Working Group Reports From Snowmass '88*, Ed. R. D. Ruth, SLAC-Report-334 (1989).
2. *Proc. of the Int. Workshop on Next-Generation Linear Colliders*, SLAC-Report-335 (1988).
3. T. O. Raubenheimer, L. Z. Rivkin and R. D. Ruth, "Damping Ring Designs for a TeV Linear Collider," in Ref. 1 and SLAC-PUB-4808.
4. S. Kheifets, R. D. Ruth and T. H. Fieguth, "Bunch Compression for TLC," SLAC-PUB-5034.
5. R. D. Ruth, "Emittance Preservation in Linear Colliders," *Lecture Notes in Physics*, **296**, Eds. M. Month, S. Turner, Springer-Verlag, Berlin, and SLAC-PUB-4436 (1988).
6. W. Spence, private communication.
7. V. Balakin, A. Novokhatsky and V. Smirnov, *Proc. of the 12th Int. Conf. on High Energy Acc.*, 119 (1983).
8. J. Tuckmantel, "Beam Tracking With RF-Focussing in CLIC," CLIC-Note 87 (1989).
9. G. Guignard, these proceedings.
10. J. Seeman et al., SLAC-PUB-4968, to be published.
11. T. Raubenheimer and R. Ruth, "A Dispersion-Free Trajectory Correction Technique for Linear Colliders," SLAC-PUB-5355 (1990), submitted for publication.
12. T. Raubenheimer, "A New Technique of Correcting Emittance Dilutions in Linear Accelerators," SLAC-PUB-5355 (1990).
13. This technique was suggested by V. Balakin.
14. J. Seeman, "New Control of Transverse Wakefield in a Linac by Displacing Accelerating Structures," these proceedings and SLAC-PUB-5337 (1990).
15. K. A. Thompson and R. D. Ruth, "Multibunch Instabilities in Subsystems of 0.5 and 1.0 TeV Linear Colliders," in Ref. 1 and SLAC-PUB-4800.
16. R. B. Palmer, "Damped Accelerator Cavities," in Ref. 1.
17. K. A. Thompson and R. D. Ruth, "Controlling Transverse Multibunch Instabilities in Linacs of High Energy Linear Colliders," *Phys. Rev. D* 41, No. 3 (1990) 964, and in SLAC-PUB-4801.
18. K. A. Thompson and R. D. Ruth, "Transverse and Longitudinal Coupled Bunch Instabilities in Trains of Closely Spaced Bunches," *Proc. of the IEEE Part. Acc. Conf.* and SLAC-PUB-4872 (1989).
19. H. Deruyter et al., "Damped Accelerator Structures," *Proc. 2nd European Part. Acc. Conf.*, SLAC-PUB-5263 (1990).
20. H. Deruyter et al., "Damped and Detuned Accelerator Structures," these proceedings and SLAC-PUB-5322, (1990).
21. K. Oide, "Final Focus System for TLC," in Ref. 1 and SLAC-PUB-4806.
22. J. Irwin, "The Applications of Lie Algebra Techniques to Beam Transport Design," to be published in *Nucl. Inst. & Meth.*, and in SLAC-PUB-5315 (1990).
23. J.J. Murray, K.L. Brown, and T.H. Fieguth, "The Completed Design of the SLC Final Focus System," *Washington PAC 1987:1331*, and SLAC-PUB-4219 (1987).
24. K. Oide, *Phys. Rev. Lett.*, Vol. 61, No. 15 (1988) 1713.
25. W. W. Ash, "Final Focus Supports for a TeV Linear Collider," in Ref. 1.
26. J. Irwin, K. Oide, private communication.
27. J. Buon et al., "Final Focus Test Beam for the Next Linear Collider," *Proc. 2nd European Part. Acc. Conf.*, and LAL-RT-90-10 (1990).

Design Study for a 500 GeV Linear Collider

Presented by T. Weiland*.

Abstract

The feasibility of a 500 $GeV_{c.m.}$ linear collider has been studied, which is based lmost entirely on conventional rf-technology. The basic components are S-band travelling wave, constant-gradient accelerating structures and 130 MW klystrons. 3 GeV damping rings are used to produce extremely small emittances in both planes which are in the same range than these of the next generation synchrotron light sources. In both cases, the envisaged methods concerning stability and feedback give rise to the assumption, that the proposed values can be reached today. Also very strong focussing and a dedicated chromatic correction scheme near the interaction region is necessary to reach spot sizes that have not been produced yet. We present a status report of the investigations that have recently been started. Already at this early stage of our studies it seems that such a collider is technically feasible and could indeed be built in this decade.

Introduction

Linear e^+-e^- colliders will open up an energy range for particle physics, which circular machines cannot reach for reasons of size and economy. The very first step in this new energy regime which only will be accessible to linear e^+-e^- colliders is generally considered to be between center of mass energies of 200 GeV and 500 GeV. This is the mass-range where the missing 6th quark, the top quark, is expected to be produced and where p-p-colliders have difficulties to search for the Higgs particle

Linear colliders are in a uniquely difficult position in so far, that the very first machine of this new kind must already be of enormous size to be of interest for particle physics. There is no slow evolution possible.

The risks in building a new project in the billion dollar range using new and untried technologies are great. New ideas [1] like two-beam accelerators, wake field accelerators, very high gradient and very high frequency accelerators might eventually mature to the point where the construction of a large collider becomes feasible, but the required time for the necessary R + D-work may be much longer than often optimistically assumed. The question is therefore of interest, what a linear collider based on present-day technology might look like and how it compares with the more daring studies presently under way elsewhere. To avoid misconceptions it must be pointed out that any linear collider with energies and luminosities of interest for high energy physics requires extensions of known technologies beyond what is available today: Damping rings must produce beams with smaller emittances than ever before, the requirements on emittance control during acceleration have to be much tighter than in the past and the final focus with linear beam size demagnifications of three orders of magnitude also requires extensive studies. While these are formidable problems, their solutions do not seem to be out of reach. Development work on existing facilities such as the one by the international collaboration on the SLAC final focus test facility FFTF might produce the required solutions in time.

In our study we assume basically a linear collider using present SLAC technology: Two S-band linacs, each of which 5 times as long as the SLAC-linac, direct their beams against each other. Each linac uses an accelerating gradient of 17 MeV/m, which may not be too far from the gradient of a cost opimized machine in which costs of total rf-power and accelerator length are balanced. In order to improve power efficiency we will use 2 μsec long current pulses with many bunches (172). The number of particles in each bunch is limited to $7 \cdot 10^9$, such that the total energy spread produced by the fundamental and higher order mode losses of $\Delta E/E = \pm 0.7\,\%$ is still within the acceptance of the final focus. This bunch charge together with the number of bunches within the rf-pulse represent an avarage pulse current of 100 mA, not unlike the currents already achieved in the SLAC-linac. The individual bunch charge is considerably smaller than that which is stably accelerated in the SLAC-linac, but multibunch instabilities will have to be carefully examined.

The R + D-work which we assume to be going on before such a study reaches the proposal stage may result in S-band klystrons of 130 MW and 3 μsec pulse duration, a modest improvement on the 130 MW, 1 μsec-klystrons already available today. Other R + D work should concentrate on economizing linac technology. Klystron modulators, the largest single cost item, might be built with hard tube pulsers, thereby avoiding the expenses for the costly pulse transformers and the low inductance pulse capacitors. A special study of a hopefully cheaper hard tube pulser is on the way.

A parameter list of the main parameters is given in table 1.

Damping Rings

The magnetic lattice for a 650 m circumference damping ring at an energy of 3.15 GeV has been designed [2].

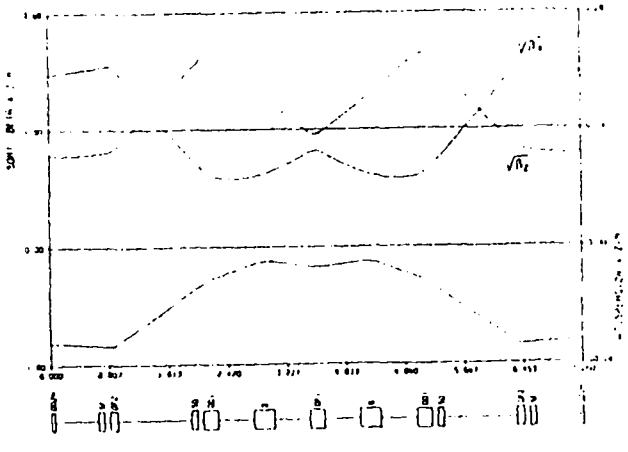

Figure 1: Unit cell of the damping ring arc structure.

* This Study is a summary of the work of groups from Deutsches Elektronensynchrotron DESY and Technische Hochschule Darmstadt THD.

General Parameters		
energy	GeV	250 + 250
luminosity (incl. crossing angle, no ehancement from disruption)	$(cm^2 sec)^{-1}$	$2.4 \cdot 10^{33}$
active length	m	29.411
repetition rate	Hz	50
number of particles per bunch		$7 \cdot 10^9$
Particle Production and Damping Rings		
damping ring energy	GeV	3.15
damping time	msec	3.8
ring circumference	m	650
invariant emittance $\gamma \epsilon_{x,y}$	m	$410/4 \cdot 10^{-8}$
energy spread	%	0.112
rf-voltage	MV	5.0
rf-frequency	MHz	500
bunch length σ_s	mm	3.6
wiggler peak field	T	2.0
wiggler period length	m	0.20
wiggler total length	m	84
dynamic acceptance	m	$4 \cdot 10^{-6}$
Main Linac		
wave length	m	0.10
average shunt impedance	MΩ/m	53.6
attenuation	neper	0.57
structure length	m	6
group velocity	% of c	4.1-1.3
filling time	μsec	0.325
maximum energy width (peak)	%	± 0.7
klystron power	MW	130
number of klystrons		2451
structures per klystron		2
klystron efficiency	%	45
total rf-pulse length	μsec	2.8
zero current energy	GeV	536
mean power	MW	94
rf-peak power	MW	271 000
average pulse current	mA	100
current pulse length	μsec	2
number of bunches per pulse		172
bunch to bunch distance	m	3.2
bunch length (rms)	mm	0.2
Final Focus and Interaction		
β-function at IP $\beta^*_{x,y}$	mm	3, 0.3
beam dimension at IP $\sigma^*_{x,y}$	nm	169, 5.48
aspect ratio		30.8
crossing angle	mrad	± 0.8
disruption parameter D_x, D_y		0.53, 16.4
luminosity enhancement		1.8
maximum disruption angle	mrad	0.77, 0.20
dilution parameter		0.38
critical energy of beamstrahl.	GeV	78
mean number of beamstrahl. photons per particle		1.1
critical radiation parameter		0.208
mean fractional energy loss		0.06
mean fract. reduct. c.m. energy		0.021
momentum acceptance	%	± 0.8

Table 1: Table of general parameters

A normalized emittance of $\gamma \epsilon_x = 4.1 \cdot 10^{-6}$ m and a transverse damping time of $\tau_{x,y} = 3.8$ msec are achieved. The layout is based on a modification of a Chasman-Green lattice and includes wiggler sections with a total active length of 84 m assuming a peak field of 2 T in the wiggler magnets (Fig. 1). The lattice is optimized for a local compensation of the nonlinear distortions caused by the sextupoles required for chromaticity correction. As particle tracking results show, this leads to a lower sensitivity of the dynamic aperture to errors than with other designs (e.g. a FODO-lattice). Both a sufficient injection acceptance (about $4 \cdot 10^{-6}$ m including the wiggler nonlinearities) and the desired small emittance coupling ratio ($\epsilon_y / \epsilon_x = 1\%$) can be achieved with a tolerance limit of 0.1 mm (rms) for transverse magnet position errors. An investigation of coherent (especially multibunch-) instability problems is on the way.

High Voltage Pulser

The high voltage pulsers are the most expensive item of the S-band linear collider. Thus some investigations have been started to develop a hard tube pulser as an alternative to the commonly used systems employing a high voltage, short pulse transformer.

In collaboration with SLAC it is planned to set up a hard tube pulser next year as a first step. Although these klystron pulsers seem to be the "least interesting" portion of a linear collider, much attention must be paid to these and they will certainly be one of the key issues of R & D work in the next year.

Accelerating Structures

The design of the structure is based on the well known features of constant-gradient travelling wave tubes with a phase advance of $2\pi/3$ per cell [3]. As a preliminary choice an attenuation of 0.57 neper is chosen. The maximum structure-length is ≈ 12 m and given by the peak power limit of one klystron. In order to have a moderate variation in group velocity (4.1 to 1.3 % of c) and shunt impedance, the length of one disk loaded structure is chosen to be 6 m. In this case the required peak power per tube is 56 MW to reach a loaded gradient of 17 MeV per meter. Using S-band frequency, conservative assumptions for the Q_0-value (13 000) and for the shunt impedance (53.6 MΩ/m) are made for the calculations.

Two possibilities are investigated: - The 130 MW Klystrons will feed two of the forward-wave structures. - The second possibility requires two 6 m structures of different type one forward-wave and one backward-wave structure with one coupler in the middle of the tube. This idea may have some advantages, for example, concerning transverse multi-bunch instabilities driven by dipole modes, which will have completely different frequencies in the two tubes. The transverse kicks in the coupling cells due to phase- and amplitude-asymmetries are avoided by feeding the coupler cell from both sides.

Transient Beam Loading

The current pulse length (2 μsec) in this type of collider is much longer than one filling time (T_f = 0.825 μsec) of the assumed 6 m long rf-structure. Starting with beam injection exactly after one filling time T_f causes a bunch to bunch energy variation during the following second filling time due to the transient beam loading. The voltage as a function of time for one tube is shown in Fig. 2. For a constant gradient structure the full energy spread is given by (1):

$$\Delta V = -\frac{R'_s \cdot i \cdot L}{2} \left[1 - \frac{2\tau e^{-2\tau}}{1 - e^{-2\tau}} \right], \qquad (1)$$

R'_s = shunt-impedance per meter
i = the average current in one pulse
L = structure length
τ = attanuation parameter,

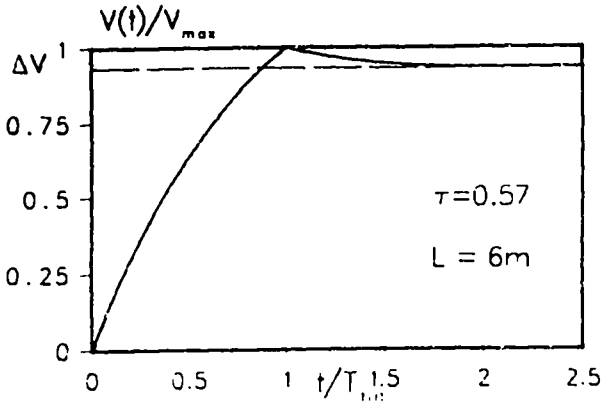

Figure 2: Voltage as a function of time for one 6 m long travelling wave tube.

and approximately 6.7 % in this case, which is far beyond the acceptance of the final focus and therefore must be compensated.

Two possible schemes have been investigated. First, injecting the bunch train after the loaded voltage V_0 has been achieved and before the structure is completely filled, which is also the proposed method for the other linear collider schemes, reduces the energy spread to 5.2 % . With the second scheme, the bunches being accelerated during the second filling time, will have different phases with respect to the crest of the wave. This method enables an almost exact compensation of the energy spread due to phase variation from bunch to bunch. Let V_{max} be the unloaded voltage, the phase angle of the first bunch is given simply by :

$$\frac{V_0}{V_{max}} = \cos(\phi_0), \qquad (2)$$

with : ϕ = 0 be the crest of the wave

and ϕ_0 = 21^0 be the phase angle of bunch # 1

Starting with the unloaded Voltage V_{max} (at t'=0 and t' = T_f+t)), the energy gain of the following bunches is given with :

$$V(t) = V_{max} \cdot \cos(\phi_0 + \Delta\phi(t')) - \frac{R_s i L}{2}\left[1 - \frac{\omega}{Q} e^{-2\tau} \cdot t' - e^{-\omega/Q \cdot t'}\right] \qquad (3)$$

with : $\phi_0 + \Delta\phi(t') = 0$ for $t' = T_f$

To provide the phase variation as a function of time, a conventional bunch compressor is used as a **'bunch to bunch'**-compressor, in order to transform a given energy spread into a distance variation according to :

$$\frac{\Delta\phi(t')}{2\pi} = \frac{\Delta s}{\lambda} = \frac{1}{\lambda} \cdot \mathrm{const}_{comp} \cdot \frac{\Delta p(t')}{p_0} \qquad (4)$$

with a typical compressor parameter of $\mathrm{const}_{comp} = 4.7/(\frac{\Delta p}{p_0})$ [mm/%] as for example presented in [4].

The required 'bunch to bunch' energy spread is in the range of 1.2 % at 3.15 GeV, the damping ring energy. The energy variation before the **'bunch to bunch'**-compressor can be produced by short low-Q cavities to make the desired fast voltage control possible, analogous to the transient beam loading $\Delta V(t)$ as a function of time. First calculations show, that the energy spread in the main linac can be reduced to less than 0.3 %. The possibility of making the first stage bunch compression and the 'bunch to bunch' compression for energy compensation in one single compressor is still investigated.

Single–Bunch Instabilities

Each of the 172 bunches in one pulse has to traverse a large number of acceleration gaps before they reach their final energy of 250 GeV. An energy spread along the bunch is induced by longitudinal wake field effects. Additionally transverse wake fields will be excited if the bunch moves off axis through an acceleration structure due to various forms of jitter. In the SLC the beam developes a corkscrew-like tail. This process of single bunch *beam breakup* is extensively studied analytically and numerically in [5]. Transverse wake fields scale roughly with the square root of the rms-bunch length. Since our bunch length (σ = 0.2 mm) is five times smaller than used in the SLC and since our bunch population is only 7×10^9 electrons (or positrons) per bunch, transverse wake fields effects will be small by design for the 2×250 GeV linear collider.

So far only estimations of this effect have been performed. The single bunch *beam breakup* can be estimated in the smooth focussing approximation using a two particle model. The equations of motion are for the head particle :

$$\frac{d}{ds}\left(\gamma \frac{d}{ds} x_1\right) + \gamma k^2 x_1 = 0 \qquad (5)$$

and for the tail particle

$$\frac{d}{ds}\left(\gamma \frac{d}{ds} x_2\right) + \gamma k^2 x_2 = \frac{e}{m_0 c^2} \frac{q}{2} x_1 W_\perp . \qquad (6)$$

x_1, x_2 are the transverse position of the head and the tail particle, γ the normalized energy, $\lambda_\beta = 2\pi/k$ the local wave length of the betatron oszillations, $q = e\,7 \times 10^9$ the total charge in the bunch and $W_\perp$ the transverse wake potential at the tail.

These equations can be solved assuming that the acceleration is adiabatic. We obtain for the relative deviation of the tail :

$$\left\|\frac{x_2 - x_1}{x_1}\right\| = \frac{\lambda_\beta}{4\pi} \frac{q}{2} e W_\perp \frac{1}{g} \ln\left(1 + \frac{g}{E_0} s\right) . \qquad (7)$$

For a gradient g of 17 MeV/m, an initial energy E_0 = 3.15 GeV, and λ_β = 100 m we have

$$\left\|\frac{x_2 - x_1}{x_1}\right\| = 91\% \qquad (8)$$

after s = 15 km. The dipol wake potential $W_\perp = 0.79 \times 10^{15}$ V/(m²C) was scaled from TBCI - results [6] for a σ = 3 mm long bunch. Numerical calculations will provide more accurate results for the 0.2 mm long bunches. So far no BNS-damping was invoked, which certainly can reduce this effect significantly.

The total (peak to peak) energy spread within one bunch due to longitudinal wake fields was found to be

$$\frac{\Delta E}{E} = 1.2\ \% . \qquad (9)$$

Due to the fact that the bunch length is very short compared to the rf wave length this energy spread cannot (and needs not to) be compensated by positioning the bunch on the rf wave scope as proposed for the SLC.

These estimates for the transverse and longitudinal single bunch beam dynamics demonstrate that the *beam breakup* effects seem to be controlable. Further studies with discrete focussing elements with the program LTRACK [5, 7] will give more detailed results and are under way.

Multibunch–Instabilities

Long current pulses with 172 bunches per pulse and a population of $7 \cdot 10^9$ particles per bunch can excite strong transverse electromagnetic fields in the structure and may limit the current due to *beam breakup* . This instability is driven by the dipole modes of the structure, which are resonantly excited by an off axis beam. Regenerative *beam breakup* will be significantly reduced by the constant-gradient structure, in which the dipole mode frequencies differe from cell to cell due to the tapering of the iris. Cumulative *beam breakup* is probably the most severe problem which is currently investigated by particle tracking.

In order avoid the use of expensive damped structures [8] where the dipole modes are coupled out by slotted irises, more simple structures are investigated. One obvious method is, to randomly destribute the dipole mode frequencies in different sections of the linac over the entire length of 15 km. This can be achieved by using slightly different geometries for the cavities, that have to be tuned for the accelerating $2\pi/3$ mode only. The use of a combined forward- and backward wave structure may be another possibility which is still investigated. This leads to two rather different passbands of the HEM-modes and can further improve the situation. At present the strength of the cumulative *beam breakup* is being investigated with tracking programs and the effects of various potential remedies are analyzed

Ground Motion - Orbit Distortions

In order to minimize the influence of transverse wake fields, strong quadrupole focussing is required. We assume that the focussing strength may be decreased with increasing energy thus avoiding extraordinarily long quadrupole magnets in the high energy end of the linac. With the average beta $\bar{\beta}$ scaling roughly as $\bar{\beta} = 0.09\,\mathrm{m} \cdot \sqrt{\gamma}$ we obtain a magnet filling factor of less than 0.05 everywhere and a total of $N \approx 1000$ quadrupole magnets. It can be shown that for any scaling law $\bar{\beta} \approx \gamma^{\epsilon}$ with $0 \leq \epsilon \leq 1$ the rms orbit distortion σ_t due to rms quadrupole motion $\sigma_{q,t}$ is estimated at [9] :

$$\sigma_t = 2\,\sigma_{q,t}\sqrt{N}, \qquad t = x, y\,. \tag{10}$$

As seen from long term measurements of ground motion in the HERA tunnel [10] we have to expect $\sigma_{(q,y)} \approx 0.1\,\mu\mathrm{m}$ during working hours (see Figure 3) resulting in $\sigma_y \approx 6\,\mu\mathrm{m}$. This would be more than twice the vertical beam size. If compared with measurements taken at numerous different places in Germany [11], this amount of vertical ground motion is not particularly high, but quite typical for ground noise close to big human settlements. Since the dominant frequency component is around 5 Hz, the 50 Hz repetition rate does not allow effective beam stabilization by means of beam position measurement and feedback. To achieve the desired vertical quadrupole stability of ≤ 20 nm for frequencies ≥ 1 Hz, we propose continuous measurement of quadrupole motion by geophones and local compensation of each orbit kick by the dipole correction magnet attached to each

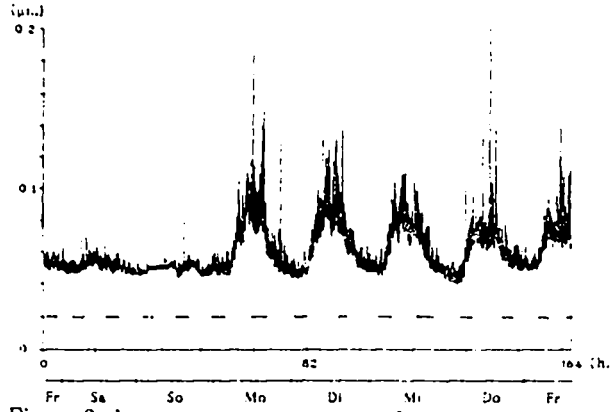

Figure 3: Long term measurement of rms-ground motion in the HERA tunnel during 1 week. The cut-off frequency of the ground motion detector is 1 Hz. The averaging time for the rms-values was one minute. The broken line represents our tolerance of uncorrelated rms vertical quadrupole motion. For the final focus quadrupoles considerably tighter tolerances will be specified.

quadrupole magnet. Alternatively, passive damping of quadrupole supports is considered.

Final Focus Lattice

Investigations of a final focus system with $\beta_x^* = 3\,\mathrm{mm}$ and $\beta_y^* = 0.3\,\mathrm{mm}$ at the interaction point have been performed. The layout is based on the CLIC lattice design by Napoly and Zotter [12] (see Fig. 4). First results show that for 250 GeV particle energy the momentum bandwidth

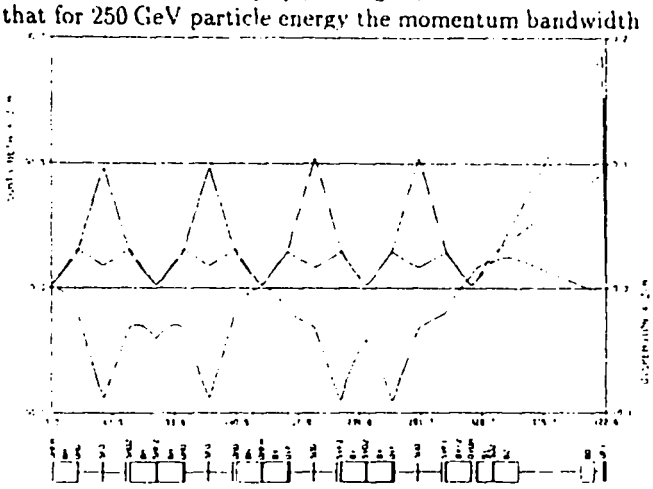

Figure 4: Lattice layout of the final focus system.

of the system can be increased to at least $\Delta p/p = \pm 0.8\,\%$ (originally $\pm 0.41\,\%$) by introducing additional sextupoles for chromaticity correction (see fig. 5).

The emittance growth caused by synchrotron radiation and sextupole nonlinearities is negligible for the ideal lattice. Studies of tolerance limits as well as practical correction algorithms have not been performed yet.

Beam–Beam effects

Due to our large aspect ratio, the disruption parameters are much different in both transverse planes [13]:

$$D_x = 0.53\,, \qquad D_y = 16.4\,.$$

In order to allow the beam to freely pass the final focus quadrupoles of the opposite beam, we have chosen a finite

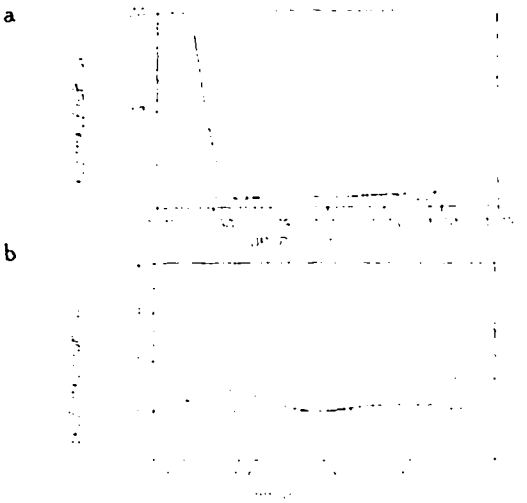

Figure 5: Relative change of the β-functions at the interaction point with momentum deviation before (a) and after (b) optimization with additional sextupoles (solid line: β_x^*, dashed line: β_y^*).

horizontal crossing angle of ± 0.8 mrad. This is considerably larger than the maximum disruption angles as estimated from [14]:

$$\theta_x = 0.77 \text{ mrad}, \qquad \theta_y = 0.20 \text{ mrad}$$

However, this estimation does not consider the effect of the finite crossing angle and the rare beamstrahlung events with photon energies much larger than the critical energy u_c of beamstrahlung. The latter has been treated in [15] to show that, with our parameters, less than one electron per interaction will experience a kick $\geq 2\theta_x$. Theory predicts a luminosity pinch enhancement H_D due to mutual focusing of the beams during interaction. Using the formula of Chen and Yokoya [10] we expect $H_D \simeq 2$. However, to be conservative, we do not include this effect in our luminosity estimation nor do we make use of it to relax orbit jitter tolerances.

The critical radiation parameter is:

$$\Upsilon = \frac{2}{3}\frac{u_c}{E_0} = 2\frac{\lambda_c}{2\pi}\frac{r_e N \gamma}{\sigma_z(\sigma_x + \sigma_y)} = 0.208 \qquad (11)$$

with :

$\lambda_c/2\pi$ = Compton wavelength of the electron
r_e = Classical electron radius
N = Number of particles per bunch

The critical beamstrahlung is formed within a distance $l_r \approx 1\mu m$ which is much smaller than the bunch length. Thus it should be insensitive to details of the particle distribution function. The mean relative energy loss is estimated to be [17]:

$$< \epsilon > = \frac{1}{3\sqrt{\pi}}\frac{r_e \sigma_z \Upsilon^2}{(\lambda_c/2\pi)^2 \gamma} \approx 0.06 \qquad (12)$$

This formula holds for $\Upsilon \ll 1$ and no pinch effect. While the first condition is satisfied quite well, we do expect some pinch. But since it will occur in the vertical plane mainly ($D_x = 0.53$) and because of $l_r \ll \sigma_z$, its influence on Υ and $< \epsilon >$ is expected to be small ($\sigma_y \ll \sigma_x$ in equation (11)).

Summary

The aim of our study is, to use where ever possible conventional technology in order to reduce the immanent risks of the first linear collider. It seems from our recently started investigations that many components may in fact be taken "off the shelf" and that such a collider of 500 GeV center of mass energy could indeed be built before the end of this century.

Acknowledgements

Scientists from many other institutes have helped with discussions and suggestions, in particular from the Stanford Linear Accelerator SLAC and from Technische Hochschule Berlin TUB.

References

[1] S. Turner, editor. Proceedings of the ECFA-CAS-IN2P3-IRF-EPS Workshop. *New Developments in Particle Accelerator Techniques*, Orsay, Frankreich, Juli 1987. ECFA 87/110. CERN 87-11, October 1987.

[2] *A Study of Low-Emittance Damping Ring Lattices*, R. Brinkmann, DESY-M/90-09. 1990.

[3] *Structure Design for a 500 GeV S-Band Linear Collider*, P. Hahne, N. Holtkamp, R. Klatt, T. Weiland, this conference.

[4] *Bunch Compression for the TLC*, S.A. Kheifets, R.D. Ruth, T.H. Figuth, SLAC-PUB-5034, 1989.

[5] *Wakefield Effects in a Linear Collider*, K.L.F. Bane, SLAC-PUB-4169, 1986.

[6] T. Weiland, *Transverse beam cavity interaction part I: short range forces*, NIM 212 (1983), p. 13-21.

[7] A. Chao, R. Cooper, Particle Accelerator 13, 1, 1983. SLAC-PUB-4169, 1986.

[8] *Damped Acceleration Cavities*, R.B. Palmer, SLAC-PUB-4542, 1988.

[9] J. Roßbach, private communication.

[10] *Measurement of Slow Closed-Orbit Motion in the HERA Electron Ring in Correlation with Ground Motion*, W. Decking, K. Flöttmann, J. Roßbach, Proc. EPAC Conf, Nice, 1990.

[11] *Systematische Untersuchung der kurzperiodischen seismischen Bodenunruhe in der Bundesrepublik Deutschland*, M. Steinwachs, Geologisches Jahrbuch, Reihe E (Geophysik), 3, 1974.

[12] *Progress Report and the CLIC Final Focus Design*, O. Napoly, B. Zotter, CERN, CLIC-Note 107, 1989.

[13] *Überblick über die Parameter der Strahl - Strahl Wechselwirkung am 2 x 250 GeV-Linear Collider*, J. Roßbach, DESY-M-VM 90-02.

[14] *Approximate Formulae for TeV Linear Colliders*, R.B. Palmer, SLAC, AAS-30, 1987.

[15] *Electron Energy Spectrum and Maximum Disruption Angle under Multi-Photon Beamstrahlung*, K. Yokoya, P. Chen, SLAC-PUB-4935, 1989.

[16] R.B. Palmer, SLAC-PUB-5195, 1990.

[17] *An Introduction to Beamstrahlung and Disruption*, P. Chen, Lecture Notes in Physics, 296, Springer, 1988

DIAGNOSTICS FOR HIGH-BRIGHTNESS BEAMS*

R. E. Shafer
Los Alamos National Laboratory, Los Alamos, NM 87545

ABSTRACT

Special techniques are required for beam diagnostics on high-brightness particle beams. Examples of high-brightness beams include low-emittance proton linacs (either pulsed or CW), electron linacs suitable for free-electron-laser applications, and future linear colliders. Non-interceptive and minimally-interceptive techniques for measuring beam current, position, profile, and transverse and longitudinal emittance will be reviewed. Included will be stripline, wire scanner, laser neutralization, beam-beam scattering, interceptive microgratings, spontaneous emission, optical transition radiation, and other techniques.

INTRODUCTION

Beam diagnostics for high-brightness beams is becoming an increasingly important topic as accelerator physicists improve the designs of low-emittance particle accelerators. The diagnostics must be able to measure the characteristics of low-emittance beams to confirm the accelerator design. Permanently-installed diagnostics must be able to characterize the beam without intercepting the beam or causing emittance dilution.

First, we need to define the characteristics of a high-brightness beam. High-brightness here means a high density of particles per unit 6-D phase space, 4 transverse and 2 longitudinal. Because high-brightness applies to individual bunches, it is not synonymous with high-average-current beams, although achieving simultaneous high brightness and high average current is often desirable. A good example of a high brightness requirement without high average beam current is the high-energy linear collider, in which individual electron and positron bunches are collided in a final focus.

There are three requirements for achieving high brightness beams; optimized accelerator operating parameters, design of accelerator and beamline components that minimize emittance degradation, and minimal variations in bunch-to-bunch characteristics.

Beam diagnostics measurements can be divided into the following three categories:

Centroid measurement	current and charge position and angle synchronous phase energy
Profile measurement	energy bunch width bunch length bunch divergence
Emittance measurement	transverse longitudinal

In addition, bunch-to-bunch jitter in any of the above centroids can lead to dilution of the single-bunch emittance, unless the jitter can be eliminated or corrected. Although beam-current jitter may not appear to be correlated to any of the 6-D emittance parameters, it can couple into them via beam loading in accelerator RF cavities as well as via space-charge effects.

This paper reviews beam diagnostics techniques for high-brightness beams, with examples given for three representative high-brightness accelerator applications: proton and H^- linear accelerators, high-energy linear colliders, and free-electron-laser linear accelerators.

Good general review papers on the subject of beam diagnostics can be found elsewhere in the literature.[1-7] Because there is not enough space in this paper to present a complete review, the reader is referred to these papers, and only a few select topics will be discussed here.

* Work supported by the US Department of Energy, Office of High Energy and Nuclear Physics.

CENTROID MEASUREMENTS

BEAM CURRENT AND CHARGE

Beam-current measurements are straight forward, and have been reviewed elsewhere.[8] Pulsed (i.e., low duty cycle) linac beams are easily measured with standard tape-wound or ferrite toroids, with the beam current representing a single-turn primary. Active feedback to the toroid secondary winding is often employed to increase the L/R time constant, and special laminating techniques are used to increase the high-frequency bandwidth. For CW applications, the non-linear properties of flux-gates have been employed to achieve a DC current-measurement capability, with accuracies of a few microamps. For single bunches, ballistic integration of the toroid signal (e.g. by shunting the toroid with a capacitor) yields a signal whose amplitude is independent of the bunch shape and proportional to the total charge. This method has been used to measure the total charge in individual sub-nanosecond-long bunches at LEP, for example.

BEAM POSITION

Generally, the largest quantity of beam diagnostics in an accelerator facility is used for beam position monitoring. Non-interceptive beam pickup electrode structures include[9]

Capacitive (also called electrostatic) pickups
Magnetic (window frame) pickups
Linear response (special form of capacitive) pickups
Button pickups (often used in electron machines)
Stripline (directional coupler) pickups
Slot-coupled (Bethe-hole-coupled) pickups
Resonant-cavity pickups

The best broad-band pickup frequency response is available in the impedance-matched stripline and slot-coupled designs, and for this reason these designs have been used in anti-proton stochastic-cooling applications. The best linearity (output amplitude vs. beam displacement from center) is available in the diagonally-cut-electrode design that has a linear difference-over-sum response to displacement. Impedance-matched designs provide the best control of beam coupling impedances, and therefore are preferred where a low "Z/n" is desired.

The choice of beam-position-processing electronics plays an important role in the overall system performance. The "standard" processing technique is the difference-over-sum method, which can be implemented either by digitizing each electrode signal separately, or by using analog or RF techniques to form RF or video (analog) difference and sum signals. These signals can then be digitized, or the ratio can be obtained using analog techniques. These circuits have a limited dynamic range and real-time bandwidth, although the acquisition bandwidth can be very high.

A second method that has been used recently on the Fermilab accelerators, and also on the LEP ring at CERN, is phase-quadrature processing (also known as amplitude-modulation-to-phase-modulation or AM/PM processing). In this method, amplitude disparities are converted to phase disparities in a passive circuit, and the phase disparity is measured using mono-pulse radar techniques. This approach, which is a frequency-domain rather than a time-domain technique, has a large dynamic range (up to 60 dB), as well as a real-time bandwidth of about 10% of the processing frequency. It is relatively costly, and requires phase matching of the signal cables. Because the circuit measures the signal-amplitude ratio from the two opposing electrodes, the output is normalized to beam current. This technique has been used on single beam bunches by using narrow-band bandpass filters that "ring" when excited by the bipolar-doublet signal from a single bunch.[10]

A third signal-processing method recently being investigated is log-ratio processing, which appears to be more linear in displacement than either difference-over-sum or AM/PM when used with stripline electrodes in a circular geometry. Like AM/PM, it is a frequency-domain method, and is more applicable to multi-bunch rather than single-bunch beams. Also, like the AM/PM method, log-ratio processing provides a real-time beam-current-normalized analog signal that is free of digitizing errors, and capable of high resolution.

In general, the resolution limit δx is determined by the signal-to-noise ratio, and may be written as

$$\delta_x = \frac{r}{2\sqrt{2}}\left(\frac{P_N}{P_S}\right)^{\frac{1}{2}}$$

where P_N and P_S are the noise and signal powers respectively, and "r" is the pickup aperture radius. For AM/PM and log-ratio, P_N is typically about 15 dB above thermal (kTB) noise because of the presence of electronic noise, when EMI and RFI are properly shielded out. For example, a 1 MHz real-time bandwidth position signal with 1-μm resolution can be obtained for a 50 mA beam in a "quarter-wavelength" stripline electrode pickup with a 1-cm aperture radius. Beam sizes in future linear colliders are expected to be in the 1 to 2 μm range[11], and the pulse-to-pulse beam position jitter must be controlled to a fraction of this. It appears that with proper design of beam position electrodes and electronics, the necessary resolution is obtainable.

Accuracy of non-intercepting beam position measurements is generally limited to about 1% of the aperture radius by such effects as mechanical tolerances and alignment, cable attenuation disparity, and electronics offsets and drifts. Direct injection of calibration signals into pickups may reduce the cable and electronic contributions by a factor of 10.

SYNCHRONOUS PHASE

The beam-synchronous-phase angle (the relative phase of the beam-bunch RF structure and the accelerator RF cavity fields) is an important measurement for optimizing the performance of linear accelerators. The synchronous-phase angle can be measured with an accuracy of about 50 ps, and with a resolution of about 5 ps (e.g., about 8° and 0.8° respectively at 425 MHz), using either stripline pickups or low-Q RF cavities.

BEAM ENERGY

Beam energy is usually obtained by measuring beam rigidity in magnetic fields. At low energies, however, where β is substantially less than 1, time-of-flight techniques can be used. An example of this is using two striplines (or low-Q RF cavities) with 50-ps time-measurement accuracy to measure the phase delay of the RF modulation between two pickups. For example, with 50-ps measurement accuracy and a flight path of 3.5 meters, the energy of a 10-MeV proton beam can be measured to about ± 10 keV.

In free-electron-laser linacs, It is also possible to use the measurement of the spontaneous emission wavelength in wigglers to measure the energy of an electron beam. The spontaneous emission wavelength is approximately the wiggler period divided by $2\gamma^2$.[12] The emission wavelength can be measured using optical spectroscopy techniques. The natural linewidth is approximately the emission wavelength divided by the number of wiggler periods, and can be less than 1% for a wiggler with over 100 periods. For example, with a 5-cm wiggler period and $\gamma = 200$, the spontaneous emission wavelength is about 600 nm. With several hundred wiggler periods, energy-measurement accuracies in the range of ±0.1% are possible.

PROFILE MEASUREMENTS

TRANSVERSE BEAM PROFILES

The wire scanner is the most widely used device for obtaining transverse beam profiles. In this method, a single 10-to-100-μm-diameter wire is moved through the beam in a controlled manner, and either the current induced in the wire or the radiation caused by the beam hitting the wire is measured. The major shortcoming of wire scanners is that the wire may not survive in high intensity beams. For low-duty-cycle accelerators, the wire is stepped through the beam in small increments, thus obtaining a profile over many beam pulses. Low-Z wires (e.g., carbon) are often used because the multiple scattering is low and the heat capacity and melting point are high. If a large radiation yield is preferred, high-Z materials (e.g., tungsten) are used. Position and profile resolution of a few μm is possible. For CW beam applications in which the stepped wire would melt, or the multiple scattering could cause excessive emittance blowup, the wire is moved through the beam at a high velocity, often exceeding 10 m/s. In this case the temporal profile of either the induced wire current or the radiation produced as a result of nuclear scattering is a good representation of the beam profile. Stepping wire scanners are now being used in the SLAC linac to check beam profile and alignment.

Wire scanners can also be used at the intersecting point of two colliding beams, such as at SLC. Because the bremsstrahlung radiation is highly collimated, the temporal overlap of the two radiation patterns is a measure of the relative alignment of the two colliding beams. Unlike beam-beam scattering (see below), the temporal profile

measurements of the two beams are not convoluted, so independent measurements of the two beam sizes are possible. The resolution of wire scanner measurements is presently limited to perhaps 10 μm or more, due to the wire diameter.

Because the beam size is so small at the collision point in linear colliders, special methods must be used to measure profiles. At SLC, the deflection of one beam by the other at the final focus as the beams are scanned across one another provides a good measure of both the beam overlap and the convoluted beam profile. Resolution of several μm has been achieved. This method does not depend on any dimension other than the beam sizes themselves, and can therefore be extended to sub-μm beams.

At SLAC, the transverse wakefield effect creates a head-tail relative displacement of the beam centroid. By placing a deflector magnets and fluorescent screens at the proper locations in the magnetic lattice, the x, x', y, and x' profiles of individual bunches can be observed on fluorescent screens.[13]

Beam profile measurements in future linear colliders pose a particularly difficult problem because the beams are expected to have rms widths of 1 to 2 μm in the linac, and 10 or 20 nm at the final focus.[11] Buon[14] has proposed observing the yield and velocities of electrons and ions in the ionized residual gas, because these parameters depend on the beam size and the electric fields surrounding the beam. This method does not seem to be extrapolatable to very small beams, however, because electric fields in excess of 10^9 V/cm will produce field-emission ionization. Another proposal is to use a target composed of many very narrow parallel stripes of high-Z material on a thin low-Z backing (e.g., gratings of gold on polymer). High-energy beam bunches will destroy the stripe, so the grating is moved continuously through the beam. The bremsstrahlung yield will depend on what percentage of the beam hits the high Z stripes. If the beam size is of the order of or smaller than the stripe spacing, there will be large pulse-to-pulse fluctuations in the bremsstrahlung yield. These fluctuations can be correlated to the beam size. Feature sizes of the order of 0.06 μm have been achieved in semiconductor lithography using synchrotron light sources, so gratings of this size are possible.

Laser beams have been used to neutralize segments of H^- beams, because the threshold for photo-dissociation of H^- is about 0.75 eV, and the maximum cross section is about 40 megabarns at 1.5 eV. A 100 ns-long, 10 mJ laser pulse focused to a narrow waist is sufficient to neutralize a longitudinal slice of the beam completely. A Nd:YAG laser at 1.06 μm has been used for this purpose.[15] After neutralization, the charged beam is separated magnetically from the neutral beam, and the yield of neutral hydrogen is measured. For transverse profile measurements, the obtainable resolution of this "massless slit" is of the order of 50 μm because of the confocal parameter of the laser beam.

Other bunch profile measurement techniques include residual gas ionization and fluorescence. The ionization measurement usually involves collecting the ions or electrons on a multi-channel plate. The residual gas fluorescence method typically uses video cameras and CCDs, sometimes with image intensifiers. These measurements suffer from senitivity to beam halos, lack of resolution, and sensitivity to the electric field of high-current beams.

For highly relativistic electron beams such as are used in free electron lasers, both spontaneous (wiggler) emission and optical transition radiation (OTR) have been successfully used to measure both beam size and beam divergence profiles. When the beam passes through a thin metallic foil, optical-wavelength radiation is emitted from both surfaces of the foil.[16] The radiation is emitted in narrow cones whose opening half-angles are about $1/\gamma$. If the foil is tilted at 45° relative to the beam, the backward radiation cone is emitted at right angles to the beam, while the forward cone is at 0°. The video image obtained by focusing at the point of emission yields a two-dimensional profile of the beam size. Focusing at infinity, however, yields a two-dimensional hollow circle representing the opening angle of the radiation cone. The width of the line is related to both the beam energy spread ($d\gamma/\gamma$) and the angular divergence. Observation of polarized coherent interference patterns in two-foil OTR interferograms yields direct information on the transverse beam divergence. In this case, the interference is between the radiation emitted from the front surface of the upstream foil, and the back surface of the downstream foil, both of which are tilted at 45° with respect to the beam. Measurement is made by observing the OTR at right angles to the beam from the back surface of the downstream foil.

BUNCH LENGTH MEASUREMENTS

Non-interceptive bunch-length measurements can be made by coupling to the electromagnetic field of the beam in either the time or frequency domain. For highly relativistic beams, the measurement is limited only by the pickup response. In the time domain, either real-time or sampling oscilloscopes can be used. In the frequency domain, spectrum analysis can be used to measure the Fourier harmonics of the beam bunching frequency.

Wall-current monitors that monitor the temporal profile of the beam-image currents in the beam-pipe wall flowing through a resistive path have achieved bandwidths up to 6 GHz.[17] The pickup is made up of 10 or more parallel resistors across a ceramic gap, and has a total resistance of a few ohms. This measurement method is generally limited to the frequencies below the beam-pipe waveguide-cutoff frequency (TE_{11} and TM_{01} modes).

For low-velocity beams, the EM field of the beam is no longer Lorentz-contracted to a TEM wave, but has a finite longitudinal extent at the beam-pipe wall, thus limiting the frequency response to (3 dB cutoff point)[18]

$$I_0\left(\frac{\omega r}{\beta\gamma c}\right) \le \sqrt{2}$$

where $\beta\gamma$ is the relativistic factor, c is the speed of light, r is the half-aperture of the pickup device, and $I_o(\text{arg})$ is the modified Bessel function of order zero. As an example, the cutoff frequency (arg = 1.22) for a 10 MeV proton beam in a 1-cm-radius aperture is about 850 MHz.

To overcome the "Bessel factor" limitation for the low-velocity beams mentioned above, it is possible to obtain good time resolution by measuring the temporal profile of secondary-emission electrons from the ions striking a thin wire. Resolution of about 1° in phase at 200 MHz (15 ps) was recently obtained at the Moscow Meson Factory on a 20-MeV proton beam.[19] In this case, the wire was biased at -4 kV, and a 600 MHz RF deflector was phase-locked to the accelerator RF to deflect the secondary-emission electrons across a narrow slit. A similar system is being built for use on the Fermilab Linac upgrade.[20]

Totally-interceptive bunch-length measurements can be made using Faraday cups either in a coaxial transmission-line geometry, or a stripline geometry in which the beam (a low-energy ion beam in this case) strikes the stripline

transversely.[21]

A laser can also be used to measure the longitudinal bunch profile of a H^- beam. In this case, very short laser pulses synchronized to the beam RF structure are required. Again, magnetic separation of the charged beam is required, and the yield of neutral hydrogen is measured. A plot of the yield of neutrals vs. the RF phase of the laser pulse provides the bunch-length-profile information.

Streak cameras, with temporal resolution under 2 ps, have been successfully used to observe the very short bunches in electron accelerators such as SLAC and free-electron-laser linacs. The signal source for streak cameras is typically spontaneous emission, synchrotron light, or Cerenkov light.

ENERGY PROFILES

Energy profile measurements generally require using a device that has momentum dispersion. An example is the energy spread measurement at SLAC, which utilizes a wiggler in a dispersive section of the magnetic lattice. The wiggler x-rays from single bunches of electrons or positrons impinge on a fluorescent screen, and are viewed by TV cameras.[13]

Very fast Nd:YAG laser pulses (<20 ps) have been used to neutralize slices of individual bunches of H^- beams.[15] At low energies, the energy profile of these slices can be measured by letting the neutral hydrogen drift to a coaxial Faraday cup many meters away. The temporal profile of the Faraday cup signal is directly related to the velocity profile, and hence the energy profile, of the neutralized beam. At higher energies, the neutrals must be stripped to protons at the entrance to a magnetic spectrometer after being separated from the H^- beam, and the momentum profile measured.

EMITTANCE MEASUREMENTS

TRANSVERSE EMITTANCE

Slit-and-collector and slit-slit systems are the traditional methods for measuring transverse emittance of high brightness ion beams, but this method is limited to beams with a low average beam power because of the slit heating. However, a slit-slit system is presently being used on the CW RFQ at CRNL.[22] Wire shadows ("negative slits") on fluorescent screens are similarly limited. For this reason, other methods have been used.

Tomographic techniques have also been used to measure transverse emittance. In this method, the transverse profile of the beam is measured at several points in a drift space or a matched strong-focusing lattice near a waist in the beam. The evolution of the transverse phase space ellipse as the beam passes through the waist can then be estimated, yielding the emittance. If the beam is space-charge dominated, then the emittance may not be preserved as the beam passes through a narrow waist, however. In this case a better measurement is obtained by measuring the beam envelope at several points in a matched strong-focusing lattice. Wire scanners can be used for this purpose.

A variation of the waist measurement mentioned above is to vary the focusing strength of the magnetic lattice in order to move the beam waist through a single profile measurement device. This method also is limited to beams in which the emittance is preserved in passing through a waist.

It is possible to reconstruct the transverse beam emittance if the second moment of the beam profile can be measured at several points. In principal, this can be done using non-interceptive electromagnetic pickups whose response is very well understood. In particular, Miller[23] proposed such a technique using stripline pickup electrodes, but no measurement using this technique has yet been reported in the literature.

For the special case of H^- beams, the laser-neutralization technique mentioned above has been used successfully in combination with a standard slit and collector.[24] In this case a 100-nsec segment of the entire beam is neutralized immediately in front of a bending magnet. A narrow slit is placed in the neutral beam immediately downstream of the magnet, and a collector, which may be a multiwire harp, a segmented Faraday cup, or a fluorescent screen, is placed at a suitable distance downstream. This approach limits the beam power on the slits. It is important in this case to minimize the distance between the neutralization point and the slits, because the emittance ellipse is shearing in the x and y coordinates between the two points, and can become quite elongated by the time it reaches the slit. Unlike the conventional slit-type transverse-emittance-measuring systems, this laser neutralization approach can be a permanently-installed diagnostic, because it has a minimal effect on the H^- beam.

LONGITUDINAL EMITTANCE

The most difficult measurement to make on particle beams is longitudinal emittance, which requires simultaneous correlated measurements on both the bunch longitudinal profile and the energy spread.

For H^- beams, it is possible to combine bunch length and energy profile measurements mentioned above using a mode-locked Nd:YAG laser at 1.06 μm. For low energies, the energy spectrum can be obtained using a pulsed laser and time of flight.[15] At higher energies, the obtainable resolution from time of flight is inadequate, and a CW mode-locked laser and a momentum spectrometer must be used.[24]

Other methods include the use of RF deflection, either of the beam itself or in a streak camera. RF deflection of a beam in a dispersive region onto a fluorescent screen provides longitudinal emittance information. In this method, the phase resolution is limited by the transverse emittance. Streak cameras can be used with a wiggler in a dispersive beamline, can also yield longitudinal emittance information.

BEAM JITTER

Although beam jitter is not a basic characteristic of beam bunches, like beam current, energy, or position, beam jitter deserves special attention because it can adversely affect the performance of the accelerator.

Sources of jitter may be vibration or ground motion (microtremors), RF amplitude or phase noise, fluctuations in magnet current, etc. Jitter in one beam parameter can couple into others. Beam current bunch-to-bunch fluctuations can cause RF-cavity-amplitude fluctuations via beam loading, and therefore couple into energy jitter. Energy jitter can couple into beam position jitter in beam optics that have residual (non-zero) dispersion. For high-brightness beams, beam profiles and emittance ellipses often depend on the space-charge density, and therefore beam current.

For these reasons, it is very important to understand the possible sources of jitter, and design the beam diagnostics to be able to observe it if it is present. Vibration and ground motion are generally below 100 Hz, but plasma oscillations in H^- sources are often in the 10 to 20 MHz range. For free-

electron-laser linacs, the beam-bunch separation is typically 10 to 50 ns, but bunch-to-bunch phase jitter must be controlled to of the order of 1 ps.

REFERENCES

1. J. Borer and R. Jung, "Diagnostics," CERN Publication 84-15, P. 385 (1984).
2. G. Lambertson, "Dynamic Devices, Pickups and Kickers," AIP Conference Proceedings #153, M. Month, Ed., P. 1413 (1987).
3. R. Littauer, "Beam Instrumentation," AIP Conference Proceedings #105, M. Month, Ed., P. 869 (1983).
4. R. H. Siemann, "Bunched Beam Diagnostics," AIP Conference Proceedings #184, M. Month, Ed., P. 430 (1989).
5. J. L. Pellegrin, "Review of Accelerator Instrumentation," Proceedings of the 10th International Conference on High Energy Accelerators, CERN, P. 459 (1980).
6. "Frontiers of Particle Beams; Observation, Diagnosis, and Correction," Proceedings of the Joint U. S. - CERN School on Particle Accelerators, M. Month and S. Turner, Eds., Springer Verlag Lecture Notes in Physics #343 (1989).
7. Proceedings of the 1989 Beam Instrumentation Workshop, AIP Conference Proceedings # 212, R. Witkover, Ed. (1990).
8. K. B. Unser, "Design and Preliminary Tests of a Beam Intensity Monitor for LEP," Proceedings of the 1989 IEEE Particle Accelerator Conference, Chicago, P. 71, (1989). See also R. Talman, "Beam Current Monitors," Ref.7, P. 1.
9. R. E. Shafer, "Beam Position Monitoring," Ref. 7, P. 26.
10. R. E. Shafer, S. P. Jachim, and R. C. Webber, "An RF Beam Position Measurement Module for the Fermilab Tevatron." Proceedings of the 1981 IEEE Particle Accelerator Conference, IEEE Trans. Nucl. Sci. Vol. NS-28, P. 2323 (1981)
11. R. D. Ruth, "Beam Dynamics in Linear Colliders," these proceedings.
12. C. A. Brau, "Free-Electron Lasers," Academic Press (1990). See also J. L. Pellegrini, "Linacs for Free-Electron Lasers," these proceedings.
13. E. J. Soderstrom et al., "Fast Energy Spectrum and Transverse Beam Profile Monitoring at SLC," Proceedings of the 1989 IEEE Particle Accelerator Conference, Chicago, P. 1864 (1989). See also J. T. Seeman, "The Stanford Linear Collider," these proceedings.
14. J. Buon, "The Possibility of Measuring Very Small Spot Sizes Using Gas Ionization at Future Linear Colliders," Particle Accelerators Vol. 31, P. 39 (1990).
15. W. B. Cottingame et al., "Non-Interceptive Techniques for Measurement of Longitudinal Parameters of Intense H^- Beams," Proceedings of the 1985 IEEE Particle Accelerator Conference, IEEE Trans. Nucl. Sci. Vol. NS-32, P. 1871 (1985).
16. R. B. Fiorito et al., "Optical Transition Radiation Measurements on the Los Alamos Free Electron Laser," Proceedings of the 1989 IEEE Particle Accelerator Conference, Chicago, P. 65 (1989).
17. C. D. Moore et al., "Single Bunch Intensity Measurement using an Improved Wall Current Monitor," Proceedings of the 1989 IEEE Particle Accelerator Conference, Chicago, P. 1513. See also R. C. Webber, Ref. 7, P. 85.
18. A. Hofmann and T. Risselada, "Measuring the ISR Impedance at Very High Frequencies," Proceedings of the 1983 IEEE Particle Accelerator Conference, IEEE Trans. Nucl. Sci. Vol. NS-30, P. 2400 (1983).
19. Private communication, A. Feschenko, INR, Academy of Sciences, USSR (1990).
20. E. S. McCrory and G. Lee, "Diagnostics for the 400 MeV FNAL Linac," these proceedings.
21. J. M. Bogaty, K. C. Pardo, and B. E. Clifft, "A very Wide Bandwidth Faraday Cup for Low Velocity Beams," these proceedings.
22. G. M. Arbique et al., "Beam Performance and Measurements on the RFQ1 Accelerator," these proceedings.
23. R. H. Miller et al., "Non-intercepting Emittance Monitor," Proceedings of the 12th International Conference on High Energy Accelerators, Fermilab, P. 602 (1983).
24. D. Sandoval, private communication (1990).

Friday

Session FR2
Chairman: S. Schriber
Invited Papers

WAKEFIELD ACCELERATORS*

J. D. Simpson
Argonne National Laboratory, 9700 S.Cass Ave., Argonne IL 60439

Abstract

The search for new methods to accelerate particle beams to high energy using high gradients has resulted in a number of candidate schemes. One of these, wakefield acceleration, has been the subject of considerable R&D in recent years. This effort has resulted in successful proof of principle experiments and in increased understanding of many of the practical aspects of the technique. Some wakefield basics plus the status of existing and proposed experimental work is discussed, along with speculations on the future of wake field acceleration.

Introduction

The motivation for the development of new acceleration methods is well documented [1]. In response to this need the accelerator community has responded with a large number of imaginative and (in some cases) clever ideas. Most of these ideas have been presented in the series of proceedings [2] generally referred to as "advanced accelerator conferences". Examination of these proceedings suggests certain trends in this field of research. One is that the number of new ideas (but hopefully not enthusiasm and effort) seemed to peak several years ago. The other is that there has been a weeding out of ideas under critical examination by the community.

Acceleration techniques may generally be classified as plasma based, near field, or far field. Plasma based schemes usually rely upon acceleration by fields which result when the charges in a plasma are redistributed, either by excitation of plasma waves by lasers as in plasma beat wave acceleration or by direct beam-plasma interaction as in plasma wakefield acceleration. The most attractive features of plasma wave based accelerators are immunity from electrical breakdown and the potential for extremely large accelerating gradients. This gradient is usually defined by the wave-breaking limit at $\approx \sqrt{n_e(cm^{-3})}$ eV/cm where n_e is the plasma electron density. Gradients of a few GeV/m are in principle obtainable for modest plasma densities.

Near field schemes use fields whose properties are determined by local boundary conditions. Conventional linac structures, grating structures, switched power devices, and non-plasma based wakefield structures are examples of near field devices. Excitation of these fields can be either from external rf power sources or, in a wakefield (WF) device, from direct interaction with an energetic beam.

Far field acceleration uses free radiation fields. Examples of this include inverse free electron lasers (IFEL) and methods based on the inverse Cherenkov effect. IFEL acceleration has been demonstrated at low level [3], and efforts are proceeding to experimentally study inverse Cherenkov acceleration [4].

Wakefield acceleration stands out as a technique which has attracted considerable interest in recent years and is the focus of several experimental programs. Possibly because the technique represents in many ways an extrapolation of well understood principles, it has also undergone relatively close examination. Its potentials and pitfalls are better understood than those of the more exotic schemes.

Wakefield Issues

If wakefield acceleration is to become a viable candidate for future accelerators, several interrelated key issues must be addressed.

- what are attainable gradients with "real" drive beams?
- are the drive beam dynamics tenable?
- can accelerated beam quality be preserved to provide useful luminosity for a linear collider?
- can it be acceptably efficient?

A wakefield accelerator is by definition a "two step" device. A more or less conventional linac is used to accelerate drive beam bunches. These in turn are used to excite EM fields in wakefield structures which accelerate "witness" bunches to high energy. In light of the fact the wall plug efficiency of a conventional linac is only marginally acceptable for a TeV collider, designing a wakefield based TeV machine with comparable efficiency is not easy.

One frequently discussed parameter of WF accelerators is the "transformer ratio", R, defined as the ratio of the peak of the accelerating wake field to the average decelerating field felt by the drive bunch. It would seem that R is therefore a handle on the efficiency, and that with some sort of transformer scheme it should be possible to obtain high gradients efficiently. Unfortunately, R, the drive bunch charge N, and the accelerating gradient G are related:

$$RG \propto N$$

Efforts to substantially increase R usually require unreasonable N if a gradient in excess of 100 MeV/m is sought.

*Work supported by U.S. Department of Energy, Division of High Energy Physics, Contract W-31-109-ENG-38

Beam dynamics problems differ between plasma wakefield and other wakefield schemes. In plasma, a two-stream type instability within the drive bunch can cause serious deterioration of the bunch. The wake, even for the case of perfect azimuthal symmetry, has strong (de)focussing effects on the accelerated beam depending upon the phase of the wake. While these forces can, in principle, provide all the desired focussing of the accelerated beam, they also place stringent requirements on the relative alignment of the driver and accelerated bunches. Any nonlinear components of the plasma wave, not unexpected if high gradients are present, will further complicate beam control.

Structure or dielectric wake devices introduce potentially serious single bunch beam break up (BBU) instabilities to the drive beam. Increasing the aperture of the device reduces BBU effects, but also reduces the gradient for a given drive bunch charge. The same wakes which produce BBU in the driver also result in effective emittance increase in the accelerated beam. Fortunately, mode damping can be designed into the devices to decouple the accelerated bunch from the deflecting modes generated by the drive beam.

The following section describes several wakefield acceleration research programs, attempting to highlight the specific ways that the above mentioned concerns are addressed.

Wakefield Experiments

The DESY/Darmstadt Wake Field Transformer- The first serious wakefield accelerator experiment was started at DESY in the early 1980s [5]. It had as one of its goals the demonstration of a wakefield transformer, schematically shown in figure 1. The underlying principle is that the energy deposited by a ring shaped drive bunch at the outer radius of the device is compressed as the wake pulse travels inward to the center. Transformer ratios of about ten are typical in the experiments to date. This experiment required the development of a hollow driving beam, pulse compression and acceleration systems, novel diagnostic devices, and the transformer itself ...each by itself a noteworthy accomplishment.

The transformer concept has been successfully demonstrated at modest levels. As an outgrowth of this work, efforts are now directed toward developing the resonant wake field transformer (RWT) as a basis for a linear collider. The RWT scheme uses a series of equally spaced hollow ring pulses to resonantly excite and "build up" fields in a wake field transformer. It is much easier to supply the requisite charge in several bunches than in a single bunch. Initial experiments with five bunches confirm the "build up" and produced a gradient of $\approx$ 1.5 MeV/m at a gun current of only 5-10 A. (The gun has delivered up to 80 A). The effect of azimuthal asymmetry in the drive beam charge density has been observed, and the experimenters acknowledge that strong transverse fields must somehow be dealt with.

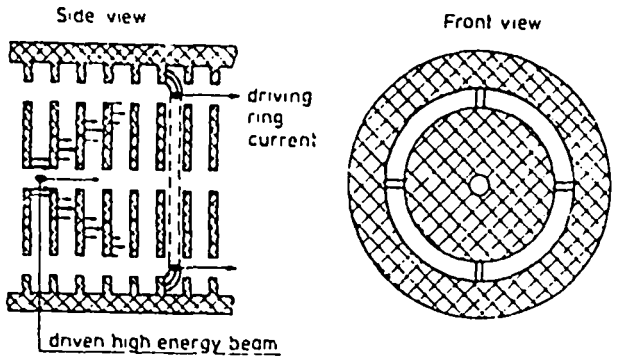

Figure 1: The wake field transformer.

Design parameters of a RWT based high energy linac suitable for high energy physics use have recently been outlined [6]. Superconducting cavities would provide the drive beam acceleration, with energy recover of drive beam energy employed to increase the overall efficiency (Figure 2). It is claimed that a TeV RWT based based collider would require only 4 km of driver cavity length.

The KEK plasma wakefield experiment- A PWFA experiment was performed at KEK [7] using a train of five 250 MeV bunches from a linac normally used by the KEK photon factory. The actual bunch separation was about 350 psec, the plasma wave period. The bunch train passed through a 1 m long plasma cell, after which the energy of each bunch in the train was measured using an innovative combination of a magnetic analyzer and a streak camera to observe Cherenkov radiation in air from the beam.

Because the interbunch spacing was fixed, resonance was established by tuning the plasma density. A 4 MeV energy shift of the fifth bunch, consistent with theory, was measured in this experiment. More experiments are possible using this apparatus such as the use of a positron witness bunch. Some of the experimental results are shown in Figure 3.

The Argonne Wakefield Program- Argonne has supported an active research program in wakefield and related effects [8]. A special facility with which wakefields could be directly measured (AATF) has permitted detailed measurements of wakefields in plasma (linear and nonlinear), in pillbox cavity arrays, and in dielectric loaded wave guides. Some of these results are shown in Figure 4.

During the past year the Argonne group has placed extensive effort on the study of dielectric loaded wave guides as wakefield devices. The attractiveness of this particular wake field scheme lies in its simplicity and potential performance characteristics. Moreover, several extensions to this technique appear to overcome some of the potentially seri-

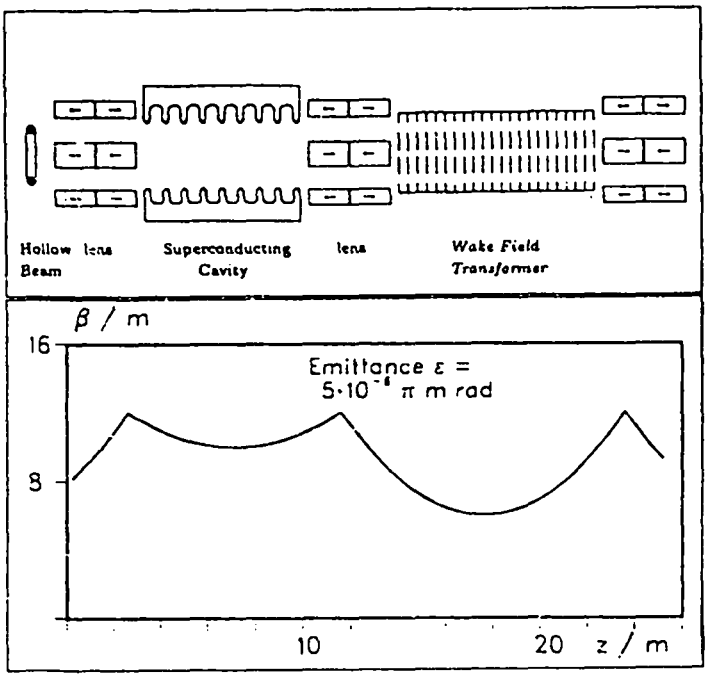

Figure 2: A RWT based cell of a high energy linac.

ous transverse wake effects. One of these is schematically shown in Figure 5. This configuration rapidly damps all but $m = 0$ modes. The longitudinal wire boundary does not affect the TM_0 accelerating mode but permits the higher order hybrid modes to leak out into the absorbing material [9]. A bunch to be accelerated need only be placed a few cycles behind the drive bunch to be "insulated" from emittance increasing deflection modes produced by the driver.

Another use of dielectric wakefield structures is in the (infelicitously named) coupled wake tube accelerator (CWTA) configuration (see Figure 6). Here the drive bunch and accelerated bunch travel along separate but parallel paths. rf energy produced in the dominant TM_{00} mode in the relatively large aperture drive section is coupled into a smaller cross section acceleration tube. Both tubes are designed to have the same luminal ($v_{ph} = c$) TM_{00} frequency. The HEM mode damping described previously can be used to suppress deflecting modes if desired.

The gradient step up ratio and length through which the bunch is accelerated (group velocity dependent) can be varied in this arrangement to adjust the transformer ratio and energy transfer efficiency. One of the more important advantages of a CWTA is that BBU in the driver can be reduced to tolerable levels while maintaining large accelerating gradients. The fact that dielectric loaded guides have an additional parameter, dielectric constant, makes them attractive for CWTA use.

Power efficiency in Argonne's wakefield accelerator concept is increased by extracting as much energy as possible from the drive linac by accelerating several pulses from a single

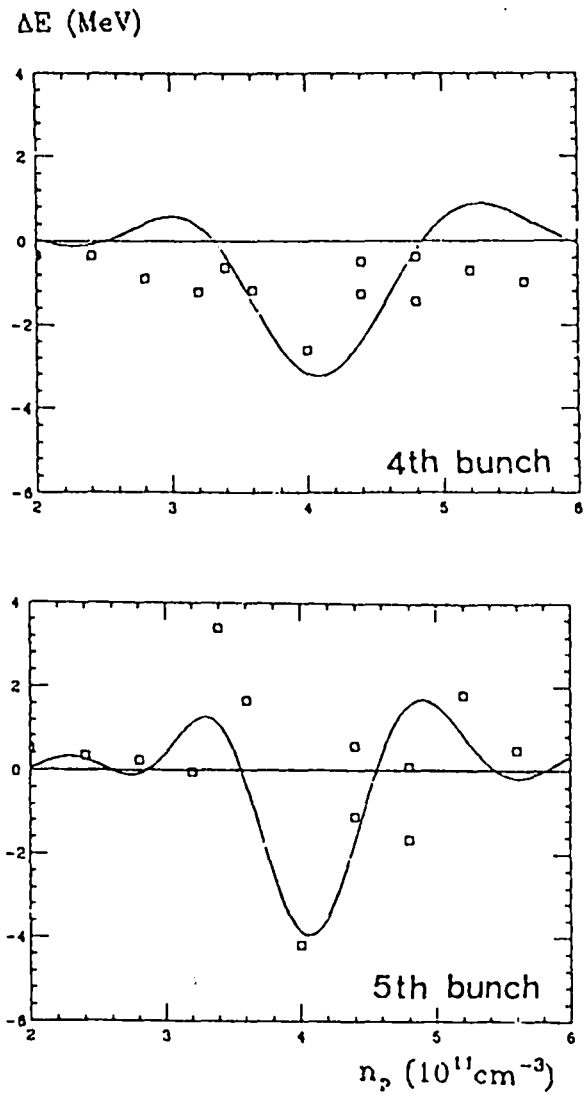

Figure 3: Observed energy shifts of the 4th and 5th bunches as functions of plasma density in the KEK PWFA experiment.

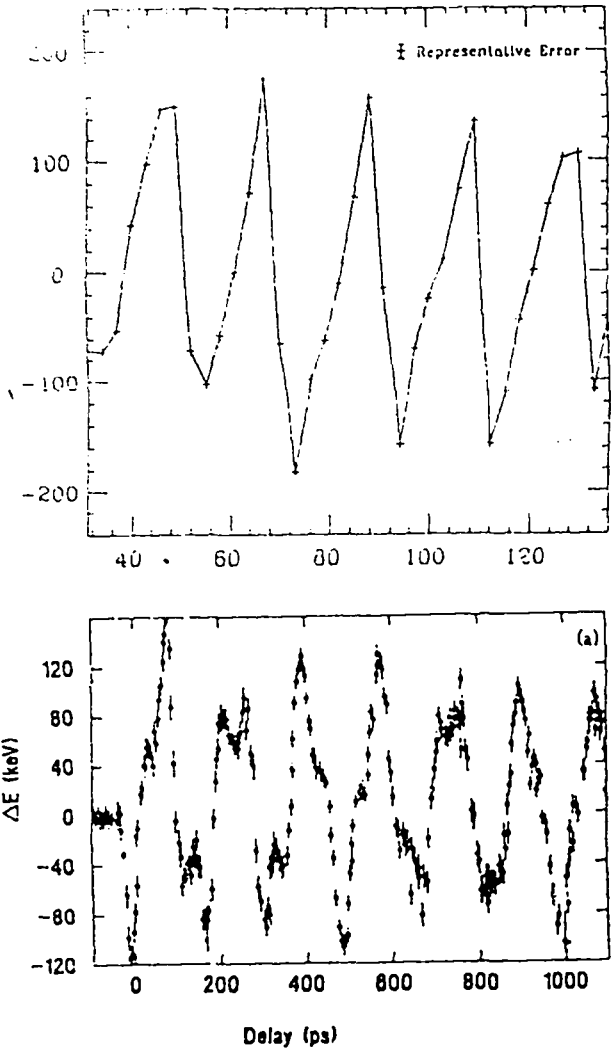

Figure 4: Examples of measured wakefields in (a)plasma (non linear regime), (b)dielectric loaded guide

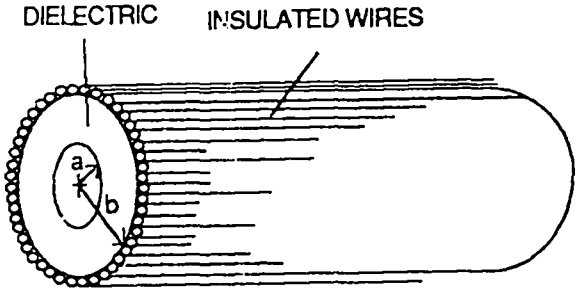

Figure 5: Deflection mode damping dielectric WF tube

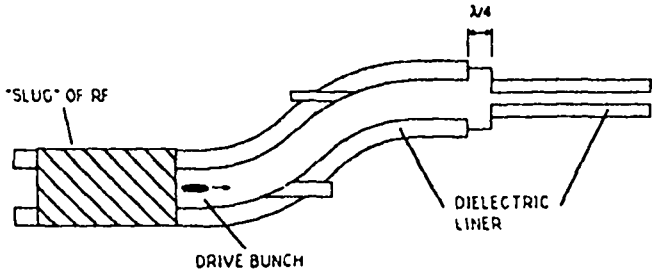

Figure 6: Schematic CWFA section

rf fill. Re-acceleration of drive pulses is not presently being considered in this design.

A new facility is being constructed at Argonne to extend wakefield and related technologies to significantly higher levels of performance than are currently possible. The new Argonne Wakefield Accelerator (AWA) facility will use a new photocathode based, intense (100 nC, 10 psec fw) electron source and a specially designed L-band linac to produce drive pulses. Research on devices with gradients in the 100 - 1000 MeV/m range will be possible at the AWA in about two years.

Comments and Conclusions

Wakefield acceleration research is being carried out in a growing number of locations. Besides the programs outlined above there are also proposals to study wakefield acceleration in the USSR at Novosibirsk and Yerevan.

Because wakefield acceleration is in some ways better understood than some of the more exotic advanced schemes, it is held to more stringent standards at this time. While accelerators based on this technique appear feasible, more research is clearly required before a credible high energy linac design can be made.

It is also interesting to note that except for plasma based devices, wakefield accelerator concepts are tending to adopt the look of the so called two beam accelerator (TBA), perhaps best represented by CERN's developing CLIC [10] scheme. It may be hoped that this research will soon define the role (if any) of wake field techniques in future high energy accelerator technology.

References

[1] As one of many examples see W. K. H. Panofsky, "What Can We Expect From Future Accelerators", AIP Conference Proceedings No. 92, 1981 (p. 13-23)

[2] Laser Acceleration of Particles, AIP Conference Proceedings No. 91, Los Alamos, 1982; Laser Acceleration of Particles, AIP Conference Proceedings No. 130, Malibu, California, 1985; Advanced Accelerator Concepts, AIP Conference Proceedings No. 156, Madison, Wisconsin, 1986; Advanced Accelerator Concepts, AIP conference Proceedings No. 193, Lake Arrowhead, California, 1989.

[3] A. Ts. Amatuni et.al., "Development of New Methods for Charged Particle Acceleration at Yerevan Physics Institute", Proceedings of the 14th International Conference on High Energy Accelerators, August 22-26, 1989, Tsukuba, Japan (p.1663-1669).

[4] W. D. Kimura et. al., "Progress on Inverse Cerenkov Laser Accelerator Experiment", Proceedings of the Workshop on Advanced Accelerator Concepts, Lake Arrowhead, California, 1989, AIP Conference Proceedings No. 198 (p.203-216)

[5] W. Bialowons et. al., "Wake Field Acceleration", Proceedings of the Symposium on Advanced Accelerator Concepts, AIP Conference Proceedings No. 156, 1986 (p. 266-280).

[6] N. Holtkamp et. al., "Longitudinal Beam Dynamics of the RWT- Collider", Submitted for Publication in the Proceedings of the 2nd European Accelerator Conference, Nice, France, 1990.

[7] H. Nakanashi et. al. "First Results of KEK Plasma Wakefield Accelerator Experiment", Proceedings of the 14th International Conference on High Energy Accelerators, Tsukuba, Japan, 1989 (p. 1645-1650).

[8] J. Simpson et.al.,"The Argonne Wakefield Accelerator", ANL-HEP-TR-89-81, plus included references and attachments.

[9] E. Chojnacki et. al., "Measurement of Deflection-Mode Dampening in an Accelerating Structure", Submitted for publication in Applied Physics Letters, September, 1990.

[10] S. van der Meer, "The CLIC Approach to Linear Colliders", CERN/PS/89-50, CLIC Note 97, August 1989.

THE BNL ACCELERATOR TEST FACILITY

Kenneth Batchelor
Brookhaven National Laboratory, Upton, New York 11973

Abstract

The design of the Brookhaven National Laboratory Accelerator Test Facility is presented including the design goals and computational results. The heart of the system is a radiofrequency electron gun utilizing a photo-excited metal cathode followed by a conventional electron linac. The Nd:YAG laser used to drive the cathode with 6 ps long pulses can be synchronized to a high peak power CO_2 laser in order to study laser acceleration of electrons. Current operational status of the project will be presented along with early beam tests.

Introduction

The Brookhaven National Laboratory Accelerator Test Facility[1] is a 50 to 100 MeV electron linear accelerator utilizing a high brightness, photoexcited cathode, radiofrequency electron gun[2] followed by two traveling wave accelerator sections operating in the $2\pi/3$ mode. The facility is designed to provide output beams suitable for studies of new methods of high gradient acceleration[3,4] or of state of the art free electron lasers[5] and nonlinear Compton scattering[6] radiation sources. Initially the electron gun and accelerating sections will be powered from a single klystron amplifier giving a maximum output energy of 50 MeV (see Fig. 1).

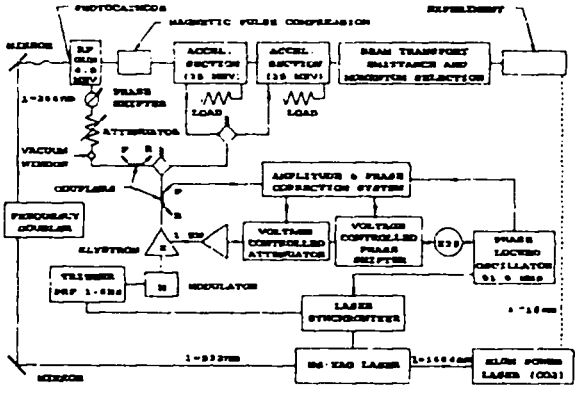

Fig. 1. Block Diagram of the Accelerator Test Facility

Design Considerations

- The electron bunch length is determined by the laser pulse width which may be small compared to the radio frequency wavelength thus eliminating the need for a buncher and permitting small energy spreads.
- The electron bunch is synchronized with the laser pulse to picosecond accuracy.
- Very low emittance beams can be produced by suitably shaping the laser pulse.
- The rf cavity can support gradients at the cathode of the order of 100 MV/m thus minimizing emittance growth due to space charge forces.
- A multicavity gun can deliver a beam of several MeV.
- The gun can operate at the same frequency as the linac.
- Optimum design of the gun cavity can minimize the emittance growth due to nonlinear components of the transverse electric and magnetic fields.

Electron Gun Design

The beam brightness is maximized by placing the cathode in the maximum electric accelerating field[7] by utilizing a half cell of a conventional disc-loaded structure followed by a suitably phased full cell (see Fig. 2). By operating in a resonant π-mode configuration and utilizing thick discs with a relatively large profile radius we are able to obtain a good approximation to the "ideal" linear dependence of the transverse fields with beam radius. By operating in π-mode and crossing the boundary between the two cells when the electric fields vanish the deflection of the beam as the bunch nears this boundary is cancelled by the opposite fields encountered as it enters the next cell. This condition determines the time at which the laser pulse should strike the cathode relative to the rf wave for minimum emittance at the gun output. Since there is no compensation for the transverse deflection at the exit of the gun essentially all of the rf induced emittance growth occurs there. The rf power is coupled to the two cells at the outer cylinder wall so that only the π-mode is coupled. The rf gun design parameters are given in Table I.

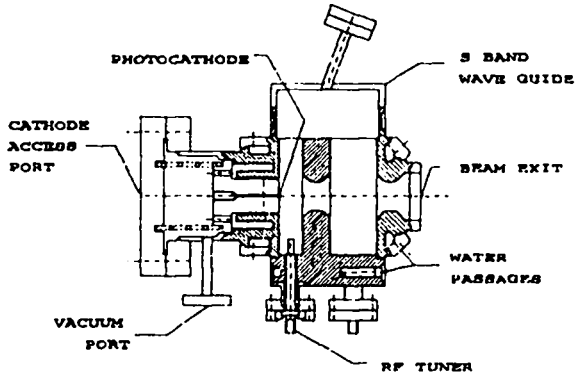

Fig. 2. Diagram of the Electron Gun

Table I. RF Gun Design Parameters

Structure type	Resonant (π-mode)
Structure inner diameter, mm	83.08
Structure length, mm	78.75
Number of cells	1+1/2
Operating frequency, GHz	2.856
Beam energy, MeV	4.65
Beam aperture, mm	20
Shunt impedance, MΩ/m	57
Cavity Q	11,900
Max. surface electric field, MV/m	119
Average accelerating gradient, MV/m	6.66
Electric field on cathode, MV/m	100
Cavity stored energy, J	4.0
Cavity peak power, MW	6.1

Photocathode Design

The photocathode requirements are as follows:

- It should have fractional picosecond response time in order to precisely follow the laser pulse form.
- It should have good quantum efficiency for operation with the laser well below damage thresholds.
- The cathode material should be robust, have good mechanical and chemical stability, and long lifetime.
- The work function should be close to and less than the photon energy of the laser.

We have chosen either a copper or yttrium metal cathode for our initial tests. Using an yttrium cathode with a work function of about 3.1 eV as compared to 4.65 eV light from a frequency quadrupoled Nd:YAG laser, the photoelectrons can emerge with up to 1.5 eV energy. If the electrons are emitted with an isotropic angular distribution at the cathode this would lead to an initial invariant emittance of 3.5π mm mrad; whereas a copper cathode with a work function of 4.3 eV would contribute a lower initial emittance but would offer a lower quantum efficiency.

Simulations of Gun Performance

The emittance of the beam from the gun has been calculated with a version of PARMELA, modified to include ejection of low energy electrons from a photocathode by a laser pulse. For electrons emitted randomly with an energy spread of a fraction of an eV, with isotropic directions and with a beam profile that is gaussian in both radius in time, as for a typical laser pulse the results are summarized in Table II for the optimized case. We use the invariant emittance, ϵ_x, defined at the bottom of this table. For these calculations the rf fields were taken from a SUPERFISH calculation and the effect of Coulomb interactions (space charge or self fields) is calculated with a point-by-point code. The effect of image charges in the cathode plane is included. The transverse and longitudinal phase space plots are given in Figures 3 and 4. It can be seen that the beam is both large in diameter and highly divergent at the gun exit.

Table II. Emittance Parameters

Laser spot radius (σ in mm)	3
Laser pulse width (σ in mm)	0.6
Charge in bunch (n Coulomb)	1
ϵ_x† at cathode (mm mrad)	3.5
$\Delta\epsilon_x$ due to self fields	6.2
$\Delta\epsilon_x$ due to rf fields	1.4
ϵ_x at exit	7.3
Beam energy spread (σ in keV)	17
Exit bunch length (σ in mm)	0.6
Exit bunch radius (σ in mm)	4.2
Exit beam angular divergence (σ in mrad)	28

$$e_x = \frac{1}{mc}\sqrt{(x^2)(xp_x^2)-(xp_x)^2} = \sqrt{(x^2)(\gamma^2\beta_x^2)-(x\gamma\beta_x)^2}$$

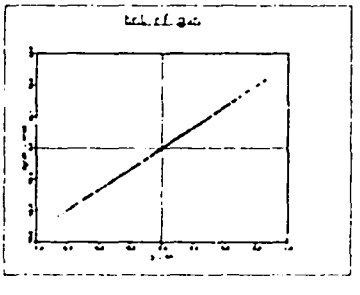

Fig.3. The transverse phase space at the gun exit for the parameters given in table II.

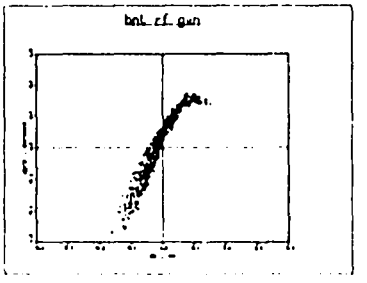

Fig.4. The longitudinal phase space at the gun exit.

Beam Transport to the LINAC

In order to allow easy access to the cathode for the photon beam it is desirable to bend the electron beam after it emerges from the electron gun. Also the longitudinal profile is such that it is possible to utilize bunch compression with a suitably designed transport system.[8] The system chosen is shown in Figure 5. It comprises two quadrupole triplets and a 180° achromatic double bend. A momentum selection slit is provided at the maximum horizontal dispersion point midway between the two 90° bending magnets. Provision for a vertical radiofrequency deflection device and beam profile and current measurement is also part of this arrangement.

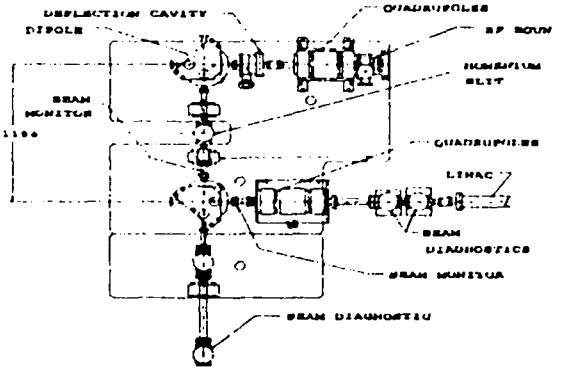

Fig. 5. Layout of the Injection System

The modeling has been done with a version of TRANSPORT with linear space charge added to study the effect of this on the beam profiles. Emittance growth in the transport line is mainly due to the following:

- mismatch caused by linear space charge forces and nonlinear space charge effects
- chromatic effects
- nonlinear magnetic fields
- spherical aberrations

The mismatch due to linear space charge can be compensated by operating the first triplet in a nonsymmetric DFD' mode. The other effects are minimized by utilizing large aperture quadrupoles with good field quality. The edges of the beam are scraped off by the beam pipe at the centers of the two quadrupole triplets at which points the pipe radius is equal to approximately 2σ horizontal beam size. The momentum slit can also be set to cut off electrons with momentum deviations down to 0.1%. For the beam parameters given in table II and the above conditions the geometric horizontal emittance (σ) growths from 0.8 mm mrad to about 2.2 mm mrad and the vertical emittance is

preserved in passing through the transport line and about 75% of electrons with momentum deviations less then 0.4% survive.

LINAC SYSTEMS

The linac comprises two 2π/3 mode, disc loaded, travelling wave sections each 3.05 meters long, excited by a single XK5 klystron delivering about 25 MW of peak power at a frequency of 2856 MHz and with a pulse duration of 3.5 μs. The rf system is designed to run at repetition rates up to 6 Hz so average power and heating is minimal. A phase locked oscillator operating at the 35th harmonic of 81.6 MHz is used to drive a series of solid state and triode amplifier stages to obtain the up to 1 KW of drive power for the klystron and also to drive and synchronize the Nd:YAG laser. A voltage controlled attenuator and phase shifter in the low level drive system may be used to vary the amplitude and phase of the radiofrequency power from the klystron during the 3.5 μs pulse. The measured bandwidth through the 1 kW stage is about 10 MHz. Amplitude stability of better than ± 0.5% and phase stability of better than 1° during a 3 μs pulse has been obtained with a preprogrammed compensation signal fed to an arbitrary function generator (see Fig. 6). Ultimately the amplitude correction signal may be obtained from a measurement of the momentum spread of the electron beam at 50 MeV and corrections applied to the subsequent pulse thus correcting for beam loading or other systematic variations during the beam macropulse. A phase correction signal from a phase comparator looking at the laser output and the klystron output may also be used for phase correction of a subsequent pulse.

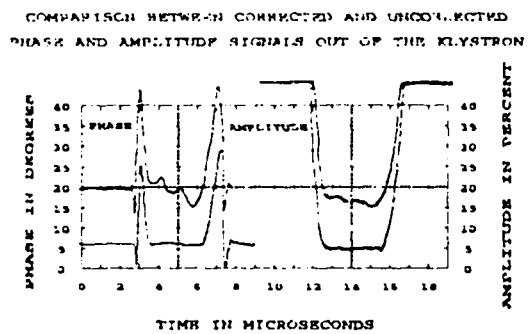

Fig. 6. Corrected Amplitude and Phase Signals at the Klystron Output

Power is fed from the klystron through a temperature controlled vacuum waveguide system using high power hybrid junctions as splitters, and phase shifters to set the correct rf phase and amplitude for acceleration. Power measurements are made with directional couplers and vacuum pumping is achieved via ion pumps connected to waveguide vacuum ports. The water cooling for the electron gun and accelerating sections is temperature controlled to 45 ± 0.02° C. Power to the electron gun is fed through a high power attenuator and phase shifter so that the power level and phase can be varied from a few KW up to a maximum of 12.5 MW.

Calculations using a modified version of the program LINAC show that for a properly matched transverse beam no increase in transverse emittance occurs in the acceleration process through the linac.

For operation in multibunch mode with 100 microbunches each separated by 12.5 ns there are a number of factors which can influence the output energy and phase spread of the electron beam[9] as follows:

a. microscopic effects within a single bunch such as:
   - rf field and phase changes during the bunch
   - longitudinal wake fields
   - space charge effects
b. macroscopic effects during a 100 bunch train of pulses such as:
   - rf field and phase changes during the macropulse due to the modulator etc.
   - input beam microbunch to microbunch energy and phase variations
   - amplitude and phase variations due to different filling times of the gun and accelerating sections
   - beam loading effects
c. macropulse to macropulse effects due to:
   - modulator pulse jitter in amplitude and time
   - temperature effects
   - laser amplitude and phase jitter

The major contribution to microscopic beam energy spread is the longitudinal wake field which for a single 6 ps bunch of 1nC charge will produce an energy charge during the pulse of about 0.4%. Proper location of the bunch centroid can reduce this wake field effect by utilizing the energy spread resulting from the rf field gradient occuring during the beam pulse.

Without correction the macroscopic effects given above, in particular beam loading effects, would produce an energy variation of about 8% during the 100 bunch macropulse. Injection phase and bunch width variations would contribute ± 0.04% energy spread in the output beam. In order to minimize amplitude and phase variations of the injected beam from the gun amplitude and phase control of the laser pulses is necessary. The final energy increases linearly with the injection energy. Changing the input phase appropriately could compensate this effect. The output energy changes nearly linearly with the square root of the input power to the accelerating sections. It is clear that the ripple during the modulator pulse must be minimized to reduce this effect. For multibunch operation with a single klystron the pulse to pulse compensation scheme proposed earlier may not be sufficient to obtain an energy spread during the 100 microbunch macropulse which is optimum for operation of a free electron laser. A second modulator and klystron allowing for separation of the electron gun and the accelerating sections is proposed for future operation of the Accelerator Test Facility.

Laser System

The laser system used for exciting the gun photocathode is a Spectraphysics CW Nd:YAG laser oscillator, mode locked to the 81.6 MHz rf reference source, with a feedback system to reduce the pulse jitter to less than 1 ps. This is followed by fiber chirping, compression and amplification stages to produce a chain of up to 200 microbunches, 5 ps long, separated by 12.25 ns. A pockels cell switching and a laser amplification system can be used to produce a single microbunch of 12 mJ energy, and of the order of 10 ps long at the laser oscillator wavelength of 1064 nm. This output is frequency doubled and then transported about 30 m to the gun hutch where a second doubling takes place. At this point there is 100 μJ of energy in a 6 ps pulse at the operating wavelength of 266 nm. This is sufficient to produce 1 nC of electron charge from the photocathode. It is also possible to produce a chain of up to 200 microbunches suitably amplified for free electron laser operation. One of the key elements in this system is a series 1000 timing stabilizer[10] purchased from Lightwave Electronics which is a phase-lock-loop feedback system for reducing pulse to pulse timing jitter, or phase noise, of the laser. The block diagram for this stabilizer is shown in Figure 7. A fast photodiode monitors a small portion of the laser output, sending this signal at the laser pulse

rate to a level detector and display and then to a precision phase detector. The phase of the laser is compared to the 81.6 MHz rf reference signal (at the same frequency). The phase detector is insensitive to laser amplitude noise, so fluctuations in its amplitude do not cause unwanted time jitter. The error signal from the phase detector is amplified and filtered before being used to drive a phase shifter that controls the timing of the mode locker drive signal. The modelocker signal is derived from a divide-by-two from the reference signal. This phase corrected signal then goes to the mode locker driver for the laser. The system has been used to reduce a timing jitter of 20 ps to less than 0.3 ps rms.

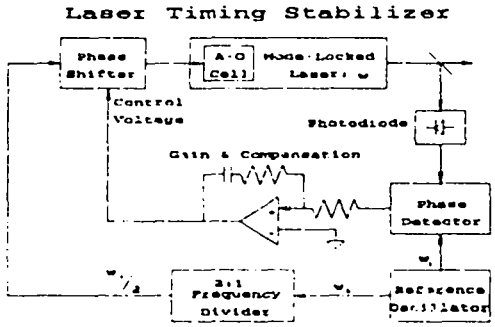

Fig.7. Phase-Lock Loop for Laser Timing Stabilization

Part of the output from the Nd:YAG at 1064 nm will be used to switch a short, synchronized CO_2 laser pulse of 6 psec duration out of a 60 ns pulse from a CO_2 oscillator by using germanium plates which change from being transmitted to reflectors when hit by 1064 nm light. A broadband CO_2 amplifier will then boost the pulse up from 10μJ to 500 mJ energy so that this may be used for laser acceleration or Compton scattering experiments.

Beam Diagnostics

ATF beam diagnostics incorporates nondestructive, strip line beam position monitors, with faraday cups for beam current measurements. Remotely insertable destructive beam profile monitors based on a phosphor screen and CCD camera system[11] are used for emittance measurement. They also give beam position information.

Momentum analysis at both 4.5 MeV and 50 MeV will be done by measuring the beam profile at the maximum dispersive points, after bending magnets. Beam profile measurement in the time domain will be done by incorporating an rf deflection cavity in the 4.5 MeV transport line and at 50 MeV by means of a fast magnetic septum pulser system and using the phosphor screen and CCD camera technique for sensing the beam.

Controls

The control system is based around a MicroVax II GPX workstation. The data acquisition and control functions use CAMAC electronics in a serial highway configuration. The control system for the ATF is built around a graphical interface and database provided by Los Alamos National Laboratory and a CAMAC driver from Kinetic Systems Corporation. All of the linac and laser systems can be driven from this system.

High Energy Beam Transport System

This system is designed to provide the desired beam parameters and beam waists at appropriate points in the three experimental beam lines and to allow for momentum analysis and transverse emittance measurements on the 50 MeV beam. The designs have been completed utilizing a version of TRANSPORT.

Operational Status

All of the electron gun and linac systems have been installed and operated at up to or close to design levels. Typical forward and reverse power waveforms for the electron gun are shown in Fig. 8 and a measured "dark current" plot for the electron gun is shown in Fig. 9. A 20 nsec pulse length excimer laser operating at a wavelength of 248 nm has been used to excite an yttrium metal cathode and the results for this mode of operation are given in Table III. The emittance measured at 3.6 MeV was less than 10 π mm mrad for a peak current of 0.6 A.

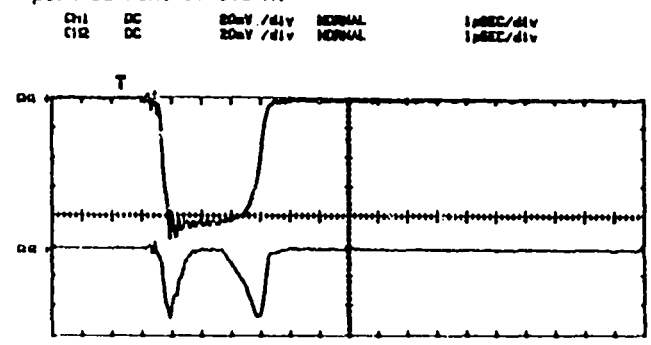

Fig.8 Forward and Reverse Power for the Electron Gun

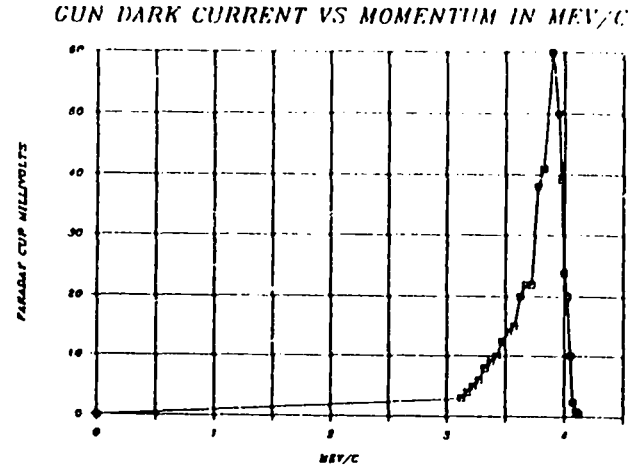

Fig.9. Measured Dark current

Table III

Brookhaven Accelerator Test Facility RF Gun Results

- 5.6 MW input RF power
- 600 μJ laser power at 248 nm
- Photo-ejected electrons accelerated to 4.2 MeV
- Measured shunt impedance = 50 MΩ/m
- dp/p = ± 0.5%
- I_{avg} = 8 mAmps
- I_{peak} = 0.6 Amps
- Initial quantum efficiency is 1.4×10^{-4}

All of the gun to linac transport elements with the exception of the vertical radiofrequency beam deflector and strip line monitors are in place and are operational from the central control computer. The magnetic components and power supplies for the high energy beam transport system are either in-house or on order. A program for measuring the magnetic field quality of all

of the transport quadrupoles is in progress. Concrete support plinths and support stands for the quadrupole magnets are already installed and the beam pipe and vacuum systems have been fabricated.

The Nd:YAG system has operated at the desired output level on the optical table in the experimental hall and the transport system and gun hutch optics are installed and operational. The CO_2 laser oscillator and amplifier systems have been delivered from Los Alamos and are being tested.

Beam studies with the electron gun and its transport system will commence as soon as operational approval has been obtained.

Experimental Area

The experimental area houses both the laser systems and the experimental beam lines. Initially two of the three beam lines shown will be implemented; namely the FEL line and the laser linac line. The first operational experiment will be the free electron laser which should give a photon source tunable over a wavelength of 500 to 1000 nm.

Future Improvements

A key element in providing a high brightness beam for the ATF experimental program is the electron gun and the transport system between it and the linac accelerating sections. Most of the emittance growth occurs at low electron energy, essentially in the first part of the first accelerating cell, and is due largely to space charge effects. A second important contribution to emittance growth is from the transport line to the linac. This growth occurs largely because of the highly divergent beam emerging from the gun giving rise to large beam radii in parts of this system. A number of corrective measures or improvements are under study as follows:

- the effect of different laser pulse longitudinal and transverse distributions on the emittance growth near the cathode.
- the effect of solenoidal focussing on the output beam divergence and emittance
- the effect of multicell gun cavities on the emittance and beam divergence
- the effect of cathode shaping
- the effect of different cathode materials on the emittance from the gun
- connecting the electron gun directly to the linac and exciting the photocathode at an angle

In addition to the gun region, for multibunch operation it will be necessary to separately control the rf amplitude and phase in the electron gun and the accelerating sections. There are plans to install a second modulator and klystron for the electron gun only and to provide for the appropriate feed forward correction scheme as provided for the accelerating sections.

Acknowledgements

The work reported results from contributions by many people who are part of the ATF design group as follows: K. Batchelor, I. Ben-Zvi, R. Fernow, J. Fischer, A. Fisher, J. Gallardo, H. Kirk, R. Palmer, Z. Parsa, J. Rogers, J. Sheehan, T. Srinivasan-Rao, T. Tsang, S. Ulc, A. VanSteenbergen, J. Veligdan and M. Woodle of Brookhaven National Laboratory; K.T. McDonald and D.P. Russell of Princeton University; C. Pellegrini and X.J. Wang of UCLA and J. Xie and R. Zhang of IHEP Beijing China. The dedicated work of our technicians, C. Biscardi, L. DeSanto, T. Monahan and H. Ratzke is also gratefully acknowledged.

References

1. K. Batchelor et al., Operational Status of the Brookhaven National Laboratory Accelerator Test Facility, Proceedings of the 1989 Particle Accelerator Conference, March 20-23, 1989, p.273.
2. K. Batchelor, H. Kirk, J. Sheehan, M. Woodle and K. McDonald, Development of a High Brightness Electron Gun for the Accelerator Test Facility at Brookhaven National Laboratory, Proceedings of 1988 European Accelerator Conference, Rome, Italy, June 2-12, 1988.
3. R.B. Palmer, A Laser Driven Grating Accelerator, Particle Accelerators 11, 81 (1980).
4. A. van Steenbergen, BNL, IFEL Demonstration Stage, BNL Report No. 42664 (1988).
5. K. Batchelor, I. Ben-Zvi, R. Fernow, J. Gallardo, H. Kirk, C. Pellegrini, A. van Steenbergen and A. Bhownik, A Microwiggler Free-Electron Laser at the Brookhaven Accelerator Test Facility, BNL Report No. 43306, 1989.
6. K.T. McDonald, Proposal for Experimental Studies of Nonlinear Quantum Electrodynamics DOE/ER/3072-38, Princeton University (Sept. 1986).
7. J.S. Fraser et al., Photocathodes in Accelerator Applications, Proceedings of the 1987 IEEE Particle Accelerator Conference, Washington D.C., March 16-19, 1987, p.1705.
8. X.J. Wang, H.G. Kirk, C. Pellegrini, K.T. McDonald and D.P. Russell, The Brookhaven Accelerator Test Facility Injection System, Proceedings of the 1989 IEEE Particle Accelerator Conference, March 20-23, 1989, p.307.
9. J. Xie and R. Zhang, Energy Spread of the ATF Beam in the Acceleration Process, BNL CAP ATF Tech Note #3.
10. M.J.W. Rodwell, D.M. Bloom and K.J. Weingarten, Subpicosecond Laser Timing Stabilization, IEEE Journal of Quantum Electronics, Vol. 25, No. 4, April 1989.
11. D.P. Russell, K.T. McDonald and B. Miller, A Beam Profile Monitor for the BNL Accelerator Test Facility, Proceedings of the 1989 Particle Accelerator Conference, March 20-23, 1989, p.1510.